cuk H01767 - 39 - P024463

AJR

39

American
Journal of
Roentgenology

April 1992

The IVC filter designed the way you'd want it to be.

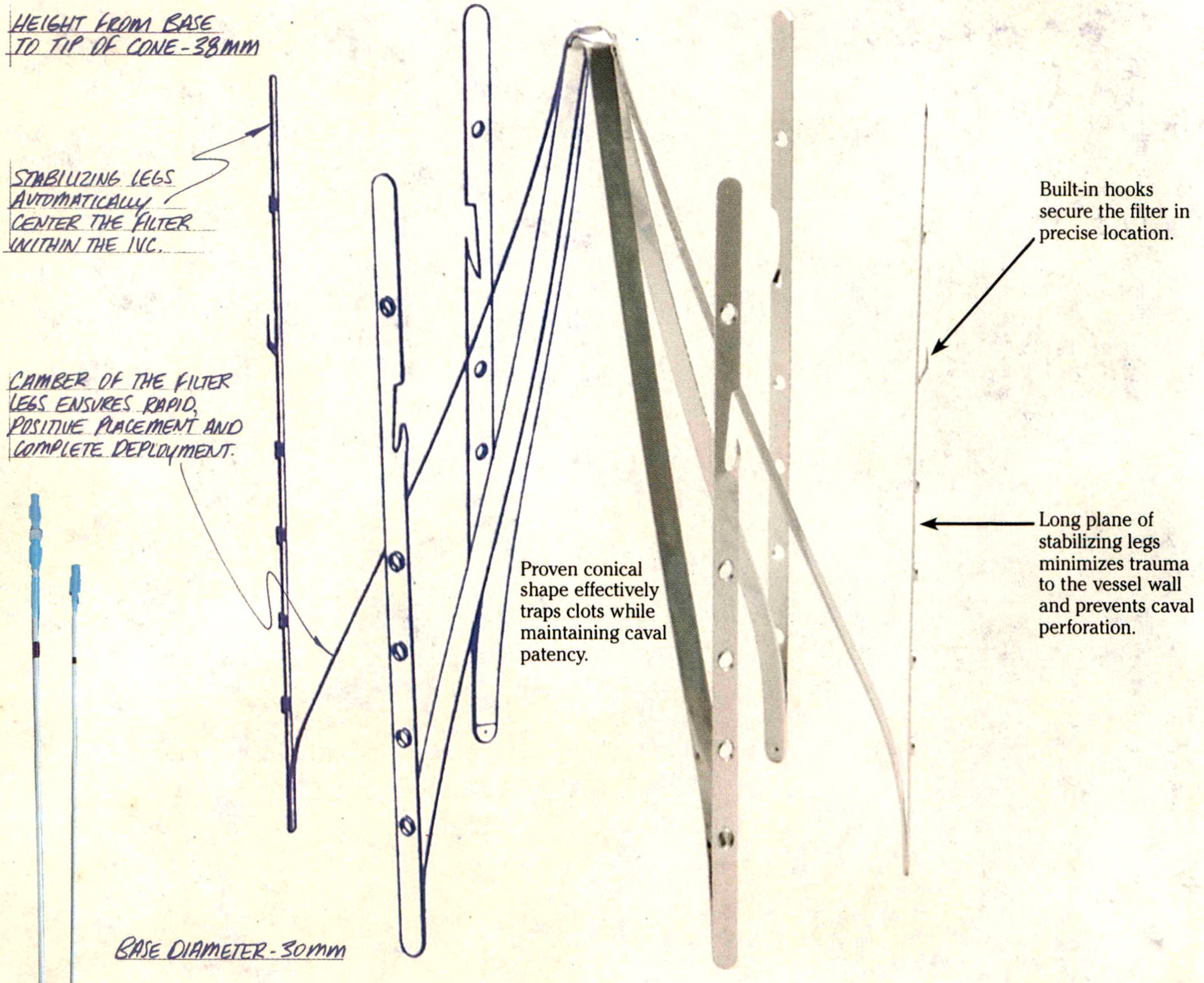

HEIGHT FROM BASE TO TIP OF CONE-38MM
STABILIZING LEGS AUTOMATICALLY CENTER THE FILTER WITHIN THE IVC.
CAMBER OF THE FILTER LEGS ENSURES RAPID, POSITIVE PLACEMENT AND COMPLETE DEPLOYMENT.
BASE DIAMETER-30MM

Built-in hooks secure the filter in precise location.

Proven conical shape effectively traps clots while maintaining caval patency.

Long plane of stabilizing legs minimizes trauma to the vessel wall and prevents caval perforation.

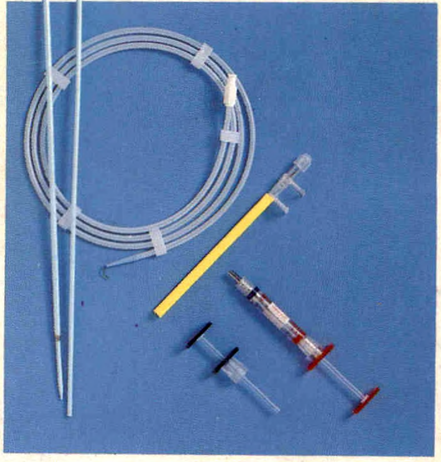

A flexible introducer facilitates the insertion procedure.

Finally, there's an IVC filter that does just what it's supposed to do.

Prevent recurrent pulmonary embolism. Maintain caval patency. And minimize procedural complications.

The Vena Tech™-LGM™ filter does it all because it's designed for success, with a proven-effective conical shape and longer stabilizing legs that ensure complete deployment. Best of all, the filter is deployed through a 10-French (ID) introducer. . . giving you and your patient a safer, easier insertion procedure.

The Vena Tech-LGM filter comes with everything you need for filter placement. And, with our unique 30D system, it can be placed from either the jugular or femoral approach.

See for yourself how easy it is. In just under ten minutes, our free video will show you how easy it is to place the Vena Tech-LGM filter. After you've seen it, you'll understand why we say the Vena Tech-LGM filter is the perfect fit—for both patient and physician.

So call 1-800-443-VENA today to receive your free video on the Vena Tech-LGM—the IVC filter that's designed for success.

B. Braun Vena Tech
1840 Oak Ave.
Evanston, IL 60201
(800) 443-VENA or (708) 866-1833
B.Braun of America Company

B.BRAUN

Vol. 158

Official Journal of the American Roentgen Ray Society

AJR

American Journal of Roentgenology
Diagnostic Imaging and Related Sciences

P24 463

Editor-In-Chief Robert N. Berk, *La Jolla, California*
University of California, San Diego
School of Medicine and Medical Center

Editor Emeritus Melvin M. Figley, *Seattle, Washington*

Associate Editor Karim Valji, *San Diego, California*

Consulting Editors A. James Barkovich, *San Francisco, California*
Edward A. Sickles, *San Francisco, California*

Statistician Charles C. Berry, *San Diego, California*

Editorial Board

Mark E. Baker
Lawrence W. Bassett
Michael A. Bettmann
Ethan M. Braunstein
Felix S. Chew
Horacio R. D'Agostino
N. Reed Dunnick
David K. Edwards
Ronald G. Evens
Sandra K. Fernbach
Richard H. Gold
Edward G. Grant
John R. Hesselink
Emanuel Kanal
Ray F. Kilcoyne
Carolyn Kimme-Smith
Melvyn T. Korobkin
Mark J. Kransdorf
Faye C. Laing
Thomas L. Lawson
Robert G. Levitt
Martin J. Lipton
Bruce L. McClennan
Richard P. Moser
Jeffrey H. Newhouse
Sven J. K. Paulin
David M. Paushter
Vassilios Raptopoulos
Donald L. Resnick
Charles A. Rohrmann, Jr.
Peter M. Ronai
Stuart S. Sagel
Sanjay Saini
Stefan C. Schatzki
William P. Shuman
Edward A. Sickles
Barry A. Siegel
M. Leon Skolnick
Edward T. Stewart
Murali Sundaram
Robert D. Tien

Director of Publications: Susan Brown Cappitelli **Editorial Staff:** Barbara Rose, *managing editor*; Katie L. Spiller, Barbara L. Halliburton, and Janine Anderson, *manuscript editors*; Nancy Rydbeck, *office manager*; Sheri Smith, *administrative assistant*; Linda J. Waggoner, *administrative secretary*

AJR, AMERICAN JOURNAL OF ROENTGENOLOGY (ISSN 0361 803X) is published monthly by the American Roentgen Ray Society, 1891 Preston White Dr., Reston, VA 22091. Annual dues include $50 for journal subscription. Second-class postage paid at Baltimore, MD, and at additional mailing offices. **POSTMASTER**, send address changes (Form 3579) to Subscription Fulfillment, AJR, 428 E. Preston St., Baltimore, MD 21202. Subscription rates $125 ($180 foreign); institutions $135 ($190 foreign); in training $25 ($80 foreign); single copy $18 ($22 foreign). The GST number for Canadian subscribers is 123394371. Airmail rates furnished on request. Indexed by *Current Contents* and *Index Medicus*. Copyright © 1992 by American Roentgen Ray Society.

0361–803X/92$3.00

AJR Business and Subscriber Information

The American Roentgen Ray Society

AJR, *American Journal of Roentgenology*, is published monthly to disseminate research on current developments in the radiologic sciences and commentary on topics related to radiology. It is published by the American Roentgen Ray Society (ARRS), 1891 Preston White Dr., Reston, VA 22091; (703) 648-8992. Address inquiries regarding Society business, the annual ARRS meeting, and membership to the Society at the above address.

Correspondence regarding editorial matters and classified advertising should be addressed to Editorial Office, AJR, 2223 Avenida de la Playa, Ste. 103, La Jolla, CA 92037-3218; telephone 1-800-348-4257 or (619) 459-2229; FAX (619) 459-8814. For information on manuscript submission, see Guidelines for Authors, pages A5–A7.

Subscriber Information

ARRS annual dues include $50 for journal subscription. Nonmember subscription rates are as follows: $125/year ($180 foreign); institutions, $135 ($190 foreign); in-training, $25 ($80 foreign). Single copies of the Journal may be purchased for $18 ($22 foreign). Airmail rates will be furnished on request. The GST number for Canadian subscribers is 123394371.

Call toll-free, 1-800-638-6423 (in Maryland call 1-800-638-4007), with subscription inquiries or problems. Please have the mailing label from your latest issue available when you call.

Report changes of address to Subscription Fulfillment, AJR, 428 E. Preston St., Baltimore, MD 21202. Damaged or unreceived issues should be reported within 60 days of publication (90 days for foreign subscribers) for replacement.

Advertising Information

All advertising is subject to approval by the publisher. Acceptance of advertising does not indicate endorsement of the products or services advertised or the claims made. For display advertising information, contact Gary Walchli, National Sales Representative, AJR, 428 E. Preston St., Baltimore, MD 21202, (410) 528-4291.

For classified advertising information, contact the Editorial Office, AJR, 2223 Avenida de la Playa, Ste. 103, La Jolla, CA 92037-3218; telephone (619) 459-2229; FAX (619) 459-8814.

Copyrights, Permissions, and Reprints

Contents of the *AJR* are copyrighted by the ARRS. No part of this publication may be reproduced without permission. Requests for such permission should be addressed to the Publications Department, ARRS, 1891 Preston White Dr., Reston, VA 22091. For reprints of a particular article, please contact the author designated in the footnotes for that article.

Indexes

The *AJR* provides volume and yearly indexes (subject and author) in the June and December issues. *AJR* articles are also indexed in *Current Contents*, *Index Medicus*, and the cumulative index published by *Radiology*.

PERSONAL COMPUTER/LASER VIDEODISC SYSTEM
to assist you in the
diagnosis of Skeletal Dysplasias

A unique collection of 400 Skeletal Syndromes
7000 Illustrations
including

- *X-rays*
- *Clinical pictures*
- *Chondro-osseous histology*

OSSUM

AN ILLUSTRATED DATABASE OF SKELETAL DYSPLASIAS

S
S
U
M

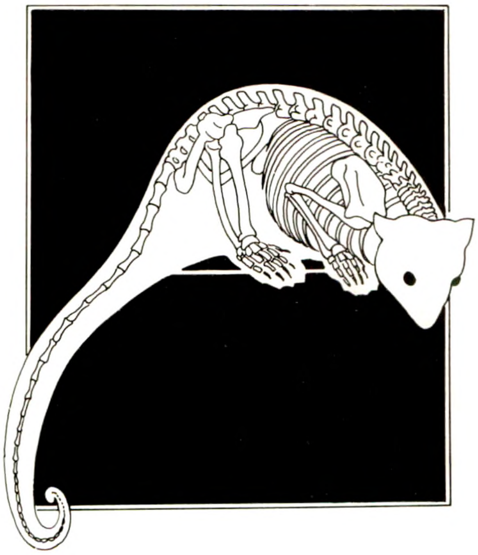

for further information contact:
Dr. Agnes Bankier – Medical Geneticist to the successful
related POSSUM system.

P O Box 1100 Parkville Victoria 3052 Australia
Phone: (03) 345 5160 Fax: (03) 348 1391

FREE DEMONSTRATION DISC
TELLS YOU HOW TO CONFORM TO JCAHO
PATIENT DOSE MEASUREMENTS DR.2.2.10.2

Call or write today for your
FREE RADCOMP™
X-Ray Entrance Skin Exposure Program
Demo Disc!

Phone 516-741-6360, FAX 516-741-5414,
or write and request
FREE RADCOMP disc #4423-44

NUCLEAR ASSOCIATES
VICTOREEN
Division of VICTOREEN, INC.
100 VOICE ROAD • P.O. BOX 349
CARLE PLACE, NY 11514-0349 U.S.A.
(516) 741-6360
FAX (516) 741-5414

TM, Victoreen, Inc.

Fellowships In Diagnostic Radiological Research.

The Diagnostic Radiology Research Program of the National Institutes of Health is accepting applications for two-year fellowship positions beginning in July 1992 and July 1993. This program provides an excellent opportunity for individuals who plan a research career in radiological sciences.

The fellowship training program emphasizes basic research in all aspects of imaging and image processing. Fellows will have no clinical responsibilities unless they are related to their project. The imaging laboratories of the Diagnostic Radiology Research Program include: state-of-the-art 0.5 and 1.5 Tesla MR units; a newly developed image analysis program with hardware support; ultrafast CT; and an experimental angiography suite. The facilities in the *In Vivo* NMR Research Center, the PET and monoclonal antibody programs of the Nuclear Medicine Department, and other laboratories on the NIH campus will be made available to the fellow, providing an opportunity to develop expertise in areas related to imaging research. Basic research in functional or metabolic imaging, contrast agents, biochemistry, biology, chemistry, immunology, physics and physiology will be encouraged. Laboratories are being developed which will include “hot” and “cold” wet labs and tissue culture facilities. Collaboration with other scientists on the NIH campus will be encouraged.

Applicants should hold the MD or PhD degree and should have completed clinical training in diagnostic radiology or nuclear medicine. Applications from individuals currently in US residency programs may also be considered for research fellowship positions. US citizenship or permanent residency is required for this full-time appointment.

Candidates should submit a Curriculum Vitae, at least two letters of reference and a preliminary statement concerning their area of research interest to Dr. Joseph A. Frank, Acting Director.

National Institutes Of Health
Diagnostic Radiology Research Program
9000 Rockville Pike, Building 10, Room 1C660, Bethesda, MD 20892 • FAX 301-496-9933
Equal Opportunity Employer

AJR Guidelines for Authors

Address new and revised manuscripts, correspondence, and classified ads to the Editor:

AJR Editorial Office
2223 Avenida de la Playa, Suite 103
La Jolla, CA 92037-3218
Telephone: (619) 459-2229; FAX: (619) 459-8814

Inquiries regarding reprints or permission to republish *AJR* material should be addressed to the publisher:

Publications Department ARRS
1891 Preston White, Dr., Reston, VA 22091

The *AJR* publishes original contributions to the advancement of medical diagnosis and treatment. Submitted manuscripts should not contain previously published material and should not be under consideration for publication elsewhere.

Manuscript decisions are based on peer review. Reviewers receive manuscripts without title pages to ensure an unbiased review. Statements made in the article, including changes made by the Editor or manuscript editor, are the responsibility of the author and not of the *AJR* or its publisher. Authors will be sent the edited manuscript, galley proof, and proofs of illustrations. If the corresponding author will be unavailable to review galleys, arrangements should be made for a coauthor or colleague to read and return the proof.

The following guidelines are based on instructions set forth in the **Uniform Requirements for Manuscripts Submitted to Biomedical Journals** (*Ann Intern Med* **1988;**108:258–265). Articles will be edited, however, to conform to the individual style of *AJR*.

General Guidelines for Major Papers

Abstract. Clearly state (in 200 words or fewer) the purpose, methods, results, and conclusions of the study. Include actual data.

Introduction. Briefly describe the purpose of the investigation and explain why it is important.

Methods. Describe the research plan, the materials (or subjects), and the methods used, in that order. Explain in detail how disease was confirmed and how subjectivity in observations was controlled.

Results. Present results in a clear, logical sequence. If tables are used, do not duplicate tabular data in text, but do describe important trends and points.

Discussion. Describe the limitations of the research plan, materials (or subjects), and methods, considering both the purpose and the outcome of the study. When results differ from those of previous investigators, explain the discrepancy.

AUTHOR'S CHECKLIST

For priority handling, complete the following checklist, sign the copyright form on the reverse side of this page, and include both with the manuscript.

________ Two copies of the manuscript (the original and a photocopy) and two complete sets of figures are submitted. One copy has been retained by the author.

________ If appropriate, *AJR* Guidelines for case reports, technical notes, pictorial essays, or letters to the Editor have been followed. (See page A7.)

________ The manuscript, including references, figure legends, and tables, is typed double-spaced on 8½ × 11 in. (21.6 × 27.9 cm) *nonerasable* paper. Right-hand margins are not justified.

________ All manuscript pages are numbered consecutively beginning with the abstract. Authors' names do not appear on the manuscript pages.

________ The manuscript is organized as follows: title page, blind title page (title only), abstract, introduction, methods, results, discussion, acknowledgments, references, tables, figure legends, and figures.

________ Informed consent has been obtained from patients who participated in clinical investigations. If experiments were performed on animals, authors complied with NIH guidelines for use of laboratory animals.

________ Use of unfamiliar acronyms and abbrevations is kept to a minimum. When abbreviations are used they are defined at first mention, followed by the abbreviation in parentheses.

________ Metric measurements are used throughout, or the metric equivalent is given in parentheses.

________ Names and locations (city and state only) of manufacturers are given for equipment and nongeneric drugs.

Title Page

________ The following information is given: title of article; names and complete addresses (including zip code) of all authors; current addresses of authors who have moved since study; acknowledgment of grant or other assistance. The corresponding author is clearly identified, and a current address, phone number, and FAX number are given.

________ A blind title page is included in each copy of the manuscript, giving only the title (without the authors' names) for use in the review process.

Abstract

________ An abstract of approximately 250 words, or one typewritten page, is organized into the following paragraphs.

Objective. In one or two sentences, indicate the specific goal or purpose of the article, and indicate why it is worthy of attention. Explain the hypothesis to be tested, the dilemma to be resolved, or the deficiency to be remedied. The objective stated here must be identical to the one given in the title and introduction of the paper.

Subjects (or materials) and methods. Describe succinctly the methods used to achieve the objective explained in the first paragraph, stating what was done, how it was done, how bias was controlled, what data were collected, and how the data were analyzed.

Results. The findings of the procedures described in the preceding paragraph are presented here. All results should flow logically from the methods described and not stray from the specific objective of the paper. Include as many specific data as possible within the overall length limitation of one typewritten page.

Conclusion. In one or two sentences, present the take-home message to be remembered when all else is forgotten. Describe the conclusion of the study, based solely on the

data provided in the body of the abstract. Conclusions must relate directly to the objective of the paper as defined in the title and first paragraph of the abstract.

________ No abbreviations or reference citations are used.

________ No abbreviations or reference citations are used.

References

________ References (not to exceed 35) are typed double-spaced starting on a separate page and are **numbered consecutively in the order in which they appear in the text.**

________ All references are cited in the text and are enclosed in brackets and typed on line with the text (not superscript).

________ Unpublished data are not cited in the reference list, but are cited parenthetically in the text, for example, (Smith DJ, personal communication), (Smith DJ, unpublished data). This includes papers submitted, but not yet accepted, for publication.

________ Papers presented at a meeting are not cited in the reference list, but are cited parenthetically in the text (e.g., Smith DJ et al., presented at the American Roentgen Ray Society meeting, May 1990). After first mention, use (Smith DJ et al., ARRS meeting, May 1990).

________ Inclusive page numbers (e.g., 333–335) are given for all references.

________ Journal names are abbreviated according to *Index Medicus*.

________ Style and punctuation of references follow the format illustrated in the following examples (all authors are listed when six or fewer; when seven or more authors, the first three are listed, followed by "et al."):

Journal article

1. Long RS, Roe EW, Wu EU, et al. Membrane oxygenation: radiographic appearance. *AJR* **1986**;146:1257–1260

Book

2. Smith LW, Cohen AR. *Pathology of tumors*, 6th ed. Baltimore: Williams & Wilkins, **1977**:100–109

Chapter in a book

3. Breon AJ. Serum monitors of bone metastasis. In: Clark SA, ed. *Bone metastases*. Baltimore: Williams & Wilkins, **1983**:165–180

Tables

________ Each table is typed double-spaced on a separate page without vertical or horizontal rules; each has a short, descriptive title. Tables do not exceed two pages in length and contain at least four lines of data.

________ Tables are numbered in the order in which they are cited in the text.

________ Abbreviations are defined in an explanatory note below each table.

________ Tables are self-explanatory and do not duplicate data given in the text or figures.

________ All arithmetic (percentages, totals, differences) has been double checked for accuracy, and tabular data agree with data given in the text.

Figures and Legends

________ Two complete sets of original figures are submitted unmounted in labeled envelopes.

________ Figures are clean, unscratched, 5 × 7 in. (13 × 18 cm) glossy prints with **white borders.** A separate print is submitted for each figure *part*.

________ All figure parts relating to one patient have the same figure number.

________ Each figure is labeled on the back with the figure number and an arrow indicating "top." For black-and-white figures, labeling is done on a gummed label, which is then affixed to the back of the print. **Never** use labels on **color** figures, but write figure number on the back lightly in pencil. *Never* use ink on front or back of any figures.

________ Authors' names are *not* written on the backs of figures.

________ Only removable (rub-on) arrows and letters are used on the figures. Symbols are uniform in size and style and are not broken or cracked.

________ Images are uniform in size and magnification.

________ Line drawings are done in black ink on a white background. They are professional in quality, and all use the same size type. (Only glossy prints are acceptable.)

________ Written permission has been obtained for use of all previously published illustrations (and copies of permission letters are included), and an appropriate credit line is given in the legends.

________ Legends are typed double-spaced, and figure numbers correspond with the order in which the figures are cited in the text.

Transfer of Copyright Agreement, Conflict of Interest Acknowledgment, Certification of Coauthors, and Exclusive Publication Statement

Complete copyright to the article entitled: ____

____

is hereby transferred to the American Roentgen Ray Society (for United States government employees to the extent transferable), effective if and when the article is accepted for publication in the *American Journal of Roentgenology*. In the case of the authors who are officers or employees of the United States government, the American Roentgen Ray Society recognizes that works prepared by officers or employees of the United States government as part of their official government duties are in the public domain.

Authors reserve all proprietary rights other than copyright, such as patent rights and the right to use all or part of this article in future works of their own. The authors retain the right of replication, subject only to crediting the original source of publication and receiving written permission from the publisher.

Authors guarantee that this manuscript contains no matter that is libelous or otherwise unlawful, invades individual privacy, or infringes any proprietary rights.

Authors understand that they will receive no royalty or other compensation from the American Roentgen Ray Society or the publisher.

Authors guarantee that the editor has been or will be informed of any proprietary or commercial interest or conflicts of interest the authors may have that relate directly or indirectly to the subject of this article.

All authors certify that they have made substantive and specific intellectual contributions to the article and assume public responsibility for its content.

Finally, the authors certify that none of the material in this manuscript has been published previously or is currently under consideration for publication elsewhere.

------------------------------	------------------------------	------------------------------
First author/date	Second author	Third author
------------------------------	------------------------------	------------------------------
Fourth author	Fifth author	Sixth author

Case Reports

A case report is a brief description of a special case that provides a message that transcends the individual patient.

Format. There is no abstract. The introduction should be a short paragraph giving the general background and the specific interest of the case. No more than one case should be described in detail (similar ones can be mentioned briefly in the discussion). Emphasis should be on the radiologic aspects; clinical information must be limited to that necessary to provide a background for the radiology. The discussion should be succinct and should focus on the specific message and relevance of radiologic methods. A review of the literature is not appropriate.

Length. Maximum of five double-spaced, typewritten pages, including the references but not the title page or figure legends.

References. Maximum of eight.

Figures. Maximum of four, unless the text is shortened accordingly. Legends must not repeat the text.

Tables and Acknowledgments. Not appropriate in case reports.

Pictorial Essays

A pictorial essay is an article that conveys its message through illustrations and their legends. Unlike other *AJR* articles, which are based on original research, pictorial essays serve primarily as teaching tools, like exhibits at a scientific meeting. They are not encyclopedic book chapters. The abstract should be a short, introductory paragraph.

Length. Maximum of four double-spaced, typewritten pages, including the references but not the title page or figure legends.

References. Maximum of four.

Figures. Maximum of 30 figure *parts*. Number should be as few as necessary to convey the message of the paper.

Tables and Acknowledgments. Not appropriate in pictorial essays.

Opinions, Commentaries, and Perspectives

Opinions, commentaries, and perspectives are special articles dealing with controversial topics or issues of special concern to radiologists.

Format. Include a title page but no abstract. Headings may be used to break up the text.

Length. Maximum of five double-spaced, typewritten pages.

References. Maximum of five.

Tables and Figures. Maximum of four.

Technical Notes

A technical note is a brief description of a specific technique or procedure, modification of a technique, or equipment of interest to radiologists.

Format. No abstract, headings, or subheadings are required. If headings are used, they should be a combination of "Case Report," "Materials and Methods," "Results," and "Discussion." A brief one-paragraph introduction should be included to give the general background. Discussion should be limited to the specific message, including the uses of the technique or equipment. Literature reviews and lengthy case reports are not appropriate.

Length. Maximum of five double-spaced, typewritten pages, including the references but not the title page or figure legends.

References. Maximum of eight.

Figures. Maximum of two, unless the text is shortened accordingly.

Tables and Acknowledgments. Not appropriate in technical notes.

Letters to the Editor and Replies

Letters to the Editor and Replies should offer objective and constructive criticism of published articles. Letters may also discuss matters of general interest to radiologists. Do not end a letter with a hand-written signature.

Format. All letters should be typed double-spaced on nonletterhead paper, with no greeting or salutation. Name and affiliation should appear at the end of the letter. Titles for letters should be short and pertinent. The title for a reply is simply "Reply."

Length. Maximum of two double-spaced, typewritten pages, including references.

References. Maximum of four.

Figures. Maximum of two.

Tables and Acknowledgments. Not appropriate in Letters to the Editor and Replies.

Computer Page Articles

Articles published on the computer page deal with practical computer applications to radiology.

Format. Include a title page and an abstract.

Length. Maximum of eight double-spaced, typewritten pages.

References. Maximum of five.

Figures and Tables. Maximum of five. Computer printouts are not acceptable. Figures must be submitted as 5 × 7 in. glossy prints.

All submissions to the *AJR* must be accompanied by a completed copy of the Author's Checklist and the signed Copyright agreement.

How can the VESS Chair help you do a better Swallow Study?

The VESS Chair is an adaptive seating device for the Modified Barium Swallow Study. For reliable Swallow Study outcomes, proper patient positioning and alignment of the head and neck is necessary. The VESS Chair provides Departments of Imaging and Speech/Language Pathology with positioning capability to effectively assess the more difficult or mobility-impaired patient.

The VESS Chair allows for both lateral and anterior-posterior viewing during videofluoroscopy. The VESS Chair's ergonomic design, narrow size, tilting flexibility and transportability will reduce the time needed in the fluoroscopy suite and contribute to patient and staff safety.

VESS
CHAIRS, INC.

New Features Include –

- IV Stand Holder
- Chart Holder
- Oxygen Tank Holder
- Foley Bag Holder
- Removeable Arms

WIDTH: 15-1/2 inches
TOTAL HEIGHT: 50 inches
TOTAL LENGTH: 52 inches
ESTIMATED WEIGHT: 110 lbs.
4 - ROTATING CASTERS

For More Information Call or Write To: ***VESS Chairs, Inc.***
1033 N. Mayfair Road; Suite 200; Wauwatosa, WI 53226
(414) 476-2488 FAX (414) 259-0423
Demonstration Video Available.

Practice opportunities are available for Radiologists seeking a challenging and rewarding career with the leading force in the healthcare industry.

Our commitment to innovative technology and resources reflects quality medicine.

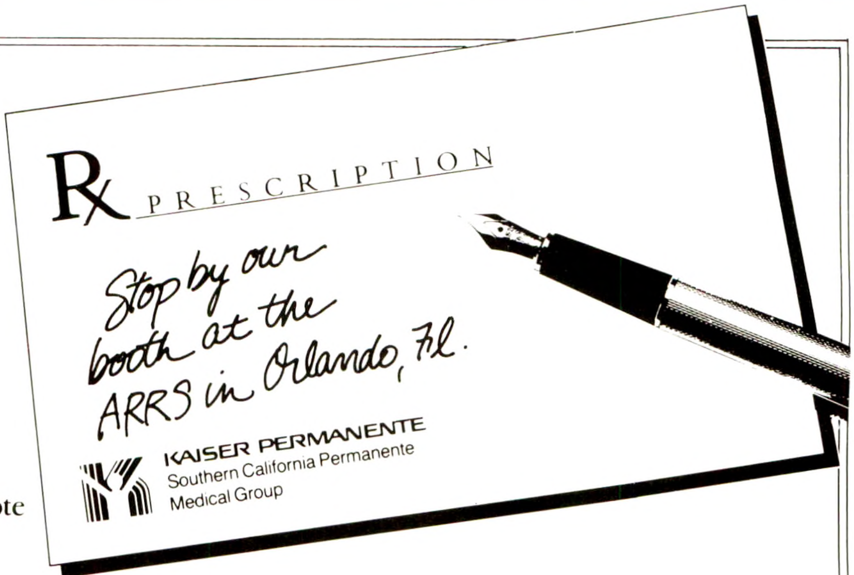
℞ PRESCRIPTION
Stop by our booth at the ARRS in Orlando, Fl.
KAISER PERMANENTE
Southern California Permanente Medical Group

- G.E. and Siemens 1.5 Tesla MRI, G.E. 9800 fully upgraded CT, Accuson with color doppler, remote fluoroscopy, digital subtraction angiography.
- Ability to practice all aspects of your practice including research opportunities.
- Relief from business and administrative responsibilities.

For more information, send your CV to: **Irwin P. Goldstein, MD, Associate Medical Director, SCPMG Dept. 612, Walnut Center, Pasadena, CA 91188-8013.**

1-800-541-7946

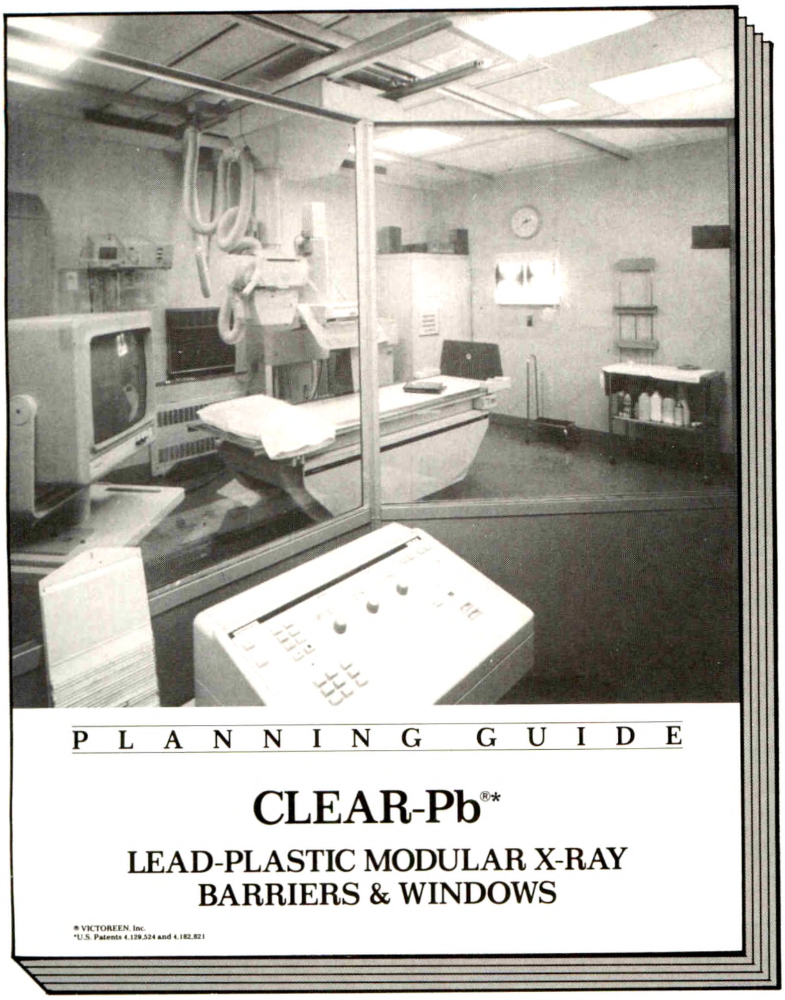

PLANNING GUIDE

CLEAR-Pb®*

LEAD-PLASTIC MODULAR X-RAY
BARRIERS & WINDOWS

® VICTOREEN, Inc.
*U.S. Patents 4,129,524 and 4,182,821

We Wrote the Book on X-Ray Room Shielding…

Ask for Your **FREE** Copy!

Our FREE PLANNING GUIDE shows how CLEAR-Pb® Transparent, Lead-Plastic Modular Barriers and Windows solve shielding problems in x-ray, CT and special procedures rooms in hospitals and therapy centers.

CLEAR-Pb is a lead-impregnated transparent plastic that is shatter-resistant. Available in 200 stock sizes up to 6×8′, and in lead equivalences from 0.3 to 2.00 mm.

Phone (516) 741-7717,
FAX (516) 741-5414, or write for
your FREE CLEAR-Pb X-Ray
Room Planning Guide 3186-44

NUCLEAR ASSOCIATES

VICTOREEN

Division of VICTOREEN, INC.
100 VOICE ROAD • P.O. BOX 349
CARLE PLACE, NY 11514-0349 U.S.A.
(516) 741-7717
FAX (516) 741-5414

® Victoreen, Inc. U.S. Patents 4,129,524 and 4,182,821

NUCLEAR ASSOCIATES…
THE RADIATION
SHIELDING SPECIALIST

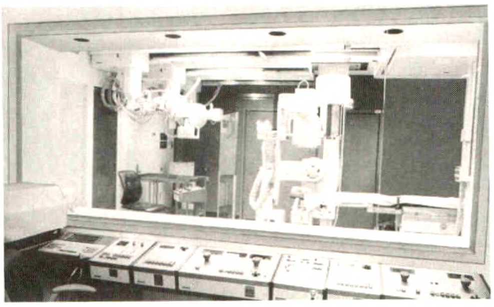

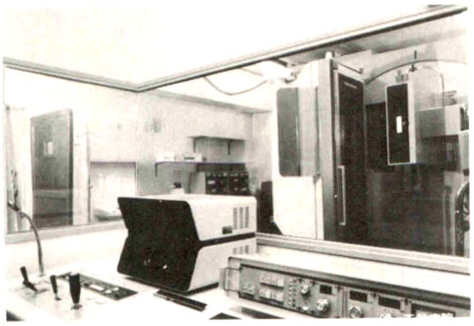

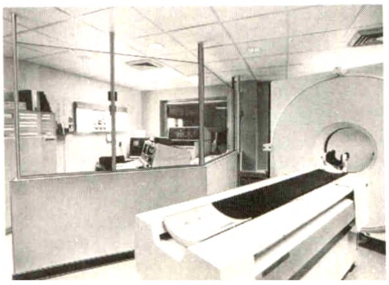

PICTURE PERFECT

IF YOUR MAMMOGRAPHY EQUIPMENT ISN'T THE "PICTURE" OF EFFICIENCY,

YOUR PRODUCTIVITY AND PERFORMANCE WILL BE OUT OF FOCUS!

For over 40 years, specially-dedicated S & S x-ray equipment and accessories have been improving Radiologists' efficiency and productivity. Specially-dedicated mammography equipment includes:

MOBILE *MOTORIZED* VIEWERS

Hold *Mammography* radiographs for random access recall and viewing within 7 seconds! Individual on-off light switches control divided viewing areas.

MODELS:

MV810-170: 10 viewing areas for 170 8x10" films
MV 1824-272: 16 viewing areas for 272 18x24cm films
MV2430-204: 12 viewing areas for 204 24x30cm films

S & S MAMMOGRAPHY ILLUMINATORS:

The standard for illumination excellence. Surface or recessed mounting is available for 1 to 6 banks—1 over 1 up to 6 over 6. Individual on-off light controls for ***each*** viewing section reduce glare and prevent spill-over. Single or two tier models for straight or angulated viewing include:

MODELS:

147000: Series for 8x10/18x24cm films
146000: Series for 24x30cm films

MAMMOGRAPH-SIZED VERTIFILE:

Doubles capacity over conventional drawer files. Adjustable partitions. Available with or without sliding door closures.

MODELS:

871: 1 shelf (2 doors) 14x30x13½"
873: 3 shelves (6 doors) 14x30x37¾"
876: 6 shelves (12 doors) 14x30x74½"

ADD-ON *MOVING GRID BUCKY SYSTEM:*

Converts existing non-Bucky mammography equipment. Improves contrast and micro-calcification visibility. Eliminates grid lines. Reduces scattered radiation.

MODELS:

MB-12: for 18x24cm film
MB-24: for 24x30cm film

See your local x-ray dealer or call S & S directly for *Picture Perfect* mammography equipment and our expanded line of radiological equipment and accessories.

S&S

S & S X-RAY PRODUCTS, INC.
1101 Linwood Street, Brooklyn, NY 11208
TOLL FREE: 800/347-XRAY ■ **NY STATE:** 718/649-8500 ■ **FAX:** 718/257-0219

Review Article

Current Use of Lymphography for Staging Lymphomas and Genital Tumors

Luceil B. North,[1] Marvin M. Lindell, Bao-Shan Jing, and Sidney Wallace

The current literature and the experience at The University of Texas M.D. Anderson Cancer Center were reviewed to determine the current status of the use of lymphography for staging of malignant disease. Lymphography continues to be used for staging and surveillance of the lymphomas and, to some extent, for staging of carcinoma of the cervix. Testicular tumors are now primarily staged and followed by CT and serum markers. Currently, other abdominal and pelvic tumors are not commonly evaluated with lymphography.

Lymphography is performed for the staging and surveillance of abdominal and pelvic lymphomas and genital tumors in men and women. With the advent of newer imaging techniques, particularly CT, lymphography has lost favor at some centers. The most recent literature on the efficacy of lymphography and the current experience at The University of Texas M.D. Anderson Cancer Center were reviewed to determine the role of this procedure in 1991. The history, anatomy, technique for performing lymphography, and interpretation of examinations have been described previously by Clouse, Harrison, Wallace, and Jing [1–7] and therefore will not be discussed here.

Lymphoma

Lymphography, when introduced, became an invaluable method for staging lymphomas because of its ability to directly show nodes and lymphatic vessels. It has proved to be particularly useful in staging Hodgkin's disease, because nodal disease predominantly occurs in the distribution of the lymphatics outlined by pedal lymphography. Overall accuracy has been reported by Castellino et al. [8] to be higher than 90% in 240 patients with histologic correlation by staging laparotomy.

Staging laparotomy has shown that approximately one third of Hodgkin's disease patients with normal lymphographic findings have abdominal disease [9]. The majority of these have disease in the spleen or upper abdominal nodes. These are usually small foci and are not detectable by any currently available imaging techniques. Normal lymphographic findings in Hodgkin's disease virtually preclude other detectable nodal disease in the abdomen or pelvis.

In non-Hodgkin's lymphoma, the prevalences of abnormal nodes outside the contrast-enhanced areas and of extranodal disease are considerably higher than in Hodgkin's disease. This is related in part to the histopathology, that is, whether the disease is follicular or diffuse. Heifetz et al. [10] found that approximately two thirds of patients with nodular (follicular) disease and normal lymphographic findings had other abdominal involvement. Approximately one quarter of patients with diffuse lymphoma and normal findings on lymphography had other abdominal disease.

Identification of all tumor sites is important in managing and staging lymphomas. In the presence of pelvic disease, the

---

Received August 14, 1991; accepted after revision November 25, 1991.

[1] All authors: Department of Radiology, The University of Texas M.D. Anderson Cancer Center, Box 57, 1515 Holcombe Blvd., Houston, TX 77030. Address reprint requests to L. B. North.

AJR 158:725–728, April 1992 0361–803X/92/1584–0725 © American Roentgen Ray Society

prognosis in Hodgkin's disease worsens [11]. Bulky sites, involvement of multiple nodal areas, or extranodal sites in the abdomen also indicate a poorer prognosis in non-Hodgkin's lymphoma [12–15].

Evaluation of nodes by lymphography has several advantages over evaluation by CT. Nodes that are small on CT may show foci of lymphoma on lymphography. Nodes that appear enlarged on CT may prove to be only hyperplastic or conglomerates of small nodes when seen on lymphography. Since the nodes generally remain opacified for at least 6 months, surveillance of nodal disease can be accomplished by abdominal radiographs. Recurrence or progression of disease is detected earlier by subtle changes in the nodes; however, the impact of earlier detection is not known.

Lymphography has at least two other advantages as compared with CT. The opacified nodes serve as markers for biopsy, which in most cases can be accomplished by fluoroscopic guidance without CT. Fine-needle aspiration is frequently performed not only for diagnostic purposes but also for obtaining lymphoma marker studies [16]. Radiation oncologists find that opacified nodes help in tailoring radiation therapy portals. Lymphography provides not only a helpful outline of areas to be covered but also information about the relationship of retroperitoneal nodes to the viscera, especially the kidneys, for shielding purposes. The importance of opacified nodes to radiotherapists has been one of the compelling reasons for continued interest in performing lymphography for lymphoma at our center.

Several comparative studies have been obtained to evaluate the efficacy of lymphography and CT for evaluation of lymphoma, and the results are mixed. Castellino et al. [17] pointed out that, because of small lesion size, they could not confirm the theoretical advantage of CT in detecting small upper abdominal nodes or liver and spleen lesions. Strijk et al. [18] concluded that lymphography was more reliable than CT in examination of the abdomen and that CT performed after lymphography adds little information.

A recent report from Australia and New Zealand [19] discussed results in 131 patients with non-Hodgkin's lymphoma who underwent both lymphography and CT. The findings were discordant in about 10% of cases, and the researchers concluded that CT could not safely replace lymphography in non-Hodgkin's lymphoma. Clouse et al. [20] concluded from a study of 54 patients with Hodgkin's disease and 18 with non-Hodgkin's lymphoma that all patients with Hodgkin's disease and patients with stage I or II non-Hodgkin's lymphoma should have lymphography because its sensitivity is higher than that of CT. Pond et al. [21] concluded that combined CT and lymphography were important in patient management and thought that lymphography should be performed in patients with newly diagnosed non-Hodgkin's lymphoma, particularly if the CT findings were normal.

In a recent study by the Southwest Oncology Group [22], the records of 139 patients with Hodgkin's disease were evaluated; all these patients had undergone lymphography and CT followed by laparotomy. They found that lymphography was more sensitive than CT in detecting abnormal lower abdominal nodes. CT had low sensitivity for detecting abnormal nodes or disease in the spleen or liver. Of interest, they noted that Hodgkin's disease was detected with CT in only three of 16 livers and 10 of 68 spleens. They concluded that lymphography provided more information in the lower abdomen than did CT, and thus lymphography should not be abandoned.

Lymphography continues to be a vital part of staging of all lymphomas at The M.D. Anderson Cancer Center and is performed on all previously untreated patients with lymphoma. For Hodgkin's disease, lymphography remains the primary staging procedure for abdominal and pelvic disease. In non-Hodgkin's lymphoma, CT is used for primary staging, and lymphography is used as the complementary procedure, especially in those patients with normal findings on CT.

In children with lymphoma, we perform lymphography only in those with Hodgkin's disease. The staging of lymphoma in children at our center has been described by Sullivan and Fuller [23, 24].

Genital Tumors in Women

Carcinoma of the cervix is the most common female genital tumor staged by lymphography. Lymphography has also been used in selecting those patients with cancer of the cervix who should receive prophylactic paraaortic radiation [25, 26].

Swart et al. [27] reported that of 54 patients with stage IB–IIA cervical carcinoma, only 29% with proved lymph node metastases had positive lymphographic findings at those sites. They decided that they would no longer perform routine lymphography for this group of patients. Boie et al. [28] thought that lymphography was not reliable for diagnosing metastases in 89 patients with stage IB cervical cancer who had had a radical hysterectomy.

Other authors have considered lymphography to be more reliable than CT for lymph node evaluation. Heller et al. [29] examined 167 patients with stage IIB–IVA carcinoma of the cervix by using CT, lymphography, and sonography. Those in whom abnormal nodes were seen on any study had fine-needle aspiration, and those with normal findings on all studies had paraaortic node dissection. They concluded that lymphography was the most reliable noninvasive examination, with a sensitivity of 79% and a specificity of 73% as compared with 34% sensitivity and 96% specificity of CT.

Smales et al. [30] concluded in a study of 205 patients that lymphography was valuable for evaluating node status and identifying high-risk patients. In their series, the prognosis of patients with positive findings on lymphography was poorer in each stage.

Ashraf et al. [31] evaluated the efficacy of lymphography in 39 patients with invasive cancer of the cervix. The results they obtained after biopsy of lymph nodes suggested that lymphography was highly predictive (93%) of absence of metastases when findings were negative, but had low predictive value (33%) when findings were positive. The majority of nodal abnormalities were due to benign conditions.

In a study of 367 patients with adenocarcinoma of the cervix, Eifel et al. [32] found a decreased rate of relapse-free survival strongly correlated with positive findings on lymphography and poorly differentiated tumor.

Lymphography is occasionally used to study other pelvic cancers in women, including those of the vulva, endometrium, and ovary. Weiner et al. [33] reported 43 patients with vulvar carcinoma who had lymphography followed by vulvectomy and lymphadenectomy. Their conclusion was that negative findings on lymphography might be helpful in predicting absence of metastases, but its poor specificity limited its use. Santoni et al. [34] analyzed 27 patients who had ovarian dysgerminomas removed and who had undergone lymphography. They thought that lymphography as well as other criteria were helpful in determining which patients required radiation therapy.

In a study of 288 patients with endometrial carcinoma, Galakhoff et al. [35] found that lymphography was not a predictor of survival when other prognostic factors were considered. They considered it of little diagnostic or prognostic value but thought it was useful for follow-up of lymph nodes treated by radiotherapy.

For staging of carcinoma of the cervix at our center, we continue to use lymphography, followed by needle biopsy of abnormal or suspicious nodes. Lymphography is not used for surveillance by our gynecology group. Lymphography is still occasionally used for staging other pelvic tumors such as carcinomas of the endometrium, ovary (especially germ cell tumors), vagina, and vulva.

Genital Tumors in Men

At M.D. Anderson Cancer Center, Wishnow et al. [36] evaluated 174 patients with early nonseminomatous tumors, and, including CT and serum tumor marker levels, lymphography detected unsuspected metastases in only 4% of the patients and provided misinformation in another 4%. When CT and serum tumor markers were normal, follow-up radiographic findings were positive in only one case. They concluded that lymphography is not necessary to assess the retroperitoneum when CT and serum tumor markers are normal.

In a separate study at M.D. Anderson Cancer Center by von Eschenbach et al. [37], CT was noted to be more accurate than lymphography in patients with nonseminomatous tumors with extensive disease, but the authors commented that the two examinations are complementary because lymphography shows internal nodal architecture. In those patients with pure seminomas, lymphography established the presence of metastases and facilitated defining radiation portals. Epstein et al. [38] reported in their series of 61 patients with seminoma that proper staging by lymphography with adequate radiation dose led to a 92% 10-year disease-free survival.

Macher and Steinfeld [39] reported that of 34 patients with seminoma, results with lymphography and CT were concordant in 21. Eleven patients had abnormal lymphographic findings and normal CT findings, and two patients had the reverse. They concluded that CT should be the first procedure, and lymphography should follow if the CT findings are negative.

In a series of 36 stage I or II patients with nonseminomatous tumors reported by Lien et al. [40], 11 patients were found to have metastases at retroperitoneal node dissection. Six of these had at least one abnormal node by palpation at surgery and the other five had microscopic disease. Dunnick and Javadpour [41] concluded that a combination of lymphography and CT provided the most accurate assessment of the paraaortic nodes in their study of 63 patients with nonseminomatous testicular tumors. Harding et al. [42] found that lymphography might result in earlier detection for nonseminomatous tumors, but with the success of salvage treatment, they concluded that lymphography could be abandoned as a staging procedure.

At our center, CT and marker studies have now replaced lymphography for staging and surveillance of patients with testicular tumors. The current literature supports this approach.

REFERENCES

1. Clouse ME. History. In: Clouse ME, Wallace S, eds. *Lymphatic imaging: lymphography, computed tomography and scintigraphy.* Baltimore: Williams & Wilkins, **1985**:1–14
2. Harrison DA, Clouse ME. Normal anatomy. In: Clouse ME, Wallace S, eds. *Lymphatic imaging: lymphography, computed tomography and scintigraphy.* Baltimore: Williams & Wilkins, **1985**:15–94
3. Clouse ME. Technique. In: Clouse ME, Wallace S, eds. *Lymphatic imaging: lymphography, computed tomography and scintigraphy.* Baltimore: Williams & Wilkins, **1985**:111–119
4. Wallace S, Jing BS, Clouse ME, Harrison DA. Interpretation. In: Clouse ME, Wallace S, eds. *Lymphatic imaging: lymphography, computed tomography and scintigraphy.* Baltimore: Williams & Wilkins, **1985**:203–223
5. Clouse ME. Lymphoma of the abdomen and retroperitoneum. In: Clouse ME, Wallace S, eds. *Lymphatic imaging: lymphography, computed tomography and scintigraphy.* Baltimore: Williams & Wilkins, **1985**:264–289
6. Jing BS, Wallace S. Lymphatic imaging of solid tumors. In: Clouse ME, Wallace S, eds. *Lymphatic imaging: lymphography, computed tomography and scintigraphy.* Baltimore: Williams & Wilkins, **1985**:290–450
7. Jing BS. Diagnostic imaging of abdominal and pelvic lymph nodes in lymphoma. *Radiol Clin North Am* **1990**;28:801–831
8. Castellino RA, Billingham M, Dorfman RF. Lymphographic accuracy in Hodgkin's disease and malignant lymphoma with a note on the "reactive" lymph node as a cause of most false-positive lymphograms. *Invest Radiol* **1990**;25:412–422
9. Gamble JF, Fuller LM, Martin RG, et al. Influence of staging celiotomy in localized presentations of Hodgkin's disease. *Cancer* **1975**;35:817–825
10. Heifetz LJ, Fuller LM, Rodgers RW, et al. Laparotomy findings in lymphangiogram-staged I and II non-Hodgkin's lymphomas. *Cancer* **1980**;45:2778–2786
11. Hagemeister FB, Fuller LM, Velasquez WS, et al. Two cycles of MOPP and radiotherapy: effective treatment for stage IIIA and IIIB Hodgkin's disease. *Ann Oncol* **1991**;2:25–31
12. Jagannath S, Velasquez WS, Tucker SL, et al. Tumor burden assessment and its implication for a prognostic model in advanced diffuse large-cell lymphoma. *J Clin Oncol* **1986**;4:859–865
13. Romaguera JE, McLaughlin P, North L, et al. Multivariate analysis of prognostic factors in stage IV follicular low-grade lymphoma: a risk model. *J Clin Oncol* **1991**;9:762–769
14. Velasquez WS, Fuller LM, Jagannath S, et al. Stages I and II diffuse large cell lymphomas: prognostic factors and long-term results with CHOP-Bleo and radiotherapy. *Blood* **1991**;77:942–947
15. Velasquez WS, Jagannath S, Tucker SL, et al. Risk classification as the basis for clinical staging of diffuse large-cell lymphoma derived from 10-

year survival data. *Blood* **1989**;74:551–557

16. Cafferty LL, Katz RL, Ordonez NG, Carrasco CH, Cabanillas FR. Fine needle aspiration diagnosis of intraabdominal and retroperitoneal lymphomas by a morphologic and immunocytochemical approach. *Cancer* **1990**;65:72–77
17. Castellino RA, Hoppe RT, Blank N, et al. Computed tomography, lymphography, and staging laparotomy: correlations in initial staging of Hodgkin disease. *AJR* **1984**;143:37–41
18. Strijk SP, Boetes C, Rosenbusch G, Ruijs JHJ. Lymphography and abdominal computed tomography in staging Hodgkin's disease. *ROFO* **1987**;146:312–318
19. Benson WJ, Ding JC, Cooper IA. Abdominal CT and lymphography in the initial staging of non-Hodgkin's lymphoma. *Aust N Z J Med* **1987**;17: 253–254
20. Clouse ME, Harrison DA, Grassi CJ, Costello P, Edwards SA, Wheeler HG. Lymphangiography, ultrasonography, and computed tomography in Hodgkin's disease and non-Hodgkin lymphoma. *J Comput Tomogr* **1985**;9:1–8
21. Pond GD, Castellino RA, Horning S, Hoppe RT. Non-Hodgkin lymphoma: influence of lymphography, CT, and bone marrow biopsy on staging and management. *Radiology* **1989**;170:159–164
22. Mansfield CM, Fabian C, Jones S, et al. Comparison of lymphangiography and computed tomography scanning in evaluating abdominal disease in stages III and IV Hodgkin's disease. *Cancer* **1990**;66:2295–2299
23. Sullivan MP, Fuller LM. Hodgkin's disease in children. In: Fuller LM, Hagemeister FB, Sullivan MP, Velasquez WS, eds. *Hodgkin's disease and non-Hodgkin's lymphomas in adults and children.* New York: Raven, **1988**:247–269
24. Sullivan MP, Fuller LM. T and B cell lymphomas in children. In: Fuller LM, Hagemeister FB, Sullivan MP, Velasquez WS, eds. *Hodgkin's disease and non-Hodgkin's lymphomas in adults and children.* New York: Raven, **1988**:365–380
25. Maor MH, Gillespie BW, Peters LJ, et al. Neutron therapy in cervical cancer: results of a phase III RTOG study. *Radiat Oncol Biol Phys* **1988**;14:885–891
26. Haie C, Pejovic MH, Gerbaulet A, et al. Is prophylactic para-aortic irradiation worthwhile in the treatment of advanced cervical carcinoma? Results of a controlled clinical trial of the EORTC radiotherapy group. *Radiother Oncol* **1988**;11:101–112
27. Swart E, Bouma J, Schuur K. The clinical value of lymphography in cervical cancer, FIGO-stage Ib-IIa. *Eur J Gynaecol Oncol* **1989**;10:85–90
28. Boie H, Jakobsen A, Petersen J, Sell A. Diagnostic value of lymphography in cervical cancer stage Ib. *Eur J Gynaecol Oncol* **1989**;10:393–395
29. Heller PB, Malfetano JH, Bundy BN, Barnhill DR, Okagaki T. Clinical-pathologic study of stage IIB, III and IVA carcinoma of the cervix: extended diagnostic evaluation for paraaortic node metastasis—a gynecologic oncology group study. *Gynecol Oncol* **1990**;38:425–430
30. Smales E, Perry CM, MacDonald JS, Baker JW. The value of lymphography in the management of carcinoma of the cervix. *Clin Radiol* **1986**;37:19–22
31. Ashraf M, Elyaderani MK, Gabriele OF, Krall JM. Value of lymphangiography in the diagnosis of paraaortic lymph node metastases from carcinoma of the cervix. *Gynecol Oncol* **1982**;14:96–104
32. Eifel PJ, Morris M, Oswald MJ, Wharton T, Delclos L. Adenocarcinoma of the uterine cervix. *Cancer* **1990**;65:2507–2514
33. Weiner SA, Lee JKT, Kao MS, Moon TE. The role of lymphangiography in vulvar carcinoma. *Am J Obstet Gynecol* **1986**;154:1073–1075
34. Santoni R, Villari N, Bisin L, Cionini L. The role of lymphography in the staging and treatment of ovarian dysgerminoma. *Acta Oncol* **1987**;26: 23–25
35. Galakhoff C, Masselot J, Dam N, Pejovic MH, Prade P, Duvillard P. Lymphography in the initial evaluation of endometrial carcinoma. *Gynecol Oncol* **1988**;31:276–284
36. Wishnow KI, Johnson DE, Tenney D. Are lymphangiograms necessary before placing patients with nonseminomatous testicular tumors on surveillance? *J Urol* **1989**;141:1133–1135
37. Von Eschenbach AC, Jing B-S, Wallace S. Lymphangiography in genitourinary cancer. *Urol Clin North Am* **1985**;12:715–723
38. Epstein BE, Order SE, Zinreich ES. Staging, treatment, and results in testicular seminoma. *Cancer* **1990**;65:405–411
39. Macher MS, Steinfeld AD. Relative role of abdominal pelvic CT and lymphangiography in staging of testicular seminoma. *Urology* **1985**;26:193–195
40. Lien HH, Kolbenstvedt A, Talle K, Fossa SD, Klepp O, Ous S. Comparison of computed tomography, lymphography, and phlebography in 200 consecutive patients with regard to retroperitoneal metastases from testicular tumor. *Radiology* **1983**;146:129–132
41. Dunnick NR, Javadpour N. Value of CT and lymphography: distinguishing retroperitoneal metastases from nonseminomatous testicular tumors. *AJR* **1981**;136:1093–1099
42. Harding M, Dall B, Corbett R, Vallance R, Kaye SB. Dose lymphangiography have any role in the management of early non-seminomatous germ cell tumors? *Clin Radiol* **1990**;41:392–394

Review Article

Diseases of the Musculoskeletal System in Children: Imaging with CT, Sonography, and MR

Alan E. Schlesinger[1] and Ramiro J. Hernandez

We reviewed the applications of CT, sonography, and MR imaging in diseases of the musculoskeletal system in children. Unique advantages of each technique are discussed, and common disease entities and practical applications of the three imaging methods are stressed. Evaluation of congenital dysplasia of the hip, hip effusion, and soft-tissue foreign bodies with sonography are emphasized. The role of CT in imaging patients with congenital dysplasia of the hip, tarsal coalition, osteomyelitis, and benign and malignant bone tumors is stressed. Common applications of MR that are emphasized include imaging of osteomyelitis, musculoskeletal tumors, normal bone marrow, and avascular necrosis. Innovations are briefly discussed, including evaluation of dermatomyositis with MR and imaging sternoclavicular dislocation, congenital vertical talus, and fractures and dislocations with sonography.

Plain film radiography is still the best initial imaging procedure for evaluating most children with musculoskeletal diseases. However, CT, sonography, and MR imaging have had a marked impact on the diagnostic workup of many musculoskeletal lesions in children. With sonography, one can noninvasively image soft tissue, cartilage, and, to a limited extent, bone. The patient can be imaged at rest or dynamically during stress maneuvers. CT provides outstanding imaging detail of cortical and medullary bone as well as the surrounding soft tissues. MR allows multiplanar imaging without ionizing radiation and the ability to image the bone marrow. This article provides an overview of applications of these techniques in the evaluation of the musculoskeletal system in children. Practical applications and common disease entities are stressed. Owing to limitations of space, only standard spin-echo MR pulse sequences are stressed. However, in some cases, faster techniques such as gradient-echo imaging [1] are supplementing or replacing standard spin-echo sequences. Other innovations that may play a role in MR imaging of musculoskeletal diseases in children in the future include MR angiography [2], three-dimensional acquisition [3], fat-suppression techniques [4], and ultrafast MR imaging techniques such as echoplanar imaging [5].

Congenital Conditions

Congenital Dysplasia of the Hip (CDH)

CDH occurs in up to 0.1% of neonates [6, 7]. Risk factors include breech presentation, family history of CDH, oligohydramnios, congenital foot anomalies, and other signs of fetal crowding. Girls are more at risk than boys, and the left hip is more frequently affected than the right.

Early detection and treatment usually result in an excellent outcome. The clinical detection of CDH was markedly improved when the Barlow and Ortolani maneuvers were introduced in the 1930s, resulting in a decrease in late diagnoses of CDH. However, despite this initial improvement in the detection rate of CDH, there has been no further clear-cut decrease in late diagnoses of CDH since 1960, despite widespread clinical screening programs [8]. Screening for CDH with conventional radiography has been attempted [9]. Radio-

---

Received September 19, 1991; accepted after revision November 5, 1991.

[1] Both authors: Department of Radiology, University of Michigan Medical Center, and Section of Pediatric Radiology, C. S. Mott Children's Hospital C3123/0252, 200 E. Hospital Dr., Ann Arbor, MI 48109-0252. Address reprint requests to A. E. Schlesinger.

AJR 158:729–741, April 1992 0361–803X/92/1584–0729 © American Roentgen Ray Society

graphic screening detects acetabular dysplasia rather than joint instability (although the two abnormalities usually occur together). The exposure to ionizing radiation and the lack of ossification of the femoral head in early infancy are limitations of radiographic screening.

The introduction of hip sonography a decade ago has stimulated much interest in the use of this procedure for screening CDH and monitoring the response to therapy. Two methods have evolved: (1) morphologic evaluation of the location of the femoral head and the degree of acetabular development and (2) dynamic evaluation of the location of the femoral head and the degree of hip instability with stress.

The morphologic approach has been developed and promoted by Graf [10, 11] and is more widely used in Europe than in the United States. A single coronal sonogram is obtained of each hip. The child is placed in the lateral position, and the hip is slightly flexed and slightly rotated internally. The coronal image includes the lateral surface of the iliac bone above the acetabulum, the deepest portion of the acetabulum, the cartilaginous acetabular roof, and the proximal femoral metaphysis. Careful application of the technique is crucial to obtaining a coronal image that demonstrates the proper anatomic landmarks through the deepest portion of the acetabulum so that reproducible measurements can be obtained. The depth of the acetabulum and the degree of lateral and/or superior displacement of the femoral head (as evidenced by elevation of the cartilaginous labrum) are measured by determining the alpha and beta angles, respectively [11] (Fig. 1). The alpha angle is measured between a baseline extending from the straight, lateral margin of the ilium above the acetabulum and a line connecting the lateral edge of the bony acetabulum and the top of the triradiate cartilage. The beta angle is measured between the same baseline and a line drawn from the lateral aspect of the bony acetabulum to the labrum. The beta angle is useful predominantly in the subclassification of the more dysplastic hips.

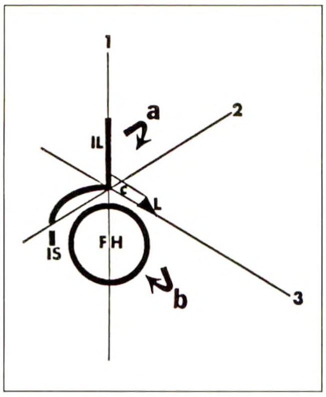

Fig. 1.—Schematic representation of coronal image of left hip shows lines and angles used for Graf classification method. Alpha angle (a) is measured between baseline (1) drawn along lateral margin of ilium (IL) above acetabulum and bony acetabular roof line (2) drawn from triradiate cartilage to lateral margin of bony acetabulum. Cartilaginous portion of acetabulum includes hypoechoic component formed from hyaline cartilage (c) and echogenic fibrocartilaginous labrum (L). Beta angle (b) is measured between baseline (1) and line drawn from lateral aspect of bony acetabulum to labrum (3). FH = femoral head, IS = ischium. (Adapted from Graf [11].)

Graf [11, 12] has developed a somewhat complex classification of hip dysplasia by using these two angles (modified in Table 1). We have found the Graf classification of hip dysplasia cumbersome to use, as the referring clinicians caring for the patients have various levels of understanding and familiarity with the classification system. To improve communication and avoid confusion, we have stressed only the alpha angle and have favored descriptive terms such as normal, physiologically immature, borderline, subluxed, and dislocated rather than type I, type IIA, type IIC, type IID, and types III or IV, respectively (Fig. 2).

The dynamic stress sonographic evaluation of the hip has been advocated by Harcke and Grissom [13]. The hip is scanned in the transverse and coronal planes with the patient supine. The transverse views are obtained in the neutral position, in flexion with abduction, and in flexion with adduction. The flexed hip is observed with real-time imaging while it is abducted and adducted. While in the adducted position, the hip is stressed with a posterior push under real-time visualization to evaluate instability (Fig. 3). In the coronal plane, the hip is viewed in flexion, and images are obtained through both the midplane of the acetabulum and posterior lip of the acetabulum. While scanning the posterior lip of the acetabulum, a posterior push is performed to assess joint instability [13]. Keller et al. [14] have shown that a certain degree of subluxability is normal in the immediate neonatal period. These views obtained in the dynamic assessment of the hip are also useful in determining the adequacy of hip reduction with the infant in a Pavlik harness [15].

We use both techniques in a complementary fashion. The Graf view provides a quantifiable evaluation of the acetabular development (the alpha angle) that is useful both in screening and in follow-up of CDH to assess the effect of therapy on acetabular development. The dynamic study provides a screen for infants with mild or no dysplasia of the acetabulum, but with significant joint instability.

Recent studies have evaluated the efficacy of screening hip sonography [16–20]. Screening programs have included either all neonates or only those with risk factors and/or abnormal physical examinations. Some researchers have shown that clinically silent dysplastic hips can be diagnosed sonographically [16, 17]. Furthermore, these studies have also suggested that clinically suspicious hips can be shown to be normal sonographically (anatomically as well as dynamically), and unnecessary therapy can be avoided [16]. Nevertheless, some studies suggest that screening hip sonography has not lowered the number of late diagnoses of CDH [20].

Applications of CT or MR or both in patients with CDH include evaluation of the concentricity of closed reduction, obstacles to closed reduction, femoral torsion, acetabular configuration, and deformity of the cartilaginous femoral head [21]. Overlying plaster makes evaluation of the concentricity of closed reduction of the hip difficult on conventional radiographs. However, the location of the unossified femoral head

TABLE 1: Sonographic Classification of Hip Dysplasia

Type	Alpha Angle	Beta Angle	Comment
I	≥60°	–	Normal
IIA	50–59°	–	Physiologic immaturity; <3 months old
IIB	50–59°	–	Delayed ossification; >3 months old
IIC	43–49°	<77°	Critical zone; labrum not everted ($\beta < 77°$)
IID	43–49°	>77°	Subluxed; labrum everted ($\beta > 77°$)
III	<43°	>77°	Dislocated
IV	<43°	>77°	Dislocated with labrum interposed between femoral head and acetabulum

Note.—Adapted from Graf [11].

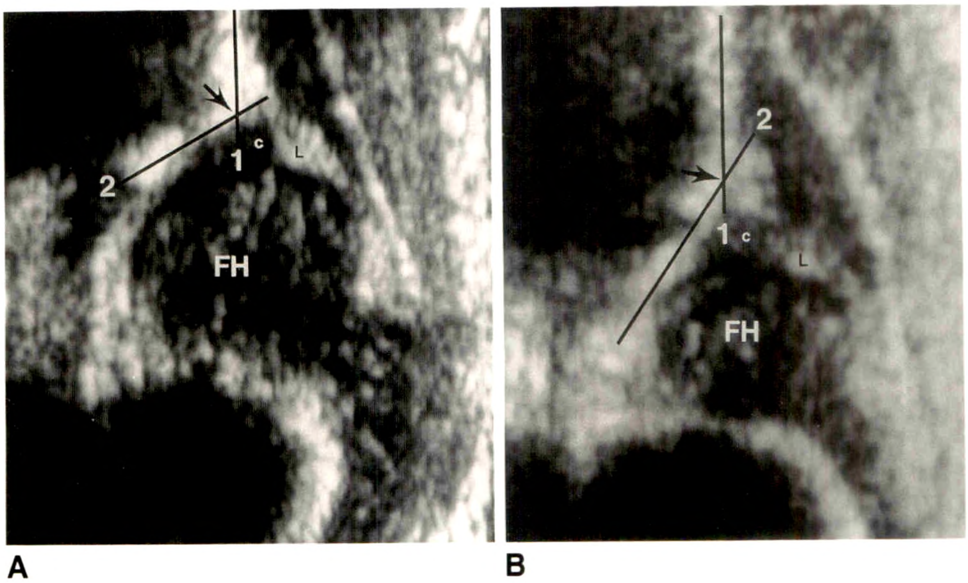

Fig. 2.—Coronal sonograms of left hip of two neonates with lines and angles of Graf method superimposed on images.

A, Normal hip (type I) shows well-developed bony acetabulum (alpha angle = 60°). Lateral aspect of bony acetabulum normally forms a sharp angle with lateral margin of ilium (*arrow*).

B, Dysplastic hip (type III) has poorly developed acetabulum (alpha angle = 34°). Lateral aspect of bony acetabulum is underdeveloped and rounded (*arrow*).

1 = baseline, 2 = bony acetabular roof line, c = hyaline cartilage of acetabular roof, L = labrum, FH = femoral head.

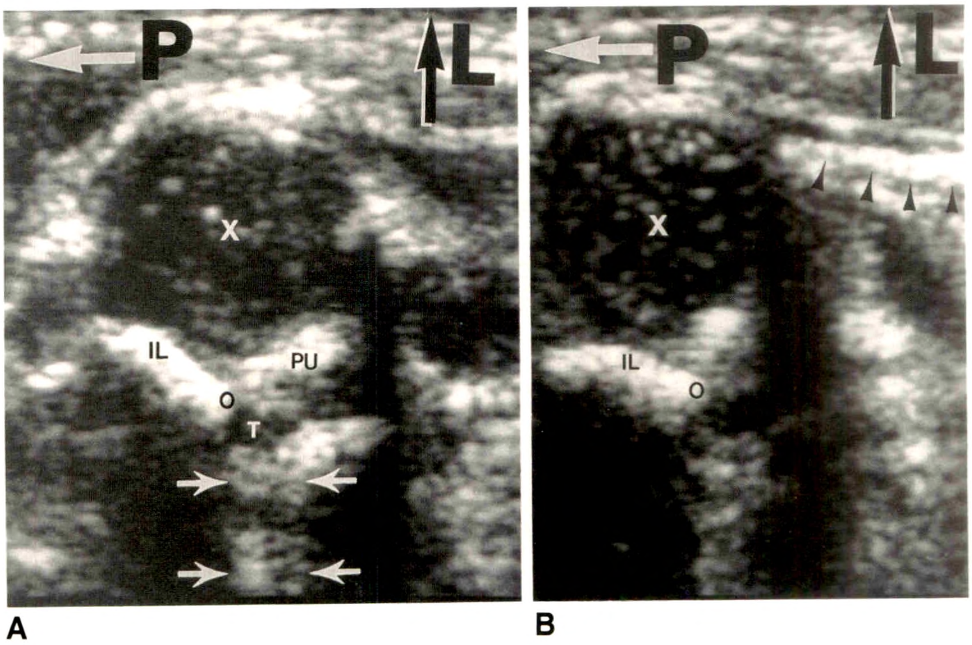

Fig. 3.—*A* and *B*, Transverse sonograms of left hip of neonate in flexion and adduction both without (*A*) and with (*B*) stress filmed on same image by using dual-image function. Lateral (L) aspect of patient is closest to transducer surface. Pubis (PU) is seen on view obtained without stress (*A*), but is obscured by ossified femoral metaphysis (*arrowheads*) on stress view (*B*). Through-transmission of sound (*white arrows*) is seen beyond triradiate cartilage (T). Without stress, center of femoral head (X) is centered over most anterior aspect (O) of ilium (IL). When hip is stressed posteriorly (P), center of femoral head (X) moves posteriorly along ilium (IL) and no longer is aligned with its most anterior aspect (O).

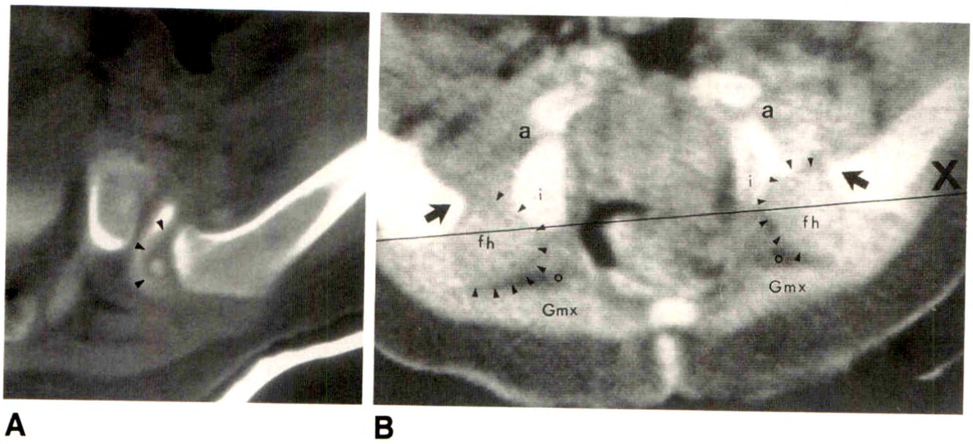

Fig. 4.—*A*, Axial CT scan above level of left acetabulum after left hip arthrogram in 18-month-old boy with left hip dislocation. Proximal femoral metaphysis has "Dutch clog" appearance. Superiorly dislocated femoral head (*arrowheads*) simulates a ball being kicked by clog. Onset of ossification of femoral head is noted.

B, Axial CT scan of hips through cast after attempted closed reduction of bilaterally dislocated hips in a 4-month-old infant. Femoral heads (fh, surrounded by *arrowheads*) are well seen just medial to ossified proximal femoral metaphyses. Although proximal femoral metaphyses do not resemble Dutch clogs as much as in *A*, upturn of anterior proximal femoral metaphyses (*arrows*) provides a landmark for axial CT section through level of cartilaginous femoral heads. Both femoral heads are posteriorly dislocated from acetabula and project posterior to ischial line. Pregluteal fat (o) is also displaced posterior to ischial line. Gmx = gluteus maximus, a = acetabula at level of triradiate cartilage, X = ischial line (tangent to ischial spines). (Reprinted with permission from Hernandez [22].)

can be easily determined by CT [22]. With the leg in the frog position, the proximal femoral metaphysis looks like a "Dutch clog" on axial CT sections. The unossified cartilaginous femoral head is located adjacent to the tip of the clog like a ball being kicked by the clogged foot. When ossification of the femoral head has begun, the location of the head is more readily identified by CT. Signs of dislocation include lateral displacement of the proximal femoral metaphysis, projection of the femoral head posterior to the ischial line (a line drawn tangent to the ischial spines), and posterior displacement of the pregluteal fat from the ischial line (Fig. 4). Because a high degree of spatial resolution is not required in these studies, a significant reduction in radiation dose is achieved when the amperage is decreased. We routinely perform these examinations at 40 mA. The dose for a single CT scan through plaster with this technique is comparable to that of conventional radiographic examinations [23].

CT and MR can identify obstacles to closed reduction of the hip [21, 24]. These obstacles can be intraarticular, such as hypertrophy of the pulvinar tissue (fibrofatty tissue at the apex of the acetabulum) or the ligamentum teres. An extraarticular obstacle to closed reduction can occur when a tight iliopsoas tendon migrates between the femoral head and the acetabulum causing infolding of the joint capsule [24].

Children with previously treated CDH may have persistent subluxation that may be related to abnormalities of femoral torsion. Femoral torsion is the angle between the long axis of the femoral neck and the coronal plane through the distal femoral condyles. This angle cannot be easily determined by conventional radiographs, but can be directly measured by CT [25, 26]. Selected axial sections are obtained both through the femoral neck and the distal femoral condyles. The axis of the neck is usually easily determined. The transcondylar plane is determined by a line bisecting the angle between two lines drawn tangentially to the anterior and posterior surfaces of the condyles, respectively. The angle between the long axis of the femoral neck and the transcondylar plane is the measure of femoral torsion (Fig. 5). If the neck of the femur is rotated anteriorly relative to the transcondylar plane, the neck is anteverted. If the neck of the femur is rotated posteriorly, it is retroverted.

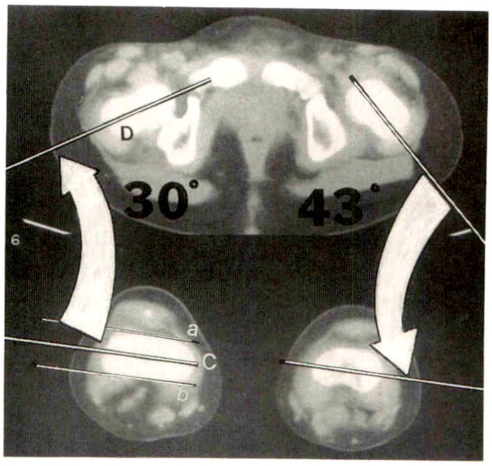

Fig. 5.—Axial CT scan through femoral necks (*top*) and distal femoral condyles (*bottom*) printed on same frame. Angles of femoral torsion (30° on right and 43° on left) are measured between long axis of femoral neck (D) and transcondylar plane (C). Transcondylar plane (C) is determined by a line bisecting angle between lines drawn tangential to anterior (a) and posterior (b) surfaces of femoral condyle. (Reprinted with permission from Hernandez [26].)

The configuration of the acetabulum can be evaluated with CT in the older child with a history of pelvic osteotomies to improve femoral head coverage. The acetabular depth can be seen readily on axial images [27]. The angle of acetabular torsion (the angle of inclination of the acetabulum relative to the sagittal plane) can also be determined from axial CT sections.

Determination of the presence of a cartilaginous head and its relation to the femoral neck may be difficult with conventional radiographs or arthrography when severe deformity exists owing to late diagnosis of CDH, poor result of prior treatment, or infection. CT arthrography or MR may be helpful in such cases [28, 29].

Tarsal Coalition

Tarsal coalition, the fibrous or bony fusion of two or more tarsal bones, is frequently associated with a spastic flat foot. The coalitions most frequently encountered are between the calcaneus and navicular bone or between the calcaneus and the talus. Calcaneonavicular tarsal coalition is usually identified easily with appropriate conventional radiographs including oblique views. However, CT scans are useful when radiographs are suboptimal or when the clinical presentation is atypical. The best way to image this type of coalition is to use thin sections parallel to the plantar surface of the foot [30]. Talocalcaneal coalitions are difficult to demonstrate with conventional radiographs, and special views or tomography was often used in the past with limited success. CT with thin sections is now the study of choice [30]. Scans perpendicular to the plantar surface of the foot best demonstrate talocalcaneal coalitions (Fig. 6). Although the middle facet of the talocalcaneal joint is the most frequently involved, coalitions occur at the posterior facet also.

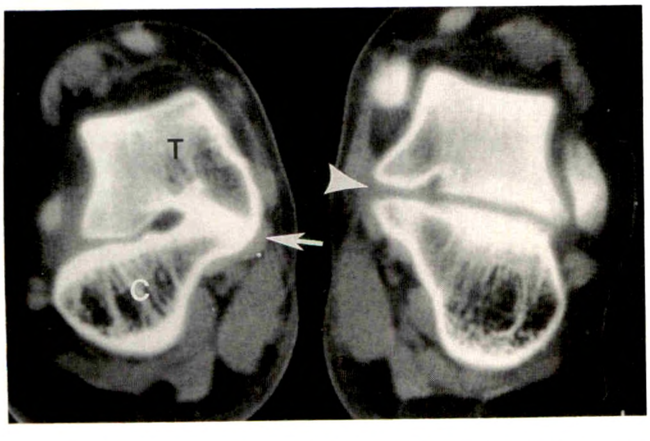

Fig. 6.—CT scan perpendicular to plantar surface of feet in 10-year-old boy with pain in right foot. Bony fusion is seen at middle facet (*arrow*) between talus (T) and calcaneus (C) on right foot. Middle facet (*arrowhead*) is normal on left foot.

Miscellaneous Congenital Conditions

In congenital vertical talus, the talus has a vertical orientation and the navicular bone is anteriorly dislocated relative to the talus. Identification of this dislocation is pivotal in the management of patients with this condition, as surgery is required to relocate the navicular bone. Because the navicular bone remains unossified during the first 2–3 years of life, orthopedic surgeons have in the past relied on indirect clues to its location. Sonography can directly image the unossified navicular bone and determine its position in relation to the talus [31].

Congenital muscular torticollis is a benign condition with focal, masslike enlargement of the sternocleidomastoid muscle [32]. The mass usually appears approximately 10–14 days after birth and is associated with head tilt and chin rotation. The diagnosis is usually readily made on physical examination, but occasionally sonography is useful to detect homogeneous, fusiform enlargement of the sternocleidomastoid muscle (Fig. 7). A similar appearance is seen with CT or MR, but the diagnosis can easily be confirmed with sonography alone.

Inflammatory Conditions

Joint Effusion in the Hip

Pediatricians often see children with a limp who do not bear weight on one leg, or who have other symptoms suggesting pain in a lower extremity. The differential diagnosis in such cases includes infection, trauma, or neoplasm in a location somewhere between the spine and the foot. Conventional radiographs should be the initial imaging procedure. If the symptoms are localized to the hip and the radiographic findings are normal or suggest a joint effusion, sonography can easily determine the presence or absence of joint fluid [33, 34]. Sonography is more reliable than conventional radiographs in detecting an effusion [33] and can thereby be used to further direct the appropriate workup.

When the presence of hip effusion is evaluated with sonography, an anterior parasagittal approach is used, paralleling the long axis of the femoral neck. Ideally, the leg should be positioned with the hip and knee in extension and the hip externally rotated. It is most important to position the two extremities symmetrically and compare the symptomatic and asymptomatic hips. Fluid tends to first accumulate in the anterior recess, where the joint capsule is most distensible. Flexion of the hip to 45° has been shown to decompress the anterior recess and result in false-negative examinations [34]

The joint capsule and iliofemoral ligament normally parallel the concave surface of the femoral neck. A joint effusion occupying the anterior recess both displaces the joint capsule/iliofemoral ligament complex from the femoral neck and changes its anteriorly concave orientation to a straight or convex orientation (Fig. 8). Although some investigators have measured the distance from the joint capsule to the femoral neck to aid in the detection of an effusion [34], many radiologists prefer to rely on a qualitative assessment of the configuration of the capsule. We have not found the relative echo-

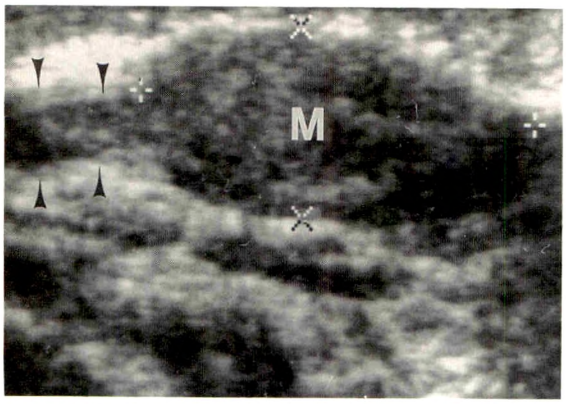

Fig. 7.—Longitudinal sonographic image of sternocleidomastoid muscle of a 1-month-old neonate with torticollis. Superior aspect of muscle has normal caliber (*arrowheads*), but inferiorly there is fusiform, masslike enlargement of muscle (M, *between calipers*). Enlarged portion of muscle is isoechoic with remainder of sternocleidomastoid muscle. Child was observed, and mass resolved over a period of 2-3 months.

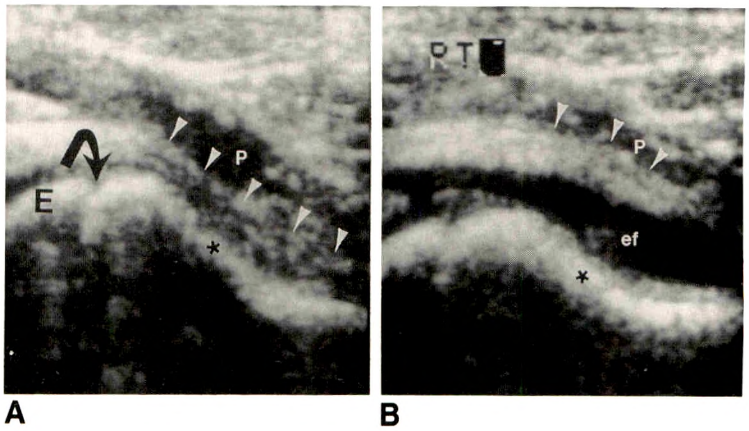

Fig. 8.—Parasagittal sonographic images along long axis of femoral neck of both hips in a 7-year-old child with right hip pain (filmed on a single image by using dual-image function).

***A*, Image of left hip shows normal course of joint capsule/iliofemoral ligament complex (*arrowheads*) paralleling anteriorly concave femoral neck (*asterisk*). E = proximal femoral epiphysis, *curved arrow* = growth plate.**

***B*, On right, large effusion (ef) displaces joint capsule/iliofemoral ligament complex (*arrowheads*) anteriorly from femoral neck. Psoas muscle (P) should not be confused with effusion in a normal hip.**

genicity of the fluid in the anterior recess to be useful in predicting the composition of the fluid in the joint [33, 34].

Osteomyelitis and Soft-Tissue Abscesses

Conventional radiographs and skeletal scintigraphy are the best initial imaging procedures in children with osteomyelitis and usually are sufficient. However, CT and MR are often needed to detect or localize a focus of infection, particularly in the flat bones [35–39]. CT findings in osteomyelitis include cortical bone destruction, periosteal new bone formation, intraosseous gas, increased attenuation of the marrow, narrowing of the medullary cavity, serpentine drainage tracts, and the presence of an involucrum or sequestrum [37, 40–43]. The presence of a punctate area of increased attenuation within a region of focal cortical destruction suggests a sequestrum and is very specific for an infectious process [37] (Fig. 9).

MR is also very sensitive in detecting osteomyelitis. The marrow space of the involved bone demonstrates decreased signal on T1-weighted images and increased signal on T2-weighted images [39]. Cortical destruction or thickening and edema or abscess formation in the soft tissues can also be demonstrated by MR. Although both an abscess and edema will have low signal on T1-weighted images and high signal on T2-weighted images, a well-demarcated border and a rim of decreased intensity are more characteristic of an abscess [44]. In chronic osteomyelitis, T2-weighted images can localize areas of active infection with high signal intensity. Findings that favor chronic infection include thickening of the cortex, a relatively sharp interface between diseased and normal marrow, and a well-defined soft-tissue abnormality [45].

Sonography has a more limited role in the evaluation of soft-tissue abscesses or osteomyelitis. An abscess limited to the soft tissues typically is predominantly hypoechoic with or without debris, but may manifest as a complex mass [46]. Gas can occasionally be present within the mass, causing acoustic shadowing. If the fluid collection is in direct contact with bone, osteomyelitis is suggested [47].

Miscellaneous Inflammatory Conditions

Sacroiliac arthritis is often difficult to image with conventional radiographs because of overlying soft tissues and the oblique orientation of the joint. In these cases, CT can be helpful in detecting joint narrowing, juxtaarticular osteopenia, loss of a sharp cortical margin, cortical erosions, intraosseous gas, and bony sclerosis [48, 49].

MR complements conventional radiography in detecting changes of juvenile rheumatoid arthritis because of its ability to directly image the cartilage and synovium. The MR findings include joint effusions (low signal on T1-weighted images, high signal on T2-weighted images), bone erosions, areas of focal cartilage loss, and intermediate signal intensity masses presumably representing hypertrophied synovium. Occasionally, areas of high signal on T2-weighted images are seen in the synovium that likely represent inflammation [50].

Pigmented villonodular synovitis is an uncommon synovial inflammatory condition that is nearly always monoarticular and commonly affects the knee. Findings on conventional radiographs include joint effusion and cystic erosions of the bone. MR can detect this entity before the appearance of radiographic changes. MR imaging reveals thickening of the synovium with signal intensity that is isointense with muscle on T1-weighted images. On long TR/long TE sequences, the shortened T2 relaxation time of hemosiderin that is deposited in the synovium leads to an overall decrease in signal intensity. However, multiple areas of high signal may also be seen on

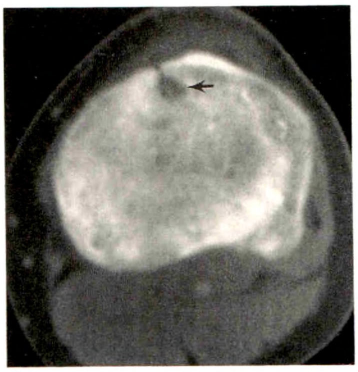

9

Fig. 9.—Axial CT scan through distal femur in 10-year-old child with leg pain. Focal region of cortical destruction (*arrow*) with small sequestrum and drainage tract to anterior cortex is diagnostic of osteomyelitis.

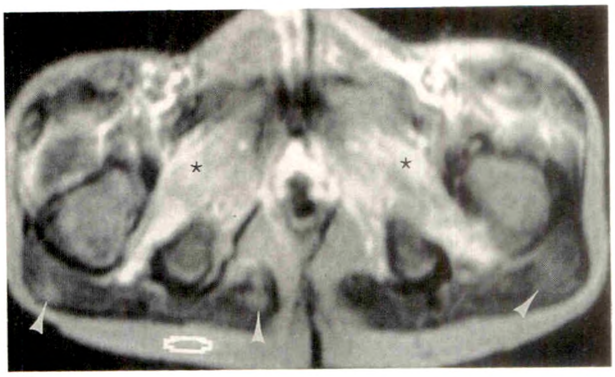

10

Fig. 10.—Axial T2-weighted MR image through pelvis in 7-year-old boy with dermatomyositis. There is a marked increase in signal in adductor muscle groups bilaterally (*asterisks*). More subtle focal areas of high signal also occur in glutei maximi (*arrowheads*) and in anterior muscles such as rectus femoris and psoas.

T2-weighted images as a result of the presence of fluid and congestion within the synovium [51].

Childhood dermatomyositis is characterized by nonsuppurative inflammation of striated muscles and skin. Documentation of the presence of muscle involvement may require muscle biopsy or electromyography. Involved muscles have normal signal intensity on T1-weighted images, but high signal intensity on T2-weighted images [52] (Fig. 10). MR imaging plays a role in initially establishing the diagnosis, monitoring the response to therapy, and determining an appropriate biopsy site.

Tumors of the Musculoskeletal System

CT and MR have greatly improved the imaging of bone and soft-tissue neoplasms. Advantages of MR over CT include superior contrast resolution, multiplanar imaging capability, and the display of blood vessels to better advantage. CT is better than MR in displaying small calcifications in soft-tissue masses, fine periosteal reaction, and the integrity of the cortex [53]. The initial imaging study should be conventional radiography. If further imaging is required, MR is often performed. However, if the internal characteristics and morphology of the lesion are inadequately demonstrated on the plain radiographs (as often occurs in the flat bones), a CT scan may be obtained instead of or in addition to an MR image [53].

At least two spin-echo sequences should be used when a bone or soft-tissue mass is evaluated by MR: a T1-weighted sequence to provide maximal contrast between the lesion and fat, and a T2-weighted sequence for improved contrast between the lesion and muscle. The bone itself is best displayed on proton-density images. A multiecho T2-weighted sequence should be obtained in the axial plane, and a T1-weighted sequence should be obtained in a longitudinal plane: sagittal if the lesion predominantly involves the anterior or posterior aspect of the bone, or coronal if the lesion predominantly involves the medial or lateral aspect of the bone. The longitudinal T1-weighted views best demonstrate the extent of the intramedullary involvement, and the axial T2-weighted sequence shows the extraosseous disease and possible involvement of the neurovascular structures to best advantage [53]. Although MR is very sensitive, the MR appearance of most bone lesions is nonspecific [54]. IV gadopentetate dimeglumine has a limited role in evaluating tumors of bone and soft tissue before and after therapy. Short inversion-time inversion-recovery (STIR) imaging increases the sensitivity of MR because of the fat-suppressing qualities of the technique. However, the increased sensitivity is accompanied by decreased specificity [55].

The CT scan should be photographed by using both soft-tissue and bone windows. A bone algorithm (with increased edge enhancement) should be used. IV contrast medium may show enhancement of a soft-tissue mass or may demonstrate abnormal vessels in a tumor of vascular origin.

Benign Bone Tumors

Most benign lesions of bone are easily diagnosed with conventional radiographs alone. On rare occasions, CT or MR may be required.

An osteoid osteoma typically has a radiolucent nidus with surrounding reactive sclerosis. Although the nidus may be identified with conventional radiographs, CT may be required for precise localization. The appearance of an osteoid osteoma is frequently atypical when the lesion occurs in a subperiosteal location or in cancellous bone, as if often the case in the femoral neck or in the spine [56]. In such cases, the reactive sclerosis may be absent, mild, or remote from the lesion, and the nidus may be obscure. CT is invaluable in identifying the nidus in such cases (Fig. 11).

Lytic lesions of bone can sometimes require investigation beyond plain films. CT has been used to differentiate a simple bone cyst from fibrous dysplasia on the basis of CT attenuation characteristics [57]. An extraosseous soft-tissue mass seen on CT or MR may be the only clue that a benign-appearing lytic lesion is in fact a purely lytic osteosarcoma rather than a simple bone cyst or an aneurysmal bone cyst [58]. A fibrous cortical defect or nonossifying fibroma may cause concern when there is increased uptake on a radionuclide bone scintigram owing to a pathologic fracture. In such cases, CT may demonstrate an otherwise occult fracture.

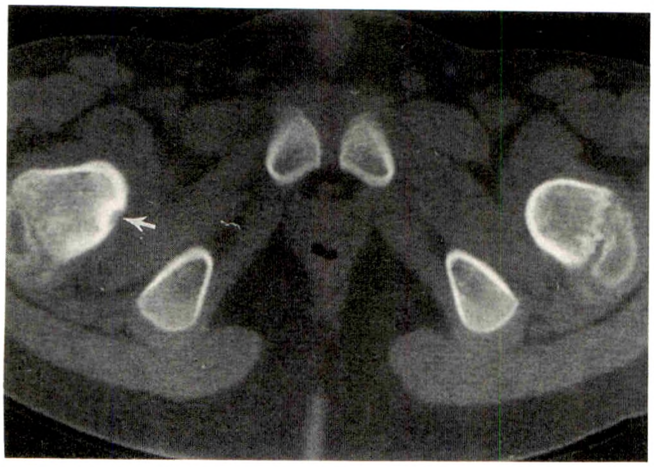

Fig. 11.—5-year-old boy with right hip and knee pain. Axial CT scan shows radiolucent nidus of an osteoid osteoma (*arrow*) with a mild amount of surrounding sclerosis. Nidus was not appreciated on plain radiographs. (Reprinted from Schlesinger and Hernandez [56].)

Malignant Bone Tumors

The most common primary malignant bone tumors in children are osteogenic sarcoma and Ewing sarcoma. Osteogenic sarcoma usually presents as a destructive lesion in a metaphyseal location. Cortical destruction, medullary extension, soft-tissue mass, and new bone formation are characteristics of this tumor. However, new bone production may not be present in the purely lytic and telangiectatic varieties of this tumor. Ewing sarcoma can be metaphyseal or diaphyseal and is often associated with an extensive extraosseous soft-tissue component; it less often has a periosteal or extraskeletal site of origin [59, 60].

CT and MR of malignant bone tumors can determine the intramedullary extension, presence of skip lesions, extent of cortical involvement, epiphyseal and joint space invasion, size and distribution of the soft-tissue mass, and response to therapy [61, 62]. Tumor involving the marrow space has higher attenuation on CT than does normal fatty marrow. The extraosseous portion of the tumor typically has CT attenuation similar to that of adjacent muscles. On MR imaging, tumor in the marrow space or in the extraosseous soft tissues has low signal intensity on T1-weighted images and high signal intensity on T2-weighted images (Fig. 12). These techniques are extremely useful in evaluating patients preoperatively and in planning amputation or limb salvage surgery [63]. MR has been shown to be more accurate than CT in measuring the intramedullary extent of tumors preoperatively [64]. MR, with its superior soft-tissue contrast resolution and ability to image in multiple planes, has a particularly important role in assessing the feasibility of limb-sparing surgery by determining the relationship of the tumor to the adjacent physis, joint, and neurovascular structures [63].

MR has played an important role in evaluating the response to preoperative chemotherapy and radiation therapy in primary malignant bone neoplasms. Measures of response to preoperative therapy include tumor volume changes, signal intensity changes [65], and changes in enhancement patterns after injection of MR contrast agents. A decrease in tumor volume after therapy is the best predictor of a favorable response [63, 66]. Early tumor response to therapy leads to increased signal on long TR/long TE images owing to replacement of tumor by a watery myxoid matrix and granulation tissue [63, 67]. However, this pattern is similar to that of recurrent tumor. Similarly, contrast enhancement is a sensitive indicator of recurrent tumor, but is nonspecific, as a similar response to MR contrast agents is seen with granulation tissue and inflammatory changes [63]. Later changes of fibrosis lead to decreasing intensity on long TR/long TE imaging, and although these findings are specific for response to therapy, they are not sensitive [63].

Soft-Tissue Tumors

MR is the imaging method of choice in the evaluation of soft-tissue masses, as it has better contrast resolution than CT [68] and has multiplanar imaging capability. However, CT can better display areas of calcification within soft-tissue

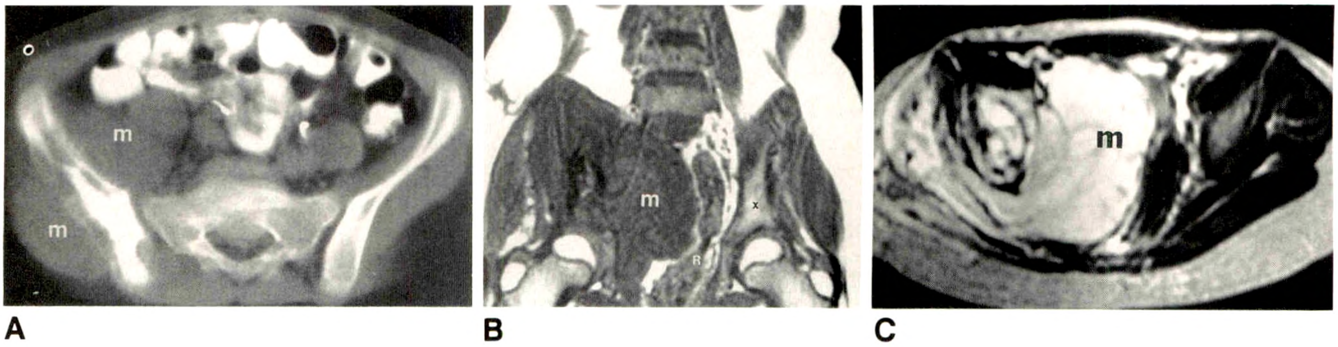

Fig. 12.—11-year-old boy with Ewing sarcoma.

***A*, CT scan through iliac wing reveals cortical destruction, periosteal reaction, and large soft-tissue mass (m).**

***B*, Coronal T1-weighted MR image reveals normal high signal in marrow of femurs and left iliac wing (X). Marrow space in right iliac wing is replaced by low-signal tumor. Large medial soft-tissue mass (m) displaces rectum (R) to left.**

***C*, Axial T2-weighted MR image shows high signal in soft-tissue mass (m). High-signal regions within soft tissues of right flank are due to edema from a recent biopsy.**

masses. CT and MR rarely can provide histologic characterization of the soft-tissue mass or distinguish benign from malignant lesions.

Most masses have low signal intensity on T1-weighted images and high signal intensity on T2-weighted images. Common exceptions include lipomas (high signal on both T1 and T2 weighting), fibrous tumors (low signal on both T1 and T2 weighting), hematomas (high signal on T2 weighting, variable signal on T1 weighting, depending on age), and hemangiomas [63, 69, 70]. Hemangiomas often appear heterogeneous, with intermediate signal intensity on short TR/short TE images and high signal intensity on long TR/long TE images. Serpentine areas of signal voids often appear within the high-signal lesions on T2-weighted images (Fig. 13). Fat is frequently present within the lesion as well and can lead to high signal intensity on both T1- and T2-weighted images.

The primary functions of CT and MR in evaluating malignant soft-tissue masses are to determine the extent of the mass, evaluate response to therapy, and detect recurrences. Although MR cannot definitely predict whether a soft-tissue mass is benign or malignant, several findings are suggestive of malignancy, including indistinct margins, an inhomogeneous signal intensity, and peritumoral edema [63, 68, 71]. Estimates of tumor size with either method may be imprecise: CT has the potential to either overestimate or underestimate the extent of disease [72, 73], whereas MR may overestimate lesion size by mistaking peritumoral edema for tumor mass [74].

Bone Marrow Imaging

MR is an excellent technique for imaging the bone marrow in children. The common applications of MR imaging of bone marrow include evaluation of avascular necrosis, myeloid hyperplasia, marrow replacement by malignant cells, and myeloid depletion. Interpretation of MR images of the marrow requires a thorough understanding of the normal evolution of the MR appearance of bone marrow of children at different ages.

MR Appearance of Normal Marrow in Children and Conversion of Red to Yellow Marrow

Normal marrow consists of myeloid and fat cells within a cancellous bone matrix. Marrow can be primarily hematopoietic (red) or fatty (yellow). The relative proportion of these two types of marrow and their distribution normally change with advancing age through childhood and young adult life [75].

Hematopoietic marrow contains approximately 40% water, 40% fat, and 20% protein [63]. The appearance of hematopoietic marrow on T1-weighted spin-echo imaging sequences ranges from low to intermediate signal intensity (less than that of muscle) in neonates to slightly increased signal intensity (greater than that of muscle) in older children. With T2 weighting, the signal of hematopoietic marrow increases slightly. These signal patterns reflect a combination of influences of the short T1 and long T2 relaxation times of fat and the long T1 and long T2 relaxation times of protein and water [76]. Fatty marrow contains approximately 15% water, 80% fat, and 5% protein [63]. The relatively short T1 and long T2 relaxation times of fat produce a high signal on T1 weighting that decreases slightly with T2 weighting [76].

The distribution of red and yellow marrow changes with age. In the neonate, essentially all of the marrow is red marrow. Conversion from red to yellow marrow begins in the infant and progresses distally (appendicular skeleton) to proximally (axial skeleton) with advancing age [75]. At birth, the red marrow of the vertebral bodies has low to intermediate signal intensity on T1-weighted images. The cartilaginous periphery of the vertebral bodies has intermediate signal [76]. The cartilage ossifies with age and becomes a signal void. With advancing age, the signal of the vertebral marrow on T1-weighted images increases, reflecting conversion from red

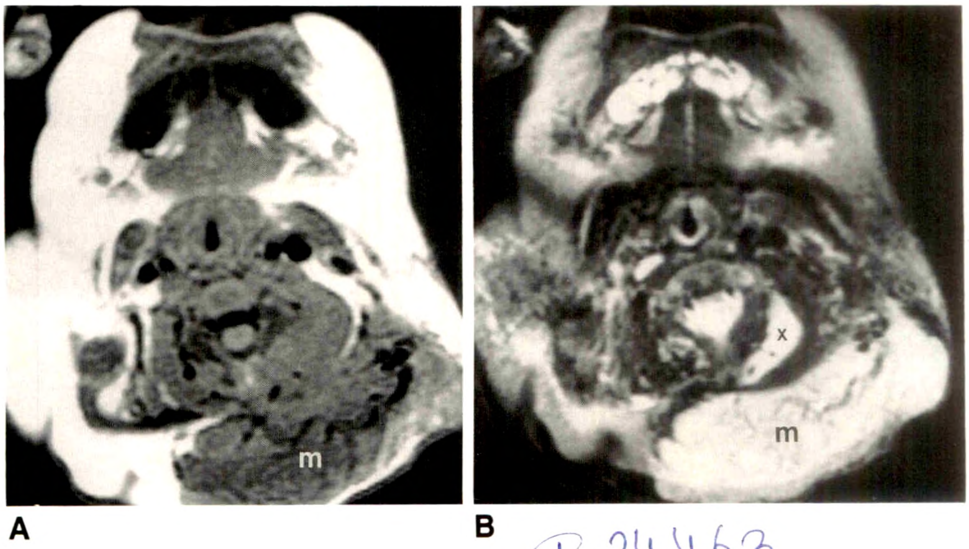

Fig. 13.—Newborn girl with large soft-tissue hemangioma of neck.

***A*, Axial T1-weighted MR image reveals mass (m) in soft tissues of posterior neck that is isointense with adjacent muscles and contains several linear, serpiginous regions devoid of signal.**

***B*, Axial T2-weighted MR image at the same level as *A* shows high signal within the hemangioma (m) with persistence of the serpiginous signal voids. In addition, a separate component of hemangioma is identified deeper in soft tissues (X).**

P 24,463

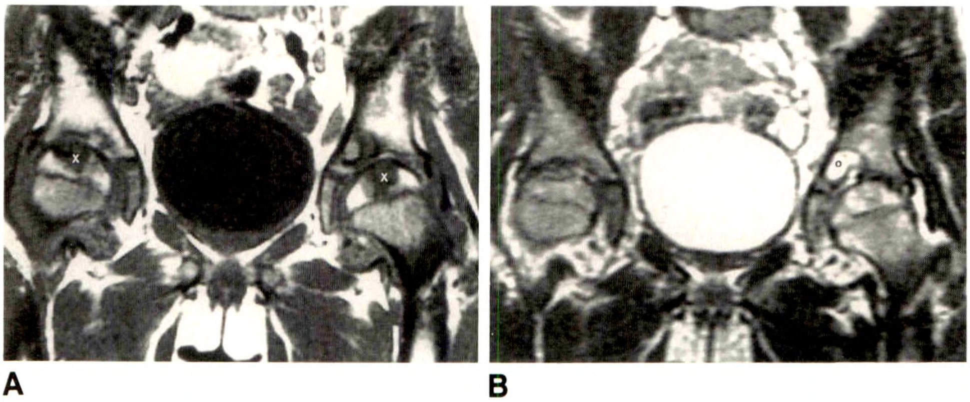

Fig. 14.—12-year-old boy with bilateral femoral head avascular necrosis caused by steroid therapy for juvenile rheumatoid arthritis.

A, Coronal T1-weighted MR image through femoral heads shows foci of low signal within normal high signal of both proximal femoral epiphyses (X).

B, Coronal T2-weighted MR image reveals heterogeneous signal in regions of femoral head avascular necrosis. Region of high signal in left iliac wing (o) is an incidental subchondral cyst related to juvenile rheumatoid arthritis.

to yellow marrow. Within individual long bones, the cartilaginous epiphyses contain red marrow for only a few months and convert to yellow marrow before other portions of the bone [77]. The shafts of the long bones convert to fatty marrow from the diaphysis toward the metaphyses. A progression through four MR bone marrow signal patterns has been described for long bones in children [78].

Myeloid Hyperplasia and Myeloid Depletion

When there is an increase in demand for hematopoiesis, there is reconversion of the yellow marrow to hematopoietic red marrow. Marrow reconversion typically occurs in chronic anemias such as sickle cell anemia or thalassemia, malignant bone marrow replacement, or severe stress. The order of the reconversion of yellow to red marrow is the opposite of the normal red to yellow progression starting in the axial skeleton and followed by the long bones in a proximal to distal sequence [63]. The conversion of yellow to red marrow results in decreasing intensity on T1 weighting and increasing intensity on T2 weighting.

Myeloid depletion states include aplastic anemia and myelofibrosis. In aplastic anemia, the hypocellular marrow is replaced by fat with accompanying high signal on both T1- and T2-weighted images [79, 80]. The fibrous tissue that fills the marrow space in myelofibrosis demonstrates decreased signal on both T1 and T2 weighting [81].

Marrow Replacement by Malignant Cells

Diffuse infiltration of the marrow with malignant cells (such as in leukemia) or focal areas of tumor involvement (as in metastases or lymphoma) will appear as decreased signal relative to normal marrow on T1-weighted images and increasing signal on T2-weighted images [76, 82, 83]. Metastases are more likely to occur in hematopoietic marrow because of its richer vascular supply relative to fatty marrow. Special imaging sequences can be used in individual cases. STIR imaging and chemical-shift imaging (fat suppression) decrease the signal of fat and thereby improve tissue contrast and conspicuity of the lesions within the bone marrow [84–86].

Avascular Necrosis

Avascular necrosis in childhood can be idiopathic (Legg-Perthes disease) or consequent to steroid use, sickle cell anemia, or Gaucher disease. The MR pattern of acute avascular necrosis can be variable. T1-weighted images can show homogeneously low signal, heterogeneous signal, rings or bands of low signal, or irregular areas of low signal [76, 87, 88]. The pattern on T2-weighted images is also variable, with some, all, or none of these regions of low signal becoming higher in signal intensity with lengthening TR and TE [76] (Fig. 14). Not only are these patterns variable but they are nonspecific for avascular necrosis [89]. However, a double-line sign on T2-weighted images (a high-signal line surrounding a zone of decreased signal with a low-signal band surrounding the high-signal line) is considered relatively specific for avascular necrosis [90]. Although MR is very sensitive in detecting acute avascular necrosis, false-negative studies do occur [91–93]. Foci of low signal on both T1- and T2-weighted images may represent either fibrosis in areas of chronic infarction or regions of marrow hyperplasia [94].

In Legg-Perthes disease, the normal high signal intensity of the epiphysis on T1-weighted images is replaced by a zone of low signal. With subsequent fragmentation, areas of mixed high and low signal will be seen, indicating inhomogeneous revascularization of the necrotic zone. Eventually there will be progressive revascularization and reossification with return of high signal intensity [95, 96]. In advanced cases, MR can be used to evaluate the thickness and shape of the femoral and acetabular cartilage, residual epiphyseal and metaphyseal deformity, and loss of containment of the femoral head [63,

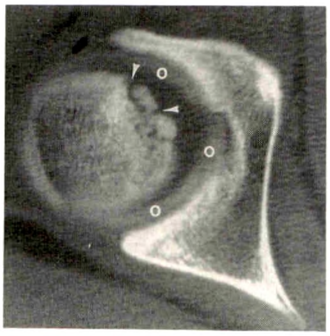

Fig. 15.—15-year-old boy with Legg-Perthes disease of right femoral head. Axial section from CT performed after arthrography reveals fragmentation of ossification center of femoral head (*arrowheads*) but no evidence of loose body in joint, as contrast material (O) in joint space does not extend into cartilaginous head to indicate disruption of cartilaginous portion of epiphysis.

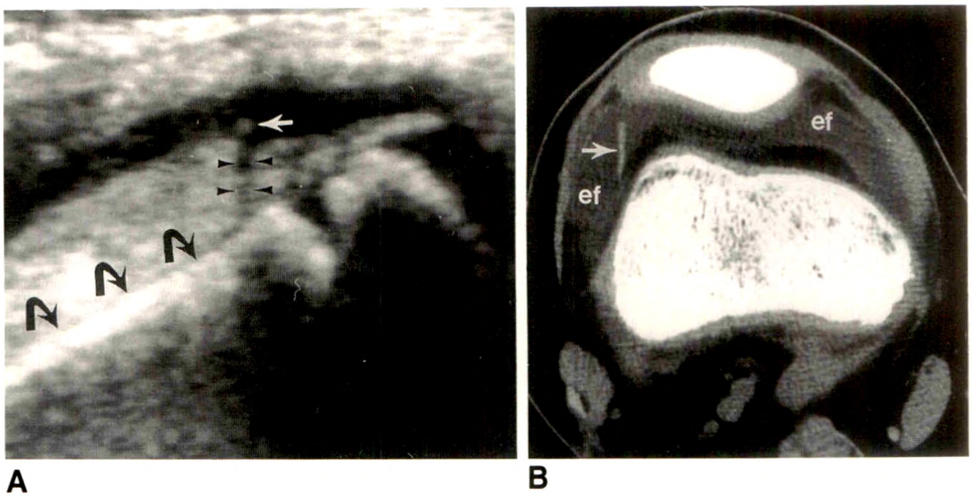

Fig. 16.—8-year-old boy with puncture wound from rose thorn with suspected residual foreign body in soft tissues.

***A*, Longitudinal sonographic image along distal femur shows echogenic structure (*straight arrow*) with acoustic shadowing (*arrowheads*) in soft tissues anterior to distal femoral metaphysis (*curved arrows*).**

***B*, Axial CT scan through knee shows thorn (*arrow*) within knee joint with surrounding joint effusion (ef).**

97]. MR also may show a frondlike structure adjacent to the joint space that most likely represents villous hypertrophy of the synovium [97].

In children with hip pain and normal radiographic findings, MR imaging of the bone marrow may reveal transient regions of low signal on T1-weighted images and high signal on T2-weighted images. These reversible changes likely represent transient bone marrow edema [98]. Similar MR changes have been described in adult patients with bone marrow biopsies that excluded avascular necrosis [99].

Patients with avascular necrosis may develop fragmentation of the epiphysis, raising the possibility of a loose bony or cartilaginous fragment. In these cases, CT combined with arthrography can play a role in detecting fractures [100] and confirming the presence or absence of a loose body in the joint (Fig. 15).

Trauma

Fractures and Dislocations in Infants

Differentiation between a dislocation or a displaced Salter I fracture can be difficult with conventional radiographs when an injury occurs in young infants prior to ossification of the cartilaginous epiphysis. When the metaphysis of the affected bone is displaced, it is not always possible to determine if the unossified epiphysis has accompanied the metaphysis (i.e., dislocation) or has maintained its normal relationship with the contralateral side of the joint (i.e., displaced Salter I fracture). Sonography is extremely useful in these cases, as the cartilaginous epiphysis can be directly imaged and its relationship with the metaphysis determined.

Foreign Bodies

Radiopaque foreign bodies such as metal or glass are well evaluated by conventional radiographs in most cases. Occasionally, sonography can be useful in guiding the surgeon in the removal of radiopaque foreign bodies such as needles or pins in the soft tissues of the foot [101]. Nonradiopaque foreign bodies are also well seen sonographically as hyperechoic foci, often with acoustic shadowing. Wood, for example, is well shown by sonography, but is only seen in a minority of cases on conventional radiography or xeroradiography. With small foreign bodies or foreign bodies in regions that cannot be well evaluated by sonography, CT or MR can also localize a foreign object (Fig. 16). CT should be performed without IV contrast material so that foreign bodies can be differentiated from vascular structures. Placement of a localization needle under sonographic or CT guidance can also help the surgeon locate a foreign body in the operating room.

Sternoclavicular Dislocation

Sternoclavicular dislocation can often be diagnosed by physical examination alone. However, imaging is often required to confirm the clinical suggestion. Conventional radiography and tomography can be difficult to interpret. CT is currently the imaging method of choice, as axial scans can readily display the relationship of the head of the clavicle to the manubrium [102]. More recently, the use of sonography to identify sternoclavicular dislocation has been reported [103].

REFERENCES

1. Erlemann R, Vassallo P, Bongartz G, et al. Musculoskeletal neoplasms: fast low-angle shot MR imaging with and without Gd-DTPA. *Radiology* **1990**;176:489–495
2. Keller PJ, Drayer BP, Fram EK, Williams KD, Dumoulin CL, Souza SP. MR angiography with two-dimensional acquisition and three-dimensional display. *Radiology* **1989**;173:527–532
3. Lang P, Steiger P, Genant HK, et al. Three-dimensional CT and MR imaging in congenital dislocation of the hip: clinical and technical considerations. *J Comput Assist Tomogr* **1988**;12:459–464
4. Hernandez RJ, Keim DR, Chenevert TL, Sullivan DB, Aisen AM. Fat suppressed magnetic resonance imaging of myositis. *Radiology* **1992**;182:217–219
5. Saini S, Stark DD, Rzedzian RR, et al. Forty-millisecond MR imaging of the abdomen at 2.0 T. *Radiology* **1989**;173:111–116
6. Novick G, Ghelman B, Schneider M. Sonography of the neonatal and infant hip. *AJR* **1983**;141:639–645
7. Harcke TH, Grissom LE. Sonographic evaluation of the infant hip. *Semin Ultrasound CT MR* **1986**;7:331–338
8. Hansson G, Nachemson A, Palmen K. Screening of children with congen-

ital dislocation of the hip joint on the maternity wards in Sweden. *J Pediatr Orthop* **1983**;3:271–279

9. Lefaure C, Maccia C, Corlobe F. Cost-effectiveness and risk associated with infants' hip dysplasia screening in France. *Ann Radiol* (*Paris*) **1986**;29:393–399
10. Graf R. The ultrasonic image of the acetabular rim in infants. *Arch Orthop Trauma Surg* **1981**;99:35–41
11. Graf R. *Guide to sonography of the infant hip.* New York: Thieme, **1987**:66–75
12. Graf R. Classification of hip joint dysplasia by means of sonography. *Arch Orthop Trauma Surg* **1984**;102:248–255
13. Harcke TH, Grissom LE. Performing dynamic sonography of the infant hip. *AJR* **1990**;155:837–844
14. Keller MS, Weltin GG, Rattner Z, Taylor KJW, Rosenfield NS. Normal instability of the hip in the neonate: US standards. *Radiology* **1988**;169:733–736
15. Grissom LE, Harcke HT, Kumar SJ, Bassett GS, MacEwen GD. Ultrasound evauation of hip position in the Pavlik harness. *J Ultrasound Med* **1988**;7:1–6
16. Berman L, Klemerman L. Ultrasound screening for hip abnormalities: preliminary findings in 1001 neonates. *BMJ* **1986**;293:719–722
17. Tônnis D, Storch K, Ulbrich H. Results of newborn screening for CDH with and without sonography and correlation of risk factors. *J Pediatr Orthop* **1990**;10:145–152
18. Castelein RM, Sauter AJM. Ultrasound screening for congenital dysplasia of the hip in newborns: its value. *J Pediatr Orthop* **1988**;8:666–670
19. Jones DA, Powell N. Ultrasound and neonatal hip screening. *J Bone Joint Surg [Br]* **1990**;72-B:457–459
20. Clarke NMP, Clegg J, Al-Chalabi AN. Ultrasound screening of hips at risk for CDH. *J Bone Joint Surg [Br]* **1989**;71-B:9–12
21. Hernandez RJ, Poznanski AK. CT evaluation of pediatric hip disorders. *Orthop Clin North Am* **1985**;16:513–541
22. Hernandez RJ. Concentric reduction of the dislocated hip: computed tomographic evaluation. *Radiology* **1984**;150:266–268
23. Guyer B, Smith DS, Cady RB, et al. Dosimetry of computerized tomography in the evaluation of hip dysplasia. *Skeletal Radiol* **1984**;12: 123–127
24. Hernandez RJ, Tachdjian MO, Dias LS. Hip CT in congenital dislocation: appearance of tight iliopsoas tendon and pulvinar hypertrophy. *AJR* **1982**;139:335–337
25. Hernandez RJ, Tachdjian MO, Poznanski A, Dias LS. CT determination of femoral torsion. *AJR* **1981**;137:97–101
26. Hernandez RJ. CT and MR imaging of the musculoskeletal system. In: Poznanski AK, Kirkpatrick JA, eds. *Diagnostic categorical course in pediatric radiology* (syllabus). Oak Brook IL: Radiologic Society of North America, **1989**:89–106
27. Browning WH, Rosenkrantz H, Tarquino T. Computed tomography in congenital dislocation. *J Bone Joint Surg [Am]* **1982**;64-A:27–31
28. Brody AS, Ball WS, Towbin RB. Computed arthrotomography as an adjunct to pediatric arthrography. *Radiology* **1989**;170:99–102
29. Johnson ND, Wood BP, Jackman KV. Complex infantile and congenital hip dislocation: assessment with MR imaging. *Radiology* **1988**;168: 151–156
30. Stoskopf CA, Hernandez RJ, Kelikian A, Tachdjian MO, Dias LS. Evaluation of tarsal coalition by computed tomography. *J Pediatr Orthop* **1984**;4:365–369
31. Schlesinger AE, Deeney VFX, Caskey PF. Sonography of the nonossified tarsal navicular cartilage in an infant with congenital vertical talus. *Pediatr Radiol* **1989**;20:134–135
32. Crawford SC, Harnsberger HR, Johnson L, Aoki JR, Giley J. Fibromatosis colli of infancy: CT and sonographic findings. *AJR* **1988**;151:1183–1184
33. Miralles M, Gonzalez G, Pulpeiro J, et al. Sonography of the painful hip in children: 500 consecutive cases. *AJR* **1989**;152:579–582
34. Marchal GJ, Van Holsbeeck MT, Raes M, et al. Transient synovitis of the hip in children: role of US. *Radiology* **1987**;162:825–828
35. Helms CA, Jeffrey RB, Wing VW. Computed tomography and plain film appearance of a bony sequestration: significance and differential diagnosis. *Skeletal Radiol* **1987**;16:117–120
36. Hernandez RJ, Conway JJ, Poznanski AK, et al. The role of computed tomography and radionuclide scintigraphy in the localization of osteomyelitis in flat bones. *J Pediatr Orthop* **1985**;5:151–154
37. Hernandez RJ. Visualization of small sequestra by computerized tomography: report of 6 cases. *Pediatr Radiol* **1985**;15:238–241
38. Fletcher BD, Scoles PV, Nelson AD. Osteomyelitis in children: detection by magnetic resonance. *Radiology* **1984**;150:57–60
39. Unger E, Moldofsky P, Gatenby R, Hartz W, Broder G. Diagnosis of osteomyelitis by MR imaging. *AJR* **1988**;150:605–610
40. Kuhn JP, Berger PE. Computed tomography diagnosis of osteomyelitis. *Radiology* **1979**;130:503–506
41. Azouz EM. Computed tomography in bone and joint infections. *Can Assoc Radiol J* **1981**;12:102–106
42. Hermann G, Rose JS. Computed tomography in bone and soft tissue pathology of the extremities. *J Comput Assist Tomogr* **1979**;3:58–66
43. Ram PC, Martinez S, Korobkin M, Breiman RS, Gallis HR, Harrelson JM. CT detection of intraosseous gas: a new sign of osteomyelitis. *AJR* **1981**;137:721–723
44. Beltran J, Noto AM, McGhee RB, Freedy RM, McCalla MS. Infections of the musculoskeletal system: high-field-strength MR imaging. *Radiology* **1987**;164:449–454
45. Cohen MD, Cory DA, Kleiman M, Smith JA, Broderick NJ. Magnetic resonance differentiation of acute and chronic osteomyelitis in children. *Clin Radiol* **1990**;41:53–56
46. Hayden CK, Swischuk LE. *Pediatric ultrasonography.* Baltimore: Williams & Wilkins, **1987**:387
47. Abiri MM, Kirpekar M, Ablow RC. Osteomyelitis: detection with US. *Radiology* **1989**;172:509–511
48. Rosenberg D, Baskies AM, Deckers PJ, Leiter BE, Ordia JI, Yablon IG. Pyogenic sacroiliitis. *Clin Orthop* **1984**;184:128–132
49. Merine D, Fishman EK, Magid D. CT detection of sacral osteomyelitis associated with pelvic abcesses. *J Comput Assist Tomogr* **1988**;12: 118–121
50. Yulish BS, Lieberman JM, Newmann AJ, Bryan PJ, Mulopulos GP, Modic MT. Juvenile rheumatoid arthritis: assessment with MR imaging. *Radiology* **1987**;165:149–152
51. Spritzer CE, Dalinka MK, Kressel HY. Magnetic resonance imaging of pigmented villanodular synovitis: a report of two cases. *Skeletal Radiol* **1987**;16:316–319
52. Hernandez RJ, Keim DR, Sullivan DB, Chenevert TL, Martel W. Magnetic resonance imaging appearance of the muscles in childhood dermatomyositis. *J Pediatr* **1990**;117:546–550
53. Sundaram M, McLeod RA. MR imaging of tumor and tumorlike lesions of bone and soft tissue. *AJR* **1990**;155:817–824
54. Bohndorf K, Reiser M, Lochner B, Feaux de Lacrox W, Steinbrich W. Magnetic resonance imaging of primary tumours and tumour-like lesions of bone. *Skeletal Radiol* **1986**;15:511–517
55. Golfieri R, Baddeley H, Pringle J, Souhami R. The role of the STIR sequence in magnetic resonance imaging examination of bone tumors. *Br J Radiol* **1990**;63:251–256
56. Schlesinger AE, Hernandez RJ. Intracapsular osteoid osteoma of the proximal femur: findings on plain film and CT. *AJR* **1990**;154:1241–1244
57. Blumberg ML. CT of unicameral bone cysts. *AJR* **1981**;136:1231–1232
58. DeSantos LA, Edeiken B. Purely lytic osteosacarcoma. *Skeletal Radiol* **1982**;9:1–7
59. Bator SB, Baer TW, Marks KE, Norris DG. Periosteal Ewing's sarcoma. *Cancer* **1986**;58:1781–1784
60. Rose JS, Hermann G, Mendelson DS, Ambinader EP. Extraskeletal Ewing sarcoma with computed tomography correlation. *Skeletal Radiol* **1983**;9:234–237
61. DeSantos LA, Bernardino ME, Murray JA. Computed tomography in the evaluation of osteogenic sarcoma: experience with 25 cases. *AJR* **1979**;132:535–540
62. Destouet JM, Gilula LA, Murphy WA. Computed tomography of long-bone osteosarcoma. *Radiology* **1979**;131:439–445
63. Moore SG, Bissett GS, Siegel MJ, Donaldson JS. Pediatric musculoskeletal MR imaging. *Radiology* **1991**;179:345–360
64. Gillespy T, Manfrini M, Ruggieri P, Spanier SS, Pettersson H, Springfield DS. Staging of intraosseous extent of osteosarcoma: correlation of preoperative CT and MR imaging with pathologic macroslides. *Radiology* **1988**;167:765–767
65. Golden P, Raymond KA, Carrasco CH, et al. Osteosarcoma: MR imaging after preoperative chemotherapy. *Radiology* **1990**;174:517–526
66. Erlemann R, Sciuk J, Bosse A, et al. Response of osteosarcoma and

Ewing Sarcoma to preoperative chemotherapy: assessment with dynamic and static MR imaging and skeletal scintigraphy. *Radiology* **1990**;175: 791–796

67. Lemmi MA, Fletcher BD, Marina NM, et al. Use of MR imaging to assess results of chemotherapy for Ewing sarcoma. *AJR* **1990**;155:343–346
68. Totty WG, Murphy WA, Lee JKT. Soft-tissue tumors: MR imaging. *Radiology* **1986**;160:135–141
69. Kaplan PA, Williams SM. Mucocutaneous and peripheral soft-tissue hemangiomas: MR imaging. *Radiology* **1987**;163:163–166
70. Sundaram M, McGuire MH, Herbold DR, Beshany SE, Fletcher JW. High signal intensity soft tissue masses on T1 weighted pulsing sequences. *Skeletal Radiol* **1987**;16:30–36
71. Berquist TH, Ehman RL, King BF, Hodgman CG, Ilstrup DM. Value of MR imaging in differentiating benign from malignant soft-tissue masses: study of 95 lesions. *AJR* **1990**;155:1251–1255
72. Eglund N, Ekeland L, Sako M, Persson B. CT of soft tissue tumors. *AJR* **1981**;137:725–729
73. Jones ET, Kuhns LR. Pitfalls in the use of computed tomography for musculoskeletal tumors in children. *J Bone Joint Surg [Am]* **1981**;63-A:1297–1303
74. Beltran J, Simon DC, Katz W, Weis LD. Increased MR signal intensity in skeletal muscle adjacent to malignant tumors: pathologic correlation and clinical relevance. *Radiology* **1987**;162:251–255
75. Kricun ME. Red-yellow marrow conversion: its effect on the location of some solitary bone lesions. *Skeletal Radiol* **1985**;14:10–19
76. Moore SG, Sebac GH. Primary disorders of bone marrow. In: Cohen MD, Edwards MK, eds. *Magnetic resonance imaging of children.* Philadelphia: Decker, **1990**:765–824
77. Jaramillo D, Laor T, Hoffer FA, et al. Epiphyseal marrow in infancy: MR imaging. *Radiology* **1990**;180:809–812
78. Moore SG, Dawson KL. Red and yellow marrow in the femur: age-related changes in appearance at MR imaging. *Radiology* **1990**;175:219–223
79. Kaplan PA, Asleson RJ, Klassen LW, Duggan MJ. Bone marrow patterns in aplastic anemia: observations with 1.5-T MR imaging. *Radiology* **1987**;164:441–444
80. McKinstry CS, Steiner RE, Young AT, Jones L, Swirsky D, Aber V. Bone marrow in leukemia and aplastic anemia: MR imaging before, during and after treatment. *Radiology* **1987**;162:701–707
81. Lanir A, Aghai E, Simon JS. MR imaging in myelofibrosis. *J Comput Assist Tomogr* **1986**;10:634–636
82. Bohndorf K, Benz-Bohn G, Gross-Fengels W, Berthold F. MRI of the knee region in leukemic children. *Pediatr Radiol* **1990**;20:179–183
83. Moore SG, Gooding CA, Brasch RC, et al. Bone marrow in children with acute lymphocytic leukemia: MR relaxation times. *Radiology* **1986**;160:237–240
84. Wismer GL, Rosen BR, Buxton R, Stark DD, Brady TJ. Chemical shift imaging of bone marrow: preliminary experience. *AJR* **1985**;145: 1031–1037
85. Rosen BR, Fleming DM, Kushner DC, et al. Hematologic bone marrow disorders: quantitative chemical shift MR imaging. *Radiology* **1988**;169:799–804
86. Brateman L. Chemical shift imaging: a review. *AJR* **1986**;146:971–980
87. Totty WG, Murphy WA, Ganz WI, Kumar B, Daum WJ, Siegel BA. Magnetic resonance imaging of the normal and ischemic femoral head. *AJR* **1984**;143:1273–1280
88. Gillespy T, Genant HK, Helms CA. Magnetic resonance imaging of osteonecrosis. *Radiol Clin North Am* **1986**;24:193–208
89. Robinson HJ, Hartleben PD, Lund G, Schreiman J. Evaluation of magnetic resonance imaging in the diagnosis of osteonecrosis of the femoral head: accuracy compared with radiographs, core biopsy, and intraosseous pressure measurements. *J Bone Joint Surg [Am]* **1989**;71-A:650–663
90. Mitchell DG, Rao VM, Dalinka MK, et al. Femoral head avascular necrosis: correlation of MR imaging, radiographic staging, radionuclide imaging, and clinical findings. *Radiology* **1987**;162:709–715
91. Beltran J, Herman LJ, Burk JM, et al. Femoral head avascular necrosis: MR imaging with clinical-pathologic and radionuclide correlation. *Radiology* **1988**;166:215–220
92. Kulkarni MV, Tarr RR, Kim EK, McArdle CB, Partain CL. Potential pitfalls of magnetic resonance imaging in the diagnosis of avascular necrosis. *J Nucl Med* **1987**;28:1052–1054
93. Elsig JP, Exner GU, von Schulthess GK, Weitzel M. False-negative magnetic imaging in the diagnosis of avascular necrosis. *J Pediatr Orthop* **1989**;9:231–235
94. Rao VM, Fishman M, Mitchell DG, et al. Painful sickle cell crisis: bone marrow patterns observed with MR imaging. *Radiology* **1986**;161: 211–215
95. Toby EB, Koman LA, Bechtold RE. Magnetic resonance imaging of pediatric hip disease. *J Pediatr Orthop* **1985**;5:665–671
96. Bluemm RG, Falke THM, Ziedses des Plantes BG, Steiner RM. Early Legg-Perthes disease (ischemic necrosis of the femoral head) demonstrated by magnetic resonance imaging. *Skeletal Radiol* **1985**;14:95–98
97. Rush BH, Bramson RT, Ogden JA. Legg-Calvé-Perthes disease: detection of cartilaginous and synovial changes with MR imaging. *Radiology* **1988**;167:473–476
98. Pay NT, Singer WS, Bartal E. Hip pain in three children accompanied by transient abnormal findings on MR imagings. *Radiology* **1989**;171: 147–149
99. Wilson AJ, Murphy WA, Hardy DC, Totty WG. Transient osteoporosis: transient bone marrow edema? *Radiology* **1988**;167:757–760
100. Mitchell DG, Kressel HY, Arger PH, Dalinka M, Spritzer CE, Steinberg ME. Avascular necrosis of the femoral head: morphologic assessment by MR imaging, with CT correlation. *Radiology* **1986**;161:739–742
101. Shiels WE, Babcock DS, Wilson JL, Burch RA. Localization and guided removal of soft-tissue foreign bodies with sonography. *AJR* **1990**;155:1277–1282
102. Destouet JM, Gilula LA, Murphy WA, Sagel SS. Computed tomography of the sternoclavicular joint and sternum. *Radiology* **1981**;138:123–128
103. Benson L, Carroll NC, Donaldson JS. The use of ultrasound in the management of posterior sternoclavicular dislocation: a case report. *J Ultrasound Med* **1991**;10:115–118

Surgeon at Work

Stefan C. Schatzki[1]

Winslow Homer, who together with Thomas Eakins was one of the most important American artists of the 19th century, was born on February 24, 1836, in Boston. In 1859, after two years as an apprentice in a lithographic firm, Homer moved to New York and soon became a well-known illustrator. He had little formal training, attending night school at the National Academy of Design briefly in 1861 and studying for about one month with the American painter Frederick Rondel. It is perhaps this absence of formal training and foreign influence that led to the unique "American" style of Homer's mature work and that set him apart from virtually all other prominent 19th century American painters.

Homer's fame began during the Civil War, when he was hired by *Harper's Weekly* to produce sketches to illustrate the conduct of soldiers in battle. His extensive works of that conflict have been the subject of a recent exhibition and book. Even though there is some question as to how close to the battlefront Homer went to produce these sketches, his artistic ability was so far superior to the other artists covering the war that his illustrations became extremely popular. The engraving reproduced here is an example of the illustrations that Homer forwarded to the readers of *Harper's Weekly*. The American publisher Louis Prang produced and sold a group of these illustrations called "Campaign Sketches." During this period, Homer began to paint in oil. Unlike his sketches that were published to illustrate actual battle scenes, these early paintings were primarily insightful genre observations of the troops behind the lines, in keeping with the other genre subjects that he would paint during the 1860s.

Following early critical acclaim, he was elected an associate academician of the National Academy at age 28, becoming a full academician two years later. During the next 46 years, until his death on September 29, 1910, Homer produced an extraordinarily varied body of work that remains unique in the artistic history of our country.

Homer's early paintings in the 1860s emphasized, though not exclusively, genre subjects. For example, a recent exhibition and publication were limited to his croquet paintings of that period. He briefly went to France, and in the next decade, in addition to the continuing genre work, began to visit and create paintings of the Adirondacks and Quebec. In the mid 1870s, a visit to Virginia led to a group of Black American studies.

In 1881, Homer went to England for one year and devoted himself to documenting the hazardous life of the North Sea fishermen and their families. On his return, in November 1882, he settled permanently in Prout's Neck, Maine. For the next 28 years, while continuing his studies of the American outdoors and recording his impression of trips to the tropics, Homer produced the marine paintings for which he is best known today. He explored the strengths, skills, and experiences of human interactions with the beauty, power, and danger of the sea. His palate frequently darkened as he painted dramatic, melancholy, and somber depictions of the drama and power of the Maine seashore. He died in Prout's Neck on September 29, 1910.

Homer produced memorable works in both oil and watercolor, but if his career had ended in the late 1860s, he would still be known today as an illustrator. He continued to produce etchings until the last decade of his life, and he never strayed from his strictly American idiom. Today the works of this celebrated American artist are honored not only in America but throughout the Western world.

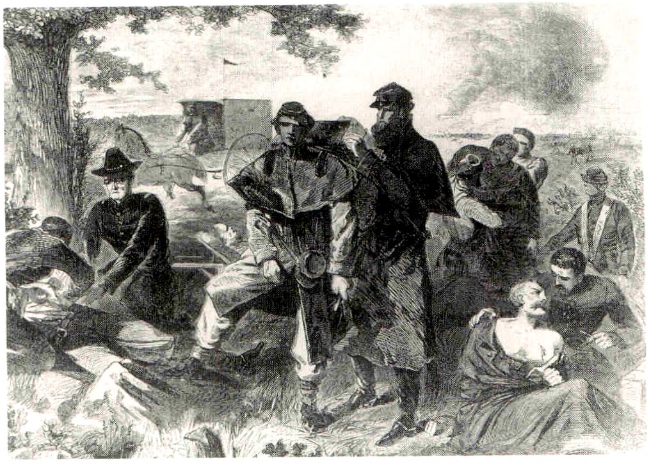

Winslow Homer (1836–1910). *Surgeon at Work at the Rear During an Engagement.* Engraving, 9½ × 14 in. (From *Harper's Weekly*, July 12, 1862.) Private collection.

---

[1] Department of Radiology, Mount Auburn Hospital, 330 Mount Auburn St., Cambridge, MA 02238.

AJR 158:742, April 1992 0361–803X/92/1584–0742 © American Roentgen Ray Society

Review Article

Infrastructure Design of a Picture Archiving and Communication System

H. K. Huang[1] and Ricky K. Taira

A picture archiving and communication system (PACS) infrastructure is the necessary framework to integrate distributed and heterogeneous imaging systems, provide intelligent data-base management of all radiology-related information, arrange an efficient means of viewing, analyzing, and documenting study results, and furnish a mechanism for effectively communicating study results to the referring physician. The PACS infrastructure consists of a basic skeleton of hardware components integrated by standardized, flexible software subsystems. This review describes these concepts and basic building blocks drawn from our original investigation, past experience, and the current clinical system in our radiology department.

A PICTURE ARCHIVING AND COMMUNICATION SYSTEM (PACS) has many definitions, depending on the user's perspective. It can be as simple as a film digitizer connected to a display station and a small image data base, or it can be as complex as a total hospital image management system. Generally speaking, a PACS consists of acquisition, storage, and display subsystems integrated by various digital networks. From 1986 to 1989, we designed three PACS modules that serviced a small subset of the total operations of the radiology department. These PACS modules were independently implemented within our institution in pediatric radiology [1], the coronary care unit [2], and neuroradiology [3]. The modules demonstrated the PACS concept and worked adequately for each of the different radiology and clinical services. However, our piecemeal approach did not address all the intricacies of connectivity and cooperation between modules. This weakness surfaced as more PACS nodes were added to the network. The maintenance, routing decisions, coordination of machines, fault tolerance, and expansibility of the system became increasingly difficult problems. The inadequacy in our design was partially due to a lack of understanding of the complexity of a large-scale PACS and to the unavailability of certain PACS-related technologies.

In the late 1980s, two new high-level PACS implementation strategies emerged. Both emphasize system connectivity. The first uses a top-down engineering approach to integrate various hospital information systems [4–7]. The second relies on building a foundation (i.e., PACS infrastructure) for a general multimedia data management system that is easily expandable, flexible, and versatile in its programmability. A hospital-wide PACS is attractive to administrators because it provides economic justification for implementing a PACS. Proponents of PACS are convinced that the cost benefit of the system should not be evaluated as a resource of the radiology department alone but should extend to the entire hospital. This concept has gained momentum during the past 2 years. A few large hospitals have obtained necessary

---

Received September 30, 1991; accepted after revision November 13, 1991.

This work was supported in part by Public Health Service Grant P01 CA 51198, awarded by the National Cancer Institute, Department of Health and Human Services.

[1] Both authors: Medical Imaging Division, Department of Radiological Sciences, University of California, Los Angeles, School of Medicine, 10833 Le Conte Ave., Los Angeles, CA 90024-1721. Address reprint requests to H. K. Huang.

AJR **158:743–749, April 1992** 0361–803X/92/1584–0743 © American Roentgen Ray Society

funding by using this strategy and are at various stages of implementation [4-7]. This review describes the second implementation strategy of the PACS infrastructure method. The PACS infrastructure is the basic design concept to ensure that PACS includes features such as standardization, open architecture, capability for future growth, connectivity, and reliability. This design philosophy can be constructed in a modular fashion. We used the PACS infrastructure designed and implemented in our department as an example to illustrate the importance of these features.

PACS Infrastructure

The goals of a PACS infrastructure are to provide the necessary framework to integrate distributed and heterogeneous imaging systems; provide intelligent data-base management of all radiology-related information; arrange an efficient means of viewing, analyzing, and documenting study results; and furnish a method for effectively communicating study results to the referring physician. The PACS infrastructure consists of a basic skeleton of hardware components (acquisition interfaces, storage devices, host computers, communication networks, display systems) integrated by standardized, flexible software subsystems. The important software subsystems include communication, data-base management, storage management, job scheduling, interprocessor communication, error handling, and network monitoring. The infrastructure as a whole is versatile and can incorporate rules to reliably perform not only basic PACS management operations but also more complex research job requests. The software modules of the infrastructure have sufficient understanding and cooperation at a system level such that the components work together as a team rather than as individual computers connected in a network.

In our design, the PACS infrastructure is physically composed of five classes of computer systems connected by various network circuits: (1) radiologic imaging systems, (2) study acquisition computers, (3) cluster controllers, (4) database servers, and (5) display workstations.

Acquisition Computers

The most troublesome PACS task to date has been the reliable and timely acquisition of image and associated study support text (information on patients, description of the study, and parameters of acquisition and image processing) from a radiologic imaging system (e.g., GE 9800 CT scanner, Milwaukee, WI). Although the ACR/NEMA (AMERICAN COLLEGE OF RADIOLOGY/NATIONAL ELECTRICAL MANUFACTURERS ASSOCIATION) standard [8] proposes to solve these difficulties, the interface is not yet mature. For example, for many imaging systems, especially computed radiography (CR), sonography, digital subtraction angiography, and film digitizer systems, this standard is not used. In our design, we impose a general-purpose computer, a CAPTURE COMPUTER, between the radiologic imaging system and the rest of the PACS network. The idea is to isolate the radiologic imaging host computers from the PACS via these capture computer gateways. The isolation is done because specialized imaging device computers lack the necessary communication and coordination software that is standardized within the PACS infrastructure. Furthermore, the radiologic imaging computers lack general PACS system knowledge that enables the PACS computers to cooperatively recover from various error conditions. The capture computer has three primary tasks: it acquires image data from the radiologic imaging system, converts the data from a manufacturer specific to a PACS standard format (header format, byte-ordering, matrix sizes) that is compliant with the proposed ACR/NEMA data formats, and forwards the image study to a CLUSTER CONTROLLER MACHINE (described later).

Two interface types exist between general-purpose PACS capture computers (e.g., SUN 4/370, Sun Microsystems, Mountain View, CA) and radiologic imaging systems (e.g., GE 9800 CT scanner). The first are PEER-TO-PEER network interfaces. For example, our GE Signa MR scanners (Milwaukee, WI) communicate with SUN 4/370 PACS capture computers by using the TCP/IP (TRANSMISSION CONTROL PROTOCOL/INTERNET PROTOCOL) ETHERNET protocol. When peer-to-peer interfaces are used, image transfers can be initiated either by the radiologic imaging system (a PUSH OPERATION) or by the destination PACS capture computer (a PULL OPERATION). The pull mode is advantageous because images may queue in the radiologic imaging system if a capture computer is down. Once the capture computer becomes operational, these queued images can be pulled and normal image flow resumed. The pull mode is the preferred mode of operation because a capture computer can be programmed to reschedule study transfers if a failure occurs (to itself or to the radiologic imaging system). This assumes sufficient data buffering is available on the imaging system. If a delay in acquisition is not acceptable, studies can be rerouted to a designated backup capture computer on the network when the primary capture computer is unavailable. We developed both types of interfaces for CT and MR with assistance from G.E. Medical System engineers.

The second interface type is a MASTER-SLAVE device-level connection such as the de facto industry standard, DR-11W. This parallel-transfer direct memory access connection is a point-to-point board-level interface. Recovery mechanisms again depend on which machine (capture computer or imaging system) can initiate a study transfer. In the case of acquiring images from a Philips PCR/SP-901 (Shelton, CT) CR system, data transfer can be initiated from the CR system only. If the capture computer is down, data may be lost. An alternative image acquisition method then must be used to acquire these images (e.g., the technologist manually sends individual images stored in the CR computer after the capture computer is brought back up, or the technologist laser scans the digital hard-copy film image).

Cluster Controller

Studies acquired by PACS capture computers are sent to machines known as cluster controllers. A cluster is logically defined as a group of computers with statistically similar case and data access patterns. For example, a pediatric radiology cluster, a neuroradiology cluster, or a chest radiology cluster

TABLE 1: Operations of a PACS Cluster Controller

- Receives images of a study from capture computers
- Extracts text information describing the received studies
- Updates a network-accessible data-base management system
- Determines the destination workstations to forward the newly generated studies
- Automatically retrieves necessary comparison images from a distributed optical disk library archive system
- Automatically corrects the orientation of computed radiographs
- Determines optimal contrast and brightness parameters for image display [9]
- Performs image data compression
- Archives new studies onto optical disk library
- Deletes images stored on remote capture computers after they have been archived
- Services archive retrieval requests from workstations and other cluster controllers

could exist as a logical entity within the PACS infrastructure. The cluster concept provides a more statistical basis for determining routing of studies and for archival strategies. At the center of each cluster is an intelligent machine termed a cluster controller. It has a central role in image acquisition, image routing, archive management, and system reliability. Cluster controllers within the University of California, Los Angeles (UCLA), PACS perform many tasks (Table 1).

Currently, we have developed two clusters—an inpatient cluster and an outpatient cluster. Each cluster controller has a Kodak optical-disk library unit with 1-terabyte archive capacity (Rochester, NY) and 4 gigabytes of PARALLEL-TRANSFER IPI (INTELLIGENT PERIPHERAL INTERFACE) MAGNETIC-DISK cache storage [3]. The large magnetic-disk cache on these cluster controllers allows the most recently acquired images to be quickly available for any PACS workstation. (Each workstation also supports a local parallel-transfer magnetic-disk cache of 2.6 gigabytes, Storage Concepts, Irvine, CA.)

Forwarding of imaging studies to the workstation has been delegated to the two cluster controllers in our PACS. This is opposed to sending images directly from the capture computers to the workstations. By using only a few central dispatchers of studies to workstations, we reduce the routing complexity, improve security, and have more central control over image routing. The decisions on routing from the cluster controllers to the workstations are shown in Figure 1. Note that a cluster is only a logical definition, and if a given cluster controller becomes disabled, capture computers can automatically reconfigure into an alternative cluster. Comparison images are also automatically retrieved and forwarded to the workstation for returning patients. We use an algorithm to calculate the degree of correlation between a new study and previous studies available for the patient. The correlation is based on organ system, imaging technique, date and time, and study type (admission image, discharge image, preoperative image, postoperative image, etc.)

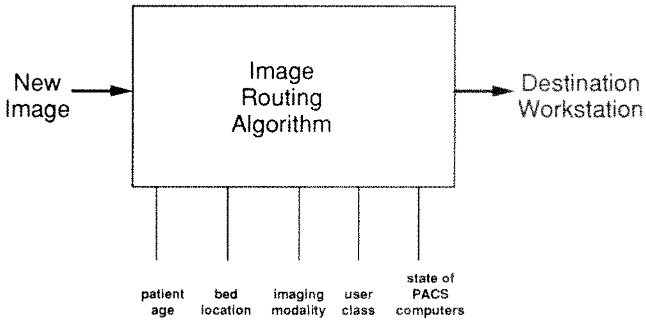

Fig. 1.—Image routing decisions from cluster controller to workstations.

Data-Base Servers

The architecture and design structure of the PACS data base is critical for the efficient access and integration of radiology operations. Table 2 provides the important guidelines for designing a good data-base management system.

The data-base schema design should include three levels of modeling. The first level is the external data model, which incorporates the local user views for each stage of the radiology process (Fig. 2). For each radiology process, the following information should be obtained: a description of the transaction or report, data items involved, priority of transaction, frequency of requests, confidentiality, routing information, processing requirements, resources required, person-

TABLE 2: Important Guidelines for Designing a PACS Data-Base Management System

Feature	Description
Integration	Sharing information among heterogeneous hardware and software systems
Performance	Access to user and program-requested data efficiently
Scalability	Easy to accommodate growth as the application scope increases
Reliability	With hardware redundancy and automatic data-base recovery capabilities
Open architecture	Ability to interface to other data-base management systems like hospital and radiology information systems
Advanced development tools	Upgradable to high-level data-base language interfaces and object-oriented tools [10]
Flexibility	Easy to make changes in data-base schema

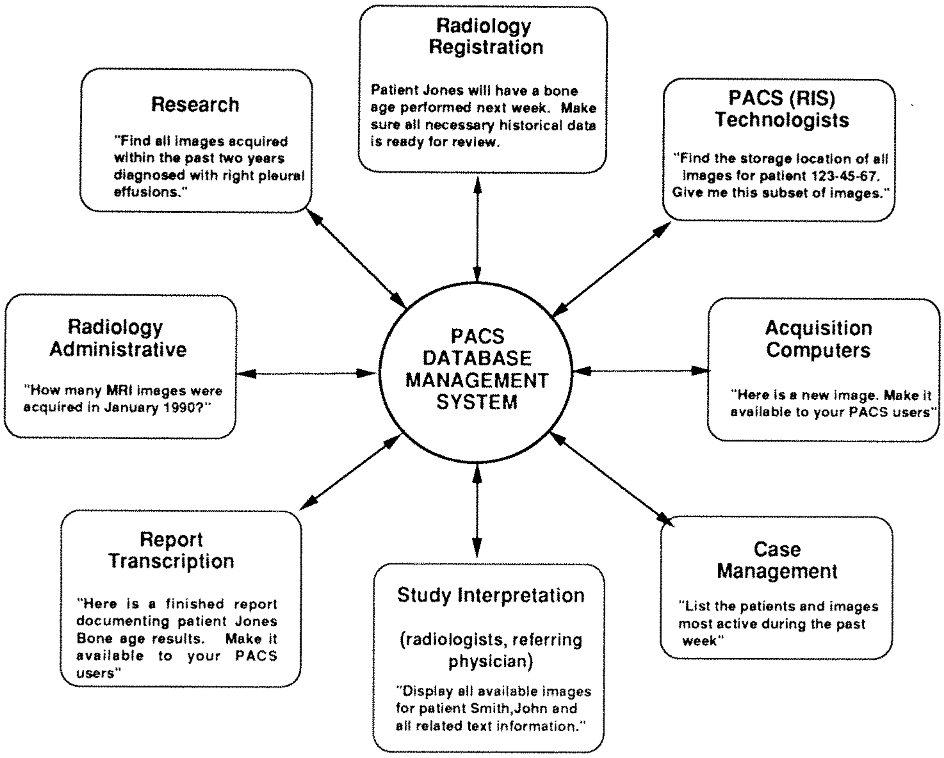

Radiology Registration

Patient Jones will have a bone age performed next week. Make sure all necessary historical data is ready for review.

Research

"Find all images acquired within the past two years diagnosed with right pleural effusions."

PACS (RIS) Technologists

"Find the storage location of all images for patient 123-45-67. Give me this subset of images."

Radiology Administrative

"How many MRI images were acquired in January 1990?"

Acquisition Computers

"Here is a new image. Make it available to your PACS users"

Report Transcription

"Here is a finished report documenting patient Jones Bone age results. Make it available to your PACS users"

Study Interpretation

(radiologists, referring physician)

"Display all available images for patient Smith,John and all related text information."

Case Management

"List the patients and images most active during the past week"

Fig. 2.—External data model incorporating local user views for each stage of radiology process.

nel required, and alternative processing and routing strategies.

Once the high-level user requirements are known, the second-level or conceptual model that consolidates the data and processing needs of the various service centers can be developed to produce an integrated global data structure capable of supporting all PACS applications. The synthesis of the conceptual data model involves determining what entities (e.g., patients, cases, studies, folders, sequences, archives) are required, what relationships exist among these entities, and what properties the entities should have.

The third level, the physical implementation model, must logically implement the conceptual model and simultaneously satisfy user performance and reliability requirements. In this model, large data items (images) and smaller data items (text) are managed differently because of differences in their storage, access, reliability, and processing requirements. In the UCLA system, small data items (e.g., patient demographics, clinical history, study description, image description, diagnostic reports) are maintained by a commercial relational database management system (Sybase Inc., Emeryville, CA). This system uses a client-server architecture [11]. All text records are centrally stored in tables maintained by mirrored database server machines [12]. Data tables may span several physical storage devices. The centralized data-base server cuts down on data redundancy and inconsistency while still maintaining fast response to user queries for text data. The server machines are dedicated processors tuned to efficiently perform data integrity checking; data-base query processing; data inserts, deletes, and updates; retrieval speed optimization; cluster table indexing; and backup and recovery of data. All nodes in the PACS network are data-base (text) clients. Client nodes send remote procedure calls from an application program over a network to the data-base server machine. The data-base language used is SQL (STRUCTURED QUERY LANGUAGE).

For large data items (images), it is important to place active files in a location where the study is most likely to be viewed. The large image files from these studies can then be allocated onto the fastest storage devices, which are local to the workstation. Images can be moved to other storage locations as their access characteristics change (such as when a patient moves from one clinical service to another or when a patient is discharged). Image files may reside on several diagnostic workstations. Factors that determine image file placement include radiology service of study, supervising radiologist, clinical service attending the patient, patient's status (inpatient, outpatient, emergency patient), type of examination, and whether the patient's case is currently active at a particular workstation.

Display Stations

PACS display stations should fully use the resources and processing power of the entire PACS network. A station includes communication, data base, display, resource management, and processing software. The fundamental workstation operations are listed in Table 3.

We use three types of display stations: (1) high-resolution 2.5K × 2K for primary diagnosis, (2) medium-resolution 1K × 1K stations for referring physicians and conferences, and (3)

TABLE 3: Operations Performed at a PACS Workstation

Operation	Description
Case preparation	Accumulation of all relevant images and information belonging to a patient examination
Case selection	Allows the selection of cases for a given subpopulation
Image arrangement	Tools for arranging and grouping images for easy review [13]
Interpretation	Measurement tools for facilitating the diagnosis
Documentation	Tools for image annotation, text, and voice reports
Case presentation	Tools for a comprehensive case presentation

high-resolution hard-copy print stations. At the primary diagnosis display workstation, images are stored on fast-access parallel-transfer magnetic disks. Each workstation maintains a local data base for managing current cases. It also has access to the global PACS data base for historical images. In addition to being a client to the global PACS text data base and distributed global image archive, the primary workstation is also a client to a centralized voice management system. Access to the voice server is instantaneous over the public telephone system. All dictation and playback functions are interfaced directly to the workstation. We integrated the primary diagnosis station by using components from various vendors and developed our own display software. In the case of medium-resolution stations, we designed and built the system in-house.

System Networking

A basic function of any computer network is to provide an access path by which end users (e.g., radiologists and clinicians) at one geographic location can access information (e.g., images, reports) at another location. The most obvious way to characterize a radiologic PACS network is to examine traffic of information between various locations and users. The important networking data needed for system design include location and function of each node, frequency of information passed between any two nodes, cost for transmission between nodes with various speed lines, desired reliability of the communication, and required throughput. The variables in the design include the network topology, line capacities, and flow assignments.

Digital communication in our infrastructure design is based on a three-tiered network architecture consisting of low-speed (10 megabits/sec signaling rate) Ethernet circuits, medium-speed (100 megabits/sec) FIBER DISTRIBUTED DATA INTERFACE (FDDI) circuits, and high-speed (1 gigabit/sec) ULTRANET network circuits (Ultra Network Technologies, San Jose, CA) [14, 15]. All three types of networks are commercially available. These networks together span three buildings housing the radiology department. All three use the TCP/IP communication protocol and are accessed by the same software calls. The local Ethernet circuits are used as a low-cost network to connect all PACS nodes. Primarily, the Ethernet circuits transmit messages, data-base query results, and images from radiologic imaging systems to capture computers. Low-speed networks are adequate for this application because most imaging system computers have relatively slow data generation and networking capabilities. FDDI is used to transmit images from the capture computers to the cluster controllers. A faster image network is used between capture computers and cluster controller machines because several imaging systems may be connected to a single capture computer. Furthermore, several local Ethernet circuits may be involved in transferring data from imaging systems to capture computers. The UltraNet system is used to transmit images between cluster controllers and from cluster controllers to display stations when long delays are not tolerable.

Process coordination between tasks running on different PACS machines is an extremely important issue in system networking. This coordination of processes running either on the same computer or on different computers is accomplished by using interprocessor communication methods implemented by using socket-level interfaces to TCP/IP. Commands are exchanged as American Standard Code for Information Interchange (ASCII) messages to ensure standard encoding of messages. Jobs requests are stuffed into disk resident priority queues, which are serviced by various DAEMON processes. The queue software has a built-in job scheduler that is programmed to retry a job several times by using either a default set of resources or alternative resources if a hardware error is detected.

Some Important PACS Design Concepts

When we planned a totally digital radiology department in 1989 and 1990, we realized the importance of system standardization, open architecture, connectivity, and reliability [16]. We were fortunate that all necessary technologies for this purpose became available at that time, allowing us to implement this concept in a clinical environment. We firmly believe that the concept of a robust PACS infrastructure is essential for small- and large-scale implementations alike.

Standardization

The first important rule in building a PACS infrastructure is to incorporate as many industry de facto standards as possible that are consistent with the overall PACS design schema. The philosophy is to minimize the developing of your own software. Furthermore, use of industry standard hardware and software increases the portability of the system to other computer platforms. For example, the following industry standards are integrated into our PACS: (1) UNIX operating system, (2) TCP/IP communication protocol, (3) SQL as the data-base query language, (4) ACR-NEMA standard (higher layers of International Standards Organization model only), (5) C programming language, (6) X WINDOWS user interface, and (7) ASCII text representation for message passing. The implications of PACS standardization include the following: Implementation of all future PACS installations is straightforward. System maintenance is easier because each module looks similar to others, if not physically, then logically. By defining the PACS primitive operations, we minimize the amount of redundant computer code within the PACS system. The code therefore is easier to debug, understand, and search. Standardizing terminology, design concepts, and so forth, facilitates system understanding and documentation among all levels of developers.

Open Architecture

If two PACS modules in the same department cannot communicate with each other, they become two isolated systems and can never be combined with other systems to form a total departmental PACS. An example is the pediatric radiology PACS module and the coronary care unit PACS module we developed earlier [1, 2]. These two modules have no means of communicating with each other. Images and patient information are isolated within each module. An open network design architecture allows a standardized method for data and message exchange between heterogeneous systems. Because computer and communications technology changes rapidly, a closed architecture would hinder system upgradability. As an example, an independent imaging console from a given manufacturer is a good addition to an MR or a CT scanner for viewing images; however, it always has a closed proprietary architecture design. As a result, no other components except those specified by the same manufacturer can be augmented to the system. This limits potential upgrading and improvement of the system. Consideration of the connectivity is important even when a small-scale PACS is planned. A yes to questions like "Can we transmit images from this PACS to other systems and vice-versa?" "Does this module use a standard data and image format?" and "Does the machine use a standard communication protocol?" means that the PACS is well designed and will allow future connectivity.

Reliability

Reliability is a major issue in a PACS for two reasons. First, a PACS has many components, so the probability of a component failing is high. Second, because the PACS manages and displays critical patient information, it cannot be down for extended periods. In designing a PACS, it is therefore important to use fault-tolerant measures, including error detection and logging software, external auditing programs (i.e., network management processes that check network circuits, magnetic-disk space, data-base status, processes status, and queue status), hardware redundancy, and intelligent software recovery blocks. Some recovery mechanisms we have used include automatic retry of failed jobs with alternative resources and algorithms and intelligent BOOTSTRAP ROUTINES that allow a PACS computer to automatically continue operations after a power outage [17]. Improving reliability is costly. How to minimize the cost while maintaining high reliability requires further study.

Security

Security is an important consideration because of the need for patient confidentiality and medicolegal issues. Three major security mechanisms include account control, privilege control, and the use of views. Most sophisticated data-base management systems have identification and authorization mechanisms that use accounts and passwords. Application programs may also supply additional layers of protection. Privilege control refers to granting and revoking the user's access to specific tables, columns, or views. These security measures provide the PACS infrastructure with a mechanism for access control to clinical and research data. With these mechanisms, the system designer can enforce departmental policy as to which persons have access to clinical studies. For example, referring clinicians may be granted image study access only after a preliminary radiology reading has been performed and attached to the image data.

Glossary

ACR/NEMA AMERICAN COLLEGE OF RADIOLOGY/NATIONAL ELECTRICAL MANUFACTURERS ASSOCIATION. The members in the ACR-NEMA committee are responsible for writing a standard for image information exchange acceptable by both ACR and NEMA.

BOOTSTRAP ROUTINE A software block executed by a computer when it is restarted.

CAPTURE COMPUTER Computer interposed between a radiologic imaging device (e.g., CT scanner) and PACS network. Its main task is to standardize the image file format.

CLUSTER CONTROLLER MACHINE The computer that maintains the optical archive for a cluster of computers (e.g., neurology cluster, pediatric cluster). Its functions are similar to those of the film library in a conventional film-based system.

DAEMON A background computer program that runs continuously. It does not affect the system operation unless a particular circumstance arises. In that case, the program will automatically change the information flow in the system. Usually each daemon performs a specific task.

ETHERNET The most common baseband communication network for connecting computers. It is a relatively slow network.

FDDI FIBER DISTRIBUTED DATA INTERFACE. A communication network that uses a ring topology. It is a medium-speed network.

IPI INTELLIGENT PERIPHERAL INTERFACE used to connect a computer to a disk drive.

MASTER-SLAVE INTERFACE The connection between two machines in which the master always initiates and requests operations to be performed by a slave device.

PACS PICTURE ARCHIVING AND COMMUNICATION SYSTEM.

PARALLEL-TRANSFER MAGNETIC DISK A magnetic-disk device typically used for images. Special magnetic-disk controllers allow the bytes of a single image to be distributed over several disks. Access to the data can be done in parallel, and this is much faster than conventional disks.

PEER-TO-PEER INTERFACE A network interface in which the communicating machines can perform reciprocal operations.

PULL OPERATION A network data transfer operation in which the computer that desires the data initiates the data transfer.

PUSH OPERATION A network data transfer operation in which the computer with the data to send initiates the data transfer.

SQL STRUCTURED QUERY LANGUAGE. It is commonly used in a later generation data base.

TCP/IP TRANSMISSION CONTROL PROTOCOL/INTERNET PROTOCOL. A standard and popular method for data communication between computers.

ULTRANET A commercial high-speed gigabit-per-second fiber-optic communication network.

UNIX A computer operating system commonly used in computers introduced in the late 1980s.

X WINDOWS A software subsystem that allows developers to construct a graphical user interface (menus, buttons, icons, etc.) for accessing text, image-processing modules.

REFERENCES

1. Taira RK, Mankovich NJ, Boechat MI, Kangarloo H, Huang, HK. Design and implementation of picture archiving and communication system for pediatric radiology. *AJR* **1988**;150:1117–1121
2. Cho PS, Huang HK, Tillisch J, Kangarloo H. Clinical evaluation of a radiologic picture archiving and communication system for a coronary care unit. *AJR* **1988**;151:823-827
3. Lou SL, Loloyan M, Weinberg W, et al. Image delivery performance of a CT/MR PACS module applied in neuroradiology. *Proc SPIE* **1991**;1446:302–311
4. Irie G, Miyasaka K. Clinical experience: 16 months of HU-PACS. *Comput Med Imaging Graph* **1991**;15:191–195
5. Masser H, Mandl A, Urban M, Hradil H, Hruby W. The Vienna Project SMZO in picture archiving and communication systems (PACS). In: Huang HK, Ratib O, Bakker AR, Witte G, eds. *NATO ASI series F, PACS in medicine*, vol. 74. New York: Springer-Verlag, **1991**:247–250
6. Glass HI, Slark NA. PACS and related research in the United Kingdom in picture archiving and communication systems (PACS). In: Huang HK, Ratib O, Bakker AR, Witte G, eds. *NATO ASI series F, PACS in medicine*, vol. 74. New York: Springer-Verlag, **1991**:319–324
7. Goeringer F. Medical diagnostic imaging support systems for military medicine in picture archiving and communication systems (PACS). In: Huang HK, Ratib O, Bakker AR, Witte G, eds. *NATO ASI series F, PACS in medicine*, vol. 74. New York: Springer-Verlag, **1991**:213–230
8. ACR-NEMA Digital Imaging and Communication Standards Committee. *Digital imaging and communications ACR-NEMA 300-1988*. Washington, DC: National Electrical Manufacturers Association, **1988**
9. McNitt-Gray MF, Taira RK, Eldredge S, Razavi M. Brightness and contrast adjustments for different tissue densities in digital chest radiographs. *Proc SPIE* **1991**;1445:468–478
10. Parsaye K, Chignell M, Khoshafian S, Wong H. *Intelligent databases*. New York: Wiley, **1989**
11. Malamud C. *INGRES: tools for building an information architecture*. New York: Von Norstrand Reinhold, **1989**
12. Taira RK, Stewart BK, Sinha U. PACS database architecture and design. *Comput Med Imaging Graph* **1991**;15:171–176
13. Ratib O, Ligier Y, Funk M, et al. PACS workstation: user interface design. In: Huang HK, Ratib O, Bakker AF, Witte G, eds. *NATO ASI series F, PACS in medicine*, vol. 74. New York: Springer-Verlag, **1991**:57–61
14. Huang HK, Lou SL, Cho PS, et al. Radiologic image communication methods. *AJR* **1990**;155:183-186
15. Stewart BK, Lou SL, Wong WK, Huang HK. An ultrafast network for communication of radiologic images. *AJR* **1991**;156:835–839
16. Huang HK, Kangarloo H, Cho PS, Taira RK, Ho BKT, Chan KK. Planning a totally digital radiology department. *AJR* **1990**;154:635–639
17. Taira RK, Chan KK, Stewart BK, Weinberg WS. PACS reliability issues. In: Huang HK, Ratib O, Bakker AR, Witte G, eds. *NATO ASI series F, PACS in medicine*, vol. 74. New York: Springer-Verlag, **1991**:149–156

Radiologic-Pathologic Conferences of Childrens Hospital Los Angeles

Tuberous Sclerosis

Beverly P. Wood,[1] Ellin Lieberman,[2] Benjamin Landing,[3] and Barry Marcus[4]

A 6-month-old girl was examined for bilaterally enlarged kidneys detected by palpation. Her development was delayed, and the parents reported recent seizures consisting of episodes of stiffening, stretching her arms, and throwing back her head. The infant's weight was in the 10th percentile, length was in the 50th percentile, and her head circumference was in the 10th percentile. The patient could not sit and had poor head control. The liver and kidneys were enlarged on palpation. The blood pressure was 140/90 and serum creatinine level was 0.1 mg/dl. Renal sonography showed bilaterally enlarged kidneys with cortical replacement by multiple cysts varying from 5 mm to 3 cm in diameter (Figs. 1A and 1B). An echocardiogram (Fig. 1C) showed multiple hyperechoic nodules in the myocardium of both ventricles. A diagnosis of tuberous sclerosis with renal parenchymal cysts and cardiac hamartomas was made and confirmed by biopsy. Therapy was started with 35 mg/kg/day of captopril; this controlled her hypertension.

Tuberous sclerosis is a heritable, autosomal dominant neurocutaneous syndrome with clinical manifestations of adenoma sebaceum, seizures, and mental retardation. Patients have hamartomas or angiofibromas involving multiple organ systems, including the skin, CNS, eye, lung, heart, and kidneys. Renal cysts are a less common manifestation of tuberous sclerosis and may have the sonographic appearance of polycystic renal disease (adult type) of autosomal dominant inheritance [1, 2]. Renal cysts may coexist with parenchymal angiomyolipomas or may be the sole renal manifestation of tuberous sclerosis [3, 4]. Cysts are differentiated from angiomyolipomata by sonographic evidence of thin-walled, anechoic areas with posterior enhancement [4]. The diagnosis is established by biopsy. Histologically, the lining of these cysts is characterized by hyperplastic clumps of eosinophilic epithelium projecting into the cyst lumen [1]. This appearance is distinctive of tuberous sclerosis and establishes the diagnosis. Cystic disease is thought to result from tubular epithelial hyperplasia with eventual hypertension and renal insufficiency. The hyperplasia may predispose to renal carcinoma [5]. The eventual diminution in renal function reflects progressive parenchymal compression by large cysts. Hypertension has been shown to be ameliorated by decompression of the renal cysts. The appearance of renal cysts may precede development of other signs of tuberous sclerosis; thus, it is important to consider and establish this diagnosis when multiple renal cysts are identified in an infant [2]. Further workup of these patients for other signs of tuberous sclerosis is warranted and future monitoring is essential.

REFERENCES

1. Bernstein J, Robbins TO. Renal involvement in tuberous sclerosis. *Ann NY Acad Sci* **1991**;615:36–49
2. Stapleton FB, Johnson D, Kaplan GW, Griswold W. The cystic renal lesion in tuberous sclerosis. *J Pediatr* **1980**;97:574–579
3. Stillwell TJ, Gomez MR, Kelalis PP. Renal lesions in tuberous sclerosis. *J Urol* **1987**;138:477–481
4. Narla LD, Slovis TL, Watts FB, Nigro M. The renal lesions of tuberosclerosis (cysts and angiomyolipoma)—screening with sonography and computerized tomography. *Pediatr Radiol* **1988**;18:205–209
5. Bernstein J, Robbins TO, Kissane JM. The renal lesions of tuberous sclerosis. *Semin Diagn Pathol* **1986**;3:97–105

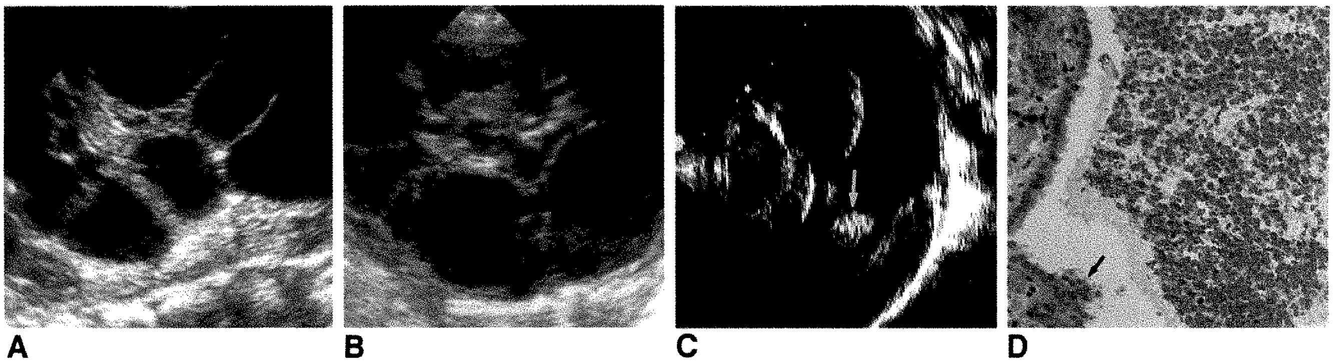

Fig. 1.—Tuberous sclerosis.
***A*, Longitudinal sonogram of right kidney shows multiple cysts replacing renal cortex.**
***B*, Transverse sonogram of right kidney shows nephromegaly and cortical cysts.**
***C*, Echocardiogram shows hyperechoic nodule (*arrow*) extending into ventricle.**
***D*, Photomicrograph of renal biopsy specimen shows hyperplastic lining of cyst wall with clumps of epithelium extending into cyst (*arrow*).**

---

[1] Department of Radiology, MS 81, Childrens Hospital Los Angeles, 4650 Sunset Blvd., Los Angeles, CA 90027. Address reprint requests to B. P. Wood.
[2] Department of Nephrology, Childrens Hospital Los Angeles, Los Angeles, CA 90027.
[3] Department of Pathology, Childrens Hospital Los Angeles, Los Angeles, CA 90027.
[4] Department of Cardiology, Childrens Hospital Los Angeles, Los Angeles, CA 90027.

***AJR* 158:750, April 1992** 0361-803X/92/1584-0750 © American Roentgen Ray Society

Pictorial Essay

MR Imaging of Thymoma: Radiologic-Pathologic Correlation

Fumikazu Sakai,[1] Shusuke Sone,[1] Kunihiro Kiyono,[1] Takashi Kawai,[1] Atsunori Maruyama,[1] Hitoshi Ueda,[1] Jun Aoki,[1] Takayuki Honda,[2] Masami Morimoto,[3] Keiko Ishii,[4] and Shu-ichi Ikeda[2]

MR images in 17 patients with surgically proved thymomas (12 malignant and five benign) were reviewed and compared with pathologic specimens. In nine cases, MR images of excised specimens also were made and evaluated. On T2-weighted images, 11 of 12 malignant thymomas had an inhomogeneous signal intensity, half with and half without a lobulated internal architecture. None of the five benign thymomas had a lobulated internal architecture, and they all had a moderately or slightly inhomogeneous signal. Cystic regions and/or hemorrhage were noted pathologically, and corresponded to areas of inhomogeneous high signal intensity seen on T2-weighted images. Examination of the excised specimens in malignant thymomas showed that the lobulated configuration seen in the tumors was caused by thick fibrous septa. Our experience suggests that, although calcification cannot be identified, MR is helpful in making a differential diagnosis of mediastinal tumors and in determining malignancy of thymoma.

Although several articles have described the MR appearance of thymic tumors [1, 2], detailed studies correlating the MR and pathologic appearances of these lesions have not yet been reported. Accordingly, we reviewed the MR images of 17 surgically proved thymomas and compared the findings with gross and microscopic findings noted in surgical specimens.

Materials and Methods

The study group comprised 12 patients with malignant thymoma and five patients with benign thymoma. The six women and 11 men were 36–75 years old (average, 55 years). All thymomas were excised, and a pathologic diagnosis was established.

Thymomas were classified as malignant when extracapsular invasion and/or pleural dissemination were seen at surgery, or when there was invasion of the capsule and/or cytologic atypia in microscopic specimens. The diagnosis of benign thymoma was made when features of malignancy were not found. Eight of 12 malignant thymomas showed macroscopic extracapsular invasion at surgery, and four had microscopic capsular invasion in the pathologic specimens. None showed pleural dissemination at surgery. Whereas two malignant thymomas showed obvious cytologic atypia, the other 10 showed no cytologic atypia.

Seventeen patients were examined with a 1.5-T superconductive MR unit (Signa, General Electric, Milwaukee, WI) or a 0.5-T superconductive unit (Resona, YMS, Tokyo, Japan). MR images were obtained with spin-echo T1-weighted imaging sequences, 500–1000/20–25 (TR/TE), and proton density–weighted and T2-weighted multiecho imaging sequences (1500–2500/20–25,50–100) by using ECG or peripheral pulse gating and respiratory compensation. The slice thickness ranged from 5 to 7 mm with a 2- to 5-mm interslice gap. MR and CT examinations were performed within 2 weeks before surgery. In nine thymomas (five malignant and four benign), T1-weighted (600/20) and T2-weighted (2000–3000/80–100) axial MR images of the excised specimens were obtained with the Signa unit

---

Received July 15, 1991; accepted after revision November 5, 1991.

[1] Department of Radiology, School of Medicine, Shinshu University, Asahi, Matsumoto, 390, Japan. Address reprint requests to F. Sakai.

[2] Department of Internal Medicine, School of Medicine, Shinshu University, Asahi, Matsumoto, 390, Japan.

[3] Department of Surgery, School of Medicine, Shinshu University, Asahi, Matsumoto, 390, Japan.

[4] Department of Laboratory Medicine, School of Medicine, Shinshu University, Asahi, Matsumoto, 390, Japan.

***AJR* 158:751–756, April 1992** 0361–803X/92/1584–0751 © American Roentgen Ray Society

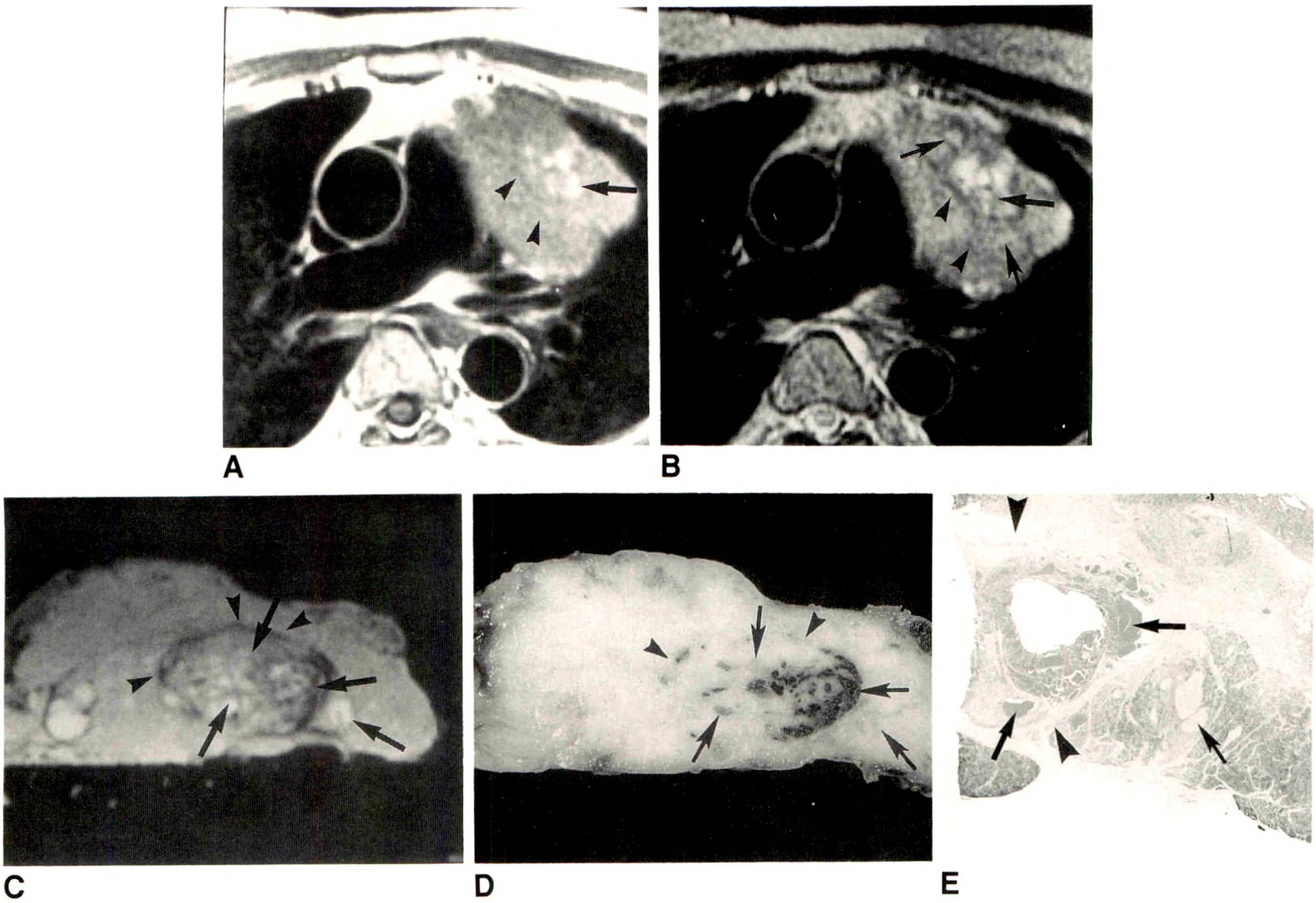

Fig. 1.—Malignant thymoma in a 41-year-old woman.

A, T1-weighted MR image (600/20) shows anterior mediastinal mass with multilobular border. Signal intensity of mass is higher than that of skeletal muscle but less than that of fat. Low-intensity lines (*arrowheads*) separate mass lesion into lobules, and high-intensity regions are present (*arrow*).

B, T2-weighted axial MR image (1800/80) shows increase in signal intensity. Intensity of mass is inhomogeneous and equal to or higher than that of fat. Lobulated internal architecture, separated by thin low-intensity lines, is visible (*arrowheads*). High-intensity regions are present (*arrows*).

C, T2-weighted MR image (2000/80) of excised specimen shows low-intensity lines (*arrowheads*) separating tumor into lobules. High-intensity regions (*arrows*) are scattered throughout mass.

D and *E*, Gross (*D*) and microscopic (*E*) specimens show lobulated configuration, separated by fibrous septa (*arrowheads*). Regions of very high intensity on T2-weighted images correspond to cystic areas (*arrows*), some of which are accompanied by hemorrhage.

or a 2.0-T chemical-shift imaging system (General Electric, Fremont, CA). Gross and microscopic specimens (hematoxylin and eosin stain) were prepared in the same planes as MR images in these nine tumors.

Preoperative MR images were compared with the pathologic findings of the resected specimens. In nine thymomas, MR images were made of the excised specimens. The homogeneity of signal intensity of tumors on T2-weighted images was determined by the consensus of two radiologists and classified into one of four grades: inhomogeneous, moderately inhomogeneous, slightly inhomogeneous, or homogeneous.

Results

Malignant thymomas ranged from 4.5 to 18 cm in maximum diameter (average, 8.2 cm). All 12 malignant thymomas had higher signal intensity than did skeletal muscle on T1-weighted images and increased signal intensity on T2-weighted images (Figs. 1A, 1B, 2A, 2B, 3A, 3B, 4A, and 4B). Eleven of the 12 malignant thymomas had inhomogeneous or moderately inhomogeneous intensities (Figs. 1B, 2B, and 3B) with scattered high-intensity regions (Figs. 1B and 2B) on T2-weighted images. The remaining one had homogeneously high intensity with several small low-intensity areas in the marginal portion of the tumor on T2-weighted images (Fig. 4B). Six of the 12 malignant thymomas had a lobulated internal architecture on T2-weighted images, with round or irregularly shaped high-intensity areas of various sizes, separated by 1- to 2-mm-thick low-intensity lines (Figs. 1B and 2B). Calcification could not be identified on the MR images. MR images of the excised specimens revealed the scattered areas of high intensity and lobulated internal architecture seen on preoperative MR images.

Scattered regions of high intensity on T2-weighted images corresponded to cystic regions with or without hemorrhage on pathologic specimens (Figs. 1E, 2D, 4D, and 4E). Marginal low-intensity areas seen on T2-weighted images of one malignant thymoma corresponded to small mural nodules attached

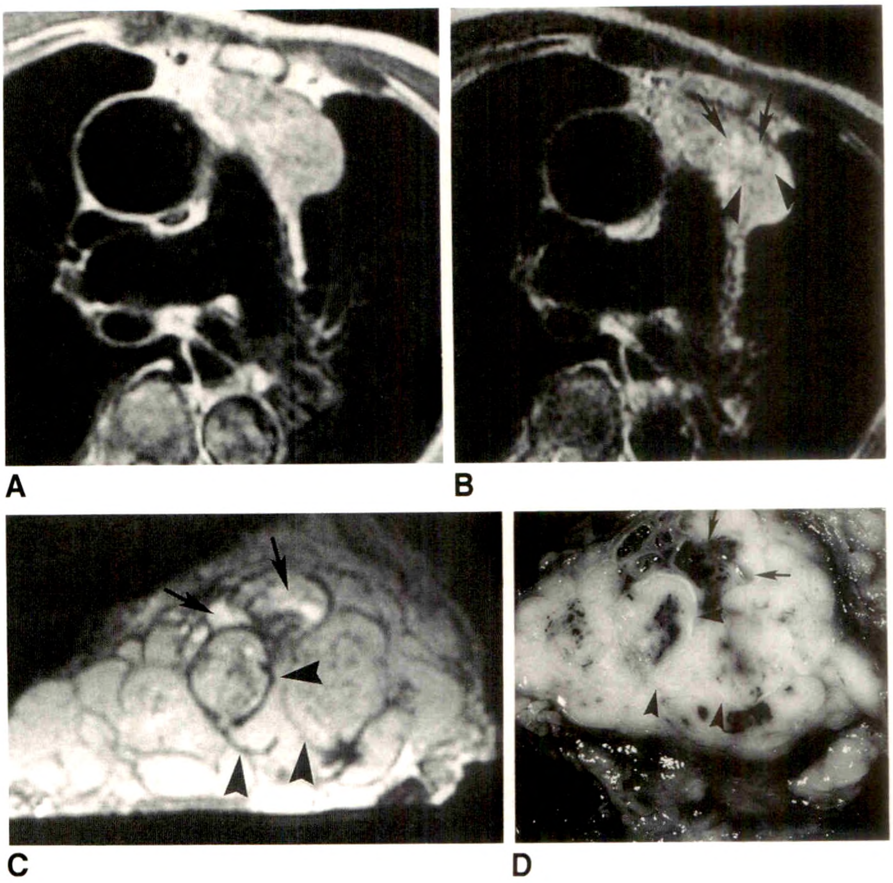

Fig. 2.—Malignant thymoma in a 75-year-old man.

A, T1-weighted axial MR image (1000/20) shows mass with intermediate signal intensity in anterior mediastinum. Calcification is not apparent.

B, T2-weighted axial MR image (2000/80) shows that mass has a lobulated internal architecture separated by low-intensity lines (*arrowheads*). Signal intensity of mass is inhomogeneous and high. Regions of high intensity are present within mass (*arrows*). Calcification is not apparent.

C, T2-weighted MR image (2000/100) of excised specimen shows a lobulated internal architecture with inhomogeneously high intensity separated by low-intensity lines (*arrowheads*). Regions of very high intensity are noted (*arrows*).

D, Pathologic specimen shows lobulated configuration, caused by fibrous septa (*arrowheads*). Cystic areas (*arrows*) correspond to regions of very high intensity on T2-weighted images.

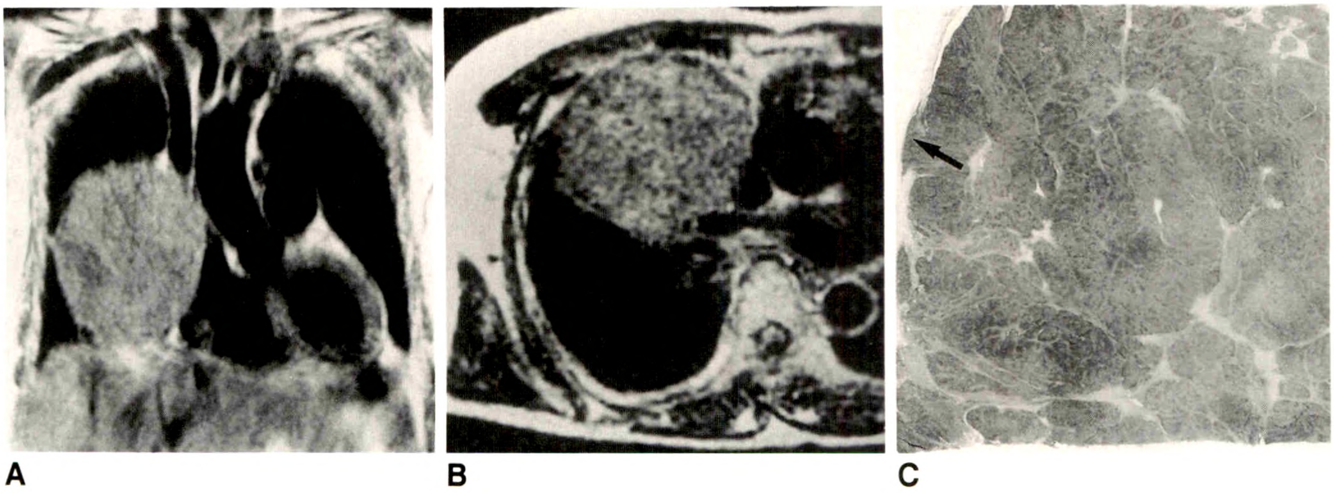

Fig. 3.—Malignant thymoma in a 50-year-old woman.

A, T1-weighted coronal MR image (500/25) shows mass of inhomogeneous signal intensity without lobulation.

B, T2-weighted MR image (1500/75) shows signal intensity of mass has increased but is less than that of fat. Signal intensity is moderately inhomogeneous. No lobulation is evident.

C, Histologic specimen shows that thin fibrous septa separate tumor into small lobules. Incomplete capsular invasion (*arrow*) is evident in specimen. Because of thin fibrous septa, lesion is not lobulated.

to the wall of a large unilocular cystic mass on pathologic specimens (Figs. 4D and 4E). The mural nodules included several small cystic regions. The lobulated architecture seen on MR images corresponded to the lobulated internal architecture seen macroscopically on the cut surface of the resected specimens (Figs. 1D and 2D). Microscopically, the lobulated architecture consisted of round or irregular areas composed of mixed lymphocytes and epithelial cells sepa-

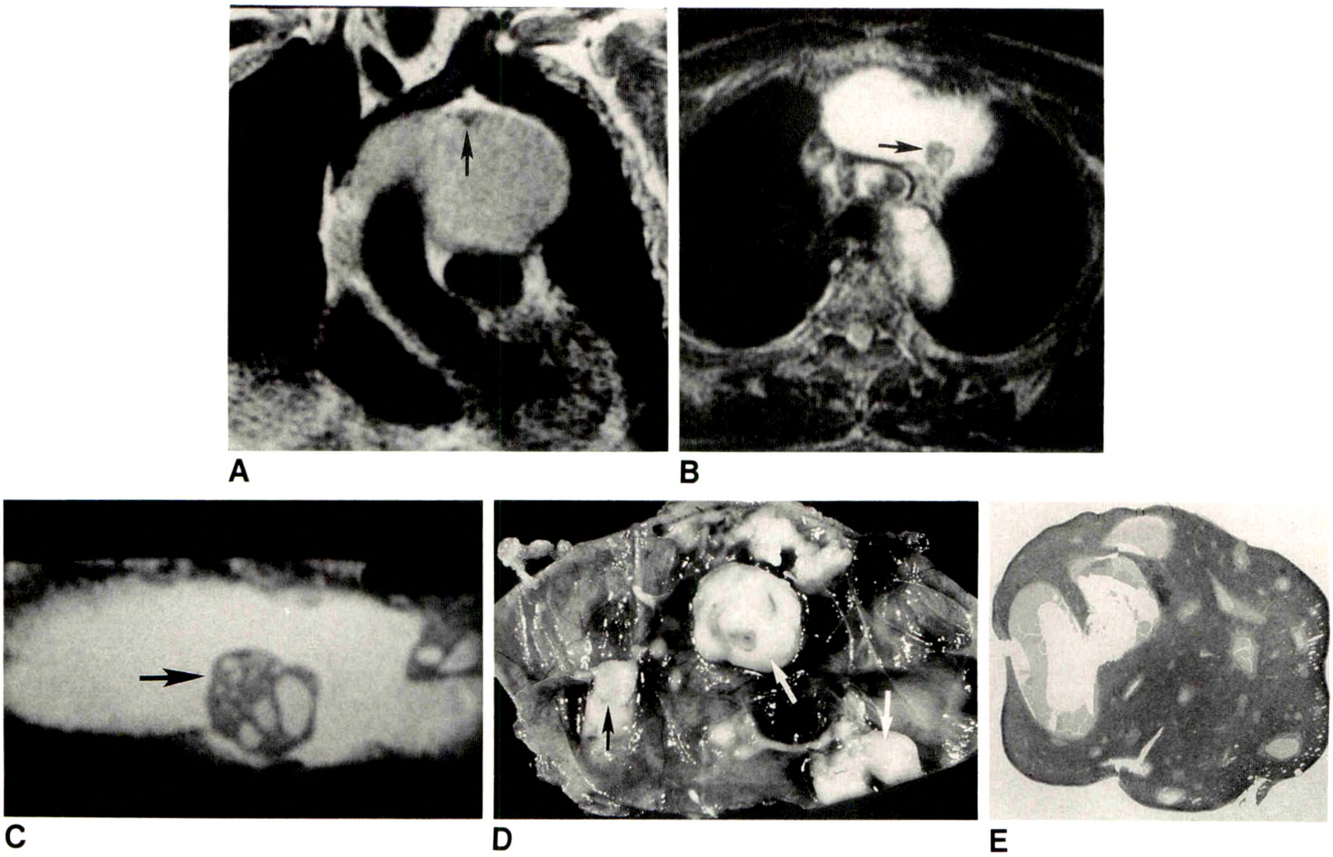

Fig. 4.—Malignant thymoma in a 50-year-old man.

A, T1-weighted coronal MR image (800/20) shows large anterior mediastinal mass with intermediate signal intensity, which is slightly higher than that of skeletal muscle. Small low-intensity area is noted in marginal portion of tumor (*arrow*).

B, T2-weighted axial MR image (1600/80) shows that signal intensity of mass is high. Area of inhomogeneously low intensity is seen in marginal portion of mass (*arrow*).

C, T2-weighted MR image (2500/100) of excised specimen shows that signal intensity of mass lesion is very high. Area of low intensity in marginal portion of mass includes small high-intensity regions (*arrow*).

D, At surgery, a large unilocular cystic mass was excised. Although no local invasion was noted at surgery, pathologic specimen showed microscopic capsular invasion. Cysts were filled with bloody fluid. Three mural nodules (*arrows*) on inner surface of capsule are visible.

E, Histologic specimen of central mural nodule in *D* shows several small cystic lesions within mural nodule.

rated by relatively thick fibrous septa (Figs. 1D and 1E). Six thymomas that showed no distinct lobulated internal architecture had no lobulated configuration or a small lobulation separated by thin fibrous septa on pathologic specimens (Fig. 3C). Calcification was noted on pathologic specimens of six malignant thymomas.

Benign thymomas ranged from 1.5 to 8 cm in maximum diameter (average, 3.1 cm). All five showed higher signal intensity than skeletal muscle on T1-weighted images. Signal intensity was increased on T2-weighted images. Four of the five benign thymomas had slightly inhomogeneous intensities, equal to or slightly lower than that of fat (Figs. 5A and 5B). The remaining one had moderately inhomogeneous intensity, higher than that of fat (Fig. 6A). None of the benign thymomas had a lobulated internal architecture. No calcification was seen in any of the five benign thymomas on MR images. On T2-weighted images of the excised specimens, four benign thymomas showed slightly inhomogeneous intensity (Fig. 5C).

On pathologic specimens of four benign thymomas in which a slightly inhomogeneous intensity was seen on MR, areas with lymphocytes and epithelial cells were mingled, without cystic regions (Fig. 5D). When compared, areas where lymphocytes predominated had the same signal intensities as areas where epithelial cells predominated (Figs. 5C and 5D). The moderately inhomogeneous intensity seen in a small benign thymoma on T2-weighted images corresponded to multiple small cystic foci in the pathologic specimens (Fig. 6). In none of the five benign thymomas was a lobulated configuration seen in pathologic specimens (Figs. 5D and 6B). A low-intensity band on the preoperative T2-weighted image of a benign thymoma corresponded to a thick fibrous septum in the pathologic specimen (Figs. 5B and 5D). No calcification was seen in pathologic specimens of benign thymomas.

Discussion

According to Rosai and Levine [3], all thymomas are composed of a mixture of lymphocytes and epithelial cells in

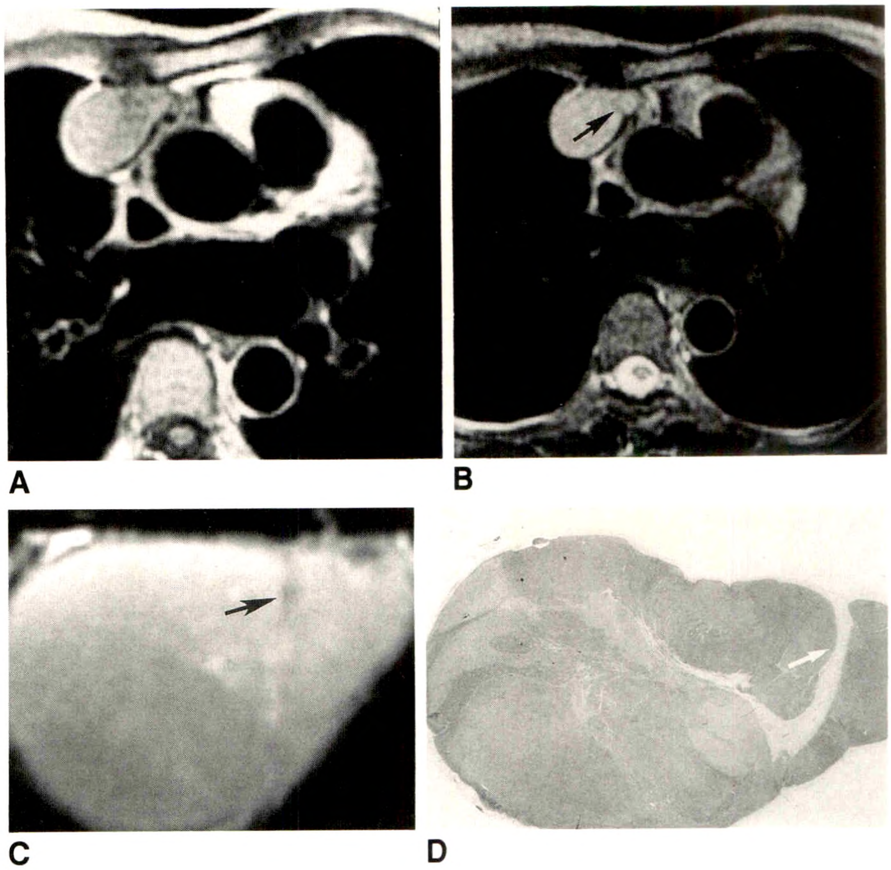

Fig. 5.—Benign thymoma in a 51-year-old woman.

A, T1-weighted axial MR image (750/20) shows a mass lesion in anterior mediastinum with signal intensity that is higher than that of skeletal muscle but lower than that of fat.

B, T2-weighted axial MR image (2250/80) shows that signal intensity of mass is high and slightly inhomogeneous. Low-intensity band is identified in medial portion of mass (*arrow*).

C, T2-weighted MR image (2500/100) of excised specimen shows relatively homogeneous pattern of signal intensity. Thick low-intensity band is seen on medial aspect of tumor (*arrow*).

D, Histologic specimen shows mixed lymphocyte and epithelial-cell components without cystic regions. Lymphocyte-predominant areas appear dark, while epithelial-cell-predominant areas appear light. Comparison with MR images of specimen shows that there is no distinct difference in signal intensity between lymphocyte and epithelial-cell-predominant areas. Low-intensity band seen on MR corresponds to relatively thick fibrous septum (*arrow*).

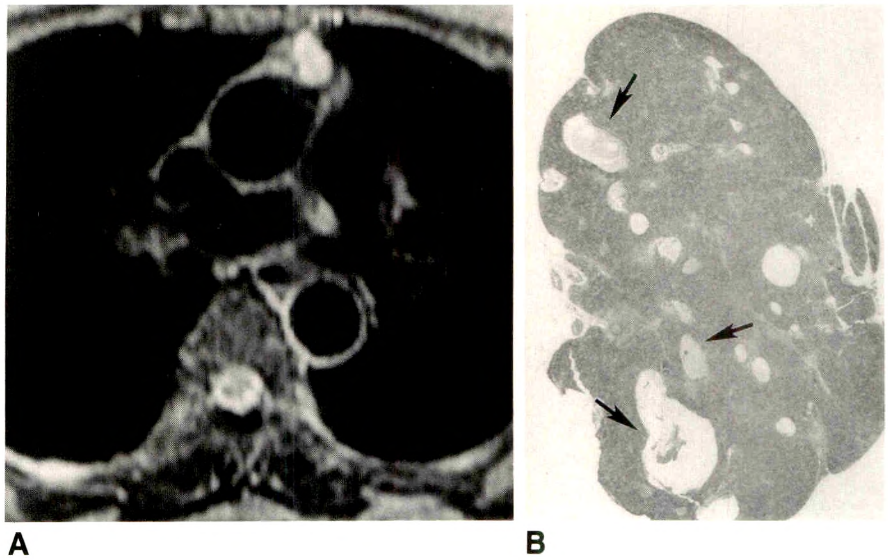

Fig. 6.—Benign thymoma in a 54-year-old woman.

A, T2-weighted axial MR image (2400/80) shows that signal intensity of mass is higher than that of fat. Mass has relatively inhomogeneous intensity without distinct lobulation.

B, Histologic specimen shows many small cystic regions (*arrows*). No lobulations are noted. Owing to limited spatial resolution of MR images, small cystic regions could not be visualized distinctly. Small cystic regions probably cause relatively inhomogeneous high-intensity appearance on T2-weighted images.

varying proportions, with scattered cystic regions of various sizes seen in 40% of thymomas pathologically. Cystic lesions in the tumor are filled with clear, proteinaceous, or bloody fluid. Larger tumors are more likely to exhibit cystic changes. The presence of sharply defined fibrous septa dividing tumors into lobules is one of the most characteristic features of thymomas, and the lobulated architecture was seen in 88% of all thymomas pathologically.

In our study, scattered high-intensity regions on T2-weighted images corresponded to cystic regions on pathologic specimens (Figs. 1B–1E and 2). On T1-weighted images, the signal intensity of cystic regions was variable, probably depending on the protein content of the cyst fluid or the presence of hemorrhage (Figs. 1A and 4A). Inhomogeneous intensity was probably caused by multiple small cystic regions (Figs. 4 and 6). On occasion, cystic changes are so extensive that solid components of the thymoma are reduced to small mural nodules attached to the capsule (Figs. 4A–4D).

The lobulated internal architecture of thymomas seen on MR images corresponded to lobulations caused by fibrous septa in pathologic specimens. Small lobulations or lobulations separated by thin fibrous septa seen in pathologic specimens could not be seen on MR images, owing to the low spatial resolution of MR.

The pathologic characteristics of thymomas were well represented on MR images. It is helpful to understand the pathologic background of the abnormalities seen on MR images of thymoma when considering a differential diagnosis. The specificity of the MR findings of the thymomas described here is to be investigated further.

Eleven of the 12 malignant thymomas had an inhomogeneous high-intensity appearance and six had a lobulated internal architecture. Four of five benign thymomas had a slightly inhomogeneous intensity and none had a lobulated architecture. Larger malignant thymomas were more likely to show the pathologic features of thymomas on MR images. The MR appearance of thymomas may be useful in assessing the malignancy of thymomas, but definitive differentiation between malignant and benign thymomas with MR currently is not possible.

ACKNOWLEDGMENTS

We thank Shun Imai and Mitushiro Momose, Department of Radiology, and Tsutomu Katsuyama, Department of Laboratory Medicine, Shinshu University, for valuable suggestions and Masayuki Haniuda, Hideki Nishimura, and Osamu Kobayashi, Department of Surgery, Shinshu University, for assistance.

REFERENCES

1. Von Schulthess GK, McMurdo K, Tscholakoff D, de Geer G, Gamsu G, Higgins CB. Mediastinal masses: MR imaging. *Radiology* **1986**;158:289-296
2. Molina PL, Siegel MJ, Glazer HS. Thymic mass on MR imaging. *AJR* **1990**;155:495-500
3. Rosai J, Levine GD. Tumors of the thymus. In: *Atlas of tumor pathology*, 2nd series, fasc 13. Washington, DC: Armed Forces Institute of Pathology, **1976**:1-166

New Format for Abstracts

Beginning in Fall 1992, the *AJR* will publish abstracts of articles in a different format, much like the ones recently adopted by the *New England Journal of Medicine* and the *Journal of the American Medical Association*. The purpose of the new design is to have abstracts present the essential elements of articles more clearly and concisely. The contents, organization, and length of the abstracts will be the same as before; however, rather than being all one paragraph except for the conclusion, abstracts will now be divided into four paragraphs, each with a title: objective, subjects (or materials) and methods, results, and conclusion.

The *AJR* Guidelines for Authors, which appears at the front of every issue of the Journal, has been revised to help you write abstracts in this new format. Please familiarize yourself with these guidelines and incorporate them into all manuscripts submitted for publication.

Robert N. Berk
Editor-in-Chief

Case Report

Pulmonary Embolism Caused by a Surgical Sponge

Nathan L. Kester[1] and Joel D. Hassien

Embolism of the pulmonary artery caused by a foreign body is an unusual but well-known phenomenon that was first described at the turn of the century [1]. Most previous cases involved bullet emboli [1–4]. Recently, intravascular catheters and catheter fragments have become more common emboli [5]. We report a unique case of a pulmonary embolism caused by a surgical sponge.

Case Report

A 40-year-old man underwent resection of a lumbar spinal pseudarthrosis with placement of an iliac crest strut graft. While harvesting the iliac crest graft, the surgeons inadvertently entered the common iliac vein. The profuse bleeding was controlled by packing with surgical sponges, and the vein was repaired.

Postoperatively, chest pain, dyspnea, and hypoxemia developed. A chest radiograph (Fig. 1A) showed a tangle of radiopaque material in the region of the left interlobar artery. This finding was not present on the preoperative film and was strongly suggestive of a surgical sponge. There was also elevation of the left hemidiaphragm, a left pleural effusion, and left lower lobe subsegmental atelectasis.

A ventilation-perfusion scan (Figs. 1B and 1C) showed marked bilateral air trapping and a large unmatched perfusion defect in the left lower lobe. The size of the defect correlated well with the location of the embolism.

Months later, the patient had CT (Fig. 1D), which clearly showed a tangle of material in the region of the left interlobar artery. The lung window settings of the same study (Fig. 1E) showed hazy opacification in the left lower lobe, extending to the pleura. Pulmonary arteriography (Fig. 1F) clearly showed the surgical sponge embolus occluding the left interlobar artery. The late arterial phase image (Fig. 1G) showed lack of perfusion of most of the left lower lobe.

A thoracotomy was done, and changes of chronic inflammation in the left lower lobe and a probable previous pulmonary infarction were seen. There was significant back-bleeding from collateral bronchial artery supply. There were numerous dense vascular adhesions of the left lower lobe to the chest wall, diaphragm, and mediastinum. These findings correlated well with the radiographic findings, although the nuclear medicine perfusion defect had been larger. A cotton sponge with surrounding organized thrombus was removed from the left interlobar pulmonary artery. Pathologic examination of the surgical specimen showed a 4 × 2 × 0.5 cm surgical sponge, and the specimen radiograph (Fig. 1H) showed the interwoven radiopaque marker.

Discussion

Most surgical sponges contain a radiopaque marker that is readily evident on plain radiographs. Description of the varied appearance of these markers is available [6], so further imaging is not usually necessary. Occasionally, however, a retained sponge may present a diagnostic problem.

CT of retained sponges in the abdomen may show a characteristic "whirllike" pattern; the complications of granuloma, abscess, or fistula; or calcification [7, 8]. Sonography may show an echogenic mass with strong posterior acoustic shadowing [8]. However, our case was a diagnostic dilemma because of the atypical intrathoracic and intravascular location of the sponge and because of the lack of a history of a previous thoracotomy (i.e., the sponge was migratory).

Although intravascular and migratory intravascular foreign bodies have been well documented, they are most often bullet emboli [1–4]. Other foreign body emboli have been described [1–5], but these have been mainly missile emboli [1–4], either from a central or peripheral vascular location [1–3] or, rarely,

---

Received August 21, 1991; accepted after revision October 7, 1991.

[1] Both authors: Department of Radiology, University of Missouri Hospital and Clinics, Columbia, MO 65212. Address reprint requests to N. L. Kester.

AJR 158:757–759, April 1992 0361–803X/92/1584–0757 © American Roentgen Ray Society

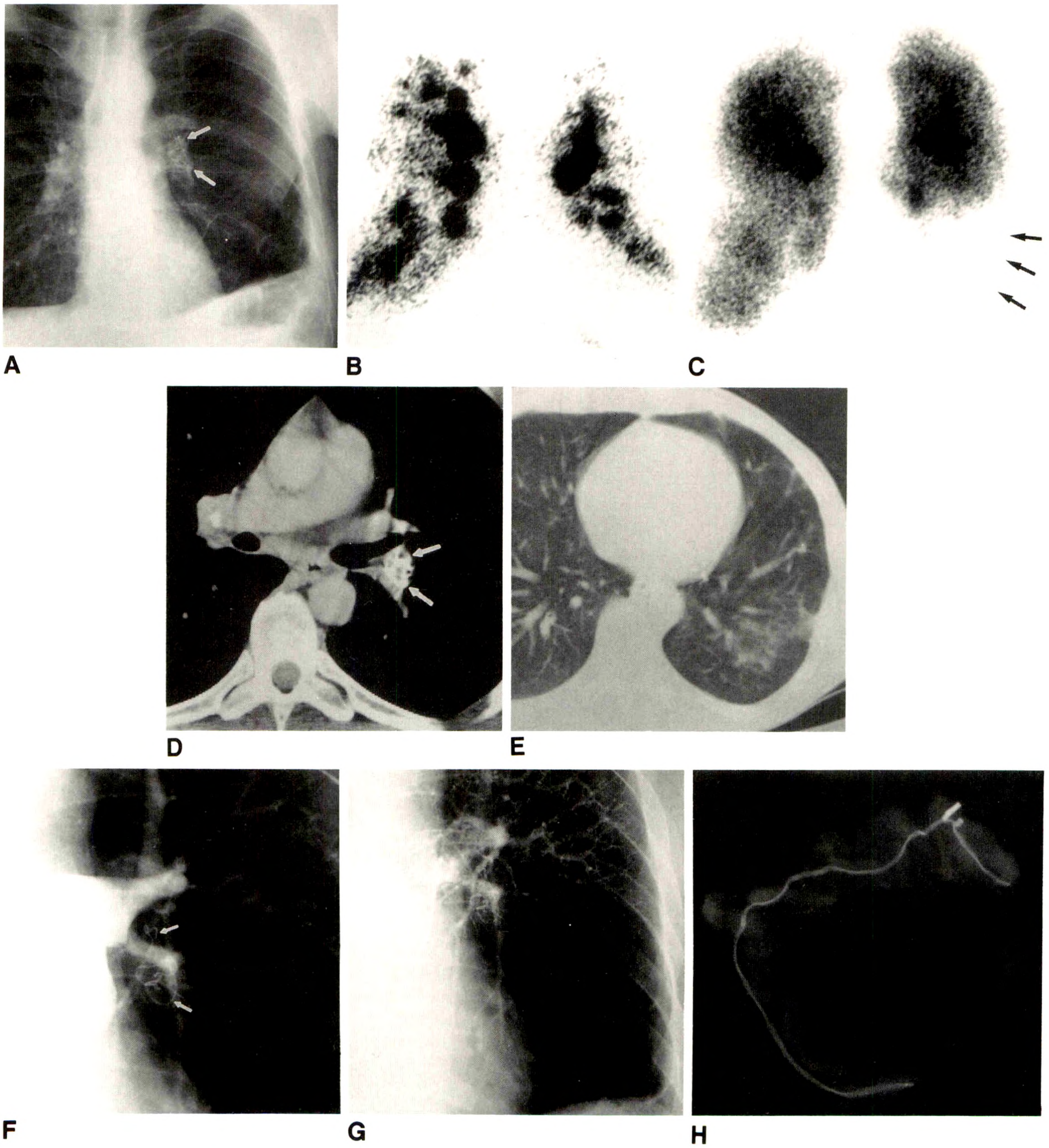

Fig. 1.—Pulmonary embolism caused by a surgical sponge.

A, Posteroanterior chest radiograph shows irregular tangle of radiopaque material (*arrows*) in left hilum, left-sided subsegmental atelectasis, and left-sided pleural effusion.

B, Ventilation portion of ventilation-perfusion scan shows extensive air trapping but no focal ventilation defect.

C, Perfusion portion of ventilation-perfusion scan shows large unmatched defect in left lower lobe (*arrows*).

D, Contrast-enhanced CT scan shows that radiopaque material seen in *A* may be in left interlobar artery (*arrows*).

E, Lung windows from CT scan in *D* show patchy opacification in left lower lobe, extending to pleura.

F, Posteroanterior magnified view from early arterial phase of left pulmonary arteriogram shows foreign body (*arrows*) occluding left interlobar artery.

G, Late arterial phase from arteriogram in *F* shows large perfusion defect in left lower lobe.

H, Radiograph of surgical specimen shows radiopaque marker in surgical sponge.

from an intracranial location [4]. Iatrogenic intravascular foreign bodies most commonly are catheter fragments [5].

The signs and symptoms in our patient and the clinical findings, especially the chest radiograph, strongly suggested the diagnosis, but CT and angiography (Figs. 1D and 1F) clearly established the location of the sponge within the central pulmonary artery. The changes that can be seen on chest radiographs in pulmonary embolism and infarction include atelectasis, pleural effusion, infiltrate, elevated hemidiaphragm, pleura-based rounded density, and regional oligemia with proximal vascular fullness or cutoff. Our patient had an elevated left hemidiaphragm, a left pleural effusion, and left lower lobe subsegmental atelectasis (Fig. 1A). The ventilation-perfusion study correlated well with the location of the embolus, but the size of the perfusion defect was larger than the findings on the chest radiograph or CT scan. This discrepancy probably can be explained by the dual vascular supply of the lung [9].

Recently, the fate of the lung in transcatheter occlusion of central and peripheral pulmonary artery branches has been described [9]. Usually, chronic central pulmonary artery occlusion will result in systemic collateral supply to the involved lobe [9]. Although these changes were seen at surgery in our patient, they were not evident radiographically. In addition, central pulmonary artery occlusion does not usually result in parenchymal infarction [9]. Therefore, the infarction seen in our patient probably was due to peripheral emboli originating at the surgical sponge, and the radiographic findings were due to the combination of chronic central pulmonary artery occlusion and superimposed chronic and recurrent thromboembolic disease.

REFERENCES

1. Barret N. Foreign bodies in the cardiovascular system. *Br J Surg* **1950**;37:416–445
2. Michelassi F, Pietrabissa A, Ferrari M, Mosca F, Vargish T, Moosa H. Bullet emboli to the systemic and venous circulation. *Surgery* **1990**;107:239–245
3. Mattox K, Beall A, Coyness E, DeBakey M. Intravascular migratory bullets. *Am J Surg* **1979**;137:192–195
4. Nehme A. Intracranial bullet migrating to pulmonary artery. *J Trauma* **1980**;20:344–346
5. Fisher R, Ferreyro R. Evaluation of current techniques for nonsurgical removal of intravascular foreign bodies. *AJR* **1978**;130:541–548
6. Williams R, Bragg D, Nelon J. Gossypiboma: the problem of the retained surgical sponge. *Radiology* **1978**;129:323–326
7. Parienty R, Pradel J, Lepreux J, Nicodeme C, Dologa M. Computed tomography of sponges retained after laparotomy. *J Comput Assist Tomogr* **1981**;5:187–189
8. Kokubo T, Itai Y, Ohtomo K, Yoshikawa K, Iio M, Atomi Y. Retained surgical sponges: CT and US appearance. *Radiology* **1987**;165:415–418
9. Remy-Jardin M, Wattinne L, Remy J. Transcatheter occlusion of pulmonary arterial circulation and collateral supply: failures, incidents, complications. *Radiology* **1991**;180:699–705

The American Academy of Roentgenology

Raymond A. Gagliardi[1]

The Japanese had bombed Pearl Harbor and the United States was involved in total war. The first Golden Age of Radiology (1920–1941) had ended, and the eventual cessation of hostilities would see a new orientation for certified specialists in all disciplines. The need of the armed services to categorize physicians' skills would reinforce the need for documented training and certification. Radiology would eventually emerge from World War II poised for a new and greater Golden Age.

The Hodges brothers, Paul C. in Chicago and Fred J. in Ann Arbor, had been active and influential in radiologic education and radiologic organizations for many years. They had already started to consider ways to strengthen radiology to ensure its continued growth toward equality with the senior clinical specialties. In their perception, one of the weaknesses in the radiologic organizational structure was the fragmentation of the specialty: too many societies with overlapping functions and members and too many journals competing for original work. We must recall that most radiology at that time was done by general radiologists, certified as equally skilled in diagnosis, radiation therapy, and the use of radium. The Hodges brothers believed that the Radiological Society of North America (RSNA), the American College of Radiology (ACR), the American Roentgen Ray Society (ARRS), and the American Radium Society (ARS) were diluting the potential influence of a single voice for all of radiology by each going its separate way. They envisioned a single monolithic society formed by the merger of the Big Four, somewhat like the AMA, with sections for special situations and the publication of a single journal.

In the beginning, there was little interest in the Hodges' proposal because the war was everyone's first priority. But as the Allies' position improved after Midway and El Alamein, more consideration could be given to the nature of the postwar world and postwar radiology in particular.

Because of wartime travel and hotel restrictions, the ARRS and RSNA agreed to hold a joint meeting in 1944. The meeting went smoothly and was highlighted by an outstanding combined Caldwell (ARRS)–Carman (RSNA) Lecture by Dr. Lawrence Reynolds, the distinguished bibliophile and Editor of the *AJR*.

The Hodges' proposal resurfaced in the aftermath of the successful joint meeting and there was now sufficient interest for Eugene Pendergrass, secretary of the ARRS, to poll his membership with a three-page questionnaire soliciting their views on the subject. The advantages seemed obvious and the proposal was endorsed by some of America's leading radiologists. Most of the ARRS membership already held places in the RSNA and the ACR. Most of the RSNA members also paid their dues to the ACR, and the ARS was largely composed of members of the other three. The responses were varied. So many of the radiologists were still in uniform that a real consensus was hard to find. Some were all for it, with one even suggesting combining *AJR* and *Radiology* into a single journal to be called the *American Journal of Radiology*, but the opposition was significant. One of those most openly and strongly opposed to union was Dr. Reynolds, who was concerned about the ARRS losing its identity in the larger and well-organized RSNA. The *AJR* was his special project and he had poured much of his soul and even his personal funds into ensuring its success. He eventually served for 22 years as Editor, longer than any other before or since. Dr. Reynolds also thought that there should be some place for the leaders in radiology who had established their credentials to congregate. He was genuinely concerned that the great strides made by competing organizations would be slowed by a single egalitarian society.

He feared that his battle might be lost and he decided to adopt a fall-back position should the major societies amalgamate. Together with the publisher, Charles C Thomas, who pioneered in the publication of radiologic texts, he conceived the idea of the American Academy of Roentgenology, incorporated in Illinois by Mr. Thomas, with its own journal edited by Dr. Reynolds and published by Thomas. This organization would be more elitist in nature, requiring defined periods of practice and evidence of scientific publication, just as was the case in the ARRS until not too many years ago. Indeed, it would not be too different from the ARRS of the time. It would be the appropriate place for the acknowledged leaders of the specialty.

The war came to a close and radiology made a series of quantum leaps forward as the technological revolution changed the face of the specialty forever. The societies gradually assumed different roles and new societies and new journals appeared almost daily. The idea of amalgamation never got off the ground, but echoes of that time recur in the Intersociety Commission of the ACR and the annual summit meetings of the subspecialty groups.

Perhaps it was a good idea. Perhaps it would have created more problems than it solved. But the incomplete application for incorporation remains in the archives. The American Academy of Roentgenology was a marvelous name for an unborn child who never was to assume it. Perhaps one day in the appropriate setting it will rise again.

In preparation for the 1995 centennial celebration of the discovery of the X-ray, the *AJR* will periodically publish History Pages, which deal with events leading up to and occurring around the time of the discovery.

[1] Department of Radiology, St. Joseph Mercy Hospital, 900 Woodward Ave., Pontiac, MI 48341-2985. Address reprint requests to R. A. Gagliardi.

Information for this article was obtained from private letters in the Society archives.

I am indebted to Nancy Knight who served as my cicerone in this endeavor.

***AJR* 158:760, April 1992** 0361–803X/92/1584–0760 © American Roentgen Ray Society

Multiple Mycotic Pulmonary Artery Aneurysms: A Complication of Invasive Mucormycosis

Laurie A. Loevner,[1] James C. Andrews, and Isaac R. Francis

Pulmonary mucormycosis is an invasive opportunistic fungal pneumonia most commonly seen in patients with hematologic neoplasms who are receiving immunosuppressive therapy and in patients with diabetes mellitus and renal failure [1]. It is frequently complicated by hemorrhagic infarction due to vascular invasion and pulmonary artery thrombosis. We report an unusual case of pulmonary mucormycosis complicated by multiple mycotic pulmonary artery aneurysms. To our knowledge, this combination has not been previously reported.

Case Report

A 30-year-old man with chronic renal failure was admitted to a local hospital with fever, chills, and night sweats. His medical history was remarkable for systemic lupus erythematosus, two failed renal transplants, splenectomy, and long-term hemodialysis. He was treated with vancomycin, gentamicin, and ceftazidime for presumed sepsis. Blood and sputum cultures were negative for bacterial and fungal growth. Serial chest radiographs showed enlarging infiltrates in the left upper and lower lobes. Bronchoscopy, performed because of persistent fevers, showed nonspecific endobronchitis. Open lung biopsy performed 4 days later showed necrotizing vasculitis associated with mucormycosis.

During the next 6 weeks, the patient remained ill and was transferred to our institution for further evaluation. On admission, he had a body temperature of 37.9°C, percussion dullness in the posterior left thorax, a WBC count of 18,200 cells/mm^3, and an oxygen tension of 59 mm Hg. Chest radiograph showed a large mass with poorly defined margins and surrounding air-space disease in the left lung (Fig. 1A). CT showed large, rounded masses in the left upper and lower lobes with homogeneous central enhancement consistent with aneurysms and dilatation of central branches of the left pulmonary artery (Fig. 1B). Pulmonary arteriography confirmed these findings and, in addition, showed aneurysmal dilatation of multiple peripheral pulmonary arteries (Fig. 1C). Pressure in the left main pulmonary artery was 44/20 mm Hg. Left bronchial arteriography showed a surrounding inflammatory reaction, but no systemic arterial supply to the aneurysms was found.

The patient had a left-sided pneumonectomy. Pathologic examination of the surgical specimen showed diffuse aneurysmal dilatation of both central and peripheral pulmonary arteries, with 7- and 5-cm pseudoaneurysms arising from pulmonary artery branches supplying the left upper and lower lobes, respectively. No evidence of rupture was seen. Microscopic sections showed organizing arterial mural thrombus containing fungal hyphae in a pattern consistent with mucormycosis and surrounding organizing pneumonia. The patient had an uneventful postoperative course and was discharged 2 weeks after surgery.

Discussion

Mucormycosis is caused by fungi belonging to the class Zygomycetes. The primary route of inoculation is inhalation of spores. Common clinical manifestations include rhinocerebral disease in patients with diabetes mellitus and pulmonary infection in immunosuppressed patients (especially those receiving cytotoxic drugs or corticosteroid therapy for hematologic neoplasms) and in patients with diabetes mellitus and renal failure [1].

The most common clinical manifestations of mucormycosis pneumonia, which occur in patients with one or more predisposing factors, are acute fever, cough, pleuritic chest pain, and, sometimes, hemoptysis [1, 2]. Patients remain ill despite conventional antimicrobial therapy [1]. Findings on chest radiograph are nonspecific and indistinguishable from those associated with other invasive fungal pneumonias. The most common abnormality is a round area of pneumonia with poorly defined margins. Other radiologic features may include nodular or lobar infiltrates, cavitation, mediastinal widening, nodule(s), or a miliary pattern. Frequently, pulmonary infection is complicated by hemorrhagic infarction resulting in wedge-shaped infiltrates [2]. To our knowledge, mycotic pulmonary artery aneurysms due to mucormycosis have not been reported previously.

Aneurysms of the pulmonary artery are rare. Noninfectious causes include trauma, pulmonary hypertension, connective

---

Received October 15, 1991; accepted after revision November 25, 1991.

[1] All authors: Department of Radiology, B1D530K, Angiography, University of Michigan Hospitals, 1500 E. Medical Center Dr., Ann Arbor, MI 48109-0030. Address reprint requests to J. C. Andrews.

AJR 158:761–762, April 1992 0361–803X/92/1584–0761 © American Roentgen Ray Society

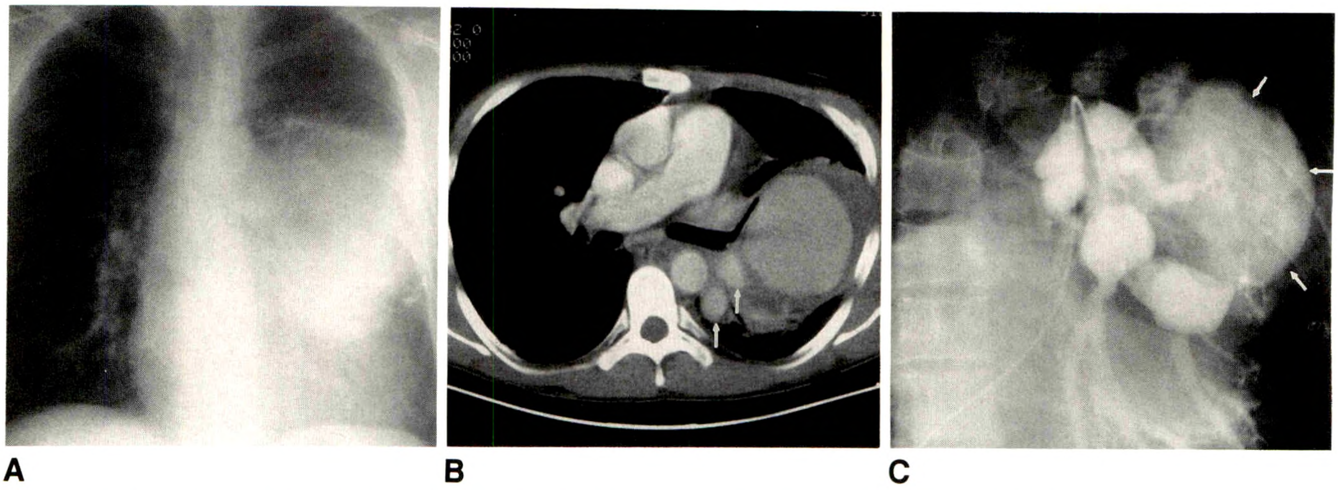

Fig. 1.—*A,* Posteroanterior chest radiograph shows poorly defined mass in left upper and lower lobes with surrounding consolidation. Note prominent left main pulmonary artery.

B, CT scan with contrast material shows homogeneously enhancing mass with irregular wall. Note marked aneurysmal dilatation of multiple central pulmonary artery branches (*arrows*).

C, Left pulmonary arteriogram shows large pseudoaneurysm corresponding to abnormalities (*arrows*) found on chest radiograph and CT scan. Note aneurysms involving multiple peripheral pulmonary artery branches.

tissue disease, and congenital alterations. Mycotic pulmonary aneurysms, the result of an invasive infection of the arterial wall in which the internal elastic lamina and media are disrupted and smooth muscle is replaced by fibrous tissue, are exceedingly rare. In a review of the literature through 1982, Navarro et al. [3] found 68 reported cases of mycotic pulmonary artery aneurysm. Aneurysms were most often solitary lesions involving the pulmonary artery trunk or its main branches; however, multiple, peripheral (intrapulmonary) aneurysms were also described. Mycotic pulmonary aneurysms are seen most often in patients with congenital heart disease with left-to-right shunts complicated by endocarditis [3, 4]. They have also been described in patients with necrotizing pneumonia and in IV drug abusers with endocarditis of the tricuspid or pulmonic valve [3, 5]. Proposed pathologic mechanisms include septic embolization to the pulmonary arteries and vasa vasorum with subsequent spread to the vessel wall and direct invasion of pulmonary arteries adjacent to a necrotizing pneumonia [2, 5]. Causative organisms are most commonly bacterial, including *Staphylococcus* and *Streptococcus*; however, treponemal, mycobacterial, and, rarely, fungal organisms, including *Aspergillus* and *Candida albicans*, have been reported [3, 5–8].

Antemortem diagnosis of mycotic pulmonary aneurysm is probably rare. Clinical manifestations are often nonspecific; hemoptysis may be the terminal event [7]. Chest radiographs may show an enlarging round or fusiform mass with poorly defined margins that may mimic pneumonia, abscess, or neoplasm. Patients with infections that do not respond to conventional therapy frequently have complex medical histories. They often have had extensive examinations that may include bronchoscopy and lung biopsy, as occurred in our case. If the diagnosis of mycotic aneurysm is not considered, the result could be inadvertent biopsy of this vascular mass, with subsequent hemorrhage and death [6, 8].

Life-threatening complications of mycotic pulmonary aneurysms include rupture and pulmonary embolism [7]. Of the 68 cases reviewed by Navarro et al. [3], 42 resulted in death. Of the 27 cases in which the cause of death was reported, 20 were due to rupture [3]. Therefore, it is imperative that the diagnosis be considered in the appropriate clinical setting. Although the diagnosis can be established on the basis of CT findings, pulmonary arteriography is necessary to accurately define the extent of disease.

Experience in the management of mycotic pulmonary aneurysms is limited because of the infrequent diagnosis. Management is usually surgical and involves aneurysmectomy plus lobectomy or, less commonly, aneurysmectomy alone [4]. Alternative nonsurgical therapeutic options, including occlusion of aneurysms with steel coils [6] or detachable balloons [5], have been reported. Transcatheter intervention performed at the time of pulmonary angiography provides rapid management, particularly in patients with massive bleeding, and may obviate surgery. In our case, surgery was chosen because of the extent of disease. Furthermore, treatment of endovascular fungal infections requires resection of infected tissue; antibiotics alone rarely result in cure.

REFERENCES

1. Myer RD, Rosen P, Armstrong D. Phycomycosis complicating leukemia and lymphoma. *Ann Intern Med* **1972**;77:871–879
2. Lipshitz HI, Pagani JJ. Aspergillosis and mucormycosis: two types of opportunistic fungal pneumonia. *Radiology* **1981**;140:301–306
3. Navarro C, Dickinson T, Kondlapoodi P, Hagstrom J. Mycotic aneurysms of the pulmonary arteries in intravenous drug addicts: report of three cases and review of the literature. *Am J Med* **1984**;76:1124–1131
4. Westaby S, Tan C, Foale R, Hallidie-Smith KA, Bentall HH. Mycotic aneurysm of the pulmonary artery: direct surgical approach with preservation of lung tissue. *J Cardiovasc Surg* (Torino) **1987**;28:596–598
5. Renie WA, Rodeheffer RJ, Mitchell S, Balke WC, White RI Jr. Balloon embolization of a mycotic pulmonary artery aneurysm. *Am Rev Respir Dis* **1982**;126:1107–1110
6. Remy J, Smith M, Lemaitre L, Marache P, Fournier E. Treatment of massive hemoptysis by occlusion of a Rasmussen aneurysm. *AJR* **1980**;135:605–606
7. Choyke PL, Edmonds PR, Markowitz RI, Kleinman CS, Laks H. Mycotic pulmonary artery aneurysm: complication of *Aspergillus* endocarditis. *AJR* **1982**;138:1172–1175
8. Rouse K, Scala-Barnett DM, Donabedian H, Freimer EH. Rupture of a pulmonary artery mycotic aneurysm associated with candidal endocarditis. *Am J Med* **1988**;84:142–144

Case Report

Tension Pneumothorax After Reversal of a Heimlich Valve

Alison R. Spouge[1] and Hollis A. Thomas

The use of small catheters to treat spontaneous and iatrogenic pneumothoraces has gained widespread acceptance in the medical community. Complications associated with their use are uncommon and are rarely life-threatening [1–4]. These small-caliber chest tubes are frequently attached to the unidirectional flutter valve developed by Heimlich [5] to prevent reaccumulation of air in the pleural cavity, allow ambulation, and simplify nursing care.

To our knowledge, no serious complications associated with the use of Heimlich valves have been previously documented. We report a tension pneumothorax resulting from inadvertent reversal of a Heimlich valve. These valves should be carefully secured to their connecting tubes, and the importance of correct orientation of the valve with respect to the connecting tube/catheter should be clearly explained to the patient and attending nursing staff.

Case Report

A 20–25% right-sided pneumothorax in a 57-year-old man developed after CT-guided biopsy of a small pulmonary nodule. The pneumothorax was evacuated with a 9-French catheter, which was then attached to a Heimlich drainage valve with a standard trumpet/Luer-Lok connecting tube. Placement of the catheter was prolonged owing to a persistent air leak. Five days after tube placement, the Heimlich valve was accidentally disconnected. The patient replaced it, unknowingly reversing the valve with respect to the connecting tube and catheter, and began to experience mild shortness of breath during the ensuing hours. A follow-up chest radiograph obtained later the same day revealed a tension pneumothorax (Fig. 1). Several hundred milliliters of air was evacuated, and the valve was replaced in the correct orientation. There were no further complications, and the catheter was removed 2 days later.

Discussion

Treatment of pneumothoraces with small-caliber chest catheters that are attached to Heimlich flutter valves is a procedure with few complications previously documented in the literature. Conces et al. [2] found no complications in a series of 79 patients treated with small-caliber chest tubes, 76 of which had Heimlich flutter valves attached. Casola et al. [3] treated 30 patients with small chest tubes, some of which were attached to Heimlich valves. The only complication in their series was severe chest pain after forceful manual aspiration of the pneumothoraces in three patients. Reinhold et al. [4] drained eight pneumothoraces with small catheters attached to Heimlich valves in a group of 42 patients who underwent percutaneous drainage of pleural collections. Their only procedure-related complications were one vasovagal reaction and conversion of one sterile pleural effusion to an empyema.

Although interventional radiologists should be aware of the danger of reversing a Heimlich valve, this potential complication has not been emphasized in the literature. When Sargent and Turner [1] first described the use of small catheters to drain pneumothoraces with Heimlich valves, they indicated the need for secure connections and emphasized that regular inspections would be required to detect inadvertent occlusion of the drainage tube. Recently, Goldberg et al. [6] also emphasized the importance of daily rounds by the radiologist after interventional procedures in the chest and abdomen.

Received October 7, 1991; accepted after revision November 1, 1991.

[1] Both authors: Department of Diagnostic Radiology, Humana Hospital–University of Louisville, 530 S. Jackson St., Louisville, KY 40202.

AJR 158:763–764, April 1992 0361–803X/92/1584–0763 © American Roentgen Ray Society

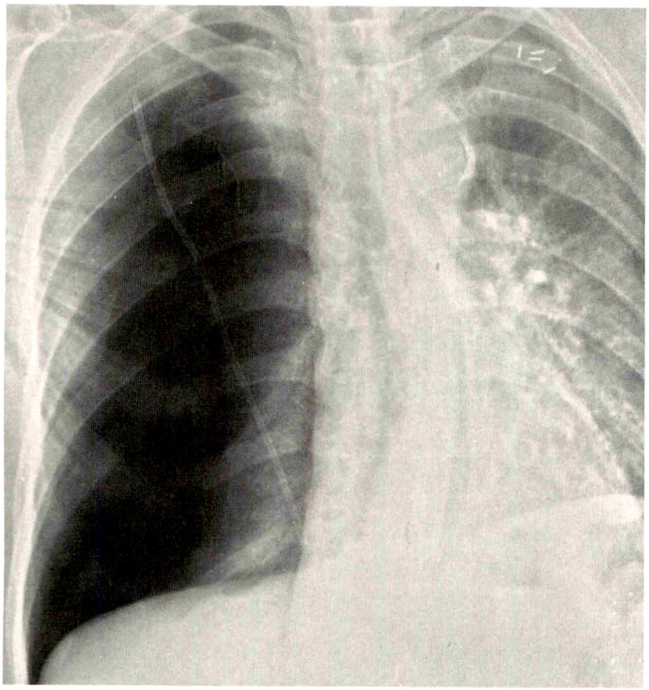

Fig. 1.—Posteroanterior chest radiograph after reversal of Heimlich valve shows right-sided tension pneumothorax with concurrent subcutaneous emphysema.

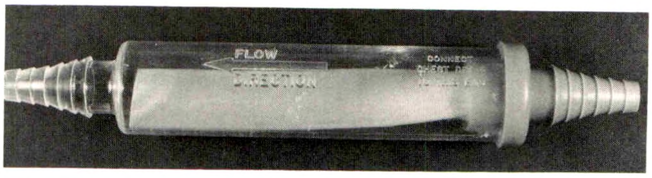

Fig. 2.—Heimlich valve design allows either end to be attached to connecting tube adapter.

The inadvertent reversal of a Heimlich valve allows ambient air to be drawn into the pleural space during inspiration with the subsequent development of a tension pneumothorax, as in our patient. We wish to reiterate the need for secure attachment of the connecting tube to the chest catheter and valve, careful follow-up by interventional radiology personnel, and education of the patient and attending health care workers regarding details of the drainage apparatus. Although the proper orientation of the Heimlich valve is indicated on the valve itself, the print is small and, if not inspected closely, is difficult to see. The design of the valve, which allows the connecting tube to be attached to either end, is potentially dangerous (Fig. 2). Manufacturers might consider redesigning the valve so that inadvertent reversal cannot occur.

REFERENCES

1. Sargent EN, Turner AF. Emergency treatment of pneumothorax: a simple catheter technique for use in the radiology department. *AJR* **1970**; 109:531–535
2. Conces DJ, Tarver RD, Gray WC, Pearcy EA. Treatment of pneumothoraces utilizing small caliber chest tubes. *Chest* **1988**;94:55–57
3. Casola G, vanSonnenberg E, Keightley A, Ho M, Withers C, Lee AS. Pneumothorax: radiologic treatment with small catheters. *Radiology* **1988**;166:89–91
4. Reinhold C, Illescas FF, Atri M, Bret PM. Treatment of pleural effusions and pneumothorax with catheters placed percutaneously under imaging guidance. *AJR* **1989**;152:1189–1191
5. Heimlich HJ. Valve drainage of the pleural cavity. *Chest* **1968**;53:282–287
6. Goldberg MA, Mueller PR, Sanjay S, et al. Importance of daily rounds by the radiologist after interventional procedures of the abdomen and chest. *Radiology* **1991**;180:767–770

CT Diagnosis of Small-Bowel Obstruction: Efficacy in 60 Patients

Tatsuro Fukuya[1]
Donald R. Hawes
Charles C. Lu
Paul J. Chang
Thomas J. Barloon

We retrospectively compared the CT findings in patients with and without surgically proved small-bowel obstruction to evaluate the role of CT in diagnosing the presence and cause of obstruction. In the patients with obstruction, we compared the CT findings with findings on plain abdominal radiographs and contrast studies of the small intestine. CT criteria used for the diagnosis of obstruction were dilated small-bowel loops proximal to the suspected site of obstruction and collapsed or normal-appearing loops of small bowel distal to the obstruction. Receiver-operating-characteristic analysis suggested the optimum balance of sensitivity and specificity was achieved when 2.5 cm was used to indicate dilatation of the small bowel. On the basis of these criteria, the presence of obstruction was correctly diagnosed in 27 (90%) of 30 patients with proved obstruction, and obstruction was not diagnosed in the patients without obstruction. The cause of the obstruction was evident on CT in 14 of the 30 obstructed patients: abscess (five), neoplastic lesion (three), peritoneal carcinomatosis (three), and other (three). Adhesions were responsible for the obstruction in 13 of 15 patients in whom the cause was not shown on CT. In six patients in whom findings on plain abdominal radiographs were normal, the CT scan was positive for obstruction. However, in the three patients whose CT scans were falsely negative for obstruction, findings suggesting obstruction were seen on plain films. Of 15 patients who had both CT and contrast studies of the small intestine, CT offered more information concerning the cause of obstruction in six (40%), primarily by demonstrating significant extraluminal abnormalities. CT and gastrointestinal contrast studies gave concordant results in eight patients with obstruction. In only one patient did the gastrointestinal contrast study give more diagnostic information.

We conclude that CT scanning demonstrates accurately the presence of high-grade small-bowel obstruction and may be the technique of choice when extraluminal abnormalities are suspected or when prompt, efficient, and comprehensive evaluation is required.

***AJR* 158:765–769, April 1992**

CT has a well-established role in the diagnosis of a variety of small-bowel diseases [1–9]. However, the ability of CT to confirm or exclude clinically suggested small-bowel obstruction (SBO) and to identify its cause has only recently been discussed in depth in the literature [10].

We studied the CT scans of 30 patients with surgically proved SBO and 30 patients with no obstruction at surgery to determine the CT findings of SBO, the optimal luminal caliber on CT for the differentiation between the normal and dilated small bowel, the ability of CT to identify a specific cause of SBO, and the efficacy of CT compared with plain abdominal radiographs and gastrointestinal contrast studies.

Materials and Methods

The medical records of all patients operated on with a clinical diagnosis of SBO at The University of Iowa Hospitals and Clinics from 1987 to 1990 were reviewed retrospectively.

Received August 12, 1991; accepted after revision November 20, 1991.

[1] All authors: Department of Radiology, The University of Iowa College of Medicine, Iowa City, IA 52242. Address reprint requests to T. Fukuya.

0361-803X/92/1584-0765
© American Roentgen Ray Society

Patients' symptoms, surgical records, and histopathologic reports were examined. Those patients with symptoms of SBO who had a CT scan before surgery were selected for this study. Thirty patients had symptoms of SBO at the time of CT and evidence of SBO at laparotomy. These nine men and 21 women were 21–75 years old (average, 50 years).

Thirty patients in whom CT was performed before laparotomy and in whom no obstruction was found at surgery also were selected, from the same time period, to determine the optimal small-bowel diameter indicative of dilatation and to determine the specificity of the CT diagnosis of SBO. None of these patients had clinical suggestion of SBO at the time of CT. To avoid a selection bias, 30 patients with consecutive numbers were selected from the listing by hospital number. Surgical diagnoses in this group of patients were lymphoma (14), ovarian or uterine carcinoma (five each), colon carcinoma (three), gastric carcinoma (two), and bile duct carcinoma (one).

CT was performed routinely with IV contrast material (58 patients), unless clinically contraindicated (two patients, both in the group with SBO). Contrast material was administered orally 2 hr and immediately before scanning, and rectally immediately before scanning. Multiple axial scans were obtained with 8- or 10-mm slice thickness at 10-mm intervals from the dome of the diaphragm to the symphysis pubis in all cases. CT scanning was performed on a Somotom DRH (Siemens, Iselin, NJ) or a Picker 1200SX (Picker International, Cleveland, OH) unit.

Findings assessed on CT were dilatation of small-bowel loops, presence of abrupt or gradual change of luminal caliber in the small bowel, and presence of any wall thickening of the small bowel or focal mass lesions at or around the level of the obstruction. An attempt was made to identify the cause of obstruction on the CT scans in each patient. CT diagnosis of SBO was based on the presence of disproportionate dilatation of small-bowel loops (dilated proximal bowel and collapsed or normal loops distally). The maximum diameter of the proximal small bowel was measured from outer wall to outer wall. Where possible, the diameter of a round cross section of distended bowel was chosen for measurement. The wall of the small bowel was considered thickened if it was more than 3 mm wide in a distended loop of bowel. The colon was considered collapsed (lumen barely identified), normal, or dilated.

Receiver-operating-characteristic (ROC) analysis was performed to determine the optimal luminal diameter indicating dilatation. CT scans in the 60 patients were reviewed in a randomized fashion. Reviewers were not aware of the clinical or surgical findings. All CT studies were reviewed by two radiologists, and a consensus was obtained if there was initial disagreement.

In the patients with proved obstruction, CT findings were compared with findings based on review of the plain abdominal films (30 patients) by two of the authors. A comparison was made between CT scans and plain films in terms of the ability to diagnose the presence of SBO. Plain films were classified as definite, nonspecific, or negative for SBO. Gastrointestinal contrast studies (15 patients) were reviewed, and, where indicated, the location and/or specific cause of obstruction were recorded. No control group of plain films or gastrointestinal contrast studies.

Results

Thirty patients with surgically confirmed SBO had CT scans preoperatively. The interval between CT and laparotomy was 0–25 days (average, 6 days). Sixteen patients had laparotomy within 2 days after CT. Twenty-six patients had laparotomy primarily to relieve symptoms related to SBO. Four patients had SBO confirmed at laparotomy, although surgery was performed primarily for other clinical indications. The interval between the onset of symptoms of SBO and CT scanning was more than 1 week in 11 patients and less than 1 week in 19 patients. Thirteen of the 19 patients had CT for an acute abdomen within 24 hr of admission.

The causes for obstruction based on laparotomy and/or pathologic examination were: adhesions (14), abscess formation (five), neoplastic lesions (four: two lymphoma and two recurrent tumor), peritoneal carcinomatosis (three), and other (four: gallstone ileus, Meckel's diverticulum, ventral hernia, and midgut volvulus).

Measurements of maximal small-bowel diameter proximal to the level of obstruction are shown in Table 1. By using a small-bowel diameter of 2.5 cm, determined by ROC analysis, to indicate dilated small bowel, and the presence of collapsed or normal-appearing small-bowel loops distal to the dilated proximal loops, we diagnosed SBO on CT scans in 27 (90%) of the 30 patients with obstruction. In the other three patients, no dilated loops were noted on CT. The causes of obstruction in these patients were abscess, lymphoma, and carcinomatosis. In none of the patients without SBO did CT suggest obstruction on the basis of these criteria.

In the 27 patients with findings meeting our criteria for SBO, the change in luminal caliber of the small bowel noted on CT was abrupt (Fig. 1) in 20 patients (74%) and gradual (Fig. 2) in seven patients (26%). Of the seven patients with a gradual transition, four had multiple adhesions, two of whom also had changes consistent with radiation effect; two had an abscess around the site of obstruction; and one had a lymphoma involving the small bowel.

In 13 of the 30 patients with SBO at surgery, the dilated loops were fluid filled on CT with little or no intestinal gas. Of the 13 patients, obstruction was in the proximal small bowel in five and in the distal small bowel in six. In two, there were multiple levels of obstruction. The colonic lumen was collapsed in 12 patients and normal appearing in 12. Four had had a total colectomy. The colon was dilated minimally in two patients with peritonitis. At laparotomy, one of these had an

TABLE 1: Maximum Diameter of the Small Bowel in Patients with and Without Obstruction

Diameter (cm)	No. of Patients	
	Obstruction	No Obstruction
>5.0	5	0
4.5–5.0	2	0
4.0–4.5	9	0
3.5–4.0	4	0
3.0–3.5	6	0
2.5–3.0	1	4[a]
2.0–2.5	3	19
1.5–2.0	0	7
Total	30	30

[a] In these four patients, CT was interpreted as negative for evidence of small-bowel obstruction because no change in luminal caliber from proximal to distal small bowel was present.

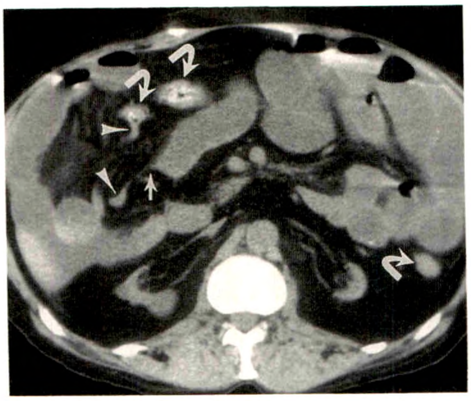

1

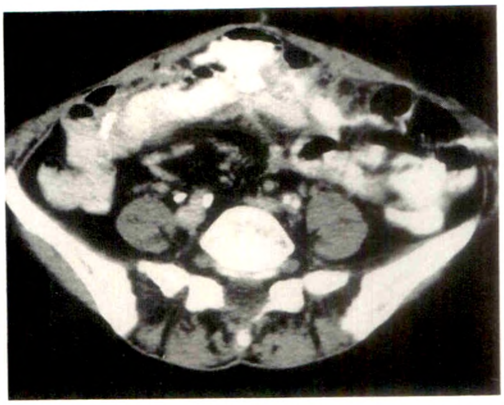

2

Fig. 1.—62-year-old man who had had renal transplantation had symptoms of small-bowel obstruction. CT scan shows abrupt transition (*straight arrow*) between dilated and collapsed loops of small bowel. Note collapsed terminal ileum (*arrowheads*) and colon (*curved arrows*), more easily appreciated when reviewing sequential images. No mass lesions are seen around site of transition. At surgery, adhesions were found to have caused obstruction.

Fig. 2.—63-year-old woman who had had right hemicolectomy for colonic cancer had symptoms of small-bowel obstruction. CT scan shows matted loops of small bowel filled with orally administered contrast material. Other slices showed nondilated distal small bowel and multiple peritoneal nodules. CT impression of peritoneal carcinomatosis causing obstruction was confirmed at laparotomy.

extensive small-bowel infarction and the other had a large abscess. Both diagnoses were made by CT.

Wall thickening of the small bowel at or around the site of obstruction was noted in 12 of 30 patients with proved SBO. Eight of these had thickening of a long segment of small bowel; that is, not confined to a single loop. Of the 12 patients, small-bowel obstruction was caused by adhesions in six, abscess in five, and lymphoma in one. Of six patients with wall thickening and adhesions, three had ischemic changes and one had radiation enteritis. This finding was unexplained in the other two. Thickening of the wall of the small bowel was seen in all five patients with an intraabdominal abscess.

CT demonstrated extraluminal findings indicating the cause of SBO in 11 of the 30 patients. Abscess formation around the site of obstruction (Fig. 3) was present in five, and a tumor mass encasing the small bowel (Fig. 4) was found in three. In three patients with peritoneal carcinomatosis, multiple nodules in the mesenteric fat and loculated ascites or peritoneal fluid collections were identified on CT.

CT correctly identified the cause of obstruction in 14 of the 30 patients: abscesses (five), tumor encasing the small bowel (three), peritoneal carcinomatosis (three), and gallstone ileus, lymphoma involving the small-bowel wall, and strangulated hernia (one each). In one patient with a known lymphoma, in whom SBO caused by adhesions was found at surgery, an incorrect diagnosis of lymphoma involving the small bowel was made because mesenteric and retroperitoneal lymph-node enlargement was seen on CT.

In the remaining 15 of the 30 patients with proved SBO, no cause for SBO was noted on CT. Thirteen of these had obstruction due to adhesions, proved at surgery, one had a twisted and impacted Meckel's diverticulum, and one had a midgut volvulus.

Plain abdominal radiographs obtained within 4 days of CT were available for all patients. In 17 patients, plain films were obtained on the same day as CT. SBO was strongly suspected on plain films in 24 patients (80%). Four plain film studies showed nonspecific findings, and two studies were normal (Fig. 4B); evidence of SBO was seen on CT in all six. In four of the six cases, CT showed little air within the dilated, fluid-filled small-bowel loops. All three patients with CT studies negative for SBO had findings positive for obstruction on plain films. The patient with abscess had been on nasogastric suction for the 5 days preceding CT. The other two patients experienced marked worsening of symptoms (5 and 12 days, respectively) after the preoperative CT scan.

Gastrointestinal contrast studies were performed in 15 patients (enteroclysis: 10; small-bowel follow-through: five), and the interval between the gastrointestinal contrast study and CT ranged from 0 to 15 days (average, 7.5 days). A correct diagnosis for the cause of SBO was made in three of seven patients for whom contrast dilution was not a problem. In the remaining four, all with obstruction caused by adhesions, differentiation between adhesions and tumor involving small bowel was impossible. In eight patients, no specific diagnosis could be made for the cause of obstruction because of marked dilution of the contrast material (Fig. 4C).

CT provided more information than contrast studies about the cause of obstruction in six of the 15 patients with obstruction who had both studies. Findings seen only on CT included extraluminal neoplastic mass lesions, abscesses, and peritoneal carcinomatosis (two patients each). In only one patient did the gastrointestinal contrast study show an abnormality, mucosal sloughing, that was not evident on CT. In one patient with a lymphoma, a diagnosis was made on both CT and gastrointestinal contrast studies with the same degree of confidence. In the remaining eight patients, neither technique allowed a specific diagnosis for the cause of obstruction. At laparotomy, all eight were found to have obstruction caused by adhesions.

Discussion

CT findings of a large variety of pathologic conditions of the small bowel have been described previously [1–9]. For evaluation of diseases of the small bowel, CT is generally

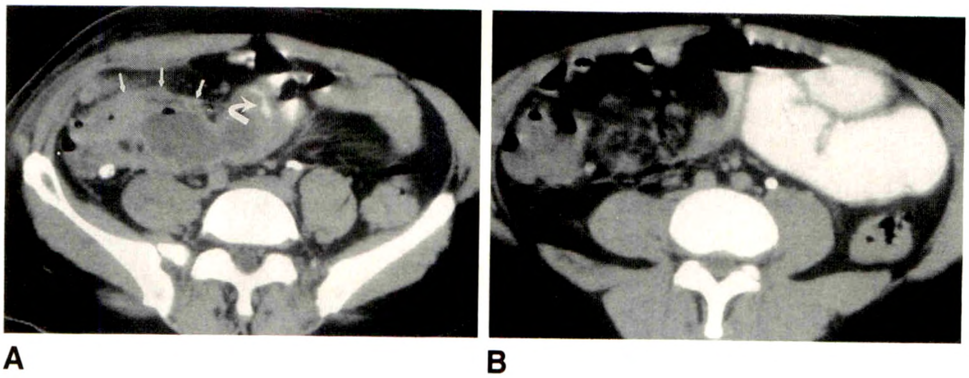

Fig. 3.—41-year-old man with pain in right lower quadrant.

***A*, CT scan shows loculated fluid collections (*straight arrows*) indicating abscess. Small-bowel loops adjacent to abscess appear to be involved, and walls of these loops show thickening (*curved arrow*). Thickened small bowel is best appreciated when reviewing sequential images.**

***B*, CT scan 5 cm cephalad to *A* shows dilated proximal small-bowel loops. Perforated appendiceal abscess was confirmed at surgery as cause of small-bowel obstruction.**

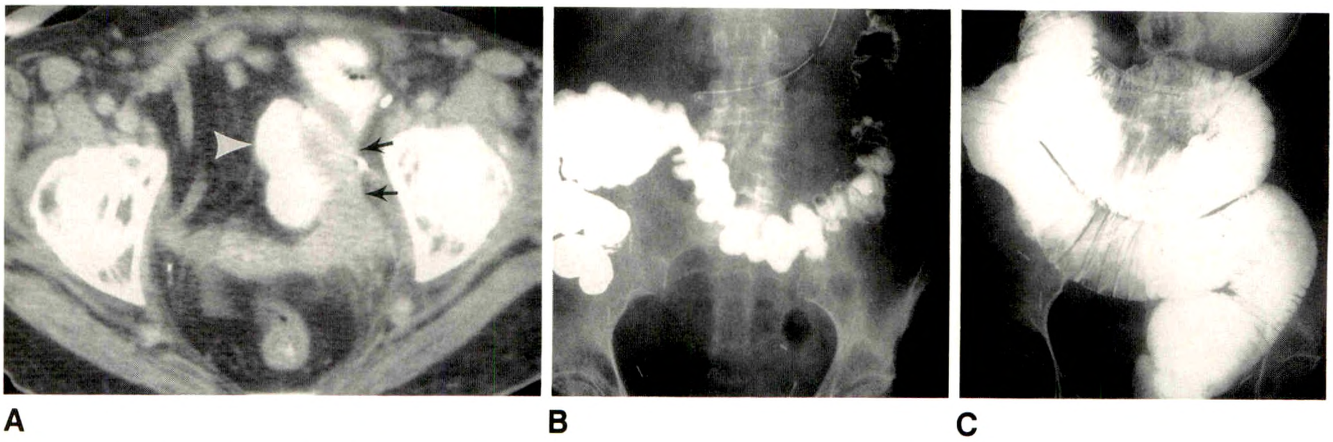

Fig. 4.—71-year-old woman who had had a total cystectomy for transitional cell carcinoma of urinary bladder.

***A*, CT scan shows pelvic side-wall lymphadenopathy (*arrows*) involving jejunal loops (*arrowhead*). CT diagnosis of nodal recurrence causing jejunal obstruction was made. Other levels showed dilated proximal jejunum filled with fluid and only a little gas.**

***B*, Abdominal plain film obtained on same day as CT scan shows normal bowel gas pattern. Barium from previous barium enema is noted within colon.**

***C*, Radiograph after enteroclysis shows almost complete obstruction of mid jejunum. Barium is diluted, and it is impossible to differentiate between adhesion and mass lesion involving the jejunum as the cause of obstruction.**

considered a supplement to gastrointestinal contrast studies [1, 8]. Until recently, however, discussion of the role of CT in the evaluation of SBO has been limited [10], and the criteria for CT diagnosis of SBO have been defined imprecisely. Our study included patients with the clinical diagnosis of SBO who subsequently had laparotomy. As a result, it is likely that all cases analyzed had high-grade SBO. We excluded patients with suspected colonic obstruction in whom barium enema was thought to be the more appropriate initial examination. We attempted to establish objective criteria for diagnosing dilated bowel by using ROC analysis. We also compared CT findings with those of plain films and gastrointestinal contrast studies, but the latter were not evaluated against a control group. Because the clinical information on our patients was obtained by retrospective chart review, it is difficult to determine how often the CT demonstration of SBO led directly to the decision for surgery.

Abdominal plain film studies have been reported to have a sensitivity of 50–65% for the diagnosis of SBO. However, false-positive and false-negative interpretations are common [11]. The selection bias of our study (that is, all our patients with obstruction presumably had high-grade obstruction) probably accounts for the high sensitivity of the plain film studies. For the same reason, however, the sensitivity of the CT studies also may be higher than in a less selective population of patients with suspected SBO, as CT cannot be used to detect obstruction in the absence of dilated bowel loops or a distinct transition in luminal diameter. The high sensitivity of interpretation in our series might also, in part, be because all plain films in our study were interpreted retrospectively by radiologists aware of the surgically proved SBO, and no control group of plain films was used.

In patients with mild degrees of SBO in whom a combination of symptoms, physical findings, and history suggests partial or early SBO, gastrointestinal contrast studies may be necessary to make a diagnosis. Contrast studies of the small intestine, especially enteroclysis, can detect minimal adhesions, small intraluminal mass lesions, and mucosal changes even when there is no bowel dilatation [12, 13]. Most of these patients can be treated conservatively. Our study did not address the possible role of CT in this group of patients.

CT findings of SBO included dilated proximal and collapsed or normal-appearing distal small-bowel loops. If a diameter of 2.5 cm is used to indicate small-bowel dilatation, 27 (90%) of our 30 patients with obstruction were diagnosed correctly by CT as having SBO. In most of these patients, the transition from dilated to collapsed or normal-appearing loops was abrupt, so that the CT diagnosis was obvious. The CT diagnosis of SBO is more difficult in patients with a gradual transition. When oral contrast material is used, delayed repeat CT may be useful to clarify the level of obstruction. In the majority of patients with obstruction, however, fluid-filled loops are present to the level of obstruction and are easily identified on CT, especially when the bowel wall is enhanced by IV contrast material. This was the case in the majority of our patients with obstruction in whom orally administered contrast material failed to reach the level of obstruction.

Thickening of the bowel wall seen on CT is considered nonspecific, and other findings such as intraluminal or extraluminal focal masses and changes in the mesentery are more important in making a specific diagnosis for the cause of the thickening [1-3, 5-8, 14]. Care must be taken to measure wall thickness where the bowel is distended, as the redundant folds in collapsed bowel may falsely appear thickened. In our study, thickening of the wall of the small bowel was nonspecific, being seen in a variety of conditions including ischemia, inflammatory processes adjacent to the small bowel, and neoplastic processes. On CT, a specific diagnosis of the cause for bowel-wall thickening must, therefore, be based on additional findings such as an associated neoplastic mass, abscess, or other findings of ischemia (i.e., pneumatosis).

In 15 patients without definite CT findings to indicate the cause of SBO, all but two were found to have obstruction due to adhesions. Therefore, our results support the assumption of Megibow et al. [10] that adhesions are likely when CT confirms the presence of obstruction and fails to demonstrate a cause. However, minimal tumor recurrence may be difficult to exclude.

In 20% of our patients, plain film studies were negative or nonspecific, whereas CT studies showed typical patterns of SBO. These six patients were among the 13 in whom CT showed predominantly fluid-filled loops of bowel. The other seven had plain film demonstration of either fluid-filled loops or small but suggestive gas collections. In patients whose plain film studies indicated SBO but whose CT studies were negative for obstruction, it is possible that decompression of the bowel proximal to the obstruction occurred before the CT scan as the result of either vomiting or nasogastric intubation.

The colon was collapsed or appeared normal in most of our patients with obstruction, supporting the diagnosis of mechanical SBO. Proportionate dilatation of small bowel and colon is indicative of an adynamic ileus rather than mechanical SBO. A minimally dilated colon was noted in two of our patients with obstruction. Both had an adynamic ileus, caused by peritonitis, in addition to the SBO. CT studies in both patients showed a change in the luminal caliber of the small bowel typical of mechanical obstruction.

CT provided more specific information about the cause of SBO in six of 15 patients with both CT and gastrointestinal contrast studies, based on the CT demonstration of characteristic extraluminal abnormality in all six. In only one case did a gastrointestinal contrast study provide more information, demonstration of the sloughing of the mucosa due to ischemia. In eight patients in whom a specific diagnosis was not made on either CT or gastrointestinal contrast studies, CT alone excluded the possibility of extraluminal disease. Contrast studies of the small bowel may be contraindicated in patients about to have surgery because the administration of high-density barium into the gastrointestinal tract may be undesirable, and a more dilute contrast material is inappropriate as dilution by fluid in the bowel is accentuated.

In patients with suspected SBO who are about to have surgery or are acutely ill, CT may be the imaging technique of choice as a diagnostic study is possible without the use of enteric contrast material. The ability of CT to demonstrate the cause of SBO could influence clinical (surgical and nonsurgical) management. Clinically, acute SBO may be mimicked by other acute abdominal diseases. It is probable that exclusion of an alternative cause of the patient's symptoms would influence management. The major advantage of CT over contrast studies in evaluating SBO, however, is its ability to demonstrate extraluminal abnormalities [1, 3, 4, 6, 8]. This is especially important in patients with malignant lesions in the abdomen.

REFERENCES

1. Megibow AJ, Balthazar EJ, Naidich DP, Bosniak MA. Computed tomography of gastrointestinal lymphoma. *AJR* **1983**;141:541-547
2. Smerud MJ, Johnson DC, Stephens DH. Diagnosis of bowel infarction: a comparison of plain films and CT scans in 23 cases. *AJR* **1989**;154: 99-103
3. James S, Balfe DM, Lee JKT, Picus D. Small-bowel disease: categorization by CT examination. *AJR* **1987**;148:863-868
4. Coscina WF, Arger PH, Levine MS, et al. Gastrointestinal tract focal mass lesions: role of CT and barium evaluations. *Radiology* **1986**;158:581-587
5. Alpern MS, Glazer GM, Francis IR. Ischemic or infarcted bowel: CT findings. *Radiology* **1988**;166:149-152
6. Gore RM, Goldberg HI. Computed tomographic evaluation of the gastrointestinal tract in diseases other than primary adenocarcinoma. *Radiol Clin North Am* **1982**;20:781-796
7. Fishman EK, Zinreich ES, Jones B, Siegelman SS. Computed tomographic diagnosis of radiation ileitis. *Gastrointest Radiol* **1984**;9:149-152
8. Balthazar EJ. CT of the gastrointestinal tract: principles and interpretation. *AJR* **1991**;156:23-32
9. Hulnick DH, Megibow AJ. Computed tomography of the small bowel. In: Herlinger H, Maglinte D, eds. *Clinical radiology of the small intestine.* Philadelphia: Saunders, **1989**:161-200
10. Megibow AJ, Balthazar EJ, Cho KC, Medwid SW, Birnbaum BA, Noz ME. Bowel obstruction: evaluation with CT. *Radiology* **1991**;180:313-318
11. Baker SR. Plain film radiology of the intestines and appendix. In: Baker SR, ed. *The abdominal plain film.* Norwalk, CT: Appleton & Lange, **1990**:155-241
12. Caroline DF, Herlinger H, Laufer I, Kressel HY, Levine MS. Small-bowel enema in the diagnosis of adhesive obstructions. *AJR* **1983**;142: 1133-1139
13. Maglinte DD, Lappas JC, Kelvin FM, Rex D, Chernish SM. Small bowel radiography: how, when, and why? *Radiology* **1987**;163:297-305
14. Thompson WM, Halvorsen RA. Computed tomographic staging of gastrointestinal malignancies. Part II. The small bowel, colon, and rectum. *Invest Radiol* **1987**;22:96-105

The reader's attention is directed to the commentary on this article, which appears on page 771.

Come to the
American Roentgen Ray Society
92nd
ANNUAL MEETING

Orlando, FL

Marriott's Orlando World Center
May 10–15, 1992

Scientific Program (200 papers)
Instructional Courses (60 hours)
Categorical Course on Neuroradiology
The Caldwell Lecture
Award Papers
Scientific Exhibits
Social, Golf, and Tennis Programs
Guest Programs

Commentary

CT Diagnosis of Small-Bowel Obstruction

Edward T. Stewart[1]

Radiologic evaluation of patients thought to have small-bowel obstruction begins with plain abdominal radiographs. In some cases, this is followed by small-bowel follow-through examination performed with barium or water-soluble contrast materials. It should come as no surprise that CT also provides valuable information in these cases. In addition to identifying dilated loops of bowel, CT has the potential to detect the cause of the obstruction.

In the preceding article, Fukuya and coworkers [1] report a retrospective study in which they evaluated the efficacy of CT to detect obstruction of the small bowel and to determine the cause of obstruction. CT scans in 30 patients with small-bowel obstruction were compared with scans in 30 control subjects. This report is certain to be compared with another study recently reported by Megibow et al. [2]. Megibow and his coworkers evaluated the CT appearance of the abdomen in 84 patients with small- or large-bowel obstruction. The results of both studies confirm the usefulness of CT in making the diagnosis of obstruction and in establishing its cause.

Obstruction of the small bowel may be acute or chronic and proximal or distal in the bowel. The cause of the obstruction may be adhesions, hernia, tumor, abscesses, inflammatory bowel disease, or other abnormalities. There is usually only one point of obstruction, but multiple points occur in some patients. Obviously, the results of any study of the efficacy of CT depend on which of these many variations predominate in the patients studied. The fact that most of the patients in Fukuya's study had well-established obstruction and some patients in Megibow's series had relatively early obstruction should bias the results toward a relatively higher sensitivity of CT among Fukuya's patients.

The vexing problem of making the diagnosis of partial bowel obstruction is not clearly addressed by either Fukuya or Megibow. Symptoms in these patients are not only vague and intermittent, but the degree of dilatation of the bowel is often not as marked as in patients with complete obstruction. Future studies may show that CT has its greatest value in these latter patients.

Both reports show that CT scans in patients with bowel obstruction provide more information about the cause of the obstruction than do either plain abdominal radiographs or small-bowel contrast studies. In addition to identifying dilatation of the bowel, CT reveals extraluminal lesions, such as tumors and abscesses, that may cause obstruction. Intramural abnormalities such as thickening of the bowel wall, due to either benign or malignant diseases, can be identified on CT, and evidence of intestinal ischemia may be apparent. Fukuya et al. used absence of such abnormalities on CT to make a diagnosis of adhesions as the cause of the obstruction by exclusion.

CT scans may be obtained specifically to detect bowel obstruction or they may be acquired primarily to detect other diseases without obstruction high on the list of diagnostic possibilities. When detection of small-bowel obstruction is the primary goal, a contrast enema should not be administered before the scan. Distension of the colon and possibly the distal small bowel with contrast material may eliminate the difference in the diameters of the bowel, proximal and distal to the obstruction, that is the basis for making the diagnosis.

The value of contrast material given orally before the CT scans is unsettled. Evidence of dilated, contrast-filled loops of small bowel may be less useful in making the diagnosis of

---

This article is a commentary on the preceding article by Fukuya et al.

[1] Department of Radiology, Froedtert Memorial Lutheran Hospital, 9200 W. Wisconsin Ave., Milwaukee, WI 53226.

AJR 158:771-772, April 1992 0361-803X/92/1584-0771 © American Roentgen Ray Society

obstruction than is the detection of dilated, air- and fluid-filled loops. IV contrast material is of value because it improves detection of edema, inflammation, and ischemia and may, therefore, help to establish the cause or the presence of a complication of the obstruction.

The findings of Fukuya et al. suggest that bowel obstruction is present when the diameter of the bowel is 2.5 cm or greater. This was the case in 90% of their patients with small-bowel obstruction, most of whom had advanced degrees of obstruction. On the other hand, Megibow et al. did not use a specific measurement to decide if the bowel was dilated. Their patients had less advanced degrees of obstruction, and their CT findings were more equivocal.

Despite the favorable results of these recent reports, it seems unlikely that CT is warranted routinely in patients with suspected bowel obstruction. CT is not indicated when the clinical and plain-film diagnoses of obstruction are unequivocal. The recent reports show that CT is valuable to determine the cause of the obstruction, but there is little practical value of knowing the cause before surgery. CT may be most important in the diagnosis of early or partial obstruction or in cases with multiple sites of obstruction.

REFERENCES

1. Fukuya T, Hawes DR, Lu CC, Chang PJ, Barloon TJ. CT diagnosis of small-bowel obstruction: efficacy in 60 patients. *AJR* **1992**;158:765–769
2. Megibow AJ, Balthazar EJ, Cho KC, et al. Bowel obstruction: evaluation with CT. *Radiology* **1991**;180:313–318

LIST OF BOOK REVIEWS

790	**Ultrasonography of the Urinary Tract,** 3rd ed. *Resnick MI, Rifkin Md, eds*
798	**Transvaginal Ultrasound.** *Dodson MG*
806	**Diagnostic Techniques in Urology.** *O'Reilly PH, George NJR, Weiss RM, eds*
836	**Handbook of Pediatric Imaging.** *Barr LL, ed*

Sonographic Detection of the Normal and Abnormal Appendix

Michel Rioux[1]

A prospective study of 170 patients with suspected appendicitis was performed to assess the value of sonography in detecting the normal and abnormal appendix. The wall thickness (normal, ≤ 3 mm), compressibility of the appendix, and echogenicity of surrounding fat were the primary criteria used to determine the status of the appendix. Of 60 patients who underwent surgery, appendicitis was proved in 45. The remaining 110 patients who did not have surgery, contacted by telephone at the end of the study, had no clinical follow-up evidence of acute appendicitis. A normal appendix was clearly identified in 102 (82%) of 125 patients without acute appendicitis. The sensitivity of sonographic examination in detecting appendicitis was 93%, the specificity was 94%, and the accuracy was 94%. The predictive value of a positive test was 86%; that of a negative test was 98%. Ruptured appendicitis was predicted in all cases (11/11).

Sonography is useful in detecting acute appendicitis and can clearly show the normal appendix more frequently than previously reported.

***AJR* 158:773–778, April 1992**

Since the original report by Puylaert [1] in 1986, the use of sonography as a tool in the diagnosis of appendicitis has become the subject of considerable study [2–12]. Sonographic findings of the abnormal appendix have been previously described; inability to visualize the appendix has been considered diagnostic of a normal appendix. However, the sensitivity of sonography in the detection of appendicitis is reported to be between 80% and 94%, and basically, more than 50% of patients (who had surgery or not) in previous studies [1, 2, 5–8, 12] were considered by the sonographer to have a normal appendix. Clinicians remain aware that a normal sonographic examination does not completely rule out appendicitis, and they still face the same dilemma in about 50% of their patients, regardless of the sonographer's conclusion.

The goals of the study were to optimize visualization of the appendix in all patients with suspected acute appendicitis and to evaluate whether visualization improved the overall accuracy of sonography in the diagnosis of a normal or abnormal appendix.

Subjects and Methods

From June 1988 to September 1989, 170 consecutive patients with clinically suspected appendicitis had sonography of the right side of the abdomen. All patients were selected by the general physician in the emergency department. Most of them also were evaluated by a surgeon. The surgeon was aware of the sonographic diagnosis in all cases, but the decision to operate was not known at the time of sonography. This study group comprised 100 females and 70 males 4–73 years old (mean, 26.5 years).

A complete examination of the abdomen and the pelvis was performed in all patients by using a 3.5-MHz sector scan transducer (Acuson 125, Mountain View, CA). The right hemiabdomen was then examined specifically with a 5-MHz linear-array transducer (Acuson

Received June 17, 1991; accepted after revision October 29, 1991.

[1] Department of Radiology, Hôpital Saint-François d'Assise, 10, rue de l'Espinay, Québec, Québec, Canada G1L 3L5. Address reprint requests to M. Rioux.

0361–803X/92/1584–0773

© American Roentgen Ray Society

125); in a few cases a 5- or 7.5-MHz sector-scan transducer (Diasonics DRF 400, Milpitas, CA) was used. The 5-MHz linear-array transducer was placed transversely below the edge of the right hepatic lobe, in front of the right kidney. Moving slowly downward to the right iliac fossa, we searched for the ascending colon. It was recognized in every patient as the largest round or oval structure delimited by a wall. The colon was either full of fluid (hypoechoic or anechoic) or, more frequently, full of feces (hyperechoic). The absence of vigorous peristalsis was often helpful in distinguishing colon from small bowel.

The ileocecal valve was then identified. Bowin's valve was often distinguished by its fatty component. The degree of peristalsis was helpful in differentiating an enlarged appendix from collapsed ileum or cecum. The appendix was finally sought in the transverse plane in the vicinity of the cecum for about 10 min, by using the graded compression technque previously described [1]. The search was made while the patient had a full bladder. If the appendix was not clearly visualized, the patient was asked to empty the bladder and scanning continued for 10 min. Even though the appendix was easiest to identify on transverse images, the origin of the appendix arising from the cecum could often be identified on longitudinal images. Scanning was done with the patient supine in the left lateral decubitus position, which was helpful in patients with a retrocecal appendix.

On the basis of our previous experience with sonographic examination of patients and pathologic specimens of the appendix, our criteria for identifying a normal appendix included a compressible, tubular, blind-ended structure; wall thickness (lumen interface to serosa) of 3 mm or less, with or without echogenic intraluminal material (gas and or feces); absence of peristalsis; and normal hyperechoic surrounding fat [2] (Fig. 1).

A diagnosis of appendicitis was made when appendiceal compressibility was reduced or absent, or when the transverse wall thickness was greater than 3 mm. Other signs of appendicitis included decreased echogenicity of the surrounding fat or the presence of a poorly defined hypoechoic round or oval structure, adjacent to the cecum and independent of loops of bowel.

Criteria for appendiceal rupture were clear asymmetry in wall thickness with indistinctness of wall layer or the presence of an air or fluid collection around the appendix (Fig. 2).

Although the number of cases in which the appendix was not visualized was tabulated, for statistical purposes, an appendix was considered normal if it was not visualized.

Sixty patients had surgery within 24 hr of the sonographic examination. Surgical specimens in 25 patients with appendicitis and nine patients with normal appendices were studied with the same sonographic transducers after the specimens were submerged in a water bath. With the assistance of a pathologist, a section of the specimen was obtained for histology at the site of optimal sonographic visualization of wall thickening or at a specific point of interest (e.g., ruptured

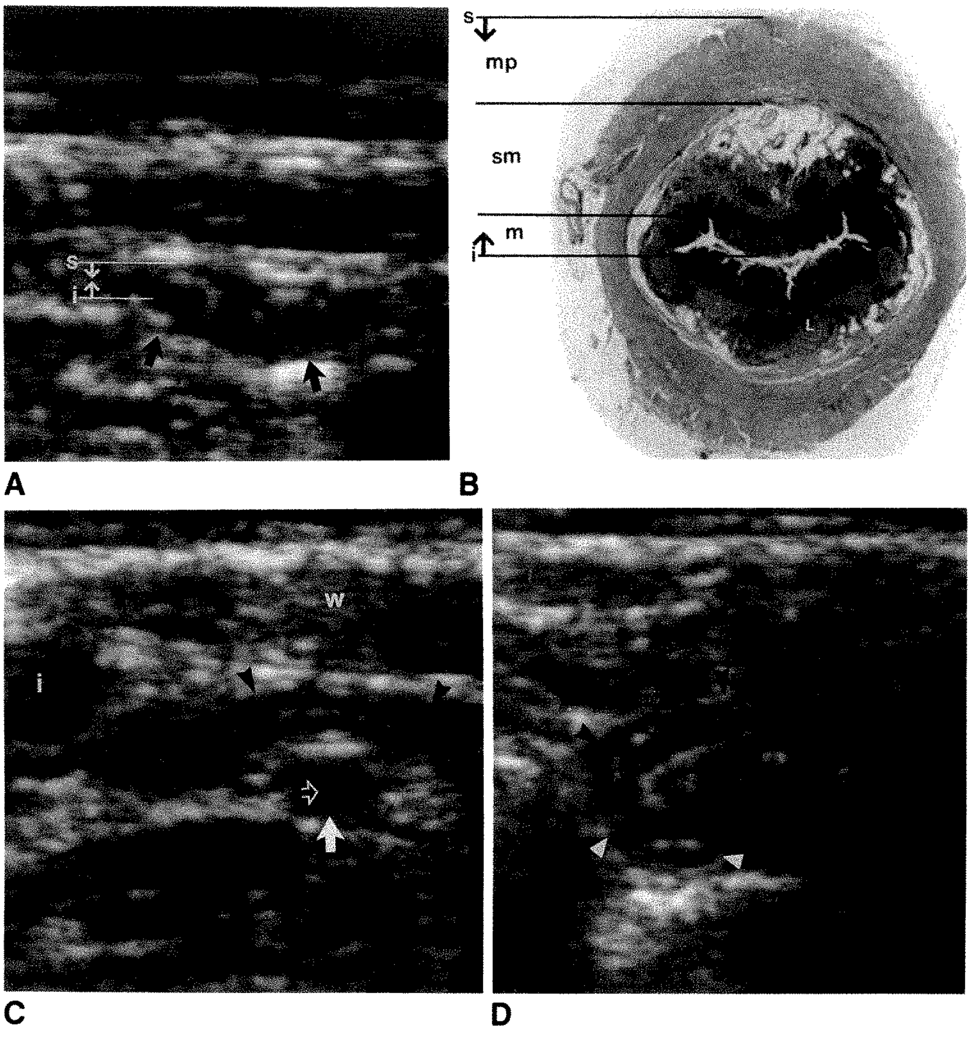

Fig. 1.—Normal appendixes.

***A*, Axial sonogram across two sections of normal but tortuous appendix (*black arrows*). Wall has typical three-ring appearance. Hyperechoic interface (i) of collapsed lumen and inner hypoechoic ring of mucosa is indicated (*lower white line*). Serosa (s) (*upper white line*) is defined as outer boundary of hypoechoic ring of muscularis propria. Wall thickness (2.2 mm) is distance between these two levels.**

***B*, Photograph of histologic specimen (transverse section) shows different layers of wall of appendix seen in *A*: m = mucosa, sm = submucosa, mp = muscularis propria, L = lymphoid follicle. Wall thickness is measured between luminal interface (i) and serosa (s).**

***C*, Sonogram of normal appendix seen both transversely (*solid arrow*) and longitudinally (*arrowheads*) in a 13-year-old boy. Inner hypoechoic ring (*open arrow*) is thicker than usual because of lymphoid hyperplasia. w = abdominal wall, i = iliac vessel.**

***D*, Sonogram clearly shows normal appendix in longitudinal section (*arrowheads*).**

area). The actual wall thickness was correlated with sonographic findings by this technique.

The 110 patients who did not have surgery were all contacted by telephone at the end of the study (mean, 8.6 months) to ascertain whether they had undergone surgery for appendicitis at another hospital.

Results

Patients Who Had Surgery

Of the 170 patients clinically suspected of having appendicitis, 60 underwent surgery. Forty-five had pathologically proved appendicitis, including five cases with histologic evidence of chronic inflammation with superimposed acute signs of inflammation of the appendix (Fig. 3). Of these patients, appendicitis was correctly diagnosed preoperatively by sonography in 42. Histologic and sonographic correlation was done in 25 cases of appendicitis. The proximal part of the appendix was the most accurate site for measuring wall thickness, and hyperechoic fat made the submucosa a useful landmark for identifying the wall on sonography. Clear distinction of the layers of the wall allowed an accurate measurement in 21 cases. The wall thickness on sonography varied between 3.3 and 7.5 mm (mean, 4.55 mm). Corresponding values by histopathology varied between 3.5 and 7.7 mm (mean, 4.58). Thirteen cases of appendicitis had advanced wall inflammation in the distal half, which was indistinguishable on sonography from hypoechoic intraluminal pus. Similarly, the appendiceal wall was not clearly visualized in four other cases, and noncompressibility as well as findings of periappendicitis were criteria used to diagnose appendicitis.

Three studies were incorrectly interpreted as normal. One false-negative examination occurred with nonvisualization of a retrocecal appendix in an obese patient, although pain occurred with transducer compression in the right lower quadrant. Another case involved an initial interpretive error; retrospectively, the sonogram showed classic signs of appendicitis with a wall thickness of 4.5 mm and hypoechoic surrounding fat with a small amount of ascites (Fig. 4). In the third case, only the proximal half of a normal appendix was

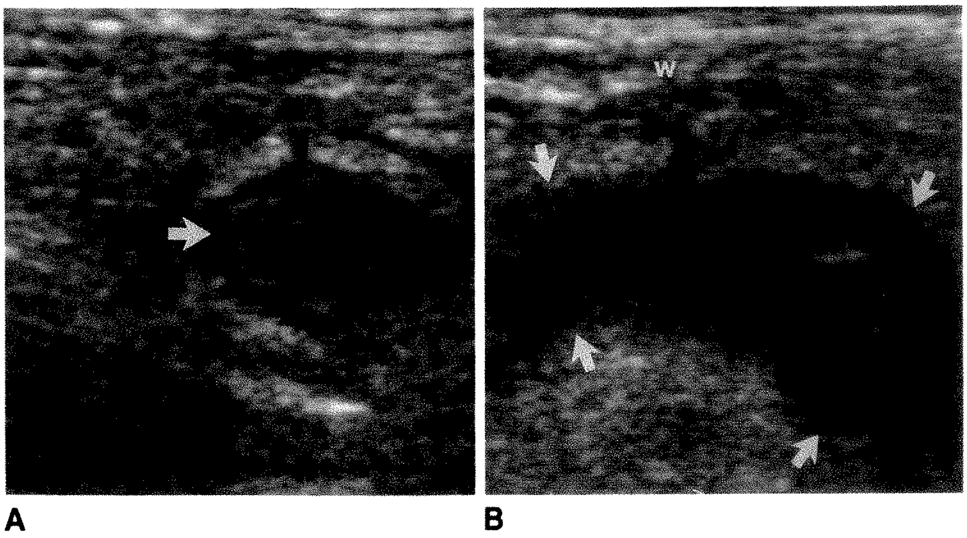

Fig. 2.—**Ruptured appendix.**
***A*, Axial sonogram of enlarged appendix (*arrow*). Right half of appendix (starting at level of *arrowheads*) shows asymmetric hypoechoic wall without hyperechoic submucosal layer. This area represents inflammatory necrosis of wall with rupture.**
***B*, Longitudinal sonogram of distal part of same appendix shows a hypoechoic, poorly defined tubular structure (*arrows*) without distinct wall visualization. w = abdominal wall.**

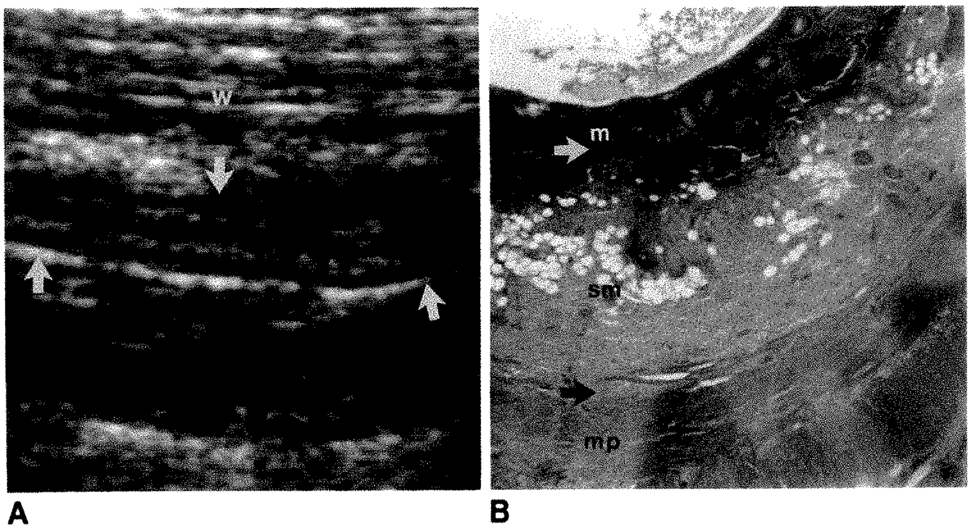

Fig. 3.—**Chronic appendicitis diagnosed on basis of sonographic findings and medical history, despite resolution of pain and leukocytosis at time of sonography and surgery.**
***A*, Longitudinal sonogram shows enlarged uncompressible appendix (*arrows*). w = abdominal wall.**
***B*, Photograph of magnified transverse histologic section of appendix shows atrophied mucosa (m). Chronic inflammation is shown by replacement of fat in submucosa (sm) by extensive fibrosis, which extends also into muscularis propria (mp). *Arrows* identify borders between mucosa and submucosa and between submucosa and muscularis propria.**

seen on sonography. Because of persistent symptoms, the patient underwent surgery and was found to have inflammatory changes in the distal appendix.

Of the 60 patients who had surgery, 15 were found to have a normal appendix at the time of the operation. Twelve cases were correctly diagnosed by sonography. Of these, a normal appendix was identified in nine cases showing identical correlation between the histopathologic specimen and such sonographic findings as clear wall distinction (nine cases), wall thickness (varying in both techniques between 0.5 and 3 mm; mean, 1.8 mm), the presence of enlarged lymphoid hyperplasia in the wall (two cases), a complete luminal collapse (three cases), or a lumen fully distended by feces (six cases); this correlation suggested that the structure visualized at sonography was indeed the appendix. In the other three cases, the appendix was not clearly identified, but was considered to be normal by sonography for statistical purposes. Three patients with normal appendixes at surgery had abnormal sonographic findings. Of note, a pericecal inflammatory process was found during surgery in all three. One patient had Meckel peridiverticulitis with a fecalith (Fig. 5), a condition easily confused with necrotized appendicitis containing a fecalith. Another patient had chronic inflammation of the right salpinx and ovary adjacent to a normal appendix. A tubular, poorly defined, hypoechoic mass was seen at sonography and confused with appendicitis; this error in diagnosis has been previously described [3] (Fig. 6). Finally, one patient had a small pericecal abscess due to cecal perforation by a foreign body. The hypoechoic mass contained increased central echoes that were falsely interpreted as a ruptured appendix (Fig. 7). This pitfall also has been described before [4]. In addition to this last case, perforation of the appendix was suggested by sonography in 11 cases and confirmed surgically in all cases.

Patients Who Did Not Have Surgery

All 110 patients who did not have surgery had clinical follow-up over a period varying between 1 and 14 months (mean, 8.6 months). Of these, 89 normal appendixes were clearly seen at sonography and another 17 cases were considered normal on sonography although the appendix was not visualized. At follow-up, none of these 106 patients had recurrent pain in the right lower quadrant. Diagnoses in four patients who did not have surgery but had abnormal sonographic findings were considered false positive for appendicitis by sonography. Sonography in all four showed the typical three-ring appearance of the appendix in transverse views, a wall thickness greater than 3 mm, and absence of compressibility.

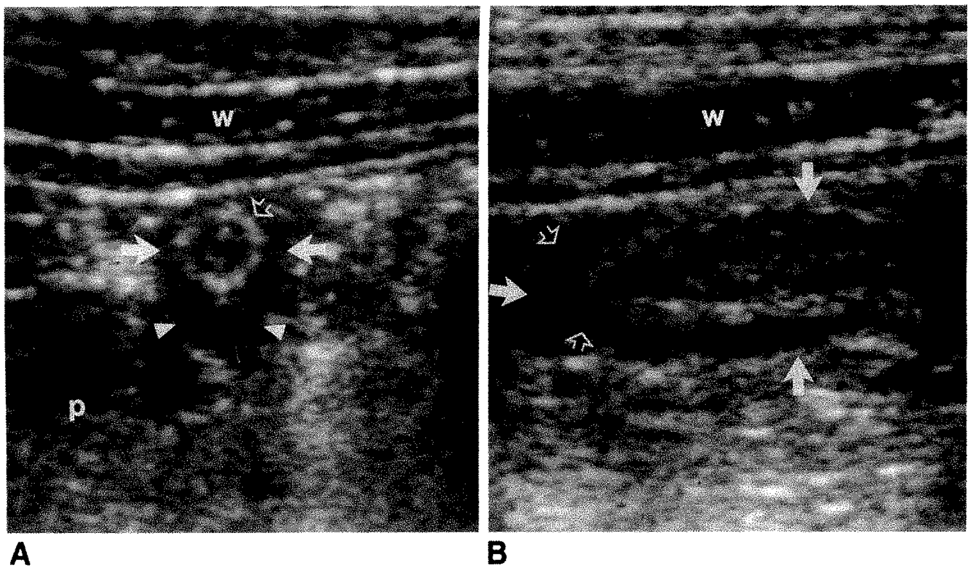

Fig. 4.—Appendicitis with periappendicitis.

***A*, Axial sonogram shows multiple-ring appearance of enlarged appendix (*solid arrows*). Although hyperechoic ring of submucosa (*open arrow*) is preserved, asymmetric hypoechoic region (*arrowheads*) represents muscular layer with periappendicitis. w = abdominal wall, p = psoas.**

***B*, Longitudinal sonogram of same enlarged appendix (*solid arrows*). Thick hypoechoic layer represents muscularis propria and periappendicitis (*open arrows*). w = abdominal wall.**

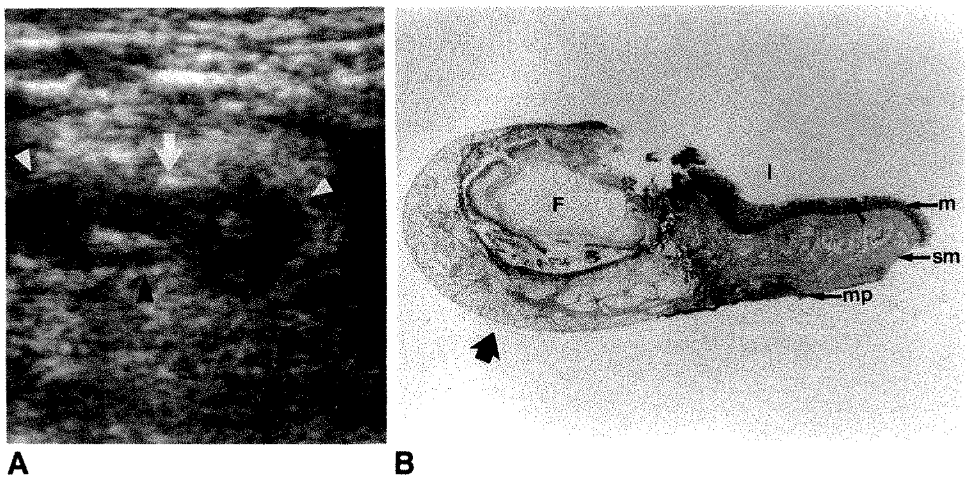

Fig. 5.—Meckel peridiverticulitis caused by fecalith misdiagnosed as appendicitis with fecalith in 39-year-old woman.

***A*, Axial sonogram of right abdominal fossa, inferior to cecum, shows hypoechoic, poorly defined mass (*arrowheads*) containing a fecalith (*arrow*).**

***B*, Photograph of histologic section of corresponding specimen shows antimesenteric wall of ileum (I = lumen, m = mucosa sm = submucosa, mp = muscularis propria). Inflamed Meckel diverticulum (*arrow*). F = fecalith.**

Fig. 6.—Pseudoappendicitis. Longitudinal sonogram shows hypoechoic, poorly defined sausagelike mass (*solid arrows*) without distinct walls adjacent to gas-filled (*open arrows*) cecum (c) mimicking appendicitis. A chronic inflammatory process of right salpinx and ovary unexpectedly located inferior to cecum was noted at surgery.

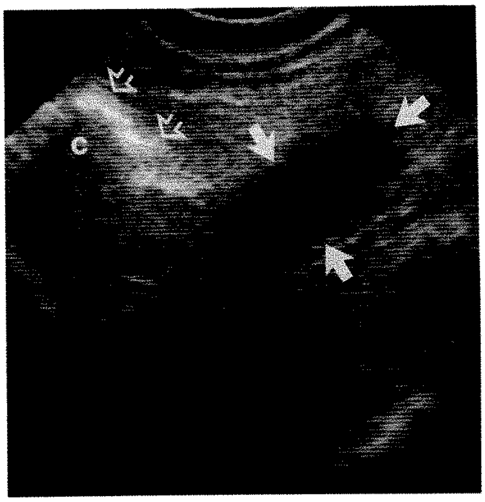

A

Fig. 7.—Pseudoappendicitis with rupture. Under collapsed cecum (c) (*arrowheads*) sonogram shows oval, hypoechoic, poorly defined mass (*arrows*) containing hyperechoic material and suggesting ruptured appendix. At surgery, a cecal perforation from foreign body with small infracecal abscess was found.

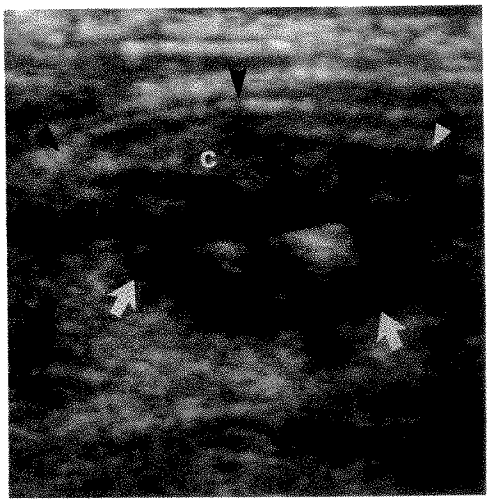

B

However, because the symptoms resolved almost completely within a few hours after sonography, the patients were released without surgery. Three of them had a chronic history of recurrent pain in the right iliac fossa. All three patients still reported recurrent episodes of abdominal pain lasting from 4 to 10 hr at the time of follow-up. The last patient with an enlarged appendix at sonography who did not have surgery had no recurrence of symptoms.

Of 125 patients without appendicitis, a normal appendix was clearly visualized in 102 cases (82%). On the other hand, our entire study group included 21 cases (12%) in which the appendix was not seen on sonography. Sonography in 170 patients enabled the diagnosis of acute appendicitis with a sensitivity of 93%, a specificity of 94%, a positive predictive value of 86%, a negative predictive value of 98%, and an accuracy of 94%.

Discussion

Preoperative diagnosis of acute appendicitis remains a difficult clinical problem. Barium enema examination is considered to be an unreliable test for acute appendicitis because of its large percentage of false-positive and false-negative results [13]. Laparoscopy is invasive and has limited use in patients who have had surgery or patients with retrocecal appendixes. Recently, CT has been used as a diagnostic tool to identify patients with appendicitis, but it is not always readily available and requires ionizing radiation and the use of IV contrast material [14]. Sonography is a readily available, inexpensive, noninvasive test, with a reported sensitivity of 80–94% in the detection of acute appendicitis [1, 2, 5, 6, 8, 10, 12]. Significant obesity and overlying loops of gas-filled bowel may give sonography a lower sensitivity in some cases.

The most frequent sonographic findings in acute appendicitis are noncompressibility of the appendix with a wall diameter greater than 6 mm [5]. However, as visualization of a normal appendix was unusual in many reported series, a nonvisualized appendix was considered normal. Recently, Vigneault et al. [12] reported the sonographic visualization of a normal appendix (diameter, ≤6 mm) in 10 of their 35 patients without appendicitis.

In our study, we identified the normal appendix by sonography in 102 (82%) of 125 patients without surgically proved appendicitis. Complete sonographic and histologic correlation in nine resected normal appendixes suggested that the structure identified at sonography was indeed the appendix. Our success in visualizing the normal appendix by sonography may be related to added effort and time spent in searching for the cecum and the appendix. Examination of patients with a full bladder and then after micturition was helpful in localizing the normal appendix in many cases, but was not useful in any case of acute appendicitis. The point of maximal tenderness was not always related to the position of the appendix in normal cases, but was useful in locating all cases of appendicitis. Finally, our early experience with sonographic inspection of surgical (colectomy and right hemicolectomy) specimens by submersion in a water bath was helpful in recognizing the sonographic appearances of the colon, the ileocecal valve, and the normal appendix.

In our series, sonography had a sensitivity of 93% and specificity of 94% in detecting acute appendicitis, comparable to those in previous studies [1–8, 12]. Identification of a normal appendix in 82% of patients and a negative predictive value of 98% had a major impact on our surgeons in increasing test credibility. We had only two false-negative cases (1.9%) out of 104 normal sonographic diagnosis *with* clear sonographic visualization of the appendix. On the other hand, of 21 normal sonographic diagnoses *without* sonographic visualization of the appendix, we had one false-negative finding (4.8%). Comparing the number of false-negative cases in our group of normal sonographic diagnoses *with* good visualization of the appendix (two of 104), and the number of false-negative cases coming from the whole group with normal sonographic diagnosis *without* visualization of the appendix (30 of 345) found in previous studies [1, 2, 5, 6, 8, 12], we found a significant difference between the two groups (chi-square value = 5.538, *df* = 1, *p* = .019). On the other hand, when we compared the number of false-negative cases in our group of normal sonographic diagnoses *without* visualization of the appendix (one of 21), and the corresponding value from the latter group (30 of 345), we found no difference between groups (chi-square value 0.315, $df = 1$, $p = .53$). Therefore, visualization of the normal appendix on sonography appears advantageous in reducing the percentage of false-negative cases; it allowed a negative predictive value of 98% in our study.

Our sonographic criteria for a normal appendix were reliable because the appendix was compressible, surrounded by normal-appearing fat, and had a distinct wall less than 3 mm thick. It is also noteworthy that six normal appendixes had a full transverse diameter of more than 6 mm because of luminal dilatation by feces, although they had a very thin wall and were compressible. Had other established criteria been used, these appendixes might have been considered abnormal because of their overall diameter.

In 35 of 42 cases of appendicitis diagnosed by sonography, the wall was clearly visualized in at least one area and was more than 3 mm thick. In the seven other cases, wall detection was difficult because the advanced mural inflammation led to a similar appearance with hypoechoic luminal contents. For that reason, the presence of a hypoechoic oval, round, or tubular noncompressible structure with indistinct borders with modified surrounding fat located in the vicinity of the cecum was used for the sonographic diagnosis of appendicitis (Fig. 2B).

Detailed analysis of our three false-negative cases of appendicitis by sonography demonstrated the importance of complete visualization of the entire appendix, because only part of it might be involved by the inflammatory process. It also indicated that in such studies, echogenicity in some patients may be inadequate, usually owing to obesity or ileus, to allow 100% safety in ruling out disease in the abdomen with sonography.

The positive predictive value of sonography for appendicitis (86%) is slightly lower than that found in other studies (between 89% and 93%) [1, 2, 5, 6, 8, 10, 12]. Of the seven patients with false-positive results, three underwent laparotomy and had inflammatory processes requiring surgery. Appendicitis was incorrectly diagnosed by sonography because of the findings of an uncompressible, hypoechoic, round or tubular structure surrounded by abnormal fat near the cecum. In none was the appendiceal wall clearly visualized.

These observations raise the possibility that the diagnosis in these three cases would not have been made if the sonographer had restricted the diagnosis of appendicitis to only those cases showing a classical appearance of an enlarged appendix (i.e., three well-visualized distinct wall rings on transverse views). Our additional abdominal sonographic criteria for appendicitis (*excluding* the wall thickness) may have slightly decreased our specificity for appendicitis, but they seem quite accurate in detecting other abnormalities mimicking appendicitis and also requiring treatment by surgery.

Four other cases were false positive on sonography, each having a noncompressible appendix clearly visualized by sonography with a wall thickness greater than 3 mm. These patients did not have surgery because of their rapidly resolving symptoms and also because three of them had previous episodes of abdominal pain with rapid resolution. The three patients still reported recurrent episodes of pain in the same location when they were contacted at the end of the study. None has been operated on so far, and none has undergone subsequent sonographic evaluation. In retrospect, we suggest that they might represent cases of subacute or chronic appendicitis [15]. To further support that hypothesis, this study reports five other similar patients who underwent surgery. Four of them were asymptomatic with a normal WBC count shortly before surgery. All patients had histologic evidence of chronic inflammation with superimposed acute signs of inflammation with various degrees of severity. We suggest that the decision for surgery in such cases was in large part conditioned by the fact that the patients were examined in the last 6 months of the study, a period correlating with the surgeon's increased confidence in our sonographic criteria for appendicitis.

In conclusion, our results suggest that a normal appendix can be visualized sonographically far more frequently than previously suspected. The wall thickness of the appendix appeared to be a useful index of the status of the appendix. The 98% negative predictive value of sonography for appendicitis in conjunction with actual visualization of the normal appendix in most cases may increase the confidence of surgeons in the use of sonography for their occasionally difficult clinical situations. In our study, a search for sonographic visualization of the normal as well as the abnormal appendix seems to significantly reduce our percentage of false-negative cases, this being one of our major goals.

REFERENCES

1. Puylaert JBCM. Acute appendicitis: US evaluation using graded compression. *Radiology* **1986**:158:355–360
2. Abu-Yousef MM, Bleichaer JJ, Maher JW, Urdaneta LF, Franken EA Jr, Metcalf AM. High resolution sonography of acute appendicitis. *AJR* **1987**;149:53–58
3. Terry J, Forest T. Sonographic demonstration of salpingitis: potential confusion with appendicitis. *J Ultrasound Med* **1989**;8:39–41
4. Machan L, Pons MS, Wood BJ, Wong AD. The "coffee bean" sign in periappendiceal and peridiverticular abscess. *J Ultrasound Med* **1987**;6:373–375
5. Jeffrey RB Jr, Laing FC, Townsend RR. Acute appendicitis: sonographic criteria based on 250 cases. *Radiology* **1988**;167:327–329
6. Jeffrey RB Jr, Laing FC, Lewis FR. Acute appendicitis: high resolution real-time US findings. *Radiology* **1987**;163:11–14
7. Gaensler EHL, Jeffrey RB Jr, Laing FC, Townsend RR. Sonography in patients with suspected acute appendicitis: value in establishing alternative diagnosis. *AJR* **1989**;152:49–51
8. Kang WM, Lee CH, Chou YH, et al. A clinical evaluation of ultrasonography in the diagnosis of acute appendicitis. *Surgery* **1989**;105:154–159
9. Fa EM, Cronan JJ. Compression as an aid in the differential diagnosis of appendicitis. *Surg Gynecol Obstet* **1989**;169:290–298
10. Bilbey JH, Gibney RG, Cooperberg PL. Ultrasonography in acute appendicitis. *J Can Assoc Radiol* **1989**;40:22–24
11. Poole GV. Appendicitis: the diagnostic challenge continues. *Am Surg* **1988**;54:609–612
12. Vigneault F, Filiatrault D, Brandt ML, et al. Acute appendicitis in children: evaluation with US. *Radiology* **1990**;176:501–504
13. Rajagopalan AE, Manson JH, Kennedy M, Pawlikowski J. The value of the baryum enema in the diagnosis of acute appendicitis. *Arch Surg* **1977**;112:531–533
14. Balthazar EJ, Megibow AJ, Siegel SE, et al. Appendicitis: prospective evaluation with high-resolution CT. *Radiology* **1991**;180:21–24
15. Dachman AH, Nichols JB, Patrick PH, et al. Natural history of the obstructed rabbit appendix: observation with radiography, sonography, and CT. *AJR* **1987**;148:281–284

Gastroepiploic Veins: CT Appearance in Pancreatic Disease

A. R. Moody[1]
P. Y. Poon

The frequency with which gastroepiploic vein (GEV) enlargement was seen on CT and its relevance to disease of the portal venous system associated with pancreatic disease were studied. We performed a retrospective study of 50 patients with proved pancreatic disease and another 50 patients without such disease. The CT examinations were done in incremental dynamic fashion after a bolus injection of contrast medium. Scans were evaluated for collateral channel formation, including GEV enlargement, and for involvement of the portal venous system by pancreatic disease. Part of the GEV arcade was visible in 36 patients without pancreatic disease, and on average measured 3.2 mm in diameter (range, 1-5.5 mm). GEV enlargement was visible in 62% of the patients with disease; 16% demonstrated a vessel 6 mm or more in diameter. Thirty-four percent of the patients with disease had portal venous complications: 26% had isolated splenic vein involvement, 2% had isolated portal vein involvement, and 6% had a combination of splenic and portal vein involvement. Of the patients with splenic vein disease, 81% had collateral channel formation, 50% of them demonstrating isolated GEV enlargement. Patients with splenic vein disease due to acute pancreatic disease had a much higher instance of GEV enlargement (83.3%).

Collateral vessels are commonly seen on CT scans of patients with splenic vein disease and most often occur via enlarged GEVs. Acute pancreatic disease is frequently associated with GEV enlargement, suggesting that the latter represents an early response to splenic vein disease. In contrast, multiple collateral pathways tend to develop in patients with chronic pancreatic disease.

AJR 158:779-783, April 1992

CT is the imaging technique of choice to evaluate pancreatic disease. Information about the gland itself, peripancreatic tissues, and associated vascular structures is best obtained with contrast-enhanced dynamic CT scanning [1]. Disease within the pancreas is prone to cause vascular complications because of the intimate relationship of the pancreas with adjacent vascular structures [2-5]. Venous complications are being increasingly recognized, with splenic occlusion seen in 45% of patients in some studies [6, 7]. Because of the rich anastomotic network that exists in the portal circulation, collateral vessels may enlarge. One such collateral channel is via the gastroepiploic veins (GEVs). These venous structures lie within the anterior two layers of the greater omentum parallel and adjacent to the greater curvature of the stomach, forming an arcade between the splenic vein and the gastrocolic trunk [8, 9] (Fig. 1). Like other tributaries of the portal system, the veins have no significant valves, and as the vessels anastomose freely with one another the direction of flow within them is directly related to the pressure within the portal system [10]. Normally, blood flows to the splenic vein in the left GEV and to the superior mesenteric vein in the right GEV.

We retrospectively reviewed the abdominal CT examinations of 50 patients with pancreatic disease and 50 patients without such disease. The objectives were to determine the frequency of visualization and the size of the GEV in these two

Received August 5, 1991; accepted after revision November 4, 1991.

Presented at the annual meeting of the American Roentgen Ray Society, Boston, May 1991.

[1] Both authors: Department of Diagnostic Imaging, St. Michael's Hospital, 30 Bond St., Toronto, Ontario, M5B 1W8, Canada. Address reprint requests to P. Y. Poon.

0361-803X/92/1584-0779
© American Roentgen Ray Society

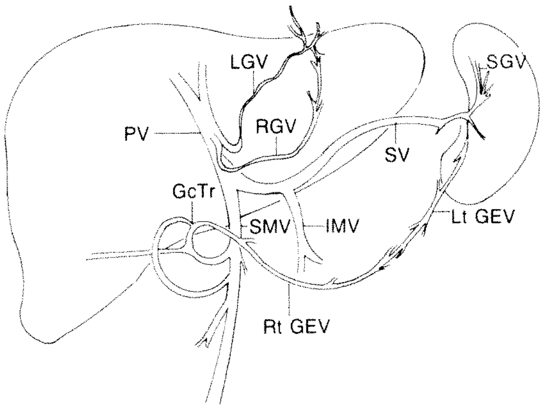

Fig. 1.—Diagram of vessels of portal venous system. Lt GEV = left gastroepiploic vein, Rt GEV = right gastroepiploic vein, GcTr = gastrocolic trunk, SGV = short gastric vessels, LGV = left gastric vein, RGV = right gastric vein, SV = splenic vein, PV = portal vein, SMV = superior mesenteric vein, IMV = inferior mesenteric vein.

groups and to correlate the presence of GEV enlargement with pancreatic disease and portal venous complications.

Materials and Methods

The abdominal CT scans of 50 consecutive patients, 28 men 33–76 years old (average, 57 years) and 22 women 27–82 years old (average, 57 years), with no clinical, biochemical, or radiologic evidence of pancreatic or liver disease were reviewed for the presence of portal venous collateral vessels. A retrospective study was made of 50 consecutive patients, 26 men 19–74 years old (average, 54 years) and 24 women 39–82 years old (average, 57 years), who were having abdominal CT scanning at our institution for investigation of possible pancreatic disease and who were subsequently proved to have such disease either biochemically, radiologically, or pathologically. Of these, 24 had acute pancreatitis (five proved at surgery), 10 had chronic pancreatitis (two proved at surgery), 13 had carcinoma of the pancreas (eight proved pathologically and five clinically), and three had peripancreatic malignant lymphadenopathy (two due to metastases and one lymphoma proved pathologically). No patients were known to have portal hypertension.

Patients were examined by contrast-enhanced dynamic CT scanning. All scans were obtained with a GE 9800 Quick (General Electric Medical Systems, Milwaukee, WI) or a Philips LX (Philips Medical Systems, Shelton, CT) scanner. All scans were obtained after administration of oral and IV contrast media. IV contrast medium consisted of 100 ml of Omnipaque 300 (Winthrop Pharmaceuticals, New York, NY) introduced via a power injector at a rate of 2 ml/sec. Dynamic incremental scanning was started after a 30-sec delay. Ten-millimeter collimated slices were obtained at 1-cm intervals through the abdomen, from the diaphragm to the pelvic inlet.

All scans were reviewed by one of us without prior knowledge of the final diagnosis. Each scan was assessed for the presence or absence of the GEV, and if present its maximum diameter was measured. The GEV could be visualized anywhere from the splenic hilum, along the greater curve of the stomach, beneath the gastric antrum, or at its junction with the gastrocolic trunk (Fig. 1); the latter two were the most common sites. Care was taken not to mistake the inferior aspect of the stomach, the left lobe of the liver, or the small bowel for the GEV. The practice of identifying the GEV at the gastrocolic trunk and following it on contiguous slices allowed for easier recognition of this vessel. Other vessels assessed for collateral channel formation included the short and left gastric veins, gastroesophageal veins, left colic vein, and omental varices.

Portal venous disease was manifested as either complete or partial occlusion. Complete occlusion was defined as obliteration of the vessel by an associated pancreatic inflammatory or neoplastic mass with no evidence of the normal enhancing vessel. Alternatively, luminal occlusion by thrombus or tumor was detected by a region of low density within the vessel surrounded by a rim of enhancement [4]. Partial occlusion appeared as narrowing of the enhancing vessel by an adjacent mass lesion or thrombus.

Correlation with surgical findings (one patient), angiographic findings (two patients), or postmortem studies (two patients) was obtained in 30% of the patients with CT evidence of portal venous abnormalities. In the remaining patients, the CT appearance alone was considered sufficient to assess the portal venous system and the presence of collateral channels.

Patients with pancreatic disease were divided into those with acute or chronic disease. The acute disease group consisted of those patients with acute pancreatitis, which was diagnosed clinically and on the basis of biochemical and radiologic investigations. The chronic disease group comprised those patients with pancreatic carcinoma or malignant peripancreatic lymphadenopathy (pathologically proved) and chronic pancreatitis, established by a clinical history of repeated attacks of acute pancreatitis and calcification seen on CT. The extent of portal venous complications and pattern of collateral channel formation, with special attention to the GEVs, were correlated with the chronicity of pancreatic disease.

Results

Some portion of the GEV arcade was visualized in 72% (36/50) of patients without liver or pancreatic disease. The vessel was most commonly seen just inferior to the gastric antrum or at the gastrocolic trunk. The size of the vessels varied between 1 and 5.5 mm (mean, 3.2 mm). A diameter of 6 mm was considered abnormal; prior CT and angiographic studies indicated upper limits of 5 and 6 mm, respectively [2, 9]. Only the short gastric vessels were otherwise visualized; none measured over 4 mm in diameter.

Sixty-two percent (31/50) of the patients with pancreatic disease had a visible GEV, 16% (8/50) being 6 mm or larger (Table 1). Thirty-four percent (17/50) of patients with pancreatic disease were found to have some form of venous complication. Isolated splenic vein disease was seen in 26% (13/50, six acute and seven chronic disease), isolated portal vein disease in 2% (1/50, chronic disease), and combined

TABLE 1: Relationship of Splenic Vein Complications and Visualization of Collateral Channels in 50 Patients with Pancreatic Disease

Collateral Channel Visualized	No. of Patients (%)	
	With Splenic Vein Disease (*n* = 16)	Without Splenic Vein Disease (*n* = 34)
Dilated gastroepiploic vein (≥6 mm)	8 (16)	0
Nondilated gastroepiploic vein	1 (2)	22 (44)
Other collateral vessels	5 (10)	1 (2)
No collateral vessels	2 (4)	11 (22)

splenic and portal vein disease was seen in 6% (3/50, all with chronic disease). In patients with pancreatic disease, splenic vein disease was associated with some kind of collateral channel formation in 81% of cases; visualization of collateral vessels was 97% specific for splenic vein disease. The presence of an enlarged GEV alone was 100% specific for splenic vein disease, with a negative predictive value of 81% but only a 50% sensitivity.

However, in patients with acute pancreatic disease causing splenic vein disease, a much higher rate of isolated GEV enlargement was demonstrated (5/6), increasing the accuracy of predicting splenic vein occlusion when the GEV is visualized (sensitivity, 83%; negative predictive value, 95%). The type of collateral channel visualized in patients with chronic pancreatic disease was much less predictable. There was little correlation between isolated GEV enlargement and splenic vein obstruction (3/10). The sensitivity was 30% and negative predictive value was 70%. The presence of any type of collateral vessel was therefore the best indicator of splenic vein occlusion in patients with chronic pancreatic disease.

Two patterns of collateral channel formation predominated in splenic vein occlusion. The GEVs were visualized in isolation (8/16, five acute and three chronic disease) (Figs. 2 and 3); in the acute pancreatic disease group this was the only type of collateral vessel seen. Alternatively, multiple vessels were seen (5/16, all chronic disease), usually involving the short gastric vessels (short and left gastric vessels, 2/16; short and left gastric and omental vessels, 2/16) (Fig. 4). A dominant GEV acting as the main collateral vessel was not, however, seen in the presence of multiple collateral vessels.

Discussion

The portal venous system is rich in anastomotic pathways that may enlarge in the face of venous obstruction. These vessels are commonly visible on CT scans of healthy patients, but when seen are always small and may be seen only in segments. Pancreatic disease commonly causes portal venous complications and often is associated with collateral

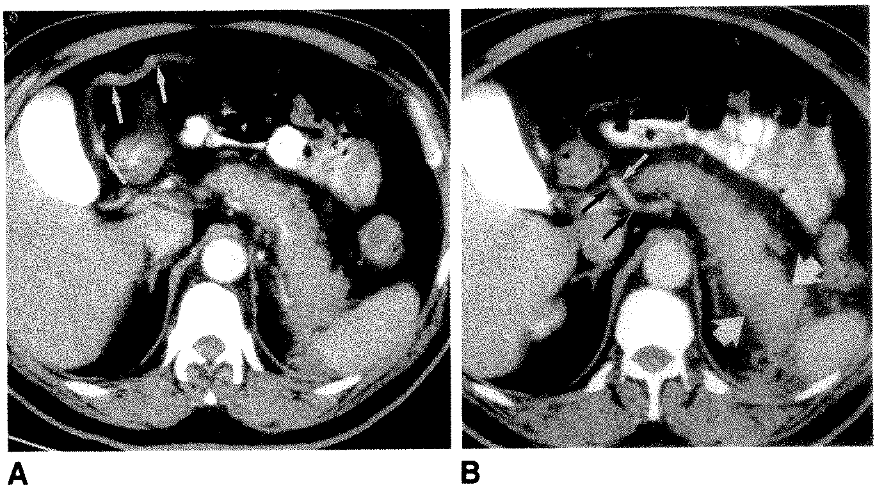

Fig. 2.—*A*, Contrast-enhanced CT scan shows gastroepiploic vein (*arrows*) anterior to gastric antrum.
B, Contrast-enhanced CT scan shows focal pancreatitis in pancreatic tail (*large arrows*). Large gastroepiploic vein is seen joining gastrocolic trunk (*small arrows*).

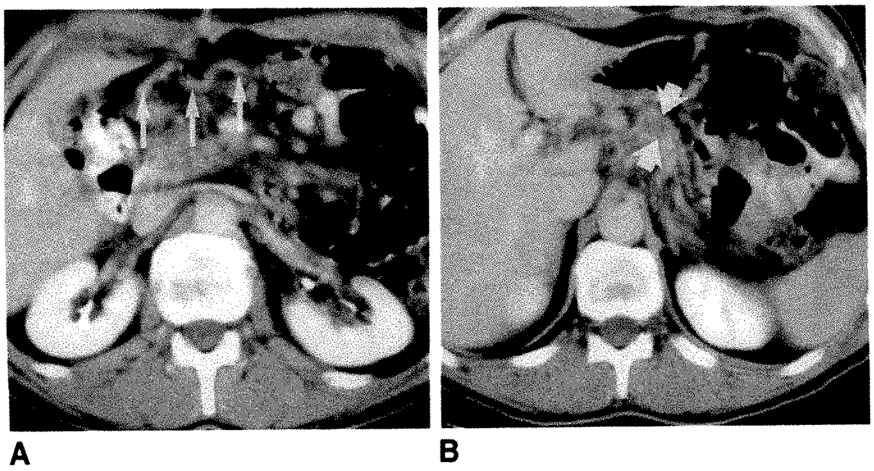

Fig. 3.—*A*, Contrast-enhanced CT scan shows tortuous, enlarged gastroepiploic vein (*arrows*) in patient with vague abdominal pain.
B, Contrast-enhanced CT scan shows small mass in pancreatic body (*arrows*), proved to be carcinoma at surgery.

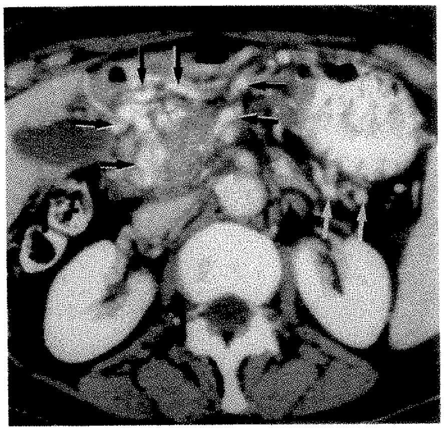

Fig. 4.—Contrast-enhanced CT scan shows a large carcinoma in head of pancreas associated with multiple collateral vessels (*arrows*).

channel formation. This study shows that splenic vein occlusion from pancreatic disease frequently produces collateral vessels visible on CT, and these may be used to aid in the diagnosis of splenic vein occlusion. As shown by splenoportography [11], a variety of channels may be formed, although two main routes are seen: one via the GEVs the other by the short gastric vessels. The observed route is dependent on a number of factors, including site of disease, anatomic variants of venous anatomy, and previous surgery [12, 13]. In addition, we think the duration of disease is also important.

In patients with acute pancreatic disease we found splenic vein occlusion was commonly seen in association with enlargement of the GEVs in isolation. Arner and Fernsterom [11] proposed that splenic vein narrowing was the precursor of complete obstruction, and this proposal has been supported by the work of Leger et al. [14]. Once the splenic vein pressure has risen above 15 cm H_2O, collateral pathways will be observed [14]. The size of the GEVs and ease of communication between them may lead to preferential dilatation before other vessels enlarge. The GEV arcade therefore seems to act as a safety valve in the early stages of splenic vein narrowing and occlusion by its rapid distension. Follow-up in one of our patients with acute pancreatitis has shown that acute dilatation of the GEV in association with splenic vein disease resolved with restoration of the normal splenic vein caliber (Fig. 5).

CT visualization of the GEVs may therefore indicate compromise of the splenic vein by early pancreatic disease. This may be caused by focal pancreatic disease, such as pancreatitis (Fig. 2), or small neoplasms in their earliest stages (Fig. 3). Because of the lack of distortion of the pancreas and the minor changes to the splenic vein itself, pancreatic disease at this early stage may be overlooked.

In patients with chronic pancreatic disease causing splenic vein obstruction, various collateral channels were formed that were visible on CT. This reflects the need to maintain splenic venous outflow in the face of persistent or worsening splenic venous hypertension. If GEV enlargement is insufficient to maintain splenic venous return, other routes will be used. Most commonly these involve the short gastric vessels that anastomose in the gastric mucosa and may produce gastric varices. A dominant GEV was never visualized in association with short gastric vein enlargement, possibly suggesting involvement of the GEV in the disease process itself. The short

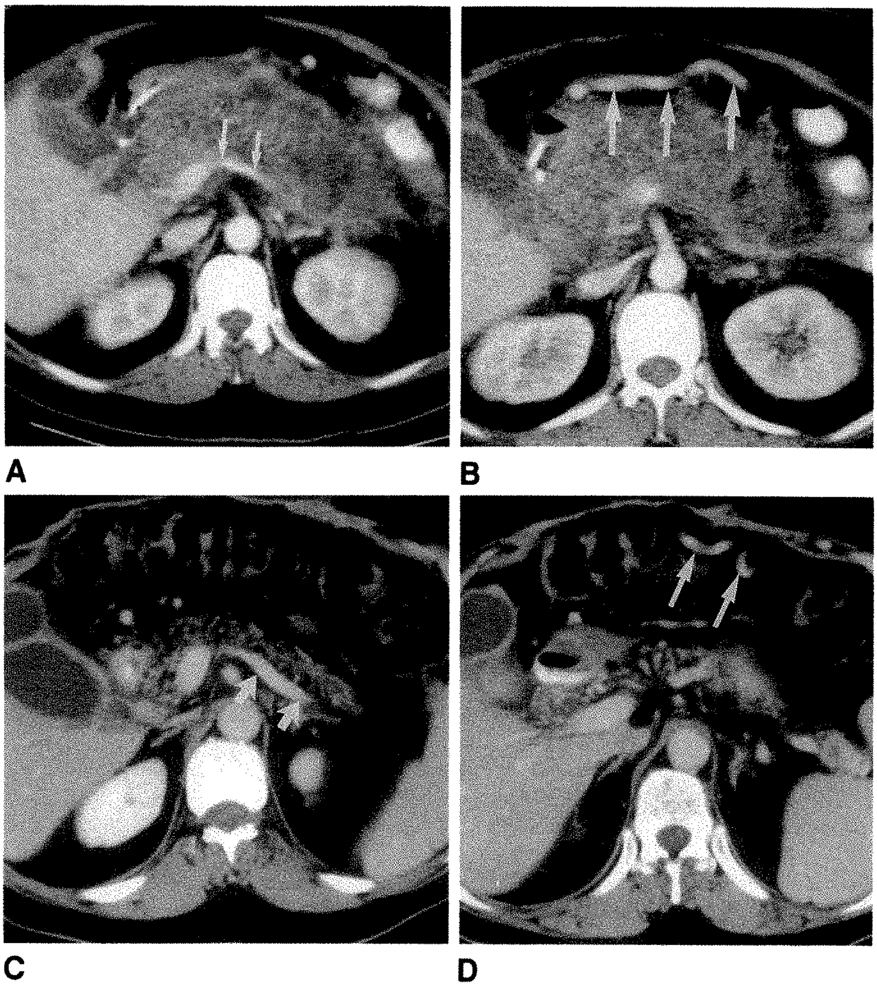

Fig. 5.—*A*, Contrast-enhanced CT scan shows severe pancreatitis causing splenic vein narrowing (*arrows*).

***B*, Contrast-enhanced CT scan shows gastroepiploic vein (*arrows*) just inferior to greater curve of stomach.**

***C*, Contrast-enhanced CT scan shows that resolution of pancreatitis results in a return to a normal-caliber splenic vein (*arrows*).**

***D*, Contrast-enhanced CT scan shows gastroepiploic vein now measures less than 6 mm in diameter (*arrows*).**

gastric veins were seen with associated omental vein enlargement; this may have arisen from, and subsequently obscured, GEV enlargement.

Although only 30% of patients with CT evidence of splenic vein disease had surgical, angiographic, or pathologic confirmation, we believe the CT appearances were sufficiently diagnostic to draw our conclusions. Only one patient with isolated portal vein occlusion was present in the pancreatic disease group. This patient had short gastric vein enlargement and represented the only false-positive scan when any type of collateral vessel was used to indicate splenic vein disease. However, it has previously been shown [2] that GEV enlargement is not a typical feature of portal hypertension, and therefore would not substantially affect the specificity of GEV enlargement as a sign of splenic vein disease.

The CT diagnosis of splenic vein occlusion may have important clinical implications. It has been advocated that patients bleeding from gastric varices associated with splenic vein disease should undergo splenectomy [15, 16]. It has also been suggested that patients with splenic vein thrombosis and significant varices should have elective splenectomy as prophylaxis against gastrointestinal hemorrhage [17]. Splenectomy, however, may be difficult in these patients because of poor access to the splenic artery and dense adhesions, which may make controlled dissection of the artery impossible [6]. It can be seen from the foregoing that careful follow-up of patients with splenic vein disease, with particular attention to the behavior of collateral vessels over time, may indicate their potential for gastrointestinal hemorrhage, and hence the need for splenectomy. Positioned in the greater and lesser omentum, the GEVs and left gastric vein are not a potential source of gastrointestinal bleeding, and correspond to the "safe" varices described by Bradley [17]. Fundal varices, however, may cause gastrointestinal bleeding, and their visualization, with no evidence of decompressive "safe" vessels elsewhere, is an indication for close follow-up and perhaps elective splenectomy.

ACKNOWLEDGMENT

We thank E. Coretti for assistance in manuscript preparation.

REFERENCES

1. Freeny PC. Radiology of the pancreas: two decades of progress in imaging and intervention. *AJR* **1988**;150:975–981
2. Marn CS, Glazer GM, Williams DM, Francis IR. CT angiographic correlation of collateral venous pathways in isolated splenic vein occlusion: new observations. *Radiology* **1990**;175:375–380
3. Mathieu D, Vasile N, Grenier P. Portal thrombosis: dynamic CT features and course. *Radiology* **1985**;154:737–741
4. Belli AM, Jennings CM, Nakielny RA. Splenic and portal venous thrombosis: a vascular complication of pancreatic disease demonstrated on computed tomography. *Clin Radiol* **1990**;41:13–16
5. Vogelzang RL, Gore RM, Anschuetz SL, Blei AT. Thrombosis of the splanchnic veins: CT diagnosis. *AJR* **1988**;150:93–96
6. Vujic I. Vascular complications of pancreatitis. *Radiol Clin North Am* **1989**;27:81–92
7. Fogartie JA, Adams DB, Vujic I, Stanley JH, Anderson MC. Splanchnic venous obstruction: a complication of chronic pancreatitis. *Am Surg* **1989**;55:191–197
8. Williams PL, Warwick R, Dyson M, Bannister LH, eds. *Gray's anatomy*, 37th ed. London: Churchill Livingstone, **1989**:818–820
9. Doehner GA, Ruzicka FF, Hoffman G, Rousselot MN. The portal venous system. Its roentgen anatomy. *Radiology* **1955**;64:675–689
10. Hollinshead WH. *Anatomy for surgeons*, vol. 2, 2nd ed. New York: Harper & Row, **1971**:450
11. Arner O, Fernsterom I. Obstruction of the splenic vein. A splenoportographic study of the clinical features of thrombosis of the splenic veins with notes on its treatment. *Acta Chir Scand* **1961**;122:66–74
12. Johnson FR, Myers RT. Etiologic factors and consequences of splenic vein obstruction. *Ann Surg* **1973**;177:736–739
13. Lemaitere G, L'hermiane C, Maillard JP, Toison F. L'hypertension portale segmentaire des pancreatites. *Lille Med* **1971**;16:928–932
14. Leger L, Lenriote JP, Lemiagia G. L'hypertension et la stase portale segmentaires dan les pancreatitis chroniques. *J Chir* (Paris) **1968**;95: 599–608
15. Longstreth GF, Newcomer AD, Green PA. Extrahepatic portal hypertension caused by chronic pancreatitis. *Ann Intern Med* **1971**;75:903–908
16. Keith RG, Mustard RA, Saibil EA. Gastric variceal bleeding due to occlusion of splenic vein in pancreatic disease. *Can J Surg* **1982**;25:301–304
17. Bradley EL. The natural history of splenic vein thrombosis due to chronic pancreatitis: indications for surgery. *Int J Pancreatol* **1987**;2: 87–92

Memorial

Esmond McDonald Mapp, 1928–1991

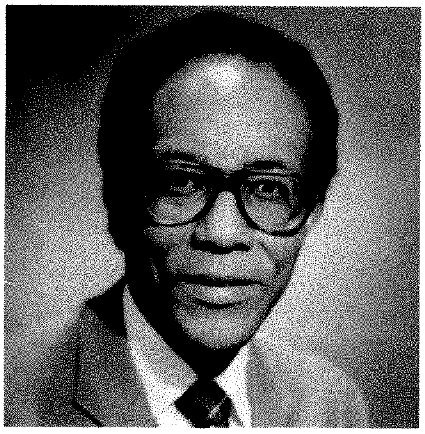

Esmond Mapp died October 15, 1991, after an 11-month struggle with colon cancer, the very disease to which he had devoted so much of his career as a gastrointestinal radiologist. Dr. Mapp was born in Port-of-Spain, Trinidad, West Indies, and received his undergraduate and medical education at Howard University, Washington, DC. After his internship at the District of Columbia General Hospital, he served in the U.S. Navy Medical Corps from 1959 to 1961. He continued as a reserve officer and was recently promoted to captain. After completion of his active military service, he was a resident at the Graduate Hospital/University of Pennsylvania Program, where his interest in gastrointestinal radiology evolved under the guidance of Drs. Finkelstein, Bockus, and Nussbaum. Dr. Mapp was certified by the American Board of Radiology in 1964 and since then held academic appointments at the Women's Medical College of Pennsylvania (now Medical College of Pennsylvania), Emory University in Atlanta, and Episcopal Hospital/Temple University Medical School in Philadelphia. In 1976, he joined the staff of Jefferson Medical College as associate professor and was promoted to professor of radiology in 1983.

Dr. Mapp had a heavy clinical and teaching schedule, but he found time to be active both at Jefferson Medical College and in the national scene in the area of medical education, specifically radiology. At Thomas Jefferson University Hospital, he was a member of the medical records and cancer committee, the admissions committee, and the graduate education committee. He also found time to be active on the advisory committee of the College of Allied Health Sciences. In addition to activities at Jefferson, he served as secretary of the section of radiology and later as national chairman of the section of radiology of the National Medical Association. He was a member of the board of directors and chairman of the program committee of the Pennsylvania Radiological Society and was a member of the nominating committee and the executive committee of the Intersociety Commission of the American College of Radiology. He was a guest examiner of the American Board of Radiology and member of the radiological devices panel of the Food and Drug Administration. He was the second vice president of Radiology Centennial Inc., among many other activities.

Before his death, he was selected to receive the first annual Outstanding Educator Award of the Philadelphia Roentgen Ray Society; the award was presented posthumously in December 1991. Although Esmond's career in radiology began with a strong interest in arteriography, he quickly concentrated his efforts on a lifelong professional commitment to gastrointestinal radiology. Within that discipline, he concentrated on diseases of the colon and rectum and was a recognized authority in defecography. He published and spoke on a wide variety of gastrointestinal clinical and imaging problems, including esophageal motility disorders, transhepatic cholangiography, abdominal aspiration procedures, and abdominal and adrenal arteriography.

Esmond was a warm, sensitive, and concerned person who was loved by virtually everyone who came in contact with him. His quiet, low-key demeanor belied a wonderful sense of humor and careful attention to detail that made him one of the most popular teachers in the department, if not the entire hospital.

Perhaps the best testimony to his steadfastness and sense of responsibility was his devotion to his full-time clinical activities despite a grim prognosis. Esmond is survived by his wife, Bette; seven children, Donald, David, Douglas, Daniel, Dorothy, Darryl, and Stacy; a brother, Elton; and his mother, Thelma Hinds. He will be sorely missed by his colleagues and friends for his strength, his sense of humor, and the wonderful example of dedication and responsibility he set for all of us.

Robert M. Steiner
Philadelphia, PA 19107

Bile Duct Disruption and Biloma After Laparoscopic Cholecystectomy: Imaging Evaluation

Andrew T. Walker[1]
Avishai W. Shapiro[1]
David C. Brooks[2]
John M. Braver[1]
Sabah S. Tumeh[1,3]

Disruption of the biliary tree after laparoscopic cholecystectomy has been reported in 0–7% of cases, and likely represents the most significant postoperative complication. Documenting the presence and extent of a bile leak is often difficult. We reviewed the first 264 laparoscopic cholecystectomies performed at our institution and found seven cases of bile extravasation and/or biloma formation (prevalence, 2.7%). All patients were first seen in the early postoperative period with abdominal pain and low-grade fever. Sonography was performed in five of seven, CT in five of seven, hepatobiliary scintigraphy with diisopropyliminodiacetic acid in five of seven, and ERCP in four of seven cases. While sonography and CT were initially helpful in determining the presence of abdominal fluid collections, they were unable to differentiate between postoperative seroma, lymphocele, hematoma, and bile leak. Hepatobiliary scintigraphy was useful in demonstrating continuity of these fluid collections with the biliary tree and guiding further therapy. Four cases were managed with endoscopic biliary decompression, with the use of sphincterotomy or nasobiliary stent placement, with good clinical result. The other three cases were treated surgically with T-tube or external drainage. All patients did well clinically, without evidence of bile reaccumulation.

Our experience suggests that sonography and CT are useful in detecting postoperative fluid collections, but cannot differentiate bile from other fluids. Hepatobiliary scintigraphy is valuable as a noninvasive means of investigating possible bile leaks and in guiding further therapy.

AJR 158:785–789, April 1992

Bilomas and bile duct disruptions have been described in association with abdominal trauma and right upper quadrant surgery. With the introduction of laparoscopic cholecystectomy, these relatively uncommon complications have increased in frequency [1, 2]. Because this procedure is being performed with increasing frequency, radiologists must increase their awareness of this potential complication and consider the development of a biloma in patients who have clinical difficulties in the early postoperative period. Bile leaks often pose a difficult diagnostic challenge. We reviewed our experience with seven bile duct disruptions and/or biloma formations occurring in the first 264 patients in whom laparoscopic cholecystectomy was performed at our institution.

Materials and Methods

We reviewed the first 264 laparoscopic cholecystectomies performed at Brigham and Women's Hospital between January 1, 1990, and March 15, 1991. Seven cases of clinically significant bile leak and/or biloma formation were found (Table 1). The group included four women and three men 26–72 years old (mean, 54 years). The most common presenting symptoms were abdominal pain, distension, and nausea. All patients had an elevated WBC count in the range of 14,000–16,000/mm^3 and low-grade temperatures ranging from 37.2°C to 37.8°C. They were first seen 3–9 days after laparoscopic cholecystectomy. Two of the seven patients had not been discharged from the hospital after the original procedure.

Received August 29, 1991; accepted after revision November 14, 1991.

[1] Department of Radiology, Harvard Medical School, Brigham and Women's Hospital, 75 Francis St., Boston, MA 02115. Address reprint requests to A. T. Walker, Department of Radiology.

[2] Department of Surgery, Harvard Medical School, Brigham and Women's Hospital, Boston, MA 02115.

[3] Present address: Department of Radiology, Eastern Virginia Medical School, Depaul Hospital, 150 Kingsley Lane, Norfolk, VA 23505.

0361-803X/92/1584-0785
© American Roentgen Ray Society

TABLE 1: Summary of Imaging and Therapy of Bile Duct Disruption After Laparoscopic Cholecystectomy

Case No.	Days Since Surgery	Sonography	CT	DISIDA	ERCP	Treatment
1	5	Small collection in gallbladder fossa	ND	ND	Accessory duct extravasation	Sphincterotomy
2	9	Complex perihepatic collection	Perihepatic collection	ND	ND	Surgery
3	5	Free peritoneal fluid	ND	Extravasation	Cystic duct extravasation	Nasobiliary catheter
4	3	ND	Peritoneal fluid	Extravasation	No extravasation	Sphincterotomy
5	7	Complex perihepatic collection	Perihepatic collection	Extravasation	ND	Surgery
6	6	Normal	Collection in gallbladder fossa	Extravasation	Cystic duct extravasation	Nasobiliary catheter
7	8	ND	Peritoneal fluid	Extravasation	ND	Surgery

Note.—DISIDA = ^{99m}Tc-diisopropyliminodiacetic acid scintigraphy; ND = not done.

Sonography was performed with 3- to 5-MHz sector transducers. Hepatobiliary scintigraphy was performed with 3–5 mCi (111–185 MBq) of ^{99m}Tc-diisopropyliminodiacetic acid (DISIDA) by using a gamma camera with a large field of view and an all-purpose collimator (Starcam, General Electric, Milwaukee, WI). Images were obtained with 450,000–500,000 counts at 5, 15, 30, 45, and 60 min. Delayed images at 90 min were obtained in all cases. CT was performed with a high-resolution Somatom 3 or Somatom Plus scanner (Siemens, Iselin, NJ). Scans were obtained with 10-mm contiguous imaging with oral but no IV contrast material.

Biloma fluid was obtained at surgery and sent for microbiological analysis and culture in three of the four patients with loculated fluid collections; the fluid was culture-positive in one case (case 2). Bile leak was documented by surgical exploration in three cases, ERCP in three cases, and hepatobiliary scintigraphy in one case.

Results

Sonography was performed in five of the seven cases, and suggested the diagnosis in four cases; the fifth study was technically limited because of the patient's extreme discomfort. We found a spectrum of sonographic findings. Two patients had anechoic, well-circumscribed collections within the gallbladder fossa and adjacent perihepatic region. One patient had a large, complex fluid collection with multiple fine internal septa that compressed the left lobe of the liver (Fig. 1). In one patient, only free peritoneal fluid within the pelvis was seen.

CT was performed in five cases. It showed discrete, fluid-attenuation collections in three patients. The smallest loculated bile accumulation was a 2-cm collection within the gallbladder fossa that could have easily been mistaken for a normal gallbladder without knowledge of the patient's previous surgery. The largest accumulation was a 15-cm complex collection that surrounded and compressed the left lobe of the liver and extended into the gallbladder fossa (Fig. 1). Two cases showed only free peritoneal fluid within the pelvis.

Biliary scintigraphy was performed in five of the seven patients and showed extrabiliary accumulation of the radiopharmaceutical in each case (Fig. 2). Two scans showed discrete, well-defined regions of perihepatic or gallbladder fossa uptake, consistent with loculated bile collections or bilomas. The other three cases showed abnormal radiotracer uptake surrounding the liver and abnormal pooling of radiotracer within the paracolic gutters and pelvis on delayed images.

ERCP was performed in four of the seven cases and showed a biliary system leak with extravasation of contrast material in three cases. In case 4, the DISIDA scan showed extrabiliary accumulation of radiopharmaceutical, consistent with a bile leak. ERCP the next day failed to demonstrate bile duct disruption, but was technically limited by problems in cannulating and maintaining position within the common bile duct, so that much of the injected contrast material escaped into the duodenum. Evaluation was also somewhat hampered by residual barium within the colon from previous CT examination (Fig. 3).

Four patients were treated with endoscopic bile duct decompression by using sphincterotomy or nasobiliary stent placement. Three patients had surgery again in hopes of definitively repairing the bile duct. In two of these cases, bile collections were found, but the specific site of bile leakage could not be identified, and external drains were placed under direct visualization. In the third case, a leak in the right hepatic duct was found at its junction with the left hepatic duct, and a T-tube was placed across the duct disruption. All patients did well clinically, with resolution of their symptoms, and none showed evidence of bile reaccumulation.

Discussion

Laparoscopic cholecystectomy has rapidly emerged as an alternative treatment of symptomatic gallstone disease. Bile duct injury and bile leaks are likely the most significant postoperative complications, and have been recently reported to occur in 0–7% of patients [1, 2]. Bile extravasation is predominantly attributed to an anatomic variation of small biliary radicles entering directly into the gallbladder bed, or the bile ducts of Luschka, reported to be present in 25–35% of patients [1]. Bile extravasation also may occur from direct injury to the biliary tree, from larger accessory ducts, or from the cystic duct remnant. In our series, bile leakage was from the cystic duct remnant in two cases, an accessory bile duct in one case, and the right hepatic duct in one case. The origin

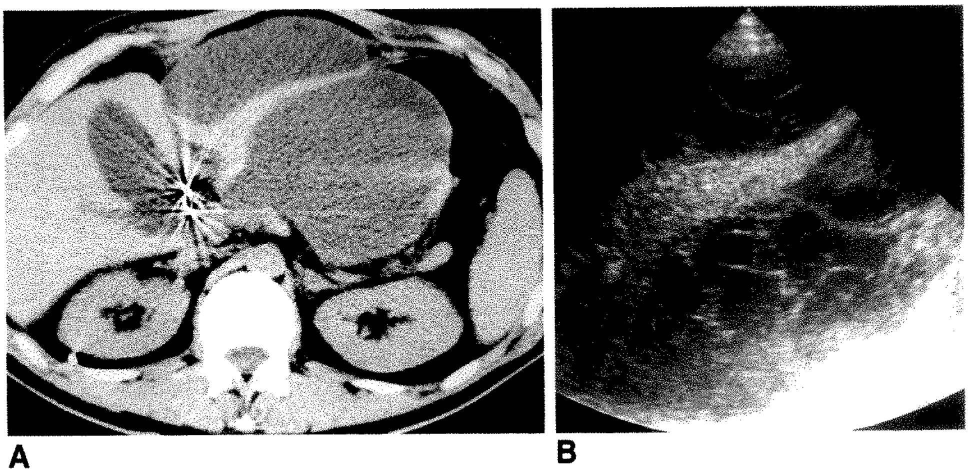

Fig. 1.—Postoperative biloma. Case 2: 44-year-old man with right upper quadrant pain and jaundice 9 days after laparoscopic cholecystectomy.

***A*, CT scan of abdomen shows large, bilobed, low-attenuation collection surrounding, and to some degree compressing, left lobe of liver.**

***B*, Sonogram of same region shows large anechoic area with multiple fine septa. Septation may be seen in infected bilomas, as here, making differentiation from postoperative hematoma difficult. At surgery, a tear in right hepatic duct was found and T-tube placed across disruption.**

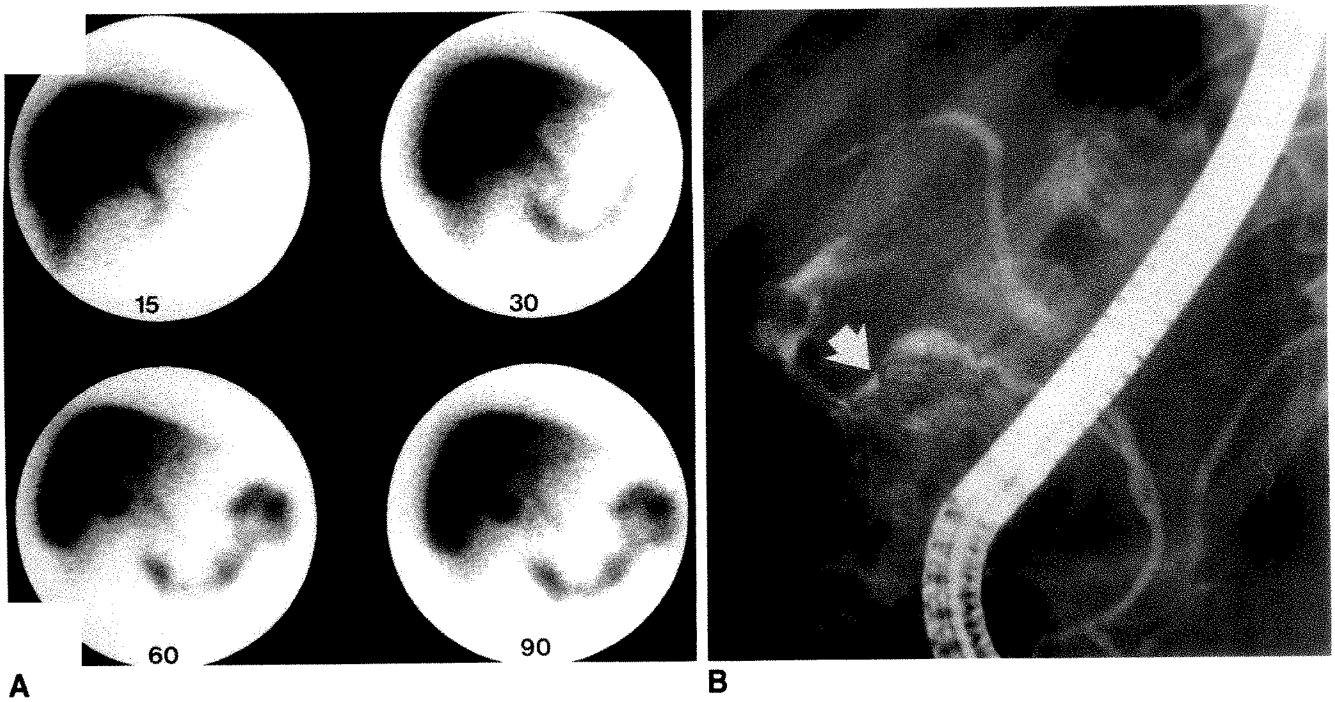

Fig. 2.—Postoperative bile leak. Case 6: 64-year-old man with abdominal pain and nausea 6 days after laparoscopic cholecystectomy.

***A*, Scintigrams 15, 30, 60, and 90 min after administration of ^{99m}Tc-DISIDA show extrabiliary accumulation of radiopharmaceutical in gallbladder fossa with extension over dome of liver. Extravasation surrounding liver can be mistaken for normal hepatic uptake on early images, but delayed images show persistent perihepatic activity as normal liver activity decreases.**

***B*, ERCP shows contrast extravasation from distal cystic duct remnant (*arrow*).**

was suggested by the DISIDA scan in the remaining three cases, but exact localization was not possible.

Clinically insignificant bile leaks are common after open cholecystectomy. Gilsdorf et al. [3] demonstrated extrabiliary accumulation of radiotracer in 44% of patients who had DISIDA scanning 2–4 hr after open cholecystectomy. Only one of the 25 patients developed symptoms and required further therapy for the bile leak. The majority of perihepatic postoperative fluid collections are small, asymptomatic, and resolve spontaneously. However, patients who develop abdominal pain, fever, jaundice, or bilious drainage from a surgical drain should be considered to have a clinically significant bile leak [4, 5]. It is in these patients that further therapy is necessary. Symptoms may be caused by local inflammatory or compressive effects of the collection, or infection. All the patients in our series had abdominal pain, fever, and mild leukocytosis on presentation, and thus were believed to have clinically significant fluid collections requiring therapy.

We found a fairly even distribution of complications throughout the study period, with a slight increase at the end. Although we did not find a clustering of complications in the first patients, representing a learning curve, others have shown strong evidence to support its presence. The Collaborative Southern Surgeons Club study cited a 2.2% preva-

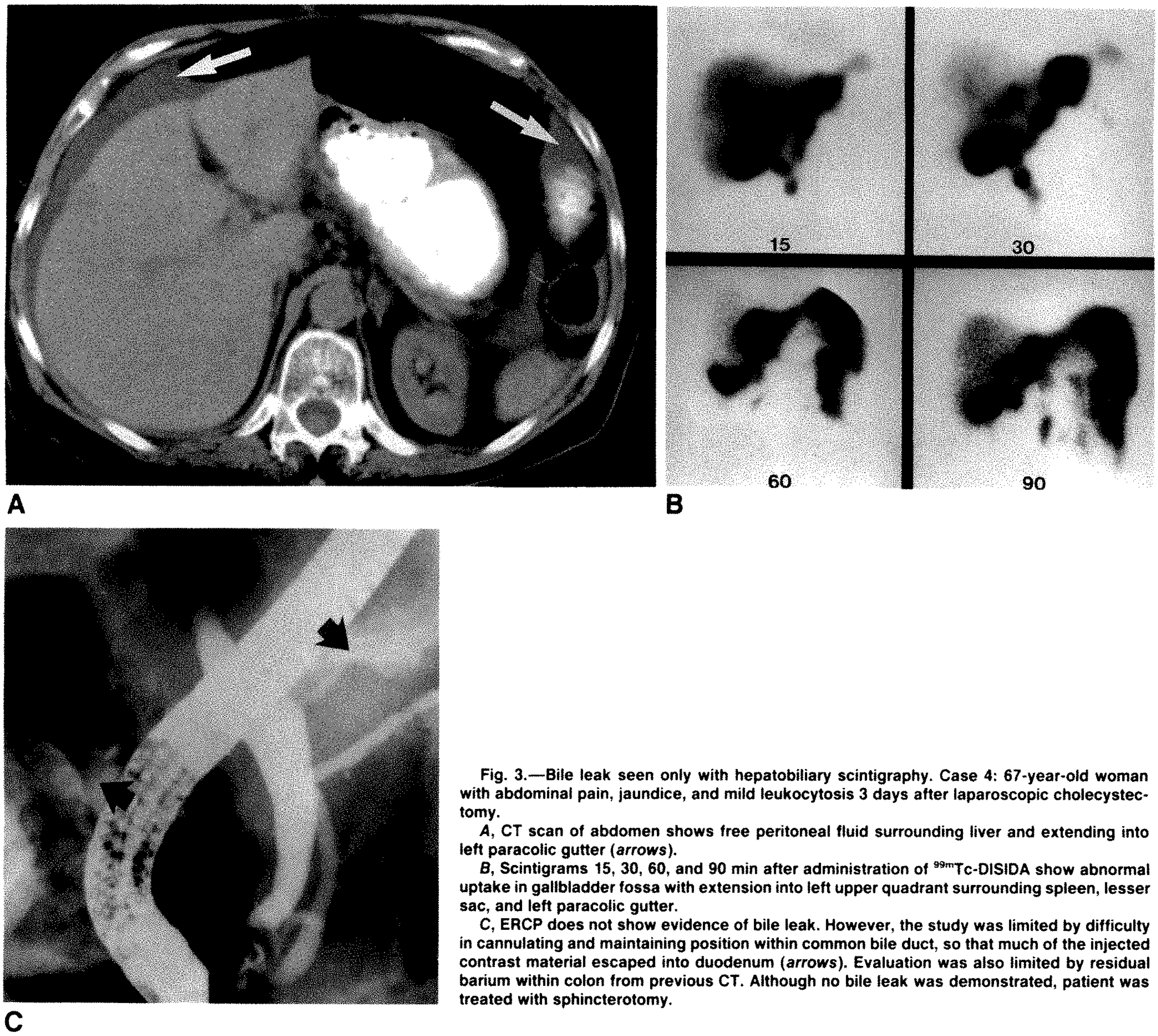

Fig. 3.—Bile leak seen only with hepatobiliary scintigraphy. Case 4: 67-year-old woman with abdominal pain, jaundice, and mild leukocytosis 3 days after laparoscopic cholecystectomy.

A, CT scan of abdomen shows free peritoneal fluid surrounding liver and extending into left paracolic gutter (*arrows*).

B, Scintigrams 15, 30, 60, and 90 min after administration of ^{99m}Tc-DISIDA show abnormal uptake in gallbladder fossa with extension into left upper quadrant surrounding spleen, lesser sac, and left paracolic gutter.

C, ERCP does not show evidence of bile leak. However, the study was limited by difficulty in cannulating and maintaining position within common bile duct, so that much of the injected contrast material escaped into duodenum (*arrows*). Evaluation was also limited by residual barium within colon from previous CT. Although no bile leak was demonstrated, patient was treated with sphincterotomy.

lence of bile duct injury among the first 13 patients operated on by each surgical group, and then a decrease to 0.1% for subsequent patients [2]. The early increased prevalence of bile leaks may also be due to early problems with the technique and the equipment itself, such as the apparatus used to place titanium clips on the cystic duct.

CT and sonography were helpful in showing perihepatic fluid collections or free peritoneal fluid. Although these tests are useful for screening, their findings are not specific and may represent other postoperative collections, such as seroma, resolving hematoma, lymphocele, abscess, or even pancreatic pseudocyst. In one case (case 2), sonography showed a large collection with multiple fine internal septa surrounding the left hepatic lobe. Complex internal septation has been described in infected bilomas [6]. This was only seen in the one case of documented infection in our series (Fig. 1). Differentiating this collection from a postoperative hematoma, which may have a similar sonographic appearance, was exceedingly difficult and required surgical confirmation.

Hepatobiliary scintigraphy was very useful in evaluating suspected postoperative bile duct disruption. It has the advantages of being physiologic, noninvasive, and usable in the setting of hyperbilirubinemia. ^{99m}Tc-iminodiacetic acid agents also have a high photon flux, allowing their detection in lower concentrations than needed for the iodinated contrast material used with conventional radiographic techniques [4]. Delayed images were often helpful in detecting small bile leaks and distinguishing extravasation from liver and small-bowel activity. Weissman et al. [5, 7] and Esensten et al. [8] stressed the importance of delayed scans whenever the diagnosis is suspected, even if findings on initial images appear normal.

When communication with the biliary tree is not demonstrated, definitive diagnosis of biloma requires aspiration and chemical analysis of the fluid. Scintigraphy still confers useful information in these instances by demonstrating that the bile leak has closed off [6]. When communication with the biliary tree has already healed, biliary decompression or surgical repair is not required.

Although hepatobiliary scintigraphy is a sensitive examination for detecting bile leaks, it is limited in anatomic resolution and often cannot show the exact site of bile extravasation. Higher resolution studies with iodinated contrast material, such as percutaneous transhepatic cholangiography (PTC) or ERCP, are necessary to provide more precise information for surgical planning [4].

The demonstration of contrast extravasation from the biliary system during ERCP also is diagnostic of bile duct disruption, obviating percutaneous aspiration. In one patient (case 4), CT showed a large perihepatic fluid collection and the DISIDA scan showed unequivocal extrabiliary accumulation of radiotracer in the perihepatic space with extension into the left paracolic gutter on delayed views (Fig. 3). ERCP the next day failed to demonstrate bile duct disruption, but was technically limited by problems in cannulating and maintaining position within the common bile duct (Fig. 3). Although a bile leak was not demonstrated, the patient was treated with sphincterotomy. She improved clinically without the need for percutaneous or surgical drainage. Thus, there remains some diagnostic discrepancy in this case. We think including it in the series is warranted by the unequivocal nature of the DISIDA scan and correlative findings on CT. When unequivocal, hepatobiliary scanning is unlikely to give false-positive results, although no rigorous study of the sensitivity and specificity of scintigraphy in bile leaks has been performed. Esensten et al. [8] used cholescintigraphy alone in four of five cases to confirm the diagnosis of biliary tree disruption in their review of posttraumatic intrahepatic bilomas.

ERCP offers the added advantage of potential therapeutic intervention. A recent review of 77 cases of endoscopically managed postoperative biliary leaks cited a 95% technical success rate [9]. The four patients treated endoscopically in our series all did well and showed no evidence of bile reaccumulation. Our experience is limited, but because the exact point of bile extravasation is often difficult to identify surgically, and morbidity is increased with an operative procedure, a trial of endoscopic management seems useful in most cases.

Needle aspiration is also a very useful diagnostic technique, although it was not used in our series [10]. It is necessary when hepatobiliary scintigraphy or ERCP fails to show communication of a loculated abdominal fluid collection with the biliary tree and the clinical suggestion of biloma remains strong. We think, however, that hepatobiliary scintigraphy is a simple, noninvasive way to detect the presence of a bile leak and should be used before more invasive steps are taken. Percutaneous drainage has been used successfully to manage bile leaks, but has the disadvantages for the patient of prolonged hospitalization and risk of infection.

Bile leak and biloma formation are important considerations in patients who develop difficulties in the early postoperative period after laparoscopic cholecystectomy. Although the number of patients in our series is small and all studies were not done in every case, a number of important considerations are demonstrated. Postoperative collections are probably common, and are not of clinical concern if found incidentally and the patient is asymptomatic. However, when patients develop clinical symptoms such as pain, fever, or jaundice, a substantial bile leak should be considered. Sonography and CT were helpful in detecting abdominal fluid collections, but could not differentiate bile from other fluids. We found hepatobiliary scintigraphy to be very useful in these patients, demonstrating disruption of the biliary tree without the need for invasive intervention. However, it is limited in anatomic resolution, and ERCP or PTC is needed to localize the exact point of bile leakage. Although only a small number of patients are reported, endoscopic management was successful in all cases in which it was used.

REFERENCES

1. Peters JH, Ellison EC, Innes JT, et al. Safety and efficacy of laparoscopic cholecystectomy. *Ann Surg* **1991**;213:3–12
2. The Southern Surgeons Club. A prospective analysis of 1518 laparoscopic cholecystectomies. *N Engl J Med* **1991**;324:1073–1078
3. Gilsdorf JR, Phillips M, McLeod MK, et al. Radionuclide evaluation of bile leakage and the use of subhepatic drains after cholecystectomy. *Am J Surg* **1986**;151:259–262
4. Rosenberg DJ, Brugge WR, Alavi A. Bile leak following an elective laparoscopic cholecystectomy: the role of hepatobiliary imaging in the diagnosis and management of bile leaks. *J Nucl Med* **1991**;32:1777–1781
5. Weissmann HS, Gliedman ML, Wilk PJ, et al. Evaluation of the postoperative patient with ^{99m}Tc-IDA cholescintigraphy. *Semin Nucl Med* **1982**;12:27–52
6. Kuligowska E, Schlesinger A, Miller KB, Lee VW, Grosso D. Bilomas: a new approach to the diagnosis and treatment. *Gastrointest Radiol* **1983**;8:237–243.
7. Weissmann HS, Chun KJ, Frand M, Koenigsberg M, Milstein DM, Freeman LM. Demonstration of traumatic bile leakage with cholescintigraphy and ultrasonography. *AJR* **1980**;133:843–847
8. Esensten M, Ralls PW, Colletti P, Halls J. Posttraumatic intrahepatic biloma: sonographic diagnosis. *AJR* **1983**;140:303–305
9. Binmoeller KF, Katon RM, Shneidman R. Endoscopic management of postoperative biliary leaks: review of 77 cases and report of two cases with biloma formation. *Am J Gastroenterol* **1991**;86:227–231
10. Mueller PR, Ferrucci JT Jr, Simeone JF, et al. Detection and drainage of bilomas: special considerations. *AJR* **1983**;140:715–720

Book Review

Ultrasonography of the Urinary Tract, 3rd ed. Edited by Martin I. Resnick and Matthew D. Rifkin. Baltimore: Williams & Wilkins, 502 pp., 1991. $95

The combined efforts of a urologist and a radiologist continue to make this book a useful blend of clinical information and state-of-the-art imaging. The introductory chapter on imaging and Doppler sonography is presented in a more conceptual than mathematical fashion and thus is more user friendly and less intimidating to the general audience. Duplex and color Doppler technologies are included.

The chapter on sectional anatomy of the genitourinary system contains a number of photographs of dissections that are of limited value. The transabdominal views of the prostate may be of some value as a general overview, but they seem somewhat superfluous in view of the book's chapter on the prostate as well as Dr. Rifkin's excellent volume on that subject for those in earnest about prostatic imaging.

In the chapter on the adrenal gland, again the line drawings are more helpful than the photographs of dissected specimens. The quality of many of the sonograms is disappointing. The use of old and black-on-white sonograms is understandable with rare entities but hardly seems necessary with such common tumors as neuroblastoma. The interrelationship between sonography and CT with respect to the adrenal gland is discussed in an evenhanded and accurate fashion. Detection of 6-mm adrenal masses by anyone but the dedicated subspecialist may be overly optimistic, however.

In the chapter on normal kidney and diffuse renal disease, the quality of the sonograms is excellent throughout, with a useful discussion of technical approaches, an excellent spectrum of normal variations, and a good discussion of cystic disease. The chapter on renal masses is liberally endowed with clinical information (e.g., the clinical manifestations of various diseases) and presents an excellent variety of the sonographic appearances of renal cell carcinoma. The descriptions of a number of the figures are somewhat cumbersome, requiring the reader to look back and forth from figure to text and sometimes to another page.

The chapter on acute and chronic renal failure provides a number of quite useful tables that list causes and separate sonographic appearances by disease process. Again the sonograms are of superb quality, and the chapter, though short, is inclusive.

The chapter on trauma contains good correlative CT scans and angiograms and an honest appraisal of the role of sonography in trauma. Speculation on the future applications of color Doppler imaging in the assessment of pedicle injury is appropriate. In the chapter on the urinary bladder, the quality of the sonograms ranges widely, and one CT scan is of marginal quality.

Although the chapter on dynamic evaluation of the lower urinary tract represents the standard practice of the authors, it is not entirely clear that this is a universal standard. This will undoubtedly be of more interest to the urologist than the radiologist. The chapter on the prostate is excellent, evenhanded and reflecting the author's well-recognized expertise in the field. The brief but complete discussion of sonography of the penis provides a good overview of the procedure and, coupled with some of the more recent writings, is a solid introduction to the topic. The chapter on pediatrics provides good CT and MR correlation with sonograms of excellent quality, and chapters on the scrotum and transplanted kidney are likewise of first-rate quality. The authors provide many practical hints, warnings, and descriptions of technique in the discussion of interventional sonography, integrating this technique with the roles of fluoroscopy and CT.

Overall, the book is of high quality, with few areas that do not measure up to the standards of the rest of the text. The bibliographies are without exception complete and current, and the index is quite functional. Although not the only good-quality volume dealing with this subject, this work continues to be a highly worthwhile addition, providing a clinical orientation not universally available.

Andrew M. Fried
University of Kentucky Medical Center
Lexington, KY 40536

Sonography of Renal Transplants in Dogs: The Effect of Acute Tubular Necrosis, Cyclosporine Nephrotoxicity, and Acute Rejection on Resistive Index and Renal Length

Myron A. Pozniak[1]
Frederick Kelcz[1]
Anthony D'Alessandro[2]
Terry Oberley[3]
Robert Stratta[2,4]

Results of studies on the accuracy of the resistive index as a predictor of acute renal transplant rejection have varied widely. Clinical evaluations are limited by the inability to control the numerous coincidental factors that affect vascular resistance. We performed a controlled study in dogs to isolate the effects of acute tubular necrosis, cyclosporine toxicity, and acute rejection on the resistive index, and to compare them with a population of normal control subjects. By doing so, we hoped to identify the patterns of change in the resistive index over time and possibly explain the wide spectrum of resistive index data reported in the literature. Resistive index, a parameter calculated from relative systolic and diastolic velocity, indicates parenchymal resistance to perfusion. Since an increase in renal length also has been reported useful in predicting rejection, we studied changes in length in each of the isolated conditions. The normal control group (four dogs) had heterotopic autotransplantation with minimal cold ischemic time. The acute tubular necrosis group (six dogs) had heterotopic autotransplantation with 1 hr of warm ischemic time. The cyclosporine toxicity group (four dogs) was allowed approximately 3 months to heal from heterotopic autotransplantation. Very high (toxic) doses of cyclosporine were then administered. The acute rejection group (five dogs) had heterotopic allografting with minimal cold ischemic time. No medications were administered. In all groups, the abnormalities induced were confirmed by biopsy. Creatinine levels were also used to monitor cyclosporine toxicity. In the normal control and acute tubular necrosis groups, resistive index increased immediately after surgery, returning to baseline within 10 days. Renal length increased slightly in both groups, but the duration of increase was longer in the acute tubular necrosis group. No significant change in resistive index or renal length was seen in the cyclosporine toxicity group. In the acute rejection group, an initial decrease in resistive index during the mild to moderate phase was followed by a rapidly progressive increase with worsening rejection. Renal length increased progressively beginning immediately after surgery.

Our study determined the patterns of change in resistance and renal length over time as caused by the isolated pathologic states. Our finding that vascular resistance decreased in mild to moderate acute rejection was unexpected, since almost all the literature reports resistive index elevation. This may explain some of the conflicting results obtained in Doppler investigations of rejection. Our results on renal length reinforce the positive clinical reports of its predictive value in rejection.

***AJR* 158:791-797, April 1992**

A reliable noninvasive means for evaluating renal transplant dysfunction has been sought for the past three decades. The primary goal has been to differentiate rejection from other conditions compromising renal function. Studies with sonographic imaging and Doppler have investigated the applicability of the use of changes in morphology, echo texture [1-9], renal size [7, 10-14], and renal arterial resistance [6, 8, 9, 15-38] in the evaluation of renal transplant dysfunction. Results have varied widely, and clinical experience has not supported the use of any one parameter.

Accordingly, we performed a controlled study in dogs that was designed to

Received July 29, 1991; accepted after revision November 13, 1991.

This work was supported in part by the general research support grant of the Medical School Research Committee of the University of Wisconsin and Sandoz Pharmaceuticals.

[1] Department of Radiology, University Hospital & Clinics, University of Wisconsin, Clinical Science Center E3/311, 600 Highland Ave., Madison, WI 53792. Address reprint requests to M. A. Pozniak.

[2] Department of Surgery, University Hospitals & Clinics, University of Wisconsin, Madison, WI 53792.

[3] Department of Pathology, University of Wisconsin, Middleton Veterans Hospital, Madison, WI 53792.

[4] Present address: Department of Surgery, University of Nebraska Medical Center, Omaha, NB 68198.

0361-803X/92/1584-0791
© American Roentgen Ray Society

isolate acute tubular necrosis, cyclosporine toxicity, and acute rejection so that the effects of these individual conditions on vascular resistance and renal length could be determined. Several different methods of calculating vascular resistance exist. Resistive index correlates peak systolic to lowest diastolic velocities. It is relatively easy to obtain and is probably the most common method in clinical use.

Materials and Methods

General

The study protocol was reviewed by the University of Wisconsin Research Animal Resource Committee, which agreed that the study conformed to the standards of the American Association for Accreditation of Laboratory Animal Care. All procedures were performed with the animals under general anesthesia. Some animals were sedated prior to induction. A preliminary measurement of resistive index was performed before and during anesthesia to ensure no measurable hemodynamic effects would be caused by the sedative or anesthetic agents. One agent (acepromazine maleate) was found to cause very high renal vascular resistance after intramuscular injection, precluding its use.

Thirty-five unrelated mongrel dogs (average weight, 25 kg) were conditioned and monitored for 10 days for signs of rabies, distemper, parasitic or infectious disease, or any limiting physical condition before entering the study. The dogs were kept in a standard laboratory environment, maintained on a standard laboratory diet, and allowed sufficient water at all times.

During the course of our study, six dogs were eliminated for nonrenal causes (two with intussusception, one with neoplasm, and three others with infections requiring antibiotics). Three were eliminated with renal problems (two with hydronephrosis and one with graft thrombosis). In addition, some data obtained early in the study were excluded because of errors in the coordination of Doppler sonographic measurements and biopsies. In 19 dogs, the experimental protocol was accurately satisfied.

All surgical procedures were performed by one of two surgeons. Two surgical assistants were present at each operation to ensure minimal renal ischemic time. All Doppler sonographic studies were performed by one of two radiologists, all biopsies were done by one radiologist, and all pathologic specimens were reviewed by one pathologist.

Normal Control Group

Four mongrel dogs had identical heterotopic autograft transplantations; that is, a kidney was removed from the renal fossa and transplanted into the iliac fossa of the same animal. The left kidney was dissected from the retroperitoneal fossa, and the renal vein and renal artery were isolated as far as the aorta and vena cava. If multiple renal arteries were detected on the left side, then the right kidney was used for transplantation. None of the transplanted kidneys had more than one renal artery.

Before the kidney was removed, the right iliac fossa was prepared, including ligation of the right external iliac artery and hypogastric vein. The kidney was then removed from the renal fossa, flushed with approximately 200–250 ml of cold heparinized saline, and immediately transplanted into the iliac fossa. The renal vein and artery were anastomosed end-to-end and end-to-side, respectively. Cold ischemic time was minimized (range, 15–20 min). The ureter was implanted into the bladder by using an anterior extravesical technique.

Aside from anesthesia, no drugs, including immunosuppressive medication, were administered to any of the dogs during the procedure or thereafter.

Acute Tubular Necrosis Group

Six mongrel dogs had heterotopic renal autograft transplantation with the use of the same surgical procedure as in the control group. Ischemic acute tubular necrosis in the transplant was produced by leaving the resected, unperfused kidney in the dog's abdominal cavity at body temperature for at least 1 hr (range, 60–90 min). The abdomen was closed temporarily with clips to minimize heat loss. The kidney was then transplanted into the same dog's iliac fossa. As with the normal control group, none of the dogs received medication.

Cyclosporine Toxicity Group

Transplantation was performed in four dogs as in the control group. Ample time (63–98 days) was allowed after the surgery for the animals to recover completely. They were then started on a progressively increasing dosage of cyclosporine. The cyclosporine, diluted in oil, was administered orally. Daily doses were started at 25 mg/kg and incrementally increased to 200 mg/kg. On day 7, when the oral cyclosporine dose was at 200 mg/kg, 250 mg of erythromycin was also administered orally on a daily basis. Erythromycin inhibits the cytochrome P_{450} enzyme system in the liver, thereby impairing cyclosporine metabolism [39]. This helps to maintain a high blood concentration of parent cyclosporine. Since the purpose of the study was to evaluate hemodynamics and not pharmacokinetics, this protocol was deemed appropriate. Renal sonography and biopsy were performed in each dog immediately before the initial dose of cyclosporine.

Acute Rejection Group

Renal allografting was performed in five unrelated mongrel dogs by using a kidney taken from one of the other dogs. No histocompatibility typing was performed. The operative procedure was identical for all five animals. Dissection of the kidney in the donor animal and preparation of the iliac fossa in the recipient were done simultaneously by two separate surgical teams in a manner similar to that described for the normal control group. Immediately after removal, the kidney was flushed with cold heparinized saline and promptly transplanted into the recipient dog. Ischemic time ranged from 15 to 20 min. No immunosuppressive medication was administered.

Sonography

Doppler sonographic examinations were performed with an Acuson 128 phased-array system with pulsed Doppler capabilities (Acuson, Mountain View, CA). Color Doppler sonography became available midway through the study and was used to facilitate vessel localization.

Doppler measurements were obtained with a 5.0-MHz linear-array transducer. Filtration was set at the lowest possible setting. Resistive index (RI), calculated by software incorporated in the Acuson scanner, is based on the formula

$$RI = [(PSV - EDV)/PSV] \times 100\%,$$

where PSV = peak systolic velocity and EDV = end diastolic velocity. A sequence of eight tracings was obtained at four different arterial levels (arcuate, interlobar, segmental, and main), with two measurements taken at each level. Variation in the resistive index value among the arteries at different levels was minimal; therefore, the eight measurements were averaged to obtain one mean resistive index for that session.

Renal length was measured with a 3.0-MHz linear-array transducer with an 8-cm length so that the entire kidney would be included within the field of view. The kidney's longest axis was approximated, the image was frozen, and the length was measured with electronic calipers. Three images were obtained, and the measurements were averaged to obtain one mean renal length for that session. If any one measurement was more than 10% less than the other two, it was excluded from the data set and the remaining data were averaged.

Immediately after surgery (within 30 min), a sonogram and baseline Doppler tracings were obtained in the normal control, acute tubular necrosis, and acute rejection groups. This examination was designated as day 0. Subsequent imaging/Doppler examinations were targeted for days 1, 2, 3, 4, 7, 9, and 11 after surgery. Sonographic imaging/Doppler examinations of the dogs in the cyclosporine group were performed just before drug administration (day 0) and then targeted for days 1, 2, 3, 4, 7, 9, 11, and 14 after the initiation of cyclosporine treatment.

Pathology

Fourteen-gauge Tru-Cut (Travenol Laboratories, Deerfield, IL) core biopsies of the renal transplants were performed under sonographic guidance. All biopsies were performed at the lower pole of the kidney to confine the area of biopsy-related complications that could alter hemodynamics, such as vascular spasm, hemorrhage, or edema.

At the beginning of the study, biopsies were done every time a sonogram was obtained. However, after the fourth or fifth procedure, it became clear that the pathologic specimens had inflammatory changes because of the trauma caused by repeated biopsies. As a result, these four dogs were excluded from the study and subsequent biopsies were done less frequently.

Biopsies were done on the day of surgery (day 0) and on postoperative days 4 and 11 for the normal control, acute tubular necrosis, and acute rejection groups. Biopsies were done on days 4, 10, and 15 in the cyclosporine group, and serum creatinine levels were monitored periodically at 3- to 5-day intervals. Biopsy samples were compared with those from a nontransplanted dog kidney.

Statistical Protocol

Two measurements for resistive index were taken at four arterial levels of each dog per session, and these eight measurements were averaged to give a mean resistive index for each dog per session. Three measurements of renal length were also obtained and averaged to yield a mean renal length for each dog per session. Baseline measurements for each dog were defined as those measurements of resistive index and renal length that were taken immediately after transplantation (within 30 min of surgery) in the normal control, acute tubular necrosis, and acute rejection groups; baseline measurements for the cyclosporine group were those taken before drug administration.

For each of the four groups (normal control, acute tubular necrosis, acute rejection, and cyclosporine toxicity), mean change from baseline with respect to resistive index and renal length was calculated for each dog per session. With respect to resistive index, mean change from baseline equals mean resistive index for a specific dog and session, minus the baseline for that dog. With respect to renal length, mean change from baseline equals mean renal length for a specific dog and session, minus the baseline for that dog. In the 12-day period after surgery or initiation of cyclosporine treatment, for each day when more than one dog was measured, one-sample t-tests were performed on the variable (i.e., mean change from baseline) with respect to both resistive index and renal length. The purpose of the t-test was to determine if mean change from baseline was significantly different from zero. No adjustments for multiple comparisons were made. The resulting *p* values are displayed in Figures 1–5. Those tests that proved the mean change from baseline to be significantly different from zero are represented by a *p* value of less than .05.

For each of the four groups, overall mean change from baseline in both resistive index and renal length was plotted against time, where time represents the number of days since surgery for the normal control, acute tubular necrosis, and acute rejection groups, or number of days since initiation of therapy for the cyclosporine group (see Figs. 1–6). Each point on these graphs represents the difference between the baseline average and the average of the dog averages for a given day (dog average equals the average of the eight measurements taken per dog per day). The standard error ($SD/\sqrt{n}$) is represented by the length of the error bars shown on each of the graphs in Figures 1–5. On days when only one dog's measurements were taken, no error bars are displayed.

Results

Normal Control Group

The resistive index increased by approximately 15% in the immediate postoperative period in the normal control group, peaking on postoperative day 2. A return to baseline was

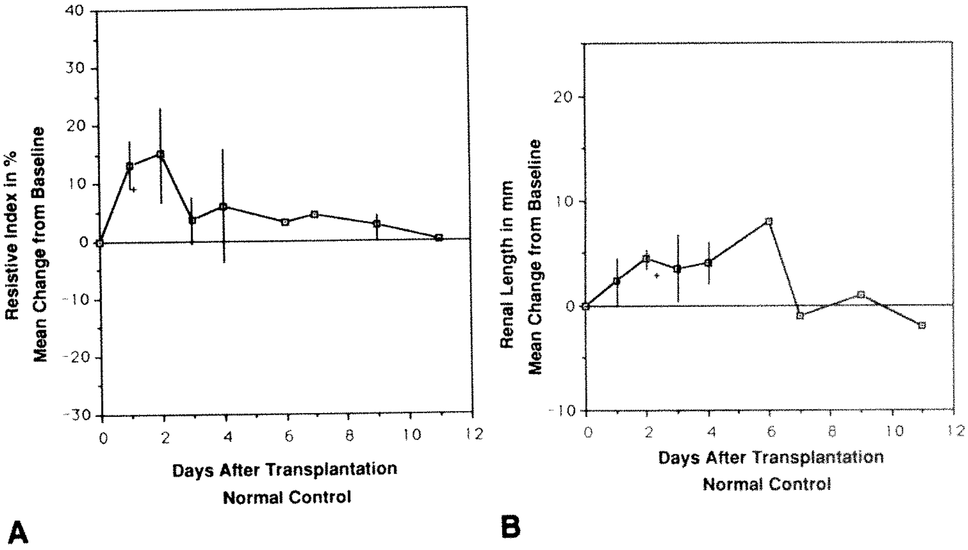

Fig. 1.—*A*, An increase in mean resistive index is seen in normal control group immediately after transplantation, with a subsequent return to baseline by day 11.

***B*, An increase in mean renal length is seen in normal control group after transplantation, with return to baseline by day 7.**

+ = $p \geq .05$ (NS).

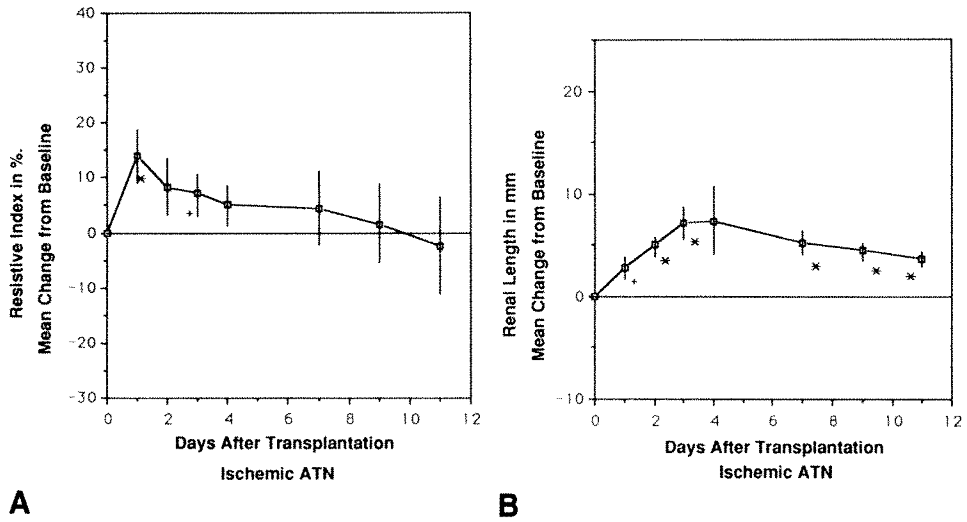

Fig. 2.—*A*, A significant ($p = .028$) increase in mean resistive index is seen in acute tubular necrosis (ATN) group immediately after transplantation with a subsequent return to baseline by day 10.

B, A significant increase in mean renal length is seen in acute tubular necrosis group after transplantation, peaking on days 3 and 4, with a slow return toward baseline.

+ = $p \geq .05$ (NS); * = $p = .01$–.05.

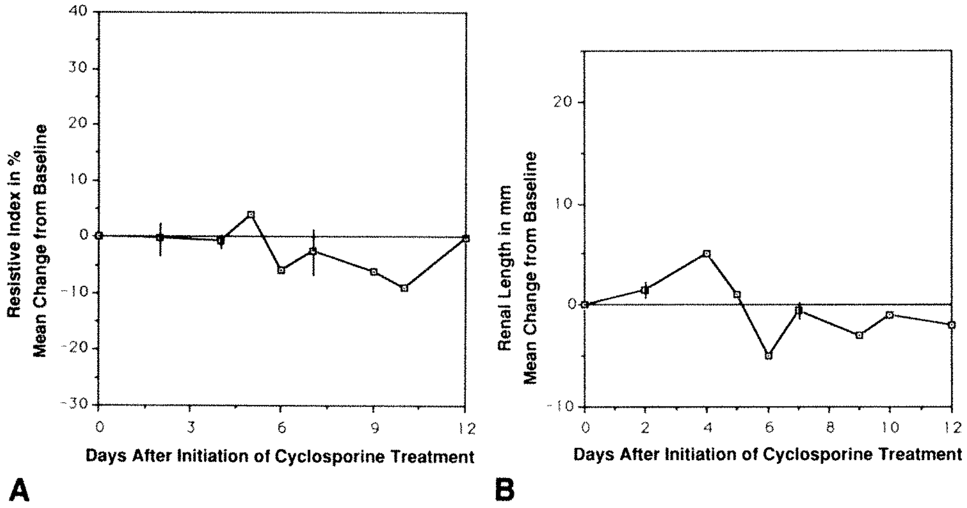

Fig. 3.—*A*, Graph shows no significant change from baseline in mean resistive index in cyclosporine toxicity group after initiation of therapy.

B, Graph shows no significant change from baseline in mean renal length in cyclosporine toxicity group after initiation of therapy.

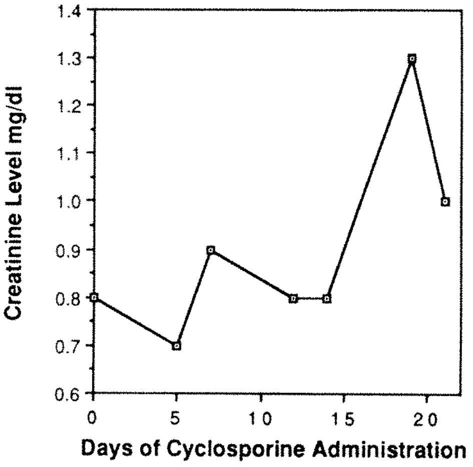

Fig. 4.—Changes in creatinine levels in dog 5 during cyclosporine toxicity phase of study.

noted by the second week (Fig. 1A). Renal length increased by an average of 5 mm during the first week after transplantation. It returned to baseline early in the second week (Fig. 1B).

The elevation of resistive index and the increase in renal length were attributed to the trauma of the surgical procedure, even though cold ischemic time was minimized. This assumption was reinforced by biopsy findings, which showed vacuolation in the distal tubules, which is consistent with mild ischemic tubular injury.

Acute Tubular Necrosis Group

Dogs with experimentally induced acute tubular necrosis also showed an approximately 15% increase in resistive index with a progressive return to baseline in week 2 (Fig. 2A). Renal length increased by approximately 8 mm soon after

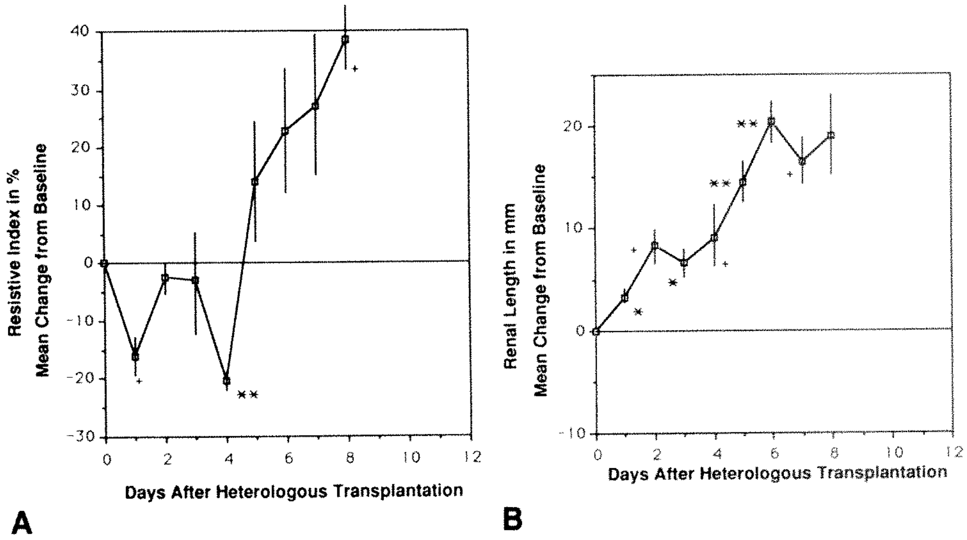

Fig. 5.—*A*, A highly significant ($p = .0019$) decrease in mean resistive index is seen in acute rejection group after transplantation during mild to moderate phase of rejection. An increase over baseline is not seen until severe stage of rejection.

B, A statistically significant increase in mean renal length is seen in acute rejection group beginning immediately after transplantation.

$+ = p \geq .05$ (NS); $** = p \leq .01$; $* = p = .01–.05$.

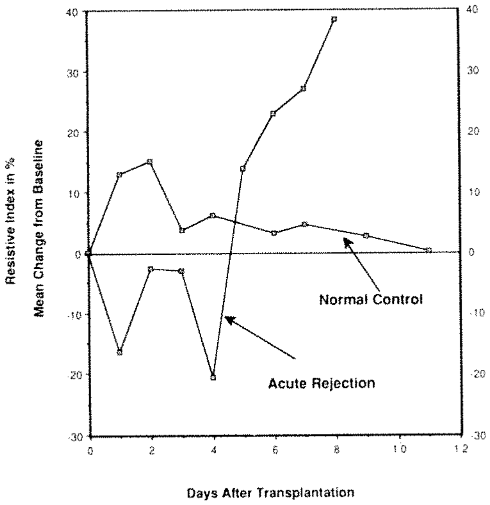

Fig. 6.—Normal control and acute rejection graphs have been overlaid to emphasize significance of downward trend in resistive index in acute rejection group. Rejecting kidneys underwent same trauma as normal control model, so a similar rise in resistance was expected but the opposite occurred.

transplantation, reaching a maximum on days 3 and 4 (Fig. 2B). There was a subsequent slow return in renal length toward baseline.

Initial biopsy findings included vacuolation, sloughing of cells in the proximal renal tubules, and congestion in the blood vessels. Later biopsies showed increased vacuolation, sloughing of tubular cells, and thickening of the basement membrane. Cellular casts were noted in both the proximal and distal tubules, indicating severe injury. No injury was seen in the glomeruli or arterial walls.

Cyclosporine Toxicity Group

No significant differences from baseline were observed in either resistive index or renal length at any time in the cyclosporine-treated animals (Fig. 3). All *p* values from t-tests performed were such that *p* was greater than .10. Creatinine levels, however, did increase (Fig. 4), and incidental sonographic observation of the liver showed it to be grossly edematous (hypoechoic and enlarged). Other evidence of systemic toxic effects included excessive salivating.

Although no universally accepted lesions exist that are absolutely diagnostic of cyclosporine nephrotoxicity, there are findings that are strongly suggestive, especially when other potential causes of decreased renal function have been eliminated. Biopsies showed vacuolation of the renal tubules and concomitant thickening of the basement membrane, indicating tubular injury. Some interstitial fibrosis also was seen. Subsequent biopsies showed chronic interstitial fibrosis with tubular atrophy and sclerosis of the renal arteries. These findings have all been described in cyclosporine toxicity [40].

Acute Rejection Group

In dogs receiving heterologous transplants, the resistive index showed a decrease of up to 20% during the first 4 days after surgery. T-test results on day 4 were highly statistically significant with *p* value equal to .0019. By day 5, the resistive index began to rise rapidly, with a 38% rise over baseline by day 8 (Fig. 5A). Unfortunately, there was a temporal variance among the dogs in their reaching the severe stage of rejection; therefore, *p* values were not as significant. By contrast, renal length began to increase immediately after transplantation and continued a very significant rise to more than 2 cm over baseline (Fig. 5B). Creatinine levels could not be used as a means of confirming rejection because a normally functioning native kidney remained in each dog. Biopsy findings were characteristic of interstitial rejection. Findings included prominent lymphocytic infiltration of the interstitium, interstitial edema, and the presence of polymorphonuclear cells.

Discussion

Research with human subjects to investigate the applicability of sonography and Doppler measurements in detecting renal transplant complications is compromised by uncontrollable extraneous factors [27, 28, 30, 36, 38] affecting the transplant. In addition, most, if not all, renal transplants undergo some period of ischemia. Finally, multiple medications are frequently administered in the perioperative period that themselves have hemodynamic effects.

Except for a few isolated studies [1, 3, 18], most reports have been based on clinical experience in patients. Conclusions were drawn regarding hemodynamic changes associated with rejection in patients receiving numerous medications and in whom the degree of ischemic injury to the transplanted organ during the surgical procedure was not measured. In these studies, no attempt was made to control or monitor the influence of the numerous extraneous factors [27, 28, 30, 36, 38] that can affect transplanted kidneys in humans.

We attempted to exclude much of the uncertainty inherent in clinical studies by using an animal model in which distinct pathologic entities could be isolated and studied in a controlled manner. These include acute tubular necrosis, cyclosporine toxicity, and acute rejection.

In the acute tubular necrosis group, the kidney was autografted after a prolonged ischemic period and the dogs were given no medications. Therefore, the possibility of rejection or cyclosporine nephrotoxicity was eliminated. Cyclosporine toxicity was tested on autotransplanted kidneys that were not ischemic and not being rejected. In the acute rejection group, ischemia was minimized, and medications, including cyclosporine, were not administered. Accurate monitoring of changes in resistive index and renal length over time was then possible in dogs with each of these isolated conditions.

Resistive Index

One of the first reports of the value of Doppler sonography in detecting renal transplant rejection and in possibly differentiating rejection from other renal complications was by Sampson [15] in 1969. However, because duplex capabilities were unavailable, accurate identification of the vessel within which flow was being evaluated was not possible. Subsequent qualitative studies [16, 17] also indicated that Doppler sonography was helpful, and in the mid-1980s Rigsby et al. [19-21] claimed that measurement of renal arterial velocity by duplex Doppler sonography could be used to accurately predict acute rejection and perhaps obviate biopsy. Although these findings were initially received with enthusiasm and supported by other authors [8, 22-24], subsequent clinical applications were disappointing [9, 25, 26, 29, 31, 34, 35], and recent criticism [37, 38] has been directed at the studies' scientific methods.

The initial postoperative increase in resistive index in our normal control group was unexpected. It suggests that some ischemic trauma occurs even when cold ischemic time is minimized. Reports have varied as to the effect of acute tubular necrosis on resistive index. Some studies stated that acute tubular necrosis did not affect resistance [23, 32] or reported mixed results [6, 25]. Others found that ischemia did raise the resistive index [26, 29, 31]. The results in our acute tubular necrosis group support these latter findings. Our findings in the cyclosporine toxicity group corroborate the findings of others [23, 24, 30, 35]. Cyclosporine toxicity does not cause any significant alteration in the resistive index.

Untreated severe rejection produced a precipitous elevation of the resistive index. However, in the early phase after transplantation as the rejection process was beginning, there was an unexpected significant decrease in resistance. This phenomenon is especially paradoxical considering that these kidneys underwent the trauma of transplantation identical to the normal control group, and should therefore be manifesting a similar resistive index elevation (Fig. 6).

The reason for this initial decrease in resistance is uncertain. A possible explanation may be in the complex autoregulatory effect of hormonal controls on renal circulation. A recent review of renal autoregulatory systems by Chou et al. [41] listed acetylcholine, the kallikrein-kinin system, adenosine, vasopressin, prostaglandins, atrial natriuretic peptide, and the renin-angiotensin system as contributing to renal hemodynamics. We can only theorize that during early mild to moderate rejection, these systems are somehow activated and may be responsible for lowering resistance to perfusion. However, as rejection progresses to a severe degree, the inflammatory process overwhelms the countereffect of the autoregulatory mechanisms and the resistive index increases dramatically.

Indeed, in the clinical scenario, antirejection medications usually prevent the process of acute rejection from reaching a full-blown crisis, so that the resistive index does not reach those high diagnostic values. Instead, the degree of rejection is kept at a mild to moderate level, where creatinine may be elevated but the autoregulatory mechanism may still exert a significant effect on hemodynamics. We theorize that this may explain the surprisingly low resistive index values obtained in acute rejection in some of the recent clinical series [9, 31].

Renal Length

In the late 1970s and early 1980s, studies [7, 10-13] indicated that changes in renal length could be used to predict acute rejection. Over the ensuing years, though, this index fell into disfavor. Precise measurement of renal length was technically difficult and results were often questionable [14].

Our study findings, however, support those earlier observations. The initial postoperative increase in renal length in the normal control group was an unexpected finding. Some change due to surgical manipulation was expected, but we did not think it would be consistently measurable or statistically significant. In conjunction with the elevation in the resistive index, it is presumably due to the mild degree of ischemic injury that occurs even under the most optimal surgical conditions. As expected, the more statistically significant increase in renal length was noted in the acute tubular necrosis group. We also confirmed previous assumptions [12] that renal length is not affected by cyclosporine toxicity. Renal length in the acute rejection group showed a progressive measurable increase in size beginning immediately after surgery. Renal size increased by as much as 30%.

Conclusions

A summary of our findings shows that the trauma of transplantation, even with optimal technique and minimal cold ischemic time, is enough to produce a brief increase in both resistive index and renal length; acute tubular necrosis, as expected, causes a brief transient increase in resistive index and renal length; high-dose cyclosporine nephrotoxicity has no significant effect on resistive index and renal length; and in untreated acute rejection during the mild to moderate phase, the resistive index initially decreases. With increasing severity of rejection, resistance begins to increase progressively and continuously. Renal length in acute rejection, however, shows a steady increase beginning immediately after surgery.

The significant decrease in resistive index identified by our study in the mild to moderate phase of acute rejection reveals the clinical limitations of the technique. As most transplant recipients maintain some degree of pharmacologically induced immune suppression, fluctuations in the degree of rejection may manifest as an elevation in creatinine level, but may not reach the degree necessary to actually elevate the resistive index. We show that vascular resistance in the renal transplant is not simply a static indicator of acute rejection but a dynamic process that fluctuates in response to many variables.

ACKNOWLEDGMENTS

We thank Allen Reed for surgical assistance, Bruce Basson and Denise Bidwell for statistical assistance, Allen Rappe for technical expertise, Daniel Faber for editorial assistance, and Carrie Poole for manuscript preparation.

REFERENCES

1. Hricak H, Toledo-Pereyra LH, Eyler WR, Madrazo BL, Zammitt M. The role of ultrasound in the diagnosis of kidney allograft rejection. *Radiology* **1979**;132:667–672
2. Hillman BJ, Birnholz JC, Busch GJ. Correlation of echographic and histologic findings in suspected renal allograft rejection. *Radiology* **1979**; 132:673–676
3. Hricak H, Toledo-Pereyra LH, Eyler WR, Madrazo BL, Sy GS. Evaluation of acute post-transplant renal failure by ultrasound. *Radiology* **1979**; 133:443–447
4. Hricak H, Cruz C, Eyler WR, Madrazo BL, Romanski R, Sandler MA. Acute post-transplantation renal failure: differential diagnosis by ultrasound. *Radiology* **1981**;139:441–449
5. Fleischer AC, James AE Jr, MacDonnell RC Jr, Johnson HK, Richie RE Jr, Hricak H. Sonography of renal transplant patients. *Crit Rev Diagn Imaging* **1982**;18(3):197–242
6. Berland LL, Lawson TL, Adams MB, Melrose BL, Foley WD. Evaluation of renal transplants with pulsed Doppler duplex sonography. *J Ultrasound Med* **1982**;1:215–222
7. Raiss GJ, Bree RL, Schwab RE, Schultz SR, Salem NG, Rosenberg BF. Further observations in the ultrasound evaluation of renal allograft rejection. *J Ultrasound Med* **1986**;5:439–444
8. Murphy AM, Robertson RJ, Dubbins PA. Duplex ultrasound in the assessment of renal transplant complications. *Clin Radiol* **1987**;38:229–234
9. Kelcz F, Pozniak MA, Pirsch JD, Oberly TD. Pyramidal appearance and resistive index: insensitive and nonspecific sonographic indicators of renal transplant rejection. *AJR* **1990**;155:531–535
10. Bartrum RJ Jr, Smith EH, D'Orsi CJ, Tilney NL, Dantono J. Evaluation of renal transplants with ultrasound. *Radiology* **1976**;118:405–410
11. Hricak H, Lieto RP. Sonographic determination of renal volume. *Radiology* **1983**;148:311–312
12. Parvin SD, Rees Y, Veitch PS, Bell PRF. Objective measurement by ultrasound to distinguish cyclosporin A toxicity from rejection. *Br J Surg* **1986**;73:1009–1011
13. Absy M, Metreweli C, Matthews C, Al Khader A. Changes in transplanted kidney volume measured by ultrasound. *Br J Radiol* **1987**;60:525–529
14. Nicholson ML, Williams PM, Bell A, Donnelly PK, Veitch PS, Bell PRF. Prospective study of the value of ultrasound measurements in the diagnosis of acute rejection following renal transplantation. *Br J Surg* **1990**; 77:656–658
15. Sampson D. Ultrasonic methods for detecting rejection of human renal allotransplants. *Lancet* **1969**;2:976–978
16. Arima M, Ishibashi M, Usami M, et al. Analysis of the arterial blood flow patterns of normal and allografted kidneys by the directional ultrasonic Doppler technique. *J Urol* **1979**;122:587–591
17. Arima M, Takahara S, Ihara H, et al. Predictability of renal allograft prognosis during rejection crisis by ultrasonic Doppler flow technique. *Urology* **1982**;14(4):389–394
18. Berland LL, Lawson TL, Adams MB. Evaluation of canine renal transplants with pulsed Doppler duplex sonography. *J Surg Res* **1985**;39:433–438
19. Rigsby CM, Taylor KJW, Weltin G, et al. Renal allografts in acute rejection: evaluation using duplex sonography. *Radiology* **1986**;158:375–378
20. Taylor KJW, Morse SS, Rigsby CM, Bia M, Schiff M. Vascular complications in renal allografts: detection with duplex Doppler US. *Radiology* **1987**; 162:31–38
21. Rigsby CM, Burns PN, Weltin GG, Chen B, Bia M, Taylor KJW. Doppler signal quantitation in renal allografts: comparison in normal and rejecting transplants, with pathologic correlation. *Radiology* **1987**;162:39–42
22. Steinberg HV, Nelson RC, Murphy FB, et al. Renal allograft rejection: evaluation by Doppler US and MR imaging. *Radiology* **1987**; 162:337–342
23. Rifkin MD, Needleman L, Pasto ME, et al. Evaluation of renal transplant rejection by duplex Doppler examination: value of the resistive index. *AJR* **1987**;148:759–762
24. Buckley AR, Cooperberg PL, Reeve CE, Magil AB. The distinction between acute renal transplant rejection and cyclosporine nephrotoxicity: value of duplex sonography. *AJR* **1987**;149:521–525
25. Needleman L, Kurtz AB. Doppler evaluation of the renal transplant. *JCU* **1987**;15:661–673
26. Allen KS, Jorkasky DK, Arger PH, et al. Renal allografts: prospective analysis of Doppler sonography. *Radiology* **1988**;169:371–376
27. Warshauer DM, Taylor KJW, Bia MJ, et al. Unusual causes of increased vascular impedance in renal transplants: duplex Doppler evaluation. *Radiology* **1988**;169:367–370
28. Pozniak MA, Kelcz F, Stratta RJ, Oberley TD. Extraneous factors affecting resistive index. *Invest Radiol* **1988**;23(12):899–904
29. Drake DG, Alford BA, Letourneau JG, et al. Duplex Doppler evaluation of pediatric renal transplants (abstr). *AJR* **1989**;153:198
30. Don S, Kopecky KK, Filo RS, et al. Duplex Doppler US of renal allografts: causes of elevated resistive index. *Radiology* **1989**;171:709–712
31. Genkins SM, Sanfilippo FP, Carroll BA. Duplex Doppler sonography of renal transplants: lack of sensitivity and specificity in establishing pathologic diagnosis. *AJR* **1989**;152:535–539
32. Skotnicki SH, van Asten WNJC, Beijneveld WJ, van Roosmalen R, Hoitsma AJ, Wijn PFF. Evaluation of renal allograft function by Doppler spectrum analysis. *Transpl Int* **1989**;2:16–22
33. Fleischer AC, Hinton AA, Glick AD, Johnson HK. Duplex Doppler sonography of renal transplants: correlation with histopathology. *J Ultrasound Med* **1989**;8:89–94
34. Drake DG, Day DL, Letourneau JG, et al. Doppler evaluation of renal transplants in children: a prospective analysis with histopathologic correlation. *AJR* **1990**;154:785–787
35. McGee GS, Peterson-Kennedy L, Astleford P, Yao JST. Duplex assessment of the renal transplant. *Surg Clin North Am* **1990**;70(1):133–141
36. Mostbeck GH, Gossinger HD, Mallek R, Siostrzonek P, Schneider B, Tscholakoff D. Effect of heart rate on Doppler measurements of resistive index in renal arteries. *Radiology* **1990**;175:511–513
37. Perella RR, Duerincky AJ, Tessler FN, et al. Evaluation of renal transplant dysfunction by duplex Doppler sonography: a prospective study and review of the literature. *Am J Kidney Dis* **1990**;15(6):544–550
38. Rubin JM, Platt JF, Adler RS. Application of Doppler ultrasound in transplant and native kidney disease. *Ultrasound Q* **1990**;8(2):95–120
39. Lensmeyer GL. Identification and analysis of nine metabolites of cyclosporine in whole blood by liquid chromatography. *Clin Chem* **1987**; 33:1841–1850
40. Striker LJ, Olson JL, Striker GE. Renal transplantation. In: *The renal biopsy*, 2nd ed. Philadelphia: Saunders, **1990**:235–237
41. Chou S-Y, Porush JG, Faubert PF. Renal medullary circulation: hormonal control. *Kidney Int* **1990**;37:1–13

Book Review

Transvaginal Ultrasound. By Melvin G. Dodson. New York: Churchill Livingstone, 273 pp., 1991. $65

This book, written by a gynecologist, is devoted completely to the technique of transvaginal sonography. Alas, it is disappointing from every standpoint and, in my opinion, is not worthy of serious consideration for inclusion in any medical library. Anyone interested in the sonography of the female pelvis and the use of the transvaginal transducer would do better to consult one of the standard texts in the field, such as the fourth edition of *Ultrasonography in Obstetrics and Gynecology* by Fleischer et al.

In the preface, the author emphasizes properly the importance of transvaginal scanning in the assessment of problems in gynecology and early pregnancy. This emphasis, however, is overblown and unnecessary, as the technique is already firmly established as standard practice, and few resist its use. However, a glance at the Contents leads the reader to hope that the book will contain thorough and systematic discussions of the technique of transvaginal sonography and the anatomy, physiology, and pathology of the female pelvis and early pregnancy. Unfortunately, the book does not deliver on this promise.

This book has many shortcomings, but its major one is poor organization. Every chapter, no matter what the subject, has weak thematic progression, with illogical and ineffective repetition, poorly defined abbreviations, and awkward grammar. The illustrations are substandard, and their captions are rambling and difficult to follow. Even the explanation of ultrasound physics, information that by now should be well understood by any author writing on the subject, is poorly conceived and unclear. Although the author is an experienced user of transvaginal ultrasound, his description of the technique of transvaginal scanning is superficial and confusing. The text abounds with numerous and extensive summaries of published data; however, in almost every instance, the summaries are so poor that the reader is lost in a morass of numbers and references. Most disappointing for me is the discussion of ovulation induction and infertility. I had hoped to gain a better understanding of the needs of the gynecologist in this area, but here the failings of the book are most obvious. The chapter is difficult to read and in the end not helpful.

In short, this is a book you can pass up. Its subject is important, but the author's efforts will not provide much aid in mastering it.

Harte C. Crow
Dartmouth-Hitchcock Medical Center
Hanover, NH 03756

Pictorial Essay

Imaging of Uterine Leiomyomas

Stephen Karasick,[1] Anna S. Lev-Toaff,[1] and Michael E. Toaff[2]

Advances in the medical and surgical treatment of uterine leiomyomas have stimulated interest in the imaging of these common tumors. The purpose of this essay is to illustrate the appearance of leiomyomas on images obtained with various techniques. The advantages of each technique in particular clinical circumstances are discussed.

Uterine leiomyomas (also called myomas and fibroids) are the most common solid uterine neoplasm, occurring in 20–40% of all women during their reproductive years [1]. They are well-circumscribed benign lesions composed primarily of smooth muscle with various amounts of fibrous connective

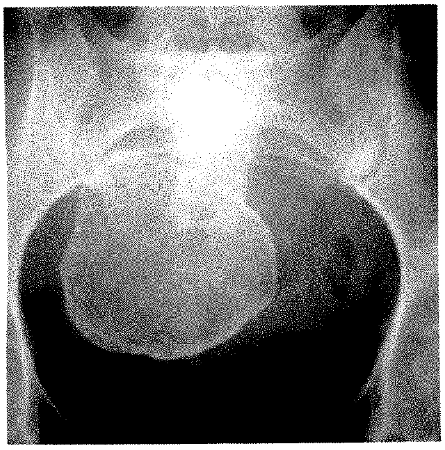

Fig. 1.—Plain radiograph of pelvis shows large, homogeneous, circumferentially calcified myoma.

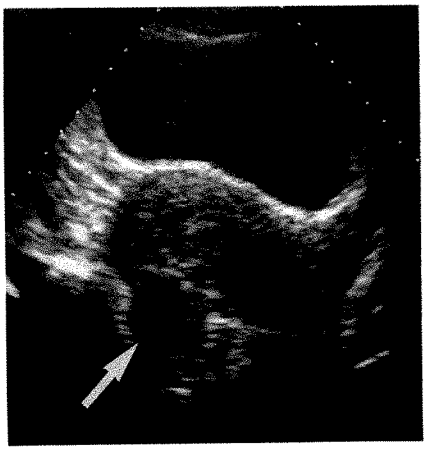

Fig. 2.—Sagittal sonogram shows hypoechoic mass (*arrow*) that could be either a fibroid or an adnexal mass. A CT scan of the same patient showed a lobulated uterus but did delineate a discrete mass. MR imaging (*not shown*) revealed a mural/subserous fibroid.

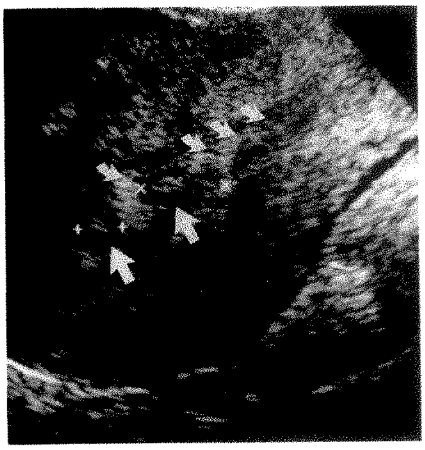

Fig. 3.—Transvaginal sagittal sonogram shows two small hypoechoic masses (*straight arrows*) distorting endometrial echo that were thought to represent either polyps or submucous fibroids. *Curved arrows* indicate interrupted endometrial echo. Submucous fibroids were found at surgery.

Received October 8, 1991; accepted after revision November 25, 1991.

[1] Department of Radiology, Thomas Jefferson University Hospital, 111 S. 11th St., Philadelphia, PA 19107. Address reprint requests to S. Karasick.

[2] Department of Obstetrics and Gynecology, Hahnemann University Hospital, Broad and Vine Sts., Philadelphia, PA 19102.

AJR 158:799–805, April 1992 0361–803X/92/1584–0799 © American Roentgen Ray Society

tissue. A pseudocapsule of areolar tissue containing one or two feeding vessels surrounds the tumor. As fibroids enlarge, they may outgrow their blood supply, resulting in ischemia and degeneration characterized as hyaline, cystic, myxomatous, fatty, or carneous. These tumors are estrogen dependent and usually regress after menopause. They are usually multiple. Leiomyomas occur most commonly in the myometrium of the uterine corpus, occasionally in the lower uterine segment, and rarely (3%) in the cervical region. According to their location with respect to the layers of the uterus, myomas are classified as submucous (under the endometrium), mural (within the myometrial wall of the uterus), or subserosal (projecting out of the uterine wall and covered by serosa). Many lesions are in a combined location (e.g., having both submucous and mural components). This classification is useful for both imaging and clinical purposes, because the signs and symptoms and the treatment options vary according to the location. From an imaging standpoint, location is also important in the differential diagnosis; for example, a subserosal pedunculated fibroid may mimic an adnexal mass. Also, a submucous fundal myoma may deform the uterine cavity so that it mimics a bicornuate uterus on hysterosalpingography.

Plain Radiography

Plain radiography of the abdomen and pelvis often does not show the uterine leiomyoma unless the tumor has undergone calcific degeneration. This type of degenerative change is more common with subserosal lesions, especially tumors with pedicles, and in leiomyomas in postmenopausal women. Occasionally, a large, nonspecific soft-tissue mass will be seen indenting the dome of the bladder or compressing the ureters at the pelvic brim, sometimes with dilatation of the

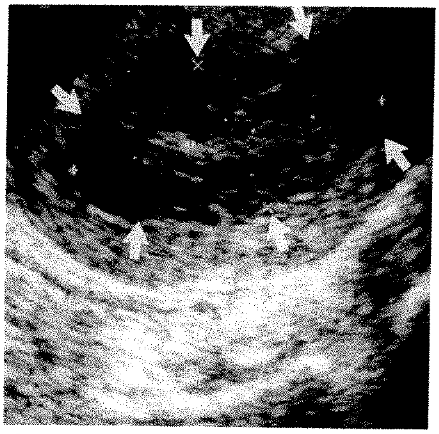

4

Fig. 4.—Transvaginal sonogram shows large hypoechoic mass in endometrial cavity (*arrows*).

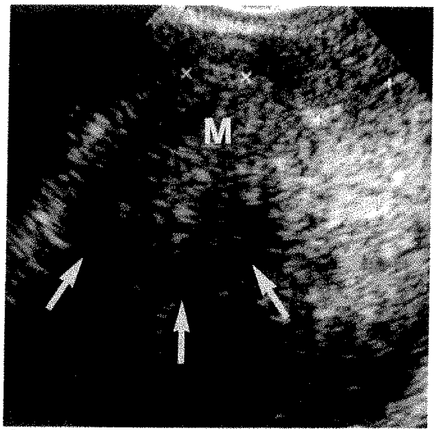

5

Fig. 5.—Transvaginal sagittal sonogram shows endometrial echo (*cursors*) draped over submucous fibroid (M). Posterior margin of mass is delineated (*arrows*).

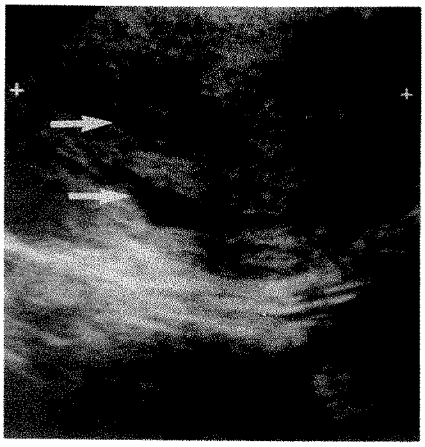

Fig. 6.—Transverse sonogram through fundal subserous myoma during third trimester of pregnancy shows signs of degeneration. Echo texture is heterogeneous, and several cystic spaces are present (*arrows*).

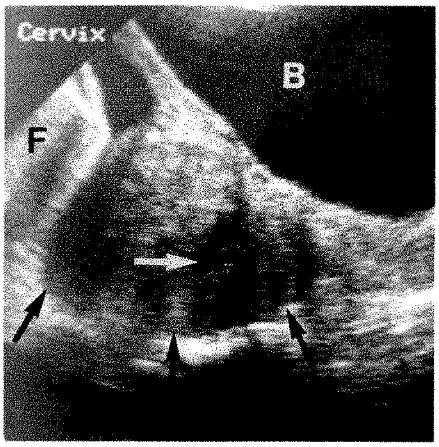

Fig. 7.—Sagittal sonogram at 31 weeks' gestation shows large fibroid (*black arrows*) in lower uterine segment posteriorly. Note heterogeneous echo texture and cystic spaces (*white arrow*). Persistent transverse fetal lie necessitated cesarean section. Lower uterine segment and cervical fibroids are associated with increased use of cesarean delivery due to malpresentation and obstructed labor. B = bladder, F = fetus.

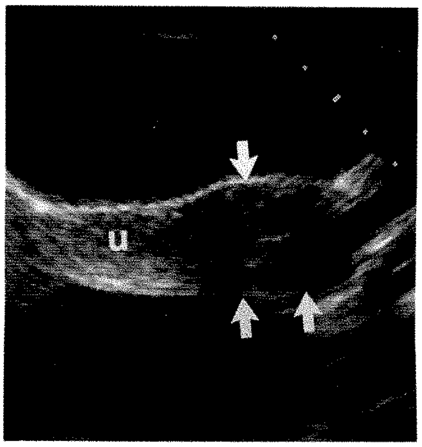

Fig. 8.—Transverse transabdominal sonogram shows lobulated hypoechoic mass (*arrows*) inseparable from left side of uterine body (u). At surgery, a subserosal myoma extending into left broad ligament was found.

upper urinary tract. Irregular coarse calcifications in the pelvis are most often caused by uterine leiomyomas. Occasionally, circumferential calcification of the lesion may occur (Fig. 1).

Sonography

Sonography is ideal to confirm clinically suggested uterine fibroids. The most common sonographic appearance is of a hypoechoic (Fig. 2) or heterogeneous uterine mass. When multiple small leiomyomas are present, sonography may merely show globular uterine enlargement. Submucous or small mural leiomyomas may distort the normally linear central endometrial echo (Fig. 3). Occasionally, a large submucous myoma will be seen as a mass within the endometrial cavity (Fig. 4), with the endometrial echoes draped over the mass (Fig. 5). The sonographic texture of leiomyomas depends on the relative ratio of fibrous tissue to smooth muscle and on the presence and type of degeneration. Hence, leiomyomas may be minimally echogenic; irregular anechoic areas are seen if cystic degeneration is present. Clusters of high-level echoes with distal acoustic shadowing are quite common with calcific degeneration. Carneous degeneration during pregnancy may cause severe pain and appear sonographically as a heterogeneous pattern with cystic spaces within the fibroid [1] (Fig. 6). Fibroids located in the lower uterine segment and cervix are associated with a higher frequency of cesarean sections and retained placentas [2] (Fig. 7). Pedunculated subserosal leiomyomas extend laterally outward between the folds of the broad ligament (intraligamentary), simulating an adnexal mass (Fig. 8).

Transvaginal sonography provides detail that surpasses that of transabdominal sonography. Transvaginal imaging can detect very small lesions and provides better differentiation of a submucous from a mural lesion, as both may produce distortion of the endometrial echo. However, because of a limited field of view, subserosal or pedunculated fibroids may be missed, and the transvaginal approach should be used in conjunction with transabdominal sonography.

Hysterosalpingography

Hysterosalpingography is considered the gold standard for identification of a submucous leiomyoma. Submucous lesions can be seen as smooth (Fig. 9) or irregular (Fig. 10), single or multiple (Fig. 11) filling defects with or without gross distortion

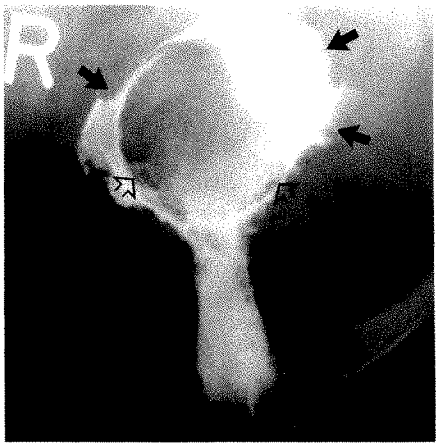

9

Fig. 9.—Hysterosalpingogram shows submucous fibroid as large polypoid filling defect (*open arrows*) in enlarged uterine cavity. Also seen is mucosal irregularity (*solid arrows*), which may be due to additional small submucous fibroids or endometrial hyperplasia. (Sonogram of this patient is shown in Fig. 4.)

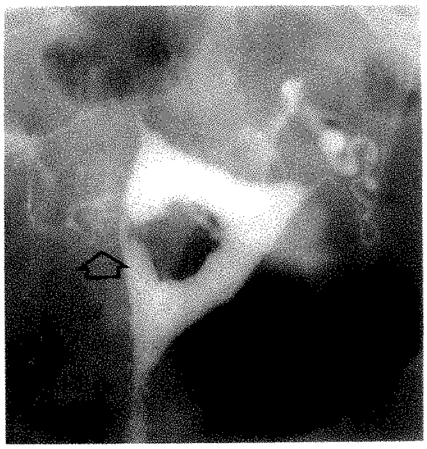

10

Fig. 10.—Hysterosalpingogram shows normal-sized uterine cavity with irregular central filling defect and venous myometrial intravasation at site of attachment to right uterine wall (*arrow*). A submucous myoma was found at surgery in addition to numerous other mural fibroids not seen on hysterosalpingography. (Sonogram of this patient is shown in Fig. 5.)

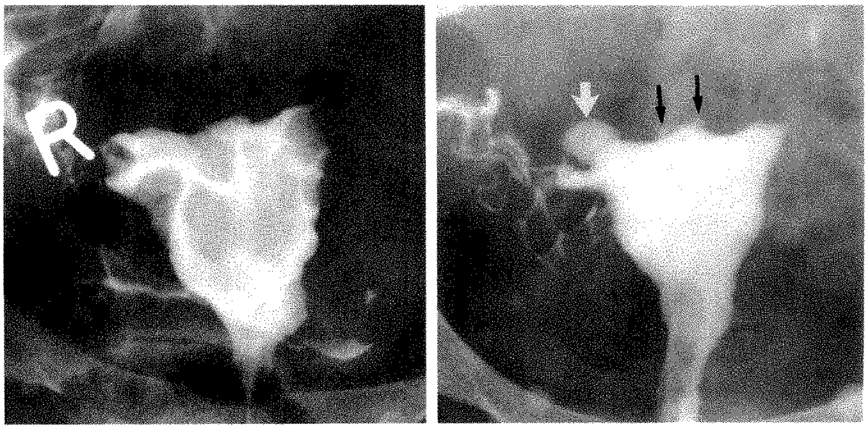

A B

Fig. 11.—Submucous myomas resembling endometrial polyps.

A, Hysterosalpingogram shows numerous filling defects in uterine cavity.

B, Hysterosalpingogram obtained after hysteroscopic myomectomy shows uterine cavity has a more normal appearance, with mucosal irregularity (*black arrows*) and diverticulum (*white arrow*), an unusual postsurgical finding.

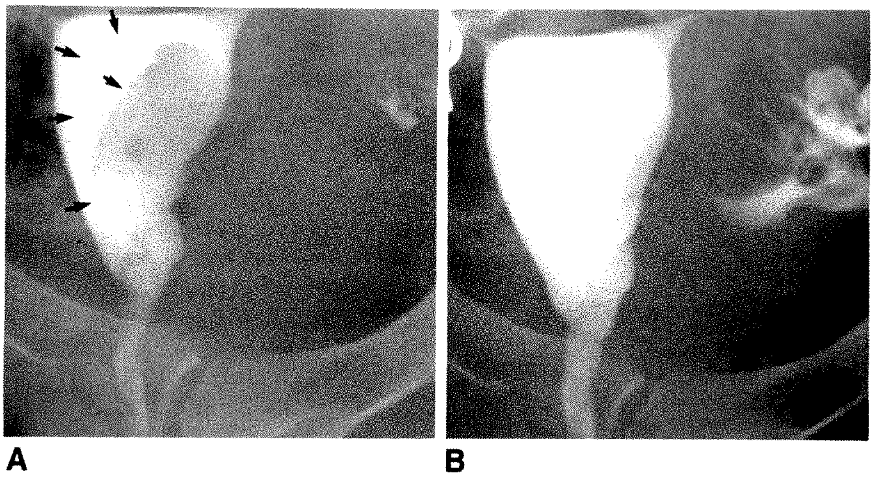

Fig. 12.—Importance of early radiograph of uterine cavity in hysterosalpingography.

A, Early filling radiograph shows large submucous fibroid in left corpus with lobulated margins (*arrows*).

B, On later radiograph, mass is nearly obscured by dense contrast material.

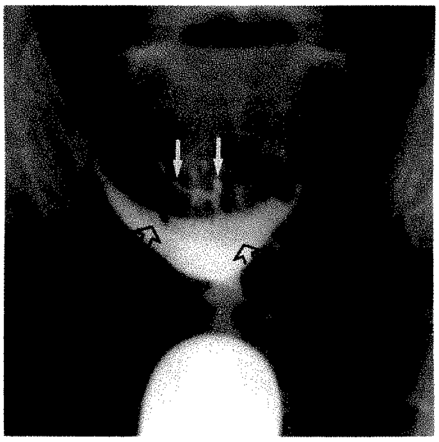

Fig. 13.—Hysterosalpingogram shows fundal submucous fibroid (*open arrows*) associated with venous myometrial intravasation of contrast medium (*solid arrows*). Later radiographs showed filling of pelvic veins; together with fundal mass effect, these findings suggest a fibroid rather than adenomyosis.

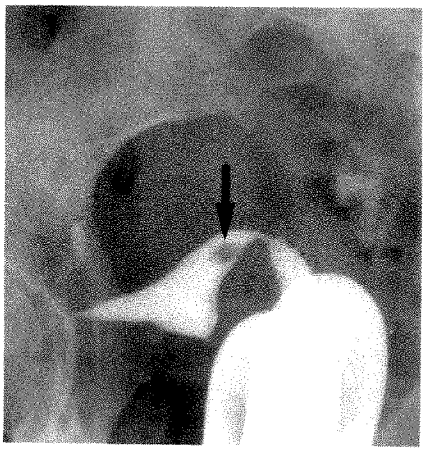

Fig. 14.—Hysterosalpingogram shows small submucous fibroid (*arrow*) simulating endometrial polyp in lower uterine segment of anteflexed uterus.

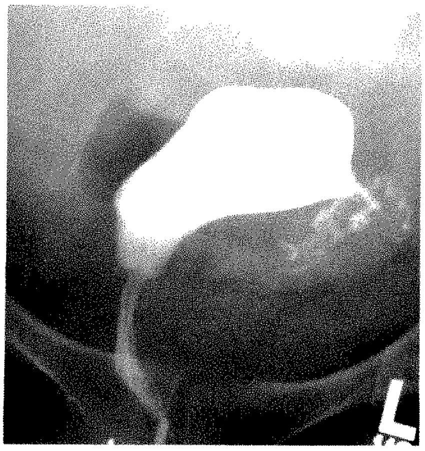

Fig. 15.—Hysterosalpingogram shows globular enlargement of uterine cavity due to mural fibroids.

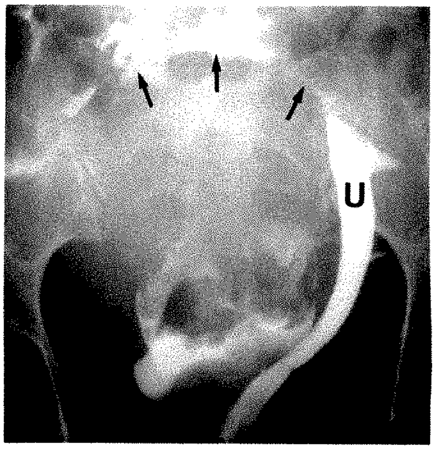

Fig. 16.—Large mural/submucous fibroid. Hysterosalpingogram shows large soft-tissue mass displacing uterus (U) to left. Crescentic impression on uterine cavity suggests a submucous component. Note elevation and draping of right fallopian tube (*arrows*) over mass.

of the uterine cavity. Attention to technique is important in the evaluation of leiomyomas; early filling radiographs of the uterus along with oblique views should be used (Fig. 12). The endometrium overlying some submucosal tumors is often thin or necrotic causing mucosal irregularity and venous myometrial intravasation (Fig. 13). Early vascular intravasation can resemble adenomyosis, but later films may show opacification of pelvic veins. Small submucous leiomyomas may be difficult to differentiate from endometrial polyps (Figs. 11A and 14). Submucous myomas, however, usually alter the uterine contour and size, whereas polyps are usually seen as a filling defect in an otherwise normal uterine cavity. Mural leiomyomas often enlarge the uterine cavity in a globular fashion (Fig. 15), and when they have a submucous component, they may produce an enlongated or crescentic configuration to the uterine cavity (Fig. 16). Fundal leiomyomas can cause an increase in the distance between the two uterine cornua, simulating a bicornuate uterus (Fig. 17). Subserosal leiomyomas usually have no definite signs on hysterography, but they can be large and be seen as soft-tissue masses that

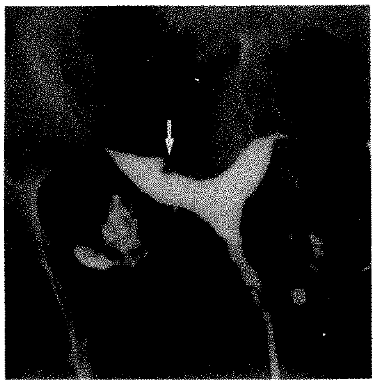

Fig. 17.—Hysterosalpingogram suggests a bicornuate uterus except for small nodular filling defect and focal mucosal irregularity (*arrow*), which is a clue to presence of fundal submucous fibroid found at surgery.

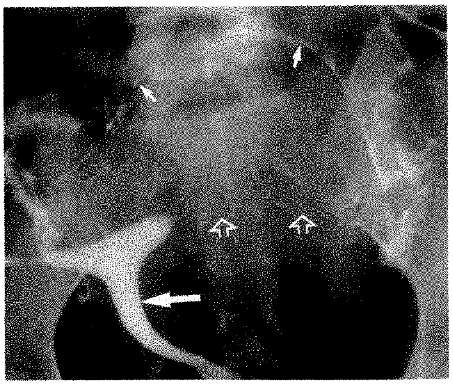

Fig. 18.—Hysterosalpingogram shows large left-sided subserosal fibroid delineated by intraperitoneal contrast material superiorly (*small solid arrows*). Note deviation of uterus to right (*large solid arrow*) and stretching of left fallopian tube (*open arrows*).

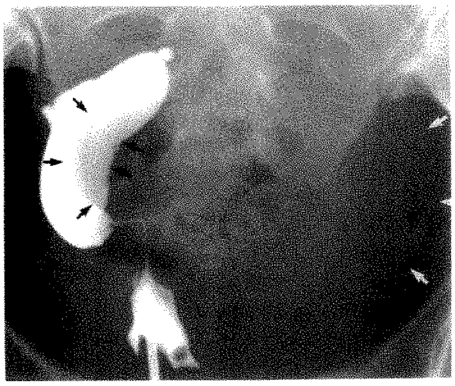

Fig. 19.—Hysterosalpingogram shows submucous myoma in left corpus (*black arrows*). Presence of large pelvic soft-tissue density suggests additional subserosal fibroids (*white arrows*). Note lack of filling of fallopian tubes.

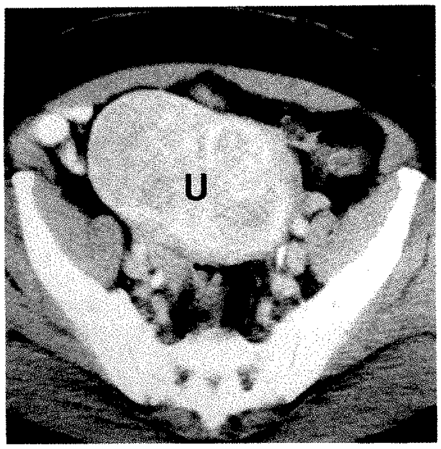

Fig. 20.—CT scan shows enlarged lobulated uterus (U) with heterogeneous enhancement. Multiple myomas are suggested, but their location is not well defined. MR in this patient clearly delineated their mural location.

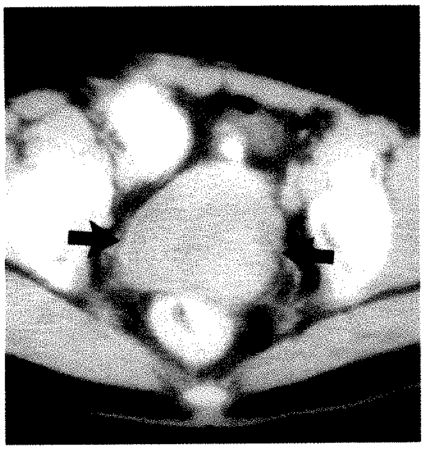

Fig. 21.—CT scan of pelvis (same patient as in Fig. 2) shows lobulated uterus (*arrows*). No discrete mass can be discerned. (Sonogram of this patient is shown in Fig. 2.)

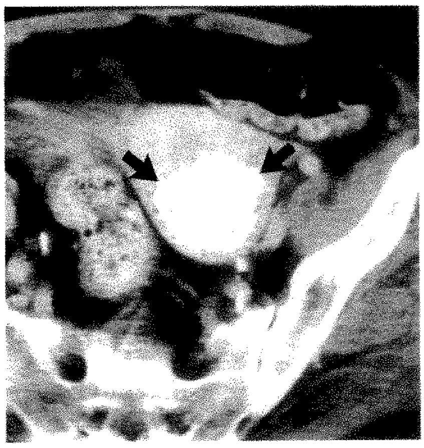

Fig. 22.—CT scan shows typical appearance of coarse, dense calcifications in uterine fundal myoma (*arrows*).

deform the uterine cavity as well as compress, displace, and occlude the fallopian tubes (Figs. 18 and 19).

CT

The most common CT findings of leiomyoma are a deformed uterine contour and an enlarged uterus (Fig. 20). Leiomyomas usually display uniformly solid consistency (Fig. 21), but they may be heterogeneous (Fig. 20) because of hyaline or cystic degeneration [3]. The presence of calcification, usually a coarse dystrophic type, is the most specific sign of leiomyoma (Fig. 22). A necrotic or degenerating leiomyoma may be seen as a low-attenuating mass in the uterus. Rarely, a leiomyoma may become infected and its central core filled with gas or purulent fluid.

MR Imaging

MR imaging provides excellent visualization and localization of uterine leiomyomas [4]. Usually the lesions are well circumscribed and have medium-intensity signal similar to that of adjacent myometrium on T1-weighted images; on T2-weighted images (e.g., 1500/40 [TR/TE]), they usually have a homogeneous low-intensity signal (Fig. 23). Degenerating leiomyomas have various nonspecific MR appearances ranging from medium to high signal on T1-weighted images to a heterogeneous, mostly high signal in the area of degeneration on T2-weighted images (Fig. 24). In patients with large or multiple myomas, MR, with its multiplanar capability, is often the best study to precisely delineate the location of each mass (Figs. 23 and 25–27). In particular, MR images are ideal to show the proximity of a myoma to the bright endometrial

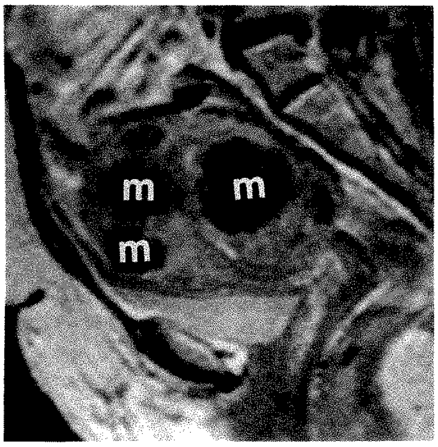

23

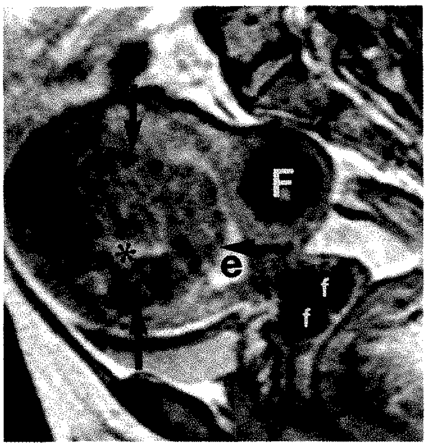

24

Fig. 23.—Sagittal MR image (1500/40) shows numerous mural myomas (m). Other images confirmed displaced but intact endometrial echo. (CT scan of this patient is shown in Fig. 20.)

Fig. 24.—Large submucous fibroid with cystic degeneration. Midsagittal MR image (1500/40) of uterus shows large submucous fibroid (*arrows*) bulging into high-signal-intensity endometrial cavity (e). High signal intensity (*asterisk*) in center of fibroid indicates cystic degeneration. Additional myomas of low signal intensity are seen in cervix (f) and posterior corpus (F).

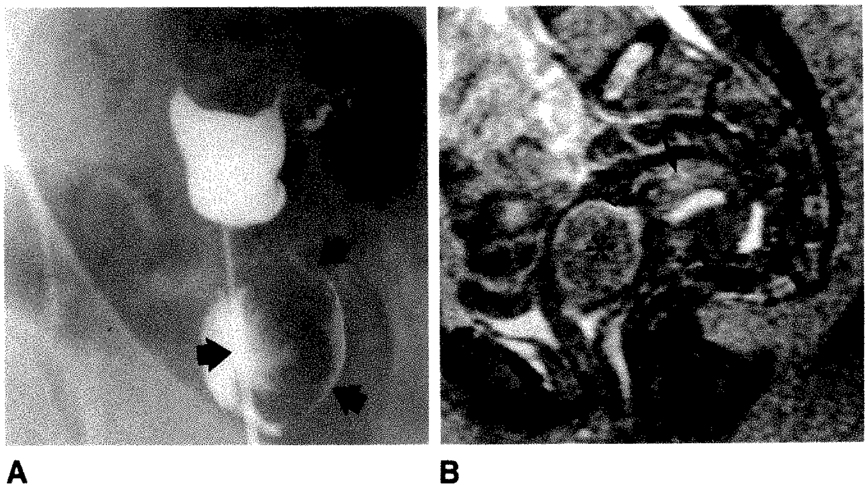

Fig. 25.—*A*, Hysterosalpingogram shows large polypoid filling defect (*arrows*) in cervical region. Cervical fibroids may be difficult to visualize unless they protrude into cervical canal.

B, Sagittal MR image (1500/40) clearly depicts myoma (*asterisk*) in anterior cervix of retroverted uterus (*solid arrows*). High-intensity rim (*open arrow*) most likely is due to vascular congestion.

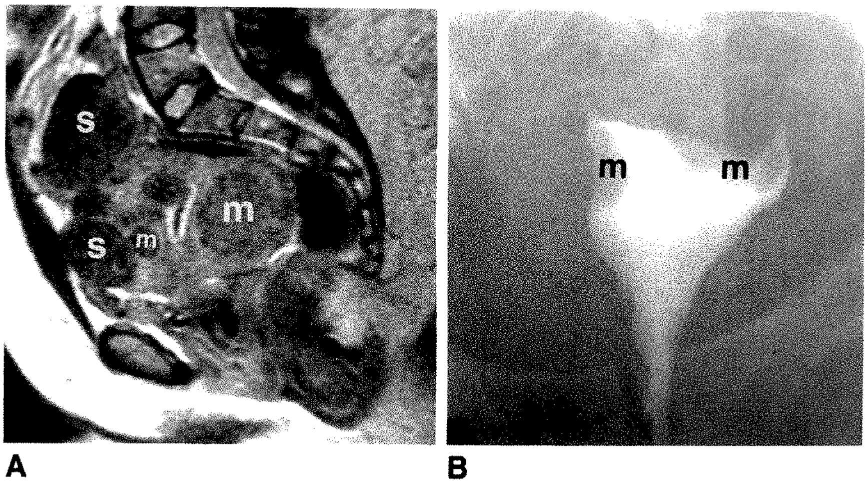

Fig. 26.—*A*, Sagittal MR image (1500/40) shows multiple low-signal-intensity masses in submucous (*asterisk*), mural (m), and subserous (s) locations. Note that submucous myoma impinges on endometrial signal. Another submucous myoma found at surgery was seen on other MR images.

B, Hysterosalpingogram shows only two submucous myomas (m).

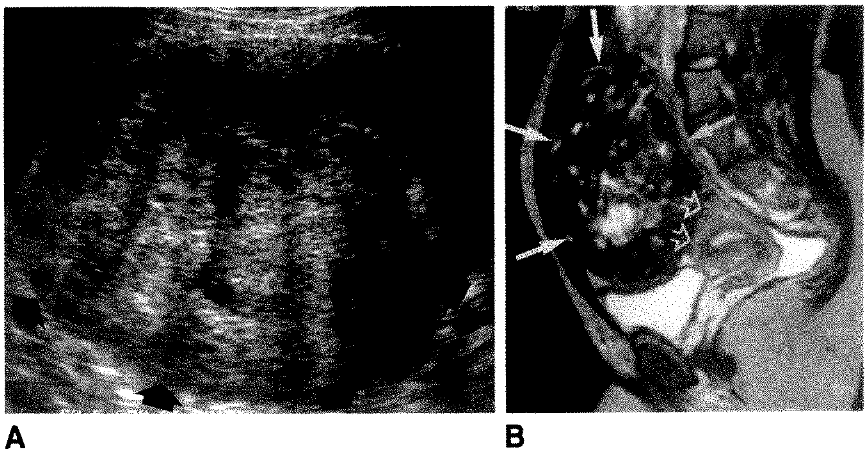

Fig. 27.—Advantage of MR for defining location of large fibroid.

***A*, Transverse transabdominal sonogram shows large, inhomogeneous mass (*arrows*), but its location is uncertain.**

***B*, Sagittal MR image (1500/40) shows intact endometrium with huge exophytic subserosal myoma (*solid arrows*) arising from fundus (*open arrows*). Mixed signal intensity is due to degeneration.**

cavity (Fig. 24). Some leiomyomas are surrounded by a high-intensity rim on T2-weighted images (Fig. 25B), most likely resulting from local vascular congestion [5].

Summary

There is no single correct approach to evaluating uterine leiomyomas. Accurate assessment of the number, size, and location of leiomyomas, especially when myomectomy is planned, is important because it often influences the type of surgical approach. CT is not a first-line imaging study; however, it often shows leiomyomas in asymptomatic patients. Hysterosalpingography and transvaginal sonography are particularly useful in the diagnosis of submucous leiomyomas. This is fundamentally important because these tumors are often missed on clinical examination, at dilatation and curettage, and on transabdominal sonography, especially if the leiomyoma is small and the patient obese. Transvaginal sonography enables follow-up study of growth or shrinkage of the leiomyoma in response to medical treatment with a gonadotropin releasing hormone agonist. MR imaging may be superior to sonography and hysterosalpingography for preoperative localization of leiomyomas, particularly in patients with multiple or large tumors.

REFERENCES

1. Altchek A. Management of uterine leiomyomata. In: Altchek A, Deligdisch L, eds. *The uterus*. New York: Springer-Verlag, **1991**:344–365
2. Lev-Toaff AS, Coleman BG, Arger PH, Mintz MC, Arenson RL, Toaff ME. Leiomyomas in pregnancy: sonographic study. *Radiology* **1987**;164: 375–380
3. Casillas J, Joseph RC, Guerra JJ. CT appearance of uterine leiomyomas. *RadioGraphics* **1990**;10:999–1007
4. Dudiak CM, Turner DA, Patel SK, Archie JT, Silver B, Norusis M. Uterine leiomyomas in the infertile patient: preoperative localization with MR imaging versus US and hysterosalpingography. *Radiology* **1988**;167: 627–630
5. Mittl RL, Yeh I-Tien, Kressel HY. High-signal-intensity rim surrounding uterine leiomyomas on MR images: pathologic correlation. *AJR* **1991**;180:81–84

Book Review

Diagnostic Techniques in Urology. Edited by Patrick H. O'Reilly, Nicholas J. R. George, and Robert M. Weiss. Philadelphia: Saunders, 640 pp., 1990. $175

This book is "how to perform" and "how to interpret." The first sections describe and evaluate diagnostic urologic procedures in such a way that readers should be able to understand both the purpose behind each examination and the practical details of how these examinations should be performed and interpreted. Topics include angiography of the urinary tract; percutaneous nephrostomy and antegrade pyelography; and evaluation of renal function, with discussions of all the current imaging techniques.

The chapter on testicular imaging is excellent. The authors point out that because the sonographic appearance of testicular tumors is so variable, it may not be possible to differentiate benign from malignant tumors when this imaging technique is used. The chapter includes updated details on the usefulness of Doppler techniques in testicular torsion and ischemia. Discussions on the current management of male impotence and infertility and the chapter on endoscopic techniques are valuable reading for general radiologists.

Nuclear medicine, long a friend of urology, takes its place of importance in the detection of urinary tract diseases. The chart on currently used renal radiopharmaceuticals (physiology and applications) is most helpful. The new technetium compound, MAG_3, the new multipurpose renal imaging agent makes it possible to observe the dynamics of renal angiography and the physiology of renal tubular function with one injection. The chapter on radiologic contrast studies is outstanding. It includes a timely review of contrast media and organ toxic effects. The proposals for the routine use of nonionic contrast medium are still controversial. The number of excretory urograms performed during the past 5 years has decreased 60%. The chapter on investigation of obstructive uropathy offers an excellent discussion on the detection of acute, and chronic (equivocal and unequivocal) obstruction and includes information on sonography, CT, and radionuclide studies.

A strong argument is presented for the place of lymphography in the detection of nodal involvement in genitourinary malignant tumors. The authors point out that currently lymphography is used in urology mostly for detection of tumors of the bladder and prostate. They also point out that sonography is the "least invasive, cheapest and one of the most accurate techniques for diagnosing renal tumors" and that Doppler techniques "may provide information on the patterns of blood flow in renal cell carcinoma."

The chapters on clinical urography include ones on perfusion pressure flow studies, cystometrics, uroflowmetry, urodynamics, endoscopy, biopsy, and cytologic techniques. Ample photomicrographs of excellent quality, pictures of instrumentation, and a goodly supply of descriptive illustrations are provided.

The book is thorough and technically excellent. Readability, index, references, charts, decision trees, and excellent quality illustrations attest to a mission accomplished. From my vantage point, the work is primarily of urology, for urology, and, for the most part, by urology. For those in uroradiology who wish to know a bit more about urology per se, this just may be the book.

Murray A. Rosenberg
Easton, CT 06612

Technical Note

Infusion of Air into the Collecting System to Avoid Needle Blockage During Percutaneous Nephrostomy After Extracorporeal Shock-Wave Lithotripsy

James H. Ellis,[1,2] David C. McKay,[1] and L. Paul Sonda[2]

Percutaneous nephrostomy after extracorporeal shock-wave lithotripsy (ESWL) can be complicated by stone fragments in the renal collecting system [1, 2]. The needle can become plugged with small stone fragments, or guidewire manipulation can be restricted by larger stone fragments. One solution to the problem of needle obstruction is to use an 18-gauge needle for the initial puncture instead of a smaller bore needle [1]. We present a patient in whom percutaneous nephrostomy after ESWL was complicated by blockage of not only the 21-gauge Cope needle used in the first puncture attempt but also an 18-gauge needle used on subsequent attempts. Air was infused into the collecting system to displace the fragment-filled urine and provide a stone-free target for access.

Case Report

A 45-year-old man was referred from another hospital after ESWL treatment of a right-sided staghorn calculus. His distal ureter had become obstructed with stone fragments (steinstrasse), and cystoscopic retrograde catheterization attempts were unsuccessful.

Percutaneous nephrostomy was performed at our institution. An initial opacification puncture was performed with a 22-gauge Chiba needle under fluoroscopic guidance from a direct posterior approach into the renal pelvis, guided by the residual stone fragments in the collecting system. After opacification, a posterolateral approach to a posterior midpole calix was chosen. Puncture was performed with a 21-gauge Cope needle (Cook Inc., Bloomington, IN). After aspiration of a small amount of urine, flow ceased and a wire could not be advanced through the needle, which had become obstructed with stone material present within the urine. A second attempt with another 21-gauge Cope needle met with the same result; even though no urine was aspirated, the needle became blocked from the fragments as urine flowed retrogradely through the needle because of internal renal pelvic pressure.

We then elected to attempt puncture with 18-gauge Hawkins-Akins blunt-tipped needles (Cook Inc.). Despite careful positioning without syringe aspiration, and rapid insertion of a guidewire, two punctures with these needles also were blocked from retrograde urine flow. Neither standard 0.035-in. (0.089-cm) nor 0.018-in. (0.046-cm) guidewires could be advanced through these needles.

We then decided to infuse air as a contrast agent. The original opacifying needle was blocked, so we placed a new 22-gauge Chiba needle from a posterolateral approach into a lower pole infundibulum. An initial attempt to pass a 0.018-in. wire was unsuccessful, but it was possible to carefully infuse a few milliliters of contrast material followed by air. With air filling the posterior (nondependent) calices, another puncture with an 18-gauge needle was made into an air-containing calix by using careful fluoroscopic positioning and no aspiration of the needle. Through this needle, a 0.035-in. wire was easily advanced into the collecting system, and tract dilatation and catheter placement were readily accomplished.

Received September 9, 1991; accepted after revision October 30, 1991.

[1] Department of Radiology, University of Michigan Medical Center, 1500 E. Medical Center Dr., Ann Arbor, MI 48109-0330. Address reprint requests to J. H. Ellis.

[2] Department of Surgery (Section of Urology), University of Michigan Medical Center, Ann Arbor, MI 48109-0330.

AJR 158:807-808, April 1992 0361-803X/92/1584-0807 © American Roentgen Ray Society

Discussion

Gas has proved to be a very useful contrast medium in percutaneous nephrostomy, with several advantages over other types of contrast material. As it is lighter than urine, it will identify the nondependent portions of the collecting system, which, with the patient in a prone, or prone-oblique position, are the target posterior calices [3]. For percutaneous stone extraction, gas has several other reported advantages over opaque contrast media: it is better for delineating small calculi, which might be obscured by opaque contrast material [4]; it prevents misidentification of areas of edema or bubbles as filling defects; and it can help differentiate small opaque caliceal stones from Randall's plaques and foci of medullary calcinosis in patients with concomitant nephrolithiasis that has been treated percutaneously [5].

In our patient, we were unable to introduce a guidewire when the lumen of the 21-gauge Cope needle used for the initial puncture became blocked by small fragments of stone that had formed a sludge in the urine in the collecting system. Two additional puncture attempts with 18-gauge needles were made, but the lumens of these needles also became occluded with stone, and we were unable to pass a wire into the collecting system. Our solution was to puncture the collecting system with a 22-gauge Chiba needle and to infuse a small amount of air before the needle became occluded. The air rose into the posterior calices, displacing the fragment-filled urine. Puncturing one of the air-filled calices enabled us to establish access to the collecting system without the lumen of the needle becoming occluded, and thus to pass a guidewire and subsequently a catheter into the collecting system.

Cochran et al. [1] have emphasized that percutaneous nephrostomy can be more difficult after ESWL because of stone fragments in the collecting system. They suggested the use of a larger bore needle for the initial puncture to obtain entry into the collecting system despite the presence of small stone fragments. In our case, access could not be obtained with either large or small needles. Percutaneous access required the use of a lighter-than-urine contrast medium to facilitate entry into the collecting system. As carbon dioxide was not readily available, after ensuring needle placement within the collecting system by infusing a small amount of contrast material, we used air to create an "air pocket" to puncture, thereby avoiding contact with the sludge of small stone fragments and preventing occlusion of the needle lumen. If readily available, carbon dioxide would be the preferred choice because of its proved safety in the event that inadvertent intravascular injection should occur, as well as the fact that it quickly diffuses away in case of extravasation and thus does not obscure visibility [3, 6]. There are no known contraindications to the use of carbon dioxide, and its use as a contrast agent has been described in a patient who had had a severe reaction to iodine [6].

In our institution, we have favored the use of percutaneous nephrostomy and endourologic techniques to debulk staghorn calculi before ESWL treatment of any remaining stone material [1]. This treatment sequence avoids the problem we describe here. However, in patients in whom ESWL is performed as the primary therapy and percutaneous nephrostomy subsequently becomes necessary, air or carbon dioxide infused into the collecting system can be a useful technique to assist in the performance of percutaneous nephrostomy.

REFERENCES

1. Cochran ST, Liu E, Barbaric ZL. Percutaneous nephrostomy in conjunction with ESWL in treatment of nephrolithiasis. *AJR* **1988**;151:103-106
2. Tegtmeyer CJ, Kellum CD, Jenkins A, et al. Extracorporeal shock wave lithotripsy: interventional radiologic solutions to associated problems. *Radiology* **1986**;161:587-592
3. Hunter DW, Salomonowitz E, Castañeda-Zuñiga WR, Young A, Mercado S, Amplatz K. Carbon dioxide as a lighter-than-urine contrast medium for percutaneous nephrostomy. *Radiology* **1984**;152:211-212
4. Khan AU, Leary FJ, Greene LF. Pneumopyelography. *Urology* **1976**;8: 92-93
5. Banner MP, Stein EJ, Pollack HM. Technical refinements in percutaneous nephroureterolithotomy. *AJR* **1985**;145:101-107
6. Salomonowitz E, Castañeda-Zuñiga WR, Lange PH, et al. Percutaneous stone removal—use of carbon dioxide as contrast material. *Radiology* **1984**;150:833-834

Percutaneous Needle Biopsy of Musculoskeletal Lesions.
1. Effective Accuracy and Diagnostic Utility

Margaret A. Fraser-Hill[1, 2]
Donald L. Renfrew[3]

The utility of a diagnostic test depends not only on its accuracy but also on how its results affect clinical management. We reviewed the results of 102 percutaneous needle biopsies to determine the accuracy, effective accuracy, and diagnostic utility of the procedure. We found percutaneous needle biopsy was similarly accurate in identifying suspected metastatic lesions (82%, $n = 44$), suspected musculoskeletal infections (90%, $n = 29$), and suspected primary musculoskeletal tumors (83%, $n = 29$). Effective accuracy, or accuracy discounted for results with limited clinical utility, was highest in identifying suspected metastatic deposits (77%), slightly lower in suspected infections (72%), and lowest in suspected primary tumors (59%). Diagnostic utility (the probability-weighted sum of the utility values of all possible outcomes of a diagnostic test) for identifying metastatic deposits and infections exceeded that for suspected primary tumors.

Percutaneous needle biopsy in patients with suspected primary tumors must be performed with the knowledge that, even though technically accurate, such biopsies may be of limited clinical value. Percutaneous needle biopsy of suspected metastatic lesions and suspected infections, on the other hand, offers high accuracy and high diagnostic utility.

***AJR* 158:809–812, April 1992**

When a diagnostic test is performed, even a highly accurate test, and the results are not used, the test adds to the expense of a patient's care without improving the quality of that care. To practice cost-effective medicine, we must know not only the accuracy of the tests we do but also their utility.

Percutaneous needle biopsy (PNB) of musculoskeletal lesions is a widely used technique with a reported accuracy ranging from 68% to 100% [1–14]. Advantages of PNB over open biopsy include lower morbidity and mortality [4, 7] and lower cost. However, PNB provides only a small quantity of tissue, and consequently, in some cases, another PNB or open biopsy is required for definitive diagnosis [4, 5]. Previous evaluations of the use of PNB have focused on the diagnostic accuracy of the technique, often without consideration of the clinical utility of PNB results. Even if the results are accurate, PNBs that do not prevent open biopsy are worse than worthless: they cause discomfort and add expense without improving care.

We undertook this study to determine the accuracy of PNB in various settings by considering the clinical utility of results. With this information, we evaluated the diagnostic utility [15] of PNB.

Materials and Methods

We retrieved the records of 102 PNBs (92 patients) of musculoskeletal lesions performed at the University of Iowa Hospitals and Clinics between 1985 and 1990. Experienced subspecialist musculoskeletal radiologists performed the PNBs using a variety of needle sizes and guidance systems. We constructed a data base using Microsoft Works (Microsoft,

Received September 9, 1991; accepted after revision November 12, 1991.

This work was supported in part by the Canadian Radiological Foundation.

[1] Both authors: Department of Radiology, College of Medicine, The University of Iowa, Iowa City, IA 52242.

[2] Present address: Department of Radiology, the Montreal General Hospital, McGill University, Montreal, Quebec, Canada H3G 1A4.

[3] Present address: Department of Radiology, Rush-Presbyterian-St. Luke's Medical Center, 1653 W. Congress Parkway, Chicago, IL 60612. Address reprint requests to D. L. Renfrew.

0361-803X/92/1584-0809
© American Roentgen Ray Society

Redmond, WA). We reviewed each patient's chart and recorded the following: (1) Demographic data. (2) Suspected diagnosis (metastatic disease, infection, or primary tumor) as determined by the clinical presentation of the patient and the process deemed most likely from the radiologic appearance of the lesion. If reports listed more than one disease process, we took the favored process or the one listed first. If different reports offered different diagnoses, we took the interpretation of the most experienced musculoskeletal radiologist as the suspected diagnosis. (3) Data related to the PNB, including the date, site, and result. Experienced subspecialist pathologists interpreted the cytologic and histologic specimens. (4) The plain film appearance of the lesion on which the biopsy was performed. (5) The date of open biopsy, if performed, and its result. (6) The ultimate pathologic or clinical outcome, as indicated by results of pathologic examinations (open biopsy, other surgical procedures, additional PNB, or autopsy) or by clinical confirmation with follow-up for 6 months or more. For example, a 55-year-old male smoker with a new pulmonary nodule had an expansile rib lesion believed to represent an enchondroma. Cytopathologic examination of material obtained with a PNB confirmed enchondroma. The patient had no chemotherapy or radiation therapy, and the appearance of the lesion remained unchanged 1 year later. Clinical follow-up in this case confirmed that the biopsy was a true-negative for metastatic disease.

We categorized PNB results as true-positive (TP), true-negative (TN), false-positive (FP), and false-negative (FN) on the basis of the cytologic findings and ultimate clinical outcome. We then determined the clinical utility (following Patton and Woolfenden [15], called here simply *utility*) of PNB results according to the effect the results had on clinical management. TP and TN results that were accepted as diagnostic and that did not require open biopsy or additional PNB for confirmation were assigned the optimum utility value (utility = +1) [15]. TP and TN results that were not accepted as diagnostic and that required open biopsy or additional PNB for confirmation were termed equivocal-positive (EP) or equivocal-negative (EN). Although PNB in these instances accurately reflected the lesion on which biopsy was performed, the pathologist could not make a definite diagnosis because of the small quantities of tissue available (EP), or the clinician did not trust the result (EN). We assigned this subset of TP and TN results, along with FN and FP results, a utility value of −1.

Using these data, we calculated the accuracy of PNB as follows:

$$\text{Accuracy} = 100\% \times (\text{TP} + \text{TN})/(\text{All results})$$

Because EP and EN results reduced diagnostic accuracy, we also calculated a second value: effective accuracy. Effective accuracy considers the clinical utility of results and better reflects the performance of PNB in the clinical setting.

$$\text{Effective accuracy} = 100\% \times [(\text{TP} - \text{EP}) + (\text{TN} - \text{EN})]/(\text{All results})$$

We used effective accuracy to calculate diagnostic utility of PNB. Diagnostic utility is a measure that considers both the clinical utility of each possible test result and the probability that each result will occur [15]:

$$\text{Diagnostic utility} = U(\text{TP})P(\text{TP}) + U(\text{EP})P(\text{EP}) + U(\text{TN})P(\text{TN}) + U(\text{EN})P(\text{EN}) + U(\text{FP})P(\text{FP}) + U(\text{FN})P(\text{FN})$$

Here, U(TP) = utility value of a TP test, and P(TP) = probability of a TP test occurring. U(EP), P(EP), U(TN), P(TN), U(EN), P(EN), U(FP), P(FP), U(FN), and P(FN) are similarly defined. When utility values of −1 and +1 are assigned, the above formula simplifies to

$$\text{Diagnostic utility} = (2 \times \text{effective accuracy}) - 100\%$$

We then formed subsets of the data according to the suspected diagnosis, and according to whether the lesions appeared to originate in soft tissue or bone. We also divided lesions by location into appendicular or axial categories. Finally, we categorized the lesions by radiologic appearance as radiolucent/lytic, sclerotic, vertebral compression fractures, and miscellaneous.

We entered 102 PNBs (92 patients) into the data base. Seven patients had two PNBs and one patient had four PNBs. Forty-six PNBs were performed on women and 56 on men. Patients were 3–90 years old (mean, 58 years).

Results

Suspected Diagnosis

As shown in Table 1, PNB demonstrated roughly equal accuracy in each of the three categories for suspected diagnosis. The effective accuracy of PNB was highest in suspected metastatic lesions. Thirty-six of these 44 patients had a known primary tumor. Effective accuracy and diagnostic utility were somewhat lower in suspected infection and much lower in suspected primary tumor. The lower effective accuracy and diagnostic utility in suspected primary tumors resulted mainly from five equivocal-positive results.

Lesion Location

Table 2 shows the results according to lesion location. The accuracy, effective accuracy, and diagnostic utility differed little with the location of the lesion.

Radiologic Features

Table 3 shows the results categorized according to radiologic features. We found the lowest values of effective accuracy and diagnostic utility in the relatively small groups of sclerotic lesions and vertebral compression fractures. Values for soft-tissue lesions were comparable to other lesions.

Discussion

PNB of musculoskeletal lesions is a relatively safe procedure that often provides critical information for patient management [1–14]. We undertook this study to determine those lesions for which PNB results would be most and least clinically useful. Past studies of PNB used accuracy to assess performance. Accuracy, however, fails to take into account the relative desirability or clinical utility of test results. Effective accuracy (which discounts for accurate but clinically useless results) and diagnostic utility are both measures that consider the clinical utility of test results [15]. Diagnostic utility is a measurement that facilitates evaluation of cost-effectiveness.

In our study, PNB provided the most useful information in the setting of suspected metastatic disease. The ideal candidate for percutaneous biopsy is a patient with a known primary tumor and either single or multiple lesions that demonstrate imaging findings consistent with metastatic deposits. Such lesions often require biopsy, because a significant proportion of them may not be metastases [11, 16]. These

TABLE 1: Results of Percutaneous Needle Biopsy According to Suspected Diagnosis

Suspected Diagnosis	TP (EP)	FN	TN (EN)	Accuracy (%)	Effective Accuracy (%)	Diagnostic Utility (%)
Metastases (44)	28 (1[a])	8	8 (1)[b]	82	77	55
Infection (29)	7[c]	3	19 (5[d])	90	72	45
Primary tumor (29)	19 (5[e])	5	5 (2[f])	83	59	17
Total (102)	54 (6)	16	32 (8)	84	71	41

Note.—TP = true-positive; EP = equivocal-positive (scientifically correct but not clinically useful); FN = false-negative; TN = true-negative; EN = equivocal-negative (scientifically correct but not clinically useful). No diagnoses were false-positive. Numbers in parentheses in column 1 = number of patients with suspected diagnosis.

[a] Poorly differentiated malignant cells identified on biopsy specimen could not be classified as sarcomatous or carcinomatous. Open biopsy showed poorly differentiated adenocarcinoma.

[b] Final diagnosis in these cases included one case of avascular necrosis, one enchondroma, one degenerative change, and five cases in which no tumor cells were seen, and which underwent no subsequent radiologic change.

[c] In six cases, cultures were positive. In the seventh, frank pus was aspirated.

[d] Open biopsy or repeat percutaneous needle biopsy confirmed absence of infection.

[e] Diagnosis at open biopsy was chondrosarcoma, chondroblastic osteosarcoma, lymphoma, Ewing sarcoma, and malignant fibrous histiocytoma. A specific diagnosis was made on the basis of cytologic examination of material from percutaneous needle biopsy in three of these cases, and malignant cells were identified in the other two. In all five cases, the pathologist requested more tissue for definitive characterization.

[f] Open biopsy confirmed the absence of tumor.

TABLE 2: Results of Percutaneous Needle Biopsy According to Location of the Lesion

Lesion Location	TP (EP)	FN	TN (EN)	Accuracy (%)	Effective Accuracy (%)	Diagnostic Utility (%)
Appendicular (69)[a]	31 (5)	11	27 (6)	85	68	36
Axial (33)[b]	23 (1)	5	5 (2)	85	76	52

Note.—TP = true-positive; EP = equivocal-positive (scientifically correct but not clinically useful); FN = false-negative; TN = true-negative; EN = equivocal-negative (scientifically correct but not clinically useful). No diagnoses were false-positive. Numbers in parentheses in column 1 = number of patients with suspected diagnosis.

[a] The most frequent sites of appendicular lesion location were the femur (16), foot (12), humerus (five), tibia (six), clavicle (four), and scapula (three).

[b] Axial lesion location included 21 in the vertebral column (five thoracic, eight lumbar, eight sacral), 10 in the ribs, and two in the soft tissues of the back.

TABLE 3: Results of Percutaneous Needle Biopsy According to Radiologic Features

Radiologic Feature	TP (EP)	FN	TN (EN)	Accuracy (%)	Effective Accuracy (%)	Diagnostic Utility (%)
Lytic or radiolucent (68)	45 (4)	10	13 (3)	85	75	50
Sclerotic (13)	1	4	8 (2)	69	54	7
Vertebral compression (6)	3	1	2 (2)	83	50	0
Soft tissue (15)	5 (2)	1	9 (1)	93	73	47

Note.—TP = true-positive; EP = equivocal-positive (scientifically correct but not clinically useful); FN = false-negative; TN = true-negative; EN = equivocal-negative (scientifically correct but not clinically useful). No diagnoses were false-positive. Numbers in parentheses in column 1 = number of patients with suspected diagnosis.

lesions often destroy the cortex and thus do not require the use of a trephine needle. The histologic monotony of these lesions makes it highly likely that the small samples obtained with PNB faithfully represent the tumor. As others have done [2, 4, 5, 7, 11], we found that PNB was accurate in about 80% of these cases and, equally important, that the pathologic readings were almost always unequivocal (Table 1).

The diagnostic success with infections exceeded the success with metastatic deposits, approaching 90% (Table 1); clinicians, however, found five TN aspirates equivocal . These patients required open biopsy or additional PNB and effective accuracy was lowered to 72%. As Murphy et al. [4] have noted, although clinicians usually accept positive results when infection is suspected, they may question or ignore negative results.

Accuracy of PNB results in suspected primary tumors closely approached the accuracy of PNB results in metastases and infections (Table 1). In five of 19 TP cases, however, the pathologist asked for more tissue to make a definitive diagnosis. This produced a markedly decreased effective accuracy (59%) and diagnostic utility (17%). Heterogeneity of primary bone lesions caused this problem. Pathologists sometimes find it difficult to classify primary skeletal lesions even when the entire lesion is available, so usefulness of cytologic diagnosis for some of these lesions is probably limited.

The location of the lesion had little effect on accuracy, effective accuracy, and diagnostic utility of PNB (Table 2). Categorizing lesions according to radiologic appearance, we found diagnostic utility of lytic or radiolucent lesions and soft-tissue lesions to be relatively high: 50% and 47%, respectively (Table 3). Chance may account for the lower success we found in the small number of sclerotic lesions (diagnostic utility = 8%) and vertebral compression fractures (diagnostic utility = 0%). These lesions are particularly challenging, however, and the lower diagnostic utility may represent the genuine difficulty in obtaining an adequate specimen.

One of the limitations of our study is that it is retrospective. The biopsies reported do not represent a random sample of all musculoskeletal lesions subject to biopsy, but rather the cases that were referred to the radiologist for biopsy. Referral patterns and patients selected for biopsy at other institutions may vary, with resulting differences in accuracy, effective accuracy, and diagnostic utility. In addition, there will be ongoing changes in accuracy, effective accuracy, and diagnostic utility with improvements in biopsy technique, cytopathologic analysis, and clinical acceptance of results. It is not, however, our goal to address these important issues here, but rather to evaluate the effective accuracy and diagnostic utility of an existing system in order to determine those lesions for which PNB is most useful.

Another possible limitation of this study is the assignment of utility values of −1 for FN, EP, and EN cases. A utility value of −1 represents the "worst" outcome according to Patton et al. [15]. Is a biopsy that yields malignant cells but that requires more tissue for definitive diagnosis (EP) or PNB results that are correctly negative but not believed (EN) as harmful as FN results? In the clinical setting, the goal generally is to use PNB to replace open biopsy. Equivocal results, although not misleading, fail to accomplish this goal and are detrimental to patients' care. We think that assigning a utility value of −1 to these outcomes is reasonable. FN results may not lead to open biopsy, but they are clearly detrimental to patients' care. Different utility values for test outcomes would result in different diagnostic utility values, but as long as equivocal results are considered to have a negative effect on clinical management (and are assigned negative utility values), the relative ranking of diagnostic utility for PNB in various settings would remain similar.

The decision to perform PNB depends on a number of variables. Past studies have provided conflicting results regarding accuracy of PNB results in different types of musculoskeletal lesions. No prior paper, to our knowledge, uses the concepts of effective accuracy and diagnostic utility to address this issue. Our study suggests that the location of a lesion has little effect on the diagnostic utility of PNB results. Lytic or radiolucent lesions were associated with a higher diagnostic utility than were sclerotic lesions and vertebral body compression lesions, but the small number of sclerotic lesions, particularly vertebral body compression lesions, makes firm conclusions difficult. Suspected diagnosis as determined from the clinical history and radiologic appearance predicted diagnostic utility well, and PNB of suspected primary tumors should be done with the knowledge that, although technically accurate, the results of such PNBs may have limited clinical usefulness. Communication with the referring physicians and the pathologist before biopsy may alert the clinicians (and patient) that additional PNB or open biopsy could be necessary. In some cases, proceeding directly to open biopsy may be prudent. PNB of suspected metastatic lesions and suspected infections, on the other hand, offers high accuracy and high diagnostic utility, with few repeated biopsies necessary.

REFERENCES

1. Thommesen P, Frederiksen P. Fine needle aspiration biopsy of bone lesions: clinical value. *Acta Orthop Scand* **1976**;47:137–143
2. Moore TM, Meyers MH, Patzakis MJ, et al. Closed biopsy of musculoskeletal lesions. *J Bone Joint Surg [Am]* **1979**;61-A:375–380
3. deSantos LA, Murray JA, Ayala AG. The value of percutaneous needle biopsy in the management of primary bone tumors. *Cancer* **1979**; 43:735–744
4. Murphy WA, Destouet JM, Gilula LA. Percutaneous skeletal biopsy 1981: a procedure for radiologists: results, review and recommendations. *Radiology* **1981**;139:545–549
5. El-Khoury GY, Terepka RH, Mickelson MR, et al. Fine needle aspiration biopsy of bone. *J Bone Joint Surg [Am]* **1983**;65-A:522–525
6. Edeiken B, deSantos LA. Percutaneous needle biopsy of the irradiated skeleton. *Radiology* **1983**;146:653–655
7. Tehranzadeh J, Freiberger RH, Ghelman B. Closed skeletal needle biopsy: review of 120 cases. *AJR* **1983**;140:113–115
8. Ayala AG, Zornosa J. Primary bone tumors: percutaneous needle biopsy. Radiologic-pathologic study of 222 biopsies. *Radiology* **1983**; 149:675–679
9. Stoker DJ, Kissin CM. Percutaneous vertebral biopsy: a review of 135 cases. *Clin Radiol* **1985**;36:569–577
10. Akerman M, Rydholm A, Persson BM. Aspiration cytology of soft tissue tumors: the 10-year experience at an orthopedic oncology center. *Acta Orthop Scand* **1985**;56:407–412
11. Mink J. Percutaneous bone biopsy in the patient with known or suspected osseous metastases. *Radiology* **1986**;161:653–655
12. White VA, Fanning CV, Ayala AG, et al. Osteosarcoma and the role of fine-needle aspiration: a study of 51 cases. *Cancer* **1988**;62:1238–1246
13. Dollahite HA, Tatum L, Moinuddin SM, et al. Aspiration biopsy of primary neoplasms of bone. *J Bone Joint Surg [Am]* **1989**;71-A:1166–1169
14. Bennet JD, Yacyshyn BJ, Haddad RC, et al. Fine-needle aspiration of bone lesions. *Can Assoc Radiol J* **1990**;41:65–72
15. Patton DD, Woolfenden JM. A utility-based model for comparing the cost-effectiveness of diagnostic studies. *Invest Radiol* **1989**;24:263–271
16. Jacobson AF, Stomper PC, Cronin EB, Kaplan WD. Bone scans with one or two new abnormalities in cancer patients with no known metastases: reliability of interpretation of initial correlative radiographs. *Radiology* **1990**; 174:503–507

Percutaneous Needle Biopsy of Musculoskeletal Lesions.
2. Cost-effectiveness

Margaret A. Fraser-Hill[1, 2]
Donald L. Renfrew[1, 3]
Peter E. Hilsenrath[4]

We compared the cost-effectiveness of fluoroscopically directed percutaneous needle biopsy (PNB) of musculoskeletal lesions, CT-guided PNB, and open biopsy. We independently assessed the following characteristics: suspected lesion type (metastatic deposit, infection, or primary neoplasm, as determined by clinical findings and radiologic appearance before biopsy); lesion location (axial or appendicular); and appearance on plain films (radiolucent or lytic, sclerotic, vertebral compression fracture, and soft-tissue lesions). In suspected primary tumors, cost-effectiveness of PNB was similar to that of open biopsy: fluoroscopically directed PNB was slightly more cost-effective than open biopsy whereas CT-directed PNB was slightly less cost-effective. Either type of PNB was cost-effective for suspected metastatic deposits and infections, axial and appendicular lesions, radiolucent or lytic lesions, and soft-tissue lesions.

We conclude that PNB is cost-effective for most musculoskeletal lesions.

***AJR* 158: 813–818, April 1992**

The cost of health care has not featured prominently in clinical decision making, especially for patients who have health insurance. Physicians, who have been trained to do everything possible to improve the health of patients, fear that cost-effectiveness means sacrificing quality in favor of lower cost. Lower cost, however, does not necessarily imply a compromise in quality. Currently, few sources identify means of lowering cost while maintaining quality. Physicians often rely on intuitive assumptions about the cost-effectiveness of techniques and therapies. In the radiologic literature, many papers [1–3] claim that percutaneous needle biopsy (PNB) of musculoskeletal lesions is cost-effective, apparently under the assumption that the lower charges and diminished number of complications make the procedure preferable to open biopsy. If we assume that PNB costs less than open biopsy when the results of PNB provide information that would otherwise be obtained only by doing an open biopsy, then PNB is cost-effective. However, when the results of PNB cannot be used to make a definite diagnosis, additional PNB or open biopsy is necessary. When these results are considered, is PNB still cost-effective? Is it possible to predict, before the procedure, whether PNB in a given case is likely to be cost-effective? This paper addresses these questions.

Materials and Methods

We determined a base cost [4] (Table 1 provides definitions of several economic and cost-effectiveness terms) of PNB performed by radiologists (both fluoroscopically directed and CT-directed techniques) and open biopsy performed by orthopedic surgeons by using microcosting techniques described by Bretland [5] and Arenson et al. [6]. (See Appendixes 1, 2, and 3.)

We made several assumptions in our costing procedure. We costed biopsies as outpatient procedures. We estimated the time, equipment, and salaried personnel (technologists, residents, and nurses) on the basis of an "average" procedure after we consulted with

Received September 9, 1991; accepted after revision November 12, 1991.

This work was supported in part by the Canadian Radiological Foundation.

[1] Department of Radiology, College of Medicine, the University of Iowa, Iowa City, IA 52242.

[2] Present address: Department of Radiology, the Montreal General Hospital, McGill University, Montreal, Quebec, Canada H3G 1A4.

[3] Present address: Department of Radiology, Rush-Presbyterian-St. Luke's Medical Center, 1653 W. Congress Parkway, Chicago, IL 60612. Address reprint requests to D. L. Renfrew.

[4] Graduate Program in Hospital and Health Administration, College of Medicine, the University of Iowa, Iowa City, IA 52242.

0361–803X/92/1584–0813
© American Roentgen Ray Society

TABLE 1: Glossary of Terms Used

Term	Definition
Cost	Value of resources used in production.
Charge	Amount requested in payment.
Base cost	The cost of personnel, time, equipment, and indirect overhead.
Microcosting	A method of determining procedure costs by directly measuring resources consumed.
Opportunity cost	The cost of using resources for a certain purpose, measured by the benefit or revenues given up by not using them in their best alternative use.
Effective cost	A measure of the dollar cost per unit of useful diagnostic information. Excluding costs of mortality and morbidity, effective cost = base cost/diagnostic utility.
Cost:charge ratio	A number calculated by dividing costs incurred by charges.
Accuracy	Given a contingency table with test results plotted against a reference standard, accuracy = (true-positives + true-negatives)/all patients studied.
Effective accuracy	Accuracy corrected for "equivocal" results; that is, results that although scientifically accurate necessitated additional testing. Effective accuracy = [(true-positives − equivocal-positives) + (true-negatives − equivocal-negatives)]/all patients studied.
Diagnostic utility	The net useful information provided by a diagnostic test. Mathematically, the probability-weighted sum of the utilities of all possible outcomes of a diagnostic test.
Utility value	A measure of the desirability of test outcome (e.g., true-positive), values go from −1 (worst possible outcome) to 1 (best possible outcome) [4].

physicians, nurses, and administrators. We calculated per hour costs for technologists, resident staff, and nurses from the yearly salary plus benefits adjusted for actual hours worked. We assumed that the costs of administration, radiation protection, and general support personnel (film librarians, darkroom technicians, supply personnel, etc.) were similar for percutaneous and open biopsy, and we did not assess value for these components.

Whenever possible, costs were used instead of charges. In the case of the fluoroscopy unit and CT scanner, we calculated equipment costs from historic costs (cost of machine at time of purchase including maintenance contracts) plus inflation (based on the Department of Commerce Producer Price Index), averaged over the expected life span of the equipment. A 7% opportunity cost of capital was included. We calculated a per hour cost by determining the number of hours per year the equipment was in use. For other items (e.g., a hand drill used for open biopsy), we used the current replacement costs. We then determined a cost per year based on the average life span of these items. We calculated a per use cost by estimating the number of times per year these items were used.

We obtained the costs of overhead (including building maintenance, housekeeping, building depreciation, plant operation, interest charges, and housekeeping) from hospital administration on a per-square-foot-per-year scale for the radiology suites used. We determined total overhead costs per hour by using the number of hours per year that a given room generated income. In determining the cost of overhead for open biopsy, we obtained cost data by using cost:charge ratios generated by our hospital's administration. We obtained the hospital charges applied for operating room time (which include overhead, maintenance, housekeeping, etc.) and adjusted them with the appropriate cost:charge ratio. We also used our hospital's cost:charge ratios to obtain cost information on recovery room time, anesthesia supplies, laboratory tests, and surgical pathology. For some items, such as electrocardiography, we used the hospital charges applied for the procedure.

We included professional costs for radiologists, orthopedic surgeons, and anesthesiologists, using an available resource-based relative-value scale for these costs [7]. These costs rely on statistical studies of time, stress, and other factors involved in performing procedures.

Because of difficulties in determining complication rates for biopsy and because dollar quantification of adverse effects is controversial, we ignored the expected direct costs [4] of morbidity and mortality associated with PNB and open biopsy. We also ignored the "downstream" costs [8] of medical therapy associated with each procedure. The occurrence of false-positive results is essentially nil [2], and although true-positive rates may vary between PNB and open biopsy, we chose to assume that the medical expenditures incurred in diseased patients would be similar for both investigative pathways.

We determined the effective cost of each procedure by using the method described by Patton and Woolfenden [4]:

$$\text{Effective cost} = (\text{Base cost})/(\text{Diagnostic utility})$$

Effective cost gives an assessment of the dollar cost per unit of useful diagnostic information provided. We determined base cost as described in the preceding paragraphs. Diagnostic utility, a measure of the net useful information provided by a diagnostic test, is the probability-weighted sum of the utility values of all possible outcomes of a diagnostic test [4]. When utility values of +1 and −1 are used, diagnostic utility is related to accuracy discounted for equivocal results (also called effective accuracy). The diagnostic performance of PNB was quantified in a review of 102 PNBs performed at our institution [9]. We formed subsets of these data according to suspected diagnosis and other features. We then determined effective accuracy (diagnostic accuracy discounted for results that required additional PNB or open biopsy for confirmation) and diagnostic utility.

We plotted the effective cost of PNB against diagnostic utility and compared the effective cost of PNB with the effective cost of open biopsy, assuming that open biopsy has a fixed effective accuracy and diagnostic utility of 100%. The effective cost of open biopsy was equal to the base cost, since we assumed a diagnostic utility of

100%. This served as a threshold below which the use of PNB was cost-effective.

Results

Appendixes 1, 2, and 3 present the line item costs for fluoroscopically directed, CT-directed, and open biopsy. Table 2 summarizes the figures from the Appendixes. Figure 1 shows effective cost vs diagnostic utility of PNB. It also shows the threshold at which PNB is favorable enough to substitute for open biopsy, assuming an accuracy and diagnostic utility of 100% for open biopsy. When fluoroscopically directed PNB has a diagnostic utility of 15% or greater, and CT-directed PNB has a diagnostic utility of 26% or greater, the effective cost of PNB is less than that of open biopsy. PNB is cost-effective in these instances. At lower levels of diagnostic utility, the effective cost of PNB is higher than the effective cost of open biopsy, and PNB is not cost-effective.

Discussion

Various authors [8, 10, 11] have offered different interpretations of cost-effectiveness. In this article we use Patton and Woolfenden's [4] definition of *effective cost*: "a measure of the actual amount of money spent [cost] per unit of diagnostic performance [effect]," which mathematically is expressed as cost (the resources consumed by a procedure) divided by diagnostic utility. Medical papers often incorrectly use charges as a substitute for cost [12]. Economists assume that in competitive markets, charges approximate cost (resources consumed). Markets that do not behave this way (e.g., medicine) may have persistently high charges that do not reflect costs. For this reason, using charge data for cost-effectiveness analysis is inappropriate. The cost of PNB and open biopsy should be calculated from resources consumed rather than charges levied for the procedures.

Diagnostic utility measures the clinical usefulness of a procedure, and depends on effective accuracy (accuracy discounted for results of limited utility) and the utility values assigned to test results. The literature provides little information on the effective accuracy of PNB, so we calculated the effective accuracy and diagnostic utility of PNB in our institution [9]. Regarding utility values, we assumed that scientifically accurate PNB results that did not prevent open biopsy or that necessitated additional PNB are as undesirable as false-negative results.

We used effective cost to compare PNB of musculoskeletal lesions (a procedure with lower diagnostic utility and lower cost than open biopsy) with open biopsy. We found that PNB had lower effective cost than open biopsy whenever the diagnostic utility exceeded 15% for fluoroscopically directed biopsy and 26% for CT-directed biopsy (Fig. 1). Our calculated diagnostic utility for all lesions was 41% [9], well within the range of cost-effectiveness. Lesions suspected of being metastases were associated with a diagnostic utility of 55%, while suspected infections were associated with a diagnostic utility of 45%. It makes eminent economic sense to perform PNB on these lesions. Diagnostic utility of PNB for suspected primary musculoskeletal lesions, however, was 17%. In this setting, despite an accuracy of 83%, the money spent per unit of useful diagnostic information obtained with CT-directed PNB exceeds the amount that would have been spent if open biopsy had been performed instead. Fluoroscopically directed PNB, with a diagnostic utility of 15%, remains cost-effective.

PNB was cost-effective for both appendicular and axial lesions, with a diagnostic utility of 36% and 52%, respectively [9]. PNB results also had high diagnostic utility for radiolucent or lytic lesions (50%) and soft-tissue lesions (47%). PNB results of sclerotic lesions and compression fractures of the vertebral body was associated with much lower diagnostic utility (8% and 0%, respectively). Only a few cases were included in either of these categories, however, and it is difficult to reach firm conclusions for sclerotic lesions or vertebral compression fractures.

Limitations of this study include the method of cost estimation. Our cost estimates should be regarded as relative, rather than absolute, costs for these procedures. We ignored costs that were difficult or impossible to measure and that we thought were of comparable magnitude for PNB and open biopsy. The cost of administration accounts for an increasing percentage of the total spending on health care [13], but we assumed administration costs are comparable for the two procedures and did not measure them. Morbidity and mortality are difficult to quantify in monetary terms. Although some

TABLE 2: Costs of Fluoroscopically Directed and CT-Directed Percutaneous Needle Biopsy and Open Biopsy

Method	Hospital Costs ($)	Physician Costs ($)	Total Costs ($)
Fluoro-PNB	136	113	249
CT-PNB	358	84	442
Open biopsy	1232	426	1658

Note.—Fluoro = fluoroscopically guided; PNB = percutaneous needle biopsy. For radiologist-performed procedures, physician costs include physician component for the radiologist and pathologist; for procedures performed by an orthopedic surgeon, this includes the surgeon, anesthesiologist, and pathologist. See Appendixes for details of cost assignment.

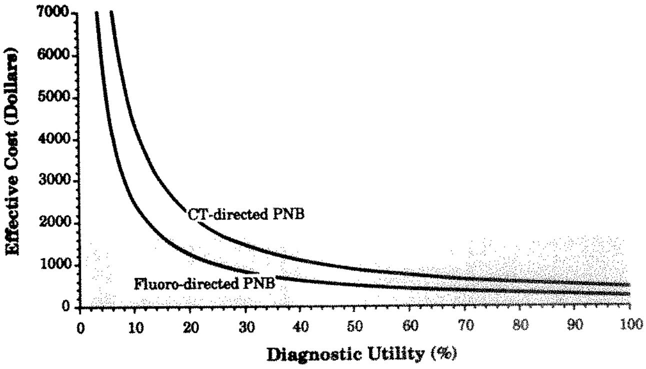

Fig. 1.—Graph shows effective costs for fluoroscopically (fluoro) directed percutaneous needle biopsy (PNB) and CT-directed PNB of bone lesions vs diagnostic utility. Shaded region represents area where PNB is cost-effective relative to open biopsy, when a diagnostic utility of 100% is assumed for open biopsy.

clinicians and patients might choose the less invasive PNB over open biopsy because of slightly decreased mortality and morbidity, other patients might consider open biopsy a better choice because the chance of an equivocal result is so small. Decision analysis [14] considers many factors such as these that are not easily quantified, and are not addressed by this study. A decision based on minimization of potential risk would likely favor PNB.

Another limitation of this study is that diagnostic utility depends on many factors, including radiologists' and pathologists' skills, and clinical acceptance. Although we offer our data as an example, site-specific data form a much better basis for calculations of diagnostic utility. Radiologists performing PNB of musculoskeletal lesions should consider auditing their own results to determine local diagnostic utility.

We also assume an accuracy, effective accuracy, and diagnostic utility of 100% for open biopsy. This assumption may be too strong. However, the effective cost of CT-directed PNB in the case of suspected primary musculoskeletal tumors is approximately $2500. For our recommendations to change, the effective cost of open biopsy must be at least $2500, and this does not occur until the accuracy of open biopsy falls to 83% (assuming no equivocal results). Our recommendations regarding cost-effectiveness thus remain the same over a wide range of accuracy for open biopsy.

In conclusion, we evaluated the cost-effectiveness of PNB relative to open biopsy for musculoskeletal lesions by comparing cost per unit of useful diagnostic information. In cases in which primary musculoskeletal tumor was considered the most likely diagnosis before biopsy, PNB and open biopsy were about equally cost-effective. In cases of suspected metastatic disease and suspected infection, PNB costs less than half as much as open biopsy. PNB was cost-effective for both appendicular and axial lesions, for radiolucent or lytic lesions, and for soft-tissue lesions.

REFERENCES

1. Schajowicz F, Derqui JC. Puncture biopsy in lesions of the locomotor system: review of results of 4050 cases, including 941 vertebra punctures. *Cancer* **1968**;2:531–548
2. Murphy WA, Destouet JM, Gilula LA. Percutaneous skeletal biopsy 1981: a procedure for radiologists. Results, review, and recommendations. *Radiology* **1981**;139:545–549
3. El-Khoury GY, Terepka RH, Mickelson MR, Rainville KL, Zaleski S. Fine-needle aspiration biopsy of bone. *J Bone Joint Surg [Am]* **1983**; 65-A:522–525
4. Patton DD, Woolfenden JM. A utility-based model for comparing the cost-effectiveness of diagnostic studies. *Invest Radiol* **1989**;24:263–271
5. Bretland PM. Costing imaging procedures. *Br J Radiol* **1988**;61:54–61
6. Arenson RL, van der Voorde F, Stevens JF. Improved financial management of the radiology department with a microcosting system. *Radiology* **1988**;166:255–259
7. Health Care Financing Administration. Medicare program: model fee schedule for physicians' services. *Federal Register.* June 5, 1991; 56:25792–25978
8. Doubilet PM. "Cost-effective:" a trendy, often misused term. *AJR* **1987**; 148:827–828
9. Fraser-Hill MA, Renfrew DL. Percutaneous needle biopsy of musculoskeletal lesions. 1. Effective accuracy and diagnostic utility. *AJR* **1992**; 158:809–812
10. Doubilet PM, Weinstein MC, McNeil BJ. Use and misuse of the term "cost effective" in medicine. *N Engl J Med* **1986**;314:253–256
11. Eisenberg JM. Clinical economics: a guide to the economic analysis of clinical practices. *JAMA* **1989**;263:2879–2886
12. Finkler SA. The distinction between costs and charges. *Ann Intern Med* **1982**;96:102–109
13. Woolhandler S, Himmelstein DU. The deteriorating administrative efficiency of the US health care system. *N Engl J Med* **1991**;324:1253–1258
14. Pauker SG, Kassirer JP. Decision analysis. *N Engl J Med* **1987**; 316:250–258

Appendix 1: Cost of Fluoroscopically Directed Percutaneous Needle Biopsy

Personnel	Time (hrs)	Cost/Hr ($)	Cost ($)
1 Technician	1	18.18	18.18
1 Radiology resident	2	15.15	30.30
Radiologist[a]			72.00
Pathologist[b]			40.93
Total			161.41
Materials[c]	Quantity	Unit Cost	Cost ($)
Proviodine 10% (ml)	5	0.002	0.01
Alcohol 70% (ml)	5	0.003	0.01
Steri-Drape	1	1.42	1.42
Gloves, sterile (pairs)	2	2.10	4.20
Lidocaine 1% (ml)	10	0.008	0.08
25-gauge needle	1	0.08	0.08
Syringe, 10 ml	2	0.06	0.12
Westcott needle	1	6.64	6.64
Franseen needle	1	15.75	15.75
Spinal needle 220-gauge	1	1.61	1.61
Arthrography tray[d]	1	1.85	1.85
Film cassette 9 × 9[e]	1	1.50	1.50
Total			33.27
Overhead and equipment	Quantity	Cost/Hr ($)	Cost ($)
Fluoroscopy suite[f]	303 sq feet	4.80	4.80
Siemens fluoroscope	1 hr	30.84	30.84
Total			35.64
Laboratory costs	Quantity	Unit Cost ($)	Cost ($)
PT/PTT[g]	1	10.71	10.71
Cytology interpretation[h]			5.44
Total			16.15
Fluoroscopically directed PNB total cost			250.47

[a] Current Procedure Terminology (CPT) code 20220 (bone biopsy, trocar/needle) used (*Physician's Current Procedure Terminology*, American Medical Association, Milwaukee, WI), using [7], adjusted by 3.5% for inflation.

[b] CPT code 88173 (interpretation of smear), modifier 26 (physician component) used, adjusted by 3.5% for inflation.

[c] Cost data used where available. We assumed a competitive market for medical equipment.

[d] Cost data unavailable. We used the charge applied for processing the tray after each use.

[e] Cost includes processing.

[f] Cost is calculated on a per sq ft basis. We assumed an average of 1 hr per procedure.

[g] PT/PTT = prothrombin and partial thromboplastin time.

[h] CPT code 88173 (interpretation of smear), modifier TC (technical component) used, adjusted by 3.5% for inflation.

Appendix 2: Cost of CT-Directed Percutaneous Needle Biopsy

Personnel	Time (hr)	Cost/Hr ($)	Cost ($)
2 Technicians	19.34	2	38.68
1 Resident	15.15	3	45.45
Radiologist[a]			43.05
Pathologist[b]			40.93
Total			168.11
Materials	**Quantity**	**Unit Cost ($)**	**Cost ($)**
Providine 10% (ml)	5	0.002	0.01
Alcohol 70% (ml)	5	0.003	0.01
Steri-Drape	1	1.42	1.42
Gloves, sterile (pairs)	2	2.10	4.20
Lidocaine 1% (ml)	10	0.008	0.08
25-gauge needle	1	0.08	0.08
Syringe, 10 ml	2	0.06	0.12
Westcott needle	1	6.64	6.64
Franseen needle	1	15.75	15.75
Spinal needle, 22-gauge	1	1.61	1.61
Arthrography tray[c]	1	1.85	1.85
Film cassette 14 × 17[d]	1	2.50	2.50
Total			34.27
Overhead and equipment	**Quantity**	**Cost/Hr ($)**	**Cost ($)**
CT suite[e]	320 sq ft	4.23	8.46
Picker CT scanner	2 hr	95.27	190.54
Total			199.00
Laboratory costs	**Quantity**	**Unit Cost ($)**	**Cost ($)**
PT/PTT[f]	1	10.71	10.71
Cytology interpretation[g]			5.44
Total			16.15
CT-directed PNB total cost			442.31

[a] CPT code 76361 (CAT scan for needle biopsy) modifier 26 (physician component) used, adjusted by 3.5% for inflation.

[b] CPT code 88173 (interpretation of smear), modifier 26 (physician component) used, adjusted by 3.5% for inflation.

[c] Cost data unavailable. We used the charge applied for processing the tray after each use.

[d] Cost includes processing.

[e] Cost is calculated on a per sq ft basis. We assumed an average of 2 hr per procedure.

[f] PT/PTT = prothrombin and partial thromboplastin time.

[g] CPT code 88173 (interpretation of smear), modifier TC (technical component) used, adjusted by 3.5% for inflation.

Appendix 3: Cost of Open Biopsy

Personnel	Time (hr)	Cost/Hr ($)	Cost ($)
1 Anesthesia resident	2	15.15	30.30
2 Orthopedic residents	4	15.15	60.60
2 Nurses	2	25.35	50.70
Anesthesiologist[a]			154.77
Orthopedic surgeon[b]			231.25
Pathologist[c]			39.74
Total			567.36
Materials	**Quantity**	**Unit Cost ($)**	**Cost ($)**
Disposable 3-gown pack	1	12.75	12.75
Basin pack	1	1.10	1.10
Arthroscopy pack	1	19.5	19.50
Skin scrub tray	1	2.59	2.59
Gloves, sterile (pairs)	7	2.10	14.70
Light handle covers	4	2.56	10.24
Sterile pillow cases	1	0.30	0.30
Lap sponge	1	1.42	1.42
4 × 4 sterile sponges	1	0.06	0.06
Asepto syringes	2	0.67	1.34
Sterile marking pen	1	0.43	0.43
Disposable pad	1	1.49	1.49
Plastic prep cup and lid	1	0.15	0.15
Sutures	3	3.51	10.53
Cautery holster	1	0.84	0.84
Instrument pouch	1	2.14	2.14
Electrocautery cleaner	1	0.24	0.24
Cautery cord and tip	1	1.48	1.48
Neomycin sulfate 1%	1	2.00	2.00
Adaptic dressing	1	0.23	0.23
Kerlix roll	1	0.57	0.57
Ace bandage (3″)	1	0.48	0.48
Total			84.58
Overhead and equipment	**Unit Cost ($)**	**Yearly Cost ($)**	**Cost ($)**
Zimmer hand drill[d]	404.00	20.20	1.68
Case for drill[d]	143.50	7.18	0.60
Drill bits (life; 1 yr)	160.09	160.09	13.34
Bone curette tray, angled[d]	344.25	17.21	0.22
Use charge	1.03	1.03	1.03
Bone curette tray, straight[d]	324.50	16.23	0.21
Use charge	1.03	1.03	1.03
Osteotome tray[d]	755.00	37.75	3.15
Use charge	1.03	1.03	1.03
Minor orthopedic tray[d]	2988.85	149.44	0.41
Use charge	1.81	1.81	1.81
Retractor tray[d]	1138.90	56.95	0.37
Use charge	1.32	1.32	1.32
Basin pack[d]	93.73	4.69	0.01
Operating room[e]			661.74
Anesthesia supplies[f]			89.20
Recovery room			145.21
Total			922.36
Laboratory costs	**Quantity**	**Unit Cost ($)**	**Cost ($)**
Complete blood count and urinalysis	1	15.01	15.01
PT/PTT[g]	1	10.71	10.71
ECG[h]	1	29.25	29.25
Chest radiograph	1	24.77	24.77
Surgical pathology[i]			4.18
Total			83.92
Open biopsy total cost			1658.22

[a] Assuming six base units and a rate/base unit of 26.87 (HCFA), adjusted 3.5% for inflation.

[b] CPT code 20250 (open biopsy), adjusted by 3.5% inflation.

[c] CPT code 88304 (interpretation of smear), modifier 26 (physician component) used, adjusted by 3.5% for inflation.

[d] Average expected lifetime: 20 years.

[e] Costs are derived from charges for ambulatory surgery, adjusted with a cost/charge ratio.

[f] Costs are derived from hospital charges adjusted with a cost/charge ratio.

[g] PT/PTT = prothrombin and partial thromboplastin time.

[h] Cost data unavailable. Hospital charges are applied.

[i] CPT code 88304 (interpretation of smear), modifier TC (technical component) used, adjusted by 3.5% for inflation.

Technical Note

Percutaneous Screw Fixation of Acetabular Fractures with CT Guidance: Preliminary Results of a New Technique

Spencer B. Gay,[1] Christopher Sistrom,[1] Gwo-Jaw Wang,[2] David A. Kahler,[2] Thomas Boman,[2] Nancy McHugh,[2] and Henry T. Goitz[2]

Treatment of acetabular fractures generally consists of either bed rest and traction for simple minimally displaced fractures, or open reduction and internal fixation for complex or significantly displaced fractures. Internal fixation permits early ambulation and can significantly reduce the amount of time spent in bed [1]. Open reduction of an acetabular fracture, however, is a significant physiological trauma to the patient and has the associated risks of postoperative infection, wound healing problems, formation of heterotopic bone, and neurologic injury. Many such patients require blood transfusion, during or after the procedure. CT is routinely used to evaluate acetabular fractures and plan treatment [2, 3]. Three-dimensional (3D) image processing also has been shown to be useful in the diagnosis and understanding of complex acetabular fractures [4]. We report a new technique for percutaneous fixation of these injuries with CT guidance. A similar technique was recently described for screw fixation of diastatic sacroiliac joints [5].

Materials and Methods

Between August 1990 and March 1991, six patients who were admitted to the orthopedic trauma service were treated with CT-guided screw fixation of their acetabular fractures. The two women and four men were 23–66 years old. Three of the fractures were in the left acetabulum and three were in the right. Four of the fractures were sagittal in orientation and involved the roof of the acetabulum with extension into the posterior column. The other two patients had coronal fractures through the roof extending into the posterior column. None of the patients had bone fragments within the hip joint itself. The interval between the injury and percutaneous fixation was 3–13 days (mean, 9.5 days). Follow-up was accomplished through review of chart notes from follow-up visits to the orthopedic clinic, chart notes from a rehabilitation center (in two patients), and verbal reports from the orthopedic surgeons involved. Follow-up has ranged from 6 to 15 months (mean, 9 months). Follow-up visits to the orthopedic clinic were made approximately every 6 weeks. Pelvic radiographs were obtained at each visit.

All patients had high-resolution CT scans of the pelvis to evaluate the geometry of the fracture and to help plan the procedure. Our protocol for these scans includes 3-mm slices through the acetabula and 5-mm contiguous slices through the rest of the pelvis. All the scans were done on a third-generation CT scanner (9800 Quick, General Electric). Image data were transferred via tape to a 3D workstation (Voxel Flinger, Reality Imaging, Solon, OH), where volumetric rendering and multiplanar reconstruction were used to visualize the geometry of the fracture and plan the procedures. The orthopedic surgeons actively participated in the 3D planning sessions.

Before the procedure, regional anesthesia was established by means of an epidural catheter and was maintained by intermittent infusion of local anesthetic; an anesthesia team was in attendance. The patients were placed prone or in the lateral decubitus (affected side up) position on the CT couch. A special stabilizing device (Vac-Pac, Olympic Equipment, Seattle, WA) was placed under the patients to maintain their position. Preliminary scans at 5-mm intervals were done with radiopaque catheters taped to the skin. The computer distance and angle measurement cursors were used to define optimal paths for the screws through the fractures and to trace these back to the skin surface. Marks were made on the skin to indicate appro-

---

Received June 14, 1991; accepted after revision October 11, 1991.

[1] Department of Radiology, Box 170, University of Virginia Hospital, Charlottesville, VA 22908. Address reprint requests to S. B. Gay.

[2] Department of Orthopedics, University of Virginia Hospital, Charlottesville, VA 22908.

AJR 158:819–822, April 1992 0361–803X/92/1584–0819 © American Roentgen Ray Society

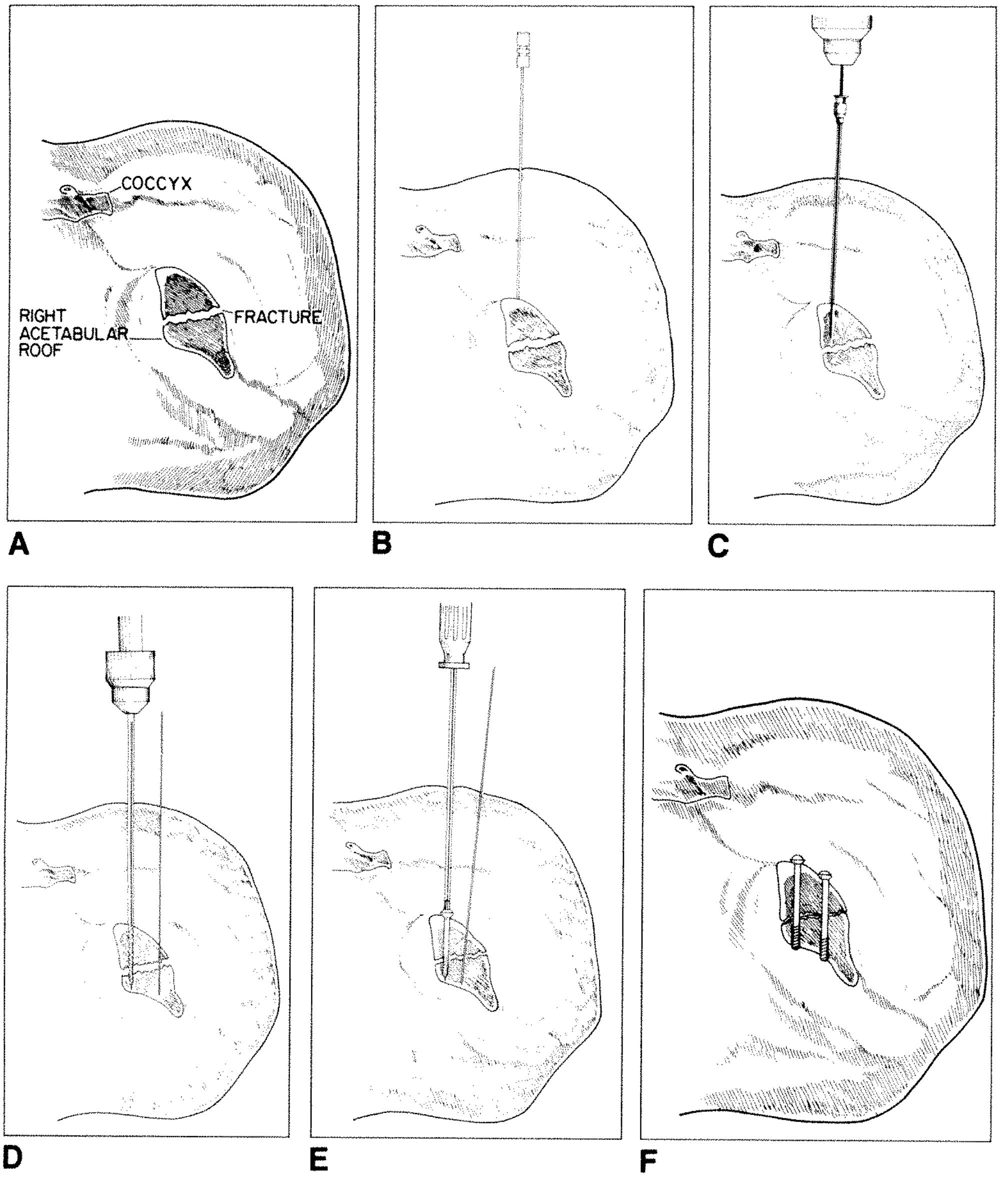

Fig. 1.—*A*, CT-guided percutaneous screw fixation of right acetabular fracture.

***B*, 20-gauge scout needle in place.**

***C*, Guiding cannula in place with Kirschner wire being drilled across fracture.**

***D*, Pilot hole being drilled over Kirschner wire. A second Kirschner wire has been placed for stabilization.**

***E*, Fixation screw being tightened across fracture.**

***F*, Final position of two screws across fracture.**

priate entry sites for the needles, guidewires, and screws. Standard sterile skin preparation and surgical draping procedures were carried out by operating room nurses.

Initially a 20-gauge removable hub needle (Cook Inc., Bloomington, IN) was placed along the previously defined path down to the bone. CT scans served to confirm the needle position (Fig. 1). When correct placement had been achieved, the hub was removed and the guiding cannula from an Ackerman bone biopsy kit (Cook Inc.) was placed over the needle shaft down to the bone. After removal of the 20-gauge needle, a 2.0-mm Kirschner guidewire (Synthes USA, Paoli, PA) was placed through this cannula and drilled by the surgeon through both fracture fragments with a pneumatic drill. The radiologist steadied the guiding cannula during this step. CT scans were used to confirm the correct angle and depth of the Kirschner wire. Usually, a second Kirschner wire was placed parallel to the first, by using the same technique, to stabilize the fragments during the subsequent steps. We found the guiding cannula useful for placement of the Kirschner wires. When the initial skin entry site was not strictly perpendicular to the cortical surface, placing the wire through the cannula helped prevent the tip from "walking" off the desired bone entry site. In addition, the stiff cannula maintained correct angulation during drilling with the Kirschner wire.

Once the Kirschner wires had transfixed the fracture, a pilot hole was drilled through both fragments. This was done with a long cannulated drill bit, marked in centimeters, and a pneumatic drill. By correlating measurements on the bit with distance measurements from the CT scans, this hole could be precisely drilled to the far cortex of the deep fragment. When the drill bit was removed after making the pilot hole, the guidewire tended to back out of the bone together with the bit. In two instances, the Kirschner wire did back out of the pilot hole in the bone. It was replaced by pushing the end against the cortical surface until the hole was found again and the wire could be repositioned.

The surgeon placed a cannulated self-tapping orthopedic screw (Richards Medical Co., Memphis, TN) of the correct length over the Kirschner wire. The correct length of the screw was estimated by measuring the distance between the proximal and distal cortices and adding approximately 5 mm. The screw was pushed down to the bone surface over the Kirschner wire and screwed through both fragments with a hollow screwdriver, thus fixing the fracture. After optimal placement was confirmed by CT, the guidewire was removed. When there was enough space in the fragments, a pilot hole was made over the second Kirschner wire and another screw was placed in tandem with the first. When indicated, these same steps were repeated to fix the second component of the fracture (three patients).

In all but one case, we placed two Kirschner wires across each fracture so that the second wire could stabilize the fracture fragments during drilling and screw placement over the first. If a second screw was placed, the first screw served to steady the fragments. Because the screws are 6.5 mm in diameter, we maintained a distance of at least 6.5 mm between the first and second guidewires to avoid entangling the threads and weakening the fixation. In one patient, we placed a screw over a single Kirschner wire into a coronal fracture of the acetabular roof that extended far up into the ileum. Both fragments were large enough to prevent rotation during the drilling or screw placement.

Results

In all cases, screws were successfully placed across the fractures chosen for percutaneous fixation (Fig. 2). In our first case, Kirschner wire placement was carried out in the CT suite, and the patient was moved to an operating room for placement of the screws. In the last five cases, we performed the entire procedure in the CT suite. The time required for the last five procedures ranged from 1.5 to 2.0 hr with about 30 min of this period devoted to transferring the patient and setting up anesthesia. Two screws were used in five cases. Three screws were placed in one patient. All six patients had coronal or sagittal fractures through the acetabular roof; all fractures were fixed with at least one screw. Four patients also had fractures of the posterior column; three of these were fixed. Although two patients had fractures of the anterior column, we did not attempt to fix either of these because intervening structures (i.e., the common femoral vessels) precluded a safe path for the hardware. Both of these fractures were of an orientation that would have required placing a very long screw through the superior pubic ramus at an awkward angle. Additionally, the cortex of the deep fragment was contiguous with the joint space, and the tip of a screw would have projected into the joint. Five of six patients had some reduction of displacement of the fracture, while the other patient had a nondisplaced fracture.

None of the patients had any significant blood loss. Five patients began to walk with crutches within 3 weeks of the procedure. All the patients are now walking, five with full weight-bearing and one with a cane. No evidence of degenerative change, shifting of the fragments, or dystrophic calcification about the hip joint has been seen on any of the follow-up pelvic radiographs. A small amount of lucency was seen around a single screw in one patient on a 5-month follow-up film. Subsequently, the patient became febrile, and the screw was removed surgically. It proved to be infected with *Staphylococcus aureus*. The patient is still walking without difficulty.

One patient had a poor technical result and did not progress to crutch-assisted walking until 2 months after the procedure. He had had a complex left acetabular fracture with posterior hip dislocation. This fracture was more displaced than the others, with a 1.2-cm maximum gap between the fragments of the sagittal acetabular roof fracture. In addition, a small bone fragment was lodged between the fragments. During percutaneous screw placement, balanced traction was maintained with femoral pins. The traction interfered with reproducible table positioning. The fragment lodged in the acetabular roof fracture prevented reduction, and in fact led to partial stripping of the bone around the screws when we attempted to fully tighten them. Nonetheless, no translation of the fragments or widening of the displacement has been seen on follow-up pelvic radiographs. The presence of contralateral tibial and fibular fractures, together with ipsilateral hip dislocation, prevented ambulation for 2 months. The patient now can walk with a cane and has a leg length discrepancy; the left leg is 1.3 cm shorter than the right. In retrospect, this patient was not a good candidate for percutaneous screw fixation.

Discussion

Currently, patients who have had acetabular fractures are treated with either open reduction and internal fixation or bed rest. When there is a widely displaced complex fracture, fragments in the hip joint, or fragments displaced into the fracture, open reduction is the procedure of choice. Conversely, a simple, minimally displaced acetabular fracture without free fragments in the joint may still be treated with bed rest and careful rehabilitation alone. The procedure we describe offers a third option. It is yet unclear which subset of patients will benefit most from percutaneous screw fixation. It would seem that mildly displaced (perhaps less than 1.0 cm) fractures through the acetabular roof and the posterior column may be best treated by this technique. Also, the alignment of the fracture fragments must be such that a smooth acetabulum can result from reduction [6].

Percutaneous fixation offers several advantages over open reduction of acetabular fractures. Soft-tissue disruption with the potential for devascularization or denervation is virtually eliminated. Blood loss is also significantly decreased, and a lower risk of infection may be anticipated owing to decreased tissue trauma and the lack of an open wound. Patients can often begin weight-bearing within 2 weeks after percutaneous fixation and do not have to recuperate from an operation. Regional anesthetic risks are equal for both procedures. It should be noted that complete reduction was not achieved in all patients, but was not considered mandatory because fixation permitted walking during recovery, which in itself promotes healing [7].

Thin-section CT scans were useful in evaluating the severity and geometry of the fractures. Such imaging is vital to exclude the presence of small free fragments of bone within the hip-joint space. When such fragments are identified, an open procedure is necessary because even small chips can cause significant damage to the joint with weight-bearing and movement [8]. Three-dimensional reconstruction was used to plan the fixation procedure in all cases and was found to be valuable in delineating the complex bony relationships. In our opinion, 3D surface rendition and multiplanar reconstruction in coronal and sagittal planes showed the relationship of all fragments more clearly. The orthopedists, who joined the planning sessions with radiologists, found the real-time interactive nature of such displays particularly helpful. Such co-

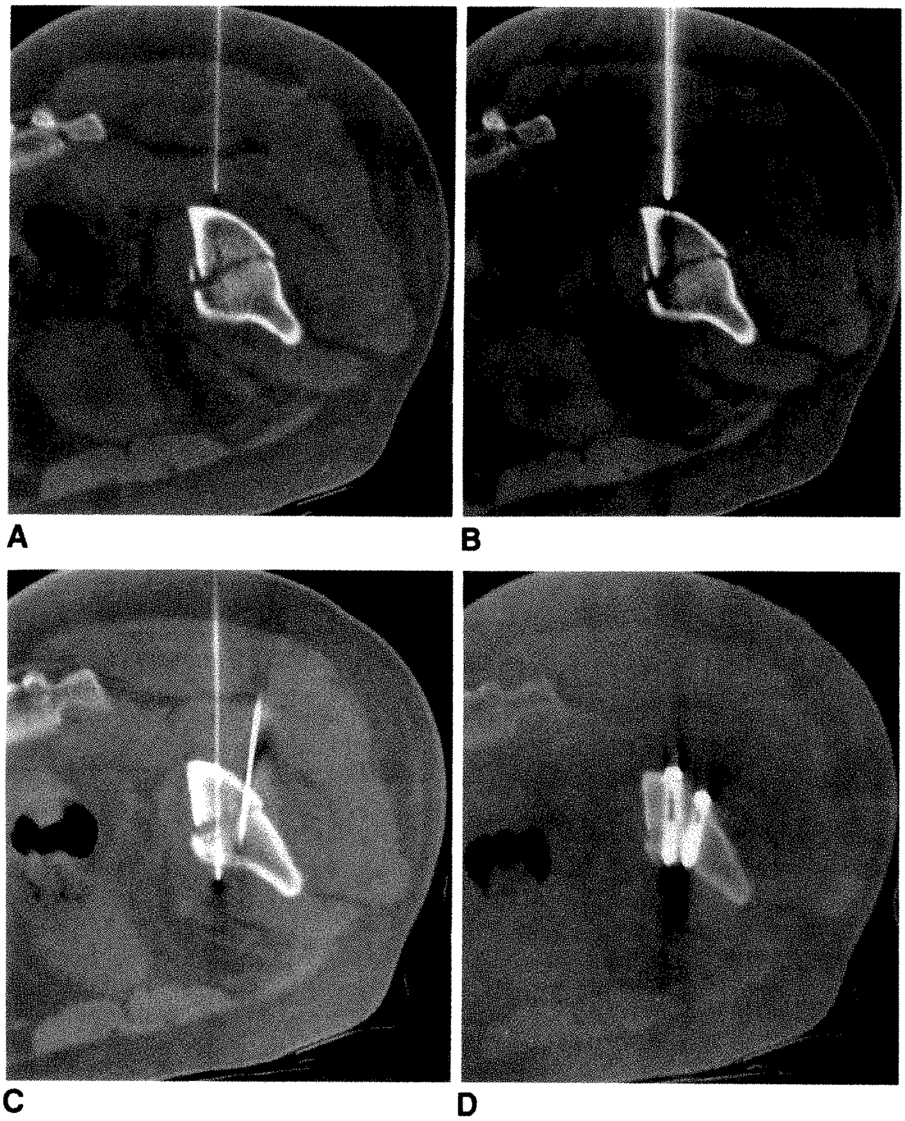

Fig. 2.—Axial CT scans through right acetabular roof during screw placement with patient prone.

***A*, 20-gauge scout needle in position with its tip contacting posterior fragment.**

***B*, Guiding cannula in place after removal of scout needle.**

***C*, Two Kirschner wires in place bridging fracture.**

***D*, Final position of two screws. Note that partial reduction has been achieved.**

operation in planning and performing these procedures is vital for optimal outcome.

We have shown that it is technically feasible to place screws across acetabular fractures under CT guidance. A combination of standard removable hub needles, a percutaneous bone biopsy set, and orthopedic guidewire and screw hardware were used. The pneumatic drills, cannulated bits, and screwdrivers used are available in most hospitals where orthopedic surgery is performed. Two radiologists, two orthopedic surgeons, and three orthopedic residents participated in the six procedures at various times, and only one technical failure occurred. The successful result suggests that the technique can be performed easily and reproducibly. The risks of the procedure are primarily those related to damage to structures found adjacent to the posteroinferior aspect of the acetabulum: the sciatic nerve and the superior and inferior gluteal artery and vein. The procedure must be planned so that the path of the hardware will not injure these structures.

The small number of patients and the relatively short follow-up preclude definitive conclusions about the indications for and the success rate of this technique. We are continuing to follow our first six patients and will perform further procedures in order to better define the role of this method in patients with acetabular fractures.

REFERENCES

1. Judet R, Judet J, Letournel E. Fractures of the acetabulum: classification and surgical approaches for open reduction. *J Bone Joint Surg [Am]* **1964**;46-A:1615–1646
2. Sauser DD, Billimoria PE, Rouse GA, Mudge K. CT evaluation of hip trauma. *AJR* **1980**;135:269–274
3. Mack LA, Harley JD, Winquist RA. CT of acetabular fractures: analysis of fracture patterns. *AJR* **1982**;138:407–412
4. Burk DL Jr, Mears DC, Kennedy WH, et al. Three-dimensional computed tomography of acetabular fractures. *Radiology* **1985**;155:183–186
5. Nelson DW, Duwelius PJ. CT-guided fixation of sacral fractures and sacroiliac joint disruptions. *Radiology* **1991**;180:527–532
6. Matta J, Merritt P. Displaced acetabular fractures. *Clin Orthop* **1988**;230:83–97
7. Mayo KA. Fractures of the acetabulum. *Orthop Clin North Am* **1987**;18:43–57
8. Epstein HC. *Traumatic dislocation of the hip*. Baltimore: Williams & Wilkins, **1980**

Case Report

Ifosfamide: A New Cause of Rickets

James E. Silberzweig,[1] Jack O. Haller,[1] and Scott Miller[2]

Ifosfamide is a chemotherapeutic agent related to the nitrogen mustards and is a synthetic analog of cyclophosphamide. Recent studies have indicated that ifosfamide is useful in the management of several recurrent tumors including Ewing's sarcoma, rhabdomyosarcoma, soft-tissue sarcomas, and Wilms' tumor [1]. It is now part of the first-line management of some of these malignant neoplasms.

Adverse effects of ifosfamide include nausea, vomiting, alopecia, myelosuppression, CNS toxicity, hemorrhagic cystitis, and nephrotoxicity [2]. Recently, hypophosphatemic rickets has been recognized as an additional complication of ifosfamide treatment [2, 3]. We saw a child with previously normal renal function and normal serum levels of calcium, phosphate, and alkaline phosphatase who developed hypophosphatemic rickets after ifosfamide treatment. To our knowledge, this occurrence has not been previously reported in the radiologic literature.

Case Report

A 2-year-old girl with normal renal function and normal serum levels of calcium, phosphate, and alkaline phosphatase underwent surgical resection, local radiotherapy, and chemotherapy for a stage III abdominal rhabdomyosarcoma. Chemotherapy consisted of ifosfamide (total cumulative dose, 175 g/m^2), vincristine, and actinomycin D at 3- to 4-week intervals for a total of 18 months. Treatment was complicated by severe myelotoxicity, but she completed therapy with no evidence of tumor recurrence and with normal renal function. However, 1 year after chemotherapy ended, a rachitic rosary was noted on physical examination. Laboratory tests revealed an elevated serum level of alkaline phosphatase and low serum level of phosphate. The serum level of calcium was normal. Radiographs of the chest and wrist (Fig. 1) confirmed the findings of rickets.

Discussion

The patient described demonstrates the rachitic changes thought to be caused by the nephrotoxicity of ifosfamide. We have also seen a 7-year-old girl with stage II Wilms' tumor who developed hypophosphatemic rickets 20 months after initiation of ifosfamide chemotherapy for tumor recurrence (Fig. 2). The specific features of the nephrotoxicity caused by ifosfamide include low serum bicarbonate and phosphate concentrations with glucosuria, aminoaciduria, and hypochloremic metabolic acidosis, otherwise known as Fanconi's syndrome [3]. The renal toxicity of ifosfamide is believed to be predominantly tubular, although glomerular abnormalities may occur [2]. Renal phosphate wasting is caused by proximal tubular damage [3]. Renal biopsies were not performed in our cases. No reversibility has been described in previous reports of nephrotoxicity in children after treatment with ifosfamide [3]. Most reported cases of ifosfamide-induced nephrotoxicity developed after several months of treatment. However, one report of a child who had severe Fanconi's syndrome after a single exposure to ifosfamide has been published [4].

The renal damage seen in ifosfamide toxicity differs from the damage seen in renal osteodystrophy. The failure of filtration seen in renal osteodystrophy causes a retention of phosphate with resulting hyperphosphatemia. The increased

---

Received August 25, 1991; accepted after revision October 7, 1991.

[1] Department of Radiology, State University of New York Downstate Medical Center, 450 Clarkson Ave., Brooklyn, NY 11203. Address reprint requests to J. O. Haller.

[2] Department of Pediatrics, State University of New York Downstate Medical Center, Brooklyn, NY 11203.

AJR 158:823–824, April 1992 0361–803X/92/1584–0823 © American Roentgen Ray Society

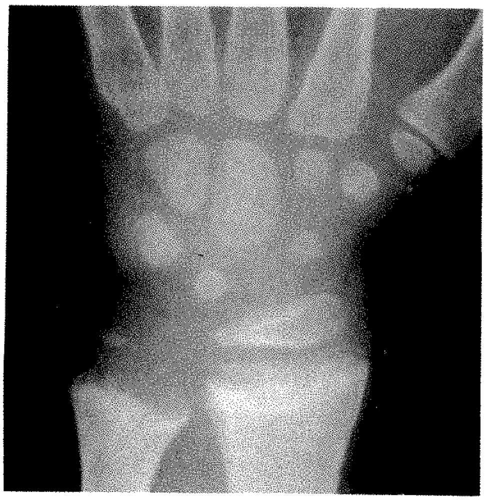

1

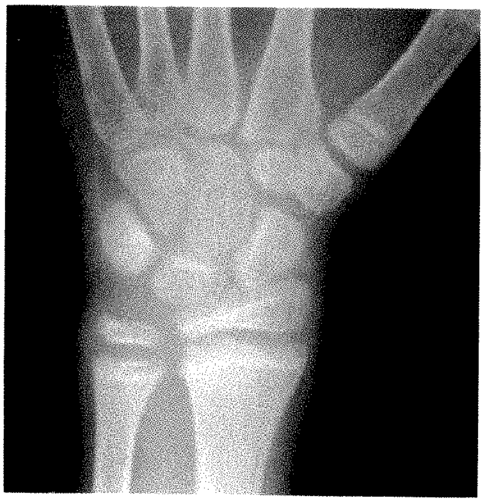

2

Fig. 1.—5-year-old girl with stage III abdominal rhabdomyosarcoma 3 years after initiation of ifosfamide chemotherapy. Radiograph of wrist shows growth-plate widening with metaphyseal fraying and cupping typical of rickets.

Fig. 2.—10-year-old girl with stage II Wilms' tumor 2 years after initiation of ifosfamide chemotherapy. Wrist radiograph shows widened growth plate and mild irregularity of metaphysis typical of rickets. (Slightly increased density at metaphysis suggests element of healing.)

phosphate causes a reduction in synthesis of 1,25-dihydroxyvitamin D and a decrease in gastrointestinal tract absorption of calcium. This decreased level of serum calcium promotes secondary hyperparathyroidism. In contrast, ifosfamide causes renal phosphate wasting with no effect on serum calcium level.

Chemically induced rickets has previously been associated with anticonvulsants. Long-term anticonvulsant treatment of epileptic children has resulted in rachitic bone changes, presumably by causing interference with vitamin D metabolism [5]. Congenital rickets has been associated with maternal IV infusion of magnesium sulfate for tocolysis. It is thought that prolonged infusion of magnesium sulfate may lead to suppression of the fetal parathyroid gland with resulting rickets [6]. Rachitic bone changes have also been noted in preterm infants receiving IV hyperalimentation. Calcium phosphate is relatively insoluble in this preparation, and the lack of available phosphate is presumed to cause rachitic changes [7]. Tumor-associated rickets also has been reported, but bone changes return to normal after tumor removal [8].

Rickets has not been described in association with any other chemotherapeutic agent [2]. Some believe that the rickets caused by ifosfamide is reversible [3]. Therefore, the radiologist should be attuned to the possibility of rickets when examining radiographs obtained for tumor surveillance.

REFERENCES

1. Miser JS, Kinsella TJ, Triche TJ, et al. Ifosfamide with mesna uroprotection and etoposide: an effective regimen in the treatment of recurrent sarcomas and other tumors in children and young adults. *J Clin Oncol* **1987**;5:1191–1198
2. Skinner R, Pearson AD, Price L, Coulthard MG, Craft AW. Nephrotoxicity after ifosfamide. *Arch Dis Child* **1990**;65:732–738
3. Burk CD, Restaino I, Kaplan BS, Meadows AT. Ifosfamide-induced renal tubular dysfunction and rickets in children with Wilms' tumor. *J Pediatr* **1990**;117:331-335
4. Devalck C, Ismaili K, Ferster A, Sariban E. Acute ifosfamide-induced proximal tubular toxic reaction (letter). *J Pediatr* **1991**;118:325–326
5. Matsuda I, Takekoshi Y, Shida N, Fujieda K, Nagai B. Renal tubular acidosis and skeletal demineralization in patients on long-term anticonvulsant therapy. *J Pediatr* **1975**;87:202–205
6. Lamm CI, Norton KI, Murphy RJ, Wilkins IA, Rabinowitz JG. Congenital rickets associated with magnesium sulfate infusion for tocolysis. *J Pediatr* **1988**;113:1078–1082
7. Binstadt DH, L'Heureux PR. Rickets as a complication of intravenous hyperalimentation in infants. *Pediatr Radiol* **1978**;7:211–214
8. Moncrieff M, Foot A. Fanconi syndrome after ifosfamide. *Cancer Chemother Pharmacol* **1989**;23:121–122

Review Article

Diagnostic Imaging of Mediastinal Masses in Children

David F. Merten[1]

Mediastinal masses are the most common thoracic masses in children. The encyclopedic list of diagnostic considerations can be distilled into a concise and practical differential diagnosis based on the location of the mass and the established prevalence of various tumors and pseudotumors in the mediastinal compartments. Malignant lymphoma, benign thymic enlargement, teratomas, foregut cysts, and neurogenic tumors make up 80% of mediastinal masses in children. Continuing advances in imaging technology have altered traditional approaches to the evaluation and diagnosis of mediastinal masses in children. Plain chest radiography remains the basic imaging examination to define location and morphology. Cross-sectional imaging subsequently clarifies the morphology and extent of the mass. In general, CT is the primary cross-sectional imaging procedure in the evaluation of most mediastinal masses in children. Exceptions to this rule include MR in children with posterior mediastinal masses or suspected vascular lesions: in such cases, MR imaging is the preferred initial postradiographic examination. Sonographic examination may be diagnostic in foregut cysts and some other mediastinal masses. Gallium-67 scintigraphy has an emerging role in management of malignant lymphoma.

The mediastinum is the most common site of chest masses in children [1, 2]. The masses are of diverse origin and pathogenesis, arising from virtually any organ or tissue in the mediastinum. The differential diagnosis includes neoplastic, developmental, inflammatory, traumatic, and cardiovascular tumors and pseudotumors and nonpathologic variations in growth and development of normal thoracic structures [3]. The mass may occur at any age, from the neonatal period through adolescence, with protean signs and symptoms that reflect both the primary pathologic condition and functional compromise of involved organs. Whatever the manifestations, a mediastinal mass in a child is an urgent clinical problem in which radiology plays a seminal diagnostic role.

During the past decade, technologic advances in imaging have greatly enhanced the capacity to localize and define the morphology and extent of the mass. Increasing experience with newer imaging techniques has altered established diagnostic approaches, and many traditional radiologic examinations have been supplanted by advanced imaging techniques. The purpose of this review is threefold: (1) to present a brief overview of the prevalence and types of mediastinal masses in children; (2) to consider developments in diagnostic imaging applicable to the evaluation and management of these masses; and (3) to describe current approaches to radiologic analysis and diagnosis of these masses, emphasizing the most commonly occurring tumors and pseudotumors.

Imaging Strategy

The principles of diagnostic imaging in the evaluation of mediastinal masses in children are simple: identify the mass; determine its location within the mediastinum; define its morphology; and delineate its extent as quickly, efficiently, and cost-effectively as possible. This requires that the radiologist be familiar with the prevalence and pathologic characteristics of various mediastinal masses that occur in children, and the relative sensitivity, specificity, and overall accuracy of applicable imaging techniques.

For purposes of radiologic analysis and diagnosis, the mediastinum in children is divided into the anterior, middle,

---

Received January 9, 1991; accepted after revision November 7, 1991.

[1] Department of Radiology, The University of North Carolina School of Medicine, Campus Box 7510, Chapel Hill, NC 27599-7510. Address reprint requests to D. F. Merten.

AJR 158:825-832, April 1992 0361-803X/92/1584-0825 © American Roentgen Ray Society

and posterior compartments of relatively equal size extending from the thoracic inlet to the diaphragm [4]. Because these masses occur with established regularity within each of the three mediastinal compartments, a concise list of diagnostic considerations can be established on the basis of the major anatomic contents of each compartment and the established prevalence of masses arising from these structures (Table 1). The anterior mediastinum contains the thymus, anterior (prevascular) lymph nodes, and anterior portions of the heart and great vessels; the middle mediastinum contains the middle group of lymph nodes, tracheobronchial tree and esophagus (which are of embryonic foregut origin), and posterior portions of the heart and great vessels; while the posterior mediastinum contains the paravertebral sympathetic nerve chain and intercostal nerves and the posterior lymph node groups [3]. In addition to these major components, each compartment contains various mesenchymal tissues, angiomatous structures, and minor nerves from which mediastinal masses may arise.

Conventional radiography remains the primary radiologic examination in the evaluation of mediastinal masses and is the foundation for all subsequent diagnostic imaging. The chest radiograph is used to identify and localize the mass to one of the mediastinal compartments and provides limited information about the morphology and extent of the lesion. Fluoroscopy and esophagography may help to further define the location of the mass and its effect on adjacent structures. Planar radiographic tomography has been used infrequently since the advent of cross-sectional imaging, and xeroradiography is seldom, if ever, indicated for evaluation of mediastinal masses in children.

TABLE 1: Primary Mediastinal Masses: Location and Prevalence in 508 Children

Location/Type of Mass	Prevalence (%)[a]
Anterior	
Malignant lymphoma (non-Hodgkin/ Hodgkin)	23
Thymus (benign enlargment, ectopy)	6
Teratoma	10
Other (angioma, cardiovascular, thymic cyst, thymoma, substernal thyroid, mesenchymal tumor, histiocytosis X)	–
Total	46
Middle	
Foregut cysts (bronchogenic, enteric)	11
Lymphadenopathy (lymphoma, granulomatous)	–
Other (angioma, cardiovascular, mesenchymal tumor)	–
Total	20
Posterior	
Neurogenic tumor (ganglion cell, nerve cell)	30
Other (angioma, lymphoma, foregut cyst, mesenchymal tumor)	–
Total	34

Note.—Data from King et al. [1] and Ravitch [2].
[a] Prevalences were not available for all types of masses.

Cross-sectional imaging is used to further define and clarify the findings on radiographs and to delineate the pathologic morphology and extent of the mass more accurately. In general, CT is the primary cross-sectional imaging technique for evaluation of most mediastinal masses in children; clinical experience with CT is extensive, the procedure is widely available, and the diagnostic accuracy is well established [5, 6]. Despite increasing application of MR in imaging children, this technique has a limited role relative to CT in the evaluation of mediastinal masses because of limitations in spatial resolution, prolonged scanning times, and relatively high cost [7]. However, specific exceptions to this general rule exist, based on the capacity of MR for multiplanar imaging and the contrast it provides between flowing blood and adjacent soft tissues [8]. Sonography may be a useful alternative to more expensive and invasive techniques in the evaluation of some supraaortic, pericardial, prevascular, paratracheal, juxtadiaphragmatic, and paraspinal masses, and sensitivity has been shown to be quite high (up to 98%) [9, 10].

Some imaging techniques such as scintigraphy appear to have emerging diagnostic roles, whereas other more specialized techniques have much diminished roles. Gallium-67 radionuclide scintigraphy is receiving increased attention in staging and follow-up of lymphoma and may be a valuable technique, especially with the use of single-photon emission CT (SPECT) [11]. Myelography, however, has been less frequently required to detect and delineate intraspinal extension of paravertebral tumors with the advent of MR imaging [12, 13]. Similarly, angiography is indicated only occasionally, since MR imaging has proved to be both accurate and efficacious in the diagnosis of many if not most vascular lesions [7].

Anterior Mediastinum

The anterior mediastinum is the most common site of mediastinal masses in children [1, 2]. The majority arise from the thymus and prevascular lymph nodes; malignant lymphomas, benign thymic enlargement, and teratomas account for 85% of all anterior mediastinal masses [1, 2] (Table 1). Other thymic masses, including cysts, thymomas, and masses of thyroid origin, rarely occur in children. Although cystic hygromas (lymphangiomas) make up 5% of all anterior mediastinal masses, these tumors usually extend into the mediastinum from the neck, and only 1% of cystic hygromas are of mediastinal origin [2].

Malignant Lymphomas and Leukemia

Malignant lymphoma is the most common anterior mediastinal mass; it accounts for 23% of all mediastinal masses in children [1, 2]. The actual prevalence is probably greater, as most large surgical series of mediastinal masses in children underreport or exclude lymphoma [2]. "Malignant lymphoma" encompasses Hodgkin disease and a heterogeneous group of other primary lymphatic tumors known as non-Hodgkin lymphomas [14]. In addition, approximately 15% of children with acute lymphoblastic leukemia have "lymphoma syndrome," which is associated with a mediastinal mass in 61% of patients [15]. Because of overlap in clinical, histologic, immunophenotypic, and cytogenic features, it is frequently difficult to determine if these patients should be classified as having leukemia with lymphomatous presentation or non-Hodgkin lymphoma with bone marrow involvement.

Overall, non-Hodgkin lymphoma is more common than Hodgkin disease in children [16, 17]. Hodgkin disease is almost invariably nodal and spreads in direct continuity: approximately 85% initially have a mediastinal mass, and 30% have hilar lymphadenopathy, which is frequently associated with direct pulmonary extension [14]. By contrast, non-Hodgkin lymphoma is usually extranodal and spreads hematogenously: there is a mediastinal mass in only 50% of newly diagnosed patients, and pulmonary involvement may occur without adjacent lymphadenopathy. Pleural fluid, present in approximately 5% of children with malignant lymphoma, may reflect lymphatic or venous compromise and does not necessarily indicate tumor involvement. By contrast, pericardial effusions are almost always due to direct tumor extension.

The initial chest radiograph is frequently diagnostic in children with malignant lymphoma, and usually shows a bulky anterior mediastinal mass that may extend into the middle or even posterior compartments (Fig. 1A). Calcification within lymphomatous tissue is nearly always associated with previous radiotherapy or chemotherapy, although primary calcification occasionally occurs in both types of lymphoma, possibly reflecting infarction and necrosis or disordered calcium metabolism related to tumor-mediated osteoclastic activity [18, 19] (Fig. 1B). CT accurately delineates tracheobronchial compromise, which may be missed on radiographs [20]. Airway compression occurs in 55% of children with newly diagnosed mediastinal lymphoma (Fig. 1C), and life-threatening airway obstruction is reported in up to 10% of patients with mediastinal lymphomas while under general anesthesia for biopsy or placement of a Broviac catheter [21, 22]. The exact amount of tracheal compromise associated with increased risk of acute obstruction has not been determined. However, it appears that endotracheal anesthesia is safe when the tracheal cross-sectional area is more than 50% of that expected [23]. In those cases with clinical or radiologic evidence of significant airway compression, preoperative pulmonary function studies or careful fiberoptic bronchoscopy may be advisable [24].

Although MR may offer some advantage over CT in more accurately showing chest wall invasion, few data support its routine use in the initial evaluation and staging of mediastinal lymphoma [8, 14]. Limited experience in adults indicates that MR determination of tumor size and signal intensity ratio (tumor to fat, tumor to muscle) before treatment can be used to predict the persistence and size of a residual mass after therapy [25]. The degree of low signal intensity before therapy appears to correlate with the amount of fibrous stroma in the primary tumor and supports the hypothesis that the size of the residual mass after therapy depends on the amount of fibrotic stroma in the original tumor. MR cannot accurately differentiate active tumor from posttherapy fibrosis in patients with a residual mediastinal mass, since radiation pneumonitis, infection, hemorrhage, and even fibrosis occasionally have a high signal intensity on T2-weighted images similar to the intensity of neoplasm [26].

The roles of other imaging techniques in the evaluation of children with mediastinal lymphoma remain to be determined. Limited experience correlating gallium-67 imaging and CT at initial presentation and follow-up indicates that scintigraphy is useful for assessing response to therapy in children with mediastinal lymphoma [27]. Both techniques consistently detected active disease with a negative predictive value of 100%; however, the positive predictive value of CT was only 46% compared with 73% in gallium-67 imaging. SPECT increases the sensitivity of gallium-67 imaging in both initial staging and follow-up of malignant lymphoma [28], although

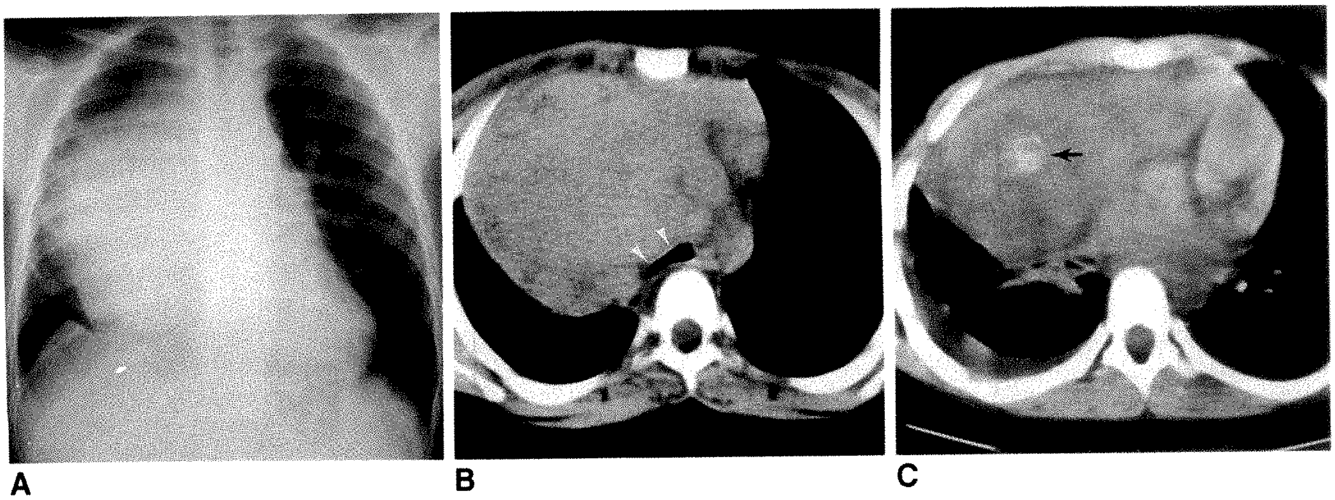

Fig. 1.—Non-Hodgkin lymphoma.

A, Chest radiograph shows large right-sided mediastinal mass obscuring right heart border. Trachea appears normal.

B, Unenhanced CT scan above carina shows tracheal compression (*arrowheads*) by inhomogeneous anterior mass extending posteriorly and to right.

C, Unenhanced CT scan at lower level than *B* shows irregular calcification within mass (*arrow*). Right-sided pleural effusion is present also. Histologic examination showed a necrotic lymphoblastic lymphoma infiltrating thymus and containing scattered calcifications.

its value in children will require additional clarification. The role of sonography in children with lymphoma is even less well defined. Although preliminary experience suggests that sonography is superior to chest radiography and comparable to CT for monitoring adults with mediastinal lymphoma [29], additional study is necessary to validate its usefulness and generality in the management of malignant lymphoma [30].

Many current imaging protocols are inefficient and make excessive use of thoracic imaging in follow-up of children with malignant lymphoma [31]. A dynamic probabilistic model developed to study optimal timing and frequency of chest radiography in the monitoring of children in remission indicates that the importance of frequent routine chest radiography for prolonged periods is minimized in the follow-up of both Hodgkin and non-Hodgkin lymphomas [32]. Implementations of a recommended optimal surveillance strategy based on this study would reduce the number of chest radiographs in currently used protocols by one half.

Benign Thymic Enlargement

Masses of thymic origin, excluding teratoma, constitute approximately 6% of all mediastinal masses in children [1, 2]. Although detection of the normal gland on radiographs is unusual in children more than 6 years old, the thymus is detected by CT and MR in virtually every child of any age [8]. Thymic size and shape are directly age related: craniocaudal size gradually increases with age, but little change occurs in width or in anteroposterior and transverse dimensions [33]. At the same time, thymic thickness decreases with increasing age, and this decrease can be used to gauge thymic enlargement. The mean thickness (measured as the largest dimension perpendicular to the long axis of the dominant left lobe) is 1.50 cm (SD = 0.46 cm) from infancy to 10 years and 1.05 cm (SD = 0.36 cm) during the second decade of life [34].

Although quantitative CT measurement of thickness is a reliable indicator of thymic enlargement (>2 SD in thickness of the left lobe above that of age-matched controls), qualitative assessment of shape, contour, and morphology correlated with clinical and other laboratory findings is usually sufficient to distinguish normal from abnormal thymus [6]. The normal thymus in children less than 5 years old is quadrilateral with smooth biconvex lateral margins and a wide retrosternal component abutting the chest wall [34]. As the child grows, the thymus gradually becomes triangular with straight or concave lateral margins and a thin chest wall attachment. However, a quadrilateral shape occasionally may persist in children 10–15 years old. The normal thymic morphology appears homogeneous on sonography, CT, and MR throughout childhood [6, 8].

Normal variations in thymic size, regrowth after cytotoxic therapy, and ectopic location may at times simulate mediastinal tumor. In children undergoing chemotherapy for malignancies, the thymus appears to atrophy during chemotherapy and regrow to its normal size during recovery [35, 36]. However, in 25% of patients, the thymus will "rebound" to an even larger size, reflecting overgrowth of normal thymic elements in normal proportions [37]. Aberrant location of normal thymic tissue in the superior mediastinum owing to incomplete descent of thymic primordia from the third pharyngeal pouch also may be manifested as a superior or posterior mediastinal mass [38, 39]. The CT, MR, and sonographic appearances of benign thymic enlargement and ectopic thymus are characterized by a smooth contour, morphologic homogeneity, and direct continuity with the normally located gland without any tissue-cleavage plane [40, 41] (Fig. 2). Although pliability is generally considered a feature of ectopic thymus, aberrant tissue at times may displace or compress adjacent structures [38].

Children with radiologic features of benign thymic enlargement or ectopy and no clinical, laboratory, or radiologic evidence of primary or recurrent disease can be followed up with chest radiography and serial scanning [42]. Lack of increase or reduction in size confirms the diagnosis of benign thymic enlargement or ectopy. Recent experience with MR indicates that signal intensities alone cannot be used to differentiate between normal and abnormal thymus reliably because of overlap on T1- and T2-weighted sequences. Signal intensity of abnormal thymus, however, is usually inhomogeneous on T2-weighted images, reflecting necrosis, hemorrhage, septations, fibrosis, or calcification [42]. Signal inhomogeneity, alteration in normal shape with focal enlargement of a lobe or multilobularity, and evidence of other thoracic lymphadenopathy are strong indicators of thymic neoplasia [43].

Teratoma

Mediastinal teratomas are derived from multipotent cells originating in the third pharyngeal pouch that have descended into the thorax with the thymus. These tumors constitute 10% of all mediastinal masses in children [1, 2]. Most (80%) are benign; determination of malignancy is based on local invasion rather than histologic examination.

The diagnosis is usually established by the demonstration on radiographs of calcification in an anterior mediastinal mass and confirmed by cross-sectional imaging with demonstration of a bulky well-defined and thick-walled cystic mass containing fat, soft tissues, and calcification [44]. The most important role for CT or MR is to distinguish between benign and malignant lesions by showing local invasion [45]. In this capacity, the multiplanar capability of MR imaging may facilitate delineation of malignant extension into surrounding tissues and organs [8].

Middle Mediastinum

Middle mediastinal masses constitute about 20% of all mediastinal masses and most frequently reflect developmental malformations of the embryonic foregut or lymphadenopathy [1, 2] (Table 1). Other, less common middle mediastinal masses include cardiovascular malformations and tumors and a variety of mesenchymal lesions.

Bronchopulmonary Foregut Cysts

Foregut cysts including bronchogenic, enteric, and neurenteric cysts represent 11% of mediastinal masses in children

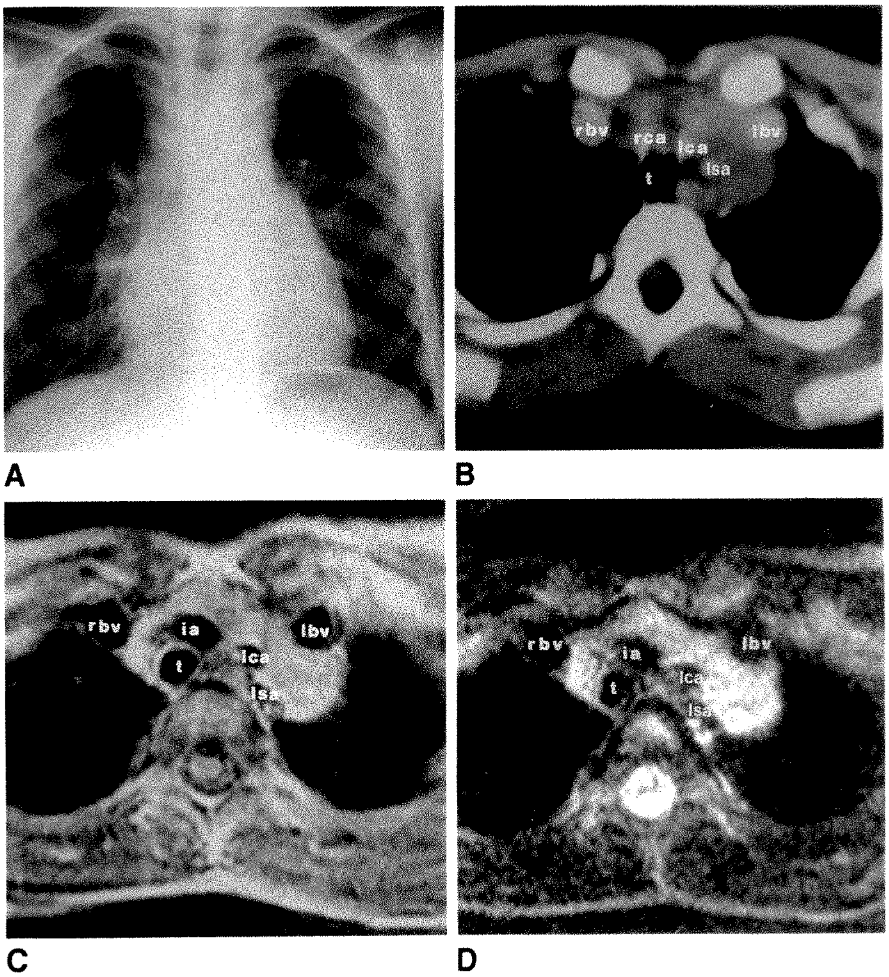

Fig. 2.—Benign thymic hyperplasia and ectopy.

***A*, Chest radiograph obtained to rule out pneumonia in otherwise well 6-year-old child shows bilateral superior mediastinal widening.**

***B*, Enhanced CT scan above level of aortic arch confirms anterior retrosternal soft-tissue mass between right (rbv) and left (lbv) brachiocephalic veins extending posteriorly behind left subclavian artery (lsa) and left brachiocephalic vein (lbv). Trachea (t), right innominate (ia), and left (lca) carotid arteries are not displaced or effaced.**

***C*, T1-weighted MR image shows thymic mass with homogeneous signal intensity slightly greater than that of muscle. Mass extends posteriorly in continuity with left lobe, without tracheal or vascular compromise.**

***D*, T2-weighted MR image confirms homogeneous signal intensity that is increased and nearly equal to that of fat, and consistent with normal thymic tissue.**

Child has remained well, and follow-up CT and chest radiography have shown gradual decrease in mediastinal widening.

and are the most common primary middle mediastinal mass [1, 2]. The most common of these is the bronchogenic cyst arising in the middle mediastinum at or near the carina [2]. The traditional approach to radiologic diagnosis has been chest radiography combined with esophagography; however, sensitivity is only 75%, and an accurate preoperative diagnosis is achieved in only 50% of cases [46]. Cross-sectional imaging provides more sensitive identification of cryptic foregut cysts, helps clarify abnormal findings on radiographs, and facilitates accurate determination of the location and cystic morphology of the mass. Sonography may accurately localize and define some cysts, and in those cases in which a typical well-defined cyst is identified, additional imaging is unnecessary [10, 47]. The CT appearance, although usually diagnostic, may be misleading when the cyst contains dense proteinaceous material and attenuation values are increased. In such cases, use of IV contrast material may help define the cystic nature by showing a sharply demarcated, low-attenuation avascular mass [48] (Fig. 3A). In general, MR provides little information over that of CT that affects diagnosis or treatment [5], although a high signal intensity on T2-weighted images can confirm the cystic mass in lesions with equivocal CT findings [49]. MR is preferable as the initial cross-sectional imaging method in patients with suspected aortic arch malformations, and may help clarify the anatomy as well as identify unsuspected anomalies that affect surgical planning [50] (Fig. 3B).

Lymphadenopathy

Middle mediastinal lymph node enlargement usually reflects lymphoma or granulomatous disease [1, 2]. Although lymphomatous involvement of paratracheal, tracheobronchial, and bronchopulmonary lymph nodes occurs frequently, the dominant mass is usually in the anterior mediastinum [16]. Masslike, granulomatous middle mediastinal lymphadenopathy occurs much less frequently than lymphoma and usually is due to tuberculosis, histoplasmosis, or sarcoidosis.

There is no size criterion for determining lymph node enlargement in children; however, the presence of identifiable mediastinal lymph nodes on CT or MR in infants and young children or enlarged nodes more than 1 cm in diameter in adolescents is considered abnormal [6]. Although CT and MR may help delineate the extent of nodal involvement and differentiate nodes from vascular structures, neither technique can differentiate between inflammatory and neoplastic lymphadenopathy [8, 51].

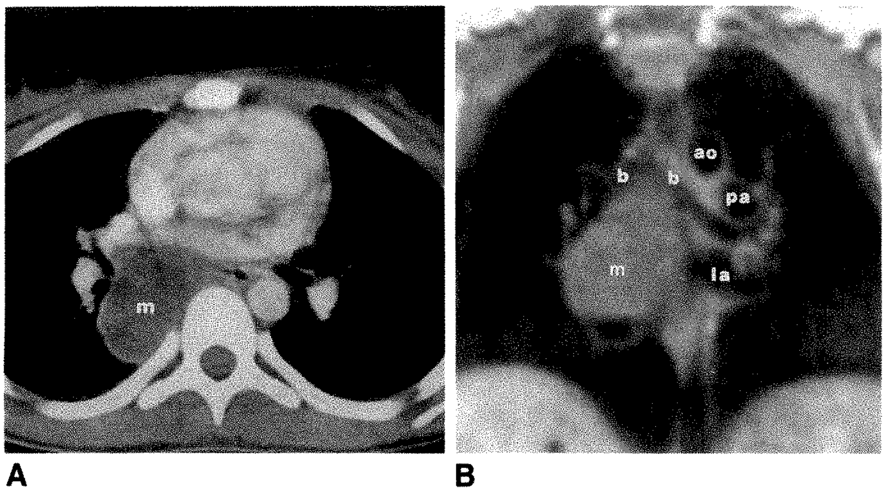

Fig. 3.—Bronchogenic cyst.
A, **Enhanced CT scan below carina shows right-sided low-density middle mediastinal mass (m) with slight rim enhancement. Mass extends into posterior mediastinum.**
B, **Coronal T1-weighted MR image clearly shows relationship of subcarinal mass (m) and bronchi (b). Cyst is distinct from pulmonary artery (pa), aorta (ao), and posterior left atrium (la).**

Posterior Mediastinum

Posterior mediastinal masses represent approximately 34% of all mediastinal masses in children [1, 2] (Table 1). Most (88%) are of neurogenic origin, and 80% of these originate from ganglion cells in the paravertebral sympathetic chain. Less common posterior masses include foregut cysts (enteric, neurenteric) and malignant lymphoma, with 5% of Hodgkin disease and 10% of non-Hodgkin lymphoma involving the posterior lymph node group [14].

Neurogenic Tumors

Tumors of ganglion cell origin are a histopathologic spectrum extending from malignant neuroblastoma to mature benign ganglioneuroma. The prevalence depends on the age of the child. Neuroblastomas usually occur in the first 5 years of life, and ganglioneuromas occur in older children (>10 years).

The chest radiograph is virtually diagnostic for neuroblastoma or ganglioneuroma when a well-circumscribed paraspinal mass, a sharp pleuropulmonary interface, and associated calcification or adjacent skeletal erosion are present (Fig. 4A). In such cases, cross-sectional imaging is used primarily to delineate the extent of the mass and more specifically to assess intraspinal involvement. Because of the intimate association with the spine, tumor extension into the spinal canal occurs frequently, and preoperative recognition is essential because any thoracic debulking procedure must be accompanied or preceded by decompressive laminectomy [2]. Although sonography may show intraspinal extension with displacement or compression of the thecal sac or spinal cord in small infants [52], CT or MR imaging is necessary to detect and delineate intraspinal involvement in older patients [6]. MR imaging has become the preferred cross-sectional imaging procedure for initial evaluation of paraspinous tumors, and CT with water-soluble contrast myelography is rarely required to evaluate intraspinal extension [53]. MR images obtained in axial and coronal planes provide accurate determination of the level and extent of intraspinal involvement, and obviate myelography in many if not all cases [7, 8] (Figs. 4B and 4C). Although less common than with anterior and middle mediastinal masses, tracheobronchial compression may occur with neurogenic tumors and should be considered before anesthesia and surgery [54].

Pleuropulmonary Pseudotumors

In a discussion of the evaluation of posterior mediastinal masses, it is appropriate to note a diagnostic pitfall posed by atypical left lower lobe pneumonia or atelectasis. This inflammatory pseudotumor reflecting left lower lobe consolidation or collapse posterior to the pulmonary ligament may occasionally be seen on radiographs as a paraspinal mass density [55] (Fig. 5A). The appearance on radiographs is thought to be due to lax or absent attachment of the pulmonary ligament to the diaphragm, permitting the lower lobe or a segment to collapse medially toward the mediastinum. In such cases, clinical findings suggesting infection in conjunction with demonstration of an irregular pleuropulmonary interface and shaggy margin on radiographs or CT scans should help differentiate the inflammatory pseudotumor from a neurogenic or other posterior mediastinal tumor (Figs. 5B and 5C).

Rational Imaging of Pediatric Mediastinal Masses

In most cases, despite technologic advances in other cross-sectional imaging, CT remains the procedure of choice to further evaluate a mediastinal mass shown on plain chest radiography [6, 8]. Because CT is still less expensive than MR, requires shorter scan times, and is more widely available, it is the preferred technique to evaluate the mediastinum after plain chest radiography. For most purposes, the information provided by MR imaging is equal to that obtained from CT, and will not materially influence patient management or outcome. Established exceptions to this general rule are posterior mediastinal neurogenic masses and vascular malformations or tumors, where better definition of intraspinal extension and superior distinction between vascular structures and soft tissues provide clear-cut indications for the initial use of MR imaging [7].

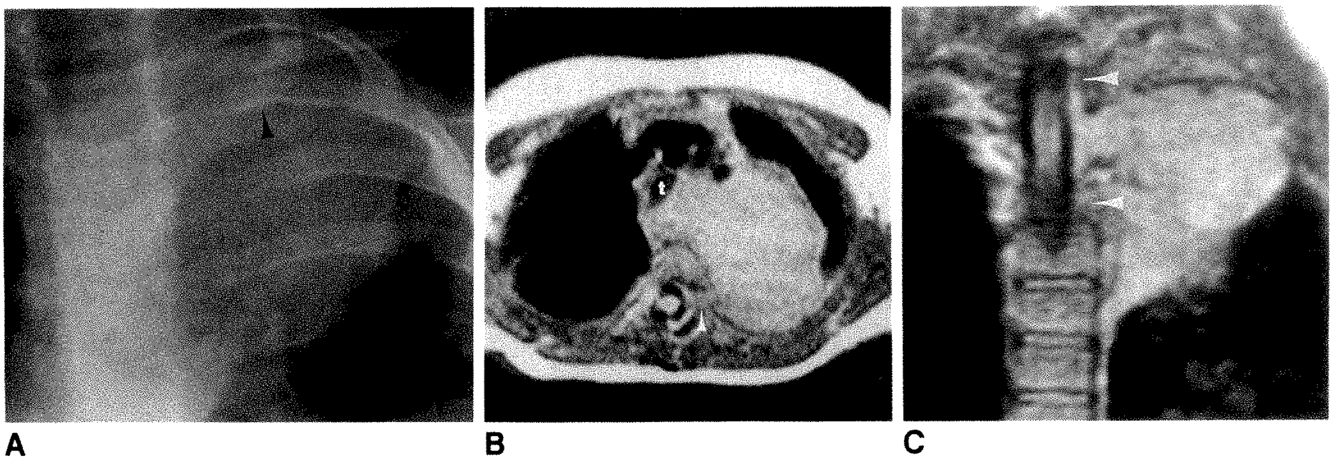

Fig. 4.—Ganglioneuroma.

A, Chest radiograph shows mass in apex of left hemithorax associated with rib erosion (*arrowhead*) and widening of intercostal space, consistent with posterior mediastinal mass.

B, Axial T1-weighted MR image shows intraspinal extension (*arrowhead*) of posterior mediastinal mass, which has a signal intensity greater than that of muscle but less than that of fat. Tumor extends anteriorly into middle mediastinum, displacing and compressing trachea (t).

C, Coronal T1-weighted MR image shows cephalocaudal extent of intraspinal tumor (*arrowheads*).

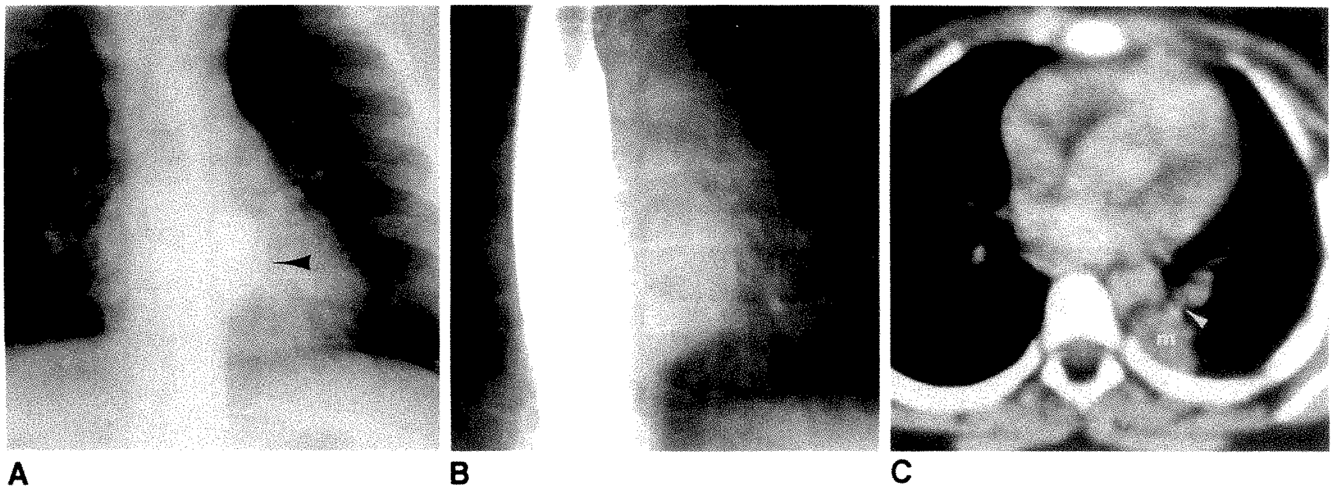

Fig. 5.—Inflammatory pseudotumor: atypical left lower lobe pneumonia.

A, Chest radiograph shows hemispheric paraspinal mass behind heart resembling neurogenic tumor (*arrowhead*).

B, Esophagogram more clearly shows mass/lung interface with somewhat shaggy margins.

C, Enhanced CT scan shows mass (m) has irregular pulmonary interface associated with adjacent patchy lung infiltrate (*arrowhead*). Mass resolved with antibiotic therapy.

Present and future fiscal constraints demand a rational and efficacious approach to the evaluation of any child with a mediastinal mass. Although precise diagnostic accuracy is generally desirable, at some point additional diagnostic information will contribute little or nothing to patient management. Few studies describing the diagnostic advantages of one or another imaging technique show that increased diagnostic accuracy leads directly to improved management and outcome or that the additional costs are justified [56]. Unfortunately, many if not most recommendations for imaging protocols in evaluation of mediastinal masses in children are based on anecdotal observations and small groups of patients, and comparative efficacy studies of imaging techniques are limited. Maximal benefit from available diagnostic imaging can be achieved only with the development of rational imaging protocols that integrate newer and established radiologic techniques into efficient, cost-effective diagnostic pathways.

REFERENCES

1. King RM, Telander RL, Smithson WA, Banks PM, Han M-T. Primary mediastinal tumors in children. *J Pediatr Surg* **1982**:17:512–520
2. Ravitch MM. Mediastinal cysts and tumors. In: Welch KJ, Randolph JG, Ravitch MM, O'Neill JA Jr, Rowe MI, eds. *Pediatric surgery*, 4th ed. Chicago: Year Book Medical, **1986**:602–618
3. Kirks DR. *Practical pediatric imaging: diagnostic radiology of infants and children*. Boston: Little, Brown, **1984**:502
4. Hope JW, Barns PE, Koop CE. Radiologic diagnosis of mediastinal masses in infants and children. *Radiol Clin North Am* **1963**:1:17–50

5. Siegel MJ, Nadel SN, Glazer HS, Sagel SS. Mediastinal lesions in children: comparison of CT and MR. *Radiology* **1986**;160:241–244
6. Siegel MJ. Pediatric applications. In: Lee JKT, Sagal SS, Stanley RJ, eds. *Computed body tomography with MRI correlation,* 2nd ed. New York: Raven, **1989**:1060–1075
7. Bisset GS III. Pediatric thoracic applications of magnetic resonance imaging. *J Thorac Imaging* **1989**;4:51–57
8. Siegel MJ, Molina PL. Respiratory system. In: Cohen MD, Edwards MK, eds. *Magnetic resonance imaging of children.* Philadelphia: Decker, **1990**:585–609
9. Liu P, Daneman A, Stringer DA. Real-time sonography of mediastinal and juxtamediastinal masses in infants and children. *Can Assoc Radiol J* **1988**;39:198–203
10. Wernecke K, Vassallo P, Potter R, Lukener HG, Peters PE. Mediastinal tumors: sensitivity of detection with sonography compared with CT and radiography. *Radiology* **1990**;175:137–143
11. Anderson KC, Leonard RC, Canellos GP, Skarin AT, Kaplan WD. High dose gallium imaging in lymphoma. *Am J Med* **1983**;75:327–331
12. Resjo IM, Harwood-Nash DC, Fitz CR, Chuang S. CT metrizamide myelography for intraspinal and paraspinal neoplasms in infants and children. *AJR* **1979**;132:367–372
13. Dietrich RB, Kangarloo H, Lenarsky C, Feig SA. Neuroblastoma: the role of MR imaging. *AJR* **1987**;148:937–942
14. Castellino RA. Diagnostic imaging evaluation of Hodgkin's disease and non-Hodgkin's lymphoma. *Cancer* **1991**;67[suppl]:1177–1180
15. Steinherz PG, Siegel SE, Bleyer A, et al. Lymphomatous presentation of childhood acute lymphoblastic leukemia. *Cancer* **1991**;68:751–758
16. Miller JH, White L. Lymphoma. In: Miller JH, White L, eds. *Imaging in pediatric oncology.* Baltimore: Williams & Wilkins, **1985**:427–460
17. Miller DR. Hematologic malignancies: leukemia and lymphoma. In: Miller DR, Baehner RL, Miller LP, eds. *Blood diseases of infancy and childhood.* St. Louis: Mosby, **1989**:661–685
18. Panicek DM, Harty MP, Scicutella CJ, Carsky EW. Calcification in untreated mediastinal lymphoma. *Radiology* **1988**;166:735–736
19. Lautin EM, Rosenblatt M, Friedman AC, Becker RD, Fromowitz FB, Yeglia W. Calcification in non-Hodgkin lymphoma occurring before therapy: identification on plain films and CT. *AJR* **1990**;155:739–740
20. Kirks DR, Fram EK, Vock P, Effmann EL. Tracheal compression by mediastinal masses in children: CT evaluation. *AJR* **1983**;141:647–651
21. Mandell GA, Lantieri R, Goodman CR. Tracheobronchial compression in Hodgkin's lymphoma in children. *AJR* **1982**;139:1167–1170
22. Azizkhan RG, Dudgeon DL, Buck JR, et al. Life-threatening airway obstruction as a complication to the management of mediastinal masses in children. *J Pediatr Surg* **1985**;20:816–822
23. Shamberger RC, Holzman RS, Griscom NT, Tarbell NJ, Weinstein HJ. CT quantitation of tracheal cross-sectional are as a guide to the surgical and anaesthetic management of children with anterior mediastinal masses. *J Pediatr Surg* **1991**;26:138–142
24. Neuman GG, Weingarten AE, Abramowitz RM, Kushins LG, Abramson AL, Ladner W. The anesthetic management of the patient with an anterior mediastinal mass. *Anesthesiology* **1984**;60:144–147
25. Nyman RS, Rehn SM, Glimelius BLG, Hagberg HE, Hemmingsson AL, Sundstrom CJ. Residual mediastinal masses in Hodgkin disease: prediction of size with MR imaging. *Radiology* **1989**;170:435–440
26. Glazer HS, Lee JKT, Levitt RG, et al. Radiation fibrosis: differentiation from recurrent tumor by MR imaging. *Radiology* **1985**;156:721–726
27. Drossman SR, Schiff RG, Kronfeld GD, McNamara J, Leonidas JC. Lymphoma of the mediastinum and neck: evaluation with Ga-67 imaging and CT correlation. *Radiology* **1990**;174:171–175
28. Tumeh SS, Rosenthal DS, Kaplan WD, English RG, Holman BL. Lymphoma: evluation with Ga-67 SPECT. *Radiology* **1987**;164:111–114
29. Wernicke K, Vassallo P, Hoffman G, et al. Value of sonography in monitoring the therapeutic response of mediastinal lymphoma: comparison with chest radiography and CT. *AJR* **1991**;156:265–272
30. Marglin SI, Laing FC, Castellino RA. Current status of mediastinal sonography in the pretreatment evaluation of patients with lymphoma. *AJR* **1991**;157:469–470
31. Cohen MD, Siddique A, Weetman R, Provisor A, Coates T. Hodgkin disease and non-Hodgkin lymphomas in children: utilization of radiological modalities. *Radiology* **1986**;158:499–505
32. Chang PJ, Parker BR, Donaldson SS, Thompson EI. Dynamic probabilistic model for determination of optimal timing of surveillance chest radiography in pediatric Hodgkin disease. *Radiology* **1989**;173:71–75
33. Francis IR, Glazer GM, Bookstein FL, Gross BH. The thymus: re-examination of age related changes in size and shape. *AJR* **1985**;145:249–254
34. St. Amour TE, Siegel MJ, Glazer HS, Nadel SN. CT appearances of normal and abnormal thymus in childhood. *J Comput Assist Tomogr* **1987**;11: 645–650
35. Cohen M, Hill CA, Cangir A, Sullivan MP. Thymic rebound after treatment of childhood tumors. *AJR* **1980**;135:151–156
36. Choyke PL, Zeman RK, Gootenberg JE, Greenberg JN, Hoffer F, Frank JA. Thymic atrophy and regrowth in response to chemotherapy: CT evaluation. *AJR* **1987**;149:269–272
37. Bode U, Scheidt W. Change of thymic size during and following cytotoxic therapy in young patients. *Pediatr Radiol* **1988**;18:20–23
38. Shackelford GD, McAlister WH. The aberrantly positioned thymus: a cause of mediastinal and neck masses in children. *AJR* **1972**;120:291–296
39. Cohen MD, Weber TR, Sequereira FW, Vane DW, King H. The diagnostic dilemma of the posterior mediastinal thymus: CT manifestations. *Radiology* **1983**;146:691–692
40. Cory DA, Cohen MD, Smith JA. Thymus in the superior mediastinum simulating adenopathy: appearance on CT. *Radiology* **1987**;162:457–459
41. Rollins NK, Currarino G. MRI imaging of posterior mediastinal thymus. *J Comput Assist Tomogr* **1988**;12:512–520
42. Siegel MJ, Glazer HS, Wiener JI, Molina PL. Normal and abnormal thymus in childhood: MR imaging. *Radiology* **1989**;172:367–371
43. Molina PL, Siegel MJ, Glazer HS. Thymic masses on MR imaging. *AJR* **1990**;155:495–500
44. Suzuki M, Takashima T, Itah H, Choutou S, Kawamura I, Watanbe Y. Computed tomography of mediastinal teratomas. *J Comput Assist Tomogr* **1983**;7:74–76
45. Levitt RG, Husbond JE, Glazer HS. CT of primary germ cell tumors of the mediastinum. *AJR* **1984**;142:73–78
46. Snyder ME, Luck SR, Hernandez R, Sherman JO, Raffensberger JG. Diagnostic dilemmas of mediastinal cysts. *J Pediatr Surg* **1985**;20: 810–815
47. Hendry PJ, Hendry GMA. Ultrasonic diagnosis of a bronchogenic cyst in a child with persistent stridor. *Pediatr Radiol* **1988**;18:338
48. Hernandez RJ. Role of CT in the evaluation of children with foregut cyst. *Pediatr Radiol* **1987**;17:265–268
49. Marin ML, Ramney BM, Franco K, Grimes MM, Smith C. Bronchogenic cyst: a case report emphasizing the role of magnetic resonance imaging. *J Thorac Imaging* **1991**;6:43–46
50. Helund GL, Bisset GS III. Esophageal duplication cyst and aberrant right subclavian artery mimicking a symptomatic vascular ring. *Pediatr Radiol* **1989**;19:543–544
51. Gamsu G, Sostman D. Magnetic resonance imaging of the thorax. *Am Rev Respir Dis* **1989**;139:254–274
52. Garcia CJ, Keller MS. Intraspinal extension of paraspinal masses in infants: detection by sonography. *Pediatr Radiol* **1990**;20:437–439
53. Siegel MJ, Jamroz GA, Glazer HS, Abramson CL. MR imaging of intraspinal extension of neuroblastoma. *J Comput Assist Tomogr* **1986**;10:593–595
54. Brown D, Magill HL, George P, Young LW. Tracheobronchial compression by thoracic neuroblastoma. *Am J Dis Child* **1986**;140:1171–1173
55. Malmgren N, Laurin S, Ivancev K, Bekassy A. Mediastinal pseudomass: pneumonia and atelectasis behind the left pulmonary ligament. *Pediatr Radiol* **1987**;17:451–453
56. Merten DF, Palmer PES, Sweet EM, Fendel H, Fauré C, Fujioka M. Rational use of diagnostic imaging in paediatrics: the report of a World Health Organization study group. *Pediatr Radiol* **1989**;19:216–218

Delayed Spontaneous Rupture of Augmented Bladder in Children:
Diagnosis with Sonography and CT

Ronald B. J. Glass[1]
H. Gil Rushton[2]

With the increasing use of augmentation enterocystoplasty to treat patients with small-capacity, noncompliant bladders, an increase in the number of cases of delayed spontaneous intraperitoneal rupture of the augmented bladder has been reported. Although patients with a ruptured bladder usually will have an acute abdomen, these clinical signs and symptoms may be masked in spina bifida patients because of their neurologic deficit. Cystography and sonography were performed in four spina bifida patients with delayed spontaneous rupture of an augmented bladder. One patient also had isotope cystography. Two patients were examined with CT. Cystographic findings were abnormal in only one case. Peritoneal fluid was identified sonographically in all four cases and also was seen in both CT studies.

Our study reveals that enhanced cystography will frequently fail to show leakage from an augmented bladder. Sonography and CT are reliable in detecting free intraperitoneal fluid, a finding that can significantly aid in the diagnosis of ruptured bladder after enterocystoplasty. Therefore, cystography with normal findings must be followed by sonography or CT in order to detect extravasated urine.

***AJR* 158:833–835, April 1992**

Bladder augmentation (enterocystoplasty) with an isolated loop of vascularized bowel or a patch of stomach is a procedure used to increase the capacity and improve the compliance of a pathologically small or contracted noncompliant bladder. Delayed spontaneous rupture of an augmented bladder is a recognized complication [1–5]. As an increasing number of patients undergo this surgery, one can expect to encounter this problem more often. Spontaneous intraperitoneal bladder rupture is a potentially fatal condition [4], and deaths have been reported [1, 3]. In spina bifida patients, the diagnosis of a ruptured bladder often may be masked or delayed because of impaired sensation [3].

Contrast-enhanced cystography may not demonstrate leakage, and diagnosis may depend on sonographic and CT demonstration of intraperitoneal fluid. We present our experience with four previously unreported cases of delayed spontaneous rupture of an augmented bladder, in which the clinical diagnosis was confirmed by sonographic and CT detection of intraperitoneal fluid.

Materials and Methods

Augmentation enterocystoplasty has been performed in 55 patients at our institution. Four patients with delayed spontaneous rupture of an augmented bladder form the basis for this report. The age range of the patients was 7–21 years. All patients had spina bifida and a noncompliant bladder augmented with a detubularized segment of ileum. None of these patients had an artificial urinary sphincter or other procedure to increase bladder outlet resistance. After enterocystoplasty, the bladder was emptied by clean intermittent catheterization. No attempt was made to maintain sterile urine with prophylactic antibiotics.

After an interval ranging from 13 months to 4 years, each of these patients was seen with

Received September 3, 1991; accepted after revision November 19, 1991.

[1] Department of Diagnostic Imaging and Radiology, Children's National Medical Center and the George Washington University School of Medicine and Health Sciences, 111 Michigan Ave., N.W., Washington, DC 20010. Address reprint requests to R. B. J. Glass.

[2] Department of Urology, Children's National Medical Center and the George Washington University School of Medicine and Health Sciences, Washington, DC 20010.

0361-803X/92/1584-0833
© American Roentgen Ray Society

acute abdominal pain and distension, vomiting, and oliguria. None had hematuria. The duration of symptoms was 24-72 hr. In two patients the diagnosis was delayed, and both underwent nondiagnostic laparotomy before they were referred to the urology department at our institution. On the basis of clinical evidence of spontaneous rupture of the augmented bladder, all patients were evaluated with sonography and cystography. The augmented bladder was fully distended with more than 350 ml of contrast medium in three cases and 300 ml in one case. Images of the full bladder were made from intermittent fluoroscopic examinations in the anteroposterior, lateral, and both oblique projections. After the contrast material was drained from the bladder, an anteroposterior overhead Bucky view of the abdomen was obtained. An isotope cystogram was also obtained in one patient. CT with IV contrast medium was performed in two cases.

Three acutely ill patients underwent laparotomy for repair of the ruptured bladder. One patient was treated nonsurgically by means of indwelling Foley catheter drainage and broad-spectrum antibiotics. He responded so well to conservative therapy that surgery was considered unnecessary.

Results

Cystography failed to demonstrate leakage from the bladder in three cases. Leakage into the peritoneal cavity was demonstrated in one patient after the bladder had been distended with 300 ml of contrast material. The one isotope cystogram also failed to show leakage.

Sonography showed intraperitoneal fluid in all four cases (Figs. 1 and 2). In one child the intraperitoneal fluid was loculated; this was distant from the site of the ventriculoperitoneal shunt tube (Fig. 3). Sonographically, the fluid was anechoic. In both CT studies, the fluid had uniformly low attenuation, with no extravasation of injected IV contrast medium from the bladder (Fig. 3).

In the three cases that required laparotomy, the ruptures were identified in the enteric component of the augmented bladder. In one case the perforation was occluded by thick tenacious mucus. Pathologic examination of the area adjacent to the tear revealed inflammatory cell infiltrate.

Discussion

Augmentation enterocystoplasty is undertaken for a wide spectrum of conditions associated with a small or noncompliant bladder. Extravasation of urine from the bladder may occur early or late in the postoperative course. Early leakage usually occurs at the anastomosis of bladder and bowel. Delayed rupture, which may take place 5 weeks to 59 months after surgery, has occurred in the augmented bladder, regardless of the segment of bowel used [2, 3]. Peritonitis, septic shock, and even death have ensued from extravasation of the chronically infected urine into the peritoneal cavity.

The etiology of spontaneous delayed rupture of the bladder is incompletely understood. It is suggested that elevated intravesical pressure caused by overdistension of the augmented bladder leads to vascular compromise and ischemia of the bowel, predisposing the augmented bladder to rupture [4-6]. Previous theories of rupture due to perivesical adhesions or traumatic catheterization are no longer considered valid by most investigators.

Once the bladder has ruptured, patients may have acute onset of abdominal discomfort or pain accompanied by abdominal distension, nausea, fever, and anorexia. Although nonspecific, these findings become highly suggestive of rupture in a patient with previous enterocystoplasty. The role of cystography in diagnosing traumatic rupture of normal bladders is well established [7]. Unfortunately, cystography is not so reliable when evaluating delayed spontaneous rupture of augmented bladders [1-3]. Contrast-enhanced cystography may be nondiagnostic if the tear in the augmented bladder seals itself or becomes occluded by mucus.

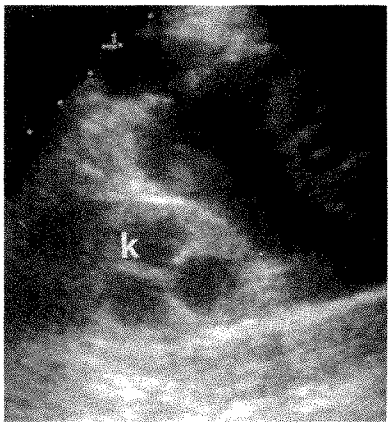

Fig. 1.—21-year-old woman with peritonitis. Longitudinal sonogram of upper abdomen reveals free fluid. k = hydronephrotic left kidney.

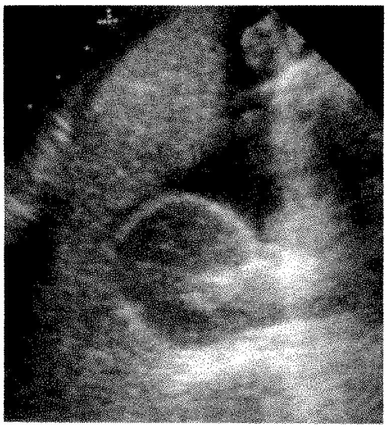

Fig. 2.—7-year-old febrile boy with abdominal pain. Transverse sonogram of left upper quadrant of abdomen shows fluid separating spleen and kidney.

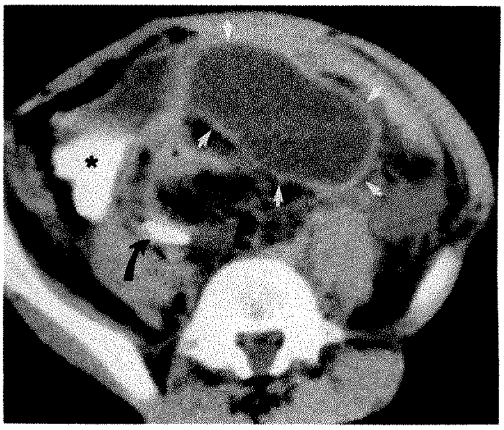

Fig. 3.—10-year-old boy with fever and abdominal pain. Enhanced CT scan through level of augmented bladder shows layered contrast material in dependent bowel component of augmented bladder (*asterisk*). Unopacified urine and loculated fluid collection (*white arrows*) have similar attenuation. Right ureter is filled with contrast material (*black arrow*).

Urine that has extravasated into the peritoneum prior to mechanical occlusion will not be seen with conventional radiography, but will be readily demonstrated by sonography or CT. Therefore, a normal appearance on the cystogram should be followed by abdominal sonography or CT in this population. CT may be more helpful than sonography in demonstrating that intraperitoneal fluid is not contiguous with a ventriculoperitoneal shunt, suggesting that this fluid does not represent CSF. Infected urine in the bladder may have increased echogenicity and may contain debris; we assume that a similar appearance may also be encountered with infected urine in the peritoneum.

CT did not help detect the site of bladder rupture in our two patients. Peritoneal fluid was identified as easily with CT as with sonography. The extravasated urine had low attenuation, with no evidence to suggest intraperitoneal leakage from the contrast-filled augmented bladder.

Delayed spontaneous rupture of an augmented bladder is associated with significant morbidity, and deaths have been reported [1, 3, 4]. We stress the importance of sonography together with a high index of suspicion in the diagnosis of a ruptured augmented bladder. Sonography will suffice in most cases to confirm the diagnosis, but when visualization is compromised by overlying bowel gas, sonography should be followed by CT examination. Prompt diagnosis of spontaneous ruptured bladder after enterocystoplasty is crucial to minimize morbidity and ensure successful treatment.

REFERENCES

1. Rushton HG, Woodard JR, Parrott TS, Jeffs RD, Gearhart JP. Delayed bladder rupture after augmentation enterocystoplasty. *J Urol* **1988**;140: 344-346
2. Sheiner JR, Kaplan GW. Spontaneous bladder rupture following enterocystoplasty. *J Urol* **1988**;140:1157-1158
3. Elder JS, Snyder HM, Hulbert WC, Duckett JW. Perforation of the augmented bladder in patients undergoing clean intermittent catheterization. *J Urol* **1988**;140:1159-1162
4. Essig KA, Sheldon CA, Brandt MT, Wacksman J, Silverman DG. Elevated intravesical pressure causes arterial hypoperfusion in canine colocystoplasty: a fluorometric assessment. *J Urol* **1991**;146:551-553
5. Dixon CM, Filmer RB, Chang CH, Perlmutter AD. Spontaneous perforation of bladder augmentation in pediatric patients. *J Urol* **1989**;141:195A
6. Crane JM, Scherz HS, Billman GF, Kaplan GW. Ischemic necrosis: a hypothesis to explain the pathogenesis of spontaneously ruptured enterocystoplasty. *J Urol* **1991**;146:141-144
7. Cass AS. Diagnostic studies in bladder rupture. Indications and techniques. *Urol Clin North Am* **1989**;16:267-273

Book Review

Handbook of Pediatric Imaging. Edited by Lori L. Barr. New York: Churchill Livingstone, 428 pp., 1991. $115

The stated intent of this book is to guide general radiologists through a "thought provoking review of pediatric radiology." The editor goes on to note that the contents have been organized to provide the "easiest method for committing imaging approaches and diagnosis to memory." The result is a synopsis of pediatric imaging that emphasizes a systematic approach to radiologic diagnosis based on the use of differential diagnostic lists and that serves as a concise review of pediatric imaging.

The book has eight chapters, of which seven are devoted to abnormalities of individual organ systems or anatomic regions. The introductory chapter by Leonard Swischuk describes a logical approach to image interpretation in infants and children that the average radiologist will find somewhat elementary. Of the remaining chapters, four are by the editor (face and neck, respiratory system, genitourinary system, CNS), two are by Susan Stansberry (gastrointestinal system, musculoskeletal system), and one is by Janet Strife (heart and great vessels). Each of these chapters includes multiple tables reflecting a broad spectrum of diagnostic gamuts based primarily on radiologic abnormalities. The differential diagnosis is in the format of pathologic fields contained in the *ACR Index for Radiological Diagnosis*. The tables are logically and systematically organized, and the accompanying text contains succinct and well-written descriptions of each diagnostic consideration. Lists of suggested reading are substituted for references at the end of each chapter.

The book has a number of problems that detract from its overall usefulness. First is the lack of consistency of style and organization of the contents, which is all too common in texts that have more than one author. The prevalence of diseases and entities that make up the diagnostic gamuts receives inconsistent attention, and little effort is made to condense the sometimes lengthy lists into more concise and practical diagnostic considerations. Only cursory consideration is given to applicable imaging techniques for evaluation of each organ system or anatomic region, and almost no effort has been made to formulate promised diagnostic imaging pathways. Some imaging recommendations are anecdotal and at odds with currently accepted concepts. For example, in the introductory paragraph of the chapter on the respiratory system, the author states that MR imaging is "superior for delineating mediastinal masses" in children. With the exception of posterior neurogenic tumors and certain vascular masses, most authorities continue to view CT as the preferred primary cross-sectional imaging approach. Further, the use of lists of suggested reading and the lack of appropriate references do not help clarify the sometimes anecdotal approaches to diagnostic imaging.

The most significant problem with this generally well-produced book is the illustrations, which are of uneven and frequently inferior quality. Reproductions of images, especially of radiographs and sonograms, are generally suboptimal, and it is often difficult, if not impossible, to detect the described findings. This problem is compounded by widespread failure to annotate the illustrations with appropriate labeling, which would help the less experienced reader find the abnormalities described in the figure legends.

In summary, this book falls well short when compared with currently available nonencyclopedic reviews of pediatric radiology. The recently published second edition of *Practical Pediatric Radiology*, edited by Donald R. Kirks, although larger and more expensive than Barr's book, is more tightly edited and avoids the usual pitfalls of a text that has several authors. Although hardly a handbook, the text edited by Kirks, with superior illustrations, complete subdivided references at the ends of chapters, and diagnostic gamuts that consider prevalence of disease, is a more practical and comprehensive reference of pediatric imaging for general radiologists. Although I cannot generally recommend purchase of *Handbook of Pediatric Imaging*, the book may be useful as an introduction to pediatric radiology for basic trainees in radiology and for those preparing for board examinations.

David F. Merten
University of North Carolina
Chapel Hill, NC 27514

The Ureterovesical Junction in Children: Sonographic Findings After Surgical or Endoscopic Treatment

F. Rypens[1]
E. F. Avni[1]
W. O. Bank[1]
C. C. Schulman[2]
J. Struyven[1]

We retrospectively analyzed pre- and postoperative sonographic and medical records of 335 children who had surgical or endoscopic treatment at the ureterovesical junction, in order to determine normal and atypical sonographic appearances. Normal sonographic findings after ureteral reimplantation include thickening of the posterior bladder wall, pseudodiverticular sacculations, bladder asymmetry, and transitory hydroureteronephrosis. Short-term or persistent (lasting more than 1 month) hydroureteronephrosis, urinoma, hematoma, bladder lithiasis, and diverticula were abnormal findings, occurring in 17% of the patients. After partial ureteronephrectomies, visualization of the residual ureter on sonograms was not possible in cases without complications; in one patient, reflux of fluid dilated the residual ureter and made the ureter visible on sonograms. After endoscopic incisions, the masslike appearance of a collapsed ureterocele was observed. Submucosally injected Teflon always appeared as a curvilinear hyperechoic area with an acoustic shadow. Marked acute or persistent hydroureteronephrosis or ectopic intracavitary Teflon particles were observed in 2% of patients. Granuloma formation was considered likely in 5% of the patients when the area of injected Teflon material was longer than 12 mm on sonograms. Submucosally injected collagen appeared less echogenic than Teflon and showed no acoustic shadowing.

The various normal sonographic appearances after treatment must be known in order to distinguish them from significant abnormalities. In patients with anatomic anomalies, such as short-term or persistent hydroureteronephrosis, urinoma, hematoma, and lithiasis, complementary uroradiologic examinations may be necessary to clarify the diagnosis.

***AJR* 158:837–842, April 1992**

Anomalies of the ureterovesical junction are common in children [1, 2]. Various surgical or endoscopic urologic procedures are used to correct vesicoureteral reflux, ureterocele, or complicated duplex systems. The intra- and extravesical segments of the terminal ureter can be visualized with sonography, and this technique can be used for follow-up after therapy [3]. The normal and atypical sonographic appearances of the treated ureterovesical junction have not been extensively reported. We describe the spectrum of sonographic findings of treated ureterovesical junctions in children and evaluate the role of sonography in the follow-up of such patients.

Materials and Methods

We performed a retrospective study of the sonographic examinations and medical records of 335 children who had endoscopic or surgical treatment of the ureterovesical junction during a 5-year period (December 1985 through December 1990). All patients had correlative uroradiologic, surgical, or clinical follow-up. The ages at the time of the first therapeutic procedures ranged from 15 days to 14 years. All children had routine sonography of the entire urinary tract before and after treatment.

The sonographic examination (Acuson 128 unit, Mountain View, CA, or Toshiba Sonolayer-L 77B unit, Amsterdam, the Netherlands) was performed with the patient supine and,

Received September 3, 1991; accepted after revision November 5, 1991.

[1] Department of Radiology, Hôpital Erasme, Université Libre de Bruxelles, 808 Route de Lennik, B-1070 Brussels, Belgium. Address reprint requests to F. Rypens.

[2] Department of Urology, Hôpital Erasme, Université Libre de Bruxelles, B-1070 Brussels, Belgium.

0361-803X/92/1584-0837
© American Roentgen Ray Society

whenever possible, with the patient's bladder full. Sagittal, transverse, and oblique sonograms were obtained with a high-resolution sector or linear transducer (at least 5 MHz). Dilatation of the urinary tract was always assessed by measuring the anteroposterior diameter of the renal pelvis on a transverse sonogram. The ureter was measured posterior to the bladder, preferably on a transverse sonogram. If some degree of hydroureteronephrosis (transverse diameter of the renal pelvis greater than 10 mm) was present, the dilatation was measured again with the patient's bladder empty [4].

The time after treatment was arbitrarily separated into two stages: the early period during the first month and late events thereafter. The sonographic findings were correlated with the results of other uroradiologic examinations and clinical and surgical follow-up.

Results

Ureteral Reimplantation

A Cohen transverse (cross-trigonal) ureteral reimplantation or a Politano-Leadbetter procedure was performed in 100 patients because of reflux or because of reflux or obstructive megaloureter [2]. In all cases, thickening of the posterior bladder wall was observed at the site of reimplantation in the immediate postoperative period, with hyperechoic foci corresponding to sutures (Fig. 1). The thickened posterior bladder wall appeared either homogeneous or had secondary sacculations with pseudodiverticula (Fig. 2). On follow-up studies (3–67 months), the thickened posterior bladder wall persisted, whereas the hyperechoic foci disappeared. An associated psoas hitch procedure was performed in 40% of patients; in these children, the bladder appeared asymmetric and deviated toward the site of reimplantation [5]. On follow-up studies, this asymmetry disappeared.

Three early complications were encountered. In two patients, a heterogeneous hypoechoic fluid collection was found around the bladder that was associated with dilatation of the upper urinary tract. The sonographic differential diagnosis included hematoma and urinoma. Excretory urography showed extravasation of contrast material into the collection, confirming the presence of a urinoma (Fig. 3). These two children were operated on again; in both patients, the distal reimplanted ureter was necrotic and compressed by the urinoma. In the third child, the bladder lumen appeared to be filled with echogenic material that bladder washing showed was blood clots; the condition resolved without sequelae.

During the early postoperative period, 32 children had hydroureteronephrosis; normalization occurred within 1 month in 20 cases. In the other 12 patients, dilatation of the urinary tract persisted for 3–17 months (mean, 6 months). Four required surgery again (three children with restenosis, one child with secondary reflux). The other eight children required no additional treatment. They had marked dilatation before surgery, and this dilatation persisted or slowly regressed after intervention.

Two children had late postsurgical complications: one true bladder diverticulum and one bladder stone. The diverticulum was noted on voiding cystourethrography (VCUG) and was confirmed on sonography. The stone was diagnosed 15 months after surgery when sonograms showed one mobile hyperechoic focus with acoustic shadowing within the bladder. The plain film confirmed the calcific nature of the focus. A 1-cm stone was removed endoscopically.

Partial Ureteronephrectomies

Ten partial ureteronephrectomies were performed in cases of nonfunctioning upper poles of duplex collecting systems with ectopic ureteroceles (six patients) or ectopic ureters (four

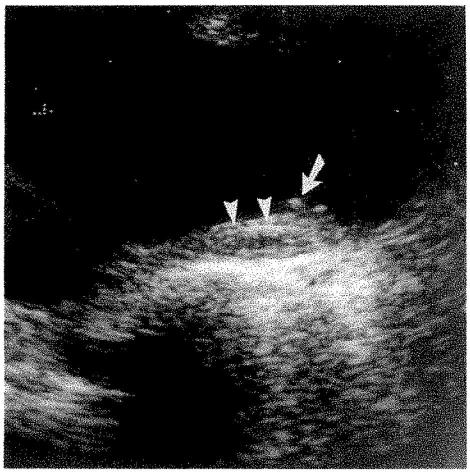

Fig. 1.—Normal appearance of ureter after reimplantation. Oblique sonogram shows thickening of posterior bladder wall with parallel tracks (tunnel sign) corresponding to submucosally reimplanted ureter (*arrowheads*), and hyperechoic suture material (*arrow*).

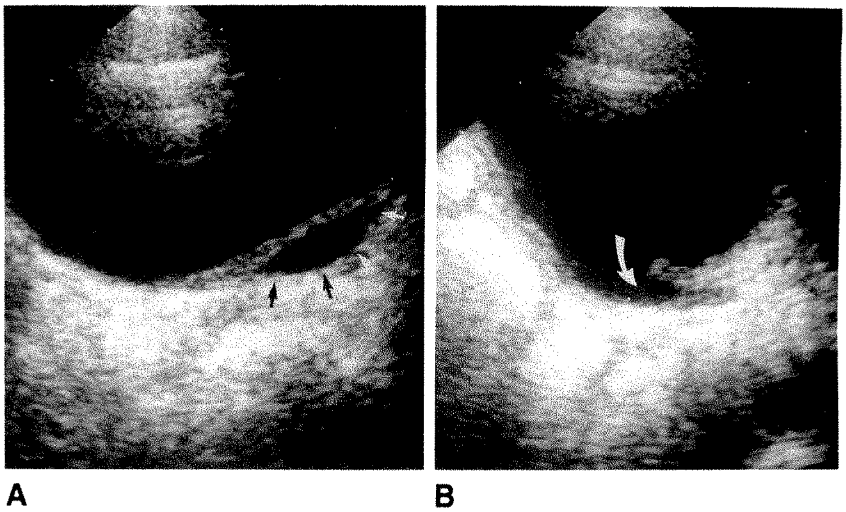

Fig. 2.—Appearance of bladder pseudodiverticulum after ureteral reimplantation.
***A*, Transverse sonogram shows diverticulumlike deformity (*arrows*).**
***B*, Sagittal sonogram shows bladder sacculation (*arrow*).**

patients) [6]. In eight children, no complications occurred, and the residual ureter was not visualized on sonography. In six patients, postsurgical sonograms showed progressive collapse of the ureterocele, leading to the appearance of a small hypoechoic mass.

In one patient, an echogenic collection was seen in the surgical area of the lumbar region. It was thought to represent a hematoma, and it resolved spontaneously within 2 weeks. In another child, sonograms showed a tubular retrovesical echogenic structure. VCUG confirmed the presence of reflux into an unused infected ureter (Fig. 4).

Endoscopic Incision of Ureterocele

In five patients with residual function in the upper pole collecting system, endoscopic incision of the ureterocele was performed [7]. Sonograms showed the collapse of these ureteroceles within the bladder, leading to a masslike appearance; dilatation of the upper urinary tract resolved in all five patients (Fig. 5).

Subureteric Injections of Teflon and Collagen

Subureteric Teflon injection (STING) was performed in 200 patients for correction of vesicoureteral reflux [8]. The Teflon paste appeared invariably as a thick linear or curvilinear hyperechoic band with acoustic shadowing within the bladder wall. On follow-up studies, the Teflon appeared less echogenic and more globular, bulging into the bladder lumen from its submucosal position (Fig. 6).

In 40 patients (20%), sonography showed dilatation of the urinary tract; in most cases, this was transitory, reverting to normal within 4 weeks. However, two patients (1%) had symptomatic acute hydroureteronephrosis and some fluid around the kidney and required surgery. In two other patients, during the first week after STING, sonograms showed hyperechoic foci in the ureter and the pyelocaliceal system without dilatation of the urinary tract, suggesting migration of the Teflon (Fig. 7). The children were asymptomatic and the sonographic appearance returned to normal after 1 week.

In 10 patients, the Teflon complex was more than 12 mm long (range, 12–20 mm). In two of these patients, the echogenic mass slowly enlarged, reaching 15 and 20 mm in length

Fig. 3.—Urinoma complicating ureteral reimplantation.
***A*, Oblique sonogram shows cystic septated mass (between *crosses*) adjacent to bladder (B).**
***B*, Postvoiding excretory urogram shows faint opacification of pelvic mass corresponding to urinoma (*arrows*). Note dilated ureter (*arrowheads*).**

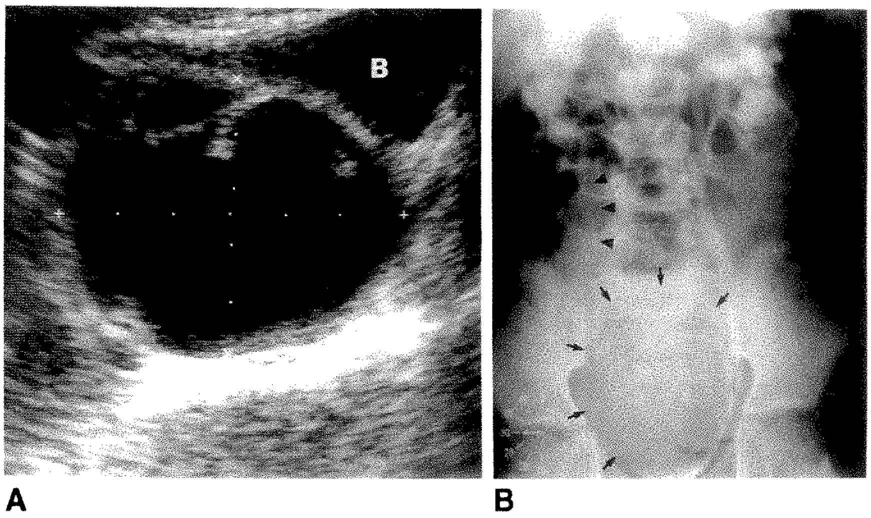

Fig. 4.—Reflux into unused ureter after partial ureteronephrectomy. Parasagittal sonogram of right side shows tubular echogenic structure with intravesical connection (*arrow*). U = ureter.

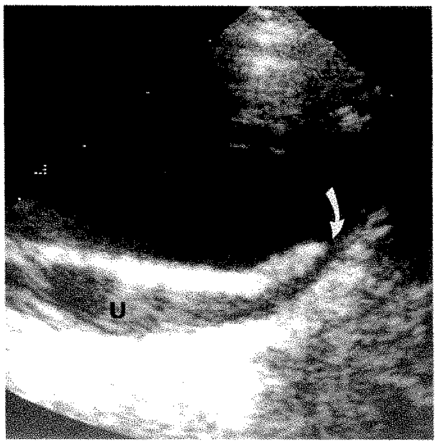

4

Fig. 5.—Normal appearance of collapsed ureterocele after endoscopic incision. Oblique sonogram shows hypoechoic mass (*arrows*) corresponding to collapsed ureterocele.

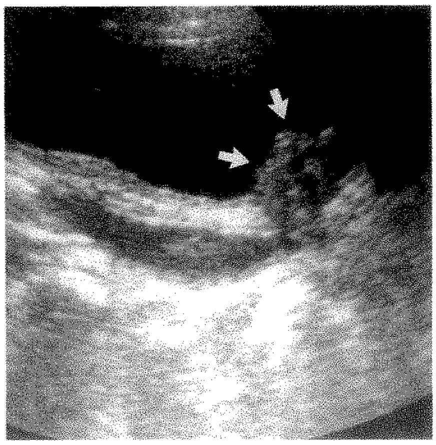

5

after 1 year. In the other eight patients, no growth of the complex was observed. No correlation between growth and the amount of Teflon injected was found. This finding was considered to represent granuloma formation, which was confirmed in five children who had to be operated on again because of persistent reflux (Fig. 8). Collagen was used for injection instead of Teflon in 20 other patients. It was less echogenic than Teflon, without acoustic shadowing (Fig. 9). No complications occurred in these patients.

Discussion

The most frequently used surgical procedures to correct reflux or distal ureteral obstruction are the Cohen (cross-trigonal) and Politano-Leadbetter procedures. In both, the ureter is reimplanted within a newly created submucosal tunnel that lengthens the ureter's intravesical segment. If necessary, the ureteral tunnel can be further lengthened by applying the psoas hitch technique [5]. The submucosal tunnel containing the reimplanted ureter is seen on sonography as thickening of the posterolateral bladder wall and has been called the tunnel sign [9] (Fig. 1). Hyperechoic foci corresponding to sutures may be detected within this thickening, and should not be confused with mobile bladder stones or polyps (Fig. 1). Unlike the calcifications occasionally formed on sutures, they are seen early in the postsurgical period. Deviation of the bladder caused by the psoas hitch procedure can be seen on sonograms, but is best shown on VCUGs or excretory urograms. Ureteral reimplantation may induce sacculations of the bladder wall that should not be misinterpreted as true bladder diverticula. Orthogonal scans may be useful in distinguishing between these two entities (Fig. 2). In the sacculation (or pseudodiverticulum), no "collar" of tissue is seen, and the wall of the sacculation is as thick as the rest of the bladder wall.

Some dilatation of the urinary tract is common after any ureteral reimplantation procedure because of postsurgical edema [4]. Its severity is proportional to the degree of preoperative dilatation, as is its rate of regression. Resolution is also related to how long the condition persists. The degree of dilatation should not exceed that seen preoperatively, and the dilatation usually disappears within 4 weeks of surgery [4]. Such transitory dilatation was observed in 20 of our children; none had complications. In 12 other patients, the dilatation persisted for more than 1 month. Among these 12 children, eight required no additional treatment. They had marked dilatation before surgery, and this dilatation persisted or slowly decreased after intervention. The remaining four were operated on again because of persistent reflux (one patient) or ureteral stenosis (three patients). Although no direct correlation exists between dilatation and function, postsurgical dilatation persisting longer than 4 weeks indicates a poorer prognosis than short-term dilatation, and complementary functional examinations should be done.

Urinomas, or urinary extravasation at the site of reimplantation, were unusual surgical complications. Only two were encountered, apparently resulting from early necrosis of the distal tapered ureter. Distinction between urinoma and hematoma could not be accomplished sonographically, necessitating excretory urography to establish the diagnosis by showing extravasation of contrast material (Fig. 3).

Late complications included one bladder stone and one bladder diverticulum. Bladder lithiasis is an unusual complication, resulting from a urinary tract infection or from a strong reaction to a suture, producing a granuloma that calcifies secondarily [10, 11]. Bladder diverticula, well-known complications of surgery at the ureterovesical junction, are caused by a weakness of the bladder wall at the site of the old ureteral meatus. They may be seen on sonograms but are best visualized on VCUGs [2].

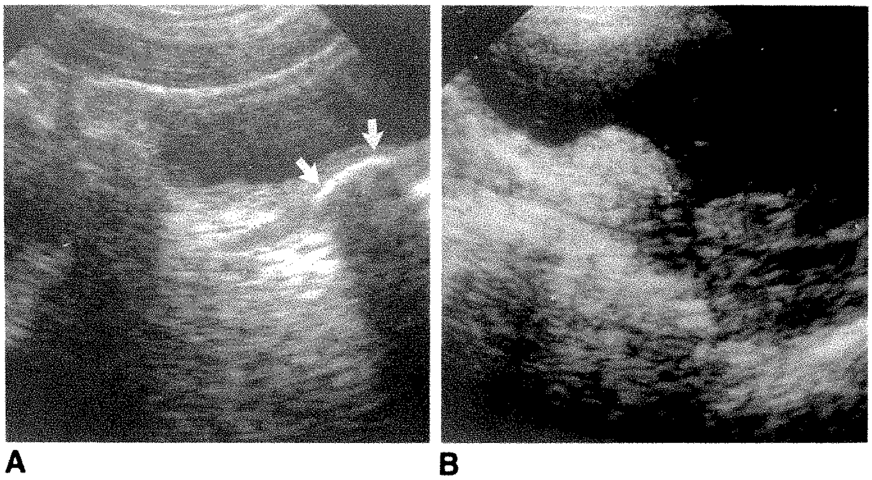

Fig. 6.—Normal appearance after subureteric injection of Teflon.
A, Oblique sonogram shows hyperechoic curvilinear band (*arrows*) with acoustic shadowing corresponding to early aspect of submucosal Teflon.
B, Oblique sonogram obtained 3 months after *A* shows a less echogenic globular mass (between *crosses*), without acoustic shadowing, corresponding to site of Teflon injection.

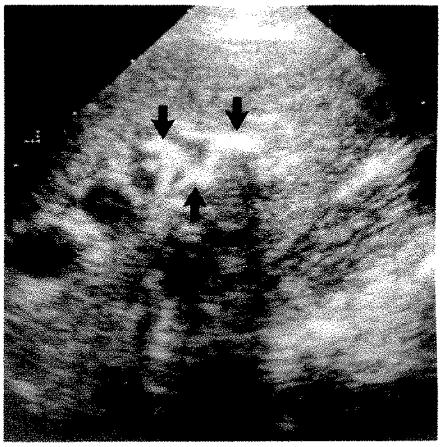

Fig. 7.—Presumed ectopic intracaliceal Teflon particles after subureteric injection of Teflon. Oblique lumbar sonogram shows hyperechoic curvilinear foci (*arrows*) within caliceal system.

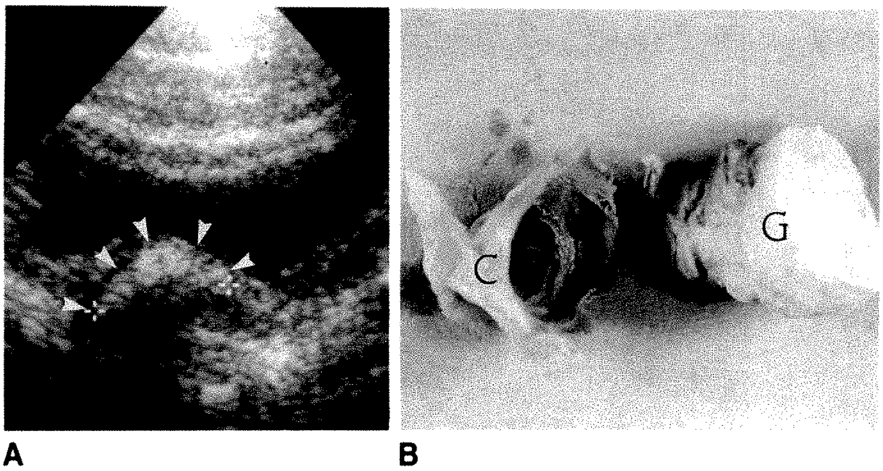

Fig. 8.—Granuloma formation complicating Teflon injection.
A, Transverse sonogram shows 15-mm echogenic mass (*arrowheads*) at ureterovesical junction (Teflon granuloma). Patient was treated surgically for persistent reflux, and granuloma was confirmed.
B, Photograph of pathologic specimen shows granuloma (G) at Teflon site, corresponding to mass described. C = capsule of granuloma.

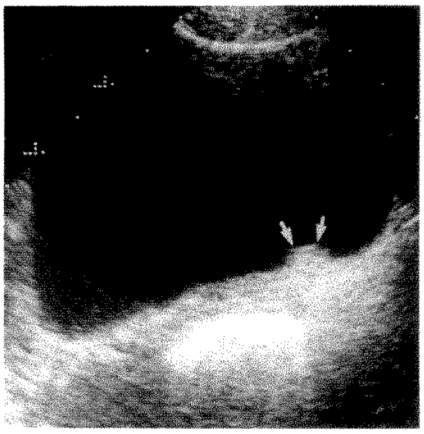

Fig. 9.—Normal appearance after subureteric injection of collagen. Oblique sonogram shows echogenic mass (*arrows*) without posterior acoustic shadowing.

In cases of duplex collecting systems with ectopic ureterocele and nonfunctioning upper poles, the usual surgical procedure is an upper pole nephrectomy with partial ureterectomy. In this technique, the distal ureter remains, and the ureterocele collapses, giving the previously undescribed appearance of an irregular echogenic mass. A normal postsurgical appearance was observed in six patients, in whom dilatation of the urinary tract resolved, and in whom the collapsed ureterocele produced a pseudotumor. Reflux may occur into the persisting ureter, and this is best diagnosed by using VCUG [12]. It is usually unsuspected on sonography unless urine or pus accumulates, producing a tubular retrovesical mass, as in one of our patients (Fig. 4).

The role of endoscopic treatment of abnormalities at the ureterovesical junction continues to increase. Important techniques include the STING procedure and ureterocele incision. The STING procedure is an endoscopic alternative to surgical correction of reflux. Teflon, injected into the submucosal part of the ureter in the bladder wall, provides better attachment to the submucosal ureter and narrows the ureteric orifice, thus preventing reflux [13]. The Teflon has a typical hyperechoic sonographic appearance with acoustic shadowing that should not be confused with urinary tract lithiasis [1, 8]. On follow-up studies, the Teflon appears less echogenic but more globular. Sonographic demonstration of the Teflon does not imply resolution of the reflux, and follow-up cystography is still necessary.

Mild dilatation of the urinary tract may occur after the STING procedure; it usually resolves rapidly, within 3–4 weeks [13]. We observed such transitory dilatation in 20% of our patients. Persistent or progressive dilatation is abnormal and must be correlated with the pretreatment examinations. Persistent ureteral dilatations in two patients were seen on sonograms, and obstruction was diagnosed on the basis of the findings on excretory urography. These two children required surgery.

Migration of Teflon inside and outside the urinary tract has been described [8]. In two of our patients, Teflon particles were detected in the ureter and the pyelocaliceal system (Fig. 7). Teflon in the ureter or renal pelvis theoretically may cause obstruction of the urinary tract, but no complication of this type was encountered in our series, and the sonographic appearance returned to normal within 1 week.

A granulomatous reaction occurs that gradually forms a fibrous capsule around the injected Teflon. Although Teflon granulomas are worrisome, complications associated with them have been observed seldom [14]. Granulomas were suspected in 10 patients in our series when the Teflon appeared as a globular echogenic mass larger than expected (from 12 to 20 mm) (Fig. 8). In two of these patients, the echogenic Teflon mass enlarged slowly. In the other eight patients, no increase in size was observed. Subsequent surgical confirmation was obtained in five children. In our retrospective study, no correlation was found between the size of the granuloma and the total volume of Teflon injected or the number of Teflon injections, as described also by Blake and O'Connell [14]. The size of the granuloma appears to depend on factors related to the patient rather than to the procedure [14]. Granuloma formation after Teflon injection may be a justification for the use of less reactive materials such as collagen. Collagen was used in 20 cases in our series, and no complications were encountered.

Modern prenatal diagnosis results in the detection of uropathies, usually before complications arise. This has led to less invasive therapy, such as endoscopic ureterocele incision instead of traditional surgery [7]. After intervention, resolution of the urinary tract dilatation can be monitored with sonography. The masslike appearance of a collapsed ureterocele seen at sonography must not be confused with a real tumor (Fig. 5).

In conclusion, sonography is useful for the follow-up of children after surgical or endoscopic procedures at the ureterovesical junction. The various normal sonographic findings after treatment must be recognized in order to distinguish them from both early and late complications. When abnormalities are major, complementary uroradiologic or functional examinations may be necessary for complete diagnosis.

REFERENCES

1. Mann Cl, Jequier S, Patriquin H, LaBerge I, Homsy YL. Intramural Teflon injection of the ureter for treatment of vesicoureteral reflux: sonographic appearance. *AJR* **1988**;151:543-545
2. Lebowitz RL. Ureter. In: *Postoperative pediatric uroradiology*. New York: Appleton-Century-Crofts, **1981**:15-36
3. Marchal GJ, Baert AL, Eeckels R, Proesmans W. Sonographic evaluation of the normal ureteral submucosal tunnel in infancy and childhood. *Pediatr Radiol* **1983**;13:125-129
4. Dinkel E, Dittrich M, Peters H, et al. Sonographic biometry in obstructive uropathy of children: preoperative diagnosis and postoperative monitoring. *Urol Radiol* **1985**;7:1-7
5. Lebowitz RL. Reconstruction of the previously diverted urinary tract. In: *Postoperative pediatric uroradiology*. New York: Appleton-Century-Crofts, **1981**:131-151
6. Lebowitz RL. Duplex collecting system. In: *Postoperative pediatric uroradiology*. New York: Appleton-Century-Crofts, **1981**:59-78
7. Viville C. Endoscopic treatment of ureterocele and antireflux injection with Teflon paste. *Eur Urol* **1990**;17:321-324
8. Giuliano CT, Cohen HL, Haller JO, Glassberg KI. The STING procedure and its complications: sonographic evaluation. *JCU* **1990**;18:415-420
9. Mezzacappa PM, Price AP, Kassner EG, Haller JO, Glassberg KI. Cohen ureteral reimplantation: sonographic appearance. *Radiology* **1987**;165:851-852
10. Lebowitz RL, Vargas B. Stones in the urinary bladder in children and young adults. *AJR* **1987**;148:491-495
11. Lebowitz RL. Bladder. In: *Postoperative pediatric uroradiology*. New York: Appleton-Century-Crofts, **1981**:37-42
12. Teele LR, Lebowitz RL, Colodny AH. Reflux into the unused ureter. *J Urol* **1976**;115:313-315
13. Schulman CS, Pamart D, Hall M, Janssen F, Avni EF. Vesicoureteral reflux in children: endoscopic treatment. *Eur Urol* **1990**;17:314-317
14. Blake NS, O'Connell E. Endoscopic correction of vesico-ureteric reflux by subureteric Teflon injection: follow-up ultrasound and voiding cystography. *Br J Radiol* **1989**;62:443-446

Radiology Outreach Foundation

The Radiology Outreach Foundation (ROF) is a nonprofit corporation whose goal is to help disadvantaged countries improve their health care by providing radiology equipment, books, consultation, education, and training to their practitioners. This assistance is on an application basis that is independent of political, ethnic, or religious orientation of the grantee. It depends on the need of the people and the ability of the ROF to meet that need. The ROF is approved by the U.S. Internal Revenue Service as a tax-exempt organization. It is endorsed by the following radiologic societies: American Association of Women Radiologists, American College of Radiology, American Roentgen Ray Society, Association of University Radiologists, Radiological Society of North America, Society of Chairmen of Academic Radiology Departments, Society for Pediatric Radiology, European Society of Pediatric Radiology.

All donations to the ROF are tax deductible. Persons who would like to contribute financially to the ROF, would be interested in being a visiting professor, would like to send books or journals to any of the institutions supported by the ROF, or would like further information about the ROF should write to Charles A. Gooding, M.D., President, Radiology Outreach Foundation, 3415 Sacramento St., San Francisco, CA 94118 USA.

Can Detection of the Yolk Sac in the First Trimester Be Used to Predict the Outcome of Pregnancy?
A Prospective Sonographic Study

Alfred B. Kurtz[1]
Laurence Needleman
Rebecca G. Pennell
Oksana Baltarowich
Maria Vilaro
Barry B. Goldberg

Recent reports have indicated that identification of the yolk sac should precede the detection of the embryo in a normal first-trimester sonographic examination and that failure to visualize a yolk sac strongly suggests an abnormal intrauterine pregnancy. A first-trimester prospective study was performed in 163 normal and 49 abnormal consecutive singleton gestations. All women were examined both abdominally and transvaginally, with pregnancy outcome determined by delivery of a normal infant or a spontaneous abortion. The yolk sac was analyzed in all patients in whom an embryo was not identified ($n = 76$). When the yolk sac was identified, the following was found: by the abdominal approach with the mean sac diameter (MSD) less than 27 mm ($n = 15$), nine gestations were normal and six were abnormal, and by the transvaginal approach with the MSD less than 18 mm ($n = 13$), seven gestations were normal and six were abnormal. The presence of a yolk sac was not consistently predictive of a normal early pregnancy. When the yolk sac was also not identified, the following was found: abdominally with the MSD less than 27 mm ($n = 41$), 19 gestations were normal and 22 were abnormal, and transvaginally with the MSD less than 18 mm ($n = 11$), six gestations were normal and five were abnormal. Absence of the yolk sac was not consistently predictive of a spontaneous abortion. When using the MSD range (20-27 mm abdominally and 7-16 mm transvaginally), over which the yolk sac but not the embryo should be identified sonographically, the yolk sac was again not consistently visualized. On abdominal sonograms, the yolk sac was present and absent in three and 10 patients, respectively, for both normal and abnormal pregnancies. On transvaginal sonograms, the yolk sac was present and absent in seven and five normal gestations and in six and four abnormal gestations, respectively.

The results of this study suggest that detection of the yolk sac in the first trimester is not an early predictor of pregnancy outcome.

***AJR* 158:843-847, April 1992**

If the appearance of the yolk sac is to be of significant clinical use in the evaluation of early pregnancy, its presence would have to routinely precede visualization of the embryo. Once the embryo is imaged and its heart motion evaluated, the importance of identifying the yolk sac lessens. Four articles [1-4] have specifically addressed this issue, comparing the size of the specific gestational mean sac diameter (MSD) with the embryo and with the yolk sac. Two studies [1, 2] evaluated only normal pregnancies with transvaginal sonography. Both detected the yolk sac in all cases, and earlier than detection of cardiac activity (presumably identifying a living embryo). The other two studies, which sonographically evaluated both normal and abnormal intrauterine pregnancies abdominally [3] and transvaginally [4], detected a yolk sac in all normal and in some abnormal pregnancies. However, when the yolk sac was not identified earlier than identification of the embryo, this was always associated with spontaneous abortion. Another study [5] compared the detection of the embryo (not the yolk sac) with the MSD by both abdominal and transvaginal sonography. In this prospective consecutive study of 163 normal singleton pregnancies, the normal embryo was always identified

Received September 23, 1991; accepted after revision November 11, 1991.

[1] All authors: Department of Radiology, Division of Diagnostic Ultrasound, Thomas Jefferson University Hospital, 111 S. 11th St., Philadelphia, PA 19107-5091. Address reprint requests to A. B. Kurtz.

0361-803X/92/1584-0843
© American Roentgen Ray Society

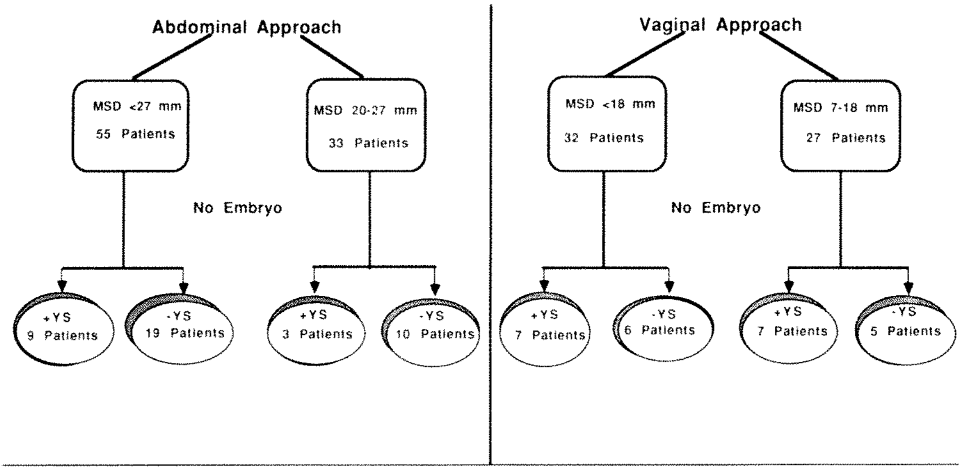

Fig. 1.—Chart depicting first-trimester sonographic detection of the yolk sac in 163 patients with normal findings. YS = yolk sac, MSD = mean sac diameter, + = present, − = absent.

abdominally when the MSD was greater than or equal to 27 mm and transvaginally when the MSD was greater than or equal to 12 mm.

Combining the results of these various series, one may conclude that by abdominal measurements [3, 5] the yolk sac should normally be identified when the MSD is greater than 20 mm and the embryo is greater than 27 mm. For transvaginal measurements [1, 2, 4, 5], the yolk sac should normally be identified when the MSD is greater than 7 mm, with the embryo normally identified at an MSD of greater than 18 mm.

As part of the previously described prospective study comparing abdominal and transvaginal sonographic findings in early pregnancy [5], we also evaluated the yolk sac in normal and abnormal singleton pregnancies. Its presence or absence was analyzed to determine whether the yolk sac could consistently predict early normal intrauterine pregnancy and pregnancy failure.

Subjects and Methods

From February to June 1987, consecutive patients were prospectively referred by clinicians for first-trimester sonographic studies [5]. These patients were examined with both abdominal and transvaginal sonography. The 224 patients with singleton gestations had adequate clinical follow-up and were categorized as to normal (175) or abnormal (49) gestations. Of the 175 patients with normal gestations, 163 had an intrauterine gestational sac noted on sonography (MSD range, 8 to 70 mm abdominally and 7 to 69 mm transvaginally) and subsequently gave birth to a healthy infant. These pregnancies constitute the normal group in the present study. The 12 other patients with normal gestations and a visible intrauterine gestational sac subsequently elected to terminate their pregnancies and were excluded from the study. The 49 abnormal gestations led to spontaneous abortions in all cases. These gestations were diagnosed as abnormal by the sonographic signs of a gestational sac without a detectable embryo or a gestational sac with an embryo but without heart motion; these patients constitute the abnormal group in the present study. All cases were proved to be abnormal by clinical examination and abnormal beta human chorionic gonadotropin (β-HCG) levels. The range of MSD for this group was 11 to 60 mm abdominally and 9 to 60 mm transvaginally.

Two experienced examiners performed the abdominal and transvaginal studies [5]. The abdominal sonogram was made from the anterior abdominal wall while the patient's bladder was full. The transvaginal examination was performed by a different sonologist without knowledge of the abdominal sonographic findings. The sonographic equipment represented a full range of standard start-of-the-art commercially available real-time units. Clinical history was available to both examiners. The findings from each study were initially recorded separately and later combined for a formal report.

The MSD was taken as an average of three orthogonal dimensions. The sac was evaluated for the presence or absence of an embryo and, when present, heart motion was sought. For the purpose of this study, the embryo was considered absent when it was either not detected or was present without heart motion. In all normal and abnormal singleton studies, the entire anechoic space within the gestational sac was imaged for the presence or absence of a cystic structure that could be identified as the yolk sac. If present, it was neither measured nor examined for unusual size or thickness. Care was taken not to confuse the normally identified amnion with the yolk sac. The actual measurement of the length of the embryo (the crown-rump length) was also obtained, but these results are not pertinent to this study.

Results

In the normal pregnancy group, the yolk sac was visualized in the majority of patients. By the abdominal approach, it was identified in 140 of the 163 patients (86%) (MSD range, 10 to 77 mm). By the transvaginal approach, the yolk sac was seen in 157 of the 163 patients (96%) (MSD range, 8 to 69 mm). In the abnormal pregnancy group, the yolk sac was identified less often. By the abdominal approach, the yolk sac was seen in 19 of the 49 patients (39%) (MSD, 16 to 52 mm). By the transvaginal approach, the yolk sac was identified in 31 of the 49 patients (63%) (MSD range, 11 to 53 mm).

Abdominal Technique

In the cases with an MSD below 27 mm, 55 intrauterine pregnancies were normal (Fig. 1) and 33 were abnormal (Fig.

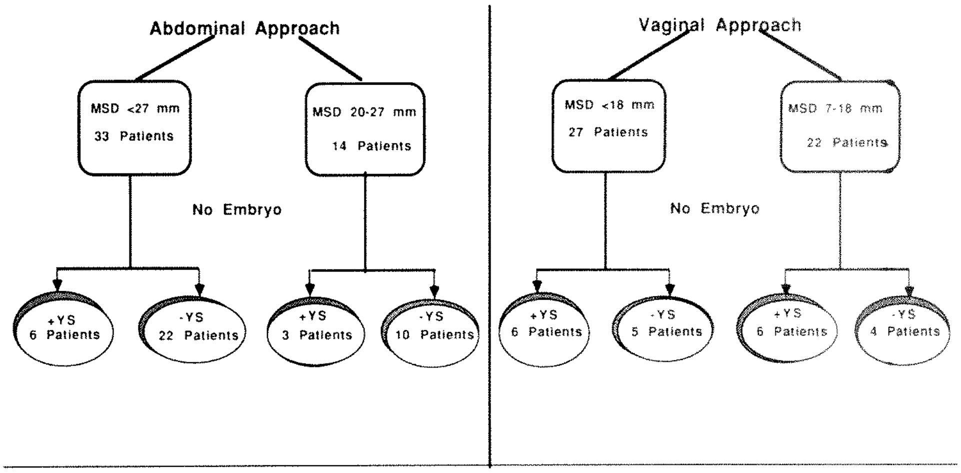

Fig. 2.—Chart depicting first-trimester sonographic detection of the yolk sac in 49 patients with abnormal findings. YS = yolk sac, MSD = mean sac diameter, + = present, − = absent.

2). The embryo was not seen in 28 normal pregnancies and in another 28 abnormal pregnancies. Reevaluated over the 20 to 27 mm MSD range, 33 pregnancies were normal (Fig. 1) and 14 were abnormal (Fig. 2). The embryo was not seen in 13 normal and in another 13 abnormal pregnancies. In all groups, normal and abnormal, findings of visualization and nonvisualization of the yolk sac were randomly distributed.

Transvaginal Technique

When using an MSD of less than 18 mm, we found 32 normal (Fig. 1) and 27 abnormal (Fig. 2) intrauterine pregnancies; the embryo was not seen in 13 normal and 11 abnormal pregnancies (Fig. 3). The yolk sac was reevaluated over the MSD range of 7 to 18 mm in 27 normal (Fig. 1) and 22 abnormal (Fig. 2) pregnancies. The embryo was not seen in 12 normal and in another 10 abnormal pregnancies. In all groups, there was again a fairly even distribution of visualization and nonvisualization of the yolk sac in both the normal and abnormal cases.

Discussion

Investigators have studied the normal sonographic appearance of the yolk sac [6–9], its proximity to the embryo [10, 11], its use in differentiating normal from abnormal intrauterine pregnancies [12], and its value in ruling out ectopic pregnancy [13–15]. Characteristics of the yolk sac have also been compared with other first-trimester parameters, including gestational age [1, 2, 16–21], gestational sac size [22, 23], the embryo and its heart motion [24, 25], and β-HCG levels [1, 2, 21]. These articles established normal growth curves for the yolk sac and detected abnormal growth in some abnormal pregnancies. While no consistent size or characteristics of the yolk sac were found, several groups stated that the yolk sac could normally be imaged at specific gestational ages, gestational sac sizes, and β-HCG levels before the embryo could be visualized [1, 2, 18, 21, 22].

The yolk sac that is imaged is actually the embryologic secondary yolk sac. The primary yolk sac is pinched off by 4 weeks' gestation and this secondary yolk sac is seen sonographically until approximately 11 weeks' gestation [6, 26]. Since the yolk sac can be identified with sonography when the prochordal plate of the evolving embryo is forming [26], the yolk sac should be routinely identified before the embryo is visualized. Despite this fact, most studies evaluating the yolk sac have not been performed very early in the pregnancy, but instead after 6 weeks' gestation [1, 16, 17, 20, 21]. Since the embryo is commonly identified by 6 weeks' gestation, visualization of the yolk sac is more important earlier. Four studies have evaluated the appearance of the yolk sac earlier, identifying it between 5 and 6 weeks' gestation [1, 2, 18, 22].

The exact MSD at which the yolk sac can first be seen by using abdominal sonography has not previously been deter-

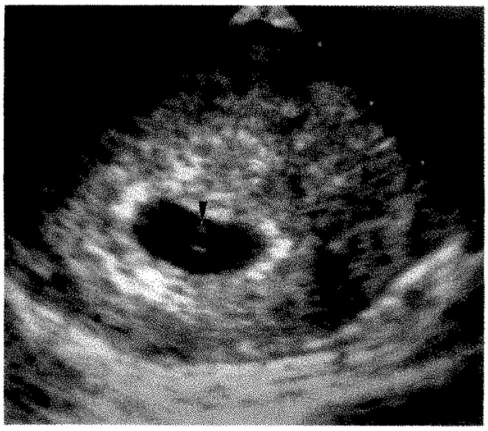

Fig. 3.—Transvaginal sonogram in a patient with a mean sac diameter (MSD) of 14 mm. Yolk sac is present (*arrowhead*) but there is no identifiable embryo. One week later, an embryo was still not seen and the MSD did not change, findings that confirmed an abnormal intrauterine pregnancy.

mined; in our study the smallest MSD at which a yolk sac could be identified was 10 mm. Transvaginally, the yolk sac was seen earlier. Cacciatore et al. [1] always visualized the yolk sac when the MSD was 10 mm and Daya et al. [2] always detected a yolk sac when the MSD was 6.7 mm. This is consistent with our findings of yolk sac identification at an MSD of 8 mm.

Two articles [3, 4] specifically evaluated the MSD in relation to the embryo and yolk sac in both normal and abnormal intrauterine pregnancies. Nyberg et al. [3], by using the abdominal approach, showed that a yolk sac was routinely imaged in normal preparations when the MSD was greater than 20 mm, a sac 5 mm smaller than when the living embryo was identified. Among 30 abnormal pregnancies, 26 had a detectable yolk sac when the MSD was greater than 20 mm. In the other four abnormal cases, a yolk sac was not identified. Levi et al. [4], by using the transvaginal approach, had similar results. The yolk sac was present in all normal pregnancies with the MSD greater than 8 mm, with a living embryo routinely identified when the MSD was greater than 16 mm. In 10 cases in which the MSD was greater than 8 mm and a yolk sac was not identified, all proved to be abnormal pregnancies; some abnormal pregnancies, however, did have an identifiable yolk sac. Both studies concluded that a yolk sac was always present in normal pregnancies above a certain MSD. Although a yolk sac could also be seen in abnormal pregnancies, the absence of a yolk sac after the expected MSD was visualized was always indicative of an abnormal pregnancy.

All four previous studies [1–4] strongly support the premise that a yolk sac should always be present in normal pregnancies and that a yolk sac may not be present in abnormal pregnancies. Although this would seem to make sense embryologically and anatomically, our findings were different. We found that yolk sacs were not predictive of either normal or abnormal pregnancies. The reasons for these discrepancies are unclear. We used state-of-the-art sonographic scanners. Our sonologists were highly skilled in abdominal pelvic sonographic examination and had at least 6 to 8 months' additional experience with transvaginal scanning before the start of our study. The anatomy of the first-trimester pregnancy was well understood and the yolk sac was carefully sought, both in the middle and at the margins of the anechoic gestational sac, and there was no confusion between the amniotic membrane and the yolk sac.

Perhaps the differences can be explained by different methodologies. Our study was a consecutive prospective first-trimester study of a group of 224 patients, and used both abdominal and transvaginal approaches. Cacciatore et al. [1] and Daya et al. [2] performed careful transvaginal prospective studies, but did not include patients with abnormal outcomes. A preselection bias may therefore have occurred, in which the entire spectrum of normal pregnancies was not evaluated. Nyberg et al. [3] performed a retrospective study of 83 pregnant women who had abdominal sonography (presumably not consecutive patients). Levi et al. [4] performed a prospective transvaginal consecutive study of 62 patients and analyzed their data retrospectively. The overall number of subjects in their patient groups is therefore smaller than ours. Using transvaginal sonography, Levi et al. [4] examined 44 patients with normal pregnancies and 15 patients with abnormal pregnancies in which the MSD was greater than 8 mm. The actual number of cases evaluated with MSDs between 8 and 16 mm is not known and may have been even smaller than our group. Nyberg et al. [3], in their abdominal analysis of 53 normal and 30 abnormal pregnancies, similarly did not indicate the number of patients with an MSD between 20 and 25 mm. More work will be needed to resolve these discrepancies.

We believe that the appearance of the yolk sac, although not as important as previously suggested, can still be useful in first-trimester studies. It has value in a number of situations, including defining normal first-trimester anatomy, determining the existence of an intrauterine pregnancy, differentiating a pseudogestational sac from a true gestational sac, and identifying the number and type of multiple gestations.

In conclusion, the most important sonographic criterion for identification of a normal first-trimester pregnancy is the presence or absence of an embryo and associated heart motion. The presence or absence of a yolk sac does not appear to have the same diagnostic impact and cannot be used to determine if the pregnancy is normal or abnormal. The yolk sac is not always visualized in normal pregnancies before the embryo can be seen. Conversely, the yolk sac may be present or absent in abnormal pregnancies.

ACKNOWLEDGMENTS

We thank the people in the statistical unit of the American College of Radiology and in particular Clare Guse for compiling and tabulating the data, and Emily Pompetti for assistance in preparation of the manuscript.

REFERENCES

1. Cacciatore B, Tiitinen A, Stenman UH, Ylöstalo P. Normal early pregnancy: serum hCG levels and vaginal ultrasonography findings. *Br J Obstet Gynaecol* **1990**;97:899–903
2. Daya S, Woods S, Ward S, Lappalainen R, Caco C. Early pregnancy assessment with transvaginal ultrasound scanning. *Can Med Assoc J* **1991**;144:441–446
3. Nyberg DA, Mack LA, Laing FC, Patten RM. Distinguishing normal from abnormal gestational sac growth in early pregnancy. *J Ultrasound Med* **1987**;6:23–27
4. Levi CS, Lyons EA, Lindsay DJ. Early diagnosis of nonviable pregnancy with endovaginal US. *Radiology* **1988**;167:383–385
5. Pennell RG, Needleman L, Pajak T, et al. Prospective comparison of vaginal and abdominal sonography in normal early pregnancy. *J Ultrasound Med* **1991**;10:63–67
6. Mantoni M, Pedersen JF. Ultrasound visualization of the human yolk sac. *JCU* **1979**;7:459–460
7. Bernard KG, Cooperberg PL. Sonographic differentiation between blighted ovum and early viable pregnancy. *AJR* **1985**;144:597–602
8. Sauerbrei E, Cooperberg PL, Poland BJ. Ultrasound demonstration of the normal fetal yolk sac. *JCU* **1980**;8:217–220
9. Coleman BG, Arger PH, Grumbach K, et al. Transvaginal and transabdominal sonography: prospective comparison. *Radiology* **1988**;168:639–643
10. Cadkin AV, McAlpin J. Detection of fetal cardiac activity between 41 and

43 days of gestation. *J Ultrasound Med* **1984**;3:499–503

11. Yeh HC, Rabinowitz JG. Amniotic sac development: ultrasound features of early pregnancy—the double bleb sign. *Radiology* **1988**;166:97–103
12. Pennell RG, Baltarowich OH, Kurtz AB, et al. Complicated first-trimester pregnancies: evaluation with endovaginal US versus transabdominal technique. *Radiology* **1987**;165:79–83
13. Dashefsky SM, Lyons EA, Levi CS, Lindsay DJ. Suspected ectopic pregnancy: endovaginal and transvesical US. *Radiology* **1988**;169:181–184
14. Nyberg DA, Mack LA, Jeffrey RB Jr, Laing FC. Endovaginal sonographic evaluation of ectopic pregnancy: a prospective study. *AJR* **1987**;149:1181–1186
15. Nyberg DA, Mack LA, Harvey D, Wang K. Value of the yolk sac in evaluating early pregnancies. *J Ultrasound Med* **1988**;7:129–135
16. Green JJ, Hobbins JC. Abdominal ultrasound examination of the first-trimester fetus. *Am J Obstet Gynecol* **1988**;159:165–175
17. Reece EA, Scioscia AL, Pinter E, et al. Prognostic significance of the human yolk sac assessed by ultrasonography. *Am J Obstet Gynecol* **1988**;159:1191–1194
18. Warren WB, Timor-Tritsch I, Peisner DB, Raju S, Rosen MG. Dating the early pregnancy by sequential appearance of embryonic structures. *Am J Obstet Gynecol* **1989**;161:747–753
19. Rempen A. Vaginale sonographie der intakten Gravidität im ersten Trimenon. *Geburtshilfe Frauenheilkd* **1987**;47:477–482
20. Crooij MJ, Westhuis M, Schoemaker J, Exalto N. Ultrasonographic measurement of the yolk sac. *Br J Obstet Gynaecol* **1982**;89:931–934
21. Bree RL, Edwards M, Böhm-Vélez M, Beyler S, Roberts J, Mendelson EB. Transvaginal sonography in the evaluation of normal early pregnancy: correlation with hCG level. *AJR* **1989**;153:75–79
22. Hurwitz SR. Yolk sac sign: sonographic appearance of the fetal yolk sac in missed abortion. *J Ultrasound Med* **1986**;5:435–438
23. Jain KA, Hamper UM, Sanders RC. Comparison of transvaginal and transabdominal sonography in the detection of early pregnancy and its complications. *AJR* **1988**;151:1139–1143
24. Ferrazzi E, Brambati B, Lanzani A, et al. The yolk sac in early pregnancy failure. *Am J Obstet Gynecol* **1988**;158:137–142
25. Levi CS, Lyons EA, Zheng XH, Lindsay DJ, Holt SC. Endovaginal US: demonstration of cardiac activity in embryos of less than 5.0 mm in crown-rump length. *Radiology* **1990**;176:71–74
26. Moore KL. *The developing human*, 3rd ed. Philadelphia: Saunders, **1982**:42–45, 128–129

Come to the
American Roentgen Ray Society
92nd
ANNUAL MEETING
Orlando, FL
Marriott's Orlando World Center
May 10-15, 1992

Scientific Program (189 papers)
60 Instructional Courses
Categorical Course on Neuroradiology
Symposium on Pediatric Radiology
Symposium featuring a New Issues Forum
The Caldwell Lecture
Award Papers
Technical Exhibits
Spouse/Guest Program on Osteoporosis
Golf, Tennis and Social Programs

American Roentgen Ray Society

92nd Annual Meeting

May 10–15, Orlando, FL

1992 Caldwell Lecturer

William J. Casarella, M.D.

"The Radiologist as a Surgeon: The Challenge of Interventional Radiology"

Review Article

Multiple Sclerosis: The Impact of MR Imaging

Carla J. Wallace,[1] T. Peter Seland,[2] and T. Chen Fong[1]

MR imaging has had a significant impact on the understanding of multiple sclerosis. The procedure now plays an important role in initial diagnostic workup, replacing some other radiologic and paraclinical tests and often confirming clinically suggested locations of lesions. It also has contributed greatly to the understanding of the natural history of this disease, allowing objective assessment of disease load, detection of asymptomatic lesions, and differentiation between acute and chronic lesions. MR imaging is highly sensitive to inflammation and demyelination caused by multiple sclerosis, and although there is a long differential diagnosis for some of the MR findings, increasing experience has defined a number of relatively specific criteria for multiple sclerosis. Recent advances may allow faster imaging and highly objective lesion quantification, which will aid in therapeutic trials.

MR imaging is the first imaging method that allows direct visualization of plaques in the brain in most patients with multiple sclerosis (MS). It is also the first imaging technique capable of noninvasive, direct sagittal and axial imaging of the spinal cord, thereby enabling the delineation of plaque formation in transverse myelitis [1, 2]. Recently, with the use of a contrast agent, gadopentetate dimeglumine, that passes through a disrupted blood-brain barrier, it has become possible to distinguish between acute inflammation in "fresh" plaques and areas of more chronic involvement [3, 4].

These features should lead to a better understanding of the natural history of this unpredictable disorder—already there have been surprising results, with considerable disease activity becoming visible in patients without clinical evidence of relapse [4-6]. Serial MR imaging, with and without contrast material, will also contribute greatly to monitoring the progress of the disease in clinical trials [5, 7]. MR imaging has already made it possible to virtually eliminate the use of other imaging techniques (e.g., CT and myelography) in excluding other diagnoses; it may eliminate some other paraclinical tests, and play a complementary role with others, in the diagnosis, management, and clinical study of this disorder.

Multiple Sclerosis: Clinical Diagnosis

MS is a common neurologic disorder that preponderantly affects young adults of Northern European extraction. Pathologically, the disease is characterized by the cyclical appearance of inflammation and then demyelination in "plaques" scattered throughout the CNS white matter. The cause of the disease is unknown, but susceptibility is determined predominantly by multiple genetic variants [8].

Clinically, most patients have a relapsing and remitting course from the outset, then shift after years into a chronic progressive phase; some courses are progressive from the start. The spectrum of clinical symptoms and signs is remarkably broad and well summarized in clinical reviews [9].

Despite the dramatic advances in the laboratory evaluation of MS, the diagnosis still rests ultimately with clinical judgment. The criteria of Schumacher et al. [10] for a diagnosis of clinically definite MS require the demonstration of clinical abnormalities implicating at least two noncontiguous CNS white matter sites, with at least two relapses or gradual progression in at least 6 months. Symptoms must be judged by an experienced physician, generally a neurologist, to be

---

Received July 25, 1991; accepted after revision October 30, 1991.

[1] Department of Radiological Sciences and Diagnostic Imaging, Foothills Hospital, 1403 29th St. N.W., Calgary, Alberta T2N 2T9, Canada. Address reprint requests to C. J. Wallace.

[2] Department of Clinical Neurosciences, Calgary General Hospital, M4-022, 841 Centre Ave. E., Calgary, Alberta T2E 0A1, Canada.

AJR 158:849-857, April 1992 0361-803X/92/1584-0849 © American Roentgen Ray Society

best explained by MS and no other disease. This judgment is based partly on the knowledge of certain sites in the CNS that are involved more frequently with MS, but mainly on the clinical demonstration of multiplicity of neurologic events, separated in time and/or space.

Few patients meet these stringent criteria, at least in the early years of the illness. So that clinical researchers could explore the entire spectrum of this disease, diagnostic criteria were expanded to include laboratory and imaging (i.e., paraclinical) findings. The criteria of Poser et al. [11] use demonstrated subclinical lesions detected by evoked potentials, CT, and MR imaging in arriving at designations of clinically definite and clinically probable MS. Where spatial or temporal criteria are not otherwise met, a finding of oligoclonal banding in the CSF often enables a designation of laboratory-supported definite or probable MS. This diagnostic classification has been extended from its research application into everyday neurologic practice.

The designation by Schumacher et al. [10] of clinically "possible" MS has been abandoned by most neurologists, because it potentially encompasses most patients with an isolated neurologic problem.

MR Criteria for Diagnosis of Multiple Sclerosis

As noted in a subsequent section, proton density-weighted images (first echo of a T2-weighted sequence) are considered most sensitive in the detection of lesions of MS, with white matter hyperintensities a characteristic finding. Unfortunately, there is a long list of differential diagnostic possibilities when these lesions are observed, as outlined in the next section. For this reason, attempts have been made to define criteria for increasing the probability of making a correct diagnosis of MS on the basis of MR imaging findings.

The textbook description of MS [12] is a description of multiple focal periventricular lesions with T1 and T2 prolongation, irregular outlines [13], a "lumpy-bumpy" appearance [14] (Fig. 1), and small size (almost always less than 2.5 cm long [15], although very large lesions can appear). The lesions may be homogeneous, or may have a thin rim of relative T2 hypointensity or T1 hyperintensity [16]. Infratentorial white matter lesions are common (Fig. 2); atrophy, both diffuse and callosal, is common in long-standing disease. Paty et al. [17] have described an MR diagnostic scale in which MR imaging is considered strongly suggestive of MS only if there are four or more areas of T2 hyperintensity longer than 3.0 mm, or three lesions, one of which is periventricular [17].

An important observation was made by Horowitz et al. [18], who noted that the great majority of MS patients (86% in their series) had at least some lesions that were ovoid and perpendicular to the long axis of the brain and lateral ventricles (Fig. 3A). They noted that this correlates well with the pathologic description of perivascular demyelination around subependymal veins, and is probably quite specific for MS. Brainstem lesions also are usually contiguous with a CSF surface, either cisternal or ventricular [19].

Involvement of the corpus callosum is common pathologically and on MR imaging (Fig. 4). Callosal or subcallosal lesions were present in 55% of cases in one series [20]; callosal atrophy was associated in 40%. A more recent study indicates a much higher frequency of involvement (93%) in well-established MS and suggests that inferior callosal lesions may be quite specific [21].

Decreased T2 in the thalamus and putamen has been reported in advanced definite MS cases, presumably owing to increased iron accumulation [22].

In the spinal cord, somewhat nonspecific focal T2 prolongation may be noted (Fig. 5), sometimes with acute swelling and chronic atrophy [2].

Differential Diagnosis of Multiple Sclerosis

The differential diagnosis of the MR imaging finding of multiple cerebral white matter lesions is quite long and primarily includes vascular and inflammatory conditions of the CNS such as white matter ischemia/infarction; "normal" aging; vasculitis; moyamoya disease; radiation injury; migraine; acute disseminated encephalomyelitis; subacute sclerosing

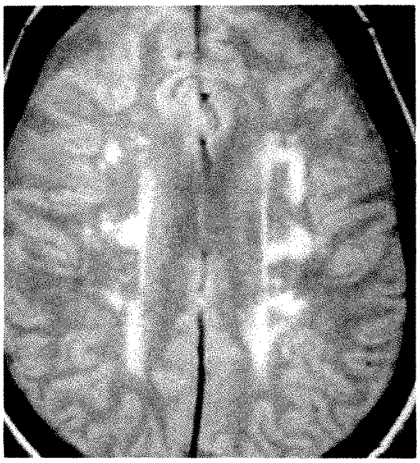
1

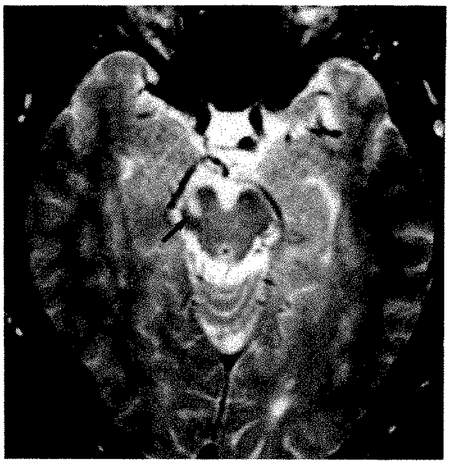
2

Fig. 1.—Typical cerebral lesions of multiple sclerosis in 64-year-old woman with sudden onset of diplopia and ataxia. Multiple periventricular lesions of multiple sclerosis, with lumpy-bumpy contour, on first echo of T2-weighted MR sequence.

Fig. 2.—Multiple sclerosis lesion in brainstem of 38-year-old man with bilateral weakness and sensory symptoms in lower extremities. T2-weighted MR image shows lesion of multiple sclerosis in right cerebral peduncle (*arrow*).

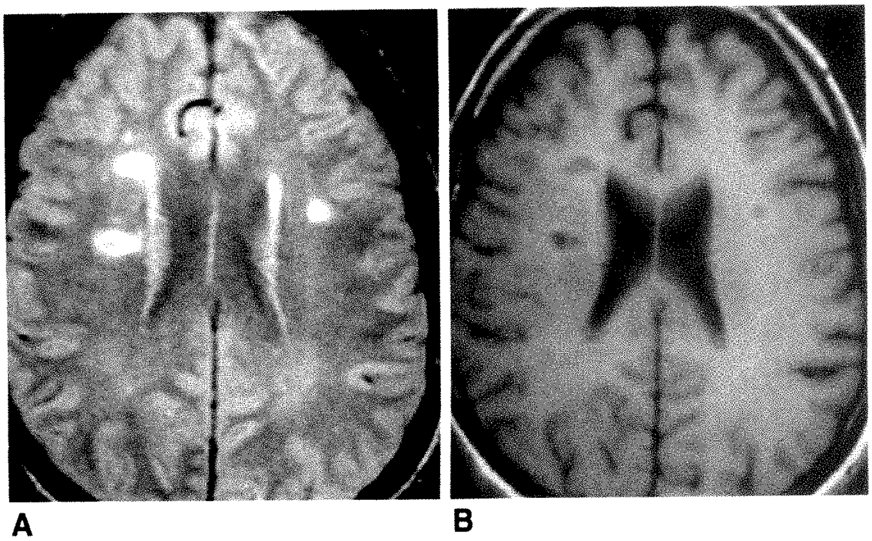

Fig. 3.—Typical ovoid periventricular lesions of multiple sclerosis in 31-year-old man with a 10-year history of relapsing-remitting neurologic symptoms.

A, First echo of T2-weighted MR sequence shows several ovoid lesions with T2 prolongation, with long axes perpendicular to ventricular walls.

B, T1-weighted MR image shows that T1 is also prolonged within lesions.

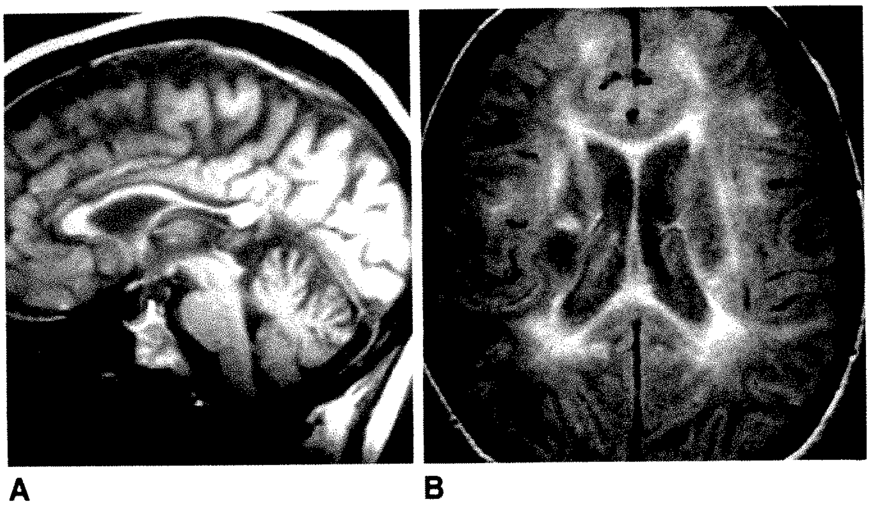

Fig. 4.—Callosal involvement with multiple sclerosis in 48-year-old woman with clinically definite multiple sclerosis for 20 years.

A, T1-weighted midline sagittal MR image shows diffuse callosal atrophy.

B, Inner callosal hyperintensity, and multiple confluent periventricular lesions, are shown on first echo of T2-weighted series.

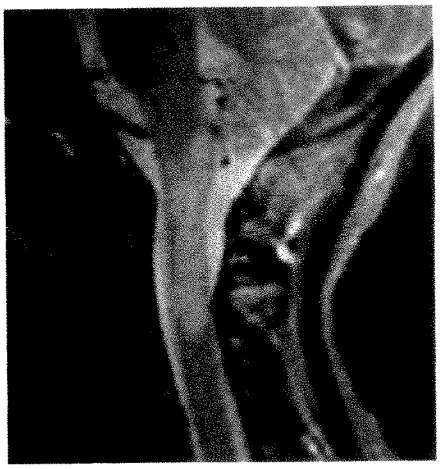

Fig. 5.—Multiple sclerosis involving upper spinal cord in 35-year-old woman with acute onset of quadriparesis. T2-weighted MR image shows a large area of demyelination in upper cervical spinal cord and cervicomedullary junction.

panencephalitis; brucellosis; borreliosis; viral encephalitis; AIDS; granulomatous diseases such as sarcoidosis and tuberculosis; and autoimmune diseases including systemic lupus erythematosus, Sjögren syndrome, and Behçet syndrome [23-33]. Other demyelinating or dysmyelinating diseases such as the leukodystrophies [34], central pontine myelinolysis [35] and vitamin B_{12} deficiency [36], and some tumors and tumorlike conditions (primary and secondary intraaxial tumor, lymphoma, and lymphomatoid granulomatosis) [33, 37], as well as head trauma [21], must also be considered.

The most common differential diagnostic possibility for multiple white matter lesions is normal aging and/or white matter ischemic lesions: small areas of increased white matter T2 signal, likely small ischemic foci, are frequently noted in healthy patients more than 50 years old [23] (Fig. 6), but they are relatively rare in healthy young people. Differentiating criteria for lesions of aging or ischemia and MS have been developed. One group achieved 100% specificity in diagnosis of MS by requiring two of three of the following: lesion diameter greater than 5.0 mm, abutting ventricular bodies, and at least one infratentorial lesion [38]. Both MS lesions and lesions seen in aging are often periventricular; vascular lesions may have a smoother contour [39], whereas MS lesions are lumpy-bumpy [14]. The focal lesions of MS may become confluent around the lateral ventricles; deep white matter infarction or ischemia may also, but it is much less commonly associated with confluence around the third and fourth ventricles and aqueduct [40]. As mentioned previously, inferior callosal lesions are very common in MS but rare in atherosclerotic disease [21].

A recent study [41] indicates that experienced neuroradiol-

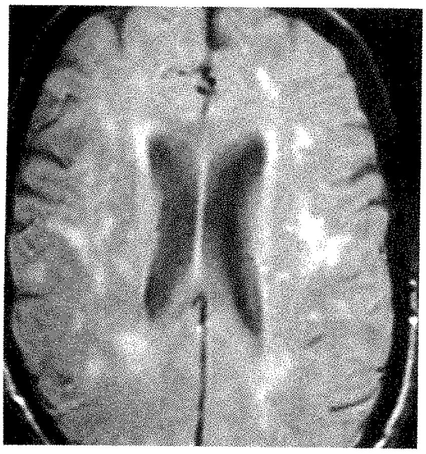

Fig. 6.—Multiple ischemic white matter lesions in 66-year-old man with symptoms of cerebellar infarction. First echo of T2-weighted MR sequence shows hyperintensities similar to those of demyelinating disease, but none are ovoid and few periventricular lesions are present.

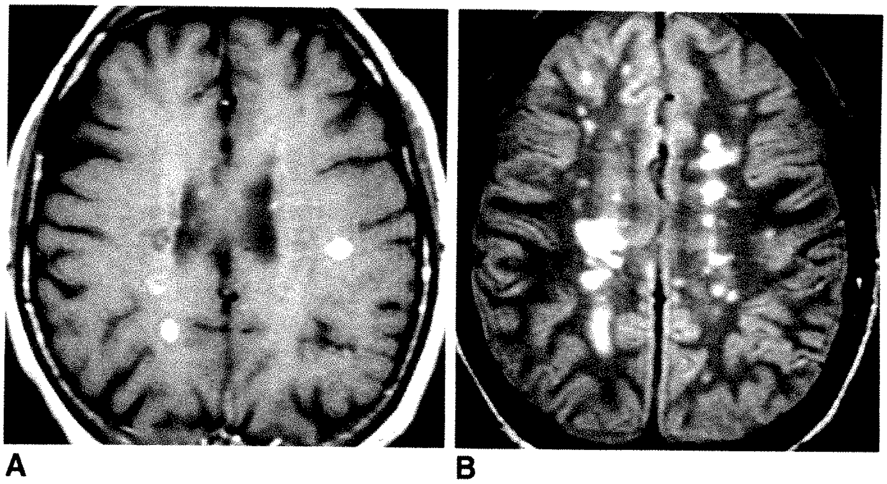

Fig. 7.—Multiple sclerosis in 42-year-old woman with clinically definite multiple sclerosis but no acute symptoms.

A, T1-weighted MR image after administration of gadopentetate dimeglumine shows several enhancing ovoid lesions in cerebral white matter bilaterally. Contrast enhancement defines areas of acute inflammation.

B, First echo of T2-weighted series at same level as *A* shows many more white matter lesions, primarily periventricular in distribution.

ogists can achieve 95–99% specificity when comparing the lesions of MS with white matter changes in elderly or hypertensive patients when age and sex are considered along with MR imaging findings. These results are encouraging. However, it must be noted that all MS patients in this study had clinically definite MS; the results thus may not apply to patients with possible or probable MS (and those patients are more often referred for MR scanning). The authors of this study acknowledge that only prospective studies of large groups of neurologic patients and control subjects will provide us with a true estimate of the accuracy of MR imaging in MS, and of the true prevalence of MS on MR imaging (which would be expected to vary by geographic region).

The addition of T1-weighted images may be helpful in differentiating vascular from MS lesions, as the latter are more commonly evident as areas of T1 prolongation when compared with white matter ischemic lesions [40] (Edwards MK et al., presented at the American Society of Neuroradiology meeting, March 1989) (Fig. 3B). However, small deep infarctions (lacunar infarcts) may certainly appear as areas of T1 prolongation.

In many disorders involving the cerebral white matter, brain involvement can be differentiated from MS only clinically or with the aid of other laboratory investigations. In some of these conditions, ancillary MR imaging findings (e.g., vascular abnormalities, symmetry of white matter involvement) help in differentiation, but in some diseases, such as encephalitis, cerebral vasculitis, and acute disseminated encephalomyelitis, differentiation from MS may not be possible with MR imaging.

Detection of lesions of varying age can be crucial in establishing a diagnosis of MS, and in differentiating it from other conditions, such as acute disseminated encephalomyelitis [26], in which lesions are usually all of similar age. This can be accomplished through serial scanning, by using IV contrast material to detect new enhancing lesions, or by investigational methods such as MR spectroscopy.

The lesions of MS may shrink or disappear on serial scans [42]; this is quite unusual in many other white matter diseases, but certainly can occur in some other inflammatory conditions. This may be due to complete resolution of an inflammatory focus [42], but it also could be due to a return of T2 toward normal levels in small plaques that can still be detected pathologically although they disappear on MR imaging [13].

Large MS lesions on MR images may be mistaken for tumors, as they may occasionally be solitary, and mass effect and peripheral enhancement may be present. Even if other small MS lesions are present, a concomitant tumor cannot always be excluded without biopsy (Batnitzky S et al., presented at the annual meeting of the American Society of Neuroradiology, June 1991) [16].

In the spine, imaging findings may also mimic tumor, with swelling and increased T2 signal [43]. As will be noted in the section on MR efficacy, brain imaging may be normal in a significant percentage of patients with spinal cord involvement, and, depending on clinical findings, these lesions may also require biopsy.

Sarcoidosis in the spinal cord can cause acute swelling and enhancement suggesting MS [44]. In tropical spastic paraparesis, areas of high T2 signal and atrophy, indistinguishable from chronic MS, may be seen in the spinal cord; brain lesions also may be present [45]. Acute disseminated encephalomyelopathy of viral origin, and vacuolar myelopathy in AIDS, can cause a focal increase in the T2 signal in the spinal cord [46].

Efficacy of MR in Multiple Sclerosis

MR imaging is by far the most sensitive imaging technique in this disease. In clinically definite MS, T2-weighted MR imaging shows white matter hyperintense lesions in a majority of patients (90–97%) in most series [47–49]. But in clinically possible or probable MS, sensitivities are reported as somewhat lower (62–94%), with the percentage increasing with clinical certainty of the diagnosis [9, 48]. Specificity of MR findings for MS has been evaluated relative to normal aging and hypertensive changes, as discussed in the section on differential diagnosis [41], but large-scale studies comparing findings in MS with those in other white matter diseases have yet to be performed.

In the selected group of patients with isolated noncompressive spinal cord symptoms suspected to be due to MS, MR imaging of the brain may still be useful. Whereas findings from direct scanning of the symptomatic spinal level may be positive for MS, scanning of the spine is still limited by technical factors, particularly in the thoracic and lumbar regions, mainly because of motion of respiratory and cardiovascular structures and CSF [2]. This results in positive findings on spinal MR scans in only 50–55% of patients with suspected spinal cord plaque [2, 50]. Results tend to be somewhat higher in the cervical region [50, 51].

Conversely, MR of the brain now has relatively few technical limitations, and clinically silent MS plaques are detectable in 43–82% of the group with isolated myelopathic symptoms [2, 50, 52, 53]; in one series [50], a significantly higher rate of lesion detection was found on brain MR imaging in patients with chronic spinal cord syndromes (82%) than in patients with acute disease (56%).

MR-Clinical Correlation

MR imaging can often pinpoint the lesions responsible for specific clinical symptoms in MS patients; however, it does not always do so, and its primary role is simply in confirming the presence of multiple lesions. Numerous case reports cite accurate detection of the "responsible" lesion on MR images in various clinical syndromes, including cranial nerve dysfunction as a result of brainstem plaques and other brainstem syndromes [54–58]. In a series of patients with various syndromes due to MS, MR has shown varying results in terms of specificity. In several series of brainstem-related symptoms, mostly retrospective (patients chosen on the basis of positive MR imaging findings), good correlation has been shown [59–62], but correlation is not consistently high [63, 64]. When present, however, lesions in the spinal cord, brainstem, and cerebellum tend to correlate quite well with clinical symptoms [2, 51, 59, 65, 66]. In contrast, supratentorial lesions tend not to correlate well with symptoms [67, 68].

A number of authors have demonstrated quite clearly that new active lesions can be seen on MR imaging with a total lack of corresponding clinical signs (Armstrong MA et al., presented at the American Society of Neuroradiology meeting, June 1991) [4, 5, 15]. In fact, serial studies [5, 69, 70] show that lesions appear and recede on MR at least five times as frequently as the occurrence of recognized clinical relapses.

Neuropsychological abnormalities are detectable in a significant percentage of MS patients. In one study, evidence of psychological morbidity was found in nearly half of MS patients [71]. MR imaging has been instrumental in showing the distribution of lesions in psychiatric patients, with significant temporal lobe involvement reported [71, 72]. Frontal and periventricular lesions may also be important [73]. Overall, psychological disability does not correlate well with the severity of MR imaging abnormalities, however [71, 72]; elation was the only specific psychological symptom that correlated with the degree of abnormality on MR imaging. Patients with MS who have only psychological symptoms have been reported [74, 75]; in this instance, MR imaging may be instrumental in making the diagnosis.

Disability as measured by several clinical scales, most commonly Kurtzke's expanded disability status scale [9], shows varying but usually positive correlation with overall extent of abnormality on MR imaging in different series [15, 47, 49, 71, 76–78]. Some authors have shown that lesions in specific sites correlate well with disability, particularly lesions in the spinal cord [2], brainstem [49, 79], corpus callosum [49], and basal ganglia [49]. Lesion confluency and infratentorial lesions were more common in patients with chronic progressive MS than in patients with benign MS in one study [80]. The lack of close correlation between clinical disability status scales and observed disease burden on MR most likely reflects the fact that the former mainly measure ambulation and upper limb function, usually primarily affected by spinal cord lesions, whereas MR studies are usually limited to the brain and are less reliable in detecting spinal cord lesions.

Long duration of disease does not consistently result in increased overall lesion load on MR images [2, 15, 47, 49, 76].

Degree of cognitive dysfunction tends to show good correlation with lesion load on MR [81, 82], although some researchers found no correlation between MR imaging findings and working memory deficit [83]. Periventricular lesions [84] and callosal atrophy [85] have both been correlated with overall cognitive dysfunction, and bilateral hippocampal demyelination has been blamed for antegrade memory decline in patients with chronic MS [86]. Cognitive dysfunction in MS was reviewed thoroughly in a recent article [81].

MR imaging has thus become crucial in understanding how the site, distribution, and extent of MS lesions contribute to patterns of symptoms; in some circumstances, this may contribute to our understanding of functional brain anatomy.

MR Imaging and Clinical Trials

The conduct of clinical trials in MS is exceedingly complex. The wide fluctuations seen in the clinical course of individual patients and the marked variability between patients make assessment of therapy very difficult. In the past, disease activity could be measured only by clinical means, and most clinical scales relied predominantly on ambulatory and upper limb function. All scales are subjective to a degree, and scores can vary according to time of day, ambient temperature, examiner, and other factors. Furthermore, MR has shown us that even the most rigorous clinical examination will detect only a fraction of the real disease burden, as demonstrated by serial prospective MR studies [4-6].

Serial MR imaging, by using the rigid techniques for head positioning and lesion delineation developed primarily by a University of British Columbia group [87], enables quantification of lesions with a reproducibility error of only 6%. MR has therefore become an indispensable complementary tool to clinical assessment.

The frequent appearance of asymptomatic new lesions in these serial studies certainly sheds new light on the natural history of the disease. However, asymptomatic new MS lesions detected on serial MR imaging may represent a management problem. The goal of current management of MS is to minimize the length and severity of clinical attacks, not to attempt to eradicate all evidence of the disease, and few neurologists would treat an asymptomatic lesion. Nevertheless, Koopmans et al. [88] emphasize the importance of further studies to assess the clinical significance of the demonstration of blood-brain barrier disruption on contrast-enhanced MR imaging, as it remains at least theoretically possible that treatment of all lesions (whether symptomatic or not) could have some effect on long-term disability.

It will be somewhat difficult to assess the efficacy of therapy for symptomatic or asymptomatic plaques with enhanced MR imaging, however, as rapid dramatic changes occur frequently in untreated patients [4], the duration of enhancement in untreated lesions is extremely variable [88], and some enhancing lesions spontaneously resolve completely without therapy [42].

MR: Technological Advances and Future Developments

Rapid technological changes have occurred in MR imaging since its introduction in 1981; discussion of these advances is beyond the scope of this review. High-field MR imaging has several advantages in scanning the brain and spine [89], mainly because of the increased signal-to-noise ratio at higher fields; high field strength also allows the use of gradient-echo sequences, which have resulted in improvements in spinal imaging [1, 90]. However, satisfactory brain imaging in MS has been performed on low-field systems [15, 17]. Pulse sequences, slice thickness and gap, and other technical factors are now quite standardized for brain imaging.

T2-weighted imaging (particularly the first echo of the T2-weighted sequence, with relatively low-intensity CSF) is generally considered optimal for detection of MS plaques, as this sequence is sensitive to the presence of abnormalities and displays the lesions as brighter than normal tissue [19, 91, 92]. T1-weighted images may be useful for lesion characterization [40] or for detection of some brainstem lesions [91]. The axial plane is used most commonly, but some authors recommend an additional T2-weighted sagittal series to improve lesion detection, particularly in the brainstem [19, 92] and corpus callosum [21]. However, addition of this series would add significantly to scanning time, and a suggested alternative is a single coronal T2-weighted sequence [93] in place of axial and sagittal scans.

Ultrathin (2.0-mm) T2-weighted axial or sagittal images may be helpful in improving lesion detectability and conspicuity in MS, and could be valuable in early or questionable cases (Watanabe AS et al., presented at the American Society of Neuroradiology meeting, June 1991).

The advent of MR contrast agents such as gadopentetate dimeglumine has contributed much to our understanding of MS. Numerous studies have shown that areas of active inflammation in acute MS plaques will enhance, whereas chronic lesions do not [4, 66, 70, 94, 95] (Fig. 7). This has been confirmed pathologically with virtually 100% correlation [16]. Enhancement is usually uniform but may be peripheral [16, 94]. Importantly, active enhancing lesions may be present with a complete absence of clinical symptoms [5, 6]. The degree of defect in the blood-brain barrier can be estimated by quantifying the change in T1 relaxation rates with administration of gadopentetate dimeglumine [96].

Quantitative scan analysis, for estimation of total plaque volume or "lesion load," has been helpful in serial evaluation of MS in clinical trials. Several methods are available [97, 98]. Computerized positioning of the patient also has been useful for standardization in follow-up studies of patients entered in clinical trials [99].

Quantification of T1 and T2 relaxation times is also of potential value in studying MS. The methods are well established [100, 101] but are currently too cumbersome for general clinical use. These values are generally elevated in focal lesions, but also have been shown to be prolonged in normal-appearing areas throughout the white matter of patients with MS [13, 102, 103]. It may be possible to distinguish acute and chronic MS plaques by their T1 and T2 values. An experimental model of gliosis in cats showed that T1 and T2 prolongation was marked in the acute phase, but much less elevated chronically [100]. Quantitative studies of human MS plaques also show this finding [13, 104], but again there is little current clinical application of T1 and T2 quantification because there is overlap between values in acute and chronic lesions, and the techniques are time-consuming.

T2*-weighted imaging [105], and ultrafast spin-echo software, which increases the speed of acquisition of conventional T2-weighted images, may improve the efficiency of screening MR studies.

Our understanding of the determinants of tissue contrast in MR imaging has been expanded by work defining the role of magnetization transfer in addition to T1 and T2 in the cerebral white matter. Myelin-bound cholesterol has a strong effect on signal on T1-weighted images due to magnetization transfer contrast [106]. To the extent that cholesterol binding and concentration is altered in acute and chronic demyelination, lesion appearance will be altered on new imaging sequences designed to emphasize magnetization transfer contrast.

Proton MR spectroscopy can provide insight into the biochemical alterations in MS lesions. MR spectroscopy is currently limited by spatial resolution, with average volumes of 2.0 cm^3 achievable at 1.5 T [107], but useful investigational data can be obtained. The detection of mobile lipids in MS lesions is most likely indicative of acute plaque formation with myelin breakdown, and is frequently seen in areas showing enhancement on MR imaging [107, 108]. Mildly decreased or normal levels of *N*-acetyl aspartate, a metabolite located primarily within neurons [109], are seen in acute plaques, with more severe decreases in older, irreversible lesions [109, 110]. Lactate may be increased in new lesions owing to impaired oxygen delivery [110].

REFERENCES

1. Enzmann DR, Rubin JB. Cervical spine: MR imaging with a partial flip angle, gradient-refocused pulse sequence. Part II. Spinal cord disease. *Radiology* **1988**;166:473–478
2. Honig LS, Sheremata WA. Magnetic resonance imaging of spinal cord lesions in multiple sclerosis. *J Neurol Neurosurg Psychiatry* **1989**;52: 459–466
3. Valk J, de Slegte RG, Crezee FC, Hazenberg GJ, Thjaha SI, Nauta JJ. Contrast enhanced magnetic resonance imaging of the brain using gadolinium-DTPA. *Acta Radiol* **1987**;28:659–665
4. Grossman RI, Braffman BH, Brorson JR, Goldberg HI, Silberberg DH, Gonzalez-Scrano F. Multiple sclerosis: serial study of gadolinium-enhanced MR imaging. *Radiology* **1988**;169:117–122
5. Willoughby EW, Grochowski E, Li DK, Oger J, Kastrukoff LF, Paty DW. Serial magnetic resonance scanning in multiple sclerosis: a second prospective study in relapsing patients. *Ann Neurol* **1989**;25:43–49
6. Koopmans RA, Li DK, Oger JJ, et al. Chronic progressive multiple sclerosis: serial magnetic resonance brain imaging over six months. *Ann Neurol* **1989**;26:248–256
7. Weiner HL, Paty DW. Diagnostic and therapeutic trials in multiple sclerosis: a new look. Summary of Jekyll Island workshop. *Neurology* **1989**;39:972–976
8. Compston A, Ebers G. The genetics of multiple sclerosis. In: Cook SD, ed. *Handbook of multiple sclerosis.* New York: Decker, **1990**:25–39
9. Swanson JW. Multiple sclerosis: update in diagnosis and review of prognostic factors. *Mayo Clin Proc* **1989**;64:577–586
10. Schumacher GA, Beebe GW, Kibler RF, et al. Problems of experimental trials of therapy in multiple sclerosis. *Ann N Y Acad Sci* **1965**;122: 552–568
11. Poser CM, Paty DW, Scheinberg L, et al. New diagnostic criteria for multiple sclerosis: guidelines for research protocols. *Ann Neurol* **1983**;13:227–231
12. Maravilla KR. Multiple sclerosis. In: Stark DD, Bradley WG, eds. *Magnetic resonance imaging.* St. Louis: Mosby, **1988**:ch. 18, 344–358
13. Ormerod IE, Miller DH, McDonald WI, et al. The role of NMR imaging in the assessment of multiple sclerosis and isolated neurological lesions. A quantitative study. *Brain* **1987**;110:1579–1616
14. Runge VM, Price AC, Kirshner HS, Allen JH, Partain CL, James AE Jr. The evaluation of multiple sclerosis by magnetic resonance imaging. *RadioGraphics* **1986**;6:203–212
15. Palo J, Ketonen L, Wikstrom J. A follow-up study of very low field MRI findings and clinical course in multiple sclerosis. *J Neurol Sci* **1988**;84: 177–187
16. Nesbit GM, Forbes GS, Scheithauer BW, Okazaki H, Rodriguez M. Multiple sclerosis: histopathologic and MR and/or CT correlation in 37 cases at biopsy and three cases at autopsy. *Radiology* **1991**;180: 467–474
17. Paty DW, Oger JJ, Kastrukoff LF, et al. MRI in the diagnosis of MS: a prospective study with comparison of clinical evaluation, evoked potentials, oligoclonal banding, and CT. *Neurology* **1988**;38:180–185
18. Horowitz AL, Kaplan RD, Grewe G, White RT, Salberg LM. The ovoid lesion: a new MR observation in patients with multiple sclerosis. *AJNR* **1989**;10:303–305
19. Brainin M, Reisner T, Neuhold A, Omasits M, Wicke L. Topological characteristics of brainstem lesions in clinically definite and clinically probably cases of multiple sclerosis: an MRI study. *Neuroradiology* **1987**;29:530–534
20. Simon JH, Holtas SL, Schiffer RB, et al. Corpus callosum and subcallosal-periventricular lesions in multiple sclerosis: detection with MR. *Radiology* **1986**;160:363–367
21. Gean-Marton AD, Vezina LG, Marton KI, et al. Abnormal corpus callosum: a sensitive and specific indicator of multiple sclerosis. *Radiology* **1991**;180:215–221
22. Drayer BP, Burger P, Hurwitz B. Magnetic resonance imaging in multiple sclerosis: decreased signal in thalamus and putamen. *Ann Neurol* **1987**;22:546–550
23. Fazekas F, Chawluk JB, Alavi A, Nurtig HI, Zimmerman RA. MR signal abnormalities at 1.5 T in Alzheimer's dementia and normal aging. *AJNR* **1987**;8:421–426
24. Revesz T, Hawkins CP, du Boulay EP, Barnard RO, McDonald WI. Pathological findings correlated with magnetic resonance imaging in subcortical arteriosclerotic encephalopathy (Binswanger's disease). *J Neurol Neurosurg Psychiatry* **1989**;52:1337–1344
25. Brady AP, Stack JP, Ennis JT. Moyamoya disease—imaging with magnetic resonance. *Clin Radiol* **1990**;42:138–141
26. Kesselring J, Miller DH, Robb SA. Acute disseminated encephalomyelitis: MRI findings and the distinction from multiple sclerosis. *Brain* **1990**;113:291–302
27. Bussone G, La Mantia L, Grazzi L, Lamperti E, Salmaggi A, Strada L. Neurobrucellosis mimicking multiple sclerosis: a case report. *Eur Neurol* **1989**;29:238–240
28. Halperin JJ, Luft BJ, Anand AK, et al. Lyme neuroborreliosis: central nervous system manifestations. *Neurology* **1989**;39(6):753–759
29. Just M, Higer HP, Kramer G, et al. Magnetic resonance imaging in infections of the brain: findings in tuberculosis, listeriosis, toxoplasmosis, subacute sclerosing panencephalitis and multiple sclerosis. *Neurosurg Rev* **1987**;10:185–190
30. Miller DH, Robb SA, Ormerod IE, et al. Magnetic resonance imaging of inflammatory and demyelinating white matter diseases of childhood. *Dev Med Child Neurol* **1990**;32:97–107
31. Trotot PM, Cabanis EA, Lavayssiere R, et al. Cerebral MRI in the study of prognostic factors in AIDS. *J Radiol* **1988**;69:193–196
32. Banna M, El-Ramahi K. Neurologic involvement in Behcet disease: imaging findings in 16 patients. *AJR* **1991**;157:867–872
33. Smith AS, Meisler DM, Weinstein MA, et al. High signal periventricular lesions in patients with sarcoidosis: neurosarcoidosis or multiple sclerosis? *AJR* **1989**;153:147–152
34. Schwankhaus JD, Patronas N, Dorwart R, Eldridge R, Schlesinger S, McFarland H. Computed tomography and magnetic resonance imaging in adult-onset leukodystrophy. *Arch Neurol* **1988**;45:1004–1008
35. Miller GM, Baker HL Jr, Okazaki H, Whisnant JP. Central pontine myelinolysis and its imitators: MR findings. *Radiology* **1988**;168:795–802
36. Haan J, Haupts M, Uhlenbrock D. Magnetic resonance imaging (MRI), cranial computerized tomography (CCT), evoked potentials and cerebrospinal fluid (CSF) analysis in five patients with funicular myelosis. *Neurosurg Rev* **1987**;10:209–211
37. Smith AS, Huang TE, Weinstein MA. Periventricular involvement in CNS lymphomatoid granulomatosis: MR demonstration. *J Comput Assist Tomogr* **1990**;14:291–293
38. Fazekas F, Offenbacher H, Fuchs S, et al. Criteria for an increased specificity of MRI interpretation in elderly subjects with suspected multiple sclerosis. *Neurology* **1988**;38:1822–1825
39. Zimmerman RD, Fleming CA, Lee BC, Saint-Louis LA, Deck MD. Periventricular hyperintensity as seen by magnetic resonance: prevalence and significance. *AJR* **1986**;146:443–450
40. Uhlenbrock D, Sehlen S. The value of T1-weighted images in the differentiation between MS, white matter lesions, and subcortical arteriosclerotic encephalopathy (SAE). *Neuroradiology* **1989**;31:203–212
41. Yetkin FZ, Haughton VM, Papke RA, Fischer ME, Rao SM. Multiple sclerosis: specificity of MR for diagnosis. *Radiology* **1991**;178:447–451
42. Poser CM, Kleefield J, O'Reilly GV, Jolesz F. Neuroimaging and the lesion of multiple sclerosis. *AJNR* **1987**;8:549–552
43. Lammoglia FJ, Short SR, Weet DE, Pay N, Abay EA II. Multiple sclerosis presenting as an intramedullary cervical cord tumor. *Kans Med* **1989**;90:219–221
44. Miller GM, Baker HL Jr, Ebersold MJ, Scheithauer BW. Spinal cord sarcoidosis: a new finding at MR imaging with Gd-DTPA enhancement. *Radiology* **1989**;173:839–843
45. Kermode AG, Rudge P, Thompson AJ, Du Boulay EP, McDonald WI. MRI of thoracic cord in tropical spastic paraparesis (letter). *J Neurol Neurosurg Psychiatry* **1990**;53:710

46. McClarty B, Sutherland S, Bertram EG. The spine. In: Kucharczyk W, ed. *MRI: central nervous system.* Philadelphia: Lippincott, **1990**:ch. 5, 1–58
47. Reese L, Carr TJ, Nicholson RL, Lepp EK. Magnetic resonance imaging for detecting lesions of multiple sclerosis: comparison with computed tomography and clinical assessment. *Can Med Assoc J* **1986**;135: 639-643
48. Paolino E, Granieri E, Tola MR, et al. The combined use of instrumental and laboratory examinations in multiple sclerosis: is the diagnostic facilitation real? *Riv Neurol* **1990**;60:73-81
49. Noakes JB, Herkes GK, Frith JA, McLeod JG, Jones MP. Magnetic resonance imaging in clinically-definite multiple sclerosis. *Med J Aust* **1990**;152:136–140
50. Miller DH, McDonald WI, Blumhardt LD, et al. Magnetic resonance imaging in isolated noncompressive spinal cord syndromes. *Ann Neurol* **1987**;22:714–723
51. Nilsson O, Larsson EM, Holtas S. Myelopathy patients studied with magnetic resonance for multiple sclerosis plaques. *Acta Neurol Scand* **1987**;76:272–277
52. Filippi M, Martinelli V, Locatelli T, et al. Acute and insidious onset myelopathy of undetermined aetiology: contribution of paraclinical tests to the diagnosis of multiple sclerosis. *J Neurol* **1990**;237:171–176
53. Miller DH, Ormerod IE, Rudge P, Kendall BE, Moseley IF, McDonald WI. The early risk of multiple sclerosis following isolated acute syndromes of the brainstem and spinal cord. *Ann Neurol* **1989**;26:635–639
54. Shea JJ III, Brackmann DE. Multiple sclerosis manifesting as sudden hearing loss. *Arch Otolaryngol Head Neck Surg* **1987**;97:335–338
55. Martyn CN, Kean D. The one-and-a-half syndrome: clinical correlation with a pontine lesion demonstrated by nuclear magnetic resonance imaging in a case of multiple sclerosis. *Br J Ophthalmol* **1988**;72:515–517
56. Tan E, Kansu T. Bilateral horizontal gaze palsy in multiple sclerosis. *J Clin Neuro Ophthalmol* **1990**;10:124–126
57. Plant GT, Kermode AG, du Boulay EP, McDonald WI. Spasmodic torticollis due to a midbrain lesion in a case of multiple sclerosis. *Mov Disord* **1989**;4:359–362
58. Yamamoto T, Imai T, Yamasaki M. Acute ventilatory failure in multiple sclerosis. *J Neurol Sci* **1989**;89:313–324
59. Ormerod IE, Bronstein A, Rudge P, et al. Magnetic resonance imaging in clinically isolated lesions of the brainstem. *J Neurol Neurosurg Psychiatry* **1986**;49:737–743
60. Bronstein AM, Rudge P, Gresty MA, Du Boulay G, Morris J. Abnormalities of horizontal gaze: clinical, oculographic and magnetic resonance imaging findings. II: Gaze palsy and internuclear ophthalmoplegia. *J Neurol Neurosurg Psychiatry* **1990**;53:200–207
61. Hutchins LG, Harnsberger HR, Hardin CW, Dillon WP, Smoker WR, Osborn AG. The radiologic assessment of trigeminal neuropathy. *AJR* **1989**;153:1275–1282
62. Valvassori GE. Diagnosis of retrocochlear and central vestibular disease by magnetic resonance imaging. *Ann Otol Rhinol Laryngol* **1988**;97:19–22
63. Baum K, Scheuler W, Hegerl U, Girke W, Schorner W. Detection of brainstem lesions in multiple sclerosis: comparison of brainstem auditory evoked potentials with nuclear magnetic resonance imaging. *Acta Neurol Scand* **1988**;77:283–288
64. Cure JK, Cromwell LD, Case JL, Johnson GD, Musiek FE. Auditory dysfunction caused by multiple sclerosis: detection with MR imaging. *AJNR* **1990**;11:817–820
65. Bradac GB, Riva A, Mortara P, Orsi L, Riccio A. Primary progressive cerebellar ataxia. *Neuroradiology* **1989**;31:16–18
66. Sze G, Krol G, Zimmerman RD, Deck MDF. Intramedullary disease of the spine: diagnosis using gadolinium-DTPA-enhanced MR imaging. *AJR* **1988**;151:1193–1204
67. Kermode AG, Thompson AJ, Tofts P, et al. Breakdown of the blood-brain barrier precedes symptoms and other MRI signs of new lesions in multiple sclerosis: pathogenetic and clinical implications. *Brain* **1990**;113: 1477–1489
68. Reese L, Carr TJ, Nicholson RL, Lepp EK. Magnetic resonance imaging for detecting lesions of multiple sclerosis: comparison with computed tomography and clinical assessment. *Can Med Assoc J* **1986**;135: 639-643
69. Isaac C, Li DK, Genton M, et al. Multiple sclerosis: a serial study using MRI in relapsing patients. *Neurology* **1988**;38:1511–1515
70. Miller DH, Rudge P, Johnson G, et al. Serial gadolinium enhanced magnetic resonance imaging in multiple sclerosis. *Brain* **1988**;111: 927–939
71. Ron MA, Logsdail SJ. Psychiatric morbidity in multiple sclerosis: a clinical and MRI study. *Psychol Med* **1989**;19:887-890
72. Honer WG, Hurwitz T, Li DK, Palmer M, Paty DW. Temporal lobe involvement in multiple sclerosis patients with psychiatric disorders. *Arch Neurol* **1987**;44:187–190
73. Reischies FM, Baum K, Brau H, Hedde JP, Schwindt G. Cerebral magnetic resonance imaging findings in multiple sclerosis: relation to disturbance of affect, drive and cognition. *Arch Neurol* **1988**;45:1114–1116
74. Salloway S, Price LH, Charney DS, Shapiro M. Multiple sclerosis presenting as major depression: a diagnosis suggested by MRI scan but not CT scan. *J Clin Psychiatry* **1988**;49:364–366
75. Kohler J, Heilmeyer H, Volk B. Multiple sclerosis presenting as chronic atypical psychosis. *J Neurol Neurosurg Psychiatry* **1988**;51:281–284
76. Baum K, Nehrig C, Girke W, Brau H, Schorner W. Multiple sclerosis: relations between MRI and CT findings, cerebrospinal fluid parameters and clinical features. *Clin Neurol Neurosurg* **1990**;192:49–56
77. Thompson AJ, Kermode AG, MacManus DG, et al. Patterns of disease activity in multiple sclerosis: clinical and magnetic resonance imaging study. *BMJ* **1990**;300:631–634
78. Kiel MK, Greenspun B, Grossman RI. Magnetic resonance imaging and degree of disability in multiple sclerosis. *Arch Phys Med Rehabil* **1988**;69:11–13
79. Baumhefner RW, Tourtellotte WW, Syndulko K. Quantitative multiple sclerosis plaque assessment with magnetic resonance imaging. Its correlation with clinical parameters, evoked potentials, and intra-blood-brain barrier IgG synthesis. *Arch Neurol* **1990**;47:19–26
80. Koopman RA, Li DK, Grochowski E, Cutler PJ, Paty DW. Benign versus chronic progressive multiple sclerosis: magnetic resonance imaging features. *Ann Neurol* **1989**;25:74–81
81. Franklin GM, Nelson LM, Filley CM, Heaton RK. Cognitive loss in multiple sclerosis: case reports and review of the literature. *Arch Neurol* **1989**;46:162–167
82. Rao SM, Leo GJ, Haughton VM, St. Aubin Faubert P, Bernardin L. Correlation of magnetic resonance imaging with neuropsychological testing in multiple sclerosis. *Neurology* **1989**;39:161–166
83. Litvan I, Grafman J, Vendrell P, et al. Multiple memory deficits in patients with multiple sclerosis. Exploring the working memory system. *Arch Neurol* **1988**;45(6):607–610
84. Anzola GP, Bevilacqua L, Cappa SF. Neuropsychological assessment in patients with relapsing-remitting multiple sclerosis and mild functional impairment: correlation with magnetic resonance imaging. *J Neurol Neurosurg Psychiatry* **1990**;53:142–145
85. Huber SJ, Paulson GW, Shuttleworth EC, et al. Magnetic resonance imaging correlates of dementia in multiple sclerosis. *Arch Neurol* **1987**;44:732–736
86. Brainin M, Goldenberg G, Ahlers C, Reisner T, Neuhold A, Deecke L. Structural brain correlates of anterograde memory deficits in multiple sclerosis. *J Neurol* **1988**;235:362–365
87. Paty DW, Bergstom J, Palmer M, et al. A quantitative magnetic resonance image of the multiple sclerosis brain. *Neurology* **1985**;35[suppl 1]:137
88. Koopmans MS, Li DKB, Oger JJF, Mayo J, Paty DW. The lesion of multiple sclerosis: imaging of acute and chronic stages. *Neurology* **1989**;39:959–963
89. Brant-Zawadzki M. MR imaging of the brain. *Radiology* **1988**;166:1–10
90. Katz BH, Quencer RM, Hinks RS. Comparison of gradient-recalled-echo and T2-weighted spin-echo pulse sequences in intramedullary spinal lesions. *AJNR* **1989**;10:815–822
91. Runge VM, Price AC, Kirshner HS, Allen JH, Partain CL, James AE. Magnetic resonance imaging of multiple sclerosis: a study of pulse-technique efficacy. *AJR* **1984**;143:1015–1026
92. Truyen L, Gheuens J, Van de Vyver FL, Parizel PM, Peersman GV, Martin JJ. Improved correlation of magnetic resonance imaging (MRI) with clinical status in multiple sclerosis (MS) by use of an extensive standardized imaging protocol. *J Neurol Sci* **1990**;96:173–182
93. Quint DJ. Multiple sclerosis and imaging of the corpus callosum. *Radiology* **1991**;180:15–17
94. Kermode AG, Totts PS, Thompson AJ, et al. Heterogeneity of blood-

brain barrier changes in multiple sclerosis: an MRI study with gadolinium-DTPA enhancement. *Neurology* **1990**;49:229-235

95. Bastianello S, Pozzilli C, Bernardi S, Bozzao L, Fantozzi LM, Buttinelli C. Serial study of gadolinium-DTPA MRI enhancement in multiple sclerosis. *Neurology* **1990**;40:591-595
96. Larsson HB, Stubgaard M, Frederiksen JL, Jensen M, Henriksen O, Paulson OB. Quantitation of blood-brain barrier defect by magnetic resonance imaging and gadolinium-DTPA in patients with multiple sclerosis and brain tumors. *Magn Reson Med* **1990**;16:117-131
97. Cline HE, Lorensen WE, Kikinis R, Jolesz F. Three-dimensional segmentation of MR images of the head using probability and connectivity. *J Comput Assist Tomogr* **1990**;14:1037-1045
98. Kapouleas I. Automatic detection of white matter lesions in magnetic resonance brain images. *Comput Methods Programs Biomed* **1990**;32:17-35
99. Badran AK, Durrani TS, Fisher AC, Paul JP. Patient realignment in magnetic resonance imaging of the head: an algorithm using mathematical morphology for feature extraction. *J Biomed Eng* **1990**;12:138-142
100. Barnes D, McDonald WI, Landon DN, Johnson G. The characterization of experimental gliosis by quantitative nuclear magnetic resonance imaging. *Brain* **1988**;111:83-94
101. Armspach JP, Gounot D, Rumbach L, Chambron J. In vivo determination of multiexponential T2 relaxation in the brain of patients with multiple sclerosis. *Magn Reson Imag* **1991**;9:107-113
102. Miller DH, Johnson G, Tofts PS, MacManus D, McDonald WI. Precise relaxation time measurements of normal-appearing white matter in inflammatory central nervous system disease. *Magn Reson Med* **1989**;11:331-336
103. Brainin M, Neuhold A, Reisner T, Maida E, Lang S, Deecke L. Changes within the "normal" cerebral white matter of multiple sclerosis patients during acute attacks and during high-dose cortisone therapy assessed by means of quantitative MRI. *J Neurol Neurosurg Psychiatry* **1989**;52:1355-1359
104. Larsson HB, Frederiksen J, Petersen J, et al. Assessment of demyelination, edema, and gliosis by in vivo determination of T1 and T2 in the brain of patients with acute attack of multiple sclerosis. *Magn Reson Med* **1989**;11:337-348
105. Stadnik TW, Luypaert RR, Neirynck EC, Osteaux M. Optimization of sequence parameters in fast MR imaging of the brain with FLASH. *AJNR* **1989**;10:357-362
106. Koenig SH. Cholesterol of myelin is the determinant of gray-white contrast in MRI of brain. *Magn Reson Med* **1991**;20:285-291
107. Wolinsky JS, Narayana PA, Fenstermacher MJ. Proton magnetic resonance spectroscopy in multiple sclerosis. *Neurology* **1990**;40:1764-1769
108. Wolinsky JS, Narayana PA. Proton magnetic resonance spectroscopy and multiple sclerosis (letter). *Lancet* **1991**;337(8732):362
109. Arnold DL, Matthews PM, Francis G, Antel J. Proton magnetic resonance spectroscopy of human brain in vivo in the evaluation of multiple sclerosis: assessment of the load of disease. *Magn Reson Med* **1990**;14:154-159
110. Miller DH. Proton magnetic resonance spectroscopy of an acute and chronic lesion in multiple sclerosis (letter). *Lancet* **1991**;337(8732):58-59

Forthcoming Articles

SPECIAL ARTICLE

Review. Detection of metastasis in cervical lymph nodes: CT and MR criteria and differential diagnosis. *Som PM*

CHEST RADIOLOGY

Review. High-resolution CT of the lungs: review of findings in various pulmonary diseases. *Swenson SJ, Aughenbaugh GL, Douglas WW, Myers JL*

Case report. Pulmonary alveolar microlithiasis: findings on high-resolution CT. *Korn MA, Schurawitzki H, Klepetko W, Burghuber OC*

CT findings in benign fibrous mesothelioma of the pleura: pathologic correlation in nine patients. *Lee KS, Im J-G, Choe KO, Kim CJ, Lee BH,*

Case report. Intrapulmonary bronchogenic cyst: spontaneous pneumothorax as the presenting symptom. *Matzinger MA, Matzinger FR, Sachs HJ*

Case report. Demonstration of pulmonary sequestration by MR angiography. *Doyle AJ*

BREAST RADIOLOGY

Perspective. Value of large-core biopsy of occult breast lesions. *Meyer JE*

Fibrosarcoma of the breast: mammographic findings in five cases. *Elson BC, Ikeda DM, Andersson I, Wattsgård C*

GASTROINTESTINAL RADIOLOGY

Changes in extrahepatic bile duct caliber in liver transplant recipients without evidence of biliary obstruction. *Campbell WL, Foster RG, Miller WJ, Lecky JW, Zajko AB, Lee KY*

Venoocclusive liver disease after bone marrow transplantation: findings at duplex sonography. *Herbetko J, Grigg AP, Buckley AR, Phillips GL*

Treatment of bile duct stones by laser lithotripsy: results in 12 patients. *Dawson SL, Mueller PR, Lee MJ, Saini S, Kelsey P, Nishioka NS*

Oriental cholangiohepatitis: correlation between portal vein occlusion and hepatic atrophy. *Kusano S, Okada Y, Endo T, Yokoyama H, Ohmiya H, Atari H*

Pictorial essay. Hepatic neoplasms: surgically relevant segmental anatomy and imaging techniques. *Gazelle GS, Haaga JR*

Occlusion and narrowing of the pharyngeal airway in obstructive sleep apnea: evaluation by ultrafast spoiled GRASS MR imaging. *Shellock FG, Schatz CJ, Julien P, et al.*

Technical note. Recurrent extraluminal rectal carcinoma: transrectal biopsy under sonographic guidance. *Nielsen MB, Pedersen JF, Hald J, Christiansen J*

Case report. *Candida* cholangitis in a diabetic woman. *Radin DR, Johnson MB*

Primary malignant small round-cell tumor of the abdomen: CT findings in five cases. *Varma DGK, McDaniel K, Ordóñez NG, Granfield CAJ, Charnsangavej C, Wallace S*

GENITOURINARY RADIOLOGY

Duplex Doppler evaluation of native kidney dysfunction: obstructive and nonobstructive disease. *Platt JF*

MR imaging in the evaluation of benign uterine masses: value of gadopentetate-dimeglumine-enhanced, T1-weighted images. *Hricak H, Finck S, Honda G, Göranson H*

Ureteric jets: evaluation of normal flow dynamics with color Doppler sonography. *Cox IH, Erickson SJ, Foley WD, Dewire DM*

Testicular microlithiasis: sonographic and clinical features. *Janzen DL, Mathieson JR, Marsh JI, et al.*

Case report. Intratesticular varicocele: sonographic findings in two patients. *Weiss AJ, Kellman GM, Middleton WD, Kirkemo A*

MUSCULOSKELETAL RADIOLOGY

Review. Lyme disease with emphasis on the radiographic findings in Lyme arthritis. *Lawson JP, Rahn DW*

Review. Digital skeletal radiography. *Buckwalter KA, Braunstein EM*

The ulnar tunnel at the wrist (Guyon's canal): normal MR anatomy and variants. *Zeiss J, Jakab E, Khimji T, Imbriglia J*

Pictorial essay. The craniovertebral junction: normal anatomy with MR correlation. *Schweitzer ME, Hodler J, Cervilla V, Resnick D*

Pictorial essay. Long bicipital tendon of the shoulder: normal anatomy and pathologic findings on MR imaging. *Erickson SJ, Fitzgerald SW, Quinn SF, Carrera GF, Black KP, Lawson TL*

PEDIATRIC RADIOLOGY

Blunt pancreatic trauma in children: CT diagnosis. *Sivit CJ, Eichelberger MR, Taylor GA, Bulas DI, Gotschall CS, Kushner DC*

Azygoesophageal recess: normal CT appearance in children. *Fitzgerald SW, Donaldson JS*

Pictorial essay. Cartilaginous epiphysis and growth plate: normal and abnormal MR imaging findings. *Jaramillo D, Hoffer FA*

Case report. Mediastinal pseudocyst secondary to pharyngeal perforation in child abuse. *Kleinman PK, Spevak MR, Hansen M*

VASCULAR RADIOLOGY

Review. The role of MR in the evaluation of acquired diseases of the thoracic aorta. *Link KM, Lesko NM*

Pictorial essay. Assessment of the thoracic aorta by spiral CT. *Costello P, Ecker CP, Tello R, Hartnell GG*

Case report. Left thyrocervical trunk bronchial artery supplying right lung: source of recurrent hemoptysis in cystic fibrosis. *Cohen AM, Antoun BW, Stern RC*

NEURORADIOLOGY

Review. Diagnosis of lumbar spinal stenosis in adults: a metaanalysis of the accuracy of CT, MR, and myelography. *Kent DL, Haynor DR, Larson EB, Deyo RA*

Epidural abscess of the cervical spine: MR findings in five cases. *Kricun R, Shoemaker EI, Chovanes GI, Stephens HW*

MR of the pituitary gland in infants and children: changes in size, shape, and MR signal with growth and development. *Tien RD, Kucharczyk J, Bessette J, Middleton M*

Crossed cerebellar diaschisis and crossed cerebellar atrophy: correlation of MR findings, clinical symptoms, and supratentorial diseases in 26 patients. *Tien RD, Ashdown BC*

Case report. MR demonstration of reversible cerebral lesions in a child with hypertensive encephalopathy caused by Wilms' tumor. *Shanley DJ, Sisler CL*

Case report. Intracranial metastatic adenoid cystic carcinoma: presumed hematogenous spread from a primary tumor in the parotid gland. *Gelber NO, Ragland RL, Knorr JR, Smith TW, Stone BB*

MEMO TO AUTHORS

The different types of articles published in the *AJR*. *Berk RN*

MR Imaging Features of Medulloblastomas

Steven P. Meyers[1]
Susan S. Kemp[1]
Robert W. Tarr[2]

The preoperative MR studies of 25 patients with surgically proved medulloblastomas were retrospectively reviewed in order to characterize these neoplasms with regard to their MR signal intensity, size, location, and appearance after contrast enhancement. Gadopentetate dimeglumine-enhanced MR images were available in 11 patients. On short TR/short TE images, medulloblastomas generally had low to intermediate signal, and were predominantly slightly hyperintense relative to muscle and hypointense relative to white matter. On long TR/long TE images, medulloblastomas generally had intermediate to moderately high signal, predominantly hyperintense relative to muscle and white matter. Tumor signal relative to gray matter varied considerably on both short TR and long TR images. Signal heterogeneity on long TR/long TE images was observed in 91% of the lesions and resulted from intratumoral cystic zones, small blood vessels, and/or calcifications. In the patients who received gadopentetate dimeglumine, the fraction of tumor volume showing enhancement was found to be less than one third in two cases, between one third and two thirds in four cases, and greater than two thirds in five cases. The mean tumor size was 3.6 × 4.0 × 3.5 cm. The most frequent location of medulloblastoma was the mid and inferior vermis.

We conclude that the unenhanced and enhanced MR characteristics of medulloblastomas are somewhat variable. Medulloblastomas should be included in the differential diagnosis when the MR findings described are present in the appropriate patient population.

AJR **158:859-865, April 1992**

Medulloblastomas are a group of primitive neuroectodermal tumors that occur in the posterior cranial fossa [1-3]. These tumors account for 33% of posterior fossa neoplasms in children, and up to 25% of all intracranial neoplasms in infants and children [3, 4]. Medulloblastomas have relatively rapid growth rates and can invade adjacent neural tissue and metastasize along CSF pathways [1-3]. Diagnostic imaging of these neoplasms is important for preoperative assessment of tumor bulk and extension.

Although the CT features of medulloblastomas are well characterized [5-8], the MR features are not. To our knowledge, the MR features have been reported in only a few cases as part of a larger series of intracranial neoplasms [9]. We retrospectively reviewed the preoperative MR studies of 25 patients with medulloblastomas in order to characterize these tumors with regard to size, position, and extension; signal intensity; and enhancement with gadopentetate dimeglumine.

Materials and Methods

We reviewed the tumor registry files and surgical and pathologic reports from two university medical centers (1985-1991) and found records of 35 patients who had initial surgical resection of medulloblastomas. For 25 of these patients, preoperative MR examinations were available for retrospective analysis. This group had 15 males and 10 females 1-42 years old

Received September 18, 1991; accepted after revision November 25, 1991.

[1] Department of Radiology, University of Pittsburgh School of Medicine, Pittsburgh NMR Institute, 3260 Fifth Ave., Pittsburgh, PA 15213. Address reprint requests to S. P. Meyers.

[2] Department of Radiology, Case Western Reserve University, 2074 Abington Rd., Cleveland, OH 44106.

0361-803X/92/1584-0859
© American Roentgen Ray Society

(mean, 10 years; median, 8 years). Fourteen patients were less than 10 years old, eight were 10–20 years old, and three were more than 20 years old. Twenty-one tumors were histologically subclassified as classical medulloblastomas and the other four as medulloblastomas with desmoplasia.

MR imaging was performed at 1.5 T for 18 patients and at 1.0 T for seven patients. Multisection spin-echo pulse sequences were used in all MR studies and included short TR/TE (450–800/15–20) for 25 patients and long TR/first-echo TE, second-echo TE (2000–3200/15–30,75–100) sequences for 23 patients. Short TR images were obtained in the axial plane for all patients and in the sagittal plane for most patients. Long TR images were acquired in the axial plane for 22 patients and in the coronal plane for one patient. MR imaging was performed immediately after the manual IV injection of gadopentetate dimeglumine (0.1 mmol/kg of body weight) for 11 of the patients; short TR/TE (500–800/20–30) MR images were obtained in sagittal and axial planes. Flow compensation was used for five enhanced examinations. For the other six enhanced examinations, signal misregistration within the tumors along the phase-encoding direction resulting from contrast-enhanced blood in the sigmoid and transverse sinuses was not encountered and gradient-moment nulling techniques were not applied. MR images were 5 mm thick with interimage gaps of 1 mm. The acquisition matrix ranged from 256 × 128 to 256 × 256.

For all images, the signal intensity of each tumor was assessed as hypo-, iso-, or hyperintense relative to muscle tissue in the field of view and relative to gray and white matter. The fraction of the tumor showing contrast enhancement was qualitatively categorized as small (less than one third), intermediate (one third to two thirds), or large (more than two thirds). Tumor signal was categorized as homogeneous, slightly heterogeneous, or markedly heterogeneous for both enhanced images and unenhanced long TR/long TE images. The size, center point, and extension of each tumor were determined. MR examinations were evaluated for the presence of associated hydrocephalus. Preoperative unenhanced CT scans were available for review in 18 of 25 cases. CT scans were obtained on third-generation scanners and were evaluated for the presence of intratumoral calcifications.

Results

Tumor Size and Configuration

Medulloblastomas ranged in size from 1.0 × 2.5 × 2.0 cm to 6.0 × 5.0 × 5.2 cm (mean, 3.6 × 4.0 × 3.5 cm) in craniocaudal, transverse, and anteroposterior dimensions, respectively. Tumor margins were mostly convex and well defined on unenhanced spin-echo images in 23 of 25 cases (Figs. 1–4). The two exceptions were lesions involving the vermis, which were seen as poorly defined zones of signal alteration on the long TR images only (Fig. 5).

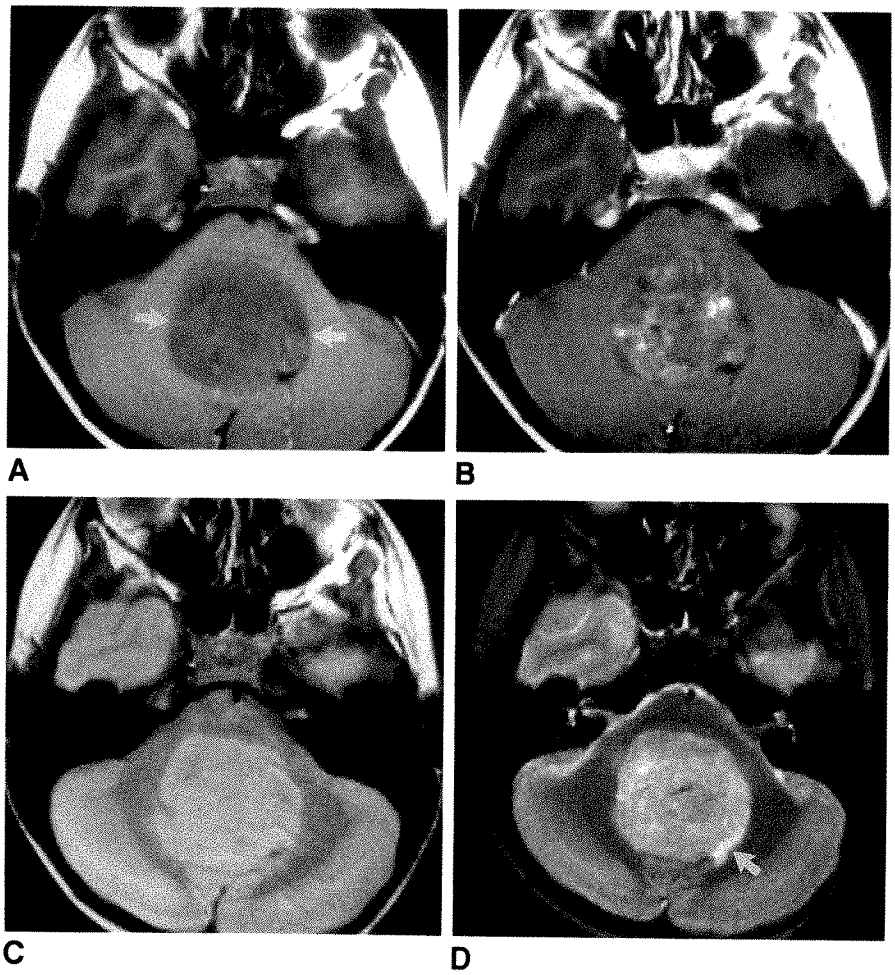

Fig. 1.—5-year-old girl with classical medulloblastoma.

A, Short TR (650/20) axial MR image shows midline mass in vermis (*arrows*). Tumor margins are well defined.

B, Enhanced short TR (650/20) axial MR image shows minimal tumor enhancement in a markedly heterogeneous pattern.

C, Long TR/short TE (2500/15) axial MR image shows mass is predominantly isointense relative to gray matter.

D, Long TR/long TE (2500/90) axial MR image shows mass has slightly hyperintense signal relative to gray and white matter. Note mild signal heterogeneity within mass and crescent-shaped peripheral zone of high signal (*arrow*).

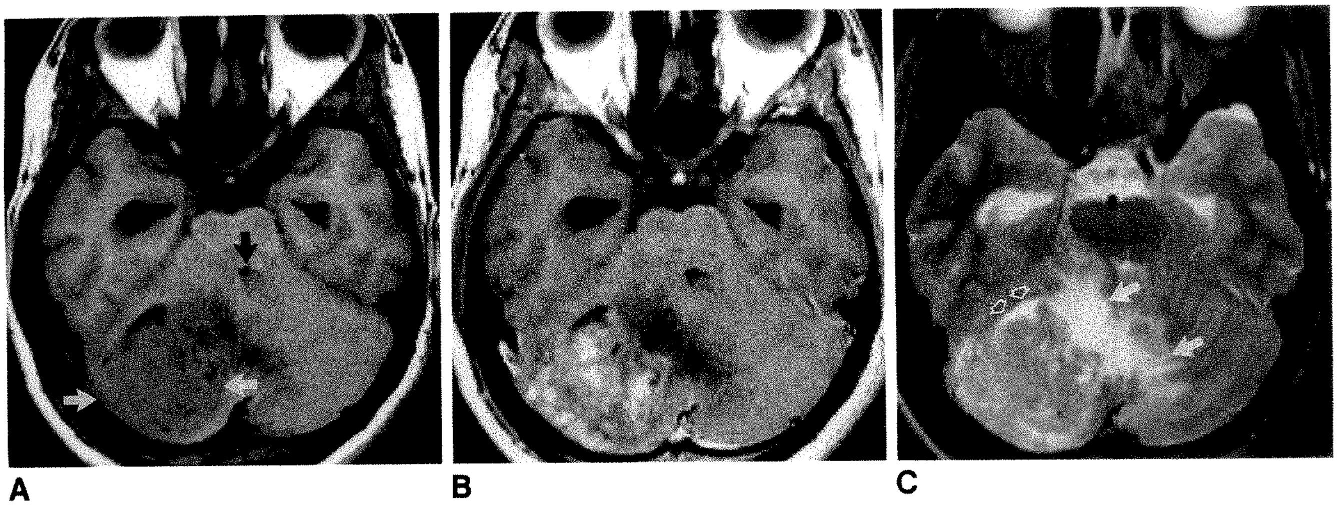

Fig. 2.—25-year-old woman with classical medulloblastoma in right cerebellar hemisphere extending into vermis.

A, Short TR (760/20) axial MR image shows mass with relatively well-defined margins (*white arrows*) that displaces fourth ventricle to left (*black arrow*).

B, Enhanced short TR (760/20) axial MR image shows moderate contrast enhancement with tumor in markedly heterogeneous pattern.

C, Long TR/long TE (2500/90) axial MR image shows mass is predominantly isointense compared with gray matter. Note small foci of very high signal within mass, surrounding high-signal white matter "edema" (*solid arrows*), and thin peripheral zone of high signal (*open arrows*) adjacent to tumor.

Fig. 3.—8-year-old boy with classical medulloblastoma.

A, Short TR (760/20) sagittal MR image shows well-marginated mass involving mid and inferior portions of vermis (*arrows*). Mass is hypointense relative to brain parenchyma and extends anteriorly, compressing fourth ventricle and resulting in a mild degree of hydrocephalus. Note mild caudal displacement of cerebellar tonsils (*arrowhead*).

B, Enhanced short TR (760/20) axial MR image shows marked tumor enhancement (*arrows*) in a mildly heterogeneous pattern.

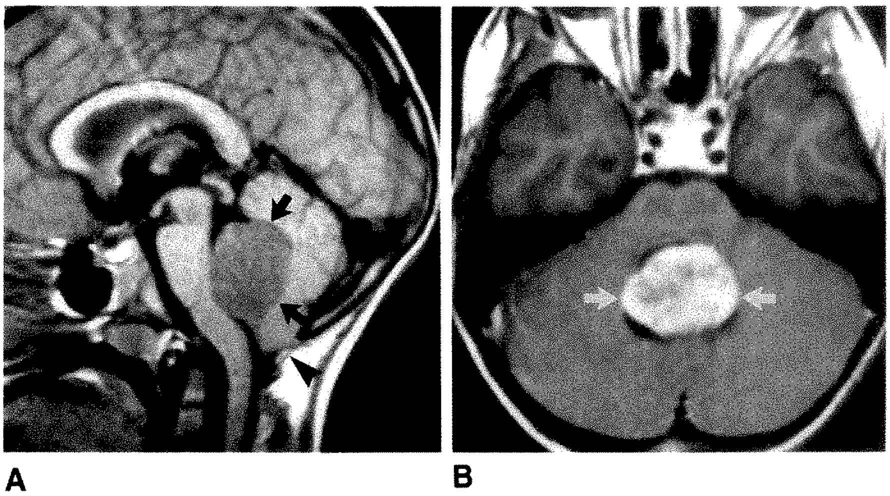

Fig. 4.—1½-year-old boy with classical medulloblastoma. Short TR (500/20) sagittal MR image shows mass (*arrows*) involving superior portion of vermis. Mass extends anteriorly, compressing cerebral aqueduct and resulting in moderate hydrocephalus.

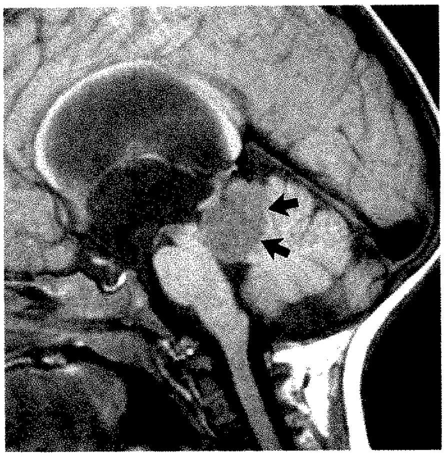

4

Fig. 5.—23-year-old man with classical medulloblastoma. Long TR (2500/75) axial MR image shows poorly marginated mass (*arrows*) within vermis that was seen on long TR images and not on short TR images. No contrast-enhanced images were available.

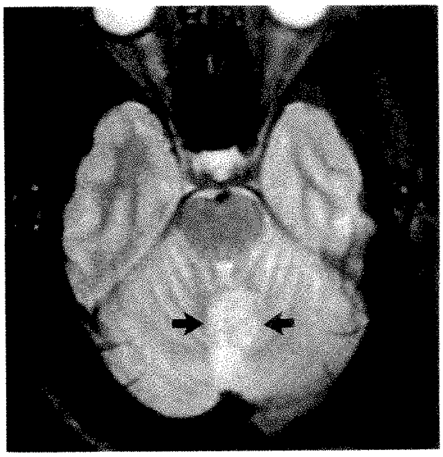

5

Tumor Location

Twenty patients (ages 1.5–23 years) had primary tumors that were midline lesions involving the anterior portion of the vermis. Nineteen of these neoplasms were located in the mid and inferior zones of the vermis (Fig. 3), and one was in the superior zone (Fig. 4). Eighteen of these tumors within the vermis were classical medulloblastomas and two were desmoplastic medulloblastomas. Two other patients (ages 17 and 42 years) had desmoplastic medulloblastomas located laterally within a cerebellar hemisphere (Fig. 6). The remaining three patients (ages 1, 5, and 25 years) had classical medulloblastomas that involved both the vermis and hemisphere (Fig. 2). Twenty-four of the 25 lesions had associated hydrocephalus. The one exception was a lesion located laterally within a cerebellar hemisphere. Herniation of cerebellar tonsils resulting from the medulloblastomas was observed in 13 cases (Figs. 3 and 7).

Signal Characteristics of Medulloblastomas

Short TR/short TE images.—On short TR/short TE images, medulloblastomas generally had low to intermediate signal intensity. In comparison with muscle, medulloblastomas were predominantly slightly hyperintense in 20 cases (80%), isointense in two (8%), and mixed in three (12%). In relation to gray matter, medulloblastomas were predominantly hypointense in 12 cases (48%), isointense in eight (32%), and mixed in five (20%). The tumors were hypointense relative to white matter in 24 cases (96%) and isointense in one (4%). None of the medulloblastomas had foci of very high signal on the short TR images that would suggest the presence of methemoglobin. One patient had several well-defined zones of low signal comparable to that of CSF involving most of the tumor (Fig. 8). Nine other patients had small foci of decreased signal within the tumors.

Long TR/short TE images.—Medulloblastomas were predominantly hyperintense relative to muscle in 23 of 23 cases. In comparison with gray matter, these tumors were predominantly hyperintense in 11 cases (48%), isointense in eight (35%), and mixed in four (17%). The tumors were hyperintense relative to white matter in 22 cases (96%) and hypointense in one (4%).

Long TR/long TE images.—On long TR/long TE images, medulloblastomas generally had intermediate to moderately high signal intensity. Medulloblastomas were predominantly hyperintense compared with muscle in 23 of 23 cases. In

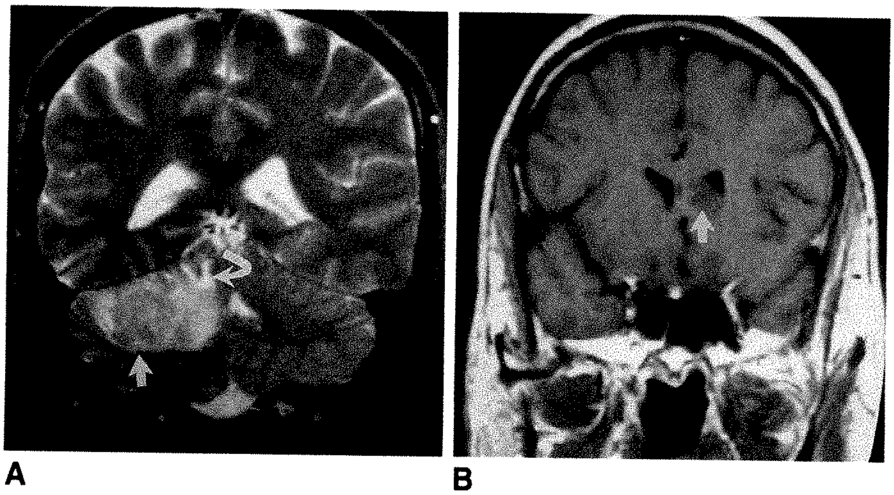

Fig. 6.—42-year-old man with desmoplastic medulloblastoma.

A, Long TR/long TE (2500/90) coronal MR image shows primary tumor (*straight arrow*) in right cerebellar hemisphere. Mass is predominantly hyperintense relative to adjacent gray and white matter. Hyperintense signal (*curved arrow*) in white matter adjacent to lesion represents "edema."

B, Enhanced short TR (800/20) coronal MR image shows metastatic lesion (*arrow*) with no definite enhancement in left lateral ventricle. Primary tumor had only a few small foci of enhancement (*not shown*).

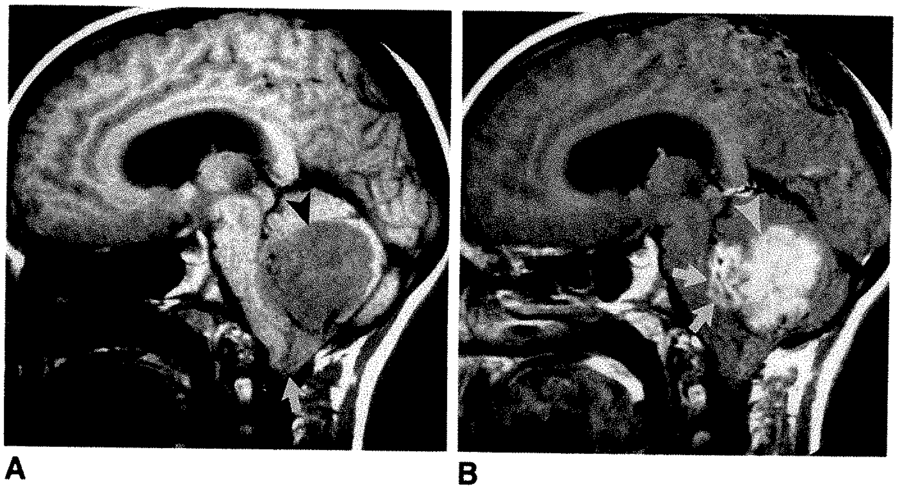

Fig. 7.—11-year-old girl with classical medulloblastoma.

A, Sagittal short TR (600/20) MR image shows a mass (*arrowhead*) in mid and inferior vermis that compresses fourth ventricle, resulting in moderate hydrocephalus. Mass causes caudal displacement of cerebellar tonsils (*arrow*).

B, Enhanced short TR (600/20) sagittal MR image shows prominent enhancement (*arrowhead*) within tumor. Abnormal enhancement (*arrows*) in posterior aspect of brainstem represents tumor invasion.

relation to gray matter, these tumors were predominantly hyperintense in 13 cases (56%), isointense in two (9%), and mixed in eight (35%). In comparison with white matter, these tumors were predominantly hyperintense in 20 cases (87%) and mixed in three (13%). No difference in signal characteristics was observed between desmoplastic and classical medulloblastomas on long TR/long TE images as well as on long TR/short TE and short TR/short TE images.

Tumor signal on long TR/long TE images was homogeneous in two cases (9%), mildly heterogeneous in 12 (52%), and markedly heterogeneous in nine (39%). Small well-defined foci with a very high signal similar to that of CSF were present in nine tumors (Fig. 9). Another patient had a tumor consisting mostly of large cystic components. Small tubular structures with signal void representing blood vessels were detected in nine of the tumors. Six tumors contained small irregular zones of decreased signal on long TR images that correlated with CT findings of clumplike calcifications (Fig. 10). Two other patients had CT scans that showed several tiny intratumoral calcifications that were not apparent on the MR images. Of the seven patients for whom CT scans were not available for comparison, none had histologic evidence of intratumoral calcifications.

Findings consistent with peritumoral white matter edema were evident for both desmoplastic medulloblastomas confined to the cerebellar hemispheres (Fig. 6) and for one of three classical medulloblastomas involving both vermis and hemisphere (Fig. 2). Thin crescent-shaped zones with signal characteristics similar to CSF were present at the periphery of 11 tumors (Figs. 1 and 2).

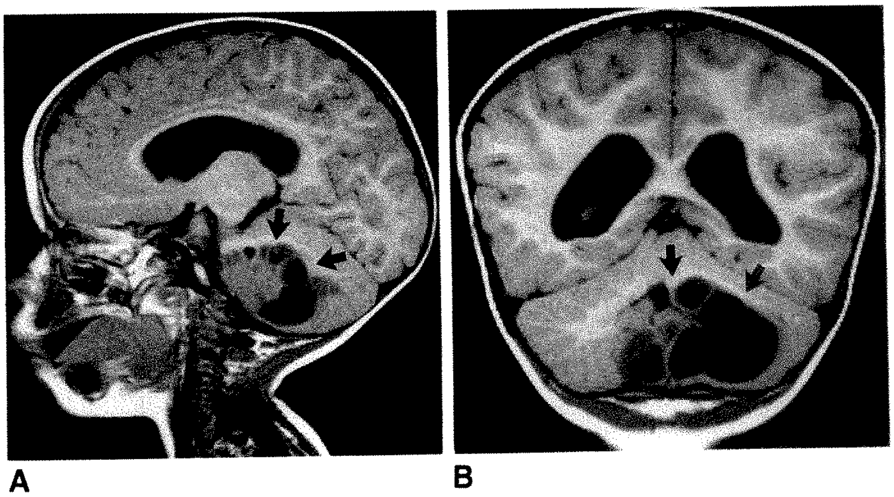

Fig. 8.—1-year-old boy with classical medulloblastoma.

***A* and *B*, Short TR (500/17) sagittal (*A*) and coronal (*B*) MR images show mass (*arrows*) involving vermis and a cerebellar hemisphere. Mass contains multiple areas with signal characteristics similar to those of CSF. Mass compresses outlet of fourth ventricle, resulting in moderate hydrocephalus.**

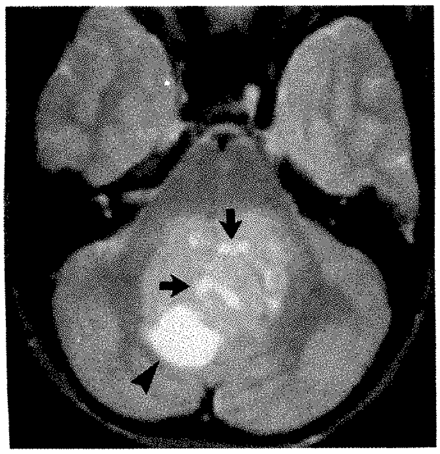

Fig. 9.—7-year-old girl with classical medulloblastoma. Long TR/long TE (2600/80) axial MR image shows small foci of high signal (*arrows*) within tumor, representing sites of cystic or necrotic degeneration, and large cystic component (*arrowhead*) at periphery of tumor.

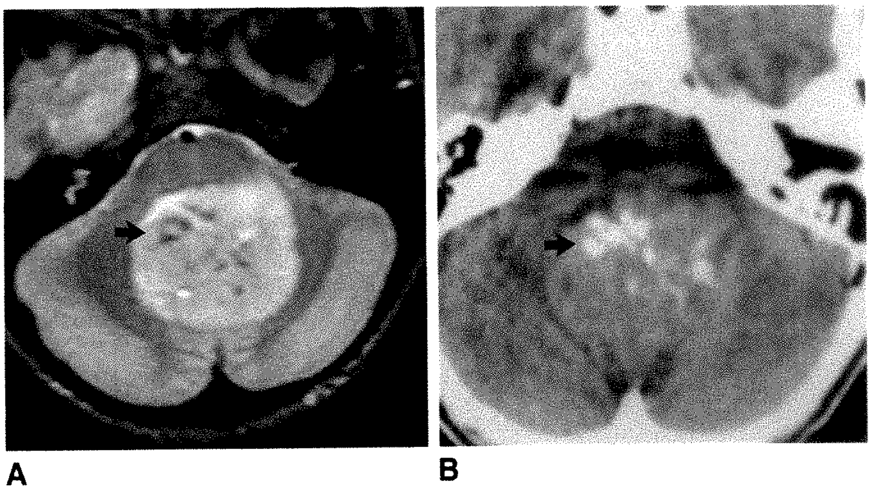

Fig. 10.—13-year-old boy with classical medulloblastoma.

A and *B*, Long TR/long TE (2400/80) axial MR image (*A*) shows small areas of decreased signal (*arrow*) within tumor that are similar in location to sites of clumplike calcification (*arrow*) on unenhanced CT scan (*B*).

Findings on Contrast-Enhanced MR Images

MR images were obtained before and after IV administration of gadopentetate dimeglumine in 11 of 25 patients. All of the medulloblastomas showed contrast enhancement. The fraction of tumor volume showing enhancement was less than one third in two cases (18%) (Fig. 1), between one third and two thirds in four (36%) (Fig. 2), and greater than two thirds in five (46%) (Figs. 3 and 7). The enhancement pattern was markedly heterogeneous in nine cases (82%) (Figs. 1 and 2) and mildly heterogeneous in two (18%) (Fig. 3). Because of the heterogeneous enhancement pattern, tumor margins were often less well delineated on the enhanced scans than on the unenhanced scans. However, enhanced scans showed abnormal enhancement at sites where signal abnormalities on unenhanced scans were not definite for tumor infiltration and could have represented peritumoral edema. These sites included the pons in one case (Fig. 7), middle cerebellar peduncle in three cases, and foramina of Luschka and Magendie in one case. Only one patient had metastatic disease at presentation. A single unenhancing metastatic lesion was observed within a lateral ventricle of a 42-year-old patient who had a primary tumor with only a few small foci of enhancement (Fig. 6).

Discussion

Primitive neuroectodermal tumors are histologically similar malignant neoplasms that occur in both intracranial and peripheral regions of the nervous system [1, 2, 10]. Medulloblastoma, which originates within the cerebellum, is the most common primitive neuroectodermal tumor of the CNS [3]. On gross pathologic examination, medulloblastomas appear as moderately well demarcated gray pink masses that may contain areas of necrosis or cystic foci [1, 3]. Histologically, the classical type of medulloblastoma is composed of sheets of small cells with scant cytoplasm and relatively large hyperchromatic round or angular nuclei [1, 3]. Medulloblastomas containing bands of connective tissue interspersed among the small malignant cells have been classified as desmoplastic medulloblastomas. Compared with classical medulloblastomas, the desmoplastic type is less common, tends to occur in older patients, and is more often lateral in position [3, 8, 10]. Tumor location and the age and sex distribution of patients with medulloblastomas in our study were similar to those reported in larger series of these neoplasms evaluated by CT [5, 8].

On MR images obtained with short TR/short TE, medulloblastomas generally had low to intermediate signal, and were predominantly hyperintense relative to muscle and hypointense relative to white matter. On long TR/short TE and long TR/long TE images, the tumors generally had intermediate to moderately high signal that was predominantly hyperintense relative to muscle and white matter. Tumor signal relative to gray matter varied considerably on both short TR and long TR images. Signal heterogeneity of medulloblastomas on long TR/long TE images was observed in 91%, and in 48% of these cases was the result of cystic or necrotic foci that were also seen histopathologically. These observations are similar to those of two large series of medulloblastomas evaluated by CT in which unenhancing areas of low attenuation representing cystic or necrotic degeneration were present in 47% and 59% of the primary tumors [5, 8]. In our series, intratumoral cystic foci were small in almost all cases (Fig. 9). The one exception was a tumor consisting predominantly of cystic components (Fig. 8). Signal heterogeneity in other medulloblastomas correlated to histopathologic findings of small intratumoral blood vessels, clumplike areas of calcification, and necrotic changes. Clumplike calcification has been reported to occur in 21% of medulloblastomas [5]. Findings of peritumoral white matter "edema" were present in three patients. Eleven patients had small crescent-shaped peripheral fluid collections adjacent to the tumors that may represent peripheral zones of necrosis, edema, or entrapped CSF. No difference in signal characteristics was observed between classical and desmoplastic medulloblastomas.

All but two of the medulloblastomas were generally well-defined masses with convex margins. The two exceptions were identified as poorly defined zones of abnormal signal relative to brain parenchyma and muscle on long TR/long TE images. Neither of the patients with these lesions had contrast-enhanced MR imaging.

The degree of gadopentetate dimeglumine enhancement within medulloblastomas varied considerably. Slightly more than half the tumors showed only small or intermediate degrees of enhancement. In addition, the enhancement pattern within tumors was heterogeneous in all 11 cases. All enhanced images in our series were acquired immediately after the manual IV injection of gadopentetate dimeglumine. Therefore, it is unknown what the effect of delaying the time between contrast administration and imaging might have on the degree and pattern of tumor enhancement. To our knowledge, the only previous report describing gadopentetate dimeglumine enhancement of medulloblastomas before surgery was a case series that included only two medulloblastomas, both of which showed intense enhancement [9]. The variable MR enhancement findings of medulloblastomas in our study are analogous to those seen with contrast-enhanced CT [5]. Enhanced MR images were useful in showing sites of tumor invasion of adjacent neural tissue. These sites of tumor invasion demonstrated on the MR examinations were confirmed at surgery.

The occurrence of intracranial metastatic disease at presentation in our study is similar to that reported by Nelson et al. [5], who found imaging evidence of metastatic disease in 5% of 233 patients with medulloblastomas evaluated by CT. Only one of 25 patients in our series had intracranial metastatic disease at the time of MR imaging. This patient had a primary desmoplastic medulloblastoma that showed only a few small foci of enhancement. The single metastatic lesion was located in a lateral ventricle and showed no evidence of contrast enhancement. This observation suggests that metastatic disease could be underestimated by reliance on only the enhancement features of these tumors. Similar limitations can also apply for recurrent medulloblastomas. Rollins et al. [11] reported that three of nine recurrent medulloblastomas showed no enhancement on either MR imaging or CT scans of the head after the administration of contrast material.

The differential diagnosis of medulloblastoma includes astrocytoma, ependymoma, metastases, and choroid plexus papilloma. The results of this study show that the unenhanced and enhanced MR characteristics of medulloblastomas are somewhat variable. Medulloblastomas should be included in the differential diagnosis when the MR findings described are present. MR, with its high contrast resolution and multiplanar imaging capability, has an important role in defining the location, size, and intracranial extent of medulloblastomas.

Effective treatment of medulloblastomas requires surgical resection of as much tumor as possible followed by high-dose radiotherapy (>5000 cGy) to the posterior fossa [3, 12]. Because medulloblastomas can invade the leptomeninges and metastasize along CSF pathways, additional postoperative radiotherapy (3500-4000 cGy) to the whole brain and spine has been reported to improve survival rates [3, 12]. In our institutions, MR imaging of the spine is routinely performed for the evaluation of intradural metastatic disease after tumor resection. The value of gadopentetate dimeglumine for detecting intradural metastases in patients with medulloblastomas is unknown and awaits future study.

ACKNOWLEDGMENT

We thank Kathryn Frazier for technical assistance in the preparation of this manuscript.

REFERENCES

1. Becker LE, Hinton D. Primitive neuroectodermal tumors of the central nervous system. *Hum Pathol* **1983**;14:538-550
2. Rorke LB. The cerebellar medulloblastoma and its relationship to primitive neuroectodermal tumors. *J Neuropathol Exp Neurol* **1983**;42:1-15
3. Russell DS, Rubenstein LJ. Medulloblastomas. In: *Pathology of tumors of the nervous system*, 5th ed. Baltimore: Williams & Wilkins, **1989**:251-279
4. Arseni C, Ciurea AV. Statistical survey of 276 cases of medulloblastoma (1935-1978). *Acta Neurochir* **1981**;57:159-166
5. Nelson M, Diebler C, Forbes WStC. Paediatric medulloblastoma: atypical CT features at presentation in the SIOP II trial. *Neuroradiology* **1991**;33:140-142
6. Zimmerman RA, Bilaniuk LT, Pahlajani H. Spectrum of medulloblastomas demonstrated by computed tomography. *Radiology* **1978**;126:137-141
7. Zee CS, Segall HD, Miller C, et al. Less common CT features of medulloblastoma. *Radiology* **1982**;144:97-102
8. Sandhu A, Kendall B. Computed tomography in management of medulloblastomas. *Neuroradiology* **1987**;29:444-452
9. Powers TA, Partain CL, Kessler RM, et al. Central nervous system lesions in pediatric patients: Gd-DTPA-enhanced MR imaging. *Radiology* **1988**;169:723-726
10. Gusnard DA. Cerebellar neoplasms in children. *Semin Roentgenol* **1990**;25:263-278
11. Rollins N, Mendelsohn D, Mulne A, et al. Recurrent medulloblastoma: frequency of tumor enhancement Gd-DTPA MR imaging. *AJNR* **1990**;11:583-587
12. Hughes EN, Shillito J, Sallan SE, Loeffler JS, Cassady JR, Tarbell NJ. Medulloblastoma at the Joint Center for Radiation Therapy between 1968 and 1984. The influence of radiation dose on the patterns of failure and survival. *Cancer* **1988**;61:1992-1998

Books Received

Receipt of books is acknowledged as a courtesy to the sender. Books considered of sufficient interest are reviewed as space permits. If the book has been reviewed in the *AJR*, the date of its review is given in parentheses.

Pediatric Sonography. Edited by Marilyn J. Siegel. New York: Raven, 419 pp., 1991. $125 (1/92)

Liver Imaging. Current Trends and New Techniques. Edited by Joseph T. Ferrucci and David D. Stark. Boston: Andover, 438 pp., 1990. $110 (1/92)

Imaging of the Thyroid and Parathyroid Glands. A Practical Guide. Edited by Brian Eisenberg. New York: Churchill Livingstone, 209 pp., 1991. $59.95 (1/92)

CT of the Immunocompromised Host. Edited by Janet E. Kuhlman. New York: Churchill Livingstone, 194 pp., 1991. $54 (1/92)

Comprehensive Textbook of Oncology, 2nd ed., vols. 1 and 2. Edited by A. R. Moossa, Stephen C. Schimpff, and Martin C. Robson. Baltimore: Williams & Wilkins, 1918 pp., 1991. $175 (1/92)

Essentials of Nuclear Medicine Imaging, 3rd ed. By Fred A. Mettler, Jr., and Milton J. Guiberteau. Philadelphia: Saunders, 339 pp., 1991. $60 (1/92)

MRI of the Extremities. An Anatomic Atlas. By Heung Sik Kang and Donald Resnick. Philadelphia: Saunders, 383 pp., 1991. $145 (1/92)

Hysterosalpingography. A Text and Atlas. By David J. Ott and Jamil A. Fayez. Baltimore: Urban & Schwarzenberg, 130 pp., 1991. $69.50 (1/92)

Nuclear Medicine Procedure Manual. Edited by William C. Klingensmith III, Dennis Eshima, and John Goddard. Englewood, CO: Oxford Medical, 466 pp., 1990. Print format, $125; disk format, $95 (1/92)

The Best of Medical Humor. A Collection of Articles, Essays, Poetry, and Letters Published in the Medical Literature. Compiled and edited by Howard J. Bennett. Philadelphia: Hanley & Belfus, 228 pp., 1991. $25 (1/92)

Easily Missed Fractures and Corner Signs in Radiology. B. Hans Olav Riddervold. Mount Kisco, NY: Futura, 400 pp., 1991. $150 (1/92)

Computers in Diagnostic Radiology. (The Institute of Physical Sciences in Medicine Report No. 62.) Edited by J. Robertson, P. F. Wankling, K. Faulkner, and M. R. Holubinka. York, England: The Institute of Physical Sciences in Medicine (available from IPSM, P. O. Box 303, York, England Y01 2WR), 164 pp., 1990. £28.50, softcover (2/92)

Head and Neck Imaging, 2nd ed. Edited by Peter M. Som and R. Thomas Bergeron. St. Louis: Mosby–Year Book, 1165 pp., 1991. $175 (2/92)

The Discipline of Curiosity. Science in the World. Edited by Janny Groen, Eefke Smit, and Juurd Eijsvoogel. New York: Elsevier, 156 pp., 1990. (2/92)

Merrill's Atlas of Radiographic Positions and Radiologic Procedures, vols. 1–3, 7th ed. By Philip W. Ballinger. St. Louis: Mosby–Year Book, 1562 pp., 1991. Vol. 1, $59.95; vols. 2 and 3, $57.95 each; set (vols. 1–3), $149.95 (2/92)

Diagnostic Radiology 1990. Edited by Charles A. Gooding. Philadelphia: Lippincott, 600 pp., 1990. $99 (2/92)

Nuclear Radiology (Fourth Series). Test and Syllabus. Section editor: James H. Thrall. Reston, VA: American College of Radiology, 684 pp., 1990. $175 (2/92)

Stone Therapy in Urology. Edited by F. Eisenberger, K. Miller, and J. Rassweiler. (Translated by Mario Kuntze.) New York: Thieme-Verlag, 171 pp., 1991. softcover (2/92)

RSNA Today Video, Vol. 5, No. 1. Oak Brook, IL: The Radiological Society of North America, 1991. $55; by subscription, 6 issues annually at $185 for RSNA members and $225 for nonmembers (VHS videotape) (2/92)

The Radiologic Clinics of North America. Radiographic Manifestations of Common Congenital Anomalies. Guest editor: Kook Sang Oh. Philadelphia: Saunders, 1991;29(2):179–435. $28, by subscription, 6 issues annually for $98 (2/92)

Radiologic and Histologic Pathology of Nontumorous Diseases of Bones and Joints, vols. 1 and 2. By James W. Milgram. Northbrook, IL: Northbrook Publishing, 1382 pp., 1990. $395 (2/92)

Understanding MRI. By Jeffrey H. Newhouse and Jonathan I. Wiener. Boston: Little, Brown, 155 pp., 1991. $42.50, softcover (2/92)

Errors in Chest Radiography. By Manuel Viamonte, Jr. New York: Springer-Verlag, 135 pp., 1991. $59, softcover (2/92)

Fast-Scan Magnetic Resonance. Principles and Applications. By Felix W. Wehrli. New York: Raven, 164 pp., 1991. $45 (3/93)

Fundamentals of Body CT. By W. Richard Webb, William E. Brant, and Clyde A. Helms. Philadelphia: Saunders, 320 pp., 1991. $39 (3/92)

Handbook of Orthopedic Terminology. By Ray F. Kilcoyne and Edward L. Farrar. Boca Raton, FL: CRC Press, 155 pp., 1991. $29.95, softcover (3/92)

Interventional Computed Tomography. By Rainer M. M. Seibel and Dietrich H. W. Grönemeyer. (Translated by Peter A. Rothschild, Jürgen Plassmann, and Hermann Sehnert.) Boston: Blackwell, 355 pp., 1990. $174.95 (3/92)

Geriatric Radiology. Edited by Manuel Viamonte, Jr. Baltimore: Williams & Wilkins, 228 pp., 1991. $65 (3/92)

Immunoscintigraphy. Practical Aspects and Clinical Applications. By A. C. Perkins and M. V. Pimm. New York: Wiley-Liss, 193 pp., 1991. $59.95 (3/93)

RSNA Today Video, Vol. 5, No. 2. Oak Brook, IL: The Radiological Society of North America, 1991. $55; by subscription, 6 issues annually at $185 for RSNA members and $225 for nonmembers (VHS videotape) (3/92)

Differential Diagnosis of Diseases of the Chest. By Robert G. Fraser, J. A. Peter Paré, P. D. Paré, Richard S. Fraser. Philadelphia: Saunders, 160 pp., 1991. $25 (3/92)

The Year Book of Diagnostic Radiology 1991. Edited by William R. Hendee, Theodore E. Keats, John A. Kirkpatrick, Jr., et al. St. Louis: Mosby–Year Book, 570 pp., 1991. $57.95 (3/92)

Grant's Atlas of Anatomy, 9th ed. By Anne M. R. Agur and Ming J. Lee. Baltimore: Williams & Wilkins, 650 pp., 1991. $49, softcover (3/92)

RSNA Today Video, Vol. 5, No. 3. Oak Brook, IL: The Radiological Society of North America, 1991. $55; by subscription, 6 issues annually at $185 for RSNA members and $225 for nonmembers (VHS videotape) (3/92)

MRI of the Musculoskeletal System. Edited by John V. Crues III. (One of 10 volumes in The Raven MRI Teaching File. Series editors: Robert B. Lufkin, William G. Bradley, Jr., and Michael Brant-Zawadzki.) New York: Raven, 255 pp., 1991. $60

Measurements in Pediatric Radiology. By Holger Pettersson and Hans Ringertz. New York: Springer-Verlag, 185 pp., 1991. $79 (3/92)

Clinical Magnetic Resonance. Imaging and Spectroscopy. By E. Raymond Andrew, Graeme Bydder, John Griffiths, Richard Iles, and Peter Styles. New York: Wiley, 220 pp., 1990. $59.95 (3/92)

WHO Model Prescribing Information. Drugs Used in Mycobacterial Diseases. By WHO. Geneva: World Health Organization, 40 pp., 1991. $8.10.

Progress in Cardiology, 4/2. Edited by Douglas P. Zipes and Derek J. Rowlands. Philadelphia: Lea & Febiger, 223 pp., 1991. $45

Diagnosis of Sturge-Weber Syndrome: Comparison of the Efficacy of CT and MR Imaging in 14 Cases

Luis Martí-Bonmatí[1]
Francisco Menor[2]
Cecilio Poyatos[1]
Hector Cortina[2]

Sturge-Weber syndrome is a neurocutaneous syndrome that includes facial and leptomeningeal angiomas. Imaging findings include cerebral lobar atrophy, brain calcifications, choroid plexus enlargement, cranial diploë prominence, and venous abnormalities. We compared the efficacy of CT and MR imaging in making the diagnosis in 14 consecutive patients. CT, with and without contrast enhancement, was performed in all patients, and 11 of the 14 had MR imaging (eight before and after administration of IV gadopentetate dimeglumine). MR imaging was better than CT in showing the extent and degree of brain parenchymal atrophy, the presumed ischemic changes affecting the gray and white matter, and the cranial diploetic prominence on the affected side. MR imaging after contrast administration permitted a better evaluation of the extent and patency of the leptomeningeal angiomatous malformation and the parenchymal venous anomalies. CT was better than MR imaging in showing the presence and extent of cortical calcifications. Enhanced CT and MR imaging were equal in evaluating the prominence of the ipsilateral choroid plexus.

Our experience indicates that contrast-enhanced MR imaging is the method of choice in the diagnosis of Sturge-Weber syndrome. Unenhanced CT should be used only if MR findings are normal, to exclude the presence of intracranial calcifications.

***AJR* 158:867–871, April 1992**

Sturge-Weber syndrome (encephalotrigeminal angiomatosis) is a neurocutaneous syndrome seen in children that is characterized by leptomeningeal angiomatosis and an ipsilateral facial nevus in the area of the trigeminal nerve, involving at least its ophthalmic division. CT has been the imaging method of choice in patients with this disorder [1, 2], but recently MR imaging also has been used [2–5]. In this study, we compared the efficacy of enhanced and unenhanced CT and MR imaging in the diagnosis of the Sturge-Weber syndrome in 14 cases.

Subjects and Methods

Fourteen consecutive children with Sturge-Weber syndrome were included in the study. The nine boys and five girls were 2–21 years old (mean, 10 years; SD, 5 years). Only one patient had a family history of the disease.

All patients had the characteristic facial angioma. This was ipsilateral to the hemispheric lesions in 12 cases, bilateral in one with a left-sided leptomeningeal angiomatosis, and contralateral to the leptomeningeal angiomatosis in another patient.

CT was performed in all 14 cases (General Electric 9800, Milwaukee, WI, and Toshiba TCT-600HQ, Nasu, Japan) without and with IV contrast agents. A bolus of contrast medium was injected by hand, a volume of 2–3 ml/kg of a 300 mg I/ml solution (Omnitrast 300, Schering AG, Berlin, Germany). Slice thickness was 10 mm. Two successive studies were made in all cases, separated by an average of 5 years; only the second CT examination was considered in this study.

MR imaging was performed in 11 children, all within 5 months of the second CT examination. A 0.5-T unit (Philips Gyroscan S5, Eindhoven, the Netherlands) was used. All patients

Received July 19, 1991; accepted after revision October 30, 1991.

[1] Unidad de Resonancia Magnética, Departamento de Diagnóstico por la Imagen, Hospital Dr Peset, E-46017 Valencia, Spain. Address reprint requests to L. Martí-Bonmatí.

[2] Servicio de Radiodiagnóstico, Hospital Infantil La Fe, Valencia, Spain.

0361-803X/92/1584-0867
© American Roentgen Ray Society

had a sagittal short TR/short TE spin-echo (SE) sequence, 505/30/4 (TR/TE/excitations), and a transverse long TR/double-echo TE (2200–2500/50,100/2) SE sequence. In eight cases, a contrast-enhanced (Magnevist, Schering AG) T1-weighted gradient-recalled echo (GRE) study, 569/16/90°/2 (TR/TE/flip angle/excitations), was carried out in the transverse and coronal planes. In five instances, a short-TI inversion-recovery (STIR) sequence, 1500/100/44/2 (TR/TI/TE/excitations), in the coronal plane also was used. Slice thickness was 7 mm in all cases, with a 256 × 256 matrix (pixel size, 0.9 × 0.9 mm). The contrast dose was always 10 ml, regardless of the patient's weight.

CT and MR images were evaluated separately by two observers. Results represent a consensus after the independent interpretations. In both CT and MR studies, cerebral lobar atrophy was graded as discrete in the case of slight volume loss, marked if the sulci also were prominent, and severe if there was marked prominence of sulci and marked decrease in volume. The CT and MR images also were evaluated for the presence of cerebral parenchymal calcifications, cerebral gray and white matter changes in signal intensity and contrast enhancement, size and homogeneity of the choroid plexus, presence of venous anomalies, enlargement of the cranial diploetic space, superior sagittal sinus hypoplasia, and retinal angioma.

Results

CT Findings

CT correctly showed cerebral involvement, except in one patient, in whom CT showed occipital involvement and MR imaging clearly showed temporooccipital involvement. Cerebral lobar atrophy was discrete in eight patients, marked in two, and severe in four. In all cases, cerebral cortical calcifications were demonstrated and were focal in six cases and

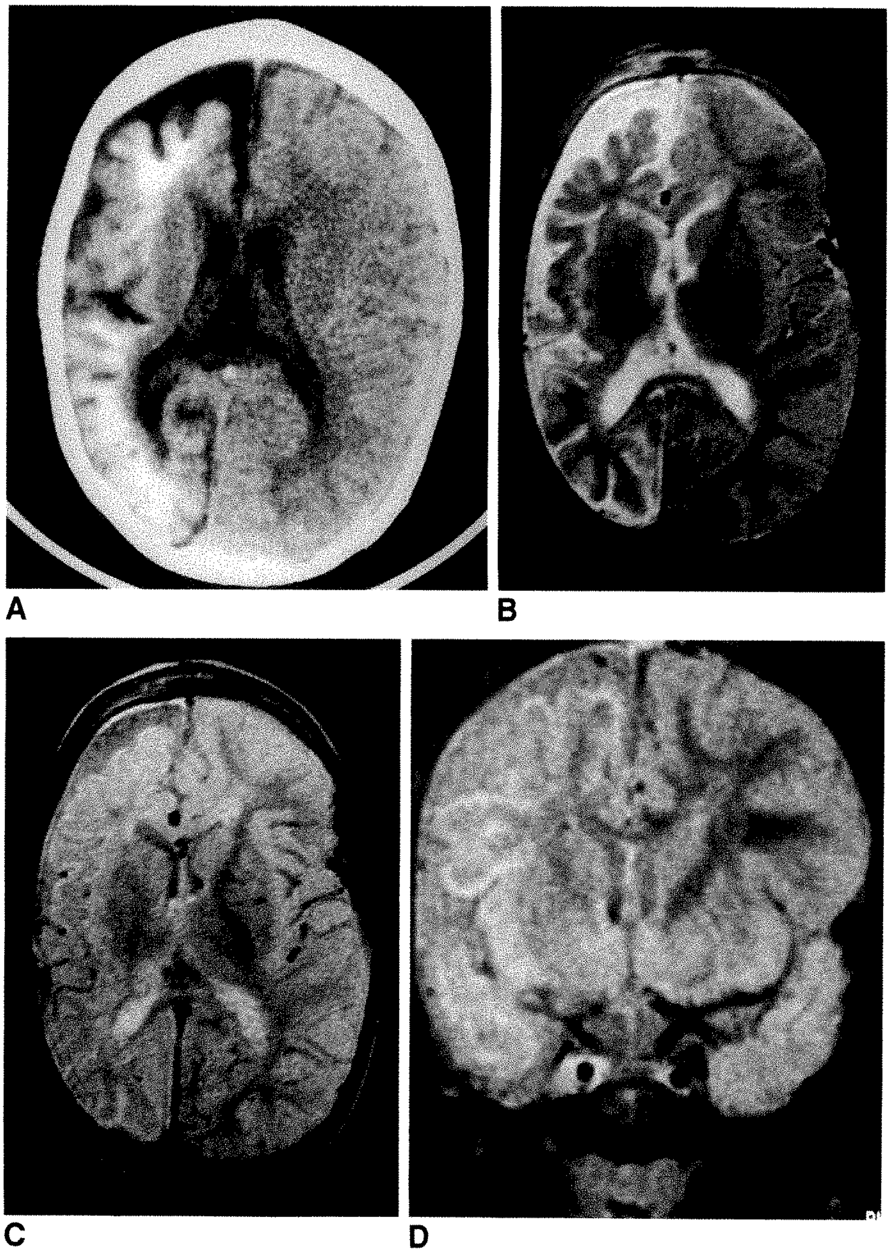

Fig. 1.—18-month-old boy with seizures, left hemiparesis, and right-sided facial angioma.

A, Unenhanced CT scan shows marked atrophy with diffuse deep cortical and white matter calcification in right cerebral hemisphere.

B and *C*, SE MR images with long TR/long TE (*B*) and medium TE (*C*) show hyperintense superficial cortical layer on both sequences, suggesting more atrophy on long TE sequence (*B*).

D, Coronal STIR image shows this superficial layer as hyperintense, as is white matter.

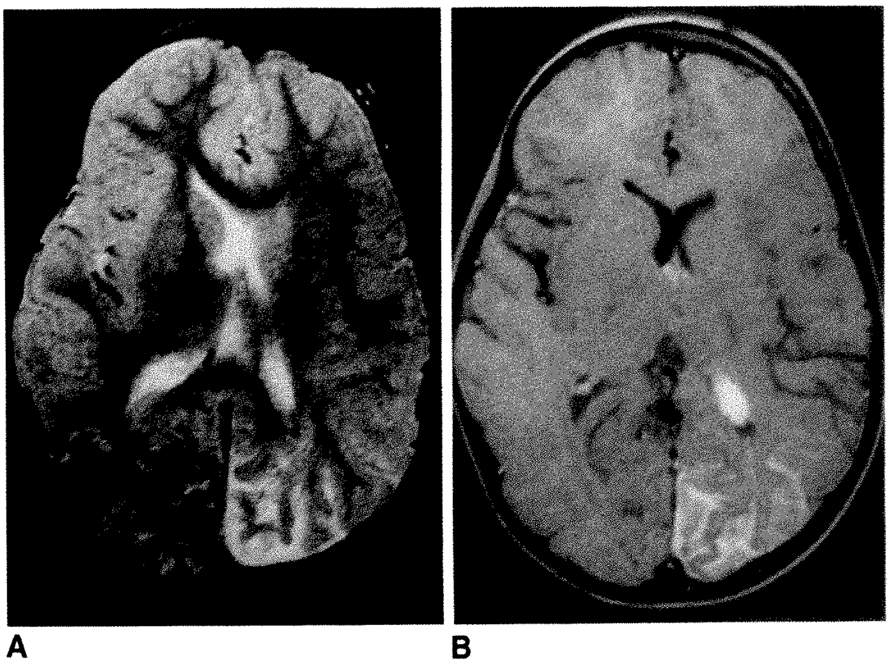

Fig. 2.—12-year-old boy with left-sided facial angioma.

A, SE MR image with long TR/long TE shows left occipital atrophy with cortical hyperintensity simulating CSF.

B, GRE T1-weighted MR image after gadopentetate dimeglumine administration showed marked enhancement of leptomeningeal angioma and superficial cortical brain.

extensive in eight (Fig. 1), making it impossible to evaluate changes in the cerebral gray and white matter.

Although contrast enhancement of the cerebral gyri was seen on CT scans in almost all patients, enhancement was not seen in either of two consecutive CT examinations in two patients. The choroid plexus, which was better evaluated on CT after contrast administration, was enlarged with respect to the contralateral plexus in all patients except one, in whom there was slight cerebral involvement. Four abnormalities in venous development were noted in three patients, consistent with prominent deep veins; one was a definite venous angioma. These anomalies were ipsilateral to the leptomeningeal angiomatosis in three of four patients.

No temporal changes were noted on serial CT scans in nine of the 14 children. In the other five, a decrease was observed in the degree of cortical contrast enhancement; three had an increase in calcifications and two had an increase in atrophy. In no case did the appearance of the choroid plexus change with time.

MR Imaging Findings

MR imaging (Figs. 1–4) easily defined the extent of cerebral lobar changes in the size and signal intensity of the gray and white matter. The involvement was temporooccipital in four, hemispheric in three, occipital in two, and parietooccipital in one. In one patient with frontoparietotemporal involvement, the occipital lobe was spared. Atrophy was discrete in five patients and marked or severe in six. Calcifications were demonstrated in eight cases, and were seen more clearly with GRE and long TR/TE SE sequences (Fig. 4). In three patients, no cortical calcification was seen. The white matter, best evaluated on SE sequences with long TR/long TE, was hyperintense relative to gray matter in five cases, isointense in four, and of normal intensity in two. The gray matter was hyperintense at the cerebral surface in six patients but normal in five. This finding was best appreciated on SE images with long TR/medium TE and STIR sequences (Fig. 1). On SE sequences with long TR/TE, gray matter changes were isointense with CSF and, thereafter, difficult to detect (Figs. 1–3).

After contrast administration, enhancement was noted in all cases (minimal or discrete in four and marked in another four). In one with moderate and another with intense contrast enhancement on MR, CT showed no uptake of iodinated contrast material. Contrast enhancement corresponded to the hyperintense cortical area, when present (Figs. 2 and 3). Although on unenhanced MR images the choroid plexus appeared normal in three cases (Figs. 1 and 2), it was enlarged after contrast administration in all cases (Figs. 2–4). MR revealed cyst formations within the plexus in two patients, also seen on CT. The patient with a normal choroid plexus on CT was not studied with MR imaging. The same anomalies in venous development (Fig. 3) that were seen on enhanced CT scans were noted on MR images. MR also visualized prominent subependymal veins in five cases that were not seen on CT.

Nine children had areas of diploë that were prominent with respect to their contralateral counterparts. This bone alteration was better visualized by MR than by CT. There was no evidence of parenchymal hemorrhage, superior sagittal sinus hypoplasia, or retinal angioma on either MR or CT images.

Discussion

In Sturge-Weber syndrome, leptomeningeal angiomata are characteristically located in the occipital lobe and on the same side as the facial angioma.

Cerebral atrophy is always present [1–5, 6]. This abnormality is seen slight better with MR imaging than with CT. In almost 50% of cases, only volume loss without prominent sulci is appreciated, making the diagnosis with CT more difficult. MR evaluation of cortical atrophy should be carried

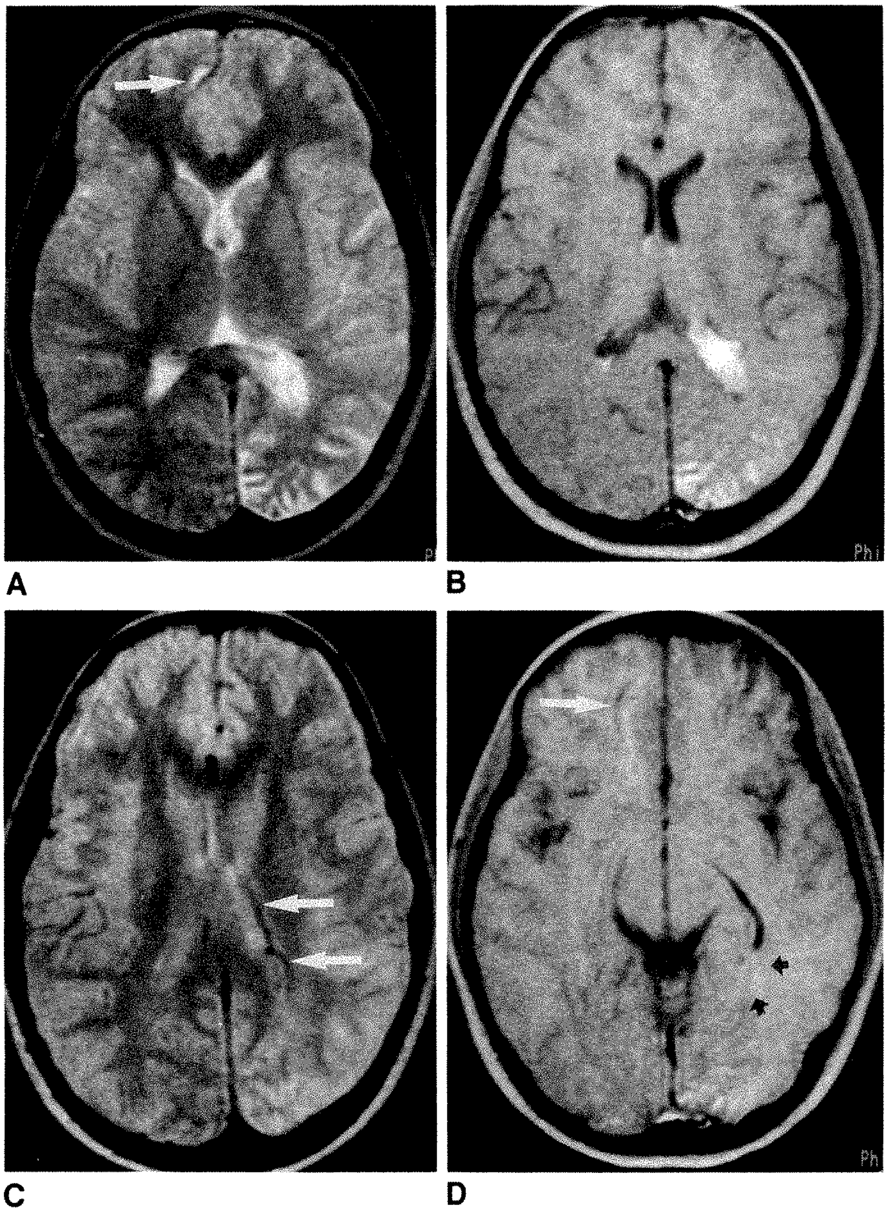

Fig. 3.—7-year-old girl with bilateral facial angioma.

A, SE MR image with long TR/long TE shows prominent choroid plexus in left parietooccipital lobe with discrete parenchymal atrophy and large deep draining vein (*arrow*) in right frontal lobe.

B, GRE T1-weighted MR image after contrast administration shows prominent uptake by choroid plexus and enhancement of area corresponding to hyperintensity on T2-weighted image, most probably representing a combination of leptomeningeal angioma and superficial cortical layer.

C, SE MR image with long TR/medium TE shows prominent subependymal draining veins (*arrows*).

D, T1-weighted GRE MR image after gadopentetate dimeglumine administration shows frontal prominent deep vein (*white arrow*) seen on *A* and deep temporal venous angioma with hyperintense feeding vessels (*black arrows*).

out with T1-weighted or STIR sequences rather than with long TR/TE SE sequences, because on T2-weighted sequences the signal intensity of CSF and the brain surface may be nearly the same (Fig. 1B).

Areas of increased signal appear in the white matter adjacent to the leptomeningeal angioma on SE long TR/long TE and STIR sequences. This hyperintensity makes the white matter appear as intense as the gray matter, if not more so. This is possibly related to ischemia resulting from long-standing cerebral hypoperfusion or disordered neuronal organization and dysmyelination of the involved brain [6, 7].

Brain surface changes are better defined by MR than by CT images. MR facilitates visualization of cortical alterations in those areas that are more difficult to evaluate with CT (e.g., the temporal lobe). The use of gadopentetate dimeglumine improves the overall superiority of MR in detecting cortical involvement, especially in those cases with cerebral calcification [4]. More importantly, CT is a poor means of evaluating enhancement of an angioma in a calcified area because it is difficult to be sure whether underlying enhancement is being masked by the heavy calcification (Fig. 4). Cortical enhancement corresponds to the hyperintense layer observed on SE long TR/medium TE and STIR sequences. This area includes the leptomeningeal angioma [5, 8] and probably also the first cortical layer affected by gliosis [6, 7, 9].

Deep to the leptomeningeal angioma and first cortical layer, a hypointense area caused by the calcification can be seen. Such hypointensity caused by the deposition of calcium is more evident on GRE and SE long TR/long TE images [2, 4]. The combination of superficial enhancement and deeper hypointensity after contrast administration on a GRE T1-weighted sequence appears to be highly characteristic of this syndrome (Fig. 2B). However, CT is better than MR in the detection of calcification.

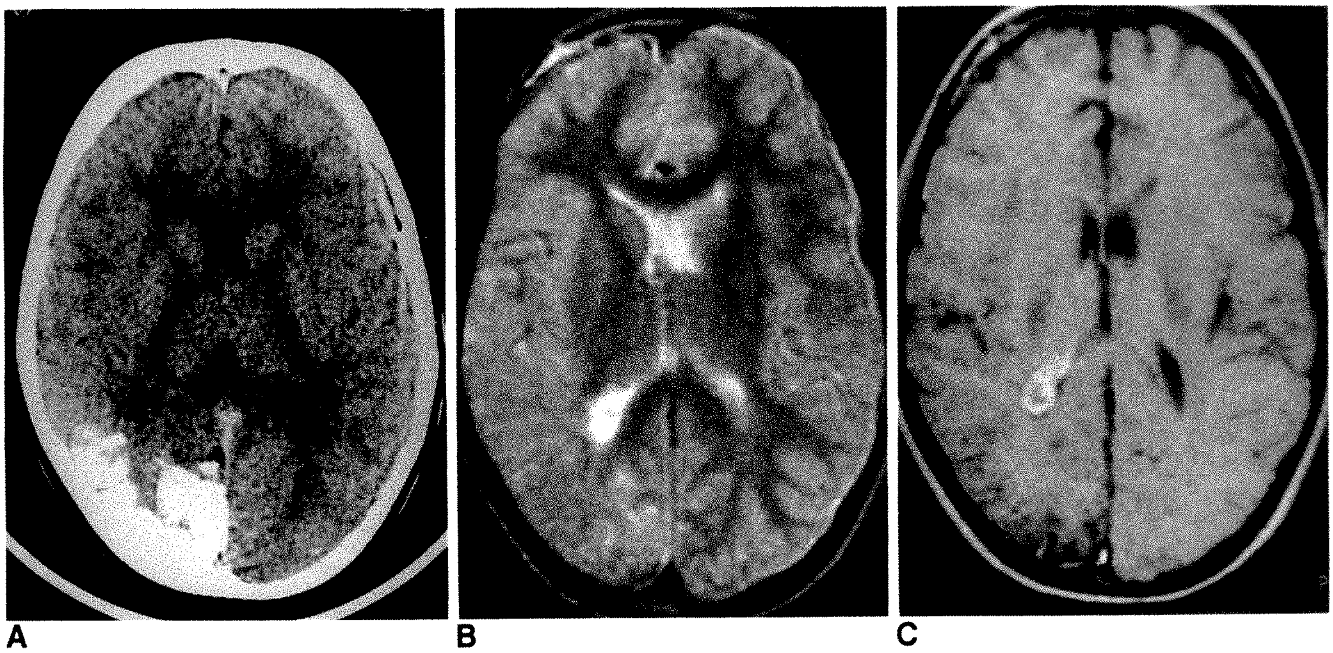

Fig. 4.—10-year-old girl with right-sided facial angioma.
A, **Unenhanced CT scan shows a dense cortical calcification in right parietooccipital lobe.**
B, **SE MR image with long TR/long TE shows discrete atrophy, isointensity of white matter with cerebral cortex, and prominent choroid plexus.**
C, **T1-weighted GRE MR image after contrast administration shows marked uptake of contrast material by choroid plexus but no enhancement and hypointensity of calcified leptomeningeal angioma, although cortical enhancement in an adjacent level was minimal.**

The enlarged, and sometimes cystic, choroid plexus is better observed after administration of contrast agents—both in CT and in MR imaging [10].

Venous abnormalities are common among patients with Sturge-Weber syndrome. The superficial venous drainage of the affected lobes is compromised by the leptomeningeal angioma, the blood shunting to the deep venous system via collateral vessels [6]. These dilated vessels may be visualized in their subependymal, periventricular, or transparenchymal location on MR images, although they are not usually detected by CT. However, the lack of superficial cortical veins cannot be demonstrated with current CT or MR techniques [2]. Venous development is also subjected to a higher rate of anomalies, such as venous angioma, and enhanced MR is more useful than CT in detecting and characterizing them.

Given the hyperintensity of yellow bone marrow with respect to cortical bone on MR images, thickening and prominence of the diploë are seen much better on MR than on CT (CT requires special windows for bone imaging).

In summary, CT was better than MR in detecting the presence and extent of cortical calcifications, and equal to MR in showing the prominent choroid plexus. MR imaging, with and without contrast administration, was better in showing the extent and degree of patency of the leptomeningeal malformation, the degree of parenchymal atrophy, the changes in the affected gray and white matter, the parenchymal venous anomalies, and the diploetic prominence on the affected side. Therefore, MR should be the imaging method of choice when this syndrome is being diagnosed [4, 5, 8]. SE with long TR/double-echo TE and T1-weighted GRE sequences after administration of contrast material are needed for optimal evaluation of these anomalies. If MR imaging does not confirm the diagnosis in a suspected case of Sturge-Weber syndrome, then CT should be done because it is more likely to show calcification that can be elusive on MR imaging.

REFERENCES

1. Diebler C, Dulac O. Neurocutaneous syndromes. In: Diebler C, Dulac O, eds. *Pediatric neurology and neuroradiology*. Berlin: Springer-Verlag, **1987**:99–104
2. Wasenko JJ, Rosenbloom SA, Duchesneau PM, Lanzieri CF, Weinstein MA. The Sturge-Weber syndrome: comparison of MR and CT characteristics. *AJNR* **1990**;11:131–134
3. Crawford SC, Boyer RS, Harnsberger HR, Pollei SR, Smoker WRK, Osborn AG. Disorders of histogenesis: the neurocutaneous syndromes. *Seminars Ultrasound CT MR* **1988**;9:247–267
4. Elster AD, Chen MY. MR imaging of Sturge-Weber syndrome: role of gadopentetate dimeglumine and gradient-echo techniques. *AJNR* **1990**;11:685–689
5. Lipski S, Brunelle F, Aicardi J, Hirsch JF, Lallemand D. Gd-DOTA-enhanced MR imaging in two cases of Sturge-Weber syndrome. *AJNR* **1990**;11:690–692
6. Barkovich AJ. Phakomatosis. In: Norman D, ed. *Pediatric neuroimaging*. New York: Raven, **1990**:123–147
7. Ton-That QT, Picard D, Bissoon-Doyal D, et al. Technetium-99m HMPAO imaging in Sturge-Weber syndrome. *Clin Nucl Med* **1990**;15:178–180
8. Sperner J, Schmauser I, Bittner R, et al. MR-imaging findings in children with Sturge-Weber syndrome. *Neuropediatrics* **1990**;21:146–152
9. Chiron C, Raynaud C, Dulac O, Tzourio N, Plouin P, Tran-Dinh S. Study of the cerebral blood flow in partial epilepsy of childhood using the SPECT method. *J Neuroradiol* **1989**;16:317–324
10. Stimac GK, Solomon MA, Newton TH. CT and MR on angiomatous malformations of the choroid plexus in patients with Sturge-Weber disease. *AJNR* **1986**;7:623–627

Case Report

Persistent Trigeminal Artery in a Patient with Sturge-Weber Syndrome

Laurie Loevner[1] and Douglas J. Quint

The primitive trigeminal artery is the most common embryonic carotid-vertebrobasilar anastomosis to persist into adulthood. It has been associated with other intracranial vascular alterations, including aneurysms and arteriovenous malformations [1], and has been implicated in a variety of clinical syndromes [2, 3]. Although persistent carotid-vertebrobasilar anastomoses have been described in association with facial capillary angiomas [4–6], in only one case has a persistent trigeminal artery been described in a patient with Sturge-Weber-Dimitri syndrome [7], a neurocutaneous disorder characterized by facial angiomata and ipsilateral leptomeningeal venous angiomatosis.

We present an unusual case of persistent trigeminal artery in a patient with Sturge-Weber-Dimitri syndrome. We discuss persistent carotid-vertebrobasilar anastomoses in association with other cranial vascular alterations and comment on the clinical and potential embryologic significance.

Case Report

A 25-year-old man with Sturge-Weber-Dimitri syndrome was admitted to our institution for embolization of a facial hemangioma before dental extractions, alveoloplasty, and dental abscess drainage. At birth he had been noted to have a large facial port-wine nevus in the distribution of all three sensory divisions of the trigeminal nerve bilaterally. At 1 year of age, he had tonic-clonic seizures. At age 2, a constellation of findings, including mental retardation, seizure disorder, enlarging facial hemangioma, and visual impairment, led to the diagnosis of Sturge-Weber-Dimitri syndrome.

A CT scan obtained during the current hospital admission showed dense bilateral temporal and parietooccipital cortical calcifications, cerebral atrophy, and a large facial hemangioma (Figs. 1A and 1B).

Right internal carotid angiography showed a persistent trigeminal artery arising from the presellar segment of the right internal carotid artery with flow into the basilar artery (Figs. 1C and 1D). Vertebral angiography showed small right and left vertebral arteries, both communicating with the basilar artery. Selective right vertebral arteriography also showed transient reflux of contrast material into the right internal carotid artery through the persistent trigeminal artery. No abnormalities were seen on angiograms of the left vertebral and left internal carotid arteries. Bilateral external carotid arteriography showed enlargement of the internal maxillary and facial arteries as well as their terminal branches in the distribution of the facial angioma. Embolization of the hemangioma was performed before oral surgery.

Discussion

Surge-Weber-Dimitri syndrome, or encephalotrigeminal angiomatosis, a neurocutaneous syndrome, is characterized clinically by facial port-wine nevus, mental retardation, seizures, and hemiparesis. Pathologically, it is characterized by cutaneous facial hemangiomas, most commonly in the ophthalmic distribution of the trigeminal nerve and ipsilateral leptomeningeal angiomatosis. Bilateral involvement is not uncommon, reported in up to 30% of cases in some series.

The trigeminal, otic, and hypoglossal arteries are well-described embryologic intracranial anastomoses between the developing primitive carotid (anterior) and vertebrobasilar (posterior) circulations. These anastomoses are each named

---

Received August 12, 1991; accepted after revision September 30, 1991.

[1] Both authors: Department of Radiology, B1D530H, Neuroradiology, University of Michigan Hospitals, 1500 E. Medical Center Dr., Ann Arbor, MI 48109-0030. Address reprint requests to D. J. Quint.

AJR 158:872–874, April 1992 0361–803X/92/1584–0872 © American Roentgen Ray Society

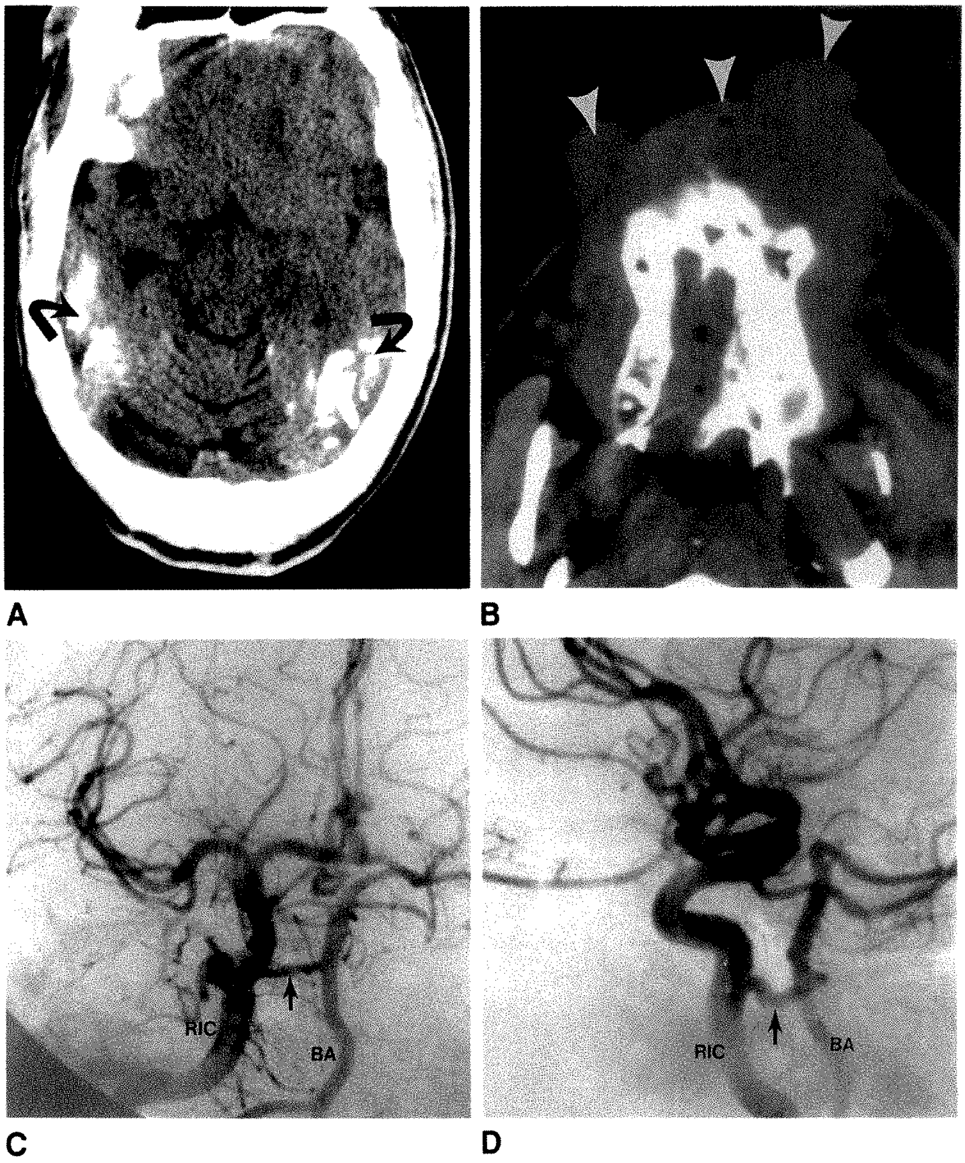

Fig. 1.—Persistent trigeminal artery in a 25-year-old man with Sturge-Weber-Dimitri syndrome.

***A*, Unenhanced head CT scan shows coarse cortical calcifications (*arrows*) involving temporal and parietooccipital regions.**

***B*, Maxillofacial CT scan shows large facial soft-tissue mass (*arrowheads*) consistent with hemangioma.**

***C* and *D*, Anteroposterior (*C*) and lateral (*D*) right internal carotid arteriograms show persistent trigeminal artery (*arrows*) arising from presellar portion of right internal carotid artery. RIC = right internal carotid artery, BA = basilar artery.**

after the cranial nerve with which they run, and appear during the development of the cranial nerve ganglia. The trigeminal arteries are present when the embryo is approximately 3 mm long (25 days). According to Padget [8], while the vertebrobasilar arterial system is evolving, blood to the hindbrain is provided predominantly by the trigeminal arteries, which arise from the primitive internal carotid arteries and supply blood to the paired posterior longitudinal neural arteries. When the embryo is approximately 5–6 mm long (29–35 days), the newly formed posterior communicating arteries provide the major blood supply to the posterior longitudinal arteries (which fuse to form the basilar artery). At this time, the trigeminal arteries begin to regress and are usually obliterated by the time the embryo is 14 mm long.

Carotid-vertebrobasilar anastomoses may persist into adulthood; persistent trigeminal artery is the most common, found on up to 0.5% of cerebral arteriograms. There may be associated hypoplasia or absence of the ipsilateral posterior communicating artery [8]. Similarly, the basilar and vertebral arteries proximal to the persistent trigeminal artery may be small, as was the case in our patient.

Although earlier literature questioned the significance of a persistent trigeminal artery, recent reports associate a variety of CNS disease with its presence. Persistent trigeminal artery occurring in association with intracranial aneurysms, arteriovenous malformations, and neoplasms [1] have been described. Persistence of a trigeminal artery has been implicated in a variety of clinical syndromes including tic douloureux, third and sixth nerve palsies [2], spontaneous subarachnoid hemorrhage, and vertebrobasilar insufficiency from atherosclerotic disease of the internal carotid artery with the persistent trigeminal artery presumably serving as the conduit to the posterior circulation [3]. Identification and an understanding of this anomalous circulation is important, as interventional neuroradiologic and neurosurgical procedures (often performed to treat many of the associated abnormalities described here) may need to be appropriately modified [2]. In particular, the blood supply to the posterior fossa must be considered before interventional procedures are performed.

Intracranial arterial alterations in Sturge-Weber-Dimitri syndrome are rare. To our knowledge, in only one case has a variant of a persistent trigeminal artery (anomalous origin of the right anterior inferior cerebellar artery from the cavernous segment of the right internal carotid artery) been described, in a 1-year-old boy with Sturge-Weber-Dimitri syndrome [7]. Interestingly, in reviewing the literature, we encountered cases of cutaneous angiomas in the trigeminal nerve distribution (in patients without other stigmata of Sturge-Weber-Dimitri syndrome) in which a variety of associated intracranial arterial abnormalities (including persistent carotid-vertebrobasilar anastomoses, absence of the internal carotid and vertebral arteries, and cerebral angiomatous malformations) were seen [5]. Four patients had persistent trigeminal arteries [4-6] (one patient also had hypoplasia of the left cerebellar hemisphere and another had a Dandy-Walker malformation).

The constellation of findings (in particular, cutaneous angiomas in the trigeminal nerve distribution and intracranial vascular alterations including persistent trigeminal artery) is curious, and one wonders (in particular, because carotid-vertebrobasilar anastomoses appear during the development of the cranial nerve ganglia) if the coexistence of these findings could be related to some underlying embryologic dysgenesis or some common insult resulting in vascular maldevelopment during the first several weeks of gestation. However, a retrospective study of a large series of patients with these abnormalities would be necessary to provide more convincing evidence that their coexistence is more than coincidental.

REFERENCES

1. Brick JV, Roberts T. Cerebral arteriovenous malformation coexistent with intracranial aneurysm and persistent trigeminal artery. *South Med J* **1987**;80:398-400
2. Morita A, Fukushima T, Miyazaki S, Shimizu T, Atsuchi M. Tic douloureux caused by primitive trigeminal artery or its variant. *J Neurosurg* **1989**;70:415-419
3. Palmer S, Güçer G. Vertebrobasilar insufficiency from carotid disease associated with a trigeminal artery. *Neurosurgery* **1981**;8:458-461
4. Miyahara S, Ohta H, Takaki T, Yonemasu Y, Yokota K. Recurrent pontine hemorrhage associated with persistent primitive trigeminal artery and facial angioma [in Japanese]. *No To Shinkei* **1977**;29:685-689
5. Pascual-Castroviejo I. The association of extracranial and intracranial vascular malformations in children. *Can J Neurol Sci* **1985**;12:139-148
6. Stoeter P, Marquardt B. Combined deformity of the brain and cerebral vessels (congenital hydrocephalus) in a 3 year old: Dandy Walker, PTA, hemangioma. *ROFO* **1978**;128:680-683
7. Ito J, Takeda N, Suzuki Y, Takeuchi S, Osugi S, Yoshida Y. Anomalous origin of the anterior inferior cerebellar arteries from the internal carotid artery. *Neuroradiology* **1980**;19:105-109
8. Padget DH. The development of the cranial arteries in the human embryo. *Contrib Embryol Carnegie Inst* **1948**;32:205-261

Pictorial Essay

Technical Problems Associated with Placement of the Bird's Nest Inferior Vena Cava Filter

Thomas Vesely,[1] Michael Darcy, Daniel Picus, and Marshall Hicks

Technical problems encountered during percutaneous placement of 165 Bird's Nest filters over 16 months are described. Filter deployment was successful in all patients. Although frequent, the technical problems were all minor with no long-term sequelae. Several problems were inherent to the design of the filter. Other problems related to the patient's anatomy were seen as well. Because deployment of the Bird's Nest filter is more operator-dependent than is deployment of other types of inferior vena cava filters, knowledge of pitfalls and means to avoid problems are particularly important.

Most of the newer inferior vena cava (IVC) filters have small introducer catheters and require relatively few steps for deployment once the catheter is in the appropriate position. Placement of the Gianturco-Roehm Bird's Nest vena cava filter (Cook Inc., Bloomington, IN) (Fig. 1) is more operator-dependent and requires deposition of an initial anchoring strut, formation of four stainless steel wires into a compact mesh, deposition of a second anchoring strut, then separation of the filter from the delivery system. Once familiar with these steps, they can be accomplished easily and quickly.

We reviewed the technical problems encountered during our initial experience with percutaneous placement of 165 Bird's Nest filters from June 1989 through October 1990. One hundred fifty-eight filters were placed through a femoral vein, seven through the right internal jugular vein. Initially, filters were placed by experienced staff interventional radiologists, but the majority were placed by radiology residents and interventional radiology fellows. Most of the problems with filter placement occurred during the first 6 months of their use at our institution. Learning to avoid problems as well as methods to remedy them has decreased the number of problems significantly.

Placement in Short Infrarenal IVC

Low-lying renal veins made insertion of the Bird's Nest filter difficult in five patients (3%). A short infrarenal IVC creates a "tight fit" for the filter, which is 6-7 cm long even when compactly deployed. Multiple or anomalous renal veins, which frequently enter the IVC close to the common iliac veins, present a similar problem (Fig. 2). A short infrarenal IVC can predispose to wire prolapse because the filter catheter cannot be withdrawn sufficiently to allow space for formation of the wire mesh caudal to the upper strut. Occasionally, even when the wire mesh is formed in the IVC, it may be necessary to place the lower strut in a common iliac vein (Fig. 3). An IVC filter with a shorter longitudinal dimension (Vena-tech, L.G. Medical, Chasseneuil, France; or Greenfield titanium filter, Medi-tech, Inc., Watertown, MA, etc.) may be desirable in such patients.

If the wire mesh is inadvertently deposited in a common iliac vein, it can be retracted into the catheter, as previously described by Roehm et al. [1], and reformed in a more optimal location (Fig. 4). When the infrarenal IVC is too short for all of our vena caval filters, we usually place Bird's Nest filters into both common iliac veins. If the common iliac veins are small, we place a suprarenal Bird's Nest filter.

Received September 10, 1991; accepted after revision November 5, 1991.

[1] All authors: Mallinckrodt Institute of Radiology, Washington University School of Medicine, 510 S. Kingshighway Blvd., St. Louis, MO 63110. Address reprint requests to T. Vesely.

AJR **158:875-880, April 1992** 0361-803X/92/1584-0875 © American Roentgen Ray Society

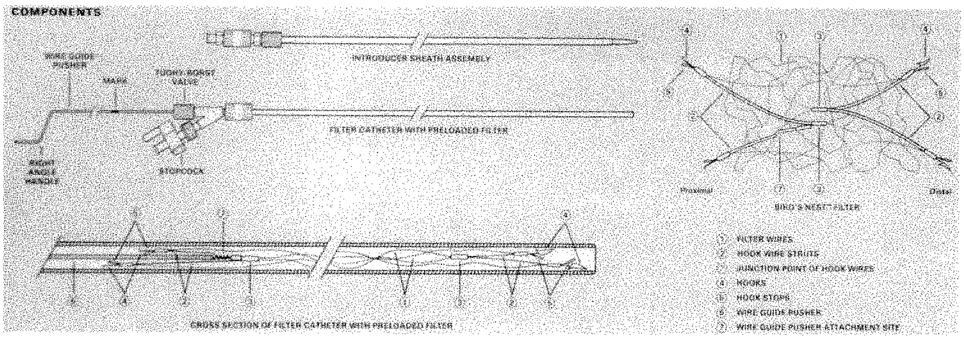
COMPONENTS
INTRODUCER SHEATH ASSEMBLY
WIRE GUIDE PUSHER
MARK
TUOHY-BORST VALVE
FILTER CATHETER WITH PRELOADED FILTER
RIGHT ANGLE HANDLE
STOPCOCK
Proximal
Distal
BIRD'S NEST™ FILTER
① FILTER WIRES
② HOOK WIRE STRUTS
③ JUNCTION POINT OF HOOK WIRES
④ HOOKS
⑤ HOOK STOPS
⑥ WIRE GUIDE PUSHER
⑦ WIRE GUIDE PUSHER ATTACHMENT SITE
CROSS SECTION OF FILTER CATHETER WITH PRELOADED FILTER

Fig. 1.—Components of the Bird's Nest filter. (Reprinted with permission from Cook Inc., Bloomington, IN.)

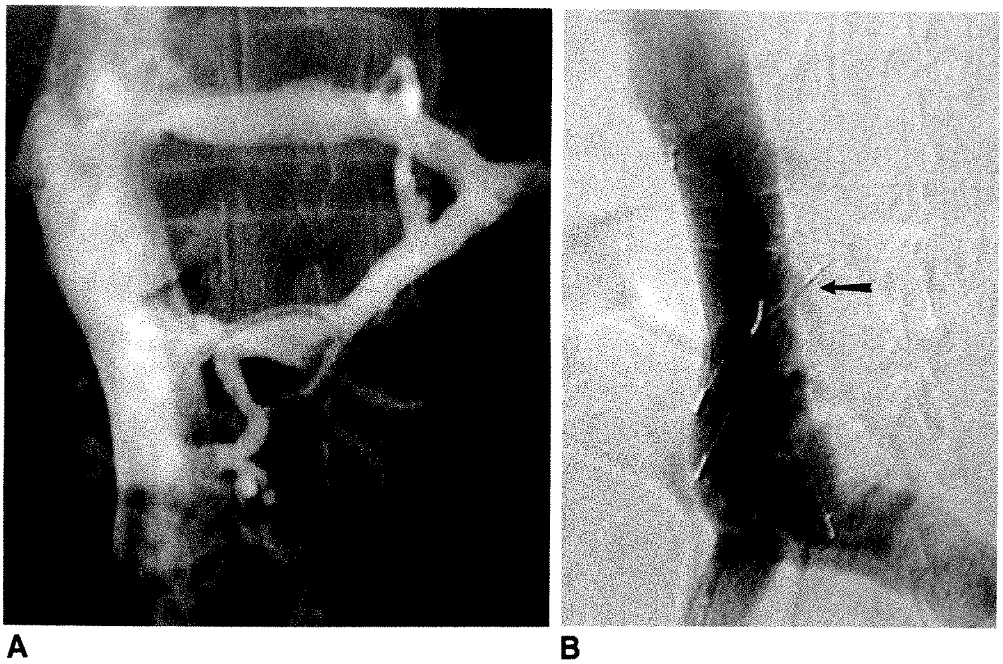

Fig. 2.—Filter placement with anomalous renal veins.

A, Angiogram after injection into inferior limb of left circumaortic renal vein. Inferior limb enters inferior vena cava just above confluence of iliac veins, creating a short infrarenal inferior vena cava.

B, Inferior venacavogram after placement of Bird's Nest filter shows one hookwire of upper strut within orifice of inferior limb of circumaortic left renal vein (*arrow*). Filter is in good position below renal veins.

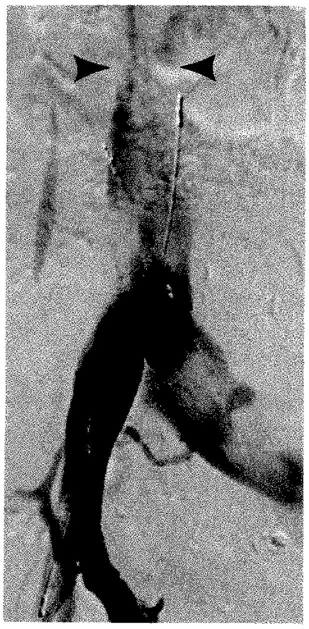

Fig. 3.—Filter placement in short infrarenal inferior vena cava. Angiogram after injection of right common iliac vein after placement of Bird's Nest filter. Streaming of contrast material is due to inflow from renal veins (*arrowheads*). Infrarenal inferior vena cava is short owing to low-lying renal veins. Wire mesh is formed at confluence of iliac veins and lower strut deposited in right iliac vein.

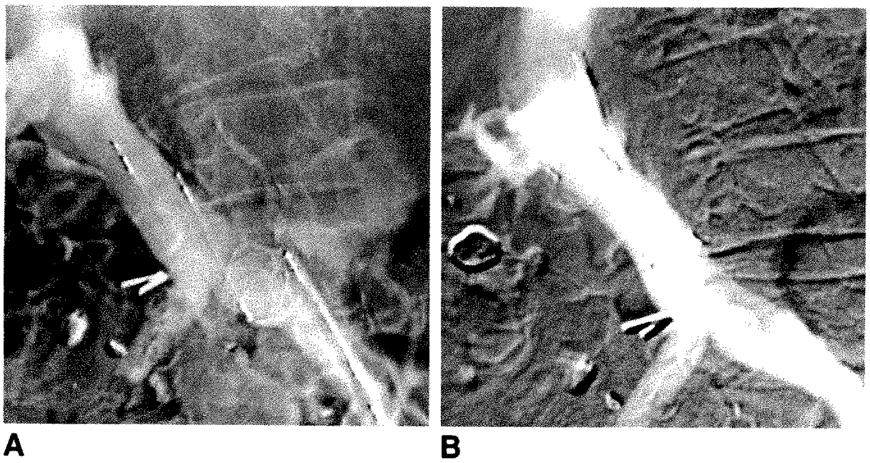

Fig. 4.—Repositioning of filter. Angiogram after injection through filter sheath in left iliac vein. Infrarenal inferior vena cava is short, renal veins are at level of L3–L4 interspace, and iliac vein confluence is at level of L5 vertebral body.

A, Upper strut is positioned in low inferior vena cava, and wire mesh is formed in left common iliac vein.

B, Wire mesh and upper strut were withdrawn into filter catheter, which was advanced more cephalad into inferior vena cava, to allow complete intracaval placement.

Sheath Kinking

In some patients, acute angulation of the iliac veins as they rise out of the pelvis to cross over the sacral promontory may be present. This angulation cannot be predicted on the basis of a frontal iliac venogram. Such acute tortuosity of the iliac veins can lead to kinking of the sheath after removal of the introducer. Sheath kinking occurred in eight patients (5%). Forceful advancement of the filter catheter through kinked segments of the sheath may result in damage to the sheath or vein (Fig. 5).

If a kink occurs in the sheath, withdrawal of the sheath while simultaneously advancing the filter catheter may straighten the kinked segment. A 16-French heavy-duty sheath (Cook Inc., Bloomington, IN) may be helpful when venous tortuosity is evident on the pelvic venogram. In our experience, if one femoral approach is unsuccessful because of sheath kinking, the contralateral approach will present

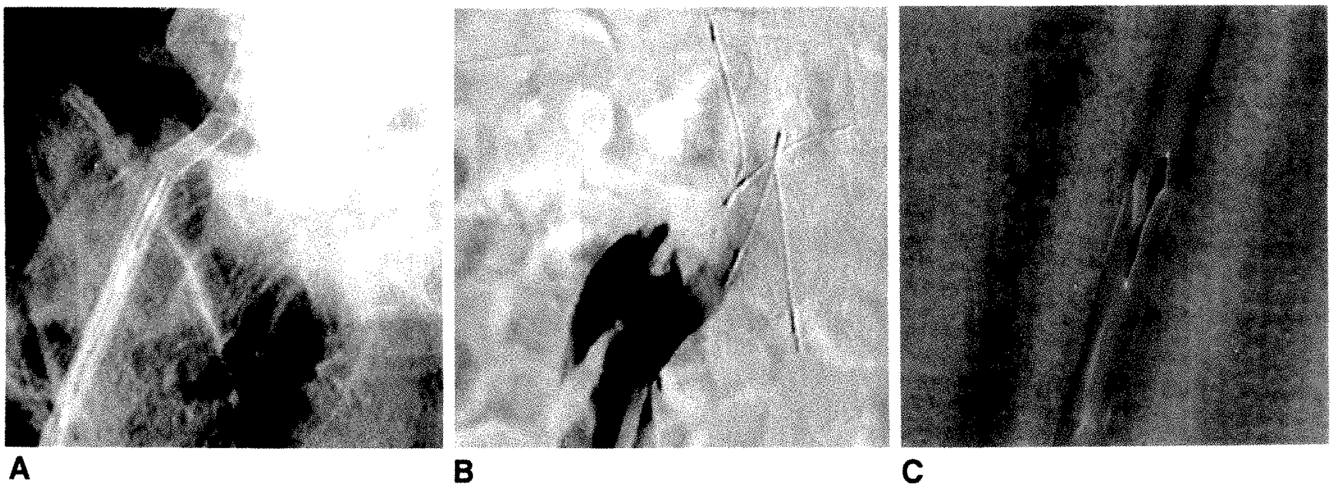

Fig. 5.—Sheath kinking.
A, **Angiogram shows severe kinking of sheath after removal of introducer. Despite many attempts, filter catheter could not be advanced past kinked segment.**
B, **Angiogram after injection into femoral filter sheath during removal reveals extravasation that did not become clinically significant. Filter was previously placed via right jugular vein.**
C, **Angiogram shows damaged femoral sheath with linear tear that was created by attempting to force filter past kinked segment.**

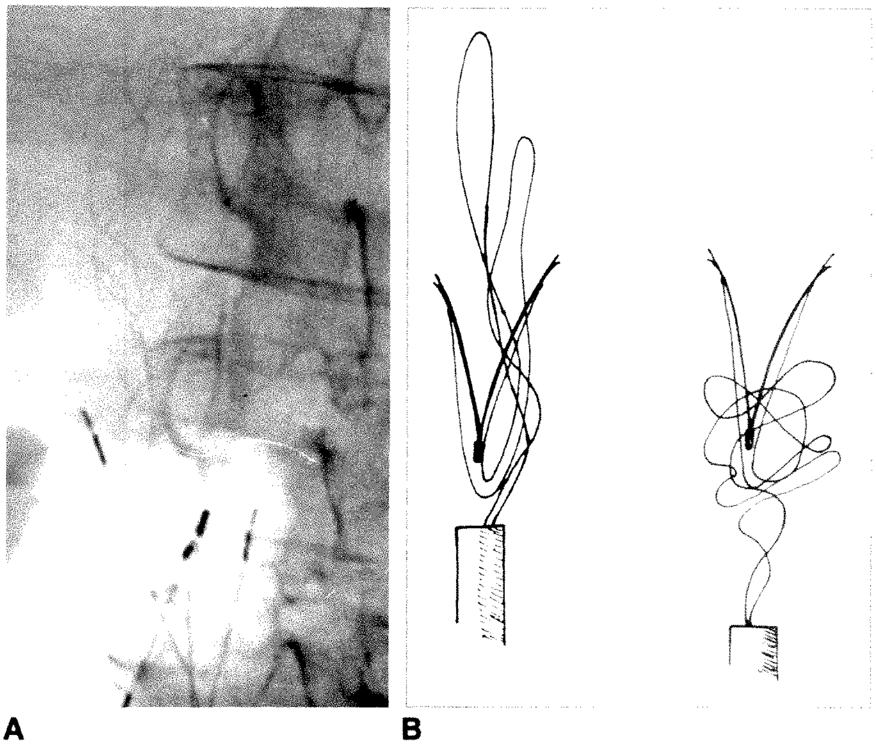

Fig. 6.—Prolapsed filtration wires.
A, **Magnified angiogram shows prolapse of filtration wires above anchoring struts.**
B, **Line drawing depicts wire prolapse. After placement of first anchoring strut, filter catheter/sheath assembly should be pulled back 3–4 cm to allow sufficient space for expansion of filtration wires (*right*). If delivery system is not withdrawn to allow sufficient space for mesh to form, wires may prolapse above upper strut (*left*).**

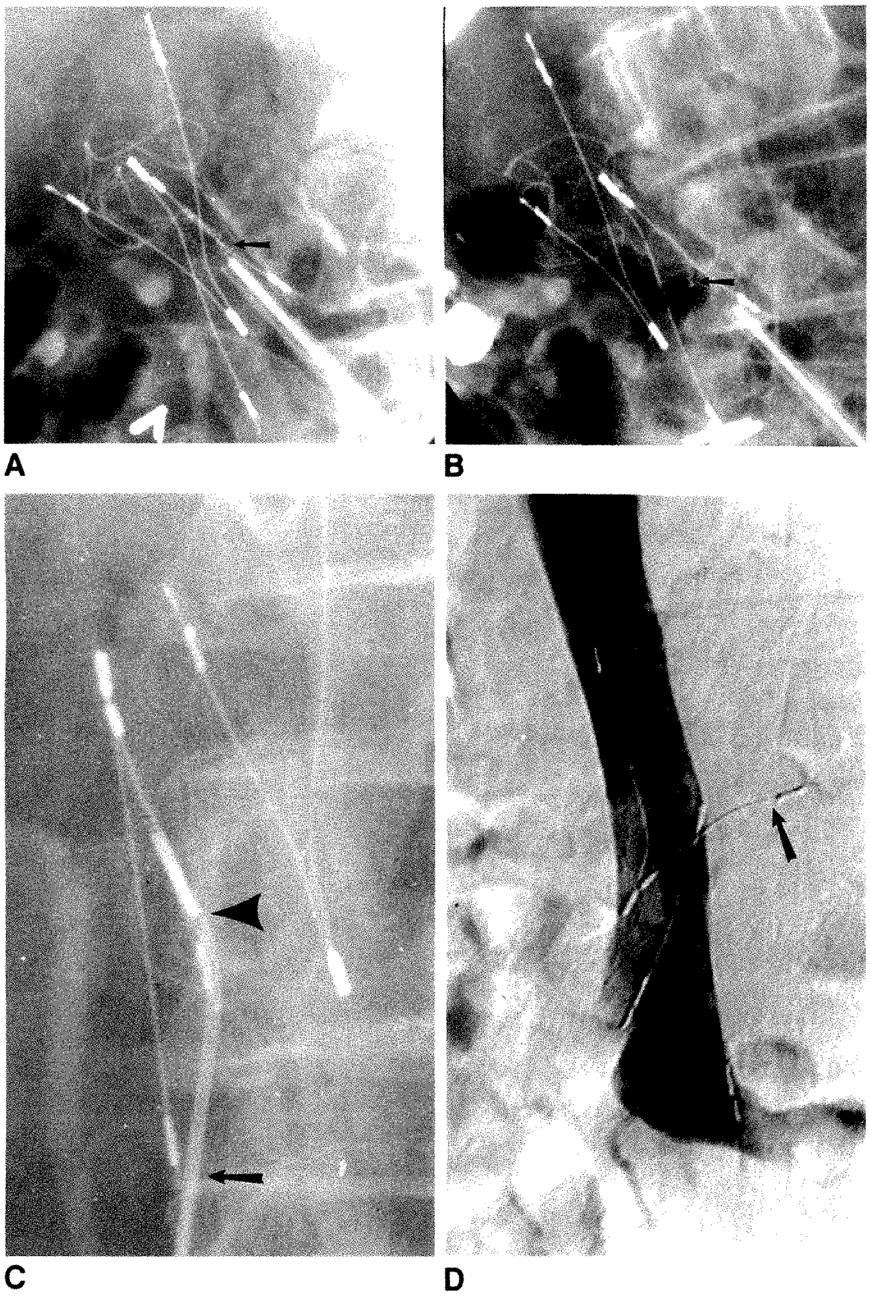

Fig. 7.—Filter release problems.

A, Magnified angiogram during filter placement. Despite multiple turns, screw tip (*arrow*) of wire guide pusher failed to disengage from filter.

B, Angiogram after continued rotation shows that wire spring on screw tip broke and remained attached to lower strut (*arrow*).

C, Magnified angiogram from another patient. After numerous turns, filter failed to release. Wire guide pusher is more lucent distally, indicating that inner mandrel (*arrow*) has separated and pulled back from metal tip (*arrowhead*). Continued rotation finally released filter.

D, Angiogram after Bird's Nest filter was placed from right internal jugular vein approach. Excessive traction on handle of wire guide pusher during filter release caused perforation of a hookwire (*arrow*) through wall of inferior vena cava.

similar difficulty. After failure of one femoral attempt, we often use a jugular approach. Filter placement problems due to unfavorable anatomy of the iliac vein are not unique to the Bird's Nest filter, and may be encountered with other types of IVC filters placed from the femoral approach.

Filter Wire Prolapse

Prolapse of filter wires cephalad to the anchoring hookwires (Fig. 6) was observed in 14 patients (8%). Prolapse is difficult to detect during deployment of a Bird's Nest filter because the filtration wires are poorly visible at fluoroscopy. A specific cause of prolapse is usually not apparent, but optimal compaction of wires occurs less frequently in patients with short infrarenal IVCs.

Prolapsed filtration wires might provide less effective clot trapping than a tight nest of wires, but the actual clot-trapping ability of prolapsed filtration wires is unknown. In vitro studies by Katsamouris et al. [2] of the Bird's Nest filter in three degrees of compaction demonstrated that prolapse did not reduce the clot-trapping capacity of the filter.

Maneuvers that may minimize wire prolapse include withdrawing the filter catheter/sheath assembly 3–4 cm after positioning the first hookwires to allow sufficient space for formation of the wire mesh; advancing the wires slowly; and rotating the entire assembly 180° after half of the filtration

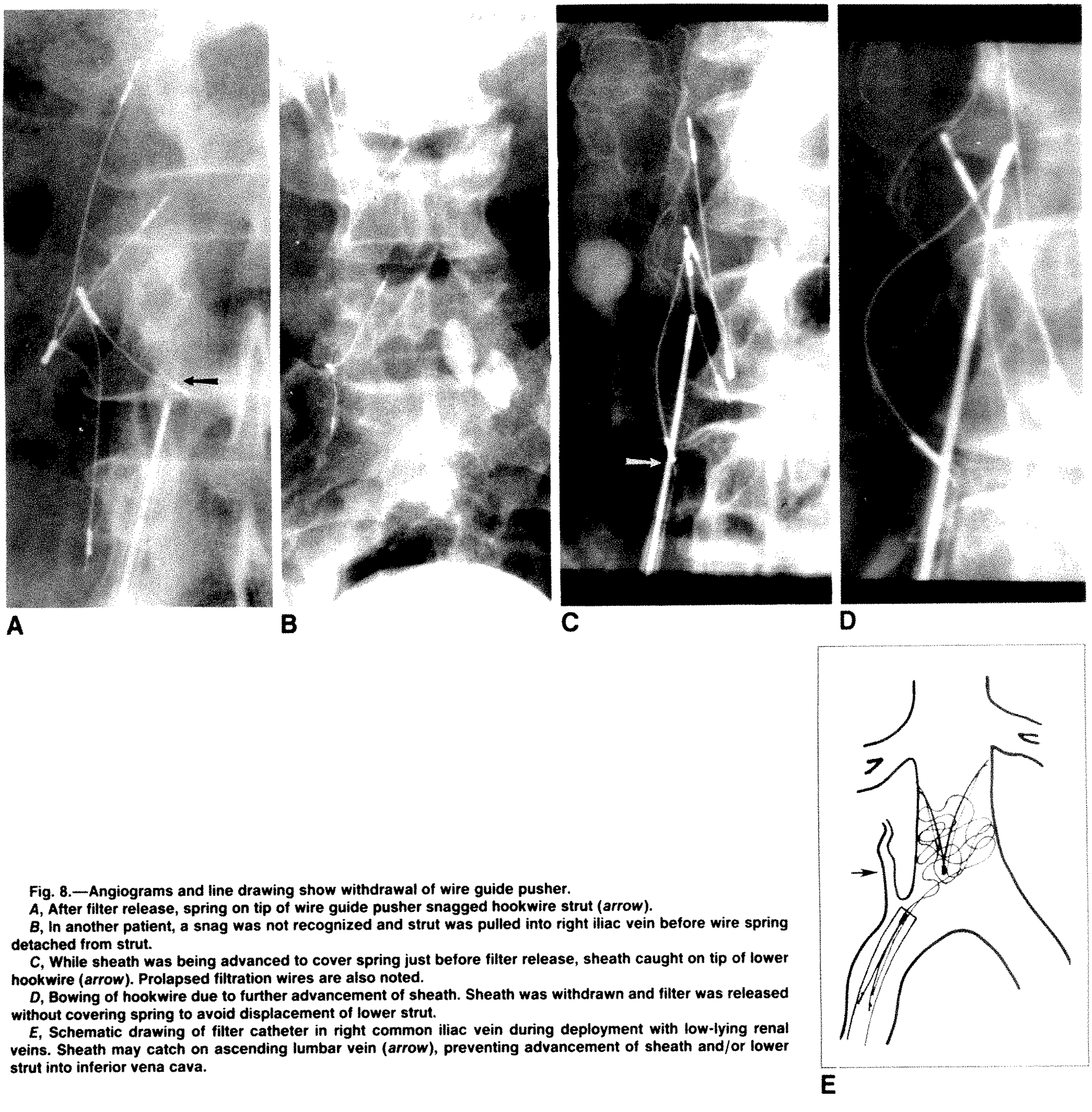

Fig. 8.—Angiograms and line drawing show withdrawal of wire guide pusher.

A, After filter release, spring on tip of wire guide pusher snagged hookwire strut (*arrow*).

B, In another patient, a snag was not recognized and strut was pulled into right iliac vein before wire spring detached from strut.

C, While sheath was being advanced to cover spring just before filter release, sheath caught on tip of lower hookwire (*arrow*). Prolapsed filtration wires are also noted.

D, Bowing of hookwire due to further advancement of sheath. Sheath was withdrawn and filter was released without covering spring to avoid displacement of lower strut.

E, Schematic drawing of filter catheter in right common iliac vein during deployment with low-lying renal veins. Sheath may catch on ascending lumbar vein (*arrow*), preventing advancement of sheath and/or lower strut into inferior vena cava.

wires are deployed, and then deploying the remainder of the wire.

Difficult Filter Release

After deployment of the filter, the handle of the wire guide pusher must be rotated counterclockwise 10 to 15 turns to disengage the filter. In one patient, the wire guide pusher failed to release despite multiple additional turns (Fig. 7). Continued rotation of the wire guide pusher caused the wire spring tip to break and remain attached to the lower hookwire.

In another patient, multiple rotations of the wire guide pusher also failed to release the filter. The mandrel of the wire guide pusher had apparently separated from the tip of the outer coils, which had then become bent slightly (Fig. 7C). Although the separated mandrel decreased the transmission of torque to the spring tip, continued rotation of the wire guide pusher handle eventually released the filter from the wire.

Gentle traction should be applied to the wire guide pusher during rotations to release the Bird's Nest filter. This traction allows separation to be visualized fluoroscopically. Excessive

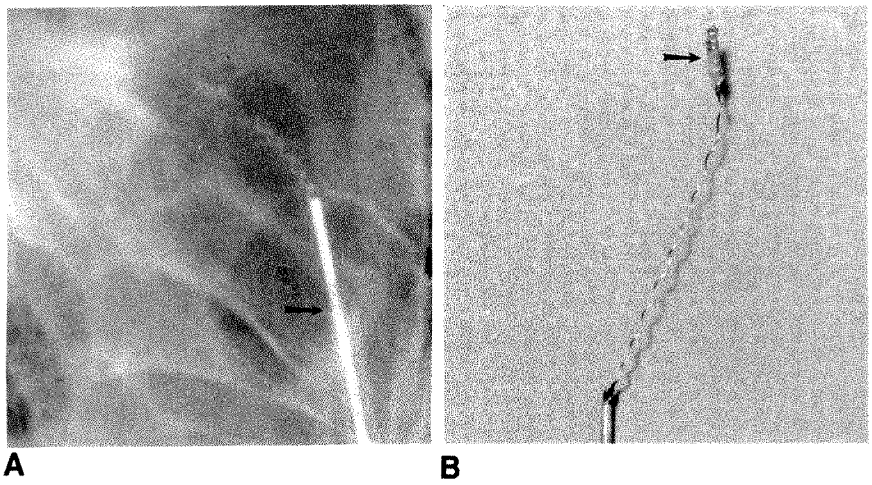

Fig. 9.—Failure to cover wire guide pusher.

A, Angiogram shows failure to cover spring wire with sheath (*arrow*) before removal. Spring wire has caught on vessel during withdrawal and become elongated.

B, Photograph shows small piece of tissue in spring wire (*arrow*) that probably was removed from vein wall during extraction.

traction, however, should be avoided. Perforation of a hookwire through the IVC wall from excessive traction on the wire guide pusher occurred during release of the filter in two patients (Fig. 7D). No clinical sequelae were observed in either case, so abdominal CT scans were not obtained to exclude retroperitoneal hemorrhage.

Release and Withdrawal of Wire Guide Pusher

After the filter has been released, the spring on the tip of the wire guide pusher may snag the hookwire or filtration wires during withdrawal into the delivery catheter. If unrecognized, the hookwire may be pulled into the iliac vein (Fig. 8). We also have observed snaring of the filtration wires in a similar fashion.

In order to avoid snagging, after the lower hookwire has been released, the sheath should be readvanced to the base of the spring tip before unscrewing. After detachment, the spring tip will then be covered by the sheath. We have found that if the spring does snag a hookwire, continued counterclockwise rotation of the wire guide pusher handle will often disengage the spring.

The sheath must be advanced carefully to cover the spring. As the sheath is readvanced it may engage the lower filter strut and could lead to displacement (Figs. 8C and 8D).

Sheath/catheter readvancement after extrusion of the filter wires or after deployment of the lower hookwire can be difficult in patients with a short infrarenal IVC. With low-lying renal veins, the filter catheter may be situated in the common iliac vein during filter deployment. Prominent ascending lumbar veins or iliac vein tortuosity may prevent advancement of the catheter to release the lower hookwire or to cover the spring tip (Fig. 8E). If the lower strut has not been deposited, the sheath may be advanced into the IVC along the filtration wires while slowly withdrawing the filter wires into the filter catheter.

The spring tip may also engage the wall of the vena cava or the iliac vein during removal if it is not completely covered by the sheath. In one patient, resistance was encountered during withdrawal of the delivery system. Fluoroscopic examination revealed that the spring tip had not been pulled into the sheath and had been elongated. A small piece of tissue that probably was removed from the vein wall was found on the spring tip (Fig. 9).

REFERENCES

1. Roehm J, Johnsrude I, Barth M, Gianturco C. The Bird's Nest inferior vena cava filter: progress report. *Radiology* **1988**;168:745–749
2. Katsamouris AA, Katsamouris A, Waltman A, Delichatsios M, Athanasoulis C. Inferior vena cava filters: in vitro comparison of clot trapping and flow dynamics. *Radiology* **1988**;166:361–366

Technical Note

Percutaneous Central Venous Catheter Placement: Use of the Blunt Needle for Subcutaneous Track Formation

E. William Akins,[1] Irvin F. Hawkins, Jr., Paul Mucciolo, James D. Overmeyer, Scott R. Kerns, and Kevin K. Murray

Percutaneous placement of central venous access catheters has recently been described [1–3]. Fluoroscopic guidance makes venous entry safe and allows proper positioning of the catheter. One step in the procedure is the creation of a subcutaneous tunnel to prevent infection [4]. A variety of surgical instruments has been used to create this tunnel, including Kelly clamps and laryngeal biopsy forceps. We report the use of a blunt needle to create a subcutaneous track for percutaneous placement of indwelling venous catheters.

Materials and Methods

The blunt needle (Cook, Bloomington, IN) consists of an 18-gauge outer cannula and inner blunt stylet [5] (Fig. 1). Needles are available in a variety of lengths (10–20 cm). After venous access is obtained, the blunt needle is inserted into the subcutaneous tissue at the expanded venotomy site. The needle is then advanced, by means of direct visual guidance and palpation, through the subcutaneous tissue toward the proposed catheter exit site. After a local anesthetic is applied, a nick is made in the skin down to the needle tip, and the blunt needle is extruded through this site. If the overlying tissue is tough at the site, the sharp stylus can be used to make the exit site for the needle.

The blunt stylus is then exchanged for a 0.035-in. (0.089-cm) guidewire, and the cannula is removed. A peel-away sheath of appropriate size is inserted through the venotomy site over the wire. The wire is removed, and the Hickman catheter is inserted through the sheath. The catheter is then pulled manually through the dilated track; care is taken to keep the Dacron cuffs well secured in the track. The distal end of the Hickman catheter is trimmed to the desired length and inserted in routine fashion via the same peel-away sheath. The skin at the puncture site is closed by two interrupted sutures; no sutures are required at the catheter entry site.

Results

The blunt needle has been used to create a subcutaneous tunnel in 22 patients requiring venous access (18 subclavian catheters and four translumbar vena cava catheters). Tracks were created successfully in all 22 cases. Local tenderness was encountered in two cases (9%), so the stylus was removed and local anesthesia was given. No complications related to the tunneling occurred. In 10 cases (45%), the needle was bent into a gentle curve to help form the track.

Subcutaneous tracks that were longer than usual were placed successfully in two patients. The first case was a 3-year-old boy who had short-bowel syndrome after repair of midgut volvulus. All conventional venous access had been exhausted. A catheter for hyperalimentation was placed into the suprarenal inferior vena cava through a translumbar route, and the catheter was tunneled to an exit site in the interscapular region of his back to prevent the patient from pulling on the catheter. The second patient was a 35-year-old woman with intestinal dysmotility syndrome who required long-term hyperalimentation and in whom no conventional venous access was possible. To provide anterior abdominal access to

---

Received August 12, 1991; accepted after revision October 7, 1991.
This work was supported in part by National Institutes of Health grant 2-T35-HLO7489.

[1] All authors: Department of Radiology, University of Florida College of Medicine, Box 100374, JHMHC, Gainesville, FL 32610-0374. Address reprint requests to I. F. Hawkins, Jr.

AJR 158:881–882, April 1992 0361–803X/92/1584–0881 © American Roentgen Ray Society

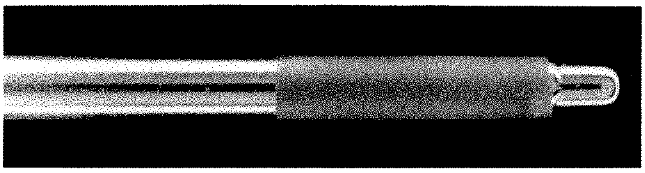

Fig. 1.—Close-up of 18-gauge blunt needle tip. Blunt stylet within cannula is highly polished. Cannula tip is roughened to improve visibility in sonographic applications.

a translumbar inferior vena caval Hickman catheter, we used a long, curved blunt needle to create a tunnel around the patient's flank to an exit site on her anterior abdominal wall.

Patients were followed up for 3 months after catheter placement. There were a variety of late catheter-related problems. In two patients (9%), infection developed at the entrance site. Subclavian vein thrombosis occurred in one case (4.5%). Three patients (14%) had sepsis that required catheter removal. These complication rates were all less than those observed in a comparable series of 23 patients with surgical catheter placement at our hospital (unpublished data). The average time between request for catheter placement and insertion was 1 day for percutaneous placement (22 patients) vs 2.4 days for surgical placement (23 patients).

Discussion

Percutaneous placement of long-term central venous catheters has several advantages over surgical placement in the operating room [1-3]. These include more accurate placement of the catheter tip under superior fluoroscopic control, increased accuracy and safety in accessing the subclavian vein, and potentially reduced cost of insertion. Regardless of the method of insertion, a subcutaneous track must be created to position the exit site of the catheter so that it can be accessed easily with minimum inconvenience to the patient. A Dacron cuff is attached to the catheter and is pulled into the subcutaneous tunnel during placement. The cuff is designed to promote tissue ingrowth to seal off the track of the catheter and create a barrier to infection.

During surgical placement of Hickman catheters, various tunneling devices are used, including laryngeal biopsy forceps [6] and Kelly clamps [7]. Standard surgical catheter sets contain a large "knitting needle" device that allows the catheter to be forcibly pulled through the track. These large devices can be cumbersome to use and cause the patient considerable pain during insertion. Errant passes create large tracks and increase the risk of hematoma.

The 18-gauge blunt needle offers several advantages over standard instruments [5]. Dilators are placed over a guidewire after the desired track has been created. With the blunt needle, the size of the skin incisions needed is reduced considerably, and only two sutures are required at the initial venous puncture site.

Trauma to the subcutaneous fascia is reduced, resulting in less discomfort for the patient. The blunt needle can be bent slightly to create a gentle curve, allowing the tunnel to follow body contours. Finally, long tracks can be created easily, which provides the option of placing catheter exit sites at the most convenient position for the patient. In uncooperative patients or in children, the catheter can be tunneled to inaccessible sites.

In conclusion, this study suggests that the blunt needle is a safe and effective means of establishing a subcutaneous track for percutaneous insertion of a central venous catheter. The technique is easy to perform and is nearly painless for the patient. The entire procedure for percutaneous placement of the Hickman catheter warrants further refinement in order to improve its safety. Modifications of the standard triple-lumen catheters and delivery systems will be needed for improved safety and long-term efficacy of percutaneously placed indwelling central catheters.

REFERENCES

1. Robertson LT, Mauro MA, Jaques PF. Radiologic placement of Hickman catheters. *Radiology* **1989**;170:1007-1009
2. Page AC, Evans RA, Kaczmarski R, Mufti GJ, Gishen P. The insertion of chronic indwelling central venous catheters (Hickman lines) in interventional radiology suites. *Clin Radiol* **1990**;42:105-109
3. Lameris JS, Post PJ, Zonderland HM, Gerritsen PG, Kappers-Klunne MC, Schutte HE. Percutaneous placement of Hickman catheters: comparison of sonographically guided and blind techniques. *AJR* **1990**;155:1097-1099
4. Flowers RH, Schwencer KJ, Kopel RF, Fisch MJ, Tucker SI, Farr BM. Efficacy of an attachable subcutaneous cuff for the prevention of intravascular catheter-related infection: a randomized, controlled trial. *JAMA* **1989**;261(6):878-883
5. Akins EW, Hawkins IF Jr, Mladinich CRJ, Siragusa RJ, Pry RJ. The blunt needle: a new percutaneous access device. *AJR* **1989**;152:181-182
6. Davis SJ, Thompson JS, Edney JA. Insertion of Hickman catheters: a comparison of cutdown and percutaneous techniques. *Am Surg* **1984**;50:673-676
7. LaBerge MT, Deppe G, Malviya VK. A simplified technique of Hickman catheter insertion at bedside in gynecological oncology patients. *Gynecol Oncol* **1987**;26:298-304

Intraarterial Papaverine for Relief of Catheter-Induced Intracranial Vasospasm

Donald A. Eckard,[1,2] Phillip D. Purdy,[1,3,4] Mark S. Girson,[1] Duke Samson,[4] Tom Kopitnik,[4] and Hunt Batjer[4]

Vasospasm of small intracranial arteries is most frequently seen in patients with subarachnoid hemorrhage associated with a ruptured aneurysm. However, vasospasm can also occur from trauma to the small intracranial vessels, commonly on an iatrogenic basis. We recently encountered a case of severe vasospasm of the distal pericallosal artery during embolization of an arteriovenous malformation (AVM). The vasospasm was relieved by the intraarterial infusion of papaverine hydrochloride.

Case Report

A 37-year-old woman was admitted because of a sudden severe headache followed by loss of consciousness. Unenhanced CT of the head showed intraventricular and subarachnoid blood. A four-vessel cerebral arteriogram showed an AVM in the left perisplenial region with arterial supply from the left posterior cerebral artery, the left pericallosal artery, the left anterior choroidal artery, and the posterior choroidal arteries bilaterally (Fig. 1A). Venous drainage was to the vein of Galen. Embolization of the left posterior cerebral artery was performed. Polyvinyl alcohol particles (Interventional Therapeutics, South San Francisco, CA) and complex helical coils (Target Therapeutics, San Jose, CA) were used. Partial superior quadrantanopia occurred, which had been predicted on the basis of testing with Amytal (amobarbital) before embolization. The left pericallosal artery was partially embolized with polyvinyl alcohol particles (355–500 μm) given through a Balt Magic Standard catheter (Balt Extrusion, Montmorency, France), which had been placed into the distal pericallosal artery adjacent to the AVM nidus. After partial embolization, the catheter became clogged. Injection through the catheter in an attempt to open it resulted in perforation approximately 2 cm proximal to the catheter tip. This created spasm in the artery with subsequent stasis of contrast material (Fig. 1B).

An attempt to withdraw the catheter resulted in severe headache and distortion of the loops in the distal pericallosal artery. Pushing on the catheter relieved the headache. A 2-in. (5-cm) nitropaste patch was applied to the patient, and attempts to remove the catheter were made over the next 15 min without success. It was decided to try to relieve the spasm by injecting papaverine through the Balt catheter. Papaverine (24 mg) was injected as two 12-mg boluses. After papaverine injection, injection of contrast material showed dilatation of the distal pericallosal artery and good distal flow. The catheter was then withdrawn intact, and the patient did not have pain during the removal. The patient's cardiac rhythm and blood pressure remained stable throughout the procedure, and the spasm resolved (Fig. 1C).

Discussion

The pathogenesis of intracranial vasospasm is unclear, and many varied treatment regimens have met with inconsistent success. Combinations of aminophylline and nitroprusside [1], isoproterenol and xylocaine [2], dopamine and nitroprusside [3], and aminophylline and isoproterenol [4] have been used with mixed results to treat posthemorrhagic intracranial vascular spasm. Papaverine hydrochloride dilates cerebral vessels and has been used as a vasodilator in cerebrovascular

---

Received August 9, 1991; accepted after revision October 1, 1991.

[1] Department of Radiology, The University of Texas Southwestern Medical Center, 5323 Harry Hines Blvd., Dallas, TX 75235-8896. Address reprint requests to P. D. Purdy.

[2] Present address: Department of Diagnostic Radiology, The University of Kansas Medical Center, 39th and Rainbow Blvd., Kansas City, KS 66103.

[3] Department of Neurology, The University of Texas Southwestern Medical Center, Dallax, TX 75235-8896.

[4] Department of Neurosurgery, The University of Texas Southwestern Medical Center, Dallas, TX 75235-8896.

AJR 158:883–884, April 1992 0361–803X/92/1584–0883 © American Roentgen Ray Society

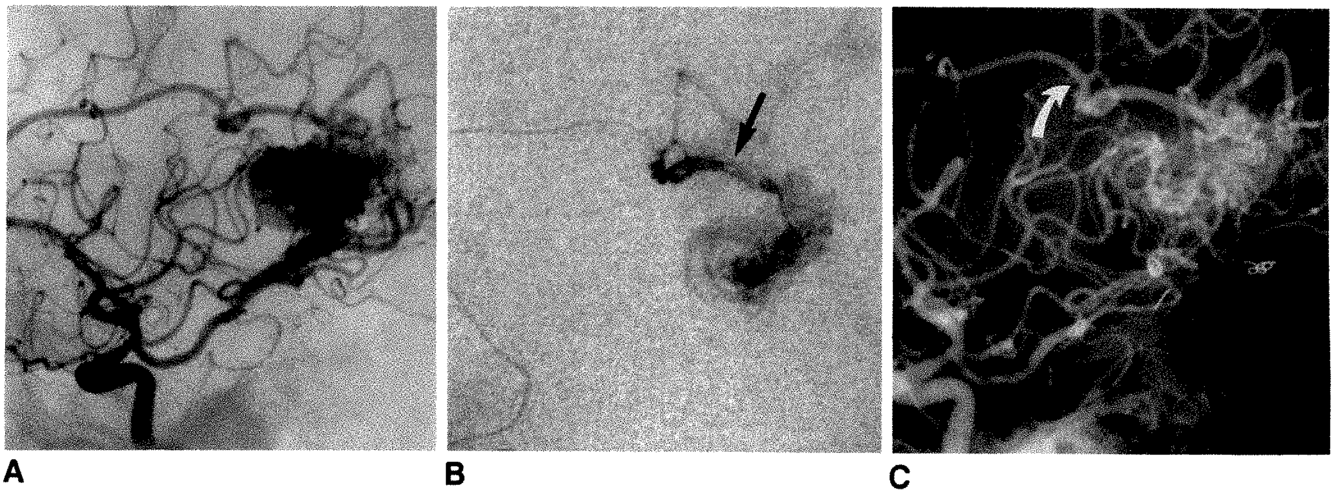

Fig. 1.—Left internal carotid artery arteriograms in 37-year-old woman who had sudden headache and loss of consciousness.
***A,* Perisplenial arteriovenous malformation with arterial supply from left pericallosal, left anterior choroidal, and left posterior cerebral arteries.**
***B,* *Balt catheter (tip indicated by arrow)* is seen in distal pericallosal artery with filling of artery through tear in catheter that developed after tip became plugged. Flow of contrast material subsequent to spasm is relatively static. Catheter could not be withdrawn.**
***C,* After embolization of other vessels, spasm of anterior cerebral artery (*arrow*) has resolved.**

disease [5]. Pool et al. [6] found that 3% topical papaverine reversed spasm induced by mechanical stimulation but was not reliable in posthemorrhagic vasospasm. Allcock [7] confirmed with angiography that intracarotid papaverine could reverse vasospasm induced by hyperventilation or intracarotid infusion of serotonin.

Papaverine is an opium alkaloid that causes relaxation of vascular smooth muscle through inhibition of phosphodiesterase and accumulation of cyclic adenosine monophosphate within the smooth muscle cell. In a canine model of vasospasm, 15 mg of intraarterial papaverine significantly reversed angiographic vasospasm, with half of the arteries returning to baseline caliber [8]. Use of animal models has been complicated by hypotension and the transitory nature of the results. An infusion of 300 mg of papaverine over 1 hr has been used without hypotensive complications and with encouraging angiographic results in both internal carotid and vertebral arteries in patients who have cerebral vasospasm after subarachnoid hemorrhage (Kopitnik TA, Kassell NF, personal communication).

In this report, infusion of papaverine provided rapid cerebral vasodilation immediately adjacent to the angiographic catheter sufficient to allow both restoration of flow and safe removal of the catheter. Restoration of flow through the distal artery is of paramount importance during catheter-related procedures. Further delay in catheter removal could have resulted in distal thrombosis or ischemic injury. Use of intraarterial papaverine in this fashion appears to be a safe and effective method of immediately reversing catheter-induced spasm, and further investigation is warranted.

REFERENCES

1. Levy WJ, Bay JW, Sawhny B, Tank T. Aminophylline plus nitroprusside and dopamine for treatment of cerebral vasospasm. *J Neurosurg* **1982**;56:646–649
2. Sundt TM, Onofrio BM, Meredith J. Treatment of cerebral vasospasm from subarachnoid hemorrhage in isoproterenol and lidocaine hydrochloride. *J Neurosurg* **1973**;38:557–560
3. Heros RC, Zervas NT, Lavyne HM, et al. Reversal of experimental cerebral vasospasm by intravenous nitroprusside therapy. *Surg Neurol* **1976**; 6:227–229
4. Flamm ES, Ransohoff J. Treatment of cerebral vasospasm by control of cyclic adenosine monophosphate. *Surg Neurol* **1976**;6:223–226
5. Russek HI, Zohman BL. Papaverine in cerebral angiospasm. *JAMA* **1948**;136:930–932
6. Pool JL, Jacobson S, Fletcher TA. Cerebral vasospasm: clinical and experimental evidence. *JAMA* **1958**;167:1599–1601
7. Allcock JM. Arterial spasm in subarachnoid hemorrhage: a clinical and experimental study. *Acta Radiol* **1966**;5:73–83
8. Kuwayama A, Zervas NT, Shintani A, Pickren KS. Papaverine hydrochloride and experimental hemorrhagic cerebral arterial spasm. *Stroke* **1972**;3: 27–33

Technical Note

Percutaneous Transaxillary Catheter Insertion for Hepatic Artery Infusion Chemotherapy

Masaharu Yoshikawa,[1] Masaaki Ebara,[1] Toshihiko Nakano,[2] Akiharu Minoyama,[1] Nobuyuki Sugiura,[1] and Masao Ohto[1]

Recently, totally implantable arterial access devices have been used for hepatic artery chemoinfusion in patients with hepatic carcinoma [1, 2]. The catheter is usually placed through direct surgical catheterization of the gastroduodenal or right hepatic artery. In this article, a new technique for percutaneous transaxillary catheterization under sonographic guidance in conjunction with placement of a totally implantable port for hepatic artery chemoinfusion is briefly described.

Subjects and Methods

Between December 1987 and March 1991, 55 patients (52 men, three women) had this catheterization procedure after informed consent for treatment of hepatic carcinoma. Fifty-one patients had hepatocellular carcinoma with underlying cirrhosis, and the remaining four had metastatic colonic cancer. The tumors were all determined by CT to be unresectable. The patients were 44–81 years old (median age, 57 years). Follow-up was obtained through May 1991; the median follow-up period was 277 days.

Technique

The infusion port and catheter are implanted under local anesthesia. After the left axillary artery is identified as a pulsating vessel just below the left clavicle and just lateral to the mid-clavicular line by sonography (3.75-MHz sector probe, Sonograph SSA-90, Toshiba, Tokyo), only the ventral wall of the artery is punctured about 2 cm lateral to the lateral border of the first rib with an 18-gauge, 15-cm-long needle (US needle, Hanako, Tokyo) whose tip is introduced into the artery (Fig. 1). The needle is replaced with a 5-French introducer catheter with the use of a 0.035-in. (0.089-cm) guidewire. A 5-French, 65-cm-long cobra catheter is inserted through the introducer into the descending thoracic aorta and advanced selectively into the hepatic artery. While the guidewire is left in the hepatic artery, the introducer and the guiding catheter are removed. A straight, heparin-coated, 6-French, 70-cm-long, end-hold catheter made of radiopaque polyurethane (Anthron P-U, type PU1470, Toray, Tokyo) is inserted into the proper hepatic artery. When bleeding around the catheter insertion site in the axillary artery is observed, the artery is manually compressed.

When the proper hepatic artery is too short to accommodate the tip of the catheter, the gastroduodenal artery is occluded at its origin with steel coils (Cook, Bloomington, IN) before common hepatic artery insertion. The same procedure is used when the right gastric artery is enlarged. These maneuvers prevent chemotherapeutic agents from flowing into nontarget vascular beds [3]. When a replaced hepatic artery is present, the vessel is occluded at its origin so that infusion of the orthotopic hepatic artery perfuses the entire liver [2].

After making a 3-cm incision parallel to the left clavicle across the puncture site, a 3- by 3-cm subcutaneous pocket is created for the implantation of the catheter and port (PORT-A-CATH, Pharmacia Deltec, St. Paul, MN) in the region of the left pectoralis major muscle. After the catheter is connected to the port, the device is sutured to the pectoral fascia with a nylon thread and then implanted into the subcutaneous pocket (Fig. 1). After the incision is closed by mattress suture with a nylon thread, prophylactic antibiotics are given for 7 days. The entire procedure is performed by radiologists while the patient is under local anesthesia. Patients were ambula-

---

Received July 22, 1991; accepted after revision October 15, 1991.

[1] First Department of Medicine, Chiba University School of Medicine, 1-8-1 Inohana Chiba-shi, Japan (280).
[2] Department of Medicine, Funabashi Central Hospital, 6-13-10 Kaijin Funabashi-shi, Chiba, Japan (273).

AJR **158:885–886, April 1992** 0361–803X/92/1584–0885 © American Roentgen Ray Society

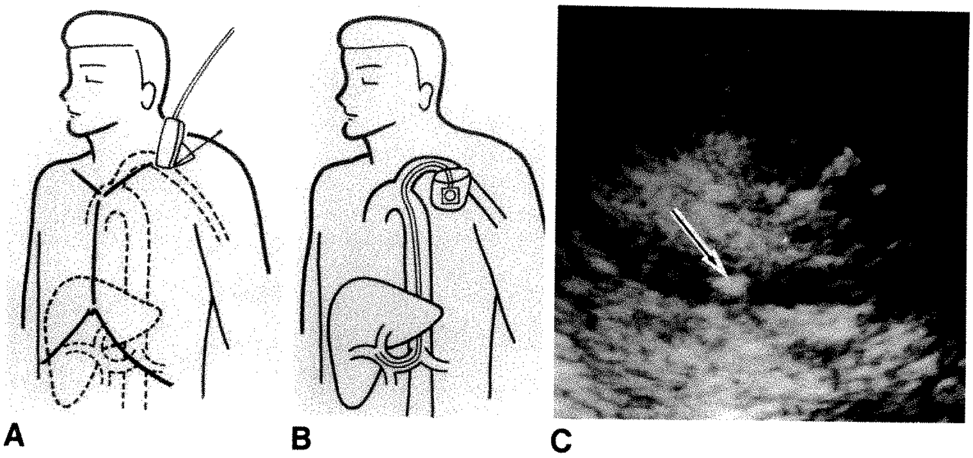

Fig. 1.—*A*, Puncture of left axillary artery under sonographic guidance.

***B*, Implantable port and catheter are in place in subcutaneous pocket in left pectoral region.**

***C*, Sonogram shows needle tip (*arrow*) being introduced into axillary artery.**

tory immediately after the procedure and were restricted from raising their left arm for 5 days. In order to prevent occlusion of the device, it is filled with 2 ml of a heparin solution (2000 units) mixed with urokinase (6000 units) every 2 or 4 weeks after percutaneous infusion of anticancer drugs; systemic antiplatelet therapy was not given during transaxillary catheterization.

Results

We successfully performed the procedure in all patients, with no procedure-related deaths. All patients were able to resume their normal activities. We placed the catheter tip in the proper hepatic artery in 48 patients, in the common hepatic artery in three, in the right hepatic artery in two, and in the left hepatic artery in two. The gastroduodenal artery was occluded by coil embolization in 20 patients, and the right gastric artery, in two patients. The occlusions were always successful. We observed no abnormal clinical symptoms related to arterial occlusion, presumably because of collateral flow from the inferior pancreaticoduodenal or left gastric arteries. We successfully occluded a replaced right hepatic artery in two patients and a replaced left hepatic artery in two patients. After occlusion, contrast medium was seen to flow to the entire liver through intrahepatic collateral arteries in these cases. The duration of catheter patency ranged from 29 to 968 days (median, 241 days).

Chest radiographs disclosed no pneumothoraces related to the arterial puncture. In two patients, large hematomas developed in the subcutaneous pocket, but resolved spontaneously within 2 weeks. No cases of distal embolization, pulse deficits of the left arm, or neurologic complications from damage to the brachial plexus during transaxillary catheterization occurred. We left the catheter and port in place until treatment was stopped in all but seven patients. The devices were successfully removed under local anesthesia because of obstruction of the hepatic artery due to injury by the catheter tip in two patients at 1 month, dislocation of the tip in two patients at 1 and 2 months, and infection in three patients at 3, 3, and 6 months after implantation. No large symptomatic hematomas developed after catheter removal, principally because of effective manual compression of the axillary artery on the first rib. A new device was reimplanted in one patient after an episode of sepsis resolved and in two patients after dislocation of the tip. No devices became obstructed and all catheters remained intact. Twenty-two patients died from hepatic failure, and three patients died from other causes. All patients had advanced cancer, mostly with underlying cirrhosis. Making the diagnosis of superimposed sclerosing cholangitis was difficult; we have no indication that this complication occurred as a result of the procedure.

Discussion

Direct surgical catheterization of the hepatic artery for chemoinfusion has usually been done to treat unresectable malignant neoplasms in the liver. The standard surgical approach to implantation of the infusion port and catheter requires laparotomy and general anesthesia [1, 2]. We successfully implanted the devices by percutaneous techniques in all cases attempted, and embolized nontarget vessels with coils as needed. We encountered procedure-related complications of hematomas, obstruction of the hepatic artery, dislocation of the tip, and infection in only a few cases. We have observed long-term patency of catheters. We believe that these favorable results are, in part, due to the use of sonography to identify the axillary artery and single-wall puncture of the artery under sonographic guidance, which greatly contributes to prevention of arterial wall damage. The use of heparin-coated catheters [4] and repeated administration of heparin solution into the port may have contributed to prevention of pericatheter thrombosis and the excellent long-term patency of the device. The advantages of the new method are the percutaneous implantation of the device under local anesthesia and the ability to embolize nontarget vessels with coils. Possible disadvantages include a slightly increased risk of catheter dislocation because the tip is not fixed, as in the direct surgical method, and the greater potential for infection.

REFERENCES

1. Buchwald H, Grage TB, Vassilopoulos PP, Rhode TD, Varco RL, Blackshear PJ. Intraarterial infusion chemotherapy for hepatic carcinoma using a totally implantable infusion pump. *Cancer* **1980**;45:866–869
2. Cho KJ, Andrews JC, Williams DM, Doenz F, Guy GE. Hepatic arterial chemotherapy: role of angiography. *Radiology* **1989**;173:783–791
3. Chuang VP, Wallace S, Stroehlein J, Yap HY, Patt YZ. Hepatic artery infusion chemotherapy: gastroduodenal complications. *AJR* **1981**; 137:347–350
4. Noishiki Y, Yamane Y, Takahashi M, et al. Prevention of thrombosis-related complications in cardiac catheterization and angiography using a heparinized catheter (Anthron^{R}). *ASAIO Trans* **1987**;10:359–365

Gadobenate Dimeglumine—a New Contrast Agent for MR Imaging:

Preliminary Evaluation in Healthy Volunteers

Thomas J. Vogl[1]
Wassili Pegios[1]
Christine McMahon[1]
Jörn Balzer[1]
Josef Waitzinger[2]
Gianpaolo Pirovano[3]
Josef Lissner[1]

Gadobenate dimeglumine (formerly known as Gd-BOPTA) is a recently developed paramagnetic contrast agent that undergoes biliary as well as renal excretion. It may, therefore, be useful in MR imaging of the liver. Its safety, tolerance, and usefulness in visualizing hepatobiliary structures were studied in eight healthy subjects. Axial abdominal images were obtained with T1-weighted spin-echo and gradient-echo sequences at 1.5 T before and after IV administration of gadobenate dimeglumine in doses of 0.005, 0.05, 0.1, and 0.2 mmol/kg body weight. Two subjects received each dose. Administration of 0.1 mmol/kg resulted in a maximum liver enhancement of 149% on the gradient-echo sequence and of 90% on the T1-weighted spin-echo sequence 60 min after injection. The contrast enhancement of the liver remained virtually constant for 2 hr. The signal-to-noise ratio of the biliary tract increased from 38 to 121 after 2 hr on gradient-echo images. In addition, there was significant contrast enhancement of the kidneys. Optimal visualization of the liver parenchyma was achieved with doses of 0.05 and 0.1 mmol gadobenate dimeglumine/kg. Mild to moderate side effects such as nausea and retching, a sense of warmth at the infusion site, and transient pruritis lasting 1 min were reported by three (38%) of the subjects.

The initial results of the first application of gadobenate dimeglumine in humans are encouraging because the contrast agent appears to be reasonably well tolerated at the doses appropriate for hepatobiliary imaging. Further clinical studies of this contrast agent are warranted to assess its effect on liver lesion conspicuity and the frequency with which side effects occur.

***AJR* 158:887–892, April 1992**

In recent years, MR imaging has been used with some degree of success for the detection and characterization of liver disease [1]. The performance of MR imaging can be improved through the use of a suitable paramagnetic contrast agent. This has generated considerable interest in finding an agent that would further extend the usefulness of MR imaging in examining the liver. To date, the largest body of clinical experience has been obtained with gadopentetate dimeglumine, a large, hydrophilic chelate that has proved extremely useful in many areas. Owing to its rapid and nonspecific redistribution from the intravascular compartment to the extracellular space and its exclusively renal elimination on IV injection, gadopentetate dimeglumine does not provide satisfactory enhancement of the liver parenchyma and biliary tract. Although it can be used for the imaging of tissue perfusion and thus has been found useful in the diagnosis of hepatic hemangiomas, in some situations, it even reduces the contrast between healthy liver tissue and tumors [2, 3]. A contrast agent that is specifically taken up by normal liver cells can be expected to yield more informative images reflecting structure and function. Gadobenate dimeglumine (formerly known as Gd-BOPTA) is a new contrast agent that is selectively taken up by hepatocytes and excreted through biliary as well as urinary routes [4, 5].

We carried out a phase 1 study of gadobenate dimeglumine in eight healthy male

Received August 5, 1991; accepted after revision November 13, 1991.

[1] Department of Radiology, University of Munich, Ziemssenstr. 1, D-8000 Munich 2, Germany. Address reprint requests to T. J. Vogl.

[2] Laboratory, Department for Pharmaceutical Research, Wegenerstr. 13, D-7910 Neu-Ulm, Germany.

[3] Research and Development Division, Bracco S.p.A., Via Egidio Folli, 50, 20134 Milan, Italy.

0361–803X/92/1584–0887
©American Roentgen Ray Society

adult volunteers in order to investigate its tolerability and efficacy in providing enhancement of the liver in MR imaging.

Subjects and Methods

Contrast Medium

Gadobenate dimeglumine (batch/lot no, R.G. 3/90; expiration date, April 1992) was supplied by Bracco S.p.A. (Milan, Italy). This compound has a stability constant (K_{ML}) of greater than 10^{-22} M^{-1}. In aqueous solution, gadobenate dimeglumine has relaxivity (r) values of $r_{T1} = 4.4$ $(mM \cdot s)^{-1}$ and $r_{T2} = 5.6$ $(mM \cdot s)^{-1}$. Its synthesis is described elsewhere [6]. The injection was formulated in a concentration of 0.25 mmol/l and had an osmolality of 0.75 Osmol/kg. The rate of injection was approximately 10 ml/min, with dose-dependent injection times ranging from 9 sec to 5 min 36 sec.

Study Design

Eight healthy male volunteers, 20–36 years old, each received a single administration of gadobenate dimeglumine in increasing doses. All eight subjects were imaged before and after administration in order to evaluate the contrast enhancement provided by the agent at each dose. Informed consent was obtained from all participants. IV gadobenate dimeglumine was administered to the eight subjects in four groups of two subjects each: group 1 received 0.005 mmol/kg body weight, group 2 received 0.05 mmol/kg body weight, group 3 received 0.1 mmol/kg body weight, and group 4 received 0.2 mmol/kg body weight. At least 1 week elapsed between administrations of the contrast material to the successive groups. Each increase in the dose was permitted only after the previous week's experiment had shown good tolerance of the substance.

The following clinical parameters were monitored before, during, and after administration of gadobenate dimeglumine: vital signs, ECG, and subjective changes in well-being (subjects were asked specifically to report discomfort at injection site, nausea, vomiting, flushing, dizziness, headache). A 12-lead ECG was performed, and blood was drawn for laboratory tests before and after injection of the contrast agent. The following laboratory tests were performed: complete blood count with differential WBC count and serum levels of electrolytes, glucose, creatinine, urea, lipids, creatine kinase, aspartate aminotransferase, alanine aminotransferase, and gamma-glutamyltransferase.

MR Imaging

MR imaging was performed with a 1.5-T superconducting unit (Magnetom 63SP, Siemens, Erlangen, Germany). For each subject, seven to nine axial abdominal sections were obtained in two acquisitions with a spin-echo pulse sequence before administration of gadobenate dimeglumine and 10, 20, 30, 40, 50, 60, and 120 min after injection. The following parameters were used for T1-weighted spin-echo sequences: 500/15 (TR/TE), 8- to 10-mm section thickness, 35- to 40-cm field of view, and matrix size of 256 × 256 pixels. Five transverse sections through the liver were obtained in suspended respiration with T1-weighted gradient-echo pulse sequences prior to and 1, 2, 3, 4, 6, 7, 8, 10, 20, 30, 40, 50, 60, and 120 min after injection. The gradient-echo imaging parameters were as follows: 120/6/80° (TR/TE/flip angle), 8- to 10-mm section thickness, 35- to 40-cm field of view, and matrix size of 128 × 256 pixels.

Signal intensities of the liver, spleen, gallbladder, renal cortex, and background with their respective standard deviations were derived from the MR images by means of the standard region-of-interest (ROI) method, under which a rectangular ROI was manually located for each image. The signal-to-noise (S/N) ratio [7, 8] and the percent enhancement of the signal intensities after Gd-BOPTA administration were calculated by using the formulas:

$$\text{S/N ratio} = (\text{SI}_{\text{tissue}} - \text{SI}_{\text{background}})/\text{SD}_{\text{background tissue}}$$

and

$$\%\ \text{Enhancement} = [(\text{SI}_{\text{enhanced}} - \text{SI}_{\text{unenhanced}})/\text{SI}_{\text{unenhanced}}] \times 100,$$

where SI = signal intensity and SD = standard deviation [9].

Results

Safety and Tolerance

Three of the eight subjects reported adverse effects of mild to moderate severity after administration of contrast material. The injection of the contrast agent and the MR imaging study were interrupted after 12 ml of a planned 16-ml dose had been administered to one of the subjects in the dose group of 0.05 mmol/kg because of nausea, retching, perspiration, and a sensation of warmth at the infusion site that lasted 11 min. The signs and symptoms resolved without specific therapy, and the examination was resumed without incident. A subject in the dose group of 0.1 mmol/kg reported mild pruritus of the head, lasting 1 min, and a feeling of emptiness in the stomach, lasting 2 min, within 5 min after the start of gadobenate dimeglumine injection. A subject in the dose group of 0.2 mmol/kg reported cramps in his right leg, lasting 2 min, occurring 2 hr 10 min after injection. No clinically relevant alterations in blood pressure, pulse, respiration rate, body temperature, or 12-lead ECG were noted during this study.

A subject in the dose group of 0.005 mmol/kg had moderate elevations in alanine aminotransferase, and a subject in the dose group of 0.2 mmol/kg showed elevations in creatine kinase, aspartate aminotransferase, and alanine aminotransferase in the blood samples drawn before gadobenate dimeglumine administration. In both cases, follow-up studies showed the serum enzyme levels to have returned to normal values. Several follow-up urine analyses from a subject who had received 0.005 mmol/kg were positive for glucose, although serum glucose levels remained within normal limits. A subject in the dose group of 0.1 mmol/kg had an elevated value of 254 mg protein in a 24-hr urine specimen collected the day after the study. The results of 24-hr urine analyses performed 3 months later in seven of the eight subjects, including the one with the previously abnormal level, were all within normal limits. Thus, the original abnormal value must be considered erroneous. Otherwise, no abnormalities were detected in laboratory studies.

MR Imaging

Liver parenchyma.—We found an appreciable increase in the relative intensities of the liver parenchyma on T1-weighted gradient-echo suspended-respiration images (Fig. 1) and on T1-weighted spin-echo images (Fig. 2).

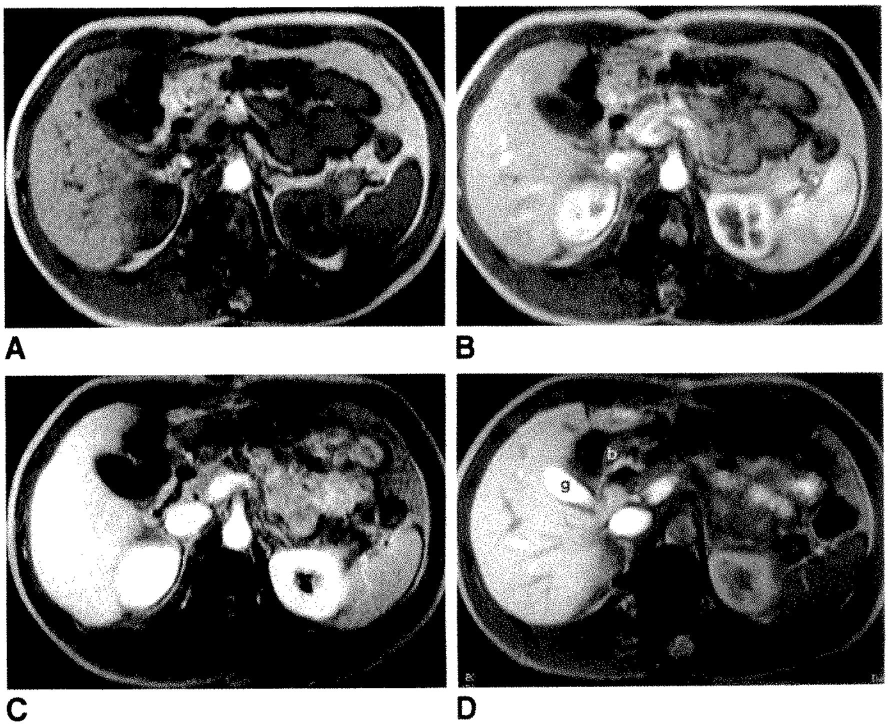

Fig. 1.—Change in signal intensity of liver on gradient-echo sequences (120/6) with administration of gadobenate dimeglumine.

***A*, Unenhanced T1-weighted MR image through abdomen at level of pancreas.**

***B*, T1-weighted MR image 1 min after injection of gadobenate dimeglumine at a dose of 0.1 mmol/kg. Liver parenchyma shows a moderate, homogeneous increase in signal intensity. Spleen and renal cortex show marked enhancement.**

***C*, T1-weighted MR image 10 min after IV administration of 0.1 mmol/kg. Signal intensity of liver parenchyma is now markedly increased. Enhancement of renal cortex persists. Signal intensity of spleen is diminishing.**

***D*, T1-weighted MR image 120 min after administration of 0.1 mmol/kg. Enhancement of liver parenchyma is still prominent. Biliary excretion causes an increase in signal intensity of gallbladder (g) and common bile duct (b). By this time, signal intensities of renal parenchyma and spleen have decreased.**

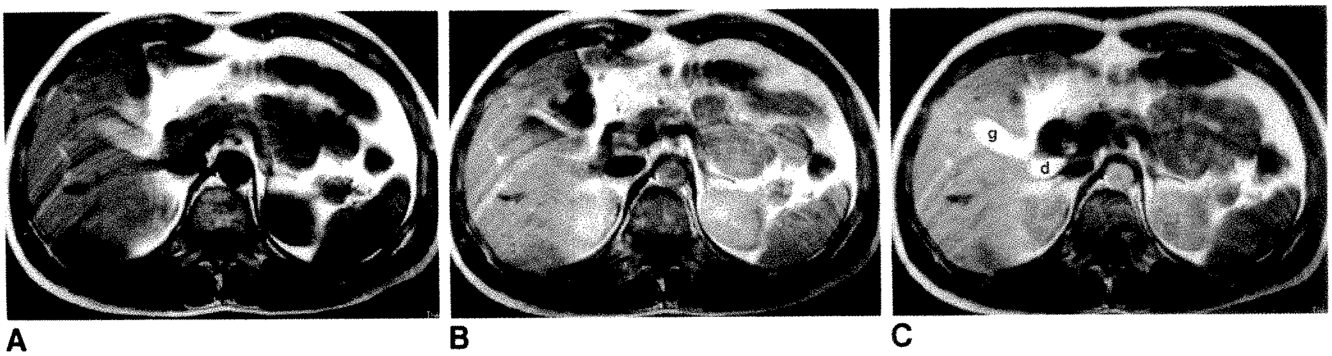

Fig. 2.—Change in signal intensity of liver on spin-echo sequences (500/15) after administration of gadobenate dimeglumine.

***A*, Unenhanced T1-weighted MR image through upper abdomen. Image quality is reduced by respiratory artifacts.**

***B*, T1-weighted MR image 20 min after IV injection of gadobenate dimeglumine 0.1 mmol/kg shows significant increase in signal intensity of liver, kidney, and spleen.**

***C*, T1-weighted MR image 2 hr after administration of 0.1 mmol/kg. Enhancement of liver parenchyma remains strong. Hepatobiliary component of elimination is documented by enhancement of gallbladder (g) and duodenum (d).**

On the gradient-echo sequence, a slight increase in the S/N ratio and weak signal intensity enhancement (24%) were observed in the first minute after gadobenate dimeglumine administration at a dose of 0.005 mmol/kg (Table 1).

At a dose of 0.05 mmol/kg, the enhancement was increased to 55% 10 min after contrast administration. The signal intensity remained constant for 2 hr after contrast injection (Table 1).

At a dose of 0.1 mmol/kg, the enhancement (65%) was comparable to that seen with the lower dose of 0.05 mmol/kg 1 min after injection (Table 1 and Fig. 1). After 10 min, the enhancement had doubled (134%), the plateau being reached after 60 min (149%). At 120 min, a slight reduction in the contrast (121%) was noted.

At a dose of 0.2 mmol/kg, a slight increase in contrast (28%), similar to that seen at the dose of 0.005 mmol/kg, was measured after the first minute (Table 1). After 60 min, the liver enhancement was similar to that obtained with the next lower dose, but the biliary elimination after 120 min was considerably higher.

On the spin-echo sequence, the smallest dose of 0.005 mmol/kg resulted in no significant changes in signal intensities on T1-weighted spin-echo images (Table 1). The most significant enhancement was seen on the T1-weighted spin-echo sequence at the doses of 0.05 and 0.1 mmol/kg. At 10 min, at a dose of 0.05 mmol/kg, the enhancement had increased to 49%, with a peak of 64% after 60 min. After 120 min, the remaining enhancement was still 49%. At a dose of 0.1 mmol/

TABLE 1: Percentage Enhancement and Signal-to-Noise (S/N) Ratios of Liver Parenchyma on T1-Weighted Gradient-Echo and T1-Weighted Spin-Echo MR Sequences Before and After IV Administration of Four Doses of Gadobenate Dimeglumine

Sequence/No. of Minutes After Enhancement	0.005 mmol/kg		0.05 mmol/kg		0.1 mmol/kg		0.2 mmol/kg	
	% Enhancement	S/N Ratio	% Enhancement	S/N Ratio	% Enhancement	S/N Ratio	% Enhancement	S/N Ratio
Gradient echo								
0	0	40	0	38	0	30	0	28
1	24	48	76	62	65	53	28	45
10	17	46	55	57	134	72	107	86
60	20	47	52	56	149	81	150	89
120	13	52	54	54	121	68	106	81
Spin echo								
0	0	25	0	29	0	20	0	17
1[a]	–	–	–	–	–	–	–	–
10	40	26	49	44	108	31	74	30
60	40	27	64	49	90	34	66	33
120	11	37	49	44	85	33	62	23

[a] Spin-echo images were not obtained 1 min after enhancement.

TABLE 2: Signal-to-Noise Ratios of Gallbladder on T1-Weighted Gradient-Echo (GRE) and T1-Weighted Spin-Echo (SE) MR Sequences Before and After IV Administration of Four Doses of Gadobenate Dimeglumine

No. of Minutes After Enhancement	0.005 mmol/kg		0.05 mmol/kg		0.1 mmol/kg		0.2 mmol/kg	
	GRE	SE	GRE	SE	GRE	SE	GRE	SE
0	46	37	29	50	38	38	23	21
1[a]	47	–	19	–	14	–	20	–
10	46	32	24	51	30	34	15	21
60	45	34	47	66	57	42	60	35
120	79	60	108	85	121	49	105	26

[a] Spin-echo images were not obtained 1 min after enhancement.

kg, the enhancement had increased to 108% at 10 min (see Fig. 2). As expected, this value is lower than that observed on the gradient-echo sequence. At the dose of 0.2 mmol/kg, both the enhancement and the S/N values were consistently lower than at the dose of 0.1 mmol/kg.

Gallbladder.—The dose of 0.005 mmol/kg provided no significant changes in the images acquired with the gradient-echo sequence. With a dose of 0.05 mmol/kg, a maximum S/N value of 108 was observed 120 min after drug administration on the gradient-echo sequence and of 85 on the T1-weighted spin-echo sequence (Table 2). With the next higher dose, 0.1 mmol/kg, a peak S/N value of 121 was recorded (Fig. 3).

Spleen.—Because the active anion of gadobenate dimeglumine is not actively taken up by reticuloendothelial tissue, the postinjection enhancement of the spleen served as a measure of the nonspecific tissue distribution of the anion owing to extracellular perfusion. The spleen showed an increase in signal intensity proportional to the dose of gadobenate dimeglumine, both on gradient-echo and spin-echo T1-weighted images (Figs. 1 and 2). Enhancement of the spleen reached its peak within 10 min after injection of contrast agent; by 2 hr, enhancement fell almost to preinjection values.

Renal parenchyma.—Enhancement of the kidneys was rapidly apparent on gradient-echo images, even at the lowest dose of 0.005 mmol/kg. Enhancement increased proportionally to the dose until a plateau was reached between 0.1 (Table 3 and Fig. 1) and 0.2 mmol/kg. The increase in enhancement was then longer lasting at the higher doses, so that with 0.2 mmol/kg a residual enhancement of 189% was present 2 hr after injection. Comparing the contrast enhancement of the left and right kidneys, only a slight variation was evident, thus serving as a control of the internal consistency of the signal intensity analysis methods used in this study (data not published here).

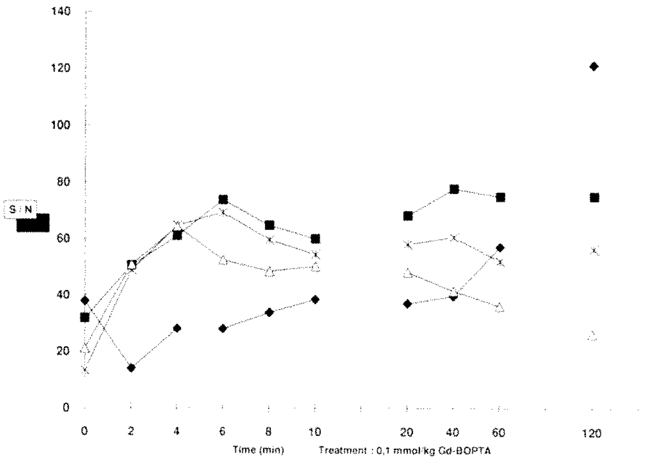

Fig. 3.—Signal-to-noise ratios (S/N) of kidney, liver, gallbladder, and spleen on gradient-echo sequences at various intervals after IV administration of 0.1 mmol of gadobenate dimeglumine per kilogram of body weight. square = liver, x = kidney, triangle = spleen, diamond = gallbladder.

TABLE 3: Percentage Enhancement and Signal-to-Noise (S/N) Ratios of Renal Parenchyma on Gradient-Echo Sequences in Suspended Respiration Before and After IV Administration of Four Doses of Gadobenate Dimeglumine

No. of Minutes After Enhancement	0.005 mmol/kg		0.05 mmol/kg		0.1 mmol/kg		0.2 mmol/kg	
	% Enhancement	S/N Ratio	% Enhancement	S/N Ratio	% Enhancement	S/N Ratio	% Enhancement	S/N Ratio
0	0	27	0	29	0	26	0	37
1	94	39	149	77	219	71	167	50
10	66	37	75	56	288	78	334	87
60	96	40	51	48	213	69	210	80
120	23	32	64	51	121	56	189	61

Discussion

Most of the paramagnetic contrast media currently under investigation exert their influence on the T1 relaxation time [10–12]. The diagnostic usefulness of gadopentetate dimeglumine in the upper abdomen is limited owing to its rapid renal excretion and virtual lack of biliary excretion; consequently, its enhancement of the liver and gallbladder is suboptimal [8, 13]. Owing to its hydrophilic properties, charge, and molecular weight, gadopentetate dimeglumine is distributed exclusively extracellularly, that is, in the intravascular and interstitial spaces. As very little gadopentetate dimeglumine is protein-bound, renal excretion by glomerular filtration is relatively fast.

Gadobenate dimeglumine differs from gadopentetate dimeglumine because of the addition of a benzyloxymethyl group, which renders the complex moleculе biliotropic. It is thought that the benzyloxymethyl moiety serves as a molecular handle that allows the recognition of the active anion of gadobenate dimeglumine by hepatic transport mechanisms at the sinusoidal membrane and access to hepatocytes, from where it is excreted unchanged into bile [4]. Pavone et al. [5] conducted a preliminary study comparing gadobenate dimeglumine and gadopentetate dimeglumine with respect to pharmacokinetics, safety, and effects on MR imaging of the liver in rats. They showed that the active anion of gadobenate dimeglumine undergoes biliary as well as renal excretion. After 6 hr, 55% of the IV load was recovered in the urine, with 39% in the bile. In contrast, 99% of an IV load of gadopentetate dimeglumine was found in the urine and 0.36% in the bile after 6 hr. The LD_{50} of gadobenate dimeglumine in mice was 5.8 mmol/kg, which compared favorably with that of gadopentetate dimeglumine (LD_{50} of 4.8 mmol/kg). However, the LD_{50} after intracerebral injection was slightly lower for gadobenate dimeglumine. On MR imaging, gadobenate dimeglumine provided strong, long-lasting enhancement of the liver [5].

Another bilitropic contrast agent, manganese(II)dipyridoxal diphosphate (Mn-DPDP), which, like the anion of gadobenate dimeglumine, accumulates selectively in functional liver parenchyma, has been shown to increase the contrast between normal liver parenchyma and diseased tissue [14, 15].

In preliminary studies of Mn-DPDP, heightened liver-lesion contrast has been reported, as well as an improved ability to detect and characterize small metastases preoperatively [16, 17].

Elizondo et al. [18] tested gadobenate dimeglumine against gadopentetate dimeglumine, Fe-HBED and Fe-EHPG for imaging metastases of hepatic adenocarcinoma in the rat and found gadobenate dimeglumine to show the greatest increase in the S/N ratio and tumor-liver contrast-to-noise ratio. Cavagna et al. [4] confirmed these results in another experiment by using a Walker carcinoma liver tumor model in rats. All authors commented on the longevity of liver enhancement by gadobenate dimeglumine.

In the current study, we found that on the whole gadobenate dimeglumine was well tolerated in a small group of human subjects with benign medical histories. Although 37% reported reactions judged as mild to moderate, these resolved without treatment and were not considered to be a threat to the subject's health. In their investigation of Mn-DPDP in 40 healthy subjects, Lim et al. [13] reported facial flushing on injection in 35, nausea in seven, vomiting in one, feelings of lightheadedness in four, heart palpitations in four, and moderate elevations in serum alanine aminotransferase in four. Further experience with gadobenate dimeglumine and Mn-DPDP involving larger numbers of subjects will be required before conclusive statements can be made about their relative safety and the frequency with which minor adverse reactions will occur.

We observed increased enhancement of the liver parenchyma after administration of gadobenate dimeglumine, both on gradient-echo and T1-weighted spin-echo images, particularly at the doses of 0.05 and 0.1 mmol/kg. At 0.2 mmol/kg, enhancement of the liver parenchyma appeared to be slightly delayed on both sequences in both subjects who received this dose. It was not until 10 min that a significant increase in liver enhancement was observed. Increasing the dose of gadobenate dimeglumine from 0.05 to 0.1 mmol/kg brought a corresponding increase in liver enhancement and in the duration of the peak enhancement attained. However, when the dose was further increased to 0.2 mmol/kg, the liver enhancement was comparable to or even lower than that of the next lower dose, 0.1 mmol/kg. This surprising reduction in liver enhancement with higher doses parallels the results of the preclinical animal trials reported by Pavone et al. [5]. In rats, they found a maximal increase in liver signal with the dose of 0.5 mmol/kg; doubling this to 1.0 mmol/kg brought about no further increase in liver signal or in residual enhancement 240 min after injection.

The dose-related effect with gadopentetate dimeglumine has also been found to be biphasic, so that the signal intensity increases proportionally to the dose at lower doses, but reaches a plateau and then decreases as the dose is further increased. This is thought to be due to the predominance of

T1 relaxation time shortening at lower doses and increasing effects of T2 relaxation time shortening at the higher doses [19]. Similarly, Lim et al. [13] reported a nonlinear increase in signal intensity with higher doses of Mn-DPDP. It is not known whether these phenomena are due to saturation of cellular uptake mechanisms or increasing T2 effects at the higher doses.

At doses of 0.05, 0.1, and 0.2 mmol/kg gadobenate dimeglumine, an increase in the contrast of the liver parenchyma was evident in all six cases for 2 hr.

In all cases, the signal intensities of the biliary tract and gallbladder were markedly increased. The signal intensities of the renal parenchyma and urinary tract increased significantly because of the component of the anion that is eliminated by the kidney. In our estimation, the doses of 0.05 and 0.1 mmol/kg, in conjunction with T1-weighted spin-echo sequences, resulted in the most anatomically informative images. Gadobenate dimeglumine enhancement made little contribution to image quality on fast T1-weighted gradient-echo sequences and no contribution on T2-weighted spin-echo sequences (data not published here).

The persistence of gadobenate dimeglumine-induced enhancement promises a long "time window" for liver imaging, sufficient for conventional MR sequences. The properties exhibited by gadobenate dimeglumine could enable it to serve a double purpose in diagnostic imaging of the liver: in the first phase after injection it can be used to characterize tissue perfusion (analogous to that obtained with gadopentetate dimeglumine); in a second phase, hepatocellular uptake and biliary excretion take place and, therefore, a new set of images can be obtained that show specific enhancement of functional liver tissue and the biliary tract (analogous to that obtained with such agents as Mn-DPDP).

The initial results of the first human application of gadobenate dimeglumine are cause for optimism. We believe that further studies are warranted to assess the effectiveness of gadobenate dimeglumine in improving liver-lesion contrast on MR images and to judge its overall performance and tolerance relative to other paramagnetic hepatotropic agents currently under investigation.

ACKNOWLEDGMENT

We thank Marianne Vorbuchner for technical assistance and help in manuscript preparation.

REFERENCES

1. Ferrucci JT. Liver tumor imaging: issues for the 1990s. In: Ferrucci JT, Stark DD, eds. *Liver imaging. Current trends and new techniques.* Boston: Andover Medical, **1990**: Ch. 1, 1–19
2. Hamm B, Fischer E, Taupitz M. Differentiation of hepatic hemangiomas from metastases by dynamic contrast-enhanced MR imaging. *J Comput Assist Tomogr* **1990**;14(2):205–216
3. Hamm B, Wolf K-J, Felix R. Conventional and rapid MR imaging of the liver with gadolinium-DTPA. *Radiology* **1987**;164:313–320
4. Cavagna F, Tirone P, Felder E, de Haën C. Hepatobiliary contrast agents for MRI. In: Ferrucci JT, Stark DD, eds. *Liver imaging. Current trends and new techniques.* Boston: Andover Medical, **1990**:384–393
5. Pavone P, Patrizio G, Buoni C, et al. Comparison of Gd-BOPTA with Gd-DTPA in MR imaging of rat liver. *Radiology* **1990**;176:61–64
6. Felder E, Uggeri F, Fumagalli L, Vittadini G. Paramagnetic chelates useful for NMR imaging. U.S. Patent No. 4,916,246 (CO7F13/00;556/1), April 10, 1990, IT 19236A/86, January 30, **1986**
7. Edelstein WA, Bottomley PA, Hart HR, Smith LS. Signal, noise, and contrast in nuclear magnetic resonance (NMR) imaging. *J Comput Assist Tomogr* **1983**;7:391–401
8. Hendrick RE, Kneeland JB, Stark DD. Maximizing signal-to-noise and contrast-to-noise ratios in FLASH imaging. *J Magn Reson* **1987**;5: 117–127
9. Raval B, Mehta S, Narayana P, Kulkarni M. Feasibility of fast MR imaging of the liver at 1.5 T. *Magn Reson Imaging* **1989**;7:203–210
10. Engelstad BL, Wolf GL. Contrast agents. In: Stark DD, Bradley WG Jr, eds. *Magnetic resonance imaging.* St. Louis: Mosby, **1988**:161–200
11. Bousquet JC, Saini S, Stark DD, et al. Gd-DOTA: characterization of a new paramagnetic complex. *Radiology* **1988**;166:693–698
12. Weinmann HJ, Brasch RC, Press WR. Characteristics of Gd-DTPA complex: a potential MR contrast agent. *AJR* **1984**;142:619–624
13. Lim KO, Stark DD, Leese PT, Pfefferbaum A, Rocklage SM, Quay SC. Hepatobiliary MR imaging: first human experience with MnDPDP. *Radiology* **1991**;178:79–82
14. Tsang YM, Chen M, Elizondo G, et al. Hepatobiliary contrast agent for hepatic MR: tissue specific biodistribution of Mn-S095 (abstr). *Magn Reson Imaging* **1988**;6:439
15. Vittadini G, Felder E, Tirone P, Lorusso V. B19036, a potential new hepatobiliary contrast agent for MR proton imaging. *Invest Radiol* **1988**;23:23[suppl 1]:246–248
16. Vogl TJ, Hamm B, Schnell B, Eibl-Eibesfeld B, Steiner S, Lissner J. Clinical efficacy of Mn-DPDP: new paramagnetic contrast agent for MRI of the liver. *Fortschr Röntgenstr* **1991**; 155:568–574
17. Lauffer RP, Vincent AC, Padmanadhaus. Hepatobiliary MR contrast agents: 5 substituted iron EHPG derivates. *Magn Reson Med* **1987**;4: 582–590
18. Elizondo G, Fretz C, Stark DD et al. Gd-BOPTA: preclinical efficacy evaluation as a hepatobiliary contrast agent for MR imaging (abstr). *Radiology* **1989**;173(P)[suppl]:253
19. Saini S, Hamm B. Contrast agents for MR imaging. In: Edelmann RR, Hesselink JR, eds. *MRI. Clinical magnetic resonance imaging.* Philadelphia: Saunders, **1990**: Ch. 7, 242

Clinicians' Access to Diagnostic Imaging Information at an Academic Center: Perceived Impact on Patient Management

David Gur[1]
William H. Straub
Rhett H. Lieberman
Rose C. Gennari

We studied the efficiency with which clinicians were able to obtain the results of radiologic studies during visits to the radiology department in an effort to determine how often delays occurred and, if so, how they were perceived to have influenced patient care. We monitored 322 physician's visits to four locations within the radiology department in search of imaging information or consultative services. The average duration of these visits was 6.2 min (range, 38 sec–55 min). Two hundred forty-three visits (75%) were completed successfully, and 10 additional visits were for consultation purposes only. In 43% of the 69 unsuccessful visits, physicians indicated that lack of access to imaging information would definitely (38%) or possibly (6%) result in delays in diagnosis and/or therapy. In 17% of the unsuccessful visits, physicians indicated that the inability to access imaging information would definitely (13%) or possibly (4%) extend the patient's length of stay in the hospital.

Our study suggests that better access to imaging information may prevent delays in patient management decisions, thereby substantially reducing costs and potentially improving patient care.

***AJR* 158:893–896, April 1992**

The complexity inherent in storing, retrieving, and reporting diagnostic information in the form of reports or images has increased significantly in larger hospitals and medical-care systems in recent years. Delayed access to imaging information has been described as resulting in an indirect or "hidden" cost, the magnitude of which has been subjectively estimated by a survey of referring physicians [1]. Although high indirect or hidden cost was suspected in that study, no actual data are available regarding clinicians' success (or efficiency) in obtaining required imaging information upon demand. In an attempt to better define clinicians' experiences while trying to access imaging information, we followed the medical staff served by the radiology department at our hospital during their visits to the department.

Methods

The study was performed in the Department of Diagnostic Radiology in our 550-bed university hospital, in which approximately 160,000 procedures are performed annually and in which a radiology information system, including a film-tracking module, has been in use during the past 4 years. During a period of 3 months, a trained staff member was stationed in several key locations within the department where referring physicians typically come to review films of their patients and to seek radiologic consultations. These locations included our main file room, general reading room, and abdominal and neurologic CT reading rooms. All locations were staffed according to predetermined schedules during the day (8:00 A.M.–5:00 P.M.) and at night (6:00 P.M.–2:00 A.M.). All nonscheduled visits during these periods were followed, timed, and monitored.

During each visit, the staff member recorded the following information about each visitor: (1) department and position of the visitor; (2) amount of time he or she spent in either the main file room or in one of the various reading rooms; (3) whether the needed patient file was

Received September 9, 1991; accepted after revision November 13, 1991.

This work was supported in part by grant no. P01 CA43684 from the National Institutes of Health.

[1] All authors: Department of Diagnostic Radiology, RC 509 Scaife Hall, University of Pittsburgh, 3550 Terrace St., Pittsburgh, PA 15261-0001. Address reprint requests to D. Gur.

0361-803X/92/1584-0893
©American Roentgen Ray Society

TABLE 1: Duration of On- and Off-Hours Visits at Different Sites

	On-Hours		Off-Hours	
	Number of Visits	Average Time (min)	Number of Visits	Average Time (min)
Main file room	80	6.9	48	6.4
Neurologic CT reading room	41	6.2	34	6.0
Abdominal CT reading room	52	6.0	18	5.3
General reading room	43	5.7	6	6.0
Total	216	6.3[a]	106	6.1[a]

[a] Weighted average.

available; (4) whether consultation was required, and, if so, whether it was available; and (5) when films were not available, whether the clinician believed that lack of timely access would result in a delay of diagnosis and/or therapy, and whether the patient's length of stay in the hospital would increase as a result of the unavailability of the films. The staff member also recorded any physician comments related to the service provided. When visits were made to the main file room, clinicians were asked to subjectively rate the overall quality of the service provided on a scale of 1 to 5, with 1 being unacceptable and 5 being excellent.

Physician's visits to the various locations (e.g., main file room, different reading rooms) were monitored according to a predetermined schedule, resulting in a different number of visits analyzed at each location. However, we required that a minimum of 40 nonscheduled visits be evaluated at each location. It should be noted that access to dictated reports or to summary information provided by our dictation system was not evaluated in this study. Visits were all initiated by clinicians who, for a variety of reasons, decided that they wished to see patients' images, review the notations (summary impressions) on patients' jackets, or consult with a radiologist.

Results

The total number of physician's visits included in the study, according to time of day (day or night) and location visited, is provided in Table 1. Of the 322 visits measured, 61 respondents (19%) were faculty members and 261 respondents (81%) were residents. Clinician's visits in this study were from the departments of medicine (38%), surgery (27%), neurosurgery (15%), neurology (7%), emergency medicine (5%), and various others (8%). Tables 2 and 3 summarize the outcomes of visits to the different sites.

Of 128 visits to the main file room, 91 (71%) were successfully completed; i.e., the needed patient film/folder was obtained. Duration of the average visit was 6.7 min (range, 38 sec–55 min). During 19 visits (15%), the physician had to search in multiple locations (e.g., he or she was told that the folder was in one of the reading rooms). In 11 visits, key films were missing in available folders; all 11 were considered "unsuccessful" visits. Consultation with a radiologist was sought in 15 instances (16%) and was readily available in 11 of these cases (73%). In addition, two physicians noted during their visits that consultation with a radiologist would have been desirable although not necessary at the time of their specific visits. In 10 instances, the most recent films were not available in the folder several hours after an X-ray procedure was performed (>2 hr). In 17 (46%) of 37 unsuccessful visits, referring physicians indicated that the inability to review the images would definitely delay patient diagnosis and/or therapy, and one stated that there could possibly be a delay in diagnosis and/or therapy. On six occasions (16%), clinicians indicated that lack of access to images would definitely result in an extended length of hospital stay for the patient, and in two other unsuccessful visits clinicians indicated there could possibly be an extension in the patient's length of stay.

The average, subjective rating of the quality of service provided at the main file room on a scale of 1 to 5 was 4.1. When grouped according to the outcome of the visit just completed, average ratings were 4.2 for successful and 3.8 for unsuccessful visits. The comments recorded included both strong praise and criticism. Most clinicians who could not obtain the needed film/folder noted that the file room personnel were very helpful and complied with their requests, but that in such a large medical center, films/folders could be in a number of various locations within the institution. A few physicians indicated that they had been staff members at other (private) hospitals and that our retrieval system was the worst they had experienced, owing to its complexity. The most common criticism of the service, however, was the amount of time needed to make recent studies available for review by referring physicians. Comments of this type may or may not be typical of many other large medical centers.

In 75 visits to the neurologic CT reading room, the average visit time was 6.1 min (range, 1–26 min). When films were successfully located (63/72, 88%), consultation with a radiologist was sought in 39 instances (62%) and was readily available in 35 (90%). On three occasions, referring physicians came to the reading room with the complete film jacket, seeking consultation only. Films could not be located in 9/72 visits (13%) (5 day/4 night). Four physicians indicated that the inability to locate needed films would result in a delay of diagnosis and/or therapy, and two indicated that it would increase length of hospital stay for the patient. One physician indicated that lack of access to films could delay diagnosis and/or therapy and could possibly increase length of stay, but was not certain at the time. In one instance, the needed films had not been sent from the emergency department, and in another instance, the entire film jacket was missing.

In 70 visits to the abdominal CT reading room, the average visit time was 5.8 min (range, 46 sec–21.6 min). Three referring physicians brought the entire jacket with them to seek consultation only. When films were successfully located in this reading room (57/67, 85%), consultation with a radiologist

TABLE 2: Outcomes of Visits to Different Sites

	File Room	Reading Rooms			Total
		Neurologic CT	Abdominal CT	General	
Successful visits[a]	91	63	57	32	243
Unsuccessful visits	37	9	10	13	69
Consultation only	0	3	3	4	10
Total visits	128	75	70	49	322
Consultations received/sought	11/15	35/39	43/44	24/26	113/124

[a] For the purpose of this study, a successful visit was one in which the clinician was able to obtain access to the needed images and/or image information.

TABLE 3: Stated Impact of Lack of Access to Image Information on Patient Diagnosis, Treatment, Length of Stay in Hospital

	File Room	Reading Rooms			Total
		Neurologic CT	Abdominal CT	General	
Definite delay in diagnosis/treatment	17	4	4	1	26
Possible delay in diagnosis/treatment	1	1	0	2	4
As percent of all visits	14%	7%	6%	7%	10%
As percent of unsuccessful visits	49%	56%	40%	23%	43%
Definite increase in LOS	6	2	1	0	9
Possible increase in LOS	2	1	0	0	3
As percent of all visits	6%	4%	2%	0%	4%
As percent of unsuccessful visits	22%	33%	10%	0%	17%

Note.—LOS = length of stay in hospital.

was sought in 44 instances (77%) and was readily available in 43 (98%). Of the 10/67 (15%) unsuccessful (6 day/4 night) visits, four physicians indicated that there would be a delay in diagnosis and/or therapy, and one indicated that there would be an increase in length of hospital stay.

In 49 visits to the general reading room, the average visit time was 5.5 min (range, 1–16 min). Four referring physicians brought the entire film jacket with them to seek consultation only, and one of those individuals wanted a particular radiologist to assist him; however, that radiologist was unavailable at the time. When films were successfully located in this reading room (32/45, 71%), radiologist consultation was sought in 26 instances (81%) and was readily available in 24 (92%). Of the 13 unsuccessful visits (29%), all of which occurred during the daytime, one physician indicated that lack of access would definitely result in a delay of diagnosis and/or therapy, while two others claimed that there could possibly be a delay. None indicated that the unsuccessful visit would result in extending the patient's length of stay in the hospital.

Discussion

Any subjective estimate of the cost of delayed access to diagnostic imaging information has inherent limitations because of potential biases. That is, in the hope of pressuring the system to improve, respondents to such surveys may overestimate the potential impact of delayed access on patient care [1]. No data are currently available on physicians' experiences while visiting the radiology department, and only preliminary data have been published concerning the time spent by file room personnel in search of ICU films [2]. Actual data are sorely needed in this area for different health care delivery systems.

While the frequency of delayed access to imaging information and the duration of a physician's visit were measured in our study, the nature of the study did not allow for actual verification of each statement concerning delay of diagnosis and/or treatment or extended length of hospital stay. This may have biased the results somewhat. We are currently conducting a separate study to assess this point through the reconstruction of patients' hospital stays from medical records.

Our time measurement included the complete length of the visit, including search, review, and/or consultation when sought and available. Typically, however, in nonscheduled visits, review and consultation times constitute a small fraction of the total visit time (≤25%). This is particularly true in the general radiology reading room and in the main file room, and it was almost always true for visits lasting more than 10 min. Unexpectedly, we found that only in 46 instances (14%) did physicians search for several patients' folders during a single visit.

The subjective rating regarding quality of our file room service must be viewed on a relative scale based on visitors' expectations from and knowledge of the institution's system. Since no norm is available in this regard, one should not compare such assessments across different institutions. The relatively high ratings, compared with the measured success rate, indicate that either our system has been improving or physicians have relatively low expectations from systems such as ours.

In spite of rapidly increasing interest in actual measurements of efficiency, effectiveness, and, ultimately, efficacy of radiology services, hardly any data are available on access to imaging information by referring physicians. Subjective assessments by radiology service users clearly indicate that in a complex medical system, there is a significant hidden cost due to delayed access to imaging information [1]. The results of our measurements are in agreement with previous observations in this regard. Physicians in our study were of the opinion that 43% of the unsuccessful visits could lead to a delay in diagnosis and/or therapy. They thought that 17% of those unsuccessful visits could lead to an extended length of stay. Increasing access to imaging information, through either conventional or electronic means, may prevent costly delays in patient-management decisions and potentially result in measurable improvements in patient care. Our findings suggest that further studies should be carried out to investigate the actual changes in costs and/or outcomes that do occur after such visits.

ACKNOWLEDGMENT

We thank Barbara C. Good for editing the manuscript.

REFERENCES

1. Straub WH, Gur D. The hidden costs of delayed access to diagnostic imaging information: impact on PACS implementation. *AJR* **1990**;155:613–616
2. Goodman LR, Pehringer J, Jacobson DR, Quebbeman E, Foley WD. ICU digital image archive and viewing. *Appl Radiol* **1991**;20:24–28

New Format for Abstracts

Beginning in Fall 1992, the *AJR* will publish abstracts of articles in a different format, much like the ones recently adopted by the *New England Journal of Medicine* and the *Journal of the American Medical Association*. The purpose of the new design is to have abstracts present the essential elements of articles more clearly and concisely. The contents, organization, and length of the abstracts will be the same as before; however, rather than being all one paragraph except for the conclusion, abstracts will now be divided into four paragraphs, each with a title: objective, subjects (or materials) and methods, results, and conclusion.

The *AJR* Guidelines for Authors, which appears at the front of every issue of the Journal, has been revised to help you write abstracts in this new format. Please familiarize yourself with these guidelines and incorporate them into all manuscripts submitted for publication.

Robert N. Berk
Editor-in-Chief

ARRS Case of the Day

The Case of the Day has always been a highlight of the American Roentgen Ray Society meeting. When Dr. A. Everette James, Jr., asked me to be responsible for this part of the meeting, I was concerned that I would not be able to achieve the high standards set by Dr. Jack O'Connor and his colleagues at Boston University School of Medicine, and before that by Dr. Margaret A. Stull and her colleagues from Georgetown University School of Medicine.

These cases have been prepared by the faculty and residents of the Department of Radiology and Radiological Sciences at Vanderbilt University Medical School. There are four cases in each of six categories, one case for each day of the American Roentgen Ray Society meeting.

If you plan to attend the meeting, submit your diagnoses at the exhibit. Winners will be acknowledged at the meeting. For those of you who will not be attending the ARRS meeting in Orlando, the answers and discussions will be presented in the June issue of the *AJR*.

Richard M. Heller
Department of Radiology
Vanderbilt University Medical Center
Nashville, TN 37232

Chest Case of the Day

John A. Worrell,[1] Dennis M. O'Donnell,[1] Frank E. Carroll,[1] Joseph P. Bruner,[2] and Jack A. Coleman, Jr.[3]

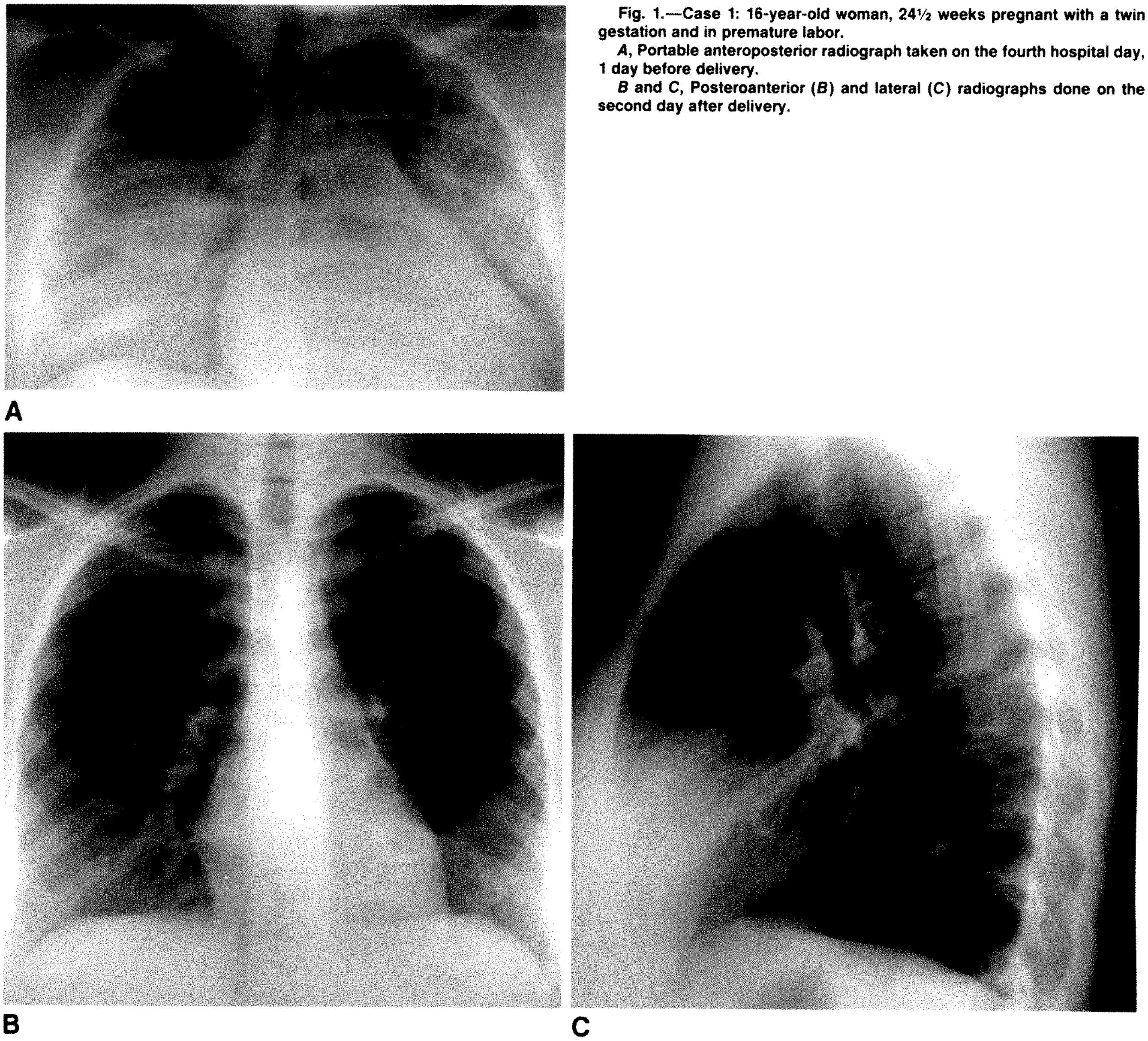

Fig. 1.—Case 1: 16-year-old woman, 24½ weeks pregnant with a twin gestation and in premature labor.

***A*, Portable anteroposterior radiograph taken on the fourth hospital day, 1 day before delivery.**

***B* and *C*, Posteroanterior (*B*) and lateral (*C*) radiographs done on the second day after delivery.**

---

[1] Department of Radiology, Vanderbilt University Medical Center, 1161 21st Ave. South, Nashville, TN 37232-2675. Address reprint requests to J. A. Worrell.
[2] Department of Obstetrics and Gynecology, Vanderbilt University Medical Center, Nashville, TN 37232-2521.
[3] Department of Otolaryngology, Vanderbilt University Medical Center, Nashville, TN 37232-2559.

Case 1 was prepared by J. A. Worrell, J. P. Bruner, D. M. O'Donnell, and F. E. Carroll; case 2 was prepared by J. A. Worrell, F. E. Carroll, and D. M. O'Donnell; case 3 was prepared by J. A. Worrell, D. M. O'Donnell, F. E. Carroll, and J. A. Coleman, Jr.; case 4 was prepared by D. M. O'Donnell, J. A. Worrell, and F. E. Carroll.

***AJR* 158:898–901, April 1992** 0361–803X/92/1584–0898 © American Roentgen Ray Society

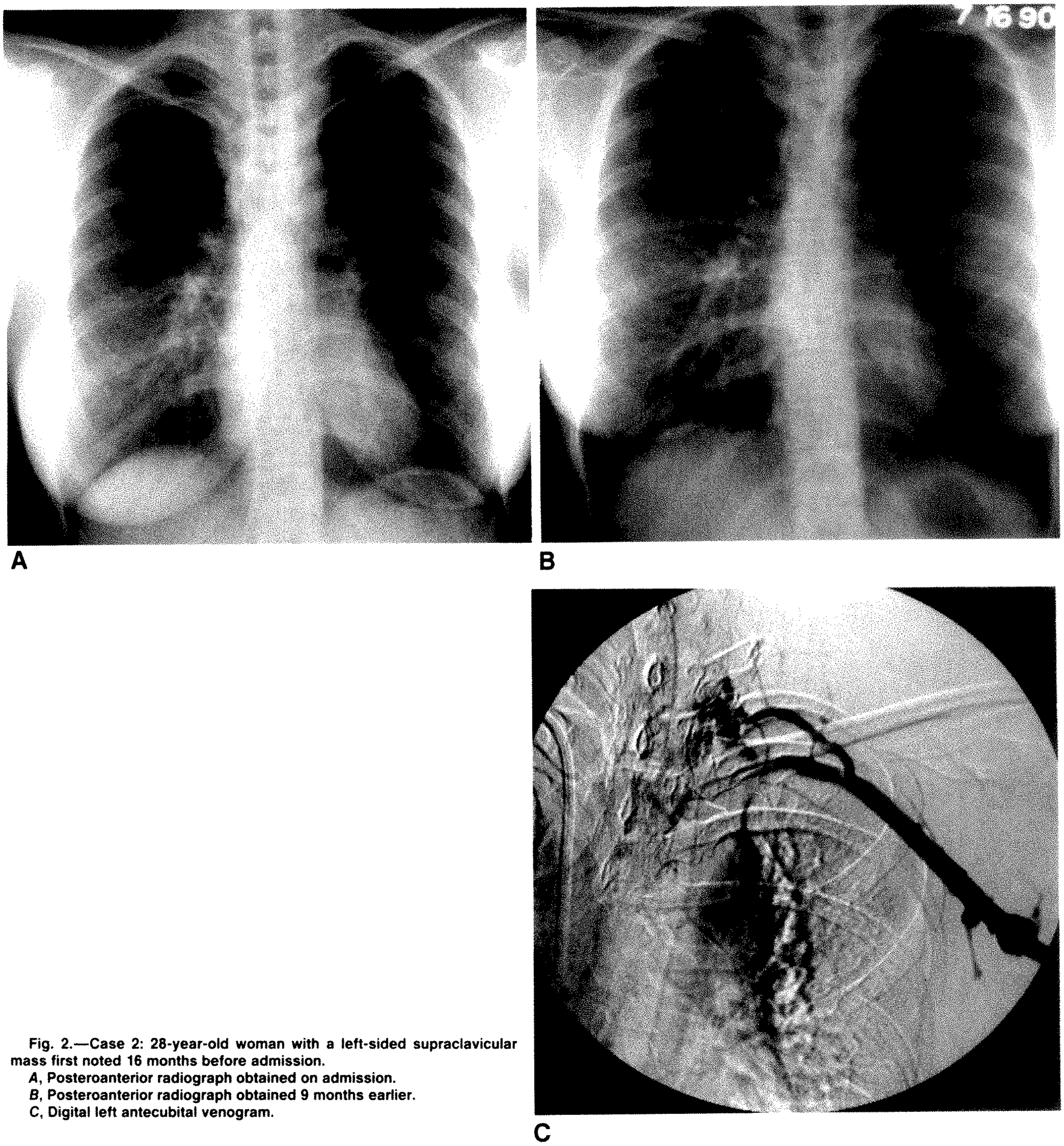

Fig. 2.—Case 2: 28-year-old woman with a left-sided supraclavicular mass first noted 16 months before admission.
A, Posteroanterior radiograph obtained on admission.
B, Posteroanterior radiograph obtained 9 months earlier.
C, Digital left antecubital venogram.

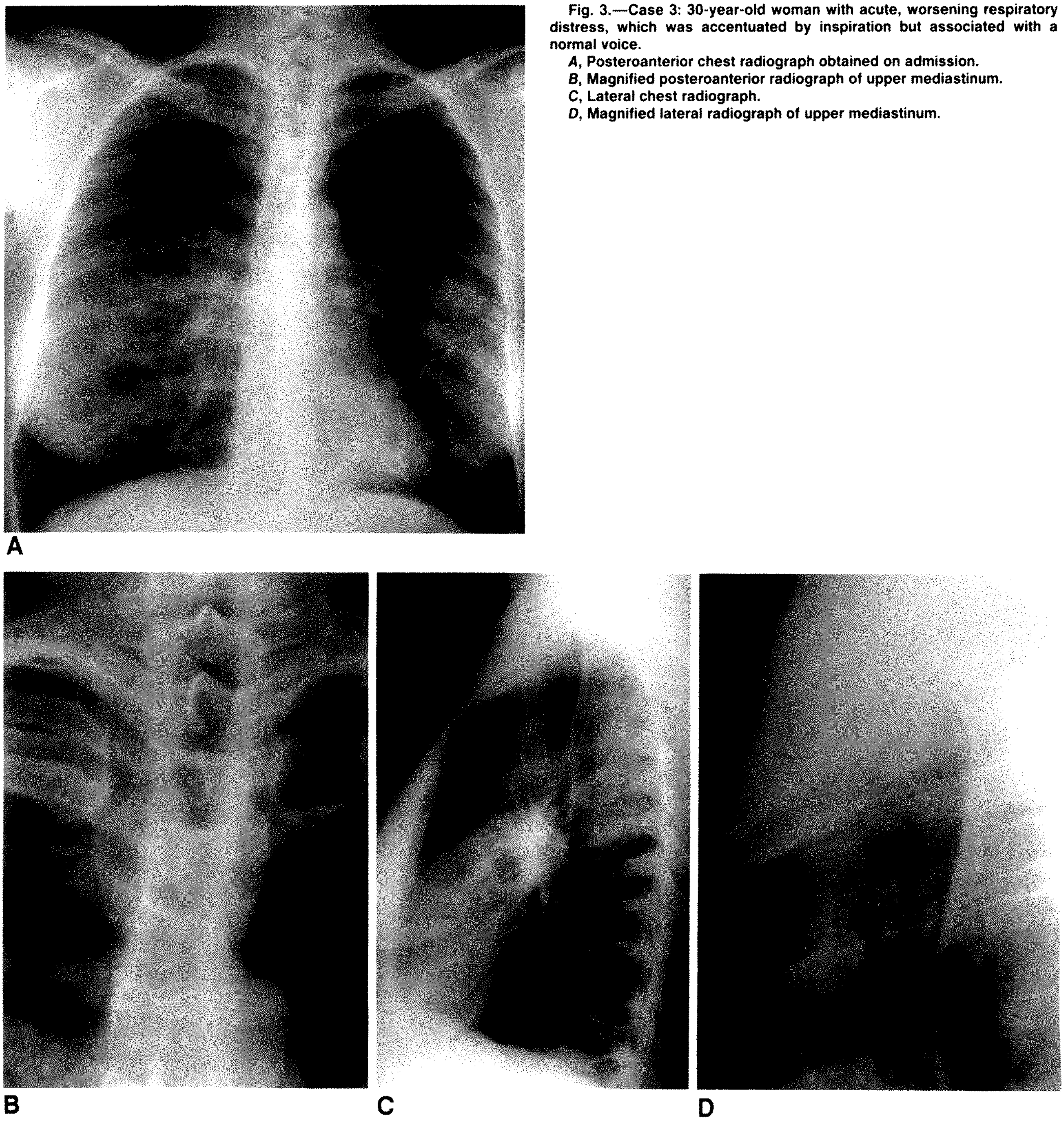

Fig. 3.—Case 3: 30-year-old woman with acute, worsening respiratory distress, which was accentuated by inspiration but associated with a normal voice.

A, Posteroanterior chest radiograph obtained on admission.

B, Magnified posteroanterior radiograph of upper mediastinum.

C, Lateral chest radiograph.

D, Magnified lateral radiograph of upper mediastinum.

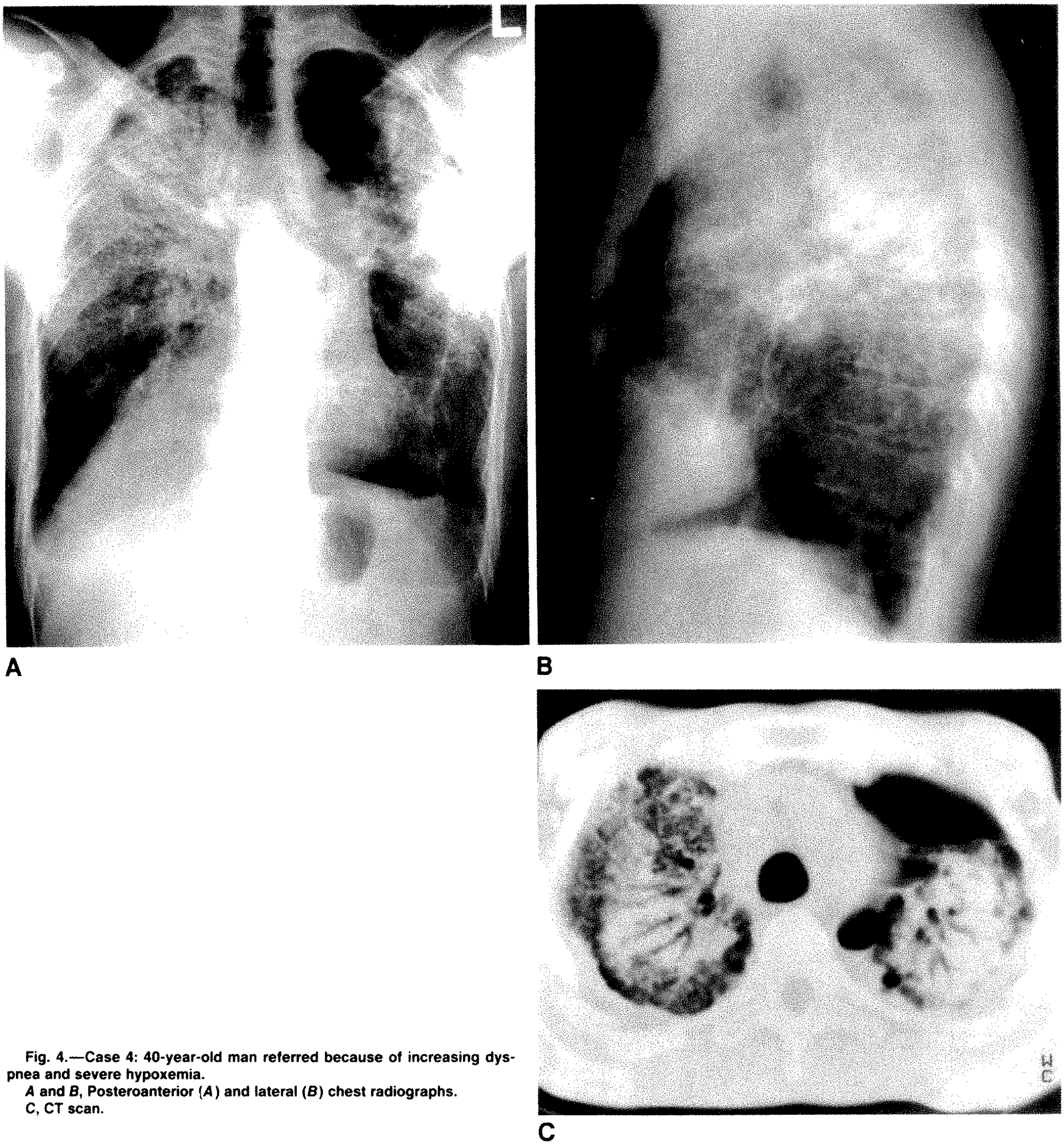

Fig. 4.—Case 4: 40-year-old man referred because of increasing dyspnea and severe hypoxemia.

A **and** ***B*****, Posteroanterior (*****A*****) and lateral (*****B*****) chest radiographs.**

C**, CT scan.**

Abdominal Case of the Day

Max I. Shaff,[1] Thomas A. Powers, Lewis B. Gilpin, and Michael E. Faulstich

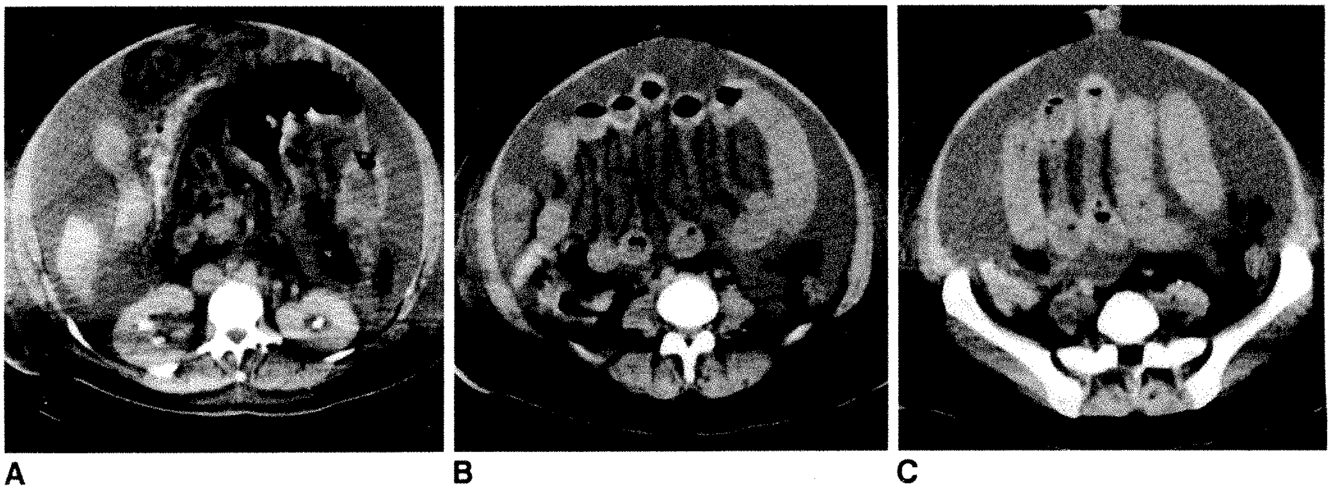

Fig. 1.—Case 1: 34-year-old woman with severe nausea, vomiting, and back pain.
***A*, Axial CT scan of midabdomen.**
***B*, Axial CT scan of abdomen just superior to iliac crests.**
***C*, Axial CT scan of lower abdomen at mid-iliac level.**

---

[1] All authors: Department of Radiology, Vanderbilt University Medical Center, 1161 21st Ave. South, Nashville, TN 37232-2675. Address reprint requests to M. I. Shaff.

Case 1 was prepared by M. E. Faulstich and M. I. Shaff; cases 2 and 3 were prepared by L. B. Gilpin and M. I. Shaff; case 4 was prepared by T. A. Powers.

AJR **158:902-904, April 1992** 0361-803X/92/1584-0902 © American Roentgen Ray Society

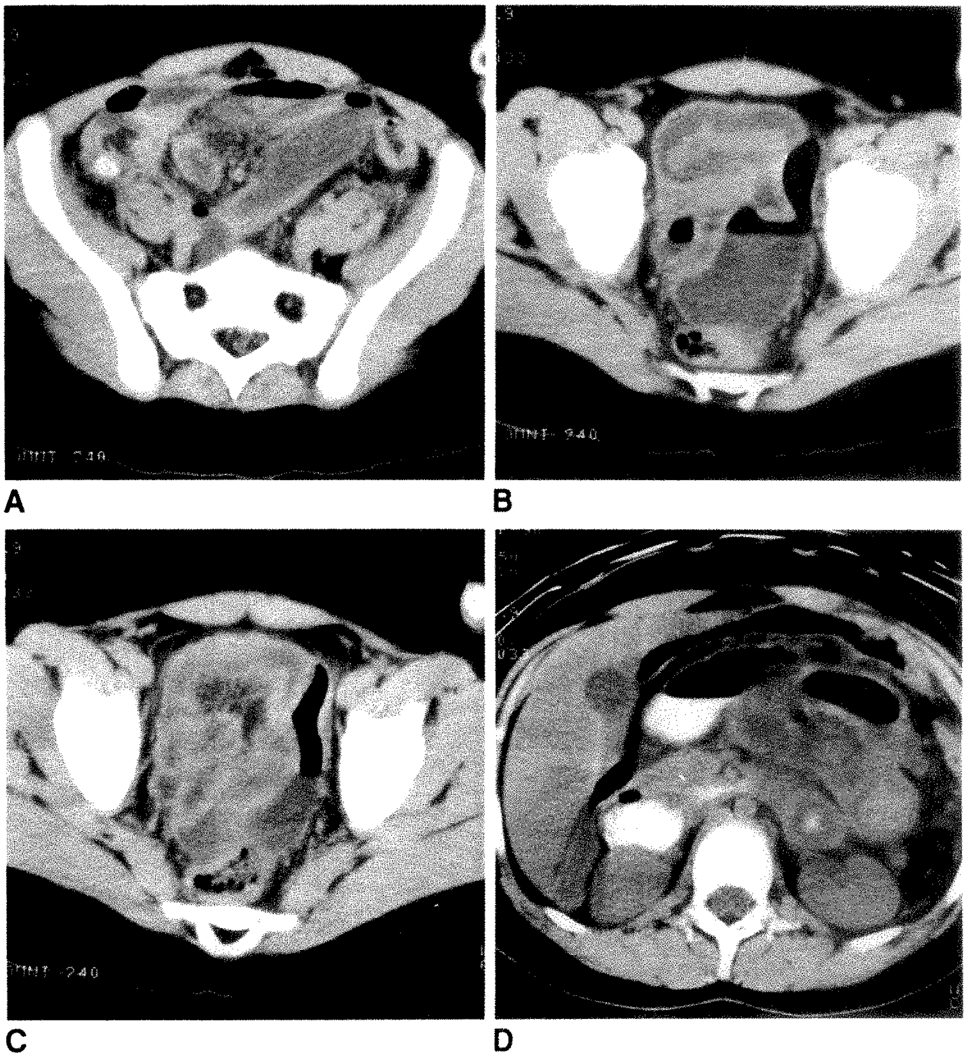

Fig. 2.—Case 2: 10-year-old boy with 2-week history of nausea, vomiting, diarrhea, and mild diffuse abdominal pain and recent onset of fever and progressive obtusion.

A, Axial CT scan through lower abdomen.

B and *C*, Axial CT scans through pelvis.

D, Axial CT scan through middle abdomen.

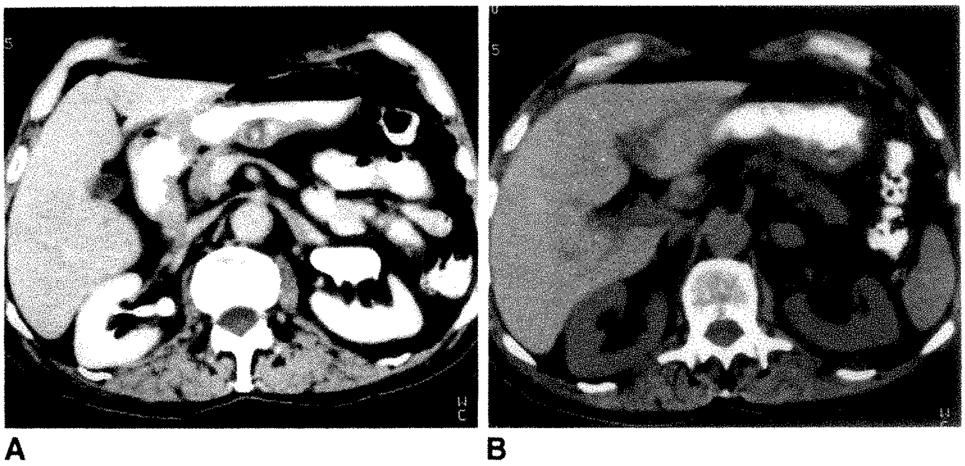

Fig. 3.—Case 3: 72-year-old man with 2-month history of weight loss and recent onset of nausea and vomiting.

A and *B*, Axial CT scans of middle abdomen.

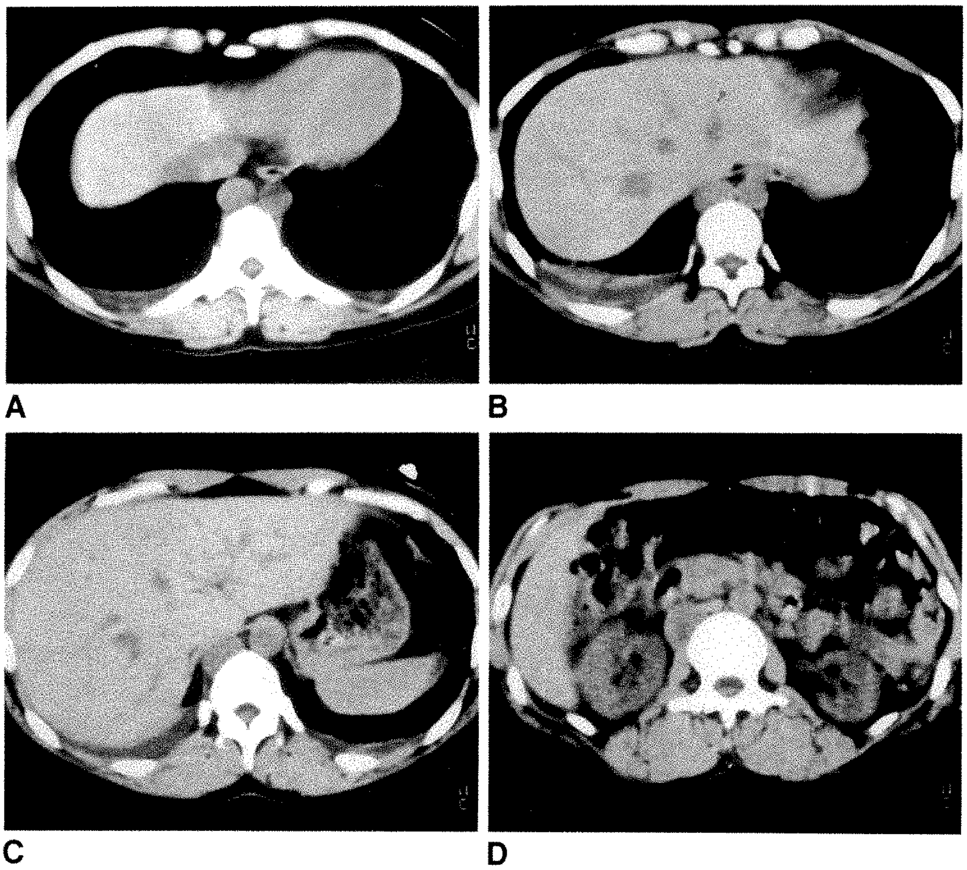

Fig. 4.—Case 4: 26-year-old woman with thrombotic thrombocytopenic purpura and right-sided paratracheal mass on a chest radiograph. CT of chest and abdomen was performed to search for presumed lymphadenopathy.

A–D, Selected CT scans of abdomen beginning at dome of liver and moving caudally to inferior edge of liver.

Skeletal Case of the Day

Stefan Tigges,[1] Roy E. Erb, and E. Paul Nance

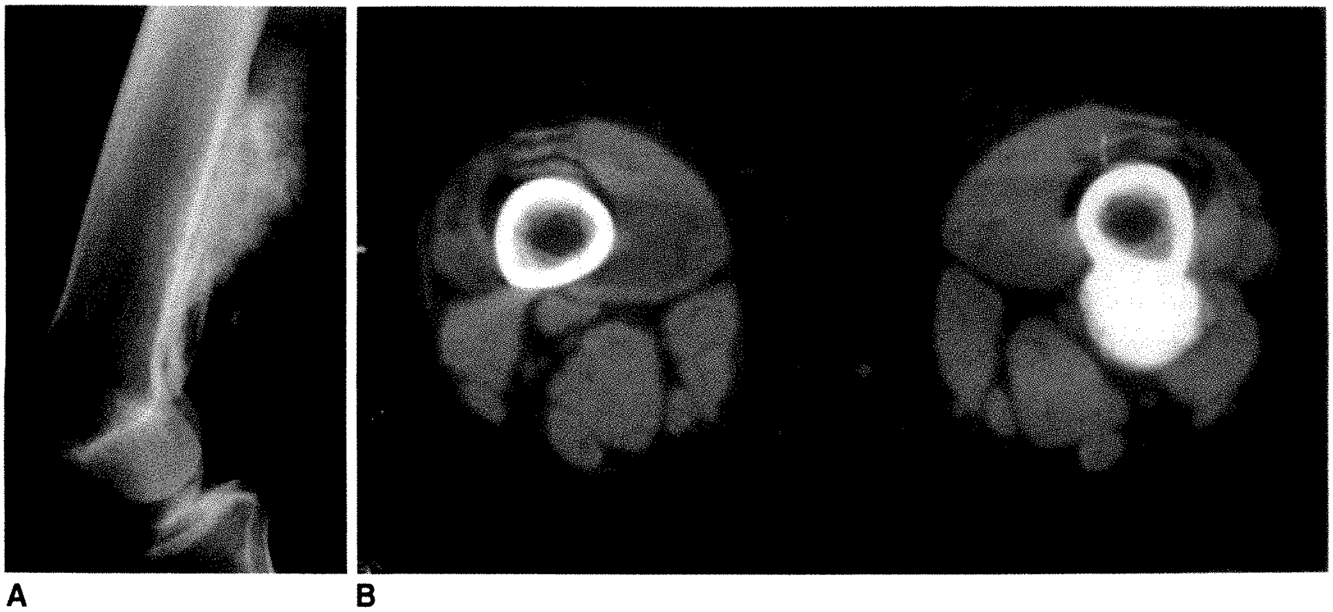

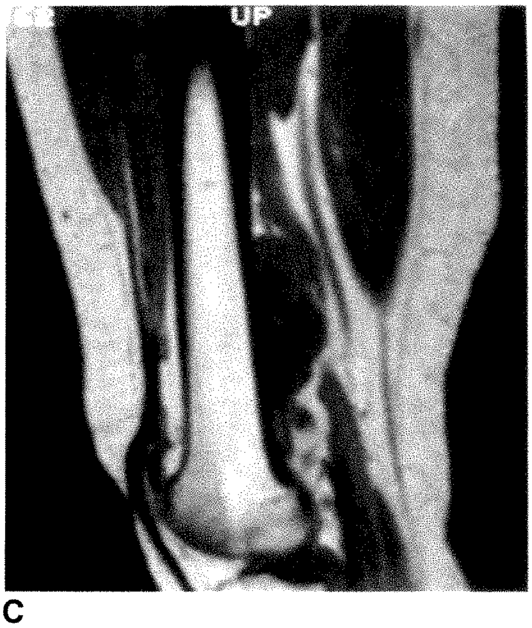

Fig. 1.—Case 1: Radiographs of left knee were obtained in this 39-year-old woman after an abnormality was noted on a bone scan obtained because of back pain.
***A*, Lateral radiograph of left distal femur.**
***B*, Axial CT scan at level of distal femur.**
***C*, Sagittal T1-weighted MR image through left distal femur.**

---

[1] All authors: Department of Radiology, Vanderbilt University Medical Center, 1161 21st Ave. South, Nashville, TN 37232-2675. Address reprint requests to E. P. Nance.

Cases 1 and 2 were prepared by S. Tigges and E. P. Nance; cases 3 and 4 were prepared by R. E. Erb and E. P. Nance.

***AJR* 158:905-906, April 1992** 0361-803X/92/1584-0905 © American Roentgen Ray Society

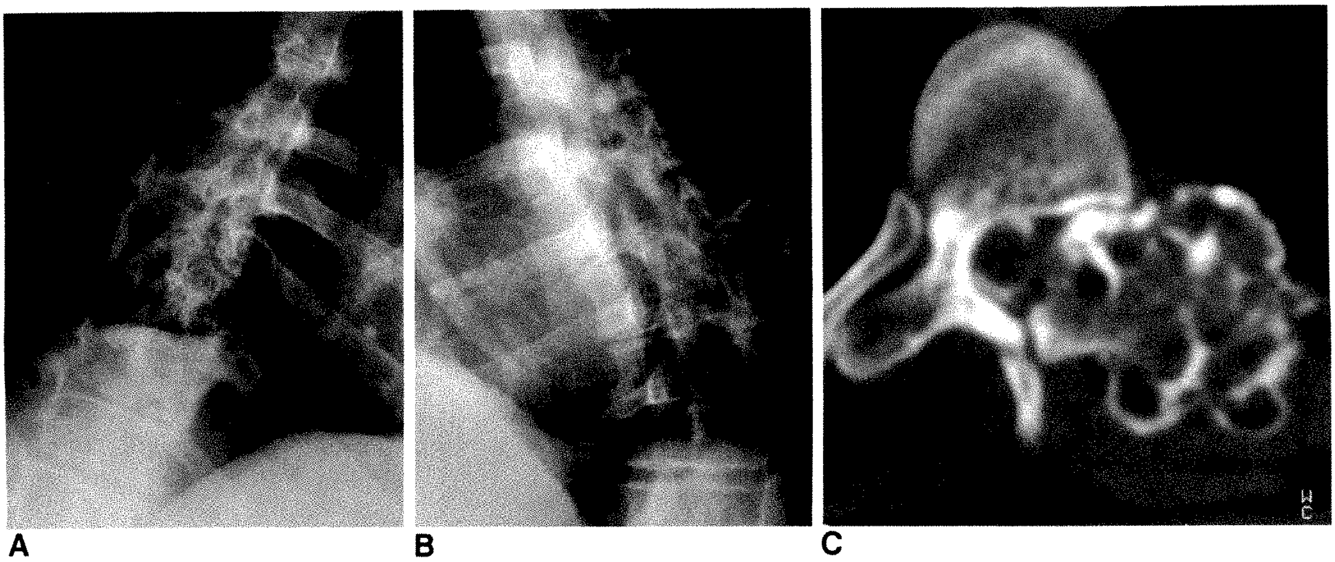

Fig. 2.—Case 2: 21-year-old man with scoliosis and vague back pain after adrenalectomy and radiation therapy for a neuroblastoma discovered at 7 months of age.
A and *B*, Oblique radiographs of lower thoracic spine.
C, Axial CT scan with intrathecal contrast medium.

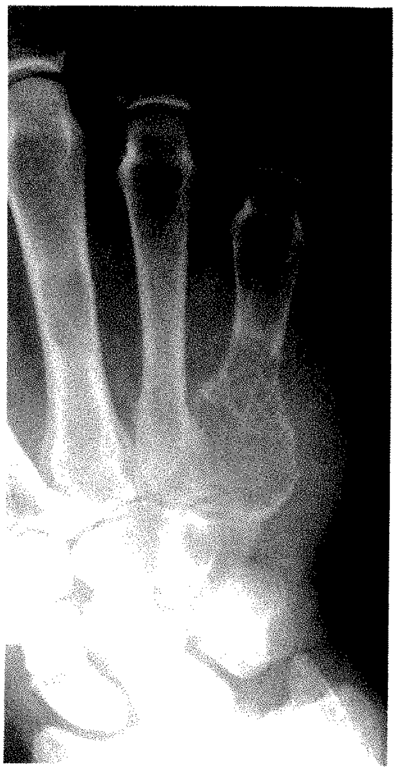

Fig. 3.—Case 3: Posteroanterior radiograph of right hand of 47-year-old man on long-term hemodialysis was obtained because of pain and swelling in right hand.

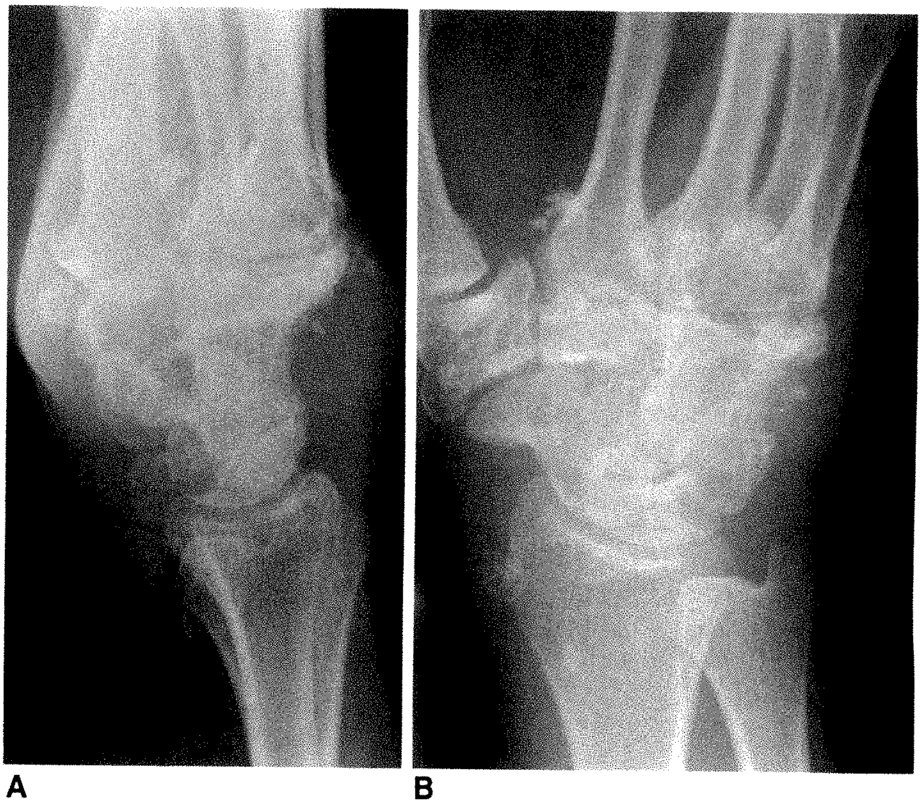

Fig. 4.—Case 4: 32-year-old woman with chronic swelling around right wrist.
A and *B*, Lateral and oblique radiographs of right wrist.

Pediatric Case of the Day

Richard M. Heller,[1] Marta Hernanz-Schulman, Joyce Johnson, Sharon M. Stein, and Sandra Kirchner

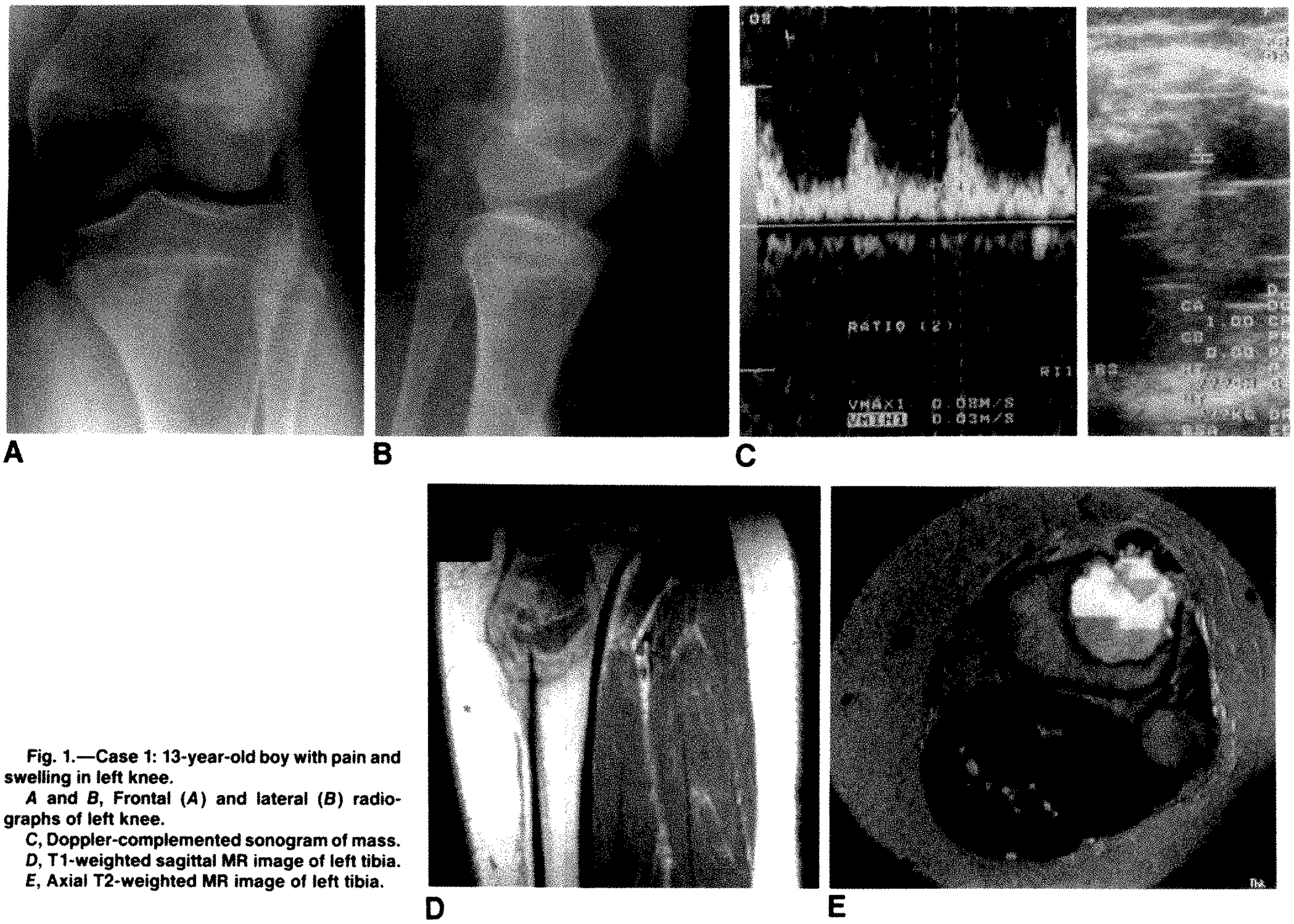

Fig. 1.—Case 1: 13-year-old boy with pain and swelling in left knee.

***A* and *B*, Frontal (*A*) and lateral (*B*) radiographs of left knee.**

***C*, Doppler-complemented sonogram of mass.**

***D*, T1-weighted sagittal MR image of left tibia.**

***E*, Axial T2-weighted MR image of left tibia.**

---

[1] All authors: Department of Radiology, Vanderbilt University Medical Center, 1161 21st Ave. South, Nashville, TN 37232-2675. Address reprint requests to M. Hernanz-Schulman.

***AJR* 158:907-910, April 1992** 0361-803X/92/1584-0907 © American Roentgen Ray Society

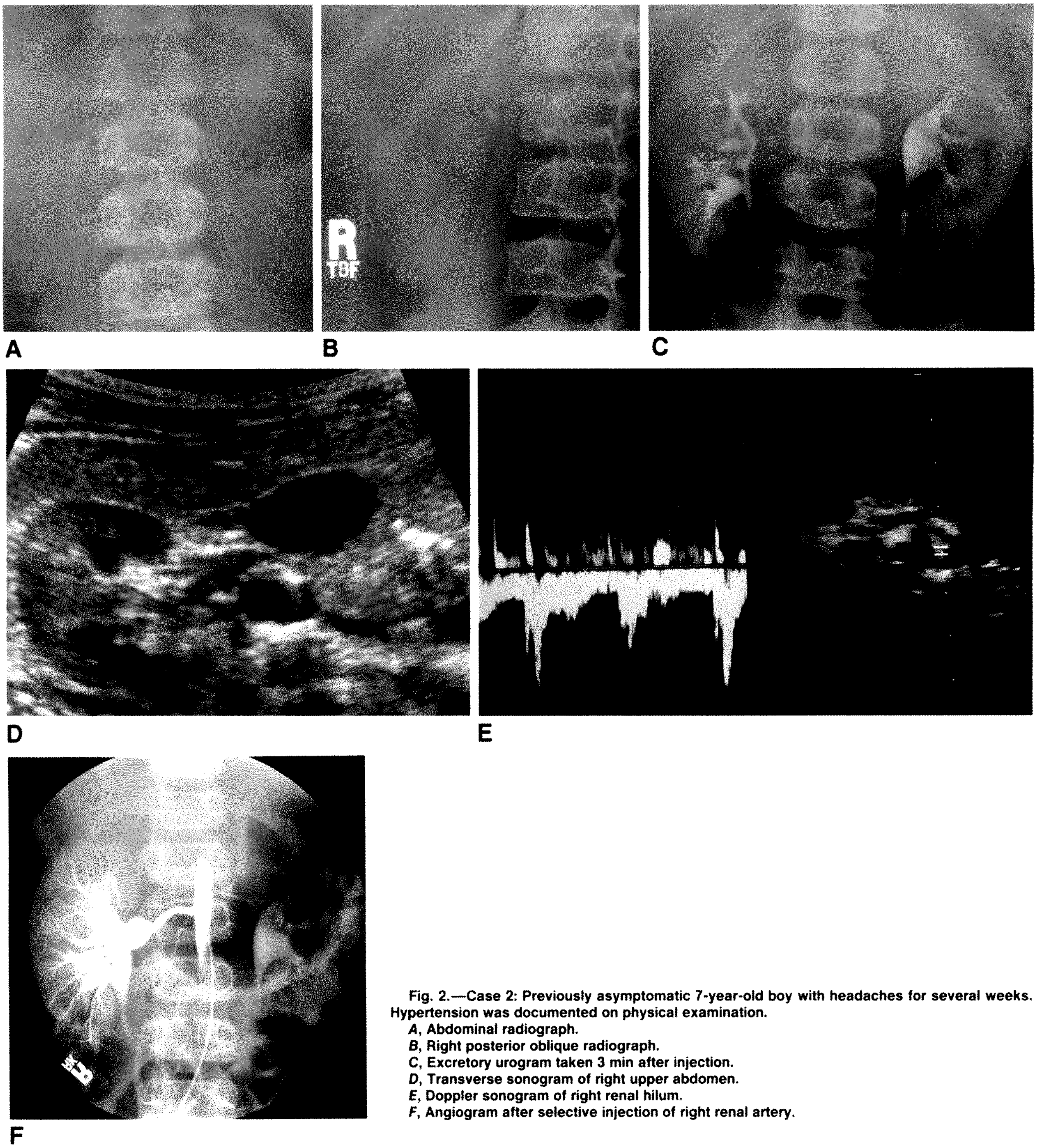

Fig. 2.—Case 2: Previously asymptomatic 7-year-old boy with headaches for several weeks. Hypertension was documented on physical examination.

A, Abdominal radiograph.
B, Right posterior oblique radiograph.
C, Excretory urogram taken 3 min after injection.
D, Transverse sonogram of right upper abdomen.
E, Doppler sonogram of right renal hilum.
F, Angiogram after selective injection of right renal artery.

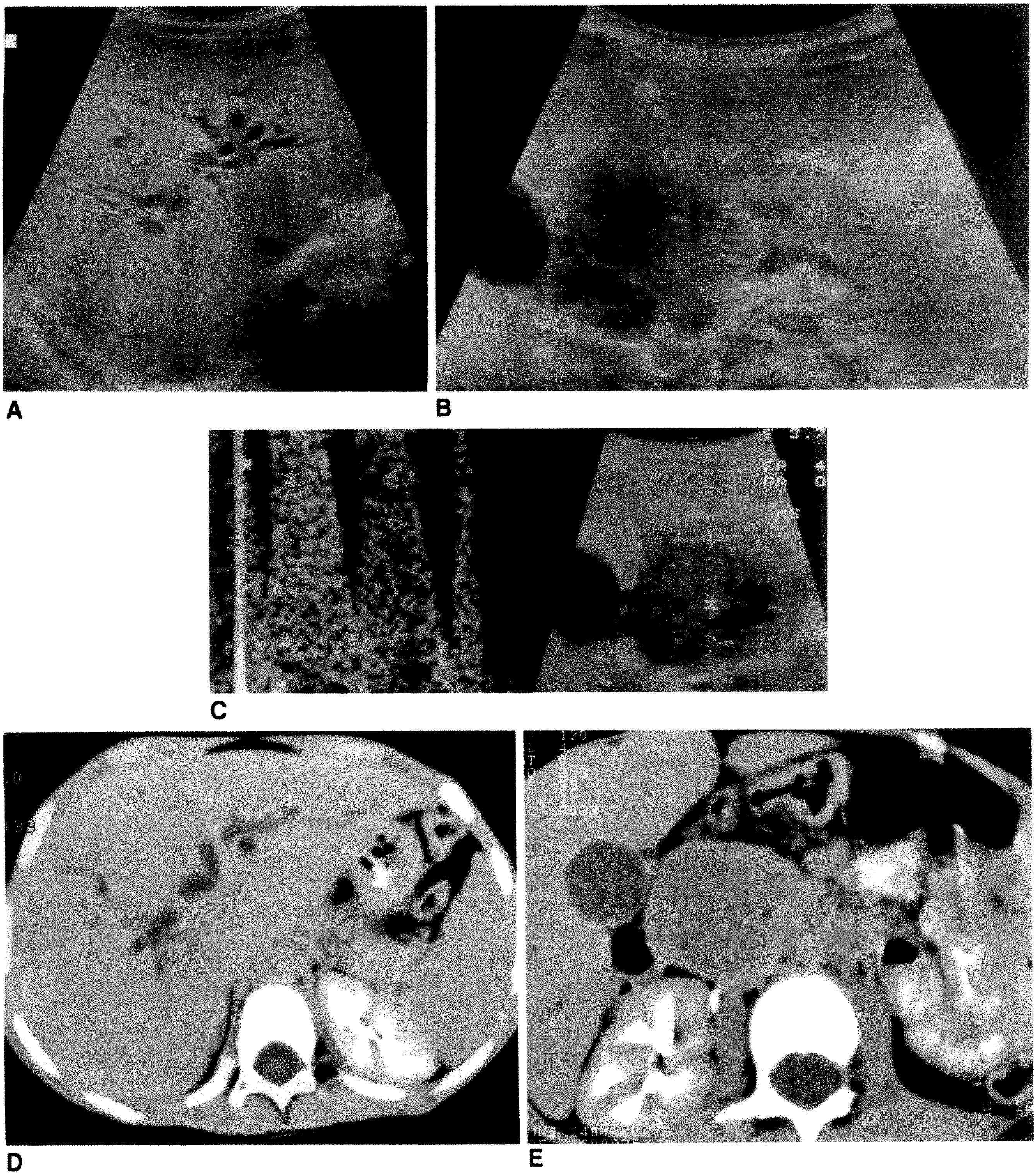

Fig. 3.—Case 3: 5-year-old girl with abdominal pain and jaundice.
A, Transverse sonogram of liver.
B, Transverse sonogram at level of pancreas.
C, Spectral Doppler sampling.
D, Contrast-enhanced CT scan through liver.
E, Magnified CT scan through head of pancreas.

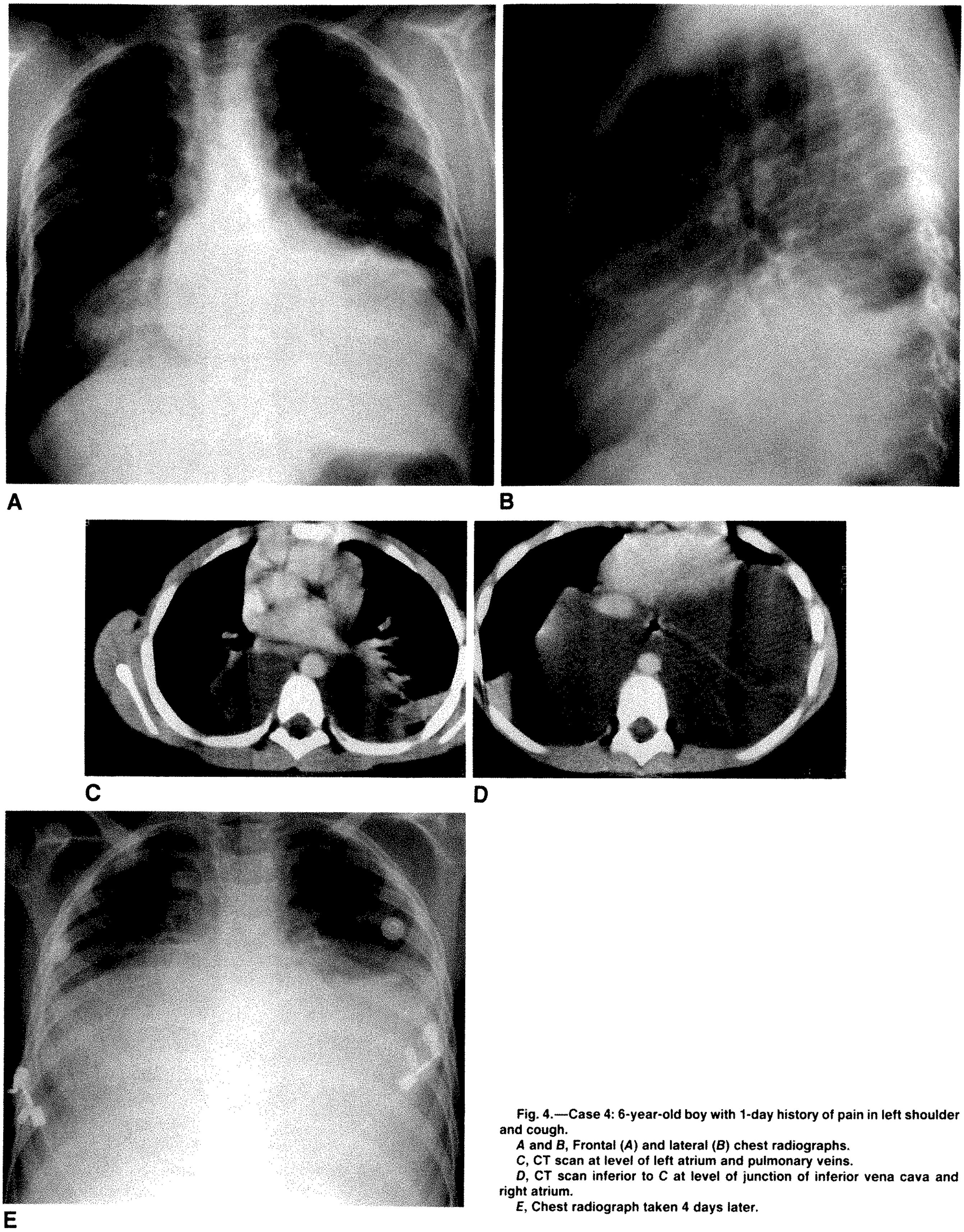

Fig. 4.—Case 4: 6-year-old boy with 1-day history of pain in left shoulder and cough.

A and *B*, Frontal (*A*) and lateral (*B*) chest radiographs.

C, CT scan at level of left atrium and pulmonary veins.

D, CT scan inferior to *C* at level of junction of inferior vena cava and right atrium.

E, Chest radiograph taken 4 days later.

Neuroradiology Case of the Day

Marc J. Lacrampe[1] and Jeff L. Creasy

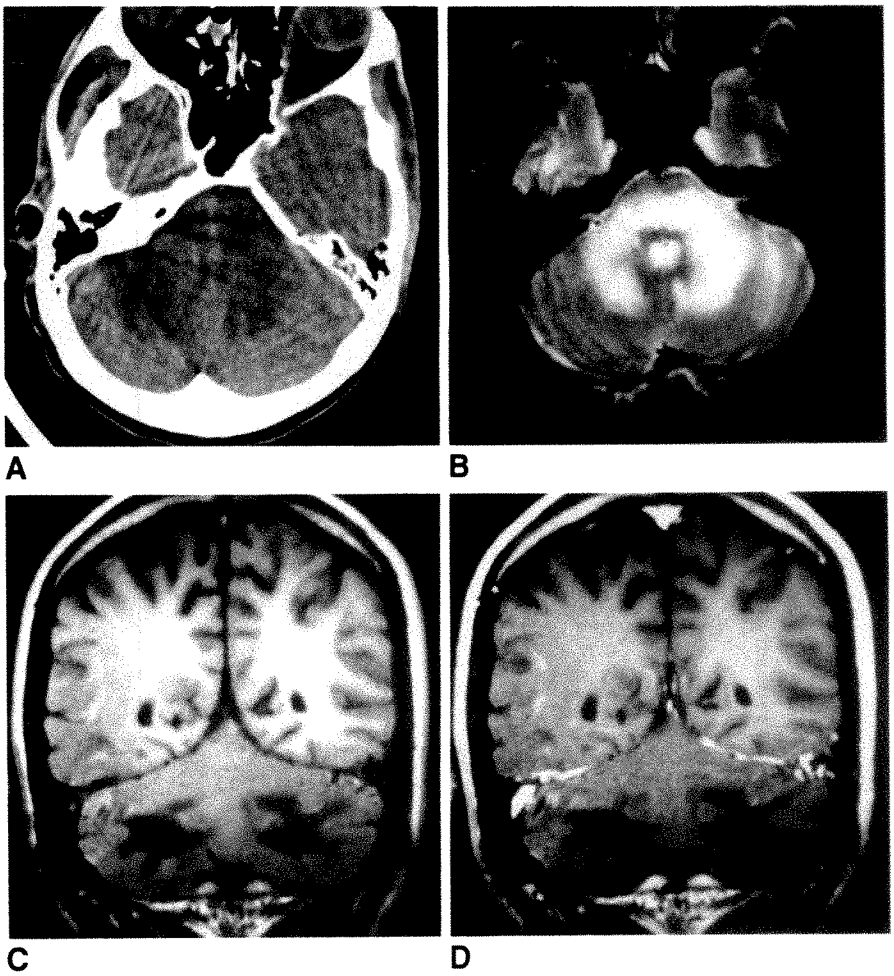

Fig. 1.—Case 1: Immunocompromised 41-year-old man with new seizure disorder.

***A*, Axial unenhanced CT scan through posterior fossa.**

***B*, Axial T2-weighted MR image through posterior fossa.**

***C* and *D*, Coronal pre- (*C*) and post- (*D*) contrast T1-weighted MR images through brainstem and posterior fossa.**

---

[1] Both authors: Department of Radiology, Vanderbilt University Medical Center, 1161 21st Ave. South, Nashville, TN 37232-2675. Address reprint requests to J. L. Creasy.

Cases 1–4 were prepared by M. J. Lacrampe and J. L. Creasy.

AJR **158:911–912, April 1992** 0361–803X/92/1584–0911 © American Roentgen Ray Society

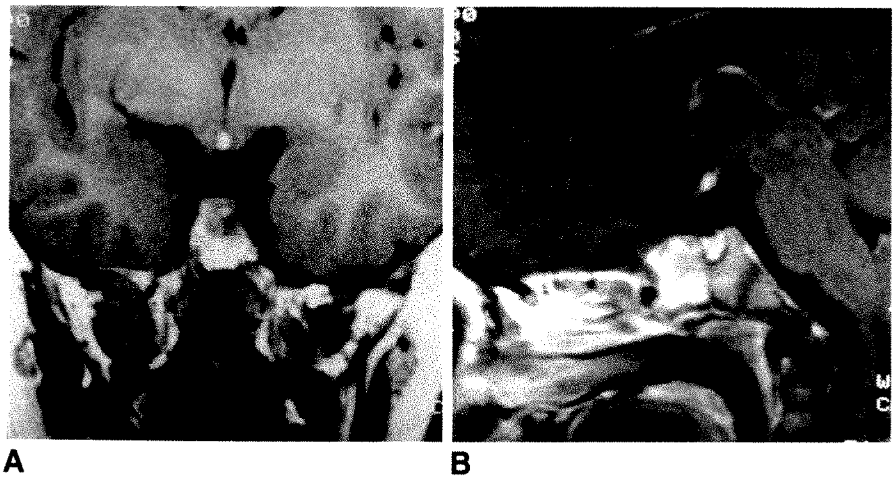

Fig. 2.—Case 2: 6-year-old boy with short stature.

A, Coronal T1-weighted image through sella region.

B, Sagittal T1-weighted image through sella region.

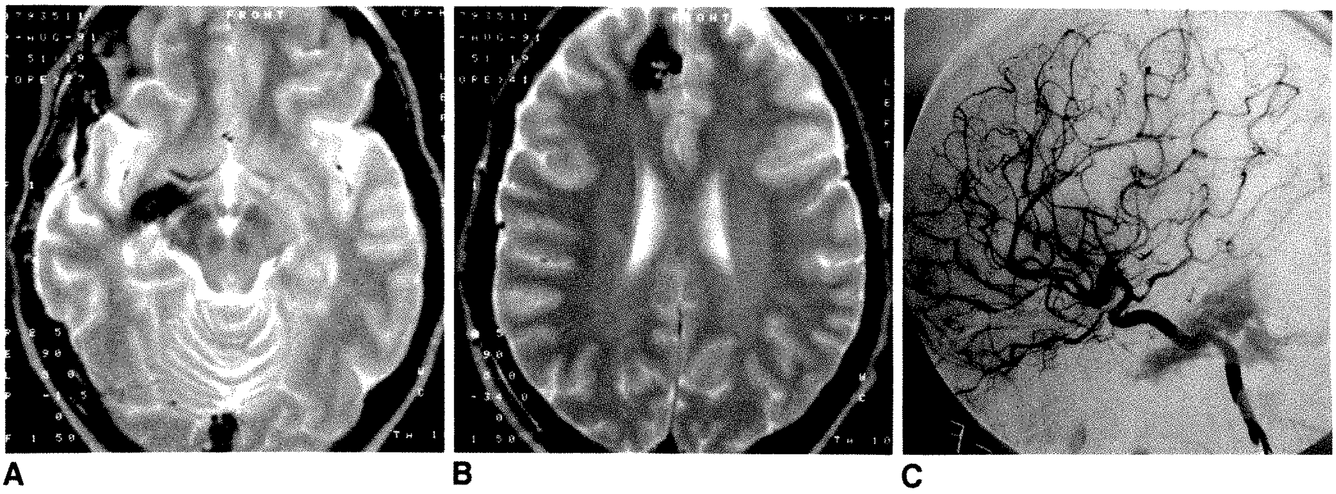

Fig. 3.—Case 3: 21-year-old woman with chronic seizure disorder.

A, Axial T2-weighted MR image at level of cerebral peduncles.

B, Axial T2-weighted image at level of lateral ventricles.

C, Subtraction image from right carotid cerebral arteriogram.

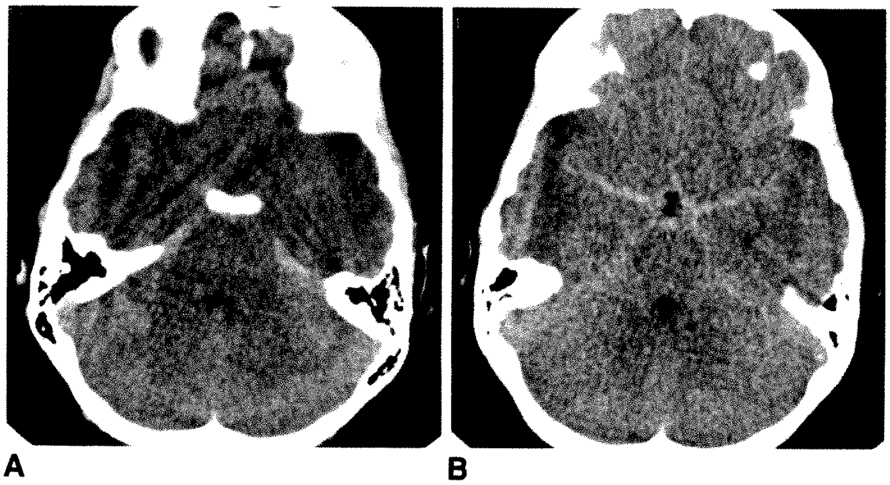

Fig. 4.—Case 4: Comatose 9-year-old boy with no history of trauma.

A, Axial noncontrast CT scan at level of fourth ventricle.

B, Axial noncontrast CT scan at level of suprasellar cistern.

Nuclear Medicine Case of the Day

Edward B. Moody,[1] Steven B. Glassman, Anne V. Hansen, Sandra K. Lawrence, and Dominique Delbeke

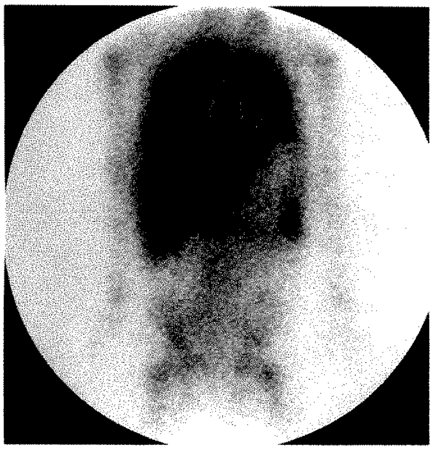

Fig. 1.—Case 1: Gallium scintigraphy in 13-month-old boy with a 1-month history of spiking fever and a 3-day history of cough with white sputum. Anterior view of chest and abdomen obtained 48 hr after IV injection of 2.5 mCi of ^{67}Ga-citrate.

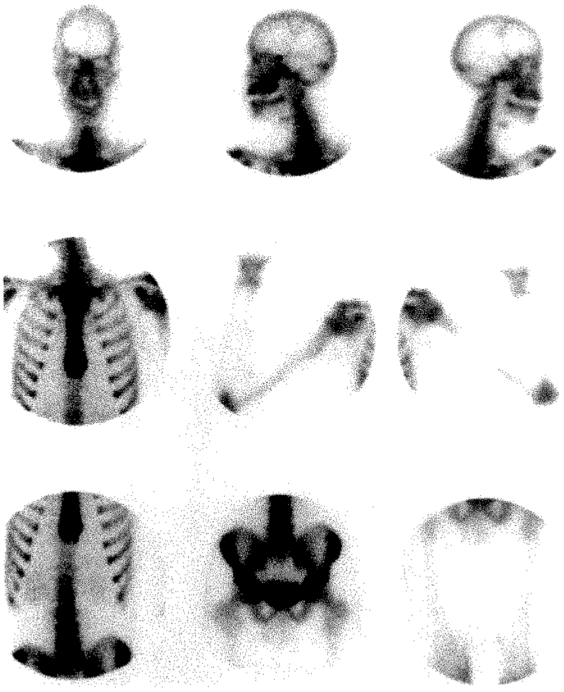

2A

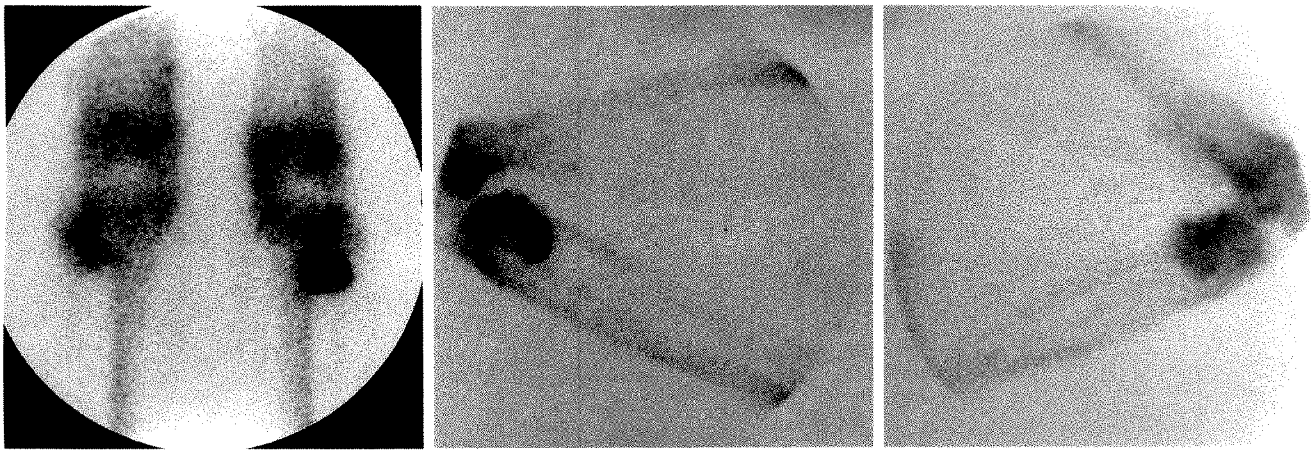

2B

2C

2D

Fig. 2.—Case 2: Bone scintigraphy in 19-year-old man with knee pain.
***A*, Multiple images obtained after IV injection of 20 mCi of ^{99m}Tc-hydroxymethylenediphosphonate.**
***B*, Anterior close-up view of knees.**
***C* and *D*, Left (*C*) and right (*D*) lateral views of knees.**

---

[1] All authors: Department of Radiology, Vanderbilt University Medical Center, 1161 21st Ave. South, Nashville, TN 37232-2675. Address reprint requests to D. Delbeke.

Case 1 was prepared by E. B. Moody and D. Delbeke; case 2 was prepared by S. B. Glassman and D. Delbeke; case 3 was prepared by A. V. Hansen and D. Delbeke; case 4 was prepared by S. K. Lawrence and D. Delbeke.

***AJR* 158:913-914, April 1992** 0361-803X/92/1584-0913 © American Roentgen Ray Society

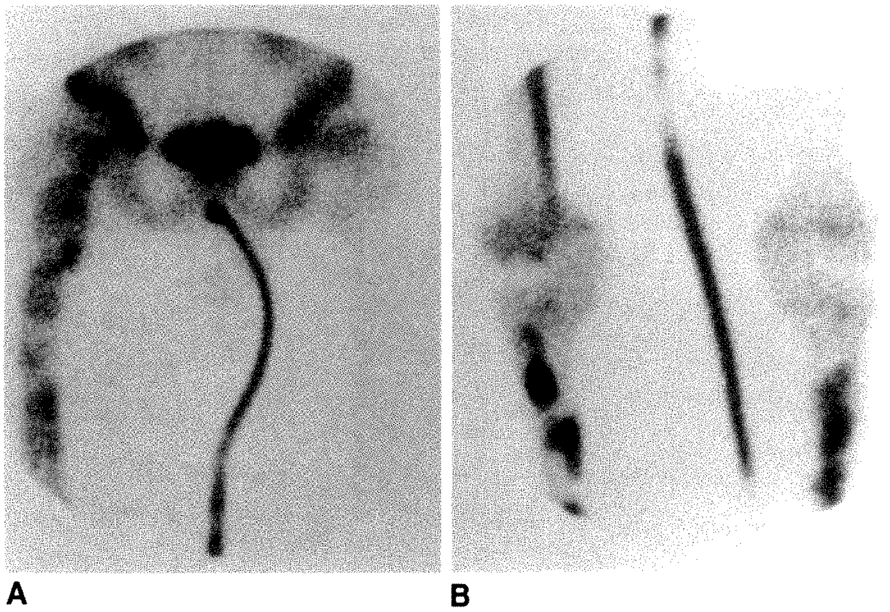

Fig. 3.—Case 3: Bone scintigraphy in 17-year-old man with neurofibromatosis.

A, Anterior view of the pelvis and lower extremities obtained after IV injection of 20 mCi of ^{99m}Tc-hydroxymethylenediphosphonate.

B, Anterior view of knees obtained as described in *A*.

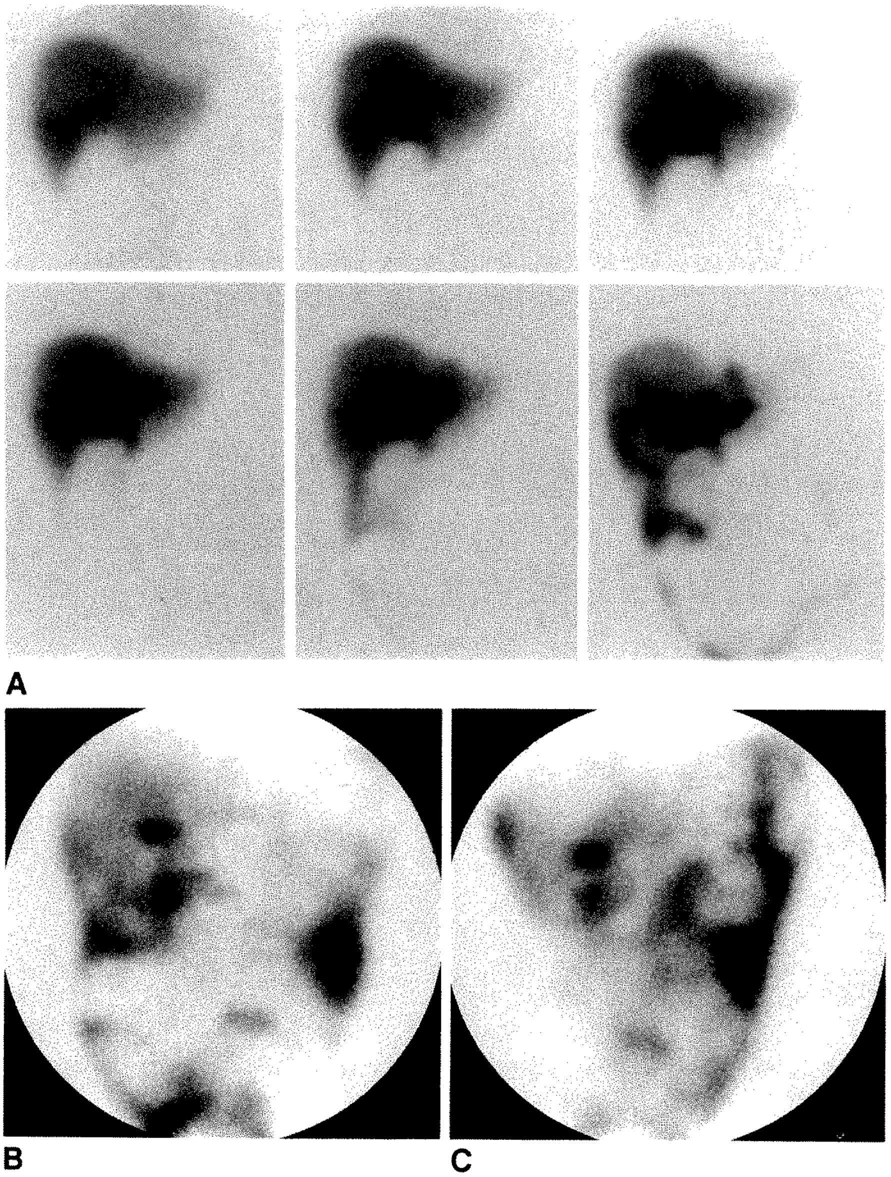

Fig. 4.—Case 4: Hepatobiliary scintigraphy in 44-year-old woman with abdominal pain after laparoscopic cholecystectomy.

A, Multiple sequential anterior views of abdomen obtained after IV injection of 5 mCi of ^{99m}Tc-disofenin.

B, 1-hr delayed anterior view of abdomen.

C, Delayed anterior view of abdomen obtained after patient had lain in left lateral decubitus position for 5 min.

Letters

Dear Journal Editor, It's Me Again

Dear Sir, Madame, or Other:

Enclosed is our latest version of Ms# 85-02-22-RRRRR, that is, the re-re-re-revised revision of our paper. Choke on it. We have again rewritten the entire manuscript from start to finish. We even changed the goddam running head! Hopefully we have suffered enough by now to satisfy even you and your bloodthirsty reviewers.

I shall skip the usual point-by-point description of every single change we made in response to the critiques. After all, it is fairly clear that your reviewers are less interested in details of scientific procedures than in working out their personality problems and sexual frustrations by seeking some kind of demented glee in the sadistic and arbitrary exercise of tyrannical power over hapless authors like ourselves who happen to fall into their clutches. We do understand that, in view of the misanthropic psychopaths you have on your editorial board, you need to keep sending them papers, for if they weren't receiving manuscripts they'd probably be out mugging old ladies or clubbing baby seals to death. Still, from this batch of reviewers, C was clearly the most hostile, and we request that you not ask him or her to review this revision. Indeed, we have mailed letter bombs to four or five people we suspect of being reviewer C, so if you send the manuscript back to them the review process could be unduly delayed.

Some of the reviewer's comments we couldn't do anything about. For example, if (as reviewer C suggested) several of my recent ancestors were indeed drawn from other species, it is too late to change that. Other suggestions were implemented, however, and the paper was improved and benefited. Thus, you suggested that we shorten the manuscript by 5 pages, and we were able to accomplish this very effectively by altering margins and printing the paper in a different font with a smaller typeface. We agree with you that the paper is much better this way.

One perplexing problem was dealing with suggestions #13–28 by reviewer B. As you may recall (that is, if you even bother reading the reviews before doing your decision letter), that reviewer listed 16 works that he/she felt we should cite in this paper. These were on a variety of different topics, none of which had any relevance to our work that we could see. Indeed, one was an essay on the Spanish-American War from a high school literary magazine. The only common thread was that all 16 were by the same author, presumably someone whom reviewer B greatly admires and feels should be more widely cited. To handle this, we have modified the introduction and added, after the review of relevant literature, a subsection entitled "Review of Irrelevant Literature" that discusses these articles and also duly addresses some of the more asinine suggestions in the other reviews.

We hope that you will be pleased with this revision and will finally recognize how urgently deserving of publication this work is. If not, then you are an unscrupulous, depraved monster with no shred of human decency. You ought to be in a cage. May whatever heritage you come from be the butt of the next round of ethnic jokes. If you do accept it, however, we wish to thank you for your patience and wisdom throughout this process and to express our appreciation of your scholarly insights. To repay you, we would be happy to review some manuscripts for you; please send us the next manuscript that any of these reviewers submits to your journal.

Assuming you accept this paper, we would also like to add a footnote acknowledging your help with this manuscript and to point out that we liked the paper much better the way we originally wrote it but you held the editorial shotgun to our heads and forced us to chop, reshuffle, restate, hedge, expand, shorten, and in general convert a meaty paper into stirfried vegetables. We couldn't, or wouldn't have done it without your input.

Roy F. Baumeister
Case Western Reserve University
Cleveland, OH 44106

Editor's note.—Although the preceding letter was written in jest, any author who has ever submitted a manuscript for publication should be able to appreciate its point. It is reprinted here in honor of April Fool's Day for your amusement. (From *Dialogue* with permission.)

Skin Ulceration from Extravasation of Low-Osmolality Contrast Medium: A Complication of Automation

Skin and soft-tissue necrosis are well-known complications of extravasation of high-osmolality contrast agents [1, 2]. Such injuries may require surgical debridement, skin grafts, and, occasionally, plastic surgery to avoid loss of limb function. Low-osmolality contrast medium is different, however. Sistrom et al. [3] recently reported 28 cases of extravasation of low-osmolality contrast medium, seven of which were "major" and nine of which were "moderate." None of the patients required medical or surgical intervention as a result of the extravasation. Our experience with extravasation of low-osmolality contrast medium is similar. In addition, we recently evaluated extravasation of contrast media in an animal mode [4]. We found that low-osmolality agents were much less injurious than high-osmolality agents when the agents extravasated and that the former did not produce cutaneous ulceration regardless of the volume of medium extravasated.

Recently, skin ulceration of moderate severity occurred in one of our patients after extravasation of a low-osmolality agent (iohexol), but under somewhat unusual circumstances. A power injector was used to administer contrast medium for a CT scan of a comatose patient. Blood pressures were being obtained at the same time by means of an automatically inflating cuff. Unknown to the physician and technologist present, the cuff inflated during the injection of contrast medium, resulting in extravasation of approximately 150 ml of medium. Cutaneous ulceration occurred as vesicular lesions over an area of 30 cm^2 in the antecubital fossa, similar to ulceration caused by a second-degree burn. The lesions resolved with topical treatment only, and no long-term sequelae occurred. Similar extravasations with high-osmolality agents would likely have resulted in a severe disfiguring injury.

Caution is mandatory when any automated device is used. Injectors for contrast medium and automatic blood pressure cuffs are clearly incompatible. The relatively inconsequential injury from extravasation seen in our case is an infrequently mentioned reason for use of low-osmolality agents.

Gerald D. Pond
Robert T. Dorr
Kelly A. McAleese
University of Arizona Health Sciences Center
Tucson, AZ 85724

REFERENCES

1. Leung PC, Cheng CY. Extensive local necrosis following intravenous use of x-ray contrast medium in the upper extremities. *Br J Radiol* **1980**;53:361–364
2. Spigos DG, Thane TT, Capek V. Skin necrosis following extravasation during peripheral phlebography. *Radiology* **1977**;123:605–606
3. Sistrom CL, Gay SB, Peffley L. Extravasation of iopamidol and iohexol during contrast-enhanced CT: report of 28 cases. *Radiology* **1991**;180:707–710
4. Elam EA, Dorr RT, Legel KE, Pond GD. Cutaneous ulceration due to contrast extravasation: experimental assessment of injury and potential antidotes. *Invest Radiol* **1991**;26:13–16

Dysphagia in the Elderly

While reading "Altered Swallowing Function in Elderly Patients Without Dysphagia: Radiologic Findings in 56 Cases," by Ekberg and Feinberg [1], in the June 1991 issue of *AJR*, I was struck by several flaws in the research design and conclusions of this article. The authors attempted to report differences in swallowing skills in elderly vs young adults. Unfortunately, almost half the subjects included in the study were neurologically impaired. In addition, no attempt was made to specifically distinguish the results in elderly patients without neurologic disease from the results in patients with dementia, Parkinson's disease, or stroke. Swallowing dysfunction in various neurogenic disorders has been well reported in the literature. For instance, Robbins et al. [2] reported that patients with Parkinson's disease do not complain of dysphagia and frequently will deny that they have dysphagia, even when silent aspiration is found on the swallowing study.

The article by Ekberg and Feinberg could have contributed useful information on the swallowing abilities of the elderly if the authors simply had used control subjects of various ages. As no attempt to do this was reported, it is impossible to consider the results of this study as representative findings associated with the normal aging process or to compare these results with the swallowing skills of young adults.

Alice K. Silbergleit
Henry Ford Hospital
Detroit, MI 48202-2691

REFERENCES

1. Ekberg O, Feinberg MJ. Altered swallowing function in elderly patients without dysphagia: radiologic findings in 56 cases. *AJR* **1991**;156: 1181–1184
2. Robbins JA, Logemann JA, Kirshner HS. Swallowing and speech production in Parkinson's disease. *Ann Neurol* **1986**;19:283–287

Reply

Ms. Silbergleit rightly points out the important differences in swallowing function in elderly vs young adults. Actually, age is probably by far the most important predictor of oral and pharyngeal dysfunction during swallowing (unpublished data). However, some neurogenic disorders cause various degrees of impaired swallowing function. The purpose of our study [1] was to highlight swallowing functions in the very elderly who did not have any dysphagia or impairment. Although patients with neurologic disease more frequently had dysfunction than those without did, the overwhelming result was the high frequency of dysfunction in patients who were asymptomatic. The relatively high frequency of abnormalities in the 31 patients without neurologic disease does contribute useful information about elderly patients who are considered "normal" because of the absence of signs and symptoms. The absence of signs and symptoms in the presence of significant dysfunction raises important issues about treatment. Should patients with a silent aspiration be considered ill and require treatment if the abnormality was discovered as part of a routine upper gastrointestinal study?

Olle Ekberg
Malmö General Hospital
S-21401 Malmö, Sweden
Michael J. Feinberg
Buffalo General Hospital
Buffalo, NY 14203

REFERENCE

1. Ekberg O, Feinberg MJ. Altered swallowing function in elderly patients without dysphagia: radiologic findings in 56 cases. *AJR* **1991**;156: 1181–1184

Spontaneous Pneumothorax in *Pneumocystis carinii* Pneumonia: Common or Uncommon?

Pneumocystis carnii is a known pathogen in patients with AIDS [1], and *P. carinii* pneumonia is the main pulmonary infection that occurs in these patients. Radiologic findings consistent with *P. carinii* pneumonia are bilateral interstitial infiltrates that rapidly progress to a confluent pulmonary edema [2]. Other less common features are a diffuse "honeycomb" pattern, localized infiltrates, cavitary disease, and hilar enlargement [3].

We emphasize that AIDS patients with *P. carinii* pneumonia have an increased prevalence of spontaneous pneumothorax. At our institution, 2200 patients known to be infected with human immunodeficiency virus (HIV) were treated between January 1, 1988, and January 1, 1991. Seventy percent (840 patients) had had *P. carinii* pneumonia at some time in the course of their disease. Of these 840, 32 (4%) had evidence on radiographs of spontaneous pneumothorax, either at the time of presentation or during their hospitalization. The pneumothorax was on the right side in 15, on the left side in 12, and bilateral in five. The prevalence of spontaneous pneumothorax in the entire group of 1200 patients with AIDS was 3%. This is 450 times higher than the prevalence in persons not infected with HIV [4]. Knowledge of the variety of patterns of *P. carinii* pneumonia on radiographs and an awareness of the frequency of spontaneous pneumothorax will be helpful in the early diagnosis of this condition and the treatment of these patients.

Terrance Truitt
Kaveh Bagheri
Benjamin H. Safirstein
Saint Michael's Medical Center
Neward, NJ 07102

REFERENCES

1. Centers for Disease Control. Update acquired immunodeficiency syndrome—United States. *MMWR* **1985**;34:245–248
2. Feinberg SB, Lester RG, Burke BA. The roentgen findings in *Pneumocystis carinii* pneumonia. *Radiology* **1961**;76:594–600
3. Delorenzo LS, Huang CT, Stone DS. Roentgenographic patterns of *Pneumocystis carinii* pneumonia in 107 patients with AIDS. *Chest* **1987**;91: 323–327
4. Melton LJ 3rd, Hepper NG, Offord KP. Incidence of spontaneous pneumothorax in Olmsted County, Minnesota: 1950–1974. *Am Rev Respir Dis* **1979**;120:1379–1382

High-Density Hepatocellular Carcinoma on Unenhanced CT

Hepatic neoplasms are usually seen as low-density or isodensity masses on unenhanced CT scans. Recently, we encountered a patient with two hepatocellular carcinomas, one of which had diffuse high density.

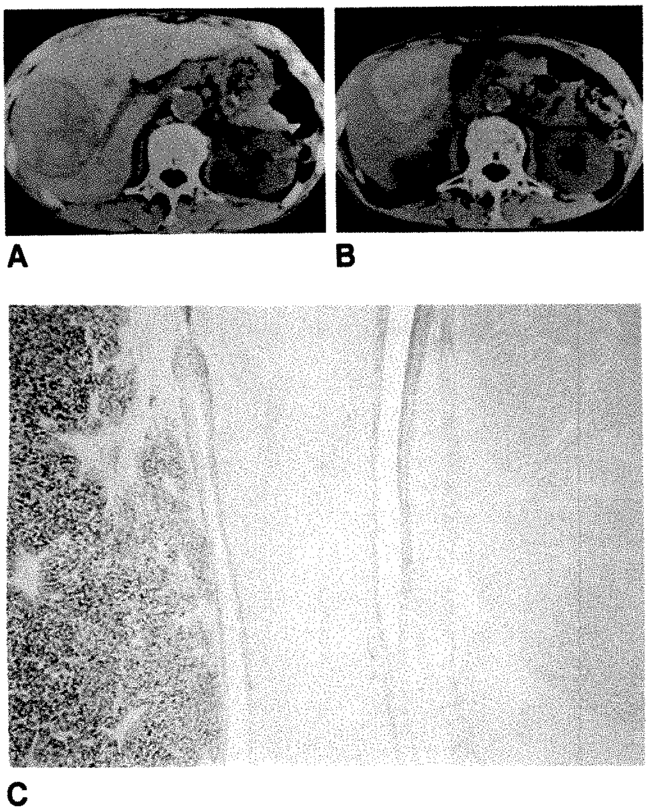

Fig. 1.—Hepatocellular carcinoma.
***A* and *B*, Unenhanced CT scans of liver show well-encapsulated 5.5 × 5.5 cm tumor (*A*) with low density in posteroinferior segment and 5.5 × 5.0 cm tumor (*B*) with diffuse high density in anteroinferior segment.**
***C*, Micrograph of both tumors shows one with high density (*left*) contains abundant orcein-positive granules.**

A 75-year-old man with chronic liver disease had hepatic tumors that had been discovered incidentally during a routine checkup. Unenhanced CT showed two liver tumors. One had a low density, and the other had a diffuse high density (129.5 H) (Figs. 1A and 1B). Partial resection of the liver was carried out, and pathologic examination showed that both tumors were hepatocellular carcinomas. No calcification or hemorrhage was seen in the high-density tumor. The high-density tumor showed diffuse and strong staining with orcein, which suggested the presence of large amounts of copper-binding protein. The low-density tumor did not stain with orcein (Fig. 1C). The concentration of copper in the tissue samples was 4.5 μg per gram of dry liver in the noncancerous liver tissue (normal, <2.0 μg/g), 2.3 μg/g in the low-density tumor, and 171.0 μg/g in the high-density tumor. No iron or zinc was found in either of the tumors.

In general, attenuation depends on a tissue's density and contents. For instance, in patients with hemochromatosis, hepatic attenuation on CT scans is greater than normal because of iron deposition. High density on CT has been reported in hepatic adenoma and in some liver metastases [1]. In these cases, hemorrhage or calcification was the main cause of the high attenuation. Recently, high-density hepatic nodules were also observed in Wilson's disease; the nodules disappeared after treatment with D-penicillamine [2]. Kitagawa et al. [3] reported three cases of high-density hepatocellular carcinoma with excessive accumulation of copper. In our case, high- and low-density hepatocellular carcinomas were detected on unenhanced CT scans in the same patient. The most remarkable difference between the two tumors was the presence of abundant cytoplasmic orcein-positive granules in the high-density tumor. Orcein-positive granules are thought to be a morphologic counterpart of copper-binding protein, and the amount of copper was prominently increased in the high-density tumor as compared with the low-density tumor or surrounding liver parenchyma. We conclude that excessive deposition of copper or copper-binding protein may be the main cause of the tumor's high attenuation on unenhanced CT scans.

Kei Yuki
Yoshiaki Kondo
Saku Central Hospital
Nagano 384-03, Japan

REFERENCES

1. Wolverson MK, Crepps LF, Sundaram M, Heiberg E, Vas WG, Shields JB. Hyperdensity of recent hemorrhage at body computed tomography: incidence and morphologic variation. *Radiology* **1983**;148:779–784
2. Ishinoda Y, Kurita M, Shigehira M. A case of Wilson disease demonstrating nodular high density area on plain CT. *Acta Hepatol Japonica* **1988**;29:156
3. Kitagawa K, Matsui O, Kadoya M, et al. Hepatocellular carcinomas with excessive copper accumulation: CT and MR findings. *Radiology* **1991**;180:623–628

Varix of the Ileum

A 49-year-old woman had maroon stools. Her history was significant for a right hemicolectomy for colonic arteriovenous malformation. The results of endoscopy of the upper gastrointestinal tract and colonoscopy were normal. Scintigraphy with ^{99m}Tc-labeled RBCs and an angiogram showed no active bleeding. Barium examination of the small bowel showed a partially obstructing, multilobulated, 3-cm mass in the proximal part of the ileum (Fig. 1A).

At surgery, a 10-mm area of abnormal rugal folds was found with an ulcer 2 mm in diameter in the center. A thin-walled vessel was visible on the serosal surface. Histologic sections showed a markedly ectatic submucosal vein with focal accumulations of fibrin and red

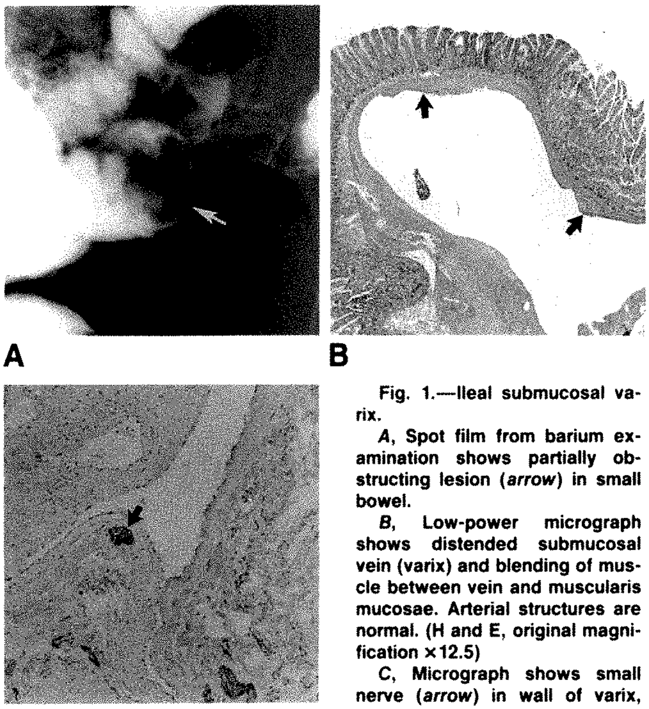

Fig. 1.—Ileal submucosal varix.

A, Spot film from barium examination shows partially obstructing lesion (*arrow*) in small bowel.

B, Low-power micrograph shows distended submucosal vein (varix) and blending of muscle between vein and muscularis mucosae. Arterial structures are normal. (H and E, original magnification ×12.5)

C, Micrograph shows small nerve (*arrow*) in wall of varix, indicating partial fusion with muscle coat of varix (anti-S-100 immunoperoxidase, original magnification ×125).

cells (Fig. 1B). A large venous space within the submucosa contained focal subintimal fibrous cushions with an abnormal incorporation of nerve fasicles into smooth muscle (Fig. 1C). The arteries were normal. The findings were consistent with a submucosal varix of the proximal ileum.

To our knowledge, this is the first case report that illustrates a submucosal varix on small-bowel barium examination. A varix or distended submucosal vein is distinct from an arteriovenous malformation because the arteries are normal. A varix is also distinct from a vascular tumor.

Bleeding small-bowel varices in the duodenum and jejunum have been reported [1, 2]. Duodenal varices are usually due to portal hypertension [1]. Diagnosis of duodenal varices is difficult; in the series of Khouqueer et al. [1], the results of endoscopy indicated the diagnosis in 44% of cases.

Jejunal varices are rare. Friedman [2] recently reported a varix in an asymptomatic man without known liver disease. Acute ileal varices have been reported after sclerotherapy and in a patient with intraabdominal adhesions [3, 4].

Raymond K. Tu
Margaret I. Fagerholm
Thomas F. C. S. Warner
University of Wisconsin Hospital and Clinics
Madison, WI 53692

REFERENCES

1. Khouqueer F, Morrow C, Jordan P. Duodenal varices as a cause of massive upper gastrointestinal bleeding. *Surgery* **1987**;102:540–542
2. Friedman E. Massive gastrointestinal bleeding from "varix" of the jejunum. *J Clin Gastroenterol* **1990**;12:482–483
3. Arst HF. Acute ileal variceal hemorrhage secondary to esophageal sclerotherapy. *J. Clin Gastroenterol* **1986**;5:603
4. Fauchuk KR, Aiello MR, Costello P. Recurrent gastrointestinal bleeding from ileal varices associated with intraabdominal adhesions: case report and review of the literature. *Am J Gastroenterol* **1982**;77:859–860

Aphthous Ulcers in Salmonella Colitis

Aphthous ulcers are a well-known feature of Crohn's disease [1] and occur in other colitides [2, 3]. We report their occurrence in a patient with salmonella colitis.

A 24-year-old man was admitted because of bloody diarrhea of 7 days' duration, weight loss, and abdominal pain. A fecal sample contained obvious blood. The serum level of immunoglobulin E was 770 Units/ml (1848 μg/l; normal, 0–200 Units/ml [0–480 μg/1]). Double-contrast barium enema showed widespread mucosal ulceration extending from the rectum to the hepatic flexure. Ulcers were distributed symmetrically and in continuity, with a loss of haustral pattern. Several aphthous ulcers were seen, particularly in the sigmoid colon (Fig. 1). Cultures of feces and blood grew *Salmonella virchow* phage type B. The patient was treated with IV ciprofloxacin and was asymptomatic when he was discharged 2 weeks later. Follow-up barium examination 3 months after discharge showed complete resolution of mucosal abnormalities and a normal haustral pattern.

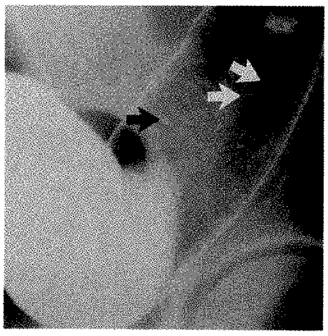

Fig. 1.—Barium examination shows aphthous ulcers (*arrows*) in sigmoid colon in a patient with salmonella colitis.

Aphthous ulcers are the earliest specific sign of Crohn's disease [1] and are not found in ulcerative colitis [2]. They occur in other infective colitides [3], but, to our knowledge, they have not been associated with salmonella colitis.

Salmonella colitis can have an appearance similar to that of ulcerative colitis [4], making it difficult to distinguish between the two types. In patients with a diffuse symmetrical colitis, the presence of aphthous ulcers should suggest the possibility of salmonella colitis.

M. A. Collins
W. C. G. Peh
N. S. Evans
Selly Oak Hospital
Birmingham, The United Kingdom B29 6JD

REFERENCES

1. Simpkins KC. Apthoid ulcers in Crohn's colitis. *Clin Radiol* **1977**;28:601–608
2. Caroline DF, Evers K. Colitis: radiographic features and differentiation of idiopathic inflammatory bowel disease. *Radiol Clin North Am* **1987**;25:47–66
3. Downey DB, Nakielny RA. Apthoid ulcers in colonic tuberculosis. *Br J Radiol* **1985**;58:561–562
4. Gardiner R, Smith C. Infective enterocolitides. *Radiol Clin North Am* **1987**;25:67–78

Tuberculosis of the Lower Genitourinary Tract: Findings on Sonography and MR

A 47-year-old man had multiple cutaneous ulcerations and a weight loss of 5 kg. Physical examination showed a large mass in the right side of the scrotum and a nodular prostate. A sonogram of the scrotum showed a serpiginous structure thought to represent enlarged epididymis adjacent to the right testis and continuous with the spermatic cord. The epididymis was also continuous with a hypoechoic area thought to represent intratesticular pathology (Fig. 1A). However, MR showed that this structure was the markedly enlarged epididymis, which had compressed the adjacent right testicle (Figs. 1B and 1C). Transrectal sonography of the prostate showed multiple hypoechoic lesions (Fig. 1D) diffusely involving the gland and asymmetric enlargement of the seminal vesicles. Diffuse, inhomogeneous enhancement of the prostate was noted on T1-weighted MR images obtained after IV administration of gadopentetate dimeglumine. Skin and urine cultures were positive for *Mycobacterium tuberculosis*, confirming the diagnosis of disseminated tuberculosis.

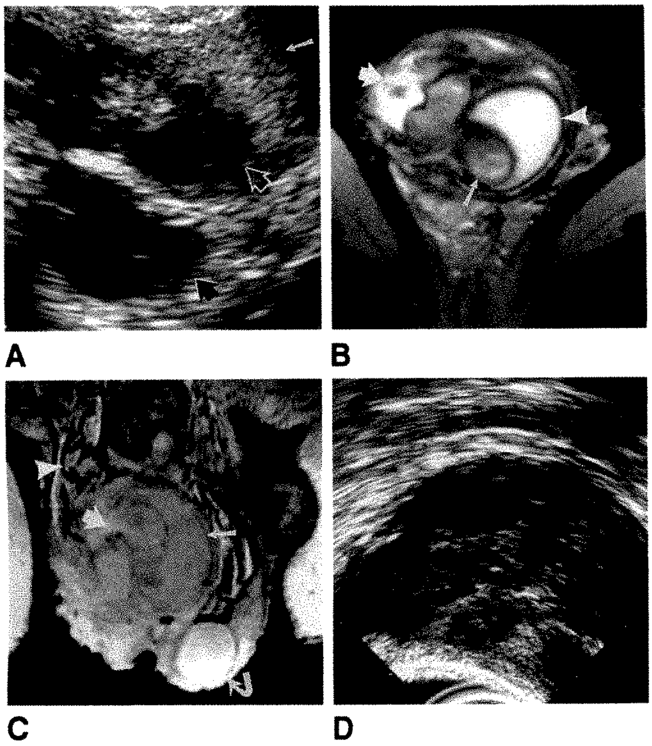

Fig. 1.—Tuberculosis of lower genitourinary tract in a 47-year-old man.

***A*, Transverse sonogram of right testicle shows thickened epididymis, which appears as a serpiginous, hypoechoic structure (*thick arrow*). A second hypoechoic area (*open arrow*) was initially thought to represent associated intratesticular disease. Subsequent MR images showed hypoechoic area actually represented enlarged epididymis compressing adjacent testicle (*thin arrow*).**

***B*, Axial MR image (SE 2000/90) shows enlarged epididymis (*thin arrow*), which has a heterogeneous but diminished signal intensity. Epididymis compresses adjacent right testicle (*arrowhead*), resulting in concave deformity of lateral aspect of testicle. Note associated hydrocele (*thick arrow*).**

***C*, Coronal MR image (GRE 60/15) shows swollen epididymis (*thick arrow*) in continuity with an enlarged, tortuous spermatic cord (*arrowhead*). Adjacent right testicle (*thin arrow*) is compressed. *Curved arrow* = left testicle.**

***D*, Axial transrectal sonogram through mid prostate shows multiple focal hypoechoic areas throughout gland.**

The radiologic findings in our case are typical of tuberculosis of the lower genitourinary tract. The multifocal nature of the process suggests an inflammatory or infectious cause. The markedly enlarged epididymis suggests epididymitis, and the diminished signal intensity on T2-weighted images indicates a chronic inflammatory process [1]. The multiple hypoechoic prostatic lesions are typical of granulomatous prostatitis, although diffuse adenocarcinoma involving the gland can mimic these findings [2]. When these radiologic findings are integrated, tuberculosis of the lower genitourinary tract becomes the primary consideration.

The number of reported cases of tuberculosis in the United States has recently increased. The affected patients have been younger than in previous cases, and a significant number have been from minority groups in urban areas [3]. Findings of multifocal disease in the lower genitourinary tract, extensive involvement of the epididymis with sparing of the testicle, and multifocal prostatic lesions (especially in patients of an age when adenocarcinoma is not a concern) suggest the diagnosis [2, 4].

Jennifer Hamrick-Turner
University of Mississippi Medical Center
Jackson, MS 39216-4505
Patricia L. Abbitt
Pablo R. Ros
University of Florda College of Medicine
Gainesville, FL 32610-0374

REFERENCES

1. Mattrey RF. Magnetic resonance imaging of the scrotum. *Semin Ultrasound CT MR* **1991**;12:95-108
2. Bude R, Bree RL, Adler RS, Jafri SZ. Transrectal ultrasound appearance of granulomatous prostatitis. *J Ultrasound Med* **1990**;9:677-680
3. Bulkner CB, Leithiser RE, Walker CW, Allison JW. The changing epidemiology of tuberculosis and other mycobacterial infections in the United States: implications for the radiologist. *AJR* **1991**;156:255-264
4. Robbins SL, Cotran RS. Male genital systems: testis and epididymis. In: *Pathologic basis of disease*. Philadelphia: Saunders, **1979**

Isolated Splenic Metastasis from Uterine Cervical Adenocarcinoma

A 55-year-old woman was admitted to our hospital with back pain. Pelvic examination showed an exophytic mass of the uterine cervix. Cervical biopsy confirmed a poorly differentiated adenocarcinoma of the endocervix. The patient received external irradiation, and 4 months later a hysterectomy and bilateral salpingo-oophorectomy were performed. Follow-up abdominal CT 14 months later showed a focal low-density lesion in the spleen (Fig. 1) and no evidence of regional tumor recurrence. The results of a CT-guided needle biopsy showed adenocarcinoma. Splenectomy was carried out, and histo-

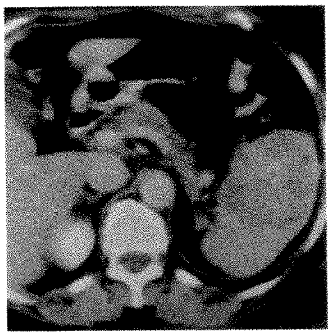

Fig. 1.—CT scan with contrast material shows a low-attenuation splenic mass with patchy areas of enhancement.

logic examination of a surgical specimen showed a poorly differentiated adenocarcinoma similar to the primary cervical cancer.

Splenic metastasis of solid tumors is infrequent, and in almost all cases, other, widespread metastases are also present [1]. In our case, the splenic mass was the only sign of recurrence; no other metastatic sites were found. Although the differential diagnosis of solitary focal lesions of the spleen must include hemangioma, lymphoma, and abscess, if the patient has or previously had a known malignant tumor, any focal lesion must be considered metastatic until proved otherwise.

CT can accurately depict parametrial invasion, tumor extension to the pelvic wall, and lymph-node metastases in patients whose cancer is stage IIb or greater [2, 3]. However, most CT scans are routinely done from the iliac crests to the symphysis pubis [3] because of the known pattern of spread of the disease through iliac and aortic lymph nodes, and the spleen is not routinely imaged. The occasional occurrence of isolated splenic metastases makes it imperative that CT examination of cervical neoplasms include the upper abdomen so that these lesions are not missed.

Carlos Valls
Joan Serra
Hospital de Bellvitge, L'Hospitalet de Llobregat
Barcelona, Spain

REFERENCES

1. Marymont JH Jr, Gross S. Patterns of metastatic cancer in the spleen. *Am J Clin Pathol* **1963**;40:58–60
2. Camilien L, Gordon D, Fruchter RG, Maiman M, Boyce JG. Predictive value of computerized tomography in the presurgical evaluation of primary carcinoma of the cervix. *Gynecol Oncol* **1988**;30:209–215
3. Kim SH, Choi BI, Lee HP, et al. Uterine cervical carcinoma: comparison of CT and MR findings. *Radiology* **1990**;175:45–51

Renal Cell Carcinoma Simulating Oncocytoma

Renal oncocytomas are uncommon neoplasms that originate from proximal tubular cells and have benign clinical features. Preoperative differentiation that would allow the surgeon to perform a more limited procedure has been emphasized in the literature [1]. We present a case of renal cell carcinoma with imaging and gross pathologic features similar to those of an oncocytoma, which led to an erroneous preoperative diagnosis.

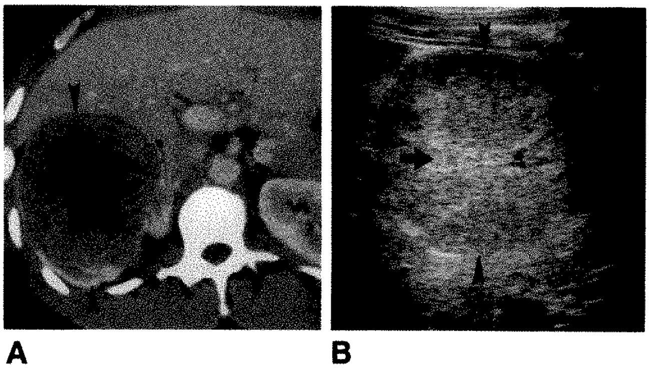

Fig. 1.—Renal cell carcinoma simulating oncocytoma.
***A*, CT scan through upper abdomen shows a large mass (*arrowheads*) in right kidney with a central stellate area of low density simulating a central scar (*arrow*) characteristic of renal oncocytoma.**
***B*, Sonogram shows a renal mass (*arrowheads*) of uniform echogenicity and a hyperechoic central zone (*arrow*).**

A previously healthy 47-year-old man had had pain in the right flank radiating anteriorly to the right lower quadrant for 2 days. The results of physical examination, renal function studies, and urinalysis were normal except for microhematuria. Dynamically enhanced CT scan showed a well-marginated, uniformly enhancing, noncalcified renal mass with a large, central, stellate, low-attenuation scar (Fig. 1A). No evidence of hepatic metastasis or retroperitoneal tumor extension was found. Sonography showed a 9.7 × 8.7 cm homogeneous mass in the right kidney with a central echogenic stellate area (Fig. 1B). MR images showed a large, well-defined, sharply marginated mass in the right kidney. The mass had a signal intensity similar to that of normal renal parenchyma, with a central stellate area of decreased signal intensity on T1-weighted images. The tumor did not extend into the inferior vena cava. Total nephrectomy was performed because the tumor involved almost the entire right kidney. The mass was 11 × 8.2 × 9.5 cm and was confined within the renal capsule. The cut surface of the gross specimen showed focal areas of peripheral hemorrhage and a central stellate white scar. Histologic examination showed a pleomorphic tumor with typical features consistent with renal cell carcinoma. No histologic evidence of oncocytoma was found.

The patient had an uneventful postoperative course and was well when discharged. Two months after surgery, follow-up examination showed no evidence of local tumor recurrence, but a pathologic fracture was discovered in the eighth right rib.

Renal oncocytomas are uncommon benign neoplasms with distinct imaging features that are often difficult to distinguish from renal cell carcinoma. Some authors [1–4] have emphasized the neeed for this preoperative differentiation, which would assist surgeons in their surgical approach. Recognition of oncocytoma will prevent the surgeon from performing a radical nephrectomy. The presence of a central stellate scar usually seen in large tumors (range, 3–16 cm; mean, 6 cm) [2] has been emphasized as the most specific characteristic feature of oncocytoma. This finding can be shown by CT, MR, and sonography. The appearance of a well-marginated, homogeneously enhancing, smoothly contoured mass with a central stellate area of decreased attenuation on CT is considered diagnostic of renal oncocytoma. In our case, the findings on the MR images correlated well with those on the CT scans.

Most studies report oncocytomas as benign. Some institutions grade oncocytomas according to how malignant the tumors are, such as renal cell carcinoma with oncocytoma features. The diagnosis indicated by the histologic findings in this case was renal cell carcinoma with scar tissue and sclerosis. The scar in oncocytomas and in renal cell carcinomas is usually the result of vascular necrosis. The peculiar features of this case are the central stellate location of the scar, the uniform enhancement, and the smooth, well-defined margins in such a large hypernephroma. This uncommon presentation of a renal cell carcinoma emphasizes the need for caution in the preoperative differentiation between hypernephroma and oncocytoma when subtotal nephrectomy is contemplated.

Carmen Endress
Michael A. Chita
Detroit Receiving Hospital
Wayne State University
Detroit, MI 48201

REFERENCES

1. Errol E, Huntrakoon M. Computed tomography of renal oncocytoma. *AJR* **1983**;141:741–746
2. Quinn MJ, Hartman DS, Friedman AC, et al. Renal oncocytoma: new observations. *Radiology* **1984**;153:49–53
3. Jasinski RW, Amendola MA, Glazer GM, Bree RL, Gikas PW. Computed tomography of renal oncocytomas. *Comput Radiol* **1985**;9:307–314
4. Curry NS, Garvin AJ, Schabel ST, Fish G. Intratumoral fat in a renal oncocytoma mimicking angiomyolipoma. *AJR* **1989**;154:307–308

Congenital Absence of a Thoracic Spine Pedicle

We read with interest the article by Wiener et al. [1] on 13 cases of congenital absence of a cervical spine pedicle, of which 55 cases have been reported in the literature. We report a case of congenital absence of a thoracic spine pedicle, which is very rare.

A 77-year-old woman had progressive muscular weakness of the lower limbs, resulting in functional disability. The results of a physical examination were normal, but the patient was anxious and depressed. The erythrocyte sedimentation rate and the results of CSF analysis were normal. Radiographs showed the absence of the left pedicle of the 10th thoracic vertebra (Fig. 1A), which had been noted some years before. Scintigrams were normal. CT confirmed the abnormality and showed the integrity of bone outline and the absence of bone destruction (Fig. 1B). The patient was treated for anxiety and eventually was able to walk again.

Reports of congenital abnormalities of the vertebral pedicles have been limited to the cervical and lumbosacral spine. Absence of a thoracic pedicle is rare (10 cases reported [2]) and frequently is discovered incidentally on radiographs. The characteristics of such abnormalities are the same for thoracic, cervical, and lumbosacral types. The congenital nature is suggested by hypoplasia of the elements of the ipsilateral neural arch and hypertrophy of various elements of the contralateral neural arches. The presence of these anatomic changes should prevent confusion with an acquired abnormality, such as neoplastic or inflammatory disease. CT allows careful analysis of the lesions and eliminates other causes of absence of a pedicle, making invasive and expensive explorations unnecessary.

Philippe Goupille
Bernard Fouquet
Philippe Cotty
Jean-Pierre Valat
CHU Trousseau
37044 Tours, France

REFERENCES

1. Wiener MD, Martinez S, Forsberg DA. Congenital absence of a cervical spine pedicle: clinical and radiologic findings. *AJR* **1990**;155:1037–1041
2. Goupille P, Cotty P, Fouquet B, Laffont J, Valat JP. Vertèbre borgne congénitale dorsale: un nouveau cas. *Ann Radiol* **1989**;32:582–585

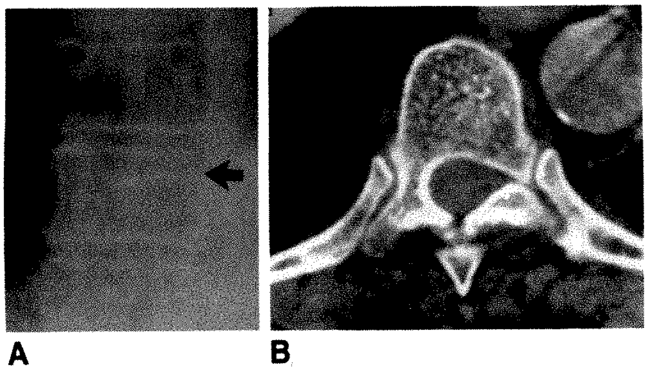

Fig. 1.—*A* and *B*, Radiograph (*A*) and CT scan (*B*) show absence of left pedicle (*arrow*) of T10. Note integrity of bone outline on *B*.

Cortical Fractures of the Femoral Head

I read with interest the paper by Richardson et al. [1] on cortical fractures of the femoral head associated with posterior hip dislocation, and I regret that it was not brought to my attention sooner. Richardson et al. are incorrect in their assertion that these injuries have not been described previously. I reported a series of 16 acetabular fractures in 1985 [2], eight of which were associated with injuries of the posterior margin. Six of the eight were in patients who had fractures of various types involving the anterior cortex of the femoral head. Some of these were remarkably similar to those described by Richardson et al. Discussion of the possible causes of such defects led me to much the same conclusions as those of Richardson et al., namely, that impaction of the dislocated femoral head against the posterior lip of the acetabulum is probably the major cause of these cortical injuries.

Richard M. Blaquière
Southampton General Hospital
Southampton SO9 4XY, United Kingdom

REFERENCES

1. Richardson P, Young JWR, Porter D. CT detection of cortical fracture of the femoral head associated with posterior hip dislocation. *AJR* **1990**;155:93–94
2. Blaquière RM. Computed tomography in acetabular trauma. *Clin Radiol* **1985**;36:5–11

Reply

In response to Dr. Blaquière's letter and having discovered his article [1], I am of course delighted to acknowledge his prior recognition of fractures of the anterior cortical head caused by impaction. I must admit that the rather small number of cases he presented, somewhat hidden within a publication dealing mainly with fractures of the acetabulum, led to the information being overlooked by both me and my coauthors. I trust that Dr. Blaquière will agree that our publication [2], which describes a much larger series of patients, is a useful addition to and corroboration of his earlier observation. Furthermore, it provides the definitive proof that the cortical fracture is due to impaction on a fragment or fragments of the posterior acetabular rim.

I am grateful to Dr. Blaquière for alerting us to his earlier and instructive publication.

Jeremy W. R. Young
University of Maryland Medical System
Baltimore, MD 21201

REFERENCES

1. Blaquière RM. Computed tomography in acetabular trauma. *Clin Radiol* **1985**;36:5–11
2. Richardson P, Young JWR, Porter D. CT detection of cortical fracture of the femoral head associated with posterior hip dislocation. *AJR* **1990**;155:93–94

Atypical Mesenchymal Hamartoma of the Liver: Prenatal Sonographic Diagnosis

The increased use of prenatal sonography has facilitated the diagnosis of a variety of fetal liver tumors, including the prenatal diagnosis of cystic hamartomas. Most mesenchymal hamartomas of the liver contain microscopic and macroscopic cysts, which can be up to 14 cm in diameter. Absence of cysts within these mesenchymal hamartomas is distinctly unusual. We describe the sonographic appearance of such a case.

A sonogram of a 27-year-old woman showed a single, live fetus of 36 weeks gestation. A solid mass 5 × 7 cm was found in the fetal liver, occupying most of the right lobe (Fig. 1). It contained medium-amplitude echoes and no cysts. Two months after an uneventful vaginal delivery, the liver mass was surgically excised. Grossly, the tumor was uniformly solid; microscopic features were consistent with the diagnosis of mesenchymal hamartoma.

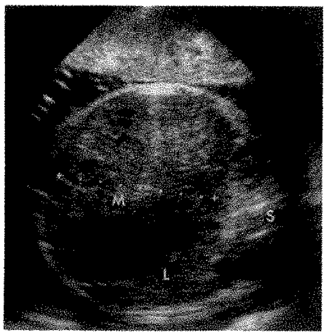

Fig. 1.—Transverse sonogram of fetal abdomen shows a mass (M) in liver (L). S = spine.

Two reports [1, 2], including one from the Armed Forces Institute of Pathology, suggest that mesenchymal hamartomas are generally solid in the early stages of development but become cystic as they enlarge. These cysts consist primarily of dilated bile ducts or fluid accumulation in areas of degenerated mesenchyme. Late appearance of cysts accounts for most cystic hamartomas reported in infants and children. The liver mass in our case might have been detected with the characteristic cystic appearance in early childhood if it had not been detected prenatally.

Gail C. Hansen
University of California, Los Angeles, School of Medicine
Los Angeles County-Olive View Medical Center
Sylmar, CA 91342
Nagesh Ragavendra
University of California, Los Angeles, School of Medicine
Los Angeles, CA 90024

REFERENCES

1. Stocker JS, Ishak KA. Mesenchymal hamartoma of the liver: report of 30 cases and review of the literature. *Pediatr Pathol* **1983**;1:245-267
2. Srouji MN, Chaten J, Schulman WM, et al. Mesenchymal hamartoma of the liver in infants. *Cancer* **1978**;42:2483-2489

MR Imaging of Patients with Migraine

We are writing in response to the article by Osborn et al., "MR of Imaging of the Brain in Patients with Migraine Headaches" [1]. In their work, Osborn et al. found white matter foci in five (12%) of 41 patients; only two of these five (5%) were less than 40 years old. Figures are cited from earlier studies in which 33% (average of three studies) of patients had white matter foci. Finally, the authors conclude that white matter foci are "found less commonly in all migraineurs than previously thought." They do not discuss why their results [1] are different from those of earlier studies, including two recent ones [2] (Prager et al., presented at the annual meeting of the Society of Magnetic Resonance in Medicine, August 1990). We wish to call attention to these studies and address why these differences have occurred.

In March 1990, Kuhn and Shekar [2] published an MR study of 74 patients with migraine. All were less than 40 years old, and 26% had white matter foci. In August 1990, Prager et al. presented an abstract of an MR study that included 100 patients with severe headache. Forty-one of the patients with migraine were less than 40 years old. Areas were considered foci only if they had greater signal intensity than CSF on both the first and second echo of the long TR sequence. Again, 26% of the patients had white matter foci. In the combined group of 115 patients less than 40 years old who had severe migraines, white matter foci were a common finding.

We think that Osborn et al. found fewer lesions because of the population of patients studied and the method used. Most of their patients were men, whereas most patients with migraine are women. Their patients were referred from a hospital clinic, whereas patients in the other studies were referred from specialty headache clinics. All the patients in the study by Prager et al. were seen at a tertiary care headache clinic and may have had more severe headaches than the patients of Osborn et al. These differences could result in two distinct groups. Finally, 14 of the patients of Osborn et al. were studied with a 0.35-T unit, and only a limited number had T2-weighted coronal imaging. All the patients of Prager et al. were studied with a 1.5-T GE Signa unit, and all had T2-weighted coronal imaging. The strength of the magnet may not be important, as some of the other studies used units with magnets of 1.5 T or less. Prager et al. found that the T2-weighted coronal images were helpful in several cases in which visualization of lesions on axial images was not clear.

In conclusion, the literature supports the contention that white matter foci occur frequently (26%) in patients with severe migraine who are less than 40 years old. The prevalence of white matter foci increases with increasing age [3]. We think that a similar prevalence was not found by Osborn et al. because of their population of patients, the size of the group, and, to a lesser extent, differences in methods.

Incidentally, in one of the cases of Osborn et al., the white matter lesion was subcortical rather than periventricular. We have found this tendency in many of our patients who have migraine, and we use the finding as a differential point. The other featured patient in the article [1] was a 66-year-old with periventricular increased signal. This case would not have qualified as white matter foci associated with migraine in the study of Prager et al. because of the location of the signal and the age of the patient.

Jordan Prager
Jordan Rosenblum
The University of Chicago
Chicago, IL 60637-1470

REFERENCES

1. Osborn RE, Alder DC, Mitchell CS. MR imaging of the brain in patients with migraine headache. *AJNR* **1991**;12:521-524, *AJR* **1991**;157:385-388
2. Kuhn MJ, Shekar PC. A comparative study of magnetic resonance imaging and computed tomography in the evaluation of migraine. *Comput Med Imaging Graph* **1990**;14:149-152
3. Evaluation of headache patients by MRI. *Headache Q* **1991**;2:192-196

Letters are published at the discretion of the Editor and are subject to editing.

Letters to the Editor must not be more than two *double-spaced*, typewritten pages. One or two figures may be included. Abbreviations should not be used. Limit the number of authors to four, or we will list only the first three and add "and colleagues" to the end of the list. See Author Guidelines.

Material being submitted or published elsewhere should not be duplicated in letters, and authors of letters must disclose financial associations or other possible conflicts of interest.

Letters concerning a paper published in the *AJR* will be sent to the authors of the paper for a reply to be published in the same issue. Opinions expressed in the Letters to the Editor do not necessarily reflect the opinions of the Editor.

Review of Current Literature

Initials and addresses of corresponding authors are provided in parentheses for each article so that the reader can obtain reprints directly. Abstracts are printed verbatim from each journal.

The New England Journal of Medicine

Effect of octreotide on intestinal motility and bacterial overgrowth in scleroderma. Soudah HC, Hasler WL, Owyang C (CO, Dept. of Internal Medicine, Gastroenterology Research Unit, University of Michigan Medical Center, 3912 Taubman Ctr., Box 0362, 1500 E. Medical Center Dr., Ann Arbor, MI 48109). *N Engl J Med* 325(21):1461-1467, Nov. 1991

Background. Patients with scleroderma may have abnormal motility of the small intestine, with pseudoobstruction and bacterial overgrowth. Standard stimulatory agents are often ineffective in such patients. Because the somatostatin analogue octreotide evokes intestinal motor activity in normal subjects, we hypothesized that it might increase motility in patients with scleroderma.

Methods. We studied the effects of octreotide on intestinal motility and plasma motilin concentrations in five fasting patients with scleroderma who had bacterial overgrowth and in six fasting normal subjects. The motor effects of octreotide were correlated with its effects on abdominal symptoms and bacterial overgrowth as determined by the level of breath hydrogen excretion.

Results. In the normal subjects, octreotide (10 μg subcutaneously) increased the mean (±SD) frequency of intestinal migrating complexes, which reflect intestinal motility, from 1.5 ± 1.0 to 4.1 ± 1.1 every three hours. In the patients with scleroderma, who had no spontaneous migrating complexes, octreotide (100 μg) induced 3.6 ± 2.3 complexes every three hours. These complexes propagated at the same velocity and had two-thirds the amplitude of the spontaneous complexes in normal subjects. Plasma motilin concentrations, which were higher in the patients with scleroderma (229 ± 74 pmol per liter) than in the normal subjects (112 ± 37 pmol per liter), were inhibited by octreotide, suggesting that intestinal activity evoked by octreotide is independent of motilin. Treatment of the patients with scleroderma with octreotide (50 μg every evening) for three weeks reduced breath hydrogen excretion while they were fasting from 25 ± 5 to 4 ± 2 ppm ($P = 0.001$) and breath hydrogen excretion after they ingested 50 g of glucose from 46 ± 24 to 8 ± 7 ppm ($P = 0.015$); these reductions were accompanied by a significant decrease in nausea, bloating, and abdominal pain and by less frequent emesis.

Conclusions. Octreotide stimulates intestinal motility in normal subjects and in patients with scleroderma. In such patients, the short-term administration of octreotide reduces bacterial overgrowth and improves abdominal symptoms. This agent may be useful for the treatment of intestinal dysmotility in patients with scleroderma.

Sickle cell disease as a cause of osteonecrosis of the femoral head. Milner PF, Kraus AP, Sebes JI, et al. (PFM, Adult Sickle Cell Clinic, Bldg. FR-100, Medical College of Georgia, Augusta, GA 30912). *N Engl J Med* 325:1476-1481, Nov. 1991

Background and Methods. Osteonecrosis of the femoral head is an important complication of sickle cell disease. We studied 2590 patients who were over 5 years of age at entry and followed them for an average of 5.6 years. Patients were examined twice a year, and radiographs of the hips were taken at least twice: at study entry and approximately three years later.

Results. At study entry, 9.8 percent of patients were found to have osteonecrosis of one or both femoral heads. On follow-up, patients with the hemoglobin SS genotype and α-thalassemia were at the greatest risk for osteonecrosis (age-adjusted incidence rate, 4.5 cases per 100 patient-years, as compared with 2.4 in patients with the hemoglobin SS genotype without α-thalassemia and 1.9 in those with the hemoglobin SC genotype). Although the rate of osteonecrosis in patients with the hemoglobin SC genotype did not differ significantly from that in patients with the hemoglobin SS genotype without α-thalassemia, osteonecrosis tended to develop in these patients later in life. Intermediate rates of osteonecrosis were observed among patients with the hemoglobin $S-\beta^0$-thalassemia and the hemoglobin $S-\beta^+$-thalassemia genotypes (3.6 and 3.3 cases per 100 patient-years, respectively). Osteonecrosis was found in patients as young as five years old (1.8 cases per 100 patient-years for all genotypes).

The frequency of painful crises and the hematocrit were positively associated with osteonecrosis. The mean corpuscular volume and serum aspartate aminotransferase level were negatively associated. Twenty-seven patients had hip arthroplasty during the study; 10 were under 25 years of age. Five of the 27 required reoperation 11 to 53 months after the initial operation.

Conclusions. Osteonecrosis of the femoral head is common in patients with sickle cell disease, with an incidence ranging from about 2 to 4.5 cases per 100 patient years. Patients with the hemoglobin SS genotype and α-thalassemia and those with frequent painful crises are at highest risk. The overall prevalence is about 10 percent. The results of hip arthroplasty are poor.

The effect of atherosclerosis on the vasomotor response of coronary arteries to mental stress. Yeung AC, Vekshtein VI, Krantz DS, et al. (ACY, Cardiovascular Division, Brigham and Women's Hospital, 75 Francis St., Boston, MA 02115). *N Engl J Med* 325(22):1551-1556, Nov. 1991

Background. Mental stress can cause angina in patients with coronary artery disease, but its effects on coronary vasomotion and blood flow are poorly understood. Because atherosclerosis affects the reactivity of coronary arteries to various stimuli, such as exercise, we postulated that atherosclerosis might also influence the vasomotor response of coronary arteries to mental stress.

Methods. We studied 26 patients who performed mental arithmetic under stressful conditions during cardiac catheterization. (An additional four patients who did not perform the mental arithmetic served as controls.) Coronary segments were classified on the basis of angiographic findings as smooth, irregular, or stenosed. In 15 of the patients without focal stenoses in the left anterior descending artery, acetylcholine (10^{-8} to 10^{-6} mol per liter) was infused into the artery to test endothelium-dependent vasodilation. Changes in coronary blood flow were measured with an intracoronary Doppler catheter in these 15 patients.

Results. The response of the coronary arteries to mental stress varied from 38 percent constriction to 29 percent dilation, whereas the change in coronary blood flow varied from a decrease of 48 percent to an increase of 42 percent. The direction and magnitude of the change in the coronary diameter were not predicted by the changes in the heart rate, blood pressure, or plasma norepinephrine level. Segments with stenoses ($n = 7$) were constricted by a mean (±SE) of 24 ± 4 percent, and irregular segments ($n = 20$) by 9 ± 3 percent, whereas smooth segments ($n = 25$) did not change significantly (dilation, 3 ± 3 percent; $P < 0.002$). Coronary blood flow increased by 10 ± 10 percent in smooth vessels, whereas the flow in irregular vessels decreased by 27 ± 5 percent. The degree of constriction or dilation during mental stress correlated with the response to the infusions of acetylcholine ($P < 0.0003$, $r = 0.58$).

Conclusions. Atherosclerosis disturbs the normal vasomotor response (no change or dilation) of large coronary arteries to mental stress; in patients with atherosclerosis paradoxical constriction occurs during mental stress, particularly at points of stenosis. This vasomotor response correlates with the extent of atherosclerosis in the artery and with the endothelium-dependent response to an infusion of acetylcholine. These data suggest that in atherosclerosis unopposed constriction caused by a local failure of endothelium-dependent dilation causes the coronary arteries to respond abnormally to mental stress.

Cancer

Cigarette smoking and lung cancer cell types. Morabia A, Wynder EL (ELW, American Health Foundation, 320 E. 43rd St., New York, NY 10017). *Cancer* 68:2074–2078, 1991

The role of tobacco smoke in the development of lung cancer is well known for squamous and small cell types, somewhat less so for adenocarcinoma, and not specifically assessed for large cell carcinoma. In the current analysis, based on 851 men and 507 women with lung cancer and their matched controls (888 men and 608 women), smoking was associated with each lung cancer cell type, and differences in smoking habits by cell types were small. However, the increase of lung cancer risk according to number of cigarettes per day was stronger for small cell and oat cell carcinoma than for adenocarcinoma. There was no increase for large cell carcinoma. For squamous cell carcinoma, this dose response was weak among men and strong among women. The strength of the association between smoking and lung cancer cell types may be related to cancer location, with more peripheral lung cancer types (such as adenocarcinoma and large cell carcinoma) showing weaker associations than more central tumors (such as squamous or small cell and oat cell carcinoma).

Reprinted by permission from the American Cancer Society.

The changing pattern of lung carcinoma. Auerbach O, Garfinkel L (OA, Veterans Administration Hospital, East Orange, NJ 07019). *Cancer* 68:1973–1977, 1991

In a study of 505 cases of lung carcinoma from a period in which there was a significant change in tobacco-smoking habits, a dramatic shift in the histologic type and location of the lung tumors was observed. Peripheral tumors, found in 30.7% of the carcinomas occurring before 1978, were found in 42% of the carcinomas from 1986 to 1989. The corresponding decrease in the centrally originating bronchial carcinoma was from 69.3% to 57.3%. The greatest change in histologic cancer type was that the incidence of bronchioalveolar carcinoma more than doubled from 9.3% in the earlier period to 20.3% in the 1986-to-1989 period. Corresponding to the decreasing incidence of lung carcinoma, there is a decrease in cancers related to cigarette smoking. A study of cases of lung carcinoma among nonsmokers and former smokers showed a decreased incidence of the bronchiogenic cancers and an increase of cancer occurring in the peripheral lung parenchyma. This finding should be validated in other population-based studies, and if confirmed, new studies should be undertaken in an attempt to discover the factors that play a role in the development of such cancers. As an example, viral oncogenes may be a possibility. Viruses were suggested in the past as being related to the development of some of these tumor types.

Reprinted by permission from the American Cancer Society.

Chest

Radiographic abnormalities in Vermont granite workers exposed to low levels of granite dust. Graham WGB, Ashikaga T, Hemenway D, Weaver S, O'Grady RV (WGBG, University of Vermont College of Medicine, Burlington, VT). *Chest* 100(6):1507–1514, Dec. 1991

The issue of whether low levels of granite dust exposure lead to radiographic abnormalities after a lifetime of exposure has not been settled. In 1983, we carried out a radiographic survey of the Vermont granite industry, consisting of quarry and stone shed workers who had been exposed to the low dust levels prevailing in the industry since 1938 to 1940. Films were read by three "B" readers, using the ILO classification system, which requires the identification of both rounded and irregular opacities, as well as combinations of both. X-ray films were taken of 972 workers, out of a total work force of approximately 1,400. Of these films, 28 (3 percent) were interpreted by either two or three of the three readers as showing abnormalities consistent with pneumoconiosis. Only seven films (or 0.7 percent of the entire cohort) showed nodular or rounded opacities of the type typically seen in uncomplicated silicosis. The remainder of the abnormal x-ray films showed irregular opacities, largely in the lower lung zones, which are of uncertain significance, but may be related to heavy cigarette smoking and aging, and possibly dust inhalation. In addition, total gravimetric dust concentrations in the workplace were measured; 417 respirable-size mass samples showed concentrations of 601 μg/cu m ± 368 μg/cu m. Using previously published estimates of 10 percent quartz in granite dust, the average quartz concentration was 60 μg/cu m. Twelve percent of the samples exceeded 100 μg/cu m, the current OSHA standard for quartz. We conclude that control of quartz exposure in the Vermont granite industry to levels which are on average less than the current OSHA standard has essentially eliminated definite radiographic changes of silicosis. The significance of the irregular opacities in the lower lung zones seen on a majority of the 28 x-ray films judged to be abnormal is not clear.

Circulation

Percutaneous balloon aortic valvuloplasty: acute and 30-day follow-up results in 674 patients from the NHLBI Balloon Valvuloplasty Registry. NHLBI Balloon Valvuloplasty Registry Participants. (Bashore TM, Box 3012, Duke University Medical Center, Durham, NC 27710). *Circulation* 84(6):2383–2397, Dec. 1991

Percutaneous balloon aortic valvuloplasty has been used as a therapeutic option for relief of valvular stenosis. This study describes patients undergoing initial percutaneous aortic balloon valvuloplasty enrolled in the National Heart, Lung, and Blood Institute (NHLBI) Balloon Valvuloplasty Registry.

Methods and Results. Extensive baseline procedural and postprocedural data were tabulated in 674 patients during a 24-month period. Functional status was captured using standard methods and an overall functional scoring system. Complications were defined and divided into procedural, acute (within 24 hours), in-hospital, and within 30 days of the procedure. The patient population was elderly and symptomatic, with 83% >70 years of age. New York Heart Association functional class (FC) III or IV congestive heart failure (CHF) was present in 76%, syncope or presyncope was present in 34%, and Canadian Heart Association class III or IV angina was present in 23%. Using an overall functional scoring system (0–100), 54% exhibited scores <50. Comorbid disease was common. Forty-five percent possessed at least one serious noncardiac disability as a reason for valvuloplasty. Eighty percent of those seen by a cardiothoracic surgeon were believed inappropriate for aortic valve replacement. Hemodynamically, the aortic valve area increased from 0.5 ± 0.2 cm^2 to 0.8 ± 0.3 cm^2 ($p < 0.0001$), accompanied by a fall in mean and peak aortic valve gradient from 55 ± 21 and 65 ± 28 mm Hg to 29 ± 13 and 31 ± 18 mm Hg, respectively (both $p < 0.0001$). Small but significant increases were observed in cardiac output, heart rate, and mean aortic pressure with minor declines in the pulmonary artery (PA) systolic and left ventricular (LV) end-diastolic pressure. One hundred sixty-seven (25%) experienced at least one significant complication within 24 hours, and 211 (31%) experienced a significant complication before discharge. Complications before hospital discharge included the need for transfusion (23%), vascular surgery (7%), cerebrovascular accident (3%), other systemic embolus (2%), myocardial infarction (2%), acute tubular necrosis (1%), or cardiac surgery (1%). Seventeen (3%) patients died during the procedure; 16 of those were due to cardiac causes. By hospital discharge, there was an additional 52 total deaths; 37 were due to cardiovascular causes. Between hospital discharge and 30 days, 23 additional deaths occurred; 18 were due to cardiac disease. At 30 days, therefore, there was a grand total of 92 (14%) deaths; 71 (11%) were due to cardiovascular-related causes. Univariate and logistic regression analysis of mortality revealed that death was most frequent in patients suffering multiorgan failure and poor LV systolic function. Thirty-day mortality was associated with a predefined high-risk subset of hypotension and NYHA class IV CHF (risk ratio, 4.4), blood urea nitrogen (BUN) >30 mg/dl (risk ratio, 3.7), use of an antiarrhythmic (risk ratio, 2.9), and cardiac output <3.0 l/min (risk ratio, 2.4). Of the survivors (86%) at 30 days, symptomatic improvement was generally present. Seventy-five percent experienced at least one functional class improvement in CHF, and 53% experienced at least a quartile improvement in overall functional status score.

Conclusions. These data reveal that percutaneous aortic balloon valvuloplasty in an elderly and debilitated population can be done with low mortality but substantial morbidity. Mortality is greatest in patients with multiorgan failure resulting from poor cardiac output. In patients with reasonably preserved LV function who are otherwise inappropriate surgical candidates because of comorbid factors, survival and early improvement in symptomatic status are frequently observed after percutaneous aortic valvuloplasty.

Single-lung transplantation for pulmonary hypertension: three-month hemodynamic follow-up. Pasque MK, Trulock EP, Kaiser LR, Cooper JD (MKP, Division of Cardiothoracic Surgery, Washington University Medical School, One Barnes Hospital Plaza, Queeny Tower Ste. 3105, St. Louis, MO 63110). *Circulation* 84(6):2275–2279, Dec. 1991

Shorter waiting times, relative technical simplicity, and satisfactory application to a broad spectrum of patients has made single-lung transplantation an attractive option in the treatment of patients with end-stage pulmonary hypertension.

Methods and Results. Seven patients with pulmonary hypertension underwent single-lung transplantation. Simultaneous closure of associated atrial septal defects was accomplished in two patients. Despite severely compromised pretransplant right ventricular function in all patients, there was no early or late mortality. Right ventricular functional recovery as characterized by hemodynamic assessment before and at a mean of 13 weeks posttransplant was nearly uniform and characterized by a drop in 1) pulmonary arterial systolic pressure from 92 ± 7 mm Hg to 29 ± 6 mm Hg ($p = 0.001$), 2) central venous pressure from 10 ± 6 mm Hg to 1 ± 2 mm Hg ($p = 0.02$), and 3) pulmonary vascular resistance index from 1,924 ± 663 to 232 ± 73 dyne·sec·cm^{-9} ($p = 0.001$). Radionuclide ventriculography before and at a mean of 17 weeks posttransplant documented a significant ($p = 0.006$) increase in right ventricular ejection fraction from 22 ± 15% to 51 ± 11%. Quantitative pulmonary perfusion scintigraphy at a mean of 17 weeks posttransplant demonstrated a significant ($p = 0.001$) increase in perfusion to the transplanted lung from 56 ± 6% to 89 ± 7%. There was a concomitant, slight but significant ($p = 0.004$) decrease in ventilation to the transplanted side from 56 ± 6% to 49 ± 8%. After transplantation, all patients returned to New York Heart Association functional class I or II from their preoperative levels of class III or IV.

Conclusions. These early follow-up data cautiously support the option of single-lung transplantation in patients with pulmonary hypertension, although long-term durability of these hemodynamic changes deserves documentation before widespread application.

Gastroenterology

Gas in gallstones: quantitative determinations and possible effects on fragmentation by shock waves. Vakil N, Everbach EC (NV, Department of Medicine, University of Rochester, Rochester, NY). *Gastroenterology* 101:1628–1634, 1991

The presence of gas in a gallstone can profoundly affect the ability of shock waves to fragment the stone by various mechanisms. In the present study, the aim was to determine the gas content of gallstones and determine if increasing the gas content of the stone affected the outcome of lithotripsy. Thirty human gallstones, transferred directly from gallbladder bile into sterile saline, were studied. The initial gas content of all stones was determined by differential weighing under saline before and after degassing. Eighteen gallstones were pairs; each pair was from a single patient and of similar size and composition. One gallstone of each of the pairs was exposed to air and the other was kept under saline. Then each of the paired gallstones was subjected to 1000 pulses at power level 3 (highest) in a Diasonics Therasonic lithotripter (Diasonics, Milpitas, CA). The volume of gas present at the beginning of the experiment in all groups of stones was 2.4 ± 2.1 mm^3, and 27% of all gallstones tested contained measurable amounts of gas initially. There was no significant difference in the volume of gas present in the paired stones at the beginning of the experiment (group A, 1 ± 0.4 mm^3; group B, 2 ± 1 mm^3). After group A stones were exposed to air, the gas content was significantly higher (36 ± 18 mm^3) than in the paired group B stones stored under saline (3 ± 2 mm^3; $P < 0.05$). Stones exposed to air fragmented more easily than stones stored under saline. The mean number of pulses required to cause initial fragmentation was significantly lower in the group of stones exposed to air (22 ± 7) compared with those stored under saline (610 ± 139; $P < 0.05$). The fragments were smaller and more numerous in the group of stones exposed to air than in those stored under saline. It is concluded that gas is present in some gallstones and that the efficacy of lithotripsy increases with increasing stone gas content. Our data suggest that alterations in the physical characteristics of gallstones can have profound effects on the outcome of lithotripsy.

Reprinted with permission by the American Gastroenterological Association.

Digestive Diseases and Sciences

Portal hypertensive colopathy: a new entity. Naveau S, Bedossa P, Poynard T, Mory B, Chaput JC (SN, Service d'Hépato-Gastroénterologie, Hôpital Antoine Béclère, 157, rue de la Porte de Trivaux, F-92141 Clamart Cedex, France). *Dig Dis Sci* 36(12):1774–1781, Dec. 1991

The aim of this paper was, first, to show in a case control study that in alcoholic cirrhotic patients colonic vascular ectasias (VE) are a complication of portal hyertension and, second, to establish in a histomorphometric study that colonic vascular ectasias and rectal varices (RV) are only endoscopic features of a new entity: portal hypertensive colopathy, the pathologic basis of which is colonic mucosal capillary ectasia. In the case control study, for each case, three age- and sex-matched controls selected from consecutive patients were used. Sixteen alcoholic cirrhotic patients, 12 men, 4 women (mean age ± SD: 62 ± 10 years) had colonic vascular ectasias. The prevalence of esophageal varices (88% vs 44%, $P < 0.005$), esophageal varices (≥ 5 mm) (44% vs 12.5%, $P < 0.01$), previous history of bleeding from esophageal varices (44% vs 8%, $P < 0.005$), and rectal varices (63% vs 6%, $P < 0.001$) was significantly greater in cases with colonic vascular ectasias than in controls without colonic vascular ectasias. The relative risk of colonic vascular ectasias in alcoholic cirrhotic patients with esophageal varices versus cirrhotic patients without esophageal varices was 14.4 (95% confidence interval 2.8–75.3). In the histomorphometric study, cirrhotic patients with vascular ectasias and/or rectal varices had a significantly higher mean diameter of vessels ($20.3 \pm 1.5\ \mu m$ vs $18.7 \pm 1.6\ \mu m$, $P < 0.05$) and a higher mean cross-sectional vascular area ($2143 \pm 396\ \mu m^2$ vs $1676 \pm 345\ \mu m^2$, $P < 0.05$) than cirrhotic patients without vascular ectasias and/or rectal varices. These results suggest that colonic vascular ectasias seem to be a complication of portal hypertension and that colonic vascular ectasias and rectal varices are endoscopic features of a new entity the portal hypertensive colopathy.

Clinical Orthopaedics and Related Research

"Hybrid" total knee arthroplasty with the Miller–Galante prosthesis: a prospective clinical and roentgenographic evaluation. Kraay MJ, Meyers SA, Goldberg VM, Figgie HE III, Conroy PA (MJK, Dept. of Orthopaedic Surgery, University Hospital of Cleveland, 2074 Abington Rd., Cleveland, OH 44106). *Clin Orthop* 273:32–41, Dec. 1991

Twenty-nine "hybrid" Miller–Galante total knee arthroplasties, in 22 patients, were evaluated prospectively and according to the clinical and roentgenographic guidelines of The Knee Society. Selection of this technique, incorporating an uncemented, porous-ingrowth femoral component and a cemented tibial component, was based on patient age, medical condition, activity level, and intraoperative assessment of bone quality and ligament competency. The average age of the patients at the time of surgery was 71 years. The average preoperative Knee Society Knee Score was 32; average pain score was 14; and the average function score, 47. After an average follow-up interval of 28 months postsurgery (minimum, 24 months), the average Knee Society Knee Score was 93; the average pain score, 47; and the average function score, 79. Range of motion averaged 110°. Only one knee, with persistent pain of obscure origin, rated an unsuccessful result. No arthroplasties were revised for any reason. Twenty-three knees had fluoroscopically guided roentgenograms to assess the bone–prosthesis and bone–cement interfaces. No significant or progressive radiolucencies were noted under any of the components. No apparent adverse bone remodeling was associated with the uncemented femoral component. The fluoroscopically guided roentgenograms were significantly more sensitive in detecting interface radiolucencies than plain ones. Clinical and roentgenographic evidence of component loosening were absent in all patients. Results of this study suggest that the hybrid fixation technique can reliably provide satisfactory pain relief and restoration of function in properly selected patients. Potential advantages of an uncemented femoral component include decreased operative time, reduction of polyethylene wear from cement debris, and avoidance of a possible adverse biologic response to polymethylmethacrylate.

The Journal of Nuclear Medicine

Clinical evaluation of a scintigraphic method for diagnosing inflammations/infections using indium-111-labeled nonspecific human IgG. Serafini AN, Garty I, Vargas-Cuba R, et al. (ANS, University of Miami, School of Medicine, Division of Nuclear Medicine (D-57), JMH Central C266, P. O. Box 016960, Miami, FL 33101). *J Nucl Med* 32:2227–2232, 1991

This study was undertaken as part of a Phase II study to assess the sensitivity and safety of ^{111}In-DTPA-human IgG, an imaging agent for the detection of inflammations and/or infections. Forty patients with infection/inflammation on the basis of clinical findings, microbiologic results, and/or the basis of results from other imaging modalities were studied. For evaluation of sensitivity, whole-body images were obtained at 6–12 hr (early) and 20–28 hr (delayed) postinjection and occasionally at 48 hr. No adverse reactions were recorded in any of the 40 patients studied. Positive results were obtained in 37 of 37 evaluable subjects (100%). The test appears to be a promising method for the detection of inflammation and/or infection.

Gastrointestinal Radiology

Diagnosis of esophageal motor disorders: a prospective study comparing barium swallow, food barium mixture, and continuous swallows with manometry. Aksglæde K, Funch-Jensen P, Vestergaard H, Thommesen P (PFJ, GI-Motility Laboratory, Depts. R and L. Århus kommunehospital, DK-8000 Århus C. Denmark). *Gastrointest Radiol* 17:1–4, 1992

Radiography and manometry of the esophagus were compared in 77 patients consecutively referred for manometric investigation on suspicion of esophageal motility disorder. Radiography and manometry were carried out simultaneously, and the results were assessed blindly. The examination comprised barium swallow, bread barium swallow, and barium swilling. Considering manometry as the standard, the overall sensitivity and specificity of the radiologic examinations were 90.4% and 92.0%, respectively. We conclude that radiology is an excellent investigation for the separation of patients with and without esophageal motility disorders, but correct subclassification often required manometry.

Journal of Ultrasound in Medicine

Contrast cholangiography versus ultrasonographic measurement of the "extrahepatic" bile duct: a two-fold discrepancy revisited. Davies RP, Downey PR, Moore WR, Jeans PL, Toouli J (RPD, Dept. of Radiology, Flinders Medical Centre, Bedford Park, SA 5042, Australia). *J Ultrasound Med* 10:653–657, Dec. 1991

The upper limit of the normal extrahepatic duct diameter when measured by sonography in our institution is less than half that when measured by endoscopic retrograde cholangiopancreatography (ERCP). The objective of this study was to locate possible sources of this discrepancy by comparing measurements obtained on the same patient by sonography, before and after ERCP. Thirty consecutive patients referred for ERCP were entered into a prospective trial; bile duct measurements were obtained independently by both techniques in 19 patients. Correcting for radiographic magnification, the ERCP measurement was more than twice that obtained by ultrasonography. Among the possible reasons for diverse results that we considered, radiographic magnification, ultrasonic underestimation, and distending effects of retrograde cholangiography (ERCP) were not found to be prominent causes for the marked discrepancy that we observed. The most likely explanation is that the duct in individual patients was being measured at a different level by the two techniques. A retrospective comparison of the studies obtained by each method suggests that the sonographic measurement is most often of the right hepatic duct. If this is the case, the two measurements show no statistically significant difference ($P > 0.05$). A prospective trial is needed to test this hypothesis.

Reprinted with permission by the American Institute of Ultrasound in Medicine.

Cardiovascular and Interventional Radiology

Bronchial arteriography and embolotherapy for hemoptysis in patients with cystic fibrosis. Tonkin ILD, Hanissian AS, Boulden TF, et al. (ILDT, Dept. of Radiology, Le Bonheur Children's Medical Center, 848 Adams Ave., Memphis, TN 38103). *Cardiovasc Intervent Radiol* 14(4):241–246, July/Aug. 1991

Bronchial arteriography and embolotherapy were performed to control hemoptysis in 11 patients with advanced stages of cystic fibrosis. Two patients suffered massive, one moderate and eight mild, but recurrent hemoptysis. The embolization procedures were performed with gelfoam, Ivalon, and coils in one to four separate procedures, altogether, nineteen of 20 procedures were successful, with follow-up, ranging from 9 months to 8 years. No serious complications were encountered except for one femoral artery pseudoaneurysm which required surgical repair. Rapid digital subtraction angiography and "road mapping" were considered helpful in avoiding the complication of reflux embolization and expediting the procedures. Bronchial embolization is a life saving procedure for severe hemoptysis in patients with cystic fibrosis and is considered safe enough to include the indications of moderate and mild/recurrent hemoptysis to improve the quality of life in these patients.

Reprinted with permission from Springer-Verlag.

News

Mammographic Interpretation

The Dept. of Radiology, Tufts–New England Medical Center is sponsoring the 1992 tutorials, Mammographic Interpretation: A Practical Approach, April 6-9, May 18-21, Sept. 14-17, and Oct. 26-29, in Boston. This intensive course is designed to teach a practical approach to mammographic interpretation and needle localization. Category 1 credit: 28 hr. Fee: $800. Information: Marc J. Homer, M.D., Box 388, Dept. of Radiology, New England Medical Center Hospitals, 750 Washington St., Boston, MA 02111; (617) 956-0045.

Visiting Fellowships in MR Imaging

The Dept. of Radiology, Hospital of the University of Pennsylvania, is sponsoring fellowships in introductory and advanced MR imaging. Dates are April 13–17, May 4–8, and June 8–12 for the introductory course and April 6–10 and May 11–15 for the advanced course. Extended stays (longer than 1 week) can be arranged. Category 1 credit: 40 hr. Fee: $1500/week; discounts available for second week. Information: Melissa Zajdel, Dept. of Radiology, Hospital of the University of Pennsylvania, 3400 Spruce St. Philadelphia, PA 19104; telephone: (215) 662-6904; fax: (215) 349-5925.

Ultrasound in Obstetrics and Gynecology

The Dept. of Radiology, The University of Michigan Medical School, is sponsoring Ultrasound in Obstetrics and Gynecology, April 8–10, at the Towsley Center, Ann Arbor, MI. The course is intended for those who have little or no experience in sonography. A broad range of introductory and advanced obstetric and gynecologic topics will be considered. The basic principles of sonography and techniques of scanning will be presented. Course director: Richard A. Bowerman. Category 1 credit: approximately 21 hr. Information: Angela Stewart, Towsley Center for Continuing Medical Education, Dept. of Post Graduate Medicine, The University of Michigan Medical School, P. O. Box 1157, Ann Arbor, MI 48106-9869; (313) 763-1400.

Clinical Seminar in Diagnostic Ultrasound

The Western Pennsylvania Hospital is sponsoring the 6th annual Clinical Seminar in Diagnostic Ultrasound, April 9–12, at the Westin William Penn Hotel, Pittsburgh. This year's seminar will be an update on duplex and Doppler imaging. Topics to be considered include vein mapping, arterial venous fistulas, carotid duplex sonography, venous duplex Doppler sonography, duplex Doppler sonography of renal arteries, transcranial Doppler imaging, pelvic transvaginal Doppler imaging, abdominal Doppler imaging, arterial duplex Doppler sonography of the lower extremities, and evaluation of transducers. Course directors: Marcela Bohm-Velez and Ellen B. Mendelson. Guest faculty: B. A. Carroll, D. O. Cosgrove, S. L. Katanick, F. W. Kremkau, C. R. B. Merritt, and D. E. Strandness, Jr. Category 1 credit: 22 hr. Fee: physicians, $495; residents, fellows, and technologists, $325. Information: CME Dept., West Penn Hospital, 4800 Friendship Ave,. Pittsburgh, PA 15224; (412) 578-7364 or (412) 578-6926.

Radiology Review Course

The University of Miami School of Medicine will present its annual Radiology Review Course, April 12–17, at the Doral Beach Resort, Miami Beach, FL. Category 1 credit: 45 hr. Information: Carol Lamarre, Seminar Coordinator, Dept. of Radiology, University of Miami School of Medicine, P. O. Box 016960 (R-109), Miami, FL 33101; telephone: (305) 585-6894; fax: (305) 325-8591.

Courses on Dysphagia

The Johns Hopkins Swallowing Center will present Basic Concepts in Dysphagia Diagnosis and Management, April 22, and Fourth Multidisciplinary Symposium on Dysphagia, April 23–24, at the Omni Inner Harbor Hotel, Baltimore. The Basic Concepts course is a special half-day introductory session for newcomers to the field of dysphagia. The symposium will discuss state-of-the-art evaluation of patients with dysphagia. Category 1 credit will be awarded. Fee (physicians/residents and allied health professionals): Basic Concepts, $125/$95; symposium, $400/$225. Information: Program Coordinator, The Johns Hopkins Medical Institutions, Office of Continuing Education, Turner Bldg., 720 Rutland Ave., Baltimore, MD 21205; telephone: (410) 955-2959; fax: (410) 955-0807.

Cleveland Conference on MR Imaging

The Dept. of Radiology, MetroHealth Medical Center and Case Western Reserve University, will present Magnetic Resonance Imaging, May 1–3, at the Forum Conference and Education Center, Cleveland. The conference will cover the basic physics of MR imaging and review current imaging in a clinical setting. The material will be presented in five half-day sessions, one each on MR physics, cardiovascular imaging, neuroimaging, musculoskeletal imaging, and advanced techniques in MR. Course chairman: E. M. Bellon. Guest faculty: A. M. Aisen, L. Eastwood, D. A. Finelli, M. Nessaiver, R. Peshock, A. S. Smith, and M. Weinstein. Category 1 credit: up to

18.25 hr. Fee: full conference: physicians, $450; residents, nurses, and technologists, $350; each half-day session: $125. Information: Educational Meeting Management, Inc., 12200 Fairhill Rd., Cleveland, OH 44120; telephone: (216) 229-2600; fax: (216) 844-7254.

Positron Emission Tomography

The Commissions on Education and Nuclear Medicine, American College of Radiology, are sponsoring Positron Emission Tomography: Applications in Cancer Management, May 15–17, at the Hilton at Walt Disney World Village, Lake Buena Vista, FL. The course will provide background information on tumor accumulation of tracers used in positron emission tomography (PET), information on PET instrumentation, and a review of specific clinical settings in which PET is showing usefulness or promise in cancer management. Program chairman: Richard L. Wahl. Information: American College of Radiology, Educational Services Division, 1891 Preston White Dr., Reston, VA 22091; (800) ACR-LINE, ext. 4961.

Yale Clinical MRI

The Dept. of Radiology, Yale University School of Medicine, will present Yale Clinical MRI, May 18–20, at the Yale-New Haven Hospital MRI Center, New Haven, CT. Topics will include neurologic, musculoskeletal, and abdominal applications of MR imaging. Course director: Ruben Kier. Category 1 credit: 21.5 hr. Fee: physicians, $575; residents, fellows, and technologists, $400. Information: Janet Wicklow, Dept. of Radiology, Yale University School of Medicine, 333 Cedar St., P. O. Box 3333, New Haven, CT 06510; (203) 785-5913.

Mammography Update: Practical Breast Imaging

The Mississippi Radiological Society (MRS) is sponsoring Mammography Update: Practical Breast Imaging, June 5–7, at the Marriott Grand Hotel, Point Clear, AL. The meeting is intended to be a refresher course in mammography for practicing radiologists. Course director: Ronald E. Gray. Category 1 credit: 10 hr. Fee: MRS members, $100; nonmembers, $250. Information: Ronald E. Gray, M.D., or Edward K. Phillips, M.D., 1405 N. State St., Jackson, MS 39202; (601) 354-4327.

Symposium on MR of the Musculoskeletal System

The 2nd International Symposium on Magnetic Resonance of the Musculo-Skeletal System will be held June 18–20 in Palma de Mallorca, Balearic Islands, Spain. The meeting will cover state-of-the-art MR of the musculoskeletal system, including the spine. Emphasis will be on normal anatomy and variants, common and uncommon conditions, sports injuries, and work in progress. Program director: J. Beltran. Guest faculty: D. Resnick, T. Masaryk, M. Rafii, M. Reiser, and Z. Rosenberg. Fee: physicians, $275; residents, $250. Information: C. Smith, Dept. of Radiology, Hospital for Joint Diseases, 301 E. 17th St., New York, NY 10003; telephone: (212) 598-6373; fax: (212) 598-6125.

Magnetic Resonance Imaging in Spain and Morocco

Hoag Memorial Hospital Presbyterian is sponsoring Magnetic Resonance Imaging in Spain and Morocco, June 28–July 1, at the Hotel Arts in Barcelona, Spain, and July 3–5, at the Sheraton Hotel, Casablanca, Morocco. Program director: Anton Hasso. Category 1 credit (pending): 28 hr. Fee (physicians/residents, fellows, and technologists): complete course, $695/$400; Barcelona only, $500/$300; Casablanca only, $500/$300. Information: Dawne Ryals, Ryals and Associates, P. O. Box 1925, Roswell, GA 30077-1925; telephone: (404) 641-9773; fax: (404) 552-9859.

Diagnostic Imaging Seminar

The Dept. of Radiology, Hospital of the University of Pennsylvania, will present its annual Diagnostic Imaging Seminar, July 13–17, at the Harbor View Hotel, Edgartown, MA (Martha's Vineyard). Category 1 credit: pending. Fee: $555. Information: Nancy Fedullo, Dept. of Radiology, Hospital of the University of Pennsylvania, 3400 Spruce St., Philadelphia, PA 19104; telephone: (215) 662-6904; fax (215) 349-5925.

Vascular Imaging and Intervention for the 90s

Stanford University Medical Center is sponsoring Vascular Imaging and Intervention for the 90s, July 17–19, at the Ritz-Carlton Resort Hotel, San Francisco. One day each will be devoted to MR angiography, color flow Doppler imaging, and vascular interventional radiology. Program directors: R. Brooke Jeffrey, Robert J. Herfkens, and Michael Dake. Category 1 credit: pending. Information: Dawne Ryals, Ryals and Associates, P. O. Box 1925, Roswell, GA 30077-1925; telephone: (404) 641-9773; fax: (404) 552-9859.

The Sharper Image in MRI

The Medical College of Wisconsin will present The Sharper Image in MRI: MR Angiography and Imaging of the Head, Spine, and Musculoskeletal System, July 27–31, at The Broadmoor Resort, Colorado Springs, CO. The course, which is the seventh in a series, will cover the newest techniques applicable to MR imaging of the brain, spine, head and neck, and musculoskeletal system. Anatomic features of each of these areas will be discussed, and important clinical features and MR findings will be stressed. Program chairmen: Victor Haughton and Robert Quencer. Category 1 credit: 25 hr. Fee: through June 5, $495; after June 5, $545. Information: Marti Carter, Course Coordinator, Continuing Medical Education, Inc., 11011 W. North Ave., Milwaukee, WI 53226; (414) 771-9520.

Contemporary Medical Imaging IX

Vanderbilt University Medical Center will present Contemporary Medical Imaging IX, Aug. 12–16, at the Mariner's Inn, Hilton Head Island, SC. The course is intended to provide an update on new clinical applications of medical imaging techniques, including MR imaging, CT, interventional radiology, and sonography. Category 1 credit: 17 hr. Fee: physicians, $570; Vanderbilt alumni, $470; technologists, $320. Information: Brenda Boner, Coordinator, Vanderbilt Division of CME, D-8211 Medical Center North, Nashville, TN 37232-2337; (615) 322-4030.

Summer Practicum

The 2nd Summer Practicum of the Society of Computed Body Tomography and Magnetic Resonance will be held at the Keystone Resort, Keystone, CO, Aug. 16–20. The course will provide updated, useful information on CT and MR of the body. Anatomy, techniques, and interventional procedures will be covered. Category 1 credit: 23 hr. Fee (through July 17/after July 17): physicians, $600/$650; residents and fellows, $500/$550. Information: Society of Computed Body Tomography and Magnetic Resonance, c/o Matrix Meetings, Inc., Barbara McLeod, CMP, Meeting Manager, P. O. Box 1026, Rochester, MN 55903; telephone: (507) 288-5620; fax: (507) 288-0014.

Barcelona 1992 Post-Games Imaging Conference

The University of California, Davis Medical Center, is sponsoring Barcelona 1992 Post-Games Imaging Conference, Aug. 17–21, at the Hotel Arts (Ritz-Carlton), Barcelona, Spain. Program directors: John P. McGahan and Elizabeth H. Moore. Category 1 credit (pending): 21 hr. Fee: physicians, $550; residents, fellows, and technologists, $475. Information: Dawne Ryals, Ryals and Associates, P. O. Box 1925, Roswell, GA 30077-1925; telephone: (404) 641-9773; fax: (404) 552-9859.

The American Board of Radiology Examinations

Written examinations for the American Board of Radiology (ABR) are scheduled for Oct. 1–2, 1992, and Oct. 14–15, 1993. Oral examinations will be held at the Executive West Hotel in Louisville, KY, June 1–5, 1992. The ABR will accept applications for admission to the examinations after July 1, but not later than Sept. 30, in the year *preceding* the year in which the examination is to be taken. For application forms and further information: Office of the Executive Director, The American Board of Radiology, 2301 W. Big Beaver Rd., Ste. 625, Troy, MI 48084.

Meeting and Course Review

For the reader's convenience, a summary of upcoming meetings and courses is provided. Detailed listings are given in the *AJR* issue given in parentheses.

Preceptorships in Ultrasound at Johns Hopkins, times arranged, Baltimore (June 1991)
Practicum in Breast Imaging, times arranged, Baltimore (Aug 1991)
Radiology in Southeast Asia and China, March 18–April 7, Singapore, Bangkok, Hong Kong, Beijing, Shanghai, and Guilin (Nov 1991)
Joint American-European Course in Davos, Switzerland, March 29–April 3, Davos (Feb)
National Council on Radiation Protection and Measurements Annual Meeting, April 1–2, Washington, DC (Dec 1991)
Pediatric Radiology 1992, April 2–4, Philadelphia (Jan)
American Cancer Society National Conference on Gynecologic Cancers, April 2–4, Orlando, FL (March)
Electronic Portal Imaging, April 3–4, Newport Beach, CA (Jan)
Wisconsin CT Conference, April 3–4, Madison (Feb)
AFIP Uroradiology Weekend, April 4–5, Washington, DC (Dec 1991)
Ultrasound 1992, April 5–8, Boston (March)
General Radiology Review Course, April 5–10, Santa Monica, CA (Dec 1991)
Advanced Mammographic Techniques and Interpretation, April 6–9, Southampton, Bermuda (Feb)
MRI Visiting Fellowships at UCLA, April 6–10, Sept. 14–18, Oct. 5–9, and Dec. 7–11, Los Angeles (Sept 1991)
Clinical Nuclear Medicine 1992, April 13–16, Cambridge, MA (March)
Residents' Radiology Review Course, April 19–24, San Diego (Dec 1991)
Radiation Oncology Clinical Research Seminar, April 23–25, Gainesville, FL (Feb)
Interventional Radiology, April 25, San Diego (Dec 1991)
Radiology in Scotland, April 26–May 3, Edinburgh and St. Andrews, Scotland (Jan)
Bone and Soft Tissue Tumors, April 27–29, San Diego (March)
Present Concepts in Radiology, April 28–May 1, San Francisco (Feb)
Spring Roentgen Conference, April 29–May 3, New Orleans (March)
Brachytherapy Symposium, May 1–2, Columbus, OH (Jan)
Ultrasound 1992—Advances in Diagnostic Imaging, May 2, Lebanon, NH (March)
Practical Interventional Radiology—1992,May 4–6, Cambridge, MA (Feb)
MRI: A State of the Art Clinical Review, May 4–8, San Francisco (Jan)
Advanced Seminars in Diagnostic Imaging, May 8–10, Laguna Niguel, CA (Jan)
Radiology Review Course, May 10–15, Miami Beach, FL (Feb)
Symposium on Diagnostic Ultrasound, May 15–17, New York City (March)
International Symposium on Diagnostic Imaging, May 18–22, Barcelona (Nov 1991)
Doppler and Duplex Imaging, May 21–24, San Diego (Jan)
Vanderbilt Sonography Symposium, May 22–23, Nashville (Jan)
Spoleto Festival Update, May 28–30, Charleston, SC (Jan)
Spanish Radiological Society National Conference, June 1–5, Seville, Spain (March)
Canadian Association of Medical Radiation Technologists 50th Anniversary Conference, June 7–12, Ottawa (Feb)
Advances in Cardiopulmonary Imaging, June 11–13, Salzburg, Austria (Nov 1991)
Concepts of Magnetic Resonance, June 20–26, Kiawah Island, SC (Feb)
Pitt Summer Imaging Course, June 21–25, Williamsburg, VA (Feb)
Workshop on Vascular Anomalies, July 1–3, Denver (March)
Paediatric Imaging Update, July 5–10, Port Douglas, Australia (March)
Course on Body Imaging, July 13–17, Santa Fe, NM (March)
Diagnostic Imaging Update, July 20–22, San Francisco, and July 23–26, Carmel, CA (March)
Clinical Imaging for Non-Radiologists, July 20–24, San Diego (March)
MRI and Musculoskeletal Imaging, July 27–Aug. 1, Laguna Niguel, CA (March)
European Symposium on Uroradiology, Aug. 24–27, Herlev, Denmark (Aug 1991)
International Skeletal Society Refresher Course, Aug. 26–29, Stockholm (March)
Congress of Asian Federation of Societies for Ultrasound in Medicine and Biology, Aug. 30–Sept. 3, Seoul, Korea (Feb)
Ultrasound Angiography 92, Sept. 2–4, University of Southampton, United Kingdom (Feb)
International Course on MR Imaging, Oct. 25–28, Riyadh, Kingdom of Saudi Arabia (March)

AJR carries announcements of courses, symposia, and meetings of interest to its readers if received a minimum of 5 months before the event. There is no charge; receipt of items by the *AJR* Editorial Office is not acknowledged. Submit items for publication typed double-spaced. Provide title, date, location, brief description, sponsor, course directors, fees, category I credit, and address and telephone number for additional information. Faculty from the host institution will not be listed. Guest faculty names will appear **only** if initials are provided. Mail news items to *AJR* Editorial Office, 2223 Avenida de la Playa, Suite 103, La Jolla, CA 92037-3218.

American Roentgen Ray Society:

Officers, Committees, and Membership Information

Officers

President: John A. Kirkpatrick, Jr.
President-elect: A. Everette James, Jr.
1st Vice-president: Andrew K. Poznanski
2nd Vice-president: George R. Leopold
Secretary: Joseph T. Ferrucci, Jr.
Treasurer: Beverly P. Wood

Executive Council: R. N. Berk, M. P. Capp, W. J. Casarella, N. R. Dunnick, R. G. Evens, J. T. Ferrucci, Jr., A. E. James, Jr., J. A. Kirkpatrick, Jr., A. M. Landry, Jr., G. R. Leopold, J. E. Madewell, T. C. McLoud, A. A. Moss, A. K. Poznanski, R. J. Stanley, J. H. Thrall, K. H. Vydareny, N. O. Whitley, B. P. Wood, R. J. Alfidi, chairman

Committees

Editorial Policy: R. N. Berk, E. Buonocore, Melvin M. Figley, C. R. B. Merritt, K. Valji, C. A. Rohrmann, Jr., W. J. Casarella, chairman

Education and Research: R. R. Hattery, C. B. Higgins, B. J. Hillman, R. J. Stanley, W. M. Thompson, N. O. Whitley, chairman

Finance and Budget: R. K. Gedgaudas-McClees, A. A. Moss, J. R. Thornbury, K. H. Vydareny, J. H. Thrall, chairman

Nominating: R. G. Evens, P. J. Fritzsche, A. A. Moss, chairman

Publications: E. Buonocore, C. R. B. Merritt, C. A. Rohrmann, Jr., W. J. Casarella, chairman

Membership: J. E. Madewell, T. C. McLoud, A. A. Moss, K. H. Vydareny, chairman

Representatives to Other Organizations

American Board of Radiology: W. J. Casarella, J. A. Kirkpatrick, Jr., L. F. Rogers

American College of Radiology: R. A. Gagliardi, J. E. Madewell, B. L. McClennan, R. J. Stanley

American Medical Association: S. F. Ochsner, delegate; K. L. Krabbenhoft, alternate; K. L. Kidd, CPT Advisory Committee

American National Standards Institute: M. E. Haskin

National Council on Radiation Protection and Measurements: F. D. Miraldi, E. L. Saenger

Armed Forces Institute of Pathology: J. E. Madewell

Meeting Arrangements

Annual Meetings: May 10–15, 1992, Marriott's World Center, Orlando, FL; April 25–30, 1993, Marriott San Francisco, San Francisco, CA

Annual Meeting Committee: J. K. Crowe, N. R. Dunnick, R. R. Lukin, N. H. Messinger, R. J. Stanley, R. D. Steele, Jr., A. M. Landry, Jr., chairman

Instructional Courses: Bruce L. McClennan, associate chairman; R. J. Stanley, chairman

Scientific Program: P. H. Arger, T. B. Hunter, D. Kushner, T. C. McLoud, L. B. Talner, J. H. Thrall, A. E. James, Jr., chairman

Scientific Exhibits: J. R. Haaga, D. S. Hartman, R. G. Ramsey, N. R. Dunnick, chairman

ARRS Membership

An application form is printed in the January issue of the Journal. For consideration at the 1993 ARRS meeting, send completed forms before February 1, 1993, to American Roentgen Ray Society, 1891 Preston White Dr., Reston, VA 22091. Active members are graduates of an approved medical or osteopathic school or hold an advanced degree in an allied science. They must practice radiology or work in an associated science in the United States or Canada and be certified by the American Board of Radiology, American Osteopathic Board of Radiology, or Royal College of Physicians of Canada or otherwise adequately document training and credentials. International members are foreign radiologists or scientists who are active in radiology or an allied science. Members-in-training are residents or fellows in radiology or postgraduate students in an allied science. Additional application forms can be obtained from the ARRS offices in Reston, VA.

Business Office

Paul Fullagar, Executive Director, American Roentgen Ray Society, 1891 Preston White Dr., Reston, VA 22091; (703) 648-8992.

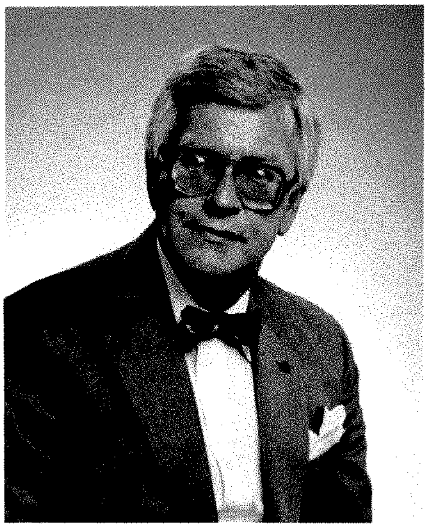

A. Everette James, Jr.

Join Your Colleagues at the 92nd Annual Meeting of the American Roentgen Ray Society

Dear Colleagues:

I am pleased to extend an invitation to all radiologists to attend the 92nd annual meeting of the American Roentgen Ray Society in Orlando, FL, May 10-15, 1992. In keeping with ARRS tradition, we have planned another outstanding scientific program in a superlative location.

From the more than 500 abstracts received, 208 scientific papers will be presented in 20 scientific sessions devoted to all major body systems, angiography, interventional techniques, sonography and mammography, as well as technologies. Special emphasis has been placed on discussion of new developments.

N. Reed Dunnick and his committee have chosen more than 300 scientific exhibits encompassing all aspects of diagnostic radiology. These exhibits will be available for viewing in the exhibit hall from early morning until late at night, and awards will be presented for the best exhibits. Technical exhibits, encompassing medical book publishers, pharmaceutical manufacturers, medical software companies and other products of interest to the radiologic community will also be on display in the exhibit hall.

One of the salient features of every ARRS meeting is the categorical course. This year's topic is Neuroradiology, and moderator Michael Huckman has assembled an outstanding faculty to present the various aspects of this field. The categorical course will begin on Sunday, May 10, and continue through Thursday, May 14.

This year for the first time, two Friday symposia will be presented. The first, entitled "Stat and Urgent Problems in Pediatrics," has been developed in conjunction with the Society for Pediatric Radiology and will be moderated by William H. McAlister. The second symposium is entitled "New Issues Forum" and features three "hot" topics of interest to the radiologic community.

Robert J. Stanley and Bruce L. McClennan have put together 60 superlative instructional courses with an outstanding faculty from across the country. There will be four Resident/Master Tutorials, with registration restricted to residents only. Robert H. Ackerman, AFIP Distinguished Scientist, will present an instructional course on cerebral vascular disease.

In 1920 the ARRS established the Caldwell Lecture named after Eugene Caldwell, an early pioneer in roentgenology and president of the ARRS in 1908. I am pleased to announce that the 1992 Caldwell Lecture will be given by William J. Casarella. Dr. Casarella is a leader in the field of interventional radiology, and I am certain that his lecture will be a highlight of the meeting.

Last year for the first time the Society presented a spouse/guest program featuring a medical topic. This program proved to be so popular that we have decided to continue the tradition. This year's program will be entitled "Osteoporosis: Assessing the Risks." Please tell your spouse or guest about this program and urge them to attend. Another innovation from last year that will be continued in 1992 is the Sunday night opening reception. Plan to attend again this year to meet and greet your colleagues.

Last, but by no means least, Abner Landry and the Annual Meeting Committee with the assistance of Convention Planning Services, Inc. have put together an outstanding array of tours of the Orlando area, as well as our traditional golf and tennis tournaments.

Marriott's Orlando World Center is a beautiful, modern facility located just minutes from Disney World and the many other attractions in the Orlando area. The weather promises to be sunny and warm, golf courses abound, and the Atlantic Ocean is within an hour's drive. I think you will agree with me that this meeting promises to be outstanding in every way. I look forward to greeting all of you in sunny Florida.

Sincerely,

A. Everette James, Jr.
President-Elect

Meeting Format

The annual meeting opens officially on Monday, May 11. However, the scientific program begins on Sunday, May 10, with a full day of the categorical course. The categorical course continues on Monday through Thursday afternoons. Also on Monday through Thursday, refresher courses are offered in both the early morning and late afternoon. Twenty scientific sessions are offered on these days, grouped in parallel sessions so that registrants may choose topics related to their interests. During the opening ceremonies on Monday morning, award-winning papers from the ARRS and sister societies will be presented. On Wednesday morning, a special ceremony will include the Caldwell Lecture and presentation of Gold Medal Awards for distinguished service to radiology. The meeting concludes on Friday morning with two symposia. Scientific and technical exhibits are open Monday through Thursday. Consult the calendar on the following page for exact times for all of these programs.

Accreditation

As an organization accredited for continuing education, the American College of Radiology has certified that this continuing medical education offering meets the criteria for Category I credit. CME credit is given on an hour-for-hour basis for attendance at the scientific programs, instructional courses, categorical course and symposia. A certificate will be included with the registration material which the attendee may have signed by an ARRS staff member to acknowledge attendance at the meeting. Each attendee is responsible for keeping track of his or her own CME credit hours.

Meeting Registration

A meeting registration form is provided on page 947 of this issue, and this form may be photocopied. Follow the instructions on page 948. Early registration is strongly suggested as enrollment in instructional courses is limited and course requests will be filled by date of receipt. Registrations will be accepted by mail or fax only until April 27. Following this date, all registration will take place on site. Fax registrations will be accepted only if accompanied by credit card information. No phone registrations will be accepted. Registration confirmations will be mailed. Fax registrations to (703) 264-8863.

Official badges, program book, course tickets and other meeting material may be picked up at the ARRS Registration Desk at the Marriott Orlando World Center beginning on Saturday, May 9, at 1:00 p.m. Consult calendar for exact dates and times registration desk is open.

Cancellation

Meeting registration fees will be refunded if cancellation is received **in writing** by April 27. Mail cancellation requests to American Roentgen Ray Society, 1891 Preston White Drive, Reston, VA 22091.

Hotel Registration

The American Roentgen Ray Society has negotiated a special rate of $150 per night, single or double, with Marriott's Orlando World Center. See page 949 of this issue for a room reservation form. This form may be photocopied. Follow the instructions on the back of the form and mail it directly to the hotel. The deadline for receipt of hotel reservations is April 13. Reservations received after that date are subject to availability. Do not mail the hotel registration form with the meeting registration form. Mailing these forms together may result in a delay in processing.

Transportation

United Airlines is offering special airfares for travel to and from Orlando from May 7 through May 18, 1992. Fares range from a 5% discount from any United available/applicable fare (MaxSavers and first class included) to a 40% discount off standard coach fares. For travel to and from Canada, United will offer published Canadian meeting fares in selected markets. This discount can be as much as 35% off normal coach fares. No discounts are permitted from Mexico, the Bahamas or the Orient. To obtain these special fares, call United toll free at 1-800-521-4041 between the hours of 8:00 a.m. and 11:00 p.m. EST and refer to Meeting I.D. #519LT.

Delta Airlines is offering special fares for travel to and from Orlando from May 6 through 19, 1992. These fares are based on Delta's published round-trip fares within the United States and San Juan, Puerto Rico, and range from a 5% discount off any published fare with certain restrictions to a 40% discount off unrestricted coach fare. Special fares are also available from Delta's Canadian cities and Delta Connection carriers. To take advantage of these discounts, call Delta toll free at 1-800-241-6760 between the hours of 8:00 a.m. and 11:00 p.m. EST, and refer to File No. M0045.

Alamo Rent A Car has been appointed the official car rental company for the 1992 meeting. Special discounted rates will be extended to meeting attendees. These rates are available one week before and after the meeting dates and include UNLIMITED FREE MILES. To make reservations call Alamo at 1-800-732-3232 and request Group I.D. #247840 and Rate Code #GA.

Fees

ARRS member (all categories)	No Fee
Scientific Exhibitor	No Fee
Scientific Paper Presenter	No Fee
Technical Exhibitor	No Fee
Course Faculty	No Fee
Non-member physician	$250
Non-member physician-in-training	$ 25
Categorical Course (all attendees)	$ 75
ACR Luncheon Programs	$ 15
Spouse/Guest Program on Osteoporosis	No fee
Social Programs	$ 16 - 100

Calendar of Events

Saturday, May 9

1:00 - 5:00	General Registration

Sunday, May 10

7:30 - 4:30	General Registration
10:00 - 12:30	**Categorical Course: Neuroradiology**
12:30 - 1:45	Lunch
1:45 - 5:45	**Categorical Course: Neuroradiology**
2:00 - 5:00	Discover Orlando*
7:00 - 8:30	**Opening Reception for all Registrants**

Monday, May 11

7:00 - 4:30	General Registration
7:45 - 10:00	**Spouse/Companion Program on Osteoporosis***
8:00 - 9:30	Instructional Courses 100 - 110
9:30 - 10:00	Coffee Break in Exhibit Hall Foyer
10:00 - 12:30	**Opening Ceremonies and Presentation of Scientific Award Papers**
10:45 - 12:30	Scientific Sessions
11:00 - Evening	Golf and Tennis Tournaments
12:30 - 1:30	Lunch (Including ACR Socio-economic Session)
1:30 - 5:45	**Categorical Course: Neuroradiology**
1:30 - 3:30	Scientific Sessions
1:30 - 4:30	Discover Orlando*
3:30 - 4:00	Coffee Break in Exhibit Hall Foyer
4:00 - 5:30	Instructional Courses 111 - 115
6:30 - 11:00	Church Street Station*

Scientific Exhibits	*7:00 a.m. - 11:00 p.m.*
Commercial Exhibits	*9:30 a.m. - 4:30 p.m.*
Companions Hospitality Suite	*8:30 a.m. - 1:00 p.m.*

Tuesday, May 12

7:00 - 4:30	General Registration
8:00 - 9:30	Instructional Courses 201 - 210
9:00 - 4:00	Kennedy Space Center*
9:30 - 3:30	Historic Winter Park/Park Avenue Shopping*
9:30 - 10:00	Coffee Break in Exhibit Hall Foyer
10:00 - 12:30	Scientific Sessions
12:30 - 1:30	Lunch (Including ACR Socio-economic Session)
1:30 - 3:30	Scientific Sessions
3:30 - 4:00	Coffee Break in Exhibit Hall Foyer
3:45 - 5:45	**Categorical Course: Neuroradiology**
4:00 - 5:30	Instructional Courses 211 - 215

Scientific Exhibits	*7:00 a.m. - 11:00 p.m.*
Commercial Exhibits	*9:30 a.m. - 4:30 p.m.*
Companions Hospitality Suite	*8:30 a.m. - 1:00 p.m.*

Wednesday, May 13

7:00 - 4:30	General Registration
8:00 - 9:30	Instructional Courses 301 - 310
9:30 - 10:00	Coffee Break in Exhibit Hall Foyer
10:00 - 12:30	**Awards Session: Scientific Exhibit Awards, Gold Medal Awards, Caldwell Lecture**
10:00 - 4:00	Cypress Gardens VIP Tour*
11:00 - 2:00	Magic of Ming*
12:30 - 1:30	Lunch (Including ACR Socio-economic Session)
1:30 - 3:30	Scientific Sessions
3:30 - 4:00	Coffee Break in Exhibit Hall Foyer
3:45 - 5:45	**Categorical Course: Neuroradiology**
4:00 - 5:30	Instructional Courses 311 - 315

Scientific Exhibits	*7:00 a.m. - 11:00 p.m.*
Commercial Exhibits	*9:30 a.m. - 4:30 p.m.*
Companions Hospitality Suite	*8:30 a.m. - 1:00 p.m.*

Thursday, May 14

7:00 - 4:30	General Registration
8:00 - 9:30	Instructional Courses 401 - 410
9:30 - 1:30	Leu Gardens/Jordan's Grove*
9:30 - 10:00	Coffee Break in Exhibit Hall Foyer
10:00 - 4:00	Hot off the Set - Universal Studios VIP Tour*
10:00 - 12:30	Scientific Sessions
12:30 - 1:30	Lunch (Including ACR Socio-economic Session)
1:30 - 3:30	Scientific Sessions
3:30 - 4:00	Coffee Break in Exhibit Hall Foyer
3:45 - 5:45	**Categorical Course: Neuroradiology**
4:00 - 5:00	Membership Business Meeting
4:00 - 5:30	Instructional Courses 411 - 415
5:00 - 6:30	Exhibitors Post-Convention Reception

Scientific Exhibits	*7:00 a.m. - 6:00 p.m.*
(Note: Scientific Exhibits close today)	
Commercial Exhibits	*9:30 a.m. - 4:30 p.m.*
(Note: Commercial Exhibits close today)	
Companions Hospitality Suite	*8:30 a.m. - 1:00 p.m.*

Friday, May 15

7:00 - 12:00	General Registration
8:00 - 12:00	**Symposium: Pediatric Radiology**
8:00 - 12:00	**Symposium: New Issues Forum**

Scientific Exhibits	*Closed*
Commercial Exhibits	*Closed*
Companions Hospitality Suite	*8:30 a.m. - 11:00 a.m.*

**Spouse/guest program. Pre-registration required.*

Categorical Course

Neuroradiology

Sunday, May 10, through Thursday, May 14, 1992

Michael S. Huckman, Director
Derek C. Harwood-Nash, Co-Director
Glenn S. Forbes, Co-Director

Sunday, May 10

10:00 - 10:30	Interpretation of Signal Intensity Changes in MRI of the Brain	*Gado*
10:30 - 11:00	Imaging Strategies in Mass Lesions of the Brain	*Kricheff*
11:00 - 11:30	The Current Role of Cerebral Angiography in Neuroradiologic Diagnosis	*Wolpert*
11:30 - 12:00	Clinical Indications for the Use of Magnetic Resonance Angiography	*Ross*
12:00 - 12:30	The Roles of MR and CT in the Evaluation of Cerebral Trauma	*Lukin*
12:30 - 1:45	Lunch	
1:45 - 2:15	Where Is the Blood in the Brain and How Old Is It?	*Hackney*
2:15 - 2:45	The Pituitary Gland: Bright Spots and Dark Spots	*Kucharzyk*
2:45 - 3:15	What Importance Should Be Attached to White Matter "Dots?"	*Heier*
3:15 - 3:45	Coffee Break	
3:45 - 4:15	Lesions of the Skin and Brain	*Elster*
4:15 - 4:45	Imaging Correlates of Brain Tumor Pathology	*Zimmerman*
4:45 - 5:15	The Many Faces of Meningeal Enhancement	*Sze*
5:15 - 5:45	Imaging of Brain Infections	*Post*

Monday, May 11

1:30 - 2:00	Imaging Cervical Lymph Nodes	*Som*
2:00 - 2:30	Neuroimaging in the Immunocompromised Patient.	*Ramsey*
2:30 - 3:00	The Role of the Radiologist in the Early Diagnosis of Stroke	*Bryan*
3:00 - 3:15	Coffee Break	
3:15 - 3:45	Evaluation of the Seizure Patient	*Bronen*
3:45 - 4:15	An Algorithm for Imaging the Orbit	*Forbes*
4:15 - 4:45	Imaging of the Temporal Bone: MR or CT?	*Chakeres*
4:45 - 5:15	Imaging of the Cerebellopontine Angle	*Hasso*
5:15 - 5:45	The Radiology of Endoscopic Sinus Surgery	*Mafee*

Tuesday, May 12

3:45 - 4:15	Evaluating Back Pain in Children	*Harwood-Nash*
4:15 - 4:45	Imaging of Hydrocephalus and Shunts	*Naidich*
4:45 - 5:15	Normal and Abnormal Patterns of Myelination in Children	*Barkovich*
5:15 - 5:45	Conduct of Invasive Outpatient Neuroimaging Procedures	*Kieffer*

Wednesday, May 13

3:45 - 4:15	Multiple Sclerosis and Its Imitators	*Brant-Zawadzki*
4:15 - 4:45	Image Correlation in Movement Disorders	*Rutledge*
4:45 - 5:15	Imaging the Aged and Demented Patient	*George*
5:15 - 5:45	Imaging Degenerative Disease of the Spine	*Haughton*

Thursday, May 14

3:45 - 4:15	Imaging of Postoperative Complications of Spine Surgery	*Davis*
4:15 - 4:45	Imaging of Cervical and Thoracic Disc Disease	*Russell*
4:45 - 5:15	Distinguishing Benign From Malignant Changes in the Vertebral Column	*Geremia*
5:15 - 5:45	Ultrasound in Neuroradiology	*Quencer*

Instructional Courses

Robert J. Stanley, Chairman, Bruce L. McClennan, Associate Chairman

Topic	Monday	Tuesday	Wednesday	Thursday
Morning Sessions 8:00 a.m. - 9:30 a.m.				
Residents/Masters Tutorial	**101.** Current Radiologic Approach to Thromboembolytic Disease. *Athanasoulis CA*	**201.** Intracranial Lesions. *Gado MH*	**301.** CT of Skeletal Trauma. *Rogers LF*	**401.** Seeing with Sound. *Leopold GR*
Technique & Technology	**102.** Teleradiology and Digital Imaging. *Templeton, AW*	**202.** Ultrafast CT Scanning: An Update. *Sheedy P*	**302.** Advances in Abdominal CT Examination Techniques. *Berland LL, Megibow AJ*	**402.** Computer-Assisted 3-D CT Imaging: State of the Art. *Fishman EK, Ney D*
Chest	**103.** Pitfalls in Plain Film and CT Analysis of the Mediastinum. *Glazer HS, Molina PL*	**203.** Interventional Techniques in the Chest. *Westcott, JL*	**303.** Imaging of Lung Cancer: Staging and Biopsy Techniques. *Sanders PC, Nath H*	**403.** Thin Section, High Resolution CT of the Lung. *Pugatch RD*
Gastrointestinal Radiology	**104.** Developmental Anomalies of the Pancreas and Biliary Tract. *Schulte SJ, Rohrmann CA Jr.*	**204.** Principles of Double Contrast Diagnosis Applied to Colorectal Cancer. *Laufer I*	**304.** CT of the GI Tract. *Balthazar EJ, Birnbaum B*	**404.** Radiologic Evaluation of the Pharynx and Esophagus. *Rubesin SE, Levine MS*
Body Imaging/GU	**105.** CT and MRI of the Retroperitoneum. *Heiken JP, Brown JJ*	**205.** CT of Gynecologic Disease. *Walsh JW*	**305.** CT and MRI of the Kidney. *Newhouse JH, Amis ES Jr.*	**405.** Renal Infarction, Infection and Venous Thrombosis. *Bosniak, MA*
Body Imaging/CT, US, MRI	**106.** CT and US-Guided Biopsies: Practical Approaches, Pitfalls and New Techniques. *Charboneau JW, Reading CC*	**206.** CT of Peritoneal Spaces and Ligaments. *Balfe DM, Brink JA*	**306.** Hepatobiliary Neoplasms. *Ros PR, Buck JL*	**406.** MRI of the Abdomen: Present Uses and Future Directions. *Kenney PJ*
Mammography	**107.** Evaluation of the Altered Breast. *Monsees B, Destouet, JM*	**207.** Screening Mammography: Historical Perspectives and Current Concepts. *Dershaw DD*	**307.** The Abnormal Mammogram: Where Do We Go From Here? *Rubin E, Dempsey PJ*	**407.** Current Concepts in Percutaneous Breast Procedures. *Parker SH, Fajardo LL*
Special Topics	**108.** Re-emphasis on the Fundamentals in Conventional Skeletal Radiology. *Jacobson HG, Edeiken J*	**208.** Medical Innovation: The Effect of Social/Technological Changes on Our Understanding of Cerebral Vascular Disease. *Ackerman, RH,* AFIP-DS.	**308.** Near-Fatal Attraction: Our Tempestuous Love Affair with Radiation and X-rays from a Historical Perspective. *DiSantis DJ*	**408.** Treatment of Acute Systemic Reactions to Contrast Media. *Bush WH, Swanson DP*
Nuclear Medicine	**109.** Hepatobiliary Imaging: Pharmacologic Intervention. *Fink-Bennett D, Juni J*	**209.** Imaging of Infection. *Alazraki, NP*	**309.** Pulmonary Thromboembolism: Modern Perspectives. *Coleman RE*	**409.** Bone SPECT. *Collier BD*
Body Imaging/Ultrasound	**110.** Transvaginal Sonography: New Applications. *Fleischer AC, Emerson DS*	**210.** Ultrasound Evaluation of the Acute Abdomen. *Wilson, SR*	**310.** Ultrasound Evaluation of the Carotid and Vertebral Vessels. *Bluth EI*	**410.** Imaging and Biopsy of the Prostate. *Papanicolaou N, Tung G*
Afternoon Sessions 4:00 p.m. - 5:30 p.m.				
Musculoskeletal	**111.** The Pelvis and Hip: Anatomic-Clinical Correlations. *Pitt MJ*	**211.** Evaluation of the Sacrum and Sacroiliac Joints. *Pope TL Jr., Brower AC*	**311.** Imaging of Bone Grafts and Joint Replacements. *Murphey MD*	**411.** MRI of Joints. *Kaye JJ, Potter HG*
Pediatric Radiology	**112.** A Practical Approach to Pediatric Abdominal Diagnosis. *Wood BP, Parisi M*	**212.** Skeletal MRI in Children. *Poznanski AK, Donaldson, JS*	**312.** Radiology of the Diaphragm in Children and Adults. *Robinson AE, Oh KS*	**412.** CT and MRI of the Pediatric Chest. *Siegel MJ*
Body Imaging/CT, US, MRI	**113.** CT, MR and US of the Subperitoneal Space: Predicting Pathways of Abdominal Disease. *Gore RM*	**213.** Adrenal Masses: Correlative Imaging With CT, MRI and Nuclear Medicine. *Korobkin MT, Francis I*	**313.** Imaging the Spectrum of Biliary Tract Disease. *Baron RL, Campbell WL*	**413.** Contemporary Imaging of the Malignant Lymphomas. *Marglin SI*
Angiography/Interventional	**114.** Clinical Assessment of Vascular Disease: The Interventionalist's Approach. *van Breda, A*	**214.** New Devices in Peripheral Vascular Intervention: Diagnosis and Therapy. *Katzen BT, Becker GJ*	**314.** Angioplasty: Principles and Technical Advances. *Saddekni S.*	**414.** Biliary Intervention: All You Ever Wanted to Know. *Hawkins IF Jr., Caridi JG*
Radiologic - Pathologic Correlation (special topics)	**115.** Intraluminal GI US: Esophagus, Stomach, Pancreas, Biliary Tree and Rectum. *Botet JF, Bree RL*	**215.** Radiologic-Pathologic Correlation of GI Tract Tumor. *Lichtenstein JE, Olmsted WW*	**315.** How To Get Your Manuscripts Published Without a Hassle. *Berk RN, Rose B, Spiller K, Valji K*	**415.** Arthropathies: Radiologic-Pathologic Correlations. *Madewell, JE*

Symposia and Special Programs

Symposia

Stat and Urgent Problems in Pediatrics

(held jointly with the Society for Pediatric Radiology)
William H. McAlister, Moderator
Friday, May 15, 1992

8:00 Sonography of Lower Abdominal Pain .... *Siegel*
8:30 Emergency Interventional Procedures in Children .... *Bisset*
9:00 Pediatric Trauma: Current Concepts in Abdominal Imaging .... *Taylor*
9:30 Emergency Sonography in the Child .... *Patriquin*
10:00 Break
10:15 Cervical Spine Trauma: Current Concepts in Imaging .... *Swischuk*
10:30 Head Trauma: Current Concepts in Imaging .... *Harwood-Nash*
11:00 Imaging of Emergencies in Immune Compromised Patients .... *Wood*
11:30 MR of Acute Musculoskeletal Injury .... *Moore*

New Issues Forum

Friday, May 15, 1992

8:00 Economic and Political Challenges for Radiologists in the '90s .... *Hillman*
9:00 The Interface of MR Imaging and Spectroscopy .... *Kressel*
10:00 PACS: Overview of Clinical Importance and Technical Feasibility .... *Kangarloo, Dwyer*

ACR Luncheon Presentations

The American College of Radiology will sponsor a series of luncheon talks on socio-economic issues Monday through Thursday, May 11-14, at 12:30 p.m. The $15 fee includes a box luncheon.

Monday, May 11	Governmental Issues for Radiology *Gary Price, ACR Director of Government Relations*
Tuesday, May 12	Practice Accreditation *Robert J. Stanley, Chairman, ACR Commission on Standards and Accreditation*
Wednesday, May 13	Current Legal Issues in Radiology *Thomas W. Greeson* *ACR Legal Counsel*
Thursday, May 14	Update on ACR Activities *James M. Moorefield* *Chairman, ACR Board of Chancellors*

Special Program

Osteoporosis: Assessing the Risks

Kay H. Vydareny, Moderator

Monday, May 11, 1992
7:45 - 10:00 a.m.

In recent years osteoporosis has become a topic of major concern to women. A report from the U.S. Preventative Services Task Force states that an estimated 1.3 million osteoporosis-associated hip fractures occur each year in the United States. Up to 70% of fractures in persons aged 45 or older are attributable to osteoporosis. Most of these occur in postmenopausal women.

The purpose of this program is to educate women about the indicators of the disease, options for diagnosis and the benefits as well as the risks associated with several treatment options available today. A panel of experts will conduct brief presentations, answer questions and identify ways to cope with the uncertainties and anxieties associated with this disease.

Topics for discussion will include:

Multiple risk factors

- Diet
- Smoking
- Exercise
- Calcium intake
- Low bone mass
- Gender

Detection and diagnosis

- Radiologic techniques for measurement of bone mass
- Effectiveness of screening programs

Prevention and treatment

- Options
- Risks
- Hormone therapy

Join us at 7:45 a.m. for a continental breakfast, followed by the program at 8:00. There is no charge to spouses and guests of registered meeting attendees. However, space is limited, and pre-registration is required.

Local Activities

The Orlando area offers a wide variety of leisure activities to visitors. The best-known of these, of course, is Disney World, which is located just minutes from our host hotel, Marriott's Orlando World Center. Many of the area's other attractions are easily accessible from the hotel via rental car or Gray Line bus shuttles.

With the assistance of Convention Planning Services, Inc., we have planned several interesting and fun activities for our own social program, and we have also arranged VIP tours of some of the major attractions. Descriptions of these tours are listed below.

Prices for the events include transportation, meals where indicated, escorts and guides, and all entrance fees, taxes and gratuities. Prices do not include alcoholic beverages with meals. Use your own judgment in deciding which tours are appropriate for young children. Special rates are available for children for the Kennedy Space Center and Cypress Gardens tours.

Reservations for the social program are limited. To avoid disappointment, send in the reservation form immediately. Reservations will be filled in the order in which they are received. Because guarantees are required for all events, reservations must be received by April 27. On Sunday, May 10, from 1:00 to 5:00 p.m. and on Monday, May 11, from 8:00 to 11:00 a.m., any remaining tickets will be sold at the meeting registration desk. These tickets may be sold at a slightly higher price. Fees will be refunded if cancellation is received in writing by April 27. Mail cancellation requests to American Roentgen Ray Society, 1891 Preston White Drive, Reston, VA 22091. No cancellations will be accepted by telephone. The ARRS reserves the right to cancel an event if registration is insufficient. If an event is cancelled, refunds will be issued.

Sunday, May 10

Discover Orlando **2:00 - 5:00 p.m.**
This tour is a great way to begin your visit to the Orlando area and help you decide what activities you would like to pursue during the rest of the week. Find out what makes Orlando the United States' number one tourist destination. The tour will highlight downtown Orlando, the "city beautiful." Your guide will discuss the history of Orlando, its growth and many points of interest. You will tour Church Street Station and Market Plaza, offering a multitude of shops, restaurants and entertainment. Fee: $16.

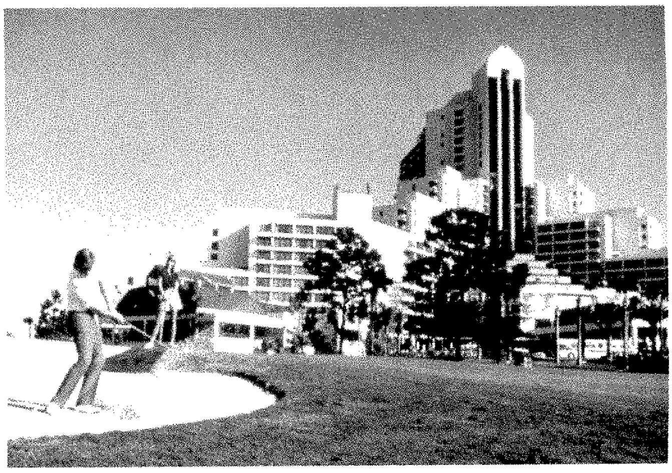
Enjoy the fun and excitement of Orlando's attractions as well as the many fine amenities available at Marriott's Orlando World Center.

Monday, May 11

Osteoporosis: Assessing the Risks **7:45 - 10:00 a.m.**
In recent years osteoporosis has become a topic of major concern to women. The purpose of this program is to educate women about the indicators of the disease, options for diagnosis and the benefits as well as the risks associated with several treatment options available today. A panel of experts will conduct brief presentations, answer questions and identify ways to cope with the uncertainties and anxieties associated with this disease. Join us at 7:45 a.m. for a continental breakfast, followed by the program at 8:00. There is no charge to spouses and guests of registered meeting attendees. However, space is limited, and pre-registration is required.

Golf Tournament **11:00 a.m. - evening**
The annual golf tournament will be held at Orlando's Bay Hill Club. Owned and operated by Arnold Palmer, the Bay Hill Club is the site of the annual Nestle Invitational and has some of the most famous and challenging holes on the pro tour. Buses will leave the hotel at 11:00 a.m. following the opening ceremonies. There will be a buffet lunch followed by a shotgun start. Participants must bring their own golf clubs and shoes. The fee includes transportation, luncheon, greens fees, cart, prizes and hors d'oeuvres and drinks following completion of play. Trophies and prizes will be awarded at this time, after which buses will return participants to the hotel. Be sure to make reservations early, as the field will be limited to 100 players. Fee: $100.

Tennis Tournament **11:00 a.m. to afternoon**
The annual men's and women's tennis tournaments will be held at the courts at Marriott's Orlando World Center. The fee of $50 includes luncheon, court fees, balls and prizes.

Discover Orlando **1:30 - 4:30 p.m.**
A repeat of Sunday's tour. See description on page 709.
Fee: $16.

Church Street Station **6:30 - 11:00 p.m.**
Let the good times roll at this exciting restaurant and shopping complex in historic downtown Orlando. Hear exciting Dixieland jazz at Rosie O'Grady's Goodtime Emporium, sample exotic drinks at Apple Annie's, savor exemplary cuisine and fine spirits at Lili Marlene's or return to the romance and glamour of the '30s in the Orchid Garden Ballroom and Dessert Cafe. Dance to the hottest sounds at Phineas Phogg's Disco or two-step and sample great BBQ at the Cheyenne Saloon and shop in style at the Bumby Arcade or Buffalo Trading Company. Sightsee and shop at Church Street Exchange with 130 shops and food marts and the Downtown Marketplace. Street entertainment and spontaneity add to the fun of this evening. Dinner not included.
Fee: $30.

Tuesday, May 12

Kennedy Space Center **9:00 a.m. - 4:00 p.m.**
The dream and commitment of space exploration is alive at the Kennedy Space Center. You will capture the spirit as you view the shuttle assembly building, launch pads, astronaut training facilities and rocket museums. A breathtaking film will be shown on a five-story IMAX screen. Ample time will be allowed for camera stops along the tour and for individual exploration among the exhibits and museums. Lunch not included. Fee: $30 adult, $25 children ages 3-11.

Historic Winter Park/Park Avenue Shopping
9:30 a.m. - 3:30 p.m.
Originally envisioned as "a beautiful winter resort for the well-to-do people," Winter Park is still the most desirable place to live in Central Florida, winter and summer. Begin the day by viewing the true beauty of Winter Park from an excursion boat as you cruise through the beautiful lakes and Venetian canals. Your guide will take you back in time and dazzle you with the magnificent homes and mansions that have lined the shores for the past 100 years. Next you will browse along Park Avenue and informally tour the "Little Europe" shopping district, a haven for boutique shoppers and gourmet palates. Enjoy the Morse Art Gallery with the largest collection of Louis B. Tiffany glass in the world. A private luncheon will be served in one of Park Avenue's fine restaurants. Fee: $48.

Wednesday, May 13

Cypress Gardens VIP Tour **10:00 a.m. - 4:00 p.m.**
Cypress Gardens is the home of the world's most photographed water ski show, combining daredevil excitement with artistry and laughter. Ski-jumping champions and hang gliders will provide the thrills, water clowns will provide the laughter and ballet aquamaids will perform with beauty and grace. Also included are a private boat tour of the lake and a tour through the lush gardens which give this attraction its name. Marvel at the more than 12 million blooming flowers and thrill to the vibrant panorama of exotic birds and animals, including the proverbial Florida gator. Lunch on your own.
Fee: $42 adult, $36 children ages 3-9.

Magic of Ming **11:00 a.m. - 2:00 p.m.**
This exclusive cooking class will give you a hands-on learning experience in the art of gourmet Chinese cuisine. The adventure begins as you prepare appetizers (complete with a spring roll competition!) and continues with a demonstration of the secrets to successful stir-fry cuisine, followed by the unveiling of hand carved garnishes prepared by the official garnee chef. After a question-and-answer session, a gourmet Chinese lunch will be served.
Fee: $43.

Thursday, May 14

"Hot off the Set" - Universal Studios VIP Tour
10:00 a.m. - 4:00 p.m.
You will be treated like a star as you are escorted into Universal Studios in a group of only 15 people to experience an hour-long studio tour. A VIP guide will escort you down the streets of New York, Hollywood and San Francisco and divulge many fun facts about your favorite movies. Lunch will be served, after which you will have three hours for leisure sightseeing and shopping. Fee: $58.

Leu Gardens/Jordan's Grove **9:30 a.m. - 1:30 p.m.**
Stroll along the meandering pathways of Harry P. Leu Botanical Gardens, through forests of camellias and avenues of giant camphors. Wind your way across gentle hills down to sparkling Lake Rowena. Relax among thousands of exotic flowers and plants. Leu Gardens is a pleasant interlude in a busy day. Following your visit to this exotic wonderland, you will be escorted to Jordan's Grove for a relaxing luncheon. Jordan's Grove is a restaurant located in a restored historic home situated on 3½ acres of land, where original recipes are created daily with only the freshest ingredients. Fee: $42.

Space Is Limited - Register Early!

Scientific Program

Monday, May 11

I Ob/Gyn Ultrasound

10:45 **001.** Antepartum Substance Abuse: Use of Duplex Doppler in a Prospective Series. *Twickler DM, Satin AJ, Little BB, Olsher DA, Soo AC, Wendel GD.*

10:57 **002.** Ovarian Masses: Evaluation by Color Doppler Endovaginal Sonography with Pathologic Correlation. *Hamper UM, Sheth S, Abbas FM, Rosenshein NB, Kurman RJ.*

11:09 **003.** Transvaginal and Transabdominal Color Doppler Sonography of Ovarian Masses: Correlation with Gross and Microscopic Pathology. *Fleischer AC, Kepple DM, Rodgers WH, Williams LC, Jones HW III.*

11:21 **004.** Comparative Reimbursements to Radiologists and Non-Radiologists for Ultrasound Examinations in the Private Office Setting. *Lev-Toaff AS, Levin DC, Edmiston RB, Rosetti G, Harford RJ.*

11:33 **005.** US Analysis of Gynecologic Structures in the 0 - 2-Year-Old: Ovaries Are Larger and More Cystic Than Previously Reported. *Shapiro M, Cohen HL, Eisenberg P, Mandel F, Haller JO.*

11:45 **006.** Renal Resistive Index in Normal Women During Pregnancy. *Nazarian GK, Platt JF, Rubin JM, Ellis JH.*

11:57 **007.** Placenta Previa: Value of Using Transperineal Ultrasound to Complement the Transabdominal Approach. *Hertzberg BS, Bowie JD, Carroll BA, Kliewer MA, Weber TM.*

12:09 **008.** Anterior Intraperitoneal Space Measurement in Evaluation of the Omentum by Sonography. *Pretorius DL, Poulton TB, Nazinitsky KJ, Peterson CL.*

II General Interest

10:45 **009.** Gallium Scanning in Adult HIV Infected Patients with Lymphocytic Infiltrative Pneumonitis (LIP). *Rosenberg ZS, Goldfarb R, Joffe S, Itescu S.*

10:57 **010.** TL-201-Spect of Cerebral Lesions in Comparison to HMPAO-Spect, CT, and MRT. *Barzen G, Hierholzer J, Debrand-Passard A, Richter W, Schubert C, Eichstadt H, Felix R.*

11:09 **011.** Incidence of Hibernating Myocardium in Patients with Irreversible Perfusion Defects: Detection by Combined RB-82 and F-18-FDG Pet Imaging. *Go RT, Cook SA, MacIntyre WJ, Neumann DR, Marwick TH, Saha GB, Antar MA, Underwood DA.*

11:21 **012.** Accuracy of Digital Teleradiology vs. Conventional Imaging for Thoracic Angiography. *Lehman CD, Goldman ML, Glickerman DJ, Richardson ML, Rowberg AH.*

11:33 **013.** Credentialing Procedure for Fluoroscopic Privileges for Non-Radiologists: Experience and Physician Reactions. *Lam SCP, Swayne LC, Filippone AL, Ambrose RB.*

11:45 **014.** PACS Demands a New Task for the Radiologic Community: The Radiology Information and Communication Coordinator. *Mosser H, Urban M, Hruby W.*

11:57 **015.** Assessment of Medical Benefits of PACS Related to the Extent of Interconnection of Imaging Devices and Information Systems. *Urban M, Hruby W, Mosser H.*

12:09 **016.** The Price of Non-Conformance (PONC): Study of Portable Unit Inefficiency in Radiology. *Correia Kamat MR, Powers J, Wheeler HE, Clouse ME.*

III Skeletal I

1:30 **017.** The Impact of Adding Cobalt-57 Transmission Imaging and TC-99M-Sulfur Colloid (SC) Marrow Scan to the Standard TC-99M-MDP/IN-111-WBC Scan Diagnosis of Osteomyelitis in Trauma Patients. *Barron B, Tran H, Browner B, Lyssy K, Lamki L.*

1:42 **018.** Bone Mineral Density Measurement in Professional Divers by Dual Energy X-Ray Absorptiometry. *Yang (S-O), Sohn SK, Lee JY, Kim KT, Lee YI.*

1:54 **019.** Phosphor Plate Arthrography: ROC Comparison with Film-Screen Technique. *Murphey MD, Quale JL, Martin NL, Cook L, Wright MJ.*

2:06 **020.** CT-Guided Bone Metastasis Pain Therapy. *Gangi A, Kastler B, Allal R, Quoix E, Mathelin C, Dietemann JL.*

2:18 **021.** Early Detection of Medullary Sclerosis: The Skeletal Silhouette Sign. *Cantor RM, Kattan KR.*

2:30 **022.** Glenohumeral Retroversion Using CT Arthrography. *Doyle AJ, Burks RT.*

2:42 **023.** Rotatory Atlantoaxial Subluxation: Plain Radiographs, Polytomes, CT, and MRI. *Mikhael MA.*

2:54 **024.** Stress Radiography of Elbow Joint Ligaments. *Rijke AM, Goitz HT, McCue FC III.*

3:06 **025.** Giant Cell Tumor of the Hands and Feet: A Review of 143 Biopsy Proven Cases. *Giudici MAI, Moser RP Jr, Kransdorf MJ.*

3:18 **026.** Complications of Long Term Allografts in a Group of Patients Who Had Surgery for Primary Bone or Soft Tissue Tumors. *Griffiths HJ, Amundson PJ, Thompson RC Jr, Detlie T, Everson L.*

IV CT - Abdomen

1:30 **027.** Primary Aldosteronism: CT Evaluation. *Dunnick NR, Gunnells JC, Leight GS Jr, Leder RA, Roubidoux MA, Paulson E, Kurylo L.*

1:42 **028.** CT of Adrenal Injury Following Blunt Trauma. *Burks D, Mirvis SE, Shanmuganathan K.*

1:54 **029.** CT of Mesenteric and Peritoneal Lymphoma. *Crawley G, Baker ME, Gulliver D, Leder R, Paulson E, Roubidoux M, Dunnick NR.*

2:06 **030.** Tissue CEA Determination From FNAB Specimens: Technique, Clinical Utility, and Comparison with Cytology. *Lee MJ, Dawson SL, McLoughlin D, Kinney T, Saini S, Hahn PF, Mueller PR.*

2:18 **031.** Evaluation of Double-Volume Low Concentration Contrast Medium and Prostaglandin E1 in CT Arterial Portography (CTAP). *Hirohashi S, Uchida H, Guo Q, Nishimura Y, Nishimine K, Yoshioka T, Ohishi H, Doi T.*

2:30 **032.** Detection of Hepatic Lesions in Patients with Abdominal Malignancy: Comparison of Bolus Contrast Enhanced Dynamic CT (BCDCT), Delayed CT (DCT), Intra-Operative Ultrasound (IOUS), and Surgical Palpation. *Marn CS, Francis IR, Knol JA, Rubin JM, Bromberg J, Chang AE.*

2:42 **033.** Diagnostic Criteria of Fatty Liver on Bolus-Enhanced Dynamic Incremental CT. *Baird AT, Korobkin M, Quint LE, Francis IR.*

2:54 **034.** Pattern of Regional Nodal Metastases in Left Colon Carcinoma: CT Evaluation. *Granfield CAJ, Charnsangavej C, Dubrow RA, Varma DGK, Wallace S.*

3:06 **035.** Portal Venous Contrast-Enhanced CT and Thin Section High Resolution CT in Preoperative Evaluation of Pancreatic Tumors. *Ibukuro K, Yoshimitsu K, Charnsangavej C, Carrasco CH, Lawrence DD, Richli W, Chuang VP.*

3:18 **036.** Abdominal Biopsy With Spiral CT: Faster Needle Tip Localization. *Silverman SG, Bloom DA, Seltzer SE, Adams DF.*

V Breast

1:30 **037.** MRI for the Evaluation of Silicone Breast Implants. *Jones MK, Clunie DA, Szumowski J, Webber B, Woltering G, Thurmond AS.*

1:42 **038.** Sonographic and Mammographic Appearance of Ruptured Breast Implants. *Rosculet KA, Ikeda DM, Forrest ME, Helvie MA, O'Neal R, Jeffries DO.*

1:54 **039.** Breast Lesions: Diagnostic Usefulness of Color Doppler Ultrasound. *Choi H, Park K, Lee S, Kim T.*

2:06 **040.** Stability of Malignant Breast Microcalcifications. *Lev-Toaff AS, Feig SA.*

2:18 **041.** Mixed Cystic and Solid Breast Masses: Sonographic Patterns as a Diagnostic Predictor. *Staiger MJ, Harris KM, Ilkhanipour ZS, Ganott MA, Wintz PW, Baratz AB, Skolnick ML.*

2:30 **042.** The Management of Patients Following Stereotactic Large Core Needle Biopsy of Non-Palpable Breast Lesions. *Evans WP III, Hall KS, Fulmer JM, Cade SH.*

2:42 **043.** The Likelihood of Malignancy for Categories of Mammographically Detected Nonpalpable Breast Lesions. *Knutzen AM, Gisvold JJ.*

2:54 **044.** Breast Cancer After Hodgkin's Disease: A Need for Earlier Radiographic Screening. *Roberts TL, Monsees BS, Wasserman T, Miller E, Destouet JM.*

3:06 **045.** Screening Mammography in Women Age 35 - 39. *Liberman L, Dershaw DD, Deutch BM, Smolek-Lippin B.*

3:18 **046.** A Study of the Effectiveness of Local Anesthetic Administration in Preoperative Needle Localizations. *Reynolds HE, Jackson VP.*

Tuesday, May 12

VI Vascular Interventional

10:00 **047.** Angioplasty Above the Aortic Arch: Indications, Technique and Results. *Selby JB, Hartwell GD, Matsumoto AH, Tribble C, Kron IL, Tegtmeyer CJ.*

10:12 **048.** Balloon Angioplasty of Severely Diseased Infrapopliteal Arteries. *Cynamon J, Parisi A, Bakal CW, Sprayregen S, Epstein SB, Veith FJ.*

10:24 **049.** Transarterial Treatment of Intrahepatic Arterioportal Fistulas (APF). *Tarazov PG.*

10:36 **050.** Transjugular Intrahepatic Portocaval Shunts (ICPS): Preliminary Results. *Maquin P, Rousseau H, Vinel JP, Pascal JP, Joffre F, Railhac JJ.*

10:48 **051.** Duplex Ultrasound Evaluation of Patients Treated with Transjugular Intrahepatic Portosystemic Stent Shunts (TIPSS). *Wagner BJ, Chintapalli K, Woodward PJ, Brantley SD, Joseph AE, Maupin WB II, Palmaz JC, Rivera FJ.*

11:00 **052.** Transjugular Intrahepatic Portosystemic Shunting (TIPS) for Portal Hypertension: Efficacy and Assessment with Color Doppler Sonography. *Chong WK, Lind C, Fleischer AC, Mazer M.*

11:12 **053.** Combined Intravascular Laser-Ultrasound Imaging Device. *Duda SH, Kreis A, Huppert PE, Fleiter T, Schmidt (K-M), Karsch KR, Claussen CD.*

11:24 **054.** Comparison of Pulsed Dye vs. Excimer Laser Angioplasty: Ablation Efficacy and Clinical Experience. *Duda SH, Huppert PE, Haase KK, Karsch KR, Claussen CD.*

11:36 **055.** MRI vs. Venography in the Detection of Deep Venous Thrombosis: A Prospective, Blinded Study in 46 Patients. *Evans AJ, Sostman HD, Knelson MH, Spritzer CE, Newman GE.*

11:48 **056.** MR Angiography in the Preoperative Evaluation of Abdominal Aortic Aneurysm. *Hackworth CA, Bova JG, Bennett WF, Durham J, Van Aman ME, Schmalbrock P, Hacker VA, Smead WL.*

12:00 **057.** Endovascular Stenting of Renal Artery Stenoses. *Saeed M, Knowles HJ, Schatz RA.*

12:12 **058.** Vasa Vasorum Changes Following Angioplasty of Experimental Arterial Stenosis. *Pisco JM, Correia M, Esperanca-Pina JA, Sousa LA.*

VII GI - Liver

10:00 **059.** Gamna-Gandy Nodules of the Spleen Identified by 0.5-TESLA MR Imaging: Clinical Significance in Cirrhotic Patients. *Fujimoto H, Murakami K, Yasuda S, Ichikawa T, Kashimada A, Ando S, Goto N, Shinozaki M, Muraoka H, Yamazaki K, Ozawa K, Arimizu N.*

10:12 **060.** Prospective Evaluation of Liposomal Gadolinium and Iron Dextran as MR Contrast Agents in a Metastatic Embryonal Cell Liver Tumor Mouse Model. *Vellet AD, Levin MF, Karlik S, Grant C, Harris R, Munk PL.*

10:24 **061.** Detection of Liver Cancer in the Presence of Hepatitis: Cell-Specific MR Contrast Agents. *Tanimoto A, Kreft BP, Baba Y, Zhao L, Finn JP, Stark DD.*

10:36 **062.** Evaluation of Oral Contrast Agents for MRI. *Kraus BB, Rappaport DC, Ros PR, Torres GM.*

10:48 **063.** Aqueous GI Contrast Agent for Ultrafast MR Imaging. *Hahn PF, Saini S, Cohen MS, Reimer P, Mueller PR.*

11:00 **064.** Contribution of MRI in Differentiation of Giant Cavernous Hemangioma from Hepatic Metastasis. *Schmutz GR, Chhem RK, Bui BT, Jeung MY, Vetter D.*

11:12 **065.** The Role of Oblique Sections in MR Angiography of the Portal Vein. *Borrello JA, Brown JJ, Siegel MJ, Lee JKT.*

11:24 **066.** Ramification Pattern of Hepatic Veins Studied by MR Imaging. *Itoh K, Hosono M, Kawakami S, Konishi J.*

11:36 **067.** The Natural History of Portal Vein Thrombosis. *Abbitt PL.*

11:48 **068.** Persistence of Portosystemic Collaterals and Splenomegaly Following Hepatic Transplantation. *Chezmar JL, Redvanly RD, Nelson RC, Henderson JM.*

12:00 **069.** Radiologic Management of Biliary Calculi. *Ho CS, Yeung E, Thurston W.*

12:12 **070.** Complications of Percutaneous Biliary Drainage After Endoscopic Failure: Is There a Relationship? *Gazelle GS, Mueller PR, Hahn PF, Lee MJ, Dawson SL, Saini S, Kabaalioglu A.*

VIII Genitourinary I

10:00 **071.** Renal Biopsies Using the Automated Biopsy Gun: Comparison with the VIM Silverman Needle. *Sateriale M, Kassner R, Cronan JJ.*

10:12 **072.** Renal Biopsy in Diffuse Renal Disease: Efficacy and Safety Using a 14-Gauge Automated Biopsy Device. *Tung KT, Downes MO, O'Donnell PJ, Path MRC.*

10:24 **073.** CT and US-Guided FNA of Renal Masses. *Miller JH, Jafri SZH, Bernacki EG, Roberts JL, Madrazo BL.*

10:36 **074.** Kidney Transplant Biopsies: Comparison of the Biopty Gun with the Tru-Cut Needle. *Mahoney MC, Racadio JM, Merhar GL, First RM.*

10:48 **075.** Prostate Cancer Detection: Comparison of Transrectal Ultrasound, Digital Rectal Examination, and Prostate Specific Antigen. *Weber TW, Dunnick NR, Robertson CN, Paulson DF, Leder RA, Roubidoux MA.*

11:00 **076.** Post Biopsy Hemorrhage in the Prostate: Friend or Foe. *Schiebler M, Schnall M, Outwater E, Pollack H.*

11:12 **077.** Sono-Histological Correlation of Contralateral (Non-Suspicious) US-Guided Prostate Biopsies. *Madrazo BL, Jafri SZH, Roberts JL, Long JC.*

11:24 **078.** Percutaneous Ureteral Stent Placement: Technical Problems and Solutions. *Lu DSK, Girard M, Papanicolaou N, Lee MJ, Yoder IC.*

11:36 **079.** Fluoroscopy-Guided Suprapubic Cystostomy: A Four-Year Experience with 45 Patents. *Lee MJ, Papanicolaou N, Valdez J, Nocks BN, Yoder IC.*

11:48 **080.** Microintervention of the Double Renal Transplant into the Adult. *Brunner MC, Matalon TAS, Patel SK, Siliunas DA, Merkel FK.*

12:00 **081.** Percutaneous Access for Endourologic Procedures in Patients With Decompressed Renal Pelvis. *Kubek R, Lang EV, Kabalin JN.*

12:12 **082.** Use of Self-Expandable Stents in the Therapy of the Recidivious Stricture of the Urethra. *Liermann D, Meyer WW, KramerW, Kirschner J, Kollath J, Jonas D.*

IX Neuroradiology I

1:30 **083.** Evaluation of Congenital Craniofacial Anomalies in the Pediatric Population: A Systematic Anatomical Approach Utilizing 3-D CT. *Wiley TE III, Hasso AN, Thompson JR, Hardesty RA.*

1:42 **084.** Comparison of Sinus Radiographs to Sinus CT in the Assessment of Paranasal Sinus Disease in Pediatric Asthma. *Gross GW, Kalman DD, McGeady SJ, Kerut T, Ehrlich SM.*

1:54 **085.** Surgical Planning of Intracranial and Skull Base Neoplasms: The Value of Contrast-Enhanced MR Angiography. *Hasso AN, Hinshaw DB Jr, Thompson JR, Holshouser B, Akamine JS, Mansfield WP.*

2:06 **086.** Anatomic and Functional Imaging in the Syndrome of Infantile Autism. *Schifter T, Hoffman JM, Hatten HP Jr, DeLong GR, Coleman RE.*

2:18 **087.** High Resolution Brain Spect Quantification Using Tc-99m HMPAO in 'Normal' Closed Head Injury, Stroke, and Epilepsy Patients. *Lamki L, Tran H, Barron B, Taylor WJ.*

2:30 088. Spiral CT in the Evaluation of the Carotid Artery Bifurcation. *Schwartz RB, Jones KM, Mukherji S, Chernoff D.*

2:42 **089.** Prediction of Cerebral Ischemia During Carotid Endarterectomy. *Schwartz RB, Ahn S, Leclercq G, Gugino L, Whittemore A.*

2:54 **090.** Adult Duplex Transcranial Doppler: Promising Technique in Evaluation of Vascular Spasm. *Hashimoto BE, Nussbaum C, Brennan L, Lewis GP.*

3:06 **091.** The Current State of the Art in Detection of Cervical Spine Injuries. *Lee C, Woodring JH.*

3:18 **092.** Incidence and Complications of Orbital Roof Fractures: A 10-Year Retrospective Analysis. *Gentry LR, Unger J.*

X Cardiac MRI

1:30 **093.** Clinical Assessment of Diffusion and Perfusion MR Images. *Le Bihan D, Douek P, Argyropoulou M, Goldberg R, Turner R, Patronas N, Fulham M, Di Chiro G.*

1:42 **094.** Gradient-Recalled MR Imaging of Vessels Adjacent to Fat. *Weinberger E, White KS, Shaw DW, Wining MK.*

1:54 **095.** Interstudy Variability of Left Ventricular Mass Measurement Comparison Between M-Mode Echography and MRI. *Kastler B, Germain P, Gangi A, Roul G, Allal R, Petrow P, Dietemann JL, Sacrez A.*

2:06 **096.** Evaluation of Ventricular Septal Defects in Congenital Heart Disease Using Septum Angulated Cine MR Imaging and Color Doppler Echocardiography. *Seelos KC, Redel DA, von Smekal A, Kaas P, Reiser M.*

2:18 **097.** Gd-DTPA Perfusion in Cardiac MR Imaging: First Results in Patients Using a Turbo Fast Scan Technique at 0.5 Tesla. *Seelos KC, von Smekal A, Gieseke J, van Vaals J, Reiser M.*

2:30 **098.** Magnetic Resonance Imaging of Left Ventricular Function: An Optimized Rapid Algorhythmic Approach. *Beyl G, von Smekal A, Seelos KC, Reiser M, Biersack HJ.*

2:42 **099.** Regional Left Ventricular Wall Stress Estimation. *Duerinckx AJ, Fujita N, Higgins CB.*

2:54 **100.** Cardiac Masses: MRI Signal Intensity Features on Spin Echo, Gradient Echo and Gd-DTPA Enchanced Spin Echo and TurboFLASH Images. *Semelka RC, Shoenut JP, Wilson M, Pellech AE, Patton JN.*

3:06 **101.** Estimation of Pulmonary Artery Pressure from Spin Echo MR Images. *Murray TI, Boxt LM, Katz J, Barst RJ.*

3:18 **102.** Use of Desktop Computers in the Enhancement of Post-Gadopentatate MR. *Carpenter WA, Stiles RG, Sheppard SK.*

XI Genitourinary II

1:30 **103.** Scintigraphy of Renal Transplants With 99M-Tc-MAG$_3$. *Meadors JN, Hubner KF, Besozzi MC, Smith GT, Goldman M, Buonocore E.*

1:42 **104.** Appearance of the Kidneys, Liver and Spleen in Paroxysmal Nocturnal Hemoglobinuria by Magnetic Resonance Imaging. *Roubidoux MA, Weber TM, Dunnick NR.*

1:54 **105.** Dynamic Gadolinium-Enhanced Ultra-Fast Gradient Refocused Echo Imaging (MPHWARPSP) of Renal Tumors. *Weber TM, Spritzer CE.*

2:06 **106.** Evaluation of MR Angiography in the Preoperative Renovascular Assessment for Potential Living-Related Kidney Donors. *Debatin JF, Spritzer CE, Grist TM, Sostman HD.*

2:18 **107.** Contrast Enhanced Computed Tomography of the Kidneys: Comparison of Nonionic vs. Ionic Contrast Media. *Sussman SK, Turner G, Illescas FF, Opalacz JP, Yirga P.*

2:30 **108.** Persistent CT Nephrogram: Correlation with Renal Insufficiency. *Love L, Johnson MS, Nelson JE, Olson MC, Bresler ME, Johnson SA, Sexton BA.*

2:42 **109.** Preoperative Assessment of Uterine Fibroids: Role of Hysterosalpingography, Ultrasound and MRI. *Karasick S, Lev-Toaff AS.*

2:54 **110.** Posttransplant Renal Artery Stenosis: Outpatient Intraarterial DSA vs. Color Coded Duplex Ultrasonography. *Duda SH, Erley CM , Wakat JP, Huppert PE, Lauchart W, Risler T, Claussen CD.*

3:06 **111.** Ovarian Cancer Imaging by PET and FDG. *Niethammer JG, Hubner KF, McDonald T, Smith GT, Gould HR, Buonocore E.*

3:18 **112.** Evaluation of Female Pelvic Masses: Value of Gadolinium-Enhanced MR Imaging. *Thurnher S.*

Wednesday, May 13

XII Skeletal II

1:30 **113.** Kinematic MRI of the Knee with Bi-Plane Acquisition. *Brown SM, Atkinson DJ, Nissenbaum MA, Song SJ, Widoff BE, Yan K, Kurzweil PR, Jackson D, Bradley WG.*

1:42 **114.** A Comparison of the MRI Findings in the Knee in Transient Osteoporosis and Spontaneous Osteonecrosis. *Schneider R, Goldman AB, Wickiewicz T, Windsor R.*

1:54 **115.** Ancillary MRI Findings in Anterior Cruciate Ligament Disruption. *Hunt JM, Vahey TN, Broome DR.*

2:06 **116.** MR Diagnosis of ACL Injury: Value of a Multiplanar Approach. *Fitzgerald SW, Remer E, Friedman H, Rogers LF, Hendrix R, Schaefer M.*

2:18 **117.** Traumatic Patellar Dislocation: MR Diagnosis. *Kirsch MD, Fitzgerald SW, Friedman H, Rogers LF.*

2:30 **118.** Cruciate Ligaments of the Knee: Magnetic Resonance (MR) - Anatomic Correlation. *Hodler J, Haghighi P, Trudell D, Resnick D.*

2:42 **119.** MR Detection of Articular Cartilage Pathology. *White EM, Kezdi PC, Sweeney HJ, Robb WG, Ghahremani GG.*

2:54 **120.** Quantitative Assessment of Hip Cartilage Using Anatomic MR Imaging Correlation: Fat Suppression Technique. *Hodler J, Pathria MN, Trudell D, Resnick D.*

3:06 **121.** Myositis Ossificans: MR Appearance with Radiologic-Pathologic Correlation. *Kransdorf MJ, Meis JM, Jelinek JS.*

3:18 **122.** Prospective Diagnostic Value of US, CT and MRI in Surgical Management of Recurrent Shoulder Dislocation. *Wrazidlo W, Lederer W, Schneider S.*

XIII Chest

1:30 **123.** Natural Radiographic History of Pulmonary Cysts in AIDS Patients with Pneumocystis Carinii Pneumonia. *Chow C, Templeton PA, White CS.*

1:42 **124.** Pleural Effusion in AIDS Patients: Correlation with Underlying Pulmonary Involvment. *Seguin N, Osborne ME, Samson L, Morisset R, Ghadirian P.*

1:54 **125.** Ultrasound Guided Thoracic Biopsy: Technique and Results. *Fundell L, D'Agostino HB, vanSonnenberg E, Sanchez RB, Oglevie S, O'Laoide R, Casola G.*

2:06 **126.** Postbiopsy Precautions Following Needle Aspiration Biopsy of the Lung. *Hanna JW, Molina PL, Glazer HS, Anderson DJ, Solomon SL, Sagel SS.*

2:18 **127.** Neodymium: Yttrium-Alumium Garnet (Nd:YAG) Laser-Assisted Thoracic Surgery: Postoperative Radiographic Findings. *Peterson MS, Cohen CS, Landreneau RJ.*

2:30 **128.** Percutaneous Needle Biopsy in Patients Status Post Heart and Heart/Lung Transplant. *Wittich G, Hamid L, Lukacs J, Lucas D, Kusnick C.*

2:42 **129.** Image-Directed Percutaneous Thoracic Biopsies with a Biopsy Gun. *Pluss JL, Mulligan JS.*

2:54 **130.** Single Lung Transplant: Correlation Between Chest Radiographs and Transbronchial Biopsy. *Chintapalli K, Levine S, Bryan C, Posteraro R, Glenn M, McCrary K.*

3:06 **131.** Evaluation of Normal Structures with a Conventional Film-Screen Chest Radiology System vs. 'Insight' Film-Screen System. *O'Keeffe M, Hudon M, Hoffman K.*

3:18 **132.** Enlarging Pleural Effusion Post Liver Transplantation. *Spizarny DL, Gross BH, McLoud T.*

XIV General CT

1:30 **133.** CT Findings in Breast Cancer Patients with Suspected Liver Metastases. *Wilson TE, Korobkin MT, Kane NM, Quint LE, Francis IR.*

1:42 **134.** T-Cell Cutaneous Lymphoma: Specific CT Findings. *Miketic LM, Chambers T, Lembersky B.*

1:54 **135.** Optimization of Nonionic IV Contrast Dose in Dynamic CT Scanning of the Abdomen and Pelvis. *Allen DA, Ros PR, Call G, Litwiller T, Torres GM.*

2:06 **136.** Assessment of Coronary Bypass Graft Patency with Volumetric Computed Tomography. *Tello R, Costello P, Ecker C, Hartnell G.*

2:18 **137.** Optimal Parameters in HRCT of Diffuse Pulmonary Disease. *Lorcher U, Peters J, Liermann D, Rautschka E.*

2:30 **138.** Chest CT of Breast Masses. *Gay SB, Langer TG, Wunder RJ.*

2:42 **139.** Extraperitoneal Hematomas: Localization at CT May Suggest Etiology. *Holland D, Quint LE, Korobkin M, Cascade PN.*

2:54 **140.** Ultrafast CT Diagnosis of Pulmonary Embolism. *Thorne DA, Geis JR, Midthun J.*

3:06 **141.** Assessment of the Thoracic Aorta by Spiral Computed Tomography. *Costello P, Ecker CP, Tello R, Hartnell GG.*

3:18 **142.** Contrast-Enhanced Spiral CT of the Chest: Initial Clinical Experience in 80 Patients. *Molina PL, Brink JA, Heiken JP, Sagel SS, DiCroce JJ.*

Thursday, May 14

XV Non-Vascular Interventional

10:00 **143.** Fine Needle Aspiration Biopsy of Abdominal Lesions: Diagnostic Yield for Different Needle Tip Configurations. *Hamper UM, Dahnert WF, Hoagland MH, Erozan YS, Peirce JC.*

10:12 **144.** Percutaneous Intraperitoneal Catheter Placement for Chemotherapy Treatment. *D'Agostino HB, vanSonnenberg E, Sanchez R, Chalmers N, O'Laoide R, Oglevie S, Fundell L.*

10:24 **145.** Evaluation of the Learning Curve for Hickman Line and Hemodialsis Catheter Insertion. *Ignotus PI, Macklin N, Gray RR.*

10:36 **146.** Long Term Benefit of Percutaneous Dilatation of Dominant Bile Duct Strictures in Primary Sclerosing Cholangitis. *Bender CE, Wiesner RH, LeRoy AJ, LaRusso NF, Nagorney DM.*

10:48 **147.** Recent Experience with Percutaneous Biliary Drainage. *Oglevie SB, vanSonnenberg E, D'Agostino H, Sanchez R, O'Laoide R, Fundell L, Tsai C, Epstein D.*

11:00 **148.** Malignant Obstruction of the Biliary Hilum: Treatment with Multiple Metallic Endoprostheses. *Vogelzang RL, Nemcek AA Jr.*

11:12 **149.** Z Stents for Treatment of Benign Biliary Strictures Following Liver Transplantation. *Goertzen TC, Lieberman RP, Ranjan D, Stratta RJ, McCowan TC, LeVeen RF.*

11:24 **150.** Chemoembolization in Hepatocellular Carcinoma with Adriamycin/Ethiodol. *Stokes KR, Stuart KR, Jenkins RL, Clouse ME.*

11:36 **151.** Selective Regional Chemotheraphy of Unresectable Hepatic Tumours Using Lipiodol. *Reddy K, Novell JR, Dusheiko G, Markham NI, Dick R, Hobbs KEF.*

11:48 **152.** Conversion of Unresectable Malignant Tumors of Liver to Resectable by Treatment of Trancatheter Hepatic Artery Embolization and Histopathological Study of the Specimens. *Teng G-J, Gao G-R, Cai X-L, Xie X-H, Nan Z-Y.*

12:00 **153.** Percutaneous Tissue Ablation with Radiofrequency Thermal Energy. *Sanchez RB, vanSonnenberg E, D'Agostino HB, Goodacre BW, Esch O, Nissenbaum M.*

12:12 **154.** Percutaneous Ethanol Injection (PEI) of Hepatic Neoplasms: Early Experience. *Dawson SL, Lee MJ, Ferrucci JT, Mueller PR.*

XVI Gastrointestinal - CT/Pancreas

10:00 **155.** Transpyloric Extension of the Gastric Tumor: Comparison between Adenocarcinoma and Lymphoma. *Cho KC, Baker SR, Alterman DD, Fusco JM, Cho S.*

10:12 **156.** Primary Colonic Lymphoma: CT and Barium Correlation. *Wyatt SH, Fishman EK, Jones B.*

10:24 **157.** Prevalence and Clinical Correlation of Opportunistic Esophagitis in HIV-Positive Patients. *Chen MYM, Hodge RG, Donati DL, Ott DJ, Gelfand DW.*

10:36 **158.** Gastrointestinal Radiology: Current Indications and Referral Patterns. *Einstein DM, Lieberman JM, Desai RK, Chilcote WA, Desberg AL, Yagan R, Motta AO.*

10:48 **159.** Dynamic Defecography and Anorectal Manometry. *Kruyt RH, Delemarre JBVM, Gooszen HG, Hermans J.*

11:00 **160.** Subcutaneous Abdominal Wall Extravasation Due to Fibrous Encasement of Intraperitoneal Catheters: Radiologic Signs. *Parisky YR, Muggia FM, Boswell WD, Russell C, Schlaerth J, Morrow CP.*

11:12 **161.** Dynamic MR in Tumor Blood Perfusion. *Sievers KW, Feldman HJ, Molls M, Lohr E.*

11:24 **162.** Dynamic MRI Anatomy of the Normal Anorectum. *Kruyt RH, Delemarre JBVM.*

11:36 **163.** Pancreatic Masses: Can MRI Contribute to Diagnosis and Staging? *Rominger MB, Kenney PJ, Koslin DB, Listinsky JJ.*

11:48 **164.** Color Doppler in the Evaluation of Peripancreatic 'Fluid' Collections: Not Everything Is Black and White. *Levin MF, Vellet AD, Munk PL, Bach DB.*

12:00 **165.** CT of Hemorrhagic Pseudocysts in Chronic Pancreatitis. *Natarajan K, Wilbur AC, Hibbeln J, Espinosa GA.*

12:12 **166.** Spiral CT Evaluation of Acute Pancreatitis: Preliminary Concepts. *Kawashima A, Fishman EK, Kuhlman JE, Ney DR.*

XVII General Ultrasound

10:00 **167.** Sonographic Evaluation of the Thickened Wall Gallbladder: Role of Color Flow Doppler. *Yee JM, Balthazar EJ.*

10:12 **168.** Transrectal Ultrasound in the Management of Rectal Villous Tumors. *Hill MC, Huntington DK, Smith LE, Orkin BA, Javitt MC.*

10:24 **169.** Color Flow Doppler Characterization of Focal Hepatic Lesions. *Nino-Murcia M, Ralls PW, Jeffrey RB Jr, Johnson M.*

10:36 **170.** Color Doppler Imaging in Differentiating Hepatocellular Carcinoma from Hemangioma and Metastatic Tumors. *Lee MG, Auh YH, Cho KS.*

10:48 **171.** Percutaneous Ethanol Injection Therapy for Hepatocellular Carcinoma. *Shiina S, Niwa Y, Komatau Y, Yoshiura K, Hamada E, Takahashi M, Shiratori Y, Terano A, Kawauchi N, Uta Y, Tagawa K, Unuma T.*

11:00 **172.** Conservative Management of Femoral Artery Pseudoaneurysms following Cardiac Catheterization: Can Color Doppler Imaging Predict Spontaneous Thrombosis? *Paulson EK, Hertzberg BS, Paine SS, Carroll BA.*

11:12 **173.** Morphologic and Hemodynamic Findings Following Transjugular Intrahepatic Porto-Systemic Shunting. *Surratt RS, Middleton WD, Darcy MD, Melson GL, Brink JA.*

11:24 **174.** Transvenous Arterial Ultrasound Imaging During and After Laser-Assisted Angioplasty. *Huppert PE, Duda SH, Braunschweig R, Claussen CD.*

11:36 **175.** In Vivo Analysis and Clinical Importance of Factors Affecting Color Doppler Detectability of Ureteral Jets. *Baker SM, Middleton WD.*

11:48 **176.** Complications of Hemodialysis Access Fistulas: Duplex and Color Doppler Ultrasound Versus Angiography. *Menanteau BP, Marcus C, Azcurra G, Lepreux A, Ladam V, Gausserand F.*

12:00 **177.** Duplex and Color Doppler Sonography of Normal Hemodialysis Fistulas and Grafts. *Finlay DE, Longley DG, Schwabacher SM, Nielsen TA, Vang K, Letourneau JG.*

12:12 **178.** Color Doppler and Duplex Ultrasound Findings in Upper Extremity Veins Following Non-Complicated Catheter Placement. *Burbidge SJ, Longley DG, Letourneau JG, Finlay DE, Leonard AS.*

XVIII Skeletal III

1:30 **179.** Rotator Cuff Disease: Complementary Roles of Plain Film and MR Imaging. *De Mouy EH, Lichtenstein RJ, Giles HW.*

1:42 **180.** MRI Saline Arthrography of the Shoulder. *De Mouy EH, Brunet ME.*

1:54 **181.** MR Imaging of Dupuytren's Disease with Surgical Correlation. *Yacoe M, Ladd A, Bjorkengren AG.*

2:06 **182.** Preoperative MRI of the Rheumatoid Wrist: Surgical Correlation with Potential for Treatment Planning. *Rubens DJ, Totterman SM, Blebea JS, Miller RJ, Delsignore J, Hooper M.*

2:18 **183.** MR-Surgical Correlation of TMJ Assessment. *Vanneroy F, Compere JF, Courtheoux P.*

2:30 **184.** Dual X-Ray Absorptiometry Analysis of the Mechanical Properties of Bone and Femoral Hip Prostheses. *Robertson DD, Lavernia C, Chan B, Eng B, Kao G, Eng M, Beck T, Scott W, Fishman E.*

2:42 **185.** MR in the Initial Diagnosis of Acute Occult Fractures. *Feldman F, Staron R, Haramati N, Zwass A.*

2:54 **186.** Applications of Fat Suppression MRI of Bone. *Erickson FA, Shih TF, Chow P, Chiu LC.*

3:06 **187.** The Limitations of MRI in Detecting Residual Soft Tissue Sarcomas After Excisional Biopsy. *Alekhteyar KM, Kim EE.*

3:18 **188.** MR Imaging of Holium: Yag Laser Discectomy in a Canine Model. *Phillips JJ, Kopchok G, Mueller M, White R.*

XIX Neuroradiology II

1:30 **189.** MRI Measurement of the Amygdala Size in Alzheimer's Disease. *Cuenod CA, Denys A, Michaud JL, Leroy-willig A, Jehenson P, Boller F.*

1:42 **190.** Radiological Features Relevant to the Diagnosis of Embryonal Cell and Other Rare CNS Tumors of the Neuroepithelium. *Lee C, Duncan V, Kirsch JE, Runge VM, Brack M, Garneau R.*

1:54 **191.** Use of Functional MRI CBV Mapping Techniques for Primary Brain Tumor Patients. *Aronen HJ, Belliveau JW, Kennedy DN, Buchbinder BR, Porkka LM, Goldberg IE, Fischman A, Alpert N, Gruber ML, Glass J, Lingood R, Weisskoff R, Brady TJ, Hochberg FH, Rosen BR.*

2:06 **192.** Comparison and Optimization of MR Venography Techniques. *Erickson KK, Lee BCP.*

2:18 **193.** Evaluation of Extracranial Head and Neck Lesions with Gadoteridol and Fat Suppression MR Imaging. *Clunie DA, Talbot JM, Szumowski J, Newcomb J.*

2:30 **194.** Hemodynamic Evaluation of Brain Tumors by Ultra-Fast MRI With High-Dose Gadoteridol at 0.3 MMOL/KG. *Lee C, Kirsch JE, Runge VM, Howard RS II.*

2:42 **195.** Detection of Spinal Metastases Using Inversion Recovery Fast Spin Echo. *Jones KM, Ahn SS, Mulkern MV, Schwartz RB, Mantello MT, Ainslie M.*

2:54 **196.** The Value of Gadolinium Enhancement in MRI of Degenerative Disease of the C-Spine on Low Field Magnet. *Dadsetan MR, Kioumehr F, Rooholamini SA, Yaghmai I.*

3:07 **197.** Fast Spin-Echo Imaging of the Brain and Spine. *Jones KM, Mulkern RV, Schwartz RB, Oshio K, Jolesz F.*

3:18 **198.** Reappearance of the Posterior Pituitary Bright Signal in Diabetes Insipidus: Clinical Correlation With MR Findings. *Lee HK, Suh DC, Chang H.*

XX Pediatrics

1:30 **199.** MR Angiography in Congenital Heart Disease: Comparison of Gated 2D-Inflow and Turbo Fast Scan Technique. *Seelos KC, Steinborn M, von Smekal A, Gieseke J, Stomp G, Redel DA, Reiser M.*

1:42 **200.** Selective Angulation in MR Imaging of Congenital Heart Disease: Comparison With Standard Orthogonal Planes. *Seelos KC, von Smekal A, Gieseke J, Kaas P, Redel DA, Reiser M.*

1:54 **201.** Gated 2D-Inflow MR Angiography for Noninvasive Diagnosis of Complex Congenital Heart Disease in Newborns and Infants. *Steinborn M, Seelos KC, von Smekal A, Gieseke J, Stomp G, Redel DA, Reiser M.*

2:06 **202.** MRI and CT: Relative Accuracy in Evaluation of Seizure Disorder in Pediatric Age Group. *Mikhael MA.*

2:18 **203.** MRI of the Pediatric Knee. *Zobel MS, Stewart NR, Siegel MJ, Borrello JA.*

2:30 **204.** Hepatobiliary Abnormalities on Sonography in Children with Cystic Fibrosis. *Quillin SP, Siegel MJ.*

2:42 **205.** Biliary Complications and Their Management in Pediatric Liver Transplantation. *Westra SJ, Zaninovic AC, Hall TR, Petrus LV, Boechat MI, Kangarloo H.*

2:54 **206.** Radiologic Assessment of RDS Complications in Surfactant Treated Infants. *Dovgan DJ, Choy OG, Herzlinger R.*

3:06 **207.** Pediatric Hepatic Injuries: Follow-Up CT Evaluation. *Bulas DI, Eichelberger MR, Sivit CJ, Wright C, Gotschall C.*

3:18 **208.** Pediatric En Bloc Renal Transplants: Imaging of Normal Anatomy and Post Transplant Complications. *Dodd GD III, Memel DS, Shaw A, Zajko AB, Jordan ML, Shapiro R, Hakala TR.*

MEETING AND ACTIVITIES REGISTRATION FORM

(Follow numbered instructions on reverse side)

(1) ____
Last Name First Name or Initials Title

____
Address

____
City State/Country Zip Code

____
Home Telephone Office Telephone

____
Spouse/Guest(s)

(2) Registration Fees

a. _____ARRS member (all categories) .. No Fee
b. _____Scientific Exhibitor .... No Fee
c. _____Scientific Paper Presenter .... No Fee
d. _____Technical Exhibitor .... No Fee
e. _____Course Faculty .... No Fee

f. _____Non-member physician $250
g. _____Non-member physician-in-training ..... $ 25

....
(Signature of Program Director to verify in-training status)

Registration Fee (if any) $__________

(3) Refresher Course Enrollment

	A.M. Choices			**P.M. Choices**		
	1st	**2nd**	**3rd**	**1st**	**2nd**	**3rd**
Monday, May 11 (100 Series)	_____	_____	_____	_____	_____	_____
Tuesday, May 12 (200 Series)	_____	_____	_____	_____	_____	_____
Wednesday, May 13 (300 Series)	_____	_____	_____	_____	_____	_____
Thursday, May 14 (400 Series)	_____	_____	_____	_____	_____	_____
Friday, May 15 (Pediatrics Symposium)	_____					
Friday, May 15 (New Issues Symposium)	_____					

(4) ___I wish to take the Categorical Course on Neuroradiology (Fee: $75) $__________

(5) ___I wish to attend the ACR luncheons as checked ($15 each): ☐ MON ☐ TUE ☐ WED ☐ THU $__________

(6) ___My spouse/guest will attend the Osteoporosis Program ______________ number of tickets

(7) Local Activities:

	Number of Tickets	
a. Discover Orlando (Sunday, May 10)	_____ @ $ 16	$__________
b. **Golf tournament (Monday, May 11)	_____ @ $100	$__________
c. Tennis tournament (Monday, May 11)	_____ @ $ 50	$__________
d. Discover Orlando (Monday, May 11)	_____ @ $ 16	$__________
e. Church Street Station (Monday, May 11)	_____ @ $ 30	$__________
f. Kennedy Space Center (Tuesday, May 12) adult admission	_____ @ $ 30	$__________
youth admission	_____ @ $ 25	$__________
g. Winter Park (Tuesday, May 12)	_____ @ $ 48	$__________
h. Cypress Gardens VIP Tour (Wednesday, May 13) adult admission	_____ @ $ 42	$__________
youth admission	_____ @ $ 36	$__________
i. Magic of Ming (Wednesday, May 13)	_____ @ $ 43	$__________
j. Universal Studios VIP Tour (Thursday, May 14)	_____ @ $ 58	$__________
k. Leu Gardens/Jordan's Grove (Thursday, May 14)	_____ @ $ 42	$__________

(8) Total Payment Enclosed $☐

**Golf tournament registrants indicate handicap:______
Foursome if desired and their handicaps

____
____
____

Method of Payment: ☐ Check (Made payable to ARRS)
☐ MasterCard ☐ Visa ☐ Amex

Card Number________________ Expiration Date________

Signature ______________________________

INSTRUCTIONS

MEETING AND ACTIVITIES REGISTRATION FORM

(Deadline: April 27)

1 Print or type your name, address and telephone number. If your spouse or guest(s) will accompany you, please list their name(s) as well. The information in this section will be used for printed badges.

2 Check the appropriate box and indicate the amount of payment required for your registration fee. **Non-member residents please note:** your training program director must sign in the place indicated in this section in order for you to receive the reduced registration fee.

3 Review the Instructional Course listings on page 707, and indicate your first, second and third choices for each time period. Courses carry Category I CME credits on a hour-for-hour basis. General registration covers all courses with the exception of the Categorical Course, for which there is a separate fee for all attendees.

4 Check this line if you wish to attend the Categorical Course on Neuroradiology and include $75 in your total payment.

5 Check the ACR luncheons you wish to attend and include fee of $15 for each in your total payment.

6 Indicate the number of complimentary tickets requested for the spouse/guest program on osteoporosis.

7 Review the local activities outlined on pages 709-710 and indicate the number of tickets you wish to purchase for each event. Golf registrants please indicate your handicap and other members of your foursome if desired. Include the total amount for social activities in your payment.

8 Total the fees in items (2) through (7) above, and indicate this amount and the method of payment. If you are paying by credit card, please indicate your card number and expiration date, and sign on the signature line. **Send completed form and payment by April 27 to:**

American Roentgen Ray Society
P.O. Box 2348
Merrifield, VA 22116

Make checks payable to American Roentgen Ray Society.

AMERICAN ROENTGEN RAY SOCIETY

1992 ANNUAL MEETING

May 10-15, 1992

Marriott's Orlando World Center, Orlando, FL

HOTEL REGISTRATION FORM

(Refer to instructions on reverse side. Complete this form and return it directly to the hotel.)

(1)

Last Name	First Name	Title (Dr., Mr., Ms., etc.)
Mailing Address		
City	State/Country	Zip Code

Name(s) of additional person(s) sharing room ____________________

(2) Arrival Date/Time ____________________ Departure Date/Time ____________________

(3) Room Categories (Circle Requested Room Size) Single $150 Double $150

Special Room Requests: ____________________

(4) **RESERVATIONS WILL BE HELD UNTIL 6:00 P.M. UNLESS ACCOMPANIED BY A DEPOSIT OR AN ACCEPTED CREDIT CARD NUMBER AND SIGNATURE.**

Please hold my reservation for (check one):

_____ 6:00 p.m. arrival
_____ Guaranteed arrival by first night's deposit (enclosed)
_____ Guaranteed arrival by credit card

Deposit of one night's rate $ ____________

(5) Method of Payment

☐ Personal Check (made payable to Marriott's Orlando World Center)

☐ MasterCard ☐ Carte Blanche ☐ Diners Club ☐ Visa ☐ Amex ☐ Discover

Card Number ____________________ Expiration Date ____________________

For Guaranteed Reservations Only

I understand that I am liable for one night's room and tax which will be deducted from my deposit or billed through my credit card in the event that I do not arrive or cancel by 6:00 p.m. on the arrival date indicated.

____

Signature

INSTRUCTIONS
HOTEL REGISTRATION FORM
(DEADLINE: APRIL 13)

Reservations must be received by the Marriott's Orlando World Center ARRS Housing Bureau by April 13. Reservations after that date are subject to availability. Written confirmation of your reservation will be sent to you by the hotel. To change or cancel reservations, please call Marriott's Orlando World Center directly at (407) 239-4200. One night's rate is required as a deposit.

Room assignments will be made in the order received by the hotel. We urge you to make your reservations promptly to be certain that you receive the room type you request.

Check-in time is 4:00 p.m. Check-out time is 11:00 a.m. Accommodations may not be available if check-in is made before 4:00 p.m.

1 Type or print name, address and telephone number for any guest reservations. If you plan to share a room, please send in only one housing form. Be sure to list the names of all occupants of rooms. Assignment is delayed until complete information is received.

2 List arrival and departure dates and times.

3 Single and double rooms are available at a flat rate of $150. Circle the desired type of accommodation. If the room type requested is not available, the next available room type will be assigned. Children under 18 are free when sharing a room with an adult.

4 One night's deposit is required, which will be applied to the last night of your scheduled stay. Enter this amount in the space provided.

5 Indicate method of payment. You may send a check with this reservation form (made payable to Marriott's Orlando World Center) or provide credit card information. The hotel accepts American Express, Diners Club, Carte Blanche, VISA, MasterCard and Discover. The deposit will hold your room until 6:00 a.m. of the morning following your scheduled arrival date. In the event of an early departure, the deposit is nonrefundable unless the hotel is notified prior to or at the time of check-in. Cancellation notice of 14 days is required for a deposit refund.

Mail reservation and check, if applicable, to:

ARRS Housing Bureau
Marriott's Orlando World Center
One World Center Drive
Orlando, FL 32821

Classified Advertisements

Positions Available

CHIEF, NUCLEAR MEDICINE, UNIVERSITY OF CALIFORNIA, SAN FRANCISCO SCHOOL OF MEDICINE—The University of California, San Francisco (UCSF) is seeking a chief of nuclear medicine. The candidate will be appointed at the level of associate professor or professor of radiology in residence (depending on qualifications) and will also serve as vice-chairman of the Dept. of Radiology at UCSF. The chief of nuclear medicine must have a demonstrated national research reputation in nuclear medicine and in PET imaging, be an excellent teacher, and be an experienced administrator who will supervise all clinical, teaching, and research programs in nuclear medicine at UCSF and Mt. Zion Hospital and Medical Center in San Francisco. Board certification in nuclear medicine and a California medical license are required. The University of California is an equal opportunity/affirmative action employer. Minority groups, women, and handicapped individuals are encouraged to apply. Send CV to Roy A. Filly, M.D., Chair, Search Committee, Dept. of Radiology, UCSF, San Francisco, CA 94143-0628. 4a

RADIOLOGIST, TYLER, TX—The University of Texas Health Center at Tyler invites applications for a clinical faculty position in the Dept. of Radiology. Some teaching, but not publishing or research, required. A progressive 4-person dept. practices general radiology (including interventional, MRI, and SPECT) and performs approximately 27,000 exams/yr. New equipment, flexible work hours, very light call, no weekend schedule. Yr-round tennis, golf, and boating are available in addition to excellent schools. Competitive first-yr salary and an unsurpassed benefits package are offered. Send CV to J. R. Shepherd, M.D., University of Texas Health Center at Tyler, P. O. Box 2003, Tyler, TX 75710; (903) 877-7100. The University of Texas Health Center at Tyler is an affirmative action, equal opportunity employer. Minorities are encouraged to apply; male/female/handicapped/disabled. 4–6a

CENTRAL NEW JERSEY, IMMEDIATE OPENING—Radiologist with fellowship training or equivalent experience in vascular/interventional and/or in MR imaging to join 6-member group. Must be willing to do other aspects of diagnostic radiology, mammography, ultrasound, CT, and nuclear medicine. Practice includes a 340-bed community hospital, a private radiology office, and an MRI facility. Area is within a 10-mi. radius of Princeton and is near New York City and Philadelphia. Competitive salary, excellent benefits, and partnership opportunity. Send CV or call Margaret M. Beck, Business Manager, 2127 Hamilton Ave., Trenton, NJ 08619; (609) 587-9410. 4–5ap

PEDIATRIC RADIOLOGIST—The Dept. of Pediatric Radiology at St. Christopher's Hospital for Children/Temple University School of Medicine is seeking a candidate for a staff/faculty appointment at the assistant professor level beginning July 1992. Individuals completing their fellowship training in June 1992 preferred. Candidates must have some experience in pediatric angiography as well as in pediatric diagnosis, CT, and ultrasound. Address inquiries to Eric N. Faerber, M.D., Dept. of Radiology, St. Christopher's Hospital for Children, Erie Ave. at Front St., Philadelphia, PA 19134-1095. Temple University is an equal opportunity/affirmative action employer and strongly encourages applications from women and minorities. 4a

GOOD LIFE, GOOD MONEY—Radiologist needed for growing practice that covers 2 hospitals and 2 free-standing clinics. Modalities include R&F, general, mammography, CT, MRI, nuclear medicine, SPECT, and special procedures. Denton, population 60,000, located 30 mi. north of Dallas/Fort Worth, has 2 recreational lakes within 15 mi. and 2 major universities. Attractive financial and benefit packages are offered. Contact Family Radiology with CV at 1614 Scripture, Ste. 2, Denton, TX 76201; (817) 387-6159. 4a

COMMUNITY HOSPITAL WITH TWO LOCATIONS IN NORTHEAST PHILADELPHIA seeks a general radiologist to perform mammography, ultrasound, CT, and nuclear medicine. Knowledge of angio helpful, but not necessary. Send CV and date available to Martin Friedman, D.O., Frankford Hospital, X-Ray Dept., Knights and Red Lion Rd., Philadelphia, PA 19114. 4–5ap

FT. WORTH, TX, DIAGNOSTIC RADIOLOGY—A 7-person, hospital-based group seeks a BC/BE radiologist. Fellowship training in neuroradiology, MRI, and nuclear medicine preferred, but other qualified candidates considered. Duties will include general diagnosis. Early partnership at modest buy-in and ample vacation. Please send CV to Clay Roberts, M.D., 1650 W. Magnolia, Ste. 117, Ft. Worth, TX 76104; (817) 927-6151. 4–5ap

RADIOLOGIST needed for South Dakota hospital-based practice. Northern Hills General Hospital features a modern, progressive radiology dept. offering radiographics, fluoroscopy, stationary mammography, and ultrasound, with mobile services available for CT and MRI. Deadwood is located in the beautiful Black Hills of western South Dakota, providing a natural setting for a diverse range of outdoor recreational activities. Financial package negotiable. Contact Charles Schulz, Administrator, Northern Hills General Hospital, P. O. Box 407, Deadwood, SD 57732; (605) 578-2313. 4a

EXCELLENT OPPORTUNITY FOR BE/BC DIAGNOSTIC RADIOLOGIST with training in all modalities to join active, 7-member group in midwestern university town with medical school affiliation. Abundance of cultural opportunities and outdoor recreation. Excellent salary with early partnership. Please send inquiries and CV to Mark Schneider, M.D., or Dean Hountras, M.D., 1000 S. Columbia Rd., Grand Forks, ND 58206-6003; (701) 780-6596. 4–6ap

CHAIRPERSON, DEPT. OF RADIOLOGY—Applications are being accepted for the position of professor and chairperson of the Dept. of Radiology, Medical College of Pennsylvania, Philadelphia. Applicants should have an M.D. degree, have successfully completed a residency in radiology approved by the ACGME, and be certified by the American Board of Radiology, or have equivalent qualifications. Applicants should demonstrate evidence of leadership and achievement in academic radiology with significant accomplishments in clinical, educational, administrative, managerial, and investigative endeavors. Ideal candidates will qualify as professor with tenure. Candidates at the associate professor level will be considered also. Please send letter of application and CV to Dr. Michael Phillips, Chairman of Radiology Search Committee, Medical College of Pennsylvania, 3300 Henry Ave., Philadelphia, PA 19129. EOE/AA. 4a

COMMUNITY-BASED, 400-BED, PROGRESSIVE HOSPITAL GROUP seeks a board-certified, fellowship-trained, interventionalist/angiographer to work in our full-service angio suite. Send CV and date available to Martin Friedman, D.O., Frankford Hospital, X-Ray, Knights & Red Lion Rd., Philadelphia, PA 19114. 4–5ap

IMAGING SCIENTIST—Ph.D. in electrical engineering or computer science and postdoctoral experience in medical image analysis with an emphasis on computer vision techniques, automated motion analysis, and mathematical optimization sought for appointment at the rank of assistant professor in the Dept. of Diagnostic Radiology. This position is in a research group working on medical image analysis in a C/UNIX/X environment. Please send applications with CV to James S. Duncan, Ph.D., Associate Professor of Diagnostic Radiology and Electrical Engineering, Yale University School of Medicine, P. O. Box 3333, New Haven, CT 06510. Yale University is an equal opportunity/affirmative action employer. Applications from women and minority group members are encouraged. Application deadline is May 31, 1992. 4–5a

COLORADO—BC/BE radiologist sought to join 2-person practice covering 2 hospitals in the central mountains of Colorado. Ample free time and excellent outdoor recreational opportunities. Contact E. J. Loeffel, M.D., P. O. Box 415, Buena Vista, CO 81211; (719) 539-3782. 4–6ap

GENERAL DIAGNOSTIC RADIOLOGIST WITH IMAGING AND MAMMOGRAPHY EXPERIENCE—William Beaumont Hospital is a modern, expanding, tertiary-care teaching medical center in southeast Michigan with approved residency and fellowship in diagnostic radiology. Excellent facilities and remuneration. We are seeking a general radiologist with training and experience in imaging and/or mammography. Please send CV to Jalil Farah, M.D., Chairman, Diagnostic Radiology, William Beaumont Hospital, 3601 W. 13 Mile Rd., Royal Oak, MI 48073. 4–6a

RADIOLOGIST/ABDOMINAL IMAGING — The Dept. of Radiology at the University of Minnesota has a full-time position available in the abdominal imaging section at the rank of tenure-track assistant or tenured associate professor beginning July 1, 1992. At the assistant professor level, minimum requirements are board certification in radiology, 1 yr postresidency specialty training or experience in abdominal imaging, and a demonstrated involvement in quality research accepted or published in peer-reviewed journals. Appointment at the rank of associate professor requires a minimum of 4 yr postresidency experience, a professional distinction in research and writing, and demonstrated effectiveness both in teaching and in advising. Responsibilities will include all facets of abdominal imaging as well as graduate and undergraduate medical instruction. Research performance will be strongly encouraged and evaluated. Salary is negotiable, competitive, and dependent on past scholarly productivity and post-M.D. experience. Applicants must be licensed or able to obtain a license to practice medicine in the state of Minnesota before appointment date. Applications will be accepted through June 15, 1992. Send letters to Dr. William M. Thompson, Professor and Chairman, Dept. of Radiology (Box 292 UMHC), University of Minnesota, 420 Delaware St., S.E., Minneapolis, MN 55455. The University of Minnesota is an equal opportunity educator and employer. 4a

RADIOLOGIST/MUSCULOSKELETAL — The Dept. of Radiology at the University of Minnesota has a full-time position available in the musculoskeletal section at the rank of tenure-track assistant professor or tenured associate professor beginning July 1, 1992. At the assistant professor level, minimum requirements are board certification in radiology, 1 yr postresidency specialty training or experience in musculoskeletal radiology, and a demonstrated involvement in quality research accepted or published in peer-reviewed journals. Appointment at the rank of associate professor requires a minimum of 4 yr postresidency experience, a professional distinction in research and writing, and demonstrated effectiveness in teaching and advising. Responsibilities will include all facets of musculoskeletal radiology as well as graduate and undergraduate medical instruction. Research performance will be strongly encouraged and evaluated. Salary is negotiable, competitive, and dependent on past scholarly productivity and post-M.D. experience. Applicants must be licensed or able to obtain a license to practice medicine in the state of Minnesota before appointment date. Applications will be accepted through June 15, 1992. Send letters to Dr. William M. Thompson, Professor and Chairman, Dept. of Radiology (Box 292 UMHC), University of Minnesota, 420 Delaware St., S.E., Minneapolis, MN 55455. The University of Minnesota is an equal opportunity educator and employer. 4a

RADIOLOGIST/PULMONARY CHIEF—The Dept. of Radiology at the University of Minnesota has a full-time position available in the pulmonary radiology section at the rank of tenure-track assistant professor or tenured associate professor beginning July 1, 1992. At the assistant professor level, minimum requirements are board certification in radiology, 1 yr postresidency specialty training or experience in pulmonary radiology, and a demonstrated involvement in quality research accepted or published in peer-reviewed journals. Appointment at the rank of associate professor requires a minimum of 4 yr postresidency experience, a professional distinction in research and writing, and demonstrated effectiveness in teaching and advising. Responsibilities will include all facets of pulmonary radiology as well as graduate and undergraduate medical instruction. Research performance will be strongly encouraged and will be evaluated. Salary is negotiable, competitive, and dependent on past scholarly productivity and post-M.D. experience. Applicants must be licensed or able to obtain a license to practice medicine in the state of Minnesota before appointment date. Applications will be accepted through June 15, 1992. Send letters to Dr. William M. Thompson, Professor and Chairman, Dept. of Radiology (Box 292 UMHC), University of Minnesota, 420 Delaware St., S.E., Minneapolis, MN 55455. The University of Minnesota is an equal opportunity educator and employer. 4a

CONNECTICUT, NEURORADIOLOGIST—Opening in July 1992 for BC/BE radiologist with fellowship training in neuroradiology. Nine-radiologist practice includes a 435-bed, university-affiliated community hospital and a 57-physician multispecialty clinic. Approximately 107,000 exams/yr including MRI, CT, nuclear medicine, ultrasound, and an active angiographic and interventional service. Excellent salary and benefits leading to full partnership after second yr. For more information, send CV to David A. Lund, M.D., Dept. of Radiology, New Britain General Hospital, 100 Grand St., New Britain, CT 06050. 3–6ap

ANGIOGRAPHER–INTERVENTIONAL RADIOLOGIST, CENTRAL MASSACHUSETTS—Radiologist with angiography and interventional skills sought to join an 11-member, private-practice group serving a 550-bed medical center and performing 150,000 exams/yr. Position involves sharing general diagnostic radiology responsibilities, including CT, ultrasound, and mammography. Please send CV to Richard Danford, M.D., Worcester Radiologists, Inc., 121 Lincoln St., Worcester, MA 01605; (508) 753-8151. 4–6ap

INSTRUCTOR, UNIVERSITY OF FLORIDA—Applications are now being accepted by the Dept. of Radiology for 3 positions at the instructor level for the 1992–93 academic yr. These are full-time, non–tenure track positions. Clinical responsibilities include teaching of house staff and medical students as well as opportunities to pursue individual research interests. Minimum requirements include an M.D. with board certification in radiology (or board eligibility), and candidates must be eligible for licensure in the state of Florida. Application deadline is June 15, 1992, with a starting date as soon as possible thereafter. Interested applicants should contact Jonathan Williams, M.D., Associate Chairman, Dept. of Radiology, Box 100374 JHMHC, Gainesville, FL 32610. An equal employment/affirmative action employer. 4a

ASSISTANT/ASSOCIATE/PROFESSOR OF RADIOLOGY, University of South Florida College of Medicine. The Dept. of Radiology is currently seeking an assistant/associate/professor. The candidate should have an M.D. degree and be board-certified in diagnostic radiology. The salary is $79,070; negotiable for a 12-mo period. This position is .15 FTE state, tenure earning and .85 FTE grant, non–tenure earning. The application deadline is April 30, 1992, and the position will begin July 1, 1992. Applications or nominations for the position should be addressed to Robert Halpert, M.D., Dept. of Radiology, H. Lee Moffitt Cancer Center, 12902 Magnolia Dr., Tampa, FL 33612; (813) 972-8425. The University of South Florida is an affirmative action/equal opportunity institution. 4ap

VASCULAR AND INTERVENTIONAL RADIOLOGIST—A 12-person, private-practice multispecialty radiology group is seeking a fellowship-trained vascular and interventional radiologist. Practice is at a university-affiliated, 700-bed, acute general hospital doing 110,000 exams/yr. Submit CV to Thomas J. Spackman, M.D., Dept. of Radiology, Saint Francis Hospital and Medical Center, Hartford, CT 06105. 4–5ap

CROSS-SECTIONAL IMAGING SPECIALIST—A 12-person, private-practice multispecialty radiology group is seeking a fellowship-trained, cross-sectional imaging specialist, with a particular interest in strengthening an ultrasound division. Practice is at a university-affiliated, 700-bed, acute general hospital doing 110,000 exams/yr. Submit CV to Thomas J. Spackman, M.D., Dept. of Radiology, Saint Francis Hospital and Medical Center, Hartford, CT 06105. 4–5ap

CENTRAL VALLEY, CALIFORNIA—Immediate opening for BC/BE diagnostic radiologist with skills in CT, MRI, interventional, ultrasound, and nuclear medicine. Join a growing practice in a 160-bed community hospital. Attractive compensation package with the opportunity for partnership. Send CV to Henderson & Associates, P. O. Box 2627, Bakersfield, CA 93303; (805) 323-6925. 4–5ap

IMMEDIATE OPENING FOR BC/BE GENERAL RADIOLOGIST with experience in basic interventional and vascular radiology. Join a group of 4 radiologists in a 160-bed hospital located in Allentown, PA, about 60 mi. northwest of Philadelphia. The daily practice includes all aspects of general radiology, CT, ultrasound, and nuclear medicine. Please call or send CV to Asad Shohadai, M.D., Allentown Osteopathic Medical Center, 1736 Hamilton St., Allentown, PA 18104; (215) 770-8700. 4xa

NEURORADIOLOGIST—Senior ASNR member needed for excellent hospital and imaging center position in Tucson, AZ. Early partnership opportunity. Send CV to Arizona State Radiology, 7250 E. Ventana Canyon Dr., Tucson, AZ 85715. 8–7ap

THE DEPT. OF RADIOLOGY AT TRIPLER ARMY MEDICAL CENTER, HONOLULU, HI, is recruiting academic radiologists for several divisions of the dept., including ultrasound, chest radiology, skeletal, neuroradiology, general diagnostic radiology, MRI, interventional radiology, and mammography. Our dept. offers a fully accredited residency program with 21 residents and 16 attending full-time staff. Numerous consultants from across the country lecture on a continuing and regular basis. The hospital is a modern, tertiary-care center serving Hawaii and the entire Pacific Basin. A strong residency program, diverse and interesting patient population, excellent equipment, and tropical lifestyle are positive aspects of the practice. Academic credentials and/or experience are necessary. Recently graduated fellows are encouraged to apply. Board certification is mandatory. Candidates should be particularly interested in patient care, teaching, and research. Salary and benefits are competitive and generous. Tripler is an EO/EEO employer. Please contact Dr. Mark F. Hansen, Col, MC, Chief, Dept. of Radiology, TAMC, HI 96859-5000; (808) 433-6393. 7–6a

THE RADIOLOGY DEPT. AT DWIGHT DAVID EISENHOWER ARMY MEDICAL CENTER is recruiting academic radiologists. The dept. provides a full range of services including angiography, ultrasound, CT (with a new GE 9800 Advantage system), and MRI (with a new 1.5-T GE Signa system). Development is underway for the installation of a digital teleradiology link to area medical facilities. The dept. is also beginning a radiology residency program in affiliation with the program at the Medical College of Georgia in Augusta. With this growth, the dept. has generated a need for several academic diagnostic radiologists. Board-certified diagnostic radiologists with academic credentials and/or experience are urged to apply. Fellowship training is desired, especially in interventional radiology and/or angiography, however candidates at all levels will be considered. Candidates should be particularly interested in patient care, teaching, and research. The medical center is located on Fort Gordon, GA, adjacent to Augusta, and is the tertiary-care hospital supporting 9 Army community hospitals of the southeastern region and Puerto Rico. The hospital supports fully accredited residency programs in family practice, general surgery, medicine, orthopedics, pathology, and psychiatry. Salary and benefits are competitive and generous. The medical center is an EO/EEO employer. Please contact Dr. Thomas M. Ralston, LtC., Chief, Radiology Dept., Eisenhower Army Medical Center, Fort Gordon, GA; (404) 791-6245. 8–7a

GADSDEN RADIOLOGY ASSOCIATES is a 3-member radiology group seeking a fourth board-certified/eligible radiologist. Gadsden Radiology covers Baptist Memorial Hospital, a 250-bed hospital performing more than 55,000 radiologic exams/yr. All radiologic modalities are available, including state-of-the-art CT, SPECT, nuclear medicine, special procedures, and MRI. Gadsden Radiology Associates also covers their private office, imaging center, and a breast center. Teleradiography is used for call. Gadsden, AL, is a safe, clean city centrally located on the Coosa River approximately 1 hr from Birmingham, 90 min from Chattanooga, and 2 hr from Atlanta, GA. Salary and vacation are excellent. Health insurance and malpractice is paid. Interested candidates contact Homer A. Spencer, M.D., 401 Bay St., Gadsden, AL; (205) 543-3200, or fax (205) 546-7908. 4ap

DIAGNOSTIC RADIOLOGIST—Immediate opening for BC/BE radiologist to join group of 6 in an active practice including 2 hospitals (480 beds) and a multispecialty clinic that performs 110,000 exams/yr. Practice includes substantial CT, nuclear medicine, ultrasound, MRI, angiography, and interventional and is located in a pleasant community on Lake Michigan with easy access to Milwaukee and Chicago. Locums needed in interval. Contact Arnold Strimling, M.D., Dept. of Radiology, St. Mary's Medical Center, 3801 Spring St., Racine, WI 53405; (414) 636-4311. 4xa

MUSCULOSKELETAL RADIOLOGIST, CHARLOTTE, NC—A 13-member, subspecialized group serving a 660-bed, private community hospital–outpatient diagnostic center desires a fellowship-trained or staff level musculoskeletal radiologist. GE 9800 CT and Signa 1.5-T equipment. Family-oriented community with warm 4-season climate, centrally located between coast and mountains. Send CV to P. O. Box 221211, Charlotte, NC 28222. 4–6ap

DIAGNOSTIC RADIOLOGIST needed for expanding practice in a 200-bed, well-equipped community hospital in Troy, MI. Must have expertise in CT, ultrasound, and mammography. Very competitive salary and benefits. Send CV to Thomas Verhelle, M.D., Troy-Beaumont Hospital, 44201 Dequindre Rd., Troy, MI 48098. 4–7ap

FACULTY POSITION IN PEDIATRIC RADIOLOGY, PENNSYLVANIA STATE UNIVERSITY, THE MILTON S. HERSHEY MEDICAL CENTER—The Pennsylvania State University, Dept. of Radiology, has an opening for an additional faculty member in pediatric radiology for July 1992. Fellowship training in pediatric radiology and ABR-certification in diagnostic radiology are required. The position provides guaranteed academic time and opportunity for research. The level of faculty appointment and salary will vary depending on the applicant's experience and training. The Pennsylvania State University Children's Hospital is a newly established, 135-bed children's hospital. There are currently 3 practicing pediatric radiologists within the Pennsylvania State University Hospital Dept. of Radiology. Applicants should respond with a letter of interest and copy of their CV to Richard P. Moser, Jr., M.D., Chief, Diagnostic Radiology, Dept. of Radiology, The Pennsylvania State University, Milton S. Hershey Medical Center, P. O. Box 850, Hershey, PA 17033; (717) 531-8039. Pennsylvania State University is an affirmative action equal opportunity employer. Women and minorities are encouraged to apply. 4a

PARTNERSHIP POSITION IN PALM SPRINGS, CA—Well-established, 9-member group has openings for 2 board-certified radiologists. A physician with a strong background in MRI is sought as director of the section of MRI. The other position requires a physician with mammography experience to direct imaging in the breast health section of a new comprehensive cancer center. The group covers a 350-bed hospital and 2 offices in a desirable, rapidly expanding area of southern California. MRI facilities include 1.5-T Picker Vista HPQ with MRA package, ViStar imaging computer, and 1.5-T GE Signa. Other equipment includes 3 CT, a Cemax image processor, 2 Acuson color-flow Doppler ultrasound, 4 nuclear cameras including 2 SPECT, and all other diagnostic modalities. Ground has just been broken on a new 25,000 sq. ft. radiology wing, which will be furnished with state-of-the-art equipment. New trauma center, cancer center, and rehab hospital being built. Excellent compensation and benefits package leading to full partnership. Beaches and large-city amenities of Los Angeles only 2 hr away. Yr-round sunny weather. Ample free time to enjoy southern California and the unparalleled recreational opportunities offered by the resort community of Palm Springs. Direct inquiries to Marvin J. Friedenberg, M.D., Desert Hospital, Dept. of Radiology, 1150 N. Indian Canyon Dr., Palm Springs, CA 92262. 4xa

ISRAEL, DIAGNOSTIC RADIOLOGY—Opportunities for 3-4 wk or longer working vacations in a number of Israeli medical centers, on a volunteer basis. Positions varied, arrangements flexible. For information contact Jonathan H. Fish, M.D., 1844 San Miguel Dr., #302, Walnut Creek, CA 94596; (510) 947-0560. 2–4xa

DIAGNOSTIC RADIOLOGIST, KNOXVILLE, TN Opportunity for full-time or permanent part-time. Outpatient diagnostic center. All modalities. No interventional. No nights or weekends. Generous compensation. Abundant vacation time. Contact B. A. Schaefer, M.D., 601 Mulvaney St., Knoxville, TN 37915; (615) 525-7100. 3–5ap

PEDIATRIC RADIOLOGY—The Medical College of Georgia seeks a general pediatric radiologist and a pediatric radiologist with expertise in pediatric imaging. These individuals will provide general and specialized pediatric radiology services, guide the integration of imaging services within pediatric radiology, and help plan and implement pediatric radiology services for the upcoming 175-bed Children's Medical Center. Tenured or nontenured positions are available at assistant, associate, or full professor levels. The senior appointee will become head of the Pediatric Radiology Section. Call or write Dr. Charles G. Howell, Jr., Pediatric Radiology Search Committee, Pediatric Surgery Section, Medical College of Georgia, Augusta, GA 30912-4070; (404) 721-3941. MCG is an equal opportunity/affirmative action employer. 4xa

SUPERB PARTNERSHIP POSITION IN LAS VEGAS—Rapidly expanding 7-member group practice covering 2 full-service imaging centers and a small hospital has an immediate opening. We are looking for an additional board-certified radiologist with an uncommon dedication to excellence in patient care. Our outpatient facilities include 2 MR, 2 CT, angio with a 4-bed recovery area, 5 ultrasound, 5 mammography, 3 SPECT, plus R&F. This is an excellent opportunity for a partnership position with a well-respected group in a growing community. Please send CV to Dr. Mark Winkler, SDMI, 2950 S. Maryland Pkwy., Las Vegas, NV 89109. 3–2ap

BC GENERAL RADIOLOGIST—Established private group in western Massachusetts is seeking a general diagnostic radiologist with experience in CT, ultrasound, MRI, and nonvascular interventional procedures. Primary assignment is at an 800-bed teaching hospital with a radiology residency program. Practice also includes 3 community hospitals and 6 private offices. Full partnership after 1 yr. Available by July 1, 1992. Interested candidates should send CV to W. Max Cloud, M.D., 130 Maple St., Springfield, MA 01103. 3–5ap

INTERVENTIONAL RADIOLOGIST, ALBUQUERQUE, NM—A well-established, 14-physician group has an immediate opening for a fellowship-trained vascular interventionalist. Initially, approximately 40–50% of work time interventional; additional interventional volume as senior physicians phase down. Practice serves a major hospital in the metro area, 2 MRI centers, 2 outpatient centers, and 3 outlying facilities. All vascular interventional work at 1 location. Candidate must have ability/desire to perform both interventional and general radiology procedures. Strong desire to live and work in the southwest a must. Competitive compensation package. Send CV with references to P. O. Box 7309, Albuquerque, NM 87194-7309. 3–4a

CONNECTICUT, ANGIO/INTERVENTIONAL RADIOLOGIST—Opening in July 1992 for BC/BE radiologist with fellowship training in angiographic procedures. Additional training or experience in other interventional procedures is desirable. Nine-radiologist practice includes a 435-bed, university-affiliated, community hospital and a 57-physician multispecialty clinic. Approximately 107,000 exams/yr, including MRI, CT, nuclear medicine, ultrasound, as well as an active angiographic and interventional service. Excellent salary and benefits leading to full partnership after second yr. For more information, send CV to David A. Lund, M.D., Dept. of Radiology, New Britain General Hospital, 100 Grand St., New Britain, CT 06050. 3–6ap

DIAGNOSTIC RADIOLOGIST, CONNECTICUT—Opening in July 1992 for BC/BE radiologist with expertise in general radiology and mammography. Additional training or experience preferred. No angiography/interventional experience is required. Nine-radiologist practice includes a 435-bed, university-affiliated community hospital and a 54-physician multispecialty clinic. Approximately 107,000 exams/yr including MRI, CT, nuclear medicine, ultrasound, and an active interventional service. Excellent salary and benefits leading to full partnership after second yr. For more information, send CV to Paul C. Lakin, M.D., Dept. of Radiology, New Britain General Hospital, 100 Grand St., New Britain, CT 06050. 3–4ap

RADIOLOGIST—A 4-physician group seeks a fifth to join our well-established and growing practice. We are located in east-central Illinois, with a 4-yr college, Jr. college, and a farming economy enhanced by numerous growing industries. We serve a rural but very modern 230-bed hospital ($25 million expansion underway) and several other sites, performing more than 80,000 exams/yr. Mattoon-Charleston is a great place to raise a family while still having access to big-city amenities. Please be BC/BE, skilled in interventional or MRI, and able to handle general diagnostic modalities competently. Please reply to Bruce Fluesmeier, Lakeland Radiologists, Ltd., 1221 Broadway, Mattoon, IL 61938; (800) 745-7701. 3–8ap

NEURORADIOLOGIST—The Section of Neuroradiology of the Dept. of Radiology at Northwestern Memorial Hospital, Chicago, IL, is seeking a full-time staff member to participate in all clinical, educational, and research activities, beginning on or before July 1, 1992. Applicants must have completed an approved residency in diagnostic radiology, be certified by the American Board of Radiology, and be eligible for senior membership in the American Society of Neuroradiology. The applicant should have experience in all aspects of clinical neuroradiology; preference may be given to applicants with expertise in current MR applications or interventional procedures. A demonstrated interest in and facility for clinical research and teaching is highly desirable. Northwestern Memorial Hospital is an 800-bed general hospital in the N. Michigan Ave. area of Chicago (near Water Tower). The section of neuroradiology has 3 neuroradiologists and 3 fellows (ACGME-approved fellowship). An active interventional neuroradiologic service is supported by an integrated clinical cerebrovascular service. Diagnostic equipment includes a new DFP 65 biplane 1024 matrix Toshiba DSA system with stereo fluoroscopic capabilities, 2 MR scanners with a 2-scanner acquisition in progress, and 3 GE 9800 CT scanners, all well-staffed with excellent ancillary personnel. Northwestern University is an affirmative action/equal opportunity employer. Hiring is contingent on eligibility to work in the United States. Salaries and benefits are maintained at high levels. Address inquiries and a current CV to Eric J. Russell, M.D., Director of Neuroradiology, Northwestern Memorial Hospital, 710 N. Fairbanks Ct., Ste. 3420, Chicago, IL 60611; (312) 908-2462. 3–4ap

DIAGNOSTIC RADIOLOGIST—Two progressive community hospitals located 17 mi. apart in north Iowa seek a diagnostic radiologist for full-time coverage. Existing volumes of 17,000 annual exams with opportunities for growth. Excellent equipment and staff. For more information, contact Tom Thompson, President/CEO, St. Joseph Community Hospital (515) 394-4121. 3–4a

GENERAL RADIOLOGY STAFF POSITION—The Dept. of Radiological Sciences at Olive View–UCLA Medical Center has openings for staff positions in general radiology and ultrasound. Candidates must be board-certified and eligible for certification in diagnostic radiology and should be eligible for licensing in the state of California. Interested candidates should contact Issa Yaghmai, M.D., Professor and Chairman, Dept. of Radiological Sciences, Olive View–UCLA Medical Center, 14445 Olive View Dr., Sylmar, CA 91342; (818) 364-4078. The University of California, Los Angeles, is an affirmative action/equal opportunity employer. 3–6a

BODY IMAGING DIAGNOSTIC RADIOLOGIST—Young, progressive group in Washington, DC, area has position immediately available for a board-certified diagnostic radiologist in an expanding and diversified hospital and office-based practice with facilities in Maryland and Virginia. Our group covers 1 hospital, 5 full-service private offices, and 2 diagnostic centers for women. All imaging modalities represented, including 3 MRIs, 6 CTs, 9 ultrasound suites including color-flow, and an ISG 3-D imaging workstation. Very attractive practice setting. Commitment to leading edge technology. Address inquiries and CV to Grant McClure, Radiology Imaging Associates, 7801 Old Branch Ave., Ste. 300, Clinton, MD 20735; (301) 856-6718. 3–5ap

ULTRASOUND/CT/MRI, LOS ANGELES—BC radiologist, with fellowship training in cross-sectional body imaging, needed to join an 8-member group in July 1992. This well-established practice includes a 300-bed hospital near downtown Los Angeles and a private office in the adjacent building. Equipment includes 2 GE 9800 CT scanners, 2 ATL Mark 9 ultrasound units, and a 2.0-T Siemens MRI. Competitive salary leading to full partnership. Contact A. K. Raja Rao, M.D., St. Vincent Medical Center, 2131 W. Third St., Los Angeles, CA 90057; (213) 484-7901. 3–4ap

BC/BE DIAGNOSTIC RADIOLOGIST—Opportunity to join a 3-person group in general radiology practice including all modalities (angio and interventional limited at this point). Hospital-based with limited itinerant schedule. Generous salary leading to early partnership in professional corporation. Outstanding benefits with liberal fringes and vacation. Wonderful, small midwestern community with great schools and bountiful cultural and recreational opportunities. Send CV to James P. Zachman, M.D., Radiology Dept., Rice Memorial Hospital, Willmar, MN 56201; (612) 231-4530. 3–5ap

PASADENA, CALIFORNIA—Immediate opening for a BC/BE radiologist. Busy outpatient imaging center including mammography, ultrasound, CT, and MRI. Call Terry Becker, M.D. at (818) 793-8189. 2–5ap

SOUTHERN OREGON—Opportunity for BC/BE, general diagnostic radiologist to join group of 5 board-certified radiologists. Experience in all modalities desired. Practice includes 2 hospitals and own private office. Competitive starting salary with early full partnership. Excellent lifestyle with many outdoor activities from Pacific Coast to Oregon Cascades. Send CV to Larry Strickland, Administrator, Roseburg Radiologists, P.C., P. O. Box 1547, Roseburg, OR 97478. 2–5ap

THE RADIOLOGIC GROUP OF NORTH JERSEY is seeking a BC radiologist with a fellowship or strong interest in pediatric radiology. This is a 7-member group with a fee-for-service arrangement at a 700-bed hospital and office. All diagnostic facilities are available. Send CV to F. Cushmore, M.D., 703 Main St., Paterson, NJ 07503. 3–5ap

CHIEF OF SECTION AND SECTION MEMBER, ANGIOGRAPHY/INTERVENTIONAL RADIOLOGY, MEDICAL COLLEGE OF VIRGINIA, DEPT. OF RADIOLOGY—An excellent opportunity is available for a dynamic individual interested in building an outstanding program already established on a strong foundation. Currently there are 2 full-time faculty members in the section plus the services of additional faculty members equaling a third full-time faculty equivalent. We are seeking to add another fellowship-trained, full-time junior faculty member and a section chief to form a 5-faculty section in charge of angiography/interventional radiology at the Medical College of Virginia and its affiliated Hunter Holmes McGuire VA Medical Center. Together the 2 institutions comprise 1800 beds. ABR certification or eligibility required. Individual should have experience working in a culturally diverse environment. Academic rank and salary commensurate with experience. Anyone interested should send CV to or phone Anthony V. Proto, M.D., Professor and Chairman, Dept. of Radiology, P. O. Box 470, Richmond, VA 23298-0470; (804) 786-7212, fax (804) 371-6129. VCU/MCV is an equal opportunity/affirmative action employer. Women and minorities are encouraged to apply. 3–4a

DEPT. OF RADIOLOGY, VIRGINIA COMMONWEALTH UNIVERSITY/MEDICAL COLLEGE OF VIRGINIA, AND THE MCGUIRE VA MEDICAL CENTER, RICHMOND, VA, seek faculty for positions in diagnostic radiology (chest, GI, mammography, CT/ultrasound/MR, musculoskeletal, ER, angio/interventional, and neuroradiology). MCV is an 1058-bed facility and a Level 1 trauma center. The McGuire VAMC is an 800-bed facility. ABR certification or eligibility is required. Individual should have experience working in a culturally diverse environment. Academic rank and salary commensurate with experience. For position description, or to submit CV, write or phone A. V. Proto, M.D., Dept. of Radiology, MCV Box 470, Richmond, VA 23298-0470; (804) 786-7212. VCU/MCV is an equal opportunity/affirmative action employer. Women and minorities are encouraged to apply. 3–4a

GENERAL RADIOLOGIST, RUIDOSO, NM—Solo practice with advantages of large group practice (CME, vacations, etc.). Small, but growing resort community in southern New Mexico. Quality outdoor lifestyle and excellent skiing. Professional support via teleradiology and vacation coverage by 14-physician group in Albuquerque. Position requires experience in general radiology, CT, mammography, and ultrasound. Strong desire to live and work in the southwest a must. Competitive compensation package. Send CV with references to P. O. Box 7309, Albuquerque, NM 87194-7309. 3–4a

PEDIATRIC RADIOLOGIST—Hahnemann University Hospital, Dept. of Diagnostic Radiology, is seeking a pediatric radiologist to provide imaging service for a very large and continuously growing Dept. of Pediatrics with a dynamic clinical and academic interactive relationship with our dept. Completion of a fellowship in pediatric radiology is required. The position is at the assistant professor or associate professor level. Salaries are very competitive and based on academic rank. Facilities include 2 GE 9800 CT scanners and a GE 1.5-T MRI. If interested, please send CV or contact Seth N. Glick, M.D., Dept. of Diagnostic Radiology, Hahnemann University Hospital, Broad and Vine Sts., Philadelphia, PA 19102; (215) 448-8719. 3–5ap

ULTRASOUND SECTION HEAD—Hahnemann University Hospital is seeking a director of ultrasound. Clinical responsibility predominantly in ultrasound with opportunity for involvement in body CT and body MRI. Approximately 11,000 ultrasound procedures previous yr with potential for expansion. Facilities include 2 state-of-the-art Acuson machines with immediate plans for additional equipment. Appointment would be at the associate professor or professor rank. Salaries are very competitive and based on academic rank. If interested, please send CV or contact Seth N. Glick, M.D., Dept. of Diagnostic Radiology, Hahnemann University Hospital, Broad and Vine Sts., Philadelphia, PA 19102; (215) 448-8719. 3–5ap

DIAGNOSTIC RADIOLOGIST(S)—Small, progressive southeastern community hospital (JCAHO-accredited) near a major metropolitan area needs at least 1 board-certified radiologist. Modern equipment, exclusive contract, good payor mix. Nuclear medicine, invasive radiologic procedures. Please send CV with cover letter and financial requirements. All inquiries will be kept strictly confidential. Write Box C30, *AJR* (see address this section). 3–5a

RADIOLOGIST NEEDED—Senior partner retired. Free-standing diagnostic medical clinic seeking second radiologist for noninterventional-type practice in small, culturally oriented community in southeast West Virginia. Rare opportunity to associate with nationally known group where highest quality medicine is the standard, under unparalleled working conditions. The Greenbrier Clinic is affiliated with world famous Greenbrier Hotel and Resort located in the Greenbrier Valley, garden spot of West Virginia. Quiet lifestyle with abundant recreational opportunities and easy access to large eastern metropolitan centers. Candidates must be board-certified in diagnostic radiology and have some practice experience. Contact Herbert Pope, M.D., The Greenbrier Clinic, White Sulphur Springs, WV 24986. 2–4ap

ASSISTANT PROFESSOR, MR RADIOLOGIST—The Dept. of Radiology at The University of Texas Medical School at Houston and the Hermann Hospital are recruiting for a full-time MRI radiologist at the assistant professor level, beginning July 1, 1992. Preference will be given to candidates with fellowship training in MRI, body imaging, neuroradiology, or 1 yr of academic MRI experience. ABR certification is required. Responsibilities will include monitoring and interpretation of both body and neuro MRI, as well as medical student, resident, and fellow teaching. Extensive clinical and basic science research opportunities are available. The dept.'s MR facilities are state-of-the-art and located in a beautiful spacious setting, which includes a 1.5-T GE Signa unit with proton spectroscopic capability. A second 1.5-T GE System, with MR angiography, fast spin echo (FSE), and phased array coils, will be installed in the first quarter of 1992. The Dept. also has an active basic science research program; research facilities include a small bore MRI system with spectroscopy capabilities. The University of Texas at Houston is an equal opportunity employer. Women, minorities, and the disabled are encouraged to apply. Please send CV and 3 references to Bharat Raval, M.D., Professor and Interim Chairman, Dept. of Radiology, The University of Texas Medical School–Houston, 6431 Fannin, Suite 2.132, Houston, TX 77030. 2–7ap

INTERVENTIONAL RADIOLOGIST — Private, multispecialty group of 125 physicians with university affiliation in upper midwest seeks second board-certified interventional radiologist. Excellent digital angiographic, CT, and MR facilities. Superb cooperation with surgical staff. At least 50% interventional with option of some general and/or neuroradiology. Salary equals 90% of partners with full partnership in 1–2 yr. City of 60,000 with referral base of 300,000. Send CV to Gerald Smyser, M.D., The United Hospital, Box 6002, Grand Forks, ND 58206-6002; (800) 437-5375. 2–4ap

THE UNIVERSITY OF ARIZONA DEPT. OF RADIOLOGY is recruiting a fellowship-trained vascular/interventional radiologist to join the faculty. Facilities at the University Hospital (300-bed), and Tucson Veteran's Hospital (300-bed), include state-of-the-art angiographic, CT, and MR units. Income and academic rank are negotiable. Contact Gerald D. Pond, M.D., Head, Section of Vascular and Interventional Radiology, University of Arizona Health Sciences Center, Tucson, AZ 85724; (602) 694-7136. Women and minorities are encouraged to apply. The University of Arizona is an EEO/AA employer. The review of applications began August 30, 1991 and will continue until position is filled. 2–4a

IMMEDIATE OPENING—BC/BE radiologist to join 8 board-certified radiologist incorporated practice covering 3 hospitals with approximately 700 beds and 100+ physician multispecialty clinic. All modalities represented. Must be willing to participate in all aspects of general diagnostic radiology. Excellent fringe benefit package with competitive salary leading to early shareholder status at modest buy-in. Practice located in Arkansas river valley. Excellent public and private schools. Send CV to or contact, June Martin, Business Manager, Radiology Services, P.A., P. O. Box 1827, Fort Smith, AR 72902; (501) 782-5035. 2–4ap

OPENING FOR A RADIOLOGIST WITH ANGIO/INTERVENTIONAL EXPERTISE—Radiology Ltd. of Tucson, AZ, is a group of 23 full-time and 2 part-time diagnostic radiologists who are the major providers of radiology services at 4 hospitals, 3 private offices, and 3 separate CT/MRI imaging centers in Tucson, AZ. We are currently recruiting another general radiologist with fellowship training in angio/interventional. This individual will be employed with 3 yr to full partnership. Individual is to be based primarily at Tucson Medical Center, the largest hospital covered by our practice. Currently TMC has the greatest load of interventional cases. Cross-coverage of advanced cases at other hospitals will be shared by this person and the other radiologists with advanced interventional skills as needed (for example when cross-coverage is needed to cover an interventionalist who is on vacation). General radiology including CT, ultrasound, and MRI is also to be performed by this individual as part of core responsibilities. If interested, send CV to Robert O. Broome, M.D., Radiology, Ltd., 6516 E. Carondelet Dr., Tucson, AZ 85710. 2–4ap

DIRECTOR OF BREAST IMAGING — The Brigham and Women's Hospital/Harvard Medical School, Dept. of Radiology, is seeking a full-time diagnostic radiologist to head the Breast Imaging Section. This hospital-based facility has 4 mammographic rooms, 2 with ultrasound. In addition, there is a mammo-test unit for performance of large core breast biopsies. More than 12,000 mammograms, 1,000 preoperative wire localizations, 500 guided aspirations, and 150 core biopsies are performed annually. This wealth of clinical material coupled with an excellent clinical staff provides unlimited opportunity for collaborative clinical investigation. Candidates must have board certification. Please contact Jack E. Meyer, M.D., Director of Diagnostic Radiology, Brigham and Women's Hospital, 75 Francis St., Boston, MA 02115; (617) 732-6269. Brigham and Women's Hospital/Harvard Medical School is an affirmative action/equal opportunity educator and employer. 2–7a

ULTRASOUND/CT/MRI—Opportunity for board-certified radiologist specializing in ultrasound, body CT, and body MRI to pursue academic career at the New York Hospital-Cornell Medical Center. Dept. provides state-of-the-art equipment, including Acuson and ATL ultrasound, GE 9800 CT, and GE Signa 1.5-T MR. Wide variety of ultrasound exams include abdominal, OB-GYN, color Doppler, small parts, neonatal head, transvaginal, and transrectal. Prefer candidate with prior fellowship in sectional imaging or ultrasound. Responsibilities include clinical practice, teaching, and research. Position available 7/1/92. Please send CV to Elias Kazam, M.D., Dept. of Radiology, New York Hospital-Cornell Medical Center, 525 E. 68th St., New York, NY 10021. 2–5a

PHYSICIAN/RADIOLOGIST—Full-time opening for a board-certified radiologist in a desirable southern New Jersey shore location. This is an active, challenging, expanding hospital and office-based practice. Must have training in CT, ultrasound, and nuclear medicine. Position available immediately. Send CV to RABC, P. O. Box 729, Mt. Holly, NJ 08060. 2–5ap

PHYSICIAN/RADIOLOGIST— A large radiology group with multiple private offices seeks a board-certified radiologist interested in a full-time position. Responsibilities include general radiography. Special training in CT, ultrasound, MRI and/or nuclear medicine is preferred. Excellent southern New Jersey location. Competitive salary and benefit package. Position available immediately. Send CV to RABC, P. O. Box 729, Mt. Holly, NJ 08060. 2–5ap

RADIOLOGIST—Second radiologist needed for a 54-physician multispecialty clinic located in the western Rockies. Experience or formal training in mammography a must. General radiologic procedures excluding CT and MRI. Offered salary and benefits generous. Four-season recreational opportunities abound. City is home of University of Montana. Send CV to Administrator, Western Montana Clinic, P.C., P. O. Box 7609, Missoula, MT 59807. 3–4a

DISCOVER WYOMING—Two young BC radiologists seek a third, recently trained BC/BE radiologist to join a growing, independent practice in a modern, 100-bed hospital. 27,000 procedures are performed annually including full-service ultrasound, nuclear medicine with SPECT, mammography, CT, and mobile MRI. Limited angiography and interventional procedures. No competing radiology groups, HMOs, or PPOs. Strong financial package with benefits including 8 wk off/yr and full partnership at 2 yr. The hospital is located in a high mountain desert community of 20,000 in southwestern Wyoming with population of 50,000 served. There is a 2-yr community college and superb outdoor and indoor community recreation facilities. School systems are ranked excellent nationally. Located 3 hr east of Salt Lake City. The surrounding area is ideal for outdoor interests such as skiing, backpacking, hunting, boating, and fishing with accessibility to Flaming Gorge recreational area and the Uintah, Wind River, and Teton Mountains. Please reply with CV to William R. Compton, M.D., Sweetwater Radiology, P.C., 1208 Hilltop Dr., #203, Rock Springs, WY 82901; (307) 382-4832. 2–5ap

POSITION AVAILABLE AT LOUIS A. WEISS MEMORIAL HOSPITAL, a 372-bed affiliate of the University of Chicago. Facilities include 2 new Acuson ultrasound machines and a GE Highlight Advantage CT. Both inpatient and outpatient areas are being redesigned. Applicants should have broad experience in general diagnostic radiology and angiography. An interest in teaching or research would be advantageous. The successful applicant will be appointed to the faculty at the University of Chicago. Academic rank and compensation commensurate with experience. Candidate should be board-certified and licensed to practice in Illinois. Interested parties should send their CV or phone James Chambliss, M.D., Dept. of Radiology, Weiss Memorial Hospital, 4646 N. Marine Dr., Chicago, IL 60640; (312) 878-8700. The University of Chicago is an equal opportunity/affirmative action employer. 2–4ap

FAIRBANKS, AK—Four diagnostic radiologists seek fifth partner for diversified practice including general radiology, ultrasound, nuclear medicine, MRI (GE 1.5-T), and CT (GE 9800). Hospital and office practice. Desirable life-style advantages in a university town. Unlimited access to the outdoors. Excellent salary, benefits, retirement, and vacation. One yr to full partnership. Contact Douglas Hutchinson, M.D., 1919 Lathrop #5, Fairbanks, AK 99701; (907) 452-5092. 2–7ap

ABDOMINAL RADIOLOGIST—The Harvard Medical School, Brigham and Women's Hospital, has a full-time faculty position for an academically inclined abdominal radiologist. Outstanding hospital setting, equipment, case mix, and research facilities make this an unusually exciting opportunity. Please contact Steven E. Seltzer, M.D., Co-Director, Abdominal Imaging, Brigham and Women's Hospital, 75 Francis St., Boston, MA 02115; (617) 732-6301. Harvard Medical School, Brigham and Women's Hospital is an affirmative action/equal opportunity educator and employer. 1–6a

NORTHERN CALIFORNIA—Seeking a radiologist who desires a semiretirement type of practice in central northern California in a geographic location equidistant from the San Francisco Bay area, Carmel-Monterey Peninsula, and Yosemite and Sierra ski areas. Full-time radiologist wishes to share practice and provide equal, bountiful time-off periods for travel, leisure, and relaxation. Call (209) 667-0216 after 6:00 p.m. (PST). 1–4ap

THE DIVISION OF NUCLEAR MEDICINE—Oregon Health Sciences University, Portland, Oregon, invites applications for a faculty position available immediately either part-time in nuclear medicine or full-time divided between nuclear medicine and another division of diagnostic radiology. Position requires that the radiologist be certified by either the American Board of Radiology (special competence in nuclear radiology) and/or the American Board of Nuclear Medicine. Send CV and references to William Weidner, M.D., Chairman, Diagnostic Radiology, UHN-72, Oregon Health Sciences University, Portland, OR 97201-3098. OHSU is an affirmative action equal opportunity employer. 1–4a

CHEST/BREAST IMAGING RADIOLOGIST—The Dept. of Radiology of the University of Miami School of Medicine is seeking an academic radiologist with subspecialty training or equivalent experience and interest in all aspects of chest imaging including CT, MR, ultrasound, and interventional procedures. Similar expertise in breast imaging including mammography, ultrasound, and needle localization required. The University of Miami/Jackson Memorial Medical Center is a tertiary-referral and level I trauma center that will soon be opening a state-of-the-art breast center. Extensive teaching is involved and an interest in clinical research is assumed. Board-certification and eligibility for, or licensure by the state of Florida is required. Academic rank and compensation commensurate with qualifications. Interested parties should forward CV to C. A. Poole, M.D., Professor and Chairman, Dept. of Radiology (R-308), P. O. Box 016960, Miami, FL 33101. The University of Miami is an equal opportunity/affirmative action employer. 1-5a

SAN ANTONIO, TX—Large group covering multiple hospitals and outpatient facilities seeks radiologists with angiography skills. Send CV to Search Committee, M&S X-Ray Associates, P. O. Box 15920, San Antonio, TX 78212-9510. 1–6ap

TRAUMA RADIOLOGISTS—The Dept. of Radiology of the University of Miami School of Medicine is recruiting for trauma radiologists to staff a new, state-of-the-art trauma center opening in the spring of 1992. The unit will be a self-contained facility within the Jackson Memorial Medical Center, a 1500-bed tertiary facility and level I trauma center. Candidates must be board-certified with fellowship training and/or experience in the management of the trauma patient, including the use of radiography, ultrasound, CT, angiography, and interventional procedures. Skill in teaching, interest in clinical research, and licensure to practice medicine in the state of Florida required. Academic rank and compensation commensurate with qualifications. Applicants should send CV to C. A. Poole, M.D., Professor and Chairman, Dept. of Radiology (R-308), University of Miami School of Medicine, P. O. Box 016960, Miami, FL 33101. The University of Miami is an equal opportunity/affirmative action employer. 1–5a

PEDIATRIC RADIOLOGY POSITION—The Dept. of Radiology, Children's Medical Center and The University of Texas Southwestern Medical Center, is seeking a fellowship-trained, pediatric radiologist for entry at an associate or assistant professor level. Applicants should be interested in expanding their areas of expertise and interest into high-tech imaging modalities. Children's Medical Center is a 263-bed, tertiary-referral hospital for Texas and the regional states. Last yr the hospital had 7700 admissions and over 112,000 outpatient visits. The hospital has a busy transplant service including heart, liver, and kidney with referrals from across the United States and South America. There is an active neurosurgical service that had over 44 children with primary brain tumors referred in over the past yr in addition to a large practice of children with congenital anomalies. The hematology-oncology team has 7 full-time physicians and a 5-day-a-wk clinic. The cardiology-cardiothoracic surgery service sees a wide range of complex congenital heart disease. The hospital has a busy pediatric surgery service in addition to general and subspecialty pediatric services staffed by private and university-affiliated pediatricians. The radiology dept. has state-of-the-art equipment including a Philips 0.5-T MRI which has MRA, cardiac, and 3D functions with a dedicated 3D work station; a Philips LX CT; Diasonics and Acuson duplex color ultrasound; a dedicated angio-interventional suite; digital fluoroscopy; and will soon acquire updated nuclear medicine equipment. The dept. of radiology performs over 49,000 exams annually including 2500 MR, nearly 4000 CT studies, over 250 interventional procedures, 3100 ultrasound, and 2200 fluoroscopic exams. Staff radiologists also cover the NNICU at Parkland Memorial Hospital, 1 of the largest NNICUs in the U.S. There are 3 radiology residents and 3-4 pediatric radiology fellows. Children's Medical Center is an exciting innovative hospital that enjoys a supportive, progressive administration and affiliation with The University of Texas Southwestern Medical School, 1 of the country's leading medical schools. Duties include clinical responsibilities in performing and interpreting pediatric radiology procedures, sharing resident and medical student teaching responsibilities, and participating in ongoing research projects. Salary and benefits are among the best offered. Flexible work schedules are available for parents with domestic demands. Direct letters of inquiry to Nancy Rollins, M.D., Director of Radiology, Children's Medical Center, 1935 Motor St., Dallas, TX 75235; (214) 902-2305. The University of Texas Southwestern Medical Center is an equal opportunity/affirmative action employer. 1–4a

BOSTON—Expanding private-practice group. No night or evening call. Need experience in mammography. Great lifestyle. Salary leading to equal partnership. Send letter and CV to Box E49, *AJR* (see address this section). 11–4a

DIAGNOSTIC RADIOLOGIST sought to join a fee-for-service group practice at 2 mid-Bronx hospitals. Board-certification with expertise in imaging and special procedures/interventional radiology preferred. Please send CV to Arthur Avenue Radiology, P.C., P. O. Box 4332, Great Neck, NY 11027. 11–4ap

DIAGNOSTIC RADIOLOGIST—A 3-member radiology group seeks a fourth radiologist with interventional skills to join them in a suburban community hospital practice in northern Ohio, 20 min from the boating and fishing pleasures of Lake Erie and its islands. Interested applicants please call or write to Dr. Matthew F. Gutowicz, Jr., 23 Patrician Dr., Norwalk, OH 44857; (419) 668-8101 ext. 6205 or 6208. 11–4ap

IMMEDIATE OPENING FOR BC/BE DIAGNOSTIC RADIOLOGIST, for night call and weekend work, to join a 2-member P.C. in a 220-bed community hospital, Birmingham, AL, area. Home video telemetry provided with few night calls. Ultrasound, CT, nuclear medicine, rare angiogram or interventional procedure, and general diagnostic radiology. No MRI. Negotiable, competitive salary with excellent benefits, insurance, and retirement plan. Full partnership potential. Contact Charles Baker, M.D., 2650 Altadena Rd., Birmingham, AL 35243; (205) 481-7193. 1–4ap

DALLAS, TX—A 12-member, subspecialty group seeks a board-certified, general radiologist for an immediate opening. Fellowship training preferred, but will consider qualified individual with special expertise. CT/ultrasound, MRI, nuclear medicine, or angiography background particularly helpful. All imaging modalities available (state-of-the-art CT, angio, ultrasound, R&F, SPECT, nuclear medicine, and MRI center). Salary and bonuses are excellent. Health and malpractice paid. No buy-in to partnership. Send CV to H. Stuart Peake, M.D., P. O. Box 814129, Dallas, TX 75381; (214) 888-7055. 11–4ap

THE DEPT. OF RADIOLOGY AT BROOKE ARMY MEDICAL CENTER, SAN ANTONIO, TX, is recruiting academic radiologists for several divisions of the dept., including ultrasound, chest, skeletal, neuroradiology, general diagnostic, interventional radiology, and mammography. Our dept. offers a fully accredited residency program with 24 residents and 16 attending full-time staff. Numerous consultants from across the country lecture on a continuing and regular basis. The hospital is a modern, tertiary-care center serving Texas, Oklahoma, and Louisiana. A strong residency program, interesting patient population, excellent equipment, teleradiology and digital radiology implementations underway, coupled with a south Texas lifestyle are positive aspects of the practice. Academic credentials and/or experience are necessary. Recently graduated fellows are encouraged to apply. Board certification is mandatory. Candidates should be particularly interested in patient care, teaching, and research. Salary and benefits are competitive and generous. Brooke is an EO/EEO employer. Please contact Dr. Billy E. Cunningham, COL, MC, Assistant Chief, Dept. of Radiology, Brooke Army Medical Center, Fort Sam Houston, TX 78234-6200; (512) 221-8418/8218. 8–7a

THE DEPT. OF RADIOLOGY AT WALTER REED ARMY MEDICAL CENTER is recruiting academic radiologists. We need board-certified radiologists to work in this famous and modern health-care center. Our dept. has a residency program consisting of 24 residents and several fellows. Subspecialists are needed in ultrasound, chest, mammography, genitourinary, gastrointestinal, pediatric, CT, MRI, and interventional radiology, as well as general radiology. Excellent opportunity to live in the nation's capital and also become an integral part of a large teaching program. Salaries are competitive and generous. Highly motivated applicants should contact Col. Mark F. Hansen, Radiology Consultant to the Army Surgeon General, Dept. of Radiology, TAMC, HI 96859-5000; (808) 433-6393. 8–7a

IMMEDIATE OPENING—BC/BE radiologist to join 2 board-certified radiologists at a 130-bed community hospital and outpatient dept. located 25 mi. east of Palm Springs, CA. Excellent salary, fringe benefits, early partnership, no buy-in, and generous vacation time. All imaging modalities including SPECT ANGER camera, MRI, and angio/interventional. Reasonable housing in resort atmosphere. Contact Stephen J. Curtis, M.D., Radiology Director, J.F.K. Memorial Hospital, 47-111 Monroe St., Indio, CA 92201; (619) 775-8066. 4–7ap

Positions Desired

SECOND YR RADIOLOGY RESIDENT (PGY3) seeks PGY4 position for July 1992. Enthusiastic, amiable, and hardworking. Desiring more challenge and diversity. Willing to relocate. Reply Box Q94, *AJR* (see address this section). 4–6bp

EXPERIENCED, YOUNG, FACULTY INTERVENTIONALIST (ABR, SCVIR) seeks private-practice position leading to full partnership. Can perform general radiology, including MRI, ultrasound, and CT. Prefer medium-sized to large hospital in urban or suburban location. Available March 1992. Reply Box P82, *AJR* (see address this section). 3–5bp

MRI OR NEURORADIOLOGY FELLOWSHIP, JULY 1992—Radiology resident in university affiliated program, seeks an MRI or neuroradiology fellowship for July 1992. Residency training in all modalities with experience in angiography. Reply Box B20, *AJR* (see address this section). 2–4bp

Fellowships and Residencies

MRI FELLOWSHIPS—Fellowship positions in MRI are available for July 1993 and July 1994 at the Johns Hopkins Dept. of Radiology and Radiological Science. Flexible fellowship programs with clinical or research emphasis are available. The MRI division is equipped with 3 1.5-T GE scanners and 2 1.5-T Siemens scanners, both with cardiac imaging and spectroscopic capabilities. Over 9000 exams are performed yearly. Over 2000 of these are body MRI studies. In addition, a 4.7-T and an 8.5-T instrument with spectroscopic and imaging capabilities are available for research. The main interests of the section are oncologic, cardiovascular, and musculoskeletal imaging. Rotating fellowships with CT and/or ultrasound or a straight MR fellowship are offered. For additional information and application, contact Janet Kuhlman, M.D., Acting Director, Body MRI, Johns Hopkins Hospital, Baltimore, MD 21205-2182; (410) 955-4419. 4–5cp

ACCREDITED FELLOWSHIPS IN PEDIATRIC RADIOLOGY—The Dept. of Radiology, St. Christopher's Hospital for Children, Philadelphia, PA, offers 1- or 2-yr accredited fellowship positions in pediatric radiology. The fellowship training covers all aspects of pediatric imaging, including cardiovascular and thoracic imaging, neuroradiology, abdominal resonance imaging, nuclear medicine, ultrasound, and angiography/interventional techniques. St. Christopher's Hospital for Children moved into a brand new facility in a new location 1 yr ago. State-of-the-art imaging equipment includes Acuson ultrasound units with Doppler and color-flow Doppler capability, GE 9800 Quick CT scanner, GE 1.5-T MRI with MRA, Gamma and SPECT nuclear cameras, and digital subtraction angiography. Salary and fringe benefits are competitive. Candidates must be board-certified or qualified. St. Christopher's Hospital for Children is an affirmative action/equal opportunity employer. Address inquiries and CV to Eric N. Faerber, M.D., Dept. of Radiology, St. Christopher's Hospital for Children, Erie Ave. at Front St., Philadelphia, PA 19134-1095; (215) 427-5230. 4–5cp

FELLOWSHIP IN ANGIO/INTERVENTIONAL IMAGING—A 1-yr fellowship program is available at Lehigh Valley Hospital Center in Allentown, PA. LVHC is a 492-bed, acute-care, university-affiliated hospital. The fellowship program offers training in CT (head and body), ultrasound, MR, angiography, and interventional radiology. For further information, contact Robert Kricun, M.D., Dept. of Radiology, Lehigh Valley Hospital Center, P. O. Box 689, Allentown, PA 18105. 4–6c

ADVANCED IMAGING FELLOWSHIP—The Dept. of Radiology and The Graduate Hospital Imaging Center are offering a 1-yr advanced imaging fellowship to include MR, CT, and ultrasound. MR and CT imaging time will be spent performing both body and neuro studies. Facilities include 2 state-of-the-art GE 1.5-T MR scanners with phased-array coils, endorectal MR, and MRA. Ultrasound includes color-flow Doppler. CTs include Elscint 2400 Elite and GE 9800. Candidates must have completed an approved 4-yr residency before commencing the fellowship. Board eligibility is a requirement. Salary will be at a PGY5 level. Interested candidates should apply to Jerome G. Jacobstein, M.D., Chairman, Dept. of Radiology, The Graduate Hospital, One Graduate Plaza, Philadelphia, PA 19146; (215) 893-2050. 4cp

FELLOWSHIP IN NEURORADIOLOGY — The Dept. of Radiology at the University of Massachusetts Medical Center has an unexpected opening for fellowship training in neuroradiology starting July 1, 1992. We also have a fellowship available starting July 1, 1993. Training is offered in neuroangiography, basic neuro interventional procedures, CT, myelography, MRI, and carotid ultrasonography. The University of Massachusetts Medical Center is a bustling 370-bed, university hospital and medical school located in Worcester, 40 mi. west of Boston. There are 22 staff, 14 residents, and 2–4 fellows. The dept. does approximately 130,000 exams/yr. The hospital is a major trauma center and is serviced by 2 life-flight helicopters. The dept. is well-equipped with 2 state-of-the-art CT, 2 1.5-T GE MR, and a 2.0-T small-bore unit for animal research. For further information, please contact Ronald L. Ragland, M.D., Chief, Division of Neuroradiology, University of Massachusetts Medical Center, 55 Lake Ave., N., Worcester, MA 01655; (508) 856-2215. The University of Massachusetts Medical Center is an affirmative action/equal opportunity employer. 4c

UNEXPECTED OPENING FOR FELLOWSHIP IN CARDIOVASCULAR-INTERVENTIONAL RADIOLOGY available July 1, 1992. A 1-yr fellowship program is available at a 750-bed teaching hospital. Extensive clinical experience involving all aspects of cardiovascular imaging, interventional vascular, and nonvascular procedures. Availability for clinical or animal research. Send CV and inquiries to Oscar H. Gutierrez, M.D., Dept. of Radiology, Box 648, University of Rochester Medical Center, Rochester, NY 14642. AA/EO/M-F employer. 4–6c

NEURO/ENT FELLOWSHIP, UNIVERSITY OF FLORIDA—The Dept. of Radiology offers several 2-yr, postresidency fellowship training positions available July 1993 and July 1994. The fellowship offers excellent clinical material, comprehensive and modern equipment, and experienced 4-person subspecialty faculty. In addition to clinical practice and training, responsibilities include graduate and undergraduate medical instruction in neuroradiology as well as participation in departmental research activities. Minimum requirements include successful completion of an accredited radiology residency. Applicants must be eligible to obtain a medical license in the state of Florida. For additional information, contact Ronald Quisling, M.D., Professor, Dept. of Radiology, Box 100374 JHMHC, Gainesville, FL 32610-0374; (904) 395-0291. The University of Florida is an equal opportunity/affirmative action employer and encourages applications from women and minorities. 3–6c

IMMEDIATE OPENING, PEDIATRIC RADIOLOGY FELLOWSHIP—Position available for 1-yr fellowship beginning July 1, 1992. Experience in all areas of imaging. Apply to Thomas E. Sumner, M.D., Dept. of Radiology, Wake Forest University, Bowman Gray School of Medicine, Medical Center Blvd., Winston-Salem, NC 27157-1088; (919) 748-2463. AA.EOE. 4–6c

FELLOWSHIP IN ULTRASOUND, BODY CT, AND MRI—July 1992 and July 1993. One-yr program featuring ultrasound, body CT, body MRI, and noninvasive vascular diagnosis. Send CV to, or for information contact, William Zwiebel, M.D., Dept. of Radiology, University of Utah Hospital, Salt Lake City, UT 84132; (801) 581-7553. 11–4c

PEDIATRIC RADIOLOGY AND MRI RESEARCH FELLOWSHIP—The University of California, San Francisco, offers a unique opportunity for a 1- or 2-yr experience focused on clinical pediatric imaging starting July 1, 1992. A significant portion of effort will also be devoted to MRI and contrast agent research as a sponsored fellow. UCSF is an equal opportunity/affirmative action employer. Minority groups, women, and handicapped individuals are encouraged to apply. Interested applicants should write or call Robert Brasch, M.D., Dept. of Radiology, UCSF, San Francisco, CA 94143; (415) 476-2275. 4c

FELLOWSHIP IN ULTRASOUND AND BODY CT/MRI, July 1, 1993, to June 30, 1994, at Hahnemann University Hospital. State-of-the-art equipment, including ultrasound color-flow imaging, 2 GE 9800 CT scanners, and Signa 1.5-T MR is provided. Applicants must have completed an approved residency in diagnostic radiology and be board-eligible or certified. For inquiries, please contact Lawrence Neustadter, D.O., Dept. of Diagnostic Radiology, Hahnemann University Hospital, Broad and Vine Sts., Philadelphia, PA 19102; (215) 448-8722. An equal opportunity employer. 4–6cp

FELLOWSHIPS AT THOMAS JEFFERSON UNIVERSITY HOSPITAL—The Dept. of Radiology at Thomas Jefferson University Hospital in Philadelphia offers the following fellowship programs each yr: (1) Ultrasound/CT/MRI—Jefferson's ultrasound division is 1 of the largest in the world and performs all currently available exams, including obstetric, vascular, lithotripsy, invasive, and endoluminal. We also operate 4 GE 1.5-T MRI units and 3 CT scanners. Contact Barry Goldberg, M.D., regarding this program. (2) Cardiovascular/interventional—this division is housed in a new suite containing Philips angio units with DSA and performs the full range of vascular and nonvascular interventional procedures. Contact Geoffrey Gardiner, Jr., M.D. (3) Neuro/ENT radiology—very active clinical services supply a wealth of material to this division, which is housed in a neurosciences imaging center containing all imaging modalities. Contact Carlos Gonzales, M.D. (4) Breast imaging—Jefferson's new breast-imaging center performs approximately 85 studies/day including ultrasound and needle localizations. Contact Stephen Feig, M.D. (5) Chest—includes biopsies and CT. Contact Robert Steiner, M.D. (6) MRI—a dedicated body MRI program including excellent research opportunities in addition to a large clinical case load. Contact Donald Mitchell, M.D. (7) Ultrasound—a dedicated ultrasound program. Contact Barry Goldberg, M.D. (8) Musculoskeletal—includes MRI of the musculoskeletal system. Contact David Karasick, M.D. All program directors listed above can be contacted at the Dept. of Radiology, Thomas Jefferson University Hospital, Philadelphia, PA 19107. Jefferson is an equal opportunity/affirmative action employer. 4xc

A FELLOWSHIP POSITION IN VASCULAR AND INTERVENTIONAL RADIOLOGY, beginning July 1, 1992, and ending June 30, 1993, has unexpectedly become available. It is offered to candidates that have recently completed a residency in radiology as well as those practicing radiologists who desire to return to an academic setting to acquire new skills in the vascular and interventional field. A very active dept. with up-to-date equipment provides an excellent opportunity for training in all interventional modalities. Contact L. B. Morettin, M.D., Director, Vascular & Interventional Radiology, University of Texas Medical Branch, Galveston, TX 77550; (409) 772-2498, fax (409) 772-3229. UTMB is an equal opportunity M/F/H/V, affirmative action employer. UTMB hires only individuals authorized to work in the United States. 3–5c

FELLOWSHIP IN ANGIO/INTERVENTIONAL RADIOLOGY—The Dept. of Radiology at the University of Florida is offering several 1-yr, postresidency clinical fellowship positions beginning in July 1993 and July 1994. Angiographic suites are available (2 have Philips C-arms with 1024 ADAC digital), and a new Toshiba vascular lab. The dept. has intravascular ultrasound color-flow Doppler and angioscopy equipment. Training includes all interventional procedures (vascular, biliary, urology, etc.), as well as experience with investigational devices such as CO_2, angioscopy, atherectomy, and holmium lasers. An animal laboratory, a full-time veterinarian, and an instrument shop are available. Applicants must be eligible for licensure in the state of Florida. For further information, contact Irvin F. Hawkins, M.D., Professor, Dept. of Radiology, Box 100374 JHMHC, Gainesville, FL 32610-0374; (904) 395-0291. The University of Florida is an equal opportunity/affirmative action employer. 3–6c

FELLOWSHIP IN BODY IMAGING/MRI—New fellowship position. The Dept. of Radiology, University of Massachusetts Medical Center, offers a 1-yr fellowship position in body imaging/MRI starting July 1, 1992. Training is offered in ultrasound, CT, and MRI. The position involves teaching of medical students and residents, with opportunity for research. The University of Massachusetts Medical Center is a 360-bed university hospital and medical school, located in Worcester, approximately 40 mi. west of Boston. The dept. consists of 24 staff, 13 residents, 2–4 fellows and does approximately 120,000 exams/yr. The hospital is a major trauma center and is serviced by 2 Life Flight helicopters. The dept. is well-equipped with 2 modern CT scanners, 2 1.5-T GE MR scanners, as well as a 2.0-T small-bore unit for animal research. The University of Massachusetts Medical Center Hospital is very active academically. Numerous radiologic, clinical, and basic science conferences are scheduled on a daily basis, and there is ample time during the course of the yr to attend many of these presentations. The fellowship position carries the title of instructor in radiology. For further information, contact Ashley Davidoff, M.D., Director, Abdominal Imaging, or David Stark, M.D., Director of MRI, University of Massachusetts Medical Center, 55 Lake Ave., N., Worcester, MA 01655; (508) 856-3154. The University of Massachusetts Medical Center is an affirmative action/equal opportunity employer. 4xc

FELLOWSHIP IN MUSCULOSKELETAL RADIOLOGY, UNIVERSITY OF FLORIDA—The Dept. of Radiology is offering a musculoskeletal fellowship position for 1 yr, beginning July 1, 1992. The fellowship currently centers on a 568-bed hospital with wide exposure to skeletal pathology, including more than 200 new musculoskeletal tumors per yr. The fellowship experience includes clinical, research, and teaching opportunities in diagnostic skeletal radiology, CT, MRI, MR spectroscopy, metabolic bone disease, TMJ pathology, and image processing. Systems available include a 1.5-T whole body spectroscopy/imager, a 1.0-T whole body imager, a 2.0-T 34-cm spectroscopy/imager, 2 GE 9800 Quick CT scanners, and an image processing workstation (DMI) for multiplanar (MPR) and 3D reformation. At the fellow's discretion, the experience could be expanded to include aspects of nuclear medicine and the adjacent 473-bed VA hospital, which is equipped with a 1.5-T whole body spectroscopy/imager and a Picker 1200 CT scanner. Send CV to William J. Montgomery, M.D., Dept. of Radiology, P. O. Box 100374, Gainesville, FL 32610-0374; or call (904) 395-0291 for further information. An equal opportunity/affirmative action employer. 3–5c

FELLOWSHIP POSITIONS—The Dept. of Radiological Sciences at Olive View–UCLA Medical Center has openings for fellowships to begin on July 1, 1992. Positions are available in neuroradiology, ultrasound, body imaging, interventional radiology, and nuclear medicine. Candidates must be board certified and eligible for certification in diagnostic radiology and should be eligible for licensing in the state of California. In addition to clinical practice and training, responsibilities will include graduate and undergraduate medical instruction in radiology as well as assisting with related departmental research projects. Interested candidates should contact Issa Yaghmai, M.D., Professor and Chairman, Dept. of Radiological Sciences, Olive View–UCLA Medical Center, 14445 Olive View Dr., Sylmar, CA 91342; (818) 364-4078. The University of California, Los Angeles, is an affirmative action/equal opportunity employer. 3–6c

ABDOMINAL IMAGING FELLOWSHIP, UNIVERSITY OF FLORIDA—The Dept. of Radiology at the University of Florida is offering 1-yr clinical fellowships in abdominal imaging beginning in July 1993 and July 1994. Minimum requirements include successful completion of an accredited radiology residency. The fellowship includes training in all aspects of abdominal imaging (gastrointestinal and genitourinary radiology, CT, MRI, and ultrasound) by a 4-person subspecialty faculty. The programs offer full clinical experience and research opportunities. Applicants must be eligible to obtain a medical license in the state of Florida. Research fellowships are also available in abdominal imaging. For additional information, contact Pablo R. Ros, M.D., Professor, Dept. of Radiology, Box J-374 JHMHC, Gainesville, FL 32610-0374; (904) 395-0288. The University of Florida is an equal opportunity/affirmative action employer and encourages applications from women and minorities. 3–6c

RESEARCH FELLOWSHIPS IN INTERVENTIONAL RADIOLOGY—Two 1-yr positions are available at Allegheny General Hospital, a 746-bed teaching hospital in Pittsburgh, for a research fellow in an innovative program in interventional radiology research beginning July 1992 and 1993. The fellow will participate in imaging studies directed at ablation of tumors in the liver, prostate, lung, and brain. Percutaneous methods of removing herniated disks also are being pursued. Clinical responsibilities will be included as well as opportunities to pursue individual research interests. Candidates must be board certified/eligible in radiology. Please send CV to Dr. Gary Onik, 320 E. North Ave., Pittsburgh, PA 15212. 11–4cp

FELLOWSHIP IN MUSCULOSKELETAL RADIOLOGY, UNIVERSITY OF FLORIDA—The Dept. of Radiology is offering musculoskeletal fellowship positions beginning July 1993 and July 1994. The fellowship currently centers on a 548-bed hospital with wide exposure to skeletal pathology, including more than 200 new musculoskeletal tumors per yr. The fellowship experience includes clinical, research, and teaching opportunities in diagnostic skeletal radiology, CT, MRI, MR spectroscopy, metabolic bone disease, TMJ pathology, and image processing. Systems available include a 1.5-T whole body spectroscopy/imager, 2 GE 9800 Advantage CT scanners, and an image processing workstation (DMI) for multiplanar (MPR) and 3D reformation. At the fellow's discretion, the experience could be expanded to include aspects of nuclear medicine and the adjacent 473-bed VA hospital, which is equipped with a 1.5-T whole body spectroscopy/imager and a Picker 1200 CT scanner. Applicants must be eligible for licensure in the state of Florida. Send CV to William J. Montgomery, M.D., Dept. of Radiology, P. O. Box 100374 JHMHC, Gainesville, FL 32610-0374; (904) 395-0291 for further information. The University of Florida is an equal opportunity/affirmative action employer. 3–6c

A FELLOWSHIP IN ULTRASOUND AND BODY CT/MRI is available July 1, 1992, to June 30, 1993, at The New York Hospital-Cornell Medical Center. The dept. provides state-of-the-art equipment, including Acuson ultrasound, GE 9800 CT, and GE Signa 1.5-T MR. Wide variety of ultrasound exams include abdominal, OB-GYN, color Doppler, small parts, neonatal head, transvaginal, and transrectal. Applicants should be ABR-eligible or certified. Send CV to Elias Kazam, M.D., Dept. of Radiology, The New York Hospital-Cornell Medical Center, 525 E. 68th St., New York, NY 10021. 2–5c

MUSCULOSKELETAL RADIOLOGY FELLOWSHIP—Applications are now being accepted for a 1-yr musculoskeletal fellowship position beginning July 1993 at the Albert Einstein College of Medicine/Montefiore Medical Center (MMC). The musculoskeletal section at MMC works closely with the active orthopedic and rheumatologic services utilizing state-of-the-art CT and MRI equipment to provide radiologic consultation in all aspects of skeletal radiology. The fellowship experience would consist of a large plain film exposure along with CT, MRI, and arthrography. Opportunities in clinical and basic imaging research are offered. Address inquiries and CV to E. Stephen Amis, Jr., M.D., Chairman, Dept. of Radiology, Montefiore Medical Center, 111 E. 210th St., Bronx, NY 10467. Einstein and Montefiore are equal opportunity/affirmative action employers. 2–4c

FELLOWSHIP IN VASCULAR AND INTERVENTIONAL RADIOLOGY—The University of Arizona is sponsoring 1-yr fellowships in vascular and interventional radiology beginning July 1, 1992, and July 1, 1993. In-depth clinical experience and training in all aspects of interventional radiology will be offered. Facilities at the University Hospital (300-bed), and Tucson Veteran's Hospital (300-bed), include state-of-the-art angiographic, CT, and MR units. Opportunities for research and teaching also provided. Interested applicants should submit a current CV and 3 letters of recommendation (including 1 from the program director) to Gerald D. Pond, M.D., Head, Section of Vascular and Interventional Radiology, University of Arizona Health Sciences Center, Tucson, AZ 85724. For further information, please contact Linda Fowler at (602) 694-7136. 2–4c

NEURORADIOLOGY FELLOWSHIP—An unexpected opening for a neuroradiology fellow is available in the Dept. of Radiology at Thomas Jefferson University Hospital beginning July 1992. The Division of Neuroradiology has close clinical and research relationships with Jefferson's very active neurology, neurosurgery, orthopedic surgery, and otolaryngology depts. Complete training in ENT radiology is part of this program. Six full-time faculty members currently staff this division. Clinical facilities include 2 dedicated CT scanners, a myelography room, a biplane angiography room with DSA, and 4 GE 1.5-T MRI units. Contact Carlos Gonzalez, M.D., Director of Neuroradiology, 1009 Main Bldg., Thomas Jefferson University Hospital, Philadelphia, PA 19107; (215) 955-5447. Jefferson is an affirmative action/equal opportunity employer. 11–6c

SPECIAL IMAGING FELLOWSHIP—The Johns Hopkins Hospital, Dept. of Radiology, is offering a unique opportunity for a yr of excellence in clinical and/or research in medical imaging starting July 1, 1993. Active body CT service (>16,000 studies/yr) on state-of-the-art equipment with special areas of interest including oncology, immunocompromised host, inflammatory bowel disease, and 3D imaging. Research in imaging includes image processing of CT and MRI data using PIXAR image computers, Sun workstations, and NeXT and Apple computers. The candidates will be able to devote a significant portion of the yr to research and will be a sponsored fellow of the Winthrop Research Fellowship. Interested applicants should write or call Elliot K. Fishman, M.D., Dept. of Radiology, The Johns Hopkins Hospital, 600 N. Wolfe St., Baltimore, MD 21205; (410) 955-5173. 1–4cp

FELLOWSHIPS AT ALBANY MEDICAL CENTER—The newly renovated and equipped Dept. of Radiology at the Albany Medical College and Center in Albany, NY offers the following fellowship positions each yr: (1) Abdominal Imaging—this fellowship encompasses all aspects of MRI, ultrasound, CT, and other advanced techniques in imaging the abdomen. Four state-of-the-art MRI and 4 CT scanners as well as 5 color Doppler ultrasound units are utilized daily. Contact James C. Peters, M.D. regarding this program. (2) Neuroradiology—This fellowship encompasses the full range of advanced neuro imaging including MRI, CT, angiography, and myelography. Contact William A. Wagle, M.D. (3) Angiography and interventional radiology—Three advanced angiographic suites are utilized daily for a full range of vascular and interventional procedures. Contact Mohammad S. Sarrafizadeh, M.D. All program directors listed above may be contacted at the Dept. of Radiology, A-113, Albany Medical Center, Albany, NY 12208; (518) 445-3277 or contact Matthew D. Rifkin, M.D., Chairman, Dept. of Radiology, A-113, at the above address. Albany Medical Center is an equal opportunity/affirmative action employer. 1–12c

FELLOWSHIP IN PEDIATRIC RADIOLOGY, UNIVERSITY OF FLORIDA—The Division of Pediatric Radiology in the Dept. of Radiology at the University of Florida offers a 1-yr fellowship training in pediatric radiology, starting July 1993 and July 1994. Three full-time pediatric radiologists provide training in conventional radiology and fluoroscopy, ultrasound, neonatal imaging, CT, MRI, and interventional/angiography techniques. Supplemental training in nuclear medicine is available. Facilities include dedicated standard r/f rooms, 4 color-Doppler ultrasound machines, 2 GE CT units, 3 MR units, ICU electronic image transfer, and computed radiography (CR). Opportunity to participate or conduct clinical and basic research is available. Applicants must be eligible for licensure in the state of Florida. Contact Jonathan L. Williams, M.D., Director of Pediatric Radiology, Dept. of Radiology, Box 100374, University of Florida, Gainesville, FL 32610-0374; (904) 395-0291. The University of Florida is an equal opportunity/affirmative action employer. 3–6c

FELLOWSHIP POSITION—The Dept. of Radiology, Division of Cardiovascular/Interventional Radiology of the Brigham and Women's Hospital/Harvard Medical School has an opening for 1- or 2-yr position beginning July 1992. We are also considering applications for 1- and 2-yr fellowships starting July 1993. The Division of Cardiovascular/Interventional Radiology is a state-of-the-art training program in peripheral angiographic techniques, vascular and nonvascular interventions of all types, vascular ultrasound, and cardiovascular MRI. Some cardiac catheterization and coronary angiography is included. Research time is available for participation in original or ongoing clinical and/or laboratory projects. Please send CV to Kris Kandarpa, M.D., Ph.D., Co-Director, Division of Cardiovascular/Interventional Radiology, Dept. of Radiology, Brigham and Women's Hospital, 75 Francis St., Boston, MA 02115. Brigham and Women's Hospital/Harvard Medical School is an affirmative action/equal opportunity educator and employer. 11–4c

MUSCULOSKELETAL RADIOLOGY FELLOWSHIP—Applications are now being accepted for a musculoskeletal fellowship position for 1993 at the Cleveland Clinic Foundation (CCF). CCF is a 1000-bed, tertiary-care, teaching medical center with a large radiology residency program. Local, national, and international patients provide for an interesting and varied mix of bone pathology. Training includes all aspects of musculoskeletal radiology, including MR, CT, arthrography, biopsy, bone densitometry, and a large plain film experience. Fellowship includes patient care, teaching, and research. There is a close working relationship with the orthopedic, rheumatology, and endocrinology depts. There are presently 4 musculoskeletal staff in the section. For further information, please contact Bradford J. Richmond, M.D., Head, Section of Musculoskeletal Radiology, Desk A-21, 9500 Euclid Ave., Cleveland, OH 44195; (216) 444-3931. 12–5cp

Tutorials/Courses

MUSCULOSKELETAL MRI, SECOND ANNUAL LOS ANGELES CONFERENCE, SEPT. 19–20, 1992—Faculty: Drs. Bradley, Brant-Zawadzki, Dietrich, Friedman, Harms, Resnick, Schlesinger. Medical Seminars International, Inc., 18981 Ventura Blvd., #303, Tarzana, CA 91356; (818) 774-9077, fax (818) 774-0244. 4–9d

PROSTATE ULTRASOUND COURSE FOR 1992—Offered April 30 and May 1, 1992. Prostate ultrasound: applications, techniques, and advances in prostate ultrasound and prostate imaging. Contact Dept. of Continuing Medical Education, A-1, Albany Medical College, 47 New Scotland Ave., Albany, NY 12208; (518) 445-5828. 4d

ALASKA 1992:CRUISE THE INLAND PASSAGE, BREAST IMAGING AT SEA, JULY 4–11, 1992, AND MRI AT SEA, JULY 11–18, 1992—Medical Seminars International, Inc., 18981 Ventura Blvd., Ste. 303, Tarzana, CA 91356; (818) 774-9077, fax (818) 774-0244. 2–6d

AJR Classified Advertisements Information

Box Responses and Address for Ad Placement:

Box ________
AJR
2223 Avenida de la Playa
Suite 103
La Jolla, CA 92037-3218

Phone (619) 459-2229
FAX: (619) 459-8814

Keep It All Together

Easily and Conveniently with Bound Volumes of the *American Journal of Roentgenology*

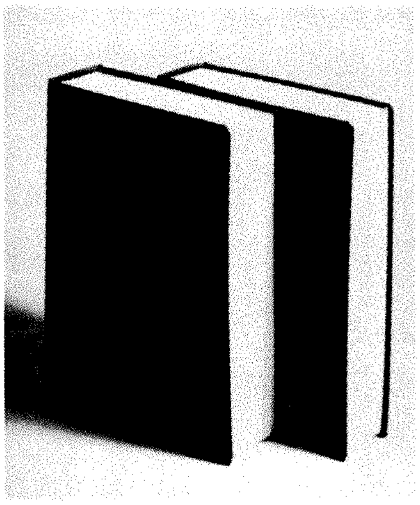

Keeping up with scientific and technological advances in radiology is more important than ever, and that's why each issue of the *American Journal of Roentgenology* is packed with up-to-the-minute information crucial to you and your practice. **Keep this important resource together for easy reference in convenient and attractive bound volumes.**

Bound volumes offer the timely coverage only a journal can provide — penetrating discussions of the topics that interest you most by the brightest names in the field — with all the durability and convenience of a hardcover edition. You'll have a year's worth of vital information all arranged and indexed in one sturdy source. And each carefully crafted volume will make a handsome addition to your permanent library.

To help you keep your reference library up to date, once a year we'll send a reminder so you can order the latest bound volumes. When you send in your paid order, a set will be reserved for you, to be sent as soon as available on 30-day approval. If you do not want the volumes for any reason, simply return them within 30 days for a courteous refund. It's that easy.

Bound volumes are available to subscribers only and are in addition to the regular subscription. For ordering information, contact *AJR* Subscription Fulfillment Department, 428 E. Preston St., Baltimore, MD 21202-3993, or call toll-free

1-800-638-6423.

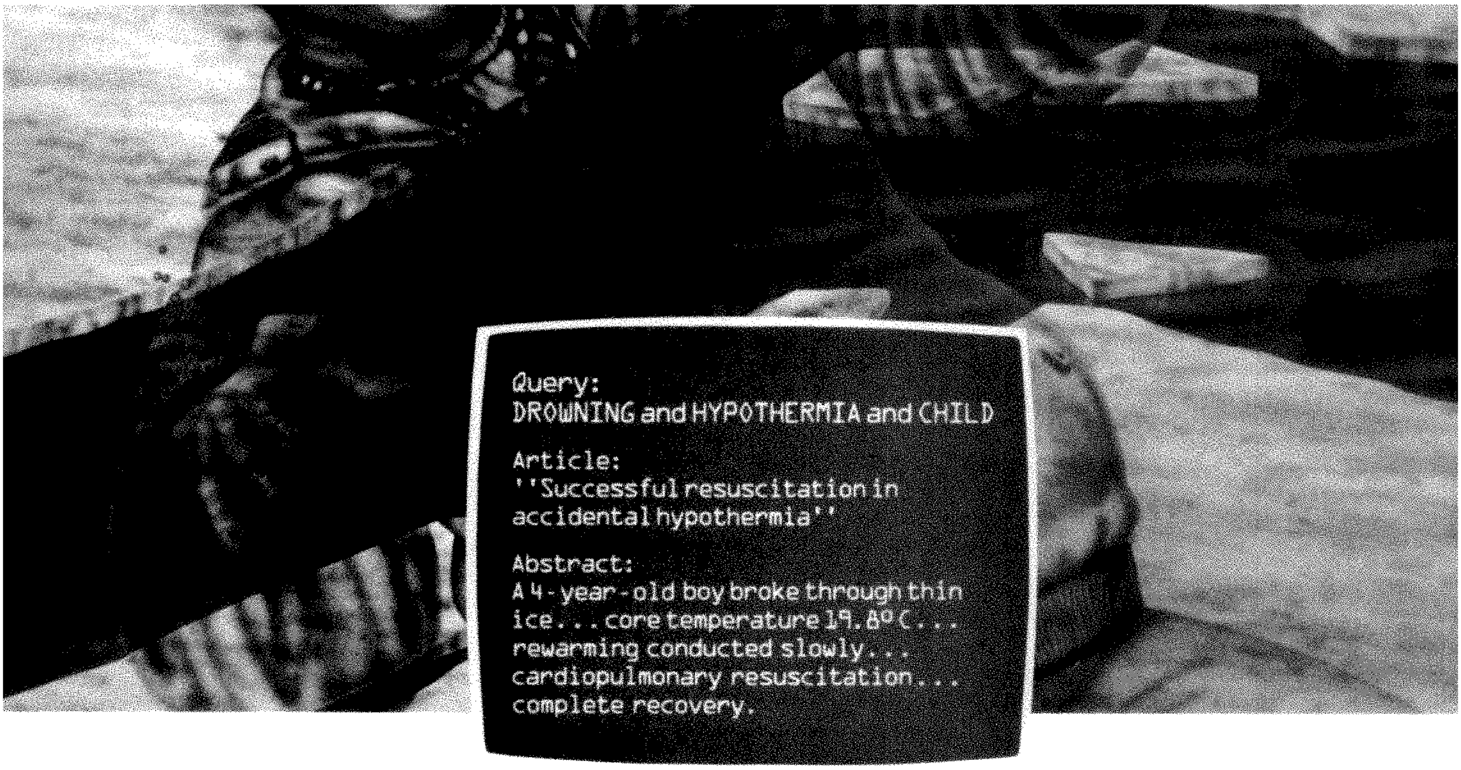

```
Query:
DROWNING and HYPOTHERMIA and CHILD

Article:
''Successful resuscitation in
accidental hypothermia''

Abstract:
A 4-year-old boy broke through thin
ice... core temperature 19.8° C...
rewarming conducted slowly...
cardiopulmonary resuscitation...
complete recovery.
```

When timing is critical, there's no time for guesswork

Comprehensive healthcare information in just minutes ...anytime you need it

As emergencies arise, you have to know what to treat, prevent, and look for immediately. Get the answers you need in just minutes through computer access to the National Library of Medicine, the largest, most complete healthcare information resource in the world.

The Friends of the NLM—a nonprofit organization—wants you, and all health professionals, to find out more about this unique link to the world's healthcare knowledge. To do so, simply use the coupon provided. You owe it to yourself and your patients.

The more you know, the better you heal

FRIENDS OF THE
NLM
NATIONAL LIBRARY
OF MEDICINE

Friends of the NLM
1529 Wisconsin Avenue N.W.
Washington, D. C. 20007

☐ Please send me more information about the NLM and the services it offers.

☐ Please enroll me in the Friends of the National Library of Medicine. My tax-deductible check for $35.00 (member) or $100.00 (sponsor) is enclosed.

(Institutional and corporate memberships are also available.)

Name ____________________

Address ____________________

City ____________ State ________ Zip ________

THE ONLY SENIOR CITIZEN NOT ELIGIBLE FOR SOCIAL SECURITY.

The American Red Cross is one of our nation's oldest, most venerated public service organizations. And since we receive no Federal appropriations for general operations, we must rely on you for donations. Which simply means, without your time and money, there will be no Red Cross. Please don't let an old friend down.

American Red Cross

Ad Council A Public Service of This Publication

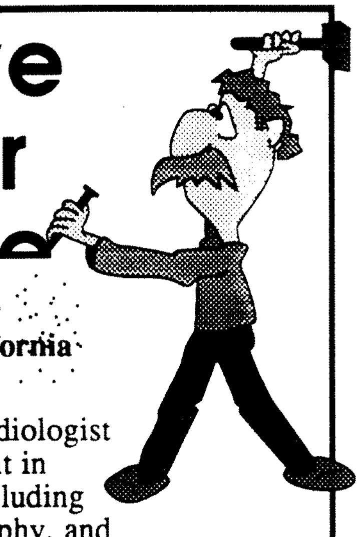

Carve Your Niche

Southern California

Growing six-physician partnership requires radiologist (BC by 7/92) competent in standard modalities including ultrasound, mammography, and CT—little or no interventional. Requires competence in MR and independent reading in multiple out-patient multi-site clinics and at central imaging center (system has 80,000+ yearly examinations and is rapidly growing). Reasonable hours, minimal weekend and call responsibilities. Excellent salary leading to full partnership. Great opportunity to enjoy career and life. Call, or submit CV to:

Ruthan Smith
(800) 338-4798 outside CA
(714) 825-4401 in CA
1826 Orange Tree Lane • Redlands, CA 92374

Gundersen Clinic: Because where you practice is as important as what you practice.

The Gundersen tradition: state-of-the-art medical care delivered by a highly qualified group of medical and dental specialists. And what sets our professionals apart from other medical staffs? Teamwork.

We are seeking General Radiologists to join our staff of 17 Radiologists who provide outreach services to those patients who visit our multiple branch community clinics in Iowa, Minnesota and Wisconsin, as well as provide care to patients in our full service main clinic in La Crosse. Last year, 191,740 radiographic examinations were performed throughout our system. It's the best of both worlds where you can combine sophisticated technology with one-on-one involvement in primary care.

Become part of the Gundersen tradition as we enter our second century serving the needs of 70,000 families through over 702,000 patient visits each year. You'll also enjoy an outstanding quality of life, competitive salaries and benefits, an excellent continuing education program and pension plan. Send your CV or **call Tim Skinner, Manager, Physician Recruitment, TOLL FREE at 1-800-362-9567, ext. 6674.** An equal opportunity employer.

1891 1991

Gundersen Clinic, Ltd.

1836 South Avenue
Dept. KK-4
La Crosse, Wisconsin 54601

Keep It All Together

Easily and Conveniently With Bound Volumes of the *American Journal of Roentgenology*

Keeping up with scientific and technological advances in radiology is more important than ever, and that's why each issue of the *American Journal of Roentgenology* is packed with up-to-the-minute information crucial to you and your practice. **Keep this important resource together for easy reference in convenient and attractive bound volumes.**

Each edition is imprinted with the year and volume number and contains six issues filled with the kind of vital research, commentary and analysis you've come to expect in the AJR.

For ordering information, contact AJR Subscription Fulfillment Department, 428 E. Preston St., Baltimore, MD 21202-3993, or call toll-free **1-800-638-6423.**

REVIEW ARTICLES

725 **Current use of lymphography for staging lymphomas and genital tumors.** *North LB, Lindell MM, Jing B-S, Wallace S*
729 **Diseases of the musculoskeletal system in children: imaging with CT, sonography, and MR.** *Schlesinger AE, Hernandez RJ*
743 **Infrastructure design of a picture archiving and communication system.** *Huang HK, Taira RK*

CHEST RADIOLOGY

751 **Pictorial essay. MR imaging of thymoma: radiologic-pathologic correlation.** *Sakai F, Sone S, Kiyono K, et al.*
757 **Case report. Pulmonary embolism caused by a surgical sponge.** *Kester NL, Hassien JD*
761 **Case report. Multiple mycotic pulmonary artery aneurysms: a complication of invasive mucormycosis.** *Loevner LA, Andrews JC, Francis IR*
763 **Tension pneumothorax after reversal of a Heimlich valve.** *Spouge AR, Thomas HA*

GASTROINTESTINAL RADIOLOGY

765 **CT diagnosis of small-bowel obstruction: efficacy in 60 patients.** *Fukuya T, Hawes DR, Lu CC, Chang PJ, Barloon TJ*
771 **Commentary. CT diagnosis of small-bowel obstruction.** *Stewart ET*
773 **Sonographic detection of the normal and abnormal appendix.** *Rioux M*
779 **Gastroepiploic veins: CT appearance in pancreatic disease.** *Moody AR, Poon PY*
785 **Bile duct disruption and biloma after laparoscopic cholecystectomy: imaging evaluation.** *Walker AT, Shapiro AW, Brooks DC, Braver JM, Tumeh SS*

GENITOURINARY RADIOLOGY

791 **Sonography of renal transplants in dogs: the effect of acute tubular necrosis, cyclosporine nephrotoxicity, and acute rejection on resistive index and renal length.** *Pozniak MA, Kelcz F, D'Alessandro A, Oberley T, Stratta R*
799 **Pictorial essay. Imaging of uterine leiomyomas.** *Karasick S, Lev-Toaff AS, Toaff ME*
807 **Technical note. Infusion of air into the collecting system to avoid needle blockage during percutaneous nephrostomy after extracorporeal shock-wave lithotripsy.** *Ellis JH, McKay DC, Sonda LP*

SKELETAL RADIOLOGY

809 **Percutaneous needle biopsy of musculoskeletal lesions. 1. Effective accuracy and diagnostic utility.** *Fraser-Hill MA, Renfrew DL*
813 **Percutaneous needle biopsy of musculoskeletal lesions. 2. Cost-effectiveness.** *Fraser-Hill MA, Renfrew DL, Hilsenrath PE*
819 **Technical note. Percutaneous screw fixation of acetabular fractures with CT guidance: preliminary results of a new technique.** *Gay SB, Sistrom C, Wang G-J, et al.*
823 **Case report. Ifosfamide: a new cause of rickets.** *Silberzweig JE, Haller JO, Miller S*

PEDIATRIC RADIOLOGY

825 **Review. Diagnostic imaging of mediastinal masses in children.** *Merten DF*
833 **Delayed spontaneous rupture of augmented bladder in children: diagnosis with sonography and CT.** *Glass RBJ, Rushton HG*
837 **The ureterovesical junction in children: sonographic findings after surgical or endoscopic treatment.** *Rypens F, Avni EF, Bank WO, Schulman CC, Struyven J*

FETAL SONOGRAPHY

843 **Can detection of the yolk sac in the first trimester be used to predict the outcome of pregnancy? A prospective sonographic study.** *Kurtz AB, Needleman L, Pennell RG, Baltarowich O, Vilaro M, Goldberg BB*

NEURORADIOLOGY

849 **Review. Multiple sclerosis: the impact of MR imaging.** *Wallace CJ, Seland TP, Fong TC*
859 **MR imaging features of medulloblastomas.** *Meyers SP, Kemp SS, Tarr RW*
867 **Diagnosis of Sturge-Weber syndrome: comparison of the efficacy of CT and MR imaging in 14 cases.** *Martí-Bonmatí L, Menor F, Poyatos C, Cortina H*
872 **Case report. Persistent trigeminal artery in a patient with Sturge-Weber syndrome.** *Loevner L, Quint DJ*

VASCULAR RADIOLOGY

875 **Pictorial essay. Technical problems associated with placement of the Bird's Nest inferior vena cava filter.** *Vesely T, Darcy M, Picus D, Hicks M*
881 **Technical note. Percutaneous central venous catheter placement: use of the blunt needle for subcutaneous track formation.** *Akins EW, Hawkins IF Jr, Mucciolo P, Overmeyer JD, Kerns SR, Murray KK*
883 **Case report. Intraarterial papaverine for relief of catheter-induced intracranial vasospasm.** *Eckard DA, Purdy PD, Girson MS, Samson D, Kopitnik T, Batjer H*
885 **Technical note. Percutaneous transaxillary catheter insertion for hepatic artery infusion chemotherapy.** *Yoshikawa M, Ebara M, Nakano T, Minoyama A, Sugiura N, Ohto M*

CONTRAST MATERIAL

887 **Gadobenate dimeglumine—a new contrast agent for MR imaging: preliminary evaluation in healthy volunteers.** *Vogl TJ, Pegios W, McMahon C, et al.*

RADIOLOGY PRACTICE

893 **Clinicians' access to diagnostic imaging information at an academic center: perceived impact on patient management.** *Gur D, Straub WH, Lieberman RH, Gennari RC*

ARRS 1992 CASE OF THE DAY QUIZ

897 **Introduction.** *Heller RM*
898 **Chest case of the day.** *Worrell JA, O'Donnell DM, Carroll FE, Bruner JP, Coleman JA Jr*
902 **Abdominal case of the day.** *Shaff MI, Powers TA, Gilpin LB, Faulstich ME*
905 **Skeletal case of the day.** *Tigges S, Erb RE, Nance EP*
907 **Pediatric case of the day.** *Heller RM, Hernanz-Schulman M, Johnson J, Stein SM, Kirchner S*
911 **Neuroradiology case of the day.** *Lacrampe MJ, Creasy JL*
913 **Nuclear medicine case of the day.** *Moody EB, Glassman SB, Hansen AV, Lawrence SK, Delbeke D*

OTHER CONTENT

742 **Medicine in American art**
750 **Radiologic-pathologic conference**
760 **History page**
772 **List of book reviews**
784 **Memorial, Esmond McDonald Mapp**
858 **Forthcoming articles**
866 **Books received**
915 **Letters**
923 **Review of current literature**
928 **News**
931 **American Roentgen Ray Society information**
932 **1992 ARRS meeting section**
951 **Classified advertisements**
A2 ***AJR* business and subscriber information**
A5 **Guidelines for authors**

American
Journal of
Roentgenology

May 1992

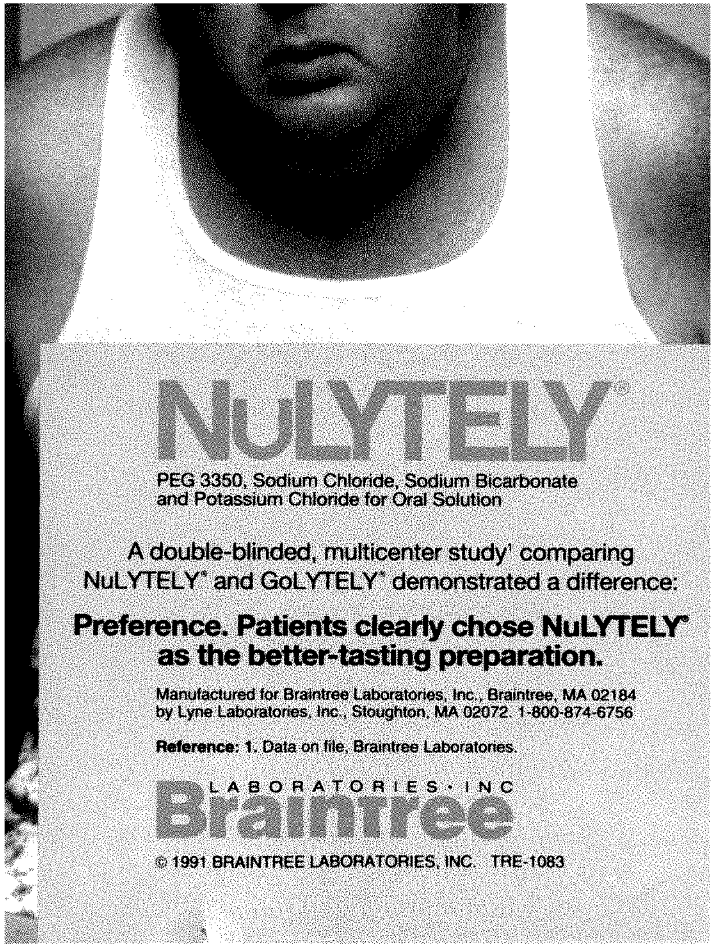

NuLYTELY®

PEG 3350, Sodium Chloride, Sodium Bicarbonate
and Potassium Chloride for Oral Solution

A double-blinded, multicenter study[1] comparing NuLYTELY® and GoLYTELY® demonstrated a difference:

Preference. Patients clearly chose NuLYTELY® as the better-tasting preparation.

Manufactured for Braintree Laboratories, Inc., Braintree, MA 02184
by Lyne Laboratories, Inc., Stoughton, MA 02072. 1-800-874-6756

Reference: 1. Data on file, Braintree Laboratories.

LABORATORIES · INC
Braintree

© 1991 BRAINTREE LABORATORIES, INC. TRE-1083

Official Journal of the American Roentgen Ray Society

AJR

American Journal of Roentgenology
Diagnostic Imaging and Related Sciences

Editor-In-Chief Robert N. Berk, *La Jolla, California*
University of California, San Diego
School of Medicine and Medical Center

Editor Emeritus Melvin M. Figley, *Seattle, Washington*

Associate Editor Karim Valji, *San Diego, California*

Consulting Editors A. James Barkovich, *San Francisco, California*
Edward A. Sickles, *San Francisco, California*

Statistician Charles C. Berry, *San Diego, California*

Editorial Board

Mark E. Baker
Lawrence W. Bassett
Michael A. Bettmann
Ethan M. Braunstein
Felix S. Chew
Horacio R. D'Agostino
N. Reed Dunnick
David K. Edwards
Ronald G. Evens
Sandra K. Fernbach
Richard H. Gold
Edward G. Grant
John R. Hesselink
Emanuel Kanal
Ray F. Kilcoyne
Carolyn Kimme-Smith
Melvyn T. Korobkin
Mark J. Kransdorf
Faye C. Laing
Thomas L. Lawson
Robert G. Levitt
Martin J. Lipton
Bruce L. McClennan
Richard P. Moser
Jeffrey H. Newhouse
Sven J. K. Paulin
David M. Paushter
Vassilios Raptopoulos
Donald L. Resnick
Charles A. Rohrmann, Jr.
Peter M. Ronai
Stuart S. Sagel
Sanjay Saini
Stefan C. Schatzki
William P. Shuman
Edward A. Sickles
Barry A. Siegel
M. Leon Skolnick
Edward T. Stewart
Murali Sundaram
Robert D. Tien

Director of Publications: Susan Brown Cappitelli **Editorial Staff:** Barbara Rose, *managing editor*; Katie L. Spiller, Barbara L. Halliburton, and Janine Anderson, *manuscript editors*; Nancy Rydbeck, *office manager*; Sheri Smith, *administrative assistant*; Linda J. Waggoner, *administrative secretary*

AJR, AMERICAN JOURNAL OF ROENTGENOLOGY (ISSN 0361 803X) is published monthly by the American Roentgen Ray Society, 1891 Preston White Dr., Reston, VA 22091. Annual dues include $50 for journal subscription. Second-class postage paid at Baltimore, MD, and at additional mailing offices. **POSTMASTER**, send address changes (Form 3579) to Subscription Fulfillment, AJR, 428 E. Preston St., Baltimore, MD 21202. Subscription rates $125 ($180 foreign); institutions $135 ($190 foreign); in training $25 ($80 foreign); single copy $18 ($22 foreign). The GST number for Canadian subscribers is 123394371. Airmail rates furnished on request. Indexed by *Current Contents* and *Index Medicus*. Copyright © 1992 by American Roentgen Ray Society.
0361-803X/92$3.00

# of choices

3M now has a laser imager to meet any user need

3M Laser Imager Systems have always been the imagers of choice of hospitals and original equipment manufacturers. After all, we were instrumental in introducing laser imaging to the medical community. And we have more placements than any other laser imager manufacturer.

But a 3M Laser Imager System is more than just the choice of those in the know, it's the only system that lets you be choosey. That's because 3M has not one, not two, but *three* models to choose from, each designed to fit your specific requirements.

The 3M Laser Imager is a fully-featured imager for single modality applications. The 3M Laser Imager Plus is a medium throughput, multi-modality-ready imager with enhanced features. And the 3M Laser Imager XL is a maximum throughput, fully integrated multi-modality system with high resolution imaging and high speed acquisition.

All accessories and options, like the 3M Laser Processor and the 3M Daylight Load Film Magazine, can be installed with any of the three systems. And there are now *four* 3M IR Laser Imaging Films, system-matched for high resolution and consistent, high quality imaging.

All of which means you can build a system that's precisely what you, your hospital and your patients need. For both today and in the future.

So make the right decision. Choose the laser imager of choice. And choices.

For more information call 1-800-328-1684 ext. 340. Or write: 3M Medical Imaging Systems Division, P.O. Box 33050, St. Paul, MN 55133-3050. In Canada, write: 3M Canada Inc., P.O. Box 5757 Terminal A, London, Ontario, Canada N6A 4T1.

Limited Time Offer!

Purchase a 3M Laser Imager for less than $50,000

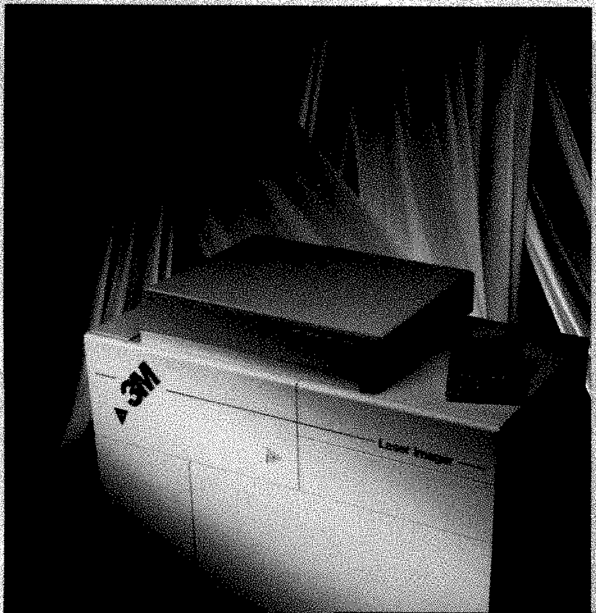

The 3M Laser Imager

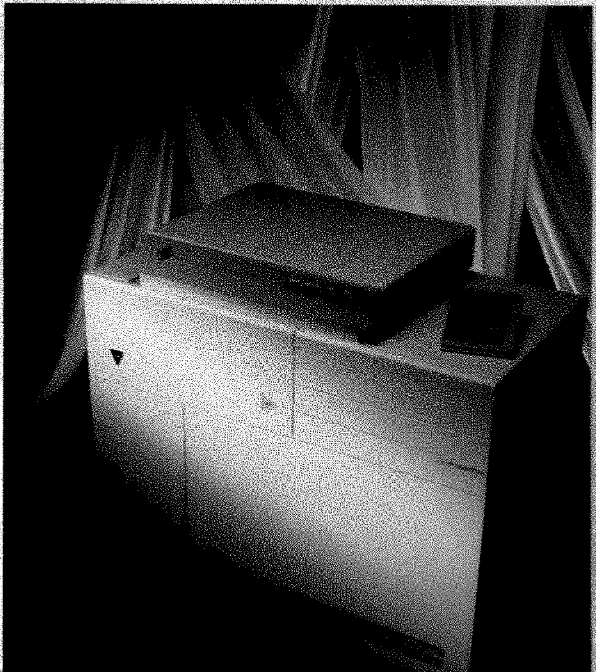

The 3M Laser Imager Plus

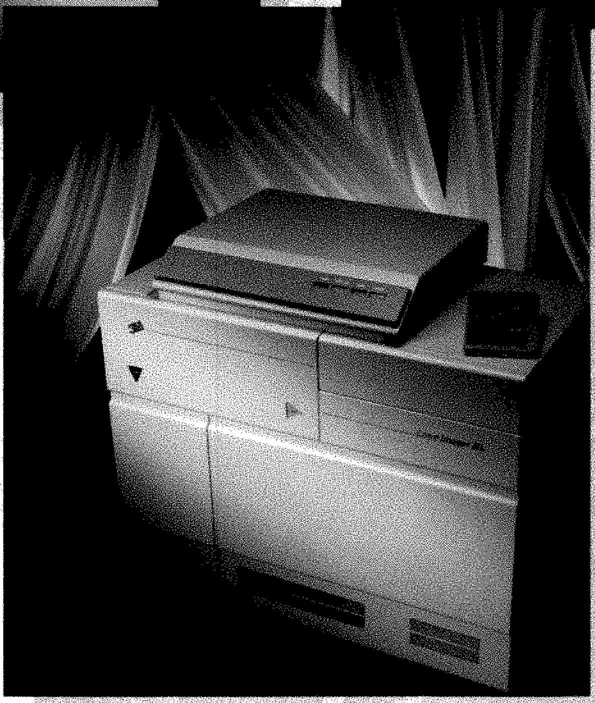

The 3M Laser Imager XL

© 3M 1991

Innovation working for you™

3M

PERSONAL COMPUTER/LASER VIDEODISC SYSTEM
to assist you in the
diagnosis of Skeletal Dysplasias

A unique collection of 400 Skeletal Syndromes
7000 Illustrations
including

• X-rays • Clinical pictures • Chondro-osseous histology

OSSUM

AN ILLUSTRATED DATABASE OF SKELETAL DYSPLASIAS

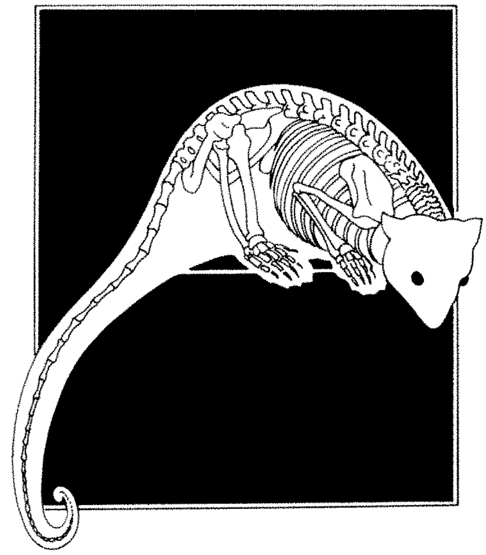

for further information contact:
Dr. Agnes Bankier – Medical Geneticist to the successful related POSSUM system.

PO Box 1100 Parkville Victoria 3052 Australia
Phone: (03) 345 5160 Fax: (03) 348 1391

© Eastman Kodak Company, 1990.

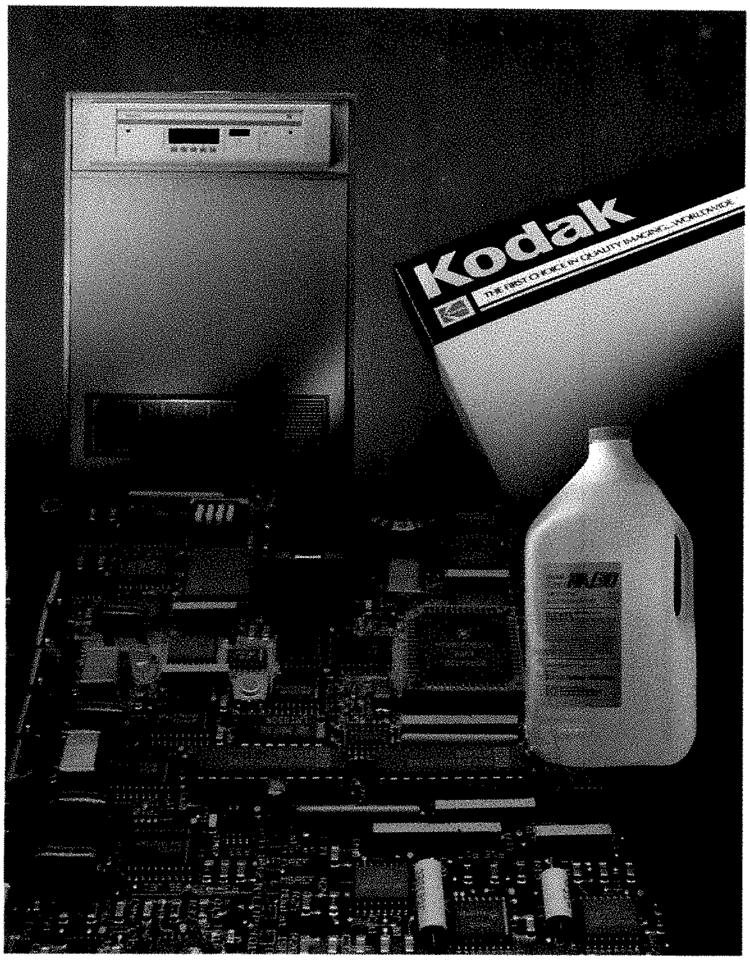

The ne
features
process
room in

It's not
of the in
consiste
X-Omat
and che
for you

Plus,
to prod
support
operato

For n
and con
System
patients,

Koda
bottom

SEE US

SEE US

MORE THA
INTRODUC
RAPID ACC
KODAK

The first choice in qual

FROM M

INCKRODT

The friendlier molecule and its pattern of protection

The toxic portion of the contrast agent molecule is the iodinated benzene ring. In modern contrast agents, the ring is sheltered by hydroxyl groups arranged around it. If the arrangement is less than optimal, it can leave "holes" in the structure.

The Optiray® molecular structure provides a superior pattern of protection from the benzene ring with six hydroxyl groups arranged symmetrically around it.[1] In addition, Optiray has no hydrophobic (lipid-soluble) methyl group as in iopamidol and iohexol molecules. These are the reasons why one investigator has called Optiray the "friendlier" contrast media molecule.[1]

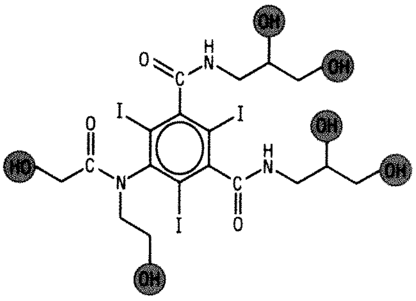

Balanced distribution of hydroxyl (OH) groups creates a pattern of protection around the toxic iodinated benzene ring.

With Optiray, you can expect a very low incidence of individual, drug-related adverse reactions.[2] Optiray also offers the safety, convenience, and cost-efficiency of the single-dose Ultraject® prefilled syringe. With all these advantages, shouldn't Optiray's friendlier molecule be your choice in a nonionic contrast agent? For more information, contact your Mallinckrodt Medical representative or call us toll free at (800) 325-3688.

All nonionic iodinated contrast media currently available inhibit blood coagulation, in vitro, less than ionic contrast media. Clotting has been reported when blood remains in contact with syringes containing nonionic contrast media. Therefore, meticulous intravascular administration technique is necessary to minimize thromboembolic events.

Please see adjacent brief summary of prescribing information.

References:

1. McClennan BL. Ionic and nonionic iodinated contrast media: evolution and strategies for use. *AJR.* 1990; 155:225-233.
2. Benamor M, Aten EM, McElvany KD, et al. Ioversol clinical safety summary. *Invest Radiol.* 1989;24 (suppl 1):S67-S72.

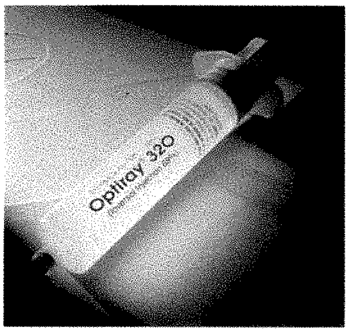

Nonionic

OPTIRAY®

(ioversol)

The friendlier molecule

OPTIRAY® 160 240 320
(Ioversol Injection)

DESCRIPTION: Each milliliter of OPTIRAY 160 (ioversol injection 34%) provides 339 mg of ioversol with 3.6 mg of tromethamine as a buffer and 0.2 mg of edetate calcium disodium as a stabilizer. OPTIRAY 160 provides 16% (160 mg/mL) organically bound iodine.

Each milliliter of OPTIRAY 240 (ioversol injection 51%) provides 509 mg of ioversol with 3.6 mg of tromethamine as a buffer and 0.2 mg of edetate calcium disodium as a stabilizer. OPTIRAY 240 provides 24% (240 mg/mL) organically bound iodine.

Each milliliter of OPTIRAY 320 (ioversol injection 68%) provides 678 mg of ioversol with 3.6 mg of tromethamine as a buffer and 0.2 mg of edetate calcium disodium as a stabilizer. OPTIRAY 320 provides 32% (320 mg/mL) organically bound iodine.

CONTRAINDICATIONS: None.

WARNINGS: Nonionic iodinated contrast media inhibit blood coagulation, in vitro, less than ionic contrast media. Clotting has been reported when blood remains in contact with syringes containing nonionic contrast media.

Serious, rarely fatal, thromboembolic events causing myocardial infarction and stroke have been reported during angiographic procedures with both ionic and nonionic contrast media. Therefore, meticulous intravascular administration technique is necessary, particularly during angiographic procedures, to minimize thromboembolic events. Numerous factors, including length of procedure, catheter and syringe material, underlying disease state and concomitant medications may contribute to the development of thromboembolic events. For these reasons, meticulous angiographic techniques are recommended including close attention to guidewire and catheter manipulation, use of manifold systems and/or three-way stopcocks, frequent catheter flushing with heparinized saline solutions and minimizing the length of the procedure. The use of plastic syringes in place of glass syringes has been reported to decrease but not eliminate the likelihood of in vitro clotting.

Serious or fatal reactions have been associated with the administration of iodine-containing radiopaque media. It is of utmost importance to be completely prepared to treat any contrast medium reaction.

As with any contrast medium, serious neurologic sequelae, including permanent paralysis, can occur following cerebral arteriography, selective spinal arteriography and arteriography of vessels supplying the spinal cord. A cause-effect relationship to the contrast medium has not been established since the patients' pre-existing condition and procedural technique are causative factors in themselves. The arterial injection of a contrast medium should never be made following the administration of vasopressors since they strongly potentiate neurologic effects.

Caution must be exercised in patients with severely impaired renal function, combined renal and hepatic disease, severe thyrotoxicosis, myelomatosis, or anuria, particularly when large doses are administered.

Intravascularly administered iodine-containing radiopaque media are potentially hazardous in patients with multiple myeloma or other paraproteinemia, particularly in those with therapeutically resistant anuria. Myeloma occurs most commonly in persons over age 40. Although neither the contrast agent nor dehydration has been proved separately to be the cause of anuria in myelomatous patients, it has been speculated that the combination of both may be causative. The risk in myelomatous patients is not a contraindication to the procedure; however, special precautions, including maintenance of normal hydration and close monitoring, are required. Partial dehydration in the preparation of these patients prior to injection is not recommended since this may predispose the patient to precipitation of the myeloma protein.

Administration of radiopaque materials to patients known or suspected of having pheochromocytoma should be performed with extreme caution. If, in the opinion of the physician, the possible benefits of such procedures outweigh the considered risks, the procedures may be performed; however, the amount of radiopaque medium injected should be kept to an absolute minimum. The blood pressure should be assessed throughout the procedure, and measures for treatment of a hypertensive crisis should be available.

Contrast media may promote sickling in individuals who are homozygous for sickle cell disease when administered intravascularly.

Reports of thyroid storm following the intravascular use of iodinated radiopaque agents in patients with hyperthyroidism or with an autonomously functioning thyroid nodule, suggest that this additional risk be evaluated in such patients before use of any contrast medium.

PRECAUTIONS: *General:* Diagnostic procedures which involve the use of iodinated intravascular contrast agents should be carried out under the direction of personnel skilled and experienced in the particular procedure to be performed. A fully equipped emergency cart, or equivalent supplies and equipment, and personnel competent in recognizing and treating adverse reactions of all types should always be available. Since severe delayed reactions have been known to occur, emergency facilities and competent personnel should be available for at least 30 to 60 minutes after administration.

Preparatory dehydration is dangerous and may contribute to acute renal failure in patients with advanced vascular disease, diabetic patients, and in susceptible non-diabetic patients (often elderly with pre-existing renal disease). *Patients should be well hydrated prior to and following the administration of OPTIRAY.*

The possibility of a reaction, including serious, life-threatening, fatal, anaphylactoid or cardiovascular reactions, should always be considered (See ADVERSE REACTIONS). Increased risk is associated with a history of previous reaction to a contrast medium, a known sensitivity to iodine and known allergies (i.e., bronchial asthma, hay fever and food allergies) or hypersensitivities.

The occurrence of severe idiosyncratic reactions has prompted the use of several pretesting methods. However, pretesting cannot be relied upon to predict severe reactions and may itself be hazardous to the patient. It is suggested that a thorough medical history with emphasis on allergy and hypersensitivity, prior to the injection of any contrast medium, may be more accurate than pretesting in predicting potential adverse reactions. A positive history of allergies or hypersensitivity does not arbitrarily contraindicate the use of a contrast agent when a diagnostic procedure is thought essential, but caution should be exercised. Premedication with antihistamines or corticosteroids to avoid or minimize possible allergic reactions in such patients should be considered. Reports indicate that such pretreatment does not prevent serious life-threatening reactions, but may reduce both their incidence and severity.

General anesthesia may be indicated in the performance of some procedures in selected patients; however, a higher incidence of adverse reactions has been reported in these patients, and may be attributable to the inability of the patient to identify untoward symptoms or to the hypotensive effect of anesthesia which can prolong the circulation time and increase the duration of exposure to the contrast agent.

In angiographic procedures, the possibility of dislodging plaques or damaging or perforating the vessel wall should be considered during catheter manipulations and contrast medium injection. Test injections to insure proper catheter placement are suggested.

Angiography should be avoided whenever possible in patients with homocystinuria because of the risk of inducing thrombosis and embolism.

Patients with congestive heart failure should be observed for several hours following the procedure to detect delayed hemodynamic

OMNIPAQUE
(iohexol)
has a
new
image

Introducing

FLEXIPAK™ (Flexible Container)

A new package for OMNIPAQUE with safety, convenience and flexibility built in

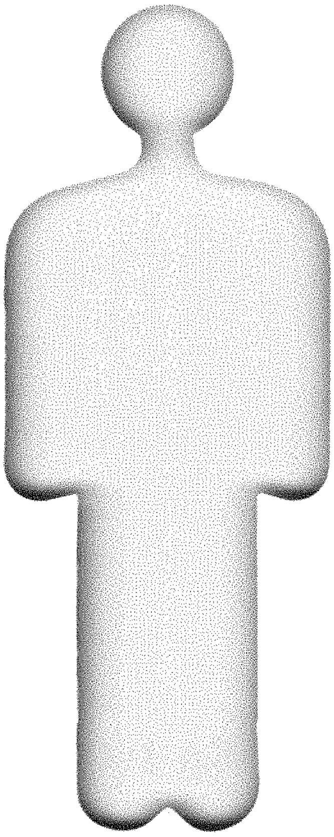

The safety package

New FLEXIPAK makes it simple to purge air from the flexible container before hanging to help reduce the potential for air emboli. The easily spiked port eliminates the possibility of infusing microscopic rubber particles from glass-bottle stoppers. And you don't need an air vent because the soft sides collapse as OMNIPAQUE flows.

The convenience package

No more waste and messy cleanups from broken glass bottles. And, FLEXIPAK is ready and easy to hang, even on crowded IV poles. FLEXIPAK lightens the load from setup to administration and all points in between.

The flexibility package

FLEXIPAK is flat and stackable for the best possible utilization of your storage space. And FLEXIPAK is available in the concentrations and sizes used most often.

	100 mL	150 mL	200 mL
OMNIPAQUE 240	X	X	X
OMNIPAQUE 300	X	X	
OMNIPAQUE 350	X	X	X

© 1991 Sanofi Winthrop Pharmaceuticals

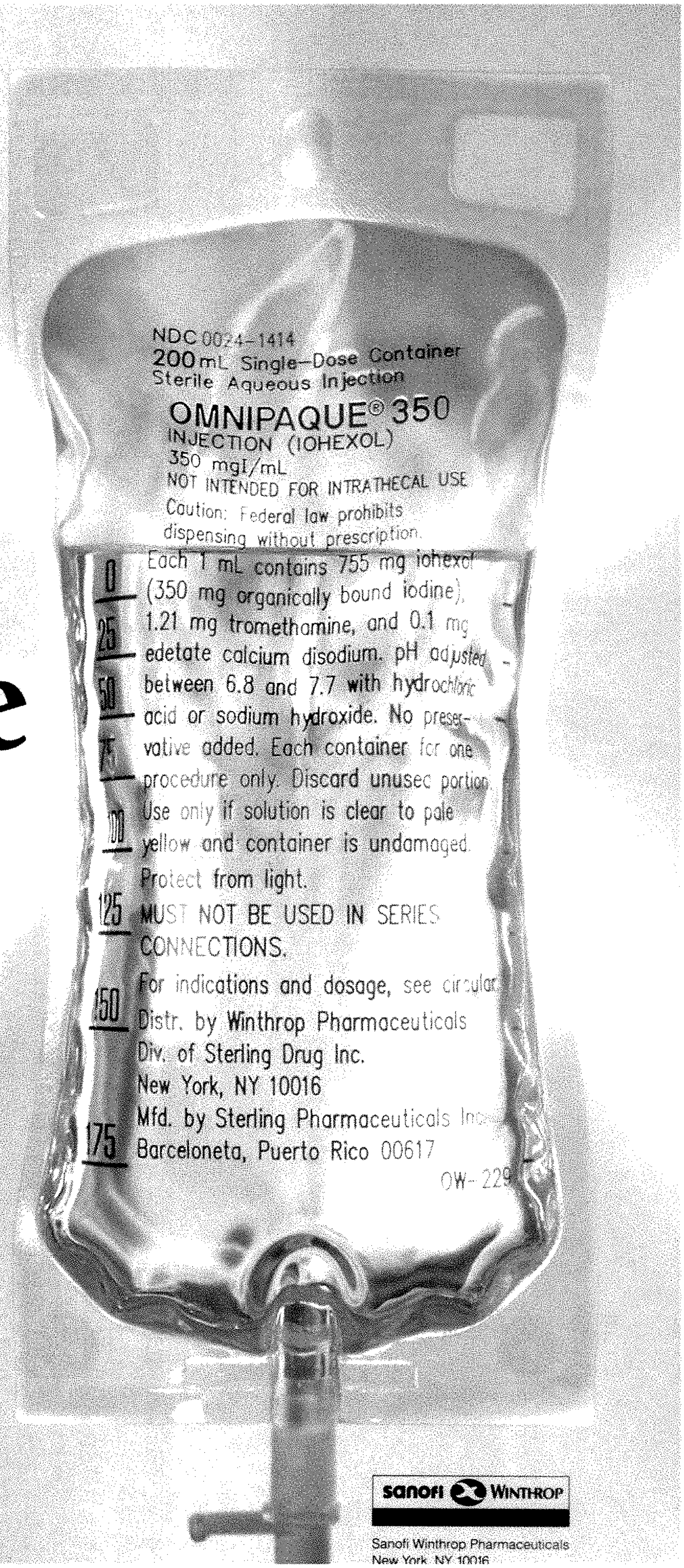
NDC 0024-1414
200 mL Single-Dose Container
Sterile Aqueous Injection
OMNIPAQUE® 350
INJECTION (IOHEXOL)
350 mgI/mL
NOT INTENDED FOR INTRATHECAL USE
Caution: Federal law prohibits dispensing without prescription.
Each 1 mL contains 755 mg iohexol (350 mg organically bound iodine), 1.21 mg tromethamine, and 0.1 mg edetate calcium disodium. pH adjusted between 6.8 and 7.7 with hydrochloric acid or sodium hydroxide. No preservative added. Each container for one procedure only. Discard unused portion. Use only if solution is clear to pale yellow and container is undamaged. Protect from light.
MUST NOT BE USED IN SERIES CONNECTIONS.
For indications and dosage, see circular.
Distr. by Winthrop Pharmaceuticals
Div. of Sterling Drug Inc.
New York, NY 10016
Mfd. by Sterling Pharmaceuticals Inc.
Barceloneta, Puerto Rico 00617
OW-229
0
25
50
75
100
125
150
175

It's all part of the package!

NONIONIC
OMNIPAQUE®
(IOHEXOL)

See last page for important product information concerning contraindications, warnings, adverse reactions, patient selection, and prescribing and precautionary recommendations.

All nonionic iodinated contrast media currently available inhibit blood coagulation, in vitro, less than ionic contrast media. Clotting has been reported when blood remains in contact with syringes containing nonionic contrast media. Therefore, meticulous intravascular administration technique is necessary to minimize thromboembolic events.

sanofi WINTHROP

Sanofi Winthrop Pharmaceuticals
New York, NY 10016

64-1121

OMNIPAQUE® 140 240 300 350
INJECTION (IOHEXOL)
INTRAVASCULAR

PLEASE CONSULT FULL PRODUCT INFORMATION BEFORE USING. A SUMMARY FOLLOWS:

DESCRIPTION: OMNIPAQUE is a sterile, pyrogen-free and preservative-free, nonionic, water-soluble radiographic contrast medium for intravascular administration in concentrations of 140, 240, 300, and 350 mgI/mL. OMNIPAQUE 140 contains 302 mg of iohexol equivalent to 140 mg of organic iodine per mL; OMNIPAQUE 240 contains 518 mg of iohexol equivalent to 240 mg of organic iodine per mL; OMNIPAQUE 300 contains 647 mg of iohexol equivalent to 300 mg of organic iodine per mL; and OMNIPAQUE 350 contains 755 mg of iohexol equivalent to 350 mg of organic iodine per mL. Each milliliter of iohexol solution contains 1.21 mg tromethamine and 0.1 mg edetate calcium disodium with the pH adjusted between 6.8 and 7.7 with hydrochloric acid or sodium hydroxide. Unused portions must be discarded. Iohexol solution is sensitive to light and should be protected from exposure.

CONTRAINDICATIONS: OMNIPAQUE should not be administered to patients with a known hypersensitivity to iohexol.

WARNINGS—General: Nonionic iodinated contrast media inhibit blood coagulation, in vitro, less than ionic contrast media. Clotting has been reported when blood remains in contact with syringes containing nonionic contrast media.

Serious, rarely fatal, thromboembolic events causing myocardial infarction and stroke have been reported during angiographic procedures with both ionic and nonionic contrast media. Therefore, meticulous intravascular administration technique is necessary, particularly during angiographic procedures, to minimize thromboembolic events. Numerous factors, including length of procedure, catheter and syringe material, underlying disease state, and concomitant medications, may contribute to the development of thromboembolic events. For these reasons, meticulous angiographic techniques are recommended including close attention to guidewire and catheter manipulation, use of manifold systems and/or three-way stopcocks, frequent catheter flushing with heparinized saline solutions and minimizing the length of the procedure. The use of plastic syringes in place of glass syringes has been reported to decrease but not eliminate the likelihood of in vitro clotting.

OMNIPAQUE should be used with extreme care in patients with severe functional disturbances of the liver and kidneys, severe thyrotoxicosis, or myelomatosis. Diabetics with a serum creatinine level above 3 mg/dL should not be examined unless the possible benefits of the examination clearly outweigh the additional risk. OMNIPAQUE is not recommended for use in patients with anuria.

Radiopaque contrast agents are potentially hazardous in patients with multiple myeloma or other paraproteinemia, particularly in those with therapeutically resistant anuria. Although neither the contrast agent nor dehydration has separately proven to be the cause of anuria in myeloma, it has been speculated that the combination of both may be causative factors. The risk in myelomatous patients is not a contraindication; however, special precautions are necessary. Partial dehydration in the preparation of these patients prior to injection is not recommended since this may predispose the patient to precipitation of the myeloma protein in the renal tubules. No form of therapy, including dialysis, has been successful in reversing the effect. Myeloma, which occurs most commonly in persons over age 40, should be considered before instituting intravascular administration of contrast agents.

Ionic contrast media, when injected intravenously or intra-arterially, may promote sickling in individuals who are homozygous for sickle cell disease.

Administration of radiopaque materials to patients known or suspected of having pheochromocytoma should be performed with extreme caution. If, in the opinion of the physician, the possible benefits of such procedures outweigh the considered risks, the procedures may be performed; however, the amount of radiopaque medium injected should be kept to an absolute minimum. The patient's blood pressure should be assessed throughout the procedure and measures for the treatment of hypertensive crisis should be readily available.

Reports of thyroid storm following the use of iodinated, ionic radiopaque contrast media in patients with hyperthyroidism or with an autonomously functioning thyroid nodule suggest that this additional risk be evaluated in such patients before use of any contrast medium.

Urography should be performed with caution in patients with severely impaired renal function and patients with combined renal and hepatic disease.

PRECAUTIONS—General: Diagnostic procedures which involve the use of radiopaque diagnostic agents should be carried out under the direction of personnel with the prerequisite training and with a thorough knowledge of the particular procedure to be performed. Appropriate facilities should be available for coping with any complication of the procedure, as well as for emergency treatment of severe reactions to the contrast agent itself. After parenteral administration of a radiopaque agent, competent personnel and emergency facilities should be available for at least 30 to 60 minutes, since severe delayed reactions have occurred (see ADVERSE REACTIONS: Intravascular—General).

Preparatory dehydration is dangerous and may contribute to acute renal failure in patients with advanced vascular disease, in diabetic patients, and in susceptible nondiabetic patients (often elderly with preexisting renal disease), infants, and small children. Dehydration in these patients seems to be enhanced by the osmotic diuretic action of urographic agents. It is believed that overnight fluid restriction prior to excretory urography generally does not provide better visualization in normal patients. *Patients should be well hydrated prior to and following administration of any contrast medium, including iohexol.*

Acute renal failure has been reported in diabetic patients with diabetic nephropathy and in susceptible nondiabetic patients (often elderly with preexisting renal disease) following excretory urography. Therefore, careful consideration of the potential risks should be given before performing this radiographic procedure in these patients.

Immediately following surgery, excretory urography should be used with caution in renal transplant recipients.

The possibility of a reaction, including serious, life-threatening, fatal, anaphylactoid or cardiovascular reactions should always be considered (see ADVERSE REACTIONS: Intravascular—General). It is of utmost importance that a course of action be carefully planned in advance for immediate treatment of serious reactions, and that adequate and appropriate personnel be readily available in case of any reaction.

The possibility of an idiosyncratic reaction in susceptible patients should always be considered (see ADVERSE REACTIONS: Intravascular—General). The susceptible population includes, but is not limited to, patients with a history of a previous reaction to contrast media, patients with a known sensitivity to iodine per se, and patients with a known clinical hypersensitivity: bronchial asthma, hay fever, and food allergies.

The occurrence of severe idiosyncratic reactions has prompted the use of several pretesting methods. However, pretesting cannot be relied upon to predict severe reactions and may itself be hazardous for the patient. It is suggested that a thorough medical history with emphasis on allergy and hypersensitivity, prior to the injection of any contrast media, may be more accurate than pretesting in predicting potential adverse reactions.

A positive history of allergies or hypersensitivity does not arbitrarily contraindicate the use of a contrast agent where a diagnostic procedure is thought essential, but caution should be exercised (see ADVERSE REACTIONS: Intravascular—General). Premedication with antihistamines or corticosteroids to avoid or minimize possible allergic reactions in such patients should be considered and administered using separate syringes. Recent reports indicate that such pretreatment does not prevent serious, life-threatening reactions, but may reduce both their incidence and severity.

Even though the osmolality of OMNIPAQUE is low compared to diatrizoate- or iothalamate-based ionic agents of comparable iodine concentration, the potential transitory increase in the circulatory osmotic load in patients with congestive heart failure requires caution during injection. These patients should be observed for several hours following the procedure to detect delayed hemodynamic disturbances.

General anesthesia may be indicated in the performance of some procedures in selected adult patients; however, a higher incidence of adverse reactions has been reported in these patients and may be attributable to the inability of the patient to identify untoward symptoms, or to the hypotensive effect of anesthesia, which can reduce cardiac output and increase the duration of exposure to the contrast agent.

Angiography should be avoided whenever possible in patients with homocystinuria, because of the risk of inducing thrombosis and embolism.

In angiographic procedures, the possibility of dislodging plaques or damaging or perforating the vessel wall should be borne in mind during the catheter manipulations and contrast medium injection. Test injections to ensure proper catheter placement are recommended.

Selective coronary arteriography should be performed only in those patients in whom the expected benefits outweigh the potential risk. The inherent risks of angiocardiography in patients with chronic pulmonary emphysema must be weighed against the necessity for performing this procedure

When OMNIPAQUE is to be injected using plastic disposable syringes, the contrast medium should be drawn into the syringe and used immediately.

If nondisposable equipment is used, scrupulous care should be taken to prevent residual contamination with traces of cleansing agents.

Parenteral products should be inspected visually for particulate matter and discoloration prior to administration. If particulate matter or discoloration is present, do not use.

Information for Patients: Patients receiving injectable radiopaque diagnostic agents should be instructed to:

1. Inform your physician if you are pregnant.
2. Inform your physician if you are diabetic or if you have multiple myeloma, pheochromocytoma, homozygous sickle cell disease, or known thyroid disorder (see WARNINGS—General).
3. Inform your physician if you are allergic to any drugs, food, or if you had any reactions to previous injections of dyes used for x-ray procedures (see PRECAUTIONS—General).
4. Inform your physician about any other medications you are currently taking, including nonprescription drugs, before you are administered this drug.

Drug/Laboratory Test Interaction: If iodine-containing isotopes are to be administered for the diagnosis of thyroid disease, the iodine-binding capacity of thyroid tissue may be reduced for up to 2 weeks after contrast medium administration. Thyroid function tests which do not depend on iodine estimation, eg, T_3 resin uptake or direct thyroxine assays, are not affected. Many radiopaque contrast agents are incompatible in vitro with some antihistamines and many other drugs; therefore, no other pharmaceuticals should be admixed with contrast agents.

Carcinogenesis, Mutagenesis, Impairment of Fertility: No long-term animal studies have been performed to evaluate carcinogenic potential, mutagenesis, or whether OMNIPAQUE can affect fertility in men or women.

Pregnancy Category B: Reproduction studies have been performed in rats and rabbits with up to 100 times the recommended human dose. No evidence of impaired fertility or harm to the fetus has been demonstrated due to OMNIPAQUE. There are, however, no studies in pregnant women. Because animal reproduction studies are not always predictive of human response, this drug should be used during pregnancy only if clearly needed.

Nursing Mothers: It is not known to what extent iohexol is excreted in human milk. However, many injectable contrast agents are excreted unchanged in human milk. Although it has not been established that serious adverse reactions occur in nursing infants, caution should be exercised when intravascular contrast media are administered to nursing women. Bottle feedings may be substituted for breast feedings for 24 hours following administration of OMNIPAQUE.

Pediatric Use: Pediatric patients at higher risk of experiencing adverse events during contrast medium administration may include those having asthma, a sensitivity to medication and/or allergens, congestive heart failure, a serum creatinine > 1.5 mg/dL, or those less than 12 months of age.

ADVERSE REACTIONS

Intravascular—General: Adverse reactions following the use of OMNIPAQUE are usually mild to moderate in severity. However, serious, life-threatening, and fatal reactions, mostly of cardiovascular origin, have been associated with the administration of iodine-containing contrast media, including OMNIPAQUE. The injection of contrast media is frequently associated with the sensation of warmth and pain, especially in peripheral angiography; pain and warmth are less frequent and less severe with OMNIPAQUE than with many contrast media.

Cardiovascular System: Arrhythmias including PVCs and PACs (2%), angina/chest pain (1%), and hypotension (0.7%). Others including cardiac failure, asystole, bradycardia, tachycardia, and vasovagal reaction were reported with an individual incidence of 0.3% or less. In controlled clinical trials involving 1,485 patients, one fatality occurred. A cause and effect relationship between this death and iohexol has not been established.

Nervous System: Vertigo [including dizziness and lightheadedness] (0.5%), pain (3%), vision abnormalities [including blurred vision and photomas] (2%), headache (2%), and taste perversion (1%). Others including anxiety, blurred vision, fever, motor and speech dysfunction, convulsion, paresthesia, somnolence, stiff neck, hemiparesis, syncope, shivering, transient ischemic attack, cerebral infarction, and nystagmus were reported, with an individual incidence of 0.3% or less.

Respiratory System: Dyspnea, rhinitis, coughing, and laryngitis, with an individual incidence of 0.2% or less.

Gastrointestinal System: Nausea (2%) and vomiting (0.7%). Others including diarrhea, dyspepsia, cramp, and dry mouth were reported, with an individual incidence of less than 0.1%.

Skin and Appendages: Urticaria (0.3%), purpura (0.1%), abscess (0.1%), and pruritus (0.1%).

Individual adverse reactions which occurred to a significantly greater extent for a specific procedure are listed under that indication in full prescribing information.

Pediatrics: In controlled clinical trials involving 391 patients for pediatric angiocardiography, urography, and contrast-enhanced computed tomographic head imaging, adverse reactions following the use of OMNIPAQUE 240, OMNIPAQUE 300 and OMNIPAQUE 350 were generally less frequent than with adults.

Cardiovascular System: Ventricular tachycardia (0.5%), 2:1 heart block (0.5%), hypertension (0.3%), and anemia (0.3%).
Nervous System: Pain (0.8%), fever (0.5%), taste abnormality (0.5%), and convulsion (0.3%).
Respiratory System: Congestion (0.3%) and apnea (0.3%).
Gastrointestinal System: Nausea (1%), hypoglycemia (0.3%), and vomiting (2%).
Skin and Appendages: Rash (0.3%).

General Adverse Reactions to Contrast Media: Physicians should remain alert for the occurrence of adverse effects in addition to those discussed above. The following reactions have been reported after administration of other intravascular iodinated contrast media, and rarely with iohexol. *Reactions due to technique:* hematomas and ecchymoses. *Hemodynamic reactions:* vein cramp and thrombophlebitis following intravenous injection. *Cardiovascular reactions:* rare cases of cardiac arrhythmias, reflex tachycardia, chest pain, cyanosis, hypertension, hypotension, peripheral vasodilatation, shock, and cardiac arrest. *Renal reactions:* occasionally, transient proteinuria; and rarely, oliguria or anuria. *Allergic reactions:* asthmatic attacks, nasal and conjunctival symptoms, dermal reactions such as urticaria with or without pruritus, as well as pleomorphic rashes, sneezing, and lacrimation; and rarely, anaphylactic reactions. Rare fatalities have occurred due to this or unknown causes. *Signs and symptoms related to the respiratory system:* pulmonary or laryngeal edema, bronchospasm, dyspnea; or *to the nervous system:* restlessness, tremors, convulsions. *Other reactions:* flushing, pain, warmth, metallic taste, nausea, vomiting, anxiety, headache, confusion, pallor, weakness, sweating, localized areas of edema (especially facial cramps), neutropenia, and dizziness. Rarely, immediate or delayed rigors can occur, sometimes accompanied by hyperpyrexia. Infrequently, "iodism" (salivary gland swelling) from organic iodinated compounds appears 2 days after exposure and subsides by the sixth day.

In general, the reactions which are known to occur upon parenteral administration of iodinated contrast agents are possible with any nonionic agent. Approximately 95% of adverse reactions accompanying the use of water-soluble intravascularly administered contrast agents are mild to moderate in degree. However, severe, life-threatening anaphylactoid reactions, mostly of cardiovascular origin, have occurred. Reported incidences of death range from 6.6 per 1 million (0.00066%) to 1 in 10,000 (0.01%). Most deaths occur during injection or 5 to 10 minutes later, the main feature being cardiac arrest, with cardiovascular disease as the main aggravating factor. Isolated reports of hypotensive collapse and shock are found in the literature. The incidence of shock is estimated to be 1 out of 20,000 (0.005%) patients.

Adverse reactions to injectable contrast media fall into two categories: chemotoxic reactions and idiosyncratic reactions.

Chemotoxic reactions result from the physicochemical properties of the contrast media, the dose, and the speed of injection. All hemodynamic disturbances and injuries to organs or vessels perfused by the contrast medium are included in this category.

Idiosyncratic reactions include all other reactions. They occur more frequently in patients 20 to 40 years old. Idiosyncratic reactions may or may not be dependent on the amount of dose injected, the speed of injection, and the radiographic procedure. Idiosyncratic reactions are subdivided into minor, intermediate, and severe. The minor reactions are self-limited and of short duration; the severe reactions are life-threatening and treatment is urgent and mandatory.

The reported incidence of adverse reactions to contrast media in patients with a history of allergy is twice that in the general population. Patients with a history of previous reactions to a contrast medium are three times more susceptible than other patients. However, sensitivity to contrast media does not appear to increase with repeated examinations.

Most adverse reactions to injectable contrast media appear within 1 to 3 minutes after the start of injection, but delayed reactions may occur.

Regardless of the contrast agent employed, the overall estimated incidence of serious adverse reactions is higher with angiocardiography than with other procedures. Cardiac decompensation, serious arrhythmias, angina pectoris, or myocardial ischemia or infarction may occur during angiocardiography and left ventriculography. Electrocardiographic and hemodynamic abnormalities occur less frequently with OMNIPAQUE than with diatrizoate meglumine and diatrizoate sodium injection.

CONSULT PACKAGE INSERT FOR A MORE DETAILED DISCUSSION OF ADVERSE REACTIONS FOR INTRAVASCULAR USE OF OMNIPAQUE.

OVERDOSAGE: Overdosage may occur. The adverse effects of overdosage are life-threatening and affect mainly the pulmonary and cardiovascular systems. The symptoms include cyanosis, bradycardia, acidosis, pulmonary hemorrhage, convulsions, coma, and cardiac arrest. Treatment of an overdosage is directed toward the support of all vital functions and prompt institution of symptomatic therapy.

The intravenous LD_{50} values of OMNIPAQUE (in grams of iodine per kilogram body weight) are 24.2 in mice and 15.0 in rats.

DOSAGE AND ADMINISTRATION: Details are provided in the package insert.

The Radiological Society of North America

Vanguard Flagship
Scholar

sanofi WINTHROP

Sanofi Winthrop Pharmaceuticals
New York, NY 10016

64-1079

Shouldn't You Be Getting Optimum Performance From Your Video Displays and Hard-Copy Cameras?

NEW MEDICAL IMAGING TEST PATTERN GENERATOR

Ensures Highest Quality Results!

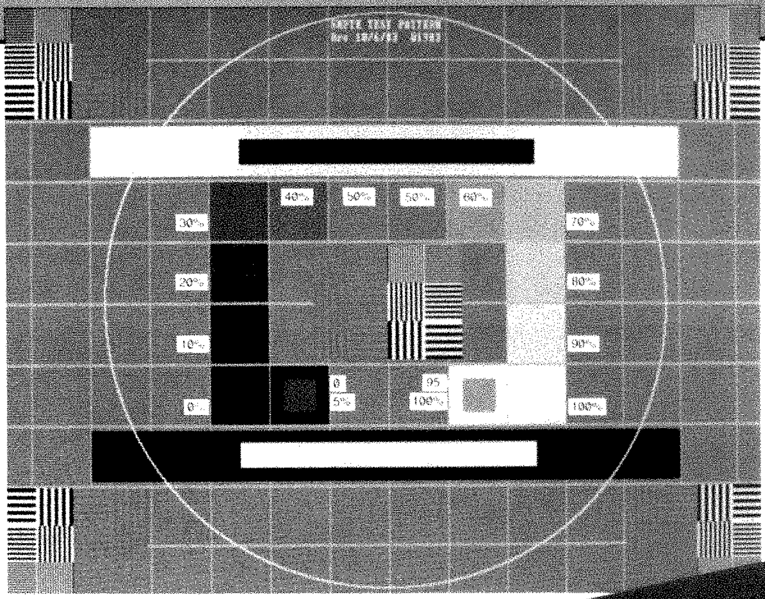

Test Pattern Produced is Used for QC and Acceptance Testing in Accordance With the SMPTE Recommended Practice

Accurately Evaluates...

- **Resolution**
- **Contrast**
- **Size**
- **Geometry**
- **Gray Scale**
- **Brightness**
- **Aspect Ratio**
- **Uniformity**

The Medical Imaging Test Pattern Generator is a portable, precision instrument that produces an electronic test pattern, designed by the Society of Motion Picture and Television Engineers (SMPTE), in accordance with *SMPTE Recommended Practice RP-133-1986.*

The electronic signal produced is at the 525/60 scan with a display aspect ratio of 4:3. The pattern is considered the "gold" standard for testing TV monitors and hard-copy recording cameras.

For more details, request Bulletin 4491-44

CINE-VIDEO QUALITY CONTROL PHANTOM AND PATIENT IDENTIFIER*

This Patient-Equivalent Phantom Provides an Easy Way to Monitor Image Quality of High Dose Cine Film and Video Tape Examinations...

- **Quality control tests for resolution, density, contrast, uniformity of focus.**
- **Patient identification information at the beginning of a cine or video study.**

For more details, request Bulletin 4581-44

* Designed by Joel E. Gray, Ph.D. Department of Radiology, Mayo Clinic, Rochester, MN 55905. Manufactured under licensing agreement with Mayo Foundation for Medical Education and Research.

NUCLEAR ASSOCIATES

VICTOREEN

Division of VICTOREEN, INC.
100 VOICE ROAD • P.O. BOX 349
CARLE PLACE, NY 11514-0349 U.S.A.
(516) 741-6360
FAX (516) 741-5414

GAIN THAT CRITICAL EDGE IN CARDIAC CATH LAB QC TESTING

Radiologists

With MRI Fellowship & General Diagnostic

The Saudi Arabian Oil Company's (SAUDI ARAMCO) Medical Services Organization in Saudi Arabia is expanding the Radiology Department.

American Board Certification and 2 years' experience after residency required.

The Dhahran Health Center (DHC) in Saudi Arabia provides comprehensive medical care to our employees and their dependents, a patient population of nearly 230,000. The DHC, recently expanded to 483 beds, has all major specialty services as well as most subspecialties and functions as a referral center. Additionally, there are five district outpatient clinics, each with emergency facilities, including one clinic with a new 80 bed hospital. Our Blood Bank is accredited by the American Association of Blood Banks. Consulting liaisons exist with the WHO in Geneva and the Centers for Disease Control in Atlanta.

As a Saudi Aramco employee, you will receive a competitive base compensation package as well as an expatriate premium. Additional benefits include noncontributory group life insurance, company-matched savings, free medical care at Saudi Aramco's hospital and clinics, housing inside a company community, and extensive recreation facilities and activities. Your eligible children will be enrolled in company schools, comparable to U.S. private schools. Annually, there are up to 13 company holidays plus you will be eligible for 36 calendar days vacation, with round-trip airfares to the U.S. or Canada for you and your family.

For consideration, **CALL OUR 24 HOUR, 7 DAYS PER WEEK TOLL-FREE NUMBER LISTED BELOW:**

1-800-221-3333, EXT. R2

SAUDI ARAMCO

Make the winning move.

The NEMOURS
CHILDREN'S
CLINIC *Reaching Out-Helping Children*

PEDIATRIC RADIOLOGISTS

The Nemours Children's Clinic, a pediatric tertiary care subspecialty clinic, located on the St. Johns River, in Jacksonville, Florida is seeking a Board Certified Pediatric Radiologist as Chairperson of the Department of Radiology. In addition, we are seeking a BC/BE staff radiologist. Nemours is affiliated with the new Children's Hospital in the development of a Children's Health Center. Nemours is also developing a system of ambulatory health care for children in Florida through a network of primary care and subspecialty clinics throughout Florida. In order to provide innovative services and additional patient care in a city of 800,000 people with a large referral base in South Georgia, Northeast Florida, and the new Children's Hospital, Nemours is expanding the Department of Radiology.

Nemours offers a stimulating and challenging setting with a unique opportunity to participate in the advancement of health care for children.

Proximity to First Coast Beaches, cultural and recreational activities, and a pleasant climate, as well as an opportunity for professional growth and participation in education and research make this a very desirable career choice.

Interested applicants should send their CV to **Ian T. Nathanson, M.D., Chairman, Search Committee, Nemours Children's Clinic, 807 Nira Street, Jacksonville, Florida 32207, (904) 390-3788.**

Radiology Group

Group of five Board-Certified Radiologists needed to provide services to 287-bed hospitals under an exclusive fee-for-service arrangement. Coverage in all modalities required.

For more information and a Request for Proposal, write to:

James B. Wood
Sr. Vice President
St. Francis Hospital
One St. Francis Drive
Greenville, SC 29601

St. Francis

Member - Franciscan Sisters of the Poor • Health System, Inc.

AJR Guidelines for Authors

Address new and revised manuscripts, correspondence, and classified ads to the Editor:

AJR Editorial Office
2223 Avenida de la Playa, Suite 103
La Jolla, CA 92037-3218
Telephone: (619) 459-2229; FAX: (619) 459-8814

Inquiries regarding reprints or permission to republish *AJR* material should be addressed to the publisher:

Publications Department ARRS
1891 Preston White, Dr., Reston, VA 22091

The *AJR* publishes original contributions to the advancement of medical diagnosis and treatment. Submitted manuscripts should not contain previously published material and should not be under consideration for publication elsewhere.

Manuscript decisions are based on peer review. Reviewers receive manuscripts without title pages to ensure an unbiased review. Statements made in the article, including changes made by the Editor or manuscript editor, are the responsibility of the author and not of the *AJR* or its publisher. Authors will be sent the edited manuscript, galley proof, and proofs of illustrations. If the corresponding author will be unavailable to review galleys, arrangements should be made for a coauthor or colleague to read and return the proof.

The following guidelines are based on instructions set forth in the **Uniform Requirements for Manuscripts Submitted to Biomedical Journals** (*Ann Intern Med* **1988;**108:258–265). Articles will be edited, however, to conform to the individual style of *AJR*.

General Guidelines for Major Papers

Abstract. Clearly state (in 250 words or fewer) the purpose, methods, results, and conclusions of the study. Include actual data.

Introduction. Briefly describe the purpose of the investigation and explain why it is important.

Methods. Describe the research plan, the materials (or subjects), and the methods used, in that order. Explain in detail how disease was confirmed and how subjectivity in observations was controlled.

Results. Present results in a clear, logical sequence. If tables are used, do not duplicate tabular data in text, but do describe important trends and points.

Discussion. Describe the limitations of the research plan, materials (or subjects), and methods, considering both the purpose and the outcome of the study. When results differ from those of previous investigators, explain the discrepancy.

AUTHOR'S CHECKLIST

For priority handling, complete the following checklist, sign the copyright form on the reverse side of this page, and include both with the manuscript.

________ Two copies of the manuscript (the original and a photocopy) and two complete sets of figures are submitted. One copy has been retained by the author.

________ If appropriate, *AJR* Guidelines for case reports, technical notes, pictorial essays, or letters to the Editor have been followed. (See page A17.)

________ The manuscript, including references, figure legends, and tables, is typed double-spaced on 8½ × 11 in. (21.6 × 27.9 cm) *nonerasable* paper. Right-hand margins are not justified.

________ All manuscript pages are numbered consecutively beginning with the abstract. Authors' names do not appear on the manuscript pages.

________ The manuscript is organized as follows: title page, blind title page (title only), abstract, introduction, methods, results, discussion, acknowledgments, references, tables, figure legends, and figures.

________ Informed consent has been obtained from patients who participated in clinical investigations. If experiments were performed on animals, authors complied with NIH guidelines for use of laboratory animals.

________ Use of unfamiliar acronyms and abbrevations is kept to a minimum. When abbreviations are used they are defined at first mention, followed by the abbreviation in parentheses.

________ Metric measurements are used throughout, or the metric equivalent is given in parentheses.

________ Names and locations (city and state only) of manufacturers are given for equipment and nongeneric drugs.

________ Upon acceptance, final version is submitted on a 5 1/4-in. DOS-compatible diskette in Wordperfect or ASCII format.

Title Page

________ The following information is given: title of article; names and complete addresses (including zip code) of all authors; current addresses of authors who have moved since study; acknowledgment of grant or other assistance. The corresponding author is clearly identified, and a current address, phone number, and FAX number are given.

________ A blind title page is included in each copy of the manuscript, giving only the title (without the authors' names) for use in the review process.

Abstract

________ An abstract of approximately one and one-half typewritten pages is organized into the following paragaphs.

Objective. In one or two sentences, indicate the specific goal or purpose of the article, and indicate why it is worthy of attention. Explain the hypothesis to be tested, the dilemma to be resolved, or the deficiency to be remedied. The objective stated here must be identical to the one given in the title and introduction of the paper.

Subjects (or materials) and methods. Describe succinctly the methods used to achieve the objective explained in the first paragraph, stating what was done, how it was done, how bias was controlled, what data were collected, and how the data were analyzed.

Results. The findings of the procedures described in the preceding paragraph are presented here. All results should flow logically from the methods described and not stray from the specific objective of the paper. Include as many specific data as possible within the overall length limitation of one typewritten page.

Conclusion. In one or two sentences, present the take-home message to be remembered when all else is forgotten. Describe the conclusion of the study, based solely on the

data provided in the body of the abstract. Conclusions must relate directly to the objective of the paper as defined in the title and first paragraph of the abstract.

________ No abbreviations or reference citations are used.

________ No abbreviations or reference citations are used.

References

________ References (not to exceed 35) are typed double-spaced starting on a separate page and are **numbered consecutively in the order in which they appear in the text**.

________ All references are cited in the text and are enclosed in brackets and typed on line with the text (not superscript).

________ Unpublished data are not cited in the reference list, but are cited parenthetically in the text, for example, (Smith DJ, personal communication), (Smith DJ, unpublished data). This includes papers submitted, but not yet accepted, for publication.

________ Papers presented at a meeting are not cited in the reference list, but are cited parenthetically in the text (e.g., Smith DJ et al., presented at the American Roentgen Ray Society meeting, May 1990). After first mention, use (Smith DJ et al., ARRS meeting, May 1990).

________ Inclusive page numbers (e.g., 333–335) are given for all references.

________ Journal names are abbreviated according to *Index Medicus*.

________ Style and punctuation of references follow the format illustrated in the following examples (all authors are listed when six or fewer; when seven or more authors, the first three are listed, followed by "et al."):

Journal article

1. Long RS, Roe EW, Wu EU, et al. Membrane oxygenation: radiographic appearance. *AJR* **1986**;146:1257–1260

Book

2. Smith LW, Cohen AR. *Pathology of tumors*, 6th ed. Baltimore: Williams & Wilkins, **1977**:100–109

Chapter in a book

3. Breon AJ. Serum monitors of bone metastasis. In: Clark SA, ed. *Bone metastases*. Baltimore: Williams & Wilkins, **1983**:165–180

Tables

________ Each table is typed double-spaced on a separate page without vertical or horizontal rules; each has a short, descriptive title. Tables do not exceed two pages in length and contain at least four lines of data.

________ Tables are numbered in the order in which they are cited in the text.

________ Abbreviations are defined in an explanatory note below each table.

________ Tables are self-explanatory and do not duplicate data given in the text or figures.

________ All arithmetic (percentages, totals, differences) has been double checked for accuracy, and tabular data agree with data given in the text.

Figures and Legends

________ Two complete sets of original figures are submitted unmounted in labeled envelopes.

________ Figures are clean, unscratched, 5 × 7 in. (13 × 18 cm) glossy prints with **white borders.** A separate print is submitted for each figure *part*.

________ All figure parts relating to one patient have the same figure number.

________ Each figure is labeled on the back with the figure number and an arrow indicating "top." For black-and-white figures, labeling is done on a gummed label, which is then affixed to the back of the print. **Never** use labels on **color** figures, but write figure number on the back lightly in pencil. *Never* use ink on front or back of any figures.

________ Authors' names are *not* written on the backs of figures.

________ Only removable (rub-on) arrows and letters are used on the figures. Symbols are uniform in size and style and are not broken or cracked.

________ Images are uniform in size and magnification.

________ Line drawings are done in black ink on a white background. They are professional in quality, and all use the same size type. (Only glossy prints are acceptable.)

________ Written permission has been obtained for use of all previously published illustrations (and copies of permission letters are included), and an appropriate credit line is given in the legends.

________ Legends are typed double-spaced, and figure numbers correspond with the order in which the figures are cited in the text.

Transfer of Copyright Agreement, Conflict of Interest Acknowledgment, Certification of Coauthors, and Exclusive Publication Statement

Complete copyright to the article entitled: ____

____

is hereby transferred to the American Roentgen Ray Society (for United States government employees to the extent transferable), effective if and when the article is accepted for publication in the *American Journal of Roentgenology*. In the case of the authors who are officers or employees of the United States government, the American Roentgen Ray Society recognizes that works prepared by officers or employees of the United States government as part of their official government duties are in the public domain.

Authors reserve all proprietary rights other than copyright, such as patent rights and the right to use all or part of this article in future works of their own. The authors retain the right of replication, subject only to crediting the original source of publication and receiving written permission from the publisher.

Authors guarantee that this manuscript contains no matter that is libelous or otherwise unlawful, invades individual privacy, or infringes any proprietary rights.

Authors understand that they will receive no royalty or other compensation from the American Roentgen Ray Society or the publisher.

Authors guarantee that the editor has been or will be informed of any proprietary or commercial interest or conflicts of interest the authors may have that relate directly or indirectly to the subject of this article.

All authors certify that they have made substantive and specific intellectual contributions to the article and assume public responsibility for its content.

Finally, the authors certify that none of the material in this manuscript has been published previously or is currently under consideration for publication elsewhere.

First author/date	Second author	Third author
Fourth author	Fifth author	Sixth author

Case Reports

A case report is a brief description of a special case that provides a message that transcends the individual patient.

Format. There is no abstract. The introduction should be a short paragraph giving the general background and the specific interest of the case. No more than one case should be described in detail (similar ones can be mentioned briefly in the discussion). Emphasis should be on the radiologic aspects; clinical information must be limited to that necessary to provide a background for the radiology. The discussion should be succinct and should focus on the specific message and relevance of radiologic methods. A review of the literature is not appropriate.

Length. Maximum of five double-spaced, typewritten pages, including the references but not the title page or figure legends.

References. Maximum of eight.

Figures. Maximum of four, unless the text is shortened accordingly. Legends must not repeat the text.

Tables and Acknowledgments. Not appropriate in case reports.

Pictorial Essays

A pictorial essay is an article that conveys its message through illustrations and their legends. Unlike other *AJR* articles, which are based on original research, pictorial essays serve primarily as teaching tools, like exhibits at a scientific meeting. They are not encyclopedic book chapters. The abstract should be a short, introductory paragraph.

Length. Maximum of four double-spaced, typewritten pages, including the references but not the title page or figure legends.

References. Maximum of four.

Figures. Maximum of 30 figure *parts*. Number should be as few as necessary to convey the message of the paper.

Tables and Acknowledgments. Not appropriate in pictorial essays.

Opinions, Commentaries, and Perspectives

Opinions, commentaries, and perspectives are special articles dealing with controversial topics or issues of special concern to radiologists.

Format. Include a title page but no abstract. Headings may be used to break up the text.

Length. Maximum of five double-spaced, typewritten pages.

References. Maximum of five.

Tables and Figures. Maximum of four.

Technical Notes

A technical note is a brief description of a specific technique or procedure, modification of a technique, or equipment of interest to radiologists.

Format. No abstract, headings, or subheadings are required. If headings are used, they should be a combination of "Case Report," "Materials and Methods," "Results," and "Discussion." A brief one-paragraph introduction should be included to give the general background. Discussion should be limited to the specific message, including the uses of the technique or equipment. Literature reviews and lengthy case reports are not appropriate.

Length. Maximum of five double-spaced, typewritten pages, including the references but not the title page or figure legends.

References. Maximum of eight.

Figures. Maximum of two, unless the text is shortened accordingly.

Tables and Acknowledgments. Not appropriate in technical notes.

Letters to the Editor and Replies

Letters to the Editor and Replies should offer objective and constructive criticism of published articles. Letters may also discuss matters of general interest to radiologists. Do not end a letter with a hand-written signature.

Format. All letters should be typed double-spaced on nonletterhead paper, with no greeting or salutation. Name and affiliation should appear at the end of the letter. Titles for letters should be short and pertinent. The title for a reply is simply "Reply."

Length. Maximum of two double-spaced, typewritten pages, including references.

References. Maximum of four.

Figures. Maximum of two.

Tables and Acknowledgments. Not appropriate in Letters to the Editor and Replies.

Computer Page Articles

Articles published on the computer page deal with practical computer applications to radiology.

Format. Include a title page and an abstract.

Length. Maximum of eight double-spaced, typewritten pages.

References. Maximum of five.

Figures and Tables. Maximum of five. Computer printouts are not acceptable. Figures must be submitted as 5 × 7 in. glossy prints.

All submissions to the *AJR* must be accompanied by a completed copy of the Author's Checklist and the signed Copyright agreement.

Subject: Technology

Point of view: Technologist

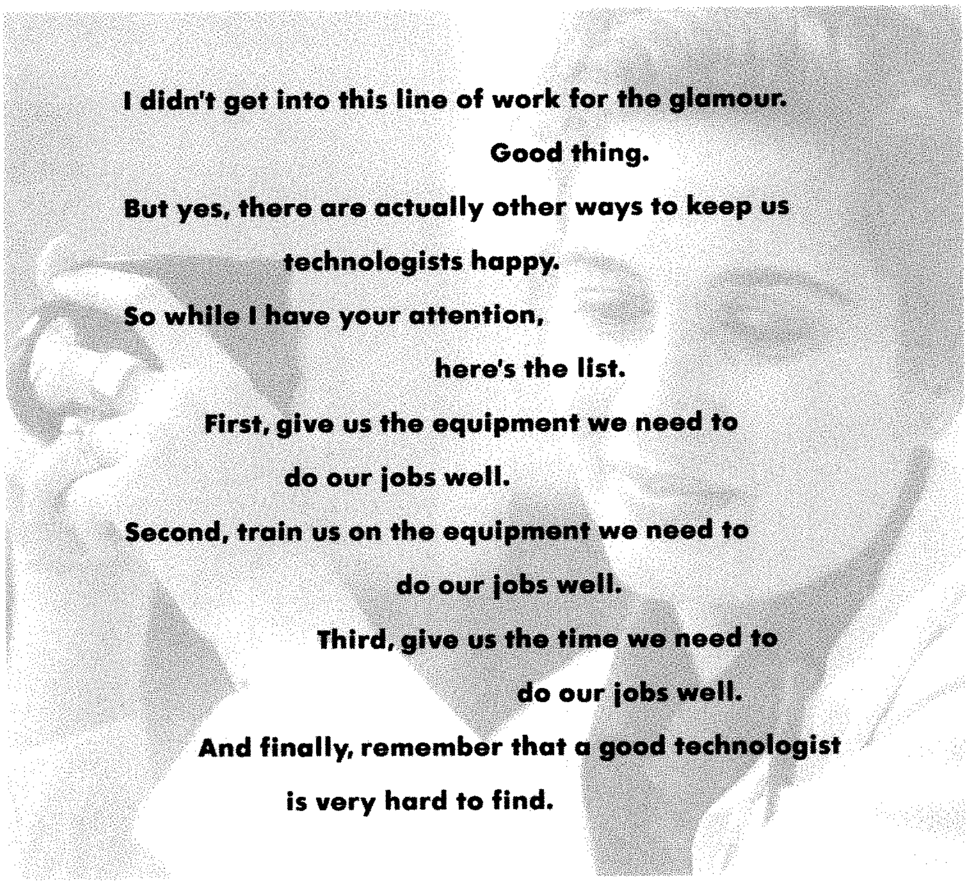

I didn't get into this line of work for the glamour.
Good thing.
But yes, there are actually other ways to keep us technologists happy.
So while I have your attention,
here's the list.
First, give us the equipment we need to do our jobs well.
Second, train us on the equipment we need to do our jobs well.
Third, give us the time we need to do our jobs well.
And finally, remember that a good technologist is very hard to find.

At Picker, our commitment is not only to developing technology. It's to developing technologists, as well. Which is why we were the first company to support the Summit on Manpower, a consortium of 18 radiological societies, in an effort to attract more technologists to the field.

PICKER
MORE THAN IMAGES. INSIGHT.

© 1991 Picker International, Inc. For reprints of this ad, or for more information, call us at 1-800-323-0550.

AJR Business and Subscriber Informa

The American Roentgen Ray Society

AJR, American Journal of Roentgenology, is published monthly to disseminate research on current developments in the radiologic sciences and commentary on topics related to radiology. It is published by the American Roentgen Ray Society (ARRS), 1891 Preston White Dr., Reston, VA 22091; (703) 648-8992. Address inquiries regarding Society business, the annual ARRS meeting, and membership to the Society at the above address.

Correspondence regarding editorial matters and classified advertising should be addressed to Editorial Office, AJR, 2223 Avenida de la Playa, Ste. 103, La Jolla, CA 92037-3218; telephone 1-800-348-4257 or (619) 459-2229; FAX (619) 459-8814. For information on manuscript submission, see Guidelines for Authors, pages A15–A17.

Subscriber Information

ARRS annual dues include $50 for journal subscription. Nonmember subscription rates are as follows: $125/year ($180 foreign); institutions, $135 ($190 foreign); in-training, $25 ($80 foreign). Single copies of the Journal may be purchased for $18 ($22 foreign). Airmail rates will be furnished on request. The GST number for Canadian subscribers is 123394371.

Call toll-free, 1-800-638-6423 (in Maryland call 1-800-638-4007), with subscription inquiries or problems. Please have the mailing label from your latest issue available when you call.

Report changes of address to Subscription Fulfillment, AJR, 428 E. Preston St., Baltimore, MD 21202. Damaged or unreceived issues should be reported within 60 da cation (90 days for foreign subscribers) for replac

Advertising Information

All advertising is subject to approval by the Acceptance of advertising does not indicate endo the products or services advertised or the claims display advertising information, contact Gary Walc Sales Representative, AJR, 428 E. Preston St., MD 21202, (410) 528-4291.

For classified advertising information, contact t Office, AJR, 2223 Avenida de la Playa, Ste. 103, L 92037-3218; telephone (619) 459-2229; FAX (619

Copyrights, Permissions, and Reprints

Contents of the *AJR* are copyrighted by the AR of this publication may be reproduced without Requests for such permission should be addres Publications Department, ARRS, 1891 Preston Reston, VA 22091. For reprints of a particular ar contact the author designated in the footnotes for

Indexes

The *AJR* provides volume and yearly indexes (author) in the June and December issues. *AJR* also indexed in *Current Contents*, *Index Medicu* cumulative index published by *Radiology*.

From the Experts.
Expect Excellence

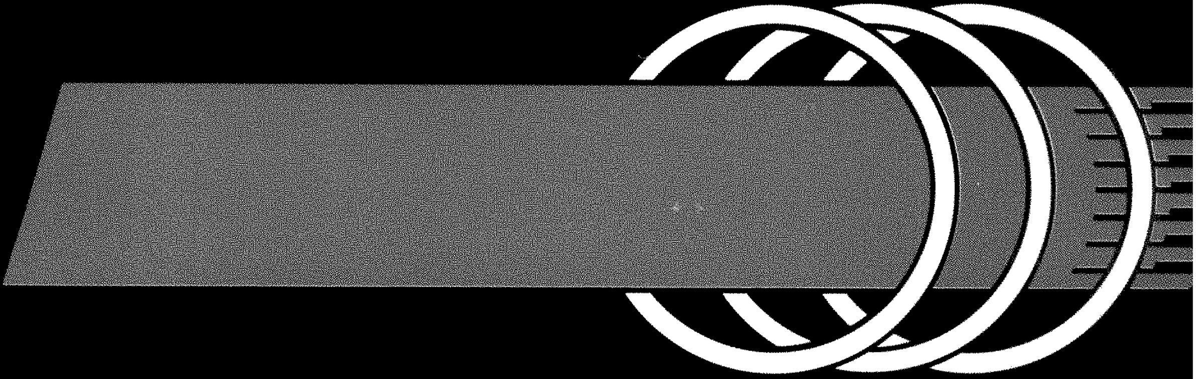

In MR Contrast
Media Research

Research at Squibb Diagnostics is exploring new pathways in the development of contrast media for MR. Our advanced technologies allow us to give our customers new products that can set new standards of care. Our research today contributes to the success of your practice tomorrow.
Squibb Diagnostics—the experts in MR contrast media research.

SQUIBB™
Diagnostics

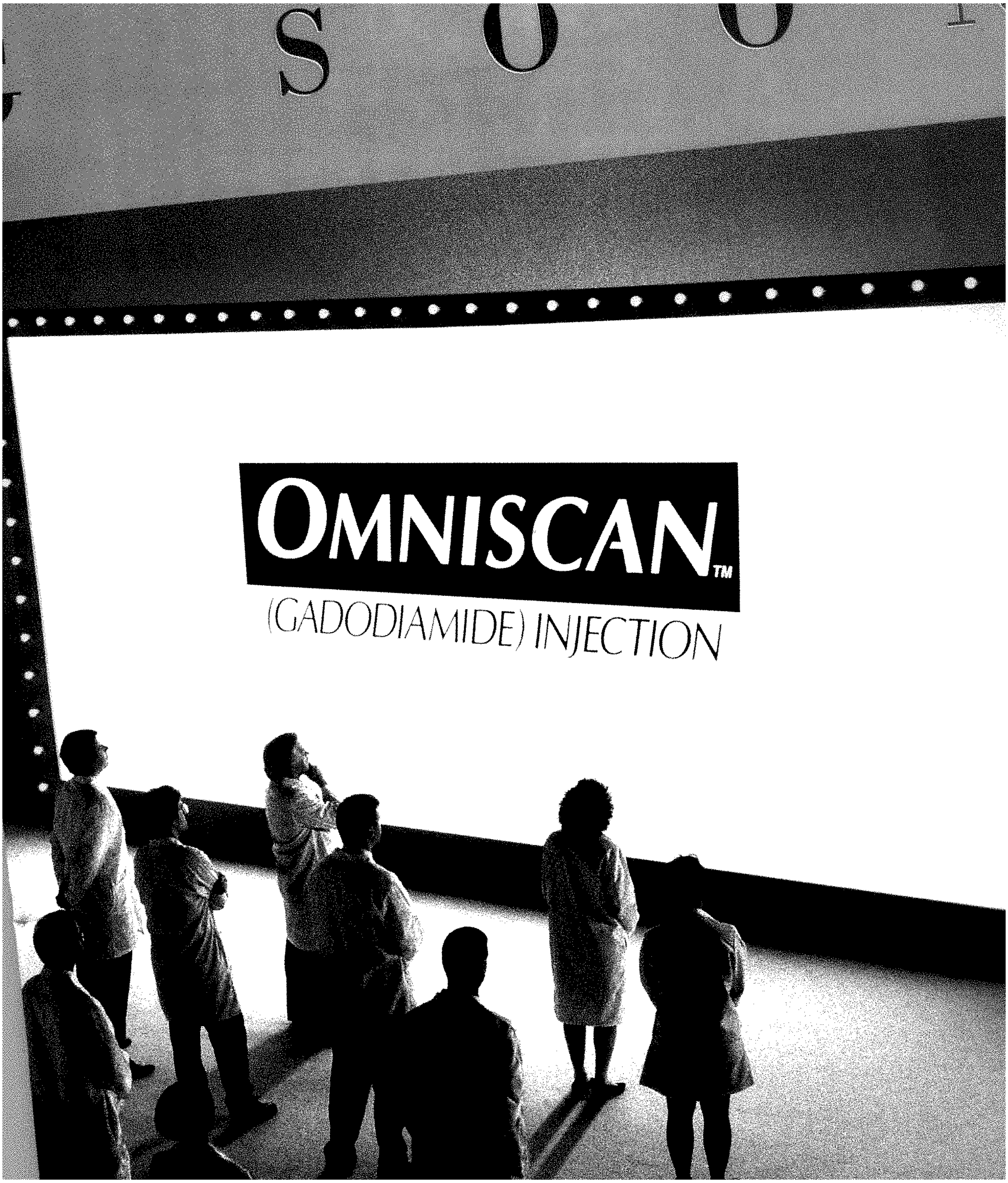
OMNISCAN™
(GADODIAMIDE) INJECTION

Fellowships In Diagnostic Radiological Research.

The Diagnostic Radiology Research Program of the National Institutes of Health is accepting applications for two-year fellowship positions beginning in July 1992 and July 1993. This program provides an excellent opportunity for individuals who plan a research career in radiological sciences.

The fellowship training program emphasizes basic research in all aspects of imaging and image processing. Fellows will have no clinical responsibilities unless they are related to their project. The imaging laboratories of the Diagnostic Radiology Research Program include: state-of-the-art 0.5 and 1.5 Tesla MR units; a newly developed image analysis program with hardware support; ultrafast CT; and an experimental angiography suite. The facilities in the *In Vivo* NMR Research Center, the PET and monoclonal antibody programs of the Nuclear Medicine Department, and other laboratories on the NIH campus will be made available to the fellow, providing an opportunity to develop expertise in areas related to imaging research. Basic research in functional or metabolic imaging, contrast agents, biochemistry, biology, chemistry, immunology, physics and physiology will be encouraged. Laboratories are being developed which will include "hot" and "cold" wet labs and tissue culture facilities. Collaboration with other scientists on the NIH campus will be encouraged.

Applicants should hold the MD or PhD degree and should have completed clinical training in diagnostic radiology or nuclear medicine. Applications from individuals currently in US residency programs may also be considered for research fellowship positions. US citizenship or permanent residency is required for this full-time appointment.

Candidates should submit a Curriculum Vitae, at least two letters of reference and a preliminary statement concerning their area of research interest to Dr. Joseph A. Frank, Acting Director.

National Institutes Of Health
Diagnostic Radiology Research Program
9000 Rockville Pike, Building 10, Room 1C660, Bethesda, MD 20892 • FAX 301-496-9933
Equal Opportunity Employer

DIAGNOSTIC RADIOLOGIST

The Department of Radiology at The George Washington University Medical Center is seeking a Board Certified Diagnostic Radiologist with experience in mammography, and other aspects of general radiology who also specializes in Nuclear Medicine or is an ABNM certified Nuclear Medicine Physician, with a record of commitment to clinical care, education and clinical research.

This is a full-time, non-tenure track position at the Assistant Professor to Associate Professor level. The George Washington University Medical Center includes a 500 bed hospital located in the Foggy Bottom area of Washington, DC, a few blocks from the White House, Kennedy Center, and Georgetown, with all medical and surgical subspecialties.

The Radiology Department is equipped with a new 1.5 Signa MR, two 9800 CT's, and state of the art Ultrasound, Angiographic, Mammographic, and General Radiographic units. Salary and rank will be commensurate with experience. Review of applications will commence on June 1, 1992 and will continue until the position is filled.

Letters of inquiry accompanied by a curriculum vitae should be sent to: David O. Davis, M.D., Professor and Chairman, Department of Radiology, The George Washington University Hospital, 901 23rd Street, NW, Washington, DC 20037. The George Washington University is an Equal Opportunity/Affirmative Action Employer.

Keep It All Together

Easily and Conveniently With Bound Volumes of the *American Journal of Roentgenology*

Keeping up with scientific and technological advances in radiology is more important than ever, and that's why each issue of the *American Journal of Roentgenology* is packed with up-to-the-minute information crucial to you and your practice. **Keep this important resource together for easy reference in convenient and attractive bound volumes.**

Each edition is imprinted with the year and volume number and contains six issues filled with the kind of vital research, commentary and analysis you've come to expect in the AJR.

For ordering information, contact AJR Subscription Fulfillment Department, 428 E. Preston St., Baltimore, MD 21202-3993, or call toll-free **1-800-638-6423.**

X-RAY ACCESSORIES

The Difference is Clear

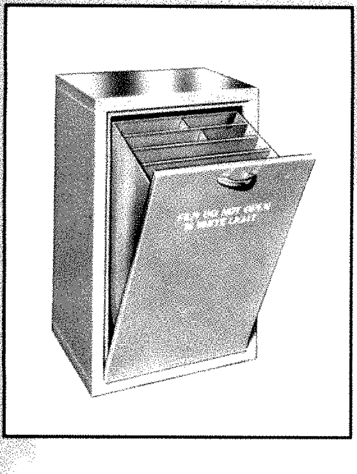

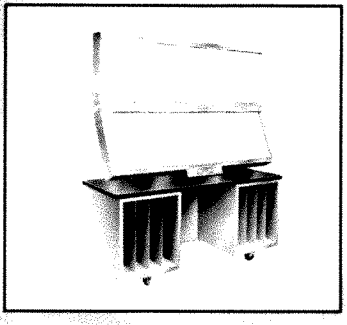

Tried, tested and trusted for over 40 years, S & S x-ray products deliver maximum proficiency and economy -- backed by quality, dependability and innovation.

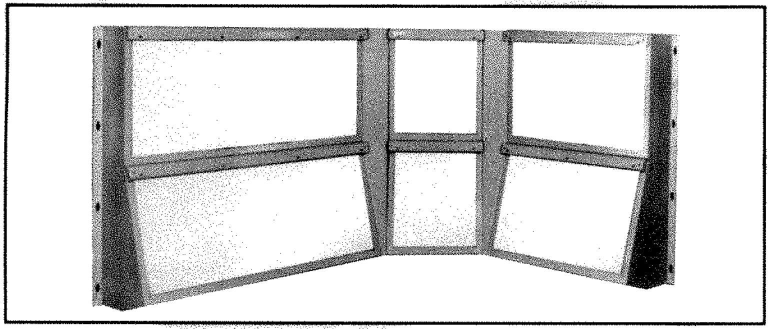

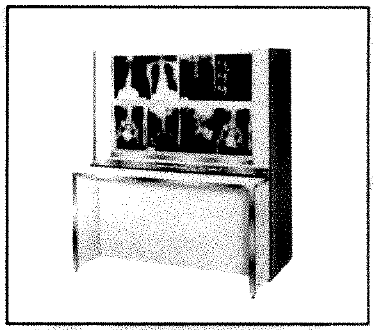

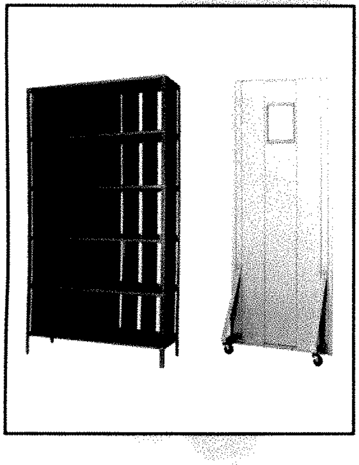

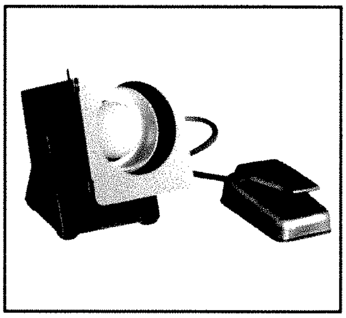

X-RAY Film Viewers ◆
X-RAY Protection ◆
X-RAY Files ◆
X-RAY Darkroom Equipment ◆
X-RAY Cabinets ◆
X-RAY Accessories ◆

For a FREE copy of our fully illustrated, 100+ page catalog, contact S & S directly or your local x-ray dealer.

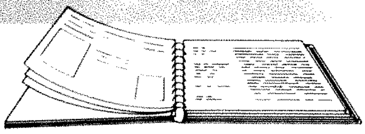

Phone: 718/649-8500
FAX: 718/257-0219
Toll Free: 800/347-XRAY

1101 Linwood Street
Brooklyn, N.Y. 11208

S&S X-RAY PRODUCTS INC
Factories in NY, NC, PA, TX

E-Z-EM®

Improve Your Image

- Local Anesthesia
- Biopsy
- Amniocentesis
- Arthrography
- Myelography

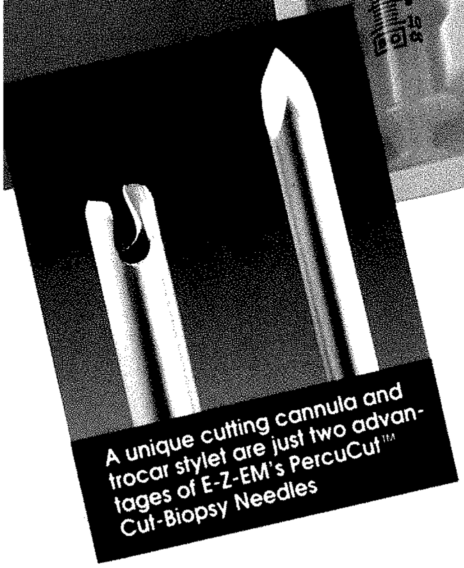

A unique cutting cannula and trocar stylet are just two advantages of E-Z-EM's PercuCut™ Cut-Biopsy Needles

The fine points of selecting procedure trays

You already know the reasons for using procedure trays: convenience, consistency and economy, to name a few. But when it comes to choosing a tray manufacturer, things aren't quite so clear.

PercuSet® procedure trays from E-Z-EM offer an advantage that should make your decision easier. You see, E-Z-EM is both a tray manufacturer and a developer of procedure needles — with innovative designs that result from listening to the needs and ideas of interventional radiologists and technologists. Patented PercuCut biopsy needles offer exclusive features others can't match. And we're the leader in developing needles for specific modalities, such as ultrasound and MRI.

So when you order trays from E-Z-EM, the finest procedure needles are an available option. But whether you order trays with needles or without, you always receive the highest quality components — logically arranged in a well-designed tray.

For more information on our trays and needles, contact E-Z-EM Customer Service today at 1-800-544-4624. To place an order, simply call your local E-Z-EM dealer.

E-Z-EM, INC., 717 Main Street, Westbury, NY 11590 • 1-800-544-4624

E-Z-EM stock is publicly traded on the NASDAQ National Market System under the symbol

For financial information, contact Investor Relations at 1-800-544-4624, ext. 345

PercuSet®

Procedure Trays

Review Article

Detection of Metastasis in Cervical Lymph Nodes: CT and MR Criteria and Differential Diagnosis

Peter M. Som[1]

Radiologists are frequently asked to evaluate cervical lymph nodes with CT or MR imaging to determine if metastases are present, how extensive the metastases are, and if they have spread from lymph nodes to critical adjacent structures such as the carotid artery and skull base. Accurate information of this type is essential if the most appropriate treatment is to be selected. The purpose of this report is to review the diagnostic criteria that are currently used with CT and MR imaging to diagnose metastases in cervical nodes by evaluating nodal size, shape, grouping, and necrosis and extranodal tumor spread. In addition, emphasis is placed on details that should be included in the CT and MR report, such as the location of the nodes, the presence of nodal calcification, and the presence of associated diseases such as parotid cysts that may suggest a specific diagnosis like HIV infection. Because optimal treatment planning depends on the combined information gleaned from the clinical evaluation and the imaging studies, it is essential that there be a close dialogue between clinicians and radiologists.

In adults, squamous cell carcinoma is the most common tumor to arise in the upper aerodigestive tract, and if the primary tumor can be controlled, the most important factor that influences a favorable outcome is the presence of metastatic cervical lymph adenopathy [1]. Regardless of the site of the primary tumor, the presence of a single metastatic lymph node in either the ipsilateral or contralateral side of the neck reduces the 5-year survival rate by about 50%. The presence of a single metastatic lymph node in each side of the neck reduces the survival rate to nearly 25% of that expected in patients without any cervical nodal metastasis [2-5].

Further complicating this situation is the presence of extranodal tumor spread, which not only is the best prognosticator of failure of local treatment of the neck, but also indicates that the survival rate is reduced by half. Thus, for most primary tumor sites in the head and neck, the presence of one metastatic lymph node in both sides of the neck with tumor extending beyond the nodal capsule in at least one node reduces survival to one eighth of that of a patient with the same primary tumor, but without any nodal metastases [2-5]. The striking effect that lymph node metastases have on prognosis and the efficacy of CT and MR imaging to detect such disease have combined to make evaluation of nodal metastases a fundamental part of the preoperative evaluation and follow-up of patients with tumors in the head and neck. The purpose of this article is to review the diagnostic criteria that are currently used to determine the presence of metastatic nodal disease in the neck by CT and MR imaging. Any sectional imaging appearance of the nodes that may suggest the site of origin of the metastases, such as the thyroid gland, is described, and the differential diagnosis of these findings is reviewed.

Detection of Microscopic Metastases and the Need for a Staging System

When tumor deposits within a node are only microscopic, detection of the tumor by CT and MR imaging is impossible. It has been estimated that it takes one billion malignant cells to create a mass of only 1 mm^3 [6]. Although tumor smaller

---

Received August 6, 1991; accepted after revision December 30, 1991.

[1] Departments of Radiology and Otolaryngology, The Mount Sinai School of Medicine of the City University of New York, One Gustave L. Levy Pl., New York, NY 10029-6574. Address reprint requests to P. M. Som, Department of Radiology, Box 1234.

AJR 158:961-969, May 1992 0361-803X/92/1585-0961 © American Roentgen Ray Society

than this can be identified microscopically, such small deposits are not visible on gross inspection of the lymph node, let alone by sectional imaging. Hence, it must be understood that CT and MR imaging cannot be used to exclude the presence of metastases. On the other hand, when metastases are large enough to be detected by CT and MR imaging, criteria are necessary to stage the disease properly.

The American Joint Committee on Cancer and the International Union Against Cancer developed a new joint tumor staging system in 1988 [7]. This tumor, node, metastasis (TNM) system is primarily used for staging lymph node involvement on the basis of clinical findings (Table 1). Although the classification fails to address a number of issues, it is the most accepted worldwide reference frame by which to compare tumor treatments.

The terminology traditionally used to describe the precise anatomic location of abnormal cervical lymph nodes has been that of Rouviere, which is based on the classical surface triangles of the neck [8]. However, in the past decade, a simpler numeric system has become the dominant nomenclature [8] (Table 2). The specific techniques used to perform the CT and MR studies have been discussed in the literature and are beyond the scope of this review [9–15].

Patients with No Clinical or Imaging Evidence of Nodal Metastases

The problem of identifying microscopic nodal disease is exemplified by the patient who has a primary tumor in the head and neck, but no metastatic cervical adenopathy evident on clinical and CT and MR examinations (N0 neck by TNM system). If all head and neck primary sites are included, approximately 15% of patients initially considered to lack cervical lymph node metastases subsequently are found by histologic examination or clinical manifestation to have such metastasis [1]. The risk of cervical metastasis depends on the site of origin of the primary tumor and varies from primary to primary. It may be as high as 32% for some oral cavity tumors [1, 9, 16, 17]. The dilemma is how to treat these patients with N0 disease. The 15% of these patients who actually have metastasis cannot be distinguished from the 85% who have no nodal metastasis. This creates the dilemma that has not been resolved [1, 9, 16, 17]. However, some evidence is available to suggest that if one waits until the nodal disease becomes evident clinically, survival is compromised.

It is hoped that monoclonal antibody tagging studies may be the vehicle to someday detect and treat such microscopic disease; however, to date, progress in this direction has been slow and relatively unrewarding [18].

TABLE 1: American Joint Committee on Cancer's System for Staging Regional Lymph Nodes (N)

Stage	Description
NX	Regional lymph nodes cannot be assessed
N0	No regional lymph node metastasis
N1	Metastasis in a single ipsilateral lymph node, 3 cm or less in greatest dimension
N2	Metastasis in a single ipsilateral lymph node, more than 3 cm but not more than 6 cm in greatest dimension; or in multiple ipsilateral lymph nodes, none more than 6 cm in greatest dimension; or in bilateral or contralateral lymph nodes, none more than 6 cm in greatest dimension
N2a	Metastasis in a single ipsilateral lymph node, more than 3 cm but not more than 6 cm in greatest dimension
N2b	Metastasis in multiple ipsilateral lymph nodes, none more than 6 cm in greatest dimension
N2c	Metastasis in bilateral or contralateral lymph nodes, none more than 6 cm in greatest dimension
N3	Metastasis in a lymph node more than 6 cm in greatest dimension

TABLE 2: Numeric Nodal Classification System

Level	Location
I	Submandibular and submental nodes (all nodes in floor of mouth)
II	Internal jugular chain (or deep cervical chain) nodes; nodes about internal jugular vein from skull base to hyoid bone (same level as carotid bifurcation)
III	Nodes about internal jugular vein from hyoid bone to cricoid cartilage (same level that omohyoid muscle crosses internal jugular chain)
IV	Infraomohyoid nodes about internal jugular vein between cricoid cartilage and supraclavicular fossa
V	Posterior triangle nodes (deep to sternocleidomastoid muscle)
VI	Nodes related to thyroid gland
VII	Nodes in tracheoesophageal groove, about esophagus extending down to superior mediastinum

Clinical Criteria: The Basis of Imaging Criteria

Because it is impossible to detect microscopic metastases other than by biopsy, the actual task is to identify gross metastatic cervical lymphadenopathy. In the era before sectional imaging, palpation was the primary method of detecting such nodal disease. The criteria used were nodal size and nodal fixation. Metastasis was suggested if a palpable node was larger than 1.5 cm in greatest diameter or if a lymph node was fixed. When the size criterion is used, the diagnosis of metastatic lymphadenopathy can be falsely negative or falsely positive 20–28% of the time.

In addition, although it was initially believed that extranodal or extracapsular tumor extension occurred only in lymph nodes larger than 3 cm in greatest diameter, CT-pathologic studies have shown that such extension actually occurs in 23% of nodes less than 1 cm in greatest diameter, in 53% of nodes 2–3 cm in greatest diameter, and in 74% of nodes greater than 3 cm in greatest diameter. Overall, a lymph node less than 3 cm in greatest diameter has microscopic or gross extracapsular disease 60% of the time [5, 19]. These clinical and pathologic observations served as the basis for the initial imaging criteria to detect metastatic lymph node disease. The criteria were based on applying the clinical size criteria to CT and scrutinizing the scans for evidence of extracapsular spread in all size lymph nodes.

CT Criteria for Nodal Metastasis

With CT, *extracapsular nodal spread* or extension of metastatic tumor beyond the lymph node capsule is diagnosed when there is enhancement of the nodal capsule and the presence of poorly defined margins around the node (Fig. 1). These criteria are accurate only if the patient has not recently had surgery, irradiation, or an active infection in the area [8, 10, 11]. Because most pathologists do not routinely comment on the presence of such extracapsular nodal spread, it is impossible to obtain precise statistics on how accurate CT is in making this diagnosis. However, it is currently agreed that if the limitations mentioned are taken into consideration, on the basis of published data CT has nearly a 100% sensitivity and thus deserves its present role as the imaging gold standard in identifying extranodal tumor spread [8–15].

CT criteria for assessing nodal metastases are based on nodal size and shape, the presence of central necrosis, and the presence of a localized group of nodes in an expected node-draining area for a specific primary tumor (grouping) [8–15]. *Nodal size criteria* can be used when nodes are homogeneous and clearly delineated (Fig. 2). The generally used upper limit of normal for the greatest nodal diameter is 1.5 cm for the jugulodigastric and submandibular nodes and 1 cm for all other cervical nodes. These criteria correspond to the earlier clinical experience described, and nodes that exceed these dimensions are metastatic about 80% of the time. Even these criteria vary, with some authors considering retropharyngeal nodes that exceed 0.8 cm in greatest diameter to be metastatic [10]. Recently, it has been suggested that a more accurate size criterion is the minimal (shortest) axial nodal diameter. If this dimension exceeds 11 mm in the jugulodigastric region and 10 mm in all other cervical nodes, metastasis is probably present [9]. Diagnosis based on imaging evaluation of nodal size is more accurate than diagnosis based on palpation alone. This is because CT can show lymph nodes that are not accessible to palpation (retropharyngeal, tracheoesophageal, and those deep to the sternocleidomastoid muscle).

If *nodal shape* is added as a criterion to nodal size, the sensitivity of CT diagnosis is improved only slightly. This criterion is based on the pathologic observation that the average hyperplastic node is "lima-bean" shaped, whereas most metastatic nodes are spherical. Thus, if a lymph node is borderline pathologic by size criteria, but is spherical, it is more likely to truly contain metastatic tumor.

Nodal grouping refers to three or more contiguous and confluent lymph nodes, each of which has a maximal diameter of 8–15 mm (or a minimal axial diameter of 8–10 mm). Such a grouping in the drainage chain of the tumor is highly suggestive of metastatic disease [9, 10].

The most accurate CT criterion for the presence of metastatic lymphadenopathy is *central necrosis*, a term that is a partial misnomer. Initially, tumor cells replace the medulla of the node, and it is only after this that necrosis of the medulla occurs. Thus, the medullary region of such a node actually has tumor cells as well as necrotic tissue. Both the tumor and the necrosis give low attenuation on CT to the medullary area of the node (Fig. 3). In part, this CT appearance is accentuated when the cortical portions of the node enhance with contrast material. On CT, the periphery of the node is usually thick, irregular, and enhances [8–15].

Both nodal lipid metaplasia and an abscessed node may simulate necrosis due to metastasis on CT. Lipid metaplasia or fatty degeneration can occur in lymph nodes after severe inflammatory disease or after irradiation. In most cases, such fat occurs in the hilum of the gland, which is peripheral rather than central. On CT, the fat usually has a lower attenuation than tumor necrosis has; however, because of its small size and volume averaging, this distinction may be difficult or impossible to make on imaging studies. Rare central lipid metaplasia can occur and usually is impossible to distinguish from metastatic nodal disease.

An abscessed node almost always occurs in a patient who has obvious symptoms of an acute inflammatory process. Such an abscessed node can have central low attenuation and a thick, irregular unsharp peripheral margin, all of which

Fig. 1.—Metastatic node with extranodal spread in a 56-year-old man with squamous cell carcinoma. Axial CT scan shows a mass in left jugulodigastric area that has slightly low-attenuation central region and unsharp, enhancing rim (*large arrow*). Mass is immediately adjacent to left common carotid artery and internal jugular vein (*small arrows*).

Fig. 2.—Multiple enlarged nodes in a 42-year-old man who is HIV positive. Axial CT scan shows multiple lymph nodes (N) bilaterally in neck involving internal jugular and posterior triangle lymph node chains. Nodes have same attenuation as muscle, are not necrotic, and are sharply outlined. Nodes happen to be hyperplastic nodes in HIV-positive patient; however, a similar CT appearance could be seen in a patient with lymphoma or sarcoid.

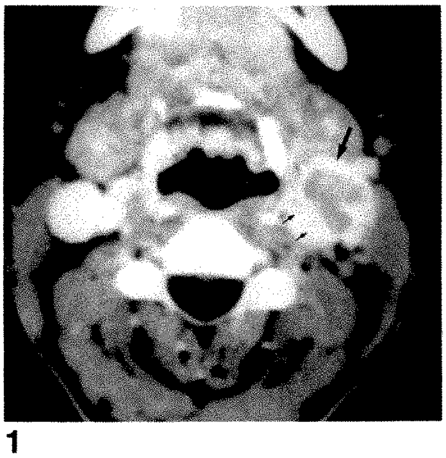

1

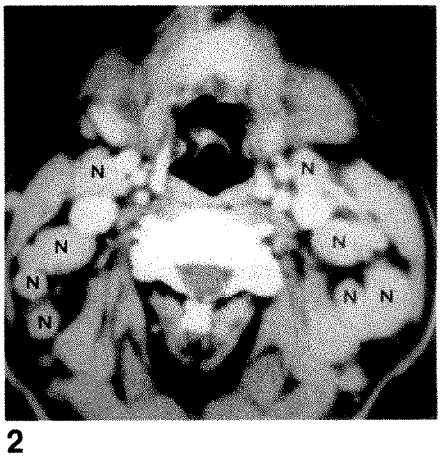

2

simulate a metastatic node (Fig. 4). A distinguishing feature may be the presence of diffuse associated cellulitis; however, in a patient who has been incompletely treated with antibiotics, this finding may be minimal or absent. Such an abscessed lymph node also can occur as an isolated finding in a lymph chain of otherwise hyperplastic nodes. Again, the primary distinguishing feature is not on the CT or MR scans, but is the patient's history.

If all of the CT criteria are used, 7–19% more metastases can be detected by CT changes than by palpation alone [8–15].

MR Imaging Criteria for Nodal Metastasis

The MR imaging evaluation of cervical nodal metastasis is less well pathologically substantiated in the literature than is the CT investigation of these nodes. A number of reports have shown that enlarged cervical lymph nodes can be identified by various MR sequences, for example, T1-weighted 500/20 (TR/TE) [20–30] (Figs. 5 and 6). However, the MR differentiation of metastatic adenopathy from hyperplastic lymph nodes remains less well documented with reference to its reliability compared with CT, the best MR sequences to use, and the benefits of the use of MR contrast material.

With the better soft-tissue resolution of MR compared with CT, one would expect lymph nodes to be very well seen on MR. However, the fat in which all cervical lymph nodes are embedded, and which contributes to their easy identification on CT, tends to decrease their perspicuity on MR. This is because the high T1-weighted signal intensity of fat obscures much nodal detail, and researchers have relied primarily on the T2-weighted signal intensities of the node for identification of tumor [21, 27]. Most hyperplastic lymph nodes have a homogeneously low signal intensity on T1-weighted images and a high signal intensity on T2-weighted images. However, nonnecrotic metastatic nodes and even some necrotic metastatic nodes may have these same signal intensities, and thus there is an overlap with the MR appearance of hyperplastic nodes. As a result, dependence on this diagnostic approach is unreliable [21, 27] (Fig. 7).

If the nodes have tumor necrosis, they usually have a nonhomogeneous MR appearance on both T1-weighted and T2-weighted studies. Sites of necrosis tend to have focally lower T1-weighted and higher T2-weighted signal intensities

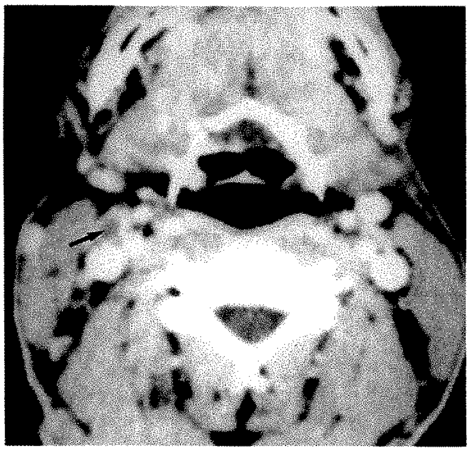

3

Fig. 3.—Unenlarged metastatic node in a 48-year-old man with squamous cell carcinoma. Axial CT scan shows unenlarged right jugulodigastric node that has central "necrosis" (*arrow*). Metastatic node was clinically assessed as being normal.

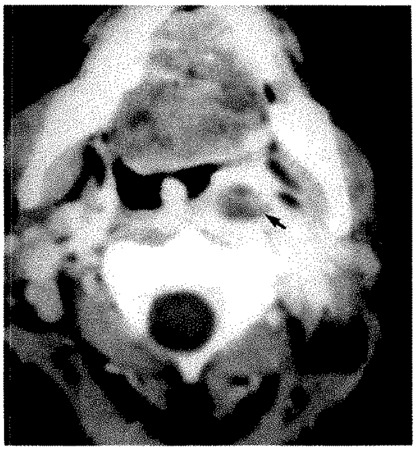

4

Fig. 4.—Retropharyngeal abscessed node in a 26-year-old woman. Axial CT scan shows low-attenuation left-sided retropharyngeal mass (*arrow*) with thick rim of enhancement that extends into left parapharyngeal space and posterior triangles.

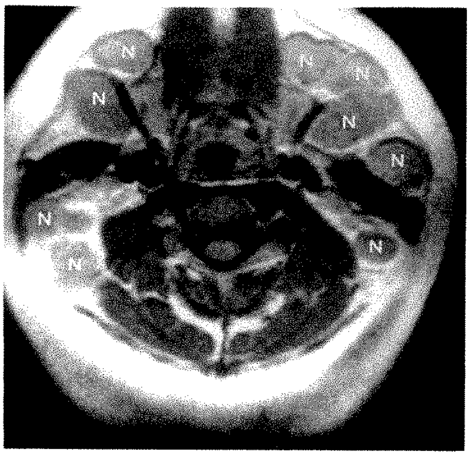

5

Fig. 5.—36-year-old woman with known sarcoid. Axial proton density-weighted (1800/30) MR image shows multiple bilateral submandibular, internal jugular, and posterior triangle chain nodes (N). These nodes had homogeneous low to intermediate T1-weighted and proton density-weighted signal intensity and higher T2-weighted signal intensity. These could be hyperplastic, lymphomatous, or sarcoid nodes.

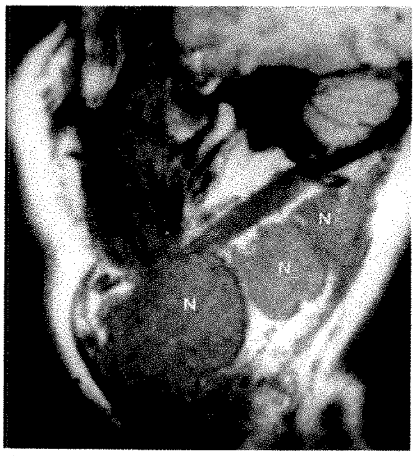

6

Fig. 6.—38-year-old woman with large-cell lymphoma. Sagittal T1-weighted (500/20) MR image shows multiple enlarged homogeneous lymph nodes (N) in posterior triangle. These nodes had signal intensities similar to those in Fig. 5.

Fig. 7.—Metastatic node in a 54-year-old man with squamous cell carcinoma.

A, Axial CT scan shows centrally necrotic sharply marginated node (*arrow*) in left posterior triangle.

B, Axial proton density–weighted (200/30) MR image shows node to be questionably unsharp with no obvious central necrosis (*arrow*).

C, Axial T2-weighted (200/80) MR image shows findings similar to those in *B*, except node has slightly higher signal intensity.

D, Axial T1-weighted (800/33), fat-suppressed, contrast-enhanced MR image shows diffuse nodal enhancement, without obvious central necrosis.

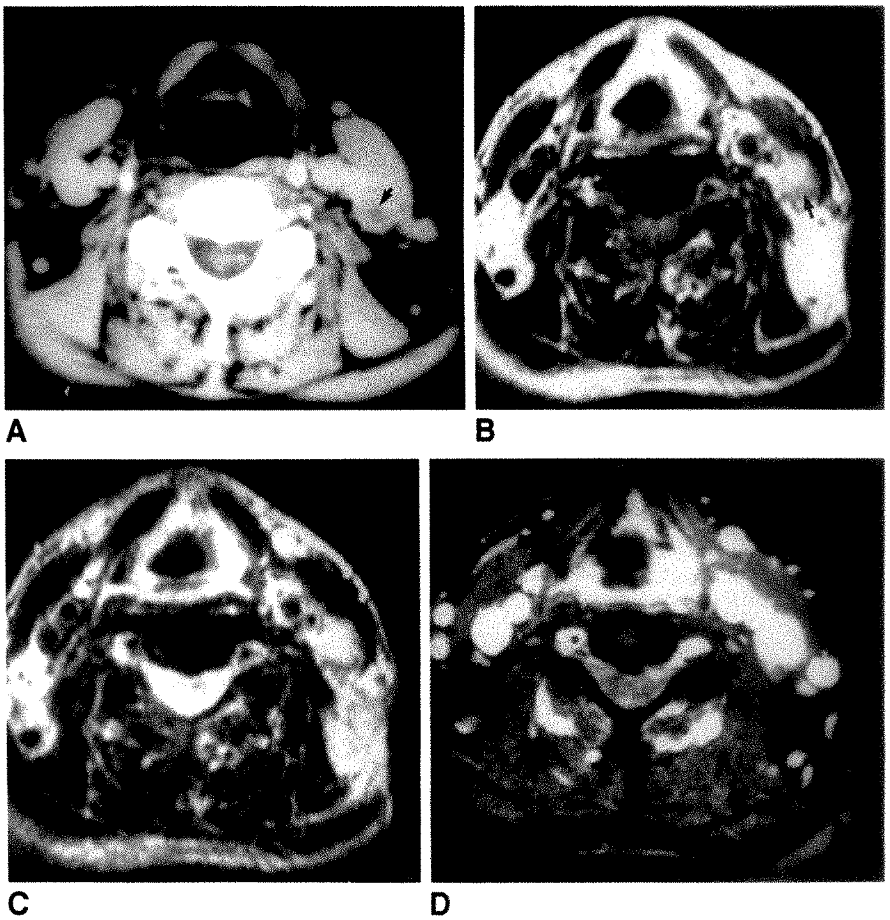

than the remainder of the lymph node. However, sites of tumor and hemorrhage may have low, intermediate, or high signal intensities that, in some cases, result in a net overall homogeneous nodal signal intensity. Thus, some nodes that clearly are necrotic on CT may appear to be homogeneous and hyperplastic on MR (Fig. 7). Purely on the basis of unenhanced signal intensity, the most reliable MR appearance suggestive of nodal metastasis is a nonhomogeneous signal intensity, especially on T2-weighted studies, with focal areas of high T2-weighted signal intensity within the node [20–30] (Fig. 8).

The use of MR contrast material has allowed necrotic nodes to have an appearance similar to that found on CT, namely, a central region of lower signal intensity and a periphery with enhancing higher signal intensity on T1-weighted images [28, 30]. Unfortunately, the high signal intensity of the nodal periphery now has decreased perspicuity when seen against the surrounding high T1-weighted signal intensity of fat. To address this problem, contrast-enhanced, fat-suppressed, T1-weighted MR studies have been proposed as the optimal MR sequence to image metastatic cervical lymph nodes [28, 30]. Such a sequence also allows extranodal tumor spread to be better seen on MR than is possible with non-fat-suppressed studies (Fig. 7).

Although contrast-enhanced T2-weighted and gradient-echo sequences have been used by some researchers, these appear overall to be less diagnostically useful than the contrast-enhanced T1-weighted, fat-suppressed studies [31].

Difficulties created by less than optimal design of the neck coil, artifacts due to patients' movement, artifacts related to the fat-suppression technique, and flow-related artifacts still present some problems that degrade MR images to various degrees. However, with continued coil development, and the faster and newer sequences that are becoming commercially available, such difficulties are becoming less significant detractions to the use of MR.

The same size and shape criteria used for CT are used for MR evaluation of cervical lymph nodes. Similarly, if contrast-enhanced, fat-suppressed, T1-weighted MR images are used, the criteria for nodal tumor necrosis and extracapsular nodal spread also apply. What remains unsubstantiated by significant clinical/pathologic/radiologic studies is how well MR compares with CT in detecting metastatic nodal disease in the neck.

Although some authors have suggested that MR currently is as good as or better than CT in assessing cervical nodal metastasis, one study indicates that MR is less accurate than CT in identifying nodal tumor necrosis and extracapsular tumor spread by about 15% [32]. It is expected, however, that these differences will continue to diminish as technologic advances in MR continue. The usefulness of sectional imaging is emphasized by a recent study, which showed that the

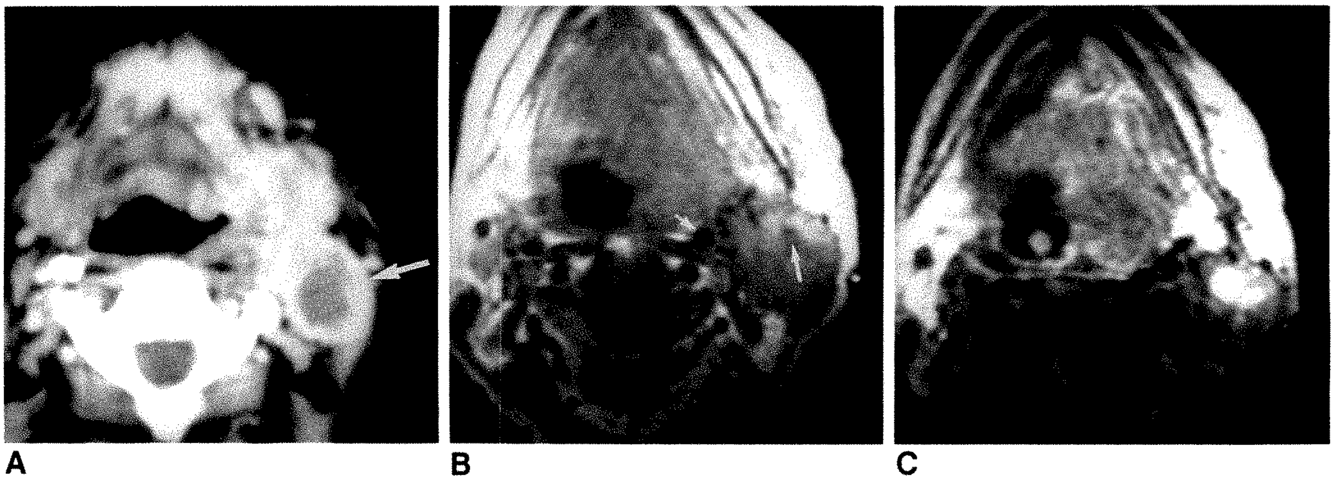

Fig. 8.—Metastatic node with extranodal spread in a 57-year-old man with squamous cell carcinoma.

***A,* Axial CT scan shows large left-sided jugulodigastric node (*arrrow*) that has central necrosis; enhancing, thick, irregular rim; and obliteration of adjacent fat planes medially and anteriorly.**

***B,* Axial T1-weighted (800/20) MR image shows mass with focal area of lower signal intensity (*long arrow*). Carotid artery (*short arrow*) is better seen than in *A*.**

***C,* Axial T2-weighted (2500/80) MR image shows nodal mass with at least two focal areas of high signal intensity. This inhomogeneous appearance is highly suggestive of a metastatic node on MR.**

sensitivity in detecting cervical nodal metastasis is about 20% better with CT and MR imaging than it is by clinical examination [33]. Further, in this study, the prevalence of undiagnosed disease by clinical examination alone was 39%, whereas the prevalence by CT and/or MR imaging was 22%. However, when clinical and sectional imaging findings were combined, the prevalence of undiagnosed disease dropped to only 12%.

Extranodal Tumor Spread

Once extracapsular tumor spread has occurred, the malignant growth can extend to involve vital structures such as the common carotid and internal carotid arteries, the last four cranial nerves, and the skull base. Involvement of any of these structures is associated with a grave prognosis, primarily because such disease cannot be oncocytically extirpated. Even if surgery can encompass such tumor, the loss of these vital structures, especially in patients 50 years old or older, is associated with significant morbidity and disability. However, recent surgical techniques have raised hope that tumor of the internal carotid artery, even after irradiation, can be safely extirpated with a reasonable chance of good palliation or, rarely, a cure [34].

Carcinomatous extension to the skull base is best seen on coronal scans. Early bone erosion is best identified on CT scans, while early intracranial or dural extension is best seen on enhanced MR images [35, 36]. Tumor involvement of the carotid artery is not diagnosed as reliably on sectional imaging. Even though the carotid artery is almost entirely encased by tumor on CT or MR images, in some cases the surgeon finds the arterial adventitia to be free of tumor. Conversely, in some patients in whom just a margin of the tumor abuts the carotid artery silhouette on sectional images, at surgery the adventitia is involved. As tumor adherence to the vessel adventitia is all that is required oncologically to cause replacement or sacrifice of the artery, the radiologist must alert the clinician to any such possible disease extension. The greater the amount of arterial circumference that is in contact with tumor, the more likely it is that tumor has invaded the arterial wall [18]. Thus, the radiologist's dictation should include a precise description of any such disease.

Some surgeons who clinically find unilateral metastatic nodal disease and plan to perform a radical neck dissection may say that a CT or MR examination to evaluate nodal disease is unnecessary. They are incorrect, because if such an imaging study demonstrates even one pathologic node in the opposite side of the neck, the treatment approach must be modified. If such surgeons find unilateral metastatic nodal disease and plan to perform one of the several types of modified neck dissections, a CT or MR scan is still useful in evaluating the neck ipsilaterally, as well as contralaterally. Most modified neck dissections do not include nodes in the posterior triangle, lower neck, or retropharyngeal areas, and the imaging demonstration of diseased nodes in any region outside of the planned surgical field will modify the surgical approach. Thus, in cancer patients, there is no logical argument against obtaining a CT scan or MR image to assist the clinician in staging the neck disease.

Nodal Ring Enhancement

The presence of areas of ring enhancement throughout a soft-tissue lesion makes it most likely that the mass represents a conglomerate group of metastatic nodes, each of which has extracapsular tumor spread (Fig. 9). This is provided that the lesion is clinically assessed as being suggestive of such nodes (hard, fixed, no bruits) or the mass is inacces-

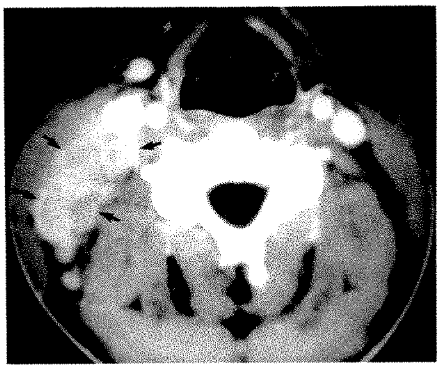

9

Fig. 9.—Posterior triangle nodes in a 24-year-old man with large-cell lymphoma. Axial CT scan shows mass in right posterior triangle that has multiple areas of ringlike enhancement that represents nodal capsular enhancement (*arrows*). This nodal mass is deep to sternocleidomastoid muscle so that it could not be well evaluated clinically.

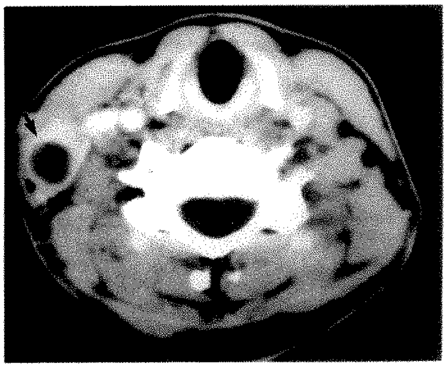

10

Fig. 10.—Cystic node in a 33-year-old woman with papillary thyroid carcinoma. Axial CT scan shows centrally low-attenuation mass in right posterior triangle that has a smooth, enhancing rim (*arrow*). Appearance is not too different from that of a benign cyst, although there is some asymmetry in nodal wall thickness.

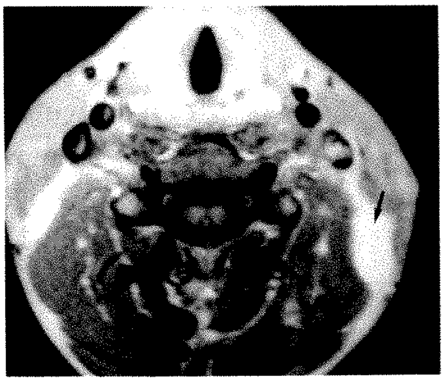

11

Fig. 11.—Metastatic posterior triangle node in a 38-year-old woman with papillary thyroid carcinoma. Axial T1-weighted (757/22) MR image shows a smooth-walled node in left posterior triangle that has homogeneously high signal intensity (*arrow*). Node also had a fairly high T2-weighted signal intensity. MR appearance in this patient with papillary thyroid carcinoma is consistent with a node full of dense thyroid protein and/or hemorrhage.

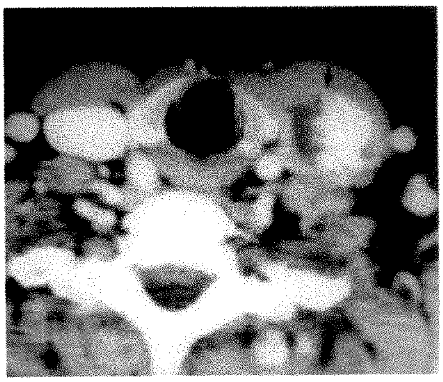

12

Fig. 12.—Hemorrhagic metastatic node in a 42-year-old woman with papillary thyroid carcinoma. Axial CT scan shows enlarged, partially enhancing, partially necrotic mass (*arrow*) in left side of neck.

sible to palpation so that such a clinical judgment cannot be made. Rarely, a large glomus vagale tumor can have areas of clot that mimic the appearance of such a conglomerate nodal mass; however, clinically such tumors are not suspected of representing metastatic cervical adenopathy.

Papillary Thyroid Nodal Metastasis

Thyroid papillary carcinoma is an unusual tumor in that it causes a variety of changes in metastatic cervical lymph nodes. The nodes may be homogeneous and either enlarged or of normal size, simulating hyperplastic adenopathy. Nodal calcifications can occur, and almost complete nodal necrosis can be present, creating a smooth-walled cystic mass that mimics a benign cyst (Fig. 10). Such a node can be filled with thyroid protein that gives a low attenuation on CT, but high signal intensity on both T1-weighted and T2-weighted MR images (Fig. 11). Last, hemorrhage into the node can occur. Such nodal hemorrhage also is rare, and the differential diagnosis of other causes includes metastatic hypernephroma and possibly Kaposi's sarcoma or Kimura's disease (angiolymphoid hyperplasia with eosinophilia). Such nodal bleeding usually has a high attenuation on CT scans and has high T1-weighted and fairly high T2-weighted MR signal intensities [37–39] (Fig. 12).

Overall, nodal calcifications are uncommon, and the most likely cause of such calcification, especially if gross, is scrofula. Metastatic tumoral calcifications are rare and usually are small or psammomatous in appearance; the most likely primary tumor is papillary thyroid carcinoma. Less likely causes of nodal calcification include irradiated lymphomatous or carcinomatous nodes and, rarely, healed abscessed inflammatory nodes [12, 15]. Such calcifications are better diagnosed on CT; they are often undetected on MR.

Lymphoma and Tuberculosis

Lymphoma produces nodes that are homogeneous and clearly delineated, like hyperplastic adenopathy; nodes that are necrotic and mimic carcinomatous nodes; or, rarely, nodes that enhance. Tuberculosis also has protean lymph node manifestations, usually producing nodes that form a conglomerate mass composed of some nodes that enhance on CT, some nodes that are isodense with muscle, and some nodes that are necrotic. There often is surprisingly little infiltration of the adjacent fat planes [40]. Such a CT appearance is most suggestive of tuberculosis; the primary differential diagnosis is large-cell lymphoma (Fig. 13).

It is unusual to find huge cervical lymph nodes that do not have necrosis (Fig. 14). As squamous cell carcinoma causes necrosis in virtually all nodes larger than 3 cm in greatest diameter, the sectional imaging finding of a large nonnecrotic node should prompt the radiologist to think of another diagnosis. Only a few diseases cause such nodes. Large-cell

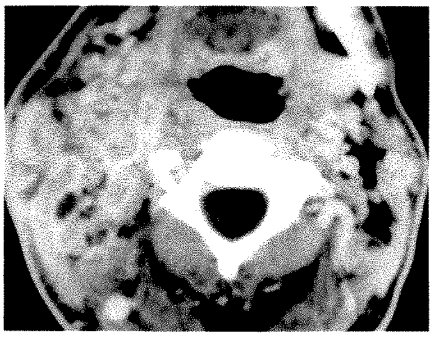
13

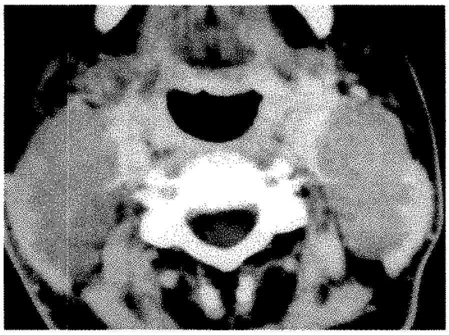
14

Fig. 13.—Multiple nodes in a 64-year-old man with tuberculosis. Axial CT scan shows multiple masses in right side of neck. Some nodes have slight enhancement, some have rim enhancement, some have attenuation of muscle, and some have lower attenuation than that of muscle. Overall, there is little obliteration of fat planes, considering size of nodal mass.

Fig. 14.—Huge lymph nodes in a 44-year-old man with sinus histiocytosis and massive lymphadenopathy. Axial enhanced CT scan shows bilateral huge lymph nodes that have only a slightly lower attenuation than that of muscle. No nodal rim is seen.

lymphoma can produce very large nodes that either are nonnecrotic or have a minimally decreased attenuation on CT. Rare diseases such as sinus histiocytosis with massive lymphadenopathy and Castleman's disease also can cause such lymph nodes [41]. Sarcoid usually produces fairly sizable nodes that are homogeneous and sharply delineated. Most of these nodes are larger than 2 cm in greatest diameter, a feature distinguishing them from hyperplastic nodes, which most often are less than 2 cm in greatest diameter [8, 11]. If the sarcoid nodes are not unusually large, they may not be differentiated from either hyperplastic or lymphomatous nodes.

HIV Nodes

HIV infection also produces diffuse cervical hyperplastic adenopathy, which is of itself nondiagnostic (Fig. 2). However, if such changes are seen in a patient who has multiple parotid cysts and large adenoidal tissue, the diagnosis of HIV infection is virtually assured [42, 43].

Conclusions

With improving CT and MR technology, the radiologist now plays an essential role in the initial evaluation of a cancer patient and in the patient's therapeutic and routine follow-up studies. The radiologist can image pathologic lymph nodes that are inaccessible on clinical examination, and because the radiologist can identify unenlarged necrotic nodes as being pathologic, the role of CT and MR in the management of cancer patients has become of paramount importance. In addition, extranodal spread of tumor to critical structures including the skull base can be routinely identified, and when noted almost always alters a prior treatment plan. As MR resolution continues to improve, scanning times shorten, and artifacts are eliminated, one can reasonably expect that MR imaging may soon be the technique of choice for examining cervical nodal disease. However, at present, the radiologist can perform a faster and more encompassing examination with CT while at the same time minimizing the chances of diagnostic error.

REFERENCES

1. Johnson JT. A surgeon looks at cervical lymph nodes. *Radiology* **1990**;175:607-610
2. Farr HW, Goldfarb PM, Farr CM. Epidermoid carcinoma of the mouth and pharynx at Memorial Sloan Kettering Cancer Center 1965 to 1969. *Am J Surg* **1980**;140:563-567
3. Spiro RH. The management of neck nodes in head and neck cancer: a surgeon's view. *Bull N Y Acad Med* **1985**;61:629-637
4. Bataskis JG. Squamous cell carcinoma of the oral cavity and the oropharynx. In: *Tumor of the head and neck: clinical and pathological considerations*, 2nd ed. Baltimore: Williams & Wilkins, **1979**: Ch. 6, 144-176
5. Bataskis JG. Parenchymal cysts of the neck. In: *Tumor of the head and neck: clinical and pathological considerations*, 2nd ed. Baltimore: Williams & Wilkins, **1979**: Ch. 11, 240-250
6. Tannock IF. Principles of cell proliferation: cell kinetics. In: De Vita VT Jr, ed. *Principles and practice of oncology*, 2nd ed. Philadelphia: Lippincott, **1988**:3-13
7. American Joint Committee on Cancer (Beahrs OH, Henson DE, Hutter RVP, Myers MH, eds). *Manual for staging of cancer*, 3rd ed. Philadelphia: Lippincott, **1988**
8. Som PM. Lymph nodes of the neck. *Radiology* **1987**;165:593-600
9. Van den Brekel MWM, Stel HV, Castelijns JA, et al. Cervical lymph node metastases: assessment of radiologic criteria. *Radiology* **1990**;177: 379-384
10. Mancuso AA, Harnsberger HR, Muraki AS, Stevens MH. Computed tomography of cervical and retropharyngeal lymph nodes: normal anatomy, variants of normal, and application in staging head and neck cancer. Part II. Pathology. *Radiology* **1983**;148:715-723
11. Reede DL, Bergeron RT. Computed tomography of cervical lymph nodes. In: Clouse ME, Wallace S, eds. *Lymphatic imaging: lymphography, computed tomography, and scintigraphy*, 2nd ed. Baltimore: Williams & Wilkins, **1985**:472-495
12. Friedman M, Shelton VK, Mafee M, Bellity P, Grybauskar V, Skolnik E. Metastatic neck disease: evaluation by computed tomography. *Arch Otolaryngol Head Neck Surg* **1984**;110:443-447
13. Close LG, Merkel M, Vuitch MF, Reisch J, Schaefer SD. Computed tomographic evaluation of regional lymph node involvement in cancer of the oral cavity and oropharynx. *Head Neck* **1989**;11:309-317
14. Stevens MH, Harnsberger R, Mancuso AA, Davis RK. Johnson LP, Parkin JL. Computed tomography of cervical lymph nodes: staging and management of head and neck cancer. *Arch Otolaryngol Head Neck Surg* **1985**;111:735-739
15. Feinmesser R, Freeman JL, Nojek AM, Birt BD. Metastatic neck disease: a clinical/radiographic/pathologic correlative study. *Arch Otolaryngol Head Neck Surg* **1987**;113:1307-1310
16. Ali S, Tiwari RM, Snow GB. False positive and false negative neck nodes. *Head Neck* **1985**;8:78-82
17. Sako K, Pradier RN, Marchetta FC, Pickren JW. Fallibility of palpation in the diagnosis of metastases to cervical nodes. *Surg Gynecol Obstet* **1964**;118:989-990
18. Eary JF. Correlative imaging in radioimmunotherapy: progress in clinical radiology. *Invest Radiol* **1991**;26:755-760
19. Snow GB, Annyas AA, Van Slooten EA, Bartelink H, Hart AA. Prognostic factors of neck node metastasis. *Clin Otolaryngol* **1982**;7:185-192
20. Dillon WP, Mills CM, Kjos B, DeGroot J, Brant-Zawadzki M. Magnetic resonance imaging of the nasopharynx. *Radiology* **1984**;152:731-738
21. Dooms GC, Hricak H, Crooks LE, Higgins CB. Magnetic resonance imaging of the lymph nodes: comparison with CT. *Radiology* **1984**;153:719-728
22. Stark DD, Moss AA, Gamsu G, Clark OH, Gooding GAW, Webb WR.

Magnetic resonance imaging of the neck. Part I: normal anatomy. Part II: pathological findings. *Radiology* **1984**;150:447–461

23. Dillon WP. Applications of magnetic resonance imaging to the head and neck. *Semin Ultrasound CT MR* **1986**;7:202–215
24. Glazer HS, Niemeyer JH, Balfe DM, et al. Neck neoplasms: MRI. Part I: initial evaluation. *Radiology* **1986**;160:343–348
25. Rafto SE, Gefter WB. MR imaging of the upper aerodigestive tract and neck. *Radiol Clin North Am* **1988**;26:547–571
26. O'Reilly BJ, Leung A, Greco A. Magnetic resonance imaging in head and neck cancer. *Clin Otolaryngol* **1989**;14:67–78
27. Dooms GC, Hricak H, Moseley MR, Bottles K, Fisher MR, Higgins CB. Characterization of lymphadenopathy by magnetic relaxation times: preliminary results. *Radiology* **1985**;155:691–697
28. Barakos JA, Dillon WP, Chew WM. Orbit, skull base, and pharynx: contrast enhanced fat suppression MR imaging. *Radiology* **1991**;179:191–198
29. Vogl TJ, Steger W, Balzer J, Dresel S, Grevers G. MRI of the neck, larynx and hypopharynx. In: Hasso AN, Stark DD, eds. *Categorical course syllabus. Spine and body magnetic resonance imaging.* Reston, VA: American Roentgen Ray Society, **1991**:99–110
30. Van den Brekel MWM, Castelijns JA, Stel HV, et al. Detection and characterization of metastatic cervical adenopathy by MR imaging: comparison of different MR techniques. *J Comput Assist Tomogr* **1990**;14: 581–589
31. Vogl T, Bruning R, Grevers G, et al. Oropharyngeal and tongue: comparison of plain and Gd-DTPA studies. *J Comput Assist Tomogr* **1988**;12:427–433
32. Yousem DM, Som PM, Schwaibold F, Hendrix R. Evaluation of cervical lymphadenopathy: MR vs CT. *Radiology* (in press)
33. Friedman M, Mafee MF, Pacella BL Jr, et al. Rationale for elective neck dissection in 1990. *Laryngoscope* **1990**;100:54–59
34. Biller HF, Urken M, Lawson W, Haimov M. Carotid artery resection and bypass for neck carcinoma. *Laryngoscope* **1988**;98:181–183
35. West MS, Russell EJ, Breit R, Sze G, Kim KS. Calvarial and skull base metastases: comparison of non enhanced and Gd-DTPA enhanced MR images. *Radiology* **1990**;174:85–91
36. Van Tassel P, Lee Y-Y. Gd-DTPA enhanced MR for detecting intracranial extension of sinonasal malignancies. *J Comput Assist Tomogr* **1991**;15:387–392
37. Som PM, Sacher M, Lanzieri CF, Shugar JMA, Biller HF. Two benign CT presentations of thyroid-related papillary adenocarcinoma. *J Comput Assist Tomogr* **1985**;9:162–166
38. Som PM, Norton KI, Shugar JMA, Norton L, Biller HF, Som ML. Metastatic hypernephroma to the head and neck. *AJNR* **1987**;8:1103–1106
39. Smith JRG, Hadgis C, Van Hasselt A, Metreweli C. CT of Kimura disease. *AJNR* **1989**;10[suppl]:34–36
40. Reede DL, Bergeron RT. Cervical tuberculous adenitis: CT manifestations. *Radiology* **1985**;154:701–704
41. Naidu RK, Urken ML, Som PM, Danon A, Biller HF. Extranodal head and neck sinus histiocytosis with massive lymphadenopathy. *Otolaryngol Head Neck Surg* **1990**;102:764–767
42. Shugar JMA, Som PM, Jacobson AL, Ryan JR, Bernard PJ, Dickman SH. Multicentric parotid cysts and cervical adenopathy in AIDS patients. A newly recognized entity: CT and MR manifestations. *Laryngoscope* **1988**;98:772–775
43. Holliday RA, Cohen WA, Schinella RA, et al. Benign lymphoepithelial parotid cysts and hyperplastic cervical adenopathy in AIDS-risk patients: a new CT appearance. *Radiology* **1988**;168:439–441

Visit from the Doctor—A Serious Case

Stefan C. Schatzki[1]

Genre paintings, which tell the story of everyday life, were extremely popular in the late 19th century. Largely forgotten during most of the first half of this century, when modernism prevailed, this style has seen a revival of interest in recent years. One of the most successful, prolific, and unusual genre painters was the Brooklyn-born artist Harry Roseland.

Roseland, who was born in 1867, was largely self-taught, studying briefly in Brooklyn and then with the noted portrait artist J. Carroll Beckwith, in New York. He began to exhibit at the National Academy at the age of 16 and four years later, in 1887, won a gold medal from the Brooklyn Art Association. For more than 20 years, spanning the end of the 19th century and the first decade of the 20th, Roseland's genre subjects were widely exhibited, earning him many prizes, until changing tastes left his paintings out of fashion in the years just before World War I. What is most unusual about Roseland is that this New Yorker, who never strayed far from his native Brooklyn, spent most of his career painting interior scenes of Afro-Americans. His early paintings, done while he was in his teens and early twenties, cover a wide range of conventional genre subjects. However, in his late twenties, Roseland began to devote himself almost entirely to subjects relating to poorer Afro-Americans. These colorful paintings portray his subjects sympathetically and present cheerful messages.

Roseland's paintings fall largely into two related categories. The best, most true to life, and most effective works are those that insightfully depict the interactions between blacks. Each painting skillfully demonstrates activities that largely occurred in or about the home and capture a way of life that has now vanished. The titles of these works, such as "The Rent Day—A Penny Short," "An Interesting Game of Chess," "A Difference of Opinion," and "Wake Up, Dad," suggest the everyday stories told by Roseland's paintings. The second category includes a large number of paintings that depict the interactions between poor blacks and elegantly dressed, young white women. These works, which primarily show palm readers, fortune tellers, or tea-leaf readings, are more stereotyped, less realistic, and less interesting.

In 1900, Roseland exhibited "Visit from the Doctor—A Serious Case" at the National Academy of Design. This unusual and delightful painting is remarkable because the entire cast of the picture, the child patient, her mother or grandmother, and the doctor, are all Afro-Americans. The charming, seemingly happy child bridges the space between the white-haired paternal physician and the older woman. The subjects are depicted with sympathy and tenderness, and the viewer feels warmth toward the scene despite the potential implications of the child's illness.

Roseland was extremely successful in the early part of his career. His paintings were popular, purchased by major collectors and museums, and were widely reproduced. However, by the time Roseland had reached his mid thirties, and particularly after the Armory show in 1913, which introduced America to the avant-garde art of Europe, Americans' tastes changed rapidly and Roseland's success waned. He continued to paint Afro-American subjects, but his later paintings were less well crafted. In addition, he produced a number of historical subjects, and a portrait of George Washington hangs today in Brooklyn's Borough Hall.

Roseland died in New York City in 1950, an example of an independent American artist who never traveled to Europe to study or observe, but rather chose his own path. During the last few years, as society has reappraised the importance of the Afro-American heritage in our history, there has been a dramatic revival of interest in Roseland's warm, sentimental, sympathetic pictures of an Afro-American era of the past.

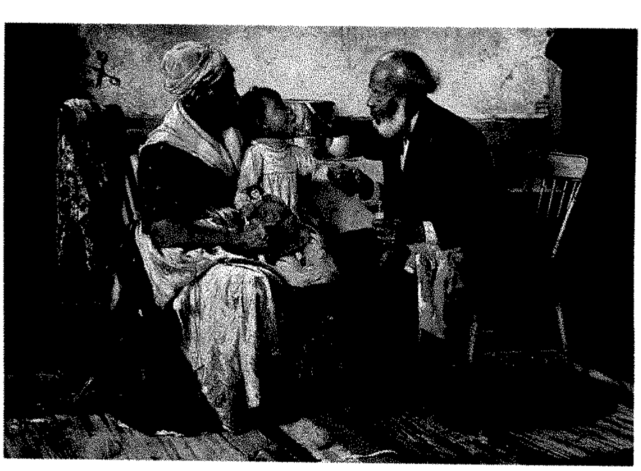

Harry Roseland (1867–1950). *Visit from the Doctor—A Serious Case*, 1898. Oil on canvas, 25 × 35 in. Private collection.

---

[1] Department of Radiology, Mount Auburn Hospital, 330 Mount Auburn St., Cambridge, MA 02238. Address reprint requests to S. C. Schatzki.

***AJR* 158:970, May 1992** 0361-803X/92/1585-0970 © American Roentgen Ray Society

Review Article

High-Resolution CT of the Lungs: Findings in Various Pulmonary Diseases

Stephen J. Swensen,[1] Gregory L. Aughenbaugh,[1] William W. Douglas,[2] and Jeffrey L. Myers[3]

High-resolution CT (HRCT) is a technique that optimizes the spatial resolution of conventional scanners. HRCT shows exquisite detail of both normal and diseased lung. The findings seen with HRCT of the lung correlate well with the microscopic and gross pathologic findings. In this review, we describe the technical features of HRCT and discuss the HRCT findings in various lung diseases.

High-resolution CT (HRCT) is a CT technique that maximizes spatial resolution. This allows superior imaging of the fine structure of the lung and its airways [1, 2].

HRCT closely reflects changes in lung structure and is well suited to evaluate the pulmonary parenchyma and airways. In the past few years, HRCT has been found useful in the evaluation of a variety of pulmonary diseases. It can be used to recognize and diagnose bronchiectasis and a number of diffuse lung diseases [3-6]. A combined examination with CT and HRCT (CT/HRCT) is particularly helpful in the detection and diagnosis of chronic diffuse lung disease [5, 6]. As with plain chest radiography, optimal radiographic technique and knowledgeable pattern recognition of disease are important in realizing the full potential of this method. In this review, we describe the pertinent technical features of HRCT and describe and illustrate the HRCT findings in several lung diseases.

Technique

HRCT uses a high-spatial-frequency reconstruction algorithm and thin CT sections to increase spatial resolution. The tradeoff is that this increases visible noise. However, increased visible noise is a negligible factor in pulmonary parenchymal imaging given the high ratio of air to tissue in the lung. The mediastinal images appear "grainy" but are diagnostically acceptable. It must be kept in mind, however, that during scanning with sections 1-1.5 mm thick at 10-mm intervals, 80-90% of the thorax is not imaged and small nodules can be missed.

The high-spatial-frequency reconstruction algorithm also has an edge enhancement effect that is most pronounced at tissue interfaces that have significantly different attenuations (e.g., air and lung parenchyma). Because of this edge enhancement artifact, HRCT may lead to erroneously high attenuation values at the periphery of a nodule and should not be used to evaluate the density of pulmonary nodules (Fig. 1).

Slice thickness with HRCT is 1.0-1.5 mm, compared with a standard CT slice thickness of 8-10 mm. A small focal spot is used with ultra-high-resolution reconstruction if available. Our technique for conventional CT is 130 kVp and 110 mA with a 2-sec scan time. For HRCT, we use 125 mA to improve image quality slightly [1].

Received March 12, 1991; accepted after revision November 25, 1991.

[1] Department of Diagnostic Radiology, Mayo Clinic and Mayo Foundation, Rochester, MN 55905. Address reprint requests to S. J. Swensen.
[2] Division of Thoracic Diseases and Internal Medicine, Mayo Clinic and Mayo Foundation, Rochester, MN 55905.
[3] Section of Surgical Pathology, Mayo Clinic and Mayo Foundation, Rochester, MN 55905.

AJR 158:971-979, May 1992 0361-803X/92/1585-0971 © American Roentgen Ray Society

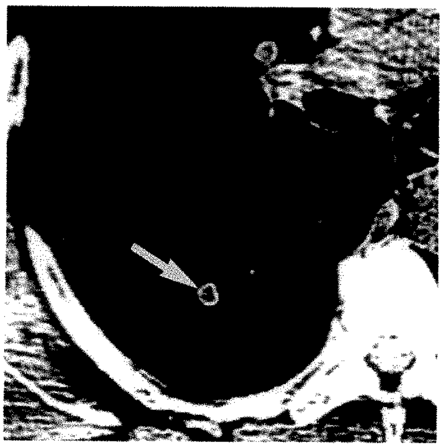

Fig. 1.—High-resolution CT scan of 1-cm pulmonary nodule. Edge enhancement artifact at periphery of nodule (*arrow*) is from high-spatial-frequency reconstruction algorithm. Artifact was not present when scan was reprocessed with standard imaging algorithm.

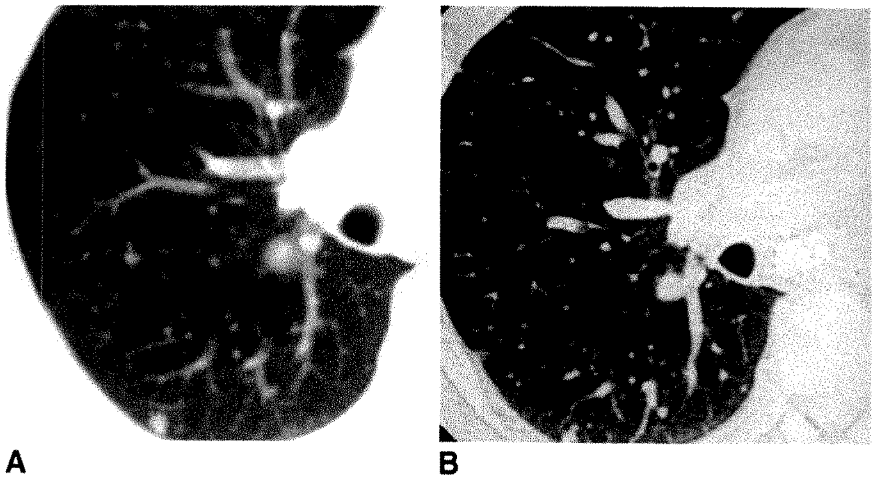

Fig. 2.—*A* and *B*, Lung metastasis from renal cell carcinoma. Small nodules are more readily identified on 10-mm-thick conventional CT scan (*A*) than on 1-mm-thick high-resolution CT scan (*B*) obtained at same level.

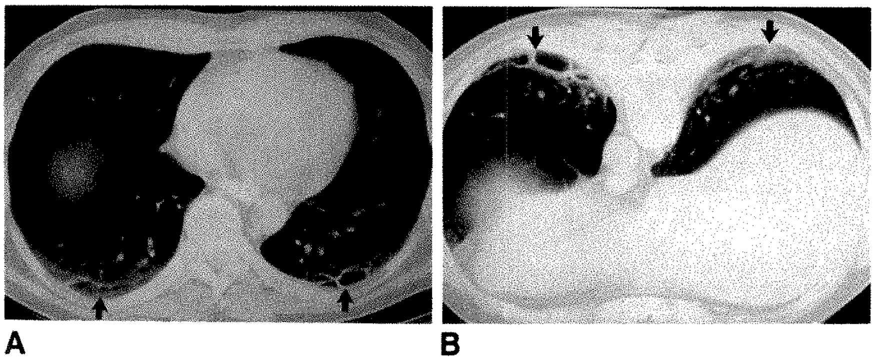

Fig. 3.—Scleroderma.

A, CT scan with patient supine shows linear opacities (*arrows*) in posterior basilar-dependent portions of lung. These opacities could be due to fibrosis, edema, or atelectasis.

B, CT scan with patient prone shows that opacities (*arrows*) persist in nondependent position and therefore are most likely fibrotic. Findings are compatible with early changes of usual interstitial pneumonia, in this case due to scleroderma.

When surveying for bronchiectasis, we obtain only HRCT scans at 1-cm intervals. Because small nodules and diffuse nodular infiltrates are more readily detected on conventional CT than on HRCT, a combination of conventional and high-resolution sections (CT/HRCT) has been recommended for evaluation of diffuse lung disease [5] (Fig. 2). When neoplasm is not suspected, we usually evaluate diffuse lung disease with alternating conventional and high-resolution sections obtained at 10-mm intervals. First, conventional 10-mm sections are obtained at 20-mm intervals through the entire chest, and then thin-section images (1–1.5 mm in thickness) are obtained at 20-mm intervals between the levels of the conventional images.

Scans are done at full inspiration and with the patient supine. When there are opacities in the dependent region of the lung, we also scan with the patient prone to differentiate gravity-dependent hypostatic pulmonary atelectasis ("airway closure") from interstitial fibrosis or infiltration (Fig. 3). Retrospective targeted images are obtained as indicated to increase spatial resolution.

Retrospective targeted reconstruction of HRCT images allows a further significant increase in spatial resolution by decreasing pixel size. The spatial resolution is approximately 1.5 times the pixel size [5]. The standard field of view of 40 cm uses a pixel of 0.78 mm. Targeting to a field of view of 12.8 cm decreases the pixel size to 0.25 mm. Further decreases in field of view do not improve the image [1, 2].

Bronchiectasis

HRCT has been used successfully in the evaluation and early detection of bronchiectasis. CT findings in bronchiectasis include thickened bronchial walls and dilated bronchi, which result in visibility of bronchi more peripherally in the lung than normal [3, 4, 7]. Bronchi accompany pulmonary arteries into the lung and have approximately equal external diameters. When bronchiectasis is present, the affected bronchus is larger than its attendant artery. The "signet ring" sign is formed when these structures are viewed in cross section (Fig. 4). This is virtually pathognomonic of bronchiectasis [7].

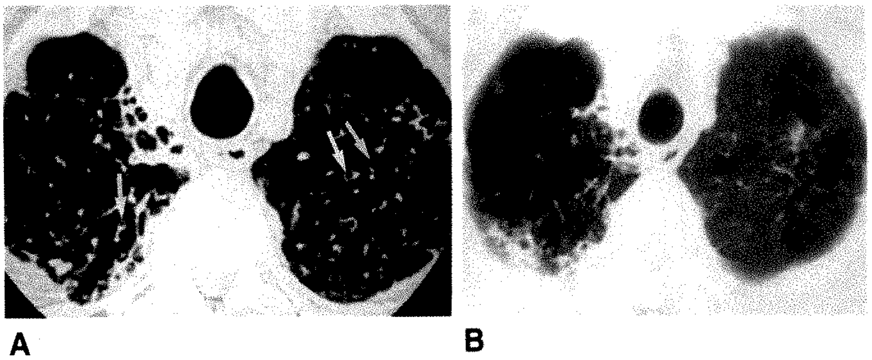

Fig. 4.—Bronchiectasis.
A, High-resolution CT scan shows multiple signet ring signs (*arrows*), which are diagnostic of bronchiectasis.
B, Shadows are much less distinct on conventional CT image (with high-spatial-frequency reconstruction algorithm) obtained on same day at same level.

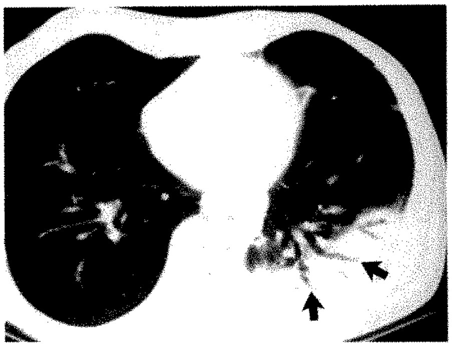

5

Fig. 5.—CT scan shows dilated bronchi (*arrows*) within consolidated region of posterior and lateral basal segments of left lower lobe. Infiltrate was bacterial pneumonia. Radiologic and clinical findings were consistent with pseudobronchiectasis.

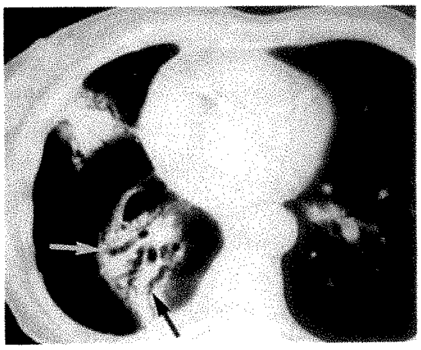

6

Fig. 6.—CT scan shows traction bronchiectasis (*arrows*) due to radiation fibrosis from treatment of lymphoma.

Bronchiectasis may also be identified as a linear array or cluster of cysts, often with air-fluid levels. Sometimes a varicose configuration can be seen when bronchi are coursing in the same plane as the CT section. Care must be taken to identify bronchiectasis with mucoid impaction, which will appear as a linear or branched solid tubular opacity when imaged in profile or as a solid signet ring when imaged in cross section.

Bronchiectasis is defined as fixed bronchial dilatation. It is important to be aware of pseudobronchiectasis, which is reversible cylindrical bronchial dilatation. Pseudobronchiectasis results from inflammatory changes typically related to bacterial pneumonia (Fig. 5). After resolution of acute pneumonia, bronchial dilatation may persist for up to 3–4 months. Consequently, HRCT examination for bronchiectasis should be performed at least 4 months after the infection has resolved to avoid this pitfall [8, 9]. Traction bronchiectasis, associated with pulmonary fibrosis, is a type of airway dilatation that should be distinguished when possible [10] (Fig. 6).

Diffuse Lung Disease

Many diffuse infiltrative lung processes have distinguishing features when studied with CT/HRCT [5, 11–13]. A nodular, cystic, polygonal, irregular linear, ground-glass (homogeneous, hazy region of increased attenuation without air bronchograms or obscuration of pulmonary vasculature) or alveolar pattern has diagnostic significance. The distribution of the parenchymal changes is also an important feature to analyze [14, 15]. Some diffuse lung diseases are distributed predominantly in the upper zones rather than in the lung bases or have peripheral rather than perihilar involvement. For example, usual interstitial pneumonia (UIP) typically has a peripheral basilar distribution, whereas silicosis has an upper, often posterior predominance.

Over 100 entities are known to cause diffuse lung disease [16]. Fortunately, fewer than 20 of these processes account for nearly 90% of all nonneoplastic disorders assessed with open lung biopsy [16, 17]. The following is a summary of the CT/HRCT features of some of the more common diffuse lung diseases.

Usual Interstitial Pneumonia

UIP is the most common abnormal finding in patients with chronic progressive infiltrating lung disease. The clinical and radiologic findings are often nonspecific. CT/HRCT is often useful in demonstrating the typical features of UIP or those of entities that can mimic this condition. UIP is a histopathologic term referring to a pattern of nonspecific interstitial fibrosis that occurs in patients with various disorders, including idiopathic pulmonary fibrosis, asbestosis, rheumatoid arthritis, mixed connective tissue disease, and scleroderma. The patient's clinical presentation determines the specific diagnosis in these situations.

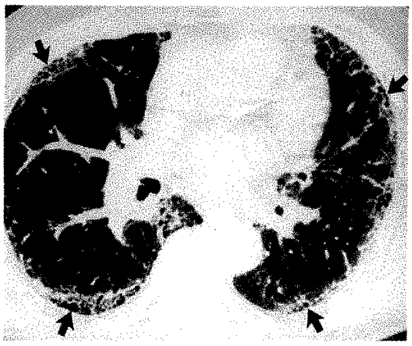

7

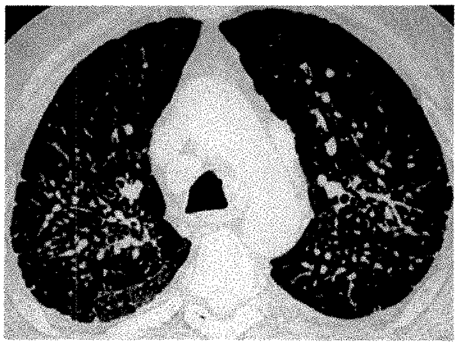

8

Fig. 7.—High-resolution CT scan of usual interstitial pneumonia. Note characteristic basilar and peripheral subpleural honeycomb pattern (*arrows*).

Fig. 8.—Silicosis. CT scan shows upper lung distribution of small nodules. Note difference in nodule distribution between silicosis and sarcoidosis (Fig. 9). Nodules in sarcoidosis have more peribronchovascular and central distribution.

CT/HRCT typically shows patchy reticular, honeycomb, and ground-glass opacities. Subpleural honeycombing is a frequent finding. The infiltrative pattern tends to have a distinctive basilar and peripheral subpleural distribution [18-20] (Fig. 7). There is generally minimal involvement of the interlobular septa [20]. Intralobular bands may be present. Enlargement of mediastinal lymph nodes is common in UIP and presumably is part of the inflammatory process [21].

CT/HRCT can assess response to steroid therapy in UIP [18]. Patients with UIP who are found to have areas of ground-glass opacity or air-space consolidation are more likely to have a response to steroid therapy than are those with only honeycombing or linear or nodular opacities [18].

Asbestosis

HRCT can depict early pulmonary fibrosis due to asbestos exposure [22]. The subpleural parenchyma of the lower lobes is the initial site of detectable abnormality by HRCT [22, 23]. Parenchymal features of asbestosis, like those of UIP, include thickened intralobular and interlobular (septal) lines, subpleural curvilinear opacities, subpleural nodular irregularities, honeycombing, and hazy patches of increased attenuation. The distribution of the parenchymal abnormalities has a basilar and peripheral predominance [22-25]. Occasionally, HRCT examinations with the patient both prone and supine are necessary to differentiate gravity-dependent subpleural opacities from fibrosis (Fig. 3). CT/HRCT is also sensitive in the detection of calcified and uncalcified pleural plaques in patients exposed to asbestos.

Silicosis and Coal Worker's Pneumoconiosis

The characteristic CT finding in silicosis and coal worker's pneumoconiosis is multiple small nodules with predominant distribution in the upper lung zones, especially posteriorly [5, 14, 26-28] (Fig. 8). Although silicosis and coal worker's pneumoconiosis are pathologically distinct entities, their radiologic findings are similar.

As simple silicosis and coal worker's pneumoconiosis progress and the number of nodules increases, nodules coalesce and the adjacent lung architecture becomes contracted and distorted. At the stage of coalescence of small nodules into large nodular opacities (diameter, ≥1 cm), simple silicosis transforms into complicated silicosis. Radiologic progression of simple silicosis to complicated silicosis is mirrored by clinical deterioration of the patient, who has increasing dyspnea and functional impairment [29].

CT is of value because it can detect the development of complicated disease early [27, 28]. Large nodular opacities can progress to form even larger conglomerate masses or progressive massive fibrosis, which is accompanied by the development of cicatricial emphysema. This further reduces lung function. The extent of emphysema correlates more closely with functional impairment than does the degree of nodular profusion (27, 30]. CT/HRCT clearly shows fibrosis and emphysema [27]. CT can monitor disease progression and evaluate for potentially curable superimposed disease, such as tuberculosis and lung cancer [26-28].

Recently, HRCT was found to differentiate focal dust emphysema, which is most commonly associated with tiny p-type nodular opacities, from centrilobular emphysema [31].

Sarcoidosis

Sarcoidosis is characterized by nonnecrotizing granulomas distributed along the lymphatic pathways of the bronchovascular bundles and interlobular septa. The opacities tend to be nodular and predominate in upper and middle lung zones. The nodules often are clustered in the perihilar, peribronchovascular region, with relative sparing of the lung periphery [13] (Fig. 9).

In later stages of sarcoidosis, cicatricial changes result in architectural distortion and fibrotic areas of consolidation [32] (Fig. 10). Sarcoidosis may occasionally be difficult to differentiate from lymphatic carcinomatosis because both can have lymphadenopathy and nodular peribronchovascular and septal thickening [13]. Cicatricial lung distortion and traction bronchiectasis are seen in sarcoidosis and can be useful in differential diagnosis. Also, nodules may be more numerous with sarcoidosis than with lymphatic carcinomatosis.

Lymphatic Carcinomatosis

CT/HRCT of lymphatic carcinomatosis is characterized by nodular thickening of the interlobular septa without cicatricial

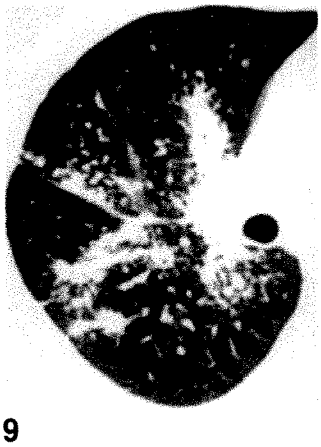

9

Fig. 9.—Typical high-resolution CT findings of stage II sarcoidosis. Note central peribronchovascular distribution of small nodules. Lung periphery is relatively spared.

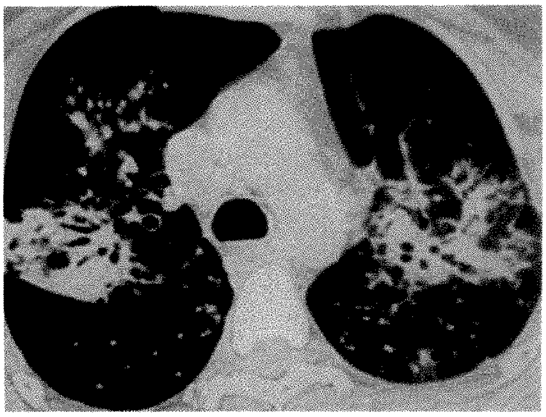

10

Fig. 10.—Stage IV sarcoidosis. High-resolution CT scan shows bilateral midlung regions of consolidation due to sarcoid granulomatous reaction and fibrosis. Secondary traction bronchiectasis and cicatricial parenchymal distortion are present. Typical small nodular changes are present in anterior segment of right upper lobe and superior segment of left lower lobe.

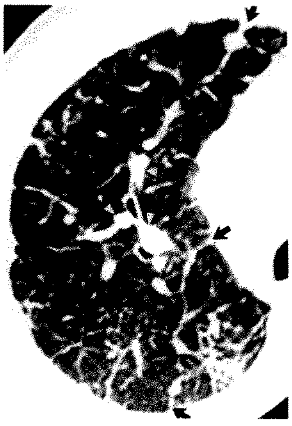

11

Fig. 11.—Lymphatic carcinomatosis. High-resolution CT scan shows typical nodular thickening of interlobular septa (*arrows*) and bronchovascular bundles (*arrowheads*).

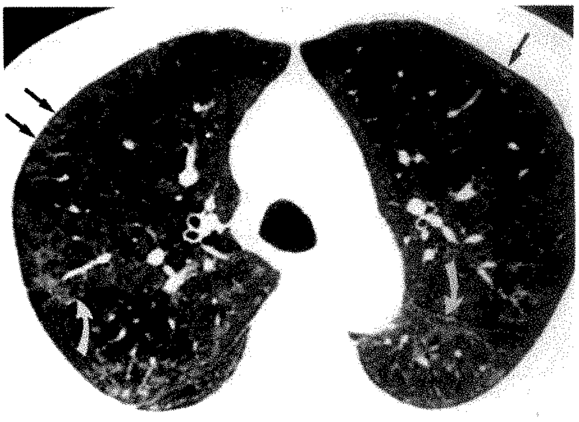

12

Fig. 12.—Pigeon breeder's hypersensitivity pneumonitis. High-resolution CT scan shows patchy areas of ground-glass opacity (*white arrows*). By definition, ground-glass opacity does not obscure bronchovascular shadows. Scattered small focal nodular opacities (*black arrows*) are present also. These high-resolution CT findings are compatible with hypersensitivity pneumonitis.

distortion of polygonal architecture. Distribution tends to be basilar. Peribronchovascular nodularity also is often evident [33, 34] (Fig. 11). CT/HRCT may locate an area of involvement that is suggestive of lymphatic carcinomatosis early in the course of the disease.

Hypersensitivity Pneumonitis (Extrinsic Allergic Alveolitis)

Acute hypersensitivity pneumonitis is characterized primarily by ground-glass and air-space opacification. Small (1.5 mm or less) or medium (1.5–3.0 mm) nodular opacities are also seen. Subacute hypersensitivity pneumonitis with disease duration measured in days or months shows both small rounded opacities and ground-glass opacity that do not obscure the underlying bronchovascular shadows (Fig. 12). Chronic hypersensitivity pneumonitis of greater than 1 year's duration has irregular fibrotic linear opacities associated with the findings of subacute disease [35].

Abnormalities are found predominantly in the middle lung zones, and the lung bases are relatively spared. No axial predilection has been noted. In the appropriate clinical setting with a history of exposure, the CT/HRCT findings in the subacute phase of hypersensitivity pneumonitis are thought to be characteristic enough to suggest the diagnosis [35]. Chest radiography has shown upper zone predominance of fibrotic changes in chronic hypersensitivity pneumonitis [36]. This finding has not yet been confirmed by CT/HRCT [35].

Cardiogenic Pulmonary Edema

Smooth subpleural and peribronchovascular thickening as well as increased thickness and number of visible interlobular septal lines without nodularity are characteristics of the interstitial abnormalities seen in pulmonary edema. The diffuse infiltrate may be dependently distributed. Various degrees of alveolar opacification representing air-space edema may also be present. The left ventricle and atrium may be enlarged. Small pleural effusions are frequently present [37].

Emphysema

CT/HRCT of emphysema is characterized by bullae or small lucent areas (or both) without the well-defined walls one would expect to see with lung cysts or honeycombing. CT/HRCT can show changes of centrilobular, panacinar, irregular, and

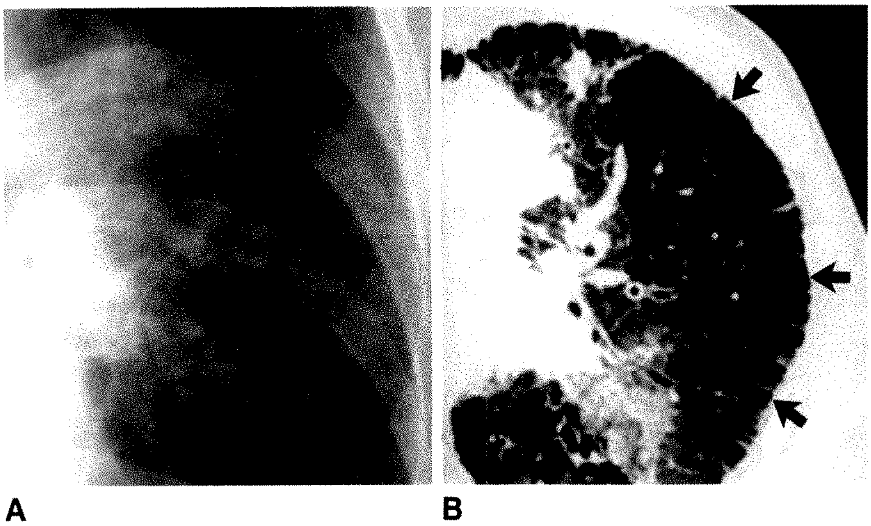

Fig. 13.—Emphysema.

A, Chest radiograph shows left hilar bronchogenic carcinoma. Linear interstitial pattern with Kerley's B lines suggested lymphatic carcinomatosis.

B, High-resolution CT scan shows central lung cancer but no evidence of lymphatic carcinomatosis. Interstitial pattern seen on chest radiograph (*A*) was due to paraseptal emphysema (*arrows*). This pattern was symmetric with contralateral lung and subsequently shown to be unchanged over several years.

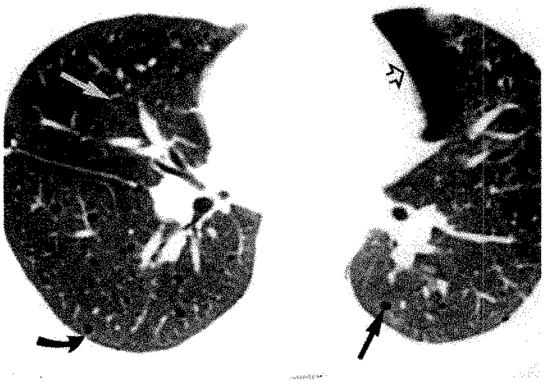

14

Fig. 14.—High-resolution CT scan of early stage of lymphangioleiomyomatosis. Small air-filled, thin-walled cysts (*solid arrows*) were uniformly distributed throughout lungs. Patients with this disease are predisposed to pneumothorax (*open arrow*).

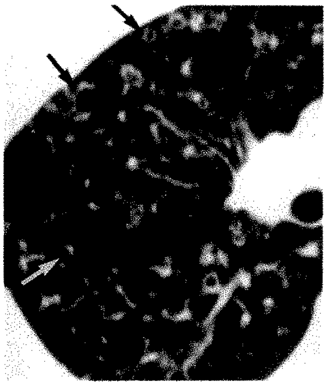

15

Fig. 15.—High-resolution CT scan of eosinophilic granuloma (histiocytosis X) shows numerous small air-filled, thin-walled cysts (*arrows*). These cysts are spherical, not tubular, and should not be confused with signet ring sign of bronchiectasis.

paraseptal emphysema [38]. There is a significant correlation between HRCT grading and pathologic grading of emphysema [39, 40]. CT/HRCT may show that apparent diffuse infiltrative lung disease on chest radiographs is due to a pleural process or a type of emphysematous lung disease (Fig. 13).

Lymphangioleiomyomatosis and Tuberous Sclerosis

Lymphangioleiomyomatosis and pulmonary involvement in tuberous sclerosis are radiologically and pathologically identical. Both are characterized by haphazard proliferation of smooth muscle cells along bronchovascular bundles, lymphatics, and pulmonary veins. Numerous small parenchymal cysts are uniformly distributed throughout the lungs and are a characteristic finding on CT/HRCT [41–46] (Fig. 14). Although not a prominent feature, septal thickening results from lymphatic engorgement, smooth muscle proliferation, and fibrosis. Additional CT/HRCT findings that may not be evident on conventional radiographs are small pneumothoraces, chylous effusions, mediastinal lymphangiomyomatous adenopathy, and renal or hepatic angiomyolipomata [41–46].

Eosinophilic Granuloma (Histiocytosis X)

The parenchymal disease of eosinophilic granuloma (histiocytosis X) tends to have an upper lung predominance [47–50]. Cystic changes and nodules are the predominant CT/HRCT finding [48]. Usually, small thin-walled, air-filled cysts or nodules are present [47, 48] (Fig. 15). Nodules may progress to cavitated nodules to cysts to confluent cysts [48]. The patients are prone to pneumothorax, probably from cyst rupture. Mild interlobular septal thickening also may occur.

The cysts found in lymphangioleiomyomatosis have a similar appearance but are not associated with nodular changes or an upper lung distribution [48]. The CT/HRCT cystic findings in eosinophilic granuloma may also resemble bronchiectasis, but examination of serial sections can differentiate tubular from spherical structures. The cysts in both lymphangioleiomyomatosis and eosinophilic granuloma do not have a peripheral distribution like honeycomb cysts of UIP.

Chronic Eosinophilic Pneumonia

Fewer than 50% of patients with chronic eosinophilic pneumonia have the classic pattern of peripheral air-space disease

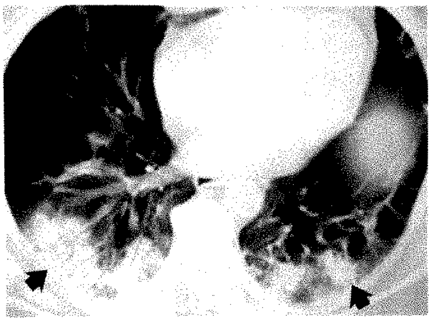
16

Fig. 16.—CT scan of bronchiolitis obliterans with organizing pneumonia. Although nonspecific, focal areas of air-space infiltrate (*arrows*) may be present, often involving outer third of lung.

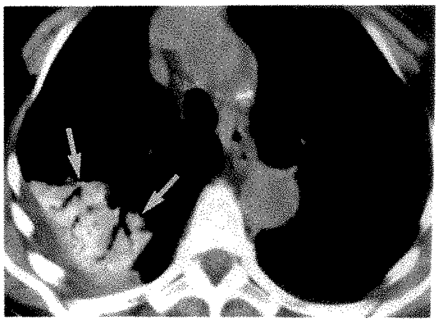
17

Fig. 17.—Unenhanced CT scan shows high-attenuation region of lung consolidation (*arrows*). Findings are characteristic of amiodarone toxicity. Air-space infiltrate was shown to be due to bronchiolitis obliterans with organizing pneumonia.

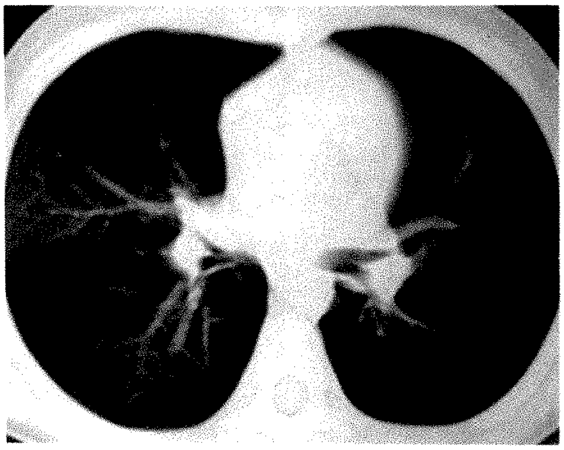
18

Fig. 18.—Obliterative bronchiolitis. CT scan shows confluent regions of hyperlucency due to hyperinflation that are primarily in lung periphery. More central regions of higher attenuation are accentuated on this expiration scan.

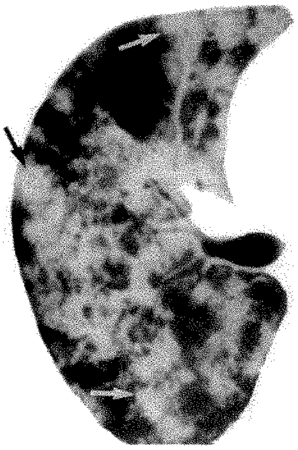
19

Fig. 19.—High-resolution CT scan of alveolar proteinosis shows predominant pattern of air-space filling. Multiple fluffy, approximately 2-cm areas of confluence (*arrows*) correspond to secondary pulmonary lobules.

involving the middle and upper lung zones on the chest radiograph [51, 52]. In patients who lack these classic findings, diagnosis and therapy can be delayed. In some cases, the absence of classic findings may even lead to unnecessary open lung biopsy. CT/HRCT can display the peripheral position of air-space infiltrates in this disorder by eliminating superimposition [53]. In the appropriate clinical setting, the diagnosis of chronic eosinophilic pneumonia can be strongly supported by the CT/HRCT findings [53]. Löffler's syndrome has a similar distribution of eosinophilic infiltrates, but they are more fleeting [54].

Bronchiolitis Obliterans with Organizing Pneumonia (BOOP)

BOOP is a relatively nonspecific pattern of intraluminal fibrosis that can be seen in various clinical contexts. In some patients, BOOP represents a primary idiopathic form of fibrosing lung disease ("idiopathic BOOP"). CT findings in patients with idiopathic BOOP include patchy areas of air-space consolidation and nodular opacities 10 mm or less in diameter (Fig. 16). Air-space consolidation and nodular opacities can be seen either alone or in combination. Air-space consolidation is usually bilateral and asymmetric but can be unilateral [55, 56]. It is common for the areas of consolidation to be subpleural, similar to the distribution with chronic eosinophilic pneumonia; however, the disease can also be restricted to more central areas without subpleural disease [55, 57]. Bronchial wall thickening and dilatation are frequently found within the areas of consolidation.

The CT/HRCT findings of idiopathic BOOP are acknowledged to be nonspecific; however, in the proper clinical setting, they can support the diagnosis. CT/HRCT can evaluate the extent of disease and its distribution. CT/HRCT may help differentiate BOOP from UIP [57].

BOOP may be a manifestation of toxicity from certain drugs, including amiodarone and bleomycin [58]. Amiodarone-induced BOOP can cause characteristic high-attenuation parenchymal-pleural abnormalities. The high attenuation is thought to be from the iodinated composition of the drug [59] (Fig. 17).

Obliterative Bronchiolitis

Obliterative bronchiolitis is a form of small-airways disease that results in chronic obstructive airways resistance. It has been associated with viral infection, exposure to toxic fumes, bone marrow transplantation, and rheumatoid arthritis [60–62]. BOOP is a distinct clinical and pathologic entity that usually has associated parenchymal infiltrates. Obliterative bronchiolitis, on the other hand, is not associated with parenchymal infiltrates, although there is widespread inhomogeneity of the lung parenchyma. CT in obliterative bronchiolitis typically shows diffuse changes consisting of patchy irregular areas of high and low attenuation that are accentuated on expiration [63]. The hyperlucent regions are presumably hyperinflated lung distal to the obstructed bronchioles. These areas tend to be in the periphery of the lobes (Fig. 18).

Alveolar Proteinosis

Alveolar proteinosis is predominantly an air-space process. The CT/HRCT appearance ranges from poorly defined acinar nodules to patchy consolidation to larger areas of confluence [64, 65] (Fig. 19). The diffuse air-space infiltrate often has a "bat wing" perihilar distribution that spares the costophrenic angles and lung periphery, but it may involve primarily the periphery. Air bronchograms are not a predominant feature, however. A background pattern of interlobular septal thickening from edema is also present in some cases [65].

Patients with alveolar proteinosis are prone to the development of pulmonary infection. CT/HRCT can be helpful in suggesting superimposed focal infection and may also show the extent of disease [64].

REFERENCES

1. Mayo JR, Webb WR, Gould R, et al. High-resolution CT of the lungs: an optimal approach. *Radiology* **1987**;163:507–510
2. Murata K, Khan A, Rojas KA, Herman PG. Optimization of computed tomography: technique to demonstrate the fine structure of the lung. *Invest Radiol* **1988**;23:170–175
3. Joharjy IA, Bashi SA, Adbullah AK. Value of medium-thickness CT in the diagnosis of bronchiectasis. *AJR* **1987**;149:1133–1137
4. Grenier P, Maurice F, Musset D, Menu Y, Nahum H. Bronchiectasis: assessment of thin-section CT. *Radiology* **1986**;161:95–99
5. Mathieson JR, Mayo JR, Staples CA, Müller NL. Chronic diffuse infiltrative lung disease: comparison of diagnostic accuracy of CT and chest radiography. *Radiology* **1989**;171:111–116
6. Grenier P, Valeyre D, Cluzel P, Brauner MW, Lenoir S, Chastang C. Chronic diffuse interstitial lung disease: diagnostic value of chest radiography and high-resolution CT. *Radiology* **1991**;179:123–132
7. Naidich DP, McCauley DI, Khouri NF, Stitik FP, Siegelman SS. Computed tomography of bronchiectasis. *J Comput Assist Tomogr* **1982**;6:437–444
8. Pontius JR, Jacobs LG. The reversal of advanced bronchiectasis. *Radiology* **1957**;68:204–208
9. Nelson SW, Christoforidis A. Reversible bronchiectasis. *Radiology* **1958**;71:375–382
10. Westcott JL, Cole SR. Traction bronchiectasis in end-stage pulmonary fibrosis. *Radiology* **1986**;161:665–669
11. Müller NL, Miller RR. Computed tomography of chronic diffuse infiltrative lung disease: part 1. *Am Rev Respir Dis* **1990**;142:1206–1215
12. Müller NL, Miller RR. Computed tomography of chronic diffuse infiltrative lung disease: part 2. *Am Rev Respir Dis* **1990**;142:1440–1448
13. Bergin CJ, Coblentz CL, Chiles C, Bell DY, Castellino RA. Chronic lung diseases: specific diagnosis by using CT. *AJR* **1989**;152:1183–1188
14. Gurney JW, Schroeder BA. Upper lobe lung disease: physiologic correlates; review. *Radiology* **1988**;167:359–366
15. Gurney JW. Cross-sectional physiology of the lung. *Radiology* **1991**;178:1–10
16. DeRemee RA. Diffuse interstitial pulmonary disease from the perspective of the clinician. *Chest* **1987**;92:1068–1073
17. McLoud TC, Carrington CB, Gaensler EA. Diffuse infiltrative lung disease: a new scheme for description. *Radiology* **1983**;149:353–363
18. Müller NL, Staples CA, Miller RR, Vedal S, Thurlbeck WM, Ostrow DN. Disease activity in idiopathic pulmonary fibrosis: CT and pathologic correlation. *Radiology* **1987**;165:731–734
19. Staples CA, Müller NL, Vedal S, Abboud R, Ostrow D, Miller RR. Usual interstitial pneumonia: correlation of CT with clinical, functional, and radiologic findings. *Radiology* **1987**;162:377–381
20. Müller NL, Miller RR, Webb WR, Evans KG, Ostrow DN. Fibrosing alveolitis: CT-pathologic correlation. *Radiology* **1986**;160:585–588
21. Bergin C, Castellino RA. Mediastinal lymph node enlargement on CT scans in patients with usual interstitial pneumonitis. *AJR* **1990**;154:251–254
22. Aberle DR, Gamsu G, Ray CS, Feuerstein IM. Asbestos-related pleural and parenchymal fibrosis: detection with high-resolution CT. *Radiology* **1988**;166:729–734
23. Akira M, Yokoyama K, Yamamoto S, et al. Early asbestosis: evaluation with high-resolution CT. *Radiology* **1991**;178:409–416
24. Friedman AC, Fiel SB, Fisher MS, Radecki PD, Lev-Toaff AS, Caroline DF. Asbestos-related pleural disease and asbestosis: a comparison of CT and chest radiography. *AJR* **1988**;150:269–275
25. McLoud TC. The use of CT in the examination of asbestos-exposed persons. *Radiology* **1988**;169:862–863
26. Remy-Jardin M, Degreef JM, Beuscart R, Voisin C, Remy J. Coal worker's pneumoconiosis: CT assessment in exposed workers and correlation with radiographic findings. *Radiology* **1990**;177:363–371
27. Bergin CJ, Müller NL, Vedal S, Chan-Yeung M. CT in silicosis: correlation with plain films and pulmonary function tests. *AJR* **1986**;146:477–483
28. Bégin R, Bergeron D, Samson L, Boctor M, Cantin A. CT assessment of silicosis in exposed workers. *AJR* **1987**;148:509–514
29. Fraser RG, Paré JAP, Paré PD, Fraser RS, Genereux GP. *Diagnosis of diseases of the chest*, 3rd ed, vol 3. Philadelphia: Saunders, **1990**: 2282–2307
30. Kinsella M, Müller NL, Vedal S, Staples C, Abboud RT, Chan-Yeung M. Emphysema in silicosis: a comparison of smokers with nonsmokers using pulmonary function testing and computed tomography. *Am Rev Respir Dis* **1990**;141:1479–1500
31. Akira M, Higashihara T, Yokoyama K, et al. Radiographic type p pneumoconiosis: high-resolution CT. *Radiology* **1989**;171:117–123
32. Zerhouni EA, Naidich DP, Stitik FP, Khouri NF, Siegelman SS. Computed tomography of the pulmonary parenchyma. Part 2: Interstitial disease. *J Thorac Imaging* **1985**;1;54–64
33. Bergin CJ, Müller NL. CT of interstitial lung disease: a diagnostic approach. *AJR* **1987**;148:9–15
34. Stein MG, Mayo J, Müller N, Aberle DR, Webb WR, Gamsu G. Pulmonary lymphangitic spread of carcinoma: appearance on CT scans. *Radiology* **1987**;162:371–375
35. Silver SF, Müller NL, Miller RR, Lefcoe MS. Hypersensitivity pneumonitis: evaluation with CT. *Radiology* **1989**;173:441–445
36. Cook PG, Wells IP, McGavin CR. The distribution of pulmonary shadowing in farmer's lung. *Clin Radiol* **1988**;39:21–27
37. Stark P, Jasmine J. CT of pulmonary edema. *Crit Rev Diagn Imaging* **1989**;29(3):245–255
38. Bergin CJ, Müller NL, Miller RR. CT in the qualitative assessment of emphysema. *J Thorac Imaging* **1986**;1:94–103
39. Hruban RH, Meziane MA, Zerhouni EA, et al. High resolution computed tomography of inflation-fixed lungs: pathologic-radiologic correlation of centrilobular emphysema. *Am Rev Respir Dis* **1987**;136:935–940
40. Kinsella M, Müller NL, Abboud RT, Morrison NJ, DyBuncio A. Quantitation of emphysema by computed tomography using a "density mask" program and correlation with pulmonary function tests. *Chest* **1990**;97:315–321
41. Aberle DR, Hansell DM, Brown K, Tashkin DP. Lymphangiomyomatosis: CT, chest radiographic, and functional correlations. *Radiology* **1990**;176:381–387
42. Müller NL, Chiles C, Kullnig P. Pulmonary lymphangiomyomatosis: correlation of CT with radiographic and functional findings. *Radiology* **1990**;175:335–339
43. Lenoir S, Grenier P, Brauner MW, et al. Pulmonary lymphangiomyomatosis and tuberous sclerosis: comparison of radiographic and thin-section CT findings. *Radiology* **1990**;175:329–334
44. Sherrier RH, Chiles C, Roggli V. Pulmonary lymphangioleiomyomatosis: CT findings. *AJR* **1989**;153:937–940
45. Rumancik WM, Bosniak MA, Rosen RJ, Hulnick D. Atypical renal and pararenal hamartomas associated with lymphangiomyomatosis. *AJR* **1984**;142:971–972
46. Merchant RN, Pearson MG, Rankin RN, Morgan WKC. Computerized

tomography in the diagnosis of lymphangioleiomyomatosis. *Am Rev Respir Dis* **1985**;131:295-297

47. Moore ADA, Godwin JD, Müller NL, et al. Pulmonary histiocytosis X: comparison of radiographic and CT findings. *Radiology* **1989**;172: 249-254
48. Brauner MW, Grenier P, Mouelhi MM, Mompoint D, Lenoir S. Pulmonary histiocytosis X: evaluation with high-resolution CT. *Radiology* **1989**;172:255-258
49. Lacronique J, Roth C, Battesti J-P, Basset F, Chretien J. Chest radiological features of pulmonary histiocytosis X: a report based on 50 adult cases. *Thorax* **1982**;37:104-109
50. Marcy TW, Reynolds HY. Pulmonary histiocytosis X. *Lung* **1985**;163: 129-150
51. Jederlinic PJ, Sicilian L, Gaensler EA. Chronic eosinophilic pneumonia: a report of 19 cases and a review of the literature. *Medicine (Baltimore)* **1988**;67:154-162
52. Pearson DJ, Rosenow EC III. Chronic eosinophilic pneumonia (Carrington's). A follow-up study. *Mayo Clin Proc* **1978**;53:73-78
53. Mayo JR, Müller NL, Road J, Sisler J, Lillington G. Chronic eosinophilic pneumonia: CT findings in six cases. *AJR* **1989**;153:727-730
54. Fraser RG, Paré JAP, Paré PD, Fraser RS, Genereux GP. *Diagnosis of diseases of the chest*, 3rd ed, vol 2. Philadelphia: Saunders, **1989**:1290-1298.
55. Müller NL, Staples CA, Miller RR. Bronchiolitis obliterans organizing pneumonia: CT features in 14 patients. *AJR* **1990**;154:983-987
56. Miki Y, Hatabu H, Takahashi M, Sadatoh N, Kuroda Y. Computed tomography of bronchiolitis obliterans. *J Comput Assist Tomogr* **1988**;12:512-514
57. Müller NL, Guerry-Force ML, Staples CA, et al. Differential diagnosis of bronchiolitis obliterans with organizing pneumonia and usual interstitial pneumonia: clinical, functional, and radiologic findings. *Radiology* **1987**;162:151-156
58. Myers JL, Kennedy JI, Plumb VJ. Amiodarone lung: pathologic findings in clinically toxic patients. *Hum Pathol* **1987**;18:349-354
59. Kuhlman JE, Teigen C, Ren H, Hurban RH, Hutchins GM, Fishman EK. Amiodarone pulmonary toxicity: CT findings in symptomatic patients. *Radiology* **1990**;177:121-125
60. Wohl MEB, Chernick V. Bronchiolitis. *Am Rev Respir Dis* **1978**;118: 759-781
61. Ramirez RJ, Dowell AR. Silo-filler's disease: nitrogen dioxide-induced lung injury; long-term follow-up and review of the literature. *Ann Intern Med* **1971**;74:569-576
62. Wyatt SE, Nunn P, Hows JM, et al. Airways obstruction associated with graft versus host disease after bone marrow transplantation. *Thorax* **1984**;39:887-894
63. Sweatman MC, Millar AB, Strickland B, Turner-Warwick M. Computed tomography in adult obliterative bronchiolitis. *Clin Radiol* **1990**;41: 116-119
64. Godwin JD, Müller NL, Takasugi JE. Pulmonary alveolar proteinosis: CT findings. *Radiology* **1988**;169:609-613
65. Murch CR, Carr DH. Computed tomography appearances of pulmonary alveolar proteinosis. *Clin Radiol* **1989**;40:240-243

History Page

The Year It Came Together

Raymond A. Gagliardi[1]

The last week of 1895 was a watershed week for Wilhelm Roentgen, medical practice, and the new science of roentgenology. As with most discoveries, much work preceded the final event. Indeed, Roentgen was not seeking new knowledge when he discovered the "new kind of ray" but only trying to duplicate the work of Philipp Lenard, who had observed fluorescence in different chemicals when they were exposed to the cathode rays of the Crookes' vacuum tube [1].

Let us review the record. In 1839, Heinrich Geissler invented a pump to produce vacuums in glass tubes. By substituting different gases for air, he produced different color effects when an electric charge passed through the tube. Twenty years later, Plucker noted an apple-green fluorescence in older Geissler tubes. Johann Hittorf then showed that Plucker's green light came from the negative electrode, and thus the term cathode ray was coined. Hittorf then placed solid matter in the path of the cathode ray and noted it cast a shadow on the opposite wall [2].

Herman Sprengel developed a superior vacuum pump and then William Crookes, using the Sprengel pump, developed a tube that retained one millionth of its original air content [3]. The apple-green effect now appeared at once, as high-tension currents passed through the higher resistance of the gasless tube. Crookes also developed a cupped target to focus the rays.

Hittorf returned to the scene, and showed that no shadow was cast when an aluminum barrier was placed in the path of the rays. The cathode ray was obviously not a new form of light, although it is interesting to note that some of the early workers seemed unaware of this work and continued to refer to "X-light" [4]. Heinrich Hertz was the first to observe that the cathode rays were not all the same and that some actually passed out of the tube with different properties, including the capacity to pass through some otherwise opaque substances. No one yet grasped the significance or potential of this latter property.

Philipp Lenard, a student of Hertz, adapted an aluminum window to the tube that directed the rays outward. In September and October of 1891, Lenard noted the rays caused crystals to fluoresce even when his hand was interposed in the beam and that the rays fogged photographic plates just as light rays would. He came ever so close but never pursued this finding [2].

It is apparent that these great men had been working with X rays and were producing X rays but did not recognize them.

Emil Grubbe, working in electrotherapy in Chicago, was using energized Crookes' tubes before Roentgen's announcement. He later claimed that he noted skin changes produced by the roentgen ray as early as 1896, although he did not realize the source. He not only claimed to be the first martyr to the new ray but attributed the origins of X-ray therapy to conclusions he had drawn from his skin problems [3]. However, the timing of his claims has cast doubt on their validity [5].

Roentgen decided in 1895 to try to duplicate Lenard's work but to eliminate the variable of ultraviolet light as the agent involved. He covered the Crookes' tube with black paper and darkened the room. Using loose crystals of barium platinocyanide in a box, he steadied the box cover with his hand. Turning on the electrical charge he saw the crystals fluoresce even with the tubes covered and observed the outline of the bones of his hands in the glowing crystals. In a sense, this was the first human fluoroscopic observation. His first report was submitted and published on November 8, 1895.

Roentgen's second discovery, just a few days later, came when he took history's first X ray. He excited the tube near a door and recorded fog on a photographic plate through the wood but only the outline of the metallic lock. It was apparent that the rays passed through the wood but did not penetrate the metal. He then repeated this experiment with his hand near the plate and produced the famous first human radiograph. Since he was uncertain of the nature of the ray, he fell back to his early algebra and called it the X ray.

Because he quickly understood the medical potential of this discovery, Roentgen chose to present his work at the Physical-Medical Society of Würzburg on December 28, 1895. To many, this is the beginning of a great story. But it was, like most discoveries, the culmination of the work of many great minds set to a great many tasks. In Roentgen's laboratory in that fateful year, it all fell into place.

REFERENCES

1. Glasser O. *William Conrad Roentgen and the early history of the roentgen rays.* Springfield, IL: Thomas, **1934**
2. Widemann M. *Z Electro-Chemie* **1895**;6:12–14
3. Grubbe E. *X-ray treatment.* St. Paul, MN: Bruce, **1949**
4. Rollins W. *Notes on x-light.* Boston: privately printed. Cited by: Brown P. *American martyrs to science through the roentgen rays.* Springfield, IL: Thomas, **1936**
5. Hodges PC. *The life and times of Emil H. Grubbe.* Chicago: University of Chicago Press, **1964**

In preparation for the 1995 centennial celebration of the discovery of the X ray, the *AJR* will periodically publish History Pages, which deal with events leading up to and occurring around the time of the discovery.

[1] Department of Radiology, St. Joseph Mercy Hospital, Pontiac, MI 48341-2985. Address reprint requests to R. A. Gagliardi.

***AJR* 158:980, May 1992** 0361-803X/92/1585-0980 © American Roentgen Ray Society

Case Report

Pulmonary Alveolar Microlithiasis: Findings on High-Resolution CT

M. A. Korn,[1] H. Schurawitzki,[1] W. Klepetko,[2] and O. C. Burghuber[3]

We report the high-resolution CT findings in a case of pulmonary alveolar microlithiasis, a disease characterized by widespread, sandlike intraalveolar calcifications. A rare lung disease, it has been reported fewer than 160 times in the literature. Although the cause is unknown, one possibility is an inborn error of metabolism [1]. The high rate of occurrence within families (>50%) suggests an autosomal-recessive hereditary factor [1].

The radiographic appearance is pathognomonic [2], but open lung biopsy is sometimes required. Plain chest radiographs show a white lung or sandstorm lung consisting of fine sandlike microcalcifications, diffusely scattered throughout both lungs with higher density at the lung bases [1-5]. The heart borders and the diaphragm are usually obliterated. Typical findings include small bullae in the apexes and a black pleural line, described by Felson [2] as a zone of increased translucence between the lung parenchyma and the ribs. However, high-resolution CT scans show that this black pleural line is due to thin-walled subpleural cysts.

Case Report

A 26-year-old woman was referred to our hospital because of recurrent pneumothoraces, which had been treated by tube thoracostomy. Eleven years earlier, an open lung biopsy confirmed a diagnosis of pulmonary alveolar microlithiasis. At the time of evaluation she had no shortness of breath at rest. Pulmonary function studies revealed the typical features of restrictive defect with reduced total lung capacity and vital capacity but without evidence of airflow obstruction. Arterial PA_{O_2} was normal at rest and deteriorated during exercise, indicating diffusion impairment.

Chest radiographs showed the typical features of alveolar microlithiasis and a small pneumothorax on the right side. Heart borders and diaphragm were obscured, small apical bullae were visible, and a small zone of radiolucency was present between the lung parenchyma and the ribs (Fig. 1A).

High-resolution CT was performed on a Somatom DR3 (Siemens, Erlangen, Germany) scanner. All images were obtained at maximal inspiration using 2-mm collimation, 125 kV, 90 mA, and a 5-sec acquisition time. Scans were taken at 20-mm intervals in the supine position; at the lower levels, additional scans were obtained in the prone position. Images were reconstructed by using bone algorithm and a 512 × 512 matrix. All scans were photographed with window/level settings of 2000/−200 and 900/−650.

Apical bullae were visible on both sides, but they were larger on the right. In addition, small thin-walled subpleural cysts, ranging from 5 to 10 mm in diameter, were seen. The cysts were ribbonlike and arranged along the mediastinal and parietal pleura on both sides extending from the apex to the costodiaphragmal sinus (Fig. 1B). The pleura itself was thickened and irregularly delineated, containing punctate calcifications. Additionally, a small residual pneumothorax was visible in the right apex 3 days after the chest tube was removed.

Lung parenchyma showed high attenuation, increasing from the apex to the lung base. In the upper and middle lung zones, the high attenuation was distributed homogeneously throughout the lung parenchyma; in the lower lung zones, however, instead of diffuse involvement, higher attenuation was seen in the dorsal zones (Fig.

Received September 4, 1991; accepted after revision October 23, 1991.

This work was supported in part by the Ludwig Boltzmann Institute for Radiological Tumor Diagnosis.

[1] Department of Radiology, University of Vienna, AKH, Währinger Gürtel 18-20, A-1090 Wien, Austria.

[2] Second Surgical Department, University of Vienna, AKH, Spitalgasse 23, A-1090 Wien, Austria.

[3] Department of Internal Medicine IV, Division of Pulmonary Medicine, University of Vienna, AKH, Währinger Gürtel 18-20, A-1090 Wien, Austria.

AJR 158:981-982, May 1992 0361-803X/92/1585-0981 © American Roentgen Ray Society

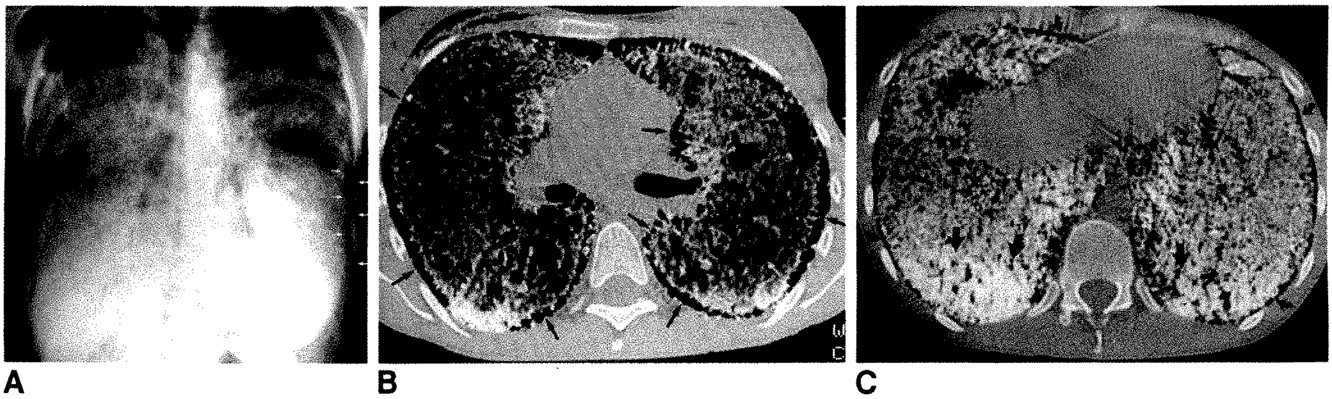

Fig. 1.—26-year-old woman with biopsy-proved pulmonary alveolar microlithiasis.

***A*, Chest radiograph shows sandstorm lung with black pleural line (*arrows*) between the ribs and lung parenchyma.**

***B*, High-resolution CT scan (middle lung zone) shows subpleural cysts (*arrows*) along the parietal and mediastinal pleura. High attenuation of lung parenchyma is due to alveolar calcifications. Soft-tissue emphysema followed right-sided pneumothorax.**

***C*, High-resolution CT scan of lower lung zone shows greater involvement than in middle lung zone (*B*), especially posteriad (*straight arrows*). *Curved arrows* show subpleural cysts.**

1C) and the higher attenuation persisted in the prone position, causing us to rule out hypostasis as a reason for the increased density. In addition to the high attenuation of the lung parenchyma, small (<5 mm) circumscribed intrapulmonary calcifications were visible. Irregularly arranged cysts smaller than 1 cm were seen throughout the lung parenchyma. The central bronchial system, the pulmonary vessels, and the heart showed no major abnormalities.

Discussion

High-resolution CT shows that the so-called black pleural line on chest radiographs is caused by thin-walled subpleural cysts, ranging from 5 to 10 mm in diameter. The cysts are ribbonlike and arranged along the parietal and mediastinal pleura from the apex to the lung bases. These subpleural cysts have not been described before; they can only be shown on high-resolution CT scans and they correlate with the so-called black pleural line seen on chest radiographs. This zone of increased translucence in the location of the parietal pleura has been considered a visual illusion created by the contrast between extreme density of lung parenchyma on one side of the pleura and the ribs on the other side [2]. Our high-resolution CT findings of small subpleural cysts not only explain the increased translucence seen on chest radiographs but also the typical recurrent pneumothoraces, as seen in our patient.

Only a few reports in the literature deal with conventional CT findings in patients with pulmonary alveolar microlithiasis [3, 5]. To our knowledge, high-resolution CT findings have not been reported. The advantages of high-resolution CT in detecting minimal structural changes in the lung parenchyma were reported previously [6, 7]. With thin-section and high-spatial-frequency (bone) algorithm, structures approximately 1 mm in size can be detected, which is not possible with conventional CT techniques [3, 6].

High-resolution CT scans show that there is a gradient of distribution of the calcifications, in which the lung bases—especially posteriad—are more involved than are the middle and upper lung zones [3, 5]. Besides high attenuation of lung parenchyma, caused by calcispherites smaller than 1 mm in diameter, calcified nodules larger than 1 mm (up to 5 mm) are visible on high-resolution CT scans. This technique can also reveal small cysts in the lung parenchyma, which have not been reported before; pleural calcification [3, 5]; and small calcispherites within the thickened pleura (irregular thickening of the pleura is due to fibrosis).

In our patient, high-resolution CT scans also showed that both the bronchial system (including small bronchioles) and the size of pulmonary vessels were normal.

REFERENCES

1. Sosman MC, Dodd GD, Jones WD, Pillmore GU. The familial occurrence of pulmonary alveolar microlithiasis. *AJR* **1957**;77:947–1012
2. Felson B. The roentgen diagnosis of disseminated pulmonary alveolar diseases. *Semin Roentgenol* **1967**;2:3–6
3. Chalmers AG, Wyatt J, Robinson PJ. Computed tomographic and pathological findings in pulmonary alveolar microlithiasis. *Br J Radiol* **1986**;59:408–411
4. Prakasch UB, Barham SS, Rosenhow EC III, Brown ML, Spencer Payne W. Pulmonary alveolar microlithiasis: a review including ultrastructural and pulmonary function tests. *Mayo Clin Proc* **1983**;58:290–300
5. Winzelberg GG, Boller M, Sachs M, Weinberg J. CT evaluation of pulmonary alveolar microlithiasis. *J Comput Assist Tomogr* **1984**;8:1029–1031
6. Schurawitzki H, Stiglbauer R, Graninger W, et al. Interstitial lung disease in progressive systemic sclerosis: high-resolution CT versus radiography. *Radiology* **1990**;176:755–759
7. Klein J, Gamsu G. High resolution computed tomography of diffuse lung disease. *Invest Radiol* **1989**;24:805–812

CT Findings in Benign Fibrous Mesothelioma of the Pleura:

Pathologic Correlation in Nine Patients

Kyung Soo Lee[1]
Jung-Gi Im[2]
Kyu Ok Choe[3]
Chang Jin Kim[4]
Byoung Ho Lee[1]

The CT findings in cases of benign fibrous mesothelioma of the pleura have been described previously, but little attention has been given to a correlation of these findings with the pathologic appearance of the tumors. Accordingly, we analyzed the CT scans in nine proved cases in which pathologic studies were available and compared the pathologic findings with the CT appearance of the tumors. On enhanced CT scans (available in eight patients), the lesions showed significant enhancement in all cases. Pathologic examination showed that the enhancement could be explained by the vascularity of the tumor. Areas of myxoid ($n = 7$) or cystic ($n = 3$) degeneration and hemorrhage ($n = 3$) seen in the pathologic specimens correlated with round or tubular low-attenuation areas on unenhanced and enhanced CT scans. On unenhanced CT scans ($n = 3$), the tumor density was the same as that of the surrounding musculature. Calcification was seen in one patient. Large lesions showed lobulated borders, but no invasion into the lung parenchyma and chest wall was noted. There was no pleural effusion.

Our experience suggests that intense enhancement of the tumors occurs because of the vascularity of the tumors. Areas of low attenuation in the tumors on CT were due to foci of myxoid or cystic degeneration and hemorrhage in the lesion.

AJR **158:983–986, May 1992**

Benign fibrous mesotheliomas of the pleura, also called solid fibrous tumors of the pleura, are rare tumors of mesodermal origin. They amount to less than 5% of all neoplasms involving the pleura [1, 2]. The tumors are usually discovered as asymptomatic lesions on routine chest radiographs. Benign fibrous mesotheliomas have a good prognosis compared with the diffuse malignant variety. Benign mesotheliomas occur in patients of all ages. There is no sex predilection and no evidence of a relationship to asbestos exposure.

Two reports describing the CT appearances of benign fibrous mesotheliomas have been published [2, 3]. To our best knowledge, however, little emphasis has been given to the CT-pathologic correlation of the tumors. The purpose of this study was to review the CT features in nine proved cases and compare them with the findings on pathologic examination of the tumors.

Materials and Methods

Eleven cases of benign fibrous mesothelioma of the pleura in 11 consecutive patients treated from January 1985 to January 1991 were collected from four institutions. Nine patients in whom pathologic confirmation was available were selected for study. The diagnosis was proved on the basis of pathologic examination in all nine cases. Histologic criteria to select the cases were minimal nuclear pleomorphism and rare or absent mitoses of the spindle-shaped fibrocytes and/or fibroblasts. The five men and four women were 23–71 years old (average, 48 years). Mild chest pain was the main complaint in five patients; the remaining four patients had no specific complaints. Hypoglycemia was seen in one patient who had a large lesion. The size of the excised tumors ranged from 3 to 20 cm in longest diameter and

Received August 22, 1991; accepted after revision November 9, 1991.

[1] Department of Radiology, College of Medicine, Soonchunhyang University, 23-20, Bongmyung-Dong, Chunan, 330-100, Korea. Address reprint requests to K. S. Lee.

[2] Department of Radiology, College of Medicine, Seoul National University, Seoul, 110-460, Korea.

[3] Department of Radiology, College of Medicine, Yonsei University, Seoul, 120-140, Korea.

[4] Department of Pathology, College of Medicine, Soonchunhyang University, Chunan, 330-100, Korea.

0361-803X/92/1585-0983
© American Roentgen Ray Society

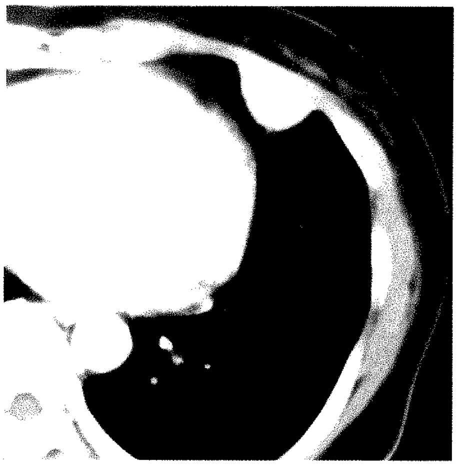

Fig. 1.—Benign fibrous mesothelioma in a 53-year-old woman. Enhanced CT scan shows homogeneous and highly enhancing mass in left anterior pleural space. Angle between mass and chest wall is obtuse.

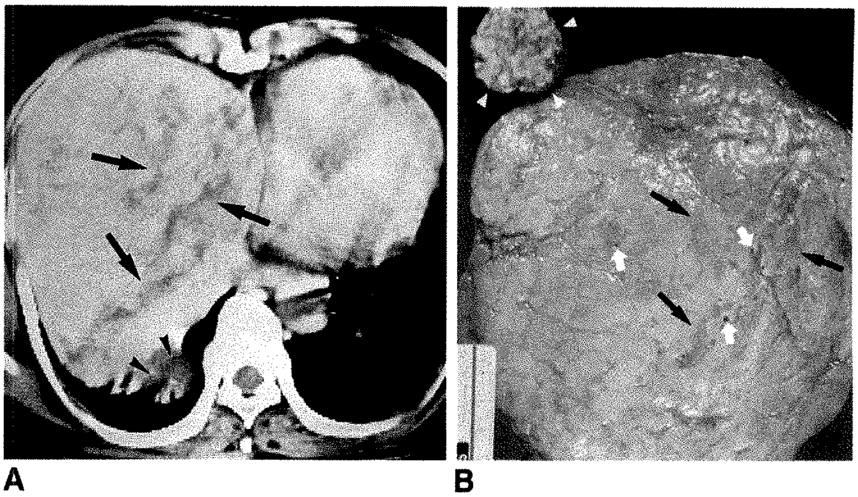

Fig. 2.—Benign fibrous mesothelioma in a 64-year-old man.

***A*, Enhanced CT scan shows large and highly enhancing mass lesion occupying right anterior and middle hemithorax. Attenuation value of lesion is same as that of heart. Multiple tubular low-attenuation areas (*arrows*), denoting areas of myxoid degeneration, are also seen. Small mixed-attenuation lesion (*arrowheads*) posterior to main lesion is incidental hamartoma in posteriorly displaced right middle lobe.**

***B*, Cut surface of gross specimen reveals a yellowish white mass lesion with scattered prominent vessels (*white arrows*). Portions of myxoid degeneration (*black arrows*) are also found. Incidental hamartoma (*arrowheads*) in right middle lobe is located and photographed in anterior aspect of main lesion.**

from 30 to 1468 g in weight. The tumor was in the left hemithorax in six patients and in the right hemithorax in three. Except for one patient who had a mass originating from the diaphragmatic pleura, all patients had tumors arising from the visceral pleura surgically and pathologically. Intrafissural tumor was seen in two patients. A short tumor pedicle was noted in three patients during surgery, but no tumors were seen to change location when conventional chest radiographs, including those obtained with the patient in the decubitus position, were reviewed. No evidence of rib destruction or chest wall invasion was seen at surgery in any of the patients. In five patients with large tumors, adhesion between the lesion and the pleura or the pericardium was noted, but surgical resection was still possible. Follow-up chest radiographs after surgical excision of the tumor were available in all patients. During the follow-up period of 4 months to 6 years (average, 24 months), no tumors recurred.

Most CT scans were obtained with a GE 9800 scanner (General Electric, Milwaukee, WI) or a CT-W 700 scanner (Hitachi Medical Corp., Tokyo). Scanning parameters were 120 kVp, 100 mA, and 3-sec scan time for the GE 9800 scanner and 120 kVp, 400 mA, and 3-sec scan time for the CT-W 700 scanner. Enhanced scans only were available in six patients and both unenhanced and enhanced scans were available in two patients. Unenhanced scans only were done in one patient. In most patients, enhanced scans were obtained with injection of 100 ml of 68.3% meglumine ioglicate (Rayvist R 300, Schering, Seoul, Korea), 50 ml in bolus before scanning and 50 ml in drip infusion during scanning. At full inspiration, contiguous scans with 10-mm collimation were obtained at 10-mm intervals. Scans photographed in narrow window (window width, 400; window level, 25) were used in CT analysis.

CT characteristics analyzed retrospectively included the attenuation values and internal architecture of the mass; the angle between the mass and the surrounding pleura or the chest wall; the contour and margin of the mass; the presence of calcification; and associated findings in the pleura, lung parenchyma, and chest wall. The attenuation value of the tumors was compared with that of the surrounding musculature. The attenuation values of the mass on CT scans were correlated with the gross pathologic features of the tumors. These specific areas of the specimens were then studied microscopically.

Results

CT Findings

The tumors showed predominantly high attenuation on enhanced scans in all patients (Figs. 1–5). The average attenuation value of the enhancing tumors, measured in four patients, was 121 H, whereas that of the surrounding musculature was 65 H. On unenhanced scans in three patients, the tumors appeared to have intermediate attenuation (mean, 38 H). The CT appearance of the tumor depended on its size. Small tumors in two patients (<6 cm in longest diameter) had a homogeneous appearance (Fig. 1). Larger tumors in seven patients had tubular or round low-density areas (Figs. 2–5). The angle between the tumor and the pleura or the chest wall was either acute or obtuse, but an acute angle was formed with large lesions in seven patients. The contour of the mass was lobulated and smooth in all cases. Dense calcification within the tumor was noted in a patient with a very large lesion (Fig. 5). In no patient was tumor invasion into the surrounding muscle or bony thorax and pleural effusion observed. Atelectatic lung was noted in two patients with very large lesions.

CT-Pathologic Correlation

The main components of the tumors on gross specimens, the yellowish or pinkish white glistening portions, appeared

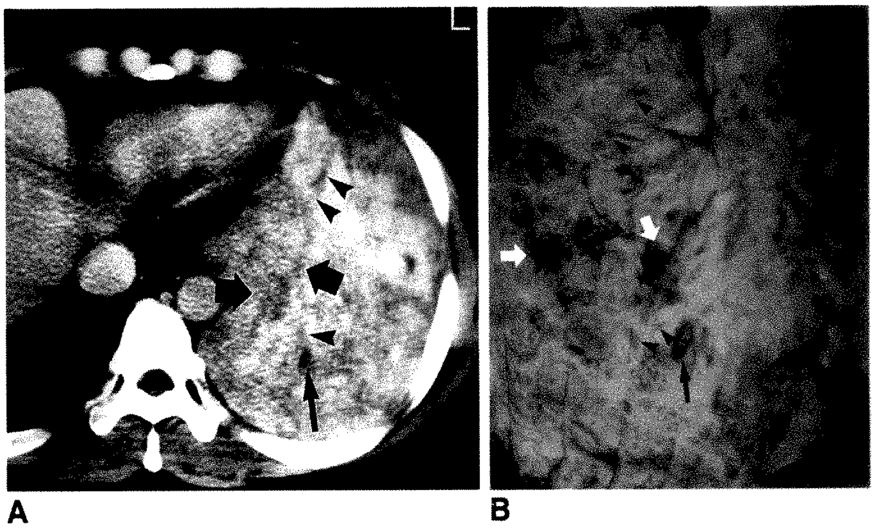

Fig. 3.—Benign fibrous mesothelioma arising from left parietal diaphragmatic pleura in a 51-year-old woman.

A, Enhanced CT scan shows large lesion occupying entire left hemithorax. High-attenuation areas prevail in lesion, although portions of low attenuation are noted. These low-attenuation areas are due to cystic (*long thin arrow*) or myxoid (*arrowheads*) degeneration and hemorrhage (*short wide arrows*), which can be correlated respectively with gross specimen.

B, Cut surface of gross specimen shows a pinkish white fibrotic lesion intermingled with minute foci of cystic (*black arrow*) and myxoid (*arrowheads*) degeneration. Large vessels with hemorrhage (*white arrows*) are prominent.

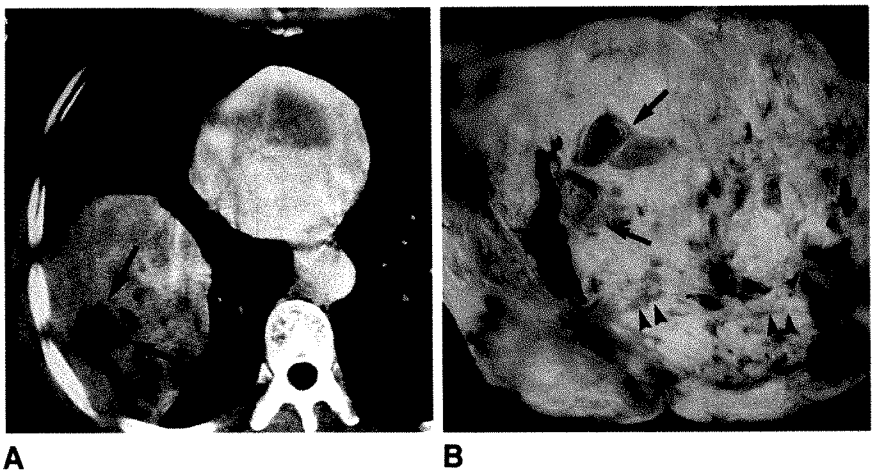

Fig. 4.—Benign fibrous mesothelioma in a 71-year-old man.

A, Enhanced CT scan shows highly enhancing mass lesion in right posterior lateral pleural space. Lesion contains multiple round and tubular low-attenuation areas. Large, round low-attenuation area (*arrows*) turned out to be area of cystic degeneration.

B, Photograph of cut section shows cystic (*arrows*) and myxoid (*arrowheads*) degeneration on yellowish white cut surface. Vessels with hemorrhage are also prominent.

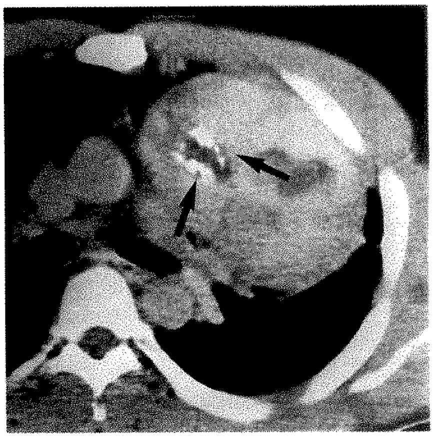

Fig. 5.—Benign fibrous mesothelioma containing areas of calcification and myxoid degeneration in a 23-year-old man. Enhanced CT scan shows large enhancing mass lesion in left anterior hemithorax. Lesion contains areas of calcification (*arrows*) and tubular low attenuation. No evidence of chest wall invasion is seen.

to be areas of mixed cellular and collagenous tissue on microscopic examination. Areas of mainly cellular or collagenous tissue were seen; in most tumors, mixed cellular and collagenous tissue formed the tumors. These areas showed intermediate attenuation on unenhanced CT scans and high intensity on enhanced scans. With CT, predominantly cellular areas cannot be distinguished from predominantly collagenous areas. Deep yellowish portions of the mass on gross specimens were areas of myxoid degeneration on microscopic examination, and these areas showed tubular or round low attenuation on either unenhanced or enhanced CT scans in seven patients (Figs. 2–5). Areas of cystic degeneration on gross specimens in three lesions were manifested as round cystic fluid-attenuation areas on CT scans (Figs. 3 and 4). Hemorrhagic areas in three cases also showed low attenuation values (Figs. 3 and 4). Vascular structures were scattered throughout the lesion either on gross or microscopic examinations in all cases. These vascular structures could be seen beside cellular and collagenous areas on microscopic examination, even in the areas of myxoid degeneration.

Discussion

CT attenuation values of benign fibrous mesotheliomas of the pleura have not been reported. These tumors are usually rounded, firm, white, and scarlike in their gross appearance. They may be highly vascular with prominent veins over the surface [4]. Histologically, they are composed of a mixture of spindle-shaped fibroblastlike cells lying within a variable amount of collagenous stroma. A whorled pattern of growth may be present focally; more commonly, however, the cells grow in a haphazard pattern [5-7].

There have been debates on the CT attenuation values of the fibrous lesions. Rubenstein et al. [8], reporting that the fibrous lesions show hyperdensity on CT, suggested two causal factors for the hyperdensity. One is the high physical density of the collagen; the other is the abundant capillary network within the lesions. However, these two characteristics could not explain the CT appearance of all fibrous lesions in their study. In a CT-pathologic correlation in nine patients with fibromatosis, Francis et al. [9] found no consistent relationship between the CT attenuation value and the amount of collagen in the fibrous lesion. In our study, unenhanced CT scans in three patients with benign fibrous mesothelioma showed intermediate attenuation values although the tumors had large amounts of collagenous tissue.

In large benign fibrous mesotheliomas, areas of prominent vascularity consisting of thin-walled venous sinusoids within the tumor and arteriovenous plexuses within the stalk are present. The substance of massive tumors is often highly vascular, with thick-walled arteries and arterioles and with vessels and veins showing luminal ectasis [4, 6, 7]. The vascular area may mimic the histologic features of an angiofibroma [7]. Hahn et al. [10] used arteriography to localize two cases of massive pleural fibrous mesothelioma and could see tumor vascularity. Tumor vascularity in these pathologic and angiographic studies may explain the highly enhancing nature of the tumors on enhanced CT scans in our study. High tumor vascularity on microscopic examination correlated with the findings on CT.

CT findings of benign fibrous mesotheliomas include well-delineated, often lobulated, noncalcified, enhancing soft-tissue masses in close relation to the pleural surface or fissure, associated crural thickening, and absence of chest wall invasion [2, 3]. Displacement and compression atelectasis of the adjacent lung parenchyma and bowing of the bronchi and pulmonary vessels around the mass also can be found. The margin at the junction of the mass with the pleura usually tapers smoothly [2]. In our study, we observed all these findings except crural thickening. In addition to these findings, we could see calcification within the tumor in one patient. Hutchinson and Friedenberg [4] observed calcification in two of their 17 cases of benign fibrous mesotheliomas, so we think calcification of the tumor is not rare.

On chest radiographs, benign fibrous mesotheliomas are seen as round or oval masses, often lobulated, located at the pleural surface [11]. Fissural mesotheliomas could be seen [12]. The tumors are pedunculated in 30-50% of cases. The presence of a pedicle may cause marked changes in the position of the mass in the thorax when the position of the patient changes [13, 14]. Although a short tumor pedicle was seen in three of our patients during surgery, no tumors changed position when the position of the patient changed.

Cellular atypia and mitoses are rare in benign fibrous mesotheliomas, but foci of degeneration and cystic change may be present, especially in large lesions [6, 7]. These areas of cystic degeneration were seen in three patients in our study and appeared as round, low-attenuation lesions on CT.

Local recurrence has been reported in up to 16% of cases, but malignant transformation is unusual [7]. In our study, no recurrent cases were seen after an average follow-up of 2 years. No malignant change was identified in our series.

ACKNOWLEDGMENTS

We thank Hak Song Rhee at Chonju Presbyterian Medical Center for one of our cases and Ji Yon Oh for secretarial assistance.

REFERENCES

1. Theros EG, Feigin DS. Pleural tumors and pulmonary tumors: differential diagnosis. *Semin Roentgenol* **1977**;12:239-247
2. Dedrick CG, McLoud TC, Shepard JO, Shipley RT. Computed tomography of localized pleural mesothelioma. *AJR* **1985**;144:275-280
3. Mendelson DS, Meary E, Buy JN, Pigeau I, Kirschner PA. Localized fibrous pleural mesothelioma: CT findings. *Clin Imaging* **1991**;15:105-108
4. Hutchinson W, Friedenberg MJ. Intrathoracic mesothelioma. *Radiology* **1963**;80:937-945
5. Battifora H. The pleura. In: Sternberg SS, ed. *Diagnostic surgical pathology*. New York: Raven, **1989**:829-885
6. Dalton WT, Zollinker T, McCaughley WTE, Jacques J, Kunnerstein M. Localized primary tumours of the pleura. *Cancer* **1979**;44:1465-1475
7. Briselli M, Mark EJ, Dickersin R. Solitary fibrous tumors of the pleura: eight new cases and review of 360 cases in the literature. *Cancer* **1981**;47:2678-2689
8. Rubenstein WA, Gray G, Auh YH, et al. CT of fibrous tissues and tumors with sonographic correlation. *AJR* **1986**;147:1067-1074
9. Francis IR, Dorovini-Zis K, Glazer GM, Lloyd RV, Amendola MA, Martel W. The fibromatoses: CT-pathologic correlation. *AJR* **1986**;147:1063-1066
10. Hahn PF, Novelline RA, Mark EJ. Arteriography in the localization of massive pleural tumors. *AJR* **1982**;139:814-817
11. Heitzman ER. *The lung*. St. Louis: Mosby, **1984**:534-536
12. Spizarny DL, Gross BH, Shepard JO. CT findings in localized fibrous mesothelioma of the pleural fissure. *J Comput Assist Tomogr* **1986**;10:942-944
13. Berne AS, Heitzman ER. The roentgenologic signs of pedunculated pleural tumors. *AJR* **1962**;87:892-895
14. Weisbrod GL, Yee AC. Computed tomographic diagnosis of a pedunculated fibrous mesothelioma. *Can Assoc Radiol J* **1983**;34:147-148

Case Report

Intrapulmonary Bronchogenic Cyst: Spontaneous Pneumothorax as the Presenting Symptom

M. A. Matzinger,[1] F. R. Matzinger,[2] and H. J. Sachs[3]

Bronchogenic cysts are thought to result from abnormal budding of the tracheal diverticulum between the third and sixth weeks of gestation [1] and consequently may be mediastinal or intrapulmonary in location. The clinical presentation is variable; some bronchogenic cysts are asymptomatic. Infants typically present with respiratory compromise due to airway compression, whereas older children present with superimposed infection [2]. Other presentations are unusual. We describe a case of a bronchogenic cyst in a 16-year-old girl in whom the presenting symptoms were caused by pneumothorax.

Case Report

A 16-year-old girl was ice skating and fell onto her anterior chest. She felt no ill effects and continued her activity. The next day, after a bout of laughing, she began having right-sided chest pain with radiation to the scapula. Chest auscultation in the emergency department revealed good air entry on both sides. The next day she presented with shortness of breath, and a chest radiograph showed a right-sided tension pneumothorax. Despite prolonged chest tube suction over many days, there was persistent air leak into the right pleural space. A chest radiograph and a CT scan showed two thin-walled cystic cavities in the right upper lobe (Fig. 1). The remainder of both lungs and the mediastinum were normal.

Surgical exploration confirmed a 0.5-cm rupture of the cyst surface. Postoperative course after right upper lobectomy was uneventful. The pathologic diagnosis was intrapulmonary subpleural bronchogenic cyst, based on examination of a bilobed cyst lined by pseudostratified ciliated columnar respiratory epithelium, which overlay parallel bundles of smooth muscle and contained mucoid proteinaceous material.

Discussion

Bronchogenic cysts are found most frequently in the mediastinum or lungs, but they can develop in extrathoracic locations, such as cervical, pericardial, paravertebral, or intra- and infradiaphragmatic sites [3].

The relative occurrence rates of intrapulmonary and mediastinal bronchogenic cysts are controversial. Studies by Reed and Sobonya [4] and by DiLorenzo et al. [5] indicated the frequency of mediastinal bronchogenic cysts was greater, whereas the series reported by Rogers and Osmer [6] and by Ramenofsky et al. [3] showed a higher frequency of pulmonary lesions.

Past reports emphasize that bronchogenic cysts may be asymptomatic. Among the 26 patients (age range, 2 months to 14 years) studied by DiLorenzo et al. [5], 27% were asymptomatic and 73% presented with respiratory symptoms such as cough, dyspnea, pain, fever, and pneumonia. Nearly all 20 patients studied by Ramenofsky et al. [3] were symptomatic, presenting with such signs and symptoms as fever, recurrent pneumonia, cervical mass, respiratory distress, frequent upper respiratory infections, and empyema.

Received September 5, 1991; accepted after revision October 30, 1991.

[1] Department of Radiology, Children's Hospital of Eastern Ontario, 401 Smyth Rd., Ottawa, Ontario, Canada K1H 8L1.
[2] Department of Radiology, Ottawa Civic Hospital, 1053 Carling Ave., Ottawa, Ontario, Canada K1Y 4E9.
[3] Department of Surgery, Ottawa Civic Hospital, 1053 Carling Ave., Ottawa, Ontario, Canada K1Y 4E9.

AJR 158:987-988, May 1992 0361-803X/92/1585-0987 © American Roentgen Ray Society

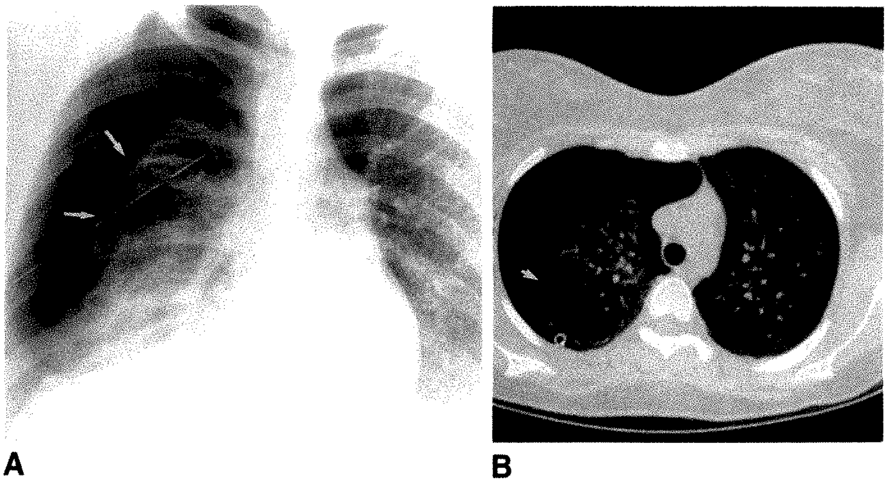

Fig. 1.—16-year-old girl with intrapulmonary bronchogenic cyst.

***A*, Chest radiograph on day chest tube was inserted shows two thin-walled right upper lobe cysts (*arrows*) and a moderately large pneumothorax.**

***B*, CT scan 11 days later shows two contiguous air-containing cavities in posterior aspect of right upper lobe. Visceral pleura overlying the more anterior cavity appears to be open (*arrow*), permitting cyst communication with pleural space.**

A literature search disclosed no previous report of spontaneous pneumothorax caused by rupture of an intrapulmonary bronchogenic cyst. Kirwan et al. [7] described catastrophic spontaneous rupture of an upper mediastinal bronchogenic cyst with leakage into the pericardium and cardiac tamponade. Adam et al. [8] described a 24-year-old woman with right pleuritic chest pain and a very small right pleural effusion presumed to result from leakage of the contents of a subcarinal cyst. Air embolism was reported in two men, with right lower lung cysts, who underwent decompression after construction work in a tunnel [9]. Since no surgery or pathologic examination of the cysts was carried out, confirmation of their congenital nature was not available.

Traumatic lung cyst and congenital pulmonary cyst were the major considerations in the differential diagnosis of our patient. Traumatic cyst typically follows blunt chest trauma with sudden compression of the elastic chest wall in a young person. Radiologically apparent within 12 to 24 hr of injury, traumatic cyst undergoes complete resolution in 2 to 16 weeks [1]. Pneumothorax is a rare complication.

Congenital cysts tend to be multiple, either limited to a lobe, or generalized, involving one or both lungs. They may be asymptomatic, or the patient may present with complications of either infection or air trapping and tension [1]. Other possible causes of thin-walled, air-containing pulmonary cysts include (1) cavities resulting from mycotic, tuberculous, or *Echinococcus* infection and (2) pneumatoceles caused by *Staphylococcus aureus* or hydrocarbon ingestion.

Chest radiography is the usual imaging method for initial detection of bronchogenic cysts, although the findings are not always diagnostic. On a chest radiograph, an intrapulmonary bronchogenic cyst typically appears as a sharply defined, thin-walled, round or oval lesion that may be air filled, have homogeneous water density, or contain an air-fluid level. CT provides optimal demonstration of cyst location, morphology, and contents. Surgical excision is the treatment of choice for both the infected and uninfected cyst to firmly establish the diagnosis and prevent future complications [1]. Our case illustrates the plain radiographic and CT features of intrapulmonary bronchogenic cyst and represents an atypical presentation of this relatively uncommon congenital lesion. Bronchogenic cyst is generally regarded as an unlikely cause of pneumothorax; perhaps, however, it is more common than previously thought.

REFERENCES

1. Shamji FM Sachs HJ, Perkins DG. Cystic disease of the lungs. *Surg Clin North Am* **1988**;68:581–620
2. Haddon MJ, Bowen A. Bronchopulmonary and neurenteric forms of foregut anomalies. *Radiol Clin North Am* **1991**;29:241–254
3. Ramenofsky ML, Leape LL, McCauley RGK. Bronchogenic cyst. *J Pediatr Surg* **1979**;14:219–224
4. Reed JC, Sobonya RE. Morphologic analysis of foregut cysts in the thorax. *AJR* **1974**;120:851–860
5. DiLorenzo M, Collin PP, Vaillancourt R, Duranceau A. Bronchogenic cysts. *J Pediatr Surg* **1989**;24:988–991
6. Rogers LF, Osmer JC. Bronchogenic cyst. A review of 46 cases. *AJR* **1964**;91:273–283
7. Kirwan WO, Walbaum PR, McCormack RJM. Cystic intrathoracic derivatives of the foregut and their complications. *Thorax* **1973**;28:424–428
8. Adam A, MacSweeney JE, Whyte MKB, Smith PLC, Ind PW. CT-guided extrapleural drainage of bronchogenic cyst. *J Comput Assist Tomogr* **1989**;13:1065–1068
9. Campbell Golding F, Griffiths P, Hempleman HV, Paton WDM, Walder DN. Decompression sickness during construction of the Dartford tunnel. *Br J Ind Med* **1960**;17:167–180

Case Report

Demonstration of Blood Supply to Pulmonary Sequestration by MR Angiography

Anthony J. Doyle[1]

The imaging of pulmonary sequestration has traditionally focused on the use of arteriography to identify abnormal systemic vessels feeding the abnormal portion of lung. More recently, several cases of pulmonary sequestration diagnosed by MR imaging have been reported [1]. MR angiography would also seem well suited for displaying the abnormal vasculature in this condition in a way that could provide a diagnosis and aid in surgical planning without the need for arteriography. The ability of MR angiography to image vessels in three dimensions should eliminate the problems caused by partial-volume averaging and nonvisualization of vessels that are not in the plane of whatever sequences are being obtained with a standard cross-sectional MR or CT imaging technique.

We report a case in which the systemic blood vessels supplying a pulmonary sequestration were imaged with this technique.

Case Report

A 35-year-old man had a 3-month history of recurrent episodes of fever, sweats, and cough that responded to antibiotics but relapsed when these were stopped. A series of CT scans made elsewhere showed a persistent area of opacity in the posterior basal segment of the left lung (Fig. 1A). A previous percutaneous biopsy of this area had yielded inflammatory cells. The diagnosis of pulmonary sequestration was considered.

We performed MR angiography in an attempt to establish the diagnosis. After initially localizing the area with a coronal T1-weighted MR sequence, we performed two-dimensional time-of-flight single breath-hold MR angiography with spoiled gradient-recalled acquisition in the steady state in 3-mm contiguous axial slices with a TR of 50 msec, TE of 10 msec, and flip angle of 60°. A license plate coil was positioned over the thoracolumbar junction. The machine used was a Signa 1.5-T superconducting magnet (General Electric Medical Systems, Milwaukee, WI). Each image was acquired as a single breath-hold on full inspiration. The patient was required to hold his breath for about 11 sec per scan. Twenty-five images were obtained.

The collapsed maximum-intensity-projection view clearly shows an abnormal vessel arising from the left side of the descending thoracic aorta and entering the abnormal area of lung (Fig. 1B). The reconstructed MR angiogram also clearly shows this vessel arising from the left of the aorta and passing superolaterally (Fig. 1C). The site of origin of the vessels just above the left hemidiaphragm was determined by reference to the individual axial slices and analysis of the reconstructed MR angiogram.

At surgery, an intralobar sequestration was found with a feeding vessel in exactly the position shown on the MR angiogram.

Discussion

The diagnosis of pulmonary sequestration rests on the demonstration of an aberrant systemic artery supplying a portion of lung. Documenting the existence and origin of this systemic blood supply is also helpful for treatment planning because the generally accepted treatment is surgery, and the surgeon needs to know where to look for the abnormal vessels [1, 2]. As in other areas of the body, MR angiography definitely should have an application in the noninvasive demonstration of abnormal blood vessels of this nature. Because the vast majority of sequestrations (both intralobar and extra-

---

Received September 18, 1991; accepted after revision November 1, 1991.

[1] Department of Radiology, University of Utah School of Medicine, 50 N. Medical Dr., Salt Lake City, UT 84132. Address reprint requests to A. J. Doyle.

AJR 158:989-990, May 1992 0361-803X/92/1585-0989 © American Roentgen Ray Society

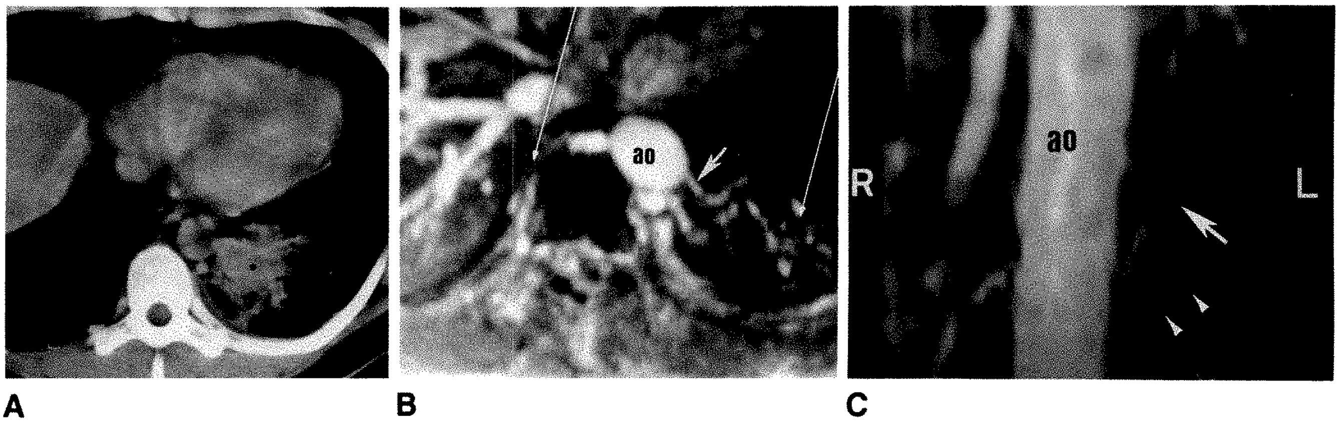

Fig. 1.—*A*, CT section through lower thorax shows poorly marginated heterogeneous opacity (*asterisk*) occupying medial portion of posterior basal segment of left lower lobe.

B, Collapsed axial maximum-intensity-projection view from MR angiogram (image produced as if looking at *C* from below) clearly shows abnormal vessel (*short arrow*) arising from left side of aorta (ao) and passing into abnormal portion of lung. *Long arrows* indicate area shown in *C* and direction from which reconstructed image is viewed.

C, Reconstructed MR angiogram as viewed from 15° left anterior oblique (rotated around inferosuperior axis) shows abnormal vessel (*arrow*) arising from aorta (ao) just above left hemidiaphragm (*arrowheads*) and ascending into abnormal portion of lung. Vertebral bodies and azygous vein are just to right of aorta. R = right, L = left.

lobar) are supplied by vessels from the lower thoracic or upper abdominal aorta, the relatively small field of view of MR angiography is not a serious limiting factor. The ability to show vessels in three dimensions and to show the high-signal vessel in the lung parenchyma should provide an advantage compared with CT or standard MR when the vessels are tortuous or their course within the lung needs to be documented [3, 4].

The most significant limitation of MR angiography in this type of application is the artifact caused by respiratory motion. Because the vessel to be demonstrated is in the lung and moves with it, any pulse sequence that requires extended time will suffer severely from respiratory motion artifact. Consequently, the most useful pulse sequence in this area is a single-slice breath-holding technique. In the case described, this was performed at full inspiration, and the amount of degradation of the image from misregistration between breath-holds was minimal. Signal from flowing arterial blood was maximized by use of a fairly thin slice thickness and relatively short TE.

We did not use a saturation band to eliminate systemic venous flow from the images because it is not possible to know prospectively where the abnormal vessels being looked for arise from. It would be at least theoretically possible to saturate out flowing blood in the vessels being looked for by use of a saturation band, thus producing a false-negative study. Once the vessels have been identified, a saturation band could be placed below them and the systemic venous flow eliminated, but this was not necessary in the case described. We also did not specifically image the pulmonary venous drainage, because no aberrant veins draining the sequestration were seen and further information was not required for surgery. Venous drainage should, however, be demonstrable by MR angiography if necessary. The localizer scan and the angiography sequence are fairly fast, and the entire examination can be completed within about 30 min.

In summary, we report a case in which MR angiography provided sufficient diagnostic information for surgical treatment of an intralobar sequestration.

REFERENCES

1. Felker RE, Tonkin ILD. Imaging of pulmonary sequestration. *AJR* **1990**;154:241-249
2. Pessar ML, Soulen RL, Kan JS, Kadir S, Zerhouni EA. MRI demonstration of pulmonary sequestration. *Pediatr Radiol* **1988**;18:229-231
3. Naidich DP, Rumancik WM, LeFleur RS, Estioko MR, Brown SM. Intralobar pulmonary sequestration: MR evaluation (case report). *J Comput Assist Tomogr* **1987**;11:531-533
4. Naidich DP, Rumancik WM, Ettenger NA, et al. Congenital anomalies of the lungs in adults: MR diagnosis. *AJR* **1988**;151:13-19

Perspective

Value of Large-Core Biopsy of Occult Breast Lesions

Jack E. Meyer[1]

The widespread use of screening mammography has resulted in the discovery of an increasing number of clinically occult breast lesions. Most impalpable solitary abnormalities have mammographic features consistent with a benign process and require no more than a follow-up examination in 6–12 months to ensure stability [1]. The radiologist may assist in further characterization of the more suspicious abnormalities by performing sonographically or mammographically guided fine-needle aspiration. In the case of solitary occult atypical cysts, this procedure is both therapeutic and diagnostic [2]. Cellular aspiration of occult solid lesions has been aided by the introduction of stereotaxic devices for more accurate needle placement [3]. The unpredictability of obtaining representative cytologic material of occult breast lesions has hindered widespread use of fine-needle aspiration. In addition, involvement of an experienced cytopathologist is an essential part of this diagnostic procedure [4].

Parker et al., who adapted an existing stereotaxic aspiration unit to perform large-core (14-gauge) biopsies, report successful tissue sampling of occult breast abnormalities [5, 6]. In these initial studies, a diagnostic accuracy equivalent to that of surgical excision may be possible in the radiology department. On the basis of these reports and my own experience, I think that, if properly implemented into the clinical practice of radiology, stereotaxic core breast biopsy will become an important tool in the management of occult breast lesions.

Indications

In my opinion, large-core biopsy should not be used as an alternative to mammographic follow-up of lesions considered benign. This would add an enormous volume of unnecessary additional procedures and expense with only a minute chance of documenting the presence of a malignant tumor.

Only those abnormalities deemed suspicious enough to warrant localization and excision should be considered for core biopsy. Solitary solid masses that are separable from the adjacent parenchyma are the easiest to sample by biopsy. Abnormalities close to the chest wall or nipple are more difficult and occasionally impossible to sample. Microcalcification clusters are considered by some to be less suited for biopsy by the large-core technique because of the potential for sampling error. However, more research into this issue will help establish firmer guidelines.

Technique

The procedure is easy to learn, safe, and well tolerated by the patient. The biopsy must be performed with the patient in the prone position. Prebiopsy hematologic evaluation is unnecessary in healthy patients. After stereotaxic localization, a small volume (<1.5 ml) of local anesthetic is injected, and a tiny skin incision is made to facilitate penetration of the 14-gauge biopsy needle. The appropriate number of cores necessary may vary with the type of occult abnormality. By submitting material from each needle pass separately to the pathologist for evaluation, we have concluded that three biopsy samples are sufficient for nearly all lesions.

After the procedure, firm compression is applied to the biopsy site for a minimum of 15 min. If a small artery or vein is transected, resulting in a hematoma, the compression and observation should be extended. The patient is then sent

---

Received November 13, 1991; accepted after revision December 16, 1991.

[1] Department of Radiology, Brigham and Women's Hospital, 75 Francis St., Boston, MA 02115. Address reprint requests to J. E. Meyer.

AJR 158:991-992, May 1992 0361-803X/92/1585-0991 © American Roentgen Ray Society

home with instructions to call in 3 days to discuss the results of the procedure with me. I do not routinely reexamine the biopsy site after the patient leaves the radiology department. I send a description of the procedure and the pathology report with my recommendations to the referring physician. The results of the biopsy may necessitate subsequent surgical excision, and the patient should always be forewarned of this possibility. If the results are benign, a follow-up mammographic examination in 6–12 months is at the discretion of the radiologist. In my experience, the procedure requires 60–75 min from acquisition of informed consent to discharge from the department.

Conclusions

Additional clinical studies are necessary to determine more specifically the appropriate use of this valuable new biopsy technique. As this evolution occurs, it is imperative that the diagnostic radiologist take the leadership role in the performance of large-core stereotaxic breast biopsy and in the management of the patient before and after the procedure. Similar to other technology-dependent interventions, this equipment should be considered only for higher volume referral centers. In the hospital, it should be in the diagnostic radiology department under the supervision of radiologists who are experienced in the diagnosis and treatment of breast disease. Protocols and referral patterns should be established in a cooperative effort with the surgical department. Close communication with the pathologist is an important component of the success of this technique.

REFERENCES

1. Sickles EA. Periodic mammographic follow-up of probably benign lesions: results in 3,184 consecutive cases. *Radiology* **1991**;179:463–468
2. Meyer JE, Christian RL, Frenna TH, Sonnenfeld MR, Waitzkin ED, Shaffer K. Image guided aspiration of occult breast "cysts." *Arch Surg* (in press)
3. Lofgren M, Andersson I, Lindholm K. Stereotactic fine-needle aspiration for cytologic diagnosis of nonpalpable breast lesions. *AJR* **1990**;154:1191–1195
4. Kopans DB. Fine-needle aspiration of clinically occult breast lesions. *Radiology* **1989**;170:313–314
5. Parker SH, Lovin JD, Jobe WE, et al. Stereotactic breast biopsy with a biopsy gun. *Radiology* **1990**;176:741–747
6. Parker SH, Lovin JD, Jobe WE, Burke BJ, Hopper KD, Yakes WF. Nonpalpable breast lesions: stereotactic automated large-core biopsies. *Radiology* **1991**;180:403–407

Fibrosarcoma of the Breast:
Mammographic Findings in Five Cases

Bruce C. Elson[1]
Debra M. Ikeda[1]
Ingvar Andersson[2]
Cecilia Wattsgård[2]

The mammographic features of fibrosarcoma of the breast, a rare malignant tumor, have not been described. Accordingly, we reviewed the mammograms, pathology reports, and medical records of five women with this tumor. All cases had surgical biopsies and a diagnosis made by histologic evaluation. The age of the patients ranged from 48 to 79 years. Histologically, three of the five fibrosarcomas were thought to have arisen from phyllodes tumor, and four were palpable. On mammograms, the tumors were dense masses with largely indistinct margins, ranging from 1.5 to 7.0 cm in diameter. One contained calcified osseous elements suggesting osseous trabeculae. Although the osseous trabeculae in that tumor strongly suggested sarcoma, most of the tumors had a nonspecific appearance on mammograms.

Fibrosarcomas of the breast have a nonspecific mammographic appearance. Surgical biopsy and histologic evaluation are necessary for definitive diagnosis.

AJR **158:993-995, May 1992**

Fibrosarcoma is a type of malignant stromal sarcoma that rarely occurs as a primary tumor within the breast [1-3]. It is composed of immature mesenchymal elements surrounded by a collagenous substance [1, 3, 4]. In this report, we describe the mammographic appearance of this tumor in five patients.

Materials and Methods

We reviewed the hospital records of five women who had a histologic diagnosis of primary fibrosarcoma of the breast and who also had mammography between 1976 and 1988 at Malmö General Hospital. The average age was 61 years (range, 48–79 years). The prior screening mammograms and mammograms obtained at the time of diagnosis were reviewed separately by two radiologists for mass size, tumor border characteristics, and calcifications. The hospital records were reviewed for clinical history and presentation, cytologic and histologic data, treatment, and follow-up. The mammograms, pathology reports, and records of the five patients were then reviewed together retrospectively. The length of follow-up varied from 4 to 12 years in four patients; the remaining patient was lost to follow-up after biopsy.

Two patients had had surgery for phyllodes tumor 8 and 22 years previously. One patient had an impalpable 1.5-cm nodule in the biopsy bed shown on screening mammography, and one had a palpable mass under the surgical scar. The remaining three patients had palpable masses in the breast, one of which had grown rapidly since a screening mammogram with normal findings 3 months before. One of these patients had both skin thickening and nipple retraction, and one had a tender breast and axillary adenopathy and had been treated with antibiotics for presumed mastitis. The palpable masses varied from 2.5 to 7.0 cm in diameter (average diameter, 4 cm).

All patients had palpable or mammographically guided fine-needle aspiration. In one patient, the cytologic findings were nonspecific, one had atypical cells, one had cells suggesting carcinoma, and two showed malignant cells suggestive of sarcoma. The five patients' masses were surgically excised, and three subsequently had a mastectomy.

Received October 17, 1991; accepted after revision December 10, 1991.

[1] Department of Radiology, The University of Michigan Hospitals, 1500 E. Medical Center Dr., Box 0326, Ann Arbor, MI 48109. Address reprint requests to D. M. Ikeda.

[2] Department of Radiology, Malmö General Hospital, S-21401 Malmö, Sweden.

0361-803X/92/1585-0993
© American Roentgen Ray Society

Histologic analysis of the specimens showed four fibrosarcomas, three of which had elements suggesting origins in phyllodes tumor, two of which were thought to represent malignant recurrences of previously resected tumors. No axillary metastases were found in the one patient with palpable axillary lymphadenopathy.

The fifth case was a fibrosarcoma thought to have arisen in a fibroadenoma or phyllodes tumor. In this fibrosarcoma, atypical cells with traits of osteoblasts forming osteoid and mineralizing bone and cartilage were seen. The significance of the bone-forming elements was not clear in this case, but the pathologist did not think that this tumor should be classified as a primary osteogenic sarcoma of the breast. No axillary metastases were found. This patient was subsequently lost to follow-up.

Three of the other four patients were alive and well 4, 8, and 12 years after diagnosis and mastectomy (two cases) or local excision with free margins (one case). No evidence of recurrence was found. Suspicious calcifications developed in the contralateral breast of the fourth patient 8 years later; ductal carcinoma in situ was found at surgery. A mass developed in the right breast 3 years later, and lobular carcinoma in situ and tubuloductal cancer were found at surgery. This patient is still alive 11 years after the diagnosis and excision of the fibrosarcoma.

Results

Three of the patients had had mammograms before that had been interpreted as showing no significant abnormality. The time intervals between the first mammogram and the mammogram obtained at the time of diagnosis were 3 months, 5 years, and 7 years. As previously stated, a rapidly growing mass was palpated in one patient 3 months after her screening study.

On mammograms, the tumors were masslike and relatively dense compared with the surrounding breast tissue. The size of the masses on mammography corresponded to those felt at physical examination, except for the impalpable 1.5-cm mass found at screening mammography. The tumor margins varied from very well defined to poorly defined (Figs. 1–3). One tumor contained a calcified structure in a pattern suggesting osseous trabeculae (Fig. 3). No microcalcifications were present.

Discussion

Our study shows that fibrosarcomas appear on mammograms as a nonspiculated, dense mass with largely indistinct borders, although some borders may be sharp, as seen in Figure 3. No specific mammographic features distinguish these from round breast carcinomas or noncalcified fibroadenomas unless bony elements are present.

Breast sarcomas are rare, accounting for 0.5 to 3.0% of malignant tumors of the breast [1–3, 5–8]. Stromal sarcomas, of which fibrosarcoma is a subtype, are always malignant, but the degree of malignancy varies. These tumors contain no epithelial component and are solid masses that can form metaplastic elements such as muscle, cartilage, and bone, sometimes with hemorrhage and necrosis [1–5, 7, 9, 10]. They may arise within breast stroma or from benign stromal tumors or phyllodes tumors, as in three of our cases. Phyllodes tumor is found only in the breast and contains mesenchymal elements, which may be either benign or malignant, and a benign epithelial component [1–3].

In the literature, 3–13% of sarcomas of the breast are reported to be osteogenic [1, 5, 7]. They have many characteristics similar to fibrosarcoma of the breast and may show typical fine spicules of bone. In our series, the diagnosis of such a sarcoma was suggested by the presence of charac-

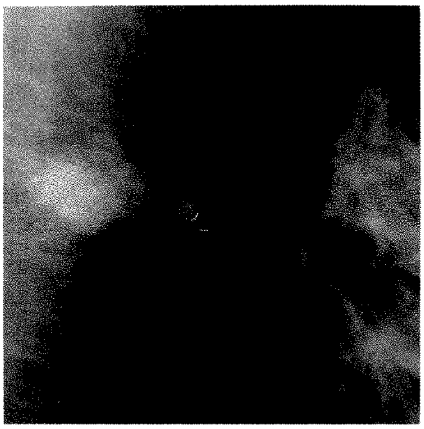

Fig. 1.—52-year-old woman with impalpable fibrosarcoma. Mediolateral oblique mammogram shows a 1.5-cm poorly defined mass. Fibrosarcoma was probably a malignant recurrence from phyllodes tumor resected 8 years earlier near biopsy bed.

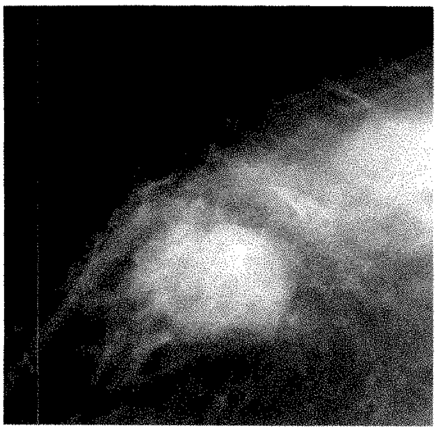

Fig. 2.—76-year-old woman with a palpable fibrosarcoma. Craniocaudal mammogram shows a 2.5-cm, dense, poorly defined mass. Fibrosarcoma probably arose from a phyllodes tumor that was resected 22 years earlier.

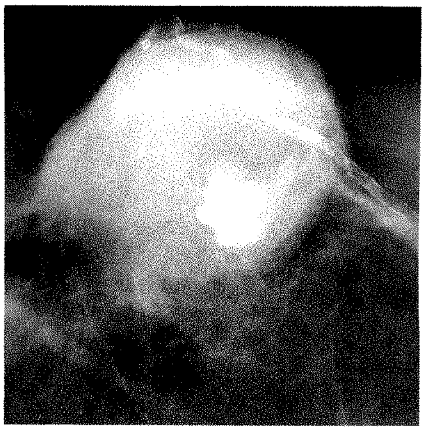

Fig. 3.—70-year-old woman with a palpable, 4-cm fibrosarcoma. Craniocaudal mammogram shows a round, well-circumscribed mass with a poorly defined posterior margin containing osseous trabeculae. Tumor contains calcified osteoid and cartilaginous elements.

teristic osseous trabeculae within the mass on the mammograms, but in our case a fibrosarcoma with chondroid and osteoid elements was found at histology.

The mean presenting age of 61 years for our patients falls within the wide reported age range (17–86 years) at presentation of breast sarcomas [1–3, 5–7, 9], and as in our series, most women presented with a palpable breast mass [1, 3, 5–7, 9]. In Roberson's study [1], approximately one third of patients presented with breast pain; the less common presenting symptoms included overlying skin inflammation and edema, elevated body temperature, and nipple inversion, which were seen in two of our patients.

The literature describes axillary lymphadenopathy occurring in approximately 25% of patients, but it is almost always due to lymphoid hyperplasia, as in our patient with enlarged lymph nodes, with only 5% of adenopathy due to metastatic disease [1–3, 6, 7, 9]. Although this did not occur in our series, metastatic tumor spread is primarily hematogenous, particularly to lung and bone, and tumors that metastasize usually do so within 5 years of diagnosis. Local tumor recurrence is common, especially if only local excision is performed, and suggested treatment for breast sarcomas is simple mastectomy with removal of underlying pectoralis fascia.

ACKNOWLEDGMENT

We thank Melanie L. Shaw for secretarial support in the preparation of this manuscript.

REFERENCES

1. Roberson GV. Fibrosarcoma of the breast. *J Arkansas Med Soc* **1973**;69:257–265
2. Barnes L, Pietruszka M. Sarcomas of the breast: a clinicopathologic analysis of ten cases. *Cancer* **1977**;40:1577–1585
3. Christensen L, Schiodt T, Blichert-Toft M, Hansen JPH, Hansen OH. Sarcomas of the breast: a clinico-pathological study of 67 patients with long term follow-up. *Eur J Surg Oncol* **1988**;14:241–247
4. Agarwal C, Maheshwari B, Kumar S, Dutta S. Cystosarcoma phyllodes with osteogenic sarcoma of the breast. *Indian J Med Sci* **1976**;30:5–7
5. Jernstrom P, Lindberg AL, Meland ON. Osteogenic sarcoma of the mammary gland. *Am J Clin Pathol* **1963**;40:521–526
6. Gogas JG, Kotslanos G, Gogas KG. Sarcoma of the breast. *Am Surg* November **1976**;42:812–816
7. Benediktsdottir K, Lagerberg F, Lundell L, Thulin A. Osteogenic sarcoma of the breast. *Acta Pathol Microbiol Scand* **1980**;88:161–165
8. Payan HM, England DM. Fibrosarcoma mimicking breast fibromatosis. *Am J Med Genet Suppl* **1987**;3:257–262
9. Ludgate CM, Anderson TJ, Langlands AO. Sarcoma of the female breast: report of a series of 30 cases. *Clin Oncol* **1977**;3:97–105
10. Lamovec J. Breast sarcoma (letter). *Am J Surg Pathol* **1987**;11:905–906

Come to the
American Roentgen Ray Society
92nd
ANNUAL MEETING
Orlando, FL
Marriott's Orlando World Center
May 10-15, 1992

Scientific Program (189 papers)
60 Instructional Courses
Categorical Course on Neuroradiology
Symposium on Pediatric Radiology
Symposium featuring a New Issues Forum
The Caldwell Lecture
Award Papers
Scientific Exhibits
Technical Exhibits
Spouse/Guest Program on Osteoporosis
Golf, Tennis and Social Programs

Changes in Extrahepatic Bile Duct Caliber in Liver Transplant Recipients Without Evidence of Biliary Obstruction

William L. Campbell[1]
Richard G. Foster[1,2]
William J. Miller[1]
James W. Lecky[1]
Albert B. Zajko[1]
Kyung Y. Lee[3]

To better understand changes in the size of the extrahepatic bile duct after liver transplantation, we retrospectively studied the luminal diameter of the extrahepatic bile duct on serial cholangiograms in 40 liver transplant recipients with choledochocholedochostomy biliary anastomoses and without biliary complications. Forty operative and 105 postoperative cholangiograms were reviewed. The average interval between operative and last postoperative cholangiogram was 5 weeks (range, 1–17 weeks). The mean diameter of the donor common hepatic duct increased from 5.5 ± 2.1 mm to 6.3 ± 2.4 mm ($p = .015$). The mean diameter of the native common bile duct increased from 5.1 ± 1.4 mm to 6.8 ± 2.4 mm ($p < .001$). The diameter of the donor common hepatic duct increased by 3 mm or more in six patients (15%); the diameter of the native common bile duct increased by 3 mm or more in nine (23%). Increased diameter of the native common bile duct was associated with T-tube migration into the duct in four cases.

The size of the extrahepatic bile duct on cholangiograms is stable or increases slightly in most liver transplant recipients. Mild increases unassociated with a specific cause of obstruction or hepatic dysfunction do not portend biliary obstruction and are clinically benign.

AJR **158:997–1000, May 1992**

Biliary obstruction after liver transplantation occurs in approximately 5% of transplants. Causes include strictures at the biliary anastomosis or in the donor biliary tree, retained internal stents, T-tube problems, and stones [1, 2]. Apparent obstruction at the ampulla of Vater with diffuse dilatation of the recipient and donor extrahepatic bile ducts and hepatic dysfunction also has been described. In such cases, cholangiography shows biliary dilatation without evidence of stricture, stone, or other specific cause for obstruction [3, 4].

Although biliary dilatation is often a valuable clue to the presence of obstruction, unexplained increases in the luminal diameters of the recipient and donor extrahepatic bile ducts occasionally develop in liver transplant recipients who apparently do not have obstruction. Documentation of such acquired changes would have implications for the imaging diagnosis of posttransplantation obstructive biliary dilatation and, possibly, for the understanding of pathophysiologic changes that might accompany choledochocholedochostomy biliary reconstructions. We therefore studied the size of the extrahepatic bile duct on serial cholangiograms in liver transplant recipients who had no clinical or pathologic evidence of biliary obstruction.

Materials and Methods

Complete imaging data and clinical follow-up were available for 49 consecutive liver transplant recipients who had postoperative cholangiography between January and July 1988. Nine of these were excluded from the study because of biliary complications that required biliary anastomotic revision to a choledochojejunostomy with Roux-en-Y loop. Forty

Received October 15, 1991; accepted after revision December 18, 1991.

[1] Department of Radiology, University of Pittsburgh School of Medicine, Presbyterian University Hospital, DeSoto at O'Hara Sts., Pittsburgh, PA 15213. Address reprint requests to W. L. Campbell.

[2] Present address: Department of Radiology, West Penn Hospital, 4800 Friendship Ave., Pittsburgh, PA 15224.

[3] Department of Biostatistics, Graduate School of Public Health, University of Pittsburgh, Pittsburgh, PA 15213.

0361-803X/92/1585-0997
© American Roentgen Ray Society

patients, 22 men and 18 women, made up the final study group. Mean age was 45 years (range, 18–71 years). All had biliary reconstructions of the end-to-end choledochocholedochostomy (duct-to-duct) type with a T-tube left in place. For each patient, a good quality operative cholangiogram and at least one postoperative cholangiogram were available for review. None of the patients was considered to have biliary obstruction on the basis of clinical, laboratory, or liver biopsy evidence; none had subsequent surgical revision of their biliary reconstructions.

Operative and postoperative T-tube cholangiography was performed by hand injection of 25% sodium diatrizoate. No attempt was made to standardize the rate of injection. Postoperative T-tube cholangiograms were recorded on conventional spot films and one overhead tube Bucky radiograph by using a 44-in. (1.1 m) target-to-film distance. Operative cholangiography was performed by using a 44-in. target-to-film distance. Percutaneous transhepatic cholangiography was performed in the standard fashion with a 40-in. (1 m) target-to-film distance.

The caliber of the extrahepatic bile duct was measured on Bucky overhead or spot film radiographs. The least magnified views that exhibited good duct filling were selected for review. For the purposes of this study, good duct filling consisted of complete distension of the extrahepatic bile ducts, as determined from several radiographs, accompanied by flow into the duodenum and filling of multiple tertiary intrahepatic duct branches. No absolute correction for magnification was made. Correction for magnification of spot radiographs relative to overhead operative and postoperative radiographs was made by measuring the lengths of the intraductal T portions of the T-tubes on anteroposterior projections. The difference between the spot and overhead radiograph measurements divided by the overhead film measurement gave the percentage of magnification of spot films compared with overhead films. This factor was used to correct duct diameters measured on spot films to the nearest millimeter to allow direct comparison with overhead radiographs. The caliber of the donor common hepatic duct was measured at a point precisely midway between the duct bifurcation and the biliary anastomosis; the caliber of the native common bile duct was measured at the midpoint between the anastomosis and the sphincter of Oddi.

Changes in diameter of the extrahepatic bile ducts were calculated for each patient by comparing the operative cholangiogram with both the postoperative study that showed the greatest diameter and the last available postoperative cholangiogram. The last postoperative cholangiographic study was used for statistical comparisons.

Statistical analyses were performed by using paired and unpaired t-tests, Mann-Whitney U, and Pearson correlation tests [5].

Results

One hundred forty-five cholangiograms were reviewed, including 40 operative and 104 postoperative T-tube studies. One postoperative percutaneous transhepatic study was performed after T-tube removal. The mean number of postoperative cholangiograms per transplant was 2.5 (range, 1–5). The average interval between the operative and last postoperative cholangiogram was 5 weeks (range, 1–17 weeks). The average length of clinical follow-up was 21.6 months (range, 0.3–33.5 months), with a mean follow-up in living patients of 29.6 months (range, 27–33.5 months). Thirteen patients (33%) died between 0.3 and 18.2 (mean, 5.0) months after transplantation.

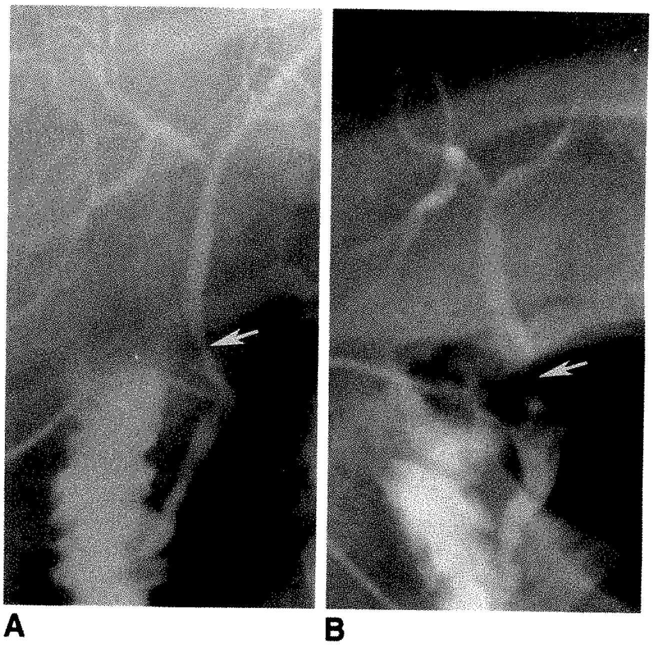

Fig. 1.—Increase in diameter of extrahepatic bile duct after uncomplicated liver transplantation.

***A*, Operative cholangiogram shows diameters of 4 mm for donor common hepatic duct and 3 mm for native common bile duct. *Arrow* = anastomosis.**

***B*, T-tube cholangiogram obtained 3 months later shows diameters of 5 mm for donor common hepatic and 6 mm for native common bile duct. *Arrow* = anastomosis.**

The mean caliber of the donor common hepatic duct on operative cholangiograms was 5.5 ± 2.1 mm (range, 2–10 mm); the mean caliber on the last postoperative cholangiogram was 6.3 ± 2.4 mm (range, 2–11 mm). The increase from 5.5 to 6.3 mm was significant ($p = .015$). The mean caliber of the native common bile duct on operative cholangiograms was 5.1 ± 1.4 mm (range, 2–8 mm); the mean caliber on the last postoperative cholangiogram was 6.8 ± 2.4 mm (range, 3–13 mm). The increase from 5.1 to 6.8 mm was statistically significant ($p < .001$) (Fig. 1). The caliber of the donor common hepatic duct increased by 3 mm or more in six (15%) of 40 patients, by 2 mm in 10 (25%), by 1 mm in five (12%), and by 0 mm in 18 (45%); in one patient in whom the T-tube had migrated to the sphincter of Oddi in a dilated native common bile duct, the donor common hepatic duct was not filled. The diameter of the native common bile duct increased by 3 mm or more in nine patients (22%), by 2 mm in 10 (25%), by 1 mm in eight (20%), and by 0 mm in 13 (32%). In three patients, the diameter of the native common bile duct was 12 mm or more on the last cholangiogram (12 mm in two patients and 13 mm in one). Increases in duct diameter in these three cases were 5, 8, and 9 mm. There were no significant differences between changes in bile duct size calculated using the postoperative cholangiogram with the greatest duct diameter and the last postoperative cholangiogram. No patients developed significant dilatation that subsequently resolved.

In four patients, the last cholangiogram showed that the T-tube had migrated into the distal common bile duct (Fig. 2). In one of these, the tube had passed into the sphincter of

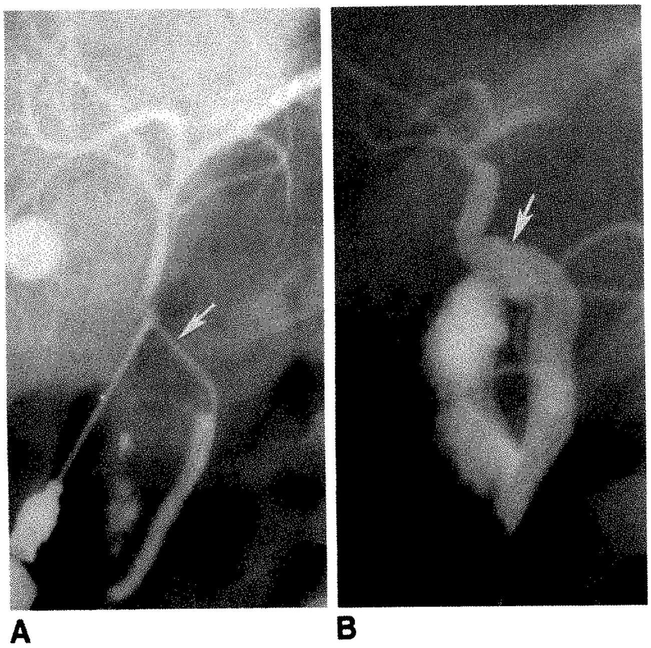

Fig. 2.—Marked increase in diameter of extrahepatic duct associated with T-tube migration in a liver transplant recipient.

***A*, Operative cholangiogram shows diameters of 3 mm for donor common hepatic duct and 4 mm for native common bile duct. *Arrow* = area of anastomosis.**

***B*, T-tube cholangiogram performed 2 months, 22 days later shows an increase in diameter of common ducts. Diameter of donor common hepatic duct is 7 mm, and diameter of native common bile duct is 12 mm. T-tube has migrated into distal common bile duct. *Arrow* = anastomosis.**

Oddi and in another it had just reached the sphincter. The mean diameter of the donor common hepatic duct in these patients was 7.7 ± 1.2 mm, compared with 6.2 ± 2.5 mm in patients without tube migration ($p = .232$). The mean diameter of the native common bile duct was 11.0 ± 1.8 mm, compared with 6.4 ± 1.9 mm in patients without tube migration ($p = .002$). The mean increase in diameter of the native common bile duct in the four patients with tube migration was 6.0 ± 2.9 mm, compared with 1.25 ± 1.7 mm in the other subjects ($p = .002$). The increase in the diameter of the donor common hepatic duct was 2.3 ± 1.5 mm in patients with tube migration compared with 0.6 ± 1.9 mm in those without migration ($p = .140$).

In 36 patients without tube migration, the mean size of the donor common hepatic duct increased from 5.6 ± 2.1 mm to 6.2 ± 2.5 mm ($p = .047$). The mean size of the native common bile duct increased from 5.1 ± 1.4 mm to 6.4 ± 1.9 mm ($p < .001$).

We found no correlation between increasing size of the native common bile duct and either the age or sex of the patient.

Discussion

Imaging of the extrahepatic bile ducts is a routine part of the postoperative management of liver transplant recipients. Early diagnosis of biliary complications such as obstruction or bile leak is essential for prompt treatment. An increase in the diameter of the bile duct may be an important clue to biliary obstruction in liver transplant recipients, as it may be in nontransplantation patients. This is particularly true in the diagnosis of so-called obstructive diffuse dilatation or ampullary obstruction, for which the main cholangiographic finding is dilatation of the extrahepatic bile ducts [4].

Although it has been assumed that the diameter of the extrahepatic bile duct normally remains stable in liver transplant recipients, occasionally both donor and native extrahepatic bile ducts have increased in size over time. Some cases, usually with more marked dilatation, have been associated with hepatic dysfunction that has improved with revision of the biliary anastomosis to a choledochojejunostomy [3, 4]. In other cases, the increase in the diameter of the bile duct has appeared to be clinically benign. The results of this study indicate that a slight increase in the size of the extrahepatic bile duct shown on cholangiograms is not unusual in liver transplant recipients, and in some patients, dilatation of the extrahepatic bile ducts develops. These findings have implications for the interpretation of posttransplantation cholangiograms and, perhaps, for a better understanding of patients with clinically significant diffuse biliary dilatation and hepatic dysfunction.

Although the degree of duct filling and radiographic magnification may affect measurements of bile duct caliber on cholangiograms, it is unlikely that the increases seen in the study patients can be entirely explained on this basis. Operative cholangiograms showed good duct distension, as evidenced by the extent of intrahepatic duct filling and the presence of flow into the duodenum; indeed, the degree of filling often was greater than in the postoperative studies. Chance variation in injection pressure could not account for observed increases in duct size as increases in diameter were statistically significant and progressive on serial studies. We corrected for magnification on spot films compared with operative and nonoperative overhead films by using the intraductal portion of the T-tube as an internal standard. Mean relative spot film magnification was 8% (range, 0–39%). As a practical matter, spot film magnification accounted for no more than 2 mm of apparent increase in duct size in any of the study patients. Whenever possible, we compared films taken in similar projections, although differences in patients' positions have a negligible influence on radiographic magnification of the extrahepatic bile ducts [6]. We analyzed change in the size of the extrahepatic bile ducts by using both the postoperative study that showed the greatest diameter (perhaps representing greatest distention or most magnification) and the last available cholangiogram; there was no significant difference between the two. For the calculation and statistical analysis of changes in diameter, we used the more conservative last examination figure to minimize any artifactual increase in measurement.

The explanation for increases in the size of the extrahepatic bile duct in liver transplant recipients is not entirely clear. Possible mechanisms include increased function of the extrahepatic bile ducts as a reservoir in the absence of a gallbladder, variations in underlying duct laxity, and subclinical low-grade obstruction. The prevalence of an acquired increase in caliber in the study patients is higher than has been reported in nontransplantation postcholecystectomy patients, particularly those studied with sonography [7-9]. Liver transplant recipients are unusual in that they may have a number of postoperative cholangiograms over several weeks or months, even in the absence of evidence of biliary obstruction; comparable serial cholangiographic observations in uncomplicated nontransplantation postcholecystectomy patients are generally lacking. Direct cholangiography distends the bile ducts, which in part explains the well-known disparity between cholangiographic and sonographic results but does not explain progressive increases in size. Dilatation forced by excessive injection pressure probably does not occur in the clinical setting and is not likely to be a factor [10]. T-tube clamping after transplantation might influence the time of development of increases in duct caliber, but data on this variable are not available.

T-tube migration into the distal common bile duct and sometimes into the ampulla of Vater was associated with significant increases in the size of the native common bile duct (3, 4, 8, and 9 mm in four patients). The largest percentages of increase in size of the native common bile duct occurred in two patients with tube migration. Migration of T-tubes in liver transplant recipients is not infrequent and is more common than in nontransplantation patients. Factors prompting tube migration may include small-caliber pliable tubes, excess intraabdominal tube length, and increasing duct diameter. Whether acquired duct dilatation usually precedes tube migration is not entirely clear, but a tube folded on itself in the native common bile duct and sometimes in the ampulla of Vater seems in some cases to lead to further dilatation of the native segment of the common bile duct. Clinical obstruction is not usually a problem, and the T-tubes are normally removed without incident within 2-3 months of the transplantation.

One must consider whether some patients with slight increases in the diameter of the extrahepatic bile duct may eventually have obstructive biliary dilatation with hepatic dysfunction. Although this must happen occasionally, the patients in this study continued to do well without evidence of biliary obstruction 2.5 years after transplantation. Diffuse obstructive biliary dilatation with hepatic dysfunction is nearly always characterized by increases in the diameter of extrahepatic ducts on cholangiograms to 12 mm or more (uncorrected for magnification) [4]. In contrast, the diameter of either the native or the donor extrahepatic duct increased to 12 mm or more (uncorrected for magnification) and would have been considered dilated in only five patients in this study, two of whom had T-tube migration. Nevertheless, some overlap exists in duct sizes between the groups with and without clinically apparent biliary obstruction.

In summary, some liver transplant recipients without biliary complications or otherwise unexplained hepatic dysfunction may have increases in the size of both native and donor extrahepatic bile ducts on postoperative cholangiograms. Increases in duct caliber occur in the first few weeks or months after transplantation and are usually slight and clinically benign. Occasionally, larger increases in duct size (to 12 mm or greater), some associated with T-tube migration, overlap with findings of obstructive extrahepatic biliary dilatation and may suggest ampullary obstruction. In managing such patients, careful attention must be paid to the diameter of the extrahepatic bile duct on baseline operative cholangiograms, results of liver function tests and liver biopsies, and the overall clinical picture.

ACKNOWLEDGMENTS

We thank Gloria Stephenson and Paula Kraft for manuscript preparation.

REFERENCES

1. Zajko AB, Bron KM, Campbell WL, Behal R, Van Thiel DH, Starzl TE. Percutaneous transhepatic cholangiography and biliary drainage after liver transplantation: a five year experience. *Gastrointest Radiol* **1987**;12: 137-143
2. Lerut J, Gordon RD, Iwatsuki S, et al. Biliary tract complications in human orthotopic liver transplantation. *Transplantation* **1987**;43:47-51
3. Stieber AC, Ambrosino G, Kahn D, et al. An unusual complication of choledochocholedochostomy in orthotopic liver transplantation. *Transplant Proc* **1988**;20[suppl 1]:619-621
4. Miller WJ, Campbell WL, Zajko AB, et al. Obstructive dilatation of extrahepatic recipient and donor bile ducts complicating orthotopic liver transplantation: imaging and laboratory findings. *AJR* **1991**;157:29-32
5. Steele R, Torrie J. *Principles and procedures of statistics*. New York: McGraw-Hill, **1960**
6. Persson B, Olsson J. Variations of common bile duct diameter after endoscopic sphincterotomy. *Gastrointest Radiol* **1991**;16:45-48
7. Graham MF, Cooperberg PL, Cohen MM, Burhenne HJ. The size of the normal common hepatic duct following cholecystectomy: an ultrasonographic study. *Radiology* **1980**;135:137-139
8. Mueller PR, Ferrucci JT Jr, Simeone JF, et al. Postcholecystectomy bile duct dilatation: myth or reality? *AJR* **1981**;136:355-358
9. Hunt DR, Scott AJ. Changes in bile duct diameter after cholecystectomy: a 5-year prospective study. *Gastroenterology* **1989**;97:1485-1488
10. Zeman RK, Burrell MI. *Gallbladder and bile duct imaging: a clinical radiologic approach*. New York: Churchill Livingstone, **1987**:403

Venoocclusive Liver Disease After Bone Marrow Transplantation:

Findings at Duplex Sonography

John Herbetko[1]
Andrew P. Grigg[2]
Anne R. Buckley[1]
Gordon L. Phillips[2]

Ascites, thickening of the gallbladder wall, and reversal of portal flow are documented sonographic findings in venoocclusive disease of the liver. The frequency and specificity of these findings and their relationship to the severity of this disease have not been studied. In an attempt to clarify these issues, 65 patients who had bone marrow transplantations were prospectively studied with serial B-scans and duplex color Doppler sonography. For all patients, assessment included liver size and texture, thickening of the gallbladder wall (>10 mm), and presence of ascites. Doppler flow velocity profiles were obtained from the portal vein, hepatic veins, and inferior vena cava. The hepatic artery resistive index (RI) was calculated. Twenty volunteers were also studied to establish normal flow values. Nineteen patients had documented venoocclusive disease, nine had hepatic graft-vs-host disease (GVHD) (five after proved venoocclusive disease), two had hepatitis, and 40 had no clinical or biochemical evidence of liver injury after bone marrow transplantation. Ascites (n = 16), thickening of the gallbladder wall (n = 8), hepatomegaly (n = 8), and altered liver texture (n = 3) were not distinguishing features of venoocclusive disease. Mean hepatic artery RI was as follows (ranges are in parentheses): control group, 0.69 (0.58–0.76); venoocclusive disease patients, 0.81 (0.75–0.87); GVHD patients, 0.69 (0.63–0.71); all other patients after bone marrow transplantation, 0.66 (0.61–0.71). The RI values in venoocclusive disease were significantly elevated, but an incremental rise in RI with increasing severity of the disease was not seen. Abnormalities in portal vein flow were seen in only two patients: In one with fatal venoocclusive disease, reversed portal flow developed, and in one with GVHD, portal vein thrombosis developed. Contrary to previous reports, no correlation between abnormalities in portal flow and venoocclusive disease was seen. Flow velocities in the hepatic veins and the inferior vena cava were not significantly different from values in the volunteer group.

These results suggest that a significant elevation of the hepatic artery RI may be a sensitive index of liver damage related to venoocclusive disease after bone marrow transplantation and an important distinguishing sonographic feature.

***AJR* 158:1001–1005, May 1992**

Venoocclusive disease of the liver results from intensive conditioning chemotherapy and radiotherapy in patients undergoing allogenic or autologous bone marrow transplantation [1–3]. The disease typically becomes manifest in the first 2 weeks after transplantation and includes weight gain caused by fluid accumulation, tender hepatomegaly, and elevated levels of bilirubin. Other liver enzymes, especially aspartate aminotransferase and alkaline phosphatase, may also be elevated. In the transplantation patient, differentiation of venoocclusive disease from other causes of liver dysfunction, particularly hepatic graft-vs-host disease (GVHD), may be difficult, because such entities may be associated with similar biochemical abnormalities. A definitive diagnosis is important because the treatment of each condition is considerably different. Treatment of hepatic venoocclusive disease is mainly supportive and involves fluid and sodium restriction, natriuresis, the use of albumin infusions, and reduction in the dose of cyclosporine. Conversely,

---

Received August 26, 1991; accepted after revision November 26, 1991.

[1] Department of Radiology, Section of Ultrasound, University of British Columbia and Vancouver General Hospital, 855 W. 12th Ave., Vancouver, B.C., Canada V5Z 1M9. Address reprint requests to Anne R. Buckley.

[2] Leukemia Bone Marrow Transplantation Program of British Columbia, Vancouver General Hospital, 910 W. 10th Ave., Vancouver, B.C., Canada V5Z 4E3.

0361–803X/92/1585–1001
© American Roentgen Ray Society

treatment of acute GVHD involves increased immunosuppression with high-dose glucocorticoids, cyclosporine, and various monoclonal antibodies against T cells. Distinction between venoocclusive disease and GVHD can generally be made histologically; however, liver biopsy in these patients is associated with an increased risk of bleeding complications because of severe thrombocytopenia or coagulation abnormalities.

Several reports [1, 2, 4–7] have described the results of gray-scale and Doppler sonography in patients with hepatic venoocclusive disease. A variety of sonographic features has been recognized, including ascites, thickening of the gallbladder wall, and reversal of portal venous flow. However, the frequency of these findings and their relationship to the severity of venoocclusive disease have not been investigated. Moreover, no studies have yet established whether these abnormalities are also seen in patients with hepatic GVHD.

In an attempt to clarify the distinguishing gray-scale and Doppler findings in hepatic venoocclusive disease, we prospectively performed serial B-scans and duplex color Doppler sonography on 65 patients before and after bone marrow transplantation.

Subjects and Methods

From February 1990 to March 1991, 65 recipients of bone marrow transplants were prospectively studied with serial B-scans and duplex color Doppler sonography of the abdomen. All examinations were performed by using an Acuson 128 (Mountain View, CA) unit with a 3.5-MHz transducer for imaging and Doppler evaluation. All patients fasted a minimum of 8 hr before the study. Sixty-two patients had a pretreatment baseline sonogram, and all 65 patients had gray-scale and Doppler assessment in the third week after transplantation. Additional sonographic studies were performed in those patients in whom biochemical evidence of hepatic venoocclusive disease developed (bilirubin ≥60 µmol/l; this bilirubin level was selected in an effort to differentiate hepatic venoocclusive disease from mild GVHD). Initial sonograms were obtained within 24 hr of tests that showed elevated levels of bilirubin. Two scans per week were obtained until either the hepatic abnormality resolved or the patient died. Venoocclusive disease was clinically graded according to criteria of Bearman et al. [8], which are based on the degree of biochemical hepatic dysfunction (bilirubin >34 µmol/l) and fluid overload (weight gain >2.5% from baseline).

Each sonographic examination included a full gray-scale assessment of the abdomen with particular attention to liver size and texture. Features noted included thickening of the gallbladder wall (>10 mm), dilatation of the biliary ducts, and ascites. Doppler flow-velocity profiles were obtained in the main portal vein; right and left portal vein branches; right, middle, and left hepatic veins; and the inferior vena cava. All Doppler data were obtained with the patient supine. The presence and direction of flow were recorded, and the peak flow velocity in each vessel was measured by using a 3.5-MHz transducer and a 30–60° angle of insonation. Flow in the hepatic artery was assessed at the point where the artery courses over the main portal vein. An absolute peak systolic velocity in the hepatic artery was not measured. Instead, the hepatic artery resistive index (RI) was calculated; this parameter is independent of the angle of insonation. The RI was calculated several times during each study, and an average value was recorded. Statistical analysis of the RI values for the different patient groups included paired t-test analysis for baseline vs maximum values in patients with venoocclusive disease, and unpaired t-test analysis for maximum values in patients with venoocclusive disease vs maximum values for other disease groups.

Twenty control subjects also were studied in order to establish normal Doppler flow values in the portal and hepatic venous systems and to determine a normal range for the hepatic artery RI.

Results

All 20 control subjects had continuous pulsatile flow within the main portal vein and its right and left branches (Fig. 1A). The mean peak portal vein velocity was 51 cm/sec (range, 15–88 cm/sec). The inferior vena cava and hepatic veins showed phasic velocity profiles reflecting hemodynamic changes in the right atrium (Fig. 1B). The mean peak velocity in the inferior vena cava was 81 cm/sec (range, 44–118 cm/sec), and the mean peak velocity in the hepatic veins was 38 cm/sec (range, 16–61 cm/sec). The mean hepatic artery RI for the control group was 0.69 (range, 0.58–0.76).

Venoocclusive disease of the liver developed in 19 of the bone marrow transplantation patients (Table 1). The diagnosis was based on histologic findings in 10 cases and on clinical and biochemical findings in nine. Hepatic GVHD developed in nine patients and was histologically proved in eight. In five

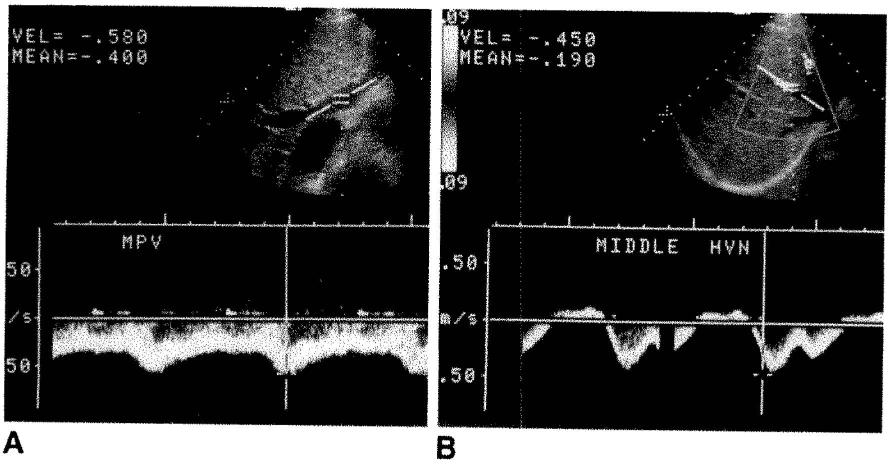

Fig. 1.—Control subject.
A, Spectral waveform shows normal continuous pulsatile flow in main portal vein. Peak and mean portal vein velocities are indicated.
B, Spectral waveform shows a normal phasic velocity profile in middle hepatic vein. Peak and mean hepatic vein velocities are indicated.

patients, GVHD developed after proved venoocclusive disease. In two patients with elevated levels of liver enzymes, hepatitis was found by liver biopsy; 40 recipients of bone marrow transplants showed no clinical or biochemical evidence of liver dysfunction.

Thickening of the gallbladder wall (>10 mm) developed in eight patients after bone marrow transplantation. This occurred in two patients with venoocclusive disease, two with GVHD, the two with hepatitis, and two with normal liver function. Ascites was detected in 16 patients, and all patients with thickening of the gallbladder wall had ascites. Ascites was detected in six patients with venoocclusive disease only, three with venoocclusive disease and subsequent GVHD, three with GVHD only, the two with hepatitis, and two with normal liver function. Hepatomegaly ($n = 8$) and altered liver texture ($n = 3$) were not specific to any disease state. No case of biliary dilatation was found.

The mean maximum hepatic artery RI for all patients with venoocclusive disease was 0.81 ± 0.037 (range, 0.75–0.87) (Table 1). An increase in RI above the initial baseline value was seen in 18 of 19 bone marrow transplant recipients in whom venoocclusive disease developed (Fig. 2). In each case, the increase in RI was detected within 24 hr of tests that showed a biochemical abnormality. In the 19th patient, poor signal quality prevented an adequate measurement of the RI. In 11 of 19 patients, the RI subsequently returned to values observed before bone marrow transplantation, and this change corresponded with resolution of the hepatic dysfunction. In seven of 19 patients, all of whom died, the last RI value obtained was elevated. The RI values in patients with venoocclusive disease were significantly higher than baseline RI values in those same patients ($p < .01$) and significantly higher than RI values in the control group ($p < .01$), in patients with isolated GVHD ($p < .01$), in patients without liver dysfunction after bone marrow transplantation ($p < .001$), and in the two patients with hepatitis ($p < .01$). However, an incremental rise in mean RI was not found with increasing clinical severity of venoocclusive disease. No significant difference was found in the mean hepatic artery RI between the group with pathologic proof of venoocclusive disease ($n = 10$) and the group with biochemical and clinical evidence of venoocclusive disease ($n = 9$). GVHD subsequently developed in five patients with histologically proved venoocclusive disease; all five had a significantly elevated hepatic artery RI during the course of venoocclusive disease, but RI values in all these patients returned to normal and remained so during the course of GVHD.

Normal flow velocities were seen in the hepatic veins and inferior vena cava in all patients during this study. We found no significant difference in the mean peak velocity flow values

TABLE 1: Hepatic Artery Resistive Index in Control Subjects and in Patients Before and After Bone Marrow Transplantation

Group	No. of Subjects	Baseline RI Mean ± SD (Range)	Maximum RI Mean ± SD (Range)
Controls	20	0.69 ± 0.043 (0.58–0.76)	—
Venoocclusive disease		0.68 ± 0.042 (0.55–0.71)	
Grade I	5 (1)		0.80 ± 0.053 (0.75–0.87)
Grade II	8 (3)		0.82 ± 0.041 (0.77–0.86)
Grade III	3 (1)		0.78 ± 0.031 (0.75–0.81)
Grade IV	3 (0)		0.80 ± 0.016 (0.79–0.83)
Graft-vs-host disease	9	0.64 ± 0.037 (0.58–0.70)	0.69 ± 0.030 (0.63–0.71)
Hepatitis	2	0.69 ± 0.028 (0.67–0.71)	0.66 ± 0.028 (0.64–0.68)
No liver dysfunction	40	0.66 ± 0.022 (0.57–0.69)	0.66 ± 0.019 (0.61–0.71)

Note.—RI = resistive index. Figures in parentheses after number of subjects indicate number of patients with subsequent graft-vs-host disease. Clinical grading of venoocclusive disease was done according to Bearman et al. [8].

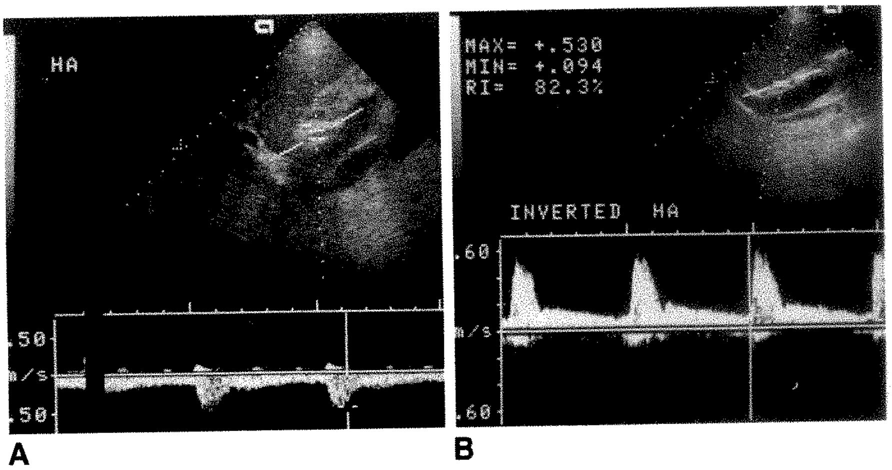

Fig. 2.—Recipient of bone marrow transplant.
***A*, Spectral analysis shows calculated baseline resistive index (RI) was normal (0.65) before conditioning chemotherapy/radiotherapy.**
***B*, Spectral analysis 8 days after bone marrow transplantation shows RI increased significantly to 0.82. Patient had biopsy-proved grade II venoocclusive disease.**

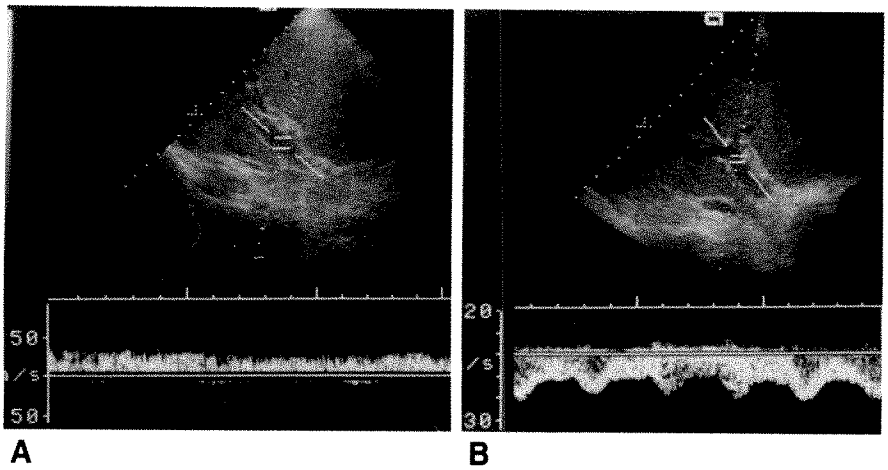

Fig. 3.—Patient with biopsy-proved grade IV venoocclusive disease after bone marrow transplantation.

A, Spectral analysis shows normal antegrade portal venous flow 7 days after bone marrow transplantation.

B, Spectral analysis shows reversed portal venous flow 20 days after bone marrow transplantation. Patient subsequently died.

between control subjects and the various groups of patients. The hepatic vein mean peak velocity was 49 cm/sec (range, 13–86 cm/sec), and the inferior vena cava mean peak velocity was 103 cm/sec (range, 26–180 cm/sec) for the combined patient groups. Normal portal venous flow was seen in 63 of 65 recipients of bone marrow transplants. In these patients, the mean peak portal vein velocity was 52 cm/sec (range, 13–90 cm/sec). Altered portal venous flow was seen in only two of the 65 recipients of bone marrow transplants. In one patient with fatal venoocclusive disease, a progressive decrease and eventual reversal of portal flow was seen (Fig. 3); this change was accompanied by a rise in RI from a baseline 0.68 to 0.82 at the onset of clinical venoocclusive disease. The RI remained elevated until the patient's death. The second patient had chronic hepatic GVHD but normal findings on serial sonographic examinations until the acute onset of massive ascites. Despite sonographic evidence of portal vein thrombosis at that time (Fig. 4A), neither a significant change in hepatic function nor any elevation in the hepatic artery RI occurred (Fig. 4B).

Discussion

Real-time sonography is frequently used in recipients of bone marrow transplants to detect the presence of ascites, to assess causes of liver dysfunction, and to determine the presence or absence of hepatic and portal vein thrombosis. The role of Doppler spectral analysis remains controversial. The pathogenesis of venoocclusive disease is thought to involve endothelial damage leading to activation of the coagulation cascade, fibrin deposition, and eventually fibrous obliteration of the terminal hepatic venules [3, 4, 9]. The hemodynamic changes occurring as a consequence of this vascular damage may, in theory, be detectable with Doppler sonography. Moreover, since GVHD mainly affects small bile canaliculi and does not cause vascular damage, it is unlikely to cause alteration in flow characteristics.

In this study, we found that an elevated hepatic artery RI after bone marrow transplantation was highly suggestive of hepatic venoocclusive disease. None of our patients had an elevated RI in the absence of venoocclusive disease. This association between altered hepatic arterial flow and venoocclusive disease has not been previously reported. We are unable to explain the strong association between an elevated hepatic artery RI and hepatic venoocclusive disease; no correlation exists between the hepatic artery RI and liver transplant rejection [10].

In our series, an abnormality in portal vein velocity was seen in only one of 19 patients with venoocclusive disease: In this patient, portal vein flow reversed 20 days after transplantation, and the patient subsequently died. Although changes in portal flow in venoocclusive disease have been reported [4, 5, 7], the frequency of these abnormalities has not been studied prospectively. Brown et al. [4] reported changes in portal flow in six of six patients with proved venoocclusive disease. Kriegshauer et al. [7] detected portal flow reversal in one case of fatal venoocclusive disease. In a study by Morris et al. [5], two of three children had reversed portal flow. The severity of venoocclusive disease in these patients was not indicated. Our observations suggest that detectable alteration of portal flow occurs infrequently even with severe (grade IV) venoocclusive disease. Portal velocity profiles were not useful in our series in distinguishing mild, moderate, or severe venoocclusive disease from GVHD. Moreover, contrary to the report by Ralls [11], our two patients with altered portal flow did not have increased systolic velocity in the hepatic artery or altered hepatic artery RI.

We cannot definitely identify the mechanism responsible for the elevated hepatic artery RI in the absence of detectable change in portal flow, a phenomenon that occurred in all but one of our 19 patients with venoocclusive disease. Possibly, endothelial damage occurring in venoocclusive disease causes an increase in resistance to flow in the hepatic artery before the development of portal hypertension. Alternatively, Doppler imaging within the portal veins may not detect small or early rises in portal pressure, and the elevated RI might result from elevated presinusoidal pressure associated with an expanded intravascular volume. However, we think that volume overload is not a sufficient explanation for these findings. First, although salt and water retention are prominent features of venoocclusive disease, most of the retained fluid is located in the extravascular space. The RI remained ele-

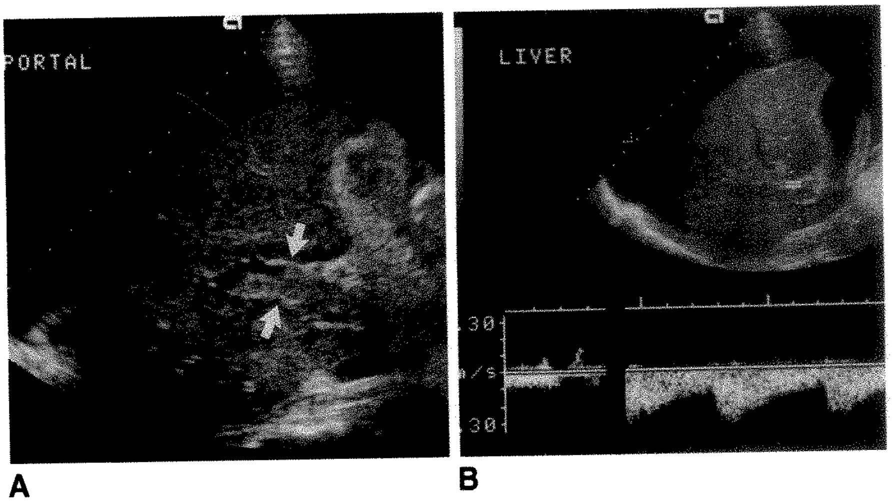

Fig. 4.—Patient with histologically proved graft-vs-host disease after bone marrow transplantation.

***A*, Sonogram shows ascites, abnormal liver texture, and portal vein thrombosis (*arrows*).**

***B*, Spectral analysis shows a normal hepatic artery waveform despite the presence of portal vein thrombosis. The calculated resistive index was normal (0.67).**

vated in six of our venoocclusive disease patients after diuretic therapy and clinical evidence of intravascular volume depletion. Moreover, RI values were normal in two patients who had severe GVHD and marked intravascular fluid overload.

Other parameters assessed in this study were not useful as distinguishing features of venoocclusive disease. Thickening of the gallbladder wall and the presence of ascites were seen both in venoocclusive disease and in other causes of hepatic dysfunction with equal frequency.

Differentiation of venoocclusive disease from GVHD may be difficult. In our experience, reversal of portal flow is an uncommon event that may occur in fatal venoocclusive disease. Elevation of the hepatic artery RI is a more sensitive index of liver damage related to venoocclusive disease and was the only distinguishing sonographic feature in our study. However, clinical grading of venoocclusive disease does not correlate with any incremental rise in the RI value.

REFERENCES

1. Jones RJ, Lee KSK, Beschorner WE, et al. Venoocclusive disease of the liver following bone marrow transplantation. *Transplantation* **1987**;44:778–783
2. McDonald GB, Sharma P, Matthews DE, Shulman HM, Thomas ED. Venoocclusive disease of the liver after bone marrow transplantation: diagnosis, incidence, and predisposing factors. *Hepatology* **1984**;4:116–122
3. Brodsky T, Topolsky D, Crilley P, Bulova S, Brodsky I. Frequency of venoocclusive disease of the liver in bone marrow transplantation with a modified busulphan/cyclophosphamide preparative regimen. *Am J Clin Oncol* **1990**;13:221–225
4. Brown BP, Abu-Yousef M, Farner R, LaBreque D, Gingrich R. Doppler sonography: a noninvasive method for evaluation of hepatic venoocclusive disease. *AJR* **1990**;154:721–724
5. Morris CL, Babcock DS, Pietryga DW, Neudorf SM. Doppler ultrasonography (DU) for evaluation of veno-occlusive disease of the liver (VOD) (abstract). *J Cell Biochem* **1990**;14A [suppl]:331
6. Matsuishi E, Anzai K, Doitmen K, et al. Sonographic diagnosis of venoocclusive disease of the liver and danazol therapy for autoimmune thrombocytopenia in an autologous marrow transplant patient. *Jpn J Clin Oncol* **1990**;20:188–192
7. Kriegshauser JS, Charboneau JW, Letenori L. Hepatic venoocclusive disease after bone-marrow transplantation: diagnosis with duplex sonography. *AJR* **1988**;150:289–290
8. Bearman SI, Appelbaum FR, Buckner CD, et al. Regimen-related toxicity in patients undergoing bone marrow transplantation. *J Clin Oncol* **1988**;6:1562–1568
9. Alperin MB, Rubin JM, Williams DM, Capek P. Porta hepatis: duplex Doppler ultrasound with angiographic correlation. *Radiology* **1987**;162:53–56
10. Longley DG, Skolnick ML, Sheahan DG. Acute allograft rejection in liver transplant recipients: lack of correlation with loss of hepatic artery diastolic flow. *Radiology* **1988**;169:417–420
11. Ralls PW. Color Doppler sonography in the hepatic artery and portal venous system. *AJR* **1990**;155:517–525

Book Review

FRCR Part 1. By Paul Butler, Charles G. Blakeney, Alan Brooks, and Robert Speller. New York: Springer-Verlag, 174 pp., 1991. softcover

This book is designed to help prepare radiologists for part 1 of the examination for Fellowship of the Royal College of Radiologists (FRCR) of the United Kingdom. Part 1 is taken by residents in England and Ireland after their first 9 months of training; it includes multiple-choice and essay questions and practical and oral examinations. *FRCR Part 1* is designed to prepare radiologists for the multiple-choice part. The book consists of five practice tests, each containing 60 multiple-choice questions. The questions are derived from a review course offered in London each year. A brief explanation of the correct and incorrect responses for each question is conveniently located on the page immediately after the questions. In keeping with the format of part 1 of the FRCR examination, the questions cover physics, anatomy, procedures, and radiographic techniques only. None of the illustrations or questions are related to disease processes or radiographic findings. *FRCR Part 1* is intended to serve as a practice examination; however, a review of the explanatory answers provides a brief review. *FRCR Part 1* should be useful to those preparing for part 1 of the FRCR examination.

Several other books are available to help European residents prepare for part 1 of the FRCR examination. *Aids to Part 1 FRCR*, by Hornsby and Winter (1988), is a concise compendium of physical, anatomic, and radiographic facts needed for part 1 of the examination. This text is small and inexpensive. It offers no explanations, but it is an excellent review and is popular among residents. *Christensen's Physics of Diagnostic Radiology*, by Curry, Dowdey, and Murray (4th edition, 1991), is a detailed physics text used by both European and U. S. residents who are studying for the physics portion of the written board examinations. The *Raphex* examination administered each year to U. S. radiology residents contains questions similar to those found on the physics section of the written board examinations, and currently residents are allowed to keep it, an excellent source of questions for study.

The premier review book for clinical material is Wolfgang Dahnert's *Radiology Review Manual* (1991). *Review of Radiology*, by the faculty of Duke University (1990), is a more concise general review, and *Aids to Radiological Differential Diagnosis*, by Chapman and Nakielny (2nd edition, 1990) provides an outstanding list of differential diagnoses. None of these include radiographs. *Clinical Imaging: An Atlas of Differential Diagnosis* by Eisenberg (2nd ed., 1992) and *Differential Diagnosis in Conventional Radiology* by Burgener and Kormano (2nd ed., 1991) provide extensive differential diagnoses with both accompanying discussion and radiographs. Unfortunately, none of these provide review questions or include a physics section; rather, they are synopses of radiologic findings, differential diagnoses, and important clinical facts. Radiology residents would be wise to own and read these books.

The books in the *American College of Radiology Syllabi*, an excellent series containing clinical questions based on radiographs, are helpful to residents preparing for the written and oral board examinations. The set is regularly updated, and each book concentrates on a specific topic. Currently, the series contains 30 volumes. Ideally, the series should be provided in duplicate by departmental libraries, and the most recent volumes read by the residents. The *ACR Teaching File* contains approximately 2000 cases with accompanying discussions and is helpful in preparing residents for the oral board examinations. No review books are available, however, that contain practice questions designed to help prepare residents for the American College of Radiology written board examinations.

FRCR Part 1 is well suited for its intended purpose of providing practice for the FRCR examination. European residents should find the practice tests and explanations useful for reviewing the material and assessing their preparedness for part 1 of the examination. Most of the questions in *FRCR Part 1* are about physics, and this book may be of some benefit to U. S. residents preparing for the physics section of the written board examinations. A library copy of *FRCR Part 1* may be useful for some, but I do not recommend that U. S. residents purchase this book.

Richard Slone
University of Florida
Gainesville, FL 32610

Treatment of Bile Duct Stones by Laser Lithotripsy: Results in 12 Patients

Steven L. Dawson[1]
Peter R. Mueller[1]
Michael J. Lee[1]
Sanjay Saini[1]
Peter Kelsey[2]
Norman S. Nishioka[2]

We used a pulsed tunable dye laser (operating at 60 mJ per pulse, 504-nm wavelength) to fragment large (0.8–4.5 cm) stones retained in the hepatic ducts or common bile duct in 12 patients after cholecystectomy. Attempts to extract stones via a T-tube or endoscope had been unsuccessful in all patients. In nine of 12 patients, all stone fragments were successfully eliminated during the initial treatment. In one patient, fragmentation occurred but debris remained, requiring endoscopic stenting. *Pseudomonas* sepsis developed in this patient 30 days after the procedure and was treated by extraction of the stone fragments. Fragments remaining after lithotripsy were cleared at the same sitting by using saline flushing or endoscopic or percutaneous basket extraction. In two of 12 patients, the treatment was unsuccessful because of laser malfunction. The treatment was performed without complications, except for clinically insignificant hyperamylasemia, which occurred in two patients.

Our experience suggests that laser lithotripsy offers a safe alternative for nonsurgical treatment of large retained biliary stones for patients in whom traditional treatments have failed.

***AJR* 158:1007–1009, May 1992**

Traditional therapy for stones retained in the common bile duct has been percutaneous or endoscopic basket extraction. Newer techniques include extracorporeal shock-wave lithotripsy (ESWL) or electrohydraulic lithotripsy. When these methods fail or cannot be performed, surgical reexploration of the duct has been necessary. Recently, tunable dye lasers have become available to fragment stones in the urinary tract and the common bile duct [1]. We present the results of fragmentation of stones retained in the intrahepatic duct or common bile duct by use of laser lithotripsy via T-tube tracks or endoscopic methods in 12 patients in whom standard percutaneous or endoscopic basket extraction was unsuccessful.

Subjects and Methods

Laser lithotripsy was performed in 12 patients in whom percutaneous or endoscopic basket removal of retained biliary stones was unsuccessful. Six women and six men between 52 and 89 years old were included in the study after giving informed consent. The laser treatment was approved by the hospital's institutional review board. Eleven patients were inpatients and one was an outpatient. The procedure was done in the radiology department under fluoroscopic guidance. One patient had epidural anesthesia, but all others were treated by IV sedation with midazolam and sublimaze. Antibiotics were not given unless clinical evidence of cholangitis was present. When necessary, IV antibiotics were given, typically ampicillin and gentamicin. Routine liver function tests and measurements of serum amylase levels were performed on all patients after the procedure. Patients had one to three stones, from 0.8 to 4.5 cm in diameter. One patient had calcified stones; two patients had intrahepatic stones. T-tube tracks were used for access in seven patients, endoscopy in five.

A tunable dye laser (60 mJ per pulse, 504-nm wavelength, 1 Hz, 3-μsec pulse length; Candela Laser Corporation, Wayland, MA) was used to fragment the stones. The laser pulses

Received August 5, 1991; accepted after revision December 23, 1991.

Presented at the annual meeting of the American Roentgen Ray Society, Boston, MA, May 1991.

[1] Department of Radiology, Massachusetts General Hospital, Harvard Medical School, 32 Fruit St., Boston, MA 02114. Address reprint requests to S. L. Dawson.

[2] Department of Gastroenterology, Massachusetts General Hospital, Harvard Medical School, Boston, MA 02114.

0361–803X/92/1585–1007
© American Roentgen Ray Society

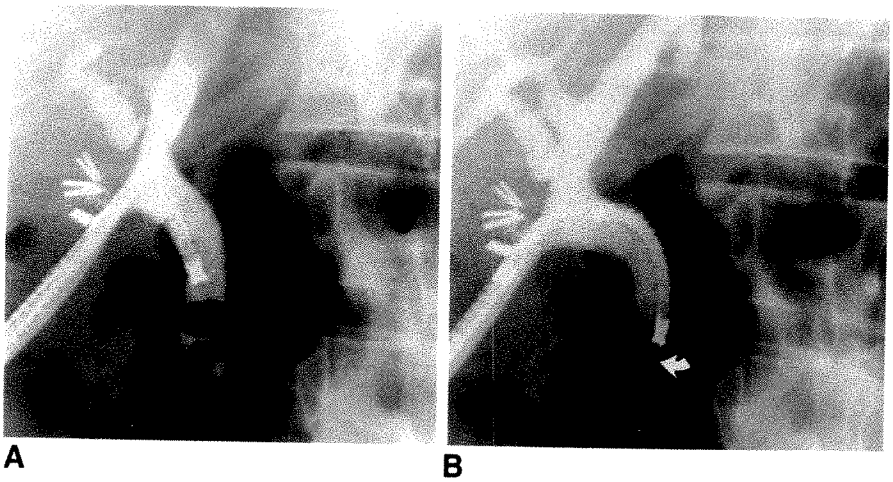

Fig. 1.—Use of choledochoscope for direct visualization during fragmentation of a stone in distal common bile duct.

***A*, Cholangiogram obtained via safety catheter shows relationship of stone to choledochoscope before laser fiber is introduced.**

***B*, Cholangiogram shows laser fiber (*arrow*) extending beyond tip of choledochoscope to contact stone.**

were conducted by a 0.4-mm-diameter quartz fiber passed to the stone. The number of pulses used to fragment the stones varied from seven to 420.

An 8.5-French ACMI choledochoscope (American Cystoscope Manufacturers Inc., Boston, MA) was inserted through the T-tube track to visualize the stone in seven patients (Fig. 1). A double endoscope system (16-mm-diameter "mother" scope with "daughter" endoscope placed through 5.5-mm working channel of mother scope) was used in all five endoscopy patients. These patients had papillotomies to allow placement of the "daughter" endoscope. In two patients, stones were held in contact with the fiber by using a modified stone basket. In the remaining eight patients, the stone was positioned against the wall of the intrahepatic, common hepatic, or common bile duct to allow consistent fiber contact with the stone. Fragments remaining after lithotripsy were extracted with stone baskets or flushed from the duct with injections of saline or contrast material. After lithotripsy, the ducts were temporarily drained with a T-tube or nasobiliary tube until follow-up cholangiography showed no residual debris. In five patients who were treated with endoscopy, fluoroscopic guidance for laser placement was used, and positioning was verified by correlating the intraprocedural cholangiogram with the fluoroscopic image. Laser lithotripsy was then performed under direct vision using a "mother-daughter" endoscope configuration. Stone disintegration was confirmed with direct vision as well as cholangiography.

Results

Stones were successfully fragmented in 10 patients, permitting subsequent basket extraction of all fragments in eight patients, or saline flushing of all fragments into the duodenum in one patient. In nine patients, the duct was free of stone debris at the conclusion of the initial procedure. In two patients, mechanical failure of the laser system precluded successful lithotripsy; procedures were aborted before lithotripsy was attempted. One of these patients subsequently underwent laparotomy and exploration of the common bile duct, and multiple stones were removed.

In one patient, several stone fragments remained after lithotripsy and could not be removed with endoscopic baskets. An 11.5-French Amsterdam stent was placed endoscopically. One month later, the patient returned with *Pseudomonas* sepsis and duodenal erosion by the stent. The stent was endoscopically removed, and all remaining fragments were basketed without further complication.

Stone size did not correlate with the number of pulses necessary for fragmentation: one 1-cm stone required seven pulses, whereas a similar-sized stone in another patient required 368 pulses. No attempts were made to characterize fragments for stone composition.

Clinically insignificant hyperamylasemia developed in two patients after lithotripsy. In one patient who had pancreas divisum and an 8-mm intrahepatic duct stone and in whom both radiologic and endoscopic approaches were used, the peak postprocedural amylase level was 1987 units (normal, 43–115 units). One patient who underwent lithotripsy (via T-tube track) of three stones from 1 to 2 cm in diameter had a peak postprocedural amylase level of 503 units.

Two patients had stones in the intrahepatic ducts: both patients were treated successfully with removal of all debris at the initial treatment session.

Discussion

Stones retained in the common bile duct are a common problem in biliary surgery. When these stones are less than 1 cm in diameter, they can often be extracted through T-tube tracks by using steerable catheters. If no T-tube is present when the stone is found, endoscopic papillotomy with basket or balloon extraction can be performed. These two techniques should be successful in approximately 90% of patients who have small stones. Dissolution with agents such as methyl *tert*-butyl ether (MTBE) is not an option for intraductal stones.

ESWL has been used to treat stones in the common bile duct [2–4] and was available in our institution during the time laser lithotripsy was studied. Although the actual lithotripsy session is noninvasive, patients require a papillotomy for passage of stone fragments, and, if fluoroscopy is used for localization, a nasobiliary catheter or percutaneous tube must be used to opacify the system. These supplementary procedures make ESWL more invasive than it appears to be. Also, targeting of stones is very difficult if sonography is used for localization. With water path, rather than water bath, ESWL, the requirement for anesthesia is lessened, but IV sedation and analgesia is still necessary. ESWL also frequently requires several sessions until patients are free of stones, whereas

TABLE 1: Comparison of Published Studies on Laser Lithotripsy

Study	Total No. of Patients	No. (%) Fragmented	No. (%) Completely Cleared	No. (%) with Single-Session Success	Immediate Complications	Subsequent Surgery	Subsequent ESWL
Cotton et al. [7]	25	23 (92)	20 (80)	12 (48)	1 (bleeding)	3	2
Ponchon et al. [9]	25	22 (88)	22 (88)	11 (44)	3 (bacteremia) 1 (duct perforation)	2	1
Present study	12	10 (83)	9 (75)	9 (75)	2 (hyperamylasemia)	1	0

Note.—ESWL = extracorporeal shock-wave lithotripsy.

laser lithotripsy has a 45–75% rate of complete stone clearance with a single treatment session [5–9] (Table 1). Because the shock wave travels across intervening organs during ESWL, there is a risk of injury to those organs, a factor that is not of concern during intracorporeal lithotripsy with pulsed dye lasers.

Pulsed dye laser lithotripsy offers a new nonsurgical option for patients in whom these other methods have failed, are unavailable, or are inappropriate.

When a stone is struck by a laser pulse, the very high energy density rapidly raises the temperature of the stone surface, causing ionization of atoms and inducing the formation of a plasma state above the stone surface. As the plasma expands, an acoustic wave is formed that fragments the stone. Thus, for most effective fragmentation, the tip should be on or very close to the surface of the stone.

With endoscopic or radiologic methods, stones in the intrahepatic and common bile duct can be localized, immobilized, and fragmented by using pulses of laser energy transmitted to the stone surface by optical fibers [1, 5–9]. The laser fiber itself measures only 0.2 mm in diameter, while the fiber plus covering measures 0.4 mm in diameter. It is easily placed through a small sheath 2- to 4-French in size. Although in many cases fluoroscopy alone might be suitable for monitoring the fiber, in this series, direct visualization through a choledochoscope or endoscope was used. The method allows fracturing of large stones into fragments small enough to permit subsequent nonoperative removal, but whether the stones were approached through the T-tube track or endoscopically, secondary maneuvers were required to remove the stone fragments: the stones approached through the T-tube track were either basketed or flushed out of the duct, and stones approached endoscopically required papillotomy and either basket extraction or balloon expulsion into the duodenum.

Earlier endoscopic or radiologic attempts at stone removal had failed in our patients because of the size of the retained stones. ESWL was not attempted in these patients. The smallest stone fragmented in this series was 0.8 cm in diameter, and the largest was 4.5 cm. The use of the coumarin green tunable dye laser allowed successful fragmentation in 10 patients and removal of stone debris during the initial session in nine of the 12 patients. The number of pulses necessary for fragmentation did not have a direct relationship to stone size. One 1-cm-diameter intrahepatic stone fragmented completely with seven pulses, whereas a 1.5-cm-diameter stone in the common bile duct required 368 pulses to be cleaved into fragments. Nishioka et al. [1] have shown that cholesterol calculi require more energy for fragmentation than pigment stones do, but we did not analyze these patients' stone debris for chemical composition.

None of our patients suffered significant immediate postprocedural morbidity. Transient hyperamylasemia developed in two patients without clinical sequela. In one of these patients, prolonged combined endoscopic and radiologic manipulations were made more difficult by the presence of pancreas divisum. One patient had *Pseudomonas* sepsis and duodenal erosion 30 days after lithotripsy and endoscopic stent placement. The acute illness responded promptly to removal of the stent and stone fragments and IV antibiotics.

In one patient, the stone could not be immobilized against the duct wall adequately to allow fiber contact without a cooperative effort. By using a catheter placed through an existing T-tube track, saline was forcefully injected onto the stone from above, displacing the stone onto the laser fiber, which had been introduced endoscopically, allowing fragmentation to occur. The cooperation of endoscopists and radiologists working as a team was crucial to success in this case.

Laser lithotripsy of large stones retained in the hepatic ducts and common bile duct expands the available nonoperative techniques for treating selected patients in whom other traditional therapies have failed. This technique can be successfully performed with an acceptable complication rate by using either radiologic or endoscopic techniques alone or with a combination of both technologies in a team approach.

REFERENCES

1. Nishioka NS, Levins PC, Murray SC, Parrish JA, Anderson RR. Fragmentation of biliary calculi with tunable dye lasers. *Gastroenterology* **1987**;93:250–255
2. Burhenne HJ, Fache JS, Gibney RG, Rowley VA, Becker CD. Biliary lithotripsy by extracorporeal shock waves: integral part of nonsurgical intervention. *AJR* **1988**;150:1279–1283
3. Staritz M, Rambow A, Grosse A, et al. Electromagnetically generated extracorporeal shock waves for fragmentation of extra- and intrahepatic bile duct stones: indications, success and problems during a 15 months clinical experience. *Gut* **1990**;31:222–225
4. Fried LA, Le Brun GP, Norman RW, et al. Extracorporeal shock wave lithotripsy in the management of bile duct stones. *AJR* **1988**;151:923–926
5. Feldman RK, Freeny PC, Kozarek RA. Pancreatic and biliary calculi: percutaneous treatment with tunable dye laser lithotripsy. *Radiology* **1990**;174:793–795
6. Berci G, Hamlin JA, Dayhovsky L, Paz-Partlow M. Common bile duct laser lithotripsy. *Gastrointest Endosc* **1990**;36:137–138
7. Cotton PB, Kozarek RA, Schapiro RH, et al. Endoscopic laser lithotripsy of large bile duct stones. *Gastroenterology* **1990**;99:1128–1133
8. Sullivan KL, Bagley DH, Gordon SJ, et al. Transhepatic laser lithotripsy of choledocholithiasis: initial clinical experience. *J Vasc Intervent Radiol* **1991**;2:387–391
9. Ponchon T, Gagnon P, Valette PJ, Henry L, Chavaillon A, Theiulin F. Pulsed dye laser lithotripsy of bile duct stones. *Gastroenterology* **1991**;100:1730–1736

Book Review

Color Doppler Flow Imaging. By W. Dennis Foley. Boston: Andover, 175 pp., 1991. $125

Written primarily by a prominent sonologist, this short monograph addresses clinical applications of color flow Doppler imaging. Complementary imaging methods are discussed when appropriate. The book consists of seven chapters: physical principles and instrumentation; neck, orbit, and neonatal head; abdomen; transplants; extremity arteries; extremity veins; and genitourinary tract. Dr. Foley is first or second author of all chapters except one, and the contributors are all connected with his institution. This facilitates a pleasingly uniform style.

The figures are mostly color sonograms with and without Doppler tracings. Quality is excellent. Ample correlative diagrams, angiograms, and CT scans are appropriately presented. The book is hardcover, with good binding and paper. The price is expensive, considering the size of the book. However, this is an unavoidable consequence of the numerous color images. The references are at the end of the chapters and are current through 1989–1990.

The first chapter starts by describing the physical principles of gray-scale sonography. A discussion of motion detection with Doppler, duplex Doppler, and color flow imaging follows. Controllable clinical parameters for image quality are explored. The second chapter, on neck, orbit, and neonatal brain, first covers normal anatomy and examination technique. Diseases of the internal and common carotid, vertebral, and innominate arteries and orbital vessels are covered. Orbital masses and pathologic vascular alterations in the neonatal brain are discussed. Gray-scale imaging of the neonatal brain is not covered. In the third chapter, technique and vascular anatomy are discussed first. Then color flow applications for the clinical evaluation of hepatic venous outflow obstruction, portal hypertension, hepatic tumors, portosystemic shunts, mesenteric angina, nontransplant renal disease, and abdominal aortic aneurysm are delineated. Again, knowledge of gray-scale applications is presumed.

The fourth chapter covers color Doppler evaluation of hepatic, renal, and pancreatic transplants and transplant postbiopsy arteriovenous fistula. Both duplex Doppler and color flow Doppler imaging of candidates for transplantation and patients who have received transplants are discussed. Radiologists who work at institutions that do these procedures will benefit from this chapter. Gray-scale applications are not evaluated. The fifth chapter, on arterial disease of the extremities, begins with an overview of competing noninvasive Doppler and plethysmographic techniques as a background. Technique and indications for color flow imaging are then presented. The role of color flow imaging and corresponding pathologic findings are presented for pseudoaneurysm, arteriovenous fistula, ischemia, detection of focal stenosis, follow-up after interventional procedures, and dialysis fistula. Knowledge of gray-scale applications is presumed.

The sixth chapter, on venous disease of the extremities, is a timely discussion of the role of color flow Doppler imaging of deep venous thrombosis compared with the roles of venography, compression B-mode imaging, duplex Doppler and continuous Doppler imaging, and other competing noninvasive tests. Radiologists with access to color flow imaging will certainly want to add this technique to compression duplex Doppler imaging, but it is unclear that it will serve as a replacement. Imaging of the upper extremities and venous insufficiency is also addressed. The final chapter, on the genitourinary system, concentrates on color Doppler imaging of the penis, scrotum, pregnant uterus, and female adnexa. The discussions of impotence and testicular ischemia are brief but comprehensive reviews emphasizing the role of color Doppler imaging, which is now the primary imaging technique in these situations. This technique should supplant radionuclide scanning for testicular torsion. The contributions of color flow Doppler imaging to gray-scale and duplex Doppler imaging of intrauterine growth retardation, fetal anomalies, ectopic pregnancy, and ovarian torsion are less well established and have briefer discussions. For those interested in reading further, good references are provided.

This monograph is excellently done and presents the physics and instrumentation of color flow and Doppler imaging and the anatomy, physiology, and pathologic changes shown by these techniques in a comprehensible format. It is easy enough for the novice and sophisticated enough for the proficient. I recommend it to trainees, sonographers, and sonologists.

Arnold C. Friedman
Temple University
Philadelphia, PA 19140

Oriental Cholangiohepatitis:

Correlation Between Portal Vein Occlusion and Hepatic Atrophy

Shoichi Kusano[1,2]
Yoshitaka Okada[1]
Takashi Endo[1]
Hisaaki Yokoyama[1]
Harumi Ohmiya[3]
Hideo Atari[4]

The angiographic features of the hepatic vasculature in patients with oriental cholangiohepatitis and their relationship to liver atrophy remain unclear. We studied 11 patients with oriental cholangiohepatitis to define the spectrum of portal vein, bile duct, and parenchymal involvement by correlating findings on cholangiography, sonography, CT, and angiography. The portal veins appeared normal in five cases, pruned in four, and completely obstructed in two. This spectrum of appearances was found to correlate with the severity of liver atrophy. No massive arterioportal shunting was found in any patients in this series. The two patients with complete obstruction of the portal veins showed no evidence of malignancy at histologic examination of the resected specimen.

It is concluded that the degree of portal vein obstruction correlates well with the degree of liver atrophy in patients with oriental cholangiohepatitis and that findings of complete central portal obstruction do not necessarily indicate associated malignancy.

***AJR* 158:1011–1014, May 1992**

Oriental cholangiohepatitis (OCH) with intrahepatic bile duct stones is commonly seen in Asia, particularly in China, Hong Kong, Korea, and Japan [1]. Differentiating between cholangitis in ordinary patients with intrahepatic bile duct stones and OCH in those with intrahepatic bile duct stones is very difficult, especially when the extrahepatic bile ducts, both proximal and distal to the stone, are diffusely dilated. Hepatic atrophy is also a common feature of OCH. Atrophy has been attributed to diminished portal venous flow, but the relationship between portal flow and parenchymal loss is not well understood. The etiologic mechanism of OCH remains unclear, but the presence of clinically occult derangement of the portal veins has been considered to be an important factor in understanding the pathogenesis of this disorder [2].

In this report, we describe the angiographic features of the hepatic vasculature in patients with OCH, correlate these findings with the degree of liver atrophy and the presence or absence of arterioportal shunting, and discuss the etiologic mechanism of this disorder and the clinical role of angiography.

Materials and Methods

From April 1980 to July 1989, 11 of 20 patients with a primary diagnosis of OCH who required surgery because of repeated episodes of biliary infection and jaundice were referred for diagnostic arteriography before hepatic resection. The group comprised seven women and four men 25–81 years old (average, 53 years). The diagnosis was proved histologically from the resected specimen in 10 cases, while in one case it was suggested intraoperatively. Six patients had had prior biliary surgery (four cholecystectomy and two cholecystectomy with T-tube drainage), whereas the remaining five had had no prior surgery.

Before angiography, all patients had abdominal sonography, CT, and either percutaneous transhepatic cholangiography or endoscopic retrograde cholangiography. These studies were evaluated together at the time of angiography. The studies were evaluated retrospectively as

Received March 8, 1991; accepted after revision December 11, 1991.

[1] Department of Radiology, Kitasato University East Hospital, 2-1-1, Asamizodai, Sagamihara, Kanagawa 228, Japan.

[2] Present address: Department of Radiology, National Defense Medical College, 3-2, Namiki, Tokorozawa, Saitama 359, Japan. Address reprint requests to S. Kusano.

[3] Department of Surgery, Kitasato University, 1-15-1, Kitasato, Sagamihara, Kanagawa 228, Japan.

[4] Department of Pathology, Kitasato University East Hospital, 2-1-1, Asamizodai, Sagamihara, Kanagawa 228, Japan.

0361–803X/92/1585–1011

© American Roentgen Ray Society

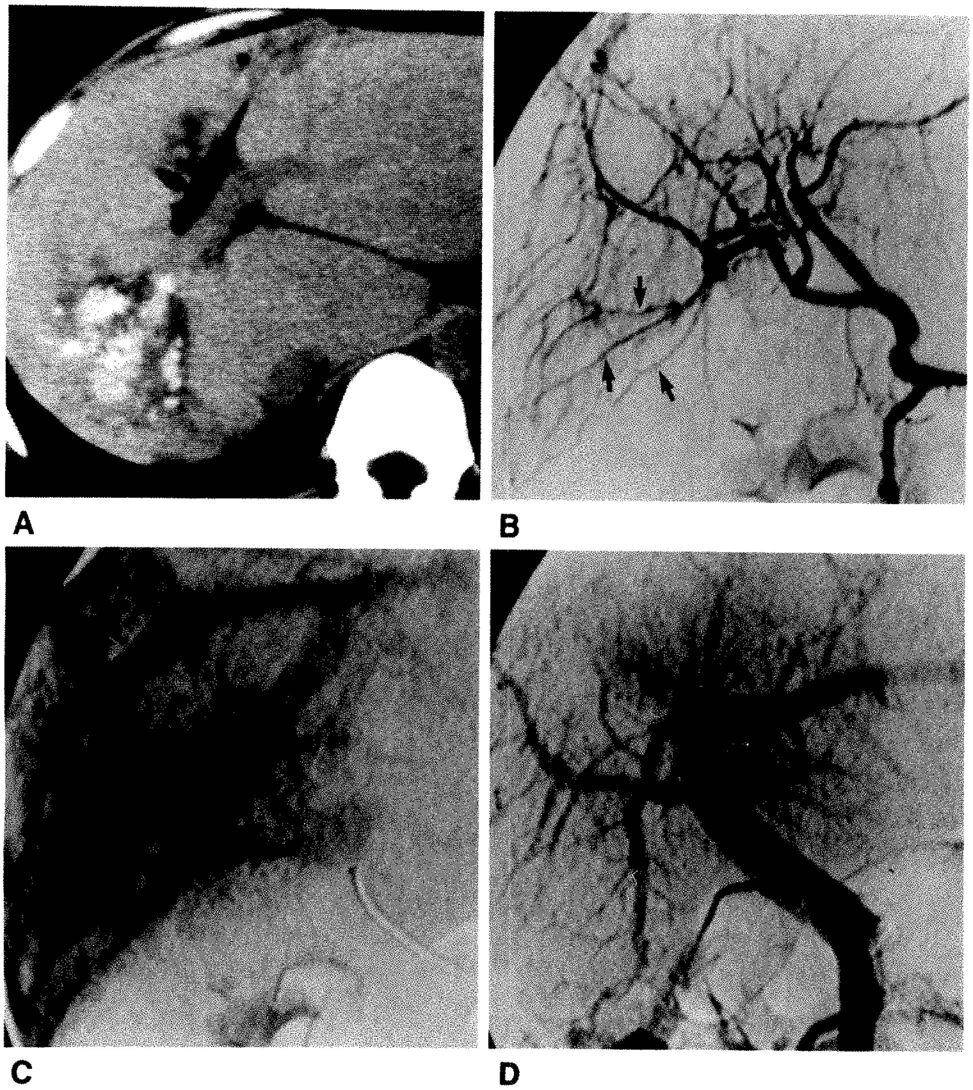

Fig. 1.—46-year-old woman with oriental cholangiohepatitis.

A, Unenhanced CT scan. Amorphous calcified stones in bile ducts of right hepatic lobe are associated with beaded dilatation and moderate loss of liver parenchyma.

B, Digital subtraction hepatic arteriogram shows fine neovascularity in right hepatic lobe and third-order branches of right posterior segmental artery (*arrows*).

C, On venous phase of *B*, parenchyma of right hepatic lobe is densely opacified with hepatic venous shunting.

D, Arterial portogram shows poor filling of third-order or smaller intrahepatic branches of right portal vein parallel to corresponding arterial branches (as shown in *B*, *arrows*). This finding represents "pruned tree" appearance.

follows. Initially, the first observer reviewed all studies independently. When findings were difficult to categorize, the opinion of a second interpreter was solicited to achieve a consensus.

The findings on sonography and cholangiography were used to assess the site of bile duct stones and the presence of biliary stricture. Both enhanced and unenhanced CT scans were obtained in all patients. None had dynamic bolus CT. The CT findings were reviewed with regard to the presence of bile duct stones, the degree of bile duct dilatation, and changes in hepatic segmental anatomy. Biliary dilatation was classified into three degrees by CT: slight tubular dilatation, moderate beaded dilatation, and marked cystic dilatation. Atrophy was diagnosed on CT as the presence of focal loss of hepatic parenchyma and was categorized as slight (identifiable loss), moderate, or marked (almost complete loss).

Celiac and superior mesenteric arteriography was performed in all patients: 10 patients also had supplementary common or proper hepatic arteriograms. Conventional film-screen angiography was performed in four patients; 30–40 ml of 76% Urografin (Schering AG, Germany) was injected into the superior mesenteric artery at a rate of 10–15 ml/sec immediately after intraarterial injection of a single 10-μg bolus of prostaglandin E_1. In the remaining seven patients, who were evaluated most recently, digital subtraction angiography was used to evaluate the hepatic vasculature. We injected 20 ml of Iopamiron 370 (Schering AG) at a rate of 4–5 ml/sec immediately after injection of a single 10-μg bolus of prostaglandin E_1 into the superior mesenteric artery. Angiograms were assessed for (1) changes in hepatic arterial blood flow and staining of the liver parenchyma and (2) segmental obstruction of the portal vein. According to the site and extent of occlusion of the portal veins as documented by arterial portography, patients were classified into one of three groups: (1) no abnormality, (2) occlusion of third-order or more distal branches of the portal veins ("pruned tree" appearance), or (3) complete obstruction of first- or second-order (main lobar or segmental) branches of the portal veins.

Results

The portal veins appeared normal in five patients, pruned in four (Fig. 1), and completely obstructed in two. None of the five patients with normal-appearing portal veins showed atrophy of the liver. Of the four patients with the "pruned tree" appearance, all had slight to moderate atrophy of the liver. Both patients with complete obstruction of the portal veins

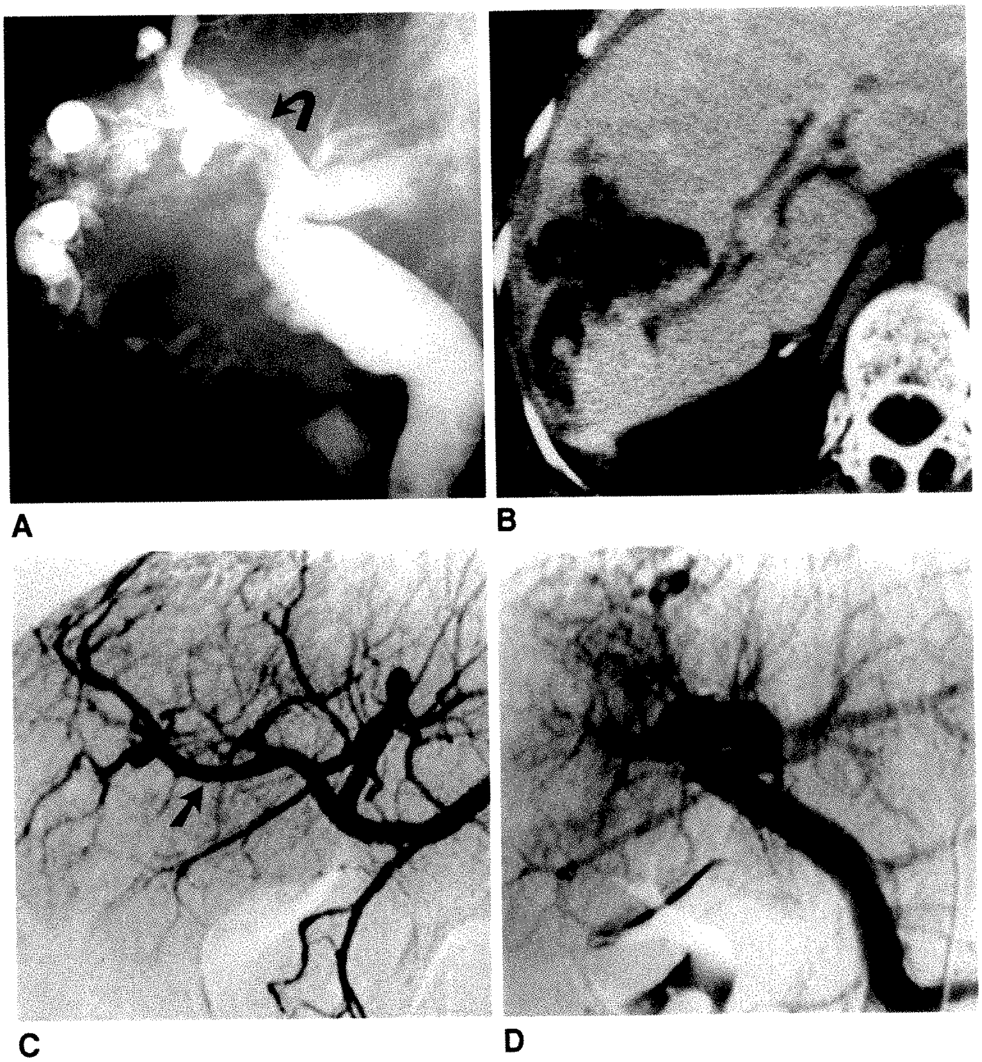

Fig. 2.—81-year-old woman with oriental cholangiohepatitis.

***A*, Percutaneous transhepatic cholangiogram shows stricture of right hepatic duct and cystic ductal dilatation with intraluminal stones distal to stenotic segment (*arrow*).**

***B*, Enhanced CT scan shows cystic dilatation of right hepatic ducts with multiple radiopaque stones and marked loss of affected liver parenchyma. Note compensatory hypertrophy of caudate lobe.**

***C*, Celiac arteriogram. *Arrow* indicates right hepatic artery. No evidence of arterioportal shunting was seen.**

***D*, Arterial portogram. Obstruction of right branch of portal vein is demonstrated by absence of portal vein branches running parallel to corresponding arterial branches.**

had marked atrophy of the liver (Fig. 2). The extent of portal vein occlusion was found to correlate with the degree of liver atrophy.

In patients with portal vein obstruction, neither hepatopetal nor hepatofugal collaterals were noted on arterial portography. In the two patients with complete obstruction of first-order branches of the portal veins, CT confirmed the absence of filling of the right branch of the portal vein; in addition, patency of the portal vein of the unaffected lobe was found (Fig. 2D). Hypervascularity of the liver (capillary staining of the parenchyma) was found in the affected segments (Figs. 1B and 1C) as well as in other segments in all degrees of liver atrophy. No massive arterioportal shunting with opacification of major branches of the portal veins was found, but hepatic venous shunting was seen in one patient (Fig. 1C).

All 11 patients had dilatation of the intrahepatic ducts and intrahepatic bile duct stones. The intrahepatic ducts were mildly dilated in three cases, moderately dilated in seven cases, and markedly dilated in one case. The degree of ductal dilatation was unrelated to the degree of portal venous involvement or hepatic atrophy.

Histologic examination of the 10 resected specimens revealed that all had chronic changes typical of OCH. Radiologic-pathologic correlation in this series, including two cases with complete obstruction of the portal veins, was not performed because of the lack of specimen angiography as a "road map" for comparing findings at arterial portography with anatomic and histologic features. There was no evidence of malignancy at histologic examination of the resected specimen in the two patients with complete obstruction of the portal vein.

Discussion

OCH has three morphologic features. The first is dilatation of intrahepatic ducts, which results from calcium bilirubinate stones, cellular debris, and mucin substances [3]. The second is stricture of intrahepatic bile ducts, infrequently associated with abscess formation. The third is some degree of atrophy of the affected lobe. Decreased blood flow in the portal veins has been implicated in liver atrophy [4–8]; however, the site and extent of portal vein obstruction has not been well investigated in patients with OCH, because this disorder is essentially a benign and relatively rare condition. Our study showed that the degree of portal vein obstruction in patients with OCH correlated with the severity of liver atrophy, and that the appearance of portal vein obstruction covered a spectrum including a normal-appearing liver with no atrophy, the "pruned tree" appearance of portal veins with slight to moderate liver atrophy, and complete obstruction of proximal portal veins with marked liver atrophy. This angiographic correlation of portal vein involvement has to our knowledge not been reported previously.

Two patients with complete obstruction of the portal veins had no evidence of malignancy on histologic examination of the resected specimen; therefore, OCH should be included in the differential diagnosis when hepatic atrophy and portal vein occlusion [1], which when combined are reported to be reliable signs of cholangiocarcinoma [5-7] and hepatic neoplasm [4, 8], are found. The finding of complete portal vein obstruction in the presence of identifiable intrahepatic stones combined with marked liver atrophy does not necessarily indicate a diagnosis of associated malignancy, which occurs in about 5-6% of patients with OCH [9, 10]. In 1953, Benz et al. [11] reported four cases of atrophy of the left lobe of the liver, caused by compression of the left trunk of the portal vein secondary to choledocholithiasis and subsequent dilatation of the left hepatic duct. However, our series showed no evidence of arterioportal shunts with retrograde opacification of the major branches of the portal vein, as is commonly found in patients with obstruction of the major portal branches due to malignancy. Freeny [12] reported one patient with acute pyogenic hepatitis in whom diffuse hypervascularity and arterioportal shunting involving the affected lobe were found on selective hepatic arteriography and in whom subsequent tolazoline-augmented arterial portography showed poor filling of multiple intrahepatic portal veins in this area. In our series, most cases showed intense hypervascularity in the liver parenchyma, but arterioportal shunting was not found in any case. This probably is because all but one patient with acute exacerbation of OCH had long-standing chronic cholangitis with intense fibroblastic proliferation.

The mechanism of bile duct dilatation in OCH continues to be controversial. One explanation is that biliary stricture is the first morphologic change leading to dilatation of the bile duct [13]. However, 37% of such patients show dilatation of the bile ducts without biliary stricture [14]. From these observations, it is difficult to explain the cause of OCH on the basis of biliary stricture alone. Another possible explanation is that portal vein obstruction triggers dilatation of the bile ducts. In experiments on rabbits that had ligation of the portal branch of the right posterior lobe and insertion of tubing into the bile duct through the duodenal papilla, marked dilatation of the biliary tree of the affected lobe was observed [2]. Takahashi et al. [15] also frequently found thrombotic obstruction due to cholangitis in the small branches of the portal vein. Our study, however, does not clarify the pathophysiology of this disease.

REFERENCES

1. Chan F-L, Man S-W, Leong LLY, Fan S-T. Evaluation of recurrent pyogenic cholangitis with CT: analysis of 50 patients. *Radiology* **1989**;170:165-169
2. Saji Y. The effect of decreased portal blood flow on the biliary system. *Jpn J Surg* **1988**;18:558-568
3. Yamamoto K. Intrahepatic periductal glands and their significance in primary intrahepatic lithiasis. *Jpn J Surg* **1982**;12:163-170
4. Heaston DK, Chuang VP, Wallace S, de Santos LA. Metastatic hepatic neoplasms: angiographic features of portal vein involvement. *AJR* **1981**;136:897-900
5. Vazquez JL, Thorsen MK, Dodds WJ, Foley WD, Lawson T. Atrophy of the left hepatic lobe caused by a cholangiocarcinoma. *AJR* **1985**;144: 547-548
6. Carr DH, Hadjis NS, Banks LM, Hemingway AP, Blumgart LH. Computed tomography of hilar cholangiocarcinoma: a new sign. *AJR* **1985**;145: 53-56
7. Takayasu K, Muramatsu Y, Shima Y, et al. Hepatic lobar atrophy following obstruction of the ipsilateral portal vein from hilar cholangiocarcinoma. *Radiology* **1986**;160:389-393
8. Lorigan JG, Charnsangavej C, Carrasco CH, Richli WR, Wallace S. Atrophy with compensatory hypertrophy of the liver in hepatic neoplasms: radiographic findings. *AJR* **1988**;150:1291-1295
9. Ohta T, Nagakawa T, Konishi I, et al. Clinical experience of intrahepatic cholangiocarcinoma associated with hepatolithiasis. *Jpn J Surg* **1988**;18:47-53
10. Koga A, Ichimiya H, Yamaguchi K, Miyazaki K, Nakayama E. Hepatolithiasis associated with cholangiocarcinoma. *Cancer* **1985**;55:2826-2829
11. Benz EJ, Baggenstoss AH, Wollaeger EE. Atrophy of the left lobe of the liver. *Arch Pathol Lab Med* **1952**;153:315-330
12. Freeny PC. Acute pyogenic hepatitis: sonographic and angiographic findings. *AJR* **1980**;135:388-391
13. Matsumoto Y, Fujii H, Yoshioka M, et al. Biliary stricture as a cause of primary intrahepatic bile duct stones. *World J Surg* **1986**;10:867-875
14. Koga A, Miyazaki K, Ichimiya H, Nakayama F. Choice of treatment for hepatolithiasis based on pathological findings. *World J Surg* **1984**;8: 36-40
15. Takahashi Y, Takahashi T, Ise H, Matsuno S, Takahashi W, Sato T. Three-dimensional morphology of intrahepatic bile ducts in patients with intrahepatic gallstones. (Japanese, abstr in English). *Nippon Geka Gakkai Zasshi* **1990**;91:86-94

Pictorial Essay

Hepatic Neoplasms: Surgically Relevant Segmental Anatomy and Imaging Techniques

G. Scott Gazelle[1] and John R. Haaga[2]

With advances in imaging and surgical techniques, the diagnosis and treatment of primary and secondary liver neoplasms have improved. Advances in imaging have contributed to the early detection of the tumors and have allowed more precise preoperative characterization and localization of the lesions. Refinements in surgical technique have permitted more extensive resections, while at the same time placing even greater importance on accurate preoperative imaging of the tumor. Presurgical planning requires precise definition of the extent of the tumor vis-à-vis hepatic segmental anatomy. The goal of this essay is to discuss the segmental anatomy of the liver, the types of segmental resections possible, and the strengths and weaknesses of the various imaging techniques used in the preoperative assessment of potential candidates for hepatic resection. Staging of hepatic malignant tumors and technical details of the imaging techniques are not discussed.

Hepatic Anatomy

The Couinaud nomenclature [1, 2], which describes hepatic segmentation based on portal venous supply and hepatic venous drainage, is illustrated in Figures 1 and 2. The liver is divided into two hemilivers, right liver and left liver; each of these is divided into two sectors. Finally, the sectors are divided into a total of seven segments; the caudate lobe is a separate eighth segment. This system differs from the perhaps more familiar "Anglo-Saxon" nomenclature (lateral left, medial left, anterior right, posterior right, caudate) by the division of the lateral segment of the left lobe into anterior and posterior subsegments by the left hepatic vein, and the division of both the anterior and posterior segments of the right lobe into superior and inferior segments by the plane of the right portal vein. This system defines segments that can

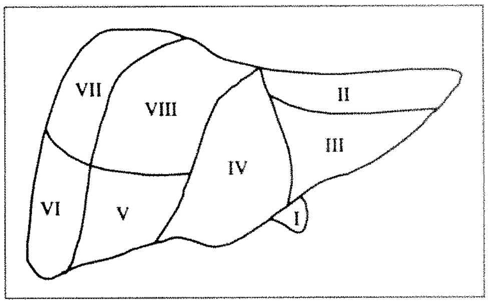

Fig. 1.—Drawing shows hepatic segmental anatomy according to Couinaud. Liver is divided into four sectors by hepatic veins; all but one of these sectors are divided into two segments. Segments II–IV (left liver) are supplied by branches of left portal vein; segments V–VIII (right liver), by branches of right portal vein. Left liver is divided into two sectors by left hepatic vein: segments III and IV are anterior; segment II is posterior. Segment III is separated from segment IV by umbilical fissure. Right liver is separated from left liver by main port scissura, or Cantlie's line, a plane that passes through inferior vena cava and long axis of gallbladder, containing middle hepatic vein. Right liver is divided into anterior (V and VIII) and posterior (VI and VII) sectors by right portal scissura, a plane containing right hepatic vein and inferior vena cava. Segments V and VI (inferior segments) are separated from segments VII and VIII (superior segments) by a plane containing right portal vein. Segment I is caudate lobe.

Received October 7, 1991; accepted after revision December 10, 1991.

[1] Department of Radiology, Massachusetts General Hospital, 32 Fruit St., Boston, MA 02114.
[2] Department of Radiology, University Hospitals of Cleveland, 2074 Abington Rd., Cleveland, OH 44106.

AJR **158:1015–1018, May 1992** 0361-803X/92/1585-1015 © American Roentgen Ray Society

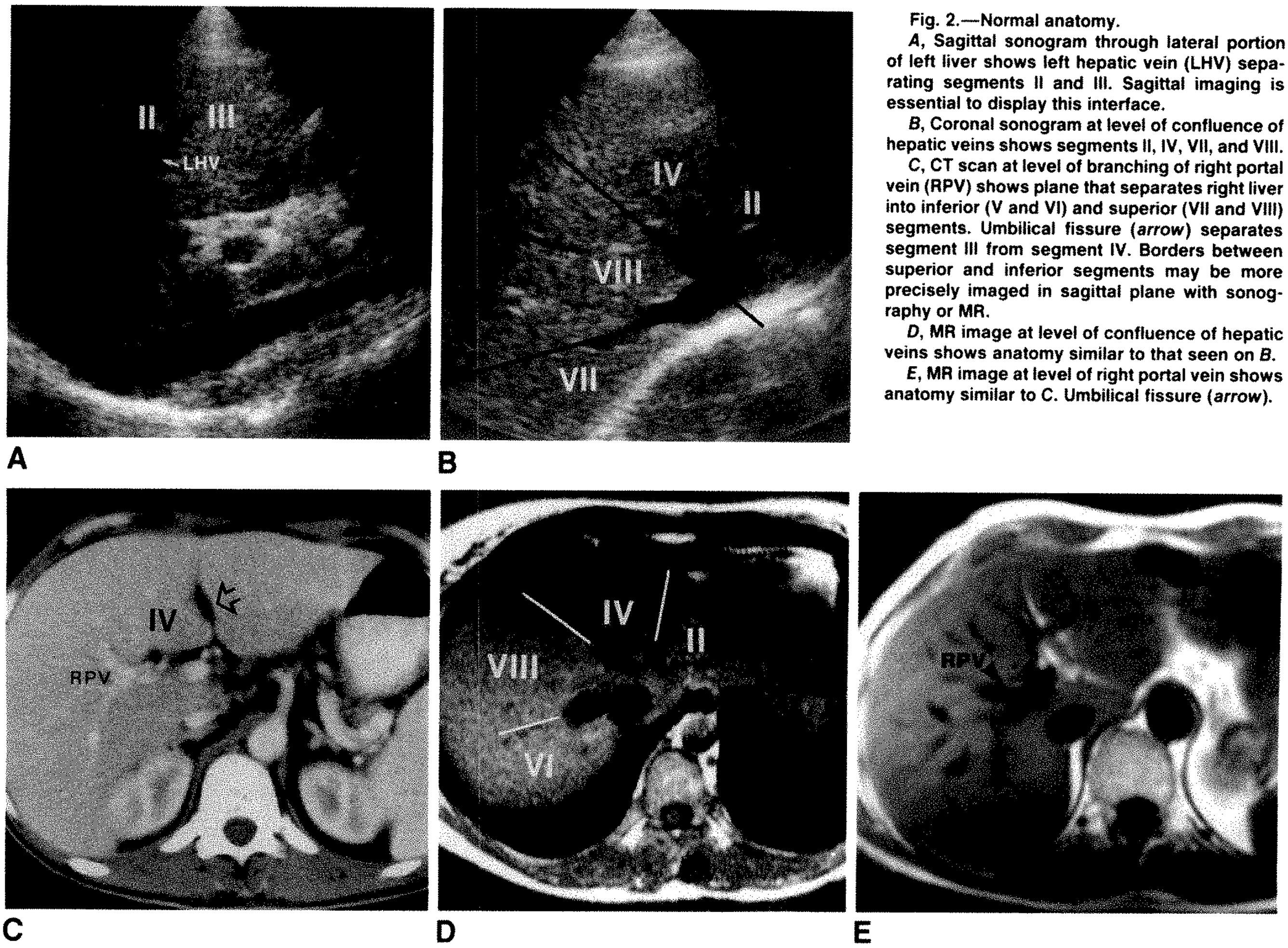

Fig. 2.—Normal anatomy.

A, Sagittal sonogram through lateral portion of left liver shows left hepatic vein (LHV) separating segments II and III. Sagittal imaging is essential to display this interface.

B, Coronal sonogram at level of confluence of hepatic veins shows segments II, IV, VII, and VIII.

C, CT scan at level of branching of right portal vein (RPV) shows plane that separates right liver into inferior (V and VI) and superior (VII and VIII) segments. Umbilical fissure (*arrow*) separates segment III from segment IV. Borders between superior and inferior segments may be more precisely imaged in sagittal plane with sonography or MR.

D, MR image at level of confluence of hepatic veins shows anatomy similar to that seen on *B*.

E, MR image at level of right portal vein shows anatomy similar to C. Umbilical fissure (*arrow*).

be resected individually and is the basis for modern segmental liver surgery.

Hepatic Resections

To perform a hepatic resection, the surgeon must be able to remove all of the tumor, with clear tissue margins, while preserving enough liver to sustain life. The minimum amount of functioning liver required for survival varies with the age of the patient and the amount of underlying hepatic dysfunction (e.g., cirrhosis). Furthermore, the vascular supply and hepatic venous and biliary drainage of the remaining liver must remain intact. Thus, tumors involving the main portal vein, proper hepatic artery, or both the left and right hepatic ducts are generally considered unresectable.

The simplest resection involves removing only a small wedge of liver tissue containing the tumor. When a lesion is not amenable to simple wedge resection owing to either its size or location, segmental resection must be performed. The most commonly performed segmental resections include right and left lobectomies, left lateral segmentectomy, transverse hepatectomy, and right trisegmentectomy. These procedures are illustrated in Figure 3.

Imaging Techniques

Sonography, because it is both widely available and relatively inexpensive, is often the initial study performed in patients with focal liver lesions. For accurate detection and localization of lesions, one must use the highest frequency transducer possible (usually 3 MHz in adults) to image both the lesion and the hepatic vasculature. By determining the location of a lesion with respect to the hepatic vasculature, one can localize it to a specific segment [3]. Scanning in both transverse and sagittal planes is essential; sagittal images may help to precisely define the cephalocaudad margins of certain segments and accurately localize lesions within them (i.e., II vs III, VIII vs V, VII vs VI). Compared with CT and MR, however, sonography is somewhat more dependent on operator expertise and may not provide the amount of detailed anatomic information required by surgeons anticipating hepatic resections. Furthermore, extremely large lesions can be difficult to localize with sonography (Fig. 4).

CT is considered the gold standard for hepatic imaging by most authors. It is highly accurate and has the additional advantage of providing a complete evaluation of the entire abdomen. Scanning must be performed in a dynamic fashion by using a rapidly injected (1 ml/sec or greater) bolus of IV

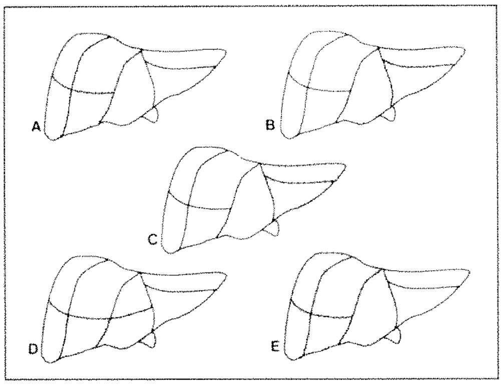

Fig. 3.—Drawing shows common hepatic segmental resections; resected segments are shaded.

A, Right lobectomy involves removal of segments V–VIII.

B, Left lobectomy involves removal of segments II–IV.

C, Left lateral segmentectomy involves removal of segments II and III only.

D, Transverse hepatectomy, often performed for gallbladder carcinoma, involves removal of segments I and IV–VI.

E, Right trisegmentectomy involves removal of segments I and IV–VIII.

contrast material (Fig. 5A), although considerable controversy exists regarding the rate and timing of this injection (in fact it should probably be tailored to the specific scanner being used). A discussion of these issues is beyond the scope of this essay and is the subject of several recent articles.

CT portography is better at detecting small lesions, defining the margins of the lesions, and defining vascular and segmental anatomy than is conventional contrast-enhanced CT [4] (Fig. 6A). To perform this technique, a catheter is placed into either the superior mesenteric or splenic artery, and scanning is performed during a continuous contrast infusion (usually 2–3 ml/sec) after an initial delay. The goal of the technique is to provide preferential portal enhancement of the hepatic parenchyma, since normal liver derives approximately 60–80% of its blood supply from the portal system, while metastases derive their blood supply completely or predominantly from the hepatic arteries. We prefer to place the catheter into the superior mesenteric artery except in patients with a replaced right hepatic artery. In these patients, the catheter must be placed in the splenic artery to avoid confusion caused by direct arterial perfusion of the right lobe of the liver. Because of its invasiveness and expense, CT portography generally is reserved for those patients in whom resection is being considered on the basis of the results of another imaging study; its role is to precisely localize the lesion(s) to be resected and to rule out the presence of others.

Delayed contrast-enhanced CT, in which scans are obtained 4–6 hr after administration of contrast material, may be useful in certain clinical situations when the results of the scans obtained during contrast administration are equivocal. It is therefore best considered an adjunct to CT portography, and may provide more information than either technique alone [4].

MR imaging has a number of advantages, although its most important role is to characterize lesions on the basis of signal characteristics (e.g., hemangioma vs metastasis). Additionally, by using sagittal images, one can sometimes better define the cephalocaudal margins of lesions falling near segmental borders. Finally, recent developments in MR angiography allow better depiction of the hepatic vasculature and excellent display of the segmental anatomy. Compared with CT, however, MR has lower spatial resolution, has longer acquisition times, is more susceptible to image degradation due to patient motion, and has problems with patient acceptance due to claustrophobia. Recent technical developments have overcome a number of these problems, but they continue to limit its more universal use.

The MR images presented in this article were acquired by using conventional T1-weighted images (Fig. 4B) as well as a recently developed short T1-weighted spin-echo pulse sequence (Figs. 5B and 6B). In this experimental sequence, 21 8-mm-thick images were obtained during a single breath-hold by using half-Fourier data collection and an effective 170 × 256 imaging matrix. Images were acquired before, during, and after injection of a bolus of gadopentetate dimeglumine. The combination of rapid acquisition, thin sections, and dynamic contrast enhancement, with the excellent contrast

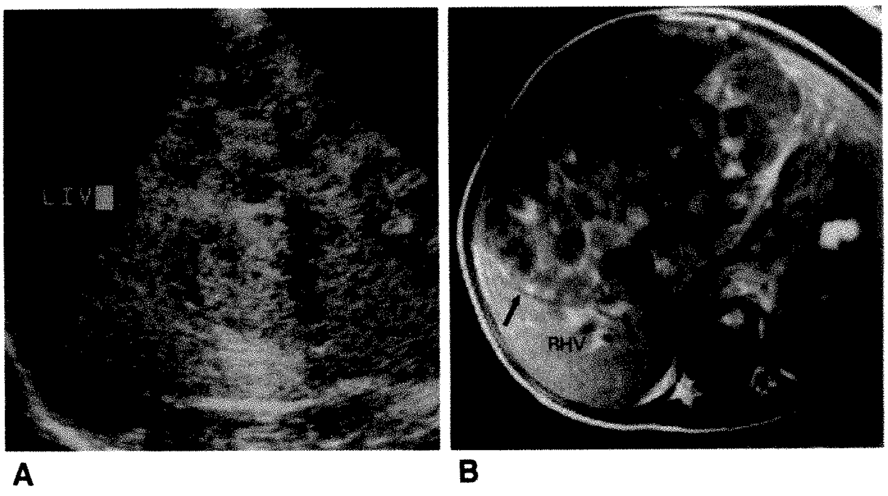

Fig. 4.—9-month-old infant who had increasing abdominal girth.

A, Sagittal sonogram shows large mass in right upper quadrant of abdomen; however, exact organ of origin and boundaries of mass cannot be determined. CT scan (*not shown*) showed a large tumor of the liver that appeared to be involving all segments of liver; thus, it was feared that resection was not possible.

B, Dynamic enhanced MR image shows that entire tumor (*arrows*) is located anterior to right hepatic vein (RHV), thus sparing segments VI and VII. Because of findings on this image, patient had a left trisegmentectomy (removal of all but segments VI and VII).

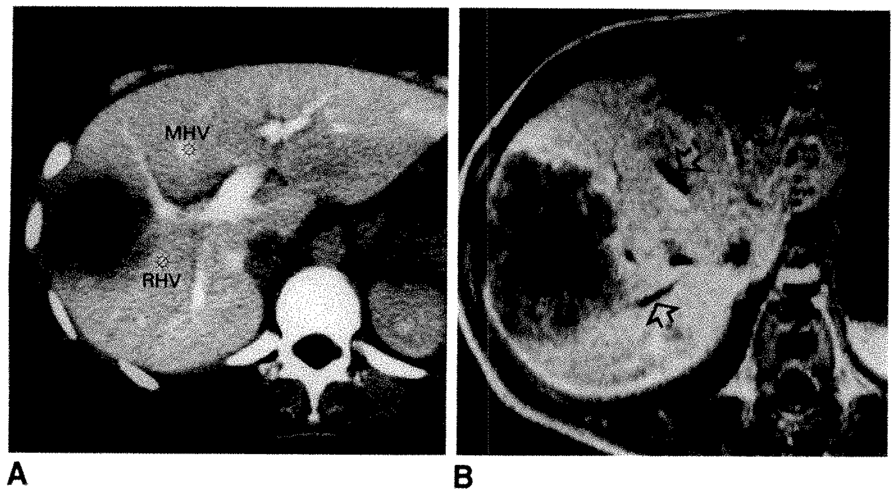

Fig. 5.—24-year-old woman who had resection of colonic carcinoma.

A, Routine follow-up CT scan shows large hypodense lesion located within right hepatic lobe. Lesion appears to be between right (RHV) and middle (MHV) hepatic veins, involving segments V and VIII.

B, Dynamic enhanced MR image shows lesion and vessels (*arrows*) clearly, once again indicating location of lesion within segments V and VIII. Patient had a right hepatectomy (removal of segments V–VIII).

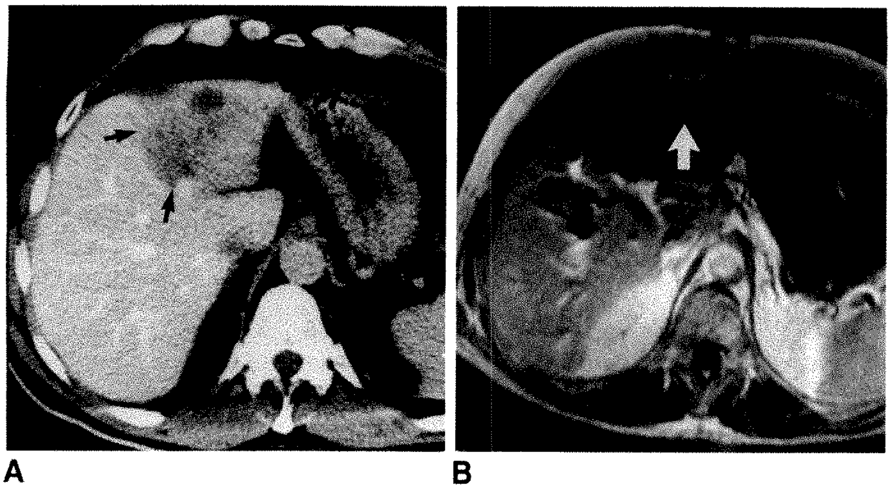

Fig. 6.—58-year-old man with a history of colon carcinoma who had rising serum levels of carcinoembryonic antigen. Sonogram (*not shown*) showed a lesion in left lobe of liver, and patient was referred for CT portography.

A, CT portogram shows diffusely decreased attenuation of segments II and III (*arrows*), as well as a focal lesion within segment II.

B, Dynamic enhanced MR image also shows focal lesion (*arrow*); global abnormality of segments II and III is not shown. At surgery, patient had diffuse involvement of segments II and III, and they were removed (lateral segmentectomy).

resolution of MR, allowed accurate lesion detection and localization.

In our practice, we use CT and CT portography for most of the workup of patients before hepatic resection. Sonography and MR are reserved for anatomic problem solving, and either MR or percutaneous biopsy is used for lesion characterization. When more than one study is performed, the later studies should make reference to the results of the other so as to avoid confusion.

REFERENCES

1. Bismuth H. Surgical anatomy and anatomical surgery of the liver. In: *Surgery of the liver and biliary tract*, vol. 1. Edinburgh: Churchill-Livingstone, **1988**:3–9
2. Couinaud C. *Le foie*. Paris: Masson & Cie, **1957**
3. Lafortune M, Madore F, Patriquin H, Breton G. Segmental anatomy of the liver: a sonographic approach to the Couinaud nomenclature. *Radiology* **1991**;181:443–448
4. Nelson R, Chezmar J, Sugarbaker P, Bernardino M. Hepatic tumors: comparison of CT during arterial portography, delayed CT, and MR imaging for preoperative evaluation. *Radiology* **1989**;172:27–34

Occlusion and Narrowing of the Pharyngeal Airway in Obstructive Sleep Apnea: Evaluation by Ultrafast Spoiled GRASS MR Imaging

Frank G. Shellock[1-3]
Charles J. Schatz[1,2]
Peter Julien[1,2]
Fred Steinberg[2]
Tom K. F. Foo[4]
Martin L. Hopp[5]
Philip R. Westbrook[2]

Morphologic abnormalities of the pharyngeal airway are frequently found in patients with obstructive sleep apnea. These structural alterations in the pharyngeal airway can be detected in awake patients by using rapid imaging techniques. Ten patients with clinically proved obstructive sleep apnea had ultrafast spoiled gradient-recalled acquisition in the steady state (GRASS) MR imaging of the pharyngeal airway to determine the presence of occlusions and/or narrowings. Twelve sequential images were obtained at one midsagittal plane and at eight transverse planes through the pharyngeal airway. The scans were obtained at the rate of one image per 1.04 sec while the patient was breathing quietly. Occlusions or narrowings of the pharyngeal airways were detected on MR images in all patients. The site(s) of the occlusions and the site(s) and extent of the narrowings varied. Six patients had occlusions and four had narrowings of one or more sites.

This study shows that ultrafast spoiled GRASS MR imaging can be used to evaluate patients with obstructive sleep apnea during tidal breathing and is useful for determining the presence of occlusions and narrowings of the pharyngeal airway.

***AJR* 158:1019–1024, May 1992**

Sleep apnea is a condition characterized by episodic cessation of breathing during sleep [1-3]. Total collapse and occlusion of the upper airway combined with respiratory efforts is a form of sleep apnea referred to as obstructive sleep apnea. Previous investigations [4-12] have shown that the pharyngeal airways are frequently occluded and the cross-sectional areas are significantly narrowed in sleeping and awake patients who have this disorder. These morphologic alterations have been studied objectively by various imaging techniques including plain film cephalometrics, fluoroscopy, conventional CT, and cine CT [2, 4, 6, 8, 9, 11].

Because the cross-sectional area of the upper airway varies with respiration [8, 9, 11, 13], total occlusion and significant narrowing (which are frequently transient processes) may be overlooked or not fully appreciated if the imaging technique used to assess these abnormalities lacks sufficient temporal resolution to show the dynamic changes in the dimensions of the upper airway [8, 9, 11]. Cine CT is particularly useful for detecting occlusion and narrowing of the pharyngeal airways of patients with obstructive sleep apnea because this technique can show changes in the size of the airway during respiration, even in tachypneic patients [8, 9, 11].

Previously, MR imaging has not been used to study dynamic alterations of the pharyngeal airway because of the poor temporal resolution of this imaging technique. However, the recent advent of rapid MR imaging techniques has provided a means of obtaining multiple images at multiple locations with sufficient image quality and temporal resolution to allow a dynamic evaluation of the pharyngeal airway [14].

This report describes the application of ultrafast spoiled gradient-recalled acquisition in the steady state (GRASS) MR imaging for evaluation of the pharyngeal

Received November 6, 1991; accepted after revision December 23, 1991.

[1] Tower Magnetic Imaging, Los Angeles, CA 90048.

[2] Department of Radiology, Cedars-Sinai Medical Center, 8700 Beverly Blvd., Los Angeles, CA 90048. Address reprint requests to F. G. Shellock, 12245 San Vicente Blvd., Los Angeles, CA 90049.

[3] Department of Radiological Sciences, University of California, Los Angeles, Medical Center, Los Angeles, CA 90024.

[4] General Electric Medical Systems, Milwaukee, WI 53201.

[5] Division of Otolaryngology, Head and Neck Surgery, Cedars-Sinai Medical Center, Los Angeles, CA 90048.

0361-803X/92/1585-1019
© American Roentgen Ray Society

airway of awake patients with known obstructive sleep apnea in order to identify occlusion and narrowing during tidal breathing.

Subjects and Methods

Subjects

The subjects included nine men (average age, 47 years; range, 40–53 years) and one woman (age, 34 years) with proved obstructive sleep apnea as determined by strict clinical criteria, including a history of habitual snoring, restless sleep, morning headaches, daytime hypersomnolence, and intellectual deterioration [1–3]. Each subject had two or more of these signs and symptoms, and each had an overnight sleep study to determine the presence of unequivocal episodes of obstructive sleep apnea. Sleep studies were performed with standardized polysomnographic techniques that included continuous monitoring of the electroencephalogram, electrooculogram, submental electromyogram, body position, body movement, ECG, oxygen saturation, oronasal air flow, sonogram, cross-sectional area changes in the chest and abdominal wall (inductive plethysmography), and anterior tibial electromyogram [1–3]. The patient was observed via closed-circuit television. For a diagnosis of obstructive sleep apnea, a cessation of air flow had to persist for a period of 20 sec or longer and occur at least 30 times during a 6-hr nocturnal sleep period, or a rate exceeding 10 episodes per hour. The mean apnea/hypopnea index for these patients was 61 episodes per hour and ranged from 48 to 72 episodes per hour. The patients examined in this study were selected because of their severe apnea/hypopnea.

MR Imaging

MR imaging was performed with the body coil of a 1.5-T, 64-MHz MR imager (General Electric Medical Systems, Milwaukee, WI) and a receive-only, wraparound anterior neck local coil (General Electric Medical Systems). This local coil was positioned over the nose, mouth, chin, and hyoid bone of the patient to optimize the signal-to-noise ratio of the images obtained of the pharyngeal airway.

An ultrafast RF phase spoiled GRASS pulse sequence [14] was used to image the pharyngeal airway during tidal breathing, as follows (General Electric 4X Advantage hardware and software upgrades are required for the implementation of this pulse sequence): In the first series, transverse images (used as a localizer), 8.4/2.9/20° (TR/TE/flip angle), were obtained with one excitation, 160 × 128 matrix, 20-cm field of view, 5-mm section thickness, and approximate imaging time of 10 sec for 10 section locations. In the second series, sagittal images (midline slice obtained in reference to the axial plane localizer), 8.4/2.9/20°, were obtained with one excitation, 160 × 128 matrix, 20-cm field of view, 5-mm section thickness, and acquisition time of approximately 12 sec for 12 images at a single section location. In the third series, transverse images (section locations obtained from the nasopharynx to the hyoid referenced to the previously obtained sagittal plane image), 8.4/2.9/20°, were obtained with one excitation, 160 × 128 matrix, 20-cm field of view, 7-mm section thickness, 2-mm interslice gap, and approximate acquisition time of 2 min 55 sec for 12 images obtained at 12 section locations.

The ultrafast spoiled GRASS pulse sequence uses a ±32-kHz digital receiver filter bandwidth and acquires a partial echo [14]. A more T1-weighted image is obtained by spoiling the residual transverse magnetization of the steady-state free precession signal [14–16]. In the pulse sequence used for this study, RF phase spoiling was used. This involved applying the RF pulses at varying phase offsets in the rotating frame, starting with an initial angle, θ, and proceeding to increment the phase angle such that the phase or spoiling offset for the nth RF pulse was $\theta + 2\theta + \ldots + n\theta$ [14–17]. As the receiver phase is advanced in synchrony with the RF pulse, no additional postprocessing is required. The phase angle for optimal contrast between various anatomic structures varies with TR and tissue T1 and T2. In the study of the pharyngeal airway, the initial spoiling or phase angle was 109.9°.

A rapidly obtained image free from significant blurring or other distortion was reconstructed from a partial echo data set by using a partial k-space reconstruction algorithm based on homodyne detection [14–17]. This allowed a reduction in the minimum TE and TR, as higher resolution images could be recovered from reduced partial-echo data sets.

For a 160 × 128 acquisition matrix (frequency samples × views), an image with an effective resolution of 256 × 128 was generated. If 256 frequency samples in a full echo were to be acquired, a minimum TE of 4.7 msec and a minimum TR of 9.0 msec could be achieved for an image with the other aforementioned imaging parameters. By using partial-echo acquisition with 160 frequency samples (i.e., by using 67% of the echo), the minimum TE and TR were 2.9 and 8.4 msec, respectively.

The very short TE used for this pulse sequence should minimize air and bone susceptibility artifacts and spurious narrowings of the soft tissue–air interface. To assess the relative accuracy of the ultrafast spoiled GRASS pulse sequence for measuring cross-sectional areas, a phantom study was conducted. The phantom contained cylinders of various sizes (cross-sectional areas ranging from 0.25 to 5.0 cm^2), filled separately with either peanut oil, copper sulfate, or air. Cross-sectional areas were determined for these cylinders by using a cursor and the software incorporated with the MR scanner. The accuracy of this measurement was ±10%.

Images obtained with this ultrafast spoiled GRASS sequence for the study of the pharyngeal airway during active respiration were acquired at the rate of one image per 1.04 sec. This temporal resolution permitted 12 images to be obtained during tidal breathing of approximately two to four respiratory cycles.

The patient was supine, with the head placed in a neutral position to ensure a consistent positioning technique for the study. Any narrowing of the pharyngeal airway seen with the head in a neutral position would be worsened by the slight flexion of the neck that normally occurs with the typical sleeping posture [5, 13]. During MR imaging, the patient was instructed to breathe through the nose with the mouth closed and to refrain from coughing or swallowing during acquisition of the images. The patient was awake during the entire procedure.

Immediately after completion of each series, images were viewed as a cine-loop display and inspected to determine if the patient coughed or swallowed during the examination. If necessary, any images that were technically inadequate were redone. The average total examination time (including setting up equipment, positioning of the patient, and explaining the study) was approximately 17 min.

Display and Evaluation of Images

The 12 images obtained at each section location for the midline sagittal and multilevel transverse plane sections were viewed as cine-loop displays in order to optimally show the alterations of the airway dimensions associated with respiration. Although the sagittal images often showed potential sites of occlusion or narrowing of the pharyngeal airway (Fig. 1), they were considered to be potentially unreliable for showing morphologic abnormalities because of the possible presence of asymmetric narrowing of the airway (i.e., narrowing may have occurred off axis). Therefore, only transverse images were used for the assessment of occlusion and narrowing.

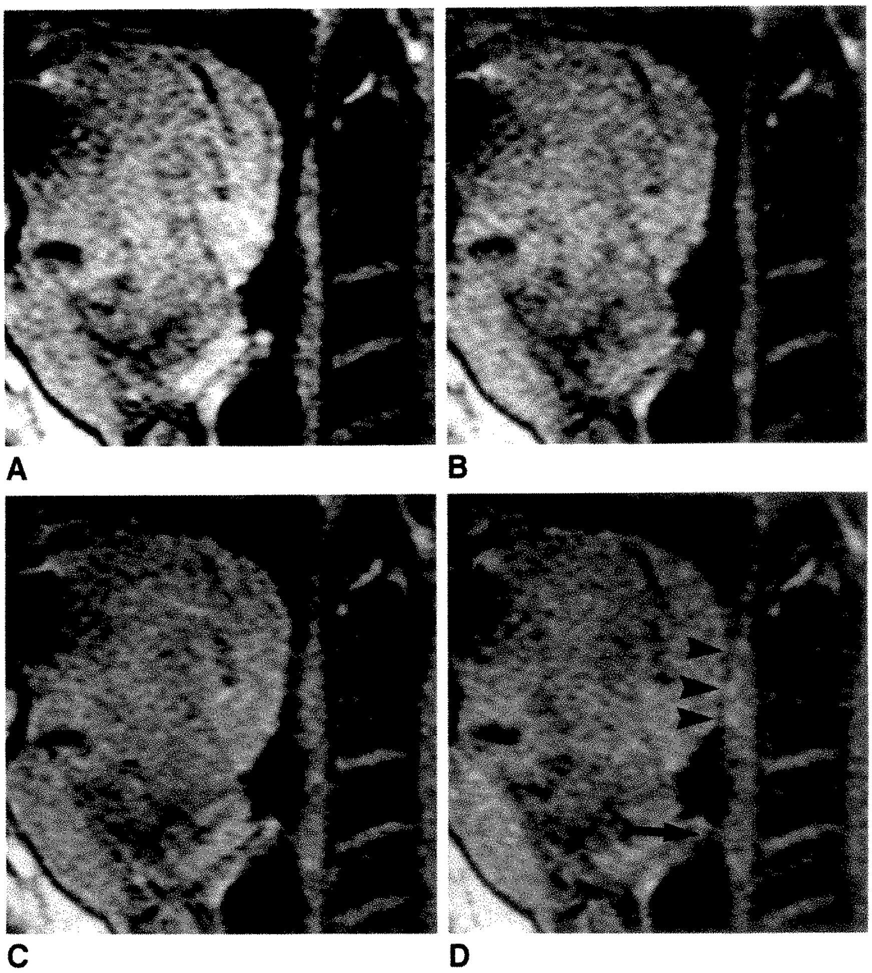

Fig. 1.—Patient with obstructive sleep apnea. *A–D*, Sagittal ultrafast spoiled GRASS MR images (8.4/2.9) obtained during respiration (four images selected from 12 images obtained at same section location during respiration) show apparent occlusions of pharyngeal airway in regions of high oropharynx, mid oropharynx, low oropharynx (*arrowheads*), and high hypopharynx (*arrow*) (*D*).

Evaluation of Images

The following eight transverse section locations obtained through the pharyngeal airway were evaluated, as previously described [9]: (1) nasopharynx, (2) hard palate, (3) soft palate, (4) high oropharynx, (5) mid oropharynx, (6) low oropharynx, (7) high hypopharynx, and (8) hyoid bone (12 transverse section locations were normally acquired in order to obtain section locations through these areas of interest, and the section locations that best depicted these anatomic locations were used for analysis) [18].

Criteria of abnormalities included (1) any occlusion of the airway seen during tidal breathing at any section location imaged and/or (2) airway cross-sectional areas less than those reported for control subjects studied by CT [4, 5, 8, 9, 11]. Determination of abnormal narrowing of the airway was based on measurement of the minimum cross-sectional area of the airway (i.e., all images obtained at a single section location were inspected to determine the one with the minimal cross-sectional area, and measurement of cross-sectional area was performed on this image) [4, 5, 8, 9, 11, 18]. As mentioned, the measurement of cross-sectional area was done by determining the area with a cursor and the software incorporated with the MR scanner. The accuracy of this measurement is ±10%.

Results

Technically acceptable results were obtained in all patients in each scan plane and section locations evaluated despite the dental materials and devices present in nine of the 10 patients (i.e., only localized artifacts were produced by the presence of metallic dental objects, and these did not affect the imaging area of interest). In each of the patients with obstructive sleep apnea, occlusion (Fig. 2) and/or narrowing (Figs. 3 and 4) of the pharyngeal airways was seen during tidal breathing. The occlusion or narrowing of the pharyngeal airway usually was seen on only two or three of the 12 images (depending on the patient's respiratory rate) obtained during tidal breathing.

The site(s) of the occlusions and the site(s) and extent of the narrowings varied (Table 1). Six of the patients had occlusions present in one or more pharyngeal airway sites: (1) high oropharynx and mid oropharynx, (2) soft palate and high oropharynx, (3) soft palate and high oropharynx, (4) high oropharynx, (5) low oropharynx, and (6) nasopharynx and high oropharynx. Of these six patients, five also had abnormal narrowing of the cross-sectional areas of the pharyngeal airways at the following sites: (1) soft palate (0.37 cm^2), (2) mid oropharynx (0.16 cm^2), (3) soft palate (0.27 cm^2), (4) soft palate (0.28 cm^2), and (5) soft palate (0.54 cm^2).

The remaining four patients had one or more abnormal narrowings of the cross-sectional areas of the pharyngeal airways at the following sites: (1) high hypopharynx (0.32

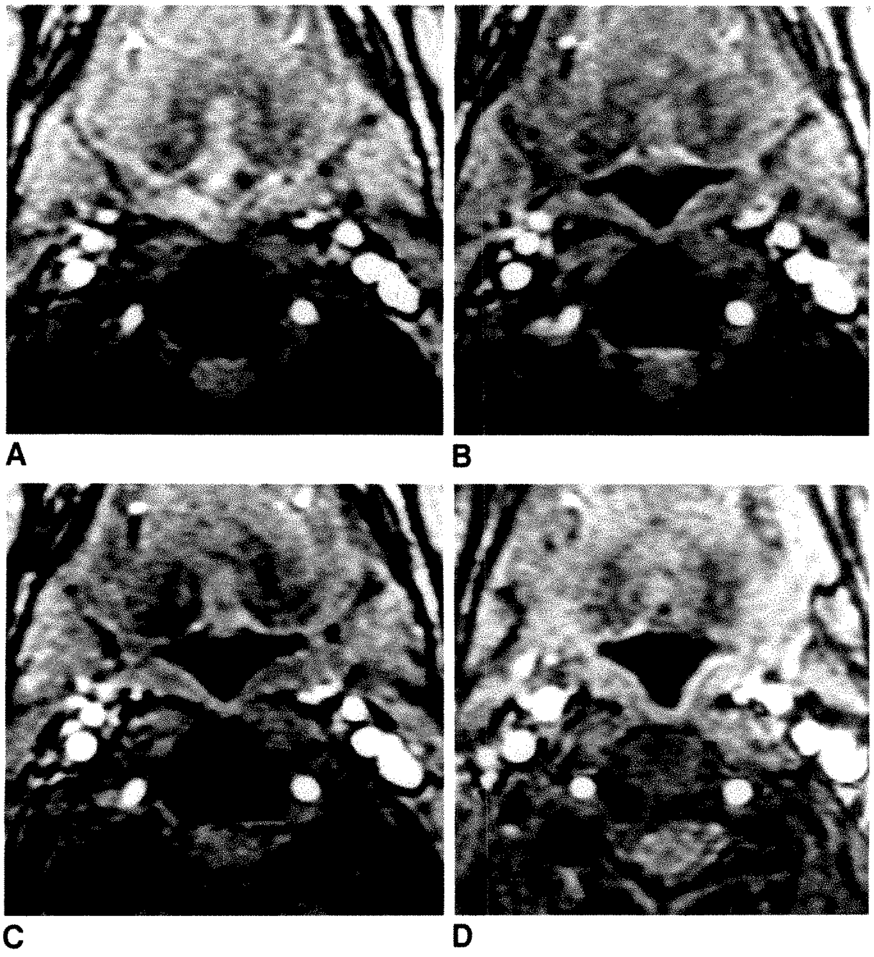

Fig. 2.—Patient with obstructive sleep apnea.
A–D, Transverse ultrafast spoiled GRASS MR images (8.4/2.9) obtained during respiration (four images selected from 12 images obtained at same section location during respiration) show occlusion of pharyngeal airway at level of mid oropharynx (images are magnified to show detail of airway). Pharyngeal airway was occluded by base of tongue (*A*).

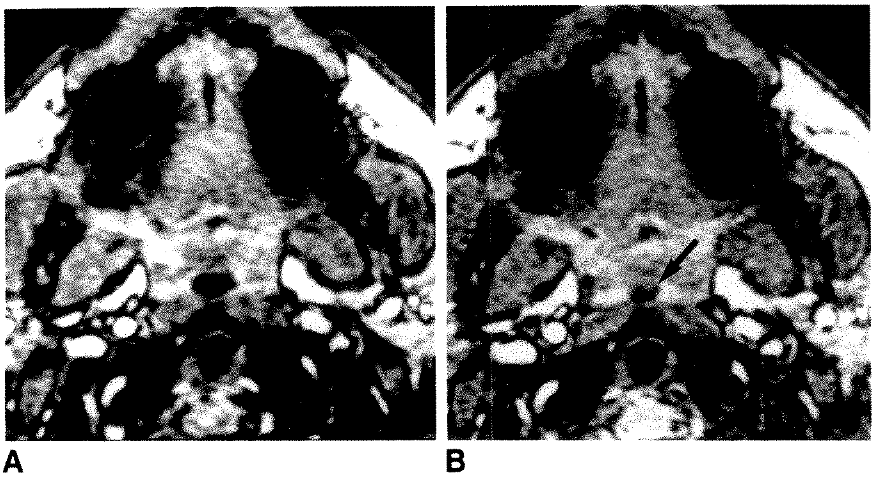

Fig. 3.—Patient with obstructive sleep apnea.
A and *B*, Transverse ultrafast spoiled GRASS MR images (8.4/2.9) obtained during respiration (two images showing largest [*A*] and smallest [*B*] cross-sectional areas selected from 12 images obtained at same section location during respiration) show narrowing (*arrow*) of pharyngeal airway at level of soft palate. (Images are magnified to show detail of airway.)

cm^2); (2) soft palate (0.79 cm^2), high oropharynx (0.44 cm^2), and high hypopharynx (0.51 cm^2); (3) soft palate (0.12 cm^2), high oropharynx (0.2 cm^2), and mid oropharynx (0.51 cm^2); and (4) soft palate (0.21 cm^2), high oropharynx (0.86 cm^2), and mid oropharynx (0.80 cm^2).

Discussion

Using a variety of assessment techniques (e.g., conventional CT, cine CT, acoustic-reflection), previous investigators established that patients with obstructive sleep apnea typi-

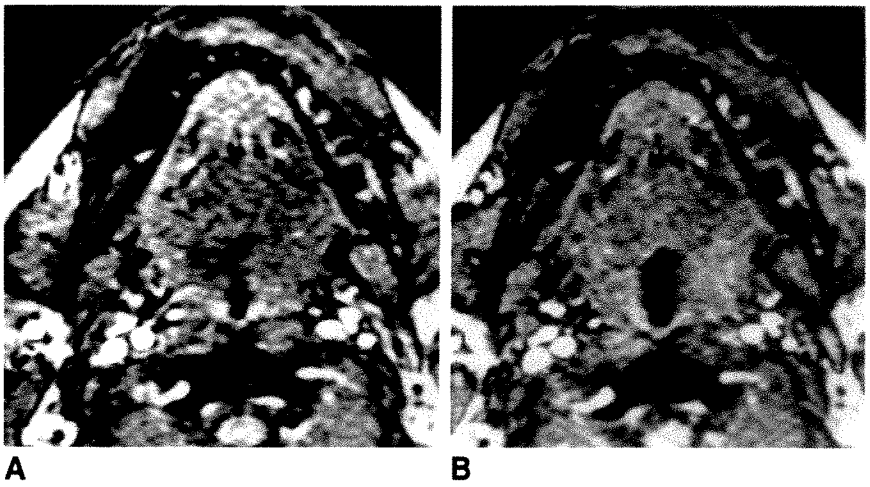

Fig. 4.—Patient with obstructive sleep apnea.
***A* and *B*, Transverse ultrafast spoiled GRASS MR images (8.4/2.9) obtained during respiration (two images showing smallest [*A*] and largest [*B*] cross-sectional areas selected from 12 images obtained at same section location during respiration) show severe vertical narrowing (*A*) of pharyngeal airway. (Images are magnified to show detail of airway.)**

cally have abnormal changes in pharyngeal airway dimensions, namely, occlusions and narrowings, compared with the pharyngeal airways of the different control groups studied (e.g., age- and weight-matched subjects; snorers vs nonsnorers) [4–9, 11, 19–21]. These abnormalities can be seen in awake patients with obstructive sleep apnea by using conventional CT [4, 5]. Occlusions and narrowings are most apparent during tidal breathing because of the dynamic alterations in the pharyngeal airway associated with changes in lung volume [8, 9, 11, 13]. Therefore, rapid imaging techniques are crucial for a thorough and accurate assessment of the pharyngeal airways of patients with obstructive sleep apnea in order to detect morphologic abnormalities, which are often transient processes [8, 9, 11, 18, 19, 21]. Otherwise, occlusions and narrowings of the pharyngeal airway may not be detected. In addition, rapid imaging techniques are especially needed for assessing the pharyngeal airways of patients with tachypneic obstructive sleep apnea [8].

Although an occlusion of the pharyngeal airway is an undeniably significant finding in the awake patient with obstructive sleep apnea, it is also important to determine if abnormal cross-sectional narrowing of the pharyngeal airway is present [4–12, 21, 22]. An abnormally narrowed pharyngeal airway observed in an awake patient with obstructive sleep apnea is thought to be a precursor to airway occlusion that may occur during sleep [9] and is an important contributing factor to the pathology of this disorder [6, 12]. This abnormal anatomic predisposition to occlusion of the pharyngeal airway is usually undetectable by clinical examination methods [5, 7]. In this study, we found abnormally narrowed pharyngeal airways in the patients with obstructive sleep apnea that were comparable in size to those reported in other studies in which cine CT and conventional CT were used [4, 5, 8, 9, 11].

The sites of occlusion and narrowings of the pharyngeal airways of patients with obstructive sleep apnea are variable; the oropharynx is the area most often affected [5, 7, 10]. In addition, multiple sites of occlusions and narrowings are common [8, 11, 18–21], similar to the findings in the obstructive sleep apnea patients we studied. The actual sites and extent of the occlusions and narrowings are important to determine in order to understand the pathologic aspects of this sleep disorder [2, 10].

Detection and characterization of the sites of occlusion and narrowing of the pharyngeal airway are of particular clinical importance insofar as the planning of therapy, especially surgical intervention, is typically based on this information [1, 2, 21, 22]. Multiple surgical procedures have been developed in an attempt to treat obstructive sleep apnea patients found to have associated structural abnormalities of the pharyngeal airways [1, 2, 21–23]. These include uvulopalatopharyngoplasty, in which the uvula and a portion of the soft palate is removed, or tracheostomy, for patients with obstruction in the hypopharyngeal area. An ultrafast spoiled GRASS MR imaging study of the pharyngeal airway may be useful for evaluating the efficacy of the selected surgical treatment of patients with obstructive sleep apnea.

The advantages of ultrafast spoiled GRASS MR imaging of the pharyngeal airway compared with cine CT include no exposure to ionizing radiation and fewer artifacts associated with metallic dental objects. Metallic dental objects can significantly obscure cine CT scans, making it difficult to interpret the findings at a particular level of the pharyngeal airway (which is usually the level of the soft palate or high oropharynx where many occlusions and narrowings tend to occur) [5,

TABLE 1: Transverse Sections Evaluated in Obstructive Sleep Apnea Patients During Dynamic Study of the Pharyngeal Airways

Location of Section	Cross-Sectional Area (cm^2)		No. of Pharyngeal Airway Occlusions[a]
	Mean	Range	
Nasopharynx	1.81	0–3.79	1
Hard palate	1.03	0.36–2.38	0
Soft palate	0.34	0–0.79	2
High oropharynx	0.37	0–1.31	5
Mid oropharynx	0.84	0–1.39	1
Low oropharynx	1.66	0–4.12	1
High hypopharynx	1.77	0.32–4.51	0
Hyoid bone	2.09	0.49–4.60	0

Note.—The minimum cross-sectional area in each subject was used.
[a] Four of the six patients with occlusions had them at two sites.

11]. By comparison, on the ultrafast spoiled GRASS MR images, artifacts caused by metallic dental objects were localized to the immediate area of the objects and did not affect the evaluation of the dimensions of the pharyngeal airway.

In addition, ultrafast spoiled GRASS MR imaging can be used to obtain a view of the pharyngeal airway in the sagittal plane, without reformatting, at an orientation that shows the entire motion of the airway, providing a different perspective of potential sites of occlusions or abnormal narrowings. Finally, the ultrafast spoiled GRASS pulse sequence is readily available on conventional MR imagers and does not require a specialized imaging device for accomplishing a dynamic study of the pharyngeal airway, such as that required for cine CT.

The expense of using ultrafast spoiled GRASS MR imaging to examine the pharyngeal airway has yet to be established. However, the time required to accomplish this study makes it a relatively efficient MR procedure that should allow a high patient throughput.

One potential limitation of our work is that we did not study the pharyngeal airways in a group of control subjects. Instead, we compared our measurements of cross-sectional area of the pharyngeal airways with previously reported values obtained in patients with obstructive sleep apnea and in different control groups assessed by other imaging techniques [4, 5, 8, 9, 11]. Nevertheless, the cross-sectional areas measured for the abnormally narrowed pharyngeal airways of our obstructive sleep apnea patients were comparable to the smallest minimum areas reported for other patients [4, 5, 8, 9, 11]. Another possible limitation is that we did not compare the ultrafast spoiled GRASS MR imaging technique with cine CT. However, we did determine the relative accuracy of using the ultrafast MR technique to determine cross-sectional areas by conducting a phantom study that yielded acceptable results.

The primary intent of this study was to show that ultrafast spoiled GRASS MR imaging can be used for dynamic study of the pharyngeal airway in patients with obstructive sleep apnea in order to detect the presence of occlusions and significant narrowings so that the potential of this imaging procedure could be determined. We acknowledge that refinement of this imaging technique and additional studies of the pharyngeal airways of obstructive sleep apnea patients and control subjects are necessary.

Because of the experimental design of this investigation, it is unknown whether dynamic study of the pharyngeal airway with ultrafast spoiled GRASS MR imaging is also useful for screening patients with suspected obstructive sleep apnea. However, this rapid imaging technique does appear to serve as a useful test that supplements the information currently obtained by physiologic testing of patients with obstructive sleep apnea.

REFERENCES

1. Kales A, Vela-Bueno A, Kales JD. Sleep disorders: sleep apnea and narcolepsy. *Ann Intern Med* **1987**;106:434–443
2. Moran WB, Orr WC. Diagnosis and management of obstructive sleep apnea. Part II. *Arch Otolaryngol Head Neck Surg* **1985**;111:650–658
3. Rechtschaffen A, Kales A, eds. *A manual of standardized terminology, techniques and scoring system for sleep stages of human subjects.* Bethesda, MD: National Institute of Neurological Diseases and Blindness Neurological Information Network, **1968**
4. Bohlman ME, Haponik EF, Smith PL, Allen RP, Bleecker ER, Goldman SM. CT demonstration of pharyngeal narrowing in adult obstructive sleep apnea. *AJR* **1983**;140:543–548
5. Haponik EF, Smith PL, Bohlman ME, Allen RP, Goldman SM, Bleecker ER. Computerized tomography in obstructive sleep apnea: correlation of airway size with physiology during sleep and wakefulness. *Am Rev Respir Dis* **1983**;127:221–226
6. Suratt PM, Dee P, Atkinson RL, Armstrong P, Wilhoit SC. Fluoroscopic and computed tomographic features of the pharyngeal airway in obstructive sleep apnea. *Am Rev Respir Dis* **1983**;127:487–492
7. Rivlin J, Hoffstein V, Kalbfleish J, McNicholas WT, Zamel N, Bryan AC. Upper airway morphology in patients with obstructive sleep apnea. *Am Rev Respir Dis* **1984**;129:355–360
8. Ell SR, Jolles H, Galvin JR. Cine CT demonstration of nonfixed upper airway obstruction. *AJR* **1986**;146:669–677
9. Stein MG, Gamsu G, de Geer G, Golden JA, Crumley RL, Webb WR. Cine CT in obstructive sleep apnea. *AJR* **1987**;148:1069–1074
10. Chaban R, Cole P, Hoffstein V. Site of upper airway obstruction in patients with idiopathic obstructive sleep apnea. *Laryngoscope* **1988**;98:641–647
11. Galvin JR, Rooholamini SA, Stanford W. Obstructive sleep apnea: diagnosis with ultrafast CT. *Radiology* **1989**;171:775–778
12. Hudgel DW. Variable site of airway narrowing among obstructive sleep apnea patients. *J Appl Physiol* **1986**;61:1403–1409
13. Brown JG, Zamel N, Hoffstein V. Pharyngeal cross-sectional area in normal men and women. *J Appl Physiol* **1986**;61:890–895
14. Foo TKF, Bernstein MA, Holsinger AE, Reiderer SJ. Ultra-fast spoiled gradient recalled (SPGR) image acquisition (abstr). In: *Book of Abstracts. Society of Magnetic Resonance in Medicine. Ninth annual meeting.* Berkeley, CA: Society of Magnetic Resonance in Medicine, **1990**:1308
15. Noll DC, Nishimura DG, Mackovski A. Homodyne detection in magnetic resonance imaging. *IEEE Trans Med Imaging* **1991**;M1-10:154–163
16. Crawley AP, Wood ML, Henkelman RM. Elimination of transverse coherences in FLASH MRI. *Magn Reson Med* **1988**;8:248–260
17. Shellock FG, Foo TKF, Deutsch AL, Mink JH. Patellofemoral joint: evaluation during active flexion with ultrafast spoiled GRASS MR imaging. *Radiology* **1991**;180:581–585
18. Shellock FG, Schatz CJ, Julien PM, et al. Dynamic study of the upper airway with ultrafast spoiled GRASS imaging. *JMRI* **1992**;2:103–107
19. Wilms D, Popovich J, Conway W, Fujita S, Zorick F. Anatomic abnormalities in obstructive sleep apnea. *Ann Otol Rhinol Laryngol* **1982**;91:595–596
20. Bradley TD, Brown IG, Grossman RF, et al. Pharyngeal size in snorers, nonsnorers, and patients with obstructive sleep apnea. *N Engl J Med* **1986**;315:1327–1331
21. Stanford W, Galvin J, Rooholamini M. Effects of awake tidal breathing, swallowing, nasal breathing, oral breathing and the Müller and Valsalva maneuvers on the dimensions of the upper airway. *Chest* **1988**;94:149–154
22. Remmers JE. Anatomy and physiology of upper airway obstruction. In: Kryger MH, Roth T, Dement WD, eds. *Principles and practice of sleep medicine.* Philadelphia: Saunders, **1989**:525–536
23. Guilleminault C, Riley RW, Powell NB. Surgical treatment of obstructive sleep apnea. In: Kryger MH, Roth T, Dement WD, eds. *Principles and practice of sleep medicine.* Philadelphia: Saunders, **1989**:571–583

Technical Note

Recurrent Extraluminal Rectal Carcinoma: Transrectal Biopsy Under Sonographic Guidance

Michael Bachmann Nielsen,[1] Jan Fog Pedersen,[1] Jesper Hald,[2] and John Christiansen[2]

Rectal endosonography is a reliable method for preoperative staging of rectal carcinoma [1]. The clinical value of this technique is perhaps even greater in postoperative management because some recurrences cannot be detected either by digital rectal examination or by rectoscopy [2-6]. Furthermore, with endosonography, biopsy can be performed under sonographic guidance.

We report our preliminary experience with rectal endosonography and transrectal endosonographically guided biopsy of suspected recurrent lesions in five patients who had undergone prior resection of the rectum for carcinoma.

Subjects and Methods

From January 1990 to February 1991, postoperative endosonographic examinations of patients with rectal carcinoma suggested an extraluminal recurrence in five of 10 examined patients, all of whom had undergone low anterior resection of the rectum for carcinoma. Pathologic staging of the five cases according to Duke's classification [7] is listed in Table 1. Because of the endosonographic findings, the five patients, all male, had sonographically guided transrectal biopsy.

Rectal endosonography was performed with the patient in the left lateral position. A Brüel & Kjær (Nærum, Denmark) sonographic scanner type 1846 with a 7-MHz rotating endoprobe type 1850 (sector, 360°; focus, 2-5 cm) was used. The biopsy specimens were obtained transrectally by using a Brüel & Kjær 7-MHz multiplanar endoprobe type 8551 (sector, 112°; focus, 1-6 cm). We used fine needles (0.8 or 1.0 mm in diameter) for aspiration biopsies in all patients; in three patients, we also performed core-needle biopsies with Surecut (TSK, Tokyo, Japan) or Biopty-gun (Bard Ltd., Sunderland, England) devices with 1.2-mm needles. IV antibiotics (gentamicin and metronidazole) were given immediately before the biopsy procedure. One patient required general anesthesia because of pain.

Results

The clinical, sonographic, and biopsy data are provided in Table 1. Like the primary rectal tumors, the detected lesions were all hypoechoic, but they showed no other specific sonographic characteristics. In one patient, the mucosa appeared slightly injected on rectoscopy; in the remaining patients, the mucosa was normal. In one patient, a stenosis had developed at the site of the anastomosis, and dilation had been performed several times; in this patient, the lesion detected on endosonography was near the stenosis.

In three patients, a recurrence was confirmed by the results of endosonographically guided biopsy (Fig. 1). In the remaining two patients, examination of the biopsy specimen showed no malignancy, and repeated endosonographic examinations showed no increase in the size of the lesion over the next 9-10 months (Fig. 2). We found no characteristics of the postoperative changes that distinguished them from recurrent lesions. We observed no complications, and the biopsy procedure was tolerated well in four patients; one patient needed general anesthesia because of pain.

Discussion

Rectal endosonography offers an opportunity for postoperative management of patients with rectal cancer who

---

Received September 27, 1991; accepted after revision November 13, 1991.

[1] Department of Radiology and Ultrasound, Glostrup Hospital, University of Copenhagen, DK-2600 Glostrup, Denmark. Address reprint requests to M. B. Nielsen.

[2] Department of Gastroenterologic Surgery D, Glostrup Hospital, University of Copenhagen, DK-2600 Glostrup, Denmark.

AJR 158:1025-1027, May 1992 0361-803X/92/1585-1025 © American Roentgen Ray Society

TABLE 1: Results of Endosonographically Guided Biopsy

Case No.	Age (yr)	Primary Duke's Classification	Time Since Surgery (months)	Rectoscopic Findings	Endosonographic Findings	Biopsy		Follow-up	
						Type	Result	Months After Biopsy	Result
1	47	C	18	Injected mucosa	4 × 4 cm extraluminal mass	AB	Tumor cells	—	NA
2	75	C	3	Normal	Extraluminal rounded mass	AB	Inflammation	10	Lesion unchanged
3	39	C	3	Normal	Thickened wall	AB	Inflammation	—	
			3.5	—	Thickened wall	CB	Tumor cells	—	NA
4	57	A	24	Stenosis, normal mucosa	Extraluminal mass	AB	Normal	—	
			26	Stenosis, normal mucosa	Extraluminal mass	AB	Normal	9	Lesion unchanged
						CB	Normal		
5	48	B	16	Normal	Extraluminal rounded confluent masses	AB CB	Tumor cells Inflammation	—	NA

Note.—AB = aspiration biopsy, CB = core biopsy, NA = not applicable. See Henrichsen and Christiansen [7] for explanation of Duke's classifications.

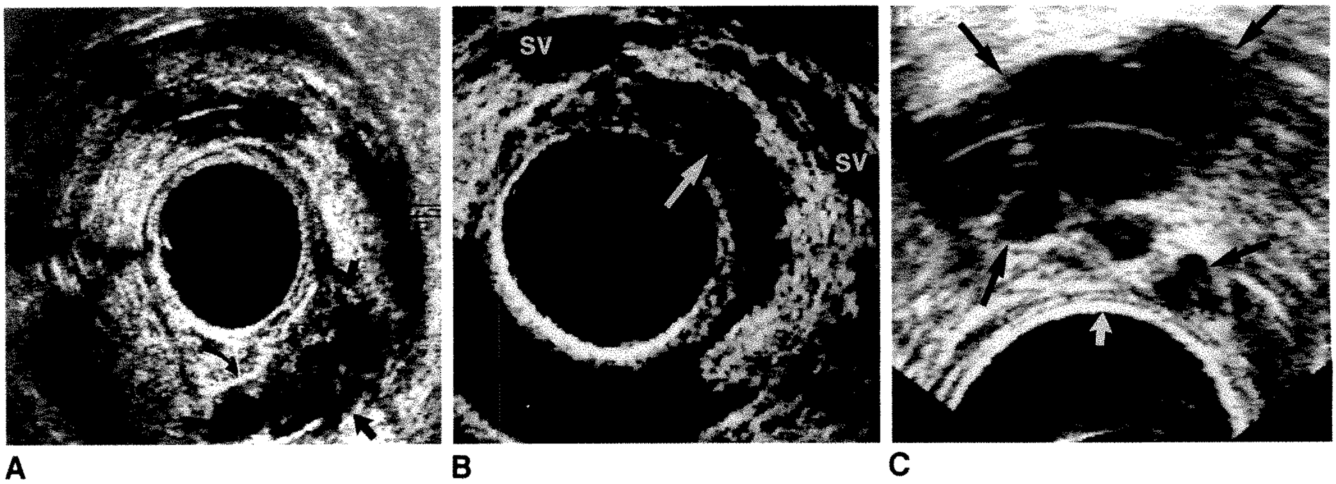

Fig. 1.—Recurrent extraluminal rectal carcinoma.

***A*, Case 1: Transverse rectal endosonogram (seen from below, up is anterior) shows 4 × 4 cm extraluminal recurrence (*arrows*) at site of resection involving part of rectal wall and extending toward sacrum.**

***B*, Case 3: Transverse rectal endosonogram shows thickening of rectal wall (up to 1 cm) anteriorly (*arrow*). Hypoechoic areas posteriorly (at 5 o'clock to 9 o'clock) are artifacts due to air in rectum. SV = seminal vesicles.**

***C*, Case 5: Transverse rectal endosonogram obtained with multiplane sector scanner shows a 4 × 2.5 cm conglomerate of rounded confluent hypoechoic masses (*black arrows*) appearing like enlarged lymph nodes. Note normal rectal wall (*white arrow*).**

undergo sphincter-preserving resection. It may be possible with routine endosonographic follow-up to detect even small local recurrences at an early stage and thus improve the chances of curative surgery.

Luminal recurrences are usually diagnosed on the basis of rectoscopic findings and biopsies performed before patients have endosonography. In these patients, endosonography can be used to detect local tumor extension or involvement of adjacent organs, findings that would affect additional treatment. Extraluminal recurrences will not be recognized at rectoscopy unless the bowel surface is involved, whereas with endosonography such recurrences can be visualized, as shown in this report.

In some patients nonmalignant postoperative changes may develop that sonographically resemble recurrent disease. Therefore, biopsy of any suspected lesion should be considered. In cases in which biopsies show nonmalignant cells, another biopsy should be considered or follow-up endosonography should be performed after several months to determine if the lesion has increased in size, suggesting tumor growth [2]. A lesion that does not increase in size may represent benign postoperative change. Some biopsies in our study suggested nonmalignant postoperative changes, which were confirmed by the subsequent clinical course.

Sonographically guided transrectal biopsy of the prostate has been performed for several years, and complications are

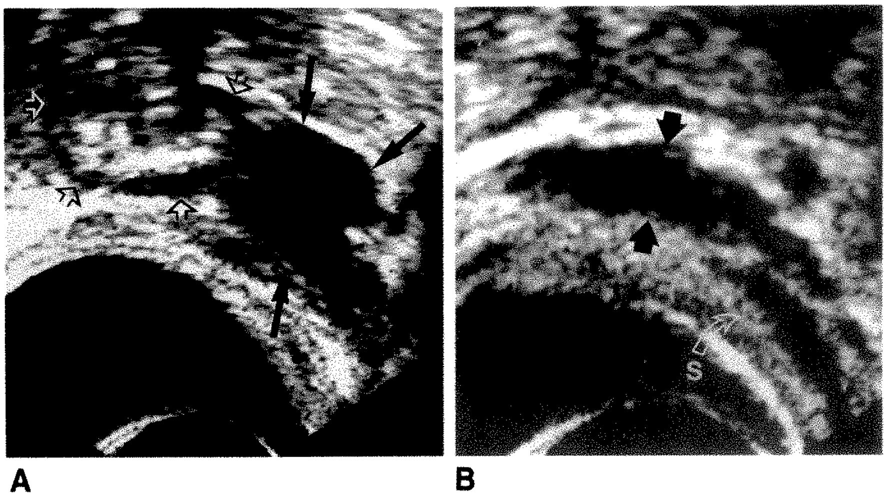

Fig. 2.—Nonmalignant postoperative changes.

***A*, Case 2: Transverse sonogram shows 1- to 1.5-cm hypoechoic extraluminal rounded mass (*solid arrows*) close to adjacent bowel wall (*open arrows*).**

***B*, Case 4: Magnification of transverse sonogram of rectal wall shows 0.5-cm-thick hypoechoic area (*arrows*) in rectal wall deep to submucosa (S).**

usually few and minor. Only a few reports [2-6, 8] have described guided biopsies of recurrent rectal cancers or recurrent pelvic masses. In some of these series, either the transperineal biopsy route was used or the biopsy procedures are not fully described [2-4].

Most endoprobes are designed for imaging of the prostate and lower rectum, so transrectal biopsies are usually confined to this part of the rectum. However, general anesthesia will provide maximal relaxation of the anal sphincter, and the endoprobe and biopsy needle then can be maneuvered to the middle or even upper part of the rectum. (This was not necessary for visualization of the recurrences in this series.) When biopsy specimens are taken from extraluminal masses, the bowel wall will be perforated, and with biopsies in the middle and upper part of the rectum, even the peritoneum may be perforated. We therefore give IV antibiotics immediately before the biopsy procedure.

We found few descriptions of the needle types used in other reports; however, Tru-Cut or Biopty-gun devices have been used [4-6]. Only one report [8] describes the use of fine-needle aspiration biopsy. We initially thought that fine-needle aspiration biopsy would provide sufficient material for cytologic studies because demonstration of tumor cells would be diagnostic. However, in one patient, an additional core biopsy was necessary to provide enough material for histologic studies. We therefore now do both fine-needle aspiration biopsies for cytologic studies (three samples) and core biopsies for histologic studies (three samples). For the latter biopsies, we use a Biopty-gun device with a 1.2-mm biopsy needle. Determination of the optimal biopsy approach awaits further study.

In summary, rectal endosonography may be useful in the postoperative management of patients with rectal carcinoma, particularly for the detection of extraluminal recurrent disease. Biopsy of any detected lesions should be considered because nonmalignant postoperative changes may resemble recurrence. Biopsy can be performed transrectally under sonographic guidance. We recommend performing both fine-needle aspiration and core biopsies in such cases. In addition, postoperative follow-up of these patients should include imaging for widespread metastatic disease.

REFERENCES

1. Romano G, De Rosa P, Vallone G, Rotondo A, Grassi R, Santangelo ML. Intrarectal ultrasound and computed tomography in the pre- and postoperative assessment of patients with rectal carcinoma. *Br J Surg* **1985**;72[suppl]:S117-119
2. Beynon J, Mortensen NJM, Foy DMA, Channer JL, Rigby H, Virjee J. The detection and evaluation of locally recurrent rectal cancer with rectal endosonography. *Dis Colon Rectum* **1989**;32:509-517
3. Hildebrandt U, Feifel G, Schwarz HP, Scherr O. Endorectal ultrasound: instrumentation and clinical aspects. *Int J Colorectal Dis* **1986**;1:203-207
4. Zainea GC, Lee F, McLeary RD, Siders DB, Thieme ET. Transrectal ultrasonography in the evaluation of rectal and extrarectal disease. *Surg Gynecol Obst* **1989**;169:153-156
5. Andersson R, Aus G. Transrectal ultrasound-guided biopsy for verification of lymph-node metastasis in rectal cancer. Case report. *Acta Chir Scand* **1990**;156:659-660
6. Mascagni D, Corbelli L, Urciuoli, Di Matteo G. Endoluminal ultrasound for early detection of local recurrence of rectal cancer. *Br J Surg* **1989**;76:1176-1180
7. Henrichsen S, Christiansen J. Prognostic staging of extraperitoneal rectal cancer. *Dis Colon Rectum* **1989**;32:214-218
8. Mandell MJ, Thieme GA, Eggli KD, Ballantine TVN. Transrectal ultrasound guided needle biopsy of recurrent vaginal mass in a 23 month old girl. *Pediatr Radiol* **1989**;20:120-121

Book Review

Gastrointestinal Radiology. By Jack Farman. Philadelphia: Lippincott, 191 pp., 1991. $59.95

If you have ever heard Jack Farman lecture, this book is thoroughly representative of his style. The introduction to the book is telltale: Its punctuated brevity typifies the remainder of the book. Although the target audience for this text is not specified in the introduction, the first sentence says, "It is impossible to encompass all of gastrointestinal (GI) imaging in a single book." Dr. Farman accomplishes the difficult task of deciding what to include or exclude in this short book, which is a cross between an atlas and an introductory text.

The book is divided into seven chapters: esophagus, stomach, duodenum and pancreas, biliary tract, small bowel, colon, and generalized disorders. Each chapter is divided into topics that cover highlights of various diseases and disorders. For example, the chapter on the esophagus discusses and illustrates benign stricture (reflux, postoperative, Barrett's), hiatal hernia (sliding), achalasia, varices, infections (*Candida*), neoplasms (leiomyoma, esophagitis cystica, carcinoma of various patterns), and other disorders (bronchogenic cyst, foregut duplication, and foreign body). A brief text is given for each topic, which may include one disorder or disease or a group, and this is followed by illustrations. The text gives an overview of the findings in each entity illustrated, with as many "pearls per page" as possible. In order to accomplish this, the text is unreferenced; it is occasionally anecdotal, but accurate by my account. Technical issues and how-to instructions are generally omitted. Discussion of pathologic or pathophysiologic changes is limited and is included only where absolutely necessary. Clinical findings are notably brief and sometimes are given by example in the legend to an illustration. In some sections, the roles of various techniques are discussed in detail to give the reader perspective. For example, in the discussion on cholelithiasis, the roles of sonography and cholecystography are expounded, and in the beginning of the section on the colon, a table is given to illustrate the roles of single-contrast, double-contrast, biphasic, and water-soluble enemas.

The illustrations are of excellent quality. Barium studies are emphasized, but CT and cholangiography are included in the appropriate chapters (pancreas and biliary tract). Arrows, when used, are an attractive and effective orange, an innovative and admirable technique. However, as the audience for this text is likely to be students and new residents, it is unfortunate that many illustrations do not have any arrows. In the section on the pancreas, an area where CT scans are used a great deal, annotated line drawings accompany many of the figures. Examples using single-contrast and double contrast imaging and enteroclysis are shown, but single-contrast images dominate the book. This is a function of the author's preference and population of patients (as described in the introduction), but I subscribe to using this balance of techniques in an introductory text such as this.

The quality of the paper and print is excellent. The size of the book (about 26 by 20 cm), although not pocket-size, is convenient for carrying around, and the length of the book (about 191 pages, paginated in decimal style) makes it readable over a weekend. The bibliography gives both the pages and the figure numbers (both are in decimal format, but the figure numbers are in boldface), which is a desirable feature to help readers find an illustration quickly.

This book differs from other introductory texts in that it does not emphasize technique and does not give laundry lists of differential diagnoses. It is a good informational introduction for beginning residents and motivated medical students who wish to acquire a fundamental fund of knowledge in gastrointestinal radiology.

Abraham H. Dachman
Uniform Services University of the Health Sciences
Bethesda, MD 20814-4799

Case Report

Candida Cholangitis in a Diabetic Woman

D. Randall Radin[1] and Meade B. Johnson

Candidiasis of the biliary tract is rare; only about a dozen well-documented cases have been published [1-3]. We report the sonographic and cholangiographic findings in a diabetic woman with *Candida* cholangitis without infection elsewhere.

Case Report

A 39-year-old woman was admitted with a third hypoglycemic episode in a week. She had a 24-year history of insulin-dependent diabetes mellitus, complicated by multiple episodes of ketoacidosis, severe retinopathy, enteropathy, neuropathy, and nephropathy, which required hemodialysis. Three weeks earlier she had been admitted to another hospital because of ascending cholangitis and had had cholecystectomy and placement of a T tube. An intraoperative cholangiogram was reported to be normal. The gallbladder contained multiple stones, and pathologic evaluation showed necrotizing acute and chronic cholecystitis. Culture of intracholecystic bile yielded *Klebsiella pneumoniae*. Fungal stains were negative. Serum bilirubin level decreased from 13.2 to 2.8 mg/dl. Hepatobiliary scintigraphy showed accumulation of radionuclide in the small bowel. The T tube was removed, and the patient was discharged 2 weeks after surgery.

On this admission, she was afebrile but icteric, with marked elevation of serum levels of alkaline phosphatase (2599 U/l) and bilirubin (14.6 mg/dl). Sonography showed thickening of the wall of the common duct and nonshadowing echogenic material throughout the lumen (Fig. 1A). Fever developed, and treatment with ampicillin, gentamicin, and metronidazole was begun. Endoscopic retrograde cholangiography showed a diffusely abnormal biliary tree with marked mural irregularity, multiple strictures, and segments of mild dilatation. Apparent dissection of contrast material in the wall of the common bile duct was seen. Differential diagnosis included infectious cholangitis and primary sclerosing cholangitis. Sphincterotomy was performed. The patient was seronegative for antibodies to HIV. Repeat endoscopic retrograde cholangiography 1 week after the sphincterotomy showed no change (Fig. 1B). Because of progressive increase of serum levels of alkaline phosphatase and bilirubin, a biliary stent was placed. Biopsy specimen of the distal common bile duct showed necrotic bile-stained tissue and debris with *Candida*. The serum level of alkaline phosphatase decreased, but the serum level of bilirubin increased. Increased biliary dilatation was seen when retrograde cholangiography was repeated 11 days after the second study. Cultures of aspirated bile yielded *Candida albicans*, *Candida krusei*, enterococcus, and *Staphylococcus epidermidis*. Treatment with amphotericin B was begun. Serum levels of alkaline phosphatase and bilirubin increased, but the patient was afebrile and did not appear to be severely ill or to have sepsis. One week later, hypothermia, hypotension, and severe hypoglycemia developed. The patient died 5 weeks after admission. Autopsy showed invasive biliary candidiasis and multiple liver abscesses caused by *C. albicans* and bacteria. No other site of *Candida* infection was present.

Discussion

Although virtually every organ may be involved, candidiasis of the biliary tract is rare, even in large series of patients with disseminated infection [1]. In 10 of 12 reported cases of biliary candidiasis ([1-3] and this case), the infection was not systemic. In 11 of the 12 patients, one or more of these predisposing factors was present: previous cholecystectomy or other major operation, treatment with broad-spectrum antibiotics, diabetes mellitus, and acute leukemia. None of the patients had AIDS. No apparent predisposing factor was present in a 3½-year-old girl who had a fungus ball in the common bile duct 2 months after blunt abdominal trauma [2].

Received August 15, 1991; accepted after revision September 23, 1991.

[1] Both authors: Department of Radiology, University of Southern California School of Medicine, Los Angeles County-University of Southern California Medical Center, 1200 N. State St., Los Angeles, CA 90033-1084.

AJR 158:1029-1030, May 1992 0361-803X/92/1585-1029 © American Roentgen Ray Society

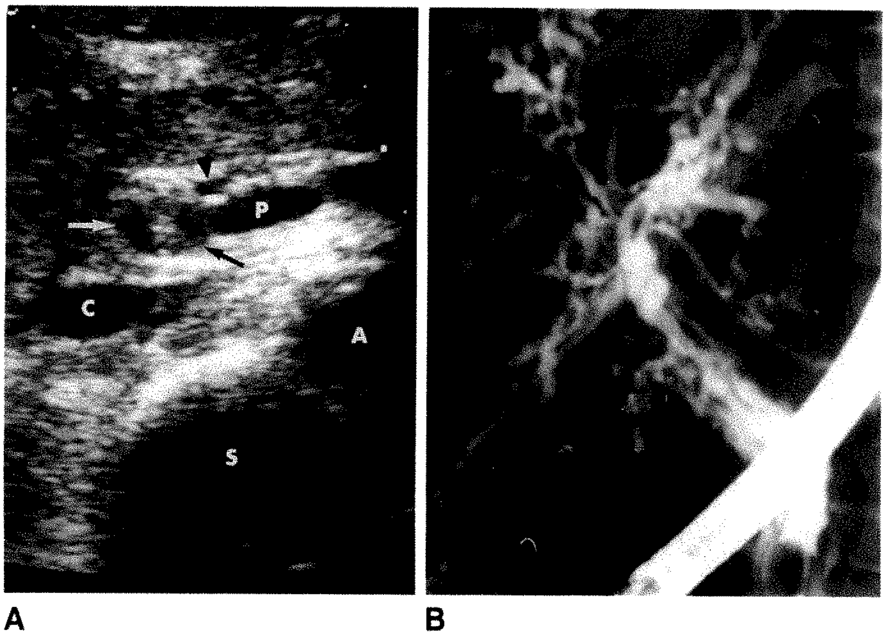

Fig. 1.—*A*, Transverse sonogram shows thickened hypoechoic wall of common duct (*arrows*) and nonshadowing echogenic material filling lumen. *Arrowhead* = hepatic artery, P = portal vein, C = inferior vena cava, A = aorta, S = spine.

B, Endoscopic retrograde cholangiogram shows involvement of entire biliary tree by marked mural irregularity with multiple strictures and segments of mild dilatation. Channels of contrast material parallel to common duct may represent intramural dissection.

In one previously reported case [2], sonography showed a nonshadowing polypoid mass of 7–8 mm in the lumen of the distal common bile duct. Pathologic examination of the contents of the common duct showed *Candida* embedded in bile sludge material. Sonographic findings in our patient differed in two respects. Thickening of the wall of the common duct reflected the invasive nature of the infection. The echogenic material filling the lumen of the entire common duct probably represented a combination of intraluminal debris and ulcerated mucosa.

Cholangiography in four reported cases of biliary candidiasis [1, 4] showed one or more intraluminal filling defects representing fungus balls in the common bile duct. In one of these cases [4], several strictures of the intrahepatic and extrahepatic bile ducts also were present. Cholangiographic findings in our patient were far more severe and extensive, consistent with diffuse invasive candidiasis. The radiologic appearance was suggestive of primary sclerosing cholangitis [5] or AIDS-related cholangitis [6]. Candidiasis was not suspected until biopsy was performed.

Although rare, the diagnosis of biliary candidiasis should be considered when radiologic findings show cholangitis or an intraluminal filling defect in the common bile duct in a patient with predisposing factors for *Candida* infection. Bile should be obtained for fungal stain and culture. With appropriate treatment, the majority of patients will make a complete recovery [1].

REFERENCES

1. Irani M, Truong LD. Candidiasis of the extrahepatic biliary tract. *Arch Pathol Lab Med* **1986**;110:1087–1090
2. Carstensen H, Nilsson KO, Nettelblad SV, Cederlund CG, Hildell J. Common bile duct obstruction due to an intraluminal mass of candidiasis in a previously healthy child. *Pediatrics* **1986**;77:858–861
3. Chen CC, Chang PY, Chen CL. Refractory cholangitis after Kasai's operation caused by candidiasis: a case report. *J Pediatr Surg* **1986**;21:736–737
4. Uflacker R, Wholey MH, Amaral NM, Lima S. Parasitic and mycotic causes of biliary obstruction. *Gastrointest Radiol* **1982**;7:173–179
5. MacCarty RL, LaRusso NF, Wiesner RH, Ludwig J. Primary sclerosing cholangitis: findings on cholangiography and pancreatography. *Radiology* **1983**;149:39–44
6. Dolmatch BL, Laing FC, Federle MP, Jeffrey RB, Cello J. AIDS-related cholangitis: radiographic findings in nine patients. *Radiology* **1987**;163:313–316

Primary Malignant Small Round Cell Tumor of the Abdomen:

CT Findings in Five Cases

Datla G. K. Varma[1]
Kelvin McDaniel[1]
Nelson G. Ordóñez[2]
Christine A. J. Granfield[1]
Chusilp Charnsangavej[1]
Sidney Wallace[1]

Malignant small round cell tumor of the abdomen is a newly described clinicopathologic entity. The features of this entity include a predilection for young men, predominant abdominopelvic location, and aggressive behavior. Pathologic analysis demonstrates a small-cell tumor unusually coexpressing desmin and keratin. This study describes CT characteristics in five patients with malignant small round cell tumor of the abdomen. All patients were young white men, 20–36 years old (mean, 28 years). In all five cases, CT scans revealed lobulated masses appearing to arise primarily from peritoneal surfaces and predominantly involving the peritoneal cavity of the abdomen (two cases) and pelvis (two cases); diffuse abdominopelvic involvement was noted in one case. The masses were centrally necrotic and enhanced inhomogeneously after administration of iodinated contrast material. Additional CT features included ascites (one case), calcifications in the dominant mass (one case), omental implants (two cases), hydronephrosis (four cases), anterior diaphragmatic lymphadenopathy (two cases), liver metastases (two cases), and retroperitoneal lymphadenopathy (two cases).

CT findings of abdominal malignant small round cell tumor are nonspecific and mimic findings noted in other conditions, such as peritoneal carcinomatosis and leiomyosarcomatosis.

***AJR* 158:1031–1034, May 1992**

A distinctive type of malignant small round cell tumor of the abdomen has been recently described in the pathologic literature [1–4]. Unique features of this neoplasm include a predilection for young men, predominant location in the peritoneal cavity with a possible predilection for the pelvic region, and aggressive behavior with high mortality despite multiple modes of therapy [2]. Immunohistochemical studies are unique in this entity in that there is coexpression of keratin and desmin indicating the presence of epithelial and muscle-associated antigens [1, 2]. To our knowledge, malignant small round cell tumor of the abdomen has not been previously reported in the radiologic literature. Abdominal CT findings in five patients with malignant small round cell tumor of the abdomen are the subject of this report.

Materials and Methods

We searched the consultation files of one of the authors and found the records of five patients with malignant small round cell tumor of the abdomen in whom CT scans of the abdomen and pelvis had been obtained. The CT scans were reviewed retrospectively. All five patients were young white men 20–36 years old (mean, 28 years). The patients had no clinical evidence of AIDS. Two patients tested negative for antibodies to HIV; the other patients were not tested. The patients had palpable abdominal and/or pelvic masses. One patient also had an enlarged metastatic left anterior cervical lymph node. Signs and symptoms were related to mass effect on contiguous organs. Diagnosis was based on pathologic examination of tissue specimens obtained during exploratory laparotomy (four cases) and from a resected cervical lymph node (one case). The histopathologic diagnosis of this tumor was done by one of the authors, who is familiar with malignant small round cell tumor of the

Received November 13, 1991; accepted after revision December 16, 1991.

[1] Department of Diagnostic Radiology, Box 57, The University of Texas M. D. Anderson Cancer Center, 1515 Holcombe Blvd., Houston, TX 77030. Address reprint requests to D. G. K. Varma.

[2] Department of Pathology, The University of Texas M. D. Anderson Cancer Center, Houston, TX 77030.

0361–803X/92/1585–1031
©American Roentgen Ray Society

abdomen [1]. Immunohistochemical studies were performed in all cases by using the avidin-biotin-peroxidase complex method [5]. The details of additional immunostaining procedures performed are described elsewhere [6]. Tissue for electron microscopy studies was available in one case.

CT scans were obtained with a GE 9800 scanner (General Electric, Milwaukee, WI) in three cases and with GE 8800 and Picker 1200 SX (Picker International, Highland Heights, OH) scanners in one case each. The scans consisted of contiguous 1.0-cm-thick sections. In all patients scans were obtained after IV infusion of 150 ml of contrast material and with oral and rectal administration of diluted barium. In three patients, IV contrast material was administered via power injector at 1.5 ml/sec with a 60-sec delay; in two patients, a rapid drip infusion technique was used. In two patients, unenhanced scans were also obtained. The CT scans were analyzed for anatomic location of tumor, morphologic characteristics, extent of disease, and associated findings.

Results

In all five cases, CT scans revealed lobulated masses appearing to arise from peritoneal surfaces and ranging in size from 5 × 4 cm to 15 × 8 cm. In two cases, the masses were located predominantly in the peritoneal cavity of the left abdomen extending inferiorly from the greater curvature of the stomach to the level of the lower pole of the kidneys (Figs. 1 and 2). The masses were centrally necrotic and enhanced inhomogeneously after administration of iodinated contrast material; one tumor demonstrated foci of calcification (Fig. 2). A smaller pelvic component posterior to the urinary bladder was also noted in one of these tumors. In two patients, large lobulated masses were identified in the pelvis posterior to the bladder and anterior to the rectum (Fig. 3), and one patient had diffuse abdominopelvic involvement. Additional CT features included ascites (one case), omental implants (two cases), hydronephrosis (four cases), anterior diaphragmatic lymphadenopathy (two cases), liver metastases (two cases), and retroperitoneal lymphadenopathy (two cases) (Figs. 2 and 4). The hydronephrosis was caused by the pelvic masses impinging on the ureters; the masses also abutted loops of bowel causing symptoms of intermittent bowel obstruction.

Pathology

Histologically, the five tumors were similar (Fig. 5). They were made up of well-defined, solid clusters of small tumor cells separated by dense fibrous stroma. The larger tumor nests had central necrosis, and mitotic figures were frequent. Immunocytochemical studies demonstrated that the tumor cells stained with keratin in all cases; in addition to keratin, most tumor cells also reacted with desmin and vimentin. No reactivity for chromogranin A or S-100 protein was seen in any of the cases.

The most striking ultrastructural feature was the presence of large amounts of intracytoplasmic intermediate filaments that often formed paranuclear bundles and whorls. No neuroendocrine granules were seen.

Discussion

Malignant small round cell tumor of the abdomen appears to be a distinct clinicopathologic entity belonging to the generic category of small round cell tumors of infancy and childhood [2, 7, 8]. The category of small round cell tumors of infancy and childhood includes Ewing's sarcoma, primitive neuroectodermal tumor, embryonal and rhabdomyosarcoma,

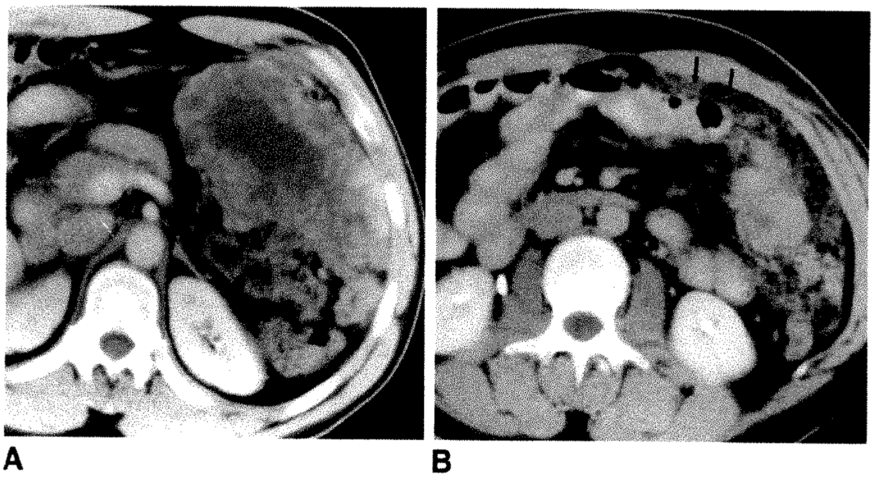

Fig. 1.—32-year-old man with increasing abdominal girth and palpable abdominal mass.

A, Contrast-enhanced CT scan shows large lobulated mass with central necrosis in left side of abdomen .

B, CT scan obtained at lower level of mass shows small omental nodules (*arrows*). Superiorly, mass extended to greater curvature of stomach.

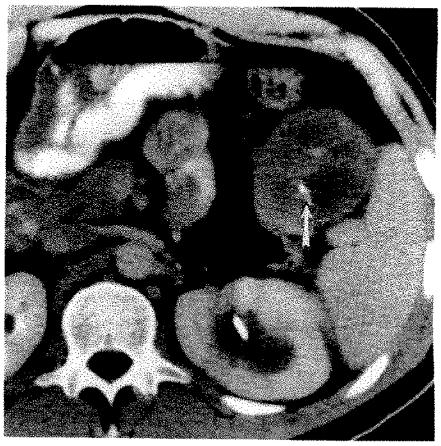

Fig. 2.—27-year-old man with signs and symptoms of bowel and urinary tract obstruction. Contrast-enhanced axial CT scan of 1-cm-thick section shows lobulated, septated, centrally necrotic mass that extended inferiorly from greater curvature of stomach. A smaller pelvic mass was the cause of hydronephrosis. A small focus of calcification (*arrow*) was also noted on an unenhanced scan.

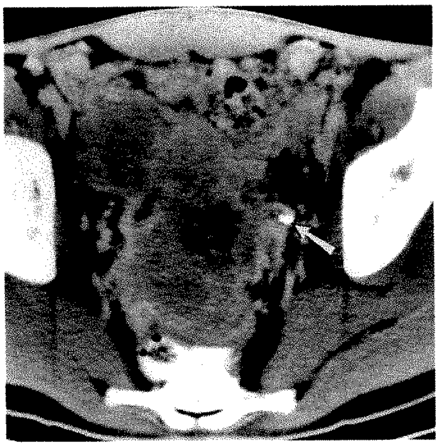

Fig. 3.—24-year-old man with palpable pelvic mass and enlarged left anterior cervical nodes. Contrast-enhanced CT scan shows large lobulated, centrally necrotic pelvic mass and dilated left ureter (*arrow*).

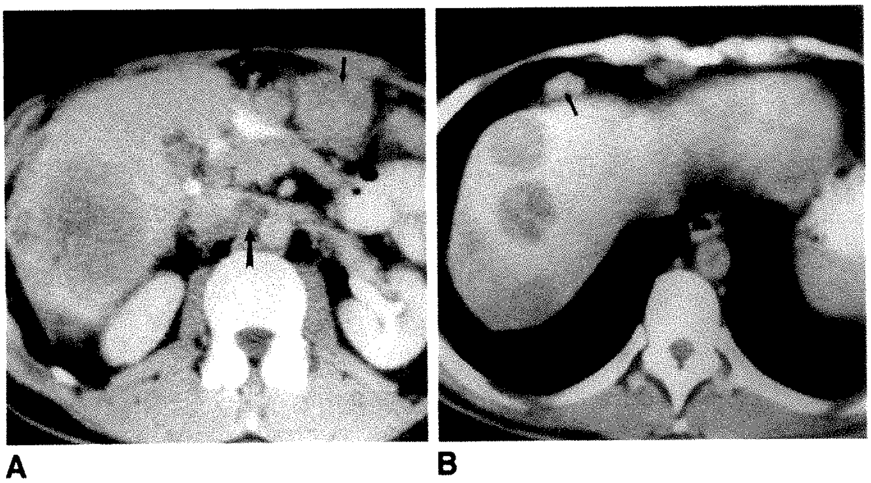

Fig. 4.—36-year-old man with tumor progression despite multidrug therapy.

A, Contrast-enhanced CT scan shows liver metastases, interaortocaval retroperitoneal lymphadenopathy (*large arrow*), and abdominal implants (*small arrow*).

B, CT scan obtained at superior aspect of liver shows anterior diaphragmatic lymphadenopathy (*arrow*) in addition to liver metastases.

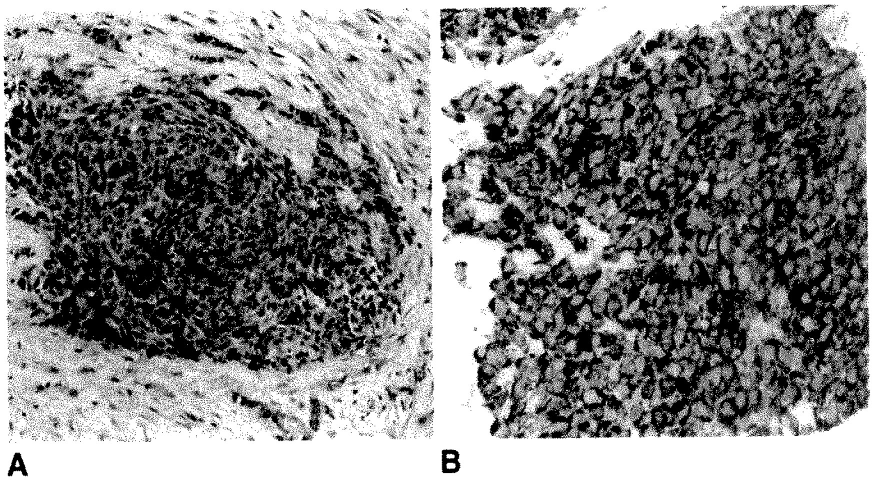

Fig. 5.—*A*, Low-power photomicrograph of malignant small round cell neoplasm shows tumor nest surrounded by dense stroma. (H and E, original magnification ×120)

B, Photomicrograph of immunocytochemical preparation shows reactivity for keratin throughout cytoplasm of tumor cells. (Avidin-biotin-peroxidase complex stain, original magnification ×300)

lymphoma, and neuroblastoma [2]. The most characteristic diagnostic feature of this tumor is the coexpression of epithelial (keratin) and mesenchymal types of intermediate filaments (desmin and vimentin). This unique immunophenotype, together with a marked predilection for young men, abdominopelvic location, and aggressive clinical behavior, supports the concept that malignant small round cell tumor of the abdomen represents a distinct clinicopathologic entity [1, 2]. The exact cell of tumor origin is not known, but in most instances, it appears to arise from the peritoneum [1, 2]. Experience in the treatment of malignant small round cell tumor of the abdomen is limited, and in our cases, no significant response was noted on multidrug chemotherapy regimens. The role of debulking surgery is yet to be determined.

The peritoneum is more often involved by metastatic disease than it is the site of origin of primary neoplasms. The common malignant lesions that cause peritoneal carcinomatosis are ovarian, colonic, and gastric carcinomas [9]. CT signs of peritoneal carcinomatosis include ascites, nodular peritoneal thickening, omental implants, and calcified peritoneal implants [9]. Nodular or masslike peritoneal involvement may also be seen in lymphoma, peritoneal leiomyosarcomatosis, and peritoneal mesothelioma [9–11]. Gastric leiomyosarcomas may be visualized on CT scanning as large necrotic exogastric masses extending into the abdominal cavity [12, 13].

The CT findings noted in our small series of patients with primary malignant small round cell tumor of the abdomen appear nonspecific and mimic findings noted in peritoneal carcinomatosis, leiomyosarcomatosis, and gastric leiomyosarcomas. Percutaneous fine-needle aspiration biopsy will probably be useful in the diagnosis of malignant small round cell tumor of the abdomen as pathologists become increasingly familiar with this entity. It is extremely important for radiologists to be aware of this newly described entity. This knowledge would help the radiologist to offer an appropriate differential diagnosis when multiple peritoneal masses are noted on abdominal CT scans, especially in young men.

REFERENCES

1. Ordóñez NG, Zirkin R, Bloom RE. Malignant small-cell epithelial tumor of the peritoneum coexpressing mesenchymal-type intermediate filaments. *Am J Surg Pathol* **1989**;13:413–421
2. Gerald WL, Miller HK, Battifora H, Mieltinen M, Silva EG, Rosai J. Intraabdominal desmoplastic small round-cell tumor: report of 19 cases of a distinctive type of high-grade polyphenotypic malignancy affecting young individuals. *Am J Surg Pathol* **1991**;15:499–513
3. Variend S, Gerrard M, Norris PD, Goepel JR. Intraabdominal neuroectodermal tumour of childhood with divergent differentiation. *Histopathology* **1991**;18:45–51
4. Gonzalez-Crussi F, Crawford SE, Chen-Chih JS. Intra-abdominal desmoplastic small cell tumors with divergent differentiation: observations on three cases of childhood. *Am J Surg Pathol* **1990**;14:633–642
5. Hsu SM, Raine L, Fanger H. Use of avidin-biotin-peroxidase complex (ABC) in immunoperoxidase technique: a comparison between ABC and unlabeled antibody (PAP) procedures. *J Histochem Cytochem* **1981**;29: 577–580
6. Ordóñez NG, Manning JT, Brooks TE. Effect of trypsinization on the immunostaining of formalin-fixed, paraffin-embedded tissues. *Am J Surg Pathol* **1988**;12:121–129
7. Unis EJ. Ewing's sarcoma and related small round cell neoplasms in children. *Am J Surg Pathol* **1986**;10[suppl 1]:54–62
8. Triche TJ. Diagnosis of small round cell tumors of childhood. *Bull Cancer* (Paris) **1988**;75:297–310
9. Walkey MM, Friedman AC, Sohotra P, Radecki PD. CT manifestations of peritoneal carcinomatosis. *AJR* **1988**;150:1035–1041
10. Choi BI, Lee WJ, Chi JG, Han JK. CT manifestations of peritoneal leiomyosarcomatosis. *AJR* **1990**;155:799–801
11. Reuter K, Raptopoulos V, Reale F, et al. Diagnosis of peritoneal mesothelioma: computed tomography, sonography, and fine-needle aspiration biopsy. *AJR* **1983**;140:1189–1194
12. Nauert TC, Zornoza J, Ordonez N. Gastric leiomyosarcomas. *AJR* **1982**;139:291–297
13. McLeod IJ, Zornoza J, Shirkhoda A. Leiomyosarcoma: computed tomography findings. *Radiology* **1984**;152:133–136

New Format for Abstracts

Beginning in Fall 1992, the *AJR* will publish abstracts of articles in a different format, much like the ones recently adopted by the *New England Journal of Medicine* and the *Journal of the American Medical Association*. The purpose of the new design is to have abstracts present the essential elements of articles more clearly and concisely. The contents, organization, and length of the abstracts will be the same as before; however, rather than being all one paragraph except for the conclusion, abstracts will now be divided into four paragraphs, each with a title: objective, subjects (or materials) and methods, results, and conclusion.

The *AJR* Guidelines for Authors, which appears at the front of every issue of the Journal, has been revised to help you write abstracts in this new format. Authors should familiarize themselves with these guidelines and incorporate them into all manuscripts submitted for publication.

Robert N. Berk
Editor-in-Chief

Review Article

Duplex Doppler Evaluation of Native Kidney Dysfunction: Obstructive and Nonobstructive Disease

Joel F. Platt[1]

Intrarenal duplex Doppler sonography can provide physiologic information reflecting the status of renal vascular resistance. Available data suggest 0.70 as a reasonable upper limit for normal intrarenal resistive index. Complete or significant partial urinary obstruction produces a prompt elevation in the resistive index that is not produced by purely nonobstructive dilatation; hence, Doppler imaging appears useful in evaluating the dilated, possibly obstructed kidney. In addition, intrarenal Doppler sonography may prove to be a useful noninvasive test to suggest the significance of partial obstruction. Nonobstructive renal disease also can cause elevation of the resistive index. Recent biopsy series, although correlating certain pathologic findings with resistive index, also indicate that renal Doppler sonography is not sensitive or specific enough to replace renal biopsy. To date, Doppler study of renal medical disease has proved most useful in two types of applications: monitoring of patients with renal disease known to produce resistive index elevation and differentiating between renal diseases where one produces more marked Doppler changes than the other. Resistive index is clearly not identical to creatinine level; in some instances the resistive index may provide unique noninvasive information regarding renal arterial resistance not available from conventional laboratory parameters.

Sonography is commonly performed to evaluate the patient with suspected or known renal disease [1-5]. Although gray-scale sonography can provide important anatomic information, it lacks the ability to provide significant physiologic data. Duplex Doppler sonography has the potential to provide physiologic information regarding renal arterial resistance, and has been extensively used in renal transplants. However, until recently, intrarenal Doppler examination of native kidney dysfunction had been largely overlooked. This review summarizes the recent advances in intrarenal duplex Doppler sonography of the native kidney and the pathophysiologic basis for these applications.

Technique

Duplex Doppler study of small intrarenal vessels, although not technically difficult, does require knowledge of the proper technique to obtain useful measurements. The majority of reported renal Doppler research has used 3-, 3.5-, or 5-MHz transducers, and has not required color Doppler imaging [6–11]. Typically, the Doppler sample volume is set at 2–5 mm. Most prior studies have concentrated on the study of distal intrarenal vessels, which are not actually seen during the examination but are detected by sampling the Doppler spectrum at the corticomedullary junction or along borders of medullary pyramids [6–11]. Prior animal renal vascular studies suggest that many pathologic processes produce the most marked alterations in resistance in these distal arterial branches [12–15]. Attention to which renal vessels were examined is crucial when analyzing Doppler studies with potentially conflicting results. These small intrarenal vessels, in general, have low flow velocities with associated relatively small frequency shifts. To detect these low velocities, the machine wall filter should be set as low as possible [11, 16]. Of even greater importance is use of the proper velocity/

Received September 12, 1991; accepted after revision December 26, 1991.

[1] Department of Radiology, The University of Michigan Medical Center, 1500 E. Medical Center Dr., Ann Arbor, MI 48109-0030. Address reprint requests to J. F. Platt.

AJR 158:1035–1042, May 1992 0361–803X/92/1585–1035 © American Roentgen Ray Society

frequency-shift scale. Optimally, the Doppler scale should be maximized by using the smallest possible frequency range (minimum pulse repetition frequency) that does not produce aliasing [11, 16]. With this technique, the deflection of the Doppler spectrum from the baseline is maximized, thus filling as much of the scale as possible. The larger the spectrum, the smaller will be the relative error produced by any error when positioning cursors or placing calipers. These simple technical adjustments are crucial, and failure to make them often results in Doppler waveforms that barely deviate from the baseline and in which measurements will be grossly inaccurate (Fig. 1). A spectrum is considered optimal if three to five consecutive similar-appearing waveforms are noted. As some renal processes may be patchy or heterogeneous in their vascular changes, we attempt to study three distinct vessels from each kidney. Both kidneys are always examined even if the renal disease is unilateral.

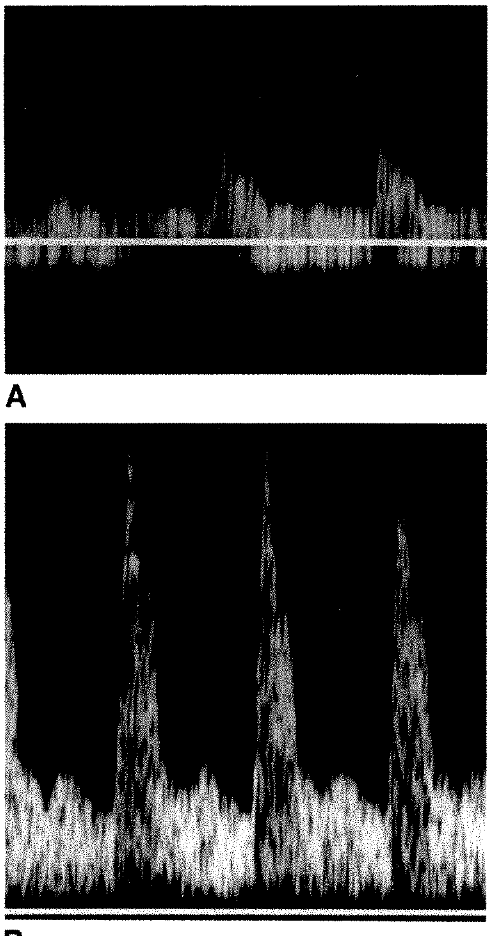

Fig. 1.—Use of appropriate Doppler velocity scale.

A, Intrarenal duplex Doppler spectrum that barely deviates from baseline could erroneously be considered a normal spectrum.

B, Doppler spectrum from same intrarenal location in same patient after properly reducing frequency-shift scale (minimizing pulse-repetition frequency). Now, actual state of elevated arterial resistance is evident in this kidney with an elevated resistive index.

To characterize the intrarenal Doppler waveform, most investigators have used the resistive index (RI). This easily calculated parameter is defined as ([peak systolic shift − minimum diastolic shift]/peak systolic shift). Increases in downstream resistance result in a relative reduction in diastolic flow compared with systolic. Hence, RI can be used as an estimate of the state of renal arterial resistance. Since normality and abnormality are based on RI measurements, it is important to actually measure the RI and not rely on qualitative waveform assessment. The presence of detectable end-diastolic flow is not sufficient to ensure a low-resistance (normal) state. Relying on a purely visual assessment of the Doppler spectrum can lead to misinterpretation of the obtained Doppler waveform. An example of this type of error was recently published (Fig. 4 in [17]).

As with any other Doppler examination, the technique is somewhat operator dependent; however, with a little experience, bilateral renal Doppler examinations are regularly completed in 10–20 min [9, 11]. Renal failure, which commonly limits or contraindicates such studies as excretory urography, contrast-enhanced CT, or scintigraphy, is not a technical limitation to the performance of the duplex Doppler examination [11].

Normal Intrarenal Blood Flow and Resistance

The renal vascular bed in a normal kidney is characterized by low impedance to blood flow resulting in continuous forward flow in diastole [18]. The largest series of normal native kidneys reported to date found a mean RI of 0.58 ± 0.05 in 109 kidneys [8] (Fig. 2). Three other studies of normal native kidneys found mean RI values of 0.64 ± 0.05 (21 patients), 0.58 ± 0.04 (15 patients), and 0.62 ± 0.04 (28 patients) [7, 19, 20].

From these normal data, 0.70 has emerged as a reasonable upper limit for a normal mean intrarenal RI. Defining a normal RI range is difficult because of limitations in the gold standard proof of normal renal status. History alone cannot suffice, as renal dysfunction can exist with minimal or nonspecific findings. A normal creatinine is suggestive but far from an infallible gold standard [21]. As Becker [21] recently reinforced, a 50%

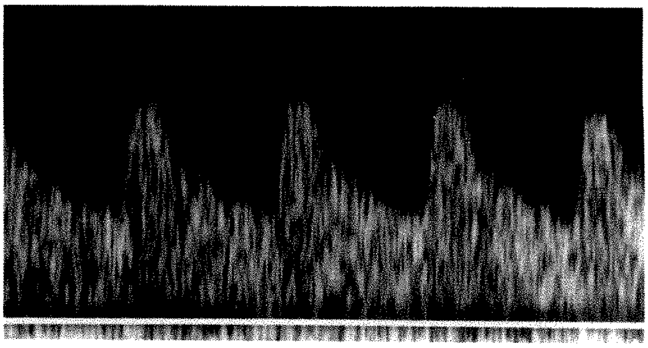

Fig. 2.—Normal intrarenal duplex Doppler spectrum from kidney in a healthy patient. Resistive index is 0.54.

decrease in renal function can occur before serum levels of creatinine will become elevated. Hence, one measurement of creatinine level is certainly not a sensitive test for mild or early renal disease. Therefore, it is possible for patients with elevated renal RIs (≥0.70) and normal creatinine levels to have elevated renal vascular resistance (RVR) as an early sign of renal disease. Defining an upper limit of normal will certainly be difficult if Doppler sonography proves in some instances to be more sensitive than measurement of creatinine levels for detecting early or mild renal diseases.

Conditions other than renal disease also can affect the RI. Significant hypotension, a markedly decreased heart rate, and a perinephric or subcapsular fluid collection can elevate the RI [22, 23]. In addition, children, especially the neonate and infant, can normally have renal RIs that would be elevated by adult standards [24, 25]. Precise definition of when the transition from pediatric to adult RVR takes place remains to be answered. It has also been suggested that aging can alter the RI in "normal" patients; however, this elevation may in fact accurately indicate the true loss of function noted in the senescent kidney, which often is not reflected in an elevated creatinine level [10, 21].

Intrarenal Duplex Doppler Sonography of the Dilated Collection System

Sonography is commonly used as the initial imaging procedure in the evaluation of the patient with possible or suspected renal obstruction [1, 2, 26–29]. Conventional sonography is indeed quite sensitive for diagnosing renal obstruction by detecting dilatation of the collecting system. However, the converse is not true, as pyelocaliectasis identified by sonography is certainly not synonymous with true obstruction [26–29]. This clinically important distinction of true renal obstruction from nonobstructive dilatation cannot in general be resolved by gray-scale sonography, and often requires the use of invasive procedures and tests [29–31]. Recent studies have evaluated the value of intrarenal Doppler in identifying true renal obstruction.

Complete or Nearly Complete Obstruction

To properly understand the observed Doppler changes, one must first look at the extensive laboratory data that exist regarding hemodynamic changes that occur with significant renal obstruction. Most studies have described a triphasic renal vascular and ureteral pressure response to obstruction [32–36].

The initial phase, occurring in the first 1–2 hr after obstruction, is characterized by a transient rise in renal blood flow and prostaglandin-mediated vasodilatation [32–36]. Although this very early stage would rarely be relevant in the clinical setting, one would expect a normal RI immediately after the onset of obstruction.

The second phase begins about 2 hr after obstruction and lasts approximately 3 hr [32–36]. This phase is characterized by elevated postglomerular RVR, decreased renal blood flow, and elevated ureteral pressures. This is the only stage in which RVR and ureteral pressure are both elevating at the same time.

The third phase, beginning after 5 hr of obstruction, is characterized by decreasing and often normalized ureteral pressures at a time when RVR is markedly rising [32–36]. This phase is characterized by an elevation in preglomerular resistance, with ureteral pressure appearing to be less important. In this phase, marked elevation of RVR and hence RI elevation would be expected. Although recently some authors have ascribed the majority of Doppler-observed changes in obstruction to elevated ureteral pressures or back pressure [7, 16, 29], it appears, on the basis of recent laboratory data, that pressure is not the major inducer of Doppler changes. It is also unlikely that nervous system reflexes or pathways are crucial to producing altered RVR, as elevated RIs have been observed in the obstructed denervated renal transplant [37, 38].

Currently, many researchers believe that the RVR changes observed with obstruction may be due to locally acting circulating vasoactive factors and hormones [12, 13, 33, 34, 39–45]. One such promising factor is thromboxane A_2 (TXA_2), a potent renal vasoconstrictor usually not found in the normal kidney. With renal obstruction, a mononuclear cell interstitial infiltrate invades the renal cortex beginning at 4 hr and peaking by 24 hr [34, 41–44]. These infiltrating cells (predominantly macrophages) significantly augment TXA_2 production, leading to marked intrarenal vasoconstriction, elevated RVR, and decreased renal blood flow [34, 41–44]. This is a local effect not observed in the contralateral normal kidney in models of unilateral obstruction [41, 42]. These data have led many to theorize that renal failure and damage due to obstruction may be largely an injury from intense intrarenal vasoconstriction [12, 13, 33, 34, 39–45]. The resultant elevation in RVR should in theory be readily detectable with intrarenal duplex Doppler analysis. Further, as the resistance changes are not dependent on ureteral pressures or pyelocaliectasis alone, purely nonobstructive dilatation should not produce RVR changes similar to true obstruction.

Recently, a few investigators have evaluated the ability of Doppler to detect these renal vascular changes. In an initial report [6], 14 proved obstructed kidneys had an elevated mean RI (0.77 ± 0.04), as compared with seven kidneys with nonobstructive dilatation (mean RI, 0.64 ± 0.04). Subsequently, data were presented from an animal model and a human clinical study, which again demonstrated an elevated RI associated with renal obstruction [7, 46].

In an effort to define a reasonably discriminatory RI value to differentiate obstructive from nonobstructive pyelocaliectasis, we reported the findings from a series of 229 kidneys [8]. Again, the obstructed kidneys had an elevated RI (0.77 ± 0.05), as compared with nonobstructive dilatation (0.63 ± 0.06) and normal kidneys (0.58 ± 0.05) (Fig. 3). On the basis of these data, 0.70 is a reasonable discriminatory level; that is, in a kidney with a dilated collecting system, an RI value of 0.70 or more is suggestive of obstruction, while RI values less than 0.70 are suggestive of nonobstructive dilatation [8]. Use of this discriminatory RI value resulted in a sensitivity

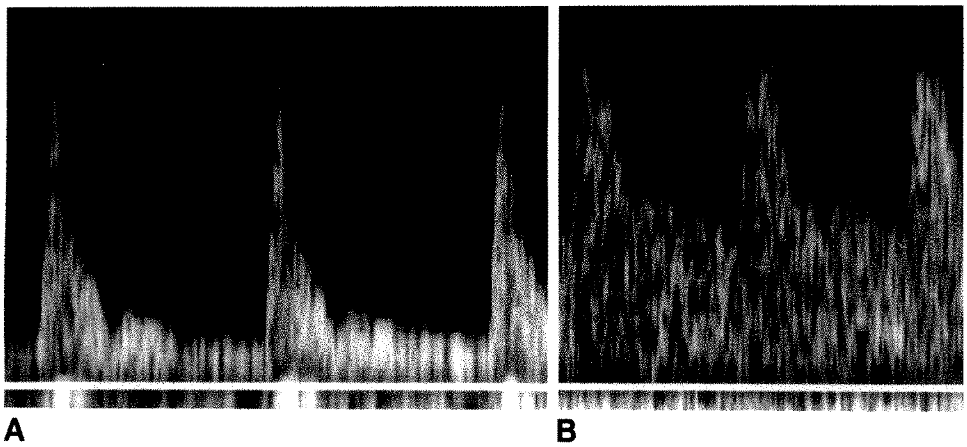

Fig. 3.—Doppler sonography in renal obstruction.

***A*, Intrarenal duplex Doppler spectrum from kidney in a patient with complete ureteral obstruction. Resistive index is elevated, measuring 0.82.**

***B*, Intrarenal duplex Doppler spectrum from contralateral kidney is normal. Resistive index is 0.50.**

of 92%, a specificity of 88%, and an overall accuracy of 90% in the diagnosis of significant obstruction [8]. As discussed later in this article, this single RI value can be even more accurate when it is compared with the RI value from the contralateral kidney.

More recently, Dodd et al. [47] studied a small number of obstructed and nonobstructed kidneys in dogs. The Doppler analysis performed over the course of 4 weeks revealed RI elevation with obstruction, but the sensitivity (74%) and specificity (77%) were lower than observed in previous clinical series [6-8, 47]. No data exist for normal renal RIs in dogs, and it is possible that the normal range in dogs may be more variable or different than in humans. It is therefore interesting to note that one dog with an obstruction and a very low baseline RI and one control dog with an elevated baseline RI together accounted for the majority of the Doppler errors. Without these two dogs the accuracy of this study approaches 90%, similar to reported clinical experience. Many of the potential problems with this dog model could have been minimized by studying the contralateral kidney and comparing the data with those from the obstructed kidney. Of perhaps greater interest, this study demonstrated that 24 hr of obstruction was sufficient time in all the dogs to elevate the RI, implying that obstruction-induced Doppler changes are a timely marker of the intrarenal vascular alterations [47].

Release of Significant Obstruction

Earlier animal data indicate that the duration of obstruction prior to relief is crucial for predicting what types of vascular changes will be observed [35, 41, 48]. In general, if obstruction is relieved within the first two phases (by 5 hr) there should be a rapid return to normal RVR and hence RI [35, 41, 48]. However, if obstruction is present for at least 18–24 hr, the normalization of RVR (RI) may not be immediate and may take days or even weeks to return to baseline levels. This continued elevation in RVR is presumably due to renal vasoconstriction caused by persisting local factors such as TXA_2 [35, 41, 48].

A previous report of 10 obstructed kidneys studied before and after nephrostomy found a significant fall in RI after nephrostomy in nine of 10 patients [6]. The other patient in fact had a blocked nephrostomy tube at the time of the follow-up study [6]. In agreement with the prior animal laboratory data, the decrease in RI was generally observed in 3–7 days and was less commonly observed in the first 36 hr after relief of obstruction.

Partial or Mild Obstruction

What constitutes significant obstruction? This is a common and challenging clinical question [29]. If one is trying to identify obstruction significant enough to cause renal atrophy and nephron loss, the most widely accepted gold standard is the Whitaker test [29–31]. However, if a different criterion for significant obstruction is used, such as sufficient to cause pyelocaliectasis or sufficient to produce any delay in excretion on an excretory urogram, the choice of gold standard will dramatically affect the sensitivity/specificity results for renal Doppler imaging.

As in complete obstruction, knowledge of existing animal renal vascular data occurring with partial obstruction is extremely helpful. Unlike significant obstruction, which appears mediated by vasoconstrictors such as TXA_2, mild partial obstruction is characterized by prostaglandin-mediated vasodilatation [39, 41, 48–50]. In one animal study, mild to moderate partial obstruction sufficient to produce pyelocaliectasis was studied. Ichikawa and Brenner [39] found no elevation in RVR and no renal atrophy despite definite collecting-system dilatation. Other researchers [49, 50] also have found that the presence or degree of pyelocaliectasis does not predict or correlate with renal atrophy and nephron loss. Clearly, the use of pyelocaliectasis as the gold standard for significant partial obstruction is not correct. Similarly, it is possible to observe ureteral narrowing sufficient to produce some delayed excretion on an excretory urogram and get normal findings on the subsequent Whitaker test. Therefore, when evaluating the usefulness of intrarenal Doppler imaging in partial obstruction, it is important to compare the RI with a gold standard that attempts to assess the significance of obstruction, such as the Whitaker test. RVR (RI) should only be elevated in partial obstruction significant enough to result in renal vasoconstriction. Milder degrees of partial obstruction mediated by renal vasodilators produce no elevation in RVR, and a normal RI would be expected.

Partial obstruction highlights the fact that Doppler analysis attempts to provide physiologic rather than anatomic information. Many cases will be observed with minimal or mild areas of ureteric narrowing or kinking with accompanying normal findings on Doppler examinations. The normal RI likely reflects the lack of obstruction of sufficient degree to produce vasoconstriction, elevate RVR, and cause renal atrophy. While a normal RI argues against significant physiologic obstruction, it does not imply that a ureter is free of any mild regions of narrowing or strictures; the renal Doppler examination alone does not suffice if precise anatomic information is required.

Pitfalls in Resistive Index Analysis of Obstruction

A few potential pitfalls in Doppler evaluation of the dilated collecting system are useful to consider. One potential pitfall that generally can be avoided is very acute obstruction. In a prior study we observed two unilateral acutely (<8 hr) obstructed kidneys with RI values less than 0.70 [8]. In both instances the difference in RI between the obstructed and the contralateral normal kidney was 0.10 or more. Therefore, the accuracy of the RI discriminatory value (0.70) can be improved by evaluation of the contralateral kidney, especially in the acute case, in which the RI may not have had sufficient time to reach 0.70. This relative limitation should be a problem only in very acute obstruction, as prior experience in animals and humans indicates an abnormal RI (>0.70) should be observed within 18–24 hr [12, 34, 45, 47].

A theoretical limitation of RI analysis is severe chronic obstruction with marked parenchymal loss. It is possible that the interstitial infiltrate thought to lead to circulating renal vasoconstrictors is lost in these cases with less elevation of RVR (RI). Such cases of end-stage obstruction will generally not be clinically problematic as the presence of obstruction will be well known.

One very important potential limitation in the use of Doppler in the evaluation of obstruction is in imaging children. Recent data strongly suggest that the RI is age dependent in the neonate and infant [24, 25]. Elevated RI values (by adult standards) are commonly observed. Despite this potential limitation, recent reports have documented encouraging results with the use of intrarenal Doppler sonography to assess the dilated collecting system in children [16] (Kessler RM et al., presented at the Society for Pediatric Radiology meeting, April 1990). In a report of 30 dilated collecting systems, Kessler et al. found high sensitivity and specificity in diagnosing obstruction similar to the reported adult experience. A third recent pediatric study, however, found less encouraging results, although in this study more proximal renal vessels were studied (Keller MS et al., presented at the Society of Pediatric Radiology meeting, April 1990). Available animal data suggest the altered renal blood flow with obstruction involves the outer portions (cortex) of the kidney to a greater degree than the medulla, so the vessels interrogated may be an important factor, especially in children [12–15].

One unavoidable limitation of Doppler analysis of possible obstruction is that RI is a nonspecific parameter. Clearly, obstruction is not the only cause of an elevated RI [8–11, 19, 20, 51]. Therefore, in the setting of known renal medical disease (RMD) and pyelocaliectasis, an elevated RI could be due either to true obstruction or to RMD with coexistent nonobstructive dilatation. This potential limitation uncommonly presents a problem clinically, and it is erroneous to assume in advance that Doppler will be useless in the patient with RMD and dilatation. If the dilatation is unilateral, the examiner can study the contralateral nondilated kidney and look for a significant difference in RI (>0.10) to suggest obstruction superimposed on RMD. Further, as will be discussed later in this article, many of these kidneys with RMD have normal RI values. Hence, a normal RI in a patient with known RMD and a dilated collecting system would still be informative, arguing against the presence of significant obstruction. The specific setting where Doppler imaging is truly limited is in the patient with bilateral pyelocaliectasis, known and usually severe RMD, and an elevated RI. Fortunately, in our experience this setting is not common; however, when it occurs the Doppler examination cannot easily discern whether obstruction or the patient's intrinsic RMD is the cause of the RI elevation.

Intrarenal Duplex Doppler Sonography of Nonobstructive Renal Disease

Obstruction is not the only renal pathologic process capable of elevating the RI: various forms of RMD can alter the Doppler waveform [8–11, 19, 20, 51]. However, it is only recently that investigators have explored pathologic factors that may correlate with RI findings to determine if intrarenal duplex Doppler sonography can provide unique diagnostic information in specific clinical settings. This section will review intrarenal Doppler studies of nonobstructive renal disease.

Hypertension and Renal Artery Stenosis

Renal artery stenosis (RAS) is the leading curable cause of hypertension, and several screening techniques have been investigated. Norris et al. [19] and Kohler et al. [52], although reporting an elevated RI in many patients with hypertensive renal disease, suggested that RI changes were not specific for RAS. Desberg et al. [53] dealt in detail with intrarenal Doppler imaging in varying degrees of RAS, and found no statistical trend between RI and increasing percentages of RAS. Therefore, although elevated RIs may be observed in hypertensive renal disease, RI does not appear predictive of the presence or degree of RAS.

Renal Vein Thrombosis

Most Doppler studies of renal vein thrombosis (RVT) have concentrated on identification of flow within the renal vein itself. In some cases, difficulty will be encountered in Doppler examination of the main renal vein, and a secondary sign of RVT would be helpful. Dubbins [18] and Parvey and Eisenberg

[54] recently reported cases of elevated RIs with acute RVT. This agrees with prior experience in renal transplant venous obstruction [55]. Parvey and Eisenberg [54] postulated the elevated RI results from intrarenal edema and venous obstruction. It is, however, interesting to note two separate animal studies of RVT that showed pathologic and renal vascular changes similar to those of obstruction [56, 57]. Histologic examination of the renal cortex revealed a similar mononuclear interstitial infiltrate capable of stimulating TXA_2 synthesis [56, 57]. Although clinical experience is limited, acute RVT can produce marked RI elevation, perhaps through mechanisms similar to those in obstruction.

Resistive Index-Biopsy Correlation in Renal Medical Disease

Some intrinsic renal processes produce marked alterations in the RI while other renal diseases are characterized by more normal RI values. In an attempt to identify specific pathologic features that do or do not affect the RI, two recent studies compared RI values with kidney biopsy results [10, 51]. One study of 41 patients found that kidneys with active disease in the tubulointerstitial and/or vascular compartment of the kidney had elevated mean RI values, while kidneys with disease limited essentially to the glomeruli had normal RIs (0.58 ± 0.05) [51]. From these preliminary data it appears that the site of the disease within the kidney may be an important factor determining the RI value [51].

The observation that glomerulonephritis (GN) generally had a normal RI is consistent with available animal data [58-60]. These data showed that following the first 24-36 hr after onset of experimentally produced GN, the RVR was essentially normal despite often marked disease [58, 59]. In agreement with the normal RVR were findings suggesting that vasodilatatory prostaglandins were crucial in GN, while vasoconstricting TXA_2 was relatively hemodynamically unimportant [58, 59]. However, with long-standing chronic GN there was eventually a fall in renal blood flow and an elevation in RVR [60]. Therefore, as in most other causes of end-stage renal disease, severe chronic GN can eventually produce marked RI elevation.

Subsequently, Mostbeck et al. [10] published a study correlating biopsy findings to RIs in 34 patients. They performed a more detailed study of precise histopathologic changes affecting RI than had previously been reported. They found RI correlated with vascular intrarenal disease, glomerular sclerosis, interstitial edema, and focal interstitial fibrosis. In agreement with the other biopsy series [51], Mostbeck et al. [10] found normal RI values in 67% of patients with GN. However, in the study of Mostbeck et al., duplex Doppler sonography did not seem capable of distinguishing tubulointerstitial from glomerular disease. The somewhat conflicting results in these two biopsy studies may reflect different patient populations (varying types and severities of renal disease and varying degrees of renal dysfunction) undergoing renal biopsy in different institutions. Certainly, neither of these studies suggests that duplex Doppler imaging can replace renal biopsy. It is also likely that studies in which intrarenal Doppler imaging is used as a screening tool for intrinsic renal disease across a heterogeneous patient population will yield disappointing results. However, it is not valid to conclude that renal Doppler sonography has no clinical utility in RMD. Rather, Doppler imaging may have tremendous diagnostic potential when used in the proper clinical setting. To date, the most promising clinical settings have been of two main types: (1) for longitudinal follow-up of patients with renal disease to provide predictive clinical information regarding recovery of renal function and (2) to differentiate two potentially clinically similar renal diseases, one of which alters the RI and another that generally does not. Hemolytic-uremic syndrome (HUS) and acute renal failure (ARF) are respective models of these two uses of Doppler sonography in RMD [9, 11].

Hemolytic-Uremic Syndrome

A recent study by Patriquin et al. [9] highlights the potential predictive ability of renal Doppler imaging. In 17 children with ARF due to HUS, these investigators invariably found elevated RIs. Of more importance they found the RI value improved (decreased) prior to clinical improvement (diuretic phase of HUS). The Doppler predictive information could potentially be used to abbreviate or in some cases cancel unneeded dialysis treatment. The authors suggested the RI elevation was due to a reduction in the arteriolar lumen observed pathologically with HUS. It is also interesting to note that TXA_2 biosynthesis is markedly elevated in acute HUS (similar to other models of RI elevation such as obstruction, RVT, and acute tubular necrosis [ATN]), falling to normal with recovery [61]. As it is known that in rats recovery from ARF is presaged by an increase in renal blood flow and a fall in RVR, it is not surprising to observe RI changes before clinical improvement [62]. It is certainly possible that Doppler monitoring will be shown to have predictive value in other forms of renal failure.

Acute Renal Failure

Sonography is commonly used early in the evaluation of patients with ARF [3-5]. Generally, the role of sonography is to exclude renal obstruction, but in clinical practice, obstruction is a rare cause of ARF [1-5]. Therefore, the vast majority of gray-scale examinations in these patients are normal [5]. A recent study investigated the use of intrarenal duplex Doppler sonography in the evaluation of ARF [11]. Elevation of the RI, seen in 69% of the ARF patients examined, was certainly much more common than abnormality on the gray-scale portion of the examination [11]. More importantly, the RI helped to differentiate the two most common forms of ARF, ATN and acute prerenal failure [11]. Distinguishing between these two leading causes of ARF can be clinically difficult, especially at initial presentation, yet it is important in terms of patient management and outcome [63]. Patients with ATN had a markedly elevated renal RI (mean, 0.85) as compared with patients with acute prerenal azotemia (mean, 0.67) [11] (Fig. 4). These data indicated 0.75 to be a reasonable discriminator between these two entities: 91% of ATN patients had mean RI values at or exceeding this level, while only 20% of the prerenal group did [11].

Although ATN encompasses many diverse disease processes, consistent features of this group are the profound hemodynamic changes. Early in the course of ATN there is a marked reduction in renal blood flow and elevation of RVR [35, 63-65]. Previous reports [35, 63-65] have noted sustained afferent arterial vasoconstriction in ATN similar to that in obstruction.

A few potential pitfalls to Doppler analysis of ARF need to be addressed. First, it is important to study both kidneys and more than one site in each, because early in the ATN process the vascular alterations can be patchy [15]. We have occasionally noted a single normal Doppler spectrum in early ATN among a group of abnormal spectra. Another potential cause for a normal RI with ATN is the phase of disease that is present. If the examination is performed in the resolution phase, a more normal waveform is observed; hence, early study of the ARF patient is recommended. It also should be pointed out that this study examined acute prerenal failure; in contrast, chronic prerenal failure appears capable of elevating the RI [11].

Resistive Index and Renal Function (Creatinine) Correlation

A very important aspect of Doppler evaluation of the kidneys is the relationship between RI and renal function as measured by creatinine level. Although degree of renal dysfunction has some effect on RI, they are not equivalent parameters.

Two biopsy correlative studies and a study of ARF patients found only a weakly positive correlation between creatinine level and RI [10, 11, 51]. However, the goal of RI determination is not to replace measurement of creatinine levels but instead to provide information on renal status that is not reflected purely by the creatinine level. For example, in the previously mentioned ARF study, 17 patients with ATN induced by nephrotoxic drugs had a mean creatinine level slightly lower than that in 30 patients with acute prerenal failure [11]. Despite these nearly identical creatinine levels, the ATN group had a statistically significantly higher RI (0.80 vs 0.67, $p < 0.01$) [11]. This illustrates that RI provides information regarding renal status not reflected by creatinine levels; optimal clinical use of this information requires an understanding of the different pathophysiologic processes affecting creatinine level and RVR.

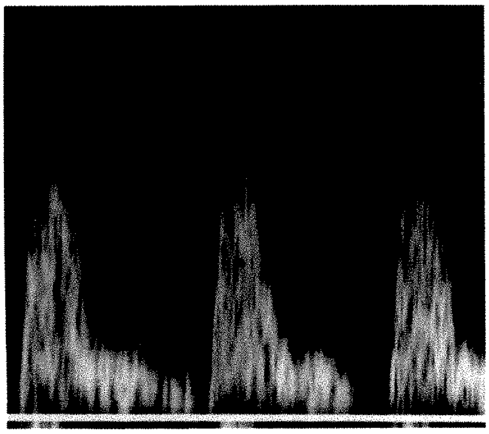

Fig. 4.—Intrarenal duplex Doppler spectrum from a kidney in a patient studied early in the course of acute tubular necrosis. Resistive index is markedly elevated, measuring almost 0.90.

Conclusions

This article has reviewed the duplex Doppler findings in normal, obstructed, and medically diseased kidneys reported to date, and the pathophysiologic basis for these findings. We conclude that intrarenal duplex Doppler sonography can provide physiologic information reflecting RVR status by means of an easily obtained and calculated parameter (RI). The Doppler examination must be performed properly to obtain useful data, with the most critical and common errors being a failure to use the full Doppler scale, minimize the wall filter, and study both kidneys.

REFERENCES

1. Stuck KJ, White GM, Granke DS, Ellis JH, Weissfeld JL. Urinary obstruction in azotemic patients: detection by sonography. *AJR* **1987**;149:1191-1193
2. Denton T, Cochlin DL, Evans C. The role of ultrasound in previously undiagnosed renal failure. *Br J Radiol* **1984**;57:673-675
3. Green D, Carroll BA. Ultrasound of renal failure. In: Hricak H, ed. *Genitourinary ultrasound: clinics in diagnostic ultrasound*, vol. 18. New York: Churchill Livingstone, **1986**:55-58
4. Hricak H. Renal medical disorders: the role of sonography. In: Sanders RC, ed. *Ultrasound annual*. New York: Raven, **1982**:43-80
5. Mittelstaedt CA. *Abdominal ultrasound*. New York: Churchill Livingstone, **1987**:286-288
6. Platt JF, Rubin JM, Ellis JH, DiPietro MA. Duplex Doppler ultrasound of the kidney: differentiation of obstructive from non-obstructive dilatation. *Radiology* **1989**;171:515-517
7. Gottlieb RH, Luhmann K, Oates RP. Duplex ultrasound evaluation of normal native kidneys and native kidneys with urinary tract obstruction. *J Ultrasound Med* **1989**;8:609-611
8. Platt JF, Rubin JM, Ellis JH. Distinction between obstructive and nonobstructive pyelocaliectasis with duplex Doppler sonography. *AJR* **1989**;153:997-1000
9. Patriquin HB, O'Regan S, Robitaille P, Paltiel H. Hemolytic-uremic syndrome: intrarenal arterial Doppler patterns as a useful guide to therapy. *Radiology* **1989**;172:625-628
10. Mostbeck GH, Kain R, Mallek R, et al. Duplex Doppler sonography in renal parenchymal disease. *J Ultrasound Med* **1991**;10:189-194
11. Platt JF, Rubin JM, Ellis JH. Acute renal failure: possible role of duplex Doppler ultrasound in distinction between acute prerenal failure and acute tubular necrosis. *Radiology* **1991**;179:419-423
12. Yarger WE, Schocken DD, Harris RH. Obstructive nephropathy in the rat. *J Clin Invest* **1980**;65:400-412
13. Klahr S. Pathophysiology of obstructive nephropathy: a 1991 update. *Semin Nephrol* **1991**;11:156-168
14. Siegel NJ, Feldwan RA, Cytton D, et al. Renal cortical blood flow distribution in obstructive nephropathy in rats. *Circ Res* **1977**;40:379-386
15. Brezis M, Rosen S, Epstein FH. Acute renal failure. In: Brenner BM, Rector FC, eds. *The kidney*, 3rd ed. Philadelphia: Saunders, **1986**:735-799
16. Patriquin H. Doppler examination of the kidney in infants and children. *Urol Radiol* **1991**;12:220-227
17. Pozniak MA, Kelcz F, Dodd GD. Renal transplant ultrasound: imaging and Doppler. *Semin Ultrasound CT MR* **1991**;12:319-334
18. Dubbins PA. Doppler ultrasound in renal disease. *Curr Imaging* **1989**;1:32-38
19. Norris CS, Pfeiffer JS, Rittgers SE, Barnes RW. Noninvasive evaluation of

renal artery stenosis and renovascular resistance. *J Vasc Surg* **1984**;1:192-201

20. Kim SH, Kim WH, Choi BI, Kim CW. Duplex sonography of the native kidney—resistive index vs serum creatinine. *J Ultrasound Med* **1990**;9:S25
21. Becker JA. Evaluation of renal function. *Radiology* **1991**;179:337-338
22. Pozniak MA, Kelcz F, Stratta RJ, Oberley TD. Extraneous factors affecting resistive index. *Invest Radiol* **1988**;23:899-904
23. Mostbeck GH, Gossinger HD, Mallek R, Siostrzonek P, Schneider B, Tscholakoff D. Effect of heart rate on Doppler measurements of resistive index in renal arteries. *Radiology* **1990**;175:511-513
24. Keller MS. Renal Doppler sonography in infants and children. *Radiology* **1989**;172:603-604
25. Wong SN, Lo RNS, Yu ECL. Renal blood flow pattern by noninvasive Doppler ultrasound in normal children and acute renal failure patients. *J Ultrasound Med* **1989**;8:135-141
26. Ellenbogen PH, Scheible W, Talner LB, et al. Sensitivity of gray-scale ultrasound in detecting urinary tract obstruction. *AJR* **1978**;130:731-733
27. Dalla-Palma L, Bazzocchi M, Pozzi-Mucelli RS, et al. Ultrasonography in the diagnosis of hydronephrosis in patients with normal renal function. *Urol Radiol* **1983**;5:221-226
28. Amis ES, Cronan JJ, Pfister RC, Yoder IC. Ultrasonic inaccuracies in diagnosing renal obstruction. *Urology* **1982**;19:101-105
29. Cronan JJ. Contemporary concepts in imaging urinary tract obstruction. *Radiol Clin North Am* **1991**;29:527-542
30. Jaffe RB, Middleton AW. Whitaker test: differentiation of obstructive from nonobstructive uropathy. *AJR* **1980**;134:9-15
31. Ryan PC, Maher K, Hurley GD, Fitzpatrick JM. The Whitaker test: experimental analysis in a canine model of partial ureteric obstruction. *J Urol* **1989**;141:387-390
32. Ryan PC, Maher KP, Murphy B, et al. Experimental partial ureteric obstruction: pathophysiological changes in upper tract pressure and renal blood flow. *J Urol* **1987**;138:674-678
33. Murphy GP, Scott WW. The renal hemodynamic response to acute and chronic ureteral obstruction. *J Urol* **1966**;95:636-657
34. Moody TE, Vaughan ED, Gillenwater JY. Relationship between renal blood flow and ureteral pressure during 18 hours of total unilateral ureteral occlusions. *Invest Urol* **1975**;13:246-251
35. Badr KF, Brenner BM. Renal circulatory and nephron function in experimental obstruction of the urinary tract. In: Brenner BM, Lazarus JM, eds. *Acute renal failure.* New York: Churchill Livingstone, **1988**:91-118
36. Klahr S, Buerkert J, Morrision A. Urinary tract obstruction. In: Brenner BM, Rector FC, eds. *The kidney*, 3rd ed. Philadelphia: Saunders, **1986**:1449-1482
37. Platt JF, Ellis JH, Rubin JM. Role of duplex Doppler in the evaluation of the renal transplant with pyelocaliectasis. *Radiology* **1991**;179:425-428
38. Don S, Kopecky KK, Filo RS, et al. Duplex Doppler US of renal allografts: causes of elevated resistive index. *Radiology* **1989**;171:709-712
39. Ichikawa I, Brenner BM. Local intrarenal vasoconstrictor-vasodilator interactions in mild partial ureteral obstruction. *Am J Physiol* **1979**;236:F131-140
40. Fitzgerald GA, Murray R, Price P, Catella F. The molecular, biochemical and human pharmacology of thromboxane A_2 in renal disease. *Adv Exp Med Biol* **1989**;259:325-360
41. Wilson DR. Pathophysiology of obstructive nephropathy. *Kidney Int* **1980**;18:281-292
42. Albrightson CR, Evers AS, Griffin AC, Needleman P. Effect of endogenously produced leukotrienes and thromboxane on renal vascular resistance in rabbit hydronephrosis. *Circ Res* **1987**;61:514-522
43. Kawasaki A, Needleman P. Contribution of thromboxane to renal resistance changes in the isolated perfused hydronephrotic rabbit kidney. *Circ Res* **1982**;50:486-490
44. Rovin BH, Harris KPG, Morrison A, Klahr S, Schreiner GF. Renal cortical release of a specific macrophage chemoattractant in response to ureteral obstruction. *Lab Invest* **1990**;63:213-220
45. Yarger WE, Griffith LD. Intrarenal hemodynamics following chronic unilateral ureteral obstruction in the dog. *Am J Physiol* **1974**;227:816-826
46. Taylor KJW, Marks W, Vasseur B, Ramos I, Feyock A. A porcine model to investigate causes for increase in renal vascular impedance. *J Ultrasound Med* **1988**;7:S63
47. Dodd GD, Kaufman PN, Bracken RB. Duplex Doppler evaluation of urinary obstruction in dogs. *J Urol* **1991**;145:644-646
48. Leahy AL, Ryan PC, Mcentee GM, Nelson AC, Fitzpatrick JM. Renal injury and recovery in partial ureteric obstruction. *J Urol* **1989**;142:199-203
49. Gonnermann D, Huland H, Schweiker U, Oesterreich FU. Hydronephrotic atrophy after stable mild or severe partial ureteral obstruction: natural history and recovery after relief of obstruction. *J Urol* **1990**;143:199-203
50. Olesen S, Madsen PD. Renal function during experimental hydronephrosis: function during partial obstruction following contralateral nephrectomy in the dog. *J Urol* **1968**;99:692-701
51. Platt JF, Ellis JH, Rubin JM, DiPietro MA, Sedman AB. Intrarenal arterial Doppler sonography in patients with nonobstructive renal disease: correlation of resistive index with biopsy findings. *AJR* **1990**;154:1223-1227
52. Kohler TR, Zierler RE, Martin RL, et al. Noninvasive diagnosis of renal artery stenosis by ultrasonic duplex scanning. *J Vasc Surg* **1986**;4:450-456
53. Desberg AL, Paushter DM, Lammert GK, et al. Renal artery stenosis: evaluation with color Doppler flow imaging. *Radiology* **1990**;177:749-753
54. Parvey HR, Eisenberg RL. Image-directed Doppler sonography of the intrarenal arteries in acute renal vein thrombosis. *JCU* **1990**;18:512-516
55. Reuther G, Wanjura D, Bauer H. Acute renal vein thrombosis in renal allografts: detection with duplex Doppler ultrasound. *Radiology* **1989**;170:557-558
56. Schwartz D, DeSchryver-Kecskemeti K, Needleman P. Renal arachidonic acid metabolism and cellular changes in the rabbit renal vein constricted kidney: inflammation as a common process in renal injury models. *Prostaglandins* **1984**;27:605-613
57. Zipser R, Myers S, Needleman P. Exaggerated prostaglandin and thromboxane synthesis in the rabbit with renal vein constriction. *Circ Res* **1980**;47:231-237
58. Lianos EA, Andres GA, Dunn MJ. Glomerular prostaglandin and thromboxane synthesis in rat nephrotoxic serum nephritis. *J Clin Invest* **1983**;72:1439-1448
59. Stork JE, Dunn MJ. Hemodynamic roles of thromboxane A_2 and prostaglandin E_2 in glomerulonephritis. *J Pharmacol Exp Ther* **1985**;233:672-678
60. Iversen BM, Ofstad J. Loss of renal blood autoregulation in chronic glomerulonephritic rats. *Am J Physiol* **1988**;254:284-290
61. Tonshoff B, Momper R, Kuhl PG, Schweer H, Scharer K, Seyberth HW. Increased thromboxane biosynthesis in childhood hemolytic uremic syndrome. *Kidney Int* **1990**;37:1134-1141
62. Myers BD, Moran SM. Hemodynamically mediated acute renal failure. *N Engl J Med* **1986**;314:97-105
63. Rose BD. Acute renal failure—prerenal disease versus ATN. In: Rose BD, ed. *Pathophysiology of renal disease*, 2nd ed. New York: McGraw-Hill, **1987**:63-117
64. Sweny P. Acute renal failure. In: Sweny P, Farrington K, Moorhead JF, eds. *The kidney and its disorders.* London: Blackwell Scientific, **1989**:316-347
65. Andreucci VE. Clinical diagnosis of acute renal failure. In: Andreucci VE, ed. *Acute renal failure.* Boston: Martinus Nijhoff, **1984**:189-200

MR Imaging in the Evaluation of Benign Uterine Masses: Value of Gadopentetate Dimeglumine–Enhanced T1-Weighted Images

Hedvig Hricak[1]
Saul Finck[1,2]
Gordon Honda[3]
Håkan Göranson[4]

Forty-six patients with surgically proved disease (115 leiomyomas, 19 cases of adenomyosis, and 14 endometrial polyps) were studied to determine if gadopentetate dimeglumine–enhanced T1-weighted MR images improve the detection and characterization of benign tumors of the uterus. Lesion detection and characterization were assessed separately for each sequence (unenhanced T1-weighted, proton-density–weighted, and T2-weighted and contrast-enhanced T1-weighted images) and for combinations of sequences (unenhanced T1- and T2-weighted images, unenhanced and contrast-enhanced T1-weighted images, and unenhanced T1- and T2-weighted and contrast-enhanced T1-weighted images). In the evaluation of leiomyomas, analysis of all three sequences provided the best detection (92%) and characterization (92%), but the improvement, except when compared with unenhanced T1-weighted images alone, was not statistically significant. The use of contrast medium did not contribute to either tumor detection or characterization. In the evaluation of adenomyosis, T2-weighted images provided significantly better lesion detection and characterization than did either unenhanced or contrast-enhanced T1-weighted images. In the evaluation of endometrial polyps, however, contrast-enhanced T1-weighted images provided significantly better lesion detection and characterization than did unenhanced images. With contrast-enhanced images, the detection rate was 79%, compared with 36% for T2-weighted images and 7% for T1-weighted images. Lesion characterization was the best (73%) when all imaging sequences were analyzed.

Our study shows that with conventional spin-echo sequences, the use of contrast-enhanced T1-weighted images does not improve the detection or characterization of uterine leiomyomas or adenomyosis but significantly improves the detection of endometrial polyps.

***AJR* 158:1043–1050, May 1992**

Leiomyomas, adenomyosis, and endometrial polyps are the three most common benign neoplasms of the uterus [1, 2]. Accurate diagnosis of these lesions facilitates the choice of therapy and assists in the design of the surgical approach. Sonography is considered an extension of the physical examination and is used as the primary imaging technique for the evaluation of benign uterine disease [3, 4]. Only when the results of sonography are inconclusive or technically limited is MR warranted [5–8]. MR imaging has been shown to be superior to sonography [5–8] or hysterosalpingography [5] for the evaluation of uterine leiomyomas and currently is the preferred technique for the diagnosis of adenomyosis [9–11]. Before the advent of MR imaging, surgical specimens were almost always needed to make a diagnosis of adenomyosis [11]. Diagnosis of endometrial polyps is mostly based on clinical findings; hysteroscopy is the most sensitive (100%) and specific (96%) procedure [12]. Transvaginal sonography is sensitive, but the findings are not specific for the diagnosis of endometrial polyps [12]. Unenhanced MR imaging is not appropriate for the detection or characterization of endometrial polyps.

Although MR is considered valuable in the diagnosis of benign uterine masses, unenhanced MR imaging has some limitations: (1) small leiomyomas cannot be

Received April 15, 1991; accepted after revision January 2, 1992.

[1] Department of Radiology, University of California, San Francisco, 505 Parnassus St., Box 0628, San Francisco, CA 94143-0628. Address reprint requests to H. Hricak.

[2] Present address: Department of Radiology, Long Beach Memorial Medical Center, Long Beach, CA 90801.

[3] Department of Pathology, University of California, San Francisco, San Francisco, CA 94143.

[4] Department of Radiology, Karolinska Institute, Stockholm, Sweden.

0361–803X/92/1585–1043
© American Roentgen Ray Society

consistently distinguished from adenomyomas, (2) endometrial polyps are often not seen, and (3) image quality can be degraded by motion because of the long time required for examination. (Currently, T2-weighted images in two planes are usually obtained for the evaluation of the uterus.)

The purpose of this study was to determine the role of gadopentetate dimeglumine–enhanced T1-weighted MR imaging in the detection and characterization of benign tumors of the uterus.

Materials and Methods

The study group consisted of 46 women 27–74 years old (average, 46 years) with surgically proved benign uterine masses. The patient list was generated from a computer data base that included female patients with a surgical-pathologic diagnosis of benign uterine tumors and a pelvic MR study that included unenhanced T1-weighted, proton-density-weighted, and T2-weighted images and contrast-enhanced T1-weighted images. The interval between an MR study and surgery did not exceed 60 days. The computer-generated list included patients imaged between November 1, 1989, and September 1, 1991. In reviews of MR requests, indications for pelvic MR included diagnosis of leiomyomas based on clinical or sonographic findings (patients sent for MR study before myomectomy) ($n = 8$), limited differentiation between uterine and adnexal lesions on sonography ($n = 11$), and evaluation of gynecologic neoplasm before surgery ($n = 21$). MR images were obtained with a 1.5-T superconducting magnet (Signa, General Electric, Milwaukee, WI). In order to minimize artifacts caused by bowel motion, each patient received 1 mg of glucagon (single dose, intramuscular injection) before the MR injection. Images were acquired by using a body coil. For unenhanced spin-echo (SE) imaging, parameters were 550–700/20 (TR/TE) for T1-weighted sequences, 2000/30 for proton-density-weighted sequences, and 2000/60 for T2-weighted sequences. Sagittal and transverse T2-weighted images and transverse T1-weighted images were obtained in each patient. Contrast-enhanced T1-weighted transverse ($n = 42$) or sagittal ($n = 30$) images were obtained immediately after administration of an IV bolus of gadopentetate dimeglumine (0.1 mmol/kg) (Magnevist, Berlex Laboratories, Wayne, NJ). Both transverse and sagittal images were acquired in 26 patients. For T2-weighted sequences, 5-mm slices with a 20% gap were used. For T1-weighted sequences, both 5- ($n = 36$) and 10- ($n = 10$) mm slices with a 20% gap were used. Two excitations were used, and the matrix size was 256 × 192. These two parameters were held constant; the field of view was 34–40 cm.

The MR images were interpreted in conference by two radiologists without knowledge of the surgical findings. The images were analyzed for both lesion detection and lesion characterization. Previously published MR criteria [5–15] were used, and each lesion was assigned a diagnosis of leiomyoma, adenomyosis, or endometrial polyp. Detection and characterization were recorded for each sequence separately. In addition, the series, including combinations of unenhanced T1- and T2-weighted images, unenhanced and contrast-enhanced T1-weighted images, and unenhanced T1- and T2-weighted images plus contrast-enhanced T1-weighted images, were ranked independently. On the contrast-enhanced images, also recorded was the visual assessment of lesion enhancement as compared with adjacent myometrium (signal intensity lower than, equal to, or higher than that of adjacent myometrium), heterogeneity or homogeneity of lesion enhancement, lesion margin (sharp or indistinct), and presence of peritumoral enhancement. In addition, tumor features shown on contrast-enhanced T1-weighted images were compared with those seen on unenhanced T2-weighted images.

Pathologic findings were collected separately by one of the authors, who reviewed the official pathologic reports and reanalyzed the histologic slides for tumor vascularity, hyaline degeneration, cellularity, fibrosis, cystic degeneration, necrosis, atrophy, and calcium. Each pathologic finding was subjectively scored on a scale of 0–3.

The collected MR and pathologic data were compared in conference. A table of the MR-pathologic correlations on lesion detection and characterization was constructed, and the chi-square test was used to analyze the differences in each sequence separately, in combined sequences, and in each single sequence with the combined sequence. If significant differences were found, Marascuilo's method of multiple comparisons was performed at the $\delta = .05$ level of significance [16].

Results

Surgical Findings

Histologic diagnoses were made on the basis of specimens obtained at hysterectomy ($n = 31$) or myomectomy ($n = 15$). A total of 115 leiomyomas were diagnosed in 35 patients. Fourteen patients had solitary leiomyomas, three patients had two leiomyomas each, and 18 had three to 15 tumors. The lesions ranged in size from 0.5 to 20 cm. Only leiomyomas greater than 0.5 cm in diameter were numerically recorded on the pathologic report. Adenomyosis was diagnosed in 16 patients. Diffuse disease was found in seven patients and focal disease in six patients. Two patients had two focal adenomyomas, and one patient had both diffuse and focal disease. The presence of microscopic foci of adenomyosis was not included in the comparative analysis. Fourteen endometrial polyps were found in nine patients. Five patients had solitary polyps, three had two polyps, and one had three polyps. Concomitant leiomyoma and diffuse adenomyosis were present in nine patients, leiomyoma and endometrial polyps were found in four patients, and both an endometrial polyp and diffuse adenomyosis were found in one patient. Leiomyoma, adenomyosis, and endometrial polyp were present in one patient.

MR Findings

Leiomyoma.—Detection and characterization of uterine leiomyomas on MR for each imaging sequence and combination is shown in Table 1.

Analysis of T1-weighted images alone revealed significantly inferior tumor detection (57%) and characterization (48%) when compared with the other single sequences or with combinations of sequences. On unenhanced T1-weighted images, detection of uterine leiomyomas was based on a lobular or irregular uterine contour in 31% (36 of 115 lesions), an enlarged uterus in 24% (28 of 115 lesions), a low-signal-intensity focus indicative of calcification ($n = 4$) or a low-signal intensity rim ($n = 5$) in 8% (nine of 115 lesions), and a localized, irregular high-signal-intensity area in 2% (two of 115 lesions). More than one MR finding was present in nine lesions. Among the 66 lesions detected, only 32 (48%) were correctly characterized as leiomyoma on unenhanced T1-weighted images. The diagnosis of leiomyoma was based on demonstration of a lobulated contour in 72% of cases, on detection of a focal

TABLE 1: MR-Pathologic Correlation of 115 Leiomyomas

Imaging Sequence(s)	No. (%)	
	Detected	Characterized
Unenhanced T1 weighted[a]	66 (57)	32 (48)
Proton-density weighted	97 (84)	87 (90)
T2 weighted	99 (86)	89 (90)
Enhanced T1 weighted	96 (83)	79 (82)
Unenhanced T1 and T2 weighted	102 (89)	93 (91)
Unenhanced and enhanced T1 weighted	99 (86)	84 (85)
Unenhanced T1 and T2 weighted, enhanced T1 weighted	106 (92)	98 (92)

Note.—The numbers of lesions characterized were derived from the totals of those detected by each sequence or combination of sequences.

[a] On unenhanced T1-weighted images, lesion detection and characterization were significantly ($p < .05$) different from the other sequences.

low-signal-intensity area (thought to represent calcification) in 6% of cases (two lesions), on detection of lobular contour and low-signal-intensity foci in 6% of cases, on detection of a curvilinear low-signal-intensity rim (thought to represent peritumoral vessels) in 3% of cases (one lesion), and on detection of lobular contour and a curvilinear low-signal-intensity rim in 12% (four cases).

No significant difference in the detection or characterization of uterine leiomyoma was observed when either proton-density-weighted, T2-weighted, or contrast-enhanced T1-weighted images were analyzed. In each sequence, detection and characterization of tumor relied on direct visualization of tumor and/or the lobular appearance of the uterine contour (Fig. 1). Lesions not seen on contrast-enhanced T1-weighted images but seen on T2-weighted images were all intramural leiomyomas ranging in size from 1 to 3 cm and having contrast enhancement similar to that of adjacent myometrium.

Detection and characterization of lesions were improved when combined sequences were reviewed, with the best lesion evaluation obtained (detection, 92%; characterization, 92%) when all three sequences were used. The addition of contrast-enhanced T1-weighted imaging to unenhanced T1- and T2-weighted sequences improved evaluation of three submucosal and one intramural leiomyomas. The improvement, however, did not reach a significant level. Nine lesions (all greater than 0.5 cm in size) were not detected on any of the imaging sequences. These included one 9-cm cervical leiomyoma, one 6-cm leiomyoma that was incorrectly diagnosed as being part of another lesion, one pedunculated calcified leiomyoma that was mistaken for a bowel loop, and six 0.5- to 2-cm intramural leiomyomas. In eight tumors, leiomyoma could not be distinguished from adenomyoma because the tumor margin was indistinct in five, numerous high-signal-intensity foci were present in two, and both indistinct margin and high-signal-intensity foci were present in one. Lesion size varied from 2 to 4 cm.

On contrast-enhanced T1-weighted images, 65% of leiomyomas had a signal intensity lower than that of adjacent myometrium (Fig. 1), 23% had a signal intensity similar to that of the adjacent myometrium (Fig. 1), and 12% had a signal intensity predominately higher than that of adjacent myometrium (Fig. 2). Signal intensity was homogeneous in 24% and heterogeneous in 76% of leiomyomas (Fig. 3). The edge or margin of the lesions was sharp in 67% of cases and poorly defined in 33% (Fig. 1). Partial (Fig. 1) or complete (Fig. 4) rim enhancement was seen in 11% of lesions. A low-signal-intensity curvilinear rim was seen in 4% of lesions.

When the appearance of leiomyoma on T2-weighted images was compared with that on contrast-enhanced T1-weighted images, it was found that tumors that demonstrated low signal intensity on T2-weighted images had either homogeneous low signal intensity (28%) or various degrees of heterogeneous medium to high signal intensity (72%) on contrast-enhanced images (Figs. 1 and 3). All the leiomyomas that were of high signal intensity on T2-weighted images had varied signal enhancement (similar to or higher than that of adjacent myometrium) on contrast-enhanced images (Fig. 2).

Correlation with histologic findings showed that tumor enhancement was associated primarily with the degree of tumor vascularity. All leiomyomas with a pathologic grade of vascularity of 2 or greater showed enhancement. Hyaline degeneration with various amounts of replacement of muscle fibers by amorphous ground substance (and occasionally collagen) was found in tumors that had a characteristic cobblestonelike

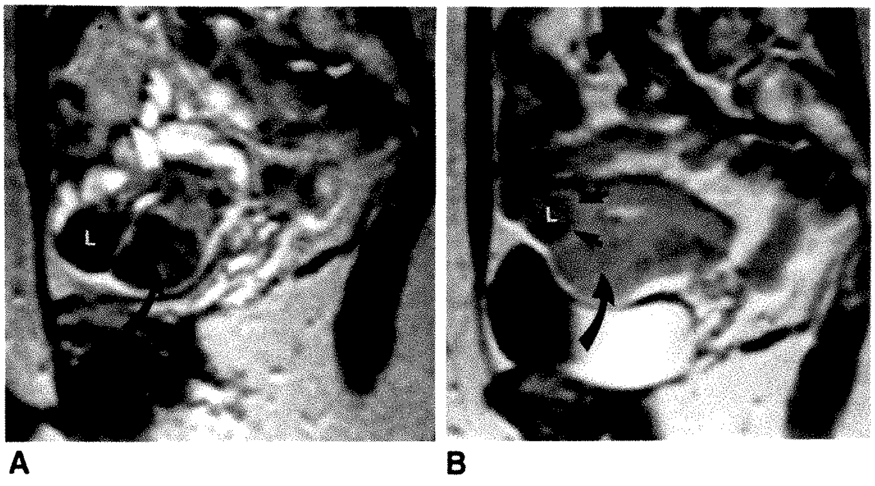

Fig. 1.—Intramural leiomyomas.

A and B, Sagittal T2-weighted (SE 2000/60) (A) and contrast-enhanced T1-weighted (SE 700/20) (B) MR images. Leiomyoma in uterine fundus (L) demonstrates homogeneous low signal intensity on T2-weighted and contrast-enhanced T1-weighted images. Peripheral rim enhancement (*straight arrows*) is seen. A second leiomyoma (*curved arrows*) shows heterogeneous but predominantly low signal intensity on T2-weighted image, but on contrast-enhanced image it shows enhancement similar to that of adjacent myometrium; lesion conspicuity is impaired on contrast-enhanced image.

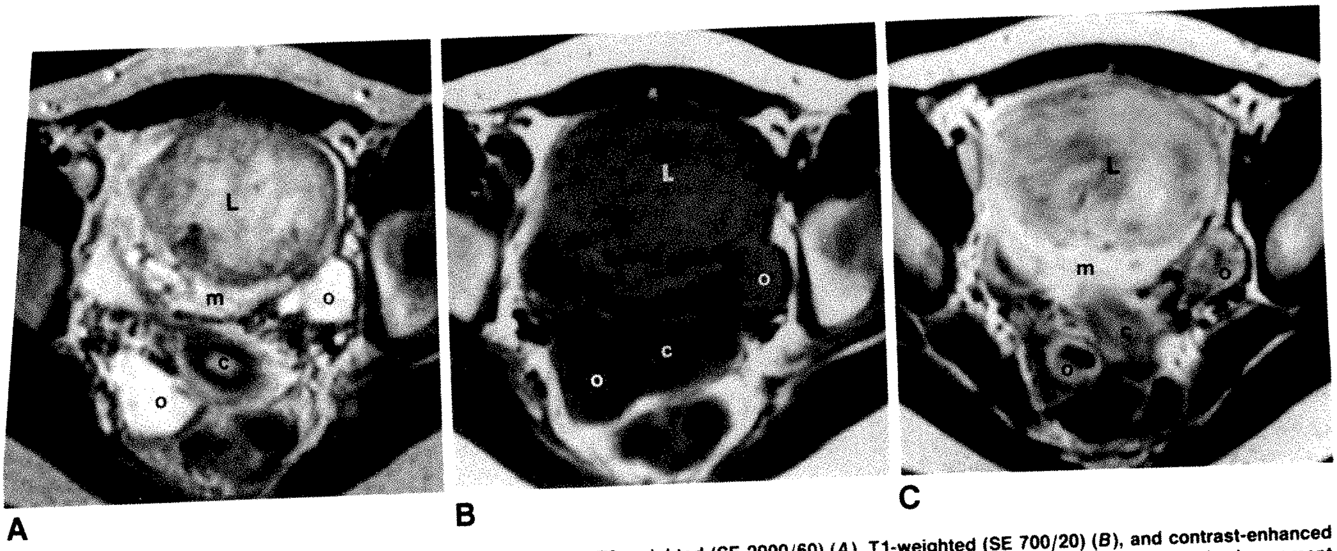

Fig. 2.—*A–C*, Large intramural degenerative leiomyoma seen on T2-weighted (SE 2000/60) (*A*), T1-weighted (SE 700/20) (*B*), and contrast-enhanced T1-weighted (SE 700/20) (*C*) MR images. Leiomyoma (L) shows heterogeneous high signal intensity on T2-weighted image and shows marked enhancement on contrast-enhanced image. m = myometrium, c = cervix, o = ovaries.

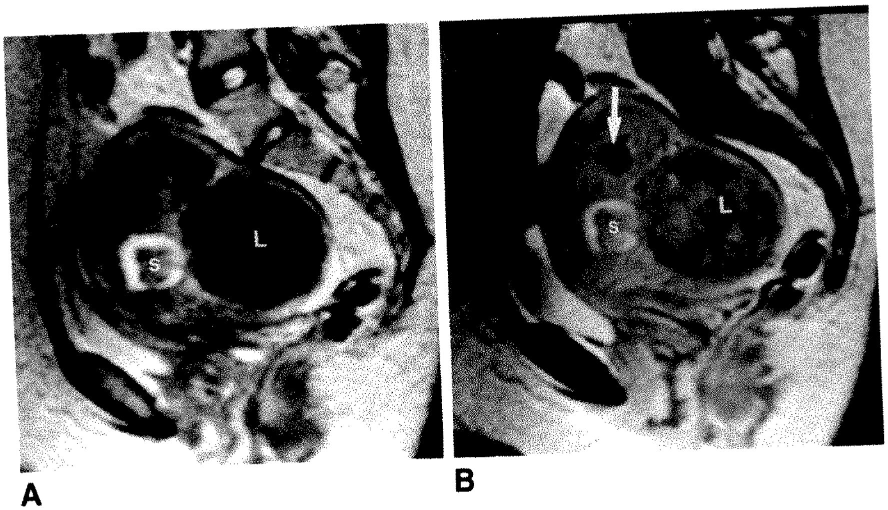

Fig. 3.—*A* and *B*, Intramural and submucosal leiomyomas seen on sagittal T2-weighted (SE 2000/60) (*A*) and contrast-enhanced T1-weighted (SE 600/20) (*B*) MR images. Two intramural leiomyomas show similar low signal intensity on T2-weighted image. On contrast-enhanced image, however, leiomyoma in posterior uterus (L) shows heterogeneous signal enhancement. Hyaline degeneration was present at histology. Fundal leiomyoma shows central area of cystic degeneration (*arrow*) not appreciated on unenhanced scan. Remainder of tumor blends with adjacent myometrium. Submucosal leiomyoma (S) is on a slender stalk.

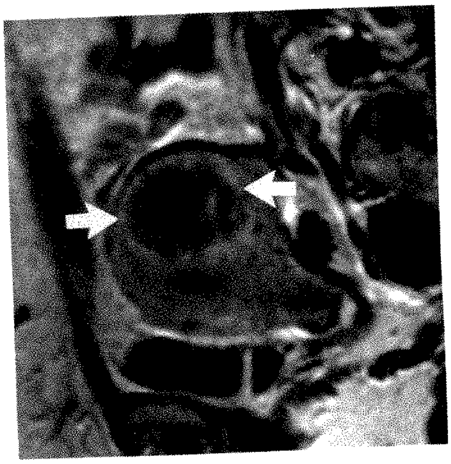

Fig. 4.—Leiomyoma with rim enhancement. Sagittal contrast-enhanced T1-weighted (SE 700/20) MR image shows rim enhancement (*arrows*) of large intramural leiomyoma.

appearance. Peritumoral rim enhancement correlated with peripheral edema in seven patients and with edema and dilated veins in four patients. When a curvilinear low-signal-intensity rim was seen, it correlated with calcium in two patients and with dilated veins in the others. On pathologic examination, focal calcifications were present in 7% of tumors detected on MR. On MR images, some of the calcifications showed low signal intensity on T1- and T2-weighted images. However, foci of calcifications were present on pathologic examination that were not recognized on MR images. Furthermore, punctate low-signal-intensity areas were seen on unenhanced T1- and T2-weighted images or contrast-enhanced T1-weighted images that at pathologic examination correlated with dilated veins.

Adenomyosis.—Detection and characterization of adenomyosis varied according to the sequence or combination of sequences used (Table 2).

When image analysis included a single unenhanced T1-weighted sequence, the results of lesion detection and characterization were significantly inferior to those obtained with proton-density-weighted images, T2-weighted images, or a combination of sequences. On unenhanced T1-weighted images, the detection of adenomyosis was based on demonstration of an enlarged uterus with a smooth outline in 32%

TABLE 1: MR-Pathologic Correlation of 115 Leiomyomas

Imaging Sequence(s)	No. (%)	
	Detected	Characterized
Unenhanced T1 weighted[a]	66 (57)	32 (48)
Proton-density weighted	97 (84)	87 (90)
T2 weighted	99 (86)	89 (90)
Enhanced T1 weighted	96 (83)	79 (82)
Unenhanced T1 and T2 weighted	102 (89)	93 (91)
Unenhanced and enhanced T1 weighted	99 (86)	84 (85)
Unenhanced T1 and T2 weighted, enhanced T1 weighted	106 (92)	98 (92)

Note.—The numbers of lesions characterized were derived from the totals of those detected by each sequence or combination of sequences.

[a] On unenhanced T1-weighted images, lesion detection and characterization were significantly ($p < .05$) different from the other sequences.

low-signal-intensity area (thought to represent calcification) in 6% of cases (two lesions), on detection of lobular contour and low-signal-intensity foci in 6% of cases, on detection of a curvilinear low-signal-intensity rim (thought to represent peritumoral vessels) in 3% of cases (one lesion), and on detection of lobular contour and a curvilinear low-signal-intensity rim in 12% (four cases).

No significant difference in the detection or characterization of uterine leiomyoma was observed when either proton-density-weighted, T2-weighted, or contrast-enhanced T1-weighted images were analyzed. In each sequence, detection and characterization of tumor relied on direct visualization of tumor and/or the lobular appearance of the uterine contour (Fig. 1). Lesions not seen on contrast-enhanced T1-weighted images but seen on T2-weighted images were all intramural leiomyomas ranging in size from 1 to 3 cm and having contrast enhancement similar to that of adjacent myometrium.

Detection and characterization of lesions were improved when combined sequences were reviewed, with the best lesion evaluation obtained (detection, 92%; characterization, 92%) when all three sequences were used. The addition of contrast-enhanced T1-weighted imaging to unenhanced T1- and T2-weighted sequences improved evaluation of three submucosal and one intramural leiomyomas. The improvement, however, did not reach a significant level. Nine lesions (all greater than 0.5 cm in size) were not detected on any of the imaging sequences. These included one 9-cm cervical leiomyoma, one 6-cm leiomyoma that was incorrectly diagnosed as being part of another lesion, one pedunculated calcified leiomyoma that was mistaken for a bowel loop, and six 0.5- to 2-cm intramural leiomyomas. In eight tumors, leiomyoma could not be distinguished from adenomyoma because the tumor margin was indistinct in five, numerous high-signal-intensity foci were present in two, and both indistinct margin and high-signal-intensity foci were present in one. Lesion size varied from 2 to 4 cm.

On contrast-enhanced T1-weighted images, 65% of leiomyomas had a signal intensity lower than that of adjacent myometrium (Fig. 1), 23% had a signal intensity similar to that of the adjacent myometrium (Fig. 1), and 12% had a signal intensity predominately higher than that of adjacent myometrium (Fig. 2). Signal intensity was homogeneous in 24% and heterogeneous in 76% of leiomyomas (Fig. 3). The edge or margin of the lesions was sharp in 67% of cases and poorly defined in 33% (Fig. 1). Partial (Fig. 1) or complete (Fig. 4) rim enhancement was seen in 11% of lesions. A low-signal-intensity curvilinear rim was seen in 4% of lesions.

When the appearance of leiomyoma on T2-weighted images was compared with that on contrast-enhanced T1-weighted images, it was found that tumors that demonstrated low signal intensity on T2-weighted images had either homogeneous low signal intensity (28%) or various degrees of heterogeneous medium to high signal intensity (72%) on contrast-enhanced images (Figs. 1 and 3). All the leiomyomas that were of high signal intensity on T2-weighted images had varied signal enhancement (similar to or higher than that of adjacent myometrium) on contrast-enhanced images (Fig. 2).

Correlation with histologic findings showed that tumor enhancement was associated primarily with the degree of tumor vascularity. All leiomyomas with a pathologic grade of vascularity of 2 or greater showed enhancement. Hyaline degeneration with various amounts of replacement of muscle fibers by amorphous ground substance (and occasionally collagen) was found in tumors that had a characteristic cobblestonelike

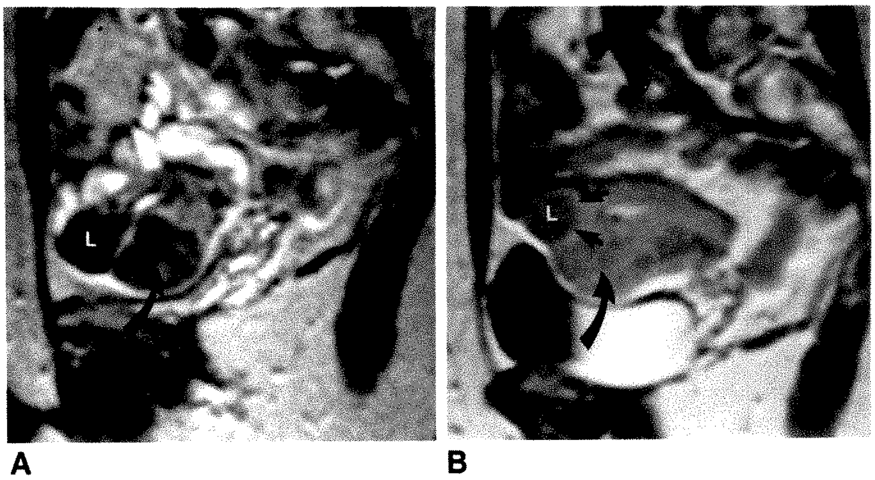

Fig. 1.—Intramural leiomyomas.
***A* and *B*, Sagittal T2-weighted (SE 2000/60) (*A*) and contrast-enhanced T1-weighted (SE 700/20) (*B*) MR images. Leiomyoma in uterine fundus (L) demonstrates homogeneous low signal intensity on T2-weighted and contrast-enhanced T1-weighted images. Peripheral rim enhancement (*straight arrows*) is seen. A second leiomyoma (*curved arrows*) shows heterogeneous but predominantly low signal intensity on T2-weighted image, but on contrast-enhanced image it shows enhancement similar to that of adjacent myometrium; lesion conspicuity is impaired on contrast-enhanced image.**

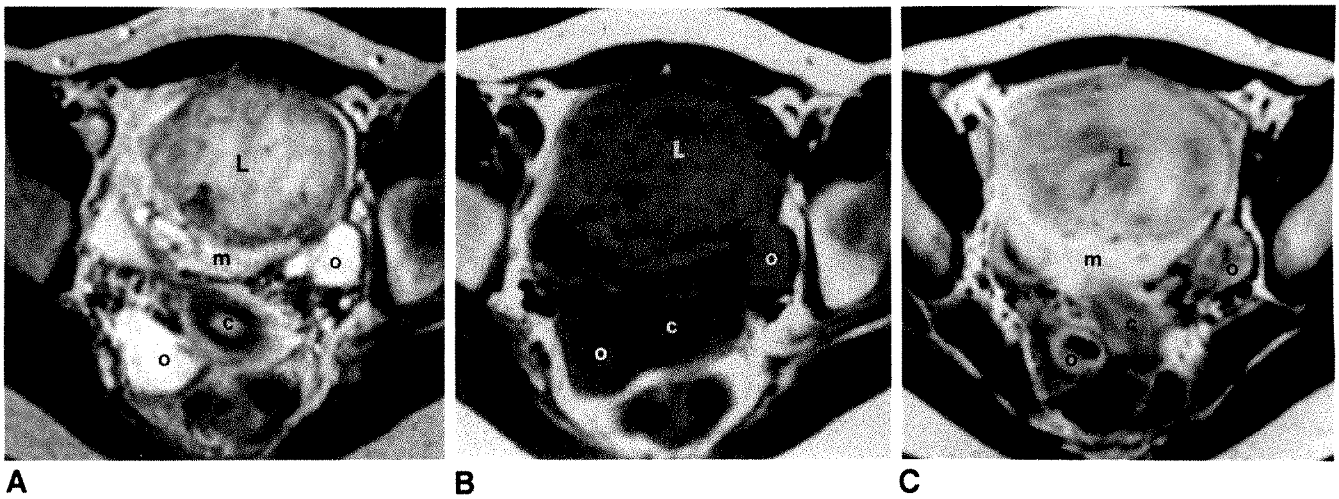

Fig. 2.—*A–C*, Large intramural degenerative leiomyoma seen on T2-weighted (SE 2000/60) (*A*), T1-weighted (SE 700/20) (*B*), and contrast-enhanced T1-weighted (SE 700/20) (*C*) MR images. Leiomyoma (L) shows heterogeneous high signal intensity on T2-weighted image and shows marked enhancement on contrast-enhanced image. m = myometrium, c = cervix, o = ovaries.

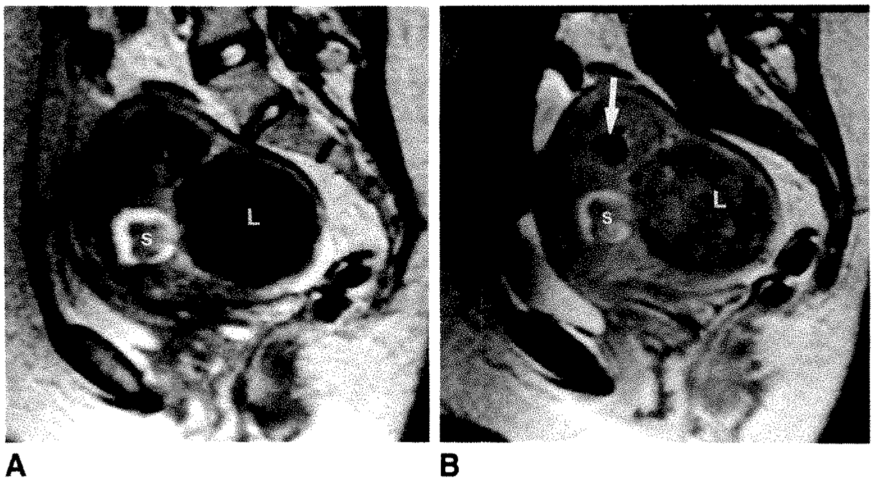

Fig. 3.—*A* and *B*, Intramural and submucosal leiomyomas seen on sagittal T2-weighted (SE 2000/60) (*A*) and contrast-enhanced T1-weighted (SE 600/20) (*B*) MR images. Two intramural leiomyomas show similar low signal intensity on T2-weighted image. On contrast-enhanced image, however, leiomyoma in posterior uterus (L) shows heterogeneous signal enhancement. Hyaline degeneration was present at histology. Fundal leiomyoma shows central area of cystic degeneration (*arrow*) not appreciated on unenhanced scan. Remainder of tumor blends with adjacent myometrium. Submucosal leiomyoma (S) is on a slender stalk.

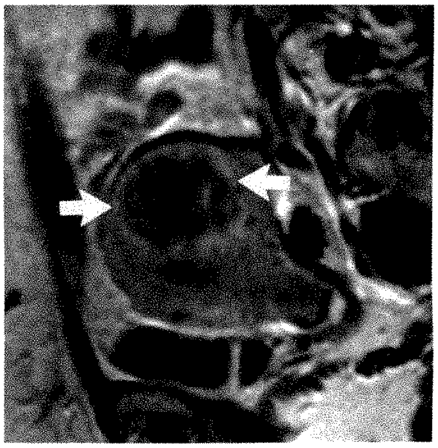

Fig. 4.—Leiomyoma with rim enhancement. Sagittal contrast-enhanced T1-weighted (SE 700/20) MR image shows rim enhancement (*arrows*) of large intramural leiomyoma.

appearance. Peritumoral rim enhancement correlated with peripheral edema in seven patients and with edema and dilated veins in four patients. When a curvilinear low-signal-intensity rim was seen, it correlated with calcium in two patients and with dilated veins in the others. On pathologic examination, focal calcifications were present in 7% of tumors detected on MR. On MR images, some of the calcifications showed low signal intensity on T1- and T2-weighted images. However, foci of calcifications were present on pathologic examination that were not recognized on MR images. Furthermore, punctate low-signal-intensity areas were seen on unenhanced T1- and T2-weighted images or contrast-enhanced T1-weighted images that at pathologic examination correlated with dilated veins.

Adenomyosis.—Detection and characterization of adenomyosis varied according to the sequence or combination of sequences used (Table 2).

When image analysis included a single unenhanced T1-weighted sequence, the results of lesion detection and characterization were significantly inferior to those obtained with proton-density-weighted images, T2-weighted images, or a combination of sequences. On unenhanced T1-weighted images, the detection of adenomyosis was based on demonstration of an enlarged uterus with a smooth outline in 32%

TABLE 2: MR-Pathologic Correlation in 19 Cases of Adenomyosis

Imaging Sequence(s)	No. (%)	
	Detected	Characterized
Unenhanced T1 weighted[a]	9 (47)	4 (44)
Proton-density weighted	14 (74)	10 (71)
T2 weighted	16 (84)	13 (81)
Enhanced T1 weighted[b]	12 (63)	8 (67)
Unenhanced T1 and T2 weighted	17 (89)	15 (88)
Unenhanced and enhanced T1 weighted	14 (74)	11 (79)
Unenhanced T1 and T2 weighted, enhanced T1 weighted	17 (89)	15 (88)

Note.—The numbers of lesions characterized were derived from the totals of those detected by each sequence or combination of sequences.

[a] The unenhanced T1-weighted sequence was significantly ($p < .05$) different for lesion detection and characterization from the proton-density-weighted and T2-weighted sequences and from the combined unenhanced T1- and T2-weighted, unenhanced and enhanced T1-weighted, and unenhanced T1- and T2-weighted and enhanced T1-weighted sequences. The unenhanced T1-weighted sequence was not significantly different from the enhanced T1-weighted sequence.

[b] The enhanced T1-weighted sequence approached significance ($p = .07$) when compared with the combined unenhanced T1- and T2-weighted sequences, and the unenhanced T1- and T2-weighted and enhanced T1-weighted sequences.

(six cases) and on demonstration of multiple high-signal-intensity foci in 21% (four cases). One patient had both an enlarged uterus and high-signal-intensity foci within it. The specific diagnosis of adenomyosis was made only in those cases where high-signal-intensity foci were present.

On contrast-enhanced T1-weighted images, in addition to demonstration of diffuse enlargement of the uterus, there was direct visualization of the widening of the junctional zone (Fig. 5) or demonstration of a lesion with focal heterogeneous signal intensity and poorly defined margin (Fig. 6). The ability to detect or characterize adenomyosis on either unenhanced or contrast-enhanced T1-weighted images was inferior to that obtained with T2-weighted images. Visualization of intratumoral high-signal-intensity foci on unenhanced T1-weighted images contributed to better lesion detection and characterization when both T1- and T2-weighted images were analyzed. However, even when all sequences were used, the detection rate was only 89% (17 of 19 lesions) and characterization was only 88% (15 of 17 lesions). Both cases not detected were the diffuse form of adenomyosis, and in both the differentiation between the normal junctional zone and presence of adenomyosis was not made. In the two patients in whom adenomyosis was detected but not accurately characterized, the differentiation between adenomyoma and leiomyoma was not possible.

In diffuse and focal adenomyosis, signal enhancement was lower than that of the adjacent myometrium in all cases detected (Fig. 5). High-signal-intensity foci, which were seen on unenhanced T2- and/or T1-weighted images, were not detected on contrast-enhanced studies (Fig. 6). At histology, all high-signal-intensity foci were found to be small hemorrhagic cysts. When the stroma associated with adenomyotic glands was collagenized, typically the lesion appeared heterogeneous with low-signal-intensity foci within it. The margins of adenomyomas were poorly defined in all cases, and no rim enhancement was seen.

Endometrial polyps.—Detection of endometrial polyps was significantly improved by the use of contrast-enhanced imaging (Table 3).

Only one lesion was detected on unenhanced T1-weighted images, and in that patient high-signal-intensity fluid within the endometrial cavity (proved to be retained blood) outlined the medium-signal-intensity endometrial polyps. However, differentiation between endometrial polyp, submucosal leiomyoma, and polypoid endometrial carcinoma was not possible. On both proton-density- and T2-weighted images, detection of endometrial polyps demonstrated an increased thickness of the endometrium in three patients, a lobular configuration of the endometrial complex in three patients, heterogeneous signal intensity within the expected endometrium in two patients, and heterogeneous but predominantly lower-signal-intensity mass in the endometrial cavity in two patients. More than one finding was present in four of five patients. On

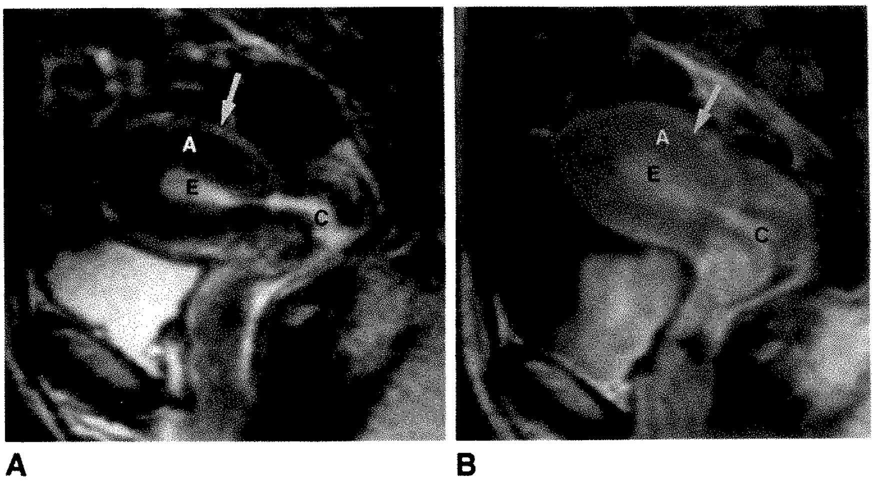

Fig. 5.—Diffuse adenomyosis seen on sagittal MR images.

***A*, T2-weighted (2000/60) image. Region of junctional zone (*arrow*) is widened and demonstrates diffuse low signal intensity characteristic of diffuse adenomyosis (A).**

***B*, Contrast-enhanced T1-weighted (SE 600/20) image. Adenomyosis (A) demonstrates signal enhancement lower than that of adjacent myometrium (*arrow*), but conspicuity of finding is inferior when compared with T2-weighted image.**

E = endometrium, C = cervix.

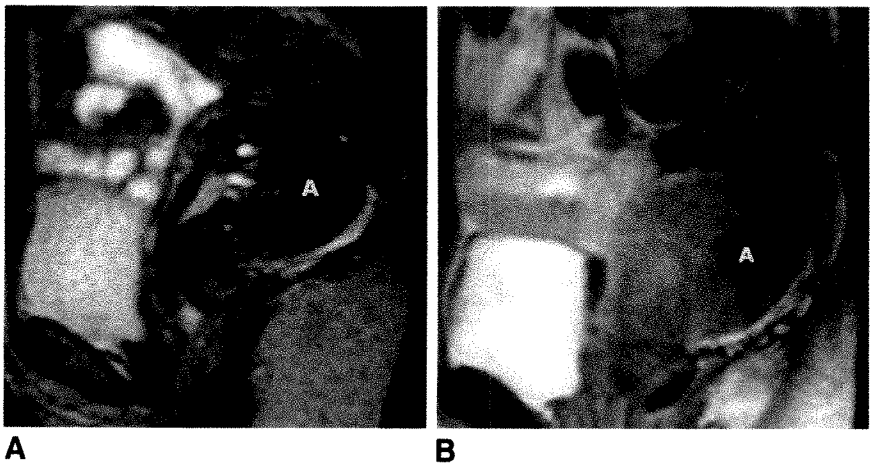

Fig. 6.—Adenomyoma seen on sagittal MR images.

***A*, T2-weighted (SE 2000/60) image shows poorly defined low-signal-intensity mass (A) with punctate foci of increased signal intensity.**

***B*, Contrast-enhanced T1-weighted (SE 700/20) image shows similar enhancement of adenomyoma (A) and adjacent myometrium, with resultant impairment in lesion conspicuity and characterization.**

unenhanced scans, lesion characterization was possible in only one patient.

The addition of contrast enhancement allowed direct visualization of the endometrial abnormality, significantly improving lesion detection to 79% (11 of 14 cases) (Fig. 7). In two patients, only one polyp was detected, yet two were present at surgery. In one patient, a small 0.5-cm polyp was not seen. Lesion characterization was significantly improved when all three sequences were analyzed. The overall improvement was attributed to a combination of findings on T2- and contrast-enhanced T1-weighted images. Seven of eight endometrial polyps that were correctly characterized as such on combined studies showed signal intensity indistinguishable from normal endometrium on T2-weighted images. In one patient, although the lesion was seen on the T2-weighted image, its signal intensity was much higher than usually seen in submucosal leiomyomas.

On contrast-enhanced images, six of the 11 endometrial polyps detected demonstrated signal intensity slightly lower than that of endometrium but higher than that of adjacent myometrium. In five tumors, signal intensity was similar to or lower than that of the adjacent myometrium. In four cases, signal intensity was homogeneous, and in seven it was heterogeneous. The margin of the polyp was smooth in seven and spiculated in four lesions. Nine lesions were pedunculated on a slender stalk, and two were broad-based. A small amount of retained secretion (demonstrating low signal intensity) was seen in association with the lesion in seven of nine patients.

TABLE 3: MR-Pathologic Correlation of 14 Endometrial Polyps

Imaging Sequence(s)	No. (%)	
	Detected	Characterized
Unenhanced T1 weighted	1 (7)	0
Proton-density weighted	5 (36)	1 (20)
T2 weighted	5 (36)	1 (20)
Enhanced T1 weighted[a]	11 (79)	6 (55)
Unenhanced T1 and T2 weighted	5 (36)	1 (20)
Unenhanced and enhanced T1 weighted[a]	11 (79)	6 (55)
Unenhanced T1 and T2 weighted, enhanced T1 weighted[b]	11 (79)	8 (73)

Note.—The numbers of lesions characterized were derived from the totals of those detected by each sequence or combination of sequences.

[a] The addition of contrast medium in a single sequence analysis or in a combination of sequences rendered significantly ($p < .05$) different detection as compared with unenhanced images.

[b] Lesion characterization on contrast-enhanced images approached significant difference when all of the imaging sequences were analyzed.

On histologic examination, all the polyps that demonstrated heterogeneous signal intensity on contrast-enhanced scans showed cystic atrophy. In addition, in one patient endometrial carcinoma was arising from the polyp (Fig. 8). Polyps that demonstrated signal intensity similar to or lower than that of the surrounding myometrium had a dense fibrotic stroma, and in one case, there was dense cellularity throughout the lesion.

Discussion

The reported sensitivity of unenhanced T1- and T2-weighted MR images in the detection of uterine leiomyomas is 86% [5], compared with 89% seen in our study. When our analysis included both leiomyomas and adenomyosis (134 lesions), the detection was 84% for unenhanced and contrast-enhanced T1-weighted images, 89% for unenhanced T1- and T2-weighted images, and 92% when all three sequences were analyzed. Although the use of contrast medium demonstrated intratumoral architecture in greater detail (Fig. 3), enhancement of leiomyomas and adenomyosis often resulted in blending margins with the surrounding myometrium and decreased conspicuity of the lesion as compared with the appearance on unenhanced T2-weighted images.

The characterization of leiomyomas on unenhanced MR has been reported to be 63% overall, increasing to 85% when the lesion demonstrated the typical low signal intensity on T2-weighted images [7]. Leiomyomas could be differentiated from adenomyosis in 83% of cases [9]. When only large lesions were analyzed, a 99% accuracy rate has been re-

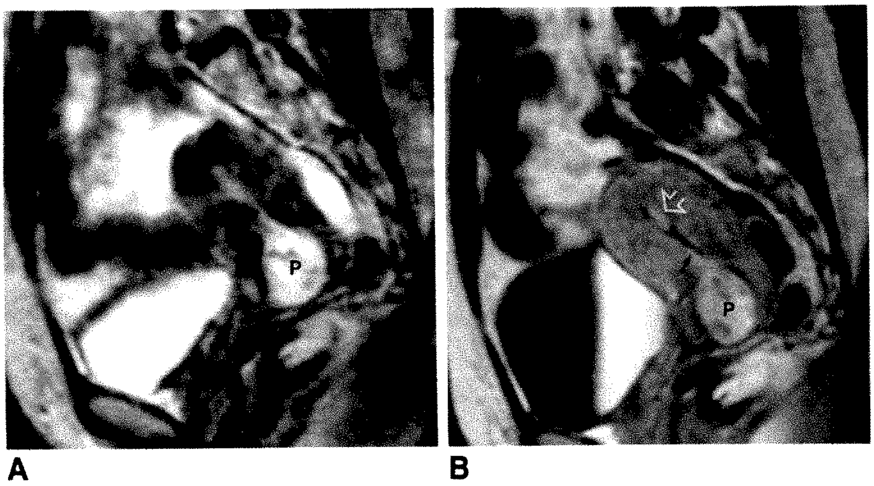

Fig. 7.—Two endometrial polyps seen on sagittal MR images.

A, T2-weighted (SE 2000/60) image shows widening of endocervical canal (P). Endometrium is unremarkable.

B, Contrast-enhanced T1-weighted (SE 700/20) image shows small broad-based, smooth-margin endometrial polyp (*open arrow*) in fundus. Enhancing lesion is contrasted by low-signal-intensity fluid. Larger polyp (P) is on a slender stalk (*solid arrow*) and is prolapsing through endocervical canal.

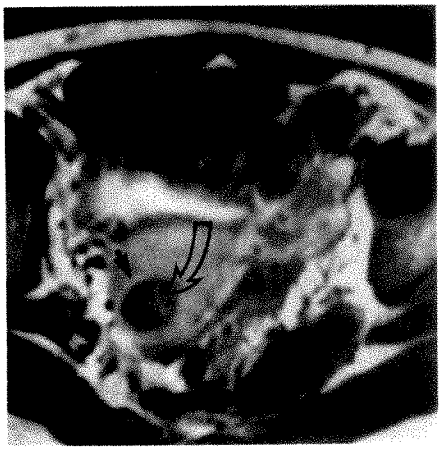

Fig. 8.—Endometrial polyp with foci of endometrial carcinoma seen on transverse contrast-enhanced T1-weighted (SE 700/20) MR image. Enhancing endometrial polyp (*curved arrow*) has spiculated margin and is surrounded by low-signal-intensity fluid. Differentiation between endometrial polyp and adenocarcinoma is not possible. Normally enhancing endometrium (*straight arrow*).

ported [10]. In our study, when unenhanced T1- and T2-weighted MR images were reviewed, characterization of leiomyomas was 91% accurate, and leiomyomas could be differentiated from adenomyosis in 91% (108/119). Lesion differentiation decreased to 84% when the analysis included unenhanced and contrast-enhanced T1-weighted images. The inferior performance of contrast-enhanced T1-weighted imaging was due to similar patterns of enhancement for both types of lesions, indistinct tumor margins in 33% of leiomyomas, and lack of demonstration of high-signal-intensity foci of adenomyosis. However, another MR imaging feature of leiomyoma, high-signal-intensity halo on T2-weighted images [15], was seen more often on contrast-enhanced T1-weighted images and not at all in adenomyosis.

Unenhanced MR imaging has been limited in the detection of endometrial polyps, and nonspecificity of signal pattern for endometrial abnormalities has been reported [14]. In this study, contrast media significantly improved the detection of endometrial polyps. While the 79% detection rate of endometrial polyps was the same when either contrast-enhanced T1-weighted images alone, unenhanced and contrast-enhanced T1-weighted images, or a combination of all three sequences was used, the lesion characterization was improved (approaching significance) when all three imaging sequences were analyzed. This was due to a combination of findings between contrast-enhanced T1-weighted and unenhanced T2-weighted images. While on contrast-enhanced T1-weighted images endometrial polyps and submucosal leiomyomas often demonstrated similar enhancement, their signal intensity differed on unenhanced T2-weighted images. On T2-weighted images, endometrial polyps most commonly demonstrated a signal intensity indistinguishable from that of the adjacent endometrium, while leiomyomas had a signal intensity lower or equal to that of the adjacent endometrium. When an endometrial polyp, however, exhibited medium signal intensity on the T2-weighted image, the differentiation between the endometrial polyp and submucosal leiomyoma was not possible. The differentiation between endometrial polyp and polypoid endometrial carcinoma is difficult when based on signal intensity, whether from unenhanced or contrast-enhanced images [17]. The analysis of tumor margin, however, may be helpful. When the tumor margin is smooth, the endometrial polyp is more likely benign, while a spiculated margin may be seen with either benign or malignant tumor. Although the prevalence of carcinoma in benign polyps has been reported to be no more than 0.5%, polyps have been found in 12–30% of uteri with endometrial carcinoma [2]. Therefore, the findings on MR should be limited to depiction of pathologic changes within the endometrial cavity, but only in rare instances can the differentiation between benign and malignant disease be made with confidence.

Conclusions

T1-weighted images alone render statistically inferior results in the evaluation of benign uterine neoplasms. Proton-density- and T2-weighted images show a similar sensitivity in the detection and characterization of benign tumors of the uterus and are essential for the evaluation of uterine leiomyomas and adenomyosis. Contrast-enhanced T1-weighted images do not improve the assessment of leiomyomas or adenomyosis except in patients in whom tumors are in an unusual location or in whom the unenhanced T2-weighted images are of inferior quality. Contrast-enhanced images, however, significantly improve the evaluation of endometrial polyps.

REFERENCES

1. Hendrickson MR, Kempson RL, eds. *Surgical pathology of the uterine corpus.* Philadelphia: Saunders, **1980**:453-529
2. Kurman RJ, ed. *Blaustein's pathology of the female genital tract*, 3rd ed. New York: Springer-Verlag, **1987**:305-310
3. Gross BH, Silver TM, Jaffe MH. Sonographic features of uterine leiomyomas: analysis of 41 proven cases. *J Ultrasound Med* **1983**;2:401-406
4. Baltarowich OH, Kurtz AB, Pennell RG, Needleman L, Vilaro MM, Goldberg BB. Pitfalls in sonographic diagnosis of uterine fibroids. *AJR* **1988**;151:725-728
5. Dudiak CM, Turner DA, Patel SK, Archie JT, Silver B, Norusis M. Uterine leiomyomas in the infertile patient: preoperative localization with MR imaging versus US and hysterosalpingography. *Radiology* **1988**;167:627-630
6. Riccio TJ, Adams HG, Munzing DE, Mattrey RF. Magnetic resonance imaging as an adjunct to sonography in the evaluation of the female pelvis. *Magn Reson Imaging* **1990**;8:699-704
7. Weinreb JC, Barkoff ND, Megibow A, Demopoulos R. The value of MR imaging in distinguishing leiomyomas from other solid pelvic masses when sonography is indeterminate. *AJR* **1990**;154:295-299
8. Zawin M, McCarthy S, Scoutt LM, Comite F. High-field MRI and US evaluation of the pelvis in women with leiomyomas. *Magn Reson Imaging* **1990**;8:371-376
9. Mark AS, Hricak H, Heinrichs LW, et al. Adenomyosis and leiomyoma: differential diagnosis with MR imaging. *Radiology* **1987**;163:527-529
10. Togashi K, Ozasa H, Konishi I, et al. Enlarged uterus: differentiation between adenomyosis and leiomyoma with MR imaging. *Radiology* **1989**;171:531-534
11. McCarthy S. MR imaging of the uterus. *Radiology* **1989**;171:321-322
12. Fedele L, Bianchi S, Dorta M, Brioschi D, Zanotti F, Vercellini P. Transvaginal ultrasonography versus hysteroscopy in the diagnosis of uterine submucous myomas. *Obstet Gynecol* **1991**;5:745-748
13. Hricak H, Tscholakoff D, Heinrichs LW, et al. Uterine leiomyomata: correlation of MR, histopathologic findings and symptoms. *Radiology* **1986**;158:385-391
14. Brown JJ, Thurnher S, Hricak H. MR imaging of the uterus: low-signal-intensity abnormalities of the endometrium and endometrial cavity. *Magn Reson Imaging* **1990**;8:309-313
15. Mittl RL Jr, Yeh I-T, Kressel HY. High-signal intensity rim surrounding uterine leiomyomas on MR images: pathologic correlation. *Radiology* **1991**;180:81-83
16. Zar JH, ed. *Biostatistical analysis.* New Jersey: Prentice-Hall, **1984**:389-402
17. Hricak H, Hamm B, Semelka RC, et al. Carcinoma of the uterus: use of gadopentetate dimeglumine in MR imaging. *Radiology* **1991**;181:95-106

Ureteric Jets: Evaluation of Normal Flow Dynamics with Color Doppler Sonography

Ian H. Cox[1]
Scott J. Erickson[1]
W. Dennis Foley[1]
Douglas M. Dewire[2]

This study was designed to investigate a variety of sonographic features of ureteric jets in order to define patterns of flow and ranges of flow values in an asymptomatic population. The following features of ureteric jets were measured during a period of up to 30 min in a group of 15 asymptomatic volunteers after oral hydration (the mean value was calculated on each side): peak velocity (mean, 57 cm/sec); jet duration (mean, 4.6 sec); and number of peaks and subpeaks (mean, 2.2). Several flow patterns were observed, including discrete jets, ureteric streaming, and rest periods. For each patient the ratios of values obtained on the left and right sides were calculated for peak velocity (1.00–1.74; mean, 1.26); jet duration (1.00–4.69; mean, 1.83); and jet frequency (1.00–1.21; mean, 1.11). The interjet interval (period between jets) ranged from 2 to 150 sec. Bolus volume and jet frequency showed simultaneous moment-to-moment variation. The frequency and velocity rather than the duration ratios may be of greatest value in identifying patients with normal ureterodynamics.

Our findings challenge two current concepts of renal pelvic and ureteral response to changes in urine output: (1) ureters have a fixed maximal discharge rate and (2) bolus volumes do not change until this rate is achieved. Asymmetric moment-to-moment fluctuations observed in jet frequency suggest that prolonged examination may be necessary to confirm normal symmetry of jet frequency in some patients with suspected ureteric obstruction.

***AJR* 158:1051–1055, May 1992**

Color Doppler sonography holds promise as a noninvasive means of investigating urodynamics [1, 2] and, in particular, of confirming or excluding ureteric obstruction. To date, reported work with color Doppler sonography in obstruction has been based entirely on the presence or absence of jets, subjective assessment of flow patterns, and relative frequency of jets [3]. Low-grade obstruction cannot be diagnosed accurately with these parameters on color Doppler sonography. We used color Doppler sonography to study urine flow dynamics in volunteers in order to elucidate normal ureterodynamics and develop a more precise method of diagnosing ureteric obstruction.

Materials and Methods

Fifteen asymptomatic volunteers (nine women, six men; ages 18–49 years; mean age, 31 years) were examined 15–30 min after drinking 600–1000 ml of water.

Initial scanning was done transversely in the midline through the bladder base with a 3-MHz linear probe (QAD 1, Quantum Medical Systems, Issaquah, WA) at medium flow-sensitivity setting. The power setting was 14 dB; slope, 1.6–3.0 dB/cm; color threshold, 15; spectral gain, 80–124; and depth, 102 or 151 mm. The seminal vesicles and mid cervix provided useful landmarks to identify the level of ureteral jets, which could then be readily traced to the ureteral orifice (Fig. 1). After at least 5 min of continuous observation of both orifices in real time, four to seven spectral traces were obtained from jets on each side. The scan axis was rotated to the axis of the jet, and spectral waveforms were obtained as close

Received July 8, 1991; accepted after revision November 26, 1991.

[1] Department of Radiology, Medical College of Wisconsin, 8700 W. Wisconsin Ave., Milwaukee, WI 53226. Address reprint requests to S. J. Erickson.

[2] Department of Urology, Medical College of Wisconsin, Milwaukee, WI 53226.

0361-803X/92/1585-1051
© American Roentgen Ray Society

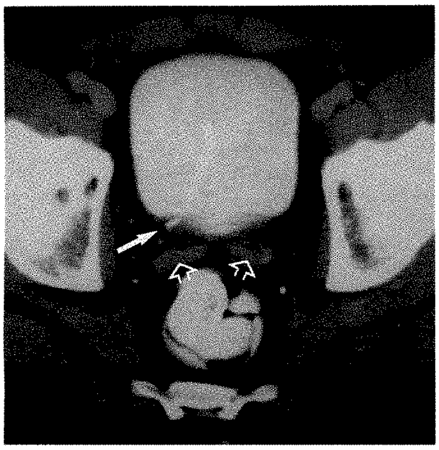

Fig. 1.—Axial CT scan of pelvis after administration of IV contrast material shows normal right ureteric jet. Scan shows transverse orientation of jet and relationship of distal ureter (*solid arrow*) to seminal vesicles (*open arrows*).

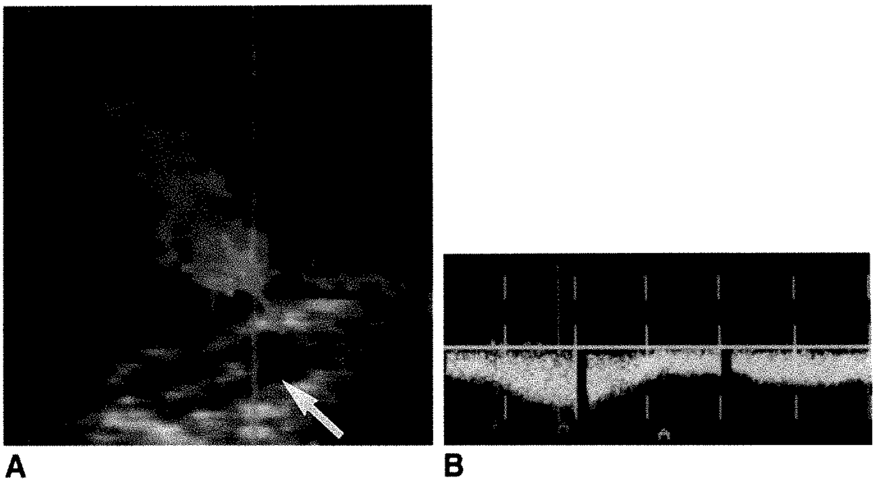

Fig. 2.—*A* and *B*, Color Doppler sonogram (*A*) and waveform (*B*) from a normal ureteric jet (duration, 8 sec; peak velocity, 76 cm/sec; two peaks). Cervix (*arrow* in *A*) served as a landmark for maintaining scanning plane on ureteric orifice between jets.

to the orifice as possible (Fig. 2). The Doppler cursor was carefully maintained directly over the ureteric orifice between jets; identification of a landmark posterior to the bladder aided this task. Slight displacement of the cursor from the center of the jet led to poor spectral waveforms, which were rejected. In subjects in whom the jets emerged more perpendicular to the bladder base, scanning had to be done from a lateral position to obtain a valid Doppler angle for spectral waveforms (Fig. 3). For 60% of ureteric jets, the Doppler interrogation angle was in the optimal range of 45–65°. In the remaining cases, the angle was between 35° and 73°. In most subjects, the ureteric jets were directly medially and close to the transverse plane, but even in subjects in whom they were angled medially and caudally, the contralateral jets remained under observation during this phase of the examination. Real-time color Doppler sonography and spectral waveforms were recorded for an average of 15 min to permit retrospective analysis. Scanning often took as long as 30 min because the sonography unit did not permit manipulation of spectral cursor position or other scanning parameters during digital recording.

The timing of each jet was determined retrospectively, permitting calculation of the interjet interval (IJI, the time interval between commencement of jets) during uninterrupted periods of recording. The jet frequency ratio between the two sides was calculated from the number of jets counted on each side during the recorded part of the examination. From the spectral waveforms, the maximum (peak) velocity and duration were determined for individual jets. Those two measurements were averaged on each side, and the ratio of the greater to the lesser average was calculated. Often a large fluctuation in instantaneous velocity occurred during each jet, so we recorded the number of "subpeaks" and correlated that value with jet duration.

Results

Ureteric jets were detected by color Doppler sonography in 14 of 15 asymptomatic volunteers. In the one volunteer who had emptied his bladder and allowed it to refill after taking the fluid load, and in two other volunteers not included in this study who had not taken a fluid load, no jets could be seen.

The measured peak velocity of individual jets varied from 16 to 150 cm/sec. The average peak velocity in 12 subjects ranged from 30 to 70 cm/sec; mean values of 20 and 122 cm/sec were calculated for the other two subjects (mean for all 14, 57 cm/sec; SD, 29.9 cm/sec). For each subject and side, peak velocity varied by 3–300% (mean, 50%) during the entire examination; in only two cases did it vary by less than 20%. In one subject, velocity varied by only 3% (1 cm/sec) during a 40-sec period (encompassing three jets) and by only 13% during a second 40-sec period 5 min later (again with three jets), but mean velocity increased by 25% between the two periods. In contrast, in five subjects, differences in velocity of 50–80% were seen in jets only 30 sec apart. The ratios between sides of mean peak velocity ranged from 1.00 to 1.74 (mean, 1.26; SD, 0.21; 95th percentile, 1.68 ± 0.21 [4]).

Duration of jets varied from 1 to 10 sec (mean, 4.6 sec; SD, 2.46 sec). In seven subjects, the duration varied on each side by only 1 sec. In the other seven subjects, it varied by 2–6 sec. At an individual orifice, an increase in duration was usually (90% of the time) accompanied by an increase in velocity, but no correlation was found between velocity and duration in individual sides and subjects (coefficient of correlation, .348 [4]). The ratio of jet duration between sides varied greatly: 1.00–2.53 in 13 subjects and 4.69 in one subject (mean in 14 subjects, 1.83; SD, 1.06; 95th percentile, 3.95 ± 1.06). When reexamined on another occasion, the subject with a ratio of 4.69 had a duration ratio of 1.20.

The frequency of jets was symmetric: the range of ratios was 1.00 to 1.21 (mean, 1.11; SD, 0.06; 95th percentile, 1.23 ± 0.06). The moment-to-moment IJI varied from 2 to 45 sec, with the exception of one IJI of 150 sec. In seven subjects, periods of up to 5 min occurred during which IJI remained very constant (varying by only 10–20%), but IJI did fluctuate asymmetrically throughout the remainder of their examinations. In the other seven subjects, the IJI fluctuated contin-

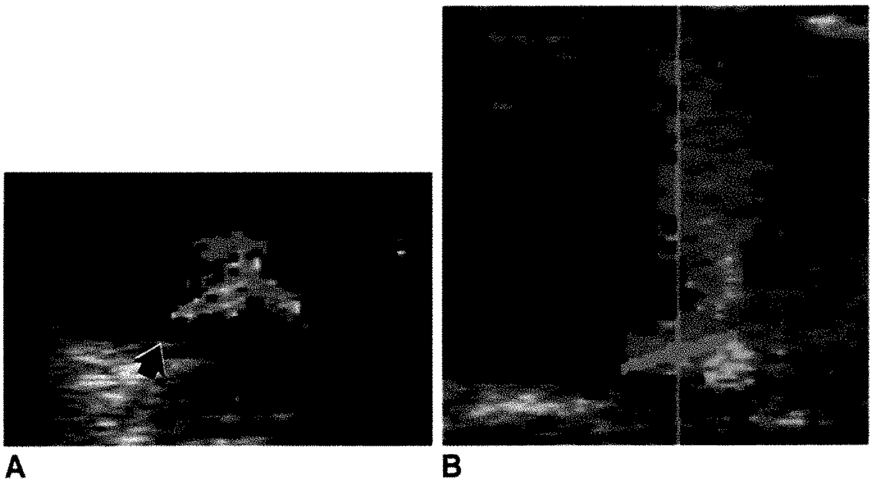

Fig. 3.—Transverse color Doppler sonograms parallel to bladder base show normal variation in orientation of bilateral ureteric jets.

***A*, Symmetrically oriented jets. Note that right jet appears to emerge a short distance above ureteric orifice (*arrow*) because some admixture of jet and bladder urine needs to occur before jet can be imaged with color Doppler sonography.**

***B*, Orientation of jets is markedly asymmetric.**

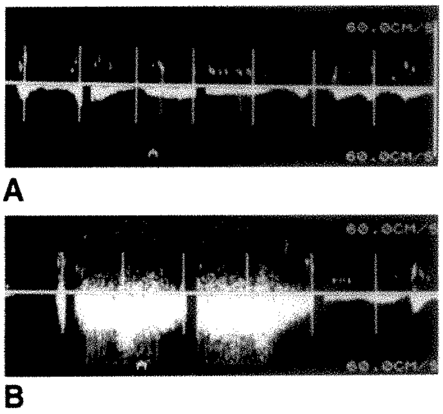

Fig. 4.—Spectral waveforms from ureteric orifice in high-flow state.

***A*, Sample of one of two episodes of ureteric streaming, each of which lasted 30 sec.**

***B*, Superimposed ureteric jet.**

ually, with no more than three jets occurring at the same period apart.

The number of peaks and subpeaks varied from 1 to 4 (mean, 2.2; SD, 1.1) and correlated directly with duration (coefficient of correlation, .768).

In one subject, a 150-sec period occurred during which no detectable flow was seen from the left ureteric orifice. This was followed by a 63-sec phase of very frequent jets (1–2 sec apart), which increased in duration from 1 to 7 sec. This pattern contrasted with the pattern of jets before and after this episode, which was 3–5 sec in duration and 20–45 sec apart. Nevertheless, in this subject, the average frequency on the two sides during 25 min was symmetric (frequency ratio, 1.07).

Thirteen subjects had discrete jets (<11 sec in duration and separated by a period of undetected flow) throughout their evaluations. One volunteer had discrete jets throughout most of a 30-min period but had two 30-sec episodes of continuous but rapidly fluctuating low-velocity streaming (at 15 cm/sec) from the same ureteric orifice on which two "normal" jets (velocity, 50 cm/sec; duration, 4 and 8 sec) were superimposed (Fig. 4). During this study, the IJI at that orifice varied from 15 to 30 sec and was 25 sec at the time that streaming occurred. The distinction between a long jet and a short episode of streaming was easily made in this and prior studies [3].

Discussion

Color Doppler sonography allows accurate enumeration and timing of ureteric jets for extended periods and documentation of other phenomena, including "rest periods" and episodes of streaming. Velocity and duration of jets can be measured, although the difficulties in positioning and maintaining the spectral sample at the ureteric orifice limit the number of jets that can be analyzed in this way. In vitro studies have shown that angle-corrected Doppler measurements correlate well with jet velocity [5]. The measured peak velocity is slightly lower than the true velocity at the ureteric orifice. This is because some mixing of the jet and bladder urine must occur before sufficient acoustic interfaces are created, and during this process viscous drag slows the jet slightly. As a result, the origin of the jet sometimes appears on color Doppler sonography to be a short distance away from the ureteric orifice (Fig. 3). Difficulty with achieving an optimal Doppler interrogation angle and of maintaining the spectral cursor precisely in the center of the jet stream are potential sources of error in velocity measurement. However, the quality of the spectral waveform deteriorates detectably with even minor displacement of the cursor from the imaged center of the jet. In this study, very similar velocity measurements were acquired from a number of jets that were in close temporal proximity, and this suggested that errors in velocity measurement were minor.

Symmetry of Ureteral Jets

In the asymptomatic population studied, the total number and hence relative frequency of jets in a 30-min period were the most consistently symmetric parameters. On the basis of renogram data revealing symmetric renal output, this implies that the average volume of jets also was symmetric. Although velocity was less symmetric than frequency, there is sufficient symmetry to suggest that it may be worth exploring this parameter in a study of ureteric obstruction. Mean jet duration and number of subpeaks were the least symmetric parameters and would appear to have less potential as ways to define abnormal ureteral dynamics.

Conspicuity of Ureteral Jets

Normal urine is devoid of microgas bubbles and particles. Sonographic visualization and production of a Doppler signal from an aparticulate jet of urine depends on differences in density and associated compressibility changes between the urine in the bladder and that in the ureter [5, 6]. The greater the density difference, the stronger the acoustic backscatter. Importantly, when the urine density in the ureter is the same as that in the bladder, the jets cannot be visualized at all. The amount of backscatter also increases with increasing velocity of the expelled urine [5]. Thus, it is necessary to create a situation in which the specific gravity of the urine being produced by the kidneys is different from that of the urine in the bladder. A simple technique is to fluid-load the patient immediately before the study. In practice, 600–1000 ml of water by mouth 15–30 min before the study was adequate hydration for this purpose. Urine produced before the resulting diuresis must be retained in the bladder. One asymptomatic volunteer in this study emptied his bladder completely soon after taking the fluid load. The bladder quickly refilled but with dilute urine identical to that subsequently delivered by the ureters, and no jets could be imaged. Burge et al. [3] encountered nonvisualization of jets in four of 47 subjects and attributed this to inadequate hydration or insufficient delay after hydration. Attention to detail in technique of prehydration is clearly an important aspect of sonographic evaluation of ureteric jets.

A possible alternative to prehydration is to fill the bladder in a retrograde fashion using a fluid that has a specific gravity different from that of the jet urine. This could be of particular value in patients with renal disease who are unable to concentrate their urine. However, prehydration has an additional advantage: an increase in the frequency and conspicuity of the jets, which greatly facilitates the examination.

Size of Ureteral Jets

Several authors [2, 3, 7] have ascribed physiologic information to the "size" or maximum spatial length and width of ureteric jets as they appear on sonographic images. However, several independent factors affect the conspicuity and hence the size of jets: flow rate (volume per unit time), velocity of jet, orientation of jet to transducer, difference in specific gravity (ureter vs bladder), and flow sensitivity of the unit. These variables suggest that measurements of jet size as imaged on color Doppler sonography might not correlate well with true jet dynamics. The orientation of jets to the bladder base and hence to the transducer is often asymmetric and differed in this study by up to 75° (Fig. 3). This can invalidate comparisons of size, even in the same patient.

Normal Ureterodynamics

Although all parts of the pelvicaliceal system and ureter can initiate a contraction, the component with the highest contraction frequency is the proximal renal pelvis, and this therefore acts as a "pacemaker" [8–15]. Only the necessary number of contractions are permitted through the physiologic "gate" at the ureteropelvic junction and into the ureter. The pelvic pacemaker continues to fire at a constant rate, and the periodicity of ureteric contractions must be equal to this rate or a whole-numeral fraction of it. At normal flow rates, as the renal pelvis fills, the pressure within it rises and urine is extruded into the upper ureter, which is initially collapsed. When a sufficient volume of urine is in the ureter, a contraction wave is allowed to pass down from the pelvis. The urine is formed into a bolus as the contraction wave moves distally down the ureter. In order to propel this bolus efficiently, the contraction wave must coapt the ureteral walls. The bolus is forced by the contraction wave across the ureterovesical junction, which does not relax, and the bolus jets into the bladder.

With increasing flow rates, the initial response of the ureter is an increase in peristaltic frequency as a greater proportion of contractions from the pelvicaliceal pacemaker are permitted to cross the ureteropelvic junction. When 1:1 transmission occurs and frequency cannot increase, the bolus volume increases, with a corresponding increase in force of ureteric contraction. With higher flow volumes, the boluses coalesce and finally the ureter becomes filled with urine. At these rates, flow is through an open tube. Continuous flow will be seen from the orifice, along with superimposed boluses from the noncoapting ureteral contractions.

Commentary

The findings in this study challenge some of the current concepts in ureteral urodynamics. According to the classical theories of urodynamics, the subject in this study who exhibited ureteric streaming must have achieved 1:1 transmission of contractions from the renal pelvis to the ureter, yet fluctuations in moment-to-moment jet frequency were observed. This suggests that the rate of discharge of his pelvic pacemaker was not fixed and it was responding relatively quickly to changes in renal output. The assumption that the frequency of jets in the bladder reflects the frequency of contractions in the proximal ureter has been based on the observation that waves of peristaltic contraction usually pass from the renal pelvis to the bladder at roughly a constant speed [11].

Although direct measurement of the volume of the bolus of urine forming the jet was not attempted in this study, some information about bolus volume can be inferred from jet duration and velocity. Almost universally, jet duration and velocity at any one orifice rose and fell together. The lack of change in resistance to flow by the ureteric orifice throughout this study suggests that the bolus volume and the force of ureteric contraction are fluctuating. We base this assumption on catheter studies in humans, which have shown that the pressure zone responsible for keeping the ureterovesical junction closed between boluses does not fluctuate from moment to moment. Even when the ureterovesical junction pressure gradient rises with bladder filling, this increase is not sufficient to significantly impede urine flow [16].

The moment-to-moment IJI (and hence jet frequency) fluctuated at some point in all subjects and ranged from 2 to 45 sec. Seven subjects also had marked fluctuations in jet duration and velocity at any one orifice. Thus, it would appear that there was simultaneous fluctuation in bolus volume and jet frequency. Either bolus volume was fluctuating before 1:1 transmission of "pacemaker" contractions, or 1:1 transmission was achieved and pacemaker frequency was fluctuating. Neither of these scenarios obeys the classical rules of urodynamics.

The subject who had no detectable flow for 150 sec was probably retaining urine in the renal pelvis or proximal ureter. Less likely explanations for cessation of observable flow are that urine output slowed dramatically or ceased, or that he achieved hydrostatic column flow with a velocity below the threshold of the color Doppler unit. The rapid, bizarre "recovery phase" jets may have been due to either noncoapting ureteric contractions superimposed on low-velocity streaming, or small coapting contractions. Short bursts of high-frequency ureteric pressure waves, interpreted as "cascade emptying of the renal pelvis," have been observed in pigs [14] but their frequency did not exceed eight per min.

The two episodes of ureteric streaming observed in one asymptomatic volunteer have been explained as a normal physiologic high-flow state. Burge et al. [3] did not observe this phenomenon in any of 17 hydrated healthy subjects studied with color Doppler sonography (for shorter periods than in this study) but did describe flow that "had a morphological appearance similar to that in the healthy subjects but continued nonstop throughout the entire examination" (5-8 min) from the contralateral ureter in four of 12 patients with high-grade ureteric obstruction. This contrasted with "low level/low intensity" continuous flow seen from two of 12 high-grade and two of 11 low-grade obstructed ureters. Burge et al. are applying a diagnostic distinction between "normal velocity" high-flow-state streaming from a kidney carrying the burden of an obstructed contralateral kidney and "low velocity" streaming from an obstructed ureter with disturbed ureterodynamics. As discussed earlier, factors other than velocity affect the intensity of the sonographic image of the urine stream. More accurate distinction between the two groups might be achieved by quantitative velocity measurement. Prolonged observation may also be of value because the high-flow stream might be expected to subside into normal jets (as was observed in this study) while an obstruction stream might not.

Summary

Color Doppler sonography can quantitate ureteric jets in most normal subjects, as long as renal function is not grossly abnormal and is an indirect noninvasive method of studying ureteric peristalsis. In the past, the acquisition of urodynamic information has been limited in humans by the invasiveness and/or poor resolution of ureteric pressure transducers, fluoroscopy, and radionuclide methods [17].

The relative frequency of jets during a 30-min period is the most consistently symmetric parameter in normal subjects. Discrete ureteric jets are not the only flow pattern observed in normal subjects. In one subject in this study, two episodes of ureteric streaming occurred, which are thought to be periods of physiologic high-flow state. Further study of this normal ureteric streaming may be necessary to accurately distinguish it from the streaming observed by Burge et al. [3] in patients with ureteric obstruction.

Although this study involved a relatively small group of subjects, the results both support and challenge the classical theory of ureteral urodynamics. The moment-to-moment frequency of jets often fluctuated during the examinations, but an underlying pattern of whole-number fractions of a "pacemaker" discharge rate was revealed in seven subjects. Our results also suggest that the pelvic pacemaker can respond more rapidly to momentary changes in urine output than previously believed and that bolus size varies before 1:1 transmission of pacemaker contractions occurs. The 150-sec episode of absent flow in one asymptomatic volunteer is probably explained by temporary retention of urine in the upper collecting system. The bizarre recovery phase jets that followed, however, are difficult to reconcile with current models of normal ureteric contraction. This 150 sec of absence of visible flow suggests that 5 min of examination (as performed by Burge et al. [3]) is not sufficient to confirm consistently the symmetry of jet frequency in healthy subjects.

REFERENCES

1. Marshall JL, Johnson ND, DeCampo MP. Vesicoureteric reflux in children: prediction with color Doppler imaging. *Radiology* **1990**;175:355-358
2. Jecquier SJ, Harriet P, Lafortune M. Ureterovesical jets in infants and children: duplex and Doppler US studies. *Radiology* **1990**;175:349-353
3. Burge HJ, Middleton WD, McLennan BL. Ureteral jets in healthy subjects and in patients with unilateral ureteral calculi: comparison with color Doppler US. *Radiology* **1991**;180:437-442
4. Royston P. Constructing time-specific reference ranges. *Stat Med* **1991**;10:675-690
5. Price Cl, Adler RS, Rubin JM. Ultrasound detection of differences in density: explanation of the ureteric jet phenomenon and implications for ultrasound applications. *Invest Radiol* **1989**;24:876-883
6. Kremer H, Dobrinski W, Mikyska M, Baumgartner M, Zollner N. Ultrasonic *in vivo* and *in vitro* studies on the nature of the ureteral jet phenomenon. *Radiology* **1982**;142:175-177
7. Elejalde BR, Mercedes de Elejalde M. Ureteral ejaculation of urine visualized by ultrasound. *JCU* **1983**;11:475-476
8. Weiss RM. Physiology and pharmacology of the renal pelvis and ureter. In: Walsh PC, Gittes RF, Perlmutter AD, Stamey TA, eds. *Campbell's urology*, 5th ed. Philadelphia: Saunders, **1986**:94-128
9. Briggs EM, Constantinou CE, Gonan DE. Dynamics of the upper urinary tract: the relationship of urine flow rate and rate of peristalsis. *Invest Urol* **1972**;56:56-62
10. Morales PA, Crowder CH, Fishman AP, Maxwell MH. The response of the ureter and pelvis to changing urine flows. *J Urol* **1952**;67:484-491
11. Griffiths DJ. Ureteral dynamics. *Semin Urol* **1987**;3:155-159
12. Constantinou CE, Hrynczuk JR. Urodynamics of the upper urinary tract. *Invest Urol* **1976**;14:233-240
13. Griffiths DJ. Flow of urine through the ureter: a collapsible, muscular tube undergoing peristalsis. *J Biochem Eng* **1989**;111:206-211
14. Tofft HP, Frokioer J, Mortensen J, Djurhuus JC. Renal pelvic peristalsis in pigs during standardized flow rate variations. *Urol Int* **1986**;41:292-298
15. Rose JG, Gillenwater JY. Pathophysiology of ureteral obstruction. *Am J Physiol* **1973**;225:830-837
16. Weiss RM, Biancani P. Characteristics of normal and refluxing ureterovesical junctions. *J Urol* **1983**;129:858-861
17. Muller-Suur R, Muller-Schauenburg W, Mesko L, Ohlson L. Urinary peristalsis investigated by radionuclide and X-ray methods: a comparison. *Scand J Urol Nephrol Suppl* **1988**;110:285-290

Radiologic-Pathologic Conferences of the Massachusetts General Hospital

Adrenal Pheochromocytoma

David G. Disler[1] and Felix S. Chew

A 62-year-old woman with a 20-year history of hypertension and occasional palpitations presented with a calcified right-upper-quadrant mass (Fig. 1). On CT, the mass involved the adrenal gland and had central necrosis. Sonography demonstrated solid and cystic regions. A rounded tumor with a pseudocapsule of compressed adrenal tissue, rim calcification, and central necrosis was resected. On microscopy the tumor resembled adrenal medullary tissue; specific histochemical and immunohistochemical stains provided the final pathologic diagnosis of pheochromocytoma.

Pheochromocytomas are rare, endocrinologically active tumors of the adrenal medulla that account for 0.5% of the cases of hypertension [1, 2]. Approximately 10% of pheochromocytomas are familial and may be components of the multiple endocrine neoplastic (MEN) syndromes, specifically type II or II(a) (medullary thyroid carcinoma, pheochromocytoma, and parathyroid adenoma) and type III or II(b) (medullary thyroid carcinoma, pheochromocytoma, mucosal neuromas, and marfanoid appearance). Pheochromocytoma may also be associated with neurofibromatosis or von Hippel-Lindau disease. About 10% of pheochromocytomas are bilateral, especially in the MEN syndromes, about 10% are extraadrenal in location, and about 10% have metastases, usually to nodes, liver, or bone [2].

Pheochromocytomas are slowly growing encapsulated tumors with a spherical shape over which residual adrenal tissue is stretched. Central necrosis and cystic change may occur. Most are several centimeters in size at the time of diagnosis, but the clinical presentation results from the tumor's uncontrolled secretion of epinephrine. Continuous or paroxysmal hypertension is consistently present, and patients typically have sweating attacks, tachycardia, or headache. The clinical diagnosis can be confirmed by measuring 24-hr urine levels of catecholamines or catecholamine metabolites, by measuring plasma catecholamine levels, by the glucagon stimulation test, or by the clonidine suppression test [1, 2]. In the proper clinical setting, most pheochromocytomas can be recognized on CT or MR imaging as round adrenal masses, 2.5 cm in size or larger. Calcification in the rim and central necrosis are common but not diagnostically specific. Bright T2 signal is usual on MR imaging. Whole-body scintigraphy with ^{131}I-metaiodobenzylguanidine may be necessary to localize extraadrenal disease [3, 4]. Surgery is curative unless metastases are present.

REFERENCES

1. Bravo EL, Gifford RW. Pheochromocytoma: diagnosis, localization and management. *N Engl J Med* **1984**;311:1298-1303
2. Gifford RW, Bravo EL, Manger WM. Diagnosis and management of pheochromocytoma. *Cardiology* **1985**;72(Suppl 1):126-130
3. Quint LE, Glazer GM, Francis IR, Shapiro B, Chenevert TL. Pheochromocytoma and paraganglioma: comparison of MR imaging with CT and I-131 MIBG scintigraphy. *Radiology* **1987**;165:89-93
4. Velchik MG, Alavi A, Kressel HY, Engelman K. Localization of pheochromocytoma: MIGB, CT, and MRI correlation. *J Nucl Med* **1989**;30:328-336

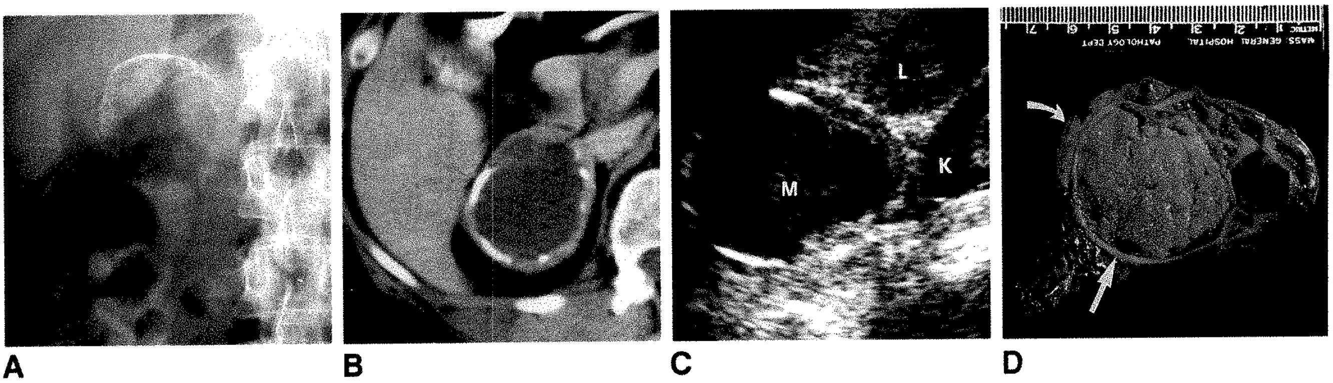

Fig. 1.—Adrenal pheochromocytoma.
***A*, Radiograph shows mass with calcified rim in right upper quadrant.**
***B*, CT scan shows adrenal mass with low-attenuation center.**
***C*, Sonogram shows that mass (M) is separate from liver (L) and kidney (K), and that it has solid and cystic components.**
***D*, Gross pathologic specimen shows a surrounding rim of normal adrenal tissue (*curved arrow*) and a calcified capsule (*straight arrow*) surrounding the tumor. There is a contiguous cystic region.**

From the weekly radiologic-pathologic correlation conferences conducted by Jack Wittenberg. Pathology editor: Andrew E. Rosenberg. Radiology editors: Felix S. Chew, William E. Palmer, Daniel P. Barboriak, Daniel I. Rosenthal.

[1] Both authors: Department of Radiology, Massachusetts General Hospital and Harvard Medical School, 32 Fruit St., Boston, MA 02114. Address reprint requests to F. S. Chew.

AJR **158:1056, May 1992** 0361-803X/92/1585-1056 © American Roentgen Ray Society

Testicular Microlithiasis:
Sonographic and Clinical Features

Dennis L. Janzen[1]
John R. Mathieson[1]
J. Ian Marsh[1]
Peter L. Cooperberg[1]
Pedro del Rio[1]
Ross H. Golding[2]
Matthew D. Rifkin[3]

Eleven cases of bilateral diffuse microlithiasis of the testes were evaluated sonographically. The presence of testicular microlithiasis was coincidental to the presence of testicular neoplasms ($n = 2$), nontesticular malignant lesion in the abdomen or chest ($n = 2$), subfertility ($n = 2$), varicocele ($n = 1$), epididymitis ($n = 1$), testicular maldescent ($n = 1$), scrotal trauma ($n = 1$), and transient scrotal pain ($n = 1$). Clinical follow-up suggested that testicular microlithiasis is an asymptomatic nonprogressive condition. Sonographic examination of testicular microlithiasis shows diffuse hyperechoic nonshadowing foci measuring 1–2 mm in diameter throughout both testes. The diagnosis of testicular microlithiasis was pathologically proved in five cases. In six cases, the diagnosis was made on the basis of the sonographic appearance ($n = 6$), clinical information and follow-up ($n = 6$), and radiologic demonstration of testicular microcalcifications ($n = 3$).

The sonographic appearance of testicular microlithiasis is specific, and we believe that biopsy or orchiectomy in these cases is unnecessary.

AJR **158:1057–1060, May 1992**

Testicular sonography is a well-accepted method of assessing testicular abnormalities. Sonography reveals homogeneous medium-level echogenicity in the normal testis. Foci of increased echogenicity may be seen in the mediastinum testis owing to invagination of the tunica albuginea and testicular vessels [1]. Focal echogenicities are occasionally seen in the testicular parenchyma; these are typically few in number and are usually due to spermatic granulomas, isolated intraluminal calcifications, or phleboliths [1, 2]. Larger diffusely hyperechoic testicular masses may represent benign processes such as fibrosis or granulomas [3, 4]. The presence of innumerable tiny echogenic foci throughout the testicle is uncommon. We present the sonographic and clinical findings in 11 patients in whom sonography showed innumerable tiny echogenic foci ("speckles") throughout both testes and in whom pathologic examination or clinical follow-up was consistent with the diagnosis of testicular microlithiasis (TM).

Materials and Methods

We analyzed retrospectively the medical records and sonographic images of bilateral diffusely speckled testes of 11 patients seen at our institutions from 1980 to 1991. In all patients, testicular sonography was performed with 7.5-MHz or 10-MHz linear-array and curved linear-array transducers, using commercially available imaging systems. We obtained testicular radiographs in three patients, using standard mammographic equipment and techniques.

In five cases, pathologic material was available, either from unilateral orchiectomy ($n = 4$) or from testicular biopsy ($n = 1$). Clinical follow-up was obtained in the remaining six patients from the primary physician and/or urologist. The patients were clinically assessed for any symptoms or signs of testicular disease. The duration of clinical follow-up ranged from 14 to 49 months.

Received September 30, 1991; accepted after revision December 12, 1991.

[1] Department of Radiology, University of British Columbia and St. Paul's Hospital, 1081 Burrard St., Vancouver, B.C., Canada V6Z 1Y6. Address reprint requests to J. R. Mathieson.

[2] Reno Diagnostic Center, 590 Eureka St., Reno, NV 89512.

[3] Department of Radiology, Albany Medical College, 47 New Scotland Ave., Albany, NY 12208.

0361-803X/92/1585-1057
© American Roentgen Ray Society

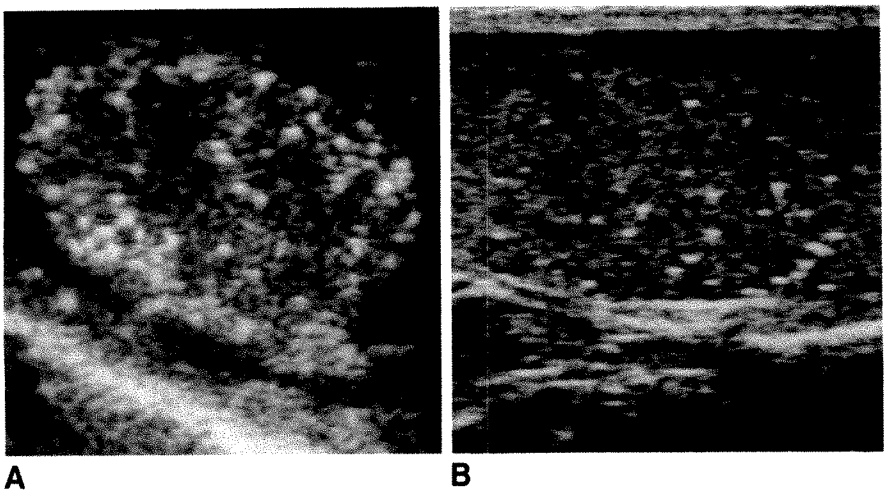
A B

Fig. 1.—Testicular microlithiasis. Sonograms from two different patients (*A* and *B*) show the typical speckled appearance of testicular microlithiasis. Multiple 1- to 2-mm hyperechoic foci are present diffusely throughout testes. The profusion of these foci is variable.

Results

The patients were 10–35 years old (mean, 28 years). The clinical indications for testicular sonography were the presence of an abdominal mass ($n = 2$), mediastinal and neck masses ($n = 1$), subfertility ($n = 2$), scrotal pain ($n = 2$), varicocele ($n = 1$), undescended testis ($n = 1$), scrotal trauma ($n = 1$), and a palpable mass in the testis ($n = 1$). None of the patients had undergone testicular sonography previously.

In all patients, sonography showed a diffuse bilateral speckled appearance in the testes studied. The hyperechoic foci were 1- to 2-mm in diameter and were randomly distributed throughout both testes. Profusion of the hyperechoic foci was variable (Fig. 1), and no acoustic shadowing was seen. The size and contour of the testes were normal, and the epididymis was normal except in one patient with epididymitis. No scrotal skin thickening or significant hydrocele was present. Use of a 7.5-MHz or 10-MHz transducer provided optimal visualization of the hyperechoic foci. Testicular radiography with mammography equipment was performed in three patients to confirm the presence of diffuse bilateral microcalcifications.

In two patients, sonography showed focal hypoechoic testicular masses, with diffuse speckled echogenic foci seen throughout both the uninvolved portions of the testicle and the entire contralateral testicle (Fig. 2). One of these patients presented with an abdominal mass, and pathologic findings showed seminoma and TM in the nonseminomatous portion of the testis. Pathologic results indicated that the patient with a palpable intratesticular mass had a seminoma as well as TM in the nonseminomatous portion of the testis. The presence of TM did not impair sonographic detection or evaluation of the hypoechoic testicular neoplasms.

Orchiectomy and pathologic examination revealed testicular microlithiasis with no evidence of malignant lesions in one of the patients who had an abdominal mass. Left testicular biopsy and pathologic examination showed TM with no evidence of malignant lesions in the patient who had neck and mediastinal masses. The neck and mediastinal masses were subsequently proved to contain large noncleaved cell lymphoma. This patient had a history of right testicular maldescent resulting in right orchiectomy at age 8. No focal hypoechoic region was found in either of these patients on testicular sonography.

Semen analysis and sperm motility studies were normal in the two patients with subfertility. One of the patients with scrotal pain had epididymal swelling and tenderness, which is consistent with epididymitis; in the second patient with scrotal pain, no cause was found. Sonograms of the patient who had had scrotal trauma showed TM; however, this diagnosis was not recognized. A unilateral orchiectomy was performed to evaluate the testes; pathologic examination showed TM. A left scrotal varicocele was seen in one patient. In another patient with an undescended left testis in the inguinal canal, sonograms showed hyperechoic foci, which were more numerous in the undescended left testis than in the normally descended right testis.

Pathologic specimens were available in five patients. Intratubular concentrically lamellated calcified bodies typical of TM were found in all cases (Fig. 3). No histologic evidence of inflammation or granulomatous disease was found.

Discussion

Testicular microlithiasis is an uncommon and nonprogressive entity that is typically discovered as an incidental finding during investigation of unrelated testicular symptoms [5]. Three previous cases have been reported in the English-language sonographic literature [5–7], and a series of five patients (three with histologic proof) has been reported in the Spanish-language literature [8]. Nine cases of pathologically proved TM without sonographic examination have been reported [9–16], and one study of autopsy specimens found testicular intraluminal calcifications in 0.05% of boys [11]. Histologic examination is probably more sensitive than sonography in detecting TM.

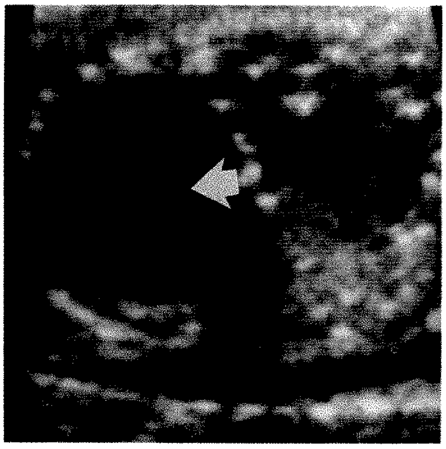

2

Fig. 2.—Longitudinal sonogram shows a hypoechoic region (*arrow*) representing seminoma. The remainder of the testis contains tiny hyperechoic foci typical of testicular microlithiasis.

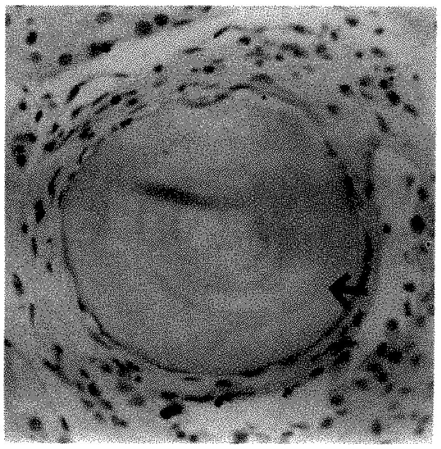

3

Fig. 3.—Photomicrograph of involved testicle shows concentrically lamellated calcific concretion (*arrow*) within lumina of seminiferous tubules. (H and E stain, original magnification ×100)

The sonographic appearance of TM is characteristic. Innumerable tiny bright foci, measuring less than 2 mm in diameter, are present diffusely throughout both testes. Acoustic shadowing is not seen, probably because of the small size of the calcifications. The hyperechoic foci correspond to the microcalcifications seen on testicular radiography and pathologic examination. There are no associated abnormalities in the epididymis or scrotal skin. Unilateral TM has not been described. The sonographic appearance of TM in our series is identical to that in previously reported cases [5–7, 17], two of which describe the same patient [6, 17].

Multiple hyperechoic regions may be seen on testicular sonography owing to calcified granulomas or focal scars; in these cases, the hyperechoic regions are larger and less numerous than those of TM [6]. Calcifications due to previous trauma or infection may be found in the epididymis or tunica vaginalis testis [4]. Solitary hyperechoic testicular masses can be caused by scar tissue, fibrosis, or benign adenomatoid tumors [3]. Hyperechoic regions can also be seen in the testicle as a result of orchitis [1], sarcoidosis [18, 19], or chronic infarction [19]; however, these hyperechoic regions are larger and less well defined than those seen in TM. Solitary hyperechoic regions greater than 5 mm in diameter have been described in nonviable primary testicular germ cell tumors [20], in intratesticular lipoma [21], and in a benign fibrous intratesticular mass [4]. Recent reviews of the sonographic appearance of diffuse infiltrating testicular diseases do not describe a speckled appearance [22, 23].

The diffuse speckled appearance seen in TM has not been described in association with any other testicular abnormality. Histologic examination of the diffusely speckled testicle has invariably documented the presence of TM [5–9, 17]. We believe that this speckled sonographic appearance is specific to TM, and therefore biopsy or excision in these cases is unnecessary. Testicular radiography may be useful to confirm the presence of intratesticular calcifications [9].

The hyperechoic foci seen on sonography represent calcified concretions within the lumina of the seminiferous tubules [5–7, 9–16, 24]. These concretions are formed from degenerating tubular epithelial cells, which slough into the tubule lumina. Lamellated concentric layers of collagenous material form within the tubule lumina, and this material serves as a site for dystrophic calcification [10]. Luminal obstruction can occur, and as many as 30–40% of the seminiferous tubules may be involved [10].

TM is frequently associated with cryptorchidism or delayed testicular descent [5, 6, 9–11]; however, the precise incidence of TM in this group is not known. Of the 23 cases reported in the English-language literature and in the present series, nine were associated with cryptorchidism or delayed descent of the testicle. TM has been found at histologic examination in two of 30 patients with cryptorchidism [10]. Associations have also been reported between TM and Klinefelter's syndrome [12, 13], male pseudohermaphroditism [12], Down's syndrome [12], and pulmonary alveolar microlithiasis [14].

TM also has been associated with subfertility/infertility [8, 15, 24]. Oligospermia or azoospermia has been documented in three patients [8]; the two subfertile patients in our series had normal semen analyses. The cause of subfertility in TM patients has not been clearly established. Subfertility and TM may both be sequelae of testicular maldescent.

TM and testicular neoplasm can coexist. A case of malignant germ cell tumor [7] and two cases of seminoma in our series have been described in association with TM. The presence of TM did not impair sonographic diagnosis of the tumors. TM does not appear to be strongly associated with testicular neoplasm: none of the patients in our series developed clinically apparent testicular neoplasms during the follow-up period. However, this entity is associated with testicular maldescent and infertility, conditions that do carry an increased risk of testicular neoplasm. Since the risk of subsequent malignancy in testicular microlithiasis is unknown, clinical or sonographic surveillance of patients with TM may be prudent [7].

In summary, TM is an uncommon asymptomatic abnormality with a characteristic sonographic appearance. Patients' symptoms should not be attributed to the presence of TM; unrelated abnormalities should be sought. This condition can be associated with genetic and urologic abnormalities. The finding of bilateral speckled testes on sonography establishes the diagnosis of TM; therefore, biopsy or excision in these cases is unnecessary.

ACKNOWLEDGMENTS

We thank D. A. Stringer (British Columbia's Children's Hospital, Vancouver, B.C.), R. Pitman (Squamish General Hospital, Squamish, B.C.), and A. R. List (Auckland Public Hospital, Auckland, New Zealand) for providing cases.

REFERENCES

1. Krone KD, Carroll BA. Scrotal ultrasound. *Radiol Clin North Am* **1985**;23:121–139
2. Doherty FJ. Ultrasound of the nonacute scrotum. *Semin US CT MR* **1991**;12:131–156
3. Vick CW, Bird KI Jr, Rosenfield AT, Viscomi GN, Taylor KJW. Scrotal masses with a uniformly hyperechoic pattern. *Radiology* **1983**;148: 209-211
4. Lipinski JK, Rao CR. Ultrasound diagnosis of a benign calcified testicular mass: report of a case. *J Can Assoc Radiol* **1986**;37:112–113
5. Jaramillo D, Perez-Atayde A, Teele RL. Sonography of testicular microlithiasis. *Urol Radiol* **1989**;11:55-59
6. Doherty FJ, Mullins TL, Sant GR, Drinkwater MA, Ucci AA. Testicular microlithiasis: a unique sonographic appearance. *J Ultrasound Med* **1987**;6:389-391
7. Kragel PJ, Delvecchio D, Orlando R, Garvin DF. Ultrasonographic finding of testicular microlithiasis associated with intratubular germ cell neoplasia. *Urology* **1991**;37:66–68
8. MacKinnon J, Coz F, Diaz L. Testicular microlithiasis: echographic diagnosis of a new cause of orchialgia and infertility. *Rev Chil Obstet Ginecol* **1990**;55:6–9
9. Weinberg AG, Currarino G, Stone IC Jr. Testicular microlithiasis. *Arch Pathol* **1973**;95:312–319
10. Vegni-Talluri M, Bigliardi E, Vanni MG, Tota G. Testicular microliths: their origin and structure. *J Urol* **1980**;124:105–111
11. Nistal M, Paniagua R, Diez-Pardo JA. Testicular microlithiasis in two children with bilateral cryptorchidism. *J Urol* **1979**;121:535-538
12. Bieger RC, Passarage E, McAdams AJ. Testicular intratubular bodies. *J Clin Endocrinol Metab* **1965**;25:1340–1343
13. Lanman JT, Sklarkin BS, Cooper HL. Klinefelter's syndrome in a ten month old mongolian idiot: report of a case with chromosomal analysis. *N Engl J Med* **1960**;263:887-892
14. Coetzee T. Pulmonary alveolar microlithiasis with involvement of the sympathetic nervous system and gonads. *Thorax* **1970**;25:637–639
15. Schantz A, Milsten R. Testicular microlithiasis with sterility. *Fertil Steril* **1976**;27:801–804
16. Priebe CJ Jr, Garret R. Testicular calcifications in a four year old boy. *Pediatrics* **1970**;46:785–786
17. Mullins TL, Sant GR, Ucci AA, Doherty FJ. Testicular microlithiasis occurring in a post-orchiopexy testis. *Urology* **1986**;27:144–147
18. McAlister WH, Sisler CL. Scrotal sonography in infants and children. *Curr Probl Diagn Radiol* **1990**;19:219–222
19. Blei L, Sihelnik S, Bloom D, Stutzman R, Chiadis J. Ultrasonographic analysis of chronic intratesticular pathology. *J Ultrasound Med* **1983**;2: 17–23
20. Shawker TH, Javadpour N, O'Leary T, Shapiro E, Krudy AG. Ultrasonic detection of "burned-out" primary testicular germ cell tumors in clinically normal testes. *J Ultrasound Med* **1983**;2:277–279
21. Hertzberg BS, Mahony BS, Bowie JD, Anderson EE. Sonography of an intratesticular lipoma. *J Ultrasound Med* **1985**;4:619–621
22. Subramanyan BR, Horii SC, Hilton S. Diffuse testicular disease: sonographic features and significance. *AJR* **1985**;145:1221–1224
23. Rifkin MD, Kurtz AB, Pasto ME, et al. The sonographic diagnosis of focal and diffuse infiltrating intrascrotal lesions. *Urol Radiol* **1984**;6:20–26
24. Sasgawa I, Nakada T, Kazama T, Satomi S, Katayama T, Matuda S. Testicular microlithiasis in male infertility. *Urol Int* **1988**;43:368–369

Case Report

Intratesticular Varicocele: Sonographic Findings in Two Patients

Alex J. Weiss,[1,2] Gary M. Kellman,[1] William D. Middleton,[3] and Aaron Kirkemo[4]

Varicocele is a common entity, with a reported occurrence rate in the normal adult population of 8–20% [1, 2]. The condition is characterized by dilatation of the veins of the spermatic cord. Varicocele may be associated with male infertility, scrotal mass, testicular pain, or atrophy. We describe two patients with the unusual finding of dilated intratesticular veins with associated ipsilateral varicocele. We refer to this finding as intratesticular varicocele. To our knowledge, this entity has not been previously reported.

Case Reports

Case 1

A 34-year-old man was referred for scrotal sonography after tenderness in his right testicle was noted during a physical examination before vasectomy. The patient experienced pain only when the testicle was palpated and reported he had experienced the pain in varying degrees since he had undergone right inguinal herniorrhaphy when was he was 5 years old.

Sonographic examination was performed with an Acuson 128 XP/10 (Mountain View, CA) and a 7.5-MHz linear-array transducer. Gray-scale and color Doppler sonographic studies were obtained at rest and during Valsalva maneuver with the patient supine.

Gray-scale images showed the right testis to be smaller and more hyperechoic than the normal left testis (Fig. 1A). The right testis also contained several abnormal hypoechoic tubular structures within and radiating from the mediastinum testis (Figs. 1A and 1B). Some of these structures contained low-amplitude echoes compatible with flowing blood. Moderately large varicocele was also present on the right side. Color Doppler sonography at rest showed symmetric flow in both testes, without demonstrable flow in the right intratesticular tubular structures. During Valsalva maneuver, a marked increase in venous flow was seen within these tubular structures (Fig. 1C). After cessation of Valsalva maneuver, the flow pattern reverted to normal. These flow characteristics paralleled those of the ipsilateral varicocele (Fig. 1C).

Case 2

A 60-year-old man presented with a periodically painful left scrotal mass. Gray-scale sonography (Advanced Technology Laboratories Ultramark 9, Seattle, WA) showed dilated left peritesticular veins. The left testis contained a serpentine hypoechoic structure arising from the mediastinum and extending into the testicular parenchyma (Fig. 2A). A subtle area of hypoechogenicity in the periphery of the left testis was also noted (Fig. 2B). The right testis appeared normal. During Valsalva maneuver, color Doppler sonography (Quantum QAD1; Isaquaah, WA) showed increased venous flow in the left peritesticular veins and in the serpentine hypoechoic structure in the left testis, confirming that this structure was a dilated intratesticular vein (Fig. 2C). In addition, the peripheral hypoechoic area in the left testis showed augmented venous flow and was thought to represent subcapsular veins that were too small to define on gray-scale imaging (Fig. 2C).

Received August 5, 1991; accepted after revision October 29, 1991.

[1] Department of Diagnostic Radiology, Henry Ford Hospital, 2799 W. Grand Blvd., Detroit, MI 48202. Address reprint requests to G. M. Kellman.

[2] Present address: Morton Plant Hospital, 323 Jeffords St., Clearwater, FL 34617.

[3] Mallinckrodt Institute of Radiology, Washington University School of Medicine, 510 S. Kingshighway, St. Louis, MO 63110.

[4] Department of Urology, Henry Ford Hospital, Detroit, MI 48202.

AJR 158:1061–1063, May 1992 0361–803X/92/1585–1061 © American Roentgen Ray Society

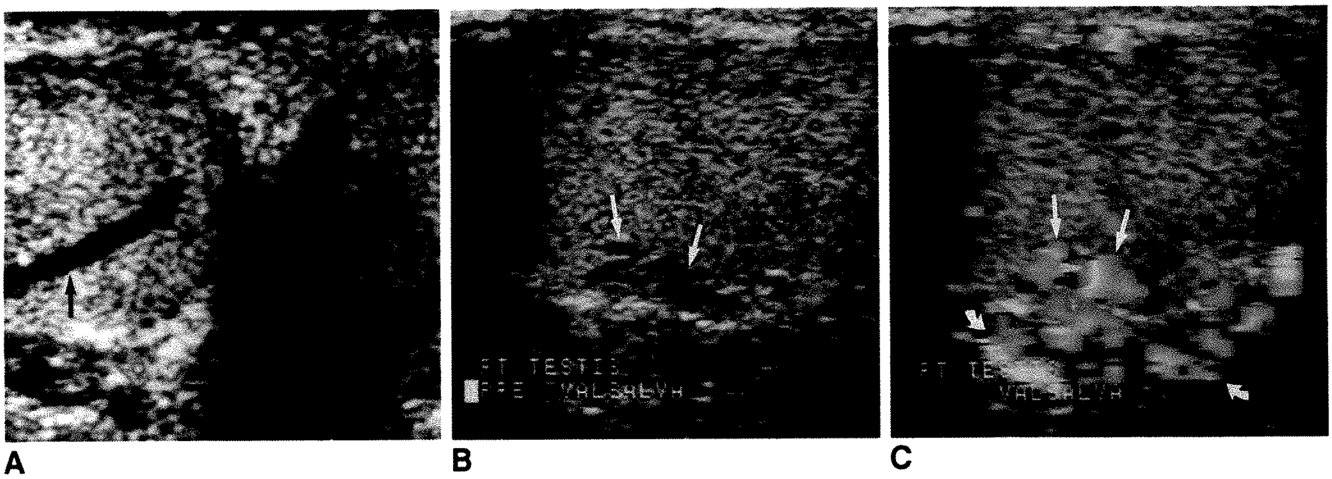

Fig. 1.—Gray-scale and color Doppler sonograms in a 34-year-old man with dilated intratesticular veins.

A, Transverse sonogram of scrotum shows a dilated vein (*arrow*) within right testis. Right testis is smaller and more hyperechoic than left testis.

B, Color Doppler image of right testis (with patient at rest) shows dilated veins near mediastinum testis (*arrows*) appearing similar to dilated rete testis.

C, Color Doppler image during Valsalva maneuver shows flow within veins confirming their vascular nature (*straight arrows*). *Curved arrows* show flow within varicocele.

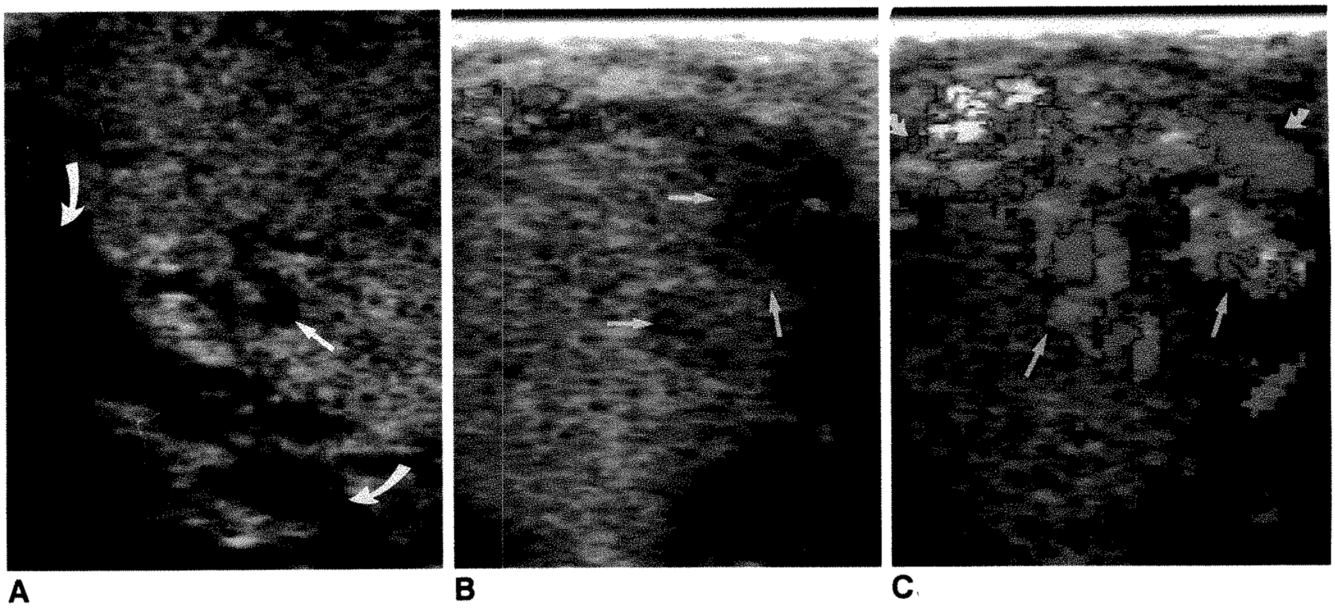

Fig. 2.—Gray-scale and color Doppler sonograms in 60-year-old man with dilated intratesticular veins.

A, Transverse sonogram of left testis shows serpentine dilated intratesticular vein (*straight arrow*) and adjacent varicocele (*curved arrows*).

B, Color Doppler image of left testis (with patient at rest) shows areas of subtle hypoechogenicity (*arrows*).

C, Color Doppler image of left testis during Valsalva maneuver shows increased flow within hypoechoic regions (*straight arrows*). This parallels the flow seen in dilated peritesticular veins (*curved arrows*).

Discussion

Varicocele is a relatively common condition that results from dilatation of veins in the pampiniform plexus. The majority of varicoceles are present on the left, and they are caused by incompetent or absent valves, venous compression, or pressure gradients [1-3].

The sonographic findings in varicocele have been well described [1-4]. The condition is seen as tubular serpentine structures exceeding 2 mm in diameter along the course of the spermatic cord or in the peritesticular region, usually posterior to the testis. These veins may enlarge further during actions that increase pressure within the spermatic venous system, such as when standing or when doing the Valsalva maneuver. Using high-frequency transducers, one can sometimes identify low-amplitude echoes from blood flow within the lumen of these dilated veins. Color Doppler sonography can facilitate the diagnosis of varicocele by demonstrating flow, either spontaneously or more commonly, when standing or doing the Valsalva maneuver.

The uniqueness of the two cases in this report lies in the patients having not only the typical findings of varicocele but also dilated intratesticular veins radiating from the mediastinum into the testicular parenchyma. To our knowledge, this finding has not been previously reported. In the first case, the veins near the mediastinum testis mimicked the appearance of tubular ectasia caused by dilatation of the rete testis [5] and the intraparenchymal veins were rather straight. In the second case, the veins appeared more serpentine; veins near the periphery of the testis were too small to resolve and appeared as an area of vague hypoechogenicity (Fig. 2B). In both cases, color Doppler sonography facilitated the recognition of these vascular structures by showing venous flow during the Valsalva maneuver, during which the flow characteristics of the extratesticular varicocele were also seen (Figs. 1C and 2C).

The differential diagnosis of hypoechoic lesions within the testicle may include neoplasm, orchitis, abscess, cyst, hematoma, and tubular ectasia. Only tubular ectasia has an appearance similar to intratesticular varicocele; use of color Doppler sonography, however, will help differentiate the two entities.

The clinical significance of an intratesticular varicocele is unknown. However, since its flow characteristics parallel those of the ipsilateral varicocele on color Doppler sonography, its pathogenesis may be similar to that of varicocele and thus may possibly affect spermatogenesis and male fertility.

In summary, intratesticular varicocele is a previously unreported entity seen as either straight or serpentine hypoechoic structures within the mediastinum testis and radiating into the testicular parenchyma. The condition may appear as a vague hypoechoic area in the testis or may mimic tubular ectasia. The condition is easily recognized by noting the presence of an ipsilateral varicocele and by confirming that the intratesticular structures are venous, which can be achieved by identifying flow with either high-resolution gray-scale imaging or preferably with color Doppler sonography. Further investigation is needed to determine the frequency and clinical significance of intratesticular varicocele in patients with typical extratesticular varicoceles.

REFERENCES

1. Rifkin MD, Foy PM, Kurtz AB, Pasto ME, Goldberg BB. The role of diagnostic ultrasonography in varicocele evaluation. *J Ultrasound Med* **1983**;2:271–275
2. Gonda RL, Karo JJ, Forte RA, O'Donnell KT. Diagnosis of subclinical varicocele in infertility. *AJR* **1987**;148:71–75
3. Shafrik A, Moftah A, Olfat S, Mohi-el-Din M, el-Sayed A. Testicular veins: anatomy and role in varicocelogenesis and other pathologic conditions. *Urology* **1990**;35:175–182
4. Wolverson MK, Houttuin E, Heiberg E, Sundaram M, Gregory J. High-resolution real-time sonography of scrotal varicocele. *AJR* **1983**;141:775–779
5. Weingarten BJ, Kellman GM, Middleton WD, Gross ML. Tubular ectasia within the mediastinum testis. *J Ultrasound Med* (in press)

Book Review

Musculoskeletal Imaging. MRI, CT, Nuclear Medicine, and Ultrasound in Clinical Practice. Edited by John A. Markisz. Boston: Little, Brown, 397 pp., 1991. $125

This book has about 600 illustrations and more than 400 references through 1989. The first section is an atlas of normal anatomy of the synovial joints. It consists of an introductory description of the gross anatomy and multiple MR images of each joint. This section makes up about one fourth of the book. The anatomic structures are depicted in multiple planes and are generously labeled, but in a considerable number of images, some of the structures are not visible or are barely visible. In addition, a few images have labeling errors, including sagittal images that are called coronal and vice versa.

The rest of the text is divided into 11 chapters, covering MR, scintigraphy, CT, and sonography. MR receives the greatest emphasis and accounts for almost 45% of the book. About 20% is devoted to scintigraphy, and the remaining 10% to CT and sonography. Selection of imaging techniques for specific clinical situations is addressed in each section.

Scintigraphy is covered in three chapters: evaluation and staging of neoplasms, imaging of bone disease in children, and diagnosis of joint pain. The chapter on evaluation of neoplasms is largely concerned with metastases and is thorough in presenting data on staging and follow-up studies of the common primary neoplasms. The chapter on bone diseases in children begins with a well-written section on methods and then presents a wide spectrum of diseases, with concise but pertinent discussions. Most of the cases presented in the chapter on joint pain not only show scintigraphic findings but also correlate other imaging findings.

The chapter on sonography presents disorders of the shoulder and includes two pages on tendons and soft tissues of the extremities. Tears of the rotator cuff receive the most attention. The quoted 90–100% sensitivity for detection of tears by experts seems to be an unduly optimistic goal for most radiologists.

The chapter on CT is divided into sections on bone tumors, soft-tissue lesions, and joint disorders. The illustrations are adequate. Most are of fractures or neoplasms. Several statements about CT are open to serious question: "With its higher resolution CT can usually confirm or disprove questionable x-ray findings." "CT is the modality of choice for evaluation of soft tissue lesions." "CT has been found to be accurate . . . in differentiating an osteochondroma . . . from a chondrosarcoma." In a concluding section in the chapter, "CT Compared with Other Modalities," MR is not included in the discussion of tumor treatment planning and posttherapy evaluation.

MR is presented in six chapters, beginning with a clear presentation of the principles of MR. A general chapter on bone disease discusses signal characteristics of normal bone and marrow and then discusses and illustrates a wide variety of pathologic changes. The soft tissues, spine, joints, and knee are each given separate chapters. Each of these chapters has an ample variety of illustrations and pertinent discussions of general principles along with specific diseases. Most of the illustrations are good to adequate. A few do not show the pathologic changes clearly.

This book on musculoskeletal imaging is heavily weighted toward MR. Currently, several textbooks on musculoskeletal MR are available, including Stoller's *Magnetic Resonance Imaging in Orthopaedics and Rheumatology* (1989, $115), Mink and Deutsch's *MRI of the Musculoskeletal System* (1990, $120), Berquist's *MRI of the Musculoskeletal System* (1990, $130), Pomeranz's *Orthopedic MRI* (1991, $90), and Beltran's *MRI of the Musculoskeletal System* (1991, $71). For readers primarily interested in MR, these texts offer more, and most are in the same price range as this book. Markisz's book, however, is an overview of all imaging techniques and can provide less experienced radiologists, residents, and clinicians with a broad but detailed introduction to musculoskeletal imaging.

Terrence C. Demos
Loyola University Medical Center
Maywood, IL 60153

Review Article

Lyme Disease and Radiologic Findings in Lyme Arthritis

Jack P. Lawson[1] and Daniel W. Rahn[2,3]

Lyme disease typically begins in the spring or summer months, with a pathognomonic skin lesion and associated flulike or meningitislike symptoms [1]. If the patient is not treated during this early stage, cardiac, neurologic, or musculoskeletal manifestations may occur weeks to months later [2]. Although the clinical picture of Lyme disease is extremely variable, the diagnosis can be made in most cases by recognizing the typical patterns of organ involvement and associated immunologic abnormalities [3].

Lyme disease is a tick-transmitted, spirochetal, infectious disease with multisystem inflammatory manifestations. It was first identified as a distinct entity in the United States in 1975 [4], but a similar illness, tick-borne meningopolyradiculitis, had been recognized in Europe decades earlier [5]. Although the precise incidence is unclear, Lyme disease is the most commonly reported vector-transmitted disease in the United States; cases have been reported from 43 of the states, particularly from the Northeast, the upper Midwest, and the Northern California coast. In fact, Lyme disease has a global distribution; it has been detected on all continents except Antarctica [6]. The causative organism, *Borrelia burgdorferi*, is transmitted by the nymph stage of infected ticks (*Ixodes dammini*, *Ixodes pacificus*, or *Ixodes ricinus*). These ticks are three-host organisms; in successive life stages, a tick may parasitize and infect a number of different animals, including mice, raccoons, and several other small mammals, in addition to the deer, which is the preferred host and breeding around for the adult ticks.

By 1988, 5000 cases of Lyme disease were being reported in the United States each year, but it is estimated that the actual incidence of the disease may be five to 10 times higher. The incidence appears to be increasing rapidly in some areas, presumably associated with urban development encroaching on the ticks' natural habitat. In certain areas of Westchester County, NY, for example, it is estimated that 25% of the deer-tick nymphs are infected; that in the wooded areas, one infected tick can be found in every 2 sq yd (1.6 m^2); and that in some urbanized areas, one infected tick can be found in every 4 sq yd (3.2 m^2) [7]. Public awareness and anxiety also have increased dramatically. In 1989, each of two commercial reference laboratories in the northeastern United States performed more than 100,000 serologic tests for Lyme disease [8].

Clinical Features

In most patients, the first evidence of Lyme disease is the appearance of the pathognomonic skin lesion, erythema chronicum migrans (ECM), at the site of a tick bite. The tick itself is no larger than a pinhead. ECM is an expanding, erythematous macular lesion with a sharply demarcated outer border and, frequently, partial clearing centrally. Although the lesions can occur anywhere on the body, they most frequently are found on the lower extremities and in the groin and axillae, sites preferred by the ticks that transmit the infection. A lesion can be up to 50 cm in diameter. *B. burgdorferi*, the causative organism, has been identified in and cultured from material from ECM lesions.

The interval between the tick bite and the appearance of ECM varies from several days to a month. However, only a

---

Received January 31, 1990; accepted December 4, 1991.

[1] Department of Diagnostic Imaging, Yale University School of Medicine, 333 Cedar St., New Haven, CT 06510. Address reprint requests to J. P. Lawson.
[2] Department of Internal Medicine, Yale University School of Medicine, New Haven, CT 06510.
[3] Present address: Department of Medicine, Medical College of Georgia, Augusta, GA 30912.

AJR 158:1065–1069, May 1992 0361–803X/92/1585–1065 © American Roentgen Ray Society

minority of patients with skin lesions recall a bite, and approximately one third of patients do not have this unique cutaneous marker of the early stage of Lyme disease. Nevertheless, ECM remains the best clinical marker of Lyme disease and often provides a definitive indication of the date of onset of the disease. Other signs and symptoms commonly associated with the early stage of Lyme disease include fever, chills, myalgias, arthralgias, headache, stiff neck, and exhaustion.

Nonspecific laboratory findings include mild leukocytosis, increased sedimentation rate, and minimally increased serum levels of transaminases. The most useful laboratory marker, however, is an increase in total serum IgM, which occurs in 33% of patients during the early stage, particularly those with systemic signs and symptoms and ECM. A persistent increase in total IgM in untreated patients is a predictor of risk for later manifestations of Lyme disease [9]. Specific antibodies against *B. burgdorferi* usually are not detectable with conventional enzyme-linked immunosorbent assays or immunofluorescence tests until 3-6 weeks after the onset of disease, so serologic tests are not generally helpful for early diagnosis [10]. Furthermore, these assays cannot distinguish between persons with active infection and persons with previous exposure without persistence of infection. The diagnosis of Lyme disease cannot be made on the basis of serologic results alone in the absence of appropriate clinical features.

Several weeks to a few months after the onset, most untreated patients have signs and symptoms of disseminated Lyme disease. In general, the sequence of organ involvement is predictable, but it can vary. Many patients do not seek treatment until late in the disease; therefore, initial clinical presentation with carditis, meningoencephalitis, or Lyme arthritis is not uncommon.

Lyme carditis typically occurs 4 weeks after the onset of the disease. It is relatively uncommon, however, affecting fewer than 10% of persons with untreated Lyme disease. The syndrome is transient; it resolves within a few days in most patients even without specific antibiotic therapy.

The neurologic manifestations of Lyme disease are variable and may occur anytime from a few days after the onset of the disease to years later. In the United States, in 10-15% of persons not treated during the early stage of the disease, neurologic signs develop within the first few months of illness. These include, in various combinations, meningitis, encephalitis, sensory and motor radiculoneuritis, and cranial neuritis. Lyme meningitis and encephalitis seem to be caused by direct borrelial infection of the CNS, and generally appropriate antibiotic therapy is rapidly effective. However, spirochetes have never been cultured from the nerves of patients who have the peripheral nervous system manifestations of Lyme disease, and antibiotic therapy is not as effective in these cases as it is in the CNS syndromes.

Lyme arthritis, the manifestation that in the United States led to the recognition of Lyme disease as a distinct illness, actually occurs late in the course of the disease for most patients. Migratory arthralgias and myalgias occur commonly early in the disease, often accompanied by ECM, but frank arthritis is rare in the first weeks of illness. In the past, some untreated patients have had migratory muscle, joint, or periarticular pain for as long as 6 years after ECM, without having joint swelling or other clinical signs and symptoms of inflammation. Migratory musculoskeletal pain is a common rheumatic complaint in persons suspected of having Lyme disease; the certainty with which this complaint can be attributed to Lyme disease is not always clear, however. In Connecticut, approximately 50% of persons with ECM who are not treated eventually have at least one attack of arthritis. The mean latency period from onset of disease to occurrence of arthritis is 6 months. The typical patient with Lyme arthritis has intermittent bouts of inflammation of one or a few large joints. The predilection is for involvement of the knees (80% of patients). Other areas involved include the shoulders, elbows, ankles, hips, wrists, small bones of the extremities, and the temporomandibular joints. Involvement of the temporomandibular joint is a diagnostically helpful feature because such involvement is rarely an early feature of other chronic arthritic disorders. The duration of these attacks of arthritis varies from several hours to a few weeks; chronic synovitis develops in only a minority of such patients. Approximately 90% of patients in whom chronic arthritis develops have DR4 or DR2 HLA alloantigens; these antigens are present in only 25% of patients in whom acute arthritis develops. The attacks are characterized clinically by short duration, swelling out of proportion to pain, and massive effusions; often 100 ml or more of joint fluid can be aspirated from the knee of a patient with acute Lyme arthritis. Joint fluid shows signs of inflammation; the number of leukocytes, which are mostly polymorphonuclear cells, is in the range of 20×10^3 cells/mm^3. *B. burgdorferi* has been detected in joint fluid and synovial biopsy samples [11]. Synovial involvement in Lyme arthritis is similar histologically to that associated with rheumatoid arthritis: synovial hyperplasia, synovial infiltration by lymphocytes, and vascular proliferation. The Lyme synovial lesion is unique, however, because perivascular tissues contain antigens of *B. burgdorferi*, which can be detected by staining with monoclonal antibodies [12].

The natural history of Lyme arthritis is variable. Episodes of inflammation, migratory pains, or chronic synovitis can recur intermittently for years. However, 10-20% of untreated patients with Lyme arthritis achieve spontaneous long-term remission yearly.

Radiologic Abnormalities in Lyme Arthritis

Since the disorder was first identified in 1976, more than 200 cases of Lyme arthritis have been studied at the Lyme disease clinic of Yale University School of Medicine. However, only 26 of the patients have had arthritic changes of sufficient duration and severity to merit radiologic examination [13]. Unfortunately the limited number of studies obtained in this small number of patients does not allow a clear description of the development and progression of the radiologic changes in this disease. Consequently, the abnormalities that have been detected represent only a qualitative assessment of the radiologic findings that may be noted in patients with severe Lyme arthritis.

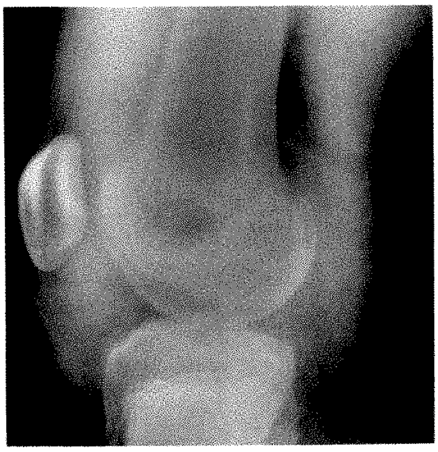

Fig. 1.—13-year-old boy with Lyme disease who had intermittent soft-tissue swelling and effusion of right knee for several months. Radiograph shows extensive soft-tissue swelling, a large effusion, areas of mottled density involving infrapatellar fat pad, and osteoporosis.

Soft-Tissue Changes

The most frequently detected abnormality in Lyme arthritis is joint effusion (Fig. 1). The most commonly affected joint is the knee; unilateral involvement occurs more frequently than bilateral involvement. Effusions of more than 100 ml may occur, and it is not uncommon for the amount of fluid to be greater than is anticipated from the patient's moderate discomfort. Arthrography may show irregular filling defects (shown surgically to be due to gelatinous chips of proteinaceous coagulum) and, frequently, a large posterior and inferior extension of the joint space (Fig. 2), similar to the giant synovial extensions associated with rheumatoid arthritis. MR imaging may show the large joint effusion and, in addition, both normal plicae and ribbonlike bands of hypertrophied synovium within the distended fluid-filled joint (Fig. 3).

A number of patients with warm and swollen joints have radiologic evidence not only of joint effusions but also of diffuse periarticular soft-tissue swelling associated with loss of musculotendinous planes (Fig. 1). This finding is frequently associated with edema of the infrapatellar fat pad and has been detected only when joint fluid or synovial thickening was present.

Many patients with radiologic evidence of joint fluid also have multiple areas of irregular, mottled density in the infrapatellar fat pad, suggesting edema (Fig. 1). MR imaging has shown that this is due to both edema of the fat and frondlike extensions of synovium and synovial fluid into the fat pad (Fig. 3).

Enthesopathic changes may be noted. Tendons around involved joints may be thickened. This thickening may be associated with loss of definition of the tendon margins and, frequently, loss of definition of adjacent soft-tissue planes. Generalized soft-tissue swelling may be present. Not surprisingly, the quadriceps tendon and the patellar ligament are the structures most frequently involved. Calcification or ossification may be detected in entheses (Fig. 4). Again, the entheses around the knee joint are the most commonly involved sites. New bone formation in the insertion of the joint capsule also has been detected (Fig. 5C). These enthesopathic changes have been shown in those patients with Lyme disease who have the most dramatic joint swelling.

Diffuse tenderness and swelling of a muscle or group of muscles may occur. The swelling can be detected on plain films and, more satisfactorily, on CT scans. On CT scans, the involved muscle groups have normal attenuation (Fig. 6A). Increased uptake of gallium-67 has been shown in the affected muscle groups of patients with Lyme disease (Fig. 6B).

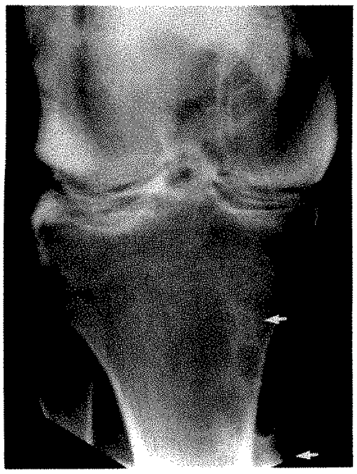

Fig. 2.—28-year-old woman with Lyme disease who had heat and swelling in right knee for 9 months. Double-contrast arthrogram shows contrast material and air (*arrows*) in an inferomedial extension of joint.

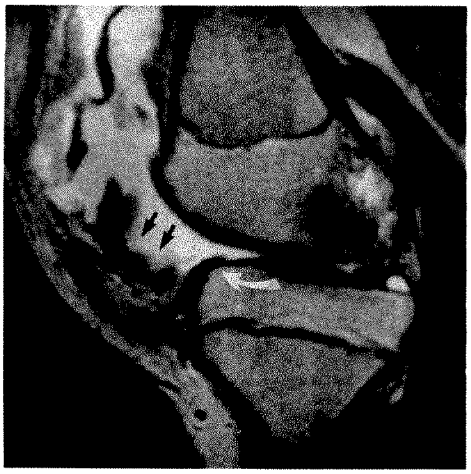

Fig. 3.—17-year-old boy with Lyme disease who had swelling of his left knee for 7 months. Sagittal T2-weighted MR image (1500/80) through medial condyle shows prominent effusion and ribbonlike folds of hypertrophied synovium. Large effusion had displaced meniscus anteriorly (*white arrow*). Frondlike extensions (*black arrows*) of synovium and synovial fluid extend into infrapatellar fat pad.

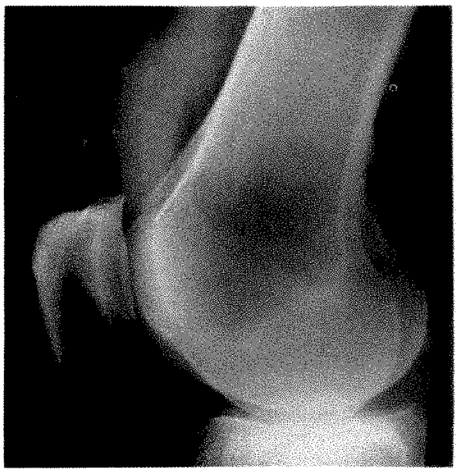

Fig. 4.—39-year-old woman with Lyme disease who had arthritis in left knee for 11 months. Radiograph shows multiple calcific densities in insertion of quadriceps tendon. (Reprinted with permission from Lawson and Steere [13].)

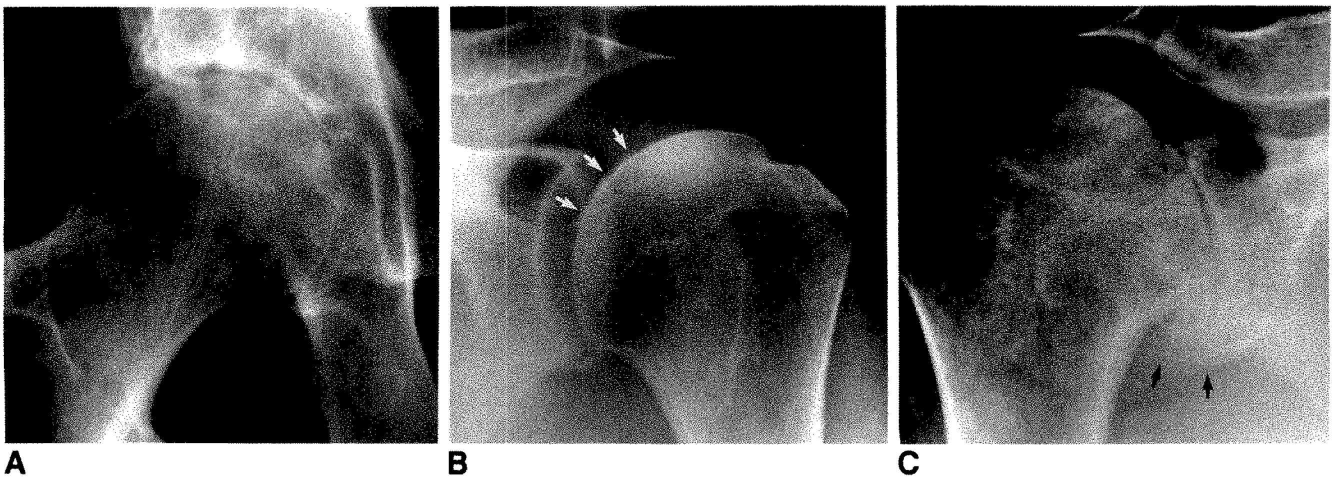

Fig. 5.—61-year-old man with Lyme disease who had arthritis in both hips and shoulders for 2 years.

A, Radiograph of right hip shows loss of articular cartilage, erosions of articular cartilage, and subarticular "cysts."

B, Radiograph of left shoulder shows calcification (*arrows*) in articular cartilage of humeral head. (Reprinted with permission from Lawson and Steere [13].)

C, Radiograph of right shoulder shows cartilage loss, erosions of articular cortex, and subarticular cysts. Note poorly defined new bone (*arrows*) at attachments of joint capsule.

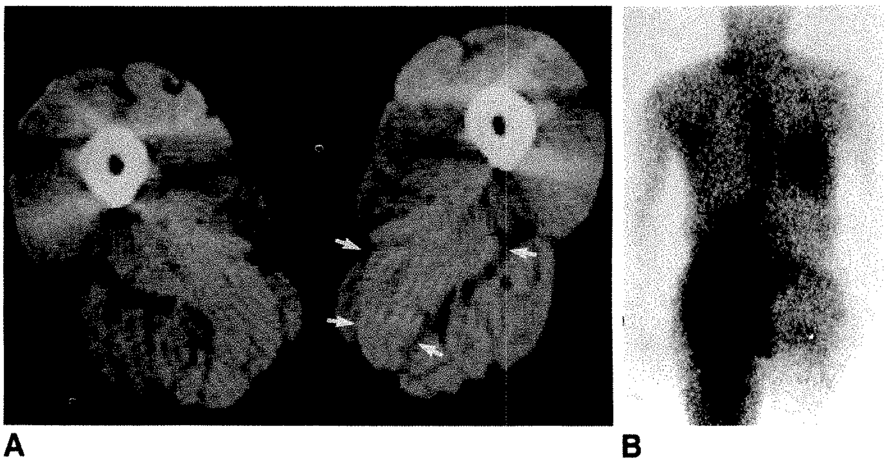

Fig. 6.—42-year-old man with Lyme disease who had muscle pain in left thigh for several months.

A, CT scan through middle of thigh shows diffuse enlargement of abductor group of muscles (*arrows*).

B, Posterior scintigram obtained 48 hr after injection of 5 mCi (185 MBq) of ^{67}Ga-citrate shows diffuse increased uptake of radionuclide in region of left gluteal, upper, and mid thigh muscles. Note cervical and axillary uptake on left side.

None of the patients with muscle tenderness or swelling have been examined by MR imaging.

Cartilaginous Changes

Loss of articular cartilage occurs in approximately 25% of patients who have chronic Lyme arthritis. This is seen most often in the knee joint but also may be detected in the shoulder and hip joints. The loss of cartilage is uniform and symmetrical and does not appear to involve the weight-bearing areas (Figs. 5A and 5C).

Chondrocalcinosis may occur. This finding has been associated with severe previous joint involvement. The finding may be fine, delicate, linear calcification of articular cartilage (Fig. 5B) or more extensive calcification of fibrocartilage (Fig. 7). In all instances, no other cause for the chondrocalcinosis could be established.

Osseous Changes

Periarticular erosions, presumably associated with synovial hypertrophy, may be seen on radiographs (Fig. 8). In addition, erosions of articular cortex, suggesting an origin in inflammatory cartilage, may be detected (Figs. 5A and 5C). These changes have been observed most often in the larger joints. However, this may simply reflect the joint distribution of the changes associated with chronic arthritis.

Osteoporosis may occur and may vary from mild to severe. It is usually juxtaarticular and most pronounced immediately adjacent to the articular cortex. The most pronounced osteoporosis has been detected in the youngest patients.

Proliferative formation of new bone may be detected, usually as formation of osteophytes. However, less well defined new bone may be seen at the joint margins. This is thought to represent a proliferative enthesopathy at the site of capsular or ligamentous attachments (Fig. 5C).

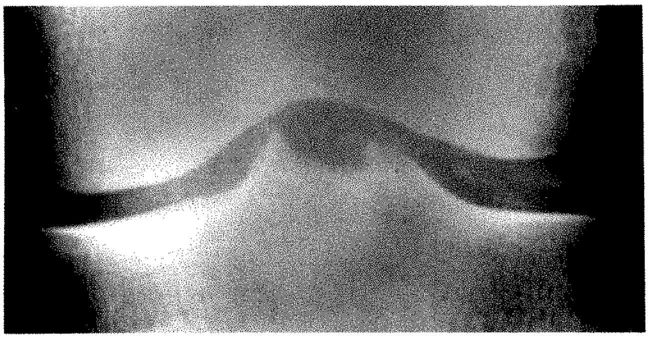

Fig. 7.—49-year-old man with Lyme disease who had intermittent clinically active arthritis in right knee for a total of 2 years. Radiograph of knee shows streaky calcification in both medial and lateral menisci.

Subarticular "cysts," particularly involving the knees and shoulder joints, may be detected. The cysts are usually small and multiple and may become confluent. Thin sclerotic margins are typical (Figs. 5A and 5C).

The constellation of osseous and cartilaginous changes found in the 26 patients with the most severe chronic Lyme arthritis suggested an inflammatory arthritis in 44%, a degenerative arthritis in 28%, and an arthritis with features of both processes in 28%. The changes may be age related. The median age of the patients with probable inflammatory arthritis was 29.5 years; the median age of the other two groups was 47 and 48.5 years, respectively.

Lyme disease has both similarities with and differences from several other rheumatic disorders. As in rheumatic fever, migratory polyarthritis and carditis may be features of the early stage of Lyme disease. However, the osteoporosis and large joint effusions, which are seen later in Lyme disease, are less marked in rheumatic fever. Furthermore, valvular involvement and the changes of Jaccoud (post-rheumatic fever) arthropathy have not been detected in Lyme disease. Although unusual, symmetrical polyarthritis, suggestive of rheumatoid arthritis, has been noted in Lyme disease. In these patients, who have not had rheumatoid factor, joint involvement has been intermittent. Because of the transient nature of these changes, radiographs have not been obtained in these patients. Both the clinical picture and the radiologic changes of Lyme arthritis may be similar to those of pauciarticular juvenile arthritis. However, in contrast to juvenile arthritis, in Lyme disease, antinuclear antibodies are rarely found, and iridocyclitis has not been detected. Prolonged monoarticular involvement without other signs and symptoms is unusual in Lyme disease, and when a patient has such involvement, Lyme disease must be distinguished from a slowly progressive infection. In adults, the asymmetrical and intermittent involvement of large joints, particularly the knee; the soft-tissue swelling; and the tendon changes all suggest Reiter's syndrome. In contrast to Reiter's syndrome, in Lyme arthritis, involvement of the joints of the feet is rare, and conjunctivitis, urethritis, mucocutaneous lesions, and involvement of the axial skeleton have not been detected.

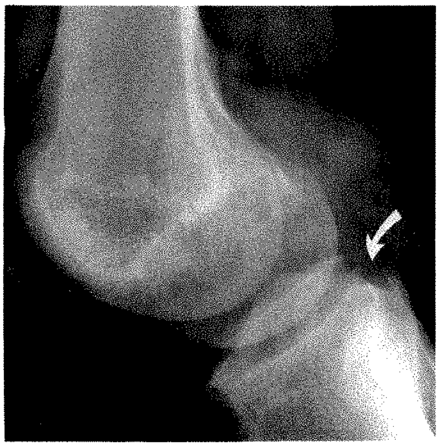

Fig. 8.—30-year-old man with Lyme disease who had intermittent arthritis for a total of 11 months. Radiograph shows erosion (*arrow*) in posterosuperior margin of tibia. Fullness in suprapatellar pouch was due to hypertrophied synovium and proteinaceous coagulum.

Recommendations for Diagnosis of Lyme Arthritis

Inflammatory changes in one or more large joints is the most common radiologic manifestation of Lyme arthritis; the knee is the joint most often involved. The disease can usually be diagnosed on the basis of the typical clinical features, namely, a history of the characteristic rash (ECM) or a flulike illness that occurs during the summer. Unfortunately, a history of tick bite is usually not obtainable. In those patients who initially seek treatment because of arthritis, the clinical picture may suggest rheumatic fever, pauciarticular juvenile arthritis (in children), or Reiter's syndrome (in adults). Serologic tests are generally not helpful in the diagnosis early in the disease but typically are positive at the time of later manifestations. Antibiotics are usually effective therapy for this potentially chronic disease. Thus, it is essential that in endemic areas, clinicians and radiologists be aware of both the usual and the less common manifestations of Lyme disease.

REFERENCES

1. Steere AC, Bartenhagen NH, Craft JE, et al. The early clinical manifestations of Lyme disease. *Ann Intern Med* **1983**;99:76–82
2. Steere AC, Malawista SE, Hardin JA, Ruddy S, Askenase PW, Andiman WA. Erythema chronicum migrans and Lyme arthritis. *Ann Intern Med* **1977**;36:685–698
3. Steere AC, Schoen RT, Taylor E. The clinical evolution of Lyme arthritis. *Ann Intern Med* **1987**;107:725–731
4. Steere AC, Malawista SE, Snydman DR, et al. Lyme arthritis: an epidemic of oligo-articular arthritis in children and adults in three Connecticut communities. *Arthritis Rheum* **1977**;20:7–17
5. Bannworth A. Zur klinik und pathogenese der "chronischen lymphozytaren Meningitis." *Arch Psychiatr Nervenkr* **1944**;117:161–185
6. Tsai TF, Bailey RE, Moore PS, Phil M. National surveillance of Lyme disease, 1987–1988. *Conn Med* **1989**;53:324–326
7. Daniels TJ, Falco RC. The Lyme disease invasion. *Nat Hist* **1989**;98:4–10
8. Schwartz BS, Goldstein MD, Ribeiro JMC, Schulze TL, Shahied SI. Antibody testing in Lyme disease. *JAMA* **1989**;262:3431–3434
9. Steere AC, Hardin JA, Ruddy S, Mummaw JG, Malawista SE. Lyme arthritis. *Arthritis Rheum* **1979**;22:471–483
10. Shrestha M, Grodzicki RL, Steere AC. Diagnosing early Lyme disease. *Am J Med* **1985**;78:235–239
11. Snydman DR, Schenkein DP, Berardi VP, Lastavica CC, Pariser KM. *Borrelia burgdorferi* in joint fluid in chronic Lyme arthritis. *Ann Intern Med* **1986**;104:798–800
12. Steere AC, Duray PH, Burcher EC. Spirochetal antigens and lymphoid cell surface markers in Lyme synovitis. *Arthritis Rheum* **1988**;31:487–495
13. Lawson JP, Steere AC. Lyme arthritis: radiologic findings. *Radiology* **1985**;154:37–43

Book Review

Orthopaedic MRI. A Teaching File. By Stephen J. Pomeranz. Philadelphia: Lippincott, 434 pp., 1991. $89.50

The author states that this book is intended to "provide a foundation for the late beginner to early intermediate orthopaedic MR reader." The format is a case presentation including one or more photographs and a specific question followed by a discussion and a diagnosis. Approximately half of the book is devoted to the knee. The remainder is fairly evenly divided between (1) shoulder; (2) hip, thigh, and proximal femur; (3) ankle, foot, and lower extremity; and (4) upper extremity and miscellaneous disorders. For any given anatomic region, more cases are generally devoted to more common problems. For example, in the section on the knee, a large number of examples of meniscal injuries and ligamentous damage provide a good overview for those relatively inexperienced in interpreting MR images. However, sufficient numbers of more difficult cases or uncommon entities keep a more advanced reader interested.

The figures are generally good to excellent, although I would prefer more T1- and T2-weighted images in the same plane at the same anatomic position. The author has thoughtfully included in almost every case a schematic line drawing illustrating the anatomy and the area of interest. This is a major strength of the book, as it facilitates evaluation of the images, something that will be appreciated by readers who are relatively inexperienced in MR.

Despite its strength, the book has several minor as well as major deficiencies. I wish it had more examples of normal anatomy, especially of areas other than the knee, where someone inexperienced in MR really would need such help. For example, one case describes disruption of the talofibular ligament in the ankle. An image of a normal ligament would be helpful for comparison. Another minor complaint is the actual arrangement of cases. Concepts are often mentioned in one section but not discussed until later in the book. For example, case 48 of the knee concerns the diagnosis of osteochondritis dissicans *extended classic type*, yet it is not until case 54 that the extended classic type of this disorder is defined.

Discussions generally address the issues and differential points associated with the images; however, the discussions are often imprecise. Sometimes the author has kept the discussion short at the cost of clarity. For example, patellar tracking and patellar abnormalities are concepts poorly understood by most radiologists. However, the discussion on the various measurements and the significance of tracking abnormalities left me with more questions than answers.

Also, inclusion of some references would be helpful. Although this book is intended to be a teaching file and not a systematic review of various diseases, I am uncertain about some discussions and frankly disagree with one or two. Appropriate references would facilitate my understanding.

However, my major concern with the book is the lack of attention to details. In particular, a number of figures are inverted, making comparisons difficult. Numerous figures are incorrectly labeled or incorrectly referred to throughout the book. The words hypointensity and hyperintensity are often interchanged. Perhaps more important, several case presentations have the wrong figures (alternatively, a paragraph from another case discussion has been inappropriately placed). The most glaring example is case 1 of the shoulder. The figures show a normal shoulder. However, the first paragraph of the discussion comments that there is no normal supraspinatous muscle, yet the next paragraph correctly labels the supraspinatous tendon. The second shoulder case contains what I think is the discussion of normal anatomy, yet the diagnosis is a tear of the rotator cuff, which is what is shown in the figure. A second example is reversal of pictures of a lipoma and a liposarcoma of a hand. Similar errors, though not so extreme, are seen throughout the book and could significantly confuse novices in MR. It is unfortunate that such errors were not detected before publication. Had they been detected and corrected, I would have said that this is an excellent book that accomplishes its task and is well worth being considered by both beginners and those more advanced in using MR. As it is, it is like many teaching files: filled with good cases, a few poor examples, and, occasionally, a film inadvertently placed in the wrong jacket.

Charles E. Spritzer
Duke University Medical Center
Durham, NC 27710

Review Article

Digital Skeletal Radiography

Kenneth A. Buckwalter[1] and Ethan M. Braunstein

Skeletal radiography accounts for a large proportion of the plain film images generated in most radiology departments, yet it has been underemphasized in the investigation of digital imaging technologies. Unique features of skeletal radiography provide a challenge in the evaluation and investigation of digital skeletal imaging. This review summarizes the results of ongoing research in digital skeletal radiography. Elementary concepts of digital imaging are reviewed to provide a foundation for discussion of nominal contrast and resolution requirements for clinically useful digital skeletal radiography. Methods of acquiring digital skeletal images are reviewed, and digital image display, image compression, and basic image processing techniques are discussed with emphasis on specific skeletal applications.

Currently, nearly 30% of the images generated in most radiology departments are in digital format [1]. This includes sonography, scintigraphy, CT, MR imaging, some angiography, and computed radiography. Most likely, the bulk of conventional projectional radiographs also will be acquired digitally in the future. Issues such as cost-effectiveness, diagnostic accuracy, and clinical efficacy need further investigation before computed radiography is universally accepted. Although much research has been conducted on digital imaging of the chest [2, 3], few articles have been published on digital skeletal imaging. This article reviews the clinically relevant research published on digital skeletal radiography.

Although chest radiography accounts for as much as 40% of all medical imaging performed in the United States [3], skeletal radiography accounts for a large fraction of the total number of plain film examinations. Thus, a large number of skeletal radiographs potentially may be digital. For this reason, it is important to understand the advantages and limitations of digital skeletal radiography before it is incorporated into general practice.

In order to understand these problems, it is necessary to review some basic concepts of digital imaging. These will be reviewed with emphasis on the spatial and contrast resolution requirements of skeletal radiography. The technologies used to acquire digital radiographs will be discussed and compared with one another. Additionally, unique features of skeletal images will be discussed in the context of image display, image archive, and image processing.

Chest vs Skeletal Radiography

Technical requirements for routine and mobile chest radiography are better defined than those for skeletal imaging. The 14 × 17 in. (36 × 43 cm) cassette is the standard size of adult chest radiographs. Film sizes for skeletal radiography vary widely. The high-kilovoltage technique and wide-latitude screen-film combination generally used in chest imaging are different from the low-kilovoltage technique and high-contrast screen-film combination used in skeletal radiography. Additionally, spatial resolution requirements for skeletal imaging vary depending on the purpose of the examination.

Unlike chest radiographs, skeletal radiographs may have uses other than diagnostic ones. Measurements obtained from the images are important for preoperative planning of joint replacement surgery. This may impede the acceptance of digital skeletal radiographs by referring orthopedists, es-

---

Received September 3, 1991; accepted after revision December 4, 1991.

[1] Both authors: Department of Radiology, Indiana University Hospital, Room X-64, 926 W. Michigan St., Indianapolis, IN 46202-5253. Address reprint requests to K. A. Buckwalter.

AJR 158:1071-1080, May 1992 0361-803X/92/1585-1071 © American Roentgen Ray Society

pecially with regard to soft-copy display and minified hard-copy images.

Digital vs Conventional Radiography

When assessing the development of computed radiography, it is important to compare it with conventional screen-film technology [4]. Film has multiple functions. Combined with the imaging screen, it serves as the X-ray detector. After development, it functions as the image archive. When placed on a light box, it displays the image. Obviously, film cannot perform all three tasks equally well. As a detector, film has excellent spatial resolution. However, the exposure latitude of screen-film combinations is limited and nonlinear. As an archival medium, film is excellent, although a single radiograph cannot be displayed in multiple locations simultaneously. As a display device, film is also excellent, showing a wide range of film densities on a properly exposed radiograph. The widespread use of conventional radiography is an indication of the success of film-screen technology.

Combining the functions of image capture, image display, and image archive requires some compromise in the optimization of each task. For example, the limited and nonlinear exposure latitude of a screen-film detector places a critical dependency on proper radiographic technique. This is particularly important for skeletal radiography, which is usually performed with a narrow-latitude technique, leaving less margin for error. Additionally, the wide variation in body and extremity thicknesses may result in underexposure in one part of a radiograph and overexposure in another part of the same radiograph. As film serves both as an archival medium and a display medium, lost, misplaced, or stolen radiographs can result in a permanent loss of information. The inability to view the original radiographic image simultaneously in two locations may compromise the delivery of clinically relevant interpretations. This is particularly important in an outpatient setting, and most of skeletal radiography is performed on outpatients. Another limitation of screen-film radiography is the inability to reproduce an exact copy of the image. Copy film does not faithfully duplicate all of the findings, particularly the more subtle ones.

Unlike conventional radiography, these film functions are uncoupled in digital radiography. Uncoupling allows optimization in the design and implementation of devices to perform each task. Each of these functions—image capture, archival, and display—will be discussed with specific applications to skeletal imaging. A review of the basic concepts of digital imaging is useful in understanding some of the problems and limitations of computed radiography.

Basic Concepts of Digital Radiography

Conventional film is an analog medium. To the naked eye, radiographic images are continuous; that is, an infinite number of elements appear to be making up the image, and each element has an infinitely variable gray value. A digital radiograph is a quantized representation of the spatial modulation of the X-ray beam after it passes through the patient. The individual sample points (pixels) are usually obtained in a rectangular pattern, with evenly spaced samples arranged in rows and columns. The number of pixels in the rows (m) and columns (n) determines the size of the image matrix, usually expressed as an m × n matrix size. The spacing of the pixels with respect to the original size of the image determines the *spatial resolution* of the image. Each pixel has an assigned gray level, and the range of available gray levels defines the image's *dynamic range*, which is determined by the number of bits per pixel. The distribution of the gray level values within the dynamic range is the *contrast resolution.*

One may express the spatial resolution of an imaging system by recording the resolving power of a line-pair phantom. Although the modulation transfer function provides a more complete assessment of spatial resolution, line-pair resolution is easier to measure. A large number of visible line-pairs per millimeter means a higher resolution. Measurements for conventional skeletal radiographs vary from 3–7.8 lp/mm [5], to 8 lp/mm [6], and 10–12 lp/mm [7]. In comparison, chest and gastrointestinal radiographs have a resolution of 4 lp/mm [6]. These measurements suggest that, aside from mammography, conventional skeletal radiography requires more spatial detail than any other plain film technique [8].

At least two pixels are required to represent the line and gap of a line-pair phantom on a digital image. In order to obtain a specific spatial resolution, it is necessary to adjust the pixel size. The size of the image will dictate the total number of pixels required to represent the image at a specific spatial resolution (see Appendix). Given equivalent-sized pixels, a larger image will require more total pixels to maintain the same spatial resolution as a smaller image. Additionally, a fixed matrix size may result in adequate detail for a smaller image but be inadequate for a larger image. This is particularly important in skeletal radiography, which requires multiple image sizes.

The dynamic range of digital images depends on the number of bits assigned to each pixel. This is typically 8, 10, or 12, representing 256, 1024, and 4096 possible gray values per pixel. Bits are grouped in 8-bit units called *bytes* for storage and computer processing. An image with 8 bits per pixel requires 1 byte, whereas an image with 10 bits per pixel requires 2 bytes for storage. Thus, a change from an 8-bit to a 10-bit per pixel image requires twice the memory or storage space.

Image transmission speed and archival space depend on the size of a digital image. Image size is the product of the number of pixels in the image matrix times the number of bytes per pixel. Doubling the spatial resolution quadruples the image size; however, increasing the gray scale range may not increase the image size in bytes. The data required for digital representation of conventional radiographic examinations may be considerable. A conservative estimate of storage requirements for a single 14 × 17 in. image is 40 megabytes [9] based on a 4096 × 4976 × 16 bit image matrix (approximately 5.7 lp/mm resolution). Because an average study requires four 14 × 17 in. image equivalents, 160 megabytes of storage would be needed for each examination. By comparison, a 30-image set of 512 × 512 × 12 bit CT images is only 16 megabytes.

Contrast and Spatial Resolution Requirements for Digital Skeletal Radiography

Several experiments have been devised to determine the effects of altered spatial and contrast resolution on diagnostic accuracy and lesion detectability in digital skeletal imaging [5–7, 10–15]. Both spatial and contrast resolution are important in determining the costs of digital radiography equipment, picture archiving and communication systems (PACS), and image workstations. These experiments suggest that resolution requirements depend on the imaging task.

Higher resolution images are needed to detect subtle changes. One particularly demanding task is the detection of subperiosteal resorption on hand radiographs. This was investigated by Murphey [11], who found that a spatial resolution of 5.7 lp/mm or less resulted in a loss of diagnostic accuracy in detecting subperiosteal resorption compared with conventional radiographs. Perhaps a more widespread application is the detection of nondisplaced fractures. Murphey et al. [6] tested a series of nondisplaced fracture images varying in resolution from 0.72 to 5.75 lp/mm and found that all fractures in a series of 56 radiographs could be detected at a resolution of 2.88 lp/mm (0.16-mm pixel size). Wilson et al. [14] compared high-resolution (5 lp/mm) photostimulable phosphor digital extremity radiographs with conventional radiographs and found conventional radiographs slightly superior in the detection of fractures. They believed that it is possible to compensate for this discrepancy during clinical practice, but concluded that conventional radiography should be available when digital images are equivocal if digital radiography is used as the primary imaging method in acute extremity trauma. Wegryn et al. [7] found that high variability between observers limited identifiable differences between digital radiographs obtained at 1.25 lp/mm resolution and conventional radiographs. Images with more subtle findings were also reviewed at 2.5 lp/mm. Wegryn et al. concluded that 1.25 lp/mm resolution was adequate for most tasks, but some subtle abnormalities required higher resolution.

Unfortunately, it is not always possible to determine how much detail will be required to make a confident diagnosis. A study comparing the effects of varying resolution on the detection of subtle gastrointestinal mucosal abnormalities suggested that more experienced observers detected abnormalities at lower levels of resolution [16]. It is not clear if the same is true with digital skeletal images. Early experience in digital skeletal radiography suggests that a resolution of 1.5 lp/mm may be sufficient for teleradiology and may result in diagnostic images such as those required for gross fracture assessment, but 2.5 lp/mm resolution is preferable [12, 17]. Greater resolution may be necessary in some instances, such as diagnosing subperiosteal resorption, subtle extremity fractures, or screening for child abuse. Magnification techniques can increase the effective resolution and may be helpful for certain examinations.

An advantage of digital imaging is the ability to alter the gray scale after the image has been acquired. To some extent, enhanced contrast resolution may partially compensate for the decreased spatial resolution [18]. One benefit is the reduction in the number of examinations repeated because of suboptimal exposure technique in conventional radiography, with a cost savings of $0.60/examination (1985 dollars) as estimated by Merritt et al. [19]. A substantial radiation savings, particularly important in children, is another advantage [20]. Serial examinations, such as scoliosis radiographs and leg-length scanograms, may be obtained at reduced exposure while maintaining diagnostic information [21, 22].

Digital Image Capture

Digital images can be acquired in several ways. In the simplest method, a conventional radiograph is converted to a digital image. One may digitize a video camera image of a radiograph with an analog-to-digital converter. Although the images can be acquired rapidly, both spatial and contrast resolution are poor, typically a 512 × 512 × 8 bit image matrix. These images are not suitable for primary image interpretation. In one series describing a clinical trial of teleradiology [23], clinically significant discrepancies between conventional and digital images were found in only 1.6% of comparisons, but a disproportionate number of these were skeletal radiographs.

Laser film digitizers are capable of performing rapid high-resolution film digitization. Radiographs are scanned line by line in "raster" fashion. The transmission of light from a small laser beam passing through the film is detected by a photo diode and converted to a digital number by an analog-to-digital converter. Typically, the size of the beam is 100–200 μm, representing a maximum spatial resolution of 2.5–5 lp/mm. Contrast resolution varies from 8 to 12 bits depending on the device.

More direct methods of image capture involve digitization of the X-ray image from an image intensifier, the standard technology used in digital angiography. Typically, 512 × 512 or 1024 × 1024 image matrices are available. The spatial resolution depends on the size of the image intensifier. Digital arthrography can be performed with these units [24–28], allowing subtraction of the bones and enhanced visibility of the contrast distribution. All three injections of a triple-compartment wrist arthrogram can be done [24] concurrently with digital subtraction. Preliminary results of K-edge digital subtraction arthrography of hip prostheses suggest that this may be a useful technique [26]. Unlike conventional temporal subtraction, which depends on rigid immobilization, K-edge subtraction can be performed at any time during an examination. Energy-selective filters are used to enhance the visibility of iodine-based contrast agents.

Limited experimental trials of large image intensifier systems measuring 47 cm or more in diameter have been conducted. Overall system resolution of one of these systems is 1.8 lp/mm [29]. A small series of patients with pulmonary nodules imaged on this system showed no statistically significant difference in detection compared with conventional chest radiographs. No large-scale series with skeletal applications has been published, but the authors of this series found the prototype unit useful in the assessment of trauma victims. Positioning is greatly facilitated by the fluoroscopy capability, but significant technical problems such as low spatial and contrast resolution, veiling glare, and poor scatter control may limit their application.

Electronic X-ray detectors offer a more direct way to capture the X-ray image in a digital format. These include spot scanners, slit and slot scanners, and charge-coupled devices (CCDs). Spot scanners produce an image by measuring the transmission of a pinpoint X-ray beam as it passes through the patient. There is essentially no scatter radiation, and there is high utilization of the X-ray dose. However, the relatively low spatial resolution and slow scan times are not suitable for imaging applications. This geometry is used in dual-energy X-ray absorptiometry equipment for measuring bone densitometry. The high precision (less than 1%) and low dose of this equipment suggest that it will displace dual-photon absorptiometry and quantitative CT in the screening and serial evaluation of patients with osteoporosis [30].

Slit scanners use a row of detectors (typically 1024 or 2048) that move in conjunction with a fan-shaped X-ray beam to scan the desired body region. Although total scan time may be several seconds for the selected anatomy, the effective exposure time is in the milliseconds range. There is low scatter with this geometry, measuring less than 1% [31]. However, conventional X-ray tubes may not produce sufficiently high X-ray output to enable penetration of thick tissues. Thus, the pelvis, lateral lumbar spine, lateral cervicothoracic junction, and other thick body parts cannot be imaged in most patients.

The slit geometry has been used by Picker (Picker International, Inc., Highland Heights, OH) in a dedicated digital chest unit. A further enhancement incorporates a dual-energy detector enabling energy subtraction radiography [32]. With this machine, it is possible to determine the mineral content of bone in nonoverlapping rib segments [33]. The accuracy of calcium quantification is high, and there is good correlation of posterior rib mineral measurements with dual-photon absorptiometry of the lumbar spine (r = .77), suggesting application in the assessment of patients with osteoporosis.

A more familiar application of digital slit radiography is found on most commercial CT scanners and allows one to obtain a scout scan to plan the position of the individual CT slices. Movement of the couch past a stationary X-ray tube and detector array creates a projection radiograph. Leg length discrepancy scanograms can be acquired in this manner with good correlation between the CT method and conventional radiographs [34, 35]. Radiation dosage is three to six times less with CT [35], and special modifications of the equipment are unnecessary. However, patients cannot be imaged in the standing position, and the table may not accommodate longer legs. A digital flying spot scanner was designed to overcome these limitations [36] and provides accurate distance and angular measurements.

Slot scanners are similar to slit scanners except that the X-ray beam and detector apertures are widened, enabling simultaneous detection of multiple lines of image data. This geometry reduces scatter compared with conventional radiography and allows more efficient use of the available X-ray beam. Slot scanners may be useful in imaging thicker body parts such as the pelvis with minimal compromise of image quality. However, the detector array is more complicated [37], and additional development is needed before a clinical device is available.

CCDs contain an integrated solid-state two-dimensional detector array. Widespread use of CCDs is common in consumer video cameras. They are small and sensitive to low light levels. Their size limits the ability to directly image most body parts except in dental radiography, although they can replace conventional television vidicon tubes in fluoroscopy equipment. Multiple CCDs can be placed end to end to form a slot scanner detector.

While most direct digital methods require special or modified equipment, it is possible to acquire digital images by using photostimulable phosphors [38] without modifying the X-ray equipment (Figs. 1 and 2). Imaging plates containing europium-activated barium fluorohalide compounds capture the

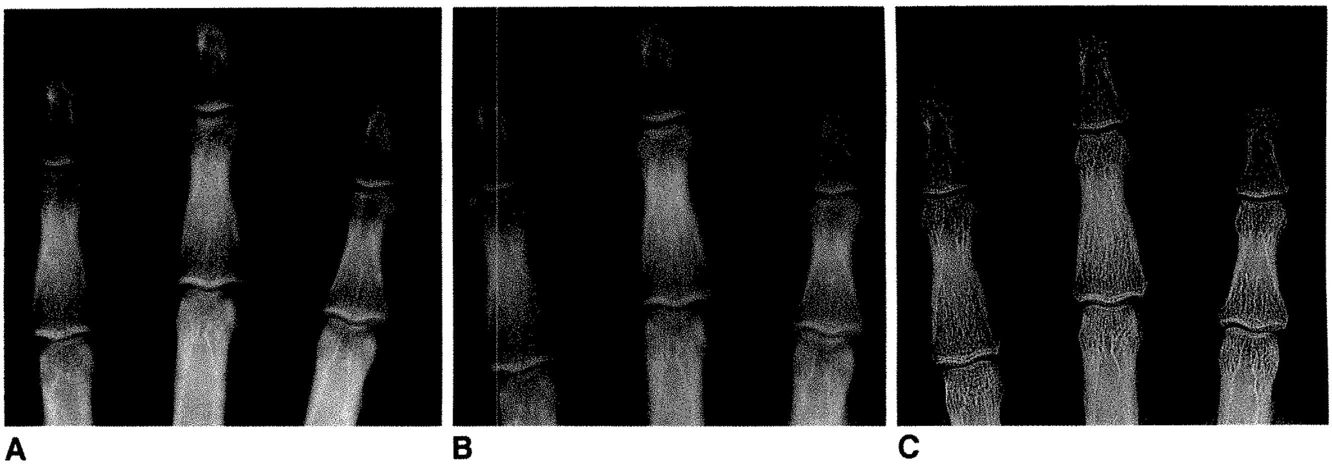

Fig. 1.—*A*, Detail view of conventional posteroanterior radiograph of the hand obtained at 52 kVp and 15 mAs by using a single-emulsion, single-screen cassette.

***B*, Computed radiograph of same hand obtained with high-resolution (5 lp/mm) storage phosphor, same technique. Default image processing produced an image with slightly less contrast than that on conventional radiograph.**

***C*, Unsharp mask filtering of image in *B*. Trabecular detail is more conspicuous and image appears to contain more detail, although resolution of these two images is identical.**

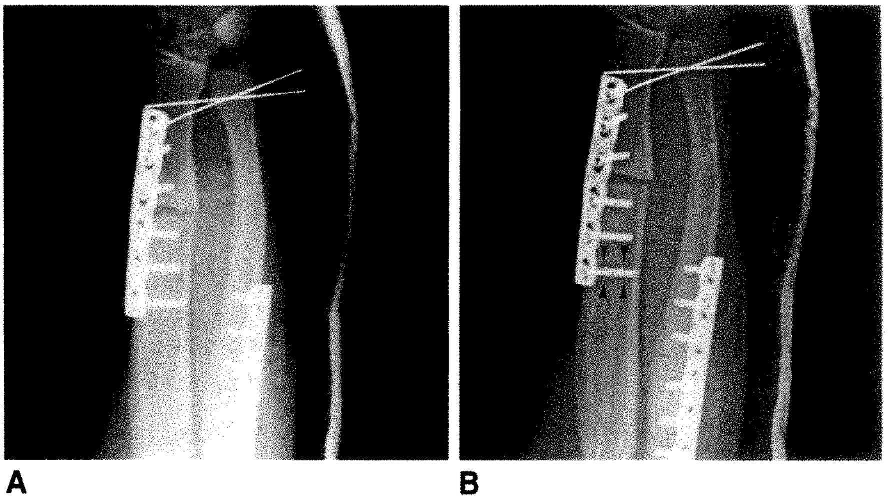

Fig. 2.—Computed radiographs of forearm 1 day after radius and ulna osteotomies.
A and *B*, Both conventional (*A*) and processed (*B*) images are printed simultaneously. Lucencies around hardware (*arrowheads*) simulate loosening, an image processing artifact.

X-ray image. These plates are similar to X-ray intensifying screens. However, conventional screens emit light when exposed to X-rays. In addition to this, photostimulable phosphors emit luminescence radiation (light) proportional to the incident X-ray exposure when excited by light, usually from a laser. Thus, a photostimulable screen stores a latent X-ray image that can be recovered from minutes to hours after the initial exposure. A special reader scans the phosphor with a laser, recording the light output emitted from the screen at each point. The phosphor plate is erased by exposure to high-intensity light and is available for immediate reuse. The phosphor plates can be used indefinitely, although repetitive handling limits their life span in practice.

The imaging plates are available in conventional cassette sizes and can be used in unmodified X-ray equipment. A commercially available computed radiography system developed by Fuji and marketed by Philips (Philips Medical Systems, Shelton, CT) has a nominal spatial resolution of 2.5 lp/mm for all image plate sizes. A 14 × 17 in. cassette size would be represented by a 1780 × 2160 image matrix size at this resolution. A high-resolution 8 × 10 in. (20 × 25 cm) plate, which has a resolution of 5 lp/mm, is available. Higher resolution systems are in development [39].

The dynamic range of photostimulable phosphor plates is more than 10,000:1 [38], much greater than for conventional screen-film radiography. In practice, this means that radiographic technique is not as critical as that in conventional radiography when using the imaging plates. This is particularly important in skeletal radiography when high-contrast, narrow-latitude screen-film combinations and low-kilovoltage technique are used. Techniques that would result in severely underexposed or overexposed radiographs can produce diagnostic images with the photostimulable plates.

There are no comprehensive published surveys of the use and distribution of digital imaging equipment. Excluding cross-sectional techniques and scintigraphy, it is likely that the most widely distributed digital technology is image intensifier based, used primarily for digital angiography. A relatively small number of digital arthrograms are performed with this equipment. Spot scanners are used almost exclusively for bone densitometry measurements, and there are approximately 430 dual-energy X-ray absorptiometry machines in the United States at present (DePass J, LUNAR Radiation Corp., Madison, WI, personal communication). More unusual devices such as slit scanners are fewer in number and usually are located in academic centers. Film digitizers are an integral part of PACS, used to convert conventional radiographs into digital form for archive and display or transmission and remote printing. These devices are located primarily in a few larger centers with a strong commitment to PACS development and implementation.

Photostimulable phosphor technology is the most widely used technology in the capture of projectional radiographic images. In 1990, 30 photostimulable phosphor imaging devices were installed in the United States, 250 in Japan, 35 in Europe, and three in parts of Asia outside Japan [40]. The acceptance of this technology is partly related to the absence of a need for specialized X-ray equipment. Photostimulable phosphor imaging can coexist with conventional radiography, and a dedicated PACS system is not mandatory for implementation. The larger number of installed systems in Japan is partly related to government subsidies associated with the use of computed radiography.

Our experience at the Indiana University Medical Center with digital radiography is concentrated at the James Whitcomb Riley Hospital for Children. A total of 71,000 imaging studies were performed at this 262-bed pediatric hospital in 1990. Of these, 27,700 (39%) were computed radiographic examinations performed with a photostimulable phosphor device. Skeletal examinations are almost exclusively performed with computed radiography and account for 9700 examinations, approximately 35% of the computed radiographic studies. The balance of the computed radiographic examinations are portable chest radiographs. The remainder of the plain film studies account for 26,980 examinations (38%). These examinations would be computed radiographs if the equipment capacity were expanded. Digital fluoroscopy and digital angiography account for 2650 (4%) of the total examinations. Cross-sectional technique account for 8550 (12%) and nuclear medicine studies account for 5200 (7%) of the examinations performed. Thus, a total of 44,120 (62%) of the examinations performed each year at this hospital generate digital images. At present, all images are photographed on film prior to interpretation. However, a remote, low-resolution television display and temporary image archive are located in the intensive care unit for immediate review of the computed radiography images by the clinical staff.

Digital Image Archiving

Archiving and transmission of digital images remain in a developmental stage. The set of image format and hardware standards developed by the American College of Radiology and the National Electronic Manufacturers' Association [41] represents an attempt to facilitate this process. Skeletal images have some unique properties that should be considered in the development of PACS. By conservative estimates, an average radiographic examination will generate approximately 40 megabytes of data [9]. Without some form of image compression, it will be impossible to store and transmit images efficiently with present technology.

Images can be compressed by reversible or nonreversible algorithms. Reversible compression results in storage of an image representation that is an exact duplicate of the original. Irreversible compression means that the stored representation is not exact. Image compression is described in terms of *compression ratios*, which represent the amount of storage required by the original image divided by the amount of storage required by the compressed image. Typically, reversible compression results in compression ratios up to 3:1 [42]. Irreversible compression ratios can be extremely high, from 15:1 to 90:1 [43], depending on the technique. However, image fidelity begins to suffer at higher compression ratios. Although the time to archive or transmit an image is reduced proportionately, more time may be required to process the images, possibly reducing the overall time savings. Experimental hardware has been designed to allow rapid compression of 1024 × 1024 and 2048 × 2048 matrix images with a compression ratio of 10:1 by using a full-frame bit-allocation algorithm [44].

The matrix size and image source determine the amount of compression that can be applied without loss of significant information [45]. In general, higher compression ratios are more acceptable with images of larger matrix size. For many compression strategies, the similarity of adjacent pixels, termed the spatial correlation, is an important factor in predicting the level of compression that can be applied. In general, images such as digital chest radiographs contain pixels with a high degree of spatial correlation and can be compressed more than CT or MR images that contain less well correlated pixels [46].

Skeletal radiographs contain many small structures such as trabecular bone as well as sharply defined, high-contrast margins such as the cortical bone–soft tissue interface. These features may be obscured with higher compression ratios [42, 44, 47]. Bramble et al. [48] investigated the effects of an irreversible compression algorithm (Fourier quantization) on the detectability of subperiosteal resorption in the hands. Compression ratios of 16:1 and 28:1 were applied to 512 × 512 × 12 bit images without a statistically significant loss in diagnostic quality. Although there was no statistically significant difference between 7- and 8-bit compressed images, the confidence of the radiologists in establishing the presence of subperiosteal resorption was reduced when interpreting the 7-bit images. The experience of these investigators suggests that empirical testing may be required to determine the optimal compression ratio allowable for a given task. Further research efforts are needed to evaluate both the effects of varying amounts and different image compression algorithms on the diagnostic accuracy of skeletal images.

Digital Image Display

Film, either used in the conventional manner or as output from a laser film printer, will remain an important means of displaying radiographic images [4]. A benefit of printing film images of digital radiographs is the ability to alter image size. Printing a 14 × 17 in. image on a 10 × 14 in. (25 × 36 cm) film results in a 41% reduction in film area. By one estimate, an overall film cost reduction of 31.5% can be achieved if chest radiographs account for 40% of the volume [20]. This number may be misleading, as it applies only to film savings and does not account for purchase of computed radiographic equipment, maintenance, and other costs.

Minified film images may cause problems in the preoperative planning of joint reconstructive surgery. Joint prosthesis templates are reproduced at specific magnification factors and may not be used on minified images without resizing the template. This is not practical, as the amount of minification may not be standardized. Additionally, distance and size measurements made from minified images are more critical because of the smaller pixel size. Template fitting could be performed electronically or automatically with computer assistance, but this would require specialized equipment in the surgeon's office.

Images may be minified by decreasing the total number of pixels comprising the displayed image or by reducing the size of each of the individual pixels in the displayed image. If the total number of pixels is decreased, there is a potential loss of information. If the size of the individual pixels is decreased, small structures may be more difficult to see, especially if the viewing distance remains constant. The effect of altered image size on the detection of specific skeletal abnormalities has not been investigated. Experiments performed with chest images suggest that this may be an important consideration. One study found a positive correlation between overall image size and the detection of small nodules from video displays [49]. A related study evaluating the detection of nodules on a chest phantom image showed no significant difference between minified film images and conventional radiographs [50]. An evaluation of storage phosphor chest radiographs vs conventional chest radiographs [51] revealed that some of the physicians participating in the study would be less confident interpreting minified film images, although the effect of image minification on diagnostic accuracy was not assessed.

Conventional television monitors cannot display high-contrast, high-resolution images. It is estimated that displays capable of 3300 × 4096 pixel resolution are needed to produce an image equivalent in quality to a radiograph [52]. At present, 2K × 2K displays are available, but 4K monitors with 72-Hz noninterlaced display rates present a technical challenge [53]. Enlargement or zooming of a portion of the image can display the image at full resolution, but requires additional time for interpretation. The lower resolution 2048 × 2048 matrix displays correspond roughly to a 0.2-mm pixel size (2.5 lp/mm) for a 14 × 17 in. radiograph. It has not been proved that this is sufficient for routine imaging. The same 2048 matrix display can be used to display a smaller format 8 × 10 in. radiograph at roughly a 4 lp/mm resolution. The issue of higher resolution monitors may be more important in chest radiography than skeletal radiography owing to the larger image format. Most high-resolution skeletal work is done on smaller body parts.

The dynamic range of television monitors limits the image display to fewer than 256 gray levels (8 bits). To some extent, windowing can overcome this limitation. Additionally, the luminance of a radiographic image displayed on a television monitor is roughly an order of magnitude less than the luminance of a conventional radiograph displayed on a view box, resulting in lower contrast sensitivity [54, 55].

The efficacy and accuracy of diagnosis of skeletal images from workstations need to be investigated. A few investigations comparing the display of chest or CT images have not demonstrated the equivalence of video monitors to film. One study comparing film to 1000-line television display of CT images showed sensitivity was better and reporting time shorter when interpreting film images [54]. A comparison between film and workstation interpretation of MR examinations of the knee showed equivalent performance, although image interpretation from a workstation required 2.7 times longer [56]. A comparison of digitized plain chest radiographs displayed on a 1000-line monitor showed equal sensitivity but greater specificity with film [57]. A receiver-operating-characteristic (ROC) study of chest radiographs that used a 2048-line display showed no significant difference between the film and video displays [58].

Image Processing

The objective of image processing is to improve diagnostic accuracy. The uncertainty about the effects of image processing on specific image features and the extra effort required have affected its acceptance in routine practice [59]. Although alteration of an image may improve the detectability of one type of abnormality, it may obscure another type, an effect observed in digital chest radiography. When unsharp masking is used, the visibility of pneumothorax is enhanced, but the detection of interstitial disease is diminished [60]. This and other examples suggest that a priori knowledge of the anticipated findings be used to select the imaging processing algorithm. However, important findings may be obscured with this approach. This has important medicolegal implications, and it suggests that an unprocessed version of the image be available at the time of interpretation. Unfortunately, this increases the time required for interpretation.

The two basic types of image manipulation are gray-scale transformation and spatial filtering. Gray-scale transformations involve the mapping of a given pixel value to a specific gray level. One of the simplest forms of image processing is a linear gray-scale transformation. This is the process that occurs when adjusting the window and level of an image. The transformation allows a specific range of pixel values to be displayed over the full dynamic range of the display device, enhancing contrast.

More complex gray-scale transformations involve analysis of the distribution of pixel values in the image. Histogram equalization is one way to reassign gray values in this manner. If the display parameters are fixed, it would be advantageous to ensure that all of the available gray values are equally used, regardless of the intensity distribution in the original image. Histogram equalization performs a gray-scale reassignment that attempts to use every available gray value equally. This tends to enhance low-contrast objects in the image, making them more visible.

Adaptive histogram equalization is a modification involving separation of an image into subregions that are individually histogram equalized. This technique has been applied to the analysis of digitized radiographs of destructive skeletal lesions [13]. Equalized images were superior in determining cortical breakthrough and presence of periosteal reaction as determined by ROC analysis. Other investigations of equalized digitized skeletal radiographs did not find the technique useful, although specific detection tasks were not investigated and only qualitative analysis was applied in the evaluation [10]. Although visually similar images can be obtained with scanning equalization radiography [61], an advantage of histogram equalization is that it is a postprocessing technique that can be applied after the image has been obtained. Additionally, no specialized radiographic equipment is required.

More complex forms of image processing involve filtering of an image. A variety of techniques can be used. One of the most popular is unsharp masking (Fig. 1C). Unsharp masking does not increase the resolution or information content of the image, although some structures in processed images appear to contain more details because of the enhancement of high spatial frequencies. In general, the contrast resolution of unsharp masked images is altered. This may obscure low-contrast objects, depending on the selection of the filter parameters [62]. One study analyzed the effect of unsharp mask filtering on the detectability of artificial cortical bone defects in human femur specimens. Computed radiographs of the specimens were obtained at 2.5 lp/mm spatial resolution with stimulable phosphor plates. Analysis of the observations with ROC methodology demonstrated that unsharp mask filtering did not help, especially with decreased kernel sizes and pronounced enhancement [5]. Aside from the effects of unsharp mask filtering, the investigators found that phosphor plate imaging was at least equal to conventional screen-film radiography with respect to contrast resolution in the detection of cortical bone defects. This is significant as spatial resolution is lower for the phosphor plate–generated images.

Conclusions

The basic principles of digital radiography have been summarized to provide a background for discussion of some of the properties of digital skeletal radiographs. Most of the research in computed radiography has been performed with chest images. However, skeletal radiography accounts for a significant proportion of the total number of plain film examinations performed in many radiology departments. Although some of the research results can be applied to skeletal imaging, unique properties of skeletal radiography require additional consideration. These properties include the high spatial resolution and high contrast of skeletal images as well as the wide variety of anatomic structures examined. Additionally, planning of joint replacement surgery from preoperative radiographs is a process unique to skeletal radiography. At present, precise matching of standard manufacturer-supplied templates to the radiographs requires near life-sized images.

An advantage of digital imaging is the ability to separate the tasks of image acquisition, image archiving, and image display. This separation facilitates optimal design of devices to perform these separate tasks. Conventional radiographic film combines these tasks, but compromises must be made. Perhaps the most severe compromise is the limited dynamic range of conventional screen-film technology. This is particularly important because conventional radiographic technique and screen-film combinations for skeletal radiography have narrow latitude with little margin for exposure error. Additionally, the use of film as both archival and display media limits the use of the radiographic image to a single site at any one time. These limitations are largely eliminated in digital imaging. Even if the images are printed on film, multiple identical copies can be generated concurrently at physically separate sites. This advantage is particularly desirable in a busy outpatient setting.

Excluding screen-film mammography, skeletal radiography requires greater spatial resolution than any other plain film technique. Nominal line-pair resolution measurements of conventional screen-film combinations for skeletal radiography vary from 8 to 12 lp/mm, while those for chest radiography are approximately 4 lp/mm. The most recent studies with digital skeletal images report that the minimum spatial resolution requirement for computed radiographs is between 2.5 and 5 lp/mm. Resolution requirements vary depending on the imaging task; unfortunately, it is not always possible to predict these requirements in advance. Higher resolution may be required in special circumstances, such as for detecting subtle subperiosteal resorption. Conversely, lower spatial resolution may be acceptable in the assessment of gross fracture alignment or scoliosis evaluation. The enhanced contrast and wider dynamic range of most digital radiography systems may partly compensate for reduced spatial resolution. Additionally, the ability to alter contrast can reduce exposure requirements and lower patient dose, particularly important in children.

Digital skeletal images can be acquired in many different ways. Some of the most important devices are laser film digitizers, image-intensified digital fluoroscopy, spot scanners, and photostimulable phosphor imaging plates. Laser film scanners convert conventional radiographs into digital images. These devices will play an important role in enabling conventional radiographs to be incorporated into a PACS environment. Image-intensified digital fluoroscopy is widespread because of digital angiography and has limited application to digital arthrography. Large-field-of-view image intensifiers have been built and can generate digital skeletal images, but technical problems limit their usefulness. Spot scanners are widely distributed and are mainly used for dual X-ray absorptiometry of the skeleton.

The most promising technology to date is one based on photostimulable phosphor imaging plates. These plates are compatible with conventional radiography equipment. Images can be filmed with a conventional laser camera. This eliminates the immediate need for a PACS environment and provides a bridge between conventional and future technologies. It may be extremely difficult to justify the purchase of such a system as it is replacement technology and does not generate additional direct revenues. Without a PACS network, some benefits of the system are lost. Careful analysis is required. The most appropriate time to consider such a commitment is in the creation, replacement, or expansion of a radiology department.

Digital images may be displayed on film or television monitors. Conventional television monitors cannot display high-contrast, high-resolution images. High-resolution 2K × 2K television monitors are currently available, but 4K monitors may be necessary to display some images at full resolution. Availability of higher resolution monitors may not be a problem with skeletal images, as most high-resolution skeletal imaging is done on smaller body parts. These images may be displayed at full resolution on a 2K monitor. High-resolution monitors are expensive, and many may be required throughout a hospital if film is to be eliminated. Film will probably remain an important means of image display because of its superior contrast and spatial resolution, although the film will originate as laser camera output.

The objective of image processing is to improve diagnostic accuracy. Two basic forms of image processing are gray-scale transformation and spatial filtering. Both have been applied to skeletal images. Adaptive histogram equalization of destructive skeletal lesions, a gray-scale transformation technique, improved detectability of cortical breakthrough and periosteal reaction. Unsharp mask filtering of cortical bone defects in human femur specimens, a spatial filtering technique, showed no improvement in detectability of the defects. Additional work is needed to determine if image processing can improve diagnostic performance.

Appendix

The following formula expresses the number of pixels (matrix size) required for a given nominal line-pair resolution and film-cassette size.

$$\text{Matrix size} = [(\text{nominal resolution in lp/mm})\ (2\ \text{pixels/lp})\ (\text{one cassette dimension in inches})\ (25.4\ \text{mm/in.})] \times [(\text{nominal resolution in lp/mm})\ (2\ \text{pixels/lp})\ (\text{other cassette dimension in inches})\ (25.4\ \text{mm/in.})].$$

As an example, a 14 × 17 in. cassette and nominal 2.5 lp/mm resolution would require an image matrix size of 1778 × 2159 pixels.

By modifying the formula, the pixel size can be obtained given the matrix size and the image field size.

$$\text{Pixel size in mm} = [(\text{image size in inches})\ (25.4\ \text{mm/in.})]/\text{matrix size}.$$

As an example, a 1024 × 1024 matrix with a 10 × 10 in. (25 × 25 cm) image size is composed of 0.25-mm pixels. To calculate the nominal line-pair resolution of such a configuration, multiply the pixel size in millimeters by two and take the reciprocal. Thus, this system has a nominal resolution of 2 lp/mm.

These calculations are useful in comparing the resolution of various systems as well as the storage requirements for images generated by different systems.

REFERENCES

1. McMillan JH, Huang HKB, Bramble JM, Siegel EL. Digital radiography. *Invest Radiol* **1989**;24:735–741
2. Fraser RG, Sanders C, Barnes GT, et al. Digital imaging of the chest. *Radiology* **1989**;171:297–307
3. Aberle DR, Hansell D, Huang HK. Current status of digital projectional radiography of the chest. *J Thorac Imaging* **1990**;5:10–20
4. Vizy KN. The roles of film in an increasingly computerized world. *Invest Radiol* **1989**;24:503–505
5. Prokop M, Galanski M, Oestmann JW, et al. Storage phosphor versus screen-film radiography: effect of varying exposure parameters and unsharp mask filtering on the detectability of cortical bone defects. *Radiology* **1990**;177:109–113
6. Murphey MD, Bramble JM, Cook LT, Martin NL, Dwyer SJ III. Nondisplaced fractures: spatial resolution requirements for detection with digital skeletal imaging. *Radiology* **1990**;174:865–870
7. Wegryn SA, Piraino DW, Richmond BJ, et al. Comparison of digital and conventional musculoskeletal radiography: an observer performance study. *Radiology* **1990**;175:225–228
8. Haus AG. Recent advances in screen-film mammography. *Radiol Clin North Am* **1987**;25:913–928
9. Cox GG, Arenson RL, Bosco HL. Current status of radiology image management systems. *Invest Radiol* **1988**;23:656–663
10. Sartoris DJ, Sommer FG. Digital film processing applications to the musculoskeletal system. *Skeletal Radiol* **1984**;11:274–281
11. Murphey MD. Digital skeletal radiography: spatial resolution requirements for detection of subperiosteal resorption. *AJR* **1989**;152:541–546
12. Bramble JM, Murphey MD. Comparison of digital and conventional musculoskeletal radiography: observer performance study (letter). *Radiology* **1990**;177:587–588
13. Braunstein EM, Capek P, Buckwalter K, Bland P, Meyer CR. Adaptive histogram equalization in digital radiography of destructive skeletal lesions. *Radiology* **1988**;166:883–885
14. Wilson AJ, Mann FA, Murphy WA, Monsees BS, Linn MR. Photostimulable phosphor digital radiograph of the extremities: diagnostic accuracy compared with conventional radiography. *AJR* **1991**;157:533–538
15. Pettersson H, Aspelin P, Boijsen E, Herrlin K, Egund N. Digital radiography of the spine, large bones and joints using stimulable phosphor. *Acta Radiol* **1988**;29:267–271
16. Kastan DJ, Ackerman LV, Feczko PJ. Digital gastrointestinal imaging: the effect of pixel size on detection of subtle mucosal abnormalities. *Radiology* **1987**;162:853–856
17. Seeley GW, Fisher HD, Stempski MO, Borgstrom M, Bjelland J, Capp MP. Total digital radiology department: spatial resolution requirements. *AJR* **1987**;148:421–426
18. Kundel HL. Digital projection radiography of the chest. *Radiology* **1986**;158:274–276
19. Merritt CRB, Tutto RH, Bell KA, et al. Clinical application of digital radiography: computed radiographic imaging. *RadioGraphics* **1985**;5:397–414
20. Kangarloo H, Boechat MI, Barbaric Z, et al. Two-year experience with a computed radiography system. *AJR* **1988**;151:605–608
21. Kushner DC, Cleveland RH, Herman TE, et al. Radiation dose reduction in the evaluation of scoliosis: an application of digital radiology. *Radiology* **1986**;161:175–181
22. Kogutt MS. Computed radiographic imaging: use in low-dose leg length radiography. *AJR* **1987**;148:1205–1206
23. Kagetsu NJ, Zulauf DRP, Ablow RC. Clinical trial digital teleradiology in the practice of emergency room radiology. *Radiology* **1987**;165:551–554
24. Quinn SF, Pittman CC, Belsole R, Greene T, Rayhack J. Digital subtraction wrist arthrography: evaluation of the multiple-compartment technique. *AJR* **1988**;151:1173–1174
25. Pittman DD, Quinn SF, Belsole R, Green T, Rayhack J. Digital subtraction wrist arthrography: use of a double contrast technique as a supplement to single contrast arthrography. *Skeletal Radiol* **1988**;17(2):119–122
26. Kelcz F, Peppler WW, Mistretta CA, DeSmet A, McBeath AA. K-edge digital subtraction arthrography of the painful hip prosthesis: a feasibility study. *AJR* **1990**;155:1053–1058
27. Resnick D, Andre M, Kerr R, et al. Digital arthrography of the wrist: a radiographic-pathologic investigation. *AJR* **1984**;142:1187–1190
28. Manaster BJ. Digital wrist arthrography: precision in determining the site of radiocarpal-midcarpal communication. *AJR* **1986**;147:563–566
29. Templeton AW, Dwyer SJ III, Cox GG, et al. A digital radiology imaging system: description and clinical evaluation. *AJR* **1987**;149:847–851
30. Sartoris DJ, Resnick D. Dual-energy radiographic absorptiometry for bone densitometry: current status and perspective. *AJR* **1989**;152:241–246
31. Tesic MM, Sones RA, Morgan DR. Single-slit digital radiography: some practical considerations. *AJR* **1984**;142:697–702
32. Barnes GT, Sones RA, Tesic MM, Morgan DR, Sanders JN. Detector for dual-energy digital radiography. *Radiology* **1985**;156:537–540
33. Friedman SE, Dubovsky EV, Dubovsky J, et al. Mineral content of bone: measurement by energy subtraction digital chest radiography. *AJR* **1987**;149(6):1199–1202
34. Helms CA, McCarthy S. CT scanograms for measuring leg length discrepancy. *Radiology* **1984**;151:802
35. Aitken AGF, Flodmark O, Newman DE, Kilcoyne RF, Shuman WP, Mack LA. Leg length determination by CT digital radiography. *AJR* **1985**;144(3):613–615
36. Wilson AJ, Ramsby GR. Skeletal measurements using a flying spot digital imaging device. *AJR* **1987**;149:339–343
37. Holdsworth DW, Gerson RK, Fenster A. A time-delay integration charge-coupled device camera for slot-scanned digital radiography. *Med Phys* **1990**;17(5):876–886
38. Sonoda M, Takano M, Miyahara J, Kato H. Computed radiography utilizing scanning laser stimulated luminescence. *Radiology* **1983**;148:833–838
39. Fuhrman CR, Gur DG, Schatzing R. High-resolution digital imaging with storage phosphors. *J Thorac Imaging* **1990**;5(1):21–30
40. Hunag HK, Cho PS, Taira R, Ho BK, Chan KK. Picture archiving and communication systems in Japan: 3 years later. *AJR* **1990**;154:415–417
41. Wang Y, Best DE, Hoffman JG, et al. ACR-NEMA digital imaging and communications standards: minimum requirements. *Radiology* **1988**;166(2):529–532
42. Lo S-C, Huang HK. Compression of radiological images with 512, 1,024, and 2,048 matrices. *Radiology* **1986**;161:519–525
43. Halpern EJ, Newhouse JH, Amis ES, Levy HM, Lubetsky HW. Evaluation of a quadtree-based compression algorithm with digitized urograms. *Radiology* **1989**;171:259–263
44. Ho BKT, Chao J, Zhu P, Huang HK. Design and implementation of a full-frame, bit-allocation image-compression hardware module. *Radiology* **1991**;179:563–567
45. Bramble JM, Huang HK, Murphey MD. Image data compression. *Invest Radiol* **1988**;23:707–712
46. Chan KK, Lou S-L, Huang HK. Full-frame transform compression of CT and MR images. *Radiology* **1989**;171:847–851
47. Lo S-C, Huang HK. Radiological image compression: full-frame bit-allocation technique. *Radiology* **1985**;155:811–817
48. Bramble JM, Cook LT, Murphey MD, et al. Image data compression in

magnification hand radiographs. *Radiology* **1989**;170:133-136
49. Fisher PD, Brauer GW. Impact of image size on effectiveness of digital imaging systems. *J Digital Imaging* **1989**;2:39-41
50. Brauer GW, Fisher PD, Hanley JA, Ritchie GW. Signal detection in digital chest-phantom images acquired with an image intensifier. *J Digital Imaging* **1989**;2:42-47
51. Fuhrman CR, Gur D, Good B, Rockette H, Cooperstein LA, Feist JH. Storage phosphor radiographs vs conventional films: interpreters' perception of diagnostic quality. *AJR* **1988**;150:1011-1014
52. Kazan B. New electronic displays and their possibilities for radiology. *Invest Radiol* **1989**;24:817-819
53. Siegel EL, Rosenthal SJ, Gold RE, et al. Interactive grayscale display workstations. *Invest Radiol* **1991**;26:479-484
54. Foley WD, Jacobson DR, Taylor AJ, et al. Display of CT studies on a two-screen electronic workstation versus a film panel alternator: sensitivity and efficiency among radiologists. *Radiology* **1990**;174:769-773
55. Siegel EL, Rosenthal SJ, Gold RE, et al. Interactive grayscale display workstations. *Invest Radiol* **1991**;26:479-484
56. Brown JJ, Malchow SC, Totty WG et al. MR examination of the knee: interpretation with multiscreen digital workstation vs hardcopy format. *AJR* **1991**;157:81-85
57. Goodman LR, Foley WD, Wilson CR, Rimm AA, Lawson TL. Digital and conventional chest images: observer performance with film digital radiography system. *Radiology* **1986**;158:27-33
58. Hayrapetian A, Aberle DR, Huang HK, et al. Comparison of 2048-line digital display formats and conventional radiographs: an ROC study. *AJR* **1989**;152:1113-1118
59. Hendee WR, Wells PNT. Visual perception as an opportunity for radiologic research. *Invest Radiol* **1989**;24:575-576
60. Goodman LR, Foley WD, Wilson CR, Tikofsky RS, Hoffmann RG. Pneumothorax and other lung diseases: effect of altered resolution and edge enhancement on diagnosis with digitized radiographs. *Radiology* **1988**;167:83-88
61. Wandtke JC, Plewes DB. Improved imaging of bone with scan equalization radiography. *AJR* **1991**;157(2):359-364
62. Loo L-ND, Doi K, Metz CE. Investigation of basic imaging properties in digital radiography. 4. Effect of unsharp masking on the detectability of simple patterns. *Med Phys* **1985**;12(2):209-214

LIST OF BOOK AND VIDEOTAPE REVIEWS

1006 **FRCR Part 1.** *Butler P, Blakeney CG, Brooks A, Speller R*
1010 **Color Doppler Flow Imaging.** *Foley WD*
1028 **Gastrointestinal Radiology.** *Farman J*
1064 **Musculoskeletal Imaging. MRI, CT, Nuclear Medicine, and Ultrasound in Clinical Practice.** *Markisz JA, ed*
1070 **Orthopaedic MRI. A Teaching File.** *Pomeranz SJ*
1086 **MRI of the Head and Neck.** *Lufkin R, Hanafee WN, eds*
1114 **Principles and Practice of Cardiovascular Imaging.** *Pohost GM, O'Rourke RA, eds*
1134 **MRI of the Spine.** *Quencer RM, ed*
1150 **MRI of the Brain III. Neoplastic Disease.** *Hasso AN, Shakudo M, Chadrycki E, eds*
1160 **MRI of Brain Tumors, parts 1 and 2.** *Solomon MA*

The Ulnar Tunnel at the Wrist (Guyon's Canal): Normal MR Anatomy and Variants

Jacob Zeiss[1]
Emery Jakab[2]
Tasneen Khimji[1]
Joseph Imbriglia[3]

The ulnar tunnel (Guyon's canal) is a fibroosseous tunnel along the anteromedial portion of the wrist that contains the ulnar nerve and artery. As with the adjacent carpal tunnel, its main clinical significance is that it may cause nerve compression. The purpose of this study was to determine whether the anatomy of this area could be depicted in sufficient detail by MR imaging for MR to be useful in the evaluation of patients with ulnar neuropathy. MR studies of 36 wrists of volunteers were reviewed with attention to the size and shape of the canal, its anatomic boundaries, the presence of anomalous muscles, the size and bifurcation of the ulnar nerve, and the presence of a fibrous or muscular arch overlying the deep motor branch of the ulnar nerve. T1-weighted transverse MR images of 3-mm-thick sections were obtained by using either an extremity coil or dedicated wrist coil. Excellent anatomic delineation was achieved. The boundaries and shape of the canal varied from proximal to distal, but no statistical differences were present in the mean cross-sectional area of the canal. Anomalous muscles were present in the canal in nine (25%) of 36 wrists; six (67%) of the nine were bilateral. The ulnar nerve had a mean diameter of 3 mm and bifurcated an average distance of 12 mm from the proximal margin of the pisiform bone. Delineation of the fibromuscular arch at the origin of the flexor digiti minimi brevis muscle was limited by imager resolution, but 50% were judged to be fibrous and 50% to be muscular.

Our results show that MR images depict the ulnar tunnel in excellent detail. Since those structures associated with ulnar neuropathy are clearly delineated by MR, the procedure should be useful in the evaluation of patients suspected of having ulnar nerve compression within the tunnel.

***AJR* 158:1081–1085, May 1992**

The ulnar nerve at the wrist passes through a fibroosseous tunnel known as Guyon's canal or the distal ulnar tunnel. The tunnel extends from the palmar carpal ligament at the proximal edge of the pisiform bone to the origin of the hypothenar muscles at the level of the hamulus, a distance of approximately 4 cm [1]. The ulnar artery and, occasionally, communicating veins accompany the nerve through the canal, which otherwise contains fat only.

The clinical importance of the tunnel is that it may become the site of ulnar nerve compression. A variety of causes have been determined, including trauma, lipoma, and false aneurysm of the ulnar artery [1–3]. Ganglion cysts causing nerve compression have recently been shown on CT and MR [4, 5]. In addition to such conditions, normal anatomic variants may predispose to compression neuropathy. One of these is the presence of abductor digiti minimi muscles coursing through the canal [6]. Another is the existence of a fibrous arch overlying the deep motor branch of the ulnar nerve as it passes under the origin of the flexor digiti minimi brevis muscle at the hook of the hamate [7].

This study was undertaken to determine the normal MR anatomy of the distal ulnar tunnel and to detect anatomic muscle variants in the region.

Received November 1, 1991; accepted after revision January 2, 1992.

[1] Department of Radiology, Medical College of Ohio, P.O. Box 10008, Toledo, OH 43699. Address reprint requests to J. Zeiss.

[2] Department of Orthopedics, Tampa General Hospital, P.O. Box 1289, Tampa, FL 33601.

[3] Department of Orthopedic Surgery, Allegheny General Hospital, 127 Anderson St., #201, Pittsburgh, PA 15212.

0361–803X/92/1585–1081
© American Roentgen Ray Society

Subjects and Methods

A total of 36 normal wrists from 26 volunteers were examined with MR imaging. One wrist was studied in 16 volunteers; both wrists were studied in 10 volunteers. The subjects were 16–38 years old, and included 13 males and 13 females. All imaging was done on a 1.5-T Signa scanner (General Electric, Milwaukee, WI) with either a General Electric extremity coil or wrist coil. Transverse sections, 3 mm thick, were done contiguously from the radiocarpal joint to the carpometacarpal joints. In those cases in which anomalous muscles were detected, both wrists were examined and imaging was extended into the forearm. T1-weighted images, 300–500/20–30 (TR/TE), were obtained with an 8- or 10-cm field of view, a 256 × 192 or 256 × 256 matrix, and two or four excitations.

Anatomic boundaries, and cross-sectional shape, dimensions, and areas of the tunnel were recorded at three levels: proximal tunnel at the mid pisiform bone, midtunnel between the pisiform bone and the hook of the hamate bone, and distal tunnel at the hook of the hamate bone. The tunnel inlet just proximal to the pisiform bone and the outlet just distal to the hamulus were also examined. Anomalous muscles within the canal were recorded. Ulnar nerve size and shape were noted at the level of the pisiform bone, and the distance from the proximal pisiform bone to the nerve bifurcation was measured. Superficial and deep branches of the nerve were traced beyond the bifurcation into separate superficial and deep canals. Finally, determination of a fibrous arch or a muscular arch overlying the deep motor nerve was attempted.

In order to correlate anatomic structures seen on the MR images, two wrists from cadavers were frozen and transverse sections 3 mm thick were compared with the MR images.

Results

The anatomic structures that defined the boundaries of the ulnar tunnel varied at each of the locations analyzed on the MR images and the cadaver sections (Figs. 1–3). The boundaries along dorsal, radial, and ulnar aspects of the canal were consistent. Volar boundaries varied, depending on the amount of hypothenar fat present and the extent of the palmaris brevis muscle anterior to the ulnar nerve and artery.

At the proximal end of the canal, the shape was generally triangular, with the base of the triangle directed toward the pisiform bone. The average transverse width of the tunnel was 11 ± 5 mm, and its greatest anteroposterior depth was 7 ± 4 mm. The mean cross-sectional area of the proximal portion of the tunnel was 32 ± 11 mm^2. The ulnar nerve and artery were clearly depicted and surrounded by fat (Fig. 1).

At the middle of the tunnel, the shape was either triangular or oval. The greatest mean transverse and anteroposterior dimensions of the tunnel were 13 ± 5 mm and 6 ± 4 mm, respectively. Cross-sectional area was 41 ± 14 mm^2. In every instance the ulnar nerve bifurcation occurred within a few millimeters of the midtunnel section (Fig. 2).

In the distal portion of the tunnel at the level of the hamulus the canal bifurcated into two separate channels: the continuation of the main ulnar tunnel containing the superficial ulnar nerve and artery and a deep tunnel containing the deep motor branch of the nerve (Fig. 3A). At the distal edge of the hamulus, there was either a fascial line or thin muscle band

Key to Abbreviations Used in Figures

ADM	abductor digiti minimi muscle
AM	anomalous accessory abductor digiti minimi muscle
DSUA	digital minimi branch of superficial ulnar artery
DSUN	digital minimi branch of superficial ulnar nerve
DUA	deep ulnar artery
DUN	deep ulnar nerve
DUNA	deep ulnar nerve and artery
FA	fibrous arch of flexor digiti minimi brevis muscle origin
FCU	flexor carpi ulnaris tendon
FDM	flexor digiti minimi brevis muscle
FR	flexor retinaculum or transverse carpal ligament
H	hamulus
ODM	opponens digiti minimi muscle
P	pisiform bone
PB	palmaris brevis muscle
PCL	palmar carpal ligament
PHL	pisohamate ligament
SUA	superficial ulnar artery
SUN	superficial ulnar nerve
TM	thenar muscles
UA	ulnar artery
UN	ulnar nerve
VV	veins

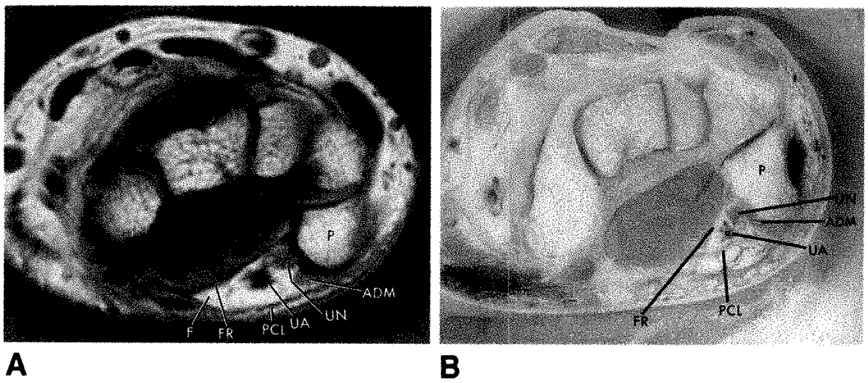

Fig. 1.—Proximal portion of ulnar tunnel. (See key for abbreviations.)

***A* and *B*, T1-weighted transverse MR image (*A*) and cadaveric section (*B*) at pisiform level show main ulnar nerve and ulnar artery coursing through fatty tissue (F) within tunnel. Anatomic structures defining boundaries of tunnel are demarcated. Cadaveric section shows significantly more palmar fat anterior to palmar carpal ligament than MR image does.**

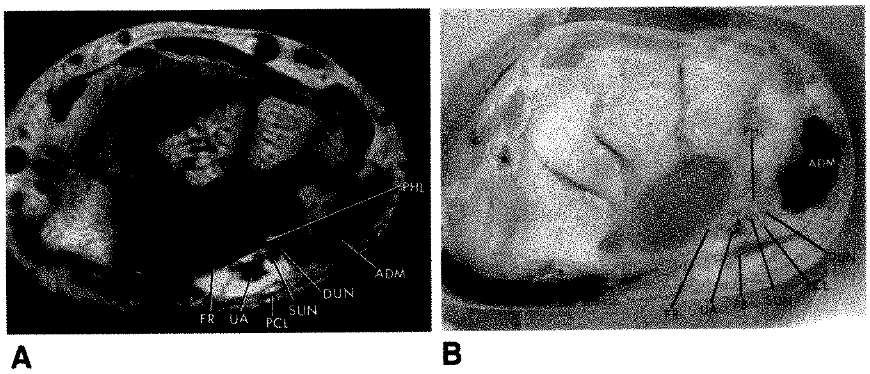

Fig. 2.—Middle portion of ulnar tunnel. (See key for abbreviations.)

***A*, T1-weighted transverse MR image shows tunnel between pisiform bone and hamulus, approximately 6–9 mm distal to tunnel in Fig. 1. Compared with proximal tunnel, pisiform bone has been replaced by abductor digiti minimi muscle, pisohamate ligament has become apparent, palmar carpal ligament has thinned, and main ulnar nerve and artery have bifurcated into superficial and deep branches.**

***B*, Corresponding cadaveric section shows similar dorsal, radial, and ulnar boundaries, but anteriorly shows palmar carpal ligament and palmaris brevis muscle embedded in larger amount of fibrofatty tissue.**

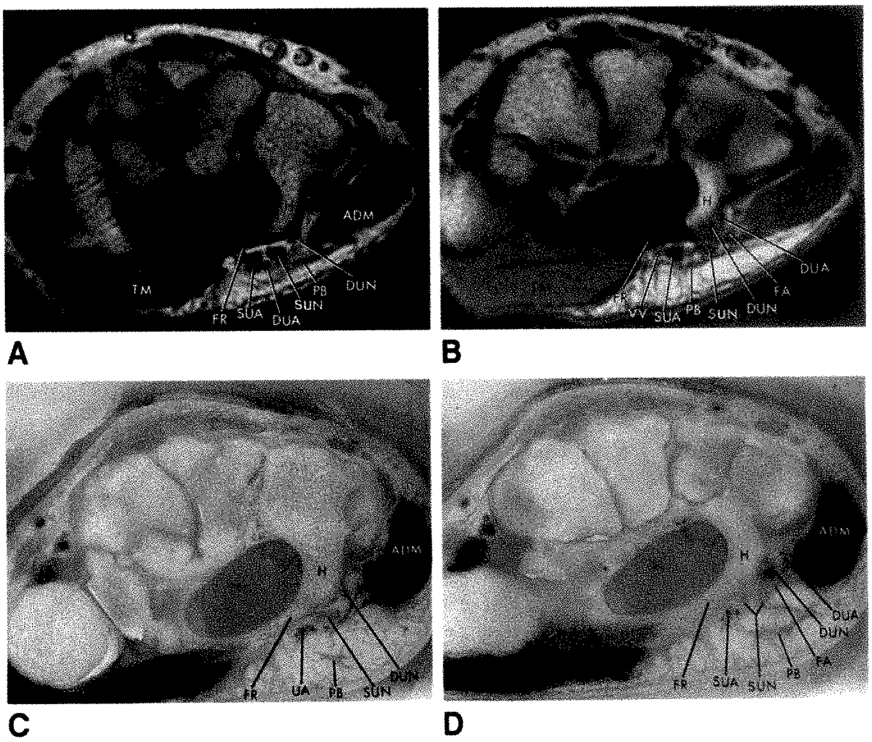

Fig. 3.—Distal portion of ulnar tunnel. (See key for abbreviations.)

***A* and *B*, T1-weighted transverse MR images show ulnar tunnel at proximal (*A*) and distal (*B*) edges of hamulus. When compared with Fig. 2A, palmaris brevis muscle rather than palmar carpal ligament muscle is volar boundary, and superficial and deep branches of ulnar nerve separate. Superficial ulnar artery can be seen anterior to superficial ulnar nerve as it courses toward deep ulnar nerve in deep tunnel. *B* is approximately 3 mm distal to *A* and shows superficial and deep branches of ulnar nerve and artery separated by fibrous arch of flexor digiti minimi brevis muscle, thereby delineating superficial and deep channels to ulnar tunnel distally.**

***C* and *D*, Corresponding cadaveric sections have similar dorsal boundaries but greater amount of hypothenar fat anteriorly, and a more poorly defined, less continuous palmaris brevis muscle.**

separating the superficial from the deep canal. This represented the fibrous arch of the flexor digiti minimi brevis muscle (Fig. 3B), or the muscle body itself attaching to the hamulus (Fig. 4). The general configuration of the superficial tunnel was biconvex or discoid. It was 14 ± 6 mm wide and 5.5 ± 2 mm deep at its greatest dimensions. The mean cross-sectional area was 44 ± 18 mm^2. The deep tunnel was generally rounded but was too indistinct to accurately characterize or measure.

The MR images depicting the inlet and outlet to the canal were consistent in appearance. The ulnar nerve was seen in the inlet just deep to the radial aspect of the flexor carpi ulnaris tendon (Fig. 5A). On the outlet view, the superficial ulnar nerve could be detected less clearly but was found just on the ulnar side of the ulnar artery, between the flexor digitorum brevis and palmaris brevis muscles (Fig. 5B). At this level, the digital branches to the small finger of the superficial ulnar nerve and artery could be seen in addition to the main branches. The deep ulnar nerve usually could not be detected here, as it was obscured by the hypothenar muscles.

Of the 36 wrists examined, anomalous muscles within the canal were found in nine wrists of six subjects, a prevalence of 25% in all wrists and 23% in all subjects. As three of the six subjects had anomalies bilaterally, those with anomalies had a 50% likelihood of bilateral lesions; the overall prevalence of bilaterality was 67%. Five of the anomalous muscles originated proximal to the ulnar tunnel along the antebrachial fascia of the forearm. Four originated from the radial side of the pisiform bone and the undersurface of the palmar carpal ligament at the proximal edge of the tunnel. All inserted with the abductor digiti minimi muscle. Figure 6 shows examples of anomalous muscle bundles from different origins coursing into the abductor digiti minimi insertion.

The ulnar nerve at the proximal canal (Fig. 1) was round or oval with a mean diameter of 3.0 ± 1 mm. The mean distance from the proximal border of the pisiform bone to the ulnar

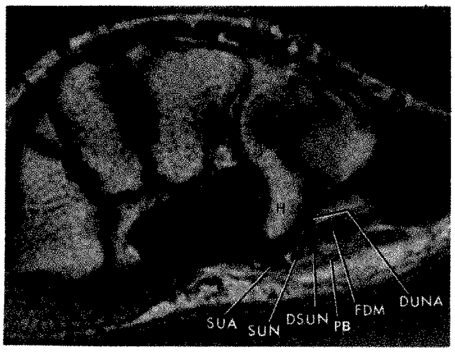

Fig. 4.—T1-weighted transverse MR image of wrist at hamulus shows muscular origin to flexor digiti minimi brevis muscle rather than fibrous arch. Compare with Fig. 3B, which shows fibrous origin to this muscle. (See key for abbreviations.)

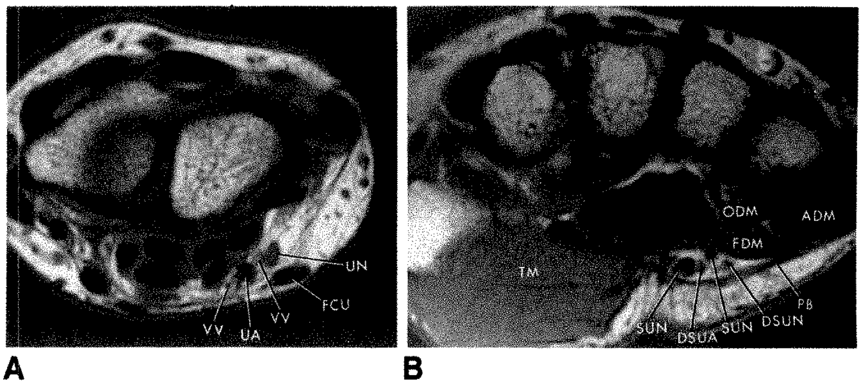

Fig. 5.—*A* and *B*, T1-weighted transverse MR images of ulnar tunnel inlet and outlet. (See key for abbreviations.)

A, At inlet, just proximal to pisiform bone, ulnar nerve and artery are deep to flexor carpi ulnaris tendon and on ulnar side of flexor digitorum tendons. Adjacent rounded structures representing veins are more numerous at this level.

B, At outlet, superficial ulnar artery and nerve have given off digital branches to small finger and can be seen between palmaris brevis and flexor digiti minimi muscles. Deep ulnar nerve and artery are obscured within hypothenar muscles.

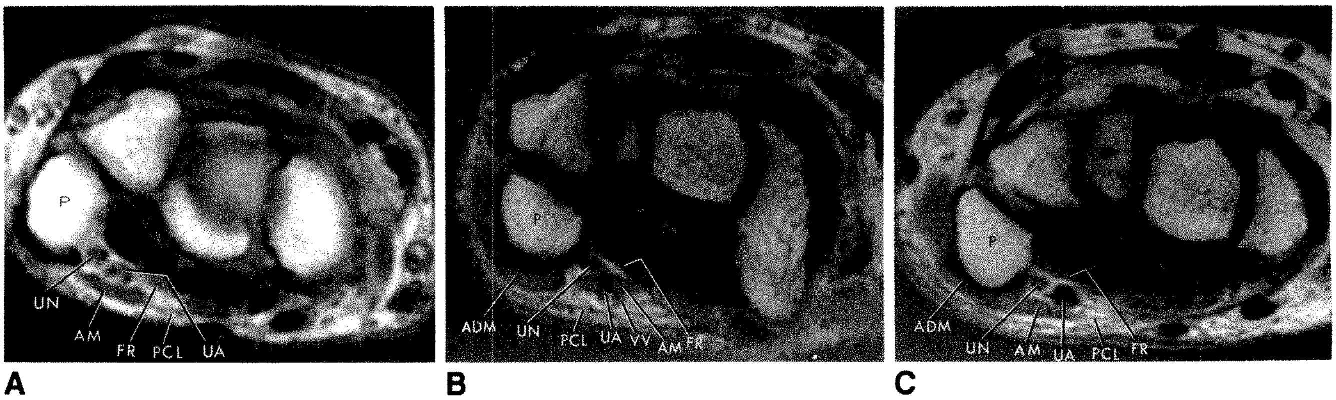

Fig. 6.—Examples of anomalous muscles passing through ulnar tunnel as seen on T1-weighted transverse MR images through tunnel at level of pisiform bone. (See key for abbreviations.)

A, Anomalous muscle located volar to both ulnar nerve and artery after originating from ulnar antebrachial fascia of distal forearm.

B, Anomalous muscle positioned between ulnar nerve and artery as muscle courses through canal. It originated from midline antebrachial fascia of mid forearm.

C, Anomalous muscle arising from proximal radial aspect of pisiform bone and palmar carpal ligament.

All muscles inserted with abductor digiti minimi muscle.

nerve bifurcation was 11.6 ± 2.5 mm. The bifurcation could be detected in virtually all cases in the mid tunnel (Fig. 2), but with varying clarity. The superficial ulnar nerve could be seen into the hand well beyond the ulnar tunnel. The deep ulnar nerve could be visualized only an average of 10 mm or less beyond the bifurcation, becoming obscured by the adjacent hypothenar muscles.

The fibromuscular arch delineating the origin of the flexor digiti minimi brevis muscle could be seen in most cases, but definition was limited by imaging plane and resolution. Approximately 50% of the volunteers had a mostly fibrous arch, and the other 50% had a muscular arch. This judgment was based on the appearance of the arch on the most proximal MR section showing it at the level of the hamulus (Figs. 3B and 4).

The dedicated wrist coil consistently provided better detail than the larger extremity coil. With both coils, images obtained with a 256 × 192 matrix and four excitations (15-min imaging time) were clearly superior to those obtained with only two excitations (10-min imaging time). However, with the dedicated wrist coil and two excitations, detail was superior to that obtained with the extremity coil and four excitations. Images obtained with a 256 × 256 matrix and four excitations (20-min imaging time) were marginally better than the 256 × 192 matrix images, but not enough to justify the additional time. The best combination of imaging time and detail was achieved with the dedicated wrist coil with 3-mm-thick sections on a 256 × 192 matrix and two excitations.

Discussion

MR imaging, especially when a dedicated wrist coil is used, offers a reliable means of evaluating the distal ulnar tunnel. Various structures define the borders of the tunnel. The most consistent boundaries were found along the dorsal aspect; the greatest variability occurred on the volar aspect (Figs. 1-3). The palmar carpal ligament, fibrofatty tissue, palmaris brevis muscle variations, and anomalous abductor digiti minimi muscles all contributed to the anterior boundaries. The ulnar nerve was consistently detected, although after its bifurcation the deep branch quickly was obscured by adjacent muscle. The average diameter of the ulnar nerve at the level of the pisiform bone was 3 mm. Ulnar nerve bifurcation occurred an average of 12 mm beyond the tunnel inlet. The latter measurement is similar to 11 mm obtained in a previous cadaveric study of distal ulnar tunnel anatomy [1]. The tunnel tended to become larger distally, with mean cross-sectional tunnel areas of 32, 41, and 44 mm^2 at proximal, midtunnel, and distal sections, respectively, but no statistically significant difference was found.

The prevalence of anomalous muscles within the tunnel in this study was 25%. This compares with 22% found in a previous cadaveric study [6]. As in that study, the anomalous muscles were found to arise anywhere from the mid forearm to the proximal part of the canal along the antebrachial fascia, undersurface of palmar carpal ligament, or radial aspect of pisiform bone. All inserted with the abductor digiti minimi muscle. They can, therefore, be considered anomalous accessories to this muscle. In our study, 67% of anomalous muscles occurred bilaterally, and affected individuals had a 50% likelihood of bilateral anomalies. In the aforementioned cadaver study, 46% of the anomalies were bilateral.

The differentiation between a fibrous and muscular origin to the flexor digiti minimi brevis muscle was of limited reliability for technical reasons and somewhat subjective in nature. The width of the fibrous edge of this muscle origin in cadaveric studies has been found to be 2 mm (range, 1-6 mm) [7]. As the MR slice thickness was 3 mm in our cases, there was almost always some degree of volume averaging between hamulus, arch, and muscle body, with blurring of detail. Nevertheless, the 50% prevalence of each in our study is similar to a previous report describing 40% of hands with a fibrous arch and 60% with a muscular arch [7].

We did not study the usefulness of MR in the evaluation of ulnar neuropathy. However, the fatty tissue within the ulnar tunnel offers a contrast on MR images against which the ulnar nerve, artery, anomalous muscles, and potential masses can be identified. As a result, MR images depict the ulnar nerve with at least as much clarity as the median nerve in the carpal tunnel. As MR has been found useful in median nerve compression [8, 9], it is reasonable to suspect that MR has a role in the diagnosis of ulnar nerve abnormality as well. In this regard, awareness of normal tunnel anatomy and recognition of anomalous muscles can be helpful.

REFERENCES

1. Gross MS, Gelberman RH. The anatomy of the distal ulnar tunnel. *Clin Orthop* **1985**;196:238-247
2. Zahrawi F. Acute compression ulnar neuropathy at Guyon's canal resulting from lipoma. *J Hand Surg [Am]* **1984**;9:238-240
3. Carlson CS, Clark GL. False aneurysm of ulnar artery in Guyon's canal. *J Hand Surg [Am]* **1983**;8:223-224
4. Subin GD, Mallon WJ, Urbaniak JR. Diagnosis of ganglion in Guyon's canal by magnetic resonance imaging. *J Hand Surg [Am]* **1989**;14:640-643
5. Giuliani G, Poppi M, Pozzati E, Forti A. Ulnar neuropathy due to a carpal ganglion: the diagnostic contribution of CT. *Neurology* **1990**;40:1001-1002
6. Dodds GA III, Hale D, Jackson WT. Incidence of anatomic variants in Guyon's canal. *J Hand Surg [Am]* **1990**;15:352-355
7. Dellon AL, Mackinnon SE. Anatomic investigations of nerves at the wrist: II. Incidence of fibrous arch overlying motor branch of ulnar nerve. *Ann Plast Surg* **1988**;21:36-37
8. Mesgarzadeh M, Schneck CD, Bonakdarpour A. Carpal tunnel: MR imaging. Part 1. Normal anatomy. *Radiology* **1989**;171:743-748
9. Mesgarzadeh M, Schneck CD, Bonakdarpour A. Carpal tunnel: MR imaging. Part 2. Carpal tunnel syndrome. *Radiology* **1989**;171:749-754

Book Review

MRI of the Head and Neck. Edited by Robert Lufkin and William N. Hanafee. (One of 10 volumes in The Raven MRI Teaching File. Series editors: Robert B. Lufkin, William G. Bradley, Jr., and Michael Brant-Zawadzki.) New York: Raven, 254 pp., 1991. $60

MRI of the Head and Neck is part of a 10-volume series known as The Raven MRI Teaching File. Each of these volumes covers the MR imaging of a specific disease or disorder or area of the body. In each volume, the editors have selected 100 cases that illustrate variable manifestations of common pathologic changes as well as the occasional and unusual case. The major problems that radiologists may encounter in the MR evaluation and interpretation of each specific disease or disorder or area are covered.

The purpose of this series is to present clinical cases in a format that allows radiologists to develop skills of observation and interpretation. Each case presented is first illustrated on the left-hand page. Readers are encouraged to try to detect the pathologic changes shown on the images before they read the discussion on the right-hand page that details the MR findings and the clinical problem.

The editors of *MRI of the Head and Neck* are well-known radiologists who have made significant contributions in the field of head and neck radiology. It is their hope that any radiologist who wishes to become knowledgeable in this area, especially in MR of this area, can use this book to enhance his or her clinical knowledge as well as MR interpretive skill. The editors have succeeded in meeting their objective.

Normal anatomy is not discussed, as it is assumed that the book's targeted readership should have a basic knowledge of normal anatomy of the head and neck. The style of the text, which is intentionally kept brief, makes reading easy. The book is packed with pearls. At the end of each case, a list of suggested reading is provided.

Image reproduction for the most part is state of the art. Most of the cases used in this book were contributed by a large number of radiologists throughout the United States. Not all the imaging was done on start-of-the-art scanners. Thus, it is not surprising that the quality of the images varies throughout the book.

Typographic errors are minimal. At least one image has been placed upside-down. Most of the illustrations have arrows pointing to the relevant abnormalities. In a few cases, however, it is difficult to see the arrows referred to in the legends.

It is universally accepted that state-of-the-art MR imaging of the cerebellopontine angle for the evaluation of suspected tumors requires the use of gadolinium. A number of cases are presented in which gadolinium was not used but would have been helpful. In one case of an acoustic neuroma, an air CT cisternogram (which is rarely obtained in 1991) and unenhanced axial T1- and T2-weighted images are inferior substitutes to show the small tumor.

MRI of the Head and Neck is not meant as a reference text of head and neck radiology. Its purpose is to serve as a teaching file, and it fulfills this purpose admirably. Despite the criticisms mentioned here, I can recommend this book. It should be useful to residents and generalists in radiology and to those in other disciplines in which MR imaging is used. At a price of $60, this book is well worth the investment. I have already recommended it to residents in radiology, neurology, neurosurgery, and head and neck surgery.

Solomon Batnitzky
University of Kansas Medical Center
Kansas City, KS, 66103

Craniovertebral Junction: Normal Anatomy with MR Correlation

Mark E. Schweitzer,[1] Jurg Hodler,[2] Vinicio Cervilla,[2] and Donald Resnick[2]

The anatomy of the craniovertebral junction, although complex, may be well visualized by routine MR imaging. This essay discusses the anatomy of the complex articulations of the craniovertebral junction. Representative MR images and gross anatomic photographs are presented to illustrate the intricate ligamentous and articular anatomy. Knowledge of the normal anatomy of the occipitoatlantoaxial region is necessary in order to understand the common disorders that affect this area. The most common disorders are trauma and arthropathies, but also include congenital abnormalities and neoplasm. The resultant abnormal mechanics may lead to neurologic sequelae or pain.

Materials and Methods

Three cadavers were sectioned at the level of the pubis with disarticulation of the upper extremities. The lower extremities were discarded. It was necessary to obtain a large specimen to minimize the amount of air in the spinal canal. Routine radiographs were used to exclude significant abnormalities. The cadaveric necks then were surveyed fluoroscopically, placed in a neutral position, and frozen. Before MR imaging, the specimens were thawed and heated to 37°C.

Each specimen was imaged with a 1.5-T imager (Signa, General Electric Medical Systems, Milwaukee, WI) in the sagittal, coronal, and axial planes through the craniovertebral junction. Images were obtained with a 10-cm field of view, a 256 × 192 matrix, and two signal acquisitions. Spin-echo sequences, 3000/35 (TR/TE), with a slice thickness of 4 mm and 1-mm interslice gap were used.

One specimen was precisely marked at the levels at which the sagittal images were obtained. This was repeated with a second specimen for the coronal levels and with a third specimen for the axial levels. After imaging, each specimen was frozen again and then sectioned with a band saw at 4-mm intervals because approximately 1 mm of tissue in each section was macerated by the saw. The resulting sections correlated closely in position and thickness with those of the MR images. The MR images were correlated with the corresponding specimen section and with anatomic texts [1–3].

MR-Anatomic Correlation

External Craniocervical Ligaments

The anterior atlantooccipital membrane extends from the upper aspect of the anterior arch of C1 to the foramen magnum. It is visualized as an intermediate-signal structure with radiating fascicles just above and anterior to the odontoid process. Although it radiates anatomically, its fascicles appear nearly parallel on MR images (Figs. 1–4). The signal intensity of the anterior atlantoaxial membrane is greater than that of the other ligaments of the craniovertebral junction.

The posterior atlantooccipital membrane is an analogous structure extending from the posterior arch of C1 to the foramen magnum. It is thinner and looser than the anterior membrane. On MR images, it is moderate in thickness and of low signal with a somewhat wavy contour (Figs. 1–4). It has apertures that allow passage of the vertebral arteries (Fig. 3).

The atlantooccipital ligaments are seen just external to the capsule of the lateral atlantooccipital joints and are oriented vertically. These ligaments as well as the joint capsule are

---

Received September 13, 1991; accepted after revision November 26, 1991.

This work was supported in part by Veterans Affairs grant SA306.

[1] Department of Radiology, Veterans Administration Medical Center, and University of California, San Diego, Medical Center, San Diego, CA 92161.

[2] Department of Radiology, Thomas Jefferson University Hospital, 132 S. 10th St., 1096 Main Bldg., Philadelphia, PA 19107. Address reprint requests to M. E. Schweitzer.

AJR 158:1087–1090, May 1992 0361-803X/92/1585-1087 © American Roentgen Ray Society

Key to Abbreviations Used in Figures

a	alar ligaments
b	anterior atlantoaxial ligament (deep portion)
b′	anterior atlantoaxial ligament (superficial portion)
c	anterior atlantooccipital membrane
C	clivus
d	anterior longitudinal ligament
D	dens (odontoid process)
e	apical ligament (in fat)
f	articular cartilage
g	atlantooccipital ligaments
h	transverse ligament of atlas
hi	inferior longitudinal fasciculus of cruciform ligament
hs	superior longitudinal fasciculus of cruciform ligament
i	capsule of anterior median atlantoaxial joint
k	capsule of atlantooccipital joint
l	capsule of lateral atlantoaxial joint
m	capsule of posterior median atlantoaxial joint
n	interspinous ligament
O	occiput
p	ligamenta flava
r	posterior atlantooccipital membrane
s	posterior longitudinal ligament
t	tectorial membrane
V	vertebral artery
1	atlas (C1)
2	axis (C2)

redundant and lax to allow rotatory motion at these articulations (Fig. 4).

The anterior atlantoaxial ligament extends from the anterior midportion of the dens to the inferior aspect of the anterior arch of C1. It consists of two distinctly visualized low-intensity fascicles separated by a high-signal-intensity fat plane (Figs. 1 and 2). Interspinous ligaments have an oblique orientation and are seen as several separate fibers of intermediate signal on midline images (Fig. 1).

Internal Craniocervical Ligaments

The tectorial membrane is the superior extension of the posterior longitudinal ligament and attaches to the anterior lateral aspect of the foramen magnum. This strong ligament is visualized as a very low signal band (Figs. 1 and 2).

The transverse ligament is a thick band with intermediate signal oriented in the coronal plane extending from a tubercle on the inner aspect of one side of the atlas to a tubercle on the opposite side. Vertical extensions extend superiorly and inferiorly to the transverse ligament (Figs. 1, 2, and 4–6). These superior and inferior fasciculi have lower MR signal than does the transverse ligament. The transverse ligament and its fasciculi have a cross shape and together constitute the cruciform ligament (Fig. 1).

The apical ligament is not directly visible on MR or anatomic sections. It lies superior to the dens extending to the occipital bone and is surrounded by fat (Fig. 2). It lies between the superior longitudinal fasciculus of the cruciform ligament and the anterior atlantooccipital membrane.

The alar ligaments are short and broad and of intermediate signal (Figs. 1 and 2). They extend outward from the superior

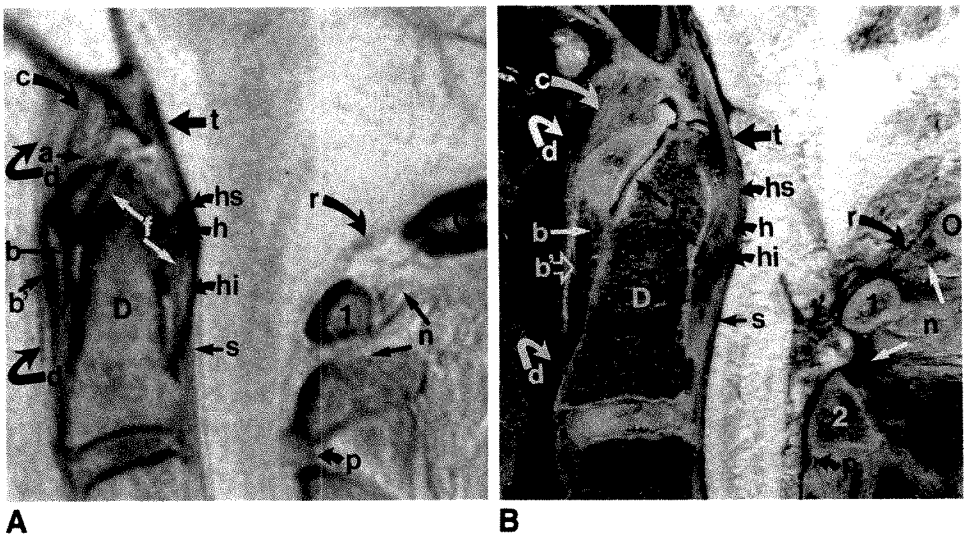

Fig. 1.—*A* and *B*, Sagittal midline MR image (*A*) and specimen photograph (*B*) show transverse ligament (h) and its superior (hs) and inferior (hi) fascicles, which together form cruciform ligament. These ligaments anchor dens and prevent instability of anterior and posterior median atlantoaxial joints. Posterior to cruciform ligament lies posterior longitudinal ligament (s) continuing cranially as strong tectorial membrane (t). Anterior to C2 lies anterior longitudinal ligament (d). Deep to this ligament is anterior atlantoaxial ligament, which attaches anterior arch of C1 to anterior body of C2. Anterior atlantoaxial ligament consists of superficial (b′) and deep (b) fibers. Posteriorly, posterior atlantooccipital membrane (r) and interspinous ligaments (n) act to attach posterior aspect of foramen magnum and spinous processes of C1 and C2, preventing hyperflexion. Ligaments cranial to dens are complex and, with exceptions of tectorial membrane (t) and alar ligament (a), are weak. Alar ligaments extend outward from dens to lie anterior to apical ligament before attaching to occipital condyles. Anterior atlantooccipital membrane (c) is superior extension of anterior atlantoaxial ligament. This membrane extends from anterior arch of C1 to clivus and is broad, densely woven fibroelastic band. Ligamenta flava (p) are not prominent in cervical spine and are not seen craniad to C1. Below C1, interspinous ligaments (n) have oblique orientation with cranial attachment more anterior than inferior attachment of each ligament. Interspinous ligament between posterior arch of C1 (1) and occiput (O) has oppositely oriented oblique course, becoming more posterior at cranial attachment. These ligaments are continuous with and are posterior extension of posterior atlantoaxial membrane (r).

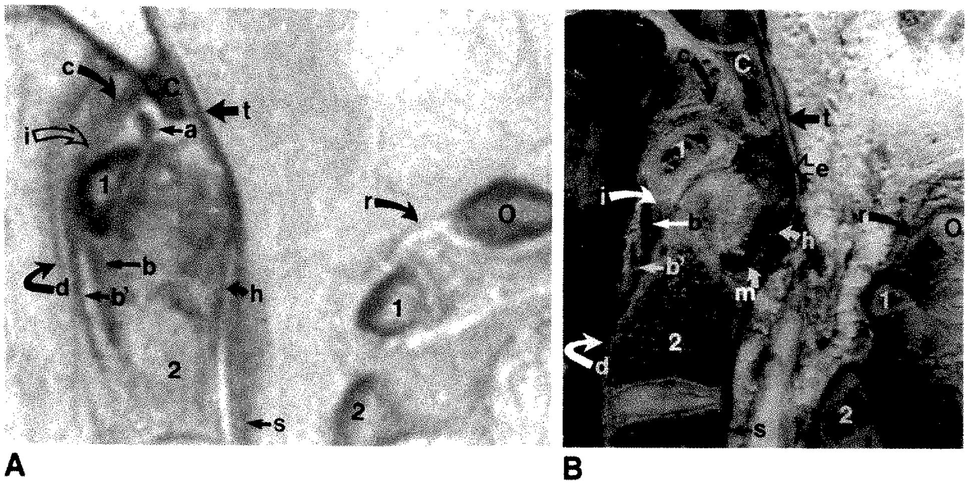

Fig. 2.—*A* and *B*, Sagittal MR image at lateral aspect of dens (*A*) and corresponding specimen photograph (*B*) show posterior atlantooccipital membrane (r), which is cranial continuation of posterior atlantoaxial ligaments. Posterior atlantooccipital membrane (r) extends from upper aspect of posterior arch of C1 (1) to posterior aspect of foramen magnum (O). It is broader, thinner, and looser than analogous structure seen anteriorly, anterior atlantooccipital membrane (c). Anteriorly lies anterior longitudinal ligament (d), which extends length of spine and becomes fixed at front of body of axis (2) and at anterior arch of atlas (1). Anterior longitudinal ligament (d) is most anterior ligamentous structure and extends to skull base. Anterior atlantoaxial ligament (b) is inferior extension of anterior atlantooccipital membrane (c). Anterior atlantoaxial ligament is a strong band extending from anterior midportion of dens to inferior aspect of anterior arch of C1. We noted both on anatomic sections; on MR images, two distinct fascicles of this ligament, one deep (b) and one superficial (b′), are separated by fat.

Fig. 3.—*A* and *B*, Sagittal MR images (*A*) and corresponding specimen photograph (*B*) show articular cartilage (f) at atlantooccipital joint. These are paired true synovial joints with prominent lax capsules (k). Anterior longitudinal ligament (d) as well as anterior atlantooccipital membrane (c) are seen on these sections since both are broad in coronal plane. Anterior atlantooccipital membrane (c) consists of densely woven fibroelastic fibers that radiate in a lateral pattern rather than linear fascicles that make up anterior longitudinal ligament (d). Ligamenta flava (p) connecting lamina of adjacent vertebrae may be seen adjacent to lateral atlantoaxial joint.

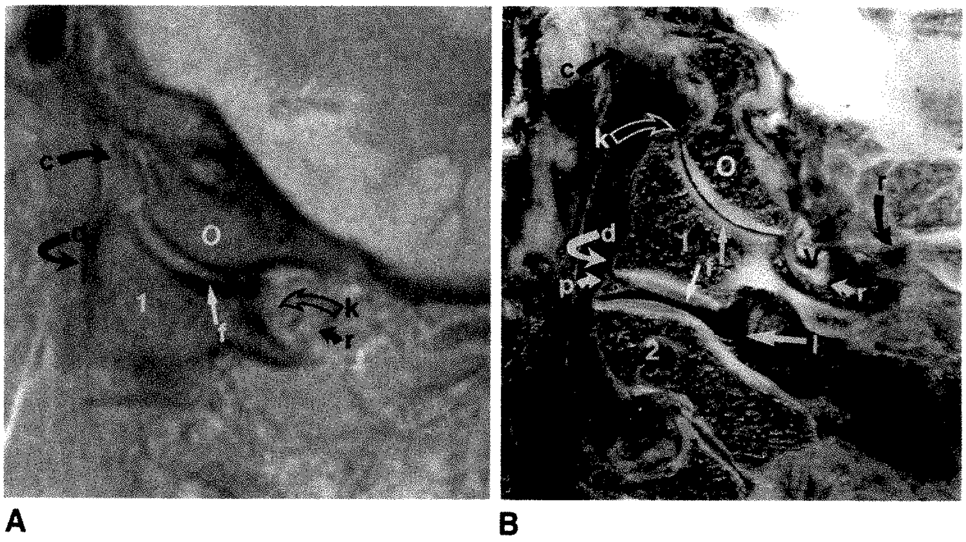

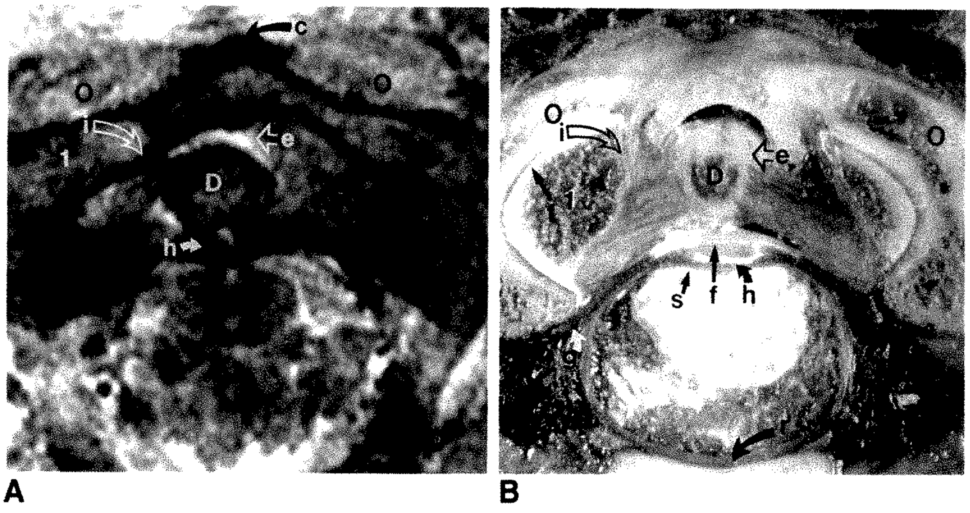

Fig. 4.—*A* and *B*, Axial MR image (*A*) and corresponding specimen photograph (*B*) show atlantooccipital joints with articular cartilage (f) formed by occipital condyles (O) and lateral masses of C1 (1). Just medial to these joints lies anterior atlantooccipital membrane (c). Posterior to this and just anterior to tip of dens (D) lies apical ligament (e), not directly discernible within adjacent fat. Lateral to apical ligament is cranial insertion of capsular fibers of anterior median atlantoaxial joint (i). Cruciform ligament (h) interdigitating with fibers of accessory ligaments is seen. These ligaments extend from lateral masses of C1 and act to reinforce lateral atlantoaxial joints and alar ligaments. Upper aspect of posterior median atlantoaxial joint with its articulating cartilage (f) is shown. Posterior to this joint and anterior to spinal cord lies posterior longitudinal ligament (s). Craniad to this level, tectorial membrane is continuation of posterior longitudinal ligament. Atlantooccipital ligaments (g) act to reinforce margins of capsule of atlantooccipital joints.

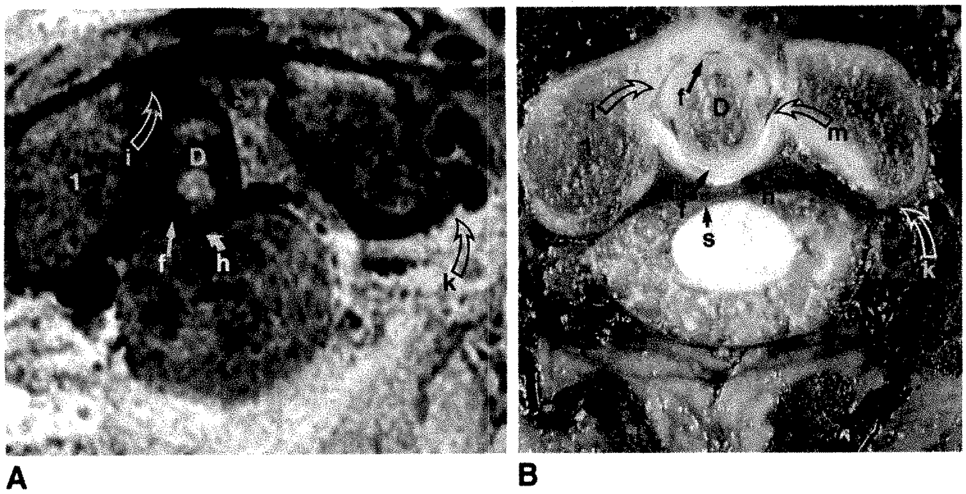

Fig. 5.—*A* and *B*, Axial MR image (*A*) and corresponding specimen photograph (*B*) show articulations of dens. Caudal capsular insertion of atlantooccipital joints (k) can be seen on these images. Anterior longitudinal ligament (d) is becoming more cordlike at this level. Deep to anterior longitudinal ligament lies anterior atlantooccipital membrane (c).

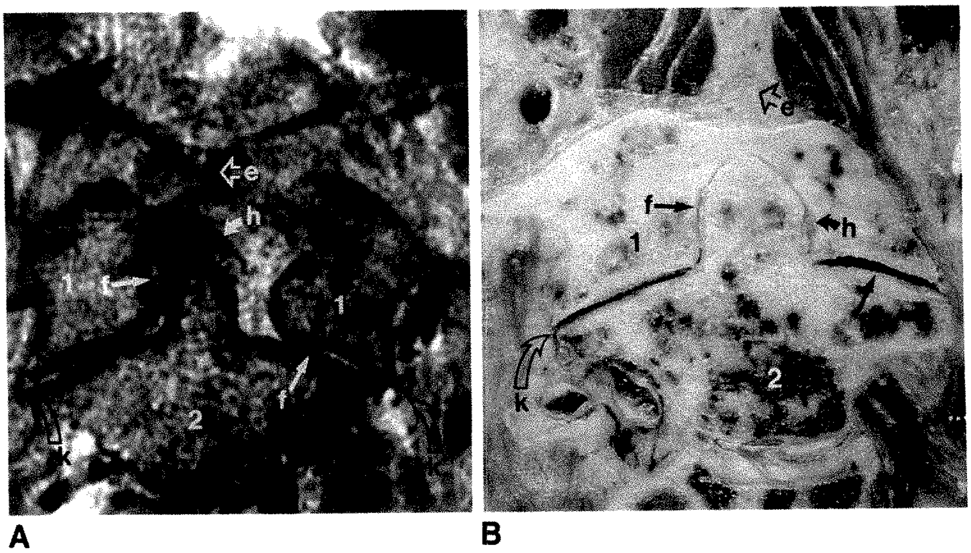

Fig. 6.—*A* and *B*, Coronal MR image (*A*) and corresponding specimen photograph (*B*) show articular cartilage (f) at posterior median and lateral atlantoaxial joints forming articulations between atlas (1) and axis (2). Apical ligament at tip of dens lies within fat (e). Capsular fibers (l) of lateral atlantoaxial joints are seen as well. Portion of cruciform ligament (h) is seen adjacent to dens. Tectorial membrane acts as primary reinforcer of upper cervical spine in flexion and extension.

and lateral aspect of the dens to the medial aspect of the occipital condyle.

Articulations

Four joints are present between the occiput and C1 and C2: the atlantooccipital joints (Fig. 4), the anterior median atlantoaxial joint (Fig. 1), the posterior median atlantoaxial joint (Figs. 1, 3, and 4), and the lateral atlantoaxial joints (Figs. 3 and 6). The first and last of these are paired. All four articulations are true synovial joints with hyaline articular cartilage and prominent lax capsules. The cartilage is seen as intermediate signal intensity usually adjacent to cortical bone. However, at the posterior median atlantoaxial joint, cartilage is seen on the anterior aspect of the transverse ligament.

REFERENCES

1. Netter RH. *The CIBA collection of medical illustrations*, vol. 8, *musculoskeletal system*, part 1. *Anatomy, physiology and metabolic disorders*. Summit, NJ: CIBA-Geigy, **1987**
2. VanGilden SC, Menezes AA, Dolon KD. *The craniovertebral junction and its abnormalities*. Mount Kisco, NY: Futura, **1987**:14–27
3. Williams PL, Warwick R, Dyston M, Banister LH. *Gray's anatomy*, 37th ed. Edinburgh: Churchill-Livingstone, **1989**

Pictorial Essay

Long Bicipital Tendon of the Shoulder: Normal Anatomy and Pathologic Findings on MR Imaging

Scott J. Erickson,[1] Steven W. Fitzgerald,[2] Stephen F. Quinn,[3] G. F. Carrera,[1] Kevin P. Black,[4] and Thomas L. Lawson[1]

The tendon of the long head of the biceps muscle (long bicipital tendon) has a complex course from its muscle belly to its insertion onto the supraglenoid tubercle/glenoid labrum. It is stabilized by numerous tendinous and ligamentous structures and is, in turn, partly responsible for maintenance of normal glenohumeral function. In this report we describe the anatomy of this tendon, correlating high-resolution MR images with cryomicrotome sections. We illustrate typical MR findings in pathologic conditions affecting the long bicipital tendon sheath, the substance of the tendon, and finally the tendon position.

The biceps muscle is composed of two muscle bellies. The short head terminates in a flat tendon that inserts onto the coracoid process adjacent to the coracobrachialis tendon. The tendon of the long head (long bicipital tendon) has a much more complex course, arcing over the humeral head as it passes intraarticularly, and finally inserting onto the supraglenoid tubercle and/or the glenoid labrum itself [1]. This structure normally maintains an intimate relationship with the adjacent rotator cuff, capsule, and capsular ligaments.

The purpose of this study is to describe the MR anatomy of the long bicipital tendon and associated structures with cryomicrotome correlation and to illustrate typical MR findings in the following pathologic conditions: tenosynovitis, synovial osteochondromatosis, tendon tear/rupture, and medial tendon dislocation.

Subjects and Methods

We performed MR imaging of the shoulder in six healthy volunteers by using a 1.5-T MR unit (Signa, General Electric Medical Systems, Milwaukee, WI) with a 3-in. (7.6-cm) planar, receive-only local coil. The coil center was placed over the expected location of the bicipital groove (intertubercular sulcus) for most sequences. T1-weighted images were obtained by using an 8–10 cm field of view, 256 × 256 matrix, 3-mm interleaved slices, four excitations, superior/inferior presaturation pulses, and 500–550/20–25 (TR/TE). Spin-density and T2-weighted images were obtained by using a 10–12 cm field of view, 256 × 192 matrix, 3-mm slice thickness with 0.5-mm interslice gaps, one excitation, superior/inferior presaturation pulses, and 2500/20,80 (TR/TE). Scan planes included direct axial, oblique axial, oblique coronal, and oblique sagittal projections. The normal images were compared with corresponding axial cryomicrotome sections (heavy-duty sledge, PMV 2250, Bromma, Sweden) and standard anatomic texts [2–4].

Representative cases of long bicipital tendon abnormalities were selected from patients examined at two institutions. All images were obtained by using either a 1.5-T Signa MR unit or a 0.5-T General Electric MAX unit. T2-weighted images were obtained in the oblique coronal, oblique sagittal, and axial planes by using a 12–16 cm field of view, 2000–2500/20,80 (TR/TE), 256 × 128 matrix, 4- or 5-mm slices, and two excitations. Axial gradient-recalled-echo (GRE) images were also obtained at one of the institutions by using 700/12/20° (TR/TE/flip angle).

Received September 9, 1991; accepted after revision November 15, 1991.

[1] Department of Radiology, Medical College of Wisconsin, 8700 W. Wisconsin Ave., Milwaukee, WI 53226. Address reprint requests to S. J. Erickson.

[2] Department of Radiology, Northwestern University Medical School, Chicago, IL 60011.

[3] Department of Radiology, Good Samaritan Hospital & Medical Center, 1015 N.W. 22nd Ave., Portland, OR 97210.

[4] Department of Orthopaedic Surgery, Medical College of Wisconsin, Milwaukee, WI 53226.

AJR 158:1091–1096, May 1992 0361–803X/92/1585–1091 © American Roentgen Ray Society

Key to Abbreviations Used in Figures

C	coracoid process
CHL	coracohumeral ligament
GL	glenoid labrum
GT	greater tuberosity
H	humerus
JC	joint capsule
LBT	long bicipital tendon
LT	lesser tuberosity
PMT	pectoralis major tendon
SBT	short bicipital tendon/coracobrachialis tendon
SGHL	superior glenohumeral ligament
ST	subscapularis tendon
THL	transverse humeral ligament

Results and Discussion

Normal Anatomy

The long bicipital tendon (Fig. 1) arises from the long head of the biceps muscle within the upper third of the arm. The tendon courses through the intertubercular sulcus (bicipital groove), and is stabilized by numerous overlying structures. The tendon of the pectoralis major muscle in part covers the intertubercular sulcus (falciform ligament) and blends with the capsular ligament (Fig. 2). More craniad, the long bicipital tendon is covered by the transverse humeral ligament—a broad band, or retinaculum, passing between the humeral tuberosities (Fig. 3). The external fibers of the subscapularis tendon may, in fact, blend into the superficial fibers of the transverse humeral ligament.

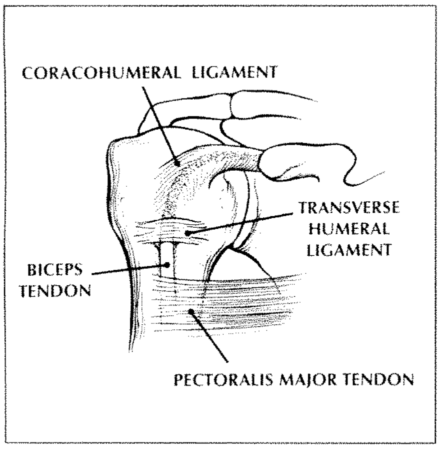

Fig. 1.—Sketch shows stabilizers of long bicipital tendon (excluding remainder of capsule and edges of supraspinatus and subscapularis tendons).

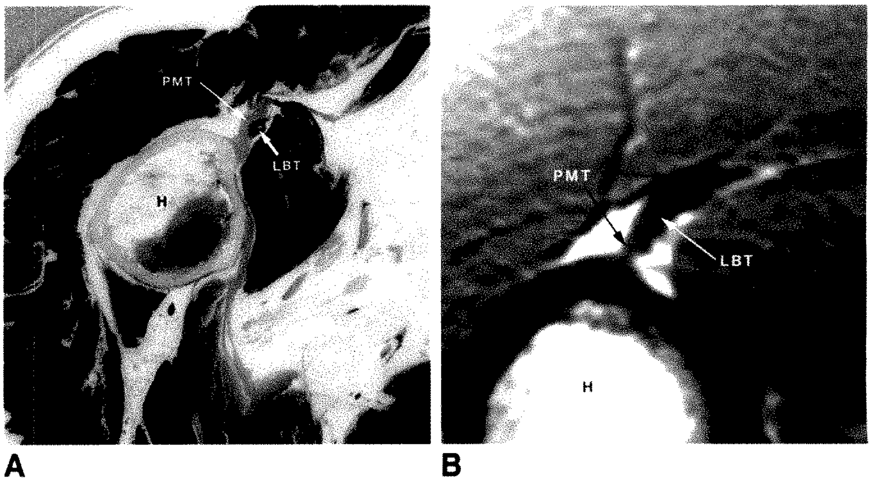

Fig. 2.—Pectoralis major tendon. (See key for abbreviations.)

A, Axial cryomicrotome section shows pectoralis major tendon coursing superficially to long bicipital tendon and inserting onto humerus.

B, Corresponding axial T1-weighted MR image (550/17).

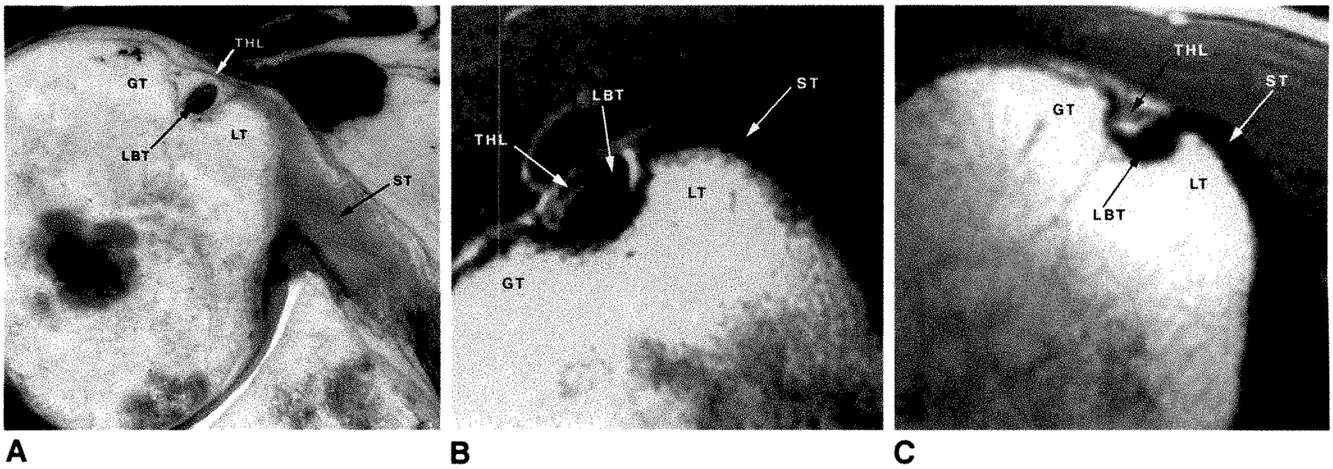

Fig. 3.—Transverse humeral ligament. (See key for abbreviations.)

A, Axial cryomicrotome section shows transverse humeral ligament attaching to both greater and lesser tuberosities. This structure is a relatively weak stabilizer of long bicipital tendon.

B, Corresponding axial T1-weighted MR image (500/20) shows intermediate signal intensity of transverse humeral ligament.

C, Corresponding axial T1-weighted MR image (500/23) in a different healthy volunteer shows a delicate, undulating transverse humeral ligament.

As the tendon traverses the intertubercular sulcus, it is invested with a double layer of synovium and becomes an intracapsular structure. It is covered anteriorly by the coracohumeral ligament, superior glenohumeral ligament, and edges of the supraspinatus and subscapularis tendons. These structures thicken the capsule and act as the chief stabilizers of the long bicipital tendon. The coracohumeral ligament arises from the posterior base of the coracoid process, blends with the supraspinatus tendon, and attaches onto both the greater and lesser tuberosities. The inferoposterior aspect of the coracohumeral ligament blends with the capsule while its anterosuperior aspect does not. This ligament not only stabilizes the long bicipital tendon but also "fills" the rotator interval, a gap that exists between the supraspinatus and subscapularis tendons (Figs. 4–9). The relatively weaker superior glenohumeral ligament parallels the long bicipital tendon, attaching onto the superomedial glenoid margin and lesser humeral tuberosity (Fig. 9).

The long bicipital tendon inserts onto the supraglenoid tubercle and/or the glenoid labrum itself (Fig. 7). The proximity of the intraarticular portion of the tendon to the above structures makes identification somewhat difficult, particularly in the nondistended joint. Furthermore, a short segment of the tendon consistently demonstrates relatively increased signal intensity on short TE sequences as it achieves the magic angle of 55° in relation to the static magnetic field (B_0) [5] (Figs. 5, 7, and 10). T2 values are significantly augmented at or near 55° with resultant increase in signal intensity when using relatively short TE times. This effect is thought to be due to the structural anisotropy of the collagen within tendons. The focus of high signal intensity may simulate a biceps or rotator cuff tear on spin-density or T1-weighted images.

Abnormalities of the Long Bicipital Tendon

Abnormalities of the tendon sheath.—The long bicipital tendon sheath may become distended by fluid, separating its visceral and parietal layers (Fig. 11). The underlying tendon may or may not be normal. Bicipital tendinitis/tenosynovitis

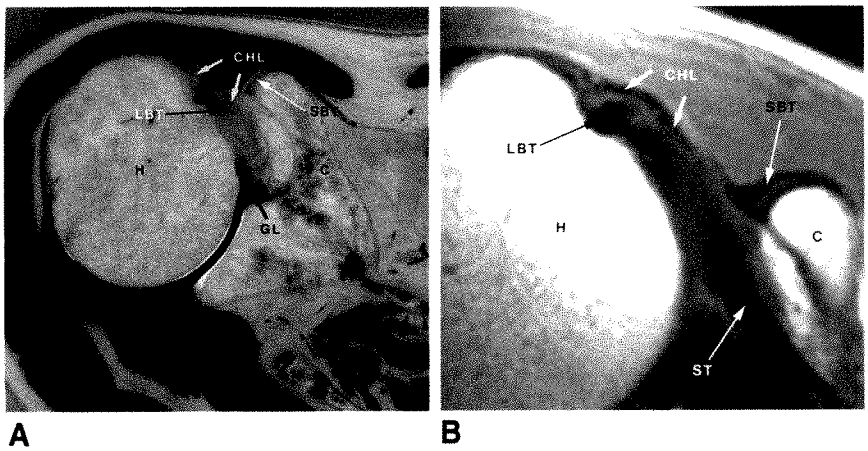

Fig. 4.—Coracohumeral ligament. (See key for abbreviations.)
***A*, Axial cryomicrotome section shows coracohumeral ligament coursing superficially to long bicipital tendon.**
***B*, Oblique axial T1-weighted MR image (500/23) shows lateral aspect of coracohumeral ligament. Medial aspect of this structure is not seen on this image.**

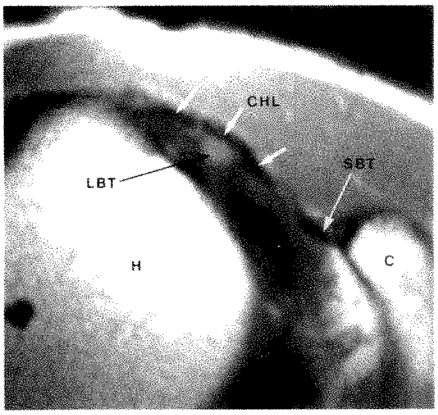

Fig. 5.—Oblique axial T1-weighted MR image (500/23) obtained at level craniad to image in Fig. 4B shows coracohumeral ligament just superficial to long bicipital tendon. Note that tendon (*arrows*) has increased signal intensity as a result of magic angle phenomenon. (See key for abbreviations.)

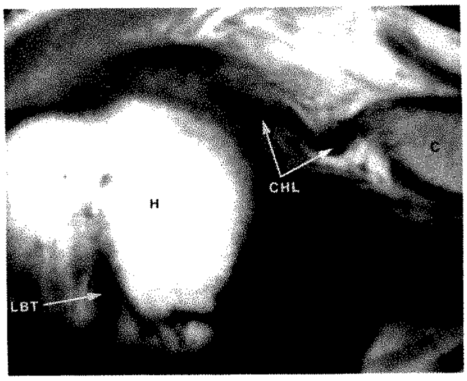

6

Fig. 6.—Oblique coronal T1-weighted MR image (550/25) shows proximal aspect of coracohumeral ligament. Short segment of long bicipital tendon is also seen. (See key for abbreviations.)

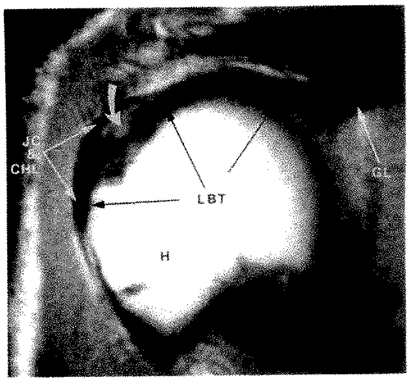

7

Fig. 7.—Oblique coronal T1-weighted MR image (500/25) at level posterior to Fig. 6 shows long segment of long bicipital tendon extending from bicipital groove to its attachment on glenoid labrum. Focal region of increased signal intensity within tendon is attributable to magic angle phenomenon (*curved arrow*). (See key for abbreviations.)

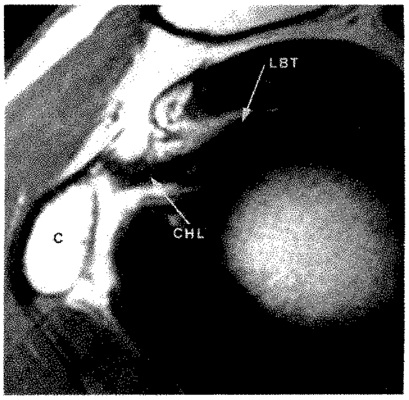

Fig. 8.—Oblique sagittal T1-weighted MR image (550/23) shows coracohumeral ligament and short segment of long bicipital tendon near insertion onto glenoid labrum. (See key for abbreviations.)

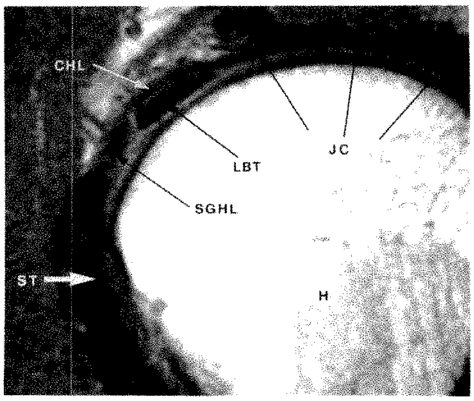

Fig. 9.—Oblique sagittal T1-weighted MR image (500/25) at level lateral to Fig. 8 shows coracohumeral ligament and superior glenohumeral ligament blending into joint capsule. Zone of intermediate signal intensity between humeral cortical bone and joint capsule represents normal hyaline cartilage. (See key for abbreviations.)

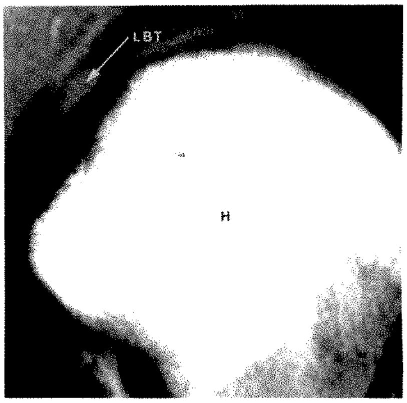

Fig. 10.—Oblique sagittal T1-weighted MR image (500/25) at level lateral to Fig. 9 shows focal region of increased signal intensity within long bicipital tendon attributable to magic angle phenomenon. This could be misinterpreted as rotator cuff tear on short TE spin-echo sequences. (See key for abbreviations.)

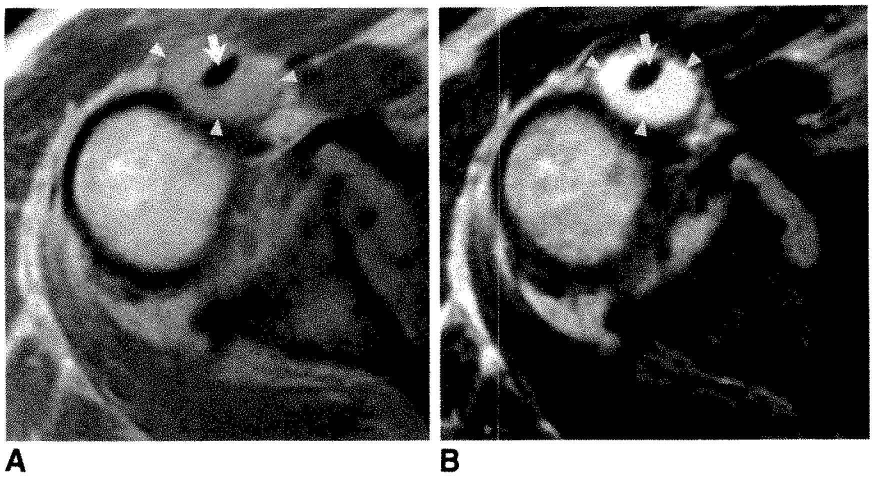

Fig. 11.—Biceps tendon sheath fluid. (See key for abbreviations.)

A, Axial spin-density MR image (2000/20) shows long bicipital tendon (*arrow*) surrounded by intermediate signal intensity fluid (*arrowheads*). Patient had coexisting rotator cuff tear.

B, Corresponding axial T2-weighted MR image (2000/80) shows tendon (*arrow*) surrounded by high signal intensity fluid (*arrowheads*).

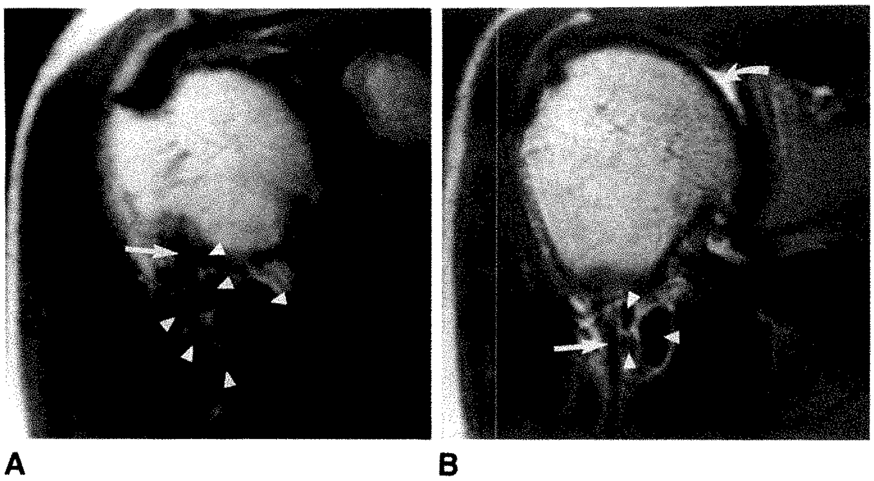

Fig. 12.—Synovial chondromatosis (surgically proved). (See key for abbreviations.)

A, Oblique coronal spin-density MR image (2000/20) shows long bicipital tendon (*arrow*) and numerous hypointense foci (*arrowheads*).

B, Oblique coronal T2-weighted MR image (2000/80) shows long bicipital tendon (*straight arrow*) and numerous hypointense foci (*arrowheads*). Note small amount of fluid within glenohumeral joint (*curved arrow*).

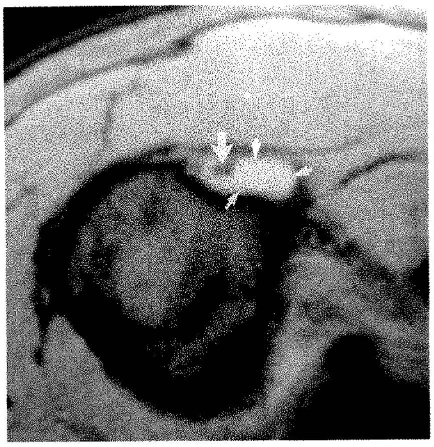

13

Fig. 13.—Partial long bicipital tendon tear (surgically proved). Axial GRE image (700/12/20°) shows linear region of increased signal intensity within long bicipital tendon representing partial tear (*large arrow*). Note distended tendon sheath (*small arrows*). (See key for abbreviations.)

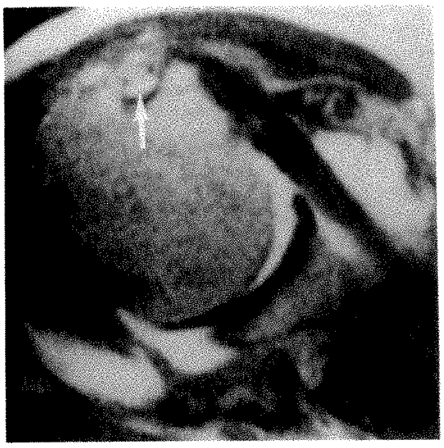

14

Fig. 14.—Biceps tendon rupture. Axial T2-weighted MR image (2500/80) shows absence of long bicipital tendon (*arrow*). Bicipital groove is filled primarily with fluid. (See key for abbreviations.)

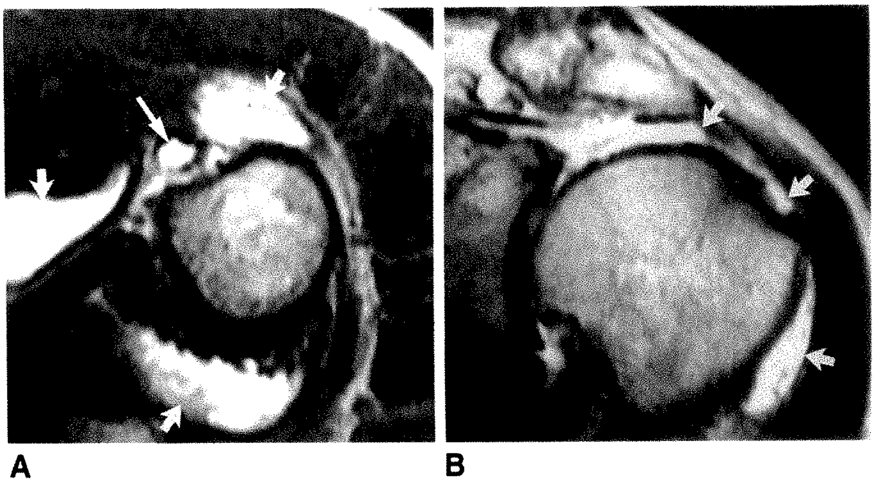

Fig. 15.—Biceps tendon rupture (clinically apparent). (See key for abbreviations.)

A, Axial T2-weighted MR image (2500/80) shows fluid-filled tendon sheath and absence of long bicipital tendon (*long arrow*). Note fluid within glenohumeral joint and subacromical-subdeltoid bursa (*short arrows*).

B, Coronal T2-weighted MR image (2500/80) shows extensive rotator cuff tear with large joint effusion extending into subacromial-subdeltoid bursa (*arrows*).

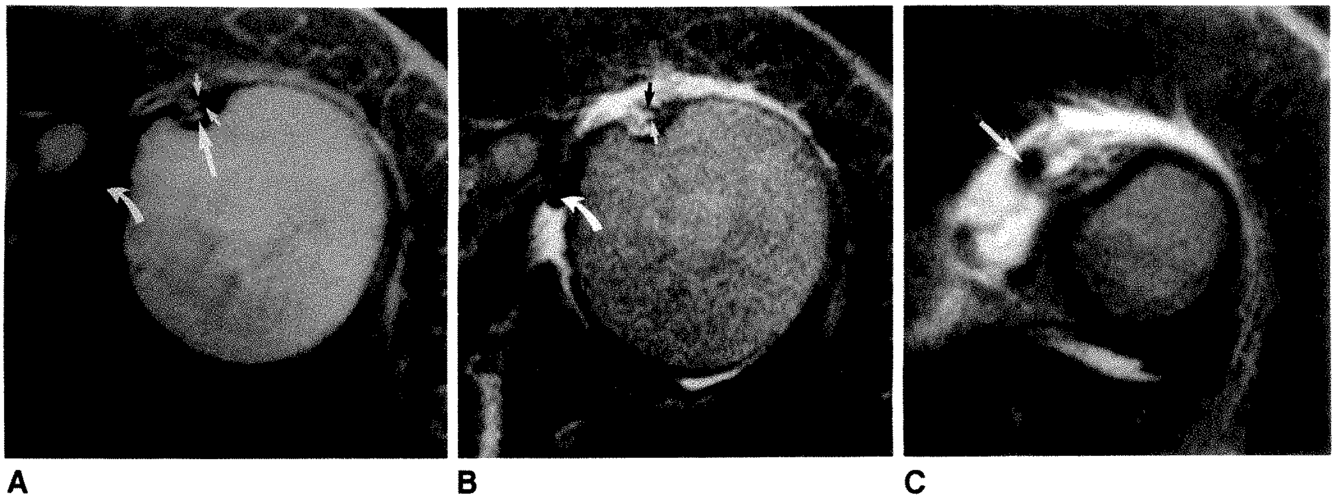

Fig. 16.—Medial long bicipital tendon dislocation with coexisting subscapularis tendon tear (surgically proved). (See key for abbreviations.)

A, Axial spin-density MR image (2500/20) shows medially dislocated long bicipital tendon (*curved arrow*). Bicipital groove (*long straight arrow*) is empty except for a few low signal intensity foci (*short straight arrows*). Insertion of normal subscapularis tendon onto lesser tuberosity is not seen.

B, Corresponding axial T2-weighted MR image (2500/80) shows increased signal intensity fluid and linear hypointense foci (*straight arrows*) to better advantage. *Curved arrow* represents long bicipital tendon.

C, Axial T2-weighted MR image (2500/80), obtained more inferiorly, shows long bicipital tendon (*arrow*) surrounded by high signal intensity material as well as strandlike hypointense foci.

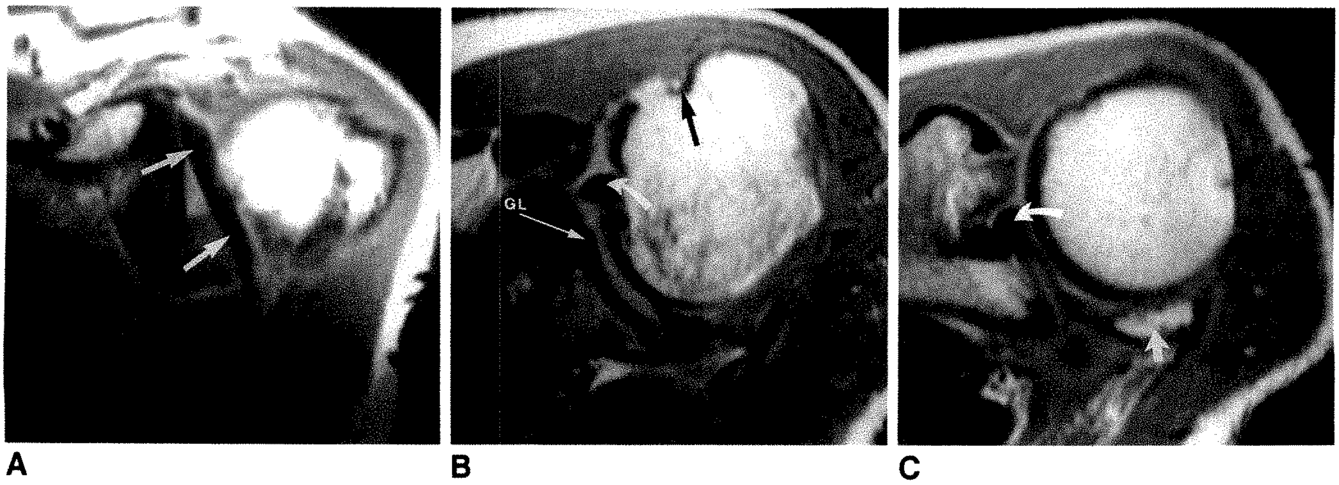

Fig. 17.—Medial dislocation of long bicipital tendon accompanying massive rotator cuff tear (surgically proved).

***A*, Oblique coronal spin-density MR image (2000/20) shows medially dislocated long bicipital tendon (*arrows*).**

***B*, Axial spin-density MR image (2000/20) shows empty bicipital groove (*straight arrow*), medially dislocated long bicipital tendon (*curved arrow*), and normal glenoid labrum. Dislocated tendon should not be mistaken for avulsed anterior glenoid labrum. (See key for abbreviation.)**

***C*, Axial spin-density MR image (2000/20) obtained at slightly higher level shows long bicipital tendon (*curved arrow*) near its insertion onto superior glenoid labrum. Fragment of bone seen posteriorly (*straight arrow*) is derived from accompanying humeral head fracture.**

frequently accompanies rotator cuff disease. The tendon sheath may likewise contain osteochondral loose bodies or be involved by synovial chondrometaplasia (Fig. 12).

Intrinsic abnormalities of the long bicipital tendon.—With rotator cuff disorders, particularly if there is a complete tear, the long bicipital tendon may become impinged between the humeral head and the coracoacromial arch. The tendon may become flattened, forming a "pseudocuff." Other findings may include tendinitis, partial tears (Fig. 13), and overt rupture (Figs. 14 and 15). Neer [6] reports that biceps tendon ruptures are extremely uncommon without coexisting rotator cuff abnormality. There may be marked retraction of the tendon through the bicipital groove resulting in a clinically obvious muscular bulge. If the tendon reattaches in the groove, however, the diagnosis may be clinically occult. Some researchers have found it difficult to distinguish fibrous tissue within the bicipital groove from the bicipital tendon itself (Saez F et al., presented at the Radiological Society of North America meeting, November 1990).

MR may prove useful in demonstrating spurs encroaching on the bicipital groove, but very small bony excrescences may be seen better with CT. Calcific tendinitis can involve either the proximal or distal aspects of the long bicipital tendon. Subtle calcification, while very apparent on plain radiographs or CT, may be overlooked on MR images. Calcifications located near the musculotendinous junction may also be difficult to distinguish from those arising in the overlying pectoralis major tendon.

Tendon dislocation.—The long bicipital tendon may dislocate if the overlying stabilizers are disrupted. Interestingly, the transverse humeral ligament, which extends between the greater and lesser tuberosities, has been shown to be a weak stabilizer of the tendon. Experiments have shown that interruption of this structure alone infrequently results in tendon dislocation. The coracohumeral ligament/capsule is thought to be the major stabilizer, whose interruption frequently results in tendinous dislocation. The long bicipital tendon will sublux superficially to the subscapularis tendon if the latter is intact. If the subscapularis tendon insertion is torn, the long bicipital tendon may slip deep to the subscapularis tendon into an intraarticular location [1, 7] (Figs. 16 and 17).

REFERENCES

1. Rockwood CA, Matsen FA. *The shoulder.* Philadelphia: Saunders, **1990**
2. Williams PL, Warwick R, Dyson M, Bannister LH. *Gray's anatomy.* Edinburgh: Churchill Livingstone, **1989**
3. Anderson JE. *Grant's atlas of anatomy.* Baltimore: Williams & Wilkins, **1978**
4. Middleton WD, Lawson TL. *Anatomy and MRI of the joints: a multiplanar atlas.* New York: Raven, **1989**
5. Erickson SJ, Cox IH, Hyde JS, Carrera GF, Strandt JA, Estkowski LD. Effect of tendon orientation on MRI signal intensity: a manifestation of the "magic angle" phenomenon. *Radiology* **1991**;181:389-392
6. Neer CS. *Shoulder reconstruction.* Philadelphia: Saunders, **1990**
7. Cervilla V, Schweitzer ME, Ho C, Motta A, Kerr R, Resnick D. Medial dislocation of the biceps brachii tendon: appearance at MR imaging. *Radiology* **1991**;180:523-526

Blunt Pancreatic Trauma in Children: CT Diagnosis

Carlos J. Sivit[1,2]
Martin R. Eichelberger[2,3]
George A. Taylor[1,4]
Dorothy I. Bulas[1,2]
Cathy S. Gotschall[3]
David C. Kushner[1,2]

The purpose of this study is to determine the efficacy of CT in the diagnosis of pancreatic injury after blunt abdominal trauma in children. Pancreatic injury was diagnosed at surgery, at autopsy, or on the basis of the development of clinical pancreatitis or a pseudocyst on follow-up imaging evaluation in 18 of 1045 consecutive children examined with CT after blunt trauma. Types of pancreatic injury included laceration in 11 children, transection in two, contusion in one, and tumor with hemorrhage in one. Three children had clinical pancreatitis without a pancreatic abnormality noted on CT. The pancreatic injury was prospectively identified on CT in 12 children (67%). The presence of fluid in the lesser sac was a useful marker for injury to the pancreas. This was noted in 13 children with pancreatic injury, whereas it was observed in only six (1%) of 1028 children in the absence of pancreatic injury (sensitivity, 72%; specificity, 99%). Fluid in the anterior pararenal space was less helpful in establishing the diagnosis of pancreatic injury (sensitivity, 44%; specificity, 98%). A pancreatic pseudocyst developed in four of the 11 survivors.

Our experience shows that direct signs of pancreatic trauma may be difficult to identify on CT. Recognition of the limitations of CT diagnosis of pancreatic injury is important in helping to reduce errors of interpretation.

***AJR* 158:1097–1100, May 1992**

CT has replaced peritoneal lavage as the method of choice in evaluating children with suspected abdominal injury after blunt trauma and has proved to be accurate in the detection and delineation of hepatic, splenic, and renal injuries [1–3]. Pancreatic injuries have proved more difficult to identify with CT [4–6]. Because pancreatic trauma is rare in children, experience regarding acute imaging findings is limited [7–9]. In this report, we analyzed data from 1045 consecutive cases of blunt trauma to determine the accuracy of CT in evaluating blunt pancreatic injury.

Subjects and Methods

Between January 1983 and June 1991, 1045 children who sustained blunt trauma and who clinically were presumed to have injury to intraabdominal organs were prospectively evaluated with abdominal CT at our institution. Pancreatic injury was diagnosed at surgery in 10 children, at autopsy in five children, and at clinical or imaging follow-up in three children. The latter group included two children who did not have laparotomy and showed a pancreatic pseudocyst on follow-up imaging examination and one additional child who did not have laparotomy and in whom clinical pancreatitis developed. Pancreatitis was defined as persistent elevation of serum amylase levels above 100 IU/l for more than 3 days [10].

Demographic data, indications for CT, and Trauma Score [10, 11] were recorded for all children at the time of admission. Injury Severity Score was recorded at the time of discharge or death [12]. Radiologic findings were recorded at the time of initial interpretation. Clinical records were reviewed to determine the type of management (operative or nonoperative), serum amylase values, and clinical outcome.

Thirteen children were male and five were female (age range, 2–13 years; mean age,

Received October 18, 1991; accepted after revision December 26, 1991.

[1] Department of Diagnostic Imaging and Radiology, Children's National Medical Center, 111 Michigan Ave., N.W., Washington, DC 20010. Address reprint requests to C. J. Sivit.

[2] The George Washington University School of Medicine and Health Sciences, 2300 I St., N.W., Washington, DC 20037.

[3] Department of Surgery, Children's National Medical Center, 111 Michigan Ave., N.W., Washington, DC 20010.

[4] Present address: Russell H. Morgan Department of Radiology, Johns Hopkins Medical Institutions, 600 N. Wolfe St., Baltimore, MD 21205.

0361–803X/92/1585–1097
© American Roentgen Ray Society

7 years). The mechanisms of injury included 11 motor vehicle-related injuries: seven of the children were pedestrians and four were passengers. Three were bicyclists, two were assaulted, one was struck while wrestling with a friend, and one fell. The median Trauma Score in these children was 3 (range, 3-16). The median Injury Severity Score was 15 (range, 5-57).

Indications for CT included abdominal tenderness (12 children), abrasions or ecchymosis (11 children), absent bowel sounds (nine children), hematuria (nine children), neurologic obtundation (nine children), abdominal distension (eight children), low hematocrit (seven children), vomiting (three children), and fractured pelvis (one child).

CT was performed on a GE 9800 CT scanner (GE Medical Systems, Milwaukee, WI) with 1-cm-thick sections obtained at 1-cm intervals through the abdomen and pelvis. Three milliliters per kilogram (maximum dose, 120 ml) of IV contrast material (iothalamate meglumine, Conray 43; Mallinckrodt, St. Louis, MO, or iohexol, Omnipaque 240, Winthrop, New York, NY) was administered by means of rapid bolus injection to opacify the solid abdominal viscera. Oral contrast material was not used during the initial CT scan. In three of these children, however, CT examination was repeated after the administration of oral contrast medium 10-60 min before scanning, because of a strong clinical suspicion of pancreatic injury.

Results

The types of pancreatic injury included laceration in 11 cases (Fig. 1), transection in two (Fig. 2), contusion in one, and tumor with hemorrhage in one (Fig. 3). Three additional children had clinical pancreatitis. The anatomic distribution of 14 pancreatic transections, lacerations, and contusions was as follows: injury limited to the pancreatic body in nine, limited to the pancreatic tail in two, limited to the pancreatic head in one, head and body combined in one, and body and tail combined in one.

CT Findings

The pancreatic injury was identified on CT scans in 12 children (67%). Three children who had a normal-appearing pancreas on CT had a pancreatic injury noted at laparotomy or autopsy (laceration in two, contusion in one). Two children who had a normal-appearing pancreas on CT and at laparotomy had postoperative pancreatitis. One additional child who had a normal-appearing pancreas on CT did not undergo laparotomy but subsequently had clinical pancreatitis.

Peripancreatic fluid collections on CT were noted in 13 children (72%) who had pancreatic injury. The fluid was in the lesser sac in all 13 children (72%), in the anterior pararenal space in eight (44%), and in the posterior pararenal space in one (6%) (Fig. 4). The location of fluid in the anterior pararenal space was bilateral in five cases and limited to the left side in three cases. Thickening of Gerota's fascia was seen in all seven children who had fluid in the anterior pararenal space. Fluid in the anterior pararenal space was always associated with fluid in the lesser sac. Peripancreatic fluid was observed in one of three children who subsequently had clinical pancreatitis.

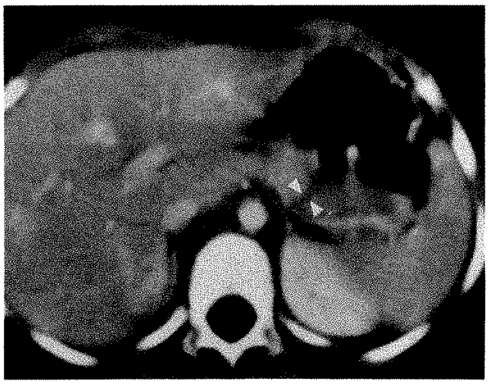

1

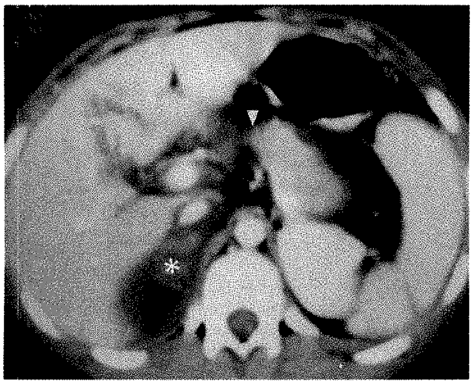

2

Fig. 1.—Pancreatic laceration with minimal separation of fracture fragments in a 5-year-old boy who was run over by a car. CT scan shows linear area of low attenuation (*arrowheads*) in pancreatic body.

Fig. 2.—Pancreatic transection with nonenhancement of head of pancreas in a 10-year-old girl injured in a motor vehicle crash. CT scan at level of pancreas shows a transection through pancreatic body (*arrowhead*) with absence of contrast enhancement of pancreatic head. Note hepatic laceration and right adrenal hematoma (*asterisk*).

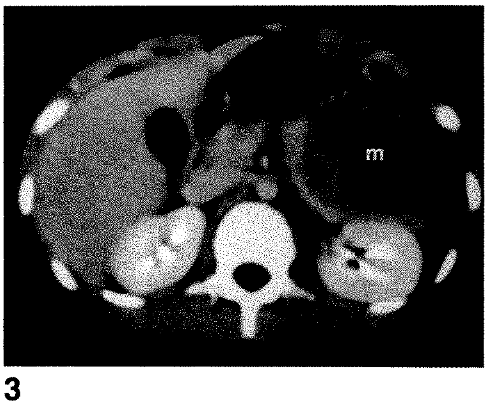

3

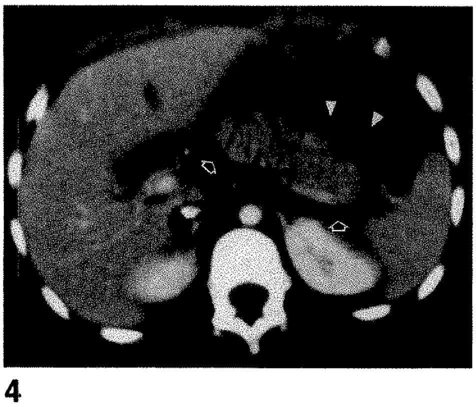

4

Fig. 3.—Pancreatic tumor with hemorrhage in a 13-year-old girl injured while wrestling. CT scan at level of pancreas shows a large pancreatic mass (m) extending anteriorly into lesser sac.

Fig. 4.—Peripancreatic fluid collections associated with pancreatic injury in a 6-year-old boy run over by an automobile. CT scan of upper abdomen shows fluid in lesser sac (*arrowheads*) and anterior pararenal space (*arrows*). Pancreas appeared normal on CT. A pancreatic laceration was noted at surgery.

Fluid in the lesser sac was observed in six (1%) of 1028 children without pancreatic injury who sustained blunt trauma and were studied with CT (Table 1; specificity for pancreatic injury, 99%). Similarly, fluid in the anterior pararenal space was seen in 18 (2%) of 1028 children without pancreatic injury studied with CT (Table 2; specificity for pancreatic injury, 98%). Fluid in the lesser sac and anterior pararenal space was observed in three children with a normal pancreas on CT and a pancreatic injury (laceration in two, contusion in one) noted at laparotomy or autopsy (Fig. 4).

Associated Injury

Six children (33%) had associated intraabdominal injuries. These included four hepatic, three bowel, three splenic, and one renal injury. In addition, dilated fluid-filled bowel loops with intense enhancement of bowel wall, mesentery, and kidneys and decreased caliber of the abdominal aorta and inferior vena cava consistent with the "hypoperfusion" complex were noted in four children [13].

Outcome

Ten children (56%) underwent surgical exploration. Of these, eight required laparotomy on an urgent basis. One had elective resection of a papillary cystic tumor of the pancreas, and one underwent drainage of a pseudocyst. Disruption of the main pancreatic duct was noted in six children who underwent surgical exploration. All six of these children had fluid in the lesser sac on the initial CT examination.

Seven children (39%) died. Of 11 survivors with pancreatic injury, five had subsequent CT or sonographic examinations 6–12 days after the injury. Indications for follow-up examinations included persistent elevation of serum amylase levels (three children), abdominal pain (two children), and fever (one child). A pancreatic pseudocyst was noted on follow-up examination in four children (lesser sac in three, intrapancreatic in one; Fig. 5). All four had a pancreatic laceration noted on the initial CT scan. Peripancreatic fluid (lesser sac in two, anterior pararenal space in one) had been noted on the initial CT examination in two of these children.

TABLE 1: Abnormalities Associated with Fluid in Lesser Sac on CT

Abnormalities	No. (%) of Patients (n = 19)
Pancreatic injury	13 (68)
No pancreatic injury	6 (31)
Isolated bowel injury	1 (5)
Isolated hepatic injury	1 (5)
Isolated hypoperfusion complex	1 (5)
Combined bowel and renal injury	1 (5)
Combined hepatic and splenic injury	1 (5)
Combined splenic and renal injury	1 (5)

TABLE 2: Abnormalities Associated with Fluid in Anterior Pararenal Space on CT

Abnormalities	No. (%) of Patients (n = 26)
Pancreatic injury	8 (31)
No pancreatic injury	18 (69)
Isolated renal injury	3 (12)
Isolated bowel injury	2 (8)
Isolated hepatic injury	2 (8)
Isolated splenic injury	1 (4)
Isolated adrenal hematoma	1 (4)
Isolated hypoperfusion complex	1 (4)
More than one abnormality	7 (27)
No abnormality detected	1 (4)

Discussion

Pancreatic injury after blunt trauma in children is uncommon, and experience with its diagnosis is limited [7–9]. We observed injury to the pancreas in approximately 2% of children who had CT examinations after blunt trauma during an 8-year period. Pancreatic injury accounted for 6% (18/292) of all injuries to solid abdominal viscera seen in these children.

In three of 14 children who had pancreatic laceration, transection, or contusion, the injury was not identified on the initial CT scan. Accurate CT-aided diagnosis of pancreatic injury in children is difficult. Delineation of the margins of the pancreas may be troublesome owing to the smallness of the organ and the relative paucity of surrounding retroperitoneal fat in children. CT signs of pancreatic trauma also may be difficult to identify [4, 5, 8]. Laceration or contusion of the pancreas may produce little change in attenuation in the acute phase of the injury [4, 5]. There may be little separation of fractured pancreatic fragments (Fig. 1) [4]. In addition, it may be difficult to distinguish a laceration in the tail of the pancreas from adjacent unopacified bowel loops.

Evidence of pancreatitis, such as focal or diffuse organ enlargement, contour irregularity, and loss of definition of adjacent fat planes, was not present on CT scans obtained immediately after injury in three children in whom pancreatitis later developed. Two of these children also had a normal-appearing pancreas on gross inspection at laparotomy. Posttraumatic pancreatitis occurs as a consequence of direct blunt force and autodigestion by liberation of pancreatic enzymes

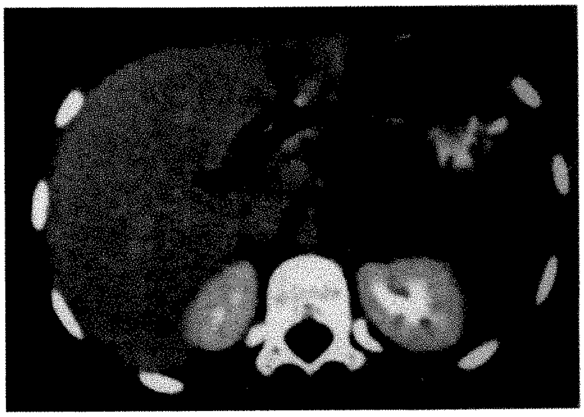

Fig. 5.—Pancreatic pseudocyst in 5-year-old injured in a motor vehicle crash. CT scan 8 days after injury shows a low-attenuation pseudocyst within body of pancreas.

after the injury [14]. As a result, pancreatic inflammatory changes evolve over time [15].

Although administration of oral contrast material for CT examination of the abdomen after blunt trauma is not routine at our institution, CT examination was repeated after the administration of oral contrast medium in three children because of a strong clinical suspicion of pancreatic trauma. Delineation of pancreatic injury in these children was not improved on the contrast-enhanced examination.

The presence of peripancreatic fluid in the absence of abdominal visceral injury should strongly suggest pancreatic injury (Fig. 4). The pancreas is located in the anterior pararenal space and forms the posterior boundary of the lesser sac. Fluid in the lesser sac was frequently seen in children with pancreatic injury and was rare in the absence of pancreatic trauma. Fluid in the anterior pararenal space was seen less frequently in children who had pancreatic injury. Four children with fluid in the lesser sac and anterior pararenal space as an isolated finding had pancreatic injury; the pancreas appeared normal on CT in all four. Unexplained fluid in the lesser sac was never seen after blunt trauma, and unexplained fluid in the anterior pararenal space was present in only one child.

Injury to the main pancreatic duct is a principal determinant in the development of significant complications after pancreatic injury [7, 9, 16]. As a result, major ductal laceration is recognized as an indication for prompt surgical intervention [8, 9, 16]. The presence of peripancreatic fluid collections may be a useful marker for major ductal injury. All six children who had injury to the main pancreatic duct noted at surgery had fluid in the lesser sac on CT examination, and four had fluid in the anterior pararenal space on the initial CT study. Additionally, two of four children in whom a pancreatic pseudocyst developed later had fluid in the lesser sac on the initial CT examination; one of these also had fluid in the anterior pararenal space.

Follow-up examination with CT or sonography was useful in identifying the development of a pancreatic pseudocyst in children with pancreatic injury who had subsequent signs and symptoms. A pseudocyst was noted on later CT or sonographic examination in four (36%) of 11 survivors with pancreatic injury (Fig. 5). The lesser sac was the most common location for these focal fluid collections.

In conclusion, pancreatic injury after blunt trauma may be difficult to identify on CT examination. The presence of fluid in the lesser sac should strongly suggest injury to the pancreas. Conversely, however, the absence of peripancreatic fluid does not exclude pancreatic trauma. Recognition of the limitations of CT diagnosis of pancreatic injury is important in helping to reduce errors of interpretation.

REFERENCES

1. Federle MP. CT of upper abdominal trauma. *Semin Roentgenol* **1984**;19:269-279
2. Taylor GA, Guion CJ, Potter BM, Eichelberger MR. CT of blunt abdominal trauma in children. *AJR* **1989**;153:555-559
3. Kaufman R, Towbin R, Babcock DS, et al. Upper abdominal trauma in children: imaging evaluation. *AJR* **1984**;142:449-460
4. Jeffrey RB, Federle MP, Crass RA. Computed tomography of pancreatic trauma. *Radiology* **1983**;147:491-494
5. Cook DE, Walsh JW, Vick CW, Brewer WH. Upper abdominal trauma: pitfalls in CT diagnosis. *Radiology* **1986**;159:65-69
6. Toombs BD, Lester RG, Ben-Menachem Y, Sadler CM. Computed tomography in blunt abdominal trauma. *Radiol Clin North Am* **1981**;19:17-35
7. Bass J, DiLorenzo M, Desjardins JG, Grignon A, Ouimet A. Blunt pancreatic injuries in children: the role of percutaneous external drainage in the pancreatic pseudocysts. *J Pediatr Surg* **1988**;23:721-724
8. Smith SD, Nakayama DK, Gantt N, Lloyd D, Rowe MI. Pancreatic injuries in childhood due to blunt trauma. *J Pediatr Surg* **1988**;23:610-614
9. Graham JM, Pokorny WJ, Mattax KL, et al. Surgical management of acute pancreatic injuries in children. *J Pediatr Surg* **1978**;105:158-163
10. Champion HR, Sacco WJ, Camazo AJ, Copes W, Fouty WJ. Trauma Score. *Crit Care Med* **1981**;9:672-676
11. Eichelberger MR, Mangubat EA, Sacco WJ, Bowman LM, Lowenstein AD. Outcome analysis of blunt trauma in children. *J Trauma* **1988**;28:1109-1113
12. Baker SP, O'Neil B, Haddon W, et al. The Injury Severity Score: a method for describing patients with multiple injuries and evaluating emergency care. *J Trauma* **1974**;14:187-196
13. Taylor GA, Fallat ME, Eichelberger MR. Hypovolemic shock in children: abdominal CT manifestations. *Radiology* **1987**;164:479-481
14. Meyers MA. Intestinal effects of pancreatitis spread along mesenteric planes. In: *Dynamic radiology of the abdomen*. New York: Springer Verlag, **1982**:243-263
15. Horst HM, Bivins BA. Pancreatic transection: a concept of evolving injury. *Arch Surg* **1989**;124:1093-1095
16. Grosfeld JL, Cooney DR. Pancreatic and gastrointestinal trauma in children. *Pediatr Clin North Am* **1975**;22:365-377

Azygoesophageal Recess: Normal CT Appearance in Children

Steven W. Fitzgerald[1]
James S. Donaldson[2]

The azygoesophageal recess is the interface of the subcarinal portion of the mediastinum and the right lower lobe. The configuration of the recess on CT can be used as a sensitive indicator of abnormality in the mediastinum. In normal adults the recess is concave. A convex contour is a normal variant, particularly in young adults. The normal appearance of the azygoesophageal recess in children has not been studied. Accordingly, we reviewed chest CT examinations performed in 253 children ranging from 1 month to 20 years old. Forty patients were excluded from further analysis either because the recess could not be evaluated properly or because underlying disease caused the mediastinum to have an abnormal configuration. An age-related spectrum of normal configurations was observed in the remaining 213 patients. A convex or straight contour was found in 96% of children less than 3 years old. Scans of children 3-12 years old revealed a spectrum of configurations. The typical adult concave configuration was seen in 78% of adolescents more than 12 years old. Overall, in only 90 (42%) of 213 children in this study was a concave recess observed on CT.

Our experience shows a convex azygoesophageal recess on CT should be considered the normal configuration in infants and young children. Recognition of this age-related variation is useful in the CT evaluation of the mediastinum in children.

***AJR* 158:1101-1104, May 1992**

The azygoesophageal recess (AER) is the interface of the subcarinal mediastinum and the right lower lobe. The AER extends from the azygous arch to the diaphragm. A variety of mediastinal, esophageal, and vascular abnormalities can affect the AER and its configuration. The configuration of the recess can be used as an indicator of disease in the mediastinum [1, 2]. The CT appearance of the AER in adults has been reported to be normally concave to the right side. A convex recess is considered a normal variant, occurring in 7-21% [3-5], especially in young adults [6]. The normal contour of the AER in children has not been described. Accordingly, this study was initiated to evaluate the configuration of the AER on CT in children.

Materials and Methods

We retrospectively reviewed 253 CT examinations of the chest performed at Children's Memorial Hospital. All examinations were done on a GE 9800 CT scanner. Infants and young children were imaged in quiet respiration. Cooperative children were scanned in suspended inspiration. All patients were scanned while they were supine. Images were obtained with 2-sec scanning times and with either 5- or 10-mm collimation at 5- or 10-mm intervals, respectively. Approximately 40% of the patients included in this study received IV contrast material (total dose of 3 ml nonionic contrast material per kilogram body weight), which was hand injected as a bolus. The patients in this study ranged from 1 month to 20 years old. The sample consisted of 142 boys and 111 girls. Eight patients were excluded from the study because we could not evaluate the AER adequately because of large pleural effusions (two patients), atelectasis in the right lower lobe (two patients), right-sided aortic arch (two patients), or azygous continuation of interruption of the inferior vena cava (two patients). A second

Received March 15, 1991; accepted after revision December 10, 1991.

Presented at the annual meeting of the Society for Pediatric Radiology, Cincinnati, April 1990.

[1] Department of Radiology, Northwestern Memorial Hospital, 710 N. Fairbanks Ct., Chicago, IL 60611. Address reprint requests to S. W. Fitzgerald.

[2] Department of Radiology, Children's Memorial Hospital, 2300 Children's Plaza, Chicago, IL 60614.

0361-803X/92/1585-1101
© American Roentgen Ray Society

TABLE 1: Indications for Chest CT in 213 Patients

Clinical Indication	No. of Patients (%)
CNS neoplasm	14 (7)
Abdominal/pelvic neoplasm	46 (22)
Musculoskeletal neoplasm	30 (14)
Lymphoproliferative disorder[a]	39 (18)
Pulmonary infection/AIDS[a]	24 (11)
Airway disorders	17 (8)
Hematologic disorders	13 (6)
Congenital anomalies[a]	13 (6)
Trauma	8 (4)
Miscellaneous[a]	9 (4)

[a] Patients with any mediastinal abnormalities on chest CT were excluded from this study.

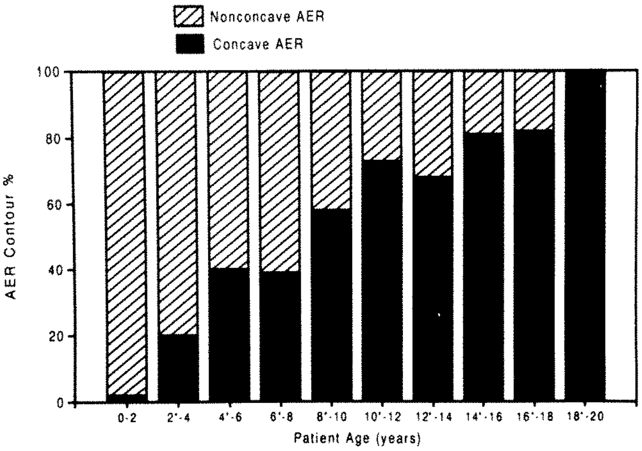

Fig. 2.—Bar graph shows distribution of azygoesophageal recess (AER) configuration by age. Nonconcave AERs include both convex and straight AER contours. Convex AERs predominate in children less than 10 years old.

group of 32 patients was excluded on the basis of an abnormal mediastinal configuration owing to obvious underlying disease. This resulted in a final group of 213 patients to serve as our normal subjects. Most of these patients did have known disease outside of the chest (Table 1). We did not include any patient in whom mediastinal disease in any compartment was noted on CT.

The configuration of the AER was assessed from hard-copy images of the mediastinum filmed at standard console settings (window = 350 H/level = 50 H). The AER was evaluated from the level of the azygous arch to the right hemidiaphragm. The contour of the AER was scored at the level of the right main bronchus as either convex, straight, or concave (Fig. 1). The appearance of the AER at all levels, as well as the location of the azygous vein, azygous node chain, and esophagus, were noted.

Results

Analysis of our review resulted in an age-related distribution of AER configurations (Fig. 2). When broken down by age groups, 85 (85%) of 100 children less than 6 years old had a convex AER. More significantly, 62 (95%) of 65 infants and children less than 3 years old were found to have a convex AER. The second group of children, ranging from 6 to 12 years old, had an intermediate distribution of convex, straight, and concave AER contours. Convex AERS were found in 25 (47%) of 53 children in this range. Finally, in adolescents 12–20 years old, the more typical adult-type concave AER was noted in 47 (78%) of 60. Overall, 123 (58%) of 213 children evaluated had a convex AER. No differences between boys and girls were observed.

Most of the convex AERs were found on the most cephalad scans, just beneath the azygous arch. The convex or straight AER configuration at this level was uniformly due to the azygous vein. The convexity extended caudad for several scans and then was noted to become concave (Fig. 3). However, some normal patients were noted to have a convex AER on the more caudal images (Fig. 4) because of the esophagus (7%); this was primarily due to esophageal reflux. No patient was found to have a convex AER extending continuously from the azygous arch to the diaphragm.

Discussion

Heitzman [7] defined the azygoesophageal recess as the intrusion of the medial aspect of the right lower lobe, the crista pulmonis, into the posterior mediastinum. The AER is well developed in most persons, and its medial boundary is readily recognized as a smooth arc, with concavity directed to the right, extending caudad from the azygous arch to the diaphragm. The concave configuration of the AER in adults

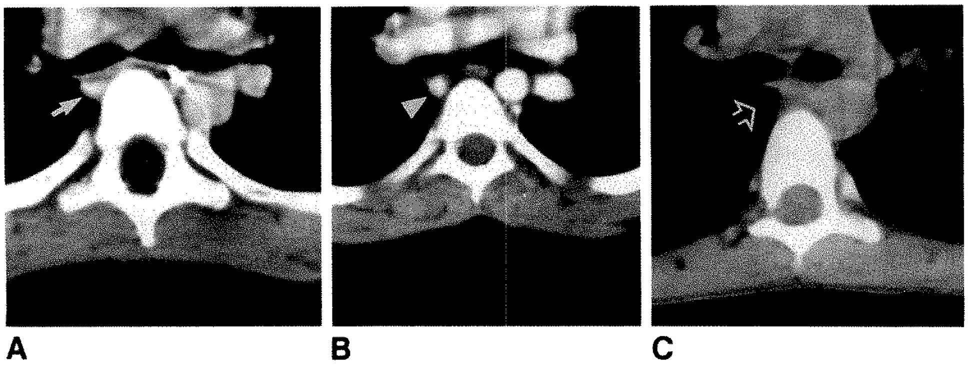

Fig. 1.—Axial CT scans of mediastinum at level of carina in three children.

A, Convex azygoesophageal recess (AER) resulting from azygous vein (*arrow*).

B, Straight AER configuration, again as a result of azygous vein (*arrowhead*).

C, Concave AER (*arrow*).

on CT examinations is well established [1, 2]. Attention to an alteration of AER contour allows detection of subtle abnormality in the mediastinum. Convex AERS have been described as a normal variant in adults in 7–21% of cases [3, 4, 6], the latter being seen in young adults.

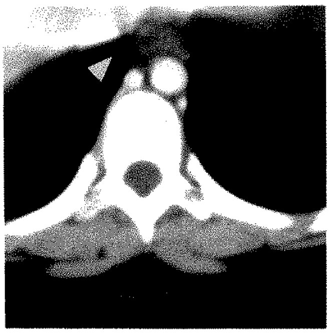

Fig. 3.—Transverse CT scan near aortic hiatus shows concave appearance of azygoesophageal recess (*arrowhead*) on more caudal scans found in most patients independently of age and configuration at level of carina.

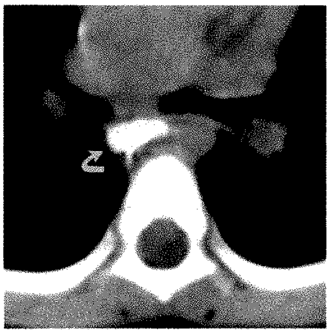

Fig. 4.—Transverse CT scan shows convexity of azygoesophageal recess caused by barium reflux in esophagus (*arrow*).

Our review shows that the configuration of the AER in children differs significantly from that seen in adults. The distribution of AER contours in our study showed a definite age-related distribution. In young children, especially infants, the AER was found to be convex in the overwhelming majority. In fact, scans in only three of 65 children less than 3 years old showed the AER to be concave. The distribution of AER contour varied with increasing age. Children 6–12 years old had an intermediate spectrum of AERs, divided nearly equally among convex, straight, and concave. In adolescents, the frequency of convex AERs dropped to 22%, a number compatible with previously reported adult studies.

The convexity of the AER in our normal patients was confined primarily to those scans just inferior to the azygous arch. The convexity of the AER was clearly related to the azygous vein at levels near the arch, while the esophagus did occasionally produce a convex AER on more caudal scans. The azygous vein was confidently identified in most patients scanned with or without IV contrast material. However, in several cases with minimal mediastinal fat, contrast administration was necessary to confirm that the azygous vein was responsible for a convex AER. Scanning at more caudal levels showed a transition to a consistently concave recess. This is related to the course of the azygous vein, which enters the chest via the aortic hiatus posteriorly and then ascends obliquely to join the superior vena cava. This helps to explain the difference in the appearance of the AER as the chest is scanned more caudally.

Consideration was given to what factors might help explain the age variation of AER contours. The obvious choice would be a variation in the size of the azygous vein itself. Unfortunately, our retrospective review did not allow determination

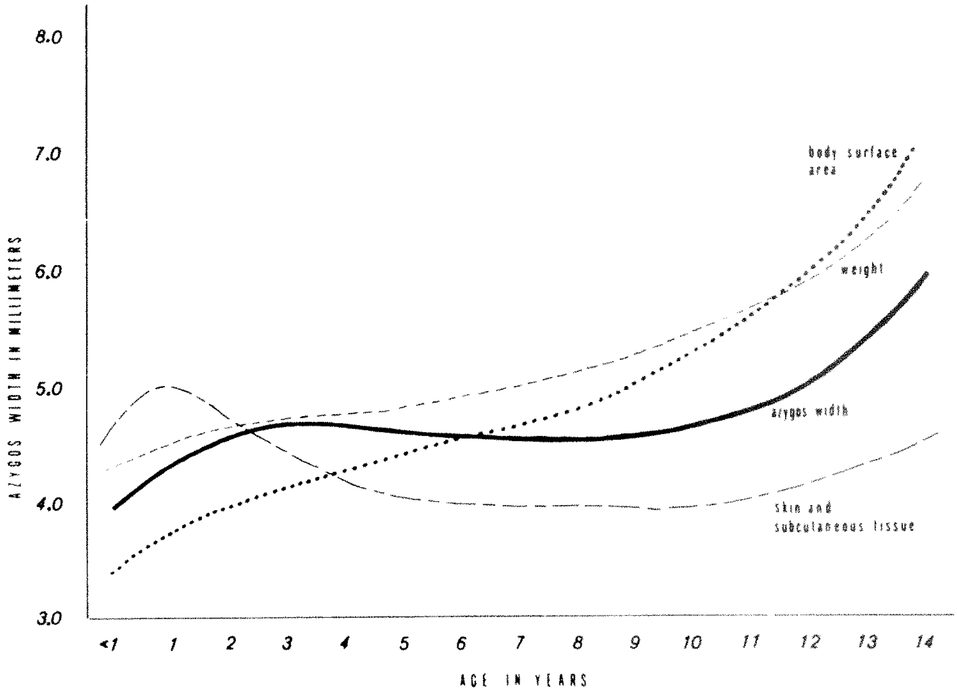

Fig. 5.—Data obtained from chest radiographs show age-related changes in azygous vein size vs other anatomic variables. A transition at age 3 in relative size of azygous vein might explain some of age-related variation in azygoesophageal recess we have observed. (Reprinted with permission from Wishart [8].)

of cardiac or fluid status, respiratory phase, or cardiac cycle. Any or all of these factors might be expected to affect the CT appearance of the azygous vein. Previously reported work on azygous vein size, as determined from chest radiographs [8], showed that the azygous vein increased in size in children from birth to 3 years of age, paralleling growth curves of soft tissue and other body structures. Beyond age 3, while other structures continued relatively constant growth rates, the size of the azygous vein was found to plateau (Fig. 5). This resulted in a relative decrease in the size of the azygous vein compared with other structures within the chest. This might help explain the age-related transition of AER configurations seen in our patients.

In summary, our findings suggest that a convex AER on CT scans is commonly observed in children. We have noted a spectrum of AER configuration with an age-related distribution in children. The azygous vein is primarily responsible for this lack of AER concavity. Recognition of the variation of the AER contour on chest CT scans is important in the accurate evaluation of the mediastinum in children.

ACKNOWLEDGMENT

We thank Susan Sloan for assistance in manuscript preparation.

REFERENCES

1. Golden RL, Heitzman ER, Proto AV. Computed tomography of the mediastinum: normal anatomy and indications for the use of CT. *Radiology* **1977**;124:235–241
2. Lund G, Lien HH. Computed tomography of the azygo-esophageal recess: normal appearances. *Acta Radiol* **1982**;23:225–230
3. Landay MJ. Azygous vein abutting the posterior wall of the right main and upper lobe bronchi: a normal CT variant. *AJR* **1983**;140:461–462
4. Lund G, Lien HH. Abnormalities of the azygo-esophageal recess at computed tomography. *Acta Radiol* **1983**;24:3–10
5. Glazer HS, Aronberg DJ, Sagel SS. Pitfalls in CT recognition of mediastinal lymphadenopathy. *AJR* **1985**;144:267–274
6. Onitsuka H, Kuhns LR. Dextroconvexity of the mediastinum in the azygoesophageal recess: a normal CT variant in young adults. *Radiology* **1980**;135:126
7. Heitzman ER. *The mediastinum*, 2nd ed. Berlin: Springer-Verlag, **1988**
8. Wishart DL. Normal azygous vein width in children. *Radiology* **1972**;104:115–118

Pictorial Essay

Cartilaginous Epiphysis and Growth Plate: Normal and Abnormal MR Imaging Findings

Diego Jaramillo[1] and Fredric A. Hoffer

The cartilaginous structures at the ends of growing bones constitute the "growth mechanism." These structures are not visible on radiographs, but they can be seen with MR imaging. Improved definition of cartilaginous abnormalities by MR imaging may permit earlier detection and treatment of these disorders and thus prevent bone deformity. This pictorial essay contains examples of normal and abnormal growth cartilage as seen with MR imaging. The indications for MR imaging in the evaluation of certain growth disorders are discussed, and the usefulness of MR imaging in certain clinical situations in which the role of this technique is still evolving is illustrated.

Normal Appearance of the Growth Cartilage on MR Images

In the infant and young child, the epiphysis is made up of concentric layers of hyaline cartilage surrounding the ossification center [1] (Fig. 1). The regions of cartilage have different signal characteristics, probably because of variation in cellularity and in the content of mineral, water, and water-binding macromolecules of the matrix [2]. The innermost cartilaginous layer is structurally similar to the growth plate and produces growth of the ossification center. It has been called the spherical growth plate [1], but it is not flat, as a plate, and it is not truly spherical but rather hemispherical. This hemispherical growth zone, like the articular cartilage and growth plate, is relatively hyperintense on both T1- and T2-weighted images (Fig 2). A broad zone of poorly organized chondrocytes, lying between the hemispherical growth zone and the articular cartilage, is hypointense with respect to the rest of the cartilaginous epiphysis on T1-weighted (e.g., 600/20 [TR/TE]) and T2-weighted (e.g., 2000/80) images (Fig. 2). On gradient-echo images (e.g., 350/13/30° [TR/TE/flip angle])

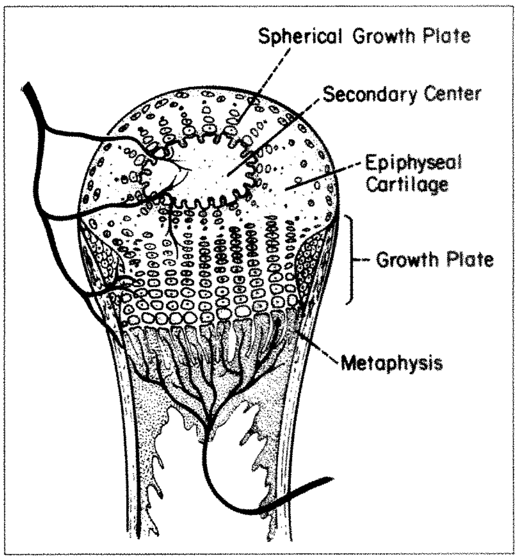

Fig. 1.—Anatomy of epiphysis and growth plate. Cartilaginous structures are largely avascular. Growth plate separates metaphyseal and epiphyseal vascular beds.

Received August 26, 1991; accepted after revision December 4, 1991.

[1] Both authors: Department of Radiology, Children's Hospital and Harvard Medical School, 300 Longwood Ave., Boston, MA 02115. Address reprint requests to D. Jaramillo.

AJR **158:1105-1110, May 1992** 0361-803X/92/1585-1105 © American Roentgen Ray Society

(Fig. 3), all the cartilaginous structures are uniformly hyperintense. Therefore, gradient-echo images are optimal for differentiating between cartilage and bone but suboptimal for distinguishing among the zones of the cartilaginous epiphysis.

In the older child, the epiphysis is almost completely ossified. The growth plate is seen as a band of higher signal between the hypointense epiphyseal bony plate and the hypointense zone of provisional calcification and primary spongiosa of the metaphysis [3, 4]. The zones of the growth plate cannot be distinguished on routine MR imaging. The signal intensity of the growth plate is intermediate on T1-weighted images and increases on "balanced" images. With progressive T2 weighting, the growth plate usually increases in signal intensity, but it may decrease.

Congenital Anomalies

Repair of congenital limb deficiencies is facilitated by imaging of the unossified structures that connect with the hypoplastic bone visible radiographically. In proximal focal femoral deficiency, the contour of the cartilaginous head can be seen on sonography and arthrography, but the growth plate and the connection with the ossified femur can be seen only on MR imaging [5].

In tibial hemimelia, the tibia is absent or hypoplastic. The decision between performing an above-knee amputation or a fibulofemoral arthroplasty depends on the degree of fibular development and of associated femoral hypoplasia [6]. We have used MR imaging to help in surgical planning in two cases of tibial hemimelia. MR imaging has shown the size and configuration of the unossified proximal fibular epiphysis, and its relationship with the distal femur (Fig. 3).

Acute Trauma

MR imaging is helpful in the evaluation of fractures that, by clinical and radiologic criteria, have a significant risk of leading to deformity [4]. Detection of cartilaginous and vascular abnormalities that precede the formation of a bony bridge allows earlier treatment of posttraumatic growth disorders. MR can define the plane of injury through the cartilage in fractures involving the growth plate. Vertical injuries through the growth plate often lead to bony bridge formation, because of the development of vascularity through the growth plate [3, 4]. The transphyseal vascularity that leads to the formation of a bony bridge has been seen on gadopentetate dimeglumine–enhanced MR imaging in rabbits [3]. Horizontal growth plate injuries that spare the cartilage immediately adjacent to the epiphysis (proliferative zone) are usually uncomplicated (Fig. 4). Severe crushing injury to the growth plate is associated with loss of signal from the cartilage, even though the growth plate may be open on radiographs (Fig. 5). MR imaging can also detect associated ligamentous injuries, which occur in half of the patients with epiphyseal separations around the knee [7] (Fig. 4).

Posttraumatic Complications

The most catastrophic complication of growth plate fractures is the formation of a bony bridge that crosses the growth plate and leads to growth arrest and deformity. Once the bony bridge develops, imaging evaluation should be directed to defining the size and location of the bridge and evaluating the severity of the growth disturbance. A very small fibrous bridge may resolve spontaneously. A small bony bridge pro-

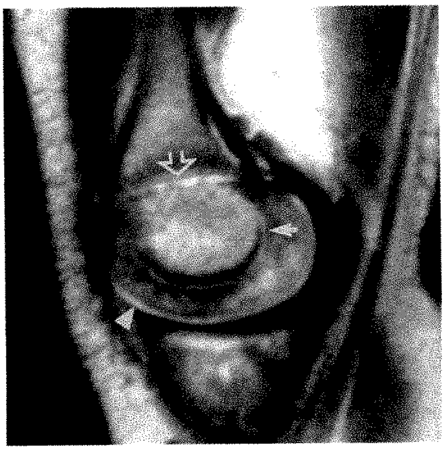

Fig. 2.—Normal epiphyseal anatomy of 4-year-old boy. Sagittal spin-echo T2-weighted 2000/80 MR image of distal femur shows hyperintense hemispherical growth zone (*solid arrow*) surrounding secondary center of ossification. Articular cartilage (*arrowhead*) and growth plate (*open arrow*) have similar signal intensity. Cartilage of inhomogeneous signal intensity lies between hemispherical growth zone and articular cartilage.

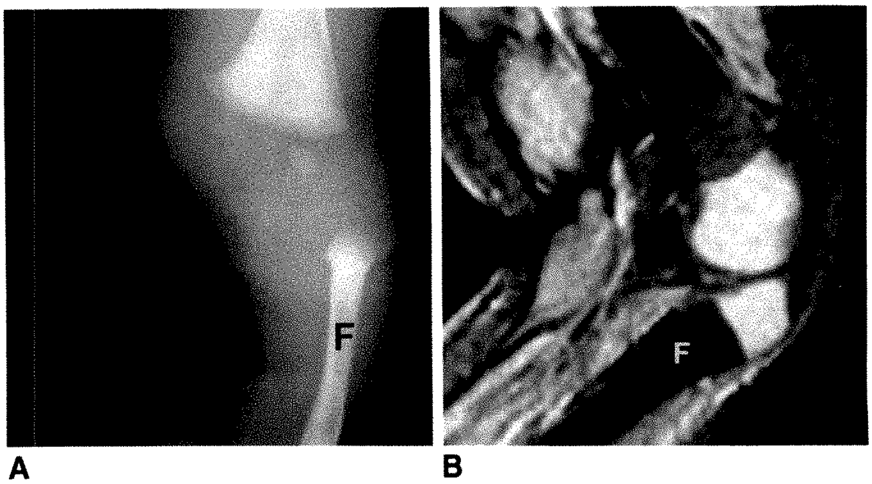

Fig. 3.—2-month-old boy with absent left tibia.

A, Anteroposterior radiograph shows wide distal femoral metaphysis and bifid distal femoral ossification center. Large fibula (F) is lateral to main axis of femur.

B, Sagittal gradient-echo 350/13/30° MR image of fibula (F). Fibular epiphysis is well formed and articulates with femur. Configuration and location of proximal fibular epiphysis make it suitable for fibulofemoral arthroplasty. Zones of cartilage cannot be differentiated on gradient-echo image.

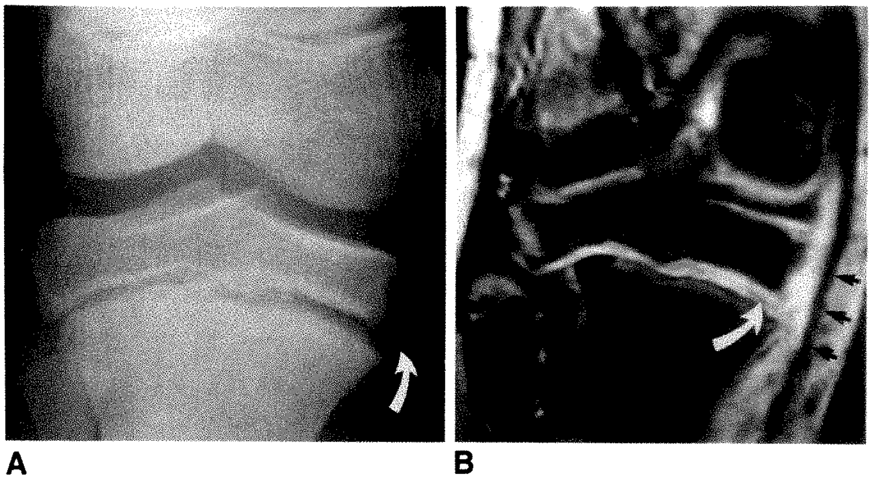

Fig. 4.—12-year-old with valgus injury to knee.
A, Anteroposterior radiograph immediately after trauma shows slight widening of medial portion of proximal tibial growth plate and small avulsed metaphyseal fragment adjacent to it (*arrow*).
B, Coronal gradient-echo 100/30/30° MR image of proximal tibia shows that medial collateral ligament has been avulsed from its tibial insertion (*black arrows*). Horizontal tear through cartilage (*white arrow*) spares epiphyseal side of growth plate. MR was performed because injuries to growth plate of proximal tibia and distal femur have high risk of a bony bridge developing.

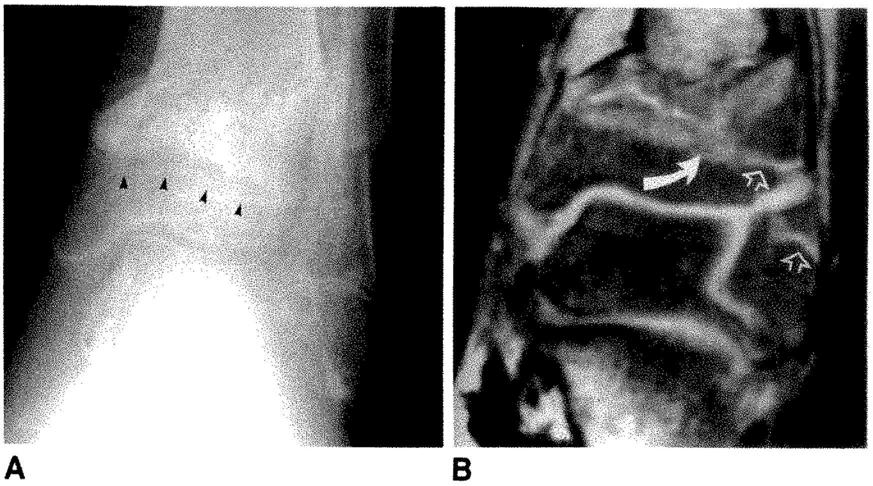

Fig. 5.—14-year-old boy with distal tibial injury sustained 6 weeks before imaging.
A, Anteroposterior radiograph shows severely comminuted metaphyseal fracture. Growth plate appears to be open (*arrowheads*). MR was performed to evaluate severity of extension of fracture into growth plate.
B, Coronal fat-suppressed spin-echo 600/20 T1-weighted MR image of distal tibia. Growth plates of fibula and uninvolved tibia are seen as bands of hyperintense signal (*open arrows*). More medially, tibial growth plate is interrupted (*solid arrow*), and normal hyperintensity of most of medial growth plate is lost. Premature closure of growth plate developed within 6 months.

ducing deformity can be resected. Multiple areas of bridging, or bridges involving the majority of the growth plate, are not resectable. We use MR imaging instead of plain tomography or CT for the preoperative evaluation of a bony bridge, as MR imaging (with cross-referencing of images in two planes) can provide a more accurate characterization and mapping of the bridge (Fig. 6). MR imaging also can provide valuable information by showing an intact growth plate in some cases where a bridge is suspected radiographically (Fig. 7).

Chronic Trauma

Chronic mechanical stress to the medial portion of the proximal tibial growth plate leads to disorganized growth and tibia vara deformity (Blount disease). Surgical treatment consists of a valgus-producing osteotomy. Patients with a bony bridge do not respond to the correcting osteotomy, and require resection of the bridge [8]. We have used MR imaging in the preoperative evaluation of five cases of Blount disease in order to see the growth plate and the unossified epiphysis, and to detect bony bridges (Fig. 8). The contour of the unossified epiphysis, which previously could only be evaluated with arthrography, is usually well preserved compared with the distorted underlying bone.

Tumor

The growth plate normally separates the metaphyseal and epiphyseal vascular territories, acting as a barrier to the spread of neoplasms. Its chondrocytes produce antiangiogenic substances that interfere with neoplastic invasion [3]. With continued tumor growth, the growth plate is overwhelmed (Figs. 9–11). Detection of transphyseal involvement by malignant tumors is essential in the planning of limb-salvage procedures. The best results are obtained when the growth plate and epiphysis are uninvolved and can be left in place. The rate of epiphyseal invasion by metaphyseal osteosarcomas is 80% as detected by MR imaging and histopathologic examination, but only 60% as determined by plain radiographs [9] (Fig. 9).

Penetration of the growth plate by benign neoplasms has been considered extremely rare, and transphyseal extension

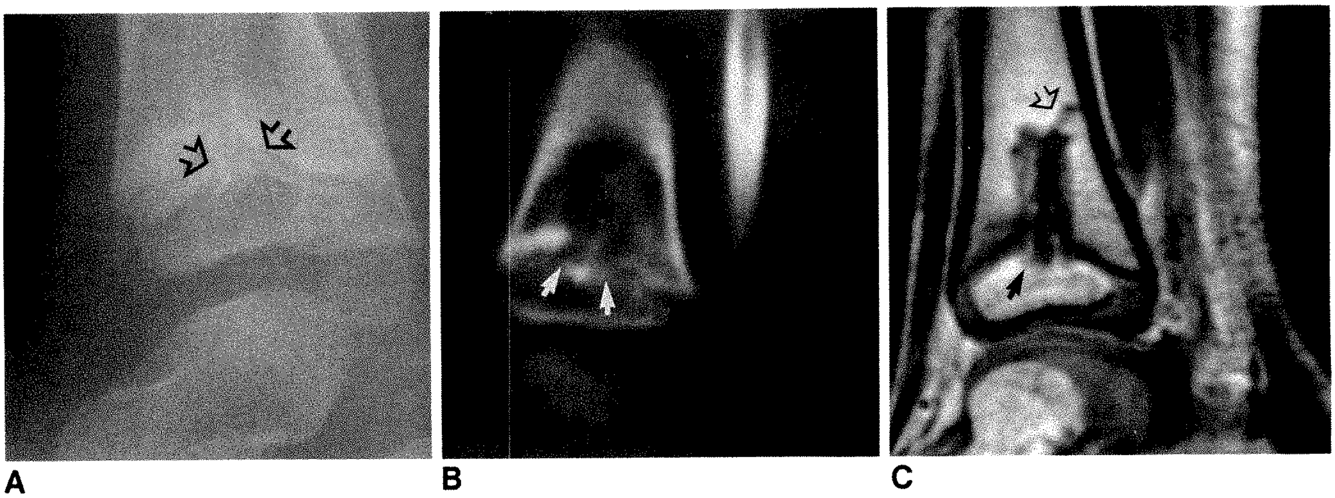

Fig. 6.—4-year-old boy with Salter II fracture of distal tibia sustained 20 months before imaging.

A, Lateral radiograph of distal tibia shows central tethering of metaphysis and epiphysis by a bony bridge (*arrows*).

B, Sagittal CT scan of distal tibia. Bony bridge (*arrows*) is better defined than in *A*. Image is not truly sagittal, and significance of metaphyseal lucency is uncertain.

C, Sagittal spin-echo 2000/30 MR image of distal tibia. Formed bridge containing fatty marrow (*solid arrow*) is better defined than on other studies. Metaphyseal abnormality corresponds to an area of abnormal ossification and a healing fracture (*open arrow*).

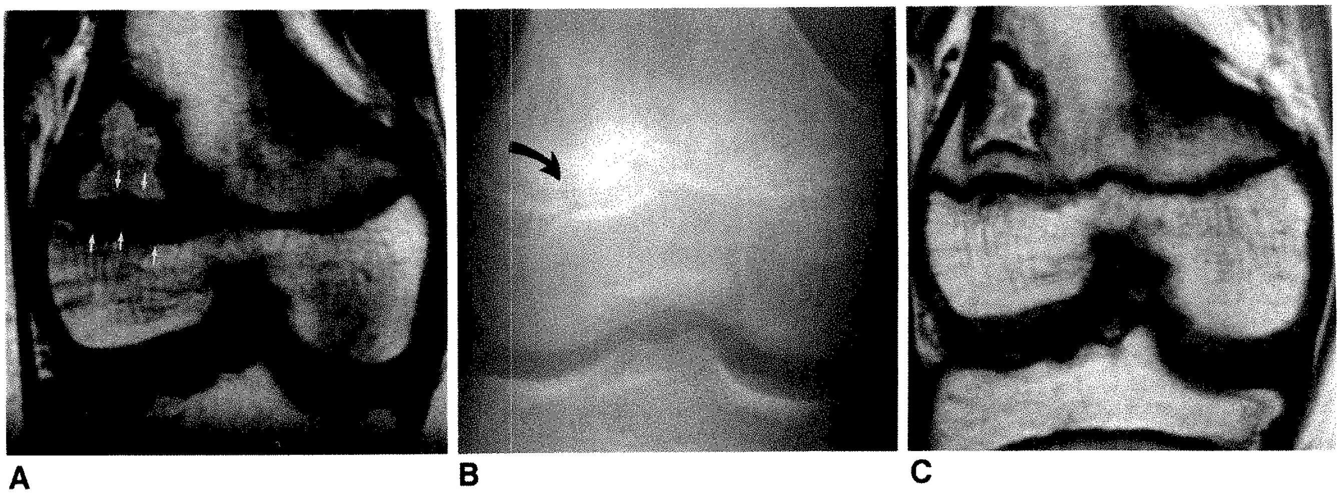

Fig. 7.—12-year-old boy with Salter II fracture of distal femur sustained 6 weeks before imaging.

A, Coronal spin-echo 600/25 T1-weighted MR image shows that medial part of growth plate is widened (*arrows*), suggesting that metaphyseal bony fragment is isolated.

B, Anteroposterior radiograph obtained 3 months after first study. Fracture has healed. Poorly defined sclerosis on medial aspect of distal femoral metaphysis (*arrow*) raises concern of a bony bridge developing.

C, Coronal spin-echo 600/25 T1-weighted MR image obtained at time of radiograph. Metaphyseal fragment has become necrotic and isolated from adjacent marrow. MR shows normal growth, which has resulted in migration of growth plate away from necrotic fragment.

has been suggested as an indicator of malignancy [10]. It is possible that, just as with osteosarcomas, epiphyseal extension of benign tumors will be detected more frequently with the use of MR imaging. We have seen two cases of benign neoplasms with epiphyseal extension that were detected by MR imaging and not seen on plain radiographs (Fig. 11).

Infection

The growth cartilage is also a partial barrier against the spread of infection. Invasion of the growth plate by the infectious process often results in growth disturbances. Bone scintigraphy continues to be the primary technique for evaluating osteomyelitis. However, involvement of the growth plate by infection is difficult to detect scintigraphically, as both the region of the growth plate and the infected area have increased activity. Plain tomograms cannot distinguish between the radiolucent growth plate and the lytic lesion in the adjacent bone (Fig. 12A). MR imaging is helpful in the evaluation of osteomyelitis when involvement of the growth plate is suspected and drainage is considered (Fig. 12B). The signal intensity of the cartilage is altered by infection. Enhancement

Fig. 8.—4-year-old boy with Blount disease who had had proximal tibial osteotomy but has persistent deformity.

A, Anteroposterior tomogram shows marked abnormality of medial growth plate, which appears to be closed (*open arrow*). Tilted growth recovery line (*arrowheads*) indicates decreased growth medially.

B, Coronal gradient-echo 30/14/30° MR image of proximal tibia shows that growth plate is open, but it curves medially in stepwise fashion (*white arrows*). Cartilaginous tibial plateau (*black arrow*) is less affected.

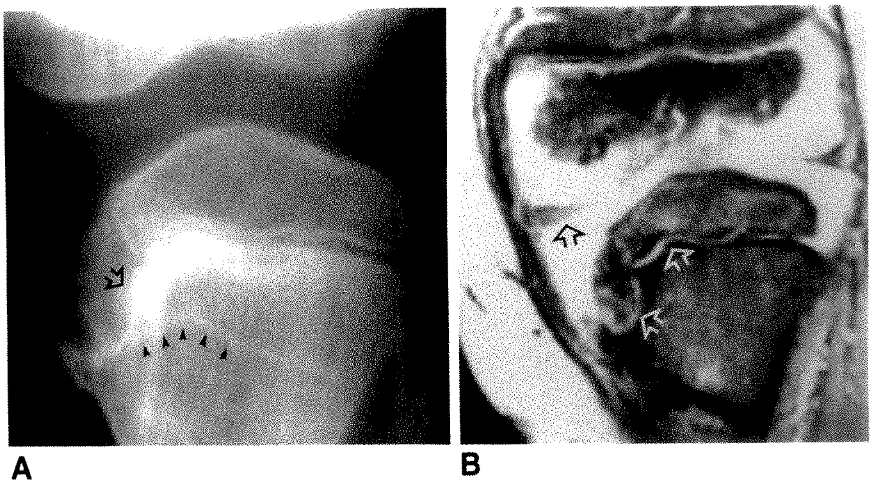

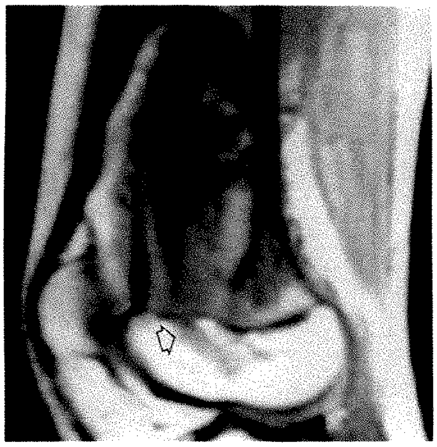

Fig. 9.—Sagittal spin-echo 600/20 T1-weighted MR image of 11-year-old girl with osteogenic sarcoma of distal femur shows tumor extending beyond growth plate into epiphysis (*arrow*). Extension was not evident radiographically.

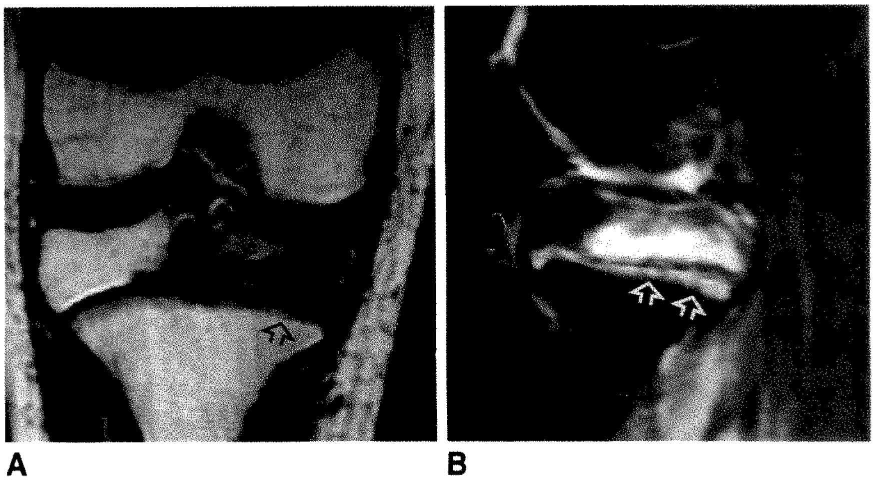

Fig. 10.—14-year-old with Ewing's sarcoma involving proximal tibial epiphysis.

A, Coronal spin-echo 700/20 T1-weighted MR image shows tumor abutting growth plate (*arrow*), but it is uncertain whether there is extension through cartilage.

B, Sagittal short TI inversion recovery 2000/140/35 (TR/TI/TE) MR image shows that signal intensity from metaphysis is also abnormal (*arrows*).

Fig. 11.—6-year-old girl with recurrent aneurysmal bone cyst of proximal tibia.

A, Anteroposterior radiograph shows predominantly lytic, expansile lesion of proximal metaphysis. Epiphysis is apparently uninvolved.

B, Coronal gradient-echo 38/17/30° MR image of tibia shows focal interruption of hyperintense signal from growth plate (*arrow*). On sagittal T2-weighted images there were multiple fluid-fluid levels within lesion, typical for aneurysmal bone cyst.

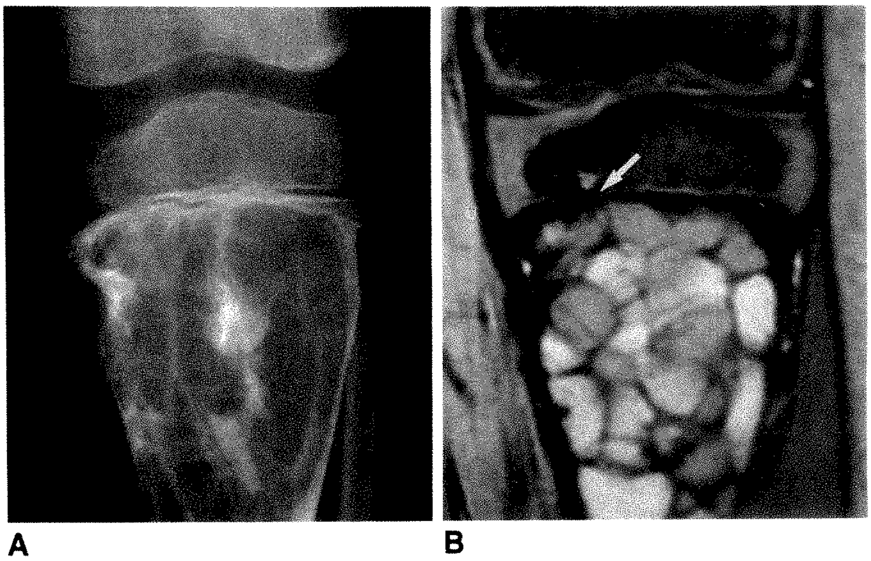

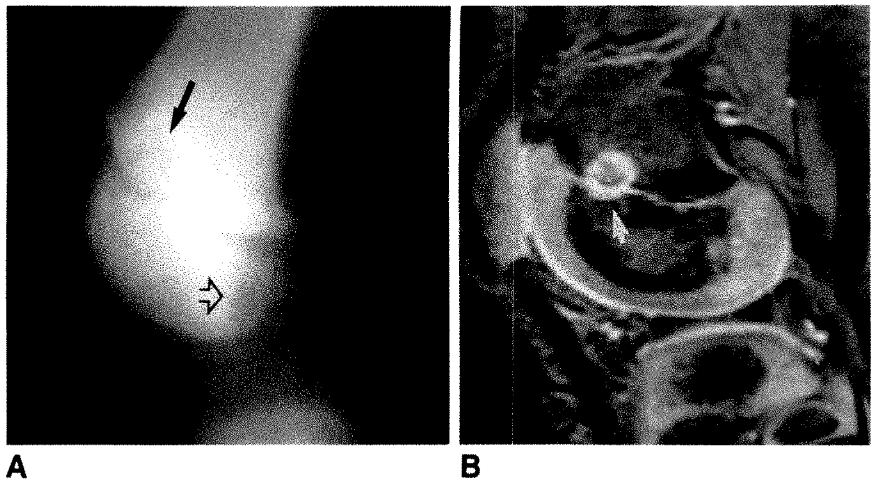

Fig. 12.—9-year-old girl with 1-month history of pain in distal femur and clinical suggestion of chronic osteomyelitis.

***A*, Lateral tomogram of distal femur shows lytic lesion in anterior metaphysis (*solid arrow*) that contains sclerotic sequestrum. Second lytic lesion is in posterior epiphysis (*open arrow*).**

***B*, Sagittal fat-suppressed fast spin-echo 2000/16 balanced MR image of distal femur. Metaphyseal lesion with sequestrum crosses growth plate and involves epiphysis (*arrow*). Posterior epiphyseal lesion had necrotic center on enhanced images. Drainage of both lesions produced pus containing *Staphylococcus aureus*.**

with gadopentetate dimeglumine shows the interruption of the growth plate and detects areas of intraosseous abscess.

REFERENCES

1. Ogden JA. Anatomy and physiology of skeletal development. In: Ogden JA. *Skeletal injury in the child,* 2nd ed. Philadelphia: Saunders, **1990**: 23–63
2. Ehrlich MG, Zaleske DJ, Armstrong AL, Sternsich A, Mankin HJ. Physeal biochemistry. In: Uhthoff HK, Wiley JJ, eds. *Behavior of the growth plate.* New York: Raven, **1988**:25–29
3. Jaramillo D, Shapiro F, Hoffer FA, et al. Posttraumatic growth-plate abnormalities: MR imaging of bony-bridge formation in rabbits. *Radiology* **1990**;175:767–773
4. Jaramillo D, Hoffer FA, Shapiro F, Rand F. MR imaging of fractures of the growth plate. *AJR* **1990**;155:1261–1265
5. Hillmann JS, Mesgarzadeh M, Revesz G, Bonakdarpour A, Clancy M, Betz RB. Proximal femoral focal deficiency: radiologic analysis of 49 cases. *Radiology* **1987**;165:769–773
6. Tachdjian MO. Congenital longitudinal deficiency of the tibia. In: Tachdjian MO, ed. *Pediatric orthopedics,* 2nd ed. Philadelphia: Saunders, **1990**: 636–651
7. Bertin KC, Goble EM. Ligament injuries assciated with physeal fractures about the knee. *Clin Orthop* **1983**;177:188–192
8. Tachdjian MO. Tibia vara. In: Tachdjian MO, ed. *Pediatric orthopedics,* 2nd ed. Philadelphia: Saunders, **1990**:2835–2850
9. Norton KI, Hermann G, Abdelwahab IF, Klein MJ, Granowetter LF, Rabinowitz JG. Epiphyseal involvement in osteosarcoma. *Radiology* **1991**;180:813–816
10. Enneking WF, Conrad EU. Tumors of the musculoskeletal system. In: Netter FH, ed. *Musculoskeletal system,* part II. Summit, NJ: Ciba-Geigy, **1990**:120–132

Case Report

Mediastinal Pseudocyst Caused by Pharyngeal Perforation During Child Abuse

Paul K. Kleinman,[1] Melissa R. Spevak,[1] and Maynard Hansen[2]

Pharyngeal and esophageal perforation caused by child abuse is rare [1-3]. All published reports have described cervical swelling, emphysema, and fever, and in two cases of a cervical abscess there was spread to the mediastinum. We report a case of child abuse in which the patient had inspiratory stridor from a mediastinal pseudocyst. Additional studies revealed evidence of prior pharyngeal perforation and widespread skeletal injury typical of child abuse.

Case Report

A 5-week-old boy was transferred to this institution because of inspiratory stridor. He was described as being well until 5 days before admission, when he awoke during the night crying inconsolably. After several visits to a physician, the infant was brought to a local emergency department where severe respiratory distress was noted. After transfer to this institution, the infant was noted to have severe substernal retractions and inspiratory stridor; respiratory rate was 60 breaths/min; heart rate, 128 beats/min; and temperature, 37.5°C. The infant was treated with oxygen and IV fluids. On the second hospital day, increased substernal retractions and expiratory wheezing were noted and were most evident while in the supine position. Radiographs of the chest revealed compression of the trachea by an apparent posterior mediastinal mass and bilateral posterior rib fractures (Figs. 1A and 1B). Barium swallow demonstrated a large posterior mediastinal soft-tissue mass compressing and displacing the esophagus and trachea. MR imaging revealed a posterior mediastinal mass with signal characteristics consistent with nonhemorrhagic fluid (Figs. 1C and 1D). The mass extended via a relatively small channel to the retropharyngeal region. A skeletal survey demonstrated fractures of the proximal and distal right tibial metaphyses as well as the bases of the left third and fourth metatarsals. A repeat barium swallow demonstrated evidence of an outpouching of contrast material in the retropharynx, and a delayed film revealed a localized area of extravasated barium (Fig. 1E). The patient remained afebrile and showed gradual improvement in respiratory symptoms without surgical drainage or antibiotics. The stridor eventually resolved. A repeat MR examination on the 12th hospital day showed almost complete resolution of the mediastinal mass. Discussions with the parents eventually suggested that the pharyngeal injury may have occurred after forceful introduction of a spoon into the infant's mouth. The patient was discharged to the custody of the Department of Social Services.

Discussion

The vast majority of radiologically documented lesions in abused infants involve the skeleton and the CNS. Visceral injuries involving the chest and abdomen do not become common until the second year of life, with the possible exception of injury to the mouth [1, 4]. Oropharyngeal trauma in the ears, nose, and throat of infants is well documented in the dental literature [5-7]. The three cases previously reported were all infants less than 10 months old. Recently,

---

Received September 24, 1991; accepted after revision November 4, 1991.

[1] Department of Radiology, University of Massachusetts Medical Center, 55 Lake Ave. N., Worcester, MA 01655. Address reprint requests to P. K. Kleinman.

[2] Department of Otolaryngology, University of Massachusetts Medical Center, Worcester, MA 01655.

AJR 158:1111-1113, May 1992 0361-803X/92/1585-1111 © American Roentgen Ray Society

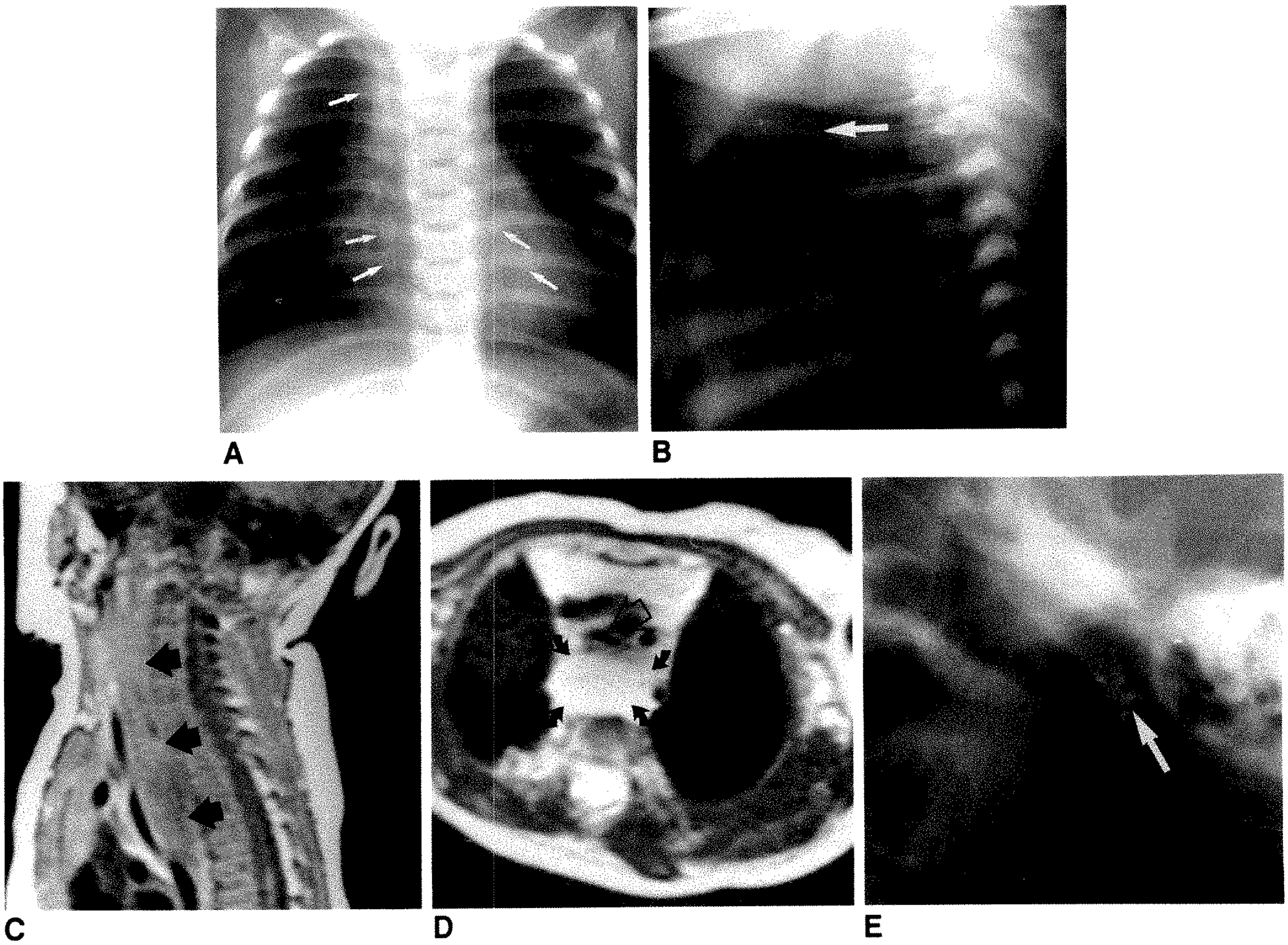

Fig. 1.—*A* and *B*, Anteroposterior (*A*) and lateral (*B*) radiographs of chest show prominence of superior mediastinal contours. Anteroposterior radiograph (*A*) shows bilateral healing fractures of seventh and eighth ribs as well as right third rib posteriorly (*arrows*). In *B*, trachea is compressed and displaced anteriorly (*arrow*) by vague soft-tissue mass.

C, Midline sagittal T1-weighted MR image shows a relatively low-signal-intensity mass in retrotracheal region extending from posterior mediastinum to neck (*arrows*).

D, T2-weighted axial image shows tracheal compression (*open arrow*) by high-signal-intensity posterior mediastinal mass (*solid arrows*).

E, Lateral view of upper airway immediately after barium swallow shows extravasated barium in retropharyngeal soft tissues (*arrow*).

Manning et al. [7] described an abused 4-month-old child with multiple oral bruises, lacerations, and a retropharyngeal abscess. Grace and Grace [6] mentioned two children with bruising of the palate and fauces, caused by forcible insertion of a spoon into the mouth. The infant reported here may have suffered the pharyngeal perforation by a similar mechanism. Insertion of a foreign object into the mouth appears to be a common mechanism of inflicted oropharyngeal injury in infants and children. Such assaults may represent a punitive measure or an attempt to suffocate the infant. The possibility of a sexual assault was raised in one reported case [3].

Pharyngeal and cervical esophageal perforation in infancy are usually iatrogenic in nature. The posttraumatic pseudodiverticulum of the esophagus is a familiar entity to pediatric radiologists and pediatric surgeons, and the clinical and radiologic findings may lead to an erroneous diagnosis of esophageal atresia [8–10]. Perforation can occur from an endotracheal tube, a suction catheter, or a nasogastric tube. Perforation can occur with digital manipulation during delivery or with an aggressive attempt to dislodge an impacted foreign body [8]. Although respiratory symptoms and evidence of abnormal air collections are frequently present, the perforation may be silent and identified only by the presence of a malpositioned nasogastric tube. However, when the perforation is unrecognized, a barium swallow study may lead to an erroneous diagnosis of a congenital pharyngeal diverticulum [8, 9]. Although surgery has been performed in some cases, particularly when an abscess is present, most perforations heal spontaneously after removal of the nasogastric tube and treatment with antibiotics.

In light of the natural history of iatrogenically induced perforations, the findings in this case of child abuse can be readily explained. After traumatic perforation of the oral pharynx, secretions flowed into the retropharyngeal soft tissues. Passage of these secretions occurred through the visceral compartment of the neck to the posterior mediastinum. With increasing size of the mediastinal collection, eosphageal and tracheal compression occurred. Although barium swallow showed the original site of perforation, no communication could be demonstrated, indicating that the process had evolved to form a mediastinal pseudocyst. Symptoms resolved and resolution was documented by the follow-up MR scan. The rib fractures were the only indication of abuse in this infant, and without this information, the true implications of the problem probably would have remained obscure.

Given the frequency of facial and oropharyngeal injuries in child abuse, pharyngeal perforation may be more common than suggested by the paucity of reports in the literature. Occult pharyngeal perforation must be included in the differential diagnosis of inspiratory stridor in the infant with a posterior mediastinal mass and tracheal compression.

REFERENCES

1. Kleinman PK. Visceral trauma. In: *Diagnostic imaging of child abuse.* Baltimore: Williams & Wilkins, **1987**:115–158
2. McDowell HP, Fielding DW. Traumatic perforation of the hypopharynx—an unusual form of abuse. *Arch Dis Child* **1984**;59:888–889
3. Ablin DS, Reinhart MA. Esophageal perforation with mediastinal abscess in child abuse. *Pediatr Radiol* **1990**;20:524–525
4. Cameron JM, Johnson HRM, Camps FE. The battered child syndrome. *Med Sci Law* **1966**;6:2–21
5. Tate RJ. Facial injuries associated with the battered child syndrome. *Br J Oral Maxillofac Surg* **1971**;9:41–45
6. Grace A, Grace S. Child abuse within the ear, nose and throat. *J Otolaryngol* **1987**;16:108–111
7. Manning SC, Casselbrant M, Lammers D. Otolaryngologic manifestations of child abuse. *Int J Pediatr Otorhinolaryngol* **1990**;20:7–16
8. Lucaya J, Herrea M, Salcedo S. Traumatic pharyngeal pseudodiverticulum in neonates and infants. *Pediatr Radiol* **1979**;8:65–69
9. Girdany BR, Sieber WK, Osman MZ. Traumatic pseudodiverticulums of the pharynx in newborn infants. *N Engl J Med* **1969**;280:237–240
10. Blair GK, Filler RM, Theodorescu D. Neonatal pharyngoesophageal perforation mimicking esophageal atresia: clues to diagnosis. *J Pediatr Surg* **1987**;22:770–774

Book Review

Principles and Practice of Cardiovascular Imaging. Edited by Gerald M. Pohost and Robert A. O'Rourke. Boston: Little, Brown, 880 pp., 1991. $175

This reference text is organized into three parts: the technology of cardiovascular imaging, the clinical applications of this technique, and a final chapter on cost-effectiveness. The introductory chapter describes the fundamental principles of sonography of all echo-Doppler applications too summarily. It is difficult to follow and superfluous, as two subsequent chapters on M-mode and two-dimensional echocardiography and conventional Doppler echocardiography cover these applications in more detail. Both chapters are well written and illustrated. The references are well organized, allowing the reader to reference subjects by content and not by order of appearance.

A significant deficit of this book is the superficial coverage of color Doppler echocardiography. This technique is covered too briefly in the technical aspects and to a lesser extent pictorially. Finally, the section on transesophageal echocardiography is short and could have explored further the potential applications of this new technique.

The section on nuclear medicine describes the most often used radionuclides and the principles of imaging the cardiovascular system by using equilibrium blood-pool and first-pass cineangiography. The section is well organized and clearly written. The reader is led sequentially through the requirements for a nuclear cardiology evaluation: the acquisition, processing, and interpretation of such studies. The most recent information on thallium-201, technetium, and antimyosin antibodies is included. Technetium-labeled isonitriles and boronic acid complexes of technetium oximes are described in several additional paragraphs in the chapter on perspectives on the future of nuclear cardiology. Other texts may cover this section in greater depth. The chapter on positron emission tomography is a good overview of the potential use of this technique in the assessment of myocardial perfusion and metabolism. It provides a good understanding of the instrumentation and isotopes available.

The section on x-ray imaging correlates clinical and radiologic techniques such as standard chest radiography, fluoroscopy, and cineangiography. This topic is addressed generally and in detail, and the most common forms of cardiovascular disease are considered. The final chapter on fast cine CT and its applications is excellent coverage of this special technology.

The section on MR imaging is excellent. It includes the basic principles of cardiovascular imaging and all potential applications for the diagnosis of cardiovascular diseases. However, it does not emphasize the conditions in which MR is comparable to other techniques or indications for its use. The section finishes with an overview of MR spectroscopy that is sufficient for the cardiologist, as the clinical applications of this technique are still to be defined.

The section on clinical application of cardiac imaging gives a general idea of what to expect from each imaging technique. It is not a structured discussion of which technique is preferable, but it gives sufficient detail to allow readers to make their own judgments. The first few chapters of this section discuss all aspects of coronary artery disease and cardiomyopathies. A particularly good chapter is the one on valvular disease. A series of clinical cases with history and other pertinent information suggests how to select an imaging technique that will provide important information and help in clinical decision making. In other cases, conflicting data provided by other imaging techniques are discussed, emphasizing the potential sources of error of each procedure. This part is followed by a description of the findings provided by each technique in the different forms of valvular disease. The book finishes with comprehensive chapters on congenital disease, pericardial disease, cardiac masses, and thrombi. All are well presented, illustrated, and referenced. The final section deals with the cost-effectiveness of using these imaging techniques and examines the potential influence of cost-containment efforts on the use and acquisition of new technologies.

The text has excellent resource and reference information. It also provides highly technical information in language that avoids jargon, and it includes glossaries of technical terminology when appropriate.

Julio F. Tubau
Henry Levenson
University of Southern California
Los Angeles, CA 90033

Review Article

The Role of MR Imaging in the Evaluation of Acquired Diseases of the Thoracic Aorta

Kerry M. Link[1] and Nadja M. Lesko[2]

Because MR imaging combines the major attributes of angiography, echocardiography, and CT, its role in the evaluation of the thoracic aorta is steadily increasing. When standard spin-echo techniques are used, flowing blood produces a signal void that allows excellent depiction of the anatomy and simultaneous evaluation of the lumen, vessel wall, and periaortic structures. On dynamic or cine MR, flowing blood generates a signal that allows visualization of the blood as it pulsates through the aorta. Turbulent blood generates a signal void, thereby allowing the detection and qualitative assessment of the pathophysiologic consequences of anatomic abnormalities. With phase-mapping techniques, blood velocity can be measured and used to calculate pressure gradients. Recent advances in the field of MR angiography will greatly enhance the overall role of MR in the evaluation of the thoracic vasculature by allowing detection and assessment of the branch vessels. Although the technique is still evolving, it has shown extraordinary potential as a tool for studying the thoracic aorta. The exact role of MR in patient care will depend on advances in transesophageal echocardiography. However, it is not unreasonable to think that someday MR imaging will be the primary technique for evaluation of the thoracic aorta.

MR imaging techniques are extremely useful for evaluating the wide spectrum of acquired abnormalities of the thoracic aorta. When "static" spin-echo (SE) techniques are used, flowing blood produces a signal void [1] throughout most of the cardiac cycle, providing a "natural" contrast agent that allows the simultaneous visualization of the lumen, vessel wall, and periaortic structures.

The pathophysiologic consequences of identified abnormalities are best studied by using dynamic imaging techniques [2-4]. With gradient-refocused-echo (GRE) or cine MR, flowing blood generates a signal that permits visualization of the blood as it pulsates through the aorta. Turbulent blood flow results in a signal void and allows the detection and qualitative assessment of valvular lesions, including stenosis and regurgitation. With phase-mapping techniques, the actual velocity of blood flow can be determined [5–7].

MR angiography will probably play a lesser role in the evaluation of the thoracic aorta itself because of the strengths of both SE and cine MR imaging techniques, but MR angiography will have definite application in the evaluation of the branch vessels and their ostia.

When used in conjunction, static and dynamic MR techniques combine the attributes of echocardiography, angiography, and CT. For these reasons, MR is arguably the imaging technique of choice for the evaluation of the thoracic aorta.

Technical Considerations

Image degradation caused by motion artifact is an inherent problem of MR imaging. In studies of the cardiovascular system, not only movement of the patient but also the natural contractile nature of the heart and normal respiratory motion must be considered. ECG gating is the primary means of overcoming these limitations; however, poor image quality remains the leading cause for the inability to diagnose thoracic

---

Received July 11, 1991; accepted after revision December 4, 1991.

[1] Department of Radiology, Bowman Gray School of Medicine, Medical Center Blvd., Winston-Salem, NC 27157-1022. Address reprint requests to K. M. Link.

[2] Department of Radiology, Northern Hospital of Surry County, P.O. Box 1101, Mt. Airy, NC 27030.

AJR 158:1115-1125, May 1992 0361-803X/92/1585-1115 © American Roentgen Ray Society

aortic disease on the basis of MR findings. In most cases the problem is patient movement or poor ECG gating; either the patient has an arrhythmia not conducive to gating or the technique is not implemented correctly.

All patients should be evaluated to determine whether sedation and/or sophisticated monitoring will be required. A multitude of sedation schemes have been advocated, reflecting the experience of a large number of institutions and the marked variability of response among patients [8, 9]. Regardless of the regimen implemented, patients must be monitored closely.

Optimal image quality is obtained with ECG-gated SE pulse sequences for static imaging and ECG-referenced GRE examination [10]. Despite the availability of these ECG-gated schemes, imaging quality may be suboptimal because of lack of attention to their implementation.

ECG patches and leads should be made of a nonferrous material. To maximize the ECG signal, the patches should be placed closely together on either the chest or the back. The leads should be coiled about one another to negate the electric flux generated about a loop in a magnetic field [11, 12].

SE Imaging

Evaluation of aortic disease should begin with an ECG-gated multislice axial SE study. An echo time (TE) of 20-30 msec is standard. The repetition time (TR) is determined on the basis of the patient's R-R interval. The field of view (FOV) will vary according to the size of the patient. Slices 8 mm thick with a 2-mm gap are used in the evaluation of adults.

With the multislice technique, the images are not obtained at the same phase of the cardiac cycle. As a result, some images may show high signal within the thoracic aortic lumen because of diastolic flow or entry or exit slice phenomena [13]. The latter is easily recognized and is not usually a problem in image interpretation. However, slow flow may be difficult to differentiate from mural thrombus or thrombus within a false lumen; therefore, the use of presaturation slabs is advisable when the thoracic aorta is examined [14]. Placing them at the level of the thoracic inlet and the diaphragm should prevent this unwanted effect.

An important view in the evaluation of the thoracic aorta, with either static or dynamic techniques, is the oblique sagittal or left anterior oblique view, which shows the entire extent of the thoracic aorta on a single image in most patients. This view is quite helpful in the evaluation of aneurysms and dissections. It is obtained by imaging through a plane that bisects the center of the ascending and descending aorta (Fig. 1). Sequential coronal views are useful in depicting the ostia of branch vessels and in the evaluation of aortic stenosis.

Cine MR

GRE techniques use narrow or low flip angles of 30-50°, short TEs on the order of 10 msec, and short TRs in the range of 20-50 msec. The low flip angle maintains signal-to-noise ratio, and the short TE, in the absence of 180° pulse, produces images in which the blood pool is white. The study is not ECG gated; however, the ECG tracing serves as a reference point for postacquisition sequencing of the images and can be used in either a prospective or a retrospective fashion [15, 16].

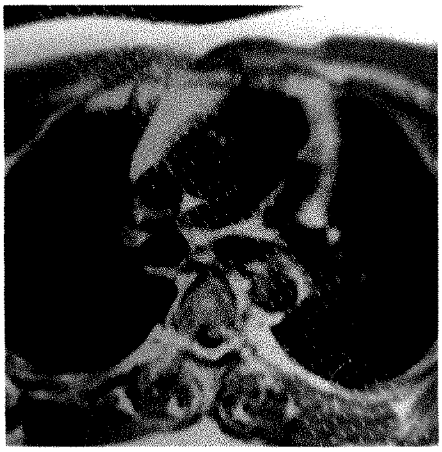

Fig. 1.—Axial MR pilot SE image for left anterior oblique view. On axial image through ascending and descending aorta, a line centered between ascending and descending aorta is used as a reference angle for acquisition of multiple left anterior oblique images (*broken lines*).

The clear advantage of using GRE techniques is that flowing blood appears white. This phenomenon occurs because the blood proton produces signal as a result of exposure to only one RF pulse, and the echo is generated by a gradient reversal. Flow-related enhancement is maintained by the constant inflow of unsaturated blood. Disturbance in blood flow results in signal loss that can be used to detect regions of abnormal flow associated with abnormalities such as aortic valvular stenosis or coarctation.

The signal loss in areas of turbulent flow is thought to be due to rapid spin dephasing. Although this phenomenon can be very useful in evaluating valvular disease, turbulent flow and subsequent signal loss can occur in the normal heart and aorta. Care must be taken when evaluating cine studies of the aorta not to mistake normal signal loss for a pathologic process. Signal void is commonly observed in the left ventricular outflow tract during early systole. It is also frequently seen just above the aortic valve during peak systole in normal subjects. In patients with aortic stenosis it is found more distally. A signal void is normally present along the inner wall of the aortic arch, extending into the proximal descending aorta [17].

Because of the fast acquisition times, multiple levels of the heart can be imaged at multiple phases of the cardiac cycle during a single acquisition. Typically, 16 phases are acquired at four different levels. A single level can be examined with a temporal resolution on the order of 50-60 frames per R-R interval. This technique becomes extremely important when the left anterior oblique projection is used to evaluate the thoracic aorta. The resultant study looks like a traditional angiogram. When played as a cine study, MR has the added advantage of showing the flow characteristics of blood as it courses through the aorta.

Recent reports have described "black blood" cine techniques, in which saturation pulses are used in conjunction with a cine study to make the blood pool appear black. This technique may be useful in differentiating between slow blood flow and thrombosis within the false lumen of an aortic dissection. However, the technique is limited by its inability to show turbulent flow [18, 19].

Phase Velocity Mapping MR

The MR signal is composed of both magnitude and phase components, and the standard MR image is produced from the magnitude component. The phase component can be used to produce images that reflect the motion of protons over a period of time. This movement or change in phase angle is proportional to the velocity of the proton. Phase display images can be formed by mapping the change in phase angle on a voxel-by-voxel basis. The protons with zero velocity (zero phase angle) are assigned to the middle of a gray scale. On the basis of their velocity, protons that move in one direction are assigned an increasing positive (white) value, and those that move in the opposite direction are assigned an increasing negative (black) value. Therefore, quantitative information is provided about both the direction and the velocity of blood flow. Because the display is recorded on a voxel-by-voxel basis, by placing a cursor at any location, an actual measurement of velocity can be obtained. Potential problems with this technique involve the phenomenon of aliasing. Because zero phase is at the middle of the gray scale, the maximum value can be +180° or −180°. Therefore, protons with velocities greater than a phase angle of 180° can be interpreted erroneously as representing slower, oppositely directed flow. This situation is usually evident as an isolated region of black that can be detected within a larger region of white or vice versa [20] (Fig. 2).

This technique can be a tremendous asset in evaluating patients with known or suspected valvular disease [6, 7]. It is useful in differentiating slow flow from thrombosis and in the evaluation of aortic dissection [21, 22]. Care must be taken not to mistake the normal blood flow pattern within the aorta for a pathologic condition. A normal diastolic flow reversal along the left posterior wall of the aortic root fills the aortic sinuses and, subsequently, the coronary arteries [3] (Fig. 2).

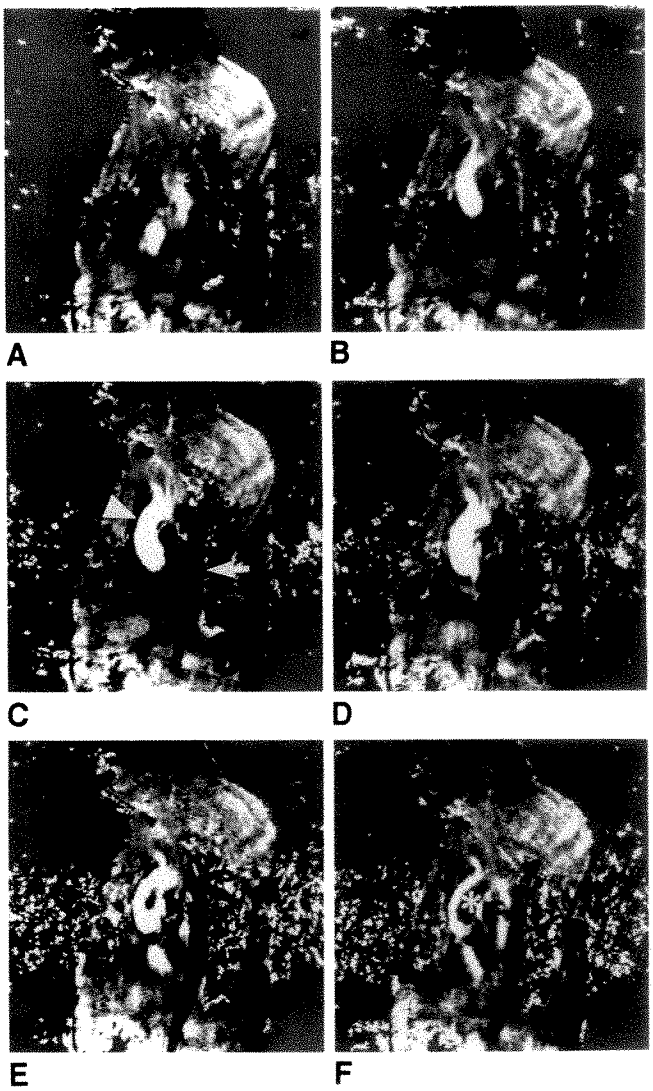

Fig. 2.—*A–F*, Selected frames of phase-mapping MR imaging through thoracic aorta at 21 (*A*), 46 (*B*), 84 (*C*), 122 (*D*), 235 (*E*), and 349 (*F*) msec performed in left anterior oblique plane. Velocity is proportional to intensity of signal. Cephalad flow (*arrowhead*) is white and caudal flow (*arrow*) is black. During early and mid systole, rapid flow of blood within aorta is evidenced by very bright signal intensity (*C* and *D*). During late systole and early diastole there is slower flow within aorta (*E* and *F*) as well as retrograde flow along posterolateral aspect of ascending aorta (*asterisk*). This retrograde flow will fill sinuses and coronary arteries.

MR Angiography

The thoracic aorta is somewhat unique in terms of blood vessels in that standard SE and cine MR techniques have been successful in depicting anatomic lesions as well as their pathophysiologic consequences. Therefore, the attributes of MR angiography for studying the aorta itself are questionable; however, these techniques may be expected to play a vital role in the evaluation of the ostia of the branch vessels and of the vessels themselves.

MR angiography is an evolving MR technique that is constantly undergoing change and modification. At present, the optimal imaging parameters are not known. Fast imaging with K-space manipulation and/or echoplanar imaging has not been fully tested and will certainly play a role in MR angiography. However, a number of techniques have been described for potential use in the evaluation of the thoracic aorta. They include two-dimensional (2D) and three-dimensional (3D) time-of-flight (TOF) methods [23–26] with and without presaturation, 3D rephase/dephase methods [27], 3D phase contrast [28], and high-speed 2D methods that use RF spoiling [29]. TOF methods followed by a maximum intensity projection provide excellent images of the aortic arch and the innominate, carotid, and subclavian arteries. The rephase/dephase and phase-contrast methods provide broader coverage of vessels with lower flow velocity extending all the way to the branchial arteries.

Imaging of the thoracic vasculature has received rather less attention than imaging of the vasculature of the head and neck. The high speed of flow in the arch and branch vessels provides nearly ideal circumstances for TOF methods so long as the motion of the vessels themselves, of the chest wall, and of the nearby heart does not produce overwhelming motion artifacts. Flow velocities within the great vessels can reach 120 cm/sec, and their sizes and positions change during the course of the cardiac cycle. Because of the divergent courses and the pulsatile nature of flow, striking differences occur in both velocity and acceleration within adjacent portions of the vasculature. Therefore, first-order motion compensation schemes may fail to retain full blood brightness. Direction of flow is roughly along the axis of the body for the ascending and descending aorta and the branch vessels. Simple axial TOF could, therefore, be expected to show these structures. The rephase/dephase and phase-contrast techniques would theoretically be much better for visualization of slower venous flow within the thorax.

Although the aorta and branch vessels possess flow characteristics amenable to MR angiography, there was initial concern over its applicability to the thoracic vasculature. Because of the significant motion of the chest, heart, and vasculature, it was expected that ECG-gated MR angiography would be required. As a result, acquisition time would be extremely long, and MR angiography would be an impractical technique. Ungated acquisition of information would be rapid, but theoretically these studies would suffer from marked motion artifacts. Despite these concerns, at least one 2D TOF method [30] (Fig. 3) has produced good-quality ungated images of the great vessels. An optimized version of this method that uses a built-in presaturation sequence allows "tuning" of sequence parameters according to the range of velocity within the region of interest [31]. A practical limitation, however, is that it must be tuned to match a predetermined range of velocities. Tuning is not a problem in normal flow systems, although the range can be difficult to predict in abnormal circumstances.

Three-dimensional first-order motion-compensation TOF methods performed in the axial view are an effective means of showing the great vessels and the branch vessels (Fig. 4). The 3D technique which is usually less tolerant of motion than 2D techniques, can consistently image these pulsatile arteries with only modest blurring. Although a short TE is preferable to offset dephasing artifacts, a TE of 7 msec may be useful for placing water and fat out of phase, thereby increasing contrast between the blood and surrounding tissue [29]. Second-order motion compensation can improve contrast and reduce blurring, but does so at the expense of an increase in TE. At present, the optimal tradeoff has not been determined.

An alternative to TOF is the rephase/dephase method in which each scan is taken once with motion compensation and once with deliberate motion-sensitive dephasing, sufficient to darken flowing blood. The images are then subtracted, the background is suppressed, and the vessels are highlighted. To obtain optimal results, it is necessary to balance a need for increased motion sensitivity against the possible flow artifacts that occur if sensitivity is too great. In addition, stronger dephasing requires an increase in TE, which also increases sensitivity to flow artifacts. It is assumed that the two corresponding scans of a given slice are aligned; therefore, gradient preemphasis must be well adjusted, minimizing eddy current effects, and the scans must be interleaved to minimize the effects of patient motion [29]. As with the TOF approach, good images have been obtained with these ungated scans, even though the technique explicitly uses motion sensitivity for one of the acquisitions (Fig. 5).

Phase-contrast MR angiography requires either six or four measurements [28] in order to sensitize in all directions. The four-measurement approach requires acquisition of a motion-compensated scan as a reference, along with three other acquisitions, each sensitized for motion along a different major axis. Ideally, the process consists of subtraction of each sensitized raw data set from the reference data set, reconstruction of the three resulting sets, and then addition of the images in quadrature. Although these methods have worked well in studies of the head, they may not be practical for studying the thoracic vasculature because of the more dramatic motion that occurs in this area. To overcome this limitation, a two-measurement (interleaved) approach can be used to minimize measurement time [29]. The tradeoff entails accepting a somewhat reduced flow sensitivity, which can be coded into a single sequence sensitized in all three directions at once, rather than a fully corrected reference scan. This

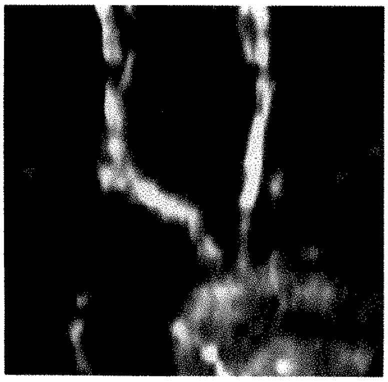

3

Fig. 3.—Coronal 2D time-of-flight MR angiogram through branch vessels. Two sets of sequential scans were acquired with presaturation zones on opposite sides and images were subtracted. In this way, simultaneous but separate visualization of venous (black) and arterial (white) flow is possible. Both venous and arterial vessels are shown; however, they can be displayed separately.

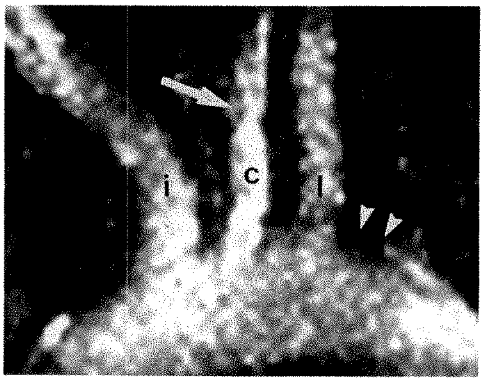

4

Fig. 4.—Ungated axial 3D time-of-flight MR angiogram through transverse aorta and branch vessels shows ostia and proximal portions of vessels. Just distal to left subclavian artery (l) is an atherosclerotic plaque (*arrowheads*). There is a stenosis (*arrow*) of proximal left common carotid artery (C). i = innominate artery.

two-measurement 3D phase-contrast technique also derives an amplitude boost from TOF effects and may be uniquely suited to ungated thoracic imaging (Fig. 6).

Implementation of newer methods and testing of other methods used to study the vasculature elsewhere within the body are continuing. One TOF variation of special interest includes dephasing the signal from static material in the slice-select direction while fully compensating for motion in all three directions [32]. Methods that increase T1 sensitivity (GRE spoiling) can improve visibility of vessels with slower flow [33]. To date, a single technique for studying the thoracic vasculature has not been discovered. For the central vessels, axial 3D TOF methods with first-order motion compensation and very short TE produce excellent-quality images with the best depiction of the vasculature when the TE places fat and water out of phase. The rephase/dephase subtraction method has been useful in the evaluation of vessels with slower flow, and the abbreviated phase-contrast approach has been useful for studying a wider range of both arterial and venous flow.

The standard study consists of a series of ECG-gated SE multislice acquisitions in both the axial and left anterior oblique orientations followed by a GRE study in an appropriate plane if a pathologic process is detected. For evaluation of the branch vessels, the coronal plane may be more advantageous than the left anterior oblique view. Under certain conditions (outlined in the following sections), the imaging would be extended to include an MR angiogram.

Clinical Application

Perhaps the greatest use for MR imaging in the evaluation of the thoracic aorta is in the realm of acquired diseases [34]. Originally this technique served as an adjunct to angiography, CT, and echocardiography for the evaluation of equivocal findings of the thoracic aorta. However, MR is rapidly emerging as the screening technique of choice for patients with mediastinal changes on sequential chest radiographs, for patients with a clinical history consistent with aortic dissection, for the follow-up of patients with aneurysmal dilatation of the thoracic aorta, and for postsurgical follow-up.

Aortic Aneurysms

Aneurysms are a common finding in adults; they are found at approximately 10% of autopsies. The leading cause of thoracic aortic aneurysms is atherosclerosis [35]. When a patient is imaged because of suspected aortic aneurysm, it is critical to characterize the lesion in an effort to delineate its cause and predict the patient's prognosis and need for surgical intervention. The true diameter of the vessel should be measured, and the aneurysm should be characterized in terms of its shape, extent, location, and relationship to the branch vessels. The aortic wall also must be evaluated for possible aortitis, mural thrombosis, and periaortic hematomas. The study is incomplete without an evaluation of the pericardium for associated hemopericardium.

The axial and left anterior oblique orientations are best for identifying aneurysms. It is also important to differentiate ectasia from an aneurysm. The normal aortic diameters are as follows: sinus of Valsalva, 3.3 cm; mid ascending aorta, 3.0 cm; aortic arch, 2.7 cm; and descending thoracic aorta, 2.4 ± 0.4 cm [36].

Ectasia and aneurysms often coexist. As with CT imaging, an erroneous diagnosis of an aneurysm can be made with axial MR imaging when there is simply ectasia and tortuosity, hence the need for the left anterior oblique acquisition. Accurate assessment of the true aortic diameter is imperative. Aneurysms greater than 6 cm in diameter have an increased prevalence of rupture and require surgical intervention, with associated high morbidity and mortality rates. Large aneurysms often alter the long axis of the ascending aorta, and axial measurements, therefore, are not accurate in determining aortic diameter. In these cases, the diameter should be measured from the left anterior oblique view.

Delineation of the shape of the aneurysm can be of great assistance in determining its etiology. Atherosclerotic aneurysms tend to have a fusiform configuration, as well as long segmental involvement of the thoracic aorta. Mycotic or false aneurysms classically are saccular rather than fusiform. Only a small number of atherosclerotic aneurysms have a saccular configuration. However, because atherosclerosis is the leading cause of thoracic aneurysms, saccular aneurysms are

Fig. 5.—Coronal 3D rephase/dephase subtraction MR angiogram of transverse aorta and of branch vessels. Proximal portion of these vessels is obscured by innominate vein.

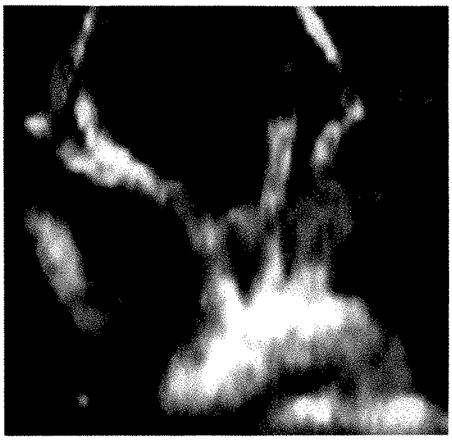

5

Fig. 6.—Two-measurement 3D phase-contrast MR angiogram of transverse aorta and proximal great vessels.

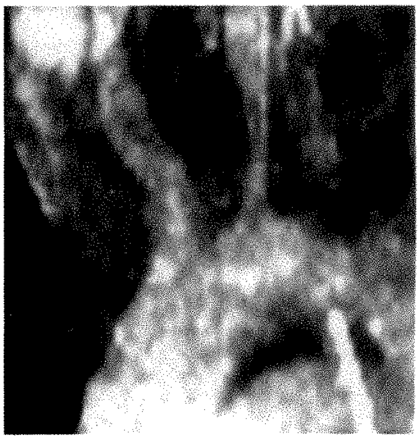

6

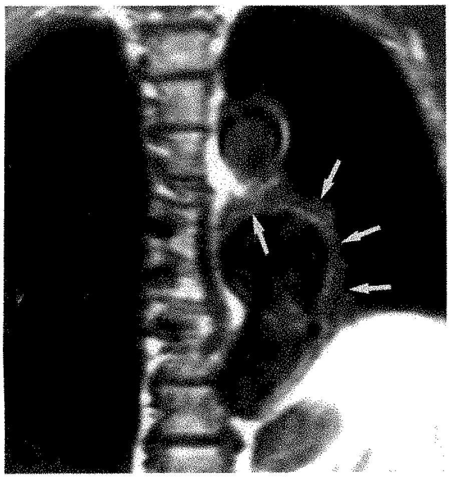

7

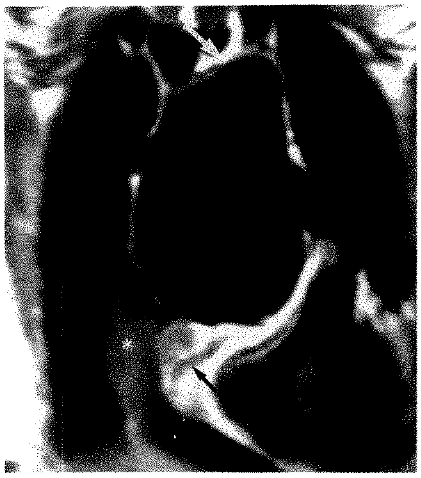

8

Fig. 7.—ECG-gated coronal SE MR image, 863/20 (TR/TE), through descending aorta in patient with surgically proved atherosclerotic saccular aneurysm. Circumferential intermediate signal around aneurysm is consistent with mural thrombosis (*arrows*).

Fig. 8.—Coronal T1-weighted SE MR image through aortic root shows large aneurysm, localized to ascending aorta, tapering to normal aortic diameter at junction of transverse aorta (*white arrow*). Keys to interpretation include obliteration of sinotubular ridge and localization to ascending aorta. In this case of annuloaortic ectasia, an acute hemopericardium, which is shown as intermediate signal intensity in right pericardium (*asterisk*), is also present. This situation requires immediate surgical intervention. *Black arrow* = right coronary artery.

usually associated with atherosclerosis (Fig. 7). Therefore, when a saccular aneurysm is encountered, the patient's clinical history must be carefully reviewed for any indication of fever, positive blood culture, or trauma.

Just as important as an aneurysm's configuration is its location. Atherosclerosis rarely involves only the ascending aorta. When an aneurysm is localized to the ascending aorta, it generally is saccular. The ability of MR to image in any plane becomes extremely important in these situations. With coronal imaging, the aortic sinuses and sinotubular ridge can be clearly depicted. This is important, as differential considerations for saccular aneurysm in the ascending aorta include syphilis, Marfan syndrome, degenerative processes of the media, and dilatation associated with valvular disease. In these cases, the patient's history is a vital piece of information, as is the evaluation of the sinotubular portion of the aortic root. Effacement of this region is noted in patients with Marfan syndrome, annuloaortic ectasia, and syphilis (Fig. 8). It is preserved in most cases of poststenotic dilatation secondary to aortic stenosis. MR has also shown that poststenotic dilatation is not always associated with congenital bicuspid aortic stenosis. It can occur in acquired disease when an eccentric jet occurs because of asymmetric thickening or calcification of the leaflets [34].

In cases of ascending aortic aneurysms, it is imperative to evaluate the pericardium for associated hemopericardium. Because of the various signal patterns, the age of the hemopericardium actually can be designated with MR. Acute processes appear as an intermediate signal on T1-weighted images and are dark on T2-weighted images. Subacute processes have a bright signal on both T1- and T2-weighted images (Fig. 8).

An aneurysm's relationship to and possible involvement of the branch vessels should also be evaluated. Although occasionally these structures can be visualized with standard *techniques*, particularly on coronal images, the techniques are somewhat limited for purposes of evaluation because of such associated problems as partial volume averaging and slow turbulent flow at the ostia. In these instances, cine MR is somewhat more useful, but its reliability in assessing the ostia is also limited. This is an arena in which MR angiography can play a vital role in the evaluation of patients with aneurysms or dissections (Fig. 9).

Compression of the trachea and other mediastinal structures is easily visualized with MR because of the large FOV. Periaortic hematomas caused by a leaking aneurysm tend to be more diffuse than hematomas associated with a false aneurysm. This is an important differential characteristic [37].

Finally, the aorta should be evaluated for the presence of mural thrombosis. With SE technique, thrombosis will have signal intensity from intermediate to high, depending on its age (Fig. 7). Usually it is easily differentiated from the aortic wall. Mural thrombosis is associated with thromboembolic disease, especially when it is exophytic; therefore, it is important to report this finding.

However, differentiating mural thrombosis from slow blood flow, both of which may have intermediate to high signal on SE images, may be difficult. Because of the large diameter of the aneurysm and the high prevalence of associated ischemic heart disease, it is common to see high signal associated with slow flow on SE images. T2 calculations can be used to differentiate thrombosis from slow flow, however, with a sensitivity of only 69% [21]. GRE and phase-mapping techniques are valuable in these situations. GRE studies graphically show the swirling blood flow pattern and the stasis that occurs in large aneurysms. With phase-mapping techniques, slow flow can be differentiated from stationary thrombosis [21].

Aortic Dissection

Aortic dissection is a disease of the elderly. It occurs most often in the sixth and seventh decades of life and more frequently in men than in women. It is found at autopsy in one of 400 patients [38]. Approximately 80% of patients with dissection have hypertension. The physical finding of differ-

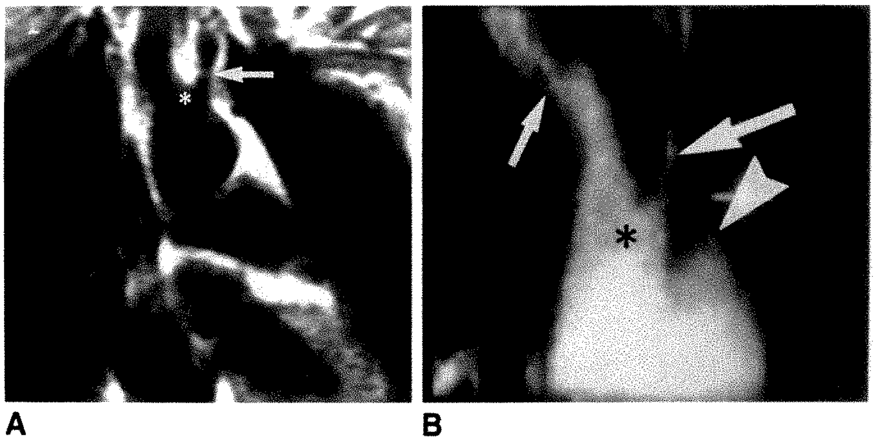

Fig. 9.—Thoracic aorta in a 40-year-old woman with Takayasu's arteritis.

***A*, Coronal T1-weighted SE MR image shows common trunk (*asterisk*) of innominate and left common carotid arteries. Stenosis is suggested just distal to origin of left common carotid artery (*arrow*).**

***B*, MR angiogram confirms findings of common trunk (*asterisk*) and stenosis of proximal aspect of left common carotid artery (*large arrow*). In addition, it shows total occlusion of left subclavian artery (*arrowhead*) as well as stenosis of right subclavian artery (*small arrow*). These findings were confirmed with angiography.**

ential pressures in the arm should alert the radiologist to examine the ostia of branch vessels for extension of the dissection into or obstruction of the ostia. Dissection is the consequence of a degenerative process of the media that results in a subintimal hemorrhage, subsequent tear in the intima because of high aortic pressures (e.g., hypertension), and subsequent extension of the false lumen. Multiple flaps (i.e., entrance and exit) occur in approximately 90% of cases [39]. In these situations, flow is usually good in both the true and the false lumina of the aorta. In approximately 10% of cases, there is a single flap, a situation that has been referred to as an incomplete dissection. Depending on the location of the entrance site, as the dissection propagates, it can involve the ostia of the branch vessels and/or the abdominal vessels. The dissection can extend into these vessels or result in occlusion of their origin.

Dissections have been classified on the basis of their location (DeBakey classification). Type I dissections arise in the ascending aorta and propagate into the descending aorta. Type II dissections are localized to the ascending aorta. Type III dissections that begin distal to the left subclavian artery are localized to the descending aorta and can extend into the abdominal aorta and common iliac arteries. It is extremely important to delineate the type of dissection with MR, as the type will greatly affect the care of these patients. Types I and II dissections are surgical emergencies, as they often are associated with dissection of the branch vessels and the coronary arteries and with aortic insufficiency and hemopericardium. Type III dissections are usually treated medically. Because they worsen over time, however, they should be evaluated regularly. MR is an excellent means of following these patients.

As types I and III dissections can involve the abdominal branch vessels, MR imaging should include an evaluation of the abdomen. SE techniques usually are not adequate for a complete evaluation; in this area, cine MR and especially 2D and 3D angiographic techniques may be quite useful.

MR is 95% sensitive and 90% specific for detecting aortic dissections [40]. It is quite common to identify the actual entrance site of the false lumen (Fig. 10). The intimal flap appears as a linear structure with intermediate signal intensity, which is contrasted by flowing blood in both lumina [39–41] (Fig. 10). If the presence of a flap is equivocal because of either slow blood flow or thrombosis within the false lumen (the prevalence is higher with incomplete dissections), cine MR techniques and/or phase velocity mapping techniques are valuable in resolving this issue. These techniques also are useful for evaluating patients with associated aortic insufficiency, which can be seen in types I and II dissections (Fig. 11). A heterogeneous signal within the false lumen is not uncommon on SE images (Fig. 10). It may represent a combination of slow flow and thrombosis or thrombosis of varying age. If the false lumen is completely thrombosed, it may be difficult to differentiate this finding from an aortic aneurysm with mural thrombosis. Indirect signs that help in the differential diagnosis include a longitudinal extension of the thrombus of more than 7 cm, a sharp demarcation between the abnormal signal and the patent lumen, a noncircular compressed lumen, and a change in the position of the thrombosis (Fig. 12). These findings are associated with aortic dissection [41, 42].

Although SE techniques can be used to detect occlusion or extension of the branch vessels on coronal images, cine MR is more effective, though not consistently reliable. Evaluation of the branch vessels is a potential application for MR angiographic techniques.

In a small number of cases, no entrance or exit site exists. This situation has been referred to as aortic dissection without intimal rupture or intramural hematoma [43]. Because of its unique contrast attributes, MR can easily show this situation, which is frequently missed with both angiography and echocardiography (Fig. 13). MR is also an excellent technique for following patients after surgery or evaluating response to medical treatment. Aneurysms at the graft insertion site and periaortic hematomas are easily detected. Patients with type III dissection should be monitored regularly for progressive dilatation of the false lumen or extension into the abdominal vasculature.

Recent reports have documented a number of artifacts that can mimic aortic dissection. These mimics are the result of normal anatomic structures (the left brachiocephalic vein, the origins of the branch vessels, the superior cardiac recess, and the azygous vein), motion artifacts [44], and fat-shift artifacts [45]. Fat-shift artifacts are most pronounced on high-

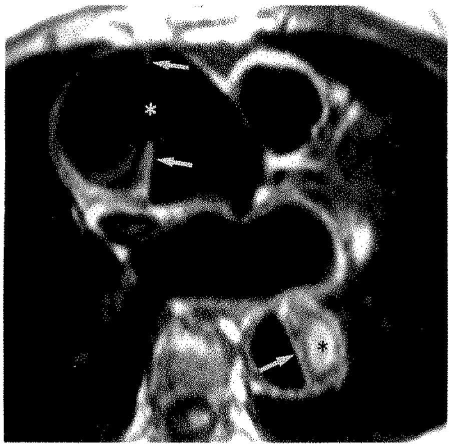

10

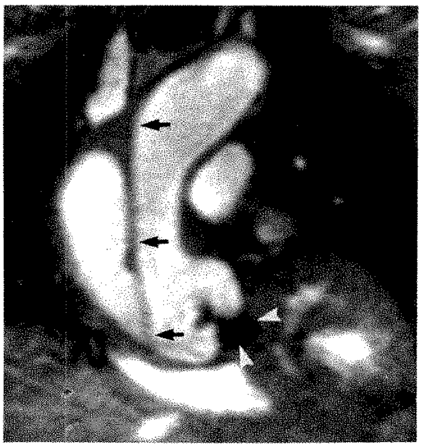

11

Fig. 10.—ECG-gated axial SE MR image through proximal ascending aorta and mid descending aorta in patient with type I aortic dissection. Entrance site (*white asterisk*) is clearly shown, as is intimal flap (*arrows*). Heterogeneous signal pattern in false lumen of descending aorta is due to combination of subacute thrombus (*black asterisk*) and slow flow.

Fig. 11.—Coronal GRE MR image through aortic root obtained during end systole in a patient with type I aortic dissection. Intimal flap begins at sinotubular junction (*arrows*). Associated aortic insufficiency appears as dark signal below aortic valve apparatus (*arrowheads*).

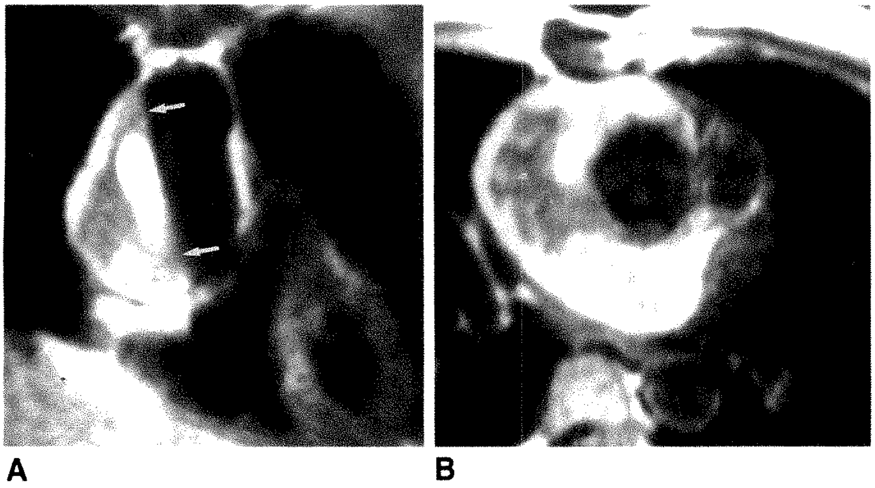

Fig. 12.—*A* and *B*, Coronal (*A*) and axial (*B*) T1-weighted SE MR images through aortic root in patient with thrombosed type II aortic dissection verified at surgery. Inhomogeneous signal within false lumen shows components of chronic (intermediate) and subacute (bright) thrombosis. Sharp demarcation with aortic lumen (due to intimal flap, *arrows*), length of thrombosis, and fact that thrombus is not circumferential (*B*) are important indirect evidence that differentiates this process from mural thrombosis of an ascending aortic aneurysm.

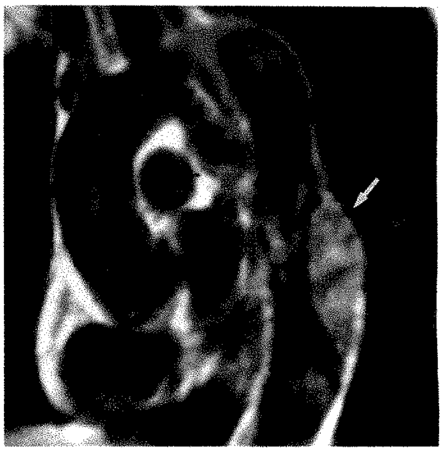

Fig. 13.—ECG-gated left anterior oblique SE MR image through thoracic aorta in patient with an intramural hematoma clearly delineates elliptical shape of hematoma within aortic wall and distinctive posterior hump (*arrow*).

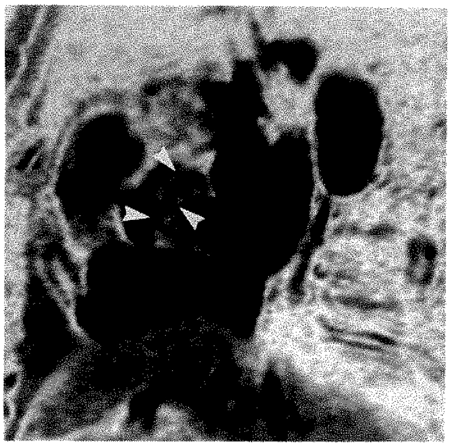

14

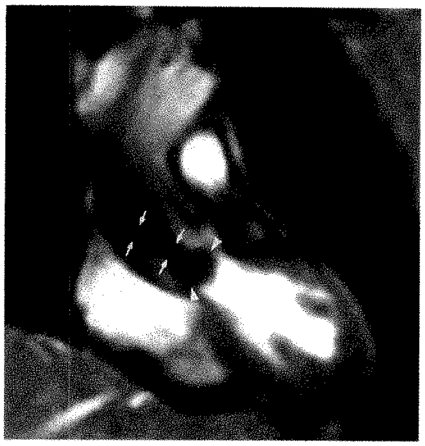

15

Fig. 14.—Oblique axial GRE MR image of fishmouth (*arrowheads*) bicuspid aortic valve stenosis. Gray-white scale has been reversed to highlight fishmouth deformity.

Fig. 15.—ECG-referenced coronal GRE cine MR image through aortic root obtained during systole in patient with acquired aortic stenosis. Fan-shaped void jet (*arrows*) is caused by turbulent flow due to stenosis. Eccentric nature of jet results in poststenotic dilatation of aortic root. Circular area of dark signal at level of valve is representative of leaflet calcification (*arrowheads*).

field-strength systems. Since the ascending aorta is surrounded by mediastinal fat and the right aspect of the descending aorta is adjacent to paraspinal fat, it is common to see a "double lumen," which must not be mistaken for dissection [45]. With fat-shift artifacts, the pseudointimal flap is identified as a discrete curvilinear signal that is parallel to the aortic wall but does not project into the aortic lumen.

Aortitis

Preliminary reports [46] have indicated that the application of MR in the evaluation of patients with aortitis is limited. Because of spatial-resolution limitations, it is not always possible to detect wall thickening or regions of stenosis. Signal changes originally thought to represent inflammatory disease have not proved to be disease specific. Even with GRE techniques, it is difficult to evaluate the branch vessel ostia for stenoses. This is an area in which MR angiography may increase the diagnostic accuracy of MR (Fig. 9).

Aortic Trauma

Deceleration injuries resulting in aortic transection are, unfortunately, relatively common [47, 48]. Transection occurs most frequently just above the aortic sinuses and at the level of the ligamentum arteriosum. Most patients with a transection involving the aortic root die from hemopericardium and subsequent cardiac tamponade. Patients who survive the initial injury often have other serious injuries and are critically ill and hemodynamically unstable. As a result, MR currently does not have a role in the initial evaluation of these patients. Documented experience in this area of aortic pathology is, therefore, limited. However, MR has proved to be useful in the evaluation of chronic traumatic pseudoaneurysms [37].

MR is also quite useful in evaluating complications of aortic surgery, including hemorrhage, graft thrombosis, perigraft infection, and pseudoaneurysm formation at graft anastomotic sites [39].

Hemorrhage and subsequent hematoma formation are usually studied in the subacute phase. On T1-weighted SE images, hematomas have an intermediate to high signal intensity and a high signal intensity on T2-weighted SE images.

Graft thrombosis is characterized by a lack of signal void on SE images. At times such thrombosis can be difficult to distinguish from slow flow, especially in patients with poor cardiac function. Cine and phase-mapping techniques are quite accurate in making this differentiation.

Perigraft infections usually have intermediate to high signal intensity on T1-weighted SE images. When an abscess has

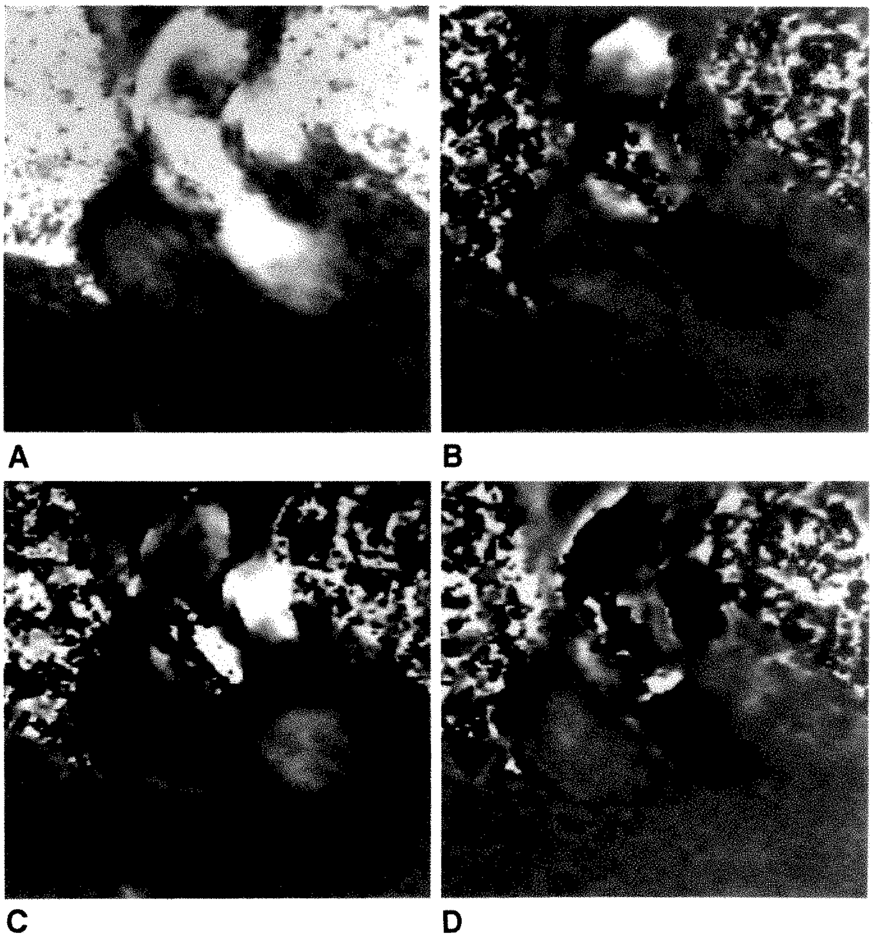

Fig. 16.—*A–D*, Coronal MR phase-mapping study through root of aorta obtained 200 msec after QRS complex. Frame *A* is a composite of flow velocities acquired in superior-inferior (*B*), left-right (*C*), and anterior-posterior (*D*) directions. With cursor placed above aortic valve apparatus, velocity can be obtained. With modified Bernoulli equation, pressure gradient across valve can be obtained.

developed, a region of low signal surrounding the process may be seen, representing a fibrous capsule.

When present, pseudoaneurysms usually occur at the graft anastomosis. Patent pseudoaneurysms are easily identified by a contained signal void connected to the vessel lumen. When there is slow flow or thrombus, there will be a variable signal pattern from intermediate to high signal intensity. Unlike perigraft hematoma, thrombosed pseudoaneurysms appear as discrete focal processes. MR is also useful in the evaluation of pseudoaneurysms involving aortocoronary bypass grafts [49] and in aortic annular pseudoaneurysm associated with bacterial endocarditis [50].

Valvular Disease

Until recently, neither static nor dynamic imaging has shown the aortic valve leaflets well enough to directly assess the presence of stenosis. Consistent visualization of the valve leaflets with an SE technique, a modified surface coil, and imaging perpendicular to the long axis of the aortic root has been reported [51]. When a dynamic study is performed in this plane, the "fishmouth" deformity of the bicuspid aortic valve and its motion during the cardiac cycle can be observed (Fig. 14). With cine MR, the turbulent jet associated with stenotic lesions is best studied in the coronal view. It appears as a focal fanlike signal void of various widths and lengths, depending on the degree of stenosis (Fig. 15). The signal void itself correlates well with catheter pressure gradients across the valve to approximately 60 mm Hg [52].

Quantitative evaluation of aortic stenosis is possible with velocity mapping techniques [6]. With either field even-echo rephasing [53] or velocity imaging with GRE [7, 54], velocity measurements can be obtained. With the latter technique, velocity vectors are calculated for the superior-inferior, left-right, and anterior-posterior planes and then added to give a single composite image (Fig. 16). With these data and a modified Bernoulli equation, a pressure gradient across the valve can be generated. Initial data obtained by using both techniques indicate excellent correlation with both echo and catheter gradient measurements [6, 7].

Similarly, dynamic techniques have been instrumental in detecting and quantifying aortic insufficiency, whether it is associated with isolated valvular disease or is a ramification of aortic dissection or aortic aneurysm [55].

Conclusions

The thoracic aorta is uniquely well suited for evaluation with MR imaging. Static SE sequences provide accurate anatomic depiction of the wide spectrum of acquired disease. Cine MR provides useful qualitative information on regurgitant and stenotic lesions of the aorta. Quantitative information can now be generated with phase velocity mapping techniques. The advent of MR angiography has brought the origin and proximal aspects of the branch vessels within the diagnostic capacity of MR imaging. In view of its noninvasive, nonionizing nature, its large FOV, its superior spatial resolution compared with echocardiography, and its phenomenal contrast resolution, MR is arguably the imaging technique of choice for thoracic aortic disease.

ACKNOWLEDGMENTS

We thank Peggy Inch and Joyce Hill for aid in the preparation of this manuscript.

REFERENCES

1. Bradley WG Jr, Waluch V. Blood flow: magnetic resonance imaging. *Radiology* **1985**;154:443-450
2. Aurigemma G, Reichek N, Schiebler M, et al. Evaluation of aortic regurgitation by cine magnetic resonance imaging (abstr). *J Am Coll Cardiol* **1988**;11(2):155A
3. Klipstein RH, Firmin DN, Underwood SR, Rees RSO, Longmore DB. Blood flow patterns in the human aorta studied by magnetic resonance. *Br Heart J* **1987**;58:316-323
4. Pettigrew RL. Dynamic cardiac MR imaging: techniques and applications. *Radiol Clin North Am* **1989**;27(6):1183-1203
5. Underwood SR, Firmin DN, Klipstein RH, Rees RSO, Longmore DB. Magnetic resonance velocity mapping: clinical application of a new technique. *Br Heart J* **1987**;57:404-412
6. Kilner PJ, Firmin DN, Rees RSO, et al. Valve and great vessel stenosis: assessment with MR jet velocity mapping. *Radiology* **1991**;178:229-235
7. Link KM. Evaluation of aortic valvular stenosis with velocity mapping (abstr). *J Magn Reson Imaging* **1991**;1:207
8. Barkovich AJ. Techniques and methods in pediatric magnetic resonance imaging. *Semin US CT MR* **1988**;9:186-191
9. Burrows PE. Magnetic resonance imaging of the aorta in children. *Semin US CT MR* **1990**;11:221-233
10. Lanzer P, Botvinick EH, Schiller NB, et al. Cardiac imaging using gated magnetic resonance. *Radiology* **1984**;150:121-127
11. Wendt RE III, Rokey R, Vick GW III, Johnston DL. Electrocardiographic gating and monitoring in NMR imaging. *Magn Reson Imaging* **1988**;6:89-95
12. Dimick RN, Hedlund LW, Herfkens RJ, Fram EK, Utz J. Optimizing electrocardiograph electrode placement for cardiac-gated magnetic resonance imaging. *Invest Radiol* **1987**;22:17-22
13. Von Schulthess GK, Fisher M, Crooks LE, Higgins CB. Gated MR imaging of the heart: intracardiac signals in patients and healthy subjects. *Radiology* **1985**;156:125-132
14. Mayo JR, Culham JAG, MacKay AL, Aikins DG. Blood MR signal suppression by preexcitation with inverting pulses. *Radiology* **1989**;173:269-271
15. White RD, Loy CA, DeBlois C, Carvlin MJ, Silver MS. Electrocardiographically triggered cine cardiovascular MR imaging (abstr). *Radiology* **1988**;169(P):110
16. Sechtem U, Pflugfelder PW, White RD, et al. Cine MR imaging: potential for the evaluation of cardiovascular function. *AJR* **1987**;148:239-246
17. Mirowitz SA, Lee JKT, Gutierrez FR, Brown JJ, Eilenberg SS. Normal signal-void patterns in cardiac cine MR images. *Radiology* **1990**;176:49-55
18. Edelman RR, Mattle HP, Wallner B, et al. Extracranial carotid arteries: evaluation with "black blood" MR angiography. *Radiology* **1990**;177:45-50
19. NessAiver MS, Murdoch JB, Kasuboski L. Presaturation used to obtain black blood cines in the left and right ventricles (abstr). *J Magn Reson Imaging* **1991**;1:207
20. Edelman RR, Mattle HP, Atkinson DJ, Hoogewoud HM. MR angiography. *AJR* **1990**;154:937-946
21. Von Schulthess GK, Augustiny N. Calculation of T2 values versus phase imaging for the distinction between flow and thrombus in MR imaging. *Radiology* **1987**;164:549-554
22. White RD, Higgins CB. Magnetic resonance imaging of thoracic vascular disease. *J Thorac Imaging* **1989**;4:34-50
23. Masaryk TJ, Modic MT, Ross JS, et al. Intracranial circulation: preliminary clinical results with three-dimensional (volume) MR angiography. *Radiology* **1989**;171:793-799
24. Masaryk TJ, Modic MT, Ruggieri PM, et al. Three-dimensional (volume)

gradient-echo imaging of the carotid bifurcation: preliminary clinical experience. *Radiology* **1989**;171:801–806

25. Link KM, Elster AD, Margosian P, Sattin B. Clinical utility of three-dimensional magnetic angiographic imaging. *Clin Neurosurg* **1991**;37:275–288
26. Gehl H-B, Bohndorf K, Klose K-C, Günther RW. Two-dimensional MR angiography in the evaluation of abdominal veins with gradient refocused sequences. *J Comput Assist Tomogr* **1990**;14:619–624
27. Laub G, Kaiser W. 3D MR angiography using bipolar gradient echoes (abstr). In: *Book of abstracts: Society of Magnetic Resonance in Medicine 1987*, vol. 1. Berkeley, CA: Society of Magnetic Resonance in Medicine, **1987**:52
28. Dumoulin CL, Souza SP, Walker MF, Wagle W. Three-dimensional phase contrast angiography. *Magn Reson Med* **1989**;9:139–149
29. Link KM, Margosian P. Thoracic aorta. In: Potchen EJ, Gottschalk A, Haacke EM, Siebert J, eds. *Magnetic resonance angiography: concepts and applications*. St. Louis: Mosby–Year Book, **1991** (in press)
30. Feiglin DH, Sattin W. Imaging of the thoracic vasculature with "saturation sandwich" MR angiography (abstr). *J Magn Reson Imaging* **1991**;1:155
31. Creasy JL, Price RR, Smith GD, Dawson RC, Kessler RM. The SAVE sequence: simultaneous arterial and venous excitation—a modification of 2D time-of-flight MR angiographic technique (abstr). *J Magn Reson Imaging* **1991**;1:155
32. Pattany PM, Wong K. Flow MR angiography with static signal suppression (FLAGS) (abstr). *J Magn Reson Imaging* **1991**;1:177
33. Chien D, Atkinson DJ, Edelman RR. Strategies for image optimization with turbo-FLASH (abstr). *J Magn Reson Imaging* **1991**;1:148
34. Link KM. The great vessels. In: Stark DD, Bradley WG Jr, eds. *Magnetic resonance imaging*, 2nd ed. St. Louis: Mosby–Year Book, **1991** (in press)
35. Joyce JW, Fairbairn II JF, Kincaid DW, Juergens JL. Aneurysms of the thoracic aorta: a clinical study with special reference to prognosis. *Circulation* **1964**;29:176–181
36. Kersting-Sommerhoff BA, Sechtem UP, Schiller NB, Lipton MJ, Higgins CB. MR imaging of the thoracic aorta in Marfan patients. *J Comput Assist Tomogr* **1987**;11:633–639
37. Moore EH, Webb WR, Verrier ED, et al. MRI of chronic posttraumatic false aneurysms of the thoracic aorta. *AJR* **1984**;143:1195–1196
38. Anagnostopoulos CE, Prabhakar MJS, Kittle CF. Aortic dissections and dissecting aneurysms. *Am J Cardiol* **1972**;30:263–273
39. Auffermann W, Olofsson P, Stoney R, Higgins CB. MR imaging of complications of aortic surgery. *J Comput Assist Tomogr* **1987**;11:982–989
40. Kersting-Sommerhoff BA, Higgins CB, White RD, Sommerhoff CP, Lipton MJ. Aortic dissection: sensitivity and specificity of MR imaging. *Radiology* **1988**;166:651–655
41. Dinsmore RE, Wedeen VJ, Miller SW, et al. MRI of dissection of the aorta: recognition of the intimal tear and differential flow velocities. *AJR* **1986**;146:1286–1288
42. Zeitler E, Kaiser W, Schuierer G, et al. Magnetic resonance imaging of aneurysms and thrombi. *Cardiovasc Intervent Radiol* **1986**;8:321–328
43. Yamada T, Tada S, Harada J. Aortic dissection without intimal rupture: diagnosis with MR imaging and CT. *Radiology* **1988**;168:347–352
44. Solomon SL, Brown JJ, Glazer HS, Mirowitz SA, Lee JKT. Thoracic aortic dissection: pitfalls and artifacts in MR imaging. *Radiology* **1990**;177:223–228
45. Lotan CS, Cranney GB, Doyle M, Pohost GM. Fat-shift artifact simulating aortic dissection on MR images. *AJR* **1989**;152:385–386
46. Miller DL, Reinig JW, Volkman DJ. Vascular imaging with MRI: inadequacy in Takayasu's arteritis compared with angiography. *AJR* **1986**;146:949–954
47. White RD, Dooms GC, Higgins CB. Advances in imaging thoracic aortic disease. *Invest Radiol* **1986**;21:761–778
48. Fisher RG, Hadlock F, Ben-Menachem Y. Laceration of the thoracic aorta and brachiocephalic arteries by blunt trauma. *Radiol Clin North Am* **1981**;19(1):91–110
49. Sherry CS, Harms SE. MR imaging of pseudoaneurysms in aortocoronary bypass graft. *J Comput Assist Tomogr* **1989**;13:426–429
50. Akins EW, Limacher M, Slone RM, Hill JA. Evaluation of an aortic annular pseudoaneurysm by MRI: comparison with echocardiography, angiography and surgery. *Cardiovasc Intervent Radiol* **1987**;10:188–193
51. Link KM, Kon ND. Presurgical evaluation of coronary artery orientation with MR imaging (abstr). *J Magn Reson Imaging* **1991**;1:169–170
52. Nishimura T, Yamada N, Itoh A, Miyatake K. Cine MR imaging in mitral regurgitation: comparison with color Doppler flow imaging. *AJR* **1989**;153:721–724
53. Nayler GL, Firmin DN, Longmore DB. Blood flow imaging by cine magnetic resonance. *J Comput Assist Tomogr* **1986**;10:715–722
54. Spritzer CE, Pelc NJ, Lee JN, Evans AJ, Sostman HD, Riederer SJ. Rapid MR imaging of blood flow with a phase-sensitive, limited-flip-angle, gradient recalled pulse sequence: preliminary experience. *Radiology* **1990**;176:255–262
55. Sechtem U, Pflugfelder PW, Cassidy MM, et al. Mitral or aortic regurgitation: quantification of regurgitant volumes with cine MR imaging. *Radiology* **1988**;167:425–430

Forthcoming Articles

SPECIAL ARTICLE

Lesions of skin and brain: modern imaging of the neurocutaneous syndromes. *Pont MS, Elster AD*

PULMONARY RADIOLOGY

Value of MR imaging in the evaluation of chronic infiltrative lung diseases: comparison with CT. *Müller NL, Mayo JR, Zwirewich CV*

Swyer-James syndrome: CT findings in eight patients. *Moore AD, Godwin JD, Dietrich PA, Verschakelen JA, Henderson WR Jr*

CT findings in lymphangitic carcinomatosis of the lung: correlation with histologic findings and pulmonary function tests. *Johkoh T, Ikezoe J, Tomiyama N, et al.*

Summer-type hypersensitivity pneumonitis: comparison of high-resolution CT and plain radiographic findings. *Akira M, Kita N, Higashihara T, Sakatani M, Kozuka T*

Case report. Thymoma with hypogammaglobulinemia (Good syndrome): an unusual cause of bronchiectasis. *Fox MA, Lynch DA, Make BJ*

BREAST RADIOLOGY

Review. Interventional procedures in diseases of the breast: needle biopsy, pneumocystography, and galactography. *Fajardo LL, Jackson VP, Hunter TB*

The role of fine-needle aspiration and pneumocystography in the treatment of impalpable breast cysts. *Ikeda DM, Helvie MA, Adler DD, Schwindt LA, Chang AE, Rebner M*

Perspective. Hidden costs of mobile mammography. Is subsidization necessary? *Wolk RB*

GASTROINTESTINAL RADIOLOGY

Rupture of hepatocellular carcinoma: predictive value of CT findings. *Kanematsu M, Imaeda T, Yamawaki Y, et al.*

Case report. Treatment of mesocaval shunt stenosis with a metallic stent. *Soyer P, Levesque M, Zeitoun G*

Case report. Peribiliary chloroma: a rare cause of jaundice after bone marrow transplantation. *Rotter AJ, O'Donnell MR, Radin DR, Marx HF*

GENITOURINARY RADIOLOGY

Cystic testicular mass caused by dilated rete testes: sonographic findings in 31 cases. *Brown DL, Benson CB, Doherty FJ, et al.*

Peyronie's disease: MR findings in 28 patients. *Helweg G, Judmaier W, Buchberger W, et al.*

Pictorial essay. Nonovarian gynecologic cysts: MR imaging findings. *Kier R*

MUSCULOSKELETAL RADIOLOGY

Intraarticular fractures of the calcaneus: value of CT findings in determining prognosis. *Janzen DL, Connell DG, Munk PL, Buckley RE, Meek RN, Schechter MT*

Do metastases in vertebrae begin in the body or the pedicles? Imaging study in 45 patients. *Algra PR, Heimans JJ, Valk J, Nauta JJ, Lachniet M, Van Kooten B*

MR imaging of the shoulder: appearance of the supraspinatus tendon in asymptomatic volunteers. *Neumann CH, Holt RG, Steinbach LS, Jahnke AH, Petersen SA*

Case report. Aneurysmal bone cyst developing after anterior cruciate ligament tear and repair. *Dagher AP, Magid D, Johnson CA, McCarthy EF, Fishman EK*

Case report. MR appearance of intramuscular injections. *Resendes M, Helms CA, Fritz RC, Genant H*

Case report. MR diagnosis of macrodystrophia lipomatosa. *Blacksin M, Barnes FJ, Lyon MM*

PEDIATRIC RADIOLOGY

Posttraumatic adrenal hemorrhage in children: CT findings in 34 patients. *Sivit CJ, Ingram JD, Taylor GA, Bulas DI, Kushner DC, Eichelberger MR*

Case report. Neonatal intestinal ischemia with bowel perforation: an in utero complication of maternal cocaine abuse. *Hall TR, Zaninovic A, Lewin D, Barrett C, Boechat MI*

Case report. Persistent infantile odontoid: a variant of abnormal atlantoaxial segmentation. *McClellan R, El Gammal T, Willing S, Lott T, Odell G*

Case report. Congenital absence of the left pulmonary artery associated with double outlet right ventricle. *Kremer S, Fayemi AB, Fish BG, Rothe WA, Spindola-Franco H*

NEURORADIOLOGY

Perspective. Fast spin-echo MR imaging of the brain and spine: current concepts. *Jones KM, Mulkern RV, Schwartz RB, Oshio K, Barnes PD, Jolesz FA*

Fractures of the nasolacrimal fossa and canal: a CT study of appearance, associated injuries, and significance in 25 patients. *Unger JM*

Neurosyphilis in HIV carriers: MR imaging findings in six patients. *Tien RD, Gean-Marton AD, Mark AS*

Rasmussen encephalitis: neuroimaging findings in four patients. *Tien RD, Ashdown BC, Lewis DV, Atkins MR, Burger PC*

Review. Role of MR imaging in the management of spinal infections. *Sharif HS*

Intradural schwannomas of the spine: MR imaging findings with emphasis on contrast-enhancement characteristics. *Friedman DP, Tartaglino LM, Flanders AE*

Case report. Schistosomal granuloma of the spinal cord: evaluation with MR and intraoperative sonography. *Silbergleit R, Silbergleit R*

ARRS 1992 CASE OF THE DAY ANSWERS

Introduction. *Heller RM*

Chest case of the day. *Worrel JA, O'Donnel DM, Carroll FE, Brunner JP, Coleman JA Jr*

Abdominal case of the day. *Shaff MI, Powers TA, Gilpin LB, Faulstich ME*

Skeletal case of the day. *Tigges S, Erb RE, Nance EP*

Pediatric case of the day. *Heller RM, Hernanz-Schulman M, Johnson J, Stein SM, Kirchner S*

Neuroradiology case of the day. *Lacrampe MJ, Creasy JL*

Nuclear medicine case of the day. *Moody EB, Glassman SB, Hansen AV, Lawrence SK, Delbeke D*

PERSPECTIVE

The information perspective of radiology. *Hendee WR*

MEETING NEWS

Thoracic imaging, 1992. *Whalen E*

Abstracts of scientific papers presented at the annual meeting of the Society of Uroradiology, January 1992. *Stanley RJ*

Pictorial Essay

Assessment of the Thoracic Aorta by Spiral CT

Philip Costello,[1] Christian P. Ecker, Richard Tello, and George G. Hartnell

A recently developed technique, spiral CT, allows rapid data acquisition through an entire anatomic region during a single breath-hold. High-quality spiral CT scans of the thoracic region have been obtained with volumes of contrast material that are small relative to those used with conventional CT. This essay illustrates the diseases of the aorta as seen on spiral CT performed with low volumes of contrast material.

A recent technologic advance called spiral CT allows rapid data acquisition through an entire anatomic region during a single breath hold [1]. The helically acquired data undergo interpolation, and transverse images may be reconstructed with slice intervals 1–10 mm apart. With a 24-sec exposure and a 10 mm/sec table feed, data are acquired over a 23-cm segment. We have demonstrated that high-quality thoracic spiral CT scans can be obtained with volumes of contrast material that are small compared with those used for conventional CT [2]. CT is an accurate, widely used technique in the assessment of aortic aneurysms and dissecting aneurysms [3–6]. The purpose of this article is to illustrate diseases of the aorta as seen on spiral CT with low volumes of contrast material.

Method of Examination

From October 1990 to September 1991, 29 patients in whom aortic disease was suspected on the basis of clinical

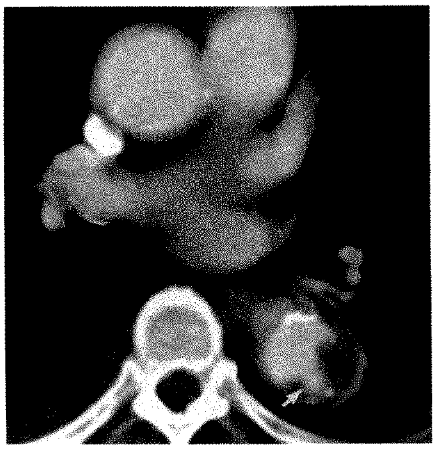

1

Fig. 1.—CT scan of 73-year-old woman with atherosclerotic aorta, mural thrombus with ulceration (*arrow*), calcified aortic wall, adjacent pulmonary atelectasis, and fluid in left pleura.

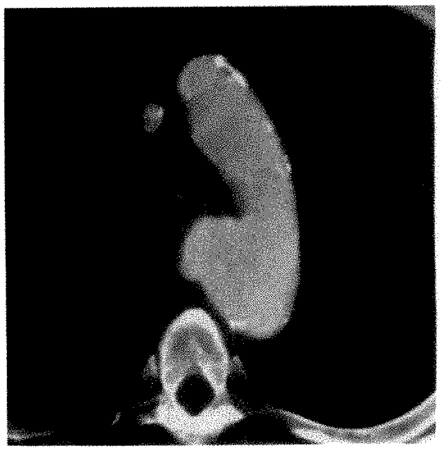

2

Fig. 2.—59-year-old man with mediastinal mass shown on chest radiograph. CT scan shows 3.5-cm atherosclerotic aneurysm of proximal descending aorta bulging into mediastinum. Extensive mural calcifications are present.

Received October 28, 1991; accepted after revision November 26, 1991.

[1] All authors: Department of Radiology, New England Deaconess Hospital, 185 Pilgrim Rd., Boston, MA 02215. Address reprint requests to P. Costello.

AJR 158:1127–1130, May 1992 0361–803X/92/1585–1127 © American Roentgen Ray Society

history or chest radiographs were assessed by means of 32 spiral CT examinations obtained on the Siemens Somatom Plus unit (Erlangen, Germany). The patients included 10 women and 19 men 46–85 years old (mean, 65 years). A 20-gauge catheter was placed in an antecubital vein and connected to a Medrad injector (Medrad Co., Inc., Pittsburgh, PA). A total of 60 ml of diatrizoate meglumine and diatrizoate sodium (Renografin 60%) was infused at 3 ml/sec for 15 sec and then 1 ml/sec. After obtaining a scout CT scan, spiral CT was initiated 2 cm above the aortic arch and continued inferiorly for 23 cm. With a single breath-hold and a 15-sec delay to scan, we could image the entire mediastinum. Patients were coached to hold their breath and instructed to take three deep respiratory excursions before scanning. When disease was demonstrated at the level of the diaphragm, spiral CT was continued with a second injection that used 60 ml of contrast material with a flow rate of 3 ml/sec for 15 sec and then 1 ml/sec for the balance of the contrast dose to study the abdominal aorta. A 30-sec delay was used to study the low thoracic and abdominal aorta. Images were reconstructed at either 2- or 4-mm intervals retrospectively when disease was demonstrated. Sagittal and coronal im-

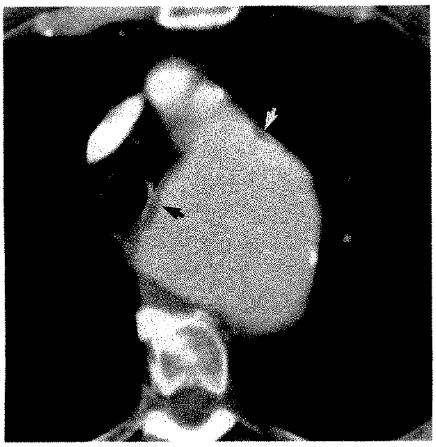
3

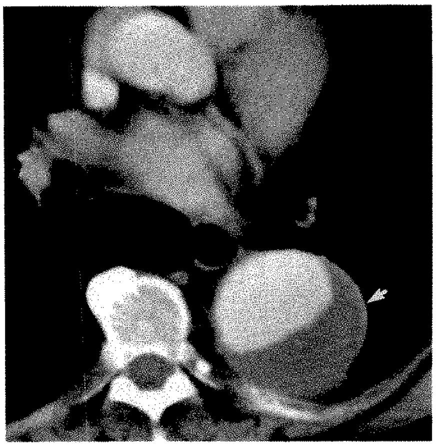
4

Fig. 3.—CT scan of 65-year-old woman clearly depicts 7.5-cm aortic arch aneurysm with small amount of mural thrombus (*arrows*).

Fig. 4.—CT scan of lower thorax in a 68-year-old woman. Large crescentric thrombus in descending thoracic aneurysm is readily distinguishable from aortic wall (*arrow*).

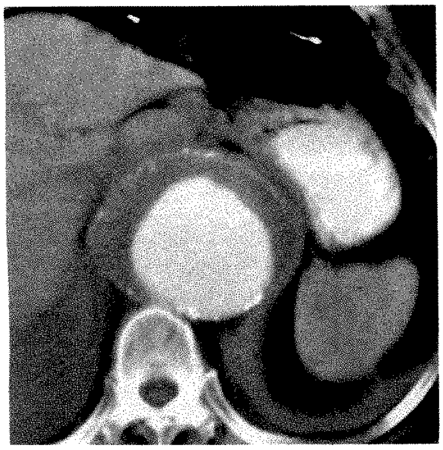

Fig. 5.—CT scan of lower thorax in a 70-year-old man with back pain shows 8-cm aneurysm lying retrocrurally and excellent differentiation of contrast-filled lumen, mural thrombus, and calcified aortic wall.

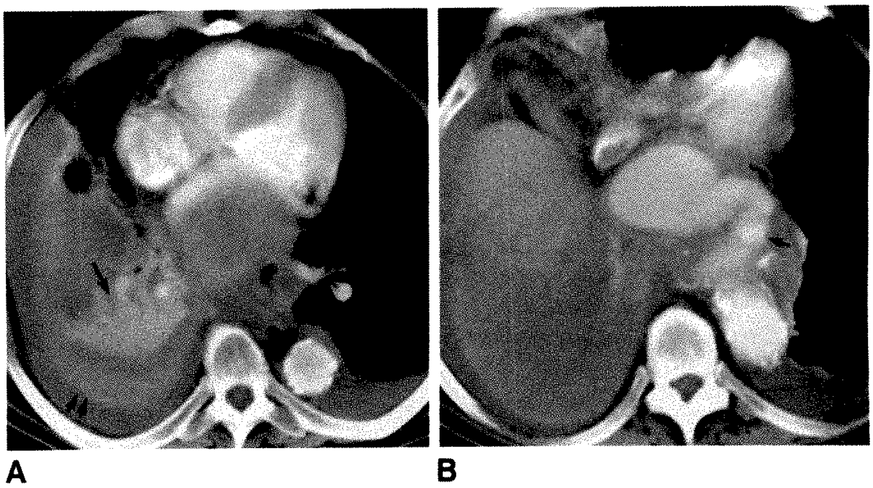

Fig. 6.—65-year-old man with chest pain and hypotension.

***A*, CT scan at level of left atrium shows soft-tissue density compressing left atrium. Right lower lobe is atelectatic (*long arrow*) and is surrounded by high-density blood in pleural space (*short arrows*).**

***B*, Transverse CT scan 3 cm inferior to *A* shows neck of contrast-filled aneurysm coursing to right side of mediastinum (*arrow*). This shows that soft-tissue density seen in *A* represents a large mural thrombus within aortic aneurysm.**

ages, and occasionally three-dimensional images, were generated.

Aortic Aneurysms, Aortic Atherosclerosis

The normal aortic wall was clearly distinguished from the contrast-filled lumen, and atherosclerotic plaques, calcifications, and ulcerations were demonstrated (Fig. 1). Pleural fluid or atelectatic lung adjacent to the aorta was easily recognized (Fig. 1). Aortic aneurysms with sizes ranging from 3.5 to 9.5 cm were shown with ready identification of the mural thrombus (Figs. 2–5). The relatively small volume of contrast material was sufficient to outline the lumen of even large aneurysms (Figs. 3 and 5). A patient with a partially thrombosed large aneurysm was examined emergently because of hypotension. The time spent within the gantry was less than 3 min for this critically ill patient, and only 60 ml of contrast material was required to depict the aneurysm's size, course, and leakage into the pleural space (Fig. 6).

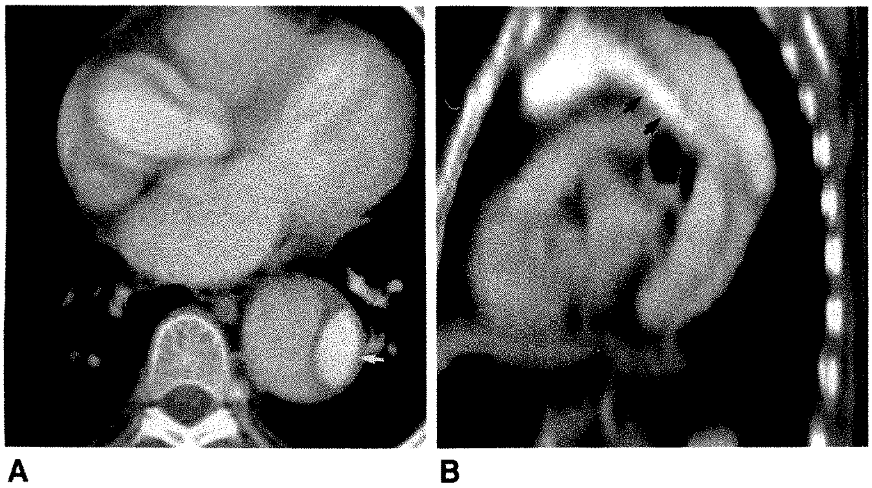

Fig. 7.—63-year-old man with type B aortic dissection.

A, CT scan at level of left atrium shows denser true lumen (*arrow*) is separated by intimal flap from false lumen.

B, Smoothly reformatted sagittal CT reconstruction reveals denser true lumen (*arrows*). Note lack of diaphragmatic motion because of successful breath-hold during spiral CT.

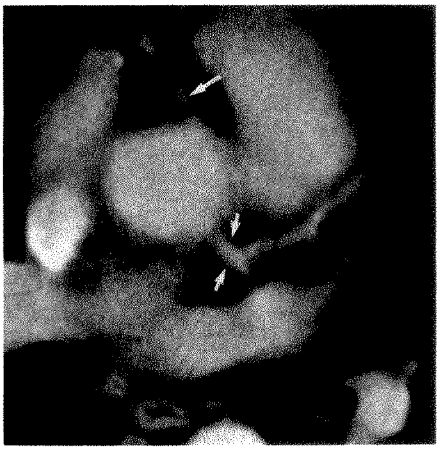

Fig. 8.—CT scan shows that ascending aorta in this 56-year-old man was replaced by a graft into which were anastomosed right (*long arrow*) and left (*short arrows*) coronary arteries. Postoperative study shows patency in both vessels.

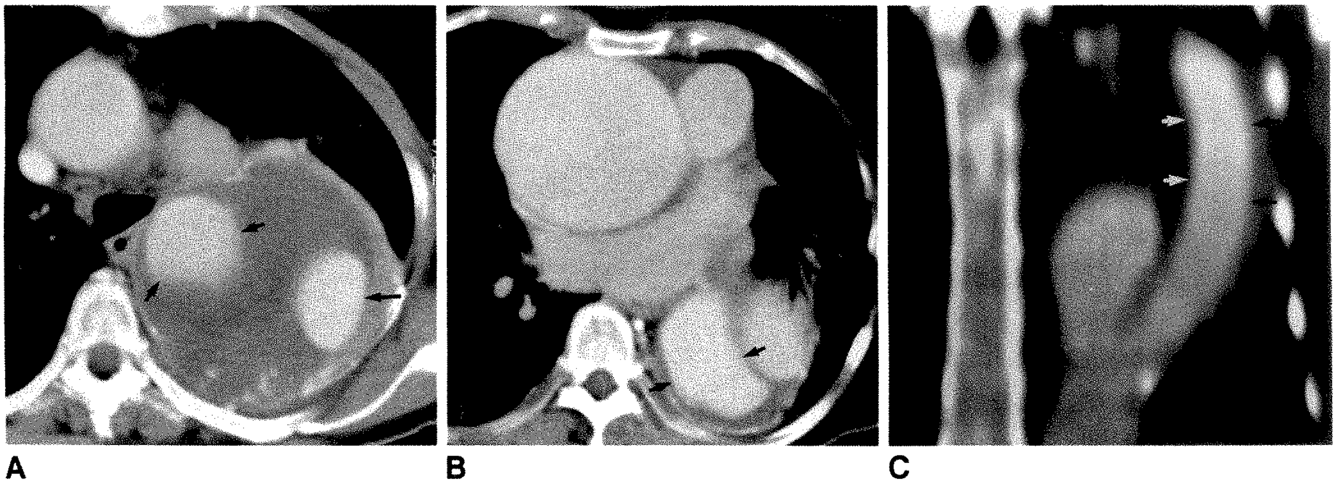

Fig. 9.—59-year-old woman with repeated respiratory infections due to collapse of left lower lobe. Surgical replacement of descending aorta from left subclavian artery to diaphragm by a 30-cm Teflon graft was performed 5 years earlier. Mediastinum had continued to enlarge over past 4 years.

A, CT scan at level of proximal descending aorta shows contrast material filling two tubular structures. Lateral contrast material is in graft (*long arrow*), whereas second lumen (*short arrows*) represents contrast material opacifying original partially clot-filled aneurysm.

B, CT scan at level of right pulmonary artery reveals tube graft laterally and original aneurysm medially filled with contrast material (*arrows*). Also note ascending aortic aneurysm.

C, Coronal CT reconstruction reveals laterally positioned tube graft (*arrows*), but there is opacification of native aneurysm through breakdown at distal anastomosis.

Thoracic Aortic Dissection

Many institutions still use single-level contrast-enhanced dynamic scanning techniques to assess aortic dissections and detect the differential opacification of true and false lumens [5]. This requires at least three bolus injections of contrast material at differing levels, and the volume used can readily approach 150 ml of 60% contrast material. The direct signs of aortic dissection were readily assessed by spiral CT with easy differentiation of the true and false lumens despite the use of only 60 ml of contrast material (Fig. 7). When a dissection was noted on the lowest slice, a second 24-sec breath-hold spiral CT study was performed with a 60-ml bolus to show the intraabdominal extent of the dissection.

Postoperative CT Examinations

In a study of six postoperative patients, we found no significant artifacts caused by aortic graft (five patients) or a ring device (one patient). Native patent coronary vessels were demonstrated anastomosed to an ascending aortic graft in one patient (Fig. 8). In one postoperative patient, continued mediastinal widening after 5 years suggested recurrent thoracic dissection. A 30-cm Teflon graft was positioned from the proximal descending aorta and anastomosed at the diaphragm to the descending aorta. Spiral CT demonstrated proximal and distal sutural dehiscence with contrast opacification of the native thoracic aortic aneurysm (Fig. 9). Coronal images of this particular problem demonstrated anastomotic breakdown exquisitely (Fig. 9C). This smoothly reformatted image was enhanced by the ability to retrospectively obtain thin-interval transverse reconstructions. Complete lack of respiratory motion artifacts was an additional factor in image improvement.

REFERENCES

1. Kalender WA, Seissler W, Klotz E, Vock P. Spiral volumetric CT with single-breath-hold technique, continuous transport, and continuous scanner rotation. *Radiology* **1990**;176:181-183
2. Costello P, Dupuy DE, Ecker CP. Spiral CT of the thorax with small volumes of contrast material: a comparative study (abstr). *Radiology* **1991**;181 (P):274
3. Demos TC, Posniak HV, Marsan RE. CT of aortic dissection. *Semin Roentgenol* **1989**;24:22-37
4. Goodwin JD, Herfkens RL, Skioldebrand CG, Federele M, Lipton MJ. Evaluation of dissections and aneurysms of the thoracic aorta by conventional and dynamic CT scanning. *Radiology* **1990**;136:125-133
5. Petasnick JP. Radiologic evaluation of aortic dissection. *Radiology* **1991**;180:297-305
6. Todd GJ, Nowgrod R, Benvemostru A, Buda J, Reemtsma K. The accuracy of CT scanning in the diagnosis of abdominal and thoracoabdominal aortic aneurysms. *J Vasc Surg* **1991**;13:302-310

Case Report

Left Thyrocervical Trunk Bronchial Artery Supplying Right Lung: Source of Recurrent Hemoptysis in Cystic Fibrosis

Alan M. Cohen,[1,2] Basim W. Antoun,[1] and Robert C. Stern[2,3]

Bronchial artery embolization is an accepted, effective method of controlling hemoptysis in patients with cystic fibrosis when more conservative means fail [1, 2]. Several studies address the typical origin of bronchial arteries from the descending aorta [3–5]. Some reports describe ipsilateral atypical or "anomalous sources" collateralizing with the bronchial [1, 3, 4, 6, 7] or systemic [8] circulation. We recently encountered a patient with cystic fibrosis in whom recurrent massive hemoptysis was caused by bleeding from bronchial arteries arising from multiple sites. One bronchial artery arose from the left thyrocervical trunk and supplied the right lung. This previously unreported occurrence is important when angiographic methods are used to control the bleeding.

Case Report

A 23-year-old man in whom cystic fibrosis was diagnosed at age 6 months had required periodic hospitalizations for pulmonary exacerbations of the disease since age 13. At age 16 the patient had increasing hemoptysis (almost daily episodes of producing 100 ml or more of bloody sputum for over 2 weeks) despite routine conservative management, including aggressive antimicrobial treatment. The patient noted a left thoracic gurgle immediately preceding each episode of hemoptysis that localized the bleeding to the left side. Angiography at this time revealed two enlarged bronchial arteries, one supplying the right lung and the other both lungs (Figs. 1A and 1B). These vessels were embolized with polyvinyl alcohol foam particles (Ivalon, Pacific Medical Industries, La Mesa, CA) of 250–590 µm in size until the blood flow slowed. Absorbable gelatin pledgets (Gelfoam, Upjohn, Kalamazoo, MI) of increasing size were then released into the artery. Hemoptysis was controlled, and the patient then had only occasional blood streaking of sputum.

At age 23 more severe hemoptysis recurred, again localized by gurgling to the left side. Conservative management failed, and angiography revealed partial recanalization of the two bronchial arteries previously embolized. These vessels were reembolized. Panangiography [1] detected two other branches supplying the left lung, one each arising from the left thyrocervical trunk and the left internal mammary artery (Fig. 1C). These vessels were embolized with polyvinyl alcohol foam followed by gelatin pledgets. Angiography showed another branch of the left thyrocervical trunk in the midline; this was not further imaged or embolized. Bleeding was again controlled.

Hemoptysis recurred 3 months later; however, the patient now felt gurgling on the right side prior to hemoptysis. Angiography demonstrated slight recanalization of the two bronchial arteries arising from the aorta. These vessels required only minimal amounts of embolic material to halt blood flow. The right thyrocervical trunk and right internal mammary arteries each had a branch embolized that supplied the bronchial arteries of the right lung (Fig. 1D). A left subclavian artery angiogram did not show recanalization of the previously embolized branches; however, a large branch of the left thyrocervical trunk supplied the right lung (Fig. 1E). This was successfully embolized from a left axillary approach by using polyvinyl alcohol foam and

---

Received October 7, 1991; accepted after revision November 6, 1991.
This work was supported in part by grant DK 27651 from the National Institutes of Health.

[1] Department of Radiology, MetroHealth Medical Center, 2500 Metro Health Dr., Cleveland, OH 44109-1998. Address reprint requests to A. M. Cohen.
[2] Department of Radiology, Case Western Reserve University, 2040 Adelbert, Cleveland, OH 44106.
[3] Cystic Fibrosis Research Center, Rainbow Babies and Children's Hospital, 2074 Abington Rd., Cleveland, OH 44106.

AJR 158:1131–1133, May 1992 0361–803X/92/1585–1131 © American Roentgen Ray Society

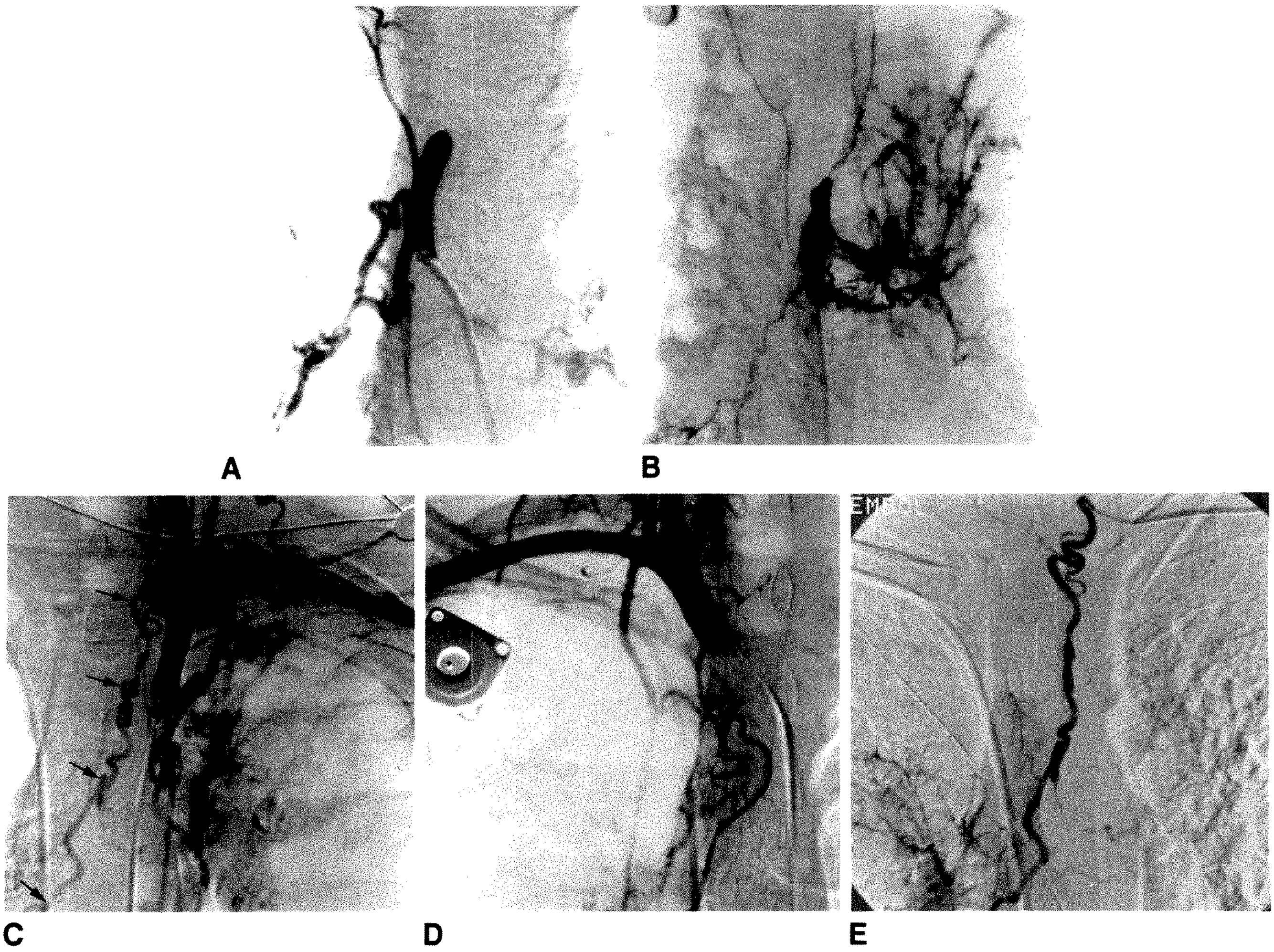

Fig. 1.—Angiographic studies in a 23-year-old man in whom cystic fibrosis was diagnosed at age 6 months.

***A* and *B*, First angiogram obtained when the patient was 16 years old shows a large bronchial artery primarily supplying right lung (*A*). A second bronchial artery supplies both lungs with predominant left lung distribution (*B*). These were embolized.**

***C*, Second angiogram obtained 7 years later included reembolization of the two vessels shown in *A* and *B*. Left subclavian arteriogram shows left lung branches from left internal mammary artery and left thyrocervical trunk; these were embolized. A midline branch of left thyrocervical trunk was present (*arrows*) but not studied further.**

***D* and *E*, Third angiogram obtained 3 months after *C* shows branches of right internal mammary artery and right thyrocervical trunk that were embolized (*D*). A branch of left thyrocervical trunk crosses midline to supply right lung (*E*). It is the same midline vessel present in *C*. This was embolized from a left axillary approach to allow better catheter stability.**

gelatin pledgets. The patient has remained free of major hemoptysis for 1 year.

Discussion

The origin of bronchial arteries is variable. In most healthy individuals, the majority of the circulation arises from the proximal descending aorta or its branches [3–5]. However, more than 20% of bronchial arteries have an anomalous origin from the great vessels and another 10% originate from the arch of the aorta [3, 4].

The bronchial artery circulation increases in regions of inflammation and tumor or in response to congenital heart disease [5–8]. Chronic inflammatory lung diseases such as cystic fibrosis result in increased bronchial artery blood flow so that small or collateral bronchial arteries enlarge [1, 2, 8]. An extensive anastomotic network exists between the bronchial arteries and the other structures in the mediastinum, as well as the head, neck, and spine [1–5]. Thus, anomalous or more likely enlarged collateral channels to the bronchial arteries originating from the great vessels can be seen at least 35–45% of the time [1, 6]. Normal collateral vessels that are not usually large enough to see angiographically become visible. Most collateral bronchial vessels supply the ipsilateral lung [1–8]. As demonstrated by our case, on rare occasions the opposite lung can form the primary anastomotic connections with aberrant bronchial arteries. While we have no proof, the multiple previous embolizations may have redirected flow, assisting in the enlargement and subsequent visualization of this anastomosis.

Knowledge of bronchial artery anatomy and its variations is essential to the angiographer attempting to control hemoptysis. Most often, control of hemoptysis follows embolization of the appropriate bronchial artery or arteries arising from the descending thoracic aorta. When this fails, a search for anomalous bronchial arteries usually entails angiographic imaging of all ipsilateral potential collateral sources, including head and neck vessels, pleural connections, and intercostal vessels [1-3, 5-8]. When routine angiography fails to show an appropriate artery, angiographic evaluation of all contralateral head and neck vessels is indicated.

REFERENCES

1. Cohen AM, Doershuk CF, Stern RC. Bronchial artery embolization to control hemoptysis in cystic fibrosis. *Radiology* **1990**;175:401-405
2. Fellows KE, Khaw KT, Schuster S, Schwachman H. Bronchial artery embolization in cystic fibrosis; technique and long-term results. *J Pediatr* **1979**;95:959-963
3. Botenga ASJ. *Selective bronchial and intercostal arteriography*. Baltimore: Williams & Wilkins, **1970**:9-159
4. Cauldwell EW, Siekert RG, Lininger RE, Anson BJ. The bronchial arteries: an anatomic study of 150 human cadavers. *Surg Gynecol Obstet* **1948**;86:395-412
5. Ulflacker R, Kaemmerer A, Picon PD, et al. Bronchial artery embolization in the management of hemoptysis; technical aspects and long-term results. *Radiology* **1985**;157:637-644
6. Keller FS, Rosch J, Loflin TG, Nath PH, McElvein RB. Nonbronchial systemic collateral arteries: significance in percutaneous embolotherapy for hemoptysis. *Radiology* **1987**;164:687-692
7. Vujic I, Pyle R, Hungerford GD, Griffin CN. Angiographic and therapeutic blockade in the control of hemoptysis: the importance of nonbronchial systemic arteries. *Radiology* **1982**;143:19-23
8. Tadavarthy SM, Klugman J, Castaneda-Zuniga WR, Nath PH, Amplatz K. Systemic-to-pulmonary collateral in pathological states. *Radiology* **1982**;144:55-59

Radiology Outreach Foundation

The Radiology Outreach Foundation (ROF) is a nonprofit corporation whose goal is to help disadvantaged countries improve their health care by providing radiology equipment, books, consultation, education, and training to their practitioners. This assistance is on an application basis that is independent of political, ethnic, or religious orientation of the grantee. It depends on the need of the people and the ability of the ROF to meet that need. The ROF is approved by the U.S. Internal Revenue Service as a tax-exempt organization. It is endorsed by the following radiologic societies: American Association of Women Radiologists, American College of Radiology, American Roentgen Ray Society, Association of University Radiologists, Radiological Society of North America, Society of Chairmen of Academic Radiology Departments, Society for Pediatric Radiology, European Society of Pediatric Radiology.

All donations to the ROF are tax deductible. Persons who would like to contribute financially to the ROF, would be interested in being a visiting professor, would like to send books or journals to any of the institutions supported by the ROF, or would like further information about the ROF should write to Charles A. Gooding, M.D., President, Radiology Outreach Foundation, 3415 Sacramento St., San Francisco, CA 94118 USA.

Book Review

MRI of the Spine. Edited by Robert M. Quencer. (One of 10 volumes in The Raven MRI Teaching File. Series editors: Robert B. Lufkin, William G. Bradley, Jr., and Michael Brant-Zawadzki.) New York: Raven, 240 pp., 1991. $60

This comprehensive MR teaching file is intended to help the practicing radiologist rapidly acquire a storehouse of experience that should aid development of proficiency in MR imaging of the spine. Designed for use as an everyday reference and study aid, the book presents 100 fully illustrated actual case studies; 450 high-resolution MR images depicting various diseases; and concise explanations of clinical history, radiologic findings, and diagnosis.

The volume illustrates a wide spectrum of spinal lesions ranging from the common to the uncommon. The discussion that accompanies each case provides a basis for understanding the pathologic changes involved and encourages the reader to delve more deeply into the subject matter presented. Cases have been carefully selected to show variable manifestations of common and unusual pathologic changes. The discussions are brief, conforming to the teaching-file format. Coverage includes trauma and postoperative complications; inflammatory changes, infection, and demyelination; congenital anomalies; neoplasms; degenerative diseases; vascular diseases and malformations; and metabolic disorders.

A number of artifacts encountered in MR imaging of the spine are also included. Short descriptions of the artifacts follow their illustration. Anatomic variants that may appear to be pathologic changes are also part of this teaching file. No attempt has been made to include every type of abnormality of the spine. Rather, cases have been selected from teaching files and from routine MR reading sessions. Discussions of the technical details of image acquisition are kept to a minimum, except when such discussion is pertinent to the diagnosis.

The editors suggest that for optimal use of this book, the reader should focus first on the left-hand page while covering the right-hand page; retention of information is thus significantly improved. Although the diagnosis in this workbook is often suggested by the clinical history and presentation of selected images, the same information is available in a convenient single videodisk in which the reader is given the option to choose either the selected images reproduced in the printed workbook or additional images, including color and movie sequences from the complete imaging file. Additionally, the videodisk format allows case presentation with or without clinical information. The videodisk is available through Medical Interactive, 936 Dewing Ave., Ste. D, Lafayette, CA 94549-4246.

Positive aspects of the book include its appealing layout, high-quality illustrations, and comprehensive subject index. Up-to-date reference lists are also provided at the end of each case. Because of its concise style, the book can easily be read cover to cover in a relatively short time.

The atlas has no apparent deficiencies and more than accomplishes the stated goals of its authors. In format and scope, when combined with other volumes in The Raven MRI Teaching File series, this work resembles the teaching file for the musculoskeletal system, by J. Mink and A. Deutsch. It is a useful companion to *Pocket Atlas of Spinal MRI*, by L. Czervionke and V. Haughton, which is limited to normal anatomy and artifacts.

This book would be a valuable acquisition for any radiology departmental library or anyone who wishes to learn or review spinal MRI imaging. In particular, residents and fellows in training will find the atlas an easy-to-use and informative study guide. The book is well worth its moderate cost, and the authors deserve praise for an outstanding contribution to the diagnostic imaging literature.

David J. Sartoris
University of California, San Diego, Medical Center
San Diego, CA 92103

Review Article

Diagnosis of Lumbar Spinal Stenosis in Adults: A Metaanalysis of the Accuracy of CT, MR, and Myelography

Daniel L. Kent,[1,2] David R. Haynor,[3] Eric B. Larson,[2] Richard A. Deyo[1,2,4]

We undertook a literature synthesis of CT, MR, and myelographic studies to evaluate what is known about the diagnostic accuracy of these imaging tests for the diagnosis of lumbar spinal stenosis in adults without prior surgery. From 116 possibly relevant studies, we reviewed 14 articles that included cases of spinal stenosis with a reference standard other than the imaging tests of interest. Of the studies we reviewed, two involved only MR, nine only CT, and three used both; six studies included myelography. Rating categories of A, B, C, or D were assigned for the quality of research methods used to estimate diagnostic accuracy. All studies received either a C or D rating. Common methodologic problems were failure to assemble a representative cohort for study, small sample size, and failure to maintain independence between image readings and reference standards. Sensitivity ranged from 0.81 to 0.97 for MR, from 0.70 to 1.0 for CT, and from 0.67 to 0.78 myelography. Studies varied greatly in case selection, definition of test and disease categories, and geographic locale, so no pooled estimates could be derived. In asymptomatic patients, abnormal findings appeared on CT or MR in 4–28% of cases and were more common in the elderly.

Published studies of the value of CT and MR for the diagnosis of lumbar stenosis lack methodologic rigor and do not permit strong conclusions about the relative diagnostic accuracies of these procedures. For the present, the choice between MR or CT depends on issues such as costs, reimbursements, access to equipment, skill of radiologists, and patient safety. Better studies will be needed to document claims for improvements in imaging accuracy as MR technologies evolve. These studies should emphasize larger sample sizes, more attention to research designs that avoid methodologic biases, and the contribution of imaging diagnoses to ultimate clinical outcome.

Clinically, lumbar spinal stenosis (LSS) is a disabling chronic illness that arises from developmental anomalies or degenerative processes in the lumbar spine [1–4]. Combinations of stenoses can arise at multiple root and intervertebral levels so symptomatology is quite variable. Modern imaging with CT and MR has produced a renaissance of interest in LSS, and has been associated with two- to threefold increases in surgery rates [5]. In this review, we compare the diagnostic accuracies of CT, MR, and myelography by using explicit criteria to evaluate the quality of the clinical research methods used in the primary studies.

CT and MR represent accurate and expensive diagnostic imaging technologies for the lumbar spine. Clinicians use CT and MR individually or together, often in conjunction with myelography. Each test has certain advantages when used as the sole image of spinal anatomy and each also may have incremental value if used in a multitest sequence. Current

---

Received September 3, 1991; accepted after revision January 2, 1992.

This research was supported by Grant No. HS06344 from the Agency for Health Care Policy and Research (the Back Pain Outcomes Assessment Team), by the John A. Hartford Foundation through the Multi-Institutional Technology Assessment Consortium (grant #88298-2H), and by the Department of Veteran Affairs through the Northwest Health Services Research and Development Field program.

[1] Health Services Research and Development Service, VA Medical Center, 1660 S. Columbian Way, Seattle, WA 98108.

[2] Division of General Internal Medicine, School of Medicine, University of Washington, Seattle, WA 98195.

[3] Department of Radiology, School of Medicine, University of Washington, Seattle, WA 98195.

[4] Department of Health Services, School of Public Health, University of Washington, Seattle, WA 98195.

AJR 158:1135–1144, May 1992 0361-803X/92/1585-1135 © American Roentgen Ray Society

reports by specialists in spine care suggest that MR is replacing myelography as the imaging test that should complement a noncontrast spinal CT scan [6, 7], and that MR may also replace CT as the first imaging test for common spinal disorders [8].

Most reviews of CT and MR enumerate the advantages of each technique [9] without explicitly reviewing the diagnostic accuracy statistics associated with each test for the major clinical syndromes causing low back or leg pain. Therefore, the clinical relevance of differences in the technical capabilities of CT, MR, or myelography remains an important research question. When working with patients who have unexplained syndromes, clinicians need to know the accuracy of the available imaging tests for the diagnoses being considered. The most helpful information for the clinician derives from prospective diagnostic accuracy studies in typical patient populations [10]. This review examines published studies related to imaging and degenerative lumbar spinal stenosis in adults. We assess the overall accuracy of CT, MR, and myelography and indicate directions for future imaging research.

Scope of Review

We limited this review to studies that included cases of lumbar spinal stenosis in adults. We included all case series with some canal, lateral recess, or foraminal stenoses. We excluded case series where the clinical syndrome was entirely acute-onset radiculopathy, where all cases had herniated disks, or where final diagnoses included fewer than 10 cases of lumbar stenosis. We retrieved all studies that used any kind of CT or MR and analyzed the diagnostic accuracy data that could be derived from these articles. Although many studies of the accuracy of myelography alone were conducted in the 1970s [11], these older studies cannot be compared with recent studies of CT or MR because the latter techniques have drastically changed case selection for imaging and surgery [5]. We reviewed myelography data when they were presented as part of a study of CT or MR. We did not review the contribution of plain films to diagnosis of lumbar spinal stenosis.

Article Retrieval and Review

"Spinal stenosis" became a search term on MEDLINE in 1983. However, many authors used other terminologies, and relevant articles may not have been indexed as spinal stenosis studies. Consequently, we searched the MEDLINE and Health Planning data bases from 1986 through July 1991 using spinal stenosis and a broader search strategy based on "spinal diseases or sciatica or backache." These disease-defining terms were combined with "tomography, X-ray, or magnetic resonance imaging" to focus on diagnostic test reports. Before 1986, MR studies were scarce, as MR for the spine was in its infancy [10]. We used a comprehensive bibliography that annotated literature through 1986 [11] and reference lists from more current retrieved articles as guides to significant articles in the older literature. For CT scanning, we carried the MEDLINE computer search back to January 1980. Bibliographies from major articles and book chapters also were reviewed for missing citations. We restricted this review to English-language articles. Articles were retained for review if they had original data on more than 10 cases of LSS imaged by CT or MR. Retained articles were read independently and rated according to standardized procedures by two reviewers. Rating discrepancies were resolved by consensus or by referral to a third reviewer.

The preceding searches yielded 783 possible citations. Based on the reviews of titles and abstracts, we excluded 667 citations immediately and obtained 116 documents for detailed readings. Most of the 667 exclusions occurred because articles identified in the broad MEDLINE search were not about adult lumbar spinal stenosis in patients without previous spinal surgery.

From the 116 articles we read, 14 were retained for analysis. Of 33 articles excluded as "not spinal stenosis," the majority were studies consisting entirely of cases with herniated or degenerated lumbar disks. Thirty-four articles were excluded because the studies lacked a reference or comparison standard. Eleven articles presented surgical findings or long-term follow-up information but did not present diagnostic imaging results for CT or MR [e.g., 12–14]. Another 22 articles were reviews or technical reports without usable clinical patient data. Two studies described obsolete CT scans done before 1980. No imaging study selected cases according to the presenting clinical syndrome, so we could not separate spinal claudication from cases of bony sciatica. When a case series included fewer than 10 final diagnoses of stenosis, we excluded the article from the diagnostic accuracy analysis [e.g., 15–17].

Quality Criteria for Evaluating Study Methodologies

Since some articles contributed more than one study to the analysis, we analyzed each study by patient group and diagnostic technology used. When different articles by the same authors reported overlapping data, we merged the findings into a single study [18, 19].

The data abstracted from each study included the source and number of patients, their clinical symptoms, physical findings, the CT or MR techniques used, surgical findings, findings from long-term clinical follow-up, and the number of patients with true or false imaging results. The quality criteria were derived from previous work on clinical research methodology [20–25]. Each study was rated as high, intermediate, or low quality in each of seven categories (see Table 1). The first three categories emphasized the technical quality of study procedures, and the latter four categories emphasized proper selection of patients and unbiased interpretation of information. These general standards for methodologic quality in the context of CT, MR, or myelography for spinal stenosis were implemented according to the following definitions.

Technical quality of the index test refers to the technical quality of the imaging procedure whose accuracy was evaluated. High-quality CT studies used slice thickness less than

TABLE 1: Distribution of Quality Ratings in Each Assessment Category

Category	Number of Studies[a]			Quality Rating	Rating Criteria
	MR	CT	Myelography		
Index test Technical quality (by test)	1	1	3	High	Best state-of-art techniques (see text).
	3	7	3	Intermediate	Average techniques found in usual practice.
	1	3	0	Low	Obsolete, technically flawed, or not described.
Reference test quality (by study)		6		High	Surgical findings or overall impression after technical imaging and follow up; explicit criteria for surgical or clinical final diagnosis.
		8		Intermediate	Surgical or clinical follow up without explicit criteria.
		0		Low	Unacceptable or unspecified reference test.
Application of reference test		12		High	Single reference test applied to all analyzed cases.
		2		Intermediate	Mixed reference tests, all cases analyzed.
		0		Low	Acceptable reference test not applied to all cases.
Independence of interpretations		3		High	Study protocol prevented both test review and diagnosis review biases.
		7		Intermediate	One of two biases present or cannot be excluded.
		4		Low	Both biases present, or no information to assure independence of test results and reference standard determinations.
Clinical description		5		High	Description includes demographics (age, sex), duration of symptoms, and percent of cases with usual symptoms and physical findings.
		5		Intermediate	Incomplete demographic or clinical description.
		4		Low	No description other than "low back pain" or "radiculopathy."
Cohort assembly		0		High	Wide spectrum of clinical severity, enrolled prospectively from typical clinical practice sources.
		8		Intermediate	Retrospective case finding; limited spectrum of types or severity, referral filtering due to enrollments after tests ordered from specialized center.
		6		Low	Workup bias present or procedure for assembling study cohort not described.
Sample size		0		High	≥35 diseased and ≥35 nondiseased.
		11		Intermediate	≥35 diseased and <35 nondiseased or reverse.
		3		Low	<35 diseased and <35 nondiseased.

[a] Of the 14 studies, five reported on MR, 11 on CT, and six on myelography.

5 mm, angled the scanner gantry to maintain the image slice perpendicular to the spinal axis, and gave explicit criteria for a positive scan and a complete description of the imaging protocol (noncontrast versus intrathecal contrast, with or without sagittal reformatting). Studies were intermediate in quality if they failed to define explicitly the criteria for a positive scan, if the scan slice thickness was between 5 and 10 mm, or if the case series mixed data from noncontrast and intrathecal contrast scans without permitting separate analyses. Poor quality CT studies involved scans whose slice thickness was greater than 10 mm. If the protocol for performing and interpreting the CT scans was not specified, the study was given a poor quality rating.

High-quality MR studies required explicit definition of protocol, high resolution (3–5 mm slices), and use of surface coils. Intermediate quality studies were surface coil MR studies with incomplete descriptions of either the technical or interpretive protocols, or with slice thicknesses of 5–10 mm. Studies were considered poor in quality if the MR protocols were not described or if scans were done with a body coil or on a low-field instrument (≤0.3 T). Whenever possible, the quality rating was corroborated with images published in the CT or MR reports.

High-quality myelography studies were those done with water-soluble contrast accompanied by descriptions of criteria for abnormalities. Myelography studies were intermediate if these descriptions were missing. Oil-based myelography studies are obsolete and were considered low-quality.

Criteria for the technical quality of tests and reference standards reflect progress made in image quality from 1980 to 1990. Mid-1980s scans were considered intermediate in quality unless the article specified that advanced machinery (e.g., GE 9800 CT scanners) was used and the images published represented excellent CT scanning techniques.

Early 1980s scans were considered inadequate assessments of diagnostic accuracy, since most of the improvements in very high resolution CT and MR with surface-coil technology have occurred in this past decade.

Technical quality of the reference test refers to the technical qualities of the tests, operations, or case review procedures that were the gold standard for diagnosis. Surgical findings of nerve root compression or constriction of the dural sac were the most rigorous gold standards. Since not all patients had surgery, a comprehensive case review using clinical follow-up and other corroborating diagnostic tests was considered an acceptable reference standard. High-quality studies reported explicit criteria for surgical findings or for clinical follow-up [19, 26–29].

Studies were intermediate in quality if the surgical or clinical follow-up criteria were incompletely defined; they received a poor rating if the procedure for defining reference test positivity was completely unspecified. Initial clinical impressions or clinically presumed diagnoses after an evaluation that did not involve supplemental tests beyond the index test were considered poor reference standards.

Uniform application of the reference test refers to complete application of the reference standard to all cases evaluated by the index test. High-quality studies used the same kind of reference test for all analyzed cases. Intermediate-quality studies used a mix of reference tests but all cases were defined by at least one acceptable gold standard. In poor-quality studies, not all cases received an acceptable reference test. In such studies, diagnostic accuracy statistics could not be calculated.

Independence of interpretations refers to separation of interpretations of the index test and reference standards. A high-quality rating required strict independence between interpretation of the index images and the reference test diagnoses. An intermediate-quality rating indicated that either test review bias (index image interpreted with knowledge of the final diagnosis) or diagnosis review bias (determination of final diagnosis affected by knowledge of the index image results) was present or could not be excluded. When studies were flawed by both test review and diagnosis review biases or did not provide information to determine whether images and reference tests were independent, they received low-quality ratings for independence of interpretations.

Clinical description refers to whether or not an article contained details of the clinical presentation of patients undergoing the test of interest. A high-quality rating required a complete clinical description, including the percentage of subjects with major signs and symptoms and demographic features of age and sex. Studies with incomplete clinical descriptions (e.g., only "bony sciatica" or "spinal claudication") or with missing demographics were rated as intermediate in quality. Studies describing patients only as having "suspected spinal stenosis" without any clinical symptom label or studies that failed to describe symptoms were rated as low in quality.

Cohort assembly refers to the procedures used to assemble the cases tested. Criteria for a high-quality rating included prospective enrollment of patients from typical primary care clinical practice referrals involving an adequate spectrum of presentations. *Spectrum* was defined as the range of clinical features found in the subjects used to test diagnostic accuracy. Thus, diseased patients should represent a range from severe stenosis with advanced symptoms to milder stenosis with modest symptoms. Patients without disease should include patients with similar symptomatologies due to lumbar strain, neuropathies, or lower extremity vascular disease. Studies that gathered cases retrospectively from a limited spectrum of patients within referral centers were rated as intermediate in quality. Similarly, studies that used the fact of testing as a case selection device were intermediate. Workup bias was present if studies used a positive index test result to determine case enrollment. These studies received a poor-quality rating, as did studies that failed to describe how their patient cohort was assembled.

Sample size refers to how many cases were included in a study. Studies were high quality if they included both 35 diseased and 35 nondiseased subjects (a total of 70). A sample size of 35 is the minimum for which the lower bound of the 95% confidence interval for a true sensitivity or specificity of 1.0 would exceed 0.9 [30]. Studies were intermediate in quality if either the diseased or nondiseased category (but not both) included fewer than 35 cases. Studies had poor-quality sample size if both the diseased and nondiseased categories included fewer than 35 cases.

An overall rating was assigned to each article on the basis of the preceding quality criteria. Studies with A ratings could be intermediate in clinical description but required high-quality ratings in all other categories. Studies with B ratings overall had high ratings in reference tests and independence but could be intermediate in all other categories. Studies with C ratings could be poor in clinical description but required intermediate ratings in all other categories. Studies falling below the criteria for C ratings in any of the seven categories were given D ratings.

Analysis

Agreement on individual features of articles was quite variable, so all ratings were reviewed until consensus was achieved. We required that studies report either sensitivity, specificity, or both as the diagnostic accuracy results of interest, or report their data in sufficient detail so that we could calculate one or both of these parameters. Sensitivity and specificity were calculated according to standard definitions: sensitivity = TPR, true-positive ratio; specificity = (1 − FPR), where FPR = false-positive ratio [21]. Exact 95% confidence intervals were taken from scientific tables [30]. Whenever possible, studies were plotted in two-dimensional receiver operating characteristic (ROC) space [31]. ROC curves plot test sensitivity and specificity to show the overall accuracy of a test (see Figs. 1–3): the *x* axis is the FPR (1 − specificity) and the *y* axis is the TPR (sensitivity). Points closer to the upper left corner of an ROC plot represent tests with greater accuracy than tests closer to the 45° diagonal of the ROC plot box. We used chi-squared tests for proportions on 2 × k contingency tables to test for heterogeneity of sensitivities or specificities [32]. Since studies varied greatly according to methods of test interpretation, case selection, and

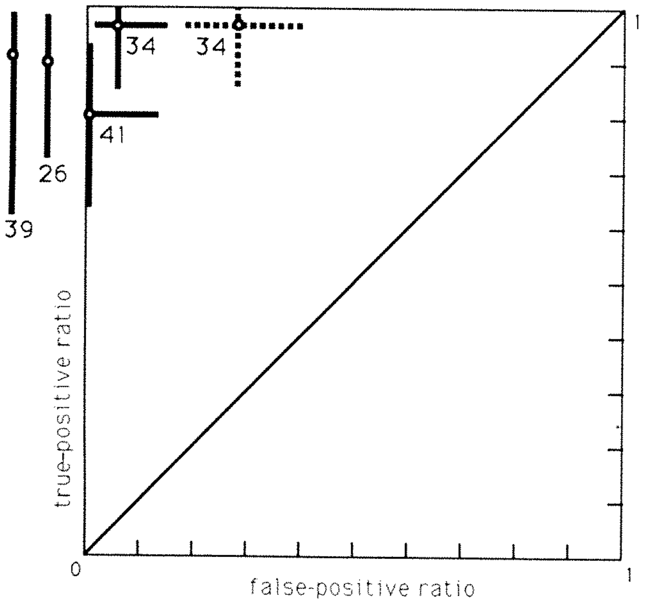

Fig. 1.—Accuracy of MR in studies of spinal stenosis. For each study, the number refers to the reference. *Open circles* indicate the actual true-positive ratio (TPR) or false-positive ratio (FPR) for each study. *Solid bars* show 95% confidence intervals. Bars to left of the receiver operating characteristic box are studies reporting only cases with disease, so no FPR could be determined. *Dotted bars* indicate an alternative interpretation of FPR data in one study. Images in this study could be interpreted as strictly positive if stenosis was the only disease found or as liberally positive if stenosis or herniated disk was found, producing a lower or higher FPR, respectively.

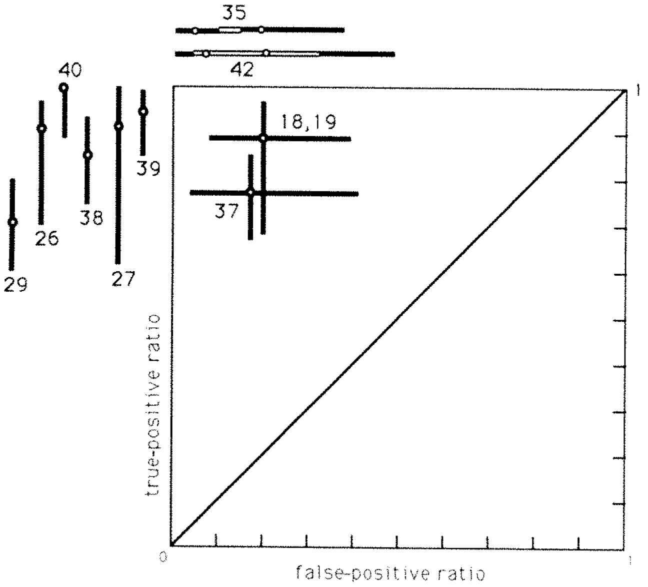

Fig. 2.—Accuracy of CT in studies of spinal stenosis. For each study, the number refers to the reference. *Open circles* indicate the actual true-positive ratio (TPR) or false-positive ratio (FPR) for each study. *Solid bars* show 95% confidence intervals. Bars to left of receiver operating characteristic box are studies reporting only cases with disease. *Overlapping bars* indicate alternative interpretations of the FPR data in two studies. The images could be interpreted as positive only if stenosis was found or if either stenosis of herniated disk was found, producing lower or higher FPRs, respectively.

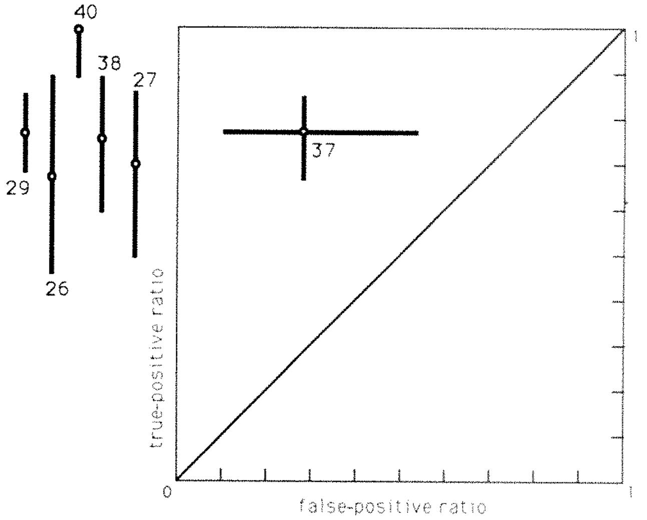

Fig. 3.—Accuracy of myelography in studies of spinal stenosis. For each study, the number refers to the reference. *Open circles* indicate the actual true-positive ratio (TPR) or false-positive ratio (FPR) for each study. Bars show 95% confidence intervals. Bars to left of receiver operating characteristic box are studies reporting only cases with disease.

geographic locale, we could not define a set of studies for derivation of pooled estimates by using metaanalysis statistics [33]. For each imaging technique, we present the TPR and FPR by study (Figs. 1–3) and offer qualitative interpretations in the text.

Findings

Of the 116 possibly relevant studies, 14 met inclusion criteria for analysis of diagnostic accuracy data (reference citations in Tables 2 and 3). Two publications appeared to be different presentations of the same case series and were treated as a single study [18, 19]. The 14 studies were done in 11 U.S. centers and in Canada, England, and the Netherlands.

Quality of Study Methodologies

Forty-eight percent of the individual ratings for the three methodology categories that involved the technical quality of procedures or imaging were considered to be high. Most studies presented average-quality MR or CT images from the mid 1980s. Some studies received high ratings for the technical quality of reference tests because the criteria for abnormal surgical findings were stated explicitly [19] and procedures for recording such findings during the surgery were described [26, 27], or because the absence of symptoms was elicited [34, 35]. Most studies received high-quality ratings for application of the reference test (see Table 1).

High methodologic quality ratings were less frequent (16%) among the four categories that reflected study design issues. Three studies maintained independence of image interpretations from reference test results by having a different radiologist interpret original images without knowledge of the diagnosis [34, 35] or by keeping detailed images from the

TABLE 2: Accuracy of CT for Spinal Stenosis[a]

Reference No.	Patients Studied	Type of CT	Comparison Standard	Ratios and 95% Confidence Intervals		Quality Rating of Study Methods	Dates of Scans[b]
				True Positive	False Positive		
[29]	122 patients, 93 disease levels found	Noncontrast	Surgery	0.71 (0.61–0.80)	NA	D	Pre 1984
[35]	52 volunteers	Noncontrast	No back symptoms on questionnaire	NA	0.19 (0.09–0.37)[c]	D	Pre 1985
[18, 19]	24 known stenosis, 30 patients with abdominal CTs	Noncontrast: cross section of dural sac	Asymptomatic for normals, surgery for diseased	0.88 (0.68–0.97)	0.20 (0.08–0.39)[c]	D	1980–1982
[26]	24 cases of stenosis	Myelo/CT, a few plain CTs	Surgery	0.88 (0.68–0.97)	NA	C	9/84–2/85
[42]	32 cases with Paget's disease	Noncontrast	Asymptomatic by interview	NA	0.20 (0.04–0.48)[c]	D	1983–1985
[40]	32 CTs done after myelogram showed complete block	Noncontrast	Surgery	1.0 (0.89–1.0)	NA	D	Pre 1987
[38]	68 cases of disk or stenosis	Myelo/CT	Surgery	0.85 (0.75–0.93)	NA	C	Pre 1986
[37]	109 cases of back and leg pain	Noncontrast	Surgery	0.77 (0.67–0.85)	0.17 (0.04–0.41)[c]	C	9/83–2/85
[27]	12 lateral stenosis cases	Noncontrast	Surgery	0.92 (0.62–1.0)	NA	D	1985–1987
[39]	60 lateral disk or stenosis cases	Noncontrast	Surgery	0.95 (0.86–0.99)	NA	D	1983–1988
[39]	(Same cases)	Myelo/CT		1.0 (0.94–1.0)	NA		

[a] Studies listed by year published.

[b] Date ranges given if in article. Date based on earliest presentation or publication if authors failed to report dates of scans.

[c] False-positive interpretations common if disk or stenosis counted. False-positive ratio was 4% to 7% when only stenosis counted.

surgeon until after he had recorded intraoperative findings for each case [27].

No study received a high-quality rating for cohort assembly. Most investigators assembled cases from a source of convenience, such as a radiology department's case files, thereby creating a retrospective case series. The few prospective studies were from highly specialized settings subject to referral filtering of cases. Only one study came close to the sample size criteria for a high-quality rating [34].

When individual quality criteria were incorporated into an overall rating, no studies qualified for A or B ratings. All studies failed at least the criterion for assembling a good cohort of study patients. Three of five studies of MR or MR and CT received C ratings [26, 34, 36], as did two studies of CT and myelography [37, 38]. Among these studies, two presented data applicable only to sensitivity [26, 38], one used a definition of disease restricted to herniations [37], and one did not present the data in a form that would permit calculation of sensitivity and specificity [36].

Availability of Sensitivity and Specificity Data

Four studies provided either the sensitivity, specificity, or both for MR (see Table 3 and Fig. 1), including two that made direct comparisons to CT scans done in the same case series [26, 39]. One study made direct comparisons of MR and CT but did not present data that permitted calculation of TPR and FPR [36]. Ten studies provided data for CT: nine for CT without contrast, and two for CT with intrathecal contrast (see Table 2 and Fig. 2). Six studies [26, 27, 29, 37, 38, 40] provided data for myelography (Fig. 3).

The results of both the CT and the MR studies suggested progressive improvements in ability to detect spinal stenosis. One early MR study [41] reported a sensitivity of 0.81, while all three later studies reported sensitivities of 0.90 or better (see Table 3). The CT studies show progressive improvements from sensitivities of 0.71 in the early 1980s to sensitivities ranging from 0.85 to 0.95 in studies from the mid 1980s (see Table 2).

Summary of ROC Results

Two studies of MR, two of CT, and one from the comparative myelography data could be plotted as points in ROC space (Figs. 1–3). The remaining studies reported only on cases with disease or without, giving data on only sensitivity or specificity, but not both. These studies are shown to the left of or above the ROC plots, respectively. In general, the

TABLE 3: Accuracy of MR for Spinal Stenosis[a]

Reference No.	Patients Studied	Type of MR (coils, T)	Comparison Standard	Ratios and 95% Confidence Intervals		Quality Rating of Study Methods	Dates of Scans[b]
				True Positive	False Positive		
[41]	20 normals, 45 cases of suspected lumbar spine disease	Body, 0.15 T	Impression from other imaging tests	0.81 (0.64–0.93)	0 (0–0.13)	D	Pre 1983
[26]	30 stenosis cases	Surface, 0.6 T	Surgery	0.90 (0.73–0.98)	NA	C	9/84–2/85
[36]	41 consecutive cases	Surface, 1.5 T	Final clinical or operative impression	NA	NA	C	6/86–3/87
[34]	67 asymptomatic volunteers and 33 patients with proved stenosis	Surface, 1.5 T	Questionnaire or operative results	0.97 (0.85–1.0)	0.06 (0.02–0.15) or 0.28 (0.18–0.41)[c]	C	4/83
[39]	24 cases of far lateral disk or stenosis	Not stated	Surgery	0.92 (0.73–0.99)	NA	D	1983–1988

[a] Studies listed by year published.

[b] Date ranges given if in article. Date based on earliest presentation or publication if authors failed to report dates of scans.

[c] False-positive interpretations common if disk or stenosis counted. False-positive ratio was 4% to 7% when only stenosis counted.

95% confidence intervals displayed for MR, CT, and myelography all overlap one another. Myelography may be worse than MR, but one cannot compare the studies directly, since they were done in different research centers and different years.

True-Positive Ratio of MR

We could not derive a pooled estimate of the TPRs for MR because the individual studies varied widely in the technical quality of the MR and methods of case selection. The single best study reported data suggesting a TPR of 0.90 [26]. A second study restricted case selection to nerve root impingement in lateral locations due to disk or stenosis and reported a similar TPR [39]. A study using reinterpretations of scans from patients with confirmed stenosis reported the highest TPR (0.97) we found [34]. In this study, two of three radiologist-readers missed known stenosis on one of 30 MR scans. Since these cases were selected for their known pathology, the series is biased toward more definitely positive scans, thereby inflating any derived estimate of TPR.

True-Positive Ratio of CT

None of the eight CT studies reporting sensitivities were sufficiently alike to permit pooling of results (see Table 2). Two studies using myelography/CT reported very similar results (0.85, 0.88) on the basis of similar approaches to tests and reference standard definitions [26, 38]. The results of two studies using noncontrast CT (0.71, 0.77) reflect obsolete CT scanning [29] and use of an idiosyncratic definition of test positivity [37]. In other CT studies, investigators selected special patient populations (e.g., patients with complete myelographic blocks [40] or far lateral root entrapments [27, 39], or restricted definitions of disease [37]).

True-Positive Ratio of Myelography

Six studies reported sensitivities for myelography as one of the imaging tests compared with MR or CT. In one, patients were enrolled for CT scans if they had myelographic blocks ([40], TPR = 1 by case selection). In another study, case selection was restricted to lateral stenoses rather than to all spine problems [27]. Three of the remaining four studies reported sensitivities of 0.77, 0.78, and 0.77 [29, 37, 38, respectively] while the fourth reported a sensitivity of myelography of 0.67 [26] with a small number of patients and a wide confidence interval (see Fig. 3).

False-Positive Images and Asymptomatic Anatomic Abnormalities

One study with MR and two studies with CT formally investigated the occurrence of abnormal scans in asymptomatic people [34, 35, 42]. In all three studies, strict interpretation of images showed asymptomatic spinal stenosis in 4–7% of cases and showed some bone disk, or ligament disease in 17–20% of cases. Two CT studies for suspected stenosis or disk confirmed the higher rate for asymptomatic disease [18, 19, 37]. In these studies of asymptomatic people, the abnormal images probably represent truly abnormal anatomy in patients without illness.

Reports of truly false-positive image interpretations (i.e., a normal scan erroneously read as abnormal) were rare. In one study, the CT scans of three patients suggested herniated disks when none were found at surgery [37]. The same study reported five false-positive myelographic images. None of the MR studies reported false-positive interpretations for spinal stenosis.

Comparative Studies of Diagnostic Accuracies

Three studies offer comparisons of CT and MR scans taken from the same patients. Two of the studies suggest that CT and MR have equivalent sensitivities, in the range of 0.88 to 0.95 [26, 39]. The third study did not offer diagnostic accuracy statistics but showed that the CT and MR agreed at 97% of disk levels investigated [36]. Thus, in the only studies in which direct comparison is possible, CT and MR had equivalent sensitivities. No study analyzed FPRs for CT and MR in the same case series.

Of five studies comparing myelography to CT or MR, three found that CT had higher sensitivity [26, 27, 38], one found no difference [37], and one early study found myelography slightly more sensitive than CT [29]. In one study, the FPR for myelography was somewhat higher than the FPR for CT in the same study [37].

Two studies reported accuracy data for myelography/CT as well as noncontrast CT. In one study [39], an abnormal CT finding on myelography probably was a requirement before surgery, and the TPR was higher than for plain CT. In the other study [26], the number of noncontrast CT scans was too small for valid comparison to myelography/CT. The same study showed that the TPR improved from 0.88 for any CT or 0.90 for MR to 0.96 when the two tests were combined. No data were found to assess the effect of combining tests on the FPR.

Conclusions

On the basis of our review of existing studies, any estimates of sensitivity of specificity must be considered imprecise, since the estimates are based on small studies whose results were flawed by several methodologic biases. Although the sensitivities and specificities of CT and MR appear comparable, at a TPR of 90% and an FPR of 20%, all sample sizes were small so confidence intervals were wide (see Figs. 1–3). More comparative studies are needed to resolve small differences (5–10%) in the TPR or FPR of MR compared with CT. Although similar problems with sample size limit conclusions about myelography, two studies [26, 27] reported TPRs for CT significantly higher than for myelography.

The imaging literature for spinal stenosis suffers particularly from failure to offer independent corroboration with a reference standard for the diagnosis. In our review, we excluded more than 30 articles with valuable imaging data because the images were not verified against any reference standard. Most often, the goal of the report was to illustrate interesting imaging findings. However, such case reporting leaves important questions unanswered. How often does such a finding occur? How often is it validated by other tests or surgical findings? Does its presence help the clinician predict operative or nonoperative patient outcomes?

In spine research, selection of reference standards is difficult, since surgical confirmation of case pathology is intimately linked to having a positive imaging test. Verification of pathology in patients who do not undergo surgery cannot be accomplished without imaging. Furthermore, the operative field is a narrow window that can confirm anatomic findings only at the levels explored and even the direct observations will be subject to some error. In future diagnostic accuracy studies, we suggest that investigators consider surgery as an imperfect reference standard. Prospective research protocols could consist of at least two imaging tests and careful follow-up information. Appropriate analysis techniques can compare individual, independently determined test results and surgical findings to a consensus developed later from all available information [43].

Unbiased assessment of diagnostic accuracy requires independence between test interpretation and determination of the final diagnosis. Three studies did not report anything about methods designed to maintain such independence. Most studies reported that imaging readings were recorded before surgery or in follow-up, thereby preserving test-review independence. However, in five studies using surgical reference standards, the confirmation of stenosis was determined by a surgeon-investigator who had seen the images that were part of the diagnostic accuracy study. Such foreknowledge may have affected the intraoperative declaration of the presence and severity of stenosis. Other investigators have eliminated this concern by asking a colleague to inspect the surgical field and catalog the findings without knowledge of the imaging tests [44] or by operating knowing only the general abnormality from the imaging test, then reviewing the entire image during surgery after recording the surgical findings [27].

The applicability of studies depends on the representativeness of the cohort assembled. For diagnostic accuracy studies, patients with and without disease must be studied. In the spinal stenosis imaging literature, most cases were assembled retrospectively as a convenience sample rather than according to clinically focused hypotheses. Collecting cases after referrals to specialists, problem back clinics, or tertiary imaging centers induces unknown referral filtering biases. With very few exceptions [34], case selection procedures in the studies we reviewed do not allow generalization to patients in primary care practice where spinal stenosis first may be suspected. The next generation of clinical studies can make a better contribution to effective use of diagnostic imaging if cohort assembly is guided by clinical entry criteria representative of both primary care and referral practices.

Most methodologic problems lead to overestimation of diagnostic accuracy. Failure to maintain independence between test and final diagnosis allows spurious correlations to inflate estimates of sensitivity and specificity. Selection of patients for imaging as they are referred for surgery enriches the study cohort with significantly diseased cases whose abnormality is larger and more obvious than would be the case when diagnostic uncertainty precludes a decision in favor of surgical treatment. Since the spinal stenosis literature we reviewed is subject to both influences, estimates for sensitivity and for specificity may be high. This inflation may be counterbalanced by ongoing improvements in imaging techniques.

Studies from one medical center may not apply in geographically or socioeconomically different locales. Furthermore, machine technologies and the interpretive skills of radiologists vary from center to center. Thus, an overall assessment of the diagnostic accuracy of either MR or CT should be a synthesis of studies from a variety of practices, preferably a mix of those pushing the technical frontiers and those doing standard examinations in usual clinical settings. All the studies we reviewed were conducted by investigator-specialists in spine care and research from centers that produce optimistic estimates of diagnostic accuracy for CT and MR.

Which tests should be used and in what order? Spinal MR and CT scanning have gained wide acceptance in clinical practice, even though their formal evaluation has not been rigorous. Since both display anatomic relationships with high fidelity, diagnostic accuracy depends as much on variations in the reader's interpretive skills as on technical features [36, 45]. We suggest that local factors, such as access to MR or CT, the skill of the radiologist operators, and the nature of the patient's complaint, should guide the clinician. From the articles we reviewed, no recommendation for CT or MR as the better test can be made on the basis of published diagnostic accuracy data. No study compared the TPR or FPR of myelography/CT to plain CT. The combination of CT and MR had a slightly higher TPR than either test alone, but this comparison has been studied only once [26]. Some centers have published reports of successful experiences of using MR to replace intrathecal imaging [46], but a recent report indicates that myelography/CT contributed to the diagnosis in 30% of cases already imaged by plain CT and MR [47].

Three voids must be filled to complete our knowledge of the optimal use of spinal imaging for suspected lumbar stenosis. First, a rigorous diagnostic accuracy study needs to be completed. Several centers working together could generate a large case-series of patients enrolled prospectively, with symptoms suggestive of bony sciatica or stenosis, and obtain two imaging tests, electrophysiologic tests, and 6 to 24 months of outcome data. If large enough, such a project would finally demonstrate the sensitivity and specificity for imaging tests in patients whose presentations were uncertain, rather than studying the extreme cases of asymptomatic normal adults or persons already referred for surgery. In particular, we need to know more about possible false-positives occurring either as a result of incidental asymptomatic abnormalities or because scans are overinterpreted. Such mishaps do occur, and they may cluster so that the CT, MR, and myelographic images all look positive [48].

The second void is lack of information about the contribution of imaging tests to predicting clinical outcomes. All the studies we reviewed presented data analyses aimed at anatomic abnormalities. No study analyzed features of the imaging findings for their prognostic significance. Are there features that might distinguish between asymptomatic abnormalities and stenoses that are causative of a patient's illness? Similarly, no studies analyzed the contribution of imaging tests relative to clinical information or electrophysiologic tests for understanding patients' responses to surgery or other treatment. Refined knowledge of the incremental value of CT and MR findings would serve the clinical need to be parsimonious in our use of diagnostic tests, avoiding redundancy, invasive testing, and unnecessary costs.

The final void to be filled is scientific rather than clinical. Plain CT or MR used as noninvasive research tools can expand our knowledge of spinal disease and the anatomic substrate of clinical outcomes if used in the context of proper epidemiologic studies. Exploratory studies have shown that substantial asymptomatic back disease is common and its prevalence increases with age [34, 45, 49]. Is this pathology prognostic for future clinical back events, or is it merely a source of confusion for the radiologist and clinician trying to determine whether or not spinal stenosis is the cause of a clinical illness? Knowing that the human spine produces asymptomatic degenerative changes means that physicians and patients will have to accept some uncertainty in the development of diagnosis and treatment plans for spinal stenosis.

ACKNOWLEDGMENTS

We thank Judy Turner, Jodie Haselkorn, John Loeser, Stan Bigos, Daniel Kido, Al Mushlin, and other members of the Back Pain Outcomes Assessment Team, and the Multi-Institutional Technology Assessment Consortium for helpful suggestions throughout this work. Tom Koepsell and Marcia Ciol assisted with statistical analyses. Mary Ersek, Laura Larsson, and John Wiesman provided logistical support, and Darlena Bursell assisted in preparation of the manuscript.

REFERENCES

1. Moreland LW, Lopez-Mendez A, Alarcon GS. Spinal stenosis: a comprehensive review of the literature. *Semin Arthritis Rheum* **1989**;19:127–149
2. Spengler DM. Degenerative stenosis of the lumbar spine. *J Bone Joint Surg [Am]* **1981**;69:305–308
3. Verbiest H. A radicular syndrome from developmental narrowing of the lumbar vertebral canal. *J Bone Joint Surg [Br]* **1954**;36:230–237
4. Arnoldi CC, Brodsky AE, Cauchoix J, et al. Lumbar spinal stenosis and nerve root entrapment syndromes: definition and classification. *Clin Orthop* **1976**;115:4–5
5. Mauersberger W, Nietgen T. Surgical treatment of lumbar stenosis: long-term results. *Neurosurg Rev* **1989**;12:291–295
6. Beltran J, Noto AM, Chakeres DW, Christoforidis AJ. Tumors of the osseous spine: staging with MR imaging vs. CT. *Radiology* **1987**;162:565–569
7. Weisz GN, LaMond TS, Kitchener PN. Spinal imaging: will MRI replace myelography? *Spine* **1988**;13:65–68
8. Modic MT, Ross JS. Magnetic resonance imaging in the evaluation of low back pain. *Orthop Clin North Am* **1991**;22:283–301
9. Consensus Conference. Magnetic resonance imaging. *JAMA* **1988**;259:2132–2138
10. Kent DL, Larson EB. Magnetic resonance imaging of the brain and spine. Is clinical efficacy established after the first decade? *Am Intern Med* **1988**;108:402–424
11. Haglund MM, Schumacher JM, Loeser JD. Spinal stenosis: an annotated bibliography. *Spine* **1988**;35:1–37
12. Alexander E, Kelly DL, Davis CH, McWhorter JM, Brown W. Intact arch spondylolisthesis. A review of 50 cases and description of surgical treatment. *J Neurosurg* **1985**;63:840–844
13. Boccanera L, Pelliccioni S, Laus M. Stenosis of the lumbar vertebral canal (a study of 25 cases operated on). *Ital J Orthop Traumatol* **1984**;10:227–236
14. Nasca RJ. Surgical management of lumbar spinal stenosis. *Spine* **1987**;12:809–816
15. Han JS, Kaufman B, El Yousef SJ, et al. MRI imaging of the spine. *AJR* **1983**;141:1137–1145
16. Raininko R. The value of CT after total block on myelography. Experience with 25 patients. *ROFO* **1983**;138:61–65
17. von Einsiedel HG, Stepan R. Magnetic resonance imaging of spinal cord syndromes. *Eur J Radiol* **1985**;5:127–132
18. Schonstrom NSR, Bolender NF, Spengler DM. The pathomorphology of spinal stenosis as seen on CT scans of the lumbar spine. *Spine* **1985**;10:806–811

19. Bolender N-F, Schonstrom NSR, Spengler DM. Role of computer tomography and myelography in the diagnosis of central spinal stenosis. *J Bone Joint Surg [Am]* **1985**;67:240–246
20. Hoffman RM, Kent DL, Deyo RA. Diagnostic accuracy and clinical utility of thermography for lumbar radiculopathy: a meta-analysis. *Spine* **1991**;16:623–628
21. Sackett DL, Haynes RB, Tugwell P. *Clinical epidemiology: a basic science for clinical medicine.* 1st ed. Toronto: Little, Brown, **1985**:47–57
22. Guyatt GH, Tugwell PX, Feeny DH, Haynes RB, Drummond M. A framework for clinical evaluation of diagnostic technologies. *Can Med Assoc J* **1986**;134:587–594
23. Ransohoff DF, Feinstein AR. Problems of spectrum and bias in evaluating the efficacy of diagnostic tests. *N Engl J Med* **1978**;299:926–930
24. Mulrow CD, Linn WD, Gaul MK, Pugh JA. Assessing quality of a diagnostic test evaluation. *J Gen Intern Med* **1989**;4:288–294
25. Wasson J, Sox HC, Neff RK, Goldman L. Clinical prediction rules: applications and methodological standards. *N Engl J Med* **1985**;313:793–799
26. Modic MT, Masaryk T, Boumphrey F, Goormastic M, Bell G. Lumbar herniated disk disease and canal stenosis: prospective evaluation by surface coil MR, CT, and myelography. *AJR* **1986**;147:757–765
27. Stockley I, Getty CJM, Dixon AK, Glaves I, Euinton HA, Barrington NA. Lumbar lateral canal entrapment: clinical, radiculographic and computed tomographic findings. *Clin Radiol* **1988**;39:144–149
28. Hall S, Bartelson JD, Onofrio BM, Baker HL, Okazaki H, O'Duffy JD. Lumbar spinal stenosis. Clinical features, diagnostic procedures, and results of surgical treatment in 68 patients. *Ann Intern Med* **1985**;103:271–275
29. Bell GR, Rothman RH, Booth RE, et al. A study of computer-assisted tomography: II. Comparison of metrizimide myelography and computed tomography in the diagnosis of herniated lumbar disc and spinal stenosis. *Spine* **1984**;9:522–556
30. Deim K, Lentner C, eds. *Documenta Geigy scientific tables.* 7th ed. Ardsley, NY: Geigy Pharmaceuticals, **1970**:85–103
31. Metz CE. Basic principles of ROC analysis. *Semin Nucl Med* **1978**;8:283–298
32. Fleiss JL. *Statistical methods for rates and proportions.* 2nd ed. New York: John Wiley, **1981**:138–141
33. Laird NM, Mosteller F. Some statistical methods for combining experimental results. *Int J Technol Assess Health Care* **1990**;6:5–30
34. Boden SD, Davis DO, Dina TS, Patronas NJ, Wiesel SW. Abnormal magnetic-resonance scans of the lumbar spine in asymptomatic subjects: a prospective investigation. *J Bone Joint Surg [Am]* **1990**;72-A:403–408
35. Wiesel SW, Tsourmas N, Feffer HL, Citrin CM, Patronas N. A study of computer-assisted tomography: 1. The incidence of positive CAT scans in an asymptomatic group of patients. *Spine* **1984**;9:549–551
36. Schnebel B, Kingston S, Watkins R, Dillin W. Comparison of MRI to contrast CT in the diagnosis of spinal stenosis. *Spine* **1989**;14:332–337
37. Slebus FG, Braakman R, Schipper J, van Dongen KJ, Westendorp-de Seriere M. Noncorresponding radiological and surgical diagnoses in patients operated for sciatica. *Acta Neurochir (Wien)* **1988**;94:137–143
38. Voelker JL, Mealey J, Eskridge JM, Gilmor RL. Metrizamide-enhanced computed tomography as an adjunct to metrizamide myelography in the evaluation of lumbar disc herniation and spondylosis. *Neurosurgery* **1987**;20:379–384
39. Epstein NE, Epstein JA, Carras R, Hyman RA. Far lateral lumbar disc herniations and associated structural abnormalities: an evaluation in sixty patients of the comparative value of CT, MRI, and myelo-CT. *Spine* **1990**;15:534–539
40. Herkowitz HN, Garfin SR, Bell GR, Bumphrey F, Rothman RH. The use of computerized tomography in evaluating non-visualized vertebral levels caudad to a complete block on a lumbar myelogram. *J Bone Joint Surg [Am]* **1987**;69:218–224
41. Modic MT, Pavilcek W, Weinstein MA, et al. Magnetic resonance imaging of intervertebral disk disease. *Radiology* **1984**;152:103–111
42. Zlatkin MR, Lander PH, Hadjipavlou AG, Levine JS. Paget disease of the spine; CT with clinical correlation. *Radiology* **1986**;160:155–159
43. Henkelman RM, Kay I, Bronskill MJ. Receiver operator characteristic (ROC) analysis without truth. *Med Decis Making* **1990**;10:24–29
44. Morris EW, DiPaola M, Vallance R, Waddell G. Diagnosis and decision making in lumbar disc prolapse and nerve entrapment. *Spine* **1986**;11:436–439
45. Deyo RA, McNiesh LM, Cone RO. Observer variability in the interpretation of lumbar spine radiographs. *Arthritis Rheum* **1985**;28:1066–1070
46. Savitz MH, Katz SS, Zablow BC. Discectomy following CT and MRI with and without myelography. *Mt Sinai J Med* **1988**;55:162–166
47. Goldberg AL, Soo MSC, Deeb ZL, Rothfus WE. Degenerative disease of the lumbar spine: role of CT-myelography in the MR era. *Clin Imaging* **1991**;15:47–55
48. DiChiro G, Doppman JL, Dwyer AJ, et al. Tumors and arteriovenous malformations of the spinal cord: assessment using MR. *Radiology* **1985**;156:689–697
49. Powell MC, Wilson M, Szypryt P, Symonds EM, Worthington BS. Prevalence of lumbar disc degeneration observed by magnetic resonance in symptomless women. *Lancet* **1986**;Dec 13:1366–1367

Epidural Abscess of the Cervical Spine: MR Findings in Five Cases

Robert Kricun[1]
Elliot I. Shoemaker[1]
George I. Chovanes[2]
Harry W. Stephens[2]

Cervical epidural abscess is an uncommon infectious process of the spinal epidural space. Although this disorder is often unsuspected clinically, the patient's signs and symptoms may suggest other diagnoses that frequently lead to an MR examination. We retrospectively reviewed the MR examinations of five patients with surgically proved cervical epidural abscess in order to assist in the diagnosis of this clinically elusive disorder. Each epidural abscess was evaluated for MR signal intensity, location, extent, delineation, and enhancement pattern. We assessed the spinal cord for compression and signal intensity and analyzed the vertebrae, intervertebral disks, and paraspinal soft tissue. Compared with the spinal cord, the abscess was isointense or hypointense on T1-weighted spin-echo images and hyperintense on T2-weighted images. The abscess was hyperintense or isointense relative to the cord on T2* gradient-echo images. Enhancement of the abscess occurred in the two patients given an IV injection of gadopentetate dimeglumine. The epidural abscess was located anteriorly in three patients, posteriorly in one, and was circumferential in one. The abscess extended from two to nine vertebral bodies in length. In each case, the abscess caused some degree of spinal cord compression, and one patient had bright signal intensity within the cord on T2-weighted images. Three patients had MR changes of accompanying osteomyelitis and paravertebral abscess.

MR imaging is useful in diagnosing cervical epidural abscess and in evaluating associated abnormality of the spinal cord, vertebral bodies, intervertebral disks, and paraspinal soft tissue.

***AJR* 158:1145–1149, May 1992**

Epidural abscess of the spine is an uncommon disorder estimated to occur in 0.2–1.3 cases per 10,000 hospital admissions [1, 2]. The cervical spine is the least frequent site of spinal epidural abscess. Although early diagnosis of epidural abscess is considered crucial for successful therapy, the clinical diagnosis is frequently unsuspected. MR imaging can be used to show an epidural process, suggest the diagnosis, and reveal the full extent of involvement. We report five patients with cervical epidural abscess and describe the MR appearance of this inflammatory process.

Materials and Methods

During a 14-month period, we examined the MR images of five patients with surgically proved cervical epidural abscess. The patient population consisted of three men and two women 32–65 years old (average, 55 years). Four of the patients had studies performed on a 1.5-T MR unit, while one patient had his examination on a 0.5-T unit. T1-weighted spin-echo (SE) images, 500–700/12–32 (TR/TE), as well as T2* gradient-echo (GRE) images were obtained in all patients. Proton-density- and T2-weighted SE images (2000–2609/35,70) were obtained in four patients. Short inversion time recovery (STIR) images, 2300/165/40 (TR/TI/TE), were obtained in one patient. Gadopentetate dimeglumine (Magnevist, Berlex Laboratories, Wayne, NJ) was injected IV in two patients in doses of 0.1 mmol/kg body weight. T1-weighted images were obtained immediately after injection.

Received October 30, 1991; accepted after revision January 2, 1992.

[1] Department of Radiology, Lehigh Valley Hospital Center, 1200 S. Cedar Crest Blvd., Allentown, PA 18103. Address reprint requests to R. Kricun.

[2] Division of Neurosurgery, Lehigh Valley Hospital Center, Allentown, PA 18103.

0361-803X/92/1585-1145
© American Roentgen Ray Society

TABLE 1: Clinical and MR Features of Cervical Epidural Abscess in Five Patients

Case No.	Age (yr)	Sex	Infection Source	Fever	Location	Extent	MR Intensity Relative to Spinal Cord			Contrast Enhancement
							T1	PD and T2	GRE	
1	62	M	Pectoral abscess	+	Anterior	C2–T2	Hypointense	Hyperintense	Isointense	Homogeneous
2	32	F	Suspected IV drug abuse	−	Anterior	C5–C6	Isointense	Hyperintense	Isointense	NA
3	65	F	Buttock abscess	−	Posterior	C1–T2	Isointense	Hyperintense	Hyperintense	NA
4	58	M	Postintubation retropharyngeal abscess	−	Anterior	C2–C3	Isointense	NA	Hyperintense	NA
5	56	M	Unknown	+	Circumferential	C1–T1	Isointense	Hyperintense	Hyperintense	Patchy, inhomogeneous

Note.—T1 = T1-weighted images; PD and T2 = proton-density- and T2-weighted images; GRE = gradient-echo images; NA = not available.

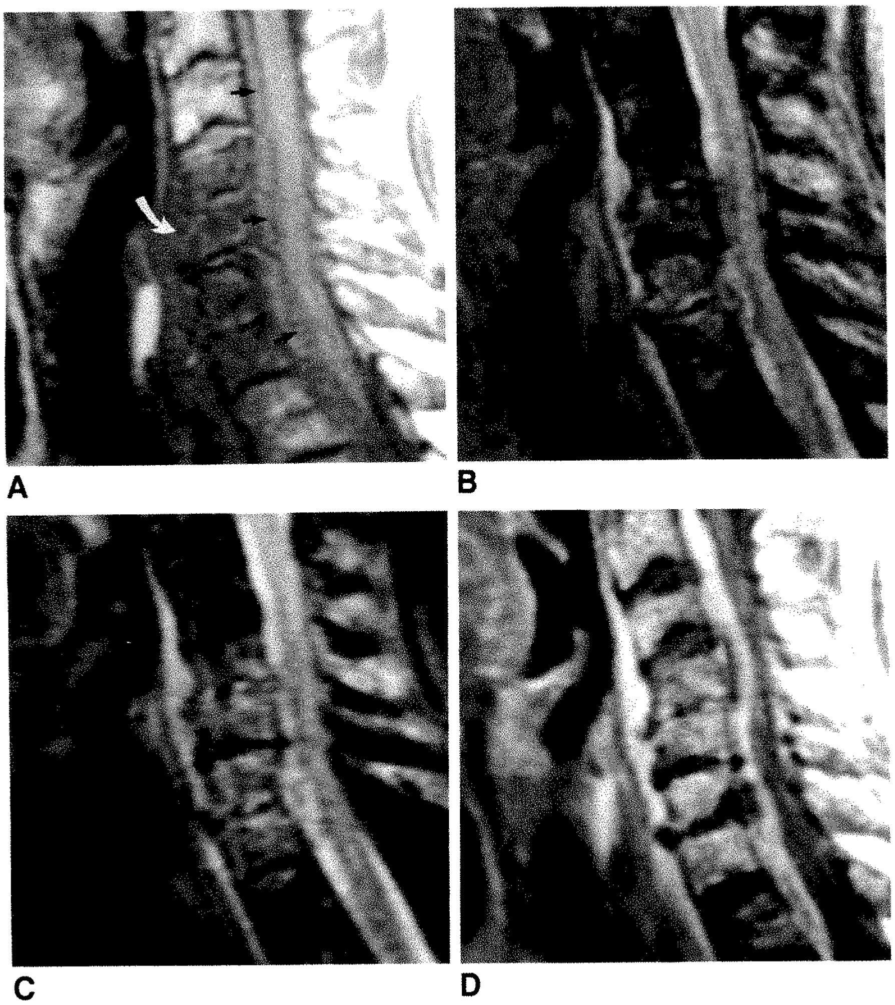

Fig. 1.—62-year-old man with epidural abscess, osteomyelitis, and prevertebral abscess. He had a pectoral abscess and a 3-week history of right shoulder and neck pain. At surgery, extensive granulation tissue was found that cultured *S. aureus*. MR images were obtained with 1.5-T magnet.

***A*, Sagittal T1-weighted image (SE 500/12) in midline shows epidural abscess (*black arrows*) and prevertebral abscess (*white arrow*) of lower signal intensity than spinal cord. Note low signal intensity of vertebral bodies from C4 to C7. Osteomyelitis at C6–C7 was proved at surgery.**

***B*, Sagittal T2-weighted image (SE 2609/70) shows increased signal intensity of abscesses and spinal cord compression. Signal intensity of involved vertebral bodies is moderately increased.**

***C*, Sagittal STIR image (2300/165/40) shows more marked increase in signal of vertebral bodies from C4 to C7 relative to very low signal of adjacent vertebrae with this fat-suppression technique. Epidural abscess and prevertebral abscess have bright signal intensity similar to that of CSF.**

***D*, Sagittal T1-weighted image (SE 600/20) after IV gadopentetate dimeglumine shows marked enhancement of epidural abscess, which extends from C1 to T2 and is causing spinal cord compression. Enhancement of prevertebral abscess and C4–C7 vertebral bodies is also seen.**

All the MR images were reviewed retrospectively. Each epidural abscess was evaluated for signal intensity, location, extent, delineation, and enhancement pattern. The spinal cord was assessed for compression and signal intensity. The vertebral bodies, intervertebral disks, and paraspinal soft tissue were examined.

Results

The clinical and MR features of our five patients are summarized in Table 1. The T1-weighted images showed the epidural abscess to be isointense relative to the spinal cord in four patients and hypointense in one patient. The abscess was hyperintense relative to CSF in all patients (Figs. 1–4). Four patients had proton-density- and T2-weighted SE images. The proton-density images showed hyperintensity of the abscess compared with the cord in all patients. Compared with CSF, there was hyperintensity in three patients and isointensity in one patient. On the T2-weighted images, the epidural abscess was hyperintense relative to the spinal cord and isointense with CSF. GRE images were obtained in all patients, with the abscess showing hyperintensity relative to the cord in three patients and isointensity with the cord in two

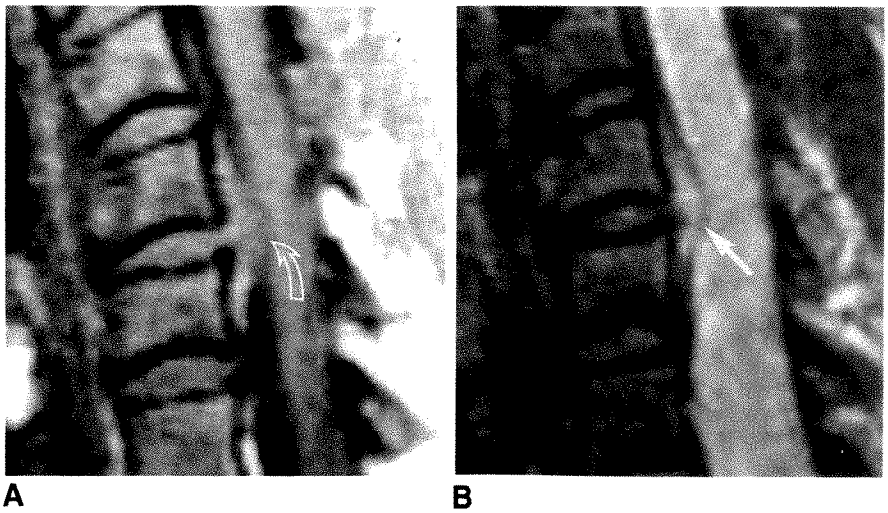

Fig. 2.—32-year-old woman with anterior cervical epidural abscess. She had a 1-week history of severe right-sided neck and arm pain that clinically was thought to be due to disk herniation. Surgery revealed pus that grew *S. aureus*. A history of IV drug abuse was suspected. MR images were obtained with 1.5-T magnet.

A, Sagittal T1-weighted image (SE 700/15) obtained 5 mm to right of midline shows anterior epidural abscess (*arrow*) of intermediate signal compressing anterior subarachnoid space and spinal cord.

B, Sagittal T2-weighted image (SE 2571/70) obtained 5 mm to right of midline shows hyperintense epidural abscess (*arrow*).

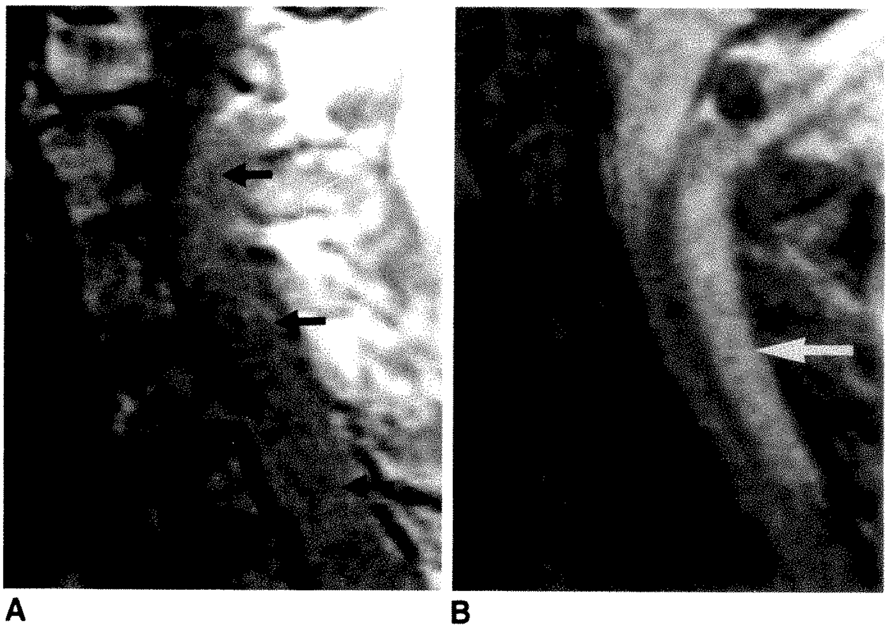

Fig. 3.—65-year-old woman with posterior cervical epidural abscess. She had a 3-day history of radicular pain radiating into posterior left arm that clinically was thought to be due to disk herniation. Surgery revealed pus that grew *S. aureus*. A buttock abscess from prior intramuscular injections was found postoperatively. MR images were obtained with 1.5-T magnet.

A, Sagittal T1-weighted image (SE 700/15) obtained near midline shows epidural abscess (*arrows*) of intermediate signal intensity obscuring visualization of spinal cord.

B, Sagittal T2-weighted image (SE 2000/70) near midline shows high-signal-intensity abscess (*arrow*) extending posteriorly through multiple cervical levels.

patients. One patient had STIR images, which showed the abscess to be hyperintense, similar to CSF (Fig. 1C).

The abscess was anterior in three patients, posterior in one patient, and circumferential in one patient. The craniocaudal extent was from two to nine vertebral bodies, with an average of six. The epidural abscess was well delineated from the adjacent cord in three patients and poorly delineated in two. The abscess was homogeneous in signal on T2-weighted images in three patients and inhomogeneous in two patients. Gadopentetate dimeglumine was injected IV in two patients. In one patient, the poorly delineated collection showed marked enhancement, allowing better distinction from the spinal cord (Fig. 1D). The enhancement pattern was homogeneous except for a few small unenhanced areas of low signal. The second patient receiving an injection had inhomogeneous, patchy enhancement. Delineation of the abscess from the spinal cord improved after contrast enhancement.

Spinal cord compression was present in all cases and was best demonstrated on T1-weighted sagittal images. One patient had central linear high signal within the cord on T2-weighted images. There was no abnormal signal within the cord on the T1-weighted images before or after injection of contrast material.

In three of the cases the marrow of two to four vertebral bodies was involved (Figs. 1 and 4). Compared with normal marrow, these vertebrae were hypointense on T1-weighted images and hyperintense on T2-weighted or GRE images. One patient had STIR images, which showed hyperintensity of the abnormal vertebrae that was more marked than on the T2-weighted images. Two of the three patients with abnormal marrow signal had T2-weighted images that showed hyperintensity of the intervertebral disk. The other patient had GRE images that showed isointensity of the disk. Paraspinal soft-tissue signal abnormality was present in all three patients and

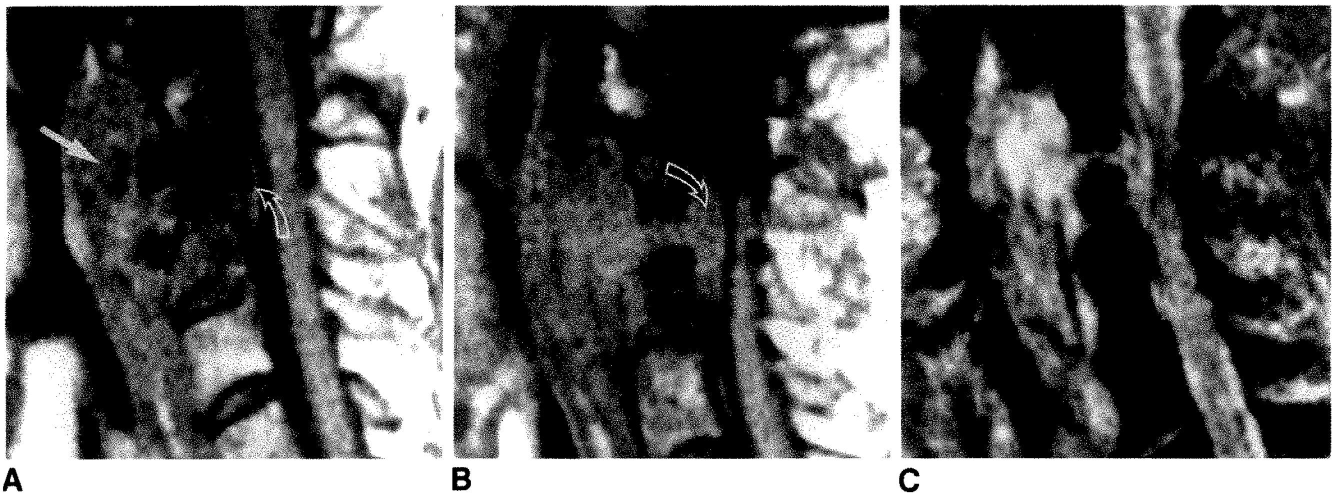

Fig. 4.—58-year-old man with anterior epidural abscess, C2-C3 osteomyelitis, and prevertebral abscess. He had severe neck pain and pain on swallowing 3 months after a traumatic intubation. A retropharyngeal mass was present on examination. MR images were obtained with 0.5-T magnet.

A and *B*, Sagittal T1-weighted images (SE 500/32) at midline (*A*) and left of midline (*B*) show large prevertebral abscess (*straight arrow*) and epidural abscess (*curved arrows*) of intermediate signal. Epidural abscess is compressing spinal cord. Low signal intensity of C2 and C3 vertebrae is due to osteomyelitis.

C, GRE image (400/25, 15° flip angle) obtained left of midline shows heterogeneous bright signal intensity of prevertebral abscess and epidural abscess.

showed hypointensity on T1-weighted images, hyperintensity on T2-weighted or GRE images, and enhancement in those receiving an injection of contrast material.

Discussion

Spinal epidural abscess is an infectious process of the epidural space that may consist of pus or granulation tissue. Sources of infection include osteomyelitis, bacteremia, and postoperative infection. Hematogenous spread is most often a result of a skin infection. Cervical epidural abscess is usually associated with a remote source of infection involving the arm, neck, or head and is frequently found with concomitant osteomyelitis [3]. *Staphylococcus aureus* is the organism most frequently implicated and was cultured in four of our patients. Gram's stain of the fifth patient's abscess revealed gram-positive cocci, although culture failed to document growth of pathologic organisms, possibly because of ongoing antibiotic therapy. The clinical course of epidural abscess has been described in four phases: spinal ache, root pain, weakness, and paralysis [4]. A sudden onset of high fever and localized severe pain should suggest the diagnosis [5]. However, patients may be afebrile or have a low-grade fever. Regardless of the initial course of the disease, weakness and paralysis can develop suddenly, thus making early diagnosis and treatment crucial in preventing neurologic damage or reversing paralysis of short duration [2, 6]. Despite this urgency, spinal epidural abscess is frequently not considered in the early evaluation of these patients [1, 2]. The clinical diagnosis of epidural abscess is correctly suspected initially in only 20–25% of cases [1, 2]. Diagnoses that may be considered include extruded disk (as in two of our patients), spinal tumor, vertebral osteomyelitis, musculoskeletal arthritis, meningitis, and transverse myelitis; these disorders frequently prompt the use of MR evaluation.

A review of several large series reveals that the primary location of spinal epidural abscess is most commonly the thoracic spine (approximately 50%) followed by the lumbar (35%) and cervical (15%) spine [2]. In our series, the extent of cervical epidural abscess ranged from two to nine vertebral bodies in length with an average of six levels involved. Cervical epidural abscess often occurs anteriorly, unlike the more common thoracic abscess, which usually occurs posteriorly. Only one abscess in our series was located completely posteriorly, while three were anterior. The other abscess surrounded the cord circumferentially, being more prominent anteriorly. The frequent anterior location of cervical epidural abscess is thought to be due to the high frequency of osteomyelitis found in these patients [3]. Three of the four patients with anterior epidural abscess had signal abnormality of the paravertebral soft tissue and adjacent vertebrae with decreased signal intensity on SE T1-weighted images and increased signal intensity on T2-weighted images consistent with paraspinal abscess and osteomyelitis. A biopsy performed in one patient proved osteomyelitis. The patient with a posterior epidural abscess did not have evidence of osteomyelitis.

A review of our case shows that an epidural abscess has low or intermediate signal intensity on SE T1-weighted images and high signal intensity on proton-density- and T2-weighted images. GRE images show the abscess as hyperintense or isointense relative to the cord. The abscess may be well delineated or poorly delineated on T2-weighted images. Delineation of the abscess was improved in the two patients who had an injection of gadopentetate dimeglumine.

At the time of surgery, the epidural abscess may consist of pus or granulation tissue. The abscess in four of our patients consisted of frank pus while the fifth had extensive granulation tissue. Some investigators [1, 2] have found pus in acute epidural abscesses and granulation tissue in the chronic stages. Others [7] have not found a correlation between the pathologic appearance and the duration of illness. Some authors [8] have shown that various components of the inflammatory process can be distinguished on T2-weighted images. The fluid portion of the abscess tends to have markedly increased signal, and the surrounding inflammatory edema and granulation tissue have inhomogeneous areas of mildly increased signal intensity. We, like others [9], did not find an exact correlation between the signal on MR and the stage of the epidural abscess. The high signal intensity of pus and more chronic granulation tissue may be similar. Rarely, hemorrhage may accompany the infection, producing heterogeneous high signal on T1- and T2-weighted images that has the appearance of an epidural hematoma [10]. None of our cases showed a hemorrhagic component.

Because both the axial and sagittal planes could be scanned, the extent of epidural involvement and the degree of compression of the thecal sac and spinal cord were readily appreciated with MR. We found some degree of spinal cord compression on MR studies of all five patients. One of our patients had bright signal intensity within the cord on T2-weighted images. This patient had sudden neurologic deterioration with weakness that rapidly led to paralysis. An emergency MR examination was obtained, and surgery was performed 5 hr after the onset of weakness. The patient made a good recovery in strength and ambulation after surgery and a lengthy course of antibiotics. Hyperintensity of the cord has been described in some patients with spinal cord compression [10]. This is of uncertain etiology, although the increased signal in the cord may be due to changes of myelitis that can regress after evacuation of the epidural collection and/or antibiotic therapy [9]. Serial MR scans after treatment can be useful in the follow-up evaluation.

Gadopentetate dimeglumine was injected IV in two patients. In one patient, this was helpful in delineating the extent of the abscess, which consisted of extensive granulation tissue that showed marked and fairly homogeneous enhancement. In the other patient, patchy and inhomogeneous enhancement of the epidural abscess aided in its delineation. Three patterns of enhancement have been described and include dense homogeneous enhancement, inhomogeneous enhancement with scattered areas of sparse or no uptake, and thin peripheral enhancement [11]. Gadopentetate dimeglumine also helps define the activity of the infectious process, and can be used to help localize an area for potential biopsy as well as to determine response to antibiotic treatment. However, an acute epidural abscess composed mainly of pus with little granulation tissue may show either no enhancement or minimal peripheral enhancement [11].

MR imaging is accurate and sensitive in the detection of accompanying osteomyelitis with disk space infection [9, 12, 13], as was shown in three of our patients. T1-weighted images show decreased signal from the marrow of two or more adjacent vertebral bodies with an indistinctness of the vertebral body endplates and narrowing of the disk space [13]. T2-weighted images show increased signal from the vertebral bodies. The signal changes of the vertebral bone marrow probably represent increased water content of the exudative process and ischemia. Some investigators [9] have stressed the importance of finding high signal intensity within the intervertebral disks on T2-weighted images, while others [13] have found variable signal intensity. STIR images have been recommended by some investigators for the evaluation of osteomyelitis [12, 13]. With this pulse sequence, an inversion time is selected that effectively suppresses the signal from fat, making the normal bone marrow appear dark. In contrast, pathologic processes of high water content such as inflammation or neoplasm appear very bright, thus providing images with high contrast between pathologic and normal tissue.

MR imaging plays an important role in the evaluation of patients with cervical epidural abscess [5, 8, 12, 13]. Although the diagnosis may not be suspected clinically, the patient's symptoms usually will lead to imaging evaluation. The MR features of epidural abscess can be used to suggest the diagnosis and guide therapy. Accompanying osteomyelitis, disk space infection, and paravertebral abscess can be evaluated with MR.

REFERENCES

1. Baker AS, Ojemann RG, Swartz MN, Richardson EP Jr. Spinal epidural abscess. *N Engl J Med* **1975**;293:463–468
2. Danner RL, Hartman BJ. Update of spinal epidural abscess: 35 cases and review of the literature. *Rev Infect Dis* **1987**;9:265–274
3. Lasker BR, Harter DH. Cervical epidural abscess. *Neurology* **1987**;37:1747–1753
4. Heusner AP. Nontuberculous spinal epidural infections. *N Engl J Med* **1948**;239:845–854
5. Erntell M, Holtas S, Norlin K, Dahlquist E, Nilsson-Ehle I. Magnetic resonance imaging in the diagnosis of spinal epidural abscess. *Scand J Infect Dis* **1988**;20:323–327
6. Verner EF, Musher DM. Spinal epidural abscess. *Med Clin North Am* **1985**;69:375–384
7. Kaufman DM, Kaplan JG, Litman N. Infectious agents in spinal epidural abscesses. *Neurology* **1980**;30:844–850
8. Angtuaco EJC, McConnell JR, Chadduck WM, Flanigan S. MR imaging of spinal epidural sepsis. *AJNR* **1987**;8:879–883, *AJR* **1987**;149:1249–1253
9. Post MJD, Quencer RM, Montalvo BM, Katz BH, Eismont FJ, Green BA. Spinal infection: evaluation with MR imaging and intra-operative US. *Radiology* **1988**;169:765–771
10. Enzmann DR. Infection and inflammation. In: Enzmann DR, DeLaPaz RL, Rubin JB, eds. *Magnetic resonance of the spine*. St Louis: Mosby, **1990**:260–300
11. Post MJD, Sze G, Quencer RM, Eismont FJ, Green BA, Gahbauer H. Gadolinium-enhanced MR in spinal infection. *J Comput Assist Tomogr* **1990**;14:721–729
12. Bertino RE, Porter BA, Stimac GK, Tepper SJ. Imaging spinal osteomyelitis and epidural abscess with short TI inversion recovery (STIR). *AJNR* **1988**;9:563–564
13. Thrush A, Enzmann D. MR imaging of infectious spondylitis. *AJNR* **1990**;11:1171–1180

Book Review

MRI of the Brain III. Neoplastic Disease. Edited by Anton N. Hasso, Miyuki Shakudo, and Edla Chadrycki. (One of 10 volumes in The Raven MRI Teaching File. Series editors: Robert B. Lufkin, William G. Bradley, Jr., and Michael Brant-Zawadzki.) New York: Raven, 216 pp., 1991. $60, softcover

This book is the third in a series of 10 volumes being published by Raven Press. The purpose of the series is to help practicing radiologists develop proficiency in MR imaging. This book consists of 450 images from a compilation of 100 cases of neoplastic disease of the CNS evaluated by using MR. In general, the quality of the images is state of the art. The scientific discussions of the diagnosis and radiologic findings are excellent, accurate, and up-to-date. Each case is printed with the MR images (and occasionally CT scans and angiograms) on the left-hand page, along with a concise clinical history. On the right-hand (facing) page is a description of the findings; the histologic diagnosis; a discussion of the case, with differential diagnosis; a brief list of one to four references; and a line crediting the person who submitted the case. The book is well indexed, not only by diagnosis but also by clinical signs and symptoms.

The images are crisp, but rather small. Most cases are pathologically proved. The images are generally presented sequentially: plain CT scan, enhanced CT scan, long TR/TE MR image, short TR/TE MR image, and, finally, gadolinium-enhanced MR image. There are deviations from this ordered plan of presentation, which may be confusing.

The authors are successful in achieving their goal of creating a "teaching file" atmosphere. However, some of the features that are helpful in a teaching file limit its usefulness as a reference. It is awkward to look at the figures without seeing the printed diagnosis, unless the facing page is intentionally covered with a piece of paper. All the radiologic images are approximately 2 × 2 in. (5 × 5 cm). Although this is necessary for cases that contain multiple figures, most cases have only four images, and this leaves large areas of the page blank. Of necessity, the book has multiple examples of the more common neoplasms. However, because the cases are all grouped together, it is more difficult to view each case as a complete unknown, rather than as one in a series of cases with the same diagnosis. Each case discussion is written to stand alone; but because the book has multiple examples of the same disease, the text tends to be a bit repetitive.

The case discussions and references (though sparse) are accurate and up-to-date, and some unreferenced comments must be derived from the editors' extensive personal experience. Overall, I recommend this book to those who enjoy an "unknown case" approach to learning. It could also be useful to those preparing for board examinations.

James G. Smirniotopoulos
Armed Forces Institute of Pathology
Washington, DC 20306-6000

MR Imaging of the Pituitary Gland in Infants and Children: Changes in Size, Shape, and MR Signal with Growth and Development

Robert D. Tien[1]
John Kucharczyk[2]
Jeffrey Bessette[3]
Michael Middleton[3]

It has been reported that on MR images of the brain in neonates the entire pituitary gland is hyperintense. This is quite different from the well-established observation that on MR images of adults only the posterior pituitary gland is hyperintense; the anterior portion is isointense. To better understand the development of the neonatal pituitary gland, we studied the timing and magnitude of changes in the size, shape, and MR signal of the pituitary gland in early childhood and infancy. The study included 76 infants and children ages 3 days to 4 years old. In each MR study, the signal intensity of the pituitary gland on T1-weighted coronal ($n = 24$) and sagittal ($n = 76$) images was compared with the signal intensity of the pons by using region-of-interest methods. The size and shape of the pituitary glands were recorded. Statistical comparisons were made for signal intensity and size of the pituitary gland between boys and girls and among age groups. The results showed that the MR signal of the posterior lobe remained hyperintense relative to the pons for all age groups represented in our study (through 4 years). However, the signal intensity of the anterior lobe gradually diminished and by approximately age 2 months was isointense with the pons. Thus, by approximately age 2 months the MR signal intensity of the infant's pituitary gland has changed from being entirely hyperintense (as seen in neonates) to isointense in the anterior lobe and hyperintense in the posterior lobe (as seen in adults). In the first 2 months of life the pituitary gland is bulbous in shape; later it has a flatter upper surface. We found no significant changes in the length or signal intensity of the pituitary gland; no differences among sexes in size, shape, or signal intensity were demonstrated.

Findings of a bulbous pituitary gland and high MR signal of the entire pituitary are normal in neonates up to 2 months of age. After that, the gland gradually flattens and the MR signal of the anterior lobe decreases until it has characteristics similar to the adult pituitary. Lack of high signal or discovery of a small pituitary gland in a neonate should alert the radiologist to the possibility of pituitary malformation or dysfunction.

***AJR* 158:1151–1154, May 1992**

To date few studies have been done on the MR appearance of the anterior lobe of the pituitary gland in normal infants. Wolpert et al. [1] reported that on T1-weighted MR images the signal intensity of the anterior lobe in neonates less than 8 weeks old was much higher than the signal intensity in older children. The purpose of this study was to correlate changes in size, shape, and MR signal intensity of the entire pituitary gland with age during infancy and early childhood in order to better understand the early postnatal growth and development of the pituitary gland.

Materials and Methods

Study Population

We retrospectively reviewed the MR images and medical histories of children less than 4 years old who were referred for routine cranial MR studies in a 24-month period. Seventy-six patients without clinical evidence of pituitary or endocrine disease and with normal images (46 boys, 30 girls) were included in the study.

Received July 25, 1991; accepted after revision December 4, 1991.

[1] Department of Radiology, Box 3808, Duke University Medical Center (North), Durham, NC 27710. Address reprint requests to R. D. Tien.

[2] Department of Radiology, Neuroradiology Section, University of California Medical Center, San Francisco, CA 94143.

[3] Department of Radiology, University of California, San Diego, Medical Center, San Diego, CA 92103.

0361–803X/92/1585–1151
© American Roentgen Ray Society

MR Imaging

Routine MR images included a midline unenhanced T1-weighted sagittal image in which both the pituitary gland and the infundibulum were seen on a single section. MR images were acquired at 1.5 T (General Electric Co., Milwaukee, WI). T1-weighted, 600/20/2-4 (TR/TE/number of excitations), spin-echo images were acquired with a head coil, a 256 × 256 or 256 × 192 matrix, a 16- or 20-cm field of view, and a 3-mm slice thickness without interslice gap. The MR viewing console was used to measure directly the maximal height and length of the pituitary gland, as shown on the midline sagittal image. The maximal width of the gland was also measured on T1-weighted images in 24 patients.

Data Analysis

In all 76 patients the signal intensity of the anterior lobe of the pituitary gland in the midsagittal plane was compared with the signal intensity of the posterior pons and graded qualitatively as follows: grade 0 = pituitary gland isointense with pons, grade 1 = pituitary gland slightly hyperintense relative to pons, and grade 2 = pituitary gland much brighter than pons. The signal intensities were graded by two neuroradiologists. Circular regions of interest (ROIs) were used to measure the anterior lobe of the pituitary gland (minimum size, at least 5 pixels) and the posterior pons centered on the longitudinal fibers (minimum size, 10 pixels) on all sagittal images. Because the posterior portion of the pons is largely myelinated at birth and changes rather slowly in the first 6 months of life, we considered the ROI value of the posterior pons as a relatively stable standard [2]. The ratio of the difference between the ROI values of the anterior lobe of the pituitary gland and that of the pons alone was used to reduce the effects of minute calibration differences (receiver attenuation) between patients.

We divided the 76 patients into four groups on the basis of the appearance of the plot of observed relative signal intensity vs age (Fig. 1): group 1 contained 19 patients up to 2 months old, group 2 contained 25 patients 3-12 months old, group 3 contained 17 patients 13-24 months old, and group 4 contained 15 patients 27-45 months old. Statistical analyses were then based on these groupings.

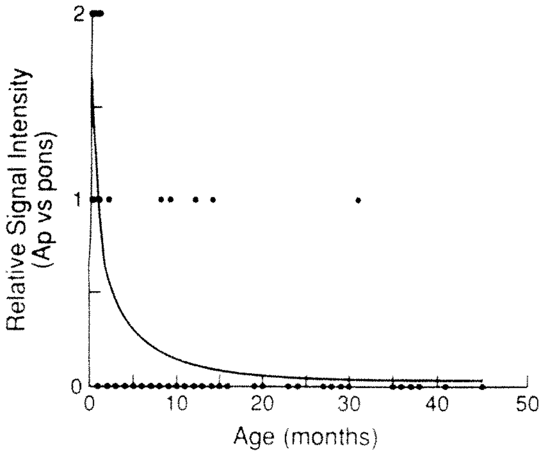

Fig. 1.—Graph shows signal intensity of anterior lobe of pituitary gland (Ap) relative to age. Grade 0 = pituitary gland isointense with pons; grade 1 = pituitary gland slightly hyperintense relative to pons; grade 2 = pituitary gland hyperintense relative to pons. *Solid line* represents curve of best fit for individual data points. Some points overlap because of convergence of individual values. A sharp decline in observed signal intensity of pituitary gland occurred between first and second postnatal months.

Bias related to sex was excluded by using appropriate statistical tests for repeated measures over time [3, 4]. The Mann-Whitney U test was used to compare the observed signal intensity and the shape of the pituitary gland because these variables were discontinuous. Pituitary length and height and the ratio of the ROIs were considered continuous variables and were analyzed with Student's t test. If the ratio of the variances (f value) of the two groups being compared was within acceptable limits, the variances were pooled and a t value was computed. Otherwise, the values of t were adjusted for the variance, and a significance level was assigned on this basis.

The means of each of the four variables relating to the pituitary gland (observed signal intensity, length, height, and measured ROI ratio) were then compared between groups in all possible combinations. Finally, Spearman's rho rank-order correlation coefficients or Pearson's r coefficients were computed for each variable in relation to the age groupings (groups 1-4), and levels of significance were obtained by using standard statistical tables [4].

Results

The anterior lobe of the pituitary gland was hyperintense (grade 2) from birth until approximately 5-6 weeks after birth and then lost some signal intensity (to grade 1) beginning 6-8 weeks after birth. After 2 months, the anterior lobe appeared isointense with the posterior portion of the pons on T1-weighted images (Figs. 2-4).

Measurements of the overall size of the neonatal pituitary gland mostly reflect the physical dimensions of its much larger anterior component. During the first 2 months after birth, the anterior lobe of the pituitary gland had a slightly bulbous appearance with a convex upper border. Although the gland's thickness (or height) was increased, the upper border became flatter with age, similar to the pituitary gland in adults. The range of thickness of the pituitary glands was 2-7 mm. In most patients, the length of the gland was rather constant in the first 4 years after birth, although individual lengths ranged from 3 to 12 mm. In 24 cases, the width of the pituitary gland was measured on coronal images; the average width was 8 mm (range, 5-10 mm).

No differences were found in the size or signal intensity of the pituitary gland in boys compared with girls, regardless of age. There was, however, a correlation between the age of the infant and the observed signal intensity of the pituitary gland for both sexes combined ($p < .01$) (Fig. 1) and for boys separately ($p < .05$). A correlation also was found between age and measured pituitary ROI intensity for boys and girls combined ($p < .001$), as well as for boys ($p < .001$) (Fig. 5) and girls ($p < .05$) separately. Finally, there was a correlation ($p < .02$) between the age of girls and pituitary length. No correlations ($p < .05$) were found between age and pituitary height in either sex.

Differences were found ($p < .001$) between the observed and measured signal intensity values of the anterior lobe of the pituitary gland in the youngest age group (group 1) compared with the other age groups studied (Figs. 1 and 5), whereas the length of the pituitary gland did not differ with age. The height of the pituitary gland was smaller in group 1 (<2 months old) girls compared with group 2 (3-12 months old) girls. Similarly, differences were seen in group 2 girls

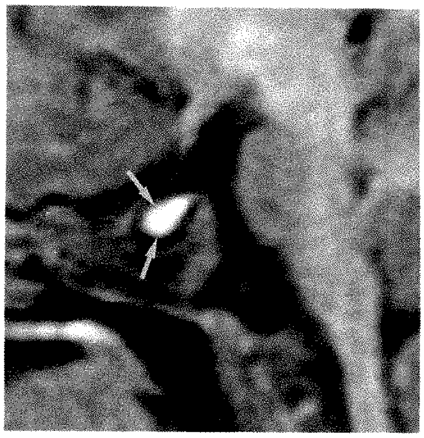

Fig. 2.—Sagittal T1-weighted MR image of a 3-day-old girl shows pituitary gland is hyperintense (grade 2) relative to posterior pons. Anterior lobe (*arrows*) is bulbous.

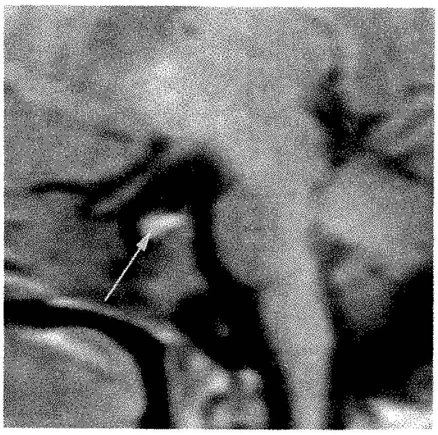

Fig. 3.—Sagittal T1-weighted MR image of a 1-month-old boy shows hyperintense (grade 1) pituitary gland (*arrow*).

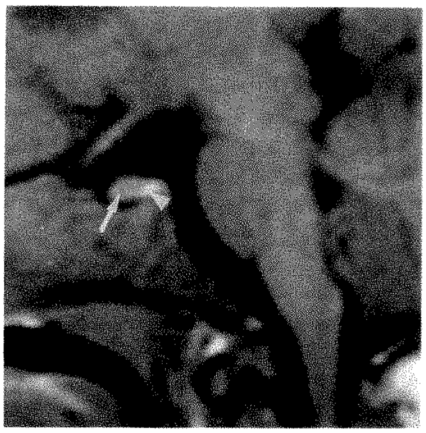

Fig. 4.—Sagittal T1-weighted MR image of 3-month-old infant shows anterior lobe of pituitary gland is isointense (grade 0) with posterior pons (*arrow*). Posterior lobe (*arrowhead*) remains relatively hyperintense.

compared with group 4 girls ($p < .001$), and in group 3 girls compared with group 4 girls ($p < .05$).

The changes in signal intensity observed in the posterior lobe of the pituitary gland were subtle (Figs. 2–4). During the first 2 months after birth, the posterior lobe was approximately isointense with the anterior lobe. Thereafter, until subjects were 4 years old, the signal intensity of the posterior lobe did not change significantly. Consequently, the posterior lobe appeared hyperintense relative to the anterior lobe and pons. The posterior lobe was generally too small for the physical dimensions to be measured accurately.

Discussion

The rapid development of MR imaging for use in biomedical research has stimulated renewed interest in neuroimaging of the pituitary gland. Most of the work to date has focused on the abnormal gland, including cases of adenoma, Rathke's cleft cyst, and Langerhans' cell histiocytosis [5–8]. Several MR imaging studies [5, 9, 10] have also investigated the nature and clinical significance of the hyperintense signal on T1-weighted images of the posterior lobe.

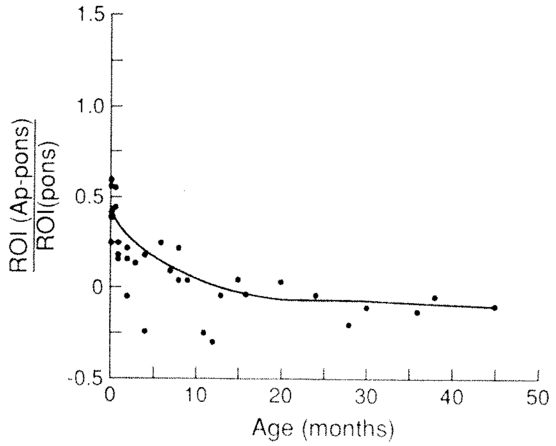

Fig. 5.—Graph shows age-related changes in signal intensity of anterior lobe of pituitary gland (Ap) and posterior pons vs posterior pons itself. Note relative signal decrease of anterior lobe of pituitary gland in early infancy. ROI = region of interest.

The fetal pituitary gland is well differentiated and capable of producing all trophic hormones by the end of the first trimester. Higher levels of growth hormone [11], prolactin [12], adrenocorticotropic hormone [13], and thyrotropin [12, 13] have been shown to be present in the pituitary gland during the second and third trimesters of fetal development, continuing through the first 2 months after birth. This corresponds to the postnatal period, during which we observed prominent hyperintensity on T1-weighted images of the anterior lobe. Our results concur with those of Wolpert et al. [1]. This hyperintensity may be the result of a shortened T1 relaxation time owing to an increase in the bound fraction of water molecules related to hormone secretion [14].

The increased secretory activity of the anterior lobe during the fetal and neonatal periods is known to stimulate hypertrophy of endocrine cells. Elevated fetal and neonatal hormone activity is accompanied by a significant increase in the number, size, and intracellular complexity of secretory cells [13]. We observed that the pituitary gland is more bulbous in the first 2 months after birth. This may be attributed to the cellular hypertrophy at this age, paralleling the finding of Elster et al. [15] of the prominent pituitary gland in adolescent girls.

These observations suggest the possibility that the high signal intensity of the anterior pituitary gland may be functionally linked to maturation of its ability to secret hormones. Further support for this view is provided by the results of a recent study by Abrahams et al. [16], who imaged the pituitary gland of four neonates (three 1 day old and one 4 weeks old) with multiple hormone abnormalities, including idiopathic growth hormone deficiency. Two of the neonates in the study by Abraham et al. had a small anterior pituitary lobe; in the remaining two neonates, the size of the hypophysis was normal. All four neonates had an ectopic posterior lobe of the pituitary gland near the median eminence. The anterior pituitary was isointense with gray matter in each case. The absence of hyperintensity in the adenohypophysis of these neonates suggests that the high signal intensity may indeed be related to normal endocrine activity in the gland. No definite evidence of tapering of the trophic hormones at 2 months is found. Thus, the disappearance of the high signal observed in the anterior pituitary gland after 2 months is still unexplained.

In contrast to the anterior lobe, the function of the posterior lobe is linked to storage and release of oxytocin and vasopressin rather than de novo hormone secretion. Thus, it is not surprising that, unlike the anterior lobe, the neurohypophysis is stable in size and in MR signal intensity during infancy and early childhood.

In summary, elevated levels of endocrine activity in healthy neonates may be a source of the observed high signal of the anterior pituitary gland and the gland's bulbous appearance. The cause of the decline in signal intensity and size of the pituitary gland at 2 months of age has not yet been determined. Absence of high signal or presence of a small pituitary gland in a neonate should alter the radiologist to the possibility of endocrine abnormalities.

REFERENCES

1. Wolpert SM, Osborne M, Anderson M, Runge VM. The bright pituitary gland: a normal MR appearance in infancy. *AJNR* **1989**;9:1–3
2. Barkovich AJ, Kjos BO, Jackson DE, Norman D. Normal maturation of the neonatal and infant brain: MR imaging at 1.5 T. *Radiology* **1988**;166:173–180
3. Downie NM, Heath RW. *Basic statistical methods*. San Francisco: Harper & Row, **1974**
4. Colon T. *Statistics in medicine*. Boston: Little, Brown, **1974**
5. Columbo N, Berry I, Kucharczyk J, et al. Posterior pituitary gland: appearance on magnetic resonance images in normal and pathologic states. *Radiology* **1987**;165:481–485
6. Kucharczyk W, Davis DO, Kelly WM, et al. Pituitary adenomas: high resolution MR imaging at 1.5 T. *Radiology* **1986**;161:761–765
7. Kelly WM, Kucharczyk W, Kucharczyk J, et al. Posterior pituitary ectopia: an MR feature of pituitary dwarfism. *AJNR* **1989**;9:453–460
8. Tien RD, Newton TH, McDermott MW, et al. Thickened pituitary stalk on MR images in patients with diabetes insipidus and Langerhans cell histiocytosis. *AJNR* **1990**;11:703–708
9. Fujisawa I, Asato R, Kawata M, et al. Hyperintense signal of the posterior pituitary on T1-weighted MR images: an experimental study. *J Comput Assist Tomogr* **1989**;13:371–377
10. Kucharczyk W, Lenkinski RE, Kucharczyk J, et al. The effect of phospholipid vesicles on the NMR relaxation of water: an explanation for the MR appearance of the neurohypophysis? *AJNR* **1990**;11:693–700
11. Kaplan SL, Grumbach MM, Aubert ML. The ontogenesis of pituitary hormones and hypothalamic factors in the human fetus: maturation of central nervous system. Regulation of anterior pituitary function. *Recent Prog Horm Res* **1976**;32:161–243
12. Asa SL, Kovacs K, Laszlo FA, et al. Human fetal adenohypophysis: histologic and immunocytochemical analysis. *Neuroendocrinology* **1986**;43:308–316
13. Fisher DA, Klein AH. Thyroid development and disorders of thyroid function in the newborn. *N Engl J Med* **1981**; 304:702–712
14. Thliveris JA, Currie RW. Observations on the hypothalamo-hypophyseal portal vasculature in the developing human fetus. *Am J Anat* **1980**;157:441–444
15. Elster AD, Chen MYM, Williams DW, Key LL. Pituitary gland: MR imaging of physiologic hypertrophy in adolescence. *Radiology* **1990**;174:681–685
16. Abrahams JJ, Trefelner E, Boulware SD. Idiopathic growth hormone deficiency: MR findings in 35 patients. *AJNR* **1991**;12;155–160, *AJR* **1991**;156:599–604

Crossed Cerebellar Diaschisis and Crossed Cerebellar Atrophy:

Correlation of MR Findings, Clinical Symptoms, and Supratentorial Diseases in 26 Patients

Robert D. Tien[1]
Boyd C. Ashdown

Crossed cerebellar diaschisis is a condition in which cerebellar hypometabolism is ascribed to functional disconnection of the contralateral hemisphere from the cerebral cortex. Interruption of the cerebropontine-cerebellar pathway is thought to be the most likely mechanism of this remote transneuronal metabolic depression. This phenomenon can be diagnosed by positron emission tomography, as there is hypometabolism in the affected cerebellar hemisphere. The morphologic features of the affected cerebellar hemisphere in patients with the diagnosis of crossed cerebellar diaschisis have not previously been studied by MR imaging. We retrospectively reviewed 26 patients in whom the diagnosis of crossed cerebellar diaschisis was suggested by positron emission tomography; these patients also had MR studies. In all 26 patients, supratentorial diseases were documented by MR imaging. Twenty-four of the 26 patients had a pathologic diagnosis. Detailed clinical history was also obtained for all patients. MR findings of morphologic change in the affected cerebellum were correlated with the patient's clinical symptoms and supratentorial disease. Of the 26 patients, eight had cerebellar atrophy; the remaining 18 patients showed no MR abnormality of the affected cerebellum. In the 18 in whom no atrophy was seen on MR imaging, the majority of the supratentorial lesions were tumors. The eight patients in whom cerebellar atrophy was demonstrated usually had significant contralateral supratentorial hemispheric atrophy. The patients with atrophy were also generally younger (average age, 14 years) than the 18 patients without cerebellar atrophy (average age, 42 years).

Our experience shows that a significant number of patients with crossed cerebellar diaschisis have morphologic changes of cerebellar atrophy shown by MR imaging. These patients usually have significant contralateral supratentorial hemispheric atrophy.

***AJR* 158:1155–1159, May 1992**

Diaschisis is an inhibition of function produced by an acute focal disturbance in a portion of the brain at a distance from the original site of injury, but anatomically connected with it through fiber tracts. Crossed cerebellar diaschisis is a phenomenon that has been identified on positron emission tomographic (PET) scans in which cerebellar hypometabolism is ascribed to functional disconnection of the contralateral hemisphere from the cerebral cortex. This phenomenon was reported by Baron et al. [1], who observed a parallel reduction in blood flow and oxygen uptake in the cerebellar hemisphere contralateral to the side of supratentorial ischemic infarction. Since that time, similar phenomena have been reported [2–4] under other clinical circumstances, including intracranial tumors, arteriovenous malformations, and hemorrhages.

While several studies have identified the PET findings in crossed cerebellar diaschisis, no study has attempted to assess the morphologic changes in the affected cerebellar hemisphere. Owing to its superior spatial resolution, MR imaging should be sensitive to subtle morphologic changes in the hypometabolic cerebellar hemisphere previously documented by PET imaging. Thus, we undertook a retrospective study to review the MR imaging findings of morphologic change in the affected cerebellum of 26 patients who had been diagnosed with crossed cerebellar

Received October 30, 1991; accepted after revision December 23, 1991.

[1] Both authors: Department of Radiology, Box 3808, Duke University Medical Center, Durham, NC 27710. Address reprint requests to R. D. Tien.

0361-803X/92/1585-1155
©American Roentgen Ray Society

diaschisis by PET imaging. We then correlated morphologic change, clinical symptoms, and supratentorial disease to investigate possible connections.

Materials and Methods

All patients in whom crossed cerebellar diaschisis was diagnosed on the basis of PET studies at our institution between 1989 and 1991 were evaluated retrospectively. Chosen for inclusion in the final study group were 26 patients who had both symmetric PET and symmetric brain MR examinations (judged by estimated symmetry of bilateral orbit and petrous bones); 24 of the patients had biopsy-proved supratentorial disease. The patients were 6–71 years old (mean, 34 years) and included 14 males and 12 females. Duration of signs and symptoms ranged from 1 month to 30 years; one patient had a seizure disorder.

None of the patients studied had a history of multiple brain lesions; the single patient with metastatic colon cancer had no cerebellar lesions. No patient had a clinical history of multiple infarctions, ethanol abuse, or multifocal encephalitis. Because many of the patients studied had a chronic seizure disorder, several of them were on long-term Dilantin therapy; however, cerebellar atrophy seen in these patients was not attributed to Dilantin therapy. Atrophy caused by Dilantin therapy would be diffuse [5]; it would not selectively affect one hemisphere of the cerebellum. Furthermore, such cerebellar atrophy would not occur in the hemisphere contralateral to the supratentorial lesion, as it does in patients with crossed cerebellar atrophy.

PET scans were obtained on an ECAT III-911 scanner (CTI, Knoxville, TN) with a full width at half-maximum resolution of approximately 8 mm. After IV administration of 10–12 mCi (370–444 MBq) of ^{18}F-fluorodeoxyglucose (FDG), the patients were placed in a dimly lit room with minimal background noise. Their eyes were not patched nor were their ears plugged during the 30-min interval allowed for uptake of FDG prior to scanning. Twelve to 15 axial images of the brain were acquired with a 6-mm slice separation.

MR studies were performed on a 1.5-T (Signa, General Electric, Milwaukee, WI) superconducting magnet and included routine axial T1-weighted (600–800/20/1 [TR/TE/number of excitations]) and T2-weighted (2500–3000/20,70/1) image sequences with 5-mm slices, interslice gap of 2 mm, 20-cm field of view, and 256 × 192 matrix. Coronal T1-weighted (600–800/20/1) images were also obtained in several patients.

A detailed clinical history as well as a biopsy-proved pathologic diagnosis (excluding two patients) were obtained for each patient. PET and MR images were examined. PET criteria for crossed cerebellar diaschisis include hypometabolism of one cerebellar hemisphere (signal intensity of the affected cerebellar hemisphere lower than that of the other hemisphere) with contralateral supratentorial lesions. Under normal circumstances the metabolism of the cerebellum should be very symmetric. MR signal intensity and morphologic change of the affected cerebellar hemisphere were carefully evaluated. MR criteria for crossed cerebellar atrophy include (1) prominent cortical sulci with parenchymal volume loss of the cerebellum, which is asymmetric (small) when compared with the normal appearance of the contralateral side, and (2) contralateral supratentorial abnormalities. For each patient, MR characteristics of the cerebellum were correlated with supratentorial diseases and clinical symptoms and signs.

Quantitative evaluation of the cerebellum was not done for two reasons. First, the MR studies were obtained by using rather thick slices with a gap, thus making volume calculation quite difficult. Because this was a retrospective study, new MR sequences could not be carried out to acquire necessary data. Second, even if volume differences between cerebellar hemispheres had been calculated, it would have been unwise to draw general conclusions because of the small sample size. However, atrophic changes in the patients' cerebellar hemispheres were not too subtle to be observed (although they could not be measured) on very symmetric MR studies.

Results

Eighteen of the 26 patients in whom unilateral cerebellar hypometabolism was identified on PET scans had no discernible MR abnormality of the cerebellum. Of these patients with contralateral supratentorial lesions, 15 had hemispheric brain tumors larger than 3 cm in diameter; one had a temporal lobe ganglioglioma approximately 2 cm in diameter. Of the remaining two patients, one had a biopsy showing large neurons and one had a large middle cerebral infarct. Of the 18 patients, 10 had motor deficits; the remaining eight had seizure disorders. The age range of the 12 males and six females with normal MR findings was 8–72 years old (average, 42 years); the duration of clinical signs and symptoms ranged from 1 month to 30 years (average, 3.5 years).

Eight of the 26 patients had abnormal MR findings demonstrating crossed cerebellar atrophy. Four of these patients had abnormal high T2 signal in portions of the affected cerebellar hemisphere. These high T2 signals may represent volume averaging from CSF in the dilated cerebellar sulci. The other four patients had normal T2 signal. All eight of these patients with abnormal cerebellar MR results had marked contralateral supratentorial hemispheric atrophy. Seven of the eight patients had biopsy-proved pathologic diagnoses. Three patients had chronic encephalitis (Fig. 1), three had Rasmussen's encephalitis (Fig. 2), and one had neuronal dysplasia and neuronal gigantism (Fig. 3). All eight patients in this group had chronic intractable focal seizures. The age range of the three males and five females with crossed cerebellar atrophy was 6–21 years old (average age, 14 years). The duration of clinical signs and symptoms ranged from 6 to 15 years (average, 9.5 years).

Among the group of 18 patients with normal cerebellar MR findings, the predominant clinical symptoms were seizures (eight patients), motor-sensory deficit (six patients), and altered mental status (four patients). In contrast, all eight patients with abnormal cerebellar MR findings had seizures. None of the 26 patients in the study had obvious cerebellar signs. The motor-sensory deficit of the six patients with normal cerebellar MR findings correlates well with the mass effect and location of their brain tumors. Seizures in these patients are induced by tumors. Seizures in patients with atrophic cerebellar MR findings are induced by encephalitis.

Discussion

In 1914, von Monakow [6] reported the diaschisis phenomenon, a transient impairment of functional activity in an area remote from the site of a primary brain lesion. It was not until 1980 that Baron et al. [1] successfully imaged the phenome-

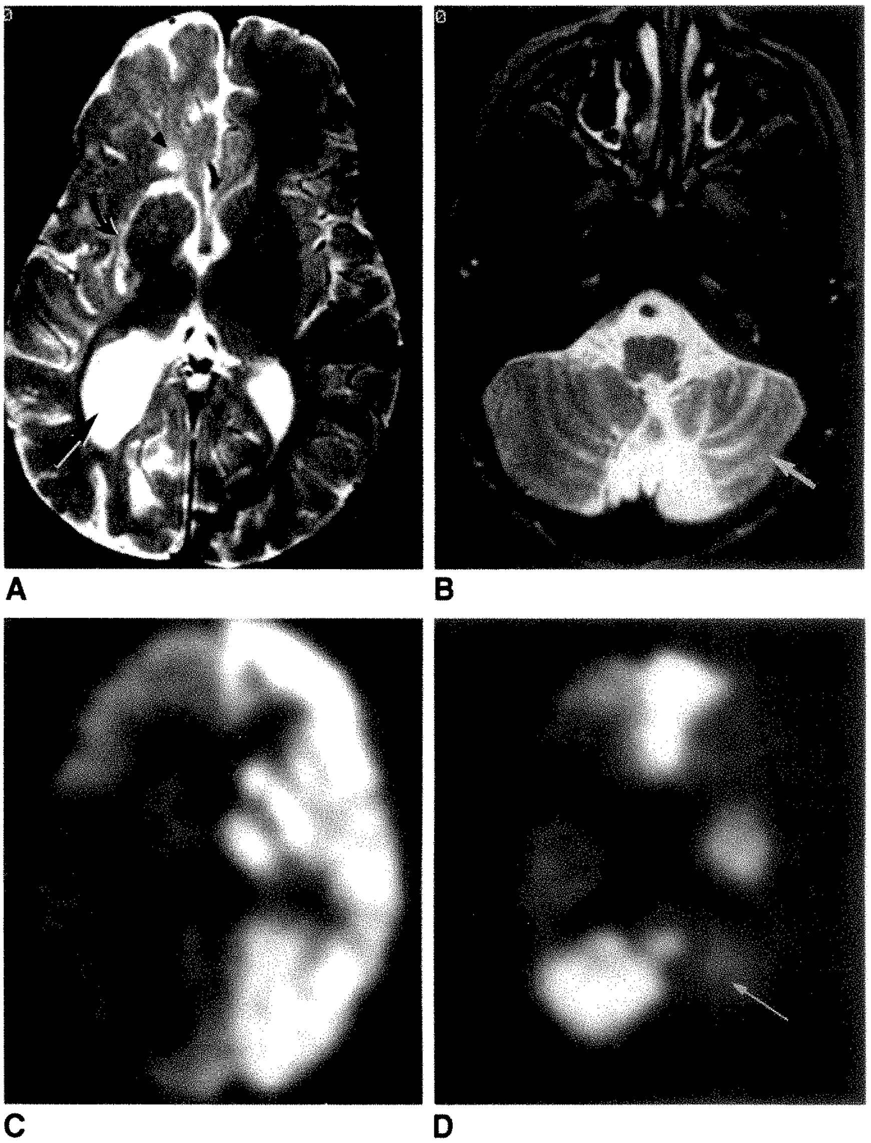

Fig. 1.—6-year-old boy with intractable focal seizure and left-sided body weakness since birth.

A, Axial T2-weighted (2500/70/1) MR image shows thinning of right supratentorial deep white matter, dilatation of right occipital horn (*straight arrow*), increased signal at right external capsule (*curved arrow*), and small focus (*arrowhead*) of increased signal at tip of right frontal horn.

B, Axial T2-weighted MR image of cerebellum shows left cerebellar hemisphere (*arrow*) is smaller than right hemisphere.

C, Axial ^{18}F-fluorodeoxyglucose (^{18}F-FDG) positron emission tomography (PET) image of supratentorial structures shows entire right hemisphere is hypometabolic compared with left.

D, Axial ^{18}F-FDG PET image of cerebellum shows left cerebellar hemisphere (*arrow*) is hypometabolic.

non with PET scans. Baron et al. described crossed cerebellar diaschisis as a parallel reduction in blood flow and oxygen uptake in the cerebellar hemisphere contralateral to the side of supratentorial ischemic infarction. Crossed cerebellar diaschisis has since been observed in a variety of brain diseases such as progressively enlarging tumors, arteriovenous malformation, and hemorrhage.

The principal mechanism of the transneuronal cerebellar metabolic depression seen in crossed cerebellar diaschisis is thought to be interruption of cerebrocerebellar pathways. This interruption is probably due to damage of the predominantly excitatory corticopontine-cerebellar projections [7], most of which originate from the frontal and parietal cortices. This hypothesis is supported by a study that found that the prevalence of crossed cerebellar diaschisis was highest in patients with infarction in the territory of the deep middle cerebral artery [2]. Although it may persist or even worsen [7], crossed cerebellar diaschisis often resolves with time. The mechanisms by which cerebellar metabolism returns to normal are unknown.

Morphologically evident atrophy has been reported in a few cases of crossed cerebellar diaschisis [8, 9]; this phenomenon was termed crossed cerebellar atrophy. Before the discovery of crossed cerebellar atrophy, clinicians believed that only fiber tracts were affected in crossed cerebellar diaschisis, while the neurons were still intact. This explained the lack of anatomic damage in the majority of reported cases of crossed cerebellar diaschisis. Observation of atrophy in patients with crossed cerebellar diaschisis suggests that this condition has characteristics that do not fit the classical definition of diaschisis (a reversible, functional phenomenon without structural change) [6]. Antegrade transneuronal degeneration has been

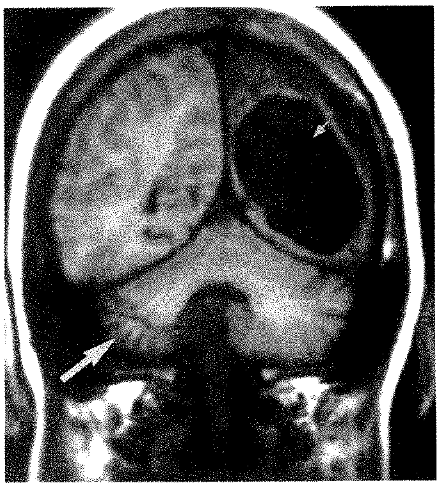

Fig. 2.—21-year-old woman with intractable partial complex seizures and right-sided weakness for 15 years. Coronal T1-weighted (600/20/1) MR image shows markedly dilated left occipital horn (*small arrow*) associated with hemiatrophy. Right cerebellar hemisphere is atrophic (*large arrow*).

suggested as a possible cause of morphologic change associated with crossed cerebellar diaschisis [8].

Eight of our patients had MR evidence of crossed cerebellar atrophy. Seven of those eight had atrophy of large portions of the contralateral supratentorial hemisphere; one had absence of a caudate nucleus. All eight had long histories of intractable focal seizures, most with onset at birth or in childhood. From our observations, atrophy is more prevalent in patients with crossed cerebellar diaschisis than was previously supposed. This is probably due to improved detection through the use of MR imaging techniques to delineate the posterior fossa. CT images of this region are obscured by beam-hardening artifact.

In all 26 of our patients, the clinical symptoms and signs were related to the supratentorial diseases; there was no obvious clinical evidence of cerebellar signs. The cerebellar hypometabolism seen in crossed cerebellar diaschisis appeared to correlate poorly with cerebellar dysfunction. Hemiparesis has been reported in some patients with crossed cerebellar diaschisis [2], and was seen in eight of our patients. Motor deficit in these patients appears to be the result of supratentorial diseases, and not induced directly by crossed cerebellar diaschisis.

Our study revealed distinct differences between patients with normal MR scans and those with evidence of crossed cerebellar atrophy: patients without atrophy averaged 42 years old with 3.5 years of symptoms; patients with atrophy averaged 14 years old with 9.5 years of symptoms. Patients without atrophy generally had contralateral brain tumors (generally larger than 3 cm in diameter); all eight patients with atrophy had significant contralateral atrophy of supratentorial

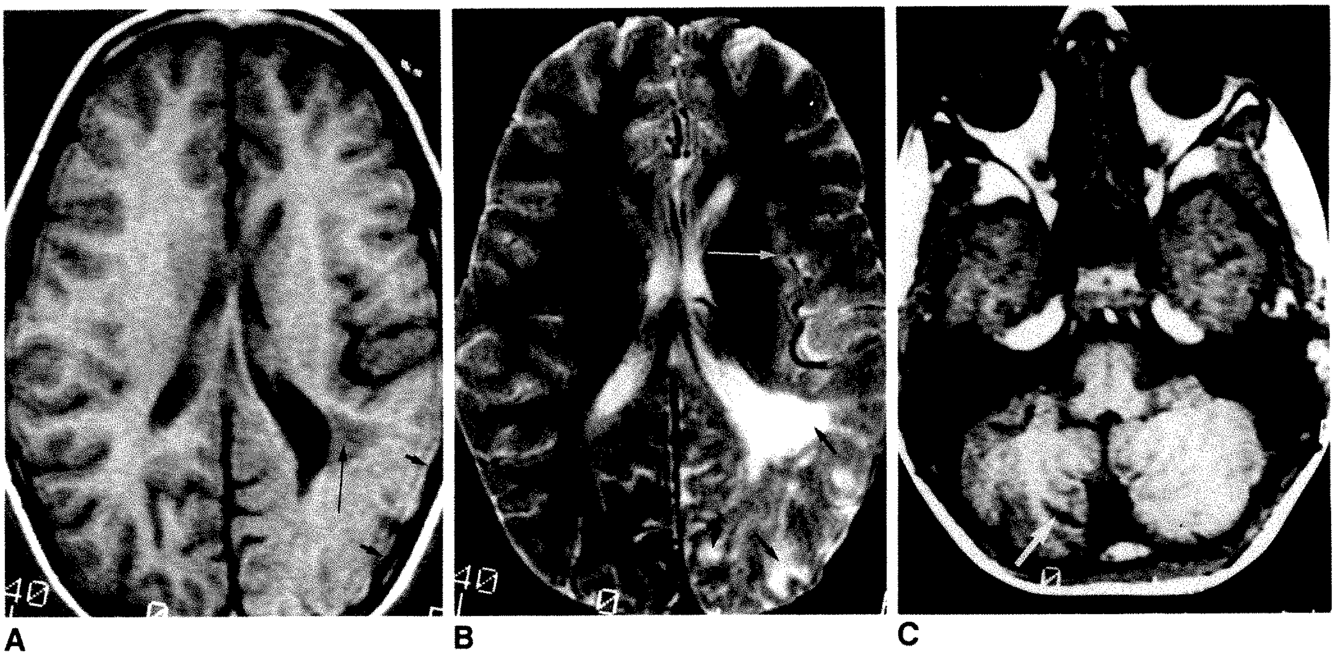

Fig. 3.—9-year-old boy with intractable complex partial seizures for 8 years.

A, Axial T1-weighted (600/20/1) MR image shows atrophy of left parietal lobe with dilatation of left trigone, and periventricular low-signal area (*long arrow*). Cortical gyri of left parietal lobe are very smooth (*short arrows*), compatible with pachygyria.

B, Axial T2-weighted (2500/70/1) MR image at same level as *A* shows diffuse abnormal high signals in left parietal lobe (*black arrows*). Signal of left insular cortex is also increasing (*white arrow*).

C, Axial T1-weighted MR image of cerebellum shows mild atrophy of right hemisphere (*arrow*).

brain and intractable seizures. This study suggests that crossed cerebellar atrophy may often be associated with long-term disease such as hemispheric atrophy with seizures. However, sequential MR studies over the duration of symptoms of our patients with crossed cerebellar atrophy are not available; therefore, we cannot draw concrete conclusions. This MR experience also suggests that crossed cerebellar diaschisis usually occurs in conjunction with large supratentorial diseases that interrupt many corticopontine-cerebellar tract fibers.

In summary, crossed cerebellar atrophy in patients with crossed cerebellar diaschisis is more prevalent than previously reported. Cerebellar hypometabolism in patients with crossed cerebellar diaschisis and crossed cerebellar atrophy correlated poorly with clinical signs and symptoms. Patients with crossed cerebellar atrophy commonly have marked supratentorial hemispheric atrophy. Detection of crossed cerebellar atrophy is greatly facilitated by use of modern MR techniques.

REFERENCES

1. Baron JC, Bousser MG, Comar D, Castaigne P. "Crossed cerebellar diaschisis" in human supratentorial infarction (abstr). *Ann Neurol* **1980**;8:128
2. Pantano P, Lenzi GL, Guidetti B, et al. Crossed cerebellar diaschisis in patient with cerebral ischemia assessed by SPECT and ^{123}I-HIPDM. *Eur Neurol* **1987**;27:142–148
3. Lenzi GL, Frackowiak RSJ, Jones T. Cerebral oxygen metabolism and blood flow in human cerebral ischemic infarction. *J Cereb Blood Flow Metab* **1982**;2:321–335
4. Patronas NJ, Di Chiro G, Smith BH, et al. Depressed cerebellar glucose metabolism in supratentorial tumors. *Brain Res* **1984**;291:93–101
5. Baier WK, Beck U, Hirsch W. CT findings following diphenylhydantoin intoxication. *Pediatr Radiol* **1985**;15(4):220–221
6. Von Monakow C. *Die Lokalisation im Grosshirn und der Abbau der Funktion durch Kortikale Herde.* Wiesbaden, Germany: Bergmann, **1914**
7. Feeney DM, Baron J-C. Diaschisis. *Stroke* **1986**;17:817–830
8. Chung HD. Retrograde crossed cerebellar atrophy. *Brain* **1985**;108:881–889
9. Baudrimont M, Gray F, Meininger V, Escourolle R, Castaigne P. Atrophie cérébelleuse croisée après lésion hémisphérique survenue à l'âge adulte. *Rev Neurol* (Paris) **1983**;139:485–495

Videotape Review

MRI of Brain Tumors, parts 1 and 2. By Murray A. Solomon. (Part of Murray Solomon's Magnetic Resonance Video Review.) Burlingame, CA: Magnetic Resonance Video Review, MRI Learning Center, (408) 925-8328, 1991. Single tape, $125; both tapes, $250; series of 6 tapes, $545 (VHS videotape)

For his series of videotapes on MR imaging, Murray Solomon has now compiled a two-videotape session on brain tumors. The viewing time for each tape is about 2 hr. The sessions are essentially videotaped slide lectures; viewers are treated to only brief glimpses of Dr. Solomon as he announces the beginnings and endings of the various segments.

These tapes cover a large territory. The lecture begins with an epidemiologic review of intracranial tumors and goes on to cover the MR appearance of various types of supra- and infratentorial gliomas, ependymomas, intracranial cysts, sellar and parasellar neoplasms, pineal tumors, abnormalities of the cerebellopontine angle, and numerous less common neoplastic diseases. The presentations are clear and simple and are at a level suitable for anyone with a minimal acquaintance with neuroanatomy and MR imaging.

The tapes have several good qualities: The lecturer pursues a logical plan with considerable consistency, a wide variety of instructive cases are demonstrated, and all statements containing facts and figures are emphasized by comprehensive word slides. However, from a generic point of view, all taped lectures suffer from an inherent disadvantage: The viewer is forced to accept and absorb the material, however complex, at a rate determined by the speaker. A moment of distraction, and the viewer must perform awkward operations to retrieve the spot where the lecturer was lost. In addition, retention of vast amounts of material, as presented on these tapes, is difficult. An ever so brief printed outline would be of great help, particularly to any novice in the field. Such handouts, easy to compile and cheap to print, ought to be provided with all videotape lectures.

In a more specific vein, these particular tapes have a few blemishes. The images shown are created simply by pointing a video camera at sequences of projected slide images. This basic technique does not provide the highest image quality. Better—although more cumbersome—methods are available in this day and age of high-resolution image transfer. Several tables are simply shot directly from articles and book pages, without editing, and the numbers are recited, hardly state-of-the-art educational technology. I happen to be allergic to spelling errors, and I experienced some histamine rushes while reading the word slides.

By and large, however, the tapes are a substantial and successful instructional effort. They are primarily intended for practicing radiologists who are beginning to do MR imaging, but the material will also be useful to residents and fellows becoming involved in neuroimaging.

Folke Brahme
Veterans Affairs Medical Center
San Diego, CA 92161

MR Demonstration of Reversible Cerebral Lesions in a Child with Hypertensive Encephalopathy Caused by Wilms' Tumor

Dean J. Shanley[1] and Cheryl L. Sisler

We report a case of reversible MR abnormalities involving the occipital lobe cortex and subcortical white matter bilaterally in a patient with severe systemic arterial hypertension associated with a Wilms' tumor. Similar findings have been described in patients with the preeclampsia-eclampsia syndrome and hypertensive encephalopathy [1-5]. Wilms-related hypertension has been attributed to elevated renin activity either due to tumor production of renin or in response to renovascular insufficiency caused by the tumor mass. Although arterial hypertension occurs in as many as 50% of cases of Wilms' tumor, to our knowledge the MR demonstration of cerebral abnormalities caused by hypertensive encephalopathy in these patients has not been described.

Case Report

A 5-year-old girl had intermittent abdominal discomfort and constipation. Physical examination showed a large right-sided abdominal mass and blood pressure of around 160/120 mm Hg. CT showed a 12 × 17 cm mass in the right kidney, and a presumptive diagnosis of Wilms' tumor with associated hypertension was made. Before antihypertensive therapy was started, the patient had several tonic-clonic seizures, which were followed by periods of deep somnolence accompanied by a transient positive Babinski's sign on the left. No persistent neurologic deficits were detected. Postictal funduscopic examination showed no evidence of papilledema, and visual fields were normal. CT of the head (Fig. 1A) showed areas of decreased density in the occipital lobes bilaterally. The brain appeared atrophic, which was attributed to poor nutritional intake and recurrent episodes of vomiting during the past several months resulting in cerebral shrinkage. MR images (Figs. 1B and 1C) obtained the next day showed areas of increased signal in the cortex and subcortical white matter of the occipital lobes bilaterally. No pathologic enhancement was detected after IV administration of gadopentetate dimeglumine.

Before surgical resection of the renal mass, the hypertension was controlled with oral medication. The pathologic diagnosis was Wilms' tumor, stage II, with a favorable histology. Antihypertensive therapy was discontinued after surgery, and the patient has remained normotensive. No further seizures have occurred. One-month follow-up MR images of the head showed complete resolution of the original abnormalities.

Discussion

A variety of CNS lesions have been described in patients with toxemia of pregnancy and hypertensive encephalopathy [1-5]. Reversible white matter changes are commonly observed in patients with toxemia of pregnancy and hypertensive encephalopathy and have been attributed to transient dysfunction of cerebral autoregulation and alteration of the normal blood-brain barrier [1, 2, 5]. The precise cause of these abnormalities is uncertain. Multiple factors, including hypoxic ischemia, vasculopathy, perivascular microhemorrhage, perivascular microinfarcts, and intracerebral hemorrhage, have been implicated on the basis of autopsy findings [6].

Severe hypertensive episodes may cause an exaggerated autoregulatory response by the cerebral vessels resulting in

---

Received September 16, 1991; accepted after revision October 21, 1991.

[1] Both authors: Department of Radiology, Tripler Army Medical Center, Honolulu, HI 96859. Address reprint requests to D. J. Shanley.

AJR 158:1161-1162, May 1992 0361-803X/92/1585-1161 © American Roentgen Ray Society

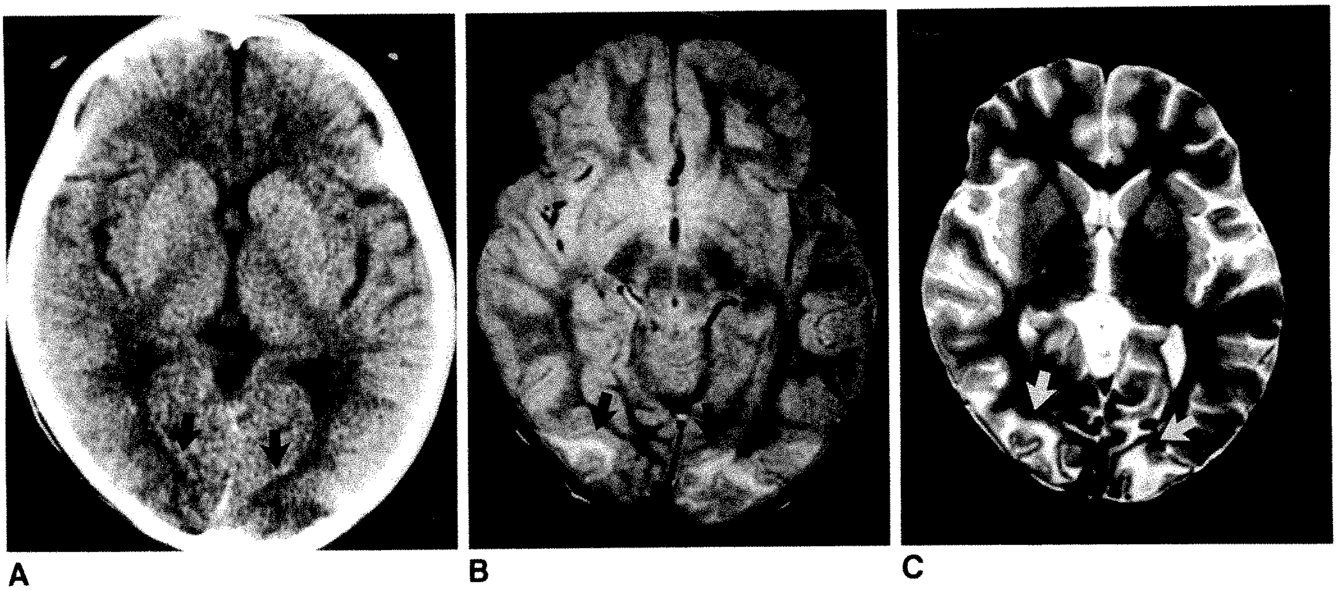

Fig. 1.—5-year-old girl with arterial hypertension associated with Wilms' tumor.

A, Unenhanced CT scan shows decreased attenuation in occipital lobes (*arrows*) bilaterally.

B and *C*, Proton-density-weighted, 2500/30 (TR/TE) (*B*), and T2-weighted, 2500/90 (*C*), MR images show increased signal (*arrows*) in both gray and white matter of occipital lobes. MR images obtained 1 month later showed complete resolution of original abnormalities.

diffuse vasoconstriction [3, 5]. The vasoconstriction leads to cerebral ischemia and cytotoxic edema, manifested on MR images as areas of increased signal involving both white and gray matter. Recent reports [7, 8] describing angiographic findings in patients with eclampsia and reversible cerebral abnormalities on MR provided further evidence in support of a vasoconstrictive cause. Dysfunction of the autoregulatory mechanism, in part due to the vasoconstriction-induced ischemia and persistent hypertension, leads to an alteration in the blood-brain barrier and extravasation of fluid into the surrounding brain parenchyma. This pattern of vasogenic edema is also seen on MR images as areas of increased signal and is classically confined to the white matter. Thus, there is a mechanism for the development of cytotoxic edema (vasoconstriction and ischemia) and vasogenic edema (disruption of the blood-brain barrier) in the setting of severe hypertensive episodes. Separation of these two patterns of edema may not always be possible with MR, and it is likely that both mechanisms are responsible for the signal abnormalities seen in patients with eclampsia and hypertensive encephalopathy.

The striking similarities in the pattern, distribution, and reversibility of MR abnormalities in our case of Wilms-related hypertension and in patients with toxemia of pregnancy suggest a similar CNS response to severe systemic hypertension. The presence of vasogenic and cytotoxic patterns of edema involving the occipital lobes is a common finding in patients with eclampsia [1, 2, 5]. Preferential involvement of the posterior cerebral circulation is not readily explainable in our case or in the previously reported cases of CNS abnormalities in patients with eclampsia [5]. Localization of the MR abnormalities in our patient, involving mostly the white matter of the occipital lobes and a lesser degree of cortical involvement, supports the concept of a dual mechanism in the development of increased brain water content; alterations in the blood-brain barrier contributed to the development of vasogenic edema, and vasoconstriction-induced ischemia resulted in cytotoxic edema. Both patterns of edema were reversible in our case, similar to previously reported cases of reversible brain lesions in eclampsia and hypertensive encephalopathy.

REFERENCES

1. Schwaighofer BW, Hesselink JR, Healy ME. MR demonstration of reversible brain abnormalities in eclampsia. *J Comput Assist Tomogr* **1989**;13:310–312
2. Raroque HG, Orrison WW, Rosenberg GA. Neurologic involvement in toxemia of pregnancy: reversible MRI lesions. *Neurology* **1990**;40:167–169
3. Hauser RA, Lacey DM, Knight MR. Hypertensive encephalopathy: magnetic resonance imaging demonstration of reversible cortical and white matter lesions. *Arch Neurol* **1988**;45:1078–1083
4. Gibby WA, Stecker MM, Goldberg HI, et al. Reversal of white matter edema in hypertensive encephalopathy. *AJNR* **1989**;10:S78
5. Saunders TG, Clayman DA, Sanchez-Ramos L, Vines FS, Russo L. Brain in eclampsia: MR imaging with clinical correlation. *Radiology* **1991**;180:475–478
6. Richards A, Graham D, Bullock R. Clinicopathological study of neurological complications due to hypertensive disorders of pregnancy. *J Neurol Neurosurg Psychiatry* **1988**;51:416–421
7. Will AD, Lewis KL, Hinshaw DB, et al. Cerebral vasoconstriction in toxemia. *Neurology* **1987**;37:1555–1557
8. Lewis LK, Hinshaw DB, Will AD, Hasso AN, Thompson JR. CT and angiographic correlation of severe neurological disease in toxemia of pregnancy. *Neuroradiology* **1988**;30:59–64

Case Report

Intracranial Metastatic Adenoid Cystic Carcinoma: Presumed Hematogenous Spread from a Primary Tumor in the Parotid Gland

Nicholas D. Gelber,[1] Ronald L. Ragland,[1] John R. Knorr,[1] Thomas W. Smith,[2] and Bernard B. Stone[3]

Intracranial extension of adenoid cystic carcinomas of the head and neck is well recognized, and typically such spread is by way of contiguous perineural invasion [1-3]. Hematogenous intracranial extension, although reported, is much less common. We report a case of hematogenous metastasis of parotid adenocystic carcinoma to the inner table of the calvaria, epidural compartment, and brain parenchyma.

Case Report

A 69-year-old man presented with ataxia of several days' duration, slurred speech, and some dizziness. Six to eight months earlier, he had undergone resection of a right parotid mass. Subsequent pathologic examination showed an adenocystic carcinoma of the parotid gland, and the patient underwent radiotherapy. No tumor spread was identified at this time.

On admission, the man was alert and his vital signs were normal. The patient's affect was blunted and his mood was depressed. His gait was slightly ataxic. No other focal neurologic signs were detected.

A CT scan showed an irregular area of focal calvarial destruction in the left frontal region. This was associated with a lobulated extraaxial mass lesion, with multiple peripheral areas of ring enhancement. Underlying this area, a focal area of vasogenic type of white matter edema was seen in the left frontal lobe with mass effect and compression of the ipsilateral frontal horn (Figs. 1A-1C).

At surgery, an infiltrating lobulated irregular soft-tissue mass was found involving the left frontal bone, the adjacent dura, and the brain parenchyma of the superficial portion of the left frontal lobe. The lesion was incompletely excised.

Pathologic examination showed tumor tissue consisting of lumen-like structures, pseudoglandular spaces, pseudocysts, and necrosis (Fig. 1D). This tumor and the original pathologic specimen of the parotid tumor had virtually identical appearances.

No evidence of lung, bone, or liver metastases was found at this time.

Discussion

Adenoid cystic carcinoma (cylindroma, adenocystic carcinoma) is a reasonably common malignant tumor of the large and small salivary glands, constituting approximately 8% of all salivary gland tumors and approximately 22% of malignant salivary gland tumors [4]. While most salivary gland lesions are commonly found in the parotid and submandibular glands, these tumors are relatively more common in the sublingual and accessory salivary glands [4].

The overall frequency of intracranial invasion of adenoid cystic carcinoma has been reported to be between 4% and 22%. However, the vast majority of these tumors spread either directly or via perineural spread [1-3]. True hematogenous metastases to the CNS are rare, even though hematogenous metastases to liver, lung, and bone are reasonably common late in the course of this disease [3].

Extraaxial intracranial metastatic adenocystic carcinoma mimicking meningioma has been reported [2, 3], and cylin-

---

Received October 23, 1991; accepted after revision December 4, 1991.

[1] Department of Radiology, University of Massachusetts Medical Center, 55 Lake Ave. N., Worcester, MA 01655. Address reprint requests to N. D. Gelber.
[2] Department of Neuropathology, University of Massachusetts Medical Center, Worcester, MA 01655.
[3] Department of Neurosurgery, University of Massachusetts Medical Center, Worcester, MA 01655.

AJR 158:1163-1164, May 1992 0361-803X/92/1585-1163 © American Roentgen Ray Society

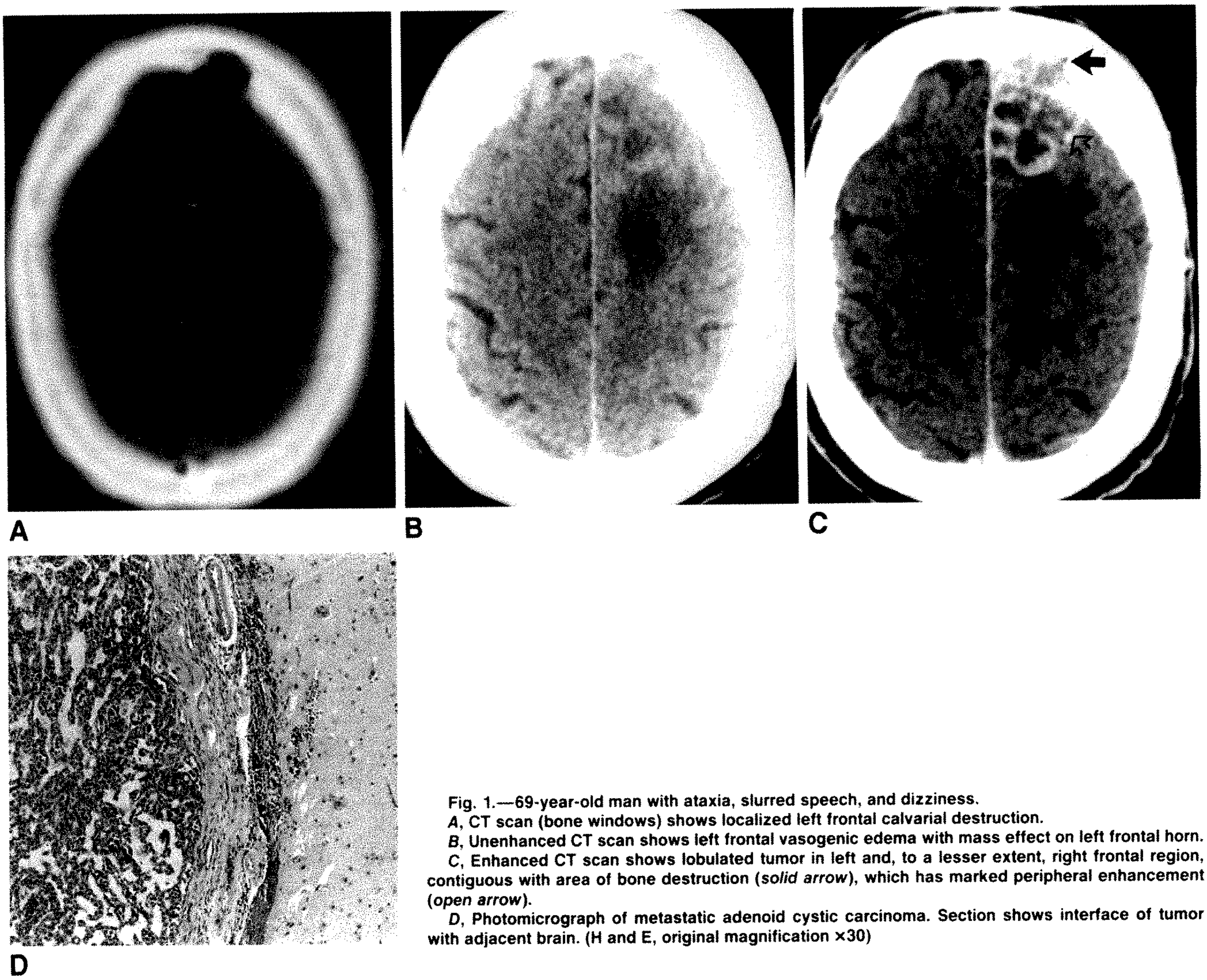

Fig. 1.—69-year-old man with ataxia, slurred speech, and dizziness.

***A*, CT scan (bone windows) shows localized left frontal calvarial destruction.**

***B*, Unenhanced CT scan shows left frontal vasogenic edema with mass effect on left frontal horn.**

***C*, Enhanced CT scan shows lobulated tumor in left and, to a lesser extent, right frontal region, contiguous with area of bone destruction (*solid arrow*), which has marked peripheral enhancement (*open arrow*).**

***D*, Photomicrograph of metastatic adenoid cystic carcinoma. Section shows interface of tumor with adjacent brain. (H and E, original magnification ×30)**

droma in the gasserian ganglion region has even been postulated to arise from auditory system mucosal cells. These reported lesions were, however, basal and therefore were consistent with the perineural invasion so typical of these tumors. The lesion in our case, while partially extraaxial, is in an anatomic position inconsistent with retrograde perineural spread from the primary site in the parotid gland. Furthermore, there was no evidence of contiguous spread of tumor at craniotomy. Koller et al. [5] reported a hematogenous brain metastasis from an adenoid cystic carcinoma of the breast, and Hara et al. [6] reported a hematogenous frontal lobe metastasis of adenoid cystic carcinoma, but no primary tumor was identified. Since adenoid cystic carcinoma can arise in other organs such as bronchial mucus glands, the prostate, lacrimal glands, Bartholin's glands, and the uterine cervix [5], the metastasis found by Hara et al. [6] may not have originated in a salivary gland. Reports of spread of adenoid cystic carcinoma to the ocular choroid plexus [7] and to the spinal cord [8] also have appeared.

In summary, our case demonstrates a histologically confirmed hematogenous metastasis of salivary gland adenoid cystic carcinoma to the meninges and brain, a particularly unusual manifestation of this tumor.

REFERENCES

1. Parker GD, Harnsberger HR. Clinical and radiologic issues in perineural tumor spread of malignant diseae of the extracranial head and neck. *RadioGraphics* **1991**;11:383–399
2. Piepmeier JM, Virapongse C, Kier EL, Kim J, Greenberg A. Intracranial adenocystic carcinoma presenting as a primary brain tumor. *Neurosurgery* **1983**;12:348–352
3. Lee Y, Castillo M, Nauert C. Intracranial perineural metastasis of adenoid cystic carcinoma of head and neck. *J Comput Tomogr* **1985**;9:219–223
4. Fitzpatrick PJ, Theriault C. Malignant salivary gland tumors. *Int J Radiat Oncol Biol Phys* **1986**;12:1743–1747
5. Koller M, Ram Z, Findler G, Lipshitz M. Brain metastasis: a rare manifestation of adenoid cystic carcinoma of the breast. *Surg Neurol* **1986**;26:470–472
6. Hara H, Tanaka Y, Tsuji T, Momose G, Kobayashi S. Intracranial adenoid cystic carcinoma. A case report. *Acta Neurochir* (Wien) **1983**;69:291–295
7. Gutmann SM, Weiss JS, Albert DM. Choroidal metastasis of adenoid cystic carcinoma of the salivary gland. *Br J Ophthalmol* **1986**;70:100–103
8. Riela AR, Meyer D, McCool JA, Pikula L Jr. Metastatic adenoid cystic carcinoma of the major salivary glands presenting as a spinal cord tumor. *Surg Neurol* **1983**;19:365–368

The Types of Articles Published in the *AJR*

Robert N. Berk[1]

The *AJR* publishes eight different kinds of articles, each one intended to serve a distinct purpose. These include major articles, reviews, pictorial essays, perspectives, opinions, case reports, technical notes, and computer pages. Each variety carries a distinctive type of message, and the manuscripts are constructed differently [1]. They are each judged by different criteria in the peer-review process.

Prudent authors make a clear decision about which type of manuscript they intend to write before beginning. Otherwise, the resulting paper is invariably bloated: it will be too long and have too many illustrations. The focus of such a paper will be inconsistent, the purpose blurred, and the message obscure. Manuscripts that are combinations of the various types are more work for authors to compose than is otherwise necessary, and the entire effort is wasted because the manuscripts are usually rejected for publication.

Following is a description of the kinds of articles published in the *AJR*. Guidelines to authors for constructing the different types of manuscripts are published monthly in the Journal [2]. Understanding the differences and writing manuscripts accordingly are certain to help authors produce trim manuscripts with clear messages. Attention to these factors will spare authors much time and frustration.

Major Paper

This is the most important type of article, because it provides new information based on original research. If the information is accurate and important and the conclusions are substantiated by the data provided, the paper serves to advance radiology. The manuscript should be divided into introduction, subjects and methods, results, and discussion.

Review Article

Reviews provide a balanced, scholarly analysis of recent developments concerning a specific topic as reported in the literature. No new information is included, and there are no opinions or descriptions of personal experiences. Reviews are not encyclopedic like a chapter in a textbook, rather they involve only the highlights.

Pictorial Essay

These are teaching exercises, with the message in the figures and their legends. The text is limited to four pages, with as many as 30 figure parts, but no new information is included. The value of the paper depends on the quality of the illustrations.

Perspective

These are articles that describe the authors' personal experience with a specific subject. The text concerns what the authors have learned in their practice or includes "how I do it" type of information. There is no original information and no analysis of the literature. Personal bias is expected. The text is longer and there are fewer figures than in a pictorial essay.

Opinion (Commentary)

Opinions are short articles (four pages or fewer) giving the author's personal judgment on a controversial topic. At most, only a few illustrations are included, and review of the litera-

---

[1] Editor-in-Chief, *American Journal of Roentgenology*, 2223 Avenida de la Playa, Suite 103, La Jolla, CA 92037. Address reprint requests to R. N. Berk.

AJR 158:1165–1166, May 1992 0361–803X/92/1585–1165 © American Roentgen Ray Society

ture is limited to those articles that serve to justify the author's opinion.

Case Report

These are descriptions of three or fewer cases. The message should transcend the individual patient described. The maximum length of the text is five pages, including the references, and there are no more than four figure parts and eight references. Only one case should be described in detail. Extensive review of the literature is inappropriate; emphasis is on the case and not on the disease.

Technical Note

These are brief descriptions of a specific technique or procedure, modification of a technique, or new equipment of interest to radiologists. There should not be more than two figure parts, and the text should not be longer than five pages.

Computers in Radiology

These articles deal with the practical application of computers in radiology. They usually are short (maximum eight pages), and proof of the value of the application is not required. Original information is not essential. When a paper involves a study designed to test a computer application, it is considered a major article.

REFERENCES

1. Berk RN. Preparation of manuscripts for radiology journals: advice to first-time authors. *AJR* **1991**;158:203–208
2. Whalen E. An author's guide to the guidelines. *AJR* **1989**;152:195–198

New Format for Abstracts

Beginning in Fall 1992, the *AJR* will publish abstracts of articles in a different format, much like the ones recently adopted by the *New England Journal of Medicine* and the *Journal of the American Medical Association*. The purpose of the new design is to have abstracts present the essential elements of articles more clearly and concisely. The contents, organization, and length of the abstracts will be the same as before; however, rather than being all one paragraph except for the conclusion, abstracts will now be divided into four paragraphs, each with a title: objective, subjects (or materials) and methods, results, and conclusion.

The *AJR* Guidelines for Authors, which appears at the front of every issue of the Journal, has been revised to help you write abstracts in this new format. Authors should familiarize themselves with these guidelines and incorporate them into all manuscripts submitted for publication.

Robert N. Berk
Editor-in-Chief

Letters

Radiology in East Africa

As members of the East African Medical Assistance Foundation, a Minneapolis-based organization that since 1987 has been raising money to improve radiologic care in Tanzania, we read with great interest the letter [1] by Mark Baker and Frederick Porter on their experience at Muhimbili Medical Center in Dar es Salaam, Tanzania. We applaud their efforts at raising the consciousness of the radiologic community regarding the complex issues involved in radiologic care in the third world. Although we agree with many of their conclusions, our experience indicates slightly different needs for donated equipment than their letter indicates. Our conclusions are based on the experience of two of our members, Helmut Diefenthal and Kevin Gustafson. Dr. Diefenthal is a retired University of Minnesota chest radiologist who has now spent 9 years in Tanzania, including 5 years as a radiologist at Kilimanjaro Christian Medical Center in Moshi, Tanzania, where he performs a full range of radiologic studies. One of our board members, Kevin Gustafson, a radiologist from Minneapolis, visited Dr. Diefenthal in Tanzania in November 1990 and worked with him for 2 weeks.

We have found that donating used, older equipment is generally a waste of time and effort. Even if the equipment arrives safely, installation is a logistic nightmare. If by chance it is installed in working condition, the first time a problem develops with the equipment is the last time the equipment is used. Service is almost nonexistent, and parts for most used radiologic equipment are unobtainable. East Africa is littered with well-intentioned white elephants.

The first thing that all of Africa needs is good basic radiographic equipment that is new, dependable, affordable, and repairable. Thus far, the radiographic equipment companies have entirely ignored this need, falsely concluding that it would not be profitable. Tanzania alone has 23 million people, and as Drs. Baker and Porter correctly pointed out, the referral hospitals and 25 regional hospitals are well organized. In addition, Tanzania has many other smaller hospitals. Each of the facilities could use a basic, dependable radiographic unit, which, in our estimation, should cost approximately $30,000–$40,000. The World Health Organization has endorsed a radiographic system that supposedly fulfills this need, but the price of the system is approximately $60,000, which is too expensive for Africa.

The second thing that is badly needed is an appropriately educated group of health care practitioners that can serve the radiologic needs of the country. Dr. Diefenthal and his associate, A. P. S. Lyimo, have been requested by the Government of Tanzania to organize a school to train assistant medical officers in radiology. Although not M.D.s, assistant medical officers function as physicians, and students will have had 5 years of formal medical training and a number of years of practical experience before they start the radiology program. They will receive 2 years of training at Kilimanjaro Christian Medical Center in interpreting radiographs and performing radiologic procedures, including sonography.

Dr. Diefenthal and the East African Medical Assistance Foundation have found that sonography is in many ways the imaging technique of choice in East Africa. It is a way of doing cross-sectional imaging that is relatively dependable, widely applicable to many clinical needs, and portable. Two other tremendous advantages are that it does not need to be installed and does not require film. Again, what is needed is an inexpensive and rugged unit in the $20,000 to $30,000 range. Several companies have machines that may fill this bill, if adequate service is available. The potential market in the developing world is large.

Currently, Dr. Diefenthal performs 30 to 35 sonographic examinations per day at Kilimanjaro Christian Medical Center and is training physicians and assistant medical officers to use sonography. The Center hosted an international conference, Ultrasound in Africa, in October and November 1991.

We agree with the comments of Drs. Baker and Porter on the need for basic radiographic accessory items, and we encourage readers to donate these through the system that has been arranged at Duke University. It has been our sad experience, however, that despite being extremely well intended, the donation of older, discarded equipment from the United States generally ends up unused in a developing country, for the reasons stated. Any further questions about our organization can be addressed to John Knoedler (612-347-2008) or Kevin Gustafson (612-924-5170).

William M. Thompson
University of Minnesota Hospital and Clinic
Minneapolis, MN 55455
Kevin D. Gustafson
Minneapolis, MN
Helmut Diefenthal
Kilimanjaro Christian Medical Center
Moshi, Tanzania
John P. Knoedler
Hennepin County Medical Center
Minneapolis, MN

REFERENCE

1. Baker ME, Porter FR. A report on radiology at Muhimbili Medical Center, Dar es Salaam, Tanzania (letter). *AJR* **1992**;157:195

Reply

We thank Drs. Thompson, Diefenthal, Gustafson, and Knoedler for their helpful and insightful letter, and for their interest in the health care needs of Tanzania. We applaud their efforts in improving the radiologic care in that country and are quite pleased with what they have already accomplished.

In September 1991, we had the opportunity and pleasure of hosting in our department the new head of radiology at Muhimbili Medical Center, R. Kazema. We agree that most equipment donated to countries like Tanzania is wasted because of the lack of appropriate parts and service. But, certain equipment is not. In fact, most of the functioning equipment at Muhimbili is donated. The problem now is that it is so old that in many respects it is no longer serviceable.

As our colleagues from Minnesota have pointed out, the major problem with any equipment (used or new) in any country, and especially in a third-world country, is a lack of consistent and reliable service. Clearly, equipment should never be sent to a country where service for the specific brand of equipment is unavailable. Perhaps some of the problems Thompson et al. have encountered with donated equipment are related to this issue. Service has been available for much of the donated equipment at Muhimbili and, up to this point, has kept the equipment running. In our opinion, what is needed is a national/international coordinated effort focused on donated equipment. If a consortium were formed to coordinate an effort for donated equipment, then hospitals and clinics with older medical equipment could determine whether this equipment would be useful and where it would be most effective.

We agree with the Minneapolis group that the basic radiologic system endorsed by the World Health Organization and sonographic equipment would be extremely helpful means of providing essential radiologic care. Unfortunately, as Thompson et al. indicated, Tanzania, as well as many other countries, does not have the hard currency necessary for even one unit. Therefore, in lieu of new units, usable, serviceable, donated equipment seems to be the only alternative. The key to this process is to appropriately match the equipment with the region.

We also agree that an appropriately educated group of health care practitioners is necessary in a country such as Tanzania. Tanzania has few physicians and even fewer radiologists. Training assistant medical officers in radiology would provide an essential service and would relieve the already overworked radiologists of some of the burden of film interpretation.

Last, we are thankful for the letter from the Minneapolis group because it will help raise the consciousness of the international radiologic community. We are pleased with the group's efforts, commitment, and monetary and physical support. In fact, we too, will soon begin an exchange program of residents and staff members with the Muhimbili Medical Center. By this exchange, understanding, education, and—we hope—tangible change will occur. For further perspective on the problem of radiology in developing countries, we strongly recommend a recent overview [1] written by Dr. Fuchs from Zurich, Switzerland.

Mark E. Baker
Eric Porter
Duke University Medical Center
Durham, NC 27710
R. Kazema
Muhimbili Medical Center
Dar es Salaam, Tanzania

REFERENCE

1. Fuchs WA. Radiology in developing countries. *Invest Radiol* **1991**;10: 906–909

Bochdalek's Hernia: CT Findings

A 53-year-old woman had a follow-up chest radiograph 1 year after a right-sided mastectomy necessitated by breast cancer. The findings were equivocal but suggested metastatic disease of the lungs. CT showed a round lesion 2 × 2 cm at the base of the left lung. At lung parenchyma window settings, the abnormality looked like a metastatic tumor (Fig. 1A). At mediastinal window settings, it was clear that the mass was herniated retroperitoneal fat (−120 H) (Fig. 1B). Scans at lower levels showed a defect in the diaphragm through which retroperitoneal fat herniated (Fig. 1C).

Several potential routes exist for protrusion of fat or other abdominal contents through the diaphragm. The foramen of Bochdalek is a developmental defect in the diaphragm posteriorly produced by failure of the retroperitoneal canal membrane to fuse with the dorsal esophageal mesentery and the body wall. The foramen of Morgagni, on the other hand, is an anterior diaphragmatic defect of developmental origin resulting from incomplete attachment of the diaphragm to the sternum between the septum transversum and the right and left costal origins of the diaphragm [1].

Hernias through the foramen of Bochdalek are the most common diaphragmatic hernias in infants; they are uncommon in adults. About 90% of Bochdalek's hernias occur in the left hemidiaphragm because of the protective effect of liver on the right side. Small Bochdalek's hernias usually contain retroperitoneal fat, kidney, or spleen; larger ones contain jejunum, ileum, or colon. Morgagni's hernia is the least common diaphragmatic hernia. It occurs in the right hemidiaphragm in more than 90% of cases, because of the protective effect of pericardium on the left side. Small Morgagni's hernias contain omentum, usually with an extension of the peritoneal sac; larger ones contain liver, stomach, small intestine, or transverse colon [1, 2].

In adults, Bochdalek's and Morgagni's hernias are usually small and asymptomatic [1, 2]. In our case, demonstration of the defect in

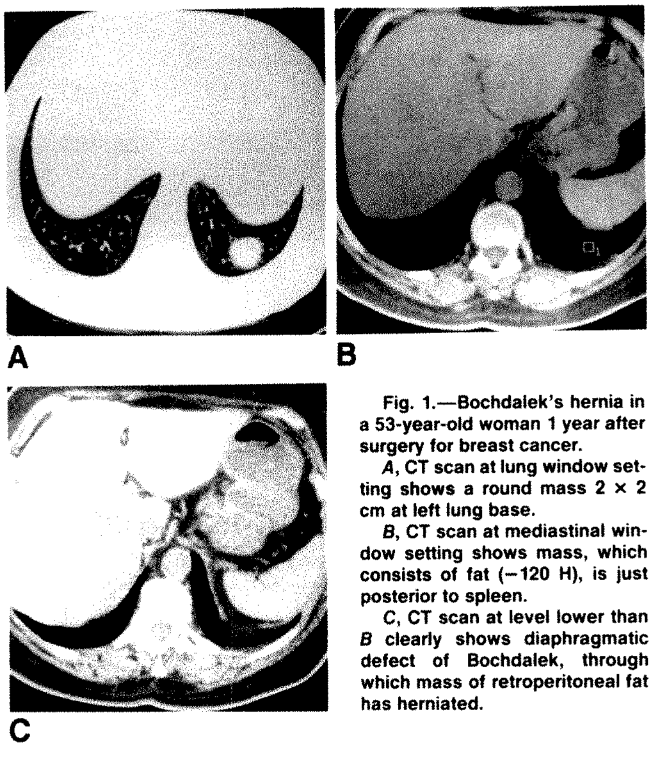

Fig. 1.—Bochdalek's hernia in a 53-year-old woman 1 year after surgery for breast cancer.

***A*, CT scan at lung window setting shows a round mass 2 × 2 cm at left lung base.**

***B*, CT scan at mediastinal window setting shows mass, which consists of fat (−120 H), is just posterior to spleen.**

***C*, CT scan at level lower than *B* clearly shows diaphragmatic defect of Bochdalek, through which mass of retroperitoneal fat has herniated.**

the left hemidiaphragm established the diagnosis of a Bochdalek's hernia.

Ziya Kumcuoglu
R. Nuri Sener
Hospital of Ege University
Bornova, Izmir, Turkey

REFERENCES

1. Gregson RHS. The mediastinum. In: Sutton D, ed. *A textbook of radiology and imaging*, 4th ed., vol. 1. Edinburgh: Churchill-Livingstone, **1987**: 368-391
2. Moss AA, Gamsu G, Genant HK. *Computed tomography of the body*. Philadelphia: Saunders, **1983**:397-398

Mammography and Malpractice

The letters by Hall, Potchen, and Edelstein [1] in the October 1991 issue of the *AJR* are reminiscent of the fable of the blind men and the elephant. Each man describes what he feels. What each describes is correct for what he feels, but none describes the animal in question.

Consider the following: (1) Screening mammography as currently propounded in the United States and the controlled trials to date are intended to reduce the mortality from breast cancer in the population. (2) The positive predictive value (PPV) is calculated as follows: PPV = number of true-positives (TP)/(number of TP + number of false-positives [FP]). (3) Expert mammographers operate along the same receiver-operating-characteristic curve, with only minor deviations [2]. (4) The annual rate of breast cancer in the United States is as follows [3]: ages 40–49 years, 158/100,000; ages 50–59, 244/100,000; and ages 60–69, 365/100,000. (5) If we assume that the TP rate for mammography is 85% and the FP rate is 1%, the PPVs for these ages will be as follows: ages 40–49, 134/1134 = 12%; ages 50–59, 207/1207 = 17%; and ages 60–69, 310/1310 = 24%. These PPVs can be changed only (1) at the expense of the TP rate or (2) if the mammographer indeed has a power of interpretation beyond that of panels of expert mammographers already tested on screening mammograms to date.

It is obvious that diagnostic populations, which have been distilled to a relatively high concentration of cancer cases either by self-selection or previous screening, will have a higher PPV. The concentration of cancers in these populations is usually more than 2–3%. If the rate is 2% and the TP rate is 85% and the FP rate is 1%, the PPV will be 63% (1700/2700).

Therefore, it is sheer folly to talk about PPVs as sacrosanct. When PPVs are discussed, a rational assessment can be made only if we know the age distribution of all women having mammograms, the size of the examined population, if clinical examination was also done, the incidence of breast cancer among all the women having mammograms, the age-specific distribution of all cancers occurring in the screened population whether at screening or within 1 year of a screening mammogram that shows no cancer, and the sensitivity and specificity. Sensitivity can be determined by taking part in a receiver-operating-characteristic analysis of a screened population of mammograms (as suggested before), or if sufficient numbers of women are enrolled in the screening program (probably 30,000 or more), an estimate of sensitivity can be determined by evaluating the number of interval cases. Unfortunately, huge populations are needed. All the women who are screened should have had independent clinical examinations, and long-term follow-up of most of the women is necessary to provide meaningful data. Data derived from populations in the diagnostic range of incidence cannot be compared with data derived from screening populations.

Controlled trials of screening have shown the following: (1) For women 40–49 years old who have mammography only (no other screening procedure) at inappropriate intervals and where PPV has been a driving factor, the mortality rates among women screened are higher than among women not screened [4]. (Modeling shows this is easily explicable as a result of the false-negative reassurance effect [5]. The false-negative reassurance effect is maximized by either inappropriate screen threshold or poor quality imaging. Screening at an inappropriate interval delays and reduces the magnitude of any reduction in mortality but has little impact on excess mortality.) (2) For women more than 50 years old, screening will be at least as good as that in the Health Insurance Plan tests, whatever method or tool is used. As the population grows older, a greater number of slower growing cancers occur, and the texture of the breasts is such that the latitude for errors in detection and diagnosis is greater.

Screening younger women is not easy. Although I happen to think such screening can be done and done effectively, making a high PPV the penultimate achievement is counterproductive. Clinical examination and breast self-examination are necessary to keep the false-negative penalty effect to a minimum. In some situations, 5-mm cancers and ductal carcinoma in situ can be found by clinical examination alone.

Myron Moskowitz
University of Cincinnati Hospital
Cincinnati, OH 45267

REFERENCES

1. Hall FM, Potchen EJ, Edelstein G. Mammography and malpractice (letters and replies). *AJR* **1991**;157:883–885
2. Swets JA, Getty DJ, Pickett RM, et al. Enhancing and evaluating diagnostic accuracy. In: *Medical decision making*. Philadelphia: Hanley & Relfus. **1991**:9–18
3. Ries LAG, Hankey BF, Miller BA, et al. *Cancer statistics review 1973–1988* (NIH publication No. 91-2789). Washington, DC: National Cancer Institute, **1991**
4. Stomper PC, Gelman RS. Mammography in asymptomatic and asymptomatic patients. *Hematol Oncol Clin North Am* **1989**;3:611–640
5. Moskowitz M. *Cancer* (in press)

Reply

We are pleased to respond to the letter of Dr. Moskowitz. He continues to pursue an area in which he has many publications. Much of what he responds to is not at issue and is not discussed in our article [1] or letter [2]. We understand that he is advocating less concern for "excessive" surgical biopsies because the primary purpose of screening mammography is to decrease deaths caused by breast cancer. In our opinion, it is not appropriate to ignore implications of "excess" surgical breast biopsies in the diagnosis of nonpalpable breast cancer. The literature on compliance suggests that some women may not seek appropriate screening mammograms if the biopsy to cancer rate is "too high." Diagnosis made on the basis of mammographic findings is imperfect. If a positive mammogram is defined as one that shows changes sufficient to warrant surgical biopsy for prospective nonpalpable cancer, then Moskowitz's claim of a 1% false-positive rate is clearly erroneous. The ability to diagnose nonpalpable breast cancers can be increased without resorting to open surgical biopsy. When this happens, more women may accept screening mammography. We advocate the Karolinska approach, which has been extremely successful. In the Karolinska program, experienced mammographers read a large number of examinations, and their interpretations are closely correlated with the clinical outcome. The major addition to Moskowitz's strategy is stereotaxic fine-needle aspiration biopsy, performed with the patient prone, when a suspected lesion is detected.

The argument that positive predictive value should not be of concern runs counter to our experience, in both containing health care costs and diminishing "disease" induced by the current diagnostic system. We completely agree with Moskowitz that the primary intention is to decrease mortality from breast cancer, but we think that this will not be possible if some women do not obtain screening mammograms because of associated morbidity. Moskowitz's caution about overemphasis of positive predictive value is a legitimate concern only if the effects of iatrogenic morbidity are ignored. We support Hall's perception that the implications of false-positive findings on mammograms also are a legitimate concern.

E. James Potchen
Arlene E. Sierra
Michigan State University
East Lansing, MI 48824

REFERENCES

1. Potchen EJ, Bissei MA, Sierra AE, Potchen JE. Mammography and malpractice (commentary). *AJR* **1991**;156:475–480
2. Hall FM, Potchen EJ, Edelstein G. Mammography and malpractice (letters and replies). *AJR* **1991**;157:883–885

MR Imaging of Hepatic Laceration

We report a case of hepatic laceration in which MR imaging was useful in assessing the injury.

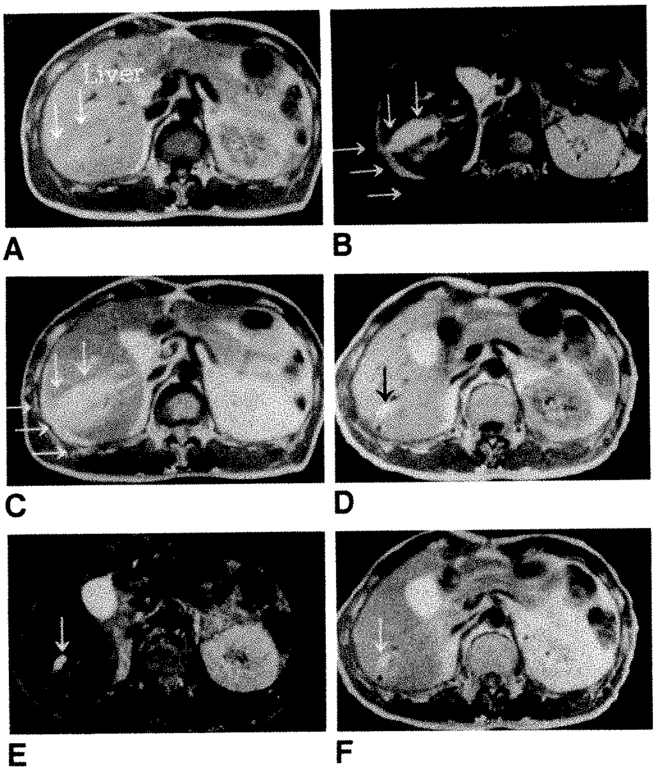

Fig. 1.—Laceration in posterior segment of right lobe of liver.

***A–C*, MR images obtained 1 hr after injury. Lesion (*arrows*) is hypointense on T1-weighted image (SE 625/25, *A*) and hyperintense on T2-weighted (SE 1800/100, *B*) and proton density-weighted (SE 1800/40, *C*) images.**

***D–F*, MR images obtained 2 months after surgery. Lesion (*arrows*) is hyperintense on T1-weighted (SE 625/25, *D*), T2-weighted (SE 1800/100, *E*), and proton density-weighted (SE 1800/40, *F*) images.**

A 52-year-old man had blunt injury to the abdomen. MR images were obtained with a 0.5-T superconducting magnet 1 hr after the injury (Figs. 1A–1C). The procedure took 15 min. At surgery, a 20-cm-long hepatic laceration in the posterior segment of the right lobe of the liver was detected and repaired. About 500 ml of blood was present in the peritoneal cavity. The patient recovered uneventfully. Follow-up MR imaging 2 months after surgery (Figs. 1D–1F) showed residual abnormality.

In this case, MR imaging was a rapid and noninvasive way to make the diagnosis of an acute laceration of the liver. The procedure took no longer than a CT scan would have required, and contrast medium was not needed [1]. In the acute stage, the laceration was slightly hypointense on T1-weighted images and was hyperintense on T2-weighted and proton density-weighted images. Within 1 month of injury, the laceration was hyperintense on all MR sequences.

Fumio Yamamoto
Yamamoto Hospital
Imari 848, Japan
Yonglin Pu
Beijing Medical University, People's Hospital
Beijing, China

REFERENCE

1. Mirvis SE, Whitley NO, Vainwright JR, Gens DR. Blunt hepatic trauma in adults: CT-based classification and correlation with prognosis and treatment. *Radiology* **1989**;171:27–32

Retained Barium Enema Balloon Tip: Proposed Treatment By Percutaneous Needle Puncture

A recent issue of the *AJR* included a letter from Kesaria [1] about a balloon tip of a barium enema kit that would not deflate. The balloon was removed by a surgeon, presumably by incising the skin and anal mucosa. Coincidentally, in the next letter in the same issue, Harned and Chezmar [2] wrote about using percutaneous puncture of a gastrostomy tube balloon to deflate the balloon and thus relieve an obstruction of the small bowel.

It occurred to me that a nondeflatable balloon of a barium enema tip can be similarly dealt with. I propose that in that situation, local anesthesia and fluoroscopically guided puncture of the balloon with a 20- or 22-gauge spinal needle could be used. This would avoid a more invasive procedure to deflate the bulb and remove the tip.

M. R. Ramakrishnan
Lonesome Pine Hospital
Big Stone Gap, VA 24219

REFERENCES

1. Kesaria AC. Retained E-Z-EM balloon barium enema tip (letter). *AJR* **1991**;157:885
2. Harned RK II, Chezmar JL. Percutaneous needle puncture for treatment of ileal obstruction caused by migration of a gastrostomy tube (letter). *AJR* **1991**;157:885–886

Reply

I appreciate the comments of Dr. Ramakrishnan. Both the surgeon and myself had attempted to puncture the balloon with a needle; however, we could not reach the inflated balloon. The surgeon then anesthetized the anal mucosa with a local anesthetic and pulled the inflated balloon out. The skin and anal mucosa were not incised.

Ashwin C. Kesaria
Firelands Community Hospital
Sandusky, OH 44870

Inadvertent IV Administration of Gadopentetate Dimeglumine During Early Pregnancy

Gadopentetate dimeglumine is a commonly used IV contrast agent for MR imaging. To the best of our knowledge, nothing is known about its safety in pregnancy, and its use during pregnancy is consequently not recommended by the manufacturer. So far the manufacturer has no data on file on the IV administration of this agent during pregnancy (J. Haustein, Schering AG Berlin, personal communication). We report the inadvertent IV administration of gadopentetate dimeglumine to a patient who was pregnant.

A 24-year-old woman with multiple sclerosis had been part of a monthly MR imaging protocol for 9 months. The protocol consisted of a precontrast long TR sequence, bolus injection of gadopentetate dimeglumine (0.2 mmol/kg), a flush with 10 ml saline, and short TR sequences [1]. At the time of the 10th study, the patient was imaged according to the standard protocol. Later, it was learned that she had been pregnant at the time of the 10th study (first day of last menstruation was 23 days before the MR imaging). She had not been aware of her pregnancy at the time of imaging but reported it at the time of the next (11th) study. She subsequently had follow-up examinations with unenhanced MR imaging only. After an uneventful pregnancy of 39 weeks, she delivered a healthy girl. The child is now 3 months old and is developing normally.

The gestational age of the (pre-) embryo when gadopentetate dimeglumine was injected was approximately 9 days (blastula stage), and the (pre-) embryo was in the process of implantation. Formation of a placenta had not started, and small molecular substances like gadopentetate dimeglumine (550 d) could have freely diffused into the (pre-) embryo. The most likely adverse effect would have been an early spontaneous abortion (rather than congenital malformations, which could have occurred with exposure in the organogenetic stage, the second and third months). Clinical use of IV gadopentetate dimeglumine during pregnancy, however, should be avoided until enough evidence is gathered about the effects of the agent on child development. The possibility of pregnancy should be excluded by means of a careful history before gadopentetate dimeglumine is injected IV. Inadvertent administration during pregnancy cannot always be avoided, as illustrated by our case. Our patient did not have early spontaneous abortion, and we have not seen any harmful effects to the child so far. Therefore, termination of a pregnancy solely because the mother inadvertently was injected with gadopentetate dimeglumine may not be justified.

Frederik Barkhof
Roel J. J. Heijboer
Paul R. Algra
and colleagues
Free University Hospital
1007 MB Amsterdam, the Netherlands

REFERENCE

1. Barkhof F, Hommes OR, Scheltens P, Valk J. Quantitative MRI changes in gadolinium-DTPA enhancement after high-dose intravenous methylprednisolone in multiple sclerosis. *Neurology* **1991**;41:1219–1221

MR Findings in Urachal Carcinoma

Carcinoma of the urachus is difficult to distinguish from common bladder tumors [1–3]. The prognosis is considerably worse than that of primary bladder carcinoma, because urachal tumors have a predilection for local invasion, and the diagnosis often is made relatively late in the disease.

Two patients with proved adenocarcinoma of the urachus had preoperative MR imaging on a 0.5-T system. T1-weighted (320/25) sagittal MR images were obtained. A 25-cm field of view, 5-mm slice thickness, an average of four signals, and a 160 × 192 matrix were used.

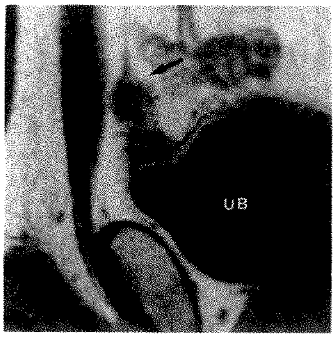

1

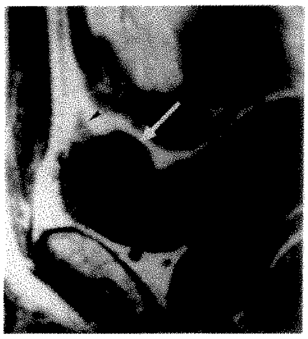

2

Fig. 1.—Sagittal MR image of 63-year-old man with urachal tumor shows a mass (*arrow*) extending from bladder wall. Mass is continuous and tapers toward umbilicus. UB = urinary bladder.

Fig. 2.—Sagittal MR image of 55-year-old man with urachal tumor shows a mass (*arrow*) in anterosuperior part of bladder wall. Triangular bud (*arrowhead*) is oriented in direction of urachal communicating ligament.

The first case was a 63-year-old man who had painless gross hematuria. The results of excretory urography were normal. Cystoscopy showed a small, smooth mass in the dome of the bladder. MR showed a tubular, 3-cm mass in the middle line of the bladder dome (Fig. 1). Partial cystectomy was done. The diagnosis was tubular adenocarcinoma of the urachus.

The second case was a 55-year-old man who had had intermittent gross hematuria for 5 years. Cystoscopy showed a broad-based 3-cm tumor in the dome of the bladder. MR showed a dumbbell-shaped mass 2.6 × 3.4 cm in the dome of the bladder (Fig. 2). Radical cystectomy was done, with excision of the urachus, communicating ligament, and umbilicus. Histologic examination showed tubular urachal adenocarcinoma.

The diagnosis of urachal carcinoma is suggested when a mass is present in the dome of the bladder associated with mostly extravesical extension in the middle line and calcification. Sagittal MR images show the shape of the tumor and the urachal ligament extending toward the umbilicus.

Hisatoshi Maeda
Tsuneo Kinukawa
Hajime Kuhara
Ryouhei Hattori
Touru Furukawa
Okazaki Municipal Hospital
Okazaki, Aichi, Japan

REFERENCES

1. Sheldon CA, Clayman RV, Gonzalez R, Williams RD, Fraley EE. Malignant urachal lesions. *J Urol* **1984**;13:1–7
2. Lee SH, Kitchens HH, Kim BS. Adenocarcinoma of the urachus: CT features. *J Comput Assist Tomogr* **1990**;14:232–235
3. Gurret JP, Ody B, Megevand M. Carcinoma of the urachus demonstrated by CT. *Eur J Radiol* **1987**;7:142–143

Large Cloisons Simulating Duplex Kidneys on CT

In 1986, Hulnick and Bosniak [1] described a CT finding they claimed was diagnostic of duplex kidneys, that is, kidneys with two collecting systems separated by a thick septum of cortical tissue [2]. As might be expected, CT scans through the upper and lower poles

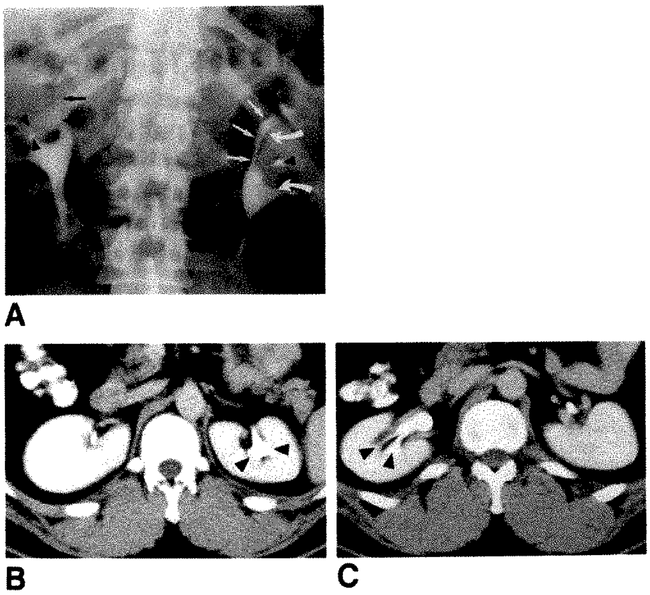

Fig. 1.—Large cloisons simulating duplex kidneys.

***A*, Excretory urogram shows long upper pole infundibula (*straight arrows*). Midzones are drained by calices (*arrowheads*) lying deep within kidneys, near renal pelves. Relatively large gaps are present between upper and midzone infundibula, occupied by large cloisons. An apparent mass (large cloison, *curved arrows*) displaces upper and lower pole infundibula on left.**

***B*, CT scan through left upper pole and right midzone shows calices and infundibula surrounded by sinus fat (*arrowheads*) within left kidney but none in right kidney, which has no renal sinus.**

***C*, CT scan through right lower pole and left midzone shows calices and infundibula surrounded by sinus fat (*arrowheads*) within right kidney but none in left kidney, which has no renal sinus.**

show calices and infundibula surrounded by sinus fat within the renal outline, whereas scans through the thick septum show renal parenchyma without calices, infundibula, or renal sinus [1].

Unduplicated kidneys, and the upper and lower poles of a duplex kidney, have thinner septa of cortical tissue, which Bertin called "cloisons" (French for septa), extending from the cortex to the renal sinus and separating the medulla into segments [3]. Hodson and Mariani [3] pointed out that cloisons had been mistranslated as "columns," and they restored Bertin's original term.

In early fetal life, a large primary cranial cloison develops between the upper pole and the midzone, but in later fetal life, all cloisons are approximately the same size [4]. A large primary cranial cloison persists in duplex kidneys, and occasionally in unduplicated kidneys, as a congenital anomaly variously referred to as large cloisons, large septa of Bertin, or lobar dysmorphism. I saw a patient with bilateral large cloisons whose CT scans closely resembled scans of duplex kidneys.

A 42-year-old man had gross hematuria. An excretory urogram showed bilateral large cloisons (Fig. 1A). CT scans between the upper and midzone infundibula showed renal parenchyma without calices, infundibula, or renal sinus on both sides, though at different levels (Figs. 1B and 1C). The reason is clear enough: duplex kidneys look this way on CT because they have large cloisons. The characteristic findings, therefore, can occur in a kidney with large cloisons, with or without duplication.

Gerald W. Friedland
Veterans Affairs Medical Center
Palo Alto, CA 94304

REFERENCES

1. Hulnick DH, Bosniak MA. "Faceless" kidney: CT sign of renal duplicity. *J Comput Assist Tomogr* **1986**;10:771-772
2. Glassberg KI, Braren V, Duckett JW, et al. Suggested terminology for duplex systems, ectopic ureters and ureteroceles. *J Urol* **1984**;132:1153-1154
3. Hodson CJ, Mariani B. Large cloisons. *AJR* **1982**;139:327-332
4. Keibel F, Mall FP. *Manual of human embryology*. Philadelphia: Lippincott, **1912**:844-845

Avascular Necrosis in a Canine Model

I just read the article by Brody et al. [1] on avascular necrosis in a canine model. I did not learn a thing, but I was upset and disturbed. Those poor beagles!!!!! I think academicians should find something else to do besides torturing innocent animals. I feel some animal experiments provide a greater good for humans. But a majority—including this one—don't. Who gives a damn what avascular necrosis looks like on days 0, 1, 7, and 23. If I see a hypointense smudge in the femoral head, I give a brief differential diagnosis. If I see a bright and dark ring, I say avascular necrosis.

Michael J. Eisenberg
Holladay Park Medical Center
Portland, OR 97232

REFERENCE

1. Brody AS, Strong M, Babikian G, Sweet DE, Seidel FG, Kuhn JP. Avascular necrosis: early MR imaging and histologic findings in a canine model. *AJR* **1991**;157:341-345

Reply

Today, we have no treatment for avascular necrosis. It is perhaps understandable, therefore, that the appearance of the earliest changes of this disease could be considered of academic interest only. My coauthors and I hope that in the future when avascular necrosis is detected during its early stages, treatment will be started immediately, and bone destruction will be prevented. Knowledge of the MR imaging appearance of the early stages will then be critically important. With the goal of bringing this time closer, we performed our investigation [1].

We surgically devascularized the distal femur of adult beagle dogs and did postoperative MR imaging and histologic studies. Using this model, we found that MR imaging can show changes in bone marrow as soon as 1 week after the onset of avascular necrosis. MR imaging showed a progression of increasing areas of low signal; the histologic findings during this time were diverse.

One goal of our research was to see if MR imaging could detect avascular necrosis in its earliest stages, when treatment would likely be most effective. A second goal was to examine the histologic changes of the early stages in order to develop MR imaging strategies and to look for histologic insights that would suggest therapies for avascular necrosis. The cellular infiltrate that we observed may provide such an insight. Host response as well as the biomechanics of the marrow space may be responsible for bone destruction.

The study was approved by our Laboratory Animal Care Committee. We took great care to minimize the animals' pain. We were very aware of the appropriate concerns that surround research that involves animals. This investigation was discussed openly at our center so that our coworkers could understand our goals and the reasons for doing this work. Only the future will reveal the true value of this research. We feel that the potential benefits in the prevention of human suffering are sufficient to justify this investigation.

Alan S. Brody
Children's Hospital of Buffalo
State University of New York at Buffalo, School of Medicine
Buffalo, NY 14222

REFERENCE

1. Brody AS, Strong M, Babikian G, Sweet DE, Seidel FG, Kuhn JP. Avascular necrosis: early MR imaging and histologic findings in a canine model. *AJR* **1991**;157:341–345

A Device for Rotation and Stabilization of the Knee During MR Imaging

We describe a simple device that we have developed to support the patient's lower leg during MR imaging of the knee. It allows accurate and reproducible positioning of the knee in external rotation so that the anterior cruciate ligament can be best imaged.

The device is constructed of Plexiglas and plastic, it has no metallic parts to cause artifacts during imaging. It consists of three separate pieces (Fig. 1). The first is a Plexiglas base that anchors the device on the imaging table and serves as the point of attachment for the rest of the device. The second part is a block that serves as a link between the leg-support piece and the Plexiglas frame. The third piece holds the patient's leg in place in full extension. It consists of a plastic sheet molded to fit the shape of a leg and three Velcro straps for securing the leg in place.

The stabilization device is easy to use and takes little time to set up. It is assembled and seated in place on the imaging table with the knee coil. The patient is placed supine on the table. The patient's leg is then strapped onto the leg-support piece and rotated externally to the desired angle, and the bolt is tightened to secure the position. The patient can relax throughout the examination and does not have to be concerned about maintaining the position of the leg. The additional time required for positioning is negligible and does not affect patient throughput.

The device allows optimal display of the anterior cruciate ligament by minimizing motion artifacts while providing a measured degree of external rotation that can be reproduced accurately with each knee study. The leg piece holds the leg snugly at the foot, ankle, and knee such that the entire lower extremity moves as a unit. Rotation of the leg piece therefore reflects the same degree of rotation of the knee. The leg is secured in full extension, the position where the anterior cruciate ligament is maximally taut and imaging is therefore optimal. The device is constructed so that the axis of rotation passes approximately through the center of the knee. This ensures that changing rotation will not move the knee out of the center of the imaging field.

Adjustments are easy. Degree of rotation is changed simply by rotating the leg and tightening a bolt. Most radiologists think that placing the knee in external rotation during MR imaging improves the study by including the entire anterior cruciate ligament in the image plane [1, 2]. At our institution, the optimal angle of the knee appears to be 15° of external rotation, although others have found that 20° is best [3]. For patients of markedly different sizes, other leg-support pieces could be constructed. Thus, all patients can be accommodated by making a few adjustments to a single device.

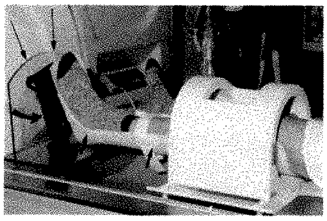

Fig. 1.—Knee stabilization device in place on MR imaging table. Patient's leg is secured onto leg piece (*short straight arrows*) joined by nylon block (*curved arrow*) to Plexiglas frame (*long straight arrows*). Frame has two supports that fit onto table of imager and a vertical piece for attachment of leg apparatus.

The device has been in use for several years at our institution, and it has improved the quality of our MR studies of the knee. The provision for accurate knee rotation and stabilization of motion results in reliable, high-quality studies that benefit both the physician and the patient. If accurate positioning is achieved and maintained, the anterior cruciate ligament can be more reliably defined.

Spencer B. Gay
Norman C. Chen
James R. Brookeman
and colleagues
University of Virginia Health Sciences Center
Charlottesville, VA 22908

REFERENCES

1. Mink JH. The ligaments of the knee. In: *Magnetic resonance imaging of the knee.* New York: Raven, **1987**:93–112
2. King CL, Hinkelman RM, Poon PY, Rubenstein J. Magnetic resonance imaging of the normal knee. *J Comput Assist Tomogr* **1984**;8:1147–1154
3. Reicher MA, Rauschning W, Gold RH, Bassett LW, Lufkin RB, Glen W Jr. High-resolution magnetic resonance imaging of the knee joint: normal anatomy. *AJR* **1985**;145:895–902

Fournier's Gangrene: Diagnosis Based on MR Findings

Fournier's gangrene is a fulminant, rapidly progressing infection of the scrotum that also involves the perineum, penis, and abdominal wall. We present a case of Fournier's gangrene that was diagnosed on the basis of MR findings.

A 71-year-old diabetic man had scrotal pain and swelling. Physical examination showed scrotal swelling and erythema with skin necrosis. Plain radiographs of the pelvis showed subcutaneous gas in the scrotum. Spin-echo MR images (1.5-T system) showed marked thickening by gas of the scrotal skin and fluid lying between the skin and the dartos muscle (Fig. 1). The dartos muscle was visible as a thickened line of low signal intensity on T2-weighted images. The fluid collection had high signal intensity on T2-weighted images and

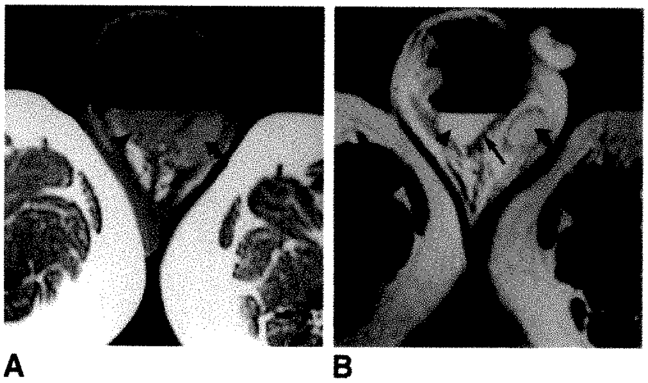

Fig. 1.—*A* and *B*, Fournier's gangrene. T1-weighted (*A*) and T2-weighted (*B*) MR images show marked gaseous thickening of scrotal skin and a fluid collection (*arrowheads*) between skin and dartos muscle. Muscle appears as a thickened line of low signal intensity (*straight arrow*) on T2-weighted image (*B*). Left testis (*curved arrows*) has normal high signal intensity on T2-weighted image and was considered to have normal function.

slightly high signal intensity on T1-weighted images. Both testes and epididymides had normally high signal intensity on T2-weighted images. The penis, including the corpora cavernosa and corpus spongiosum, also had homogeneously high signal intensity on T2-weighted images. The transition zone of the prostate was enlarged, but no areas of abnormal signal intensity were seen in the peripheral or transition zones on T2-weighted images. Sonograms could not be obtained because of the skin necrosis. Debridement was performed, and 3 weeks later, the patient had recovered fully.

Fournier's gangrene was originally described as a fulminating disease of unknown origin that devastated the genitalia of young male subjects. However, the disease may affect both healthy young males and elderly men, especially those who have diabetes, advanced liver or kidney disease, or immunosuppression [1-3]. The gangrene commonly develops as a periurethral or perianal infection. Sometimes the point of origin is obscure, possibly a minute scrotal abrasion. The soft-tissue infection usually begins as an area of cellulitis adjacent to the portal of entry of the causative organism. The infection then begins to involve the deep fascia and spreads beyond the entry point. As fascitis develops, the overlying skin becomes involved [1-3]. The cause of the gangrene in our patient is not certain. However, a combination of two mechanisms may have been responsible for its development, as he had diabetes and had been massaging his scrotum for 1 month.

Fournier's gangrene causes marked thickening of the scrotal skin and, most importantly, air in the subcutaneous tissues. However, it can be confused with epididymitis, orchitis, and scrotal cellulitis [1, 2]. Therefore, evaluation of the testes, epididymides, and scrotum is essential for making the correct diagnosis of this condition. The mortality rate is still significant. Early aggressive antibiotic therapy with debridement of all necrotic tissue is important, and further debridement must be done when indicated [1-3]. Knowledge of the extent of the necrosis is necessary when surgery is required.

In our case, MR images showed marked thickening of the scrotal skin, extensive subcutaneous gas, and fluid accumulation. Both testes, the epididymides, the penis, and the abdominal wall were normal. Because the gangrene was confined to the scrotum, we decided that debridement was the only treatment needed.

Thickening of scrotal skin and air in the subcutaneous tissues can be shown by sonography also [4]. Both sonography and MR are highly accurate for assessment of testicular lesions. However, MR is more useful than sonography; it allows a wider field of view, and it can be used in patients who have advanced skin necrosis. MR also can show extension of disease to the perineum, abdominal wall, and buttocks more accurately than sonography can. Sonography should continue to be the primary imaging technique for the diagnosis of Fournier's gangrene. However, MR should be used in patients who may have spread of gangrene beyond the scrotum or who have advanced skin lesions.

Hiromi Okizuka
Kazuro Sugimura
Takeshi Yoshizako
and colleagues
Shimane Medical University
Izumo, 693, Japan

REFERENCES

1. Jones RB, Hirschmann JV, Brown GS, Tremann JA. Fournier's syndrome: necrotizing subcutaneous infection of the male genitalia. *J Urol* **1979**;122:279-282
2. Banks DW, O'Brien DP III, Amerson JR, Hester TR Jr. Gracli's musculocutaneous flap scrotal reconstruction after Fournier's gangrene. *Urology* **1986**;29:582-585
3. Spirnak JP, Resnick MI, Hampel N, Perskey L. Fournier's gangrene: report of 20 patients. *J Urol* **1984**;131:289-291
4. Begley MG, Shawker TH, Robertson CN, Bock SN, Wei JP, Lotze MT. Fournier gangrene: diagnosis with sacral US. *Radiology* **1988**;169: 387-389

Percutaneous Transluminal Angioplasty of the Subclavian Arteries

I read with interest the article by Hebrang et al. [1] on percutaneous transluminal angioplasty of the subclavian arteries. In the introduction, the authors state that they will report technical success, complications, and long-term follow-up of percutaneous transluminal angioplasty in a series of 52 patients. Despite this promise, I was unable to clearly determine the prevalence of complications. In discussing the subgroup of patients who required inflation of the balloon across the vertebral artery, the authors report that their results were "similar" to those of Vitek [2]. Does this mean that they had no complications? What about when the balloon was inflated proximal to the vertebral artery? Also, in discussing heparinization, the authors state that "no differences in complication rates were observed between patients treated with heparin and those not treated with it." What, then, was the complication rate?

Karen T. Brown
St. Luke's/Roosevelt Hospital Center
New York, NY 10019

REFERENCES

1. Hebrang A, Maskovic J, Tomac B. Percutaneous transluminal angioplasty of the subclavian arteries: long-term results in 52 patients. *AJR* **1991**;156:1091-1094
2. Vitek JJ. Subclavian artery angioplasty and origin of the vertebral artery. *Radiology* **1989**;170:407-409

Reply

Dr. Brown writes that the article by me and my colleagues on percutaneous transluminal angioplasty of the subclavian arteries [1] had no data on the prevalence of complications. In the first version of the manuscript, such data were included in table form (Table 1). The editor asked us to delete the data because the complications and side effects associated with percutaneous transluminal angioplasty of the subclavian arteries are well known. Consequently, in the final draft of the article, we mentioned only that we did not have serious complications.

A. Hebrang
Clinical Hospital "Dr. O. Novosel"
41000 Zagreb, Croatia

TABLE 1: Side Effects and Complications Associated with Percutaneous Angioplasty of the Subclavian Arteries in 52 Patients

Side Effects and Complications	Patients Treated with Heparin		Total
	Yes	No	
Transient pain	6	4	10
Groin hematoma	1	0	1
Distal ischemia	0	1	1
Headache	0	1	1
Tremor	2	2	4
Total	9	8	17

REFERENCE

1. Hebrang A, Maskovic J, Tomac B. Percutaneous transluminal angioplasty of the subclavian arteries: long-term results in 52 patients. *AJR* **1991**;156:1091–1094

A Theoretical Explanation of Asymmetry of the Frontal Horns of the Lateral Ventricles

A familiar occasional finding on CT scans and MR images of the brain is the asymmetric appearance of the frontal horns of the lateral ventricles in healthy subjects. In Figure 1, the septum pellucidum is seen just left of the midline, and that is why the frontal horns appear asymmetric. This situation reminds me of the "cavum septi pellucidi." This is a potential space located between the two nonfused leaves of the septum pellucidum and is regularly present in the developing fetus. It begins to involute just before birth in order to fuse completely at exactly the midline to form a single leaf of septum pellucidum. It reportedly persists throughout life in 5–15% of the population [1–3]. In Figure 1, if an arbitrary line is drawn just right of the midline, as a mirror image of the present (left) septum pellucidum, the result would be an imaginary cavum septi pellucidi within two (left and right) leaves of the septum pellucidum.

This concept suggests that the asymmetry of the frontal horns reflects a developmental disorder. If one of the two leaves of the septum pellucidum is congenitally absent, then a normally expected "midline fusion" will not take place (because only one leaf would be present). The single leaf that is present, located off the midline, would create an apparent asymmetry of the frontal horns, as shown in Figure 1. In addition, the posterior extension of the cavum septi pellucidi, when present, is termed a cavum vergae and is located between the bodies of the lateral ventricles [1–3]. Another familiar but rare finding on CT scans and MR images in healthy subjects, an asymmetry of the bodies of the lateral ventricles, can represent a similar event with the cavum vergae and can be caused by the same mechanism discussed before. I think that asymmetric frontal horns or bodies of the lateral ventricles represent maldevelopment of the septum pellucidum in otherwise healthy subjects.

R. Nuri Sener
Hospital of Ege University
Bornova 35100, Izmir, Turkey

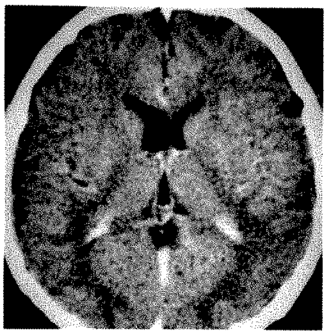

Fig. 1.—Contrast-enhanced CT scan in healthy 21-year-old man shows apparent asymmetry of frontal horns due to orientation of septum pellucidum off midline to left. This finding suggests maldevelopment of septum pellucidum: Lack of one of its two leaves, which should normally fuse at midline during infancy, prevents midline fusion, and a single leaf persists on one side off midline, creating an asymmetric ventricle.

REFERENCES

1. Williams AL, Haughton VM. *Cranial computed tomography*. St. Louis: Mosby, **1985**:317–319
2. Lee SH, Rao KCVG. *Cranial computed tomography and MRI*, 2nd ed. New York: McGraw-Hill, **1987**:202
3. Silverman FN. *Caffey's pediatric X-ray diagnosis*, 8th ed., vol. 1. Chicago: Year Book Medical, **1985**:157–161

Reply

Asymmetric appearance of the lateral ventricles, particularly of the frontal horns, as described by Dr. Sener, has intrigued us also. This appearance simulates unilateral obstructive hydrocephalus and may suggest an obstructive lesion at the foramen of Monro. In more than one instance at our institution, patients have had surgery because of a presumed foraminal lesion (Fig. 1), but no obstructive lesion has been found. (Incidentally, both septal leaves were present.) Curiosity about this asymmetry stimulated us to review the normal position of the septum pellucidum in an effort to explain this appearance. We reviewed the coronal T1-weighted (600/20 [TR/TE], 3-mm slice thickness) MR images of 57 otherwise healthy patients who were having MR for evaluation of abnormalities of the hypothalamic-pituitary axis. The septum was deviated in 17 patients (to the right in 12 and to the left in five). The average deviation from midline was 2.00 mm (range, 1–7 mm). A cavum septi pellucidi was present anteriorly and superiorly in 20 patients, and, in most patients with septal deviation, both septal leaves were detected on the coronal MR image. We also evaluated the size of the temporal horns of the lateral ventricles. Our hypothesis was that the temporal horn would be dilated in those patients with obstructive unilateral hydrocephalus and not in patients without this disorder. The temporal horn was asymmetric in only four patients with septal deviation. In none of these were the temporal horns sufficiently dilated to suggest hydrocephalus. However, a review of the images of six patients with unilateral obstructive hydrocephalus showed obstructing lesions at the foramen of Monro, with contralateral septal deviation and associated dilatation of the lateral ventricle, including marked dilatation of the temporal horn of the lateral ventricle.

Pathologic examples of septal deviation and asymmetric enlargement of the frontal horns (Fig. 2) show asymmetric dilatation of the frontal horn and contralateral septal deviation. The specimens clearly show that both septal leaves are present. The body and the anterior columns of the fornices are asymmetrically placed within the larger ventricle, perhaps slightly narrowing the left interventricular foramen and causing mildly increased unilateral ventricular pressure, with resultant asymmetric fusion of the septal leaves. The forniceal asymmetry, however, may merely be a result of the septal deviation.

Our data suggest that bowing of the septum pellucidum is a common occurrence and probably represents a benign developmental

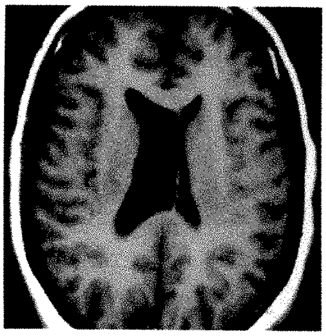

1

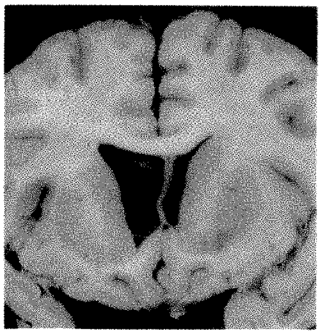

2

Fig. 1.—Axial spin-echo MR image (600/20) shows asymmetry of lateral ventricles caused by deviation of septum pellucidum. At surgery, both leaves of septum were present. No obstructing lesion was found at foramen of Monro.

Fig. 2.—Pathologic specimen from a person who died of unrelated causes shows asymmetry of frontal horns of lateral ventricles. Both leaves of septum pellucidum are clearly present. (Courtesy of Hideo Itabashi, Los Angeles, CA.)

variant. Both septal leaves seem to be present in most cases. We think that one possible explanation for this variant is that the two leaves of the septum pellucidum fuse asymmetrically (possibly because of a mild pressure differential between the two lateral ventricles), such that a bowed, asymmetric septum results. The result is unilateral enlargement of the frontal horn of the lateral ventricle and asymmetry of the fornices, without significant dilatation of the ipsilateral temporal horn. The asymmetry can be pronounced and can simulate unilateral hydrocephalus, but in the absence of dilatation of the temporal horn, it should be recognized as a developmental variant rather than a pathologic condition. We emphasize that when concomitant dilatation of the ipsilateral temporal horn is present, the region of the foramen of Monro should be examined carefully to exclude an obstructing lesion. Congenital webs, stenosis, and tumors of this region have been described [1]. In a symptomatic patient with unilateral ventricular enlargement that includes the temporal horn, exploration may be indicated. We compliment Dr. Sener for bringing this interesting variant to our attention.

William P. Dillon
A. James Barkovich
University of California, San Francisco
San Francisco, CA 94143-0628

REFERENCE

1. Mampalam T, Harsh GR, Tien RD, Dillon WP, Wilson CB. Unilateral hydrocephalus in adults. *Surg Neurol* **1991**;35:14–19

MR Findings in an AIDS Patient with Cytomegalovirus Retinitis

A 28-year-old man with AIDS had had ataxia, decreased vision in the right eye, and fever for 10 days. A previous episode of cytomegalovirus (CMV) retinitis had resulted in complete blindness in the left eye despite treatment with ganciclovir. At that time, the right eye was normal. At this admission, with the right eye, the patient could detect gross hand motion only. Funduscopy showed early signs of CMV retinitis. Electroencephalographic findings indicated diffuse encephalopathy. Axial and coronal T1-weighted MR images were obtained. Unenhanced images showed thickening of the retinochoroid layer of the left eye as compared with that of the right eye (Figs. 1A and 1B). Images obtained after the IV administration of gadopentetate dimeglumine showed enhancement of the layer in the left eye (Figs. 1C and 1D). The patient was treated with ganciclovir, but his vision did not improve.

Cytomegalovirus is one of the most common opportunistic infections in patients with AIDS and is found at autopsy in approximately 90% of AIDS patients [1]. Although often asymptomatic, CMV infections can cause significant morbidity and mortality. Retinitis is one of the most common manifestations of CMV infection; it causes decreased visual acuity and may lead to blindness. Funduscopic examinations show small, white, granular retinal lesions that coalesce to form fluffy, white exudates. Clinical diagnosis of CMV retinitis is based on funduscopic findings and recovery of the virus from any body site [1]. So far, radiology has had no definite role in the diagnosis of CMV retinitis or in the follow-up of these patients. Although MR findings at various stages of CMV retinitis have not been described, our case suggests that enhancement of the retinochoroid layer is a late finding.

Robert J. Monette
David J. Czarnecki
Brian P. Buggy
St. Luke's Medical Center
Milwaukee, WI 53215

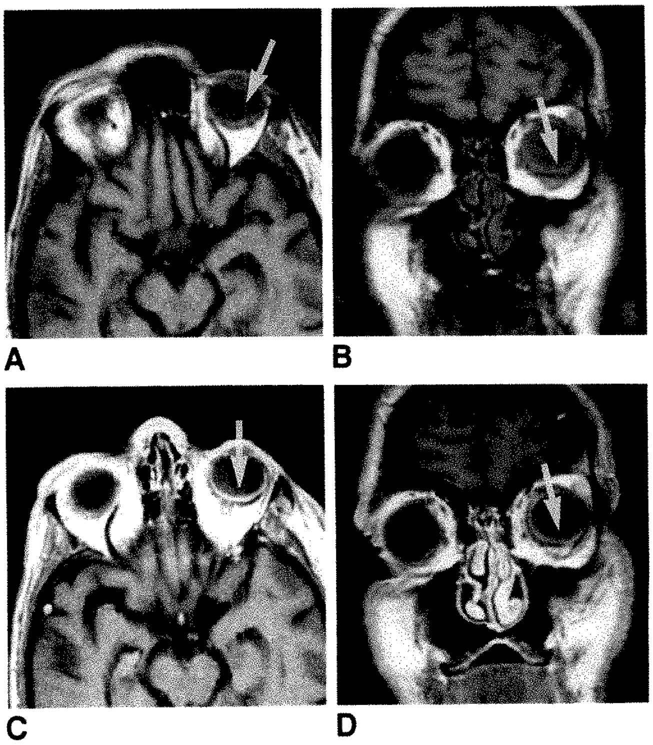

Fig. 1.—*A–D*, T1-weighted axial (670/20, *A* and *C*) and coronal (500/20, *B* and *D*) MR images in an AIDS patient with cytomegalovirus retinitis. Retinochoroid layer (*arrows*) of left eye is thickened (*A–D*) and shows enhancement (*C* and *D*) after administration of IV gadopentetate dimeglumine.

REFERENCE

1. Jacobson MA, Mills J. Serious cytomegalovirus disease in the acquired immunodeficiency syndrome (AIDS). *Ann Intern Med* **1988**;108:585–594

Pachygyria: CT Findings

We report a case of pachygyria, a rare congenital malformation characterized by abnormal gyral development in which a few, coarse, broad gyri are separated by a decreased number of sulci. The patient was a 6-month-old neonate with seizures, psychomotor retardation, and failure to thrive. CT showed multiple broad gyri separated by a few sulci throughout the anterior half of the brain and widened subarachnoid space (Fig. 1). An unusual ventricular configuration was evident: absence of the septum pellucidum, small and parallel frontal horns separated by medially located abnormal gyri, and widely separated tubular bodies of the lateral ventricles. The separation of the frontal horns and the bodies of the lateral ventricles suggested dysgenesis of the corpus callosum. The falx was present.

Pachygyria may be localized to a small area of the brain, or it may involve a large portion. Extreme pachygyria is termed agyria or lissencephaly (smooth brain); the cortical surface is totally agyrial except for a wide, shallow sylvian fissure. Pachygyria without associated areas of agyria usually causes less severe clinical manifestations than agyria does and is considered a separate entity [1–6].

Pachygyria is a hereditary (autosomal recessive) disorder of sulcation and migration. Neurons fail to migrate from the periventricular

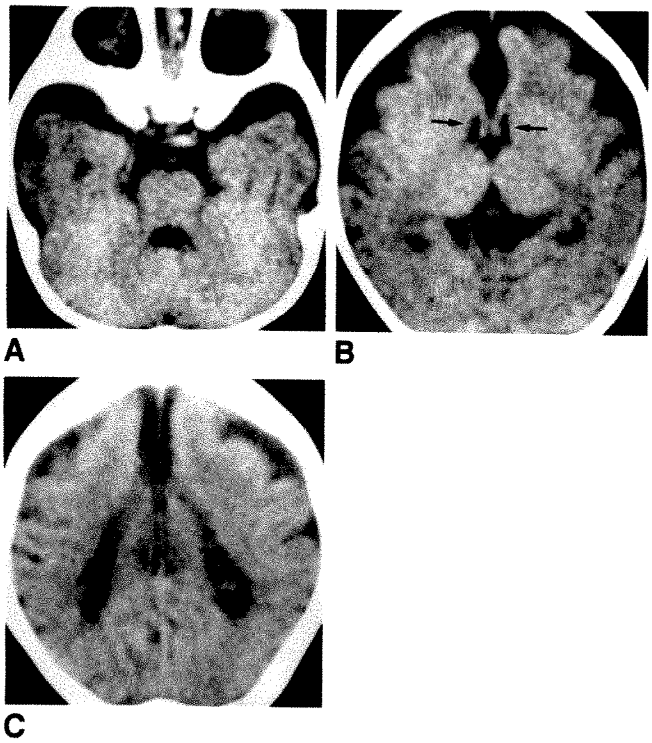

Fig. 1.—CT scans show pachygyria throughout anterior halves of cerebral hemispheres adjacent to widened subarachnoid spaces.

A, Scan through pons shows bilateral thickened temporal gyri.

B, Scan through thalami shows pachygyria of frontal and parietal lobes. Frontal lobes of lateral ventricles are small and have an unusual parallel configuration (*arrows*). Abnormal gyri extend from anterior frontal lobe to medial surfaces of frontal horns, which show no evidence of indentation of heads of caudate nuclei. Sylvian fissures are not detectable except for a shallow, narrow sulcus on left. Thalami appear normal.

C, Scan shows tubular shape of bodies of lateral ventricles, which are widely separated and are converging anteriorly. This finding along with appearance of frontal horns (*B*) suggests dysgenesis of corpus callosum and absence of septum pellucidum.

germinal matrix to the cortical surface of the brain during the period of normal gyral formation at 26–28 weeks of gestation. The result is cessation of cerebral and cerebellar cortical development, with abnormal formation of gyri and sulci and hypoplasia of the white matter. Accompanying anomalies are schizencephaly, polymicrogyria, and heterotopic gray matter [1–6].

The CT findings in pachygyria have recently been described [1–4]: broad gyri; a wide, shallow sylvian fissure; wide subarachnoid space; enlarged ventricles with colpocephaly; calcification in the septum pellucidum; and sparse white matter. Diagnosis of pachygyria based on CT findings can be difficult in premature infants because on CT scans the surface of the brain appears to be smoother in premature infants than in full-term neonates [5]. Also, it is difficult to detect schizencephaly (in fused-lip form), polymicrogyria, and heterotopic gray matter on CT scans [6]. MR is the best technique for evaluation of such disorders of sulcation and migration, especially in cases in which the CT findings are equivocal.

This case illustrates the typical CT findings of pachygyria. In contrast to previous observations, wide sylvian fissures and enlarged ventricles were not seen. Instead, the septum pellucidum was absent, and dysgenesis of the corpus callosum was present. The unusual ventricular configuration might reflect a primary error in ventricular morphogenesis or might be due to dysgenesis of the corpus callosum with surrounding abnormal gyria.

R. Nuri Sener
Aynur Dagdeviren
Rahmi Akyol
and colleagues
Hospital of Ege University
Bornova, Izmir, Turkey

REFERENCES

1. Byrd SE, Osborn RE, Bohan TP, Naidich TP. The CT and MR evaluation of migrational disorders of the brain. Part I. Lissencephaly and pachygyria. *Pediatr Radiol* **1989**;19:151–156
2. Williams JP, Joslyn JN. Lissencephaly: computed tomographic diagnosis. *CT* **1983**;7:141–144
3. Ohno K, Enomoto T, Imamoto J, Takeshila K, Arima M. Lissencephaly (agyria) on computed tomography. *J Comput Assist Tomogr* **1979**;3:92–95
4. Garcia CA, Dunn D, Trevor R. The lissencephaly (agyria) syndrome in siblings: computed tomographic and neuropathological findings. *Arch Neurol* **1978**;35:608–611
5. Williams AL, Haughton VM. *Cranial computed tomography*. St. Louis: Mosby, **1985**:348
6. Latchaw RE. *Computed tomography of the head, neck, and spine*. Chicago: Year Book Medical, **1985**:473–474

Letters are published at the discretion of the Editor and are subject to editing.

Letters to the Editor must not be more than two *double-spaced*, typewritten pages. One or two figures may be included. Abbreviations should not be used. Limit the number of authors to four, or we will list only the first three and add "and colleagues" to the end of the list. See Author Guidelines.

Material being submitted or published elsewhere should not be duplicated in letters, and authors of letters must disclose financial associations or other possible conflicts of interest.

Letters concerning a paper published in the *AJR* will be sent to the authors of the paper for a reply to be published in the same issue. Opinions expressed in the Letters to the Editor do not necessarily reflect the opinions of the Editor.

Review of Current Literature

Initials and addresses of corresponding authors are provided in parentheses for each article so that the reader can obtain reprints directly. Abstracts are printed verbatim from each journal.

The New England Journal of Medicine

Aspirin use and reduced risk of fatal colon cancer. Thun MJ, Namboooodiri MM, Heath CW Jr. (MJT, Dept. of Epidemiology and Statistics, American Cancer Society, 1599 Clifton Rd., Atlanta, GA 30329). *N Engl J Med* 325(23):1593–1596, Dec. 1991

Background and Methods. Experiments in animals and two epidemiologic studies in humans suggest that aspirin and other nonsteroidal antiinflammatory drugs (NSAIDs) may be protective against colon cancer. We tested this hypothesis in a prospective mortality study of 662,424 adults who provided information in 1982 on the frequency and duration of their aspirin use. Death rates from colon cancer were measured through 1988. The possible influence of other risk factors for colon cancer was examined in multivariate analyses for 598 case patients and 3058 matched control subjects drawn from the cohort.

Results. Death rates from colon cancer decreased with more frequent aspirin use in both men and women. The relative risk among persons who used aspirin 16 or more times per month for at least one year was 0.60 in men (95 percent confidence interval, 0.40 to 0.89) and 0.58 in women (95 percent confidence interval, 0.37 to 0.90). The risk estimates were unaffected when we excluded persons who reported at entry into the study that they had cancer, heart disease, stroke, or another condition that might influence both their aspirin use and their mortality. Adjustment for dietary factors, obesity, physical activity, and family history did not alter the findings significantly. No association was found between the use of acetaminophen and the risk of colon cancer.

Conclusions. Regular aspirin use at low doses may reduce the risk of fatal colon cancer. Whether this is due to a direct effect of aspirin, perhaps mediated by the inhibition of prostaglandin synthesis, or to other factors indirectly associated with aspirin use is unclear.

A comparison of angioplasty with medical therapy in the treatment of single-vessel coronary artery disease. Parisi AF, Folland ED, Hartigan P (AFP, Miriam Hospital, 164 Summit Ave., Providence, RI 02906). *N Engl J Med* 326:10–16, Jan. 1992

Background. Despite the widespread use of percutaneous transluminal coronary angioplasty (PTCA), only a few prospective trials have assessed its efficacy. We compared the effects of PTCA with those of medical therapy on angina and exercise tolerance in patients with stable single-vessel coronary artery disease.

Methods. Patients with 70 to 99 percent stenosis of one epicardial coronary artery and with exercise-induced myocardial ischemia were randomly assigned either to undergo PTCA or to receive medical therapy and were evaluated monthly. The patients assigned to PTCA were urged to have repeat angioplasty if their symptoms suggested restenosis. After six months, all the patients had repeat exercise testing and coronary angiography.

Results. A total of 107 patients were randomly assigned to medical therapy and 105 to PTCA. PTCA was clinically successful in 80 of the 100 patients who actually had the procedure with an initial reduction in mean percent stenosis from 76 to 36 percent. Two patients in the PTCA group required emergency coronary-artery bypass surgery. By six months after the procedure, 16 patients had had repeat PTCA. Myocardial infarction occurred in five patients assigned to PTCA and in three patients assigned to medical therapy. At six months 64 percent of the patients in the PTCA group (61 of 96) were free of angina, as compared with 46 percent of the medically treated patients (47 of 102; $P < 0.01$). The patients in the PTCA group were able to increase their total duration of exercise more than the medical patients (2.1 vs. 0.5 minutes, $P < 0.0001$) and were able to exercise longer without angina on treadmill testing ($P < 0.01$).

Conclusions. For patients with single-vessel coronary artery disease, PTCA offers earlier and more complete relief of angina than medical therapy and is associated with better performance on the exercise test. However, PTCA initially costs more than medical treatment and is associated with a higher frequency of complications.

P-glycoprotein expression as a predictor of the outcome of therapy for neuroblastoma. Chan HSL, Haddad G, Thorner PS, et al. (HSLC, Division of Hematology-Oncology, Hospital for Sick Children, 555 University Ave., Toronto, Ontario, M5G 1X8, Canada). *N Engl J Med* 325(23):1608–1614, Dec. 1991

Background and Methods. Multidrug resistance in chemotherapy for cancer is characterized by increased genetic expression of P-glycoprotein, which acts as an ATP-dependent drug-efflux pump. To determine whether P-glycoprotein levels are of prognostic value in such cases, we measured these levels immunohistochemically in a retrospective study of sequential tumor samples from 67 children with neuroblastoma.

Results. P-glycoprotein was not detected in pretreatment samples from either of the 2 patients with Stage I disease, any of the 21 with Stage II disease, or any of the 8 with Stage IVS disease, but it was detected in the samples from 1 of the 17 patients with Stage III disease (6 percent) and 12 of the 19 with Stage IV disease (63 percent). Of the 44 patients with nonlocalized neuroblastoma (Stage III, IVS, or IV), 26 of the 31 who were negative for P-glycoprotein had a complete response to primary treatment, as compared with 6 of the 13 who were positive for P-glycoprotein (84 percent vs. 46 percent, $P = 0.0232$ by Fisher's exact test). Log-rank analysis of outcome, with simultaneous stratification according to tumor stage and age, showed that the group that was negative for P-glycoprotein had significantly longer relapse-free survival ($P = 0.0011$) and overall survival ($P = 0.0373$) than the group that was positive.

Conclusions. Expression of P-glycoprotein before treatment may predict the success or failure of therapy for nonlocalized neuroblastoma. Neuroblastoma may be a promising tumor to treat with anticancer drug therapy combined with a chemosensitizing agent capable of reversing P-glycoprotein–mediated multidrug resistance.

Cancer

The new International Federation of Gynecology and Obstetrics surgical staging and survival rates in early endometrial carcinoma. Gal D, Recio FO, Zamurovic D (DG, Gynecologic Oncology, Obstetrics and Gynecology, North Shore University Hospital, 300 Community Dr., Manhasset, NY 11030). *Cancer* 69:200-202, 1992

The medical records of patients with clinical Stage I endometrial adenocarcinoma who were treated at the Maimonides Medical Center between October 1979 and October 1987 were reviewed. There was sufficient surgical-pathologic information to allow a reclassification based on the new International Federation of Gynecology and Obstetrics (FIGO) surgical staging in 93 patients. These are the subjects of analysis. Twenty-one patients (23%) were found surgically to have more than Stage I disease. The 5-year survival rate for the whole group (N = 93) was 90%. However, it was significantly better for patients with surgical Stage I disease (98%) than for patients with surgical Stage III disease (60%) ($P < 0.001$). There was no significant statistical difference in survival among patients with different substages within surgical Stage I (*i.e.*, IA, 100%; IB, 100%; and IC, 88%), whereas the distribution of adjuvant therapy among these substages was not statistically different ($P = 0.17$). Thus, survival was not significantly affected by depth of myometrial invasion in patients who had negative peritoneal washing and no involvement of lymph nodes or the peritoneal cavity.

Reprinted by permission from the American Cancer Society.

Chest

Acute pulmonary edema induced by overdosage of phenothiazines. Li C, Gefter WB (WBG, Hospital, University of Pennsylvania, 3400 Spruce St., Philadelphia, PA 19104). *Chest* 101(1):102-104, Jan. 1992

Three schizophrenic adults with previous histories of using phenothiazine derivatives developed acute pulmonary edema after taking large amounts of these drugs. The clinical manifestations included coma (three), hypothermia (two), tachycardia (two), miosis (two) and hypotension (one). All three patients underwent gastric lavage and were treated supportively. The fulminant pulmonary edema in the three cases resolved within 18 to 40 h. The etiology of pulmonary edema following overdosage of phenothiazines remains unknown. The authors hypothesize that the most likely pathogenesis is a drug-induced neurogenic pulmonary edema resulting from a disturbance of hypothalamic function.

Gastroenterology

Staging of pancreatic and ampullary carcinoma by endoscopic ultrasonography: comparison with conventional sonography, computed tomography, and angiography. Rösch T, Braig C, Gain T, et al. (TR, Dept. of Internal Medicine II, Technical University of Munich, Munich, Germany). *Gastroenterology* 102:188-199, 1992

In a prospective study, endoscopic ultrasonography was compared with transabdominal ultrasonography, computed tomography, and angiography in 60 consecutive patients with pancreatic ($n = 46$) and ampullary ($n = 14$) cancer considered to be candidates for surgery. The diagnostic value of these imaging procedures in determining local resectability was assessed. The diagnosis of ampullopancreatic malignancy was made by operation ($n = 40$) or puncture/biopsy ($n = 20$). In the 40 patients who underwent surgery, endoscopic ultrasonography was significantly superior to abdominal ultrasonography and computed tomography in determining tumor size and extent and lymph node metastases of pancreatic and ampullary cancer. Furthermore, involvement of the portal venous system as judged by histopathology or surgical exploration was correctly assessed by endoscopic ultrasonography in 95%, whereas angiography (85%), computed tomography (75%) and abdominal ultrasonography (55%) were less sensitive. Of 11 cases of portal venous infiltration found at surgery, endoscopic ultrasonography correctly predicted 10, abdominal ultrasonography only 1, computed tomography 4, and angiography 5 ($P < 0.05$ for all three comparisons). Twenty patients did not undergo surgery for different reasons: of those, 9 patients were excluded from operation because of portal venous involvement as shown by angiography. Endoscopic ultrasonography detected portal venous invasion in all these cases. In contrast to the venous system, arterial encasement was less reliably detected by endoscopic ultrasonography. In conclusion, endoscopic ultrasonography is the most effective single imaging procedure for local tumor staging in pancreatic and ampullary cancer. Thus, endoscopic ultrasonography will improve the assessment of tumor resectability and further decrease the need for explorative laparotomy.

Reprinted with permission by the American Gastroenterological Association.

Distal colonic hyperplastic polyps do not predict proximal adenomas in asymptomatic average-risk subjects. Rex DK, Smith JJ, Ulbright TM, Lehman GA (DKR, Division of Gastroenterology/Hepatology, Dept. of Medicine, Indiana University Medical Center, Indianapolis IN). *Gastroenterology* 102:317-319, 1992

The significance of distal colonic hyperplastic polyps was investigated in 482 asymptomatic average-risk subjects, aged 50–75 years, in whom fecal occult blood test results were negative and who underwent screening colonoscopy. The incidence of adenomas in the colon proximal to the sigmoid-descending colon junction in subjects with hyperplastic polyps distal to that point was 18% and was similar to the incidence of proximal colonic adenomas in subjects with no distal colonic polyps (15%). The incidence of proximal colonic adenomas in subjects with distal colonic adenomas was 38% and was significantly greater than the incidence found in individuals with no distal colonic polyps or only hyperplastic polyps. Our data do not support distal colonic hyperplastic polyps as markers for proximal colonic adenomas in asymptomatic average-risk subjects.

Reprinted with permission by the American Gastroenterological Association.

Digestive Diseases and Sciences

Methyl *tert*-butyl ether in the endoscopic treatment of common bile duct radiolucent stones in elderly patients with nasobiliary tube. Diaz D, Bories P, Ampelas M, Larrey D, Michel H (DD, Service des Maladies de l'Appareil Digestif, Hôpital Saint-Eloi, 34059 Montpellier, France). *Gastroenterology* 37(1):97-100, Jan. 1992

Methyl *tert*-butyl ether is an effective dissolution agent for cholesterol stones. The aim of this work was to evaluate the effect of methyl *tert*-butyl ether on radiolucent common bile duct stones in patients in whom endoscopic extraction has failed. From September 1985 to September 1987, 1374 patients underwent endoscopic retrograde cholangiopancreatography in our Liver Unit. An endoscopic sphincterotomy was indicated in 195 patients with common bile duct (CBD) stones because of an age over 65 years and/or surgical contraindications. Endoscopic sphincterotomy was efficient in 187 patients, allowing complete stone removal in association with conventional endoscopic methods and mechanical lithotripsy in 170 patients. Twelve of the 17 patients with failure of conventional endoscopic treatments were either older than 75 years (11 patients; mean age, 86 ± 4.5 years) or exhibited a surgical contraindication. Stones completely obstructed CBD in six patients and had a diameter exceeding 25 mm in the six other patients. These subjects were selected for stone dissolution by methyl *tert*-butyl ether (MTBE) according to the following protocol. MTBE was directly infused into CBD through a nasobiliary catheter, twice daily for 4–13 days (mean, seven days). Bile duct opacification, repeated after MTBE treatment, revealed the complete disappearance of CBD stones in one patient, a decrease in stone size in five patients and no change in the six other patients. MTBE treatment was well tolerated except in three patients who complained from transient abdominal pains and nausea. At the second attempt of endoscopic treatment, CBD stones were found to be softened and easily broken up, allowing a complete clearance in six patients. MTBE treatment failed to improve stone extraction in the five other patients. These results show that, in patients with large radiolucent stones in the CBD, unextractable by conventional endoscopic methods, the direct infusion of MTBE in CBD rarely led to a complete stone dissolution; however, this treatment partially solubilizes stones, enabling their complete endoscopic extraction thereafter in half the patients.

The Journal of Bone and Joint Surgery

Hydroxyapatite-coated femoral stems: histological analysis of components retrieved at autopsy. Bauer TW, Geesink RCT, Zimmerman R, McMahon JT (TWB, Dept. of Pathology, Cleveland Clinic Foundation, 9500 Euclid Ave., Cleveland, OH 44195-5138). *J Bone Joint Surg [Am]* 73-A(10):1439–1452, Dec. 1991

Plasma-sprayed coatings of hydroxyapatite are biocompatible and, because of their osteoconductive properties, may contribute to the early fixation of total joint prostheses. To evaluate this interface, we histologically analyzed five hydroxyapatite-coated femoral stems which, along with the surrounding bone, were retrieved from three humans at autopsy.

The five femoral components had been *in situ* for a mean duration of twelve months (range, almost five to twenty-five months) and had been inserted for osteonecrosis (two), osteoarthrosis (two), and as an uncemented revision for failure of a cemented stem. The three patients had had a good or excellent clinical result and had died of causes unrelated to the joint arthroplasty.

A coating of hydroxyapatite was identified on each stem. There was a variable amount of apposition of bone (32 to 78 per cent of available surface per section). The deposition of bone was most prominent on the surface of the prosthesis that was close to the endosteal surface of the bone, especially in areas that are predicted by Wolff's law (anterior and medial aspects of the implant, and at lateral-oblique corners). There were occasional foci of bone-remodeling around the implant, including osteoclast-mediated removal of the coating of hydroxyapatite along with adjacent bone. Occasional particles of ceramic were present within macrophages in the adjacent bone marrow. Other areas showed formation of new bone with a few areas of bone directly against the metal substrate.

The over-all histological features suggest mechanically stable implants with bone-remodeling at the surface of the bone-implant interface.

The Journal of Pediatrics

Acute adenovirus hepatitis in liver transplant recipients. Cames B, Rahier J, Burtomboy G, et al. (E. M. Sokal, Pediatric Hepatology, Dept. of Pediatrics, Université Catholique de Louvain, St. Luc Hospital 1301, 10 av Hippocrate, B-1200 Brussels, Belgium). *J Pediatr* 120:33-37, 1992

An acute or fulminant adenovirus hepatitis developed in 5 of 224 pediatric patients who were recipients of orthotopic liver transplants. All had received prednisolone, azathioprine, and cyclosporine as basal immunosuppression, and four received monoclonal (OKT3) or polyclonal (antithymocyte globulin) antibodies for steroid-resistant rejection episodes. These patients initially had high fever and a worsening condition for a mean of 73 days after transplantation (range 44 to 140 days). Results of biochemical tests showed very high serum levels of lactate dehydrogenase. Aspartate aminotransferase values were always markedly more elevated than those of alanine aminotransferase. Two patients had severe leukopenia. Results of histologic studies of the liver showed extensive areas of confluent necrosis and targetlike hepatocyte nuclei. Typical intranuclear viral inclusions were observed on electron microscopy. Adenovirus was cultured in all patients and in two relatives. Two patients died of liver failure; others recovered after cessation of immunosuppression. We conclude that adenovirus hepatitis can be fatal in liver transplant recipients. There is no specific treatment, and immunosuppression must be discontinued.

A prospective, multicenter, randomized study of high versus low positive end-expiratory pressure during extracorporeal membrane oxygenation. Keszler M, Ryckman FC, McDonald JV Jr, et al. (MK, Division of Neonatology, Georgetown University Medical Center, 3800 Reservoir Rd. N.W., Washington, DC 20007). *J Pediatr* 120:107–113, 1992

To test the hypothesis that increased positive end-expiratory pressure (PEEP) could prevent deterioration of pulmonary function and lead to more rapid recovery of lung function, we randomly assigned 74 patients undergoing extracorporeal membrane oxygenation (ECMO) at four centers to receive either high (12 to 14 cm H_2O) or low (3 to 5 cm H_2O) PEEP. The two groups were similar in terms of weight, gestational age, diagnosis, and pre-ECMO course. All other aspects of care were identical. Dynamic lung compliance was measured at baseline and every 12 hours. Radiographs of the chest were obtained daily. Survival rates were similar in the two groups: 36 of 40 for low PEEP and 34 of 34 for high PEEP. The duration of ECMO therapy was 97.4 ± 36.3 hours in the high-PEEP group and 131.8 ± 54.5 hours in the low-PEEP group ($p < 0.01$). Dynamic lung compliance throughout the first 72 hours of ECMO was significantly higher in patients receiving high PEEP. Radiographic appearance of the lungs correlated well with lung compliance: patients receiving high PEEP had significant deterioration of the radiographic score less frequently than those receiving low PEEP. High PEEP also was associated with significantly fewer complications. We conclude that PEEP of 12 to 14 cm H_2O safely prevents deterioration of pulmonary function during ECMO and results in more rapid lung recovery than traditional lung management with low PEEP.

Gastrointestinal Radiology

Cirrhosis: diagnosis by liver surface analysis with high-frequency ultrasound. Ferral H, Male R, Cardiel M, Munoz L, Quiroz Y, Ferrari F (HF, Dept. of Radiology, University of Minnesota, Box 292, UMHC, 420 Delaware St. S.E., Minneapolis, MN 55455). *Gastrointest Radiol* 17:74–78, 1992

To determine the sensitivity, specificity, and predictive values of the sonographic analysis of liver surface irregularities for the diagnosis of cirrhosis, the authors conducted a prospective and blinded study in 70 subjects with abnormal liver function tests. All patients included underwent liver biopsy within 15 days of the sonographic study. Twenty-three subjects with no signs or symptoms of liver disease were examined to assess the sonographic appearance of normal liver surface. Studies were performed with a small-parts probe, high-frequency transducer (7.5 MHz). Three basic patterns of liver surface were found: type I, normal; type II, focal abnormality; and type III, diffuse irregularity. Considering diffuse surface irregularity as an objective sonographic sign of cirrhosis, the study's sensitivity was 87.5%, specificity 81.5%, and positive and negative predictive values were 80% and 88.5%, respectively. Disease prevalence for cirrhosis was 45%. We conclude that sonographic analysis of the liver surface is a useful noninvasive test for the diagnosis of cirrhosis in the appropriate clinical setting.

Journal of Ultrasound in Medicine

The fetal thyroid: normal and abnormal sonographic measurements. Bromley B, Frigoletto FD Jr, Cramer D, Osathanondh R, Benacerraf BR (BB, Diagnostic Ultrasound Associates, 333 Longwood Ave., Boston, MA 02115). *J Ultrasound Med* 11:25–28, Jan. 1992

The thyroid of 31 fetuses at low risk for perinatal thyroid disease was evaluated sonographically. The transverse width and circumference of the fetal thyroid was measured prospectively to provide normative values for each gestational age. In addition, the thyroids of 23 fetuses at risk for thyroid disease were examined sonographically and compared to the control group. At birth, 18 of the neonates had no evidence of thyroid dysfunction, whereas 5 newborns had goiters and abnormal thyroid function. The fetal thyroid measurements for these 5 neonates were above the upper limit of the 95% confidence interval compared to the control group. The other 18 fetuses in the group at risk for thyroid disease but without evidence of thyroid dysfunction at birth had fetal thyroid measurement within the normal range.

Reprinted with permission by the American Institute of Ultrasound in Medicine.

News

Society for Pediatric Radiology Annual Meeting

The Society for Pediatric Radiology (SPR) will hold its 35th annual meeting May 14–17 at the Westin Hotel and Resort, Lake Buena Vista, FL. The meeting will include 60 short papers, 45 long papers, 24 scientific updates, 40 poster exhibits, a book corner, a videotape corner, and a case of the day. The Neuhauser Lecture, Diseases of the Pediatric Bone Marrow—MRI Observations, will be presented by W. E. Berdon. Fee: Physicians: SPR members, $270; nonmembers, $495; residents and fellows (letter required), no fee. Information: Lynne K. Tiras, CMP, Meeting Manager, International Meeting Managers, Inc., 4550 Post Oak Pl., Ste. 248, Houston, TX 77027; telephone: (713) 965-0566; fax: (713) 960-0488.

Clinical MRI: 1992 Update

Massachusetts General Hospital and Harvard Medical School will present Clinical MRI: 1992 Update, May 20–22, at the Four Seasons Hotel, Boston. The course, which is designed for practicing radiologists, will offer an approach to the interpretation of MR images that takes full advantage of new and emerging technologies. Category 1 credit: 29 hr. Information: Dept. of Continuing Medical Education, Harvard Medical School, P. O. Box 825, Boston, MA 02117; (617) 432-1525.

Tutorial in Scotland and Ireland

The Dept. of Radiology, Cornell University Medical College, and The New York Hospital, in conjunction with the University of Edinburgh, are sponsoring Tutorial in Scotland and Ireland, May 24–29, in St. Andrew's, Scotland, and Dublin, Ireland. Current, state-of-the-art imaging techniques and clinical aspects of orbital disease will be emphasized. Course director: Joseph P. Whalen. Category 1 credit: 30 hr. Fee: physicians, $475; residents and fellows, $275. Information: Dept. of Radiology, Cornell University Medical College, 1300 York Ave., New York, NY; telephone: (212) 746-2522; fax: (212) 746-8645.

Yale Symposium on Duplex and Color Doppler Ultrasound

Yale Symposium on Duplex and Color Doppler Ultrasound will be presented June 18–19 at Yale University, New Haven, CT. Course directors: Kenneth J. W. Taylor and Lynwood W. Hammers. Guest speaker: B. Thiele. Category 1 credit: 14 hr. Fee: physicians, $350; residents and sonographers, $300. Information: Kenneth J. W. Taylor, M.D., Ph.D., Dept. of Diagnostic Radiology, Yale University School of Medicine, 333 Cedar St., P. O. Box 3333, New Haven, CT 06510.

Practicum in Mammography for Technologists

The Dept. of Radiology, University of California, San Diego School of Medicine, is offering 5-day practicums in mammography for technologists. Beginning dates are June 22, Sept. 28, and Oct. 19. The course emphasizes clinical application and is designed to train technologists to perform high-quality mammographic examinations that satisfy the standards set by the American College of Radiology and the State of California Rules of Good Practice. The curriculum includes technical factors, quality assurance, basic and advanced positioning of the patient, patient relations and history, early detection of breast cancer, film critique, and extensive clinical experience. Medical director: Linda Olson. Course director: Louise Miller. CME credit (American Society of Radiologic Technologists): 40 hr. Fee: $500. Information: Ms. Shelley Van Buren, Dept. of Radiology, UCSD Medical Center, 225 Dickinson St., San Diego, CA 92103; (619) 543-6768.

Imaging Courses at Sea

The Dept. of Radiology, Monrovia Community Hospital, Monrovia, CA, is sponsoring Alaska '92—Cruise the Inland Passage: Breast Imaging at Sea, July 4–11, and Magnetic Resonance Imaging—Musculoskeletal Imaging at Sea, July 11–18. The course on breast imaging will be presented by Edward Sickles; the course on MR, by Donald L. Resnick. Category 1 credit is pending. Fee: either course alone: physicians, $495; residents, interns, nurses, and technologists (letter required), $395; both courses: physicians, $790; residents, interns, nurses, and technologists (letter required), $590. Information: Alaska 92—Breast Imaging at Sea or Alaska 92—Magnetic Resonance Imaging at Sea, Medical Seminars International, Inc., 18981 Ventura Blvd., Ste. 303, Tarzana, CA 91356; telephone: (818) 774-9077; fax: (818) 774-0244.

Mackinac Island Imaging Conference

The Dept. of Diagnostic Radiology, William Beaumont Hospital, Royal Oak, MI, is sponsoring Mackinac Island Imaging Conference, Aug. 3-6, at the Grand Hotel, Mackinac Island, MI. The conference is intended to be a refresher course and an update in the practical aspects of modern radiologic imaging and interventional techniques. Guest faculty: W. G. Bradley, Jr., R. Dietrich, T. L. Lawson, and M. D. Rifkin. Category 1 credit: 21 hr. Fee: physicians, $400; residents and Beaumont alumni, $200. Information: Program Coordinator, Miss Mary Anne Smith, William Beaumont Hospital, Royal Oak, MI 48073; (303) 551-6199.

Cardiovascular and Interventional Radiological Society of Europe Annual Meeting and Postgraduate Course

The Cardiovascular and Interventional Radiological Society of Europe will hold its annual meeting and postgraduate course Aug. 30-Sept. 3 at Hotel Gran Sitges, Palacio de Congressos, Sitges (Barcelona), Spain. Information: CIRSE, P. O. Box 201, CH 8028 Zürich, Switzerland; telephone: (01) 262 24 04; fax: (01) 261.05.78 or M. Delors Puig, Roger de LLuria, 120, 2n, E-08037 Barcelona, Spain; telephone: 34 3 258 19 21; fax: 34 3 207 67 60.

Radiation, Physics, and Biology

Radiation, Physics, and Biology will be presented Aug. 31-Sept. 4 at NYU Medical Center, New York City. The course, designed specifically for residents in diagnostic radiology and nuclear medicine, is an intensive review of physics and biology basic to radiology. The emphasis is on concepts. Category 1 credit: 34 hr. Fee: $600. Information: NYU Medical Center, Post-Graduate Medical School, 550 First Ave., New York, NY 10016; telephone: (212) 263-5295; fax: (212) 263-5293.

Pacific Northwest Diagnostic Ultrasound: OB/GYN Symposium

The American Institute of Ultrasound in Medicine and Swedish Hospital Medical Center, Seattle, are cosponsoring Pacific Northwest Diagnostic Ultrasound: OB/GYN Symposium, Sept. 10-12, at the Sheraton Hotel, Seattle. The symposium will provide timely and useful information on obstetric and gynecologic sonography and Doppler imaging, including detection of ovarian cancer. Course directors: David A. Nyberg and Barry S. Mahony. Category 1 credit: 19 hr. Fee: (3-day course/Saturday only): physicians, $400/$250; residents and sonographers, $275/$150. Information: Renee Schutter, 1229 Madison St., #1150, Seattle, WA 98104; telephone: (206) 386-6300, ext. 426; fax: (206) 386-6312.

Pittsburgh Breast Imaging Seminar

The 12th annual Pittsburgh Breast Imaging Seminar will be held Sept. 10-13 at the Westin William Penn Hotel, Pittsburgh. Course codirectors: Kathleen M. Harris, Ellen B. Mendelson, Ingrid E. Naugle, and William R. Poller. Category 1 credit: 28 hr. Information: Pittsburgh Breast Imaging Seminar, Dept. of Continuing Medical Education, West Penn Hospital, 4800 Friendship Ave., Pittsburgh, PA 15224; (412) 578-6926.

Symposium on Transrectal Ultrasound

Huron Valley Radiology, Catherine McAuley Health Systems, Ann Arbor, MI, will present the 7th International Symposium on Transrectal Ultrasound in the Diagnosis and Management of BPH and Prostate Cancer, Sept. 11-13, at the Fairmont Hotel, Chicago. Category 1 credit: 18 hr. Information: Diversified Conference Management, Inc., P. O. Box 2508, Ann Arbor, MI 48106; (313) 665-2535 or (800) 458-2535.

Vancouver Imaging Update 1992

The Dept. of Radiology, University of British Columbia, is sponsoring Vancouver Imaging Update 1992, Sept. 13-17, at the Pan Pacific Hotel, Vancouver. The conference will include lectures on a wide variety of topics in diagnostic and interventional radiology. Neuroradiology, musculoskeletal radiology, sonography, and interventional radiology will be emphasized. Guest faculty: C. A. Helms, W. Kucharczyk, F. C. Laing, and E. vanSonnenberg. Category 1 credit: 24 hr. Fee: physicians, $500; residents, fellows, and technologists, $300. Information: Dr. P. L. Cooperberg, Chief, Dept. of Radiology, St. Paul's Hospital, 1081 Burrard St., Vancouver, B.C., Canada V6Z 1Y6; telephone: (604) 631-5026; fax: (604) 631-5283.

Dose, Time, and Fractionation in Radiation Oncology

The American Association of Physicists in Medicine and the Dept. of Human Oncology, University of Wisconsin, will present the 4th International Conference on Dose, Time, and Fractionation in Radiation Oncology, Sept. 16-19, at the Edgewater Hotel, Madison, WI. The topic of the conference will be "Prediction of Response in Radiation Therapy: Radiosensitivity and Repopulation." Information: Bhudatt Paliwal, Ph.D., Conference Chairman, Dept. of Human Oncology and Medical Physics, University of Wisconsin, 600 Highland Ave., K4/B100, Madison, WI 53792; (608) 263-8506.

Update in Film Screen Mammography

The University of Virginia will present its 7th annual postgraduate course, Update in Film Screen Mammography, Sept. 30-Oct. 2, at the Jefferson Hotel, Richmond, VA. Category 1 credit: 20 hr. Fee: physicians, $450; technologists, $325. Information: R. L. Boswell, Programs Director, Dept. of Radiology, Box 170, University of Virginia Health Sciences Center, Charlottesville, VA 22908; telephone: (804) 924-9387; fax: (804) 982-1618.

Fall Foliage Imaging Seminar

The Dept. of Radiology, University of Vermont, will present Fall Foliage Long Weekend Imaging Seminar, Oct. 9-11, at the Sheraton Hotel and Conference Center, Burlington, VT. Guest faculty: W. Berdon, P. Cooperberg, and M. Federle. Category 1 credit: 12 hr. Fee: $250. Information: Linda Saia, CME, University of Vermont, 233 Rowell Bldg., Burlington, VT 05405-0068; (802) 656-2292.

Radiological Society of North America 1992 Officers and Board of Directors

The Radiological Society of North America officers for 1992 are as follows: president, Robert G. Parker; president-elect, Thomas S. Harle; first vice-president, Derek C. Harwood-Nash; second vice-president, James E. Marks; third vice-president, John S. Laughlin; and historian, William R. Eyler. The chairman of the board of directors is O. Wayne Houser. Other members of the board are liaisons for the annual meeting, Seymour H. Levitt and Helen C. Redman; secretary-treasurer, Ernest J. Ferris; liaison for education, Michael A. Sullivan; liaison for publications, David B. Fraser; and members, Parker, Houser, and Harle.

The American Board of Radiology Examinations

Written examinations for the American Board of Radiology (ABR) are scheduled for Oct. 1-2, 1992, and Oct. 14-15, 1993. Oral examinations will be held at the Executive West Hotel in Louisville, KY, June 1-5, 1992. The ABR will accept applications for admission to the examinations after July 1, but not later than Sept. 30, in the year *preceding* the year in which the examination is to be taken. For application forms and further information: Office of the Executive Director, The American Board of Radiology, 2301 W. Big Beaver Rd., Ste. 625, Troy, MI 48084.

Meeting and Course Review

For the reader's convenience, a summary of upcoming meetings and courses is provided. Detailed listings are given in the *AJR* issue given in parentheses.

Preceptorships in Ultrasound at Johns Hopkins, times arranged, Baltimore (June 1991)
Practicum in Breast Imaging, times arranged, Baltimore (Aug 1991)
Radiology in Scotland, April 26-May 3, Edinburgh and St. Andrews, Scotland (Jan)
Present Concepts in Radiology, April 28-May 1, San Francisco (Feb)
Spring Roentgen Conference, April 29-May 3, New Orleans (March)
Brachytherapy Symposium, May 1-2, Columbus, OH (Jan)
Cleveland Conference on MR Imaging, May 1-3, Cleveland (April)
Ultrasound 1992—Advances in Diagnostic Imaging, May 2, Lebanon, NH (March)
Practical Interventional Radiology—1992, May 4-6, Cambridge, MA (Feb)
MRI: A State of the Art Clinical Review, May 4-8, San Francisco (Jan)
Visiting Fellowships in MR Imaging: introductory, May 4-8 and June 8-12; **advanced,** May 11-15; Philadelphia (April)
Advanced Seminars in Diagnostic Imaging, May 8-10, Laguna Niguel, CA (Jan)
Radiology Review Course, May 10-15, Miami Beach, FL (Feb)
Symposium on Diagnostic Ultrasound, May 15-17, New York City (March)
Positron Emission Tomography, May 15-17, Lake Buena Vista, FL (April)
Yale Clinical MRI, May 18-20, New Haven, CT (April)
Mammographic Interpretation, May 18-21, Sept. 14-17, and Oct. 26-29, Boston (April)
International Symposium on Diagnostic Imaging, May 18-22, Barcelona (Nov 1991)
Doppler and Duplex Imaging, May 21-24, San Diego (Jan)
Vanderbilt Sonography Symposium, May 22-23, Nashville (Jan)
Spoleto Festival Update, May 28-30, Charleston, SC (Jan)
Spanish Radiological Society National Conference, June 1-5, Seville, Spain (March)
Mammography Update: Practical Breast Imaging, June 5-7, Point Clear, AL (April)
Canadian Association of Medical Radiation Technologists 50th Anniversary Conference, June 7-12, Ottawa (Feb)
Advances in Cardiopulmonary Imaging, June 11-13, Salzburg, Austria (Nov 1991)
Symposium on MR of the Musculoskeletal System, June 18-20, Palma de Mallorca, Balearic Islands, Spain (April)
Concepts of Magnetic Resonance, June 20-26, Kiawah Island, SC (Feb)
Pitt Summer Imaging Course, June 21-25, Williamsburg, VA (Feb)
Magnetic Resonance Imaging in Spain and Morocco, June 28-July 1, Barcelona, and July 3-5, Casablanca (April)
Workshop on Vascular Anomalies, July 1-3, Denver (March)
Paediatric Imaging Update, July 5-10, Port Douglas, Australia (March)
Course on Body Imaging, July 13-17, Santa Fe, NM (March)
Diagnostic Imaging Seminar, July 13-17, Edgartown, MA (Martha's Vineyard) (April)
Vascular Imaging and Intervention for the 90s, July 17-19, San Francisco (April)
Diagnostic Imaging Update, July 20-22, San Francisco, and July 23-26, Carmel, CA (March)
Clinical Imaging for Non-Radiologists, July 20-24, San Diego (March)
The Sharper Image in MRI, July 27-31, Colorado Springs, CO (April)
MRI and Musculoskeletal Imaging, July 27-Aug. 1, Laguna Niguel, CA (March)
Contemporary Medical Imaging IX, Aug. 12-16, Hilton Head Island, SC (April)
Summer Practicum, Aug. 16-20, Keystone, CO (April)
Barcelona 1992 Post-Games Imaging Conference, Aug. 17-21, Barcelona (April)
European Symposium on Uroradiology, Aug. 24-27, Herlev, Denmark (Aug 1991)
International Skeletal Society Refresher Course, Aug. 26-29, Stockholm (March)
Congress of Asian Federation of Societies for Ultrasound in Medicine and Biology, Aug. 30-Sept. 3, Seoul, Korea (Feb)
Ultrasound Angiography 92, Sept. 2-4, University of Southampton, United Kingdom (Feb)
MRI Visiting Fellowships at UCLA, Sept. 14-18, Oct. 5-9, and Dec. 7-11, Los Angeles (Sept 1991)
International Course on MR Imaging, Oct. 25-28, Riyadh, Kingdom of Saudi Arabia (March)

AJR carries announcements of courses, symposia, and meetings of interest to its readers if received a minimum of 5 months before the event. There is no charge; receipt of items by the *AJR* Editorial Office is not acknowledged. Submit items for publication typed double-spaced. Provide title, date, location, brief description, sponsor, course directors, fees, category I credit, and address and telephone number for additional information. Faculty from the host institution will not be listed. Guest faculty names will appear **only** if initials are provided. Mail news items to *AJR* Editorial Office, 2223 Avenida de la Playa, Suite 103, La Jolla, CA 92037-3218.

American Roentgen Ray Society:
Officers, Committees, and Membership Information

Officers

President: John A. Kirkpatrick, Jr.
President-elect: A. Everette James, Jr.
1st Vice-president: Andrew K. Poznanski
2nd Vice-president: George R. Leopold
Secretary: Joseph T. Ferrucci, Jr.
Treasurer: Beverly P. Wood

Executive Council: R. N. Berk, M. P. Capp, W. J. Casarella, N. R. Dunnick, R. G. Evens, J. T. Ferrucci, Jr., A. E. James, Jr., J. A. Kirkpatrick, Jr., A. M. Landry, Jr., G. R. Leopold, J. E. Madewell, T. C. McLoud, A. A. Moss, A. K. Poznanski, R. J. Stanley, J. H. Thrall, K. H. Vydareny, N. O. Whitley, B. P. Wood, R. J. Alfidi, chairman

Committees

Editorial Policy: R. N. Berk, E. Buonocore, M. M. Figley, C. R. B. Merritt, K. Valji, C. A. Rohrmann, Jr., W. J. Casarella, chairman

Education and Research: R. R. Hattery, C. B. Higgins, B. J. Hillman, R. J. Stanley, W. M. Thompson, N. O. Whitley, chairman

Finance and Budget: R. K. Gedgaudas-McClees, A. A. Moss, J. R. Thornbury, K. H. Vydareny, J. H. Thrall, chairman

Nominating: R. G. Evens, P. J. Fritzsche, A. A. Moss, chairman

Publications: E. Buonocore, C. R. B. Merritt, C. A. Rohrmann, Jr., W. J. Casarella, chairman

Membership: J. E. Madewell, T. C. McLoud, A. A. Moss, K. H. Vydareny, chairman

Representatives to Other Organizations

American Board of Radiology: W. J. Casarella, J. A. Kirkpatrick, Jr., L. F. Rogers

American College of Radiology: R. A. Gagliardi, J. E. Madewell, B. L. McClennan, R. J. Stanley

American Medical Association: S. F. Ochsner, delegate; K. L. Krabbenhoft, alternate; K. L. Kidd, CPT Advisory Committee

American National Standards Institute: M. E. Haskin

National Council on Radiation Protection and Measurements: F. D. Miraldi, E. L. Saenger

Armed Forces Institute of Pathology: J. E. Madewell

Meeting Arrangements

Annual Meetings: May 10–15, 1992, Marriott's World Center, Orlando, FL; April 25–30, 1993, Marriott San Francisco, San Francisco, CA

Annual Meeting Committee: J. K. Crowe, N. R. Dunnick, R. R. Lukin, N. H. Messinger, R. J. Stanley, R. D. Steele, Jr., A. M. Landry, Jr., chairman

Instructional Courses: Bruce L. McClennan, associate chairman; R. J. Stanley, chairman

Scientific Program: P. H. Arger, T. B. Hunter, D. Kushner, T. C. McLoud, L. B. Talner, J. H. Thrall, A. E. James, Jr., chairman

Scientific Exhibits: J. R. Haaga, D. S. Hartman, R. G. Ramsey, N. R. Dunnick, chairman

ARRS Membership

An application form is printed in the January issue of the Journal. For consideration at the 1993 ARRS meeting, send completed forms before February 1, 1993, to American Roentgen Ray Society, 1891 Preston White Dr., Reston, VA 22091. Active members are graduates of an approved medical or osteopathic school or hold an advanced degree in an allied science. They must practice radiology or work in an associated science in the United States or Canada and be certified by the American Board of Radiology, American Osteopathic Board of Radiology, or Royal College of Physicians of Canada or otherwise adequately document training and credentials. International members are foreign radiologists or scientists who are active in radiology or an allied science. Members-in-training are residents or fellows in radiology or postgraduate students in an allied science. Additional application forms can be obtained from the ARRS offices in Reston, VA.

Business Office

Paul Fullagar, Executive Director, American Roentgen Ray Society, 1891 Preston White Dr., Reston, VA 22091; (703) 648-8992.

Classified Advertisements

Positions Available

IMMEDIATE OPENING FOR BC/BE GENERAL DIAGNOSTIC RADIOLOGIST to join 2-person group in private office and 160-bed hospital. Practice includes all aspects of diagnostic radiology including MRI. Located on the lovely southern Oregon coast. Competitive compensation, fringe benefits, and partnership in 2 yr. Send CV to Michael Quinn, M.D., South Coast Radiology, 2650 N. 17th, Coos Bay, OR 97420; (503) 267-5411. 5–6ap

ANGIO/INTERVENTIONAL SECTION CHIEF—Fill by June 30, 1992. Busy division. 2500 exams/yr. Rank based on experience. Unlimited potential. Reply Box D40, *AJR* (see address this section). 5–6a

NEURO/MRI RADIOLOGIST—Excellent opportunity in the resort community of Palm Springs, CA. Expanding radiology practice at 350-bed medical center with new dept. and on-campus outpatient facilities under construction. Radiology group seeks established authority in neuroradiology and MRI to lead expanding section into the future. Current dept. equipped with 2 state-of-the-art 1.5-T MRI units (GE and Picker) and associated modalities for complete neuroradiology services. A dynamic individual, well-versed in community relations, will be given top consideration. Generous compensation including near-partner salary with early partnership contemplated. Contact Sharon Tanabe, Korn/Ferry International, 100 E. Wardlow Rd., Ste. 100, Long Beach, CA 90807; (310) 595-1101, fax (310) 427-4225. 5ap

HOSPITAL-BASED, BC/BE RADIOLOGIST IS needed to join newly planned subregional medical center (campus). Must be proficient in general diagnostic radiology, ultrasound, nuclear medicine, CT, and MRI. Excellent opportunity plus attractive financial package. Located in east, central Montana along the Yellowstone River. Great outdoors for recreation, hunting, and fishing. Excellent education system. Lifestyle is rural and family-oriented. Send CV to Vice-President, Business Services, Holy Rosary Hospital, 2101 Clark, Miles City, MT 59301. 5–7ap

NEURORADIOLOGIST—A 25-person radiology group in central New Jersey seeks a fourth neuroradiologist well-versed in all neuroimaging modalities and procedures. Senior member status or eligibility in the ASNR is required. Practice includes 2 450-bed hospitals, 3 offices, 3 MRI scanners, 5 CT scanners, a radiology residency, and medical student teaching. Send CV to Richard Feinstein, M.D., c/o Kathy McGrath, Radiology Group of New Brunswick, 230 Old Bridge Tpk., South River, NJ 08882. 5–6a

VETERANS AFFAIRS MEDICAL CENTER, AUGUSTA, GA, is seeking a physician, board-eligible/certified in radiology. Subspecialty interest in chest, skeletal, GI, or interventional radiology is desirable but not essential. This 1142-bed, tertiary-care medical center is affiliated with the Medical College of Georgia. Faculty appointment commensurate with qualifications and experience. Augusta enjoys a moderate climate, reasonable cost of living, numerous recreational facilities, and institutions of higher learning. An equal opportunity employer. For additional information, contact George T. Jamarik, M.D., Chief, Radiology Service, (404) 823-2236. 5a

DENVER, CO—Diagnostic radiologist needed to replace a retiring partner in an outpatient practice with Denver's largest multispecialty group. General radiology practice, with mammography, ultrasound, and nuclear medicine. Future expansion to include CT and possibly outpatient interventional radiography. Moving to a new facility in Cherry Creek in the summer of 1992. Send CV to Kari Miller, Accord Medical Centers, 1555 Clarkson, Denver, CO 80203. 5a

GOOD LIFE, GOOD MONEY—Radiologist needed for growing practice that covers 2 hospitals and 2 free-standing clinics. Modalities include R&F, general, mammography, CT, MRI, nuclear medicine, SPECT, and special procedures. Denton, population 60,000, located 30 mi. north of Dallas/Fort Worth, has 2 recreational lakes within 15 mi. and 2 major universities. Attractive financial and benefit packages are offered. Contact Family Radiology with CV at 1614 Scripture, Ste. 2, Denton, TX 76201; (817) 387-6159. 5a

CALIFORNIA, CENTRAL COAST (POP. 60K)—BC radiologist sought for a small hospital with an active outpatient service. Routine radiology with mammography and ultrasound. Solo position. Relief coverage available. Generous salary. Full-time or 6–8 mo/yr. Write Box D44, *AJR* (see address this section). 5–6ap

RADIOLOGISTS—This 911-bed medical center, affiliated with University of Miami, is seeking a board-eligible/certified radiologist with training and experience in diagnostic, CT, interventional, neuroradiology, and/or MRI. An interest in clinical and academic programs and in basic research is desirable. Candidates should send CV to VA Medical Center, Personnel Service (05C3), Jean Little, 1201 N.W. 16th St., Miami, FL 33125; (305) 324-4455, ext. 3617. EOE. 5a

BOSTON—Expanding private-practice group. No night or evening call. Need experience in mammography. Great lifestyle. Salary leading to equal partnership. Send letter and CV to Box E49, *AJR* (see address this section). 5–10a

INTERVENTIONAL RADIOLOGIST, ALBUQUERQUE, NM—A well-established, 14-physician group has an immediate opening for a fellowship-trained vascular interventionalist. Initially, approximately 40–50% of work time interventional; additional interventional volume as senior physicians phase down. Practice serves a major hospital in the metro area, 2 MRI centers, 2 outpatient centers, and 3 outlying facilities. All vascular interventional work at 1 location. Candidate must have ability/desire to perform both interventional and general radiology procedures. Strong desire to live and work in the southwest a must. Competitive compensation package. Send CV with references to P. O. Box 7309, Albuquerque, NM 87194-7309. 5–6a

GENERAL RADIOLOGIST, RUIDOSO, NM—Solo practice with advantages of large group practice (CME, vacations, etc.). Small, but growing resort community in southern New Mexico. Quality outdoor lifestyle and excellent skiing. Professional support via teleradiology and vacation coverage by 14-physician group in Albuquerque. Position requires experience in general radiology, CT, mammography, and ultrasound. Strong desire to live and work in the southwest a must. Competitive compensation package. Send CV with references to P. O. Box 7309, Albuquerque, NM 87194-7309. 5–6a

NORTHERN CALIFORNIA—The Permanente Medical Group, Inc., is seeking a BC radiologist with multimodality interests and fellowship training in MR to join a 12-person group serving a 337-bed acute-care hospital and 2 outpatient clinics. Teaching opportunities are available with residents of subspecialty services on rotation from Stanford University Hospital, as well as our own medical residents. We have sited a GE 1.5-T MRI system. Competitive salary and excellent benefits. Please send inquiries and CV to Bruce Baker, M.D., Chief, Dept. of Radiology, Kaiser Permanente Medical Center, 900 Kiely Blvd., Santa Clara, CA 95051; (408) 236-4444. EOE. 5–7a

DIAGNOSTIC RADIOLOGIST, ABDOMINAL IMAGING—The University of Missouri–Columbia Hospital and Clinics is seeking a radiologist with expertise in abdominal imaging (GI, CT, ultrasound, and MRI). Board-certification required. Fellowship desirable. Tenure and nontenure tracks available at assistant and associate professor levels. Address inquiries to Robert J. Churchill, M.D., Dept. of Radiology, University of Missouri–Columbia Hospital and Clinics, One Hospital Dr., Columbia, MO 65212. An equal opportunity/affirmative action employer. 5–10ap

RADIOLOGY DEPT. HEAD—St. Joseph Mercy Hospital (SJMH), a 554-bed teaching hospital in Ann Arbor, MI, is seeking a qualified radiologist to serve as head of radiology. The selected candidate will provide leadership to the 36-member Dept. of Radiology and serve as administrative director for hospital radiology services. Candidates must have both clinical and administrative expertise, including board certification. SJMH is part of the Catherine McAuley Health System, affiliated with the Sisters of Mercy Healthcare Corporation. The 720 members of the SJMH medical staff provide state-of-the-art care to a wide service area, with specialized programs in cardiothoracic surgery, oncology, and rehabilitation. The Dept. of Radiology offers comprehensive inpatient and outpatient diagnostic imaging including angiography, CT, and MRI. Interested candidates should send CV to S. J. Weber, St. Joseph Mercy Hospital Staff Services, P. O. Box 995, Ann Arbor, MI 48106. Equal opportunity employer. 5ap

SKELETAL RADIOLOGIST—The College of Physicians and Surgeons of Columbia University is searching for a staff radiologist for our skeletal division. A multimodality approach is used, including state-of-the-art MRI. Salary and academic rank will be commensurate with experience and qualifications. Responsibilities include patient care, teaching, supervising residents, and involvement in research. Requirements include board certification in diagnostic radiology and experience or fellowship in skeletal radiology. New York state medical license required; narcotics license desirable. Please send resume to Philip O. Alderson, M.D., Dept. of Radiology, 622 W. 168th St., New York, NY 10032. Columbia University is an affirmative action/equal opportunity employer. 5a

PIEDMONT, NORTH CAROLINA—A 6-member amicable group covering all radiology subspecialty areas has an immediate opening due to sudden retirement. Fellowship preferred, but not mandatory. New regional medical center on I-85/I-40 to be completed in 1995. Rapidly growing, nice family area with excellent schools and recreational opportunities. Send CV to Edward J. Duszlak, M.D., Dept. of Radiology, Alamance County Hospital, 319 N. Graham Hopedale Rd., Burlington, NC 27215. 5ap

DIRECTOR, DIVISION OF ULTRASOUND—The Dept. of Radiology, The University of Texas Medical Branch, is looking for a director of diagnostic ultrasound at the associate professor or professor entry level. The Division of Ultrasound, in our dept., is poised for growth and expansion. We require a leader with drive, initiative, and vision, and 1 who is still in his or her growing career phase. The University of Texas Medical Branch employs more than 8400 employees, and Dept. of Radiology performs more than 200,000 exams/yr. The campus provides a fertile environment for those wishing to pursue an academic career. The clinical material and academic support are excellent. The dept. boasts many peer-reviewed publications and textbooks resulting from an inherent feature of the institution that allows 1 to pursue academic interests with freedom. Galveston is a very comfortable community with few large-city problems. It has an extremely pleasant climate, with the Gulf breeze making it exceptionally attractive throughout the yr. Outdoor activities abound, including boating, sailing, fishing, and tennis. The winters are extremely mild. More than half of the present faculty have lived in this area for 15 yr or more. The dept. and institution are quite stable and have proved an excellent place for many of us to pursue academic careers. The position we offer has the foundation for the development of a truly superior academic career. Interested persons should send their CV to Leonard E. Swischuk, M.D., Chairman Ad-Interim, Dept of Radiology, The University of Texas Medical Branch, Galveston, TX 77550. UTMB is an equal opportunity, affirmative action employer, M/F/H/V. UTMB hires only individuals authorized to work in the United States. 5–7a

MRI RADIOLOGIST, ATLANTA, GA—Radiologist trained in MRI needed for free-standing MRI facility. State-of-the-art equipment and experienced techs. Income potential to $250,000+. Send CV to P. O. Box 88532, Dunwoody, GA 30356. 5ap

FULL-TIME BC/BE DIAGNOSTIC RADIOLOGIST needed to replace retiring senior partner in a friendly, cooperative, 4-person group in south-central Idaho. 165-bed hospital with GE Signa 1.5-T MR, GE 9800 Quick CT, Acuson XP, and good technical staff. General radiology including angio, interventional, and nuclear medicine. Good income and vacation schedule, 1 yr to partnership. Nice community with extensive nearby skiing, hunting, fishing, etc. 80 mi. from Sun Valley, 4-hr drive from Yellowstone. Send CV and references to Dr. Evan Thomas, Southern Idaho Radiology, P. O. Box AB, Twin Falls, ID 83303. 5–7ap

DIAGNOSTIC RADIOLOGIST FOR TOP-FIVE CITY (MONEY MAGAZINE OCTOBER '91)—Progressive, well-established group of 9 board-certified radiologists has position immediately available for a recently trained BC diagnostic radiologist. Fellowship training preferred, but will consider qualified individual with special expertise in body imaging; angiographic experience is optional. Practice includes 2 tertiary hospitals (850 and 350 beds), private office, and 2 imaging centers. State-of-the art equipment includes 2 GE 1.5-T MRI units; ATL, Toshiba, and Acuson duplex color ultrasound; and 5 GE 9800 CT. High plains offer moderate climate, and surrounding area is ideal for outdoor interests, including skiing, hunting, boating, and fishing. Excellent compensation and benefits package leading to full partnership. Please reply with CV to Todd R. Samuels, M.D., Lubbock Radiology Associates, 3707 21st St., Lubbock, TX 79410. 5–8ap

BC/BE GENERAL DIAGNOSTIC RADIOLOGIST needed to join 3 radiologists in 70-physician multispecialty clinic. Also responsible for radiology services at 250-bed hospital connected to clinic. All radiology modalities available, including CT and MR. Competitive first-yr guarantee with excellent benefit package. Eligibility for shareholdership after 1 full fiscal yr. Community of 52,000 in beautiful Mississippi River Valley. Send CV to P. Stephen Shultz, M.D., Medical Director, Skemp Clinic, Ltd., 800 West Ave., S., La Crosse, WI 54601; (608) 782-9760, ext. 6329. 5–7ap

DIAGNOSTIC RADIOLOGIST, FLORIDA—Staff radiologist is being sought by the University of Florida Health Science Center/Jacksonville for a full-time faculty position. Special interest, expertise, or fellowship training in CT, ultrasound, MR, pediatric, interventional, or nuclear radiology is preferable. Salary and fringe benefits are excellent. An academic appointment will be at the rank of instructor/assistant professor/associate professor/professor, depending on training, background, and experience. Application recruiting deadline is June 1, 1992. Send CV and references to Chairman, Search Committee, Dept. of Radiology, University Medical Center, 655 W. 8th St., Jacksonville, FL 32209. AA/EOE. 5a

TWO DIAGNOSTIC RADIOLOGISTS, WASHINGTON—prominent, 100-physician multispecialty clinic in Pacific Northwest seeks both a diagnostic radiologist and an interventional radiologist. Interventional radiologist should have fellowship training and/or extensive experience in interventional radiology. Diagnostic radiologist should have general radiology experience to include all full-scope imaging services. Guaranteed salary and partnership track available. Excellent benefit package. Abundant 4-season recreational opportunities. Send CV to Fred Bockenstedt, M.D., P. O. Box 489, Wenatchee, WA 98807. 5ap

DIAGNOSTIC RADIOLOGIST, TOLEDO, OH—Expanding 23-radiologist group seeks BC radiologist with 1 or more yr fellowship experience. Interest/expertise in either pediatric radiology, mammography, or nuclear medicine would be helpful. Position requires no special procedures and leads to equal partnership. Our group values quality of work as well as personal time and offers an excellent salary with very generous time off. Coverage includes 850-bed tertiary hospital, 350-bed suburban hospital, and 3 outpatient offices with more than 240,000 exams/yr. All modalities are represented. Excellent family-oriented community with great schools. Send CV to Drs. David Parker or Keith Wilson, Roemer Bldg., 3912 Sunforest Ct., Toledo, OH 43623; (419) 471-4438 days. 5–7ap

THE UNIVERSITY OF OKLAHOMA HEALTH SCIENCES CENTER is seeking a staff radiation oncologist in the Dept. of Radiation Therapy. The position will be available July 1, 1992. The closing date for applications is June 15, 1992. Salary level is open. A list of requirements follows: board certification in radiation oncology by the American Board of Radiology, experience working in a teaching institution, experience with brachytherapy, 3-dimensional treatment planning, electron therapy, and resident teaching. Inquiries should be directed to Carl R. Bogardus, Jr., M.D., Chairman, University of Oklahoma Health Sciences Center, Dept. of Radiological Sciences, Division of Radiation Therapy, P. O. Box 26901, Oklahoma City, OK 73190; (405) 271-5641. The University of Oklahoma is an equal opportunity/affirmative action employer. 5a

PARTNERSHIP POSITION IN PALM SPRINGS, CA—Well-established, 9-member group has openings for 2 board-certified radiologists. A physician with a strong background in MRI is sought as director of the section of MRI. The other position requires a physician with mammography experience to direct imaging in the breast health section of a new comprehensive cancer center. The group covers a 350-bed hospital and 2 offices in a desirable, rapidly expanding area of southern California. MRI facilities include 1.5-T Picker Vista HPQ with MRA package, ViStar imaging computer, and 1.5-T GE Signa. Other equipment includes 3 CT, a Cemax image processor, 2 Acuson color-flow Doppler ultrasound, 4 nuclear cameras including 2 SPECT, and all other diagnostic modalities. Ground has just been broken on a new 25,000 sq. ft. radiology wing, which will be furnished with state-of-the-art equipment. New trauma center, cancer center, and rehab hospital being built. Excellent compensation and benefits package leading to full partnership. Beaches and large-city amenities of Los Angeles only 2 hr away. Yr-round sunny weather. Ample free time to enjoy southern California and the unparalleled recreational opportunities offered by the resort community of Palm Springs. Direct inquiries to Marvin J. Friedenberg, M.D., Desert Hospital, Dept. of Radiology, 1150 N. Indian Canyon Dr., Palm Springs, CA 92262. 5xa

EXCELLENT OPPORTUNITY FOR BE/BC DIAGNOSTIC RADIOLOGIST with training in all modalities to join active, 7-member group in midwestern university town with medical school affiliation. Abundance of cultural opportunities and outdoor recreation. Excellent salary with early partnership. Please send inquiries and CV to Mark Schneider, M.D., or Dean Hountras, M.D., 1000 S. Columbia Rd., Grand Forks, ND 58206-6003; (701) 780-6596. 4–6ap

IMAGING SCIENTIST—Ph.D. in electrical engineering or computer science and postdoctoral experience in medical image analysis with an emphasis on computer vision techniques, automated motion analysis, and mathematical optimization sought for appointment at the rank of assistant professor in the Dept. of Diagnostic Radiology. This position is in a research group working on medical image analysis in a C/UNIX/X environment. Please send applications with CV to James S. Duncan, Ph.D., Associate Professor of Diagnostic Radiology and Electrical Engineering, Yale University School of Medicine, P. O. Box 3333, New Haven, CT 06510. Yale University is an equal opportunity/affirmative action employer. Applications from women and minority group members are encouraged. Application deadline is May 31, 1992. 4–5a

IMMEDIATE OPENING FOR BC/BE GENERAL RADIOLOGIST with experience in basic interventional and vascular radiology. Join a group of 4 radiologists in a 160-bed hospital located in Allentown, PA, about 60 mi. northwest of Philadelphia. The daily practice includes all aspects of general radiology, CT, ultrasound, and nuclear medicine. Please call or send CV to Asad Shohadai, M.D., Allentown Osteopathic Medical Center, 1736 Hamilton St., Allentown, PA 18104; (215) 770-8700. 5xa

ISRAEL, DIAGNOSTIC RADIOLOGY—Opportunities for 3- to 4-wk or longer working vacations in a number of Israeli medical centers, on a volunteer basis. Positions varied, arrangements flexible. For information contact Jonathan H. Fish, M.D., 1844 San Miguel Dr., #302, Walnut Creek, CA 94596; (510) 947-0560. 5–7xa

PEDIATRIC RADIOLOGY—The Medical College of Georgia seeks a general pediatric radiologist and a pediatric radiologist with expertise in pediatric imaging. These individuals will provide general and specialized pediatric radiology services, guide the integration of imaging services within pediatric radiology, and help plan and implement pediatric radiology services for the upcoming 175-bed Children's Medical Center. Tenured or nontenured positions are available at assistant, associate, or full professor levels. The senior appointee will become head of the Pediatric Radiology Section. Call or write Dr. Charles G. Howell, Jr., Pediatric Radiology Search Committee, Pediatric Surgery Section, Medical College of Georgia, Augusta, GA 30912-4070; (404) 721-3941. MCG is an equal opportunity/affirmative action employer. 5xa

UNIVERSITY OF CALIFORNIA, SAN FRANCISCO, DIRECTOR, RADIOLOGICAL INFORMATICS—The Dept. of Radiology at the University of California, San Francisco, is searching for a director for the newly created Section of Radiological Informatics. The Director of Radiological Informatics will lead a group of computer scientists and other professionals to provide both research and clinical service in picture archiving and communication systems (PACS), radiology information systems (RIS), office automation, computer-assisted instruction (CAI) with digital imaging, expert system applications, image processing, and speech-recognition applications. These activities will focus on software design and implementation, but some hardware fabrication on the board level will also be anticipated. A new imaging laboratory, which will be the primary site for this team, will begin construction shortly. The director will be appointed at the level of associate professor or professor of radiology in residence (depending on qualifications) and will also serve as vice-chairman and a member of the executive committee of the Dept. of Radiology at UCSF. The director should have a Ph.D. degree in a related field, several yr of experience in a related position, an established track record in terms of publications and peer-reviewed funding, experience in teaching postdoctoral students, and demonstrated leadership of a research group in radiological informatics. The University of California, San Francisco is an equal opportunity/affirmative action employer. Minority groups, women, and handicapped individuals are encouraged to apply. Send CV to Charles A. Gooding, M.D., Chair, Search Committee, UCSF, Dept. of Radiology, San Francisco, CA 94143-0628. 5a

COMMUNITY HOSPITAL WITH TWO LOCATIONS IN NORTHEAST PHILADELPHIA seeks a general radiologist to perform mammography, ultrasound, CT, and nuclear medicine. Knowledge of angio helpful, but not necessary. Send CV and date available to Martin Friedman, D.O., Frankford Hospital, X-Ray Dept., Knights and Red Lion Rd., Philadelphia, PA 19114. 4–5ap

GENERAL DIAGNOSTIC RADIOLOGIST WITH IMAGING AND MAMMOGRAPHY EXPERIENCE—William Beaumont Hospital is a modern, expanding, tertiary-care teaching medical center in southeast Michigan with approved residency and fellowship in diagnostic radiology. Excellent facilities and remuneration. We are seeking a general radiologist with training and experience in imaging and/or mammography. Please send CV to Jalil Farah, M.D., Chairman, Diagnostic Radiology, William Beaumont Hospital, 3601 W. 13 Mile Rd., Royal Oak, MI 48073. 4–6a

RADIOLOGIST, TYLER, TX—The University of Texas Health Center at Tyler invites applications for a clinical faculty position in the Dept. of Radiology. Some teaching, but not publishing or research, required. A progressive 4-person dept. practices general radiology (including interventional, MRI, and SPECT) and performs approximately 27,000 exams/yr. New equipment, flexible work hours, very light call, no weekend schedule. Yr-round tennis, golf, and boating are available in addition to excellent schools. Competitive first-yr salary and an unsurpassed benefits package are offered. Send CV to J. R. Shepherd, M.D., University of Texas Health Center at Tyler, P. O. Box 2003, Tyler, TX 75710; (903) 877-7100. The University of Texas Health Center at Tyler is an affirmative action, equal opportunity employer. Minorities are encouraged to apply; male/female/handicapped/disabled. 4–6a

CENTRAL NEW JERSEY, IMMEDIATE OPENING—Radiologist with fellowship training or equivalent experience in vascular/interventional and/or in MR imaging to join 6-member group. Must be willing to do other aspects of diagnostic radiology, mammography, ultrasound, CT, and nuclear medicine. Practice includes a 340-bed community hospital, a private radiology office, and an MRI facility. Area is within a 10-mi. radius of Princeton and is near New York City and Philadelphia. Competitive salary, excellent benefits, and partnership opportunity. Send CV or call Margaret M. Beck, Business Manager, 2127 Hamilton Ave., Trenton, NJ 08619; (609) 587-9410. 4–5ap

COMMUNITY-BASED, 400-BED, PROGRESSIVE HOSPITAL GROUP seeks a board-certified, fellowship-trained, interventionalist/angiographer to work in our full-service angio suite. Send CV and date available to Martin Friedman, D.O., Frankford Hospital, X-Ray, Knights & Red Lion Rd., Philadelphia, PA 19114. 4–5ap

FT. WORTH, TX, DIAGNOSTIC RADIOLOGY—A 7-person, hospital-based group seeks a BC/BE radiologist. Fellowship training in neuroradiology, MRI, and nuclear medicine preferred, but other qualified candidates considered. Duties will include general diagnosis. Early partnership at modest buy-in and ample vacation. Please send CV to Clay Roberts, M.D., 1650 W. Magnolia, Ste. 117, Ft. Worth, TX 76104; (817) 927-6151. 4–5ap

COLORADO—BC/BE radiologist sought to join 2-person practice covering 2 hospitals in the central mountains of Colorado. Ample free time and excellent outdoor recreational opportunities. Contact E. J. Loeffel, M.D., P. O. Box 415, Buena Vista, CO 81211; (719) 539-3782. 4–6ap

DIAGNOSTIC RADIOLOGIST needed for expanding practice in 200-bed, well-equipped community hospital in Troy, MI. Must have expertise in CT, ultrasound, and mammography. Very competitive salary and benefits. Send CV to Thomas Verhelle, M.D., Troy-Beaumont Hospital, 44201 Dequindre Rd., Troy, MI 48098. 4–7ap

MUSCULOSKELETAL RADIOLOGIST, CHARLOTTE, NC—A 13-member, subspecialized group serving a 660-bed, private community hospital–outpatient diagnostic center desires a fellowship-trained or staff level musculoskeletal radiologist. GE 9800 CT and Signa 1.5-T equipment. Family-oriented community with warm 4-season climate, centrally located between coast and mountains. Send CV to P. O. Box 221211, Charlotte, NC 28222. 4–6ap

ANGIOGRAPHER–INTERVENTIONAL RADIOLOGIST, CENTRAL MASSACHUSETTS—Radiologist with angiography and interventional skills sought to join an 11-member, private-practice group serving a 550-bed medical center and performing 150,000 exams/yr. Position involves sharing general diagnostic radiology responsibilities, including CT, ultrasound, and mammography. Please send CV to Richard Danford, M.D., Worcester Radiologists, Inc., 121 Lincoln St., Worcester, MA 01605; (508) 753-8151. 4–6ap

VASCULAR AND INTERVENTIONAL RADIOLOGIST—A 12-person, private-practice multispecialty radiology group is seeking a fellowship-trained vascular and interventional radiologist. Practice is at a university-affiliated, 700-bed, acute general hospital doing 110,000 exams/yr. Submit CV to Thomas J. Spackman, M.D., Dept. of Radiology, Saint Francis Hospital and Medical Center, Hartford, CT 06105. 4–5ap

CROSS-SECTIONAL IMAGING SPECIALIST—A 12-person, private-practice multispecialty radiology group is seeking a fellowship-trained, cross-sectional imaging specialist, with a particular interest in strengthening an ultrasound division. Practice is at a university-affiliated, 700-bed, acute general hospital doing 110,000 exams/yr. Submit CV to Thomas J. Spackman, M.D., Dept. of Radiology, Saint Francis Hospital and Medical Center, Hartford, CT 06105. 4–5ap

CENTRAL VALLEY, CALIFORNIA—Immediate opening for BC/BE diagnostic radiologist with skills in CT, MRI, interventional, ultrasound, and nuclear medicine. Join a growing practice in a 160-bed community hospital. Attractive compensation package with the opportunity for partnership. Send CV to Henderson & Associates, P. O. Box 2627, Bakersfield, CA 93303; (805) 323-6925. 4–5ap

DIAGNOSTIC RADIOLOGIST, KNOXVILLE, TN Opportunity for full-time or permanent part-time. Outpatient diagnostic center. All modalities. No interventional. No nights or weekends. Generous compensation. Abundant vacation time. Contact B. A. Schaefer, M.D., 601 Mulvaney St., Knoxville, TN 37915; (615) 525-7100. 3–5ap

IMMEDIATE OPENING—BC/BE radiologist to join 2 board-certified radiologists at a 130-bed community hospital and outpatient dept. located 25 mi. east of Palm Springs, CA. Excellent salary, fringe benefits, early partnership, no buy-in, and generous vacation time. All imaging modalities including SPECT ANGER camera, MRI, and angio/interventional. Reasonable housing in resort atmosphere. Contact Stephen J. Curtis, M.D., Radiology Director, J.F.K. Memorial Hospital, 47-111 Monroe St., Indio, CA 92201; (619) 775-8066. 4–7ap

SUPERB PARTNERSHIP POSITION IN LAS VEGAS—Rapidly expanding 7-member group practice covering 2 full-service imaging centers and a small hospital has an immediate opening. We are looking for an additional board-certified radiologist with an uncommon dedication to excellence in patient care. Our outpatient facilities include 2 MR, 2 CT, angio with a 4-bed recovery area, 5 ultrasound, 5 mammography, 3 SPECT, plus R&F. This is an excellent opportunity for a partnership position with a well-respected group in a growing community. Please send CV to Dr. Mark Winkler, SDMI, 2950 S. Maryland Pkwy., Las Vegas, NV 89109. 3–2ap

BC GENERAL RADIOLOGIST—Established private group in western Massachusetts is seeking a general diagnostic radiologist with experience in CT, ultrasound, MRI, and nonvascular interventional procedures. Primary assignment is at an 800-bed teaching hospital with a radiology residency program. Practice also includes 3 community hospitals and 6 private offices. Full partnership after 1 yr. Available by July 1, 1992. Interested candidates should send CV to W. Max Cloud, M.D., 130 Maple St., Springfield, MA 01103. 3–5ap

CONNECTICUT, ANGIO/INTERVENTIONAL RADIOLOGIST—Opening in July 1992 for BC/BE radiologist with fellowship training in angiographic procedures. Additional training or experience in other interventional procedures is desirable. Nine-radiologist practice includes a 435-bed, university-affiliated, community hospital and a 57-physician multispecialty clinic. Approximately 107,000 exams/yr, including MRI, CT, nuclear medicine, ultrasound, as well as an active angiographic and interventional service. Excellent salary and benefits leading to full partnership after second yr. For more information, send CV to David A. Lund, M.D., Dept. of Radiology, New Britain General Hospital, 100 Grand St., New Britain, CT 06050. 3–6ap

DIRECTOR OF BREAST IMAGING—The Brigham and Women's Hospital/Harvard Medical School, Dept. of Radiology, is seeking a full-time diagnostic radiologist to head the Breast Imaging Section. This hospital-based facility has 4 mammographic rooms, 2 with ultrasound. In addition, there is a mammo-test unit for performance of large core breast biopsies. More than 12,000 mammograms, 1,000 preoperative wire localizations, 500 guided aspirations, and 150 core biopsies are performed annually. This wealth of clinical material coupled with an excellent clinical staff provides unlimited opportunity for collaborative clinical investigation. Candidates must have board certification. Please contact Jack E. Meyer, M.D., Director of Diagnostic Radiology, Brigham and Women's Hospital, 75 Francis St., Boston, MA 02115; (617) 732-6269. Brigham and Women's Hospital/Harvard Medical School is an affirmative action/equal opportunity educator and employer. 2–7a

CONNECTICUT, NEURORADIOLOGIST—Opening in July 1992 for BC/BE radiologist with fellowship training in neuroradiology. Nine-radiologist practice includes a 435-bed, university-affiliated community hospital and a 57-physician multispecialty clinic. Approximately 107,000 exams/yr including MRI, CT, nuclear medicine, ultrasound, and an active angiographic and interventional service. Excellent salary and benefits leading to full partnership after second yr. For more information, send CV to David A. Lund, M.D., Dept. of Radiology, New Britain General Hospital, 100 Grand St., New Britain, CT 06050. 3–6ap

RADIOLOGIST—A 4-physician group seeks a fifth to join our well-established and growing practice. We are located in east-central Illinois, with a 4-yr college, Jr. college, and a farming economy enhanced by numerous growing industries. We serve a rural but very modern 230-bed hospital ($25 million expansion underway) and several other sites, performing more than 80,000 exams/yr. Mattoon-Charleston is a great place to raise a family while still having access to big-city amenities. Please be BC/BE, skilled in interventional or MRI, and able to handle general diagnostic modalities competently. Please reply to Bruce Fluesmeier, Lakeland Radiologists, Ltd., 1221 Broadway, Mattoon, IL 61938; (800) 745-7701. 3–8ap

GENERAL RADIOLOGY STAFF POSITION—The Dept. of Radiological Sciences at Olive View–UCLA Medical Center has openings for staff positions in general radiology and ultrasound. Candidates must be board-certified and eligible for certification in diagnostic radiology and should be eligible for licensing in the state of California. Interested candidates should contact Issa Yaghmai, M.D., Professor and Chairman, Dept. of Radiological Sciences, Olive View–UCLA Medical Center, 14445 Olive View Dr., Sylmar, CA 91342; (818) 364-4078. The University of California, Los Angeles, is an affirmative action/equal opportunity employer. 3–6a

BC/BE DIAGNOSTIC RADIOLOGIST—Opportunity to join a 3-person group in general radiology practice including all modalities (angio and interventional limited at this point). Hospital-based with limited itinerant schedule. Generous salary leading to early partnership in professional corporation. Outstanding benefits with liberal fringes and vacation. Wonderful, small midwestern community with great schools and bountiful cultural and recreational opportunities. Send CV to James P. Zachman, M.D., Radiology Dept., Rice Memorial Hospital, Willmar, MN 56201; (612) 231-4530. 3–5ap

THE RADIOLOGIC GROUP OF NORTH JERSEY is seeking a BC radiologist with a fellowship or strong interest in pediatric radiology. This is a 7-member group with a fee-for-service arrangement at a 700-bed hospital and office. All diagnostic facilities are available. Send CV to F. Cushmore, M.D., 703 Main St., Paterson, NJ 07503. 3–5ap

PEDIATRIC RADIOLOGIST—Hahnemann University Hospital, Dept. of Diagnostic Radiology, is seeking a pediatric radiologist to provide imaging service for a very large and continuously growing Dept. of Pediatrics with a dynamic clinical and academic interactive relationship with our dept. Completion of a fellowship in pediatric radiology is required. The position is at the assistant professor or associate professor level. Salaries are very competitive and based on academic rank. Facilities include 2 GE 9800 CT scanners and a GE 1.5-T MRI. If interested, please send CV or contact Seth N. Glick, M.D., Dept. of Diagnostic Radiology, Hahnemann University Hospital, Broad and Vine Sts., Philadelphia, PA 19102; (215) 448-8719. 3–5ap

ULTRASOUND SECTION HEAD—Hahnemann University Hospital is seeking a director of ultrasound. Clinical responsibility predominantly in ultrasound with opportunity for involvement in body CT and body MRI. Approximately 11,000 ultrasound procedures previous yr with potential for expansion. Facilities include 2 state-of-the-art Acuson machines with immediate plans for additional equipment. Appointment would be at the associate professor or professor rank. Salaries are very competitive and based on academic rank. If interested, please send CV or contact Seth N. Glick, M.D., Dept. of Diagnostic Radiology, Hahnemann University Hospital, Broad and Vine Sts., Philadelphia, PA 19102; (215) 448-8719. 3–5ap

PHYSICIAN/RADIOLOGIST—A large radiology group with multiple private offices seeks a board-certified radiologist interested in a full-time position. Responsibilities include general radiography. Special training in CT, ultrasound, MRI and/or nuclear medicine is preferred. Excellent southern New Jersey location. Competitive salary and benefit package. Position available immediately. Send CV to RABC, P. O. Box 729, Mt. Holly, NJ 08060. 2–5ap

DIAGNOSTIC RADIOLOGIST(S)—Small, progressive southeastern community hospital (JCAHO-accredited) near a major metropolitan area needs at least 1 board-certified radiologist. Modern equipment, exclusive contract, good payor mix. Nuclear medicine, invasive radiologic procedures. Please send CV with cover letter and financial requirements. All inquiries will be kept strictly confidential. Write Box C30, *AJR* (see address this section). 3–5a

ASSISTANT PROFESSOR, MR RADIOLOGIST—The Dept. of Radiology at The University of Texas Medical School at Houston and the Hermann Hospital are recruiting for a full-time MRI radiologist at the assistant professor level, beginning July 1, 1992. Preference will be given to candidates with fellowship training in MRI, body imaging, neuroradiology, or 1 yr of academic MRI experience. ABR certification is required. Responsibilities will include monitoring and interpretation of both body and neuro MRI, as well as medical student, resident, and fellow teaching. Extensive clinical and basic science research opportunities are available. The dept.'s MR facilities are state-of-the-art and located in a beautiful spacious setting, which includes a 1.5-T GE Signa unit with proton spectroscopic capability. A second 1.5-T GE System, with MR angiography, fast spin echo (FSE), and phased array coils, will be installed in the first quarter of 1992. The Dept. also has an active basic science research program; research facilities include a small bore MRI system with spectroscopy capabilities. The University of Texas at Houston is an equal opportunity employer. Women, minorities, and the disabled are encouraged to apply. Please send CV and 3 references to Bharat Raval, M.D., Professor and Interim Chairman, Dept. of Radiology, The University of Texas Medical School–Houston, 6431 Fannin, Suite 2.132, Houston, TX 77030. 2–7ap

PHYSICIAN/RADIOLOGIST—Full-time opening for a board-certified radiologist in a desirable southern New Jersey shore location. This is an active, challenging, expanding hospital and office-based practice. Must have training in CT, ultrasound, and nuclear medicine. Position available immediately. Send CV to RABC, P. O. Box 729, Mt. Holly, NJ 08060. 2–5ap

FAIRBANKS, AK—Four diagnostic radiologists seek fifth partner for diversified practice including general radiology, ultrasound, nuclear medicine, MRI (GE 1.5-T), and CT (GE 9800). Hospital and office practice. Desirable life-style advantages in a university town. Unlimited access to the outdoors. Excellent salary, benefits, retirement, and vacation. One yr to full partnership. Contact Douglas Hutchinson, M.D., 1919 Lathrop #5, Fairbanks, AK 99701; (907) 452-5092. 2–7ap

BODY IMAGING DIAGNOSTIC RADIOLOGIST—Young, progressive group in Washington, DC, area has position immediately available for a board-certified diagnostic radiologist in an expanding and diversified hospital and office-based practice with facilities in Maryland and Virginia. Our group covers 1 hospital, 5 full-service private offices, and 2 diagnostic centers for women. All imaging modalities represented, including 3 MRIs, 6 CTs, 9 ultrasound suites including color-flow, and an ISG 3-D imaging workstation. Very attractive practice setting. Commitment to leading edge technology. Address inquiries and CV to Grant McClure, Radiology Imaging Associates, 7801 Old Branch Ave., Ste. 300, Clinton, MD 20735; (301) 856-6718. 3–5ap

ULTRASOUND/CT/MRI—Opportunity for board-certified radiologist specializing in ultrasound, body CT, and body MRI to pursue academic career at the New York Hospital-Cornell Medical Center. Dept. provides state-of-the-art equipment, including Acuson and ATL ultrasound, GE 9800 CT, and GE Signa 1.5-T MR. Wide variety of ultrasound exams include abdominal, OB-GYN, color Doppler, small parts, neonatal head, transvaginal, and transrectal. Prefer candidate with prior fellowship in sectional imaging or ultrasound. Responsibilities include clinical practice, teaching, and research. Position available 7/1/92. Please send CV to Elias Kazam, M.D., Dept. of Radiology, New York Hospital–Cornell Medical Center, 525 E. 68th St., New York, NY 10021. 2–5a

SOUTHERN OREGON—Opportunity for BC/BE, general diagnostic radiologist to join group of 5 board-certified radiologists. Experience in all modalities desired. Practice includes 2 hospitals and own private office. Competitive starting salary with early full partnership. Excellent lifestyle with many outdoor activities from Pacific Coast to Oregon Cascades. Send CV to Larry Strickland, Administrator, Roseburg Radiologists, P.C., P. O. Box 1547, Roseburg, OR 97478. 2–5ap

CHEST/BREAST IMAGING RADIOLOGIST—The Dept. of Radiology of the University of Miami School of Medicine is seeking an academic radiologist with subspecialty training or equivalent experience and interest in all aspects of chest imaging including CT, MR, ultrasound, and interventional procedures. Similar expertise in breast imaging including mammography, ultrasound, and needle localization required. The University of Miami/Jackson Memorial Medical Center is a tertiary-referral and level I trauma center that will soon be opening a state-of-the-art breast center. Extensive teaching is involved and an interest in clinical research is assumed. Board-certification and eligibility for, or licensure by the state of Florida is required. Academic rank and compensation commensurate with qualifications. Interested parties should forward CV to C. A. Poole, M.D., Professor and Chairman, Dept. of Radiology (R-308), P. O. Box 016960, Miami, FL 33101. The University of Miami is an equal opportunity/affirmative action employer. 1–5a

TRAUMA RADIOLOGISTS—The Dept. of Radiology of the University of Miami School of Medicine is recruiting for trauma radiologists to staff a new, state-of-the-art trauma center opening in the spring of 1992. The unit will be a self-contained facility within the Jackson Memorial Medical Center, a 1500-bed tertiary facility and level I trauma center. Candidates must be board-certified with fellowship training and/or experience in the management of the trauma patient, including the use of radiography, ultrasound, CT, angiography, and interventional procedures. Skill in teaching, interest in clinical research, and licensure to practice medicine in the state of Florida required. Academic rank and compensation commensurate with qualifications. Applicants should send CV to C. A. Poole, M.D., Professor and Chairman, Dept. of Radiology (R-308), University of Miami School of Medicine, P. O. Box 016960, Miami, FL 33101. The University of Miami is an equal opportunity/affirmative action employer. 1–5a

SAN ANTONIO, TX—Large group covering multiple hospitals and outpatient facilities seeks radiologists with angiography skills. Send CV to Search Committee, M&S X-Ray Associates, P. O. Box 15920, San Antonio, TX 78212-9510. 1–6ap

THE DEPT. OF RADIOLOGY AT BROOKE ARMY MEDICAL CENTER, SAN ANTONIO, TX, is recruiting academic radiologists for several divisions of the dept., including ultrasound, chest, skeletal, neuroradiology, general diagnostic, interventional radiology, and mammography. Our dept. offers a fully accredited residency program with 24 residents and 16 attending full-time staff. Numerous consultants from across the country lecture on a continuing and regular basis. The hospital is a modern, tertiary-care center serving Texas, Oklahoma, and Louisiana. A strong residency program, interesting patient population, excellent equipment, teleradiology and digital radiology implementations underway, coupled with a south Texas lifestyle are positive aspects of the practice. Academic credentials and/or experience are necessary. Recently graduated fellows are encouraged to apply. Board certification is mandatory. Candidates should be particularly interested in patient care, teaching, and research. Salary and benefits are competitive and generous. Brooke is an EO/EEO employer. Please contact Dr. Billy E. Cunningham, COL, MC, Assistant Chief, Dept. of Radiology, Brooke Army Medical Center, Fort Sam Houston, TX 78234-6200; (512) 221-8418/8218. 8–7a

THE RADIOLOGY DEPT. AT DWIGHT DAVID EISENHOWER ARMY MEDICAL CENTER is recruiting academic radiologists. The dept. provides a full range of services including angiography, ultrasound, CT (with a new GE 9800 Advantage system), and MRI (with a new 1.5-T GE Signa system). Development is underway for the installation of a digital teleradiology link to area medical facilities. The dept. is also beginning a radiology residency program in affiliation with the program at the Medical College of Georgia in Augusta. With this growth, the dept. has generated a need for several academic diagnostic radiologists. Board-certified diagnostic radiologists with academic credentials and/or experience are urged to apply. Fellowship training is desired, especially in interventional radiology and/or angiography, however candidates at all levels will be considered. Candidates should be particularly interested in patient care, teaching, and research. The medical center is located on Fort Gordon, GA, adjacent to Augusta, and is the tertiary-care hospital supporting 9 Army community hospitals of the southeastern region and Puerto Rico. The hospital supports fully accredited residency programs in family practice, general surgery, medicine, orthopedics, pathology, and psychiatry. Salary and benefits are competitive and generous. The medical center is an EO/EEO employer. Please contact Dr. Thomas M. Ralston, LtC., Chief, Radiology Dept., Eisenhower Army Medical Center, Fort Gordon, GA; (404) 791-6245. 8–7a

THE DEPT. OF RADIOLOGY AT WALTER REED ARMY MEDICAL CENTER is recruiting academic radiologists. We need board-certified radiologists to work in this famous and modern health-care center. Our dept. has a residency program consisting of 24 residents and several fellows. Subspecialists are needed in ultrasound, chest, mammography, genitourinary, gastrointestinal, pediatric, CT, MRI, and interventional radiology, as well as general radiology. Excellent opportunity to live in the nation's capital and also become an integral part of a large teaching program. Salaries are competitive and generous. Highly motivated applicants should contact Col. Mark F. Hansen, Radiology Consultant to the Army Surgeon General, Dept. of Radiology, TAMC, HI 96859-5000; (808) 433-6393. 8–7a

PASADENA, CALIFORNIA—Immediate opening for a BC/BE radiologist. Busy outpatient imaging center including mammography, ultrasound, CT, and MRI. Call Terry Becker, M.D. at (818) 793-8189. 2–5ap

PHYSICIAN/RADIOLOGIST—Full-time opening for a board-certified radiologist in a desirable southern New Jersey shore location. This is an active, challenging, expanding hospital and office-based practice. Must have training in CT, ultrasound, and nuclear medicine. Position available immediately. Send CV to RABC, P. O. Box 729, Mt. Holly, NJ 08060. 2–5ap

NEURORADIOLOGIST—Senior ASNR member needed for excellent hospital and imaging center position in Tucson, AZ. Early partnership opportunity. Send CV to Arizona State Radiology, 7250 E. Ventana Canyon Dr., Tucson, AZ 85715. 8–7ap

THE DEPT. OF RADIOLOGY AT TRIPLER ARMY MEDICAL CENTER, HONOLULU, HI, is recruiting academic radiologists for several divisions of the dept., including ultrasound, chest radiology, skeletal, neuroradiology, general diagnostic radiology, MRI, interventional radiology, and mammography. Our dept. offers a fully accredited residency program with 21 residents and 16 attending full-time staff. Numerous consultants from across the country lecture on a continuing and regular basis. The hospital is a modern, tertiary-care center serving Hawaii and the entire Pacific Basin. A strong residency program, diverse and interesting patient population, excellent equipment, and tropical lifestyle are positive aspects of the practice. Academic credentials and/or experience are necessary. Recently graduated fellows are encouraged to apply. Board certification is mandatory. Candidates should be particularly interested in patient care, teaching, and research. Salary and benefits are competitive and generous. Tripler is an EO/EEO employer. Please contact Dr. Mark F. Hansen, Col, MC, Chief, Dept. of Radiology, TAMC, HI 96859-5000; (808) 433-6393. 7–6a

Positions Desired

A FELLOWSHIP-TRAINED NEUROINTERVENTIONIST, senior member of the ASNR, would like to join academic or private radiologists or neurosurgeons wishing to add this expertise to their practice. Reply to Box D42, *AJR* (see address this section). 5–6bp

SECOND YR RADIOLOGY RESIDENT (PGY3) seeks PGY4 position for July 1992. Enthusiastic, amiable, and hardworking. Desiring more challenge and diversity. Willing to relocate. Reply Box Q94, *AJR* (see address this section). 4–6bp

EXPERIENCED, YOUNG, FACULTY INTERVENTIONALIST (ABR, SCVIR) seeks private-practice position leading to full partnership. Can perform general radiology, including MRI, ultrasound, and CT. Prefer medium-sized to large hospital in urban or suburban location. Available March 1992. Reply Box P82, *AJR* (see address this section). 3–5bp

Fellowships and Residencies

FELLOWSHIP PROGRAM IN INTERVENTIONAL RADIOLOGY—The fellowship offered is a 1-yr training program in interventional radiology. A high volume of studies provides excellent experience for the fellowship training program. The 1-yr appointment is intensive, supervised, and allows for graded responsibility in performance and interpretation of studies including angioplasty, atherectomy, arterial and biliary stents, and all drainage procedures. The fellowship training involves performance of interventional procedures under sonographic and CT guidance as well as fluoroscopy. Inquiries should be addressed to Gordon K. McLean, M.D., Director, Interventional Radiology, The Western Pennsylvania Hospital, 4800 Friendship Ave., Pittsburgh, PA 15224. 5–12c

ULTRASOUND, CT, AND MR IMAGING FELLOWSHIP TO BEGIN JULY 1993—More than 140,000 exams are performed yearly in the radiology dept. of this 578-bed teaching hospital. The imaging fellowship emphasizes diagnostic ultrasound, with all areas represented, including OB-GYN, urology, and vascular, significantly integrating MRI and body CT. Fellows also have the opportunity to participate in teaching, conference presentations, and research projects, many of which culminate in publications. Inquiries should be addressed to Marcela Bohm-Velez, M.D., Director of Imaging Fellowship Program, Dept. of Radiology, The Western Pennsylvania Hospital, 4800 Friendship Ave., Pittsburgh, PA 15224. 5–12c

WOMEN'S IMAGING FELLOWSHIP POSITION—High-volume breast imaging (mammography, breast ultrasound, interventional procedures), and ultrasound emphasizing obstetric and gynecologic sonography. A 1-yr fellowship to start in July 1993. Fellows also have the opportunity to participate in teaching, conference presentations, and research projects, many of which culminate in publications. Inquiries should be addressed to Ellen B. Mendelson, M.D., Chief, Mammography and Women's Imaging, The Western Pennsylvania Hospital, 4800 Friendship Ave., Pittsburgh, PA 15224. 5–12c

INTEGRATED CHEST RADIOLOGY FELLOWSHIP AT JOHNS HOPKINS UNIVERSITY HOSPITAL—The Dept. of Radiology, Division of Thoracic Imaging, Johns Hopkins University, is offering a 1- to 2-yr academically oriented fellowship in chest radiology. The fellowship offers an integrated experience in cross-sectional imaging including more than 4000 chest CT exams/yr and 1000 thoracic MRI exams/yr. Strong research interests in high-resolution CT, MRI, and interventional thoracic radiology offer the potential candidate an exciting working environment. The fellowship is available starting July 1, 1993. Contact Janet E. Kuhlman, M.D., Director of Chest Radiology, Dept. of Radiology, Johns Hopkins Hospital, Baltimore, MD 21205; (410) 955-4419. 5–7cp

FELLOWSHIP POSITION—The Charles Dotter Institute of Interventional Therapy has an additional opening for a 1-yr fellowship in interventional radiology to start July 1, 1992. The fellowship includes all aspects of vascular and interventional radiology and affords the opportunity for animal research in a well-equipped laboratory. Please send CV to Frederick S. Keller, M.D., Oregon Health Sciences University, Interventional Radiology L-605, 3181 S.W. Sam Jackson Park Rd., Portland, OR 97201; (503) 494-7660. 5c

FELLOWSHIP POSITIONS—The Dept. of Radiology of the Brigham and Women's Hospital-Harvard Medical School has 1- or 2-yr fellowship positions in the following areas: (1) cardiovascular and interventional, (2) neuroradiology, (3) CT/ultrasound/MR/interventional, (4) oncoradiology, (5) chest, (6) bone, (7) nuclear medicine, and (8) computer science. For more information, please send CV specifying your area of interest to B. Leonard Holman, M.D., Chairman, Dept. of Radiology, Brigham and Women's Hospital, 75 Francis St., Boston, MA 02115. Harvard Medical School and Brigham and Women's Hospital are equal opportunity, affirmative action employers. 5–4c

FELLOWSHIP IN ONCORADIOLOGY/MAMMOGRAPHY—The Dept. of Radiology at the Dana-Farber Cancer Institute and Brigham and Women's Hospital, which are Harvard Medical School affiliates, offers a 1-yr fellowship position beginning July 1, 1993. All imaging modalities involved in the diagnosis, staging, and follow-up of patients with malignant disease are integrated into this program. An additional feature is a concentrated experience in the performance of interventional breast diagnostic procedures. Please contact Jack E. Meyer, M.D., Director of Diagnostic Radiology, Brigham and Women's Hospital and Dana-Farber Cancer Institute, 75 Francis St., Boston, MA 02115; (617) 732-6269. Brigham and Women's Hospital/Dana Farber Cancer Institute/Harvard Medical School is an affirmative action/equal opportunity educator and employer. 5–4c

A FELLOWSHIP IN ULTRASOUND AND BODY CT/MRI is available July 1, 1992, to June 30, 1993, at The New York Hospital-Cornell Medical Center. The dept. provides state-of-the-art equipment, including Acuson ultrasound, GE 9800 CT, and GE Signa 1.5-T MR. Wide variety of ultrasound exams include abdominal, OB-GYN, color Doppler, small parts, neonatal head, transvaginal, and transrectal. Applicants should be ABR-eligible or certified. Send CV to Elias Kazam, M.D., Dept. of Radiology, The New York Hospital-Cornell Medical Center, 525 E. 68th St., New York, NY 10021. 2–5c

FELLOWSHIP IN BODY IMAGING/MRI—New fellowship position. The Dept. of Radiology, University of Massachusetts Medical Center, offers a 1-yr fellowship position in body imaging/MRI starting July 1, 1992. Training is offered in ultrasound, CT, and MRI. The position involves teaching of medical students and residents, with opportunity for research. The University of Massachusetts Medical Center is a 360-bed university hospital and medical school, located in Worcester, approximately 40 mi. west of Boston. The dept. consists of 24 staff, 13 residents, 2–4 fellows and does approximately 120,000 exams/yr. The hospital is a major trauma center and is serviced by 2 Life Flight helicopters. The dept. is well-equipped with 2 modern CT scanners, 2 1.5-T GE MR scanners, as well as a 2.0-T small-bore unit for animal research. The University of Massachusetts Medical Center Hospital is very active academically. Numerous radiologic, clinical, and basic science conferences are scheduled on a daily basis, and there is ample time during the course of the yr to attend many of these presentations. The fellowship position carries the title of instructor in radiology. For further information, contact Ashley Davidoff, M.D., Director, Abdominal Imaging, or David Stark, M.D., Director of MRI, University of Massachusetts Medical Center, 55 Lake Ave., N., Worcester, MA 01655; (508) 856-3154. The University of Massachusetts Medical Center is an affirmative action/equal opportunity employer. 5xc

MRI FELLOWSHIPS—Fellowship positions in MRI are available for July 1993 and July 1994 at the Johns Hopkins Dept. of Radiology and Radiological Science. Flexible fellowship programs with clinical or research emphasis are available. The MRI division is equipped with 3 1.5-T GE scanners and 2 1.5-T Siemens scanners, both with cardiac imaging and spectroscopic capabilities. Over 9000 exams are performed yearly. Over 2000 of these are body MRI studies. In addition, a 4.7-T and an 8.5-T instrument with spectroscopic and imaging capabilities are available for research. The main interests of the section are oncologic, cardiovascular, and musculoskeletal imaging. Rotating fellowships with CT and/or ultrasound or a straight MR fellowship are offered. For additional information and application, contact Janet Kuhlman, M.D., Acting Director, Body MRI, Johns Hopkins Hospital, Baltimore, MD 21205-2182; (410) 955-4419. 4–5cp

ACCREDITED FELLOWSHIPS IN PEDIATRIC RADIOLOGY—The Dept. of Radiology, St. Christopher's Hospital for Children, Philadelphia, PA, offers 1- or 2-yr accredited fellowship positions in pediatric radiology. The fellowship training covers all aspects of pediatric imaging, including cardiovascular and thoracic imaging, neuroradiology, abdominal resonance imaging, nuclear medicine, ultrasound, and angiography/interventional techniques. St. Christopher's Hospital for Children moved into a brand new facility in a new location 1 yr ago. State-of-the-art imaging equipment includes Acuson ultrasound units with Doppler and color-flow Doppler capability, GE 9800 Quick CT scanner, GE 1.5-T MRI with MRA, Gamma and SPECT nuclear cameras, and digital subtraction angiography. Salary and fringe benefits are competitive. Candidates must be board-certified or qualified. St. Christopher's Hospital for Children is an affirmative action/equal opportunity employer. Address inquiries and CV to Eric N. Faerber, M.D., Dept. of Radiology, St. Christopher's Hospital for Children, Erie Ave. at Front St., Philadelphia, PA 19134-1095; (215) 427-5230. 4–5cp

IMMEDIATE OPENING, PEDIATRIC RADIOLOGY FELLOWSHIP—Position available for 1-yr fellowship beginning July 1, 1992. Experience in all areas of imaging. Apply to Thomas E. Sumner, M.D., Dept. of Radiology, Wake Forest University, Bowman Gray School of Medicine, Medical Center Blvd., Winston-Salem, NC 27157-1088; (919) 748-2463. AA.EOE. 4–6c

FELLOWSHIP IN PEDIATRIC RADIOLOGY, UNIVERSITY OF FLORIDA—The Division of Pediatric Radiology in the Dept. of Radiology at the University of Florida offers a 1-yr fellowship training in pediatric radiology, starting July 1993 and July 1994. Three full-time pediatric radiologists provide training in conventional radiology and fluoroscopy, ultrasound, neonatal imaging, CT, MRI, and interventional/angiography techniques. Supplemental training in nuclear medicine is available. Facilities include dedicated standard r/f rooms, 4 color-Doppler ultrasound machines, 2 GE CT units, 3 MR units, ICU electronic image transfer, and computed radiography (CR). Opportunity to participate or conduct clinical and basic research is available. Applicants must be eligible for licensure in the state of Florida. Contact Jonathan L. Williams, M.D., Director of Pediatric Radiology, Dept. of Radiology, Box 100374, University of Florida, Gainesville, FL 32610-0374; (904) 395-0291. The University of Florida is an equal opportunity/affirmative action employer. 3–6c

FELLOWSHIPS AT THOMAS JEFFERSON UNIVERSITY HOSPITAL—The Dept. of Radiology at Thomas Jefferson University Hospital in Philadelphia offers the following fellowship programs each yr: (1) Ultrasound/CT/MRI—Jefferson's ultrasound division is 1 of the largest in the world and performs all currently available exams, including obstetric, vascular, lithotripsy, invasive, and endoluminal. We also operate 4 GE 1.5-T MRI units and 3 CT scanners. Contact Barry Goldberg, M.D., regarding this program. (2) Cardiovascular/interventional—this division is housed in a new suite containing Philips angio units with DSA and performs the full range of vascular and nonvascular interventional procedures. Contact Geoffrey Gardiner, Jr., M.D. (3) Neuro/ENT radiology—very active clinical services supply a wealth of material to this division, which is housed in a neurosciences imaging center containing all imaging modalities. Contact Carlos Gonzales, M.D. (4) Breast imaging—Jefferson's new breast-imaging center performs approximately 85 studies/day including ultrasound and needle localizations. Contact Stephen Feig, M.D. (5) Chest—includes biopsies and CT. Contact Robert Steiner, M.D. (6) MRI—a dedicated body MRI program including excellent research opportunities in addition to a large clinical case load. Contact Donald Mitchell, M.D. (7) Ultrasound—a dedicated ultrasound program. Contact Barry Goldberg, M.D. (8) Musculoskeletal—includes MRI of the musculoskeletal system. Contact David Karasick, M.D. All program directors listed above can be contacted at the Dept. of Radiology, Thomas Jefferson University Hospital, Philadelphia, PA 19107. Jefferson is an equal opportunity/affirmative action employer. 5xc

FELLOWSHIP POSITIONS—The Dept. of Radiological Sciences at Olive View–UCLA Medical Center has openings for fellowships to begin on July 1, 1992. Positions are available in neuroradiology, ultrasound, body imaging, interventional radiology, and nuclear medicine. Candidates must be board certified and eligible for certification in diagnostic radiology and should be eligible for licensing in the state of California. In addition to clinical practice and training, responsibilities will include graduate and undergraduate medical instruction in radiology as well as assisting with related departmental research projects. Interested candidates should contact Issa Yaghmai, M.D., Professor and Chairman, Dept. of Radiological Sciences, Olive View–UCLA Medical Center, 14445 Olive View Dr., Sylmar, CA 91342; (818) 364-4078. The University of California, Los Angeles, is an affirmative action/equal opportunity employer. 3–6c

MUSCULOSKELETAL RADIOLOGY FELLOWSHIP—Applications are now being accepted for a musculoskeletal fellowship position for 1993 at the Cleveland Clinic Foundation (CCF). CCF is a 1000-bed, tertiary-care, teaching medical center with a large radiology residency program. Local, national, and international patients provide for an interesting and varied mix of bone pathology. Training includes all aspects of musculoskeletal radiology, including MR, CT, arthrography, biopsy, bone densitometry, and a large plain film experience. Fellowship includes patient care, teaching, and research. There is a close working relationship with the orthopedic, rheumatology, and endocrinology depts. There are presently 4 musculoskeletal staff in the section. For further information, please contact Bradford J. Richmond, M.D., Head, Section of Musculoskeletal Radiology, Desk A-21, 9500 Euclid Ave., Cleveland, OH 44195; (216) 444-3931. 12–5cp

FELLOWSHIP IN MUSCULOSKELETAL RADIOLOGY, UNIVERSITY OF FLORIDA—The Dept. of Radiology is offering musculoskeletal fellowship positions beginning July 1993 and July 1994. The fellowship currently centers on a 548-bed hospital with wide exposure to skeletal pathology, including more than 200 new musculoskeletal tumors per yr. The fellowship experience includes clinical, research, and teaching opportunities in diagnostic skeletal radiology, CT, MRI, MR spectroscopy, metabolic bone disease, TMJ pathology, and image processing. Systems available include a 1.5-T whole body spectroscopy/imager, 2 GE 9800 Advantage CT scanners, and an image processing workstation (DMI) for multiplanar (MPR) and 3D reformation. At the fellow's discretion, the experience could be expanded to include aspects of nuclear medicine and the adjacent 473-bed VA hospital, which is equipped with a 1.5-T whole body spectroscopy/imager and a Picker 1200 CT scanner. Applicants must be eligible for licensure in the state of Florida. Send CV to William J. Montgomery, M.D., Dept. of Radiology, P. O. Box 100374 JHMHC, Gainesville, FL 32610-0374; (904) 395-0291 for further information. The University of Florida is an equal opportunity/affirmative action employer. 3–6c

FELLOWSHIP IN ULTRASOUND AND BODY CT/MRI, July 1, 1993, to June 30, 1994, at Hahnemann University Hospital. State-of-the-art equipment, including ultrasound color-flow imaging, 2 GE 9800 CT scanners, and Signa 1.5-T MR is provided. Applicants must have completed an approved residency in diagnostic radiology and be board-eligible or certified. For inquiries, please contact Lawrence Neustadter, D.O., Dept. of Diagnostic Radiology, Hahnemann University Hospital, Broad and Vine Sts., Philadelphia, PA 19102; (215) 448-8722. An equal opportunity employer. 4–6cp

ABDOMINAL IMAGING FELLOWSHIP, UNIVERSITY OF FLORIDA—The Dept. of Radiology at the University of Florida is offering 1-yr clinical fellowships in abdominal imaging beginning in July 1993 and July 1994. Minimum requirements include successful completion of an accredited radiology residency. The fellowship includes training in all aspects of abdominal imaging (gastrointestinal and genitourinary radiology, CT, MRI, and ultrasound) by a 4-person subspecialty faculty. The programs offer full clinical experience and research opportunities. Applicants must be eligible to obtain a medical license in the state of Florida. Research fellowships are also available in abdominal imaging. For additional information, contact Pablo R. Ros, M.D., Professor, Dept. of Radiology, Box J-374 JHMHC, Gainesville, FL 32610-0374; (904) 395-0288. The University of Florida is an equal opportunity/affirmative action employer and encourages applications from women and minorities. 3–6c

UNEXPECTED OPENING FOR FELLOWSHIP IN CARDIOVASCULAR-INTERVENTIONAL RADIOLOGY available July 1, 1992. A 1-yr fellowship program is available at a 750-bed teaching hospital. Extensive clinical experience involving all aspects of cardiovascular imaging, interventional vascular, and nonvascular procedures. Availability for clinical or animal research. Send CV and inquiries to Oscar H. Gutierrez, M.D., Dept. of Radiology, Box 648, University of Rochester Medical Center, Rochester, NY 14642. AA/EO/M-F employer. 4–6c

NEURO/ENT FELLOWSHIP, UNIVERSITY OF FLORIDA—The Dept. of Radiology offers several 2-yr, postresidency fellowship training positions available July 1993 and July 1994. The fellowship offers excellent clinical material, comprehensive and modern equipment, and experienced 4-person subspecialty faculty. In addition to clinical practice and training, responsibilities include graduate and undergraduate medical instruction in neuroradiology as well as participation in departmental research activities. Minimum requirements include successful completion of an accredited radiology residency. Applicants must be eligible to obtain a medical license in the state of Florida. For additional information, contact Ronald Quisling, M.D., Professor, Dept. of Radiology, Box 100374 JHMHC, Gainesville, FL 32610-0374; (904) 395-0291. The University of Florida is an equal opportunity/affirmative action employer and encourages applications from women and minorities. 3–6c

FELLOWSHIP IN ANGIO/INTERVENTIONAL IMAGING—A 1-yr fellowship program is available at Lehigh Valley Hospital Center in Allentown, PA. LVHC is a 492-bed, acute-care, university-affiliated hospital. The fellowship program offers training in CT (head and body), ultrasound, MR, angiography, and interventional radiology. For further information, contact Robert Kricun, M.D., Dept. of Radiology, Lehigh Valley Hospital Center, P. O. Box 689, Allentown, PA 18105. 4–6c

FELLOWSHIP IN MUSCULOSKELETAL RADIOLOGY, UNIVERSITY OF FLORIDA—The Dept. of Radiology is offering a musculoskeletal fellowship position for 1 yr, beginning July 1, 1992. The fellowship currently centers on a 568-bed hospital with wide exposure to skeletal pathology, including more than 200 new musculoskeletal tumors per yr. The fellowship experience includes clinical, research, and teaching opportunities in diagnostic skeletal radiology, CT, MRI, MR spectroscopy, metabolic bone disease, TMJ pathology, and image processing. Systems available include a 1.5-T whole body spectroscopy/imager, a 1.0-T whole body imager, a 2.0-T 34-cm spectroscopy/imager, 2 GE 9800 Quick CT scanners, and an image processing workstation (DMI) for multiplanar (MPR) and 3D reformation. At the fellow's discretion, the experience could be expanded to include aspects of nuclear medicine and the adjacent 473-bed VA hospital, which is equipped with a 1.5-T whole body spectroscopy/imager and a Picker 1200 CT scanner. Send CV to William J. Montgomery, M.D., Dept. of Radiology, P. O. Box 100374, Gainesville, FL 32610-0374; or call (904) 395-0291 for further information. An equal opportunity/affirmative action employer. 3–5c

NEURORADIOLOGY FELLOWSHIP—An unexpected opening for a neuroradiology fellow is available in the Dept. of Radiology at Thomas Jefferson University Hospital beginning July 1992. The Division of Neuroradiology has close clinical and research relationships with Jefferson's very active neurology, neurosurgery, orthopedic surgery, and otolaryngology depts. Complete training in ENT radiology is part of this program. Six full-time faculty members currently staff this division. Clinical facilities include 2 dedicated CT scanners, a myelography room, a biplane angiography room with DSA, and 4 GE 1.5-T MRI units. Contact Carlos Gonzalez, M.D., Director of Neuroradiology, 1009 Main Bldg., Thomas Jefferson University Hospital, Philadelphia, PA 19107; (215) 955-5447. Jefferson is an affirmative action/equal opportunity employer. 11–6c

FELLOWSHIP IN ANGIO/INTERVENTIONAL RADIOLOGY—The Dept. of Radiology at the University of Florida is offering several 1-yr, postresidency clinical fellowship positions beginning in July 1993 and July 1994. Angiographic suites are available (2 have Philips C-arms with 1024 ADAC digital), and a new Toshiba vascular lab. The dept. has intravascular ultrasound color-flow Doppler and angioscopy equipment. Training includes all interventional procedures (vascular, biliary, urology, etc.), as well as experience with investigational devices such as CO_2, angioscopy, atherectomy, and holmium lasers. An animal laboratory, a full-time veterinarian, and an instrument shop are available. Applicants must be eligible for licensure in the state of Florida. For further information, contact Irvin F. Hawkins, M.D., Professor, Dept. of Radiology, Box 100374 JHMHC, Gainesville, FL 32610-0374; (904) 395-0291. The University of Florida is an equal opportunity/affirmative action employer. 3–6c

A FELLOWSHIP POSITION IN VASCULAR AND INTERVENTIONAL RADIOLOGY, beginning July 1, 1992, and ending June 30, 1993, has unexpectedly become available. It is offered to candidates that have recently completed a residency in radiology as well as those practicing radiologists who desire to return to an academic setting to acquire new skills in the vascular and interventional field. A very active dept. with up-to-date equipment provides an excellent opportunity for training in all interventional modalities. Contact L. B. Morettin, M.D., Director, Vascular & Interventional Radiology, University of Texas Medical Branch, Galveston, TX 77550; (409) 772-2498, fax (409) 772-3229. UTMB is an equal opportunity M/F/H/V, affirmative action employer. UTMB hires only individuals authorized to work in the United States. 3–5c

FELLOWSHIPS AT ALBANY MEDICAL CENTER—The newly renovated and equipped Dept. of Radiology at the Albany Medical College and Center in Albany, NY offers the following fellowship positions each yr: (1) Abdominal Imaging—this fellowship encompasses all aspects of MRI, ultrasound, CT, and other advanced techniques in imaging the abdomen. Four state-of-the-art MRI and 4 CT scanners as well as 5 color Doppler ultrasound units are utilized daily. Contact James C. Peters, M.D. regarding this program. (2) Neuroradiology—This fellowship encompasses the full range of advanced neuro imaging including MRI, CT, angiography, and myelography. Contact William A. Wagle, M.D. (3) Angiography and interventional radiology—Three advanced angiographic suites are utilized daily for a full range of vascular and interventional procedures. Contact Mohammad S. Sarrafizadeh, M.D. All program directors listed above may be contacted at the Dept. of Radiology, A-113, Albany Medical Center, Albany, NY 12208; (518) 445-3277 or contact Matthew D. Rifkin, M.D., Chairman, Dept. of Radiology, A-113, at the above address. Albany Medical Center is an equal opportunity/affirmative action employer. 1–12c

Tutorials/Courses

MUSCULOSKELETAL MRI, SECOND ANNUAL LOS ANGELES CONFERENCE, SEPT. 19–20, 1992—Faculty: Drs. Bradley, Brant-Zawadzki, Dietrich, Friedman, Harms, Resnick, Schlesinger. Medical Seminars International, Inc., 18981 Ventura Blvd., #303, Tarzana, CA 91356; (818) 774-9077, fax (818) 774-0244. 4–9d

KONA, HAWAII 1992—Seventeenth annual International Body Imaging Congress, Oct. 10–17. CME 1. Mauni Lani Bay Hotel. Contact Medical Seminars International, Inc., 18981 Ventura Blvd., Ste. 303, Tarzana, CA 91356; (818) 774-9077, fax (818) 774-0244. 5–10d

ALASKA 1992:CRUISE THE INLAND PASSAGE, BREAST IMAGING AT SEA, JULY 4–11, 1992, AND MRI AT SEA, JULY 11–18, 1992—Medical Seminars International, Inc., 18981 Ventura Blvd., Ste. 303, Tarzana, CA 91356; (818) 774-9077, fax (818) 774-0244. 2–6d

AJR Classified Advertisements Information

Box Responses and Address for Ad Placement

Write Box ______, *AJR*, 2223 Avenida de la Playa, Suite 103, La Jolla, CA 92037-3218; Telephone: (619) 459-2229; FAX: (619) 459-8814.

How to Place an Ad

AJR accepts classified advertising for Positions Available, Positions Desired, Fellowships and Residencies, and Tutorials/Courses. Ads must be submitted typed double spaced. Ads are accepted by mail or FAX.

Rates: \$6.00/line with a \$30 minimum charge. Box service is \$10 additional for each month the ad appears. There are discounts for multiple insertions: 10% for 2-3 insertions; 20% for 4 or more. To estimate lines, count all words and divide by 7.

Billing: Ads *must* be prepaid, or advertisers will be billed after the ad appears, *providing* a purchase order number is submitted with the advertising copy. Terms are net 30 days.

Deadlines: 6 weeks before the issue date. For specific deadlines, telephone the *AJR* editorial office.

Estimating Ad Charges

Line charge: divide total words by 7 and
multiply by \$6.00 .... \$ ________

Multiple insertions? If so, multiply by number .... x ________
Subtotal .... \$ ________

Discount applies to two or more insertions.
Subtract 10% if ad appears 2-3 months;
20% if 4 months or more .... – ________
Subtotal .... \$ ________

Box response requested? If so, multiply number
of months by \$10.00 .... + ________

Approximate advertising charge .... \$ ________

Keep It All Together

Easily and Conveniently with Bound Volumes of the *American Journal of Roentgenology*

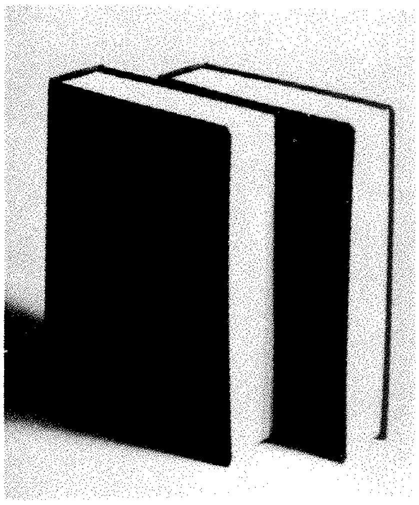

Keeping up with scientific and technological advances in radiology is more important than ever, and that's why each issue of the *American Journal of Roentgenology* is packed with up-to-the-minute information crucial to you and your practice. **Keep this important resource together for easy reference in convenient and attractive bound volumes.**

Bound volumes offer the timely coverage only a journal can provide — penetrating discussions of the topics that interest you most by the brightest names in the field — with all the durability and convenience of a hardcover edition. You'll have a year's worth of vital information all arranged and indexed in one sturdy source. And each carefully crafted volume will make a handsome addition to your permanent library.

To help you keep your reference library up to date, once a year we'll send a reminder so you can order the latest bound volumes. When you send in your paid order, a set will be reserved for you, to be sent as soon as available on 30-day approval. If you do not want the volumes for any reason, simply return them within 30 days for a courteous refund. It's that easy.

Bound volumes are available to subscribers only and are in addition to the regular subscription. For ordering information, contact *AJR* Subscription Fulfillment Department, 428 E. Preston St., Baltimore, MD 21202-3993, or call toll-free

1-800-638-6423.

No one ever said a lot of knowledge is a dangerous thing.

IN FACT, for radiologists, the only danger is not keeping up with what's new. **AJR: American Journal of Roentgenology** is your monthly guide to the latest advances, with articles that are timely, succinct, and relevant to daily practice.

AJR
American Journal of Roentgenology
Published monthly
Robert N. Berk, M.D., Editor
The University of California, San Diego

Call toll-free to order: **1-800-638-6423**
from anywhere in the U.S. or Canada.
Or clip and mail this coupon to
Waverly, Inc. ATTN: AJR

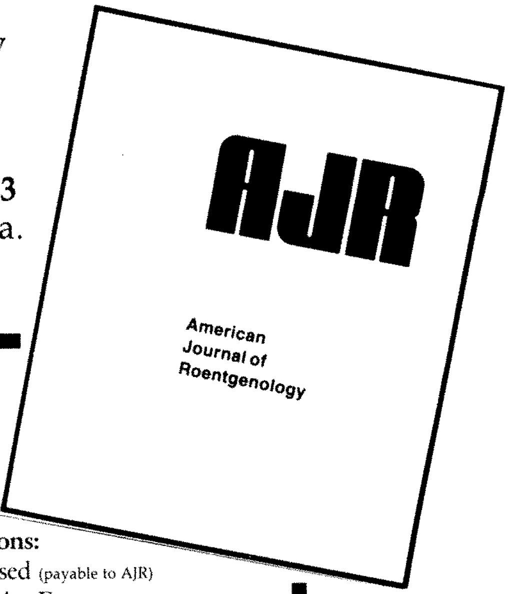

Subscribe to **AJR** now. (Current rates available for up to three years.)

☐ Individual $125/year
☐ Institutional $135/year
☐ In-training* $25/year
(Add $55/year outside the U.S.; in Canada, also add 7% GST.)
☐ 3 years ☐ 2 years ☐ 1 year
Maryland residents add 5% sales tax. Subscriptions outside the U.S. must be prepaid in U.S. dollars. Rates valid through October 31, 1992.

Name
Address
City/State/Zip
*Please specify institution and training status

AJR 592

Payment Options:
☐ Check enclosed (payable to AJR)
☐ Bill me ☐ AmEx
☐ MasterCard ☐ VISA

Card # Exp. Date
Signature

Return coupon to:
Waverly, Inc. ATTN: AJR
P.O. Box 23291, Baltimore, MD 21203-9990

AJR: AMERICAN JOURNAL OF ROENTGENOLOGY is the official journal of the American Roentgen Ray Society.

There are two foundations for PACS.

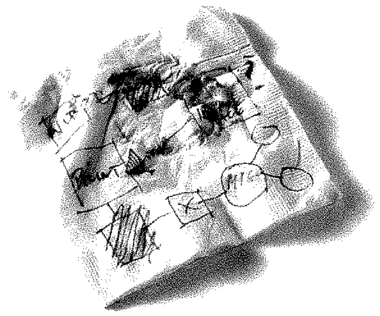

Theirs.

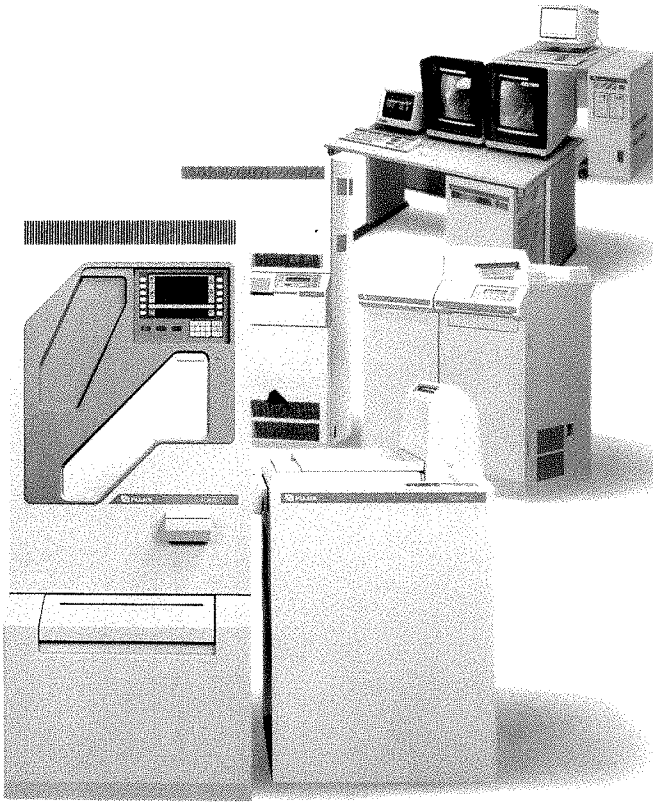

Ours.

Introducing Fuji RACS (Radiology Acquisition and Communication Systems), today's affordable foundation for the PACS networks of tomorrow. With Fuji RACS, Computed Radiography (CR) images can be acquired, displayed, transmitted and stored throughout the hospital.

Building on ten years development and clinical experience, Fuji extends the benefits of CR technology to your hospital *today*.

Commit to RACS from Fuji--the company that is delivering complete Computed Radiography Systems, not just promises. For more information on Fuji RACS, call (800) 431-1850 today. We'll provide the right foundation for your PACS.

A new way of
seeing things.

SPECIAL ARTICLE

961 **Review. Detection of metastasis in cervical lymph nodes: CT and MR criteria and differential diagnosis.** *Som PM*

CHEST RADIOLOGY

971 **Review. High-resolution CT of the lungs: findings in various pulmonary diseases.** *Swensen SJ, Aughenbaugh GL, Douglas WW, Myers JL*

981 **Case report. Pulmonary alveolar microlithiasis: findings on high-resolution CT.** *Korn MA, Schurawitzki H, Klepetko W, Burghuber OC*

983 **CT findings in benign fibrous mesothelioma of the pleura: pathologic correlation in nine patients.** *Lee KS, Im J-G, Choe KO, Kim CJ, Lee BH*

987 **Case report. Intrapulmonary bronchogenic cyst: spontaneous pneumothorax as the presenting symptom.** *Matzinger MA, Matzinger FR, Sachs HJ*

989 **Case report. Demonstration of blood supply to pulmonary sequestration by MR angiography.** *Doyle AJ*

BREAST RADIOLOGY

991 **Perspective. Value of large-core biopsy of occult breast lesions.** *Meyer JE*

993 **Fibrosarcoma of the breast: mammographic findings in five cases.** *Elson BC, Ikeda DM, Andersson I, Wattsgård C*

GASTROINTESTINAL RADIOLOGY

997 **Changes in extrahepatic bile duct caliber in liver transplant recipients without evidence of biliary obstruction.** *Campbell WL, Foster RG, Miller WJ, Lecky JW, Zajko AB, Lee KY*

1001 **Venoocclusive liver disease after bone marrow transplantation: findings at duplex sonography.** *Herbetko J, Grigg AP, Buckley AR, Phillips GL*

1007 **Treatment of bile duct stones by laser lithotripsy: results in 12 patients.** *Dawson SL, Mueller PR, Lee MJ, Saini S, Kelsey P, Nishioka NS*

1011 **Oriental cholangiohepatitis: correlation between portal vein occlusion and hepatic atrophy.** *Kusano S, Okada Y, Endo T, Yokoyama H, Ohmiya H, Atari H*

1015 **Pictorial essay. Hepatic neoplasms: surgically relevant segmental anatomy and imaging techniques.** *Gazelle GS, Haaga JR*

1019 **Occlusion and narrowing of the pharyngeal airway in obstructive sleep apnea: evaluation by ultrafast spoiled GRASS MR imaging.** *Shellock FG, Schatz CJ, Julien P, et al.*

1025 **Technical note. Recurrent extraluminal rectal carcinoma: transrectal biopsy under sonographic guidance.** *Nielsen MB, Pedersen JF, Hald J, Christiansen J*

1029 **Case report. *Candida* cholangitis in a diabetic woman.** *Radin DR, Johnson MB*

1031 **Primary malignant small round cell tumor of the abdomen: CT findings.** *Varma DGK, McDaniel K, Ordóñez NG, Granfield CAJ, Charnsangavej C, Wallace S*

GENITOURINARY RADIOLOGY

1035 **Review. Duplex Doppler evaluation of native kidney dysfunction: obstructive and nonobstructive disease.** *Platt JF*

1043 **MR imaging in the evaluation of benign uterine masses: value of gadopentetate dimeglumine–enhanced T1-weighted images.** *Hricak H, Finck S, Honda G, Göranson H*

1051 **Ureteric jets: evaluation of normal flow dynamics with color Doppler sonography.** *Cox IH, Erickson SJ, Foley WD, Dewire DM*

1057 **Testicular microlithiasis: sonographic and clinical features.** *Janzen DL, Mathieson JR, Marsh JI, et al.*

1061 **Case report. Intratesticular varicocele: sonographic findings in two patients.** *Weiss AJ, Kellman GM, Middleton WD, Kirkemo A*

MUSCULOSKELETAL RADIOLOGY

1065 **Review. Lyme disease and radiologic findings in Lyme arthritis.** *Lawson JP, Rahn DW*

1071 **Review. Digital skeletal radiography.** *Buckwalter KA, Braunstein EM*

1081 **The ulnar tunnel at the wrist (Guyon's canal): normal MR anatomy and variants.** *Zeiss J, Jakab E, Khimji T, Imbriglia J*

1087 **Pictorial essay. Craniovertebral junction: normal anatomy with MR correlation.** *Schweitzer ME, Hodler J, Cervilla V, Resnick D*

1091 **Pictorial essay. Long bicipital tendon of the shoulder: normal anatomy and pathologic findings on MR imaging.** *Erickson SJ, Fitzgerald SW, Quinn SF, Carrera GF, Black KP, Lawson TL*

PEDIATRIC RADIOLOGY

1097 **Blunt pancreatic trauma in children: CT diagnosis.** *Sivit CJ, Eichelberger MR, Taylor GA, Buias DI, Gotschall CS, Kushner DC*

1101 **Azygoesophageal recess: normal CT appearance in children.** *Fitzgerald SW, Donaldson JS*

1105 **Pictorial essay. Cartilaginous epiphysis and growth plate: normal and abnormal MR imaging findings.** *Jaramillo D, Hoffer FA*

1111 **Case report. Mediastinal pseudocyst caused by pharyngeal perforation during child abuse.** *Kleinman PK, Spevak MR, Hansen M*

VASCULAR RADIOLOGY

1115 **Review. The role of MR imaging in the evaluation of acquired diseases of the thoracic aorta.** *Link KM, Lesko NM*

1127 **Pictorial essay. Assessment of the thoracic aorta by spiral CT.** *Costello P, Ecker CP, Tello R, Hartnell GG*

1131 **Case report. Left thyrocervical trunk bronchial artery supplying right lung: source of recurrent hemoptysis in cystic fibrosis.** *Cohen AM, Antoun BW, Stern RC*

NEURORADIOLOGY

1135 **Review. Diagnosis of lumbar spinal stenosis in adults: a metaanalysis of the accuracy of CT, MR, and myelography.** *Kent DL, Haynor DR, Larson EB, Deyo RA*

1145 **Epidural abscess of the cervical spine: MR findings in five cases.** *Kricun R, Shoemaker EI, Chovanes GI, Stephens HW*

1151 **MR imaging of the pituitary gland in infants and children: changes in size, shape, and MR signal with growth and development.** *Tien RD, Kucharczyk J, Bessette J, Middleton M*

1155 **Crossed cerebellar diaschisis and crossed cerebellar atrophy: correlation of MR findings, clinical symptoms, and supratentorial diseases in 26 patients.** *Tien RD, Ashdown BC*

1161 **Case report. MR demonstration of reversible cerebral lesions in a child with hypertensive encephalopathy caused by Wilms' tumor.** *Shanley DJ, Sisler CL*

1163 **Case report. Intracranial metastatic adenoid cystic carcinoma: presumed hematogenous spread from a primary tumor in the parotid gland.** *Gelber ND, Ragland RL, Knorr JR, Smith TW, Stone BB*

MEMO TO AUTHORS

1165 **The types of articles published in the *AJR*.** *Berk RN*

OTHER CONTENT

970 **Medicine in American Art**
980 **History page**
1056 **Radiologic-pathologic conference**
1080 **List of book and videotape reviews**
1126 **Forthcoming articles**
1167 **Letters**
1178 **Review of current literature**
1181 **News**
1184 **American Roentgen Ray Society information**
1185 **Classified advertisements**
A15 **Guidelines for authors**

AJR

American
Journal of
Roentgenology

June 1992

This time, you'll take NuLYTELY, the better-tasting lavage!

NuLYTELY®

PEG 3350, Sodium Chloride, Sodium Bicarbonate and Potassium Chloride for Oral Solution

A double-blinded, multicenter study[1] comparing NuLYTELY® and GoLYTELY® demonstrated a difference:

Preference. Patients clearly chose NuLYTELY® as the better-tasting preparation.

BRIEF SUMMARY: Before prescribing, see complete prescribing information.

INDICATIONS AND USAGE: NuLYTELY is indicated for bowel cleansing prior to colonoscopy.

CONTRAINDICATIONS: NuLYTELY is contraindicated in patients with gastrointestinal obstruction, gastric retention, bowel perforation, toxic colitis or toxic megacolon.

WARNINGS: No additional ingredients, e.g. flavorings, should be added to the solution. NuLYTELY should be used with caution in patients with severe ulcerative colitis.

PRECAUTIONS: General: Patients with impaired gag reflex, unconscious, or semiconscious patients, and patients prone to regurgitation or aspiration should be observed during the administration of NuLYTELY, especially if it is administered via nasogastric tube. If a patient experiences severe bloating, distention or abdominal pain, administration should be slowed or temporarily discontinued until the symptoms abate. If gastrointestinal obstruction or perforation is suspected, appropriate studies should be performed to rule out these conditions before administration of NuLYTELY.

ADVERSE REACTIONS: Nausea, abdominal fullness and bloating are the most common adverse reactions (occurring in up to 50% of patients) to administration of NuLYTELY. Abdominal cramps, vomiting, and anal irritation occur less frequently. These adverse reactions are transient and subside rapidly. Isolated cases of urticaria, rhinorrhea and dermatitis have been reported with a related drug (GoLYTELY®) which may represent allergic reactions.

CAUTION: Federal law prohibits dispensing without prescription.

STORAGE: Store in sealed container at 25°C. When reconstituted, keep solution refrigerated. Use within 48 hours. Discard unused portion. NDC 52268-0300-01

Manufactured for Braintree Laboratories, Inc. Braintree MA 02184 by Lyne Laboratories, Inc., Stoughton MA 02072.

Reference: 1. Data on file, Braintree Laboratories.

LABORATORIES • INC

Official Journal of the American Roentgen Ray Society

AJR

American Journal of Roentgenology

Diagnostic Imaging and Related Sciences

Editor-In-Chief	Robert N. Berk, *La Jolla, California* *University of California, San Diego* *School of Medicine and Medical Center*
Editor Emeritus	Melvin M. Figley, *Seattle, Washington*
Associate Editor	Karim Valji, *San Diego, California*
Consulting Editors	A. James Barkovich, *San Francisco, California* Edward A. Sickles, *San Francisco, California*
Statistician	Charles C. Berry, *San Diego, California*

Editorial Board

Mark E. Baker
Lawrence W. Bassett
Michael A. Bettmann
Ethan M. Braunstein
Felix S. Chew
Horacio R. D'Agostino
N. Reed Dunnick
David K. Edwards
Ronald G. Evens
Sandra K. Fernbach
Richard H. Gold
Edward G. Grant
John R. Hesselink
Emanuel Kanal
Ray F. Kilcoyne
Carolyn Kimme-Smith
Melvyn T. Korobkin
Mark J. Kransdorf
Faye C. Laing
Thomas L. Lawson
Robert G. Levitt
Martin J. Lipton
Bruce L. McClennan
Richard P. Moser
Jeffrey H. Newhouse
Sven J. K. Paulin
David M. Paushter
Vassilios Raptopoulos
Donald L. Resnick
Charles A. Rohrmann, Jr.
Peter M. Ronai
Stuart S. Sagel
Sanjay Saini
Stefan C. Schatzki
William P. Shuman
Edward A. Sickles
Barry A. Siegel
M. Leon Skolnick
Edward T. Stewart
Murali Sundaram
Robert D. Tien

Director of Publications: Susan Brown Cappitelli **Editorial Staff:** Barbara Rose, *managing editor*; Katie L. Spiller, Barbara L. Halliburton, and Janine Anderson, *manuscript editors*; Nancy Rydbeck, *office manager*; Sheri Smith, *administrative assistant*; Linda J. Waggoner, *administrative secretary*

AJR, AMERICAN JOURNAL OF ROENTGENOLOGY (ISSN 0361 803X) is published monthly by the American Roentgen Ray Society, 1891 Preston White Dr., Reston, VA 22091. Annual dues include $50 for journal subscription. Second-class postage paid at Baltimore, MD, and at additional mailing offices. **POSTMASTER**, send address changes (Form 3579) to Subscription Fulfillment, AJR, 428 E. Preston St., Baltimore, MD 21202. Subscription rates $125 ($180 foreign); institutions $135 ($190 foreign); in training $25 ($80 foreign); single copy $18 ($22 foreign). The GST number for Canadian subscribers is 123394371. Airmail rates furnished on request. Indexed by *Current Contents* and *Index Medicus*. Copyright © 1992 by American Roentgen Ray Society.

0361-803X/92$3.00

AN IDEA OF WHAT TO EXPECT FROM OUR NEW CT SYSTEM.

Quite simply, speed and power. Routine one second scans and a one second interscan delay — with no compromise in image quality. That's the kind of performance you can expect from the new CT HiSpeed Advantage.™

Slip-ring technology has made faster rotation possible, but in reality, slip rings are only a small part of the story. Our new 48 kW generator and x-ray tube provide the power needed to obtain these uncompromised one second images. This high power technology, coupled with the high quantum efficiency of GE's exclusive HiLight Detector, means new clinical capabilities such as cluster and helical scanning will have even greater possibilities.

As with other GE CT systems, the HiSpeed Advantage is backed by our revolutionary Continuum philosophy. So your system can be cost-effectively upgraded to keep up with the latest clinical advancements. In fact, all CT 9800 series systems are upgradeable to the new HiSpeed Advantage.

So, if you're considering a fast CT scanner, only one choice is clear. The HiSpeed Advantage.

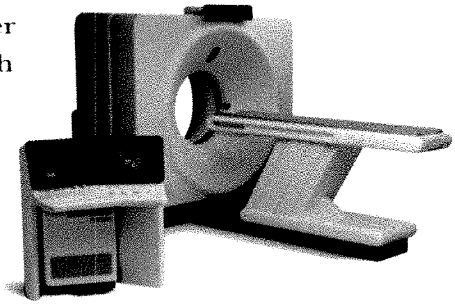

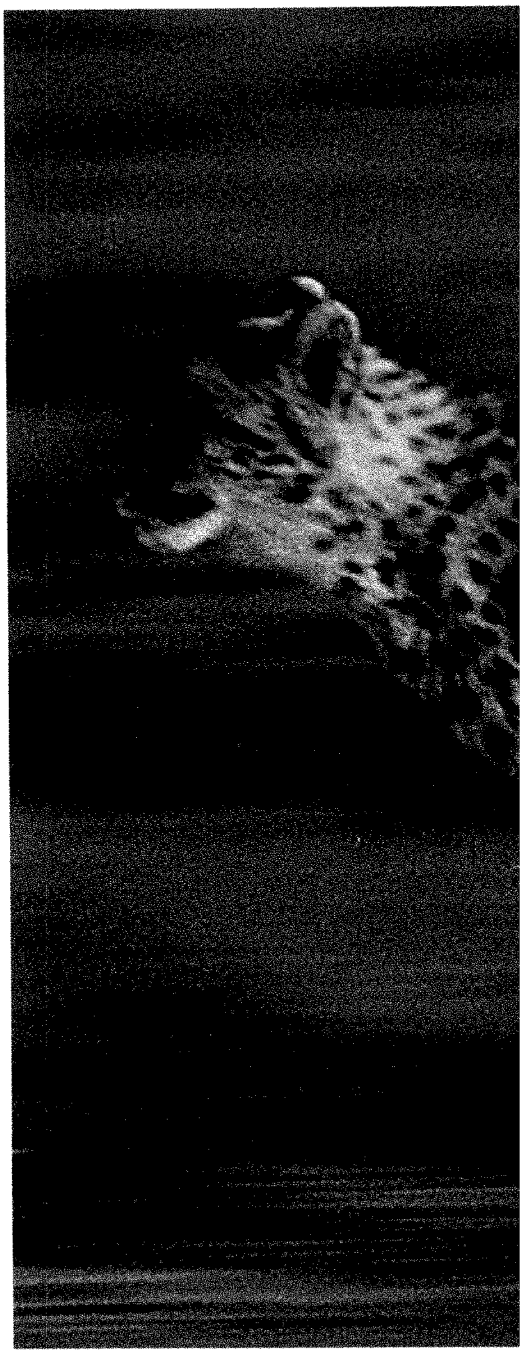

GE Medical Systems

We bring good things to life.

Address new and revised manuscripts, correspondence, and classified ads to the Editor:

AJR Editorial Office
2223 Avenida de la Playa, Suite 103
La Jolla, CA 92037-3218
Telephone: (619) 459-2229; FAX: (619) 459-8814

Inquiries regarding reprints or permission to republish *AJR* material should be addressed to the publisher:

Publications Department ARRS
1891 Preston White, Dr., Reston, VA 22091

The *AJR* publishes original contributions to the advancement of medical diagnosis and treatment. Submitted manuscripts should not contain previously published material and should not be under consideration for publication elsewhere.

Manuscript decisions are based on peer review. Reviewers receive manuscripts without title pages to ensure an unbiased review. Statements made in the article, including changes made by the Editor or manuscript editor, are the responsibility of the author and not of the *AJR* or its publisher. Authors will be sent the edited manuscript, galley proof, and proofs of illustrations. If the corresponding author will be unavailable to review galleys, arrangements should be made for a coauthor or colleague to read and return the proof.

The following guidelines are based on instructions set forth in the **Uniform Requirements for Manuscripts Submitted to Biomedical Journals** (*Ann Intern Med* **1988;**108:258–265). Articles will be edited, however, to conform to the individual style of *AJR*.

General Guidelines for Major Papers

Abstract. Clearly state (in 250 words or fewer) the purpose, methods, results, and conclusions of the study. Include actual data.

Introduction. Briefly describe the purpose of the investigation and explain why it is important.

Methods. Describe the research plan, the materials (or subjects), and the methods used, in that order. Explain in detail how disease was confirmed and how subjectivity in observations was controlled.

Results. Present results in a clear, logical sequence. If tables are used, do not duplicate tabular data in text, but do describe important trends and points.

Discussion. Describe the limitations of the research plan, materials (or subjects), and methods, considering both the purpose and the outcome of the study. When results differ from those of previous investigators, explain the discrepancy.

AUTHOR'S CHECKLIST

For priority handling, complete the following checklist, sign the copyright form on the reverse side of this page, and include both with the manuscript.

________ Two copies of the manuscript (the original and a photocopy) and two complete sets of figures are submitted. One copy has been retained by the author.

________ If appropriate, *AJR* Guidelines for case reports, technical notes, pictorial essays, or letters to the Editor have been followed. (See page A6.)

________ The manuscript, including references, figure legends, and tables, is typed double-spaced on 8½ × 11 in. (21.6 × 27.9 cm) *nonerasable* paper. Right-hand margins are not justified.

________ All manuscript pages are numbered consecutively beginning with the abstract. Authors' names do not appear on the manuscript pages.

________ The manuscript is organized as follows: title page, blind title page (title only), abstract, introduction, methods, results, discussion, acknowledgments, references, tables, figure legends, and figures.

________ Informed consent has been obtained from patients who participated in clinical investigations. If experiments were performed on animals, authors complied with NIH guidelines for use of laboratory animals.

________ Use of unfamiliar acronyms and abbrevations is kept to a minimum. When abbreviations are used they are defined at first mention, followed by the abbreviation in parentheses.

________ Metric measurements are used throughout, or the metric equivalent is given in parentheses.

________ Names and locations (city and state only) of manufacturers are given for equipment and nongeneric drugs.

________ Upon acceptance, final version is submitted on a 5 1/4-in. DOS-compatible diskette in Wordperfect or ASCII format.

Title Page

________ The following information is given: title of article; names and complete addresses (including zip code) of all authors; current addresses of authors who have moved since study; acknowledgment of grant or other assistance. The corresponding author is clearly identified, and a current address, phone number, and FAX number are given.

________ A blind title page is included in each copy of the manuscript, giving only the title (without the authors' names) for use in the review process.

Abstract

________ An abstract of approximately one and one-half typewritten pages is organized into the following paragaphs.

Objective. In one or two sentences, indicate the specific goal or purpose of the article, and indicate why it is worthy of attention. Explain the hypothesis to be tested, the dilemma to be resolved, or the deficiency to be remedied. The objective stated here must be identical to the one given in the title and introduction of the paper.

Subjects (or materials) and methods. Describe succinctly the methods used to achieve the objective explained in the first paragraph, stating what was done, how it was done, how bias was controlled, what data were collected, and how the data were analyzed.

Results. The findings of the procedures described in the preceding paragraph are presented here. All results should flow logically from the methods described and not stray from the specific objective of the paper. Include as many specific data as possible within the overall length limitation of one typewritten page.

Conclusion. In one or two sentences, present the take-home message to be remembered when all else is forgotten. Describe the conclusion of the study, based solely on the

data provided in the body of the abstract. Conclusions must relate directly to the objective of the paper as defined in the title and first paragraph of the abstract.

________ No abbreviations or reference citations are used.

________ No abbreviations or reference citations are used.

References

________ References (not to exceed 35) are typed double-spaced starting on a separate page and are **numbered consecutively in the order in which they appear in the text.**

________ All references are cited in the text and are enclosed in brackets and typed on line with the text (not superscript).

________ Unpublished data are not cited in the reference list, but are cited parenthetically in the text, for example, (Smith DJ, personal communication), (Smith DJ, unpublished data). This includes papers submitted, but not yet accepted, for publication.

________ Papers presented at a meeting are not cited in the reference list, but are cited parenthetically in the text (e.g., Smith DJ et al., presented at the American Roentgen Ray Society meeting, May 1990). After first mention, use (Smith DJ et al., ARRS meeting, May 1990).

________ Inclusive page numbers (e.g., 333–335) are given for all references.

________ Journal names are abbreviated according to *Index Medicus*.

________ Style and punctuation of references follow the format illustrated in the following examples (all authors are listed when six or fewer; when seven or more authors, the first three are listed, followed by "et al."):

Journal article

1. Long RS, Roe EW, Wu EU, et al. Membrane oxygenation: radiographic appearance. *AJR* **1986**;146:1257–1260

Book

2. Smith LW, Cohen AR. *Pathology of tumors*, 6th ed. Baltimore: Williams & Wilkins, **1977**:100–109

Chapter in a book

3. Breon AJ. Serum monitors of bone metastasis. In: Clark SA, ed. *Bone metastases*. Baltimore: Williams & Wilkins, **1983**:165–180

Tables

________ Each table is typed double-spaced on a separate page without vertical or horizontal rules; each has a short, descriptive title. Tables do not exceed two pages in length and contain at least four lines of data.

________ Tables are numbered in the order in which they are cited in the text.

________ Abbreviations are defined in an explanatory note below each table.

________ Tables are self-explanatory and do not duplicate data given in the text or figures.

________ All arithmetic (percentages, totals, differences) has been double checked for accuracy, and tabular data agree with data given in the text.

Figures and Legends

________ Two complete sets of original figures are submitted unmounted in labeled envelopes.

________ Figures are clean, unscratched, 5 × 7 in. (13 × 18 cm) glossy prints with **white borders.** A separate print is submitted for each figure *part*.

________ All figure parts relating to one patient have the same figure number.

________ Each figure is labeled on the back with the figure number and an arrow indicating "top." For black-and-white figures, labeling is done on a gummed label, which is then affixed to the back of the print. **Never** use labels on **color** figures, but write figure number on the back lightly in pencil. *Never* use ink on front or back of any figures.

________ Authors' names are *not* written on the backs of figures.

________ Only removable (rub-on) arrows and letters are used on the figures. Symbols are uniform in size and style and are not broken or cracked.

________ Images are uniform in size and magnification.

________ Line drawings are done in black ink on a white background. They are professional in quality, and all use the same size type. (Only glossy prints are acceptable.)

________ Written permission has been obtained for use of all previously published illustrations (and copies of permission letters are included), and an appropriate credit line is given in the legends.

________ Legends are typed double-spaced, and figure numbers correspond with the order in which the figures are cited in the text.

Transfer of Copyright Agreement, Conflict of Interest Acknowledgment, Certification of Coauthors, and Exclusive Publication Statement

Complete copyright to the article entitled: ____

____

is hereby transferred to the American Roentgen Ray Society (for United States government employees to the extent transferable), effective if and when the article is accepted for publication in the *American Journal of Roentgenology*. In the case of the authors who are officers or employees of the United States government, the American Roentgen Ray Society recognizes that works prepared by officers or employees of the United States government as part of their official government duties are in the public domain.

Authors reserve all proprietary rights other than copyright, such as patent rights and the right to use all or part of this article in future works of their own. The authors retain the right of replication, subject only to crediting the original source of publication and receiving written permission from the publisher.

Authors guarantee that this manuscript contains no matter that is libelous or otherwise unlawful, invades individual privacy, or infringes any proprietary rights.

Authors understand that they will receive no royalty or other compensation from the American Roentgen Ray Society or the publisher.

Authors guarantee that the editor has been or will be informed of any proprietary or commercial interest or conflicts of interest the authors may have that relate directly or indirectly to the subject of this article.

All authors certify that they have made substantive and specific intellectual contributions to the article and assume public responsibility for its content.

Finally, the authors certify that none of the material in this manuscript has been published previously or is currently under consideration for publication elsewhere.

------------------------------	------------------------------	------------------------------
First author/date	Second author	Third author
------------------------------	------------------------------	------------------------------

Case Reports

A case report is a brief description of a special case that provides a message that transcends the individual patient.

Format. There is no abstract. The introduction should be a short paragraph giving the general background and the specific interest of the case. No more than one case should be described in detail (similar ones can be mentioned briefly in the discussion). Emphasis should be on the radiologic aspects; clinical information must be limited to that necessary to provide a background for the radiology. The discussion should be succinct and should focus on the specific message and relevance of radiologic methods. A review of the literature is not appropriate.

Length. Maximum of five double-spaced, typewritten pages, including the references but not the title page or figure legends.

References. Maximum of eight.

Figures. Maximum of four, unless the text is shortened accordingly. Legends must not repeat the text.

Tables and Acknowledgments. Not appropriate in case reports.

Pictorial Essays

A pictorial essay is an article that conveys its message through illustrations and their legends. Unlike other *AJR* articles, which are based on original research, pictorial essays serve primarily as teaching tools, like exhibits at a scientific meeting. They are not encyclopedic book chapters. The abstract should be a short, introductory paragraph.

Length. Maximum of four double-spaced, typewritten pages, including the references but not the title page or figure legends.

References. Maximum of four.

Figures. Maximum of 30 figure *parts*. Number should be as few as necessary to convey the message of the paper.

Tables and Acknowledgments. Not appropriate in pictorial essays.

Opinions, Commentaries, and Perspectives

Opinions, commentaries, and perspectives are special articles dealing with controversial topics or issues of special concern to radiologists.

Format. Include a title page but no abstract. Headings may be used to break up the text.

Length. Maximum of five double-spaced, typewritten pages.

References. Maximum of five.

Tables and Figures. Maximum of four.

Technical Notes

A technical note is a brief description of a specific technique or procedure, modification of a technique, or equipment of interest to radiologists.

Format. No abstract, headings, or subheadings are required. If headings are used, they should be a combination of "Case Report," "Materials and Methods," "Results," and "Discussion." A brief one-paragraph introduction should be included to give the general background. Discussion should be limited to the specific message, including the uses of the technique or equipment. Literature reviews and lengthy case reports are not appropriate.

Length. Maximum of five double-spaced, typewritten pages, including the references but not the title page or figure legends.

References. Maximum of eight.

Figures. Maximum of two, unless the text is shortened accordingly.

Tables and Acknowledgments. Not appropriate in technical notes.

Letters to the Editor and Replies

Letters to the Editor and Replies should offer objective and constructive criticism of published articles. Letters may also discuss matters of general interest to radiologists. Do not end a letter with a hand-written signature.

Format. All letters should be typed double-spaced on nonletterhead paper, with no greeting or salutation. Name and affiliation should appear at the end of the letter. Titles for letters should be short and pertinent. The title for a reply is simply "Reply."

Length. Maximum of two double-spaced, typewritten pages, including references.

References. Maximum of four.

Figures. Maximum of two.

Tables and Acknowledgments. Not appropriate in Letters to the Editor and Replies.

Computer Page Articles

Articles published on the computer page deal with practical computer applications to radiology.

Format. Include a title page and an abstract.

Length. Maximum of eight double-spaced, typewritten pages.

References. Maximum of five.

Figures and Tables. Maximum of five. Computer printouts are not acceptable. Figures must be submitted as 5 × 7 in. glossy prints.

All submissions to the *AJR* must be accompanied by a completed copy of the Author's Checklist and the signed Copyright agreement.

THE UNITED STATES OF A
THIS NOTE IS LEGAL TENDER FOR ALL DEBTS, PUBLIC AND PRIVATE
B14303059B
FRANKLIN
SERIES 1985
ONE HUNDRED DOLLAR

HOW MUCH IS YOUR TIME WORTH?

If, like most Radiologists, you spend 30% or more of your day **handling** films, let us show you how S & S Motorized Viewers eliminate those COSTLY WASTED HOURS!

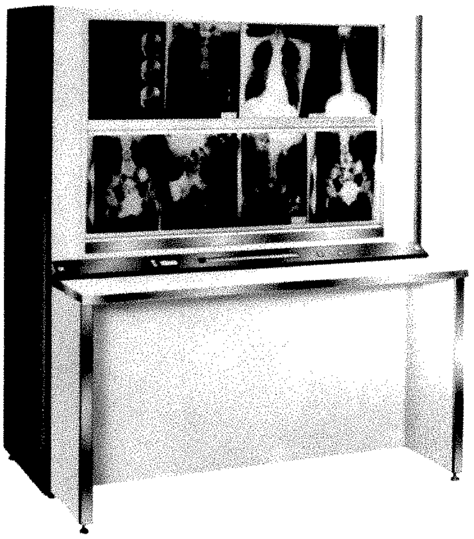

Model MV216

- From 48 up to 324 14" x 17" films can be pre-loaded and stored in proper sequence to be recalled when needed for viewing in as little as 7 seconds—by simply pressing a button!
- All 12 models feature illumination brighter than most other viewers, plus individual panel light controls which promote viewer concentration and increase reading efficiency.
- Some models feature an optional "floating bright spot" which illuminates dense area—at the touch of a button.
- Optional remote controls eliminate need to stand directly in front of viewer to operate it.
- Smaller capacity units on casters provide room-to-room mobility as needed.
- Specially dedicated models are also available for MAMMOGRAPHY, ULTRASOUND, CT and NUCLEAR FILM VIEWING.

Ideal for Teaching, Lecturing or Consultation, S & S Motorized Viewers turn waste into efficiency. **How much is YOUR time worth?** Call S & S or your local x-ray dealer **today**.

S & S X-RAY PRODUCTS INC.
1101 Linwood Street
Brooklyn, NY 11208
800/347-XRAY
718/649-8500
FAX 718/257-0219

The NEMOURS
CHILDREN'S
CLINIC *Reaching Out-H*

PEDIATRIC RADIOLC

The Nemours Children's Clinic, a pediatric te
specialty clinic, located on the St. Johns River,
Florida is seeking a Board Certified Pediatric
Chairperson of the Department of Radiology.
are seeking a BC/BE staff radiologist. Nemours i
the new Children's Hospital in the developmen
Health Center. Nemours is also developing a sy
tory health care for children in Florida throug
primary care and subspecialty clinics throug
order to provide innovative services and additio
in a city of 800,000 people with a large referr
Georgia, Northeast Florida, and the new Chil
Nemours is expanding the Department of Radio

Nemours offers a stimulating and challengin
unique opportunity to participate in the advanc
care for children.

Proximity to First Coast Beaches, cultural a
activities, and a pleasant climate, as well as an
professional growth and participation in ed
search make this a very desirable career choic

Interested applicants should send their CV to **la**
M.D., Chairman, Search Committee, Nemours
807 Nira Street, Jacksonville, Florida 32207, (

BODY

Mau

Octobe

The seventeenth edition of this hig
Lani Bay Hotel,on the island of Kc
Famous." A renowned invited facul
S. Harms, D. Kumpe, M. L. Manco-
Tomography, Ultrasonography, Ma
ties. A special focus section on **Brea**
approximately 25 Category I CM

Michael L. Manco-Jo
University of Colorado Health
Program Coordin

Registration Information: US $
and Nurses with letter may deduc
For further travel information:

Pacifica Plaza Travel, I
(800) 92

For registration and further meeti

18981

OMNIPAQUE
(iohexol)
has a
new
image

Introducing

FLEXIPAK™ (Flexible Container)

A new package for OMNIPAQUE with safety, convenience and flexibility built in

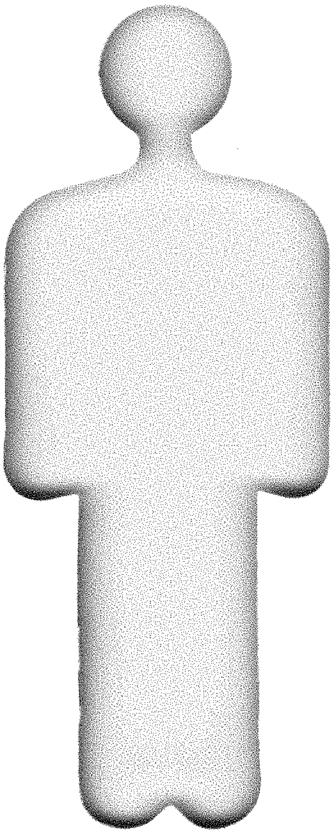

The safety package

New FLEXIPAK makes it simple to purge air from the flexible container before hanging to help reduce the potential for air emboli. The easily spiked port eliminates the possibility of infusing microscopic rubber particles from glass-bottle stoppers. And you don't need an air vent because the soft sides collapse as OMNIPAQUE flows.

The convenience package

No more waste and messy cleanups from broken glass bottles. And, FLEXIPAK is ready and easy to hang, even on crowded IV poles. FLEXIPAK lightens the load from setup to administration and all points in between.

The flexibility package

FLEXIPAK is flat and stackable for the best possible utilization of your storage space. And FLEXIPAK is available in the concentrations and sizes used most often.

	100 mL	150 mL	200 mL
OMNIPAQUE 240	X	X	X
OMNIPAQUE 300	X	X	
OMNIPAQUE 350	X	X	X

© 1991 Sanofi Winthrop Pharmaceuticals

It's all part of the package!

NONIONIC
OMNIPAQUE®
(IOHEXOL)

See last page for important product information concerning contraindications, warnings, adverse reactions, patient selection, and prescribing and precautionary recommendations.

All nonionic iodinated contrast media currently available inhibit blood coagulation, in vitro, less than ionic contrast media. Clotting has been reported when blood remains in contact with syringes containing nonionic contrast media. Therefore, meticulous intravascular administration technique is necessary to minimize thromboembolic events.

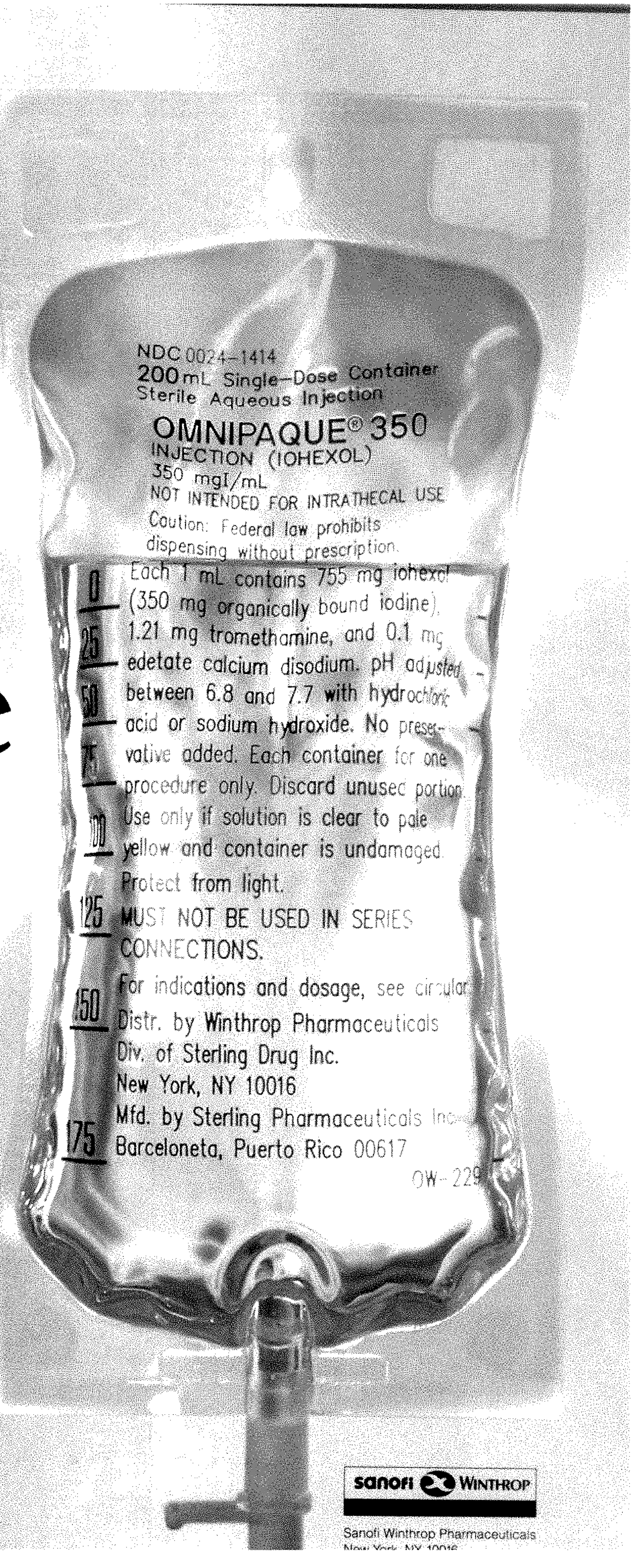

NDC 0024-1414
200 mL Single-Dose Container
Sterile Aqueous Injection
OMNIPAQUE® 350
INJECTION (IOHEXOL)
350 mgI/mL
NOT INTENDED FOR INTRATHECAL USE
Caution: Federal law prohibits dispensing without prescription.
Each 1 mL contains 755 mg iohexol (350 mg organically bound iodine), 1.21 mg tromethamine, and 0.1 mg edetate calcium disodium. pH adjusted between 6.8 and 7.7 with hydrochloric acid or sodium hydroxide. No preservative added. Each container for one procedure only. Discard unused portion. Use only if solution is clear to pale yellow and container is undamaged. Protect from light.
MUST NOT BE USED IN SERIES CONNECTIONS.
For indications and dosage, see circular
Distr. by Winthrop Pharmaceuticals
Div. of Sterling Drug Inc.
New York, NY 10016
Mfd. by Sterling Pharmaceuticals Inc.
Barceloneta, Puerto Rico 00617
OW-229

sanofi WINTHROP

Sanofi Winthrop Pharmaceuticals
New York, NY 10016

64-1121

OMNIPAQUE® 140 240 300 350

INJECTION (IOHEXOL)
INTRAVASCULAR

PLEASE CONSULT FULL PRODUCT INFORMATION BEFORE USING. A SUMMARY FOLLOWS:

DESCRIPTION: OMNIPAQUE is a sterile, pyrogen-free and preservative-free, nonionic, water-soluble radiographic contrast medium for intravascular administration in concentrations of 140, 240, 300, and 350 mgI/mL. OMNIPAQUE 140 contains 302 mg of iohexol equivalent to 140 mg of organic iodine per mL; OMNIPAQUE 240 contains 518 mg of iohexol equivalent to 240 mg of organic iodine per mL; OMNIPAQUE 300 contains 647 mg of iohexol equivalent to 300 mg of organic iodine per mL; and OMNIPAQUE 350 contains 755 mg of iohexol equivalent to 350 mg of organic iodine per mL. Each milliliter of iohexol solution contains 1.21 mg tromethamine and 0.1 mg edetate calcium disodium with the pH adjusted between 6.8 and 7.7 with hydrochloric acid or sodium hydroxide. Unused portions must be discarded. Iohexol solution is sensitive to light and should be protected from exposure.

CONTRAINDICATIONS: OMNIPAQUE should not be administered to patients with a known hypersensitivity to iohexol.

WARNINGS—General: Nonionic iodinated contrast media inhibit blood coagulation, in vitro, less than ionic contrast media. Clotting has been reported when blood remains in contact with syringes containing nonionic contrast media.

Serious, rarely fatal, thromboembolic events causing myocardial infarction and stroke have been reported during angiographic procedures with both ionic and nonionic contrast media. Therefore, meticulous intravascular administration technique is necessary, particularly during angiographic procedures, to minimize thromboembolic events. Numerous factors, including length of procedure, catheter and syringe material, underlying disease state, and concomitant medications, may contribute to the development of thromboembolic events. For these reasons, meticulous angiographic techniques are recommended including close attention to guidewire and catheter manipulation, use of manifold systems and/or three-way stopcocks, frequent catheter flushing with heparinized saline solutions and minimizing the length of the procedure. The use of plastic syringes in place of glass syringes has been reported to decrease but not eliminate the likelihood of in vitro clotting.

OMNIPAQUE should be used with extreme care in patients with severe functional disturbances of the liver and kidneys, severe thyrotoxicosis, or myelomatosis. Diabetics with a serum creatinine level above 3 mg/dL should not be examined unless the possible benefits of the examination clearly outweigh the additional risk. OMNIPAQUE is not recommended for use in patients with anuria.

Radiopaque contrast agents are potentially hazardous in patients with multiple myeloma or other paraproteinemia, particularly in those with therapeutically resistant anuria. Although neither the contrast agent nor dehydration has separately proven to be the cause of anuria in myeloma, it has been speculated that the combination of both may be causative factors. The risk in myelomatous patients is not a contraindication; however, special precautions are necessary. Partial dehydration in the preparation of these patients prior to injection is not recommended since this may predispose the patient to precipitation of the myeloma protein in the renal tubules. No form of therapy, including dialysis, has been successful in reversing the effect. Myeloma, which occurs most commonly in persons over age 40, should be considered before instituting intravascular administration of contrast agents.

Ionic contrast media, when injected intravenously or intra-arterially, may promote sickling in individuals who are homozygous for sickle cell disease.

Administration of radiopaque materials to patients known or suspected of having pheochromocytoma should be performed with extreme caution. If, in the opinion of the physician, the possible benefits of such procedures outweigh the considered risks, the procedures may be performed; however, the amount of radiopaque medium injected should be kept to an absolute minimum. The patient's blood pressure should be assessed throughout the procedure and measures for the treatment of hypertensive crisis should be readily available.

Reports of thyroid storm following the use of iodinated, ionic radiopaque contrast media in patients with hyperthyroidism or with an autonomously functioning thyroid nodule suggest that this additional risk be evaluated in such patients before use of any contrast medium.

Urography should be performed with caution in patients with severely impaired renal function and patients with combined renal and hepatic disease.

PRECAUTIONS—General: Diagnostic procedures which involve the use of radiopaque diagnostic agents should be carried out under the direction of personnel with the prerequisite training and with a thorough knowledge of the particular procedure to be performed. Appropriate facilities should be available for coping with any complication of the procedure, as well as for emergency treatment of severe reactions to the contrast agent itself. After parenteral administration of a radiopaque agent, competent personnel and emergency facilities should be available for at least 30 to 60 minutes, since severe delayed reactions have occurred (see ADVERSE REACTIONS: Intravascular—General).

Preparatory dehydration is dangerous and may contribute to acute renal failure in patients with advanced vascular disease, in diabetic patients, and in susceptible nondiabetic patients (often elderly with preexisting renal disease), infants, and small children. Dehydration in these patients seems to be enhanced by the osmotic diuretic action of urographic agents. It is believed that overnight fluid restriction prior to excretory urography generally does not provide better visualization in normal patients. *Patients should be well hydrated prior to and following administration of any contrast medium, including iohexol.*

Acute renal failure has been reported in diabetic patients with diabetic nephropathy and in susceptible nondiabetic patients (often elderly with preexisting renal disease) following excretory urography. Therefore, careful consideration of the potential risks should be given before performing this radiographic procedure in these patients.

Immediately following surgery, excretory urography should be used with caution in renal transplant recipients.

The possibility of a reaction, including serious, life-threatening, fatal, anaphylactoid or cardiovascular reactions should always be considered (see ADVERSE REACTIONS: Intravascular—General). It is of utmost importance that a course of action be carefully planned in advance for immediate treatment of serious reactions, and that adequate and appropriate personnel be readily available in case of any reaction.

The possibility of an idiosyncratic reaction in susceptible patients should always be considered (see ADVERSE REACTIONS: Intravascular—General). The susceptible population includes, but is not limited to, patients with a history of a previous reaction to contrast media, patients with a known sensitivity to iodine per se, and patients with a known clinical hypersensitivity: bronchial asthma, hay fever, and food allergies.

The occurrence of severe idiosyncratic reactions has prompted the use of several pretesting methods. However, pretesting cannot be relied upon to predict severe reactions and may itself be hazardous for the patient. It is suggested that a thorough medical history with emphasis on allergy and hypersensitivity, prior to the injection of any contrast media, may be more accurate than pretesting in predicting potential adverse reactions.

A positive history of allergies or hypersensitivity does not arbitrarily contraindicate the use of a contrast agent where a diagnostic procedure is thought essential, but caution should be exercised (see ADVERSE REACTIONS: Intravascular—General). Premedication with antihistamines or corticosteroids to avoid or minimize possible allergic reactions in such patients should be considered and administered using separate syringes. Recent reports indicate that such pretreatment does not prevent serious, life-threatening reactions, but may reduce both their incidence and severity.

Even though the osmolality of OMNIPAQUE is low compared to diatrizoate- or iothalamate-based ionic agents of comparable iodine concentration, the potential transitory increase in the circulatory osmotic load in patients with congestive heart failure requires caution during injection. These patients should be observed for several hours following the procedure to detect delayed hemodynamic disturbances.

General anesthesia may be indicated in the performance of some procedures in selected adult patients; however, a higher incidence of adverse reactions has been reported in these patients and may be attributable to the inability of the patient to identify untoward symptoms, or to the hypotensive effect of anesthesia, which can reduce cardiac output and increase the duration of exposure to the contrast agent.

Angiography should be avoided whenever possible in patients with homocystinuria, because of the risk of inducing thrombosis and embolism.

In angiographic procedures, the possibility of dislodging plaques or damaging or perforating the vessel wall should be borne in mind during the catheter manipulations and contrast medium injection. Test injections to ensure proper catheter placement are recommended.

Selective coronary arteriography should be performed only in those patients in whom the expected benefits outweigh the potential risk. The inherent risks of angiocardiography in patients with chronic pulmonary emphysema must be weighed against the necessity for performing this procedure.

When OMNIPAQUE is to be injected using plastic disposable syringes, the contrast medium should be drawn into the syringe and used immediately.

If nondisposable equipment is used, scrupulous care should be taken to prevent residual contamination with traces of cleansing agents.

Parenteral products should be inspected visually for particulate matter and discoloration prior to administration. If particulate matter or discoloration is present, do not use.

Information for Patients: Patients receiving injectable radiopaque diagnostic agents should be instructed to:

1. Inform your physician if you are pregnant.
2. Inform your physician if you are diabetic or if you have multiple myeloma, pheochromocytoma, homozygous sickle cell disease, or known thyroid disorder (see WARNINGS—General).
3. Inform your physician if you are allergic to any drugs, food, or if you had any reactions to previous injections of dyes used for x-ray procedures (see PRECAUTIONS—General).
4. Inform your physician about any other medications you are currently taking, including nonprescription drugs, before you are administered this drug.

Drug/Laboratory Test Interaction: If iodine-containing isotopes are to be administered for the diagnosis of thyroid disease, the iodine-binding capacity of thyroid tissue may be reduced for up to 2 weeks after contrast medium administration. Thyroid function tests which do not depend on iodine estimation, eg, T_3 resin uptake or direct thyroxine assays, are not affected. Many radiopaque contrast agents are incompatible in vitro with some antihistamines and many other drugs; therefore, no other pharmaceuticals should be admixed with contrast agents.

Carcinogenesis, Mutagenesis, Impairment of Fertility: No long-term animal studies have been performed t evaluate carcinogenic potential, mutagenesis, or whether OMNIPAQUE can affect fertility in men or women.

Pregnancy Category B: Reproduction studies have been performed in rats and rabbits with up to 100 times th recommended human dose. No evidence of impaired fertility or harm to the fetus has been demonstrated due t OMNIPAQUE. There are, however, no studies in pregnant women. Because animal reproduction studies are not alway predictive of human response, this drug should be used during pregnancy only if clearly needed.

Nursing Mothers: It is not known to what extent iohexol is excreted in human milk. However, many injectable contras agents are excreted unchanged in human milk. Although it has not been established that serious adverse reactions occur i nursing infants, caution should be exercised when intravascular contrast media are administered to nursing women. Bottl feedings may be substituted for breast feedings for 24 hours following administration of OMNIPAQUE.

Pediatric Use: Pediatric patients at higher risk of experiencing adverse events during contrast medium administration ma include those having asthma, a sensitivity to medication and/or allergens, congestive heart failure, a serum creatinine > 1. mg/dL, or those less than 12 months of age.

ADVERSE REACTIONS

Intravascular—General: Adverse reactions following the use of OMNIPAQUE are usually mild to moderate in severit However, serious, life-threatening, and fatal reactions, mostly of cardiovascular origin, have been associated with th administration of iodine-containing contrast media, including OMNIPAQUE. The injection of contrast media is frequent associated with the sensation of warmth and pain, especially in peripheral angiography; pain and warmth are less freque and less severe with OMNIPAQUE than with many contrast media.

Cardiovascular System: Arrhythmias including PVCs and PACs (2%), angina/chest pain (1%), and hypotension (0.7% Others including cardiac failure, asystole, bradycardia, tachycardia, and vasovagal reaction were reported with an individu incidence of 0.3% or less. In controlled clinical trials involving 1,485 patients, one fatality occurred. A cause and effe relationship between this death and iohexol has not been established.

Nervous System: Vertigo [including dizziness and lightheadedness] (0.5%), pain (3%), vision abnormalities [includi blurred vision and photomas] (2%), headache (2%), and taste perversion (1%). Others including anxiety, blurred visio fever, motor and speech dysfunction, convulsion, paresthesia, somnolence, stiff neck, hemiparesis, syncope, shiverin transient ischemic attack, cerebral infarction, and nystagmus were reported, with an individual incidence of 0.3% or less

Respiratory System: Dyspnea, rhinitis, coughing, and laryngitis, with an individual incidence of 0.2% or less.

Gastrointestinal System: Nausea (2%) and vomiting (0.7%). Others including diarrhea, dyspepsia, cramp, and d mouth were reported, with an individual incidence of less than 0.1%.

Skin and Appendages: Urticaria (0.3%), purpura (0.1%), abscess (0.1%), and pruritus (0.1%).

Individual adverse reactions which occurred to a significantly greater extent for a specific procedure are listed under th indication in full prescribing information.

Pediatrics: In controlled clinical trials involving 391 patients for pediatric angiocardiography, urography, and contras enhanced computed tomographic head imaging, adverse reactions following the use of OMNIPAQUE 240, OMNIPAQUE 3 and OMNIPAQUE 350 were generally less frequent than with adults.

Cardiovascular System: Ventricular tachycardia (0.5%), 2:1 heart block (0.5%), hypertension (0.3%), and anemia (0.3%

Nervous System: Pain (0.8%), fever (0.5%), taste abnormality (0.5%), and convulsion (0.3%).

Respiratory System: Congestion (0.3%) and apnea (0.3%).

Gastrointestinal System: Nausea (1%), hypoglycemia (0.3%), and vomiting (2%).

Skin and Appendages: Rash (0.3%).

General Adverse Reactions to Contrast Media: Physicians should remain alert for the occurrence of adverse effec in addition to those discussed above. The following reactions have been reported after administration of other intravascul iodinated contrast media, and rarely with iohexol. *Reactions due to technique:* hematomas and ecchymoses. *Hemodynam reactions:* vein cramp and thrombophlebitis following intravenous injection. *Cardiovascular reactions:* rare cases of cardi arrhythmias, reflex tachycardia, chest pain, cyanosis, hypertension, hypotension, peripheral vasodilatation, shock, a cardiac arrest. *Renal reactions:* occasionally, transient proteinuria; and rarely, oliguria or anuria. *Allergic reaction* asthmatic attacks, nasal and conjunctival symptoms, dermal reactions such as urticaria with or without pruritus, as well pleomorphic rashes, sneezing, and lacrimation; and rarely, anaphylactic reactions. Rare fatalities have occurred due to th or unknown causes. *Signs and symptoms related to the respiratory system:* pulmonary or laryngeal edema, bronchospas dyspnea; or *to the nervous system:* restlessness, tremors, convulsions. *Other reactions:* flushing, pain, warmth, metal taste, nausea, vomiting, anxiety, headache, confusion, pallor, weakness, sweating, localized areas of edema (especially fac cramps), neutropenia, and dizziness. Rarely, immediate or delayed rigors can occur, sometimes accompanied by hyp pyrexia. Infrequently, "iodism" (salivary gland swelling) from organic iodinated compounds appears 2 days after expos and subsides by the sixth day.

In general, the reactions which are known to occur upon parenteral administration of iodinated contrast agents possible with any nonionic agent. Approximately 95% of adverse reactions accompanying the use of water-solu intravascularly administered contrast agents are mild to moderate in degree. However, severe, life-threatening anaphylact reactions, mostly of cardiovascular origin, have occurred. Reported incidences of death range from 6.6 per 1 milli (0.00066%) to 1 in 10,000 (0.01%). Most deaths occur during injection or 5 to 10 minutes later, the main feature bei cardiac arrest, with cardiovascular disease as the main aggravating factor. Isolated reports of hypotensive collapse and sh are found in the literature. The incidence of shock is estimated to be 1 out of 20,000 (0.005%) patients.

Adverse reactions to injectable contrast media fall into two categories: chemotoxic reactions and idiosyncratic reactio

Chemotoxic reactions result from the physicochemical properties of the contrast media, the dose, and the speed injection. All hemodynamic disturbances and injuries to organs or vessels perfused by the contrast medium are include this category.

Idiosyncratic reactions include all other reactions. They occur more frequently in patients 20 to 40 years old. Idiosyncr reactions may or may not be dependent on the amount of dose injected, the speed of injection, and the radiogra procedure. Idiosyncratic reactions are subdivided into minor, intermediate, and severe. The minor reactions are self-limi and of short duration; the severe reactions are life-threatening and treatment is urgent and mandatory.

The reported incidence of adverse reactions to contrast media in patients with a *history of allergy is twice that in* general population. Patients with a history of previous reactions to a contrast medium are three times more susceptible th other patients. However, sensitivity to contrast media does not appear to increase with repeated examinations.

Most adverse reactions to injectable contrast media appear within 1 to 3 minutes after the start of injection, but dela reactions may occur.

Regardless of the contrast agent employed, the overall estimated incidence of serious adverse reactions is higher w angiocardiography than with other procedures. Cardiac decompensation, serious arrhythmias, angina pectoris, myocardial ischemia or infarction may occur during angiocardiography and left ventriculography. Electrocardiographic a hemodynamic abnormalities occur less frequently with OMNIPAQUE than with diatrizoate meglumine and diatrizoate sodi injection.

CONSULT PACKAGE INSERT FOR A MORE DETAILED DISCUSSION OF ADVERSE REACTIONS FOR INTR VASCULAR USE OF OMNIPAQUE.

OVERDOSAGE: Overdosage may occur. The adverse effects of overdosage are life-threatening and affect mainly pulmonary and cardiovascular systems. The symptoms include cyanosis, bradycardia, acidosis, pulmonary hemorrha convulsions, coma, and cardiac arrest. Treatment of an overdosage is directed toward the support of all vital functions a prompt institution of symptomatic therapy.

The intravenous LD_{50} values of OMNIPAQUE (in grams of iodine per kilogram body weight) are 24.2 in mice and 15 rats.

DOSAGE AND ADMINISTRATION: Details are provided in the package insert.

THE RADIOLOGICAL SOCIETY OF NORTH AMERICA

Vanguard Flagship Scholar

sanofi WINTHRO

Sanofi Winthrop Pharmaceutic
New York, NY 10016

The Problem: OBTAINING MEASUREMENTS OF FLUOROSCOPIC AND RADIOGRAPHIC DOSAGES RECEIVED BY YOUR PATIENTS.

The Solution: THE NUCLEAR ASSOCIATES' DIAMENTOR M2 PATIENT X-RAY EXPOSURE MEASUREMENTS SYSTEM.

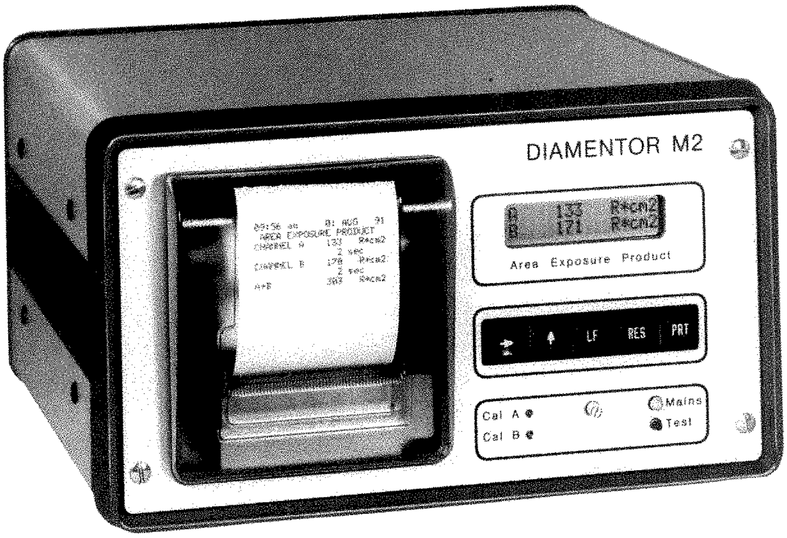

You know this story because you live it every day. Government regulations that require you to provide your patients with information about the actual dosages they receive from radiographic procedures.

But there are problems.

Measurement problems arise due to the differences between fluoroscopic and radiographic procedures.

Until now.

Now there's the Diamentor M2.

This unique x-ray exposure measurement system gives you the only means of truly evaluating the total exposure your patient receives during a radiologic procedure.

Whether it's fluoroscopic or radiographic, the Diamentor M2 measures the exposure to your patient without any connection whatsoever to the x-ray generator machine. The ionization chamber for the Diamentor M2 is mounted to the x-ray collimator assembly, so that it is positioned between the collimator and the patient. And because it is transparent, the Diamentor M2 allows you to visualize the radiographic field without any obstruction.

This state-of-the-art microprocessor-based instrument has two independent measuring circuits so it can be connected to two ionized chambers. This means you can monitor the Area Exposure Product for one or two x-ray tubes simultaneously on a large, easy-to-read display.

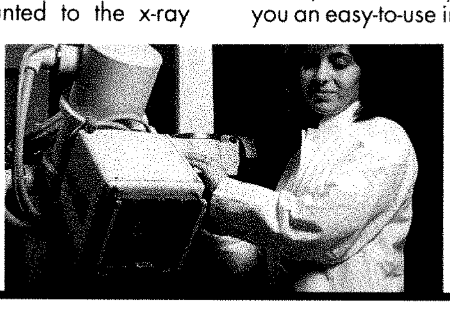

Display information consists of:

- AEP Channel A
- AEP Channel B
- Total of AEP Channels A and B

The Diamentor M2's built-in printer records:

- Date and Time
- AEP for Channel A and Channel B
- Total of AEP Channel A and Channel B
- AEP Measurement Units (cGy•cm2) or (R•cm2)
- Exposure Time Channel A and Channel B

We also offer a Diamentor M2 AEP software package that can operate on any IBM™ PC-compatible computer. It gives you an easy-to-use interface for making measurements, storing patient exposure data on disk, and making hard copies for review and filing.

So if you're looking for the solution to give your patients the best possible treatment while conforming to forthcoming Government regulations, you should be looking at the Diamentor M2 from Nuclear Associates. It's a real problem solver.

For more information, request Bulletin 454-44

IBM™, International Business Machines, Inc.

NUCLEAR ASSOCIATES

Division of VICTOREEN, INC.
100 VOICE ROAD • P.O. BOX 349
CARLE PLACE, NY 11514-0349

AJR Business and Subscriber Information

The American Roentgen Ray Society

AJR, American Journal of Roentgenology, is published monthly to disseminate research on current developments in the radiologic sciences and commentary on topics related to radiology. It is published by the American Roentgen Ray Society (ARRS), 1891 Preston White Dr., Reston, VA 22091; (703) 648-8992. Address inquiries regarding Society business, the annual ARRS meeting, and membership to the Society at the above address.

Correspondence regarding editorial matters and classified advertising should be addressed to Editorial Office, AJR, 2223 Avenida de la Playa, Ste. 103, La Jolla, CA 92037-3218; telephone 1-800-348-4257 or (619) 459-2229; FAX (619) 459-8814. For information on manuscript submission, see Guidelines for Authors, pages A4–A6.

Subscriber Information

ARRS annual dues include $50 for journal subscription. Nonmember subscription rates are as follows: $125/year ($180 foreign); institutions, $135 ($190 foreign); in-training, $25 ($80 foreign). Single copies of the Journal may be purchased for $18 ($22 foreign). Airmail rates will be furnished on request. The GST number for Canadian subscribers is 123394371.

Call toll-free, 1-800-638-6423 (in Maryland call 1-800-638-4007), with subscription inquiries or problems. Please have the mailing label from your latest issue available when you call.

Report changes of address to Subscription Fulfillment, AJR, 428 E. Preston St., Baltimore, MD 21202. Damaged or unreceived issues should be reported within 60 days of publication (90 days for foreign subscribers) for replacement.

Advertising Information

All advertising is subject to approval by the publisher. Acceptance of advertising does not indicate endorsement of the products or services advertised or the claims made. For display advertising information, contact Gary Walchli, National Sales Representative, AJR, 428 E. Preston St., Baltimore, MD 21202, (410) 528-4291.

For classified advertising information, contact the Editorial Office, AJR, 2223 Avenida de la Playa, Ste. 103, La Jolla, CA 92037-3218; telephone (619) 459-2229; FAX (619) 459-8814.

Copyrights, Permissions, and Reprints

Contents of the *AJR* are copyrighted by the ARRS. No part of this publication may be reproduced without permission. Requests for such permission should be addressed to the Publications Department, ARRS, 1891 Preston White Dr., Reston, VA 22091. For reprints of a particular article, please contact the author designated in the footnotes for that article.

Indexes

The *AJR* provides volume and yearly indexes (subject and author) in the June and December issues. *AJR* articles are also indexed in *Current Contents*, *Index Medicus*, and the cumulative index published by *Radiology*.

The IVC filter designed the way you'd want it to be.

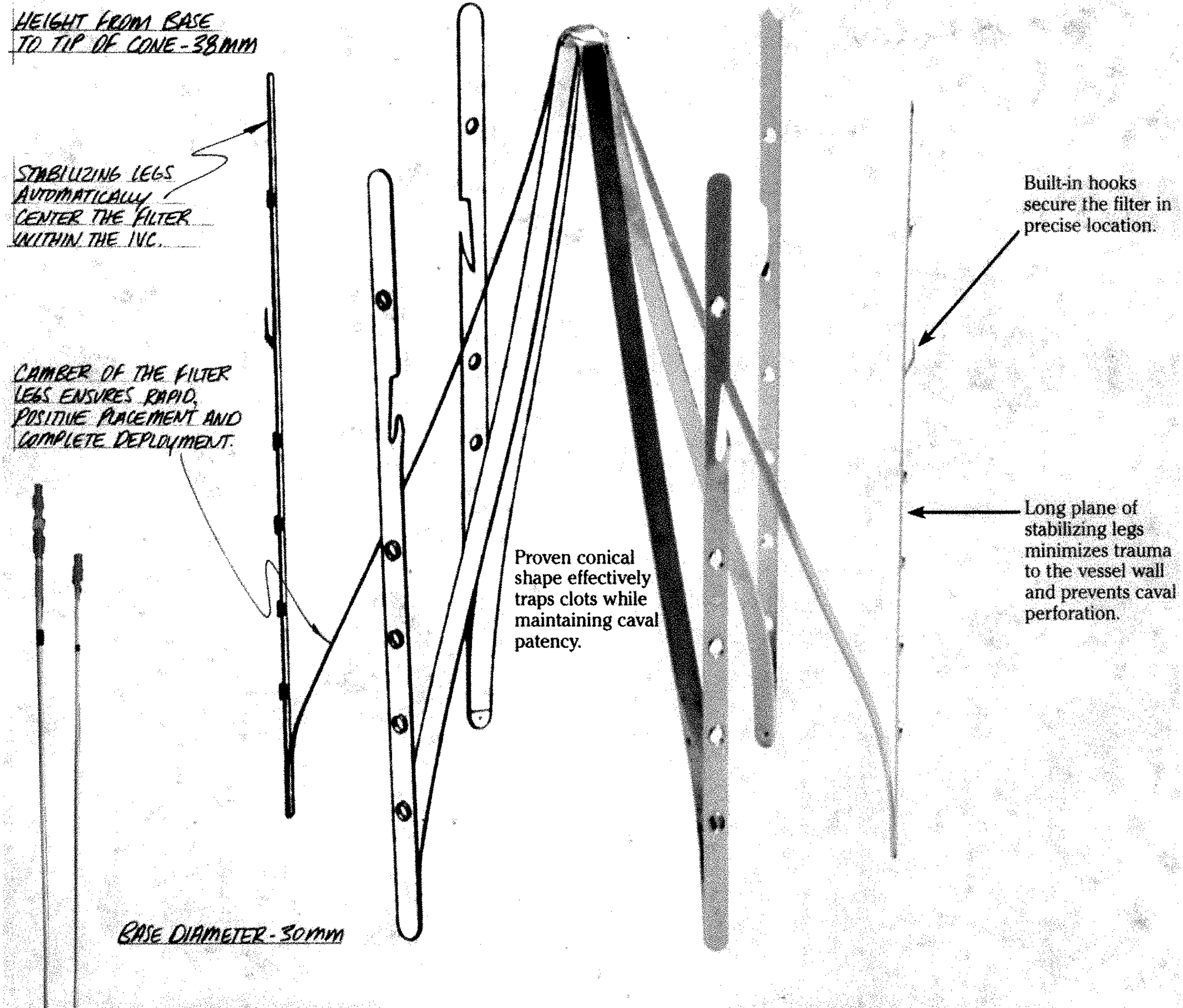
HEIGHT FROM BASE TO TIP OF CONE - 38mm
STABILIZING LEGS AUTOMATICALLY CENTER THE FILTER WITHIN THE IVC.
CAMBER OF THE FILTER LEGS ENSURES RAPID, POSITIVE PLACEMENT AND COMPLETE DEPLOYMENT.
BASE DIAMETER - 30mm

Built-in hooks secure the filter in precise location.

Long plane of stabilizing legs minimizes trauma to the vessel wall and prevents caval perforation.

Proven conical shape effectively traps clots while maintaining caval patency.

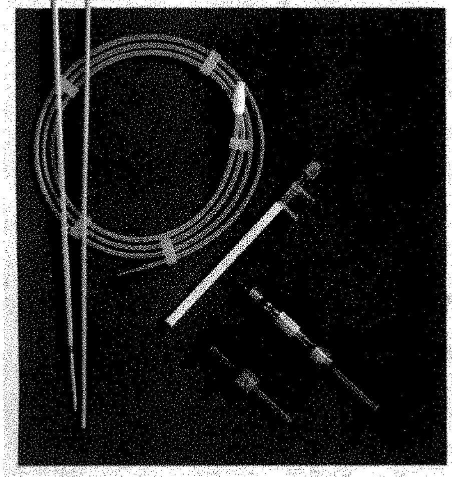

A flexible introducer facilitates the insertion

Finally, there's an IVC filter that does just what it's supposed to do.

Prevent recurrent pulmonary embolism. Maintain caval patency. And minimize procedural complications.

The Vena Tech™-LGM™ filter does it all because it's designed for success, with a proven-effective conical shape and longer stabilizing legs that ensure complete deployment. Best of all, the filter is deployed through a 10-French (ID) introducer . . . giving you and your patient a safer, easier insertion procedure.

The Vena Tech-LGM filter comes with everything you need for filter placement. And, with our unique 30D system, it can be placed from either the jugular or femoral approach.

See for yourself how easy it is. In just under ten minutes, our free video will show you how easy it is to place the Vena Tech-LGM filter. After you've seen it, you'll understand why we say the Vena Tech-LGM filter is the perfect fit—for both patient and physician.

So call 1-800-443-VENA today to receive your free video on the Vena Tech-LGM—the IVC filter

B. Braun Vena Tech
1840 Oak Ave.
Evanston, IL 60201
(800) 443-VENA or (708) 866-1833

BRAUN

No one
ever said
a lot of knowledge
is a dangerous
thing.

IN FACT, for radiologists, the only danger is not keeping up with what's new. **AJR: American Journal of Roentgenology** is your monthly guide to the latest advances, with articles that are timely, succinct, and relevant to daily practice.

AJR
American Journal of Roentgenology
Published monthly
Robert N. Berk, M.D., Editor
The University of California, San Diego

Call toll-free to order: **1-800-638-6423**
from anywhere in the U.S. or Canada.
Or clip and mail this coupon to
Waverly, Inc. ATTN: AJR

Subscribe to **AJR** now. (Current rates available for up to three years.)

☐ Individual $125/year
☐ Institutional $135/year
☐ In-training* $25/year
(Add $55/year outside the U.S.; in Canada, also add 7% GST.)
☐ 3 years ☐ 2 years ☐ 1 year
Maryland residents and 5% sales tax. Subscriptions outside the U.S. must be prepaid in U.S. dollars. Rates valid through October 31, 1992.

Name ____
Address ____
City/State/Zip ____
*Please specify institution and training status ____

Payment Options:
☐ Check enclosed (payable to AJR)
☐ Bill me ☐ AmEx
☐ MasterCard ☐ VISA

Card # ____ Exp. Date ____
Signature ____

Return coupon to:
Waverly, Inc. ATTN: AJR
P.O. Box 23291, Baltimore, MD 21203-9990

AJR: AMERICAN JOURNAL OF ROENTGENOLOGY is the

There are a handful of reasons you should use the 3M Digital Imager System.

This is just one.

Digital Imager Disk
3M
High Capacity Flexible Disk Cartridge

Now you have a choice of how to store 80 ultrasound images.

On the one hand ... or in both hands ... you've got five film cassettes.

On the other hand ... or between index finger and thumb... you have the compact 3M Digital Imager Disk. And that leaves plenty of fingers for counting the benefits of the 3M Digital Imager System.

It's easy to use. You don't have to lug around film cassettes or load and unload them in the darkroom. You can store and review up to 80 diagnostic images on a single disk, play them back, edit them, and print on film only the images you need.

With the 3M Digital Imager System you can print up to 99 originals at the touch of a button. No more costly duplication. No more sacrificin resolution with second generation copies.

The highest resolution on the market. Built-in reliability. Professional support.

A handful of benefits instead of a handful of cassettes.

That's the advantage of the 3M Digital Imager System.

To find out more about the 3M Digital Imager System, call 1-800-328-1684 ext. 340. Or write 3M Medical Imaging Systems Division, P.O. Box 33050, St. Paul, MN 55133-3050.
In Canada, write: 3M Canada Inc., P.O. Box 5757 Terminal A, London, Ontario, Canada N6A 4T1.

© 3M 1990

Innovation working for yo

3M

Keep It All Together

Easily and Conveniently with Bound Volumes of the *American Journal of Roentgenology*

Keeping up with scientific and technological advances in radiology is more important than ever, and that's why each issue of the *American Journal of Roentgenology* is packed with up-to-the-minute information crucial to you and your practice. **Keep this important resource together for easy reference in convenient and attractive bound volumes.**

Bound volumes offer the timely coverage only a journal can provide — penetrating discussions of the topics that interest you most by the brightest names in the field — with all the durability and convenience of a hardcover edition. You'll have a year's worth of vital information all arranged and indexed in one sturdy source. And each carefully crafted volume will make a handsome addition to your permanent library.

To help you keep your reference library up to date, once a year we'll send a reminder so you can order the latest bound volumes. When you send in your paid order, a set will be reserved for you, to be sent as soon as available on 30-day approval. If you do not want the volumes for any reason, simply return them within 30 days for a courteous refund. It's that easy.

Bound volumes are available to subscribers only and are in addition to the regular subscription. For ordering information, contact *AJR* Subscription Fulfillment Department, 428 E. Preston St., Baltimore, MD 21202-3993, or call toll-free

1-800-638-6423.

Radiation Oncologist

The University of South Florida and the H. Lee Moffitt Cancer Center & Research Institute are seeking an experienced radiation oncologist with experience working in a multi-disciplinary setting. The tenure earning associate professor position will be based at Moffitt Cancer Center, which maintains active research programs in head and neck radiotherapy, monoclonal antibodies, laboratory studies of tumor kinetics and radiosensitivity, intraoperative radiation and breast conservation therapies.

The successful candidate will be qualified to serve at the associate professor level or higher in a tenure earning position, with experience in head and neck cancers and cooperative clinical trials. Board certification in radiation oncology or therapeutic radiology is required.

Send inquiries and current Curriculum Vitae: **Harvey M. Greenberg, M.D., Chief, Radiation Oncology, or John C. Ruckdeschel, M.D., Center Director, Address: Search Committee; Office of Faculty Recruitment, H. Lee Moffitt Cancer Center & Research Institute, P.O. Box 280179, Tampa, FL 33682-0179. Deadline for receipt is July 1, 1992.**

H. LEE MOFFITT CANCER CENTER
& RESEARCH INSTITUTE
University of South Florida College of Medicine

Moffitt Cancer Center is an Equal Opportunity Employer.
The University of South Florida is an Affirmative Action Equal Opportunity Employer.

CHANGE OF ADDRESS?

Please notify us eight weeks in advance. Send us your mailing label or your account number, along with your new address and the date the change of address is to take effect.

AJR
at your service.

For customer assistance,
call TOLL-FREE:
1-800-638-6423
(from anywhere in the U.S. or Canada)
Or write:
Subscription Fulfillment Department
428 East Preston Street

E-Z-EM® Single-patient bottles of Liquid E-Z-Paque® can make your routine upper GI studies more efficient, more economical and more consistent. Easy to stock and inventory, with no mess or waste, each bottle of pre-mixed Liquid E-Z-Paque gives you a consistent suspension for completely repeatable results. Make the move to single-patient liquids. Call your E-Z-EM Distributor or one of our Customer Service Specialists at 1-800-544-4624.

E-Z-EM, Inc.
717 Main Street
Westbury, NY 11590
Tel: 1-800-544-4624
Fax: 516-333-8278

E-Z-EM INTEGRITY • E-Z-EM DEDICATION • E-Z-EM INNOVATION • 30 Years of Quality and Service to Radiology

LESS IS MORE.

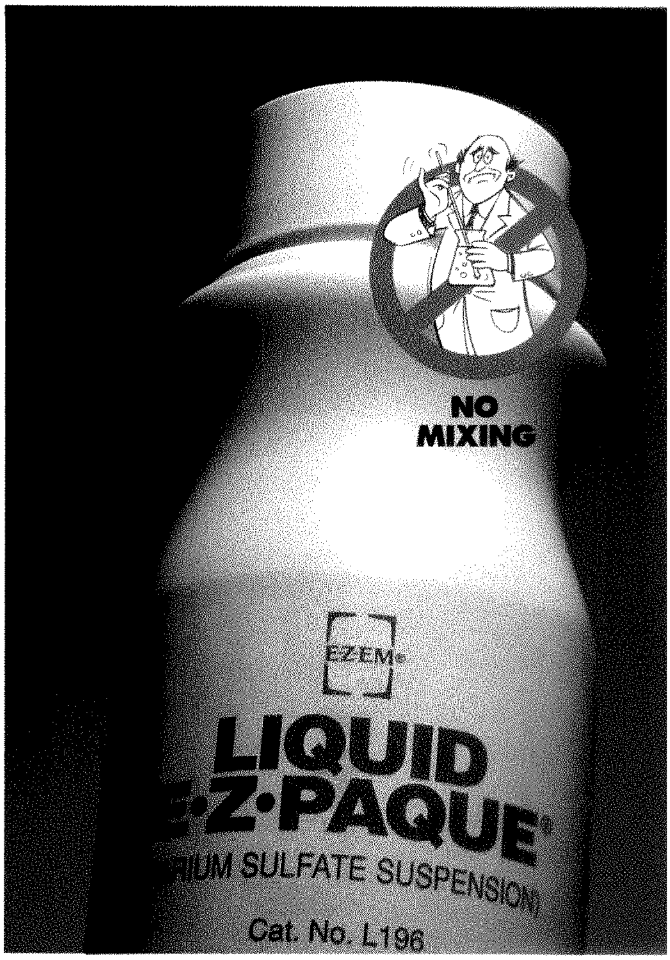

E-Z-EM stock is publicly traded on the NASDAQ National Market System

© Eastman Kodak Company, 1990

Two leaders in image technology present one advanced system for managing all your diagnostic imaging information.

Eastman Kodak Company and Vortech Data, Inc. have joined forces to clear a path through the confusion and uncertainty of diagnostic imaging information management.

This strategic alliance brings together Kodak's proven excellence in diagnostic imaging with Vortech's established leadership in medical image management.

The result is a system to take you from wherever you are to wherever you want to be in managing diagnostic imaging information.

Today and tomorrow. Whatever your needs. No matter how many modalities you use. Or who manufactured the equipment. For details, call your local Kodak representative.

The resources are in place.
The path is clear.
The next step is yours.

THE PATH IS CLEAR. KODAK

Watch "Radiology Update" on Lifetime Medical Television, sponsored in part by Kodak's Health Sciences Division and Sanofi Winthrop.

Quality imaging worldwide

Review Article

Lesions of Skin and Brain: Modern Imaging of the Neurocutaneous Syndromes

Michael S. Pont[1] and Allen D. Elster

The neurocutaneous syndromes, or phakomatoses, are a diverse group of disorders affecting the skin and CNS. This review highlights some important but lesser known aspects of the more common phakomatoses while concentrating on rarer and more recently discovered syndromes. The roles of newer imaging techniques such as contrast-enhanced MR imaging and three-dimensional CT in the evaluation of these disorders also are discussed.

In the 1920s and 1930s, van der Hoeve [1] first recognized a characteristic pattern of involvement of the skin and multiple organs shared by several hereditary diseases—neurofibromatosis (NF), tuberous sclerosis (TS), Sturge-Weber syndrome (SWS), and von Hippel-Lindau (VHL) disease—and called them phakomatoses (after the Greek word *phakos* meaning "mole" or "birthmark") [1]. Since that time, many new diseases have been described that exhibit prominent involvement of both the skin and CNS, and can be classified as neurophakomatoses, neurocutaneous syndromes, or neuroectodermal dysplasias (Table 1). The cranial imaging findings seen in the more common phakomatoses have been the subject of several excellent recent articles [2–4]. This review highlights some important but lesser known aspects of the common neurocutaneous syndromes, and gives proportionately more space to many recently discovered or rare disorders that are now recognized as part of this spectrum. We also attempt to demonstrate the role of newer imaging techniques such as contrast-enhanced MR imaging and three-dimensional CT (3DCT) in the evaluation of patients with lesions of skin and brain.

Neurofibromatosis

In the 100 years since von Recklinghausen [5] first described this entity, it has become clear that NF is actually a group of heterogeneous diseases [6–8]. In 1982, Riccardi [7] proposed a new working classification for NF based on mod-

TABLE 1: Principal Neurocutaneous Syndromes

- Neurofibromatosis
- Tuberous sclerosis
- Sturge-Weber syndrome
- Other vascular phakomatoses
  - Wyburn-Mason syndrome
  - Ataxia-telangiectasia
  - Osler-Weber-Rendu disease
  - Multiple hemangiomatoses
  - Klippel-Trenaunay-Weber syndrome
  - Meningioangiomatosis
- Von Hippel-Lindau disease
- Melanocytic phakomatoses
  - Neurocutaneous melanosis
  - Oculodermal melanosis
  - Incontinentia pigmenti
  - Hypomelanosis of Ito
- Epidermal nevus syndrome
- Cowden's disease

Received November 18, 1991; accepted after revision January 9, 1992.

Dr. Elster is supported in part as a Winthrop Pharmaceuticals/RSNA Scholar.

[1] Both authors: Department of Radiology, Bowman Gray School of Medicine, Wake Forest University, Medical Center Blvd., Winston-Salem, NC 27157-1022. Address reprint requests to A. D. Elster.

AJR 158: 1193–1203, June 1992 0361–803X/92/1586–1193 © American Roentgen Ray Society

ern genetic and epidemiologic investigations, dividing NF into eight categories. On the basis of this research and recombinant DNA studies, the National Institutes of Health Consensus Conference on NF [6] recommended the adoption of uniform clinical criteria (Table 2) for the diagnosis of the two subtypes, denoted NF-1 and NF-2, which account for over 99% of all cases of NF (Table 3).

Neurofibromatosis Type 1

Neurofibromatosis type 1 (NF-1) typifies classic von Recklinghausen's disease, being characterized by multiple cutaneous skin lesions (café-au-lait spots, neurofibromas), mesodermal dysplasias (dural ectasia), and CNS tumors (principally gliomas) [7, 8]. This form of NF is transmitted as an autosomal-dominant trait in approximately one half of cases; in others it presumably results from a spontaneous mutation of a genetic locus on chromosome 17.

Plexiform neurofibromas are the most common extracranial tumors found in NF-1. They are usually locally aggressive and course along the entire nerve of origin [4, 9]. Orbital plexiform neurofibromas typically involve the eyelid and orbital contents, frequently causing proptosis and extending retrogradely into the ipsilateral cavernous sinus (Fig. 1A). Sphenoid wing dysplasia is often associated with orbital plexiform neurofibromas, yielding the classic empty orbit sign or harlequin eye on conventional skull radiographs. MR and 3DCT may also reveal this dysplasia to good advantage and be useful for planning surgical reconstruction (Fig. 1B). It should be emphasized that the empty orbit appearance is nearly always a result of an associated mesodermal dysplasia and is only rarely caused by direct erosion from a neurofibroma or other neoplasm [9].

CNS tumors of glial origin represent a potentially life-threatening complication of NF-1. Optic nerve gliomas are the most common central tumor and have been estimated to occur in between 5% and 15% of patients with NF-1 [10]. Conversely, of all patients presenting with an optic glioma, about 25% will have NF-1. CT and MR imaging have generally proved equivalent in our experience for diagnosing and delineating optic gliomas confined to the orbit. When these tumors extend intracranially, however, MR imaging holds considerable advantage over CT, particularly for assessing involvement of the optic chiasm, tracts, and radiations by the glioma (Fig. 2).

Other central tumors of glial cell origin also frequently occur in NF-1 and include ependymomas, glioblastomas, and lower grade astrocytomas of the brainstem, spinal cord, and basal ganglia [3, 7, 8, 11, 12]. MR has proved superior to CT for detecting these lesions, defining their full extent and location, and providing critically important surgical information such as the presence of vascular encasement. Because many benign pilocystic astrocytomas of the brainstem have enhancing components, MR images enhanced with gadopentetate dimeglumine have not proved particularly useful in predicting malignancy. However, contrast enhancement can guide the surgeon in selected cases toward identifying the highest yield site for stereotaxic biopsy or assessing the most vascular portions of a given tumor preoperatively [13].

TABLE 2: Diagnostic Criteria for the Neurofibromatoses[a]

Type of Neurofibromatosis/Criteria for Diagnosis
Type 1 (two or more criteria required for diagnosis)
Six or more café-au-lait macules over 5 mm in greatest diameter (prepubertal) or over 15 mm (postpubertal)
Two or more neurofibromas of any type *or* one plexiform neurofibroma
Freckling in the axillary or inguinal region
Optic glioma
Two or more Lisch nodules (iris hamartomas)
A distinctive osseous lesion (sphenoid dysplasia, cortical thinning of a long bone, pseudarthrosis)
A first-degree relative (parent, sibling, or offspring) with neurofibromatosis type 1 by the above criteria
Type 2 (one criterion required for diagnosis)
Bilateral cranial nerve VIII schwannomas
A first-degree relative with neurofibromatosis type 2 and *either*
A unilateral cranial nerve VIII schwannoma *or*
Any two of the following: neurofibroma, meningioma, glioma, schwannoma, juvenile posterior subcapsular lenticular opacity

[a] From National Institutes of Health Consensus Development Conference [6].

A relatively new finding [3, 14, 15] of great radiologic significance has been the discovery on MR images of multiple focal lesions in patients with NF-1, located especially in the cerebellar peduncles, basal ganglia, brainstem, and optic radiations (Fig. 3). These lesions generally have high signal on T2-weighted MR images (e.g., 2800/80 [TR/TE]) and are difficult or impossible to see on CT. There is generally no evidence of surrounding mass effect, edema, or contrast enhancement.

Considerable controversy surrounds the nature of these lesions, and the notion [3] that they represent hamartomas, heterotopias, schwannosis, or glial nests has only weak pathologic support and fits poorly with their natural history. These lesions may increase in size and number throughout childhood, but are virtually never seen in adults [15]. Because of

TABLE 3: Comparison of the Features of Neurofibromatoses Types 1 and 2

Feature	Neurofibromatosis Type 1	Neurofibromatosis Type 2
Gene location	Chromosome 17	Chromosome 22
Presentation	Children and young adults	Adults
Prevalence	1/3000	1/50,000
Skin lesions	Numerous	Sparse
CNS lesions	Glial-type tumors (gliomas, neurofibromas)	Nerve sheath/meningeal tumors (schwannomas, meningiomas, ependymomas)
Bone lesions	Common (sphenoid dysplasia, pseudarthroses)	Rare
Other CNS dysplasias	Common (aqueductal stenosis, buphthalmos)	Rare

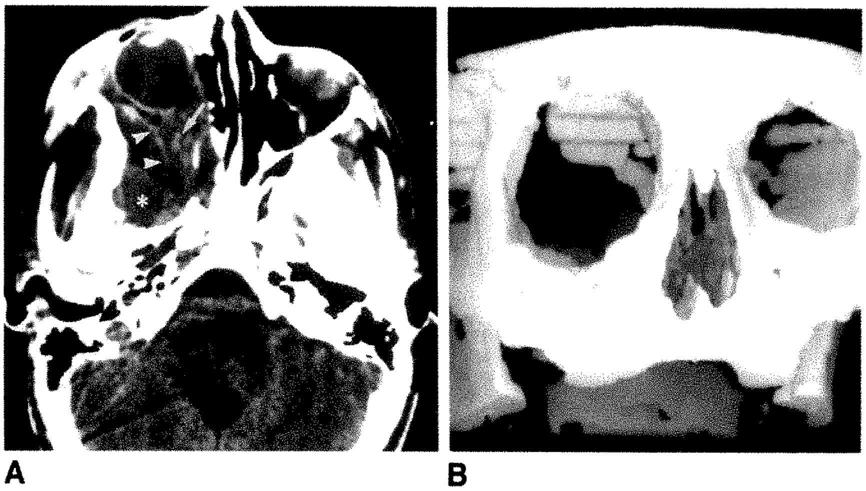

Fig. 1.—14-year-old child with plexiform neurofibroma of the orbit.

A, Transverse CT scan shows proptosis of right globe and infiltration of orbital soft tissues by plexiform neurofibroma (*arrow*). Greater sphenoid wing is dysplastic, with herniation of meninges (*arrowheads*) and brain (*asterisk*) through defect.

B, Three-dimensional CT reformation shows sphenoid wing dysplasia to good advantage.

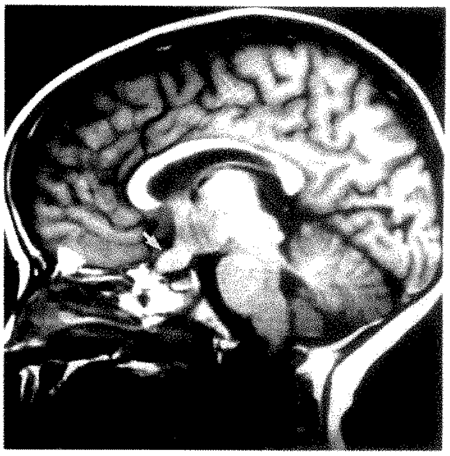

Fig. 2.—T1-weighted (600/20) sagittal MR image of a child with neurofibromatosis type 1 shows chiasmatic glioma (*arrow*).

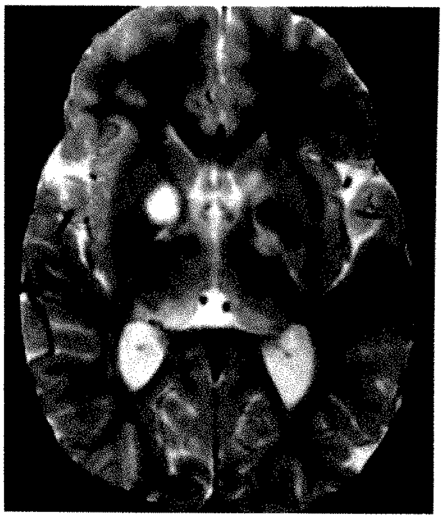

3

Fig. 3.—T2-weighted (2800/80) MR image of multifocal high-signal lesions that are frequently encountered in basal ganglia of neurofibromatosis type 1 patients and are generally thought to represent glial dysplasias or areas of dysmyelination.

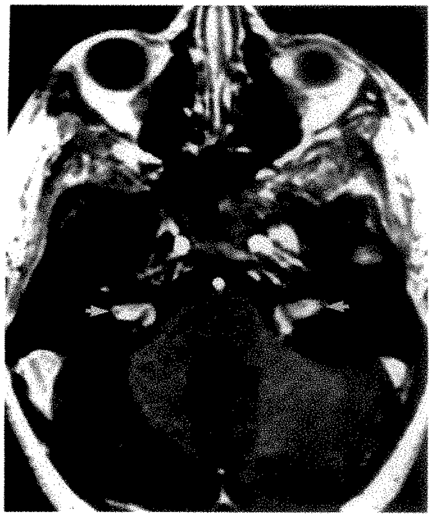

4

Fig. 4.—Contrast-enhanced MR image shows bilateral acoustic schwannomas (*arrows*), the hallmark of neurofibromatosis type 2.

their transient and uncertain nature, we prefer to call them UNOs (unidentified neurofibromatosis objects). Since the risk of neoplastic transformation is extremely low, one is probably safe in ignoring small UNOs without mass effect or enhancement that are encountered as the sole abnormality on initial MR images in children with NF-1.

Neurofibromatosis Type 2

Neurofibromatosis type 2 (NF-2) is now recognized as a distinct form of the disease that must be separated from NF-1, because its genetic basis and natural history are unique [3, 5, 16]. NF-2 is transmitted as an autosomal-dominant trait with nearly 100% penetrance, caused by a genetic defect on the long arm of chromosome 22. The hallmark of NF-2 is bilateral acoustic schwannomas (Fig. 4), which typically present in the third or fourth decade of life. In contrast to NF-1, in which glial tumors predominate, the neoplasms found in NF-2 arise principally from the coverings of the CNS. Schwannomas of the cranial and spinal nerves are the most common tumors, followed by meningiomas, which are frequently multiple. Most of the meningiomas seen in NF-2 are of the fibroblastic subtype, and hence have low signal on T2-weighted images [17].

Neurofibromatosis Type 5

Segmental neurofibromatosis (NF-5) is characterized by the presence of neurofibromas, schwannomas, and café-au-lait spots over a limited dermatomal distribution [18, 19]. Pain

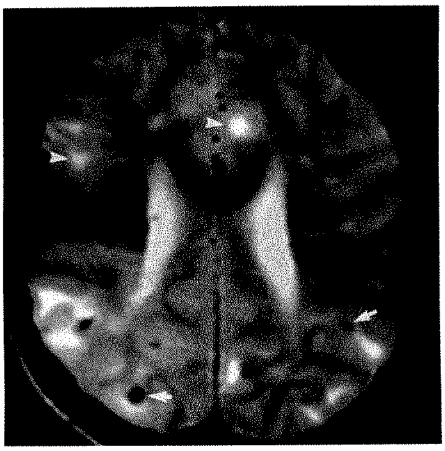

Fig. 5.—T2-weighted (2500/80) MR image shows calcified (*arrows*) and noncalcified (*arrowheads*) parenchymal tubers of tuberous sclerosis.

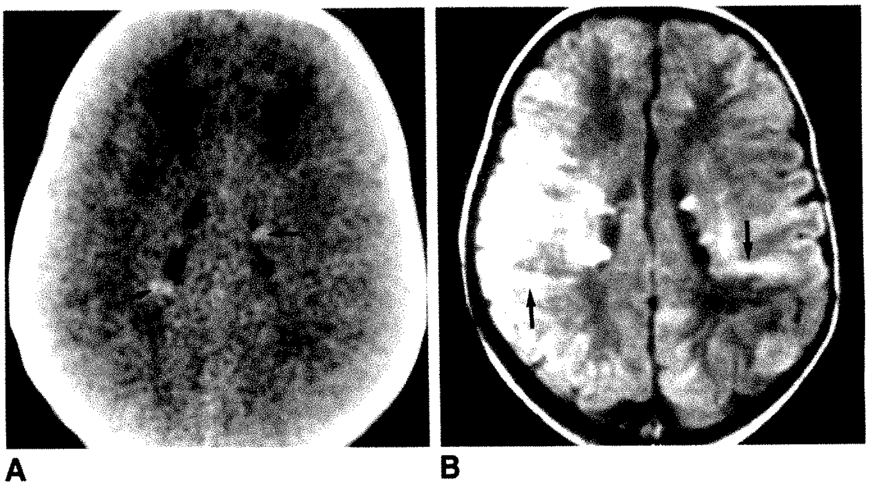

Fig. 6.—Neonate with clinical stigmata of tuberous sclerosis.
A, Transverse CT scan shows small periventricular calcifications (*arrows*).
B, T1-weighted (700/20) MR image shows paradoxical high signal of tubers. Linear bands or striations in white matter (*arrows*) adjacent to tubers represent coexisting migrational anomaly.

and pruritus (due to the presence of large numbers of mast cells in the neurofibromas) are the presenting symptoms in most of these patients. Cases reported in the radiologic literature have shown segmental involvement in the lumbosacral plexus or scalp by neurofibromas [18, 19].

Tuberous Sclerosis

Tuberous sclerosis (TS) is an autosomal-dominant disorder originally described by Bourneville [20] in 1880. In 1908, Vogt [21] described the classical clinical triad of seizures, adenoma sebaceum, and mental retardation in several patients with the disorder. Recent recombinant DNA research has subsequently identified the genetic defect of TS to be on chromosome 11 near the gene for tyrosinase [22]. Since the enzyme tyrosinase is intimately involved with the synthesis of melanin, this genetic locus may help explain the associated pigment abnormalities in the skin of patients with TS.

Although fewer than one third of patients will demonstrate all the features of Vogt's classic triad, at least 95% will exhibit some cutaneous manifestations, including facial angiofibromata (adenoma sebaceum), fibromas, hypopigmented maculas, or shagreen patches. Seizures are the most common clinical sign, present in 80–100% of patients. Although mental deficiency was previously thought to be an invariable feature of this syndrome, an increasing number of patients with TS are now being reported with normal or above average intelligence [23]. This trend may be a reflection of recognition of TS in noninstitutionalized patients and in those with formes frustes of the disease.

Cortical tubers are the most frequently encountered cerebral lesions, seen in approximately 95% of patients. *Tuber* is a gross pathologic description given to these firm nodular masses within the brain. A direct correlation between the number of cortical tubers and the degree of mental retardation has been demonstrated [24, 25]. Histologically, tubers represent hamartomatous lesions, composed of variable amounts of disordered glial tissue, heterotopic neurons, giant cells, and dystrophic calcifications. The imaging features of a given lesion will therefore depend on the relative proportions of each of these components within the tuber. When calcified, cortical tubers are easy to detect by their high density on CT and their low signal on MR (Fig. 5). Noncalcified tubers, however, which represent the vast majority of lesions, are difficult to detect by CT, and when seen usually appear as subtle, low-density subcortical masses. MR imaging has been shown to be far superior to CT for the detection of these lesions, which usually have low signal on T1-weighted images and high signal on T2-weighted images. These signal characteristics presumably result from increased central free water content caused by the tubers' loose connective stromal architecture and adjacent disordered myelination. In neonates, however, this signal pattern is reversed; the tubers appear hyperintense on T1-weighted images and hypointense on T2-weighted images [23] (Fig. 6).

White matter lesions are seen in approximately 90% of patients with TS, in direct proportion to the number of cortical tubers [2]. These lesions usually take the form of linear bands or striations (Figs. 6B and 7A), but may be wedge shaped or tumefactive [26]. Approximately 10% of these white matter lesions will enhance homogeneously after administration of gadopentetate dimeglumine. The distribution of abnormal giant cells along the usual migratory pathway of neurons within the white matter and common association with overlying cortical tubers imply a shared dysgenetic migrational origin.

Subependymal nodules are found in approximately 95% of patients with TS and are usually bilateral [2, 27]. They tend to calcify progressively with time and hence are easily detected by CT (Fig. 6A). MR usually shows these nodules as isointense or hypointense relative to gray matter on T1-

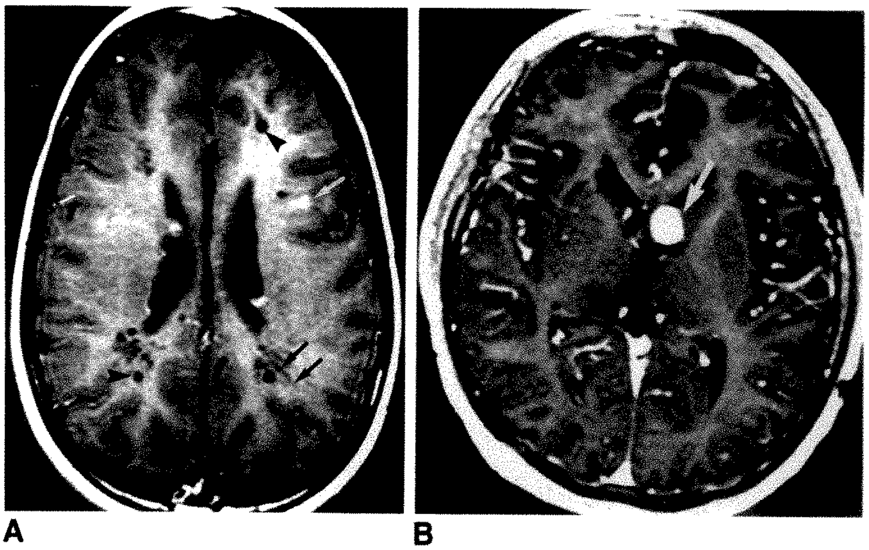

Fig. 7.—Enhanced MR images of brain in two patients with tuberous sclerosis.

A, Multiple calcified tubers (*arrowheads*) and unenhancing linear striations (*black arrows*) are shown. Several periventricular and one parenchymal tuber show enhancement (*white arrow*) not portending malignancy.

B, Giant-cell astrocytoma (*arrow*) at left foramen of Monro also enhances.

weighted sequences and hypointense on T2-weighted sequences. A relative signal reversal is again recorded in the neonate [2, 27, 28]. As an interesting discordant finding between imaging techniques, subependymal nodules virtually never enhance on CT but enhance frequently (30%) on MR [2, 29]. It is thought that this discordance is merely a manifestation of the higher sensitivity of MR relative to CT for detecting small quantities of their respective contrast media. Furthermore, although contrast enhancement of a subependymal nodule seen on CT has traditionally been considered a sign of neoplastic transformation, the same cannot be said when enhancement is seen on MR.

Subependymal giant-cell astrocytomas (Fig. 7B) occur in about 15% of patients with TS and are nearly always located near the foramen of Monro with a slight right-sided predominance [23, 30–33]. The classic CT appearance of these lesions is a 2–3 cm partially calcified mass with contrast enhancement [2, 28]. MR signal characteristics are indistinguishable from those of other benign subependymal nodules, but contrast enhancement with gadopentetate dimeglumine is invariably seen. Serpentine flow voids representing dilated tumor vessels may be detected in up to one third of cases, revealing the origin of these tumors near the vascular germinal matrix [2]. Because of the tendency of subependymal giant-cell astrocytomas to develop in patients with TS, we recommend screening such patients every 1–2 years with contrast-enhanced CT or MR, or more frequently if clinical conditions warrant. This regimen should be followed at least from ages 8 to 18, which is the most likely time for giant-cell tumors to develop [14, 28].

Sturge-Weber Syndrome (Encephalotrigeminal Angiomatosis)

Sturge-Weber syndrome (SWS) consists of a facial vascular nevus in the territory of the trigeminal nerve (predominantly the distribution of V1), together with leptomeningeal angiomatoses, angiomas of the choroid plexus and the ocular choroid, disordered venous drainage, and cerebral cortical calcifications [4, 34–37]. Imaging findings on CT include cerebral atrophy with secondary bone and sinus hypertrophy, intracranial calcifications (with a classic tram-track configuration), leptomeningeal thickening, and choroid plexus enlargement. Early reports stressed the complementary roles of MR and CT in the evaluation of patients with SWS; specifically, CT was thought necessary to detect calcifications and leptomeningeal angiomas that could be missed on a conventional unenhanced MR examination. However, the development of newer MR techniques (such as gradient-echo imaging and the use of paramagnetic contrast agents) has significantly diminished, if not eliminated, the contribution and necessity for CT in the evaluation of this disorder.

This issue was formally treated by Elster and Chen [34], who performed CT, gradient-echo MR, and contrast-enhanced MR imaging in five patients with SWS. These authors concluded contrast enhancement was absolutely necessary in the evaluation of patients with suspected SWS, because the full extent and even existence of the vascular lesion may not be apparent on MR without enhancement (Fig. 8). Calcifications were well shown by both CT and gradient-echo MR imaging. The latter technique was even found superior to CT in one case in which the calcifications were small and diffusely distributed (Fig. 9).

Other Vascular Phakomatoses

Wyburn-Mason Syndrome

As originally described by Bonnet-Dechaume-Blanc in 1937 and Wyburn-Mason in 1943, this disorder consists of a facial vascular nevus together with a cerebral arteriovenous malformation [38, 39]. The arteriovenous malformation usually involves the visual pathways, including the retina, orbital soft tissues, visual pathways, and midbrain. Clinical findings in-

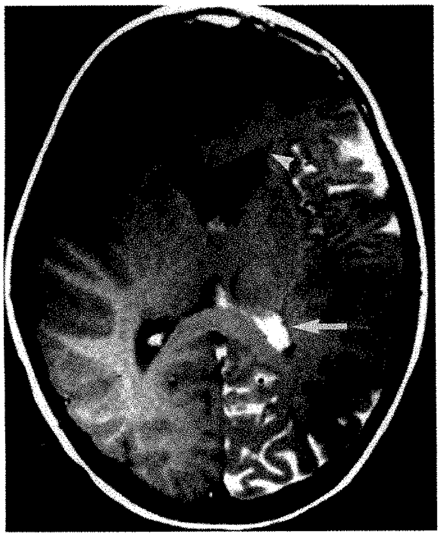

Fig. 8.—Enhanced MR image in patient with Sturge-Weber syndrome shows extensive unilateral leptomeningeal enhancement. There is also angiomatous enlargement of ipsilateral choroid plexus (*arrow*). Note also disordered venous drainage in left frontal lobe (*arrowhead*).

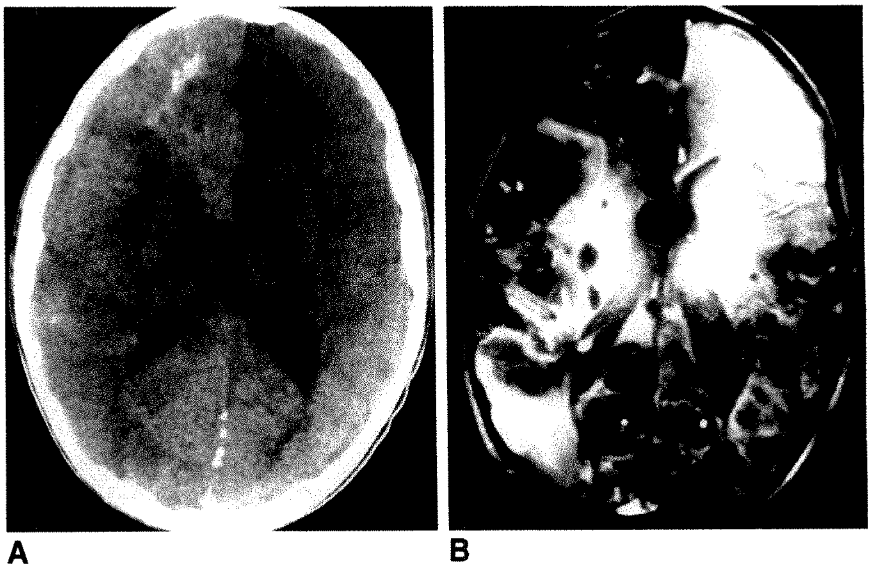

Fig. 9.—Extensive Sturge-Weber syndrome in a 3-year-old boy.

***A*, Unenhanced CT scan shows areas of definite and suspected calcifications bilaterally. Full extent of abnormality is difficult to determine.**

***B*, Gradient-echo MR image (300/18/30° [TR/TE/flip angle]) shows low signal from distributed microcalcifications to better advantage than even CT does.**

clude headache, visual disturbances, seizures, and subarachnoid hemorrhage.

Ataxia Telangiectasia (Louis-Bar Syndrome; Boder-Sedgwick Disease)

This disorder, described by Louis-Bar in 1941 and Boder and Sedgwick in 1957, consists of oculocutaneous telangiectasias and cerebellar ataxia [40–43]. Although symptoms of cerebellar ataxia usually begin in childhood, the telangiectasias of the face and conjunctiva may not appear until years later. Pathologically there is marked cerebellar atrophy that predominantly affects the anterior vermis, with defective maturation of Purkinje cells and granular neurons; dilated veins in the cerebellar and spinal leptomeninges with perivascular areas of necrosis; multiple, small capillary telangiectasias in the cerebral white matter and brainstem; atrophy of the dentate and olivary nuclei; and degeneration of the posterior columns of the spinal cord.

Osler-Weber-Rendu Disease

Osler-Weber-Rendu disease, or hereditary hemorrhagic telangiectasia, is an autosomal-dominant neurocutaneous syndrome that usually appears in adolescence [44]. This disease is characterized by multiple dermal, mucosal, and visceral telangiectasias that are prone to hemorrhage. Approximately two thirds of the patients have pulmonary arteriovenous fistulas, and about one third have vascular malformations (telangiectasias, arteriovenous malformations, or aneurysms) of the brain or spinal cord. MR may show the larger uncomplicated telangiectasias and angiomas as areas of hyperintensity on T2-weighted images that show enhancement [45, 46]. Infarcts, septic emboli, and brain abscesses occurring as complications of the pulmonary fistulas all have characteristic appearances on CT and MR and usually become more conspicuous after contrast administration.

Multiple Hemangiomatosis Syndromes

Several syndromes have been described that are closely related to Osler-Weber-Rendu disease but differ in that their vascular lesions are hemangiomas rather than telangiectasias (Table 4). The situation is complicated even further by the fact that pathologically intermediate forms between cavernous hemangiomas and telangiectasias have recently been demonstrated. Opinion is growing among many neuropathologists that a telangiectasia-hemangioma spectrum exists, and that *capillary malformation* should be applied to all such lesions [48]. It may very well be that Osler-Weber-Rendu disease and the multiple hemangiomatosis syndromes also merge and overlap with one another in a pathologic continuum.

When they involve the brain, multiple hemangiomas have a characteristic appearance (Fig. 10). On CT they are typically well circumscribed and hyperdense relative to brain with punctate or diffusely distributed microcalcifications. Contrast enhancement is typical, but may be somewhat obscured on CT by the calcifications. The MR appearance of cerebral hemangiomas is nearly pathognomonic [49], although hemorrhagic lesions simulating these malformations have been reported [50]. MR signal characteristics include either a cen-

TABLE 4: Multiple Hemangiomatosis Syndromes[a]

Syndrome	Description
Bean	Blue rubber bleb nevi (hemangiomas) of skin and mucosa, occasional CNS involvement
Burke	Disseminated hemangiomatosis (skin, brain, liver, kidney)
Familial cerebral angiomatosis	Multiple cavernous angiomas of brain with or without skin lesions
Familial retinal angiomatosis	Hemangiomas of skin, retina, optic nerve, and brain
Kasabach-Merritt	Hemangiomas of skin, viscera, skeleton, and occasionally brain with thrombocytopenia
Riley	Hemangiomas of skin and brain with macrocephaly and pseudopapilledema

[a] Adapted from Taybi [47].

tral cystic focus of isointensity or high intensity on both T1- and T2-weighted images, with peripheral hypointensity surrounding the central focus, or a focus of low-intensity signal, fading peripherally on both T1- and T2-weighted images.

Klippel-Trenaunay-Weber Syndrome

The Klippel-Trenaunay-Weber syndrome (KTWS) consists of cutaneous angiomata, soft-tissue or bony hypertrophy, and a deep parenchymal vascular malformation (arteriovenous or capillary) [51, 52]. A number of patients with KTWS have now been identified who have prominent involvement of the CNS as well. Over 40 cases of combined KTWS and SWS have been reported, and evidence is increasing that KTWS and SWS are probably disembryoplasias that differ only in the location of the lesion and severity of involvement [53]. Cranial CT and MR findings in KTWS are variable and include vascular lesions, angiomas, and hemimegalencephaly. Williams and Elster [53] noted a striking pattern of deep white matter and subcortical calcifications together with leptomeningeal and choroid plexus enhancement in two of their patients (Fig. 11). Often, however, the cranial findings will resemble the more common SWS, and the diagnosis of KTWS rests on supportive clinical findings (e.g., limb hypertrophy, peripheral varicosities, and skin lesions).

Meningioangiomatosis

Meningioangiomatosis is part of a spectrum of hamartomatous, meningeal-based lesions that involve the meninges, blood vessels, and adjacent brain. The primary histopathologic features consist of focal meningovascular proliferation on the surface of the cerebral cortex with spread along the Virchow-Robin spaces [54, 55]. The leptomeninges become thickened with proliferating meningothelial cells and psammomatous calcifications, resembling an en plaque meningioma. The typical clinical presentation is in a teenager or young adult with seizures, headache, and vertigo. About half the reported cases of meningioangiomatosis have occurred in patients with NF, and some authors even consider meningioangiomatosis to be a forme fruste of NF [54, 56, 57]. Imaging findings of meningioangiomatosis reported on CT include focal regions of linear or granular meningeal and cortical calcifications with peripheral or gyriform enhancement [53]. Cerebral angiography may reveal small clusters of abnormal vessels in the meninges. T2-weighted MR images have documented white matter edema in a reaction to the leptomeningeal fibrous and vascular proliferation [54].

Von Hippel-Lindau Disease

In 1926 Lindau conducted an investigation into the nature of cerebellar cysts that were associated with a mural nodule,

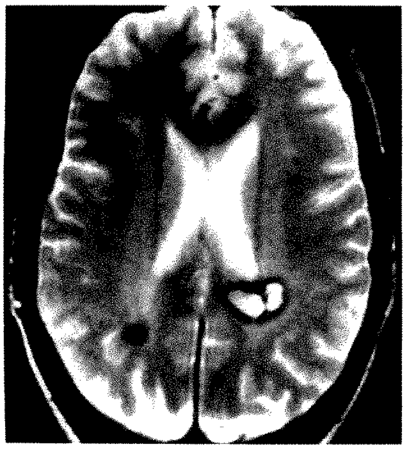

Fig. 10.—Multiple cerebral hemangiomatoses in a 36-year-old man. Dark areas on T2-weighted (2800/80) MR image correspond to deposition of hemosiderin and ferritin from previous subclinical hemorrhages.

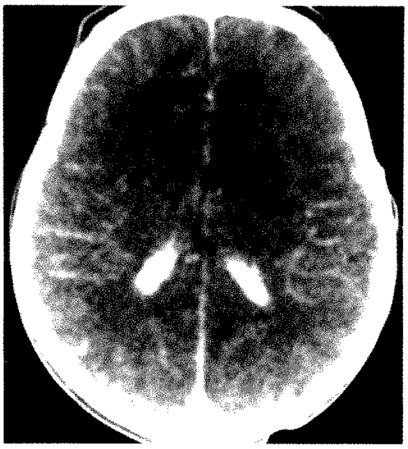

Fig. 11.—Klippel-Trenaunay-Weber syndrome in 3-month-old child with hemihypertrophy of right upper extremity and seizures. Contrast-enhanced CT scan shows extensive meningeal enhancement bilaterally and angiomatous enlargement of both choroid plexi.

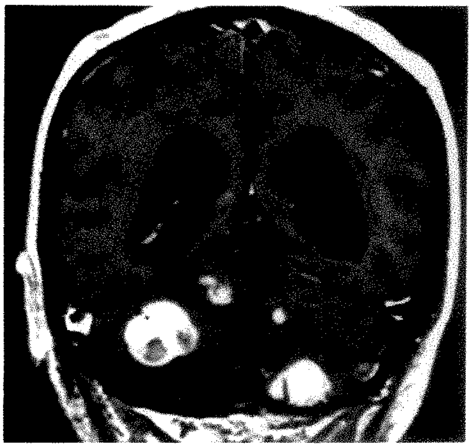

Fig. 12.—MR image shows four brightly enhancing cerebellar hemangioblastomas in this 56-year-old patient with von Hippel-Lindau disease.

proving them to be capillary hemangioblastomas [8, 9, 58]. Von Hippel subsequently described retinal angiomas that were associated both with visceral cysts (of the pancreas, kidney, liver, lung, and epididymis) and hemangioblastomas of the brain and spinal cord [59]. This complex of lesions became known as von Hippel-Lindau (VHL) disease.

VHL disease is inherited as an autosomal-dominant disorder with incomplete penetrance linked to a defect on chromosome 3 [60]. The most recent criteria for the diagnosis of VHL disease include two or more hemangioblastomas of the CNS, one hemangioblastoma plus a visceral manifestation, or one central or visceral manifestation in conjunction with a positive family history [61, 62]. Although skin lesions (such as café-au-lait spots and hemangiomas) are infrequent, their occurrence does suggest that VHL be classified as a neurocutaneous syndrome. At least one remarkable kindred has also been reported in which both NF and VHL disease were present in members of the same family and even coexisted in one patient [62]. Renal cell carcinomas occur in up to 30% of patients with VHL disease, and are bilateral or multiple in 10-50% [8]. The histopathology of metastatic renal cell carcinomas and hemangioblastomas are extremely similar, suggesting a shared genetic origin for these two lesions.

Hemangioblastomas in VHL disease may involve the cerebellum (65%), brainstem (20%), or spinal cord (15%) and are multiple in up to 40% [4, 63]. Hemangioblastomas in patients with VHL disease tend to appear a decade or two earlier in life (mean age at presentation, 32 years) than those occurring in patients without VHL [63]. Approximately 60-70% are cystic and the rest are solid. Solid tumors are more common in the brainstem and supratentorially. Cystic tumors usually have a small (<15 mm diameter) hypervascular mural nodule that abuts the pial surface.

Because nearly all hemangioblastomas occur in the posterior fossa or spinal cord, MR imaging is clearly superior to CT for the evaluation of such lesions [63, 64]. Solid tumors show intermediate to high signal on T2-weighted images and enhance homogeneously with contrast administration (Fig. 12). Cystic tumors have mural nodules that are usually isointense with gray matter on T1-weighted images, are hyperintense on T2-weighted images, and brilliantly enhance with contrast administration. Serpentine vessels supplying the mural nodules may be seen in up to 60% of cases. The cyst wall is generally thin and should not enhance. A thick or enhancing wall should strongly suggest that the tumor is not a hemangioblastoma but another tumor such as a cystic astrocytoma or metastasis.

Melanocytic Phakomatoses

Giant hairy nevi, mongolian spots, and infantile malignant melanomas are congenital skin lesions that result from disordered development of melanocytes or their precursors. Similarly, several rare neurocutaneous syndromes are also thought to be based on defective melanocyte or melanoblast proliferation and migration.

Neurocutaneous Melanosis

This rare disease consists of one or more large, cutaneous hairy or deeply pigmented nevi in association with diffuse melanosis of the leptomeninges [65, 66]. Primary malignant melanoma of the CNS will develop in approximately 40% of patients with neurocutaneous melanosis (NCM), often during the first year of life. It should be stressed, however, that NCM is essentially a diagnosis of exclusion, and the possibility that one is merely observing diffuse intracranial metastases from an occult melanoma arising outside the CNS must be ruled out. Additionally, NCM must be distinguished pathologically from the other primary melanin-containing tumors of the skull, brain, and meninges (pigmented meningioma, melanocytic schwannoma, meningeal melanocytoma, and melanotic neuroectodermal tumor of infancy) [8].

Reported cases of NCM imaged with CT have shown only diffuse meningeal enhancement [67]. One MR case also showed only diffuse meningeal enhancement and no abnormality on unenhanced images [68]. A second MR case showed a focal temporal lobe lesion with signal characteristics suggestive of melanin or hemorrhage (slightly hyperintense on T1-weighted images, slightly hypointense on T2-weighted images) [69].

Oculodermal Melanosis (Nevus of Ota Syndrome)

The nevus of Ota is a characteristic blue gray lesion in the V1 or V2 dermatomes, associated with abnormal meningeal pigmentation, meningeal melanocytomas, melanomas of the choroid and ciliary body, and primary malignant melanomas of the nervous system [70-74]. It should be noted that in contrast to NCM, meningeal pigmentation in the nevus of Ota syndrome is generally confined to the dura and periosteum, with sparing of the pial membranes.

Incontinentia Pigmenti

Incontinentia pigmenti is a rare neurocutaneous disorder that appears in infancy with erythematous vesicular skin lesions that later become verrucous and pigmented [75, 76]. The mode of inheritance is X-linked dominant and is usually fatal in males; hence, it has a 37:1 predilection for females. Cranial imaging manifestations reported to date have included microcephaly, hydrocephalus, optic nerve atrophy, encephalitis, and skull deformities.

Hypomelanosis of Ito

Hypomelanosis of Ito, also called incontinentia pigmenti archromians, consists of bizarre hypopigmented skin lesions that histologically have a decreased size and number of melanosomes and melanocytes [77]. Neuropathologic studies in patients with hypomelanosis of Ito have revealed cerebral atrophy, migrational anomalies, disordered cortical laminations with extensive gliosis, and widespread white matter involvement similar to that found in the leukodystrophies. Findings on cranial MR or CT imaging have included hemimegalencephaly, heterotopias, white matter abnormalities, parenchymal cysts, agenesis of the corpus callosum, porencephaly, and macrocephaly [78–80] (Fig. 13).

Epidermal Nevus Syndrome

Epidermal nevi are congenital skin lesions with a predilection for the midline or paramedian regions of the face. At least seven subtypes of these lesions are known, the most common being the linear sebaceous nevus. This syndrome is therefore sometimes referred to as the linear sebaceous nevus syndrome (of Jadassohn) [81–83]. The clinical triad of mental retardation, seizures, and midface sebaceous nevi closely resembles the findings in TS. Intracranial abnormalities include hemimegalencephaly (ipsilateral to the dermal nevus), gyral malformations (pachygyria and polymicrogyria), and heterotopias [81–84] (Fig. 14). A multitude of underlying vascular dysplasias have been described, including leptomeningeal angiomas, arteriovenous malformations, berry aneurysms, and absence of dural sinuses. Secondary underlying brain parenchymal abnormalities (infarcts, atrophy, dystrophic calcifications, and porencephalic cysts) may be seen and are thought to be the sequelae of these vascular events.

Cowden's Disease

Cowden's disease, also called multiple hamartoma syndrome, is a rare hereditary condition characterized by multiple hamartomas and neoplasms of ectodermal, mesodermal, and endodermal origins [85]. Abnormalities include facial polyps, hemangiomas, and tricholemmomas; gastrointestinal polyps; breast lesions (carcinoma, fibrocystic disease); thyroid tumors; ovarian cysts; hepatic lesions (hamartomas, hemangiomas); neurofibromas; and meningiomas.

Recently, two groups of investigators independently recognized the coexistence of Cowden's disease and a rare disorder of the cerebellum (Lhermitte-Duclos disease) in some of their patients [86, 87]. Lhermitte-Duclos disease is known under a variety of names (dysplastic cerebellar gangliocytoma, purkinjeoma) and behaves like a low-grade neoplasm. Although extremely rare, Lhermitte-Duclos disease has such a characteristic imaging appearance that the diagnosis should be entertained preoperatively [87–90]. The tumor has a marked propensity to involve the left rather than right cerebellar hemisphere, and the degree of mass effect is usually slight considering the average size of the lesion (3–5 cm). CT reveals an unenhancing, hypodense mass that may contain focal calcifications. On MR imaging the lesion is typically of moderately high signal on T2-weighted images and slightly hypointense relative to brain on T1-weighted images. The presence of parallel linear striations on the surface of the lesion, presumably representing thickened, dysplastic cerebellar folia, is nearly pathognomonic (Fig. 15). A supportive finding is the presence of prominent draining veins on the pial surface of the mass. Megalencephaly, heterotopias, polymicrogyria, and venous angiomas also may be seen.

Conclusions

A relatively large number of phakomatoses are now recognized, primarily manifest by lesions of skin and brain. These disorders serve to remind us of the fascinating and complex embryologic development of the neuroectoderm, illustrating how a single genetic error may appear as abnormalities in multiple organ systems. Because many of these syndromes have nearly pathognomonic cutaneous or radiologic appearances (but not both), their proper diagnosis hinges on good communication between two groups of physicians who oth-

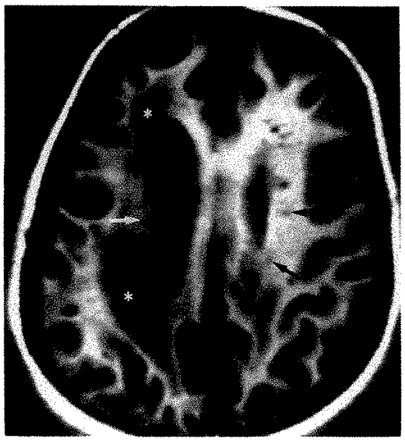

Fig. 13.—13-year-old patient with hypomelanosis of Ito. T1-weighted inversion-recovery MR image shows diffuse right hemisphere white matter disease (*asterisks*) and multiple periventricular cysts (*white arrow*) and heterotopias (*black arrows*).

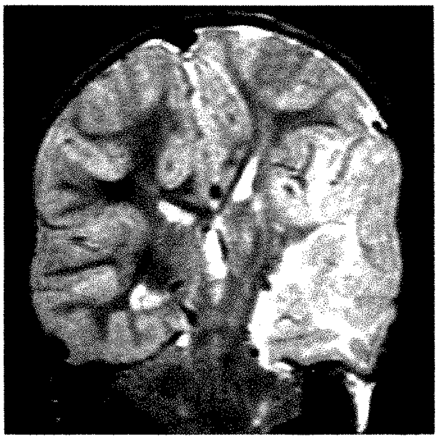

Fig. 14.—Epidermal nevus syndrome in 4-year-old boy with extensive pigmented nevus over most of his torso and upper extremities and chronic seizures. Coronal T2-weighted (2800/80) MR image shows enlargement of left temporal lobe with cortical thickening and abnormal signal representing a focal pachygyria and migrational anomaly. (Case courtesy of S. T. Auringer.)

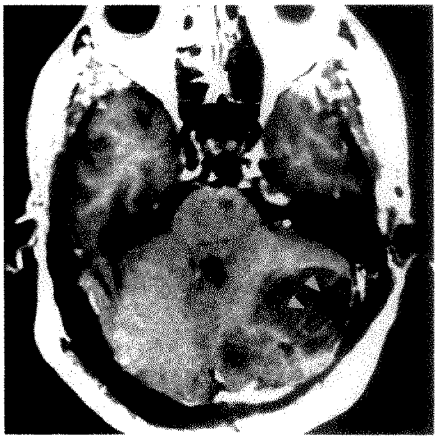

Fig. 15.—Lhermitte-Duclos disease may be associated with Cowden's disease. MR image shows unenhancing mass in left cerebellar hemisphere with characteristic linear striations (*arrowheads*) representing thickened, dysplastic cerebellar folia.

erwise only infrequently interact (dermatologists and radiologists). Further collaborative research will not only allow us to understand better the natural history of these rare diseases but may reveal patterns of embryologic development that will lead to uncovering their true genetic bases.

REFERENCES

1. Van der Hoeve. Les phakomatoses de Bourneville, de Recklinghausen et de von Hippel Lindau. *J Belge Neurol Psychiatr* **1933**;33:752-762
2. Braffman BH, Bilaniuk LT, Naidich TP, et al. MR imaging of tuberous sclerosis: pathogenesis of this phakomatosis, use of gadopentetate dimeglumine, and literature review. *Radiology* **1992**;183:227-238
3. Aoki S, Barkovich AJ, Nishimura K, et al. Neurofibromatosis types 1 and 2: cranial MR findings. *Radiology* **1989**;172:527-534
4. Braffman BJ, Bilaniuk LT, Zimmerman RA. MR of central nervous system neoplasia of the phakomatoses. *Semin Roentgenol* **1990**;25:198-217
5. Crump T, trans. Ueber die multiplen Fibrome der Haut und ihre Bezeihung zu den multiplen Neuromen by F. V. Recklinghausen [transl of case reports in English]. *Adv Neurol* **1988**;29:259-275
6. National Institutes of Health Consensus Development Conference. Neurofibromatosis Conference Statement. *Arch Neurol* **1988**;45:575-588
7. Riccardi VM. Neurofibromatosis: clinical heterogeneity. *Curr Probl Cancer* **1982**;7:1-34
8. Mulvihill JJ. Neurofibromatosis 1 (Recklinghausen disease) and neurofibromatosis 2 (bilateral acoustic neurofibromatosis). *Ann Intern Med* **1990**;113:39-52
9. Russell DS, Rubinstein LJ. *Pathology of tumors of the nervous system*, 4th ed. Baltimore: Williams & Wilkins, **1977**:766-808
10. Lott IT, Richardson EP. Neuropathogenesis and the biology of neurofibromatosis. *Adv Neurol* **1981**;29:23-31
11. Jacoby CG, Go RT, Beren RA. Cranial CT of neurofibromatosis. *AJR* **1980**;135:553-557
12. Klatte EG, Franken EA, Smith JA. The radiographic spectrum in neurofibromatosis. *Semin Roentgenol* **1976**;11:17-33
13. Elster AD, Rieser GD. Gadolinium-DTPA-enhanced cranial MR imaging in children: initial clinical experience and recommendations for its use. *AJNR* **1989**;10:1027-1030, *AJR* **1989**;153:1265-1268
14. Elster AD. Radiologic screening in the neurocutaneous syndromes: strategies and controversies. *AJNR* **1992** (in press)
15. Sevick RJ, Barkovich AJ, Edwards MS, Koch TK, Lempert T, Norman D. Neurofibromatosis type I: temporal evolution of white matter lesions (abstr). *Radiology* **1991**;181(P):193
16. Rouleau GA, Wertelecki W, Haines JL, Superneau DW, Martuzza RL, Gusella R. Genetic linkage of bilateral acoustic neurofibromatosis 2 (bilateral acoustic neurofibromatosis) to a DNA marker on chromosome 22. *Nature* **1987**;329:246-248
17. Elster AD, Challa VR, Gilbert TC, Richardson DN, Contento J. Meningiomas: MR and histopathologic features. *Radiology* **1989**;170:857-862
18. Friedman D. Segmental neurofibromatosis (NF-5): a rare form of neurofibromatosis. *AJR* **1991**;12:971-972
19. Trattner A, David M, Hodak E. Segmental neurofibromatosis. *J Am Acad Dermatol* **1990**;23:1-38
20. Bourneville DM. Sclerose tubereuse des circonvolutions cerebrales: idiotie et epilepsie hemiplegique. *Arch Int Neurol* **1880**;1:81-91
21. Vogt H. Zur Pathologie und pathologishen Anatomie der ver schiedenen idiotie-formen: II. Tuberose sklerose. *Monatsschr Psychiatr Neurol* **1908**;24:106-150
22. Smith MS, Smalley S, Cantor R, et al. Mapping of a gene determining tuberous sclerosis to human chromosome 11g14-11g23. *Genomics* **1990**;6:105-114
23. Altman NR, Purser RK, Post MJD. Tuberous sclerosis: characteristics at CT and MR imaging. *Radiology* **1988**;167:527-532
24. Roach ES, Williams DP, Laster DW. Magnetic resonance imaging in tuberous sclerosis. *Arch Neurol* **1987**;44:301-303
25. Roach ES. Usefulness of magnetic resonance imaging in tuberous sclerosis. *Arch Neurol* **1988**;45:830-831
26. Iwasaki S, Nakagawa H, Kichikawa K, et al. MR and CT of tuberous sclerosis: linear abnormalities in the cerebral white matter. *AJNR* **1990**;11:1029-1034
27. Nixon JR, Houser OW, Gomez MR, Okazaki H. Cerebral tuberous sclerosis: MR imaging. *Radiology* **1989**;170:869-873
28. McMurdo SK, Moore SG, Brant-Zawadzki M, et al. MR imaging of intracranial tuberous sclerosis. *AJR* **1987**;148:791-796
29. Martin N, Debussche C, DeBroucker T, Mompoint D, Marsault C, Nahum H. Gadolinium-DTPA enhanced MR imaging in tuberous sclerosis. *Neuroradiology* **1990**;31:492-497
30. Bell DG, King BF, Hattery RR, Charboneau JW, Hoffman AD, Houser OW. Imaging characteristics of tuberous sclerosis. *AJR* **1991**;156:1081-1086
31. DeRecondo J, Haguenau M. Neuropathologic survey of the phakomatoses and allied disorders. In: Vinken RJ, Bruyn GW, eds. *Handbook of clinical neurology*, Vol. 14. *The phakomatoses*. Amsterdam: North Holland, **1972**:19-71
32. Frerebeau PH, Benezech J, Segnarbieux F, Harbi H, Desy A. Intraventricular tumors in tuberous sclerosis. *Childs Nerv Syst* **1985**;1:45-48
33. Palmieri A, DeVecchio E, Pirolo R, Gardeur D, Ambrosio A. The current potential of neuroradiology in the diagnosis of tuberous sclerosis. *Ital J Neurol Sci* **1982**;3:229-233
34. Elster AD, Chen MY. MR imaging of Sturge-Weber syndrome: role of gadopentetate dimeglumine and gradient-echo techniques. *AJNR* **1990**;11:685-689
35. Bilaniuk LT, Zimmerman RA, Hochman M, et al. MR of the Sturge-Weber syndrome (abstr). *AJNR* **1987**;8:945
36. Stimac GK, Solomon MA, Newton TH. CT and MR of angiomatous malformations of the choroid plexus in patients with Sturge-Weber disease. *AJNR* **1986**;7:623-627
37. Chamberlain MC, Press GA, Hesselink JR. MR imaging and CT in three cases of Sturge-Weber syndrome: prospective comparison. *AJNR* **1989**;10:491-496
38. Lalonde G, Duquette P, Laflamme P, Vezina J. Bonnet-Dechaume-Blanc syndrome. *Can J Ophthalmol* **1979**;14:47-50
39. Wyburn-Mason R. Arteriovenous aneurysm of midbrain and retina, facial naevi and mental changes. *Brain* **1943**;66:163
40. Louis-Bar D. Sur un syndrome progressif comprenant des télangiectasies capillaries cutanées et conjonctivales symétriques, à disposition naevoide et des troubles cérébelleux. *Stereotact Funct Neurosurg* **1941**;4:32-42
41. Boder E, Sedgwick RP. Ataxia-telangiectasia: familial syndrome of progressive cerebellar ataxia, oculo-cutaneous telangiectasia and frequent pulmonary infection. *USC Med Bull* **1957**;9:15-27
42. Aguilar MJ, Kamoshita S, Landing BH, Boder E, Sedgwick RP. Pathological observations in ataxia-telangiectasia: a report on five cases. *J Neuropathol Exp Neurol* **1968**;27:659
43. Hosking G. Ataxia telangiectasia. *Dev Med Child Neurol* **1982**;24:77-80
44. Roman G, Fisher M, Perl DP, Poser CM. Neurological manifestations of hereditary hemorrhagic telangiectasia (Rendu-Osler-Weber disease): report of 2 cases and review of the literature. *Ann Neurol* **1978**;4:130
45. Kucharczyk W, Lemme-Pleghos L, Brant-Zawadzki M, Dooms GC, Norman D. Intracranial vascular malformations: MR and CT imaging. *Radiology* **1985**;156:383-389
46. Aesch B, Lioret E, de Toffal B, Jan M. Multiple cerebral and Rendu-Osler-Weber diseaes: case report. *Neurosurgery* **1991**;29:599-602
47. Taybi H. *Radiology of syndromes and metabolic disorders*, 2nd ed. Chicago: Yearbook Medical, **1983**:404-405
48. Rigamonte D, Johnson PC, Spetzler RF, Hadley MN, Drayer BP. Cavernous malformations and capillary telangiectasia: a spectrum within a single pathological entity. *Neurosurgery* **1991**;28:60-64
49. Gomori J, Grossman RI, Goldberg HI, Hackney DB, Zimmerman RA, Bilaniuk LT. Occult cerebral vascular malformations: high-field MR imaging. *Radiology* **1986**;158:707-713
50. Sze G, Krol G, Olsen WL, et al. Hemorrhagic neoplasms: MR mimics of occult vascular malformations. *AJNR* **1987**;8:795-802
51. Klippel M, Trenaunay P. Du naevus variqueux osteophypetrophique. *Arch Gen Med* **1900**;3:641-642
52. Parke-Weber F. Angioma formation in connection with hypertrophy of the limbs and hemihypertrophy. *Br J Dermatol* **1907**;19:231-232
53. Williams DW III, Elster AD. Cranial CT and MR in the Klippel-Trenaunay-Weber syndrome. *AJNR* **1992**;13:291-294
54. Aizpuru RN, Quencer RM, Norenberg M, Altman N, Smirniotopoulas J. Meningioangiomatosis: clinical, radiologic and histopathologic correlation. *Radiology* **1991**;179:819-821

55. Worcester-Drought C, Dickson WEC, McMenemy WH. Multiple meningeal and perineural tumors with analogous changes in the glia and ependyma. *Brain* **1937**;60:85–117
56. Kasantikul V, Brown WJ. Meningioangiomatosis in the absence of von Recklinghausen's disease. *Surg Neurol* **1981**;15:71–75
57. Kunishio K, Yamamoto Y, Sunami N, et al. Histopathologic investigation of a case of meningioangiomatosis not associated with von Recklinghausen's disease. *Surg Neurol* **1987**;27:575–579
58. Lindau A. Discussion on vascular tumors of the brain and spinal cord. *J R Soc Med* **1930**;24:363–370
59. Von Hippel E. Die anatomische Grund lage der von mir beschriebenen sehr seltenen Erkrankung der Netzhaut. *Graefes Arch Clin Exp Ophthalmol* **1911**;79:350
60. Hosoe S, Brauch H, Latif F, et al. Localization of the von Hippel–Lindau disease to a small region of chromosome 3. *Genomics* **1990**;8:634–640
61. Melmon KL, Rosen SW. Lindau's disease: review of the literature and study of a large kindred. *Am J Med* **1964**;36:595–617
62. Horton WA, Wong V, Eldridge R. Von Hippel–Lindau disease: clinical and pathological manifestations in nine families with 50 affected members. *Arch Intern Med* **1976**;136:769–777
63. Elster AD, Arthur DW. Intracranial hemangioblastomas: CT and MR findings. *J Comput Assist Tomogr* **1988**;12:736–739
64. Sato Y, Yaziri M, Smith W, et al. Hippel-Lindau disease: MR imaging. *Radiology* **1988**;166:241–246
65. Barbieri F, Santangelo R, Indaco A, DeFurio M, Buscaino GA. Neurocutaneous melanosis, neurofibromatosis and spinal meningioma: an unusual association. *Acta Neurol* (Napoli) **1990**;12:115–221
66. Fox H. Neurocutaneous melanosis. In: Vinken RJ, Bruyn GW, eds. *Handbook of clinical neurology,* Vol. 14. *The phakomatoses.* Amsterdam: North Holland, **1972**:414–428
67. Crisp DE, Thompson JA. Primary malignant melanomatosis of the meninges. *Arch Neurol* **1981**;38:528–529
68. Rhodes RE, Friedman HS, Hatten HP, et al. Contrast-enhanced MR imaging of neurocutaneous melanosis. *AJNR* **1991**;12:380–382
69. Sebag G, Dubois J, Pfister P, Brunelle F, St Rose C. Neurocutaneous melanosis and temporal lobe tumor in a child: MR study. *AJNR* **1991**;12:699–700
70. Ota M. Naevus fusco-caeruleus ophthalmo-maxillaris. *Nippon Hifuka Gakkai Zasshi* **1939**;46:360–361
71. Botticelli AR, Villani M, Angiari P, Peserico L. Meningeal melancytoma of Meckel's cave associated with ipsilateral Ota's nevus. *Cancer* **1983**;51:2304–2305
72. Albert EM, Scheie HC. Naevus of Ota with malignant melanoma of the choroid. *Arch Ophthalmol* **1963**;69:774–777
73. Hadasa A. Malignant melanoma in a case of bilateral naevus of Ota. *Arch Ophthalmol* **1970**;84:176–178
74. Horsey WJ, Bilbao JM, Nethercott J, Myers R, Hoffman HJ. Oculodermal melanosis (naevus of Ota) complicated by multiple intracranial tumors. *Can J Neurol Sci* **1980**;7:101–107
75. Federico A, Fabrizi GM, Dotti MT, et al. Neurocutaneous syndromes with pigmentary abnormalities and central nervous system involvement. *Acta Neurol* (Napoli) **1990**;12:264–272
76. Bloch B. Egentumliche bisher night beschriebene pigmentaffektion (incontinentia pigmenti). *Schweiz Med Wochenschr* **1926**;56:404–405
77. Ito M. Studies on melanin. XI. Incontinentia pigmenti achromians, a singular case of nevus dipigmentosus systematicus bilateris. *Tohoku J Exp Med* **1952**;55[suppl]:57–59
78. Williams DW, Elster AD. Cranial MR imaging in hypomelanosis of Ito. *J Comput Assist Tomogr* **1991**;14:981–983
79. Moss C, Burn J. Genetic counseling in hypomelanosis of Ito: case report and review. *Clin Genet* **1988**;34:109–115
80. Dunn V, Mock T, Bell WE, Smith W. Detection of heterotopic gray matter in children by magnetic resonance imaging. *Magn Reson Imaging* **1986**;4:33–39
81. Pavone L, Curatolo P, Rizzo R, et al. Epidermal nevus syndrome: a neurologic variant with hemimegalencephaly, gyral malformation, mental retardation, seizures and facial hemihypertrophy. *Neurology* **1991**;41:266–271
82. Feuerstein RC, Mims LC. Linear nevus sebaceous with convulsions and mental retardation. *Am J Dis Child* **1962**;104:675–679
83. Barth PG, Valk J, Kalsbeek GL, Blom A. Organoid nevus syndrome (linear nevus sebaceous of Jadassohn): clinical and radiological study of a case. *Neuropediatrics* **1977**;8:418–428
84. Chalhub EG, Volpe JJ, Gado MH. Linear nevus sebaceous syndrome associated with porencephaly and nonfunctioning major cerebral venous sinuses. *Neurology* **1975**;28:857–860
85. Lloyd KM, Dennis M. Cowden's disease: a possible new symptom complex with multiple system involvement. *Ann Intern Med* **1963**;58:136–142
86. Padberg GW, Schot JDL, Vielvoye GJ, Bots AM, de Beer FC. Lhermitte-Duclos disease and Cowden disease: a single phakomatosis. *Ann Neurol* **1991**;29:517–523
87. Williams DW, Elster AD, Ginsberg LE, Stanton C. Recurrent Lhermitte-Duclos disease: report of two cases and associations with Cowden's disease. *AJNR* **1992**;13:287–290
88. Ashley DG, Zee C-S, Chandrasoma PT, Segall HD. Lhermitte-Duclos disease: CT and MR findings. *J Comput Assist Tomogr* **1990**;14:984–987
89. Smith RR, Grossman RI, Goldberg HI. MR imaging of Lhermitte-Duclos disease: a case report. *AJNR* **1989**;10:187–189
90. Reeder RF, Saunders RL, Roberts DW, Fratkin JD, Cromwell LD. Magnetic resonance imaging in the diagnosis and treatment of Lhermitte-Duclos disease (dysplastic gangliocytoma of the cerebellum). *Neurosurgery* **1988**;23:240–245

AJR
AMERICAN JOURNAL OF ROENTGENOLOGY

MELVIN M. FIGLEY FELLOWSHIPS IN RADIOLOGY JOURNALISM
1993

The American Roentgen Ray Society announces two one-month fellowships in radiology journalism in the La Jolla editorial office of the *AJR*. Board-certified radiologists with special academic promise are invited to apply.

PURPOSE

The purpose of the fellowship is (1) to stimulate bright young radiologists to continue with an academic career, to accelerate their progress, and to stimulate their interest in good radiology journalism and (2) to improve the quality of radiology journals by teaching the fundamentals of medical journalism to academicians, training manuscript reviewers and future editors, and providing core teachers of medical journalism in radiology departments around the country.

CURRICULUM

Through hands-on experience in the editorial office, the fellows will be taught the fundamentals of medical writing, manuscript preparation, peer review, manuscript editing, the ethics of scientific journalism, and journal publication and printing in personal tutorials given by the *AJR* editors and editorial staff. They will visit Waverly Press in Maryland to observe the publication and printing process.

STIPEND

The successful candidates will each be awarded $10,000, which includes the cost of travel to La Jolla and Maryland, living expenses for the month, and an honorarium.

APPLICATIONS

Candidates should apply in writing to Robert N. Berk, M.D., Editor-in-Chief, *AJR* Editorial Office, 2223 Avenida de la Playa, Suite 103, La Jolla, CA 92037. The letter must include a curriculum vitae and a description of the candidate's goals during the fellowship. Letters of recommendation from his or her department chairman and one other senior person are required. Deadline for receipt of applications is Sept. 1, 1992. The successful candidates will be notified Oct. 1, 1992.

Value of MR Imaging in the Evaluation of Chronic Infiltrative Lung Diseases: Comparison with CT

Nestor L. Müller[1]
John R. Mayo
Charles V. Zwirewich

The value of MR imaging was compared with that of high-resolution CT in assessing chronic infiltrative lung disease in 25 patients. The cases included nine patients with usual interstitial pneumonia, six with sarcoidosis, four with hypersensitivity pneumonitis, and six with miscellaneous conditions. The diagnosis was proved by biopsy ($n = 17$) or by means of clinical, laboratory, and radiologic criteria ($n = 8$). All patients had 1.5-T MR imaging and CT of the chest. Cardiac-gated T1-, proton density-, and T2-weighted spin-echo sequences were obtained. Initially, the MR images were assessed independently; later they were compared directly with the corresponding CT scans. In six patients, MR images and CT scans were obtained before open lung biopsy, and the images and scans were assessed prospectively. CT was superior to MR imaging in the anatomic assessment of the lung parenchyma and in showing fibrosis. However, areas of air-space opacification (ground-glass opacities) were seen as well on MR as on high-resolution CT. In the six patients who had open lung biopsy, areas of air-space opacification seen on MR and on CT corresponded to areas of active alveolitis or air-space infiltrates pathologically. Follow-up in six patients showed equal degrees of change in the air-space opacification over time on MR and CT.

We conclude that, although MR imaging is inferior to high-resolution CT in the assessment of chronic infiltrative lung diseases, it may play a role in the assessment and follow-up of patients with air-space opacification.

***AJR* 158:1205–1209, June 1992**

High-resolution CT (HRCT, 1- to 2-mm collimation, high-spatial-frequency reconstruction algorithm) has been shown to accurately reflect the macroscopic pathologic abnormalities in patients with chronic infiltrative lung disease [1–4]. In idiopathic pulmonary fibrosis, sarcoidosis, and hypersensitivity pneumonitis, areas of air-space opacification (ground-glass opacities) have been shown to correlate with active alveolitis [5–10]. The use of CT in the assessment of disease activity and in the follow-up of patients is limited, however, particularly in young patients, by the radiation dose.

The aim of the present study was to compare MR with HRCT in the assessment of chronic infiltrative lung diseases. MR was compared with HRCT, as HRCT is currently the best technique for the assessment of disease pattern and distribution in vivo. In those patients undergoing open lung biopsy, the CT scans and MR images were correlated with the pathologic findings.

Subjects and Methods

The study included 24 adults (13 men and 11 women) 30–76 years old (mean ± SD, 56 ± 13 years) and one 5-year-old boy. All patients had MR and CT. In all cases, CT was performed as part of the clinical evaluation of proved or suspected chronic infiltrative lung disease. MR imaging in the 24 adults was performed as part of a research project to evaluate the potential usefulness of MR in the assessment of infiltrative lung disease. All patients having CT of the

Received November 19, 1991; accepted after revision December 23, 1991.

This work was supported by a B.C. Health Care Research Foundation grant. J. R. Mayo is supported by a Sterling-Winthrop Imaging Research Institute career scientist award; C. V. Zwirewich is supported by a B.C. Lung Association and Canadian Association of Radiologists fellowship.

[1] All authors: Department of Radiology, University of British Columbia and Vancouver General Hospital, 855 W. 12th Ave., Vancouver, B.C., Canada V5Z 1M9. Address reprint requests to N. L. Müller.

0361–803X/92/1586–1205
© American Roentgen Ray Society

chest for assessment of chronic infiltrative lung disease who could be studied without interfering with their treatment and who agreed to undergo research MR imaging were included in the study. Approval for the project was obtained from the university and hospital ethics committees, and signed informed consent was obtained from the 24 patients. The 5-year-old boy was from an outside hospital, and MR was performed as part of his clinical assessment. Informed consent was obtained from the child's parents.

The patients included nine with usual interstitial pneumonia (six idiopathic pulmonary fibrosis and three associated with collagen vascular disease), six with sarcoidosis, four with hypersensitivity pneumonitis, two with lymphangitic carcinomatosis, two with drug reactions, one with desquamative interstitial pneumonia, and one with Churg-Strauss syndrome. In 17 patients, diagnosis was proved by biopsy; in two cases of hypersensitivity pneumonitis, it was based on clinical history and positive serologic tests for thermophilic actinomycetes. In the remaining six patients, including two with idiopathic pulmonary fibrosis, three with interstitial fibrosis associated with collagen vascular disease, and one with drug reaction to amiodarone, the diagnosis was based on clinical, radiologic, and CT findings.

All MR studies were performed on a 1.5-T MR imager (Signa, Software 3.39, General Electric Medical Systems, Milwaukee, WI). Cardiac-gated proton density–weighted and relatively T2-weighted images, 1714–2903/30,80 (TR/TE), were obtained at two or three R-R intervals. Two excitations, a 256 × 192 matrix, flow compensation, respiratory compensation, and spatial presaturation above and below the transverse image plane were used for all sequences. The slice thickness was 10 mm, with a 1- or 2-mm interslice gap. Images were prescribed caudad to craniad.

The cardiac-gated T1-weighted images were obtained at one R-R interval (TR range, 571–1176 msec). The TE used was changed over the course of the study. In the first 13 patients, T1-weighted images were obtained with a TE of 30 msec, two excitations, a 256 × 192 matrix, flow compensation, respiratory compensation, and spatial presaturation. In the next 12 patients, a TE of 20 msec, spatial presaturation, four excitations, and no flow or respiratory compensation were used. Scan location and interslice gap were the same as for the proton density–weighted and T2-weighted sequences.

CT scans were obtained by using 1.5-mm collimation scans, a high-spatial-frequency reconstruction algorithm, and 10-mm intervals through the chest in 23 patients and by using conventional 10-mm collimation scans, 10-mm intervals, and the high-spatial-frequency algorithm in two cases. The CT scans were photographed at levels appropriate for lung parenchyma (mean, −600 to −700 H; width, 1500 H) and mediastinum (mean, 30–50 H; width, 350–500 H). The MR images were photographed at windows and levels appropriate for lung parenchyma and mediastinum.

In eight patients, the CT scans and MR images were obtained on the same day, and in the remaining 17 patients, the scans were obtained 2–90 days apart (median, 5 days).

The MR images and CT scans were reviewed by two chest radiologists who reached a decision by consensus. Ability to visualize the following features was assessed on the MR images and CT scans: central and peripheral vessels; lobar, segmental, and subsegmental bronchi; interlobular septa or veins and centrilobular arteries; interstitial abnormalities, including reticulation, honeycombing, septal thickening, and small nodules; distribution of abnormalities as peribronchovascular, peripheral, diffuse, or patchy; and air-space abnormalities, including ground-glass opacity and consolidation (Table 1). These parameters were chosen to compare MR images with HRCT scans in the visualization of normal pulmonary parenchymal structures and in the assessment of the known HRCT pattern and distribution of findings associated with the most common infiltrative lung diseases [1, 2, 11, 12]. Ground-glass opacity was defined as an area of hazy, increased density on CT and increased signal intensity on MR without obscuration of underlying pulmonary vascular markings. Air-space consolidation was considered to be present when the vascular markings were obscured. Visualization of these various parameters was assessed independently on T1-weighted, proton density–weighted, and T2-weighted images. Observers recorded the MR sequences in which these parameters were visualized and, subsequently, whether the findings were detected on CT. Subsequently, the MR images were compared directly with the CT scans, and the observers recorded whether each parameter was visualized better on MR, better on CT, or equally on both.

In six patients, the MR images and CT scans were obtained within 9 days before open lung biopsy and were used as a guide to the biopsy site. In these patients, the MR and CT findings at the biopsy site were correlated with the pathologic findings. In the remaining patients, open lung biopsy was not performed or the time interval between lung biopsy and MR or CT did not allow pathologic correlation. In six patients, follow-up CT and MR were performed within 6–12 months of the initial study. Indications for the follow-up CT scans were based exclusively on clinical criteria and included interval clinical deterioration or lack of improvement despite therapy, as well as being part of an evaluation to determine whether the patient's treatment could be discontinued.

Results

MR imaging allowed assessment of normal parenchymal structures and visualization of the interstitial and air-space abnormalities in the majority of cases (Table 1, Figs. 1 and 2). However, when directly compared with CT, MR was consist-

TABLE 1: Comparison of MR and CT in 25 Patients with Chronic Infiltrative Lung Disease

Findings	No. of Patients by Imaging Study			
	CT	T1	PD	T2
Vessels				
Central	25	25	24	24
Peripheral	25	25	18	3
Airways				
Lobar	25	25	25	25
Segmental	25	21	20	8
Subsegmental	25	8	5	4
Secondary pulmonary lobule				
Interlobular septum or vein	25	19	15	7
Centrilobular arteriole	25	11	5	1
Interstitial abnormality				
Reticulation	15	13	12	4
Honeycombing	10	9	6	0
Septal thickening	16	12	11	4
Nodules	6	5	6	5
Distribution of interstitial abnormalities				
Peribronchovascular	4	4	4	4
Peripheral	11	10	10	9
Diffuse	7	7	7	7
Patchy	4	5	5	4
Air-space abnormality				
Ground-glass opacity	18	19	18	17
Consolidation	5	5	5	5

Note.—The numbers refer to the number of patients in whom the various findings were detected when the scans and images were assessed independently. In the six patients who had follow-up CT and MR, only the findings in the initial study are included in the table. CT = CT scans, T1 = T1-weighted MR imaging, PD = proton density–weighted MR imaging, T2 = T2-weighted MR imaging.

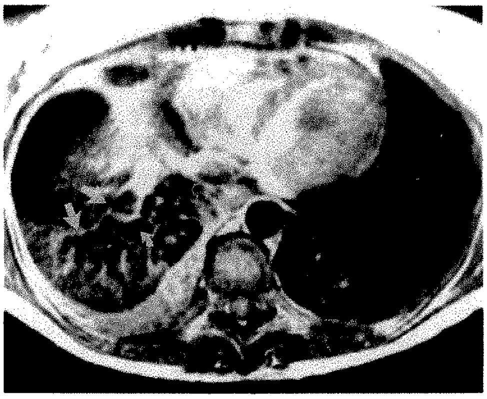

Fig. 1.—Interlobular septal thickening in a 44-year-old woman with lymphangitic carcinomatosis involving mainly right lower lobe. MR image (2118/30) shows thickening of interlobular septa (*straight arrows*) and centrilobular structures (*curved arrow*), a right-sided pleural effusion, and a few poorly defined nodules in left lower lobe.

ently inferior in the anatomic assessment of lung parenchyma and in showing interstitial abnormalities, particularly fibrosis (Table 1). Furthermore, areas of mild interstitial abnormalities seen on CT were often not apparent on MR. It was possible to assess distribution of disease as being mainly peribronchovascular, peripheral, diffuse, or patchy on MR, although it was often not as readily apparent as on CT (Table 1). Visualization of normal parenchymal structures and interstitial abnormalities on T1-weighted MR images was usually comparable to that on proton density-weighted images and considerably better than on T2-weighted images (Table 1).

MR was comparable to CT in the assessment of air-space abnormalities (Table 1, Figs. 3 and 4). In all patients, areas with ground-glass opacities or air-space consolidation on CT corresponded to areas of increased signal intensity on MR. Six patients had open lung biopsy 0–9 days after MR imaging. Five of the six had areas of ground-glass opacity (i.e., hazy, increased density without obscuration of the vascular markings) on CT and MR. These five patients had areas of active alveolitis pathologically and included three with usual interstitial pneumonia, one with hypersensitivity pneumonitis, and one with cyclophosphamide-induced inflammatory pulmonary drug reaction. In one of the six patients, peripheral air-space consolidation was seen equally well on MR and CT (Fig. 4). Open lung biopsy proved that this patient had Churg-Strauss syndrome. This patient had a prominent eosinophilic air-space infiltrate and necrotizing granulomas.

Follow-up MR and CT in six patients showed improvement of the ground-glass opacities in one patient with sarcoidosis (Fig. 5), one with hypersensitivity pneumonitis, and one with idiopathic pulmonary fibrosis corresponding to clinical improvement; increased air-space opacification in one patient with idiopathic pulmonary fibrosis corresponding to clinical deterioration; and no appreciable change in one patient with hypersensitivity pneumonitis and one patient with sarcoidosis. In all six cases, the areas of air-space opacification on the initial and follow-up MR images were comparable to those on the corresponding HRCT scans.

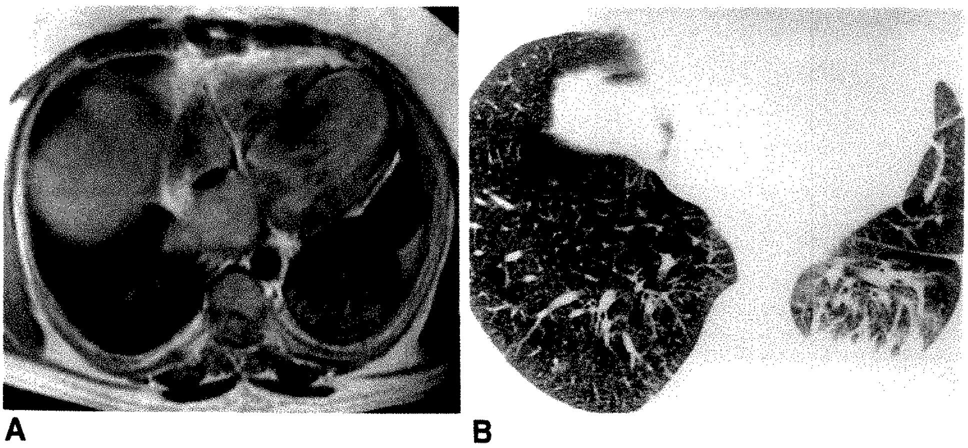

Fig. 2.—Parenchymal and pleural abnormalities in a 37-year-old man with pulmonary toxic reaction to amiodarone.

A, MR image (2400/30) shows loss of volume in left lung and curvilinear densities in left lower lobe radiating posteriorly. Also noted are mild pleural thickening and small pleural effusion.

B, High-resolution CT findings are similar to those seen on MR image.

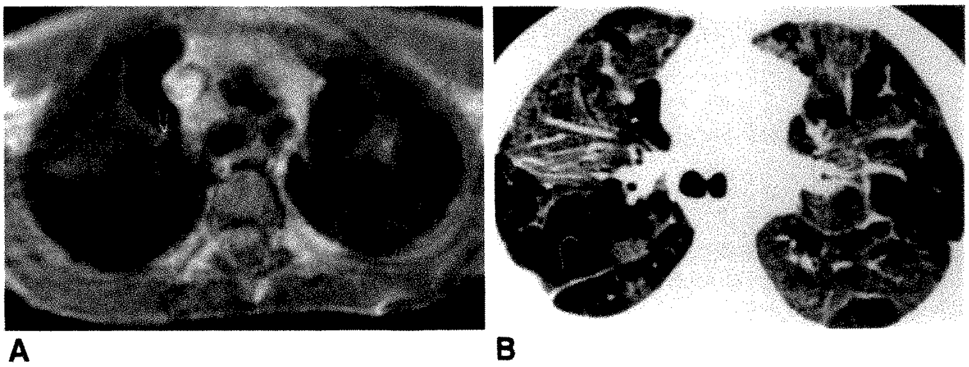

Fig. 3.—Comparison of MR imaging and CT in assessing air-space opacification in a 5-year-old boy with hypersensitivity pneumonitis.

A, MR image (1782/30) at level of great vessels above aortic arch shows extensive bilateral areas of increased signal intensity.

B, CT scan (10-mm collimation) shows distribution of areas of air-space opacification similar to that seen on MR image.

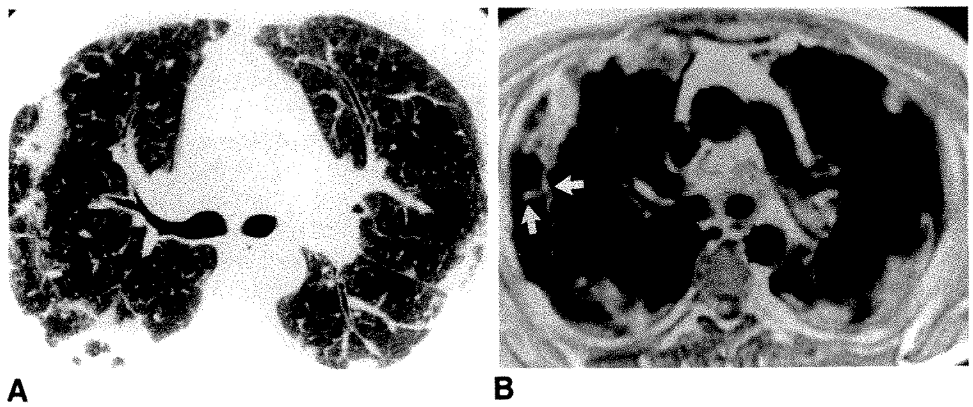

Fig. 4.—Comparison of high-resolution CT and MR imaging in assessment of air-space consolidation.

A, High-resolution CT scan at level of right upper lobe bronchus shows peripheral air-space consolidation.

B, MR image (759/20) at same level as *A* shows air-space consolidation similar to that seen on *A* and thickening of interlobular septa (*arrows*). On open lung biopsy, consolidation was centered on subpleural regions and interlobular septa.

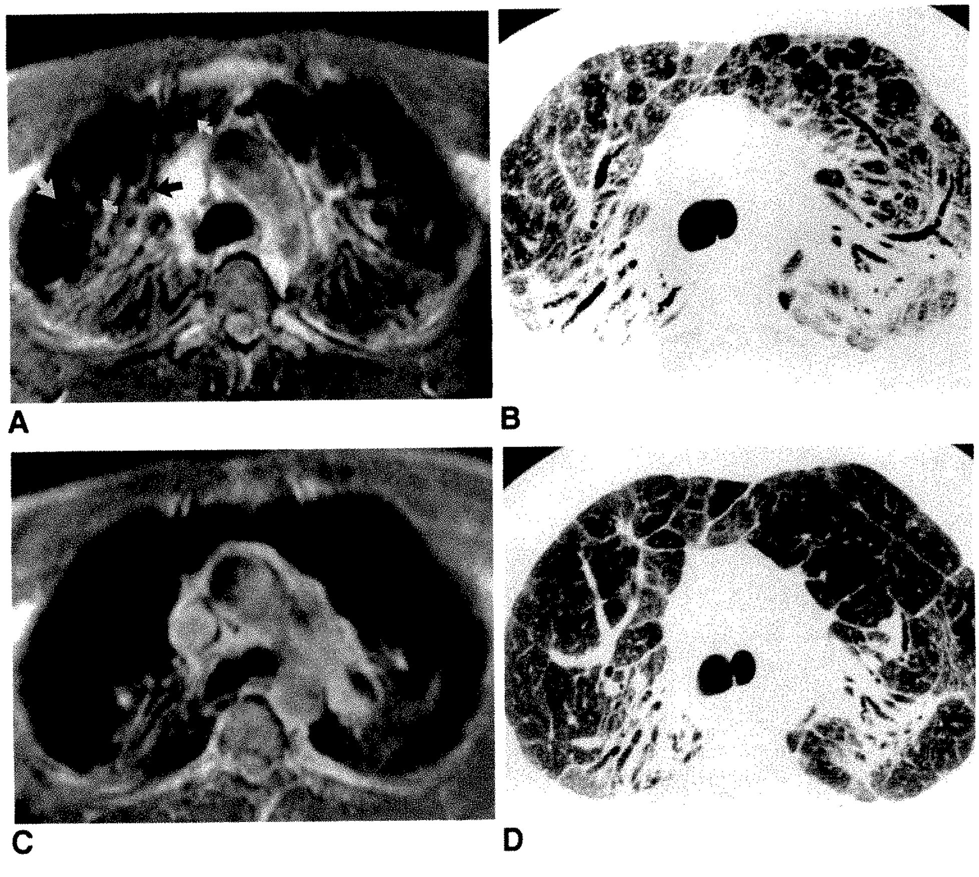

Fig. 5.—Comparison of MR images and high-resolution CT scans in assessment of parenchymal abnormalities and follow-up in a 32-year-old man with sarcoidosis.

A, MR image (2771/30) at level of tracheal carina shows extensive bilateral parenchymal abnormalities. Increased signal intensity is present particularly in posterior half of lungs and is associated with traction bronchiectasis. Note thickened interlobular septa (*straight arrows*) and thickening of centrilobular structures (*curved arrows*).

B, High-resolution CT scan at same level as *A* shows fibrosis with distortion of lung architecture and air-space opacification. Thickening of interlobular septa and milder abnormalities anteriorly are seen more easily on *B* than on *A*.

C and *D*, MR image (2571/30) (*C*) and high-resolution CT scan (*D*) obtained 6 months after *A* and *B* show marked improvement of parenchymal abnormalities after treatment.

Discussion

A number of studies have shown that by eliminating superimposition of structures, cross-sectional imaging with HRCT allows better assessment of pattern and distribution of disease than is possible with the chest radiograph [13]. Irregular linear opacities giving a reticular pattern and architectural distortion with traction bronchiectasis have been shown to reflect the presence of fibrosis [1–4]. In chronic infiltrative lung diseases, areas of air-space opacification (ground-glass opacity) have been shown to correlate with the presence of active alveolitis [5–10]. Alveolitis is thought to play a central role in the pathogenesis of pulmonary fibrosis and to represent a potentially reversible stage of disease [14, 15]. CT scans obtained after response to treatment have shown a decrease or resolution of the areas of ground-glass opacity [6–8].

MR imaging is currently inferior to CT in the anatomic assessment of lung parenchyma. Most normal lungs show little or no MR signal above background [16]. However, when the relative amount of air is decreased by the presence of pulmonary infiltrates such as edema, pneumonia, atelectasis, infarcts, and chronic infiltrative lung disease, a substantial increase in signal intensity occurs [17–19].

McFadden et al. [19] were the first to suggest a potential role for MR in patients with chronic infiltrative lung disease. They showed that the most severely affected patients had the greatest signal intensity on MR. A decrease in signal intensity seen after treatment in four patients correlated with clinical improvement. Their study included 34 patients with a variety of chronic infiltrative lung diseases. However, these patients were imaged with a 0.15-T resistive magnet without cardiac gating or respiratory compensation. McFadden et al. did not distinguish signal intensity due to fibrosis from that due to active alveolitis. Despite these limitations, they found that qualitative MR was as useful as chest radiography, pulmonary function tests, and gallium scans in predicting the clinical course and was superior to bronchoalveolar lavage.

Our study shows that conventional proton density–weighted and T1-weighted MR images are inferior to CT scans in the anatomic assessment of the lung parenchyma and may fail to show mild interstitial fibrosis. However, these MR sequences do allow the gross assessment of the pattern and distribution of disease in the majority of patients and are comparable to CT scans in the assessment of air-space opacification. Air-space opacification detected prospectively on the basis of CT and MR findings in six of our patients before open lung biopsy was shown to reflect the presence of potentially reversible active alveolitis or air-space infiltration pathologically. In six other patients, follow-up CT and MR 6–12 months after the initial studies showed equally well the improvement, stability, or deterioration of the parenchymal abnormalities.

T2-weighted MR images yielded no signal from normal or mildly infiltrated lung because of susceptibility-induced magnetic field gradients. As a result, current sequences do not allow accurate measurements of T2 relaxation times of lung parenchyma. The T2-weighted images were useful only in characterizing the T2 contrast in lesions that were densely infiltrated, solid, or fluid. They also were helpful in distinguishing dense peripheral infiltrates from small pleural effusions.

Our study had several limitations. Ideal pathologic correlation with MR findings would require open lung biopsy after every MR study, but this was not clinically warranted. However, the results do show that proton density–weighted and T1-weighted MR images are comparable to CT scans in the assessment of air-space opacification, and open lung biopsy in five patients showed that areas of air-space opacification did correspond to areas of active alveolitis. The study included MR and CT follow-up in only six patients. Clinical, radiologic, and MR follow-up in a larger group of patients will be required to determine the potential role of MR in the differentiation of irreversible from reversible parenchymal abnormalities in chronic infiltrative lung disease.

As a result of the relatively low signal intensity and the inevitable presence of some motion artifacts on all images (respiratory, cardiac), no attempt was made to quantify the T1 and T2 relaxation times. Experimental studies in animals suggest that in the early or active alveolitis stage of infiltrative lung disease, a marked increase in signal intensity occurs that is directly proportional to lung wet weight [20]. As inflammation decreases and fibrosis develops, the signal intensity and relaxation times (T1 and T2) decrease; the signal intensity of mature fibrosis is quite low [20–22]. Therefore, measurements of T1 and T2 relaxation times may be helpful in distinguishing active inflammation from irreversible fibrosis. However, at this time, technical and patient factors (i.e., patient motion) prevent accurate and reproducible assessment of these relaxation parameters.

In summary, our preliminary results suggest that although current spin-echo MR imaging is inferior to HRCT in the anatomic assessment of the lung parenchyma, it is comparable in the assessment of air-space opacification. This has been shown to correlate with disease activity in patients with chronic infiltrative lung disease. The main advantage of MR over CT is the lack of ionizing radiation. Although currently cost is a major limitation of MR, this cost is much less than that of invasive procedures, such as open lung biopsy, currently used to diagnose disease activity.

ACKNOWLEDGMENT

We thank Gordon Culham from the B.C. Children's Hospital for allowing us to include one of his patients.

REFERENCES

1. Müller NL, Miller RR. State of the art. Computed tomography of chronic diffuse infiltrative lung disease. Part 1. *Am Rev Respir Dis* **1990**;142:1206–1215
2. Müller NL, Miller RR. State of the art. Computed tomography of chronic diffuse infiltrative lung disease. Part 2. *Am Rev Respir Dis* **1990**;142:1440–1448
3. Webb WR, Stein MG, Finkbeiner WE, Im J-G, Lynch D, Gamsu G. Normal and diseased isolated lungs: high-resolution CT. *Radiology* **1988**;166:81–87
4. Meziane MA, Hruban RH, Zerhouni EA, et al. High resolution CT of the lung parenchyma with pathologic correlation. *RadioGraphics* **1988**;8:27–54
5. Müller NL, Staples CA, Miller RR, Vedal S, Thurlbeck WM, Ostrow DN. Disease activity in idiopathic pulmonary fibrosis: computed tomographic–pathologic correlation. *Radiology* **1987**;165:731–734
6. Lynch DA, Webb WR, Gamsu G, Stulbarg M, Golden J. Computed tomography in pulmonary sarcoidosis. *J Comput Assist Tomogr* **1989**;13:405–410
7. Hansell DM, Kerr IH. The role of high resolution computed tomography in the diagnosis of interstitial lung disease. *Thorax* **1991**;46:77–84
8. Vedal S, Welsh EV, Miller RR, Müller NL. Desquamative interstitial pneumonia: computed tomographic findings before and after treatment with corticosteroids. *Chest* **1988**;93:215–217
9. Klein JS, Webb WR, Gamsu G, Warnock M, Park CK. Hazy increased density in diffuse lung disease: high-resolution CT (abstr). *Radiology* **1989**;173(P):140
10. Silver SF, Müller NL, Miller RR, Lefcoe MS. Computed tomography in hypersensitivity pneumonitis. *Radiology* **1989**;173:441–445
11. Mathieson JR, Mayo JR, Staples CA, Müller NL. Chronic diffuse infiltrative lung disease: comparison of diagnostic accuracy of CT and chest radiography. *Radiology* **1989**;171:111–116
12. Grenier P, Valeyre D, Cluzel P, Brauner MW, Lenoir S, Chastang C. Chronic diffuse interstitial lung disease: diagnostic value of chest radiography and high-resolution CT. *Radiology* **1991**;179:123–132
13. Müller NL. Clinical value of high-resolution CT in chronic diffuse lung disease. *AJR* **1991**;157:1163–1170
14. Hunninghake GW, Garrett KC, Richerson HB, et al. State of the art. Pathogenesis of the granulomatous lung diseases. *Am Rev Respir Dis* **1984**;130:476–496
15. Cherniack RM, Crystal RG, Kalica AR. Current concepts in idiopathic pulmonary fibrosis: a road map for the future. *Am Rev Respir Dis* **1991**;143:680–683
16. Gamsu G, Sostman D. State of the art. Magnetic resonance imaging of the thorax. *Am Rev Respir Dis* **1989**;139:254–274
17. Moore HM, Webb WR, Müller NL, Sollitto R. MRI of pulmonary airspace disease: experimental model and preliminary clinical results. *AJR* **1986**;146:1123–1128
18. Herold CJ, Kuhlman JE, Zerhouni EA. Pulmonary atelectasis: signal patterns with MR imaging. *Radiology* **1991**;178:715–720
19. McFadden RG, Carr TJ, Wood TE. Proton magnetic resonance imaging to stage activity of interstitial lung disease. *Chest* **1987**;92:31–38
20. Vinitski S, Pearson MG, Karlik SJ, et al. Differentiation of parenchymal lung disorders with in vitro proton nuclear magnetic resonance. *Magn Reson Med* **1986**;3:120–125
21. Inch WR, Prato FS, Butland TS, Frei JV. Use of nuclear magnetic resonance to monitor lung injury by x-radiation: a preliminary study. *Respir Care* **1986**;31:388–394
22. Lee JKT, Glazer HS. Controversy in the MR imaging appearance of fibrosis. *Radiology* **1990**;177:21–22

Anatomical Lectures by Dr. William W. Keen

Stefan C. Schatzki[1]

"To draw the human figure," stated Thomas Eakins, "it is necessary to know as much as possible about it, about its structure and its movement, its bones and its muscles, how they are made and how they act." Anatomic study has been part of the academic curriculum since the beginning of formal artistic education in America. Lectures were offered as early as 1812 at the Pennsylvania Academy, and Dr. Frederick Gore King began to teach anatomy at the National Academy soon after its foundation in 1825. In 1845, Dr. Robert Watts, professor of anatomy at the National Academy, invited his art students to study with him at the medical college. In 1857, Dr. A. R. Thomas moved his lectures from the Pennsylvania Academy to a local medical school, beginning the Pennsylvania Academy's tradition of teaching scientific anatomy to art students. Dr. Thomas's Programme of Anatomical Studies was wide-ranging, including such subjects as the anatomical knowledge of the ancients, dissections of the cadaver, and finally the passions and emotions and their impact on the anatomy and expression of the face.

Dr. William W. Keen, a lecturer on surgical pathology and professor of surgery at Jefferson Medical School, was also the director of the Philadelphia School of Anatomy from 1866 to 1875. In about 1873, he introduced a course on artistic anatomy at that school and in 1876 became a lecturer in artistic anatomy at the Pennsylvania Academy of Fine Arts. Excerpts from Keen's first report to the directors of the Academy in April 1877 indicate some of the methods that he used. "I have also had an excellent male model and after showing the parts of the skeleton on the subject, I have at once demonstrated them on the living model calling the muscles into place by using dumbbells, weights, rings, etc. I have used the galvanic battery to call special muscles into contraction and thus illustrate their function. . . I have had the dissected subjects with the muscular attachments on the bone. . . . A large plaster cast of the muscles . . . has been carefully painted from the dissection of the body by Mr. Eakins. . . . I have had the skeleton and a number of plaster casts, partly my own and partly those from the antique collection." Finally, his report states, "I beg to leave to renew my former suggestion as to the opportunities for dissections." Scientific anatomy taught to art students at the Pennsylvania Academy was very similar to the course attended by medical students of the day.

In September 1879, William C. Brownell, one of the leading art critics of the time, wrote an article in Scribner's *Monthly Illustrated* discussing Thomas Eakins' teaching methods. The illustrations for Brownell's article were painted in black and white, *en grissaile*, by students at the Pennsylvania Academy. The paintings illustrated the different classes taught at the academy and included this work by Charles H. Stephens illustrating the anatomic lectures by Dr. Keen. This painting includes most of the items that Dr. Keen had listed in his 1877 report, including "an excellent male model," "the dissected subject," "the skeleton," "the plaster cast," and the "plaster from the antique collection."

This small black and white oil painting is an important document in the history of art education and has been frequently reproduced. However, very little information remains today about Charles H. Stephens. Most of what is known about this obscure artist comes from the lives of other members of his family. His brother Frank married Thomas Eakins's sister. The illustration of the women's life class in Brownell's 1879 article was painted by Alice Barber. Ten years later she married Charles Stephens, who was now a teacher of drawing and painting at the Academy. Alice Barber Stephens subsequently became a well-known illustrator and impressionistic artist. Nothing else is known about Charles Stephens except for his participation in some of the politics of the Philadelphia artistic community and the presence of a few of his illustrations in the collection of the New York public library.

The scientific anatomy instruction at the Pennsylvania Academy of Fine Arts was the framework on which Thomas Eakins built his brilliant career, which in turn led to the most illustrious era in the history of the Pennsylvania Academy.

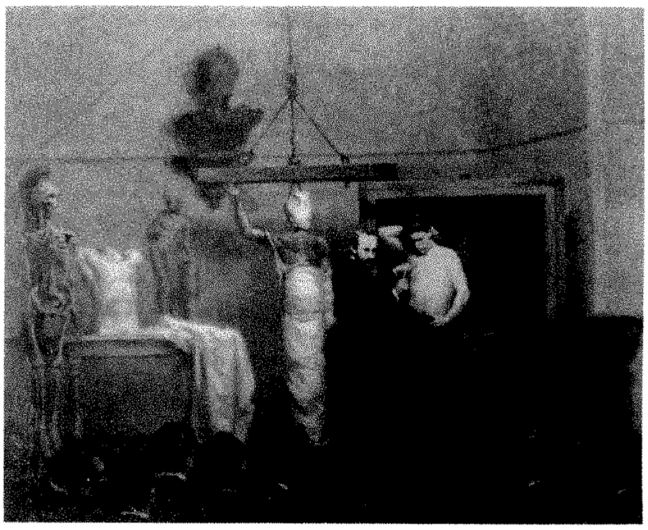

Charles H. Stephens (ca. 1855–1931). *Anatomical Lectures by Dr. William Williams Keen*, 1879. Oil on board, 8½ × 11 in. (The Pennsylvania Academy of the Fine Arts.) Gift of the artist.

---

[1] Department of Radiology, Mount Auburn Hospital, 330 Mount Auburn St., Cambridge, MA 02238.

***AJR* 158:1210, June 1992** 0361-803X/92/1586-1210 © American Roentgen Ray Society

Swyer-James Syndrome: CT Findings in Eight Patients

Aynsley D. A. Moore[1,2]
J. David Godwin[1]
Peter A. Dietrich[3]
Johny A. Verschakelen[4]
William R. Henderson, Jr.[5]

To determine the importance of chest CT findings in patients with Swyer-James syndrome (unilateral small lung with air trapping) and to compare these findings with those on chest radiographs and scintigrams, we reviewed the CT scans, chest radiographs, and scintigrams of eight patients with the syndrome. Radiographs showed unilateral hyperlucency in seven patients and bilateral asymmetric hyperlucency in one. CT showed that the hyperlucency was unilateral in only three and that hyperlucent regions on radiographs contained patches of normal lung attenuation in five patients. Conversely, in four patients, CT also showed small hyperlucencies in regions considered normal on radiographs. These lucencies usually had poorly defined margins and irregular shapes (five patients), but sometimes were peripheral, wedge shaped, and sharply demarcated (two patients). CT also showed subtle abnormalities not visible on radionuclide scans in two patients. Air trapping in hyperlucent regions was confirmed by a lack of change in volume on expiratory CT scans in five cases. Bronchiectasis was found in only three patients.

CT helps to exclude central bronchial obstruction, cysts, and vascular disease as causes of hyperlucency. By excluding central obstruction, CT may make bronchoscopy unnecessary in some patients. CT is more sensitive than radiographs and radionuclide scans in detecting hyperlucent regions and in showing their distribution. Our experience suggests that bronchiectasis is not a necessary component of the Swyer-James syndrome.

***AJR* 158:1211–1215, June 1992**

Swyer-James (Macleod's) syndrome (SJS), as originally described [1, 2], is characterized on radiographs by a unilateral small lung with hyperlucency and air trapping. The condition typically follows a viral respiratory infection in infancy or childhood [3–5]. Thus, it is a postinfectious form of bronchiolitis obliterans [6].

Few reports of the CT findings in SJS have been published [7–11]. We describe the CT findings in eight patients and compare these findings with those on plain radiographs and scintigrams.

Materials and Methods

Eight cases gathered retrospectively from several institutions were reviewed. The criteria for inclusion were (1) unilateral or asymmetric hyperlucency shown on radiographs or CT scans to be due to air trapping, (2) presumed or documented antecedent lung infection or injury, and (3) exclusion of other causes of hyperlucency by CT and clinical evaluation. The study population included four males and four females 8–44 years old (mean, 25 years). The patients were initially examined because of dyspnea ($n = 5$), cough ($n = 2$), and hemoptysis ($n = 1$).

Seven patients gave histories of previous lung disease. These included respiratory distress syndrome complicated by left-lower-lobe pneumonia in a child born prematurely, "chest infection" during infancy in two patients, pneumonia at age 1 in two patients (tuberculous in one), and pneumonia at age 7 in one. One adult was exposed to Agent Orange 3 years

Received November 20, 1991; accepted after revision January 9, 1992.

Presented at the annual meeting of the American Roentgen Ray Society, Washington, DC, May 1990.

[1] Department of Radiology, SB-05, University of Washington, Seattle, WA 98195. Address reprint requests to J. D. Godwin.

[2] Present address: Department of Radiology, Nelson Hospital, Nelson, New Zealand.

[3] Department of Radiology, Medical Center Hospital of Vermont, Burlington, VT 05401.

[4] Department of Radiology, University Hospitals K.U.L., Herestraat 49, 3000 Leuven, Belgium.

[5] Department of Medicine (Division of Infectious Diseases), University of Washington, Seattle, WA 98195.

0361–803X/92/1586–1211
©American Roentgen Ray Society

before onset of symptoms and was also a 25-pack-year cigarette smoker; he had also had left lower lobectomy because of bronchiectasis and recurrent pneumonia. The eighth patient had classic radiographic findings of SJS, but could not recall an episode of childhood infection.

Pulmonary function tests (four patients) revealed decreased forced vital capacity (FVC) in three (40–79% of predicted) and normal FVC in one (103%). The ratio of forced expiratory volume in 1 sec (FEV_1) to FVC (FEV_1/FVC) was decreased, indicating airway obstruction, in all four. The obstruction was mild in two (68% and 77%, respectively) and severe in two (44% and 54%, respectively). In all three patients in whom the residual volume (RV) and the ratio of RV to total lung capacity (RV/TLC) were measured, both values were elevated. RV was 124–176% of predicted and RV/TLC was 126–175% of predicted. Diffusing capacity (measured in two patients) was slightly decreased (75% and 90%, respectively, of predicted). Bronchoscopy (performed in four patients) revealed no obstructing lesions.

Chest radiographs obtained in inspiration were available for all eight patients. Radiographs in expiration were also available in five patients. Ventilation-perfusion radionuclide studies were available in five patients, bronchograms in three, and pulmonary angiograms in two.

CT was performed without contrast enhancement on a variety of scanners, most often a GE 9800 unit (five cases). A high-resolution technique was used in seven cases (1.5- to 2.0-mm collimation, most with high-resolution image reconstruction), at a varying number of levels. Scans were obtained in inspiration in all cases, and also in expiration in five cases.

CT scans were evaluated with particular attention to airways and lung parenchyma. Airways were evaluated for central obstruction and bronchiectasis. Parenchyma was assessed for evidence of hyperlucency (low attenuation). Hyperlucent regions were examined carefully for surrounding walls that would indicate that they were actually cysts or bullae. Air trapping was identified by a lack of change of attenuation between expiratory and inspiratory scans. In one case, air trapping was identified on an inspiratory scan by displacement of vessels and fissures away from a hyperlucent region. Coexisting abnormalities, such as bronchiectasis, were noted.

Results

Inspiratory radiographs showed bilateral hyperlucency in one case and unilateral hyperlucency in seven (five left, two right) (Fig. 1). In one case, hyperlucency was confined to the upper lung. The hyperlucent lung was smaller than the contralateral lung on inspiratory radiographs in five cases, including the four in which superimposed lower lobe disease or previous lobectomy was apparent. Hyperlucent lungs were abnormally large on inspiratory radiographs in two cases, including the one with bilateral changes. In the one case with hyperlucency confined to the right upper lung, the volume of this lung was normal overall. The mediastinum shifted away from the hyperlucent lung, and the difference in density between the two lungs increased on expiratory radiographs (Figs. 1–3) in all five cases in which they were obtained.

Ventilation-perfusion radionuclide scans showed matched defects in the lungs that were hyperlucent on radiographs, and showed some small defects that were not visible radiographically. Bronchograms showed various degrees of atelectasis and lower lobe bronchiectasis in all three cases in which they were obtained. Pulmonary arteriography showed a small right pulmonary artery with attenuated branches in the patient with bilateral hyperlucent lungs and right lower lobe atelectasis, and similar changes in the left pulmonary artery in the patient with a hyperlucent left lung and previous left lower lobectomy.

CT confirmed the low attenuation of radiographically hyperlucent lungs in all eight cases, including the one with bilateral disease. Hyperlucency was uniform and unilateral in three cases (excluding changes related to bronchiectasis and partial atelectasis in the lower lobes in two). CT scans also showed regions of low attenuation in three lungs that appeared normal on radiographs (Figs. 1 and 2). In two of these three cases, CT showed hyperlucent regions that were not detected on radionuclide scans. Abnormalities on CT scans were more pronounced in the lungs that manifested hyperlucency on radiographs.

In five cases, all with bilateral hyperlucency on CT scans, normal and low-attenuation regions were seen together in the same lung. Islands of normal lung attenuation were present in regions that were predominantly hyperlucent (Figs. 1 and 2), and patchy hyperlucency was present in relatively spared regions (Figs. 1 and 2). Lucent regions with poorly defined margins and various shapes were seen in all five cases. In two cases, several of the lucencies were peripheral, wedge shaped, and sharply demarcated. The boundaries of some hyperlucent regions corresponded to interlobular septa.

In all eight cases, CT showed that the lucent regions had no surrounding walls, indicating that they were not bullae or cysts. Lung vessels were thin and sparse within the hyperlucent regions in all cases (Fig. 3). In two cases, some moderately large regions without visible lung vessels were observed, but there were no visible walls to indicate that the lucent regions were bullae.

Air trapping was found in all five cases in which inspiratory and expiratory scans were obtained. In all, the mediastinum shifted contralaterally on expiration (Fig. 3).

Expiratory CT scans showed regions of hyperlucency more dramatically than inspiratory scans did (Figs. 1–3), but in only one case did they show more extensive disease than was visible on the inspiratory scans. On all expiratory CT scans, normal lung increased in attenuation and the caliber of vessels increased, but diseased lung showed little change.

Coexisting lung abnormalities were present in seven cases. Atelectasis was present in the ipsilateral lower lobe in four cases, with associated bronchiectasis in three of these cases. Bronchiectasis was also present in the hyperlucent upper lobe in one of these cases. Small foci opacities, most likely chronic infection or residual scars from previous pneumonia, were found in the hyperlucent lung in five cases and in the contralateral lung in three. No evidence of central bronchial obstruction was shown by CT scan in any patient.

Discussion

We reserve the term Swyer-James syndrome for cases in which radiographs show asymmetric or patchy hyperlucency and air trapping when postinfectious bronchiolitis obliterans is documented or suspected as the most likely cause. How-

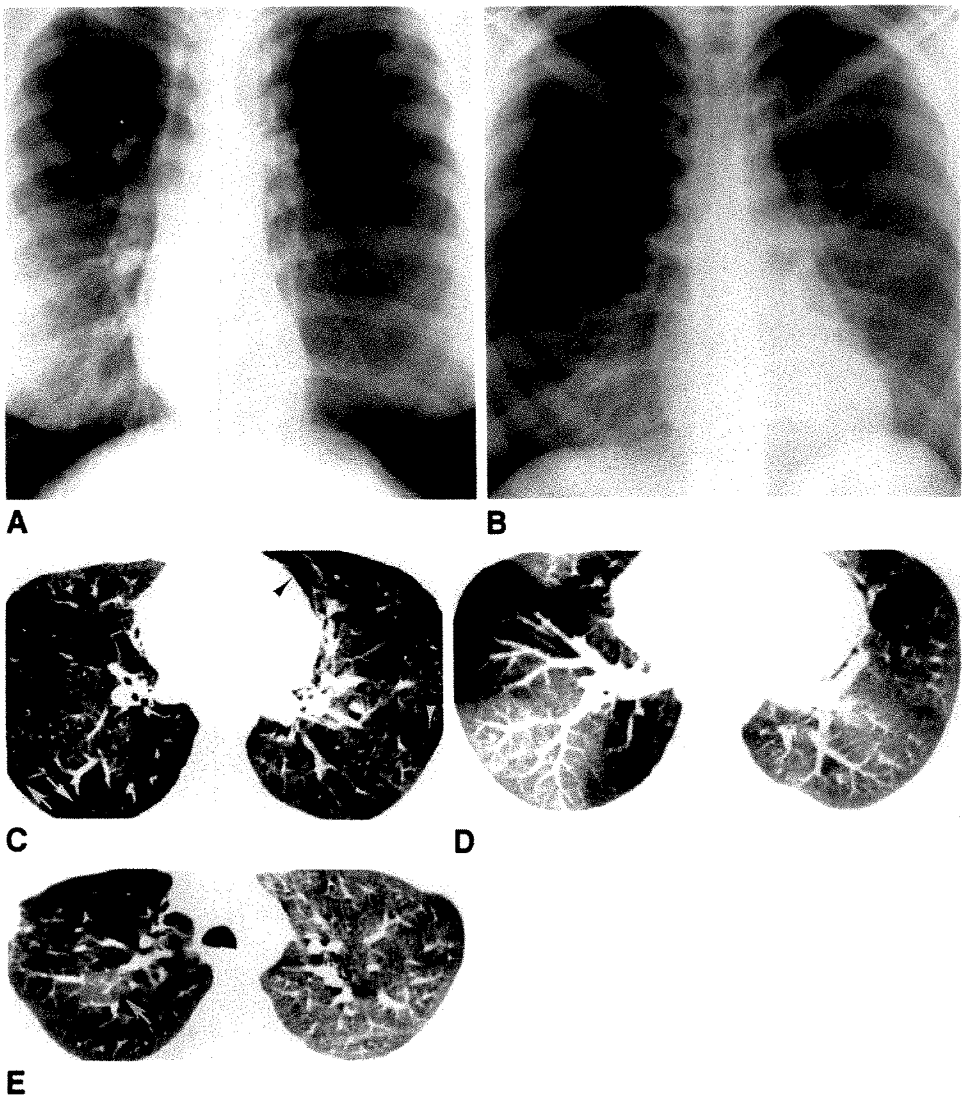

Fig. 1.—22-year-old woman with Swyer-James syndrome has mild dyspnea on exertion.
A, Inspiratory radiograph shows hyperlucency and sparse, attenuated vessels in right upper lung.
B, Expiratory radiograph shows no change in volume of hyperlucent region and shows shift of mediastinum toward left; both findings indicate air trapping. Attenuation and sparsity of vessels in hyperlucent region are accentuated on expiration.
C, Inspiratory CT scan (1.5-mm collimation) shows hyperlucent right lower lobe containing island of normal lung marginated by interlobular septa (*arrows*). Vessels in hyperlucent region are sparse and attenuated. Subtle, less clearly demarcated hyperlucent regions are present in left lung (*arrowheads*).
D, Expiratory CT scan a few millimeters lower shows clearer demarcation and greater attenuation differences between normal and hyperlucent lung on both sides.
E, Expiratory CT scan shows hyperlucent right lung apex containing a small central patch (*arrow*) of more normal lung attenuation, which is partly defined by an interlobular septum. Lung vessels are smaller in caliber than corresponding ones on left.

ever, bronchiolitis obliterans has many other causes, including nonviral infections, aspiration, toxic fumes, and organ transplantation [5, 6].

SJS is uncommon. Gosink et al. [12] found only two cases of hyperinflation in 52 patients with bronchiolitis obliterans. In another series, SJS developed in only three of 69 children with adenoviral lung infection [13]. The diagnosis is usually based on radiologic and clinical findings rather than on the results of pathologic examination. When pathologic specimens have been examined, they have shown bronchiolitis obliterans with various degrees of chronic inflammation, fibrosis, and dilatation of airways and air spaces distal to the obstructed bronchioles [1, 5, 14]. The air trapping results from gas entering the air spaces by collateral air drift but being unable to exit because of the bronchiolar obstruction [14]. In diagnosing SJS, the clinician needs to exclude other causes of air trapping [6], such as obstructing tumor or foreign body. We believe that CT can substitute for bronchoscopy or bronchography in excluding central obstruction.

Bronchiectasis is present in some cases diagnosed as SJS, and there are several explanations for this. First, bronchiolitis obliterans can cause atelectasis or scarring that in turn leads to bronchial dilatation [4, 13–15]; when bronchiolitis is the primary process, one expects the air trapping to be more

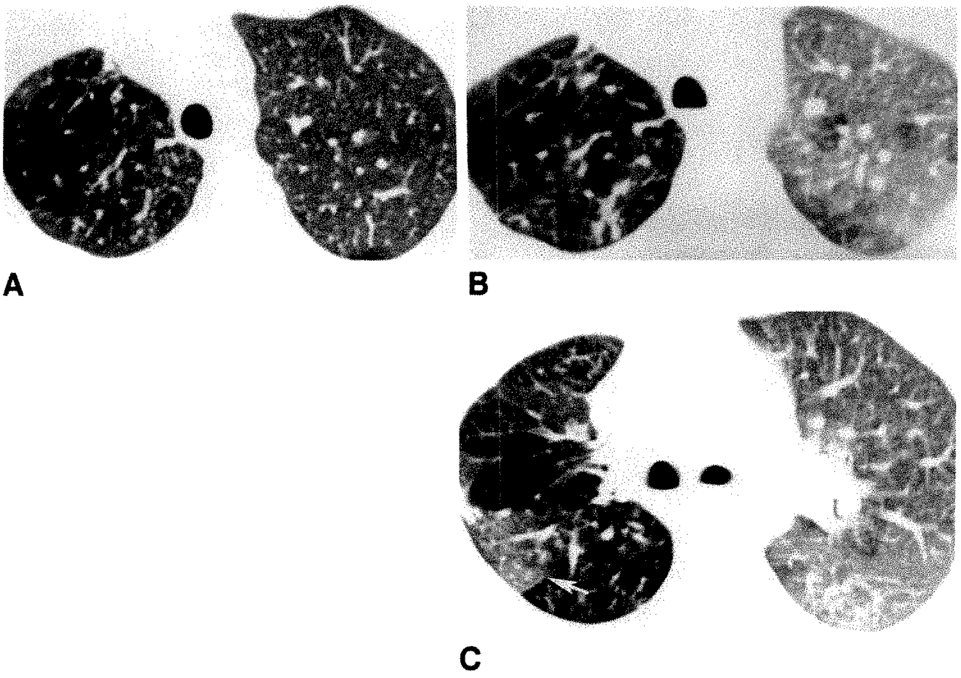

Fig. 2.—30-year-old woman with histologically proved bronchiolitis obliterans in right upper and middle lobes.

A, Inspiratory CT scan shows patchy hyperlucency in right lung apex. Patient also had right lower lobe bronchiectasis and atelectasis.

B, Expiratory CT scan better shows patchiness of right upper lobe hyperlucent regions. As in Fig. 1, boundaries between hyperlucent and normal lung tissue may be interlobular septa. Patches of hyperlucency are seen in left lung.

C, Expiratory CT scan at lower level shows patch of normal lung (*arrow*) within hyperlucent right upper lobe.

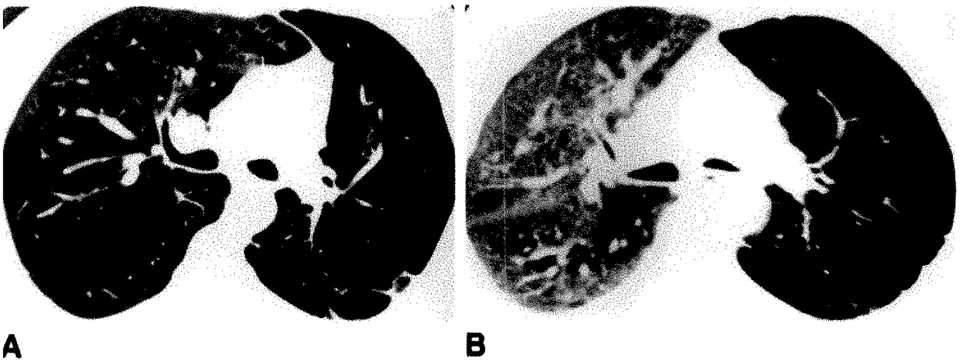

Fig. 3.—30-year-old man with Swyer-James syndrome involving left lung.

A, Inspiratory CT scan shows hyperlucency and small size of left lung. Vessels are sparse and attenuated.

B, Expiratory CT scan shows shift of mediastinum back to midline and no change in left lung attenuation.

extensive than any associated bronchiectasis. Second, bronchiectasis can cause chronic infection that spreads peripherally to small airways, leading to obliteration [6, 15–19]; when bronchiectasis is the primary process, the air trapping should be limited to lung segments with demonstrable bronchiectasis. Third, the initiating viral infection might damage both bronchioles and bronchi simultaneously [14, 19]; the early result is air trapping, reflecting bronchiolar obstruction, and bronchiectasis follows over weeks and months [4, 14], often promoted by secondary bacterial infection [16].

In a recent series, bronchiectasis, sometimes severe, was found in all nine cases of SJS examined by CT [10], but in our series, bronchiectasis occurred in only three of the eight cases. We speculate that some of the patients in the previous series might have had bronchiectasis as the primary disease and bronchiolitis obliterans as a secondary complication, whereas the patients in our series who had no bronchiectasis had primary bronchiolitis. The difference between the two series makes clear that bronchiectasis is not an invariable finding in SJS.

Radiographic, Scintigraphic, and CT Findings

On radiographs, the hyperlucency is usually confined to one lobe or lung, even though bronchography and radionuclide scans show that the abnormality is often patchy and bilateral [3, 4]. Radiographs showed unilateral disease in seven of our cases and bilateral disease in one, but both radionuclide and CT scans showed that radiographs underestimated the extent of disease.

Radionuclide ventilation scans show delayed entry and washout in regions of air trapping [20]. Perfusion and ventilatory abnormalities are matched. Unsuspected regions of bronchiolitis in the contralateral lung are often demonstrated [3], as in two of our cases.

CT showed hyperlucent regions in both lungs in five of our patients, whereas radiographs showed bilateral changes in only one. CT visualized regions of air trapping not detected by radionuclide scans in two cases. Thus, CT provided the best determination of extent and distribution of disease. In addition, CT in many cases showed islands of normal tissue within generally hyperlucent regions. This patchiness in distribution and the small size of many of the spared or affected regions reflect that the obstruction is in the small airways rather than in segmental or larger bronchi.

As on radiographs, air trapping was manifest on CT scans as persisting low attenuation of lung tissue in affected regions at end exhalation. Low attenuation without air trapping might represent compensatory overexpansion caused by lobectomy or atelectasis. Compensatory overexpansion was a consideration in five of our cases because four had ipsilateral lower lobe atelectasis and one had undergone lower lobectomy. However, CT scans or radiographs obtained on expiration showed air trapping in each of these cases, indicating that airway obstruction was indeed present.

CT helps in the differential diagnosis of hyperlucency. Contiguous scans effectively exclude central airway obstruction. Bullae and cysts have clearly defined walls. Vascular diseases can usually be excluded. In the cases of pulmonary embolism and congenital interruption of a pulmonary artery that we have examined, CT has shown a lesser degree of lung hyperlucency than occurs in SJS. Furthermore, there is no air trapping, and the vascular anomaly is clearly shown. Diseases of small airways, such as asthma and chronic bronchitis, probably cannot be distinguished from SJS by CT.

The experience of Marti-Bonmatí et al. [10] differs from ours not only in that they found bronchiectasis in all nine cases but also that they found bilateral disease in only one case, whereas we found it in five of eight. A possible explanation beyond differences in patient populations is that small patches of bilateral disease were missed because these investigators used wider collimation (8–10 mm) than we did and thus did not achieve high resolution.

From this preliminary experience with CT in SJS, we have found CT more sensitive than radiography and scintigraphy in detecting hyperlucent lung regions and superior in showing their extent and distribution. CT is helpful in excluding other causes of hyperlucency, and, by excluding central obstruction, it can spare some patients bronchoscopy. It can also delineate accompanying conditions such as bronchiectasis.

REFERENCES

1. Swyer PR, James GCW. A case of unilateral pulmonary emphysema. *Thorax* **1953**;8:133–136
2. MacLeod WM. Abnormal transradiancy of one lung. *Thorax* **1954**;9:147–153
3. Daniel TL, Woodring JH, Vandiviere MH, Wilson HD. Swyer-James syndrome: unilateral hyperlucent lung syndrome. *Clin Pediatr* (Phila) **1984**;23:393–397
4. Reid L, Simon G, Zorab PA, Seidelin R. The development of unilateral hypertransradiancy of the lung. *Respir Med* **1967**;61:190–194
5. Reid L, Simon G. Unilateral lung transradiancy. *Thorax* **1962**;17:230–239
6. McLoud TC, Epler GR, Colby TV, Gaensler EA, Carrington CB. Bronchiolitis obliterans. *Radiology* **1986**;159:1–8
7. Narita H, Kikuchi T, Sukekawa K, Yoshida J, Fukui A. A case of Swyer-James syndrome [in Japanese]. *Kokyu To Junkan* **1987**;35:341–345
8. Ikezoe J, Morimoto S, Arisawa J, Kuriyama K, Akira M. CT of unilateral hyperlucent lung (Swyer-James syndrome) [in Japanese]. *Jpn J Clin Radiol* **1985**;30:825–828
9. Shimamoto Y, Shimamoto H, Matsuura Y, et al. A case of Swyer-James syndrome, with reference to pathophysiologic and etiologic aspect. *Hiroshima J Med Sci* **1986**;35:163–166
10. Marti-Bonmati L, Perales RF, Catala F, Mata JM, Calonge E. CT findings in Swyer-James syndrome. *Radiology* **1989**;172:477–480
11. Norton KI, Mendelson DS, Hodes D, Kattan M. Computed tomography findings in the Swyer-James syndrome. *Clin Imaging* **1989**;13:48–50
12. Gosink BB, Friedman PJ, Liebow AA. Bronchiolitis obliterans. Roentgenologic-pathologic correlation. *AJR* **1973**;117:816–832
13. Gold R, Wilt JC, Adhikari PK, MacPherson RI. Adenoviral pneumonia and its complications in infancy and childhood. *Can Assoc Radiol J* **1969**;20:218–224
14. Becroft DMO. Bronchiolitis obliterans, bronchiectasis, and other sequelae of adenovirus type 21 infection in young children. *J Clin Pathol* **1971**;24:72–82
15. Thurlbeck WM. Chronic airflow obstruction. In: Thurlbeck WM, ed. *Pathology of the lung*. New York: Thieme Medical, **1988**:519–575
16. Barker AF, Bardana EJ. Bronchiectasis: update of an orphan disease. *Am Rev Respir Dis* **1988**;137:969–978
17. Culiner MM. Obliterative bronchitis and bronchiolitis with bronchiectasis. *Chest* **1963**;44:351–361
18. Reid L. Reduction in bronchial subdivision in bronchiectasis. *Thorax* **1950**;5:233–247
19. Whitwell F. A study of the pathology and pathogenesis of bronchiectasis. *Thorax* **1952**;7:213–239
20. O'Dell CW, Taylor A, Higgins CB, Ashburn WL, Schillaci RF, Alazraki NP. Ventilation-perfusion lung images in the Swyer-James syndrome. *Radiology* **1976**;121:423–426

Book Review

Computed Tomography and Magnetic Resonance of the Thorax, 2nd ed. By David P. Naidich, Elias A. Zerhouni, Stanley S. Siegelman, and Jerald P. Kuhn. New York: Raven, 606 pp., 1991. $125

This is a great new textbook. The authors have written a useful, informative, authoritative, and complete text on CT and MR of the chest. It is more than an update, more than the usual second edition rewrite. It is a completely new textbook. The second edition has new illustrations, new drawings, new charts, and new references. Many of the references are from 1990. The authors set out to include the "remarkable advances in our understanding and use of CT and MR to evaluate thoracic disease."

The book starts with a lucid chapter explaining the principles and techniques of thoracic CT and MR. This is an important part of the book and should not be overlooked, as many references throughout the text are made to techniques discussed in this chapter. In this edition, the chapter on the mediastinum includes information on the aorta and great vessels and provides an excellent discussion of mediastinal anatomy and of pathologic changes. Liberal use is made of studies that illustrate the great potential of MR for imaging mediastinal abnormalities. The chapter on the airways has been updated with clearer pictures and includes discussions on the role of CT in bronchiectasis and hemoptysis and how CT findings correlate with findings from fiberoptic bronchoscopy. Lobar collapse and the role of MR in differentiating central tumor from collapsed lung are discussed. The chapter on the hila has been updated by adding information on faster scanning techniques, better contrast boluses, and the impact MR has had on the evaluation of the hila. The MR images are so good that the usual photographs of injected anatomic specimens are not needed or included. A whole new chapter has been added on CT and MR in the diagnosis and staging of lung cancer. MR imaging of lung cancer, including the pros and cons of using this technique, are discussed. Evaluation of solitary pulmonary nodules including use of a phantom, is covered, as well as evaluation of other focal lung abnormalities, from metastases to hamartomas.

Diffuse lung disease and the use of high-resolution CT are covered, with an excellent discussion and images. The chapter on the pleura and chest wall includes more than the first edition on the imaging of asbestos-related diseases, and the number of illustrations of diseases of the chest wall has been greatly expanded. Included is a section on the normal axilla. The chapter on the diaphragm is good, with a helpful discussion on the differentiation of peridiaphragmatic fluid collections. An entirely new chapter, an excellent review, has been added on the thorax in children. Another new chapter has been added on imaging the heart. Because of the advancements in MR imaging, this is an important new area for the thoracic radiologist to become familiar with. This chapter provides the basis for understanding the anatomy and techniques for MR imaging of the heart.

This textbook should be read by anyone involved in imaging the thorax. Radiologists, thoracic surgeons, and pulmonologists would benefit from reading this textbook. It should be in every radiology department. I can find nothing wrong about this text, and I enthusiastically recommend it to anyone involved with chest diseases.

Robert D. Tarver
Wishard Memorial Hospital
Indiana University Medical Center
Indianapolis, IN 46202

CT Findings in Lymphangitic Carcinomatosis of the Lung:

Correlation with Histologic Findings and Pulmonary Function Tests

Takeshi Johkoh[1]
Junpei Ikezoe[1]
Noriyuki Tomiyama[1]
Tomohumi Nagareda[2]
Nobuaki Kohno[1]
Noriyuki Takeuchi[1]
Hidetoshi Yamagami[1]
Shoji Kido[1]
Shodayu Takashima[1]
Jun Arisawa[1]
Takahiro Kozuka[1]

The purpose of this study was to analyze the CT findings in lymphangitic carcinomatosis and to determine how the abnormalities seen on CT correlated with histologic findings and the results of pulmonary function tests. Accordingly, we reviewed CT findings in 20 proved cases and correlated them with histologic findings and with results of pulmonary function tests (available in 11). Special attention was given to the extent and degree of thickening of the peripheral and/or axial interstitium as seen on CT. In 15 of 20 patients, CT scans showed marked thickening of axial interstitium and subtle or no thickening of peripheral interstitium (four diffuse and 11 localized). In three cases, CT showed marked thickening of both axial and peripheral interstitium (two diffuse and one localized). In two cases, CT showed marked thickening of peripheral interstitium and subtle or no thickening of axial interstitium (one diffuse and one localized). These CT findings correlated with the pathologic findings. Marked impairment of vital capacity and alveolar-arterial oxygen gradient was observed in three patients (one with diffuse and peripheral interstitial thickening and two with diffuse and both peripheral and axial interstitial thickening).

We conclude that CT findings in patients with lymphangitic carcinomatosis are variable and that marked impairment of pulmonary function occurs in patients with diffuse and peripheral interstitial thickening. Marked impairment of pulmonary function can be predicted from CT findings.

***AJR* 158:1217–1222, June 1992**

CT findings in patients with pulmonary lymphangitic carcinomatosis accurately show the fine details of the peripheral pulmonary structure in relation to the secondary pulmonary lobules [1–10]. However, some cases of lymphangitic carcinomatosis are difficult to diagnose on the basis of CT scans. This may be due to variation in the CT findings, including (1) focal, diffuse, or asymmetric distribution of the disease; (2) preferential involvement of the peripheral (interlobular septal, subpleural) or axial (bronchovascular) compartments; or (3) variation in severity of the disease [11–15]. Some patients have marked impairment of pulmonary function beginning early in the disease when no radiographic abnormalities are apparent, while others have impairment of pulmonary function only in the late stage.

To clarify the spectrum of CT findings in lymphangitic carcinomatosis and to determine which CT abnormalities are related to impairment of pulmonary function, we reviewed CT findings in 20 patients with histologically proved pulmonary lymphangitic carcinomatosis. We classified the CT findings according to the degree of involvement of the peripheral and/or axial portions of the lung. In 11 of the 20 cases, the CT findings were correlated with the results of pulmonary function tests.

Materials and Methods

We retrospectively reviewed the chest CT scans of 11 men and nine women 28–84 years old (mean, 56 years) who had proved pulmonary lymphangitic carcinomatosis. None of the

Received October 16, 1991; accepted after revision January 2, 1992.

[1] Department of Radiology, Osaka University Medical School, 1-1-50, Fukushima, Fukushima-ku, Osaka 553, Japan. Address reprint requests to T. Johkoh.

[2] Department of Pathology, Osaka Prefectural Hospital, 3-1-56, Bandai-Higashi, Sumiyoshi-ku, Osaka 558, Japan.

0361-803X/92/1586-1217
© American Roentgen Ray Society

atients had a history of tobacco use or underlying pulmonary diseases. The primary lesions in these 20 patients were bronchogenic arcinoma (10), breast carcinoma (three), adenocarcinoma of the tomach (two), nasopharyngeal carcinoma (two), cholangiocarcinoma ɔne), malignant melanoma of the skin (one), and hemangiopericytoma ɔne). Thirteen of the 20 cases were adenocarcinomas. Histologic roof of the diagnosis of lymphangitic carcinomatosis was available ı all 20 patients (16 transbronchial biopsy, four autopsy).

CT studies were performed with a CT/T 8800 scanner (General lectric Medical Systems, Milwaukee, WI) or a CT 9000 or Quantex canner (Yokogawa Medical Systems, Tokyo). Contiguous 1-cm-ollimation scans were obtained from the lung apices to the diahragm by using the standard algorithm, and additional 1.5- or 2.0-ım-collimation scans were obtained at selected levels specific to ach case. These thin-section images were reconstructed by using igh-resolution algorithms (bone algorithm, high-resolution CT). All cans were photographed at windows and levels appropriate for the ıng parenchyma (level, −550, −700 H; window, 1000–1500 H).

In 11 patients, either pulmonary function tests were done or arterial lood gases were measured; nine patients had both. All laboratory ɜsts and measurements and CT were performed within a 5-day eriod. Vital capacity was measured with a spirometer fixed to the ıouth. Forced vital capacity and forced expiratory volume at 1 sec lso were measured by using a pneumotachygraph with an integrated ow signal display volume meter. Vital capacity and forced expiratory olume at 1 sec were considered normal if they were more than 80% nd 70%, respectively, of predicted values. Blood gases and the lveolar-arterial oxygen gradient were measured in room air when atients were resting.

High-resolution CT scans were independently analyzed by three adiologists with knowledge of the diagnoses. The radiologists were sked to determine the following: (1) Did the disease involve predomıantly the peripheral or axial compartment? (2) How extensive were ıe findings? (3) Was the involvement diffuse or localized? Disagreements among the three radiologists were discussed and a consensus reached. The abnormalities were then classified according to the degree of involvement of the peripheral and/or axial portion of the lung, and the relationship between these CT findings and the results of pulmonary function tests were analyzed.

Pathologic and CT correlation was performed in all patients, especially in two patients for whom autopsy materials were available, paying special attention to the degree of involvement of the peripheral and/or axial interstitium of the lung. Survival time also was correlated with CT findings in 10 patients for whom this information was available.

Results

High-resolution CT scans showed bilateral diffuse interstitial changes in seven patients. The disease was confined to one lobe in seven, to two lobes in three, and to one lung in three. The predominant finding on CT scans was thickening of the bronchovascular bundle (19 patients). CT scans in 17 patients showed thickening of interlobular septa.

Four of 20 patients had discrete nodules on CT. Eight had pleural effusion and 18 had hilar lymphadenopathy. CT in one patient showed thickened interlobular septal lines adjacent to the chest wall.

The CT findings were classified on the basis of the degree of involvement of the interlobular septa and bronchovascular bundles (Fig. 1). In 15 patients, CT scans showed marked thickening of bronchovascular bundle (axial interstitium) and subtle or no thickening of the interlobular septa (peripheral interstitium). Three of the 15 had no evidence of thickening of the interlobular septa, and the other 12 had localized and

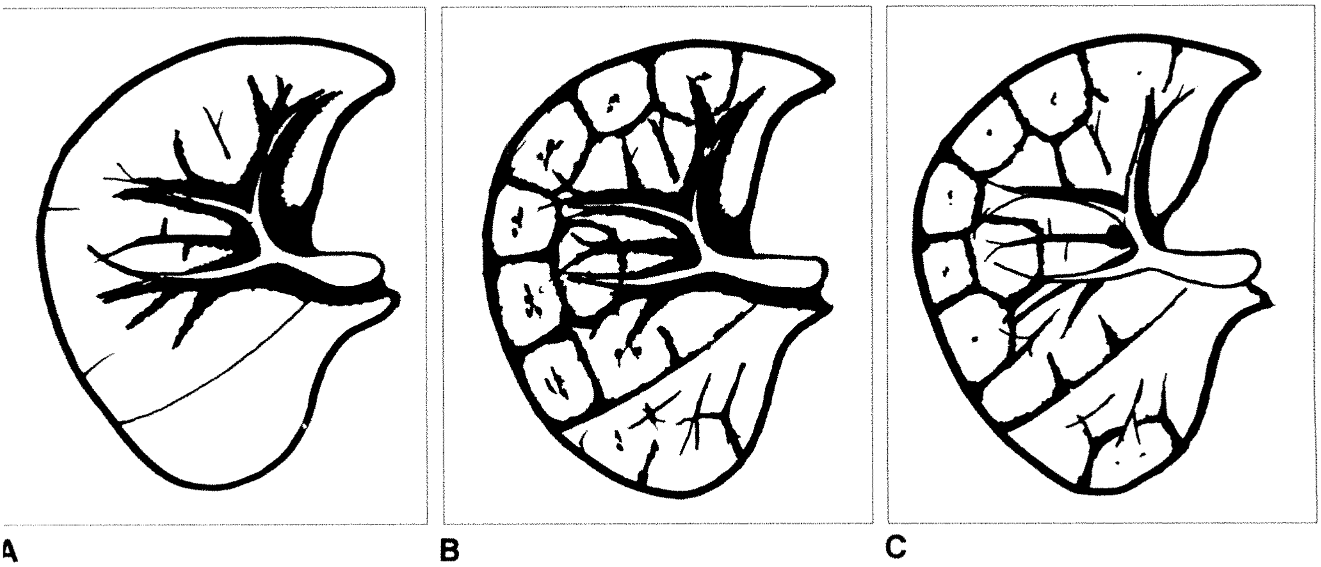

Fig. 1.—Schematic illustrations of CT types of lymphangitic carcinomatosis.

***A*, Uneven thickening of bronchovascular bundles is observed from hilum to periphery, but thickened peripheral interlobular septal lines are subtle or ıot shown.**

***B*, Both thickened peripheral interlobular septa and thickening of bronchovascular bundles are observed.**

***C*, Thickened peripheral interlobular septa and polygonal lines are prominent, and thickening of bronchovascular bundles is subtle or not shown.**

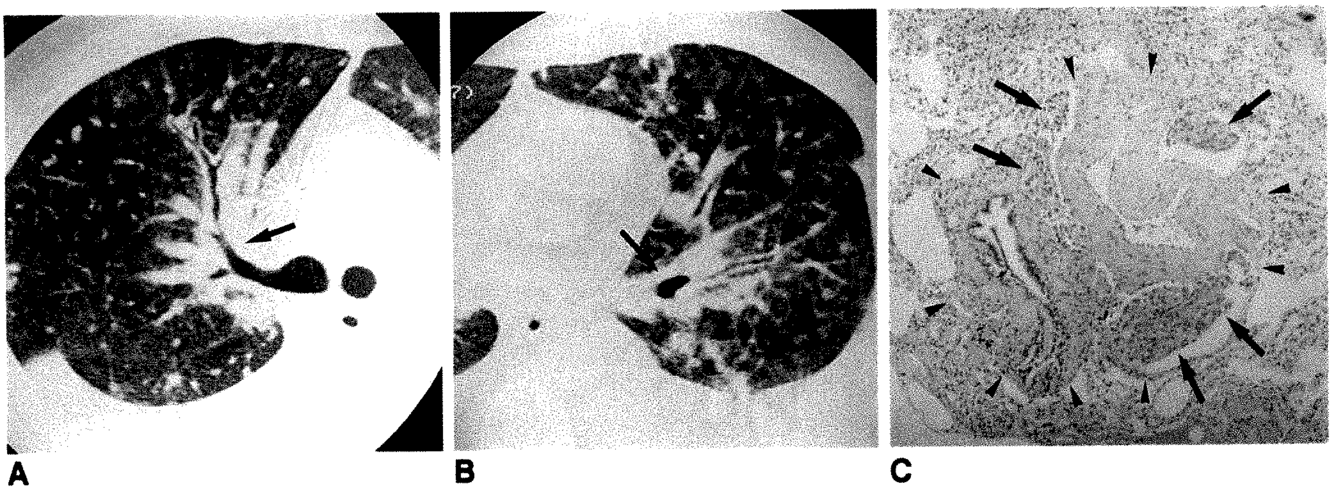

Fig. 2.—36-year-old man with lymphangitic carcinomatosis with thickening of bronchovascular bundle and subtle thickening of interlobular septa. Primary lesion was bile duct carcinoma.

A, CT scan of right lung shows marked thickening of bronchovascular bundles from hilum to periphery (*arrow*). Thickening of interlobular septa is not seen at all. Pleural effusion is present.

B, CT scan of left lung shows uneven thickening of bronchovascular bundles (*arrow*) and subtle thickening of peripheral interlobular septa (*arrowheads*).

C, Photomicrograph of transbronchial biopsy specimen shows thickening of bronchovascular interstitium (*arrowheads*). Lymphatic vessels are occluded by clusters of tumor cells (*arrows*). (Original magnification ×40)

faint thickening of the interlobular septa (Fig. 2). Four of the 15 had diffuse disease, and the other 11 had localized disease. In three patients, CT showed marked thickening of both bronchovascular and interlobular septa. Two had diffuse disease and one had focal disease (Fig. 3). All 18 of these patients had bilateral hilar lymphadenopathy. Six of the 15 with axial interstitial thickening and all three with both axial and peripheral interstitial thickening had pleural effusion. In the remaining two patients, CT showed marked thickening of the interlobular septa and subtle or no thickening of the bronchovascular bundle. One had localized disease with a metastatic lesion in the chest wall. In this case, thickening of the bronchovascular bundle was not observed. The other patient had diffuse disease in which faint thickening of the bronchovascular bundle was found (Fig. 4). These two patients had no hilar lymphadenopathy and no pleural effusion.

Autopsy specimens were available for one patient in whom both axial and peripheral interstitial thickening was observed on CT and one in whom peripheral interstitial thickening was seen on CT. Transverse sections of an inflation-fixation lung in the first patient clearly showed both peribronchovascular and interlobular interstitial thickening (Fig. 3). In the latter patient, microscopic examination showed marked interlobular and subpleural interstitial desmoplastic thickening with many lymphatic vessels occluded by tumor cells, and faint thickening of the alveolar wall and peribronchovascular interstitium due to desmoplastic reaction (Fig. 4). In these cases, the CT findings clearly reflected the pathologic findings.

The vital capacity markedly decreased in all three with both axial and peripheral interstitial thickening and in one patient with peripheral interstitial thickening, in which thickened peripheral interlobular septal lines and polygonal lines were marked. Forced expiratory volume at 1 sec was normal in all 11 patients who had pulmonary tests. However, all 11 showed widening of alveolar-arterial oxygen gradients. Three of four patients with peripheral interstitial thickening, or both axial and peripheral interstitial thickening, had marked widening of alveolar-arterial oxygen gradients, as did four of seven with axial interstitial thickening. No correlation between the widening of alveolar-arterial oxygen gradients and the types of CT abnormalities was found. Both a marked decrease of vital capacity and a striking widening of alveolar-arterial oxygen gradients were observed in three of six patients with diffuse disease who had peripheral interstitial thickening or both axial and peripheral interstitial thickening. These findings could not be properly analyzed for statistical significance because of the small number of patients.

In five patients with peripheral interstitial thickening or both axial and peripheral interstitial thickening, two had breast carcinomas, two had gastric carcinomas, and one had bronchogenic carcinoma. Of the 15 patients with axial interstitial thickening, nine had bronchogenic carcinomas (the most frequent primary lesion). Eight of the 10 with bronchogenic carcinoma had localized disease and the other two had diffuse disease.

The mean survival time of the 10 patients whose survival times were available was 142 days. One patient with diffuse disease and peripheral interstitial thickening died 12 days after CT examination (14 days after histologic diagnosis was confirmed). One patient with diffuse disease and both peripheral and axial interstitial thickening died 18 days after CT examination (11 days after histologic diagnosis was confirmed), and the patient with localized disease and both peripheral and axial interstitial thickening died 4 weeks after CT examination. The cause of death in these three cases was respiratory failure. Seven patients with diffuse or localized profusion and axial interstitial thickening died 3–9 months after CT examination.

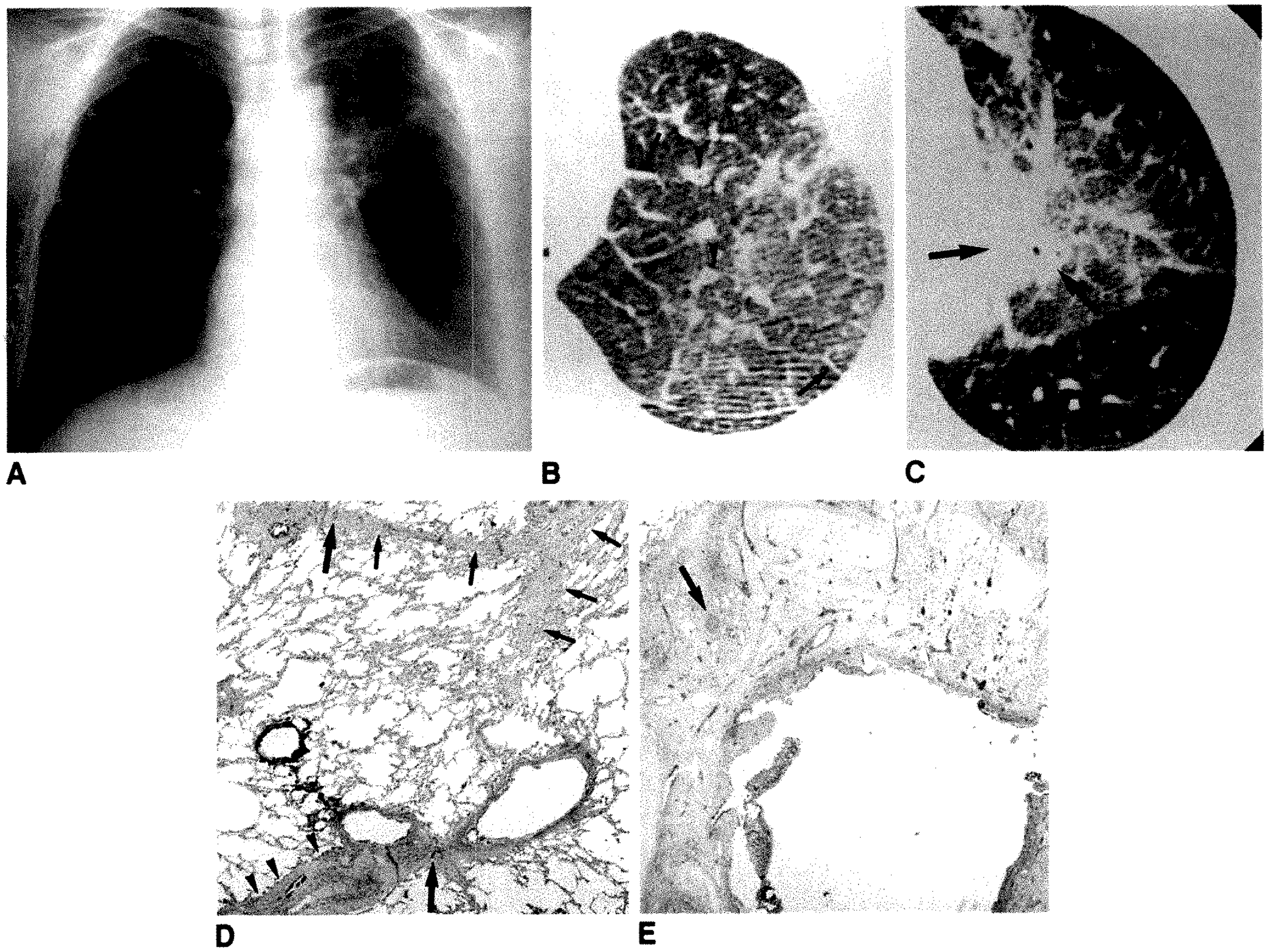

Fig. 3.—63-year-old woman with lymphangitic carcinomatosis with thickening of both bronchovascular and interlobular interstitium. She had right-sided mastectomy for breast cancer 3 years earlier.

***A*, Posteroanterior chest radiograph shows perihilar haziness suggestive of bronchovascular thickening in left upper lobe of lung. Lymphadenopathy in left hilum is also present.**

***B*, CT scan shows thickening of interlobular septa and polygonal lines (*arrows*), as well as thickening of bronchovascular bundles from hilum to periphery (*arrowheads*).**

***C*, CT scan at level of left hilum shows marked thickening (*arrows*) of bronchovascular interstitium.**

***D*, Photomicrograph of autopsy specimen shows thickening of interlobular septa (*small arrows*) and perivascular interstitium (*arrowheads*) caused by reactive fibrous change. Some small lymphatic vessels are occluded by tumor cells (*large arrows*). (Original magnification ×40)**

***E*, Photomicrograph of more central bronchial wall shows thickening of bronchial wall. Some lymphatic vessels are occluded by tumor cells (*arrow*).**

Discussion

The high-resolution CT findings and the distribution of pulmonary lymphangitic carcinomatosis varied. For this reason, we classified the CT findings according to the relative prominence of involvement within the peripheral (interlobular and subpleural) or axial (peribronchovascular) interstitial compartments.

Histologically, the essential findings for pulmonary lymphangitic carcinomatosis are thickening of the interlobular septa and thickening of the peribronchovascular interstitium; these are caused by infiltration of tumor cells into the lymphatic vessels [1–4, 15–20]. These pathologic findings correlate well with the two types of lymphatic drainage systems. Although these drainage systems are independent, they have many anastomoses. Consequently, the relative prominence of thickening within the subpleural, interlobular septal, or peribronchovascular interstitium varies from patient to patient. This is one of the reasons why CT findings in lymphangitic carcinomatosis are not uniform. Furthermore, thickening may be due to tumor cell infiltration, desmoplastic reaction, edema caused by lymphatic obstruction, or some combination of these pathologic findings.

In our series, it was difficult to diagnose lymphangitic carcinomatosis in both patients with only peripheral interstitial thickening. One had localized peripheral disease with metastatic disease in the adjacent chest wall. In this case, no hilar lymphadenopathy and no axial interstitial thickening were

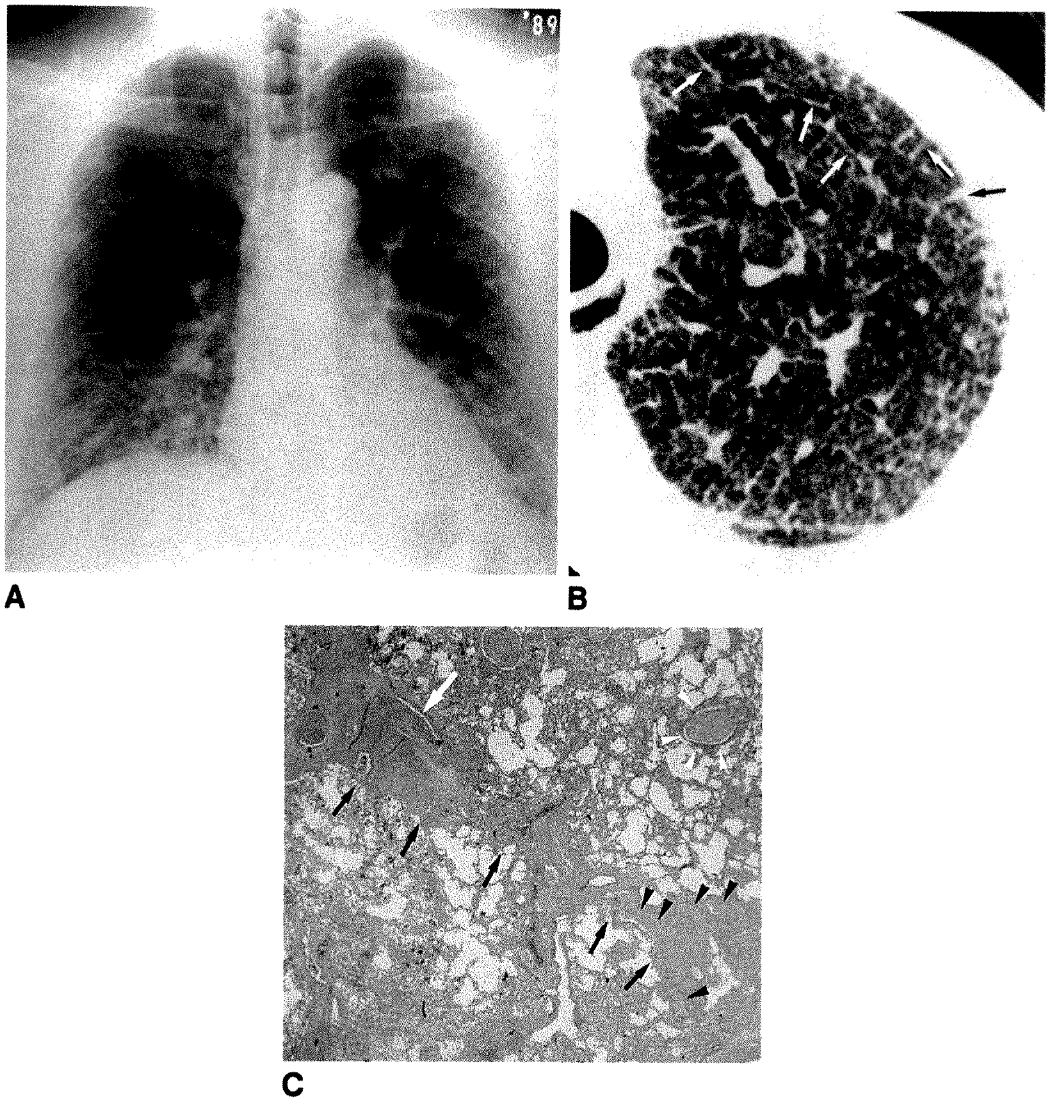

Fig. 4.—51-year-old man with lymphangitic carcinomatosis with thickening of interlobular septa and subtle thickening of bronchovascular bundle. Primary lesion was gastric carcinoma.

***A*, Posteroanterior chest radiograph shows diffuse reticulonodular shadowing throughout both lungs. Hilar and mediastinal lymphadenopathy cannot be seen.**

***B*, CT scan shows thickened peripheral interlobular septa and polygonal lines (*arrows*). Thickening of bronchovascular bundles is faint.**

***C*, Photomicrograph of autopsy specimen shows thickening of interlobular septa (*black arrows*) and subpleural interstitium, caused by desmoplastic reaction or edema. Many lymphatic vessels occluded by tumor cells are observed in interstitium (*black arrowheads*). Pulmonary vein (*white arrow*); pulmonary artery (*white arrowhead*). (Original magnification ×40)**

observed; only smooth interlobular interstitial thickening was seen. The other patient with peripheral interstitial thickening had smooth thickening of interlobular interstitium and faint thickening of the bronchovascular bundle without hilar lymphadenopathy. These two patients had interstitial disease, but it was not specific for lymphangitic carcinomatosis. Diagnosis was easy in the 18 patients with either axial interstitial thickening or both axial and peripheral interstitial thickening because they had hilar lymphadenopathy and thickening of the peribronchovascular interstitium with or without peripheral interstitial disease.

It is not certain whether these three types of lymphangitic carcinomatosis represent a continuum that might be observed in any patients or whether they are truly distinct.

In terms of their distribution, CT abnormalities were diffuse in both lungs in seven patients. They were confined to a single lobe in seven patients, to two lobes in three, and to one lung in three. Unilateral lung disease was found in 11 patients, in the right lung in 10 and in the left in one. No reason was found for this predominance on the right side. Bilateral lung disease was found in eight patients.

The impairment of pulmonary function varied. Some cases showed marked impairment of pulmonary function from the early stage of lymphangitic carcinomatosis, but others showed impairment of pulmonary function only in the late stage of the disease. For this reason we correlated CT findings with pulmonary function test results to determine which CT findings were related to impairment of pulmonary function. Vital capacity is a fundamental index for the evidence of restrictive ventilatory defects [21]. We found that the more widespread the thickened peripheral interlobular septal lines and polygonal lines were, the more severely vital capacity was diminished. Thickened interlobular septal lines in the periphery and thickened polygonal lines are thought to reflect pathologic thickening of the interlobular septa [1-3]. Therefore, restrictive ventilatory defects observed in patients with lymphangitic carcinomatosis are thought to occur because thickened interlobular septa prevent the lung from expanding in the lobular level. The widening of alveolar-arterial oxygen gradients was observed in all patients, and it was correlated with neither the type nor distribution of CT abnormalities. The widening of alveolar-arterial oxygen gradients observed in lymphangitic carcinomatosis is thought to be due to defects in diffusion from alveolus to capillary, as well as to an arteriovenous shunt in the periphery [22]. Histologically, in lymphangitic carcinomatosis, a desmoplastic reaction caused by tumor cells or chronic interstitial pulmonary edema occurs within the interstitium [3, 15-20]. Although the alveolar walls have no lymphatic vessels, lymphatic vessels surrounding the peripheral venules (juxtaalveolar lymphatics) are adjacent to the alveolus [23]. Therefore, one of the possible explanations for the diffusion defects observed in lymphangitic carcinomatosis is edema or a desmoplastic reaction in the alveolar walls. Both marked decrease of vital capacity and marked widening of alveolar-arterial oxygen gradients were observed in three patients with bilateral diffuse disease who had either peripheral interstitial thickening or both axial and peripheral interstitial thickening.

In our series, patients with peripheral interstitial thickening had immediate respiratory failure and had a poor prognosis relative to patients with axial interstitial thickening.

Our results show that CT findings in patients with lymphangitic carcinomatosis of the lung vary depending on the extent and degree of thickening of the peripheral and/or axial interstitium. Marked impairment in pulmonary function occurs in patients with diffuse and peripheral interstitial thickening. It is important for radiologists to recognize the variation in CT findings in this disease and to know which CT abnormalities are related to impairment in pulmonary function, because marked impairment in pulmonary function and a poor prognosis could be predicted from CT findings alone.

REFERENCES

1. Stein MG, Mayo J, Muller N, Aberle DR, Webb WR, Gamsu G. Pulmonary lymphangitic spread of carcinoma: appearance on CT scans. *Radiology* **1987**;162:371-375
2. Munk PL, Muller NL, Miller RR, Ostrow DN. Pulmonary lymphangitic carcinomatosis: CT and pathologic findings. *Radiology* **1988**;166:705-709
3. Ren H, Hruban RH, Kuhlman JE, et al. Computed tomography of inhalation-fixed lungs: the beaded septum sign of pulmonary metastases. *J Comput Assist Tomogr* **1989**;13:411-416
4. Fraser RG, Paré JAP, Paré PD, Fraser RS, Genereux GP. *Diagnosis of diseases of the chest*, 3rd ed. Philadelphia: Saunders, **1990**:1632-1640
5. Bergin C, Rogyli V, Coblentz CL, Chiles C. The secondary pulmonary lobule: normal and abnormal CT appearance. *AJR* **1988**;151:21-25
6. Bergin C, Coblentz CL, Chiles C, Bell DY, Castellino RA. Chronic lung diseases: specific diagnosis by using CT. *AJR* **1989**;152:1183-1188
7. Mathieson JR, Mayo JR, Stoples CA, Muller NL. Chronic diffuse infiltrative lung diseases: comparison of diagnostic accuracy of CT and chest radiography. *Radiology* **1989**;171:111-116
8. Murata K, Kahn A, Herman PG. Pulmonary parenchymal disease: evaluation with high-resolution CT. *Radiology* **1989**;170:629-635
9. Klein J, Gamsu G. High resolution computed tomography of diffuse lung disease. *Invest Radiol* **1989**;24:805-812
10. Todo Y, Murata K, Itoh S, Torizuka K. Computed tomography of diffuse pulmonary disease (in Japanese). *Nippon Igaku Hoshasen Gakkai Zasshi* **1986**;46:1281-1295
11. Trapnell DH. Radiological appearance of lymphangitis carcinomatosa of the lung. *Thorax* **1964**;19:251-260
12. Janower ML, Blennerhassett JB. Lymphangitic spread of metastatic cancer to the lung. *Radiology* **1971**;101:261-273
13. Yang SP, Lin CC. Lymphangitic carcinomatosis of the lungs. *Chest* **1972**;62:179-187
14. Matsumoto M. Radiological and pathological studies of pulmonary metastases—in relation to lymphangitic spread (in Japanese). *Haigan* **1976**;16:111-127
15. Heitzmann ER. *The lung: radiologic-pathologic correlations*, 2nd ed. St. Louis: Mosby, **1984**:915-921
16. Spencer H. *Pathology of the lung*, 4th ed. Oxford, England: Pergamon, **1985**:1085-1090
17. Churg A. Tumors of lung. In Thurlbech WM, ed. *Pathology of the lung*. Stuttgart: Thieme, **1988**:410-411
18. Flint A, Colby TV. *Surgical pathology of diffuse infiltrative lung disease*. Philadelphia: Saunders, **1987**:145-146
19. Kawabata Y, Shishido S, Iwai K. Pathological studies on carcinomatous lymphangiosis of the lung from the standpoint of the route of spread (in Japanese). *Haigan* **1982**;22:27-34
20. Satoh T, Matsubara O, Kasuga T. A clinico-pathological study of the mode of evolution of lymphangiosis carcinomatosa (in Japanese). *Nippon Kyobu Shikkan Gakkai Zasshi* **1988**;26:1243-1248
21. Cherniack RM. Physiologic disturbances in interstitial lung disease. In: Schwarz MI, King TE eds. *Interstitial lung disease*. Toronto: BC Decker, **1988**:37-44
22. Emirgil C, Zsoldos S, Heinemann HO. Effect of metastatic carcinoma to the lung on pulmonary function in man. *Am J Med* **1964**;36:382-394
23. Nagaishi C, Okada Y. The pulmonary lymphatic system. In: Fishmann AD, ed. *Pulmonary disease and disorders*, 2nd ed. New York: McGraw-Hill, **1988**:901-908

Summer-Type Hypersensitivity Pneumonitis: Comparison of High-Resolution CT and Plain Radiographic Findings

Masanori Akira[1]
Nobuhiko Kita[2]
Tokuro Higashihara[3]
Mitsunori Sakatani[2]
Takahiro Kozuka[4]

Summer-type hypersensitivity pneumonitis is an immunologic disease that occurs only in Japan. It is a form of hypersensitivity pneumonitis in which the clinical symptoms appear in the summer and subside spontaneously in mid autumn. The purpose of our study was to determine the CT findings in this condition, to compare the CT findings with those on chest radiographs, and to assess the variations in the CT findings over time. Accordingly, high-resolution CT scans and chest radiographs of 15 patients with summer-type hypersensitivity pneumonitis were retrospectively studied. Seven patients had sequential CT examinations 18–37 days apart. The CT scans and chest radiographs were reviewed by two observers independently. CT findings included diffuse micronodules ($n = 15$), slightly elevated lung density ($n = 13$), and patchy air-space consolidation ($n = 13$). In one patient, the findings on a chest radiograph were normal, while CT showed parenchymal abnormalities. In two cases, follow-up CT showed micronodular abnormalities after findings on the chest radiograph had returned to normal.

Our results show that high-resolution CT findings of summer-type hypersensitivity pneumonitis include pulmonary micronodules, increased lung density, and air-space consolidation. High-resolution CT appears to be more useful than plain chest radiographs in the evaluation of pulmonary parenchymal abnormalities in this condition.

***AJR* 158:1223–1228, June 1992**

Summer-type hypersensitivity pneumonitis is the most prevalent type of hypersensitivity pneumonitis in Japan [1]. It is characterized by symptoms that appear during the summer months, repeated episodes during subsequent seasons for many years, provocation of symptoms when at home, familial occurrence, and other manifestations similar to those of other types of hypersensitivity pneumonitis. Seasonal atmospheric microbiologic pollution is a possible cause, but the offending antigen has not yet been defined. Environmental factors, such as the muggy weather during early summer in Japan and the type of housing—mostly old wooden structures—have been considered as causes [1, 2]. Shimazu et al. [3] and Soda et al. [4] have suggested that *Trichosporon cutaneum* is a likely causative agent of summer-type hypersensitivity pneumonitis. However, this remains a matter of controversy.

Recently, Silver et al. [5] showed that CT is superior to radiography in the assessment of lung abnormalities in patients with hypersensitivity pneumonitis. We retrospectively evaluated chest radiographs and high-resolution CT (HRCT) scans in 15 patients with proved summer-type hypersensitivity pneumonitis. The purpose of the study was to describe the pulmonary abnormalities observed on HRCT scans, to evaluate the contribution of CT relative to chest radiography, and to assess the variations in the HRCT findings over time with follow-up examinations.

Materials and Methods

HRCT scans of 15 patients (three men, 12 women) with histologically confirmed summer-type hypersensitivity pneumonitis were retrospectively studied. All patients were symptomatic.

Received September 3, 1991; accepted after revision January 2, 1992.

[1] Department of Radiology, National Kinki Chuo Hospital for Chest Diseases, 1180 Nagasone-cho, Sakai City, Osaka 591, Japan. Address reprint requests to M. Akira.

[2] Department of Medicine, National Kinki Chuo Hospital for Chest Diseases, Sakai City, Osaka 591, Japan.

[3] Department of Radiology, Kansai Rosai Hospital, Amagasaki 660, Japan.

[4] Department of Radiology, Osaka University School, 1-1-50, Fukushima-ku, Osaka 553, Japan.

0361-803X/92/1586-1223
© American Roentgen Ray Society

The criteria for establishing the diagnosis included compatible clinical and radiographic evidence, negative results in bacterial and fungal studies, and histologic evidence. Histologic proof was obtained by means of transbronchial lung biopsy (*n* = 13) or open lung biopsy (*n* = 2). The patients were 31-67 years old (mean, 48 years) at the time of examination.

Seven patients had sequential HRCT examinations 18-37 days apart (mean, 29 days). Four of these seven had a third HRCT examination 9-42 days after the second examination (mean, 22 days). In two patients with repeated episodes during the summer months, several follow-up HRCT scans were obtained over 2 years. Thus, this study is based on a total of 29 HRCT scans in 15 patients. In three patients, HRCT was performed after clinical improvement. In one patient, who had repeated episodes during the summer months, HRCT scans were obtained during the chronic stage (interval since onset of the disease, 6 years).

CT scans were obtained on an 8800 (11 patients) or 9800 (four patients) scanner (General Electric Medical Systems, Milwaukee, WI). All patients had HRCT scanning with sections 1.5 mm thick and 20-mm interslice gap. Eight patients also had CT scanning with sections 10 mm thick. Scanning was performed from the apex of the lungs to the diaphragm. Targeted reconstruction was then performed with a field of view of 16-25 cm, depending on the size of the lung. Images were reconstructed by using the bone algorithm. All images were observed and photographed at lung (level, −700 H; width, 1000 H) and mediastinal (level, 20 H; width, 300 H) windows. Additional settings were used as needed.

Evaluation included posteroanterior radiographs and HRCT scans in all patients. The radiographs obtained on the same day as three of the 29 HRCT scans were not available. CT scans and chest radiographs were obtained on the same day in 26 instances, and were assessed by means of a descriptive system. The six areas of the lung included the upper zones, above the level of the carina; the middle zones, between the level of the carina and the level of the inferior pulmonary veins; and the lower zones, under the level of the inferior pulmonary veins. The severity of parenchymal abnormalities was scored in each area by using a modification of the four basic categories defined by McLoud et al. [6]: 0 = normal, 1 = slight, 2 = moderate, 3 = advanced.

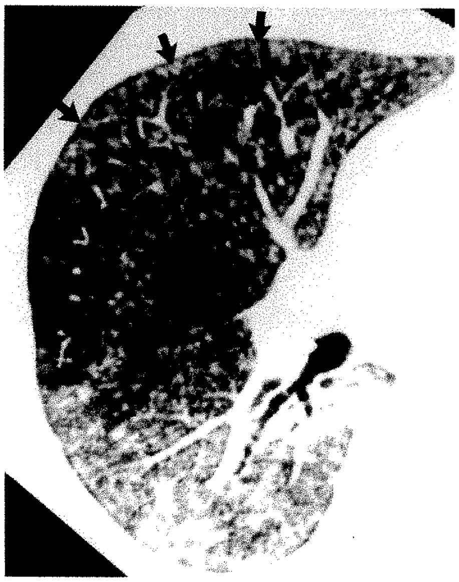

Fig. 1.—43-year-old woman with summer-type hypersensitivity pneumonitis. High-resolution CT scan shows diffuse micronodules, increased lung density, and patchy air-space consolidations. Nodules are located a few millimeters away from pleura and outer margin of a large vessel. Some are concentrated near peripheral branches of pulmonary artery (*arrows*).

In category 1, the opacities were definitely present but few, and the normal lung markings were usually visible. In category 2, the opacities were numerous, and normal lung markings were partially obscure. In category 3, the opacities were very numerous, and normal lung markings were usually totally obscured. Category 1 denoted a fine hazy pattern of density, with normal markings usually visible (i.e., ground-glass pattern), whereas in category 3, there was a high level of density with normal markings totally obscured (i.e., air-space opacification).

The chest radiographs and CT scans were viewed independently by two observers who reached a decision by consensus. The overall radiographic and CT scores were determined by using a weighted average of the severity in each zone multiplied by the number of zones assessed and a correlation factor for the different volume of each zone. The ratio of the volumes of the upper, middle, and lower lung zones (1.0:1.6:1.3) was used as the correction factor for lung volume according to the ratio described by Müller et al. [7].

Arterial blood gas values at rest were measured with an automated blood gas analyzer. The arterial oxygen tension obtained on the day of radiographic and CT examinations (*n* = 13) was used. Radiographic and CT scores were correlated with the arterial blood gas values by means of Spearman's rank correlation test and paired t test.

Results

In all patients, CT showed micronodules that affected both central and peripheral portions of the lungs diffusely. In 13 patients, slightly increased lung density and patchy air-space consolidations were also present on the initial scans (Fig. 1). In three patients who had severe hypoxemia, CT showed diffuse increased lung density and air-space consolidations, and micronodules were fine and ambiguous. However, thin-section (1.5 mm) HRCT scans showed nodularities more clearly than plain radiographs and 10-mm-section CT scans did, especially in less affected lung. In two patients whose initial scans were obtained after clinical improvement, micronodules were the only abnormality.

Most of the pulmonary nodules seen on HRCT were about 3 mm in diameter. These nodules seldom attached to the pleura or to the outer margin of a large bronchus or vessel, although they occurred near the pleura and vessels. No irregular interfaces of pleura, bronchi, or vessels were observed. The nodules were concentrated near the centers of secondary lobules (Fig. 1). Slightly hyperattenuated areas, or ground-glass opacities, in which vessels and bronchi remained visible, were observed diffusely on one scan (Fig. 2). When the lung density was slightly increased, the contrast between the air of the bronchi and the affected lung increased more than normal, and the peripheral airways, which were not seen in normal lung, could be visualized (Fig. 2). Polygonal areas of less affected parenchyma were seen in the affected lung (Fig. 3). On radiographs, the abnormalities were symmetrically distributed in all patients. The main sites of the lesions were the middle or lower lung zones.

All the sequential HRCT scans (seven patients) showed micronodules and regression of increased density. The air-space consolidations had cleared, leaving irregular linear

Fig. 2.—54-year-old woman with summer-type hypersensitivity pneumonitis.

***A*, Chest radiograph shows bilateral lower-lobe coarse reticulonodular infiltration.**

***B–D*, High-resolution CT scans show diffuse increased lung density with visible underlying pulmonary markings and poorly defined micronodules in upper to lower lung and patchy air-space consolidation with vascular markings totally obscured in lower lung.**

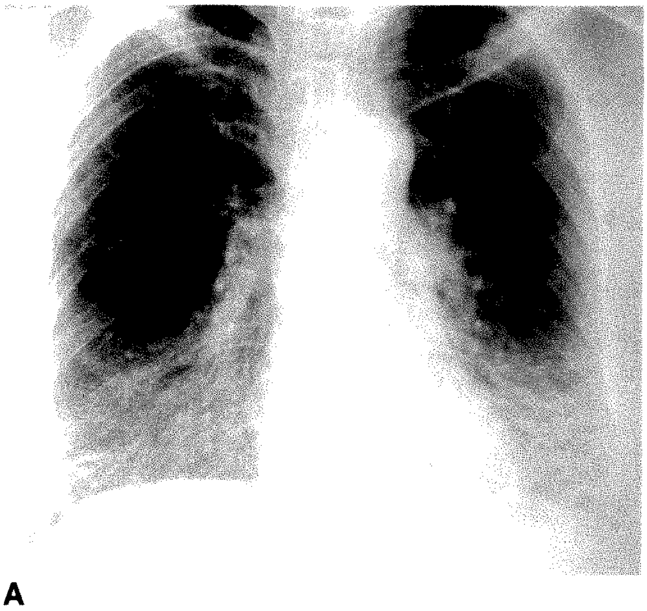

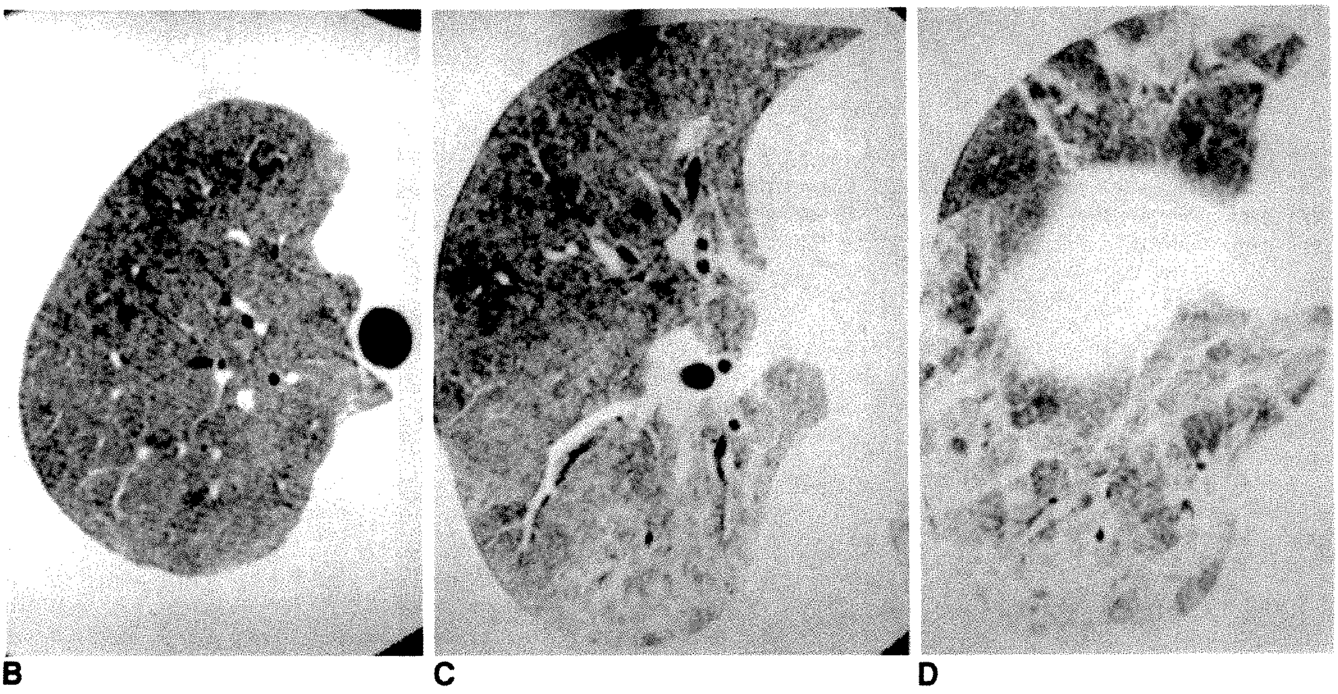

opacities that eventually disappeared. The micronodules remained after clinical improvement, although their number and diameter decreased.

In the patient whose initial CT scans were obtained during the chronic stage, micronodular abnormalities were not a prominent feature, and the scans showed irregular linear opacities, a honeycomb appearance, and formation of bullae.

In the 15 patients studied, chest radiographs showed rounded nodular opacities with or without patchy air-space consolidation in eight, reticulonodular opacities in three, ground-glass opacities with air-space consolidation in two, reticular opacities in one, and no abnormalities in one. Micronodular abnormalities and slightly increased lung density were noted on HRCT scans in areas in which the pulmonary parenchyma appeared normal on radiographs. CT scans showed that micronodules and increased density were underestimated on the plain radiographs. In one patient with no parenchymal changes on the radiograph, parenchymal abnormalities were detected on HRCT scans (Fig. 4). In two other cases, follow-up CT showed micronodular abnormalities even after the chest radiograph had returned to normal.

A significant correlation was found between arterial oxygen tension and the CT visual score ($r = .89$, $p < .01$). The correlation coefficient between arterial oxygen tension and

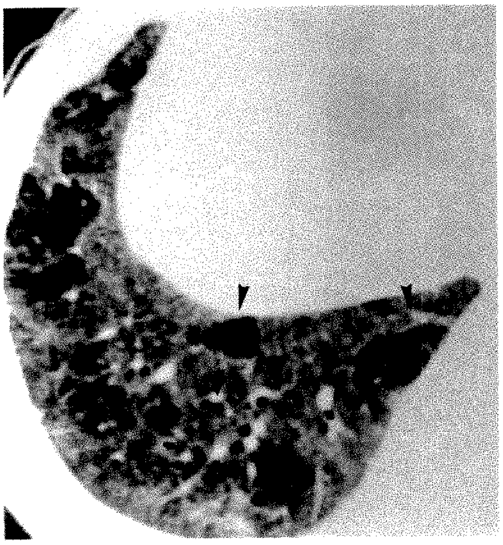

Fig. 3.—53-year-old woman with summer-type hypersensitivity pneumonitis. Thin-section CT scan shows polygonal areas of less affected parenchyma (*arrowheads*) in affected lung.

the radiographic visual score was .78 (Fig. 5). The radiographic visual score correlated relatively well with arterial oxygen tension; a disparity between the two was found in four cases. The correlation between the CT scores and arterial oxygen tension was better than the correlation between the CT scores and the plain radiographic scores ($p < .05$).

Discussion

Hypersensitivity pneumonitis is an immunologic disorder characterized by granulomatous interstitial pneumonia associated with exposure to occupational or environmental antigens. A unique form of hypersensitivity pneumonitis, summer-type hypersensitivity pneumonitis, in which signs and symptoms appear in the summer and subside spontaneously in mid autumn, is the most prevalent form found in Japan.

In this study, characteristic HRCT findings included diffuse micronodules and slightly increased lung density. In the symptomatic period, patchy air-space consolidation was also seen. In the earlier period, characterized by diffuse increased lung density and air-space consolidation, micronodules were small, fine, and poorly defined. However, thin-section (1.5-mm collimation) HRCT scans showed micronodules even when results were difficult to obtain on chest radiography and CT scanning with 10-mm collimation. Nodularity is a useful diagnostic finding in hypersensitivity pneumonitis. Follow-up CT scans showed that the air-space consolidation cleared first; this was followed by regression of increased lung density. Diffuse micronodules remained even after clinical improvement. The micronodular opacities probably reflect cellular bronchiolitis and granulomas [5]. Slightly increased lung density may reflect diffuse interstitial infiltrates of chronic inflammatory cells and granulomas. Patchy air-space consolidation may also indicate foci of obstructive pneumonia with foamy histiocytes in air spaces [8]. None of the features we observed is specific for the disease. However, in the appropriate clinical setting, the combination of diffuse micronodules with no interface irregularity and sometimes concentrated in the center of the secondary lobule, slightly increased lung density, and patchy

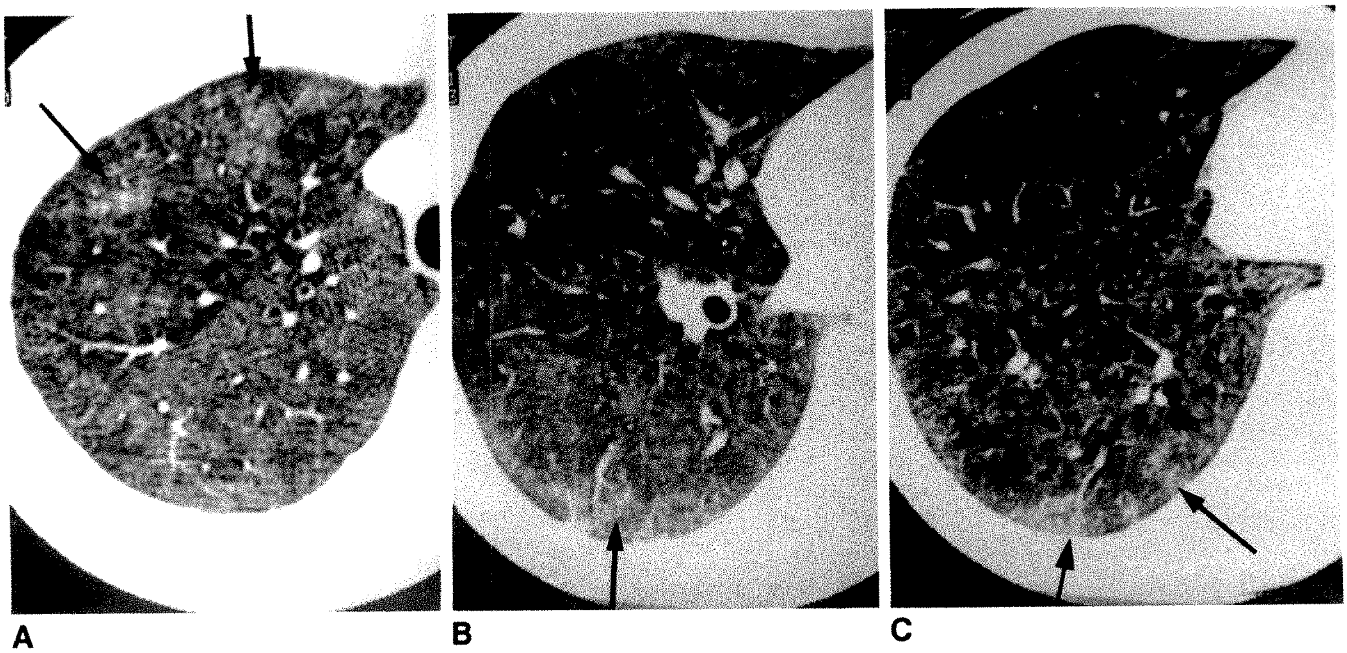

Fig. 4.—45-year-old woman with summer-type hypersensitivity pneumonitis.
A–C, High-resolution CT scans show some fine micronodules (*arrows*). Findings on chest radiograph were normal.

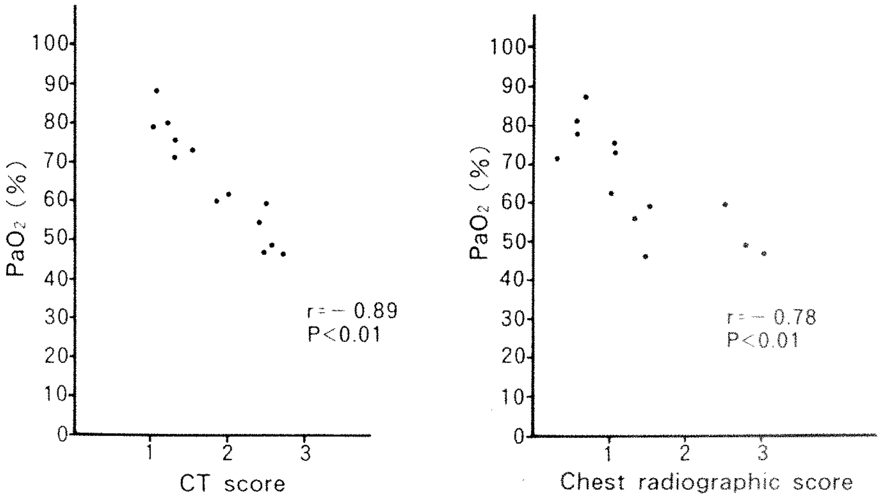

Fig. 5.—Graphs show relationship between arterial oxygen tension (Pao$_2$) and radiographic or CT score in 13 patients with summer-type hypersensitivity pneumonitis.

air-space consolidation in the prominent symptomatic period may indicate summer-type hypersensitivity pneumonitis.

Thin-section HRCT may permit localization of pathologic changes within the lobule [9–11]. Micronodules that have a centrilobular distribution are characteristic in diffuse panbronchiolitis [12]. Such nodules are sometimes seen in a number of other conditions, including hypersensitivity pneumonitis, eosinophilic granuloma [13], p-type pneumoconiosis [14], chronic berylliosis, and endobronchial tuberculosis [15].

The most difficult disease to differentiate from hypersensitivity pneumonitis clinically is sarcoidosis [16–18]. However, the CT features of the nodules in summer-type hypersensitivity pneumonitis can be distinguished from those of nodules seen in sarcoidosis. In the latter, the nodules are concentrated along the bronchovascular bundles, and irregularity of the interface is a prominent feature [19, 20]. In summer-type hypersensitivity pneumonitis, the micronodules seldom attach to the pleura or the outer margins of a large bronchus or vessels, and the lung-pleural interface remains sharp.

In hypersensitivity pneumonitis, the changes on radiographs vary with the stage of the disease. Parkes [21] stated that initial changes consisted of either fine pinpoint opacities in the central two thirds or lower zones of the lung fields, frequently sparing the costophrenic angles, with blotchy shadowing in an acute attack. Chronic changes were described as reticular or reticulonodular shadowing, radiating from the hilum with evidence of loss of volume in the upper lobe in advanced disease. Reports of the distribution of pulmonary shadowing in farmer's lung are inconsistent [22]. In hypersensitivity pneumonitis, chest radiographic findings may be normal [23–25].

In our study, CT showed parenchymal abnormalities in one patient who had a normal chest radiograph. In two cases, follow-up CT scans showed micronodular abnormalities even after the chest radiograph had returned to normal. Moreover, the patterns seen on HRCT scans and chest radiographs were inconsistent. In the prominent symptomatic period, air-space consolidation and diffuse lung density were prominent and micronodules were fine and ambiguous on radiographs, and the presence of micronodules and slightly increased density was underestimated. It is not known how prevalent normal findings on HRCT scans are in patients with hypersensitivity pneumonitis who have pulmonary symptoms.

The HRCT characteristics of hypersensitivity pneumonitis also vary with the stage of the disease. In the acute stage, the CT findings were nonspecific air-space opacification. In the subacute stage, they included small, rounded opacities and patchy, soft air-space opacification that did not obscure underlying interstitial markings [5]. The CT appearance of summer-type hypersensitivity pneumonitis depended on the time during the course of the disease at which the scans were made.

Summer-type hypersensitivity pneumonitis has a high recurrence rate [1, 26]. In one of our subjects, repeated recurrences have led to irreversible lung fibrosis. CT findings during the chronic stage are nonspecific and more difficult to differentiate from the CT findings of other conditions.

Lung function may continue to be impaired even after findings on the chest radiograph have returned to normal [27]. In four cases, we found a disparity between the radiographic score and arterial oxygen tension. When findings on the chest radiograph appear normal or indicate mild parenchymal abnormality despite the patient's severe signs and symptoms, HRCT may be useful to account for the physiologic-radiographic disparity.

HRCT was more sensitive and more accurate than plain radiography and conventional CT in the evaluation of parenchymal abnormalities in summer-type hypersensitivity pneumonitis. HRCT may be more useful than conventional radiography, not only in the differential diagnosis but also in the evaluation of responses to therapy or provocation tests.

REFERENCES

1. Kawai T, Tamura M, Murao M. Summer-type hypersensitivity pneumonitis: a unique disease in Japan. *Chest* **1984**;85:311–317
2. Miyagawa T, Ochi T, Takahashi H. Hypersensitivity pneumonitis with

antibodies to *Cryptococcus neoformans*. *Clin Exp Allergy* **1978**;8:501–509

3. Shimazu K, Ando M, Sakata T, Yoshida K, Araki S. Hypersensitivity pneumonitis induced by *Trichosporon cutaneum*. *Am Rev Respir Dis* **1984**;130:407–411
4. Soda K, Ando M, Shimazu K, Sakata T, Yoshida K, Akaki S. Different classes of antibody activities to *Trichosporon cutaneum* antigen in summer-type hypersensitivity pneumonitis by enzyme-linked immunosorbent assay. *Am Rev Respir Dis* **1986**;133:83–87
5. Silver SF, Müller NL, Miller RR, Lefcoe MS. Hypersensitivity pneumonitis: evaluation with CT. *Radiology* **1989**;173:441–445
6. McLoud TC, Carrington CB, Gaensler EA. Diffuse infiltrative lung disease: a new scheme for description. *Radiology* **1983**;149:353-363
7. Müller NL, Mawson JB, Mathieson JR, Abboud R, Ostrow DN, Champion P. Sarcoidosis: correlation of extent of disease at CT with clinical, functional, and radiographic findings. *Radiology* **1989**;171:613–618
8. Coleman A, Colby TV. Histologic diagnosis of extrinsic allergic alveolitis. *Am J Surg Pathol* **1988**;12:514–518
9. Murata K, Khan A, Herman PG. Pulmonary parenchymal disease: evaluation with high-resolution CT. *Radiology* **1989**;170:629-635
10. Bergin C, Roggli V, Coblentz C, Chiles C. The secondary pulmonary lobule: normal and abnormal CT appearances. *AJR* **1988**;151:21–25
11. Webb WR, Stein MG, Finkbeiner WE, Im JG, Lynch D, Gamsu G. Normal and diseased isolated lungs: high-resolution CT. *Radiology* **1988**;166:81–87
12. Akira M, Kitatani F, Lee YS, et al. Diffuse panbronchiolitis: evaluation with high-resolution CT. *Radiology* **1988**;168:433–438
13. Moore AD, Godwin JD, Muller NL, et al. Histiocytosis X: comparison of radiographic and CT findings. *Radiology* **1989**;72:249-254
14. Akira M, Higashihara T, Yokoyama K, et al. Radiographic type p pneumoconiosis: high-resolution CT. *Radiology* **1989**;171:117–123
15. Murata K, Itoh H, Togo G, et al. Centrilobular lesions of the lung: demonstration by high-resolution CT and pathologic correlation. *Radiology* **1986**;161:641–645
16. Burke GW, Gaensler EA, Carrington CB, Gupta R, Fitzgerald MX. Hypersensitivity pneumonitis or sarcoidosis. *Chest* **1976**;70:421
17. Cohen SH, Fink JN, Carancis JC, Hensley GT, Barboriak JJ, Schlueter DP. Sarcoidosis in hypersensitivity pneumonitis. *Chest* **1977**;72:588–592
18. König G, Baur X, Fruhmann G. Sarcoidosis or extrinsic allergic alveolitis. *Respiration* **1981**;42:150–154
19. Müller NL, Kullnig P, Miller RR. The CT findings of pulmonary sarcoidosis: analysis of 25 patients. *AJR* **1989**;152:1179–1182
20. Brauner MW, Grenier P, Mompoint D, Lenoir S, Cremoux H. Pulmonary sarcoidosis: evaluation with high-resolution CT. *Radiology* **1989**;172:467–471
21. Parkes WR. *Occupational lung disorders*, 2nd ed. London: Butterworth, **1982**
22. Cook PG, Wells IP, McGavin CR. The distribution of pulmonary shadowing in farmer's lung. *Clin Radiol* **1988**;39:21–27
23. Hargreave F, Hinson KF, Reid L, Simon G, McCarthy DS. The radiological appearances of allergic alveolitis due to bird sensitivity (bird fancier's lung). *Clin Radiol* **1972**;23:1–10
24. Unger GF, Scanlon GT, Fink N, Unger JDB. A radiologic approach to hypersensitivity pneumonias. *Radiol Clin North Am* **1973**;11:339-356
25. Epler GR, McLoud TC, Gaensler EA, Mikus JP, Carrington CB. Normal chest roentgenograms in chronic diffuse infiltrative lung disease. *N Engl J Med* **1978**;298:934-939
26. Lee YS, Kitatani F. Prevention from recurrence of summer-type hypersensitivity pneumonias. *Chest* **1985**;87:273–274
27. Williams JV. Inhalation and skin tests with extracts of hay and fungi in patients with farmer's lung. *Thorax* **1963**;18:182–196

Case Report

Thymoma with Hypogammaglobulinemia (Good's Syndrome): An Unusual Cause of Bronchiectasis

Michael A. Fox,[1] David A. Lynch,[1] and Barry J. Make[2]

There is general agreement that CT scanning is the optimal noninvasive technique for diagnosis and assessment of bronchiectasis [1]. However, CT seldom exposes a cause for bronchiectasis. Bronchiectasis may be due to cystic fibrosis, impaired immunity, immotile-cilia syndrome, allergic bronchopulmonary aspergillosis, or prior infection. In older patients, recurrent aspiration and previous infection are the most common causes. Hypogammaglobulinemia is not usually considered as a cause of bronchiectasis in the elderly.

We report a case of bronchiectasis associated with an anterior mediastinal mass in a patient with hypogammaglobulinemia. The mass proved to be a spindle-cell thymoma associated with hypogammaglobulinemia, consistent with the diagnosis of Good's syndrome [2]. We describe the CT appearance of this disorder.

Case Report

A 71-year-old woman was evaluated after several years of dyspnea and sinusitis. Investigation showed anemia, a hemoglobin level of 10.8 g/dl (108 g/l; normal, 12.0–16.0 g/dl [120–160 g/l]), and a hematocrit of 32% (normal, 38–47%). The platelet count was moderately elevated at 1130 × 10^9/l (normal, 150–375 × 10^9/l). The patient had hypogammaglobulinemia, manifested by an immunoglobulin G level of 220 mg/dl (2.20 g/l; normal, 706–1451 mg/dl [7.06–14.51 g/l]), an immunoglobulin A level of 29 mg/dl (0.29 g/l; normal, 78–340 mg/dl [0.78–3.40 g/l]), and an immunoglobulin M level of 38 mg/dl (0.38 g/l; normal 52–280 mg/dl [0.52–2.80 g/l]). Immunoglobulin E levels were at the lower limits of normal.

Chest radiograph (Fig. 1A) revealed bronchial wall thickening and an abnormal soft-tissue density along the right border of the heart. High-resolution CT scans showed bronchiectasis in the right middle and lower lobes (Fig. 1B). A rounded, 4 × 4 × 2.5 cm mass containing several small foci of calcification was present adjacent to the right atrium (Fig. 1C). Percutaneous CT-guided biopsy of the mass was performed. The cytologic appearances were consistent with spindle-cell thymoma. The findings of thymoma and hypogammaglobulinemia were consistent with Good's syndrome, which in this patient was manifested by recurrent sinopulmonary disease [2]. Thymectomy was not performed because the spindle-cell type of thymoma, in association with Good's syndrome, is rarely malignant and surgery does not alleviate the immunodeficiency.

Discussion

The thymus, consisting predominantly of an epithelial cell framework housing a sea of lymphocytes, is responsible for over a dozen different histologically identifiable neoplasms and is the most frequent site of primary neoplasms in the anterior mediastinum [3]. Up to 50% of thymomas are undetectable on the posteroanterior chest radiograph. Thymomas can cause several different paraneoplastic syndromes, including neuromuscular disorders, hematologic and endocrine disorders, and connective tissue diseases [3]. The most commonly associated disorder is myasthenia gravis (35% of patients), followed by pure red cell aplasia (5% of patients) and hypogammaglobulinemia (5% of patients) [3, 4]. Conversely, 15% of patients with myasthenia gravis, 50% of those with

---

Received September 30, 1991; accepted after revision December 10, 1991.

[1] Department of Radiology, Box A030, University of Colorado Health Science Center, 4200 E. Ninth Ave., Denver, CO 80262.

[2] Department of Medicine, National Jewish Center for Immunology and Respiratory Medicine, 1400 Jackson St., Denver, CO 80206.

AJR 158:1229–1230, June 1992 0361-803X/92/1586-1229 © American Roentgen Ray Society

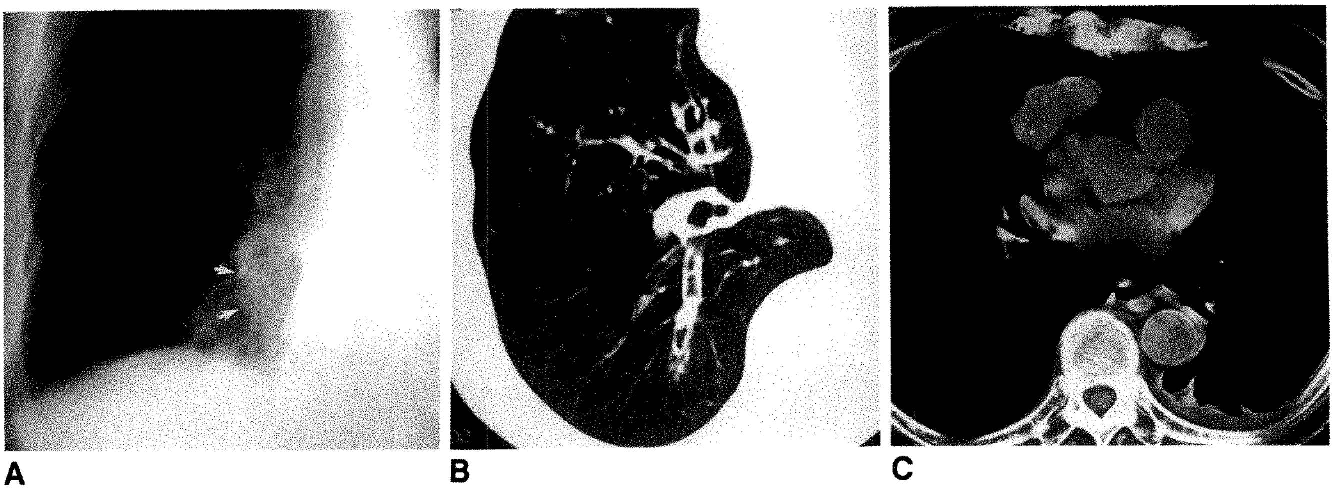

Fig. 1.—*A*, Chest radiograph shows bronchial wall thickening and a subtle bulge (*arrows*) along right border of heart.
***B*, Thin-section CT scan shows cylindrical bronchiectasis in right middle and lower lobes.**
***C*, CT scan shows mass anterolateral to heart with focus of calcification. Small pleural effusion is seen on left side.**

pure red cell aplasia, and 10% of those with hypogammaglobulinemia have a thymoma. The simultaneous occurrence of thymoma and hypogammaglobulinemia, first described in 1954 [2], is referred to as Good's syndrome.

Good's syndrome is generally recognized when a patient with the manifestations of hypogammaglobulinemia is subsequently found to have a mediastinal mass. The most common clinical presentation of Good's syndrome is with sinopulmonary disease [5]. However, diarrhea is also a common manifestation [6], and it may be a consequence of either the infection or the immunodeficiency. Moffat [5] reviewed the radiologic changes in this syndrome and recommended that the diagnosis should be considered when a paracardiac or anterior mediastinal mass occurs in combination with pulmonary infiltrates and/or an exudative enteropathy on small bowel examination. Other reported features of Good's syndrome have included an immunoglobulin G gammopathy, disorders of cell-mediated immunity, polyarthropathy, lichen planus, and hemolytic anemia. Disseminated cytomegalovirus or varicella pneumonia may be fatal in this condition. Bronchiectasis seems to be common in Good's syndrome and is usually thought to be due to recurrent bronchopulmonary infections [5]. The cause of the anemia in this patient is unclear, but it is unlikely to have been due to red cell aplasia, as it resolved spontaneously. No features of hemolytic anemia were present.

Of the various cell types that can constitute a thymoma, the spindle-cell type of epithelial tumor usually behaves in a benign manner and is commonly associated with red cell aplasia and hypogammaglobulinemia. Whereas thymectomy frequently alleviates the symptoms of myasthenia gravis, it only occasionally results in remission of pure red cell aplasia and never improves hypogammaglobulinemia [3, 5].

CT scanning, which identifies nearly 100% of thymomas, is far more sensitive than the chest radiograph [7]. The major role of CT scanning with regard to thymoma is to define the extent of tumor and to identify pleural or pulmonary metastases [7]. In our case, CT scanning provided an evaluation of the extent and severity of the patient's bronchiectasis in addition to evaluating the thymoma.

CT-guided fine-needle aspiration can avert the need for thoracotomy to diagnose thymoma [8]. Should the biopsy lead to a diagnosis of Good's syndrome, surgery can sometimes, as in this case, be avoided, as it provides no relief from the hypogammaglobulinemia and the behavior of the tumor is usually benign.

REFERENCES

1. Grenier P, Lenoir S, Brauner M. Computed tomographic assessment of bronchiectasis. *Semin Ultrasound CT MR* **1990**;11:430–441
2. Good RA. Agammaglobulinemia: a provocative experiment of nature. *Bull Univ Minn Hosp Minn Med Found* **1954**;26:1–19
3. Rosenow EC, Hurley BT. Disorders of the thymus. *Arch Intern Med* **1984**;144:763–770
4. Masaoka A, Hashimoto T, Shibata K, et al. Thymomas associated with pure red cell aplasia. *Cancer* **1989**;64:1872–1878
5. Moffat RE. Radiologic changes in the thymoma-hypogammaglobulinemia syndrome. *AJR* **1976**;126:1219–1222
6. Sherman JD, Banas JS, Edwards TL, McMahon HE, Patterson JF. A syndrome of diarrhea, thymoma and hypogammaglobulinemia. *Gastroenterology* **1966**;51:681–688
7. Ellis K, Austin JHM, Jaretski A. Radiologic detection of thymoma in patients with myasthenia gravis. *AJR* **1988**;151:873–881
8. Weisbrod GL. Percutaneous fine-needle aspiration biopsy of the mediastinum. *Clin Chest Med* **1987**;8:27–41

Perspective

Interventional Procedures in Diseases of the Breast: Needle Biopsy, Pneumocystography, and Galactography

Laurie L. Fajardo,[1] Valerie P. Jackson,[2] and Tim B. Hunter[1]

This article discusses the roles of mammography-guided needle biopsy of the breast, pneumocystography, and galactography in further defining breast lesions that have been detected with mammography. For each procedure, indications for its use, proper technique, complications, interpretation, and role in clinical practice are described. Use of these procedures is warranted for some patients to provide detail beyond that available with mammography and sonography.

Mammography is clearly the most sensitive method available for detecting abnormalities of the breast. In many instances, the nature of mammographically detected lesions can be further defined by additional interventional procedures. Breast sonography, the most useful adjunct to mammography [1, 2], and preoperative needle localization of breast lesions [3-11] have been well reviewed. Other breast procedures, including breast needle biopsy, pneumocystography, and galactography, are reviewed here.

Mammography-Guided Breast Needle Biopsy

Mammography is currently the best method for detecting impalpable breast abnormalities. However, distinguishing between malignant and benign lesions on the basis of mammography alone may be difficult, and, therefore, excisional biopsy—with preoperative needle-wire localization—is often recommended. The positive rate for surgical breast biopsies performed for mammographically identified impalpable abnormalities is 11–36% [3–13]. Significant costs are related to diagnosing impalpable breast lesions, including costs to health care insurers and patients' morbidity. In addition, a breast may show abnormal findings after a surgical biopsy (most often, architectural distortion due to scarring) that can mimic a cancer and make interpretation of subsequent mammograms difficult. As an alternative to surgical biopsy, we and others advocate the use of mammography-guided needle biopsy to diagnose impalpable breast lesions.

Indications

Breast needle biopsy is indicated for the following types of impalpable breast lesions:

1. Well-defined masses that appear benign, if needle biopsy is preferred over follow-up mammography by the patient, referring physician, or mammographer. This situation commonly occurs with women who have a strong family history of breast cancer, or when the mass is relatively large (i.e., larger than 1 cm) and no prior mammogram is available for comparison. In these cases, an unexpected carcinoma may be diagnosed on the basis of needle biopsy, but far more often biopsy results verify the benign nature of the mass, which can safely be followed up by mammography without surgical excision.
2. For lesions exhibiting characteristics suggestive of carcinoma (i.e., a mass with a partially obliterated border or a well-defined mass with less than five microcalcifications), breast needle biopsy determines the benign vs malignant

---

Received July 8, 1991; accepted after revision January 15, 1992.

[1] Department of Radiology, University of Arizona, 1501 N. Campbell Ave., Tucson, AZ 85724. Address reprint requests to L. L. Fajardo.

[2] Department of Radiology, Indiana University School of Medicine, Indianapolis, IN 46202.

AJR **158:1231-1238, June 1992** 0361-803X/92/1586-1231 © American Roentgen Ray Society

nature of such masses and may provide information for staging and guiding surgical therapy.

3. For lesions highly suggestive of carcinoma on mammography, needle biopsy may confirm the presence of malignant cells and may show tumor invasion. This information can be used to determine whether inpatient or outpatient surgical excision can be performed, depending on whether the need for lymph node dissection is known a priori.

Because the patient must remain motionless for about 30 min during a biopsy, women with kyphosis or severe arthritis may not tolerate the positioning required with either upright or prone stereotaxic devices. In addition, lesions located deep within the breast may not be suitable for biopsy with stereotaxic imaging. Breast biopsy in these cases can be accomplished with sonographic guidance [14]. In a few cases, surgical excision may be the only option. We do not perform biopsy on patients taking anticoagulants.

Before needle biopsy, all patients are seen by a breast surgeon. If a needle biopsy result warrants further surgical intervention, this allows the patient to establish a relationship with her surgeon. In addition, it is important that the surgeon examine the patient before the procedure, as findings may be temporarily altered after a needle biopsy.

Technique and Complications

At the University of Arizona, we use both fine-needle aspiration cytology (FNAC) and core biopsy to evaluate impalpable breast lesions. Methods for localizing impalpable breast abnormalities for needle biopsy include sonography [14], conventional mammography [15, 16], and stereotaxic mammography [17–22]. We use stereotaxic imaging most often (Fig. 1). Most stereotaxic devices calculate the three-dimensional location of a breast lesion from two images obtained 30° apart. The major difference between devices is in the patient's positioning (upright or prone). To achieve the greatest success with this procedure, close cooperation between the mammographer, a cytopathologist experienced in breast disease [23], the breast surgeon, and the surgical pathologist is important [24].

After the location of a breast abnormality is calculated in three dimensions, the skin is prepared, and a small amount of 2% lidocaine (0.5–1.0 ml) is administered. Four to six passes for FNAC are obtained with 22-gauge, 3½-in. (9-cm) spinal needles (Sherwood Medical, St. Louis, MO). Depending on the size of the lesion, the mammographer may wish to adjust the needle entry position slightly between passes to sample all areas of the mass. By having the mammography technologist apply suction with a 20-ml syringe attached to the needle by plastic tubing (K50L, Baxter Healthcare, Valencia, CA), the mammographer has both hands free to manipulate the needle up and down through the lesion 10 to 20 times with slight rotation of the needle between excursions. The needle also should be angled 5–10° between excursions in a fanlike fashion to avoid sampling the same needle track repeatedly. In addition, the amplitude of the needle excursions should be about 1 cm (always greater than 5–6 mm) [25, 26]. Depending on the type of stereotaxic device used for localization, this distance may need to be factored into the needle depth calculation. For example, if the center of the 10-mm lesion is calculated to be 22 mm from the skin surface, the needle guide should be adjusted so that the needle enters the breast to a depth of 27–28 mm to ensure passage through the entire lesion. Suction is released and the plastic tubing is disconnected from the aspiration needle before it is removed from the breast. After expressing the FNAC sample onto a

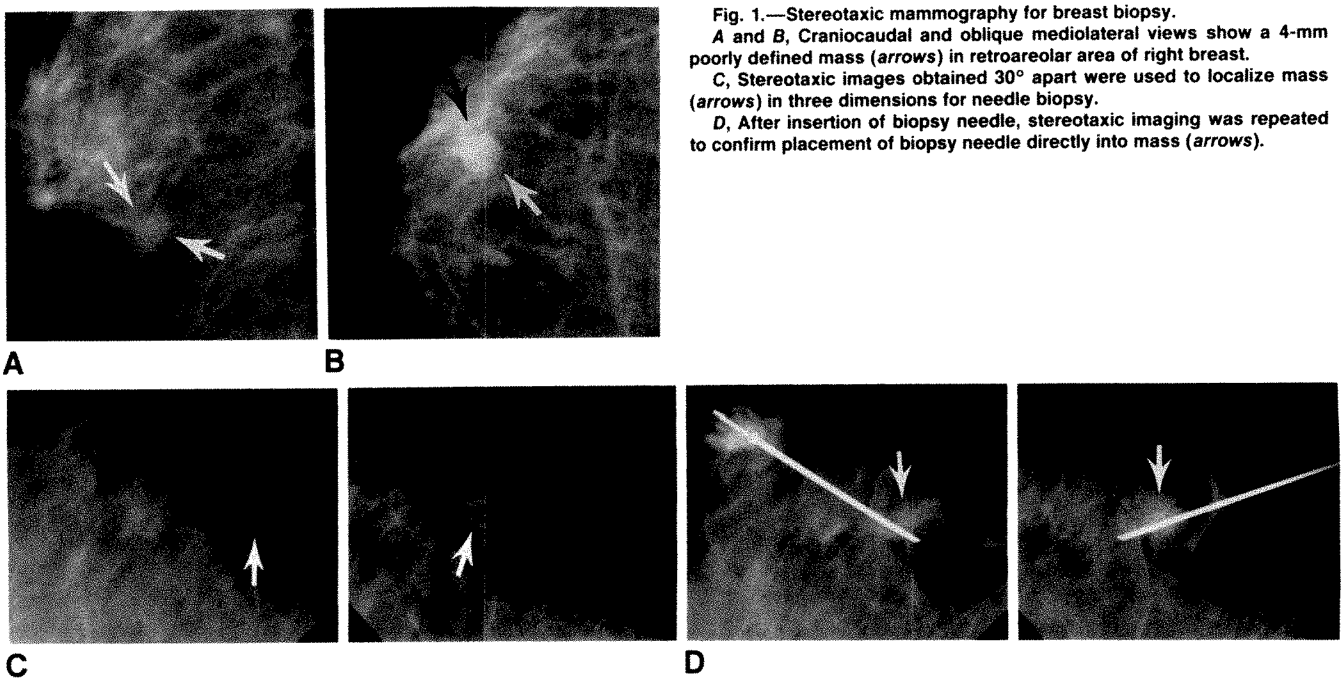

Fig. 1.—Stereotaxic mammography for breast biopsy.

A and *B*, Craniocaudal and oblique mediolateral views show a 4-mm poorly defined mass (*arrows*) in retroareolar area of right breast.

C, Stereotaxic images obtained 30° apart were used to localize mass (*arrows*) in three dimensions for needle biopsy.

D, After insertion of biopsy needle, stereotaxic imaging was repeated to confirm placement of biopsy needle directly into mass (*arrows*).

glass slide, the needle is then flushed with 50% ethanol into a plastic tube for a cell block. The position of the biopsy needle is confirmed and documented by at least one set of stereotaxic images obtained during the procedure (Fig. 1).

We routinely obtain three to four aspiration biopsy specimens, which are prepared and stained in the mammography suite. These are immediately examined for adequacy and suggestive findings. If the FNAC samples do not contain adequate ductal cells for evaluation, additional aspirates are obtained. If cells suggestive of malignancy are seen, 14-gauge needle core biopsy samples are obtained with a "long throw" (23-mm excursion) Biopty gun (distributed by Bard Urological, Covington, GA; manufactured by Radiplast, Uppsala, Sweden). We do not routinely perform core biopsies on every patient. Rather, we use the FNAC findings to determine whether a core biopsy is necessary.

Several types of needles have been used for breast aspiration or core biopsy [14-22]. We find ordinary spinal needles to be an inexpensive choice for aspiration cytology. In about 4-5% of patients, adequate samples are not obtained on the initial passes and additional samples are needed. In these instances, it is useful to try a different type of needle for the repeat aspiration. As a second choice, we most often use a 22- or 20-gauge, 3½-in. "Westcott" style of biopsy needle (MWN 2003, Manan Medical Products, Northbrook, IL) with good results. In our experience, adequate diagnostic material is obtained on the initial four passes in 95-96% of patients; only 1% have required more than six passes. A maximum number of eight passes was necessary for each of two widespread lesions. In both cases, the greater number of samples was obtained to ensure that an adequate area was sampled, not because of inadequate specimen retrieval.

At the completion of the procedure, patients are given written instructions for postbiopsy breast care and follow-up. They are warned to expect slight bruising or discoloration at the biopsy site for 7-10 days. In our experience with more than 250 breast needles biopsies, we have had no serious bleeding complications. In a previous study, we performed FNAC on 100 patients before breast needle localization and surgical excision [19]. Although evidence of minor local hematoma was apparent at surgery in 35% of these patients, this did not interfere with pathologic evaluation or receptor analysis.

Postbiopsy infection is a possible complication, but we have not encountered this problem.

Interpretation

A preliminary FNAC interpretation is made at the end of the procedure; the final diagnosis is available the next day. Cytologic samples are evaluated for cellularity, cellular arrangements, nucleocytoplasmic ratio, and characteristics of cell nuclei and nucleoli. They are classified on a scale of 1-4 as follows: 1 = benign; 2 = atypical, benign; 3 = suggestive of malignancy; 4 = malignant [19, 27]. Histologic core biopsy samples are used to confirm malignancy suggested by FNAC (FNAC diagnosis, 3), and to determine whether a tumor is invasive.

Role in Clinical Practice

We recommend combining mammographic findings with the results of needle biopsy in the management of patients with impalpable breast lesions. If strict diagnostic criteria are developed for each of these examinations, consistent patient management can be facilitated. When the needle biopsy findings are consistent with an invasive malignant lesion (cytologic diagnosis, 4), the patient undergoes a definitive inpatient surgical procedure with lymph node sampling. When an in situ carcinoma is suspected from the core biopsy, or FNAC is suggestive (cytologic diagnosis, 3) but the core biopsy is not definitive, the patient undergoes an outpatient biopsy. Some of these patients will subsequently be found to have invasive carcinoma and will require a second inpatient surgical procedure.

If the needle biopsy result is benign (cytologic diagnosis, 1 or 2), but mammography suggests malignancy (mammographic diagnosis, 3 or 4), the possibility of a sampling error must be considered. In such cases, we currently take a conservative approach by performing outpatient excisional biopsy. Further studies are needed to investigate the cost-effectiveness of this approach.

When initially instituting breast needle biopsy in the evaluation of impalpable breast lesions, we recommend a trial period of correlation between needle biopsy and surgical biopsy in 50 to 100 patients. This is especially important when the cytologist is not familiar with breast disease and the radiologist is inexperienced at breast needle biopsy. In such cases, a significant learning curve should be expected. In addition, the radiologist can use mammographic criteria to select cases that are likely to yield the best results. In our experience, we have found that the accuracy of needle biopsy correlates well with the findings on mammography (Fajardo LL, unpublished data). The most accurate cytologic yield is obtained from stellate masses with microcalcifications, well-defined masses, and stellate masses that are well depicted on mammography. Accuracy has been lower with poorly defined masses and clustered microcalcifications without an associated mass. Our poorest results have occurred with architectural distortions and "radial scar" types of lesions. These abnormalities frequently occupy relatively large areas in the breast and often are predominantly benign pathologically, but contain foci of carcinoma. If significant fibrosis is present, the FNAC samples may be relatively acellular, requiring a greater number of passes, and, because of their size, these lesions are difficult to sample in their entirety by either FNAC or core biopsy. The frequency of acellular or inadequate breast FNAC specimens varies from 0% to 36% in reported series [14-22]. If cytologic evaluation of aspirates can be done immediately, the occurrence of scanty or inadequate specimens can be eliminated.

Several recent studies have compared the diagnosis of impalpable breast abnormalities by using FNAC with results from surgical biopsy [14, 15, 18-21]. Sensitivity for FNAC has varied from 0.68 to 0.93, and specificity has varied from 0.88 to 1.00. In analyzing these reports, it should be noted that data from patients in whom specimens are inadequate are quite often omitted in these calculations [28]. Likewise, the recommendations for follow-up of patients for whom needle biopsy results are negative are also variable. Our routine is to obtain follow-up mammograms 6, 12, and 24 months after the procedure. This protocol is identical to that used for mammographic follow-up of our patients after lumpectomy.

Pneumocystography

Pneumocystography is a mammographic air-contrast study involving aspiration of fluid from a breast cyst followed by injection of air. This technique is useful in the workup of cystic breast masses that show wall irregularity, nodular excrescences, an intracystic solid component, or internal debris on sonography. It is also useful in the diagnosis and therapy of recurrent cysts. The prevalence of tumor within breast cysts ranges from 1.3% to 6.0% [29–31], and, because cytologic evaluation of cyst fluid is unreliable [30], pneumocystography is a useful adjunct to breast sonography in evaluating cystic breast masses.

Indications

Pneumocystography is generally not indicated for evaluating masses that fulfill sonographic criteria for a simple cyst. It is useful in evaluating masses that are "indeterminate" on sonography. The procedure may be therapeutic for large, symptomatic, or recurrent simple cysts. Because intracystic tumors are uncommon, breast masses selected for pneumocystography must be carefully selected to realize a reasonable cost-benefit ratio. Asymptomatic masses that are benign, simple cysts on sonography can be safely followed up with routine mammography and/or sonography, depending on the patient's age.

Technique and Complications

Palpable breast lesions can be manually aspirated and injected with air. For impalpable lesions, pneumocystography can be performed by using either sonographic or mammographic guidance. In our experience, the mammographic technique is the most efficient when either conventional or stereotaxic methods are used to localize the mass. The breast is positioned in the mammography unit to provide the shortest route of access to the cyst and compressed with a localizing grid. The breast should not be compressed too vigorously or the cyst will flatten, limiting access and aspiration. After localization by mammography or sonography (impalpable lesions) or manual technique (palpable lesions), the skin is cleansed and the cyst punctured with a 20- to 22-gauge needle. In general, local anesthesia is not necessary for breast aspiration, unless multiple punctures are performed. After aspirating the fluid, a second syringe is attached without dislodging the needle, and the cyst cavity is insufflated with a volume of air slightly less than the amount of fluid that was aspirated. Coned magnification images are then obtained in two orthogonal views.

Incomplete aspiration of a breast cyst will be evident as an air-fluid level on the pneumocystogram. Although it is still possible to evaluate the cyst walls, the cyst may recur. In our experience, incomplete aspiration most often occurs when a craniocaudal approach is chosen for the needle entry or when excessive breast compression is used. Puncture of the lower half of the cyst, by way of a lateromedial or mediolateral approach, avoids incomplete aspiration, except in the case of noncommunicating, septated, or multiloculated lesions. These lesions require additional needle punctures for complete drainage. If a cystic mass is small (<1 cm), it may be difficult to maintain the needle position within the cyst cavity for injecting air. In such cases, the air may be injected into the parenchyma and will look similar to subcutaneous emphysema.

Interpretation

A pneumocystogram of a normal breast will show a smooth inner wall (Fig. 2). The most common intracystic abnormalities are intracystic papilloma and intracystic carcinoma. It is difficult to distinguish a benign from a malignant intracystic mass on pneumocystography because both can appear as a lobular or irregular mass protruding into the air-filled cystic cavity [32, 33] (Fig. 3). Once a filling defect is confirmed, biopsy is indicated to determine whether the lesion is benign or malignant. We do not submit aspirated fluid for examination unless it is bloody because of the high false-negative rate for cytologic evaluation of cyst fluid. This experience has been confirmed by others. In a series of 13 patients with intracystic malignant lesions diagnosed by pneumocystography, only three had suggestive or positive cytologic findings [30].

Role in Clinical Practice

If the findings on the pneumocystogram are normal and the aspirated fluid is not bloody, the patient is followed up with routine screening mammography. If the fluid is bloody but the cytologic finding is negative and the pneumocystographic findings are normal, we obtain a 6-month follow-up mammogram of the affected breast to evaluate for a recurrent lesion. If results of the follow-up examination are normal, routine screening is recommended. If the cyst recurs, pneumocystography and cytology are repeated. If results of these studies are again normal, the same follow-up procedure is used. If the cyst recurs again, particularly if the fluid remains bloody, surgical excision is performed.

Some studies indicate that performing pneumocystography in conjunction with cyst puncture is of therapeutic value in preventing cyst recurrence [30, 32, 34]. It is suggested that the presence of intracystic air and disruption of the epithelial lining of the cyst by needle puncture induces collapse of the cavity, adherence of the opposing stroma, and sclerosis of the wall. In our experience with 89 pneumocystograms with normal findings obtained in 73 patients, there were five recurrent cysts [35]. Three have not recurred after a second aspiration/pneumocystogram during a follow-up time of 18–24 months. Two recurred after the second procedure and were subsequently excised surgically. Both were benign.

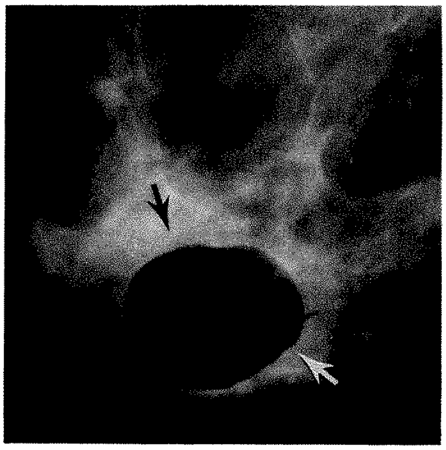

2

Fig. 2.—Pneumocystogram of normal breast shows smooth cyst walls (*arrows*) and no evidence of intracystic mass.

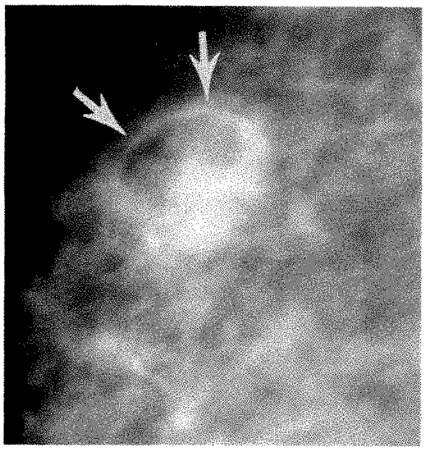

3

Fig. 3.—8-mm intracystic papilloma (*arrows*) is seen as a filling defect on pneumocystogram.

Galactography

Galactography or ductography is a mammographic study involving the injection of contrast material into a duct. According to a literature review by Tabar et al. [36], there is a 10% frequency of carcinoma in women operated on for nipple discharge. This frequency is higher for bloody discharge (13%) than for serous discharge (7%). While some researchers advocate the use of cytology for evaluation of nipple discharge, Tabar et al. [36] found this unreliable. Only two of their 18 cases of carcinoma had positive cytologic results. We do not routinely send discharge fluid for cytology at the time of galactography.

Indications

Galactography may be helpful for evaluation of spontaneous nipple discharge that is bloody, serous, or clear in nature, originating from one or two ducts; other types of discharge are not associated with tumors [36]. The procedure is not indicated for women with any type of discharge from multiple ducts bilaterally, or for pregnant or lactating women. Some authors stress that significant discharge is *spontaneous* and does not require manipulation for its production [37–39]. Galactography should not be performed in a woman with active mastitis, as it may worsen the inflammatory process [37].

Technique and Complications

Preliminary mammograms of good quality must be available. Patients are asked to check for nipple discharge on the day of the study. Nipple discharge must be present during the cannulation and therefore is confirmed by the patient and radiologic staff before the procedure.

A 27- or 30-gauge blunt needle–catheter system, as used for sialography, is filled with contrast medium. Full-strength contrast material (meglumine diatrizoate or a nonionic contrast agent) is used for galactography. The catheter is connected to a 3- or 5-ml syringe via a stopcock so that the system can be filled and closed to prevent air from entering the needle tip. The system must be completely filled and free of air bubbles before injection, because air bubbles will appear as filling defects that simulate intraductal tumors.

A gooseneck lamp provides additional light for better visualization during duct cannulation, and its warmth may relax the ductal sphincter and facilitate entry into the duct orifice. The woman may be supine or seated for the contrast injection. At our institution, we perform the procedure with the patient seated and her breast supported as for the craniocaudal view on the mammography unit. The compression paddle and collimator are removed to provide more working space. The cassette holder is covered with a sterile towel. After cleansing the breast, the mammographer gently expresses a small drop of discharge onto the nipple surface. The catheter is carefully guided into the discharging duct. Because of the smallness of the needle, preliminary enlargement of the duct orifice with sialographic dilators is not necessary. The needle may enter only the first several millimeters of the duct and, to avoid duct perforation, should not be forced. A slow injection rate is necessary because of the smallness of the catheter and the viscosity of the contrast material. When the patient experiences fullness or discomfort [36], or when clear fluid—indicating reflux of contrast material—appears at the nipple surface, the injection is stopped. Craniocaudal and 90° lateral magnification mammograms are obtained with mild to moderate compression. One can tape the needle to the nipple, leaving it in place for the mammograms. However, in our experience, the catheter frequently dislodges and becomes contaminated during positioning. We prefer to remove the needle before filming; reinsertion is usually straightforward if another injection is necessary. In addition, we have found that little or no contrast material leaks during the positioning for mammography after the needle has been removed. When the procedure is performed with the patient supine, it may be helpful to have her compress the nipple after removal of the catheter to prevent leakage while she is transferred to the mammography unit.

The patient is given sterile gauze pads to place in her bra after the procedure. She is told to expect more discharge than usual for a day or more after the procedure and that she may even have new bloody discharge. She is instructed to call her referring physician or the breast imaging center immediately if signs of mastitis develop.

The most serious potential complication from galactography is perforation of the duct. This necessitates termination of the procedure, usually before any diagnostic information has been obtained. The other potential complication from galactography is inflammation or mastitis, which may occur if careful sterile technique is not used. Strict attention to aseptic technique will minimize this possibility.

Interpretation

Galactography of the normal breast shows filling of the arborizing ductal system, frequently with contrast medium in the small acinar or lobular structures (Fig. 4). Generalized dilatation of the ducts may occur in secretory disease [38, 40, 41], and occasionally small cysts will fill from the duct system (Fig. 4). The most common abnormal finding is one or more smooth, often lobulated filling defects within the duct. These are usually papillomas and may be solitary or multiple (Fig. 5). Less commonly, these may represent carcinoma. Occasionally, a large papilloma may completely obstruct the duct, preventing the passage of contrast agent beyond the lesion. Ductal carcinoma may produce wall irregularity, abrupt luminal changes, and cutoff of the column of contrast material [37, 38, 42] (Fig. 6). In our experience, it is not usually possible to differentiate reliably between a carcinoma and a papilloma on galactography. Thus, any filling defect or abrupt duct termination requires surgical biopsy. However, a solitary filling defect is usually benign, whereas multiple abnormalities are more suggestive of malignancy.

Role in Clinical Practice

The utility of galactography is controversial. Some surgeons do not require preoperative galactography, preferring to merely dissect along the discharging duct. However, other surgeons prefer to have a preoperative "road map" to guide them to the site of the tumor. In addition, some surgeons find it helpful to have the duct reinjected on the day of biopsy. At that time, the contrast material is mixed with methylene blue before injecting the abnormal duct. This allows identification of the duct by mammography and by visual inspection at surgery [37]. Others advocate placement of a segment of proline suture material into the duct. The length can be estimated from the galactograms so that the segment ends near the lesion. Another alternative is needle or wire localization of the filling defect on a second galactogram on the day of surgery.

In most published series, if the patient with spontaneous bloody nipple discharge has normal galactographic findings and cytology of the fluid is negative, biopsy is not performed. Rather, clinical follow-up is advocated. However, in a series reported by Ciatto et al. [42], two patients with infiltrating ductal carcinoma found at biopsy had persistent bloody discharge but normal mammographic, galactographic, and cytologic findings. These authors nonetheless concluded that "bloody nipple discharge alone does not justify surgical excision of the discharging duct, which should be limited to selected cases on the basis of cytology (evidence of suspect cells), or galactography (evidence consistent with breast cancer or multiple papillomas)." Thus, the correct course of

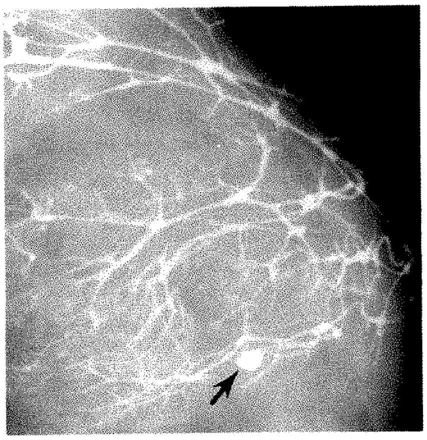

Fig. 4.—Galactogram of normal breast. Contrast material fills normal arborizing duct system, with little acinar filling in this case. A single small cyst is filled with contrast material (*arrow*).

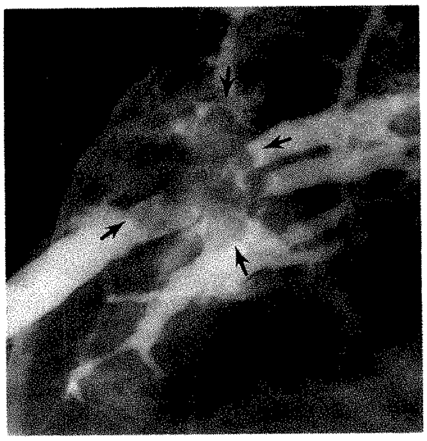

Fig. 5.—65-year-old woman with bloody discharge from nipple. Magnification craniocaudal galactogram shows ductal ectasia and a large lobulated filling defect (*arrows*). A large papilloma was found at surgery.

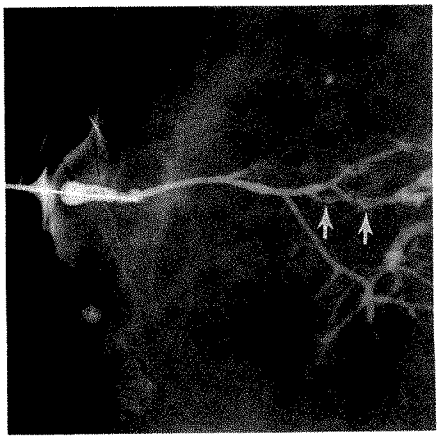

Fig. 6.—50-year-old woman with bloody discharge from nipple. Galactogram shows multiple small filling defects (*arrows*), wall irregularity, and abrupt cutoff of contrast column. These findings are highly suggestive of malignancy. The patient refused biopsy and 9 years later was seen with infiltrating ductal carcinoma involving most of breast.

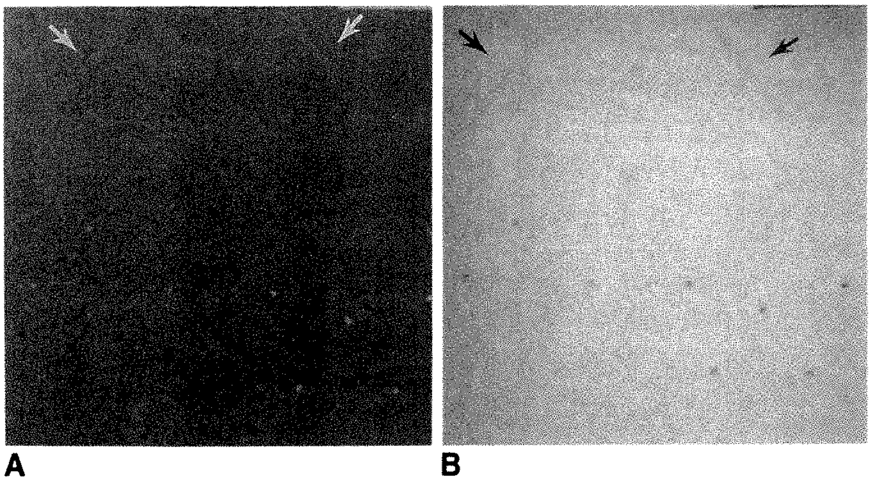

Fig. 7.—*A* and *B*, Images of a portion of breast phantom (RMI model 156) obtained by conventional screen-film (*A*) and digital charge-coupled device (*B*) mammography techniques show two fibrils (*arrows*) and two clusters of microcalcification.

management of women with normal results of diagnostic studies remains unclear.

Future Technology for Breast Interventional Procedures: Charge-Coupled-Device Mammography

Fluoroscopic mammography has not been possible thus far owing to the low kilovoltage required for breast imaging and the high radiation doses that would result. Likewise, digital techniques for breast radiography have limited use because of the lack of adequate electronic receptors and the need for high spatial resolution [43, 44]. However, charge-coupled devices (CCDs) offer promise for digital mammography and for "pseudo–real-time" mammography [45].

CCDs are small electronic chips that range in size from approximately 0.5 to 4 cm^2 and typically contain pixel matrices of 512 × 512 to 1028 × 1028. Exquisitely sensitive to visible and infrared light, CCD imaging systems offer wide dynamic range, high signal-to-noise ratio, high spatial resolution, and increased low-contrast resolution when compared with other digital systems [46, 47]. Because CCD chips are very efficient receptors and mammography screens emit considerable light with low-kilovoltage exposures, radiation doses with CCD mammography should be no more (and perhaps considerably less) than those with conventional mammography. CCD images of breast phantoms consistently show more dynamic range than comparable film-screen images do [45]. This increased image contrast may improve detection of breast abnormalities.

At the University of Arizona, we have built a CCD-based mammography imaging system. X-rays generated from a standard mammography unit pass through the breast and strike a standard mammography screen positioned with its phosphorescent side facing down. Light emitted from the screen is then fiberoptically coupled to the CCD camera system, which displays the resultant image in 2–4 sec on a high-resolution CRT screen. Thus, a type of pseudo–real-time mammography is possible. Initial phantom studies have shown that rapid, high-resolution, high-contrast images are possible for limited areas (Fig. 7).

Breast imaging with CCDs will be useful for needle localizations and mammography-guided needle biopsy procedures because there will no longer be a 4- to 5-min turnaround time for acquiring and developing images. The ability to do procedures in pseudo–real time will increase patients' tolerance and enhance the efficiency and accuracy of breast interventional procedures. In addition, when the CCD chip is optically coupled to a small area of breast tissue (approximately 5 × 5 cm), superb magnification views on the order of three to four times are possible (Fig. 8).

Because CCD-acquired magnification images contain greater spatial resolution than standard film-screen magnification images do [45], this technology will be useful for specimen radiography and magnification views also. For these applications to be realized, the prototype systems must be converted into systems that are simple to operate. Our experience with CCD imaging techniques shows that nearly instantaneous, high-quality, low-dose images of breast phantoms are possible, particularly when one or two skilled engineers are present to adjust the equipment and display monitor. Once CCD technology becomes more user-friendly, it should have a major impact on breast imaging and intervention.

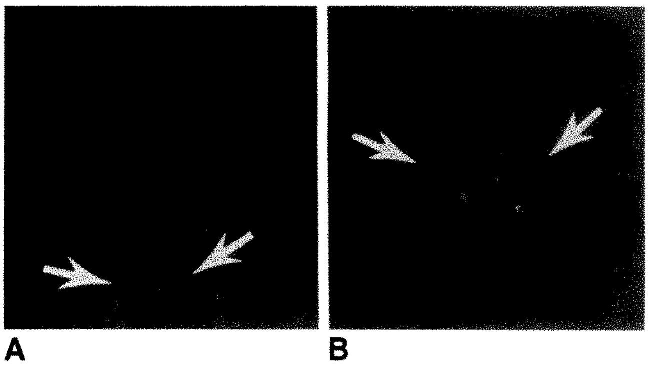

Fig. 8.—*A* and *B*, Conventional (*A*) and digital charge-coupled device (*B*) mammograms of microcalcification inserts that have been placed in tissue-equivalent research breast phantom (CIRS). Conventional image was produced with small focal spot and magnification technique (×1.8). Charge-coupled device image was filmed as it appeared on CRT screen. *Arrows* indicate same microcalcification group on each image.

REFERENCES

1. Bassett LW, Kimme-Smith C. Breast sonography. *AJR* **1991**;156:449–455
2. Jackson VP. The role of US in breast imaging. *Radiology* **1990**;177:305–311
3. Meyer JE, Kopans DB, Stomper PC, Lindfors KK. Occult breast abnormalities: percutaneous preoperative needle localization. *Radiology* **1984**;150:335–337
4. Grisvold JJ, Martin JK. Prebiopsy localization of nonpalpable breast lesions. *AJR* **1984**;143:477–481
5. Proudfoot RW, Mattingly SS, Stelling CB, Fine JG. Nonpalpable breast lesions: wire localization and excisional biopsy. *Am Surg* **1986**;52:117–122
6. Schwartz GF, Patchefsky AS, Feig SA, Schwartz AB. Clinically occult breast cancer: multicentricity and implications for treatment. *Ann Surg* **1980**;191:8–12
7. Hermann G, Janus C, Schwartz IS, Krivisky B, Bier S, Rabinowitz JG. Nonpalpable breast lesions: accuracy of prebiopsy mammographic localization. *Radiology* **1987**;165:323–326
8. Bigelow R, Smith R, Goodman PA, Wilson GS. Needle localization of nonpalpable breast masses. *Arch Surg* **1985**;120:565–569
9. Hoehn JL, Hardacre JM, Swanson MK, Williams GH. Localization of occult breast lesions. *Cancer* **1982**;49:1142–1144
10. Homer MJ, Smith TJ, Marchant DJ. Outpatient needle localization and biopsy for nonpalpable breast lesions. *JAMA* **1984**;252:2452–2454
11. Baker LH. Breast Cancer Detection Demonstration Project: five-year summary report. *CA* **1982**;32:194–225
12. Wilhelm MC, de Paredes ES, Pope T, Wanebo HJ. The changing mammogram: a primary indication for needle localization biopsy. *Arch Surg* **1986**;121:1311–1314
13. Landercasper J, Gunderson SB, Gunderson AL, Cogbill TH, Travelli R, Struttt P. Needle localization and biopsy of nonpalpable lesions of the breast. *Surg Gynecol Obstet* **1987**;164:452–456
14. Fornage BD, Faroux MJ, Simatos A. Breast masses: US-guided fine-needle aspiration biopsy. *Radiology* **1987**;162:409–414
15. Evans WP, Cade SH. Needle localization and fine needle aspiration biopsy of nonpalpable breast lesions with use of standard and stereotactic equipment. *Radiology* **1989**;173:53–56
16. Hann L, Ducatman BS, Wang HE, Fein V, McIntire JM. Nonpalpable breast lesions: evaluation by means of fine-needle aspiration cytology. *Radiology* **1989**;171:373–376
17. Dowlatshahi K, Gent HJ, Schmidt R, Jokich PM, Biobbo M, Sprenger E. Nonpalpable breast tumors: diagnosis with stereotaxic localization and fine-needle aspiration. *Radiology* **1989**;170:427–433
18. Schmidt R, Morrow M, Bibbo M, Cox S. Benefits of stereotactic cytology. *Admin Radiol* **October 1990**:35–42
19. Fajardo LL, Davis JR, Wiens JL, Trego DC. Mammography-guided stereotactic fine-needle aspiration cytology of nonpalpable breast lesions: prospective comparison with surgical biopsy results. *AJR* **1990**;155:977–981
20. Parker SH, Lovin JD, Jobe WE, et al. Stereotactic breast biopsy with a biopsy gun. *Radiology* **1990**;176:141–147
21. Helvie MA, Baker D, Adler DD, et al. Radiographically guided fine-needle aspiration of nonpalpable breast lesions. *Radiology* **1990**;174:657–661
22. Jackson VP, Littman JS. Stereotactic breast biopsy precisely locates lesions. *Diagn Imaging* **November 1989**:182–185
23. Cohen MB, Rodgers RPC, Hales MS, et al. Influence of training and experience in fine-needle aspiration biopsy of breast: receiver operating characteristics curve analysis. *Arch Pathol Lab Med* **1987**;111:518–520
24. Hunter TB, Villar HV, Bjelland JC, Leong SPL, Barteau LL. Combined surgery-mammography conference: a way to optimize patient care. *AJR* **1987**;149:1081–1082
25. Kreula J. A new method for investigating the sampling technique of fine needle aspiration biopsy. *Invest Radiol* **1990**;25:245–249
26. Kreula J. Effect of sampling technique on specimen size in fine needle aspiration biopsy. *Invest Radiol* **1990**;25:1294–1299
27. McDivitt R, Stewart F, Berg J. Tumors of the breast. In: *Atlas of tumor pathology*. Washington, DC: Armed Forces Institute of Pathology, **1969**:22–86
28. Fornage BD. Guided fine-needle aspiration biopsy of nonpalpable breast lesions: calculation of accuracy values (letter). *Radiology* **1990**;177:884–885
29. Gatchell FG, Dockerty MB, Clagett OT. Intracystic carcinoma of the breast. *Surg Gynecol Obstet* **1958**;106:347–352
30. Tabar L, Pentek Z, Dean PB. The diagnostic and therapeutic value of breast cyst puncture and pneumocystography. *Radiology* **1981**;141:659–663
31. Czernobilsky B. Intracystic carcinoma of the female breast. *Surg Gynecol Obstet* **1967**;124:93–98
32. Hoeffken W, Lanyi M. *Mammography*. Philadelphia: Saunders, **1977**:100–109
33. Tabar L, Pentek Z. Pneumocystography of benign and intracystic growths of the female breast. *Acta Radiol* **1976**;17:829–831
34. Hoeffken W, Hintzen C. Die Diagnostik der Mammazysten durch Mammographie and Pneumozystographie. *ROFO* **1970**;112:9–18
35. Leong PL, Fajardo LL, Rappaport WD, Villar HV. Stereotactic localization and aspiration of nonpalpable breast cysts prior to preoperative needle localization and biopsy. *Surg Gynecol Obstet* (in press)
36. Tabar L, Dean PB, Pentek Z. Galactography: the diagnostic procedure of choice for nipple discharge. *AJR* **1983**;149:31–38
37. Threatt B. Ductography. In: Bassett LW, Gold RH, eds. *Breast cancer detection: mammography and other methods in breast imaging*, 2nd ed. Orlando, FL: Grune & Stratton, **1987**:119–129
38. Funderburk WW, Syphax B. Evaluation of nipple discharge in benign and malignant diseases. *Cancer* **1969**;24:1290–1296
39. Diner WC. Galactography: mammary duct contrast examination. *AJR* **1981**;137:853–856
40. Nunnerley HB, Field S. Mammary duct injection in patients with nipple discharge. *Br J Radiol* **1972**;45:717–725
41. Tabar L, Dean PB. Interventional radiologic procedures in the investigation of lesions of the breast. *Radiol Clin North Am* **1979**;17:607–621
42. Ciatto S, Bravetti P, Berni D, Catarzi S, Bianchi S. The role of galactography in the detection of breast cancer. *Tumori* **1988**;74:177–181
43. Chan HP, Vyborny CJ, MacMahon H, et al. Digital mammography: ROC studies on the effects of pixel size and unsharp-mask filtering on the detection of subtle microcalcifications. *Invest Radiol* **1987**;22:581–589
44. Oestmann JW, Kopans D, Hall DA, et al. A comparison of digitized storage phosphors and conventional mammography in the detection of microcalcifications. *Invest Radiol* **1988**;23:725–728
45. Fajardo LL, Hunter TB. Digital genitourinary, gastrointestinal, and breast radiology. In: Newell JD, Kelsey CA, eds. *Digital imaging in diagnostic radiology*. New York: Churchill Livingstone, **1990**:43–70
46. Herron JM, Kennedy WH, Gur D, Good WF. X-ray imaging with two-dimensional charge-coupled device (CCD) arrays. *Proc SPIE* **1984**;486:141–145
47. Herron JM, Daxon EG, Gur D, et al. X-ray imaging with a 2048 × 2048 CCD array. In: *Proc SPIE Medical Imaging IV: Image Formation*. Society of Photo-Optical Instrumentation Engineers, **1990**:1231–1233

The Role of Fine-Needle Aspiration and Pneumocystography in the Treatment of Impalpable Breast Cysts

Debra M. Ikeda[1]
Mark A. Helvie[1]
Dorit D. Adler[1]
Laura A. Schwindt[1]
Alfred E. Chang[2]
Murray Rebner[1,3]

Prior studies have suggested that the recurrence rate is lower in breast cysts treated by pneumocystography (injection of air into cyst cavities after cyst aspiration) than in cysts treated by fine-needle aspiration alone. To determine if this is the case for impalpable breast cysts, we reviewed the hospital records and mammograms of 38 women with 41 impalpable cysts. Mammograms obtained immediately after aspiration show that pneumocystography was successful in 18 and unsuccessful in 20 of the 41 cysts. Four cysts were excluded from the study: one cyst that recurred after aspiration and was sampled by biopsy and three cysts for which immediate postaspiration mammograms were unavailable but which had recurred or persisted 3 years after aspiration. Review of follow-up mammograms made 4 months to 3 years after the aspiration showed that three (17%) of 18 cysts in the group with successful pneumocystography recurred and 11 (58%) of 19 cysts in the unsuccessful group recurred ($p = .02$). No difference was found in the number of recurrent cysts in relation to estrogen therapy or menopausal status.

Our results indicate that impalpable breast cysts treated by pneumocystography are less likely to recur than are cysts treated by aspiration alone.

***AJR* 158:1239–1241, June 1992**

The instillation of air into a breast cyst after aspiration of the cystic fluid (pneumocystography) has been reported to decrease the recurrence rate of the cyst. In these studies, aspiration was done using palpation for guidance, and cyst recurrences were detected by mammography or palpation [1, 2]. Because previous studies of impalpable cysts focused on mammographically guided aspiration for cytologic diagnosis rather than as a therapy for cysts, the rates of impalpable cyst recurrence after pneumocystography have not been reported [3–5]. The effect of exogenous estrogen administration on cyst recurrence after pneumocystography is also unknown.

Accordingly, we determined the long-term (4 months–3 years) recurrence rates of 41 breast cysts treated by fine-needle aspiration and pneumocystography. All cysts were initially detected only by mammography.

Materials and Methods

We reviewed the hospital records of women who had impalpable breast cysts diagnosed and treated by mammographically guided fine-needle aspiration between September 1985 and August 1987. Additional requirements for inclusion in the study included the following: (1) the initial mammograms were available for review, (2) the fine-needle aspirations revealed clear fluid with no malignant cells on cytologic examination, and (3) the patients had follow-up mammograms performed for at least 3 years after fine-needle aspiration. Thirty-eight women with 41 cysts qualified for the study and are the subject of this report. The average age of the patients was 52 years (range, 37–82 years). The average duration of follow-up was 41 months (range, 36–60 months), and the median cyst size was 15 mm (range, 8–60 mm). Recurrence of the cyst was determined by detection of a mass in the same location as

Received September 25, 1991; accepted after revision January 21, 1992.

[1] Department of Radiology, University of Michigan Hospitals, Box 0326, 1500 E. Medical Center Dr., Ann Arbor, MI 48109-0326. Address reprint requests to D. M. Ikeda.

[2] Department of Surgery, University of Michigan Hospitals, 1500 E. Medical Center Dr., Ann Arbor, MI 48109.

[3] Present address: Henry Ford Hospital, W. Grand River Blvd., Detroit, MI 48202.

0361-803X/92/1586-1239
© American Roentgen Ray Society

the original cyst on follow-up mammograms as reported separately by two radiologists. Disagreements were settled by consensus.

Cyst aspiration and pneumocystography were performed at the same time. Aspirations were performed under the guidance of dedicated screen-film mammographic equipment (500 T; General Electric CGR, Columbia, MD) with a fenestrated alphanumeric plate by a method previously described by Novak [6]. Some of the earliest aspirations were performed with a Mamex DC Mag unit (Technomed USA, Bayshore, NY) with similar equipment. Generally, only one 22-gauge needle was passed into the cyst until fluid was aspirated, and subsequently, an equal amount of air was injected into the cyst cavity (pneumocystography). Craniocaudal and mediolateral mammograms usually were obtained after the procedure to evaluate for an intracystic mass.

Although pneumocystography was attempted in all cysts except for three cases in which the needle was thought to have moved out of the cyst before air injection, not every cyst was completely emptied at aspiration nor was pneumocystography accomplished in every case. As such, two radiologists categorized the postaspiration films as either having a complete pneumocystogram (12 cases), partial pneumocystogram with air-fluid levels (six cases), complete disappearance of the cyst mass but no air in the cyst cavity (14 cases), cyst size smaller than on preaspiration films (six cases), or no postaspiration films obtained (three cases). Follow-up mammograms were scheduled for 4, 12, 24, and 36 months after aspiration to check for cyst recurrence.

Some authors have suggested that pneumocystography prevents recurrence of palpable breast cysts. We tested the hypothesis that the probability of cyst recurrence was the same in the cysts for which pneumocystograms were obtained and cysts for which pneumocystograms were not obtained by using Fisher's exact test [7].

Fisher's exact test also was used to determine if the presence of endogenous or exogenous estrogens had an effect on cyst recurrence after aspiration. At the time of cyst aspiration, 24 women were postmenopausal, three were perimenopausal, and 11 were premenopausal. Ten women were taking exogenous estrogens at the time of fine-needle aspiration. After fine-needle aspiration, eight women continued taking hormones, two discontinued estrogen treatments, and five began hormone replacement.

Results

Of the 41 cysts punctured under mammographic guidance, 25 (61%) did not recur by 3 years (average size, 17 mm). Fifteen of the 25 had complete or partial pneumocystography (average size, 19 mm), including the largest (60-mm) cyst. Of the other 10 cysts, seven were completely drained at fine-needle aspiration without successful pneumocystography (average size, 13 mm); no postaspiration films were available for two, and one was smaller after aspiration. One recurrent cyst was surgically removed after a second fine-needle aspiration.

Overall, 15 (37%) of the 41 cysts persisted (five cases) or recurred (10 cases) within 3 years. Five cysts were smaller after the procedure, leaving a small residual cyst on postaspiration films (average size, 16 mm). Fewer of the recurrent or persistent cysts had either partial or complete pneumocystography (three cysts, average size, 16 mm) or complete aspiration with no pneumocystography (six cysts, average size, 14 mm), or no postaspiration films (one case).

We also evaluated the data by separating the cysts into groups with pneumocystography or without pneumocystography on the postaspiration mammograms. Complete or partial pneumocystograms were available in 18 cases, and of these, 12 cysts (67%) never recurred after complete pneumocystography (seven cases) or partial pneumocystography (five cases). The other six cysts recurred but three of these resolved by 36 months either after a second aspiration (one case) or spontaneously (two cases).

Pneumocystography was not achieved in the remaining 23 cases, despite the presence of the needle in the cyst cavity at fine-needle aspiration and the aspiration of fluid. Three of the radiologic reports indicated that the needle probably moved out of the cyst cavity after aspiration, with subsequent collapse of the cyst cavity; no explanation was given for the others. Postaspiration films showed complete resolution of the cystic shadow in 14 of the 23 cases; six of these never recurred and the other eight recurred at various time intervals, four occurring at the 4-month follow-up. By 36 months, one of the eight recurrent cysts had resolved spontaneously, a surgical biopsy was done on one, and the other six persisted.

The remaining nine of these 23 cases either had no postaspiration films (three cases) or showed smaller cyst shadows on postaspiration films (six cases). Not unexpectedly, seven (78%) of these nine cysts were still present on the 4-month follow-up mammogram. One persistent cyst resolved spontaneously by 36 months after aspiration (for a total of three resolved cysts); the other six were still present.

Fisher's exact test was used to test the hypothesis that the probability of cyst recurrence was the same in the groups with complete and/or partial pneumocystography and those without; the analysis excluded three cysts for which postaspiration mammograms were not obtained and the one cyst from the group that was sampled by biopsy and for which no pneumocystogram was obtained. Fifteen (83%) of the 18 cysts with pneumocystograms had resolved by 3 years after aspiration, and eight (42%) of 19 cysts without pneumocystograms had resolved. The *p* value of the two-tailed test was .02, so the hypothesis of no difference was rejected. If cysts in both groups that had reaspiration are excluded, 14 of 16 cysts in the group with pneumocystograms and eight of 18 cysts in the group without pneumocystograms resolved at 3 years. The *p* value of the two-tailed test was .013, so the hypothesis of no difference between the two groups was rejected.

Interestingly, the age at menopause or the administration of exogenous hormone therapy did not influence which women had recurrent cysts. One postmenopausal woman on estrogen replacement had one cyst refill and one cyst resolve in the same breast. Of 17 women in whom breast cysts never recurred, nine (55%) were either on exogenous estrogen therapy or were premenopausal. Eleven (55%) of 20 women with recurrent cysts were either on exogenous estrogen replacement or were premenopausal.

Although other authors [8] have indicated that exogenous hormonal therapy may increase the occurrence of breast cysts, this factor, or the presence of endogenous estrogens, did not increase cyst recurrence after aspiration in the population under observation. Fisher's exact test showed no difference in cyst recurrence between the groups with and without endogenous estrogens or estrogen replacement therapy.

Discussion

Fine-needle aspiration under mammographic guidance proved that 41 cysts seen on mammograms were simple cysts, and fine-needle aspiration was therapeutic in 12 of 18 cysts with technically successful pneumocystography. Three additional cysts with successful pneumocystography resolved by 3 years, in contrast to 39% cyst persistence or recurrence when pneumocystography was unsuccessful.

Pneumocystography has been described as almost always successful in the treatment of simple benign cysts [1]. It has been postulated that after cyst aspiration, the injection of air into the cyst cavity causes the cyst to collapse and scar down, leading to fewer cyst recurrences [9]. Previous investigators did not distinguish between aspirations of palpable or impalpable cysts. Successful pneumocystography might have been somewhat easier to achieve by using palpation, because there is more tactile control over the position of the needle in relation to the cyst, and in general, palpable cysts are larger than those that are impalpable. With mammographically guided aspiration, pneumocystography may be difficult if the needle should move out of the cyst cavity before air is injected. Breast compression during mammographically guided fine-needle aspiration also flattens the overall cyst size, leaving a flatter volume of fluid to be punctured. Advancement of the needle into the deepest portion of the cyst cavity to completely empty the cyst fluid may be necessary for complete aspiration.

Fine-needle aspiration of palpable breast cysts has been described in the surgical and obstetric literature [10], and usually the palpable mass resolves after fluid is aspirated from the cyst. Routine physical examinations of the breast are performed 1-3 months after cyst aspiration to exclude cyst recurrence [10]. Recurrent palpable cysts are usually reaspirated or, after multiple aspirations, may be considered for surgical removal [2, 10-12]. Because the prevalence of malignant disease is extremely low in recurrent palpable cysts, there appear to be very few indications for their removal. These indications would include the persistence of a palpable mass after aspiration, aspiration of bloody cystic fluid, cytologic findings that suggest malignancy, or evidence of an intracystic mass lesion on pneumocystography.

In this study, impalpable cysts diagnosed on the basis of the results of fine-needle aspiration were considered benign at aspiration, just as impalpable breast cysts detected by screening mammography, and subsequently diagnosed on the basis of sonographic findings, are so considered. However, in the cases of cysts diagnosed on the basis of the results of fine-needle aspiration, we routinely evaluated for cyst recurrence (using mammography), similar to evaluation by physical examinations as part of postaspiration management of palpable cysts described in the surgical literature. Subsequent management of impalpable breast cyst recurrences was varied, with surgical biopsies performed on some cysts, some aspirated again, and some followed up mammographically, depending on the clinical situation, the patient, and her referring physician. For impalpable recurrent cysts, the indications for excision include aspiration of bloody cyst fluid or evidence of an intracystic mass by pneumocystography. If a patient has not had pneumocystography for a recurring palpable or impalpable breast cyst, then this procedure should be considered to determine if cyst excision is necessary.

ACKNOWLEDGMENT

Many thanks to Melanie L. Shaw for secretarial support.

REFERENCES

1. Tabár L, Péntek Z, Dean PB. The diagnostic and therapeutic value of breast cyst puncture and pneumocystography. *Radiology* **1981**;141:659-663
2. Dyreborg U, Blichert-Toft M, Boegh L, Kiaer H. Needle puncture followed by pneumocystography of palpable breast cysts: a controlled clinical trial. *Acta Radiol* **1985**;26:277-281
3. Ikeda DM, Bondeson L, Helvie MA, Rebner M, Adler DD. Evaluation of non-palpable breast nodules: 4-month mammographic follow-up vs. x-ray guided fine needle aspiration. *Breast Dis* **1991**;4:205-218
4. Helvie MA, Baker DE, Adler DD, et al. Radiographically guided fine-needle aspiration of nonpalpable breast lesions. *Radiology* **1990**;174:657-661
5. Löfgren M, Andersson I, Bondeson L, Lindholm K. X-ray guided fine needle aspiration for the cytologic diagnosis of nonpalpable breast lesions. *Cancer* **1988**;61:1032-1037
6. Novak R. Position-controlled needle aspiration biopsy at mammography. *ROFO* **1979**;131:659-671
7. Argresti A. *Categorical data analysis*. New York: Wiley, **1990**:59
8. Stomper PC, Van Voorhis BJ, Ravnikar VA, Meyer JE. Mammographic changes associated with postmenopausal hormone replacement therapy: a longitudinal study. *Radiology* **1990**;174:487-490
9. Hoeffken W, Lanyi M. *Mammography*. Philadelphia: Saunders, **1977**:39
10. Rosemond GP, Maier WP, Brobyn TJ. Needle aspiration of breast cysts. *Surg Gynecol Obstet* **1969**;28:351-354
11. Devitt JE. Association of breast cysts and breast cancer. *Can J Surg* **1988**;31:356-358
12. Haagensen CD. The relationship of gross cystic disease of the breast and carcinoma. *Ann Surg* **1977**;185:375-376

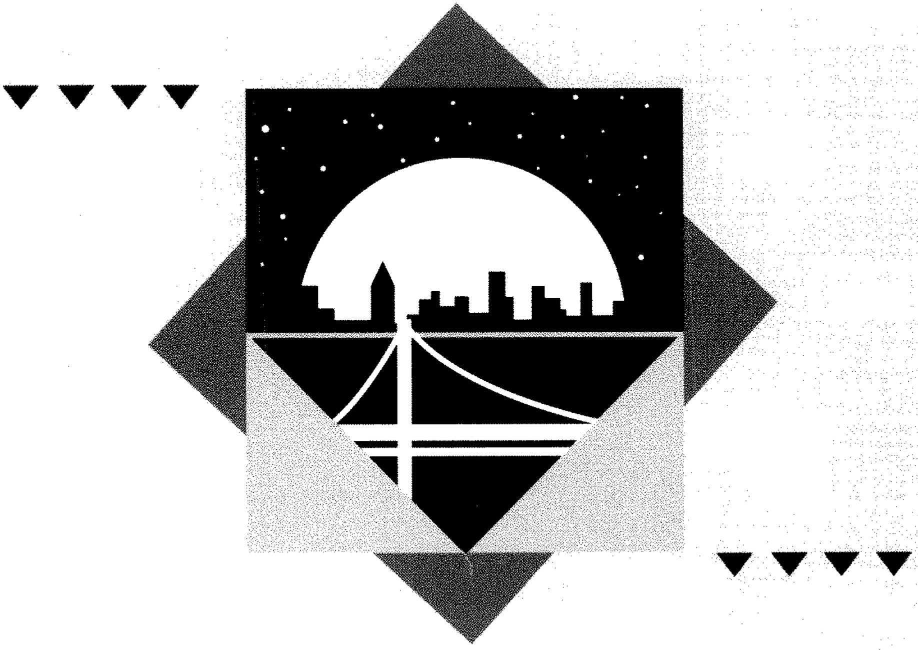

San Francisco

American Roentgen Ray Society
93rd Annual Meeting
April 25–30, 1993

San Francisco Marriott • San Franciso, CA

Perspective

Hidden Costs of Mobile Mammography: Is Subsidization Necessary?

Richard B. Wolk[1]

Two major impediments to an effective mammography program are inaccessibility and cost. This article itemizes the expenses associated with providing a mobile screening program accredited by the American College of Radiology (ACR) during a 3-year period. Mobile Diagnostics Inc. established a mobile mammography service in April 1987. A 36-ft (11-m) van is staffed by two registered technologists. The unit includes on-board processing and educational videotapes. Analysis of expenses for the years 1988, 1989, and 1990 does not include interpretation fees. A total of 3522 patients were examined in 1988, 4232 in 1989, and 5005 in 1990. Fixed operating expenses in 1988 were $70/examination and variable expenses were $13/examination, resulting in an average total cost per examination of $83. Fixed costs in 1989 were $63, variable costs were $15, and total costs were $78 per examination. Fixed costs in 1990 were $55, variable costs were $14, and total costs were $69 per examination.

Many third parties, including Medicare, are contemplating a global screening fee in the $50–$60 range. An average payment of $55 would require examination of more than 6500 patients a year or 28 patients a day to break even. Our experience suggests that some form of subsidization may be necessary to sustain a mobile mammography service at those reimbursement levels.

Two major impediments to an effective mammography program are inaccessibility and cost [1]. Mobile mammography has the potential of overcoming the problems of accessibility while increasing community awareness of the program. Women may avail themselves of state-of-the-art facilities in a convenient, nonthreatening environment that requires little time lost from daily activities because the service is provided locally. Much has been written about methods of reducing costs of mammographic screening [2, 3]. This report details the expenses associated with providing a mobile screening program accredited by the American College of Radiology (ACR) during a 3-year period.

Materials and Methods

Mobile Diagnostics Inc., an independent corporation in Wellesley, MA, established a mobile mammography service in April 1987. A 36-foot (11-m) van is staffed by two registered technologists. The unit includes dedicated mammography equipment, on-board processing, and educational videotapes, and it is accredited by the ACR. The sales, educational programs, and personnel are supervised by a full-time manager. The educational programs include free seminars for patients several days before arrival of the van, and on-board videotapes. No physical examination is performed. A full-time office manager handles processing of reports, data analysis, film control, scheduling, and bookkeeping. We reviewed the expenses, exclusive of interpretation fees, involved in operating the service for the years 1988, 1989, 1990. We assume 230 working days per year although the number of patients examined each month fluctuates significantly. Time lost for preventive maintenance, equipment malfunction, and inclement weather also contribute to the assumption of 230 working days.

Operating expenses are those that relate solely to the mobile unit and are further divided into fixed and variable categories. Administrative expenses are those that relate to all other aspects of the service, including sales, office, and billing functions, and are similarly divided into fixed and variable categories.

Received November 4, 1991; accepted after revision January 9, 1992.
Presented at the annual meeting of the American Roentgen Ray Society, Boston, MA, May 1991.

[1] Department of Radiology, Metro-West Medical Center Leonard Morse Campus, 67 Union St., Natick, MA 01760.

AJR **158:1243–1245, June 1992** 0361-803X/92/1586–1243 © American Roentgen Ray Society

Results

A total of 3522 patients were examined in 1988, 4232 in 1989, and 5005 in 1990. Fixed administrative costs rose from $64,300 in 1988 to $110,600 in 1990 (Table 1). Salaries accounted for the major change, as raises and the onset of pension plan contributions had an incremental impact of $25,500 during that time span. Annual office rent of $3600 was paid first in 1989, and medical insurance and worker's compensation for administrative personnel cost $12,000 in 1989. Costs relating to payroll taxes, telephone, legal and accounting services, furniture depreciation, and other taxes rose a total of $5200 between 1988 and 1989. Fixed administrative costs were $18 per examination for 3522 patients in 1988, $24 per examination for 4232 patients in 1989, and $22 per examination for 5005 patients in 1990.

Variable administrative expenses (Table 2) are those that depend on the number of patients examined and include office staff overtime, supplies, travel, temporary help, and billing fees. These costs have ranged from $23,500 in 1988 to $32,600 in 1990, although the cost per examination has remained relatively constant in the $6.50 range. Business consultant services amounted to $11,500 in 1988 and were dropped in 1989. However, these figures include the 1989 onset of yearly billing charges of $14,400. Ninety percent of our charges are billed to third parties because of market conditions and the fact that Massachusetts has mandated that screening mammography be covered by insurance. Many states have similar mandates, and other mobile mammography providers have found patients to be quite willing to pay at the time of service and seek reimbursement from their insurers. Such a system would lower our costs by $3 per examination. We also visit inner-city health centers. Many, if not most, of those patients would not have a mammogram if a cash advance was necessary. Our experience leads us to conclude that patients in Massachusetts strongly prefer us to bill their insurance carriers directly, and failure to comply would decrease the number of patients seen.

Fixed operating expenses (for the truck) have fallen from $183,200 in 1988 to $162,300 in 1990. This is largely due to a drop in the van's depreciation from $80,000 to $18,000 during the same interval (Table 3). Salary raises accompanied by the onset of pension contributions resulted in a $20,000 increase between 1988 and 1990. Special note should be taken of the fact that worker's compensation insurance amounts to 10% of salaries ($7000 per year) because that rate is mandated in Massachusetts for all personnel working on trucks. Truck repair and liability insurance has been steady, with each costing $6000 per year (Table 3). Mammographic units are exposed to constant mechanical stresses due to motion while being required to function at high volume, resulting in repair service charges greater than would be the case in a fixed site facility. Our mammography equipment repairs have varied between $3700 and $22,800. The latter was associated with a $17,000 charge for a new tube. Although cheaper tubes may be available, examination of 5000 patients per year will require periodic tube changes at substantial cost. As the number of examinations has increased, the fixed operating cost per examination has fallen from $52 in 1988 to $39 in 1989 to $32 in 1990.

Variable operating expenses rose from $22,000 in 1988 to $37,800 in 1990, but the cost per patient has remained steady, averaging $7.50 per patient throughout this period, with film being the main expense (Table 4). Supplies such as chemicals and film folders cost $3400 this past year. We operated for 3 months without on-board processing and found it to be a less efficient and less satisfying process for our mammographers. Our need for repeated films, owing to technical problems, was greater than 2%. Batch processing also required an additional 1–2 hr of personnel time to develop the films and match them with the appropriate histories and film jackets. With on-board processing, we are able to schedule five patients per hour, and we are skeptical that batch processing would enhance efficiency. Unexpected variables that may preclude operation include weather and disaster situations; for example, our truck was destroyed by an engine fire while en route to a scheduled site and has been replaced by a used vehicle.

TABLE 1: Fixed Administrative Expenses in Thousands of Dollars

Expense	1988	1989	1990
Salaries	50.0	67.1	75.5
Other expenses (medical insurance, taxes, rent, accounting, worker's comp.)	14.3	35.0	35.1
Total	64.3	102.1	110.6

TABLE 2: Variable Administrative Expenses in Thousands of Dollars

Expense	1988	1989	1990
Office supplies	4.3	6.4	10.2
Billing fees	0.0	14.4	14.4
Travel	3.2	2.9	3.7
Miscellaneous (overtime, consultants, temporary help)	16.0	6.1	4.3
Total	23.5	29.8	32.6

TABLE 3: Fixed Operating (Truck) Expenses in Thousands of Dollars

Expense	1988	1989	1990
Depreciation	80.0	48.0	17.9
Interest	22.4	19.0	11.8
Salaries	50.0	60.0	69.5
Taxes (payroll, worker's comp.)	5.2	7.3	14.2
Mammography equipment repair	7.5	3.7	22.8
Truck repair and liability	13.1	12.9	11.7
Miscellaneous (medical insurance, phone, sales taxes)	5.0	13.3	14.4
Total	183.2	164.2	162.3

TABLE 4: Variable Operating (Truck) Expenses in Thousands of Dollars

Expense	1988	1989	1990
Film	9.5	14.8	17.0
Overtime	3.6	3.8	8.0
Supplies (chemicals, folders, gowns)	5.4	6.2	4.7
Miscellaneous (travel, gas, temporary help)	3.4	6.7	8.1
Total	21.9	31.5	37.8

Discussion

We have described the costs of providing an ACR-accredited mobile mammography service in the Northeast. Our market is not totally free. Massachusetts has one of the highest rates of health maintenance organization (HMO) participation in the nation. HMOs may restrict patients' access to specific facilities and may choose not to participate with mobile programs. This practice has limited the number of persons who use our service, particularly in the industrial setting, and has hampered growth in the daily number of patients examined.

We discovered many hidden costs that have not been noted or itemized in previous reports [4, 5]. They include rent, worker's compensation, overtime, and marketing and educational services. If reimbursement levels are restricted, other sources of income may need to be sought to cover expenses.

Only market conditions and society can determine if a mobile program, with its attendant costs, is worthwhile and merits subsidization. Subsidization may occur in many ways. We were provided free office space for our first year. Sponsoring institutions or medical groups may provide personnel, processing facilities, publicity, funds, and even entire mobile units. Failing to acknowledge such aid masks the true cost of providing the service.

TABLE 5: Cost per Examination, in Dollars

Expense	1988	1989	1990
Operating			
Fixed	52	39	33
Variable	6	8	8
Administrative			
Fixed	18	24	22
Variable	7	7	6
Total	83	78	69

Note.—In 1988, 3522 patients were seen; in 1989, 4232 patients; in 1990, 5005 patients.

Fixed operating expenses (Table 5) in 1988 were $70 per examination and variable expenses were $13 per examination resulting in an average total cost per examination of $83. Fixed costs in 1989 were $63, variable costs were $15, and total costs were $78 per examination. Fixed costs in 1990 were $55, variable costs were $14, and total costs were $69.

Medicare has established a global screening fee of $55, and similar fees have been suggested by others [6, 7]. Because fixed costs are so sizable, mobile mammography is financially feasible only when operating at high volume, which may take several years to achieve. An average payment of $55 would require examination of more than 7580 patients per year or 28 patients per day to break even, assuming fixed costs of $36, variable costs of $14, and an interpretation fee of $5 per patient. Owing to seasonal and daily fluctuations in number of patients examined, a daily average of 28 patients may take a long time to achieve and be difficult to sustain. This fact affects the capitalization required to establish such a program. Our experience suggests that some form of subsidization may be necessary to sustain such a service at those reimbursement levels.

ACKNOWLEDGMENT

I thank Daniel Kopans for his help in reviewing this paper.

REFERENCES

1. Dodd GR. Breast cancer detection and community practice. *Cancer* **1989**;64:2639–2640
2. Sickles EA, Weber WN, Galvin HB, Ominsky SH, Sollito RA. Low-cost mammography screening. *Cancer* **1987**;60:1688–1691
3. Rubin E, Frank MS, Stanley RJ, Bernreuter WK, Han SY. Patient-initiated mobile mammography. *South Med J* **1990**;83:178–184
4. Sickles EA, Weber WN, Galvin HB, Ominsky SH, Sollito RA. Mammographic screening: how to operate successfully at low cost. *Radiology* **1986**;160:95–97
5. Bird RE, McClelland R. How to initiate and operate a low cost screening mammography center. *Radiology* **1986**;161:43–47
6. Dodd GD. Cost reduction in mammography. *Cancer* **1989**;64:2667–2670
7. Kron ES, Moskowitz H, McConner D, Loveland JA. Mobile mammography: the first six-months experience at Mount Sinai Hospital. *Conn Med* **1989**;53:71–72

AJR to Use Diskettes Instead of Hard-Copy Manuscripts for Editing and Printing

Beginning with the January 1993 issue, accepted papers to be published in the *AJR* will be edited and printed by using computer diskettes rather than hard copies of the manuscripts. This change will expedite the editing and publication process and result in less delay between submission of manuscripts and their appearance in the Journal. Also with the new system, authors will receive page proofs rather than galleys prior to publication. This will enable them to see exactly what their final article will look like.

Effective immediately, upon *acceptance* of manuscripts for publication, authors will be asked to send a copy of their revised manuscript on a 5¼-inch DOS-compatible diskette in Wordperfect or ASCII format along with the hard copy of the revision. Articles will be edited directly on the diskettes. Changes will be highlighted electronically; as before, a hard copy of the edited manuscript and figure proofs will be mailed to authors for approval before publication. Note that hard copies of manuscripts will still be required for the peer-review and revision processes.

The *AJR* already takes great pride in the speed with which the peer review process is accomplished (mean time 3.4 weeks) and in the amount of time between submission of manuscripts and their final appearance in print (6 months). This is nearly twice as fast as many other journals. With the new system, these intervals will be even shorter. Authors will see their work in print faster, and the timeliness of the Journal will be greater than ever.

Robert N. Berk
Editor-in-Chief

Rupture of Hepatocellular Carcinoma: Predictive Value of CT Findings

Masayuki Kanematsu[1]
Takeyoshi Imaeda[1]
Yoshiharu Yamawaki[1]
Matsuzo Seki[1]
Hiroo Goto[1]
Yasuhiro Sone[2]
Gen Iinuma[1]
Ryozo Mochizuki[1]
Hidetaka Doi[1]

To assess the value of CT in predicting spontaneous rupture of hepatocellular carcinoma, we reviewed CT scans obtained within 3 months before the rupture of hepatocellular carcinoma in 23 patients (rupture group) and within 3 months before death of any cause other than rupture of hepatocellular carcinoma in 20 patients with tumor contacting or protruding out of the liver margins (nonrupture group). All the carcinomas in the rupture group were located in the periphery of the liver. They protruded out of the liver margins in 18 cases and contacted the liver margins without protrusion in five cases. For the rupture and nonrupture groups, respectively, mean numbers of involved liver segments were 4.2 ± 2.3 and 2.3 ± 1.3 ($p < .01$); mean maximal tumor areas were 102.0 ± 57.0 cm^2 and 57.7 ± 50.9 cm^2 ($p < .05$); frequencies of tumor protrusion was 78% and 50% (NS); mean maximal lengths of protruded margins of the tumor were 188.1 ± 81.4 mm and 77.2 ± 50.3 mm ($p < .01$); frequencies of extrahepatic invasion of the tumor were 44% and 20% (NS); and frequencies of ascites were 78% and 50% (NS). No significant differences in age or sex of the patients and clinical stage of the cancer were evident between the two groups. Multiple regression analysis ($p < .005$, $r^2 = .428$) indicated that, of the CT findings, maximal length of protrusion correlated best ($p < .05$) with subsequent rupture.

We conclude that increased tumor size and extent of extrahepatic protrusion are associated with an increased risk for rupture of hepatocellular carcinoma.

***AJR* 158:1247–1250, June 1992**

About 10% of patients with hepatocellular carcinoma (HCC) have spontaneous rupture of the tumor [1], and most of them rapidly lapse into a critical condition because of substantial intraabdominal bleeding [2–4]. Attempts to treat such patients by means of surgery or transcatheter arterial embolization have been made [2–5], but have not been successful in the vast majority of cases. The ability to predict HCC rupture with high likelihood might improve the treatment of such patients. CT findings after HCC rupture have been described in numerous articles [3, 4, 6, 7]; however, no reports evaluating the use of CT in predicting HCC rupture have been published. We undertook such a study.

Materials and Methods

From 1980 through 1991, HCC was diagnosed in 203 consecutive patients on the basis of CT, sonographic, angiographic, or MR findings, serum level of α-fetoprotein, or results of biopsy or autopsy. In 23 of these patients (rupture group), a rupture of HCC developed, which was confirmed by abdominal paracentesis or autopsy. Another group of 20 patients with HCC contacting or protruding out of the liver margins (nonrupture group) died of causes other than HCC rupture (hepatic coma, nine cases; intestinal bleeding, eight cases; other causes, three cases) between 1986 and 1991. CT scans in both groups had been obtained within 3 months before HCC rupture or death. The CT scans were reviewed for the site of tumor, number of involved segments among the eight liver segments, maximal tumor area, presence of protrusion of the tumor, maximum length of protruded margins of the tumor,

Received November 6, 1991; accepted after revision January 9, 1992.

[1] Department of Radiology, University of Gifu School of Medicine, Gifu City, 500 Japan. Address reprint requests to M. Kanematsu.

[2] Department of Diagnostic Radiology, Aichi Cancer Center, Nagoya City, 464 Japan.

0361-803X/92/1586-1247
© American Roentgen Ray Society

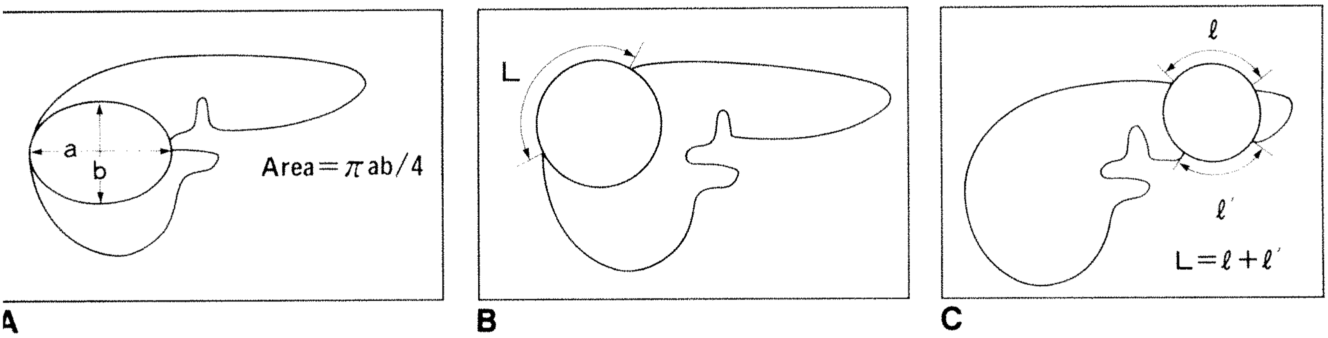

Fig. 1.—Drawings show methods of measurement of maximal tumor area and of maximal length of protruded margins of tumor on CT.
***A*, Area of tumor is calculated approximately as area of an ellipse. a = major axis, b = minor axis of tumor on CT scan.**
***B*, Maximal length (L) of protruded margins of tumor is measured along most protruded segment on CT scan.**
***C*, When tumor protrudes along more than one surface, maximal length (L) of protruded margins is obtained by adding lengths of individual protrusions (ℓ) together.**

presence of extrahepatic invasion, and presence of ascites. Maximal tumor area on CT was calculated approximately as the area of an ellipse by measuring the major and minor axes of the tumor on the CT scan (Fig. 1A). Maximal length of protruded margins of the tumor was measured along the most protruded segment on the CT scan (Fig. 1B). When the tumor protruded along more than one surface, the maximal length of protrusion was obtained by adding the lengths of each protrusion (Fig. 1C). Extrahepatic invasion was considered to be present when the tumor mass shown on CT was associated with thickening of the contiguous diaphragm or abdominal wall (Figs. 2–4). The mean values of numbers of involved liver segments, maximal tumor areas, and maximal lengths of protrusion between the two groups were compared by using an unpaired Student's t-test. The frequencies of protrusion, extrahepatic invasion, and ascites in the two groups were compared by using a chi-square test. Further, we performed multiple regression analysis with CT findings (number of involved segments, maximal tumor area, presence of protrusion, maximal length of protrusion, presence of invasion, presence of ascites) as independent variables, and occurrence of rupture as the dependent variable.

Results

The rupture group consisted of 22 men and one woman. The age range was 40–69 years (mean, 56 years). The nonrupture group had 19 men and one woman. The age range was 38–73 years (mean, 58 years). All the HCCs in the rupture group were located in the periphery of the liver. They protruded out of the liver contours in 18 cases and contacted the liver margins without protrusion in five cases. The HCCs in the rupture group involved significantly more ($p < .01$) segments of the liver than in the nonrupture group. Results of comparison of CT measurements in the rupture group and nonrupture group are given in Table 1 and Figure 5. (Values are expressed as mean ± SD.) The mean maximal tumor area on CT in the rupture group was significantly greater ($p < .05$) than that in the nonrupture group. The mean maximal length of protruded margins of the tumor in the rupture group was significantly longer ($p < .01$) than that in the nonrupture group.

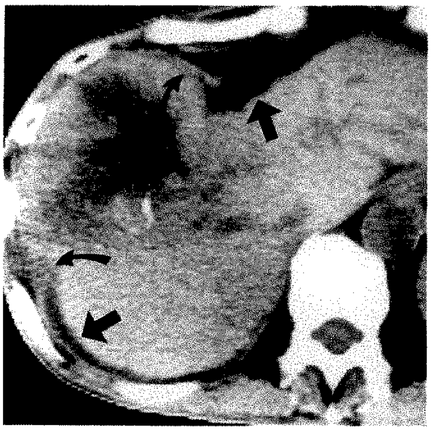

Fig. 2.—CT scan of patient with hepatocellular carcinoma in whom tumor subsequently ruptured shows tumor protrusion, extrahepatic invasion (*curved arrows*), and ascites (*straight arrows*).

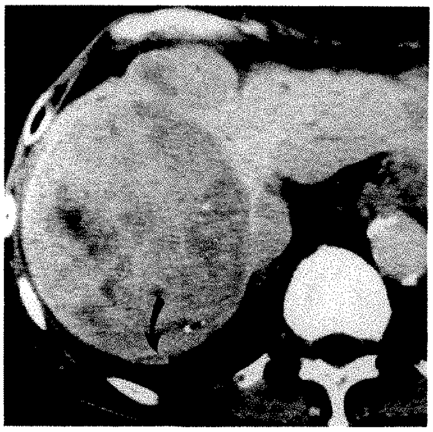

Fig. 3.—CT scan of patient with hepatocellular carcinoma with subsequent tumor rupture shows tumor protrusion and extrahepatic invasion (*arrow*).

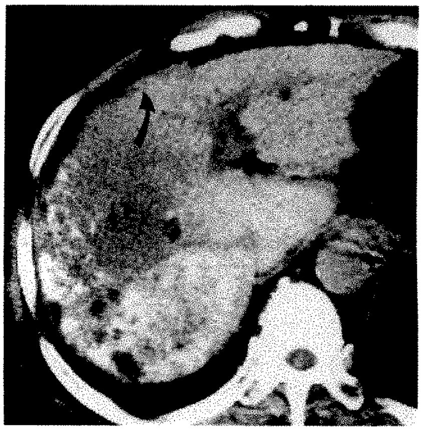

Fig. 4.—CT scan of patient with hepatocellular carcinoma without subsequent tumor rupture shows extrahepatic invasion (*arrow*) without tumor protrusion.

TABLE 1: CT Findings in Groups with and Without Subsequent Rupture of Hepatocellular Carcinoma

Findings	Rupture Group ($n = 23$)	Nonrupture Group ($n = 20$)	Statistical Analysis
Tumor site			
Right lobe	15	17	
Left lobe	1	1	NS[a]
Both lobes	7	2	
Number of involved liver segments	4.2 ± 2.3	2.3 ± 1.3	$p < .01$[b]
Maximum tumor area (cm^2)	102.0 ± 57.0	57.7 ± 50.9	$p < .05$[b]
Protrusion from liver periphery	18 (78%)	10 (50%)	NS[a]
Maximum length of protrusion (mm)	188.1 ± 81.4	77.2 ± 50.3	$p < .01$[b]
Extrahepatic invasion	10 (44%)	4 (20%)	NS[a]
Ascites	18 (78%)	10 (50%)	NS[a]

[a] Statistical analyses between the two groups were performed by chi-squared test. NS = not significant.

[b] Statistical analyses between the two groups were performed by unpaired Student's t-test.

The frequency of protrusion of the tumor, extrahepatic invasion, and ascites tended to be higher in the rupture group than in the nonrupture group, although these differences were not statistically significant. Multiple regression analysis ($p < .005$, $r^2 = .428$) indicated the predictive value of the CT findings for rupture; of the six independent variables, maximal length of protrusion correlated best with subsequent rupture ($p < .05$). The other CT findings had no significant correlation with occurrence of rupture.

Low-attenuation areas compatible with necrotic degeneration inside the tumor were seen on CT in all the tumors of both groups. Tumors were clinically staged according to the TNM classification as follows: stage I, zero and one case; stage II, zero and one case; stage III, four and four cases; stage IVA, seven and two cases; stage IVB, 12 and 13 cases; for the rupture and nonrupture groups, respectively.

Discussion

It is believed that a tear in the tumor surface or rupture of a parasitic feeding artery causes HCC rupture and resulting hemoperitoneum. In Japan, HCC often grows expansively, especially when the tumor has an encompassing fibrous capsule [8]. In such cases, pressure within the tumor may be relatively high, predisposing the tumor to rupture. Further, when HCC protrudes out of the liver contours, a tumor might tear more easily than in cases in which HCC is entirely surrounded by liver parenchyma. A parasitic feeding artery may rupture in conjunction with development of ascites. Ascites in the space between the liver and the diaphragm may cause separation of these structures, leading to tearing of adhesive surfaces or rupture of an adjacent artery.

We initially hypothesized that size of tumor, extent of contact of tumor with the surface of the liver, extent of protrusion out of the liver contours, presence of extrahepatic invasion of HCC, and presence of ascites might correlate with HCC rupture. In this study, the estimated maximal tumor area on CT was used as an approximation of tumor volume.

The results showed a significant difference in maximal tumor area measured on CT between the rupture and nonrupture groups. Similarly, the maximal lengths of protruded margins of the tumor measured on CT also showed a significant difference between the two groups. The frequency of protrusion of the tumor, extrahepatic invasion, and ascites tended to be higher in the rupture group than in the nonrupture group, although these differences were not significant.

Multiple regression analysis indicated that all of the CT findings predicted rupture to a certain extent ($p < .005$, $r^2 = .428$). As an independent variable, maximal length of protrusion correlated best with occurrence of rupture ($p < .05$). However, the other CT findings, including maximal tumor area, had no significant correlation. We now strongly consider maximal length of protrusion rather than maximal tumor area for predicting rupture.

We limited our review to an evaluation of CT scanning in this study. However, as CT usually offers only axial images, it may fail to depict protrusion or invasion of HCC in the craniocaudal direction. MR imaging, however, can be done in various planes and may enable evaluation of contact or protrusion of the tumor in all directions. For evaluation of extrahepatic invasion of HCC in the craniocaudal direction, MR imaging, sonography, and angiography are of greater value. In particular, angiography can delineate parasitic feeding vessels such as the inferior phrenic, gastroepiploic, right colic, or intercostal arteries.

Several limitations of the study must be considered. We cannot exclude the effect of selection bias on the results we obtained. One must consider the possibility that patients in the nonrupture group who died of other causes might have had tumor rupture if they had lived. In addition, despite the significant differences in maximal tumor area and protrusion length between the two groups, the distribution of values still shows significant overlap (Fig. 5). When a cutoff level of maximal tumor area is set at 80 cm^2, the sensitivity and specificity of this finding are 61% and 65%, respectively, and when a cutoff level of maximal length of protrusion is set at 133 mm, sensitivity and specificity are 78% and 70%, respectively.

When a high possibility of rupture is suggested by CT findings, preventative therapeutic intervention such as

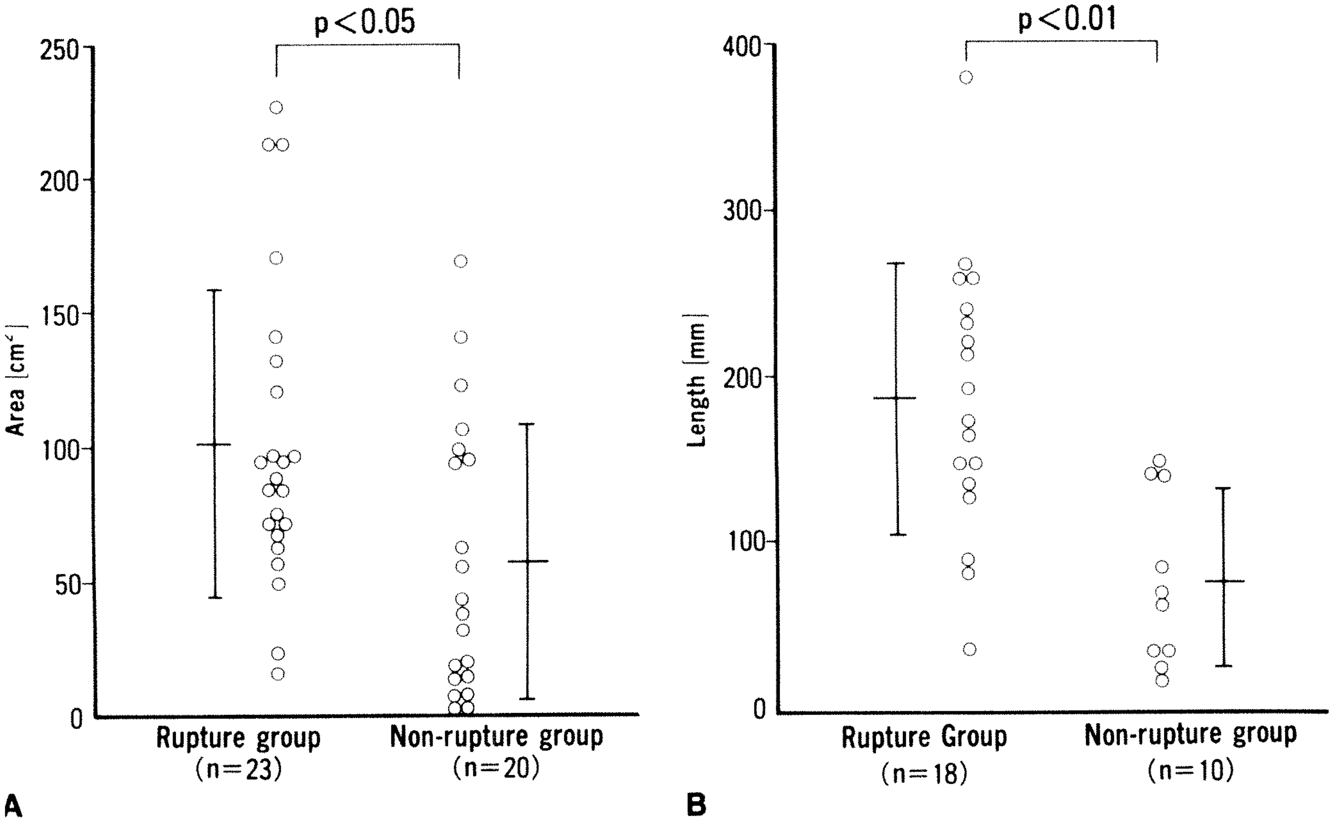

Fig. 5.—Distribution of CT measurements for groups with and without subsequent rupture of hepatocellular carcinoma.
***A*, Maximal tumor areas on CT scans.**
***B*, Maximal lengths of protruded margins of tumor on CT scans.**

transcatheter arterial embolization directed at reduction of tumor volume, or Lipiodol chemoembolization through parasitic feeding vessels such as the inferior phrenic artery may be indicated.

ACKNOWLEDGMENT

We thank Toshiyuki Sawa, Second Department of Internal Medicine, for assistance in statistical analyses in this study.

REFERENCES

1. The Liver Cancer Study Group of Japan. Primary liver cancer in Japan: sixth report. *Cancer* **1987**;60:1400–1411
2. Takano S, Tesima Y, Murata I, et al. A study of spontaneous rupture of hepatocellular carcinoma. *J Jpn Pract Surg Soc* **1987**;48:989–994
3. Cates JD, Thorsen MK, Foley WD, Lawson TL. CT diagnosis of massive hemorrhage from hepatocellular carcinoma. *J Comput Assist Tomogr* **1987**;11:81–82
4. Uchida K, Nakata S, Iwase H, Yamamoto H, Kasahara H, Konagaya T. Imaging diagnosis of ruptured site in hepatocellular carcinoma. *Jpn J Gastroenterol* **1989**;86:1287–1291
5. Kitsuki H, Okazaki M. Successful experience in transcatheter arterial embolization (TAE) after visualizing extravasation due to rupture of hepatocellular carcinoma. *Jpn J Clin Radiol* **1988**;33:727–730
6. Merine D, Fishman EK, Zerhouni EA. Spontaneous hepatic hemorrhage: clinical and CT findings. *J Comput Assist Tomogr* **1988**;12:397–400
7. Siskind BN, Malat J, Hammers L, et al. CT findings of hemorrhagic malignant liver tumors. *J Comput Assist Tomogr* **1987**;11:766–770
8. Okuda K, Nakashima T. Primary carcinoma of the liver. In: Berk JE, ed. *Bockus gastroenterology*, 4th ed., vol. 5. Philadelphia: Saunders, **1985**:3315–3376

Case Report

Treatment of Mesocaval Shunt Stenosis with a Metallic Stent

Philippe Soyer,[1] Marc Levesque,[1] and Guy Zeitoun[2]

Percutaneous transluminal angioplasty (PTA) has been proposed for the treatment of occluded or stenosed mesocaval shunts [1, 2]. Unfortunately, reocclusion or restenosis frequently occurs after PTA [3]. Most of the time, reocclusion or restenosis may benefit from repeated PTA, but failure after several attempts prompts the surgeon to place a new mesocaval shunt. In those cases, the use of a metallic stent that would exert constant outward force on the affected shunt might be of benefit [3]. To our knowledge, intravascular stenting as a means of providing definitive treatment of mesocaval shunt stenosis has not been described. We report a case of stenosis of a mesocaval shunt that was successfully treated by percutaneous insertion of a metallic stent after failure of PTA.

Case Report

A 52-year-old woman was admitted to our hospital with jaundice, hypotension, hepatomegaly, and marked ascites. No hematemesis or melena was observed. Laboratory blood tests showed elevated levels of liver enzymes, low serum levels of protein, slightly increased creatinine levels, and an increased platelet count. The patient had no history of alcohol abuse. Upper endoscopic examination revealed moderate esophageal varices. Occlusion of the hepatic veins and patency of the inferior vena cava (IVC) were shown with Doppler sonography, CT, MR imaging, and angiography. The diagnosis of Budd-Chiari syndrome was confirmed by liver biopsy. Transhepatic portography with pressure measurement showed an increased pressure in the portal vein (17 cm saline). Pressure in the IVC was 6 cm saline.

The patient was treated with surgical construction of a mesocaval shunt. The bypass operation was performed with a venous graft constructed from the patient's own external jugular vein. After surgery, the patient deteriorated clinically and had persistent ascites (>4 l/day). On the 15th postoperative day, after ascites was drained, direct portography showed narrowing of the shunt with filling of collateral veins (Fig. 1A). The stenosis was located on the portal side of the shunt. The intrahepatic portal pressure was 18 cm saline while pressure in the IVC was 6 cm saline. Subsequently, PTA of the shunt was performed with a 10 mm × 4 cm balloon catheter (Ultra-thin, Medi-Tech/Boston Scientific, Watertown, MA). Controlled balloon inflation was achieved with a pressure of 10 atm (1.01×10^6 Pa) over 30 sec for three inflations. After the dilatation, control portography showed residual stenosis (Fig. 1B) even when the pressure gradient fell to 4 cm saline. In the following days, the patient continued to have abundant ascites. Portography 10 days later showed restenosis (Fig. 1C) and pressure measurements confirmed intraportal hypertension. A second PTA was performed with the same short-term results. After this second rapid recurrence of the stenosis, it was decided that a more definitive treatment was needed. During both PTA procedures, it was noted that the stenosis was easy to dilate, and immediately after the procedure, the shunt was patent with diminished pressure gradient.

Before stent implantation, the patient was informed of the risks and benefits of the procedure, and consent was obtained. The patient was treated with an anticoagulant (heparin) for 1 day before and 2 days after stent placement. On the 35th postoperative day, the stent was inserted under local anesthesia, after puncture of the right femoral vein and placement of an 11-French introducer sheath. After PTA, a balloon-expandable flexible metallic stent (Strecker; Meditech/Boston Scientific, Watertown, MA) was placed across the shunt. The Strecker stent is a tube knitted from a single metallic filament

---

Received October 23, 1991; accepted after revision December 11, 1991.

[1] Department of Radiology, Hôpital Louis Mourier, 178 rue des Renouillers, 92701 Colombes, France. Address reprint requests to P. Soyer.

[2] Department of Surgery, Hôpital Louis Mourier, 92701 Colombes, France.

AJR 158:1251-1253, June 1992 0361-803X/92/1586-1251 © American Roentgen Ray Society

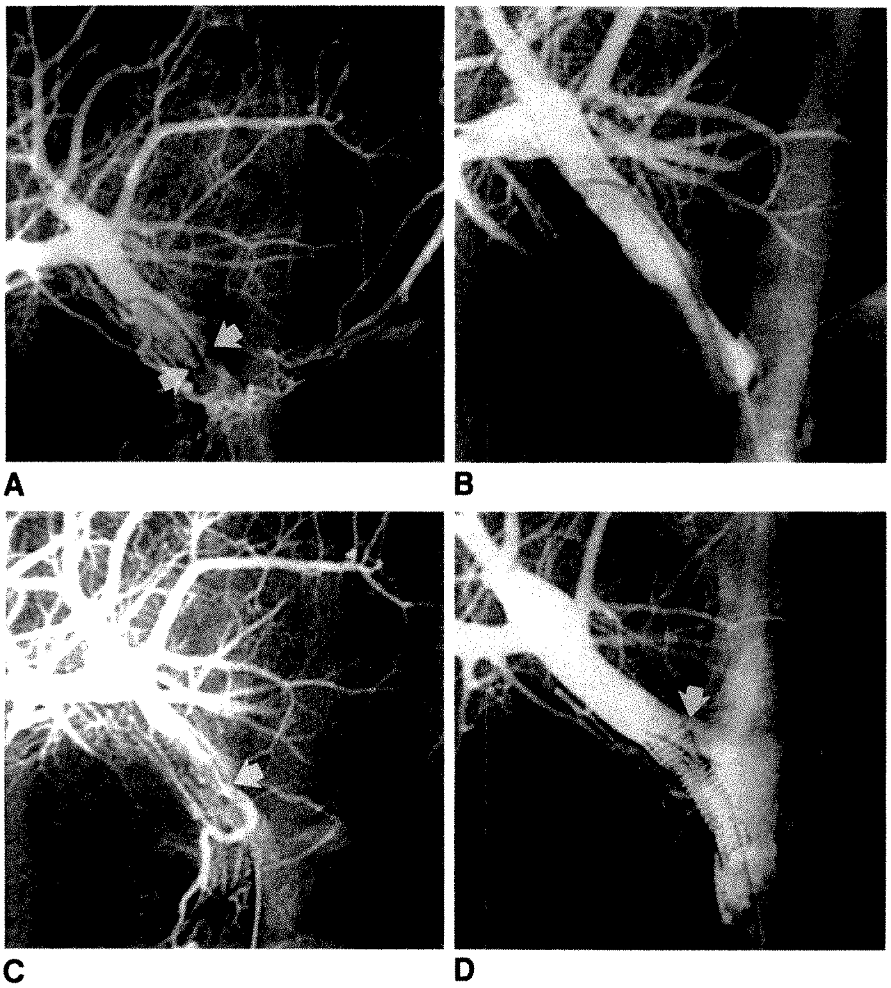

Fig. 1.—*A*, Portogram obtained with catheter in portal vein shows marked stenosis of shunt (*arrows*) with virtual occlusion and filling of collateral veins. Portal pressure is 18 cm saline when pressure in inferior vena cava is 6 cm saline.

B, Portogram obtained after dilatation with a 10-mm balloon catheter shows stenosis is incompletely resolved, but pressure gradient dropped to 4 cm saline.

C, 10 days after first transluminal angioplasty, portogram shows recurrence of previously dilated stenosis (*arrow*). A 12-cm saline pressure gradient is present.

D, Portogram obtained immediately after placement of stent confirms wide patency of shunt and shows good opacification of inferior vena cava. A 1-cm saline pressure gradient is present. Reflux in splenic vein (*arrow*) is visible.

made of tantalum; the filament is 0.1 mm in diameter, and the stent is 40 mm long. The stent was loaded onto a 7-French, 11 mm × 4 cm polyethylene balloon catheter and advanced through the shunt. This flexible stent, which was also flexible even when mounted on its delivery balloon-catheter, permitted easy access through the shunt to the area of stenosis. The stent expanded to the size of the balloon (11 mm) as the balloon was inflated, and remained expanded after the balloon was deflated. The final length of the stent was 36 mm. After stent placement, portography showed the stent completely open (Fig. 1D); intraportal pressure dropped to 7 cm saline, resulting in a pressure gradient of 1 cm saline. The patient had no complications and was considered improved clinically during the first 2 weeks, because ascites lessened and results of liver function tests improved. Four months after stent placement, the patient was free of symptoms.

Discussion

Mesocaval shunts are constructed to palliate symptomatic portal hypertension and to decompress the hepatic vasculature. Occlusion of mesocaval shunts may be caused by thrombosis, kinking, extrinsic compression, or collapse due to reduced blood flow. The rate of shunt failure is reported to be 5–15% [3], but these values are probably underestimates of the true frequency because many patients do not have recurrent symptoms.

The use of PTA to preserve the function of surgically created mesocaval shunts is well established. Unfortunately, this procedure has to be repeated in many patients, partly because PTA itself causes a proliferative response after intimal and medial disruption with subsequent restenosis [3]. Cope [2] reported a series of 16 patients with mesocaval shunt dysfunction, of whom 11 had initially successful balloon dilatation. Six of those 11 patients required repeated balloon dilatation. Martin et al. [3] reported a series of six patients with Budd Chiari syndrome in whom PTA was used. All patients had clinical and hemodynamic improvement after each PTA, but during a follow-up period of 12–92 months (mean, 43 months), all patients required multiple dilatations (mean, 3.2) because of restenosis at the angioplasty site. Cope [2] and Martin et al. [3] suggest that PTA is not the definitive therapy but serves to moderate the severity of the disease. Restenosis and rethrombosis after PTA of mesocaval shunts restrict the usefulness of this procedure even when one considers its low morbidity.

The results obtained after placement of a metallic stent in this case are encouraging. Avoiding surgery in such patients is highly desirable, as the repair of venous obstructive lesions may be difficult because of extensive endovenous and perivenous fibrosis. It is usually necessary to sacrifice the occluded shunt and place a new graft. We believe that graft stenting may be an alternative to surgery for treating restenosis of mesocaval shunts. This technique may add a new dimension to the management of some patients with mesocaval shunt because it avoids the stress of a major surgical procedure and reduces the cost of increased hospital stay. Nevertheless, PTA should be the preferred treatment for initial graft stenosis because it is feasible and well-tolerated.

The possible immediate or long-term complications of this technique need to be evaluated. Sigwart et al. [5] showed that 6 months after they placed an intraarterial stent, the Medinvent stent was firmly embedded in the arterial wall; the neointima smoothly filled the pores between the stent filaments and the endothelial surface was similar to the arterial endothelium. Gunther et al. [6] described a series of patients with venous stenoses in dialysis shunts in whom intima hyperplasia, associated with narrowing of the stent lumen, was noted within 4 months of stent placement. Because portal blood flow differs from arterial flow and flow within a dialysis shunt, the pathologic changes occurring in a stented mesocaval shunt cannot be extrapolated from observations in other vascular beds. Nevertheless, intimal hyperplasia may be a limitation of stent placement in mesocaval shunts. In the study reported by Richter et al. [7] regarding transjugular intrahepatic portosystemic stent shunt, autopsy in the two patients who died showed patent stent shunts but early neoendothelial incorporation. Further studies will determine the long-term benefits of this new approach.

REFERENCES

1. Cope C. Balloon dilatation of closed mesocaval shunts. *AJR* **1980**;135:989-993
2. Cope C. Dilatation of mesocaval shunts. *Ann Radiol* **1986**;29:178-180
3. Martin LG, Henderson JM, Millikan WJ Jr, Casarella WJ, Kaufman SL. Angioplasty for long term treatment of patients with Budd-Chiari syndrome. *AJR* **1990**;154:1007-1010
4. Dowling JB. Ten years' experience with mesocaval grafts. *Surg Gynecol Obstet* **1979**;149:518-522
5. Sigwart U, Puel J, Mirkovitch V, Joffre F, Kappenberger L. Intravascular stents to prevent occlusion and restenosis after transluminal angioplasty. *N Engl J Med* **1987**;316:701-706
6. Gunther RW, Vorwerk D, Bohndorf K, et al. Venous stenoses in dialysis shunts: treatment with self-expanding metallic stents. *Radiology* **1989**;170:401-405
7. Richter GM, Noeldge G, Palmaz JC, Roessle M. The transjugular intrahepatic portosystemic stent-shunt (TIPSS): results of a pilot study. *Cardiovasc Intervent Radiol* **1990**;13:200-207

Videotape Review

RSNA Today Video, Vol. 5, No. 5. Oak Brook, IL: The Radiological Society of North America, 1991. $55; by subscription, 6 issues annually at $185 for RSNA members and $225 for nonmembers (VHS videotape)

This videotape consists of four sections introduced by William J. Casarella. The first section, presented by Donald Resnick, is on MR imaging of the shoulder. Dr. Resnick first reviews basic anatomy of the shoulder, including the muscular attachments and the ligaments, and then the stabilizing mechanisms of the shoulder: the rotator cuff, labrum, ligaments, and coracoacromial arch. The optimal MR technique for imaging the shoulder is then discussed, with consideration given to individualizing the examination for specific conditions and to the use of surface coils. In order, Dr. Resnick then discusses and gives examples of rotator cuff problems—impingement syndromes and instability problems—and their respective classifications and associated abnormalities. This complex topic is surprisingly well covered in such a short space, and is done so with great clarity, a hallmark of Dr. Resnick's presentations. Some recently recognized subtleties, such as increased signal normally occurring in the supraspinatus tendon critical zone and the anterior labrum, are beyond the scope of this introductory presentation, and the various types of normal attachment of the glenohumeral ligaments (which can overlap with pathologic changes) are not covered. Perhaps Dr. Resnick will consider a follow-up lesson on these and other points of refinement.

The second section, by Phillip O. Alderson, is on problems of pleural effusions in the scintigraphic diagnosis of pulmonary embolism. Displacement and compression of normal lung by pleural effusions are common problems, and Dr. Alderson discusses the pitfalls and avoidance methods in ventilation-perfusion lung scintigraphy in cases in which pleural effusions exist, or seem to exist. Effusions, of course, are not always visible on the necessary contemporaneous plain radiograph of the chest and may be suspected, or erroneously suspected, on the basis of scintigraphic findings. The accuracy and differential diagnostic considerations of the "fissure sign" and the effects of gravity on effusions are discussed, as are the use of special positioning of the patient during scanning to avoid mistakes in diagnosis. This presentation is clear and concise and covers a limited topic well suited to the video presentation format.

The third section, by R. Nick Bryan, is on MR imaging of the orbit. After discussing MR techniques of orbital imaging and a few relative advantages and disadvantages vis-à-vis CT scanning, Dr. Bryan covers special considerations that apply to MR imaging. Appropriately angled additional views, surface coils, gadolinium, and various pulse sequences are all clearly discussed. Examples, in the form of interesting cases, are used to clarify the points made; this makes for a high-quality presentation of a complex topic distilled to its imperatives. A follow-up presentation on pathologic changes would be of interest.

The final presentation on MR imaging of intramuscular hemangiomas, by Mark J. Kransdorf, although short, is a clear, concise review of a limited topic. After defining and reviewing the classification and histology of hemangiomas, one of the most common soft-tissue tumors, Dr. Kransdorf clearly demonstrates the pertinent MR features of these tumors. The characteristic patterns of hemangiomas on various pulse sequences are described, many examples are shown to illustrate these patterns, and their pathologic correlation is stressed. This presentation also, being limited in scope, is well suited to the video format.

Hano A. Siegel
Mercy Hospital
San Diego, CA 92103

Case Report

Peribiliary Chloroma: A Rare Cause of Jaundice After Bone Marrow Transplantation

Arnold J. Rotter,[1] Margaret R. O'Donnell,[2] D. Randall Radin,[3] and Howard F. Marx[1]

The onset of jaundice after bone marrow transplantation most frequently is due to graft-vs-host disease of the liver or hepatic venoocclusive disease [1]. Recurrent leukemia forming a mass of leukemic cells, or chloroma, surrounding the intrahepatic biliary tree has not been reported before as a cause of jaundice after bone marrow transplantation. The radiologic findings of intrahepatic peribiliary chloroma are the subject of this report.

Case Report

A 45-year-old man with chronic myelogenous leukemia in blast crisis underwent allogeneic bone marrow transplantation. Bone marrow biopsy on day 32 showed no evidence of leukemia. On day 69, he was admitted with anorexia and jaundice. Sonography showed thickening of the gallbladder wall and mild intrahepatic biliary dilatation. Hepatobiliary scintigraphy showed poor hepatic uptake with no biliary excretion. Liver biopsy was not performed because of thrombocytopenia. A presumptive diagnosis of hepatic graft-vs-host disease was made, and the patient was given immunosuppressive therapy with cyclosporine and prednisone. Bone marrow biopsy showed no morphologic evidence of leukemia, but subsequent cytogenetic analysis showed a recurrence of one of the pretransplantation chromosomal abnormalities.

Because of rising serum levels of bilirubin, alkaline phosphatase, and aminotransferases, more intensive immunosuppression with anti-T-cell monoclonal antibody was begun 5 days after admission. Ten days after admission, CT showed marked intrahepatic biliary dilatation and a heterogeneous hypoattenuating mass anterior to the bifurcation of the portal vein (Fig. 1). Two days later, endoscopic retrograde cholangiography showed complete obstruction of the proximal common hepatic duct with a tapered appearance. Transhepatic cholangiography and bilateral percutaneous biliary drainage showed complete obstruction of the right and left hepatic ducts near the porta hepatis. Several hours later, the patient had bloody biliary drainage and hypotension. At emergent surgery, blood was found oozing diffusely from the liver. Intraoperative biopsy of a mass at the bifurcation of the common hepatic duct showed sheets of blast cells. The patient died several hours after surgery.

At autopsy, the liver showed a dense infiltrate of myeloid blast cells centered around the intrahepatic biliary tree. The hepatic parenchyma was otherwise normal.

Discussion

Following bone marrow transplantation, as many as 25% of patients have an elevated serum bilirubin level at some time in their course [2]. The most common causes for jaundice are hepatic venoocclusive disease during the first 3 weeks after bone marrow transplantation, and hepatic graft-vs-host disease thereafter. Other, less common causes include calculous or acalculous cholecystitis, pancreatitis with biliary obstruction, or hepatic fungal abscesses.

The cause of jaundice in our patient was biliary obstruction due to isolated extramedullary recurrence of leukemia infiltrating the intrahepatic biliary tree. Recurrence of leukemia can occur at any time from 30 days to years after bone

---

Received October 15, 1991; accepted after revision December 4, 1991.

[1] Department of Radiology, City of Hope National Medical Center, 1500 E. Duarte Rd., Duarte, CA 91010. Address reprint requests to A. J. Rotter.

[2] Department of Hematology and Bone Marrow Transplantation, City of Hope National Medical Center, Duarte, CA 91010.

[3] Department of Radiology, University of Southern California School of Medicine, Los Angeles County–University of Southern California Medical Center, 1200 N. State St., Los Angeles, CA 90033-1084.

AJR 158:1255–1256, June 1992 0361–803X/92/1586–1255 © American Roentgen Ray Society

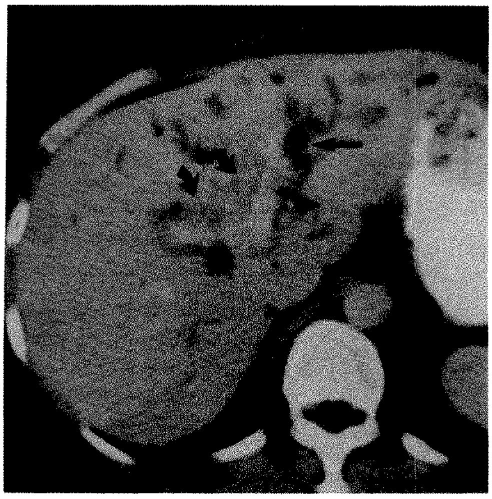

Fig. 1.—45-year-old man with recurrent chronic myelogenous leukemia after bone marrow transplantation. Contrast-enhanced CT scan shows mildly hypoattenuating heterogeneous soft tissue (*curved arrows*) anterior to bifurcation of portal vein causing dilated intrahepatic bile ducts (*straight arrow*). At surgery, peribiliary tissue was a mass of leukemic cells (chloroma).

marrow transplantation. In a previous case report of obstructive jaundice after bone marrow transplantation [3], recurrent leukemia involved the duodenum, intrapancreatic portion of the common bile duct, and bone marrow, but did not involve the intrahepatic biliary tree.

Extramedullary involvement in the form of chloromas occurs in up to 10% of patients at some time in their course, most commonly when there is extensive marrow involvement. Isolated extramedullary leukemic infiltration is very unusual and most frequently involves skin, testes, bone, lymph nodes, breast, and CNS [4]. This is the first report of intrahepatic peribiliary recurrent leukemia with a morphologically normal bone marrow. The initial mild intrahepatic biliary dilatation on sonography and the lack of biliary excretion on scintigraphy were initially attributed to an unusual periductal sclerotic reaction from graft-vs-host disease, which can mimic primary sclerosing cholangitis [5]. This resulted in administration of intensive immunosuppressive therapy for graft-vs-host disease instead of chemotherapy or irradiation directed at the recurrent leukemia.

Additional differential diagnostic considerations in this case include primary biliary carcinoma; secondary neoplasm to the periportal region; and, after bone marrow transplantation, Epstein-Barr virus–related lymphoma [6]. Each of these requires biopsy proof.

Awareness of peribiliary chloroma as a rare cause of jaundice following bone marrow transplantation is clinically important. The therapy for recurrent leukemia is quite different from that given for more common diagnostic considerations such as graft-vs-host disease, venoocclusive disease, biliary stone disease, fungal liver abscesses, and viral hepatitis. Thus, recurrent leukemia should be included in the differential diagnosis when cross-sectional imaging or cholangiography shows biliary obstruction or peribiliary abnormality after bone marrow transplantation.

REFERENCES

1. McDonald GB, Shulman HM, Wolford JL, Spencer GD. Liver disease after human marrow transplantation. *Semin Liver Dis* **1987**;7:210–229
2. McDonald GB, Sharma P, Mathew DE, Shulman HM, Thomas ED. The clinical course of 53 patients with venoocclusive disease of the liver after bone marrow transplantation. *Transplantation* **1985**;29:603–608
3. Lipshutz GR, Katon RM, Lee TG. Obstructive jaundice after bone marrow transplant. *Gastroenterology* **1977**;73:565–569
4. Williams WJ, Beutler E, Erslev AJ, Lichtman MA. *Hematology*, 4th ed. New York: McGraw-Hill, **1990**:214–215, 252–253
5. Geubel AP, Cnudde A, Ferrant A, Latinne D, Rahier J. Diffuse biliary tract involvement mimicking primary sclerosing cholangitis after bone marrow transplantation. *J Hepatol* **1990**;10:23–28
6. Martin PJ, Shulman HM, Schuback WH, et al. Fatal Epstein-Barr virus associated proliferation of donor B cell, after treatment of acute graft versus host disease with a murine anti-T-cell antibody. *Ann Intern Med* **1984**;101:310

Cystic Testicular Mass Caused by Dilated Rete Testis: Sonographic Findings in 31 Cases

Douglas L. Brown[1]
Carol B. Benson[1]
Frederick J. Doherty[2]
Peter M. Doubilet[1]
Donald N. DiSalvo[1]
Gretchen A. Van Alstyne[1]
Martyn A. Vickers[3]
Kevin R. Loughlin[3]

We reviewed the scrotal sonograms of 31 patients who had a testicular mass consisting of multiple small spherical or tubular anechoic structures in the region of the mediastinum testis. The median age of the patients was 62 years (range, 31–76 years). The abnormality was unilateral in 22 patients and bilateral in nine. Thirty-four (85%) of the 40 involved testicles had coexisting epididymal abnormalities: 32 with epididymal cysts and two with epididymitis. Follow-up sonograms were available in five patients and showed no change up to 4.5 years after the initial diagnosis. Surgical and histologic findings were available in one other patient and showed dilatation of the rete testis.

The sonographic appearance and location of the lesions, the frequent presence of an epididymal abnormality, and the surgical and histologic findings in one case suggest that the lesion is due to dilatation of the rete testis, probably associated with obstruction in the epididymis. Recognition of this entity on sonograms may prevent unnecessary orchiectomy.

***AJR* 158:1257–1259, June 1992**

Sonography is frequently the initial imaging technique for the evaluation of many scrotal diseases. Most masses within the testicle are malignant neoplasms [1–7]. Occasionally, however, a benign cause of a testicular mass is recognized sonographically, and orchiectomy is averted [8]. We describe the sonographic findings in a series of patients with a testicular mass due to dilatation of the rete testis.

Materials and Methods

The study group consisted of 31 patients, selected retrospectively from review of a log of sonograms with abnormal findings, in whom scrotal sonography showed a peripheral, elongated mass within the testicle. The mass in each case consisted of a cluster of small spherical, ovoid, or tubular anechoic spaces, in or immediately adjacent to the mediastinum testis (Figs. 1–3). All sonograms except two were obtained by using an Acuson 128 (Acuson; Mountain View, CA) scanner with a 5-MHz linear-array transducer. Two patients had been scanned with a Diasonics Widevue (Diasonics; Milpitas, CA) with a 7.5-MHz sector transducer. For each patient, we recorded age and indication for sonography. Sonographic features recorded included laterality of the lesion, size of the involved portion of the testis, diameter of the largest individual cystic area within the lesion, presence or absence of detectable blood flow within the lesion (when pulsed or color Doppler imaging had been performed), and any extratesticular abnormality. Sonographic and pathologic follow-up were obtained when available.

Results

Patients were between 31 and 76 years old, with a mean age of 58 years and a median age of 62 years. Indications for sonography included evaluation of suspected hydrocele (13 patients), suspected epididymal cyst or spermatocele (11),

Received November 8, 1991; accepted after revision January 15, 1992.

[1] Department of Radiology, Brigham and Women's Hospital and Harvard Medical School, 75 Francis St., Boston, MA 02115. Address reprint requests to D. L. Brown.

[2] Department of Radiology, New England Medical Center, 750 Washington St., Boston, MA 02111.

[3] Department of Urology, Brigham and Women's Hospital and Harvard Medical School, 75 Francis St., Boston, MA 02115.

0361-803X/92/1586-1257
© American Roentgen Ray Society

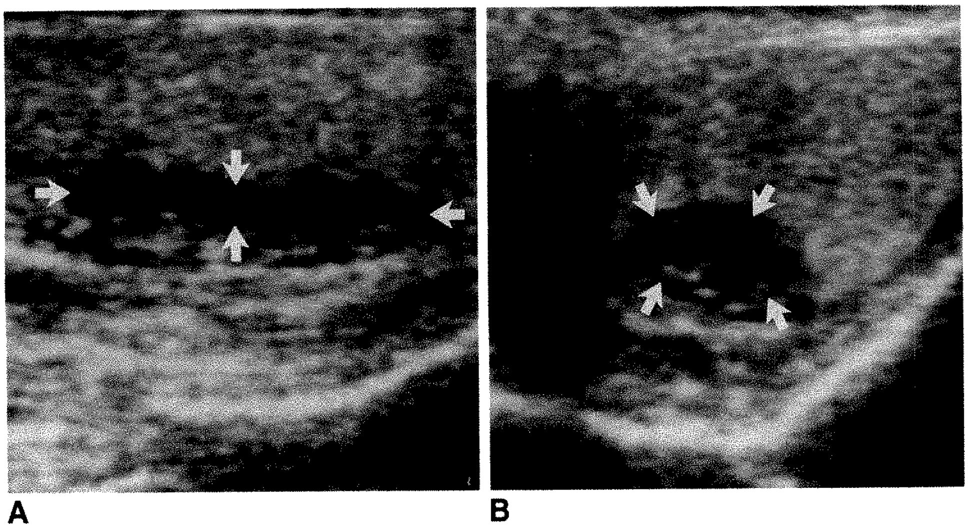

Fig. 1.—*A* and *B*, Sagittal (*A*) and nearly transverse (*B*) sonograms of testicle show a peripheral, elongated, hypoechoic area (*arrows*) consisting of several tiny cystic spaces. This appearance was typical of most cases.

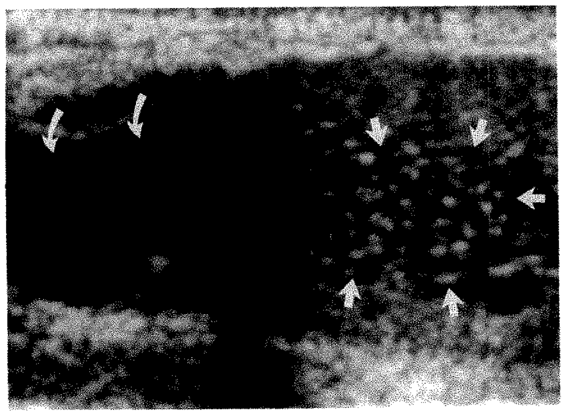

2

Fig. 2.—Oblique sagittal sonogram of testicle shows a large cluster (*straight arrows*) of multiple tiny cystic spaces. Cysts (*curved arrows*) are also present in head of epididymis.

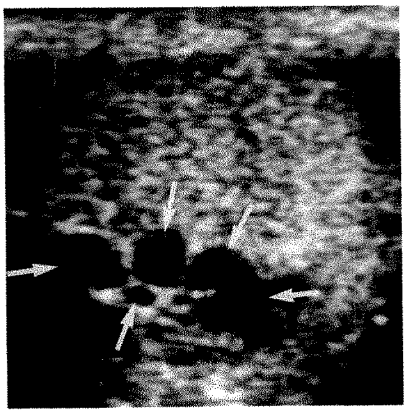

3

Fig. 3.—Sagittal sonogram shows several large cystic spaces (*arrows*) radiating from mediastinum testis. This testicle contained the largest individual cystic spaces seen in our series.

epididymis (two), infertility (one), trauma (one), routine follow-up after contralateral orchiectomy for neoplasm (one), and unknown reasons (two). No patient was referred because of a palpable testicular mass. Three patients had had a vasectomy in the distant past.

The abnormality was present in 40 testicles in 31 patients. It was unilateral in 22 patients and bilateral in nine. Of the unilateral lesions, 14 were in the left testicle and eight were in the right testicle. In 33 of the 40 testicles, the entire lesion was less than 3 cm in sagittal dimension and less than 1 cm in both transverse and anteroposterior dimensions (Fig. 1). In seven testicles, the area of involvement was larger (Fig. 2), up to 4.3 × 2.0 × 1.0 cm. In 37 lesions, the largest diameter of any individual cystic area within the mass was equal to or less than 0.3 cm. In three lesions, the cystic spaces were larger and variable in size (Fig. 3); the largest was 1.8 cm in greatest diameter. Pulsed and/or color Doppler imaging of the cystic spaces was performed in 21 lesions and did not show flow in any case.

Thirty-four (85%) of the 40 involved testicles had coexisting epididymal abnormalities, including 32 with one or more cysts (or spermatoceles) in the head of the epididymis and two with an enlarged epididymis consistent with epididymitis. The epididymal cysts varied from 0.5 to 6.7 cm in greatest diameter. The two lesions with associated epididymal enlargement occurred in a patient with bilateral lesions who had epididymitis clinically. None of the patients had a solid testicular mass.

Five patients, all with a unilateral abnormality, had follow-up sonography 1 to 4.5 years after the initial diagnosis. No change in the sonographic findings was seen in any of these patients.

Two patients had surgery to remove large symptomatic spermatoceles. In one, surgical and histologic findings from a wedge resection of the testis revealed dilated rete testis. This patient also had ipsilateral absence of the vas deferens discovered at surgery. The other surgical patient refused biopsy of the testicle. The testicle was normal to intraoperative palpation and visual inspection.

Discussion

The sonographic demonstration of a mass within the testicle most often indicates a malignant testicular neoplasm [1–6]. Benign testicular masses are uncommon and usually cannot be reliably distinguished from a malignant neoplasm on the basis of sonographic findings [1–8]. Occasionally, the clinical setting and other sonographic findings suggest that the mass is benign [7, 8], allowing deferment of biopsy or orchiectomy pending clinical and sonographic follow-up. In this series, we describe another benign cause of a testicular mass seen on sonography that is most likely due to dilatation of the rete testis.

In the normal testis, the seminiferous tubules merge at the apex of each lobule and connect with the tubuli recti. The tubuli recti then enter the mediastinum testis, forming irregular anastomosing spaces known as the rete testis. Several efferent ductules arise from the rete testis to form the head of the epididymis [9, 10]. Obstruction in the epididymis or efferent ductules may lead to pathologic changes in the more proximal ductal system. Spermatoceles and epididymal cysts are thought to represent cystic dilatation of tubules of the efferent ductules or aberrant ducts, along the course of the efferent ductules or epididymis, possibly because of obstruction [9, 10]. Dilatation [11] and cysts [12–14] of the rete testis have been observed histologically, usually in association with epididymal obstruction.

Several reports [14–16] have described the sonographic appearance of cystic lesions within the testicle. Most of those cases, unlike the ones in our series, had a single simple cyst. A few of the cases in two series [14, 15] and all the cases in one study [16] did have multiple cystic areas. Although the cause was not always known, some were proved or believed to be due to dilatation of the rete testis. The sonographic appearance of dilatation of the rete testis also has been described in a patient with an epididymal cystadenoma [17].

Although lack of histologic correlation in all but one case is a limitation of our study, several findings support our conclusion that this sonographic abnormality is in fact due to dilatation of the rete testis. Because each lesion consists of multiple small cystic spaces, is located in the area of the mediastinum testis, and frequently occurs with a potentially obstructing lesion in the epididymis, dilatation of the rete testis is the most likely cause. The histologic and surgical findings in one case provide supportive evidence. Absence of blood flow within these structures, as shown by Doppler imaging, is evidence against a vascular cause.

Distinguishing this benign entity from a neoplasm should be possible on the basis of its sonographic appearance (i.e., cystic spaces without a focal solid component). Also, this benign lesion is always located peripherally in the region of the mediastinum testis. Neoplasms may occasionally contain cystic areas, but the areas are usually within a larger, primarily solid mass [14, 18]. This distinction most likely also holds true for the rare adenocarcinoma of the rete testis, which is the neoplasm most likely to have a sonographic appearance similar to dilatation of the rete testis [10, 19, 20]. One should, however, sonographically exclude the presence of an adjacent solid mass, as, rarely, tumor infiltration has been reported to cause dilatation of the rete testis due to occlusion of the ductal system by tumor [14]. The patients in our series also differed from the typical patient with primary testicular neoplasm; most were older and none had a palpable testicular mass. Cystic dysplasia of the testis [10, 21–24] is a rare nonneoplastic entity that also may appear sonographically and histologically similar to the lesion we describe. Whether these two entities are truly different is unclear, although most authors believe cystic dysplasia is a congenital abnormality because it is usually diagnosed in children.

In summary, we describe 31 patients with an elongated cluster of small anechoic spaces in the region of the mediastinum testis. This appearance, along with a relatively older age of the patient and the frequent presence of an epididymal abnormality, suggests that the pathologic process is dilatation of the rete testis, probably caused by obstruction in the epididymis. As the frequency of testicular neoplasm is relatively low in this older age group, we recommend conservative management and follow-up when a lesion with the sonographic appearance described is found within the testicle.

REFERENCES

1. Krone KD, Carroll BA. Scrotal ultrasound. *Radiol Clin North Am* **1985**;23:121–139
2. Arger PH, Mulhern CB, Coleman BG, et al. Prospective analysis of the value of scrotal ultrasound. *Radiology* **1981**;141:763–766
3. Carroll BA, Gross DM. High-frequency scrotal sonography. *AJR* **1983**;140:511–515
4. Rifkin MD, Kurtz AB, Pasto ME, et al. The sonographic diagnosis of focal and diffuse infiltrating intrascrotal lesions. *Urol Radiol* **1984**;6:20–26
5. Benson CB. The role of ultrasound in diagnosis and staging of testicular cancer. *Semin Urol* **1988**;6:189–202
6. Rifkin MD, Kurtz AB, Pasto ME, Goldberg BB. Diagnostic capabilities of high-resolution scrotal ultrasonography: prospective evaluation. *J Ultrasound Med* **1985**;4:13–19
7. Lentini JF, Benson CB, Richie JP. Sonographic features of focal orchitis. *J Ultrasound Med* **1989**;8:361–365
8. Bird K, Rosenfield AT. Testicular infarction secondary to acute inflammatory disease: demonstration by B-scan ultrasound. *Radiology* **1984**;152:785–788
9. Gondos B, Wong TW. Non-neoplastic diseases of the testis and epididymis. In: Murphy WM, ed. *Urological pathology*. Philadelphia: Saunders, **1989**:249–313
10. Nistal M, Paniagua R. *Testicular and epididymal pathology*. New York: Thieme-Stratton, **1984**;52–62, 81–83, 278–286, 331–332
11. Nistal M, Paniagua R, Regadera J, Santamaria L. Obstruction of the tubuli recti and ductuli efferentes by dilated veins in the testes of men with varicocele and its possible role in causing atrophy of the seminiferous tubules. *Int J Androl* **1984**;7:309–323
12. Gelberg HB, McEntee K. Cystic rete testis in a cat and fox. *Vet Pathol* **1983**;20:634–636
13. Tejada E, Eble JN. Simple cyst of the rete testis. *J Urol* **1988**;139: 376–377
14. Hamm B, Fobbe F, Loy V. Testicular cysts: differentiation with US and clinical findings. *Radiology* **1988**;168:19–23
15. Gooding GAW, Leonhardt W, Stein R. Testicular cysts: US findings. *Radiology* **1987**;163:537–538
16. Weingarten BJ, Kellman GM, Middleton WD, Gross ML. Tubular ectasia of the mediastinum testis. *J Ultrasound Med* **1991**;10:S17
17. Choyke PL, Filling-Katz MR, Shawker TH, et al. Von Hippel-Lindau disease: radiologic screening for visceral manifestations. *Radiology* **1990**;174: 815–820
18. Schwerk WB, Schwerk WN, Rodeck G. Testicular tumors: prospective analysis of real-time US patterns and abdominal staging. *Radiology* **1987**;164:369–374
19. Fukunaga M, Aizawa S, Furusato M, Akasaka Y, Machida T. Papillary adenocarcinoma of the rete testis: a case report. *Cancer* **1982**;50: 134–138
20. Smith SJ, Vogelzang RL, Smith WM, Moran MJ. Papillary adenocarcinoma of the rete testis: sonographic findings. *AJR* **1987**;148:1147–1148
21. Cho CS, Kosek J. Cystic dysplasia of the testis: sonographic and pathologic findings. *Radiology* **1985**;156:777–778
22. Leissring JC, Oppenheimer ROF. Cystic dysplasia of the testis: a unique congenital anomaly studied by microdissection. *J Urol* **1973**;110:362–363
23. Fisher JE, Jewett TC, Nelson SJ, Jockin H. Ectasia of the rete testis with ipsilateral renal agenesis. *J Urol* **1982**;128:1040–1043
24. Nistal M, Regadera J, Paniagua R. Cystic dysplasia of the testis: light and electron microscopic study of three cases. *Arch Pathol Lab Med* **1984**;108:579–583

Videotape Review

RSNA Today Video, Vol. 5, No. 4. Oak Brook, IL: The Radiological Society of North America, 1991. $55; by subscription, 6 issues annually at $185 for RSNA members and $225 for nonmembers (VHS videotape)

This tape, moderated by William J. Casarella, contains three sections. In the first section, Morton A. Bosniak discusses the use of CT in imaging obstruction of the ureteropelvic junction. CT is used when the results of routine IV urography do not conclusively indicate the cause of the obstruction. Dr. Bosniak discusses the potential causes in adults (e.g., tumor or congenital causes) and the CT findings that can be used to distinguish between the causes. Using the CT findings of congenital obstruction of the ureteropelvic junction as a baseline, Dr. Bosniak describes and illustrates the findings in various other causes of this disease.

In the second section, Barbara A. Carroll discusses many aspects of color Doppler imaging of the carotid arteries. The advantages of color Doppler imaging, which combines gray-scale anatomy with color flow physical effects, in supplying an overview and information on the direction and velocity of blood flow are reviewed. Color assignment and saturation in relationship to frequency and phase changes in the RBC "targets" are explained. Dr. Carroll then discusses the limitations of pulsed Doppler sonography, the many factors affecting color assignment, and the requirements that must be met in order to provide the best results. A typical examination is demonstrated, and aspects related to the usefulness of color Doppler imaging are examined. Dr. Carroll points out that with color Doppler imaging, the time needed for an examination is decreased and confidence in the accuracy of diagnosis is increased. She also mentions that duplex Doppler sonography is still necessary because peak velocity rates are used to calculate the degree of stenosis of a vessel. Color Doppler imaging is theta angle dependent, and so luminal patency can be overestimated.

In the third section, Dr. Casarella discusses the indications for transluminal interruption of the inferior vena cava, and then Morris Simon discusses the Simon nitinol filter. Dr. Simon first briefly reviews previous and current filters and their configurations. Then, he discusses the properties of the nickel-titanium alloy used to make the nitinol filter and the filter's other advantages, such as the size of the catheter used to insert the filter, the filter's nonferromagnetic properties, and the filter's ability to resume its original shape at body temperatures. A typical insertion is demonstrated, along with a test system with which to test filter materials for efficiency and potential complications. The advantages of using the nitinol filter as opposed to anticoagulation are also discussed.

Although the last two topics covered in this tape may both be of interest to vascular interventional radiologists, it is difficult to justify inclusion of the first topic, which is of interest to a limited audience. Although the illustrative cases are interesting, differentiating benign from malignant disease in this one region (i.e., the ureteropelvic junction) hardly seems inclusive enough or challenging enough to test the formidable teaching skills of Dr. Bosniak. Dr. Carroll's review of color Doppler imaging of the carotid arteries is a well-presented, relatively complete overview of physical principles, advantages and disadvantages, and limitations of the examination. Dr. Simon's review of the state of the art and description of the fascinating physical characteristics of the nitinol coil are interesting and potentially quite useful for anyone likely to be called on to place a vena caval filter.

Hano A. Siegel
Mercy Hospital
San Diego, CA 92103

Peyronie's Disease: MR Findings in 28 Patients

G. Helweg[1]
W. Judmaier[2]
W. Buchberger[2]
K. Wicke[1]
H. Oberhauser[1]
R. Knapp[1]
O. Ennemoser[3]
D. Zur Nedden[1]

Induratio penis plastica (Peyronie's disease) is a chronic fibrotic process involving the penis. Proper treatment of the disease requires assessment of the degree of inflammation preceding or accompanying the fibrous Peyronie's plaques. Owing to its high tissue contrast and its multiplanar capability, MR imaging offers excellent visualization of penile anatomy. To determine the usefulness of MR imaging in the diagnosis and staging of Peyronie's disease, we used MR imaging with a surface coil to examine 28 consecutive patients with clinical evidence of the disease. Eighteen patients had contrast-enhanced MR imaging with gadopentetate dimeglumine. In seven patients who subsequently had surgery or biopsy, MR findings were correlated with histopathologic findings. On unenhanced images, fibrous plaques were shown in 20 patients. Enhanced MR images showed focal contrast enhancement around or within the plaques in seven patients. Images in three patients with plaques showed no enhancement. Images in five patients showed focal areas of contrast enhancement without evidence of plaques. Histologic studies demonstrated that the degree of contrast enhancement correlated with the extent of inflammatory cell infiltration. In two patients with unenhancing plaques on MR, histology confirmed the absence of inflammation.

Our results suggest that MR imaging not only depicts the localization and extent of fibrous plaques in patients with Peyronie's disease but also reveals the presence of inflammation. This makes MR imaging the technique of choice for planning therapy and for evaluating the response to conservative treatment.

***AJR* 158:1261–1264, June 1992**

Induratio penis plastica, a fibrotic process involving the penis, was first described in 1743 by the French physician François de la Peyronie. Histopathologically, Peyronie's disease is characterized by a focal inflammatory reaction with progressive fibrosis, formation of sclerotic plaques, and, occasionally, calcification [1–3].

Various imaging methods, including autophotography [4], plain film radiography, CT [5], and sonography [6–8], have been used to provide an objective basis for planning therapy. Of these, sonography has been the most useful, as it can show the localization and extent of sclerotic plaques with great accuracy. However, it cannot be used to distinguish reliably between active inflammatory and quiescent stages of the disease.

A previous report demonstrates that MR imaging clearly depicts the normal anatomy of the penis [9]. The purpose of this study was to determine the usefulness of MR in the diagnosis and staging of Peyronie's disease.

Subjects and Methods

Over a 3-year period from 1989 to 1991, 28 consecutive patients with clinical evidence of Peyronie's disease were examined with MR. The patients were 19–79 years old (mean, 48 years). Sixteen gave a history of painful erections, 23 had abnormal curvature of the penis, and 18 had a palpable induration or mass.

Received November 8, 1991; accepted after revision January 16, 1992.

[1] Department of Diagnostic Radiology and CT, University Clinic of Internal Medicine, Anichstrasse 35, A-6020 Inssbruck, Austria.

[2] Institute of Magnetic Resonance Imaging and Spectroscopy, University of Innsbruck, A-6020 Innsbruck, Austria.

[3] University Clinic of Urology, A-6020 Innsbruck, Austria.

0361-803X/92/1586-1261

© American Roentgen Ray Society

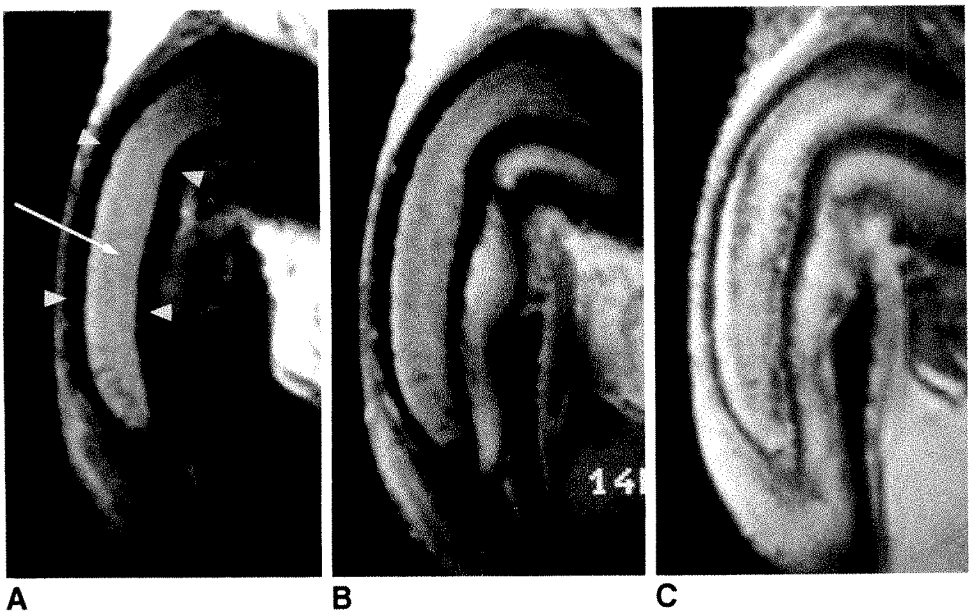

Fig. 1.—Sagittal MR images of normal left corpus cavernosum in 49-year-old man with penile deviation but without palpable penile plaque.

***A*, Unenhanced T1-weighted (550/15) image shows homogeneous signal intensity of corpus cavernosum (*arrow*) and normal tunica albuginea (*arrowheads*).**

***B*, Contrast-enhanced T1-weighted image shows no focal enhancement.**

***C*, T2-weighted (2000/90) image shows inhomogeneous signal intensity of corpus cavernosum.**

MR imaging was performed with a 1.5-T superconducting system (Magnetom, Siemens, Erlangen, Germany) and an 8.5-cm surface coil. During imaging, the patients were supine, with the penis taped on a plastic pad and the surface coil positioned on the penis anteriorly. Images were acquired in the sagittal and axial planes; a 256 × 256 matrix, two repetitions, and a 20-cm field of view were used. Ten to 15 contiguous 3- to 5-mm-thick slices were obtained. The pulse sequences used were a spin-echo format with 550/15 (TR/TE) for T1-weighted images and 2000/90 for T2-weighted images. In 18 patients, T1-weighted images were obtained before and 5 min after IV injection of gadopentetate dimeglumine at a dose of 0.2 mmol/kg. The unenhanced and enhanced images were evaluated visually by three observers for the presence of plaques, and for the presence and type of enhancement. Correlation of unenhanced and contrast-enhanced MR images with histopathology was possible in seven patients. Five patients underwent surgery, and in two patients biopsy was performed at the site of contrast enhancement.

Results

MR showed penile structures satisfactorily in all cases (Fig. 1). On T1-weighted images, the tunica albuginea and the septum penis had low signal intensity and could be distinguished from the medium-signal-intensity corpora cavernosa and corpus spongiosum. The contrast between the corpora cavernosa and the tunica albuginea was increased on T2-weighted images when compared with T1-weighted images.

Localized thickening and irregularities of the tunica albuginea suggesting plaques were shown on unenhanced images in 20 patients (Figs. 2–4). Without exception, the plaques were of low signal intensity. Thirteen patients had solitary plaques; seven patients had two or more plaques. The plaques varied in size from 0.8 to 5.0 cm (median, 2.0 cm). The dorsal aspect of the penis was involved in 14 cases and the septum penis in six cases. The signal intensity of the corpora cavernosa was homogeneous on T1-weighted images in all patients and inhomogeneous on T2-weighted images in nine patients (Fig. 1). In three patients with extensive plaques, the corpora cavernosa had a very low signal intensity compared with that of the corpus spongiosum. This finding might indicate fibrosis; however, histopathologic confirmation was not available.

Eighteen patients had MR imaging with gadopentetate dimeglumine. Peyronie's plaques were apparent on unen-

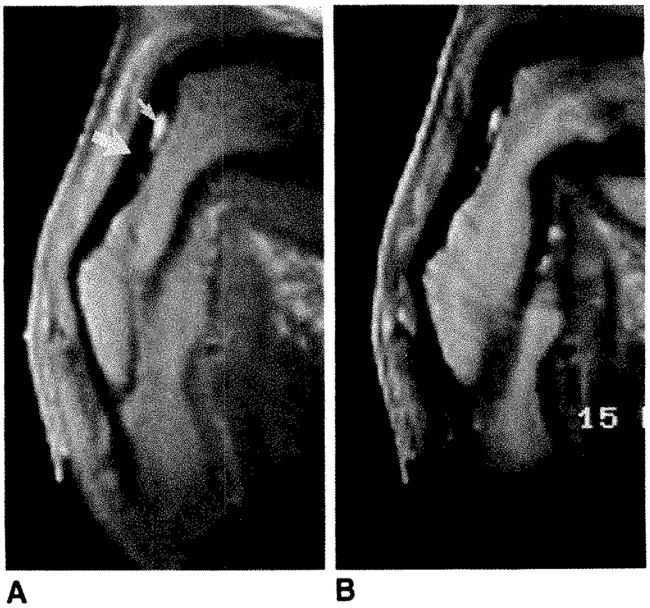

Fig. 2.—T1-weighted (550/15) sagittal MR images of right corpus cavernosum in 57-year-old man with Peyronie's disease and large palpable penile plaque.

***A*, Unenhanced image shows focal thickening of tunica albuginea (*large arrow*) with area of high signal intensity, probably due to hemorrhage (*small arrow*).**

***B*, Contrast-enhanced image shows no enhancement. Histology confirmed absence of inflammation.**

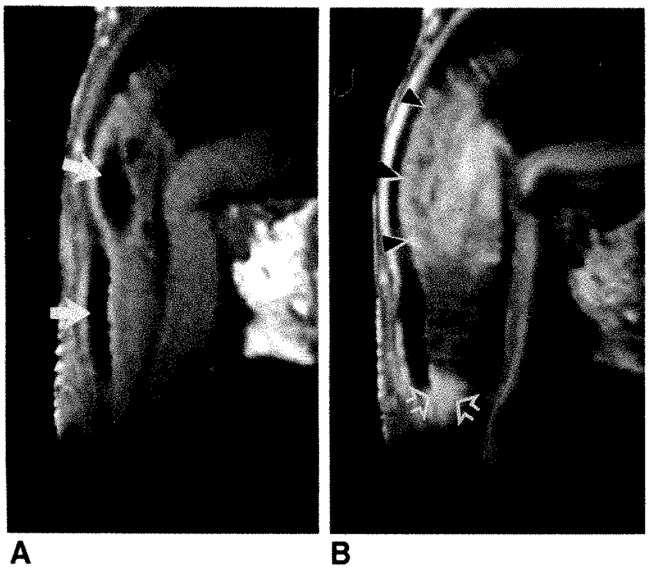

Fig. 3.—T1-weighted (550/15) sagittal MR images of right corpus cavernosum in 45-year-old man with Peyronie's disease and palpable penile plaques.

A, Unenhanced image shows low-signal-intensity plaques proximally and distally (*arrows*).

B, Contrast-enhanced image shows marked focal and perifocal enhancement of plaque in proximal corpus cavernosum (*arrowheads*); second abnormal area of enhancement is apparent in periphery of distal plaque (*open arrows*). Histology proved inflammation.

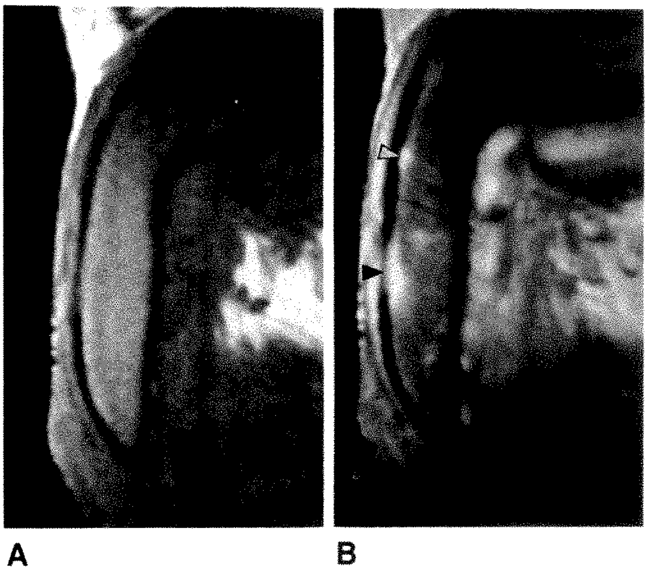

Fig. 5.—T1-weighted (550/15) sagittal MR images of right corpus cavernosum in 49-year-old patient with Peyronie's disease but no palpable penile plaques.

A, Unenhanced image shows homogeneous signal intensity of corpus cavernosum.

B, Contrast-enhanced image shows abnormal enhancement of tunica albuginea and adjacent corpus cavernosum (*arrowheads*). Biopsy proved inflammation.

hanced images in 10 of these patients, whereas findings on unenhanced MR images were normal in eight. Seven patients had focal contrast enhancement around or within plaques (Figs. 3 and 4). In addition, focal areas of contrast enhancement within the tunica albuginea, the septum penis, or the adjacent corpus cavernosum were seen in five patients whose unenhanced images were normal (Fig. 5). Three patients showed Peyronie's plaques, but no focal enhancement (Fig. 2). In three patients, neither the unenhanced nor the contrast-enhanced images showed any abnormal findings.

In five patients, histologic examination confirmed inflammatory cell infiltration and edema. On contrast-enhanced MR images, focal contrast enhancement adjacent to plaques was seen in four patients and enhancement without evidence of plaques was seen in one. In two patients with plaques but without focal enhancement with gadopentetate dimeglumine, histopathology proved the absence of inflammation.

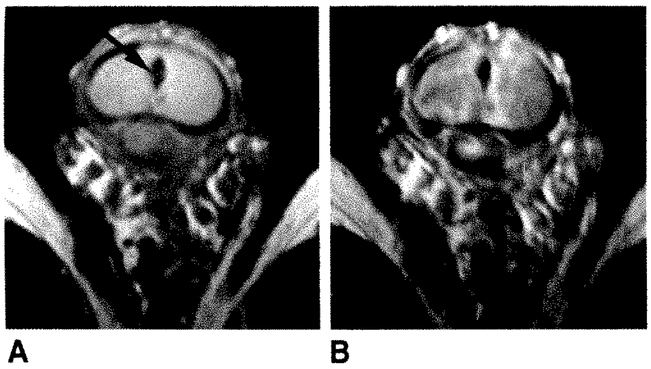

Fig. 4.—T1-weighted (550/15) axial MR images of penis in 39-year-old man with Peyronie's disease but no palpable penile plaques.

A, Unenhanced image shows focal thickening of septum penis (*arrow*).

B, Contrast-enhanced image shows focal enhancement adjacent to plaque and of corpora cavernosa. Histology proved inflammation.

Discussion

Peyronie's disease accounts for 0.3–0.7% of all urologic disorders [1]. It occurs most often in the fourth to sixth decades of life, and occasionally in men less than 20 years old [1, 2]. Patients usually have increasingly painful erection and deviation of the penis. The main clinical findings are hard, well-demarcated plaques in the region of the tunica albuginea enclosing the corpora cavernosa and of the septum penis [1]. The cause of the disease is still not fully explained, although some evidence suggests that repeated microtrauma, hormonal dysfunction, metabolic disorders (diabetes, gout), and a general fibroplastic disposition may play a role in the pathogenesis [1, 2, 10–12]. Various forms of treatment have been suggested, including the administration of estrogens, vitamin E, and potassium *para*-aminobenzoate; local infiltration of steroids; and radiation therapy, but none has proved fully satisfactory [13–15]. More recently, local application of superoxide dismutase (orgotein) has provided good results [16, 17]. Surgical treatment is required for advanced stages of the disease [13, 18].

The results of various histopathologic [2, 19] studies suggest that Peyronie's disease usually begins as a vasculitis in the connective tissue sleeve between the corpus cavernosum and the tunica albuginea. In an early stage of the disease, the lesions show evidence of an endangiitic and perivascular lymphoplasmatic cellular infiltrate, perivascular edema, and fibrinous exudate. In the advanced stage, fibrosis is prevalent with sclerosed, hyalinized, and, occasionally, calcified connective tissue plaques adjacent to the tunica albuginea and encroaching on the corpus cavernosum [2, 20]. Inflammation may persist in the periphery of the plaques, or it may cease entirely [1, 2].

MR imaging showed either a diffuse or localized plaquelike thickening of the tunica albuginea in all 18 patients with palpable indurations. In addition, small impalpable plaques were shown on MR in two patients. On contrast-enhanced MR, seven patients had focal enhancement around or within Peyronie's plaques, suggesting florid inflammation. Five patients without evidence of plaques had focal enhancement of the tunica albuginea or the corpora cavernosa, possibly representing early stages of the disease. Three patients had typical Peyronie's plaques but showed no enhancement with gadopentetate dimeglumine. These observations suggest that contrast-enhanced MR can be used to detect early changes in Peyronie's disease that are usually missed by palpation and sonography. In addition, with MR, fibrous plaques with persistent inflammatory infiltration can be distinguished from plaques in which inflammation has ceased. The diagnostic value of T2-weighted images in the evaluation of Peyronie's disease is quite limited. Although plaques were distinguished more easily on T2-weighted images than on T1-weighted images, none would have been missed on T1-weighted images alone. In nine patients, the signal intensity of the corpora cavernosa was inhomogeneous on T2-weighted images. However, a wide range of signal intensity of the corpora cavernosa is also demonstrable in healthy subjects [9]. Low signal intensity of the corpora cavernosa in three of our patients may indicate fibrosis, although this finding can also be due to decreased blood flow [9]. We therefore think that when the time required for examination is taken into account, unenhanced and contrast-enhanced T1-weighted images should constitute an adequate imaging strategy.

In summary, MR imaging opens new diagnostic possibilities for the diagnosis and staging of Peyronie's disease. As our limited study indicates, contrast-enhanced MR not only shows the localization and extent of Peyronie's plaques but also the presence or absence of inflammation. This makes MR imaging the technique of choice for planning therapy and for evaluating the response to conservative therapy.

REFERENCES

1. Schneider HJ, Rugendorff EW, Röhrborn C. Pathogenesis, diagnosis and therapy of induratio penis plastica (IPP). *Int Urol Nephrol* **1985**;17:235-244
2. Smith BH. Peyronie's disease. *Am J Clin Pathol* **1966**;45:670-678
3. Chesney J. Peyronie's disease. *Br J Urol* **1975**;47:209-218
4. Kelami A. Classification of congenital and acquired penile deviation. *Urol Int* **1983**;38:229-233
5. Rollandi G, Tentarelli T, Vespier M. Computed tomographic findings in Peyronie's disease. *Urol Radiol* **1985**;7:153-156
6. Gelbrand M, Sarti P, Kaufmann JJ. Ultrasound imaging of Peyronie's plaques. *J Urol* **1981**;125:44-46
7. Helweg G, Rauschmeier H, Zur Nedden D, Judmaier W, Sief R. Die Wertigkeit der Sonographie in der Therapieüberwachung der Induratio penis plastica (Peyronie's disease). *ROFO* **1989**;151:298-300
8. Altaffer LF, Jordan GH. Sonographic demonstration of Peyronie's plaques. *Urology* **1981**;17:292-295
9. Hrizak H, Marotti M, Gilbert TJ, et al. Normal penile anatomy and abnormal penile conditions: evaluation with MR imaging. *Radiology* **1988**;169:683-690
10. Smith BH. Subclinical Peyronie's disease. *Am J Clin Pathol* **1969**;52:385-390
11. Hinman F. Etiologic factors in Peyronie's disease. *Urol Int* **1980**;35:407-413
12. Chilton CP, Castle WM, Westwood CA, Pryor JP. Factors associated in the etiology of Peyronie's disease. *Br J Urol* **1982**;54:748-750
13. Palomar JM, Halikiopoulos H, Thomas R. Evaluation of the surgical management of Peyronie's disease. *J Urol* **1980**;123:680-682
14. Zarafonatis CJ, Horrax TM. Treatment of Peyronie's disease with potassium *para*-aminobenzoate (Potaba®). *J Urol* **1959**;81:770-772
15. Williams G, Green NA. The non-surgical treatment of Peyronie's disease. *Br J Urol* **1980**;52:392-395
16. Bartsch G, Menander-Huber KB, Huber W, Marberger H. Orgotein, a new drug for the treatment of Peyronie's disease. *Eur J Rheumatol Inflamm* **1981**;4:250-259
17. Gustafson H, Johansson B, Edsmyr F. Peyronie's disease: experience of local treatment with orgotein. *Eur Urol* **1981**;7:346-348
18. Coughlin PWF, Culley C, Carsom II, Paulson DF. Surgical correction of Peyronie's disease: the Nesbit procedure. *J Urol* **1984**;131:282-285
19. Byström J, Rubio C. Induratio penis plastica (Peyronie's disease): clinical features and etiology. *Scand J Urol Nephrol* **1976**;10:12-20
20. Poutasse EF. Peyronie's disease. *J Urol* **1972**;107:419-422

Pictorial Essay

Nonovarian Gynecologic Cysts: MR Imaging Findings

Ruben Kier[1]

MR imaging has improved the detection and characterization of cysts arising in the ovaries. Although they are less common, cysts also can develop in the endocervical glands (nabothian cysts), labia (Bartholin's cysts), vaginal wall (Gartner's cysts), and broad ligament (paratubal cysts). Findings on pelvic MR imaging were reviewed to determine the prevalence and MR features of gynecologic cysts arising outside the ovary.

Materials and Methods

From January 1990 to June 1991, 458 women had MR imaging of the pelvis at Yale-New Haven Hospital. MR imaging reports were reviewed to determine cases in which nabothian cysts, Bartholin's cysts, or Gartner's cysts were diagnosed on the basis of MR detection of a cystic structure in the appropriate anatomic site [1, 2]. Because imaging studies may not allow distinction of cysts in the broad ligament from cysts in the adjacent ovary [3], surgical pathology reports were reviewed to identify cases in which cysts seen on MR images were determined pathologically to be paratubal cysts.

All patients were studied on a 1.5-T system (Signa, General Electric, Milwaukee, WI). All patients were studied with both T1-weighted (400–600/13–20) images in either the axial or coronal plane and T2-weighted (spin echo 1700–2117/20, 80 or fast spin echo 2900–4500/126) images in both the sagittal and axial planes. Images were acquired with a 128 × 256 matrix, two excitations, 5-mm slice thickness, 2.5-mm interslice gap, 28-cm field of view, spatial presat-

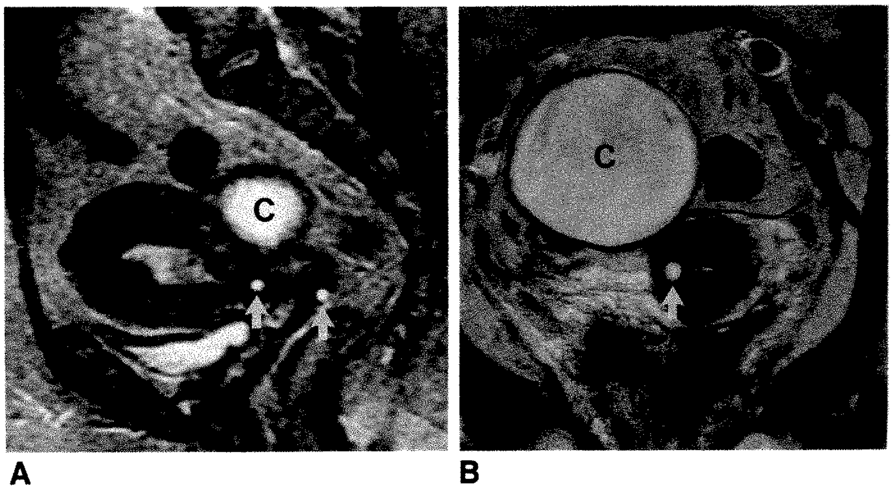

Fig. 1.—Nabothian cysts in a 55-year-old woman.
***A*, Sagittal T2-weighted (2000/80) MR image shows two small nabothian cysts (*arrows*) appearing as small well-circumscribed high-signal structures adjacent to cervical canal. C = ovarian cyst.**
***B*, Coronal T2-weighted (3000/100) fast spin-echo MR image shows a 6-mm nabothian cyst (*arrow*) within cervical fibrous stroma.**

Received November 25, 1991; accepted after revision January 10, 1992.
Presented as a scientific exhibit at the annual meeting of the American Roentgen Ray Society, Orlando, FL, May 1992.

[1] Department of Radiology, Yale University School of Medicine, 333 Cedar St., New Haven, CT 06510. Address reprint requests to R. Kier.

AJR 158:1265–1269, June 1992 0361-803X/92/1586-1265 © American Roentgen Ray Society

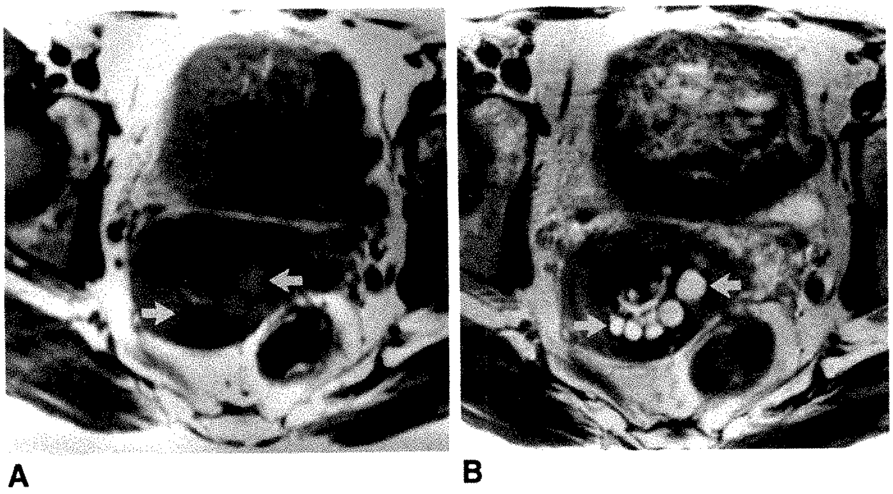

Fig. 2.—Nabothian cysts in a 47-year-old woman.

A, Axial T1-weighted (500/20) MR image shows multiple cysts (*arrows*) near external cervical os with a signal intensity similar to that of muscle.

B, Axial T2-weighted (4500/126) fast spin-echo MR image shows multiple cysts (*arrows*) that are hyperintense relative to fat.

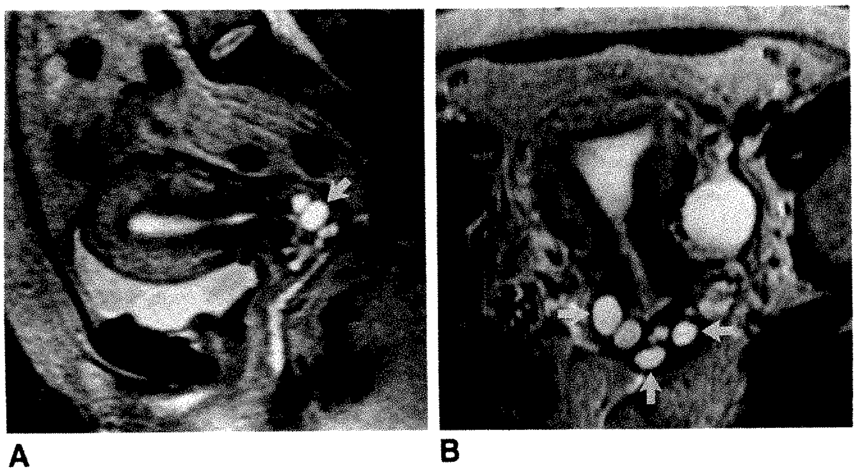

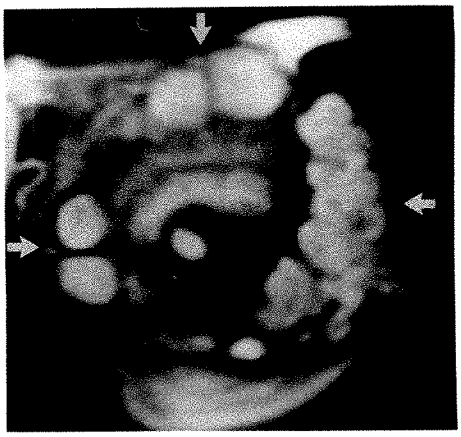

Fig. 3.—*A* and *B*, Unusually large nabothian cysts in a 44-year-old woman. Sagittal (*A*) and axial (*B*) T2-weighted (2000/80) MR images show multiple discrete nabothian cysts (*arrows*) in cervix, most prominently near external os.

Fig. 4.—Unusually large nabothian cysts in a 44-year-old woman. T2-weighted (2000/80) transverse MR image of a surgical uterine specimen shows multiple cysts (*arrows*) near external cervical os. Histologic examination showed marked acute and chronic cervicitis.

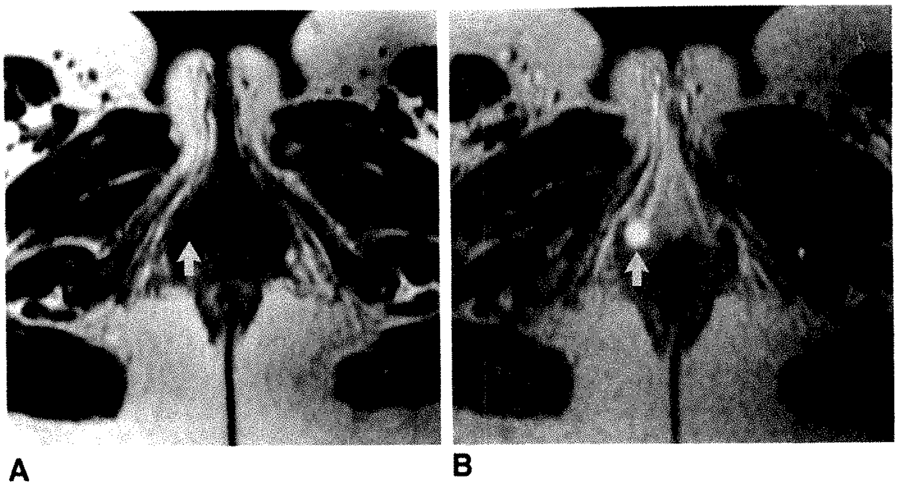

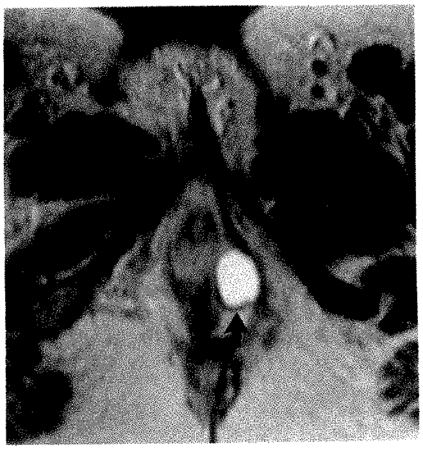

Fig. 5.—*A* and *B*, Bartholin's cyst in a 37-year-old woman. Cyst (*arrow*) in right labium has low signal intensity on T1-weighted (400/13) axial MR image (*A*) and high signal intensity on T2-weighted (2000/80) axial MR image (*B*).

Fig. 6.—Bartholin's cyst in a 35-year-old woman. T2-weighted (2117/80) axial MR image shows 2-cm cyst (*arrow*) in left labium that is hyperintense relative to fat.

uration superior and inferior to the imaging volume, and respiratory compensation.

Results and Discussion

Nabothian Cysts

Nabothian cysts were detected in 57 patients, for a prevalence of 12%. This may differ from the frequency with which nabothian cysts are seen on physical examination because (1) MR imaging can be used to detect cysts above the external os that are not detectable on physical examination and (2) small cysts may be below the resolution of routine MR imaging with the body coil. On MR images, nabothian cysts appeared as single or multiple well-circumscribed cystic lesions in the cervical fibrous stroma (Figs. 1 and 2) that were up to 1.7 cm in diameter (Figs. 3 and 4). All were hyperintense relative to fat on T2-weighted images. On T1-weighted images, most were isointense with urine or muscle. None of these patients were referred specifically for evaluation of nabothian cysts.

Nabothian cysts are retention cysts of the cervical glands. They are caused by chronic inflammation with scarring of the cervix, which leads to occlusion of the lumen of the cervical glands. Cystic accumulation of mucus within the dilated glands accounts for the MR appearance [1].

Bartholin's Cysts

Bartholin's cysts were detected in six cases, for a prevalence of 1.3%. This corresponds closely to the prevalence of

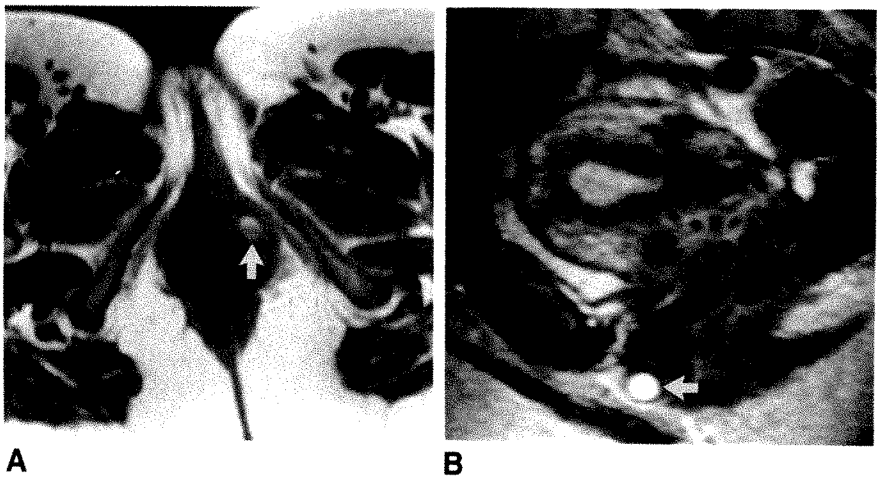

Fig. 7.—Bartholin's cyst in a 38-year-old woman.

***A*, Axial T1-weighted (433/17) MR image shows cyst (*arrow*) in left labium. Hyperintensity of cyst may reflect hemorrhagic, proteinaceous, or mucinous content.**

***B*, Sagittal T2-weighted (2117/80) MR image shows cyst (*arrow*) hyperintense relative to fat.**

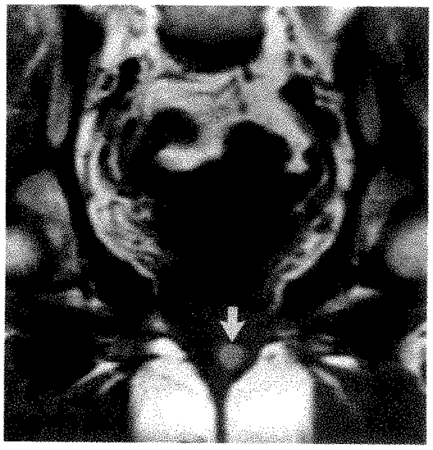

Fig. 8.—Bartholin's cyst in a 41-year-old woman. Coronal T1-weighted (500/20) MR image shows cyst (*arrow*) in left labium that is hyperintense relative to muscle.

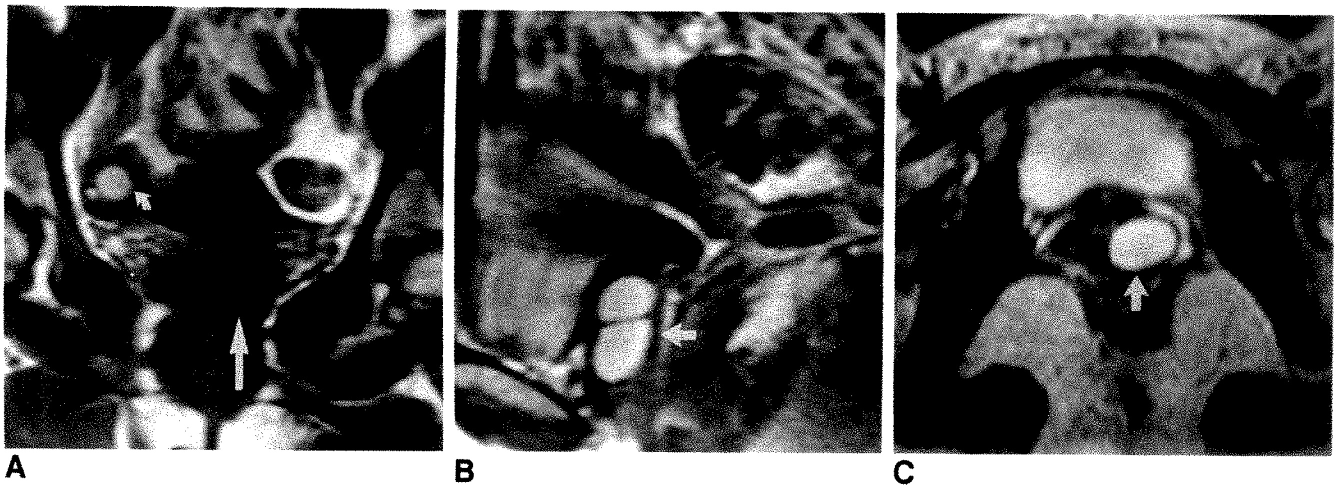

Fig. 9.—Gartner's cyst in a 39-year-old woman.

***A*, Coronal T1-weighted (400/13) MR image shows septated low-signal structure (*large arrow*) in left wall of vagina. Note also small hemorrhagic cyst (*small arrow*) in right ovary.**

***B*, Sagittal T2-weighted (1700/80) MR image shows septated high-signal structure (*arrow*) in vicinity of vagina.**

***C*, Axial T2-weighted (2000/80) MR image shows high-signal cystic structure (*arrow*) in left lateral wall of vagina, findings consistent with Gartner's cyst.**

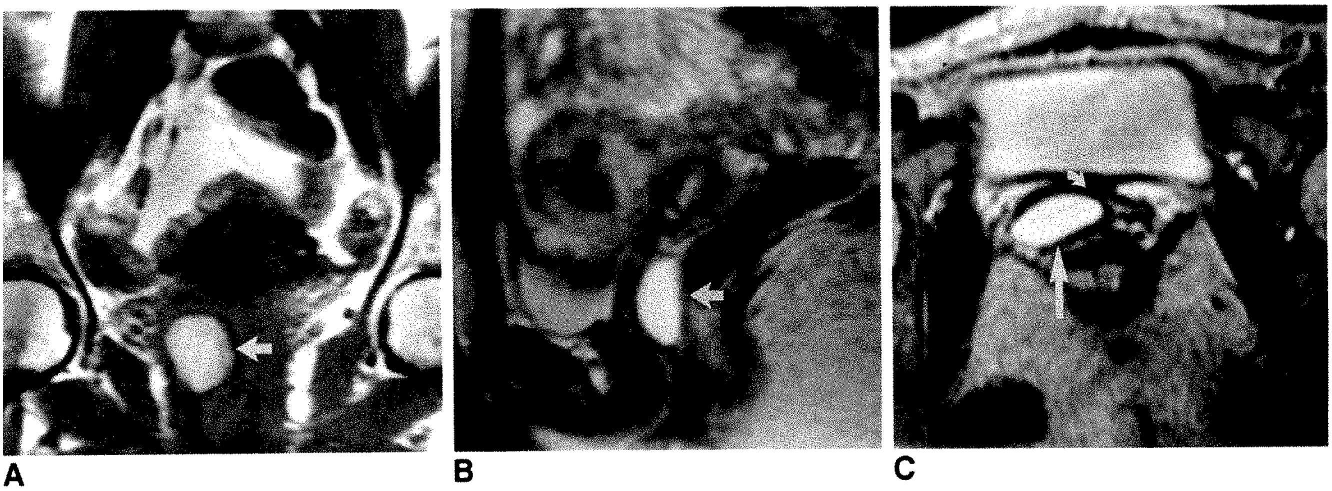

Fig. 10.—Gartner's cyst in a 42-year-old woman.

A, Coronal T1-weighted (500/20) MR image shows high-signal structure (*arrow*) in right wall of vagina, suggesting either hemorrhagic, proteinaceous, or mucinous content.

B, Sagittal T2-weighted (1700/80) MR image shows high-signal structure (*arrow*) in vicinity of vagina.

C, Axial T2-weighted (2000/80) MR image shows close relationship of cyst (*large arrow*) to right wall of vagina (*small arrow*), consistent with Gartner's cyst.

2% that has been reported for detection by physical examination [2]. These cysts appeared as discrete cystic structures in the labia. All were hyperintense relative to fat on T2-weighted images. On T1-weighted images, signal intensity was similar to that of urine (one case), muscle (three cases), or fat (two cases), presumably reflecting differences in protein or mucin content (Figs. 5–8). Clinically, none of the cysts were symptomatic at the time of MR imaging.

Bartholin's cysts arise from the duct system of Bartholin's glands. Most cysts involve the main duct only and thus are unilocular. Bartholin's cysts are unilateral, nontender, tense, palpable masses 1–4 cm in diameter. Most contain sterile fluid and are located in the posterior part of the labia majora. The cysts are often asymptomatic unless they become enlarged or infected [2].

Gartner's Cysts

Gartner's cysts were detected in six patients, for a prevalence of 1.3%. This is similar to the prevalence of approximately 1% for their detection on physical examination. They appeared as ovoid (five cases) or septated (one case) cystic lesions located within the wall of the vagina (Figs. 9 and 10). All were hyperintense relative to fat on T2-weighted images. On T1-weighted images, four were hypointense or isointense with muscle, and two were isointense with fat. Clinically, no patients had symptoms attributable to Gartner's cysts before MR imaging. On physical examination, the Gartner's cyst was detected before MR imaging in three cases. In another case, the cyst was drained after MR imaging, and 20 ml of clear fluid was aspirated (Fig. 9).

True Gartner's cysts develop from remnants of the vaginal portion of the mesonephric (wolffian) ducts. If parts of these ducts fail to regress, secretory activity gives rise to cystic tumors within the wall of the vagina. Clinically indistinguishable from "true" Gartner's cysts, paramesonephric cysts can arise in the vaginal wall from vestiges of the paramesonephric (müllerian) ducts. Both types of vaginal cysts are usually asymptomatic, and their gross appearances are similar, so their precise origin is not of major clinical significance. Most are solitary, smaller than 2 cm in diameter, and located in the anterolateral wall of the vagina [2].

Paratubal Cysts

Three patients with surgically proved paratubal cysts had MR imaging preoperatively (Figs. 11–13). The prevalence of these cysts on MR imaging studies is difficult to calculate because paratubal cysts seen on MR images may be misdi-

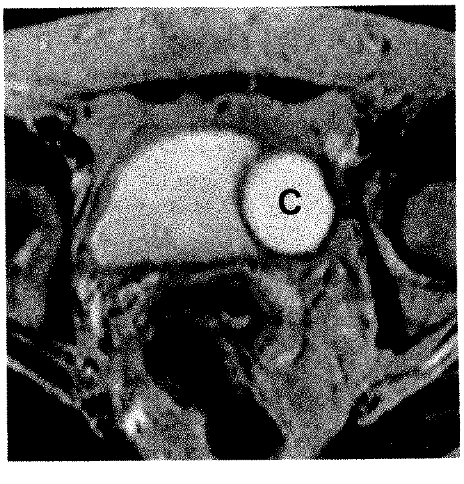

Fig. 11.—Paratubal cyst in a 59-year-old woman. T2-weighted (2000/80) axial MR image shows 4-cm left adnexal cyst (C). Because left ovary could not be detected as a separate structure, lesion was misdiagnosed as an ovarian cyst.

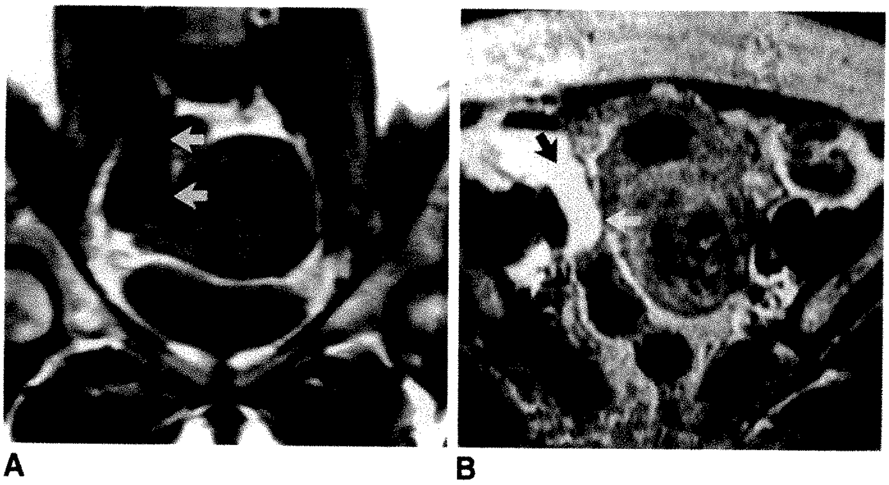

Fig. 12.—Paratubal cyst in a 48-year-old woman.

***A*, Coronal T1-weighted (500/20) MR image shows elongated structure (*arrows*) adjacent to right side of uterus.**

***B*, Axial T2-weighted (2000/80) MR image shows elongated oval structure (*arrows*) with high signal intensity, suggesting fluid contents. Elongated shape prospectively suggested nonovarian origin.**

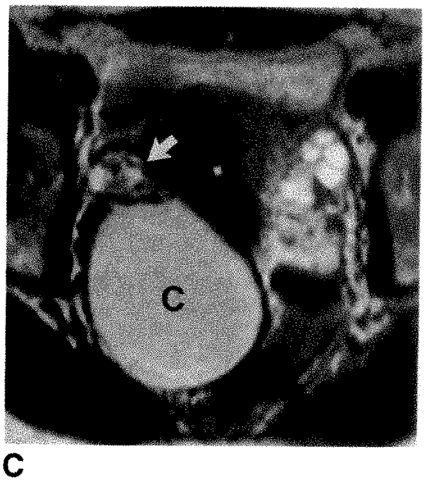

Fig. 13.—Paratubal cyst in a 25-year-old woman. T2-weighted (3000/126) fast spin-echo MR image shows large cyst (C) posterior to right ovary (*arrow*). Because cyst was separate from ovary, a paratubal cyst was diagnosed prospectively.

agnosed as ovarian cysts (Fig. 11), and not all patients with a diagnosis of ovarian cysts based on MR findings have surgery. Surgical data suggest that paratubal cysts account for 10–20% of adnexal masses. On MR images, two of the lesions could be differentiated prospectively from ovarian lesions because of an elongated configuration of the cyst (Fig. 12) or an anatomically normal ipsilateral ovary (Fig. 13).

Paratubal (paraovarian or parovarian) cysts develop within the broad ligament. They arise most commonly from either the mesothelial epithelium of peritoneal inclusions or vestiges of the paramesonephric ducts and rarely from remnants of the mesonephric ducts [4]. Complications of these cysts can develop, including hemorrhage, torsion, and rupture, similar to those associated with ovarian cystic lesions. On sonograms, uncomplicated paratubal cysts may be indistinguishable from simple ovarian cysts [3]. In some cases, either transvaginal sonography or MR imaging may show that the paratubal cyst is separate from a normal ipsilateral ovary.

REFERENCES

1. Jones HW, Jones GS. *Novak's textbook of gynecology*, 10th ed. Baltimore: Williams & Wilkins, **1981**:282–295
2. Kaufman RH, Friedrich EG, Gardner HL. *Benign diseases of the vagina and vulva*. Chicago: Year Book Medical, **1989**:237–285
3. Alpern MB, Sandler MA, Madrazo BL. Sonographic features of parovarian cysts and their complications. *AJR* **1984**;143:157–160
4. Genadry R, Parmley T, Woodruff JD. The origin and clinical behavior of the parovarian tumor. *Am J Obstet Gynecol* **1977**;129:873–880

When the Solution Is the Problem: A Brief History of the Shoe Fluoroscope

Council A. Nedd II[1]

Few events in the history of science and technology have brought about so many consequences as did the fortuitous discovery of the X-ray by Wilhelm Roentgen in November 1895. The following year saw more than 1000 publications produced on the subject, demonstrating the impact of the X-ray on the world's scientific community. The general public was affected as well and constantly came up with new uses for the X-ray. During the late 1890s, for example, X-rays of the hand were considered to be a new form of portraiture, and an X-ray was once used to locate a lost ring that had mistakenly been baked in a cake [1]. In another case, a radiologist was approached about the feasibility of using a "frisking fluoroscope" on patrons of a gambling establishment for the purpose of flushing out concealed weapons [2].

While fascination with the X-ray crossed social and economic boundaries, it was primarily the scientific community and the monied classes that had access to X-ray apparatuses. Thomas Edison's battery of experiments with the X-ray eventually compelled him to define his role with relation to Roentgen. In a *New York Times* article, Edison stated, "[Roentgen] needs men like myself, whose chief aim is to turn the great discoveries to practical use and adapt them, so that the world will receive the benefit of them" [3]. Unwittingly, an answer to Edison's call for application of the new technology was evolving, reaching an important plateau in 1927. In that year, Arthur H. Compton won the Nobel Prize for his discovery of wavelength change in diffused X-rays, and that same year the fluoroscope was being put to an odd use in some of the better shoe stores in America.

In 1927 a patent was granted to Jacob Lowe for a machine that would visually determine the "fit of footwear." Lowe stated that his machine effects a means "whereby the salesman, the purchaser and even a purchaser's advisory friend can visually know exactly how well a shoe is fitting, both under pressure and otherwise." Lowe went on to state that, "With this apparatus in his shop, a shoe merchant can positively assure his customers that they need never wear ill-fitting boots and shoes; that parents can visually assure themselves as to whether they are buying shoes for their boys and girls which will not injure and deform the sensitive bone joints" [4].

The shoe fluoroscope emerged as one of more successful marketing devices in the history of shoe sales. The polished wooden cabinet with the metal viewing scopes at first glance is reminiscent of a nickelodeon. The relatively high purchase price of $2000 was thought to be well worth it when weighed against the amount of sales that resulted from people simply wanting access to the machine.

The fluoroscope reached its height of popularity during the years immediately following World War II. However, radiation studies conducted just before the explosion of the atomic bomb prompted investigation into the effects of prolonged and repeated exposure to low voltage X-rays. It was determined that the two populations most at risk from the X-rays put out by the shoe fluoroscope were store clerks and children being fitted for new shoes. Nevertheless, not until 1949 was there any attempt to regulate the volume of X-rays emitted from the fluoroscopic units. Scattered radiation from the foot holes of the fluoroscopes could exceed 100 mR/hr at 10 ft from the machine.

Store clerks faced the danger of chronic radiation injury to the hematopoietic tissue and reproductive organs from prolonged exposure. But children, whose feet were placed in the machine, were at much greater risk. A child who tried on several pairs of shoes per visit, several times a year, with one or both feet in the machine from 10 to 45 sec, at a dose ranging from 0.5 to 5.8 R/sec, could be exposed to radiation doses ranging from 10 to 116 R in a 20-sec period [5]. This level of exposure can cause radiation burns of the skin; but worse, it can damage the epiphyseal cartilage in the feet, resulting in stunted bone growth or deformation.

The lack of an effective means for regulating the radiation produced by the machines forced the Food and Drug Administration to ban the machine in 1953. How ironic an end—the shoe fluoroscope was banned for causing the exact thing it was designed to prevent: damage to the foot.

REFERENCES

1. Anonymous. Cakes under the X-ray. *Lancet* January 23, 1897:289
2. Grigg ERN. *The trail of the invisible light*. Springfield, IL: Thomas, **1965**:55
3. Edison TA. *The New York Times*, February 9, 1896:9
4. Lowe JJ, inventor. *Method and means for visually determining the fit of footwear*. U.S. patent 1,614,988. Washington, DC: United States Patent Office: **1927**
5. Williams CR. Radiation exposure from the use of shoe-fitting fluoroscopes. *N Engl J Med* **1949**;241:333–335

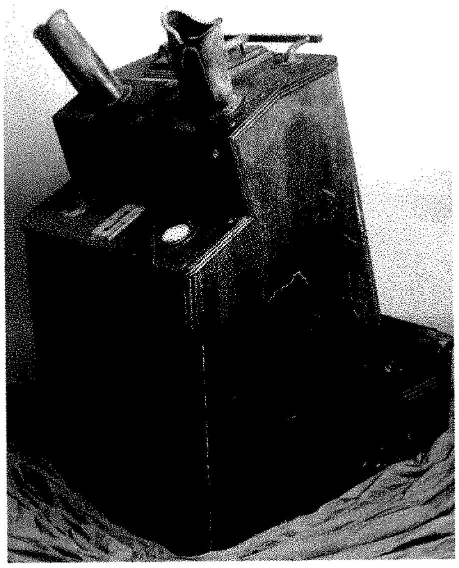

The Adrian Corp. shoe fluoroscope model no. 2544 type AC. This machine was once used in the Boyce & Lewis shoe store in Washington, DC.

In preparation for the 1995 centennial celebration of the discovery of the X-ray, the *AJR* will periodically publish History Pages, which deal with events leading up to and occurring around the time of the discovery.

The opinions or assertions contained herein are the private views of the author and are not to be construed as being official or as reflecting the views of the Department of the Army or the Department of Defense.

[1] Department of National Museum of Health and Medicine, Historical Collections, Armed Forces Institute of Pathology, Washington, DC 20306-6000. Address reprint requests to Council A. Nedd II.

0361-803X/92/1586-1270 © American Roentgen Ray Society

Intraarticular Fractures of the Calcaneus: Value of CT Findings in Determining Prognosis

Dennis L. Janzen[1]
Douglas G. Connell[1]
Peter L. Munk[1,2]
Richard E. Buckley[3]
Robert N. Meek[3]
Martin T. Schechter[4]

The prognosis of intraarticular calcaneal fractures is variable, ranging from severe functional impairment and pain to complete return of normal function. Clinical assessment and CT scanning were performed 1-11 years after fracture in 45 patients (51 fractures) to determine the relationship between the CT findings and clinical status. Conservatively treated ($n = 18$) and surgically treated ($n = 33$) fractures were assessed. Clinical assessment included evaluation of subjective parameters (pain, activity, gait, and use of orthotics) and objective measurement of subtalar motion. CT evaluation included assessment of abnormalities in the posterior subtalar joint, loss of calcaneal height, tendon abnormalities, and calcaneocuboid joint abnormalities. A poor clinical outcome, caused by loss of subtalar motion, was more common when CT showed incongruity or degeneration of the posterior facet ($p = .04$) and when Bohler's angle was decreased ($p = .0006$). Other CT findings, such as loss of calcaneal height and tendon abnormalities, did not correlate with clinical outcome. An unexpected finding was that surgical screws were intraarticular in eight (24%) of 33 surgically treated patients; however, this finding was not significantly associated with poor clinical outcome.

Our findings indicate that the CT findings of degenerative change and incongruity of the posterior subtalar joint correlate significantly with poor clinical outcome.

***AJR* 158:1271-1274, June 1992**

Calcaneal fractures are intraarticular in 56-75% of cases [1, 2]. Intraarticular calcaneal fractures are complex injuries, with multiple bone and soft-tissue abnormalities. No clear consensus exists regarding the management of these difficult fractures [3-5]. Open reduction and internal fixation have been recommended in recent articles [5-11]. In both conservatively and surgically treated patients, 15-50% have long-term pain, loss of joint mobility, and functional disability after intraarticular calcaneal fracture [1, 3, 4, 6]. The prognostic significance of the various anatomic derangements is controversial [4, 12]. Knowledge about the functional significance of the various anatomic derangements would be useful in the treatment and prognostication of acute intraarticular calcaneal fractures.

CT is superior to plain radiographs in the assessment of acute intraarticular calcaneal fractures [2, 13-18]; however, only one case report on the use of CT to evaluate intraarticular calcaneal fractures after treatment has been published [19]. The purpose of this study is to evaluate the correlation between the CT findings (as seen on CT at the time of follow-up) and the clinical outcome of intraarticular calcaneal fractures.

Subjects and Methods

Patients with acute intraarticular calcaneal fractures evaluated at our institution and the local Worker's Compensation Board between March 1978 and December 1988 were contacted and asked to return for clinical and radiologic assessment. Patients with other

Received September 23, 1991; accepted after revision December 26, 1991.

This work was supported by the Worker's Compensation Board of British Columbia.

[1] Department of Radiology, University of British Columbia and Vancouver General Hospital, Vancouver, B.C., Canada V5Z 1M9.

[2] Present address: Department of Radiology, University Hospital, London, Ontario, Canada N6A 5A5.

[3] Department of Orthopedic Surgery, University of British Columbia and Vancouver General Hospital, Vancouver, B.C., Canada V5Z 1M9.

[4] Department of Health Care and Epidemiology, Faculty of Medicine, University of British Columbia, Vancouver, B.C., Canada V6T 1Z3.

0361-803X/92/1586-1271
© American Roentgen Ray Society

concurrent fractures in the lower limbs or spine were excluded from study. Forty-five patients returned for clinical and CT examination. The interval between the time of the acute fracture and the time of clinical and radiologic assessment ranged from 1 to 11 years (average, 4.5 years). Six of these patients had bilateral intraarticular calcaneal fractures; therefore, 51 intraarticular calcaneal fractures were analyzed. Bilateral fractures were analyzed as independent injuries.

All patients were men. The average age at time of injury was 37 years (range, 14–61 years). All patients had displaced "tongue"-type (*n* = 14) or joint depression-type (*n* = 37) intraarticular fractures according to the Essex-Lopresti classification [1]. The degree of displacement of the surface of the posterior subtalar joint (as determined by CT at the time of injury) was less than 2 mm in five fractures and greater than 2 mm in 46 fractures. Eighteen fractures were treated without surgery. In nine cases, the limb was immobilized in a cast for 6 weeks; the other nine had no cast but weight bearing was avoided for 6 weeks. Thirty-three fractures were treated surgically: seven with screw fixation, four with Kirschner wires, and 22 with a combination of lateral plate, screws, and Kirschner wires. Of the 33 surgically treated fractures, the surgeon's report indicated anatomic reduction in 23, joint surface incongruity of 1–2 mm in nine, and incongruity greater than 2 mm in one patient. The surgeon's assessment of the success of surgical reduction was based on open inspection of the joint surface and intraoperative fluoroscopy.

The clinical examinations were done at the time of the CT examinations by an orthopedic surgeon who had not been involved in the initial treatment of any of the patients and was not aware of the CT findings. The Carter-Rowe scoring system [7, 20] was used in the clinical examination. This scoring system assesses pain, activities, occupational function, gait, use of orthotics, and use of medications. In this scoring system, a higher score indicates a more favorable outcome. A clinical score of 90–100 points was judged to be a good result; 70–90 points, a fair result; and less than 70 points, a poor result.

The average clinical score was 80.2 ± 13.0 (range, 40–100) with a median of 81, indicating a lack of skewness in this variable. A good result was present in 13 fractures (25%), a fair result in 27 (53%), and a poor result in 11 (22%). Forty-six (90%) of the 51 intraarticular calcaneal fractures caused residual pain. In 28 cases (55%), the patient had pain on motion of the subtalar joint, which was felt centrally in the calcaneus or over the lateral aspect of the posterior subtalar joint. Eighteen patients (35%) described restriction of occupational or recreational activities; most of this group had a "poor" result clinically. The range of motion of the subtalar joint was determined by the McMaster method [21]. The mean subtalar motion observed at follow-up was 57% of normal.

The CT scans were obtained at the time of clinical assessment. CT was performed on a GE 9800 scanner (General Electric, Milwaukee, WI) with 3-mm collimation at 3-mm intervals in transverse and coronal planes [14, 15, 18]. Sagittal 3-mm reconstructions were made from the coronal scans. The CT scans were assessed by three observers (two experienced muscoloskeletal radiologists and one radiology resident) who were unaware of the clinical scores. Radiologic scoring was determined by consensus. The anatomic parameters and scoring of the various categories were as follows: posterior facet incongruity (none = 0 points; 1–2 mm = 1 point; >2 mm = 2 points), posterior facet degeneration (none = 0 points; mild = 1 point; severe = 2 points), calcaneocuboid incongruity (none = 0 points; 1–2 mm = 1 point; >2 mm = 2 points), calcaneal height (normal = 0 points; 5–25% loss = 1 point; >25% loss = 2 points), tendons (normal = 0 points, displaced = 1 point, impinged or entrapped = 2 points). In all the radiologic parameters, a higher score indicates a more severe abnormality. The posterior facet CT score was 0 if posterior facet incongruity or degeneration was absent; 2 if incongruity (> 2 mm) and/or degeneration was severe; and 1 otherwise (Figs.

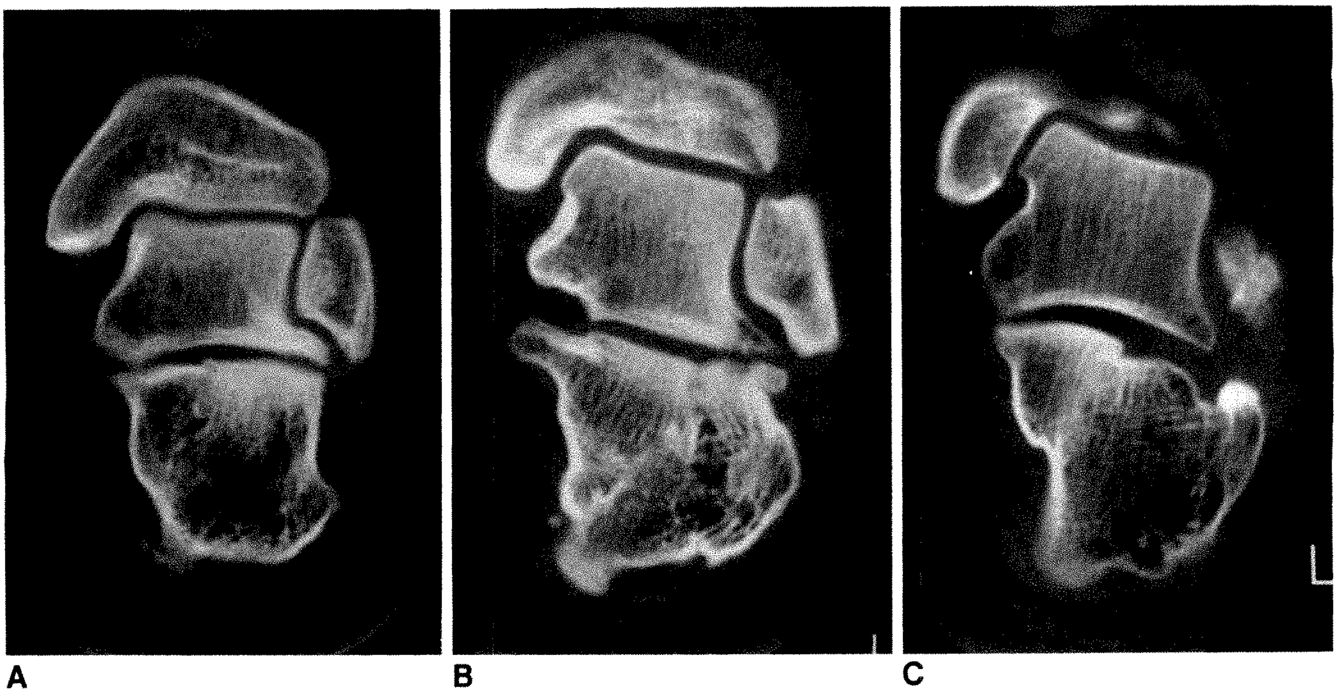

Fig. 1.—CT scans show appearances of posterior subtalar joint, which correlated with clinical status.
***A*, No significant irregularity or incongruity of posterior subtalar joint.**
***B*, Moderate incongruity (1–2 mm) and degenerative change in posterior subtalar joint. Note osteophytes arising from lateral aspect of joint.**
***C*, Severe incongruity (>2 mm), degenerative change, and gas in posterior subtalar joint.**

1A–1C). The presence of gas or surgical screws in the joint space was recorded. The fracture type (as determined from plain radiographs at the time of initial injury) was noted.

Analysis of the CT images according to the various factors revealed the following results. Posterior facet incongruity was absent in 20 cases (39%), 1–2 mm in 27 cases (53%), and greater than 2 mm in four cases (8%). Posterior facet degeneration was absent in three cases (6%), mild in 39 cases (76%), and severe in nine cases (18%). Calcaneocuboid incongruity was absence in 38 cases (78%), 1–2 mm in 11 cases (22%), and greater than 2 mm in two cases (4%). The calcaneal height was normal in 18 cases (35%), decreased by 5–25% in 28 cases (55%), and decreased by more than 25% in five cases (10%). The tendons were normal in 35 cases (69%), displaced in 12 cases (23%), and entrapped in four cases (8%).

Bohler's angles in the fractured and normal foot were measured from the sagittal CT reconstructions. In the unfractured foot, the angle averaged 31° (range, 26–40°). This measurement was compared with Bohler's angle as measured on the plain radiographs [6, 14, 15]. Statistical analysis confirmed that Bohler's angle can be reliably measured on sagittal CT reconstructions. In the fractured foot, the angle measured 30–40° in six cases (12%), 20–30° in 14 cases (27%), 10–20° in 13 cases (26%), 0–10° in eight cases (16%), and less than 0° in nine cases (18%).

Gas was present in the posterior subtalar joint in nine (18%) of the intraarticular calcaneal fractures (Fig. 2). Surgical screws were present in the posterior subtalar joint in eight (24%) of the 33 surgically treated patients (Fig. 3).

Descriptive statistics are presented as simple proportions and as mean plus or minus SD unless otherwise indicated. The distribution of clinical scores was examined for normality. Univariate regression models were fit, treating all independent predictors as either binary or continuous variables. After bivariate relationships were identified, multiple regression models were fit to examine the effects of confounding variables.

Results

Two variables were significantly associated with improved clinical score: increased range of subtalar joint motion ($p = .0005$) and tongue-type (as opposed to joint depression–type) fractures ($p = .0063$). No significant association was found between clinical score and calcaneal height, tendon abnormalities, or the surgeon's intraoperative assessment of the posterior subtalar joint. No significant association was found between the surgeon's intraoperative assessment of the subtalar joint and the CT appearance of the joint. Failure to detect significant associations may reflect a lack of statistical power due to the small number of fractures studied.

Because range of subtalar joint motion was an important correlate of clinical score, we conducted a second multiple regression analysis using range of subtalar motion as the dependent variable. Significant and independent predictors of loss of subtalar joint motion were an elevated posterior facet CT score ($p = .037$), decreased Bohler's angle ($p = .0006$), and surgical treatment (as opposed to conservative therapy; $p = .0007$).

CT evaluation showed intraarticular screws in the posterior subtalar joint in eight (24%) of the 33 surgically treated patients. It is of note that even retrospectively this intraarticular position could not be seen on the plain radiographs. The presence of an intraarticular screw was not significantly as-

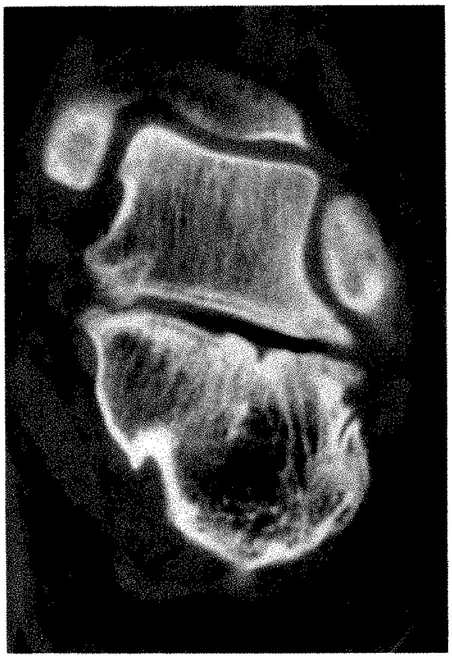
2

Fig. 2.—CT scan shows gas in posterior subtalar joint. Note incongruity of posterior facet joint surface and lateral osteophyte formation, indicating degenerative changes.

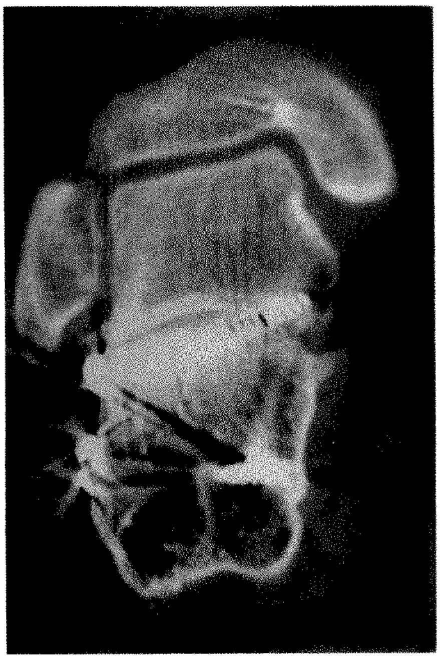
3

Fig. 3.—CT scan shows a surgical screw in posterior subtalar joint. Screws typically entered medial aspect of subtalar joint.

sociated with a poor clinical score (mean score of patients without screw in joint, 80.6; mean score of patients with screw in joint, 78.3; $p = .11$). Failure to detect significant associations may reflect lack of statistical power due to the small number of patients in this subgroup.

Discussion

The superiority of CT over plain radiographs in imaging acute intraarticular calcaneal fractures is well established [2, 13-18]. Our experience indicates that CT is also superior in evaluating healed intraarticular calcaneal fractures, especially the posterior subtalar joint and the soft-tissue structures (tendons).

The presence of gas in the posterior subtalar joint has not been reported before. This abnormality was present in 18% of our cases and was undetectable on plain radiographs. This finding showed a weak correlation with posterior subtalar joint degeneration; however, no association with pain, clinical score, or subtalar motion was found. Intraarticular position of surgical screws also has not been reported. This was present in 24% of the surgically treated patients (Fig. 3). It is difficult to accurately assess the position of screws in relation to the curved surface of the posterior subtalar joint on plain radiographs. The use of plain radiographs underestimates the frequency of intraarticular position of screws. During surgical reduction, the surgeon attempts to position the screw in the dense subchondral bone immediately subjacent to the articular surface. Also, the surgeon (using a lateral approach) cannot visualize the medial aspect of the joint. These factors most likely explain the frequent finding of screws entering the medial aspect of the posterior subtalar joint. No association was found between clinical score and the presence of an intraarticular screw in our study; however, the presence of an intraarticular screw in a markedly symptomatic patient may justify removal of the screw.

Tendon displacement or entrapment as detected on CT or during surgery has been described as a major prognostic variable [11, 12]. In our study, tendon abnormalities were not significantly associated with pain or clinical score; however, failure to detect significant associations may reflect lack of statistical power due to the small number of fractures studied.

In our study, the strongest correlates of clinical score were subtalar motion and principal fracture type. The patients who had the most impairment of motion in the subtalar joint and a pattern of centrolateral joint depression had the poorest clinical scores. The findings of incongruity and degeneration of the posterior subtalar joint and smaller Bohler's angle on CT correlated significantly with loss of subtalar joint motion. These findings strongly suggest that the CT appearance and mobility of the posterior subtalar joint is a prime factor in predicting clinical outcome. A recent study of the correlation between preoperative CT appearance and clinical outcome of intraarticular calcaneal fractures also concluded that the status of the posterior subtalar joint was prognostically important [22]. The significance of this result is that the diagnosis and treatment of intraarticular calcaneal fractures should focus on identifying and correcting abnormalities of the posterior subtalar joint.

REFERENCES

1. Essex-Lopresti P. The mechanisms of reduction techniques and results in fractures of the os calcis. *Br J Surg* **1952**;39:395–419
2. Heger L, Wulff K, Seddiqi MSA. Computed tomography of calcaneal fractures. *AJR* **1985**;145:131–137
3. Giachino AA, Uhtohoff HK. Intra-articular fractures of the calcaneus. *J Bone Joint Surg [Am]* **1989**;71-A:784–787
4. Paley D, Hall H. Calcaneal fracture controversies: can we put Humpty Dumpty together again? *Orthop Clin North Am* **1989**;20:665–677
5. Hammesfahr JFR. Surgical treatment of calcaneal fractures. *Orthop Clin North Am* **1989**;20:679–689
6. Stephenson JR. Treatment of displaced intra-articular calcaneal fractures. *J Bone Joint Surg [Am]* **1987**;69-A:115–130
7. Rowe CR, Sakellarides HT, Freeman PAA, Sorbie C. Fractures of the os calcis: a long term follow-up study of 146 patients. *JAMA* **1963**;184:920–923
8. Burdeaux BD. Reduction of calcaneal fractures by the McReynolds medial approach technique and its experimental basis. *Clin Orthop* **1983**;177:87–103
9. Leung KS, Chan WS, Shen WY, Pah PP, So WS, Leung PC. Operative treatment of intra-articular fractures of the os calcis: the role of internal fixation and primary bone grafting. *J Orthop Trauma* **1989**;3:232–240
10. Harding D, Waddell JP. Open reduction in depressed fractures of the os calcis. *Clin Orthop* **1985**;199:124–131
11. Soeur R, Remy R. Fractures of the calcaneus with displacement of the thalamis portion. *J Bone Joint Surg [Br]* **1975**;57-B:413–421
12. Pozo JL, Kirwan E, Jackson AM. The long-term results of conservative management of severely displaced fractures of the calcaneus. *J Bone Joint Surg [Br]* **1984**;66-B:386–390
13. Rosenberg ZS, Feldman F, Singson R. Intra-articular calcaneal fractures: computed tomographic analysis. *Skeletal Radiol* **1987**;16:105–113
14. Guyer BH, Levinsohn EM, Fredricksen BE, Bailey GL, Formikell M. Computed tomography of calcaneal fractures: anatomy, pathology, dosimetry, and clinical relevance. *AJR* **1985**;145:911–919
15. Sartoris DJ, Resnick D. Diagnostic imaging approach to calcaneal fractures. *J Foot Surg* **1987**;26:524–529
16. Lowrie IG, Finlay BB, Brenke IJ, Gregg PJ. Computed tomographic assessment of the subtalar joint in calcaneal fractures. *J Bone Joint Surg [Br]* **1988**;70-B:247–250
17. Heger L, Wulff K. Computed tomography of the calcaneus: normal anatomy. *AJR* **1985**;145:123–129
18. Segal D, Marsh JL, Leiter B. Clinical application of computerized axial tomography (CAT) scanning to calcaneal fractures. *Clin Orthop* **1985**;199:114–123
19. Techner LM, Eannace RJ. Computed tomography in the evaluation of old calcaneal fractures. *J Am Podiatr Med Assoc* **1987**;77:243–245
20. Buckley RE, Meek RN. Comparison of open versus closed reduction of intraarticular calcaneal fractures: a matched cohort study in workmen. *J Orthop Trauma* (in press)
21. McMaster M. Disability of the hindfoot after fracture of the tibial shaft. *J Bone Joint Surg [Br]* **1976**;58-B:90–93
22. Crosby LA, Fitzgibbons T. Computerized tomography scanning in acute fractures of the calcaneus. *J Bone Joint Surg [Am]* **1990**;72-A:852–859

Do Metastases in Vertebrae Begin in the Body or the Pedicles?

Imaging Study in 45 Patients

Paul R. Algra[1,2]
Jan J. Heimans[3]
Jaap Valk[1]
Jos J. Nauta[4]
Monique Lachniet[3]
Barend Van Kooten[3]

We analyzed CT scans of the spine obtained in patients with vertebral metastases to determine what specific portion of the vertebra is initially involved by metastasis. The CT findings were then correlated with the abnormalities seen on plain films. Forty-five patients with histologically proved metastases in 95 vertebrae were included in the study. In all patients, CT scans and plain films of the spine were obtained within 1 week of each other. Analysis of the CT scans showed that the vertebral body was the portion of the vertebra that was most frequently destroyed by the metastases. Destruction of a pedicle was never identified in the absence of involvement of the body. The opposite was true on plain films, in which the most common finding was destruction of the pedicles. CT showed that the position of the metastases in the vertebra correlated with the sites of entry of the vertebral vessels.

Our results show that the initial anatomic location of metastases within vertebrae is in the posterior portion of the body. Analysis of CT scans shows that the body is involved before the pedicles, although destruction of the pedicles is the most common finding on plain films. The pedicles are not the primary site of metastatic involvement. Destruction of the pedicles occurs only in combination with involvement of the vertebral body.

***AJR* 158:1275–1279, June 1992**

Skeletal metastases have a tendency to develop in the axial skeleton in a distribution that correlates with the location of red bone marrow [1]. Loss of contours of the vertebral pedicle on plain films of the spine has been described as an early radiologic sign of vertebral metastases [2]. However, the vertebral pedicle consists mainly of cortical bone and contains virtually no bone marrow. The vertebral body, containing most of the red bone marrow, is more likely to harbor and develop blood-borne metastases than are other parts of the vertebra [3].

To establish the initial location of metastases within vertebrae and to determine the association between pedicle destruction and involvement of other parts of the vertebra by metastases, we performed a retrospective analysis of CT and plain film findings in patients in whom spinal metastases were identified for the first time. The location of destruction seen on CT was compared with the location of destruction seen on plain films. Special attention was paid to the location of destruction seen on CT in patients in whom destruction of a pedicle was seen on plain films.

We tested the hypothesis that the observed location of vertebral destruction followed the sites of entry of the vertebral vessels.

Materials and Methods

During the years 1987–1989, 201 patients in our hospital were examined radiologically for skeletal metastases. From this group, we selected 86 patients in whom symptoms and/or signs of vertebral metastases were identified for the first time, and in whom both CT scans and plain films of the spine were obtained within a period of 1 week (maximum interval between both examinations, 7 days; average, 2.1 days). We excluded from evaluation 41

Received November 18, 1991; accepted after revision January 13, 1992

[1] Department of Diagnostic Radiology, Free University Hospital, Boelelaan 1117, 1081 HV Amsterdam, the Netherlands.

[2] Present address: Medisch Centrum Alkmaar, Wilhelminalaan 12, 1815 GD Alkmaar, the Netherlands. Address reprint requests to P.R. Algra.

[3] Department of Neurology, Free University Hospital, 1081 HV Amsterdam, the Netherlands.

[4] Department of Theory of Medicine, Epidemiology and Biostatistics, Free University Hospital, 1081 HV Amsterdam, the Netherlands.

0361-803X/92/1586-1275
© American Roentgen Ray Society

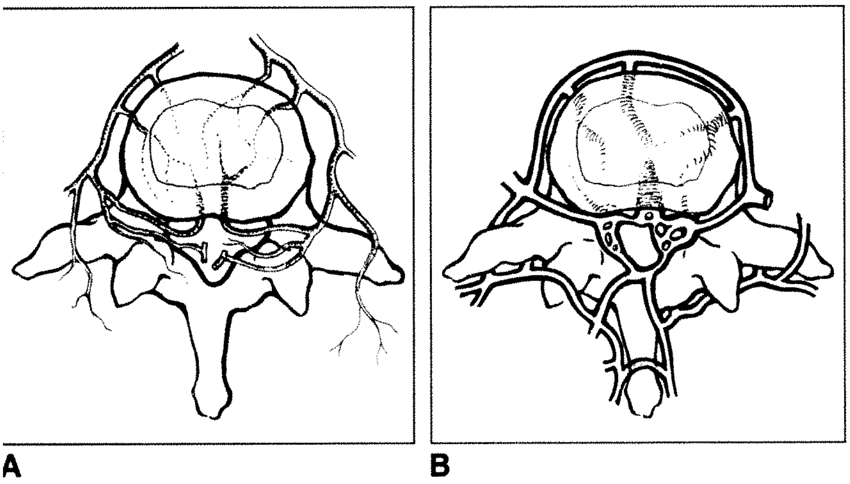

Fig. 1.—*A* and *B*, Drawings show that main arterial (*A*) and venous (*B*) vessels supplying vertebra enter anterior and posterior parts of vertebral body. Hematogenous spread of metastases occurs most likely via these posterior and anterior vessels.

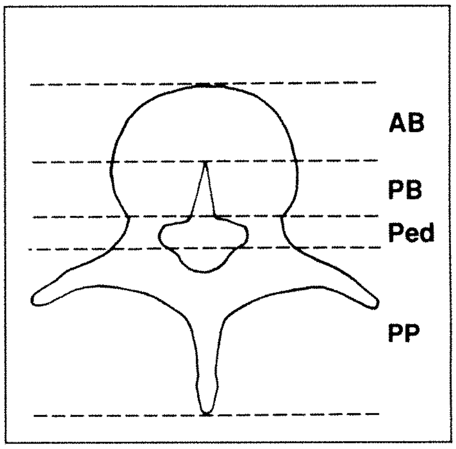

Fig. 2.—Drawing shows four sections of vertebra that were used to establish location of destruction as assessed by CT. AB = anterior part of vertebral body, PB = posterior part of vertebral body, Ped = pedicles, PP = posterior part of the vertebra consisting of spinous and transverse processes and laminae.

patients who had been treated with chemotherapy or hormonal agents or had radiation therapy on the spine.

In this retrospective study, we included 45 patients (27 men and 18 women; mean age, 59 years; age range, 37–71 years) known to have malignancy with vertebral metastatic disease. The diagnosis of skeletal metastases was histologically proved by iliac crest biopsy in 31 patients, by trephine vertebral biopsy in seven patients, by bone marrow biopsy from a lytic lesion in the femur in three patients and biopsy from a lytic lesion in the shoulder in one patient, and by autopsy in three patients.

The patients were known to have a primary tumor for an average period of 4 years (range, 6 months to 16 years). The primary tumors included 13 carcinomas of the breast, nine carcinomas of the lung, four carcinomas of the kidney, three carcinomas of the prostate, three carcinomas of the larynx, two melanomas, two carcinomas of the colon, two carcinomas of the endometrium, one carcinoma of the parotid gland, one carcinoma of the adrenal gland, one carcinoma of the urinary bladder, one carcinoma of the oropharynx, and three that were unknown.

Reasons for radiologic examination included back pain (39/45) and signs of compressive radiculopathy or myelopathy, such as irradiating pain (28/45), abnormal or lost reflexes (26/45), loss of sensation (23/45), and loss of strength (20/45).

We compared CT scans with plain films of the spine, which were routinely obtained as part of myelography. In the assessment of location of destruction, we reviewed the vertebrae showing destruction on CT. We evaluated a total of 95 affected vertebrae: five cervical, 26 thoracic, and 64 lumbar. The average number of vertebrae imaged in each patient was 2.1. Ninety vertebrae (43 patients) showed lytic metastases, and five (two patients) showed mixed (sclerotic and lytic) forms.

CT scans were obtained on a Tomoscan 350 scanner (Philips, Shelton, CT). Slice thickness was 4.5 mm in the thoracic and lumbar regions and 3.0 mm in the cervical spine. Slices were continuous; a standard bone setting with a window level of 120 and window width of 600 was used.

Both lateral and frontal plain films had been obtained in each patient. The plain films were assessed with regard to the presence of lysis or destruction of the vertebral body; loss of vertebral height; and destruction of pedicles, transverse and spinous processes, and laminae.

CT scans and plain films were reviewed separately by two radiologists. The radiologist who reviewed the plain films of a patient was unaware of the CT findings and vice versa.

We supposed that the location of vertebral bone destruction followed the entry sites of the vertebral vessels. The main vessels supplying the vertebra enter at the posterior and anterior parts of the vertebral body (Fig. 1). A simplified outline of a standard vertebra was used to indicate the location of destruction as established by CT (Figs. 2 and 3). The standard vertebra was divided into four sections: anterior vertebral body, posterior vertebral body, pedicles, and posterior part of the vertebra consisting of spinous and transverse processes and laminae.

If hematogenous metastases enter the vertebra via the vertebral body, the anterior plus posterior part of the body would be primarily involved in the destruction. Subsequently, a progression of the destruction can involve the pedicles and the posterior part of the vertebra. In our model in which a vertebra is separated into four sections, a total of 15 sections or combinations of sections are possible. The six most probable locations or combinations of locations of vertebral destruction when the entry sites of the vertebral vessels are taken into consideration are: (1) posterior body, (2) anterior body, (3) posterior + anterior body, (4) posterior + anterior body + pedicle, (5) posterior body + pedicle, and (6) posterior body + pedicle + spinous and transverse processes and laminae.

The null hypothesis was defined as follows: Destruction of bone by metastases occurs in a random fashion, or the frequency of each section involved in destruction or any combination of sections involved is equally distributed. If the null hypothesis is correct, the previously described locations (which are likely to be involved when the entry sites of the vertebral vessels are taken into consideration) would occur in six (40%) of the 15 possibilities. To test the null hypothesis, we computed the percentage of vertebrae that supported our hypothesis for each patient separately. The overall percentage ($\bar{p}$) was computed as the weighted average of these individual percentages, with the numbers of the vertebrae per patients as weights.

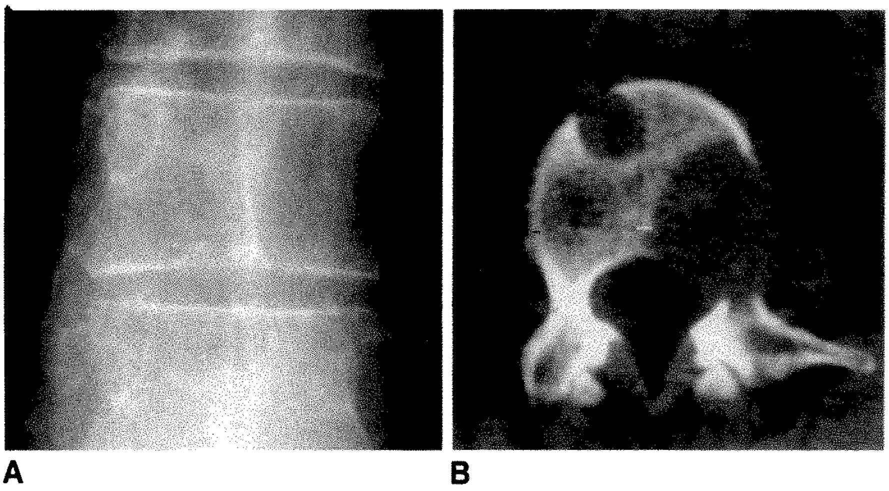

Fig. 3.—*A*, Plain film shows destruction of left pedicle by lytic metastasis in second lumbar vertebra.
B, In addition to pedicle destruction, CT scan shows lytic lesions in anterior and posterior parts of vertebral body.

The formula for the standard error of $\bar{p}$, SE($\bar{p}$), is given by Snedecor and Cochran [4]. Next, it was tested if $\bar{p}$ deviated significantly from 40% by referring the value of $(\bar{p} - 0.4)/\mathrm{SE}(\bar{p})$ to the standard gaussian distribution.

Results

The distribution of lesions in the 95 affected vertebrae is given in Table 1. CT showed lesions confined to one section in six vertebrae. In five vertebrae, the posterior part of the vertebral body was the only affected site, and in one vertebra, the anterior part of the vertebral body was the only affected site. The other 89 vertebrae had combinations of sections involved in the metastatic process. The most frequent combination of sections affected was the posterior part of the vertebral body in combination with the anterior part; next most frequent was the posterior part and anterior part in combination with the pedicles (Table 1). The pedicle showed destruction in 53 vertebrae (left pedicle in 17, right pedicle in 12, both pedicles in 24). Involvement of the pedicle was never present without involvement of the posterior part of the vertebra. The location of destruction in the vertebra, as established by CT, was the same in each level imaged; that is, the location of destruction observed in the cervical vertebrae was the same as in the thoracic and lumbar vertebrae. In only one of the 95 vertebrae was the posterior part of the body not involved. In 20 instances, the anterior part of the body was not involved.

Plain films of the 95 affected vertebrae showed destruction of the pedicle in 29 vertebrae (left pedicle in 13, right pedicle in nine, both pedicles in seven). Loss of vertebral body height or lytic lesions were observed in 52 vertebral bodies (posterior body was involved in 27 vertebrae, anterior body in 25 vertebrae), and destructive lesions in the laminae and spinous process in five vertebrae (Table 2). In none of the 45 patients were lesions seen on plain films that were not visible on CT.

Comparing the distribution of parts of the vertebra involved in the metastatic process as assessed by plain films and by CT, we found the pedicle the most affected part on plain films, whereas on CT, the posterior part of the vertebral body was the most frequently involved part (Fig. 4). In the 57 vertebrae in which CT showed involvement of the pedicle, plain films confirmed destruction of the pedicle in 28 vertebrae. Only when CT showed cortical destruction of the pedicle was loss of visibility of the pedicle noted on plain films. In addition, there was extensive destruction of trabecular bone within the vertebral body that was visible on CT only.

In 32 patients we found that location of destruction in 100% of the vertebrae followed the entry sites of the vertebral vessels. This percentage was 75% in one patient, 60% in two patients, 50% in six patients, 40% in one patient, and 0% in three patients. The overall percentage of vertebrae in favor of

TABLE 1: Locations of Vertebral Destruction by Metastases as Assessed by CT

Part(s) of Vertebra	No. of Vertebrae Involved
Posterior + anterior body	32
Posterior + anterior body + pedicles	24
Posterior + anterior body + pedicles + spinous, transverse processes and laminae	18
Posterior body + pedicles	12
Posterior body	5
Posterior body + pedicles + spinous, transverse processes and laminae	3
Anterior body	1
Total	95

TABLE 2: Frequency of Involvement of Each Vertebral Section by Metastases as Established by CT and Plain Films

Part of Vertebra	No. (%) (*n* = 95)	
	CT Scans	Plain Films
Posterior body	94 (99)	27 (28)
Anterior body	75 (79)	25 (26)
Pedicle (left or right)	57 (60)	29 (30)
Spinous, transverse processes and laminae	21 (22)	5 (5)

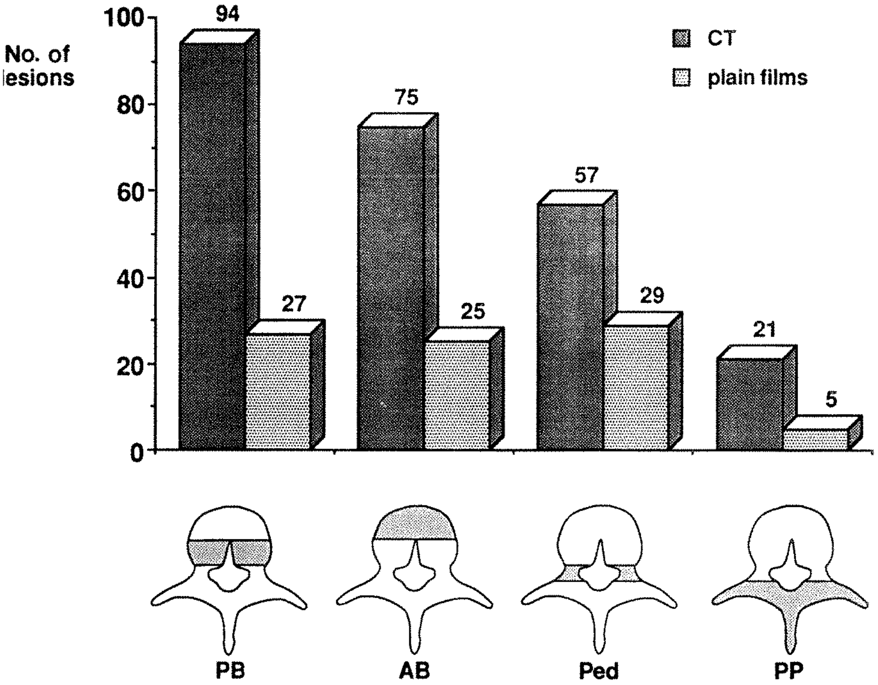

Fig. 4.—Bar graph shows frequency of involvement of each part of the 95 vertebrae evincing destruction on CT scans and plain films. Data are derived from Table 2. PB = posterior part of body, AB = anterior part of body, Ped = pedicles, PP = spinous and transverse processes and laminae.

our hypothesis was 81%. If the null hypothesis is correct, the expected percentage of these vertebrae would be 40%. The observed percentage (81%) in our study deviates significantly ($p < .0001$, one sided) from the expected one (40%). Hence, the null hypothesis could be rejected in favor of our alternative hypothesis.

Discussion

For the selection of patients, we used strict criteria so as to be sure that the group of patients studied consisted solely of patients seen for the first time with symptoms or signs suggesting vertebral metastases. By doing so, the location of lysis we observed can be considered as the initial pathway of metastatic vertebral destruction. By excluding patients who had been treated with chemotherapeutic or hormonal agents and patients who received spinal radiation therapy, interpretation errors caused by recalcification after therapy were avoided.

We found that the lumbar part of the spine was the area most frequently affected by metastases; next were the thoracic and cervical portions. The level of the vertebral column involved by the metastatic process is not primarily related to the amount of bone [5]. Additional venous pathways (Batson veins) for hematogenous metastases may also contribute to the high frequency of lumbar metastases [6, 7].

The part of the vertebra affected most often is the body, which constitutes the major part of the vertebra. This partly explains the high frequency of involvement of the body in the metastatic process. Other factors such as the location of red bone marrow, which is more abundant in the body than in the posterior complex, and the concomitant blood supply, which is more intensive in the body than in the remaining parts of the vertebra, make the vertebral body prone to harbor and develop metastases.

In our series, the posterior part was affected more often than the anterior part. This might be explained by assuming that the posteriorly located basivertebral vein serves as an entrance site for hematogenous spread of metastases [6–8]. Neoplastic spread by way of the Batson plexus to the basivertebral veins has been detected on CT [9]. This mode of metastatic spread also has been corroborated in experimental studies [10].

In combinations of sections of the vertebra involved in the destruction, the section involved most frequently was the posterior part of the vertebral body. The pedicles were always involved in combination with the posterior part of the vertebral body; this suggests that invasion and destruction of the pedicle by the metastatic process occurs only via the vertebral body.

Although destruction of the pedicle is an easily appreciated sign of metastases on plain films, the loss of contours of the pedicle occurs rather late in the metastatic process and often accompanies extensive destruction of trabecular bone in the vertebral body. As has been shown in experimental studies, loss of trabecular bone is hard to visualize on plain films: 50–70% of the trabecular bone must be destroyed before lysis is visible on plain films [11–14]. This might explain why loss of visibility of the pedicle has been interpreted as an early sign of lytic metastases [2]; the concomitant destruction of trabecular bone within the vertebral body remained undetected on plain films.

The frequent involvement of the pedicle in the metastatic process, originally described by Jacobson et al. [2], might be caused by patient selection. As more than 90% of the patients described in the study of Jacobson et al. showed involvement of the pedicles, and only 30% in our group (Table 2) did, it must be assumed that the group of patients studied by Jacobson et al. consisted of patients in an advanced stage of metastatic disease. Unfortunately, Jacobson et al. gave no data as to when the patients were known to have metastatic disease. If they indeed included patients in advanced stages of metastatic disease, their observation of early involvement of the pedicle by metastases might suggest that destruction of the body remained undetected when plain films only were used.

In our patients, the pedicle was the part of the vertebra most often affected on plain films. Thus, the pedicle sign remains a valuable radiologic indicator of metastases on plain films, although CT showed that the posterior part of the vertebral body is more often involved in the destruction than is the pedicle. CT finds metastases earlier than plain films do, before there is destruction of cortical bone of the pedicles.

Braunstein and Kuhns [15] used CT to evaluate the location of vertebral destruction in 33 patients. They found that vertebral body destruction without involvement of the pedicle occurred in 22 of the 33 patients. In 11 cases there was destruction of both the vertebral body and one or both pedicles. In none of the cases was a pedicle involved alone. In 11 cases plain films were compared with CT. In nine of these CT showed bone destruction while plain films were normal.

Our CT findings of early metastatic spread to vertebral bodies rather than to the pedicles correlate well with autopsy and MR imaging [16] findings: metastatic tumor may fill the marrow cavity and leave the cortical bone intact, a circumstance more easily detected on CT or MR imaging than on conventional radiographs. Bone marrow infiltration probably precedes osseous destruction [17].

REFERENCES

1. Kricun ME. Red-yellow marrow conversion: its effect on the location of some solitary bone lesions. *Skeletal Radiol* **1985**;14:10–19
2. Jacobson HG, Poppel MH, Shapiro JH, Grossberger S. The vertebral pedicle sign: a roentgen finding to differentiate metastatic carcinoma from multiple myeloma. *AJR* **1958**;80:817–821
3. Shackman R, Harrison CV. Occult bone metastases. *Br J Surg* **1948**;35:385–389
4. Snedecor GW, Cochran WG. *Statistical methods*, 7th ed. Iowa City: Iowa State University Press, **1980**:202
5. Cumming J, Hacking N, Fairhurst J, Ackery D, Jenkins JD. Distribution of bony metastases in prostatic carcinoma. *Br J Urol* **1990**;66:411–414
6. Batson OV. The function of the vertebral veins and their role in the spread of metastases. *Ann Surg* **1940**;112:138–149
7. Batson OV. The vertebral vein system. *AJR* **1957**;78:195–212
8. Coman DR, De Long RP. Role of the vertebral venous system in the metastasis of cancer to the spinal column: experiments with tumor cell suspensions in rats and rabbits. *Cancer* **1951**;4:610–618
9. Sartoris DJ, Resnick D, Guerra J. Vertebral venous channels: CT appearance and differential considerations. *Radiology* **1985**;155:745–749
10. Arguello F, Baggs RB, Duerst RE, Johnstone L, McQueen K, Frantz CN. Pathogenesis of vertebral metastasis and epidural spinal cord compression. *Cancer* **1990**;65:98–106
11. Ardran GM. Bone destruction not demonstrable by radiography. *Br J Radiol* **1951**;24:107–109
12. Edelstyn GA, Gillespie PJ, Grebell FS. The radiological demonstration of osseous metastases: experimental observations. *Clin Radiol* **1967**;18:158–162
13. Haller J, Andre P, Resnick D, et al. Detection of thoracolumbar vertebral body destruction with lateral spine radiography. Part 1. Investigation in cadavers. *Invest Radiol* **1990**;25:517–522
14. Haller J, Andre P, Resnick D, et al. Detection of thoracolumbar vertebral body destruction with lateral spine radiography. Part 2. Clinical investigation with computed tomography. *Invest Radiol* **1990**;25:523–532
15. Braunstein EM, Kuhns LR. Computed tomographic demonstration of spinal metastases. *Spine* **1983**;8:912–915
16. Asdourian PL, Weidenbaum M, Dewald RL, Hammerberg KW, Ramsey RG. The pattern of vertebral involvement in metastatic vertebral breast cancer. *Clin Orthop* **1990**;250:164–170
17. Kamby C, Guldhammer B, Vejborg I, et al. The presence of tumor cells in bone marrow at the time of first recurrence of breast cancer. *Cancer* **1987**;60:1306–1312

Book Review

MRI of the Shoulder. By Michael B. Zlatkin. New York: Raven, 174 pp., 1991. $89

This text is intended as a state-of-the-art review of what is currently known about MR imaging of the shoulder, emphasizing those areas that have received the most clinical interest: the rotator cuff and the glenoid labrum. The author, Michael B. Zlatkin, is a well-known and highly regarded authority on MR imaging of the shoulder.

The book is divided into six chapters. Chapter 1, by Mitchell D. Schnall, is an excellent overview of the basic physics and principles of MR imaging and how they apply specifically to imaging of the shoulder joint. Chapter 2, by Dr. Zlatkin, is a review of the anatomy of the shoulder. Rather than just presenting the MR anatomy, he makes considerable use of corresponding anatomic drawings and cadaveric specimens. This is followed by a nice review of common variations in normal anatomy and pitfalls in the interpretation of MR images. Chapter 3, by Joseph P. Iannotti, an orthopedic surgeon, discusses the clinical examination of patients with shoulder pain and presents algorithms for the evaluation and treatment of rotator cuff impingement syndrome and recurrent glenohumeral instability.

Chapters 4–6, by Dr. Zlatkin, are the main focus of the text. They cover disease of the rotator cuff and shoulder instability (emphasizing those areas in which MR imaging has had the most clinical impact) and other glenohumeral disorders. The last are a diverse group that includes biceps tendon disorders, posttraumatic disorders, glenohumeral arthritis, osteonecrosis, crystal deposition disease, and bone and soft-tissue tumors. These chapters are well written, with material presented in a logical and comprehensive manner. Detailed MR protocols for rotator cuff disease and shoulder instability are also provided. The chapters have a large number of high-quality, well-labeled illustrations. Arrows are used liberally to highlight pathologic changes and subtle findings.

The book is logically laid out, easy to read, well referenced, and well indexed. It is comprehensive, and Dr. Zlatkin has done an excellent job in showing the spectrum of disease, rather than just classic examples. When grading systems are presented, they are well explained and illustrated.

Although this is an MR text, a few more correlating CT athrograms might be useful for those most experienced with the latter technique. The book also has a few minor editing errors. For example, some figures are cited out of order, and others are not cited in the text; figure 5D in chapter 4 is cited in the text but not illustrated; figure 30C in chapter 6 is probably printed backward. The short section on bone and soft-tissue tumors is too brief to be of value. Compared with the overall text, however, these are minor deficiencies.

I recommend this book to all those interested in MR evaluation of the shoulder. It is reasonably priced, considering the high quality of the images. It would be an excellent addition to any personal library or to the academic library of any teaching program.

Mark J. Kransdorf
Armed Forces Institute of Pathology
Washington, DC 20306-6000

MR Imaging of the Shoulder:

Appearance of the Supraspinatus Tendon in Asymptomatic Volunteers

Christian H. Neumann[1,2]
R. Gary Holt[1,3]
Lynne S. Steinbach[1,2]
Arlon H. Jahnke, Jr.[4]
Steve A. Petersen[5]

MR imaging has been shown to be accurate in the diagnosis of rotator cuff disruption and tear. Uncertainty remains about the significance of increased signal intensity in the critical zone of the supraspinatus tendon without visible disruption of tendon fibers and about the significance of other secondary findings commonly encountered with rotator cuff abnormalities, such as musculotendinous retraction or obliteration and fluid in the subacromial space. We evaluated proton density–weighted and T2-weighted coronal images (obtained on a 1.5-T superconductive MR imager) of 55 shoulders in 32 asymptomatic volunteers for signal intensity in the supraspinatus tendon, location of the musculotendinous junction, fluid in the subacromial-subdeltoid space, and appearance of the fat plane. In 89% of shoulders, the supraspinatus tendon showed focal, linear, or diffuse increased signal intensity with or without loss of the low-signal-intensity tendon margin on proton density–weighted images. None of these findings were confirmed on T2-weighted images. The musculotendinous junction was always located within an area 15° medial to 30° lateral to the highest point (12 o'clock) on the humeral head convexity. A peribursal fat plane was poorly defined or absent in 49%, and fluid in the subacromial-subdeltoid space was found in 20%.

Increased signal intensity in the supraspinatus tendon on proton density–weighted images without a corresponding increase on T2-weighted images, the presence of small amounts of fluid in the subacromial space, and the lack of preservation of the subdeltoid fat plane are common findings in asymptomatic shoulders and by themselves are poor predictors of rotator cuff disease.

AJR **158:1281–1287, June 1992**

Since 1986, a number of articles have appeared detailing the technical, anatomic, and pathologic considerations for high-quality surface-coil MR imaging of the shoulder [1–5]. MR has been shown to be useful in the diagnosis of rotator cuff tears and appears to be gaining wide clinical acceptance [6–10]. Despite these advances, a great deal of uncertainty remains about the normal appearance of the rotator cuff on MR images and, specifically, about the clinical significance of areas of increased signal intensity in the critical zone of the supraspinatus tendon. Although a number of publications have described the normal supraspinatus tendon as possessing little or no signal intensity [2, 4, 5, 9, 11], areas of increased signal are frequently seen in patients having no further MR findings to support the diagnosis of rotator cuff disease [12]. We undertook this study to describe the variability of signal patterns in the supraspinatus tendon of asymptomatic subjects in order to assist in the differentiation of normal variation from clinically significant rotator cuff disease.

Subjects and Methods

All MR examinations were performed on a 1.5-T superconducting MR scanner (Signa, General Electric, Milwaukee, WI) operating on software versions 3.0 to 4.0. The patients

Received January 2, 1992; accepted after revision February 3, 1992.

[1] San Francisco Magnetic Resonance Center, 3333 California St., Ste. 105, San Francisco, CA 94118. Address reprint requests to C. H. Neumann, Ste. 105.

[2] Department of Radiology, University of California, San Francisco, 505 Parnassus Ave., San Francisco, CA 94143.

[3] Present address: Northern Nevada Radiologists, Reno, NV 89502.

[4] Orthopaedic Surgery Service, Letterman Army Medical Center, Presidio of San Francisco, CA 94119.

[5] Department of Orthopedic Surgery, Wayne State University, Detroit, MI 48202.

0361-803X/92/1586-1281
© American Roentgen Ray Society

were placed supine with the arm at the side and thumb pointing upward or rotated slightly outward. Two 5-in. (13-cm) surface coils were applied in Helmholtz configuration over the anterior and posteior surfaces of the shoulder joint and connected through a standard decoupler (Model A66GE, Wide Band Engineering Co., Phoenix, AZ). After acquisition of a T1-weighted, large-field-of-view body-coil localzer in the coronal projection, four subsequent sequences were performed: (1) an axial proton density-weighted multiplanar gradient-ecalled acquisition in the steady state sequence, 300/10/4 (TR/TE/excitations), with a 90° flip angle, 256 × 192 matrix, 14-cm field of view (FOV), 4-mm slice thickness, and 0-mm interslice gap; (2) an axial proton density-weighted and T2-weighted, 2000/10-70/2, sequence with a 256 × 192 matrix, 14-cm FOV, 4-mm slice thickness, and 1-mm interslice gap; (3) an oblique coronal proton density–weighted and T2-weighted, 1800/25-80/2, sequence along the diection of the supraspinatus muscle with a 256 × 192 matrix, 14-16 cm FOV, 5-mm slice thickness, and 5-mm interslice gap with rectangular pulse profile (contiguous space multiecho multiplane [CSMEMP]); and (4) an oblique sagittal T1-weighted sequence, perpendicular to he oblique coronal sequence, 700/10/1, with a 256 × 128 matrix, 8-cm FOV, 5-mm slice thickness, and 2-mm interslice gap.

This study includes MR images of 55 shoulders in 32 asymptomatic young, active, and healthy men and women in medical services or enlisted in the Armed Forces. The 23 men and nine women were 22–5 years old (mean, 26 years). Thirty-one right and 24 left shoulders were scanned. Informed consent was obtained from all subjects.

The images were reviewed by radiologists experienced in musculoskeletal MR imaging. The supraspinatus tendon was evaluated for signal intensity and signal patterns on both proton density-weighted and T2-weighted images according to the grading system used by Farley et al. [10] (Table 1). Within these tendon types, additional attention was paid to patterns such as increased signal intensity with preservation of low-signal-intensity tendon margins, increased signal ntensity with poor definition of either the superior or inferior tendon margin, and increased signal intensity without continuity of tendon margins.

The location of the musculotendinous junction of the supraspinatus endon was recorded and defined as the most distal point at which muscle could be identified along with tendinous fibers. The most cranial point (12 o'clock) on the convexity of the humeral head was used as a reference to describe the position of the musculotendinous unction. The location of the musculotendinous junction was then recorded in intervals of 15° medial and lateral to this (12 o'clock) reference point.

Additionally, the subacromial-subdeltoid space was evaluated for presence, continuity, and signal intensity of the fat stripe and for the presence of fluid in the bursa. When present, changes suggesting reactive thickening or osteophytes on the inferior cortex of the overlying acromion were recorded, as were inferior osteophytes and other degenerative changes of the acromioclavicular joint.

Results

In only five (9%) of the 55 shoulders did the supraspinatus tendon appear as a solid low-signal-intensity structure on proton density-weighted and T2-weighted images, conforming with the type 0 pattern (Fig. 1). Forty-nine shoulders (89%) exhibited variations of the type 1 pattern in the supraspinatus tendon, with diffuse, linear, or focal increased signal intensity on proton density-weighted and variable but proportional low signal intensity on T2-weighted images compared with subacromial fat and joint fluid, when present. In addition, 22 of the 49 shoulders with the type 1 pattern (40% of all shoulders) had distinct low-signal-intensity tendon margins on proton density-weighted images, clearly delineating the tendon margin against the intrasubstance signal and subdeltoid stripe and humeral head cartilage surface (type 1A) (Figs. 2-4). Twenty-two shoulders (40%) had an indistinct superior or inferior tendon margin (type 1B) (Fig. 5). The remaining five shoulders (9%) appeared to have short, complete discontinuations in both otherwise distinct low-signal-intensity tendon margins (type 1C) (Fig. 6). One volunteer (2%) had a type 2 pattern in the right supraspinatus tendon, showing a small fluid collection or cyst within the substance of the distal tendon (Fig. 7, Table 1). In none of these tendons was any evidence of focal thinning, surface defects, or tendinous gaps seen.

The musculotendinous junction was found over the center of the humeral head at the 12 o'clock position in 30 (55%) of 55 shoulders (Figs. 2 and 8). In 18 shoulders (33%), the

TABLE 1: Signal Patterns of the Supraspinatus Tendon in 55 Asymptomatic Shoulders

Type	Appearance on MR		No. (%) of Shoulders	Clinical Interpretation[a]
	Proton Density-Weighted Images	T2-Weighted Images		
0	Signal void	Signal void	5 (9)	Normal
1	Focal, linear, diffuse intermediate signal[b]	Signal void, faint signal less than signal of fat & water	49 (89)	Normal, degeneration, "magic angle" artifact
2	Focal, linear, diffuse intermediate signal	Focal, linear, diffuse increased signal equivalent to that of water, less than full thickness	1 (2)	Partial tear
3	Focal, linear diffuse intermediate signal	Focal, linear increased signal equivalent to that of water extending through full thickness of tendon	0	Full tear

Note.—Classification adopted from Farley et al. [10], modified from Zlatkin et al. [3].

[a] Secondary corroborating findings such as musculotendinous retraction and atrophy of the muscle and tendon may suggest more severe disease.

[b] With or without low-signal tendon margin (types 1A–1C).

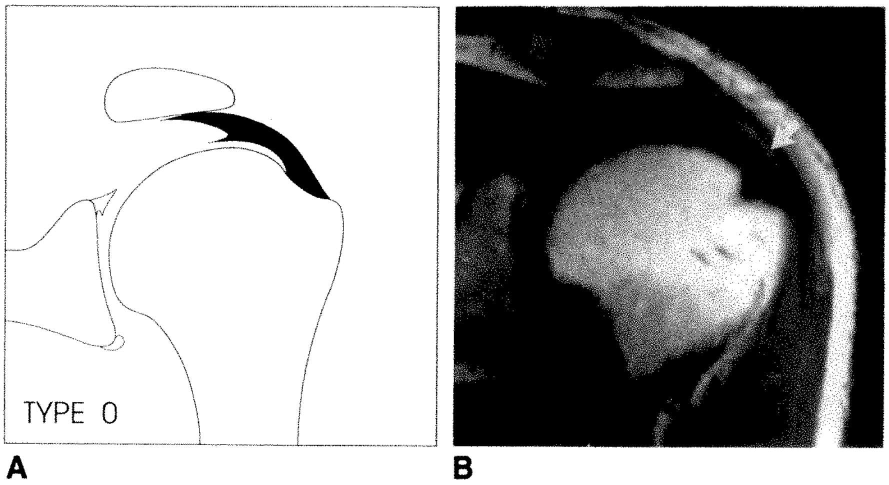

Fig. 1.—Type 0 signal pattern in supraspinatus tendon, seen in 9% of study group. Poorly defined subdeltoid fat stripe (*arrow*) is of intermediate signal intensity compared with subcutaneous fat and bone marrow.

***A*, Artist's depiction of type 0 signal pattern in supraspinatus tendon.**

***B*, Proton density-weighted oblique coronal MR image through central portion of supraspinatus tendon. Diffuse homogeneous low signal intensity throughout supraspinatus tendon was matched by second-echo T2-weighted image (*not shown*).**

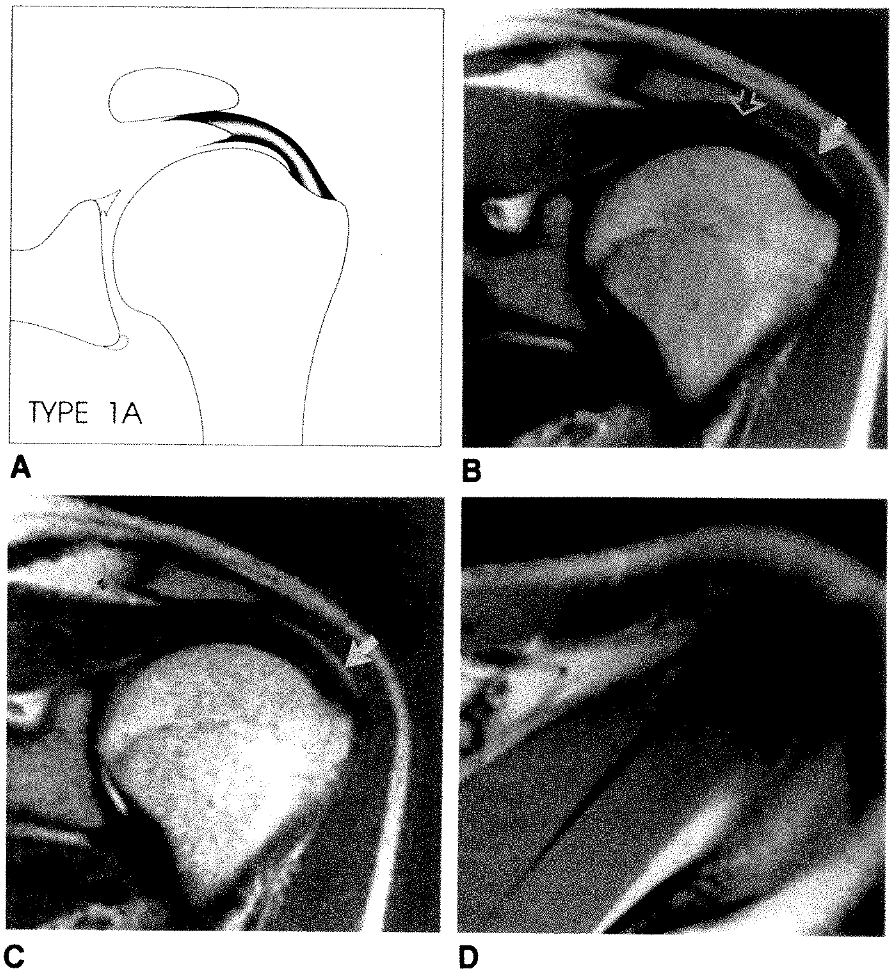

Fig. 2.—Diffuse type 1A signal pattern in supraspinatus tendon with intermediate signal throughout central portion of tendon on proton density-weighted images and distinct low-signal tendon margins. Subdeltoid stripe is of intermediate signal intensity on proton density-weighted images (*solid arrow*), somewhat lower than signal intensity of fatty tissue; however, signal on T2-weighted images (*solid arrow*) is subtle but definitely increased, indicating a thin rim of fluid in subacromial subdeltoid bursa. Musculotendinous junction (*open arrow*) is at 0° (12 o'clock) position over humeral head.

***A*, Artist's depiction of diffuse type 1A signal pattern.**

***B*, Proton density-weighted oblique coronal MR image of supraspinatus tendon shows diffuse intermediate signal intensity similar to that of musculature throughout central portion of tendon with distinct low-signal-intensity tendon margins.**

***C*, Second-echo T2-weighted MR image in same location as *B* shows only faint foci of intermediate signal in center of supraspinatus tendon, clearly lower in intensity than fatty tissue or joint fluid.**

***D*, Axial T1-weighted MR image through supraspinatus muscle shows two separate muscle bellies, whose fascicles are running at a slight angle to each other before joining into common tendon.**

musculotendinous junction was 15° lateral (Figs. 3 and 8); in four shoulders (7%), 30° lateral; and in three shoulders (6%), 15° medial to the 12 o'clock position (Figs. 6 and 8). In none of the cases was the musculotendinous junction found more than 15° medial to the 12 o'clock position.

The deltoid portion of the subdeltoid-subacromial fat stripe appeared as a contiguous line of variable thickness with typical signal characteristics for fat in 28 (51%) of the 55 shoulders (Fig. 6). In 21 shoulders (38%), it was poorly defined and of higher signal intensity than musculature but lower signal intensity than subcutaneous fat on proton density-weighted and T2-weighted images, making it difficult to delineate it clearly from tendon and muscular surfaces (Fig. 1). In six shoulders (11%) incompleteness, discontinuity, or ab-

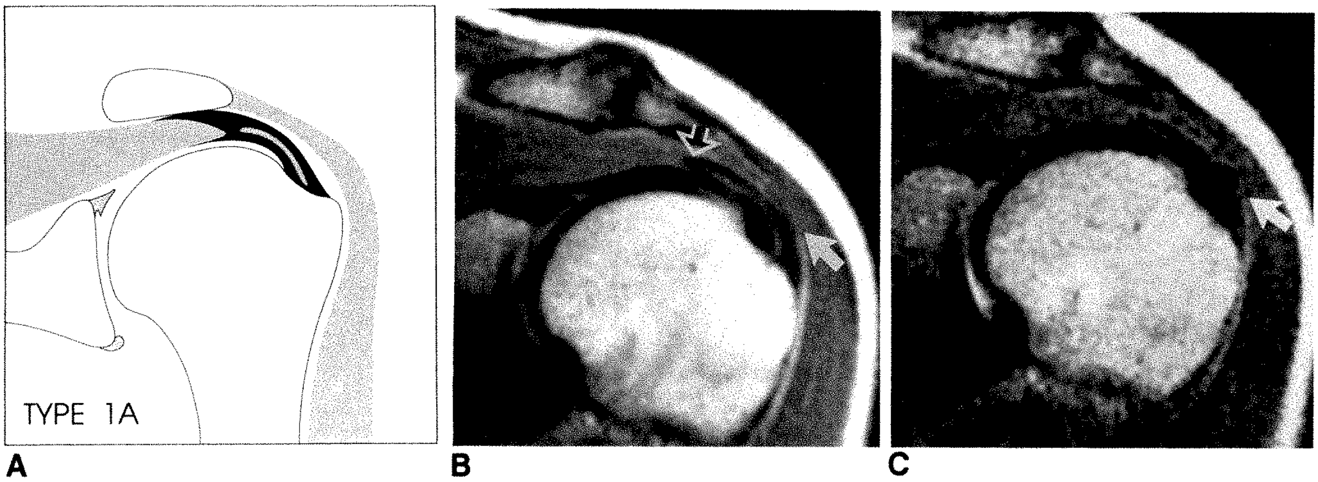

Fig. 3.—Linear type 1A signal pattern in supraspinatus tendon with distinct low-signal tendon margins. Musculotendinous junction lies 15° laterally over humeral head (*open arrow*). Subdeltoid fat stripe is focally disrupted (*solid arrows*).

A, Artist's depiction of linear type 1A signal pattern.

B, Proton density-weighted oblique coronal MR image through anterior third of supraspinatus tendon shows a continuous band of intermediate and slightly higher signal intensity than that of musculature within supraspinatus tendon, which is bordered on each side by clearly defined low-signal-intensity tendon margin.

C, Second-echo T2-weighted oblique coronal MR image at same location shows nearly homogeneous low signal intensity throughout supraspinatus tendon.

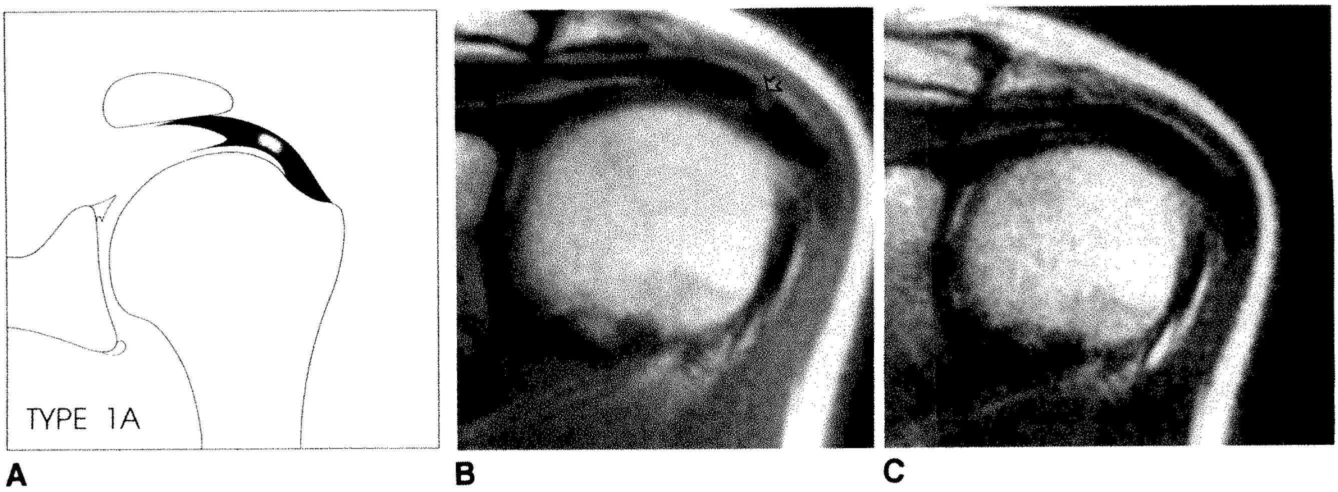

Fig. 4.—Focal type 1A signal within substance of supraspinatus tendon is well demarcated against low-signal-intensity tendon margins (*arrow*).

A, Artist's depiction of focal type 1A signal pattern.

B, First-echo proton density-weighted oblique coronal MR image through supraspinatus tendon with focal increased intrasubstance signal and distinct low-signal-intensity tendon margins (*arrow*).

C, Second-echo T2-weighted MR image at same location shows relative signal void in same area.

sence of a fat plane was seen between the subdeltoid muscle and the supraspinatus tendon (Figs. 3 and 7). Continuity between the subdeltoid and subacromial fat stripe was found in only five shoulders (9%).

In 11 shoulders (20%), fluid was identified in the subacromial-subdeltoid bursa on T2-weighted images. In six shoulders, the amount of fluid was minimal (2–3 mm in largest dimension) and seen on one image only. In the remaining five shoulders, fluid was clearly seen up to 2 × 4 mm in dimension or as a thin linear band in the subdeltoid space (Fig. 2). The fluid was seen in nine patients with the type 1 pattern and in one patient each with types 0 and 2.

The inferior cortex of the anterior acromion was smooth and equal in thickness to the superior cortex in 28 (51%) of 55 shoulders (Fig. 2). In eight shoulders (15%), the inferior cortical surface was smooth and relatively thicker (Fig. 1), while in 19 (35%) it was thicker and irregular (Fig. 4). In only two cases was evidence found of subacromial osteophyte formation. A spectrum of mild degenerative changes of the acromioclavicular joint was observed. Seventeen shoulders

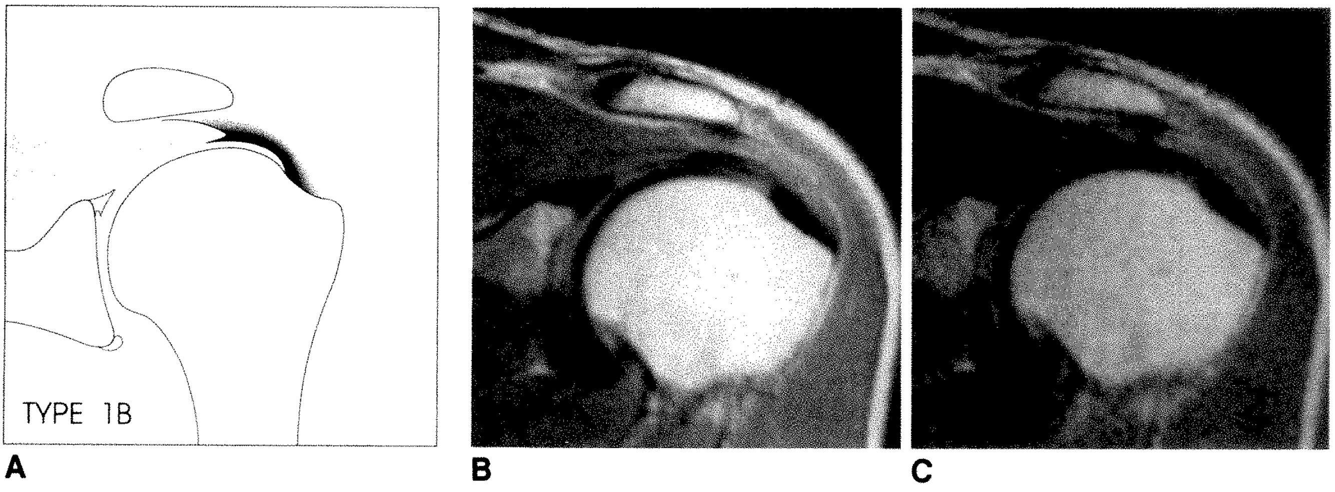

Fig. 5.—Type 1B signal (40% of study group) with intermediate signal intensity within upper half of tendon and indistinct upper tendon margin.
A, Artist's depiction of type 1B signal pattern.
B, First-echo proton density-weighted oblique coronal MR image through mid supraspinatus tendon shows a relatively thick tendon with a distinct low-signal-intensity inferior margin and diffuse intermediate signal throughout upper half of tendon. Upper margin of tendon is poorly defined.
C, Second-echo T2-weighted oblique coronal MR image at same location shows similar intermediate signal or mild signal decrease within upper part of tendon that is clearly lower than that of subcutaneous fat or marrow and joint fluid (not present on this image).

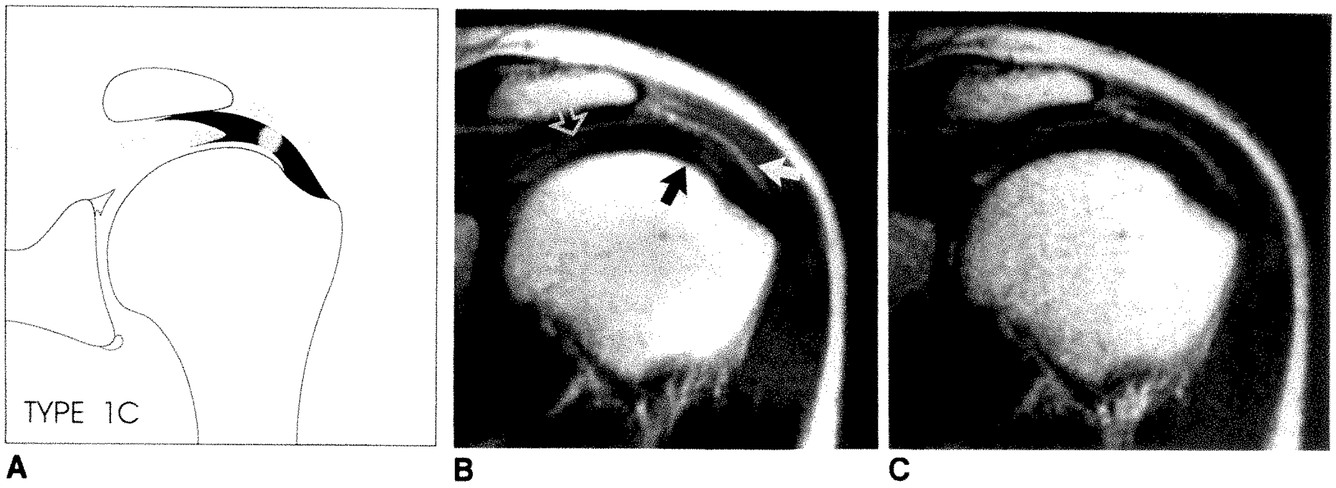

Fig. 6.—Focal type 1C signal pattern (9% of study group) of supraspinatus tendon with focal intermediate signal in tendon substance and indistinct overlying upper and lower tendon margins (*black arrow*). Subdeltoid fat stripe (*solid white arrow*) is well delineated. Musculotendinous junction is 15° medial to 12 o'clock point of humeral head (*open arrow*).
A, Artist's depiction of type 1C signal pattern.
B, First-echo proton density-weighted image through mid third of supraspinatus tendon shows a band of intermediate signal within otherwise low-signal-intensity tendon. This extends from superior to inferior surface with lack of continuity of otherwise distinct low-signal-intensity margin (*black arrow*).
C, Second-echo T2-weighted image at same location shows relative decrease in signal within tendon compared with *B*.

(31%) showed mild bulges of the joint capsule. Inferior bulging of the capsule with mild inferior bony proliferation was seen in seven shoulders (13%).

Discussion

Most supraspinatus tendons (89%) in these 55 asymptomatic shoulders fell into the type 1 pattern described by Farley et al. [10] (Table 1). Among the volunteers with a type 1 pattern, subsets of signal patterns were found, including diffuse, linear, and focal increased signal intensity on proton density-weighted images within the substance of the tendon with and without disruption or absence of a distinct superior or inferior low-signal-intensity tendon margin (types 1A–1C). In none of these tendons, however, was a significant increase in signal intensity to a level comparable with that of water noted on T2-weighted images. All showed distinct low-signal-intensity tendon margins on T2-weighted images. Disease such as inflammation, degeneration, and partial tearing has been attributed to the type 1 pattern and its variations, with some investigators using only T1-weighted coronal images

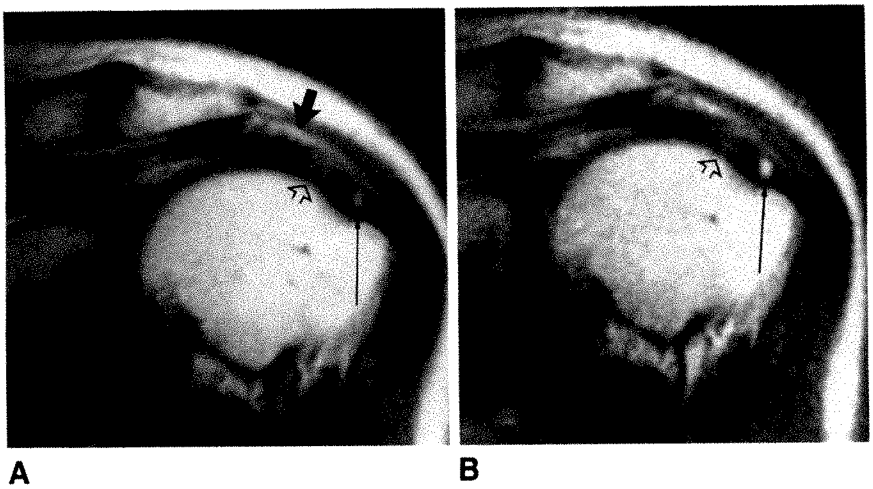

Fig. 7.—Type 2 pattern (2% of study group) of supraspinatus tendon shows a focal collection of fluid within tendinous substance (*long arrows*). This appearance is often considered diagnostic of an intrasubstance partial tear or cyst in patients with clinical signs and symptoms. Subdeltoid fat stripe is foreshortened and distally obliterated (*short solid arrow*).

A, First-echo proton density-weighted oblique coronal MR image through anterior third of shoulder shows a sharply defined focal area of intermediate signal in distal portion of supraspinatus tendon surrounded by otherwise low signal intensity (*long arrow*). In addition, a band of intermediate signal is seen more proximally (*open arrow*), extending from inferior to superior surface of tendon.

B, Second-echo T2-weighted oblique coronal MR image at same location shows marked increase of signal in peripheral locule (*long arrow*), suggesting a fluid collection. More proximal vertical band of intermediate signal on proton density-weighted images shows proportional decrease of signal similar to that shown in Fig. 6, characteristic of type 1C pattern (*open arrow*).

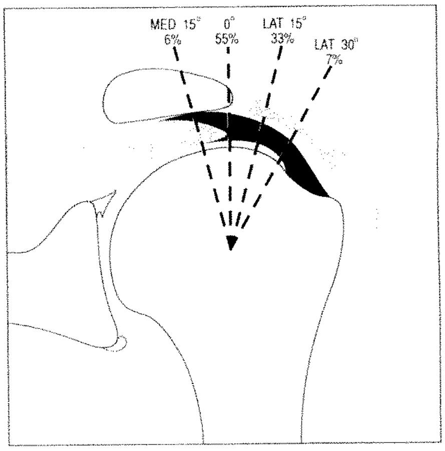

Fig. 8.—Artist's depiction of a musculotendinous junction at 0° (12 o'clock), including results of this study regarding its occurrence at points 15° medial (MED) to 30° lateral (LAT) to highest point on humeral head.

for assessment of the tendon. Our results indicate that the type 1 pattern with its variations is commonly found in asymptomatic persons [12]. This supports the impression of others [10] that this pattern is of low predictive value for the diagnosis of clinically significant rotator cuff disease even if it is associated with small amounts of subacromial fluid. Furthermore, it indirectly supports the opinion that T1-weighted or proton density-weighted imaging of the rotator cuff without acquisition of T2-weighted images is insufficient as it does not allow differentiation of normal variation of tendon signal from partial or complete tears of the rotator cuff (signal types 2 and 3) [7].

Volunteers were selected carefully for this study, excluding persons who had a history of trauma or shoulder problems. Nevertheless, the possibility that an asymptomatic volunteer could have had an asymptomatic rotator cuff injury in the past cannot completely be excluded. This investigation therefore has a drawback intrinsic to similar studies trying to define the normal by examining asymptomatic volunteers in that no pathologic proof was available. A histologic explanation for the variation in type 1 signal patterns is therefore not provided. Kjellin et al. [13] have attributed similar type 1 changes in cadaveric shoulders to eosinophilic, fibrillary, or mucoid degeneration in the tendon or its surface [13], with the extent of signal increase on proton density-weighted images proportional to the severity of degeneration. Without clinical correlation and with a much higher mean age in their sample group, their results, however, do not explain the same signal changes occurring in a much younger population in which degenerative changes are not expected. As described by Erickson et al. [14], tendons deviating in their course significantly from the axis of the main magnetic field exhibit an increase in signal on T1-weighted and proton density-weighted images. This phenomenon is most obvious at 55° ("magic angle") and is due to structural anisotropy of collagen fibers having a T2 relaxation time dependence on their orientation in the main (B_0) magnetic field [14, 15]. Owing to their anatomic orientation, rotator cuff tendons are always imaged at a significant angle to the B_0 field. Some of the signal changes within the tendon substance and in its surface observed in this study could be explained by this phenomenon. At times, however, we observed these signal changes involving a large segment of the tendon diffusely despite a progressive change in orientation in the B_0 field due to the normal course of the tendons (Figs. 2 and 3). A decrease in signal intensity would have been expected in those parts of the tendon that orient themselves at an angle less close to the magic angle (55°) and closer to 0° or 90° to the B_0 field. At the same time, tendons with the type 0 pattern do not exhibit this phenomenon at all (Fig. 1).

Another factor that could contribute to the signal changes in the supraspinatus tendon is that fascicles of the supraspinatus muscle may form two or more individual bundles that run at a slight angle to each other before joining into the common tendon (Fig. 2D). One bundle may form the undersurface while the other forms the upper surface of the tendon. The connective tissue between the muscle and tendon layers could conceivably contribute to the variable pattern in the substance or surface of the tendons found in this study. The potential effect of internal rotation of the shoulder on the appearance of the supraspinatus tendon with overlap from the infraspinatus tendon [16] was carefully avoided in our study by positioning the arm meticulously in neutral position or slightly external rotation.

Although none of these studies or suggestions give a complete explanation for the type 1A signal pattern found in this study, they contribute and complement each other insofar as they suggest that these signal changes are to be expected in asymptomatic subjects and are without clear clinical pathologic significance, if not accompanied by other corroborating findings such as large amounts of bursal fluid, musculotendinous retraction, and atrophy of the muscle and tendon, as shown by Farley et al. [10] and Kjellin et al. [13].

Ninety-three percent of all musculotendinous junctions in this asymptomatic group were found in a 30° radius around the 12 o'clock reference point on the humeral head (Fig. 8). In the remaining four shoulders, muscular tissue could be seen up to 30° lateral to the midline. This supports findings by others that retraction of the musculotendinous junction beyond 15° medial to the 12 o'clock position on the humeral head indicates significant disease and full-thickness rotator cuff tearing [10].

Continuity of the subacromial-subdeltoid fat stripe was an uncommon occurrence. Variability of the subdeltoid fat stripe signal pattern was frequent, contradicting results of other investigators who have attributed rotator cuff disease to disruption of the subdeltoid fat stripe [3, 7].

In 20% of the shoulders in this study group, small amounts of fluid were identified in the subacromial-subdeltoid bursa. Although this finding is reportedly of high sensitivity for the presence of rotator cuff tear, its presence may be misleading because of its low specificity [10].

In 49% of the shoulders, some focal or broad thickening of the cortex of the undersurface of the distal anterior acromion was found; this may be related to a somewhat thickened attachment of the coracoacromial ligament or deltoid muscle, or it may be a normal variant. The possibility of some of this being artifactual owing to the direction of the gradients was unlikely because the frequency direction was predetermined by the software in the oblique direction when using an oblique coronal imaging plane. Mild capsular bulges and mild bony proliferation at the margins of the acromioclavicular joint were seen in these asymptomatic subjects and may not necessarily indicate impingement even in association with type 1 signal within the tendon.

Our observations allow added insight to the MR appearance of the rotator cuff, providing baseline information from an asymptomatic population. These observations should be helpful to those who deal with MR examinations of the shoulder on a day-to-day basis and should contribute to a critical reevaluation of the criteria selected for definition of disease.

ACKNOWLEDGMENTS

We thank the technical staff of the San Francisco Magnetic Resonance Center and the Orthopaedic Surgery Service at Letterman Army Medical Center for providing the technical and administrative support that made this study possible; we also thank Kara Reynolds for careful preparation of the manuscript and Gill Gardner for artwork.

REFERENCES

1. Holt RG, Helms CA, Steinbach LS, Neumann CH, Munk PL, Genant HK. Magnetic resonance imaging of the shoulder: rationale and current applications. *Skeletal Radiol* **1990**;19:5–14
2. Seeger LL, Ruszkowski JT, Basset LW, et al. MR imaging of the normal shoulder: anatomic correlation. *AJR* **1987**;148:83–91
3. Zlatkin MB, Dalinka MK, Kressel HY. Magnetic resonance imaging of the shoulder. *Magn Reson Q* **1989**;5:3–22
4. Middleton WD, Kneeland JB, Carrera GF, et al. High-resolution magnetic resonance imaging of the normal rotator cuff. *AJR* **1987**;148:559–564
5. Kieft GJ, Bloem JL, Obermann WR, Verbout AL, Rozing PM, Dornbos J. Normal shoulder: MR imaging. *Radiology* **1986**;159:741–745
6. Burk DL, Karasick D, Kurtz AB, et al. Rotator cuff tears: prospective comparison of MR imaging with arthrography, sonography, and surgery. *AJR* **1989**;153:87–92
7. Zlatkin MG, Iannotti JP, Roberts MC, et al. Rotator cuff tears: diagnostic performance of MR imaging. *Radiology* **1989**;172:223–229
8. Evancho AM, Stiles RG, Fajman WA. MR imaging diagnosis of rotator cuff tears. *AJR* **1988**;151:751–754
9. Seeger LL, Gold RH, Bassett LW, Ellman H. Shoulder impingement syndrome: MR findings in 53 shoulders. *AJR* **1988**;150:343–347
10. Farley TE, Neumann CH, Steinbach LS, Jahnke AH, Petersen SA, Morgan FW. Full-thickness tears of the rotator cuff of the shoulder: diagnosis with MR imaging. *AJR* **1992**;158:347–351
11. Kieft GJ, Bloem JL, Rozing PM, Obermann WR. Rotator cuff impingement syndrome: MR imaging. *Radiology* **1988**;166:211–214
12. Mirowitz SA. Normal rotator cuff: MR imaging with conventional and fat-suppression techniques. *Radiology* **1991**;180:735–740
13. Kjellin J, Ho CP, Cervilla V, et al. Alteration of the supraspinatus tendon at MR imaging: correlation with histopathologic findings in cadavers. *Radiology* **1991**;181:837–841
14. Erickson SJ, Cox HJ, Hyde JS, et al. Effect of tendon orientation on MR imaging signal intensity: a manifestation of the "magic angle" phenomenon. *Radiology* **1991**;181:389–392
15. Fullerton GD, Cameron IL, Ord VA. Orientation of tendons in the magnetic field and its effect on T2 relaxation times. *Radiology* **1985**;155:433–435
16. Davis SJ, Fereri LM, Bradley WG, Resler JA, Ross TE. Effect of arm rotation on MR imaging of the rotator cuff. *Radiology* **1991**;181:265–268

Book Review

Radiology of Trauma. By Salvatore J. A. Sclafani. Philadelphia: Lippincott, 155 pp., 1991. $59.95

This attempt to produce a user-friendly textbook on the radiology of trauma fails on most counts. The text is oversimplified and too brief to provide adequate coverage of basic radiologic diagnostic principles and classifications of injuries. The paucity of images results in a failure to show some important injuries and significant variations. The images are often too small, too closely cropped, and too poorly exposed or poorly photographed to disclose sufficient detail. The accompanying line drawings, some with a smattering of enlivening color, tend to be so lacking in detail as to be superfluous rather than useful. The book has no introduction or preface to delineate the audience for whom it is intended. It also does not have any references or recommendations for further reading.

The book is divided into two sections: skeletal trauma and nonskeletal trauma. The first section takes the reader through the skeletal system from head to foot, beginning with a few basic definitions and principles. Some of these are rather naive: "The presence of a fracture is indicated by a break in or abrupt angulation of the cortex, discontinuity of the bony trabeculae, a radiolucent fracture line," and "A fracture may be open (compound) or closed, depending upon whether it produces an open wound to the skin, or not." Later on, comes the statement, "Dislocations of the knee are usually produced by major deforming forces." Numerous statements are not followed up with needed explanation; for example, "the Salter-Harris classification is useful for fractures involving the growth plate." Although the various types of physeal features are diagramed, the book has no discussion of why the classification is useful (i.e., to prognosticate future disability). Some statements are overgeneralized; for example, "To evaluate an ankle fracture properly, the radiologist must obtain radiographs of the entire leg, including the knee joint." Although this is understandable for a suspected Maisonneuve fracture, it is an unnecessary expenditure of radiation and money for other ankle fractures in the absence of clinical findings associated with the knee. No mention is made of the basic radiographic projections for each examination or of the positioning required to achieve them. The mortise view of the ankle is not described.

The chapter on facial fractures illustrates the various views but does not show how to obtain them. In the chapter on the cervical spine, poor-quality radiographs are somewhat compensated for by inclusion of diagrams of how to position patients, but the angles of the central ray are unspecified. In the chapter on the upper extremity, no attempt is made to describe the entire Neer or Rockwood classifications of shoulder injuries or their significance, even though a Rockwood type III acromioclavicular dislocation and a Neer four-part fracture-dislocation of the proximal humerus are illustrated and the types are indicated in the captions. Trauma to the wrist is given exceptionally short shrift. The text has no explanation of avascular necrosis of the scaphoid. Triquetral fracture, the second most common carpal fracture, is not even mentioned. A perilunate dislocation is illustrated in a lateral view only, without any discussion of the high likelihood of an accompanying fracture of the scaphoid. The pathophysiologic mechanism of lunate-perilunate dislocations and the pitfalls that hamper radiologic analysis of these injuries are not discussed. "Navicula" is mistakenly substituted for the carpal "navicular" in several places. In the chapter on pelvic fractures, an illustration of bilateral avulsions of the ischial tuberosities should have been labeled as bilateral fatigue fractures caused by repeated trauma, as evidenced by their massive overgrowth. How could simultaneous bilateral acute fractures occur in a hurdler, as described in the caption?

The second section of the book, on nonskeletal trauma, contains separate chapters on injuries to the head and neck, chest, abdomen and gastrointestinal tract, retroperitoneum and urinary tract, and blood vessels. The chapter on chest trauma presents a useful checklist for evaluating the supine chest radiograph, and the major injuries are briefly summarized. Although most of the CT scans are reasonably clear, the radiographs are too small, and some lesions cannot be adequately seen. In the chapter on abdominal trauma, the use of CT is briefly reviewed, but slice thicknesses and intervals are not discussed. The radiographs lack detail. In the chapter on genitourinary trauma, the three types of urethral injuries in males are illustrated, but the type I injury is not defined. The indications for particular types of imaging examinations are not always made clear. Figure 10.5 is upside-down. The arrow that is supposed to delineate a perinephric hematoma in Figure 10.13 actually points to a shadow posterior to the hematoma. In the chapter on vascular trauma, the indications for angiography do not include bruit or ischemia.

To whom might this book prove useful? Its lack of sophistication would seem to make it of questionable value to all but medical students, and even they might be discouraged by its lack of textual detail and the poor illustrations. Regarding value for dollar, this book may seem relatively inexpensive by today's inflated prices, but as it contains a mere 155 pages of dubious content, caveat emptor!

Richard H. Gold
University of California, Los Angeles
Los Angeles, CA 90024

Case Report

Aneurysmal Bone Cyst Developing After Anterior Cruciate Ligament Tear and Repair

Azar P. Dagher,[1] Donna Magid,[1,2] Carl A. Johnson,[2] Edward F. McCarthy, Jr.,[3] and Elliot K. Fishman[1]

Aneurysmal bone cysts can occur either as isolated lesions or with coexistent bone lesions, or they can develop subsequent to acute fracture [1, 2]. We report a case of an aneurysmal bone cyst in the distal femoral metaphysis that occurred 4 years after surgery to repair a tear of the ligament. Plain film, CT, MR, and pathologic findings are presented. The appearance of the lesion 4 years after surgery suggests that the cyst occurred either as a complication of the surgery, which to our knowledge has never been reported, or as a complication of the initial nonfracture injury, which also is rare.

Case Report

A 22-year-old woman sustained an acute rupture of the anterior cruciate ligament of her right knee as a result of an athletic injury. Preoperative radiographs showed no bone abnormality. Surgery was performed to repair the avulsed femoral attachment of the ligament by using nonabsorbable sutures (#2 Ethibond) to reattach the ligament to its anatomic femoral insertion. Sutures placed in the ligament were passed through two small drill holes from the intercondylar notch through the lateral femoral condyle and tied over a polyethylene button lateral to the femur. Radiographs obtained 2 years later showed the drill holes in the distal femur but were otherwise unremarkable.

Approximately 5 years after surgery the patient was seen for evaluation of diffuse intermittent knee pain. Plain radiographs revealed a new 5 × 5 cm expansile lesion in the distal femoral metaphysis with a thin sclerotic margin (Fig. 1A). CT with two- and three-dimensional reformatting showed a sharply defined lytic lesion with a matrix of soft-tissue attenuation and minimal septa (Figs. 1B and 1C). The cortex was interrupted posteriorly. MR imaging at 1.5 T showed a lobulated lesion with multiple fluid-fluid and fluid-blood levels in locules (Figs. 1D and 1E). Aspirate of the cyst produced a brownish fluid tinged with blood. Open biopsy was done and samples were obtained of the lateral thigh soft-tissue scar and suture material, of a window made into the cyst wall, and of the brownish blood-tinged cyst fluid.

The cyst was curettaged and packed with autologous bone graft. Symptoms resolved in the postoperative period; follow-up radiographs at 10 months showed incorporation of the graft without evidence of recurrence.

Discussion

The differential diagnosis of an expansile lytic lesion in the distal femur of a young adult includes aneurysmal bone cyst, giant-cell tumor, atypical eosinophilic granuloma, infection, chondroblastoma, metastasis, or, given this patient's history, a subchondral degenerative cyst, a hemorrhagic bone cyst, or a reaction granuloma to suture material. The site of surgery was too remote and the clinical picture inconsistent with infection. The lesion only minimally apposed the articular surface, which decreased the likelihood of a giant-cell tumor. In the posttraumatic setting, coincident degenerative changes in the joint would suggest a subchondral cyst; however, arthritic changes were not present. Fluid-fluid levels are most suggestive of aneurysmal bone cyst but may be seen, less

---

Received October 3, 1991; accepted after revision November 13, 1991.

[1] Russell H. Morgan Department of Radiology and Radiological Science, The Johns Hopkins Medical Institutions, 600 N. Wolfe St., Baltimore, MD 21205. Address reprint requests to D. Magid.

[2] Department of Orthopaedic Surgery, The Johns Hopkins Medical Institutions, Baltimore, MD 21205.

[3] Department of Pathology, Sinai Hospital, Baltimore, MD 21215.

AJR 158:1289–1291, June 1992 0361–803X/92/1586–1289 © American Roentgen Ray Society

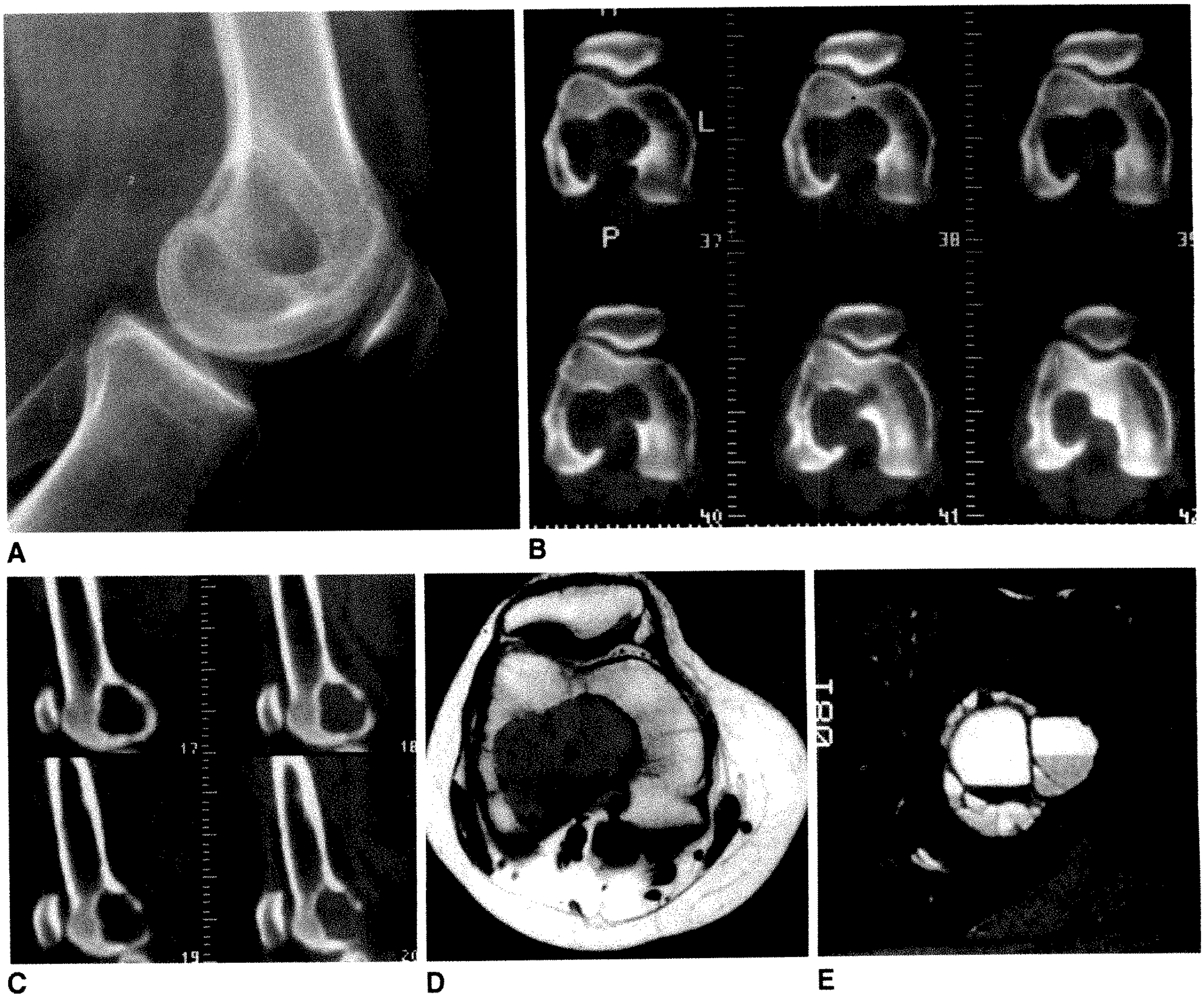

Fig. 1.—*A*, Lateral radiograph of right knee shows large, sharply defined bubbly lesion of metaepiphyseal distal femur, with few apparent loculations, and no evidence of periosteal reaction, cartilaginous matrix, or soft-tissue mass.

B, Serial axial images define a fine sclerotic margin, minimal scattered high-attenuation foci compatible with bone fragments or calcific matrix, and a lower attenuation matrix mass, which has extended through posterior cortex but is sharply demarcated from adjacent muscle.

C, Serial reformatted sagittal CT images confirm the sharp sclerotic margins, slight matrix heterogeneity, posterior cortical destruction, and preservation of posterior fascial planes.

D, Axial T1-weighted MR image (800/20 [TR/TE]) at 1.5 T shows an intraosseous matrix of slightly mixed intermediate signal that does not invade popliteal fossa. Low-signal sclerotic rim is less clearly defined than on CT anteriorly and laterally.

E, Sagittal T2-weighted MR image (2700/80) at 1.5 T shows multiple loculations or septa and fluid-fluid levels of at least three distinct signal intensities (low, intermediate, and high). Posterior compartment integrity is again confirmed.

commonly, in other bone lesions. Histologic findings were diagnostic of aneurysmal bone cyst [1].

Aneurysmal bone cyst occurring as a consequence of fracture is unusual but has been well documented [1, 2], with the suggested cause being posttraumatic altered hemodynamics in bone. Venous obstruction and arteriovenous fistula resulting from the fracture have been implicated. In the cases reviewed by Moore et al. [2], the lesion occurred within 6 months of the initial trauma. Aneurysmal bone cyst occurring as a consequence of relatively minor trauma with no fracture is much rarer; only two case reports could be found [3, 4]. Presentation of the aneurysmal bone cyst in both these case reports was also within 6 months of injury.

Bone resorption and enlargement of the femoral osseous tunnel 1 year after anterior cruciate ligament reconstruction with an ethylene oxide–sterilized allograft has previously been reported [5]. In the case reported here, primary repair of the ligament was accomplished without allograft by using nonabsorbable suture material to secure the native ligament to bone. The possibility that the cyst formed in reaction to the suture material was considered but was not substantiated by the histology of the lesion.

The present case is one of an aneurysmal bone cyst occurring 5 years after cruciate repair surgery. This temporal relationship suggests that the lesion occurred either because of the anterior cruciate ligament tear and associated minor bone injury or as a consequence of the repair surgery, which involves broaching the cortex of the distal femur. In the first possibility (i.e., the lesion occurred as a consequence of the initial ligamentous injury), one could theorize a mechanism in which a subclinical bone injury led to a small hemorrhage in the bone that subsequently sealed itself off. Vascular compromise, be it from vascular obstruction or an arteriovenous fistula, recurrent hemorrhages, or the physical stresses of daily use, could then lead to expansion of cysts and formation of new cysts. Remissions between hemorrhages would allow the fibrous and giant-cell response to develop. Alternatively, the initial compromise in the cortex from cruciate repair surgery may have initiated the process, with a similar subsequent sequence of events.

REFERENCES

1. Resnick D, Niwagama G. *Diagnosis of bone and joints disorders*, 2nd ed. Philadelphia: Saunders, **1988**;3831–3842
2. Moore TE, King AR, Travis RC, et al. Post-traumatic cysts and cyst-like lesions of bone. *Skeletal Radiol* **1989**;18:93–97
3. Kushner DC, Zebulon V, Kirkpatrick JA. Case report 103. *Skeletal Radiol* **1979**;4:240–243
4. Burnstein MI, De Smet AA, Gholam RH, et al. Case report 611. *Skeletal Radiol* **1990**;19:294–297
5. Jackson DW, Windler GE, Simon TM. Intraarticular reaction associated with the use of freeze-dried, ethylene oxide–sterilized bone-patella tendon-bone allografts in the reconstruction of the anterior cruciate ligament. *Am J Sports Med* **1990**;18:1–11

LIST OF BOOK AND VIDEOTAPE REVIEWS

1216 **Computed Tomography and Magnetic Resonance of the Thorax,** 2nd ed. *Naidich DP, Zerhouni EA, Siegelman SS, Kuhn JP*
1254 **RSNA Today Video,** Vol. 5, No. 5. *The Radiological Society of North America*
1260 **RSNA Today Video,** Vol. 5, No. 4. *The Radiological Society of North America*
1280 **MRI of the Shoulder.** *Zlatkin MB*
1288 **Radiology of Trauma.** *Sclafani SJA*
1298 **Abominal Sonography.** *Koenigsberg M, Hoffman-Tretin J*
1308 **Pediatric Cardiovascular Imaging.** *Tonkin ILD*
1346 **Magnetic Resonance Test and Syllabus.** *Bradley WG Jr, ed*
1354 **Quality Assurance in Radiotherapy Physics. Proceedings of an American College of Medical Physics Symposium.** *Starkschall G, Horton JL, eds*
1390 **Cardiac Imaging. A Companion to Braunwald's Heart Disease.** *Marcus ML, Schelbert HR, Skorton DJ, Wolf GL, eds*

Memorial

James G. Lorman, 1920–1991

James G. Lorman, professor emeritus of radiology at the University of Kentucky Medical Center, lost a protracted battle with cancer on May 16, 1991. Jim, a beloved friend of many both inside and outside medicine, was an excellent clinician and teacher who devoted 15 years to clinical service at the University of Kentucky Medical Center and to the direction of its radiology residency training program, a duty he found exceptionally gratifying and to which he made a lasting contribution.

Dr. Lorman was born in Connersville, IN, September 13, 1920, and attended the local primary and secondary schools. He obtained his bachelor's degree from Indiana University in Bloomington and his M.D. degree also from Indiana University. After military service in Korea, during which he was introduced to radiology, he returned to Indianapolis for his radiology training with Jack Campbell.

For many years he was a highly successful practitioner in the Ft. Wayne, IN, area. During these years, he spent some time teaching radiology in India. His colleagues at the University of Kentucky were both happy and fortunate to obtain his services in 1974. He was rapidly promoted to professor and was equally acclaimed for his activities in local political radiologic activities. Jim was proud of the fact that he served as president of both the Indiana and the Kentucky chapters of the American College of Radiology, possibly the only person who was at some time president of two such state organizations.

The medical students recognized his teaching accomplishments by awarding him on two occasions the Golden Apple for excellence in teaching. He was similarly honored by the radiology residents in the yearly election of him as Best Teacher on several occasions. He served for many years as a guest examiner of the American Board of Radiology.

Besides his professional activities, Jim was active in the Presbyterian Church and had a host of friends. He was an accomplished woodworker. The esteem in which he was held is manifested by the fact that considerable money already has been donated to a scholarship fund in his honor for medical students at the University of Kentucky Medical Center who have an interest in radiology. In addition to many devoted friends and neighbors, he leaves his wife, Phyllis, three children, and five grandchildren. He is sorely missed by all.

Harold D. Rosenbaum
Andrew M. Fried
Lexington, KY 40536-0084

Case Report

MR Appearance of Intramuscular Injections

Mariela Resendes,[1] Clyde A. Helms, Russell C. Fritz, and Harry Genant

Many commonly used medications are given intramuscularly. On MR, these injections can cause signal changes within the muscles and surrounding tissue that can be mistaken for a number of abnormalities, including biopsy sites. We describe a patient who had abnormalities in the soft tissues of the thigh on MR images due to intramuscular injections of commonly used medications.

Case Report

A 19-year-old man was admitted because of pain in his lower back and right hip 4 days after a skiing injury. Radiographs of the lumbar spine and hip were normal. Review of the patient's history indicated that the patient had received intramuscular injections of Demerol (meperidine) and Vistaril (hydroxyzine pamoate) into his quadriceps

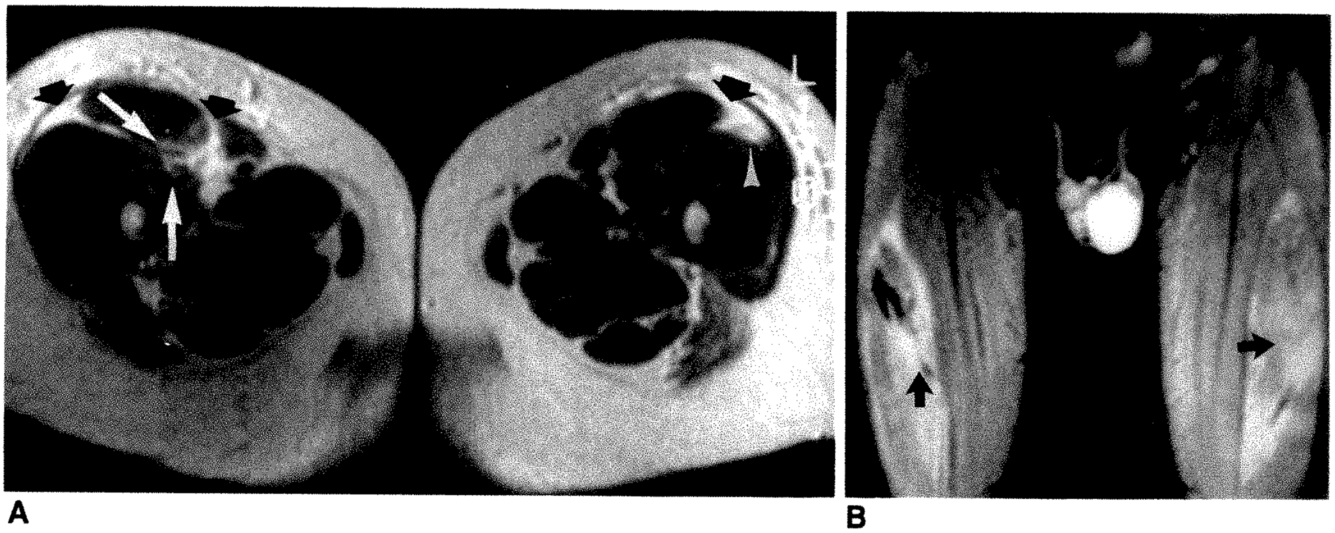

Fig. 1.—19-year-old man after recent intramuscular injections of Demerol and Vistaril.

A, Axial MR image (2000/80) of thighs shows increased signal intensity in vastus lateralis muscle on left (*arrowhead*), in vastus medialis and rectus femoris muscles on right (*white arrows*), and in subcutaneous fat and intermuscular septa bilaterally (*black arrows*).

B, Coronal MPGR MR image (400/20/30°) shows increased signal within quadriceps muscles bilaterally (*arrows*).

Received June 21, 1991; accepted after revision November 21, 1991.

[1] All authors: Department of Radiology, M-392, University of California, San Francisco, San Francisco, CA 94143. Address reprint requests to M. Resendes.

AJR 158:1293–1294, June 1992 0361-803X/92/1586-1293 © American Roentgen Ray Society

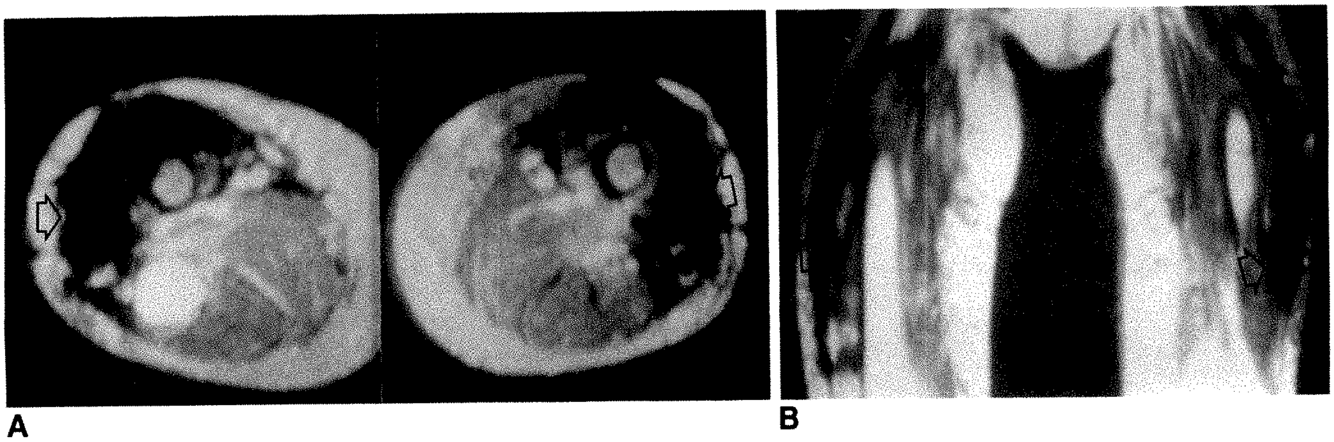

Fig. 2.—35-year-old diabetic man who had intramuscular insulin injections over a long period.
***A*, Axial T1-weighted MR image (400/20) of thigh shows decreased signal in vastus lateralis muscle bilaterally (*arrows*).**
***B*, Coronal MPGR MR image (400/20/30°) shows decreased signal within quadriceps muscles bilaterally (*arrows*).**

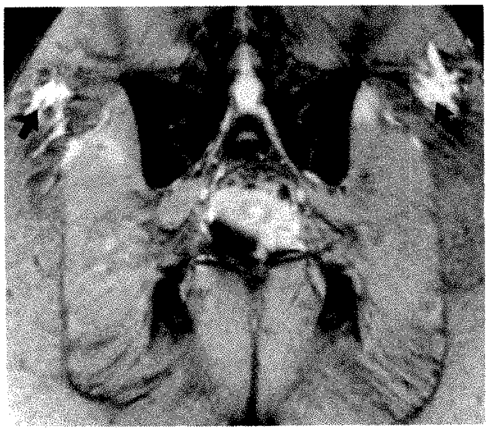

Fig. 3.—32-year-old woman after intramuscular Demerol injections. Coronal MPGR MR image (400/20/30°) shows symmetrically increased signal within gluteus maximus muscles bilaterally (*arrows*).

muscles on four separate occasions after the injury (two to each thigh).

MR images of the hips were obtained as axial spin-echo images, 2000/20,80 (TR/TE); coronal multiplanar gradient-recalled (MPGR) images, 400/20/15° (TR/TE/flip angle); and coronal spin-echo images, 400/20. The scans showed markedly increased signal on the T2-weighted and MPGR sequences in the vastus lateralis and intermedius muscles, intermuscular septa, and adjacent subcutaneous tissue (Fig. 1). The abnormalities had isointense signal on T1-weighted images. The patient had no symptoms referable to the abnormal areas.

Discussion

Descriptions of MR abnormalities in the soft tissue after intramuscular injections of medications are rare. Huber et al. [1] reported MR abnormalities caused by injection of a children's sedative (DPT, a mixture of Demerol, Phenergan, and Thorazine).

Changes in the appearance of soft tissue after the intramuscular injection of drugs should be seen on MR images fairly often, because the use of intramuscular pain medications is common. These changes can mimic muscular tears [2], infection [3, 4], infarction [5], or even an infiltrating tumor. Diabetics may have chronic changes in the soft tissues from hemorrhage, as seen in a patient who was receiving intramuscular insulin (Fig. 2).

The most frequent site of intramuscular injections is the anterior thigh or the upper outer quadrant of the buttocks (Fig. 3). Other sites, such as the deltoid muscle, may also be used. The dissection of the injected material along intermuscular fascial planes, absence of distortion of the muscle, and typical location are clues to the diagnosis. Sometimes the actual needle tract is seen. The cause of the high signal seen on MR in our patient may be due to the drug itself or may be the result of an associated inflammatory tissue reaction, with or without hemorrhage. The interval after the initial injection in our patient was short (4 days); however, these changes have been reported to persist for up to 36 days after injection [1].

REFERENCES

1. Huber DJ, Sumers E, Klein M. Soft tissue pseudotumor following intramuscular injection of "DPT": a pitfall in magnetic resonance imaging. *Skeletal Radiol* **1987**;16:469–473
2. De Smet A, Fisher DR, Heiner JP, Keene JS. Magnetic resonance imaging of muscle tears. *Skeletal Radiol* **1990**;19:283–286
3. Tang JSH, Gold RH, Bassett LW, Seeger LL. Musculoskeletal infection of the extremities: evaluation with MR imaging. *Radiology* **1988**;166:205–209
4. Beltran J, Noto AM, McGhee RB, Freedy RM, McCalla MJ. Infections of the musculoskeletal system: high-field-strength MR imaging. *Radiology* **1987**;164:449–454
5. Lamminen AE, Hekali PE, Tiula E, Suramo I, Ossi A. Acute rhabdomyolisis: evaluation with magnetic resonance imaging compared with computed tomography and ultrasonography. *Br J Radiol* **1989**;62:326–330

Case Report

MR Diagnosis of Macrodystrophia Lipomatosa

Marcia Blacksin,[1] Frederick J. Barnes,[2] and Michael M. Lyons[3]

Macrodystrophia lipomatosa is a congenital form of localized gigantism characterized by an increase in all mesenchymal elements, particularly fibroadipose tissue. MR imaging can be used to examine the soft tissues and detect the fibrous and fatty hypertrophy that characterizes this condition. To our knowledge, this is the first reported case of macrodystrophia lipomatosa diagnosed on the basis of MR findings and confirmed at reconstructive surgery.

Case Report

A 12-year-old girl was noted to have atraumatic enlargement of the right upper arm and index finger when she was 4 years old. For several years before the present evaluation she had noticed disproportional growth of her upper arm. Ulnar deviation of the right index finger made it difficult for her to write.

Physical examination showed enlargement of the right upper arm, ventrally and laterally. The midhumeral circumference of the right upper arm was 30 cm, 4 cm larger than that of the left arm. The right index finger and dorsal forearm were also enlarged (Fig. 1A). No skin nodules, pitting edema, or cafe-au-lait spots were present on the right arm or body. No audible bruits or thrills were heard at the elbow or wrist, and the radial and antecubital pulses were normal. The results of neurologic examination were unremarkable.

Radiographs of the right hand showed ulnar deviation of the second digit. A soft-tissue mass containing mottled lucencies was noted adjacent to the radial aspect of the distal phalanx of the second digit (Fig. 1B). Focal enlargement of the finger extended from the base of the digit to the fingertip.

The cause of the macrodactyly was unclear, and MR imaging was performed to characterize the soft-tissue masses. MR imaging, performed on a G.E. 1.5-T Signa scanner, showed an asymmetric accumulation of adipose tissue in the right upper arm. The fat displaced the biceps brachii and the brachialis muscles medially but did not insinuate itself between these muscles (Fig. 1C). No identifiable capsule was seen on either the axial or coronal images (Fig. 1D).

MR examination of the second digit showed excessive fat along the ventral and radial aspects of the second digit, greater at the tip of the index finger than at the base. A central focus of low signal intensity was present within the fat (Fig. 1E) on both T1- and T2-weighted images. It ran the length of the second digit and was thought to be fibrous tissue.

Discussion

Macrodystrophia lipomatosa was first described by Feriz in 1925 [1]. In 1967, Barsky [2] offered a classification system for "true macrodactyly," dividing it into two forms. The first form is present at birth, and the size of the involved digit increases proportionally in relation to the rest of the body. The second, less common type can be complicated by fatty overgrowth in the palm, dorsum of the hand, and forearm. It is identical to Feriz's description of macrodystrophia lipomatosa. In the second form, the degree of overgrowth increases faster than the normal growth pattern [2]. Our patient has the second type.

This condition is found in both the upper and lower extremities. Involvement of more than one digit is the most frequent finding; often adjacent digits are affected. Most cases involve the middle and index fingers, corresponding to the territory supplied by the branches of the median nerve [1, 2].

Received October 8, 1991; accepted after revision November 26, 1991.

[1] Department of Radiology, University of Medicine and Dentistry, New Jersey Medical School, 150 Bergen St., Newark, NJ 07103. Address reprint requests to M. Blacksin.

[2] Department of Orthopedics, University of Medicine and Dentistry, New Jersey Medical School, Newark, NJ 07103.

[3] Department of Pathology, University of Medicine and Dentistry, New Jersey Medical School, Newark, NJ 07103.

AJR 158:1295–1297, June 1992 0361-803X/92/1586-1295 © American Roentgen Ray Society

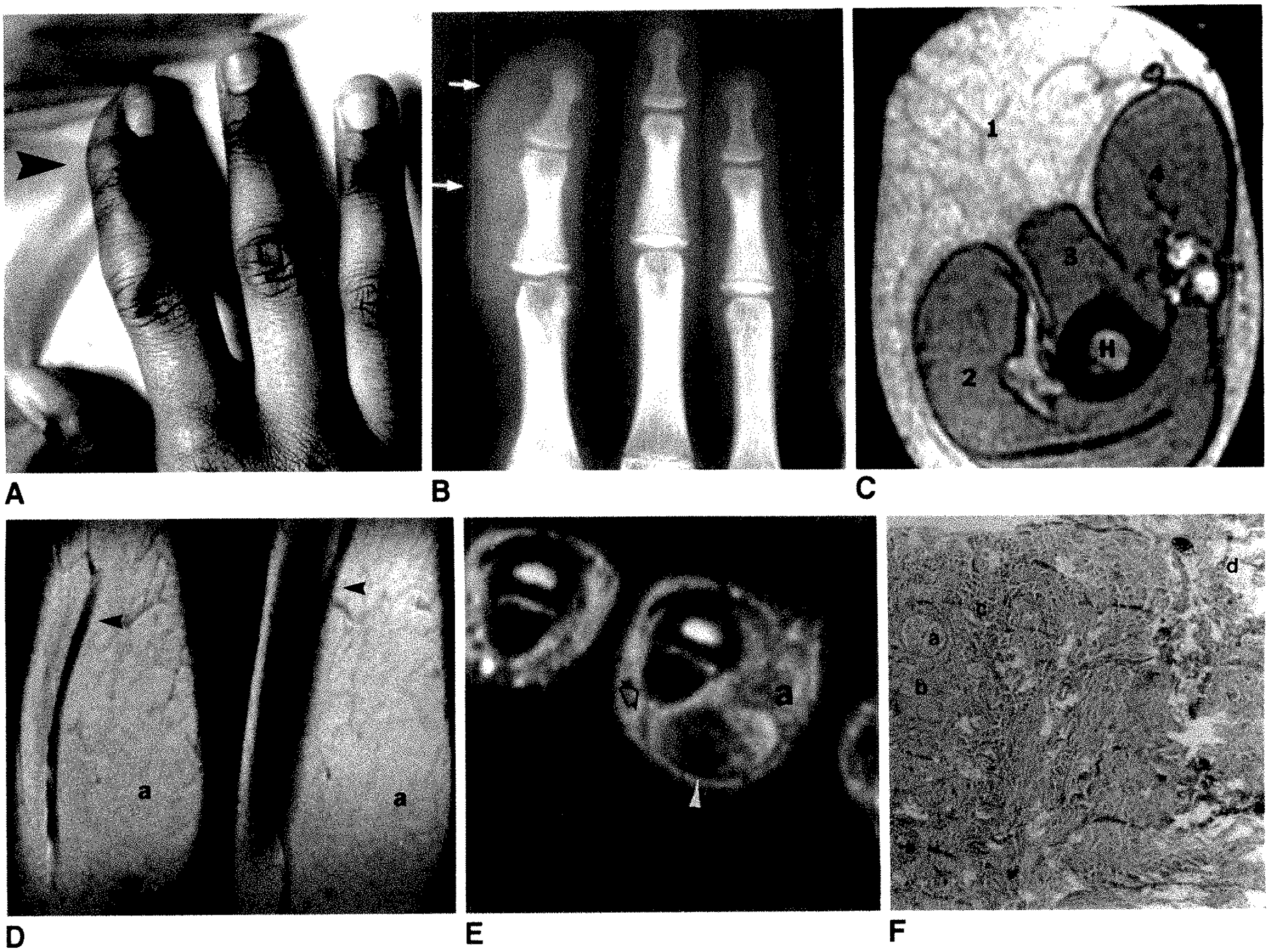

Fig. 1.—Macrodystrophia lipomatosa in a 12-year-old girl.

A, Preoperative photograph of affected right hand shows macrodactyly and slight ulnar deviation of second digit (*arrowhead*).

B, Radiograph of affected hand shows ulnar deviation and mottled lucency in soft-tissue mass along radial aspect of second digit (*arrows*).

C, Axial gradient-recalled acquisition in the steady state MR image, 50/18/30° (TR/TE/flip angle), of right upper arm shows asymmetric accumulation of adipose tissue (1). 2 = triceps brachii, 3 = brachialis muscle, 4 = biceps brachii, H = humerus.

D, Coronal T1-weighted spin-echo MR image, 600/20 (TR/TE), through right upper arm shows asymmetric accumulation of adipose tissue (a) without evidence of a capsule. *Arrowheads* = blood vessel.

E, T2-weighted spin-echo MR image, 2000/80 (TR/TE), at level of distal phalanges shows focal accumulation of adipose tissue (a) with central area (*arrowhead*) of low signal intensity along radial aspect of second digit. *Arrow* = flexor tendon.

F, Photomicrograph of soft tissue from right second digit shows cluster of nerves (one marked a) enmeshed in dense fibrous tissue (b), occasional strips of striated muscle (c), and surrounding adipose tissue (d).

The differential diagnosis includes neurofibromatosis, Klippel-Trenaunay-Weber syndrome, lymphangiomatosis, hemangiomatosis, and fibrolipomatous hamartoma of the nerve. Both neurofibromatosis and macrodystrophia lipomatosa can demonstrate limb deformity and enlargement. The latter does not share the neurocutaneous or familial prevalence of neurofibromatosis. Digital overgrowth ceases at puberty with macrodystrophia lipomatosa, and cosmesis is the primary reason for surgery. Bony changes in neurofibromatosis include thinned bone shafts and wavy cortices as opposed to the phalangeal enlargement and syndactyly seen in macrodystrophia lipomatosa [3]. MR imaging allows distinction between the two entities, as neurofibromas show marked hyperintensity on T2-weighted images and are close to the nerves. No such lesion was seen on our T2-weighted images [4].

Klippel-Trenaunay-Weber syndrome can be diagnosed by virtue of its unilateral cutaneous capillary hemangiomas and varicose veins. These lesions were not noted on physical examination or on the MR study of our patient. The lack of bruits speaks against hemangiomatosis, but MR imaging was useful in demonstrating the absence of these lesions. Long TR/TE sequences would show a striated-septated configuration of high-signal-intensity channels that correlate with the vascular channels and fibrous strands found in hemangiomas [5]. Diffuse swelling and pitting edema, characteristic findings of lymphangiomatosis, were not seen in the patient. Lymphangiomas can display high signal intensity relative to skeletal muscle on T1-weighted images, and they are hyperintense relative to fat on T2-weighted images [6]. These types of lesions were not seen on our MR images, and the areas of highest signal intensity corresponded only to fatty deposits.

When confined to the hand, fibrolipomatous hamartoma of the nerve and macrodystrophia lipomatosa may be indistinguishable on the basis of the MR findings. Both these lesions can be found in the median nerve distribution, and both will demonstrate fibrous thickening of the nerve on MR images. Histologically, both lesions can demonstrate endoneural and perineural fibrosis, with axons that are normal in size and number [7, 8]. These findings were noted in our patient (Fig. 1F). The fibrolipomatous hamartoma displays fat deposits within the nerve sheath, whereas macrodystrophia lipomatosa can demonstrate fat deposits within the whole limb. The MR images demonstrated just such a fat deposit in our patient's upper arm (Figs. 1C and 1D) and index finger (Fig. 1E). The hamartoma occasionally can be seen in association with macrodactyly, and in these cases, consideration of this lesion as a pathologic entity separate from macrodystrophia lipomatosa may be unnecessary [8].

MR imaging is uniquely suited to the investigation of macrodactyly. Accurate soft-tissue characterization will confine the differential diagnosis to only a few possibilities. A redundancy of fatty tissue and fibrous thickening of a nerve, in the presence of macrodactyly, should lead to a diagnosis of macrodystrophia lipomatosa.

REFERENCES

1. Kelikian H. *Congenital deformities of the hand and forearm.* Philadelphia: Saunders, **1974**;610–635
2. Barsky AJ. Macrodactyly. *J Bone Joint Surg [Am]* **1967**;49-A:1255–1265
3. Pitt MJ, Mosher JF, Edeiken J. Abnormal periosteum and bone in neurofibromatosis. *Radiology* **1972**;103:142–146
4. Cerofolini E, Landi A, DeSantis G, Maiorana A, Canossi G, Romagnoli R. MR of benign peripheral nerve sheath tumors. *J Comput Assist Tomogr* **1991**;15:593–597
5. Cohen E, Kressel H, Perosio T, et al. MR imaging of soft tissue hemangiomas: correlation with pathologic findings. *AJR* **1988**;150:1079–1081
6. Kransdorf MJ, Jelinek JS, Moser RP Jr, et al. Soft-tissue masses: diagnosis using MR imaging. *AJR* **1989**;153:541–547
7. Minkowitz S, Minkowitz F. A morphological study of macrodactylism: a case report. *J Pathol* **1965**;90:323–328
8. Silverman TA, Enzinger FM. Fibrolipomatous hamartoma of nerve. *Am J Surg Pathol* **1985**;9:7–14

Book Review

Abdominal Sonography. By Mordecai Koenigsberg and Janet Hoffman-Tretin. Philadelphia: Lippincott, 143 pp., 1991. $49.95

As the authors of this book point out in their introduction, recognition of normal structures and of abnormalities on sonograms continues to be one of the more difficult skills in imaging for many physicians. One of the main aims of this text is to enhance such recognition in the context of abdominal sonography.

The book is divided into nine chapters, each dealing with a specific region or organ system: the liver and intrahepatic vessels, the gallbladder and biliary tree, the pancreas, the spleen, the peritoneal cavity, the retroperitoneum, the great vessels, the kidney and lower urinary tract, and the adrenal glands. Each chapter begins with a discussion of the corresponding anatomy and normal sonographic features and some suggestions as to scanning technique. A discussion of the more common pathologic entities affecting each region or organ, and their sonographic appearances, then follows.

The book is lavishly illustrated, with more than 200 sonograms and diagrams. The sonograms are well reproduced and of good quality. However, more than half the sonograms are compound static images and thus do not reflect what would be considered current or state-of-the-art practice. However, the compound images are used appropriately, providing for teaching purposes a greater field of view and thus a more comprehensive picture of organs and anatomic relationships than would be possible with real-time sector images.

One of the helpful features of this text is the manner in which a problem common to many imaging texts is handled. For illustrations of imaging findings, the image can be left intact, free of arrows and the like, and the findings can be described in the text. The disadvantage of this approach is that the reader may have difficulty correlating the description with the image. Alternatively, the image can be labeled, but this in a sense makes it too easy for those trying to learn to recognize normal anatomy and pathologic findings. A third technique is used by the authors of this book: Many images, particularly those with more complex anatomy or difficult findings, are accompanied by a corresponding diagram, and labels and legends are applied to the diagram rather than the image. Thus, readers can examine the unaltered image and test their interpretive skills before checking the labeled figure.

For experienced sonographers, this book offers little. The images portray basic anatomy and, for the most part, common examples of pathologic changes. The book makes little mention of and has no illustrations of duplex or color Doppler imaging. The text aims successfully for brevity, but it is too general for use as a comprehensive reference. The bibliography is limited: a list of 21 references is given at the end of the book, but references are cited infrequently in the text itself.

For beginning sonographers (radiology residents or sonographic technologists early in their training) or for those inexperienced in abdominal sonography (nonradiologists, or radiologists with little background in interpreting sonograms), this would be a reasonable introductory text and a useful text to have handy when studying sonograms. For these reasons, it likely will find a useful niche in the library of a radiology department or medical center.

Albert A. Nemcek, Jr.
Northwestern Memorial Hospital
Northwestern University Medical School
Chicago, IL 60611

Posttraumatic Adrenal Hemorrhage in Children:

CT Findings in 34 Patients

Carlos J. Sivit[1,2]
J. David Ingram[1,3]
George A. Taylor[1,4]
Dorothy I. Bulas[1,2]
David C. Kushner[1,2]
Martin R. Eichelberger[5]

The medical records and CT scans of 34 children with posttraumatic adrenal hemorrhage were reviewed. Adrenal hemorrhage was unilateral in 32 children; most injuries were on the right side. Bilateral hemorrhage was present in two children. The injured gland was oval in 27 cases and triangular in nine. Gland size ranged from 7 to 45 mm long and 4 to 30 mm wide. All adrenal hemorrhages had decreased attenuation relative to liver and spleen on contrast-enhanced CT. Ipsilateral diaphragmatic crural thickening was a frequent (61%) associated finding. Ipsilateral intraabdominal (61%) and intrathoracic (44%) injuries were often present. Clinical signs of adrenocortical insufficiency were not observed in any child.

In summary, posttraumatic adrenal hemorrhage is uncommon in children. The hemorrhage is usually unilateral, right sided, and associated with ipsilateral visceral injury.

***AJR* 158:1299–1302, June 1992**

CT is the most frequently used imaging method in the examination of children with suspected blunt intraabdominal injury [1–3]. Its usefulness in the determination of the presence and extent of solid and hollow viscus injuries has been well documented [1–6]. Despite the widespread use of abdominal CT in children with blunt trauma, hemorrhage of the adrenal gland has been described infrequently [7]. We describe the frequency and CT characteristics of posttraumatic adrenal hemorrhage in a large group of children.

Materials and Methods

Between January 1983 and November 1991, 1155 consecutive children with blunt trauma who were clinically suspected of having injury to intraabdominal organs had CT at our institution. Thirty-four (3%) of these children had an adrenal hemorrhage observed on CT. These 34 children form the basis for this report.

Demographic data, indications for CT, and trauma score were recorded at the time of initial CT examination [8, 9]. Indications for CT included abdominal tenderness (22), hematuria (21), abdominal distension (18), neurologic obtundation such that the clinical examination was considered unreliable (12), absent bowel sounds (11), abdominal abrasion (seven), low hematocrit (seven), and vomiting (three). The number of indications for CT per child ranged from two to seven; the median number of indications per child was three. CT findings originally reported at the time of the examination were used for data collection. Clinical outcome was determined by retrospective review of medical records.

The CT examination was performed by using a GE 9800 CT scanner (General Electric Medical Systems, Milwaukee, WI) with 1-cm-thick slices obtained at 1-cm intervals from the diaphragm through the symphysis pubis. Contrast medium (iothalamate meglumine, Conray 43, Mallinckrodt, St. Louis; or iohexol, Omnipaque 240, Winthrop, New York) was administered by rapid manual IV bolus injection at a dose of 3 ml/kg body weight (maximum dose, 120 ml).

Results

The 34 children with adrenal injury included 19 girls and 15 boys 2 months to 16 years old (median age, 5 years). The mechanism of injury included 25 motor

---

Received November 20, 1991; accepted after revision January 9, 1992.

[1] Department of Diagnostic Imaging and Radiology, Children's National Medical Center, 111 Michigan Ave., N.W., Washington, DC 20010. Address reprint requests to C. J. Sivit.

[2] Department of Diagnostic Imaging and Radiology, The George Washington University School of Medicine and Health Sciences, Washington, DC 20052.

[3] Present address: Department of Radiology, The Children's Hospital, 1056 E. 19th Ave., Denver, CO 80218.

[4] Present address: Russell H. Morgan Department of Radiology, Johns Hopkins Medical Institutions, 600 N. Wolfe St., Baltimore, MD 21205.

[5] Department of Surgery, Children's National Medical Center, Washington, DC 20010, and The George Washington University School of Medicine and Health Sciences, Washington, DC 20052.

0361-803X/92/1586-1299
© American Roentgen Ray Society

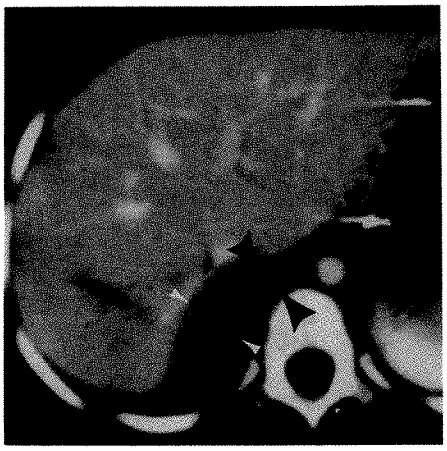

Fig. 1.—7-year-old girl injured in a motor vehicle crash. CT scan of upper abdomen shows an oval hematoma in right adrenal gland. Both limbs of injured gland are shown (*white arrowheads*). Note associated hepatic laceration and ipsilateral crural thickening (*black arrowheads*).

vehicle-related injuries; 14 children were pedestrians and 11 were passengers. Five children were assaulted, two had a fall, one was riding a bicycle, and one was riding a sled. The median trauma score was 14 (range, 5–16).

Adrenal hemorrhage was unilateral in 32 children and bilateral in two. A right-sided hemorrhage was noted in 31 children and a left-sided hemorrhage was observed in five. All injured glands were of decreased attenuation relative to liver and spleen on contrast-enhanced CT. The injured gland was oval in 27 cases (Fig. 1) and triangular in nine (Fig. 2A). Hematomas were 7–45 mm long (mean, 26 mm) and 4–30 mm wide (mean, 15 mm). Both limbs of the adrenal gland could be detected in eight injured glands (22%) (Fig. 1); only the posterior limb was seen in 14 (39%) and only the anterior limb in three (8%) (Fig. 2a). Thickening of the ipsilateral diaphragmatic crus was noted in 22 cases (61%) (Fig. 1).

Associated Injuries

An ipsilateral solid viscus was injured in 22 cases (61%), including the liver (17), kidney (five), and spleen (six) (Fig. 1). The location of the hepatic injury was in the posterior segment of the right lobe in 15 and the medial segment of the left lobe in two. All renal injuries involved the upper pole. Ipsilateral lower chest injury was seen in 16 cases (44%), including pulmonary contusion (13), rib fracture (three), hemothorax (three), and pneumothorax (two). Peritoneal fluid or blood was noted in 19 children (56%), and retroperitoneal fluid or blood was observed in seven (21%). The fluid or blood was found in the anterior pararenal space in six, in the perirenal space in three, and in the posterior pararenal space in two. Associated hepatic, renal, splenic, or bony pelvic injury was present in all cases observed to have peritoneal and retroperitoneal fluid.

Outcome

One child (3%) died. Of 33 survivors with adrenal hemorrhage, 11 had subsequent CT (six) or sonography (five) 2 days to 3 months after the injury. The adrenal gland appeared normal on follow-up examination in five children. The injured gland remained abnormal in the other six children. On follow-up CT, a rounded area of decreased attenuation relative to liver was noted in the center of the gland in one child and a bulbous tip of the posterior limb was noted in another (Fig. 2B). On follow-up sonographic evaluations, the hematoma appeared as an area of mixed echogenicity with areas that were hyperechoic and isoechoic relative to liver (Figs. 3 and 4). Adrenal gland calcifications were not observed on follow-up CT or sonography.

Clinical signs of adrenocortical insufficiency, including hyponatremia, hypokalemia, acidosis, or hypotension in the absence of concurrent severe hemorrhagic injury, were not observed in any child. Cortisol levels were not measured in any case.

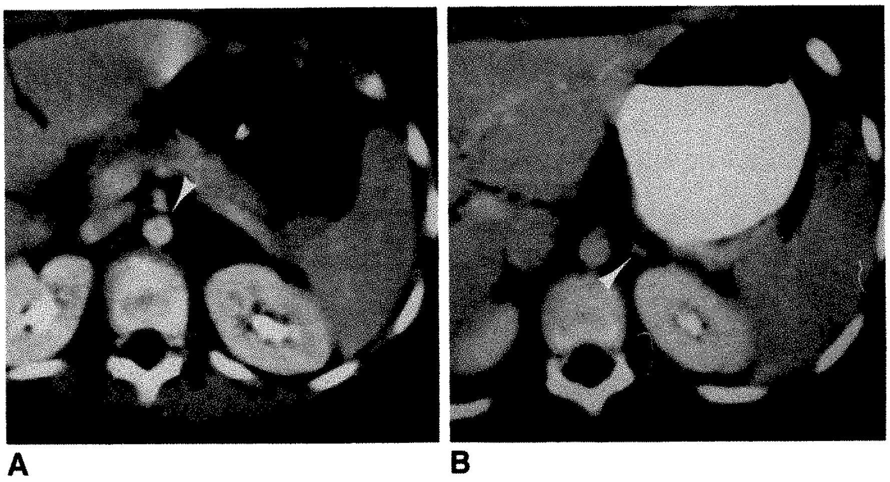

Fig. 2.—10-year-old boy who was run over by a car.

A, CT scan of upper abdomen shows a triangular hematoma in left adrenal gland. Anterior limb of injured gland (*arrowhead*) is seen.

B, Follow-up CT scan 2 months after injury shows residual bulbous tip of posterior limb of left adrenal gland (*arrowhead*).

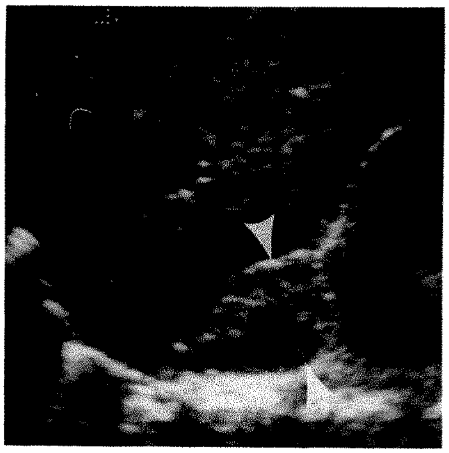

3

Fig. 3.—Follow-up sagittal sonogram through right upper quadrant obtained 2 days after injury shows a homogeneously echogenic right-sided suprarenal mass (*arrowheads*).

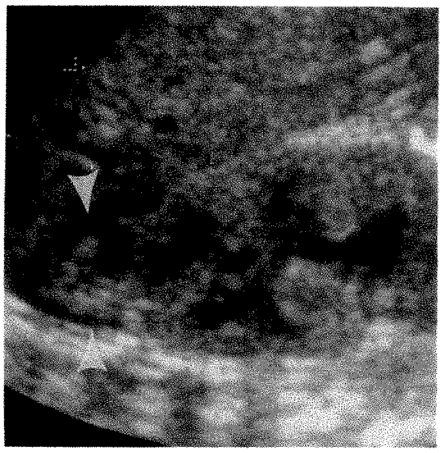

4

Fig. 4.—Follow-up sagittal sonogram through right upper quadrant obtained 6 days after injury shows a right-sided suprarenal mass of mixed echogenicity (*arrowheads*).

Discussion

The diagnosis of posttraumatic adrenal hemorrhage has been made at autopsy in up to 25% of severely injured patients [10]. With the widespread use of abdominal CT in the examination of patients who have sustained blunt trauma, unsuspected injury to the adrenal gland is being observed after less severe injury [7, 11, 12]. In an 8-year period, we observed adrenal hemorrhage in approximately 3% of children who had CT after blunt trauma.

Posttraumatic adrenal hemorrhage has seldom been diagnosed before death because specific signs and symptoms are usually absent. Abdominal tenderness and hematuria were the most common indications for CT in children with an adrenal injury in our series. They were also the most common indications for CT in children studied after blunt trauma who did not have adrenal hemorrhage (unpublished data); therefore, the criteria are not selective for the detection of adrenal injury. Additionally, none of our children had signs of adrenocortical insufficiency on follow-up clinical evaluation. This most likely was because injury was unilateral in nearly all children.

The cause of posttraumatic adrenal hemorrhage may be multifactorial. Several mechanisms have been proposed. These include direct compression of the gland between the spine and liver by direct trauma to the upper abdomen and flank, shearing of small vessels that perforate the adrenal capsule because of deceleration forces, and a short-term rise in intraadrenal venous pressure due to compression of the inferior vena cava [7, 11, 12]. Support for direct compression or shearing of the gland as a mechanism of injury is found in the high frequency of associated ipsilateral intraabdominal (61%) and intrathoracic (44%) injuries. The adrenal glands are located deep in the abdominal cavity and are protected by the surrounding solid viscera and vertebra. These adjacent structures are also likely to be injured by external blunt force that is severe enough to injure the adrenal gland. Support for a short-term rise in intraadrenal venous pressure from compression of the inferior vena cava as a mechanism of injury is found in the more frequent occurrence of hemorrhage in the right adrenal gland (86%). The right adrenal vein drains directly into the inferior vena cava while the left adrenal vein drains into the left renal vein. As a result, it is speculated that the right adrenal gland would be more affected by a sudden rise in intracaval pressure than would the left.

CT findings of adrenal hemorrhage in our experience are similar to those in previous reports [7, 11–17]. Most hemorrhages are in the right gland; are small, focal, and oval or triangular; and have decreased attenuation relative to liver, spleen, and kidneys on contrast-enhanced CT. The hemorrhage may obliterate the normal contour of the organ; however, in 69% of cases at least one limb of the adrenal gland was visualized. Thickening of the ipsilateral diaphragmatic crus was a frequent secondary finding; it was present in 61% of cases.

Recognition that adrenal hemorrhage may be seen after blunt trauma and familiarity with its associated CT features are helpful in permitting its differentiation from an adrenal neoplasm. These features include the presence of an ipsilateral visceral injury, thickening of the ipsilateral diaphragmatic crus, and peritoneal and retroperitoneal fluid or blood. If any question about the diagnosis remains, follow-up examination with sonography or CT should be performed, and the hemorrhage should be followed to resolution.

The correct characterization of the abnormality on CT as an adrenal hemorrhage will also help prevent needless additional imaging examinations. The adrenal gland can easily be overlooked because of its smallness, and the abnormality may be mistaken for localized retroperitoneal blood. This, in turn, may prompt a search for associated visceral injury. Additionally, the abnormality may be incorrectly identified as an injury to the liver or to the upper pole of the ipsilateral kidney. In either case, an error in diagnosis may lead to further diagnostic tests and a longer hospitalization.

In summary, adrenal hemorrhage is rare in children after blunt abdominal trauma. The hemorrhage is usually unilateral, in the right gland, small, and associated with ipsilateral intraabdominal and intrathoracic injuries. It should not be incorrectly identified as an adrenal neoplasm, retroperitoneal blood, or hepatic or renal injury. Clinical signs of adrenocortical insufficiency were not observed in any child with posttraumatic adrenal hemorrhage.

REFERENCES

1. Kaufman RA, Towbin R, Babcock DS, et al. Upper abdominal trauma in children: imaging evaluation. *AJR* **1984**;142:449-466
2. Taylor GA, Fallat ME, Potter BM, Eichelberger MR. The role of computed tomography in blunt trauma in children. *J Trauma* **1988**;20:1660-1664
3. Berger PE, Kuhn JP. CT of blunt abdominal trauma in childhood. *AJR* **1981**;136:105-110
4. Federle MP, Goldberg HI, Kaiser JH. Evaluation of abdominal trauma by computed tomography. *Radiology* **1981**;138:637-644
5. McCort JJ. Caring for the major trauma victim: the role of radiology. *Radiology* **1987**;163:1-9
6. Toombs BD, Sandler CM, Rauschkolb EN, Stax R, Haile TS. Assessment of hepatic injuries with computed tomography. *J Comput Assist Tomogr* **1982**;6:72-75
7. Murphy BJ, Casillas J, Yrizarry JM. Traumatic adrenal hemorrhage: radiologic findings. *Radiology* **1988**;169:701-703
8. Champion HR, Sacco WJ, Camazo AJ, Copes W, Fouty WJ. Trauma score. *Crit Care Med* **1981**;9:672-676
9. Eichelberger MR, Mangubat EA, Sacco WJ, Bowman LM, Lowenstein AD. Outcome analysis of blunt trauma in children. *J Trauma* **1988**;28:1109-1113
10. Sevitt S. Post-traumatic adrenal apoplexy. *J Clin Pathol* **1955**;8:185-194
11. Wilms G, Marchal G, Baert A, Adisoejoso B, Mangkuwerdojo S. CT and ultrasound features of post-traumatic adrenal hemorrhage. *J Comput Assist Tomogr* **1987**;11:112-115
12. Scully RE, Mark EJ, McNeely BU. Case 38, case records of the Massachusetts General Hospital: weekly clinicopathological exercises. *N Engl J Med* **1984**;311:783-790
13. Solomon N, Sumkin J. Right adrenal gland hemorrhage as a complication of liver transplantation: CT appearance. *J Comput Assist Tomogr* **1988**;12:95-97
14. Bowen A, Keslar PJ, Newman B, Hashida Y. Adrenal hemorrhage after liver transplantation. *Radiology* **1990**;176:85-88
15. Albert SG, Wolverson MK, Johnson FE. Bilateral adrenal hemorrhage in the adult: demonstration by computed tomography. *JAMA* **1982**;247:1737-1739
16. Wolverson MK, Kannegiesser H. CT of bilateral adrenal hemorrhage with acute adrenal insufficiency in the adult. *AJR* **1984**;142:311-314
17. Ling D, Korobkin M, Silverman PM, Dunnick NR. CT demonstration of bilateral adrenal hemorrhage. *AJR* **1983**;141:307-308

New Format for Abstracts

Beginning in Fall 1992, the *AJR* will publish abstracts of articles in a different format, much like the ones recently adopted by the *New England Journal of Medicine* and the *Journal of the American Medical Association*. The purpose of the new design is to have abstracts present the essential elements of articles more clearly and concisely. The contents, organization, and length of the abstracts will be the same as before; however, rather than being all one paragraph except for the conclusion, abstracts will now be divided into four paragraphs, each with a title: objective, subjects (or materials) and methods, results, and conclusion.

The *AJR* Guidelines for Authors, which appears at the front of every issue of the Journal, has been revised to help you write abstracts in this new format. Authors should familiarize themselves with these guidelines and incorporate them into all manuscripts submitted for publication.

Robert N. Berk
Editor-in-Chief

Case Report

Neonatal Intestinal Ischemia with Bowel Perforation: An In Utero Complication of Maternal Cocaine Abuse

Theodore R. Hall,[1] Alejandra Zaninović,[1] David Lewin,[2] Cynthia Barrett,[3] and M. Ines Boechat[1]

The differential diagnosis for pneumoperitoneum in a neonate typically includes meconium peritonitis, malrotation and midgut volvulus, and acute gastric perforation caused by ulcer. With the increased recreational use of crack cocaine, pneumoperitoneum or meconium in the peritoneum at birth may be the result of cocaine-induced bowel perforation. We report such a case in a term neonate born to a mother addicted to crack cocaine.

Case Report

A 1.19-kg second male twin of 28 weeks' gestation was born by emergency cesarean delivery after preterm labor and breech presentation. Apgar scores were 1 at 1 min, 2 at 5 min, and 3 at 10 min. The mother was 28 years old, gravida 1, para 1, and had a history of cocaine abuse. Urine tests of the mother and the twins were positive for cocaine. Respiratory distress syndrome developed in the second twin and was treated with surfactant administered by endotracheal

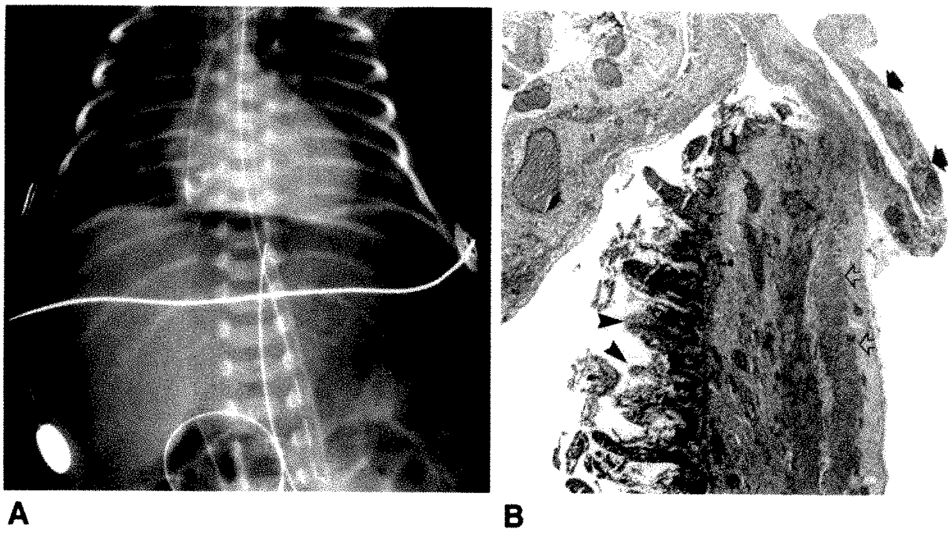

Fig. 1.—Intestinal ischemia and bowel perforation in a neonate exposed to cocaine in utero.

***A*, Supine chest radiograph obtained at birth shows large pneumoperitoneum.**

***B*, Photomicrograph of histologic specimen obtained from perforations in distal ileum shows loss of mucosa and underlying longitudinal and transverse muscle layers at site of perforation. Degree of muscle loss is consistent with an ischemic event that occurred days before bowel perforation and surgery. *Arrowheads* = mucosa, *open arrows* = muscularis mucosa, *solid arrows* = fibrinous serosal covering at site of perforation.**

Received October 7, 1991; accepted after revision November 20, 1991.

[1] Department of Radiological Sciences, University of California, Los Angeles, School of Medicine, 10833 Le Conte Ave., CHS B2-248, Los Angeles, CA 90024-1721. Address reprint requests to T. R. Hall.

[2] Department of Pathology, University of California, Los Angeles, School of Medicine, Los Angeles, CA 90024-1721.

[3] Department of Pediatrics, University of California, Los Angeles, School of Medicine, Los Angeles, CA 90024-1721.

AJR 158:1303–1304, June 1992 0361–803X/92/1586–1303 © American Roentgen Ray Society

tube; patent ductus arteriosus was treated with IV indomethacin. Cranial sonography showed no evidence of intracerebral hemorrhage.

At 7 days of age, the patient had not yet been fed orally, even though normal stools were observed soon after birth. Physical examination revealed jitteriness and a distended abdomen with absence of bowel sounds. A radiograph of the chest and abdomen (Fig. 1A) showed massive free intraperitoneal air without evidence of pneumatosis intestinalis. At surgery, two round perforations 5 mm in diameter were found in the distal ileum. Histologic examination indicated ischemia (Fig. 1B). A 2.5-cm resection of the distal ileum and an end-to-end bowel anastomosis were performed.

During the postoperative period, the neonate had persistent jitteriness and a soft abdomen. Oral feedings were started on the eighth postoperative day. One day later, distension of the abdomen and free peritoneal air were noted again. A second operation revealed disruption at the site of the anastomosis. An end ileostomy along with a mucus fistula was performed. When the neonate was 20 days old, oral feedings were begun.

Discussion

The increased use of crack cocaine has resulted in a higher prevalence of fetal exposure to cocaine. Maternal use during pregnancy affects the mother [1, 2], the fetus [3], and the infant [4, 5]. Cocaine acts both centrally and peripherally. In the peripheral circulation, cocaine is a powerful vasoconstrictor. Detoxification of cocaine in the plasma and liver is facilitated by cholinesterase. Because plasma cholinesterase has extremely low activity in fetuses, neonates, the elderly, pregnant women, and patients with liver disease, the blood level of the drug is sustained in these groups [6]. In the fetus and the neonate, episodes of transient or prolonged ischemia may result in peripheral effects on the intestine, integument, cardiovascular system, or brain [5]. Cocaine-related perforation of the small bowel in adult crack cocaine abusers is thought to be related to bowel ischemia [7]. In the reported cases of gastroduodenal perforation, a comparison between crack users and those without a history of crack abuse showed a younger average age, a less frequent history of peptic ulcer disease, and a higher ratio of males to females in the crack cocaine group [8].

Prolonged in utero exposure of the fetus to high concentrations of cocaine can lead to ischemic changes in the bowel, with perforation and subsequent meconium peritonitis. Although this association has not been reported, this may be because clinically silent in utero perforations heal before birth. As the prevalence of cocaine abuse in the general population increases, more pregnant women and their fetuses will be at risk for this complication.

In fetuses and neonates exposed to cocaine, the initial manifestations of intestinal perforation may be evidence on abdominal radiographs of pneumoperitoneum or calcified meconium within the peritoneum or the scrotal sac. In addition to acute gastric perforation, meconium peritonitis, and midgut volvulus with perforation, the differential diagnosis for these radiographic findings should include cocaine-induced intestinal ischemia with bowel perforation.

REFERENCES

1. Rosen TS, Johnson HL. Drug-addicted mothers, their infants, and SIDS. *Ann N Y Acad Sci* **1988**;533:89–95
2. Rosenak D, Diamant YZ, Yaffe H, Hornstein E. Cocaine: maternal use during pregnancy and its effect on the mother, the fetus, and the infant. *Obstet Gynecol Surv* **1990**;45:348–359
3. Dominquez R, Vila-Coro AA, Slopis JM, Bohan TP. Brain and ocular abnormalities in infants with in utero exposure to cocaine and other street drugs. *Am J Dis Child* **1991**;145:688–695
4. Lipshultz SE, Frassica JJ, Orav EJ. Cardiovascular abnormalities in infants prenatally exposed to cocaine. *J Pediatr* **1991**;118:44–51
5. Dixon SD, Bejar R. Echoencephalographic findings in neonates associated with maternal cocaine and methamphetamine use: incidence and clinical correlates. *J Pediatr* **1989**;115:770–778
6. Stewart D, Inaba J, Lucassen M, Kalow W. Cocaine metabolism: cocaine and norcocaine hydrolysis by liver and serum esterases. *Clin Pharmacol Ther* **1979**;25:464–468
7. Endress C, Kling GA. Cocaine-induced small bowel perforation (letter). *AJR* **1990**;154:1346–1347
8. Lee HS, Lamaute HR, Pizzi WF, Picard DL, Luks FI. Acute gastroduodenal perforations associated with use of crack. *Ann Surg* **1990**;211:15–17

Persistent Infantile Odontoid Process: A Variant of Abnormal Atlantoaxial Segmentation

Russell McClellan,[1] Taher El Gammal,[1] Steven Willing,[1] Thomas Lott,[2] and George Odell[1]

Congenital anomalies of the vertebral column can make diagnosis difficult, particularly when trauma has occurred [1–4]. Most of the congenital variants encountered in the cervical spine involve the first two cervical vertebrae [1]. We report a case in which an anomaly of the second cervical vertebra was seen that, to our knowledge, has not been described previously. The pathogenesis is based on abnormal embryologic development of the second cervical vertebra.

Case Report

An 18-year-old man experienced neck pain after a motor vehicle accident. Tenderness in the upper cervical region was elicited on physical examination. Cervical spine radiographs revealed an abnormality of C2 thought to represent either fracture or a congenital anomaly. Gardner-Wells tongs were applied before further evaluation. Findings on complex motion tomography and CT (Fig. 1) revealed an apparent elongated odontoid process with a wide base and a shouldered appearance. The articulation of the lateral masses of C2 with C1 appeared L shaped instead of having the normal oblique configuration. The lateral masses of C1 were large and the lateral masses of C2 were small. No fractures were noted. The tongs were removed and the patient was released for clinical follow-up.

Discussion

Radiographic features of the case described include an odontoid process that has the appearance of being elongated and shouldered. The lateral masses of C2 are shortened while the lateral masses of C1 are lengthened. Atlantoaxial articulations are L shaped instead of having the normal oblique configuration.

These features can be explained embryologically by abnormal segmentation of the lateral masses of both the axis and atlas. The lateral masses of C1 are lengthened owing to inclusion of tissues that would normally form the superior aspects of the lateral masses of C2. Loss of these tissues from C2 leads to shortening of the C2 lateral masses. The small, short lateral mass of C2 now fuses with the body of C2, leaving the base of the odontoid process bare and unfused. Normally, the adult odontoid fusion occurs not only inferiorly at the subdental synchondrosis but also laterally with the normal lateral C2 mass at the neurocentral synchondrosis. This results in the incorporation (assimilation) of the adult odontoid base in the upper body of C2 [2] (Fig. 2). The persistent infantile anomaly results in an apparently long odontoid process because of the inferior displacement of the neurocentral synchondrosis leaving a bare (unassimilated) odontoid base. The appearance is similar to the infantile odontoid process before fusion of the synchondrosis (Fig. 2A). This also results in a change in the appearance of the lateral atlantoaxial articulation, whereby the base of the odontoid process will be part of this articulation resulting in an L-shaped appearance. The vertical component is from articulation between the C1 lateral mass and the odontoid base. A unilateral form of this anomaly was found in another case (Fig. 3), where the left side of the base of the odontoid process remained bare and unassimilated. The left lateral atlantoaxial joint had an L-shaped appearance.

Several authors have published cases of irregular atlan-

Received September 27, 1991; accepted after revision November 26, 1991.

[1] Department of Radiology, University of Alabama at Birmingham, 619 S. 19th St., Birmingham, AL 35233. Address reprint requests to T. El Gammal.

[2] Department of Radiology, University Hospital, Augusta, GA 30910.

AJR 158:1305–1307, June 1992 0361-803X/92/1586-1305 © American Roentgen Ray Society

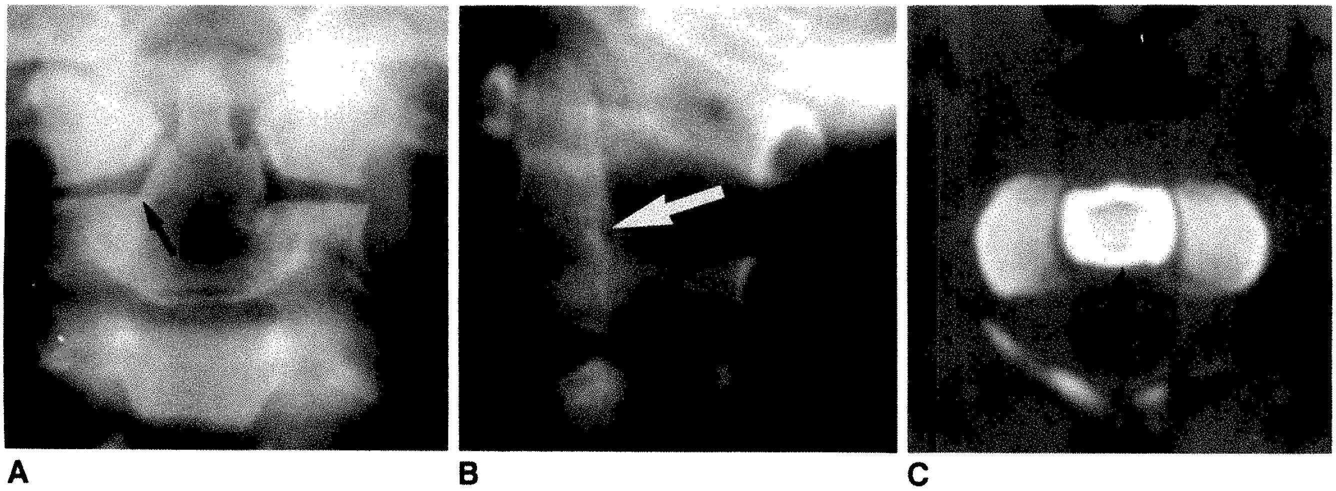

Fig. 1.—Persistent infantile odontoid process bilaterally in an 18-year-old man who had neck pain after a motor vehicle accident.

A and *B*, Pluridirectional tomograms, anteroposterior (*A*) and midsagittal (*B*) views, show a long broad-based odontoid process with shouldered appearance. Note L-shaped atlantoaxial articulation (*arrow, A*). On lateral view (*B*), the only abnormality is an apparent defect (*arrow*) mimicking impacted fracture. This is seen at junction of broad-based odontoid process with body of C2.

C, Axial CT scan through "bare" broad-based odontoid process (*arrow*).

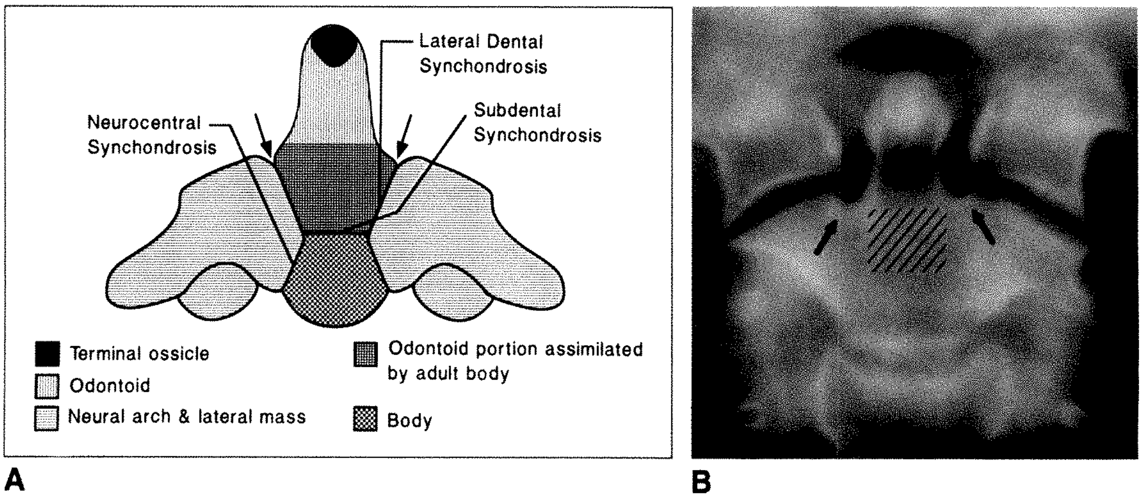
Lateral Dental Synchondrosis
Subdental Synchondrosis
Neurocentral Synchondrosis
■ Terminal ossicle
▨ Odontoid
▨ Neural arch & lateral mass
▨ Odontoid portion assimilated by adult body
▨ Body
A
B

Fig. 2.—Normal C2: assimilation of broad odontoid base.

A, Diagram of infantile C2 shows sites of synchondrosis before assimilation of odontoid base into body of C2.

B, Anteroposterior tomogram of adult C2. *Shaded areas* and *arrows* show assimilation of infantile odontoid base into upper body of C2. Normal adult odontoid process is smaller and shorter than infantile one. Note normal oblique atlantoaxial articulation.

(Reprinted with permission from El Gammal and Brooks [2].)

toaxial segmentation [3–7]. Unilateral odontoid deformities, with some features similar to our second case, have been described [2, 3, 5, 6]. Von Torklus and Gehle [5] have diagrammed three cases of unilateral abnormal atlantoaxial segmentation. The features of their first diagram are similar to our description of persistent infantile odontoid process except for concurrent atlantooccipital synostosis. The second diagram is similar except that it lacks the shouldered appearance of the wide odontoid base shown in our cases. The third diagram shows abnormal segmentation involving unilateral shortening of the lateral mass of C1. Gehweiler [3] included a single case of scoliotic dens dysplasia with associated asymmetric atlantoaxial joints. In this case the usual sulcus at the base of the dens was filled with a hummock of bone producing unilateral widening of the odontoid base. The lateral atlantoaxial joints, however, were not L shaped. Wackenheim [6] reported several cases of asymmetry and hemivertebra of the axis. Only one of these had an L-shaped atlantoaxial articulation, but its odontoid process did not have a shouldered appearance. Two cases of anomalous development of the base of the odontoid were reported by Keats [4]. However, the odontoid process did not have an elongated appearance in either case. One case had a unilaterally large, lengthened lateral mass of C1 and L-shaped atlantoaxial articulation. The odontoid process appeared short on the side of the anomaly, probably owing to an anomalous lateral C2 mass with higher fusion and assimilation of the lower odontoid shaft.

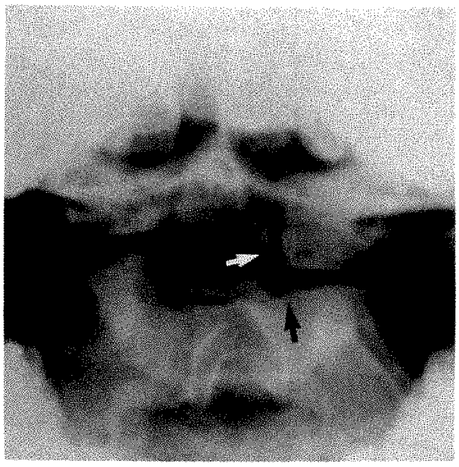

Fig. 3.—Persistent infantile odontoid process unilaterally in a 24-year-old man evaluated for possible neck fracture when neck pain developed after a heavy box fell on his head. Plain anteroposterior radiograph shows unassimilated base because small left lateral mass of C2 has fused with body of C2 below bare unassimilated unfused odontoid base. Note L-shaped atlantoaxial articulation (*arrows*).

We found no previous report of bilateral abnormal atlantoaxial segmentation as seen in our case with the wide-based, shouldered, and elongated appearance where the infantile odontoid process persisted in the adult. This type of anomaly should not be mistaken for fracture to avert unnecessary drastic treatment such as halo placement.

REFERENCES

1. Daffner RH. *Imaging of vertebral trauma*. Rockville: Aspen, **1988**:147–153
2. El Gammal T, Brooks BS. Anatomy of the craniovertebral junction. In: Taveras JM, Ferrucci JT, eds. *Radiology*, vol. 3. *Neuroradiology and radiology of the head and neck*. Philadelphia: Lippincott, **1986;** ch. 78:1–8
3. Gehweiler JA Jr. *The radiology of vertebral trauma*. Philadelphia: Saunders, **1980**:55–58, 138–139, 170–172
4. Keats TE. *Atlas of normal roentgen variants that may simulate disease*. Chicago: Yearbook Medical, **1988**:191–202
5. Von Torklus D, Gehle W. *The upper cervical spine*. New York: Grune & Stratton, **1972**:42–50
6. Wackenheim A. *Roentgen diagnosis of the craniovertebral region*. New York: Springer-Verlag, **1974**:91–93, 197–207, 217–219, 253–260
7. Schmidt H, Fischer E. Uber partielle einseitige synastosen zwischen Atlas und Axis. *ROFO* **1960**:92;380

Book Review

Pediatric Cardiovascular Imaging. By Ina Lynn Dyer Tonkin. Philadelphia: Saunders, 288 pp., 1992. $85

In *Pediatric Cardiovascular Imaging*, a recognized authority in the field presents a review of current imaging techniques used to evaluate congenital heart disease. Well-trained and widely traveled, Dr. Tonkin has been able to gather material from a wide source of friends and colleagues eminently involved in pediatric cardiovascular and interventional radiology.

A short, well-written chapter by Dr. Tonkin on embryology of the cardiovascular system and fetal circulation provides an overview of the development of the systemic venous system, atria, ventricles, and pulmonary veins. Discussion of the great arteries and the aortic arch, fetal circulation, and circulatory changes accompanying birth complete the chapter. Chapter 2 introduces the radiographic approach to congenital heart disease based on the presence of cyanosis or acyanosis and the appearance of the pulmonary vasculature. The authors, however, fail to emphasize that the wide use of prostaglandins to maintain ductal patency and pulmonary blood flow in neonates with cyanotic heart disease means that "decreased pulmonary blood flow" is rarely seen on chest radiographs today. The classic division of cyanotic heart disease into two categories, diseases associated with increased and decreased pulmonary blood flow, should be revised, as it is no longer accurate. Also, the term "pulmonary vascularity" is used imprecisely throughout this chapter and the text. On page 13, the authors state that "increased vascularity . . . refers exclusively to overcirculation or pattern shunt vascularity." Yet, the legend for Figure 2-20 notes that "the pulmonary vascularity is increased, showing mild to moderate pulmonary venous hypertension." Also, the legend for Figure 2-22 states that with transposition of the great arteries, the pulmonary vascularity cannot be "increased in this cyanotic newborn" because of the normal or elevated pulmonary vascular resistance present at birth. Other images presented in the chapter, such as chest radiographs of truncus arteriosus (Fig. 2-23) and total anomalous pulmonary venous return (Fig. 2-24), are no longer seen today and can be found only in radiology teaching files, as patients with these abnormalities have surgical repair at an early age.

Chapters on echocardiography (beautifully illustrated) and cine and digital subtraction angiography make up the body of the text, describing various lesions and their pathophysiology in detail. Chapters on ultrafast CT, MR imaging, postoperative chest radiography, interventional procedures, and fetal echocardiography complete the text. Notable for its absence is a chapter on nuclear medicine, which is especially useful in the evaluation of patients with cardiomyopathy and myocardial ischemia.

The organization of the text has several noticeable inherent weaknesses. Considerable duplication of material is present, as various entities are discussed repeatedly in each chapter. The most noticeable weakness with the organization is that a discussion of individual imaging techniques is not clinically relevant to current imaging of congenital heart disease in children. As the reader goes through the individual chapters, each repetitively illustrating and discussing various lesions in detail, the lack of a recommended integrated imaging approach becomes apparent. Chapter 3 begins with the comment, "Echocardiography has changed the practice of pediatric cardiology profoundly." The authors also should have mentioned the practice of the radiologist, and this dominant fact should have been the basis for the organization of the text.

I believe that Dr. Tonkin would have served the readers better if she had separately recommended, and then illustrated, the integrated imaging of each pathologic lesion, beginning with the diagnosis established on the basis of echocardiograms and chest radiographs. What are the indications for catheterization and angiography in patients with complete transposition? After angiography, why are certain patients referred for MR imaging? What are the common operations and associated complications for complete transposition, and how can these be recognized and best imaged? Which of these complications can be treated by interventional procedures?

The text is well illustrated, and figures are clearly labeled. Some chest radiographs in chapters 2 and 7 are too small, and the fine points of pulmonary vascularity are obscured. Most of the MRI images were obtained 5–7 years ago and are not up to current standards of clarity and definition. Two-dimensional and color Doppler illustrations, on the other hand, represent state-of-the-art imaging.

For those interested in the imaging of congenital heart disease, the well-written chapters on echocardiography and cine and digital subtraction angiography are useful reference material. A more complete and detailed reference of angiocardiography of congenital heart disease is available in *Angiocardiography of Congenital Heart Disease* by Freedom, Culham, and Moes, and an approach to integrated imaging may be found in the ninth edition of *Caffey's Pediatric X-Ray Diagnosis*, soon to be published.

Richard B. Jaffe
Primary Children's Medical Center
Salt Lake City, UT 84113

Case Report

Congenital Absence of the Left Pulmonary Artery Associated with Double-Outlet Right Ventricle

Sarah Kremer,[1] Ayodeji B. Fayemi,[1] Bernard G. Fish,[2] William A. Rothe,[3] and Hugo Spindola-Franco[1]

Congenital unilateral absence of a pulmonary artery is a rare anomaly often associated with intracardiac defects, such as tetralogy of Fallot and truncus arteriosus. Approximately 160 cases have been reported in the literature [1-8]. We report a case of unilateral absence of the left pulmonary artery occurring with a double-outlet right ventricle. To our knowledge, this has not been described previously.

Case Report

An 11-year-old boy was referred to our institution for evaluation of dyspnea and cyanosis. He was born at term by uncomplicated vaginal delivery after a normal pregnancy; his birth weight was 3.6 kg. Shortly after delivery, he had peripheral cyanosis. At 18 months, he was admitted to a local hospital with diarrhea, dehydration, and cyanosis. A diagnosis of tetralogy of Fallot was made. The patient became progressively dyspneic until the time of admission, when he was almost completely bedridden. He frequently had phlebotomies for polycythemia.

Physical examination showed a thin child with central cyanosis. The blood pressure was 107/64 mm Hg, pulse rate was 100 beats per minute, and respirations were 24 per minute. A right ventricular lift was present. A single loud second heart sound was heard with a II/VI harsh systolic ejection murmur at the left lower sternal border. Breath sounds were normal.

The ECG showed marked right-axis deviation, severe right ventricular hypertrophy, and a strain pattern. Chest radiographs (Figs. 1A and 1B) showed mild cardiomegaly with bilateral pulmonary undercirculation and hypoplasia of the left lung with herniation of the right lung into the left hemithorax. An echocardiogram showed a large ventricular septal defect with a double-outlet right ventricle. The aorta was anterior and slightly toward the right. Marked subvalvular pulmonic stenosis was present. Angiocardiograms (Figs. 1C and 1D) showed a double-outlet right ventricle with a subaortic ventricular septal defect and severe subpulmonic obstruction. The left pulmonary artery was absent. No large vessel supplied the left lung. Instead, it was supplied by small systemic collateral vessels arising from the descending aorta and the intercostal arteries. Wedge injection of a left pulmonary vein showed no retrograde opacification of a central left pulmonary artery. MR images (Fig. 1E) confirmed double-outlet right ventricle with severe subpulmonic osbtruction and unilateral absence of the left pulmonary artery.

The double-outlet right ventricle was repaired surgically with an intracardiac Dacron tunnel used to divert left ventricular flow to the aorta and to obliterate the ventricular septal defect. Excess muscle was excised from the right ventricular infundibulum. The postoperative course was uncomplicated, and the patient was improved and stable when discharged.

Discussion

Unilateral absence of a pulmonary artery was first reported by Fraentzel in 1868 (cited by Pool et al. [1]). The disorder has no hereditary component or sex predilection. Although most instances are manifested in infancy or childhood, cases have been diagnosed up to age 68 [6].

The pulmonary artery is formed by the ventral bud from the aortic sac and contributions from the postbranchial plexus.

Received December 9, 1991; accepted after revision January 15, 1992.

[1] Department of Radiology, Montefiore Medical Center, Albert Einstein College of Medicine, 111 E. 210th St., Bronx, NY 10467. Address reprint requests to H. Spindola-Franco.

[2] Department of Pediatrics, Section of Pediatric Cardiology, New York Medical College, Valhalla, NY 10595.

[3] Department of Pediatrics (Cardiology), Montefiore Medical Center, Albert Einstein College of Medicine, Bronx, NY 10467.

AJR 158:1309-1311, June 1992 0361-803X/92/1586-1309 © American Roentgen Ray Society

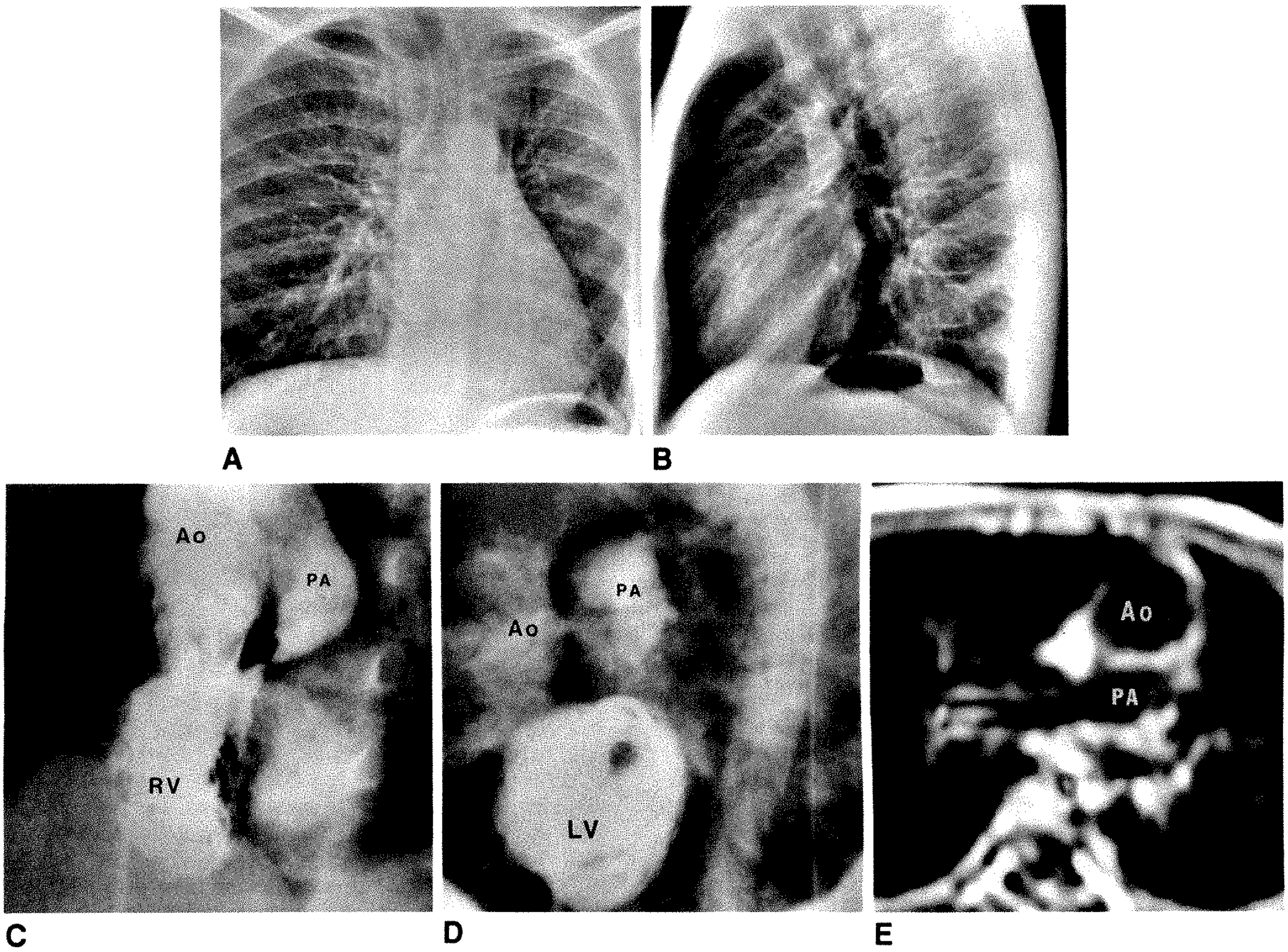

Fig. 1.—Congenital absence of left pulmonary artery and double-outlet right ventricle in an 11-year-old boy.

***A*, Frontal chest radiograph shows hypoplastic left lung and shift of mediastinum to left. Right lung herniates over midline toward left.**

***B*, Lateral chest radiograph shows left pulmonary artery is absent.**

***C*, Left anterior oblique right ventriculogram with cranial angulation shows that aorta (Ao) and pulmonary artery (PA) arise from right ventricle (RV). Severe subpulmonic stenosis is present. Left pulmonary artery is absent. Left ventricle opacifies faintly by way of ventricular septal defect.**

***D*, Lateral left ventriculogram shows that no great vessel arises from left ventricle (LV). Aorta (Ao) opacifies by way of ventricular septal defect. Right pulmonary artery (PA) is visualized; no left pulmonary artery is present.**

***E*, Axial spin-echo MR image, 750/20 (TR/TE), just inferior to carina shows right pulmonary artery (PA), but no left pulmonary artery is visualized. Ao = ascending aorta.**

The dorsal bud forms the ductus arteriosus on the left and does not persist on the right. The truncus arteriosus rotates so that the left pulmonary artery is pulled anteriorly and to the right to form a major portion of the main pulmonary artery. It is thought that unilateral absence of a pulmonary artery is caused by failure of development of the ventral bud, with persistence of the dorsal connections to the postbranchial plexus providing supply to the lung via bronchial vessels. If the lung is supplied by a vessel from the aortic arch, this is most likely due to persistence of the dorsal portion of the pulmonary arch. If blood supply to the affected lung is from the ascending aorta, this is probably due to failure of migration of the ventral portion of the pulmonary arch rather than to failure of formation of the pulmonary artery. The relatively frequent association of unilateral absence of the left pulmonary artery with tetralogy of Fallot has been attributed to the contribution made by the left pulmonary artery to the formation of the main pulmonary artery. The other anomalies associated with an absent right or left pulmonary artery have not been explained on the basis of their embryogenesis [1, 2].

Clinical findings include respiratory distress, recurrent pulmonary infection, and hemoptysis. Occasionally, abnormal findings on routine chest radiographs will prompt investigation.

Bahler et al. [3] divided absent right pulmonary artery into three groups: (1) patients with associated left-to-right shunt, usually patent ductus arteriosus, who have congestive heart failure and respiratory problems in infancy; (2) patients with isolated absence of the right pulmonary artery and pulmonary hypertension who die in infancy; and (3) patients with isolated absence of the right pulmonary artery without pulmonary hypertension whose condition is diagnosed when they are adults—when they have hemoptysis or when abnormal findings are seen on chest radiographs.

Physical examination may show a small hemithorax with decreased breath sounds, shift of the heart and mediastinum, or signs of pulmonary hypertension. The ECG is usually normal, but may show right-axis deviation. The findings on plain films of the chest include decreased vascularity in one lung, absent hilar density, shift of the heart or mediastinum, small hemithorax with narrowed intercostal spaces, elevated diaphragmatic leaflet, and lacy pattern suggestive of bronchial arteries. Ventilation and perfusion scintigraphy will show absent perfusion in one lung with relatively normal ventilation. Pulmonary angiocardiography shows which circulatory structures are absent, and aortography may show an anomalous supply to the affected lung.

The left pulmonary artery and the right pulmonary artery are absent with approximately equal frequency. Absence of the left pulmonary artery is most often associated with tetralogy of Fallot [1] and can be associated with right-sided aortic arch [2]. Unilateral absence of the right pulmonary artery is isolated in approximately 50% of cases, and if associated with an anomaly is most often associated with patent ductus arteriosus [1]. Defects associated with absence of either artery include atrial and ventricular septal defects, coarctation of the aorta, aorticopulmonary window, truncus arteriosus, and, in one instance, supracardiac total anomalous pulmonary ventricular return [1, 2]. Our review of the literature showed a larger proportion of isolated absence of both right and left pulmonary arteries than previously reported [1, 2]. This may be because many of these cases were diagnosed in adults, who must have had less severe or no associated anomalies in order to survive and have signs and symptoms so late in life.

Treatment of unilateral absence of a pulmonary artery includes pneumonectomy, ligation of abnormal vessels, and anastomosis of the remaining peripheral pulmonary artery with the main pulmonary trunk. Embolization might be useful in selected cases.

The association of unilateral absence of the left pulmonary artery with a double-outlet right ventricle has not previously been described. Nevertheless, a strong association has been shown between an absent left pulmonary artery and other abnormalities of the bulbus cordis, such as tetralogy of Fallot and truncus arteriosus [1]. Therefore, in the presence of a double-outlet right ventricle and other similar cardiac defects, unilateral absence of the left pulmonary artery should be excluded, especially if the left lung is hypoplastic. This anomaly is likely to be missed on echocardiography because the left pulmonary artery is surrounded by lung, which makes it inaccessible to ultrasound. MR techniques are useful in excluding a central pulmonary artery branch but cannot delineate the source of blood flow in the abnormal lung. Angiography is definitive in the diagnosis of an absent left pulmonary artery and is generally necessary before repair of complex cardiac defects such as double-outlet right ventricle, in which anomalies of the coronary arteries may be present.

REFERENCES

1. Pool, PE, Vogel JHK, Blount SF Jr. Congenital unilateral absence of a pulmonary artery: the importance of flow in pulmonary hypertension. *Am J Cardiol* **1962**;10:706–732
2. Sherrick DW, Kincaid OW, DuShane JW. Agenesis of a main branch of the pulmonary artery. *AJR* **1962**;10:917–928
3. Bahler RC, Carson P, Traks E, Levene A, Gillespie D. Absent right pulmonary artery: problems in diagnosis and management. *Am J Med* **1969**;46:64–71
4. Byrne RJR, Bloom DL, Morristown NJ. Absence of the right pulmonary artery as a cause of hemoptysis. *J Thorac Cardiovasc Surg* **1970**;59:264–268
5. Borgeson E, Vogel J. Congenital unilateral absence of the left pulmonary artery. *Chest* **1980**;77:106–107
6. Currarino G, Williams B. Causes of unilateral pulmonary hypoplasia: a study of 33 cases. *Pediatr Radiol* **1985**;15:15–24
7. Cogswell TL, Singh S. Agenesis of the left pulmonary artery as a cause of hemoptysis. *Angiology* **1986**;37:154–159
8. Weg JG, Krumholz RA, Hackleroad LE. Unilateral hyperlucent lung: a physiologic syndrome. *Ann Intern Med* **1965**;62:675–676

Radiologic-Pathologic Conferences of the Massachusetts General Hospital

Rathke's Cleft Cyst

William B. Crenshaw[1] and Felix S. Chew

A 15-year-old girl with labile hypertension, bitemporal visual field deficits, and occasional dizziness and headaches presented with a neck mass. The lesion was an incidental hemangioma, but a sellar mass was discovered on MR images of the cervical spine. The 3-cm, nonenhancing, well-circumscribed lesion expanded the sella and pushed into the suprasellar cistern with mass effect on the optic chiasm (Fig. 1). The infundibulum was midline, but the neurohypophysis was displaced posteriorly. The signal characteristics were similar to CSF. CT scans showed no calcification. The differential diagnosis included intrasellar arachnoid cyst, Rathke's cleft cyst, cavitated pituitary adenoma, and cystic craniopharyngioma. Fenestration and drainage of the sellar lesion were done through a right pterional craniotomy. A simple cyst lined with epithelium and containing clear fluid was found, and the final pathologic diagnosis was Rathke's cleft cyst. The patient's signs and symptoms remitted.

Rathke's pouch, an upgrowth of oral ectoderm, is the embryologic precursor of the anterior lobe, pars intermedia, and pars tuberalis of the pituitary gland. Rathke's cleft cysts are derived from or are remnants of Rathke's pouch. Sellar and juxtasellar epithelial cysts comprise a spectrum of lesions that range from craniopharyngioma (aggressive and complex) to Rathke's cleft cyst (simple and indolent).

Intra- and suprasellar in location, Rathke's cleft cysts have well-defined margins and midline location. The thin walls are lined by a single layer of epithelium. Mucin-secreting goblet cells may be present. Depending on the activity of the goblet cells and the rate of epithelial desquamation, the material within the cyst ranges from serous to mucoid. This variation in content is reflected on CT, where the attenuation is low (serous) to intermediate (mucoid), and on MR, where lesions are hypointense on T1-weighed images and hyperintense on T2-weighted images (serous) or hyperintense on T1-weighted images and isointense on T2-weighted images (mucoid) [1–3]. Hyperintensity on both T1- and T2-weighted images suggests the presence of blood. A small area of hypo- or isointensity may indicate thickening of the cyst wall or aggregation of cellular debris. The lesions are noncalcified. Occasionally, the cyst wall may enhance.

Before CT, Rathke cleft cysts were usually incidental discoveries at autopsy. The typical size is less than 1 cm, and symptoms are rare. When signs or symptoms occur, they result from compression of the pituitary gland, pituitary stalk, optic chiasm, or hypothalamus and may include hypopituitarism, diabetes insipidus, visual disturbances, and headache. If asymptomatic, and if endocrine function is normal and extrasellar structures are not compressed, these lesions may be safely ignored; otherwise, surgical drainage and partial excision are necessary [4]. The recurrence rate is low.

REFERENCES

1. Voelker JL, Campbell RL, Muller J. Clinical, radiographic, and pathological features of symptomatic Rathke's cleft cysts. *J Neurosurg* **1991**;74:535–544
2. Asari S, Ito T, Tsuchida S, Tsutsui T. MR appearance and cyst content of Rathke cleft cysts. *J Comput Assist Tomogr* **1990**;14:532–535
3. Nakasu Y, Isozumi T, Nakasu S, Handa J. Rathke's cleft cyst: computed tomographic scan and magnetic resonance imaging. *Acta Neurochir* **1990**;103:99–104
4. Kucharczyk W, Peck WW, Kelly WM, Norman D, Newton TH. Rathke cleft cysts: CT, MR imaging, and pathologic features. *Radiology* **1987**;165:491–495

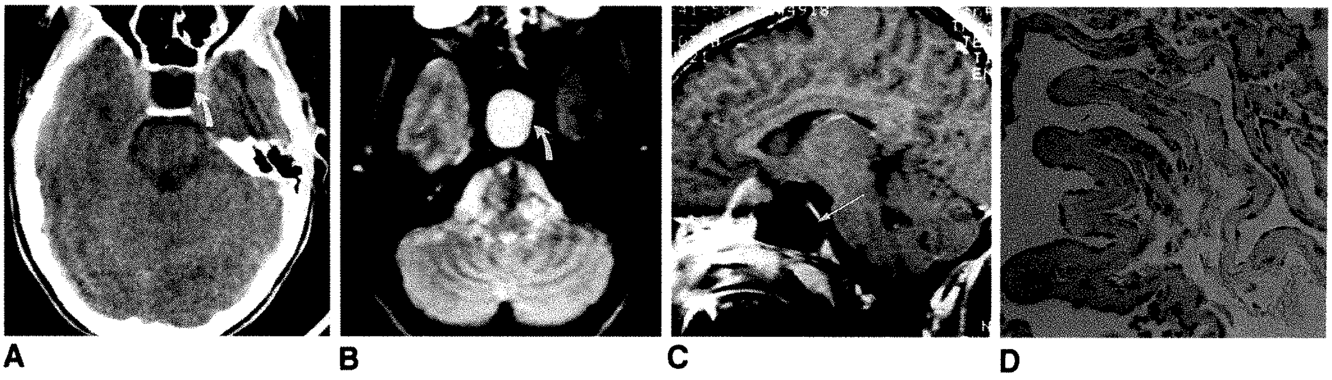

Fig. 1.—Rathke's cleft cyst.
***A*, CT scan shows low-density mass (*arrow*) enlarging sella.**
***B*, Axial T2-weighted MR image shows bright signal in mass (*arrow*).**
***C*, Sagittal T1-weighted MR image shows low signal in mass (*arrow*).**
***D*, Lesion was filled with fluid. Photomicrograph of lesion wall shows single layer of epithelial cells.**

From the weekly radiologic-pathologic correlation conferences conducted by Jack Wittenberg. Pathology editor: Andrew E. Rosenberg. Radiology editors: Felix S. Chew, William E. Palmer, Daniel P. Barboriak, Daniel I. Rosenthal.

[1] Both authors: Department of Radiology, Massachusetts General Hospital and Harvard Medical School, 32 Fruit St., Boston, MA 02114. Address reprint requests to F. S. Chew.

***AJR* 158:1312, June 1992** 0361–803X/92/1586–1312 © American Roentgen Ray Society

Perspective

Fast Spin-Echo MR Imaging of the Brain and Spine: Current Concepts

Kendall M. Jones,[1] Robert V. Mulkern,[2] Richard B. Schwartz,[1] Koichi Oshio,[1] Patrick D. Barnes,[2] and Ferenc A. Jolesz[1]

Fast spin-echo (FSE) sequences are recently developed modifications of the rapid acquisition relaxation enhanced (RARE) sequences initially described by Henning et al. [1–4]. The basic pulse sequence underlying all RARE/FSE methods is the Carr-Purcell-Meiboom-Gill (CPMG) echo train. This sequence was originally introduced over 30 years ago in order to make transverse relaxation time (T2) measurements that would be largely free from errors introduced by imperfect refocusing pulses [5], the latter being accomplished by making a 90° phase shift between the excitation pulse and ensuing refocusing pulses. In RARE/FSE sequences, each echo of the CPMG train is phase encoded with a distinct phase-encode gradient, read out in the presence of a frequency-encoding gradient, and phase "unwound" after readout [1]. It has now been shown that with a judicious selection of the number of echoes per train and tailored phase-encode reordering algorithms, FSE sequences can be fashioned to yield high-quality T1-weighted, proton density–weighted, and T2-weighted images far more rapidly than is possible with conventional spin-echo (CSE) sequences [6–10]. Furthermore, FSE images retain true spin-echo T2 contrast features rather than the T2* contrast features associated with gradient-echo methods.

A number of clinical studies are currently under way, and several have been completed comparing FSE and CSE sequences. The results have shown a promising correlation between the two sequences [9, 10], with the implication that the slower CSE sequences will ultimately be replaced by selected FSE sequences. Improvements in image quality and FSE sequence innovations have been so rapid, however, that many of the techniques implemented and images obtained for comparative purposes have become almost outdated before the completion of controlled clinical trials.

This article describes current concepts concerning the optimization of FSE pulse sequences in the brain and spine and comments on the strengths and weaknesses of FSE. State-of-the-art and potential future applications of this pulse sequence are discussed from a practical perspective.

Fast Spin-Echo MR Imaging of the Brain

During the past 10 months, CSE images were supplemented when feasible with FSE images by using 1.5-T Signa scanners equipped with a 4.6 hardware/software configuration (General Electric Medical Systems, Milwaukee, WI). For the past several months, all proton density–weighted and T2-weighted images have been obtained by using only selected FSE sequences. The primary FSE sequence used for brain studies during this time consisted of an eight-echo CPMG train in which the first four echoes were used for proton density–weighted images and the second four for T2-weighted images. Various combinations of scanning parameters TR/pTE1,pTE2 were used. Here, pTE is the pseudo–echo time as determined by the specific phase-encode reordering algorithm introduced by Melki et al. [7]. An extremely useful

---

Received December 12, 1991; accepted after revision January 17, 1992.

[1] Department of Radiology, Brigham and Women's Hospital, Harvard Medical School, 75 Francis St., Boston, MA 02115. Address reprint requests to K. M. Jones.

[2] Department of Radiology, The Children's Hospital, Harvard Medical School, Boston, MA 02115.

AJR 158:1313–1320, June 1992 0361–803X/92/1586–1313 © American Roentgen Ray Society

combination for obtaining 28 slices through the adult brain is a 2500/18,90 combination with an 18-msec echo spacing and one signal average per phase encode. This allows 14 slice locations to be acquired with 256 × 192 image matrices in only 2 min 6 sec. We have used a 5-mm slice thickness with a 5-mm interslice gap in an interleaved manner to acquire 5-mm contiguous proton density-weighted and T2-weighted images at 28 slice locations in only 4 min 12 sec. Early studies with this sequence that used 256 × 128 matrices reduced the total acquisition time to 2 min 40 sec. However, a number of problems with Gibbs (ringing) artifacts and blurring on proton density-weighted images were encountered that have been reduced or eliminated by using a 192 or 256 image matrix. Several early studies also used a pTE1 of 30 msec [9]. However, the resulting proton density-weighted images showed high CSF signal that could obscure periventricular lesions, leading to the adoption of pTE1s between 15 and 20 msec.

Although modifications with respect to TR and matrix size were made that lengthened acquisition times, our current sequence produces a threefold time savings as compared with CSE methods that use identical imaging parameters. Summarizing our current optimized protocol for adult brain imaging, proton density-weighted and T2-weighted images of the entire brain (2500/18,90, one acquisition, 256 × 192 matrix, 5-mm/0-mm slice/gap, 28 slice locations) are obtained in 4 min 12 sec. Overall image quality has been excellent, with reduced motion artifact and nearly identical lesion conspicuity compared with CSE images. We have observed no significant differences in the imaging characteristics of extraaxial (Fig. 1) or intraaxial masses, infarcts, inflammatory lesions, or white matter disease, such as multiple sclerosis (Fig. 2). Clinical trials are under way to determine if subtle differences are seen in imaging characteristics between CSE and the updated FSE sequence, but we have found no significant differences in lesion conspicuity to date with the possible exception of some cases of intracranial hemorrhage (discussed later).

Many users do not require zero-gap studies of the entire brain. We have found that the eight-echo FSE sequence that uses a 5-mm/2.5-mm slice/gap (14 slices) and a 2000-msec TR can be used quite efficiently for brain imaging in children [9]. The 2000-msec TR renders CSF hypointense relative to brain parenchyma on the proton density-weighted image, helping to separate subependymal and subpial lesions from CSF and to distinguish CSF-containing structures from other water-containing lesions when both appear hyperintense on T2-weighted images (e.g., arachnoid cyst vs low-grade astrocytoma). A more recent modification has been the implementation of a six-echo FSE sequence in which the first three echoes are used for the proton density-weighted image and the last three are used for the T2-weighted image. The shorter echo train allows 18 slices to be acquired in a 2000-msec TR, yielding full-volume coverage with a five-skip 2.5-mm slice setting. The sequence is now acquired with two signal averages per phase-encode step and is restricted to 256 × 192 image matrices. Excellent proton density-weighted and T2-weighted images that use 18 slice locations with 5-mm slice thickness are now acquired in 4 min 18 sec, permitting acquisitions in both the axial and coronal planes in less time than is required for a single CSE acquisition with a 256 × 128 image matrix, two signal averages, and a 2000-msec TR (8 min 56 sec).

Despite the overall similarity between CSE and FSE images, some important differences between them deserve comment. The most favorable difference results from faster scanning times, with concomitant reduction in motion artifact and, in some cases, reduced phase artifact from flowing blood. In

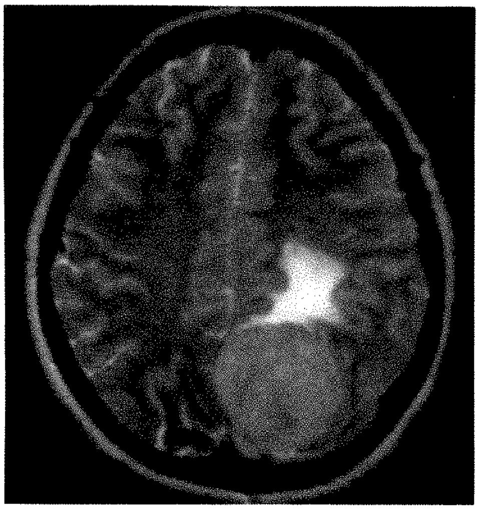

Fig. 1.—FSE (2500/90) MR image of brain shows a meningioma. Signal intensity of tumor is same as that of gray matter. Prominent area of edema is present anterior to lesion.

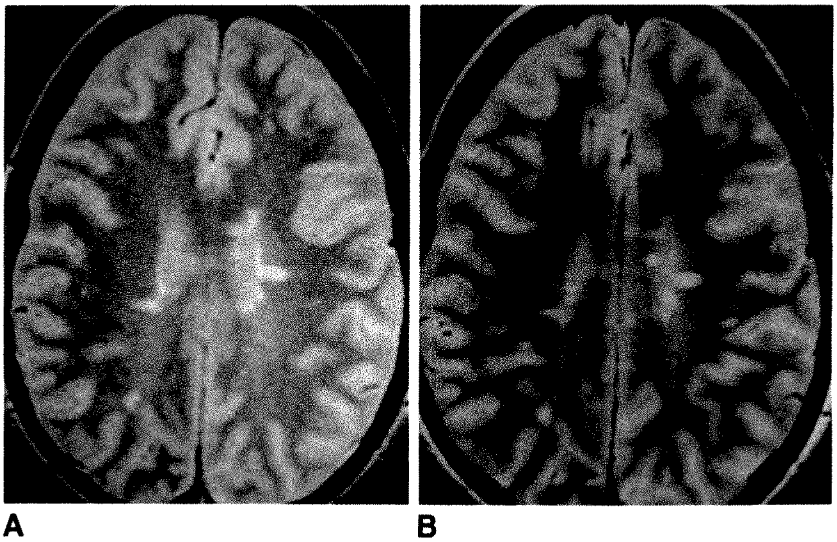

Fig. 2.—*A* and *B*, CSE (3000/30, *A*) and FSE (3000/30, *B*) MR images of brain both show periventricular white matter lesions of multiple sclerosis.

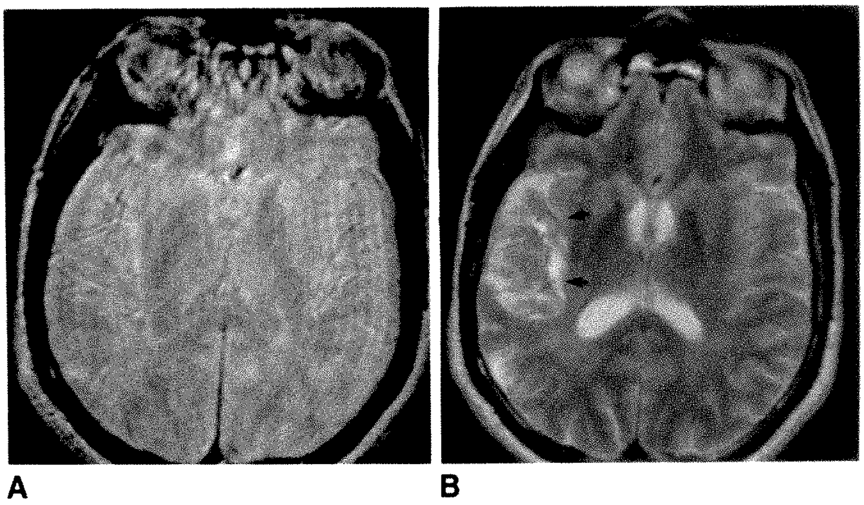

Fig. 3.—*A*, CSE MR image of brain (2000/30) shows severe motion artifact. T2-weighted images were uninterpretable and were never filmed.

B, FSE MR image (2000/80) at same level obtained immediately after CSE MR image clearly shows right superior temporal infarct (*arrows*).

some instances, excellent images were obtained by using FSE when CSE images were uninterpretable (Fig. 3). The greatest disparity between FSE and CSE images is the markedly increased signal from fatty tissues in FSE. Although the cause for this increased signal has not been established definitively, we believe that the mechanism responsible is a decreased contribution from spin-spin splittings among lipid protons to the T2 decay process because of the multiple, closely spaced 180° refocusing pulses used in FSE. Theoretical and experimental support for this hypothesis may be found in the literature [11, 12]. We have not found the bright fat signal to be a problem in brain imaging, although a lipoma or other fat-containing structure might conceivably be mistaken for a subacute hemorrhage. One possibility for making the distinction would be to look for the presence or absence of the standard chemical-shift artifact along the read-gradient direction. Such artifacts are bandwidth dependent but are the same in FSE as in CSE, since both encode spatial information along the read axis in precisely the same manner. An alternative and more straightforward approach is to apply fat-suppression techniques, as discussed later.

Another important observation is the slight reduction in magnetic susceptibility loss with FSE compared with CSE images, an effect again attributed to the use of closely spaced 180° pulses in FSE [7, 10, 13, 14]. This has both advantages and disadvantages for FSE imaging. Perhaps the most important disadvantage is the reduction in signal loss associated with hemorrhagic blood products (Fig. 4). In a recent study, slightly higher signal intensity measurements were obtained in hemorrhagic foci and iron-containing nuclei on FSE images when compared with CSE counterparts [10]. Although all hemorrhages were detected in this series, it is quite possible that a small hemorrhagic lesion might not be seen on FSE images or might be mistaken for edema or some other abnormality. Additional sequences (e.g., gradient echo) may be useful if subtle brain hemorrhage is of significant concern. On the positive side, decreased magnetic susceptibility effects have proved advantageous when imaging such structures as the sinuses or skull base, or such artifact-producing metallic objects as dental braces, orthopedic hardware, aneurysm clips, or metallic ventricular shunt components.

Since FSE uses echoes with different T2 weightings to form the raw k-space data matrix [15], a leakage of signal along the phase-encode direction is unavoidable [16, 17]. The end result is a structured noise component along the phase-encode direction with concomitant decreased signal to noise when compared with CSE images produced with comparable scanning parameters. Measurements indicate reductions of signal-to-noise ratios (SNRs) for brain tissue that are on the order of 25% [9, 10]. In brain imaging, this reduction is not readily apparent owing to the routine use of quadrature coils with a resultant high SNR. In spine imaging, however, where volume coils are used in conjunction with surface receiver coils, noisier images are often observed, particularly when a small number of acquisitions or shorter TRs are used. This issue is addressed more fully in the next section.

Of the advantages of FSE in brain imaging, perhaps the greatest is the versatility resulting from the reduced acquisition times. The time savings may be used purely to obtain faster images with similar image quality compared with CSE, or to provide greatly improved image quality (e.g., increased signal to noise, increased spatial resolution, or improved image contrast) in a comparable time period. If speed is of utmost importance, scanning times may be reduced even further through the use of longer echo trains or by eliminating either proton density–weighted or T2-weighted images. For example, by lengthening the echo train to 16 and using all 16 echoes for a T2-weighted image, 14 slice locations (2000/75, 15-msec echo spacing, 256 × 256 matrix) can be imaged in only 66 sec with excellent image quality (Fig. 5). Such an adjunct sequence might be quite useful for rapidly obtaining additional coronal images in cases of temporal lobe epilepsy, or for obtaining images in additional planes to assist in surgical planning.

There are, of course, limitations to how far an echo train can be usefully extended, and to how much the interecho interval can be reduced. As the echo train is extended, more heavily T2-weighted echoes are used to fill k-space data lines,

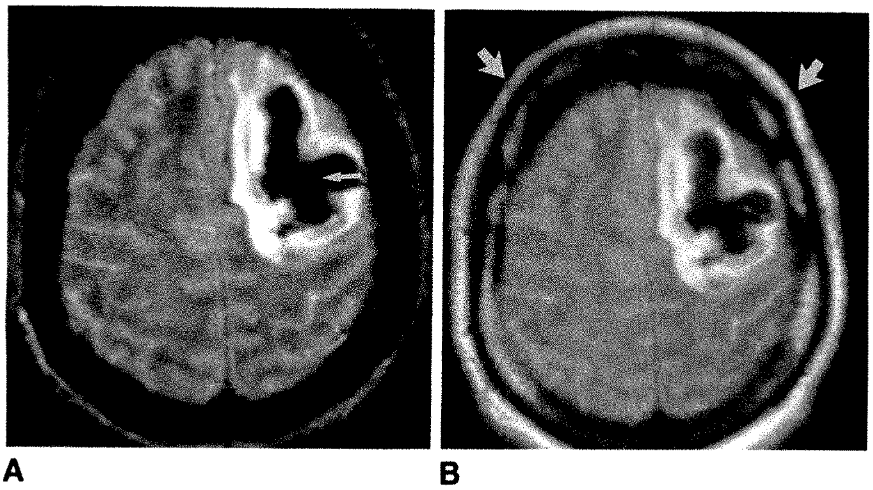

Fig. 4.—*A*, CSE MR image of brain (2000/80) shows right frontal hemorrhage with central deoxyhemoglobin (*arrow*).

B, Central deoxyhemoglobin appears and measures slightly higher in signal intensity on corresponding FSE MR image with identical scan parameters. Scalp fat appears very bright (*arrows*).

(Reprinted with permission from Jones et al. [10].)

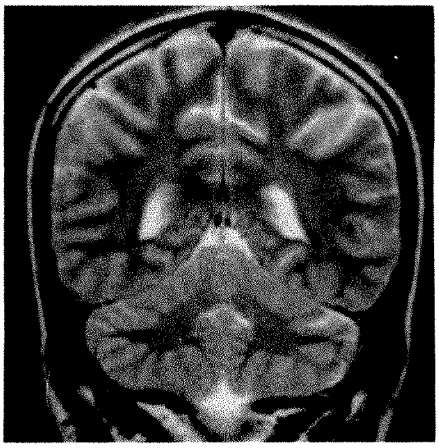

Fig. 5.—FSE T2-weighted coronal MR image (2000/75) of brain in a healthy volunteer. Total imaging time was 66 sec.

leading to increased blurring, or edge enhancement and ringing artifacts [6, 7, 16, 17]. These effects have not been observed on T2-weighted images for echo-train lengths of up to 16, although for proton density–weighted images such effects become noticeable for echo-train lengths greater than four [7, 17].

High-Resolution Brain Imaging

If speed is of less concern than image quality, increased signal averaging with FSE may be used to provide superior images compared with CSE in comparable acquisition times. Such an approach is especially useful for obtaining high-spatial-resolution images (e.g., 512 × 512 image matrices, 1- to 3-mm slice thicknesses) with their inherently small voxels and reduced SNR.

The use of multiple acquisitions (four, eight, or even 12 repetitions) affords excellent signal even with very thin slices or small voxel size, formerly not practical with CSE owing to long acquisition times. For instance, a 512 × 512 image matrix acquired with a 16-echo train, four signal averages, and a 2000/90 TR/pTE may be acquired in only 4 min 16 sec.

In addition to increasing the number of acquisitions and reducing the voxel size or slice thickness, a small field of view (FOV) may be used to obtain fine structural detail in a specific anatomic region of interest. We have used FOVs as small as 8–16 cm in combination with a 1- to 3-mm slice thickness and four to 12 acquisitions to obtain detailed anatomic information in small regions of interest such as the pituitary fossa, cavernous sinuses, internal auditory canal, and brainstem. Such a protocol may be very useful for delineation of specific cranial nerves or to confirm the presence of a very small or equivocal lesion (Fig. 6). In addition to increasing spatial resolution or SNR, FSE allows the manipulation of contrast options normally not considered. For example, we have used a TR as long as 6000 msec to increase conspicuity of multiple sclerosis lesions. Such a long TR would not be practical with CSE owing to the excessive motion artifact.

In summary, FSE provides images similar in contrast characteristics to CSE images, but allows much greater flexibility in setting image parameters. This flexibility may be used to obtain very rapid dual-echo images in any plane, or to improve spatial resolution or overall image quality.

Fast Spin-Echo MR Imaging of the Spine

For the past 4 months, we have replaced CSE with FSE sequences specifically designed for routine spine imaging in adults. Our routine screening examination consists of sagittal T1-weighted and T2-weighted FSE images with supplemental CSE axial proton density–weighted or gradient-echo images. T1-weighted FSE images can be obtained simply by decreasing the TR, and we have obtained excellent images in 1 min 59 sec (600/12, 256 × 192 matrix, four-echo train length, four acquisitions, 4-mm/0.5-mm slice/gap, 10 slice locations). Since T1-weighted images can already be rapidly obtained with conventional techniques, the time savings is not as impressive with T1-weighted FSE images as with T2-weighted FSE images. In addition, the whole-body transmit coil–surface receive coil combination used for the spine makes reduced SNR more apparent than on FSE brain images obtained with a quadrature coil. For this reason, we routinely obtain four acquisitions for both T1- and T2-weighted FSE images. In addition, the T1- and T2-weighted FSE spine sequences do not use zero phase-encode reordering [6, 7], and the effective TE is the central echo of the CPMG train [8].

With the T2-weighted FSE sequence, 14 images are obtained in 3 min 16 sec (4000/102, 256 × 192 matrix, 16-echo train length, four acquisitions, 4-mm/0.05-mm slice/gap). We have found that the long TR provides improved contrast and

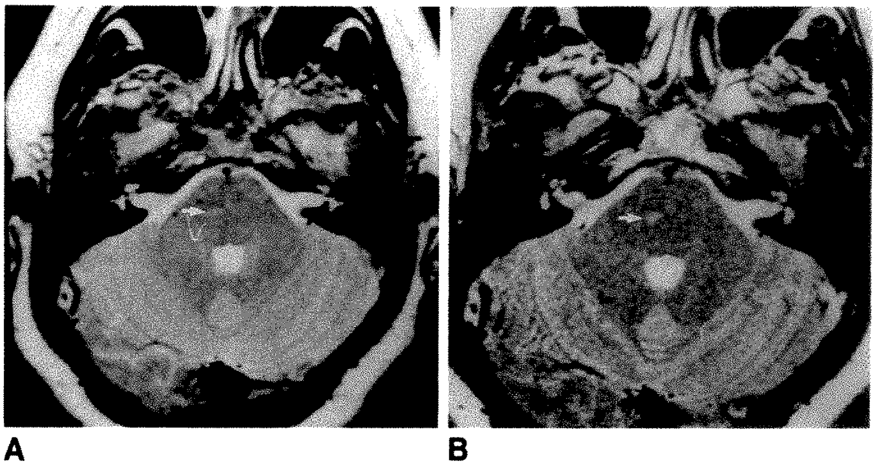

Fig. 6.—*A*, Axial FSE MR image of brainstem shows questionable lesion in right pons (*arrow*).

B, Corresponding high-resolution FSE MR image clearly shows right pontine lesion (*arrow*). Increased noise is due to use of only four acquisitions. Right pontine infarct was suspected clinically.

increased SNR. With a shorter TR (e.g., 3000 msec), images tended to have a "noisy" appearance owing to lower SNR. The use of a 256 × 256 matrix has also provided significant improvement in image quality with only a small time penalty.

We have found the uniformly bright appearance of fat on all FSE sequences (T1-, proton density–, and T2-weighted images) to be the most dramatic difference between conventional and FSE images of the spine. Although marrow may appear relatively dark in young patients with hematopoietic (red) marrow, the marrow often appears remarkably bright in older patients with fatty (yellow) marrow, even on heavily T2-weighted images. As might be expected, this appearance on T1-weighted images can be quite useful in the case of marrow metastases, since most lesions appear dark on this sequence. These dark lesions are, therefore, highly conspicuous against a background of bright marrow (Fig. 7A). Given the generally brighter appearance of fat on T1-weighted FSE sequences, metastatic lesions often appear more conspicuous than on T1-weighted CSE sequences owing to the higher contrast between the low-intensity lesions and the very bright marrow background.

On T2-weighted images, however, bright fat may pose a disadvantage in the evaluation of both marrow disease and degenerative disease. Metastatic lesions (usually bright on T2-weighted images) are often poorly seen against the background of bright fatty marrow. In the case of degenerative spine disease in an older patient with bright (fatty) marrow, the posterior vertebral margins (including osteophytes) are poorly seen adjacent to the bright CSF. Fat suppression imaging performed with a frequency-selective pulse (250-Hz bandwidth) and gradient dephasing (chemical-shift selective saturation, CHESS) has proved most helpful in rendering marrow dark on T2-weighted FSE images, and can be performed without time or slice penalty. Although the more superficial fat adjacent to the coil remains bright, the deeper structures including fatty vertebral marrow spaces appear dark. Posterior osteophytes are now clearly seen, and high-signal marrow metastases are easily identified (Fig. 7B).

The short TI inversion-recovery (STIR) FSE sequence has also been a useful adjunct for spine imaging. The STIR FSE sequence places a 180° inversion pulse 100 msec before the T2-weighted FSE sequence, nulling the fat signal. Conventional STIR has proved useful in many clinical settings [18–21], although long scanning times and motion artifact have hindered widespread use. With STIR FSE, we have obtained excellent images in 2 min 30 sec (16-echo train length, 3104/110/90 [TR/TI/TE], 256 × 192 matrix, four acquisitions, 4-mm/0.5-mm slice/gap, seven slice locations).

Because T1 and T2 contrast are additive with STIR imaging, lesion conspicuity is often enhanced. Fat suppression is more complete when using STIR FSE than when using T2-weighted FSE with CHESS. However, our early experience has demonstrated nearly identical contrast-to-noise ratios for the two techniques when measuring the signal intensities of metastatic lesions, normal adjacent marrow, and noise posterior to the spine (Fig. 7C). In general, we have not found a significant difference in lesion conspicuity when using STIR FSE and T2-weighted FSE with CHESS pulse fat saturation. Lesions often appear slightly brighter on the T2-weighted images, probably owing to greater overall signal, but marrow often appears darker on STIR FSE, and background noise is slightly reduced. STIR FSE is more prone to artifact, especially motion and flow-related artifact, and overall image quality appears slightly inferior to that on T2-weighted FSE images. The use of aliasing-suppression software with STIR FSE is essential. Gradient-moment nulling, although not yet available, should improve image quality significantly. For T2-weighted images, however, we have not encountered significant flow-related artifact, even though gradient-moment nulling has not yet been implemented. Intrinsic cord lesions are very well seen on T2-weighted FSE, perhaps in part owing to the use of a relatively long TR (4000 msec). Intrinsic cord tumors, syringomyelia, demyelination, cord infarction, and cord compression (Fig. 8) have all been well shown with this sequence. Degenerative disk disease, including disk herniation, also is well seen on FSE (Fig. 9). For reasons that are not entirely clear, FSE appears to be quite sensitive to changes associated with degenerative disk disease. Although normal disks appear appropriately bright, even mild degenerative changes may render disk material quite dark on FSE.

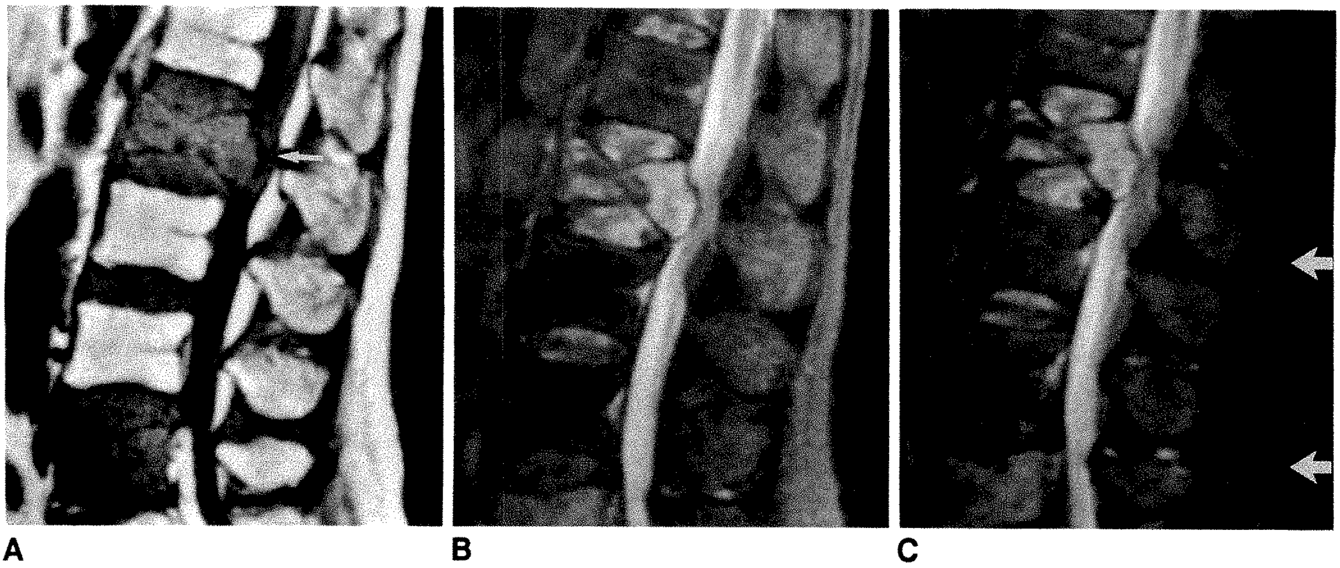

Fig. 7.—*A*, T1-weighted FSE MR image of spine (600/12, 256 × 256 matrix, four acquisitions, 2:37 min) shows dark vertebral metastases with retropulsion at L2 level (*arrow*). Normal vertebral marrow appears very bright.

B, T2-weighted FSE MR image with CHESS fat suppression (3000/102, 256 × 256, four acquisitions, 3:15 min) shows increased signal in corresponding metastases.

C, STIR FSE MR image (4105/90, 256 × 192, four acquisitions, 3:18 min) shows similar findings. Overall image quality appears slightly inferior to T2-weighted study, but fat suppression is more complete (*arrows*).

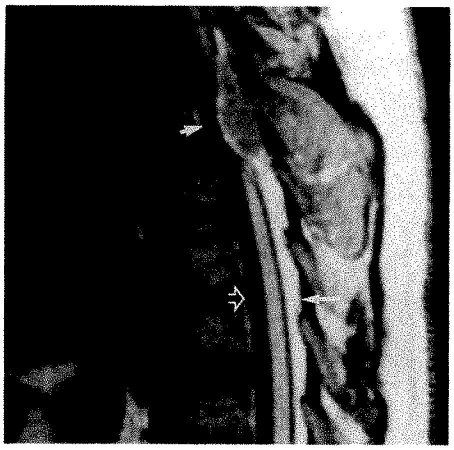

8

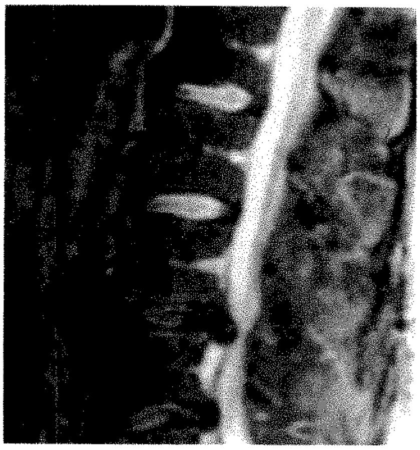

9

Fig. 8.—T2-weighted FSE MR image of thoracic spine (3000/102) without fat suppression shows cord compression from metastatic embryonal cell carcinoma (*short solid arrow*). CSF is outlined by dark spinal cord anteriorly (*open arrow*) and bright fat posteriorly (*long solid arrow*). Marrow remains dark despite lack of fat suppression owing to young age of this patient (23 years).

Fig. 9.—T2-weighted FSE MR image of lumbar spine (4000/102) with CHESS fat suppression shows disk herniations at L4–L5 and L5–S1. Herniated or otherwise degenerative disks often appear quite dark on FSE images, as in this case.

We have not found this to be a problem, although conceivably some difficulty may be encountered in differentiating herniated disk material from a posterior osteophyte.

To obtain high-definition brain or axial spine images, we have used a novel three-dimensional (3D) multislab volume technique that allows for oblique slab prescription [8]. Excellent image quality with less than 2-mm slice thickness has been obtained with this technique (Fig. 10). Although the technique is still under investigation, early results are promising. Three-dimensional FSE poses a theoretical advantage over 3D gradient-echo techniques in that magnetic susceptibility effects are reduced. In a recent study, axial gradient-echo 3D sequences overestimated neuroforaminal stenosis in spine images owing to increased magnetic susceptibility effects [22]. In addition, the degree of overestimation was increased with motion, whereas motion artifact is generally reduced with FSE techniques. It is unclear whether the reduction of magnetic susceptibility effects will have a significant effect on the conspicuity or appearance of vertebral osteophytes, although posterior osteophytes (dark on routine fat-suppressed images) appear quite conspicuous adjacent to the bright posterior CSF. The addition of a phased-array spine coil has afforded high-resolution imaging of the entire cord in less than 4 min (Fig. 11).

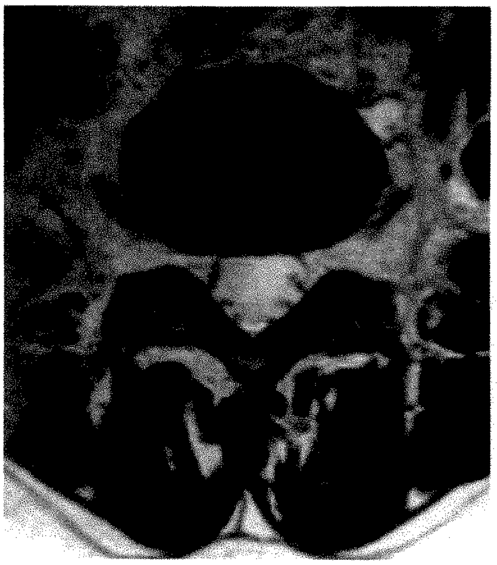

10

Fig. 10.—3D FSE axial MR image of lumbar spine (2500/110), 1.8 mm in thickness. Individual nerve roots are seen adjacent to bright CSF. Aliasing artifact is seen laterally.

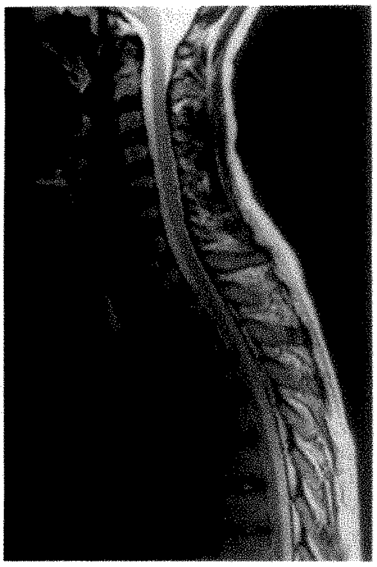

11

Fig. 11.—T2-weighted FSE MR image of spine (3000/90) was obtained in 3:19 min with 512 × 512 matrix and phased-array coil. Posterior fat is bright owing to lack of fat suppression.

Conclusions

FSE is a promising technique for the rapid acquisition of images with true spin-echo contrast features. Depending on the desired protocol, FSE images may be obtained approximately three to 16 times faster than CSE images. Advantages aside from the rapid imaging include decreased motion artifact; decreased magnetic susceptibility effects when imaging metallic objects, skull base, or neuroforamina; and versatility. Disadvantages include reduced magnetic susceptibility effects in hemorrhagic lesions and the bright appearance of fat on T2-weighted images, although this latter problem may be easily overcome by using fat suppression. This may be accomplished by using CHESS pulse fat saturation, or by using STIR FSE, with the additional benefit of additive T1 and T2 contrast. STIR FSE spine images, however, appear more prone to motion and flow-related artifact.

For routine brain imaging in the adult patient, we obtain dual-echo FSE images with the following protocol: 2500/18,90, one acquisition, 256 × 192 matrix, 5-mm/0-mm slice/gap, 28 slice locations, and eight-echo train length (4 min 12 sec). For routine spine images, we obtain sagittal T1-weighted FSE images (600/12, four acquisitions, 256 × 192 matrix, 4-mm/0.5-mm slice/gap, four-echo train length, 10 slice locations in 1 min 59 sec). These are supplemented with sagittal T2-weighted FSE images (4000/102, four acquisitions, 256 × 192 matrix, 4-mm/0.5-mm slice/gap, 16-echo train length, 14 slice locations in 3 min 16 sec). Axial FSE T1-weighted or proton density–weighted images also may be obtained. We perform CHESS fat suppression on all T2-weighted spine sequences, including suspected metastases (dark marrow vs bright lesion) and degenerative disk disease (improved conspicuity of posterior osteophytes).

Rapid imaging is possible with longer echo trains or by acquiring single-contrast (e.g., T2-weighted) images. High-resolution images of specific anatomic regions of interest may be obtained by using a small FOV (8–16 cm), multiple acquisitions (four to 12), smaller matrix size, or thin slice profiles (1–3 mm). Three-dimensional imaging is now feasible without the disadvantages of gradient-echo imaging. Applications in both brain and spine include image reconstruction and manipulation for surgical planning, and detailed evaluation of focal regions of disease or anatomic structures such as specific cranial nerves.

Further refinements in both hardware and software should provide improvements in FSE techniques, and many applications, including rapid spectroscopic imaging [23], remain to be explored. Reductions in interecho interval should be possible, reducing artifact and permitting the collection of longer useful echo trains, although at the expense of increased bandwidth and reduced SNR.

At our institutions, replacement of CSE sequences with FSE has significantly reduced the patient's waiting time for elective MR examination. While further refinements are clearly to be expected, FSE is already a practical alternative to CSE imaging, providing nearly identical lesion conspicuity with far greater versatility. Controlled clinical trials should provide more information about the potential usefulness of this technique and also should determine if more subtle differences are seen in lesion conspicuity that have not as yet been appreciated.

ACKNOWLEDGMENTS

We thank Gordon Sze, Todd Constable, and Robert Smith for providing us with the inversion-recovery FSE sequence used for the FSE STIR studies described herein.

REFERENCES

1. Hennig J, Naureth A, Friedburg H. RARE imaging: a fast imaging method for clinical MR. *Magn Reson Med* **1986**;3:823–833

2. Hennig J, Friedburg H, Strobel B. Rapid non-tomographic approach to MR myelography without contrast agents. *J Comput Assist Tomogr* **1986**;10:375–378
3. Hennig J, Friedburg H, Ott D. Fast three dimensional imaging of cerebrospinal fluid. *Magn Reson Med* **1987**;5:380–383
4. Hennig J, Friedburg H. Clinical applications and methodological developments of the RARE technique. *Magn Reson Imaging* **1988**;6:391–395
5. Meiboom S, Gill D. Modified spin-echo method for measuring nuclear relaxation times. *Rev Sci Instrum* **1958**;29:688–691
6. Mulkern RV, Wong STS, Winalski C, Jolesz FA. Contrast manipulation and artifact assessment of 2D and 3D RARE sequences. *Magn Reson Imaging* **1990**;8:557–566
7. Melki PS, Mulkern RV, Panych LP, Jolesz FA. Comparing the FAISE method with conventional dual echo sequences. *J Magn Reson Imaging* **1991**;1:319–326
8. Oshio K, Jolesz FA, Melki PS, Mulkern RV. T2 weighted thin slice imaging with multi-slab 3D RARE. *J Magn Reson Imaging* **1991**;1:695–700
9. Ahn SS, Mantello MT, Jones KM, et al. Rapid MR imaging of pediatric brain using fast spin-echo technique. *AJNR* (in press)
10. Jones KM, Mulkern RV, Mantello MT, et al. Evaluation of brain hemorrhage: comparison of fast spin-echo and conventional dual spin-echo images. *Radiology* **1992**;182:53–58
11. Allerhand A. Analysis of Carr-Purcell spin-echo NMR experiments on multiple spin-systems. I. The effect of homonuclear coupling. *J Chem Phys* **1966**;44:1–9
12. Hinks RS, Henkelman RM. Problems with organic materials for magnetic resonance imaging phantoms. *Med Phys* **1988**;15:61–63
13. Bendell P. Spin-echo attenuation by diffusion in non-uniform field gradients. *J Magn Reson* **1990**;86:509–515
14. Gomori JM, Grossman RJ, Yu-Ip C, Asakura T. NMR relaxation times of blood: dependence on field strength, oxidation state, and cell integrity. *J Comput Assist Tomogr* **1987**;11:684–690
15. Tweig DB. The k-space trajectory formulation of the NMR imaging process with applications in analysis and synthesis of imaging methods. *Med Phys* **1983**;10:610–621
16. Mulkern RV, Melki PS, Jakab P, Higuchi N, Jolesz FA. Phase-encode order and its effect on contrast and artifact in single-shot RARE sequences. *Med Phys* **1991**;18:1032–1037
17. Melki PS, Jolesz FA, Mulkern RV. Partial RF echo planar imaging with the FAISE method: I. Experimental and theoretical assessment of artifact. *Magn Reson Med* (in press)
18. Unger EC, Moldofsky P, Hartz WK, Clair M, Silver M, McGlone J. MR imaging of bone marrow disease using STIR. *Radiology* **1987**;165 (P):274
19. Shuman WP, Patten RM, Baron RL, Liddell RM, Conrad EU, Richardson ML. Comparison of STIR and spin-echo imaging at 1.5T in 45 suspected extremity tumors: lesion conspicuity and extent. *Radiology* **1991**;179:247–252
20. Shuman WP, Baron RL, Peters MJ, Tazioli PK. Comparison of STIR and spin-echo MR imaging at 1.5 T in 90 lesions of the chest, liver, and pelvis. *AJR* **1989**;152:853–859
21. Jones KM, Unger EC, Granstrom P, Seeger JF, Carmody RF, Yoshino M. Bone marrow imaging using STIR at 0.5T and 1.5T. *Magn Reson Imaging* (in press)
22. Tsuruda JS, Remley K. Effects of magnetic susceptibility artifacts and motion in evaluating the cervical neural foramina on 3DFT gradient-echo MR imaging. *AJNR* **1991**;12:237–241
23. Mulkern RV, Melki PS, Lilly HS, Hoffer FA. 1D Spectroscopic imaging with RF echo planar (SIRFEN) methods. *Magn Reson Imaging* **1991**;9:909–916

Erratum

In the article "MR Imaging of the Stellate Ganglion: Normal Appearance," by Hogan and Erickson (*AJR* **1992**;158:655–659) an error was made in captioning several of the figures. The legends to Figures 6, 7, and 8 are transposed with those to Figures 11, 12, and 13. *AJR* and Waverly Press apologize for this error.

Fractures of the Nasolacrimal Fossa and Canal: A CT Study of Appearance, Associated Injuries, and Significance in 25 Patients

June M. Unger[1]

The bony nasolacrimal fossa and canal, which protect the more distal excretory portion of the lacrimal apparatus, the nasolacrimal sac and duct, are contained within the medial portion of the orbit and lateral aspect of the nose, sites that are commonly injured in facial trauma. The CT scans of 25 patients who sustained fractures of the nasolacrimal fossa and/or canal as a result of motor vehicle accidents were reviewed to determine the appearance of the fractures and to determine types of facial fractures also present. The patients' clinical records were reviewed to determine the frequency of associated complications. Thirty-six fractures of the nasolacrimal fossa and canal were found in the 25 patients. In 20 patients these were associated with complex fractures of the midportion of the face; the other five patients had simple unilateral facial fractures. Three kinds of nasolacrimal fractures were identified: avulsion of the fossa, comminution of the fossa or canal, and linear fractures of the canal. Of the 19 fractures involving the nasolacrimal fossa, 15 consisted of an avulsed fragment of bone containing the nasolacrimal sac and four had comminution of the nasolacrimal fossa. The majority of the fractures of the nasolacrimal canal (15 patients) were comminuted.

Our results show that nasolacrimal fractures occur in association with simple unilateral facial fractures and with more complex fractures of the midface and that the fractures follow certain patterns. Complications related to injury to the nasolacrimal sac and duct were documented in five patients. Although this number is significant, it is fewer than we expected, considering the severity of the injuries.

***AJR* 158:1321–1324, June 1992**

Before the availability of thin-section CT, fractures of the nasolacrimal fossa and nasolacrimal canal could not be detected with any degree of accuracy. As a result, the presence of these fractures usually was unsuspected clinically until complications associated with nasolacrimal duct obstruction, such as epiphora, dacryocystitis, or lacrimal mucocele, developed.

It is our impression that, although CT examination of the facial bones is commonly performed in patients with severe facial fractures, nasolacrimal duct and canal fractures may occasionally be overshadowed by more profound facial injuries. Accordingly, we reviewed the CT scans of 25 patients with these fractures to determine the CT findings and the prevalence of associated fractures. We then reviewed the patients' clinical records to establish the frequency of complications related to ductal obstruction.

Materials and Methods

Twenty-five patients with evidence of nasolacrimal fractures on CT scans were identified from a review of patients who had incurred facial bone fractures during motor vehicle accidents and survived. The group included 19 men and six women 17–74 years old (mean age, 30).

All patients had thin-section (2–3 mm) axial CT scans of the facial bones done on one of three CT scanners (Siemens DR3 or DRH, Erlangen, Germany, or GE 9800 Advantage 2, General Electric Medical Systems, Milwaukee, WI). The diagnosis of nasolacrimal fossa or

Received November 22, 1991; accepted after revision February 3, 1992.

[1] Department of Radiology, University of Wisconsin–Madison, Medical School, E3/311 Clinical Science Center, 600 Highland Ave., Madison, WI 53792. Address reprint requests to J. M. Unger.

0361–803X/92/1586–1321

© American Roentgen Ray Society

canal fracture was established at the time of the original interpretation in some of the patients; in others, these fractures were not initially distinguished from other facial fractures.

To determine the significance of the nasolacrimal fractures in these patients, we reviewed hospital and outpatient charts. Clinical evidence of lacrimal duct obstruction, particularly epiphora, was accepted as an indication of injury of the nasolacrimal sac or duct.

Results

Thirty-six fractures of the nasolacrimal fossa and/or nasolacrimal canal, 11 of which were bilateral, were identified in 25 patients. Of the 36 fractures, 19 involved fractures of the nasolacrimal fossa and 17 of the nasolacrimal canal. Seven fractures primarily involved the nasolacrimal fossa, while 17 were limited to the nasolacrimal canal; the remaining 12 occurred as unilateral or bilateral combined fractures of both the fossa and canal in seven patients.

Three types of fractures were identified: the avulsed fragment, comminuted fractures, and linear fractures. The avulsed fragment was created by fractures through the lacrimal bone and frontal process of the maxilla that effectively separated the major portion of the bone of the nasolacrimal from adjacent osseous structures while leaving the groove for the nasolacrimal sac intact (Fig. 1). The comminuted fractures involved either the walls of the nasolacrimal fossa or canal, but the linear fractures involved only the nasolacrimal canal (Figs. 2–5).

The predominant type of fracture of the nasolacrimal fossa was the avulsed fragment, which occurred in 15 of the 19 nasolacrimal fossa fractures. Of the 17 fractures involving the nasolacrimal canal, 15 were comminuted and two were linear. Five patients had bilateral nasolacrimal fractures among seven patients who had fractures that involved both the fossa and canal.

All nasolacrimal fractures were associated with other facial fractures. Most of the associated fractures (20) were of the complex midfacial type; the 11 patients who had bilateral nasolacrimal fractures were in this group. The nasolacrimal fractures in five patients with unilateral facial fractures all occurred on the ipsilateral side.

Review of the patients' charts documented unilateral nasolacrimal duct complications in five patients, two of whom had bilateral nasolacrimal fossa/canal fractures. Three of

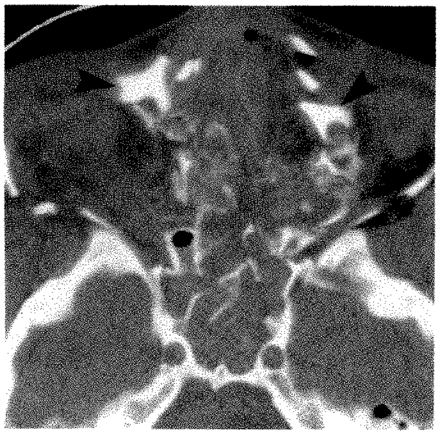

Fig. 1.—Axial CT scan of panfacial fracture shows marked comminution with bilateral avulsed nasolacrimal fossa fragments (*arrowheads*). Fossa margins are intact.

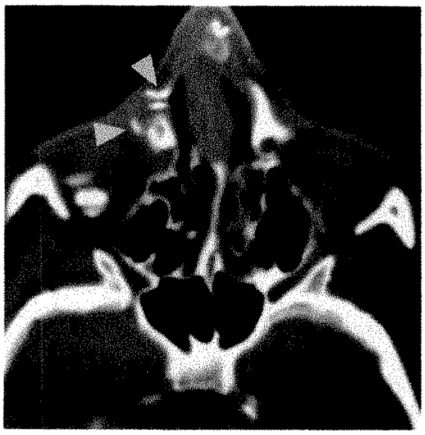

Fig. 2.—Axial CT scan of Le Fort II fracture shows comminution of walls of right nasolacrimal fossa (*arrowheads*). Left side is intact.

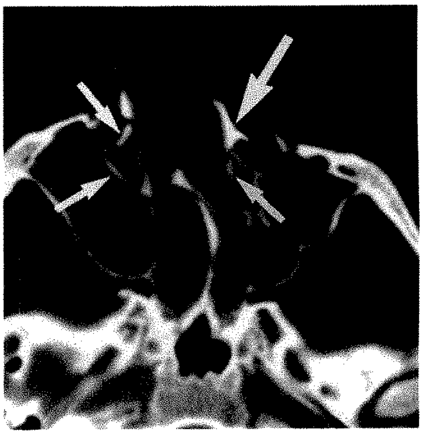

Fig. 3.—Axial CT scan of nasoethmoidal fracture shows bilateral comminuted fractures of nasolacrimal canals (*small arrows*). Avulsed fragment containing nasolacrimal fossa is indicated on left (*large arrow*).

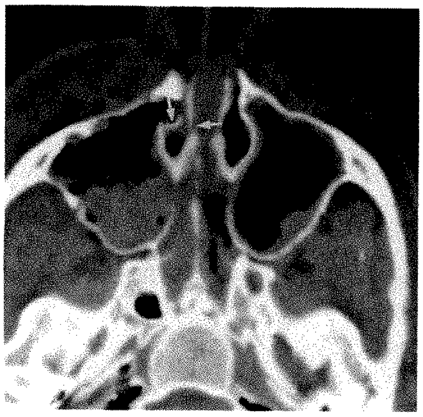

4

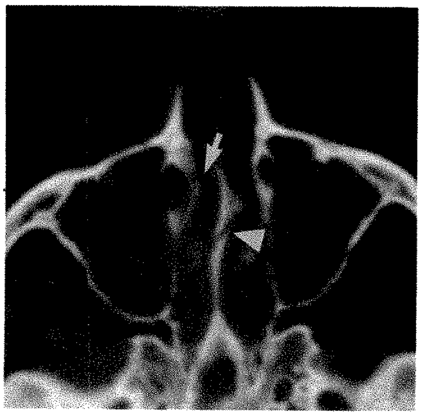

5

Fig. 4.—Axial CT scan of right tripod fracture shows comminuted fracture of right nasolacrimal canal (*arrows*).

Fig. 5.—Axial CT scan of nasal septal fracture (*arrowhead*) shows undisplaced linear fracture involving medial wall of right nasolacrimal canal (*arrow*). Patient was severely brain damaged in a motor vehicle accident and was thought to have acquired these fractures while extubating himself.

these patients had Le Fort II, III, or combined II–III fractures; one had a panfacial fracture; and the fifth patient had a unilateral fracture of the maxillary sinus and nasal septum. All five patients had epiphora, which, as an isolated finding, is also consistent with obstruction of the lacrimal canaliculi. Although mucopurulent fluid was expressed from the lacrimal sac of one of these patients during a follow-up visit, no clinical evidence of lacrimal sac or duct infection in the other four was found. None of the patients developed a lacrimal sac mucocele. Three patients were treated with dacryocystorhinostomy and one was managed conservatively; the ultimate management of the last patient was not indicated in the chart.

Discussion

The intraosseous portion of the lacrimal excretory system, the nasolacrimal fossa and canal, begins in the medial wall of the orbit and terminates just beneath the inferior turbinate [1–3] (Figs. 6 and 7). The orbital depression for the nasolacrimal

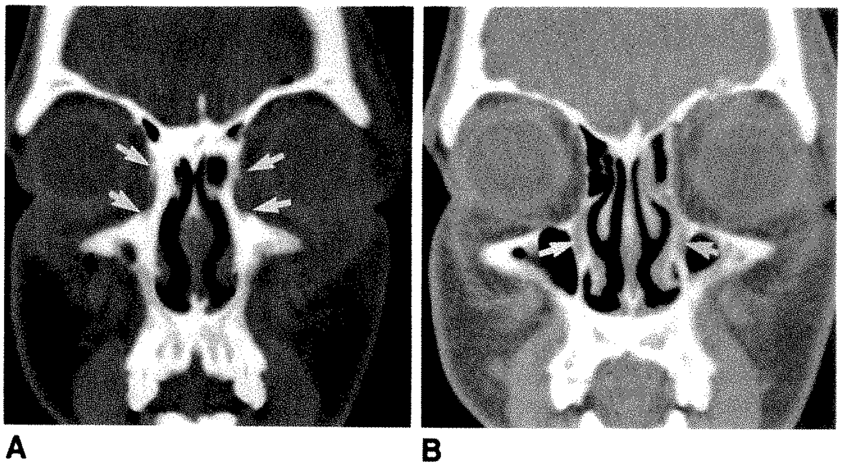

Fig. 6.—*A* and *B*, Coronal CT scans of normal nasolacrimal fossae (between *arrows*, *A*) and canals (upper portions, *arrows*, *B*). Entire canal is not visible because of normal 5° anteroposterior inclination of canal in craniocaudal direction.

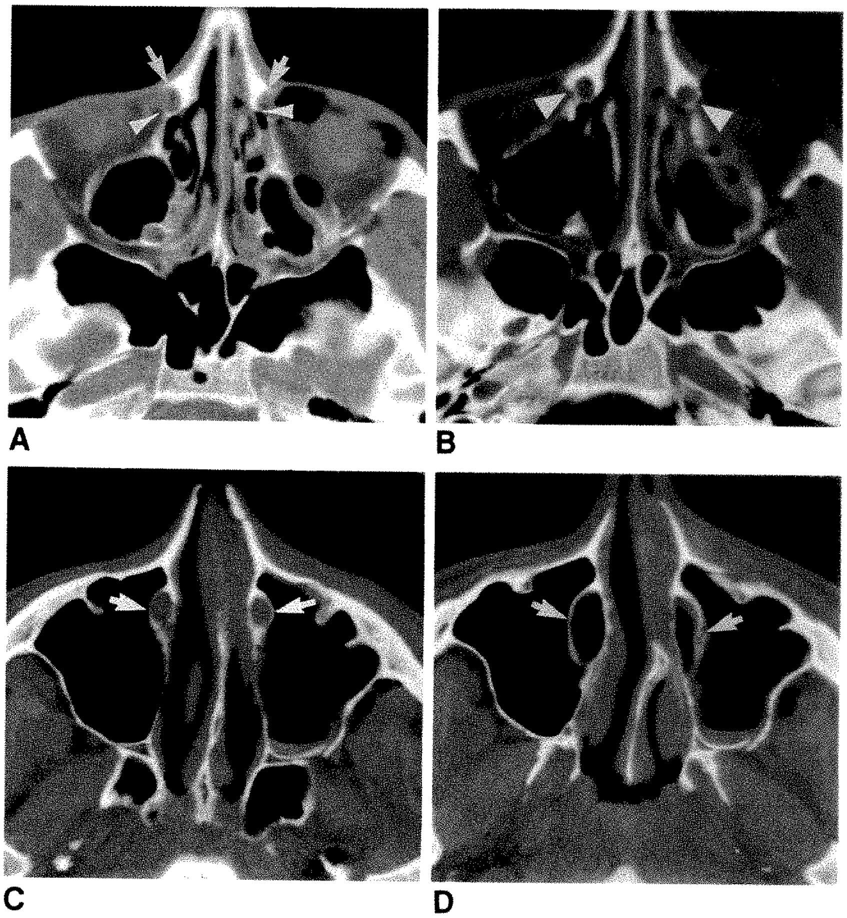

Fig. 7.—Axial CT scans show normal nasolacrimal fossae and canals.

A, Nasolacrimal fossa (compare with Fig. 1). Lacrimal crest of frontal process of maxilla (*arrows*); lacrimal crest of lacrimal bone (*arrowheads*).

B, Most superior aspect of nasolacrimal canals (*arrowheads*).

C, Midportion of nasolacrimal canals (*arrows*).

D, Level of inferior orifice of nasolacrimal canal (*arrows*). Normal admixture of air and secretions in ducts is seen in parts *B* and *D*.

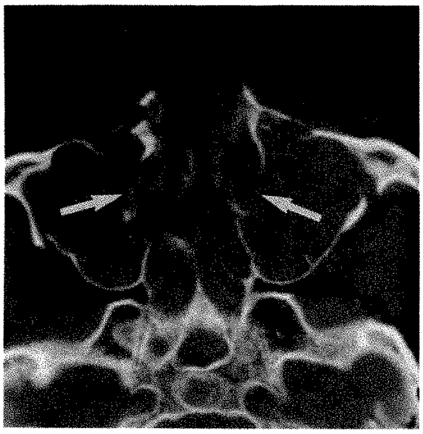

Fig. 8.—Axial CT scan of Le Fort III fracture shows marked comminution of thin walls of distal nasolacrimal canals (*arrows*).

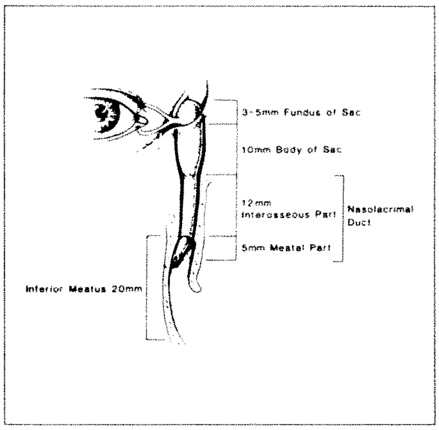

Fig. 9.—Drawing of lacrimal drainage apparatus. (Reprinted with permission from Russell et al. [1].)

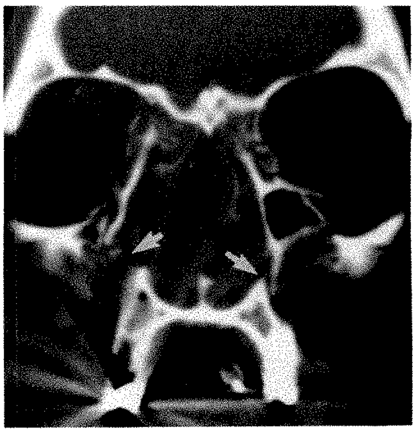

Fig. 10.—Coronal CT scan shows panfacial fracture with marked comminution of nasolacrimal canals bilaterally (*arrows*). No subsequent clinical evidence of nasolacrimal duct obstruction was found.

fossa is formed anteriorly by the lacrimal crest of the frontal process of the maxilla, and posteriorly by the lacrimal crest of the lacrimal bone. The nasolacrimal fossa, therefore, consists of relatively strong bone that maintains its integrity as an avulsed fragment when traumatically separated from the more fragile components of the adjacent orbital and nasal bones.

The nasolacrimal canal is also formed superiorly by the lacrimal bone and maxilla, but continues inferiorly within the thinner bone of the nasal surface of the maxilla. Comminution of the walls appears to be the most common type of nasolacrimal canal fracture, with the degree of comminution occasionally increasing as the canal wall becomes thinner inferiorly, and the canal sometimes appearing shattered close to its termination beneath the inferior nasal concha (Fig. 8).

The membranous lacrimal sac, which is contained within the lacrimal fossa, consists of a fundus and body. It receives the secretions from the lacrimal gland via the lacrimal canaliculi that begin within the lid margins. The major portion of the connecting nasolacrimal duct is contained within the nasolacrimal canal (Fig. 9).

Complications resulting from injury to the nasolacrimal sac and duct were present in only five patients. Although this finding is significant, it is less common than we expected before we reviewed the charts, especially given the degree of displacement and comminution of fragments present in many of the fractures (Fig. 10). Because the length of the follow-up varied, however, complications that were not documented may have eventually developed in some patients. Open reduction and internal fixation of orbital fractures were performed in only one of these patients; therefore, it is unlikely that the lacrimal duct complications had any cause other than the primary injury in the remaining four patients [4].

Although injury to the nasolacrimal excretory system is an accepted feature of nasoethmoidal fractures [5, 6], it is not generally considered an important component of other facial fractures. In our patients, 10 were classified as having nasoethmoidal fractures (if one includes the panfacial injuries), but the remaining 15 had fractures that principally involved other portions of the midface; five of these fractures were simple rather than complex. It would therefore appear important to consider the possibility of damage to the nasolacrimal system when imaging anyone with a potentially serious central facial fracture.

In addition, the fracture patterns identified in this study may help to explain why dacryocystorhinostomy, a surgical procedure that bypasses obstruction at the level of the nasolacrimal duct, is so often successful in patients with lacrimal obstruction caused by facial fractures. Avulsion of the nasolacrimal fossa with preservation of the space within the fossa would tend to protect the lacrimal sac, even if the sac were dislodged or severed from its attachment to the nasolacrimal duct. Because the structure of the lacrimal sac is preserved, successful dacryocystorhinostomy is more likely.

REFERENCES

1. Russell EJ, Czervionke L, Huckman M, Daniels D, McLachlan D. CT of the inferomedial orbit and the lacrimal drainage apparatus: normal and pathologic anatomy. *AJR* **1985**;145:1147–1154
2. Gray H. *Anatomy of the human body*, 30th American ed., vol. 2. Philadelphia: Lea & Febiger, **1985**:1311–1312
3. Zinreich SJ, Kennedy DW, Rosenbaum AE, Gayler BW, Kumar AJ, Stammberger H. Paranasal sinuses: CT imaging requirements for endoscopic surgery. *Radiology* **1987**;163:769–775
4. Paskert JP, Manson PN, Iliff NT. Nasoethmoidal and orbital fractures. *Clin Plast Surg* **1988**;15:2:209–223
5. Hughes SM. Sequelae of orbital fractures. *Adv Ophthalmic Plast Reconstruct Surg* **1987**;6:313–341
6. Gruss JS, Hurwitz JJ, Nik NA, Kassel EE. The pattern and incidence of nasolacrimal injury in naso-orbital-ethmoid fractures: the role of delayed assessment and dacryocystorhinostomy. *Br J Plast Surg* **1985**;38:116–121

Neurosyphilis in HIV Carriers:
MR Findings in Six Patients

Robert D. Tien[1]
Alisa D. Gean-Marton[2]
Alexander S. Mark[3]

Neurosyphilis, a sexually transmitted disease that can cause neurologic damage, has become increasingly prevalent in the AIDS era. HIV carriers can contract neurosyphilis without the presence of other concurrent opportunistic infections. Because MR findings of neurosyphilis are seldom reported, we retrospectively reviewed and evaluated contrast-enhanced MR images of six young (average age, 33 years) HIV-positive men with high serum and CSF VDRL titers indicative of neurosyphilis. All six patients tested negative for concurrent opportunistic infections. Five patients had acute or subacute strokelike symptoms involving the basal ganglia or middle cerebral arteries; one had a parietal convexity mass mimicking meningioma with headache and ataxia. Contrast-enhanced MR images showed patchy enhancement involving the basal ganglia and middle cerebral artery territories in the first five patients and the convexity mass in the sixth patient. On the basis of brain biopsy, a convexity mass was diagnosed in the patient with syphilitic gumma. The imaging findings of the remaining five patients represented ischemic infarct caused by meningovascular syphilis. After penicillin treatment, serum and CSF VDRL titers decreased, and neurologic signs and symptoms improved in all six patients. A follow-up MR study in the patient with the gumma showed that the lesion resolved almost completely.

In young HIV patients with stroke symptoms or a convexity mass, neurosyphilis should be considered. Contrast-enhanced MR can reveal the extent of involvement by neurosyphilis and should be used to facilitate diagnosis and proper treatment.

***AJR* 158:1325–1328, June 1992**

Syphilis is one of the major sexually transmitted diseases and is caused by the spirochete *Treponema pallidum.* It is a chronic systemic infection with three well-characterized stages. If the disease is treated early, current methods can effectively eliminate late complications and can cure all but exceptional cases. Neurosyphilis can occur at any stage of the disease. Without treatment, 5–10% of persons with syphilis will have clinical CNS involvement.

The prevalence of infectious syphilis in the United States has risen rapidly during the AIDS era. In 1983, homosexual men accounted for 40–45% of all patients with syphilis. Between the last quarter of 1986 and the end of 1989, the incidence rose sharply in both men and women. The overall increase since 1985 is attributable to a dramatic rise in infections among AIDS patients and among people of low socioeconomic status. Neurosyphilis is difficult to diagnose because most patients with the disease are asymptomatic. Also, many physicians are unfamiliar with the presenting features of neurosyphilis because classic forms of the disease have changed since the advent of antibiotics. For these reasons, the radiologic features of the varied manifestations of neurosyphilis are important to recognize so that proper management can be instituted. We report the contrast-enhanced MR findings in six HIV-positive patients with neurosyphilis.

Received October 16, 1991; accepted after revision January 9, 1992.

[1] Department of Radiology, Duke University Medical Center, Box 3808, Durham, NC 27710. Address reprint requests to R. D. Tien.

[2] Department of Radiology, San Francisco General Hospital, San Francisco, CA 94110.

[3] Department of Radiology, Washington Hospital Center, Washington, DC 20010-2975.

0361-803X/92/1586-1325
© American Roentgen Ray Society

Materials and Methods

We retrospectively reviewed the MR findings in six young male HIV carriers with documented neurosyphilis (average age, 33 years) who were examined in our institutions from 1988 to 1991. All six tested negative for opportunistic organisms (e.g., toxoplasma, cryptococci, and mycobacteria) and for tumors (e.g., lymphomas). Five patients had motor deficits, such as hemiparesis and bilateral leg weakness, and one of them also had seizures. The sixth patient had headache and ataxia. In the first five patients, analysis of CSF and sera indicated neurosyphilis. In the sixth patient, the VDRL test was positive for serum but negative for CSF; an MR study at another hospital showed that the patient had a parietal convexity mass. The diagnosis of neurosyphilis in this patient was established when the results of the biopsy of this mass done in our institution were compatible with syphilitic gumma and after penicillin treatment, the patient's serum VDRL test became negative and the brain mass resolved. After penicillin treatment, follow-up examination in all six patients showed that the VDRL titers had decreased significantly and clinical neurologic signs and symptoms had improved.

MR studies in these patients were done on a 1.5-T superconducting magnet (Signa, General Electric, Milwaukee, WI). Both T1-weighted, 600–800/20/1 (TR/TE/excitations), and T2-weighted (2000–2800/30,80/1) images were obtained. Additional imaging parameters included 5-mm slice thickness, 2.5-mm interslice gap, 20-cm field view, and 256 × 192 matrix. After administration of gadopentetate dimeglumine (0.1 mmol/kg, Berlex), axial T1-weighted images were obtained in all patients. The patient with a convexity mass had a follow-up MR study, and three neuroradiologists carefully reviewed the MR images of all six patients and correlated imaging findings with clinical information.

Results

Five patients had motor deficits and stroke. Four of these five had subtle enhancing lesions in the bilateral basal ganglia corresponding to the vascular territories of the lenticulostriate arteries (Fig. 1). One patient had imaging evidence of an infarct with gyriform enhancement subacute in the left middle cerebral artery (Fig. 2). After contrast enhancement, all lesions generally corresponded well to the abnormal high-signal areas seen on the T2-weighted images. On the basis of clinical symptoms and signs, a vascular ischemic event caused by inflammatory neurosyphilitic vasculitis was diagnosed in these five patients. The sixth patient had headache, ataxia, and an enhancing dura-based mass in the right parietal lobe with a large amount of edema (Fig. 3). A biopsy was done on this mass, and syphilitic gumma was diagnosed. After penicillin treatment, a follow-up MR study showed that the mass had resolved completely.

Discussion

Neurosyphilis develops in one third of the patients who progress to late stages of syphilis. The CNS may be involved at almost any stage of the disease; it may occur from weeks to decades after the initial infection. Neurosyphilis may result from small-vessel endarteritis of the meninges, brain, and spinal cord with gradual degeneration of nerve tissue [1], or it may develop after HIV-induced cell-mediated immunodeficiency adversely affects the course of primary syphilis.

Symptomatic cases of neurosyphilis can be divided into four types on the basis of predominant clinical findings: meningeal, vascular, general paresis, and tabes dorsalis. Although various combinations of these types are not uncommon [1], neurosyphilis most commonly takes the meningeal or vascular form. Meningeal neurosyphilis generally has the clinical features of any acute meningitis, including cranial neuritis, hydrocephalus, and formation of focal leptomeningeal granulomas (gummas) of various sizes. Vascular neurosyphilis is usually characterized by headache and transient hemiparesis followed by an acute or subacute vascular event [2] and abnormal CSF findings.

In all six patients in this study, acute or subacute neurologic deficits were directly correlated with the areas of involvement by neurosyphilis. In five patients, MR imaging of the brain showed abnormally high signals on T2-weighted images in the basal ganglia regions (Figs. 1A and 2A). Contrast-enhanced MR images showed patchy enhancement in the basal ganglia in four patients (Fig. 1B) and gyriform enhancement

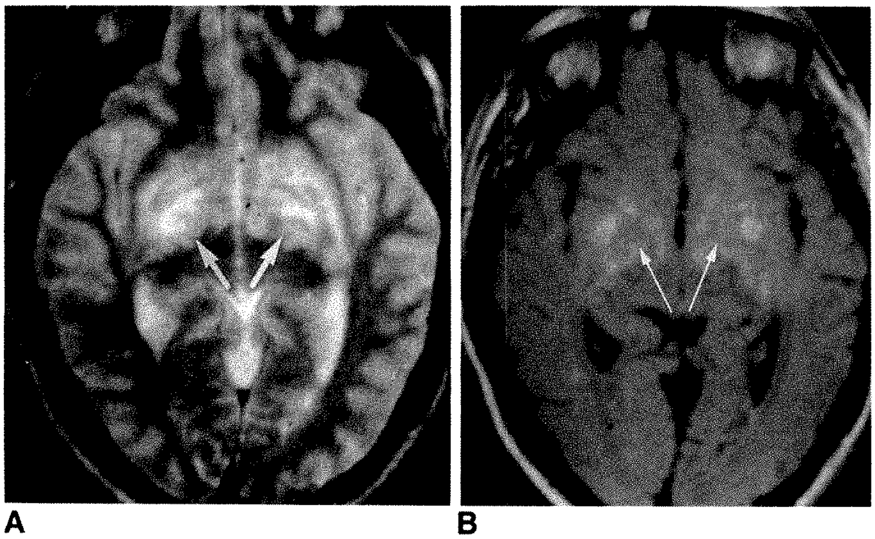

Fig. 1.—42-year-old HIV-positive man with weakness of both legs and dizziness.

A, Axial T2-weighted MR image (2500/80/1) shows abnormal high signal in bilateral basal ganglia and thalamic region (*arrows*).

B, Axial T1-weighted enhanced MR image (600/20/1) at same level as *A* shows bilateral patchy enhancement in same region (*arrows*).

Diagnosis of neurosyphilis was based on positive CSF VDRL test of 1:16; serum VDRL test of 1:256; reactive fluorescent treponemal antibody absorption test; and negative tests for opportunistic organisms such as mycobacteria, toxoplasma, and cryptococci. CSF VDRL titer decreased after penicillin treatment.

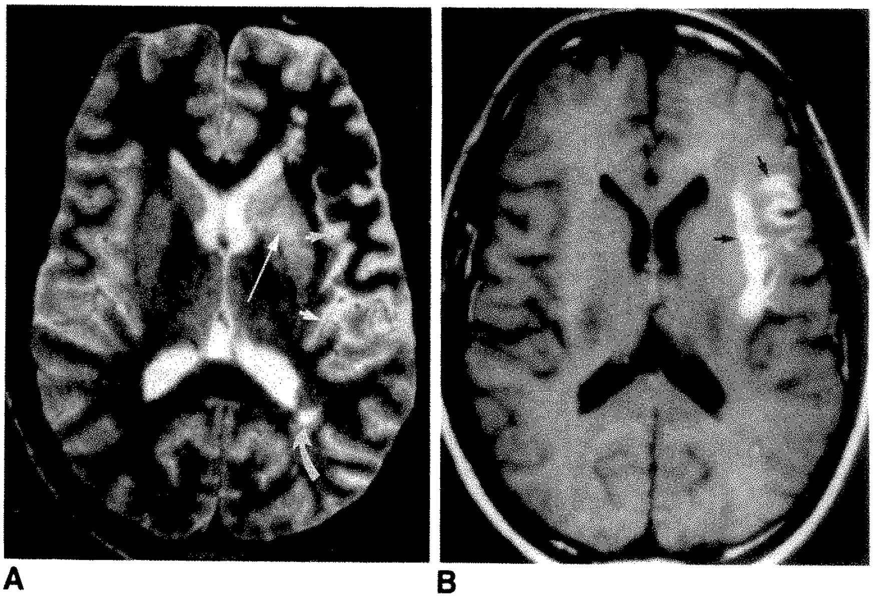

Fig. 2.—32-year-old HIV-positive man with subacute right hemiplegia and expressive aphasia.

A, Axial T2-weighted MR image (2500/80/1) shows abnormally increased signal in left basal ganglia (*long straight arrow*), insular cortex (*short straight arrows*), and white matter near left trigone (*curved arrow*).

B, Axial contrast-enhanced T1-weighted MR image (600/20/1) at same level as *A* shows abnormal gyriform enhancement at left insular and frontal opercular region (*arrows*).

Diagnosis of neurosyphilis was based on positive CSF VDRL test of 1:8; CSF VDRL titer decreased after penicillin treatment, and tests for other opportunistic organisms were negative.

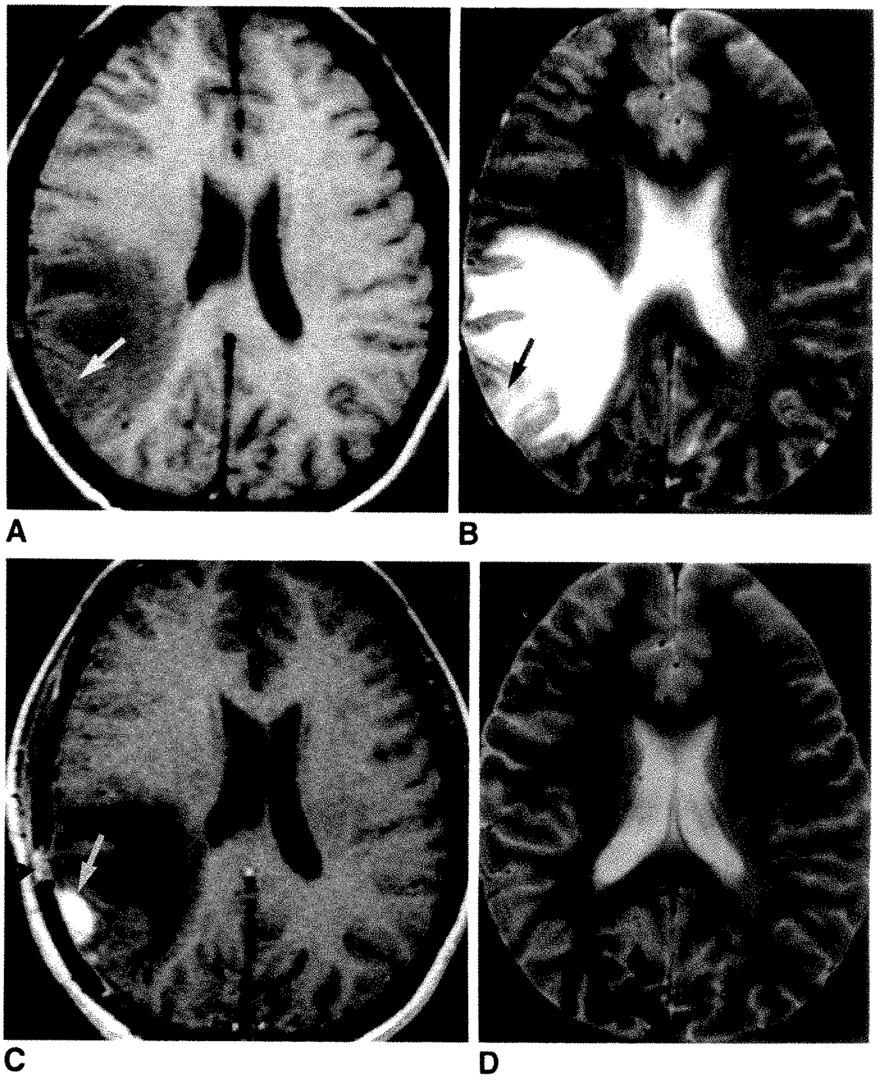

Fig. 3.—22-year-old HIV-positive man with headache and ataxia for several months.

A and *B*, Axial T1-weighted MR images, 800/200/1 (*A*) and 2500/80/1 (*B*), show dura-based mass (*arrows*) that is isointense with gray tissue on T1-weighted image and hyperintense on T2-weighted image with large amount of edema.

C, Contrast-enhanced T1-weighted MR image shows mass is intensely enhanced (*arrow*). Craniotomy defect from prior biopsy can be seen (*arrowhead*).

D, Follow-up enhanced T2-weighted MR image after penicillin therapy shows complete resolution of mass and edema.

Diagnosis of neurosyphilis was based on positive serum VDRL test of 1:64, biopsy result of convexity mass (syphilitic gumma), decreased VDRL titers, and resolution of gumma after penicillin treatment. Tests for various opportunistic organisms were negative.

in the temporal lobe in one patient (Fig. 2B). These MR findings suggest breakdown of blood-brain barriers in the basal ganglia and luxury perfusion in the temporal lobe, and most likely represent infarction caused by neurosyphilis-induced vasculitis.

Few reports of angiographic findings of vascular neurosyphilis include segmental constriction and occlusion of the supraclinoid carotid artery [2, 3]. In these large arteries, the stenoses may be concentric or asymmetric, occasionally resulting in a beaded appearance. In the smaller arteries, particularly the sylvian branches of the middle cerebral artery, focal stenoses and aneurysmal dilatation may be shown [2, 3]. Multiple syphilis-induced infarcts can occur throughout the brain [2]. The only report that included unenhanced MR findings described one case of basal ganglia infarct [2]. Our experience supports the idea that the infarcts in these patients are mostly in the basal ganglia and middle cerebral artery territory.

One of six patients in our study had a dura-based enhancing mass with significant peritumoral edema. When a biopsy was done, this mass was diagnosed as syphilitic gumma, which resolved after penicillin treatment. Although syphilitic gummas usually enhance on CT, angiography provides nonspecific findings [4], and surrounding edema is common. Similarly, one MR study found only nonspecific characteristics (isointense on T1-weighted images and hyperintense on T2-weighted images [5]). For these reasons, it can be quite difficult to distinguish syphilitic gumma from other cerebral tumors. However, other dura-based tumors such as meningioma or metastasis are statistically less likely to occur in young men. Another possibility is CNS lymphoma, which tends to occur in HIV carriers, but lymphomas are usually located in the periventricular regions. Generally, CNS gummas resolve rapidly after proper treatment with penicillin.

Syphilis also can induce cranial neuritis, particularly in the second (optic) and eighth cranial nerves. Especially with fat-suppression techniques, contrast-enhanced MR imaging has demonstrated its usefulness in detecting optic neuritis and perineuritis. Contrast-enhanced MR can show syphilitic cochlear vestibulitis also [6]. Recent recognition of aggressive forms of syphilis such as optic nerve gumma and syphilitic orbital periostitis in HIV-seropositive patients warrants renewed emphasis on considering ocular syphilis and neurosyphilis in the differential diagnosis [7, 8].

Laboratory diagnosis of neurosyphilis is typically based on a positive serum fluorescent treponemal antibody absorption test, CSF pleocytosis, elevated protein levels, or a positive VDRL test. A positive CSF VDRL test is highly specific for active neurosyphilis, but the test is negative in about half of neurosyphilis patients. The serum VDRL test reportedly is negative in one third to one half of all cases [1, 9, 10]. An increase in levels of lymphocytes and immunoglobulin in the CSF supports a diagnosis of neurosyphilis, but these findings are nonspecific. Caution should be exercised because the difficulty of diagnosing neurosyphilis on the basis of serologic tests increases in immunocompromised patients [10].

The differential diagnosis of strokelike motor deficits in a young patient could encompass a wide variety of entities, including premature atherosclerosis caused by diabetes, embolus from a cardiac source, IV drug use, coagulopathy, complicated migraine, and inflammatory arteriopathy (e.g., syphilis, tuberculosis, cocaine and amphetamine abuse, systemic lupus erythematosus, periarteritis nodosa, and rheumatoid arthritis) [11]. Usually, HIV-positive patients with opportunistic infections or tumors (e.g., toxoplasmosis or lymphoma) have parenchymal masses that may create the symptoms of stroke owing to their mass effect, but these patients do not typically have imaging findings of vasculitis or infarct. Also, the ischemic lesions in patients with neurosyphilis tend to involve the basal ganglia region and middle cerebral artery territories. Therefore, in a young HIV carrier with stroke and MR findings of ischemic infarct, neurosyphilis should be high on the list of differential diagnoses.

In conclusion, strokelike symptoms in conjunction with MR findings suggestive of vascular ischemic lesions in a young HIV patient should alert the radiologist to the possibility of meningovascular syphilis so that proper management can be instituted immediately.

REFERENCES

1. Herrmann C. Neurosyphilis. In: Rowland LP, ed. *Merritt's textbook of neurology*, 7th ed. Philadelphia: Lea & Febiger, **1984**:123–130
2. Holland BA, Perrett LV, Mills CM. Meningovascular syphilis: CT and MR findings. *Radiology* **1986**;158:439–442
3. Vatz K, Scheibel R, Keiffer S, Ansari K. Neurosyphilis and diffuse cerebral angiography: a case report. *Neurology* **1974**;24:472–476
4. Kaplan JG, Sterman AB, Horoupian D, Leeds NE, Zimmerman RD, Gade R. Luetic meningitis with gumma: clinical, radiographic, and neuropathologic features. *Neurology* **1981**;31:464–467
5. Agrons GA, Han SS, Husson MA, Simeone F. MR imaging of cerebral gumma. *AJNR* **1991**;11:80–81
6. Seltzer S, Mark AS. Contrast enhancement of the labyrinth on MR scans in patients with sudden hearing loss and vertigo: evidence of labyrinthine disease. *AJNR* **1991**;12:13–16
7. Zaidman GW. Neurosyphilis and retrobulbar neuritis in a patient with AIDS. *Ann Ophthalmol* **1986**;18:260–261
8. Lawton Smith J, Frazier Byrne S, Cambron CR. Syphiloma/gumma of the optic nerve and human immunodeficiency virus seropositivity. *J Clin Neuro Ophthalmol* **1990**;10:175–184
9. Simon RP. Neurosyphilis. *Arch Neurol* **1985**;42:606–613
10. Fujimara NJ. Human immunodeficiency virus infection and syphilis. *J Am Acad Dermatol* **1989**;21:141–142
11. Hart RG, Miller VT. Cerebral infarction in young adults: a practical approach. *Stroke* **1982**;17:110–114

Rasmussen's Encephalitis:

Neuroimaging Findings in Four Patients

Robert D. Tien[1]
Boyd C. Ashdown[1]
Darrell V. Lewis, Jr.[2]
Mark R. Atkins[3]
Peter C. Burger[3]

Rasmussen's encephalitis is a devastating disease of childhood causing progressive neurologic deficits and intractable seizure activity. Patients frequently have episodes of epilepsia partialis continua and, much less frequently, generalized status epilepticus. The seizures are intractable despite aggressive medical management. In advanced cases, hemispherectomy appears to be the only option to control the seizures. Permanent physical and mental impairments are inevitable. The cause of this disease is unknown, although pathologic specimens demonstrate nonspecific changes that are compatible with viral encephalitis. The progressive brain damage is typically so insidious in onset and gradual in course that it is difficult to make an accurate diagnosis on the basis of clinical evidence. We retrospectively evaluated the CT, xenon CT, positron emission tomographic, and MR neuroimaging findings in four young patients with pathologically suspected Rasmussen's encephalitis (three patients had CT scans, two had xenon CT scans, two had MR scans, and one had a positron emission tomogram). All studies showed abnormalities of the involved cerebral hemisphere: CT and MR revealed nonspecific atrophy, xenon CT showed decreased cerebral blood flow, and positron emission tomography revealed a hypometabolic state.

Rasmussen's encephalitis is a diagnosis of exclusion; however, the information obtained from neuroimaging studies in combination with the clinical course should suggest this disorder.

***AJR* 158:1329–1332, June 1992**

Rasmussen's encephalitis was first characterized by Rasmussen et al. in 1958 [1]. These investigators described a series of 27 children who had severe and progressive focal epilepsy, often with episodes of epilepsia partialis continua. The patients had no clinical findings of encephalitis, but histologic study of the brain revealed viral encephalitis. In patients with Rasmussen's encephalitis, partial motor seizures are predominant, although a mixture of other types can be seen. The patients have a progressive motor deficit as well as mental deterioration. This chronic viral encephalitis is rare and not easily diagnosed. We reviewed the imaging manifestations in four patients in whom pathologic changes suggested Rasmussen's encephalitis.

Materials and Methods

We retrospectively reviewed the imaging findings, including CT, MR, positron emission tomography (PET), and xenon CT, of four patients with the histologic diagnosis of Rasmussen's encephalitis. The patients were 8½–21 years old (average age, 17); three were young adults (one man and two women) and one was an 8½-year-old girl. All patients had a history of intractable focal motor seizures unresponsive to medical therapy. The average age at onset of symptoms was 6 years. Two patients had had a partial hemispherectomy, and, after a seizure-free period of several years, frequent seizures recurred; these patients are now scheduled for total hemispherectomy. Two other patients had had a complete hemispherec-

Received October 17, 1991; accepted after revision January 3, 1992.

[1] Department of Radiology, Duke University Medical Center, Box 3808, Durham, NC 27710. Address reprint requests to R. D. Tien.

[2] Department of Pediatrics, Division of Neurology, Duke University Medical Center, Durham, NC 27710.

[3] Department of Pathology, Duke University Medical Center, Durham, NC 27710.

0361-803X/92/1586-1329
© American Roentgen Ray Society

tomy and are seizure-free. Three patients had unenhanced CT studies, two had unenhanced MR studies, two had xenon CT studies, and one had a PET study.

CT studies were performed on a GE 9800 scanner (General Electric Medical Systems, Milwaukee, WI). MR studies were performed on a 1.5-T GE Signa superconducting magnet. Xenon CT cerebral blood flow (CBF) data were determined by using the GE 9800 Xenon Blood Flow System. Flow map images were derived from calculations of the time-dependent changes in pixel intensity; averaged baseline pixel data were subtracted from pixel data on the xenon-enhanced images. The ^{18}F-fluorodeoxyglucose (FDG) PET scans were obtained on an ECAT III-911 scanner (CTI, Knoxville, TN) with a full-width at half-maximum resolution of 8 mm. After IV administration of 10–12 mCi (370–444 MBq) of FDG, 12 to 15 axial images of the brain were acquired with 6-mm slice separations.

All four patients had normal CSF studies. EEG results for each patient were abnormal, corresponding to the affected hemisphere. The pathologic findings of these four patients were almost identical and showed marked perivascular lymphocytic cell infiltration; clusters of chronic inflammatory cells (glial nodules) in the brain parenchyma consistent with viral encephalitis (Fig. 1) were also found.

The clinical history and imaging and pathologic findings were correlated for each patient.

Results

The two patients with xenon CT CBF studies showed selectively decreased CBF to the affected hemisphere despite rather unremarkable CT studies. In another patient, CT and MR showed remarkable atrophy of the left hemisphere (Figs. 2A and 2B) with decreased FDG tracer uptake in the left hemisphere (Fig. 2C). CT and MR studies in the fourth patient showed severe left hemispheric atrophy (Fig. 3). MR also demonstrated remarkable gliosis in the basal ganglia region and the periventricular area. The abnormal hemisphere seen on imaging studies correlated well with EEG results. The

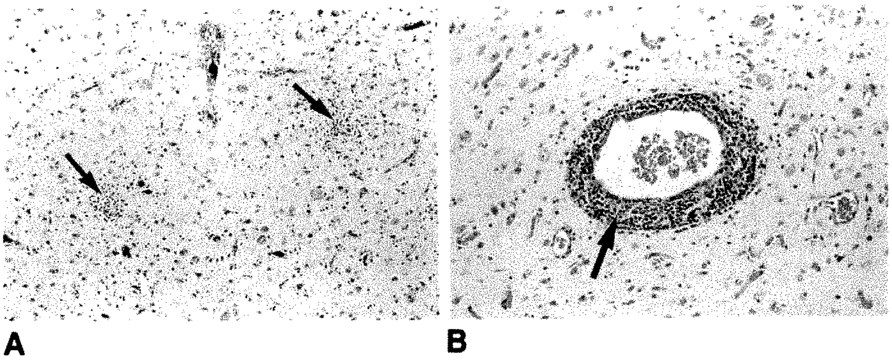

Fig. 1.—21-year-old woman with intractable partial tonic clonic seizure.

***A*, Photomicrograph of pathologic specimen from brain shows multiple clusters of chronic inflammatory cells (glial nodules) (*arrows*). (H and E, original magnification ×170)**

***B*, Photomicrograph shows perivascular cuffs of lymphocytes (*arrow*) are prominent throughout specimen. (H and E, original magnification ×130)**

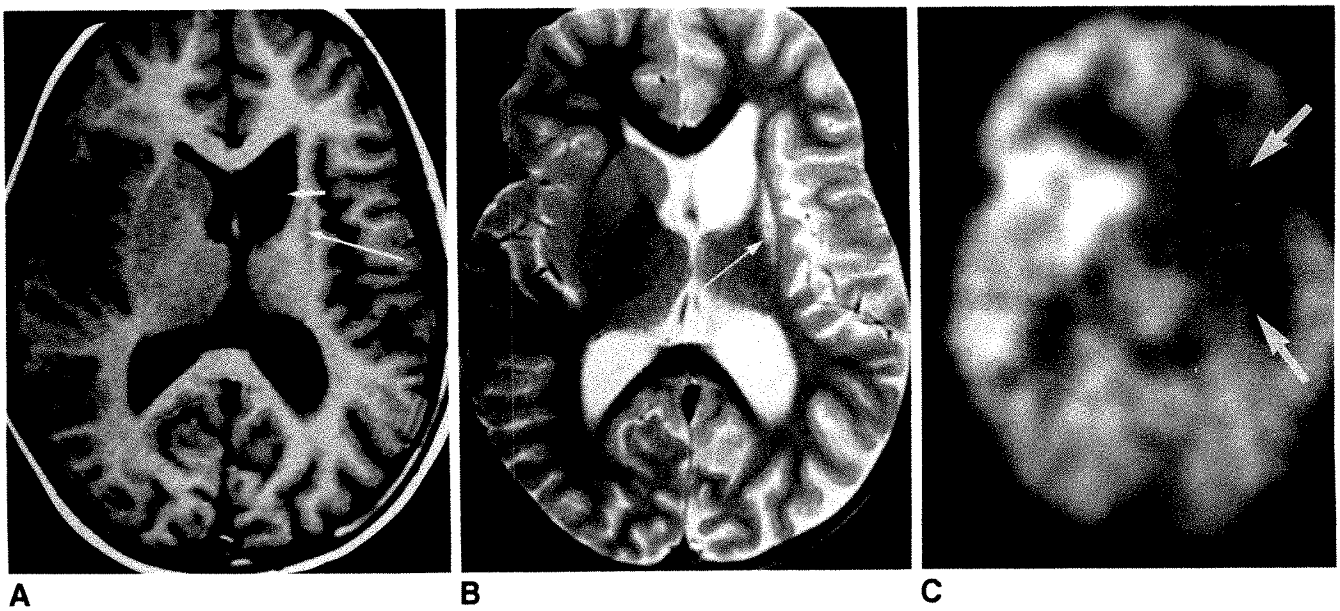

Fig. 2.—8½-year-old girl with intractable focal motor seizure.

***A*, Axial T1-weighted MR image, 600/20/1 (TR/TE/excitations), shows atrophic left hemisphere. Left frontal horn (*short arrow*) is dilated owing to caudate nucleus atrophy. Left putamen is extremely atrophic (*long arrow*).**

***B*, Axial T2-weighted MR image (2500/80/1) shows left atrophic basal ganglia has abnormal high signal (*arrow*) that might represent gliosis.**

***C*, ^{18}F-FDG positron emission tomograms show marked decreased tracer uptake in left frontotemporal area (*arrows*).**

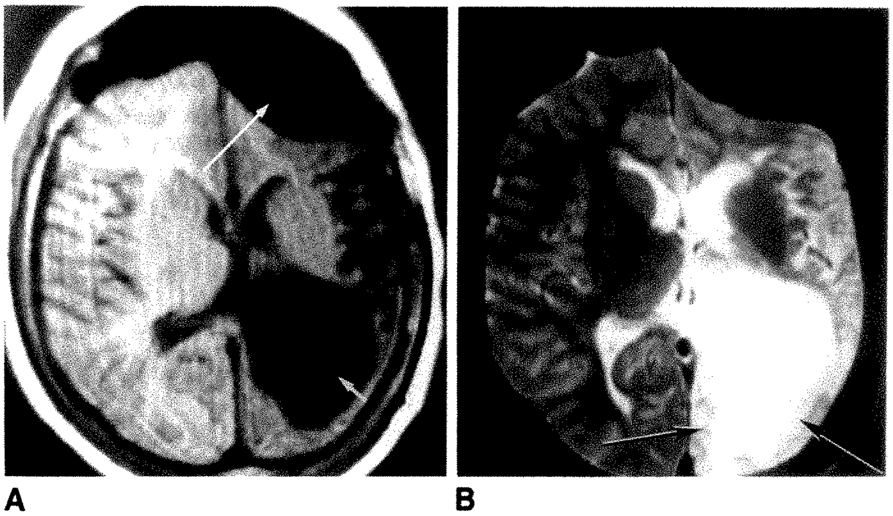

Fig. 3.—MR findings in a 21-year-old woman with intractable partial seizure.

***A*, Axial T1-weighted image shows marked atrophic left hemisphere. Left occipital horn is markedly enlarged (*short arrow*). Frontal sinus is also very prominent, especially on left side (*long arrow*).**

***B*, Axial T2-weighted image shows abnormal periventricular high signal (*arrows*), probably representing gliosis.**

diagnosis of Rasmussen's encephalitis was based on these clinical, imaging, and pathologic findings.

Discussion

Rasmussen et al. [1] first reported patients with intractable focal seizure activity caused by chronic encephalitis in 1958. This disease is primarily an event of childhood, with onset occurring at 10 years of age or younger in 85% of patients. In the studies of Rasmussen et al., the median age at onset was 5 years. Although it has been reported to present initially with bilateral cerebral involvement [2], Rasmussen's encephalitis tends to localize in one hemisphere. The disease is rarely fatal; however, in only 10% of patients is it self-limiting before permanent neurologic deficit occurs [2]. Varying degrees of hemiparesis, dysphasia, hemianopia, and mental deterioration can also occur in patients with Rasmussen's encephalitis.

The cause of Rasmussen's encephalitis is uncertain. A viral origin, possibly a slow virus similar to the etiologic agent found in subacute, sclerosing panencephalitis, has been suggested [2]. In more recent studies, Rasmussen et al. [2, 3] have reported that in approximately two thirds of patients, there may be an infectious or inflammatory episode in the patient or a close family member immediately before onset of seizures. Epstein-Barr virus and cytomegalovirus have been suggested as a possible cause in some cases [4].

The prominent microscopic features are perivascular lymphocytic cuffing of round cells, scattered glial nodules, and diffuse proliferation of microglia in the cortical layers and in the white matter. All these changes are commonly seen in viral infections; however, rickettsial infection can also mimic this change. As the disease progresses, cortical atrophy with scattered areas of spongy degeneration and neuronal loss with no evidence of inflammatory cells is noted.

Results of radiologic examinations carried out at, or soon after, the initial onset of seizures are usually normal. However, in one reported patient, a CT scan obtained at the end of the first week of illness showed patchy low attenuation and swelling in the right temporal region. CT studies performed at 4 weeks showed atrophy of the same area [5]. Even when CT findings are unremarkable, the xenon CT scan may demonstrate subtly decreased CBF to the affected hemisphere, as seen in our patients. In chronic cases, cerebral CT studies can show focal atrophy of the frontal, temporal, and parietal regions [5, 6]. One study found progressive atrophy of the involved hemisphere in 17 (89%) of 19 cases [2].

Few MR studies of Rasmussen's encephalitis patients have been reported in the English language literature [5, 7]. One MR study showed the atrophic change around the right ventricle and the right sylvian fissure [5]. In another case report [7], initial MR findings obtained with and without administration of gadopentetate dimeglumine were normal. A later MR study demonstrated increased signal intensity in the left temporal lobe, as well as the left parietal lobe on T2-weighted images, suggestive of edema. A PET study performed after the onset of seizure depicted a focal hypermetabolic area over the left centroparietal head region [5]. However, this abnormal hypermetabolic activity of brain may be directly caused by seizure. It is also likely that the area of hypermetabolism seen on PET may eventually become hypometabolic and atrophic as the disease progresses. In our study, the PET and MR findings showed the morphologically atrophic hemisphere with decreasing metabolic activity. The abnormally high signals noted in the putamen in one patient and periventricular area in another on T2-weighted images have not been reported before. These abnormal signals are likely the result of gliosis caused by chronic brain damage.

We believe that PET scans, which can illustrate the brain's metabolism, may be used in the monitoring as well as the diagnosis of Rasmussen's encephalitis. However, caution must be exercised, because PET findings merely reflect the hypometabolism of the affected brain portions and are not specific to this disorder.

Single-photon emission CT (SPECT) with ^{99m}Tc-hexamethylpropyleneamine oxime, together with ^{123}I-amphetamine, is also a useful technique for evaluating this disease [5, 7]. SPECT imaging can reveal an area of hypoperfusion that corresponds to the anatomic location of the epileptogenic foci found by clinical assessment. Proton MR spectroscopy, yet another imaging technique, reveals decreased *N*-acetylaspartate concentration in patients with Rasmussen's encephalitis. This finding correlates well with brain atrophy and neuronal loss [8].

As a rule, medication with antiepileptic drugs is palliative at best and may contribute to the general deterioration in function that is seen. Although deterioration may be rapid or may take years, Rasmussen's encephalitis eventually results in intractable seizures and hemiparesis, at which time surgical intervention (usually hemispherectomy) is required.

Diagnosis of Rasmussen's encephalitis depends on recognition of the clinical symptoms: the appearance of progressive partial motor seizures in a previously healthy child. Brain biopsy of persons with Rasmussen's encephalitis may be useful in differentiating these patients from those with disorders that have similar clinical symptoms and radiologic findings, such as Davidoff-Dyke-Mason syndrome. For instance, the biopsy would reveal viral encephalitic changes associated with Rasmussen's encephalitis or indicate histologic changes from intrauterine ischemia or trauma that cause some cases of Davidoff-Dyke-Mason syndrome.

In summary, MR, SPECT, PET, and other new techniques of neuroimaging can offer hope in developing criteria for early diagnosis of Rasmussen's encephalitis. These imaging techniques may also provide keys to monitor the disease process. The presence of an extensive area of functional abnormality on xenon CT, SPECT, and PET (with or without structural atrophy) may alert the clinician to the possibility of Rasmussen's encephalitis early in the course of this devastating disease and facilitate proper management.

REFERENCES

1. Rasmussen T, Olszweski J, Lloyd-Smith D. Focal seizures due to chronic localized encephalitis. *Neurology* **1958**;8:435–455
2. Rasmussen T, Andermann F. Update on the syndrome of "chronic encephalitis" and epilepsy. *Cleve Clin J Med* **1989**;56[suppl]:181–184
3. Oguni H, Andermann F, Rasmussen T. The natural history of the syndrome of chronic encephalitis and epilepsy: a study of the MNI series of 48 cases. *Neurology* **1989**;39[suppl 1]:155
4. Power C, Poland SD, Blume WT, Girvin JP, Rice GPA. Cytomegalovirus and Rasmussen's encephalitis. *Lancet* **1990**;336:1282–1284
5. English R, Soper N, Shepstone BJ, Hockaday JM, Stores G. Five patients with Rasmussen's syndrome investigated by single-photon-emission computed tomography. *Nucl Med Commun* **1989**;10:5–14
6. Piatt JH, Hwang PA, Armstrong DC, Becker LE, Hoffman HJ. Chronic focal encephalitis (Rasmussen's syndrome): six cases. *Epilepsia* **1988**;29:268–279
7. Zupanc ML, Handler EG, Levine RL, et al. Rasmussen encephalitis: epilepsia partialis continua secondary to chronic encephalitis. *Pediatr Neurol* **1990**;6:397–401
8. Mattews PM, Andermann F, Arnold DL. A proton magnetic resonance spectroscopy study of focal epilepsy in humans. *Neurology* **1990**;40:985–989

Review Article

Role of MR Imaging in the Management of Spinal Infections

Hassan S. Sharif[1]

Infection of the spine is a major category of spinal disease that is difficult to differentiate clinically from degenerative disease, noninfective inflammatory lesions, and spinal neoplasm. The infection can affect the vertebrae, intervertebral disks, paraspinal soft tissues, the epidural space, the meninges, and/or the spinal cord. Specific causative organisms include bacteria (pyogenic, granulomatous), fungi, parasites (*Echinococcus*, *Schistosoma*), and viruses. Early diagnosis and prompt treatment are essential to prevent permanent neurologic deficit and/or spinal deformity. Imaging plays an important role in the overall evaluation of these lesions, and the ideal technique is expected to provide information that will help characterize and delineate the disease process, guide biopsy and/or drainage procedures, suggest method of treatment (medical vs surgical), and assess response to therapy. The aim of this article is to review the advantages and limitations of MR imaging in the management of spinal infections.

MR Imaging Technique

In the diagnosis of spinal infections and their sequelae, MR imaging has become an established imaging technique [1-4]. MR has been shown to be at least as sensitive as bone scintigraphy for detecting infections of the vertebrae and is comparable to CT for visualizing extent of disease [1, 3-5]. High contrast resolution, direct multiplanar imaging, usefulness in detecting marrow infiltration, and ease by which intradural disease can be assessed are definite advantages. Depending on the location of the spinal lesion (extradural, intradural extramedullary, intramedullary), the MR technique should be modified to obtain adequate visualization and delineation. A sagittal, multisection, two-dimensional, spin-echo (SE) sequence with short TRs and TEs (T1-weighted sequence) can be used as a localizer. These slices can show alterations in the morphology of the vertebral body and disk, prevertebral soft tissues, epidural space, and size of the spinal cord in most affected spines [4, 6]. Changes in vertebral marrow signal can also be observed [1, 4-7]. Information provided by this pulse sequence will help to point out the area of involvement and hence dictate the rest of the MR examination.

After the first sequence is obtained, patients with extradural disease (vertebral osteomyelitis, diskitis, epidural abscess, paraspinal soft-tissue infection) benefit from multisection sagittal images with either long TR/TE (T2-weighted sequence) or a fat-suppression technique (short TI inversion recovery [STIR]) [1, 4-9]. All affected areas will exhibit increased signal intensity on these sequences by virtue of the increased water content caused by the infection [1, 4, 6]. The STIR technique has a slightly higher sensitivity for detecting areas of involvement than T2-weighted images do, but it has been found to be generally less specific [10, 11]. No definite advantage has been recorded from obtaining both sequences together. Although these sequences can help in showing vertebral and disk disease, epidural extension may not be adequately assessed, because the abnormal signal obtained may be isointense with the high signal of CSF [5]. The first echo of the long TR study can sometimes show higher signal intensity from an epidural abscess than from CSF, presumably because of the higher protein content of the inflammatory exudate [4].

An additional sagittal multisection T1-weighted sequence done immediately after IV administration of gadopentetate

---

Received October 30, 1991; accepted after revision December 26, 1991.

[1] Department of Radiology, Riyadh Armed Forces Hospital, P.O. Box 7897, Riyadh 11159, Kingdom of Saudi Arabia. Address reprint requests to H. S. Sharif.

AJR 158:1333-1345, June 1992 0361-803X/92/1586-1333 © American Roentgen Ray Society

dimeglumine in a concentration of 0.1 mmol/kg body weight is a necessary adjunct to the previous two sequences because it will help show the presence and extent of epidural disease [4, 12]. It will also help to characterize tuberculous spondylitis and is essential for the detection and delineation of intradural disease [4, 13].

Although sagittal images clearly display prevertebral soft-tissue abnormalities, the paraspinal soft tissues are best assessed on coronal sections [4, 14]. A multisectional coronal T1-weighted sequence obtained after the sagittal enhanced images can show alterations in morphology in the paraspinal soft tissues. Abscess loculations are visualized because of rim enhancement [4].

Extradural Disease (Infective Spondylitis)

Infective spondylitis is an infection that involves one or more of the extradural components of the spine and can be caused by bacterial, fungal, or parasitic organisms. Vertebral bodies are most frequently affected, but the posterior osseous elements, disks, epidural space, and paraspinal soft tissues can also be either primarily or secondarily involved [15]. Mechanisms of infection include blood borne, spread from a contiguous site, and direct implantation [16]. Hematogenous spread results in lodgment of organisms in the vertebral marrow. The venous (Batson's plexus) and arterial systems have both been implicated in carrying the pathogens, but the latter is recognized as the more important method of transmission [17]. Involvement of the disk by blood-borne pathogens occurs only in the pediatric age groups (below 20 years old) because of persistent blood supply to the disk [6, 18, 19]. In older patients, disk infection is invariably caused by direct spread from neighboring vertebrae or soft tissue [12, 17].

Clinically, infective spondylitis is extremely difficult to differentiate from other causes of spinal disease because of the paucity of distinctive signs and symptoms. Back pain is a common early symptom, frequently associated with localized tenderness and stiffness with or without neurologic abnormality [15, 16]. A high erythrocyte sedimentation rate (ESR) is invariably present, and the patient may or may not be febrile. Early diagnosis and prompt treatment are essential to prevent permanent neurologic deficit and/or spinal deformity [12, 20].

Bacterial Infections

Pyogenic spondylitis.—There has been a major increase in the reported incidence of pyogenic spondylitis in the last decade [6, 15]. Elderly diabetic patients 40–70 years old (men slightly more than women) are most frequently affected, but immunocompromised persons and drug abusers are also at risk [16]. *Staphylococcus aureus* is the most common organism identified; *Escherichia coli*, *Salmonella*, *Pseudomonas aeruginosa*, and *Klebsiella pneumoniae* have also been implicated [15]. The infection occurs anywhere in the spine, but the lumbar region is the area of predilection [15, 16]. Two major criteria are essential for establishing the diagnosis of pyogenic spondylitis: (1) the presence of characteristic imaging features of spine infection and (2) the isolation of the offending organism from blood or the affected site [15]. The great majority of cases respond promptly and adequately to antibiotic therapy; surgical decompression is rarely needed [20].

The findings on unenhanced MR images of hematogenous pyogenic spondylitis are characteristic and correctly reflect the pathophysiologic changes [1, 6, 21]. The increase in extracellular fluid within vertebral marrow—a manifestation of the inflammatory reaction—is responsible for the abnormal signal, which is relatively low on T1-weighted images (e.g., SE 500/30 [TR/TE]) and high on T2-weighted images (e.g., SE 1800/100); this abnormal signal is usually diffusely distributed throughout the whole vertebra [6] (Fig. 1). Vertebral collapse and spinal deformity are extremely rare, and affected vertebrae do not seem to lose their cortical margin (Sharif HS et al., presented at the Radiologic Society of North America meeting, November 1990). Classically, two consecutive vertebrae and the intervening disk are involved. The disk is invariably reduced in height and shows high signal intensity on T2-weighted images in the absence of a nuclear cleft (normal anatomic structure that on T2-weighted images appears as a signal void area in the center of lumbar disks in subjects 30 years or older; its absence in the presence of increased signal intensity indicates disk-space infection) [22]. Disk material could herniate into the softened neighboring endplates or into the spinal canal [5].

Pyogenic spondylitis is usually confined to the vertebral marrow with no significant extension into the paraspinal region. Moderate granulation tissue can be produced; this gets distributed evenly and circumferentially around the vertebral body [23]. Epidural extension is infrequent and could be suspected on T1-weighted sagittal images as an isointense mass obliterating the echo void area between the vertebral bodies and the cord and formed by the vertebral cortex, posterior spinal ligaments, dura, and CSF [5]. On T2-weighted images, epidural collections can become isointense with the high signal of CSF and hence can be missed [12].

Administration of gadopentetate dimeglumine has recently been shown to be an important adjunct to MR imaging of this disease [12]. Epidural extension and associated meningeal inflammation can be established with confidence only on enhanced examination [4, 12, 24]. In addition, most infected disks seem to enhance, a fact that increases observer's confidence for establishing the diagnosis of infective spondylitis [12]. Activity and severity of infection can also be judged by the degree of enhancement. This may prove useful in assessing response to therapy [12].

Affected marrow enhances diffusely in pyogenic spondylitis. The increased signal produced seems to cause less tissue contrast between normal and abnormal vertebrae than what could be detected on T1- and T2-weighted images [25]. Fat-suppression techniques in conjunction with IV contrast agents have recently been recommended, as they may improve the conspicuity of enhancing structures by obliterating the signal from neighboring fatty tissue [26].

The great majority of cases of infective spondylitis (also called diskitis) in the pediatric age group are caused by

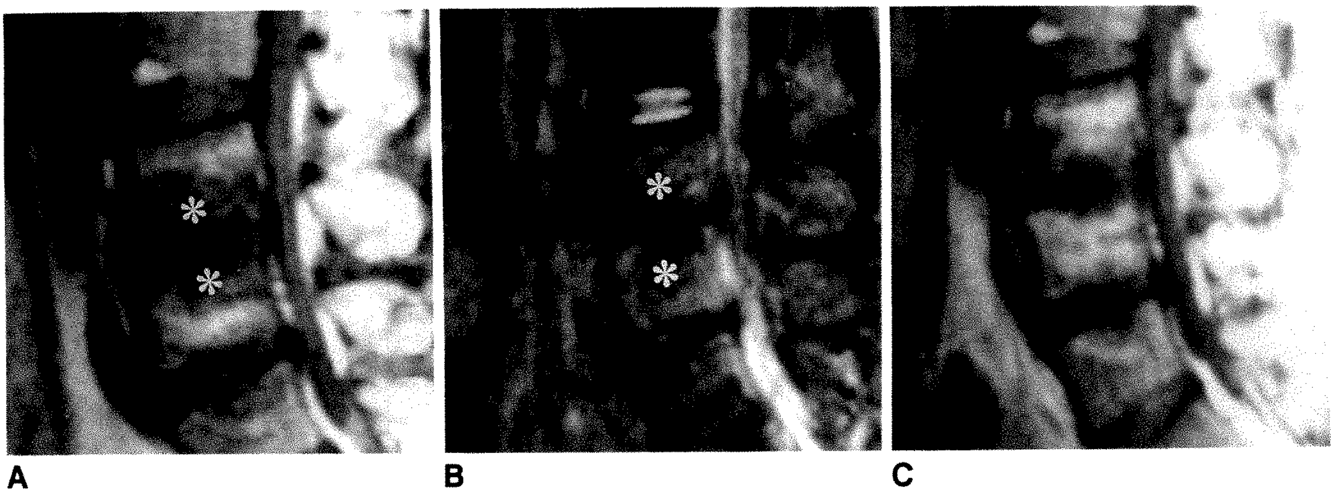

Fig. 1.—34-year-old man with pyogenic spondylitis of the lumbar spine who had back pain and fever. *Staphylococcus aureus* was isolated from blood culture.

A, Midsagittal MR image (SE 500/30) shows decreased signal in L3 and L4 vertebral bodies (*asterisks*) and in superior endplate of L5. L3–L4 disk appears to be moderately reduced in height.

B, Midsagittal MR image (SE 1800/100) shows moderate increased signal from L3 and L4 vertebrae (*asterisks*). No signal could be obtained from intervening disk.

C, Midsagittal MR image (SE 500/30) obtained 6 months after admission. Patient is completely asymptomatic. Increased signal from bodies of L3 and L4 indicates decrease in cellular marrow (presumably destroyed by infective process).

pyogenic organisms [18, 19]. It is more difficult to diagnose in children than in adults, and the causative organism may be difficult to isolate from blood or from the site of the lesion [15, 18, 19, 27, 28]. Most of these children respond promptly and adequately to broad-spectrum antibiotics [16]. The absence of ionizing radiation makes MR imaging an ideal method for examining these children and for assessing response to treatment. The features are similar to those of the adult disease and are diagnostic [27] (Fig. 2).

Hematogenous spread of pyogenic organisms can rarely cause an epidural abscess in the absence of detectable bone or disk disease [29]. MR is superior to other imaging methods for early recognition and delineation of the lesion. A T1-weighted image will show an extradural mass isointense with vertebral marrow compressing the thecal sac [29, 30]. On the first echo of the long TR study, an epidural abscess may exhibit higher signal intensity than CSF, presumably because of higher protein content of the inflammatory exudate. On long TR/long TE and STIR images, the epidural collection could be completely silhouetted by the high signal of CSF. Gadopentetate dimeglumine enhancement improves the detection and delineation of these lesions [4, 12]. Signal abnormalities by themselves are nonspecific for recognizing the infective nature of the mass; the presence of relevant clinical signs and symptoms (e.g., immunosuppressed or diabetic patient with high ESR, septicemia), together with the MR findings, leads to early diagnosis and prompt treatment [31, 32].

Pyogenic spondylitis can be caused by direct spread from neighboring infected organs (e.g., oropharynx, pleural cavity, thoracoabdominal wall) and also by direct postoperative implantation of pathogens [15, 33]. MR imaging is an ideal method for detecting and delineating the extent of these lesions. Involvement of small bones such as ribs, spinous processes, and iliac bone could, however, be missed on MR because of partial-volume averaging from the high signal of surrounding abscess collections [33].

Follow-up in cases of pyogenic spondylitis can easily and conveniently be done with MR imaging [4]. T2-weighted sagittal images may demonstrate a decrease in the abnormal high signal noted on the first examination. The presence of increased signal intensity on T1-weighted images from previously infected vertebrae reflects replacement of cellular marrow by fat and indicates healing, a process that has been described after radiotherapy, trauma, and degenerative disease [4, 7]. T1-weighted images are therefore essential in the posttherapy follow-up of these lesions [4] (Fig. 1). T2-weighted images may still be required early in the disease in order to assess the presence or absence of residual inflammation.

Granulomatous spondylitis.—A granulomatous reaction is a nonspecific response of tissues to an antigenic stimulus. Such a reaction has been identified in a wide range of diseases including bacterial, viral, and fungal infections; neoplasia; and autoimmune and idiopathic disorders [15]. Bacterial granulomatous organisms that have been implicated in spinal infections include *Mycobacterium tuberculosis* and *Brucella* species [4, 34].

Tuberculous spondylitis is of worldwide distribution, but the prevalence in developing countries is considerably higher than in the United States or western Europe [20, 35]. Middle-aged adults (with no sex predominance) are most frequently affected, especially those with predisposing conditions such as debilitation, alcoholism, drug addiction, and immunosuppression [5, 15, 35, 36].

The diagnosis of tuberculous spondylitis is established by isolating the tuberculous bacillus from the site of the infection and/or by characteristic histopathologic changes [5, 15, 35,

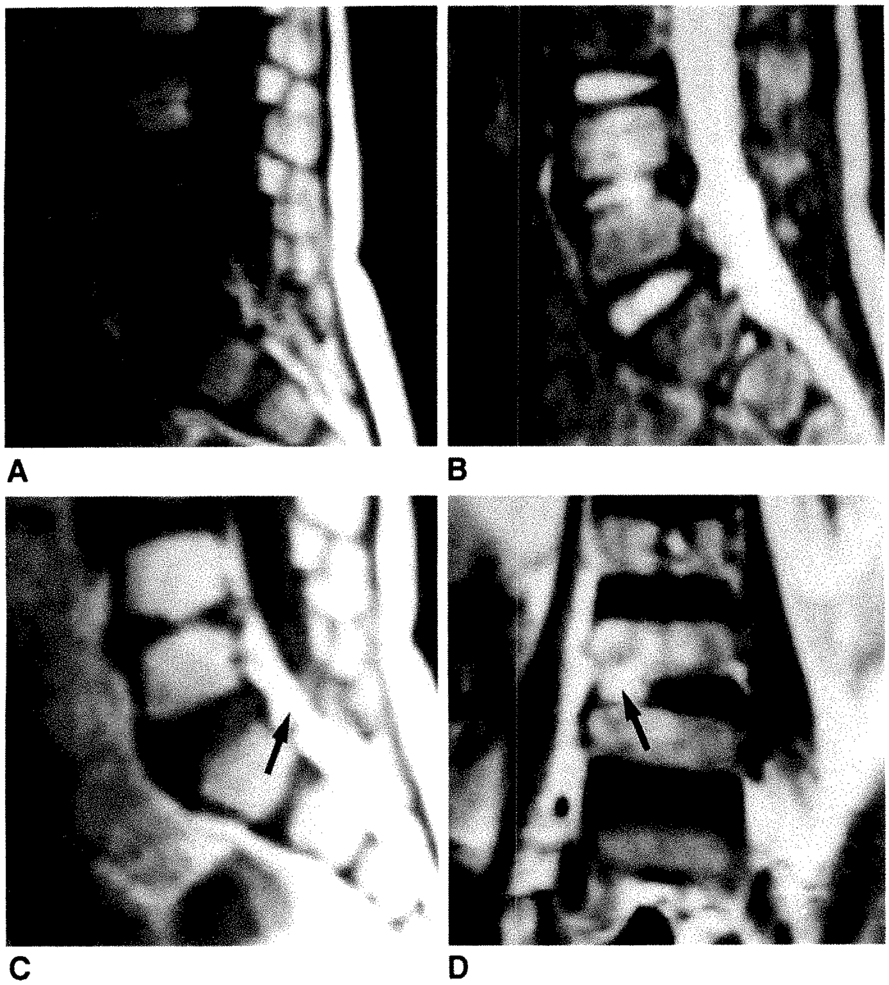

Fig. 2.—3-year-old girl with pyogenic spondylitis of lower lumbar spine who had abdominal pain and difficulty walking. No organisms were isolated from blood cultures or from percutaneous biopsy. Patient was treated with broad-spectrum antibiotics on basis of MR findings and was free of symptoms 2 weeks later.

A, Midsagittal MR image (SE 500/30) shows decreased signal from bodies of L4 and L5 and loss of height of intervening disk.

B, Midsagittal MR image (SE 2000/100) shows diffusely high signal from L4 and L5 vertebral bodies. L4–L5 disk shows moderate bulge causing displacement of posterior spinal ligament and high signal intensity, features indicative of diskitis.

C, Midsagittal MR image (SE 500/30) obtained after IV administration of gadopentetate dimeglumine shows diffuse enhancement of L4 and L5 up to isointensity with normal vertebral bodies. Intense homogeneous enhancement of granulation tissue and/or dura in lumbosacral region (*arrow*) is best appreciated by comparison with *A*.

D, Coronal postcontrast MR image (SE 500/30) shows enhancement of L4 and L5 and right aspect of intervening disk (*arrow*). Paraspinal soft tissues are minimally enhanced on right side, but psoas muscles are normal.

36]. Adequate response to antituberculous chemotherapy is another recognized method of establishing the diagnosis.

The treatment of tuberculous spondylitis is controversial, particularly in patients with minimal or absent neurologic deficits [36, 37]. Together with antituberculous chemotherapy, surgery aimed at draining the abscesses, removing necrotic tissue, decompressing the thecal sac, and fusing the spine remains the preferred method in many centers [35, 37]. In poor-risk patients, percutaneous drainage of paraspinal abscesses may help with early recovery [4].

The morphologic and pathophysiologic changes encountered in spinal tuberculosis are the most severe among infective spondylitides and are also the most varied. Tuberculosis can selectively affect part or all of a vertebral body (pedicle, lamina, posterior elements) without involving neighboring disks [4, 6, 12]. Skip lesions, large abscesses, epidural extension, and subligamentous spread are seen more frequently in this disease than in any other spinal infection [4, 6, 12]. On MR images, vertebral intraosseous abscesses, paraspinal soft-tissue abscesses that extend beyond the confines of the affected vertebrae and disks, vertebral and disk collapse, spinal deformity (gibbus), skip lesions, encroachment on spinal canal and nerve roots, and involvement of the posterior elements are all readily detectable [4] (Fig. 3).

In tuberculous spondylitis, the cortical definition of affected vertebrae is invariably lost, in contradistinction to pyogenic spondylitis [4]. T1-weighed images usually show decreased signal from the affected vertebral marrow, reduced disk height, morphologic alteration of paraspinal soft tissues, and epidural extension. On T2-weighted images, an indiscriminate increase in signal intensity is noted from the vertebrae, disks, and soft tissues. Enhanced MR studies are particularly useful for characterizing tuberculous spondylitis [4]. Rim enhancement around intraosseous and paraspinal soft-tissue abscess had not been demonstrated in other spinal infections [4] (Sharif HS et al., RSNA meeting, November 1990). Epidural extension and meningeal involvement are seen to better advantage on enhanced examinations [4].

Planning the surgical approach can be facilitated by MR imaging because of the clear display of the extent of the active infection and its complications [4]. Posttherapy follow-up can also be done ideally with MR. Similar to other spinal infections, increased signal intensity on T1-weighed images from previously affected vertebrae indicates healing and has

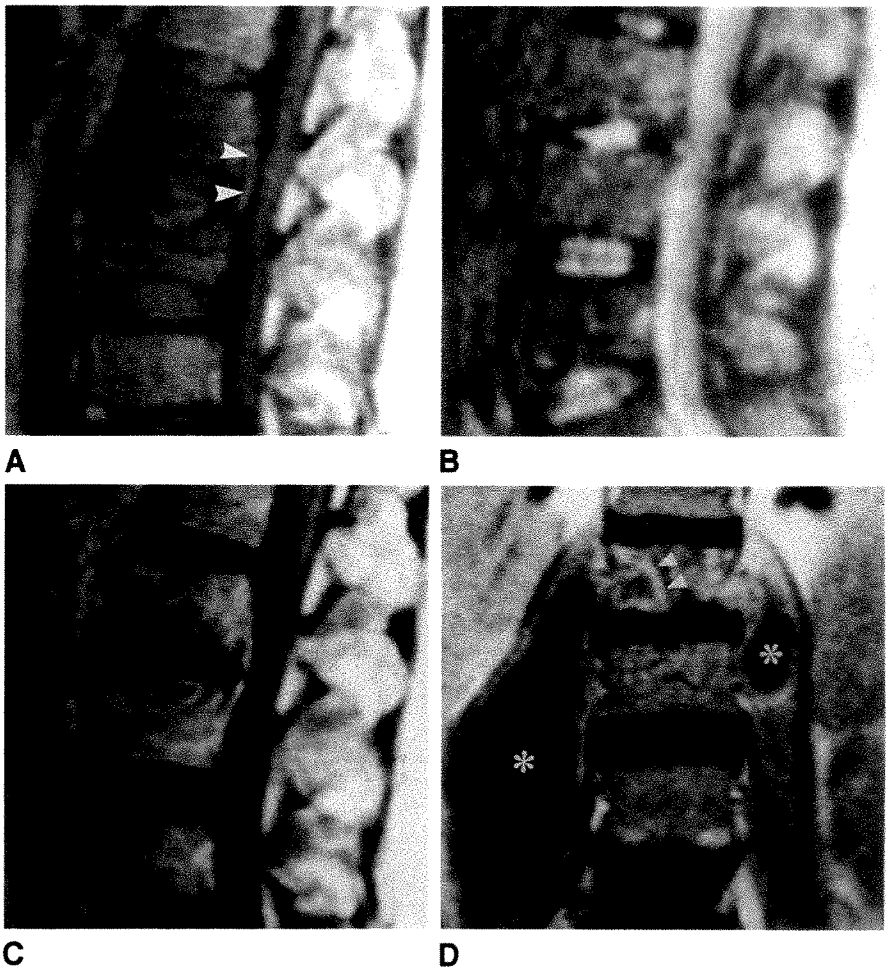

Fig. 3.—Tuberculous spondylitis in a 47-year-old man.

***A*, Midsagittal MR image (SE 500/30) shows heterogeneous decrease in signal intensity in bodies of L2 and L3 with poor demarcation of vertebral disk junction. Note moderate epidural extension (*arrowheads*).**

***B*, Midsagittal MR image (SE 2000/100) shows diffuse moderately increased signal in bodies of L2 and L3 and intervening disk in absence of a nuclear cleft.**

***C*, Midsagittal MR image (SE 500/30) after gadopentetate dimeglumine administration shows fairly diffuse enhancement of bodies of L2 and L3 to level of isointensity with normal vertebrae. Enhancement of posteriorly displaced dura is also present at L2–L3 interspace, best appreciated by comparison with *A*. Note that intervening disk did not enhance although it showed increased signal on *B*.**

***D*, Coronal MR image obtained after *C* shows classic intraosseous (*arrowheads*) and bilateral psoas abscesses (*asterisks*), which were proved surgically. Features on coronal image are diagnostic of tuberculous spondylitis.**

been found to correlate well with clinical signs and symptoms [4].

Percutaneous drainage of large paraspinal abscesses is a recognized method for enhancing healing and has been found to be a convenient alternative to surgery [4]. Enhanced coronal images are extremely helpful for delineating these abscesses, but the actual drainage procedure cannot be performed with ease with MR guidance [4].

Brucellosis is a zoonosis of worldwide distribution that is caused by small, gram-negative, nonencapsulated coccobacilli of the genus *Brucella* [5, 38]. Of the four species implicated in human infection, *Brucella melitensis* is the most common, the most invasive, and the one most frequently associated with infective spondylitis [5, 38]. Ingestion of unpasteurized contaminated milk and milk products is the most common form of transmission in countries in which the disease is endemic [5, 38, 39]. In the United States and in western Europe, brucellosis is mostly an occupational hazard among animal handlers, slaughterhouse workers, and veterinarians [38]. The diagnosis is established by detecting definite elevation of anti-*Brucella* antibodies and the presence of characteristic imaging features [5, 38]. Isolation of the organism from blood culture and/or from tissues removed from the site of involvement is extremely rare, and histopathologic changes show nonspecific inflammatory changes in the presence or absence of small granulomata [5, 38, 40]. Patients respond promptly and adequately to anti-*Brucella* chemotherapy; surgical intervention is rarely needed [5].

Brucella spondylitis is unique among the different forms of infective spondylitis because it can manifest as either focal or diffuse [4, 5]. In the focal form, the osteomyelitis is localized to the anterior aspect of an endplate (classically L4) at the diskovertebral junction [5]. In the diffuse form, the infection initially involves an osseous endplate and ultimately extends to involve two consecutive vertebrae and the intervening disk [4, 5]. The lower lumbar spine is the area of predilection, but other areas of the spine can be affected. The focal form of the disease is self-limiting, and in the great majority of cases is seen as an incidental finding on lumbar spine radiographs [5].

The MR features of the diffuse form of *Brucella* spondylitis are similar but less severe than those of pyogenic spine infections (Fig. 4). Vertebral body morphology and cortical margins are intact despite evidence of osteomyelitis; no associated spinal deformity is present; moderate granulation tissue is produced, which may herniate into the spinal canal; and the disk is reduced in size and shows an increase in signal intensity on heavily weighted T2-weighted images in

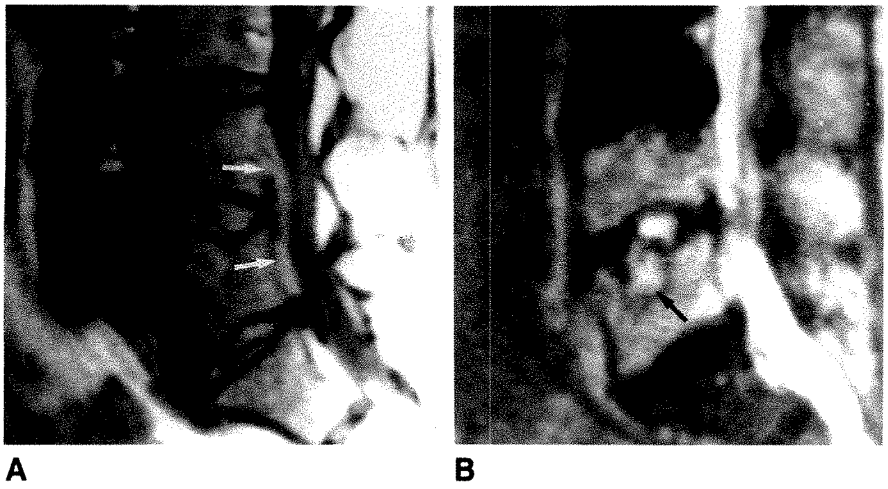

Fig. 4.—Man with classic *Brucella* spondylitis of lower lumbar spine.

A, Midsagittal MR image (SE 500/30) shows minimally decreased signal from bodies of L4 and L5. Moderate epidural extension (*arrows*) most probably represents granulation tissue. Cortical margins of anterior aspect of superior endplate of L5 and posterior aspect of L4 are obliterated. These are unusual findings in brucellosis.

B, Midsagittal MR image (SE 2000/100) shows diffuse high signal intensity from L4 and L5. Note increased signal intensity from intervening disk and absence of a nuclear cleft. Note also localized area of high signal intensity in superior endplate of L5 (*arrow*), most probably representing intervertebral disk herniation. No evidence of paraspinal disease was noted on coronal scan (*not shown*).

the absence of a nuclear cleft [5]. The presence of paraspinal abscesses is exceedingly rare [4, 5]. Enhanced images do not seem to provide information additional to the T2-weighted images except in demonstrating epidural extension and meningeal involvement, which are infrequent [4].

As with other spinal infections, posttherapy follow-up demonstrates increased signal intensity on T1-weighted images from previously affected vertebrae. This is a reflection of partial destruction of the cellular marrow with a predominance of the signal from the fatty component, and this has been noted to correlate well with healing of the disease [4].

Fungal Infections of the Spine

Infections of the spine caused by fungus and funguslike organisms are rare [15]. They have been reported with actinomycosis, nocardiosis, coccidioidomycosis, aspergillosis, and maduromycosis [34, 41, 42]. Routes of contamination vary from direct implantation by external or internal injuries to hematogenous spread from lesions elsewhere in the body [33, 41, 43]. Immunocompromised and debilitated individuals seem to have a higher risk for developing such infections [15].

Some fungi are distributed worldwide, and others are endemic only in certain geographic locations [15, 33]. The diagnosis is established by isolation of the organism and/or by the presence of characteristic histopathologic changes [15, 33, 42]. In the event of neurologic complications, decompressive surgery may be needed; otherwise, antifungal therapy can be effective in improving survival and decreasing recurrence rates [41, 42].

Certain organisms (blastomycosis, aspergillosis) may produce radiologic findings that are indistinguishable from those of tuberculosis, such as bone destruction, abscess formation, and gibbus deformity; others (actinomycosis, cryptococcoses, coccidioidomycosis, mycetoma) will affect the vertebral bodies by producing patchy destruction or sclerosis but will spare the disks [15]. Rib involvement seems to be more frequent in these infections than in the bacterial type of spinal infections [15].

Because of the rarity of this infection, very little has been written about the MR appearance of fungal spine infections. The two mycetoma cases I have seen were caused by external injury (sharp thorn) with implantation of the pathogen in the subcutaneous tissue [4]. The infective process led to the gradual destruction (over several years) of subcutaneous tissue and muscles and replacement by granulation tissue. MR delineated the extent of the soft-tissue abnormalities and adequately demonstrated the epidural extension. Vertebral bodies and disks were spared, but infiltration of the periosteum resulted in bizarre osteophyte formation. Rib changes (sclerosis and obliteration of marrow cavity) were not detected on the MR study [33, 43].

Parasitic Infections of the Spine

Hydatid disease is caused by the parasitic tapeworm *Taenia echinococcus*. Two main forms have been implicated with human infection: *Echinococcus multilocularis* and *E. granulosus*. The liver and lungs are the organs most frequently affected: liver, 75%; lungs, 15%; and the rest of the body, 10%. The skeleton is involved only in about 1% of all cases and the spine is the area of predilection (50%) [44, 45].

Because of the rigid nature of bone, the hydatid cysts do not form into the typical spherical shape but rather permeate and slowly destroy cancellous bone. In the spine, the disease starts in the vertebral body and may spread later to the neural arch and adjacent ribs. If the cortex is breached, the cyst may invade the extradural space and cause neurologic deficits. The dura always remains intact [44, 46, 47].

Spinal echinococcosis is a rare disease, and the imaging features of the reported cases do not seem to follow a recognized pattern. There is bone destruction with extension into soft tissues and the epidural space, but the disks are usually not involved [48, 49] (Fig. 5). Occasionally, the hydatid cysts can localize in the epidural space without involving the osseous spine [47]. On MR imaging, the osseous and soft-tissue extent will be depicted on sagittal, coronal, and axial views. The findings can be extremely difficult to differentiate from neoplasia. Posttherapy follow-up can ideally be done by means of MR imaging [47–51].

Differential Diagnosis in Extradural Spine Infections

Disease processes that can simulate infective spondylitis on MR include Modic type I degenerative disk disease, post-intradiskal chymopapain injection, and spinal neoplasm [52, 53]. In Modic type I disease, the vertebral endplates around a degenerated disk demonstrate decreased signal intensity on T1-weighted images and increased signal on T2-weighted image [52]. Although these changes can simulate a mild form of spinal infection, the degenerated disks tend to show low signal on T1- and T2-weighted images and hence are easily differentiated from the classic form of disk infection. In addition, most infected disks tend to enhance strongly after IV contrast administration, whereas degenerated disks rarely enhance (presumably because of infiltration by granulation tissue) [25, 30].

In differentiating infection from neoplasm on MR imaging of the spine, pitfalls can be encountered in spinal neoplasms affecting consecutive vertebrae (lymphomas), neoplasms affecting consecutive vertebrae and disks (multiple myeloma, chordoma), and infections complicating spinal neoplasms. Bizarre infections like fungal disease and echinococcosis of the spine do not have characteristic features and can be difficult to differentiate from neoplasms. Infections and neoplasms caused by direct spread from affected paraspinal organs can also be difficult to distinguish on MR.

Tuberculous spondylitis can selectively involve part or all of a vertebral body (pedicle, lamina, posterior elements) without affecting neighboring disks [4, 6, 12]. Skip lesions are also not unusual in this disease. On unenhanced MR images, these features can mimic primary or secondary neoplasms [4, 6, 12]. Since tuberculous spondylitis is invariably associated with paraspinal collections, IV contrast material can demonstrate rim enhancement around these abscesses, a finding that is diagnostic of this infection [4, 6, 9, 12, 14, 24].

Epidural abscesses that are not associated with an osseous lesion can have an appearance similar to that of epidural metastases on unenhanced MR images. IV contrast enhancement can help in the diagnosis if rim enhancement is present. If the enhancement is diffuse, differentiation with MR alone can be extremely difficult [6, 24].

Differentiation of a postoperative disk-space infection from normal immediate postoperative changes can be extremely difficult because both enhance after contrast administration and their appearances on T1- and T2-weighted images are identical [12].

Noninfective inflammatory conditions like ankylosing spondylitis can also be difficult to differentiate from infective spondylitis on unenhanced MR images [6].

Intradural Extramedullary Disease

Infections of spinal meninges can be caused by bacterial (pyogenic, granulomatous), fungal, parasitic, and viral organisms [54]. Transmission occurs either by the hematogenous route or by direct spread from infective spondylitis, cranial meningitis, and/or parenchymal brain or spinal cord infections [54]. Meningeal involvement may or may not coexist with spinal cord or nerve root infection.

The nature and course of this illness varies a great deal, and depends on the virulence of the offending organism, the number of organisms released in the subarachnoid space, and the immunologic response of the patient [54–56]. Fever and malaise are observed in severe cases with acute onset, but the most important clinical feature is that of radiculomyelopathy. The symptoms and signs are a mixture of back pain, radicular pain, and progressive paraplegia or tetraplegia depending on the location and extent of the lesion. An elevated ESR is frequently present with or without leukocytosis [54–56]. A lumbar puncture may prove to be "dry" or yield only few drops of xanthochromic fluid. The CSF protein levels are invariably raised and the sugar level may be low with a varying increase in the number of cells [54–56].

Bacterial Infections

Pyogenic leptomeningitis.—Pyogenic leptomeningitis is the most common bacterial infection of the spinal axis [55]. The vast majority of these cases occur as part of cerebral men-

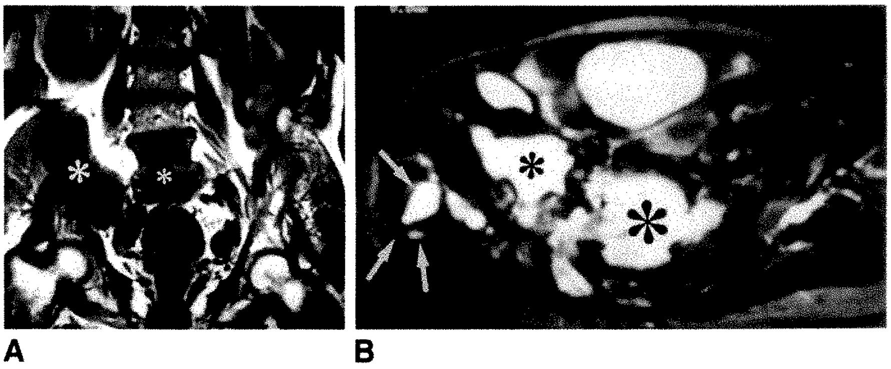

Fig. 5.—50-year-old man with hydatid disease involving lower lumbar spine and right iliac bone who had lower back pain radiating to right lower extremity. Immunologic tests were positive for *Echinococcus multilocularis*.

***A*, Coronal MR image (SE 500/30) shows evidence of replacement of body of L5 by a mass isointense with muscles (*small asterisk*). Similar mass is seen arising from right iliac crest (*large asterisk*).**

***B*, Axial image (SE 2000/100) at level of L5 shows markedly increased signal from affected fifth lumbar vertebra (*large asterisk*) and neighboring soft tissues, right iliac bone (*small asterisk*), and gluteus muscle (*arrows*). At surgery, several hydatid cysts were removed from body of L5, neighboring soft tissues, and right iliac region.**

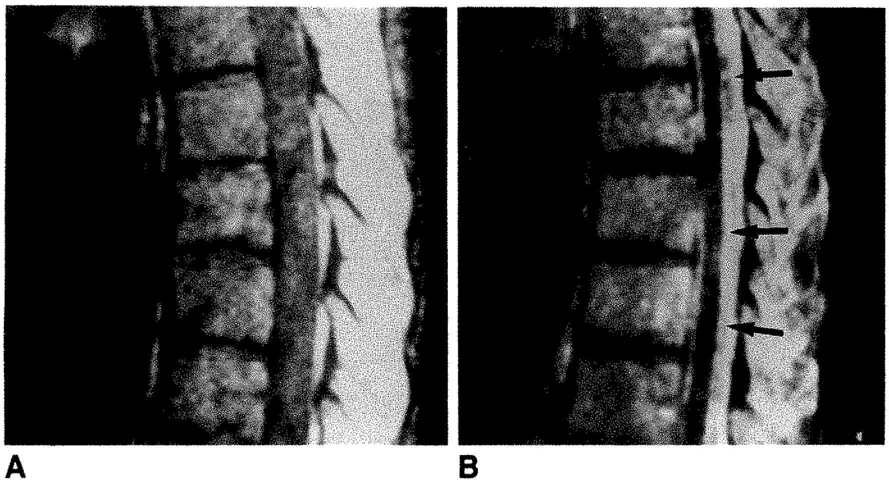

Fig. 6.—26-year-old man with enterococcal meningitis who had fever and, subsequently, sepsis and quadriparesis. Gram-positive cocci were present on a CSF smear and enterococci were grown from blood.

A, Midsagittal MR image (SE 400/20) in midthoracic region shows loss of normal spinal cord-CSF interface and poor characterization of underlying disease. Compare with Figs. 1A and 2A.

B, Midsagittal MR image (SE 400/20) obtained after IV gadopentetate dimeglumine shows diffuse circumferential dural enhancement (*arrows*) surrounding spinal cord. Disease is localized in intradural extramedullary compartment.

(Reprinted from Gero et al. [13].)

ingitis. Organisms implicated in the adult disease include *Neisseria meningitidis*, *Diplococcus pneumoniae*, *Staphylococcus aureus*, and *Streptococcus*. In children, *Haemophilus influenzae* and *Escherichia coli* are the most common [54].

The diagnosis in children can be reached by characteristic clinical features and positive CSF and blood test results. In the adult population, the clinical findings can be misleading, and CSF could demonstrate the presence of inflammation [55]. Because pyogenic leptomeningitis is rarely associated with infective spondylitis, plain radiographs, unenhanced CT, and bone scintigraphy provide limited help in the detection and delineation of this disease. Myelography may show partial or complete obstruction depending on the severity of the lesion [55].

In the absence of associated bone infection, unenhanced MR images rarely suggest the presence of meningeal disease [13] (Fig. 6). On T1-weighted images, obliteration of the area of low signal surrounding the cord should raise the possibility of a dural lesion. The increased signal intensity of CSF may obscure that obtained from the affected meninges on T2-weighted images [13]. With the administration of gadopentetate dimeglumine, enhancement of the inflamed dura and/or nerve root sheath will invariably be noticed, together with possible areas of involvement of the spinal cord [13] (Fig. 6).

Three patterns of enhancement of intradural extramedullary infections have been noted: linear, nodular, and diffuse [13]. No correlation was found between the patterns of enhancement and the severity of disease or the type of offending organisms [13]. The degree of meningeal enhancement has been shown to correlate well with the severity of the inflammatory lesion on histopathologic sections intracranially. This has not so far been verified for spinal meningeal infections, but it can be presumed [13].

Granulomatous leptomeningitis.—Tuberculous leptomeningitis remains an important clinical problem in many developing countries [56, 57]. Although it is rare in the Western world, it is by no means eradicated. The disease differs from other meningitides in the frequency of associated involvement of the spinal cord and nerve roots, so much so that it has been designated in the literature as radiculomyelitis [56, 57].

Intradural tuberculous infections occur invariably as an extension of basal meningitis or extension from infective spondylitis [56, 57]. In a recent publication, Chang et al. [57] reported 13 cases with tuberculous radiculomyelitis, for which 85% had documented intracranial meningitis and 8% had associated vertebral infection. Early in the disease the meninges may show a variable degree of congestion and exudation. The spinal cord and nerve roots may also be involved and show various degrees of edema and inflammation [57].

Tuberculoma formation may occur anywhere on the inner aspect of the dura mater. The lesion tends to dig a crater in the spinal cord so that it may be difficult to distinguish between dural disease and an intramedullary tuberculoma [57].

Tuberculous leptomeningitis can be diagnosed either by isolation of acid-fast bacilli from CSF or by definite evidence of old or active intracranial or vertebral body tuberculosis [56, 57]. The presence of radiculomyelopathy and characteristic imaging features are essential to localize the lesion [57]. The presence of caseating granulomas on pathologic specimens obtained from affected meninges and/or an adequate response to antituberculous chemotherapy are additional important diagnostic alternatives [56, 57].

As in pyogenic intradural extramedullary disease, enhanced MR imaging should be the method of first choice for assessing these lesions [57]. It is superior to IV contrast-enhanced CT for detecting and delineating meningeal involvement as well as associated spinal cord disease [57]. These features are indistinguishable from those described for pyogenic infections [13] (Fig. 7). Associated abnormalities of the nerve roots within the thecal sac in patients with ineffective arachnoiditis (edema, adhesions, tuberculous nodules) can, however, be difficult to identify on MR images [13, 57]. Conventional myelography remains the best method for demonstrating these findings [57].

Another bacterial granulomatous infection that could affect spinal meninges is syphilis [58]. MR features in a patient with syphilitic meningitis were recently described by Gero et al. [13], and the findings were similar to those associated with other meningitides [13].

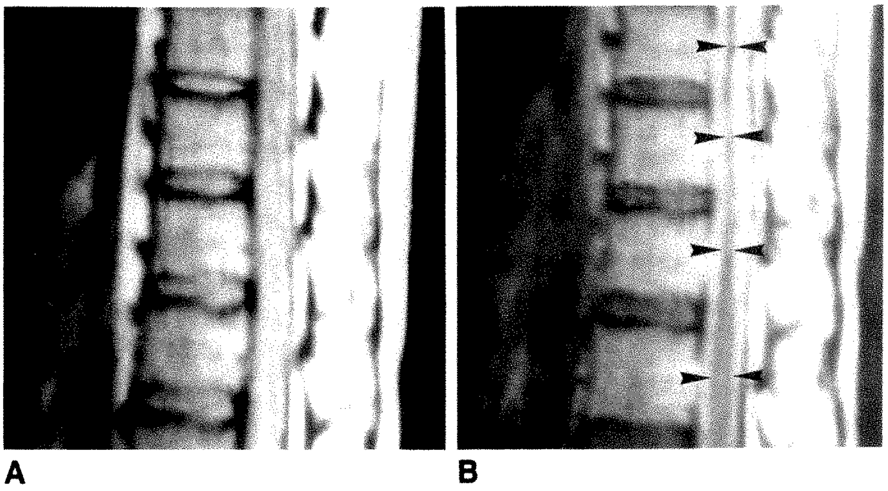

Fig. 7.—28-year-old man with extensive tuberculous meningitis who had bilateral leg weakness. Samples of CSF showed increased lymphocytes and low sugar, erythrocyte sedimentation rate measured 100 mm, and tuberculin test was positive. Significant gradual improvement in the neurologic status was achieved a few weeks after antituberculous therapy was begun.

***A*, Midsagittal MR image (SE 500/30) shows loss of normal spinal cord–CSF interface.**

***B*, Midsagittal MR image (SE 500/30) obtained after IV administration of gadopentetate dimeglumine shows circumferential meningeal enhancement extending from lower cervical to upper lumbar region. Spinal cord (*arrowheads*) is sandwiched within inflamed dura.**

Fungal Meningitis

Cases of fungal meningitis are exceedingly rare. Gero et al. [13] examined a case of fungal meningitis by using MR imaging. The findings were indistinguishable from those of other meningitides.

Viral Meningitis

Cases of viral meningitis are rare, but they have clinical presentations similar to those of other meningitides [59]. The diagnosis is confirmed by isolating the virus from CSF or by demonstrating an elevated titer in the CSF [59]. No description of the MR features of documented viral meningitis has been given in the literature.

Parasitic Meningitis

Involvement of spinal meninges by cysticercosis is rare and manifests by subarachnoid cyst formation and/or arachnoiditis [60–62]. The infection is thought to spread from intracranial disease via the posterior fossa [60]. The cervical, thoracic, and lumbar regions are affected equally [60]. Diagnosis is usually established by CSF studies, which show eosinophilia, positive reaction to complement fixation test for cysticercosis, and elevated protein [61, 63]. No description of the MR findings in meningeal cysticercosis in the spine has appeared in the literature.

Differential Diagnosis in Intradural Extramedullary Disease

The MR findings in patients with intradural extramedullary infections are virtually indistinguishable from those of leptomeningeal tumor spread [13]. Although contrast administration increases the sensitivity of MR in detecting and delineating intradural extramedullary disease, it does not improve the diagnostic specificity. Fine linear enhancement on the cord surface has been detected in various infections as well as in sarcoidosis [13].

Spinal Cord Infections

Multiple agents have been implicated in spinal cord infections, as they have in infections involving brain parenchyma. These include bacterial (pyogenic, granulomatous), fungal, parasitic, and viral organisms [63]. The hematogenous route is the most frequent method of transmission, but extension from brain and meningeal infections as well as vertebral osteomyelitis have been observed. The clinical presentation can be acute or chronic depending on the type of offending organism [55]. In the acute form, back pain is not severe and is followed immediately by paresthesia with a rising level of sensory impairment until complete transverse myelitis develops. Disturbance of sphincter function is an early finding [55].

Subacute or chronic intramedullary infections tend to mimic the clinical presentation of neoplasms with regard to the fluctuation of symptoms [13]. Recurrent bouts of radiculomyelitis with intervals of normal neurologic function may be present for months or years.

Peripheral blood count reveals findings of inflammation in acute cases but is usually normal in subacute and chronic cases. CSF analysis can show early pleocytosis with an increased number of polymorphonuclear leukocytes. Increased protein is invariably present, with normal or low glucose levels depending on the type of organism [55].

Bacterial Intramedullary Infections

Pyogenic myelitis.—Intramedullary pyogenic abscesses of the spinal cord are exceedingly rare [55]. The thoracic cord is the area of predilection. Predisposing conditions include pneumonia, bronchiectasis, pelvic infections, and immunosuppression [55]. Many pathologists suggest that the lesion starts as spinal venous thrombosis with resultant ischemic infarction that is later complicated by bacterial colonization [55]. MR imaging is the method of choice for assessing these lesions because it should provide optimal detection and delineation, although characterization may not be possible. To

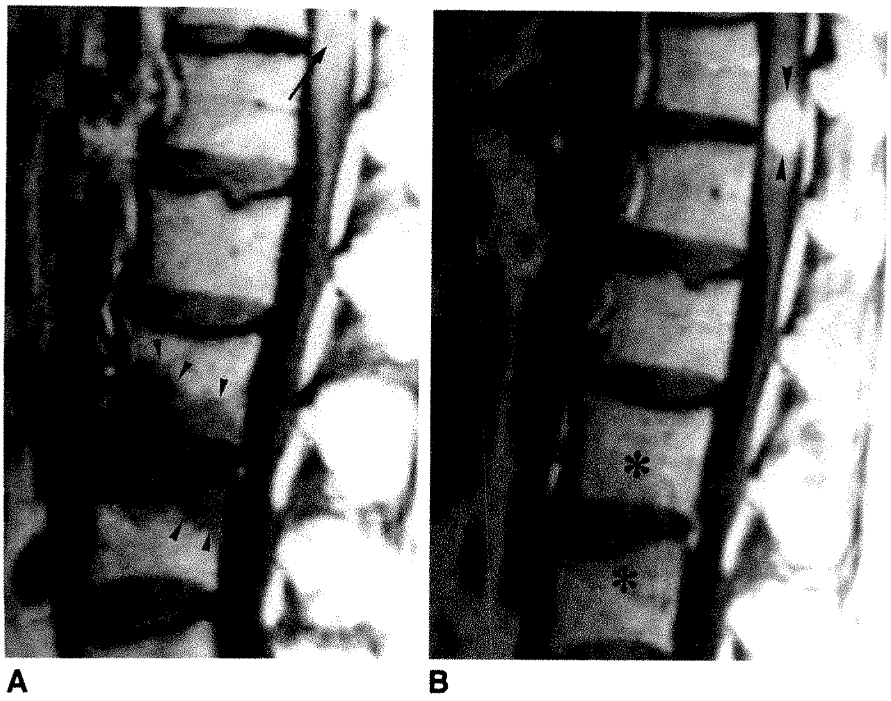

Fig. 8.—47-year-old man with tuberculoma of conus medullaris and infective spondylitis at L4–L5 who had bilateral leg weakness and progressive urinary retention. Examination was performed to exclude disk herniation.

A, Midsagittal MR image (SE 450/30) of lumbar spine shows decreased signal in vertebral bodies around L4–L5 disk (*arrowheads*). Note focal enlargement of conus (*arrow*). Long TR/TE study (*not shown*) showed moderately increased signal from L4 and L5 and nodular high signal from lesion in conus, with surrounding poorly defined higher signal.

B, Midsagittal MR image (SE 450/30) obtained after IV gadopentetate dimeglumine shows nodular enhancement of lesion in conus (*arrowheads*). Note also enhancement of affected vertebrae to level of isointensity with normal vertebrae (*asterisks*). Similar nodules were seen in several locations in brain. Cord and brain nodules as well as spondylitis disappeared 6–8 months after antituberculous therapy was begun.

(Reprinted from Gero et al. [13].)

date, no cases of documented intramedullary pyogenic abscesses have been evaluated by MR.

Bacterial granulomatous infection of the cord.—The overall rate of intramedullary granulomatous infections is low, and tuberculosis is probably the most common cause of such lesions [13]. Gero et al. [13] recently described the MR appearances in four patients with this disease, all with associated intracranial tuberculomas. Focal spinal cord swelling was identified on T1- and T2-weighted images and nodular enhancement was detected after contrast administration [13] (Fig. 8). Gradual decrease in the size was noted on posttherapy follow-up [13]. Similar lesions were described by Chang et al. [57], but these were associated with spinal meningitis. An intramedullary syphilitic nodule also diagnosed by contrast-enhanced MR was recently described by Tashiro et al. [64].

Viral Intramedullary Infections

Viruses are the most commonly organisms to directly involve the cord [13, 65]. Poliomyelitis, coxsachievirus A and B, herpes zoster, and rabies have been implicated [66]. Cytomegalovirus, herpes simplex, and human T-cell lymphocytotropic virus III have been isolated from CSF and/or cord parenchyma in patients with AIDS [67–69]. Irrespective of the offending viral agent, the response of the cord parenchyma to the infection is similar: edema with vessel thrombosis leading to ischemia and infarction [13, 70]. Pathologically, the affected cord segment exhibits perivascular inflammation with myelin degeneration of neighboring nerve fibers; the axons are normally spared.

On MR images two sets of findings have been described. In the first set the cord may show diffuse swelling over numerous segments with or without skip areas [13, 63, 69]. A subtle increase in signal intensity may be seen on T1-weighted images, probably related to petechial hemorrhage [13]. T2-weighted images will demonstrate diffuse high signal intensity in the affected areas (Fig. 9). Diffuse, peripheral, or speckled enhancement may be detected on enhanced images [13]. In the second set, the cord may not show enlargement and T2-weighted images may demonstrate diffuse or focal areas of high signal intensity. Faint nodular enhancement can be present after contrast administration [13] (Fig. 9).

Parasitic Intramedullary Infections

Schistosoma myelitis.—Spinal cord disease is a rare manifestation of schistosomiasis and is usually caused by *Schistosoma mansoni* or *Schistosoma haematobium* [71–73]. Patients have pain and associated radiculomyelopathy of the lower extremities with or without sphincteric problems.

Ova carried by mesenteric venules are deposited into the substance of the cord, where a granulomatous reaction is induced [71–73]. This reaction is the major factor responsible for the pathologic and clinical features of *Schistosoma* myelitis.

Dupuis et al. [71] recently described a proved case of *Schistosoma* myelitis in which MR was the only examination that documented the cord abnormalities. Mild enlargement was seen on T1-weighted images, and diffuse increased signal intensity was demonstrated from the affected cord segment on T2-weighted images. Heterogeneous enhancement was noted on enhanced images [71].

Spinal cord cysticercosis.—Intramedullary spinal cord cysticercosis is extremely rare and thought to occur as a result of hematogenous dissemination [61, 74]. Parenchymal cord

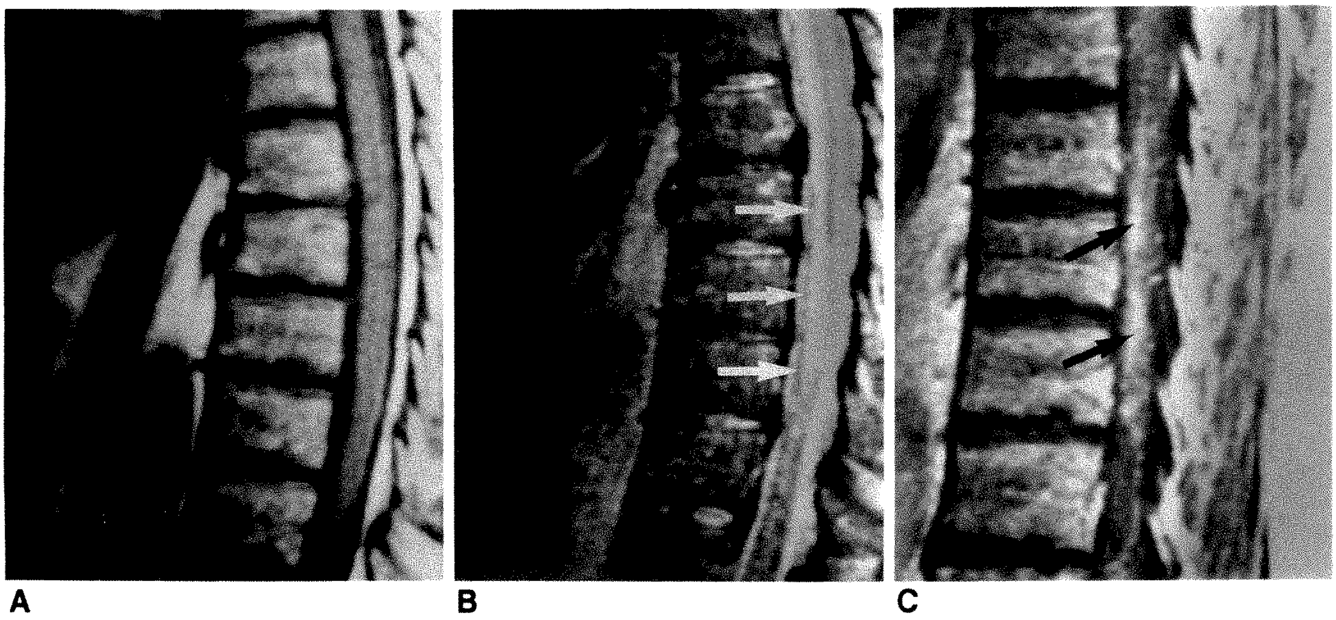

Fig. 9.—41-year-old man with herpes zoster myelitis who had bilateral progressive leg weakness. Concomitant herpes zoster skin papules were present. Acyclovir therapy resulted in moderate clinical improvement.

***A*, Midsagittal MR image (SE 600/30) in thoracic region shows minimal swelling of cord.**

***B*, Midsagittal MR image (SE 600/30) shows increased signal from cord to a level of isointensity with CSF (*arrows*).**

***C*, Midsagittal MR image (SE 600/30) obtained after IV administration of gadopentetate dimeglumine shows speckled pattern of enhancement within cord (*arrows*).**

(Reprinted from Gero et al. [13].)

lesions are similar to those of the brain and tend to produce neurologic symptoms by virtue of the inflammatory reaction and edema caused by parasite metabolites, the mass effect of the cyst, and/or cord degeneration [74, 75].

Castillo et al. [74] recently described the MR changes in a proved case of *Cysticercus* myelitis. The cord demonstrated fusiform widening in the cervical, thoracic, and lumbar regions [74]. T1-weighted images showed low signal intensity at the three levels and T2-weighted images showed hyperintensity in the thoracic and conus medullaris lesions. The lesion in the conus was shown to be a *Cysticercus cellulosae* vesicle. The other levels were not explored [74].

Differential Diagnosis in Intramedullary Infections

Several pathologic entities can produce MR imaging findings that are indistinguishable from those of infective myelitis. Intramedullary tumors can produce changes that are similar to those of spinal cord granulomas with regard to the fusiform dilatation of the cord and the pattern of enhancement [13]. Although both lesions can have an insidious onset, the presence of well-documented old or associated intracranial infection, meningitis, or infective spondylitis should favor the diagnosis of infection. CSF findings of pleocytosis, increased protein, and low sugar will also favor an infective cause.

Although the MR features of nongranulomatous infective myelitis are relatively easy to differentiate from those of intramedullary neoplasms (mild cord enlargement with patchy enhancement in myelitis vs severe enlargement and marked enhancement in tumor), they are virtually indistinguishable from inflammatory conditions of unestablished cause such as sarcoidosis, multiple sclerosis, and acute idiopathic transverse myelitis [13]. Patients with intramedullary stroke may also have similar MR findings. CSF antigen titers and viral cultures can help if positive, but they often take a long time before they are available. Even open biopsy may sometimes fail to isolate the causative agent when the pathologic changes are consistent with myelitis.

Conclusions

MR imaging is an ideal method for evaluating infections of the spine. It is extremely sensitive in detecting and delineating infective lesions irrespective of their spinal location. Evidence on MR of involvement of two consecutive vertebrae and the intervening disk is virtually diagnostic of infective spondylitis. Rim enhancement around abscess loculations within the vertebral bodies and/or paraspinal soft tissues is strongly suggestive of tuberculous spondylitis. In addition, the features of acute infective myelitis on MR are fairly characteristic.

Limitations of MR include the difficulty by which interventional procedures can be performed under its guidance (biopsy and/or drainage procedures); a low diagnostic specificity for distinguishing granulomatous myelitis and intradural extramedullary infections from neoplasia; and the difficulty of differentiating infective myelitis from lesions like sarcoidosis, multiple sclerosis, and idiopathic transverse myelitis.

ACKNOWLEDGMENT

I thank Rose Avecilla-Cansanay for assistance in manuscript preparation.

REFERENCES

1. Modic MT, Feiglin DH, Piraino DW, et al. Vertebral osteomyelitis: assessment using MR. *Radiology* **1985**;157:157–166
2. Smith FW, Runge V, Permezel M, Smith CC. Nuclear magnetic resonance (NMR) imaging in the diagnosis of spinal osteomyelitis. *Magn Reson Imaging* **1984**;2:53–56
3. Modic MT, Pfanze W, Feiglin DH, Belhobek G. Magnetic resonance imaging of musculoskeletal infections. *Radiol Clin North Am* **1986**;24: 247–258
4. Sharif HS, Clark DC, Aabed MY, et al. Granulomatous spinal infections: MR imaging. *Radiology* **1990**;177:101–107
5. Sharif HS, Aideyan OA, Clark DC, et al. Brucellar and tuberculous spondylitis: comparative imaging features. *Radiology* **1989**;171:419–425
6. Smith AS, Blaser SI. Infectious and inflammatory process of the spine. *Radiol Clin North Am* **1991**;29:809–827
7. Smith SS, Weinstein MA, Mizushima A, et al. MR imaging characteristics of tuberculous spondylitis vs vertebral osteomyelitis. *AJR* **1989**;153:399–405
8. Bertino RE, Porter BA, Stimac GK, Tepper SJ. Imaging spinal osteomyelitis and epidural abscess with short TI inversion recovery (STIR). *AJNR* **1988**;9:563–564
9. Thrush A, Enzman D. MR imaging of infectious spondylitis. *AJNR* **1990**;11:1171–1180
10. Dwyer AJ, Frank JA, Sank VJ, Reining JW, Hickey AM, Doppman JL. Short-T1 inversion-recovery pulse sequence: analysis and initial experience in cancer imaging. *Radiology* **1988**:827–836
11. Baker LL, Goodman SB, Perbash I, Lane B, Enzman D. Benign versus pathologic compression fractures of vertebral bodies: assessment with conventional spin echo, chemical shift, and STIR MR imaging. *Radiology* **1990**;174:495–502
12. Post MJD, Sze G, Quencer RM, Eismont FJ, Green BA, Gahbauer H. Gadolinium enhanced MR in spinal infection. *J Comput Assist Tomogr* **1990**;14:721–729
13. Gero B, Sze G, Sharif H. MR imaging of intradural inflammatory diseases of the spine. *AJNR* **1991**;12:1009–1019
14. De Roos A, van Meerten EP, Bloem JL, Bluemm RG. MRI of tuberculous spondylitis. *AJR* **1986**;146:79–82
15. Resnick D, Niwayama G. Osteomyelitis, septic arthritis and soft tissue infection: the axial skeleton. In: Resnick D, Niwayama G, eds. *Diagnosis of bone and joint disorders*. Philadelphia: Saunders, **1988**:2619–2754
16. Sutton MJ. Pyogenic osteomyelitis of the vertebral body. *J Am Osteopath Assoc* **1984**;83:724–728
17. Wiley AM, Trueta J. The vascular anatomy of the spine and its relationship to pyogenic vertebral osteomyelitis. *J Bone Joint Surg [Br]* **1959**;41-B:796–809
18. Sartoris DJ, Moskowitz PS, Kaufman RA, Ziprkowski MN, Berger PE. Childhood diskitis: computed tomographic findings. *Radiology* **1983**;149:701–707
19. Fischer GW, Popich GA, Sullivan DE, Mayfield G, Mazat BA, Patterson PH. Diskitis: a prospective diagnosis analysis. *Pediatrics* **1978**;62: 543–548
20. Fredrickson B, Yuan H, Olans R. Management and outcome of pyogenic vertebral osteomyelitis. *Clin Orthop* **1978**;131:160–167
21. Bruns J, Maas R. Advantages of diagnosing bacterial spondylitis with magnetic resonance imaging. *Arch Orthop Trauma Surg* **1989**;108:30–35
22. Aguila LA, Piraino DW, Modic MT, Dudley AW, Duchesneau PM, Weinstein MA. The internuclear cleft of the intervertebral disk: magnetic resonance imaging. *Radiology* **1985**;155:155–158
23. Van Lom KJ, Kellerhouse LE, Pathria MN, et al. Infection versus tumor in the spine: criteria for distinction with CT. *Radiology* **1988**;166:851–855
24. Beltran J, Chandnani V, McGhee RA, Kursunoglu Brahme S. Gadopentetate dimeglumine-enhanced MR imaging of the musculoskeletal system. *AJR* **1991**;156:457–466
25. Saini S, Modic MT, Hamm B, Hahn PF. Advances in contrast-enhanced MR imaging. *AJR* **1991**;156:235–254
26. Simon JH, Szumowski J. Chemical shift imaging with paramagnetic contrast material enhancement for improved lesion depiction. *Radiology* **1989**;171:539–543
27. Heller RM, Szalay EA, Green NE, Horev GD, Kirchner SD. Disc space infection in children: magnetic resonance imaging. *Radiol Clin North Am* **1988**;26:207–209
28. Hoffer FA, Strand RD, Gebhardt MC. Percutaneous biopsy of pyogenic infection of the spine in children. *J Pediatr Orthop* **1988**;8:442–444
29. Angtuaco EJ, McConnel JR, Chadduck WM, Flanigan S. MR imaging of spinal epidural sepsis. *AJNR* **1987**;8:879–883
30. Donovan Post MJ, Quencer RM, Montalvo BM, Katz BH, Eismont FJ, Green BA. Spinal infection: evaluation with MR imaging and intraoperative US. *Radiology* **1988**;169:765–771
31. Curling OD, Gower D, McWhoter JM. Changing concepts in spinal epidural abscess: a report of 29 cases. *Neurosurgery* **1990**;27:185–192
32. Halvin ML, Kaminski HJ, Ross JS, Ganz E. Spinal epidural abscess: a ten year perspective. *Neurosurgery* **1990**;27:177–184
33. Sharif HS, Clark DC, Aabed MY, Aideyan OA, Haddad MC, Mattsson TA. MR imaging of thoracic and abdominal wall infections: comparison with other imaging procedures. *AJR* **1990**;154:989–995
34. Pritchard DJ. Granulomatous infections of bones and joints. *Orthop Clin North Am* **1975**;6:1029–1047
35. Weaver P, Lifeso RM. The radiological diagnosis of tuberculosis of the adult spine. *Skeletal Radiol* **1984**;12:178–186
36. Hsu LCS, Yau ACMC, Hodgson AR. Tuberculosis of the spine. In: Evarts CM, ed. *Surgery of musculoskeletal system*, vol. 4. New York: Churchill Livingstone, **1983**:153–168
37. Sixth Report of the Medical Research Council Working Party on Tuberculosis of the Spine. Five-year assessment of controlled trials of ambulatory treatment, debridement and anterior spinal fusion in the management of tuberculosis of the spine. *J Bone Joint Surg [Br]* **1979**;60-B:163–177
38. Madkour MM, Sharif HS, Aabed MY, Al Fayez MA. Osteoarticular brucellosis: results of bone scintigraphy in 140 patients. *AJR* **1988**;150: 1101–1105
39. Lifeso RM, Harder E, McCorkell SJ. Spinal brucellosis. *J Bone Joint Surg [Br]* **1985**;67-B:345–351
40. Akhtar M. Brucellosis: histopathological features. In: Madkour M, ed. *Brucellosis*. London: Butterworths, **1989**:59–69
41. Dalinka MK, Dinnenberg S, Greendyke WH, Hopkins. Roentgenographic features of osseous coccidioidomycosis and differential diagnosis. *J Bone Joint Surg [Am]* **1971**;53-A:1157–1164
42. Mariat F. The mycetomas: clinical features, pathology, etiology and epidemiology. *Contrib Microbiol Immunol* **1977**;4:1–39
43. Sharif HS, Clark DC, Aabed MY, et al. MR imaging of mycetoma: comparison with CT. *Radiology* **1991**;178:865–870
44. Charles RW, Grovender S, Maidoo KS. Echinococcal infection of the spine with neural involvement. *Spine* **1988**;13:47–49
45. Claudon M, Bracard S, Plenat F, Regent D, Bernadac P, Picard L. Spinal involvement in alveolar echinococcosis: assessment of two cases. *Radiology* **1987**;162:571–572
46. Levack B, Kernohan J, Edgar MA, Ransford OA. Observations on the current and future surgical management of the hydatid disease affecting the vertebrae. *Spine* **1986**;11:583–590
47. Jena A. Primary spinal echinococcosis causing paraplegia: case report with MR and pathologic correlation. *AJNR* **1991**;12:560
48. Beggs I. The radiology of hydatid disease. *AJR* **1985**;145:639–648
49. Michael MA, Ciric IC, Tarkington JA. MR imaging in spinal echinococcosis. *J Comput Assist Tomogr* **1985**;9:398–400
50. Pau A, Simonetti G, Tortori-Donati P, Turtas S, Viale GL. Computed tomography and magnetic resonance imaging in spinal hydatidosis. *Surg Neurol* **1987**;29:365–369
51. Kaoutzanis M, Anagnostopoulos D, Apostolou A. *Acta Neurochir* (Wien) **1989**;98:60–65
52. Modic MT, Mazaryk TJ, Ross JS, Carter JR. Imaging of degenerative disk disease. *Radiology* **1988**;168:177–186
53. De Ross A, Kressel H, Spritzer C, Dalinka M. MR imaging of marrow changes adjacent to end plates in degenerative lumbar disk disease. *AJR* **1987**;149:531–534
54. Walton J. Diseases of the meninges. In: Walton J, ed. *Brain's diseases of*

the nervous system. Oxford: Oxford University Press, **1985**:237–348

55. D'Angelo CM, Whisler W. Bacterial infections of the spinal cord and its coverings. In: Vinken PJ, Bruyn GW, eds. *Handbook of clinical neurology*, vol. 33. Amsterdam: North-Holland, **1978**:187–194
56. Tandon PN. Tuberculous meningitis (cranial and spinal). In: Vinken PJ, Bruyn GW, eds. *Handbook of clinical neurology*, vol. 33. Amsterdam: North Holland, **1978**:195–262
57. Chang KH, Han MH, Choi YW, Kim IO, Han MC, Kim CW. Tuberculous arachnoiditis of the spine: findings on myelography, CT, and MR imaging. *AJNR* **1989**;10:1255–1262
58. Johnson KP. Syphilitic infections of the central nervous system. In: Wyngaarden JB, Smith LH, eds. *Cecil textbook of medicine*. Philadelphia: Saunders, **1988**:2187–2191
59. Price RW. Acute viral meningitis and encephalitis. In: Wyngaarden JB, Smith LH, eds. *Cecil textbook of medicine*. Philadelphia: Saunders, **1988**:2192–2194
60. Enzmann DR. Infection and inflammation. In: Enzmann DR, De La Paz RL, Rubin JB, eds. *Magnetic resonance of the spine*. St. Louis: Mosby, **1990**:260–300
61. Trelles JO, Trelles L. Cysticercosis of the nervous system. In: Vinken PJ, Bruyn GW, eds. *Handbook of clinical neurology*, vol. 35. Amsterdam: North Holland, **1978**:291–318
62. Sotelo J, Marin C. Hydrocephalus secondary to cysticercotic arachnoiditis. *J Neurosurg* **1987**;66:686–689
63. Merine D, Wang H, Kumar AJ, Zinreich SJ, Rosenbaum AE. CT myelography and MR imaging of acute transverse myelitis. *J Comput Assist Tomogr* **1987**;11:606–608
64. Tashiro K, Moriwaka F, Sudok, Akino M, Abe H. Syphilitic myelitis with its MRI verification and successful treatment. *Jpn J Psychiatry Neurol* **1987**;41:269–272
65. Elghazawi AK. Clinical syndromes and differential diagnosis of spinal disorders. *Radiol Clin North Am* **1991**;29:651–661
66. Appel B, Moens E, Lowenthal A. MRI of the spine and spinal cord: infectious and inflammatory pathology. *J Neuroradiol* **1988**;15:325–334
67. Awerbuch G, Feinberg WM, Ferry P, Komar N, Clements J. Demonstration of acute post-viral myelitis with magnetic resonance imaging. *Pediatr Neurol* **1987**;3:367–369
68. Tucker T, Dix RD, Katzen C, Davis RL, Schmidley JW. Cytomegalovirus and herpes simplex virus ascending myelitis in a patient with acquired immune deficiency syndrome. *Ann Neurol* **1985**;18:74–79
69. Shabas D, Gerard G, Cunha B, Malhotra V, Leeds N. MR imaging of AIDS myelitis. *AJNR* **1989**;10:S51–S52
70. Walton J. Virus infections of the nervous system. In: Walton J, ed. *Brain's diseases of the nervous system*. Oxford: Oxford University Press, **1985**:274–294
71. Dupuis MJ, Atroni S, Dooms GC, Gonsette RE. MR imaging of schistosomal myelitis. *AJNR* **1990**;11:782–783
72. Efthimiou J, Denning D. Spinal cord disease due to schistosoma mansoni successfully treated with oxamniquine. *BMJ* **1984**;288:1343–1344
73. Scrimgeour EM, Gajdusek DC. Involvement of the central nervous system in *Schistosoma mansoni* and *S. haemotobium* infection. *Brain* **1985**;108:1023–1038
74. Castillo M, Quencer RM, Post MJD. MR of intramedullary cysticercosis. *AJNR* **1988**;9:393–395
75. Lotz J, Hewlett R, Alheit B, Bowen R. Neurocysticercosis: correlative pathomorphology and MR imaging. *Neuroradiology* **1988**;30:35–41

Book Review

Magnetic Resonance Test and Syllabus. Section chairman: William G. Bradley, Jr. Reston, VA: American College of Radiology, 658 pp., 1991. Residents, $90; ACR members, $110; nonmembers, $175

Magnetic Resonance Test and Syllabus is one of the latest volumes in the well-known series of the American College of Radiology (ACR) syllabi. It is edited by William G. Bradley, Jr., and the coauthors include Drs. Brant-Zawadzki, Hasso, Herfkens, Lee, Modic, Murphy, and Stark. Dr. Bradley mentions that there was initially some debate about the need for a technique-oriented syllabus on MR imaging. This impressive volume more than justifies the decision of the ACR to proceed with such a project. The book discusses many aspects of MR imaging that would have been difficult to cover in organ-specific syllabi.

The book follows the standard format of ACR syllabi. It commences with a series of 172 multiple-choice questions, linked to 38 clinical cases. The questions are relatively difficult, even for a good fourth-year resident. The body of the book is composed of detailed answers to each question. This format allows the authors to cover a wide range of MR issues, with succinct and clear discussions of basic principles, hemorrhage, flow, MR angiography, administration of contrast material, signal-to-noise ratio, safety issues, artifacts, and surface coils. Because the discussion of each of these issues is linked to a specific set of images, the reader can immediately grasp the practical relevance of the text. The succinct integration of the theory and practice of MR imaging is one of the outstanding features of this book and represents a refreshing change from standard textbooks on MR in which readers must wade through at least two chapters of basic principles before being allowed to see images.

About one third of the cases included in the syllabus are related to the brain. The remaining systems covered, in various detail, include the spine, head and neck, cardiovascular system, chest, pelvis, liver, kidneys, and bone. Two of the cases (breast cysts, and imaging of acute myocardial infarction) are primarily of academic interest. The syllabus format places an inevitable limit on the depth and range of coverage of some topics. Areas omitted or only minimally discussed include imaging of the brachial plexus, soft-tissue tumors, imaging of congenital brain lesions and brain lesions in children, imaging of the orbit, and imaging of congenital heart disease. In addition, musculoskeletal MR seems underrepresented. More detailed coverage of these topics will presumably be found in the organ-specific syllabi. This book is not intended as, and should not be used as, a substitute for one of the standard textbooks on MR imaging.

The quality of the images, apart from a few of the body images, is good. Almost all images are clearly labeled with the imaging parameters. Each section is followed by a comprehensive list of readings, which in most cases has been updated to 1989 or 1990. This is important, as the searching questions provide a strong stimulus to further reading.

Why read this book? For residents and practicing radiologists, the book offers a valuable method for evaluating the depth of their knowledge and correcting misconceptions. The lucid discussions of basic principles are an adequate justification for buying rather than borrowing this book. For practicing radiologists, the book also provides an inexpensive method of gaining 20 hours of continuing medical education credit.

Any book on MR imaging runs the risk of being outdated by the time it is published. The rate of growth of MR makes this partial obsolescence inevitable. If the limitations of publication time are considered, this book is reasonably up-to-date in its coverage of standard spin-echo, contrast-enhanced, and gradient-echo imaging. Discussion of developing areas such as fast MR imaging and MR angiography must await the next edition.

This book is already in heavy demand in our library, and it will be useful to third- and fourth-year residents who are grappling with the challenges of MR imaging. I recommend it also to radiologists who wish to bring themselves up to speed on aspects of MR imaging.

David A. Lynch
University of Colorado Health Sciences Center
Denver, CO 80262

Intradural Schwannomas of the Spine: MR Findings with Emphasis on Contrast-Enhancement Characteristics

David P. Friedman[1]
Lisa M. Tartaglino
Adam E. Flanders

Intradural extramedullary schwannomas are nerve sheath neoplasms that consist of focal proliferations of Schwann cells involving a spinal nerve. We reviewed the MR findings in seven patients with pathologically proved intradural schwannomas. The contrast-enhancement characteristics on MR images were determined and compared with the histologic features of the tumor. Six lesions were variably hyperintense on T2-weighted images and one was uniformly hypointense compared with the signal intensity of the spinal cord. Signal on T1-weighted images ranged from hypointense to isointense. All seven tumors showed heterogeneous enhancement; in five, the enhancement involved only the periphery of the lesion. The pattern of enhancement did not correlate with the signal characteristics noted on unenhanced T1- and T2-weighted images. Pathologically, hyaline thickening of vessel walls and cyst formation were prevalent in the peripherally enhancing lesions. However, enhancement did not correlate with the relative proportion of Antoni type A and type B tissue.

Recognition of the MR characteristics of intradural extramedullary schwannomas may be helpful in the differential diagnosis of spinal tumors. In particular, peripheral contrast enhancement of an intradural extramedullary tumor on MR images should suggest the diagnosis of schwannoma.

AJR 158:1347–1350, June 1992

Nerve sheath tumors include schwannoma and the more common neurofibroma. The two lesions are often combined in regard to description of their MR appearance, particularly as it relates to enhancement characteristics [1–5]. Consequently, we reviewed the MR appearance of seven pathologically proved intradural spinal schwannomas. The MR and pathologic findings were compared, and the value of the contrast-enhancement characteristics of schwannomas in the differential diagnosis of intradural extramedullary neoplasms was studied.

Materials and Methods

Seven consecutive cases of pathologically proved intradural schwannomas studied with enhanced MR imaging at our institution were retrospectively reviewed. The studies were performed between December 1988 and August 1991. Unenhanced MR examinations of intradural schwannomas performed before 1988 were excluded from review. The patients were 29–78 years old; four were women and three were men. Scans were obtained with a 1.5-T superconducting magnet (General Electric Medical Systems, Milwaukee, WI). Double-echo T2-weighted, 1800–2000/30,80/2 (TR/TE/excitations), sagittal images were obtained in all cases, and for one patient, T2-weighted (1800/30,80/2) axial images were obtained also. T1-weighted axial (400–650/11–20/4) and sagittal (500–600/11–20/2) images were obtained before and after IV administration of gadopentetate dimeglumine (0.1 mmol/kg body weight; Berlex Laboratories, Wayne, NJ). The enhanced scans were obtained immediately after injection. Slice thickness was 4–5 mm for both sagittal and axial imaging. Flow compensation was used in all cases.

Received December 6, 1991; accepted after revision January 17, 1992.

[1] All authors: Department of Radiology, Jefferson Medical College and Thomas Jefferson University Hospital, Room 1072, Main Bldg., 132 S. 10th St., Philadelphia, PA 19107. Address reprint requests to D. P. Friedman.

0361–803X/92/1586–1347
© American Roentgen Ray Society

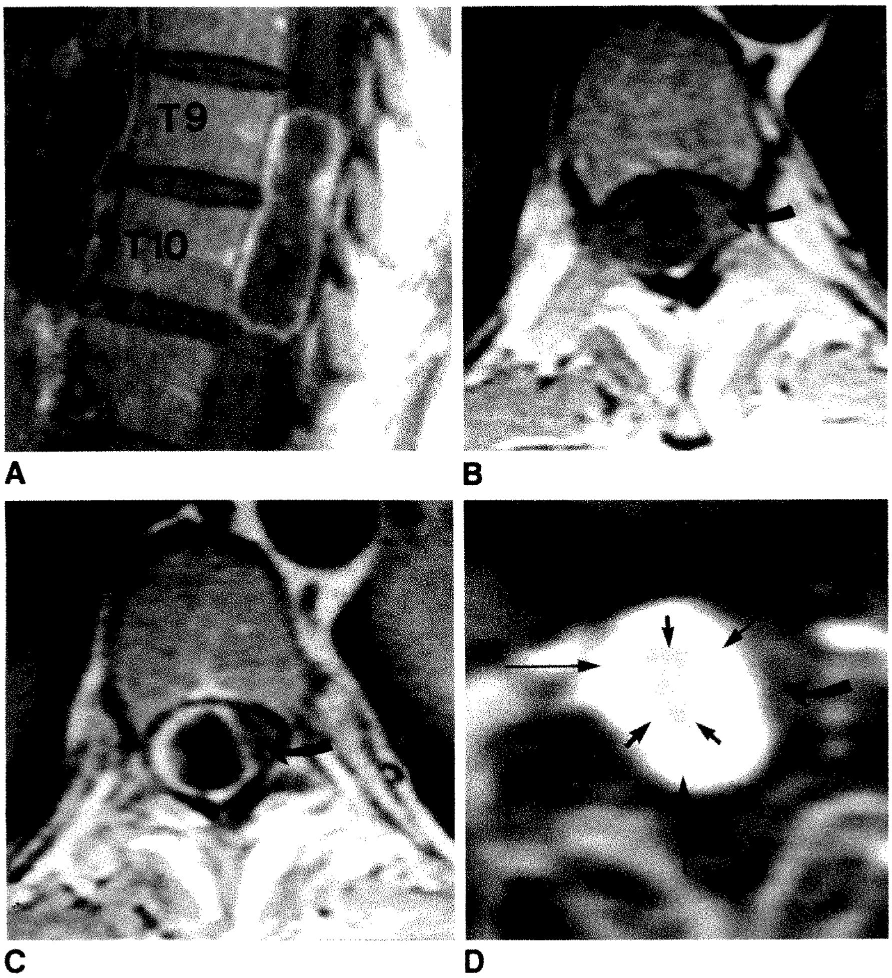

Fig. 1.—42-year-old woman with T9–T10 schwannoma.

***A*, Enhanced sagittal T1-weighted (500/11) MR image shows large, hypointense, peripherally enhancing mass in intradural extramedullary compartment.**

***B* and *C*, Axial T1-weighted (650/11) MR images obtained before (*B*) and after (*C*) administration of contrast material confirm extramedullary location of lesion. Cord is compressed and displaced to left (*arrows*). Enhancing ring is quite thin.**

***D*, Axial T2-weighted (1800/80) MR image shows periphery of mass (*long straight arrows*) is markedly hyperintense as compared with central portion (*short straight arrows*). Cord is displaced to left (*curved arrow*). Pathologic examination showed thickening of vessel walls, microcystic spaces, and areas of necrosis; more Antoni type A tissue was noted.**

The scans were reviewed by three neuroradiologists. Location, signal characteristics, and enhancement pattern were recorded for each tumor. Four lesions were located in the lumbosacral spine, two were in the thoracic spine, and one was at the level of the conus medullaris. The histologic features of the tumors were then compared with the imaging findings. The retrospective nature of the study precluded exact correlation of the gross pathology with the MR appearance.

Results

With respect to the cord signal, six lesions were variably hyperintense on T2-weighted images (Fig. 1D) and one was uniformly hypointense (Fig. 2). Three lesions were isointense on T1-weighted images, three were hypointense, and one was iso- to hypointense. All tumors showed heterogeneous enhancement, and in five cases, peripheral (ring) enhancement was the only feature seen (Figs. 1A, 1C, 3, and 4). The pattern of enhancement did not correlate with either the signal characteristics on the unenhanced T1- and T2-weighted images or the size of the tumor.

Pathologically, all of the tumors showed both Antoni type A and type B tissue; the latter pattern did not always predominate, even in neoplasms with peripheral enhancement. However, hyaline thickening of vessel walls, cyst formation, and myxoid change in Antoni type B tissue were frequently seen in the peripherally enhancing lesions. We found no evidence of malignancy in any of these neoplasms.

Discussion

Schwannomas and neurofibromas account for 16–30% of all intraspinal masses; most are intradural and extramedullary [5]. In the literature, the tendency has been to combine all nerve sheath tumors, regardless of their location and histologic features, when their MR appearance is discussed. This is particularly true with regard to enhancement characteristics; it has been stated that nerve sheath tumors in the spine "enhance intensely and fairly homogeneously" [5]. Our experience in the past 3 years with contrast-enhanced imaging of these lesions provided several exceptions, which prompted this study.

Intradural schwannomas tend to have signal intensity equal to or less than that of the spinal cord on T1-weighted images and mild to marked hyperintensity on T2-weighted images. Focal areas of even greater hyperintensity on T2-weighted images often correspond to cystic portions, whereas hypoin-

Fig. 2.—55-year-old woman with T4 schwannoma. Sagittal T2-weighted (2000/80) MR image shows a hypointense, dorsally situated intradural extramedullary mass (*arrow*); provisional diagnosis was meningioma. Enhanced scans (*not shown*) showed ring enhancement, which is more consistent with a diagnosis of schwannoma. Pathologic examination showed cystic changes and more Antoni type A tissue.

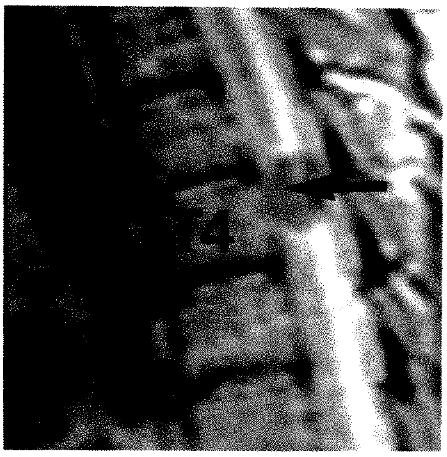

2

Fig. 3.—78-year-old woman with L3–L4 schwannoma. Enhanced sagittal T1-weighted (567/11) MR image shows large, peripherally enhancing mass filling spinal canal. Pathologic examination showed mostly Antoni type A tissue, myxoid changes in Antoni type B areas, and markedly thickened vessel walls.

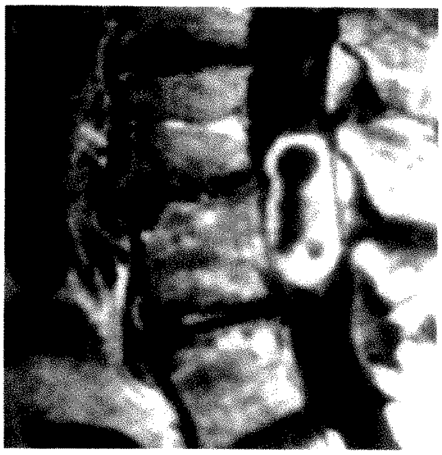

3

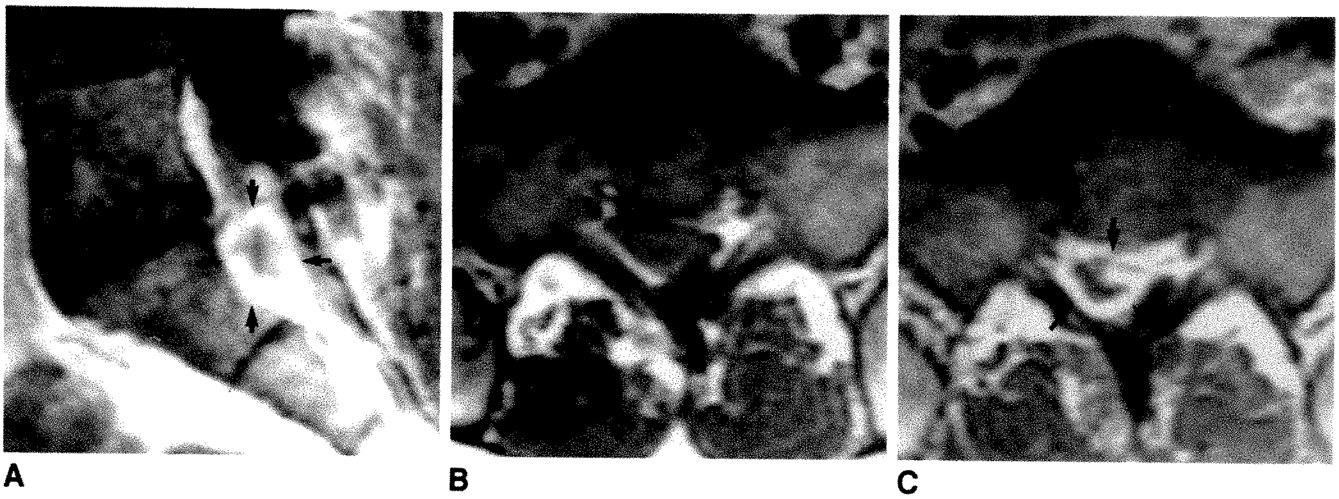

Fig. 4.—37-year-old man with S1 schwannoma.
A, Enhanced sagittal T1-weighted (500/20) MR image shows small, peripherally enhancing mass filling distal canal (*arrows*).
B and *C*, Axial T1-weighted (600/20) MR images obtained before (*B*) and after (*C*) administration of contrast material. Enhancing ring (*arrows*) is moderately thick. Pathologic examination showed mixture of Antoni type A and type B tissue.

tensity may represent hemorrhage, dense cellularity, or collagen deposition [5, 6]. Tumor heterogeneity does not necessarily indicate malignant change [7]. The histology of these neoplasms explains their varied MR appearances. Schwannomas may be composed of both Antoni type A and type B patterns. Antoni type A tissue is rich in cells and is composed of compact bundles of fibrillated cells. Antoni type B tissue is hypocellular and is composed of a loosely textured stroma; in addition, cystic degeneration or xanthomatous change may be present [6, 8]. Both types of tissue often coexist in the same tumor; this pattern was seen in all of our cases. Pathologically, intraspinal schwannomas have necrosis and cyst formation much more frequently than their intracranial and peripheral nerve counterparts do [6, 8]. Cystic acoustic and paraspinal schwannomas are well described in the CT literature, but are uncommon [7, 9, 10].

Recently, Demachi et al. [6] reported that it was impossible to establish a correlation between Antoni type A and type B tissue in spinal schwannomas and signal characteristics on MR. In the same study, heterogeneous contrast enhancement (including one case with ring enhancement) was reported in three of five patients. Other authors [11, 12] have attempted to correlate the histologic features of acoustic schwannomas with their MR appearance. All seven lesions in our review had heterogeneous enhancement, and in five cases, peripheral enhancement was the sole feature. Importantly, peripheral enhancement is not synonymous with cyst formation and necrosis; it may reflect poor central vascularity and/or increased compactness of the tumor (with decreased extracellular space available for contrast accumulation) [13]. Sze et al. [13] showed that most intramedullary spinal tumors tend to increase in enhancement with delayed scanning. In addition, lesions that may initially appear to have peripheral enhancement can later fill in. Our patients were scanned immediately after contrast injection; more uniform enhancement might have occurred with delayed scanning. For clinical purposes, however, immediate enhanced imaging is likely to yield the most diagnostic information.

Although the Antoni type B pattern is prone to cystic degeneration, we did not necessarily find predominance of this tissue in peripherally enhancing lesions (Figs. 1-4). Several factors may account for this finding. First, even in small schwannomas, the incorporated blood vessels often show focal sinusoidal dilatation, cavernous or telangiectatic formations, and hyaline thickening of their walls. These abnormal vessels, which occur in type A and type B tissue, are liable to spontaneous thrombosis with consequent hemorrhage, necrosis, and cyst formation [8]. Second, areas of Antoni type B tissue that undergo extensive cystic change may be poorly recognizable as such at pathologic examination. Finally, as previously described, peripheral enhancement does not always equate with cystic degeneration.

The pure neurofibroma is a solid tumor; areas of cystic change and xanthomatous material are uncommon [8]. The more uniform histologic appearance typical of these lesions is reflected in their appearance on unenhanced and enhanced MR scans [1-5, 14]. Frequently, central areas of decreased signal intensity, which may reflect dense central areas of collagenous stroma [5, 14], are noted on T2-weighted images.

Meningioma is the second most common intradural extramedullary neoplasm. These tumors can show a variety of signal characteristics, but usually they are isointense or hypointense relative to the cord on T2-weighted scans. Enhancement is generally intense and uniform [1-5]. One of our patients was a 55-year-old woman with a hypointense dorsal intradural extramedullary lesion of the thoracic cord (Fig. 2); the provisional diagnosis was meningioma. The pattern of ring enhancement seen on the enhanced images, however, suggested the correct diagnosis.

Mucinous degeneration is frequent in myxopapillary ependymoma, a distinct clinicopathologic variant of ependymoma seen exclusively in the conus medullaris and filum terminale. These neoplasms are often highly vascular and prone to hemorrhage [8]. Moreover, because of their location outside the cord, filum ependymomas appear to be in the intradural extramedullary compartment. These considerations suggest that caution should be exercised in distinguishing filum ependymomas from cauda equina schwannomas on the basis of MR imaging findings. Three myxopapillary ependymomas seen at our institution showed slightly heterogeneous enhancement.

In conclusion, the MR appearance of seven intradural spinal schwannomas has been reviewed. The heterogeneous appearance of these tumors is explained by their pathologic features. Recognition of the MR characteristics of this subset of nerve sheath neoplasms should be helpful in the differential diagnosis of spinal lesions. In particular, peripheral enhancement of an intradural extramedullary tumor should suggest the diagnosis of schwannoma.

REFERENCES

1. Scotti G, Scialfa G, Colombo N, Landoni L. MR imaging of intradural extramedullary tumors of the cervical spine. *J Comput Assist Tomogr* **1985**;9:1037-1041
2. Dillon WP, Norman D, Newton TH, Bolla K, Mark A. Intradural spinal cord lesions: Gd-DTPA-enhanced MR imaging. *Radiology* **1989**;170:229-237
3. Valk J. Gd-DTPA in MR of spinal lesions. *AJNR* **1988**;9:345-350
4. Breger RK, Williams AL, Daniels DL, et al. Contrast enhancement in spinal MR imaging. *AJNR* **1989**;10:633-637
5. Sze G, Twohig M. Neoplastic disease of the spine and spinal cord. In: Atlas SW, ed. *Magnetic resonance imaging of the brain and spine.* New York: Raven, **1991**:921-965
6. Demachi H, Takashima T, Kadoya M, et al. MR imaging of spinal neurinomas with pathological correlation. *J Comput Assist Tomogr* **1990**;14: 250-254
7. Cohen LM, Schwartz AM, Rockoff SD. Benign schwannomas: pathologic basis for CT inhomogeneities. *AJR* **1986**;147:141-143
8. Russell DS, Rubinstein LJ. *Pathology of tumors of the nervous system.* 5th ed. Baltimore: Williams & Wilkins, **1989**:203-206, 533-571
9. Haughton VM, Daniels DL. The posterior fossa. In: Williams AL, Haughton VM, eds. *Cranial computed tomography.* St. Louis: Mosby, **1985**:350-443
10. Johansen JG, Stenwig JT. Paraspinal schwannoma with cystic appearance on CT. *Neuroradiology* **1987**;29:314
11. Goldberg HI. Extraaxial brain tumors. In: Atlas SW, ed. *Magnetic resonance imaging of the brain and spine.* New York: Raven, **1991**:327-378
12. Daniels DL, Millen ST, Meyer GA, et al. MR detection of tumor in the internal auditory canal. *AJNR* **1987**;8:249-252
13. Sze G, Bravo S, Krol G. Spinal lesions: quantitative and qualitative temporal evolution of gadopentetate dimeglumine enhancement in MR imaging. *Radiology* **1989**;170:849-856
14. Barkovich AJ. *Pediatric neuroimaging.* New York: Raven, **1990**:285-286

Case Report

Schistosomal Granuloma of the Spinal Cord: Evaluation with MR Imaging and Intraoperative Sonography

Robert Silbergleit[1] and Richard Silbergleit[2]

Symptomatic spinal cord involvement is a rare but well-documented manifestation of schistosomiasis [1]. Patients typically have lower back pain and progressive neurologic impairment of the lower extremities, bowel, and bladder [2, 3]. An intramedullary mass in the caudal spinal cord is the most common finding. Radiologic findings are not specific for schistosomal infection, but are strongly suggestive in the appropriate clinical setting. Radiologic and clinical diagnosis of this syndrome may permit medical therapy and eliminate the need for laminectomy.

Case Report

A 7-year-old girl had sudden onset of lower back and bilateral lower extremity pain, paresthesias, and weakness that began 1 week before admission and progressed rapidly. The patient lost function of the lower extremity and had disturbed function in the bowel and bladder.

The patient lived with her American parents in Sierra Leone, an area endemic for schistosomiasis. Medical and family history was unremarkable. She had lived in Africa for more than 1 year. Water in the family's home was filtered for schistosome cercariae, but the patient had lived with a native family for 5 months in a hut not equipped with such filters.

Physical examination was unremarkable except for the neurologic examination. Lower extremity strength was decreased, and deep tendon reflexes were absent at the knee and ankle. Tactile sensation over the lower extremities was diminished. Admission laboratory studies were unremarkable. There was no peripheral eosinophilia.

Lumbar myelography performed on admission revealed an irregular intramedullary mass at the T11–T12 level that delayed the flow of contrast material but did not cause a complete block. CSF examination revealed mild eosinophilia with normal chemistry and negative stains and cultures. On the patient's second hospital day, surface coil MR imaging was performed at 1.5 T (General Electric, Milwaukee, WI). T1-weighted images (617/20/2 [TR/TE/excitations]) best showed enlargement of the caudal cord with nodular and confluent enhancement, especially anteriorly after IV administration of gadopentetate dimeglumine (Figs. 1A and 1B). Inhomogeneous high signal intensity was seen in the enlarged portion of the cord on T2-weighted images (Fig. 1C).

The patient was taken to the operating room on her third hospital day. The anterior aspect of the mass was hyperechoic on intraoperative sonography (Fig. 1D). Laminectomy from T9 to L1 was performed, with subtotal resection of a soft yellow mass. Pathologic examination showed granulomatous inflammation containing *Schistosoma mansoni* ova. Postoperatively, multiple urine and fecal schistosome screens were negative, but the diagnosis of chronic schistosomal infection was confirmed by a positive *S. mansoni* serum antibody test by enzyme-linked immunosorbent assay (57 activity units/μl; cutoff, >10 units).

The patient was treated with praziquantel (three doses of 20 mg/kg for 1 day) with concurrent dexamethasone for 7 days. At discharge on hospital day 72, the patient had improved lower extremity strength and was able to ambulate short distances with a walker. Six months after presentation, the patient was ambulatory with resolution of her

---

Received October 2, 1991; accepted after revision December 17, 1991.

Presented in part at the annual meetings of the Western Neuroradiological Society, Santa Fe, NM, October 1990, and the American Society of Neuroradiology, Washington, DC, June 1991.

[1] The University of Michigan Medical School, Ann Arbor, MI 48109.

[2] Department of Diagnostic Radiology, Henry Ford Hospital, 2799 W. Grand Blvd., Detroit, MI 48202. Address reprint requests to Richard Silbergleit.

AJR 158:1351–1353, June 1992 0361–803X/92/1586–1351 © American Roentgen Ray Society

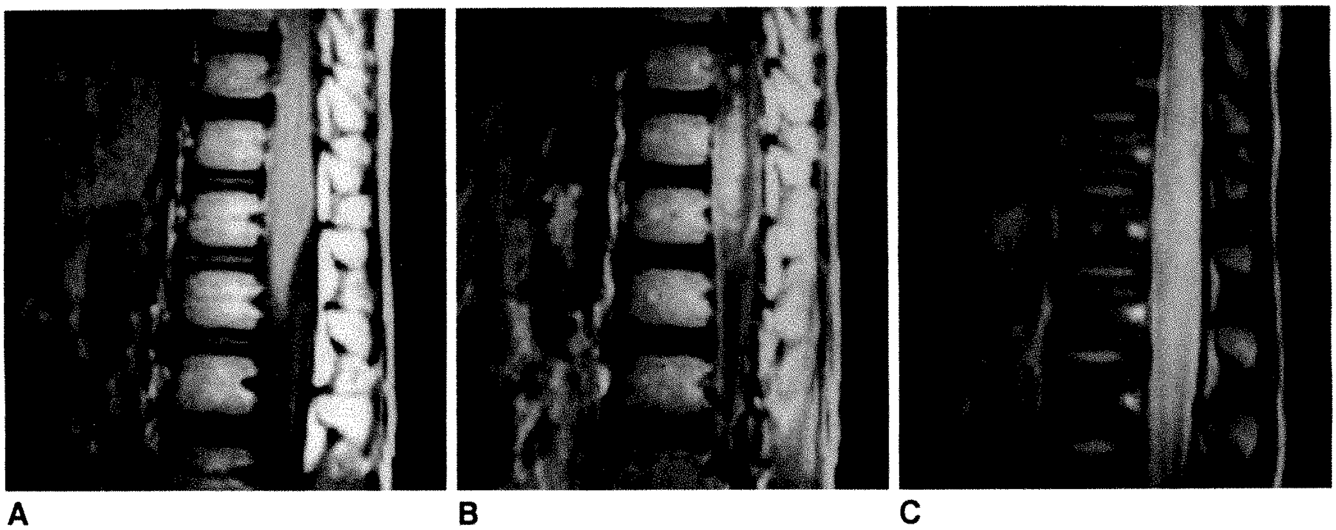

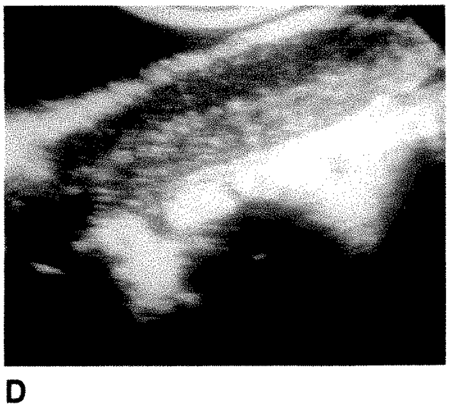

Fig. 1.—7-year-old girl with spinal cord schistosomiasis.

***A*, Sagittal T1-weighted (617/20/2) MR image shows markedly enlarged conus medullaris.**

***B*, Enhanced sagittal T1-weighted (600/20/2) MR image shows heterogeneous enhancement of enlarged conus medullaris. Enhancement is more prominent anteriorly.**

***C*, Sagittal T2-weighted (2250/90/2) MR image shows inhomogeneously increased signal intensity within conus medullaris.**

***D*, Intraoperative sonogram, sagittal orientation, shows hyperechoic area in anterior portion of lesion corresponding to enhancing portion of lesion on MR.**

(*A* and *B* reprinted with permission from Selwa et al. [4].)

neurogenic bladder and with only minimal residual weakness of the hip flexor.

Discussion

The three human blood flukes, *S. mansoni*, *Schistosoma haematobium*, and *Schistosoma japonicum*, are increasingly prevalent in endemic areas of Arabia and Africa (*S. mansoni* and *S. haematobium*); South America and the Caribbean (*S. mansoni*); and Japan, China, and the Philippines (*S. japonicum*). The prevalence of human schistosomiasis in the United States is estimated to be greater than 400,000, occurring mainly in immigrants from endemic areas, but also occurring in travelers to those areas [1].

Schistosomes are released from snails, enter humans through the skin, and migrate through blood vessels and lymphatics to the lung and liver, where they mature and then descend to their final habitat in the venous system of the rectum, intestines, and urinary bladder. Characteristically shaped eggs are usually expelled in urine and feces, but ectopic ova may be carried via the venous system leading to granulomatous infestation in the intestine, liver, ureters, or bladder. Pulmonary and CNS lesions are less common [1].

The incidence and prevalence of spinal cord schistosomiasis remain uncertain. Since it was first described early in this century, less than 100 cases have been reported. Pathologically, four manifestations of schistosomiasis of the spinal cord are described in the literature: (1) confluent granulomatous intramedullary mass of the caudal cord; (2) radicular involvement with granulomatous changes surrounding the conus medullaris and cauda equina; (3) diffuse granulomatous changes with necrosis, atrophy, and hemorrhage causing an acute transverse myelitis without cord enlargement; and (4) asymptomatic deposition of ova in the cord [2]. Granulomatous masses of the caudal cord and conus medullaris are most common, and are responsible for symptoms in approximately 78% of the reported cases [3].

MR findings of schistosomal transverse myelitis and the granulomatous schistosomal mass have recently been reported [4, 5]. The MR appearance of the granulomatous lesion in our case was of an intramedullary mass with inhomogeneous signal hyperintensity on T2-weighted images. There was heterogeneous enhancement after administration of gadopentetate dimeglumine. Although these findings are relatively nonspecific indicators of inflammatory or neoplastic processes, they are suggestive of schistosomal disease in patients with the appropriate exposure history and clinical presentation.

Definitive diagnosis and treatment in the majority of reported cases of spinal cord schistosomiasis included laminectomy with partial resection of the lesion, definitive antiparasitic medical therapy, and occasionally concurrent corticosteroid administration [3]. It has been suggested that if the diagnosis of spinal cord schistosomiasis can be made on the basis of clinical presentation and radiologic evidence, medical therapy alone with imaging follow-up is an appropriate and less invasive treatment [6]. Treatment with schistosomicidal medication with or without laminectomy or steroids is usually effective and curative, especially if given soon after the onset of neurologic symptoms. Residual neurologic deficits are usually minimal or absent [2].

Spinal cord schistosomiasis must be included in the differential diagnosis of intramedullary masses of the caudal spinal cord in patients with a history of possible exposure. Correct identification of these lesions by clinical and radiologic evidence may spare the patient the need for diagnostic laminectomy and myelotomy.

REFERENCES

1. Mahmoud AA. Trematodes (schistosomiasis, other flukes). In: Mandell GL, Douglas RG, Bennett JE, eds. *Principles and practice of infectious diseases*, 2nd ed. New York: Wiley Medical, **1985**:1573–1579
2. Blansjaar BA. Schistosomiasis. In: Vinken PJ, Bruyn GW, Klawans HL, Harris AA, eds. *Handbook of clinical neurology*, vol. 52, rev. 8: *Microbial disease*. Amsterdam: Elsevier, **1988**:535–543
3. Scrimgeour EM, Gajdusek DC. Involvement of the central nervous system in *Schistosoma mansoni* and *S. haematobium* infection: a review. *Brain* **1985**;108:1023–1038
4. Selwa LM, Brumberg JA, Mandell SH, Garofalo EA. Spinal cord schistosomiasis: a pediatric case mimicking intrinsic cord neoplasm. *Neurology* **1991**;41:755–757
5. Dupuis MJ, Atrouni S, Dooms GC, Gonsette RE. MR imaging of schistosomal myelitis. *AJNR* **1990**;11:782–783
6. Haribhai HC, Bhigjee AI, Bill PL, Cosnett JE. Schistosoma in the spinal cord. *J Neurol Neurosurg Psychiatry* **1988**;51:158

American Roentgen Ray Society Residents' Award Papers, 1993

The ARRS announces competition for the 1993 President's Award and two Executive Council Awards for the best papers concerning the clinical application of the radiologic sciences.

Awards

The winner of the President's Award will receive a certificate and a $2000 prize. The winners of the two Executive Council Awards will each be given a certificate and a prize of $1000. The winners will be announced on March 15, 1993. Winning papers will be presented at the ARRS annual meeting at the San Francisco Marriott, San Francisco, CA, April 25–30, 1993. Winning papers will be submitted for early publication in the *American Journal of Roentgenology*. All other papers will be returned to the authors.

Regulations

Eligibility is limited to residents or fellows in radiology who have not yet completed 4 years of approved training in a radiologic discipline. A letter from the resident's department chairman attesting to this status must accompany the manuscript. The resident must be the sole or senior author and be responsible for all or most of the project.

Submitted manuscripts must not exceed 5000 words and have no more than 10 illustrations. Four copies of the manuscript and illustrations are required. Submitted manuscripts should not contain previously presented or published material and should not be under consideration for publication elsewhere.

Deadline for submissions is February 12, 1993. Send papers to

Nancy O. Whitley, M.D.
Chairman, Committee on Education & Research
American Roentgen Ray Society
Department of Radiology
University of Maryland Medical Systems Hospital
22 S. Greene St.
Baltimore, MD 21201

Book Review

Quality Assurance in Radiotherapy Physics. Proceedings of an American College of Medical Physics Symposium, May 1991. Edited by George Starkschall and John L. Horton. Madison, WI: Medical Physics Publishing, 387 pp., 1991. $55

The editors of this book state in the foreword that "the purpose of this document is to provide the individual engaged in practice sufficient information on both the basis of radiotherapy physics quality assurance and the allied procedures to establish and administer a quality assurance program." The book accomplishes this objective quite well.

The material is organized into three categories. The first includes establishing and administering specific procedures for a quality assurance program in radiotherapy physics. It begins with a chapter on equipment specification, acceptance testing, and commissioning and continues with chapters on quality assurance of external beam megavoltage radiotherapy equipment, computer control systems, simulators, CT and MR for treatment planning, dosimetry, treatment aid fabrications, and chart review. Included also are chapters on intraoperative radiotherapy, Linac-based stereotaxic radiosurgery, low-dose-rate brachytherapy, and hyperthermia. Although this section is already comprehensive, some topics are inadvertently omitted, such as high-dose-rate remote afterloading brachytherapy and gamma-knife cobalt radiosurgery, presumably because their use is not yet widespread. Most of these discussions follow a practical format, outlining procedural steps and, more importantly, the recommended frequency of these quality assurance procedures.

The second category generally deals with the administrative aspects of quality assurance. Departmental support of a quality assurance program, regulatory requirements, legal ramifications, and the establishment of standards are discussed. It is estimated that the total cost for a quality assurance program may come to approximately 3% of the annual billings of combined technical and professional charges. The chapter on the legal risks of a physicist discusses the hypothetical trial of a case of alleged negligence and strict liability and concludes that careful adherence to steps such as those found in *Physics Aspects of Quality Assurance in Radiation Therapy* (American Association of Physicists in Medicine, Report No. 13) would be convincing demonstration of the fulfillment of the physicist's responsibilities. Another chapter provides a convincing argument for establishing a standard of practice for medical physicists, from the professional and the legal perspectives.

The third category includes "how we do it" topics. The various authors describe their experience and perspectives of how quality assurance programs are organized and conducted in different types of facilities, including a large radiotherapy clinic, a large facility with several affiliated clinics, a medium-sized facility, and a consulting practice that services many small clinics. Despite the different requirements of these institutions, it is obvious that quality delivery of radiation therapy can be assured by having medical physicists diligently follow certain established guidelines.

The writing style of the authors is uniformly clear, with a minimal amount of jargon. The diagrams and tables are all useful to the understanding of the chapter contents. Specially worth mentioning is the deliberate step-by-step outlining of the quality assurance programs on a daily, weekly, monthly, semiannual, and annual bases. This book presents not only the concepts of quality assurance but also the practical aspects of how to carry it out.

One minor criticism is the brevity of some of the chapters. Perhaps this is an attempt by the editors and the publishers to limit the size of the book to a certain number of pages. If so, then some valuable information may have been sacrificed in the process. An important area in which more details are needed is quality assurance of the software that controls the machinery and treatment planning programs.

Overall, this is a valuable and timely publication that will be welcomed by medical physicists, radiation oncologists, dosimetrists, and radiation therapy technologists. For most physicians, however, the technical details may not be relevant for a clinical quality assurance program. For someone who is starting a physics quality assurance program, this book is an excellent starting point. Others who have already developed a program can use the book to evaluate their program for completeness, or to prepare a new program for a new piece of equipment. The subject matter is so important that purchasing this book for the department or the interested individual would be most worthwhile.

Kenneth H. Luk
City of Hope National Medical Center
Duarte, CA 91010

ARRS Case of the Day

The correct diagnoses and discussions of the Case of the Day series featured at the Orlando meeting of the ARRS are presented in this issue of the *AJR*. We have repeated the images as unknowns and discussed the important features of each case.

The cases have been prepared by the faculty and residents of the Department of Radiology and Radiologic Sciences of Vanderbilt University Medical School. They have been selected to demonstrate a wide range of abnormalities and it is hoped that this has been an enjoyable and instructive exercise.

Congratulations to those of you who were successful at recognizing the conditions shown in the Case of the Day exhibit at the ARRS meeting and published in the April issue of the *AJR*.

I thank Barbara Heilman and John Bobbitt for their invaluable assistance and A. Everette James, Jr., for the invitation to organize the Case of the Day project.

Richard M. Heller
Department of Radiology
Vanderbilt University Medical Center
Nashville, TN 37232

Chest Case of the Day

John A. Worrell,[1] Dennis M. O'Donnell,[1] Frank E. Carroll,[1] Joseph P. Brunner,[2] and Jack A. Coleman, Jr.[3]

Case 1: Pulmonary Edema Associated with Tocolytic Therapy

This 16-year-old was a late registrant for prenatal care when she was noted on sonography to have twin fetuses of approximately 20 weeks' gestational age. She presented at 24$\frac{5}{7}$ weeks with uterine contractions. Physical examination at this time revealed cervical dilatation of 4 cm with bulging membranes, but no fluid leakage. Temperature was 37.8°C, pulse 105 beats per minute, blood pressure 124/77. The WBC count was 11,900/dl (11.9×10^9/l) with 78% segmented neutrophils. She was treated with bed rest, and tocolytic therapy with IV magnesium sulfate was initiated. She also received betamethasone in an effort to accelerate fetal lung maturity and empiric antibiotic coverage as a precaution against subclinical amnionitis. On the third day in the hospital, she became short of breath, and decreased urine output was noted. Arterial blood gases on room air revealed a pH of 7.44, Pco$_2$ of 33, Po$_2$ of 67, and −0.6 base excess. A positive fluid balance was discovered, and 40 mg furosemide was administered IV. The patient responded with a brisk diuresis and improved respirations, but the uterus continued to be irritable. Furosemide was administered again on the fourth day, but with poor response.

An anteroposterior portable chest radiograph at this time (Fig. 1A) showed diffuse bilateral alveolar edema with the heart larger than normal for the gravid state. The patient's contractions increased in frequency with further cervical dilatation to 7 cm. At this point, the IV tocolytic therapy was discontinued. The membranes ruptured spontaneously the next day, and the cervix dilated to 9 cm. Subcutaneous terbutaline was administered twice, but the labor persisted. Live-born twin male neonates were delivered, but both died later of complications of extreme prematurity. Furosemide was again administered, and the pulmonary edema had resolved by the second day after delivery (Figs. 1B and 1C). The subsequent postpartum course was uneventful.

The occurrence of pulmonary edema in association with tocolytic therapy has been noted in the obstetric literature for the past 10 years [1, 2]. Agents used to inhibit uterine contractility include the beta-mimetics terbutaline, isoxsuprine, ritodrine, fenoterol, salbutamol, and the calcium antagonist magnesium sulfate [2]. In addition to suppressing uterine contractions, these medications can cause tachycardia, hyperglycemia, hypokalemia, antidiuresis, pulmonary edema, cardiac arrhythmias, and hypotension as a result of β_1- and β_2-receptor effect as well as other more complex and incompletely understood mechanisms [3, 4].

The infusion of large volumes of saline in the healthy young adult should not result in pulmonary edema, nor should betamimetic therapy in nongravid patients [3, 5]. This pulmonary edema, unique to the gravid state, may be due to a combination of factors. Simply assuming the supine position, for example, decreases sodium and water excretion. In addition, tocolytic agents increase the secretion of antidiuretic hormone, and the twin pregnancy may be at special risk because the physiologic increase in intravascular volume is greater than in the singleton pregnancy [1]. Neither a direct cardiac effect with left ventricular failure nor a decrease in the pulmonary lymphatic flow has been substantiated [1, 3]. The combination of fluid overload, decreased plasma colloid oncotic pressure, and the physiologic alterations of pregnancy is sufficient to account for this predisposition to pulmonary edema. Increased capillary permeability, especially in the presence of a bacterial infection such as amnionitis, also may contribute [1–4].

Pisani and Rosenow [1] have divided the criteria for diagnosis of pulmonary edema associated with tocolysis into major and minor criteria (Table 1). Mothers at increased risk include those with hypertension, diabetes, coronary and valvular heart disease, and obstructive cardiomyopathy. Other risk factors include multiple pregnancy, amniotic fluid infection, and possibly smoking [4]. The differential diagnosis of dyspnea of acute onset in the pregnant patient includes venous thromboembolism, amniotic fluid embolization, adult respiratory distress syndrome, peripartum cardiomyopathy, and pneumomediastinum [1].

John A. Worrell
Joseph P. Brunner
Dennis M. O'Donnell
Frank E. Carroll

---

[1] Department of Radiology, Vanderbilt University Medical Center, 1161 21st Ave., S., Nashville, TN 37232-2675. Address reprint requests to J. A. Worrell.
[2] Department of Obstetrics and Gynecology, Vanderbilt University Medical Center, 1161 21st Ave., S., Nashville, TN 37232-2675.
[3] Department of Otolaryngology, Vanderbilt University Medical Center, 1161 21st Ave., S., Nashville, TN 37232-2675.

AJR 158:1356–1362, June 1992 0361–803X/92/1586–1356 © American Roentgen Ray Society

Fig. 1.—Case 1: Pulmonary edema associated with tocolytic therapy.

***A*, Anteroposterior portable chest radiograph shows a diffuse bilateral pattern of alveolar pulmonary edema with heart larger than normal for gravid state.**

***B* and *C*, Findings on posteroanterior (*B*) and lateral (*C*) chest radiographs taken on second day after delivery are normal. Pulmonary edema has resolved, and size of heart is normal.**

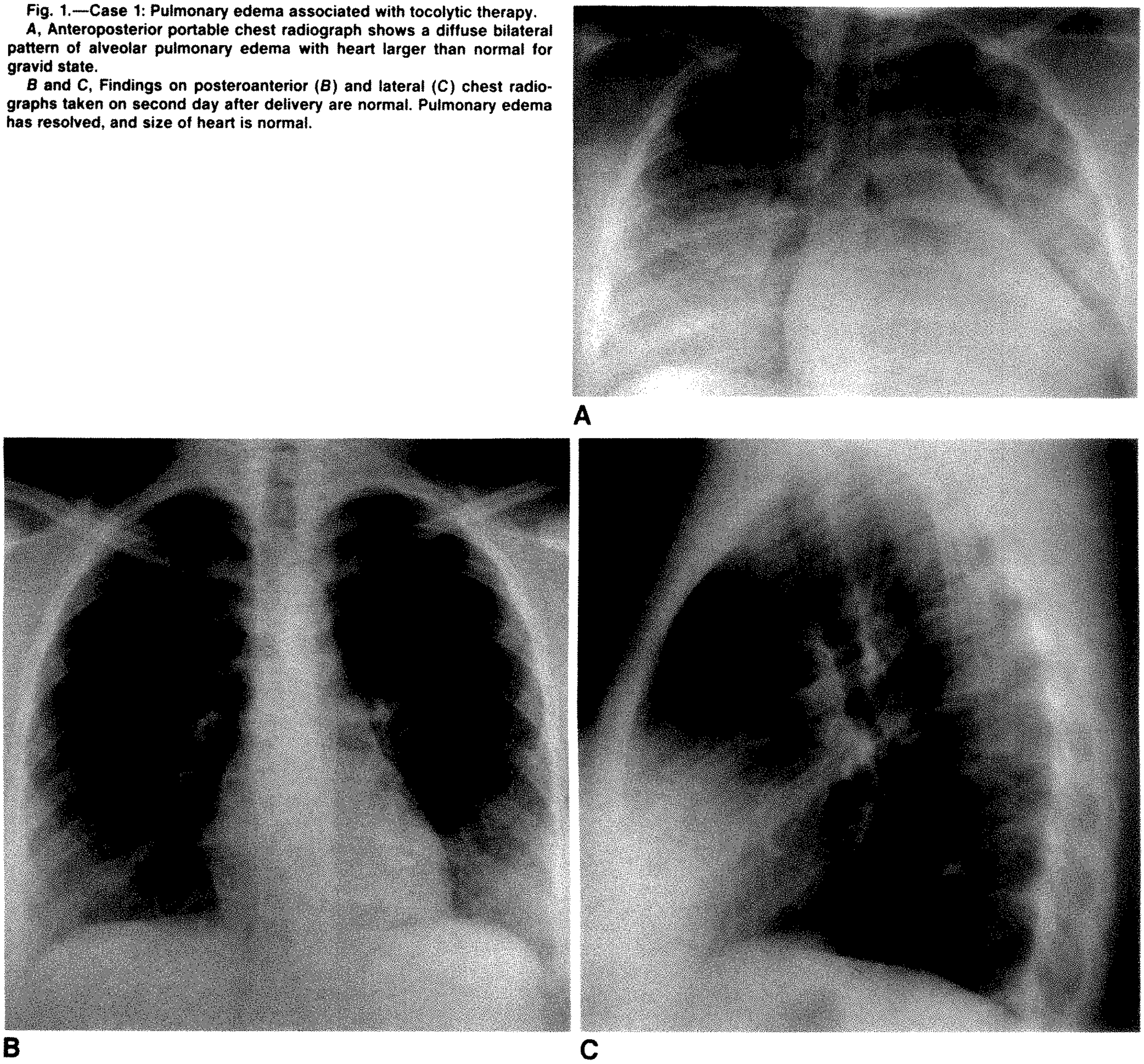

TABLE 1: Criteria for Diagnosis of Pulmonary Edema Associated with Tocolytic Therapy

- Major criteria
  - Recent (<24 hr) or current use
  - Dyspnea occurring before delivery or less than 12 hr postpartum in women who deliver despite tocolysis
  - A chest radiograph showing unilateral or bilateral alveolar opacities
  - Evidence of hemodilution (decreased hematocrit or hypokalemia)
  - Rapid clinical response (<24 hr) to treatment with diuretics and oxygen
- Minor criteria
  - Normal findings on ventilation/perfusion lung scan
  - Normal findings on echocardiogram
  - Evidence of fluid overload

Note.—From Pisani and Rosenow [1].

REFERENCES

1. Pisani RJ, Rosenow EC III. Pulmonary edema associated with tocolytic therapy. *Ann Intern Med* **1989**;110:714–718
2. Hankins GDV. Complications of beta-sympathomimetic tocolytic agents. In: Clark SL, Cotton DB, Hankins GDV, Phelan JP, eds. *Critical care obstetrics*, 2nd ed. Boston: Blackwell Scientific Publ., **1991**:223–250
3. Ingemarrsson I, Arulkumaran S, Kottegoda SR. Complications of betamimetic therapy in preterm labour. *Aust N Z J Obstet Gynaecol* **1985**;25: 182–189
4. Watson NA, Morgan B. Pulmonary edema and salbutamol in preterm labour: case report and literature review. *Br J Obstet Gynaecol* **1989**;196: 1445–1448
5. Hardy CC, Lorigan P, Ratcliffe A, Carroll KB. Asthma in pregnancy complicated by iatrogenic pulmonary oedema. *Postgrad Med J* **1989**;65: 407–409

Case 2: Obstruction of the Left Brachiocephalic Vein

This 28-year-old woman had a left-sided supraclavicular mass 16 months before admission. Biopsy of this mass revealed nodular sclerosing Hodgkin's lymphoma, which was subsequently staged as IVA. The patient underwent chemotherapy, but 3 months before admission had mediastinal recurrence confirmed at mediastinoscopy. She presented at this time for bone marrow transplantation. Results of physical examination on admission were normal, with the comment that no jugular venous distension was noted.

A posteroanterior chest radiograph showed a widened superior mediastinum with a prominent aortic "nipple" (Fig. 2A). A comparison radiograph from 9 months earlier showed that the aortic "nipple" had appeared since then (Fig. 2B). The patient subsequently underwent contrast venography via the Hickman catheter, which showed a patent superior vena cava below the level of the catheter tip (not shown). Contrast venography via the left antecubital vein, however, confirmed occlusion of the left brachiocephalic vein. Collateral flow through the superior intercostal vein into the accessory hemiazygos system accounted for the appearance of the aortic nipple (Fig. 2C).

Because of the aggressive nature of the patient's disease, the clinical decision was made to proceed with the patient's chemotherapy. The patient's hospitalization was prolonged by fever of unknown origin, anemia, and thrombocytopenia. Anticoagulant therapy was withheld, and after 6 weeks, the patient was discharged.

The aortic nipple sign is caused by the left superior intercostal vein as it courses around the aortic arch before joining the left brachiocephalic vein [1]. It may be seen as an anatomic

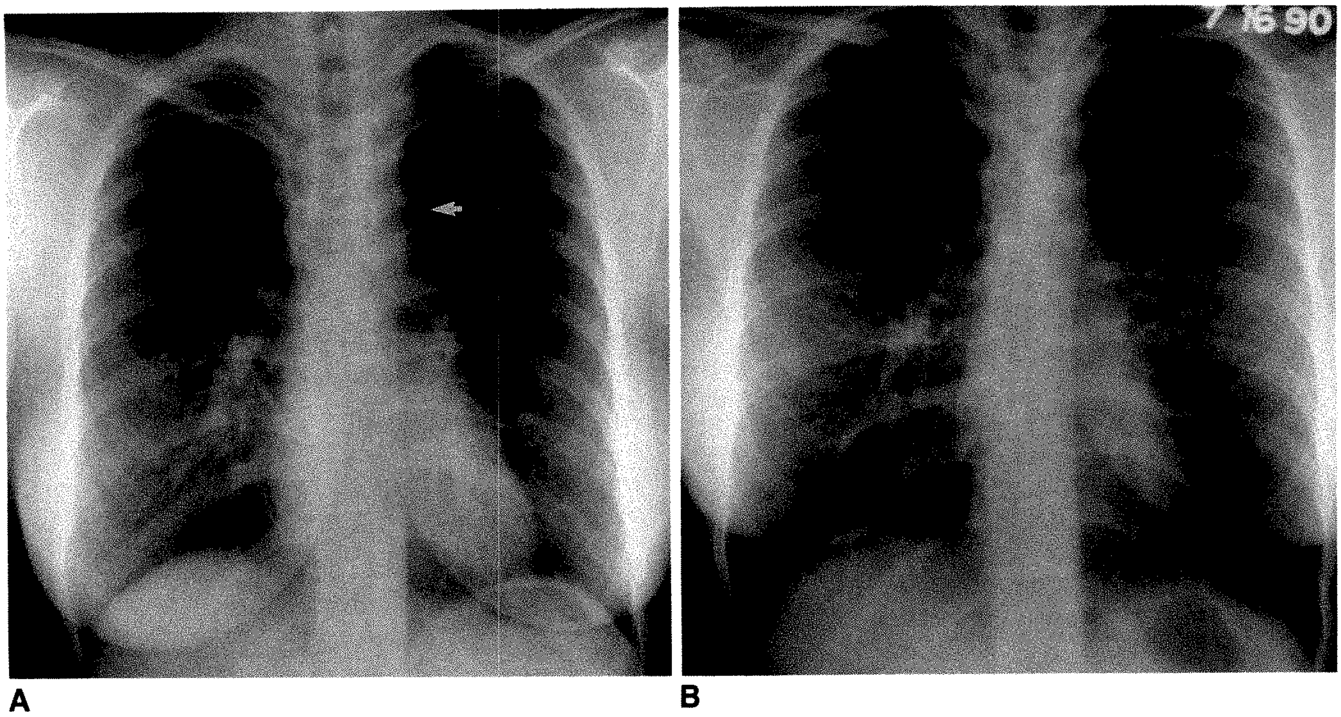

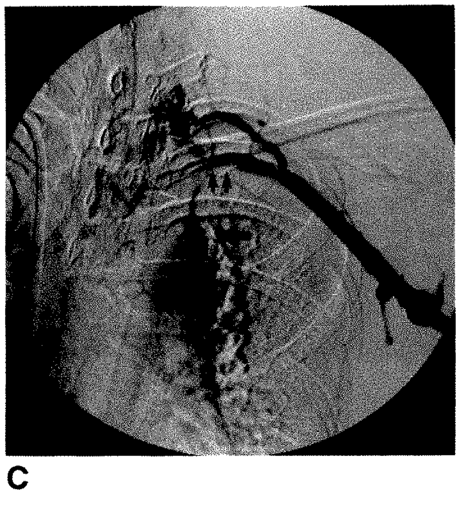

Fig. 2.—Case 2: Obstruction of left brachiocephalic vein.

A, Posteroanterior chest radiograph obtained at admission shows Hickman catheter in left subclavian vein. Superior mediastinum is widened, and an aortic "nipple" (*arrow*) is noted lateral to aortic arch.

B, Posteroanterior chest radiograph taken 9 months earlier shows a normal aortic arch with no "nipple" seen.

C, Digital left antecubital venogram shows obstruction of proximal left subclavian and innominate veins (*small arrows*). Collateral flow goes through superior intercostal vein to hemiazygos system. As superior intercostal vein courses around aortic arch, its shadow creates aortic "nipple" (*large arrow*).

variant, with reports of its prevalence in healthy patients ranging from 1.4% to 9.5% [2, 3].

The differential diagnosis of pathologic enlargement of the left superior intercostal vein includes states characterized by increased venous flow, such as portal venous hypertension, caval anomalies with azygos or hemiazygos continuation, and anomalous venous return. Also included in the differential diagnosis are states with increased venous resistance, such as congestive heart failure and obstruction of the superior or inferior vena cava or left brachiocephalic vein [2–4].

Carter et al. [4] reported periods of 7 and 10 weeks, respectively, between the appearance of the aortic nipple on radiographs and the physical findings of the clinical superior vena caval syndrome in their two patients. It is important to recognize the appearance of a new aortic nipple as a potential indication of obstruction of the superior vena cava or left brachiocephalic vein so that appropriate diagnostic confirmation can be made and treatment begun without waiting for the clinical appearance of the superior vena caval syndrome.

John A. Worrell
Frank E. Carroll
Dennis M. O'Donnell

REFERENCES

1. Lane EJ, Heitzman ER, Dinn WM. The radiology of the superior intercostal veins. *Radiology* **1974**;120:263-267
2. Ball JB Jr, Proto AV. The variable appearance of the left superior intercostal vein. *Radiology* **1982**;144:445-452
3. McDonald CJ, Castellino RA, Blank N. The aortic "nipple." *Radiology* **1970**;96:533-536
4. Carter MM, Tarr RW, Mazer MJ, Carroll FE. The "aortic nipple" as a sign of impending superior vena caval syndrome. *Chest* **1987**;6:775-777

Case 3: Respiratory Tract Papillomatosis

This 30-year-old woman arrived in the emergency department with acute, worsening respiratory distress that was accentuated by inspiration but was associated with a normal voice. Physical examination revealed bilateral wheezes and upper airway inspiratory stridor with retractions in the neck and chest musculature. Her medical history was remarkable for multiple resections of respiratory tract papillomas, with the last treatment 3 weeks before this admission. The posteroanterior chest radiograph obtained at admission showed bilateral nodular and cystic changes in the lung parenchyma as well as a more subtle tracheal mass below the level of the glottis at the thoracic inlet (Figs. 3A and 3B). The lateral view confirmed the nodular and cystic changes in the lung, as well as the subglottic mass in the trachea (Figs. 3C and 3D).

Direct laryngoscopy and tracheoscopy revealed multiple papillomas beginning 3 cm below the vocal cords. The papillomas were excised down to and just past the level of the carina with a carbon dioxide laser. At the time of the excisions, more papillomas were noted extending beyond the bifurcation of the trachea with more severe involvement of the left main bronchus. Pathologic examination of multiple tissue fragments revealed multiple squamous papillomas. The patient's subsequent recovery was uneventful, and she was asymptomatic when discharged from the hospital.

Respiratory papillomas (also known as juvenile laryngeal papillomas) are the most common tumors in the respiratory tree in infants and children, but can occur in adults also [1–3]. These benign tumors consist of a central fibrous connective tissue core covered by squamous epithelium and are apparently caused by human papillomaviruses, especially types six and 11. These papillomas have similarities to the condyloma acuminata of the female genital tract, but a direct causal link has not been established [3]. The lesions are more likely to recur if the patient is less than 16 years old when the lesions are excised. Although lesions in the upper airway may regress spontaneously at puberty, no regression of pulmonary lesions has been reported [4, 5]. The prognosis is particularly grim in patients less than 6 months old, with all four of the patients reported by Chipps et al. [6] dying within 2 years of diagnosis. Tracheostomy should be avoided because of the marked predilection for recurrence at the tracheostomy site [2].

The lesions commonly manifest as single or multiple masses involving the true vocal cords and are more rarely seen in the supraglottic and subglottic regions [5]. Five percent of patients exhibit extension into the trachea or proximal bronchi, and in less than 1% lesions will develop in the lung parenchyma [7].

The appearance of the laryngeal and tracheal tumors on plain radiographs is that of large fungating masses. The parenchymal lesions appear as solid or cystic nodules ranging in size from a few millimeters to several centimeters in diameter, and they may exhibit either moderately thick or thin walls [5, 7]. CT may be useful in detecting pulmonary lesions before they are visible on plain radiographs [7] and also in establishing the relationships of lesions to the vascular structures in the mediastinum, especially when laser ablation is contemplated, in order to minimize the risk of hemorrhage [8]. When laser ablation is used, a postoperative chest radiograph must be obtained and reviewed before the patient leaves the recovery room in order to rule out a pneumothorax, should the tracheal wall be damaged.

The differential diagnosis for the tracheal and bronchial lesions includes carcinoma, carcinoid, lymphoma, and granulomatous diseases. Differential considerations for the pulmonary nodules and cavities include metastatic disease, septic emboli, tuberculosis and fungal diseases, Hodgkin's disease, Wegener's granulomatosis, and bronchiectasis [5].

Treatment is primarily surgical, and current surgical recommendations include aggressive initial laser resection to reduce the papilloma burden, with additional therapy as required thereafter [9]. A single removal is curative in most cases, but recurrences often lead to a prolonged course of multiple resections, pneumonia, hemoptysis, and bronchiectasis [4]. Death is usually associated with complications of surgical procedures or respiratory failure due to disease progression [6].

John A. Worrell
Dennis M. O'Donnell
Frank E. Carroll
Jack A. Coleman, Jr.

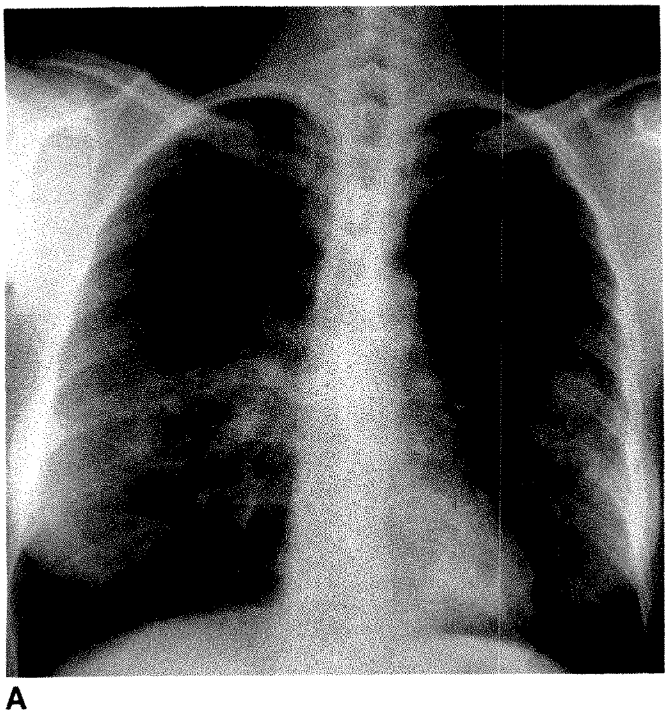

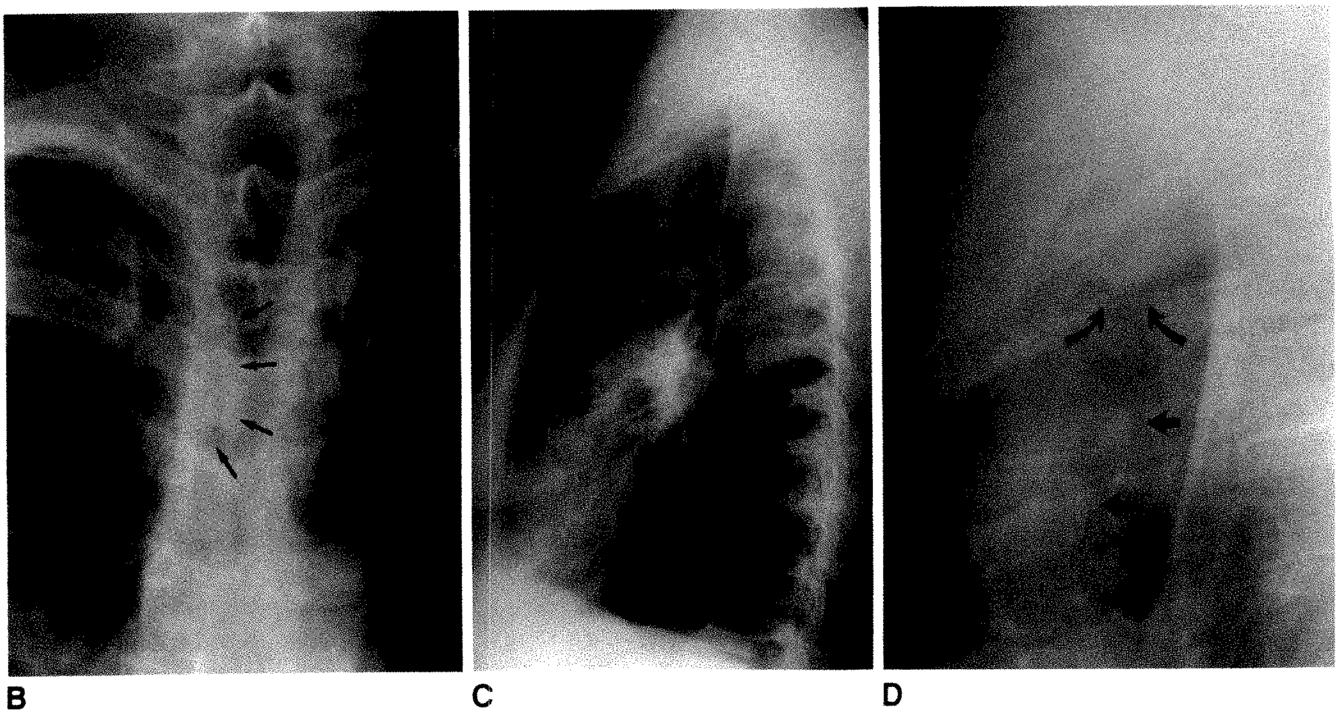

Fig. 3.—Case 3: Respiratory tract papillomatosis.

***A*, Posteroanterior chest radiograph obtained at admission shows multiple parenchymal nodules of various sizes, some of which suggest cavitation.**

***B*, Magnified posteroanterior radiograph of upper mediastinum shows a tracheal mass (*arrows*) encroaching on tracheal air column from right side.**

***C*, Lateral chest radiograph shows multiple nodular irregularities involving trachea. Nodular changes are seen over cardiac shadow.**

***D*, Magnified lateral radiograph of upper mediastinum shows subglottic tracheal mass (*curved arrows*) nearly occluding tracheal air column. More nodules (*arrows*) are present in trachea below this lesion.**

REFERENCES

1. Kerley SW, Buchon-Zalles C, Moran J, Fishback JL. Chronic cavitary respiratory papillomatosis. *Arch Pathol Lab Med* **1989**;113:1166–1169
2. Singer DB, Greenberg SD, Harrison GM. Papillomatosis of the lung. *Am Rev Resp Dis* **1966**;94:777–781
3. Healy GB, Gelber RD, Trowbridge AL, Grundfast KM, Ruben RJ, Price KN. Treatment of recurrent respiratory papillomatosis with human leukocyte interferon: results of a multicenter randomized clinical trial. *N Engl J Med* **1988**;319:401–407
4. Rosenbaum HD, Alavi SM, Bryant LR. Pulmonary parenchymal spread of juvenile laryngeal papillomatosis. *Radiology* **1968**;90:654–660
5. Sweriduk ST, Deluca SA. Juvenile laryngotracheal papillomatosis. *Am Fam Physician* **1986**;33:155–156
6. Chipps BE, McClurg FLD Jr, Freidman EM, Adams GL. Respiratory papillomas: presentation before six months. *Pediatr Pulmonol* **1990**;9:125–130
7. Kramer SS, Wehunt WD, Stocker JT, Kashima H. Pulmonary manifestations of juvenile laryngotracheal papillomatosis. *AJR* **1985**;144:687–694
8. Naidich DP. CT/MR correlation in the evaluation of tracheobronchial neoplasia. *Radiol Clin North Am* **1990**;28:555–571
9. Hunt JM, Pierce RJ. Tracheal papillomatosis treated with Nd-YAG laser resection. *Aust N Z J Med* **1988**;18:781–784

Case 4: Acute Silicosis

A 40-year-old man was referred to the hospital because of increasing dyspnea and severe hypoxemia. Two years earlier, the patient had begun working as a sandblaster in a small blue jeans factory. The patient's job entailed using fractured sand in sandblasting the jeans to produce a "stone-washed" appearance.

The patient's primary form of respiratory protection was a simple painter's mask. The patient noted that the masks quickly became obstructed by the fine sand, making it difficult to breathe. Because of this, the workers would frequently remove their masks soon after starting work.

The patient performed this work for 9 months. For the ensuing 7 months, the patient was relatively asymptomatic, but in October 1990, the patient presented to his local hospital with fever and dyspnea. After a subsequent evaluation, it was decided that the patient had silicosis. The patient's condition rapidly deteriorated, with progressively worsening dyspnea on exertion such that during the 4 months before admission, the patient was essentially bedridden.

Posteroanterior and lateral chest radiographs (Figs. 4A and 4B) obtained at admission showed multiple small nodular densities coalescing into confluent opacities with air bronchograms in the upper lobes. A large left-sided pneumothorax is present. The pneumothorax and bronchograms are seen on a representative CT scan (Fig. 4C) also.

Silicosis is a lung disease caused by the inhalation of very small particles of crystalline silica (silicon dioxide). Silica comprises approximately 25% of the earth's crust, and thus, any

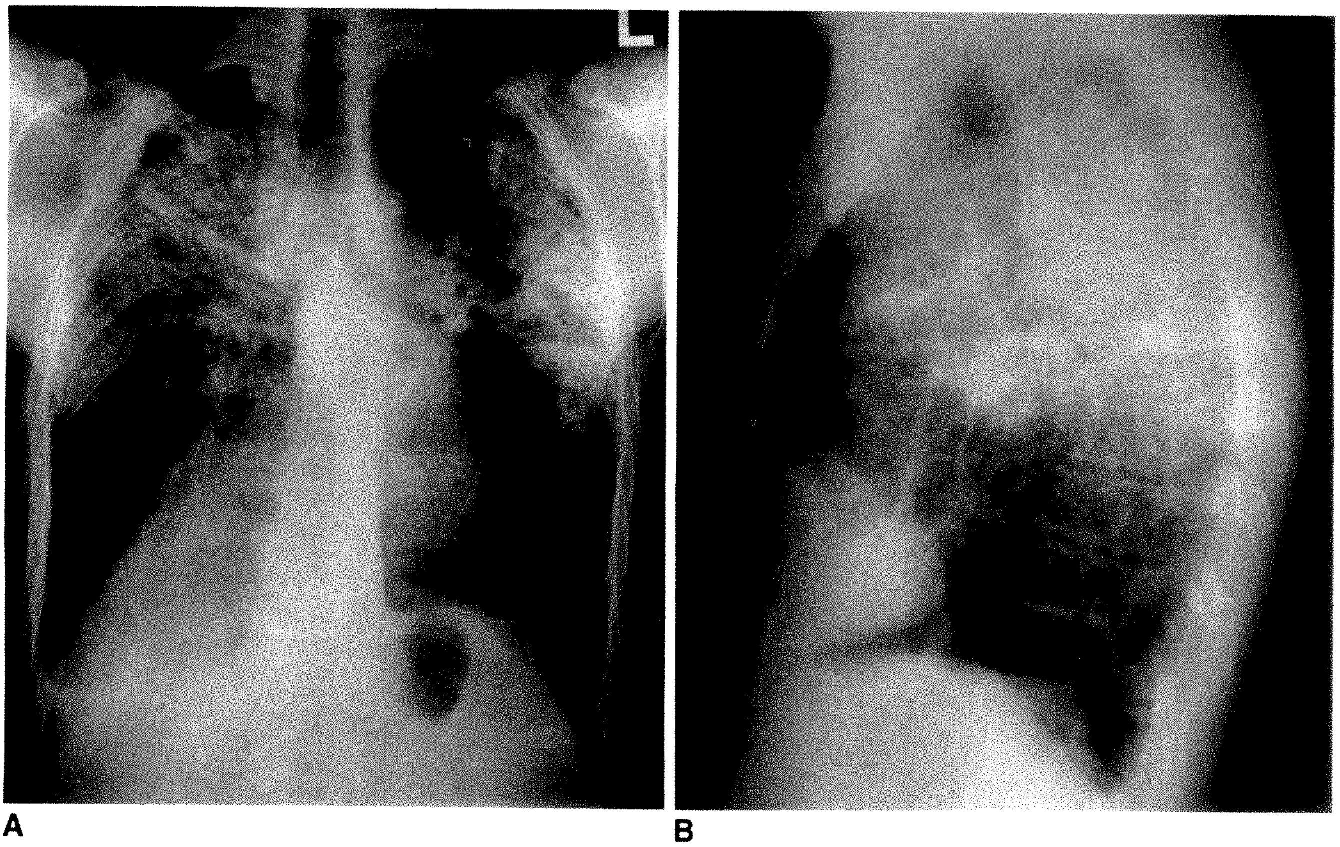

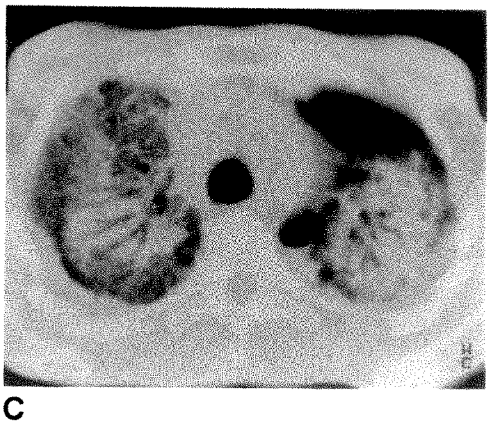

Fig. 4.—Case 4: Acute silicosis.
A and *B*, Posteroanterior and lateral chest radiographs obtained at admission show a large left-sided pneumothorax. There are coalescent alveolar opacities in upper lobes and reticulonodular opacities in mid and upper zones of lung.
C, CT scan shows left-sided pneumothorax and shows more clearly both interstitial and alveolar opacities, with air bronchograms centrally and posteriorly.

person in a mining occupation is at risk for the development of this disease [1]. Other high-risk occupations include sandblasting, stone cutting, foundry work, glassmaking, and stone polishing. Sand is also used in the manufacture of paints, cosmetics, and plastics. Because of the well-recognized dangers of silica inhalation, sand is seldom used as the abrasive in sandblasting. In spite of this, there can be considerable exposure from the dust of architectural stone [2].

Silicosis is the lung's reaction to the deposition of silica particles in the terminal airways and alveoli. The smaller the particle is when inhaled, the greater the potential for pulmonary injury. The critical size appears to be 1-3 μm, and it is this size particle that has the greatest potential for deposition in the peripheral airways [2].

Silicosis can be clinically classified into three subtypes: chronic, accelerated, and acute. The form of the disease that one develops depends mostly on the severity and duration of exposure to the respirable silica particles. The diagnosis is based on the appearance on radiographs and the history of exposure to silica. Pulmonary function testing is used to assist in determining the severity of the disease, the degree of functional impairment, and the progression of the disease [2, 3].

Chronic silicosis is the most common form. It is the result of exposure to lower levels of silica over a long period. The course of the disease is usually from 10 to 30 years. Often, the disease can progress even after the exposure is discontinued. The characteristic appearance on chest radiographs is of multiple small nodular densities, which are sharply defined and preponderant in the upper lobe. Occasionally, these nodules coalesce to form large areas of opacity and fibrosis, usually greater than 2-3 cm in diameter. This is termed progressive massive fibrosis. Hilar adenopathy with the classic "eggshell" calcification also can be seen, but this is not a common occurrence.

The accelerated form of silicosis has a shorter time course, usually over several years. The appearance on radiographs is similar to that of chronic silicosis, but the clinical progression is more rapid.

Acute silicosis is a much more rapidly progressive disease, usually measured in months to a few years. It is most likely the result of a very large exposure to silica dust. The radiologic and clinical presentations are distinctly different than in the chronic or accelerated forms. Radiographs show alveolar opacities with indistinct margins preponderant in the upper lobe. Air bronchograms can be seen within these opacities, and the density of the opacities is relatively inhomogeneous. Reticulonodular opacities also may be present, again mostly in the upper lobe. Pneumothoraces are common [3-5]. Pathologically, there is a proteinaceous and cellular alveolar exudate similar in character to that of alveolar proteinosis. Extensive fibrotic and nodular interstitial changes also are present.

Clinically, these patients have a rapid downhill course. In spite of discontinuing the exposure, respiratory impairment progresses and hypoxia increases, with death due to respiratory failure occurring in months to a few years.

This patient's clinical course, exposure, history, and radiologic presentation are all most consistent with acute silicosis. Often this diagnosis is difficult to make on the basis of radiographs alone, as an appropriate exposure history and clinical course are needed. The treatment is supportive, with lung transplantation as an investigational option.

Dennis M. O'Donnell
John A. Worrell
Frank E. Carroll

REFERENCES

1. Silicosis: cluster in sandblasters. *MMWR* **1990**;39:433-437
2. Murray JF, Nadel JA, eds. *Textbook of respiratory medicine.* Philadelphia: Saunders, **1988**
3. Bergin CJ, Muller NL, Vedal S, Chan-Yeung M. CT in silicosis: correlation with plain films and pulmonary function tests. *AJR* **1986**;146:477-483
4. Dee P, Suratt P, Winn W. The radiographic findings in acute silicosis. *Radiology* **1978**;126:359-363
5. Begin R, Bergeron D, Samson L, Boctor M, Cantin A. CT assessment of silicosis in exposed workers. *AJR* **1987**;148:509-514

Abdominal Case of the Day

Max I. Shaff,[1] Thomas A. Powers, Lewis B. Gilpin, and Michael E. Faulstich

Case 1: Superior Mesenteric Venous Thrombosis

A 34-year-old woman with severe nausea, vomiting, and back pain had CT of the abdomen after IV administration of contrast material. Presence of marked ascites and edematous mesentery are noted (Figs. 1A–1C). On an axial CT scan (Fig. 1A), thrombosis in the superior mesenteric vein can be seen as a low-attenuation intraluminal lesion surrounded by a wall of higher attenuation. Further axial CT scans (Figs. 1B and 1C) show an unusual small-bowel configuration with loops of small bowel exhibiting a parallel distribution from left to right. Exploratory laparotomy documented presence of thrombosis in the superior mesenteric vein and extensive small-bowel infarction.

Several predisposing pathologic conditions are associated with mesenteric venous occlusion, including hypercoagulable states, mechanical obstruction, abdominal inflammation, and postsurgical/posttraumatic conditions. The main complication of thrombosis in the superior mesenteric vein is the development of intestinal infarction. Interestingly, it has been shown that in approximately half these patients bowel infarction may not occur because of the development of multiple portosystemic venous connections [1].

Early diagnosis of mesenteric infarction can be a difficult clinical and radiologic problem. Abdominal CT is useful through identification of bowel wall thickening, bowel dilatation, pneumatosis, and abdominal vascular gas. However, these findings can be nonspecific, and normal CT findings do not exclude the diagnosis of ischemic or infarcted bowel [2]. In the present case, the bowel infarction manifested as edematous, parallel loops surrounded by marked ascites. The CT appearance of thrombosis in the superior mesenteric vein has been previously described, but the diagnostic sensitivity of CT is yet to be determined [3, 4]. Therefore, when clinical suspicion is high, angiographic or surgical evaluation should not be delayed.

Michael E. Faulstich
Max I. Shaff

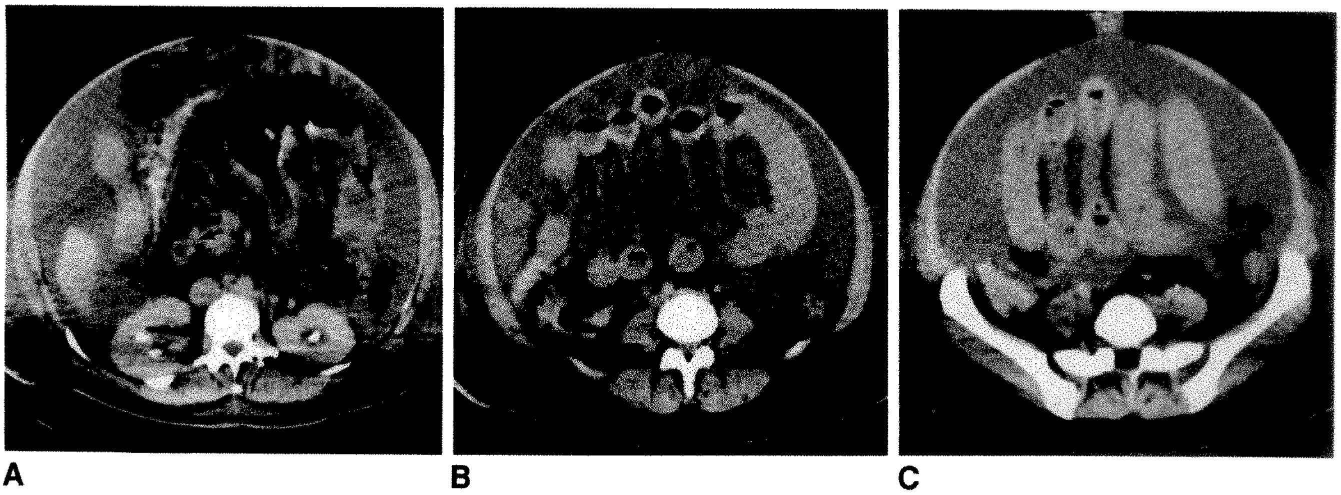

Fig. 1.—Case 1: Superior mesenteric venous thrombosis in a 34-year-old woman with severe nausea, vomiting, and back pain.
***A*, Axial CT scan shows thrombosis in superior mesenteric vein as a low-attenuation intraluminal lesion (*arrow*).**
***B* and *C*, Axial CT scans show edematous, parallel loops of small bowel surrounded by marked ascites.**

---

[1] All authors: Department of Radiology, Vanderbilt University Medical Center, 1161 21st Ave., S., Nashville, TN 37232-2675. Address reprint requests to M. I. Shaff.

***AJR* 158:1363–1367, 1992** 0361–803X/92/1586–1363 © American Roentgen Ray Society

REFERENCES

1. Ottinger LW, Austen WG. A study of 136 patients with mesenteric infarction. *Surg Gynecol Obstet* **1967**;124:251-261
2. Alpern MB, Glazer GM, Francis IR. Ischemic or infarcted bowel: CT findings. *Radiology* **1988**;166:149-152
3. Rosen A, Korobkin M, Silverman P, et al. Mesenteric venous thrombosis: CT identification. *AJR* **1984**;143:83-86
4. Franquet T, Bescos J, Reparaz B. Non-invasive methods in the diagnosis of isolated superior mesenteric vein thrombosis: US and CT. *Gastrointest Radiol* **1989**;14:321-325

Case 2: Complicated Appendicitis

Equivocal findings on plain films of the abdomen showing a possible mass in the right lower quadrant led to a CT examination. Axial CT scans of the abdomen were obtained after IV and oral administration of contrast material. Multiple loculated fluid collections, thickened bowel loops, and interloop abscesses were evident throughout the abdomen and pelvis (Figs. 2A–2D).

Up to 6% of the population will have appendicitis during a lifetime, and 75% will experience uncomplicated appendicitis, in which the appendix has not perforated before surgery. The most common CT finding, seen in 58–88% of patients, is periappendiceal or pericecal inflammation. Other important CT findings are abnormal appendix, thickening of the cecal or small-bowel wall, thickened renal fascial planes or abdominal muscle walls, and enlargement and blurring of the right psoas muscle. Appendicoliths are detected much more often on CT than on plain films. They are single or multiple and appear as calcifications on CT. They were found in 80% of cases with appendiceal abscesses (complicated appendicitis) [1].

Complicated appendicitis occurs much less often than the uncomplicated type. Perforation results in variable amounts of abdominal abscesses and peritonitis. Pathognomonic for complicated appendicitis is an appendicolith within an inflammatory mass, which may be seen on CT in 25–80% of cases [1].

This case is an example of complicated appendicitis, with the findings documented by CT. However, sonography is also

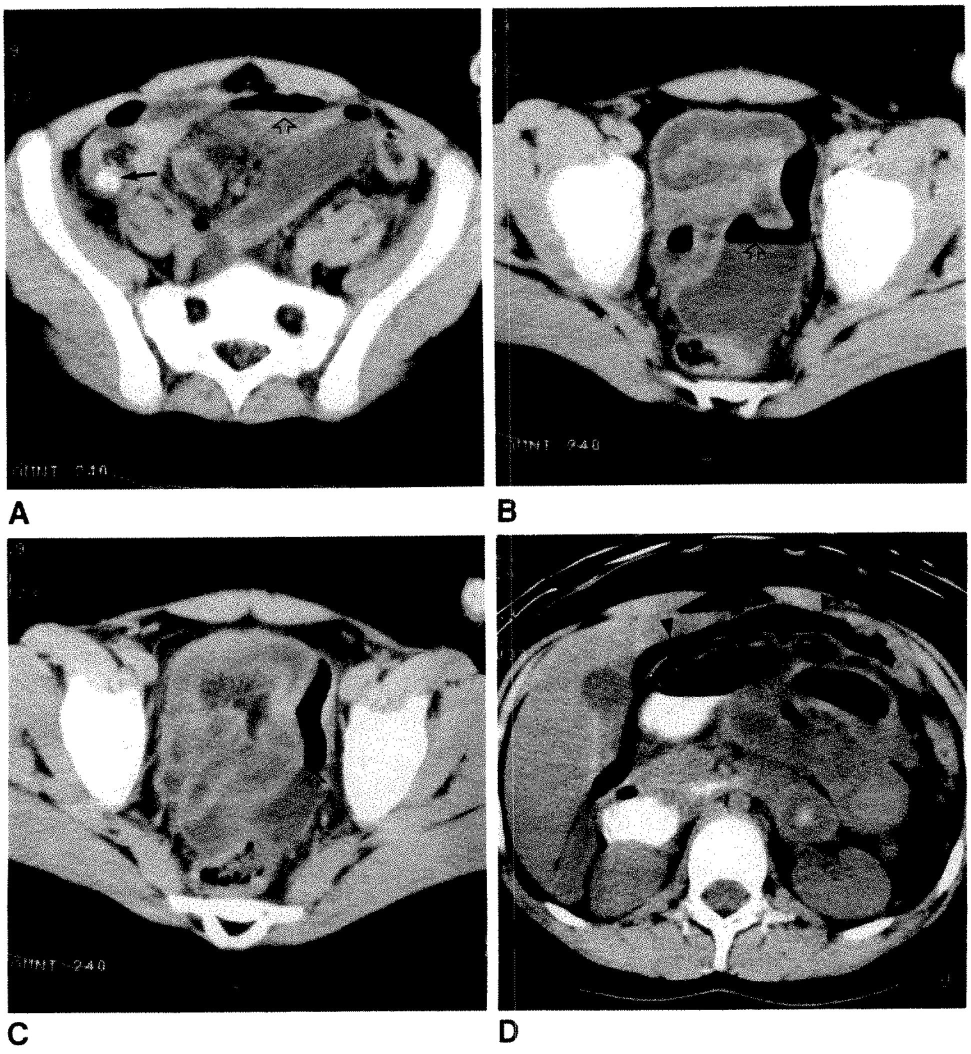

Fig. 2.—Case 2: Complicated appendicitis in a 10-year-old boy with a 2-week history of nausea, vomiting, and mild diffuse abdominal pain and recent onset of fever and progressive obtusion.

***A–C*, Axial CT scans of pelvis and abdomen show multiple loculated fluid collections, thickened bowel loops, and interloop abscesses (*open arrows*). Axial CT scan of lower abdomen (*A*) also shows a calcified appendicolith (*solid arrow*).**

***D*, Axial CT scan of middle abdomen shows free intraperitoneal air (*arrowheads*).**

an excellent imaging technique for diagnosis of appendicitis [2]. CT can also be very beneficial in CT-guided percutaneous drainage of well-localized periappendiceal abscesses [3, 4].

Lewis B. Gilpin
Max I. Shaff

REFERENCES

1. Shapiro MP, Gale ME, Gerzof SG. CT of appendicitis: diagnosis and treatment. *Radiol Clin North Am* **1989**;27:753-762
2. Vignault F, Filiatrault D, Brandt ML et al. Acute appendicitis in children: evaluation with US. *Radiology* **1990**;176:501-504
3. Jeffrey RB Jr, Federle MP, Tolentino CS. Periappendiceal inflammatory masses: CT-directed management and clinical outcome in 70 patients. *Radiology* **1988**;167:13-16
4. Garcia CJ, Rosenfield NS, Markowitz RJ, et al. Appendicitis in children: accuracy of the barium enema (abstr). *Radiology* **1988**;168:296

Case 3: Gastric Adenocarcinoma

Axial CT scans of the abdomen were obtained after administration of oral and IV contrast material. Thickening and ulceration are seen in the posterior wall of the gastric antrum (Figs. 3A and 3B). A left-sided adrenal mass 1 × 2 cm in diameter also was present. A similar scan of the lung showed a mass associated with extensive consolidation and atelectasis of the left lower lobe and involving the left hilum near the esophagus and aorta.

Poorly differentiated adenocarcinoma was identified in the transverse colon, small intestine, stomach, and lesser omental nodes.

This case generated considerable discussion concerning the evolution of carcinoma in this patient. Because of the pathology report of poorly differentiated adenocarcinoma in each sample, the true primary site remains unclear. One likely scenario, because lung adenocarcinoma very seldom metastasizes to the stomach [1], describes two primary tumors: one in the stomach and one in the lung. Lung adenocarcinoma can metastasize to the adrenal gland. Gastric adenocarcinoma can metastasize to small bowel and large bowel and to the adrenal gland. Because the pathology of the masses in the lung and adrenal gland are not determined as yet, the following discussion will be limited to gastric adenocarcinoma and its metastatic pattern.

Adenocarcinoma is certainly the most common primary malignant tumor of the stomach. Although the prevalence in the United States has decreased in recent years, this silent disease has a poor 5-year survival rate of 10-20%. Although our case involved a localized area of mural thickening with ulceration, the process may also be circumferential or diffuse. Mural thickening varies from 6.0 mm to more than 4.0 cm and is a predictor of transmural extension when greater than 2 cm. Gastric carcinoma can invade directly any of the organs located nearby, including liver, diaphragm, spleen, duodenum, and adrenal glands. Lymphatic metastases occur in the peripancreatic lymph nodes, gastrohepatic ligament, and the cardiophrenic angles [2-4].

Lewis B. Gilpin
Max I. Shaff

REFERENCES

1. Taveras J, Ferrucci J. GI, general abdominal and pelvic, and genitourinary radiology. *Radiology* **1991**;4:4-5
2. Shapiro MP, Gale ME, Gerzof SG. CT of the stomach and duodenum, CT of the small bowel and mesentery. *Radiol Clin North Am* **1989**;27: 687-715
3. Ming SC. Tumors of the esophagus and stomach. In *Atlas of tumor pathology*, 2nd ser., vol. 7. Washington, DC: Armed Forces Institute of Pathology, **1973**:253-255
4. Seaman WB. Stomach and duodenum. In: Margulis AR, Burhenne HJ, eds. *Alimentary tract radiology*, 4th ed. St. Louis: Mosby, **1989**:622-624

Case 4: Interruption of the Inferior Vena Cava with Azygos Continuation

The inferior vena cava (IVC) develops in a complex series of events, beginning with the appearance of paired posterior cardinal veins that drain the dorsal and inferior portions of the

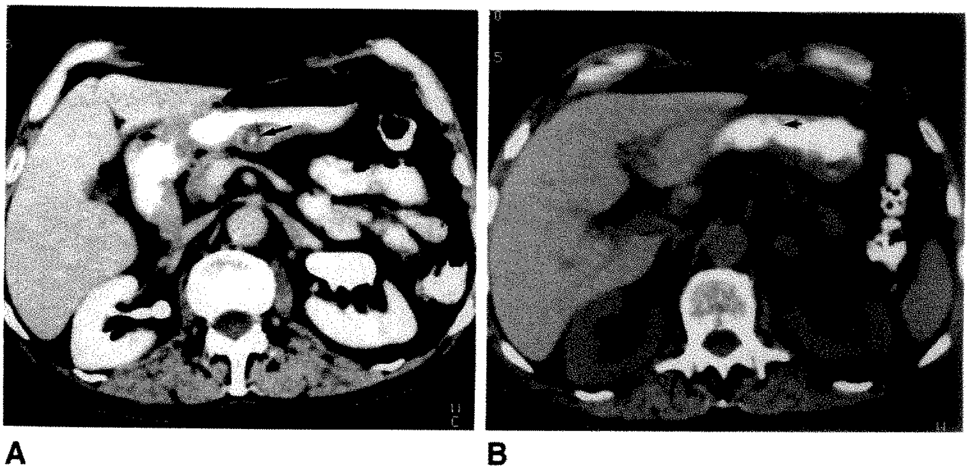

Fig. 3.—Case 3: Gastric adenocarcinoma in a 72-year-old man with a 2-month history of weight loss and recent onset of nausea and vomiting.

***A* and *B*, Axial CT scans of middle abdomen show thickening and ulceration in posterior wall of gastric antrum with a central speck of contrast material (*arrow*) in ulcer surrounded by edema.**

embryo. These vessels anastomose with the medially situated subcardinal veins, which subsequently become the route of preferred drainage as the posterior cardinal veins regress. The right hepatic vein is formed by hepatic sinusoids and becomes the hepatic segment of the IVC. The right subcardinal vein anastomoses with the right hepatic vein and persists to become the prerenal segment of the IVC. Supracardinal veins also develop medial to the posterior cardinal veins and dorsolateral to the subcardinal veins. The right supracardinal vein persists as the postrenal segment of the IVC. The renal segment of the IVC develops from anastomoses between the supracardinal and subcardinal veins [1].

Failure of regression of the early venous channels may lead to various congenital anomalies of the IVC. In the postrenal segment, persistence of both supracardinal veins results in a duplicated IVC, while regression of the right supracardinal vein and persistence of the left supracardinal vein gives a left-sided IVC. A persistent right posterior cardinal vein results in

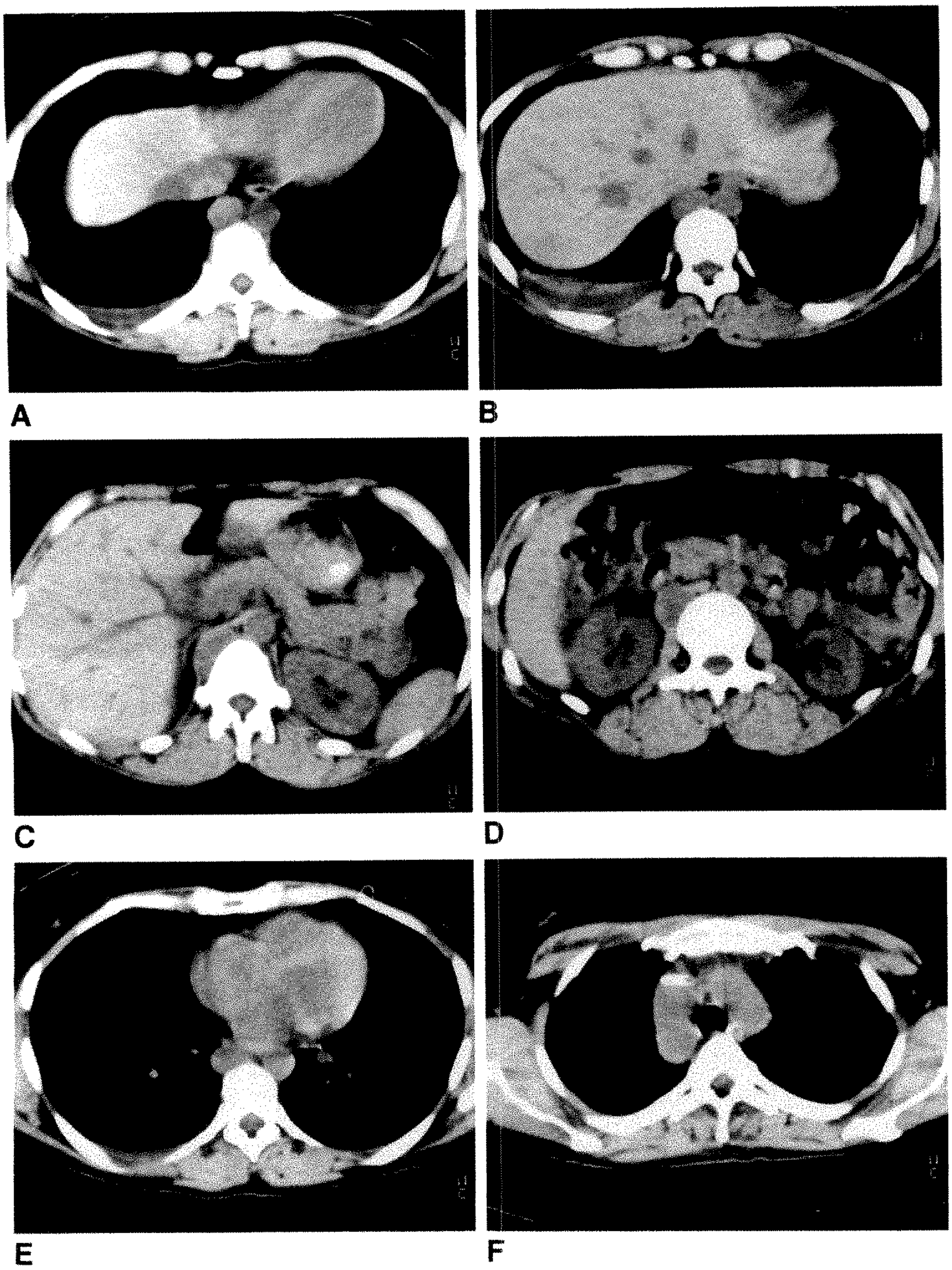

Fig. 4.—Case 4: Interruption of inferior vena cava with azygos continuation. This 26-year-old woman with thrombotic thrombocytopenic purpura was noted to have a right-sided paratracheal mass on chest radiographs.

A–D, Selected CT scans of abdomen beginning at dome of liver and moving caudally to inferior edge of liver. Note enlarged azygos vein in right retrocrural region.

E, CT scan at level of left atrium.

F, CT scan at level of aortic arch.

a retrocaval ureter. Anomalies of the supracardinal and subcardinal anastomoses may produce a circumaortic venous ring in the renal segment.

The situation in the present case is known as interruption of the IVC with azygos continuation and results from failure of formation of the hepatic segment of the IVC. CT scans show the absence of the IVC above the level of the renal veins. The intrahepatic IVC is absent, and the hepatic veins drain directly into the right atrium (Figs. 4A and 4B). Blood is carried toward the heart through an enlarged azygos vein, which can be followed in the right retrocrural region and azygoesophageal recess to the level of the enlarged azygos arch (Figs. 4C–4F). (A left subclavian catheter is present just inside the azygos arch.) The enlarged arch accounts for the mistaken diagnosis of right-sided paratracheal adenopathy on the chest radiograph.

This anomaly is associated with congenital heart disease in approximately 85% of cases; frequently, the polysplenia syndrome [2]. The lateral chest radiograph may give a clue to the diagnosis when the normal intrathoracic portion of the IVC is not seen adjacent to the right atrium [3]. Hemiazygos continuation of a left-sided IVC also has been described, which results in a dilated left superior intercostal vein that can simulate an aortic aneurysm or dissection [4].

Thomas A. Powers

REFERENCES

1. Chuang VP, Mena CE, Hoskins PA. Congenital anomalies of the inferior vena cava: review of embryogenesis and presentation of a simplified classification. *Br J Radiol* **1974**;47:206–213
2. Churchill RJ, Wesby GW III, Marsan RE, et al. Computed tomographic demonstration of anomalous inferior vena cava with azygos continuation. *J Comput Assist Tomogr* **1980**;4:398–402
3. Heller RM, Dorst JP, James AE Jr, Rowe RD. A useful sign in the recognition of azygos continuation of the inferior vena cava. *Radiology* **1971**;101:519–522
4. Cohen MI, Gore RM, Vogelzang RL, et al. Accessory hemiazygos continuation of the left inferior vena cava: CT demonstration. *J Comput Assist Tomogr* **1984**;8:777–779

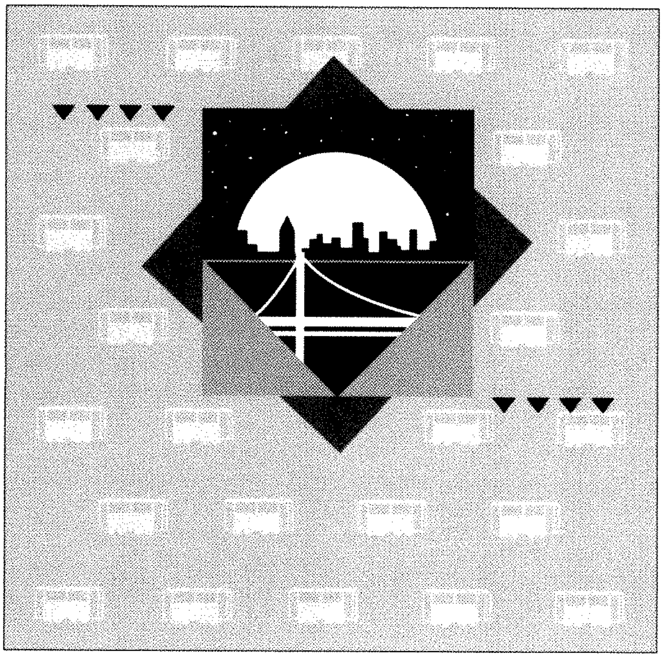

San Francisco
American Roentgen Ray Society
93rd Annual Meeting
April 25–30, 1993
San Francisco Marriott
San Francisco, CA

Skeletal Case of the Day

Stefan Tigges,[1] Roy E. Erb, and E. Paul Nance

Case 1: Parosteal Osteosarcoma

A 39-year-old woman had an abnormality noted on a bone scan obtained to assess back pain. The radiologic and clinical features of this case nicely illustrate the differences between myositis ossificans, osteochondroma, and surface osteosarcomas. Often, patients with myositis ossificans give a history of trauma, although in many cases the trauma may have been forgotten. Radiologically, myositis ossificans has a more mature (ossified) periphery with a radiolucent center [1, 2].

Osteochondromas are benign neoplasms typically arising from the metaphyses of long bones. The periosteum, cortex, and marrow are continuous with that of the underlying bone. These lesions stop growing after skeletal maturity. Any growth after this time should suggest possible malignant degeneration [1, 2].

This patient had a biopsy-proved parosteal osteosarcoma, one of three types of surface osteosarcomas. In addition to parosteal osteosarcoma, surface osteosarcomas also include periosteal osteosarcoma and high-grade conventional osteosarcoma. Surface high-grade conventional osteosarcomas are identical to conventional osteosarcomas histologically and in terms of prognosis; the only distinction between the two is location. Periosteal osteosarcomas are rare lesions that most often involve the diaphysis of long bones, especially the tibia. These tumors arise juxtacortically and typically have a "hair on end" appearance with spicules of bone perpendicular to the cortex. The medullary cavity is typically uninvolved. Clinically, patients tend to be somewhat older than those with conventional osteosarcoma, and the prognosis is better [1, 2].

Parosteal osteosarcomas also occur in older patients and have a better prognosis than do conventional osteosarcomas. They are more common than periosteal osteosarcomas but still represent only 3–4% of all osteosarcomas. The location of the tumor in this patient was typical; approximately two thirds of these osteosarcomas involve the posterior distal femoral metaphysis (Figs. 1A–1C). These lesions are typically large, lobulated, and contain a densely sclerotic matrix with the more mature elements located centrally (Fig. 1D). Parosteal osteosarcomas are often extremely large when detected and can grow to encircle the underlying bone. Finally, as our case demonstrates, the tumor may be relatively asymptomatic [1, 2].

Stefan Tigges
E. Paul Nance

REFERENCES

1. Hudson TM. *Radiologic pathologic correlation of musculoskeletal lesions.* Baltimore: Williams and Wilkins, **1987**:79–95
2. Resnick D, Kyri-kos M, Greenway GD. Tumors and tumor-like lesions of bone: imaging and pathology of specific lesions. In: Resnick D, Niwayama G, eds. *Diagnosis of bone and joint disorders*, 2nd ed. Philadelphia: Saunders, **1988**:3668–3677

Case 2: Radiation-Induced Osteochondroma

A 21-year-old man who had had radiotherapy for a neuroblastoma at age 7 months now had scoliosis and vague pain. Even without knowing the history, the patient's scoliosis and hypoplastic lower thoracic vertebral bodies (Figs. 2A and 2B) should suggest prior radiotherapy. Both these changes are well-known consequences of radiotherapy. Tumors may occur in irradiated bones also, most commonly osteochondromas, but also chondrosarcoma, osteosarcoma, and fibrosarcoma. In most cases these tumors will have distinctive features; osteosarcomas and chondrosarcomas may have osteoid and chondroid calcifications, respectively, and osteochondromas have elements of normal cortical and medullary bone (Fig. 2C). In addition, osteosarcomas and chondrosarcomas will appear aggressive relative to osteochondromas, which are well circumscribed and nondestructive in the absence of malignant degeneration [1, 2].

Radiation-induced osteochondromas arise only in patients who received radiotherapy as children, and they are radiologically and histologically indistinguishable from spontaneous osteochondromas. They may occur in any growing bone included in the radiation port. In the series of Libshitz and Cohen [3], osteochondromas were reported to occur in 12% of patients who were irradiated as children, and they are often

---

[1] All authors: Department of Radiology, Vanderbilt University Medical Center, 1161 21st Ave., S., Nashville, TN 37232-2675. Address reprint requests to E. P. Nance.

AJR 158:1368–1371, June 1992 0361–803X/92/1586–1368 © American Roentgen Ray Society

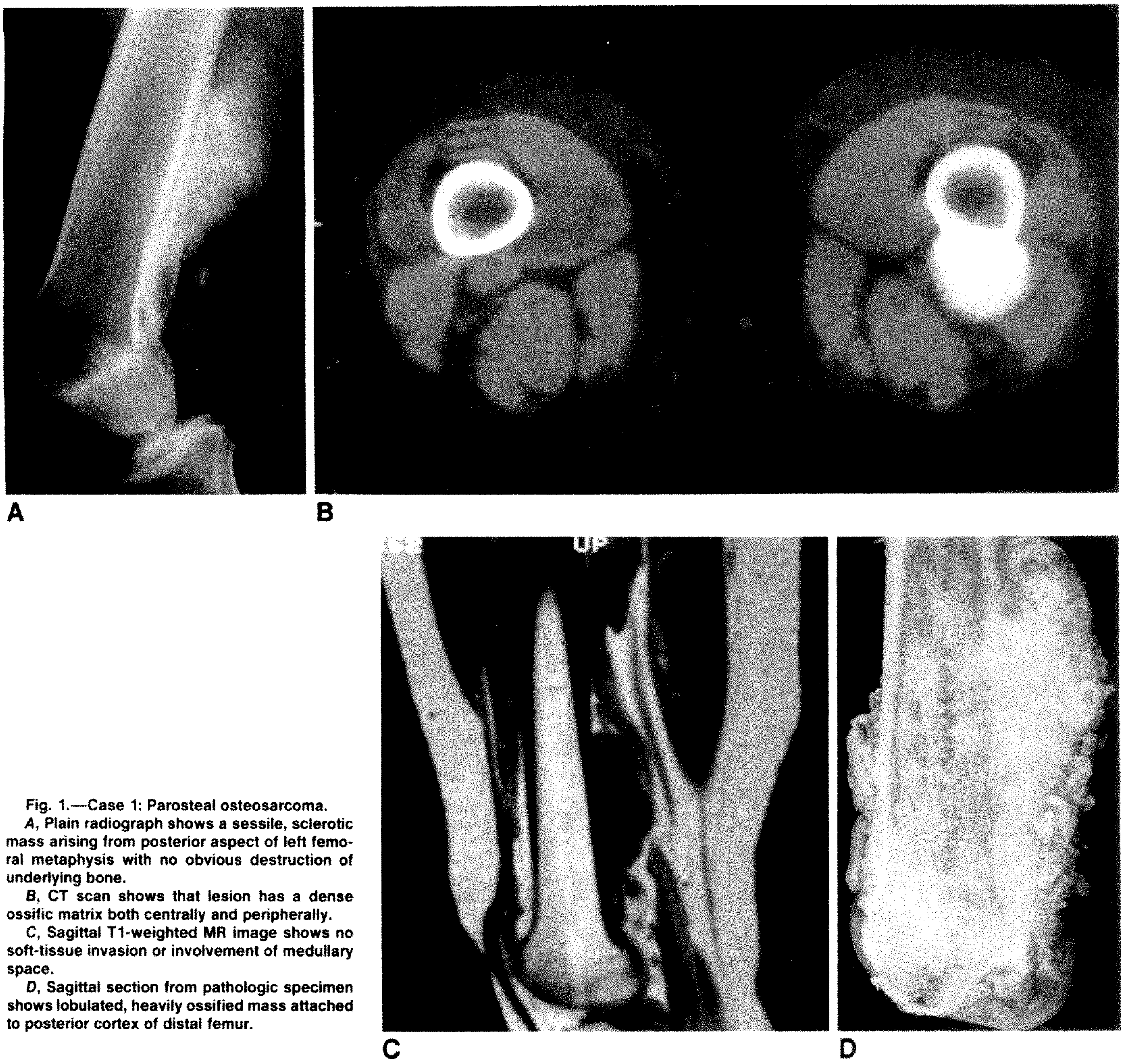

Fig. 1.—Case 1: Parosteal osteosarcoma.

***A*, Plain radiograph shows a sessile, sclerotic mass arising from posterior aspect of left femoral metaphysis with no obvious destruction of underlying bone.**

***B*, CT scan shows that lesion has a dense ossific matrix both centrally and peripherally.**

***C*, Sagittal T1-weighted MR image shows no soft-tissue invasion or involvement of medullary space.**

***D*, Sagittal section from pathologic specimen shows lobulated, heavily ossified mass attached to posterior cortex of distal femur.**

multiple. Malignant degeneration of those tumors appears to be extremely rare. Nevertheless, unexpected growth or the appearance of a soft-tissue mass and symptoms of pain should suggest this possibility [1, 2].

Stefan Tigges
E. Paul Nance

REFERENCES

1. Rutherford H, Dodd GD. Complications of radiation therapy: growing bone. *Semin Roentgenol* **1974**;9:15–28
2. Dalinka MK, Neustadter LM. Radiation changes. In: Resnick D, Niwayama G, eds. *Diagnosis of bone and joint disorders*, 2nd ed. Philadelphia: Saunders, **1988**:3043–3052
3. Libshitz HI, Cohen MA. Radiation-induced osteochondromas. *Radiology* **1982**;142:643–647

Case 3: Brown Tumor

A 47-year-old man on long-term hemodialysis had pain and swelling in the right hand. Brown tumors, or osteoclastomas, are benign osseous lesions frequently seen in primary hyperparathyroidism and less frequently observed in secondary hyperparathyroidism [1]. These lesions occur in all age groups and are most often found in the pelvis, ribs, clavicle, facial bones, femurs, or digits. Although osteoclastomas typically occur as solitary lesions, multiple lesions can be found in both primary and secondary hyperparathyroidism [2]. Histologically, the tumors are composed of fibrous tissue and giant cells.

The clinical presentation of brown tumors varies depending on the site of the tumor. The lesions may be clinically occult or cause local pain. Pathologic fractures can occur, as can

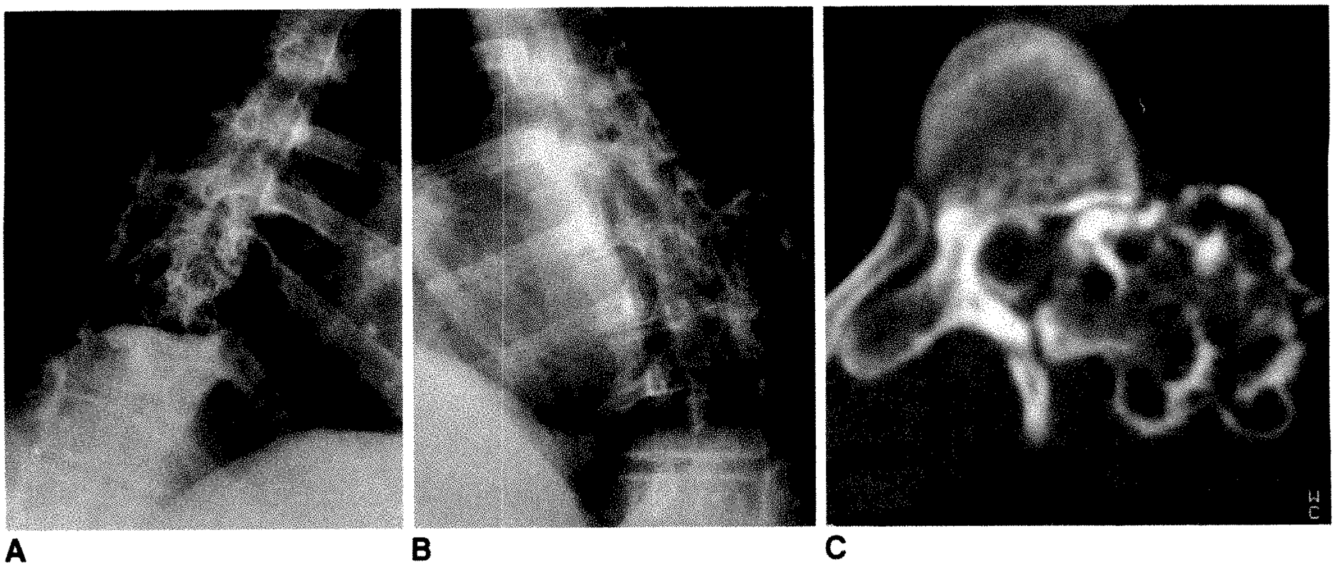

Fig. 2.—Case 2: Radiation-induced osteochondroma.
***A* and *B*, Oblique plain radiographs of thoracic spine show an expansile, lobulated bony mass involving one of lower thoracic vertebral bodies. Adjacent vertebrae are hypoplastic.**
***C*, CT scan shows that lobulated lesion consists of medullary bone centrally with a rim of cortical bone. Mass displaces thecal sac to right.**

local symptoms due to mass effect of the tumor in regions such as the orbit or spine [3].

Radiologically, brown tumors are typically well demarcated, lytic lesions that can be expansile (Fig. 3). When the underlying hyperparathyroidism is treated, these lesions may show healing with increased sclerosis.

Roy E. Erb
E. Paul Nance

REFERENCES

1. Resnick D, Niwayama G. Parathyroid disorders and renal osteodystrophy. In: Bone and joint imaging. Philadelphia: Saunders, **1989**
2. Brown TW, et al. Multiple brown tumors in a patient with chronic renal failure and secondary hyperparathyroidism. *AJR* **1977**;128:131–134
3. Levine MR, Clin A, Abdul-Karin F. Brown tumor and secondary hyperparathyroidism. *Arch Ophthalmol* **1991**;109:847–849

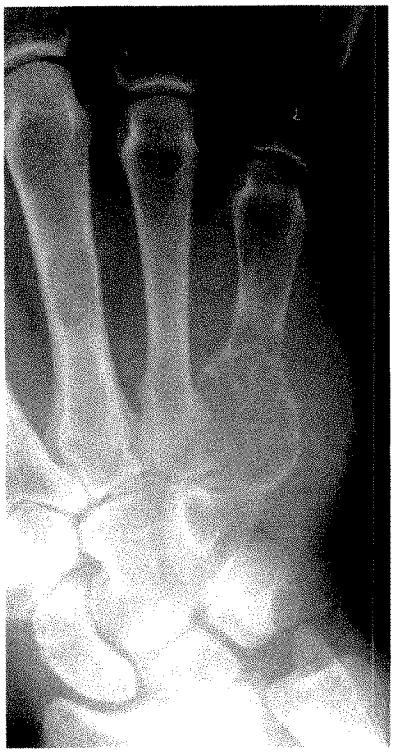

Fig. 3.—Case 1. Brown tumor. Posteroanterior radiograph of hand reveals an expansile destructive lesion involving base of fifth metacarpal. There is no matrix calcification or ossification.

Case 4: Synovial Osteochondromatosis

A 32-year-old woman had chronic swelling about her right wrist. Synovial osteochondromatosis is an idiopathic condition that affects synovial joints and tendon sheaths. It is generally considered to be associated with metaplasia of the synovium. It is typically a monoarticular process that most commonly involves the knee, hip, or elbow, although any joint, bursa, or tendon sheath may be affected. Most patients are 30–50 years old and have chronic pain and limited motion in a joint [1]. The condition is more common in men than in women.

The cause of synovial osteochondromatosis is unknown. Nodules of cartilaginous tissue develop in the synovium and later calcify or ossify while attached to the synovium. The nodules may extend intraarticularly via a thin pedicle. The pedicle may break, resulting in "loose bodies" within the joint. These intraarticular masses then derive their nutrition from the synovial fluid [2].

Findings on plain radiographs typically include multiple calcified juxtaarticular or intraarticular densities measuring less than 3 cm (Fig. 4). Early in the disease, the nodules may not

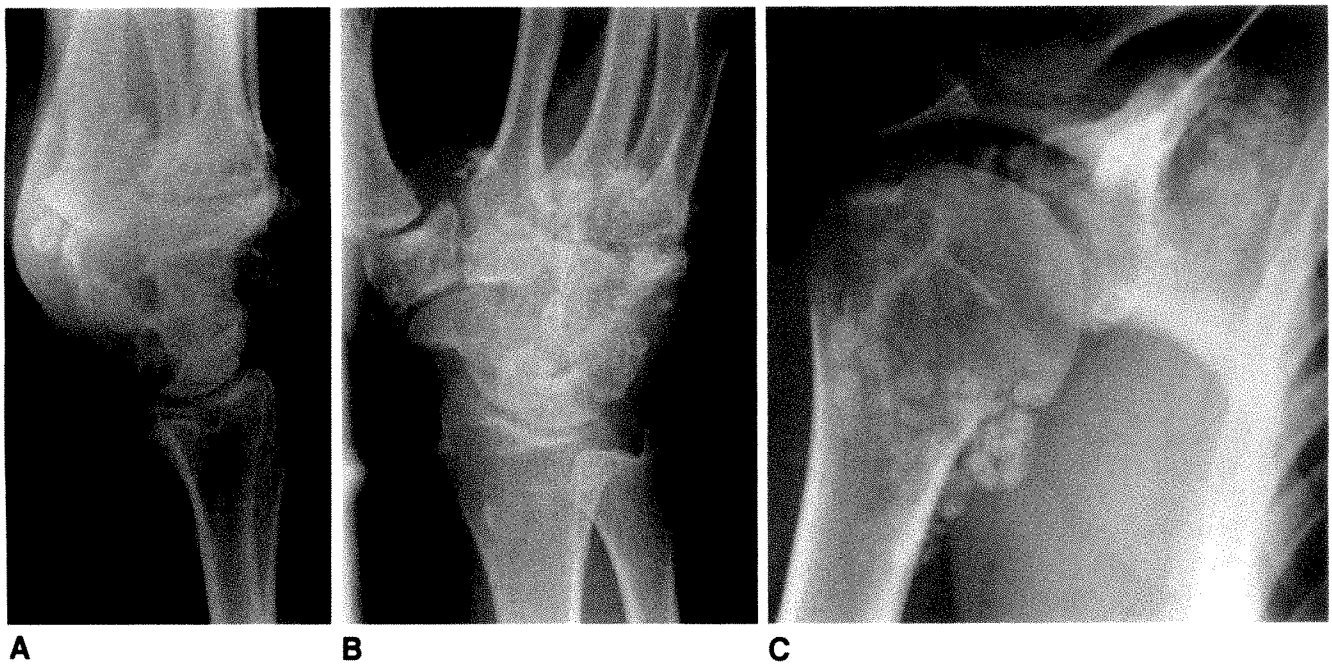

Fig. 4.—Case 4: Synovial osteochondromatosis.
***A* and *B*, Lateral and oblique radiographs of right wrist reveal "nodular" soft-tissue swelling and multiple calcifications or ossifications around wrist. Underlying bones and joints appear normal.**
***C*, Anteroposterior radiograph of shoulder in a patient with long-standing pain and limitation of motion shows multiple ossified nodules.**

be calcified or ossified. Secondary findings may include joint erosions and joint-space widening.

Treatment usually consists of surgical or arthroscopic removal of the nodules or synovectomy in recurrent cases [3].

Roy E. Erb
E. Paul Nance

REFERENCES

1. Madewell JE, Sweet DE. Tumors and tumor-like lesions in or about joints. In: Resnick D, Niwayama G, eds. *Diagnosis of bone and joint disorders*, 2nd ed. Philadelphia: Saunders, **1988**
2. Alexander JE, et al. Synovial osteochondromatosis. *Am Fam Physician* **1987**;35:157–161
3. Milgram JW. Synovial osteochondromatosis. *J Bone Joint Surg [Am]* **1977**; 59A:792–801

Pediatric Case of the Day

Richard M. Heller,[1] Marta Hernanz-Schulman,[1] Joyce Johnson,[2] Sharon M. Stein,[1] and Sandra Kirchner[1]

Case 1: Aneurysmal Bone Cyst

A 13-year-old boy had pain and swelling in his left knee. The frontal and lateral radiographs of the left knee show a lytic lesion in the proximal tibial metaphysis (Figs. 1A and 1B). Sonography shows multiple fluid-fluid interfaces (Fig. 1C). MR images show the lesion to be of heterogeneous signal intensity, expanding, obliterating, and extending anterior to the cortex of the tibia (Fig. 1D). The T2-weighted images show high signal intensity within the lesion; the multiple fluid-fluid levels are well shown.

This child has an aneurysmal bone cyst, a benign, nonneoplastic solitary lesion of bone [1]. Hypotheses as to the cause relate to an abnormal vascular physiology such as venous obstruction or arteriovenous communication, resulting in dilatation of the medullary space [1, 2]. It is noteworthy that

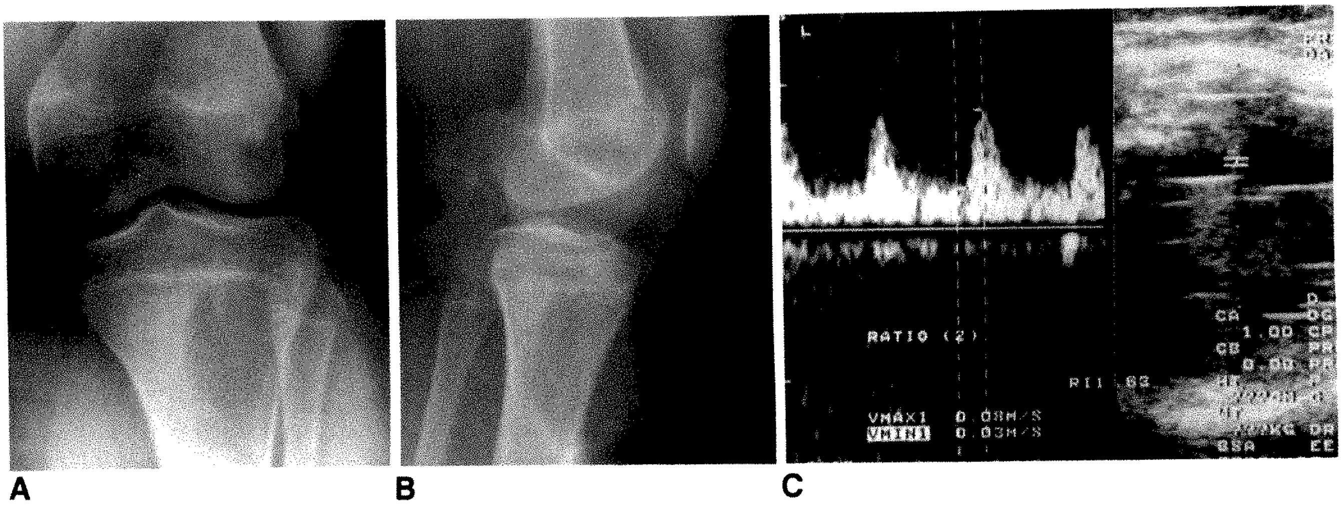

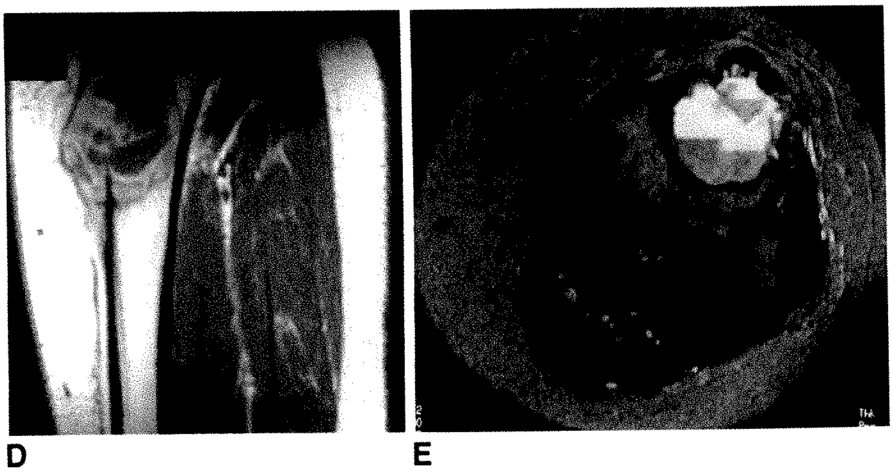

Fig. 1.—Case 1: Aneurysmal bone cyst.

A and *B*, Frontal and lateral radiographs of left knee show a lytic lesion involving anterolateral metaphysis of tibia, with minimal sclerosis of edges of lesion.

C, Sonography of mass shows multiple fluid-fluid interfaces. Within internal septa, arterial and venous flow could be identified. Note echogenic, concave posterior bony border of mass.

D, Sagittal T1-weighted MR image of mass shows its multiple compartments of mixed signal intensity and its anterior extension.

E, Axial T2-weighted MR image shows fluid-fluid levels previously documented on sonography. Note high-intensity signal from fluid.

---

[1] Department of Radiology, Vanderbilt University Medical Center, 1161 21st Ave., S., Nashville, TN 37232-2675. Address reprint requests to M. Hernanz-Schulman.

[2] Department of Pathology, Vanderbilt University Medical Center, 1161 21st Ave., S., Nashville, TN 37232-2675.

AJR **158:1372–1377, June 1992** 0361–803X/92/1586–1372 © American Roentgen Ray Society

aneurysmal bone cyst may be seen in association with other bone tumors such as giant-cell tumor, fibrous dysplasia, unicameral bone cyst, chondroblastoma, and nonossifying fibroma [1].

Clinical symptoms may result from pressure on adjacent structures or from pathologic fracture. The condition affects males and females equally and usually is discovered in the first three decades of life. Approximately half the cases occur in the long bones, about a third occur in the spine, and the rest arise in tubular or flat bones [1].

Four stages of development are evident on plain radiographs [1]. The first phase consists of an oval, lytic lesion that may be central or eccentric. In the second stage, rapid growth occurs, which yields the "blowout" appearance with concurrent expansion and destruction of bone. In the third stage, multiple bony trabeculae are observed, and finally in the fourth stage, the cyst undergoes calcification and, ultimately, ossification.

Sonography is useful for outlining the soft-tissue extent of the lesion and characterizing the fluid-fluid interfaces. Interestingly enough, it should be noted that such fluid-fluid interfaces are nonspecific, and although they have been reported in aneurysmal bone cysts, they also have been described in other tumors originating in bone and in soft tissues. They are believed to be the result of previous episodes of hemorrhage [3].

CT can be done, especially in cases in which no "window" of destroyed cortex is available to access the bony lesion with sonography.

MR imaging is very useful, and the diagnosis is strongly suggested by the following four criteria [4]: (1) a young patient; (2) expansile lesion, with a low-signal-intensity border; (3) high signal intensity on T2-weighted images; and (4) the lesion is commonly lobulated, and fluid-fluid interfaces may be evident.

The treatment choices include surgical excision with possible embolization to reduce bleeding. Embolotherapy may be used as definitive therapy for inoperable lesions [5].

REFERENCES

1. Waitzkin ED, Deluca SA. Aneurysmal bone cyst. *Am Fam Physician* **1986**;33:137-138
2. Munk PL, Helms CA, Hoit RG, Johnston J, Steinbach L, Neumann C. MR imaging of aneurysmal bone cysts. *AJR* **1989**;153:99-101
3. Tsai JC, Dalinka MK, Fallon MD, et al. Fluid-fluid level: a nonspecific finding on tumors of bone and soft tissue. *Radiology* **1990**;175:779-782
4. Beltran J, Simon DC, Levy M, et al. Aneurysmal bone cysts: MR imaging at 1.5 T. *Radiology* **1986**;158:689-690
5. Cory DA, Fritsch SA, Cohen MD, et al. Aneurysmal bone cysts: imaging findings and embolotherapy. *AJR* **1989**;153:369-373

Case 2: Fibromuscular Dysplasia (Intimal Fibroplasia) with Aneurysm

A previously asymptomatic 7-year-old boy had been having headaches for several weeks. Examination at his pediatrician's office revealed hypertension.

Preliminary radiographs (Fig. 2) showed a calcification related to the right renal hilum. Results of a "hypertensive" excretory urogram were normal. Further investigation with sonography revealed that the calcification was in fact the calcified wall of an aneurysm in the renal artery. Angiography and histopathologic evaluation revealed intimal fibromuscular dysplasia with aneurysm, involving the middle and distal thirds of the right renal artery as well as multiple intrarenal branches.

Both fibromuscular dysplasia and aneurysms of the renal artery are very rare in children. Aneurysms of the renal arteries have many causes, including large-vessel arteritis such as polyarteritis nodosa and Takayasu's arteritis, infection, trauma, neurofibromatosis, and fibromuscular dysplasia. A search of the literature reveals the rarity of this condition in childhood [1-4]. Six well-documented cases are published [2]; an additional eight cases [3] are listed as arterial dysplasia, although the description of the disease does not identify any proliferative collagenous or muscular elements to indicate fibromuscular dysplasia.

Fibromuscular dysplasia is usually found in females (5:1) in the third and fourth decades of life. Nevertheless, it is the most common cause of renal vascular hypertension in children [2, 5].

Fibromuscular dysplasia is an interesting lesion of unknown cause that has several histologic and angiographic manifestations. It is divided into three main groups: intimal fibroplasia, medial fibromuscular dysplasia, and periarterial fibroplasia. Medial fibroplasia in turn is divided into four subtypes. These are (1) medial hyperplasia, (2) medial dissection, (3) medial fibroplasia with aneurysm, and (4) perimedial fibroplasia [2, 6]. The most common type of fibromuscular dysplasia (60-70% of all lesions) is the third subtype of medial fibroplasia: medial fibroplasia with aneurysm. It is characterized by aneurysms that bulge beyond the expected diameter of the renal artery. In children, the most common type is intimal fibroplasia, which is rarely associated with aneurysm; to our knowledge, only one such case has been reported [1].

Fibromuscular dysplasia is bilateral in 60-70% of the cases. When it is unilateral, as in the present case, it involves the right renal artery three times more commonly than the left. Most types of fibromuscular dysplasia are known to be progressive; its initiation in previously normal vessels has been documented. For this reason, and because of its prevalence in multiparous, premenopausal women, a relationship to estrogen has been postulated but not proved. A recent report [7] has demonstrated a familial link and a correlation with cigarette smoking. The familial link is believed to be most consistent with an autosomal dominant trait with variable penetrance [2].

While calcification in the wall of aneurysms associated with fibromuscular dysplasia is known to occur in adults, we have not found a previous report of this disorder in a child.

The imaging examination of children with renal vascular hypertension is best done angiographically. As in this case, the "hypertensive" excretory urogram is often insensitive in the identification of renal vascular lesions. Sonography can be very helpful in identifying aneurysms of the main renal artery. However, it cannot stand alone, and subsequent angiography is mandatory.

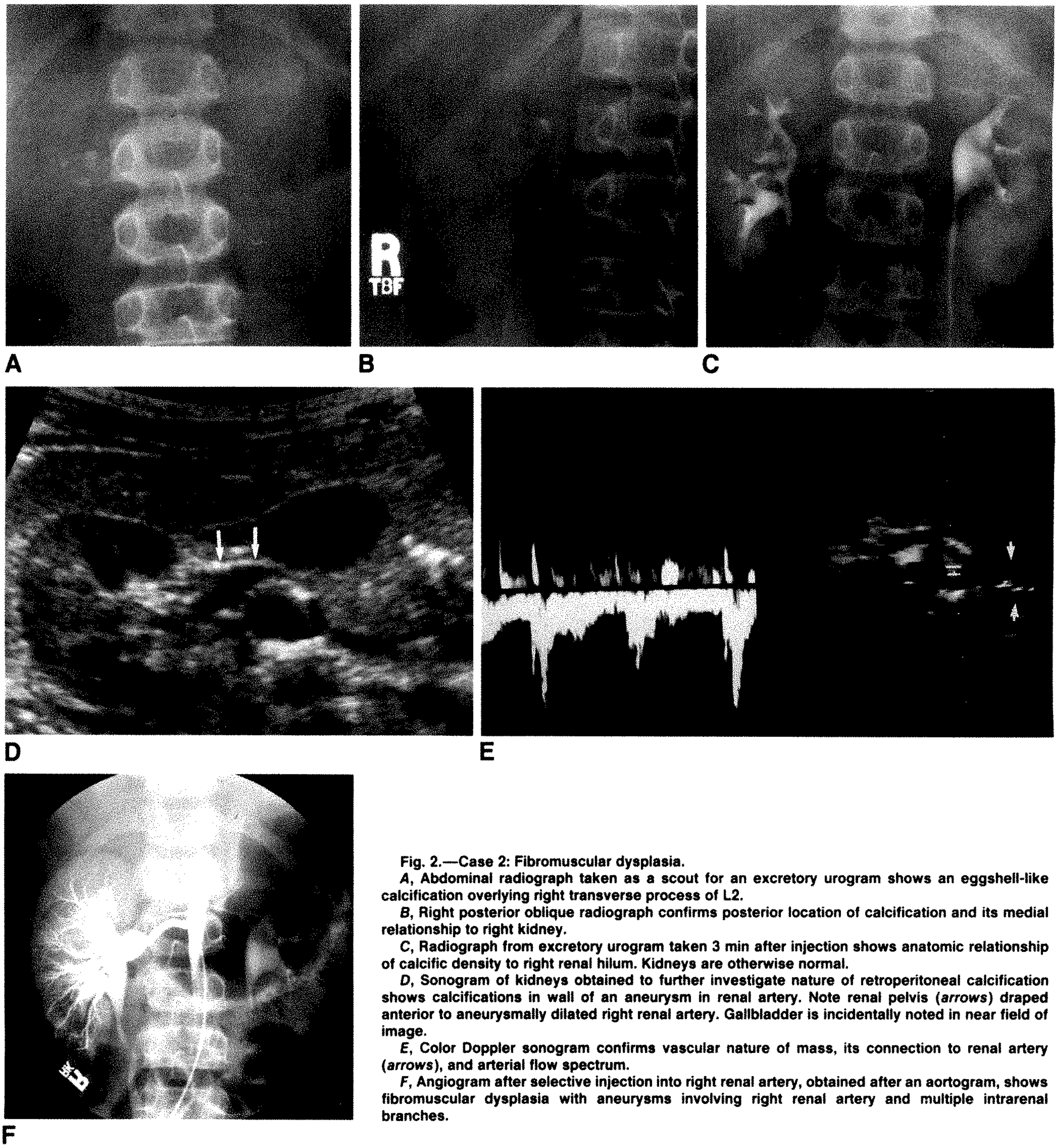

Fig. 2.—Case 2: Fibromuscular dysplasia.

***A*, Abdominal radiograph taken as a scout for an excretory urogram shows an eggshell-like calcification overlying right transverse process of L2.**

***B*, Right posterior oblique radiograph confirms posterior location of calcification and its medial relationship to right kidney.**

***C*, Radiograph from excretory urogram taken 3 min after injection shows anatomic relationship of calcific density to right renal hilum. Kidneys are otherwise normal.**

***D*, Sonogram of kidneys obtained to further investigate nature of retroperitoneal calcification shows calcifications in wall of an aneurysm in renal artery. Note renal pelvis (*arrows*) draped anterior to aneurysmally dilated right renal artery. Gallbladder is incidentally noted in near field of image.**

***E*, Color Doppler sonogram confirms vascular nature of mass, its connection to renal artery (*arrows*), and arterial flow spectrum.**

***F*, Angiogram after selective injection into right renal artery, obtained after an aortogram, shows fibromuscular dysplasia with aneurysms involving right renal artery and multiple intrarenal branches.**

REFERENCES

1. Bunchman TE, Walker HSJ III, Joyce PF, Danter ME, Silberstein MJ. Sonographic evaluation of renal artery aneurysm in childhood. *Pediatr Radiol* **1991**;21:312–313
2. Park SH, Chi JG, Choi Y. Primary intimal fibroplasia with multiple aneurysms of renal artery in childhood. *Child Nephrol Urol* **1991**;10:51–55
3. Sarkar R, Coran AG, Cilley RE, Lindenauer SM, Stanley JC. Arterial aneurysms in children: clinicopathologic classification. *J Vasc Surg* **1991**;13:47–57
4. Walsh JS, Hendry GMA, Utley WS. Unusual clinical presentations of bilateral renal artery aneurysms in a child: the value of ultrasound in diagnosis. *Pediatr Radiol* **1987**;17:436–437
5. Novick AC. Management of renovascular disease: a surgical perspective. *Circulation* **1991**;83[suppl 2]:167–171
6. Abrams HL, ed. *Abrams angiography: vascular and interventional radiology*, vol 2, 3rd ed. Boston: Little, Brown, **1983**:1252–1264
7. LaMendola CL, Culliford AT, Harris LF, Amendo MR. Multiple aneurysms of the coronary arteries in a patient with systemic aneurysmal disease. *Ann Thorac Surg* **1990**;49:1009–1010

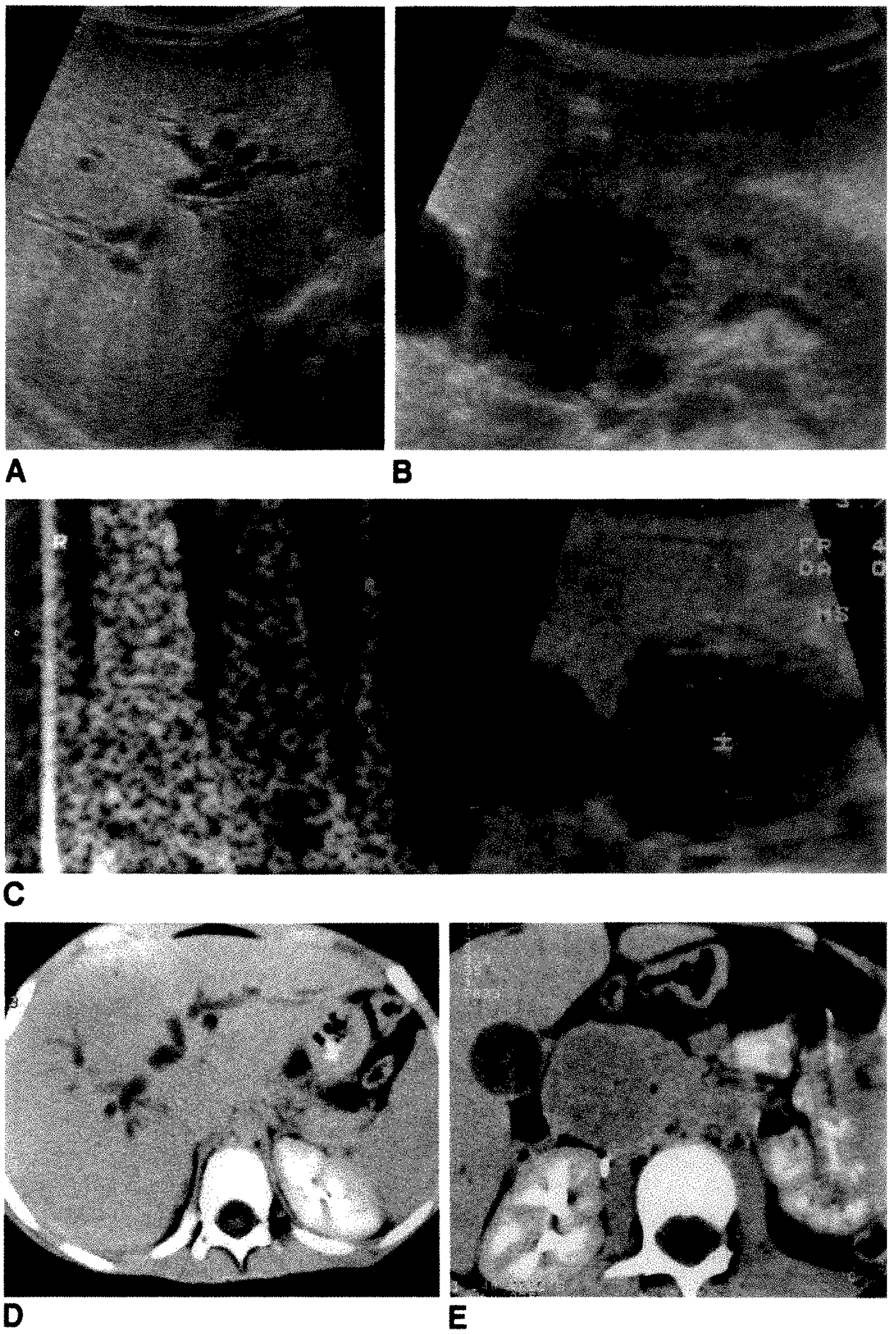

Fig. 3.—Case 3: Non-Hodgkin's lymphoma in the pancreas.

***A*, Transverse sonogram of liver shows dilatation of intrahepatic ducts.**

***B*, At level of pancreas, sonogram shows a hypoechoic, "cystic-appearing" mass involving head of pancreas. Note dilatation of pancreatic duct.**

***C*, Doppler sampling shows vascular structures within mass, suggesting that it is solid rather than cystic.**

***D*, Contrast-enhanced CT scan through liver shows dilated intrahepatic biliary tree previously shown sonographically.**

***E*, Magnified CT scan through head of pancreas after administration of contrast material confirms location of mass within head of pancreas as well as its solid structure. Note that mass enhances to a lesser extent than does surrounding pancreatic parenchyma.**

Case 3: Non-Hodgkin's Lymphoma in the Pancreas

A 5-year-old girl had a brief history of abdominal pain and jaundice. Her imaging studies (Fig. 3) showed a solid, hypoechoic mass within the head of the pancreas, obstructing the biliary and pancreatic ducts.

Childhood lymphomas constitute about 10% of malignant tumors in children in developed countries and represent the third most common pediatric neoplasm after leukemia and brain tumors [1]. Two main types of lymphoma are seen in children: Hodgkin's disease and non-Hodgkin's lymphoma; the latter includes B-cell and Burkitt's lymphoma. Burkitt's lymphoma may be considered a subtype of B-cell lymphoma with similar imaging manifestations.

In B-cell lymphoma, pancreatic involvement is an uncommon presenting manifestation, although it is often a finding at autopsy. Lymphoma presenting as acute pancreatitis has been reported [2]. The case shown here, with a pancreatic mass being the sole site of involvement, is most rare [3].

The behavior and imaging manifestations of B-cell lymphoma and Burkitt's lymphoma are similar. In these two forms of non-Hodgkin's lymphoma, intrinsic involvement of the gas

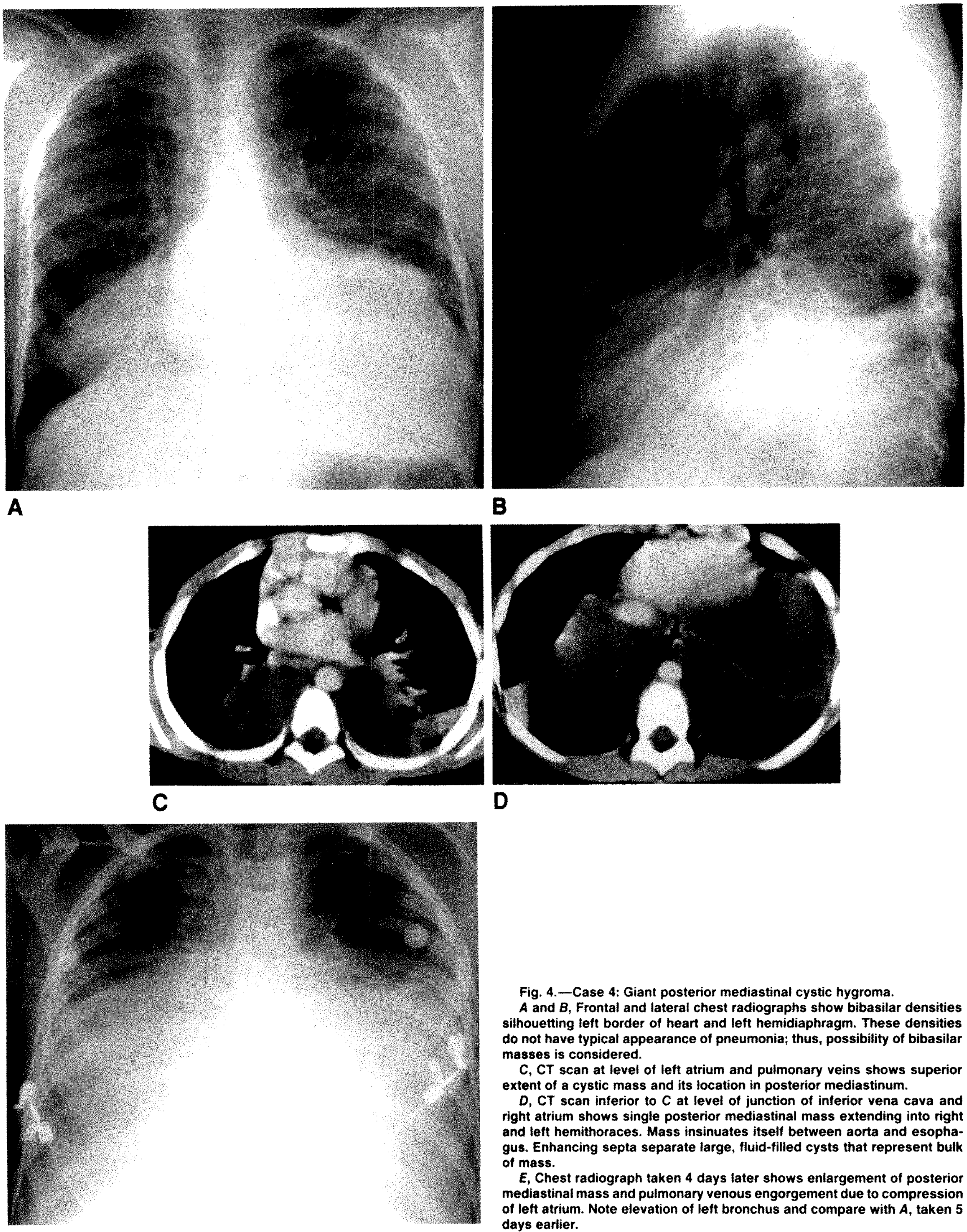

Fig. 4.—Case 4: Giant posterior mediastinal cystic hygroma.

A and *B*, Frontal and lateral chest radiographs show bibasilar densities silhouetting left border of heart and left hemidiaphragm. These densities do not have typical appearance of pneumonia; thus, possibility of bibasilar masses is considered.

C, CT scan at level of left atrium and pulmonary veins shows superior extent of a cystic mass and its location in posterior mediastinum.

D, CT scan inferior to *C* at level of junction of inferior vena cava and right atrium shows single posterior mediastinal mass extending into right and left hemithoraces. Mass insinuates itself between aorta and esophagus. Enhancing septa separate large, fluid-filled cysts that represent bulk of mass.

E, Chest radiograph taken 4 days later shows enlargement of posterior mediastinal mass and pulmonary venous engorgement due to compression of left atrium. Note elevation of left bronchus and compare with *A*, taken 5 days earlier.

trointestinal tract is most often centered in the small bowel, especially in the terminal ileum [4]; occasionally the stomach or colon is involved [5]. Other abdominal findings include masses in the liver, porta hepatis, spleen, and mesentery [4]. In the genitourinary tract, the most common abnormalities relate to obstructive uropathy, but bilateral enlargement of the kidneys and renal masses can occur [4]. In the chest, the most common radiologic abnormality is pleural effusion, usually without mediastinal or hilar adenopathy [4]. When the skeleton is involved, a permeative diaphyseal pattern of destruction, which may be accompanied by periosteal reaction, is often seen.

In summary, non-Hodgkin's lymphoma should be considered in children with gastrointestinal masses, especially masses involving the terminal ileum but sparing the retroperitoneal nodes, and should be investigated by a combination of sonography and CT.

REFERENCES

1. Pizzo PA, Poplack DG. *Principles and practice of pediatric oncology*. Philadelphia: Lippincott, **1989**:417
2. Francis IR, Glazer GM. Burkitt's lymphoma of the pancreas presenting as acute pancreatitis. *J Comput Assist Tomogr* **1986**;6:395–397
3. Kotwall CA, Brow JR, Keith RG. Lymphoma pancreatitis: a real entity. *Can J Surg* **1989**;32:375–377
4. Vade A, Blane CE. Imaging of Burkitt lymphoma in pediatric patients. *Pediatr Radiol* **1985**;15:123–126
5. Dunnick NR, Reaman GH, Head GL, Shawker TH, Ziegler JL. Radiographic manifestations of Burkitt's lymphoma in American patients. *AJR* **1979**;132:1–6

Case 4: Giant Posterior Mediastinal Cystic Hygroma

A 6-year-old boy had had pain in the left shoulder and a cough for 1 day.

Posterior bibasilar densities that do not correspond to a typical pattern of lobar consolidation are shown on radiographs (Fig. 4). A CT scan at the level of the left atrium shows bilateral septated cystic masses. A scan at a lower level shows that these masses are contiguous across the midline between the aorta and the esophagus, which is markedly displaced anteriorly. A portable radiograph obtained 5 days after the initial radiograph shows marked increase in size of the densities and evidence of pulmonary venous congestion.

This is an example of a massive or giant posterior mediastinal cystic hygroma. This lesion occurs commonly in the neck (75%) and axilla (20%), although it is stated that 5% can occur elsewhere, including the mediastinum, extremities, mouth, larynx, and trunk [1–3]. In the mediastinum, they usually occupy the anterior compartment; this case is thus truly exceptional.

Histologically, cystic hygromas are benign lesions that are lined by flat endothelial cells and are commonly filled with lymph. Cystic hygromas are locally invasive and tend to infiltrate adjacent tissues and structures, rendering excision difficult. These lesions have a tendency to become infected and to bleed. It has been postulated that posterior mediastinal giant cystic hygromas arise from an error in embryogenesis of the cisterna chyli or in the formation of the paired thoracic ducts [4]. This theory has the advantage of explaining both the retropleural nature of the lesion and its bilateral extension.

Included in the differential diagnosis of mediastinal cystic hygroma are bronchogenic cysts, which are most often found near the trachea or carina. Enteric duplication cysts are frequently located near the esophagus in the posterior mediastinum and can extend into both hemithoraces [5, 6].

REFERENCES

1. Raffensberger JG. Mediastinal masses. In: *Swenson's pediatric surgery*, 4th ed. New York: Appleton-Century-Crofts, **1980**:375–385
2. Moore TC, Cobo JC. Massive symptomatic cystic hygroma confined to the thorax in early childhood. *J Thorac Cardiovasc Surg* **1985**;89:459–468
3. Sumner TE, Volberg FM, Kiser PE, Shaffner LD. Mediastinal cystic hygroma in childhood. *Pediatr Radiol* **1981**;11:160–162
4. Curley SA, Ablin DS, Kosloske A. Giant cystic hygroma of the posterior mediastinum. *J Pediatr Surg* **1989**;24:398–400
5. Shin MS, Berland LL, Ho KJ. Mediastinal cystic hygromas: CT characteristics and pathogenetic consideration. *J Comput Assist Tomogr* **1985**;9:297–301
6. Korman MJ, Steiner R, Fish JE. Dyspnea and stridor in a young woman. *Chest* **1986**;89:579–581

Neuroradiology Case of the Day

Marc J. Lacrampe[1] and Jeff L. Creasy

Case 1: Progressive Multifocal Leukoencephalopathy

A 41-year-old man died of a new seizure disorder. At autopsy, a limited pathologic examination of the intracranial contents showed progressive multifocal leukoencephalopathy.

Progressive multifocal leukoencephalopathy is a viral illness caused by a papovavirus (the JC virus) in patients who have abnormal cell-mediated immunity. On CT scans (Fig. 1), characteristic lesions appear as focal areas of low density that do not enhance [1]. No mass effect is noted, and the lesions tend to occur posteriorly. These lesions are characteristically round or ovoid, and the distribution is asymmetric.

On T2-weighted MR images, the abnormal areas appear as regions of high signal [2–4]. As in CT, the lesions are multifocal, located in white matter, round or ovoid, have no

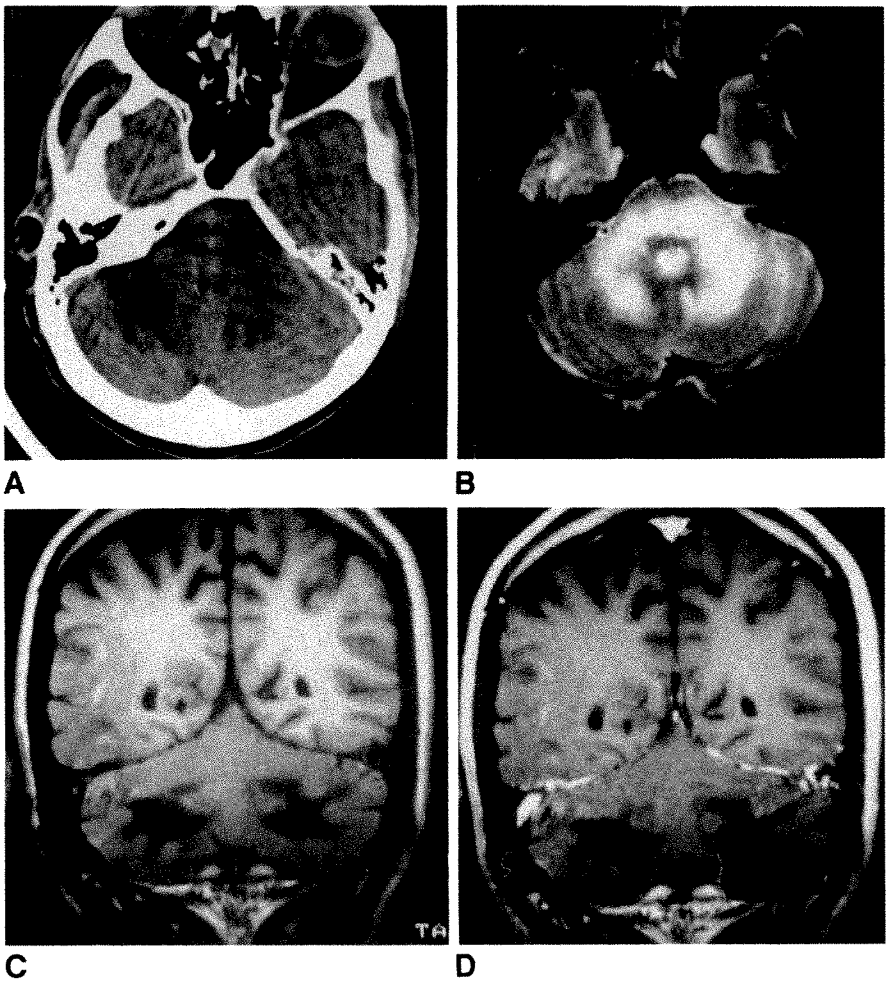

Fig. 1.—Case 1: Progressive multifocal leukoencephalopathy.

***A*, Unenhanced CT scan of head shows decreased density throughout cerebellar white matter.**

***B* and *C*, Signal is increased on T2-weighted MR image (*B*) and decreased on T1-weighted MR image (*C*) in cerebellar white matter, peduncles, and extending into pons.**

***D*, MR image after contrast administration shows no enhancement.**

---

[1] Both authors: Department of Radiology, Vanderbilt University Medical Center, 1161 21st Ave., S., Nashville, TN 37232-2675. Address reprint requests to J. L. Creasy.

***AJR* 158:1378–1381, June 1992** 0361–803X/92/1586–1378 © American Roentgen Ray Society

mass effect, do not enhance, and are asymmetrically distributed.

The differential diagnosis of these lesions includes other viral infections, toxic causes of demyelination, and CNS lymphoma.

REFERENCES

1. Carroll BA, Lane B, Norman D, Enzmann D. Diagnosis of progressive multifocal leukoencephalopathy by computed tomography. *Radiology* **1977**;122:137–141
2. Guilleux MH, Steiner RE, Young IR. MR imaging in progressive multifocal leukoencephalopathy. *AJNR* **1986**;7:1033–1035
3. Olsen WL, Longo FM, Mills CM, Norman D. White matter disease in AIDS: findings at MR imaging. *Radiology* **1988**;169:445–448
4. Mark AS, Atlas SW. Progressive multifocal leukoencephalopathy in patients with AIDS: appearance on MR images. *Radiology* **1989**;173: 517–520

Case 2: Ectopic Posterior Lobe of Pituitary Gland Associated with Panhypopituitarism

On T1-weighted MR images (Fig. 2) of a short 6-year-old boy, the posterior lobe of the pituitary gland demonstrated typical high signal intensity. The cause of this "bright" signal has been a matter of some debate; recent articles suggest that it is due to the vasopressin-neurophysin complex [1] or to intracellular lipid in pituicytes [2]. Vasopressin and oxytocin are produced in the supraoptic and paraventricular nuclei of the hypothalamus. These hormones are transported to the posterior lobe of the pituitary gland in combination with the carrier protein neurophysin, via the hypothalamicohypophysial tract in the infundibulum. If the infundibulum is interrupted, the neurosecretory products are retained at the base of the infundibulum in the region of the median eminence.

The infundibulum can be disrupted by a variety of causes. The infundibulum may be congenitally absent or hypoplastic, perhaps due to vascular injury [3]. Hypophysectomy and pituitary tumors also may disrupt the infundibulum, resulting in an ectopic posterior lobe of the pituitary gland [4]. Regardless of the cause, if the hypophysial portal system is interrupted as well, function of the anterior lobe of the pituitary gland also is affected. In particular, release of human growth hormone is depressed, resulting in pituitary dwarfism in the child. A number of cases of ectopic posterior lobe of the pituitary gland have been associated with dwarfism [5–7]. However, this finding can occur in biochemically normal persons also [8].

The differential diagnosis for a small high-signal lesion in this location should include lipoma, small craniopharyngioma, or focus of hemorrhage. However, given the clinical history of short stature and typical appearance of this lesion, the diagnosis of ectopic posterior lobe of the pituitary gland is made.

REFERENCES

1. Fujisawa I, Asato R, Nishimura K, et al. Anterior and posterior lobes of the pituitary gland: assessment by 1.5 T MR imaging. *J Comput Assist Tomogr* **1987**;11:214–220
2. Kucharczyk J, Kucharczyk W, Berry I, et al. Histochemical characterization and functional significance of the hyperintense signal on MR images of the posterior pituitary. *AJNR* **1988**;9:1079–1083
3. Fujisawa I, Kikuchi K, Nishimura K, et al. Transection of the pituitary stalk: development of an ectopic posterior lobe assessed with MR imaging. *Radiology* **1987**;165:487–489
4. Gammal TE, Brooks BS, Hoffman WH. MR imaging of the ectopic bright signal of posterior pituitary regeneration. *AJNR* **1989**;10:323–328
5. Kelly WM, Kucharczyk W, Kucharczyk J, et al. Posterior pituitary ectopia: an MR feature of pituitary dwarfism. *AJNR* **1988**;9:453–460
6. Abrahams JJ, Trefelner E, Boulware SD. Idiopathic growth hormone deficiency: MR findings in 35 patients. *AJNR* **1991**;12:155–160
7. Kuroiwa T, Okabe Y, Hasuo K, Yasumori K, Mizushima A, Masuda K. MR imaging of pituitary dwarfism. *AJNR* **1991**;12:161–164
8. Benshoff ER, Katz BH. Ectopia of the posterior pituitary gland as a normal variant: assessment with MR imaging. *AJNR* **1990**;11:709–712

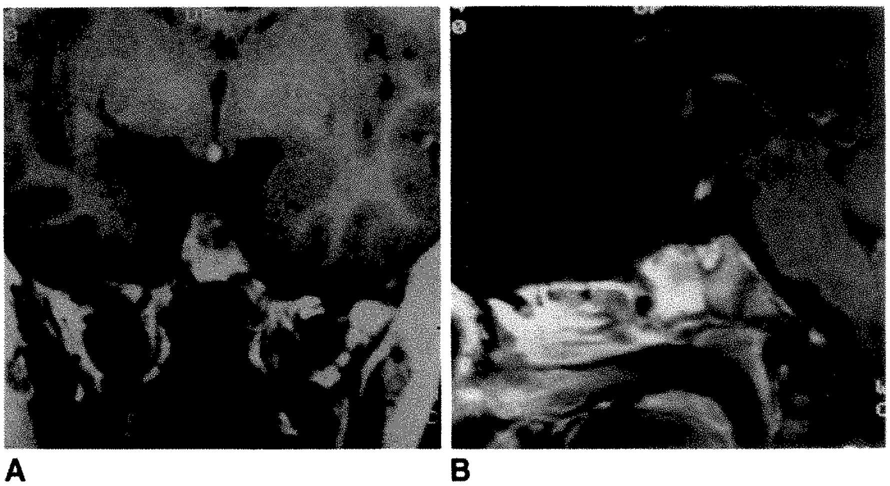

Fig. 2.—Case 2: Ectopic posterior lobe of pituitary gland associated with panhypopituitarism.

***A* and *B*, In pituitary fossa, normally bright signal in posterior pituitary area is absent. Instead, coronal (*A*) and sagittal (*B*) MR images show single focus of increased signal at level of base of infundibular stalk, just below hypothalamus. Infundibulum is hypoplastic. No suprasellar masses or hypothalamic abnormalities are present.**

Case 3: "Cryptic" Arteriovenous Malformations

A 20-year-old woman had a chronic seizure disorder. Cryptic or occult arteriovenous malformations are a group of vascular lesions that include thrombosed arteriovenous malformations, capillary telangiectasias, venous angiomas, and cavernous angiomas. These lesions are composed of vascular structures with low-velocity flow, focal areas of calcification, and surrounding regions of hemorrhage of variable age. Clinically, these lesions cause a wide range of signs and symptoms, including transient neurologic deficits, seizures, and headaches. Hemorrhage is often not clinically suspected.

A common feature of these malformations is the absence of abnormal vessels on angiography; consequently they are referred to as occult or cryptic lesions. Both CT and MR are useful in detecting these lesions. On CT, small isodense or hyperdense masses are seen, often containing punctate calcifications, which enhance mildly. These findings suggest a vascular malformation, but the differential diagnosis often includes low-grade astrocytoma, oligodendroglioma, or granulomatous infection [1]. The findings on MR (Fig. 3) include central focal areas of signal void, which may be due to calcifications, paramagnetic effects, or flow voids [2, 3]. Surrounding regions of signal intensity characteristic for hemorrhages of variable age also are seen; this is useful in confirming the diagnosis of cryptic arteriovenous malformation because the lesions in the CT differential list rarely hemorrhage to this degree. MR imaging is thus valuable in evaluating these lesions and may obviate biopsy, particularly for lesions in critical anatomic locations. In addition, MR imaging may depict lesions not seen on CT. MR may be useful in follow-up of these lesions over time [4].

In the case presented, a biopsy of the lesion in the temporal lobe was done. The tissue diagnosis was arteriovenous malformation with surrounding reactive astrocytosis. The patient was treated with computerized photon knife therapy.

REFERENCES

1. New PFJ, Ojemann RG, Davis KR, et al. MR and CT of occult vascular malformations of the brain. *AJR* **1986**;147:985-993
2. Gomori JM, Grossman RI, Goldberg HI, Hackney DB, Zimmerman RA, Bilaniuk LT. Occult cerebral vascular malformations: high-field MR imaging. *Radiology* **1986**;158:707-713
3. Lemme-Plaghos L, Kucharczyk W, Brant-Zawadzki M, Uske A, Edwards M, Norman D. MR imaging of angiographically occult vascular malformations. *AJNR* **1986**;7:217-222
4. Sigal R, Krief O, Houtteville JP, Halimi P, Doyon D, Pariente D. Occult cerebrovascular malformations: follow-up with MR imaging. *Radiology* **1990**;176:815-819

Case 4: Meningitis Caused by *Neisseria meningitidis*

A limited number of conditions produce increased density within the subarachnoid space on MR images (Fig. 4). The most commonly encountered condition is subarachnoid hemorrhage, which is diagnosed easily in the acute phase on the basis of the high-density material visible throughout this space on CT. This is most commonly seen in trauma victims. If no trauma has occurred, the most likely causes are aneurysm or rupture of an arteriovenous malformation.

CT scans obtained within 1-2 days of water-soluble myelograms will show a similar appearance. This is because of

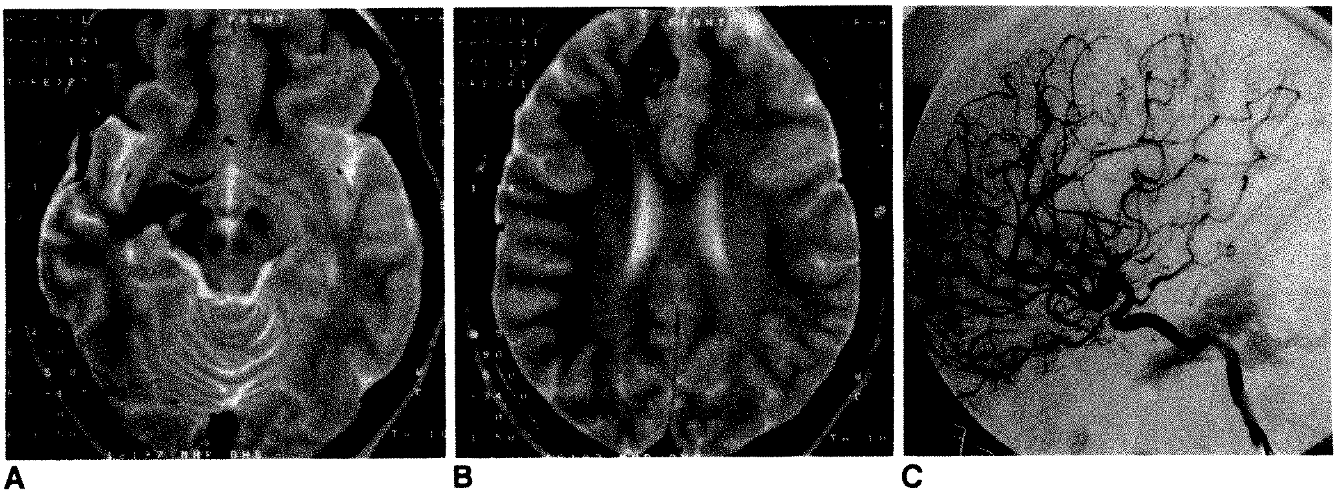

Fig. 3.—Case 3: "Cryptic" arteriovenous malformations.

***A* and *B*, MR images show two areas of abnormal signal, located in parasagittal right frontal lobe and medial right temporal lobe. These lesions are characterized by central areas of mildly increased signal surrounded by a band of low signal on T2-weighted images. Within central high signal area are areas of low signal, due to calcification or paramagnetic effects. These features are characteristic of a vascular malformation that has bled before this time.**

***C*, Findings on cerebral angiogram are normal.**

Fig. 4.—Case 4: Meningitis caused by *Neisseria meningitidis*.
***A* and *B*, Axial unenhanced MR images show diffuse areas of increased density filling subarachnoid spaces. Appearance is similar to that seen in severe subarachnoid hemorrhage. In addition, basilar cisterns and sulci are partially effaced, suggesting diffuse cerebral edema.**

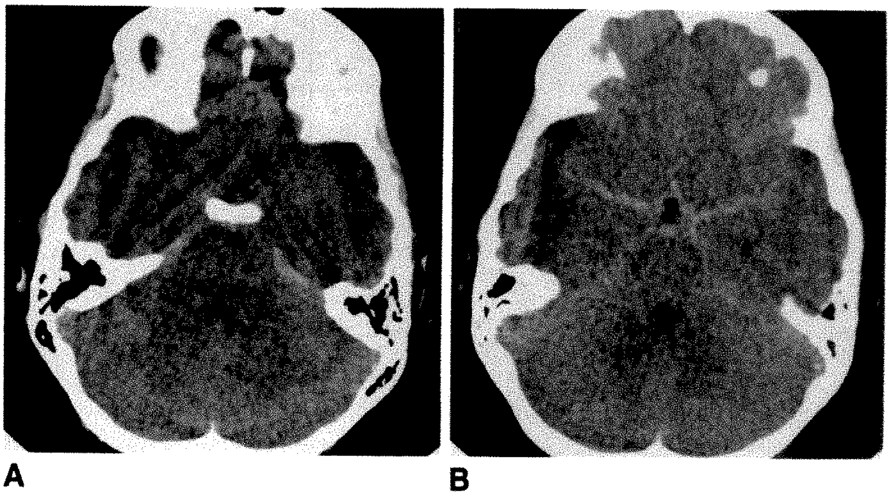

the normal clearance pathway of CSF, and hence of contrast material, from the CNS. This flow occurs over the convexities toward the parasagittal region.

In this case, the increased density is due to a hemorrhagic inflammatory exudate caused by the infectious agent. The inclusion of an infectious process in the differential diagnosis is important in acutely comatose patients, as some may respond to very aggressive antibiotics and supportive therapy. Unfortunately, this patient died shortly after this examination, owing to the fulminant nature of the infection.

Nuclear Medicine Case of the Day

Edward B. Moody,[1] Steven B. Glassman, Anne V. Hansen, Sandra K. Lawrence, and Dominique Delbeke

Case 1: Miliary Tuberculosis

The distribution of gallium in infectious lesions is thought to result from transcapillary exudation of transferrin-bound gallium with subsequent binding to leukocytes or bacteria [1]. Lactoferrin, elaborated by and bound to the surface of leukocytes, has a high binding affinity for gallium. Gallium is also bound to the surface of bacteria by siderophores and is ultimately transported into the bacterium [2]. Because of this dual mechanism of gallium uptake, gallium scintigraphy is a sensitive indicator for the presence of either inflammatory exudates or bacteria.

Diffuse homogeneous pulmonary uptake of gallium has been attributed to a number of causes. Infectious causes include bacterial pneumonia, viral pneumonitis (most often due to cytomegalovirus), *Pneumocystis carinii*, fungal infections, and tuberculosis. Noninfectious causes include connective tissue diseases, radiation pneumonitis, and drug-induced pneumonitis (bleomycin, amniodarone, and nitrofurantoin). Diffuse pulmonary uptake of gallium also may be seen after administration of lymphangiographic contrast material. In this case, the diagnosis of miliary tuberculosis was made on the basis of the appearance of the chest radiograph (Fig. 1) and a strongly positive tuberculin skin test. Cultures later confirmed the diagnosis.

Gallium scanning is a sensitive indicator of the presence of active tuberculosis. Abnormal patterns of gallium uptake may precede radiographic abnormalities, and the sensitivity of gallium for the detection of active pulmonary disease is reported to be 97% [2]. Because gallium uptake is rarely seen in inactive tuberculosis, imaging with this agent is superior to conventional radiography in assessing the response to chemotherapy or establishing reactivation of the disease. Successful treatment of pulmonary tuberculosis results in marked reduction of gallium uptake within a few months [2]. Disseminated tuberculosis may involve numerous organs, including bone, liver, spleen, lymph nodes, kidneys, meninges, and pelvic organs. Gallium scintigraphy has proved useful in the identification of distant sites of tuberculous involvement and in assessing the response to therapy. In the case presented, the only site of extrapulmonary disease identified was in a cervical lymph node. Useful information on the differential diagnosis of various patterns of pulmonary uptake of gallium is available [3–5].

Edward B. Moody
Dominique Delbeke

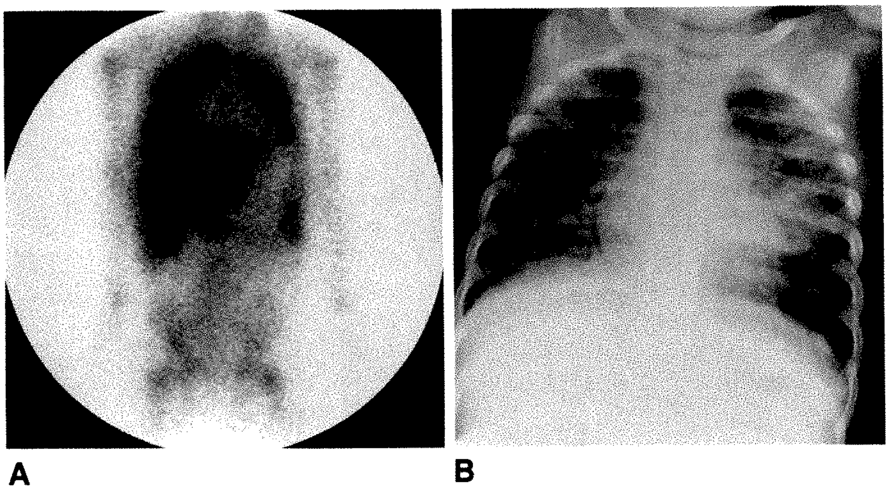

Fig. 1.—Case 1: Miliary tuberculosis.

_A_, Gallium scintigram. Anterior view of chest and abdomen obtained 48 hr after IV injection of 2.5 mCi of ^{67}Ga-citrate shows markedly diffuse increased uptake of gallium throughout both lungs. Intensity of gallium uptake was approximately equal to that in liver. It could not be determined if uptake was increased in hilar lymph nodes.

_B_, Chest radiograph shows a miliary pattern throughout both lung fields, with a superimposed alveolar opacity in superior segment of left lower lobe.

---

[1] All authors: Department of Radiology, Vanderbilt University Medical Center, 21st and Garland Aves., Nashville, TN 37232-2405. Address reprint requests to D. Delbeke.

AJR 158:1382–1386, June 1992 0361–803X/92/1586–1382 © American Roentgen Ray Society

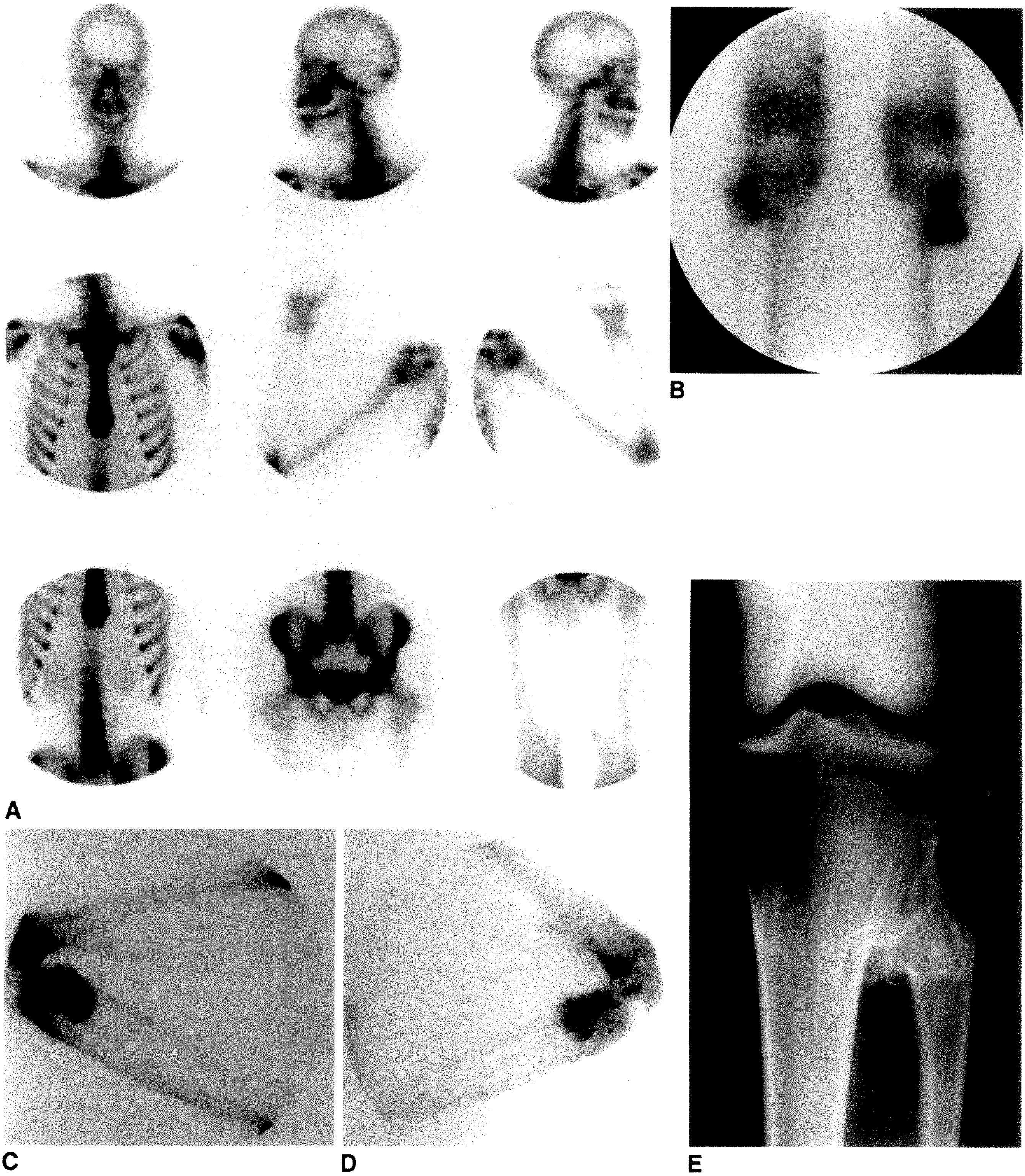

Fig. 2.—Case 2: Hereditary multiple exostoses.

A, Bone scintigram. Multiple images obtained after IV injection of 20 mCi of ^{99m}Tc-hydroxydiphosphonate show deformities of proximal humeri, proximal femurs, and knees. A characteristic exostosis is noted projecting from medial aspect of distal left femur.

B, Bone scintigram. Anterior view from bone scan of knees shows an area of increased uptake of radionuclide in exostosis protruding from posterolateral aspect of proximal left tibia.

C and *D*, Bone scintigrams. Left (*C*) and right (*D*) lateral views of the knees show another projection of same findings as on *B*.

E, Bone radiograph. Anteroposterior view of left knee shows an osteochondroma projecting from proximal tibia.

REFERENCES

1. Gottschalk A, Hoffer PB, Potchen EJ, Berger HJ. *Diagnostic nuclear medicine*, vol 2. Baltimore: Williams & Wilkins, **1988:**1111-1112
2. Higasi T, Nakayami Y. Clinical evaluation of ^{67}Ga-citrate scanning. *J Nucl Med* **1972**;13:196-201
3. Siemsen JK, Grebe SF, Waxman AD. The use of gallium-67 in pulmonary disorders. *Semin Nucl Med* **1978**;8:235-249
4. Thrall JH, Alderson PO, Brown ML, et al. *Nuclear radiology (fourth series) test and syllabus.* Reston, VA: American College of Radiology, **1990:**3-16
5. Silberstein EB, McAfee JG. *Differential diagnosis in nuclear medicine.* New York: McGraw-Hill, 1984:

Case 2: Hereditary Multiple Exostoses

A 19-year-old man with bone pain had multiple exostoses shown on bone scintigrams (Fig. 2). Uptake of radionuclide was increased in an osteochondroma of the left knee, raising the question of malignant degeneration. The bone radiograph confirmed the diagnosis of multiple exostoses, but no evidence of sarcomatous degeneration was found.

Osteochondromatosis, also known as hereditary multiple exostoses or diaphyseal aclasis, is an autosomal dominant disorder characterized by multiple bony excrescences that grow out from the bone cortex. The lesions of osteochondromatosis most frequently arise from the expanded metaphyses of the tubular bones, but the flat bones of the pelvis, the scapula, the ribs, and the vertebrae also can be involved. Osteochondromas usually increase in size during childhood and adolescence, but new exostoses do not appear and existing exostoses do not enlarge after closure of the neighboring growth plate. Occasionally, one finds evidence of activity well into adult life, but it is usually impossible to determine whether this is independent growth or whether there is still activity in the normal epiphysis. Reactivation should be viewed with suspicion and presumed to represent malignant change until determined otherwise [1].

Various complications are associated with osteochondromas; for example, growth disturbances, compression and irritation of adjacent nerves, vessels, and tendons, and urinary or intestinal obstruction. The most serious possible complication is sarcomatous degeneration. Malignant degeneration most commonly occurs in the pelvis or shoulder region and is associated with pain and an enlarging soft-tissue mass. Radiographs show evidence of growth and irregularity of the excrescence. Malignant transformation in cases of solitary osteochondromas is rare (<1%); however, in osteochondromatosis the risk of a malignant tumor developing can be as high as 20% [2].

On radiographs, exostoses appear as projections composed of cortical and medullary components that are continuous with the underlying bone. The projection may be on a pedunculated stalk or a sessile base and typically points away from the joint. The cartilaginous cap is usually radiolucent, but after puberty, irregular zones of calcification may appear. Extensive calcification with irregularities of the cap should suggest the possibility of malignant change [3].

Steven B. Glassman
Dominique Delbeke

REFERENCES

1. Aegerter E, Kirkpatrick J Jr. *Orthopedic diseases: physiology, pathology, radiology*, 4th ed. Philadelphia: Saunders, **1975**:121-128
2. Resnick D. Tumors and tumor-like lesions of bone. In: Resnick D, Niwayama G, eds. *Diagnosis of bone and joint disorders*, vol 3. Philadelphia: Saunders, **1988**:2653-2654
3. Hennekam R. Hereditary multiple exostoses. *J Med Genet* **1991**;28: 262-266

Case 3: Fibrous Dysplasia in a Patient with Neurofibromatosis

Although neurofibromatosis and polyostotic fibrous dysplasia have some characteristics in common, they are distinct diseases and generally speaking, do not overlap. The finding of fibrous dysplasia in this patient with neurofibromatosis is coincidental.

Neurofibromatosis was classically considered to be a neuroectodermal dysplasia, but is now recognized to be a mesodermal dysplasia with diffuse systemic expressions [1]. The classic clinical triad of neurofibromatosis includes cutaneous lesions, mild mental deficiency, and skeletal deformities. The most common skeletal manifestations are localized to the spine and skull and include kyphoscoliosis, hypoplasia of the posterosuperior orbital wall, and deformities of the left lambdoidal suture. Other skeletal abnormalities also reflect the mesodermal dysplasia basic to the disease. Pseudoarthrosis and bowing of the tibia occur, as well as deficient growth or overgrowth of bones [2] (Fig. 3).

Fibrous dysplasia is a developmental anomaly of bone-forming mesenchyme that may affect one or many bones. It can exist independently, or the polyostotic form can be associated with skin, skeletal, CNS, and endocrine abnormalities (the McCune-Albright syndrome) [3].

The most common sites of monostotic fibrous dysplasia are the proximal femur, tibia, ribs, and face. Fifty percent of patients with polyostotic fibrous dysplasia have skull involvement. Unlike neurofibromatosis, fibrous dysplasia rarely involves the spine. The long bone lesions are diametaphyseal and located within the medullary cavity of the bone. Histologically, the lesions consist of fibrous collagenous tissue, within which are found disorganized spicules of woven bone that may be well mineralized. The radiolucency, radiopacity, or ground-glass appearance on radiographs is determined by the relative amounts of fibrous vs ossified tissue present in the lesion. The intense uptake of bone-seeking radionuclide reflects hyperemia and active bone remodeling. Malignant degeneration occurs in 0.4 to 1.0% of the cases.

Anne V. Hansen
Dominique Delbeke

REFERENCES

1. Feldman F. Tuberous sclerosis, neurofibromatosis, and fibrous displasia. In: Resnick D, Niwayama G, eds. *Diagnosis of bone and joint disorders.* Philadelphia: Saunders, **1981**;2931-2959
2. Hunt JC, Pugh DG. Skeletal lesions in neurofibromatosis. *Radiology* **1961**;76:1-20
3. Albright F, Butler AM, Hampton AO. Syndrome characterized by osteitis fibrosa disseminata, areas of pigmentation, and endocrine dysfunction with precocious puberty in females. *N Engl J Med* **1937**;216:727-746

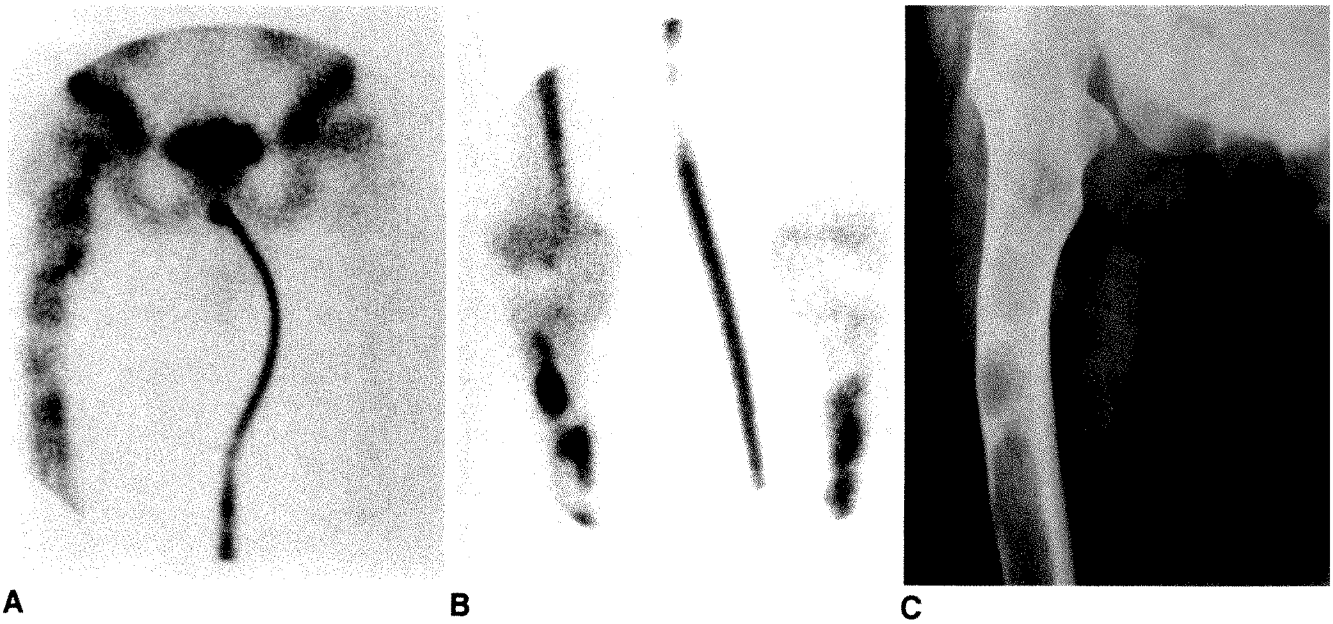

Fig. 3.—Case 3: Fibrous dysplasia in a 17-year-old patient with neurofibromatosis.

***A*, Bone scintigram. Anterior view of pelvis and lower extremities obtained after IV injection of 20 mCi of ^{99m}Tc-hydroxydiphosphonate shows intensely increased uptake of radionuclide in a geographic distribution in tibia and right femur. In addition, right femur is deformed.**

***B*, Bone scintigram. Anterior view of knees, obtained as in *A*, shows similar findings.**

C, Bone radiograph. Anteroposterior view shows classical changes of fibrous dysplasia. Disease causes structural weakening, resulting in bowing of this weight-bearing bone. Lesions have a "ground glass" appearance with a sclerotic rim. They are expansile, with associated cortical thinning.

Case 4: Bile Leak After Laparoscopic Cholecystectomy

Cholescintigraphy was performed after IV administration of 5 mCi of ^{99m}Tc-disofenin, with sequential anterior abdominal images obtained every 5 min for 30 min (Fig. 4). The images showed a progressive accumulation of radionuclide in the gallbladder fossa and along the right pericolic gutter. The 1-hr delayed anterior abdominal image showed presence of the radionuclide diffusely in the abdomen. An additional delayed anterior abdominal image, obtained after the patient had lain in the left lateral decubitus position for 5 min, showed displacement of the radionuclide into the left pericolic gutter, illustrating free-flowing bile in the peritoneal cavity. ERCP was performed and confirmed brisk extravasation of contrast material from a small, short cystic duct.

More than 500,000 cholecystectomies are performed every year in the United States. Laparoscopic cholecystectomy offers a minimally invasive and economically advantageous treatment, with a reduced hospital stay, decreased recovery interval, and diminished postoperative discomfort when compared with open cholecystectomy [1]. However, the prevalence of injury of the common bile duct during laparoscopic cholecystectomy (0.5–2.7%) is higher than that during open cholecystectomy (0.2%) [2]. Sequelae of bile extravasation include subhepatic fluid collection, abscess formation, fistula formation, and peritonitis [3]. Cystic duct leaks resulting from dislodgement of a loosely placed clip or ligature may not be recognized for several days after the procedure and can be lethal because of bile peritonitis [4, 5]. Thus, the potential morbidity and mortality associated with bile extravasation make rapid diagnosis and proper management of bile leakage essential.

Although sizable fluid collections within the abdomen can be shown on CT or sonographic studies, the fluid cannot be positively identified as bile [3, 5]. Hepatobiliary scintigraphy with ^{99m}Tc-labeled iminodiacetic acid (IDA) derivatives is a superior technique for early specific evaluation of postsurgical complications from hepatobiliary procedures [4–7]. IDA scans provide good visualization of the intrahepatic and extrahepatic ductal anatomy, surgical anastomosis of the biliary duct, evidence of partial or complete obstruction of bile flow, or evaluation of traumatic injuries of the biliary tree with or without biloma. The newer IDA agents produce excellent images even at bilirubin levels of 30 mg/dl. In patients with bile leakage, the small bowel is usually visualized, unless all of the bile excreted by the liver is being extravasated [6]. Very slow or small leaks that can be hidden in early images of normal activity may require extra delayed images. Fortunately, radioactivity in abnormal bile collections persists even after liver parenchyma and the biliary tract are no longer visible, which aids in their recognition [6]. Activity that accumulates in the duodenum may interfere with accurate identification of a bile leak. This can be overcome by oblique views, delayed views, ingestion of water to wash out duodenal activity, or standing views, which promote intestinal transit and displace bowel loops downward [7]. Different image patterns of large bile leakage have been described, including perihepatic accumulation without peritoneal activity, diffuse biliary ascites, and biloma [6].

Management of small, sterile, and adequately drained in-

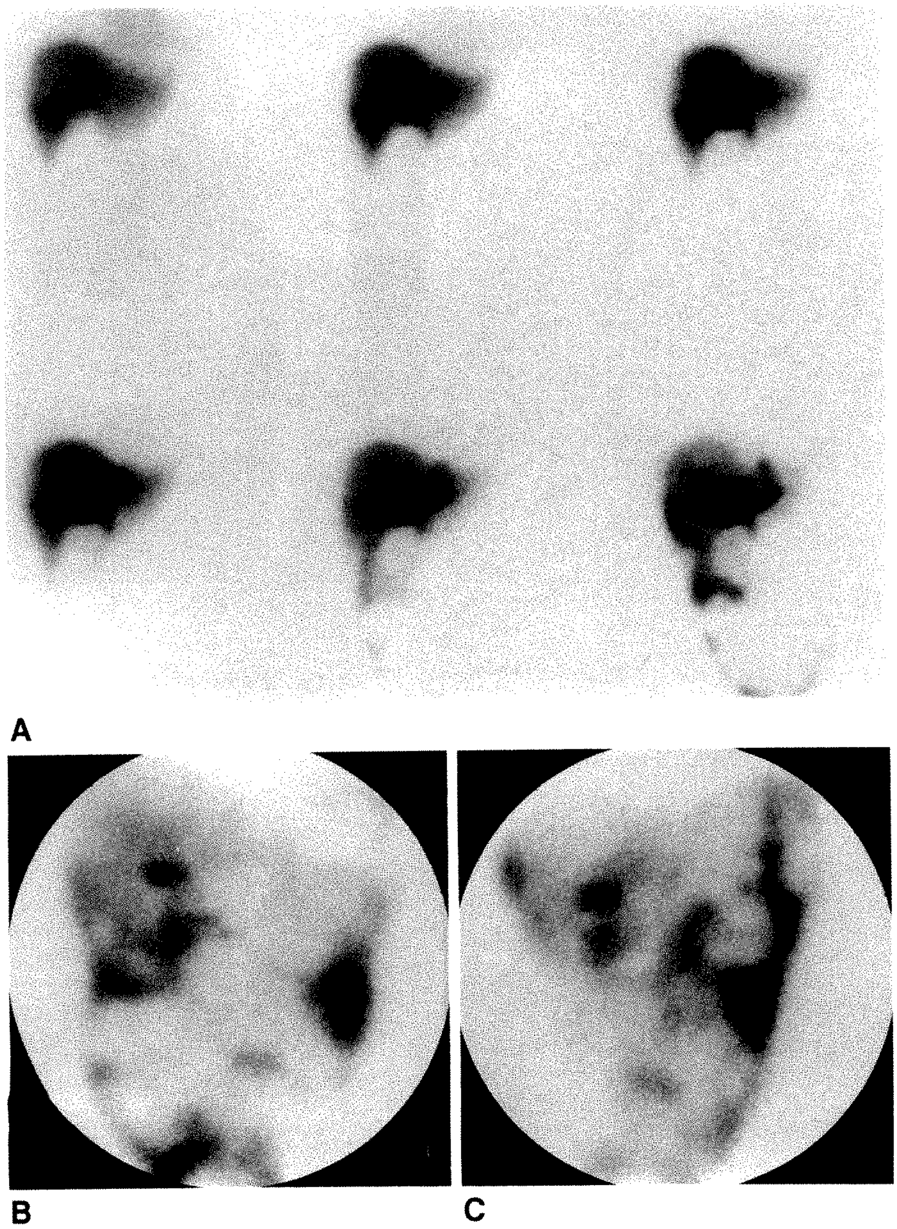

Fig. 4.—Case 4: Bile leak after laparoscopic cholecystectomy.

***A*, Hepatobiliary scintigrams. Multiple sequential anterior views of abdomen obtained after IV injection of 5 mCi ^{99m}Tc-disofenin show progressive accumulation of radionuclide in gallbladder fossa and along right pericolic gutter.**

***B*, Hepatobiliary scintigram. One-hour delayed anterior view of abdomen shows presence of radionuclide diffusely in abdomen.**

***C*, Hepatobiliary scintigram. Delayed anterior view of abdomen, after patient had lain in left lateral decubitus position for 5 min, shows displacement of radionuclide into left pericolic gutter, illustrating free-flowing bile in peritoneal cavity.**

traabdominal leaks usually heal spontaneously and may be expectantly observed [3-5]. Patients with larger leaks, small leaks that do not respond to conservative therapy, or fistulous tracts can be managed with open abdominal surgery, percutaneous transhepatic biliary drainage, or endoscopic sphincterotomy and stent placement [3].

Sandra K. Lawrence
Dominique Delbeke

REFERENCES

1. Brandon JC, Velez MA, Teplick SK, et al. Laparascopic cholecystemtomy: evolution, early results, and impact on nonsurgical gallstone therapies. *AJR* **1991**;157:235-239
2. Hunter JD. Avoidance of bile duct injury during laparoscopic cholecystectomy. *Am J Surg* **1991**;162:71-75
3. Rosenberg DJ, Brugge WR, Alan A. Bile leak following an elective laparoscopic cholecystectomy: the role of hepatobiliary imaging in the diagnosis and management of bile leaks. *J Nucl Med* **1991**;32:1777-1781
4. Ponsky JL. Complications of laparoscopic cholecystectomy. *Am J Surg* **1991**;161:393-395
5. Lorenz R, Beyer D, Peters PE. Detection of intraperitoneal bile accumulations: significance of ultrasonography, CT, and cholescintigraphy. *Gastrointest Radiol* **1984**;9:213-217
6. Siddiqui AR, Ellis JH, Madura JA. Different patterns for bile leakage following cholecystectomy demonstrated by hepatobiliary imaging. *Clin Nucl Med* **1986**;11:751-753
7. Lette J, Morin M, Heyen F, et al. Standing views to differentiate gallbladder or bile leak from duodenal activity on cholescintigrams. *Clin Nucl Med* **1990**;4:231-236

The Information Perspective of Radiology

William R. Hendee[1]

How well an industry such as radiology responds to challenges and adapts to change depends in large measure on how it views itself. The railroad industry has not thrived in the United States, largely because it has viewed itself for decades as a railroad industry. It would have fared better if it had thought of itself as an industry dedicated to efficient and effective transportation of people and products and followed through with the organizational and functional changes necessary to improve its efficiency and effectiveness. As an opposite example, IBM has done very well over the years by conceptualizing its business not as making computers but as facilitating the acquisition and use of information. Eastman Kodak has remained strong in the photographic products market because it has presented itself less as a film industry and more as an industry dedicated to memorializing events such as family activities and significant public happenings.

The challenge to any industry is to understand and appreciate the fundamental needs and desires of its market and then to develop and characterize products that meet those needs and desires [1]. To attempt to mold the marketplace to one's product line is to court disaster, as was discovered by the U.S. auto industry in the early 1970s when it ignored the growing public demand for smaller, more fuel-efficient cars. To build and maintain a viable position in the marketplace for the long term, an industry must position its product line in response to the market, rather than try to mold the market to its product line.

Radiology is an industry with a market that has specific needs and desires. How we in radiology view our discipline defines in large measure how well those needs and desires are satisfied and therefore how well our profession will fare in the future. The question then is: How do we in radiology view our discipline?

Perspectives of Radiology

There are many different perspectives on radiology. Some persons think that radiology is primarily a discipline in which sophisticated imaging technologies are used for the study of human disease and injury. This "technology perspective" focuses on mastering the principles and applications of imaging technologies and sometimes ends up as an infatuation with the technologies themselves. Persons with this orientation may become more interested in the gadgetry of technologies than in how and why the technologies are useful in caring for patients. Those who work in radiology principally because they are enamored with radiology's technologies are the technocrats of the discipline.

Some persons define radiology as the process of producing diagnostic images that are helpful in determining what might be wrong with patients. This "image perspective" operates under the assumption that high-quality images are the desired products of the radiologic process. Persons with this image perspective are devoted to performing comprehensive examinations that yield the highest quality images possible. They are satisfied only with the best pictures and the most complete diagnostic information attainable from a radiologic study.

Other radiologists might suggest that images are meaningful only when they are interpreted and a report of findings is

---

Received November 21, 1991; accepted after revision January 9, 1992.

[1] Office of Research and Technology, Medical College of Wisconsin, 8701 Watertown Plank Rd., Milwaukee, WI 53226. Address reprint requests to W. R. Hendee.

AJR 158:1387–1389, June 1992 0361–803X/92/1586–1387 © American Roentgen Ray Society

prepared. This "diagnostic perspective" implies that radiologic diagnoses constitute the mission of radiology and that anything short of such opinions is a misperception of the true purpose of radiology. Persons with the diagnostic perspective are dedicated to acquiring accurate and complete radiologic data and weaving the data into a diagnosis prepared as a dictated report.

Radiology viewed from any one of these three perspectives represents a way of thinking about the discipline that falls short of meeting the needs and desires of the radiology marketplace. This shortcoming could erode the base of medical support for radiology and threaten its survival over the long term. Radiology certainly is a profession for all radiologists and perhaps a calling for some. But it is also an industry, albeit one that contains strong elements of compassion and caring. All of us, physicians, physicists, technologists, and manufacturers, are in the business of radiology. And because we are in the business, we had better understand just what business we are in.

The Business of Radiology

The business of radiology is providing diagnostic information about patients to all who need it. Radiology has the responsibility not only to provide useful information but also to facilitate the use of this information in the care of patients. This "information perspective" of radiology implies that our discipline is in the information business, in the sense not only of acquiring information but also of ensuring that the information is delivered, accepted, and used by those who need it. The market for information, the true product of radiology, is composed of other physicians who care for patients and ultimately of the patients themselves. The definition of information is "that which informs." So the business of radiology is to create and serve an informed market of physicians and patients, where informed means much more than "communicated to." "Informed" means that physicians and patients form opinions and take appropriate actions on the basis of the work of the professionals in radiology, including radiologists, physicists, technologists, business managers, and others.

Characterization of the radiology market is not so difficult. The market needs information that is (1) relevant to the medical problem being addressed, (2) as accurate as possible, (3) complete enough to contribute to decision making by physicians and patients and to provide assurance that correct decisions are being made, (4) delivered in a timely (real-time) fashion, and (5) reinforceable through follow-up consultation with a radiologist.

Market Demands for Radiology Services

Radiology has many tools and techniques available to satisfy the needs and desires of its market. The challenge to radiology is how to use these resources in the most effective and efficient fashion with every patient. An even greater challenge is the need for radiology to view itself from the information perspective, and to create the training and clinical service environments consistent with this perspective.

For most of its history, radiology has functioned principally as an off-line, batch-processing operation. Patients are examined and films are taken, processed, and brought to the reading room for interpretation and dictation. The dictated reports are typed and distributed to appropriate clinical services, where they are inserted into patients' charts and sometimes brought to the attention of the primary care physician. Typically, the time between examination of the patient and the availability of a report to the referring physician is 24 hr or longer.

Occasionally, the dissemination of radiologic information is expedited by interpreting films "wet" and telephoning reports to the requesting physician. But, in general, the acquisition, interpretation, and communication of radiologic information lumbers along at a rather leisurely pace. In the past, that pace may have been acceptable. In today's world of instant communications and data sharing, it no longer is. In fact, it is unlikely to be gracefully accommodated much longer, as, much later than it should have, medicine is at last entering the era of computer-based decision making and rapid communication.

Most persons working in radiology do not think of their activities as proceeding at a leisurely pace. In fact, radiology activities often are more frenetic than leisurely. It is not that the pace of work is leisurely—far from it. It is just that the rate of information flow is leisurely. It simply takes too long to produce radiologic information and get it to those who want and need it. The pace of information flow is too slow—not the pace of work. The pace of information flow in radiology is gradually fading out of synchrony with the needs of physicians who have on-line responsibilities for care of patients. The needs and desires of these physicians are creating a "clinical imperative" for radiology to become an on-line, real-time information service rather than an off-line batch-processing operation. This imperative promises to be a major influence on how radiology is structured in the future, including the character of the technologies that support it and the work habits of those who provide it. Already it is a force driving radiology toward digitization of radiologic images and the real-time interpretation and networking of these images, and decisions about them, to referring physicians.

Role of Digital Radiology

In radiology, considerable debate has occurred about the feasibility and desirability of capturing and presenting radiologic images in digital rather than analog form. Much of this debate focuses on current technical limitations of digital imaging systems, including the less-than-optimal spatial resolution of digital detectors and whether new receptor systems will overcome this limitation at reasonable cost. Photostimulable detectors, scan projection receptors, and other devices to produce digital images are promising, but they have not addressed all the concerns about spatial resolution [2]. Efforts are under way in several institutions to develop improved digital systems, including multiple-detector arrays and high-resolution image intensifiers. A major benefit of digital imaging is that the image receptor is decoupled from the image display. Decoupling offers opportunities to present digital radiologic images with adequate spatial resolution and the capability to suppress noise, enhance contrast, and manipulate the image further [3].

In all likelihood, satisfactory detectors for digital radiography will not be a long-standing technical challenge. Adequate display technology already is available, as is evident in the exquisite digital systems developed to produce and display images in the defense, space, and surveillance industries. The major question is whether these display systems, or something close to them, can be developed in quantity at a reasonable cost for use in radiology.

Digital systems offer several potential advantages over film for display of radiologic images. They provide an essentially infinite gray scale, so that visualization of structures of interest is not lost because the structures are on the toe or shoulder of a characteristic curve. They permit facile application of intensity-equalization techniques to reveal subtle abnormalities that might otherwise remain hidden in the image. They provide algorithms for edge enhancement, noise suppression, and density windowing of the image. These features, and others as well, emphasize the need for continued development and use of digital techniques for acquisition and display of radiologic images.

What Else Is Needed?

It is one thing to automate the acquisition and presentation of radiologic data so that these processes can be moved into an on-line, real-time operation. It is another to facilitate the interpretative and transmission processes so that information of equal or improved accuracy can be furnished to physicians in a more rapid and useful manner. This challenge might be surmountable in part through the presentation of images on display stations and the use of computer assistance in their interpretation. Computer-assisted diagnosis for interpretation of mammograms and chest radiographs is being explored in several institutions, with the objective of improving the frequency of detection of abnormalities (i.e., enhancing the sensitivity) and reducing the number of false-positive and suggestive findings (i.e., improving the specificity) [4, 5]. Methods of computer diagnosis are not yet advanced enough to provide the discrimination needed for such computer-based decision making. They may be available in the future, however. Such computer codification programs do not have to be perfect; they need only be as good as the average radiologist.

Digital systems for acquisition and display of radiologic images and the use of computer-assistance algorithms in the interpretation of images are promising approaches to helping radiology move into the information perspective. But they alone are not sufficient to accomplish the transition. They must be accompanied by an increased responsiveness among radiologists to the growing clinical imperative for the discipline to reposition itself into the critical path of medical decision making and care of patients. A commitment to continuous, on-line, real-time radiology services to the physicians and patients who need them is part of this responsiveness. Another part is recognition that the technology of radiology is not an end in itself, but that it exists to serve the needs of primary care physicians and patients.

Much attention is focused today on efforts to improve the accuracy of radiology and reduce the time required to get radiologic information to those who need it. This attention is a driving force toward digitization of the acquisition and display of radiologic information. Technical limitations resisting this force probably will be overcome in the near future. Changes needed for radiologists to become comfortable with digital radiology and the provision of on-line, real-time services may take somewhat longer. However, the clinical imperative will eventually force radiology into accommodating these changes. When that happens, radiology will be more appropriately aligned with the information perspective of the discipline.

REFERENCES

1. Ries A, Trout J. *Positioning: the battle for your mind.* New York: McGraw-Hill, **1986**
2. Nishikawa RM, Mawdsley GE, Fenster A, Yafte MJ. Scanned projection digital mammography. *Med Phys* **1987**;14:717–727
3. Lee KR, Siegel EL, Templeton AW, Dwyer SJ III, Murphey MD, Wetzel LH. State-of-the-art digital radiography. *RadioGraphics* **1991**;11:1013–1025
4. Chan HP, Doi K, Vyborny CJ, et al. Improvement in radiologists' detection of clustered microcalcifications on mammograms: the potential of computer-aided diagnosis. *Invest Radiol* **1990**;25:1102–1110
5. Gale AG. HCI in breast cancer screening. In: Lemke HU, Rhodes MC, Jaffe CC, Felix R, eds. *Computer assisted radiology.* Berlin: Springer-Verlag, **1991**:499–504

Book Review

Cardiac Imaging. A Companion to Braunwald's Heart Disease. Edited by Melvin L. Marcus, Heinrich R. Schelbert, David J. Skorton, and Gerald L. Wolf. Philadelphia: Saunders, 1344 pp., 1991. $110

This book will serve for many years as an excellent reference on all aspects of cardiac imaging. It contains 69 chapters covering most aspects of cardiac imaging. The 118 contributors are recognized authorities in their respective areas. The 1349 illustrations are of fair to good quality.

The book is organized into 10 specific parts: introduction, conventional radiography, coronary angiography, digital angiography, echocardiography, ultrafast CT, cardiac nuclear MR imaging, conventional radionuclide imaging, new developments in cardiac radionuclide imaging, and positron emission tomography. The introduction includes brief overviews of cardiac physiology and biochemistry and chapters on imaging processing and the perceptual aspects of imaging. Each of the remaining nine parts generally contains at least one chapter that discusses basic information on the specific imaging devices and related physics. In general, it is assumed that the reader has a fair working knowledge of the basic physics. Basic X-ray physics, for example, is really not covered, though digital and CT technology are discussed. The basic aspects of MR are covered more thoroughly than those of other techniques. Pharmaceuticals used for cardiac imaging are discussed for X-ray, MR, radionuclide, sonographic, and positron emission tomographic imaging. These chapters on pharmaceuticals provide overviews on the mode of action and the use of the agents. The remaining chapters describe the application of the different imaging techniques to specific diagnostic questions related to vascular anatomy and myocardial perfusion and for quantifying myocardial function. As a researcher who has limited exposure to clinical procedures, I found these chapters of great value. The extensive use of figures facilitates comprehension of the material.

One thing missing from this book is a thorough, unified discussion of the relative advantages and disadvantages of the various imaging techniques and procedures for specific diagnostic questions.

The scope of this book makes it a relatively unique resource for physicians and scientists interested in cardiac imaging and heart disease. The book will be most useful to those who have some working knowledge of one or more of the various imaging techniques. The organization of the book and the broad scope of the chapters can provide rapid access to appropriate information related to procedures of which the readers are less knowledgeable. As with all such books, some topics are not included, and experts in a specific area may not find all the topics they would have included. However, the book will be useful as a convenient and detailed source of information on areas of cardiac imaging in which the readers are not expert.

Thomas W. Morris
University of Rochester Medical Center
Rochester, NY 14642

Meeting News

Thoracic Imaging, 1992

Elizabeth Whalen[1]

The tenth annual meeting and postgraduate course of the Society of Thoracic Radiology, "Thoracic Imaging 1992," was held January 19-23, 1992, at the Ritz-Carlton Hotel, Laguna Niguel, CA. At this meeting, participants could attend postgraduate courses, scientific sessions, a research symposium, workshops, discussions of unknown cases of the day, and the annual Benjamin Felson Lecture. The postgraduate course included seven plenary sessions that provided detailed reviews of state-of-the-art techniques concerning thoracic neoplasms, CT and MR imaging of the thorax, cardiovascular disease, pulmonary disease, imaging the lung, pediatric imaging, and acute lung disease. The two scientific sessions featured 42 presentations of original scientific investigations in thoracic imaging. Also offered were four workshops and daily cases of the day to challenge the diagnostic skills of the attendees. Two annual highlights of the meeting were the Scanlon Memorial Research Symposium (a 2-hr discussion of high-resolution CT of the lung) and the Benjamin Felson Lecture, this year presented by Joel D. Cooper (St. Louis, MO), a pioneer in lung transplantation.

Because Journal space is limited, we cannot include coverage of all the activities provided at this 5-day meeting. However, the following pages contain summaries of nine of the presentations of original scientific research, 12 of the up-to-date reviews given in the postgraduate plenary sessions and Scanlon Symposium, and the Felson Lecture. The material that follows is grouped by subject matter.

Acute Lung Disease

In the plenary session on acute lung disease, Richard J. Wechsler (Philadelphia, PA) discussed "monitoring the monitors"—the radiologic imaging of thoracic venous catheters, which are almost always inserted blindly. After each catheter is inserted, chest radiographs are routinely needed to avoid complications such as inaccurate measurement of central venous pressure, arrhythmia, thrombosis, infection, catheter knotting and fragmentation, catheter migration, and pneumothorax. The cause of thrombosis may be endothelial entry of the catheter, alterations in blood flow, or hypercoagulability. Thrombosis is found in up to 71% of patients who have catheters in for 7 days or more, and use of the Hickman-Broviak catheter reduces but does *not* totally eliminate the possibility of thrombosis. If chest radiographs show widening of the mediastinum, pleural effusion, and collateral flow, then thrombosis should be suspected. Sonography is the method of choice to check for thrombosis in catheterized patients because it will show clot or dampening of the waveform, and CT also can help detect thrombosis by showing vascular occlusion with collateral development.

An estimated 50,000 cases of catheter-related septicemia occur each year, with a mortality rate of 10–20%. These infections result from bacterial or fungal colonization at the skin/catheter interface or the catheter hub itself. Complications from catheter knotting include perforation, thrombosis,

---

[1] Contributing editor, *American Journal of Roentgenology*, Ste. 103, 2223 Avenida de la Playa, La Jolla, CA 92037.

Editor's note.—"Meeting News" articles report the highlights of important national radiology meetings. The articles will not undergo the peer review usually required of *AJR* publications, nor will they offer a critique of the information provided. The sole purpose of the series is to provide Journal readers with succinct, substantive, and accurate reviews of topics of current interest, written in a readable fashion and published promptly after the meeting.

158:1391–1398, June 1992 0361–803X/92/1586–1391 © American Roentgen Ray Society

and catheter breakage. Because a loose knot is always easier to untie than a tight knot, it helps to diagnose and fix these complications as soon as possible. Catheter fragmentation may result from improper insertion technique, and 71% of patients in whom this occurs have serious or fatal complications if the catheter is not removed. After thoracic catheter insertion, the complication most frequently found is pneumothorax; its prevalence is 1–12%. On supine radiographs, pneumothoraces may be apparent and should be looked for in the anteromedial and subpulmonic recesses. For vascular injection and perforation, the radiologic findings include apical cap, pleural effusion, and mediastinal widening. A gentle arc at the tip of the catheter may suggest that it is lying against a vessel wall, which predisposes the vessel to erosion and perforation; knowledge of mediastinal anatomy is helpful in diagnosing these perforations.

Even correctly placed catheters do not always stay in the same place, and radiologists need to look for catheter migration. In one example shown, a migrated catheter was bathing the patient's spinal cord with a chemotherapeutic agent. One general point that Dr. Wechsler made was that thoracic venous catheters that are *not* in the brachiocephalic vein are either complications or impending complications. He shared an image of his "favorite" catheter complication: a clinician had just kept inserting a catheter continuously, trying to place it correctly, so that the radiograph shows a chest containing a convoluted catheter that was as long as the patient was tall. Dr. Wechsler suggested that sometimes the most difficult aspect of catheter complications is convincing the unbelieving physician that the device was inserted incorrectly.

CT in Blunt Chest Trauma

Irena Tocino (New Haven, CT) attempted to answer the question "Is there a role for CT in acute chest trauma?" Currently, the mortality rate resulting from direct injuries to the chest is 30%, and from indirect injuries to the chest it is 50%. Chest trauma is often occult, and the first imaging examination (supine chest radiograph) often does not provide all the information needed. For the past 8 years, Dr. Tocino and her colleagues have used CT to distinguish hemorrhagic from nonhemorrhagic mediastinal widening. The distinction between the two on chest radiographs may be difficult because of fat, lordotic position, pleural effusions, infiltrates, and normal variations in vascular structures, but CT scans clearly show blood in the mediastinum in cases of hemorrhagic mediastinal widening.

Other uses of CT in acute chest trauma include the following: localizing hemorrhage, evaluating catheter or tube placement (e.g., endotracheal tube, Swan-Ganz catheter, nasogastric tube, and chest tube), looking for abnormal air collections, assessing skeletal injuries (e.g., sternoclavicular dislocations, sternal fracture, rib fracture, flail chest, dorsal spine), and occasionally finding parenchymal disease not shown on chest radiographs (e.g., contusion, laceration, aspiration, and atelectasis).

Traumatic Lacerations of the Aorta and Great Vessels with a Radiographically "Normal" Mediastinum

A. M. Cohen (Cleveland, OH) explained the rationale of this study conducted by himself and J. R. Crass as follows: (1) the chest radiograph is the first study performed in blunt chest trauma, and (2) a "normal" radiograph often affects the decision to proceed to angiography. Therefore, the researchers proposed this hypothesis: A lacerated aorta or great vessel may be present in patients whose mediastinum appears "normal" radiographically. The hypothesis was tested by using the experience of fellow radiologists: a questionnaire was sent to all 1991 members of the Society of Thoracic Radiology, a letter containing identical questions was published in the Spring 1991 issue of the journal of the Society of Cardiovascular and Interventional Radiology (SCVIR), and a literature search was undertaken to find relevant cases.

Of 327 questionnaires sent, 77 were returned: 69 respondents had never seen a normal mediastinum in the presence of a tear of the aorta or great vessel, and eight respondents described different cases in which a normal mediastinum was seen with a lacerated aorta or great vessel; no responses were received from the letter published in the SCVIR journal. The literature search yielded 23 references, of which 16 showed aortic tears and two showed great-vessel tears in patients with normal mediastina. The researchers were able to contact 21 of 23 authors; in one case of dual authorship, the radiologist said that the mediastinum was *not* normal on the radiograph while the surgeon said that it *did* look normal on the radiograph, confirming that "normal" depends heavily on who is interpreting the image (or, "Normal is in the eye of the beholder").

This survey study indicated that a lacerated aorta or great vessel can occur with a radiographically "normal" mediastinum, but the frequency of this event (infrequent to rare in any case) depends on the interpreter of the radiograph. Therefore, practical application of this conclusion in triage would suggest obtaining an angiogram to check for tears in unstable patients who have an appropriate mechanism of injury and applying more options for the stable patient, depending on the appearance of the chest radiograph, the index of suspicion for a tear, and whether or not the mediastinum appears normal. Discussion of this study included an informal survey of participants concerning whether CT should be used in these patients; the opinion appeared to be evenly split among members present.

CT-Guided Drainage of Pneumothoraces in Patients with Severe Pulmonary Compromise

Eight patients with severe respiratory disease who were undergoing CT-guided drainage of pneumothoraces were studied by Eric vanSonnenberg and colleagues (H. D'Agostino, R. Sanchez, R. O'Laoide, L. Fundell, S. Oglevie, all in San Diego, CA). The eight patients (trauma, four; carcinoma, one; AIDS, one; IV drug abuse, two) had different types of pulmonary diseases, including adult respiratory disease syndrome, pneumonia, septic emboli, and lung abscess. In two patients, the pneumothorax encompassed less than 25% of the hemithorax; in five, 25–50%; and in one, more than 50%. The pneumothorax was on the right side in five and on the left side in three patients. In all patients, the trocar technique was used; the catheter size ranged from 8- to 28-French (12-French was used most often), and the volume of air initially removed varied from 150 to 1000 ml. Reexpansion occurred in all patients; reexpansion was immediate and complete in five patients. Although one tube was exchanged, no major complications occurred, and the catheters were removed within 1 week in six patients and within 2 weeks in the other two patients. The experience with this small group of patients indicates that CT-guided drainage of localized pneumothoraces is successful in patients with severe lung disease. The measures of this success include improvement in the appearance of the lung on both radiographs and CT scans and the reduction of ventilatory factors.

Thoracic Neoplasms

Past, Present, and Future of Lung Cancer

Sanford Rubin (Galveston, TX) began his talk by warning that it was not really a "radiology" talk, but his discussion provided an excellent background and philosophical outlook for the other reviews about imaging of thoracic neoplasms. Although lung cancer is truly a "20th century disaster" because of tobacco use, this entity was first noted medically in the 15th and 16th centuries as a pulmonary disease ("Bergkrankheit" or "Bergsucht") that killed many miners (in Schneeberg, Germany) at a young age. In 1879, Harting and Hesse performed autopsies on 20 miners who had died of Bergsucht, and labeled the cause of death "pulmonary sarcoma." This disease, which Adler in 1912 found to be so rare that he questioned the value of writing about it (he had found 374 cases worldwide), will cause a predicted 143,000 deaths in the United States in 1992.

As Dr. Rubin discussed the current diagnosis of lung cancer, he noted that MR imaging may prove to be better than CT for staging in some instances (e.g., detecting invasion of the mediastinum, chest wall, vascular structures, or heart; Pancoast's tumor; and recurrence after therapy). Screening, however, may or may not improve mortality significantly; screening of high-risk patients may be best accomplished by routine chest radiography. Patients may be helped more by research to develop a clearer understanding of lung cancer and more effective therapeutic methods (which have improved significantly since 1821, when Anthony performed the first deliberate thoracotomy for partial pulmonary resection without benefit of anesthetic). However, Dr. Rubin emphasized that prevention is the key to resolving the problem of continued deaths due to lung cancer: The medical evidence is clear, but it does not seem sufficient to overcome the powerful forces that cause people to start smoking and to continue to smoke. Both political and social pressures can be used to discourage the use of tobacco and thus to decrease significantly the diagnostic and treatment problems concerning lung cancer in the future.

Diagnostic Imaging Techniques for the Solitary Pulmonary Nodule

As defined by Poonam Batra (Los Angeles, CA), a solitary pulmonary nodule is a single focal opacity up to 6 cm in diameter (usually <3 cm) that is located within the lung parenchyma and has a well-defined margin. The goal of imaging such a nodule is to establish its nature, guide biopsy, and determine its resectability. Among possible imaging methods are chest radiography, fluoroscopy, tomography, CT, high-resolution CT, MR imaging, and digital, dual-energy imaging. The current procedures of choice are chest radiography and either CT or high-resolution CT. CT should be used to supplement plain radiographs and help localize single pulmonary nodules, define morphology, detect calcification and fat, and provide densitometric values; however, its role in staging single malignant pulmonary nodules is controversial. In high-resolution CT, the technique for imaging these nodules includes thin collimation, 1.5-mm contiguous slices, and reformatting data with a high-spatial-frequency reconstruction algorithm. Fluoroscopy is helpful when the initial radiographic findings are equivocal. The role of MR imaging for these nodules is still limited. Use of the digital and dual-energy techniques is a current research topic.

The characteristics of malignancy in a single pulmonary nodule include the following: size greater than 3 cm, spiculated margin, absence of calcification or presence of eccentric or fine stippled calcification, and increasing size over time (doubling time, 30–490 days). On the other hand, benign solitary pulmonary nodules have diffuse, central, laminar, "popcorn" calcification; their margins are smooth and well-defined; and they may be round, oval, angular, or linear. Other indications of benignity include absence of growth on chest radiographs for 2 years, a size of less than 2 cm, and presence of satellite lesions.

Metastatic Lung Disease

Gordon L. Weisbrod (Toronto, Ontario, Canada) noted that the high frequency of pulmonary metastases (30–53% of autopsies of patients who died of cancer) is due to the rich vascular supply to lung and direct systemic venous drainage from tumor sites. Several routes exist for cancer to spread to the lung, and some of the more common cancers in which lung metastases are found include choriocarcinoma (70–100%), renal cell carcinoma (50–75%), Wilms' tumor (60%), Ewing's sarcoma (77%), osteosarcoma (75%), and testicular carcinoma (70–80%). For diagnosis of lung metastases, whole-lung tomography has now been replaced by CT; most nodules detected by CT are malignant. Spontaneous pneumothorax occurs with pulmonary metastases; such pneumothoraces most commonly occur with osteosarcoma, often develop during or after chemotherapy, and may antedate radiologic evidence of metastases. The main cause of cavitation in pulmonary metastases is vascular invasion and ischemic necrosis.

Among other topics covered by Dr. Weisbrod in his comprehensive presentation were the following: lymphangitic carcinoma (which is shown on high-resolution CT by irregular or nodular thickening of bronchovascular bundles, polygonal lines, increased number and thickness of interstitial lines, nodules, thickening and irregularity of fissures, and sometimes adenopathy), endobronchial metastases (seen in 2-5% of patients dying of metastatic disease and clinically important because it may simulate bronchogenic carcinoma), thoracic metastases from renal cell carcinoma (which is important because 30-45% of patients with renal cell carcinoma metastatic to the lung will have *no kidney symptoms*), thyroid carcinoma (which may have a favorable prognosis), choriocarcinoma (which is seen in 45-87% of patients, is characterized by multiple poorly defined or well-defined nodules, pulmonary infarction, and pulmonary hypertension, and whose remission rate after chemotherapy may be up to 88%), and breast carcinoma (which is very common and is associated with lymphangitic carcinoma, mediastinal/hilar adenopathy, and pleural effusions).

Resectability of Lung Carcinoma Involving the Heart

In a paper presented by M. G. Baron (researchers: J. A. Ziffer, P. Symbas, E. Cheung, M. G. Baron; all from Atlanta, GA), new evidence suggests that some patients with lung cancer involving the left atrium may be surgical candidates. These findings conflict with the accepted American Joint Committee on Cancer staging criteria that define these types of cancers as T4 lesions, which cannot be successfully treated by complete surgical resection. Cine MR imaging was used to select three patients for this study (two with bronchogenic carcinoma and one with primary germ cell tumor of the lung); all three patients had extension of tumor into the left atrium. The decision to operate on these patients was based on MR gradient-echo movies that showed that the mass was moving independently of the atrial walls, which indicated a lack of infiltration. Resection of the mass was successful in two of the patients and required removal of only a small segment of the atrial wall; in the third patient, mediastinal lesions were found at surgery and resection was not attempted.

This preliminary study indicates that involvement of the heart in lung cancer does not necessarily indicate invasion; false-positive results of "cardiac invasion" may deny some of these patients their best chance of cure. Venous extension of resectable tumor is not rare, particularly with hypernephroma; therefore, radiologists should consider performing cardiac-gated MR studies in patients who have a lung tumor that abuts the mediastinum because if the heart is involved by extension through a pulmonary vein, the patient may be a candidate for successful surgical resection.

Pediatric Thoracic Imaging

Emergency Radiology of the Pediatric Chest

Donald R. Kirks (Cincinnati, OH) began the plenary session on pediatric imaging with an informative discussion of emergency radiology of the chest in children. Chest radiography is still the "foundation" of thoracic imaging. In older, cooperative children, posteroanterior and lateral views should be obtained; many immobilization devices are available to assist the radiologist attempting to obtain radiographs of a child who is uncooperative or very young (<4 years old). Proper technique to achieve high-quality radiographs involves the considerations of centering, sufficient penetration (the intervertebral disk spaces should be visible through the heart but the pulmonary vessels should not be obscured), and attention to inspiration and motion factors. The radiologist should evaluate all anatomic portions of the chest radiograph, examining the parenchyma *last* because it is usually the area that is the focus of the examination. Normal variants to be remembered include the thymus (which reaches its maximum weight at puberty but its maximum volume compared with thoracic volume at 1-2 years) and expiration artifacts (which may mimic pneumonia). Among the unique features of the infant lung are smaller and collapsible airways, decreased conductance, increased mucus production, and poor collateral ventilation.

Dr. Kirks advised radiologists to beware of diagnosing pneumonia or airways disease in a young child unless hyperinflation is present, because much that is called pneumonia or airways disease in these patients is actually underaeration or atelectasis. Another entity that may mimic pneumonia in children aged 9 months to 12 years is a foreign body in the airway. This problem peaks in children 1-2 years old; the site is more often the right hemithorax than the left, and only 10% of the foreign bodies found are opaque. Vegetable foreign bodies make up 84% of those found stuck in airways—and peanuts are the worst offenders. The most common finding in foreign body obstruction is air trapping, and a large foreign body can completely obstruct the airway. In cases of a suspected foreign body in the airway, an expiration film is needed, either fluoroscopy, decubitus (well-centered), or inspiration/expiration. If a radiologist sees consolidation and air block, he or she should raise the possibility of foreign body aspiration. Complications of asthma in children also are seen by emergency department radiologists; these include pneumonia (uncommon), air block (pneumomediastinum, pneumothorax), obstructive emphysema, and atelectasis. In emergency pediatric patients, the thoracic radiologist also needs to know the radiologic features of pulmonary infection, hydrocarbon pneumonitis, and near drowning.

The First Newborn Chest Film: A Practical Approach

According to Ronald Ablow (New York, NY), "Respiratory difficulty is the most common neonatal problem." The chest radiograph provides the best approach for assessing these difficulties; in general, laboratory and physical findings are not helpful. In this lecture during the Pediatric Imaging plenary session, Dr. Ablow addressed the thoracic radiologists who are not specialists in neonatal radiography but who may need to make a diagnosis very quickly to save the life of a neonate in respiratory distress. The theoretical problem is that at least 31 differential diagnoses must be considered in the face of neonatal tachypnea. Fortunately, the practical approach espoused in this talk showed that only *nine* of these diagnoses are potential surgical emergencies: diaphragmatic hernia and eventration, congenital adenomatoid malformation, chylothorax, lobar emphysema, pneumomediastinum, pneumothorax, pneumopericardium, compression of the trachea, and congenital heart disease. Missing one of these conditions can be disastrous. A missed radiographic interpretation with the much larger nonsurgical group of possibilities should be far less serious.

Ventilatory therapy, antibiotics, suction, surfactant, and so forth are used depending more on the infant's symptoms and perinatal history than on the radiographic findings. Prenatal sonography can detect the most serious diaphragmatic hernia when the stomach is seen above the diaphragm. The radiologist may not always be able to distinguish between hernia and eventration (sometimes surgeons themselves cannot), but in either case, the infant may require surgery. In congenital cystic adenomatoid malformation, cysts are present within the hemithorax and may contain fluid; this potentially fatal problem also may need immediate surgical attention. Prenatal sonography can help detect a chylothorax, allowing immediate postnatal intervention. Instead of the "classic textbook" appearance of lobar emphysema, another surgical emergency, films obtained soon after birth show the mediastinum shifted and the involved lobe filled with fluid (very rarely is this a lower-lobe problem); subsequent films show the pulmonary fluid replaced with air.

Pneumothorax and other complications of air block in the neonate may be very tricky and important: one subtle sign of a pneumothorax is a medial lucency in a child lying on his or her back; on lateral, cross-table views, the radiologist can see anterior air collections and a depressed thymus. With a large pneumothorax, the cross-table lateral view may show a lung "pancaked" posteriorly, a very important finding. Dr. Ablow strongly advised that a child in respiratory distress should never be put on his or her side for a decubitus view, because if the child lies on the "good side," breathing is made even more difficult. Also, radiologists should remember that pneumothorax may contribute to the development or degree of cerebral hemorrhage. Tracheal compression is small and sometimes difficult to see but must be considered in these patients; and, for congenital heart disease, sonography is the safest method of diagnosis.

Radiographic Congestive Heart Failure After Extracorporeal Membrane Oxygenation

George W. Gross (Philadelphia, PA; co-authors: M. S. Kornhouser, J. Cullen) presented a paper describing a study of 90 neonates being treated by extracorporeal membrane oxygenation (ECMO). The patients all satisfied the requirements for undergoing ECMO: severe respiratory failure not responding to maximum medical support, 34 weeks or greater gestational age, and 2000 g or greater birth weight. (Contraindications for ECMO include bleeding disorders and congenital abnormalities not compatible with "reasonable quality of life.") Of the 90 neonates studied, nine showed post-ECMO radiographic congestive heart failure (CHF), which is generally in a stage of resolution 4 days after it is evident on radiographs. To evaluate the etiology and significance of CHF after ECMO, these researchers compared the nine patients with nine other ECMO-treated neonates in whom CHF did not develop. Significant differences were found in net weight gain during ECMO (CHF patients: 797 g and control subjects: 374 g), in mean positive end-expiratory pressure (PEEP, which was lower in CHF patients), and in mean FIO_2. The researchers concluded that radiographic CHF is associated with increased respiratory requirement (at least temporarily) and that the lower PEEP in CHF patients during ECMO may result in increased fluid retention (indicated by the increased weight gain), causing cardiomegaly, pulmonary edema, and CHF.

High-Resolution CT in Thoracic Imaging

Techniques of High-Resolution CT

John R. Mayo (Vancouver, B.C., Canada) led off the Scanlon Symposium with a comprehensive lecture on the technical aspects of high-resolution CT, which potentially offers solutions for the technical problems of two other methods of lung imaging: Chest radiography of the lung is limited because of the overlapping structures within the lung, and the 10-mm slices of conventional CT do not provide sufficient spatial resolution for imaging of lung parenchyma. In the high-contrast environment of the lung parenchyma, high-resolution CT can be optimized for maximum spatial resolution. The spatial resolution of CT depends on machine factors (focal spot size, geometry of tube and detector array, size of detector window, and frequency of data sampling) and user factors (scan collimation, reconstruction algorithm, and field of view [FOV]). The radiologist can control the user factors: Scan collimation makes the greatest difference (1–2 mm collimation provides much better image quality than does 10-mm collimation). Reconstruction algorithms can be configured for either maximum spatial resolution (high spatial frequency or bone algorithm) or maximum contrast (standard or soft-tissue algorithm).

Since the lung structures provide naturally high contrast, the thoracic radiologist should prefer the high spatial frequency or bone algorithm. Although the image-display factor is less important than the other two user factors, the optimal matching of FOV to spatial resolution uses two pixels for the smallest resolvable object; therefore, decreasing the FOV increases spatial resolution, and a 20-cm FOV was suggested to better identify small areas of nodularity. High-resolution CT scans may contain artifacts, including linear-streak, star, and double-fissure. To maximize image quality and minimize artifacts, Dr. Mayo recommends use of a scanner with maximum spatial resolution of less than 0.5 mm, collimation of 1–2 mm, a scan time of less than 3 sec/scan, and use of a high spatial frequency or bone reconstruction algorithm.

Normal and Abnormal Anatomy in Diffuse Lung Disease

After illustrating normal lung anatomy, W. Richard Webb (San Francisco, CA) discussed the four categories of abnormalities seen on high-resolution CT in diffuse lung disease:

reticular opacities, ground-glass opacities, nodules, and cysts. First, reticular opacities may indicate lymphangitic spread of cancer (interlobular septal thickening, nodularity, or bronchovascular interstitial thickening ["cuffing"], prominent intralobular interstitium, and—very importantly—*no* architectural distortion), interstitial fibrosis (irregular septal thickening, irregular interfaces, intralobular interstitial thickening, visible intralobular bronchioles, architectural distortion, and honeycombing), or pulmonary edema (histology similar to lymphangitic spread, smooth interlobular thickening, no architectural distortion—usually diagnosed clinically rather than radiologically).

Second, when high-resolution CT scans show ground-glass opacities, the disease is usually at a treatable stage; however, the finding is nonspecific and may indicate minimal interstitial disease, minimal air-space consolidation, or associated diseases (e.g., active alveolitis, bronchiolitis obliterans with organizing pneumonia, usual interstitial pneumonia, desquamative interstitial pneumonia). Third, nodular or reticulonodular opacities may occur in a variety of diseases, including lymphangitic spread of cancer, sarcoidosis, histiocytosis X, and extrinsic alveolitis. In cases of sarcoidosis, high-resolution CT frequently shows interstitial nodules (3–10 mm); these appear on the scans as subpleural nodules, nodular thickening of the peribronchovascular interstitium, or nodular or irregular thickening of interlobular septa. Fourth, cystic or low-attenuation lesions are present in patients with honeycombing, and they may also be shown by high-resolution CT in patients with histiocytosis X, lymphangiomyomatosis or tuberous sclerosis, emphysema, bronchiectasis, airway disease with air trapping, or other diseases. Radiologists need to remember that cysts can be complex in shape, and multiple cysts can appear to join into one, oddly shaped cyst.

Differential Diagnosis of Chronic Diffuse Infiltrative Lung Disease

Nestor L. Müller (Vancouver, B.C., Canada) discussed the use of high-resolution CT in diagnosing chronic diffuse lung disease. Although chest radiography is still the best imaging method for these diseases because of its low cost and low radiation dose, radiographic findings may be normal in patients with lung disease, and rates of agreement among interpreters may be low (70% in one study). Therefore, high-resolution CT is indicated when chest radiographic findings are (1) normal in a patient with suspected lung disease, (2) nonspecific or questionable, or (3) not compatible with clinical findings and lung function. In a study by Dr. Müller and his colleagues, radiographs and high-resolution CT scans were obtained in 118 patients with chronic infiltrative lung disease: Significant differences were found in correct first-choice diagnosis (57% on radiography, 76% on high-resolution CT), in achieving a high degree of confidence in the diagnosis (23% of radiographs and 49% of high-resolution CT scans), and in making a correct diagnosis when confident (77% on radiography, 93% on high-resolution CT).

In general, the definite diagnosis of chronic infiltrative lung disease should be made on the basis of a combination of clinical and laboratory findings, chest radiography, high-resolution CT (which sometimes can preclude biopsy, depending on the clinical situation, or can help determine biopsy site), and lung biopsy. The indications for high-resolution CT in emphysema are limited because this disease can usually be diagnosed on the basis of clinical, functional, and radiographic findings. High-resolution CT can be useful in diagnosing emphysema in patients with dyspnea or impaired gas transfer and normal findings on chest radiographs and in patients about to undergo bullectomy (bullectomy is most helpful in patients with large bullae—>⅓ of hemithorax—and high-resolution CT can show the size of the bullae and visualize the rest of the lungs). In summary, high-resolution CT can be used in patients with chronic infiltrative lung disease to confirm diagnosis when findings on the chest radiograph are normal or nondiagnostic, to help determine whether transbronchial or open-lung biopsy is appropriate, to determine the best biopsy site, and to guide therapy by indicating extent of disease activity and superimposed complications. Perhaps the most important of these uses is determining the site for biopsy, and high-resolution CT should be used routinely in patients before biopsy.

Pulmonary Edema in Pigs

One of the scientific presentations on potential uses of high-resolution CT dealt with the different mechanisms of pulmonary edema. Dr. J.-G. Im (Seoul, Korea), presenting a paper for himself and his co-authors (Y. J. Yu, M. C. Han, J. H. Park, S. W. Choo, and Y. S. Oh), listed three possible mechanisms of pulmonary edema: increased hydrostatic pressure, decreased colloid osmotic pressure, and increased capillary permeability. In this study, 10 Yorkshire pigs were studied to compare the findings on high-resolution CT (1.5-mm slices) in hydrostatic edema (induced in four pigs) and permeability edema (induced in four pigs); two pigs were used as controls. The scans of the pigs were analyzed for distribution of edema (whole lung or secondary lobule; diffuse, peripheral, or central) and for vascular response (diameter of pulmonary arteries and veins; thickening of bronchial walls).

In distribution of edema caused by increased hydrostatic pressure, high-resolution CT showed an early peribronchovascular collection of extravascular lung water with prominent centrilobular structures and—later—gravity-dependent air-space consolidation; in the secondary lobule, air-space consolidation around the central core and interlobular septa was seen. Permeability edema, on the other hand, was gravity-independent and showed randomly distributed air-space consolidation that was multifocal and patchy; in the secondary lobule, the edema was predominantly peripheral (66%) with a tendency to diffuse. The diameter of the pulmonary artery increased significantly in hydrostatic edema (from 0.65 to 0.87 mm) but did not change in permeability edema. The pulmonary vein also increased in diameter in hydrostatic edema (from 0.65 to 0.80 mm) and decreased significantly in permeability edema (from 0.80 to 0.60 mm). High-resolution CT appears to differentiate between hydrostatic and permeability edema on the basis of their different distributions and vascular responses.

Metastatic Pulmonary Nodules

K. Hirakata (Kitakyushu-shi, Japan) presented a paper written by herself and H. Nakata in which findings on high-resolution CT were correlated with pathologic findings in 87 metastatic pulmonary nodules from 11 inflation-fixed lungs (all from autopsies). Each nodule was classified into one of five histopathologic growing-pattern categories: expanding, alveolar-space-filling, alveolar-cell type, interstitial proliferation type, or mixed type. Also, nodular margins as shown by high-resolution CT were classified into one of four categories: well-defined and smooth, well-defined and irregular, poorly defined and smooth, or poorly defined and irregular.

Correlations showed that all 18 nodules with well-defined and smooth margins showed expanding growth patterns; well-defined and smooth margins also were seen on seven of nine nodules that were classified as alveolar-space-filling. In contrast, 11 (92%) of 12 alveolar-cell nodules had poorly defined margins on high-resolution CT. The high-resolution CT findings also may help distinguish metastatic nodules of hepatocellular carcinoma from those of adenocarcinoma: 22 (76%) of 29 metastatic nodules of hepatocellular carcinoma had well-defined and smooth margins, while 15 (65%) of 23 metastatic nodules of adenocarcinoma had poorly defined and irregular margins; 71% of metastatic nodules of squamous cell carcinoma had irregular margins. These researchers concluded that metastatic nodules show certain different marginal growth patterns on high-resolution CT scans that correlate well with histologic type.

New Techniques in Thoracic Imaging: Three Scientific Papers

Quantitative CT Assessment of Air Trapping in Asthmatic Patients

John Newell (Denver, CO) presented this study of the value of quantitative CT in asthmatic patients (coauthors: K. B. Newman, D. A. Lynch, L. Newman, D. C. Ellegood). Imaging and CT findings were reviewed for 42 adult nonsmokers, 19 of whom had asthma. In all subjects, CT scans (1.5-mm and 10-mm slices, bone algorithm, 30–40 cm field of view) were obtained at the level of the transverse aorta and just above the diaphragm at both end inspiration and end expiration; a density-mask technique was used to calculate the pixel index. (The mosaic pattern on high-resolution CT was evident only in patients with severe asthma.) Other measurements on all subjects included pulmonary function tests and forced expiratory volume in 1 sec, forced vital capacity, functional residual capacity, residual volume, and total lung capacity.

These researchers found that their pixel index was not useful for inspiratory images. However, a clear difference was found between the two groups on expiratory images, for which the pixel index was significantly greater for asthmatic patients: On 1.5-mm slices, pixel index for asthmatic patients was 9.81 vs 1.20 for control subjects; on 10-mm slices, pixel index for asthmatic patients was 4.31 vs 0.19 for control subjects. Dr. Newell stressed that for this pixel technique to be successful, it must be used on the slice just above the diaphragm at expiration. This research indicates that expiratory quantitative CT (1) helps assess air trapping in asthmatic patients, (2) provides pixel indexes that correlate well with residual volume measurements, and (3) may help assess other airways, also.

Detection of Air-Space Consolidation with Advanced Multiple Beam Equalization Radiography

Advanced multiple beam equalization radiography (AMBER) was compared with conventional radiography for detection of air-space consolidation in a study presented by R. D. Nichols (Omaha, NE; co-author: J. Gurney). In AMBER, computer-controlled attenuators equalize film exposure, which results in a chest film that is properly exposed for both the lung and the mediastinum. These researchers wanted to check the possibility that AMBER may be less sensitive than conventional radiography for detecting alveolar consolidation because of AMBER compensation.

Examinations of 30 volunteers (83 lavaged lobes) who had retained lavage fluid were interpreted by three observers using a five-point rating scale. Sixty radiographs were divided into six sets, and AMBER and conventional radiographs were interpreted separately. No difference in observer performance was found, but sensitivity for both imaging methods was low. However, the average grade of consolidation was significantly higher on conventional radiography than on AMBER; also, the correlation with retained fluid was less on AMBER than on conventional radiography (right lung: conventional = 0.487, AMBER = 0.27; left lung: conventional = 0.411, AMBER = not significant). Finally, a significant difference was found in the detectability thresholds of the two methods: of the 262 AMBER zones graded as normal, 17% were graded as definitely abnormal on the correlative conventional radiographs. In contrast, only 8% of the zones graded normal on conventional radiography were graded as abnormal on AMBER. In summary, AMBER appeared to be inferior to conventional radiography for detecting subtle air consolidation, but neither technique has high sensitivity for this entity.

Precise Portable Alignment: The Conundrum and a Solution

Peter B. O'Donovan (Cleveland, OH) presented a grid method of improving the quality of radiographs obtained with mobile equipment (co-authors: G. J. Skipper, A. Salupo, J. Litchney, S. Park). The possible problems faced with mobile radiographic equipment include an upside-down-focused grid, lateral decentering, focus-grid-distance decentering, off-level grid, and (perhaps the most common problem) combined lateral and focus-grid-distance decentering. They used a slip-on focused-linear grid with a focal range of 34–44 in. (resolution = 103 lines/in.; grid ratio = 10:1). In their proposed method, the necessary equipment includes a compact electronic level attached to the grid cassette, a second identical level attached to the collimator housing of the mobile unit and aligned parallel to the central beam, and a counterweight system attached to the second sensor to overcome possible compound-angle error.

Dr. O'Donovan listed some steps that will help provide close-to-precise alignment with mobile radiographic equipment: (1) Ensure focal spot distance is in the range of the grid. (2) Place grid cassette transversely behind the patient. (3) The transverse illuminated cross hair should intersect lines on the handle (midpoint of the short axis of the cassette) and on the "smart" level (midpoint of the opposite short axis). This will ensure no lateral decentering. (4) Activate the electronic level on the grid cassette and note the angle. Minutely adjust the collimator housing until the angle on this sensor matches that of the grid cassette. This ensures no off-level centering. The researchers asked one radiologist a series of six questions about a set of 28 portable radiographs on 14 patients; in each set one radiograph was obtained by using the above-described method and the second radiograph was obtained without a grid. Radiographs were obtained within 48 hr of each other. In *every* case, the radiographs obtained by using their method of alignment were considered significantly better than the radiographs obtained without a grid.

The History and Current Status of Lung Transplantation: The 1992 Benjamin Felson Lecture

As described by Joel D. Cooper (St. Louis, MO), a thoracic surgeon and leader in lung transplantation, early attempts at lung transplantations were not successful: In the 1940s and 1950s, H. Métras worked on lung transplantations in dogs, and J. Hardy first attempted the procedure in humans in the early 1960s. The number of attempted human lung transplantations increased from two in 1963 to seven in 1969 before beginning to decrease steadily to one each in 1975 and 1976. This decrease was due to general lack of success of these transplantations, with the "Achilles heel" being bronchial disruption. Bronchial healing after lung transplantation was affected by rejection, ischemia, and immunosuppression. Once again, researchers turned to studies of canine lung transplants and found that (1) steroids adversely affect wound healing and (2) when transplanted lung was wrapped with omentum, bronchial blood supply was restored within 3 days by collateral vessels from the omentum.

After these experiments, researchers were ready to try lung transplantation in humans again—a procedure that now had a failure rate of 100% (44/44). Tom Hall, a respirator-dependent patient in Toronto, "volunteered to be number 45." He received a lung from the victim of a Montreal traffic accident and survived 6.5 years (dying eventually of renal failure). In 1984, the second successful lung transplantation was done; a young woman given only 1 month to live received a donor's lung that at first seemed "too big." At this point, however, Dr. Cooper and colleagues discovered the wonderful adaptability of the human body, and the "big" lung was successfully transplanted. Dr. Cooper was happy to hear later that Monica, the recipient, was riding a bicycle for exercise, but less happy when he heard she had ridden a motorcycle (his words to her: "Don't you know? Motorcycle riding is for donors, not for recipients").

After these two successful cases were published in *The New England Journal of Medicine*, many pleas for transplants arrived from possible recipients, some of whom needed double-lung rather than single-lung transplantation. Researchers used the heart-lung (or lung-heart) transplantation techniques developed by Shumway at Stanford, but sometimes were replacing the heart in patients who had a good heart but two bad lungs (i.e., they needed "a heart-lung transplant—hold the heart"). In November 1986, the first double-lung transplantation was performed, and that patient still enjoys good health. Of the first seven such procedures performed in 1986, six recipients are still healthy. Despite the two big advantages of double-lung transplantation (increased availability of donor hearts for heart transplantations and preservation of the native heart in the double-lung recipient), several complications of double-lung transplantation caused Dr. Cooper to reconsider use of the procedure. These problems included airway ischemia, bleeding (cystic fibrosis), postoperative cardiac dysfunction, and cardiac denervation. At this point, they stopped doing double-lung transplantations, but, to avoid wasting a donor lung, they successfully began to use a new process called "twinning," in which both lungs from a donor are used, but in two different people who each need single-lung transplants.

Currently, Dr. Cooper's group no longer does en bloc double-lung transplantations; they do, however, perform sequential bilateral lung transplantations during the same operation to replace both lungs in a patient when needed. They tend to use single-lung procedures in patients with such diseases as emphysema, pulmonary hypertension, and pulmonary fibrosis and to use bilateral sequential procedures in patients with cystic fibrosis, in some younger patients with emphysema, and in patients with certain other diseases associated with bilateral infection. They have achieved an 83% 2-year survival rate for single-lung transplantation and a 70% 2-year survival rate for the bilateral procedure.

In the last 7 years, the number of lung transplantations has risen exponentially around the world (one transplantation in 1983 to 340 in 1990). By October 1991, 890 lung transplantations had been performed worldwide in that year, including 191 for emphysema, 119 for emphysema A-1, 180 for idiopathic pulmonary fibrosis, 116 for cystic fibrosis, and 71 for primary pulmonary hypertension. Worldwide, the survival rate (60–68%) of hospitalized patients is increasing with the learning curve.

Radiologic studies in lung transplantations are needed to size donor lungs (although the recipient chest wall does adjust amazingly well to smaller or larger lungs) and to evaluate the status of the transplant. Routine radiologic studies in lung recipients should include chest radiography, quantitative ventilation-perfusion scan, chest CT (particularly helpful in patients with postoperative complications and airway problems), nuclear ventriculography, MR imaging (for pulmonary hypertension cases), and positron emission tomography (currently for research purposes). Dr. Cooper stressed the importance of an immediate posttransplantation study to determine the function of the transplanted lung.

Abstracts of Scientific Papers Presented at the Annual Meeting of the Society of Uroradiology, January 1992

The following are abstracts of presentations made at the annual meeting of the Society of Uroradiology, which was held January 11–12, 1992, in Scottsdale, AZ. They were provided by Robert J. Stanley, who served as chairman of the scientific program, and are reprinted here verbatim.

1. The Imaging Evaluation for Laparoscopic Nephrectomy: *McClennan BL*, Clayman RV (Mallinckrodt Institute of Radiology, St. Louis, MO)

Laparoscopic nephrectomy and later nephroureterectomy were developed after a series of animal studies and first performed successfully in humans at Washington University Medical Center by Drs. Clayman, Kavoussi and colleagues in June, 1990 and May, 1991, respectively. Two unique developments, 1) an organ entrapment device (nonpermeable nylon bag, Lapsac; Cook Urological, Inc.) and 2) an electrical tissue morcellator (Cook Ob-GYN, Inc.) have allowed removal of the kidney—through an 11 mm trocar site. Fifteen (n = 15) adult patients have been evaluated, treated and currently followed (range 2–18 months) to date. A variety of imaging studies were performed prior to and after the laparoscopic procedures. The purposes of this report are:

I. Examine the pre-laparoscopic nephrectomy imaging evaluation in the setting of an evolving (experimental) technique and report the diagnostic efficacy and imaging algorithms in accordance with the growth/learning curve of the procedure.
II. To identify unique anatomic/pathologic requirements for preoperative imaging for laparoscopic nephrectomy patients compared with standard procedures, e.g., open surgical vs. endoscopic dissection/resection.
III. Examine and define the post-operative imaging requirements and complications in this unique patient population.

2. Radiologic Evaluation of the "Miami Pouch": *Amendola MA*, Joseph RC, Guerra JJ, Bejani D, Bloch W, Penalver M (University of Miami School of Medicine, Miami, FL)

Continent urinary diversions are becoming increasingly popular as an alternative to the ileal conduit. The "Miami Pouch" is a new type of continent colonic diversion characterized by its technical simplicity, adequate capacity and high continence rate (over 98%). This paper illustrates the role of radiology in the diagnostic evaluation of the Miami Pouch and in the management of its complications based on our experience with 75 patients. Follow-up ranged from 3 to 66 months. In addition to its typical postoperative radiologic appearance, we will demonstrate examples of complications of the Miami Pouch including: ureterocolonic anastomotic leaks, ureteral obstruction treated with percutaneous dilatation, abdominal abscesses drained percutaneously, and pouch calculi.

3. Pelvic Support in Women: *Barbaric ZL*, Raz S (UCLA School of Medicine, Los Angeles, CA)

The anatomical description of the female pelvic floor in major textbooks and atlases does not correspond to actual findings at surgery. In particular, the levator muscles and tendinous arch in the anterior compartment of the true pelvis are depicted wrongly.

Ten volunteers and ten patients with poor support (moderate to major cystocele and urethrocele) were imaged in oblique coronal plane (MR, T1 weighted images) so that the tendinous arch was in central transverse plane of each image.

The most striking finding in this plane was the lack of space between internal obturator and vagina, and the absence of any appreciable levator musculature. The more posterior levator ani are funnelled, rather than cupped, as presented in the literature.

The obturator fascia in a number of cases was separate from internal obturator muscle, and the space between filled with fat. The internal obturators in patients with cystocele had demonstrative atrophy.

Using both intraoperative and MR findings, we conclude that levator fascia condenses into pubo-urethral, urethro-pelvic, vesico-pelvic, and cardinal ligaments. Condensed fascias, rather than levator muscles, perhaps with the bulk of the obturator muscles, contribute to urethral, bladder and vaginal support.

4. Contrast Extravasation Without Renal Laceration After Blunt Trauma: *Sandler CM*, Lutzker S (University of Texas, LBJ General Hospital, Houston, TX)

Contrast material extravasation on urography and/or body computed tomography from the kidney in patients who have suffered blunt abdominal trauma is generally an indication of a renal parenchymal laceration which involves the collecting system. Two other conditions, however, may result in this finding: 1) avulsion of the ureteropelvic junction and 2) benign pyelosinus extravasation.

We reviewed urograms and/or CT scans in 5 patients who demonstrated contrast extravasation without a renal laceration after blunt trauma. There were 3 cases of UPJ avulsion [2 adults (1 partial, 1 complete), 1 child (complete)] and 2 cases of benign pyelosinus extravasation. In each instance an accurate diagnosis can be made by CT. UPJ avulsion either shows non-filling of the ureter (complete avulsion) or that the contrast extravasation originates outside the kidney near the UPJ. This may be distinguished from benign pyelosinus extravasation in which the UPJ appears intact and the origin of the extravasated contrast material may be traced into the renal sinus. Benign pyelosinus extravasation after blunt trauma has not been previously well described. It presumably results from clot caused obstruction of the collecting system or ureter following a renal contusion. In one of our cases, a relative UPJ obstruction associated with a horseshoe kidney may have been a contributing factor.

5. Natural History of von Hippel Lindau Associated Renal Lesions: Observations on Serial Computed Tomography: *Choyke P*, Weiss G, Walther M, Glenn G, Zbar B, Thakore K, Linehan WM (National Institutes of Health, Bethesda, MD)

The objective of this study was to determine the natural history of renal lesions in von Hippel Lindau (VHL) disease. To date, 280 patients have been screened for VHL as part of a linkage study to isolate the genetic defect in this disease. Enhanced abdominal CT was employed in all cases and revealed renal lesions in 59 patients, 6 of whom had renal cysts but did not have evidence of VHL by either other imaging or linkage criteria. Twenty-three patients had solid renal masses and cystic lesions while the remaining patients had only cystic lesions. Of the 53 patients (ages 22–84) with VHL associated renal lesions, 20 have had follow-up CT scans over a period ranging from 8 months to 6 years (mean 1.8 years). During this period no lesion has metastasized. In 16 patients several lesions have enlarged; in 5 of these new lesions developed. In 4 patients there has been no change. A decrease in size of one or more cysts was seen in 5 patients and a scar formed at the site of the former cyst. The progression of a complex cyst to solid lesion was observed in only two patients followed over 4–6 years. The pathologic material available (7 patients) supports the concept that there is great diversity among the VHL associated lesions.

This study shows a range of biologic activity in VHL associated renal lesions and suggests that the process of lesion development, growth and involution is dynamic and complex. These results may have implications for understanding molecular genetic abnormalities associated with initiation and progression of this malignancy as well as for growth patterns in sporadic renal tumors.

Drs. Choyke et al. received first prize and a $5000 research award.

6. Phase III Clinical Trial of Iodixanol (Non-ionic, Isotonic) as a Body CT Contrast Agent: Genitourinary and General Results: *Thornbury JR* (University of Wisconsin Hospital & Clinics, Madison, WI)

A Phase III, randomized, double-blind, 3 group, parallel IV contrast study is being conducted at the University of Wisconsin from July through November, 1991. The contrast is Iodixanol, a water soluble, non-ionic, isotonic dimer (Sterling Research Group). Seventy-five adult patients will be recruited (with 20 patients consenting through August). All are outpatients in stable condition already requiring body CT examination. Each patient receives either Iodixanol 270 or 320 or Omnipaque 300 (3 randomized groups of 25 patients each). All examinations are done on the newest software version of a 9800 Advantage GE CT system. Blood pressure, pulse, and blood and urine parameters pre- and post-injection are obtained. Examinations are being evaluated in concert by two radiologists blinded to which contrast agent was received. Results represent forced choice consensus of the two observers. Genitourinary tract as well as related anatomic visualization is graded for quality of imaging features. Results of this evaluation and reaction rates and types will be presented.

7. Renal Colic: Ultrasonography and Plain Film And/Or IV Urography? *Dalla-Palma L*, Stacul F, Bazzocchi M (University of Trieste, Cattinara Hospital, Trieste, Italy)

Urography (IVU) is considered a primary tool in patients with renal colic, but in the last years ultrasonography (US), possibly associated with the plain film (PF) of the abdomen, was suggested as an alternative approach.

On the basis of a previous research carried out in our department by experienced uroradiologists, we personally supported the idea of investigating these patients with US and PF (diagnostic accuracy 85%). More recently, we began a prospective study to see if this approach could be suggested in an Emergency Department, where several radiologists with different levels of experience are involved. All patients with firm diagnosis of renal colic who arrived at the Emergency Department in 1991 were enrolled. They immediately underwent PF and US (kidneys and bladder). One hundred and six patients were investigated up to June 30 and underwent a clinical and radiological follow-up.

Our preliminary data in this prospective study suggest: 1) PF and US together are a good screening test (sensitivity 97%, specificity 70%); 2) IVU is useless when stones passed (20% in the first 48 hours); 3) IVU is useless when PF and US are negative (negative predictive value 98%); 4) IVU is to be performed only when a non-medical treatment is advisable; and 5) IVU is redundant in at least 70% of the cases.

8. Imaging of the Hemi-Kock Ileal Bladder Substitute: *Dorph S*, Steven K, Thomsen HS (Herlev Hospital, Herlev, Denmark)

Bladder substitution with Hemi-Kock pouch was carried out in male patients after radical cystectomy for bladder cancer without involvement of the prostate.

The Kock pouch used for continent diversion is provided both with an afferent reflux preventing valve and an efferent valve to achieve continence. They are created by invaginating the afferent and efferent ileal segments into the reservoir and securing the intussusceptions with staples.

In contrast, the Hemi-Kock pouch only has an afferent valve while the outlet consists of a direct anastomosis between the pouch and the posterior urethra. Continence is achieved by the external urethral sphincter situated just distal to the anastomosis. The procedure is not applicable in females, since radical cystectomy requires excision of the entire urethra.

Since 1987, 44 male patients have undergone Hemi-Kock urinary diversion to the urethra at our institution. Each patient was evaluated radiographically in the immediate postoperative period and at regular postoperative intervals. The radiographic appearance of the normal Hemi-Kock pouch is demonstrated and the postoperative complications reviewed. In addition, the relation between capacity, shape and function of the mature Hemi-Kock pouch is described by cystometry and cystography in selected patients.

9. The Value of Measuring Renal Parenchymal Thickness Before Renal Biopsy: *Webb JAW*, Roger SD, Beale AM, Cattell WR (St. Bartholomew's Hospital, London UK)

Reduced renal length is widely used to diagnose chronicity in patients with renal impairment. A length of 9 cm or less is considered to indicate chronic irreversible disease. We noted that some patients with normal renal length had thin parenchyma and decided to correlate ultrasonographically measured renal length and parenchymal thickness with histology obtained at renal biopsy.

Fifty-four patients aged 16 to 76 years who had had renal biopsy were evaluated retrospectively. Histology was considered in five categories: I—Interstitial nephritis (8), II—Glomerulonephritides (26), III—Diabetes mellitus/metabolic (6), IV—Chronic renal disease (CRD) (11), V—Vascular (3).

There was good linear correlation between renal length and mean parenchymal thickness ($r = 0.64$, $p < 0.001$). Both were reduced most in patients with CRD. Seven of the 11 patients (64%) with CRD had parenchymal thickness 1.5 cm or less, compared to 33% in Group V, 16.5% in Group III, 12.5% in Group I and 7.7% in Group II. Although 8/31 (25%) of patients whose serum creatinine had increased 3 months post biopsy had parenchymal thickness 1.5 cm or less, so did 4/19 (21%) whose creatinine decreased.

Like renal length, parenchymal thickness gives an indication of the chronicity of renal failure. However, some patients with parenchymal thickness 1.5 cm or less, still have potential for improvement.

10. Renal Transplant Biopsy: Comparison of Trucut Needle and Monopty Device: *Baumgartner BR*, Carlock K (Emory University Hospital, Atlanta, GA)

Various imaging modalities have been proposed for the evaluation of renal transplant dysfunction. Renal biopsy, however, remains an essential part of this evaluation in patients with suspected transplant rejection. This study compares the efficacy and safety of two biopsy techniques. All biopsies were performed in the ultrasound suite after the kidney transplant was localized with sonography and the position marked.

Over a 16-month period, 57 transplant biopsies were performed in 56 consecutive patients using a 14-gauge Trucut needle. The number of passes ranged from 1-5. Over a subsequent 8-month period, 91 transplant biopsies were performed in 68 consecutive patients using the disposable 18-gauge Monopty device. The number of passes ranged from 2-7. Adequate tissue was obtained in 53/57 (93%) Trucut biopsies and 88/91 (97%) Monopty biopsies. Eleven complications occurred with the Trucut needle. Seven were minor (gross hematuria without transfusion), but four were major and included bleeding requiring transfusion, ureteral obstruction by clots resulting in nephrostomy or nephrectomy or elevated creatinine. Eight complications (9%) occurred with the Monopty gun; seven were minor and only one major (hematuria requiring transfusion). Renal transplant biopsy with the Monopty device appears to be a simple procedure with very high yield of adequate tissue cores and fewer major complications than the Trucut needle biopsy.

11. Spectrum of Hysterosalpingography Findings After Myomectomy: *Karasick S*, Lev-Toaff AS, Ehrlich S (Thomas Jefferson University Hospital, Philadelphia, PA)

After myomectomy for infertility, approximately 60% of women fail to become pregnant. Postoperative hysterosalpingography (HSG) is then performed to evaluate the uterine cavity, particularly in regard to recurrent myoma, uterine synechia, and tubal obstruction. The purpose of this study is to describe the spectrum of HSG findings in post-myomectomy patients.

In 22 women, HSG findings after myomectomy were reviewed and correlated with the location of the myomata at surgery. Abnormalities of the uterine cavity were noted in 19 of 22 patients; 3 normal studies were seen in patients with pedunculated subserous myomas. Eleven (50%) had abnormalities consisting of small mass impressions suggesting residual/recurrent myomas. Mucosal irregularity, seen in 13 of 22 patients (59%), is of uncertain significance when found alone, but probably suggests the diagnosis of myoma when there is concomitant distortion or mass effect (8 of 13). Five patients (23%) had gross distortion of the uterine cavity while four (18%) had myometrial contrast intravasation. One patient had uterine synechiae. There were no cases of proximal tubal occlusion. Resection of submucous and intramural myomas were often associated with mucosal irregularity, uterine distortion and suggestion of residual/recurrent myoma; mucosal irregularity and uterine distortion occasionally followed resection of subserous fibroids, perhaps related to surgical technique.

Hysterosalpingography is frequently used to evaluate infertile patients after myomectomy. Familiarity with the spectrum of post-operative HSG findings is useful in interpretation of these studies and may assist in the clinical management of these patients.

12. Excretion of Contrast Media During Renal Failure: *Golman K* (Malmo General Hospital, Malmo, Sweden)

In order to use contrast media for measurement of the glomerular filtration rate, it is important to know how much of the given dose that leaves the body extrarenally. This is especially important if the GFR is close to zero.

We have examined the extrarenal clearance of all commonly used contrast media in a rabbit model where renal failure has been imitated. In order to understand the mechanism of the extrarenal excretion, some experimental iodinated contrast media and new NMR contrast media were included in the study. During total absence of renal function all the examined contrast media were excreted with a rate of <2% of the dose/hour. Large differences between the individual contrast media were found. The reason for this will be discussed based on our knowledge of membrane physiology.

Dr. Golman tied for third prize and received $500 (half the $1000 award).

13. Primary Aldosteronism: CT Evaluation: *Dunnick NR*, Gunnells JC, Leight GS Jr, Leder RA, Roubidoux MA, Kurylo L (Duke University Medical Center, Durham, NC)

Primary aldosteronism is an uncommon but curable cause of hypertension. Patients with an aldosterone secreting adenoma must be distinguished from those with bilateral adrenal hyperplasia, as surgical removal of the adenoma is curative while hyperplasia is treated medically. In order to assess the ability of CT to detect and localize aldosterone secreting adenomas, our experience with this disease over the past eight years was reviewed.

Twenty-seven patients with biochemically proven primary aldosteronism were studied. Fifteen patients were found to have an aldosterone secreting adenoma at surgery. CT correctly identified the adenoma in 13 of these patients (sensitivity 87%). The two false negative studies underwent surgery based on a lateralizing adrenal venous hormone sampling. They were found to have small adenomas measuring 0.9 cm and 1.1 cm in diameter.

There were no false positive CT examinations in the ten patients with bilateral adrenal hyperplasia. Two of these patients underwent surgery for either an equivocal CT finding or a lateralizing adrenal venous hormone sampling. In both of these patients, adrenal cortical hyperplasia with small nodules was confirmed histologically.

We conclude that CT is a sensitive method of detecting aldosterone secreting adenomas. Contiguous 5 mm collimation is recommended, with narrower collimation for equivocal examinations.

14. CT and US Guided FNA of Renal Masses: Miller JH, *Jafri SZH*, Bernacki EG, Roberts JL, Madrazo BL (William Beaumont Hospital, Royal Oak, MI)

Fine needle aspirations of renal masses guided by computed tomographic and sonographic means were reviewed. Ninety-six patients studied from January of 1985 through August of 1991 at our institution included 65 patients guided by CT and 31 by US. In 51 patients, renal lesions were classified as solid, the remaining 45 cases were not definable as simple cyst by sonography or CT and therefore, warranted additional workup. Disease entities diagnosed included: renal cell, transitional cell and squamous cell carcinoma, lymphoma, metastasis, oncocytoma, angiomyolipoma and abscess. Complications were minimal and included 2 pneumothoracis. The technique, limitations, success and results of fine needle aspiration of renal masses will be discussed.

15. Antegrade Urethral Catheterization: *Lee WJ*, Badlani GH (Long Island Jewish Medical Center, New Hyde Park, NY)

Retrograde urethral access is the standard way to access the bladder. Frequently, retrograde access is not possible due to various clinical situations such as impassable urethral stricture, false passage, and the presence of a prosthetic device in the penis. Antegrade urethral access can be achieved by percutaneous puncture of the bladder. Percutaneous bladder access is an extension of the endourological techniques learned for the upper tract. The access to the bladder may be obtained by one of three methods: under fluoroscopic guidance, under direct vision using flexible cystoscopy, and if necessary, under ultrasonic guidance. Most of our procedures have been performed either under fluoroscopic guidance, and/or under direct cystoscopic control. We present the technique in representative cases of antegrade catheterization and manipulation using fluoroscopy in seven patients and a combination of cystoscopy and fluoroscopy in ten patients. The success rate is high and morbidity is significantly lower than performing these procedures in an open surgical manner. These access techniques have been combined with other endourological techniques of lower urinary tract manipulation such as urethral stents, etc.

16. Ureteral Stenting with a Self-Expandable Stent: *Castaneda WR*, Hunter DW, Maynar M, Hulbert J, Gonzalez R (University of Minnesota Medical School, Minneapolis, MN)

The use of balloon expandable and/or self-expandable stents in the ureter has not been recommended in the ureter due to early occlusion of the stent lumen by hyperplastic urothelium. This problem has been reported in animals with normal ureteric peristalsis. We report in four patients in whom a fibrotic, rigid, segment of ureter was dilated and subsequently stented as a last result after multiple failed balloon dilations and prolonged stenting in four patients with post-surgical strictures. The results and long-term follow-up will be presented.

17. Follow-Up of 70 Patients with Benign Ureteric Strictures Treated by Percutaneous Transluminal Dilatation: Predictive Factors for Long Term Success: *Beckmann CF*, Roth RA (Lahey Clinic Medical Center, Burlington, MA)

Balloon dilatation of benign ureteric strictures was performed in 70 patients followed by placement of 7-10F stents for four to eight weeks. During the follow-up period of one to 69 months, the overall success rate was 73%. The success rate in primary strictures at the ureteropelvic junction was 77%. Among 26 patients with post-surgical anastomotic (pyeloplasty, ureteroenterostomy, ureteroneocystostomy) strictures, dilatation remained successful in 61%. Of seven patients with post-operative strictures following calculus removal by ureterolithotomy or pyelolithotomy, five (71%) had good results. All patients with iatrogenic, post ureteroscopic strictures (nine patients) or accidental ureteral ligation (three patients) had a normal follow-up pyelogram. The success rate in acute strictures of less than three months durations is 85%; in strictures of longer than three months duration the success rate was 67%. On the average, failures occurred within ten months of the dilatation.

Etiology, length, and duration of the stricture are the primary determinants of success. Early intervention with balloon dilatation is suggested.

18. Renal Embolotherapy: Parenchymal Sparing Techniques: *Mitty HA*, Javit DJ, Train JS, Abramson AF (Mount Sinai Medical Center, New York, NY)

Renal artery embolotherapy has a vital role in the management of A-V fistulas, bleeding, or renal lesions which are prone to bleed. Basic to this form of treatment is the desirability of sparing as much normal parenchyma as possible. Newer catheters and guidewire systems have made this an attainable goal. Most notable among these technical advances are smaller catheters in the range of 3 French or less such as the Tracker system. In addition, use of conventional 4 or 5 French catheters with hydrophilic coated guidewires also allows good subselectivity. Newer coils which are compatible with these small catheter systems are available as embolic agents along with polyvinyl alcohol foam (PVF), alcohol, and Gelfoam particles.

Ten patients with indications for parenchymal sparing embolotherapy were treated with these newer catheter techniques. Four patients had persistent post renal biopsy bleeding and one had a post biopsy A-V fistula causing renal failure. Two patients had symptomatic angiomyolipomas embolized as the sole form of treatment. One patient had a vascular malformation embolized with PVF. One patient with a solitary kidney and a mass requiring resection had preoperative devascularization of the segment of kidney to be resected. In each instance, the choice of catheter-guidewire system and embolic agent resulted in successful management of the pathology with minimum damage to adjacent normal parenchyma.

19. Transcalyceal Brush Biopsy of Renal Parenchymal Tumors: *Banner MP*, Ramchandani P, Pollack HM (University of Pennsylvania School of Medicine and Hospital, Philadelphia, PA)

While fluoroscopically-guided, retrograde transureteral brush biopsy of pyelocalyceal filling defects is currently a standard method of establishing the diagnosis of urothelial renal neoplasms, the procedure has had, traditionally, an otherwise limited range of usefulness. We have encountered three problematic cases in which the diagnosis of suspected urothelial tumor could not be confirmed by means of noninvasive imaging, including retrograde pyelography with fluorscopically-guided brush biopsy. Transcalyceal advancement of a wire guide and catheter into an upper pole renal mass allowed for brush biopsy of the interior of a renal tumor. Cytology was positive in each case. No complications were encountered. Insertion of a Teflon sheath in the ureter facilitated retrograde catheter advancement and parenchymal puncture.

This technique, a logical extension of brush biopsy methodology, eliminated the risks associated with passage of a ureteroscope to the upper pole collecting system or of percutaneous biopsy of a possible urothelial or vascular parenchymal neoplasm. It allowed us to diagnose a transitional cell carcinoma which had completely obstructed the upper pole infundibulum, differentiate between renal cell carcinoma and invasive transitional cell neoplasm, and between renal and adrenal carcinoma in a patient with hematuria following flank trauma.

20. Doppler Sonography of Severe Renal Artery Stenosis: Slowed Systole in the Downstream Vascular Bed: *Patriquin H*, Fontaine A, Filiatrault D, Garel S, O'Regan S (Hopital Ste. Justine, Montreal, Quebec, Canada)

Purpose: Severe stenosis of an artery slows systolic flow in the arterial bed distal to it. Handa described an Acceleration Index (AI), which provides a measurement of the slope of systole seen on Doppler spectral display. The AI relates the systolic upsweep to time and to the frequency of the systolic Doppler shift. Does severe renal artery stenosis slow systole in intrarenal arteries in children? Does the AI reflect this slowing?

Methods: We examined the intrarenal arteries of 16 children with suspected stenosis of the main renal artery with renal angiography and duplex Doppler ultrasound. The AI of 3 segmental arteries in each kidney was calculated.

Results: Nine children (13 arteries) showed abnormal, slowed, blunted systolic Doppler curves with AIs ranging from 0.7–2.7. Nine children (12 arteries) showed a >80% reduction in vessel diameter at angiography, and one had a 360° turn of the renal artery. Seven children (11 arteries) had normal Doppler curves (AI > 3.8, ranging from 3.8–10). At angiography, 10 of these renal arteries were normal, and one had a stenosis estimated at 60–70%. Five stenotic arteries were treated. Systolic Doppler curves returned to normal at the first post-treatment examination (1–10 days later).

Conclusion: The Doppler examination of the intrarenal arteries mirrors the effects of severe renal arterial stenosis and may prove to be a valuable part of the examination for severe renal artery stenosis.

Drs. Patriquin et al. received second prize and a $3000 research award.

21. Transvaginal and Transabdominal Color Doppler Sonography of Ovarian Masses: A Correlation with Gross and Microscopic Pathology: *Fleischer AC*, Kepple DM, Rodgers WH, Williams LC, Jones HW III (Vanderbilt University Medical Center, Nashville, TN)

This study correlates the transvaginal and transabdominal color Doppler sonography of 50 excises ovarian masses with their gross and microscopic pathology. Color Doppler sonography was performed either with a 5 Mhz curvilinear transvaginal or 3.75 Mhz transabdominal transducer connected to a Toshiba 270 scanner. The vascular signals were evaluated according to three main parameters including (1) impedance—low PI less than 1.0, intermediate—1.0 to 1.5 or high—greater than 1.5, (b) location, peripheral or central (within 1 cm from the capsule) and (c) maximum systolic velocity (low—less than 15 cm per second, high—greater than 15 cm per second).

Of the 11 malignancies included in this study, all had low impedance, four had peripheral and four central vascularity, four having high maximum systolic velocity, four low. In contrast, of the 33 benign lesions, 24 had high impedance, 5 low impedance, and only 2 had areas of vascularity within septa. Using these parameters, a specificity of 92%, sensitivity of 100%, negative predictive value of 100%, positive predictive value of 79% was obtained.

Microscopic evaluation indicated that abnormal flow and vessels even less than 1 mm could be detected if the velocity was sufficient (1 cm/s). Vessels with low impedance tended to have a paucity of smooth muscle intima although some rapidly growing benign tumors and ones associated with vasodilatation also demonstrated low impedance.

This work will describe the potentials and limitations of this technique for distinguishing benign versus malignant ovarian lesions.

22. Lasix-Enhanced Renal Ultrasound—Can it Diagnose Obstructive Processes?: *Fernbach SK*, Maizels M, Riden D, Conway JJ (The Children's Memorial Hospital, Chicago, IL)

Neonates (babies less than eight weeks of age) with prenatally diagnosed hydronephrosis undergo many studies to confirm the diagnosis and to differentiate between the many causes of hydronephrosis. Voiding cystourethrography is routine. Diuresis renography has been an important and commonly used tool to diagnose urinary tract obstruction. We have performed a conventional nonhydrated urinary tract ultrasound in 20 neonates and correlated it with renography and ultrasound performed after standardized IV hydration and Lasix injection. The appearance of the post-Lasix ultrasound was specifically correlated with 1) the T ½ clearance of the almost simultaneous diuresis renography and 2) the surgical/pathological findings in the population. This was done to determine if hydrated ultrasound could be used to diagnose urinary tract obstruction.

The post-Lasix ultrasound demonstrated many anatomic changes in appearance: the development of hydronephrosis, an increasing degree of hydronephrosis, changes in the morphology of a previously dilated system, dilatation of the distal ureter. We will present the grading systems used in the study and the results of the correlative studies.

23. Histopathologic Correlation of Resistive Index in Patients with Intrinsic Renal Disease: *Cronan JJ*, Deyoe LA, Esparza A (Rhode Island Hospital, Providence, RI)

Purpose: To correlate resistive index (RI) with histopathologic changes in patients with intrinsic renal disorders.

Materials & Methods: Forty-two patients with renal disease due to intrinsic disorders underwent duplex ultrasound at the time of percutaneous renal biopsy. Renal length, assessment of cortical echogenicity, RI, age and serum creatinine were obtained. The specimens were placed into minimal, mild, moderate, and severe categories based on the grading (0–4) of the following: arteriosclerosis, arterial vasculitis, interstitial fibrosis, interstitial edema, interstitial infiltrate. Glomerular pathology was graded separately (0–4) based on cell proliferation, inflammatory infiltrate, sclerosis, and crescents.

Results: Eleven patients had an elevated RI (range .74–.86, mean .79). Thirty-one patients had a normal RI (range .50–.69, mean .55). An elevated RI correlated with a significantly more severe, arterial or interstitial histopathology, and an elevated serum creatinine. There was no statistically significant difference in severity of glomerular histopathology. A normal RI in a patient with a normal serum creatinine was significantly associated with a minimal or mild histopathologic grade. No significant correlation was seen between RI and renal length or cortical echogenicity.

Conclusion: Patients with suspected intrinsic renal disease and an elevated serum creatinine correlated with severe interstitial or vascular histopathology. Patients with a normal serum creatinine and a normal RI correlated with a minimal or mild interstitial or vascular histopathology.

24. Transrectal Ultrasound Evaluation of Patients Following Radical Prostatectomy: *Hattery RR*, King BF, Wilson TM (Mayo Clinic and Mayo Foundation, Rochester, MN)

Transrectal ultrasound is employed as a method of evaluation of the prostatic fossa and vesicle neck following radical prostatectomy for prostatic carcinoma. Transverse had longitudinal ultrasound images are obtained for evaluation of recurrent neoplasm and as an adjunct to ultrasound-guided transrectal needle biopsy to obtain tissue for diagnosis. Normal postoperative anatomy of the vesicle neck and prostatic fossa will be reviewed. The results of transrectal ultrasound will be compared with tissue obtained with transrectal needle biopsy. The ultrasound findings related to neoplasm will be illustrated and, in selected cases, correlated with CT and MR examinations. Data obtained on approximately 30 patients will be reviewed as part of the presentation.

25. Virchows' Node (Left Supraclavicular Lymph Node) in Retroperitoneal Neuroblastoma—US, CT and MRI Findings: *Berdon WE*, Ruzal-Shapiro C (Babies Hospital, New York City, NY)

Stage IV neuroblastoma kills ... There are, however, a group of neuroblastoma patients with spread beyond the abdomen but not to bone but to lymph nodes; we report six such patients with left supraclavicular nodes either at DX (5) or later (1) ... 5/6 survive! The term IVN (for nodal) has been suggested; the use of MRI has probably increased the detection before surgery.

26. Urinary Tract Infection in Infants in Spite of the Prenatal Diagnosis of Hydronephrosis: Dacher JN, Mandell J, *Lebowitz RL*, (Children's Hospital, Boston, MA)

Prenatal diagnosis of hydronephrosis by obstetrical ultrasonography offers the potential benefit of preventing postnatal urinary infection by means of continuous antibiotic prophylaxis. To examine the efficacy of this approach, we prospectively studied 426 such infants who underwent postnatal uroradiologic evaluation between January 1984 and June 1991. Boys treated at birth for posterior urethral valves (13) were excluded. Thirteen of the remaining 413 infants (3.1%) presented with urinary infection in the first six months of life. Ten were boys and 7 of these were not circumcised. Only 2 of the 13 were breast fed. Bacteriology results were available for 10 infections; urine and/or blood cultures grew *E. coli* in 4, *Staphylococcus* in 3, *Enterobacter* in 2, and *Klebsiella* in 1. All of the bacteria were resistant *in vitro* to ampicillin, the most commonly prescribed antibiotic for prophylaxis in neonates. The causes for hydronephrosis were vesicoureteral reflux in 6 (3 with the so-called megacystics megaureter association), ureteropelvic junction obstruction in 6 (with coexisting ipsilateral reflux in 4, 3 mild and 1 severe), and primary megaureter in 1. The presence of reflux, the foreskin, formula feeding, and resistant organisms all seem to be important risk factors. Four categories of "management failure" were identified: not communicating the prenatal diagnosis (2), not prescribing antibiotics (4), antibiotics prescribed but not administered (2), and urinary infection in spite of prophylaxis (5). The overall success of continuous antibiotic prophylaxis is good. However, communication, treatment, and follow-up can be improved. Infection with an organism resistant to the commonly used prophylactic antibiotic remains a problem.

27. Ectopic Ureterocele in Adults with a Comparison of the Anomaly in Children: Amitai M, *Hertz M*, Jonas P, Apter S, Heyman Z (Chaim Sheba Medical Center, Tel-Hashomer, Israel)

Ectopic ureteroceles, while not uncommon in children, have been reported only rarely in adults. We present 5 adults with ectopic ureteroceles with emphasis on the varied clinical and radiographic manifestations. These findings will be compared with those in 32 children with ectopic ureterocele.

It was found that the clinical presentation differed in adults and children, but the radiological findings were similar. The diagnosis was in some cases delayed for many years. The anomaly could not be detected by imaging means in 2 of 5 adults and 8 of 32 children, and was found only at surgery.

28. Differentiation of Oncocytoma from Carcinoma by Computed Tomography: *Davidson AJ*, Hayes WS, Hartman DS, Davis CJ Jr (Armed Forces Institute of Pathology, Washington, DC)

We studied the hypothesis that oncocytoma and carcinoma of the kidney can be differentiated by CT criteria and that differences would become more apparent as tumors enlarged. On enhanced scans, homogeneous density throughout the tumor and a centrally placed, sharply defined, stellate area of lower density were considered radiologic analogues respectively of absence of necrosis and a central scar and predictors of a tissue diagnosis of oncocytoma. Any inhomogeneous density except for a stellate, central pattern was used as an analogue for necrosis and a predictor of carcinoma. Numerical scores were assigned for each criteria by three independent observers. Tissue from each tumor was evaluated independently by a pathologist. Sixty-four oncocytomas and 64 carcinomas were evaluated. For proven oncocytomas larger than 9 square centimeters, 65% exhibited the radiologic criteria for oncocytoma and 35% met the criteria for carcinoma; for small oncocytomas, the respective results were 90% and 10%. For large carcinomas, 85% fulfilled the criteria for malignancy and 15% were incorrectly predicted to be oncocytomas. The respective results for small carcinoma were 50% for each category. It is concluded that the computed tomographic criteria used in this study are poor discriminants in predicting the diagnosis of oncocytoma or carcinoma regardless of tumor size.

29. Male Urethral Trauma: The Need for a New Unified Classification Encompassing Pure Anterior, Pure Posterior and Combined Anterior-Posterior Injuries: *Goldman SM* (Francis Scott Key Medical Center, Baltimore, MD)

Most uroradiologists (and uroradiology textbooks) currently use the McCallum and Colapinto Classification for defining traumatic injuries to the urethra. This classification fails to include anterior urethral injuries. More important, the McCallum and Colapinto Type III injury really is a combined anterior-posterior injury and should be classified separately from the purely membranous injuries. We believe that there is a need for a single unified classification of urethral injuries which combines this concept. We believe this approach to be more pathologically correct and more easily understood by radiology and urology residents, as well as practicing radiologists and urologists. We suggest the following:

I. Pure Anterior Urethral Injuries
II. Pure Posterior Urethral Injuries
   A. Urethra intact but stretched with prostatic avulsion (the McCallum and Colapinto Type I Injury)
   B. Rupture of the membranous urethra above the congenital diaphragm (old classic posterior urethral injury, the McCallum and Colapinto Type II Injury)
III. Combined Anterior Posterior Urethral Injury with Disruption of the UG Diaphragm (McCallum and Colapinto Type III Injury)

30. The Cost of Self-Referral for Uroradiological Examinations: A New Evaluation of Patients Presenting with Difficulty Urinating and Urinary Tract Infections: *Hillman BJ*, Olson G, Griffith P, Sunshine J, Joseph CA, Kennedy S, Bernhardt LB (Univ of Arizona Med Ctr, Tucson, AZ)

In previous research, we assessed the effect of non-radiologists' ownership of imaging technology on their utilization of imaging in evaluating men with difficulty urinating. Physicians self-referring their patients for imaging performed four times as many examinations as physicians who referred their patients to radiologists.

Using a new insurance claims database (United Mine Workers of America Health and Retirement Funds) representing a more rural, older population, and evaluating a broader range of technologies, we used our previous methods to evaluate both men having difficulty urinating and patients with possible urinary tract infections. We compared the frequency of imaging, the charges per episode of medical care, and the charges per relative value unit of the examinations performed attributable to self- and radiologist-referring physicians.

For both clinical presentations studied, self-referring physicians performed imaging more than twice as frequently as radiologist-referring physicians. Imaging-related charges per episode of difficulty urinating were 2.3 times as great for self-referring physicians as radiologist-referring physicians, 2.2 times as great per episode of possible urinary tract infection. Charges when corrected for the complexity of examinations were higher for self-referring physicians than radiologist-referring physicians in office practice. All of these results were statistically significant ($P < 0.01$, unpaired t test).

These results both validate and expand the results of our previous work in a very different patient population. Self-referral for diagnostic imaging results in higher utilization, higher charges, and greater overall cost per episode of care.

Drs. Hillman et al. tied for third prize and received $500 (half the $1000 award).

31. Pelvic CT Findings After Radical Prostatectomy: Summers RM, *Korobkin MT*, Ellis JH, Quint LE (University of Michigan Medical Center, Ann Arbor, MI)

Purpose: To evaluate the CT appearance of the pelvis after radical prostatectomy in patients, with and without clinical evidence of local tumor recurrence.

Materials and Method: Pelvic CT scans were retrospectively reviewed in 22 patients who underwent radical prostatectomy for prostate cancer from 1 month to 4 years earlier.

Results: The bladder base was in a retropubic location, in the bed of the resected prostate, in 20 patients. Soft tissue simulating normal seminal vesicles was present in 20 and a transversely oriented bar of soft tissue density between the bladder base and the rectum was present in 14. Four of the 5 patients with clinical and/or pathologic evidence of local tumor recurrence had findings not seen in the other 17 patients: asymmetry or abnormal thickening of the rectal wall in 2, and a soft tissue nodule in the bed of the resected prostate or seminal vesicle in the other 2.

Conclusions: Knowledge of the normal variations in the CT appearance of the pelvis after radical prostatectomy is necessary to correctly identify local tumor recurrence. Tissue in the bed of the seminal vesicles and between the bladder base and the rectum are normal findings. Nodular asymmetry of this tissue and rectal wall abnormalities suggest recurrent tumor.

32. Postoperative Abdominal CT Evaluation Following Radical Nephrectomy for Renal Cell Carcinoma (RCC): Ramchandani P, *Pollack HM*, Coleman BG, Banner MP (The Hospital of the University of Pennsylvania, Philadelphia, PA)

Postoperative abdominal CT scans on patients who had undergone radical nephrectomy for RCC were reviewed to determine the frequency of recurrent disease in the abdomen as detected by CT scanning, and thereby, reassess the need for annual CT scans of the abdomen (as is common practice). We also attempted to identify the normal structures which migrate into the renal bed and which can simulate the appearance of a recurrence ("pseudomass"). Three hundred forty postoperative abdominal CT scans on 100 patients were reviewed. Scans were obtained 1–21 years after surgery.

Renal bed recurrence was seen in 5 patients, all of whom had carcinomas initially larger than 6 cm. Malignant ascites with peritoneal seeding was seen in 2. No neoplasms were detected in the contralateral kidney in the study period. A new adrenal mass developed in one patient.

The liver, colon, duodenum, and bowel migrated into the right renal fossa. The spleen, pancreatic tail, duodenum, and bowel did so on the left. On serial scans, postoperative anatomy was consistent. Problematic "pseudomasses" were seen most often on the left.

In this series, renal bed recurrence of renal cell carcinoma was uncommon, related to original tumor size and usually occurred within 2 years of nephrectomy. Annual CT surveillance may reach a point of diminishing cost effectiveness when carried out for many years.

33. Correlation of CT and Ultrasound of Perirenal and Abdominal Regions with Insulin Resistance: Preliminary Results: *Rosenfield AT*, Camp A, Black HR (Yale Univ. School of Medicine, New Haven, CT)

The correlation of CT and ultrasound of perirenal and abdominal regions in patients with insulin resistance was evaluated to further define the relationship of metabolic process with fat distribution and texture.

Insulin resistance has been shown to have an association with hypertension, as well as to be a significant cardiovascular risk factor. An android body fat distribution has also been shown to correlate with coronary artery disease; the CT scan is the most precise measurement of central obesity. Ultrasound provides a sensitive method of identifying the echogenicity of fat in the perirenal and subcutaneous regions. The purpose of our study was to evaluate abdominal fat distribution both intra-abdominal and subcutaneous as well as central and peripheral; in addition, the texture in several regions including subcomponents of the perirenal space such as within the renorenal fascia and within the bridging fascial planes, and the pararenal spaces was studied. These were all correlated with insulin resistance.

Seven patients were initially studied with the euglycemic insulin clamp and hyperglycemic clamp to test insulin sensitivity. On the same day, ultrasound and computed tomograms of the abdomen including the perirenal and subcutaneous regions were obtained. Slices through the nipple level, the umbilical level, and the mid thigh on CT also were performed. These patients were subsequently put on therapy with celiprolol, a vasodilating beta blocker, which is a selective B_1-adrenoreceptor antagonist and B_2-adrenoreceptor agonist. At the end of six weeks, the insulin resistance studies, CT, and ultrasound were then repeated. Correlation was determined between the echogenicity of perinephric and subcutaneous regions on ultrasound, the distribution of fat on CT, and insulin resistance.

34. Diuresis Renography: Recent Advances and Recommended Protocols: *O'Reilly, PH* (Stepping Hill Hospital, Stockport, Cheshire, England)

Diuresis renography is widely accepted as a useful technique for the evaluation of dilated upper urinary tracts and to distinguish between obstructed and non-obstructed systems. In our unit, an equivocal rate of 15% has been found making management decisions difficult in this group. In addition, some concern has been felt over poor correlation in the literature with perfusion pressure flow studies.

Recent work has been directed towards reducing the equivocal rate and improving interpretation of the renogram. This has been comprised of detailed analysis of urinary flow rates at differing levels of renal function, the timing of furosemide for optimum washout responses, and investigation of the choice of radiopharmaceutical with particular reference to the use of 99mTc-MAG3. These studies have led to improved technique and interpretation with a reduction in the equivocal rate to less than 5%. They have also enabled the production of a series of standard protocols for the performance and interpretation of diuresis renography in clinical practice.

35. The Results of a Standardized Diuretic Renogram Protocol for Neonatal Hydronephrosis: *Conway JJ*, Maisels M, Weiss S, Fernbach S, Everett J (The Children's Memorial Hospital, Chicago, IL)

A consortium of members of the Society of Fetal Urology and the Pediatric Nuclear Medicine Club cooperated to formulate a standardized diuretic renogram protocol in an effort to define in a uniform manner those factors which best relate to the diagnosis and management of obstructive urinary tract disease in the newborn.

Twenty-five hospitals in the United States and Great Britain are enrolled in this program. Approximately 400 neonates with hydronephrosis have been entered into the registry since 1989 and approximately 150 of the infants since the fall of 1990 have been studied using the standardized diuretic renogram protocol.

Eighty-five of these children were examined at The Children's Memorial Hospital. Sixteen have had surgery and form the basis for this report. A good correlation of the surgical findings is found with the subjective impression of obstruction which utilizes multiple findings such as the degree or grade of hydronephrosis (3 or 4), the estimated loss of renal function in the affected kidney and the diuretic response ½ time. Our data indicates an eight-fold increase in urine output is observed following hydration and the use of furosemide in the neonate.

The consortium of subspecialists in Pediatric Urology and Nuclear Medicine provides a unique opportunity for future scientific research which can form the basis for other studies in Uroradiology.

36. Urine Profiles and Kidney Histology Following Mannitol and Different Doses of Iohexol in Gentamicin Nephropathy During the Degeneration Phase: *Thomsen HS*, Dorph S, Golman K, Larsen S, Horn T, Svendsen O, Skaarup P, Hemmingsen L (Herlev Hospital, University of Copenhagen, Herlev, Denmark)

The effect of intravenous saline, mannitol (16%), and iohexol 350 mg I/ml (1 ml/kg BW, 2-½ ml/kg BW, 5 ml/kg BW, and 10 ml/kg BW) on urine profiles (albumin, glucose, sodium and the enzymes: NAG, LDH, BG, GGT, AP, and AAP), serum profiles (iohexol conc. (3 h post injection), potassium, sodium, creatinine, albumin, glucose, and urea) and kidney histology (light and electron microscopy) was studied in 80 male rats with gentamicin nephropathy (a tubulointerstitial nephritis). The contrast medium, mannitol and saline were injected during the beginning of the degeneration phase of gentamicin nephropathy (= after 8 daily injections of 40 or 20 mg/kg BW gentamicin).

The preliminary results show varying effects of various doses. The dose of 2,5 and 5,0 ml/kg BW caused a higher increased excretion of some of the urine components and more histologic changes than 10 ml/kg BW. Also a small dose 1 ml/kg BW caused significant changes compared to saline and other doses. In contrast, lowering the dose of gentamicin by 50% was an effective method of avoiding changes in the excretion of various urine components as well as the histologic changes.

The final results will be presented at the meeting.

Forthcoming Articles

FELIX FLEISCHNER LECTURE

Imaging the respiratory system in the first few years after the discovery of the X-ray: the contributions of Francis H. Williams, M.D. *Greene R*

MALLINCKRODT SYMPOSIUM

The Edward Mallinckrodt Institute of Radiology: 60th anniversary rededication program. *Murphy WA Jr*

Government and radiology during the next 60 years. *Evens RG*

Radiology research: a strategic plan for the 90's. *Vannier MW*

Radiology ethics. *Armstrong JD II*

The hidden curriculum. *Anderson DJ*

SPECIAL ARTICLE

Perspective. Radiologic evaluation of a Renaissance painting. *Robbins AH, Wetzner SM, Marini M*

CARDIOPULMONARY RADIOLOGY

Value of sonography in determining the nature of pleural effusion: analysis of 320 cases. *Yang P, Luh K, Chang D, Wu H, Yu C, Kuo S*

Case report. Lung torsion after percutaneous needle lung biopsy. *Graham RJ, Heyd RL, Raval VA, Barrett TF*

Pleuropulmonary paragonimiasis: radiologic findings in 71 patients. *Im J, Whang HY, Kim WS, Han MC, Shim Y, Cho S*

Pictorial essay. CT evaluation of poststernotomy complications. *Templeton PA, Fishman EK*

BREAST RADIOLOGY

Case report. Mammographic appearance of loiasis. *Britton CA, Sumkin J, Math M, Williams S*

GASTROINTESTINAL

Epithelioid hemangioendothelioma of the liver: imaging findings with pathologic correlation. *Miller WJ, Dodd GD III, Federle MP, Baron RL*

Hereditary hemorrhagic telangiectasia: findings in the liver with color Doppler sonography. *Ralls PW, Johnson MB, Radin DR, Lee KP, Boswell WD*

Case report. Langerhans cell histiocytosis of the liver: imaging findings. *Radin DR*

Pictorial essay. Operative cholangiography in patients undergoing laparoscopic cholecystectomy: unique radiographic findings. *Balachandran S, Goodman P, Saydjari R, Hogge MW, Leonard MH*

Pictorial essay. Mucocele of the appendix: imaging findings. *Madwed D, Mindelzun R, Jeffrey RB*

Case report. Bowel ischemia and perforation after cocaine use. *Endress C, Gray DG, Wollschlaeger G*

GENITOURINARY RADIOLOGY

Calcified renal stones and cyst calcifications in autosomal dominant polycystic kidney disease: clinical and CT study in 84 patients. *Levine E, Grantham JJ*

Diagnosis of placenta previa during the third trimester: role of transperineal sonography. *Hertzberg BS, Bowie JD, Carroll BA, Kliewer MA, Weber TM*

Ovarian cysts are common in premenarchal girls: a sonographic study of 101 children 2–12 years of age. *Cohen HL, Eisenberg P, Mandel F, Haller JO*

Case report. Prolapsing inverted papilloma of the prostatic urethra. Diagnosis by transrectal sonography. *Occhipinti K, Kutcher R, Gentile RL*

MUSCULOSKELETAL RADIOLOGY

Pictorial essay. Diseases of the lumbar spine: findings on fat-suppression MR imaging. *Tien RD, Olson EM, Zee CS*

Case report. Ewing's sarcoma of the hand. *Escobedo EM, Bjorkengren AG, Moore SG*

VASCULAR RADIOLOGY

3D time of flight MR angiography using a surface coil: evaluation in 12 subjects. *Hendrix LE, Strandt JA, Daniels DL, et al.*

MR imaging of symptomatic peripheral vascular malformations. *Rak KM, Yakes WF, Ray RL, et al.*

Budd-Chiari syndrome: detection with color Doppler sonography. *Ralls PW, Johnson MB, Radin DR, Boswell WD, Lee KP, Halls JM*

Extrinsic compression of the superficial femoral artery at the adductor canal: evaluation with intravascular sonography. *The SH, Wilson RA, Gussenhoven EJ, et al.*

Insertion of Hickman central venous catheters by using angiographic techniques in patients with hematologic disorders. *Cockburn JF, Eynon CA, Virji N, Jackson JE*

Atherectomy of the distal aorta using a "kissing balloon" technique for the treatment of blue-toe syndrome. *Clugston RA, Eisenhauer AC, Matthews RV*

Technical note. Misplaced Wallstent during transjugular placement of an intrahepatic portosystemic shunt: retrieval using a loop snare. *Sanchez RB, Roberts AC, Valji K, Lengle S, Bookstein JJ*

INTERVENTIONAL RADIOLOGY

Occult glove perforations: frequency during interventional radiologic procedures. *Hansen ME, McIntire DD, Miller GL*

NEURORADIOLOGY

Review. CNS complications of cocaine abuse: incidence, pathophysiology, and neuroradiology. *Brown E, Prager J, Lee H, Ramsey RG*

Review. MR imaging of the spinal cord: current status and future advances. *Sze G*

Review. MR imaging in the management of extracranial malignant tumors of the head and neck. *Hudgins PA, Gussack GS*

Evolution of white matter lesions in neurofibromatosis type 1: MR findings. *Sevick RJ, Barkovich AJ, Edwards MS, Koch T, Berg B, Lempert T*

Cerebellar and cerebral abnormalities in Rett syndrome: a quantitative MR analysis. *Murakami JW, Courchesne E, Haas RH, Press GA, Yeung-Courchesne R*

High-signal foci in brain MR: observer variability in their quantification. *Yetkin FZ, Haughton VM, Fischer ME, et al.*

Case report. Iatrogenic air in the cavernous sinus. *Adams M, Quint DJ, Eldevik OP*

Perspective. Current role of cerebral angiography in the diagnosis of cerebrovascular diseases. *Wolpert SM, Caplan LR*

COMPUTERS IN RADIOLOGY

A PACS-based interactive teaching module for radiological sciences. *Sinha S, Sinha U, Kangarloo H, Huang HK*

MEMO TO AUTHORS

The composition of abstracts for *AJR* articles. *Berk R*

MEETING NEWS

Society of Gastrointestinal Radiologists, 21st annual meeting: February 1992. *Whalen E*

Letters

Adverse Reaction to Contrast Material in a Patient Treated with Local Interleukin-2

Systemic treatment with interleukin-2 (IL-2) can result in sensitization to contrast material [1, 2]. We report a case of an adverse reaction to contrast material in a patient treated with local IL-2; that is, IL-2 applied at a high and constant concentration at a tumor site.

A 78-year-old man with advanced carcinoma of the bladder was treated with continuous local perfusion of the bladder with high doses of natural IL-2 (Biotest, Germany) for 6 weeks. The procedure was a modification of one described previously [3]. A portable infusion pump (Deltec CADD-1; Pharmacia, Piscataway, NJ) allowed perfusion of the bladder via a suprapubic catheter on an outpatient basis. At the time IL-2 treatment was started, excretory urography with 100 ml of Conray 30 (Byk Gulden, Konstanz, Germany) showed that the left kidney was nonfunctional. CT scans obtained after 6 weeks of treatment showed that the bladder tumor had regressed; however, a new pelvic mass was present in the left kidney. Percutaneous urography with 20 ml of Urografin 30% (Schering, Berlin, Germany) showed hydronephrosis of the left kidney, no evidence of a tumor, and no extravasation. One hour after the procedure, the patient's condition deteriorated rapidly; he became dyspneic and began vomiting. Six hours after the procedure, his blood pressure had increased to 220/120 mm Hg. Intensive care was necessary because of possible cardiac failure. A chest radiograph showed pulmonary edema. No evidence of cardiac decompensation or general infection was found. The diagnosis was hypersensitivity reaction to contrast material. The patient responded quickly to corticosteroids and symptomatic treatment, and 2 days later, local treatment with IL-2 was tolerated as before.

Reactions to contrast material can occur in patients treated with IL-2 who have not had toxic reactions to IL-2, and such reactions clearly have been associated with IL-2 therapy. We have developed methods of IL-2 treatment that are highly effective and do not result in toxic reactions to IL-2 [3, 4]. When we began administering IL-2 by inhalation for treatment of pulmonary metastases of renal cell carcinoma, the first three patients became hypersensitive to contrast material during the first 6 weeks of treatment. All had hypertension, vomiting, dyspnea, and skin edema, and all responded to corticosteroids and symptomatic treatment. We were using excretory urography to monitor response to IL-2 treatment, and each patient had received nonionic contrast material (6–10 ml of Angiografin; Schering) several times.

REFERENCES

1. Zukiwski AA, David CL, Coan J, et al. Increased incidence of hypersensitivity to iodine-containing radiographic contrast media after interleukin-2 administration. *Cancer* **1990**;65:1521–1524
2. Oldham RK, Brogley J, Braud E. Contrast medium "recalls" interleukin-2 toxicity. *J Clin Oncol* **1990**;8:942–943
3. Huland E, Huland H. Local continuous high dose interleukin 2: a new therapeutic model for the treatment of advanced bladder carcinoma. *Cancer Res* **1989**;49:5469–5474
4. Huland E, Huland H, Heinzer H. Interleukin-2 by inhalation: local therapy for metastatic renal cell carcinoma. *J Urol* **1992**;147:344–348

Hans Heinzer
Edith Huland
Hartwig Huland
University Clinic Eppendorf
D-2000 Hamburg 20, Germany

A Useful Sign for Distinguishing Clustered Skin Calcifications from Calcifications Within the Breast on Mammograms

Recognition of skin calcifications in the breast is essential in order to avoid unnecessary biopsies. When the breast is compressed during mammography, calcifications in the skin are often projected within the breast on several views, giving the impression that the calcifications are intramammary. Several clues to a benign intradermal origin have been described [1–3]. They include peripheral location in at least one projection, round or polygonal shape, low particle density, central radiolucencies, multiplicity, and bilaterality.

In the absence of these well-recognized features, distinguishing an isolated cluster of skin calcifications from malignant microcalcifications can be difficult. When morphologic analysis is unreliable, a biopsy may be recommended. However, clustered skin calcifications have another characteristic that, to my knowledge, has not been described previously.

A cluster of microcalcifications inside the breast is contained in a volume of tissue that has three dimensions. Thus, the arrangement of the particles on the film is determined by the projection and is different in each view. Because skin is thin, dermal calcifications can be thought of as being distributed in a plane or a disk that has only two dimensions. When projected within the breast, the disk of skin containing the calcifications is nearly perpendicular to the incident beam and is seen en face. As a result, the arrangement of particles appears the same regardless of which projection is used (Fig. 1).

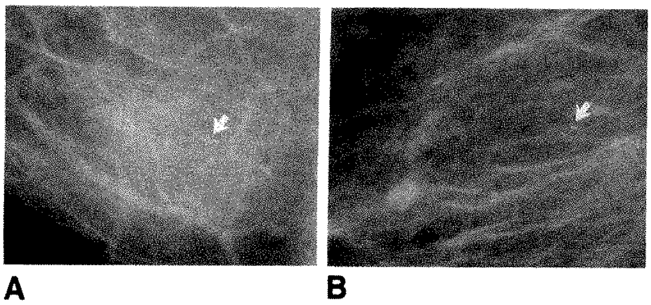

Fig. 1.—*A* and *B*, Close-ups of craniocaudal (*A*) and 45° oblique (*B*) mammograms show isolated cluster (*arrows*) of microcalcifications projected within breast. Note that patterns formed by the particles are identical.

I have observed this characteristic often in the past 2 years. Each time the correct nature of the calcifications was confirmed by using a localizing grid to place an opaque marker on the skin and then obtaining a tangential view of the area [4]. In several instances, recognizing the presence of identical patterns of calcific particles resulted in the cancellation of biopsies that would have been unnecessary.

Steven B. Sitzman
The Malden Hospital
Malden, MA 02148

REFERENCES

1. Kopans DB, Meyer JE, Homer MJ, Grabbe J. Dermal deposits mistaken for breast calcifications. *Radiology* **1983**;149:592-594
2. Homer MJ, Marchant DJ, Smith TJ. The geographic cluster of microcalcifications of the breast. *Surgery* **1985**;161:532-534
3. Rebner M. Breast calcifications: differential diagnosis. In: Feig SA, ed. *AARS Categorical Course Syllabus*. Reston, VA: American Roentgen Ray Society, **1988**
4. Berkowitz JE, Gatewood OMB, Donovan GB, Gayler BW. Dermal breast calcifications: localization with template-guided placement of skin markers. *Radiology* **1987**;163:282

Motion Artifact Simulating Aortic Dissection

I read with interest the article by Burns et al. [1], "Motion Artifact Simulating Aortic Dissection on CT." The authors state that an artifact was seen with scanners with 1-sec scan time but not with scanners with 1.2- to 5-sec scan times and postulated that the finding was caused by motion of the aortic wall during systole and diastole. It was not seen when several heartbeats occurred during the image acquisition. My colleagues and I are quite familiar with this artifact, having observed it many times with an ultrafast CT scanner with imaging times of 50 msec (Fig. 1). We too are uncertain as to the cause of the artifact, but we concur with Burns et al. that it is important to be aware that such an artifact may occur with various types of scanners. As in their cases, we found that the artifact was generally confined to one or two slices at the level of the main pulmonary artery. Our slices were 8 mm thick.

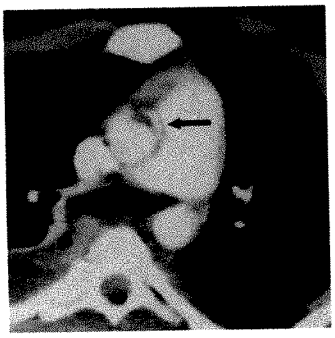

Fig. 1.—Ultrafast CT scan (acquisition time, 50 msec) obtained at level immediately above aortic valve shows a simulated aortic dissection (*arrow*).

William Stanford
University of Iowa College of Medicine
Iowa City, IA 52242

REFERENCE

1. Burns MA, Molina PL, Gutierrez FR, Sagel SS. Motion artifact simulating aortic dissection on CT. *AJR* **1991**;157:465-467

A Giant Meckel's Diverticulum in an Adult

Meckel's diverticulum is an unusual cause of abdominal distress in adults and may be difficult to diagnose in this age group. We describe a case of a giant Meckel's diverticulum in an adult.

A 63-year-old man had had intermittent, crampy abdominal pain for 4-5 days. Physical examination showed diffuse, vague sensitivity to abdominal palpation with maximum tenderness in the right lower quadrant. An abdominal radiograph obtained with the patient erect showed multiple air-fluid levels in the small bowel. A CT scan showed a mass 6 × 9 × 7 cm adjacent to and above the right posterior wall of the urinary bladder (Fig. 1). A sonogram showed a thick-walled, fluid-filled pelvic mass with many internal echoes; the mass was thought to be an abscess. A drainage catheter was inserted percutaneously. Initially, the material draining from the catheter was cloudy yellow, but it soon became feculent and bile stained. Contrast material injected through the catheter flowed into the small bowel. At surgery, a Meckel's diverticulum 12 × 9 × 6 cm was found. The drainage catheter penetrated the wall of the diverticulum and extended into the lumen. Peritoneal leakage had occurred around the catheter, with omental encasement of the area.

Meckel's diverticulum is the most common congenital abnormality of the small bowel; it occurs in approximately 2% of the general population. The lifetime complication rate associated with Meckel's diverticulum varies greatly, from 15% to 33%. Most complications occur in children [1].

In an adult, Meckel's diverticulum is usually asymptomatic and frequently is found incidentally at laparotomy performed for another reason. Few of the diverticula in adults contain gastric mucosa, and compared with diverticula in children, fewer are detected with radionuclide scanning. In adults, enteroclysis is more useful than scintigraphy is for diagnosis. A Meckel's diverticulum typically appears as a blind pouch of the distal ileum and contracts like the adjacent bowel. Preoperative diagnosis of an inflamed Meckel's diverticulum based on CT findings was recently reported [2].

Giant Meckel's diverticulum is rare, accounting for less than 0.5% of all the vitelline duct remnants. Two forms have been described.

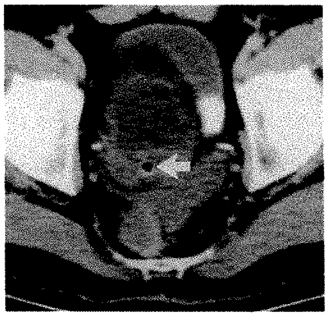

Fig. 1.—Giant Meckel's diverticulum in a 63-year-old man. CT scan of pelvis shows a mass displacing urinary bladder toward left. Note solitary dependent gas bubble (*arrow*) in mass.

Type I is a long lesion, with a transverse diameter approximately equal to that of the ileum. Type II is an ovoid pouch [3]. Some authors [4] reserve the term "giant" for type II lesions that are more than 5–6 cm in diameter. Obstruction and volvulus are the most common complications in giant Meckel's diverticulum, even in children.

The appropriate treatment for asymptomatic Meckel's diverticulum has been a topic of debate in the literature. In one of the largest reported series of cases in adults, Leijonmarck et al. [1] concluded that asymptomatic Meckel's diverticulum found incidentally should not be resected. In their study, the complication rate from resection was 6%. Projected complication rates for in situ Meckel's diverticulum were calculated at 2% for patients 30 years old and near 0% for older patients.

B. S. Rose
D. L. Pretorius
Aultman Hospital
Canton, OH 44710

REFERENCES

1. Leijonmarck CE, Bonman-Sanselin K, Frisell J, Raf L. Meckel's diverticulum in the adult. *Br J Surg* **1986**;73:146–149
2. Nigogosyan M, Dolinskas C. CT demonstration of inflamed Meckel diverticulum. *J Comput Assist Tomogr* **1990**;14:140–142
3. Miller DL, Becker MH, Eng K. Giant Meckel's diverticulum. *Radiology* **1981**;140:93–94
4. Torii Y, Hisatsune I, Imamura K, Morita K, Kumagaya N, Nakata H. Giant Meckel diverticulum containing enteroliths diagnosed by computed tomography and sonography. *Gastrointest Radiol* **1988**;14:167–169

Spontaneous Resolution of Peliosis of the Liver and Spleen in a Patient with HIV Infection

An uncommon condition characterized by multiple blood-filled cavities in the hepatic parenchyma, peliosis hepatis occurs in association with chronic wasting disorders and usage of a variety of drugs [1]. Peliosis also occurs in other parts of the reticuloendothelial system and elsewhere. Resolution appears to be rare [1, 2]. Spontaneous resolution of a previously reported case of peliosis of the liver and spleen in a patient with HIV infection [3] is the subject of this letter.

CT scans of a 34-year-old man who was seropositive for antibodies to HIV showed hepatosplenomegaly, diffuse small hypodense hepatic and splenic nodules, and portal and retroperitoneal lymphadenopathy. Most of the liver lesions became isodense after administration of IV contrast material. Most of the splenic lesions did not enhance. Liver biopsy indicated peliosis hepatis. No treatment was given. The patient returned 18 months later with fever and cough. CT scans showed resolution of hepatosplenomegaly and of the focal hepatic and splenic lesions. Cephalocaudal liver span had decreased from 19 cm to 16 cm. Cephalocaudal spleen span had decreased from 18 cm to 12 cm. Hepatic and splenic parenchyma was homogeneous both before and after administration of contrast material. Portal and retroperitoneal lymph nodes had decreased in size but were still enlarged. Sonography showed normal homogeneous echogenicity of the hepatic and splenic parenchyma. Cultures of sputum, stool, and blood specimens grew *Mycobacterium avium-intracellulare*. A lesion on the hard palate was thought to be Kaposi's sarcoma. Antituberculous therapy was begun, and the patient was discharged to an AIDS hospice facility. Liver biopsy was not performed.

Groos et al. [2] reported a case of peliosis associated with long-term use of oxymetholone. Resolution of hepatomegaly and restoration of normal liver function occurred when oxymetholone was discontinued. Spontaneous regression of hepatic lesions, as shown by CT and decrease of serum alkaline phosphatase level, was reported in an elderly woman with peliosis hepatis thought to be due to rapid weight loss [1]. Although peliosis hepatis has been described in other patients with HIV infection [4, 5], evidence of resolution of the lesions has not been reported. However, spontaneous disappearance of cutaneous Kaposi's sarcoma has been described in a man with AIDS. The disappearance was coincident with worsening of his immune status, as indicated by the onset of pulmonary tuberculosis, *Pneumocystis carinii* pneumonia, and cerebral toxoplasmosis [6]. It has been suggested that in patients with HIV infection, both Kaposi's sarcoma and peliosis hepatis might be due to abnormal angiogenesis promoted by the inappropriate secretion of immunoregulatory factors that act on vascular endothelium [4, 5]. Spontaneous resolution of peliosis and Kaposi's sarcoma suggests that the effects of the endothelial stimulation are somehow reversible.

D. Randall Radin
Los Angeles County-University of Southern California Medical Center
Los Angeles, CA 90033-1084

REFERENCES

1. Simon DM, Krause R, Galambos JT. Peliosis hepatis in a patient with marasmus. *Gastroenterology* **1988**;95:805–809
2. Groos G, Arnold OH, Brittinger G. Peliosis hepatis after long-term administration of oxymetholone. *Lancet* **1974**;1:874
3. Radin DR, Kanel GC. Peliosis hepatis in a patient with human immunodeficiency virus infection. *AJR* **1991**;156:91–92
4. Devars du Mayne JF. Hepatic vascular lesions in AIDS. *JAMA* **1985**;254:53–54
5. Scoazec JY, Marche C, Girard PM, et al. Peliosis hepatis and sinusoidal dilatation during infection by the human immunodeficiency virus (HIV): an ultrastructural study. *Am J Pathol* **1988**;131:38–47
6. Janier M, Vignon MD, Cottenot F. Spontaneously healing Kaposi's sarcoma in AIDS. *N Engl J Med* **1985**;312;1638–1639

Retroperitoneal Fibrosis

I read with interest Dr. Amis's excellent review article on retroperitoneal fibrosis [1]. It describes in detail the possible causes and the clinical and pathologic findings and emphasizes with beautiful examples the importance of cross-sectional imaging in the diagnosis of this disease.

Historically, it is true that Albarran (1905) was the first to describe retroperitoneal fibrosis and that Ormond rediscovered the disease in 1948. In the interim, however, in the French and German literature, several authors reported cases of retroperitoneal fibrosis. Bachrach, in his German textbook of urology (1928), distinguished two forms of retroperitoneal fibrosis: one diffusely involving the retroperitoneum and one limited to the periureteral region.

Additional cases were reported by Pérard and Orsini (1937), Rischar (1937), Lebbin (1942), and Dieckow (1942). In some of these cases as in the one by me and a colleague in 1988 [2], perirenal-peripelvic localization was a finding.

References to the reports on retroperitoneal fibrosis published before Ormond's article, from 1928 to 1942, can be found in my article of 1966 [3].

Juri V. Kaude
University of Florida, College of Medicine
Gainesville, FL 32610-0374

REFERENCES

1. Amis ES Jr. Retroperitoneal fibrosis. *AJR* **1991**;157:321–329
2. Yancey JM, Kaude JV. Diagnosis of perirenal fibrosis by MR imaging. *J Comput Assist Tomogr* **1988**;12:335–337
3. Kaude J. Retroperitoneal fibrosis. *Acta Radiol [Diagn]* **1966**;4:331–343

Hemoperitoneum Due to Traumatic Avulsion of a Pedunculated Uterine Leiomyoma

A 50-year-old woman was brought to the emergency department after being struck by a car when she was crossing the street. She had severe pelvic and moderate lower abdominal pain. Her abdomen protruded slightly and was slightly tender on palpation. Her blood pressure was 110/40 mm Hg, and her pulse rate was 112 beats per minute. The initial hematocrit was 34% (0.34); it dropped to 30% within 1 hr.

Abdominal and pelvic CT scans with oral and IV contrast material were obtained at 10-mm contiguous intervals. They showed a moderate amount of free intraperitoneal fluid, pelvic fractures, and no significant retroperitoneal hematoma. Discrete round masses surrounded by free intraperitoneal fluid were present within the pelvis (Fig. 1A). These were thought to represent leiomyomas. Because of the absence of apparent injury to other intraperitoneal organs, a ruptured or avulsed leiomyoma was suggested as the possible source of intraperitoneal bleeding.

At laparotomy, the peritoneal cavity contained approximately 2 l of free blood. The bleeding site was a transected vessel supplying a large pedunculated uterine leiomyoma (one of two) that had been partially avulsed at its base. A hysterectomy and bilateral salpingo-oophorectomy were performed. The patient's postoperative course was uneventful.

Pathologic examination of the uterus after surgery showed multiple uterine leiomyomas. The uterine cavity was obliterated by a large leiomyoma. Several small leiomyomas were present in the subserosa, and two pedunculated leiomyomas 7 cm in diameter extended inferiorly and laterally on each side of the uterus. The leiomyoma on the right side was partially avulsed, with transection of the feeding vessels (Fig. 1B).

The size and calcium content of the leiomyomas and a fracture of the pelvis in the absence of injury to other organs led us to suggest avulsed leiomyoma as the cause of the intraperitoneal bleeding. We found only one previous report [1] of traumatic avulsion of a uterine leiomyoma in a patient with pelvic trauma.

Jeff Drutman
University of Utah Hospital
Salt Lake City, UT 84132
Daniel M. Fruechte
Holy Cross Hospital
Salt Lake City, UT 84114

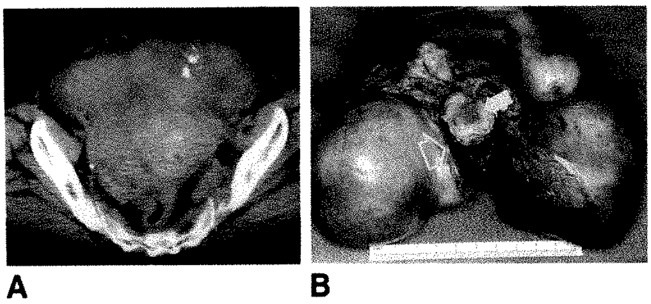

Fig. 1.—Hemoperitoneum due to traumatic avulsion of a pedunculated uterine leiomyoma.

***A*, CT scan shows large calcified leiomyoma, adjacent intraperitoneal blood, and fracture of left iliac wing.**

***B*, Anterior view of gross specimen shows two large pedunculated leiomyomas extending inferiorly and laterally on either side of uterine cervix (*solid arrow*) and partial avulsion of leiomyoma (*open arrow*) on right side. Several more leiomyomas are present in uterine body and fundus.**

REFERENCE

1. Venables CW, Craft IL. Haemoperitoneum after traumatic avulsion of uterine fibroid. *BMJ* **1967**;3:723–724

Hysterosalpingography in England

We read with interest the review article by Yoder and Hall [1], "Hysterosalpingography in the 1990s." We recently did a survey by mail in the Merseyside region of England to ascertain the techniques used in departments that perform hysterosalpingography. We thought it would be useful to compare the techniques used on the two sides of the Atlantic.

Eight centers (seven district general hospitals and one university teaching hospital) replied. The number of hysterosalpingographic examinations performed in 1 year ranged from 48 to 127 (mean, 96). Thirty-eight percent of the examinations were performed by gynecologists and radiologists working together, 38% by gynecologists working alone, and 25% by radiologists working alone.

All respondents indicated that the Leech-Wilkinson cannula was the one used most often for instillation of contrast medium. Fifty percent sometimes altered their technique to incorporate use of a balloon catheter, which was preferred by gynecologists. A Cusco's speculum was used for visualization of the cervix in 88% of cases and a Sims's speculum in 13%. All examinations were performed with the patient supine. Sedation was given routinely in 25% of cases. Most centers obtained three hysterosalpingograms: one to show uterine filling, one to show tubal filling, and one (delayed) to show peritoneal spillage. All respondents emphasized that screening was kept to a minimum. One center regularly used antispasmodic agents (e.g., glucagon) to overcome tubal spasm, and one indicated that turning the patient to the prone position was done to try to overcome tubal obstruction of the flow of contrast medium. No centers were using tubal catheterization techniques.

All centers used water-soluble contrast media; low-osmolar agents were used in 63% of cases. Only one center obtained transvaginal sonograms before hysterosalpingography was performed. No centers were using insufflated air as the contrast agent. The new sonographic contrast agent (Echovist) is currently undergoing trials before release in the United Kingdom [2].

D. E. Roberts
G. C. Markham
Royal Liverpool Hospital
Liverpool, England

REFERENCES

1. Yoder IC, Hall DA. Hysterosalpingography in the 1990s. *AJR* **1991**;157:675–683
2. Schlief R, Deichert U. Hysterosalpingo-contrast sonography of the uterus and fallopian tubes: results of a new contrast medium in 120 patients. *Radiology* **1991**;178:213–215

Reply

We appreciate the comments from Drs. Roberts and Markham. Their small survey suggests that in Liverpool as in the United States no more than a quarter of hysterosalpingograms are done by radiologists alone, and that the majority are performed by a gynecologist alone or jointly with a radiologist. We hoped that, among other things, our review [1] would encourage more radiologists to become involved in hysterosalpingography. We think that radiologists' skills in imaging, in fluoroscopic technique, and in the interpretation of transvaginal sonograms and MR images are essential to successful performance and interpretation in this procedure.

It is of interest to us that all the respondents in the Roberts and Markham survey preferred the cannula technique and used water-soluble contrast media. We use and recommend the balloon catheter. This type of catheter allows removal of the speculum and enables the patient to move easily on the fluoroscopy table so that oblique and supine views, which better show uterine and tubal abnormalities, can be more readily obtained. Multiple views avoid the pitfall of a single-dimension projection and thus increase the diagnostic accuracy of the procedure. We would not sacrifice that accuracy for fear of excessive exposure to radiation, as careful fluoroscopic technique will minimize exposure. Finally, we do advocate the use of water-soluble contrast medium, but we do not use low-osmolar agents routinely because of their high cost in the United States.

Isabel C. Yoder
Deborah A. Hall
Massachusetts General Hospital
Boston, MA 02114

REFERENCE

1. Yoder IC, Hall DA. Hysterosalpingography in the 1990s. *AJR* **1991**; 157:675–683

Retrieval of a Coil Embolus: The Enemy of Good Is Better

Embolization is a safe and effective technique for treatment of acute gastrointestinal hemorrhage [1]. Recently, we treated acute hemorrhage from a proximal branch of the gastroduodenal artery by placing three 3-mm stainless steel coils (Cook, Inc., Bloomington, IN) in the artery. The third coil produced near occlusion of the bleeding branch, and *one last coil* (a fourth coil) was positioned just above it to ensure complete occlusion. Placement of the fourth coil was uneventful, but as the catheter tip was withdrawn, the coil was partially dislodged, occluding the hepatic artery (Fig. 1A). The patient had cirrhosis with portal hypertension, varices, ascites, and abnormal liver function. Occlusion of the hepatic artery was therefore considered a potentially serious complication. The dislodged fourth coil was immediately retrieved by using a 0.018-in. (0.46 mm) guidewire looped inside a catheter to form a snare. The coil was captured and removed through a femoral sheath. Patency of the hepatic artery was restored (Fig. 1B).

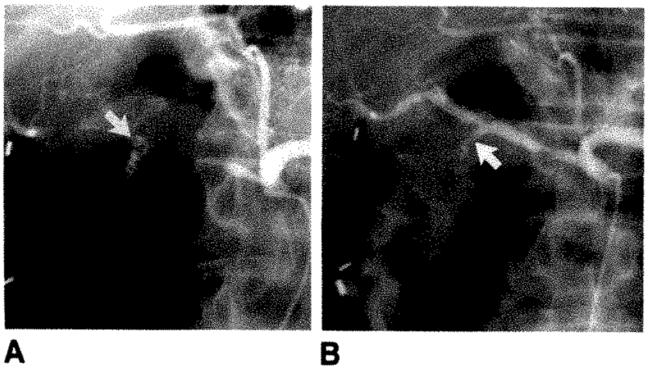

Fig. 1.—*A*, Angiogram shows poor position of fourth of four 3-mm coils placed in gastroduodenal artery to control hemorrhage. Coil is partly in gastroduodenal artery and partly in hepatic artery (*arrow*), which was occluded as a result.

***B*, Angiogram obtained after retrieval of poorly placed coil shows patent hepatic artery. Gastroduodenal artery remains occluded (*arrow*).**

Although many reports [2–4] of malpositioned coils have been published, we found only two [3, 4] on retrieval of coil emboli. In those cases, the coils were lost on the venous side and were retrieved from the right side of the heart or from the pulmonary artery. To our knowledge, the case reported here is the first one in which an arterial coil was placed incorrectly and then removed, restoring patency of an occluded artery. However, that is not the most important lesson of this case. Rather, it points out the need to overcome the temptation to improve on an already good result. The fourth coil was not really necessary, and a serious complication was only narrowly avoided. This case illustrates why the expression "the enemy of good is better" is so frequently heard in the interventional suite.

Gerald D. Pond
Steven H. Smyth
Thomas P. Bocchini
University of Arizona Health Sciences Center
Tucson, AZ 85724

REFERENCES

1. Athanasoulis CA. Upper gastrointestinal bleeding of arteriocapillary origin. In: Athanasoulis CA, Pfister RS, Greene RE, Roberson GH, eds. *Interventional radiology*. Philadelphia: Saunders, **1982**:55–89
2. Hemingway AP, Allison DJ. Complications of embolization: analysis of 410 procedures. *Radiology* **1988**;166:669–672
3. Radojkovic S, Kamenica S, Jasovic M, Draganic M. Catheter-aided extraction of a steel coil accidentally lodged in the right ventricle. *Cardiovasc Intervent Radiol* **1980**;3:153–155
4. Chomyn JJ, Craven WM, Groves BM, Durham JD. Percutaneous removal of Gianturco coil from the pulmonary artery with use of flexible intravascular forceps. *J Vasc Intervent Radiol* **1991**;2:105–106

Indications for Radiography in Acute Ankle Injuries

A recent article by Auletta et al. [1] concludes that "a brief but thorough physical examination can eliminate the need for a large percentage of radiographs ordered in patients with acute ankle trauma." Their examination included a short interview and "required less than 5 min to perform." My experience suggests that similar results may be obtained even with a *nonthorough* physical examination.

For a brief period in the late 1970s, my department asked on-call radiology residents to examine patients who were having ankle radiographs because of acute injury. This was done before the radiographs were obtained or before they were interpreted. The residents determined if the point of maximum tenderness was category 1: distal to (below) the medial or lateral malleolus, category 2: at the malleolus, or category 3: elsewhere or of uncertain location. Residents were encouraged to spend no more than 30 sec and if the findings were at all uncertain to simply assign the patient to category 3. Of 89 patients examined, 30 (34%) had maximal tenderness distal to the malleoli, and only one of these had an acute fracture: a small cortical avulsion of the lateral malleolus without clinical implication. In the series of Auletta et al., a solitary talar avulsion fracture was the only fracture found in 101 (50%) of 201 patients classified as having inadequate indications for radiographs.

This information will come as no surprise to most orthopedists, and its dissemination among radiologists or even emergency department physicians will, as suggested by Auletta et al., have little impact on current practice in the United States. This is because of our current medicolegal climate, patients' unrealistic expectations, and our relatively open-ended policy of medical reimbursement. I hope that studies "of academic interest only," like the one by Auletta et al., will someday help form the basis for decisions on medical care in this country.

Ferris M. Hall
Beth Israel Hospital
Harvard Medical School
Boston, MA 02215

REFERENCE

1. Auletta AG, Conway WF, Hayes CW, Guisto DF, Gervin AS. Indications for radiography in patients with acute ankle injuries: role of the physical examination. *AJR* **1991**;157:789–791

Reply

We thank Dr. Hall for his letter both confirming and expanding the ideas expressed in our recent article [1]. A couple of points in the letter, however, need expansion. We agree with Dr. Hall that the physical examination can be streamlined even more than the one described in our paper. However, we would add to his suggestions for physical examination careful palpation of the base of the fifth metatarsal. In our experience, patients with fractures of the base of the fifth metatarsal often complain of "ankle pain." If these fractures are missed on physical examination and no radiographs are obtained, the clinical consequences could be serious.

Dr. Hall suggests that studies such as ours have little impact on current practice in the United States because of "our current medicolegal climate, patients' unrealistic expectations, and our relatively open-ended policy of medical reimbursement." In the setting of a teaching institute, we would add to this list residents' inexperience and consequent lack of confidence in doing physical examinations. Over the past year, even armed with the data from our study, we still have had great difficulty convincing surgical residents in our own emergency department to trust and therefore act on the results of physical examinations in cases of acute ankle injuries. In a setting such as this, we think that a reasonable alternative might be having orthopedically trained physician assistants on staff in the emergency department. These assistants would be responsible for the triage of all patients with orthopedically related trauma. Because of the specialized training they receive, physician assistants perhaps would be better equipped and more motivated to perform and act on the results of an adequate physical examination.

In conclusion, we join Dr. Hall in hoping that studies such as ours will eventually convince clinicians to curb the overuse of certain radiology services. Until then, we will have to either grimace and bear it or come up with imaginative alternatives.

William F. Conway
Curtis W. Hayes
Ann G. Auletta
Medical College of Virginia
Richmond, VA 23298

REFERENCE

1. Auletta AG, Conway WF, Hayes CW, Guisto DF, Gervin AS. Indications for radiography in patients with acute ankle injuries: role of the physical examination. *AJR* **1991**;157:789–791

Percutaneous Lumbar Nerve Root Blocks

I read with interest the article by El-Khoury and Renfrew [1] on percutaneous procedures for the diagnosis and treatment of lower back pain. The article, however, did not mention percutaneous lumbar nerve root blocks, which may be of diagnostic and, occasionally, therapeutic value when findings from conventional imaging studies are equivocal or nondiagnostic or show multilevel disease [2]. These procedures can be easily performed with fluoroscopic guidance. Small-gauge needles are used to inject small volumes (0.2–0.5 ml) of Marcaine around lumbar nerve roots where the roots pass inferior to the pedicles (Fig. 1) or through sacral foramina. The therapeutic response can be assessed immediately and may help surgeons decide on the level of disease responsible for patients' sciatic symptoms or the clinical significance of abnormalities seen on myelograms, CT scans, or MR images.

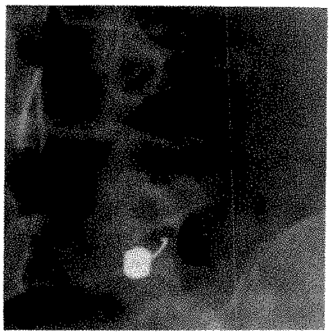

Fig. 1.—Oblique radiograph shows needle position for right L5 nerve root block. Slight curve on tip of 22-gauge needle facilitates placement just inferior to pedicle of L5 and also helps placement of needle in nerve root foramen for S1 nerve root blocks.

Over the past 12 months, my colleagues and I have performed 58 nerve blocks in 55 patients; block was obtained in 97%. Complete or nearly complete relief of pain was obtained in 63% of the patients, and the results had an effect on surgical intervention in 56%. Of the 11 patients who have had surgery, nine have had excellent clinical outcomes, with follow-up to 1 year. Although these are preliminary findings on a small number of patients, our experience indicates that this technically simple procedure can help in the subsequent surgical management of patients with lower back pain of complex origin.

David M. Pelz
The University of Western Ontario
London, Ontario, Canada N6A 5A5

REFERENCES

1. El-Khoury GY, Renfrew DL. Percutaneous procedures for the diagnosis and treatment of lower back pain: diskography, facet-joint injection, and epidural injection. *AJR* **1991**;157:685–691
2. Quinn SF, Murtagh FR, Chatfield R, Kori SH. CT-guided nerve root block and ablation. *AJR* **1988**;151:1213–1215

Reply

We are delighted that Dr. Pelz is interested in percutaneous procedures for the diagnosis and treatment of lower back pain. In the review [1], we limited our discussion to major procedures that radiologists may be asked to perform in the usual clinical setting. Despite the many percutaneous procedures that we perform, we are seldom asked to do nerve blocks. Experience with this technique appears to be meager; not much material on the subject is available in the literature. We anxiously await publication of Dr. Pelz's series.

We differ with Dr. Pelz when he characterizes percutaneous lumbar nerve root blocks as simple. The nerve blocks we performed were difficult. It was almost impossible to get a clean radiculogram. The responses of the patients to the injections were not convincing and were sometimes confusing. We are also not certain the technique described by Dr. Pelz is the orthodox way of performing this procedure. He places the needle tip within the neural foramina rather than in the nerve sheath. Most authorities [2–4] think that the provocative portion of the test, in which placing the needle in the nerve sheath reproduces the patient's exact pain, is important.

Georges Y. El-Khoury
Donald L. Renfrew
The University of Iowa College of Medicine
Iowa City, IA 52242

REFERENCES

1. El-Khoury GY, Renfrew DL. Percutaneous procedures for the diagnosis and treatment of lower back pain: diskography, facet-joint injection, and epidural injection. *AJR* **1991**;157:685-691
2. Tajima T, Furukawa K, Kuramochi E. Selective lumbosacral radiculography and block. *Spine* **1980**;5:68-77
3. Dooley JF, McBroom RJ, Taguchi T, MacNab I. Nerve root infiltration in the diagnosis of radicular pain. *Spine* **1987**;13:79-83
4. Stanley D, McLaren MI, Euinton HA, Getty CJM. A prospective study of nerve root infiltration in the diagnosis of sciatica: a comparison with radiculography, computed tomography, and operative findings. *Spine* **1990**;15:540-543

Hemisection of the Cervical Spinal Cord Caused by a Stab Wound: MR Findings

Stab wounds causing spinal cord injury are rare [1, 2], and to our knowledge, this case is the first report of MR imaging of a hemisection of the cervical spinal cord caused by a stab wound.

A 28-year-old woman was brought to our hospital 3 days after she had been stabbed. She had left-sided hemiplegia at the C7 level and six stab wounds posterolaterally on the neck over the trapezius muscle on the left side. MR imaging was performed with a 1.5-T system, and spin-echo T1-weighted and multiplanar gradient-recalled T2*-weighted images were obtained. A horizontally oriented laminar area with sharp borders, hypointense on T1-weighted images and hyperintense on T2-weighted images was seen on the left side of the spinal cord at the C6–C7 level. This finding represented liquid in the wound, inside the spinal cord on the left side (Fig. 1). The patient was treated conservatively. Eight months after the injury, she had Brown-Séquard syndrome with left-sided hemiplegia at the C7 level and was ambulating with the aid of a brace on her left lower extremity.

MR imaging allows visualization of the traumatized spinal cord and can be helpful in distinguishing irreversible damage from potentially reversible damage, as proposed by Bondurant et al. [3] and Kulkarni et al. [4]. They concluded that neurologic recovery in patients with cord hemorrhage is poor and that the prognosis is better in patients with cord edema. In our case, MR imaging confirmed the cord hemisection, and the MR findings correlated with the neurologic findings.

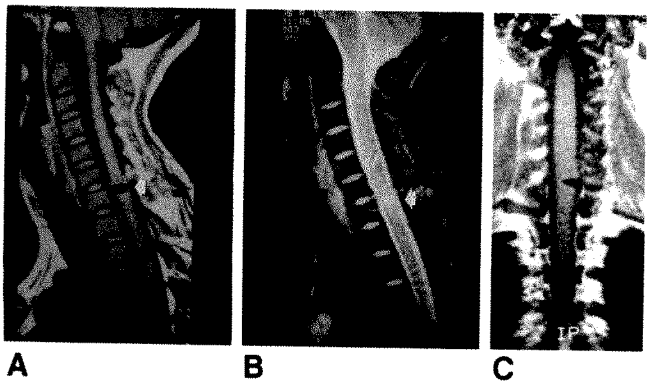

Fig. 1.—*A–C*, Sagittal T1- and T2-weighted (*A* and *B*, respectively) and coronal T1-weighted (*C*) MR images show hemisection (*arrows*) of spinal cord at C6–C7.

Tarcisio E. P. Barros
Reginaldo P. Oliveira
Laercio A. Rosemberg
Alvaro C. A. Magalhães
Hospital das Clínicas
School of Medicine, University of São Paulo
05403 São Paulo, Brazil

REFERENCES

1. Larson SJ. Evaluation and treatment of acute cervical spinal cord injury. In: The Cervical Spine Research Society, Ed. Committee. *The cervical spine*. Philadelphia: Lippincott, **1989**
2. Sett P, Crockard HA. The value of magnetic resonance imaging (MRI) in the follow-up management of spinal injury. *Paraplegia* **1991**;29:396-410
3. Bondurant FJ, Cotler HB, Kulkarni MV, McArdle CB, Harris JH. Acute spinal cord injury: a study using physical examination and magnetic resonance imaging. *Spine* **1990**;15:161-168
4. Kulkarni M, McArdle C, Kopanicky D, et al. Acute spinal cord injury: MR imaging at 1.5 T. *Radiology* **1987**;164:837-843

Multiple Meningiomas

A 35-year-old woman was referred to our department after surgery elsewhere for a left-sided acoustic schwannoma. Contrast-enhanced CT scans showed five masses. Two were located in the falx (Figs.

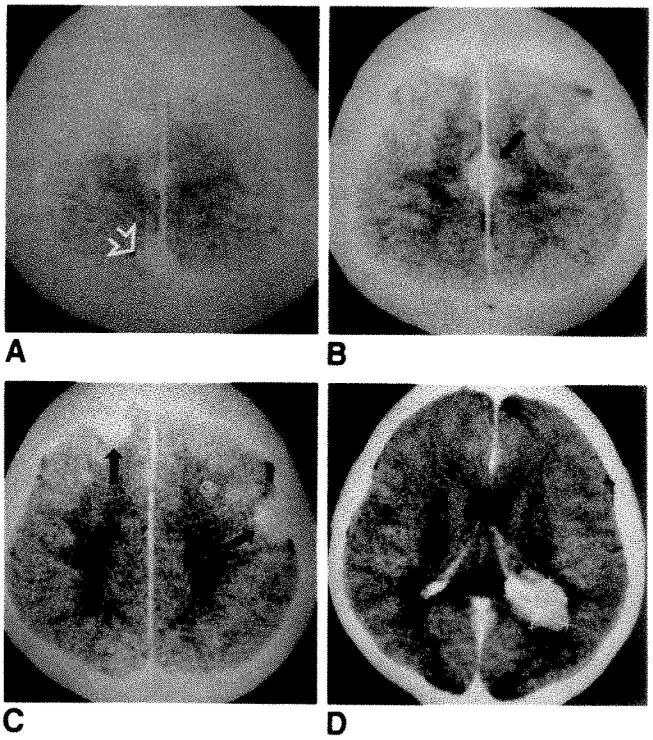

Fig. 1.—*A–D*, Contrast-enhanced CT scans show masses (*arrows*) in posterior (*A*) and mid (*B*) falx, two dura-based masses (*arrows*) in right frontal and left parietal regions (*C*), and a mass (*cursors*) with calcified margins and a homogeneously enhancing core in trigone of left lateral ventricle (*D*). Presence of these meningiomatous masses and history of unilateral acoustic schwannoma suggest neurofibromatosis type 2.

1A and 1B), a typical location for meningiomas. Two others were dura-based masses in the right frontal and left parietal regions (Fig. 1C). These four lesions showed homogeneous contrast enhancement. The fifth tumor, which originated from the trigone of the left lateral ventricle, showed peripheral calcification with a homogeneously enhancing core (Fig. 1D). Information on neurofibromatosis in the patient's family was not available.

Recently, the National Institutes of Health (NIH) Consensus Development Conference [1] classified neurofibromatosis as two separate and distinct disorders: NF-1 and NF-2. NF-1 is mainly a disease of astrocytes and neurons, in which astrocytomas, optic gliomas, and hamartomas usually develop. Its prevalence is about 1 in 4000 persons. NF-2 is primarily a disease of the coverings of the CNS, in which acoustic schwannomas, other schwannomas, and meningiomas develop. Its prevalence is 1 in 50,000 persons. In a recent study, Aoki et al. [2] found increased frequency of multiple meningiomas in NF-2, in addition to bilateral or unilateral acoustic schwannomas. The study also showed that intraventricular meningiomas occur commonly in NF-2.

The NIH criterion for NF-2 is the presence of one of the following: (1) bilateral eighth nerve masses seen with CT or MR or (2) NF-2 in a first-degree relative and either a unilateral eighth nerve mass or two of the following: neurofibroma, meningioma, glioma, schwannoma, or juvenile posterior subcapsular lenticular opacity [1]. Although the findings in our patient do not fit the criteria for NF-2 exactly, particularly because her family history was incomplete and she had only one of the specified tumors, a left-sided acoustic schwannoma, we think that the presence of multiple meningiomas along with unilateral (excised) acoustic schwannoma can be classified as NF-2.

R. Nuri Sener
Can Dundar
Mustafa Ozturk
and colleagues
Hospital of Ege University
Bornova, 35100, Izmir, Turkey

REFERENCES

1. National Institutes of Health Consensus Development. Neurofibromatosis. *Arch Neurol* **1988**;45:575–578
2. Aoki S, Barkovich AJ, Nishimura K, et al. Neurofibromatosis types 1 and 2: cranial MR findings. *Radiology* **1989**;172:527–534

Letters are published at the discretion of the Editor and are subject to editing.

Letters to the Editor must not be more than two *double-spaced*, typewritten pages. One or two figures may be included. Abbreviations should not be used. Limit the number of authors to four, or we will list only the first three and add "and colleagues" to the end of the list. See Author Guidelines.

Material being submitted or published elsewhere should not be duplicated in letters, and authors of letters must disclose financial associations or other possible conflicts of interest.

Letters concerning a paper published in the *AJR* will be sent to the authors of the paper for a reply to be published in the same issue. Opinions expressed in the Letters to the Editor do not necessarily reflect the opinions of the Editor.

Review of Current Literature

Initials and addresses of corresponding authors are provided in parentheses for each article so that the reader can obtain reprints directly. Abstracts are printed verbatim from each journal.

The New England Journal of Medicine

Treatment of postmenopausal osteoporosis with calcitriol or calcium. Tilyard MW, Spears GFS, Thomson J, Dovey S (MWT, RNZCGP Research Unit, Dept. of General Practice, University of Otago, P. O. Box 913, Dunedin, New Zealand). *N Engl J Med* 326(6):357–362, Feb. 1992

Background and Methods. Osteoporosis is a common problem whose management is controversial. To evaluate the efficacy and safety of calcitriol (1,25-dihydroxyvitamin D_3) in the treatment of postmenopausal osteoporosis, we conducted a three-year prospective, multicenter, single-blind study in 622 women who had one or more vertebral compression fractures. The women were randomly assigned to receive treatment with calcitriol (0.25 μg twice a day) or supplemental calcium (1 g of elemental calcium daily) for three years. New vertebral fractures were detected by means of lateral roentgenography of the spine each year, and calcium absorption was measured in 392 of the women.

Results. The women who received calcitriol had a significant reduction in the rate of new vertebral fractures during the second and third years of treatment, as compared with the women who received calcium (second year, 9.3 vs 25.0 fractures per 100 patient-years; third year, 9.9 vs. 31.5 fractures per 100 patient-years; $P<0.001$). This effect was evident only in women who had had five or fewer vertebral fractures at base line (second year, 5.2 vs. 25.3 fractures per 100 patient-years; third year, 4.2 vs. 31.0 fractures per 100 patient-years; $P<0.0001$). The groups also differed significantly in the number of peripheral fractures; 11 such fractures occurred in 11 women in the calcitriol group, whereas 24 occurred in 22 women in the calcium group ($P<0.05$). There was no significant difference between the groups in the incidence of side effects requiring withdrawal of treatment (8.6 percent in the calcitriol group vs. 6.5 percent in the calcium group).

Conclusions. Continuous treatment of postmenopausal osteoporosis with calcitriol for three years is safe and significantly reduces the rate of new vertebral fractures in women with this disorder.

Mortality over a period of 10 years in patients with peripheral arterial disease. Criqui MH, Langer RD, Fronek A, et al. (MHC, Dept. of Community and Family Medicine, Division of Epidemiology-0607, University of California, San Diego, School of Medicine, La Jolla, CA 92093-0607). *N Engl J Med* 326(6):381–386, Feb. 1992

Background. Previous investigators have observed a doubling of the mortality rate among patients with intermittent claudication, and we have reported a fourfold increase in the overall mortality rate among subjects with large-vessel peripheral arterial disease, as diagnosed by noninvasive testing. In this study, we investigated the association of large-vessel peripheral arterial disease with rates of mortality from all cardiovascular diseases and from coronary heart disease.

Methods. We examined 565 men and women (average age, 66 years) for the presence of large-vessel peripheral arterial disease by means of two noninvasive techniques—measurement of segmental blood pressure and determination of flow velocity by Doppler ultrasound. We identified 67 subjects with the disease (11.9 percent), whom we followed prospectively for 10 years.

Results. Twenty-one of the 34 men (61.8 percent) and 11 of the 33 women (33.3 percent) with large-vessel peripheral arterial disease died during follow-up, as compared with 31 of the 183 men (16.9 percent) and 26 of the 225 women (11.6 percent) without evidence of peripheral arterial disease. After multivariate adjustment for age, sex, and other risk factors for cardiovascular disease, the relative risk of dying among subjects with large-vessel peripheral arterial disease as compared with those with no evidence of such disease was 3.1 (95 percent confidence interval, 1.9 to 4.9) for deaths from all causes, 5.9 (95 percent confidence interval, 3.0 to 11.4) for all deaths from cardiovascular disease, and 6.6 (95 percent confidence interval, 2.9 to 14.9) for deaths from coronary heart disease. The relative risk of death from causes other than cardiovascular disease was not significantly increased among the subjects with large-vessel peripheral arterial disease. After the exclusion of subjects who had a history of cardiovascular disease at base line, the relative risks among those with large-vessel peripheral arterial disease remained significantly elevated. Additional analyses revealed a 15-fold increase in rates of mortality due to cardiovascular disease and coronary heart disease among subjects with large-vessel peripheral arterial disease that was both severe and symptomatic.

Conclusions. Patients with large-vessel peripheral arterial disease have a high risk of death from cardiovascular causes.

The prevalence of ulcerated plaques in the aortic arch in patients with stroke. Amarenco P, Duyckaerts C, Tzourio C, Hénin D, Bousser MG, Hauw JJ (PA, Service de Neurologie, Hôpital Saint-Antoine, 184 rue du Faubourg Saint-Antoine, 75571 Paris, CEDEX 12, France). *N Engl J Med* 326(4): 221–225, 1992

Background and Methods. The cause of cerebral infarction is obscure in up to 40 percent of patients with this disorder who are studied prospectively. In this investigation, we determined the frequency of ulcerated plaques in the aortic arch and explored the part they may play in the formation of cerebral emboli. Using an autopsy data bank, we studied the prevalence of ulcerated plaques in the aortic arch in 500 consecutive patients with cerebrovascular and other neurologic diseases who were studied at autopsy.

Results. Ulcerated plaques were present in 26 percent of the 239 patients with cerebrovascular disease but in only 5 percent of the 261 patients with other neurologic diseases ($P<0.001$). After we controlled for age and heart weight, the adjusted rates were 16.9 percent and 5.1 percent, respectively (adjusted odds ratio, 4.0; 95 percent confidence interval, 2.1 to 7.8; $P<0.001$). Among the patients with cerebrovascular disease, the prevalence of ulcerated plaques in the aortic arch was 28 percent in the 183 patients with cerebral infarcts and 20 percent in the 56 patients with brain hemorrhage. The prevalence of ulcerated plaques was 61 percent among the 28 patients with no known cause of cerebral infarction, as compared with 22 percent among the 155 patients with a known cause of cerebral infarction ($P<0.001$). After adjustment for covariates, the prevalence was 57.8 percent among patients with no known cause of cerebral infarction and 20.2 percent among those with a known cause (adjusted odds ratio, 5.7; 95 percent confidence interval, 2.4 to 13.6; $P<0.001$). The presence of ulcerated plaques in the aortic arch was not correlated with the presence of extracranial internal-carotid-artery stenosis, suggesting that these were two independent risk factors for stroke.

Conclusions. Ulcerated plaques in the aortic arch may play a part in causing cerebral infarction, especially in patients in whom cerebral infarction has no known cause.

Cancer

The leukocyte count and risk of lung cancer. Phillips AN, Neaton JD, Cook DG, Grimm RH, Shaper AG (ANP, MRC UK Centres for Coordinating Epidemiological Research on AIDS and HIV, Academic Dept. of Genito-Urinary Medicine, University College and Middlesex School of Medicine, James Pringle House, 73–75 Charlotte St., London W1N 8AA, England). *Cancer* 69:680–684, 1992

The association between leukocyte count and subsequent risk of lung cancer was evaluated in three large cohorts from the United States and Britain. A total of 309 lung cancer events occurred among 28,181 men whose cases were followed-up for 7 to 12 years. In all three cohorts, there was a marked increase in risk of lung cancer with increasing leukocyte count, after adjustment for age and the number of cigarettes smoked per day. The adjusted relative odds in the three cohorts, for a 2000/μl difference in leukocyte count, were 1.58 ($P = 0.0001$), 1.29 ($P = 0.003$) and 1.20 ($P = 0.02$). These relative odds persisted when current smokers were considered alone, when serum markers of cigarette smoking exposure were adjusted for, and when men with lung cancer events during the first 5 years of follow-up were excluded. The leukocyte count appears to be linked to the pathogenesis of smoking-related lung cancer.

Reprinted by permission from the American Cancer Society.

Chest

Impact of transesophageal echocardiography on the treatment of patients with aortic dissection. Chan KL (KLC, University of Ottawa Heart Institute, Ottawa, Canada). *Chest* 101(2):406–410, Feb. 1992

To determine the impact of transesophageal echocardiography (TE) on the treatment of patients with aortic dissection, the clinical course and outcome of 18 patients with TE diagnosis of dissection were analyzed. Ascending aortic dissection was present in nine patients, of whom six had surgery with confirmation of TE findings. Angiography was performed in only two of these patients and was falsely negative in one patient. Angiography was not performed in the three patients who were not surgical candidates. In the nine patients who had descending aortic dissection, angiography was performed in seven patients, of whom two underwent surgery. Information provided by angiography did not change the treatment of these patients. Thus, TE provides a prompt and accurate diagnosis in aortic dissection obviating the need for angiography in most patients.

Circulation

One-year results of the Thrombolysis in Myocardial Infarction Investigation (TIMI) Phase II Trial. Williams DO, Braunwald E, Knatterud G, et al. (DOW, Division of Cardiology, Rhode Island Hospital, 593 Eddy St., Providence, RI 02903). *Circulation* 85(2):533–542, Feb. 1992

Background. The Thrombolysis in Myocardial Infarction (TIMI) Phase II Trial randomized 3,339 patients to either an invasive (INV, $n=1,681$) or a conservative (CON, $n=1,658$) strategy after intravenous recombinant tissue-type plasminogen activator (rt-PA) for acute myocardial infarction.

Methods and Results. The patients assigned to the INV strategy routinely underwent cardiac catheterization, and when anatomically appropriate, percutaneous transluminal coronary angioplasty (PTCA) or coronary artery bypass grafting 18–48 hours after infarction. CON patients had these procedures only in response to the occurrence of spontaneous or provoked ischemia. One-year follow-up data are available in 3,316 patients (99.3%). The primary trial end point, death and nonfatal reinfarction, occurred in 14.7% of INV patients and in 15.2% of CON patients (p=NS). When analyzed individually, there was no difference (p=NS) in death (INV, 6.9%; CON, 7.4%) or recurrent infarction (INV, 9.4%; CON, 9.8%) between the two groups. Anginal status at 1 year was also similar. Cardiac catheterization and PTCA were performed more often in INV (98.0% and 61.2%, respectively) compared with CON (45.2% and 20.5%, respectively) patients. At 1 year, the cumulative number of patients who underwent coronary bypass surgery (INV, 17.5%; CON, 17.3%) was similar in the two groups.

Conclusions. The INV and CON strategies resulted in similar favorable outcomes at 1 year of follow-up. In particular, the rates of mortality and reinfarction were not different and were impressively low in both groups. One possible advantage of the INV strategy was detected in subgroup analyses. In patients with a history of myocardial infarction, the data are suggestive that 1-year mortality was lower in INV patients (10.3%) than in CON patients (17.0%) ($p=0.03$).

Gastroenterology

Extracorporeal shock-wave lithotripsy of pancreatic calculi. Delhaye M, Vandermeeren A, Baize M, Cremer M (MD, Medicosurgical Dept. of Gastroenterology, Erasme Hospital, Free University of Brussels, Brussels, Belgium). *Gastroenterology* 102:610–620, 1992

Extracorporeal shock-wave lithotripsy (ESWL) has been used to disintegrate pancreatic stones located in the main pancreatic duct for 123 patients with severe chronic pancreatitis. Endoscopic management following ESWL is aimed at restoring the pancreatic flow to the duodenum. Stone disintegration was achieved in 122 patients, whereas a decrease in the main pancreatic duct diameter resulted in 111, and complete clearance of the main pancreatic duct was obtained in 72. Pain relief, complete (40/88) or partial (35/88), correlated significantly with the results of the endoscopic drainage of the main pancreatic duct (e.g., decrease in main pancreatic duct diameter). Relapsing pain was most often related to recurrent pancreatic duct obstruction. Of 76 patients whose body weight had decreased before ESWL, 54 gained weight. Improvement of the exocrine function, evaluated by the [^{14}C]triolein breath test before and 11 months, on the average, after ESWL, was observed in 12 patients among 22 for whom this test was performed before and after treatment. Improvement of the endocrine function after relief of obstruction of the main pancreatic duct was less frequently recorded (4/41). ESWL of pancreatic stones is a new, safe, and highly effective method of facilitating the endoscopic procedures for relief of pancreatic duct obstruction in severe chronic pancreatitis.

Reprinted with permission by the American Gastroenterological Association.

Digestive Diseases and Sciences

Outcome of hepatic amebic abscesses managed with three different therapeutic strategies. Filice C, Di Perri G, Strosselli M, et al. (CF, Istituto di Clinica delle Malattie Infettive dell'Universita' di Pavia, IRCCS—Ospedale Policlinico "San Matteo," Piazzale Golgi n. 2, 27100 Pavia, Italy). *Dig Dis Sci* 37(2):240–247, Feb. 1992

Three different approaches to hepatic abscesses due to *Entamoeba histolytica* were compared in 51 patients. The three modes of therapy utilized were: medical therapy with nitroimidazoles ($N = 11$ patients), open surgical drainage ($N = 9$ patients), and percutaneous drainage using ultrasound guidance followed by intralesional nitroimidazole administration ($N = 31$ patients). The results with each form of therapy were assessed clinically and by abdominal ultrasound. Patients receiving combined US-guided drainage and intralesional chemotherapy experienced a faster and overall better clinical response, which was confirmed also by sonographic follow-up of the hepatic lesions. This better response was associated with faster resolution, fewer relapses, and less residual hepatic scarring than either with medical therapy alone or open surgical drainage combined with medical therapy.

Gastrointestinal Endoscopy

Endoscopic stenting for post-operative biliary strictures. Davids, PHP, Rauws EAJ, Coene PPLO, Tytgat GNJ, Huibregtse K (PHPD, Dept. of Hepato-gastroenterology, Academic Medical Center, Meibergdreef 9, 1105 AZ Amsterdam, the Netherlands). *Gastrointest Endosc* 38:12–18, 1992.

This study evaluates the efficacy of endoscopic stenting in 70 patients with noncomplete post-operative biliary strictures. The treatment consisted of placement of two 10 F gauge straight endoprostheses with elective exchange trimonthly, for a 1-year period. Successful endoprosthesis placement was accomplished in 66 of 70 patients (94%). In all 66 patients jaundice subsided. During the stenting period six patients had an operation and six died. In 46 patients the endoprostheses were removed. The mean period of follow-up was 42 months (range, 4 to 99 months). Excellent (asymptomatic, normal, or stable liver enzymes) and good (only one episode of cholangitis) responses were achieved in 83%; restricturing occurred after stent removal in 17%. Prolonged biliary stenting appears to be a safe and effective treatment modality for benign post-operative strictures and a valid alternative to surgery.

Clinical Orthopaedics and Related Research

The mechanism of loosening of cemented acetabular components in total hip arthroplasty. Schmalzried TP, Kwong LM, Jasty M, et al. (W. H. Harris, Orthopaedic Biomechanics Laboratory, Massachusetts General Hospital, Boston, MA 02114). *Clin Orthop* 274:60–78, Jan. 1992

Late aseptic loosening of cemented acetabular components is governed by the progressive, three-dimensional resorption of the bone immediately adjacent to the cement mantle. This process begins circumferentially at the intraarticular margin and progresses toward the dome of the implant. Evidence of bone resorption at the cement-bone interface was present even in the most well-fixed implants before the appearance of lucent lines on standard roentgenographic views. The mechanical stability of the implant was determined by the three-dimensional extent of bone resorption and membrane formation at the cement-bone interface. The leading edge of the membrane is a transition zone from regions of membrane interposition between the cement and the bone to regions of intimate cement–bone contact. Histologic analysis revealed that progressive bone resorption is fueled by small particles of high density polyethylene (HDP) migrating along the cement–bone interface and bone resorption occurs as a result of the macrophage inflammatory response to the particulate HDP. Evidence in support of a mechanical basis for failure of fixation was lacking. The mechanism of late aseptic loosening of a cemented acetabular component is therefore biologic in nature, not mechanical. This is exactly opposite to the mechanism of loosening on the femoral side of a cemented total hip replacement, which is mechanical in nature.

The Journal of Urology

Clinical aspects of polycystic kidney disease. Higashihara E, Aso Y, Shimazaki J, Ito H, Koiso K, Sakai O (EH, Dept. of Urology, The University of Tokyo, Yokyo, Japan). *J Urol* 147:329–332, Feb. 1992

A total of 316 patients (167 men and 149 women) with autosomal dominant polycystic kidney disease was studied retrospectively by a multi-institute group. With advancing patient age renal function decreased, and blood pressure, prevalence of liver cysts and probability of end stage renal failure increased. The probability of end stage renal failure was 39% in the patients in their sixties. Regression analysis indicated that polycystic kidney disease patients could expect to lose 1.1 ml. per minute of creatinine clearance per year, reaching a level of 10 ml. per minute, a point of end stage renal failure, by the age of 72.7 years. The better prognosis in our study than that reported previously in white patients might be due to the inclusion of more asymptomatic persons and/or milder genotypic expression of polycystic kidney disease in Japan. There was no sex difference in the prevalence of liver cysts (54.6%), pancreatic cysts (7.1%), intracranial aneurysms (8.0%) and hypertension (63.6%). The occurrence of pancreatic cysts was significantly associated with liver cysts. Our study clarifies several clinical characteristics of polycystic kidney disease in Japan.

Journal of Ultrasound in Medicine

Varix of the fetal intra-abdominal umbilical vein: comparison with normal. Mahony BS, McGahan JP, Nyberg DA, Reisner DP (BSM, 1229 Madison St., #1150, Seattle, WA 98104). *J Ultrasound Med* 11:73–76, Feb. 1992

To compare the normal extrahepatic portion of the fetal intra-abdominal umbilical vein (FIUV) with varix of the FIUV, we prospectively measured the diameter of the FIUV in 150 uncomplicated second and third trimester pregnancies and compared these results with retrospective review of nine fetuses with varix of the FIUV as an isolated prenatal sonographic finding. The diameter of the normal FIUV increases linearly from approximately 3 mm at 15 menstrual weeks to approximately 8 mm at term ($R = 0.92$). The nine fetuses with FIUV varix had a FIUV diameter 6 to 12 standard deviations above the mean for age. Four (44%) of the nine fetuses with FIUV varix subsequently died, including one with trisomy 21. One of the remaining fetuses developed severe hydrops 2 weeks after the initial detection of the FIUV varix. FIUV varix appears to carry an increased risk of adverse fetal outcome, including fetal demise.

Reprinted with permission by the American Institute of Ultrasound in Medicine.

Journal of Computer Assisted Tomography

Sedation for pediatric patients undergoing CT and MRI. Hubbard AM, Markowitz RI, Kimmel B, Kroger M, Bartko MB (AMH, Dept. of Radiology, Children's Hospital of Philadelphia, 34th St. and Civic Center Blvd., Philadelphia, PA 19104). *J Comput Assist Tomogr* 16(1):3–6, Jan./Feb. 1992

Adequate sedation remains one of the most important parts of performing high quality cross-sectional imaging in children. This is a noncomparative retrospective analysis of existing sedation protocols used in 1,158 children between the ages of 1 day and 18 years, checking for safety and efficacy. The most commonly used drugs were chloral hydrate (60–120 mg/kg) by mouth for infants <18 months and intravenous Nembutal (2–6 mg/kg) for older children. Sedation was successful in 97% of patients.

Pre- and postcontrast MR studies in tuberous sclerosis. Wippold FJ II, Baber WW, Gado M, Tobben PJ, Bartnicke BJ (FJW, Mallinckrodt Institute of Radiology, Washington Medical Center, 510 S. Kingshighway, St. Louis, MO 63110). *J Comput Assist Tomogr* 16(1):69–72, Jan./Feb. 1992

The MR findings in eight patients with intracranial manifestations of tuberous sclerosis are reported. There were subependymal lesions in seven patients and peripheral lesions (i.e., cortical and subcortical) in all patients. All lesions were supratentorial. We emphasize two findings that have not been previously stressed. The signal intensity patterns of the subependymal lesions varied from patient to patient, but in all patients receiving intravenous contrast medium, the majority of these lesions enhanced. Although this finding may signify early breakdown of the blood-brain barrier with potential for lesion growth, the high frequency of enhancement challenges earlier concepts of equating this phenomenon with existence of actively growing giant cell astrocytomas. The peripheral lesions were more numerous than subependymal lesions. These lesions were nearly always hyperintense in the proton density weighted and T2-weighted images. Most notable is the fact that, in half of the lesions, signal intensity was also elevated in the T1-weighted image, an observation that has not been emphasized in previous reports. Although not pathologically confirmed this signal pattern may represent early stages of calcification within these lesions. Finally, unlike subependymal lesions, none of the peripheral lesions showed contrast enhancement.

Clinical Materials

Contrast media for angiography: physicochemical properties, pharmacokinetics and biocompatibility. Eloy R, Corot C, Belleville J (RE, Unit 37 INSERM, 18 avenue Doyen Lépine, 69500 BRON, France). *Clin Materials* 7:89–197, 1991

Contrast agents are used as diagnostic molecules for the visualization of the vascular system. Despite their rapid pharmacokinetic distribution, and their excretion within a few minutes, their injection is associated with clinical symptoms of relative bioincompatibility. Allergoid reactions and disturbances of the hemostatic system represent the main fields of biological investigations. Due to the extent of clinical and experimental works the ubiquitous interactions between these molecules and cellular and/or protein systems have emerged.

The development of a new family of low osmolality ionic or nonionic contrast molecules had decreased the incidence of minor reactions, but did not modify the frequency of severe accidents and even led to the emergence of new iatrogenic syndromes. Despite extensive laboratory investigations there are still no predictive criteria nor any specific therapeutic prevention of these allergoid reactions.

The suggested future line of investigation concerns the physicochemical interaction of CM and targeted biological systems which may allow the analysis and predictivity of these interactions at the molecular level.

Reprinted by permission from Elsevier Science Publishers Ltd.

News

1992 Marie Curie Award

The American Association for Women Radiologists (AAWR) is accepting nominations for the 1992 Marie Curie Award. The award is given annually to a radiologist, radiation oncologist, or other person who has been a mentor, role model, or leader in radiology. The nominee need not be a member of the AAWR. The nomination should include the candidate's curriculum vitae and a letter of support addressing the unique role the nominee has undertaken in clinical care, teaching, or research and the accomplishments that set him or her apart. The deadline for nominations is July 1. The award will be presented in December at the AAWR membership luncheon meeting during the 1992 annual meeting of the Radiological Society of North America. The AAWR will pay the winner's expenses (airfare and per diem) to accept the award. Information: Ann R. Wieseneck, Executive Director, American Association for Women Radiologists, 1891 Preston White Dr., Reston, VA 22091; telephone: (703) 648-8939; fax: (703) 391-0397.

AAWR Distinguished Resident Award

The American Association for Women Radiologists (AAWR) is asking directors of residency programs to submit nominations for the 1992 Distinguished Resident Award. Nominees must be members of AAWR as of Jan. 1, 1992. Nominations are limited to one per residency program. The nomination package should include a completed application; a nominating letter from the residency director, with notation of what year the candidate will be in residency at the time of the award ceremony; a letter of concurrence from the departmental chair; and a copy of the candidate's curriculum vitae. Nominees will be evaluated on the basis of outstanding contributions, whether in clinical care, teaching, research, or public service. The award will be presented in December 1992 at the AAWR annual meeting. It will include a prize of $500 and expenses (air fare and per diem) for attending the meeting for the acceptance ceremony. Nominations should be sent to Ann R. Wieseneck, Executive Director, American Association for Women Radiologists, 1891 Preston White Dr., Reston, VA 22091. The deadline for submissions is July 1, 1992.

Symposium on Breast Disease

The Dept. of Radiology, The University of Michigan Medical School, is sponsoring the 6th annual Symposium on Breast Disease: Diagnostic Imaging and Current Management, July 12–15, at the Grand Traverse Resort Village, Grand Traverse Resort, MI. The course will present the newest developments in breast imaging and diagnostic techniques, including mammography, other breast imaging techniques, and fine-needle aspiration biopsy; an update on breast cancer screening; and a summary of the latest medical, radiation, and surgical oncologic approaches to breast cancer. Workshops will allow small group discussions on various diagnostic, management, and technical issues. Course director: Dorit D. Adler. Category 1 credit: 15 hr. Information: Edwina Borde, Towsley Center for Continuing Medical Education, Dept. of Postgraduate Medicine, The University of Michigan Medical School, P. O. Box 1157, Ann Arbor, MI 48106-1157; (313) 763-1400.

Courses on Prostate Ultrasound

Prostate Ultrasound: Applications, Techniques, and Advances in Prostate Ultrasound and Prostate Imaging will be presented July 31–Aug. 1 and Oct. 16–17 at Albany Medical College, Albany, NY. Information: Dept. of Continuing Medical Education, A-1, Albany Medical College, 47 New Scotland Ave., Albany, NY 12208; (518) 445-5828.

Midwest Interventional Radiology Seminar

Midwest Institute for Interventional Therapy, Saint Francis Medical Center, and The University of Illinois College of Medicine at Peoria are sponsoring Midwest Interventional Radiology Seminar, Aug. 7–9. The seminar will include a wide range of topics in interventional radiology. Category 1 credit: 20 hr. Fee: physicians, $425; fellows, residents, and technologists, $225. Information: Kathy Klein, University of Illinois College of Medicine at Peoria, Office of Statewide Programming, P. O. Box 1649, Peoria, IL 61656; (309) 671-8475.

Northern Imaging 1992 Radiology Seminar

The Dept. of Radiology, The University of Manitoba, will present the 5th annual Northern Imaging 1992 Radiology Seminar, Aug. 7–10, at Knee Lake Lodge in Manitoba. The focus of the course will be current concepts in diagnostic sonography. Participation is limited to 50 registrants. Course director: E. A. Lyons. Guest faculty: G. Leopold, P. Mueller, J. W. Charboneau, C. C. Reading, and B. Lewis. Category 1 credit: 12 hr. Fee: $1695 (includes airfare from Winnipeg). Information: Randy Duvell, Ste. 3-1791 Dublin Ave., Winnipeg, Manitoba, Canada R3H 1A9; telephone: (204) 632-6098; fax: (204) 632-6204.

Symposium on Diagnostic Imaging

The Department of Diagnostic Imaging, Rhode Island Hospital, and Brown University School of Medicine will present their 13th annual

Symposium on Diagnostic Imaging, Aug. 8–12, at the Newport Islander Doubletree Hotel, Newport, RI. The course will devote 3 days to mammography and 2 days to the fundamentals of MR imaging. Category 1 credit: mammography course, 15 hr; MR imaging course, 9 hr. Fee (through July 1/after July 1): both courses: physicians, $600/$625; residents, fellows, and technologists (letter required), $475; mammography course only: physicians, $450/$475; residents, fellows, and technologists (letter required), $375; MR imaging course only: physicians, $250/$275; residents, fellows, and technologists (letter required), $200. Information: Mrs. Gayle Pascetta, Dept. of Radiology, Main—3rd Floor, Rhode Island Hospital, 593 Eddy St., Providence, RI 02903; (401) 277-5184.

Mammography Update

Lovelace Medical Center is sponsoring Mammography Update, Sept. 7–11, at the Eldorado Hotel, Santa Fe, NM. Program director: Arvis Williams. Information: Dawne Ryals, Ryals and Associates, P. O. Box 1925, Roswell, GA 30077-1925; telephone: (404) 641–9773; fax (404) 552-9859.

Ultrasound and Cardiovascular Technology Review Conference

The Dept. of Radiology, University of California, San Diego School of Medicine, is offering the 8th annual Ultrasound and Cardiovascular Technology Registry Review Conference, Sept. 11–13, at the Town & Country Hotel, San Diego. The 3-day program has two purposes: (1) to provide an overview of anatomy, physiology, pertinent laboratory values, pathophysiology, and current applications for persons who are planning to take the national board examinations in ultrasound or cardiovascular technology and (2) to provide practicing physicians and sonographers with an update on current applications in ultrasound physics, abdominal ultrasound, obstetric and gynecologic ultrasound, echocardiology in adults, vascular technology, and invasive cardiovascular technology. Program director: Sandra L. Hagen-Ansert. Category 1 credit will be awarded. Fee (postmarked by Aug. 16/after Aug 16): entire course: physicians, $350/$400; sonographers and cardiovascular technologists, $250/$300; 1-day session only: $175. Information: Dawne Ryals, Ryals and Associates, P. O. Box 1925, Roswell, GA 30077–1925; telephone: (404) 641-9773; fax: (404) 552–9859

Musculoskeletal and Neuroradiological MRI

The University of Alabama at Birmingham is sponsoring Musculoskeletal and Neuroradiological MRI, Sept. 21–26, at the Westin Resort Hotel, Hilton Head Island, SC. Program directors: Taher El Gammal, William W. Daniel, and Phillip Kenney. Category 1 credit (pending): 25 hr. Fee: physicians, $625; residents, fellows, and technologists, $395. Information: Dawne Ryals, Ryals and Associates, P. O. Box 1925, Roswell, GA 30077-1925; telephone: (404) 641–9773; fax: (404) 552-9859.

Practical Radiology

The Dept. of Radiology, University of Virginia, will present its 15th annual postgraduate course, Practical Radiology, Oct. 12–15 at the Boar's Head Inn, Charlottesville, VA. Program director: Theodore E. Keats. Guest faculty: J. Beltran, R. B. Dyer, S. A. Feig, and N. E. Leeds. Category 1 credit: 20 hr. Fee: $425. Information: R. L. Boswell, Program Coordinator, Dept. of Radiology, Box 170, University of Virginia Health Sciences Center, Charlottesville, VA 22908; (804) 924-9387.

Nuclear Cardiology Symposium and Workshop

The Cardiovascular Disease Section, University of Wisconsin School of Medicine, Milwaukee Clinical Campus; Sinai Samaritan Medical Center; Continuing Medical Education, University of Wisconsin, Madison; and University of Wisconsin-Extension are sponsoring the 17th annual Nuclear Cardiology Symposium and Workshop, Oct. 14–16, at the Marc Plaza Hotel, Milwaukee. The course will provide a comprehensive review of current techniques in nuclear cardiology for physicians and technologists who are involved in cardiovascular imaging. Category 1 credit: 17 hr. Information: Sarah Aslakson, Continuing Medical Education, 2715 Marshall Ct., Madison, WI 53705; (608) 263-2856.

Progress in Magnetic Resonance

Progress in Magnetic Resonance, the 10th annual meeting of the European Magnetic Resonance Forum, will be held Oct. 15–17 at the Grand Hotel, Locarno, Switzerland. The meeting will be an overview of selected topics of state-of-the-art MR imaging. Basic courses on MR imaging will be provided in English, German, and Italian. The deadline for registration is Sept. 20. Fee: SFr 575 plus SFr 220 for the basic course. Information: European Magnetic Resonance Forum, P. O. Box 1235, CH 6648 Minusio-Locarno, Switzerland; telephone and fax: +41-93-67 6295.

Society of Radiologists in Ultrasound Postgraduate Course

The Society of Radiologists in Ultrasound is sponsoring its first postgraduate course, Oct. 23–25, at the Fairmont Hotel, Chicago, The foci of the course will be advanced obstetric sonography and state-of-the-art Doppler sonography. Information: Society of Radiologists in Ultrasound, 1101 Market St., Philadelphia, PA 19107; telephone: (215) 574-3183.

American College of Nuclear Physicians New Officers

The American College of Nuclear Physicians has installed Robert J. Lull as president of the society for the 1992 term. Other officers are Conrad E. Nagle, president-elect, and William H. McCartney, treasurer.

The American Board of Radiology Examinations

Written examinations for the American Board of Radiology (ABR) are scheduled for Oct. 1–2, 1992, and Sept. 23–24, 1993. Oral examinations will be held at the Executive West Hotel in Louisville, KY, June 1–5, 1992, and June 7–10, 1993. The ABR will accept applications for admission to the examinations after July 1, but not later than Sept. 30, in the year *preceding* the year in which the examination is to be taken. For application forms and further information: Office of the Executive Director, The American Board of Radiology, 2301 W. Big Beaver Rd., Ste. 625, Troy, MI 48084.

Meeting and Course Review

For the reader's convenience, a summary of upcoming meetings and courses is provided. Detailed listings are given in the *AJR* issue given in parentheses.

Practicum in Breast Imaging, times arranged, Baltimore (Aug 1991)
Spanish Radiological Society National Conference, June 1-5, Seville, Spain (March)
Mammography Update: Practical Breast Imaging, June 5-7, Point Clear, AL (April)
Canadian Association of Medical Radiation Technologists 50th Anniversary Conference, June 7-12, Ottawa (Feb)
Visiting Fellowships in MR Imaging: introductory, June 8-12, Philadelphia (April)
Advances in Cardiopulmonary Imaging, June 11-13, Salzburg, Austria (Nov 1991)
Yale Symposium on Duplex and Color Doppler Ultrasound, June 18-19, New Haven, CT (May)
Symposium on MR of the Muscoloskeletal System, June 18-20, Palma de Mallorca, Balearic Islands, Spain (April)
Concepts of Magnetic Resonance, June 20-26, Kiawah Island, SC (Feb)
Pitt Summer Imaging Course, June 21-25, Williamsburg, VA (Feb)
Practicum in Mammography for Technologists, beginning dates: June 22, Sept. 28, and Oct 19, San Diego (May)
Magnetic Resonance Imaging in Spain and Morocco, June 28-July 1, Barcelona and July 3-5, Casablanca (April)
Workshop on Vascular Anomalies, July 1-3, Denver (March)
Imaging Courses at Sea, breast imaging, July 4-11; **MR imaging—musculoskeletal imaging**, July 11-18 (May)
Paediatric Imaging Update, July 5-10, Port Douglas, Australia (March)
Course on Body Imaging, July 13-17, Santa Fe, NM (March)
Diagnostic Imaging Seminar, July 13-17, Edgartown, MA (Martha's Vineyard) (April)
Vascular Imaging and Intervention for the 90s, July 17-19, San Francisco (April)
Diagnostic Imaging Update, July 20-22, San Francisco, and July 23-26, Carmel, CA (March)
Clinical Imaging for Non-Radiologists, July 20-24, San Diego (March)
The Sharper Image in MRI, July 27-31, Colorado Springs, CO (April)
MRI and Musculoskeletal Imaging, July 27-Aug. 1, Laguna Niguel, CA (March)
Mackinac Island Imaging Conference, Aug. 3-6, Mackinac Island, MI (May)
Contemporary Medical Imaging IX, Aug. 12-16, Hilton Head Island, SC (April)
Summer Practicum, Aug. 16-20, Keystone, CO (April)
Barcelona 1992 Post-Games Imaging Conference, Aug. 17-21, Barcelona (April)
European Symposium on Uroradiology, Aug. 24-27, Herlev, Denmark (Aug 1991)
International Skeletal Society Refresher Course, Aug. 26-29, Stockholm (March)
Congress of Asian Federation of Societies for Ultrasound in Medicine and Biology, Aug. 30-Sept. 3, Seoul, Korea (Feb)
Cardiovascular and Interventional Radiological Society of Europe Annual Meeting and Postgraduate Course, Aug. 30-Sept. 3, Sitges (Barcelona), Spain (May)
Radiation, Physics, and Biology, Aug. 31-Sept. 4, New York City (May)
Ultrasound Angiography 92, Sept. 2-4, University of Southampton, United Kingdom (Feb)
Pacific Northwest Diagnostic Ultrasound: OB/GYN Symposium, Sept. 10-12, Seattle (May)
Pittsburgh Breast Imaging Seminar, Sept. 10-13, Pittsburgh (May)
Symposium on Transrectal Ultrasound, Sept. 11-13, Chicago (May)
Vancouver Imaging Update 1992, Sept. 13-17, Vancouver, B.C. (May)
Mammographic Interpretation, Sept. 14-17 and Oct. 26-29, Boston (April)
MRI Visiting Fellowships at UCLA, Sept. 14-18, Oct. 5-9, and Dec. 7-11, Los Angeles (Sept 1991)
Dose, Time, and Fractionation in Radiation Oncology, Sept. 16-19, Madison, WI (May)
Update in Film Screen Mammography, Sept. 30-Oct. 2, Richmond, VA (May)
Fall Foliage Imaging Seminar, Oct. 9-11, Burlington, VT (May)
International Course on MR Imaging, Oct. 25-28, Riyadh, Kingdom of Saudi Arabia (March)

AJR carries announcements of courses, symposia, and meetings of interest to its readers if received a minimum of 5 months before the event. There is no charge; receipt of items by the *AJR* Editorial Office is not acknowledged. Submit items for publication typed double-spaced. Provide title, date, location, brief description, sponsor, course directors, fees, category I credit, and address and telephone number for additional information. Faculty from the host institution will not be listed. Guest faculty names will appear **only** if initials are provided. Mail news items to *AJR* Editorial Office, 2223 Avenida de la Playa, Suite 103, La Jolla, CA 92037-3218.

Mark Your Calendar Now!

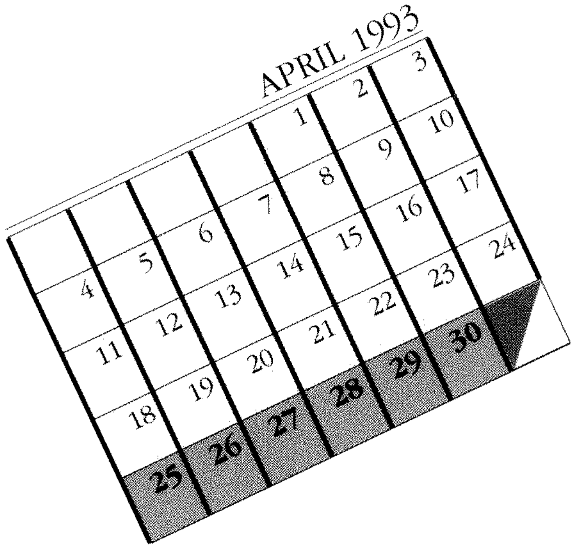

The American Roentgen Ray Society will return to San Francisco in 1993, and plans are already underway for what promises to be an educationally fulfilling and socially enjoyable week in the city by the bay. Look for the San Francisco logo in the next several issues of the *AJR* for updated meeting information.

Call for Papers

Abstracts of papers to be considered for the scientific program must be submitted by November 1, 1992. Abstract forms and instructions for submission are included in this issue and will also appear in the July through October issues. The *AJR* has first rights to all papers accepted for presentation at the ARRS meeting.

Call for Scientific Exhibits

The deadline for submission of abstracts to be considered for scientific exhibits is November 1, 1992. Abstract forms and instructions for submission are included in this issue and will also appear in the July through October issues.

Categorical Course

The topic of the 1993 Categorical Course is Ultrasound. A summary of topics and faculty for this course will appear in the February 1993 issue of the *AJR*.

Refresher Courses

Plans are underway to present at least 60 instructional courses on various topics of interest to the radiology community. A summary of these courses will be included in the February *AJR*. Early registration is strongly suggested, as these courses fill up quickly.

Resident Award Papers

The society offers three cash awards for the best scientific papers prepared by residents in radiology. The President's Award has a cash prize of $2,000, and there are two Executive Council Awards with a cash prize of $1,000 each. The winners of these three awards are invited to present their papers during the opening ceremonies at the annual meeting. Papers must be submitted by February 12, 1993, for consideration in this competition. Additional information on these awards will be mailed to all residency program directors in July.

Local Arrangements

The San Francisco area offers many opportunities for sightseeing, shopping and entertainment. Check the February *AJR* for detailed information on local tours developed especially for ARRS meeting attendees.

Registration and Hotel Reservations

All meeting activities will take place in the beautiful new San Francisco Marriott, centrally located on Market Street. The society has negotiated special room rates for meeting attendees, and the February *AJR* will contain meeting registration and hotel reservation forms. As in previous years, early registration is strongly suggested.

Travel

The society will make arrangements with United Airlines and a major car rental firm for preferred rates for meeting attendees. Taking advantage of these special rates benefits both you and the society – you save money on your reservations, and the society receives discounts to send staff and supplies to the meeting. Plan now to check the February issue of the *AJR* for details.

Classified Advertisements

Positions Available

VETERANS AFFAIRS MEDICAL CENTER, AUGUSTA, GA, is seeking a physician, board-eligible/certified in radiology. Subspecialty interest in chest, skeletal, GI, or interventional radiology is desirable but not essential. This 1142-bed, tertiary-care medical center is affiliated with the Medical College of Georgia. Faculty appointment commensurate with qualifications and experience. Augusta enjoys a moderate climate, reasonable cost of living, numerous recreational facilities, and institutions of higher learning. An equal opportunity employer. For additional information, contact George T. Jamarik, M.D., Chief, Radiology Service, (404) 823-2236. 6a

RADIOLOGIST—Eight-person group seeks general radiologist with fellowship training and special interest in MRI for 92-bed hospital and several imaging centers. Practice in the rapidly growing north San Diego and Temecula Valley areas. Send CV to North Coast Imaging Radiology Medical Group, Inc. 1582 W. San Marcos Blvd., Ste. 104, San Marcos, CA 92069; (619) 744-6442. 6ap

EXCITING RADIOLOGY OPPORTUNITIES NATIONWIDE!—Now is the time to make your move! Absolutely no cost to you. We specialize in radiology, so we understand your needs. Both group and private practice opportunities are available. We give you the inside tracks! Fax your CV to (214) 258-1092 or mail to Snelling Search Medical Group, 1301 Walnut Hill Ln., Ste. 103, Irving, TX 75038. For information on specific positions, call toll free (800) 259-5973. 6–7a

RADIOLOGY FACULTY POSITIONS—The University of Tennessee, Memphis, in conjunction with UT Medical Group, Inc., is actively recruiting radiologists in diagnostic radiology, pediatric radiology, ultrasonography, angiography and interventional radiology, and magnetic resonance. Applicant must be board-certified or eligible. Competitive salaries, excellent benefits, and research/clinical opportunities. Blacks, women, handicapped, and other minorities are encouraged to apply. The University of Tennessee, Memphis, is an equal opportunity/Title IX/Section 504/ADA affirmative action employer. Send CV to Barry Gerald, M.D., Chairman, Dept. of Radiology, The University of Tennessee, Memphis, 800 Madison Ave., Memphis, TN 38163. 6–7a

CT/ULTRASOUND/MRI, VASCULAR/INTERVENTIONAL, NEURORADIOLOGISTS—The Medical College of Pennsylvania is seeking BC/BE radiologists with expertise in the above specialty areas. Responsibilities involve clinical work, teaching (resident and medical students), and research as desired. Competitive salary and benefits. Immediate full/part-time openings. Please contact Mindy M. Horrow, M.D., Dept. of Radiologic Sciences, Medical College of Pennsylvania, 3300 Henry Ave., Philadelphia, PA 19129; (215) 842-6578. 6–7a

ASSOCIATE PROFESSOR OR PROFESSOR, DEPT. OF RADIOLOGY—Faculty position. Willing to start 7/1/92. Willing to start without a chairman named for the dept. Chief of angiographic interventional radiology section. Must have proven track record as teacher and publisher. Generous reimbursement package commensurate with experience and qualifications. Busy and diverse clinical load. Reply Box E62, *AJR* (see address this section). 6ap

CHAIRMAN—The University of Texas Medical Branch at Galveston is seeking applications and nominations for the position of chairman, Dept. of Radiology. The radiology dept. chairman will be responsible for the academic leadership of the dept. in clinical care, research, and education. Candidates must be highly qualified radiologists with clinical experience, research excellence, and service orientation. There is an opportunity to recruit new faculty members and obtain new equipment. Resources include state and institutional funding sources, access to foundation support, and broad clinical research population. Applicant must be certified by the American Board of Radiology. Applications will be accepted until a suitable candidate is selected. Interested candidates should submit a CV to Don W. Powell, M.D., Chairman, Search Committee for Radiology Chair, Dept. of Internal Medicine, 4.108 JSH (Rt. E67), UTMB, Galveston, TX 77555-0567. EO/AA employer, M/F/H/V. UTMB hires only individuals authorized to work in the U.S. 6a

DIAGNOSTIC RADIOLOGIST—The Dept. of Radiology at the University of Washington invites applications for academically oriented faculty positions in the area of general radiology, musculoskeletal radiology, chest/mammography, CT/ultrasound, and MRI. Responsibilities include instructing medical students and residents and conducting research. Applicants must possess board certification in radiology. The dept. has recently undergone major expansion with new facilities at the University Hospital, Children's Hospital Medical Center, Harborview Medical Center, and the Veteran's Administration Hospital. Salary is commensurate with rank based on established level of the University of Washington School of Medicine. Submit CV to Albert A. Moss, M.D., Professor and Chairman, Dept. of Radiology, SB-05, University of Washington, Seattle, WA 98195. The University of Washington is an equal opportunity/affirmative action employer. 6a

ASSISTANT PROFESSOR OF RADIOLOGY IN RESIDENCE, THORACIC IMAGING, UNIVERSITY OF CALIFORNIA, SAN FRANCISCO—UCSF is seeking a radiologist with expertise in thoracic imaging for the San Francisco Veteran's Administration Medical Center, 1 of 3 core integrated teaching hospitals. The candidate will be appointed at the level of assistant professor of radiology. Responsibilities include clinical service, teaching, and research. Requirements include expertise in thoracic imaging, board-certification, and a California medical license. In addition, this position requires teaching proficiency, clinical expertise, and productivity in focused research leading to publications. UCSF and the San Francisco VAMC are equal opportunity/affirmative action employers. Minority groups, women, and handicapped individuals are encouraged to apply. Send CV to Gordon Gamsu, M.D., Chairman, Search Committee, Dept. of Radiology, UCSF, San Francisco, CA 94143-0628. 6a

PART-TIME PEDIATRIC/GENERAL RADIOLOGIST, CENTRAL MASSACHUSETTS—Radiologist sought with special competence in pediatric radiology to join an 11-member group. We serve a 550-bed medical center that includes the regional 40-bed neonatal intensive care unit. Position involves sharing general responsibilities including CT, ultrasound, and mammography. Part-time position may become full-time. Please send CV to Richard Danford, M.D., Worcester Radiologists, 121 Lincoln St., Worcester, MA 01605; (508) 753-8151. 6–8ap

PHILADELPHIA—Full- or part-time opportunity for diagnostic radiologist at an outpatient clinic affiliated with the Medical College of Pennsylvania. Modalities include general radiology, mammography, and ultrasound. This individual would rotate through the main dept. with teaching responsibilities for the residency program. Send CV or call Mindy M. Horrow, M.D., Dept. of Radiologic Sciences at the MCP, Main Clinical Campus, 3300 Henry Ave., Philadelphia, PA 19129; (215) 842-6578. 6a

VASCULAR/INTERVENTIONAL RADIOLOGIST—Temple University Hospital and School of Medicine is seeking a board-certified vascular/interventional radiologist with fellowship training for a faculty position at the assistant professor rank in the academic yr 1992–1993. This position involves responsibilities in patient care and teaching. Additionally, those candidates with research skills would be preferred. Applicants should contact Francis J. Shea, M.D., Deputy Chairperson, Dept. of Diagnostic Imaging, Temple University Hospital, 3401 N. Broad St., Philadelphia, PA 19140. Temple University Hospital and School of Medicine is an affirmative action/equal opportunity employer. 6xa

PEDIATRIC RADIOLOGY—Emory University School of Medicine is seeking applicants for a position as a pediatric radiologist. The division is staffed by 5 full-time radiologists and 1 part-time radiologist. Salary and faculty position commensurate with experience. Please direct all inquiries to William J. Casarella, M.D., Professor and Chairman, Dept. of Radiology, Emory University School of Medicine, 1364 Clifton Rd., N.E., Atlanta, GA 30322. Emory University is an AA/EEO employer. 6a

DIAGNOSTIC RADIOLOGIST, PITTSBURGH, PA—Immediate opening for general diagnostic radiologist with imaging fellowship or practice experience to join 14-member, private-practice group in 523-bed teaching hospital. Must have interest in ultrasound and nuclear medicine. Responsible for dept. residents and administrative tasks in the ultrasound division. Competitive salary and excellent benefits leading to partnership position. Contact B. A. Carlin, M.D., Diagnostic Imaging Associates, Ltd., 2041 Blvd. of the Allies, Pittsburgh, PA 15219. 6ap

BOSTON UNIVERSITY SCHOOL OF MEDICINE is seeking board-certified/eligible radiologists in ultrasound, CT, MRI, and general radiology with an opportunity to work in more than 1 section. Please send CV to Dr. Anthony Carter, Radiology Dept., The University Hospital, 88 E. Newton St., Boston, MA 02118; (617) 638-6610. An equal opportunity employer. 6ap

NEURORADIOLOGIST—Position available at the staff level. The dept. has 4 full-time neuroradiologists and 2 fellows. The practice is based at Boston City Hospital and The University Hospital. The appointment will be at the assistant or associate professor level. The candidate should be interested in teaching; research will be encouraged. Must be eligible for Massachusetts state license. Please send CV and a letter of inquiry to Dr. Jerome Shapiro, Chairman, The University Hospital, Dept. of Radiology, 88 E. Newton St., Boston, MA 02118; (617) 638-6610. An equal opportunity employer. 6ap

PEDIATRIC RADIOLOGIST—The Dept. of Radiology at the University of Minnesota has a full-time position available in the pediatric section at the rank of tenure-track assistant professor or tenured associate professor beginning as soon as possible. At the assistant professor level, minimum requirements are board-certification in radiology, a minimum of 1-yr post-residency specialty training or experience in pediatrics, and a demonstrated involvement in quality research accepted or published in peer-reviewed journals. Appointment at the rank of associate professor requires a minimum of 4 yr postresidency experience, a professional distinction in research and writing, and demonstrated effectiveness in teaching and advising. Responsibilities will include all facets of pediatric radiology as well as graduate and undergraduate medical instruction. Research performance will be strongly encouraged and evaluated. Salary is negotiable and competitive, and is dependent on past scholarly productivity and post-M.D. experience. Applicants must be licensed or able to obtain a license to practice medicine in the state of Minnesota before appointment date. Applications will be accepted through Aug. 31, 1992. Send letters to Dr. William M. Thompson, Professor and Chairman, Dept. of Radiology (Box 292 UMHC), University of Minnesota, 420 Delaware St., S.E., Minneapolis, MN 55455. The University of Minnesota is an equal opportunity educator and employer. 6a

RADIOLOGIST—Established northeastern PA radiology practice seeking fifth radiologist for hospital and private practice. Applicant should have experience in CT, MRI, ultrasound, mammography, nuclear medicine, angiography, and interventional radiology. Potential for partnership. Candidate should be board-certified/eligible and licensed in PA. Address inquiries and current CV to Box E60, *AJR* (see address this section). 6–8ap

DIRECTOR, RADIOLOGY SERVICE—The Dept. of Radiology at Columbia-Presbyterian in New York City is searching for a Director of Radiology for the Allen Pavilion practice site. The Allen Pavilion is a 300-bed, medical-surgical hospital built in 1988 that is owned and operated by the Presbyterian Hospital. It is located about 2 mi. from the Presbyterian Hospital at the northern tip of Manhattan within Columbia University's athletic complex. The Allen Radiology Service functions as a semiautonomous division within the Dept. of Radiology of Columbia-Presbyterian Medical Center. The Allen Service performs 36,000 procedures/yr including CT (GE 9800 Quick), ultrasound (Acuson), nuclear medicine (Picker SPECT), mammography (GE-ACR accredited), fluoroscopy, radiography, and angiography. Teleradiology to the main dept. provides overnight coverage. Residents from the main dept. rotate to Allen on a continuous basis. All staff radiologists at Allen participate regularly in CME and academic programs in radiology at the main dept. and have full-time appointments at Presbyterian Hospital and Columbia University. There are 3 staff radiologists at Allen in addition to the director. We are seeking a director who will participate in and organize the daily work, supervise the residents' experience, and administer the service. Salary and academic rank will be commensurate with experience and qualifications. Board certification in diagnostic radiology and a New York state medical license required; narcotics license desirable. Please send resume to Philip O. Alderson, M.D., Dept. of Radiology, 622 W. 168th St., New York, NY 10032. Columbia University is an affirmative action/equal opportunity employer. 6a

BC DIAGNOSTIC RADIOLOGIST—Affluent practice. Excellent salary, benefits, and partnership. Investigate now before socialized medicine becomes a reality! This 395-bed hospital, second largest in the beautiful state of Delaware, is centrally located on the East Coast. This is a rapidly expanding, high-powered group practice. Subspecialty training in interventional, imaging, or mammography desired. Open to F/M with 1–2 yr of postgrad experience. Send resume to or contact Ben Hollander, M.D., Dept. of Radiology, St. Francis Hospital, 7th & Clayton Sts., Wilmington, DE 19805; (302) 421-4304. 6–8ap

ST. LOUIS, MO—Excellent opportunity for a solo general diagnostic radiologist in a rapidly growing, privately owned, free-standing imaging center equipped with ultrasound, CT, nuclear medicine, mammography, general diagnostics, and mobile MRI. Competitive salary and benefits. Send CV to Linda Flanders, AMTS, 235 Dunn Rd., Florissant, MO 63031. 6ap

IMMEDIATE OPENING FOR BC/BE DIAGNOSTIC RADIOLOGIST, NEW ENGLAND to join a 6-member group, leading to partnership, in an active community, university-affiliated hospital Over 100,000 exams/yr. Practice includes CT, ultrasound, nuclear medicine, MRI, angiography, and interventional. Locum needed in interval. Located in New England close to boating and skiing, 1 hr from Boston. Contact Allan M. Deutsch, M.D., Dept. of Radiology, The Miriam Hospital, 164 Summit Ave., Providence, RI 02906; (401) 331-8500, ext. 4400. 6–8ap

DIRECTOR OF PEDIATRIC RADIOLOGY—The Division of Pediatric Radiology, Oregon Health Sciences University, Portland, OR, invites applications for a section director. Completion of an approved fellowship in pediatric radiology and ABR certification is required. Please send CV to Frederick Keller, M.D., Oregon Health Sciences University, Diagnostic Radiology, L340, 3181 S.W. Sam Jackson Park Rd., Portland, OR 97201-3098; (503) 494-4498. The OHSU is an affirmative action, equal opportunity employer. 6–8a

RADIOLOGY—Marshfield Clinic, Dept. of Radiology, is seeking a fellowship-trained or experienced abdominal imager to join its 16 members. Interest in high-risk OB ultrasound is desirable. The dept. is subspecialized and provides services to more than 380 clinic physicians in all branches of medicine and surgery. This challenging, state-of-the-art practice opportunity is located in a friendly, small-town atmosphere. For additional information, please send CV to William Manor, D.O., Dept. of Radiology, Marshfield Clinic, 1000 N. Oak Ave., Marshfield, WI 54449; (715) 387-5261 collect. 6a

DIAGNOSTIC RADIOLOGIST—Private practice opportunity with 2 radiologists. Senior partner retiring. Excellent salary and early partnership. All imaging modalities including MRI. Angio experience desired. University community of 100,000 with abundant outdoor recreation. CV to Dan Davidson, M.D., 3000 W. Deborah Dr., Monroe, LA 71201; (318) 388-7810. 6–9ap

NUCLEAR MEDICINE PHYSICIAN—Active, affiliated VA Medical Center is seeking BC/BE physician to join our nuclear medicine staff. Competitive salary and benefits. Excellent location; diverse outdoor recreational opportunities. Send resume to E. J. Towbin, M.D., Ph.D., Chief of Staff, VA Medical Center, 4300 W. 7th St., Little Rock, AR 72205; (501) 661-1202, ext. 2092. EOE. 6a

LIVE WHERE YOU CAN PLAY, THE SMOKY MOUNTAINS OF WESTERN NC—A 5-person group seeks a BC/BE diagnostic radiologist with experience in all modalities. Special interest in angio/interventional or nuclear medicine desired. Competitive salary leading to early full partnership. State-of-the-art equipment. Friendly, small-town atmosphere in 75,000+ population county. Plentiful amenities and diverse recreational activities in the immediate area. Moderate 4-season climate. Position available at this time, but would hold for suitable candidate. Send CV or call Dr. Ronald Liljedahl, Hendersonville Radiological Consultants, 807 N. Justice, Hendersonville, NC 28739; (704) 696-1045, work; (704) 697-6741, home. 6ap

IMMEDIATE OPENING FOR BC/BE GENERAL DIAGNOSTIC RADIOLOGIST to join 2-person group in private office and 160-bed hospital. Practice includes all aspects of diagnostic radiology including MRI. Located on the lovely southern Oregon coast. Competitive compensation, fringe benefits, and partnership in 2 yr. Send CV to Michael Quinn, M.D., South Coast Radiology, 2650 N. 17th, Coos Bay, OR 97420; (503) 267-5411. 5–6ap

MRI/CT/ULTRASOUND—The State University of New York/Health Science Center at Brooklyn seeks a board-certified/eligible physician to join the faculty in cross-sectional imaging. The medical center is a 1700-bed facility including Kings County Hospital and the State University Hospital. The medical center performs over 250,000 diagnostic procedures/yr. Currently, we have 4 state-of-the-art CT scanners with a fifth to be installed shortly. A GE Signa was recently installed and a second is planned. Seventeen ultrasound units are in clinical use. Research time and facilities are available. The 2 hospitals are connected with a PACS system via a microwave link. Rank and salary are commensurate with qualifications. CV should be addressed to Joshua A. Becker, M.D., Professor and Chairman, Dept. of Radiology, SUNY/Health Science Center at Brooklyn, 450 Clarkson Ave., Brooklyn, NY 11203. Equal opportunity employer. 6–7ap

INTERVENTIONAL RADIOLOGIST, ALBUQUERQUE, NM—A well-established, 14-physician group has an immediate opening for a fellowship-trained vascular interventionalist. Initially, approximately 40–50% of work time interventional; additional interventional volume as senior physicians phase down. Practice serves a major hospital in the metro area, 2 MRI centers, 2 outpatient centers, and 3 outlying facilities. All vascular interventional work at 1 location. Candidate must have ability/desire to perform both interventional and general radiology procedures. Strong desire to live and work in the southwest a must. Competitive compensation package. Send CV with references to P. O. Box 7309, Albuquerque, NM 87194-7309. 5–6a

VASCULAR/INTERVENTIONAL RADIOLOGIST–The Dept. of Radiology at Graduate Hospital is looking for a vascular/interventional radiologist, either fellowship-trained or with extensive experience in this subspecialty. The successful applicant will join a 13-person radiology group in a tertiary-care hospital affiliated with the University of Pennsylvania. A new, state-of-the-art angiography suite has just been installed. Inquiries and CV should be addressed to Jerome G. Jacobstein, M.D., Chairman, Dept. of Radiology, Graduate Hospital, One Graduate Plaza, Philadelphia, PA 19146; (215) 893-2050. 6ap

RADIOLOGIST—Active/affiliated VA Medical Center seeks BC/BE radiologist for diagnostic radiologic work. Full, unrestricted license and current registration. Salary based on qualification. Excellent fringe benefits. Contact David Harshfield, M.D., VA Medical Center, 4300 W. 7th St., Little Rock, AR 72205; (501) 661-1202, ext. 2009. EOE. 6a

MAMMOGRAPHY FACULTY POSITION—The Dept. of Radiology at the University of Rochester Medical Center has a faculty position available in mammography. The mammography practice is in Strong Memorial Hospital and 2 private offices. One of the offices has over 30,000 exams/yr. The section offers a strong potential for academic growth with emphasis on original research and teaching. Academic time is available for faculty interested in developing a strong academic career. Support, resources, and opportunities are available for research. The radiologist can also participate in other aspects of radiology. Academic rank and salary will be determined by previous experience. Contact John C. Wandtke, M.D., Acting Chair, Dept. of Radiology, Box 648, University of Rochester Medical Center, Rochester, NY 14642; (716) 275-2733. EO/AA/M-F. 6–8a

NEURORADIOLOGIST—A faculty position is available in the Dept. of Radiology at the University of Rochester Medical Center, Strong Memorial Hospital, a 725-bed university hospital. An appointment as assistant professor or higher is available at a level appropriate to experience. A fellowship is required. The neuroradiology section consists of 5 faculty members and 1–2 fellows. Research and teaching opportunities are available in a strong academic dept. with state-of-the-art radiologic equipment. Contact John C. Wandtke, M.D., Acting Chair, Dept. of Radiology, Box 648, University of Rochester Medical Center, Rochester, NY 14642; (716) 275-2733. EO/AA/M-F. 6–8a

RADIOLOGY DEPT. CHIEF, DEPT. OF VETERAN AFFAIRS MEDICAL CENTER, LOUISVILLE, KY—The VA Medical Center in Louisville, which is a major, affiliated hospital of the University of Louisville, School of Medicine, is seeking applications for the chief of diagnostic radiology. The radiology dept. is equipped with state-of-the-art equipment, which is the result of a recent $13 million clinical and education addition. The dept. includes facilities for digital vascular imaging, computerized tomography, ultrasound, and all noncardiac nuclear medicine imaging. The radiology dept. is staffed by a group of 6 physicians and performs approximately 50,000 exams/yr. Qualifications include board certification in diagnostic radiology and eligibility for an academic appointment at the University of Louisville, School of Medicine. Please send CVs in confidence by July 15, 1992, to Chief of Staff (11), VA Medical Center, 800 Zorn Ave., Louisville, KY 40206-1499. An equal opportunity/affirmative action employer. 6a

CENTRAL WISCONSIN—Established radiology group in independent practice is seeking 2 additional radiologists for growing practice in central Wisconsin. All imaging modalities. Competitive first yr salary with full partner status available second yr. Full benefits. Excellent schools, recreation, and quality of life. Contact David E. Enerson, M.D., 900 Illinois Ave., Stevens Point, WI 54481; (715) 346-5140 or Andrew M. Lucas, M.D., 410 Dewey St., Wisconsin Rapids, WI 54495-8080; (715) 423-6060. 6xa

GREENVILLE, SC—Metro Radiology, a large multistate practice in the southeast, will begin providing professional services in Greenville, SC, at the St. Francis Hospital, the St. Francis Women's Hospital, and its affiliate outpatient center beginning Sept. 1. We will be adding 4 additional radiologists to our staff to provide services at these facilities. The hospitals are modern and well-equipped and have a total of 287 beds. We are seeking radiologists who are bright, talented, and energetic. They must be board-certified and should possess subspecialty experience. Greenville is a metropolitan community of over 200,000 people. It is adjacent to the Blue Ridge Mountains and is readily accessible to Atlanta and Charlotte. Greenville is an excellent family community with fine schools and is the home of a major university. Our radiologists receive excellent compensation and have a full benefit package including complete insurance programs and retirement programs. We will be filling these positions very soon, so please contact us immediately. Please call Denise Rinderer or Franklin Zirkle at (800) 662-6387. Please send your CV to Metro Radiology, NCNB Plaza, 7 N. Laurens St., Ste. 300, Greenville, SC 29601. 6ap

ISRAEL, DIAGNOSTIC RADIOLOGY—Opportunities for 3- to 4-wk or longer working vacations in a number of Israeli medical centers, on a volunteer basis. Positions varied, arrangements flexible. For information contact Jonathan H. Fish, M.D., 1844 San Miguel Dr., #302, Walnut Creek, CA 94596; (510) 947-0560. 5–7xa

ANGIO/INTERVENTIONAL SECTION CHIEF—Fill by June 30, 1992. Busy division. 2500 exams/yr. Rank based on experience. Unlimited potential. Reply Box D40, *AJR* (see address this section). 5–6a

ULTRASOUND/NONINVASIVE VASCULAR DIAGNOSTIC RADIOLOGIST—Progressive radiology group practice expansion has created an immediate opportunity for a board-certified diagnostic radiologist with subspecialty strength in diagnostic ultrasound, high-risk obstetrical, and noninvasive vascular imaging. Our established hospital and full-service private offices are located in the Washington, DC, areas from western Loudoun County, through northern Virginia, and into southern Maryland. OB/GYN exams comprise approximately 60% of volume. Special expertise with high-risk obstetric exams required. Noninvasive vascular, prostate imaging, and prostate biopsy programs represent another strong component. We are committed to the use of leading edge technologies including Diasonics Spectra and Acuson 128 XP Systems, 4 MRI systems, SOPHA nuclear SPECT and cardiac programs, ISG 3-D workstation, ACR-accredited women's centers, and Philips CT scanners and radiographic/fluoroscopic systems. Very attractive, comfortable practice setting for individual with exceptional commitment to excellence and a desire to lead. Address inquiries and CV to Radiology Imaging Associates, Attn: Grant McClure, 7801 Old Branch Ave., Ste. 300, Clinton, MD 20735; (301) 856-6718. 6ap

NEURORADIOLOGIST—A 25-person radiology group in central New Jersey seeks a fourth neuroradiologist well-versed in all neuroimaging modalities and procedures. Senior member status or eligibility in the ASNR is required. Practice includes 2 450-bed hospitals, 3 offices, 3 MRI scanners, 5 CT scanners, a radiology residency, and medical student teaching. Send CV to Richard Feinstein, M.D., c/o Kathy McGrath, Radiology Group of New Brunswick, 230 Old Bridge Tpk., South River, NJ 08882. 5–6a

PARTNERSHIP POSITION IN PALM SPRINGS, CA—Well-established, 9-member group has openings for 2 board-certified radiologists. A physician with a strong background in MRI is sought as director of the section of MRI. The other position requires a physician with mammography experience to direct imaging in the breast health section of a new comprehensive cancer center. The group covers a 350-bed hospital and 2 offices in a desirable, rapidly expanding area of southern California. MRI facilities include 1.5-T Picker Vista HPQ with MRA package, ViStar imaging computer, and 1.5-T GE Signa. Other equipment includes 3 CT, a Cemax image processor, 2 Acuson color-flow Doppler ultrasound, 4 nuclear cameras including 2 SPECT, and all other diagnostic modalities. Ground has just been broken on a new 25,000 sq. ft. radiology wing, which will be furnished with state-of-the-art equipment. New trauma center, cancer center, and rehab hospital being built. Excellent compensation and benefits package leading to full partnership. Beaches and large-city amenities of Los Angeles only 2 hr away. Yr-round sunny weather. Ample free time to enjoy southern California and the unparalleled recreational opportunities offered by the resort community of Palm Springs. Direct inquiries to Marvin J. Friedenberg, M.D., Desert Hospital, Dept. of Radiology, 1150 N. Indian Canyon Dr., Palm Springs, CA 92262. 6xa

PEDIATRIC RADIOLOGY—The Medical College of Georgia seeks a general pediatric radiologist and a pediatric radiologist with expertise in pediatric imaging. These individuals will provide general and specialized pediatric radiology services, guide the integration of imaging services within pediatric radiology, and help plan and implement pediatric radiology services for the upcoming 175-bed Children's Medical Center. Tenured or nontenured positions are available at assistant, associate, or full professor levels. The senior appointee will become head of the Pediatric Radiology Section. Call or write Dr. Charles G. Howell, Jr., Pediatric Radiology Search Committee, Pediatric Surgery Section, Medical College of Georgia, Augusta, GA 30912-4070; (404) 721-3941. MCG is an equal opportunity/affirmative action employer. 6xa

CALIFORNIA, CENTRAL COAST (POP. 60K)—BC radiologist sought for a small hospital with an active outpatient service. Routine radiology with mammography and ultrasound. Solo position. Relief coverage available. Generous salary. Full-time or 6–8 mo/yr. Write Box D44, *AJR* (see address this section). 5–6ap

BOSTON—Expanding private-practice group. No night or evening call. Need experience in mammography. Great lifestyle. Salary leading to equal partnership. Send letter and CV to Box E49, *AJR* (see address this section). 5–10a

GENERAL RADIOLOGIST, RUIDOSO, NM—Solo practice with advantages of large group practice (CME, vacations, etc.). Small, but growing resort community in southern New Mexico. Quality outdoor lifestyle and excellent skiing. Professional support via teleradiology and vacation coverage by 14-physician group in Albuquerque. Position requires experience in general radiology, CT, mammography, and ultrasound. Strong desire to live and work in the southwest a must. Competitive compensation package. Send CV with references to P. O. Box 7309, Albuquerque, NM 87194-7309. 5–6a

NORTHERN CALIFORNIA—The Permanente Medical Group, Inc., is seeking a BC radiologist with multimodality interests and fellowship training in MR to join a 12-person group serving a 337-bed acute-care hospital and 2 outpatient clinics. Teaching opportunities are available with residents of subspecialty services on rotation from Stanford University Hospital, as well as our own medical residents. We have sited a GE 1.5-T MRI system. Competitive salary and excellent benefits. Please send inquiries and CV to Bruce Baker, M.D., Chief, Dept. of Radiology, Kaiser Permanente Medical Center, 900 Kiely Blvd., Santa Clara, CA 95051; (408) 236-4444. EOE. 5–7a

DIAGNOSTIC RADIOLOGIST, ABDOMINAL IMAGING—The University of Missouri– Columbia Hospital and Clinics is seeking a radiologist with expertise in abdominal imaging (GI, CT, ultrasound, and MRI). Board-certification required. Fellowship desirable. Tenure and nontenure tracks available at assistant and associate professor levels. Address inquiries to Robert J. Churchill, M.D., Dept. of Radiology, University of Missouri—Columbia Hospital and Clinics, One Hospital Dr., Columbia, MO 65212. An equal opportunity/affirmative action employer. 5–10ap

INTERVENTIONAL RADIOLOGIST needed for large, private-practice group in northern New York suburb area. Salary leading to partnership. Send CV to Kenneth S. Schwartz, M.D., Northern Metropolitan Radiology Associates, P.C., 3630 Hill Blvd., Jefferson Valley, NY 10535; (914) 245-8935. 6ap

HOSPITAL-BASED, BC/BE RADIOLOGIST needed to join newly planned subregional medical center (campus). Must be proficient in general diagnostic radiology, ultrasound, nuclear medicine, CT, and MRI. Excellent opportunity plus attractive financial package. Located in east, central Montana along the Yellowstone River. Great outdoors for recreation, hunting, and fishing. Excellent education system. Lifestyle is rural and family-oriented. Send CV to Vice-President, Business Services, Holy Rosary Hospital, 2101 Clark, Miles City, MT 59301. 5–7ap

BC/BE GENERAL DIAGNOSTIC RADIOLOGIST needed to join 3 radiologists in 70-physician multispecialty clinic. Also responsible for radiology services at 250-bed hospital connected to clinic. All radiology modalities available, including CT and MR. Competitive first-yr guarantee with excellent benefit package. Eligibility for shareholdership after 1 full fiscal yr. Community of 52,000 in beautiful Mississippi River Valley. Send CV to P. Stephen Shultz, M.D., Medical Director, Skemp Clinic, Ltd., 800 West Ave., S., La Crosse, WI 54601; (608) 782-9760, ext. 6329. 5–7ap

FULL-TIME BC/BE DIAGNOSTIC RADIOLOGIST needed to replace retiring senior partner in a friendly, cooperative, 4-person group in south-central Idaho. 165-bed hospital with GE Signa 1.5-T MR, GE 9800 Quick CT, Acuson XP, and good technical staff. General radiology including angio, interventional, and nuclear medicine. Good income and vacation schedule, 1 yr to partnership. Nice community with extensive nearby skiing, hunting, fishing, etc. 80 mi. from Sun Valley, 4-hr drive from Yellowstone. Send CV and references to Dr. Evan Thomas, Southern Idaho Radiology, P. O. Box AB, Twin Falls, ID 83303. 5–7ap

DIRECTOR, DIVISION OF ULTRASOUND—The Dept. of Radiology, The University of Texas Medical Branch, is looking for a director of diagnostic ultrasound at the associate professor or professor entry level. The Division of Ultrasound, in our dept., is poised for growth and expansion. We require a leader with drive, initiative, and vision, and 1 who is still in his or her growing career phase. The University of Texas Medical Branch employs more than 8400 employees, and Dept. of Radiology performs more than 200,000 exams/yr. The campus provides a fertile environment for those wishing to pursue an academic career. The clinical material and academic support are excellent. The dept. boasts many peer-reviewed publications and textbooks resulting from an inherent feature of the institution that allows 1 to pursue academic interests with freedom. Galveston is a very comfortable community with few large-city problems. It has an extremely pleasant climate, with the Gulf breeze making it exceptionally attractive throughout the yr. Outdoor activities abound, including boating, sailing, fishing, and tennis. The winters are extremely mild. More than half of the present faculty have lived in this area for 15 yr or more. The dept. and institution are quite stable and have proved an excellent place for many of us to pursue academic careers. The position we offer has the foundation for the development of a truly superior academic career. Interested persons should send their CV to Leonard E. Swischuk, M.D., Chairman Ad-Interim, Dept of Radiology, The University of Texas Medical Branch, Galveston, TX 77550. UTMB is an equal opportunity, affirmative action employer, M/F/H/V. UTMB hires only individuals authorized to work in the United States. 5–7a

DIAGNOSTIC RADIOLOGIST FOR TOP-FIVE CITY (MONEY MAGAZINE OCTOBER '91)—Progressive, well-established group of 9 board-certified radiologists has position immediately available for a recently trained BC diagnostic radiologist. Fellowship training preferred, but will consider qualified individual with special expertise in body imaging; angiographic experience is optional. Practice includes 2 tertiary hospitals (850 and 350 beds), private office, and 2 imaging centers. State-of-the art equipment includes 2 GE 1.5-T MRI units; ATL, Toshiba, and Acuson duplex color ultrasound; and 5 GE 9800 CT. High plains offer moderate climate, and surrounding area is ideal for outdoor interests, including skiing, hunting, boating, and fishing. Excellent compensation and benefits package leading to full partnership. Please reply with CV to Todd R. Samuels, M.D., Lubbock Radiology Associates, 3707 21st St., Lubbock, TX 79410. 5–8ap

COLORADO—BC/BE radiologist sought to join 2-person practice covering 2 hospitals in the central mountains of Colorado. Ample free time and excellent outdoor recreational opportunities. Contact E. J. Loeffel, M.D., P. O. Box 415, Buena Vista, CO 81211; (719) 539-3782. 4–6ap

TWO DIAGNOSTIC RADIOLOGISTS, WASHINGTON—Prominent, 100-physician multispecialty clinic in Pacific Northwest seeks both a diagnostic radiologist and an interventional radiologist. Interventional radiologist should have fellowship training and/or extensive experience in interventional radiology. Diagnostic radiologist should have general radiology experience to include all full-scope imaging services. Guaranteed salary and partnership track available. Excellent benefit package. Abundant 4-season recreational opportunities. Send CV to Fred Bockenstedt, M.D., P. O. Box 489, Wenatchee, WA 98807. 5-10ap

DIAGNOSTIC RADIOLOGIST, TOLEDO, OH—Expanding 23-radiologist group seeks BC radiologist with 1 or more yr fellowship experience. Interest/expertise in pediatric radiology, mammography, or nuclear medicine would be helpful. Position requires no special procedures and leads to equal partnership. Our group values quality of work as well as personal time and offers an excellent salary with very generous time off. Coverage includes 850-bed tertiary hospital, 350-bed suburban hospital, and 3 outpatient offices with more than 240,000 exams/yr. All modalities are represented. Excellent family-oriented community with great schools. Send CV to Drs. David Parker or Keith Wilson, Roemer Bldg., 3912 Sunforest Ct., Toledo, OH 43623; (419) 471-4438 days. 5–7ap

EXCELLENT OPPORTUNITY FOR BE/BC DIAGNOSTIC RADIOLOGIST with training in all modalities to join active, 7-member group in midwestern university town with medical school affiliation. Abundance of cultural opportunities and outdoor recreation. Excellent salary with early partnership. Please send inquiries and CV to Mark Schneider, M.D., or Dean Hountras, M.D., 1000 S. Columbia Rd., Grand Forks, ND 58206-6003; (701) 780-6596. 4–6ap

RADIOLOGIST, TYLER, TX—The University of Texas Health Center at Tyler invites applications for a clinical faculty position in the Dept. of Radiology. Some teaching, but not publishing or research, required. A progressive 4-person dept. practices general radiology (including interventional, MRI, and SPECT) and performs approximately 27,000 exams/yr. New equipment, flexible work hours, very light call, no weekend schedule. Yr-round tennis, golf, and boating are available in addition to excellent schools. Competitive first-yr salary and an unsurpassed benefits package are offered. Send CV to J. R. Shepherd, M.D., University of Texas Health Center at Tyler, P. O. Box 2003, Tyler, TX 75710; (903) 877-7100. The University of Texas Health Center at Tyler is an affirmative action, equal opportunity employer. Minorities are encouraged to apply; male/female/handicapped/disabled. 4–6a

SAN ANTONIO, TX—Large group covering multiple hospitals and outpatient facilities seeks radiologists with angiography skills. Send CV to Search Committee, M&S X-Ray Associates, P. O. Box 15920, San Antonio, TX 78212-9510. 1–6ap

GENERAL DIAGNOSTIC RADIOLOGIST WITH IMAGING AND MAMMOGRAPHY EXPERIENCE—William Beaumont Hospital is a modern, expanding, tertiary-care teaching medical center in southeast Michigan with approved residency and fellowship in diagnostic radiology. Excellent facilities and remuneration. We are seeking a general radiologist with training and experience in imaging and/or mammography. Please send CV to Jalil Farah, M.D., Chairman, Diagnostic Radiology, William Beaumont Hospital, 3601 W. 13 Mile Rd., Royal Oak, MI 48073. 4–6a

MUSCULOSKELETAL RADIOLOGIST, CHARLOTTE, NC—A 13-member, subspecialized group serving a 660-bed, private community hospital–outpatient diagnostic center desires a fellowship-trained or staff level musculoskeletal radiologist. GE 9800 CT and Signa 1.5-T equipment. Family-oriented community with warm 4-season climate, centrally located between coast and mountains. Send CV to P. O. Box 221211, Charlotte, NC 28222. 4–6ap

ANGIOGRAPHER–INTERVENTIONAL RADIOLOGIST, CENTRAL MASSACHUSETTS—Radiologist with angiography and interventional skills sought to join an 11-member, private-practice group serving a 550-bed medical center and performing 150,000 exams/yr. Position involves sharing general diagnostic radiology responsibilities, including CT, ultrasound, and mammography. Please send CV to Richard Danford, M.D., Worcester Radiologists, Inc., 121 Lincoln St., Worcester, MA 01605; (508) 753-8151. 4–6ap

DIAGNOSTIC RADIOLOGIST needed for expanding practice in 200-bed, well-equipped community hospital in Troy, MI. Must have expertise in CT, ultrasound, and mammography. Very competitive salary and benefits. Send CV to Thomas Verhelle, M.D., Troy-Beaumont Hospital, 44201 Dequindre Rd., Troy, MI 48098. 4–7ap

SUPERB PARTNERSHIP POSITION IN LAS VEGAS—Rapidly expanding 7-member group practice covering 2 full-service imaging centers and a small hospital has an immediate opening. We are looking for an additional board-certified radiologist with an uncommon dedication to excellence in patient care. Our outpatient facilities include 2 MR, 2 CT, angio with a 4-bed recovery area, 5 ultrasound, 5 mammography, 3 SPECT, plus R&F. This is an excellent opportunity for a partnership position with a well-respected group in a growing community. Please send CV to Dr. Mark Winkler, SDMI, 2950 S. Maryland Pkwy., Las Vegas, NV 89109. 3–2ap

CONNECTICUT, ANGIO/INTERVENTIONAL RADIOLOGIST—Opening in July 1992 for BC/BE radiologist with fellowship training in angiographic procedures. Additional training or experience in other interventional procedures is desirable. Nine-radiologist practice includes a 435-bed, university-affiliated, community hospital and a 57-physician multispecialty clinic. Approximately 107,000 exams/yr, including MRI, CT, nuclear medicine, ultrasound, as well as an active angiographic and interventional service. Excellent salary and benefits leading to full partnership after second yr. For more information, send CV to David A. Lund, M.D., Dept. of Radiology, New Britain General Hospital, 100 Grand St., New Britain, CT 06050. 3–6ap

CONNECTICUT, NEURORADIOLOGIST—Opening in July 1992 for BC/BE radiologist with fellowship training in neuroradiology. Nine-radiologist practice includes a 435-bed, university-affiliated community hospital and a 57-physician multispecialty clinic. Approximately 107,000 exams/yr including MRI, CT, nuclear medicine, ultrasound, and an active angiographic and interventional service. Excellent salary and benefits leading to full partnership after second yr. For more information, send CV to David A. Lund, M.D., Dept. of Radiology, New Britain General Hospital, 100 Grand St., New Britain, CT 06050. 3–6ap

RADIOLOGIST—A 4-physician group seeks a fifth to join our well-established and growing practice. We are located in east-central Illinois, with a 4-yr college, Jr. college, and a farming economy enhanced by numerous growing industries. We serve a rural but very modern 230-bed hospital ($25 million expansion underway) and several other sites, performing more than 80,000 exams/yr. Mattoon-Charleston is a great place to raise a family while still having access to big-city amenities. Please be BC/BE, skilled in interventional or MRI, and able to handle general diagnostic modalities competently. Please reply to Bruce Fluesmeier, Lakeland Radiologists, Ltd., 1221 Broadway, Mattoon, IL 61938; (800) 745-7701. 3–8ap

GENERAL RADIOLOGY STAFF POSITION—The Dept. of Radiological Sciences at Olive View–UCLA Medical Center has openings for staff positions in general radiology and ultrasound. Candidates must be board-certified and eligible for certification in diagnostic radiology and should be eligible for licensing in the state of California. Interested candidates should contact Issa Yaghmai, M.D., Professor and Chairman, Dept. of Radiological Sciences, Olive View–UCLA Medical Center, 14445 Olive View Dr., Sylmar, CA 91342; (818) 364-4078. The University of California, Los Angeles, is an affirmative action/equal opportunity employer. 3–6a

ABDOMINAL RADIOLOGIST—The Harvard Medical School, Brigham and Women's Hospital, has a full-time faculty position for an academically inclined abdominal radiologist. Outstanding hospital setting, equipment, case mix, and research facilities make this an unusually exciting opportunity. Please contact Steven E. Seltzer, M.D., Co-Director, Abdominal Imaging, Brigham and Women's Hospital, 75 Francis St., Boston, MA 02115; (617) 732-6301. Harvard Medical School, Brigham and Women's Hospital is an affirmative action/equal opportunity educator and employer. 1–6a

IMMEDIATE OPENING—BC/BE radiologist to join 2 board-certified radiologists at a 130-bed community hospital and outpatient dept. located 25 mi. east of Palm Springs, CA. Excellent salary, fringe benefits, early partnership, no buy-in, and generous vacation time. All imaging modalities including SPECT ANGER camera, MRI, and angio/interventional. Reasonable housing in resort atmosphere. Contact Stephen J. Curtis, M.D., Radiology Director, J.F.K. Memorial Hospital, 47-111 Monroe St., Indio, CA 92201; (619) 775-8066. 4–7ap

ASSISTANT PROFESSOR, MR RADIOLOGIST—The Dept. of Radiology at The University of Texas Medical School at Houston and the Hermann Hospital are recruiting for a full-time MRI radiologist at the assistant professor level, beginning July 1, 1992. Preference will be given to candidates with fellowship training in MRI, body imaging, neuroradiology, or 1 yr of academic MRI experience. ABR certification is required. Responsibilities will include monitoring and interpretation of both body and neuro MRI, as well as medical student, resident, and fellow teaching. Extensive clinical and basic science research opportunities are available. The dept.'s MR facilities are state-of-the-art and located in a beautiful spacious setting, which includes a 1.5-T GE Signa unit with proton spectroscopic capability. A second 1.5-T GE System, with MR angiography, fast spin echo (FSE), and phased array coils, will be installed in the first quarter of 1992. The Dept. also has an active basic science research program; research facilities include a small bore MRI system with spectroscopy capabilities. The University of Texas at Houston is an equal opportunity employer. Women, minorities, and the disabled are encouraged to apply. Please send CV and 3 references to Bharat Raval, M.D., Professor and Interim Chairman, Dept. of Radiology, The University of Texas Medical School–Houston, 6431 Fannin, Suite 2.132, Houston, TX 77030. 2–7ap

FAIRBANKS, AK—Four diagnostic radiologists seek fifth partner for diversified practice including general radiology, ultrasound, nuclear medicine, MRI (GE 1.5-T), and CT (GE 9800). Hospital and office practice. Desirable life-style advantages in a university town. Unlimited access to the outdoors. Excellent salary, benefits, retirement, and vacation. One yr to full partnership. Contact Douglas Hutchinson, M.D., 1919 Lathrop #5, Fairbanks, AK 99701; (907) 452-5092. 2–7ap

DIRECTOR OF BREAST IMAGING—The Brigham and Women's Hospital/Harvard Medical School, Dept. of Radiology, is seeking a full-time diagnostic radiologist to head the Breast Imaging Section. This hospital-based facility has 4 mammographic rooms, 2 with ultrasound. In addition, there is a mammo-test unit for performance of large core breast biopsies. More than 12,000 mammograms, 1,000 preoperative wire localizations, 500 guided aspirations, and 150 core biopsies are performed annually. This wealth of clinical material coupled with an excellent clinical staff provides unlimited opportunity for collaborative clinical investigation. Candidates must have board certification. Please contact Jack E. Meyer, M.D., Director of Diagnostic Radiology, Brigham and Women's Hospital, 75 Francis St., Boston, MA 02115; (617) 732-6269. Brigham and Women's Hospital/Harvard Medical School is an affirmative action/equal opportunity educator and employer. 2–7a

THE DEPT. OF RADIOLOGY AT BROOKE ARMY MEDICAL CENTER, SAN ANTONIO, TX, is recruiting academic radiologists for several divisions of the dept., including ultrasound, chest, skeletal, neuroradiology, general diagnostic, interventional radiology, and mammography. Our dept. offers a fully accredited residency program with 24 residents and 16 attending full-time staff. Numerous consultants from across the country lecture on a continuing and regular basis. The hospital is a modern, tertiary-care center serving Texas, Oklahoma, and Louisiana. A strong residency program, interesting patient population, excellent equipment, teleradiology and digital radiology implementations underway, coupled with a south Texas lifestyle are positive aspects of the practice. Academic credentials and/or experience are necessary. Recently graduated fellows are encouraged to apply. Board certification is mandatory. Candidates should be particularly interested in patient care, teaching, and research. Salary and benefits are competitive and generous. Brooke is an EO/EEO employer. Please contact Dr. Billy E. Cunningham, COL, MC, Assistant Chief, Dept. of Radiology, Brooke Army Medical Center, Fort Sam Houston, TX 78234-6200; (512) 221-8418/8218. 8–7a

THE RADIOLOGY DEPT. AT DWIGHT DAVID EISENHOWER ARMY MEDICAL CENTER is recruiting academic radiologists. The dept. provides a full range of services including angiography, ultrasound, CT (with a new GE 9800 Advantage system), and MRI (with a new 1.5-T GE Signa system). Development is underway for the installation of a digital teleradiology link to area medical facilities. The dept. is also beginning a radiology residency program in affiliation with the program at the Medical College of Georgia in Augusta. With this growth, the dept. has generated a need for several academic diagnostic radiologists. Board-certified diagnostic radiologists with academic credentials and/or experience are urged to apply. Fellowship training is desired, especially in interventional radiology and/or angiography, however candidates at all levels will be considered. Candidates should be particularly interested in patient care, teaching, and research. The medical center is located on Fort Gordon, GA, adjacent to Augusta, and is the tertiary-care hospital supporting 9 Army community hospitals of the southeastern region and Puerto Rico. The hospital supports fully accredited residency programs in family practice, general surgery, medicine, orthopedics, pathology, and psychiatry. Salary and benefits are competitive and generous. The medical center is an EO/EEO employer. Please contact Dr. Thomas M. Ralston, LtC., Chief, Radiology Dept., Eisenhower Army Medical Center, Fort Gordon, GA; (404) 791-6245. 8–7a

THE DEPT. OF RADIOLOGY AT WALTER REED ARMY MEDICAL CENTER is recruiting academic radiologists. We need board-certified radiologists to work in this famous and modern health-care center. Our dept. has a residency program consisting of 24 residents and several fellows. Subspecialists are needed in ultrasound, chest, mammography, genitourinary, gastrointestinal, pediatric, CT, MRI, and interventional radiology, as well as general radiology. Excellent opportunity to live in the nation's capital and also become an integral part of a large teaching program. Salaries are competitive and generous. Highly motivated applicants should contact Col. Mark F. Hansen, Radiology Consultant to the Army Surgeon General, Dept. of Radiology, TAMC, HI 96859-5000; (808) 433-6393. 8–7a

NEURORADIOLOGIST—Senior ASNR member needed for excellent hospital and imaging center position in Tucson, AZ. Early partnership opportunity. Send CV to Arizona State Radiology, 7250 E. Ventana Canyon Dr., Tucson, AZ 85715. 8–7ap

THE DEPT. OF RADIOLOGY AT TRIPLER ARMY MEDICAL CENTER, HONOLULU, HI, is recruiting academic radiologists for several divisions of the dept., including ultrasound, chest radiology, skeletal, neuroradiology, general diagnostic radiology, MRI, interventional radiology, and mammography. Our dept. offers a fully accredited residency program with 21 residents and 16 attending full-time staff. Numerous consultants from across the country lecture on a continuing and regular basis. The hospital is a modern, tertiary-care center serving Hawaii and the entire Pacific Basin. A strong residency program, diverse and interesting patient population, excellent equipment, and tropical lifestyle are positive aspects of the practice. Academic credentials and/or experience are necessary. Recently graduated fellows are encouraged to apply. Board certification is mandatory. Candidates should be particularly interested in patient care, teaching, and research. Salary and benefits are competitive and generous. Tripler is an EO/EEO employer. Please contact Dr. Mark F. Hansen, Col, MC, Chief, Dept. of Radiology, TAMC, HI 96859-5000; (808) 433-6393. 7–6a

Positions Desired

FELLOWSHIP-TRAINED NEUROINTERVENTIONIST, senior member of the ASNR, would like to join academic or private radiologists or neurosurgeons wishing to add this expertise to their practice. Reply to Box D42, *AJR* (see address this section). 5–6bp

SECOND YR RADIOLOGY RESIDENT (PGY3) seeks PGY4 position for July 1992. Enthusiastic, amiable, and hardworking. Desiring more challenge and diversity. Willing to relocate. Reply Box Q94, *AJR* (see address this section). 4–6bp

Fellowships and Residencies

FELLOWSHIP IN NEURORADIOLOGY—Boston University Dept. of Radiology has an opening for a fellowship in neuroradiology to begin July 1992. The dept. is based at Boston City Hospital and The University Hospital. The candidate must be eligible for Massachusetts state license and must be interested in teaching and research. Some coverage of general vascular radiology in evenings and weekends will be required. Send a CV and a letter of inquiry to Dr. Shripad Tilak, The University Hospital, Dept. of Radiology, 88 E. Newton St., Boston, MA 02118; (617) 638-6610. An equal opportunity employer. 6cp

FELLOWSHIPS IN PEDIATRIC RADIOLOGY—The Dept. of Diagnostic Imaging and Radiology, Children's National Medical Center, Washington, DC, is soliciting applications for postgraduate fellowship training in pediatric radiology beginning 1994. The dept. performs over 70,000 exams/yr in 1 of the 4 largest children's hospitals and ambulatory practices in North America. The dept. has 11 faculty, 4 fellows, and many resident trainees. Imaging services and training include state-of-the-art radiography, fluoroscopy, ultrasound, nuclear medicine, cardiovascular imaging, interventional radiology, CT, and MRI. There are many opportunities for rewarding careers in pediatric radiology in either academic or practice environments. If you wish to receive more information about the fellowship or careers in pediatric radiology, please contact David C. Kushner, M.D., Chairman, Dept. of Diagnostic Imaging and Radiology, Children's National Medical Center, 111 Michigan Ave., N.W., Washington, DC 20010; (202)745-5080. EOE. 6c

WAYNE STATE UNIVERSITY, BODY MRI FELLOWSHIP—The Dept. of Radiology, Wayne State University, is offering a new fellowship in body MRI commencing July 1, 1992. The MR Center includes a 4.7-T animal imager and state-of-the-art 1.0-T and 1.5-T magnets with a second 1.5-T magnet to be installed in fall 1992. One whole-body magnet is dedicated to research. In addition, the physically connected Children's Hosptial has a 0.35-T magnet dedicated to pediatric patients. The medical center has 1200 beds and a broad referral base, leading to a busy clinical service covering all ages and all body systems. There is an active research program in both imaging and spectroscopy with a full-time MR physicist, a biochemist, and graduate students. The fellowship is a 1-yr program with a potential second yr for a fellow with strong research interests. Interested candidates should contact Renate L. Soulen, M.D., MR Center, Harper Hospital, 3990 John R., Detroit, MI 48201; (313) 745-9542. 6c

ADVANCED IMAGING FELLOWSHIP—The Dept. of Radiology and The Graduate Hospital Imaging Center are offering a 1-yr advanced imaging fellowship to include MR, CT, and ultrasound. Positions are available for July 1992 and July 1993. MR and CT imaging time will be spent performing both body and neuro studies. Facilities include 2 state-of-the-art GE 1.5-T MR scanners with phased array coils, endorectal MR, and MRA. Ultrasound includes color-flow Doppler. CTs include Elscint 2400 Elite and GE 9800. Candidates must have completed an approved 4-yr residency before commencing the fellowship. Board eligibility is a requirement. Salary will be at a PGY-5 level. Interested candidates should apply to Jerome G. Jacobstein, M.D., Chairman, Dept. of Radiology, The Graduate Hospital, One Graduate Plaza, Philadelphia, PA 19146; (215) 893-2050. 6cp

FELLOWSHIP POSITIONS—The Dept. of Radiology and Radiological Sciences of Vanderbilty University School of Medicine is offering fellowship positions for 1993–94 in angiography, neuroradiology, chest, and pediatric radiology. Research opportunities are available and encouraged. Candidates must be board-certified or board-qualified in diagnostic radiology and must obtain a Tennessee medical license. Address inquiries and CV to Martin P. Sandler, M.D., Director, Fellowship Programs, Dept. of Radiology and Radiological Sciences, Vanderbilt University, Nashville, TN 37232-2675. An equal opportunity/affirmative action employer. 6–7c

PEDIATRIC RADIOLOGY FELLOWSHIP—The Vanderbilt University Children's Hospital offers a 1-yr fellowship, with an option for a second yr, in pediatric radiology beginning July 1, 1992. This is a 210-bed facility with a staff with strong clinical and academic interests. It is both a primary care center and a tertiary referral facility; it is the only pediatric hospital in middle Tennessee with a catchment area extending into southern Kentucky. Training includes conventional radiography, digital fluoroscopy, computerized tomography, MRI, and all aspects of pediatric sonography. Flexible opportunities to participate in either clinical or basic research will be available. The Dept. of Radiology presently has 3 CT scanners, 3 MRI units, and a PET facility. Candidates must be board-certified or board-eligible in diagnostic radiology and must obtain a Tennessee medical license. Address all correspondence to Dr. Richard M. Heller, Dept. of Radiology, Medical Center North, Vanderbilt University Medical Center, Nashville, TN 37232-2675. An equal opportunity/affirmative action employer. 6–7c

BODY IMAGING FELLOWSHIP—Unexpected opening for a 1-yr fellowship position is available starting July 1, 1992, at Beth Israel Medical Center, Dept. of Radiology, in New York City. Beth Israel Medical Center is a nearly 1000-bed teaching hospital affiliated with Mount Sinai School of Medicine. Fellowship offers extensive clinical training in ultrasound, CT, and MRI on state-on-the-art equipment, which includes 7 ultrasound units providing color-flow Doppler, transvaginal and transrectal scanning, 2 GE 9800 CT scanners, and 1.5-T GE Signa MRI. Experience offered in CT- and ultrasound-guided interventional procedures. Applicants must have completed an approved residency in diagnostic radiology. For inquiries, please contact Helene Goldfarb, M.D., Beth Israel Medical Center, Dept. of Radiology, First Ave. at E. 16th St., New York, NY 10003; (212) 420-4580. An equal opportunity employer committed to a smoke-free environment. 6c

IMMEDIATE OPENING, PEDIATRIC RADIOLOGY FELLOWSHIP—Position available for 1-yr fellowship beginning July 1, 1992. Experience in all areas of imaging. Apply to Thomas E. Sumner, M.D., Dept. of Radiology, Wake Forest University, Bowman Gray School of Medicine, Medical Center Blvd., Winston-Salem, NC 27157-1088; (919) 748-2463. AA.EOE. 4–6c

WOMEN'S IMAGING FELLOWSHIP POSITION—High-volume breast imaging (mammography, breast ultrasound, interventional procedures), and ultrasound emphasizing obstetric and gynecologic sonography. A 1-yr fellowship to start in July 1993. Fellows also have the opportunity to participate in teaching, conference presentations, and research projects, many of which culminate in publications. Inquiries should be addressed to Ellen B. Mendelson, M.D., Chief, Mammography and Women's Imaging, The Western Pennsylvania Hospital, 4800 Friendship Ave., Pittsburgh, PA 15224. 5–12c

MUSCULOSKELETAL RADIOLOGY FELLOWSHIP—July 1, 1993. Training in ultrasound, CT, MRI, arthrography, myelography, discography, conventional tomography, bone denistometry, and plain film radiography. Offered in multiple areas, including general adult and pediatric orthopedics, congenital dysplasias, joint replacement, spine, and arthritis. Competitive salary and excellent benefits. Send CV to J. Beltran, M.D., Chairman, Dept. of Radiology, Hospital for Joint Diseases Orthopaedic Institute, 301 E. 17th St., New York, NY 10003. An equal opportunity employer. 6c

ONCORADIOLOGY/MAMMOGRAPHY FELLOWSHIP—The Dept. of Radiology at the Dana-Farber Cancer Institute and Brigham and Women's Hospital, which are Harvard Medical School affiliates, offers a 1-yr fellowship position beginning July 1, 1993. All imaging modalities involved in the diagnosis, staging, and follow-up of patients with malignant disease are integrated into this program. An additional feature is a concentrated experience in the performance of interventional breast diagnostic procedures. Please contact Jack E. Meyer, M.D., Director of Diagnostic Radiology, Brigham and Women's Hospital and Dana-Farber Cancer Institute, 75 Francis St., Boston, MA 02115; (617) 732-6269. Brigham and Women's Hospital/Dana Farber Cancer Institute/Harvard Medical School is an affirmative action/equal opportunity educator and employer. 5–4c

INTEGRATED CHEST RADIOLOGY FELLOWSHIP AT JOHNS HOPKINS UNIVERSITY HOSPITAL—The Dept. of Radiology, Division of Thoracic Imaging, Johns Hopkins University, is offering a 1- to 2-yr academically oriented fellowship in chest radiology. The fellowship offers an integrated experience in cross-sectional imaging including more than 4000 chest CT exams/yr and 1000 thoracic MRI exams/yr. Strong research interests in high-resolution CT, MRI, and interventional thoracic radiology offer the potential candidate an exciting working environment. The fellowship is available starting July 1, 1993. Contact Janet E. Kuhlman, M.D., Director of Chest Radiology, Dept. of Radiology, Johns Hopkins Hospital, Baltimore, MD 21205; (410) 955-4419. 5–7cp

ULTRASOUND, CT, AND MR IMAGING FELLOWSHIP TO BEGIN JULY 1993—More than 140,000 exams are performed yearly in the radiology dept. of this 578-bed teaching hospital. The imaging fellowship emphasizes diagnostic ultrasound, with all areas represented, including OB-GYN, urology, and vascular, significantly integrating MRI and body CT. Fellows also have the opportunity to participate in teaching, conference presentations, and research projects, many of which culminate in publications. Inquiries should be addressed to Marcela Bohm-Velez, M.D., Director of Imaging Fellowship Program, Dept. of Radiology, The Western Pennsylvania Hospital, 4800 Friendship Ave., Pittsburgh, PA 15224. 5–12c

FELLOWSHIP IN MUSCULOSKELETAL RADIOLOGY, UNIVERSITY OF FLORIDA—The Dept. of Radiology is offering musculoskeletal fellowship positions beginning July 1993 and July 1994. The fellowship currently centers on a 548-bed hospital with wide exposure to skeletal pathology, including more than 200 new musculoskeletal tumors per yr. The fellowship experience includes clinical, research, and teaching opportunities in diagnostic skeletal radiology, CT, MRI, MR spectroscopy, metabolic bone disease, TMJ pathology, and image processing. Systems available include a 1.5-T whole body spectroscopy/imager, 2 GE 9800 Advantage CT scanners, and an image processing workstation (DMI) for multiplanar (MPR) and 3D reformation. At the fellow's discretion, the experience could be expanded to include aspects of nuclear medicine and the adjacent 473-bed VA hospital, which is equipped with a 1.5-T whole body spectroscopy/imager and a Picker 1200 CT scanner. Applicants must be eligible for licensure in the state of Florida. Send CV to William J. Montgomery, M.D., Dept. of Radiology, P. O. Box 100374 JHMHC, Gainesville, FL 32610-0374; (904) 395-0291 for further information. The University of Florida is an equal opportunity/affirmative action employer. 3–6c

***FELLOWSHIPS AT THOMAS JEFFERSON UNIVERSITY HOSPITAL**—The Dept. of Radiology at Thomas Jefferson University Hospital in Philadelphia offers the following fellowship programs each yr: (1) Ultrasound/CT/MRI—Jefferson's ultrasound division is 1 of the largest in the world and performs all currently available exams, including obstetric, vascular, lithotripsy, invasive, and endoluminal. We also operate 4 GE 1.5-T MRI units and 3 CT scanners. Contact Barry Goldberg, M.D., regarding this program. (2) Cardiovascular/interventional—this division is housed in a new suite containing Philips angio units with DSA and performs the full range of vascular and nonvascular interventional procedures. Contact Geoffrey Gardiner, Jr., M.D. (3) Neuro/ENT radiology—very active clinical services supply a wealth of material to this division, which is housed in a neurosciences imaging center containing all imaging modalities. Contact Carlos Gonzales, M.D. (4) Breast imaging—Jefferson's new breast-imaging center performs approximately 85 studies/day including ultrasound and needle localizations. Contact Stephen Feig, M.D. (5) Chest—includes biopsies and CT. Contact Robert Steiner, M.D. (6) MRI—a dedicated body MRI program including excellent research opportunities in addition to a large clinical case load. Contact Donald Mitchell, M.D. (7) Ultrasound—a dedicated ultrasound program. Contact Barry Goldberg, M.D. (8) Musculoskeletal—includes MRI of the musculoskeletal system. Contact David Karasick, M.D. All program directors listed above can be contacted at the Dept. of Radiology, Thomas Jefferson University Hospital, Philadelphia, PA 19107. Jefferson is an equal opportunity/affirmative action employer. 6xc

NEURO/ENT FELLOWSHIP, UNIVERSITY OF FLORIDA—The Dept. of Radiology offers several 2-yr, postresidency fellowship training positions available July 1993 and July 1994. The fellowship offers excellent clinical material, comprehensive and modern equipment, and experienced 4-person subspecialty faculty. In addition to clinical practice and training, responsibilities include graduate and undergraduate medical instruction in neuroradiology as well as participation in departmental research activities. Minimum requirements include successful completion of an accredited radiology residency. Applicants must be eligible to obtain a medical license in the state of Florida. For additional information, contact Ronald Quisling, M.D., Professor, Dept. of Radiology, Box 100374 JHMHC, Gainesville, FL 32610-0374; (904) 395-0291. The University of Florida is an equal opportunity/affirmative action employer and encourages applications from women and minorities. 3–6c

ABDOMINAL IMAGING FELLOWSHIP, UNIVERSITY OF FLORIDA—The Dept. of Radiology at the University of Florida is offering 1-yr clinical fellowships in abdominal imaging beginning in July 1993 and July 1994. Minimum requirements include successful completion of an accredited radiology residency. The fellowship includes training in all aspects of abdominal imaging (gastrointestinal and genitourinary radiology, CT, MRI, and ultrasound) by a 4-person subspecialty faculty. The programs offer full clinical experience and research opportunities. Applicants must be eligible to obtain a medical license in the state of Florida. Research fellowships are also available in abdominal imaging. For additional information, contact Pablo R. Ros, M.D., Professor, Dept. of Radiology, Box J-374 JHMHC, Gainesville, FL 32610-0374; (904) 395-0288. The University of Florida is an equal opportunity/affirmative action employer and encourages applications from women and minorities. 3–6c

FELLOWSHIP IN ANGIO/INTERVENTIONAL IMAGING—A 1-yr fellowship program is available at Lehigh Valley Hospital Center in Allentown, PA. LVHC is a 492-bed, acute-care, university-affiliated hospital. The fellowship program offers training in CT (head and body), ultrasound, MR, angiography, and interventional radiology. For further information, contact Robert Kricun, M.D., Dept. of Radiology, Lehigh Valley Hospital Center, P. O. Box 689, Allentown, PA 18105. 4–6c

FELLOWSHIP IN ULTRASOUND AND BODY CT/MRI, July 1, 1993, to June 30, 1994, at Hahnemann University Hospital. State-of-the-art equipment, including ultrasound color-flow imaging, 2 GE 9800 CT scanners, and Signa 1.5-T MR is provided. Applicants must have completed an approved residency in diagnostic radiology and be board-eligible or certified. For inquiries, please contact Lawrence Neustadter, D.O., Dept. of Diagnostic Radiology, Hahnemann University Hospital, Broad and Vine Sts., Philadelphia, PA 19102; (215) 448-8722. An equal opportunity employer. 4–6cp

FELLOWSHIP POSITIONS—The Dept. of Radiological Sciences at Olive View–UCLA Medical Center has openings for fellowships to begin on July 1, 1992. Positions are available in neuroradiology, ultrasound, body imaging, interventional radiology, and nuclear medicine. Candidates must be board certified and eligible for certification in diagnostic radiology and should be eligible for licensing in the state of California. In addition to clinical practice and training, responsibilities will include graduate and undergraduate medical instruction in radiology as well as assisting with related departmental research projects. Interested candidates should contact Issa Yaghmai, M.D., Professor and Chairman, Dept. of Radiological Sciences, Olive View–UCLA Medical Center, 14445 Olive View Dr., Sylmar, CA 91342; (818) 364-4078. The University of California, Los Angeles, is an affirmative action/equal opportunity employer. 3–6c

FELLOWSHIP IN PEDIATRIC RADIOLOGY, UNIVERSITY OF FLORIDA—The Division of Pediatric Radiology in the Dept. of Radiology at the University of Florida offers a 1-yr fellowship training in pediatric radiology, starting July 1993 and July 1994. Three full-time pediatric radiologists provide training in conventional radiology and fluoroscopy, ultrasound, neonatal imaging, CT, MRI, and interventional/angiography techniques. Supplemental training in nuclear medicine is available. Facilities include dedicated standard r/f rooms, 4 color-Doppler ultrasound machines, 2 GE CT units, 3 MR units, ICU electronic image transfer, and computed radiography (CR). Opportunity to participate or conduct clinical and basic research is available. Applicants must be eligible for licensure in the state of Florida. Contact Jonathan L. Williams, M.D., Director of Pediatric Radiology, Dept. of Radiology, Box 100374, University of Florida, Gainesville, FL 32610-0374; (904) 395-0291. The University of Florida is an equal opportunity/affirmative action employer. 3–6c

UNEXPECTED OPENING FOR FELLOWSHIP IN CARDIOVASCULAR-INTERVENTIONAL RADIOLOGY available July 1, 1992. A 1-yr fellowship program is available at a 750-bed teaching hospital. Extensive clinical experience involving all aspects of cardiovascular imaging, interventional vascular, and nonvascular procedures. Availability for clinical or animal research. Send CV and inquiries to Oscar H. Gutierrez, M.D., Dept. of Radiology, Box 648, University of Rochester Medical Center, Rochester, NY 14642. AA/EO/M-F employer. 4–6c

FELLOWSHIP PROGRAM IN INTERVENTIONAL RADIOLOGY—The fellowship offered is a 1-yr training program in interventional radiology. A high volume of studies provides excellent experience for the fellowship training program. The 1-yr appointment is intensive, supervised, and allows for graded responsibility in performance and interpretation of studies including angioplasty, atherectomy, arterial and biliary stents, and all drainage procedures. The fellowship training involves performance of interventional procedures under sonographic and CT guidance as well as fluoroscopy. Inquiries should be addressed to Gordon K. McLean, M.D., Director, Interventional Radiology, The Western Pennsylvania Hospital, 4800 Friendship Ave., Pittsburgh, PA 15224. 5–12c

FELLOWSHIP IN ANGIO/INTERVENTIONAL RADIOLOGY—The Dept. of Radiology at the University of Florida is offering several 1-yr, postresidency clinical fellowship positions beginning in July 1993 and July 1994. Angiographic suites are available (2 have Philips C-arms with 1024 ADAC digital), and a new Toshiba vascular lab. The dept. has intravascular ultrasound color-flow Doppler and angioscopy equipment. Training includes all interventional procedures (vascular, biliary, urology, etc.), as well as experience with investigational devices such as CO_2, angioscopy, atherectomy, and holmium lasers. An animal laboratory, a full-time veterinarian, and an instrument shop are available. Applicants must be eligible for licensure in the state of Florida. For further information, contact Irvin F. Hawkins, M.D., Professor, Dept. of Radiology, Box 100374 JHMHC, Gainesville, FL 32610-0374; (904) 395-0291. The University of Florida is an equal opportunity/affirmative action employer. 3–6c

FELLOWSHIP POSITIONS—The Dept. of Radiology of the Brigham and Women's Hospital-Harvard Medical School has 1- or 2-yr fellowship positions in the following areas: (1) cardiovascular and interventional, (2) neuroradiology, (3) CT/ultrasound/MR/interventional, (4) oncoradiology, (5) chest, (6) bone, (7) nuclear medicine, and (8) computer science. For more information, please send CV specifying your area of interest to B. Leonard Holman, M.D., Chairman, Dept. of Radiology, Brigham and Women's Hospital, 75 Francis St., Boston, MA 02115. Harvard Medical School and Brigham and Women's Hospital are equal opportunity, affirmative action employers. 5–4c

FELLOWSHIPS AT ALBANY MEDICAL CENTER—The newly renovated and equipped Dept. of Radiology at the Albany Medical College and Center in Albany, NY offers the following fellowship positions each yr: (1) Abdominal Imaging—This fellowship encompasses all aspects of MRI, ultrasound, CT, and other advanced techniques in imaging the abdomen. Four state-of-the-art MRI and 4 CT scanners as well as 5 color Doppler ultrasound units are utilized daily. Contact James C. Peters, M.D. regarding this program. (2) Neuroradiology—This fellowship encompasses the full range of advanced neuro imaging including MRI, CT, angiography, and myelography. Contact William A. Wagle, M.D. (3) Angiography and interventional radiology—Three advanced angiographic suites are utilized daily for a full range of vascular and interventional procedures. Contact Mohammad S. Sarrafizadeh, M.D. All program directors listed above may be contacted at the Dept. of Radiology, A-113, Albany Medical Center, Albany, NY 12208; (518) 445-3277 or contact Matthew D. Rifkin, M.D., Chairman, Dept. of Radiology, A-113, at the above address. Albany Medical Center is an equal opportunity/affirmative action employer. 1–12c

NEURORADIOLOGY FELLOWSHIP—An unexpected opening for a neuroradiology fellow is available in the Dept. of Radiology at Thomas Jefferson University Hospital beginning July 1992. The Division of Neuroradiology has close clinical and research relationships with Jefferson's very active neurology, neurosurgery, orthopedic surgery, and otolaryngology depts. Complete training in ENT radiology is part of this program. Six full-time faculty members currently staff this division. Clinical facilities include 2 dedicated CT scanners, a myelography room, a biplane angiography room with DSA, and 4 GE 1.5-T MRI units. Contact Carlos Gonzalez, M.D., Director of Neuroradiology, 1009 Main Bldg., Thomas Jefferson University Hospital, Philadelphia, PA 19107; (215) 955-5447. Jefferson is an affirmative action/equal opportunity employer. 11–6c

Tutorials/Courses

ALASKA 1992:CRUISE THE INLAND PASSAGE, BREAST IMAGING AT SEA, JULY 4–11, 1992, AND MRI AT SEA, JULY 11–18, 1992—Medical Seminars International, Inc., 18981 Ventura Blvd., Ste. 303, Tarzana, CA 91356; (818) 774-9077, fax (818) 774-0244. 2–6d

FOURTH ANNUAL CONFERENCE ON ADVANCED INTERVENTIONAL TECHNIQUES FOR PERIPHERAL VASCULAR DISEASE—Sept. 16–19, 1992; Hyatt Regency Oak Brook, Oak Brook, IL. Course Director is Amir Motarjeme, M.D. Contact Karin Bodenhagen, R.N., Midwest Vascular Institute of Illinois, 3815 Highland Ave., Downers Grove, IL 60515; (708) 963-0660, (708) 963-8348 (fax). 6xd

KONA, HAWAII 1992—Seventeenth annual International Body Imaging Congress, Oct. 10–17. CME 1. Mauni Lani Bay Hotel. Contact Medical Seminars International, Inc., 18981 Ventura Blvd., Ste. 303, Tarzana, CA 91356; (818) 774-9077, fax (818) 774-0244. 5–10d

MUSCULOSKELETAL MRI, SECOND ANNUAL LOS ANGELES CONFERENCE, SEPT. 19–20, 1992—Faculty: Drs. Bradley, Brant-Zawadzki, Dietrich, Friedman, Harms, Resnick, Schlesinger. Medical Seminars International, Inc., 18981 Ventura Blvd., #303, Tarzana, CA 91356; (818) 774-9077, fax (818) 774-0244. 4–9d

• NOTICE •

New Business Office for AJR

All inquires and correspondence regarding classified ads should be sent to:

AJR Classifieds
1891 Preston White Drive
Reston, VA 22091
Attn: Terry Fitterer
Phone: (703) 648-8992
FAX: (703) 264-8863

Author Index
Volume 158

Authors of *AJR* articles are also included in the 5-year cumulative index published in *Radiology*.

A

Abbasoğlu O, **158**:635
Abbitt PL, **158**:77, **158**:919
Abdelwahab IF, **158**:119
Abe H, **158**:599
Abramson SJ, **158**:125
Adler DD, **158**:1239
Agarwal R, **158**:75
Ahmadjian JM, **158**:129
Aizenstein RI, **158**:575
Akhan O, **158**:635
Akins EW, **158**:881
Akira M, **158**:1223
Akyol R, **158**:1176
Albanese MA, **158**:669
Alexander E III, **158**:399
Algra PR, **158**:1171, **158**:1275
Alper H, **158**:213
Andersson I, **158**:993
Andrews JC, **158**:427, **158**:761
Angeloni U, **158**:151
Antoun BW, **158**:1131
Aoki J, **158**:751
Applegate GR, **158**:692
Apstein MD, **158**:456
Araki Y, **158**:587
Arisawa J, **158**:1217
Ashdown BC, **158**:1155, **158**:1329
Atari H, **158**:1011
Atkins MR, **158**:1329
Atkinson GO Jr, **158**:613
Atlas SW, **158**:391
Aughenbaugh GL, **158**:971
Auletta AG, **158**:1412
Avni EF, **158**:837

B

Bagheri K, **158**:210, **158**:916
Baker KS, **158**:689
Baker ME, **158**:1168
Baker SP, **158**:273
Balkanci F, **158**:635
Ball TI Jr, **158**:613
Baltarowich O, **158**:843
Balthazar EJ, **158**:550
Balzer J, **158**:887
Bank WO, **158**:837
Barkhof F, **158**:1171
Barkovich AJ, **158**:1175
Barloon TJ, **158**:765
Barnes FJ, **158**:1295
Barnes PD, **158**:1313
Barrett C, **158**:1303
Barros Fo TEP, **158**:1413
Barth KH, **158**:199
Bass SH, **158**;669
Bassett LW, **158**:688
Bastianello S, **158**:151
Batjer H, **158**:883
Batnitzky S, **158**:282, **158**:1086
Baumeister RF, **158**:915
Beabout JW, **158**:331
Bechtold RE, **158**:493
Belloni C, **158**:565
Bennett MR, **158**:515
Benson CB, **158**:1257
Berbaum KS, **158**:431
Berdon WE, **158**:125
Berk RN, **158**:203, **158**:1165, **158**:1246
Bernardino ME, **158**:535, **158**:644, **158**:665
Bero L, **158**:209
Berquist TH, **158**:581
Berry M, **158**:212
Bessette J, **158**:1151
Bisset GS III, **158**:75, **158**:693
Black KP, **158**:1091
Blacksin M, **158**:1295
Blaquière RM, **158**:921
Blickman JG, **158**:137
Bloch SM, **158**:62
Blum JE, **158**:558, **158**:668
Bluth EI, **158**:37
Bocchini TP, **158**:1411
Boden SD, **158**:335
Boechat MI, **158**:1303
Boman T, **158**:819
Bowen A, **158**:692
Bozzao L, **158**:151
Brahme F, **158**:1160
Bramble JM, **158**:19
Braun MA, **158**:309
Braunstein EM, **158**:1071
Braver JM, **158**:785
Bray HJ, **158**:81
Brink JA, **158**:41
Brody AS, **158**:1172
Brody JM, **158**:609
Broecker BH, **158**:613
Brookeman JR, **158**:1173
Brooks DC, **158**:785
Brower AC, **158**:609
Brown DL, **158**:1257
Brown JJ, **158**:95
Brown KT, **158**:1174
Brown LR, **158**:331
Brown PC, **158**:665
Bruner JP, **158**:898
Brunner JP, **158**:1356
Bruno L, **158**:598
Bryan PJ, **158**:458
Buchberger W, **158**:1261
Buchholz DW, **158**:283
Buckley AR, **158**:179, **158**:1001
Buckley RE, **158**:1271
Buckwalter KA, **158**:1071
Buggy BP, **158**:1176
Bulas DI, **158**:1097, **158**:1299
Burger PC, **158**:1329
Burghuber OC, **158**:981
Burhenne HJ, **158**:45
Burks DW, **158**:503

C

Cáceres J, **158**:458
Çakmakçi M, **158**:635
Caldwell B, **158**:363
Campbell WL, **158**:997
Caplan LR, **158**:158
Caron KH, **158**:75
Carrera GF, **158**:1091
Carroll FE, **158**:898, **158**:1356
Carvalho PA, **158**:399
Cascade PN, **158**:352
Casola G, **158**:91, **158**:191
Cerqueira MD, **158**:58
Cervilla V, **158**:1087
Chang AE, **158**:1239
Chang PJ, **158**:457, **158**:765
Charnsangavej C, **158**:1031
Chen NC, **158**:1173
Cheong I, **158**:619
Chew FS, **158**:62, **158**:330, **158**:570, **158**:1056, **158**:1312
Chezmar JL, **158**:535
Chita MA, **158**:920
Choe KO, **158**:983
Chovanes GI, **158**:1145
Christiansen J, **158**:1025
Chuang K-S, **158**:443
Clark RA, **158**:527
Cleveland RH, **158**:137
Cohen AM, **158**:673, **158**:1131
Cohen IT, **158**:129
Coleman JA Jr, **158**:898
Collins MA, **158**:918
Collins MB, **158**:309
Colon E, **158**:299
Concepcion R, **158**:293
Connell DG, **158**:1271
Connell RK, **158**:210
Connolly JL, **158**:269
Constantinou C, **158**:137
Conway WF, **158**:1412
Cook LT, **158**:19
Cooperberg PL, **158**:81, **158**:1057
Cortell ED, **158**:41
Cortina H, **158**:867
Costello P, **158**:1127
Cotty P, **158**:459, **158**:921
Coumas JM, **158**:591
Cox IH, **158**:1051
Cragg AH, **158**:431
Crass JR, **158**:673
Creasy JL, **158**:911, **158**:1378
Crenshaw WB, **158**:330, **158**:1312
Crow HC, **158**:798
Cullen J, **158**:353
Czarnecki DJ, **158**:1176

D

Dachman AH, **158**:574, **158**:1028
Daffner RH, **158**:100
Dagdeviren A, **158**:1176
Dagher AP, **158**:1289
D'Agostino HR, **158**:91, **158**:634
D'Alessandro A, **158**:791
Darcy M, **158**:875
Das KM, **158**:327, **158**:571
Dawson SL, **158**:41, **158**:1007
Deck J, **158**:163
de Lange EE, **158**:287
Delbeke D, **158**:913, **158**:1382
DelMaschio A, **158**:565
Demlow T, **158**:641
Demos TC, **158**:1064
Denys A, **158**:215
de Rio P, **158**:1057
Deutsch AL, **158**:335
Dewire DM, **158**:1051
Deyo RA, **158**:1135
Diefenthal H, **158**:1167
Dietrich PA, **158**:1211
Dietrich R, **158**:363
Dillon WP, **158**:405, **158**:1175
DiSalvo DN, **158**:1257
Disler DG, **158**:1056
Dodds WJ, **158**:691
Doherty FJ, **158**:1257
Doi H, **158**:1247
Donaldson JS, **158**:1101
Donnay M, **158**:694
Donner MW, **158**:283
Dorr RT, **158**:915
Doubilet PM, **158**:1257
Douglas WW, **158**:971
Doyle AJ, **158**:989
Drutman J, **158**:1410
Druy E, **158**:199
Dubinsky TJ, **158**:212
Dundar C, **158**:1413
Dunkley B, **158**:641
Dwyer SJ III, **158**:19

E

Ebara M, **158**:885
Eckard DA, **158**:883
Ecker CP, **158**:1127
Edge SB, **158**:287

Edge V, **158**:133
Edwards DK III, **158**:519
Eichelberger MR, **158**:63, **158**:1097, **158**:1299
Eisenberg MJ, **158**:1172
Ekberg O, **158**:916
Elam EA, **158**:509
El Gammal T, **158**:1305
El-Khoury GY, **158**:1412
Ellis JH, **158**:807
Elson BC, **158**:993
Elster AD, **158**:173, **158**:1193
Endo T, **158**:1011
Endress C, **158**:920
Ennemoser O, **158**:1261
Epstein DM, **158**:515
Erb RE, **158**:905, **158**:1368
Erickson SJ, **158**:655, **158**:1051, **158**:1091
Ernst RJ, **158**:645
Evans NS, **158**:918
Evans WP, **158**:51

F

Fagerholm MI, **158**:917
Fajardo LL, **158**:509, **158**:1231
Fantozzi LM, **158**:151
Farley TE, **158**:347
Faulstich ME, **158**:902, **158**:1363
Fayemi AB, **158**:1309
Fechner RE, **158**:287
Feigin DS, **158**:508
Feinberg MJ, **158**:916
Ferrari DA, **158**:591
Fetsch JF, **158**:581
Feuerstein I, **158**:293
Fieschi C, **158**:151
Filly RA :**158**:133
Finck S, **158**:1043
Finkbeiner WE, **158**:265
Fish BG, **158**:1309
Fishman EK, **158**:143, **158**:603, **158**:665, **158**:1289
Fitzgerald SW, **158**:1091, **158**:1101
Flamig DP, **158**:631
Flanders AE, **158**:1347
Fleischer D, **158**:199
Foley WD, **158**:1051
Folkerth R, **158**:399
Fong S, **158**:619
Fong TC, **158**:849
Foo TKF, **158**:1019
Foreman ML, **158**:631
Foster RG, **158**:997
Fouquet B, **158**:459, **158**:921
Fox MA, **158**:1229
Francis IR, **158**:761
Fraser-Hill MA, **158**:809, **158**:813
Freed H, **158**:437
Fried AM, **158**:90, **158**:790
Friedland GW, **158**:279, **158**:547, **158**:1171
Friedman AC, **158**:308, **158**:1028
Friedman DP, **158**:1347
Fritz RC, **158**:1293
Fruechte DM, **158**:1410
Fukuya T, **158**:765
Furukawa T, **158**:587, **158**:1171

G

Gagliardi RA, **158**:302, **158**:760, **158**:980
Gambino J, **158**:363
Garancini P, **158**:565
Gay SB, **158**:819, **158**:1173
Gazelle GS, **158**:1015
Gean-Marton AD, **158**:1325
Gelber ND, **158**:1163
Gelfand DW, **158**:211
Genant H, **158**:1293
Gennari RC, **158**:893
Getachew MM, **158**:133
Gibbon WW, **158**:692
Gilbert MS, **158**:119
Gilliam JH III, **158**:243
Gilpin LB, **158**:902, **158**:1363
Girson MS, **158**:883
Giuliano AE, **158**:688
Glass RBJ, **158**:833
Glassman SB, **158**:913, **158**:1382
Godwin JD, **158**:1211
Goitz HT, **158**:819
Gold RH, **158**:688, **158**:1288
Goldberg BB, **158**:843
Goldberg JD, **158**:133
Golding RH, **158**:1057
Goldschmidt P, **158**:694
Goldstein RB, **158**:133
Goodman P, **158**:80
Göranson H, **158**:1043
Gore RM, **158**:62, **158**:59 Palmer WE
Goss TP, **158**:591
Goto H, **158**:1247
Gotschall CS, **158**:1097
Goupille P, **158**:459, **158**:921
Gragg LA, **158**:437
Graham CM, **158**:265
Granfield CAJ, **158**:1031
Grant EG, **158**:195
Griffey RH, **158**:631
Grigg AP, **158**:1001
Griscom NT, **158**:1
Groskin SA, **158**:326
Gross GW, **158**:353
Gur D, **158**:893
Gustafson KD, **158**:1167
Gutierrez ED, **158**:95
Guttentag AR, **158**:637

H

Haaga JR, **158**:1015
Haggar AM, **158**:693
Hahn PF, **158**:41
Hald J, **158**:1025
Hale JC, **158**:437
Hall DA, **158**:1410
Hall F, **158**:458, **158**:1411
Hall TR, **158**:1303
Haller JO, **158**:823
Hamed MM, **158**:303
Hamilton PA, **158**:691
Hamm B, **158**:183, **158**:303
Hamrick-Turner J, **158**:77, **158**:919
Hanafee W, **158**:564
Hansen AV, **158**:913, **158**:1382
Hansen GC, **158**:921
Hansen M, **158**:1111
Hantraye P, **158**:215
Harms SE, **158**:631
Harrow MM, **158**:359
Hartman TE, **158**:581
Hartnell GG, **158**:1127
Hassien JD, **158**:757
Hattori R, **158**:1171
Hawes DR, **158**:315, **158**:765
Hawkins IF Jr, **158**:881
Hayes CW, **158**:1412
Haynor DR, **158**:1135
Hebrang A, **158**:1174
Heijober RJJ, **158**:1171
Heimans JJ, **158**:1275
Heller RM, **158**:897, **158**:907, **158**:1355, **158**:1372
Helms CA, **158**:1293
Helvie MA, **158**:1239
Helweg G, **158**:1261
Hendee WR, **158**:1387
Henderson WR Jr, **158**:1211
Henriquez G, **158**:129
Herbetko J, **158**:1001
Hermann G, **158**:119
Hernandez RJ, **158**:729
Hernanz-Schulman M, **158**:907, **158**:1372
Hicks ME, **158**:547, **158**:875
Higashihara T, **158**:1223
Hillman BJ, **158**:509
Hilsenrath PE, **158**:813
Hirasa M, **158**:65
Hirsh MP, **158**:129
Hislop TG, **158**:45
Ho C-S, **158**:251
Hodler J, **158**:106, **158**:1087
Hoffer FA, **158**:1105
Hogan QH, **158**:655
Holman BL, **158**:399
Holt RG, **158**:1281
Holtz P, **158**:559
Honda G, **158**:1043
Honda T, **158**:751
Hopp ML, **158**:1019
Horii SC, **158**:442
Howe MA, **158**:693
Hricak H, **158**:1043
Hsu BY, **158**:519
Huang HK, **158**:443, **158**:743
Huang WX, **158**:210
Huland H, **158**:1407
Hunter DW, **158**:623
Hunter TB, **158**:1231
Hussmann P, **158**:183

I

Ibrahim ME, **158**:303
Ibuki Y, **158**:65
Iinuma G, **158**:1247
Ikeda DM, **158**:993, **158**:1239
Ikeda S, **158**:751
Ikezoe J, **158**:1217
Im J-G, **158**:983
Imaeda T, **158**:1247
Indudhara R, **158**:327, **158**:571
Ingram JD, **158**:1299
Inoue S, **158**:541
Ishii K, **158**:460, **158**:751

J

Jabra AA, **158**:143
Jackson VP, **158**:1231
Jacobson A, **158**:380
Jaffe RB, **158**:1308
Jahnke AH Jr, **158**:347, **158**:1281
Jahre C, **158**:645
Jaile JC, **158**:125
Jain R, **158**:212
Janda RC, **158**:315
Janzen DL, **158**:1057, **158**:1271
Jaramillo D, **158**:137, **158**:1105
Jeffrey RB Jr, **158**:665
Jelinger E, **158**:199
Jing B-S, **158**:725
Johkoh T, **158**:1217
Johnson CA, **158**:1289
Johnson J, **158**:907, **158**:1372
Johnson MB, **158**:1029
Jokl P, **158**:101
Jolesz FA, **158**:1313
Jones B, **158**:283
Jones EC, **158**:535
Jones KM, **158**:1313
Jorion JL, **158**:694
Judmaier W, **158**:1261
Julien P, **158**:1019

K

Kadoya M, **158**:311
Kahler DA, **158**:819
Kaji Y, **158**:214
Kanal E, **158**:692
Kanematsu M, **158**:1247
Kang K, **158**:212
Kangarloo H, **158**:363, **158**:443
Kanzaria PK, **158**:591
Kaplan S, **158**:456
Kapur S, **158**:63
Karasick S, **158**:799
Kashida H, **158**:65
Kassner EG, **158**:661
Kaude JV, **158**:1409
Kaul U, **158**:417
Kawai T, **158**:751
Kawamori Y, **158**:311
Kazema R, **158**:1168
Keck GM, **158**:413
Kelcz F, **158**:791
Keller MA, **158**:163
Kellman GM, **158**:1061
Kelsey P, **158**:1007
Kemp SS, **158**:859
Kent DL, **158**:1135
Kerns SR, **158**:881
Kernzer B, **158**:63
Kerr R, **158**:335
Kesaria AC, **158**:1170
Keskey TS, **158**:58
Kester NL, **158**:757
Kido S, **158**:1217
Kier R, **158**:101, **158**:321, **158**:457, **158**:1265
Kikuchi Y, **158**:691
Kim CH, **158**:983
Kim EE, **158**:40
Kim RC, **158**:170
Kimble KJ, **158**:663
Kimme-Smith C, **158**:195, **158**:268
Kimura T, **158**:551
Kinder B, **158**:457
King JN, **158**:413
Kinukawa T, **158**:1171
Kirchner S, **158**:907, **158**:1372
Kirkemo A, **158**:1061
Kita N, **158**:1223
Kitagawa K, **158**:311
Kiyono K, **158**:751
Kleinman PK, **158**:129, **158**:1111
Klepetko W, **158**:981
Knapp R, **158**:1261
Knoedler JP, **158**:1167
Knorr JR, **158**:1163
Kohno N, **158**:1217
Kondo Y, **158**:917
Kono M, **158**:460
Kopans DB, **158**:521
Kopitnik T, **158**:883
Korn MA, **158**:981
Kornhauser MS, **158**:353
Kozuka T, **158**:1217, **158**:1223
Kransdorf MJ, **158**:108, **158**:1280
Kremer S, **158**:1309
Kricun R, **158**:1145
Krolikowski, **158**:273
Kucharczyk J, **158**:1151
Kucharczyk W, **158**:163
Kudo M, **158**:65
Kuhara H, **158**:1171
Kumcuoglu Z, **158**:1168
Kurtz AB, **158**:843
Kusano S, **158**:1011
Kushner DC, **158**:1097, **158**:1299
Kuster GGR, **158**:87
Kwong JS, **158**:179

L

Lachman RS, **158**:412
Lachniet M, **158**:1275
Lacrampe MJ, **158**:911, **158**:1378
Lail VJ, **158**:81

Landing B, **158**:750
Lang EV, **158**:547
Larson EB, **158**:1135
Laub G, **158**:381
Laverdiere JT, **158**:87
Lawrence SK, **158**:913, **158**:1382
Lawson JP, **158**:1065
Lawson TL, **158**:1091
Lecky JW, **158**:997
Lee BH, **158**:983
Lee C, **158**:113
Lee JKT, **158**:95
Lee KS, **158**:983
Lee KY, **158**:997
Lee MJ, **158**:41, **158**:1007
Leonidas JC, **158**:128
Leroy-Willig A, **158**:215
Lesko NM, **158**:1115
Letourneau JG, **158**:623
Levenson H, **158**:1114
Levesque M, **158**:1251
Levin M, **158**:179
Levin T, **158**:125
Lev-Toaff AS, **158**:799
Lewin D, **158**:1303
Lewin JS, **158**:381
Lewis DV Jr, **158**:1329
Lieberman E, **158**:750
Lieberman RH, **158**:893
Lin DTC, **158**:179
Lindell MM, **158**:725
Link KM, **158**:1115
Lissner J, **158**:887
Litt AW, **158**:389
Liu T-H, **158**:688
Loeffler JS, **158**:399
Loevner LA, **158**:761, **158**:872
Longley DG, **158**:623
Lossef SV, **158**:199
Lott T, **158**:1305
Loughlin KR, **158**:1257
Lu CC, **158**:315, **158**:765
Luk KH, **158**:1354
Lynch DA, **158**:1229, **158**:1346
Lynch KJ, **158**:101
Lyons, MM, **158**:1295

M

Maden N, **158**:687
Maeda H, **158**:1171
Maeda K, **158**:460
Magalhães ACA, **158**:1413
Magid D, **158**:603, **158**:1289
Mahfouz AE, **158**:303
Make BJ, **158**:1229
Maloney K, **158**:509
Manoogian C, **158**:553
Marcus B, **158**:750
Marik P, **158**:687
Marincola F, **158**:293
Mark AS, **158**:391, **158**:1325
Markham D, **158**:1410
Marsh JI, **158**:1057
Marti-Bonmatí L, **158**:867
Martin NL, **158**:19
Maruoka S, **158**:599
Maruyama A, **158**:751
Marx HF, **158**:1255
Marx MV, **158**:427, **158**:547
Mata JM, **158**:458
Mathieson JR, **158**:1057
Matsui O, **158**:311
Matsuura K, **158**:551
Matzinger FR, **158**:987
Matzinger MA, **158**:987
Maves CK, **158**:75
Mayo JR, **158**:1205
McAleese KA, **158**:915
McCarthy EF Jr, **158**:1289
McCarthy SM, **158**:321
McCauley TR, **158**:101
McClellan R, **158**:1305
McClennan BL, **158**:675
McDaniel K, **158**:1031
McHugh N, **158**:819
McKay DC, **158**:807
McLoud TC, **158**:637
McMahon C, **158**:887
McNeill K, **158**:509
Meek RN, **158**:1271
Mehta SN, **158**:417
Menor F, **158**:867
Meredith JW, **158**:493
Merritt CRB, **158**:37
Merten DF, **158**:825, **158**:836
Meyer CA, **158**:299
Meyer JE, **158**:991
Meyers SP, **158**:859
Meziane MA, **158**:437
Middleton M, **158**:1151
Middleton WD, **158**:1061
Miller S, **158**:823
Miller WJ, **158**:997
Milne N, **158**:456
Mimura J, **158**:65
Mink JH, **158**:335
Minoyama A, **158**:885
Mirich DR, **158**:163
Miron SD, **158**:673
Mirvis SE, **158**:503
Misugi K, **158**:541
Mitomo M, **158**:587
Mitsu S, **158**:551
Miyake H, **158**:423
Miyata M, **158**:551
Mochizuki R, **158**:1247
Molina EJ, **158**:623
Monette RJ, **158**:1176
Moody AR, **158**:779
Moody EB, **158**:913, **158**:1382
Moore ADA, **158**:1211
Moore B, **158**:191
Mori H, **158**:423
Morimoto M, **158**:751
Morparia H, **158**:456
Morris E, **158**:335
Morris TW, **158**:1390
Morrison MC, **158**:41
Moser RP Jr, **158**:346
Moskowitz M, **158**:688, **158**:1169
Mucciolo P, **158**:881
Mueller PR, **158**:41, **158**:1007
Mulkern RV, **158**:1313
Müller NL, **158**:1205
Munk PL, **158**:179, **158**:1271
Murphey MD, **158**:19
Murray KK, **158**:881
Myers JL, **158**:971
Myers SM, **158**:663

N

Nadel S, **158**:213
Nadler JL, **158**:553
Nagai J, **158**:551
Nagareda T, **158**:1217
Nakagawa N, **158**:431
Nakamura M, **158**:599
Nakano T, **158**:885
Nance EP, **158**:905, **158**:1368
Napp TE, **158**:575
Nauta JJ, **158**:1275
Nedd CA II, **158**:1270
Needleman L, **158**:843
Nelson RC, **158**:535
Nemcek AA Jr, **158**:1298
Neumann CH, **158**:347, **158**:1281
Nielsen MB, **158**:1025
Nino-Murcia M, **158**:279, **158**:457
Nishioka NS, **158**:1007
North LB, **158**:725
Novelline RA, **158**:191
Numata K, **158**:541

O

Oberhauser H, **158**:1261
Oberly T, **158**:791
O'Connell P, **158**:619
Odell G, **158**:1305
O'Donnell DM, **158**:898, **158**:1356
O'Donnell MR, **158**:1255
Ogawa Y, **158**:599
Ohaki Y, **158**:541
Ohmiya H, **158**:1011
Ohto M, **158**:885
Okabe Y, **158**:65
Okada Y, **158**:1011
Okizuka H, **158**:214, **158**:1173
Oliveira RP, **158**:1413
Ootani F, **158**:587
Ootani M, **158**:587
Ordóñez NG, **158**:1031
Orrison WW, **158**:413
Oshio K, **158**:1313
Ott DJ, **158**:211, **158**:243
Overmeyer JD, **158**:881
Oyar O, **158**:213, **158**:687
Özenç A, **158**:635
Özer H, **158**:687
Ozturk M, **158**:1413

P

Pappas AM, **158**:591
Patrick LE, **158**:613
Patten RN, **158**:86
Pauls CC, **158**:694
Pedersen JF, **158**:1025
Pegios W, **158**:887
Peh WCG, **158**:918
Pelsang RE, **158**:315
Pelz DM, **158**:1412
Peng RL, **158**:210
Pennell RG, **158**:843
Perella RR, **158**:195
Perkash I, **158**:457
Pessin MS, **158**:158
Petersen SA, **158**:347, **158**:1281
Peters GN, **158**:51
Phillips GL, **158**:1001
Picus D, **158**:547, **158**:875
Pierallini A, **158**:151
Piraino DW, **158**:437
Pirovano G, **158**:887
Pitman RG, **158**:690
Platt JF, **158**:1035
Pollack HM, **158**:559
Pond GD, **158**:915, **158**:1411
Pont MS, **158**:1193
Poon PY, **158**:779
Porter E, **158**:1168
Potchen EJ, **158**:1169
Powers C, **158**:437
Powers TA, **158**:902, **158**:1363
Poyatos C, **158**:867
Pozniak MA, **158**:791
Prager J, **158**:922
Premkumar A, **158**:293
Pretorius DL, **158**:1408
Prince MR, **158**:570
Provost T, **158**:299
Pu Y, **158**:1170
Purdy PD, **158**:883

Q

Quale JL, **158**:19
Quinn SF, **158**:641, **158**:1091
Quint DJ, **158**:872

R

Radin DR, **158**:553, **158**:1029, **158**:1255, **158**:1409
Ragavendra N, **158**:195, **158**:921
Ragland RL, **158**:1163
Rahbar G, **158**:443
Rahn DW, **158**:1065
Rajani M, **158**:417
Rajwanshi A, **158**:571
Ramakrishnan MR, **158**:1170
Raptopoulos V, **158**:458
Ratcliffe JF, **158**:619
Ravich WJ, **158**:283
Razavi M, **158**:443
Rebner M, **158**:1239
Rehm K, **158**:509
Renfrew DL, **158**:669, **158**:809, **158**:813, **158**:1412
Rennie D, **158**:209
Resendes M, **158**:1293
Resnick D, **158**:106, **158**:1087
Resnik CS, **158**:109
Reuter KL, **158**:273
Riche D, **158**:215
Richmond BJ, **158**:437
Rifkin MD, **158**:559, **158**:1057
Rioux M, **158**:773
Roberts DE, **158**:1410
Roberts GM, **158**:692
Rock MG, **158**:331
Ros PR, **158**:77, **158**:919
Rose BS, **158**:1408
Rosemberg LA, **158**:1413
Rosenbaum HD, **158**:1292
Rosenberg MA, **158**:806
Rosenblum J, **158**:922
Rosenquist CJ, **158**:320
Rothe WA, **158**:1309
Rotter AJ, **158**:1255
Rushton HG, **158**:833
Ruzal-Shapiro C, **158**:125
Rypens E, **158**:837

S

Sachs HJ, **158**:987
Safirstein BH, **158**:210, **158**:916
Saini S, **158**:41, **158**:368, **158**:1007
Sakai F, **158**:751
Sakamoto K, **158**:599
Sakatani M, **158**:1223
Samson D, **158**:883
Sanders L, **158**:293
Sandhu FS, **158**:405
Saremi F, **158**:83
Sartoris DJ, **158**:1134
Sawhney S, **158**:212
Saxena A, **158**:417
Sayre JW, **158**:443
Scanlan KA, **158**:460
Scharling ES, **158**:493
Schatz CJ, **158**:1019
Schatzki SC, **158**:518, **158**:742, **158**:970, **158**:1210
Schauwecker DS, **158**:9
Schechter MT, **158**:1271
Schiebler ML, **158**:559
Schils J, **158**:437
Schlesinger AE, **158**:729
Schluchter MD, **158**:437
Schmidt JD, **158**:563
Schulman CC, **158**:837
Schurawitzki H, **158**:981
Schwabacher S, **158**:623
Schwartz RB, **158**:399, **158**:1313
Schwartzentruber D, **158**:293
Schweitzer ME, **158**:1087
Schwindt LA, **158**:1239
Scott R, **158**:694
Seeger LL, **158**:339
Seki M, **158**:1247
Seland TP, **158**:849
Seltzer S, **158**:391
Sener RN, **158**:213, **158**:214,

158:215, **158**:1168, **158**:1175, **158**:1176, **158**:1413
Serra J, **158**:919
Shaff MI, **158**:902, **158**:1363
Shalaby-Rana E, **158**:63
Shanley DJ, **158**:1161
Shanmuganathan K, **158**:109, **158**:503
Shannon FB, **158**:609
Shapiro AW, **158**:785
Sharif HS, **158**:1333
Sharma S, **158**:417
Shellock FG, **158**:335, **158**:663, **158**:1019
Shepard J-AO, **158**:637
Sherman JL, **158**:299
Shoemaker EI, **158**:1145
Shramek JK, **158**:661
Sickles EA, **158**:55
Siegel HA, **158**:426, **158**:540, **158**:1260, **158**:1254
Siegel ME, **158**:398
Siemers PT, **158**:631
Sierra AE, **158**:1169
Sigdestad CP, **158**:380
Silbergleit AK, **158**:916
Silbergleit Richard, **158**:1351
Silbergleit Robert, **158**:1351
Silberzweig JE, **158**:823
Simons M, **158**:443
Sinha S, **158**:339
Sironi S, **158**:565
Sisler CL, **158**:1161
Sistrom C, **158**:819
Sitzman SB, **158**:1407
Sivit CJ, **158**:1097, **158**:1299
Siwek J, **158**:209
Slone RM, **158**:202, **158**:1006
Smirniotopoulos JG, **158**:1150
Smith RC, **158**:321
Smith TP, **158**:431
Smith TW, **158**:1163
Smyth SH, **158**:1411
Snyder RD, **158**:413
Som PM, **158**:961
Sonda LP, **158**:807
Sone S, **158**:751
Sone Y, **158**:1247
Soyer P, **158**:1251
Spaulding CA, **158**:287
Spencer RP, **158**:50
Spevak MR, **158**:129, **158**:1111
Spindola-Franco H, **158**:1309
Spouge AR, **158**:763
Spritzer CE, **158**:559, **158**:1070
Sproat I, **158**:427
Stackhouse DJ, **158**:109
St. Amour S, **158**:691
Stanford W, **158**:1408
Steen RG, **158**:259
Stein SM, **158**:907, **158**:1372
Steinbach LS, **158**:347, **158**:1281
Steinberg F, **158**:1019
Steiner RM, **158**:784
Stelling CB, **158**:689
Stephens HW, **158**:1145
Stephenson CA, **158**:613
Stern EJ, **158**:265
Stern RC, **158**:1131
Stewart ET, **158**:771
Stomper PC, **158**:269
Stone BB, **158**:1163
Stratta R, **158**:791
Straub WH, **158**:893
Strife JL, **158**:693
Strum WB, **158**:87
Struyven J, **158**:837
Sugimura K, **158**:214, **158**:1173
Sugiura N, **158**:885
Suzuki K, **158**:423
Swensen SJ, **158**:971

T

Taccagni G, **158**:565
Taira RK, **158**:443, **158**:743
Takahashi S, **158**:599
Takamura Y, **158**:541
Takashima S, **158**:1217
Takashima T, **158**:311
Takebayashi S, **158**:541
Takeda H, **158**:423
Takeuchi N, **158**:1217
Talner LB, **158**:91
Talwar KK, **158**:417
Tanaka K, **158**:541
Tanaka O, **158**:551
Tarr RW, **158**:859
Tartaglino LM, **158**:1347
Tarver RD, **158**:618, **158**:1216
Taupitz M, **158**:183, **158**:303
Taylor GA, **158**:143, **158**:1097, **158**:1299
Teal PA, **158**:158
Tekin :auU, **158**:687
Tello R, **158**:1127
Tempany C, **158**:559
Tessler FN, **158**:195
Thomas HA, **158**:763
Thompson WM, **158**:1167
Tien RD, **158**:369, **158**:651, **158**:1151, **158**:1155, **158**:1325, **158**:1329
Tigges S, **158**:905, **158**:1368
Toaff ME, **158**:799
Tobias ME, **158**:459, **158**:694
Tochio H, **158**:65
Todo A, **158**:65
Tomita S, **158**:65
Tomiyama N, **158**:1217
Tomoda K, **158**:587
Towers MJ, **158**:691
Trambert MA, **158**:519
Tristń TA, **158**:388
Truitt T, **158**:916
Tsukaguchi I, **158**:587
Tu RK, **158**:460, **158**:917
Tubau JF, **158**:1114
Tubbs WS, **158**:331
Tumeh SS, **158**:785

U

Ueda H, **158**:751
Ueda S, **158**:423
Unger JM, **158**:1321
Unni KK, **158**:331

V

Vaidyanathan S, **158**:327, **158**:571
Valat J-P, **158**:921
Valk J, **158**:1275
Valls C, **158**:919
Van Alstyne GA, **158**:1257
Van Kooten B, **158**:1275
vanSonnenberg E, **158**:87, **158**:91, **158**:191
VaPat JP, **158**:459
Varma DGK, **158**:1031
Varma JR, **158**:211
Varney RR, **158**:91
Vellet AD, **158**:179
Verschakelen JA, **158**:1211
Vesely T, **158**:875
Vickers MA, **158**:1257
Vilaro M, **158**:843
Vogel VG, **158**:51
Vogl TJ, **158**:887

W

Wacquez M, **158**:694
Wagner S, **158**:183
Waite RJ, **158**:591
Waitzinger J, **158**:887
Walker AT, **158**:785
Walker-Andrews SC, **158**:427
Wallace CJ, **158**:849
Wallace S, **158**:722, **158**:1031
Walot I, **158**:363
Wang G-J, **158**:819
Warner TFCS, **158**:917
Warren Burhenne LJ, **158**:45
Wattsgård C, **158**:993
Webb WR, **158**:265
Weber A, **158**:213
Webster E, **158**:137
Weingarten K, **158**:645
Weiss AJ, **158**:1061
Westbrook PR, **158**:1019
Whalen E, **158**:449, **158**:679, **158**:1391
White SS, **158**:661
Whitis BM, **158**:669
Wicke K, **158**:1261
Wilbur AC, **158**:575
Willams DM, **158**:427
Willing S, **158**:1305
Winzelberg GG, **158**:150, **158**:598
Withers CE, **158**:691
Wittich GR, **158**:91
Wolf K-J, **158**:183
Wolfmman NT, **158**:493
Wolfson PJ, **158**:353
Wolk RB, **158**:1243
Wood BP, **158**:660, **158**:750
Woodard JR, **158**:613
Woodring JH, **158**:113
Worrell JA, **158**:898, **158**:1356
Wung JT, **158**:125

Y

Yamada Y, **158**:423
Yamagami H, **158**:1217
Yamahana T, **158**:311
Yamamoto F, **158**:1170
Yamamoto T, **158**:587
Yamawaki Y, **158**:1247
Yankaskas BC, **158**:559
Yao L, **158**:339
Yaquinto JJ, **158**:631
Yedlicka JW, **158**:623
Yeung EY, **158**:251
Yoder IC, **158**:1410
Yokoyama H, **158**:1011
Yorulmaz I, **158**:213
Yoshikawa M, **158**:885
Yoshizako T, **158**:1173
Young GP, **158**:243
Young JWR, **158**:109, **158**:586, **158**:608, **158**:921
Young LW, **158**:612
Yuki K, **158**:917

Z

Zagoria RJ, **158**:243
Zajko AB, **158**:997
Zaninović A, **158**:1303
Zeitoun G, **158**:1251
Zerhouni EA, **158**:559
Zimmerman RD, **158**:645
Zur Nedden D, **158**:1261
Zwiebel WJ, **158**:29
Zwirewich CV, **158**:1205

Subject Index
Volume 158

AJR articles are also included in the 5-year cumulative index published in *Radiology*.

Index Key: a = abstract, b = book review, e = editorial, l = letter, m = memorial, p = pictorial essay, v = videotape review

Subjects in this index are cataloged by body part where possible. Disease entities unique to a body part are listed by that part; other more general diseases have separate listings by name. Technical procedures are also listed by part, as appropriate. Because of general interest, subjects dealing with CT, MR imaging, sonography, radionuclide imaging, and pediatric radiology are listed under those headings as well as under appropriate body part and/or disease.

A

Abdomen
  infection, technetium-99m-HMPAO labeled leukocytes (a), **158:**698
  upper
    blunt trauma, adrenal injury and, CT, **158:**503
    blunt trauma, CT, **158:**493
Accessory occipital ventricle, CT scans (l), **158:**694
Acetabular fractures, percutaneous screw fixation, CT guidance, **158:**819
Adenoid cystic carcinoma, intracranial metastatic, primary tumor in parotid gland, **158:**1163
Adrenal gland
  pheochromocytoma, **158:**1056
  posttraumatic adrenal hemorrhage, children, **158:**1299
Adrenoleukodystrophy, adrenomyeloneuropathy and, MR imaging, **158:**413
Adrenomyeloneuropathy, adrenoleukodystrophy and, MR imaging, **158:**413
AIDS
  cytomegalovirus retinitis with, MR findings in (l), **158:**1176
  musculoskeletal infections in, CT (p), **158:**603
  tiny echogenic foci, liver and kidney, **158:**81
  visceral calcifications in (l), **158:**691
Airway, pharyngeal, occlusion and narrowing, obstructive sleep apnea and, **158:**1019
ALD, *see* Adrenoleukodystrophy
American Journal of Roentgenology, types of articles published, **158:**1165
American Roentgen Ray Society
  Figley Fellows in Radiology Journals, 1992, **158:**502
  information and application for membership, **158:**228
  1992 meeting, Orlando, FL, **158:**225, **158:**471, **158:**703
    calendar of events, **158:**473
    summary, **158:**227
  officers, committees, and membership information, **158:**224, **158:**469, **158:**702, **158:**931, **158:**1184
AMN, *see* Adrenomyeloneuropathy
Amniotic bands, amputations of fingers, congenital constricting ring and (l), **158:**215
Amniotic cavity, enlarged, early embryonic death, sonography, **158:**359
Amyloidosis, diffuse alveolar septal, CT, **158:**265
Angina pectoris, unstable, restenosis after coronary angioplasty (a), **158:**462
Angiography
  contrast media for (a), **158:**1418
  digital subtraction, vs film-screen, lower limbs, **158:**431
  middle cerebral artery, hemorrhagic infarction, **158:**151, **158:**158
  MR
    arterial injury from penetrating trauma, **158:**631
    blood supply to pulmonary sequestration, **158:**989
    intracranial, three time-of-flight techniques, **158:**381, **158:**389
Angioplasty
  balloon, coarctation of aorta (a), **158:**218
  bypass surgery and amputation, peripheral vascular disease (a), **158:**217
  comparison with medical therapy, coronary artery disease (a), **158:**1178
  coronary, restenosis after, unstable angina pectoris (a), **158:**462
  percutaneous transluminal
    mesocaval shunt stenosis, **158:**1251
    subclavian arteries (l), **158:**1174
    Takayasu disease, **158:**417
Ankle, acute injuries, radiography in (l), **158:**1411
Anterior cruciate ligament, tear, aneurysmal bone cyst after, **158:**1289
Aortic arch, ulcerated placques, stroke patients (a), **158:**1415
Aphthous ulcers, salmonella colitis (l), **158:**918
Apnea, obstructive sleep, occlusion and narrowing of airway, **158:**1019
Appendix, normal and abnormal, sonographic detection, **158:**773
Arterial thrombi, peripheral, sonography (a), **158:**697
Arteriography, normal findings, massive upper gastrointestinal hemorrhage with, **158:**547
Arteritis, nonspecific, renal artery stenosis caused by, MR imaging, **158:**417
Arthritis, Lyme, radiologic findings, **158:**1065
Arthroplasty
  hip, cemented acetabular components in (a), **158:**1417
  hybrid total knee, Miller-Galante prosthesis (a), **158:**926
  knee, metal-induced synovitis as a complication (a), **158:**219
Aspirin, colon cancer risk and (a), **158:**1178
Atherosclerosis, vasomotor response to mental stress and, coronary arteries (a), **158:**923
Avascular necrosis, canine model (l), **158:**1172
Azygos lobe, imaging (l), **158:**458

B

Back pain, lead apron use and, radiologists, **158:**191
Barium studies
  esophageal motor disorder diagnosis (a), **158:**926
  latex retention balloon for (l), **158:**691
  retained balloon tip, treatment by percutaneous needle puncture (l), **158:**1170
Bicipital tendon, long, shoulder, MR imaging (p), **158:**1091
Bile duct
  disruption, after laparoscopic cholecystectomy, **158:**785
  extrahepatic, changes after liver transplant, **158:**997
  stones, treatment by laser lithotripsy, **158:**1007
Biliary duct, interventional endoscopy, **158:**243
Biliary endoprostheses, expendable metallic, hot-tip laser probes in, **158:**199
Biliary stones, percutaneous extraction, air-bubble artifacts during, **158:**309
Biliary strictures
  postoperative
    after liver transplant, **158:**997

  endoscopic stenting for (a), **158**:1417
Biliary sump syndrome, imaging (p), **158**:315
Biloma, bile duct disruption and, after laparoscopic cholecystectomy, **158**:785
Biopsy
  fine-needle, sonographically guided, **158**:195
  large-core, value in occult breast lesions, **158**:991
  needle
    diseases of the breast, **158**:1231
    impalpable breast cysts, **158**:1239
  percutaneous needle, musculoskeletal lesions, **158**:809, **158**:813
  Temno needle, **158**:641
  transrectal, sonographic guidance, rectal carcinoma, **158**:1025
Bladder, augmented, delayed spontaneous rupture, children, **158**:833
Bochdalek's hernia, CT (l), **158**:1168
Bone
  benign giant-cell tumor, pulmonary metastases with, **158**:331
  density measurement methods, osteoporosis and (a), **158**:463
  nontumorous diseases of bones and joints (b), **158**:346
Bone cyst
  aneurysmal
    after anterior cruciate ligament tear, **158**:1289
    case of the day, **158**:1368
Bone marrow
  hematopoietic hyperplasia, MR images, **158**:335
  transplant
    jaundice after, peribiliary chloroma, **158**:1255
    venoocclusive liver disease after, duplex sonography, **158**:1001
Book reviews
  abdominal sonography, **158**:1298
  cardiac imaging, **158**:1390
  clinical magnetic resonance, **158**:564
  color Doppler flow imaging, **158**:1010
  comprehensive textbook of oncology, 2nd ed, **158**:40
  computed tomography and magnetic resonance of the thorax, **158**:1216
  computers in diagnostic radiology, **158**:443
  CT of the immunocompromised host, **158**:80
  diagnostic radiology 1990, **158**:326
  diagnostic techniques in urology, **158**:806
  differential diagnosis of diseases of the chest, **158**:508
  early missed fractures and corner signs in radiology, **158**:108
  errors in chest radiography, **158**:352
  essentials of nuclear medicine imaging, **158**:58
  fast-scan magnetic resonance, **158**:644
  FRCR part 1, **158**:1006
  fundamentals of body CT, **158**:550
  gastrointestinal radiology, **158**:1028
  geriatric radiology, **158**:668
  Grant's atlas of anatomy, **158**:574
  handbook of orthopedic terminology, **158**:608
  handbook of pediatric imaging, **158**:836
  head and neck imaging, 2nd ed, **158**:282
  hysterosalpingography, **158**:90
  imaging of the thyroid and parathyroid glands, **158**:50
  immunoscintigraphy, **158**:598
  interventional computed tomography, **158**:634
  liver imaging, **158**:86
  magnetic resonance test and syllabus, **158**:1346
  measurements in pediatric radiology, **158**:612
  Merrill's atlas of radiographic positions and radiologic procedures, **158**:388
  MRI of the brain III, **158**:1150
  MRI of the extremities, **158**:100
  MRI of the head and neck, **158**:1086
  MRI of the musculoskeletal system, **158**:586
  MRI of the shoulder, **158**:1280
  MRI of the spine, **158**:1134
  musculoskeletal imaging, **158**:1064
  nuclear medicine procedure manual, **158**:150
  orthopaedic MRI, **158**:1070
  pediatric cardiovascular imaging, **158**:1308
  pediatric sonography, **158**:128
  principles and practice of cardiovascular imaging, **158**:1114
  quality assurance in radiotherapy physics, **158**:1354
  radiologic and histologic pathology of nontumorous diseases of bones and joints, **158**:346
  radiologic clinics of North America, radiographic manifestations of common congenital anomalies, **158**:412
  radiology of trauma, **158**:1288
  stone therapy in urology, **158**:308
  the best of medical humor, **158**:202
  the discipline of curiosity, **158**:320
  the year book of diagnostic radiology 1991, **158**:618
  transvaginal ultrasound, **158**:798
  ultrasonography of the urinary tract, **158**:790
  understanding MRI, **158**:368
Bowel
  benign gaseous distension, after nasal continuous airway pressure, premature infants, **158**:125
  small, diagnosis of obstruction, CT, **158**:765, commentary, **158**:771
Brain
  fast spin-echo MR imaging, **158**:1313
  lesions, modern imaging, **158**:1193
Brainstem, deep cerebral infarction, MR contrast enhancement in, **158**:173
Breast
  calcifications, mammograms (l), **158**:1407
  Coumadin-induced fat necrosis, mammographic appearance of (l), **158**:689
  diseases, interventional procedures in, **158**:1231
  economic issues in mammography, **158**:527
  fibrosarcoma, mammographic findings, **158**:993
  impalpable cysts, fine-needle aspiration and pneumocystography in, **158**:1231
  infiltrating ductal carcinoma, mammographic features, **158**:269
  lesions, occult, large-core biopsy value in, **158**:991
  mammographically detected carcinomas, positive predictive values (l), **158**:688
  National Cancer Institute breast imaging workshop, **158**:268
  positive predictive value of mammography, **158**:521
Breast cancer
  mammography screening
    British Columbia, **158**:45, commentary, **158**:55
    low-cost project, **158**:51, commentary, **158**:55
  risk factors, women undergoing mammography, **158**:273
Bronchial artery, left thyrocervical trunk, recurrent hemoptysis in cystic fibrosis, **158**:1131
Bronchiolitis obliterans, organizing pneumonia, migratory pulmonary infiltrates, **158**:515
Bronchogenic cyst, intrapulmonary, spontaneous pneumothorax and, **158**:987
Bronchopulmonary dysplasia, early life, survival in adulthood, **158**:1
Budd-Chiari syndrome, interruption of inferior vena cava, combined saccular aneurysm and, **158**:635

C

Calcaneus, intraarticular fractures, **158**:1271
Calcinosis, idiopathic tumoral, **158**:330
Calcitriol, treatment, postmenopausal osteoporosis (a), **158**:1415
Calcium, treatment, postmenopausal osteoporosis (a), **158**:1415
Calvaria, osteogenic sarcoma, MR imaging, **158**:661
Carbon dioxide, microbubbles, intraarterial infusion, sonography with, **158**:65
Cardiovascular imaging, principles and practice (b), **158**:1114
Carotid stenosis, high-grade, carotid endarterectomy in (a), **158**:217
Case of the day
  abdominal, **158**:902, **158**:1363
  chest, **158**:898, **158**:1356
  neuroradiology, **158**:911, **158**:1378
  nuclear medicine, **158**:913, **158**:1382
  pediatric, **158**:907, **158**:1372
  skeletal, **158**:905, **158**:1368
Catheter
  image-guided, drainage of pleural space (a), **158**:464
  intracranial vasospasm induced by, intraarterial papaverine for relief of, **158**:883
  percutaneous central venous, placement, **158**:881
  percutaneous transaxillary, hepatic artery infusion chemotherapy, **158**:885
  peripherally inserted central, upper arm approach, protracted venous abscess, **158**:427
  pulmonary artery pseudoaneurysm induced by, CT, **158**:637
  pulmonary embolectomy in, massive pulmonary embolism (a), **158**:218
  small-bore, sclerotherapy of malignant pleural effusion, **158**:41
Central nervous system, sarcoidosis, contrast-enhanced MR imaging, **158**:391
Cerebellum, crossed diaschisis, crossed atrophy and, MR imaging, **158**:1155
Cerebral arteries, duplex sonography of, **158**:29
Cerebral infarction, brainstem, MR contrast enhancement in, **158**:173
Chemotherapy, hepatic artery infusion, percutaneous transaxillary catheter for, **158**:885
Child abuse
  long-bone fractures (a), **158**:219
  mediastinal pseudocyst, caused by pharyngeal perforation, MR, **158**:1111
Chloroma, peribiliary, jaundice after bone marrow transplant, **158**:1255
Cholangiocarcinoma, intrahepatic, MR imaging, **158**:77
Cholangiohepatitis, Oriental, **158**:1011
Cholangitis, *Candida*, diabetic woman, **158**:1029
Cholecystectomy
  laparoscopic, bile duct disruption and biloma after, **158**:785
  percutaneous laparoscopic, CT findings (a), **158**:464
Cholecystitis, gangrenous, sonography, **158**:698
Cholelithiasis
  gas in (a), **158**:925
  measurement of, sonography (a), **158**:220
Chondromalacia patellae, MR imaging, **158**:101
  commentary, **158**:106
Cinefluorography, swallowing dysfunction, postpolio syndrome, **158**:283
Cirrhosis, surface analysis diagnosis, high-frequency sonography (a), **158**:1180
Cocaine, maternal abuse, neonatal intestinal ischemia and bowel perforation, **158**:1303
Colitis
  hemorrhagic, *Escherichia coli*, **158**:551
  salmonella, aphthous ulcers in (l), **158**:918
Colitis, ulcerative, colonic contour changes, commentary, **158**:59
Colon
  cancer
    aspirin use and (a), **158**:1178
    radiologic screening. economics of (l), **158**:211
  hyperplastic polyps, prediction of proximal adenoma and (a), **158**:1179
Colopathy, portal hypertensive (a), **158**:925

Computed radiography, musculoskeletal imaging, **159:**19
Computers
  diagnostic radiology (b), **158:**442
  HyperCard coding system, ACT *Index for Radiological Diagnosis*, **158:**669
  three-dimensional imaging system based on, radiologic application of, **158:**673
Contrast media
  adverse reaction (l), **158:**1407
  angiography (a), **158:**1418
  low-osmolality, skin ulceration from extravasation (l), **158:**915
  new, preliminary evaluation in healthy volunteers, **158:**887
Coronary artery
  vasomotor response to mental stress, atherosclerosis effects (a), **158:**923
  visualization of, transvenous sonography (a), **158:**696
Coronary artery disease, single vessel, angioplasty and medical therapy compared (a), **158:**1178
Corticosteroids, injections, facet joints in chronic low back pain (a), **158:**462
Coumadin, fat necrosis induced by, breast, mammographic appearance of (l), **158:**689
Craniovertebral junction, normal anatomy, MR imaging (p), **158:**1087
Crohn's disease, transrectal sonography (a), **158:**697
CT
  fine-needle aspiration, percutaneous, grid for (l), **158:**459
  fundamentals (b), **158:**550
  immunocompromised host (b), **158:**80
  interventional (b), **158:**634
  iohexol 300, diatrizoate meglumine 60 comparison, **158:**665
CT, abdomen
  blunt trauma, **158:**493
    acute adrenal injury after, **158:**503
  hydatid cyst, follow-up of cystogastric fistula (l), **158:**212
  jejunoduodenogastric intussusception (l), **158:**212
  localized fat collection, inferior vena cava, **158:**423
  primary hyperaldosteronism, **158:**553
  primary malignant small round cell tumor, **158:**1031
  small bowel obstruction, **158:**765
    commentary, **158:**771
  tuboovarian abscess (p), **158:**575
  uncomplicated percutaneous laparoscopic cholecystectomy (a), **158:**464
CT, adrenal, posttraumatic hemorrhage, children, **158:**1299
CT, aorta, motion artifact simulating dissection (l), **158:**1408
CT, bladder, augmented, delayed spontaneous rupture, children, **158:**833
CT, cervical lymph nodes, detection of metastasis, **158:**961
CT, cranium
  intracranial metastatic adenoid cystic carcinoma, primary tumor of parotid gland, **158:**1163
  lateral ventricles, asymmetry of frontal horns (l), **158:**1175
  pachygyria, infant (l), **158:**1176
  Sturge-Weber syndrome, children, **158:**867
CT, face, nasolacrimal fossa and canal fractures, **158:**1321
CT, head and neck, hemorrhagic infarction, middle cerebral artery, **158:**151, **158:**158
CT, kidney, duplex, large cloisons simulating (l), **158:**1171
CT, leg, calcaneus, intraarticular fractures, **158:**1271
CT, liver
  hepatocellular carcinoma (l), **158:**917
  hepatocellular carcinoma, **158:**1247
  hypoplasia of left lobe (l), **158:**213
  lesions, small, frequency and significance of, **158:**535
  macronodular tuberculoma, **158:**311
  masses, infants and children (p), **158:**143
CT, lung
  benign fibrous mesothelioma, pleura, **158:**983
  chronic infiltrative disease, MR imaging comparison, **158:**1205
  high-resolution
    alveolar microlithiasis, **158:**981
    various pulmonary diseases, **158:**971
  hypersensitivity pneumonitis, summer-type, **158:**1223
  lymphangitic carcinomatosis, **158:**1217
  Swyer-James syndrome, **158:**1211
CT, mediastinum, azygoesophageal recess, children, **158:**1101
CT, musculoskeletal
  diseases in children, **158:**729
  hemophilia, **158:**119
  infections, AIDS patients (p), **158:**603
CT, pancreas
  blunt trauma, children, **158:**1097
  gastroepiploic veins, **158:**779
  pleomorphic pancreatic sarcoma, mimicking pancreatic pseudocyst, **158:**87
CT, pediatric, sedation (a), **158:**1417
CT, pelvis, acetabular fractures, percutaneous screw fixation, **158:**819
CT, shoulder, labral capsular ligamentous complex (p), **158:**591
CT, spine
  lumbar spinal stenosis, **158:**1135
  metastases, vertebrae, **158:**1275
CT, thorax
  Bochdalek's hernia (l), **158:**1168
  diffuse alveolar septal amyloidosis, **158:**265
  MR imaging and (b), **158:**1216
  ruptured pulmonary hydatid cysts, folded membrane and (l), **158:**687
  spiral, thoracic aorta assessment (p), **158:**1127
Cyst, *see* specific organ or site
Cystic fibrosis
  bronchial arteriography, embolotherapy and (a), **158:**927
  early life, survival in adulthood, **158:**1
  recurrent hemoptysis in, bronchial artery embolization, **158:**1131
Cystogastric fistula, follow-up, hydatid disease (l), **158:**212
Cystourethrography, voiding, digital fluoroscopy in reducing radiation dose, **158:**137
Cytodiagnosis
  fine-needle, renal tuberculosis (a), **158:**463
  sonographically guided aspiration, renal tuberculosis, **158:**571

D

Desmoids, extraabdominal, MR imaging, **158:**581
Dexamethasone, chronic lung disease, neonate (a), **158:**219
Diabetes, *Candida* cholangitis, woman, **158:**1029
Diaphragm, congenital hernia, survival in adulthood, **158:**1
Diaschisis, cerebellar, crossed atrophy and, MR imaging, **158:**1155
Diatrizoate meglumine 60, iohexol 300 comparison, body CT, **158:**665
Dipyridamole thallium-201, image quality, exercise effects (a), **158:**220
Dysphagia, elderly patients (l), **158:**916

E

Echocardiography, transesophageal, treatment of aortic dissection (a), **158:**1416
Edema, tumor perfusion and, **158:**259
Embolization
  prophylactic, left gastric artery, **158:**547
  transcatheter arterial, hepatocellular carcinoma, color Doppler sonography, **158:**541
Encephalitis, Rasmussen's, neuroimaging in, **158:**1329
Endarterectomy, carotid (a), **158:**217
Endometrium
  carcinoma
    International Federation of Gynecology and Obstetrics surgical staging and survival rates (a), **158:**1179
    myometrial invasion by, MR imaging, **158:**565
Endoscopy
  interventional, biliary and pancreatic ducts, **158:**243
  pancreatic ductal stones (a), **158:**463
Epiphysis, cartilaginous, growth plate and, MR imaging (p), **158:**1105
Escherichia coli, hemorrhagic colitis, **158:**551
Esophageal atresia, tracheoesophageal fistula, survival in adulthood, **158:**1
Esophagus
  motor disorders, diagnostic comparisons (a), **158:**926
  postcricoid impression of (l), **158:**690
Ewing sarcoma, acute abdomen (l), **158:**692
Exercise, supplementation, dipyridamole thallium-201 image quality (a), **158:**220
Extracorporeal membrane oxygenation
  positive end-expiratory pressure during, pediatric (a), **158:**1180
  thoracic complications, chest radiographs and sonograms (p), **158:**353
Extracorporeal shock-wave lithotripsy
  pancreatic calculi (a), **158:**1416
  percutaneous nephrostomy after, needle blockage, **158:**807
Eye, ocular trauma, sonography, **158:**179

F

Femoral head
  cortical fractures (l), **158:**921
  osteonecrosis, sickle cell disease and (a), **158:**923
Femoral stem, hydroxyapatite-coated (a), **158:**1180
Fibrosarcoma, breast, mammographic findings, **158:**993
Filters, inferior vena cava, Bird's Nest, placement (p), **158:**875
Fluoroscope, shoe, history page, **158:**1270
Fluoroscopy, digital, voiding cystourethrography, children, **158:**137
Fournier's gangrene, MR imaging (l), **158:**1173

G

Gadobenate dimeglumine, preliminary evaluation, healthy volunteers, **158:**887
Gadopentetate dimeglumine
  dynamic MR imaging
    benign uterine masses, **158:**1043
    liver, spleen, stomach, and pancreas, **158:**303
  inadvertent administration, during pregnancy (l), **158:**1171
Galactography, diseases of the breast, **158:**1231
Gallbladder, contractility, spinal cord injury and (l), **158:**456
Gastric carcinoma, *Helicobacter pylori* (a), **158:**696
Gastroepiploic veins, CT appearance, pancreatic disease, **158:**779
Gastrointestinal hemorrhage, coil embolus, retrieval of (l), **158:**1411
Gastrointestinal tract
  abnormalities, spinal cord injury patients, **158:**279
  massive hemorrhage, normal findings on arteriography and, **158:**547
Gastrostomy, percutaneous, transgastric jejunostomy and, **158:**251

- **Gastrostomy tube,** complication, jejunoduodenogastric intussusception (l), **158:**212
- **Genitourinary tuberculosis,** sonography (p), **158:**327
- **Glioma,** high-grade recurrent, vs radiation necrosis, **158:**399
- **Good's syndrome,** thymoma with, **158:**1229
- **Gradient-recalled echo techniques,** MR imaging of joints, **158:**339
- **Granite dust,** exposure, radiographic abnormalities with (a), **158:**924
- **Growth plate,** cartilaginous epiphysis, MR imaging (p), **158:**1105
- **Gynecologic cysts,** nonovarian, MR (p), **158:**1265

H

- **Halo sign,** CT, pulmonary artery pseudoaneurysm, **158:**637
- **Hatam, Ahmad (m), 158:380**
- **Heart,** imaging (b), **158:**1390
- **Heart rate,** monitoring, fiber-optic pulse oximeter during MR imaging, **158:**663
- **Heart ventricle, right,** double-outlet, congenital absence of left pulmonary artery and, **158:**1309
- **Heimlich valve,** reversal of, tension pneumothorax after, **158:**763
- ***Helicobacter pylori*,** risk of gastric carcinoma (a), **158:**696
- **Hematoma,** intrahepatic, ultrasound-detected (a), **158:**219
- **Hemolytic-uremic syndrome,** *Escherichia coli* preceding, hemorrhagic colitis and, **158:**551
- **Hemoperitoneum,** traumatic avulsion of pedunculated uterine leiomyoma (l), **158:**1410
- **Hemophilia,** musculoskeletal involvement, CT, sonography, and MR imaging, **158:**119
- **Hemorrhagic infarction,** middle cerebral artery, early angiographic and CT findings, **158:**151, **158:**158
- **Hepatocellular carcinoma**
  - color Doppler sonography, before and after transcatheter arterial embolization, **158:**541
  - CT, **158:**1247
  - high-density, unenhanced CT (l), **158:**917
  - intraoperative sonography (a), **158:**220
- **Herman, Richard (m), 158:124**
- **Hinman syndrome,** psychogenic urinary retention, pediatric (l), **158:**460
- **History page, 158:**302, **158:**760, **158:**980, **158:**1270
- **Human immunodeficiency virus**
  - carriers of, neurosyphilis in, MR findings, **158:**1325
  - drug addict seropositive for, lung cancer in (l), **158:**210
  - peliosis of liver and spleen (l), **158:**1409
- **Huntington disease,** MR appearance of neural grafts, primate model (l), **158:**215
- **Hydatid cyst**
  - CT (l), **158:**212
  - percutaneous drainage, new cutting device, **158:**83
  - ruptured pulmonary, folded membrane and, CT (l), **158:**687
- **Hyperaldosteronism,** primary, CT findings and endocrinologic studies, **158:**553
- **Hypertension,** pulmonary, single-lung transplantation for (a), **158:**925
- **Hypogammaglobulinemia,** thymoma with, **158:**1229
- **Hysterectomy,** normal and abnormal vagina after, MR imaging, **158:**95
- **Hysterosalpingography**
  - England (l), **158:**1410
  - text and atlas (b), **158:**90

I

- **Ifosfamide,** rickets and, **158:**823
- **Ileum,** varix (l), **158:**917
- **Immunoglobulin G,** indium-111-labeled nonspecific human, diagnosing of inflammations/infections (a), **158:**926
- **Infantile odontoid process,** persistent, **158:**1305
- **Insulinoma,** MR imaging, STIR sequences and motion suppression (l), **158:**457
- **Interleukin-2,** local, adverse reaction to contrast media (l), **158:**1407
- **International Skeletal Society,** eighteenth annual refresher course, September 1991, **158:**449
- **Intestine**
  - ischemia, neonatal, bowel perforation and, maternal cocaine abuse, **158:**1303
  - stricture, lap-belt injury, **158:**63
- **Intramuscular injections,** MR appearance of, **158:**1293
- **Intussusception,** plain film diagnosis, **158:**618
- **Iohexol 300,** diatrizoate meglumine 60 comparison, body CT, **158:**665
- **Irradiation**
  - insufficiency fractures induced by, pelvic, **158:**599
  - preoperative, rectal carcinoma, MR imaging, **158:**287
  - radiation necrosis, vs high-grade recurrent glioma, **158:**399

J

- **Jaundice,** after bone marrow transplant, peribiliary chloroma, **158:**1255
- **Jefferson fracture,** unstable variant atlas, **158:**113
- **Jejunostomy,** transgastric, percutaneous gastrostomy, **158:**251
- **Joints,** nontumorous diseases of bones and joints (b), **158:**346

K

- **Karyotypic abnormalities,** omphalocele contents and, sonography, infant, **158:**133
- **Kidney**
  - duplex, large cloisons simulating on CT (l), **158:**1171
  - dysfunction, native, duplex Doppler evaluation, **158:**1035
  - lymphoma, **158:**570
  - polycystic disease (a), **158:**1417
  - stones, ochronosis and (l), **158:**214
  - symptomatic renal obstruction, or urosepsis during pregnancy, sonography, **158:**91
  - tiny echogenic foci, AIDS patients, **158:**81
  - transplant
    - dogs, sonography, **158:**791
    - vertebral mineral density after (a), **158:**218
  - tuberculosis
    - fine needle cytodiagnosis (a), **158:**463
    - sonographically guided aspiration cytology, **158:**571
- **Knee,** meniscal tears, MR diagnosis of, **158:**587

L

- **Laser lithotripsy,** treatment of bile duct stones, **158:**1007
- **Laser probe,** hot-tip, occluded expandable metallic biliary endoprostheses, **158:**199
- **Leiomyoma,** uterine, imaging of (p), **158:**799
- **Lipomatosis,** endobronchial lipoma associated with (l), **158:**210
- **Liver**
  - amebic abscesses, three different therapeutic strategies (a), **158:**1417
  - atrophy, portal vein occlusion correlation, **158:**1011
  - atypical mesenchymal hamartoma, sonography (l), **158:**921
  - cirrhosis, high-frequency sonography (a), **158:**1180
  - dynamic MR imaging, gadopentetate dimeglumine, **158:**303
  - imaging (b), **158:**86
  - laceration, MR imaging (l), **158:**1170
  - left lobe, hypoplasia, CT (l), **158:**213
  - lesions, small, frequency and significance of, CT, **158:**535
  - macronodular tuberculoma, CT and MR imaging, **158:**311
  - masses, infants and children, CT (p), **158:**143
  - neoplasms (p), **158:**1015
  - peliosis, HIV patient (l), **158:**1409
  - surgical segmental anatomy, PRISE in, **158:**299
  - tiny echogenic foci, AIDS patients, **158:**81
  - transplant
    - acute adenovirus hepatitis in, pediatric (a), **158:**1180
    - changes in extrahepatic bile duct caliber in, **158:**997
    - sonography vs MR imaging, pediatric (l), **158:**692
  - tumors, sonography with carbon dioxide microbubbles, **158:**65
  - venoocclusive disease, after bone marrow transplant, duplex sonography, **158:**1001
- **Lorman, James G. (m),** **158:**1292
- **Lumbar nerve root blocks,** percutaneous (l), **158:**1412
- **Lung**
  - cancer
    - changing patterns of (a), **158:**924
    - cigarette smoking and (a), **158:**924
    - drug addict seropositive for HIV (l), **158:**210
    - leukocyte count and risk of (a), **158:**1416
  - chronic infiltrative disease, MR imaging, CT comparison, **158:**1205
  - intrapulmonary bronchogenic cyst, spontaneous pneumothorax and, **158:**987
  - pleura, benign fibrous mesothelioma, pleura, **158:**983
  - radiographic abnormalities, exposure to granite dust and (a), **158:**924
  - transplant, single, hypertension and (a), **158:**925
  - various diseases, high-resolution CT, **158:**971
- **Lyme disease,** radiologic findings, Lyme arthritis and, **158:**1065
- **Lymphangitic carcinomatosis,** lung, CT findings, **158:**1217
- **Lymph nodes,** cervical, metastasis detection in, **158:**961
- **Lymphography,** staging lymphomas and genital tumors, **158:**725
- **Lymphomas**
  - renal, **158:**570
  - staging, lymphography, **158:**725

M

- **Macrodystrophia lipomatosa,** MR diagnosis, **158:**1295
- **Macronodular tuberculoma,** liver, CT and MR imaging, **158:**311
- **Malpractice,** mammography and (l), **158:**1169
- **Mammography**
  - calcifications, clustered skin distinguished from (l), **158:**1407
  - carcinoma detected by, positive predictive values (l), **158:**688
  - Coumadin-induced fat necrosis (l), **158:**689
  - economic issues in, **158:**527
  - extensive intraductal component, early-stage infiltrating ductal carcinoma, **158:**269
  - fibrosarcoma of breast, **158:**993
  - malpractice and (l), **158:**1169
  - mobile, hidden costs, **158:**1243
  - National Cancer Institute breast imaging workshop, **158:**268
  - occult breast lesions, large-core biopsy and, **158:**991
  - positive predictive value of, **158:**521
  - risk factors before breast cancer, **158:**273
  - screening program
    - British Columbia, **158:**45, commentary, **158:**55
    - low-cost project, **158:**51, commentary, **158:**55

Manometry
- continuous swallows, esophageal motor disorder diagnosis (a), **158**:926
- percutaneous transhepatic, sphincter of Oddi (a), **158**:463

Mapp, Esmond McDonald (m), **158**:784

Meckel's diverticulum, giant, adult (l), **158**:1408

Mediastinum
- azygoesophageal recess, children, CT, **158**:1101
- masses, diagnostic imaging, children, **158**:825
- pseudocyst, pharyngeal perforation and, child abuse, **158**:1111

Medicine in American Art, **158**:518, **158**:742, **158**:970, **158**:1210

Medullablastoma, MR imaging in, **158**:849

Melanoma, malignant, visceral metastases, MR imaging, **158**:293

Memorials
- Ahmad Hatam, 1923–1991, **158**:380
- Esmond McDonald Mapp, 1928–1992, **158**:784
- James G. Lorman, 1920–1991, **158**:1292
- Richard Herman, 1946–1991, **158**:124
- Scot I. Rowe, 1958–1991, **158**:660

Ménétrier disease, radiologic-pathologic conference, **158**:62

Meningioma
- multiple (l), **158**:1413
- residual or recurrent, after surgery, MR imaging, **158**:645

Mesocaval shunt stenosis, metallic stent in, **158**:1251

Mesothelioma, benign fibrous, pleura, CT findings, **158**:983

Methyl *tert*-butyl ether, endoscopic treatment, common bile duct stones (a), **158**:1179

Microlithiasis
- pulmonary alveolar, high-resolution CT, **158**:981
- testicular, sonography, **158**:1057

Migraine, MR imaging in (l), **158**:922

Motor vehicle accident, lap-belt injury, intestinal stricture, **158**:63

MR imaging
- angiography, arterial injury from penetrating trauma, **158**:631
- clinical (b), **158**:564
- extremities (b), **158**:100
- fast-scan (b), **158**:644
- fat-suppression, neuroradiology, **158**:369
- fiber-optic pulse oximeter, heart rate and oxygen saturation during, **158**:663
- ^{1}H-, edema and tumor perfusion, **158**:259
- HIV carriers, neurosyphilis in, **158**:1325
- intracranial angiography, three time-of-flight techniques, **158**:381, **158**:389
- intramuscular injections, **158**:1293
- magnetic resonance test and syllabus (b), **158**:1346
- rectal carcinoma, preoperative irradiation, **158**:287
- sexual differentiation, congenital disorders (p), **158**:363
- understanding of (b), **158**:368

MR imaging, abdomen
- extraabdominal desmoids, **158**:581
- gadopentetate dimeglumine, liver, spleen, stomach, and pancreas, **158**:303
- nonovarian gynecologic cysts (p), **158**:1265
- technetium-99m-HMPAO labeled leukocytes, fast diagnosis (a), **158**:698
- visceral metastases, malignant melanoma and, **158**:293

MR imaging, bone, cartilaginous epiphysis, growth plate and (p), **158**:1105

MR imaging, cervical lymph nodes, detection of metastasis, **158**:961

MR imaging, CNS, contrast-enhanced, sarcoidosis, **158**:391

MR imaging, cranium
- brain (b), **158**:1150
- brain, fast spin-echo, **158**:1313
- brain tumors (v), **158**:1160
- craniovertebral junction (p), **158**:1087
- crossed cerebellar diaschisis, crossed cerebellar atrophy and, **158**:1155
- lateral ventricles, asymmetry of frontal horns (l), **158**:1175
- medulloblastomas, **158**:859
- migraine patients (l), **158**:922
- multiple sclerosis, **158**:849
- reversible cerebral lesions, hypertensive encephalopathy caused by Wilms' tumor, **158**:1161
- Sturge-Weber syndrome, children, **158**:867
- tuberous sclerosis (a), **158**:1418

MR imaging, eye, cytomegalovirus retinitis, AIDS and (l), **158**:1176

MR imaging, genitourinary, tuberculosis (l), **158**:919

MR imaging, hand, macrodystrophia lipomatosa, **158**:1295

MR imaging, head and neck
- deep cerebral infarction, brainstem, **158**:173
- meningioma, residual or recurrent, after surgery, **158**:645
- neural grafts, Huntington disease, primate model (l), **158**:215
- osteogenic sarcoma, calvaria, **158**:661
- pituitary gland, sequence of enhancement of various portions, **158**:651
- teaching file (b), **158**:1086

MR imaging, joints, GRE techniques at 1.5 T, **158**:339

MR imaging, knee
- bone marrow, hematopoietic hyperplasia, **158**:335
- chondromalacia patellae, **158**:101
  - commentary, **158**:106
- meniscal tears, **158**:587
- rotation and stabilization device (l), **158**:1173

MR imaging, liver
- intrahepatic cholangiocarcinoma, **158**:77
- laceration (l), **158**:1170
- macronodular tuberculoma, **158**:311
- magnetization prepared gradient-echo (a), **158**:464
- splenic and hepatic peliosis, **158**:75

MR imaging, lung, chronic infiltrative disease, CT comparison, **158**:1205

MR imaging, mediastinum, pseudocyst, pharyngeal perforation and, child abuse, **158**:1111

MR imaging, musculoskeletal
- diseases in children, **158**:729
- hemophilia, **158**:119
- orthopaedic (b), **158**:1070
- review of applications (b), **158**:586

MR imaging, ovary, lipid- and water-suppression, ovarian masses, **158**:321

MR imaging, pancreas, insulinoma, STIR sequences and motion suppression (l), **158**:457

MR imaging, pediatric, sedation (a), **158**:1417

MR imaging, pelvis, looking-down view (l), **158**:693

MR imaging, penis, Peyronie's disease, **158**:1261

MR imaging, physeal bars, premature partial physeal arrest (a), **158**:698

MR imaging, pituitary, growth and development, infants and children, **158**:1151

MR imaging, prostate, adenocarcinoma, determining stage C disease, **158**:559, **158**:563

MR imaging, scrotum, Fournier's gangrene (l), **158**:1173

MR imaging, shoulder
- full-thickness tears of rotator cuff, **158**:347
- labral capsular ligamentous complex (p), **158**:591
- long bicipital tendon, normal anatomy and pathologic findings (p), **158**:1091
- review (b), **158**:1280
- supraspinatus tendon, asymptomatic volunteers, **158**:1281

MR imaging, spine
- ALD-AMN complex, **158**:413
- comprehensive teaching file (b), **158**:1134
- contrast-enhanced
  - epidural abscess, **158**:405
  - intradural schwannoma, **158**:1347
- epidural abscess, cervical spine, **158**:1145
- hemisection of cervical spinal cord, stab wound (l), **158**:1413
- lumbar spinal stenosis, **158**:1135
- management of infections, **158**:1333
- schistosomal granuloma, **158**:1347
- subacute necrotizing myelopathy, **158**:163, **158**:170

MR imaging, thorax
- CT and (b), **158**:1216
- pulmonary hemorrhage, complicating systemic lupus erythematosus, **158**:519
- retained surgical sponge (l), **158**:460
- stellate ganglion, normal appearance (p), **158**:655
- thoracic aorta, acquired diseases, **158**:1115

MR imaging, thymus, thymoma (p), **158**:751

MR imaging, urachus, carcinoma (l), **158**:1171

MR imaging, uterus
- adenofibroma, mimicking endometrial carcinoma (l), **158**:214
- contrast-enhanced, benign masses, **158**:1043
- endometrial carcinoma, myometrial invasion by, **158**:565

MR imaging, vagina, normal and abnormal, after hysterectomy, **158**:95

MR lymphography, iron oxide particles, **158**:183

Mucormycosis, invasive, multiple mycotic pulmonary artery aneurysms and, **158**:761

Multiple sclerosis, MR imaging in, **158**:849

Myelography, lumbar spinal stenosis, **158**:1135

Myelopathy, subacute necrotizing, MR, **158**:163, **158**:170

N

Nasal continuous positive airway pressure, benign gaseous distension of bowel after, premature infants, **158**:125

Nasobiliary tube, common bile duct radiolucent stones with, elderly patients, methyl *tert*-butyl ether for (a), **158**:1179

Nasolacrimal fossa, fractures, CT, **158**:1321

National Cancer Institute, breast imaging workshop, **158**:268

Nephrostomy
- percutaneous
  - needle blockage during, after extracorporeal shock-wave lithotripsy, **158**:807
  - sonographically guided, **158**:91

Neuroblastoma, outcome of therapy, P-glycoprotein expression as a predictor of (a), **158**:1178

Neurocutaneous syndromes, modern imaging, **158**:1193

Neuroimaging, Rasmussen's encephalitis, **158**:1329

Neuroradiology
- case of the day, **158**:911, **158**:1378
- fat-suppression MR imaging, **158**:369

Neurosyphilis, HIV carriers, MR imaging, **158**:1325

Nuclear medicine
- case of the day, **158**:913, **158**:1382
- essentials of imaging (b), **158**:58
- procedure manual (b), **158**:150

Nutcracker syndrome, pathophysiology, diagnosis and treatment (a), **158**:219

O

Ochronosis, urinary tract, prostatic and renal stones (l), **158**:214

Octreotide, intestinal motility and bacteria, scleroderma (a), **158**:923

Omphalocele, contents, karyotypic abnormalities and, sonography, infant, **158**:133

Oncocytoma, renal cell carcinoma simulation of (l), **158**:920

Oncology, comprehensive textbook (b), **158**:40

Osteogenic sarcoma, primary, calvaria, MR imaging, **158:**661
Osteoma, epiphyseal osteoid, **158:**609
Osteomyelitis
  scintigraphic diagnosis, **158:**9
  sickle-cell disease and (a), **158:**697
Osteoporosis
  bone density measurement methods and (a), **158:**463
  postmenopausal
    calcitriol or calcium treatment (a), **158:**1415
    prevention (a), **158:**696
Osteosarcoma
  parosteal, case of the day, **158:**1368
  surface (a), **158:**463
Ovary, masses, lipid- and water-suppression MR images, **158:**321
Oximeter, fiber-optic pulse, heart rate and oxygen saturation during MR imaging, **158:**663
Oxygen saturation, monitoring, fiber-optic pulse oximeter during MR imaging, **158:**663

P

Pachygyria, infant, CT findings (l), **158:**1176
Pancreas
  blunt trauma, CT, children, **158:**1097
  calculi, extracorporeal shock-wave lithotripsy (a), **158:**1416
  disease, CT appearance, **158:**779
  dynamic MR imaging, gadopentetate dimeglumine, **158:**303
  pleomorphic sarcoma, mimicking pancreatic pseudocyst, CT, **158:**87
  stone morphology, pancreatic lithiasis patients (a), **158:**697
Pancreatic duct
  interventional endoscopy, **158:**243
  stones, successful endoscopy (a), **158:**463
Papaverine, intraarterial, catheter-induced intracranial vasospasm, **158:**883
Parathyroid gland, imaging (b), **158:**50
Parotid gland, primary tumor, intracranial metastatic adenoid cystic carcinoma, **158:**1163
Patient management, imaging information, clinician's access to, **158:**893
Pediatric radiology
  amniotic bands, amputations of fingers and congenital constricting ring (l), **158:**215
  aneurysmal bone cyst, case of the day, **158:**907, **158:**1368
  augmented bladder, delayed spontaneous rupture, sonography and CT, **158:**833
  azygoesophageal recess, CT, **158:**1101
  blunt pancreatic trauma, CT, **158:**1097
  cardiovascular imaging (b), **158:**1308
  chest radiographs, receiver-operating-characteristic study, children, **158:**443
  child abuse, pharyngeal perforation, mediastinal pseudocyst caused by, **158:**1111
  extracorporeal membrane oxygenation, positive end-expiratory pressure during (a), **158:**1180
  fetal thyroid, sonographic measurements (a), **158:**1180
  fever of unknown origin, scanning procedures for diagnosis (a), **158:**464
  handbook of pediatric imaging (b), **158:**836
  hepatic masses, CT (p), **158:**143
  hypertrophic pyloric stenosis, sonography, infant, **158:**129
  liver transplant recipients, acute adenovirus hepatitis in (a), **158:**1180
  long-bone fractures, young children (a), **158:**219
  measurements (b), **158:**612
  mediastinal masses, diagnostic imaging, **158:**825
  MR imaging and CT, sedation for (a), **158:**1417
  musculoskeletal system, CT, sonography, and MR imaging, **158:**729
  neonatal chronic lung disease, dexamethasone (a), **158:**219
  neonatal intestinal ischemia, bowel perforation and, maternal cocaine abuse, **158:**1303
  omphalocele contents karyotypic abnormalities and, sonography, **158:**133
  pachygyria, infant, CT findings (l), **158:**1176
  pediatric sonography (b), **158:**128
  persistent infantile odontoid process, **158:**1305
  pituitary gland, growth and development, MR imaging, **158:**1151
  posttraumatic adrenal hemorrhage, CT, **158:**1299
  premature infants, benign gaseous distension of bowel, nasal continuous airway pressure, **158:**125
  psychogenic urinary retention, Hinman syndrome (l), **158:**460
  respiratory problems, survival in adulthood, **158:**1
  reversible cerebral lesions, hypertensive encephalopathy caused by Wilms' tumor, MR imaging, **158:**1161
  scrotum, normal and abnormal, sonography, **158:**613
  solid tumors, symptom onset and diagnosis differences (a), **158:**698
  sonography vs MR imaging, pediatric liver transplantation (l), **158:**692
  Sturge-Weber syndrome, CT and MR imaging comparison, **158:**867
  tuberous sclerosis, **158:**750
  ureterovesical junction, sonography, after surgery or endoscopy, **158:**837
  voiding cystourethrography, digital fluoroscopy in reducing radiation dose, **158:**137
Peliosis, splenic and hepatic, MR imaging, **158:**75
Pelvis
  fractures and trauma, diagnosis, **158:**109
  radiation-induced insufficiency fractures, **158:**599
Penis, Peyronie's disease, MR imaging, **158:**1261
Peripheral arterial disease, mortality over 10 years (a), **158:**1415
Peripheral vascular disease, angioplasty, bypass surgery, and amputation use in (a), **158:**217
Peyronie's disease, MR imaging, **158:**1261
P-glycoprotein, expression, neuroblastoma outcome and (a), **158:**1178
Pharynx, perforation, mediastinal pseudocyst caused by, child abuse, **158:**1111
Phenothiazines, overdosage, acute pulmonary edema and (a), **158:**1179
Pheochromocytoma, adrenal, **158:**1056
Physeal bars, premature partial arrest, MR imaging (a), **158:**698
Picture archiving and communication system, infrastructure design of, **158:**743
Pituitary gland
  growth and development, infants and children, MR imaging, **158:**1151
  sequence of enhancement of various portions, gadolinium-enhanced MR imaging, **158:**651
Pneumocystis carinii, tiny echogenic foci in liver and kidney, AIDS patients, **158:**81
Pneumocystography
  diseases of the breast, **158:**1231
  impalpable breast cysts, **158:**1239
Pneumonia
  bronchiolitis obliterans organizing, migratory pulmonary infiltrates, **158:**515
  Pneumocystis carinii, spontaneous pneumothorax in (l), **158:**916
Pneumonitis, hypersensitivity, summer-type, CT, **158:**1223
Pneumopyopericardium, after penetrating chest injury (l), **158:**687
Pneumothorax
  digital radiography for, **158:**509
  spontaneous
    intrapulmonary bronchogenic cyst and, **158:**987
    Pneumocystis carinii pneumonia (l), **158:**916
  tension, after reversal of Heimlich valve, **158:**763
  thoracentesis and (l), **158:**458
Portal vein, occlusion, hepatic atrophy correlation and, **158:**1011
Postpolio syndrome, swallowing dysfunction in, cinefluorographic study, **158:**283
Pregnancy
  inadvertent gadopentetate dimeglumine administration during (l), **158:**1171
  outcome, sonographic detection of yolk sac and, **158:**843
  urosepsis during, or symptomatic renal obstruction, sonography, **158:**91
Prostate
  adenocarcinoma, determining stage C disease, MR imaging, **158:**559, **158:**563
  stones, ochronosis and (l), **158:**214
Pulmonary artery
  embolism
    embolectomy, by catheter device (a), **158:**218
    surgical sponge, **158:**757
    ventilation/perfusion lung scans in (a), **158:**218
  multiple mycotic aneurysms, complication of invasive mucormycosis, **158:**761
  pseudoaneurysm, catheter-induced, CT, **158:**637
Pulmonary artery, left, congenital absence, double-outlet right ventricle and, **158:**1309
Pulmonary edema
  overdosage of phenothiazines and (a), **158:**1179
  tocolytic therapy and, case of the day, **158:**1356
Pulmonary function tests, CT correlation, lymphangitic carcinomatosis, **158:**1217
Pulmonary sequestration, blood supply to, demonstration by MR angiography, **158:**989
Pyloric muscle, hypertrophic stenosis, sonography, infant, **158:**129

R

Radiography
  computed, musculoskeletal imaging, **159:**19
  digital
    pneumothorax detection, **158:**509
    skeletal, **158:**1071
  digitized images vs plain films, joints of the fingers, **158:**437
  pelvic fractures, patients with acute trauma, **158:**109
  thorax, receiver-operating-characteristic study, children, **158:**443
  unstable Jefferson variant atlas fractures, unrecognized cervical injury, **158:**113
Radiologists, lead apron use, back pain and, **158:**191
Radiology
  atlas of positions and procedures (b), **158:**388
  East Africa (l), **158:**1167
  environment and (l), **158:**456
  gastrointestinal (b), **158:**1028
  information perspective on, **158:**1387
  screening for colonic cancer, economics of (l), **158:**211
  trauma (b), **158:**1288
Radiology department, clinician's access to diagnostic imaging information, at an academic center, **158:**893
Radiology journals
  advice to first time authors of manuscripts, **158:**203
  controlled circulation (l), **158:**209
Radiology Summit Meeting, 1991, 158:675
Rathke's cleft cyst, 158:1312
Rectum
  carcinoma
    preoperative irradiation, MR, **158:**287
    recurrent extraluminal, transrectal biopsy, **158:**1025
Renal artery stenosis, nonspecific arteritis and, percutaneous transluminal angioplasty, **158:**417
Renal cell carcinoma, simulating oncocytoma (l), **158:**920

Retroperitoneal fibrosis (l), 158:1409
Rickets, ifosfamide and, **158:**823
Rotator cuff, full-thickness tears, MR imaging, **158:**347
Rowe, Scot I. (m), 158:660

S

Salmonella, colitis, aphthous ulcers in (l), **158:**918
Sarcoidosis, CNS, contrast-enhanced MR imaging, **158:**391
Schwannoma, intradural, spine, contrast-enhanced MR, **158:**1347
Scleroderma, bacterial overgrowth, intestinal motility and, octreotide effects (a), **158:**923
Sclerotherapy, malignant pleural effusion, sonography, small-bore catheter, **158:**41
Scrotum, normal and abnormal, pediatric, color Doppler sonography, **158:**613
Sexual differentiation, congenital disorders, MR imaging (p), **158:**363
Shoulder, long bicipital tendon, MR imaging, normal anatomy and pathologic findings (p), **158:**1091
Sickle-cell disease
  osteomyelitis and (a), **158:**697
  osteonecrosis and, femoral head (a), **158:**923
Single-photon emission computed tomography, radiation necrosis, vs high-grade recurrent glioma, **158:**399
Skin, lesions, modern imaging, **158:**1193
Small round cell tumor, malignant, abdomen, CT, **158:**1031
Society of Thoracic Radiology, meeting news, 1992, **158:**1391
Society of Uroradiology, annual meeting, January, 1992, abstracts of scientific papers, **158:**1399
Sonography
  color Doppler, hepatocellular carcinoma, transcatheter arterial embolization, **158:**541
  color Doppler flow imaging (b), **158:**1010
  duplex Doppler, native kidney dysfunction, **158:**1035
  fine-needle biopsy, new electronically enhanced system, **158:**195
Sonography, abdomen
  appendix, normal and abnormal, **158:**773
  endoscopic, pancreatic and ampullary (a), **158:**1179
  gallstones (a), **158:**220
  gangrenous cholecystitis, **158:**698
  hypertrophic pyloric stenosis, infant, **158:**129
  introduction (b), **158:**1298
  urinary tract (b), **158:**790
  yolk sac detection, first trimester, outcome of pregnancy and, **158:**843
Sonography, bladder, augmented, delayed spontaneous rupture, children, **158:**833
Sonography, cerebrovascular
  duplex
    commentary, **158:**37
    efficacy, limitations, and indications, **158:**29
Sonography, eye, ocular trauma, **158:**179
Sonography, genitourinary
  tuberculosis (p), **158:**327
  tuberculosis (l), **158:**919
Sonography, kidney
  renal transplants, dogs, **158:**791
  symptomatic renal obstruction, urosepsis during pregnancy and, **158:**91
Sonography, liver
  atypical mesenchymal hamartoma (l), **158:**921
  carbon dioxide microbubbles, intraarterial microbubbles, **158:**65
  duplex, venoocclusive disease after bone marrow transplant, **158:**1001
  high-frequency, surface analysis diagnosis of cirrhosis (a), **158:**1180
  intrahepatic hematoma, Tru-cut needle liver biopsy (a), **158:**219
  intraoperative, hepatocellular carcinoma (a), **158:**220
  pediatric candidates for transplantation (l), **158:**692
Sonography, lung, malignant pleural effusion, sclerotherapy, **158:**41
Sonography, musculoskeletal
  diseases in children, **158:**729
  hemophilia, **158:**119
Sonography, pregnancy, enlarged amniotic cavity, early embryonic death, **158:**359
Sonography, scrotum, color Doppler, normal and abnormal children, **158:**613
Sonography, spine, intraoperative, schistosomal granuloma, **158:**1347
Sonography, testicular
  cystic mass, dilated rete testis and, **158:**1257
  intratesticular varicocele, **158:**1061
  microlithiasis, **158:**1057
Sonography, thorax
  color duplex, thoracic outlet syndrome, **158:**623
  complications, extracorporeal membrane oxygenation (p), **158:**353
  pneumothorax, thoracentesis and (l), **158:**458
Sonography, thyroid, fetal, measurements of (a), **158:**1180
Sonography, transrectal
  biopsy, rectal carcinoma, **158:**1025
  Crohn's disease (a), **158:**697
Sonography, transvaginal
  color Doppler, ovarian tumor vascularity (a), **158:**220
  technique (b), **158:**798
  urethra, leiomyoma of (l), **158:**694
Sonography, transvenous, visualization of coronary arteries (a), **158:**696
Sonography, ureter
  color Doppler, normal flow dynamics, **158:**1051
  ureterovesical junction, after surgery or endoscopy, children, **158:**837
Sphincter of Oddi, percutaneous transhepatic manometry of (a), **158:**463
Sphincterotomy, endoscopic, complications of (a), **158:**219
Spine
  ALD-AMN complex, MR imaging, **158:**413
  cervical, epidural abscess, MR imaging, **158:**1145
  epidural abscess, contrast-enhanced MR imaging, **158:**405
  fast spin-echo MR imaging, **158:**1313
  injury
    abnormalities in gastrointestinal tract, **158:**279
    gallbladder contractility and (l), **158:**456
  intradural schwannoma, contrast-enhanced MR, **158:**1347
  lumbar, stenosis, CT, MR, and myelography in diagnosis of, **158:**1135
  management of infections, MR role in, **158:**1333
  metastases, vertebrae, CT, **158:**1275
  schistosomal granuloma, MR and intraoperative sonography, **158:**1347
  thoracic, congenital absence of pedicle (l), **158:**921
Spinous process, erosion, after surgery (l), **158:**459
Spleen
  dynamic MR imaging, gadopentetate dimeglumine, **158:**303
  peliosis, HIV patient (l), **158:**1409
Stellate ganglion, normal appearance, MR imaging (p), **158:**655
Stomach, dynamic MR imaging, gadopentetate dimeglumine, **158:**303
Sturge-Weber syndrome
  CT and MR imaging comparison, **158:**867
  persistent trigeminal artery in, **158:**872
Subclavian vessels, evaluation, thoracic outlet syndrome, sonography, **158:**623
Superior mesenteric venous thrombosis, case of the day, **158:**1363
Superparamagnetic iron oxide, MR lymphography, **158:**183
Supraspinatus tendon, appearance in asymptomatic volunteers, MR imaging, **158:**1281
Swallowing, dysfunction, postpolio syndrome, **158:**283
Swyer-James syndrome, CT findings, **158:**1211
Synovitis, metal-induced, complication of arthroplasty of knee (a), **158:**219
Systemic lupus erythematosus, pulmonary hemorrhage complicating, MR imaging in, **158:**519

T

Takayasu disease, percutaneous transluminal angioplasty, **158:**417
Target sign, prevalence, plain film diagnosis of intussusception, **158:**619
Testicles
  cystic mass, dilated rete testis and, **158:**1257
  microlithiasis, sonography, **158:**1057
Thoracic aorta
  acquired diseases, MR imaging, **158:**1115
  assessment, spiral CT (p), **158:**1127
Thoracic empyema, image-guided catheter drainage of (a), **158:**464
Thoracic outlet syndrome, color duplex sonography, **158:**623
Thorax
  diseases, differential diagnosis (b), **158:**508
  errors in chest radiography (b), **158:**352
  penetrating injury, pneumopyopericardium after (l), **158:**687
  radiography, complications of extracorporeal membrane oxygenation (p), **158:**353
Thrombolysis, myocardial infarction (a), **158:**1416
Thymoma
  hypogammaglobulinemia with, **158:**1229
  MR imaging (p), **158:**751
Thymus, tumors, MR imaging (p), **158:**751
Thyroid
  fetal, sonographic measurements (a), **158:**1180
  imaging (b), **158:**50
Trauma
  pancreatic, blunt, children, **158:**1097
  radiology (b), **158:**1288
  stab wound, hemisection of cervical spinal cord, MR imaging (l), **158:**1413
Tuberculosis
  lower genitourinary tract, sonography and MR imaging (l), **158:**919
  miliary, case of the day, **158:**1382
Tuberous sclerosis, children, **158:**750
Tuboovarian abscess, CT (p), **158:**575

U

Umbilical vein, intra-abdominal, varix, fetal (a), **158:**1417
Urachus, carcinoma, MR imaging (l), **158:**1171
Ureteric jets, normal flow dynamics, color Doppler sonography, **158:**1051
Ureterovesical junction, children, after surgery or endoscopy, sonography, **158:**837
Urethra, leiomyoma, transvaginal sonography (l), **158:**694
Urinary tract, upper, tumors (a), **158:**698
Urology, diagnostic techniques (b), **158:**806
Uterus
  adenofibroma, mimicking endometrial carcinoma, MR (l), **158:**214
  benign masses, contrast-enhanced MR imaging, **158:**1043
  cervical adenocarcinoma, isolated splenic metastasis from (l), **158:**919
  leiomyomas, imaging of (p), **158:**799
  pedunculated leiomyoma, traumatic avulsion, hemoperitoneum due to (l), **158:**1410

V

Vagina, normal and abnormal, after hysterectomy, MR imaging, **158:**95
Valvuloplasty, percutaneous balloon aortic (a), **158:**924
Vena cava
  inferior
    Bird's Nest filter placement (p), **158:**875
    interruption of, Budd-Chiari syndrome, **158:**635
    localized fat collection, CT, **158:**423
Venous abscess, protracted, upper arm approach, peripherally inserted central catheters for, **158:**427
Videotape reviews
  MRI of brain tumors, **158:**1160
  RSNA Today video, vol. 5, no. 1, **158:**426
  RSNA Today video, vol. 5, no. 3, **158:**540
  RSNA Today video, vol. 5, no. 2, **158:**558
  RSNA Today video, vol. 5, no. 5, **158:**1254
  RSNA Today video, vol. 5, no. 4, **158:**1260

W

Western Neuroradiological Society, 23rd annual meeting, October 1991, **158:**679
Wilms' tumor, hypertensive encephalopathy caused by, reversible cerebral lesions, pediatric, **158:**1161

Volume 158

Official Journal of the American Roentgen Ray Society

AJR

American Journal of Roentgenology

Diagnostic Imaging and Related Sciences

Editor-In-Chief Robert N. Berk, *La Jolla, California*
University of California, San Diego
School of Medicine and Medical Center

Editor Emeritus Melvin M. Figley, *Seattle, Washington*

Associate Editor Karim Valji, *San Diego, California*

Consulting Editors A. James Barkovich, *San Francisco, California*
Edward A. Sickles, *San Francisco, California*

Statistician Charles C. Berry, *San Diego, California*

Editorial Board

Mark E. Baker
Lawrence W. Bassett
Michael A. Bettmann
Ethan M. Braunstein
Felix S. Chew
Horacio R. D'Agostino
N. Reed Dunnick
David K. Edwards
Ronald G. Evens
Sandra K. Fernbach
Richard H. Gold
Edward G. Grant
John R. Hesselink
Emanuel Kanal
Ray F. Kilcoyne
Carolyn Kimme-Smith
Melvyn T. Korobkin
Mark J. Kransdorf
Faye C. Laing
Thomas L. Lawson
Robert G. Levitt
Martin J. Lipton
Bruce L. McClennan
Richard P. Moser
Jeffrey H. Newhouse
Sven J. K. Paulin
David M. Paushter
Vassilios Raptopoulos
Donald L. Resnick
Charles A. Rohrmann, Jr.
Peter M. Ronai
Stuart S. Sagel
Sanjay Saini
Stefan C. Schatzki
William P. Shuman
Edward A. Sickles
Barry A. Siegel
M. Leon Skolnick
Edward T. Stewart
Murali Sundaram
Robert D. Tien

Director of Publications: Susan Brown Cappitelli **Editorial Staff:** Barbara Rose, *managing editor*; Katie L. Spiller, Barbara L. Halliburton, and Janine Anderson, *manuscript editors*; Nancy Rydbeck, *office manager*; Sheri Smith, *administrative assistant*; Linda J. Waggoner, *administrative secretary*

AJR, AMERICAN JOURNAL OF ROENTGENOLOGY (ISSN 0361 803X) is published monthly by the American Roentgen Ray Society, 1891 Preston White Dr., Reston, VA 22091. Annual dues include $50 for journal subscription. Second-class postage paid at Baltimore, MD, and at additional mailing offices. **POSTMASTER**, send address changes (Form 3579) to Subscription Fulfillment, AJR, 428 E. Preston St., Baltimore, MD 21202. Subscription rates $125 ($180 foreign); institutions $135 ($190 foreign); in training $25 ($80 foreign); single copy $18 ($22 foreign). The GST number for Canadian subscribers is 123394371. Airmail rates furnished

Final No.

Call for Scientific Papers

Date Received

Tracking No.

American Roentgen Ray Society
1993 Annual Meeting
April 25 – 30, 1993
San Francisco, CA

ADDRESS OF PRESENTING AUTHOR

Department

Institution

Street

City State Zip

Phone

Type title, authors, and abstract in the space provided below. (Instructions are on reverse side of this page. Abstract should not exceed 300 words.

Select one category:

☐ Angio/Interventional ☐ Breast ☐ Sonography ☐ CT ☐ Gastrointestinal Tract ☐ Genitourinary Tract
☐ Neuroradiology ☐ Skeletal ☐ Chest ☐ MR ☐ Pediatrics ☐ Medical Physics

Projection Requirements: ☐ 35mm– single or double (circle one) ☐ 16mm silent film ☐ VHS (½") ☐ VHS (¾")

Has this been presented elsewhere? ☐ Yes ☐ No If yes, where?

Instructions for Scientific Paper Abstracts

1. Type information single-spaced. Underline the name of the presenting author. Append as a last line of the abstract any research grant support, if applicable (e.g. Supported by USPHS Grant HE-80144). If the abstract is accepted, it will appear in the program book exactly as typed. Use the following format:

   MR IMAGING OF THE SPINE AND NECK
   F.S. Lau, M.D., A.N. Kirk, M.D., R.A. Beck, Ph.D.
   University of California, Bakersfield, Bakersfield, CA 92338

2. Abstracts should include four paragraphs devoted sequentially to the following topics: (1) object or purpose of the study; (2) materials, methods and procedures; (3) results; and (4) significance of the results and conclusions. The text should not exceed 300 words. Specific data are essential. The abstract should be a succinct summary of work done rather than a promissory note.

3. The Scientific Program Committee will grade each abstract and determine acceptance. Letters indicating acceptance or rejection will be mailed to all applicants in mid-January, together with meeting registration information.

Deadline for submission of abstracts is November 1, 1992. Mail **one** copy of abstract to

ARRS President-Elect
c/o Susan Roberts, Projects Manager
American Roentgen Ray Society
1891 Preston White Drive
Reston, VA 22091

Although mail submission is preferable, abstracts will be accepted by fax at (703) 264-8863. When faxing an application, **do not** mail a confirmation copy, as this results in unnecessary duplication of paper work.

Final No.

Call for Scientific Exhibits

Date Received

Tracking No.

American Roentgen Ray Society
1993 Annual Meeting
April 25 – 30, 1993
San Francisco, CA

ADDRESS OF PRESENTING AUTHOR

Department

Institution

Street

City State Zip

Phone ____

Type title, authors, and abstract in the space provided below. (Instructions are on reverse side of this page.)

Select one category: ☐ Cardiovascular ☐ Breast ☐ Sonography ☐ Gastrointestinal ☐ Genitourinary ☐ Chest
☐ Neuroradiology ☐ Bone ☐ Pediatric ☐ Nuclear medicine ☐ Medical physics

What Type of Exhibit is Proposed? (Check one and fill in all appropriate blanks.)

____ **Free-standing.** This is a self-contained display created in total by the exhibitor. It may be a fold-open unit, a unit shipped in cases and assembled on site, or a tabletop unit. Standard free-standing space is 10' x 10'. Indicate linear feet required ____.

____ **Poster Board (Backboard panels).** Backboard panels are 4 x 8 ft. (1.2 x 2.5m). Number of panels required ____. If two panels are needed, there will be a ¼-in. frame separating the panels, thus requiring a separation in the presentation.

____ **Viewbox.** Mounted materials (radiographs and other transparencies) for display on the society's illuminators. Each illuminator is 39.5 x 59.5 in. (100 x 151 cm). Number of illuminators required

Instructions for Scientific Exhibit Abstracts

1. Type information single-spaced. Underline the name of the presenting author. Append as a last line of the abstract any research grant support, if applicable (e.g. Supported by USPHS Grant HE-80144). If the abstract is accepted, it will appear in the program book exactly as typed. Use the following format:

   MR IMAGING OF THE SPINE AND NECK
   F.S. Lau, M.D., A.N. Kirk, M.D., R.A. Beck, Ph.D.
   University of California, Bakersfield, Bakersfield, CA 92338

2. The abstract should be a brief paragraph that states the purpose, principal information and conclusions of the exhibit. Promissory statements are not acceptable. Brevity is desirable but not at the expense of specific information. Exhibits will be chosen on the basis of the quality of the abstract and exhibit space available. Poster board exhibits are encouraged as they do not require a viewbox or electricity.

3. The Scientific Exhibits Committee will grade each abstract and determine acceptance. Letters indicating acceptance or rejection will be mailed to all applicants in mid-January, together with meeting registration information. Exhibitors will receive instructions for exhibit preparation.

Deadline for submission of abstracts is November 1, 1992. Mail **one** copy of abstract to

N. Reed Dunnick, M.D.
Chairman, Scientific Exhibits Committee
c/o Susan Roberts, Projects Manager
American Roentgen Ray Society
1891 Preston White Drive
Reston, VA 22091

Although mail submission is preferable, abstracts will be accepted by fax at 703-264-8863. When faxing an application, **do not** mail a confirmation copy, as this results in unnecessary duplication of paper work.

PERSONAL COMPUTER/LASER VIDEODISC SYSTEM
to assist you in the
diagnosis of Skeletal Dysplasias

A unique collection of 400 Skeletal Syndromes
7000 Illustrations
including

- *X-rays*
- *Clinical pictures*
- *Chondro-osseous histology*

OSSUM

AN ILLUSTRATED DATABASE OF SKELETAL DYSPLASIAS

S
S
U
M

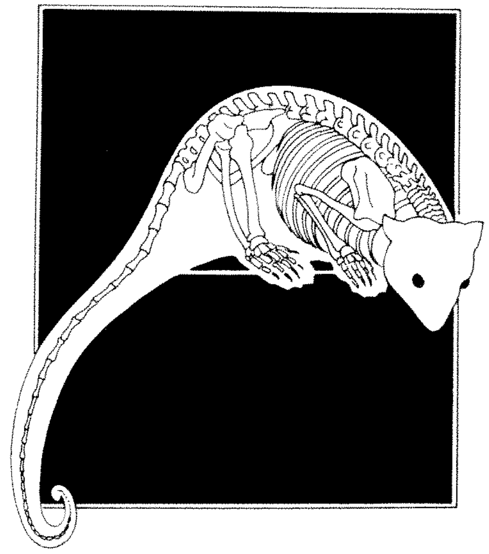

for further information contact:

Dr. Agnes Bankier – Medical Geneticist to the successful related POSSUM system.

PO Box 1100 Parkville Victoria 3052 Australia
Phone: (03) 345 5160 Fax: (03) 348 1391

Volume 158 **American Journal of Roentgenology** **June 1992**

SPECIAL ARTICLE

1193 **Review. Lesions of skin and brain: modern imaging of the neurocutaneous syndromes.** *Pont MS, Elster AD*

PULMONARY RADIOLOGY

1205 **Value of MR imaging in the evaluation of chronic infiltrative lung diseases: comparison with CT.** *Müller NL, Mayo JR, Zwirewich CV*

1211 **Swyer-James syndrome: CT findings in eight patients.** *Moore ADA, Godwin JD, Dietrich PA, Verschakelen JA, Henderson WR Jr*

1217 **CT findings in lymphangitic carcinomatosis of the lung: correlation with histologic findings and pulmonary function tests.** *Johkoh T, Ikezoe J, Tomiyama N, et al.*

1223 **Summer-type hypersensitivity pneumonitis: comparison of high-resolution CT and plain radiographic findings.** *Akira M, Kita N, Higashihara T, Sakatani M, Kozuka T*

1229 **Case report. Thymoma with hypogammaglobulinemia (Good's syndrome): an unusual cause of bronchiectasis.** *Fox MA, Lynch DA, Make BJ*

BREAST RADIOLOGY

1231 **Perspective. Interventional procedures in diseases of the breast: needle biopsy, pneumocystography, and galactography.** *Fajardo LL, Jackson VP, Hunter TB*

1239 **The role of fine-needle aspiration and pneumocystography in the treatment of impalpable breast cysts.** *Ikeda DM, Helvie MA, Adler DD, Schwindt LA, Chang AE, Rebner M*

1243 **Perspective. Hidden costs of mobile mammography: is subsidization necessary?** *Wolk RB*

GASTROINTESTINAL RADIOLOGY

1247 **Rupture of hepatocellular carcinoma: predictive value of CT findings.** *Kanematsu M, Imaeda T, Yamawaki Y, et al.*

1251 **Case report. Treatment of mesocaval shunt stenosis with a metallic stent.** *Soyer P, Levesque M, Zeitoun G*

1255 **Case report. Peribiliary chloroma: a rare cause of jaundice after bone marrow transplantation.** *Rotter AJ, O'Donnell MR, Radin DR, Marx HF*

GENITOURINARY RADIOLOGY

1257 **Cystic testicular mass caused by dilated rete testis: sonographic findings in 31 cases.** *Brown DL, Benson CB, Doherty FJ, et al.*

1261 **Peyronie's disease: MR findings in 28 patients.** *Helweg G, Judmaier W, Buchberger W, et al.*

1265 **Pictorial essay. Nonovarian gynecologic cysts: MR imaging findings.** *Kier R*

MUSCULOSKELETAL RADIOLOGY

1271 **Intraarticular fractures of the calcaneus: value of CT findings in determining prognosis.** *Janzen DL, Connell DG, Munk PL, Buckley RE, Meek RN, Schechter MT*

1275 **Do metastases in vertebrae begin in the body or the pedicles? Imaging study in 45 patients.** *Algra PR, Heimans JJ, Valk J, Nauta JJ, Lachniet M, Van Kooten B*

1281 **MR imaging of the shoulder: appearance of the supraspinatus tendon in asymptomatic volunteers.** *Neumann CH, Holt RG, Steinbach LS, Jahnke AH Jr, Petersen SA*

1289 **Case report. Aneurysmal bone cyst developing after anterior cruciate ligament tear and repair.** *Dagher AP, Magid D, Johnson CA, McCarthy EF Jr, Fishman EK*

1293 **Case report. MR appearance of intramuscular injections.** *Resendes M, Helms CA, Fritz RC, Genant H*

1295 **Case report. MR diagnosis of macrodystrophia lipomatosa.** *Blacksin M, Barnes FJ, Lyons MM*

PEDIATRIC RADIOLOGY

1299 **Posttraumatic adrenal hemorrhage in children: CT findings in 34 patients.** *Sivit CJ, Ingram JD, Taylor GA, Bulas DI, Kushner DC, Eichelberger MR*

1303 **Case report. Neonatal intestinal ischemia with bowel perforation: an in utero complication of maternal cocaine abuse.** *Hall TR, Zaninović A, Lewin D, Barrett C, Boechat MI*

1305 **Case report. Persistent infantile odontoid process: a variant of abnormal atlantoaxial segmentation.** *McClellan R, El Gammal T, Willing S, Lott T, Odell G*

1309 **Case report. Congenital absence of the left pulmonary artery associated with double-outlet right ventricle.** *Kremer S, Fayemi AB, Fish BG, Rothe WA, Spindola-Franco H*

NEURORADIOLOGY

1313 **Perspective. Fast spin-echo MR imaging of the brain and spine: current concepts.** *Jones KM, Mulkern RV, Schwartz RB, Oshio K, Barnes PD, Jolesz FA*

1321 **Fractures of the nasolacrimal fossa and canal: a CT study of appearance, associated injuries, and significance in 25 patients.** *Unger JM*

1325 **Neurosyphilis in HIV carriers: MR findings in six patients.** *Tien RD, Gean-Marton AD, Mark AS*

1329 **Rasmussen's encephalitis: neuroimaging findings in four patients.** *Tien RD, Ashdown BC, Lewis DV Jr, Atkins MR, Burger PC*

1333 **Review. Role of MR imaging in the management of spinal infections.** *Sharif HS*

1347 **Intradural schwannomas of the spine: MR findings with emphasis on contrast-enhancement characteristics.** *Friedman DP, Tartaglino LM, Flanders AE*

1351 **Case report. Schistosomal granuloma of the spinal cord: evaluation with MR imaging and intraoperative sonography.** *Silbergleit R, Silbergleit R*

ARRS 1992 CASE OF THE DAY ANSWERS

1355 **Introduction.** *Heller RM*

1356 **Chest case of the day.** *Worrell JA, O'Donnell DM, Carroll FE, Brunner JP, Coleman JA Jr*

1363 **Abdominal case of the day.** *Shaff MI, Powers TA, Gilpin LB, Faulstich ME*

1368 **Skeletal case of the day.** *Tigges S, Erb RE, Nance EP*

1372 **Pediatric case of the day.** *Heller RM, Hernanz-Schulman M, Johnson J, Stein SM, Kirchner S*

1378 **Neuroradiology case of the day.** *Lacrampe MJ, Creasy JL*

1382 **Nuclear medicine case of the day.** *Moody EB, Glassman SB, Hansen AV, Lawrence SK, Delbeke D*

PERSPECTIVE

1387 **The information perspective of radiology.** *Hendee WR*

MEETING NEWS

1391 **Thoracic imaging, 1992.** *Whalen E*

1399 **Abstracts of scientific papers presented at the annual meeting of the Society of Uroradiology, January 1992.**

OTHER CONTENT

1204 **Figley Fellowship announcement**
1210 **Medicine in American Art**
1270 **History page**
1291 **List of book and videotape reviews**
1292 **Memorial. James G. Lorman**
1312 **Radiologic-pathologic conference**
1320 **Erratum**
1353 **ARRS 1993 residents' award papers information**
1406 **Forthcoming articles**
1407 **Letters**
1415 **Review of current literature**
1419 **News**
1422 **1993 ARRS meeting information**
1423 **Classified advertisements**
1431 **Index, Volume 158**
A13 **Guidelines for authors**
A20 ***AJR* business and subscriber information**